Cover Picture

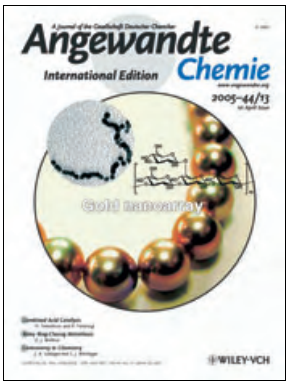

Ah-Hyun Bae, Munenori Numata, Teruaki Hasegawa, Chun Li, Kenji Kaneko, Kazuo Sakurai, and Seiji Shinkai*

A linear array of nanoparticles can be generated by the use of an appropriate template. The cover picture shows a TEM image of such a 1D array of gold nanoparticles, aligned by the use of the β-1,3-glucan polysaccharide schizophyllan, which adopts a triple-helical structure in aqueous solution. In their Communication on page 2030 ff., S. Shinkai and co-workers describe how the hydrophobic inner cavity of the helix hosts the hydrophobic nanoparticles and aligns the guests along its length.

Planned Catalysis
Combinations of Brønsted and Lewis acids can provide enantioselective catalysts with unique reactivity and versatility. The latest developments in "designer acids" for asymmetric synthesis are discussed in the Review by H. Yamamoto and K. Futatsugi on page 1924 ff.

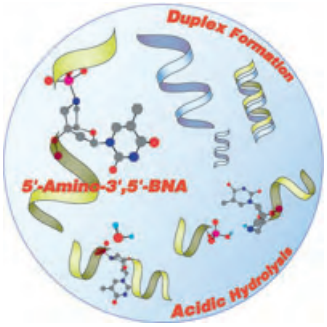

Bridged Nucleic Acids
In their Communication on page 1944 ff, T. Imanishi and co-workers describe the consequences of a conformational restriction brought about by introducing a methylene bridge into an oligonucleotide P3′→N5′ phosphoramidate.

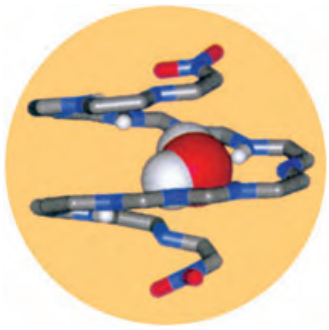

Molecular Encapsulation
An amide helix with terminal quinoline units is described by I. Huc and co-workers in their Communication on page 1954 ff. The resulting helix resembles an apple peel and encapsulates a water molecule.

Contents

VIP *The following Communications have been judged by at least two referees to be "very important papers" and will be published online at www.angewandte.org soon:*

*Kendric J. Nelson, Ian D. Giles, William W. Shum, Atta M. Arif, Joel S. Miller**
The Myth of Cyanide Always Being a Strong Field Ligand: Synthesis and Structural Characterization of Homoleptic S = 2 Pentacyanochromate(II), $[Cr^{II}(CN)_5]^{3-}$, and Nonacyanodichromate(II), $[Cr^{II}_2(CN)_9]^{5-}$

Andrew J. Wilson, Mitsutoshi Masuda, Rint P. Sijbesma, E. W. Meijer**
Chiral Amplification in the Transcription of Supramolecular Helicity into a Polymer Backbone

*Mark Gandelman, Eric N. Jacobsen**
Highly Enantioselective Catalytic Conjugate Addition of N Heterocycles to α,β-Unsaturated Ketones and Imides

*Sang Hyuk Im, Yun Tack Lee, Benjamin Wiley, Younan Xia**
Large-Scale Synthesis of Silver Nanocubes: The Role of HCl in Promoting Cube Perfection and Monodispersity

*Sridhar Narayan, John Muldoon, M. G. Finn, Valery V. Fokin, Hartmuth C. Kolb, K. Barry Sharpless**
"On Water": Unique Reactivity of Organic Compounds in Aqueous Suspensions

*Tetsuro Murahashi, Christopher R. Clough, Joshua S. Figueroa, Christopher C. Cummins**
A Ligand Comprised of Dinitrogen and Methyldiphenylphosphine in a Cationic Molybdenum Complex

News

Distinctions for G. Férey ——— **1908**

M. Inoue Gives the Merck Banyu Lecture ——— **1908**

K. C. Nicolaou to Head Biopolis Laboratory ——— **1908**

Books

Energetic Materials — Ulrich Teipel — *reviewed by M.-J. Crawford, T. M. Klapötke, J. Welch* ——— ***1909***

Modern Allene Chemistry — Norbert Krause, Stephen K. Hashmi — *reviewed by G. Maas* ——— ***1909***

Highlights

Synthetic Methods

D. J. Wallace* ——— **1912 – 1915**

Relay Ring-Closing Metathesis—A Strategy for Achieving Reactivity and Selectivity in Metathesis Chemistry

How can uncooperative alkenes be rendered more susceptible to metathesis reactions? The realization that what is difficult in an intermolecular sense can become straightforward when transposed to a kinetically favorable intramolecular reaction has led to development of relay ring-closing metathesis (see scheme). This provides a method for directing initiation and propagation of previously unattainable metathesis sequences.

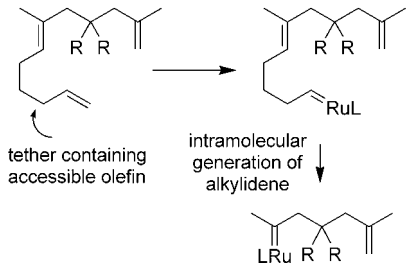

Essays

History of Science

J. A. Labinger,* S. J. Weininger* ——— **1916 – 1922**

Controversy in Chemistry: How Do You Prove a Negative?—The Cases of Phlogiston and Cold Fusion

Believe it or not: It can sometimes be difficult to prove an idea is wrong once it has caught the human imagination. This situation is demonstrated for the two temporally separated cases of phlogiston and cold fusion. Although there are clear differences between the two cases, they both illustrate how difficult it can be to prove the non-existence of a conceived idea.

Reviews

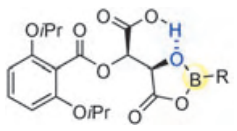

An ideal couple: The intramolecular combination of Brønsted and Lewis acids (e.g. acyloxyborane catalyst shown), or of two Lewis acids, or of two Brønsted acids could become a particularly useful tool for the design of asymmetric catalysts with high reactivity, selectivity, and versatility. The inherent reactivity of the associated components is maintained, and the highly organized structures provide an efficient asymmetric environment.

Designed Catalysis

H. Yamamoto,*
K. Futatsugi _____ **1924 – 1942**

"Designer Acids": Combined Acid Catalysis for Asymmetric Synthesis

Communications

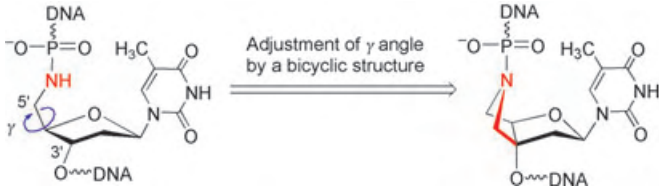

Bridge to the right angle: A methylene bridge between the C3′ and N5′ atoms restricts the γ dihedral angle of an oligonucleotide P3′→N5′ phosphoramidate within the +*sc* orientation (see scheme), which improves duplex-forming ability and accelerates hydrolytic cleavage.

Bridged Nucleic Acids

S. Obika, M. Sekiguchi, R. Somjing,
T. Imanishi* _____ **1944 – 1947**

Adjustment of the γ Dihedral Angle of an Oligonucleotide P3′→N5′ Phosphoramidate Enhances Its Binding Affinity towards Complementary Strands

Nucleation by chiral polyimide surfaces leads to finite enantioselectivity in the B_4 phase of achiral banana mesogen molecules (see optical micrograph). An *ee* value of 10% was obtained with rubbed chiral polyimide surfaces. This technique opens up new possible ways of controlling chirality in chemical and biological systems.

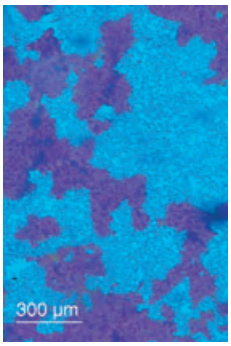

Liquid Crystals

K. Shiromo, D. A. Sahade, T. Oda,
T. Nihira, Y. Takanishi, K. Ishikawa,
H. Takezoe* _____ **1948 – 1951**

Finite Enantiomeric Excess Nucleated in an Achiral Banana Mesogen by Chiral Alignment Surfaces

For the USA and Canada:
ANGEWANDTE CHEMIE International Edition (ISSN 1433-7851) is published weekly by Wiley-VCH PO Box 191161, D 69451 Weinheim, Germany. Air freight and mailing in the USA by Publications Expediting Inc. 200 Meacham Ave., Elmont, NY 11003. Periodicals postage paid at Jamaica NY 11431. US POSTMASTER: send address changes to *Angewandte Chemie*, Wiley-VCH, 111 River Street, Hoboken, NJ 07030. Annual subscription price for institutions: US$ 4948.00/4498.00 (valid for print and electronic / print or electronic delivery); for individuals who are personal members of a national chemical society, or whose institution already subscribes, or who are retired or self-employed consultants, print only: US$ 394.00. Postage and handling charges included. All Wiley-VCH prices are exclusive VAT.

 © 2005 Wiley-VCH Verlag GmbH & Co. KGaA, Weinheim

The best in chemistry –

for more than a hundred years

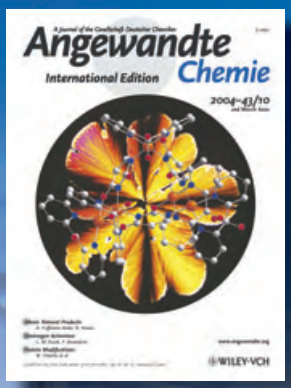

A Journal of the Gesellschaft Deutscher Chemiker

Angewandte International Edition **Chemie**

www.angewandte.org

1888: ***The beginning of a success story***

Constant Innovations

1962: *First issue of the International Edition*
1976: *Graphical abstracts*
1979: *Cover pictures*
1988: *Centenary of Angewandte*
1989: *Routine use of color*
1991: *New section: Highlights*
1992: *Computerized editorial tracking system*
1995: *Internet service for readers*
1998: *Regular press service; full-text online*
2000: *New section: Essays; EarlyView: Communications available online ahead of the printed version*
2001: *New section: Minireviews*
2002: *Online submission of manuscripts*
2003: *Weekly publication; new section: News; new layout*
2004: *Backfiles (1962-1997); ManuscriptXpress: Online system for authors and referees*

Angewandte's advisors...

Stefan Marcinowski
BASF AG
Ludwigshafen

» *In our company* ***Angewandte Chemie*** *is seen as an outstanding journal that combines first class performance in publishing innovative chemistry with a high international visibility. With its global recognition* ***Angewandte Chemie*** *functions as a seed cell for innovative technologies to be applied on a commercial basis in the future.* «

Angewandte Chemie International Edition *is a journal of the German Chemical Society (GDCh)*

GDCh

WILEY InterScience® DISCOVER SOMETHING GREAT

WILEY-VCH

1186104_gu

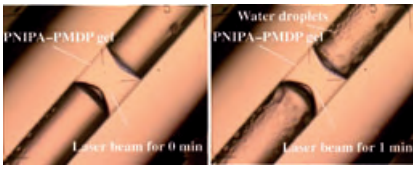

Pump up the volume: Poly(*N*-isopropylacrylamide) gel containing poly(2-(methacryloyloxy)decyl phosphate) surfactant (NIPA-PMDP gel) shows a rapid reversible volume decrease above its phase-transition temperature. The gel also undergoes an abrupt volume change on laser irradiation, which results in expulsion of a stream of water (see pictures). The gel can be used in fluid control systems, such as drug delivery.

Polymer–Surfactant Gels

H. Yan,* H. Fujiwara, K. Sasaki, K. Tsujii* ——— **1951 – 1954**

Rapid Swelling/Collapsing Behavior of Thermoresponsive Poly(*N*-isopropylacrylamide) Gel Containing Poly(2-(methacryloyloxy)decyl phosphate) Surfactant

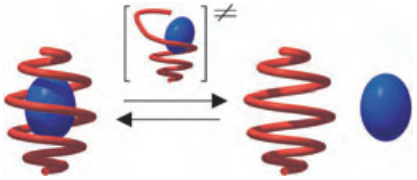

It's a wind up: Peeling the skin of an apple into a single helical ribbon gives a sort of shell that can be wound back around the apple. Such a shell can be constructed at the molecular scale using a helix with a reduced diameter at both ends which behaves as a capsule and entraps a small guest such as water (see picture).

Molecular Recognition

J. Garric, J.-M. Léger, I. Huc* ——— **1954 – 1958**

Molecular Apple Peels

Change and change about: Highly porous, homochiral metal–organic frameworks (MOFs) undergo reversible single-crystal to single-crystal and single-crystal to amorphous to single-crystal structural transformations when exposed to solvent vapors or air. These results suggest that true heterogeneous asymmetric catalysts can be built from homochiral MOFs.

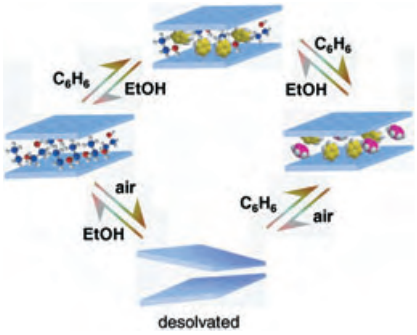

Porous Materials

C.-D. Wu, W. Lin* ——— **1958 – 1961**

Highly Porous, Homochiral Metal–Organic Frameworks: Solvent-Exchange-Induced Single-Crystal to Single-Crystal Transformations

Biporous materials: Two distinct large channels form within a 3D coordination network. Each channel adsorbs its own preferred guest from a mixture of two guests, such as cyclohexane and naphthalene, to form two independent columnar arrays of guests in the crystal (see figure).

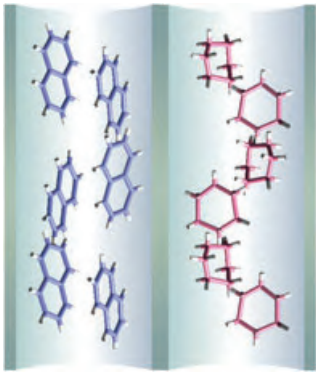

Host–Guest Systems

O. Ohmori, M. Kawano,* M. Fujita* ——— **1962 – 1964**

A Two-in-One Crystal: Uptake of Two Different Guests into Two Distinct Channels of a Biporous Coordination Network

 © 2005 Wiley-VCH Verlag GmbH & Co. KGaA, Weinheim

Contents

Surface Structures

C. Whitehouse,* J. Fang, A. Aggeli, M. Bell, R. Brydson, C. W. G. Fishwick, J. R. Henderson, C. M. Knobler, R. W. Owens, N. H. Thomson, D. A. Smith, N. Boden* _____ **1965 – 1968**

Adsorption and Self-Assembly of Peptides on Mica Substrates

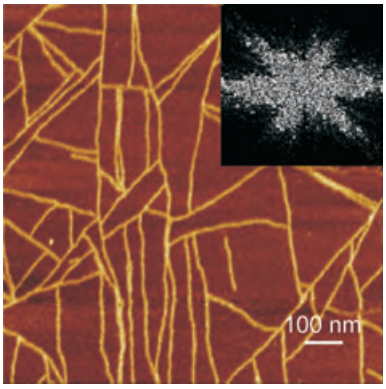

Self-assembled tapes: Adsorption and self-assembly of peptides on mica substrates produces tapes, a single molecule in thickness, with a cross-β-sheet structure (see picture). A variety of surface morphologies may be produced depending on the preparation procedure. One of these, a close-packed monolayer of parallel-aligned tapes, may be of practical utility as a functionalized protein-like surface.

Controlled Fibril Assembly

J. M. Smeenk, M. B. J. Otten, J. Thies, D. A. Tirrell, H. G. Stunnenberg, J. C. M. van Hest* _____ **1968 – 1971**

Controlled Assembly of Macromolecular β-Sheet Fibrils

Blocking out aggregation: Triblock copolymers consisting of a central β-sheet polypeptide block with the repeating $[(AlaGly)_3GluGly]_n$ sequence and poly(ethylene glycol) (PEG) of $M_n = 750\ g\,mol^{-1}$ were prepared and the assembly properties in the solid state were investigated. Attachment of PEG prevented the macroscopic aggregation of the β-sheet polypeptide portion and,

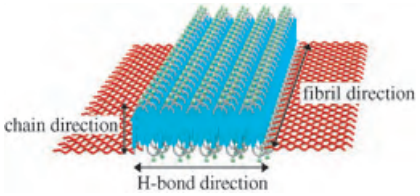

instead, resulted in the formation of well-defined fibrils.

Mixed-Metal Clusters

M. Koutmos, D. Coucouvanis* _____ **1971 – 1974**

Metal Clusters as Ligands: Substitution of Fe ions in Fe/Mo/S Clusters by Thiophilic Cu^{I} Ions To Give Clusters with $[Cu_4Mo_2Fe_2S_8]^{4+}$ and $[Cu_5Mo_3Fe_4S_{11}]^{6+}$ Cores

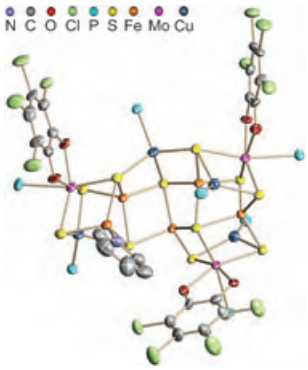

The reactivity of Fe/S and Fe/Mo/S clusters, similar or analogous to those occurring in biological systems, with thiophilic metal ions is explored. The synthesis of two heteropolynuclear clusters with different coordination geometries at different sites is reported. The new clusters contain Fe^{III}, Mo^{V}, and Cu^{I} centers in pseudotetrahedral, pseudooctahedral, and pseudotrigonal coordination environments, respectively (see structure).

Electrochromism

H. Tokudome, M. Miyauchi* _____ **1974 – 1977**

Electrochromism of Titanate-Based Nanotubes

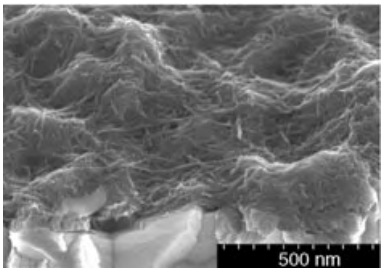

A transparent thin film of titanate nanotubes turns brown under cathodic polarization in water. This electrochromism arises from the creation of Ti^{3+} centers by proton intercalation into the interlayer separation of nanotubes. The significant color change of the titanate nanotubes is a consequence of their layered nanostructure.

 © 2005 Wiley-VCH Verlag GmbH & Co. KGaA, Weinheim

A chameleonic, redox-switchable carrier molecule: A [4,4]ferrocenophane ligand can selectively recognize Mg^{2+} ions through complexation. This ligand can transport and release Mg^{2+} ions by application of an external electrochemical stimulus across a CH_2Cl_2 liquid membrane (see picture). Furthermore, dramatic color changes are seen, which allow the potential for "naked-eye" detection.

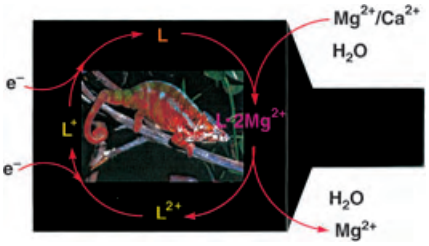

Sensors

A. Caballero, V. Lloveras, A. Tárraga, A. Espinosa, M. D. Velasco, J. Vidal-Gancedo, C. Rovira, K. Wurst, P. Molina,* J. Veciana* —— **1977 – 1981**

An Electroactive Nitrogen-Rich [4.4]Ferrocenophane Displaying Redox-Switchable Behavior: Selective Sensing, Complexation, and Decomplexation of Mg^{2+} ions

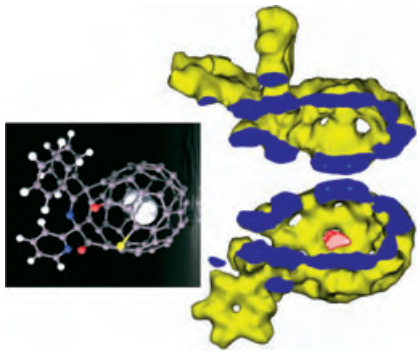

Open-mouthed fullerene swallows H_2 whole: Direct observation of a H_2 molecule that is fully encapsulated by a derivative of an aza–thia open-cage fullerene (see model) is achieved by synchrotron X-ray diffraction analysis of single crystals. A 3D electron-density map obtained by the maximum entropy method shows a single H_2 molecule (red) floating in the center of a hollow cavity in the open-cage fullerene molecule (yellow).

Fullerenes

H. Sawa,* Y. Wakabayashi, Y. Murata, M. Murata, K. Komatsu —— **1981 – 1983**

Floating Single Hydrogen Molecule in an Open-Cage Fullerene

Like an organic molecule! A chemically inert ruthenium complex acts as a metallopharmaceutic inhibitor of the protein kinase GSK-3 by targeting its ATP-binding site. It is shown to switch on the Wnt signal transduction pathway inside living cells and in *Xenopus* embryos, which developed a hyperdorsalized phenotype (see picture, top; bottom: control specimen) on administration of the complex.

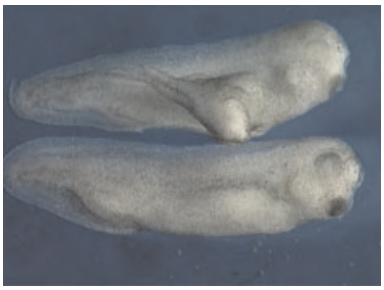

Enzyme Inhibitors

D. S. Williams, G. E. Atilla, H. Bregman, A. Arzoumanian, P. S. Klein, E. Meggers* —— **1984 – 1987**

Switching on a Signaling Pathway with an Organoruthenium Complex

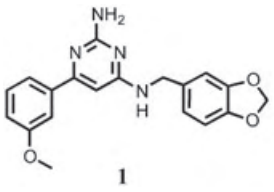

1

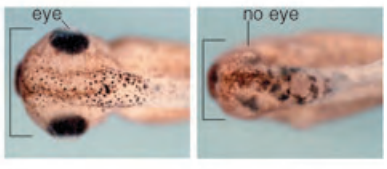

A new tool for developmental biology: A screen of combinatorial chemical libraries identified the 2-amino-4,6-disubstituted pyrimidine **1** as a dose-dependent agonist of Wnt signaling. Tadpoles that developed from embryos treated with **1** had substantial head defects (see right-hand image; left = control). Compound **1** appears to mimic the effects of a Wnt ligand in a *Xenopus* model and may be a useful tool in the study of physiological processes that involve the Wnt pathway.

Cell Signaling

J. Liu, X. Wu, B. Mitchell, C. Kintner, S. Ding,* P. G. Schultz* —— **1987 – 1990**

A Small-Molecule Agonist of the Wnt Signaling Pathway

 © 2005 Wiley-VCH Verlag GmbH & Co. KGaA, Weinheim

Contents

Polymerization

G. A. Metselaar, J. J. L. M. Cornelissen,* A. E. Rowan,* R. J. M. Nolte **1990 – 1993**

Acid-Initiated Stereospecific Polymerization of Isocyanopeptides

Recognition with a twist: The acid-initiated polymerization of dipeptide-derived isocyanides (see scheme) is found to be an exceptionally stereospecific process that requires a helical template. The reaction is very sensitive to the acid concentration. At high acid concentrations, the template is destroyed and a competing cyclization reaction becomes predominant.

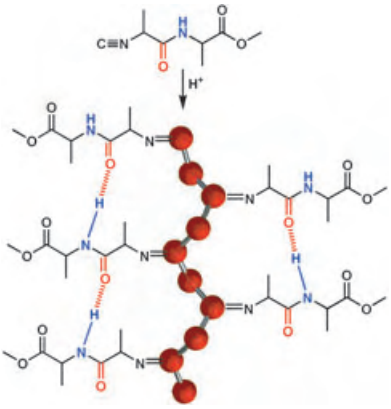

Host–Guest Systems

X. Liu, G. Chu, R. A. Moss,* R. R. Sauers,* R. Warmuth* **1994 – 1997**

Fluorophenoxycarbene inside a Hemicarcerand: A Bottled Singlet Carbene

Long live the carbene: Longevity is granted to fluorophenoxycarbene when it is generated photochemically from fluorophenoxydiazirine (see picture) inside a hemicarcerand. This fleeting, and otherwise nonisolable, singlet carbene is the first electron-deficient species that has been stabilized by trapping. NOE experiments suggest that the carbene adopts the intrinsically less stable *cis* conformation in the confined inner phase.

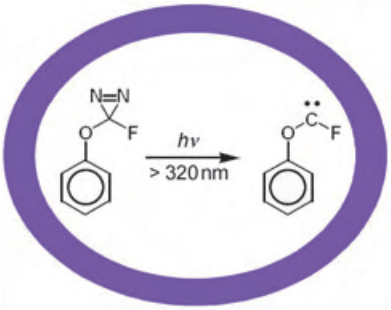

Molecular Magnetism

Y. Yukawa,* G. Aromí,* S. Igarashi, J. Ribas, S. A. Zvyagin, J. Krzystek **1997 – 2001**

[$GdNi_6$] and [$LaNi_6$]: High-Field EPR Spectroscopy and Magnetic Studies of Exchange-Coupled Octahedral Clusters

The competition between ferromagnetic and antiferromagnetic exchange for Ni–Gd and Ni–Ni interactions, respectively, leads to spin frustration and a degenerate $S = 13/2$ spin ground state for the symmetric [$GdNi_6$] cluster in $(NMe_4)[GdNi_6(pro)_{12}](ClO_4)_4$ (Hpro = proline; octahedral core shown). The influence of the Ni–Ni coupling was probed with the analogous cluster [$LaNi_6$]. In this case the lanthanide is diamagnetic, and one observes an $S = 0$ ground state.

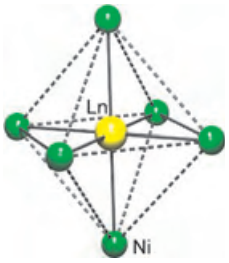

Enzyme Inhibition

B. G. Reddy, Y. D. Vankar* **2001 – 2004**

The Synthesis of Hybrids of D-Galactose with 1-Deoxynojirimycin Analogues as Glycosidase Inhibitors

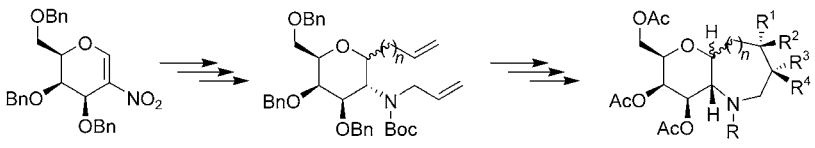

Sweet stop: Sugar–azasugar hybrids as enzyme inhibitors and leads for drug discovery are presented. Three hybrids **3** of D-galactose with analogues of 1-deoxynojirimycin were prepared from 3,4,6-tri-*O*-benzyl-2-nitro-D-galactal (**1**) by using ring-closing metathesis as a key reaction (see scheme); Bn = benzyl, Boc = *tert*-butoxycarbonyl, $n = 0,1$, R = Ac/Boc, R^1 = H/OAc, R^2 = H/OAc, R^3 = H/OAc, R^4 = H/OAc.

 © 2005 Wiley-VCH Verlag GmbH & Co. KGaA, Weinheim

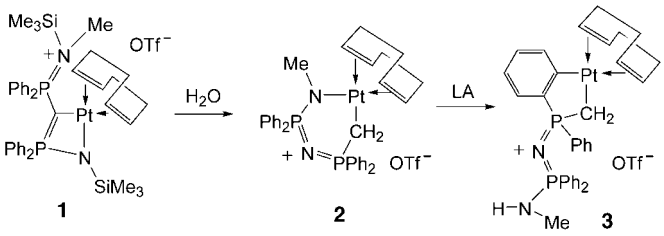

An unusual synthetic route to the first example of a six-membered M-N-P-N-P-C metallacycle (M = metal atom) is reported which involves a water-induced rearrangement of the methylated Pt-N-P-C-P-N carbene **1** to the unique Pt-N-P-N-P-C platinacyclocarbaphosphazene **2**. In the presence of a Lewis acid (LA), **2** converts into its orthometalated isomer **3** quantitatively. (OTf = CF_3SO_3).

Metallacycles

M. Fang, N. D. Jones, M. J. Ferguson, R. McDonald, R. G. Cavell* . **2005 – 2008**

Water-Induced Rearrangement of a Platinacyclic Carbene Produces a Platinacyclic Carbaphosphazene with an Intraannular Pt–C Bond in a Pt–N–P–N–P–C Ring

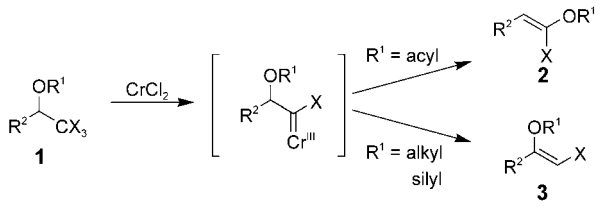

Reduction of trihalomethylcarbinols 1 with $CrCl_2$ affords good to excellent yields of (*Z*)-α-haloenol esters **2** and (*Z*)-β-haloenol ethers **3** through acyl or hydrogen migration, respectively. The reaction is proposed to proceed through regio- and stereoselective rearrangement of a chromium(III) Fischer carbene. (R^2 = H, alkyl, aryl; X = F, Cl, Br).

Organometallic Chemistry

R. Bejot, S. Tisserand, L. M. Reddy, D. K. Barma, R. Baati, J. R. Falck,* C. Mioskowski* _____ **2008 – 2011**

Stereoselective Transformations of Trihalomethylcarbinols Induced by Chromous Chloride

A new secondary building unit with edge-sharing 3-rings of BO_4 and GeO_4 tetrahedra (shown in the picture in turquoise and yellow, respectively) forms the basis of the framework of SU-16, a borogermanate with zeolite topology. SU-16 has three-dimensional intersecting 12-ring and 8-ring channels. In particular the unusual elliptical 12-ring channels may make this zeolite structure interesting for shape selectivity.

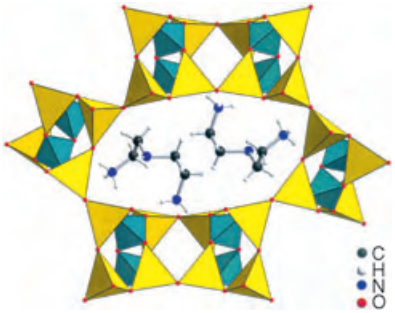

Zeolites

Y. Li, X. D. Zou* _____ **2012 – 2015**

SU-16: A Three-Dimensional Open-Framework Borogermanate with a Novel Zeolite Topology

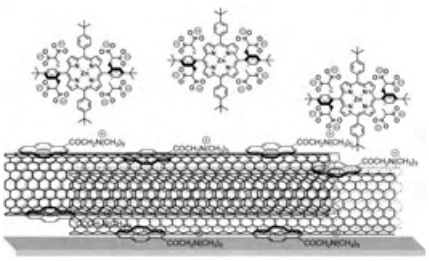

Light at the end of the tunnel: Single-wall carbon nanotubes—covalently and non-covalently functionalized with positively and negatively charged groups—associated with porphyrin counterparts are absorbed onto transparent electrodes (see scheme) to yield photochemical devices that exhibit monochromatic power conversion efficiencies of up to 8.5%.

Functional Materials

D. M. Guldi,* G. M. A. Rahman, M. Prato, N. Jux, S. Qin, W. Ford ____ **2015 – 2018**

Single-Wall Carbon Nanotubes as Integrative Building Blocks for Solar-Energy Conversion

 © 2005 Wiley-VCH Verlag GmbH & Co. KGaA, Weinheim

Contents

Molecular Switches

D. Sud, T. B. Norsten, N. R. Branda* ——— 2019 – 2021

Photoswitching of Stereoselectivity in Catalysis Using a Copper Dithienylethene Complex

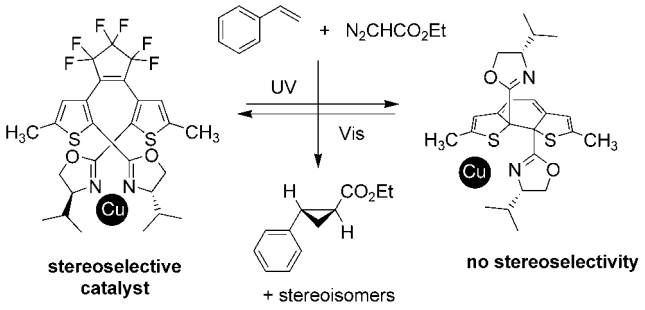

Light controls the outcome of a stereoselective reaction. Only in the ring-open form can the shown chelate copper(I) complex transfer its chirality to the cyclopropanation of styrene with ethyl diazoacetate. Irradiation with UV light triggers the ring-closing reaction of the ligand rendering it ineffective (see scheme).

Ruthenium-Catalyzed Reactions

R. Aoun, J.-L. Renaud, P. H. Dixneuf, C. Bruneau* ——— 2021 – 2023

Concomitant Monoreduction and Hydrogenation of Unsaturated Cyclic Imides to Lactams Catalyzed by Ruthenium Compounds

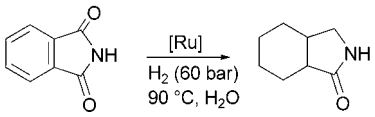

One for two: $[Ru_4H_6(p\text{-cymene})_4]Cl_2$ and $[RuCl_2(p\text{-cymene})]_2$, [Ru], are efficient catalyst precursors for the selective transformation of cyclic imides into saturated lactams (see scheme). The catalytic systems operate with the same reagent (H_2) to perform two transformations, namely, monoreduction of the carbonyl groups and hydrogenation of C=C bonds, with the release only of water, which is the solvent of the reaction.

Polyoxotungstates

A. Bagno,* M. Bonchio ——— 2023 – 2026

Vicinal Tungsten–Tungsten Coupling Constants in Polyoxotungstates: DFT Calculations Challenge an Empirical Rule

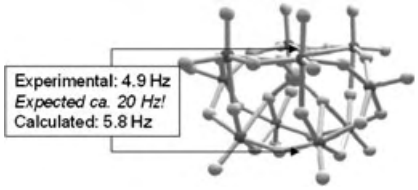

Smaller than expected: The empirical rule that edge and corner junctions give rise to small and large vicinal NMR tungsten–tungsten coupling constants, respectively, in polyoxometalates has led to the assumption that the W-O-W angle is the sole factor involved. Why then is the corner $^2J_{WW}$ coupling in γ-$[SiW_{10}O_{36}]^{8-}$ (see picture) so small? Relativistic DFT calculations show why this is indeed expected.

Palladium Catalysts

J. W. Sprengers, J. Wassenaar, N. D. Clement, K. J. Cavell, C. J. Elsevier* ——— 2026 – 2029

Palladium–(N-Heterocyclic Carbene) Hydrogenation Catalysts

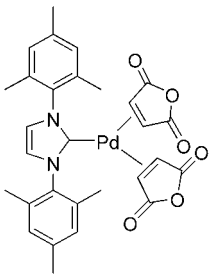

Low-valent palladium compounds with N-heterocyclic carbenes (NHCs) formed from $[Pd(NHC)(\eta^2\text{-alkene})_2]$ (see example) are amazingly selective catalysts for the hydrogenation of several alkynes to *Z* alkenes. One such complex, [Pd{1,3-(2,6-diethylphenyl)imidazol-2-ylidene}], has been employed for the selective (95%) hydrogenation of 1-phenyl-1-propyne to (*Z*)-1-phenyl-1-propene.

 © 2005 Wiley-VCH Verlag GmbH & Co. KGaA, Weinheim

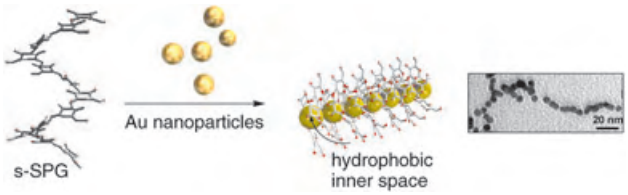

Forming an orderly line: Au nanoparticles can be aligned in one dimension by their incorporation into the helical structure of a natural polysaccharide, schizophyllan (s-SPG, see picture). The hydrophobic inner cavity of the helix hosts the hydrophobic nanoparticles and aligns the guests along its length (≈200 nm).

Nanostructures

A.-H. Bae, M. Numata, T. Hasegawa, C. Li, K. Kaneko, K. Sakurai, S. Shinkai* _____ **2030 – 2033**

1D Arrangement of Au Nanoparticles by the Helical Structure of Schizophyllan: A Unique Encounter of a Natural Product with Inorganic Compounds

The issues for March 2005 appeared online on the following dates:
Issue 9: February 15. · Issue 10: February 22. · Issue 11: March 2. · Issue 12: March 11

Sources

Product and Company Directory

You can start the entry for your company in "Sources" in any issue of *Angewandte Chemie*.

If you would like more information, please do not hesitate to contact us.

Wiley-VCH Verlag – Advertising Department
Tel.: 0 62 01 - 60 65 65
Fax: 0 62 01 - 60 65 50
E-Mail: MSchulz@wiley-vch.de

Service

Keywords _____ ***2034***

Authors _____ ***2035***

Sources _____ ***A15***

Preview _____ ***2037***

Corrigenda

While referring to Breslow's work on catalysis by nucleophilic carbenes derived from thiamine and model systems, the authors inadvertently left out his work on imidazolium and oxazolium ions.[1] The authors also wish to emphasize that Breslow was the first to observe catalysis by nucleophilic carbenes of any kind.
In Equation (18), which refers to work by Enders et al., the reference should be [32]. The references associated with Equation (19) are [32] and [33].
The omissions and errors are regretted by the authors.

[1] R. Breslow, *J. Am. Chem. Soc.* **1958**, *80*, 3719.

N-Heterocyclic Carbenes: Reagents, Not Just Ligands!

V. Nair,* S. Bindu, V. Sreekumar _____ **5130–5135**

Angew. Chem. Int. Ed. **2004**, *43*

DOI 10.1002/anie.200301714

An error in the references cited in the published article was noticed. The correct citation for ref. [5i] is provided below. The authors apologize for the oversight.

[5] i) W. H. Binder, M. J. Kunz, C. Kluger, G. Hayn, R. Saf, *Macromolecules* **2004**, *37*, 1749; W. H. Binder, M. J. Kunz, E. Ingolic, *J. Polym. Sci. Polym. Chem. Ed.* **2004**, *42*, 162.

Supramolecular AD Diblock Copolymers

X. Yang, F. Hua, K. Yamato, E. Ruckenstein, B. Gong,* W. Kim, C. Y. Ryu* _____ **6471–6474**

Angew. Chem. Int. Ed. **2004**, *43*

DOI 10.1002/anie.200460472

 © 2005 Wiley-VCH Verlag GmbH & Co. KGaA, Weinheim

Corrigenda

While referring to Breslow's work on catalysis by nucleophilic carbenes derived from thiamine and model systems, the authors inadvertently left out his work on imidazolium and oxazolium ions.[1] The authors also wish to emphasize that Breslow was the first to observe catalysis by nucleophilic carbenes of any kind.
In Equation (18), which refers to work by Enders et al., the reference should be [32]. The references associated with Equation (19) are [32] and [33].
The omissions and errors are regretted by the authors.

[1] R. Breslow, *J. Am. Chem. Soc.* **1958**, *80*, 3719.

N-Heterocyclic Carbenes: Reagents, Not Just Ligands!

V. Nair,* S. Bindu, V. Sreekumar — **5130–5135**

Angew. Chem. Int. Ed. **2004**, *43*

DOI 10.1002/anie.200301714

 © 2005 Wiley-VCH Verlag GmbH & Co. KGaA, Weinheim

Distinctions for G. Férey

Gérard Férey (University of Versailles, France) has been elected member of the French Academy of Sciences and will receive a Humboldt Research Award. Recipients of this award, which is intended to make it possible for esteemed foreign scientists to undertake half- to full-year research projects in collaboration with colleagues in Germany, are selected by the Alexander von Humboldt Foundation on the basis of nominations.

G. Férey

Férey studied in Caen (France) and completed his PhD in 1977 in Le Mans under the guidance of R. de Pape. From 1981 he was professor at the Université du Maine (Le Mans), but spent a period from 1988 to 1992 as deputy director of the chemistry department of the CNRS in Paris. In 1996 he took up his current position as professor at the University of Versailles and director of the Institut Lavoisier de Chimie Inorganique that he set up there. He is a knight of the French Legion of Honor and has been a full member of the Academy of Sciences since 2003, having been a corresponding member since 1996. He received a sword as a sign of his membership at the end of 2004.

Férey's research encompasses inorganic chemistry, in particular the chemistry of porous and hybrid solids. In issue 46/2004 of *Angewandte Chemie* he published three Communications on the targeted preparation and computer simulation of tailor-made crystalline solids with hierarchically ordered pores.[1] Further focal points of his research are magnetism and the chemistry of fluorine.

M. Inoue Gives the Merck Banyu Lecture

Masayuki Inoue (Tohoku University, Sendai, Japan) has received the Merck Banyu Lectureship Award, with which he has been recognized for his creative research in the area of natural product synthesis. The 14-person jury particularly emphasized the value of his contributions to the development of efficient methods and strategies for the total synthesis of structurally complex and biologically important substances, such as TMC-95A, merrilactone, and ciguatoxin. In issue 47/2004 of *Angewandte Chemie* he reported a formal total synthesis of (+)-pinnatoxin A and the synthesis of a chromophore framework through an atropselective macrolactonization.[2]

M. Inoue

Inoue studied chemistry at the University of Tokyo and completed his PhD in 1998 under the guidance of K. Tachibana. From 1998 to 2000 he undertook postdoctoral studies in the research group of S. Danishefsky at the Sloan-Kettering Institute for Cancer Research in New York. Since his return to Japan he has been assistant professor, lecturer (2003), and associate professor (since 2004) at Tohoku University. In 2004 he received the Chemical Society of Japan Award for Young Chemists.

K. C. Nicolaou to Head Biopolis Laboratory

K. C. Nicolaou is to direct the Biopolis Chemical Synthesis Laboratory in Singapore. The Singaporean government has been constructing the research center Biopolis since 2001 through the Agency for Science, Technology and Research with allocations amounting to several billion dollars. Nicolaou will remain concurrently Professor of Chemical Biology and Chemistry at The Scripps Research Institute in La Jolla, CA and Professor of Chemistry at the University of California, San Diego (USA). He is well known for his outstanding multifaceted research in organic synthesis, in particular in the stereoselective synthesis of natural products. He has co-authored numerous Reviews in *Angewandte Chemie* and books on this topic. His Review entitled "Chasing Molecules That Were Never There: Misassigned Natural Products and the Role of Chemical Synthesis in Modern Structure Elucidation" appeared recently.[3]

K. C. Nicolaou

Nicolaou was born in Cyprus and studied chemistry in London, where he completed his PhD in 1972 at University College under the guidance F. Sondheimer and P. J. Garratt. He then moved to the USA, where he undertook postdoctoral research in the groups of T. Katz at Columbia University in New York and E. J. Corey at Harvard University in Cambridge, MA. In 1977 he became professor at the University of Pennsylvania in Philadelphia, where he remained until 1989, when he moved to La Jolla. Nicolaou is a member of the International Advisory Board of *Angewandte Chemie*.

[1] a) C. Serre, F. Millange, S. Surblé, G. Férey, *Angew. Chem.* **2004**, *116*, 6445; *Angew. Chem. Int. Ed.* **2004**, *43*, 6285; b) C. Mellot-Draznieks, J. Dutour, G. Férey, *Angew. Chem.* **2004**, *116*, 6450; *Angew. Chem. Int. Ed.* **2004**, *43*, 6290; c) G. Férey, C. Serre, C. Mellot-Draznieks, F. Millange, S. Surblé, J. Dutour, I. Margiolaki, *Angew. Chem.* **2004**, *116*, 6456; *Angew. Chem. Int. Ed.* **2004**, *43*, 6296.

[2] a) M. Inoue, T. Sasaki, S. Hatano, M. Hirama, *Angew. Chem.* **2004**, *116*, 6662; *Angew. Chem. Int. Ed.* **2004**, *43*, 6500; b) S. Sakamoto, H. Sakazaki, K. Hagiwara, K. Kamada, K. Ishii, T. Noda, M. Inoue, M. Hirama, *Angew. Chem.* **2004**, *116*, 6667; *Angew. Chem. Int. Ed.* **2004**, *43*, 6505.

[3] a) K. C. Nicolaou, E. J. Sorensen, *Classics in Total Synthesis*, Wiley-VCH, Weinheim, **1996**; b) K. C. Nicolaou, S. A. Snyder, *Classics in Total Synthesis II*, Wiley-VCH, Weinheim, **2003**; c) K. C. Nicolaou, S. A. Snyder, *Angew. Chem.* **2005**, *117*, 1036; *Angew. Chem. Int. Ed.* **2005**, *44*, 1012.

 © 2005 Wiley-VCH Verlag GmbH & Co. KGaA, Weinheim DOI: 10.1002/anie.200500679

Synthetic Methods

Relay Ring-Closing Metathesis—A Strategy for Achieving Reactivity and Selectivity in Metathesis Chemistry

*Debra J. Wallace**

Keywords:
alkenes · cyclization · dienynes · metathesis · ruthenium

The power of metathesis chemistry in organic synthesis is undeniable. Over the past ten years technology has developed to promote ring-closing, ring-opening, and cross metathesis reactions.[1] In particular, ring-closing reactions using the air-stable, commercially available ruthenium alkylidene catalysts such as **1**,[2] **2**,[3] and **3**[4] have achieved widespread use to promote a range of cyclizations (Scheme 1). Alkenes, alkynes, and enynes have been used as substrates and the selective formation of one or even multiple rings has been reported in numerous papers. Despite the many successful applications, in some instances reactions can still be less than satisfactory, due to low reactivity and/or low selectivity. To elevate ring-closing metathesis (RCM) to a universally applicable procedure, development of methods to overcome these shortcomings is ongoing in many laboratories, and relay RCM is one such recent development.

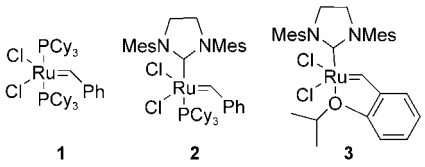

1 2 3

Scheme 1. Commercially available ruthenium alkylidene catalysts. Cy = cyclohexyl, Mes = 2,4,6-trimethylphenyl.

Historically, products that proved difficult to access via RCM using the first generation catalyst **1** were tetrasubstituted alkenes such as **4** (Scheme 2).

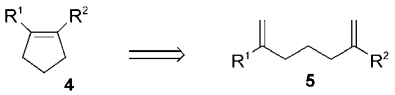

4 ⟹ 5

Scheme 2. A well-known difficult process: the sythesis of tetrasubstituted alkenes by RCM.

This was largely due to the difficulty of initiating the catalytic process on either of the sterically hindered acyclic alkenes in diene **5**.[5] Even with the development of second-generation catalysts,[6] the formation of some tetrasubstituted olefins remained elusive,[7] and this provided one impetus for development of the relay RCM method.

The rational behind this strategy rests on the fact that although initiation of the catalytic cycle between two sterically demanding alkenes as in **5** is a challenge, the intramolecular reaction of a ruthenium alkylidene onto such an alkene is attainable, as is the subsequent reaction of the previously inaccessible alkylidene. As such, if a method was available to generate the initial alkylidene in an intramolecular fashion the reaction could proceed.[8] The relay approach involves incorporation of a temporary tether containing a sterically unencumbered olefin for initiation of the catalytic cycle. The olefin is positioned such that a kinetically favorable formation of a five-membered ring is used to deliver the ruthenium onto the sterically hindered position with concomitant extrusion of the ring. The use of this method to address such a problem was demonstrated by Hoye et al., and is exemplified in Scheme 3.[9] Diene **6** does not undergo cyclization promoted by catalyst **1**; however when armed with the relay moiety, as in compound **7**, the unencumbered terminal alkene became the site for initial reaction with the catalyst,[10] leading to intramolecular delivery of the ruthenium onto the traditionally less accessible position. The desired ring-closing reaction then proceeded to give **8**.

The application of this principle to other substrates, many of which would be unreactive to standard RCM conditions, at least with the originally employed first generation catalyst, has been carried out by the same research group.[9] For example, the butenolide **9** can be prepared from either of the

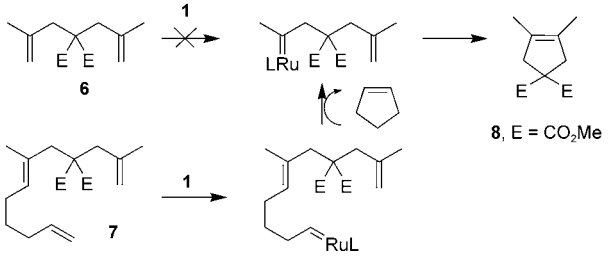

6 → 8, 7 → 8

Scheme 3. Relay RCM to give tetrasubstituted olefins.

[*] Dr. D. J. Wallace
Department of Process Research
Merck Sharp and Dohme Research Laboratories
Hertford Road, Hoddesdon, Hertfordshire, EN11 9BU (UK)
Fax: (+44) 199-247-0437
E-mail: debra_wallace@merck.com

 © 2005 Wiley-VCH Verlag GmbH & Co. KGaA, Weinheim DOI: 10.1002/anie.200462753

starting materials **10** or **11** using catalyst **1** via initial reaction with the terminal olefins incorporated into the tethers (Scheme 4). In this instance, the relay procedure overcame both a steric and an electronic deactivation, as the intermolecular reaction of catalyst **1** with electron-deficient double bonds cannot usually be achieved, even when they are unsubstituted.[11]

In some cases, formation of unsubstituted cyclic alkenes can also be challenging if the starting alkenes are substituted. In an interesting approach to a diastereoselective RCM reaction, Robinson et al. installed a trigger in **12** to promote initiation of the ring-closing event via delivery of the ruthenium onto the desired double bond.[12] This also ensured that the stereodifferentiating step was the intramolecular cyclization, rather than an intermolecular differentiation between two diastereotopic groups and the catalyst (Scheme 5). The reaction did not proceed with the truncated derivative **13**, although it is likely that substrate **14** would have been a suitable starting material for this transformation using second-generation catalysts **2** or **3**.

A different reactivity issue may be encountered when the ruthenium catalyst reacts with an alkene to afford a particularly stabilized alkylidene, which then does not react in the subsequent ring-closing reaction. Such a problem could be overcome by blocking of the non-productive site, or by relay activation of the alternate more reactive position. In a recent synthesis of oximidine II Porco et al. attempted the RCM of substrates such as **15** (Scheme 6).[13] In **15**, preferential reaction of either catalyst **1** or **2** with the *trans*-diene component afforded a stabilized alkylidene **16** that was unreactive to further reaction. Blocking of this position by introduction of substitution, as in **17**, allowed the catalytic cycle to initiate at the *cis*-diene and the desired macrocycle was formed, albeit in modest yield. However, when this approach was applied to the closely related synthesis of oximidine III, compound **18** did not give the desired ring-closed product even with second-generation catalysts.[14] This was again attributed to the formation of the stabilized alkylidene **19**, which did not undergo significant further reaction,

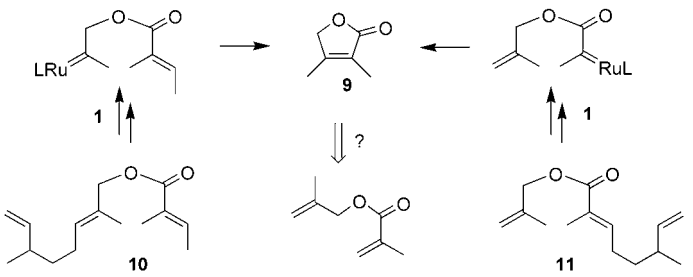

Scheme 4. Use of relay RCM by Hoye et al. to overcome both steric and electronic deactivation.

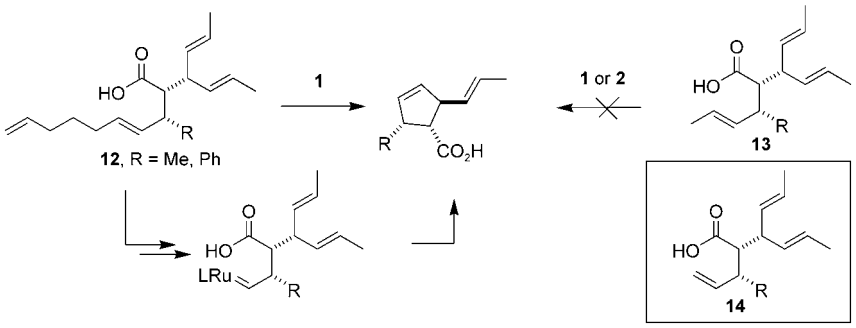

Scheme 5. Intramolecular differentiation of diastereotopic groups is achieved by using a relay procedure.

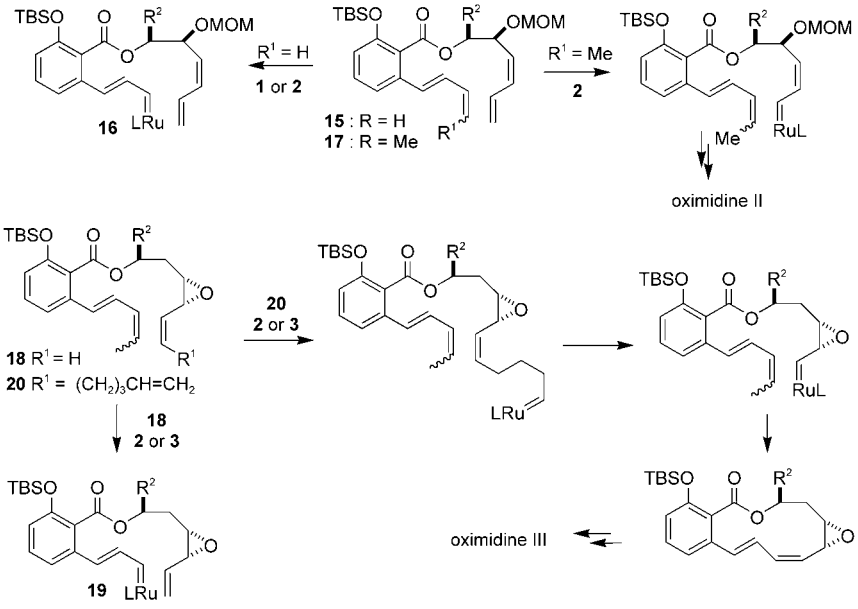

Scheme 6. Synthesis of oximidine III by Porco et al. illustrates the use of relay RCM to avoid generation of the unproductive alkylidene **19**. MOM = methoxymethyl, TBS = *tert*-butyldimethylsilyl.

suggesting that the vinyl epoxide moiety was too hindered for satisfactory catalyst interaction even when compared with a trisubstituted olefin. The problem was overcome by introduction of a relay moiety onto the vinyl epoxide side in compound **20**, which allowed delivery of the ruthenium onto the aforementioned vinyl epoxide position. The subsequent ring-closing reaction proceeded smoothly and was more efficient than the corresponding cyclization in the oximidine II route.

 © 2005 Wiley-VCH Verlag GmbH & Co. KGaA, Weinheim

A similar strategy has also been used by Lee et al. to increase reactivity and yields in cross metathesis reactions (Scheme 7).[15] The reaction of enyne **21** with alkene **22** afforded the cross metathesis product **23** in good *Z*-selectivity but suffered from low yield and reactivity, (18 h, 34%). The authors propose that the initiation site is the alkene and low reactivity of the conjugated enyne towards the propagating alkylidene is detrimental to the reaction progress. To bias the system towards generation of the conjugated enyne alkylidene, the tethered substrate **24** was prepared, allowing relay generation of the previously unattainable alkylidene **25**, which was expected to react more readily with the alkene. Indeed, a more efficient reaction was now observed (6 h, 64%). A reduced *Z*-selectivity was obtained for all substrates examined when using the relay method, supporting the proposal that different reacting species were responsible for the outcomes.

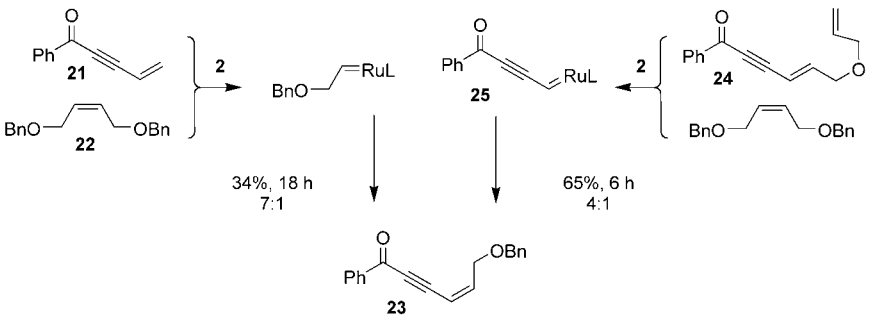

Scheme 7. Different propagating species lead to differing reactivities and selectivities in a cross metathesis reaction. Bn = benzyl.

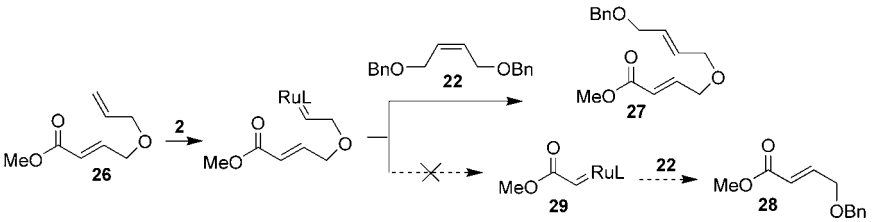

Scheme 8. Cross metathesis with alkene **22** takes place in preference to the intramolecular ring-closing reaction.

This work highlights one limitation of the relay procedure which can arise when the intramolecular formation of the five-membered ring to generate the "difficult" alkylidene is not sufficiently favorable to take preference over an alternate intra- or intermolecular reaction. As shown in Scheme 8 reaction of alkene **26** with **22** afforded **27** rather than the expected **28**, indicating that cyclization onto the electron-deficient olefin to give alkylidene **29** was slower than the competing intermolecular cross metathesis process.[16]

Selectivity issues can arise in metathesis chemistry when more than one ring is formed during a ring-closing process. For example, a key factor in determining the outcome of dienyne RCM is the site of initiation of the catalyst. Controlling this position can aid in achieving the desired product.[17] In Scheme 9, substrate **30** afforded a 1:1 mixture of products **31** and **32** on treatment with **2**, due to non-discriminatory interaction of the catalyst with either of the unhindered terminal olefins.[18] In many cases this lack of selectivity can be addressed by biasing the initial reaction by introduction of either steric hindrance or electronic deactivation on one olefin. In the above example, compound **33** afforded a 6:1 mixture of

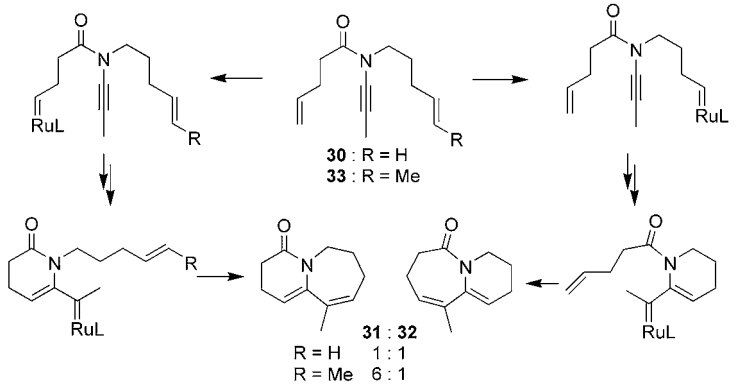

Scheme 9. The outcome of a dienyne metathesis can be influenced by biasing the site of catalyst interaction.

31:**32**; other examples of controlling dienyne metathesis in this way abound.[19]

An alternative strategy for controlling the outcome of dienyne metathesis is the introduction of a relay moiety to direct the initial reaction of the catalyst.[9] As shown in Scheme 10, the dienyne **34** gave a 1:2 ratio of **35**:**36** when treated with catalyst **2**. However, the relay substrates **37** or **38** gave ratios of 1:7 and 5:1, respectively, when using the same catalyst and near total selectivity with the less reactive first-generation catalyst **1**. Given that the olefins in this substrate are substituted the alternate strategy of introducing a blocking group to either of the alkenes, such as in **39**, would probably have led to low reactivity, although some directionality might have been achieved.

In conclusion, relay RCM has recently been developed as a method to overcome both reactivity and selectivity issues in metathesis chemistry. The installation of a "tether" containing a reactive alkene has provided a mechanism to replace challenging intermolec-

 © 2005 Wiley-VCH Verlag GmbH & Co. KGaA, Weinheim

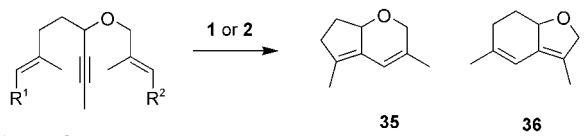

34 ; $R^1 = H$, $R^2 = H$
37 : $R^1 = CH_2OCH_2CH{=}CH_2$, $R^2 = H$
38 : $R^1 = H$, $R^2 = CH_2OCH_2CH{=}CH_2$
39 : $R^1 = Me$, $R^2 = H$

Scheme 10. Use of the relay procedure to control dienyne metathesis.

ular reactions between commonly used alkylidene catalysts and electronically or sterically deactivated alkenes, with favorable intramolecular variants. This has allowed previously unattainable transformations to be realized, and also provided a mechanism for controlling the outcome of dienyne cyclizations. Given the relative ease of synthesis of the relay substrates it seems likely that further examples of this strategy will continue to emerge in this field.

Published online: February 2, 2005

[1] For recent reviews on metathesis reactions see: a) *Tetrahedron*, **1999**, *55*, 8141 (*Symposium in Print*; Eds.: M. L. Snapper, A. H. Hoveyda); b) "Alkene Metathesis in Organic Synthesis": *Top. Organomet. Chem.* **1998**, 1; c) S. Blechert, *Pure Appl. Chem.* **1999**, *71*, 1393; d) A. Fürstner, *Angew. Chem.* **2000**, *112*, 3140; *Angew. Chem. Int. Ed.* **2000**, *39*, 3012; e) T. M. Trnka, R. H. Grubbs, *Acc. Chem. Res.* **2001**, *34*, 18; f) S. J. Connon, S. Blechert, *Angew. Chem.* **2003**, *115*, 1944; *Angew. Chem. Int. Ed.* **2003**, *42*, 1900; g) R. E. Schrock, A. H. Hoveyda, *Angew. Chem.* **2003**, *115*, 4740; *Angew. Chem. Int. Ed.* **2003**, *42*, 4592; h) A. Deiters, S. F. Martin, *Chem. Rev.* **2004**, *104*, 2199.

[2] a) P. Schwab, M. B. France, J. W. Ziller, R. H. Grubbs, *Angew. Chem.* **1995**, *107*, 2179; *Angew. Chem. Int. Ed. Eng.* **1995**, *34*, 2039; b) P. Schwab, R. H. Grubbs, J. W. Ziller, *J. Am. Chem. Soc.* **1996**, *118*, 100.

[3] M. Scholl, S. Ding, C. W. Lee, R. H. Grubbs, *Org. Lett.* **1999**, *1*, 953.

[4] a) S. B. Garber, J. S. Kingsbury, B. L. Gray, A. H. Hoveyda, *J. Am. Chem. Soc.* **2000**, *122*, 8168; b) S. Gessler, S. Randl, S. Blechert, *Tetrahedron Lett.* **2000**, *41*, 9973.

[5] T. A. Kirkland, R. H. Grubbs, *J. Org. Chem.* **1997**, *62*, 7310.

[6] a) See references [3–5]; b) M. Scholl, T. M. Trnka, J. P. Morgan, R. H. Grubbs, *Tetrahedron Lett.* **1999**, *40*, 2247; c) A. Briot, M. Bujard, V. Gouverneur, S. P. Nolan, C. Mioskowski, *Org. Lett.* **2000**, *2*, 1517; d) H. Wakamatsu, S. Blechert, *Angew. Chem.* **2002**, *114*, 2509; *Angew. Chem. Int. Ed.* **2002**, *41*, 2403; e) A. Michrowska, R. Bujok, S. Harutyunyan, V. Sashuk, G. Dolgonos, K. Grela, *J. Am. Chem. Soc.* **2004**, *126*, 9318.

[7] In some cases use of molybedum catalyst can be used to overcome these issues, for example: S. E. Denmark, S.-M. Yang, *Tetrahedron* **2004**, *60*, 9695.

[8] Geminal-disubstituted ruthenium alkylidenes are generated and react in dienyne RCM reactions: S.-H. Kim, W. J. Zuercher, N. B. Bowden, R. H. Grubbs, *J. Org. Chem.* **1996**, *61*, 1073.

[9] T. R. Hoye, C. S. Jeffrey, M. A. Tennakoon, J. Wang, H. Zhao, *J. Am. Chem. Soc.* **2004**, *126*, 10210.

[10] a) M. Ulman, R. H. Grubbs, *Organometallics* **1998**, *17*, 2484; b) T. R. Hoye, H. Zhao, *Org. Lett.* **1999**, *1*, 1123.

[11] a) M. Ulman, T. R. Belderrain, R. H. Grubbs, *Tetrahedron Lett.* **2000**, *41*, 4689; b) T.-L. Choi, C. W. Lee, A. K. Chatterjee, R. H. Grubbs, *J. Am. Chem. Soc.* **2001**, *123*, 10417; c) K. Basu, J. A. Cabral, L. A. Paquette, *Tetrahedron Lett.* **2002**, *43*, 5453.

[12] J. Robinson, A. D. Piscopio, L. Zhu, *Abstracts of Papers*, 226th National Meeting of the American Chemical Society, New York, American Chemical Society, Washington, DC; ORGN-118.

[13] X. Wang, J. A. Porco, Jr., *J. Am. Chem. Soc.* **2003**, *125*, 6040.

[14] X. Wang, E. J. Bowman, B. J. Bowman, J. A. Porco, Jr., *Angew. Chem.* **2004**, *116*, 3685; *Angew. Chem. Int. Ed.* **2004**, *43*, 3601.

[15] E. C. Hansen, D. Lee, *Org. Lett.* **2004**, *6*, 2035.

[16] In contrast, the cyclization of **11** in Scheme 4 does achieve a cyclization onto an electron-deficient olefin in preference to competing reactions.

[17] For reviews of enyne metathesis see: a) C. S. Poulsen, R. Madsen, *Synthesis* **2003**, 1; b) S. T. Diver, A. J. Giessert, *Chem. Rev.* **2004**, *104*, 1317.

[18] J. Huang, H. Xiong, R. P. Hsung, C. Rameshkumar, J. A. Mulder, T. P. Grebe, *Org. Lett.* **2002**, *4*, 2417.

[19] For example, see: a) C.-J. Wu, R. J. Madhushaw, R.-S. Liu, *J. Org. Chem.* **2003**, *68*, 7889; b) T. Honda, H. Namiki, K. Kaneda, H. Mizutani, *Org. Lett.* **2004**, *6*, 87.

 © 2005 Wiley-VCH Verlag GmbH & Co. KGaA, Weinheim

History of Science

Controversy in Chemistry: How Do You Prove a Negative?—The Cases of Phlogiston and Cold Fusion**

Jay A. Labinger and Stephen J. Weininger**

Keywords:
cold fusion · energy conversion · history of science · oxygen

In our first essay in this series, the two cases of controversy in stereochemistry we examined were temporally widely separated—one from the very beginnings of the field and one quite recent—and also quite different in terms of overall scope and impact, not to mention the disparity in experimental methodology and conceptual framework available to the participants. Nonetheless, as we tried to show, they are actually closely related with respect to a most fundamental issue in the historical development of a discipline—namely, how the community comes to agree upon what counts as evidence in resolving disputes.

For our second study we have again chosen two stories that appear to be about as disparate as one could possibly arrange. One, the overthrow of the theory of phlogiston, dates from the origins of modern chemistry, and is now universally considered a central development therein. The other, the cold fusion episode, is only 15 years old, and is now generally (though by no means universally) considered as just a stumble in the long historical march of chemistry. Why have we paired them? Because we feel that, as with the previous study, closer examination reveals certain connections that are instructive for a general understanding of how controversies play out and, in doing so, serve as a powerful engine for the advancement of science. The question of what counts as evidence is important here as well, but we will focus in particular on the persistence of belief, associated with the difficulty of demonstrating the *non-existence* of a theoretical or hypothetical entity.

[*] Dr. J. A. Labinger
Beckman Institute
California Institute of Technology, 139-74
Pasadena, CA 91125 (USA)
Fax: (+1) 626-449-4159
E-mail: jal@its.caltech.edu
Prof. S. J. Weininger
Worcester Polytechnic Institute
Worcester, MA 01609-2280 (USA)
Fax: (+1) 508-831-5933
E-mail: stevejw@wpi.edu

[**] Controversy in Chemistry, Part II. For Part I, see Ref. [25].

Case 1: The Eventual Death of Phlogiston—What are the Lessons?

Phlogiston has long served as a hobby horse that various commentators have ridden for their own purposes, particularly textbook authors, who often use historical incidents as vehicles for their personal philosophies. This situation is hardly a new phenomenon. For example, Roscoe and Schorlemmer, like many 19th century chemists, were concerned with the status of chemistry. In their *Treatise on Chemistry* of 1881 they asserted that "It is only after Stahl's labours [on phlogiston] that a scientific chemistry becomes possible".[1] Closer to our own time, Linus Pauling also emphasized the strengths of Stahl's conception in providing a coherent theoretical framework for chemistry:

> *"The phlogiston theory thus provided a general explanation of the chemical processes of oxidation and reduction ... It is interesting to consider the other ways in which chemical phenomena were accounted for by the phlogiston theory. The success of the theory in providing these explanations explains the fact that it had many strong adherents".*[2]

These appreciative comments are not, however, representative of the general opinion among textbook authors. The history of phlogiston is usually presented as a cautionary tale: "The phlogiston theory … long outlived its usefulness, and the tenacity with which it maintained itself is an instructive illustration of the difficulty which most men have of freeing their minds from the authority of a long held theory", a theory that "delayed the development of chemistry as an exact science for three-quarters of a century".[3]

In addition to what the phlogiston episode supposedly tells us about the frailties of the human mind, it has the additional merit (according to some authors) of highlighting the virtues of science:

> *"Although the phlogiston theory is of no importance today, the way in which it was discarded is a good illustration of the manner in which the scientific method operates ... It remained for Lavoisier, who had developed good equipment and a facility for accurate experimentation, to deliver the crushing blow to the theory".*[4]

Since the phlogiston theory is generally believed to have expired by 1800, it would seem to have little relevance today. Yet the lessons encapsulated in its history apparently have not been appreciated sufficiently by all scientists. Thus, in 1991 the journal *Chemtech* thought it necessary to recount the story yet again under the headline, "A timely analysis of the persistence of lousy ideas".[5] In this part of our article we will address two questions: Was the phlogiston theory indeed a lousy idea, and why did it persist for a century or more?

 © 2005 Wiley-VCH Verlag GmbH & Co. KGaA, Weinheim DOI: 10.1002/anie.200462084

We can begin answering the first question by noting how misleading the *Chemtech* headline is—a situation not at all uncommon in the treatment of this subject. The article itself is an adaptation of a chapter by James Bryant Conant, one of the major historians of phlogiston.[6] Nowhere in Conant's work does the phrase "lousy idea" appear, and he neither sneers at the theory nor derides its advocates. Rather, he notes that the concept "provided a pattern into which a mass of otherwise unrelated phenomena could be fitted".[7] As we shall see, Conant's respectful treatment of phlogiston and the phlogistonists was entirely appropriate.[8]

Although the conceptual structure of the phlogiston hypothesis was laid down by Johann Joachim Becher in the mid-17th century, phlogiston only became a centerpiece of chemical thinking through the efforts of his student Georg Ernst Stahl, later Professor of Medicine at the University of Halle (1694–1715), who coined the term phlogiston.[9] The concept was founded upon a common contemporary belief, namely, that the properties of substances were a consequence of their containing *carriers* of those properties, which were called *principles*. For example, substances that were metallic, saline, or acidic had those characteristics because they contained the principles for metallicity, salinity, and acidity, respectively. A single principle could be the carrier of more than one property, and the diversity of substances was accounted for by the differing proportions of the principles that were present in each substance.[10]

The exact nature of these principles was a matter of dispute. Some authors categorized them as purely hypothetical, some as real but imponderable (most assigned phlogiston to this category), and some as real and ponderable (late on, phlogiston was in this category as well). The general view was that principles could not be isolated in an uncombined state, but instead were passed from one substance to another during chemical reactions.

The doctrine of principles was in fact able to make sense of a wide range of well-established phenomena, many of them connected with practical arts such as mining and metallurgy. For example, it was common knowledge that flammable substances such as charcoal and sulfur would convert earthy, metallic ores (called calces) into shiny, ductile metals. Stahl and his followers attributed this conversion to the transfer of phlogiston (the principle of flammability and metallicity) from the charcoal or sulfur to the ore. Note that according to this theory, metals (which consisted of a calx and phlogiston) were more complex than their calces (oxides). The oxygen theory maintained just the opposite—that metals were less complex than their calces. This difference was to be a major point of disagreement between the phlogistonists and antiphlogistonists.

Describing the reduction of metal ores by charcoal in terms of phlogiston transfer was more than mere word play. It was supported empirically by the observation of reversible chemical transformations, such as the combustion of sulfur to sulfuric acid and its eventual recovery from the derived potassium sulfate by reaction of the salt with charcoal. The phlogistonists asserted that since the combustion of sulfur involved the loss of phlogiston, the sulfur could be regained by combining the product with a phlogiston-rich material such as charcoal—which is exactly what was observed [Eq. (1)].[11]

$$\mathrm{S} \xrightarrow[\text{[phlogiston lost]}]{\text{air, water, heat}} \mathrm{H_2SO_4} \xrightarrow{\mathrm{K_2CO_3}} \mathrm{K_2SO_4} \xrightarrow[\text{[phlogiston regained]}]{\text{charcoal, heat}} \mathrm{K_2CO_3} + \mathrm{KS}_n \xrightarrow{\text{vinegar}} \mathrm{S} \quad (1)$$

The phlogiston theory also enabled Stahl to realize that the reverse of ore reduction (the calcination of metals) was a form of combustion that differed from the burning of charcoal only in its rate. Even Stahl's most determined opponents conceded that this was a discovery of prime importance. Furthermore, Stahl included respiration under the rubric of phlogiston transfer, thus making a conceptual bridge between the animate and inanimate realms. He further believed that phlogiston was conserved, so that when charcoal or sulfur was burned in air (then thought to be a single substance) the emitted phlogiston was absorbed by the air. For the air itself to remain respirable, the phlogiston was in turn absorbed by living organisms, thus establishing a complete phlogiston cycle in nature.[12] Finally, it is noteworthy that the phlogiston theory was the first truly chemical theory of chemical phenomena, deliberately set in opposition to the prevailing mechanical theory, which could not convincingly explain the qualitative changes so characteristic of chemical processes. Thus, in 1770, at about the time that Lavoisier began to interest himself in the problem of combustion, the phlogiston theory "was not a decaying relic tradition … but a work that symbolized for most chemists the achievement of autonomy for chemistry".[13]

Phlogiston's most passionate advocate was Joseph Priestley, who continued to believe in it up to the time of his death in 1804.[14] Phlogiston's most effective and implacable opponent was Antoine-Laurent Lavoisier, who in 1772 began a series of experiments that would eventually convince him, and subsequently the chemical community, that the phlogiston concept was completely superfluous.[15] Yet Priestley and Lavoisier relied on the same set of experiments to buttress their contradictory conclusions.

Many of these experiments involved the production and differentiation of a variety of new gases ("airs", as they were then known). One of the most important, which led to the discovery of a new "air", was the thermal decomposition of HgO to give "an eminently respirable air" that supported combustion and living organisms far better than ordinary air. To Priestley the gas was "dephlogisticated air"—ordinary air deprived of phlogiston. To Lavoisier it was "oxygen", a "simple substance" that combined with materials undergoing combustion or calcination. Deciding between these alternatives involved observing and interpreting the behavior of various airs under different chemical and biological conditions.

In the standard version of phlogiston's fall from credibility Lavoisier is supposed to have discovered unexpectedly that substances gain weight when they burn, even though they are allegedly losing phlogiston. This discovery then forced the adherents of phlogiston to embrace an absurdity—that phlogiston had negative weight—which then convinced all but a few diehards of the superiority of the oxygen theory of combustion.

 © 2005 Wiley-VCH Verlag GmbH & Co. KGaA, Weinheim

As is often the case, the actual history is not nearly so tidy. It had been established already in 1630 by Jean Rey that metallic calces weighed more than the metals from which they were derived, and 18th-century investigators further confirmed this observation.[16] Phlogistonists did not view this result as fatal for their theory, but rather as an observation that could be explained within the theory's framework.

There were in fact several competing explanations that all relied on the plausible assumption that phlogiston was lighter than air. For example, one explanation held that, as a metal was calcined, air replaced phlogiston in its internal spaces, thus leading to the weight increase. The fact that weight increases were not invariably observed in calcination—temperatures were sometimes high enough to vaporize portions of the product leading to a weight decrease—further blunted the impact of this line of attack.

Other experimental results were also thought to have invalidated the phlogiston hypothesis. As noted above, one particularly important set of data concerned the thermal decomposition of the calx of mercury (HgO).[17] In this experiment, a gas is released and metallic mercury is left as a residue. To Lavoisier the results furnished decisive support for the oxygen theory, since mercury regained its metallic state without any external source of phlogiston such as charcoal. However, the phlogistonists had an alternative explanation at hand. By the 1780s most of them accepted the proposition that during calcination air replaced phlogiston within the pores of the metal. This so-called "fixed air" (about whose composition there was much disagreement) was presumed to be rich in phlogiston. Upon heating the sample, the phlogiston was supposed to be transferred to the mercury calx, thus restoring it to the metallic state. The dephlogisticated air that remained was expelled, as observed.

The picture that emerges from even this abbreviated history is that of two competing theories, one of which eventually prevailed by a steady accretion of new experimental results linked to a more coherent explanatory framework.[18] Lavoisier's balance sheet method, which accounted for the weights of all reactants and products and showed that nothing ponderable was created or destroyed, was very effective in converting other chemists to his system. Yet the rigorous application of this method required Lavoisier to adopt some premises of the scheme he had set out to overthrow. For example, to account for the three states of matter and for the heat released in oxidation reactions, Lavoisier posited that all substances contain varying amounts of caloric, the material basis of heat. Since he obtained nearly perfect agreement between the weights of reactants and products—to the extent that some of his opponents had understandable doubts about his claim[19]—Lavoisier found it necessary to assume that caloric, although real, was an imponderable fluid. Shades of phlogiston!

In fact, it was precisely with respect to the imponderable aspects of chemical phenomena, such as heat, light, and electricity, that the oxygen theory was found wanting. Thus, a small band of natural philosophers was able to welcome oxygen as being "among the greatest discoveries in physics" (in the words of the eminent geologist James Hutton) while still embracing phlogiston. The reality of phlogiston, Hutton claimed, would always be hidden from "those philosophers, who, with the balance in their hands refuse to admit into the rank of chymical elements substances which do not ponderate…".[20] Until the elaboration of the energy concept in the mid-19th century, Hutton's critique could not be totally dismissed.

In addition, phlogiston's fortunes were temporarily boosted by the unraveling of parts of Lavoisier's system. For example, caloric was rendered superfluous by the kinetic theory of heat.[21] An even harsher blow resulted from the discovery that oxygen was not an essential component of acids. It is often forgotten that Lavoisier's theory was as much about acidity as it was about combustion.[22] (The word "oxygen" was derived from the Greek words for "acid former".) Lavoisier described oxygen as the principle of acidity, which uncomfortably echoes Stahl's description of phlogiston as the principle of flammability. When Humphrey Davy showed in 1810 that muriatic acid (HCl) contained no oxygen and that so-called "oxygenated muriatic acid" was in fact elemental chlorine, doubts arose in some quarters about the viability of the oxygen theory.[23] Davy himself entertained a sympathetic attitude toward phlogiston in the first decade of the 19th century, and his results with HCl and Cl_2 provoked concerns that "future discoveries shall … utterly destroy the merits of the later improvements in pneumatic chemistry and bring us back to the doctrine of phlogiston …".[24]

Yet the oxygen theory of combustion, the nomenclatural reform, and other pillars of the Chemical Revolution remained unshaken. As we noted in an earlier report, it usually takes more than just experimental disconfirmations to destroy a theory that has had predictive success with respect to crucial issues.[25] So, at the end of the day, how can we explain the contrasting fates of the oxygen and phlogiston theories? By the last two decades of the 18th century, phlogistonists could do no more than provide explanations of known results, while Lavoisier and his adherents were able to predict as yet unknown phenomena. To even account for those experimental data that played so conclusive a role in the struggle between the two theories, phlogistonists had constant recourse to ad hoc hypotheses. Ultimately, Lavoisier was fully justified in characterizing phlogiston as "a veritable Proteus that changes its form every instant!"[26] Yet the longevity of this protean concept was derived in large part from the great difficulty involved in proving its nonexistence.[27]

Case 2: The Short Life (but Longer Afterlife) of Cold Fusion

Our previous essay dealt with a recent controversy, that of bond–stretch isomerism, which was relatively unfamiliar even to the majority of practicing chemists, and completely unknown outside their ranks. The roughly contemporaneous case of cold fusion was entirely the opposite. For several months in 1989 it was one of the hottest topics around—not just in scientific journals, but also in newspapers, popular magazines, TV shows, etc. We can think of no chemistry story that has attained comparable vis-

 © 2005 Wiley-VCH Verlag GmbH & Co. KGaA, Weinheim

ibility. Indeed, how it played out in the public eye would merit a fascinating and valuable examination in its own right, but one that would far exceed the scope of this Essay. Nor do we have space to consider the claims and counterclaims in any detail; in any case, most readers are probably fairly familiar with at least the basic outline. We present below a very brief summary. For those who want to know more, several full-length book accounts, written from a variety of perspectives (including scientist–nonbeliever,[28] scientist–agnostic/skeptic,[29] scientist/science writer–nonbeliever,[30] scientist/science writer-believer,[31] and science writer–nonbeliever[32]) were published within the first few years. There are also a number of internet-based bibliographies which can easily be located on-line.

The controversy opened in March 1989, when University of Utah electrochemists Stanley Pons and Martin Fleischmann held a press conference to announce that electrolysis of D_2O at a palladium electrode produced anomalous effects, including liberation of energy in excess of the input—in one case to such an extreme extent as to melt the Pd cathode and destroy the apparatus. A publication appearing shortly afterwards (but submitted prior to the press conference) provided some details and also reported neutron fluxes, γ-rays at the right energy to indicate proton–neutron reactions, and accumulation of tritium in the electrolyte.[33] Related, but much less dramatic, findings (many fewer neutrons, no excess heat) were published around the same time by Steve Jones, a physicist at Brigham Young University.[34] (The two research groups were aware of each other's work; concerns over priority issues—patent rights in particular—no doubt prompted the unorthodox publication-by-press-conference and substantially set the tone for ensuing developments.) The authors concluded that nuclear fusion, which had been somehow catalyzed within the Pd lattice, was the only possible explanation for these observations.

The clear potential importance of such a discovery, coupled with the apparent experimental simplicity, inspired many to attempt replication. Within a matter of weeks a number of positive findings were announced (mostly by press release, like the original), including excess heat (Texas A&M, Stanford), neutrons (Georgia Tech), and tritium (Washington, a different group at Texas A&M). A special session on cold fusion at the April 1989 ACS national meeting attracted an audience of around 7000 (mostly) enthusiastic chemists. Almost immediately, though, strong skepticism set in, as several of the highly publicized "confirmations" were retracted, with explanations of the experimental problems responsible. A special session at the American Physical Society meeting at the beginning of May featured a number of negative presentations; one in particular (by Nate Lewis, subsequently published[35]) reported his research group's inability to detect any excess heat, possible experimental reasons why one *might* (erroneously) detect excess heat, and a deconstruction of the assumptions used by Pons and Fleischmann that, he argued, led to deducing excess heat evolved from unconvincing data. Later in May, a publication appeared demonstrating that the claimed γ-ray signature was artifactual.[36]

Over the next year or so the controversy continued, as further positive as well as negative results appeared regularly. A Department of Energy (DOE) panel investigated the topic during the summer, and issued its report—strongly negative—in October. In August 1989 the National Cold Fusion Institute (NCFI) was inaugurated in Salt Lake City, funded by the state of Utah (after federal support was refused). The First Annual Conference on Cold Fusion was held there in March 1990; the participants were primarily (by design) those with positive findings to report. In any case the majority of critics had concluded there was little left that needed to be criticized, and ceased paying much attention. By late 1990 both Pons and Fleischmann had left Utah, and the NCFI closed the following June. The cold fusion controversy was effectively over.

But *not* cold fusion. Research has continued at a moderate level of activity right up to the present day. A good deal of the work has been published in non-mainstream journals (some created for the purpose) or electronically; but occasionally papers have appeared in prestigious locations, such as the 1993 paper by Pons and Fleischmanns on calorimetry, which was accepted by *Physics Letters A*.[37] This publication merits notice on further grounds: it reports what appears to be the last joint experimental work by Fleischmann and Pons on cold fusion. Perhaps more importantly, it is one of the last reports to be formally challenged on technical grounds by a cold fusion skeptic.[38] Subsequent claims have been almost completely ignored by the scientific mainstream, and the popular media has generally followed suit, with a few exceptions. Compilations of this work may be found on a number of websites, notably the LENR–CANR (low energy nuclear reactions/chemically assisted nuclear reactions) site,[39] which features bibliographic material and summaries, written from the strong proponents' point of view. A quite different (and intriguing) perspective may be found in a recent book by the sociologist of science Bart Simon, who proposes a new model for understanding how and why research persists beyond the point where the vast majority of the community considers the field finished: he calls it "Undead Science".[40]

Two somewhat less fanciful, but rather contradictory, conceptual models have been offered for the consideration of scientific controversies: one from an internal point of view and one more external. In fact they *both* seem to fit the cold fusion saga pretty well. The first is that of "pathological science", first described by Irving Langmuir in a 1953 lecture (a transcription was republished in *Physics Today* in 1989[41]) and subsequently reprised and updated by Denis Rousseau.[42] According to Rousseau, pathological science has three fundamental characteristics:

1. Observed effects are near the limits of detectability and/or statistically marginally significant; their magnitudes cannot be controlled in any systematic way by varying experimental parameters.
2. Incompatibility with accepted theories or principles is readily ignored.
3. Investigators avoid carrying out critical, potentially disconfirming experiments, and refuse to accept any such experiments carried out by others as conclusive.

 © 2005 Wiley-VCH Verlag GmbH & Co. KGaA, Weinheim

Rousseau argued that all three applied to Pons and Fleischmann (the other two cases he examined were "polywater" and Benveniste's "infinite dilution"), in which he called particular attention to the complete lack of correspondence between the excess heat claimed and the levels of nuclear by-products detected (point 2), and the failure to perform any control experiments with ordinary water (point 3). The first point applies to the question of excess heat itself (although Rousseau does not specifically comment on that): even in the original paper[33] some of the data (Table 2) appear to show effects varying inversely with input, and subsequent analysis established that many of the most striking claims were actually tiny numbers inflated by dubious assumptions.[35]

A quite different perspective has been proposed by the sociologist of science Harry Collins. The "Experimenter's Regress", which was introduced in a discussion of the search for gravity waves, argues that it is impossible to separate questions about the existence or non-existence of a novel phenomenon from questions about the validity of the experiments designed to detect it:

"When the normal criterion—successful outcome—is not available, scientists disagree about which experiments are competently done.
Where there is disagreement about what counts as a competently performed experiment, the ensuing debate is coextensive with the debate about the proper outcome of the experiment".[43]

Clearly this may be applied to cold fusion (as Collins and a colleague did[44]): any negative finding can always be (and has been) challenged as incorrectly performed, such as claims that the wrong kind of electrode was used, etc.

The fact that these dueling descriptors are both operative has much to do with the continued survival of cold fusion research—if only as a ghostly entity, as Simon would have it. How should we view the more recent findings in light of the earlier, substantially discredited work? Pons and Fleischmann, and others, made some rather major errors that led to reports of large effects—excess heat exceeding 1000%, high levels of neutrons or tritium—so a skeptic comfortably concludes that the generally much smaller effects now claimed are the result of more subtle errors. Conversely, proponents can reasonably argue that their later experimental designs *do* take previous criticisms into account, and should not be automatically assumed to be tainted by the same old mistakes; but they never get the opportunity to defend themselves, since nobody even bothers to criticize them. A (rather plaintive) letter to this effect, published in *Chemical & Engineering News* in 2003,[45] elicited no response at all. As Simon comments:

"No matter what kinds of new experiments and data CF researchers present, their critics (if even listening) always drag them back to debates from 1989. There seems to be no escape ... Their collective identity as a group as well as their scientific practice is organized to a large degree around reclaiming scientific legitimacy by constantly revisiting the criticisms of 1989–1990. In part they have no choice, since there are few extant criticisms of work after 1990 that they can address".[46]

Another factor in the post-mortem survival of cold fusion has been its decidedly chimerical nature. Which of the various phenomena that have been reported in the context of cold fusion—excess heat, neutrons, tritium, X-rays, γ-rays, helium, even transmutation[47]—are fundamental to whatever (if anything) is going on? At least some of these reports are indisputably erroneous, but what does that imply about others? For example, the philosopher of science William McKinney, in arguing that one *can* escape from the "Experimenter's Regress" on the basis of objective analysis of experiments, suggested that the unequivocal demonstration of the artifactual γ-ray signature (thus undermining the claim for neutrons) was the real "knockout blow" for cold fusion.[48] However, cold fusion researchers are committed to no theory, so (on their account) excess heat need not be tied to neutrons. Since nobody has seriously claimed to understand the phenomena on the basis of any unifying theory, there need not be any real links between the various types of phenomena studied. From a strictly logical point of view, every individual experiment would need to be evaluated on its own merits: if one set of claims is debunked to everyone's satisfaction, that does not necessarily disprove another.

Indeed, one of the more recent studies (by the above-cited letter-writer Melvin Miles) reports detecting ^{4}He along with excess heat in more or less commensurate amounts, if it is assumed that the heat is produced by fusion of two deuterons to produce ^{4}He and energy [Eq. (2)]. Furthermore, he claims that although the generation of excess heat is not always reproducible, the two phenomena correlate well, and the long-demanded control experiment *was* performed: light-water experiments exhibit neither excess heat nor ^{4}He.[49] Of course, in "standard" D + D fusion, Equation (2) represents a very low-probability pathway compared to reactions that generate neutrons and tritium,[50] and one would also need to explain why the energy liberated shows up entirely as heat rather than radiation (and many more things besides). But *if* one is willing to accept the possibility of some kind of nonstandard nuclear process going on within the Pd lattice (a big if for many, but one that does not seem to have much troubled cold fusion researchers), there are no apparent a priori grounds for dismissing these and other findings. They might well be subject to criticism on a variety of experimental grounds; but as noted above, work from the last ten years or more has received little, if any, scrutiny at all.

$$D + D \rightarrow {}^4He + \gamma\,(23.77\,MeV) \qquad (2)$$

So there matters stand: no cold fusion researcher has been able to dispel the stigma of "pathological science" by rigorously and reproducibly demonstrating effects sufficiently large to exclude the possibility of error (for example, by constructing a working power generator), nor does it seem possible to conclude unequivocally that *all* the apparently anomalous behavior can be attributed to error. Under these circum-

 © 2005 Wiley-VCH Verlag GmbH & Co. KGaA, Weinheim

stances, the DOE has decided to carry out another review, which is underway at the time of writing (summer 2004). From the range of comments made in response to that announcement,[51] though, it seems most unlikely that their report will settle matters:

"There are quite a few people who are putting their time into this. They are working under conditions that are bad for their careers. They think they are doing something that may result in some important new finding. I think scientists should be open minded. Historically, many things get overturned with time."

"The critical question is, How good and different are [the cold fusion researchers'] new results? If they are saying, 'We are now able to reproduce our results', that's not good enough. But if they are saying, 'We are getting 10 times as much heat out now, and we understand things', that would be interesting. I don't see anything wrong with giving these people a new hearing."

"I think a review is a waste of time. But if you put together a credible committee, you can try to put the issue to bed for some time. It will come back. The believers never stop believing."

There are clear differences between our two cases: whereas the phlogiston controversy involved choosing the best theoretical framework to rationalize a set of experimental observations, with cold fusion there are essentially no theoretical frameworks among which to choose. Instead we have a set of observations that cannot be rationalized in terms of existing standard theory, and need to decide whether they (or some fraction thereof) are real anomalies that require new ideas, or mere mistakes. The majority of the scientific community has (explicitly or implicitly) opted for the second interpretation, just as the majority decided against phlogiston at the end of the 18th century. But the minority positions, then and now, were sustained for a considerable period. It is easy, but (as we have tried to show) much too simplistic, to invoke irrationality to explain this persistence of heterodoxy. Instead, these two cases illustrate that, once the human imagination has conceived an idea, it can sometimes be very difficult to prove its non-existence.

[1] H. E. Roscoe, C. Schorlemmer, *Treatise on Chemistry*, *Vol. 1*, Macmillan, London, **1881**, p. 14.

[2] L. Pauling, *General Chemistry: An Introduction to Descriptive Chemistry and Modern Chemical Theory*, *2nd ed.*, W. H. Freeman, San Francisco, **1953**, p. 120.

[3] A. Findlay, *The Spirit of Chemistry: An Introduction to Chemistry for Students of the Liberal Arts*, Longman Green, London, **1930**, p. 143.

[4] R. A. Day, Jr., R. C. Johnson, *General Chemistry*, Prentice-Hall, Englewood Cliffs, **1975**, p. 5.

[5] J. B. Conant, *Chemtech* **1991**, 592–596.

[6] a) J. B. Conant, *Science and Common Sense*, Yale University Press, New Haven, **1951**; b) Conant's major work on phlogiston is one of his famous case studies: "The Overthrow of the Phlogiston Theory: The Chemical Revolution of 1775–1789": *Harvard Case Studies in Experimental Science*, *Vol. 1* (Eds.: J. B. Conant, L. K. Nash), Harvard University Press, Cambridge, **1966**, pp. 65–115.

[7] Ref. [5], p. 592.

[8] The phlogiston story has been of great interest to those in science studies as well as to scientists themselves. It has served as a paradigmatic case for one controversial philosophical theory of scientific change: T. S. Kuhn, *The Structure of Scientific Revolutions*, *2nd ed.*, enlarged, University of Chicago Press, Chicago, **1970**, pp. 52–56, 69–72. An early sociological study is by H. G. McCann, *Chemistry Transformed: The Paradigmatic Shift from Phlogiston to Oxygen*, Ablex, Norwood, **1978**. Two additional books that deal significantly with phlogiston (although it does not appear in their titles) are E. Ströker, *Theoriewandel in der Wissenschaftsgeschichte: Chemie im 18. Jahrhundert*, Klostermann, Frankfurt am Main, **1982**; and K. Hufbauer, *The Formation of the German Chemical Community (1720–1795)*, University of California Press, Berkeley, **1982**.

[9] W. H. Brock, *The Norton History of Chemistry*, W. W. Norton, New York, **1993**, pp. 79–84.

[10] a) B. Bensaude-Vincent, I. Stengers, *A History of Chemistry*, Harvard University Press, Cambridge, **1996**, pp. 57–63; b) for an extensive discussion of principles and their role in chemistry, see M. G. Kim, *Affinity, That Elusive Dream: A Genealogy of the Chemical Revolution*, MIT Press, Cambridge, **2003**, pp. 84–110.

[11] Ref. [9], p. 82. We thank Professors Lawrence Principe and William Brock for helpful correspondence about this process.

[12] Ref. [9], p. 83.

[13] Ref. [10a], p. 58.

[14] T. L. Davis, *J. Chem. Educ.* **1927**, *4*, 176–183.

[15] There was of course a third party who played a major role in the discovery of oxygen, the Swedish apothecary Carl Wilhelm Scheele (1742–1786): W. A. Smeaton, *Endeavour* **1986**, *45*, 28–30; W. A. Smeaton, *Endeavour* **1992**, *51*, 128–131. Although the first to isolate the gas, Scheele worked in relative obscurity and died before both Lavoisier and Priestley, and was thus not a major participant in the phlogiston controversy. The near simultaneous discovery of oxygen by three independent investigators has provided prime material for examinations of the meaning of "discovery": A. Musgrave in *Method and Appraisal in the Physical Sciences* (Ed.: C. Howson), Cambridge University Press, Cambridge, **1976**, pp. 181–209, on pp. 194–195. The three contenders have even been turned into characters in a drama: C. Djerassi, R. Hoffmann, *Oxygen*, Wiley, New York, **2001**.

[16] Musgrave, Ref. [15], pp. 182–185.

[17] Ref. [6b], pp. 93–104.

[18] F. L. Holmes, *Isis* **2000**, *91*, 735–753.

[19] J. Golinski in *The Values of Precision* (Ed.: N. M. Wise), Princeton University Press, Princeton, **1995**, pp. 72–91. Several of the doubters took the quotation of these incredibly precise numbers (to eight places of decimals!) to be nothing more than a rhetorical device.

[20] D. Allchin, *Ambix* **1992**, *39*, 110–116, on pp. 110, 112.

[21] S. Brush, *The Kind of Motion We Call Heat: A History of the Kinetic Theory of Gases in the 19th Century*, North-Holland, Amsterdam, **1986**.

[22] H. E. Le Grand, *Ann. Sci.* **1972**, *29*, 1–18; M. Crosland, *Isis* **1973**, *64*, 306–325.

[23] D. M. Knight, *The Transcendental Part of Chemistry*, Dawson, Folkestone, **1978**, pp. 125–153.

[24] Quoted from the *Edinburgh Review*, **1811**, in Ref. [23], pp. 139–140.

[25] J. A. Labinger, S. J. Weininger, *Angew. Chem.* **2004**, *116*, 2664–2672, on p. 2668; *Angew. Chem. Int. Ed.* **2004**, *43*, 2612–2619, on p. 2616.

[26] Ref. [9], p. 112.

[27] An example from the 1950s and 1960s, which has been characterized as a "twentieth-century phlogiston", was the fruitless search for non-existent high-energy molecules in the cell: D.

 © 2005 Wiley-VCH Verlag GmbH & Co. KGaA, Weinheim

Allchin, *Perspect. Sci.* **1997**, *5*, 81 – 127. Here again, the task of proving the nonexistence of substances for which there was supporting evidence and a substantial intellectual investment was arduous.
[28] J. R. Huizenga, *Cold Fusion: the Scientific Fiasco of the Century*, University of Rochester Press, Rochester, **1992**.
[29] N. Hoffman, *A Dialogue on Chemically Induced Nuclear Effects: A Guide for the Perplexed about Cold Fusion*, American Nuclear Society, La Grange Park, **1995**.
[30] F. Close, *Too Hot to Handle: The Race for Cold Fusion*, Princeton University Press, Princeton, **1991**.
[31] G. Mallove, *Fire from Ice: Searching for the Truth Behind the Cold Fusion Furor*, Wiley, New York, **1991**.
[32] G. Taubes, *Bad Science: The Short Life and Weird Times of Cold Fusion*, Random House, New York, **1993**.
[33] M. Fleischmann, S. Pons, *J. Electroanal. Chem.* **1989**, *261*, 301 – 308.
[34] S. E. Jones, E. P. Palmer, J. B. Czirr, D. L. Decker, G. L. Jensen, J. M. Thorne, S. F. Taylor, J. Rafelski, *Nature* **1989**, *338*, 737 – 740.
[35] N. S. Lewis, C. A. Barnes, M. J. Heben, A. Kumar, S. R. Lunt, G. E. McManis, G. M. Miskelly, R. M. Penner, M. J. Sailor, P. G. Santangelo, G. A. Shreve, B. J. Tufts, M. G. Youngquist, R. W. Kavanagh, S. E. Kellog, R. B. Vogelaar, T. R. Wang, R. Kondrat, R. New, *Nature* **1989**, *340*, 525 – 530; G. M. Miskelly, M. J. Heben, A. Kumar, R. M. Penner, M. J. Sailor, N. S. Lewis, *Science* **1989**, *246*, 793 – 796.
[36] R. D. Petrasso, X. Chen, K. W. Wenzel, R. R. Parker, C. K. Li, C. Fiore, *Nature* **1989**, *339*, 183 – 185
[37] M. Fleischmann, S. Pons, *Phys. Lett. A* **1993**, *176*, 498 – 502.
[38] D. R. O. Morrison, *Phys. Lett. A* **1994**, *185*, 118 – 129.
[39] http://www.lenr-canr.org/.
[40] B. Simon, *Undead Science: Science Studies and the Afterlife of Cold Fusion*, Rutgers University Press, New Brunswick, **2002**.
[41] I. Langmuir (Ed.: R. N. Hall), *Physics Today* **1989**, *42*, 36 – 48.
[42] D. L. Rousseau, *Am. Sci.* **1992**, *80*, 54 – 63.
[43] H. M. Collins, *Changing Order: Replication and Induction in Scientific Practice*, University of Chicago Press, Chicago, **1992**, p. 89.
[44] H. Collins, T. Pinch, *The Golem: What Everyone Should Know About Science*, Cambridge University Press, Cambridge, **1993**, pp. 57 – 78.
[45] M. H. Miles, Letter to the Editor, *Chem. Eng. News* **2003**, *81* (24 November), 6.
[46] Ref. [40], p. 217.
[47] Ref. [40], pp. 150–153.
[48] W. J. McKinney in *A House Built on Sand: Exposing Postmodernist Myths about Science* (Ed.: N. Koertge), Oxford University Press, Oxford, **1998**, pp. 133 – 150.
[49] M. Miles, *Correlation Of Excess Enthalpy And Helium-4 Production: A Review. Tenth International Conference on Cold Fusion*, Cambridge, **2003**. Available at http://www.lenr-canr.org/LibFrame1.html.
[50] Ref. [28], pp. 6–7.
[51] T. Feder, *Phys. Today* **2004**, *57*, 27 – 28.

 © 2005 Wiley-VCH Verlag GmbH & Co. KGaA, Weinheim

> Designed Catalysis

"Designer Acids": Combined Acid Catalysis for Asymmetric Synthesis

Hisashi Yamamoto and Kentaro Futatsugi*

Keywords:
asymmetric catalysis · Brønsted acids · catalysis design · cooperative effects · Lewis acids

 © 2005 Wiley-VCH Verlag GmbH & Co. KGaA, Weinheim DOI: 10.1002/anie.200460394

Lewis and Brønsted acids can be utilized as more-effective tools for chemical reactions by sophisticated engineering ("designer acids"). The ultimate goal of such "designer acids" is to form a combination of acids with higher reactivity, selectivity, and versatility than the individual acid catalysts. One possible way to take advantage of such abilities may be to apply a "combined acids system" to the catalyst design. The concept of combined acids, which can be classified into Brønsted acid assisted Lewis acid (BLA), Lewis acid assisted Lewis acid (LLA), Lewis acid assisted Brønsted acid (LBA), and Brønsted acid assisted Brønsted acid (BBA), can be a particularly useful tool for the design of asymmetric catalysis, because combining such acids will bring out their inherent reactivity by associative interaction, and also provide more-organized structures that allow an effective asymmetric environment.

From the Contents

1. Introduction 1925

2. Combined Acid Catalysis: Introduction and Background 1925

3. Brønsted Acid Assisted Lewis Acid Catalysts (BLA) 1926

4. Lewis Acid Assisted Lewis Acid Catalysts (LLA) 1931

5. Lewis Acid Assisted Brønsted Acid Catalysts (LBA) 1937

6. Brønsted Acid Assisted Brønsted Acid Catalysts (BBA) 1940

7. Conclusions and Outlook 1941

1. Introduction

In 1923 Lewis laid the foundation for our modern understanding of acid catalysis. His definition of the valence-bond principle encompasses all chemical phenomena. The designation of electron-pair donors and acceptors as Lewis bases and Lewis acids, respectively, is firmly ingrained in the chemical language. However, the true power and elegant applications of this reagent to asymmetric synthesis[1] has only begun to be realized. The developments continue unabated, and nowadays many different Lewis acid catalysts have been elaborated and cover almost all the metals in the periodic table.

This Review summarizes a program of research that has been carried out in our laboratories at Nagoya and Chicago over the past two decades with the objective of extending the research of Lewis acid catalysis to new domains, specifically targeting combined acid catalysis for asymmetric synthesis and a much deeper understanding of the fine mechanistic details and pathways of these reagents. Many other research groups have also been active in this field of asymmetric synthesis, and the science of organic synthesis has benefited greatly from the development of new reagents and catalysts for other types of enantioselective reactions.

2. Combined Acid Catalysis: Introduction and Background

Coordination of a ketone or aldehyde to a Lewis acid can promote enolization by virtue of the enhanced acidity of the α-hydrogen atoms in the complex. The practical utility of these types of Lewis acid activation is well developed. For example, changes in acidities of up to 24 pK_a units are observed by combining the measured gas-phase acidities with the calculated solvation energies for these species (Figure 1).[2] This example can be described as a typical case for a Lewis acid activation of a weak Brønsted acid.

Similar activations can be readily found in various reports as combined acid complexes. Clark showed that the catalytic activity of silica-supported $AlCl_3$ arose from Lewis acid activation of the Brønsted acidic site on the silica surface (Figure 2).[3]

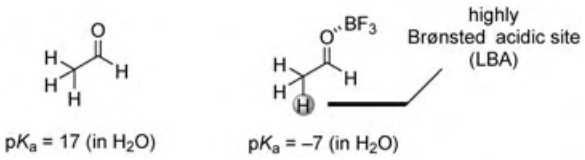

Figure 1. Lewis acid activation of a weak Brønsted acid.

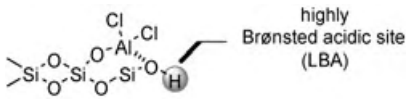

Figure 2. Brønsted acidity arising from Lewis acid complexation on a silica surface.

Negishi reported the principle of activation of Lewis acids or electrophiles through association (Figure 3).[4] He described that coordinatively unsaturated monomers are far more Lewis acidic than doubly bridged coordinatively saturated dimers. However, the same compounds can readily generate a species that is even more Lewis acidic than the monomer through the formation of a singly bridged dimer. This species is also an example of a combined acid catalyst.

[*] Prof. H. Yamamoto, K. Futatsugi
Department of Chemistry
University of Chicago
5735 South Ellis Avenue, Chicago IL 60637 (USA)
Fax: (+1) 773-702-0805
E-mail: yamamoto@uchicago.edu

 DOI: 10.1002/anie.200460394 © 2005 Wiley-VCH Verlag GmbH & Co. KGaA, Weinheim

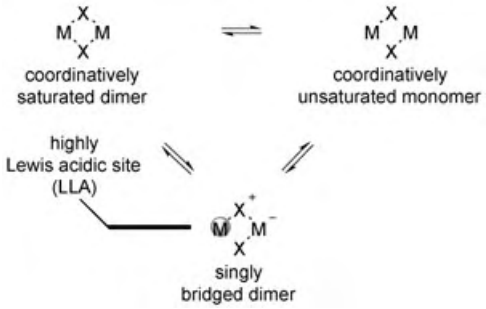

Figure 3. State of association of Lewis acid M-X.

Classic acid-catalyzed reactions, such as the addition of HCl to alkenes, often show a second-order dependence on the acids. In that sense, the involvement of dimeric acids such as HCl···HCl might be speculated (Figure 4).[5] The same principle of activation of Brønsted acids plays an important role in many cases, a number of which are regarded as Brønsted acid assisted Brønsted acid systems.

These combined acid catalysts can be classified as shown in Table 1. It should be emphasized that we anticipated a more or less intramolecular assembly of such combined systems rather than intermolecular arrangements. Thus, a correct design of the catalyst structure is essential for success.

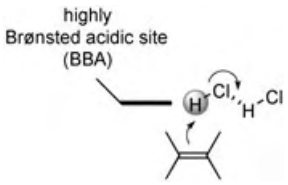

Figure 4. Plausible involvement of dimeric acids in acid-catalyzed addition of HCl to alkenes.

3. Brønsted Acid Assisted Lewis Acid Catalysts (BLA)

When Lewis acids and Brønsted acids are combined, conjugate Friedel–Crafts acids are produced (e.g. anhydrous $HF{\cdot}BF_3$ and $HCl{\cdot}AlCl_3$). They effectively catalyze hydrocarbon transformations. In the early 1960s, much stronger acids were prepared. Magic acid ($HSO_3F{\cdot}SbF_5$) and fluoroantimonic acid ($HF{\cdot}SbF_5$) are two well-known examples.[6]

Table 1: General classifications of combined acid catalysis.

Catalyst system	General structure	Examples
Brønsted acid assisted Lewis acid catalyst (BLA) Enhancement of Lewis acidity by the combination with Brønsted acid		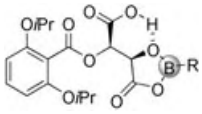
Lewis acid assisted Lewis acid catalyst (LLA) Enhancement of Lewis acidity by the combination with Lewis acid		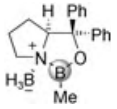
Lewis acid assisted Brønsted acid catalyst (LBA) Enhancement of Brønsted acidity by the combination with Lewis acid		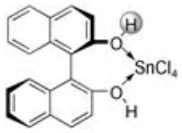
Brønsted acid assisted Brønsted acid catalyst (BBA) Enhancement of Brønsted acidity by the combination with Brønsted acid		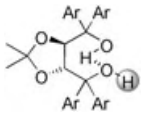

Hisashi Yamamoto received his BSc from Kyoto University and his PhD from Harvard University (Prof. E. J. Corey). He held academic positions at Kyoto University and at the University of Hawaii, before he moved to Nagoya in 1980, where he became Professor (1983). In 2002, he was appointed Professor at the University of Chicago. He has been honored with the Prelog Medal (1993), the Chemical Society of Japan Award (1995), the Max-Tishler Prize (1998), Le Grand Prix de la Fondation Maison de la Chimie (2002), the National Prize of the Purple Medal (Japan) (2002), and the Yamada Prize (2004).

Kentaro Futatsugi received his BSc from Nagoya University in 2001 under the supervision of Professor Hisashi Yamamoto. He is currently carrying out research towards his PhD in organic chemistry at the University of Chicago under the supervision of Professor Hisashi Yamamoto. His research is directed toward the development of stereoselective reactions with a Lewis acid assisted chiral Lewis acid (LLA) system and their application to the synthesis of biologically important compounds.

 © 2005 Wiley-VCH Verlag GmbH & Co. KGaA, Weinheim

Our results suggested that several characteristics of the chiral Lewis acid catalyst are enhanced significantly by attachment of a Brønsted acid. In 1986 we reported the asymmetric Diels–Alder reaction of naphthoquinone derivatives and various dienes in the presence of a chiral boron reagent derived from $B(OMe)_3$ and (*R*,*R*)-(+)-tartaric acid diamide (Scheme 1).[7] The reagent has been described as a

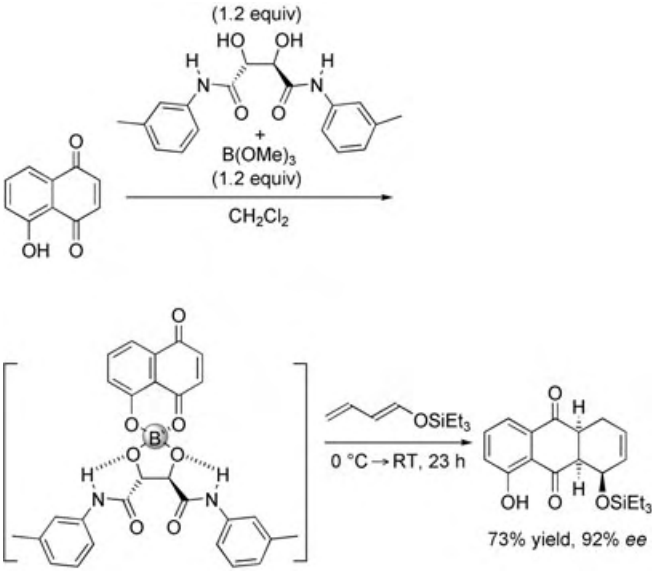

Scheme 1. Asymmetric Diels-Alder reaction promoted by a tartaric acid diamide derived chiral boron reagent.

model for the enantioselective preparation of important tetracycline natural products. Both the rate enhancement and the high enantioselectivity observed for this type of auxiliary can be ascribed to the novel intramolecular hydrogen bonding between the hydrogen atom of the amide and the oxygen atom attached to the boron center.

In 1988 we first reported a chiral boron catalyst based on a tartaric acid ligand (Figure 5).[8] The high reactivity of the chiral acyloxyborane (CAB) catalysts **1a–c** may originate

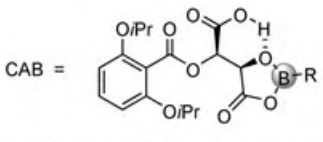

Figure 5. Representative CAB (chiral acyloxyborane) catalysts.

from intramolecular hydrogen bonding of the terminal carboxylic acid to the alkoxy oxygen atom. The CAB catalysts are uniformly effective for aldol, Diels–Alder, and allylation reactions (Scheme 2). Based on a series of NOE experiments, it was established that the effective shielding of the CAB-coordinated aldehydes arises from π stacking of 2,6-diisopropoxybenzaldehyde ring and the coordinated aldehyde (Figure 6).

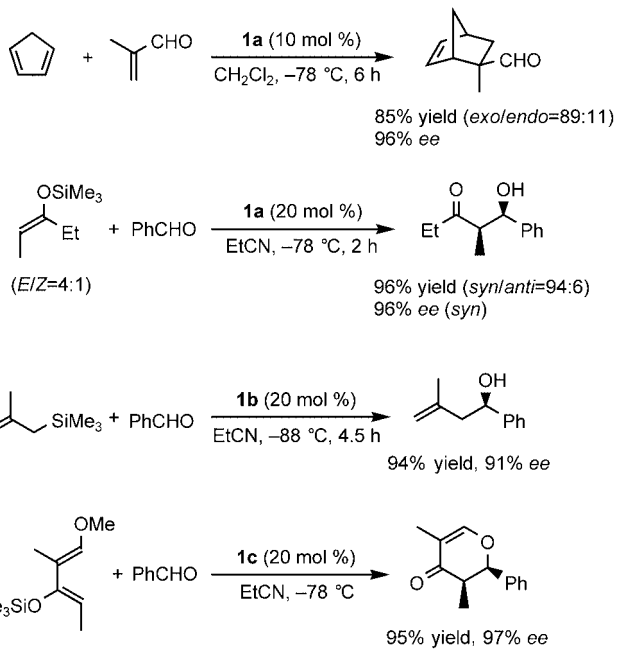

Scheme 2. Asymmetric reactions promoted by CAB catalysts.

Brønsted acid assisted chiral Lewis acid (BLA) **2** was proposed to promote high selectivity through the dual effects of intramolecular hydrogen-bonding interactions and attractive π–π donor–acceptor interactions in the transition state (Scheme 3).[9] Extremely high enantioselectivity (up to >99% *ee*) and *exo* selectivity (up to >99% *exo*) are obtained for cycloadditions of α-substituted α,β-enals with dienes in the presence of BLA **2**. The absolute stereochemical preference in the

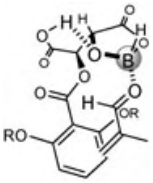

Figure 6. CAB–methacrolein complex.

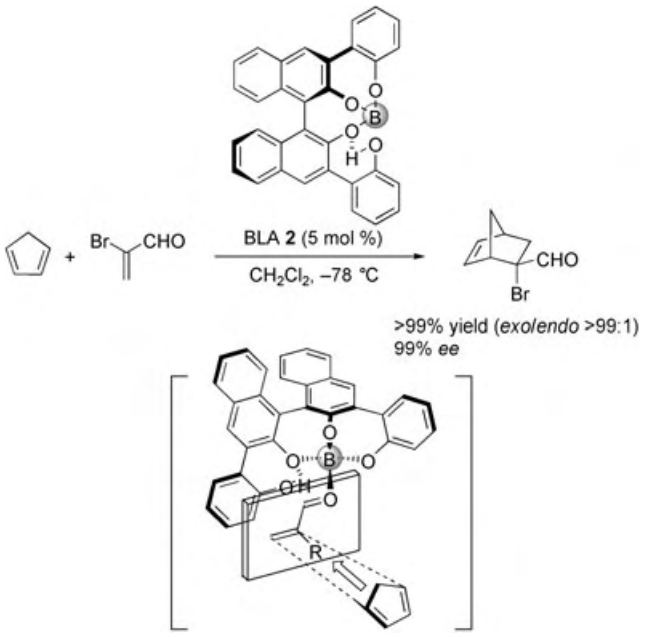

Scheme 3. Diels–Alder reaction catalyzed by BLA **2**.

 © 2005 Wiley-VCH Verlag GmbH & Co. KGaA, Weinheim

reaction can be easily understood in terms of the most favorable transition-state assembly shown in Scheme 3. The coordination of a proton of the 2-hydroxyphenyl group with an oxygen atom of the adjacent B–O group in the complex plays an important role in asymmetric induction; this hydrogen-bonding interaction through a Brønsted increases the Lewis acidity of boron and the π basicity of the phenoxy moiety.

Diels–Alder reactions of α-unsubstituted α,β-enals with BLA **2** as well as most other chiral Lewis acids exhibit low enantioselectivity and/or reactivity. We developed BLA **3**, which was prepared from a chiral triol and 3,5-bis(trifluoromethyl)benzeneboronic acid to overcome this deficiency.[10] This catalyst was extremely effective in the enantioselective cycloaddition of both α-substituted and -unsubstituted α,β-enals with various dienes (Figure 7). The Brønsted acid in the new BLA **3** catalyst clearly improves the scope of this cycloaddition.

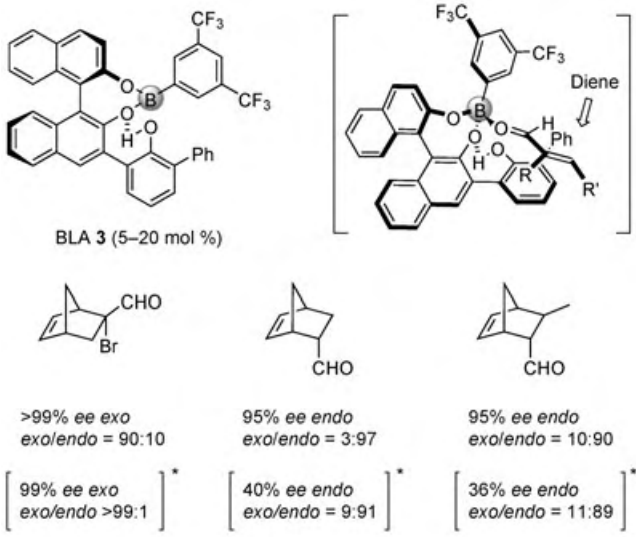

Figure 7. Asymmetric Diels–Alder reactions catalyzed by BLA **3**.

BLA **4**, which is prepared from a trialkyl borate and optically pure binol (1,1′-binaphthol) in a 1:2 molar ratio, is also an excellent chiral promoter for the aza-Diels–Alder reaction of chiral imines with the Danishefsky diene (Scheme 4).[11] The structure of this BLA **4** was identified by X-ray crystallographic analysis.

BLA **4** is also very useful in the double stereochemical differentiation of Mannich-type reactions of chiral imines. The Mannich reaction with the trimethylsilyl ketene acetal derived from *tert*-butyl acetate proceeds with high diastereoselectivity (Scheme 5).

In 2000 Shibasaki and co-workers successfully developed a stable, storable, and reusable La–binol complex for the asymmetric Michael reaction (up to >99% *ee*) with broad generality (Scheme 6).[12] After 4 weeks of storage, this powdered complex was still highly effective in the catalytic asymmetric Michael reaction. Furthermore, the complex is

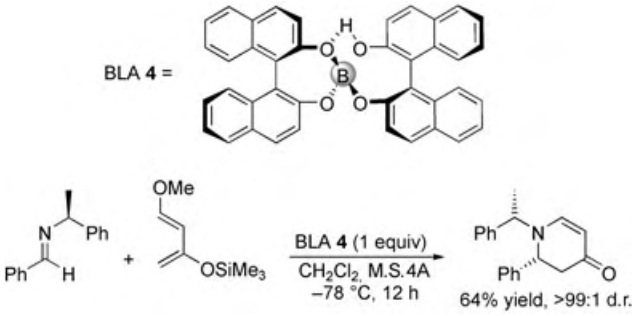

Scheme 4. Asymmetric aza-Diels–Alder reaction promoted by BLA **4**.

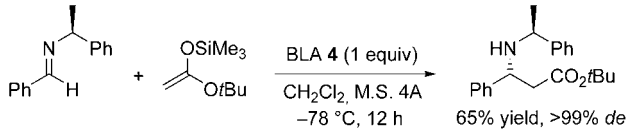

Scheme 5. Mannich-type reaction promoted by BLA **4**.

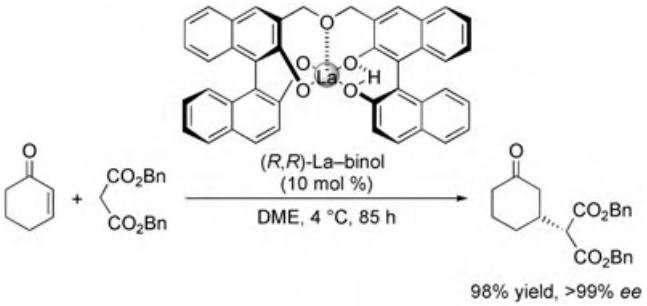

Scheme 6. Asymmetric Michael addition reaction catalyzed by (*R*,*R*)-La–binol. DME = 1,2-dimethoxyethane, Bn = benzyl.

recoverable and recyclable still gives the desired product with very high *ee* values even after the fourth cycle. These catalysts are typically considered to be activated by Brønsted acids located in favored positions. On the other hand, the *intermolecular* activation of the Lewis acid catalysts by external Brønsted acids could be achieved by the appropriate choice of 1) a chiral Lewis acid that has Brønsted basic sites in the optimum position to activate the Lewis acidic center, and 2) an external Brønsted acids of sufficient Brønsted acidity for the desired reactivity.

Mukaiyama and co-workers reported that proline derivatives combined with BBr_3 produce a promising catalyst for Diels–Alder reactions (Scheme 7).[13] The chiral catalyst is believed to be the HBr adduct salt of the amino boron derivative.

In 2002 Corey and co-workers reported that chiral proline-derived oxazaborolidines combined with trifluoromethanesulfonic acid (TfOH) produce very reactive catalysts **5a** and **5b** (Figure 8) for Diels–Alder reactions (Scheme 8).[14] The high activity of the catalysts is derived from the cationic nature of the nitrogen ligand and the fact that a very strong acid is required for their efficient generation. The absolute stereochemical outcome of the Diels–Alder reactions medi-

 © 2005 Wiley-VCH Verlag GmbH & Co. KGaA, Weinheim

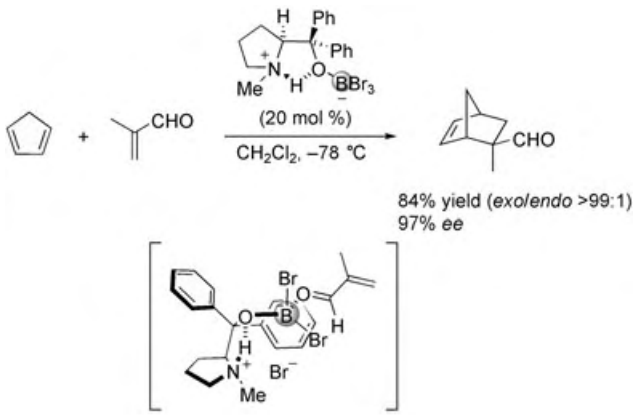

Scheme 7. Chiral proline-based catalyst reported by Mukaiyama and co-workers.

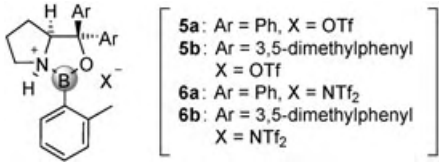

Figure 8. Cationic oxazaborolidines generated by protonation of chiral proline-derived oxazaborolidines with strong Brønsted acids (TfOH or Tf_2NH).

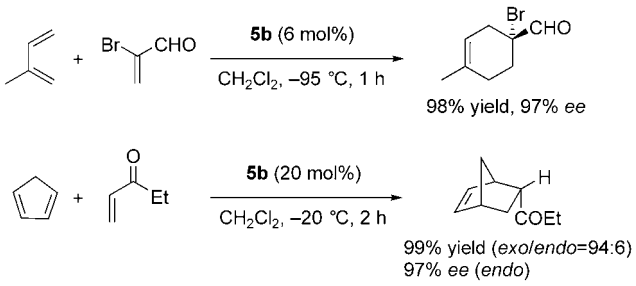

Scheme 8. Diels–Alder reactions catalyzed by cationic oxazaborolidine **5b** (see Figure 8).

ated with these catalysts was successfully predicted on the basis of the pre-transition-state assemblies shown in Figure 9.

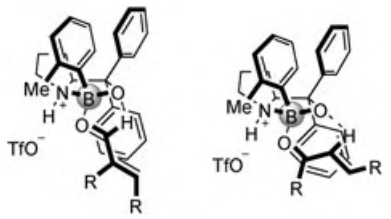

Figure 9. Proposed pre-transition-state assemblies for **5b**.

Later, Corey reported that the strong Brønsted acid triflimide ($(CF_3SO_2)_2NH$) protonates chiral oxazaborolidines to form superactive, stable, chiral Lewis acids **6a** and **6b** (Figure 8), which are highly effective catalysts for a wide variety of enantioselective Diels–Alder reactions that were previously beyond the reach of synthetic chemists (Scheme 9).[15]

The hydrogen bonding within BLA catalysts participates not only in the activation of the Lewis acidic center but also in the effective transmission of the chiral scaffold to other molecules. Kobayashi and co-workers developed a series of chiral Lewis acid catalysts in which Brønsted acids are utilized in an intramolecular fashion to transmit chiral information to the other organic molecules (Figure 10). Kobayashi and co-workers also reported the chiral Lewis acid catalyst **7a** (prepared from $Sc(OTf)_3$, (*R*)-binol, and a tertiary amine),

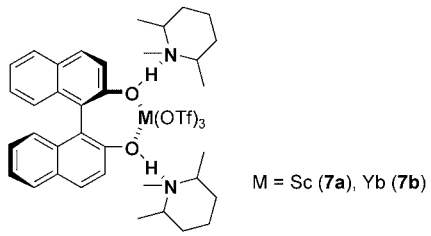

Figure 10. Chiral Diels–Alder catalysts (Kobayashi and co-workers).

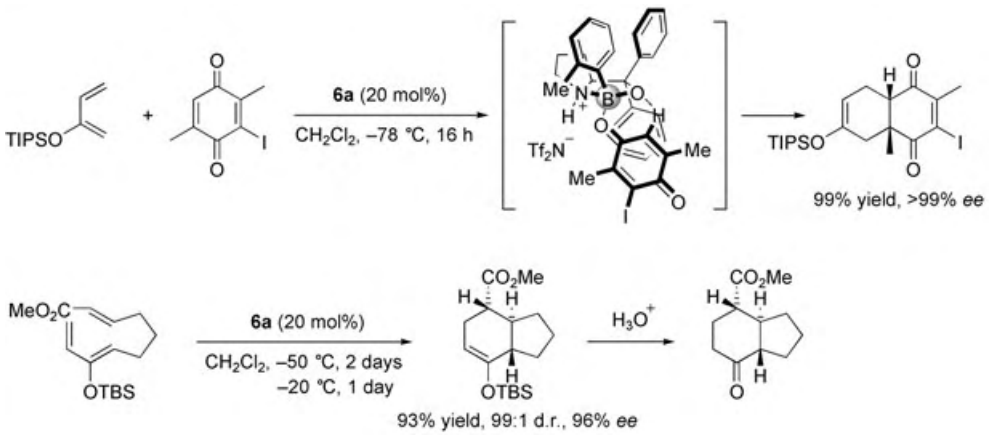

Scheme 9. Representative examples for the Diels–Alder reaction catalyzed by cationic oxazaborolidine **6a**. TBS = *tert*-butyldimethylsilyl, TIPS = triisopropylsilyl.

 © 2005 Wiley-VCH Verlag GmbH & Co. KGaA, Weinheim

which was quite effective in the enantioselective Diels–Alder reactions of acyl-1,3-oxazolidin-2-ones with dienes in dichloromethane (Scheme 10).[16] A unique coordination mode, which has never been observed in other Lewis acid

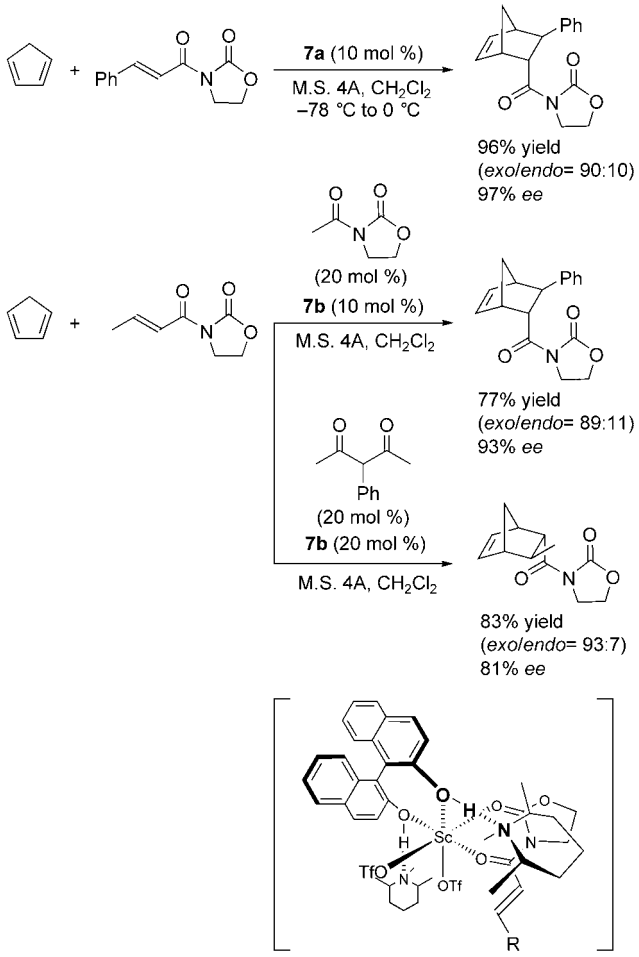

Scheme 10. Diels–Alder reaction catalyzed by chiral Diels–Alder catalysts **7a** and **7b** (see Figure 10).

catalysts, was indicated from several experiments. In the chiral catalyst, the axial chirality of (*R*)-binol is postulated to be transferred to the amine part, which would work as a "wall" in the transition state to shield one side of the dienophile.

Using a similar design, Kobayashi and co-workers found that both enantiomers of the Diels–Alder reaction between 3-acyl-1, 3-oxazolidin-2-ones and cyclopentadiene could be prepared in the presence of chiral lanthanide (III) **7b** from the same chiral source, (*R*)-binol (Scheme 10).[17] It should be noted that the chiral catalysts with reverse enantiofacial selectivities could be prepared by using the same chiral source with an appropriate choice of achiral ligands.

In 1996 Kobayashi reported that in the presence of a catalytic amount of chiral ytterbium Lewis acid, which was prepared from $Yb(OTf)_3$, (*R*)-binol, DBU (1,8-diazabicyclo-[5.4.0]undec-7-ene), and an additive, achiral imines reacted with achiral dienophiles to afford the corresponding tetrahydroquinoline derivatives in high yields with high diastereo- and enantioselectivities (Scheme 11).[18] This is the first example of aza-Diels–Alder reactions in the presence of a catalytic amount of a chiral source.

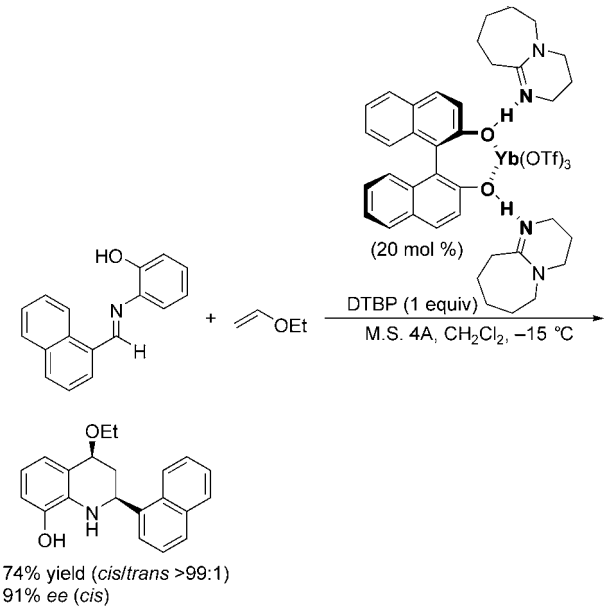

Scheme 11. Aza-Diels–Alder reaction catalyzed by chiral Yb catalyst. DTBP = 2,6-di-*tert*-butylpyridine.

Later, catalytic enantioselective 1,3-dipolar cycloadditions of nitrones with alkenes in the presence of a novel heterochiral Yb^{III} catalyst were developed by Kobayashi and Kawamura (Scheme 12).[19] The combination of (*S*)-binol and the newly prepared chiral amine (*R*)-MNEA, *N*-methyl-bis[(*R*)-1-(1-naphthyl)ethyl]amine, led to the *endo* adduct in excellent yield (92%), enantioselectivity (96% *ee*), and diastereoselectivity (*endo*/*exo* = 99:1) by. The chiral Yb^{III} catalyst thus prepared has two independent chiral units (heterochiral Yb^{III} catalyst, vide below), and it was found that the sense of the chiral induction in these reactions was mainly

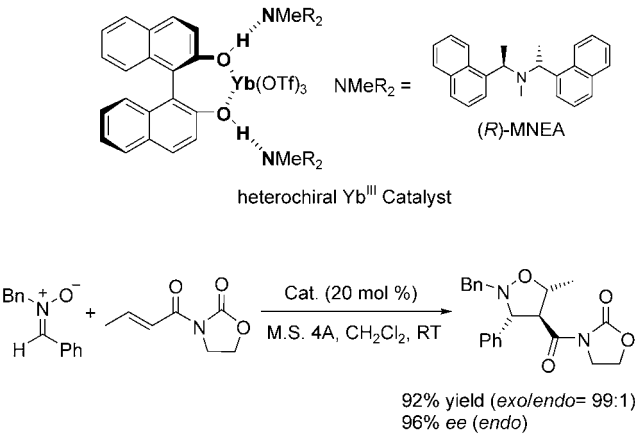

Scheme 12. 1,3-Dipolar cycloaddition in the presence of heterochiral Yb^{III} catalyst.

 © 2005 Wiley-VCH Verlag GmbH & Co. KGaA, Weinheim

determined by binol and that the chiral amine increased or decreased the induction relatively. Actually, the existence of hydrogen bonds between the phenolic hydrogen atoms of (*S*)-binol and the nitrogen atoms of (*R*)-MNEA was confirmed by the IR spectrum of the catalyst.

4. Lewis Acid Assisted Lewis Acid Catalysts (LLA)

Reactive Lewis acid assisted Lewis acid catalysts are relatively well known. Electron-deficient metal compounds can be further activated as electrophiles through hetero- and homodimeric associative interaction. In several instances, naked metal cations can be generated. In fact, this has been widely encountered in many acid-catalyzed reactions including the Friedel–Crafts reaction and the Ziegler–Natta polymerization. However, its full recognition as a synthetically powerful tool does not appear to be widespread as of yet. It may be further extended to include asymmetric catalysis design.

These associative interactions are crucial not only for higher reactivity but also for the construction of the well-organized chiral environment. Representative examples of Lewis acid assisted Lewis acid catalysts that have higher reactivities and/or highly organized transition states by the aid of associative interactions will be discussed in this section.

Our results suggested that several characteristics of Lewis acid catalysts are enhanced significantly in the presence of another Lewis acid. In 1998 we reported the remarkable enhancement of the catalyst activity of trialkylsilyl triflate in the Mukaiyama aldol synthesis by the addition of the bulky aluminum reagent MABR (Scheme 13).[20] Thus, a strongly Lewis acidic species forms from two different Lewis acids, namely the bulky organoaluminum reagent and Me_3SiOTf. One plausible active species in which MABR might act as an activator for Me_3SiOTf by coordinating to the triflate counter anion is shown in Scheme 13. Thus, MABR might act as MAO does in Ziegler–Natta catalysts.

A chiral dialuminum Lewis acid, which is effective as an asymmetric Diels–Alder catalyst, has been prepared from organoaluminum reagents and binol derivatives (Scheme 14).[21] The catalytic activity of this catalyst is significantly greater than that of monometallic reagents. The catalyst achieves high reactivity and selectivity by an intramolecular interaction of two aluminum Lewis acids.

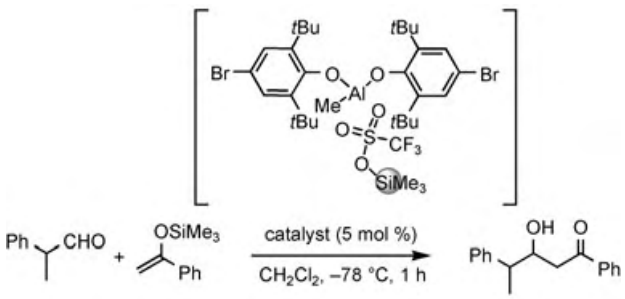

Catalyst	Yield [%] (*syn*/*anti*)
MABR	7 (42:58)
Me_3SiOTf	15 (75:25)
MABR + Me_3SiOTf	76 (89:11)

Scheme 13. Mukaiyama aldol reaction catalyzed by MABR–TMSOTf.

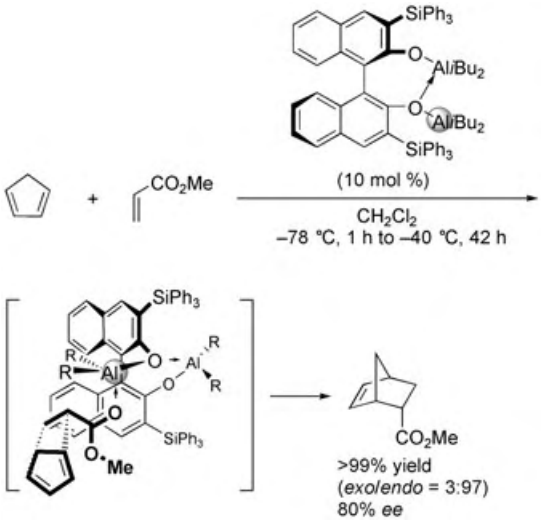

Scheme 14. Chiral dialuminum Lewis acid as an asymmetric Diels–Alder catalyst. R = *i*Bu.

Similarly, a chiral trialuminum compound was quantitatively formed from optically pure 3-(2,4,6-triisopropylphenyl)binaphthol (2 equiv) and Me_3Al (3 equiv) in CH_2Cl_2 at room temperature (Scheme 15).[21] The novel structure of this complex was ascertained by ^1H NMR spectroscopic analysis and measurement of the methane gas evolved. This trinuclear chiral aluminum complex is effective for the Diels–Alder reaction of methacrolein with cyclopentadiene. Diels–Alder adducts were obtained in 99% yield with 92% *exo* selectivity. Under optimum reaction conditions, the *exo* adduct was obtained with 75% *ee*. Intramolecular association of aluminum Lewis acids as shown in Scheme 15 might lead to

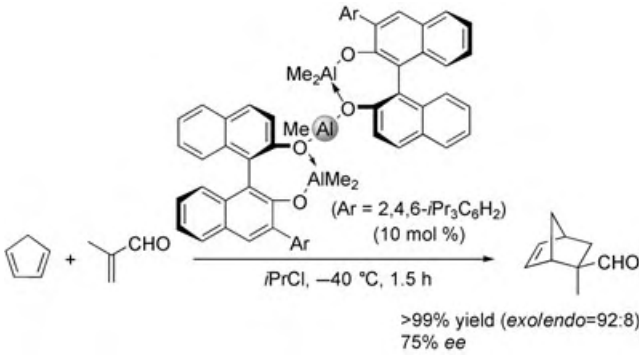

Scheme 15. Asymmetric Diels–Alder reaction catalyzed by a chiral trialuminum catalyst.

 © 2005 Wiley-VCH Verlag GmbH & Co. KGaA, Weinheim

enhanced Lewis acidity of the aluminum atom located in the center of the chiral scaffold (shown in the gray circle).

Catalytic enantioselective Strecker-type reactions of aldimines with tributyltin cyanide (Bu_3SnCN) proceeded smoothly in the presence of a novel chiral zirconium catalyst to afford α-amino nitrile derivatives with high enantioselectivities (Scheme 16).[22] Later, hydrogen cyanide (HCN) was successfully used instead of Bu_3SnCN as the cyanide source.[23] The catalytic asymmetric Strecker amino acid synthesis starting from achiral aldehydes, amines, and HCN in the presence of chiral zirconium catalyst has also been

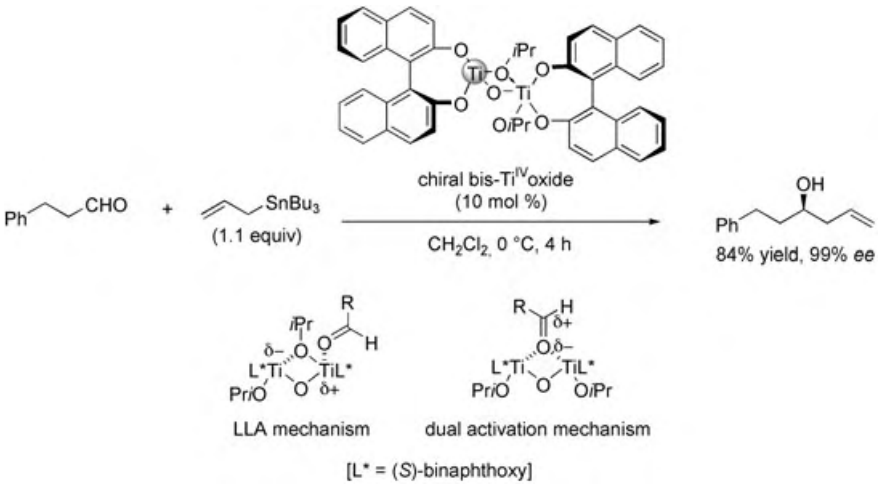

Scheme 17. Chiral bis-Ti^{IV} oxide catalyzed asymmetric allylation reaction.

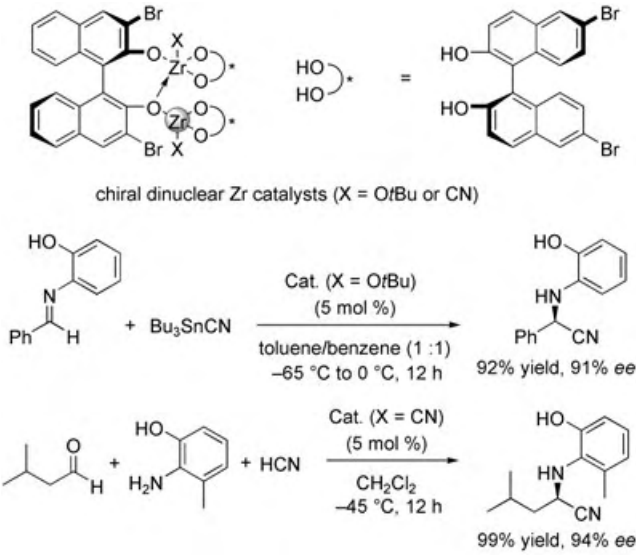

Scheme 16. Enantioselective Strecker reactions in the presence of chiral dinuclear zirconium catalysts.

achieved. Although mechanistic details of this catalytic reaction are not yet clear, the two binuclear zirconium complexes shown in Scheme 16 are postulated to be active chiral catalysts in the reactions of aldimines with Bu_3SnCN and in the three-component reactions.

A new chiral bis-Ti^{IV} oxide was successfully designed by Maruoka and co-workers and can be utilized for strong activation of aldehydes, thereby allowing a new catalytic enantioselective allylation of aldehydes with allyltributyltin (Scheme 17).[24] The chiral bis-Ti^{IV} catalyst can be readily prepared either by treatment of bis(triisopropoxy)titanium oxide [(*i*PrO)$_3$Ti–O–Ti(*i*OPr)$_3$] with (*S*)-binol or by reaction of ((*S*)-binaphthoxy)isopropoxytitanium chloride with silver(I) oxide. The reaction of 3-phenylpropanal with allyltributyltin (1.1 equiv) under the influence of chiral bis-Ti^{IV} oxide (10 mol %) generated in situ in CH_2Cl_2 at 0 °C for 4 h afforded 1-phenyl-5-hexen-3-ol in 84 % yield with 99 % *ee*. This asymmetric approach provides a very useful way for obtaining high reactivity and selectivity by the simple introduction of the M-O-M unit in the design of chiral Lewis acid catalysts. The authors proposed that the high reactivity of this chiral bis-Ti^{IV} oxide might be ascribed to the intramolecular coordination of one isopropoxy oxygen atom to the other titanium center, thereby enhancing the otherwise weak Lewis acidity of the original Ti^{IV} center for carbonyl activation. This mode of activation is a typical example of the Lewis acid assisted Lewis acid mechanism. Alternatively, a dual activation of the carbonyl group by the simultaneous coordination of two Ti centers was also proposed as the origin of the high reactivity.

Marhwald et al. recently reported that ligand exchange of titanium(IV) alkoxides with optically active α-hydroxy acids presents an unexpected and novel approach to enantioselective direct aldol reactions of aldehydes and ketones (Scheme 18).[25] The aldol products were isolated with a high degree of *syn* diastereoselectivity. High enantioselectivities were observed when using simple optically pure α-hydroxy acids. Based on the X-ray crystallographic analysis of this Ti(O*i*Pr)$_4$/(*R*)-mandelic acid complex and on the absolute configuration found in the aldol products, they proposed the LLA-like species shown in Scheme 18.

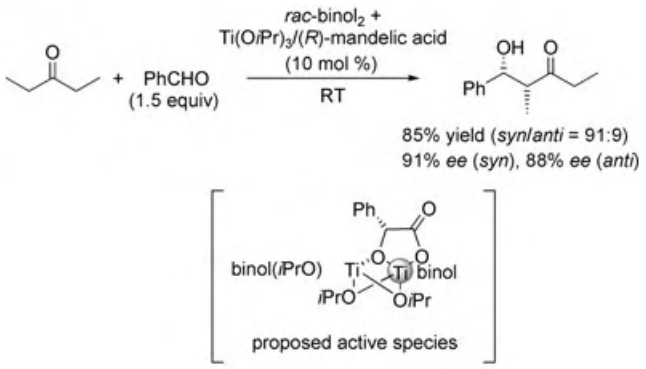

Scheme 18. Asymmetric direct aldol reaction promoted by a chiral Ti^{IV} catalyst.

 © 2005 Wiley-VCH Verlag GmbH & Co. KGaA, Weinheim

Oh and Reilly reported that chiral Lewis acids derived from 1,8-naphthalenediylbis(dichloroborane), a novel bidentate Lewis acid, have been found to be active catalysts for the asymmetric Diels–Alder reaction (Scheme 19).[26] Chiral

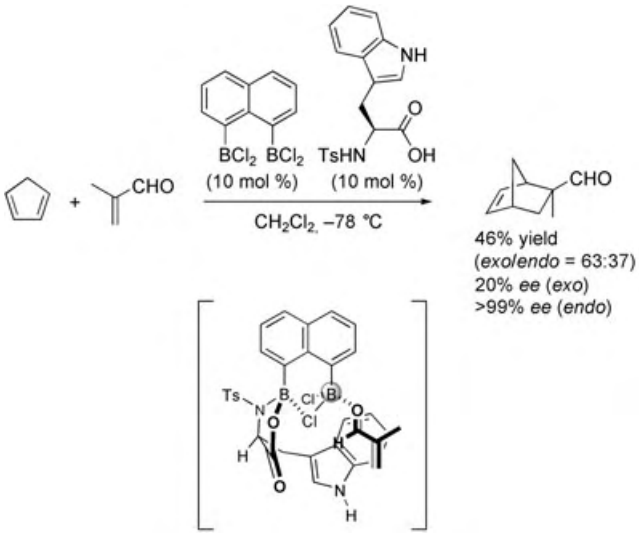

Scheme 19. Asymmetric Diels–Alder reaction catalyzed by chiral dinuclear boron catalyst.

ligands derived from amino acids resulted in a range of enantioselectivities in the reaction of cyclopentadiene with various α,β-unsaturated aldehydes. The authors proposed a transition-state assembly that includes chloride bridging between two boron atoms. Such an interaction should trigger the enhancement of the Lewis acidity of the ligand-free borane center.

The development of chiral heterobimetallic catalysts, which could be considered as examples of LLAs, has been studied extensively.[27a] In this section, representative examples will be disclosed.

The chiral heterobimetallic complex,[27a,b] $LaLi_3$-tris(binaphthoxide) (LLB), is an efficient asymmetric catalyst for direct aldol reactions of aldehydes and unmodified ketones (Scheme 20).[28] The LLB catalyst functions not only as a base to remove an α proton from the ketone, but also as a Lewis acid, giving the aldol product in high yield with high enantioselectivity. The LLB catalyst also works well for the direct aldol reaction of aldehydes with α-hydroxy ketones to provide 1,2-dihydroxyketones with high enantiomeric excess.[29]

A practical and efficient Michael addition for the large-scale synthesis of enantiomerically pure (*R*)-3-[bis(methoxycarbonyl)methyl]cyclohexanones in the presence of an (*R*)-Al-Li-bis(binaphthoxide) complex ((*R*)-ALB)[30] was developed (Scheme 21).[31] The Michael reaction of 2-cyclohexe-

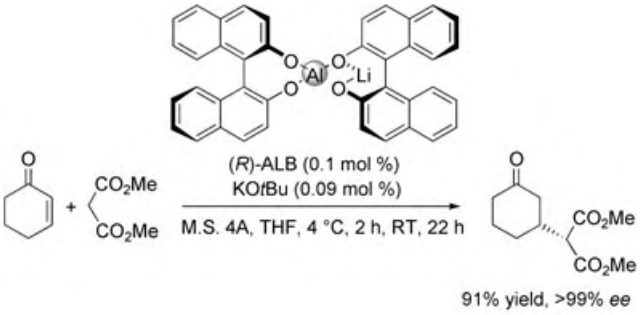

Scheme 21. Asymmetric Michael addition catalyzed by (*R*)-ALB.

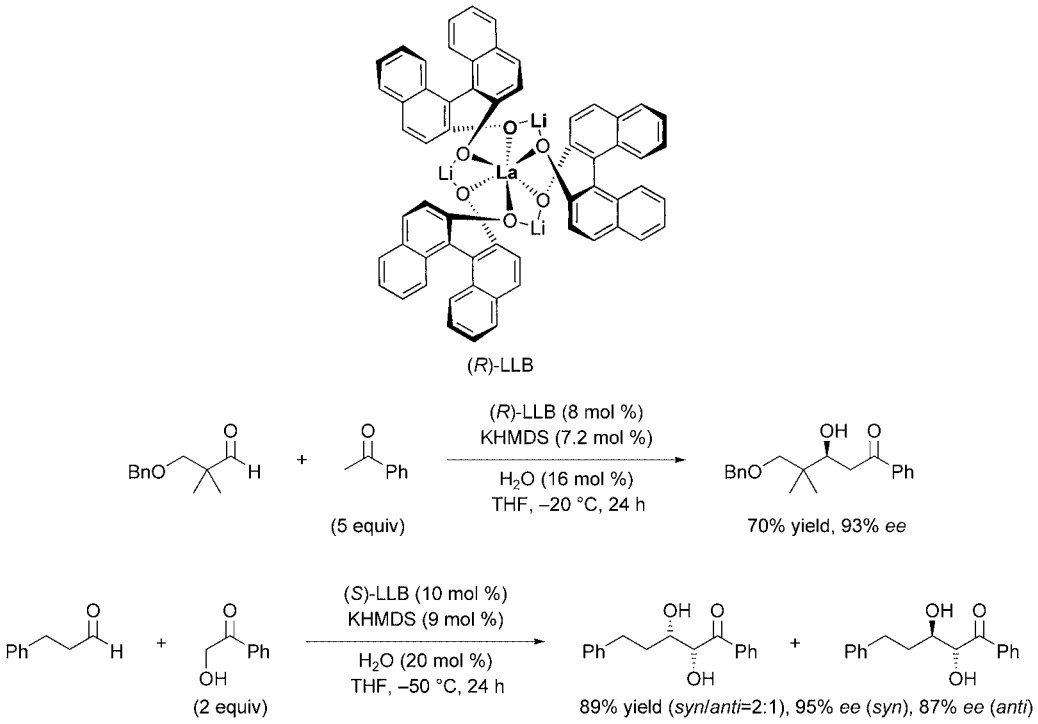

Scheme 20. Asymmetric direct aldol reaction in the presence of (*R*)-LLB. KHMDS = potassium hexamethyldisilazide.

 © 2005 Wiley-VCH Verlag GmbH & Co. KGaA, Weinheim

none (6.0 mol, 581 mL) with dimethyl malonate (6.0 mol, 686 mL) was completed in 24 h at ambient temperature when using 0.1 mol% of the catalyst with 0.09 mol% of KO*t*Bu and 4-Å molecular sieves to afford more than 1 kg of the enantiomerically pure product in 91% yield after three successive crystallizations.

The direct catalytic asymmetric Mannich reaction of unmodified ketones was achieved by the cooperative catalysis of a heterobimetallic asymmetric complex of ALB and $La(OTf)_3 \cdot n H_2O$ in the presence of 3-Å molecular sieves (Scheme 22).[32] The reactivity and selectivity were greatly improved by addition of $La(OTf)_3 \cdot n H_2O$ to ALB. The association of ALB and $La(OTf)_3 \cdot n H_2O$ was indicated by means of LDI-TOF mass spectrometry.

A variety of epoxide-opening reactions were found to proceed smoothly in the presence of a bridged (*R*,*R*)-Ga-Li–binol complex (3–10 mol%), affording products in 67–94% yield with 66–96% *ee* (Scheme 23).[33] The structure of the LiCl-free Ga- and Li-linked binol complex was elucidated by X-ray crystallographic analysis and was shown to have a monomeric tetracoordinated structure similar to that of ALB.

A mixture of Et_2Zn and bridged (*S*,*S*)-binol (4:1) with 3-Å molecular sieves was developed as an effective catalyst system for the direct aldol reaction of hydroxyketones (Scheme 24).[34] As little as 0.1 mol% of the bridged (*S*,*S*)-binol species and 0.4 mol% of Et_2Zn promoted the direct aldol reaction smoothly, using only 1.1 equiv of hydroxyketones as a donor (substrate/ligand = 1000:1). In terms of catalyst loading, this is the most efficient asymmetric catalyst for the direct catalytic asymmetric aldol reaction.

Based on the transition-state model initially proposed by Noyori and co-workers, Shibasaki developed a new enantioselective catalyst for the addition of Me_2Zn to α-ketoesters (Scheme 25).[35] The introduction of the *cis* hydroxy group into the prolinol ligand might induce more *organized aggregation* of Zn species, resulting in high catalyst activity and enantioselectivity. (The original concept stems from the increased nucleophilicity of the alkyl zinc species by the proximal zinc alkoxide, which might act as an additional Lewis base).

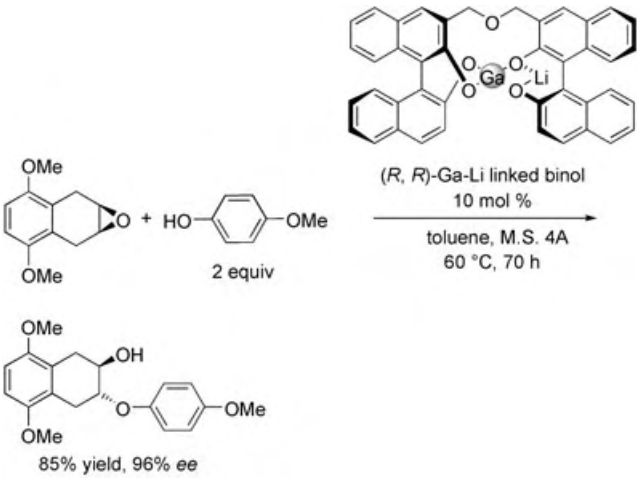

Scheme 23. Catalytic enantioselective epoxide-opening reaction with (*R*,*R*)-Ga,Li-linked binolate.

Trost and co-workers reported a series of novel dinuclear zinc complexes (Figure 11), which are effective catalysts for asymmetric direct aldol reactions,[36a,b,c] Mannich-type reactions,[36d] and desymmetrizations of 1,3- and 1,4-diols, as shown in Scheme 26.[36e] These catalysts might be regarded as a type of LLA, because the synergistic effect discussed above could be assumed for the addition stage. In these systems, the *intramolecular* interaction of the Lewis acids through the attached heteroatom should enhance the Lewis acidity efficiently in the chiral environment. In contrast, the *intermolecular* activation of the Lewis acid assisted by either catalytic or stoichiometric amounts of the other Lewis acid is also possible.

The discovery that Group IV metallocenes can be activated by methylaluminoxane (MAO),[37] an extremely strong Lewis acid and cocatalyst in olefin polymerization, has

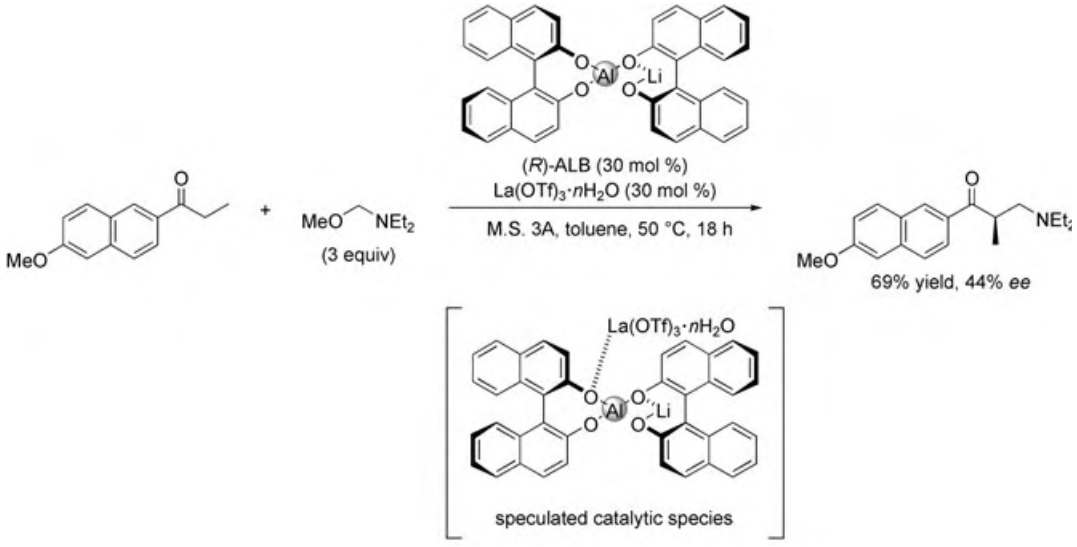

Scheme 22. Asymmetric direct Mannich reaction catalyzed by (*R*)-ALB and $La(OTf)_3 \cdot n H_2O$.

 © 2005 Wiley-VCH Verlag GmbH & Co. KGaA, Weinheim

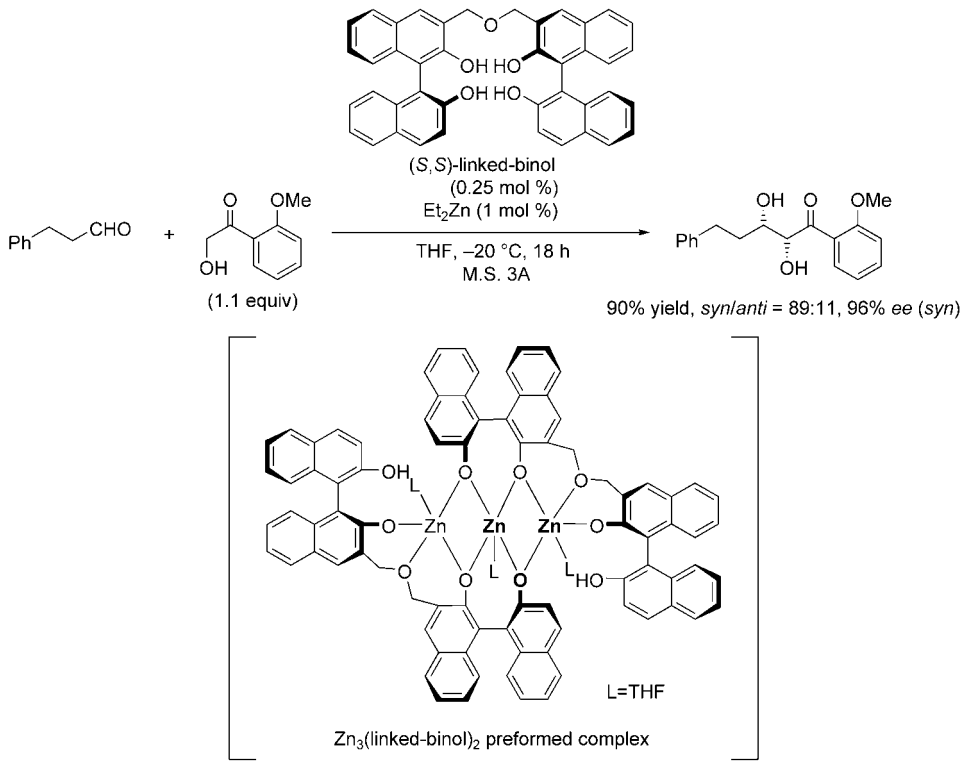

Scheme 24. Asymmetric direct aldol reaction catalyzed by an (*S*,*S*)-Zn–binol complex.

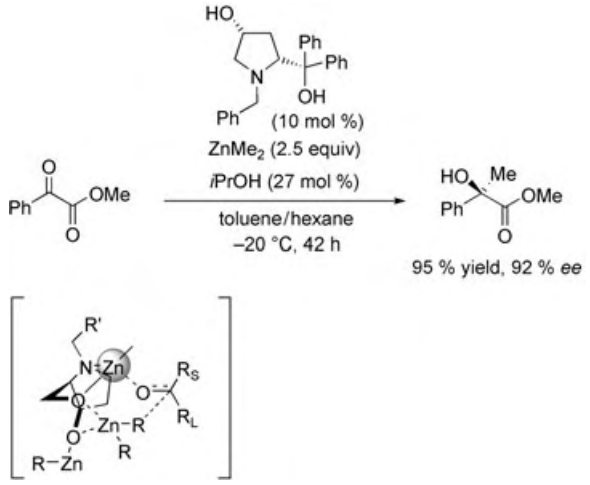

Scheme 25. Asymmetric addition of $ZnMe_2$ with a chiral prolinol-derived ligand.

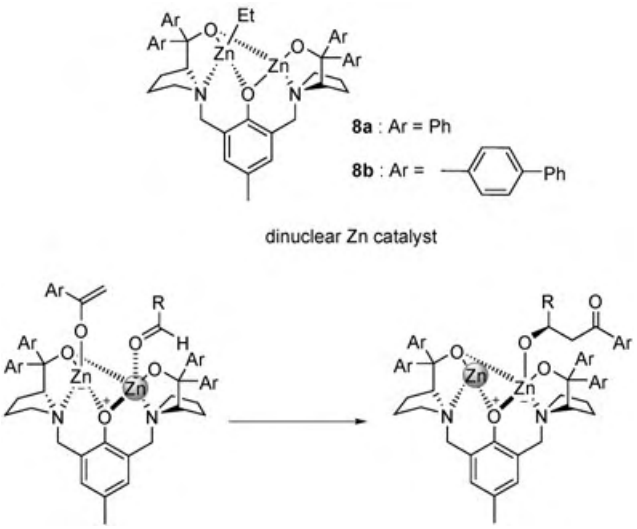

Figure 11. Structure of dinuclear zinc catalysts and their plausible synergistic effect.

stimulated a renaissance in Ziegler–Natta catalysis. These combined Lewis acid catalysts could also be regarded as a typical type of LLAs (Figure 12). The (*R*)-zirconocene catalyst/MAO reported by Pino et al. for the asymmetric oligomerization of propylene, 1-pentene, and 4-methyl-1-pentene using hydrogen as a chain-transfer reagent is a representative example (Scheme 27).[38]

Highly enantioselective carboalumination of alkenes was achieved with the Erker non-bridged chiral zirconocene catalyst by Negishi and co-workers (Scheme 28).[39] An impressive range of alkyl aluminum complexes can be added with high efficiency and excellent enantioselectivity. A different reaction medium changes the mechanism so that the catalytic alkylations proceed through carbometallation of the alkene (direct addition of cationic alkylzirconium to the olefin, followed by Zr–Al ligand exchange), rather than involving the formation of a metallacyclopentane.

Ishiyama and Miyaura reported that the addition of pinacol allylboronic esters to aromatic and aliphatic aldehydes occurred smoothly at −78 °C in toluene in the presence

 © 2005 Wiley-VCH Verlag GmbH & Co. KGaA, Weinheim

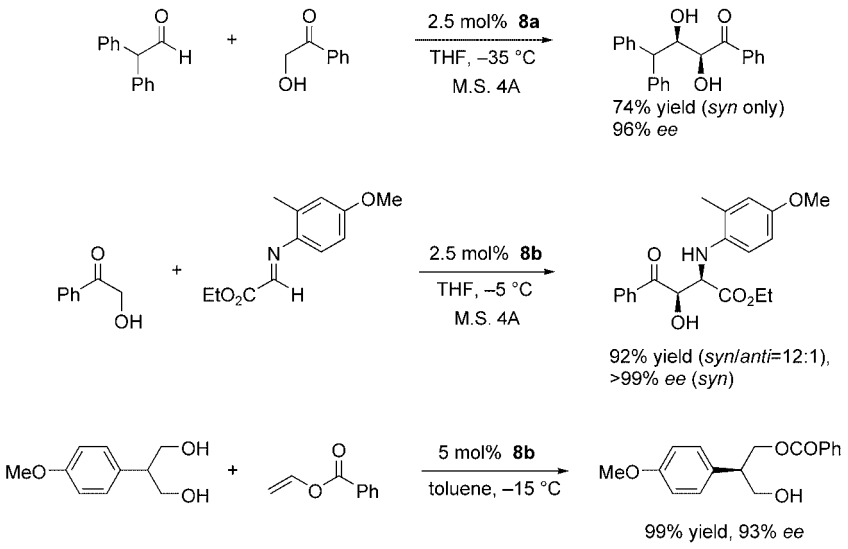

Scheme 26. Some applications of dinuclear zinc catalysts to asymmetric synthesis.

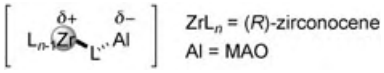

Figure 12. Mode of activation for Ziegler–Natta catalysts.

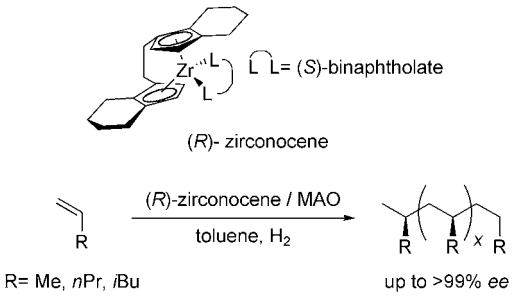

Scheme 27. Asymmetric oligomerization catalyzed by (*R*)-zirconocene/MAO.

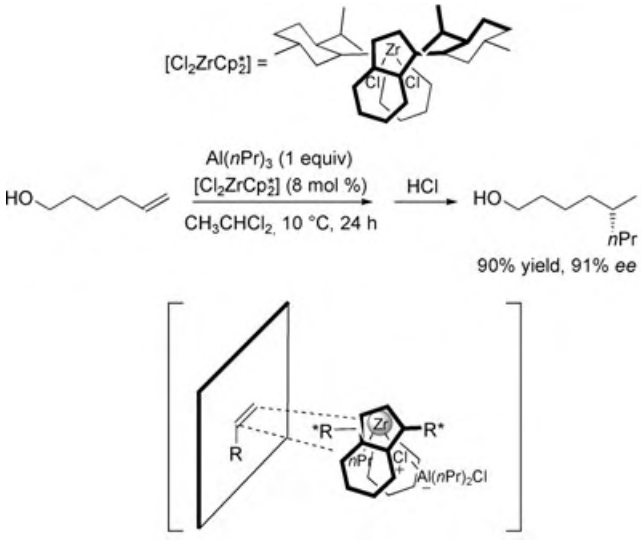

Scheme 28. Enantioselective carboalumination of alkenes in the presence of a chiral zirconocene catalyst.

of a catalytic amount of $AlCl_3$ or $Sc(OTf)_3$ (10 mol%) to give the corresponding homoallyl alcohols in high yields (Scheme 29).[40] The reactions proceeded regio- and diastereospecifically, yielding the isomerically pure *syn* and *anti* homoallyl alcohols from (*Z*)- and (*E*)-allylboronic esters, respectively. The protocol was also applied to enantioselective reactions in the presence of a chiral Lewis acid catalyst. Although the origin of activation remains unclear, the chiral Lewis acid might coordinate to the oxygen atom of the allyl boron reagent, resulting in dramatic increase in the Lewis acidity of the boron center.

Hall and co-workers reported a remarkably general and practical aldehyde allylation method based on the $Sc(OTf)_3$-catalyzed reaction of stable chiral allylboronates (Scheme 30).[41a,b] This approach is unrivaled in many ways, particularly in its efficient control of both diastereo- and

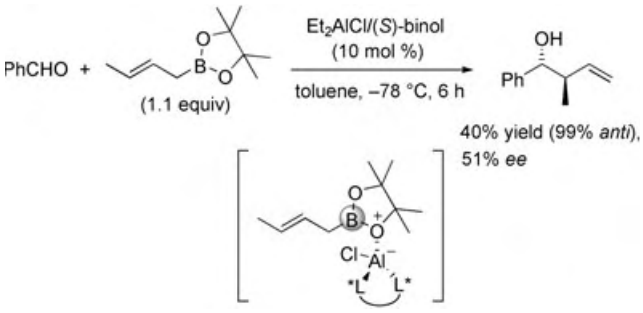

Scheme 29. Asymmetric allylation with achiral allyl boron reagent catalyzed by a chiral Lewis acid. L*–L* = (*S*)-binol.

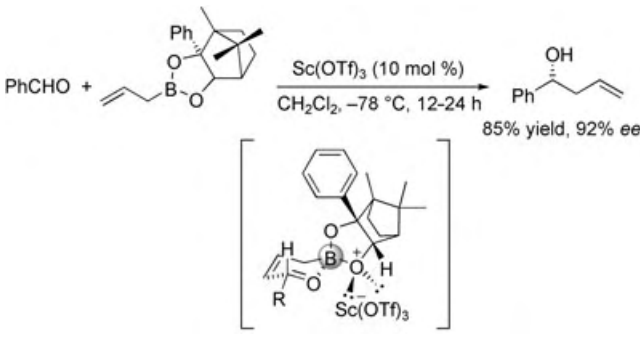

Scheme 30. Asymmetric allylation with a chiral allyl boron reagent catalyzed by $Sc(OTf)_3$.

enantioselectivity. The precise mechanistic nature of this Lewis acid catalyzed process and the mode of stereoinduction are unknown. On the basis of preliminary arguments presented earlier and the fact that the diastereospecificity of the uncatalyzed reaction is preserved, the allylboration is thought to proceed via the usual cyclic transition state, with electrophilic boron activation by metal coordination to the boronate oxygen atoms.[41b]

 © 2005 Wiley-VCH Verlag GmbH & Co. KGaA, Weinheim

Promising results obtained by Itsuno and co-workers in the 1980s with mixtures of chiral 1,2-amino alcohols and borane paved the way for the discovery of oxazaborolidines as chiral catalysts for the borane-mediated enantioselective reduction of a wide variety of achiral ketones (CBS reduction) (Scheme 31).[42] In the general mechanistic model, the coordination of the electrophilic BH_3 to the nitrogen atom of the oxazaborolidine serves to activate BH_3 as a hydride donor and also to increase strongly the Lewis acidity of the endocyclic boron atom. The strongly Lewis acidic complex then readily binds to the ketone at the more sterically accessible electron lone pair and *cis* to the vicinal BH_3 group. The reaction has been applied in numerous syntheses.[43]

Noyori and co-workers reported that in the presence of (−)-3-*exo*-(dimethylamino)isoborneol (DAIB), the reaction of dialkyl zinc complexes and aldehydes is markedly accelerated to give, after hydrolysis, the corresponding *S* alcohols with high enantiomeric purity (Scheme 32).[44] The alkylation proceeds via a dinuclear zinc species containing the DAIB auxiliary, an aldehyde ligand, and three alkyl groups; it is the bridging alkyl group, rather than the terminal alkyls, that migrates from zinc to the aldehyde carbon atom. The operation of a synergistic effect in the bimetallic complex serves to activate the central Zn as a Lewis acid while concomitantly increasing the nucleophilicity of the diorganozinc reagent in the transition state.

A possible transition state for titanium-catalyzed enantioselective additions of alkyl groups to aldehydes was proposed by Walsh and co-workers (Scheme 33).[45] Because of the tendency of the binolate–titanium complexes to associate, the formation of a binuclear intermediate was proposed.

Carreira and co-workers demonstrated the unique reactivity of a fluorotitanium complex as a catalyst for the asymmetric addition of Me_3Al to aldehydes (Scheme 34).[46] Importantly, in contrast to known alkyl metal additions to aldehydes involving Ti^{IV} catalysts, the fluorotitanium complex obviates the need for stoichiometric quantities of $Ti(OR)_4$ as additive. It is conceivable that fluoride on a Lewis acid center could also serve to participate as a bridging component and provide bimetallic complexes that function in a manner similar to the dialkyl zinc complexes described above.

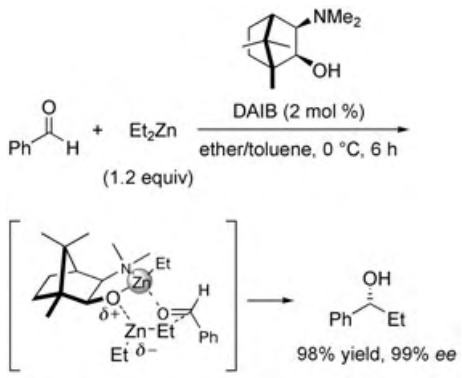

Scheme 32. Enantioselective addition of diethylzinc to aldehydes with DAIB.

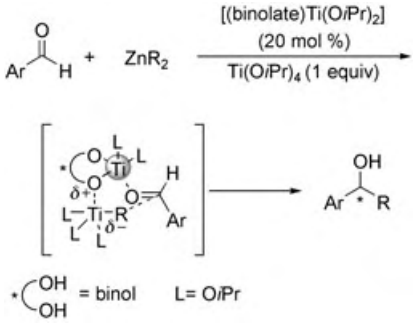

Scheme 33. Asymmetric alkylation with dialkylzinc reagent catalyzed by Ti–binol.

5. Lewis Acid Assisted Brønsted Acid Catalysts (LBA)

The combination of Lewis acids and Brønsted acids gives Lewis acid assisted Brønsted catalysts and provide an opportunity to design a "unique proton",[47] that is, the

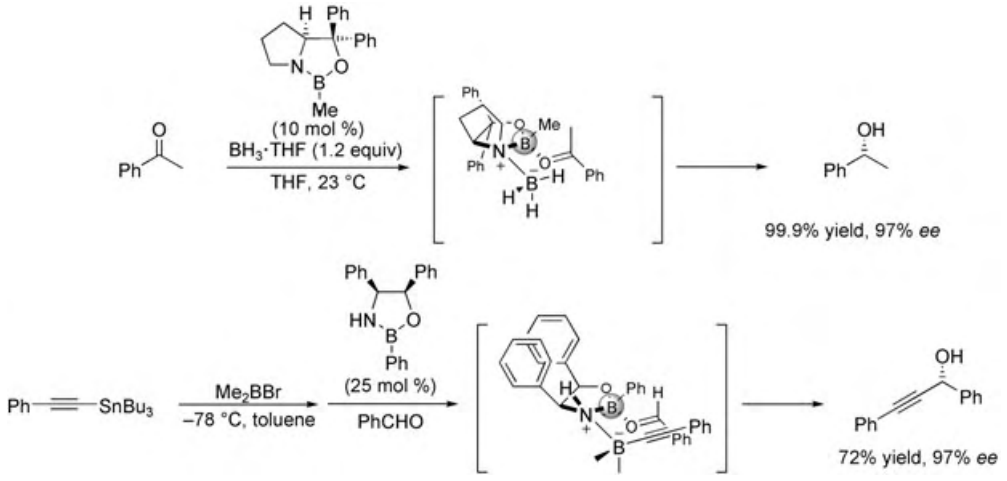

Scheme 31. Representative examples of chiral oxazaborolidine-mediated asymmetric reactions.

 © 2005 Wiley-VCH Verlag GmbH & Co. KGaA, Weinheim

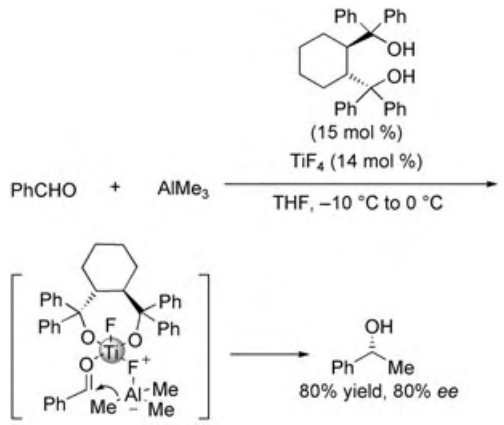

Scheme 34. Enantioselective alkylation with Me_3Al catalyzed by chiral titanium complex.

coordination of a Lewis acid to the heteroatom of the Brønsted acid could increase the acidity of the latter.

In 1994, we reported that such LBAs can be generated in situ from optically pure binol and $SnCl_4$ in toluene and is stable in solution, even at room temperature.[48a,b] In the presence of a stoichiometric amount of (*R*)-LBA, the protonation of the silyl enol ether derived from 2-phenylcyclohexanone proceeded at −78 °C to give the *S* isomer with 97 % *ee* (Scheme 35). This reagent is also applicable to various ketene

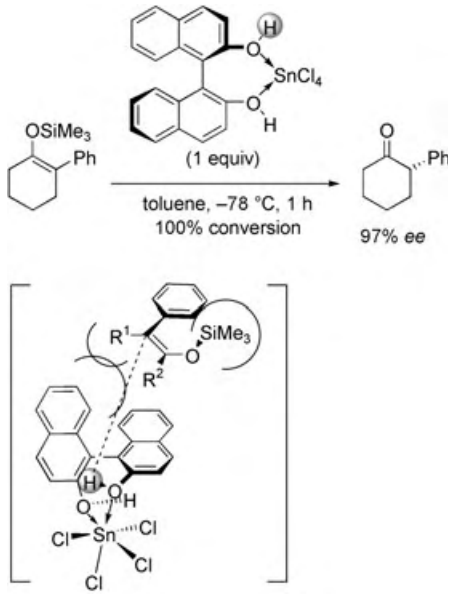

Scheme 35. Enantioselective protonation with chiral LBA generated from (*R*)-binol and $SnCl_4$.

bis(trialkylsilyl) acetals derived from α-aryl carboxylic acids. The sense of stereoinduction can be understood in terms of the proposed transition-state assembly shown in Scheme 35. The trialkylsiloxy group is directed opposite to the binaphthyl moiety to avoid any steric interaction, and the aryl group is stacked on this naphthyl group. In further studies, enantioselective protonation with a stoichiometric amount of an

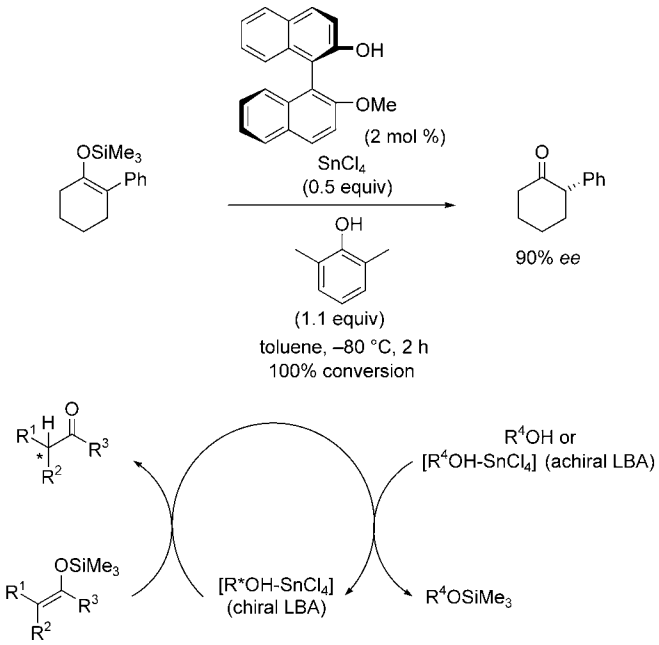

Scheme 36. Catalytic enantioselective protonation with chiral LBA generated from monoprotected binol derivative and $SnCl_4$.

achiral proton source and a catalytic amount of the chiral LBA was possible (Scheme 36).[48a,c]

The synthetic utility of LBAs is not only limited to asymmetric synthesis. We also developed the regio- and stereoselective isomerization of a "kinetic" silyl enol ether to a "thermodynamic" one catalyzed by an achiral LBA (Scheme 37).[48d] "Kinetic" TBDMS enol ethers were isomer-

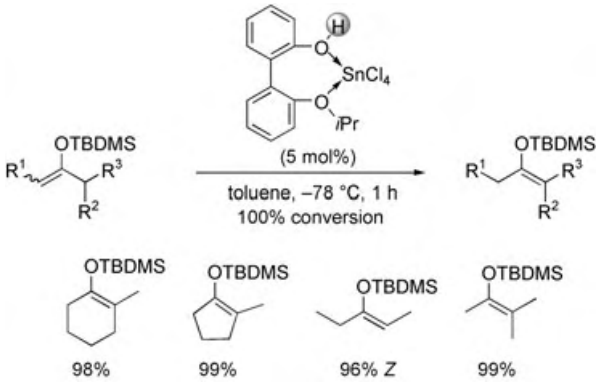

Scheme 37. Isomerization of silyl enol ethers catalyzed by achiral LBA. TBDMS = *tert*-butyldimethylsilyl.

ized to "thermodynamic" species in the presence of catalytic amounts of the coordinate complexes of $SnCl_4$ and the monoalkyl ethers of binol or biphenol. For the various structurally diverse substrates, the isomerization proceeded cleanly in the presence of 5 mol % of the achiral LBA.

In 2003, optically active 1,2-diarylethane-1,2-diol·$SnCl_4$ derivatives were designed as a new type of LBA for enantioselective protonation (Scheme 38).[47e] A variety of optically active 1,2-diarylethane-1,2-diols could be readily

 © 2005 Wiley-VCH Verlag GmbH & Co. KGaA, Weinheim

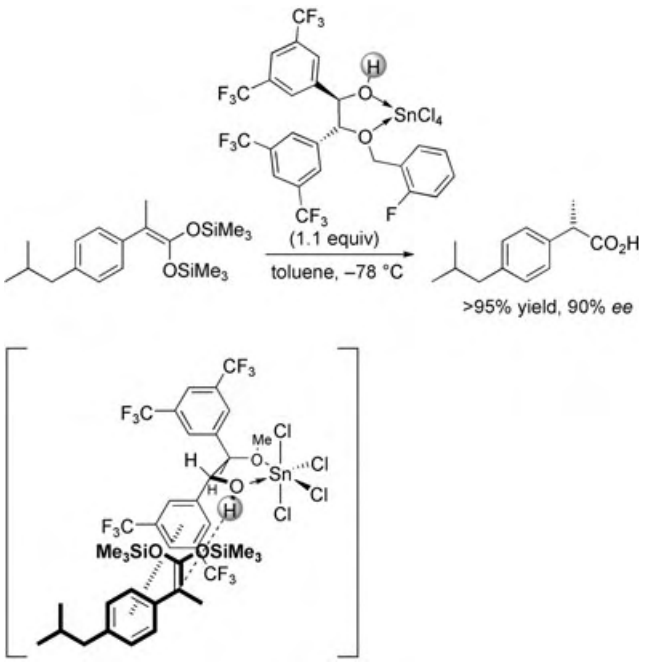

Scheme 38. Enantioselective protonation with chiral LBA generated from chiral hydrobenzoin derivative and $SnCl_4$.

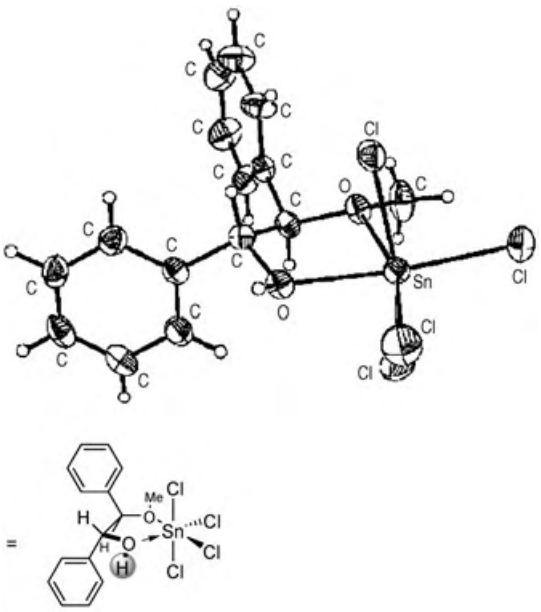

Figure 13. X-ray structure of LBA generated from monomethylated chiral hydrobenzoin and $SnCl_4$.

prepared by asymmetric *syn* dihydroxylation, which is advantageous to the use of binol for the flexible design of a new LBA. The most significant finding is that we were able to specify the conformational direction of the H–O bond of LBA by X-ray diffraction analysis (Figure 13). The stereochemical outcome of the enantioselective protonation of silyl enol ethers with this LBA could be controlled by a linear OH–π interaction with in the initial step (Scheme 38).

Despite extensive studies on acid-catalyzed diastereoselective polyene-cyclizations, the corresponding enantioselective processes have not yet been reported. Very recently, we succeeded in the first enantioselective biomimetic cyclization

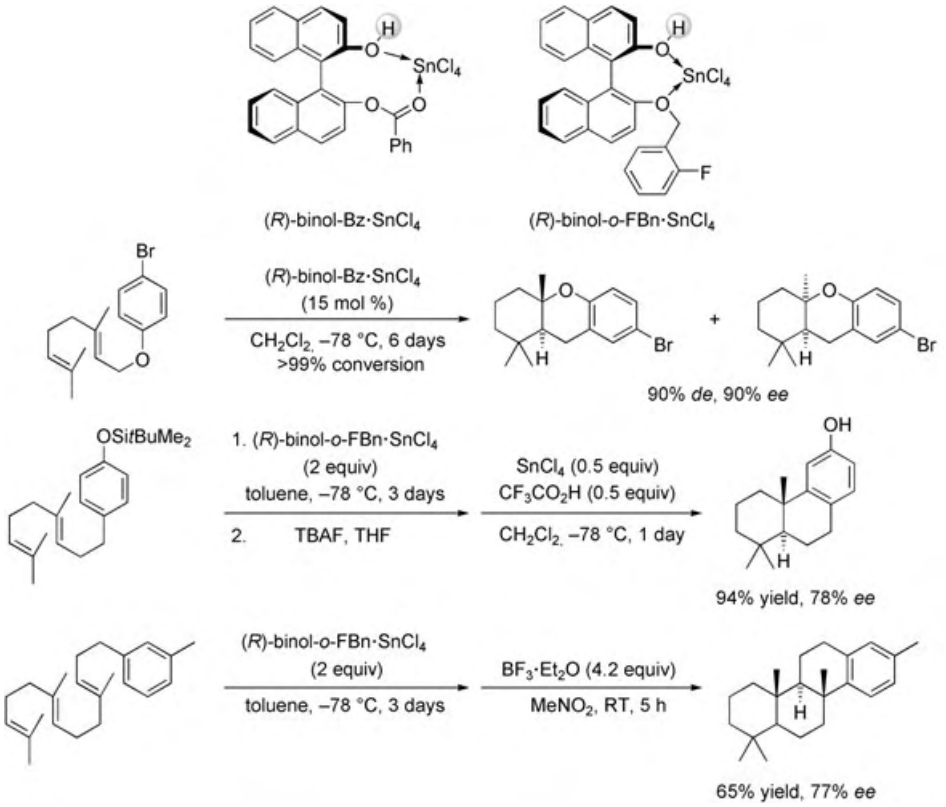

Scheme 39. Biomimetic cyclizations catalyzed by chiral LBAs.

 © 2005 Wiley-VCH Verlag GmbH & Co. KGaA, Weinheim

of polyprenoids catalyzed by chiral LBA (Scheme 39). This is the first example of a proton-induced enantioselective ene cyclization in synthetic chemistry.[49a,b] Geranyl phenyl ethers, *o*-geranylphenols, and geranylacetone derivatives were directly cyclized at −78 °C in the presence of (*R*)-binol derivatives and $SnCl_4$. During the cyclization, unusual [1,3] Claisen rearrangements often took place, with up to 90 % *ee*. These chiral LBAs recognize a trisubstituted terminal olefin enantiotopically and generate site-selective carbocations on the substrates.

The enantioselective cyclization of homo(polyprenyl)arenes was also induced by (*R*)-binol–*o*-FBn·$SnCl_4$ (Scheme 39).[49c,d] Several optically active podocarpa-8,11,13-triene diterpenoids and (−)-tetracyclic polyprenoids of sedimentary origin were synthesized by the enantioselective cyclization of homo(polyprenyl)benzene derivatives induced by this catalyst and subsequent diastereoselective cyclization induced by $BF_3{\cdot}Et_2O/EtNO_2$ or $CF_3CO_2H{\cdot}SnCl_4$ (75–80 % *ee*).

6. Brønsted Acid Assisted Brønsted Acid Catalysts (BBA)

Hydrogen bonding plays a crucial role in the organization of the three-dimensional structure of enzymes and is often involved in the reaction at the active site. An ideal example is a concerted proton transfer in the rate-limiting step of heme-oxygenase catalysis, which was recently elucidated (Figure 14).[50]

Such an elegant principle could be applicable to asymmetric catalysis. Especially for Brønsted acid catalysis, the design of these catalysts would result not only in the formation of a highly organized chiral cavity but also in an increase in the Brønsted acidity of the terminal proton in a much milder way than that of the LBA system.

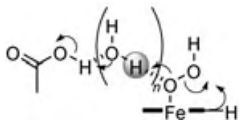

Figure 14. Concerted proton transfer in the rate-limiting step of heme oxygenase.

An example of intramolecular hydrogen bonding is also observed in the small organic molecule taddol[51] (Figure 15), which is one of the most efficient chiral backbones for asymmetric synthesis. Within this molecule, one of the hydrogen atom of the alcohol group participates in an intramolecular hydrogen bond and the other one is free for intermolecular interactions. These unique features have been confirmed by X-ray crystallographic analysis.

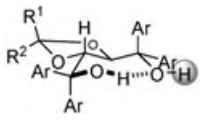

Figure 15. Intramolecular hydrogen bonding within taddol.

This excellent candidate was utilized as a chiral BBA catalyst by Rawal and co-workers.[52a] They showed that hetero-Diels–Alder reactions in the presence of taddol are highly enantioselective and generate only one of the enantiomers of the dihydropyran product (e.g. Scheme 40, top). This type of catalysis mimics the action of enzymes and antibodies, in contrast to traditional, metal-based catalysts used in organic chemistry. An interesting feature of this catalyst is that the monomethyl ether derivatives of taddol showed poor enantioselectivity, indicating that the *intramolecular* hydrogen bonding network within the catalyst must be crucial for higher asymmetric induction.

This BBA catalyst is also highly effective for the enantioselective Diels–Alder reactions of α, β-unsaturated aldehydes (Scheme 40, bottom).[52b] After the two-step transformations from the initial cycloadducts, a variety of chiral cyclohexenones were obtained with high enantioselectivities (up to 92 % *ee*).

A proposed working model for the taddol-catalyzed Diels–Alder reactions is shown in Figure 16. Well-defined internal hydrogen bonding may organize the asymmetric environment of the taddol derivative, coupled with an increase in Brønsted acidity of the other hydroxy proton, which coordinates to the carbonyl oxygen atom.[53] The resulting electron-deficient dienophile is stabilized through

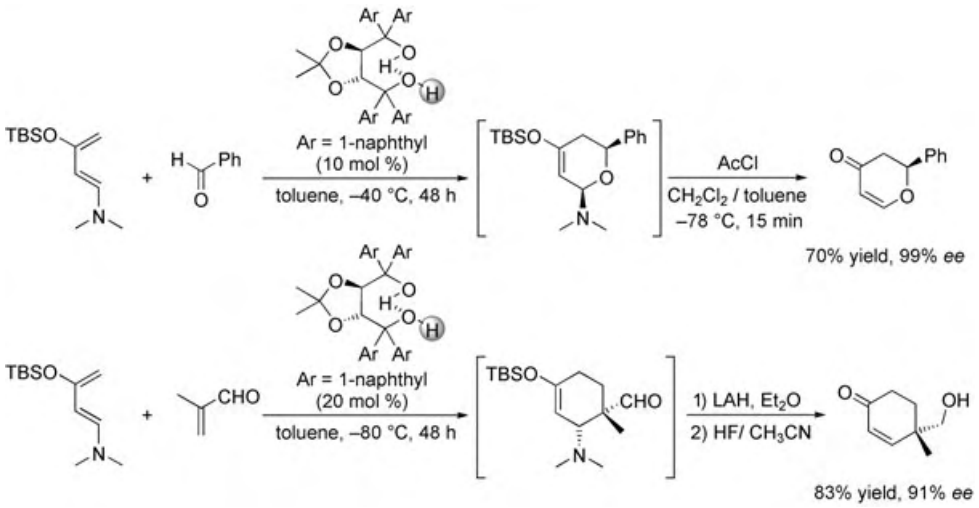

Scheme 40. Asymmetric Diels–Alder reactions catalyzed by a taddol derivative. LAH = lithium aluminum hydride.

 © 2005 Wiley-VCH Verlag GmbH & Co. KGaA, Weinheim

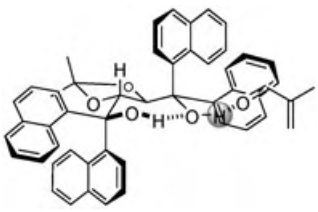

Figure 16. Proposed working model for the taddol-catalyzed Diels–Alder reactions.

π–π donor–acceptor interactions with the proximal 1-napthyl ring, which shields one enantiofacial side of the dienophile.

Chiral binol-derived Brønsted acids catalyze the enantioselective asymmetric Morita–Baylis–Hillman (MBH) reaction of cyclohexenone with aldehydes (Scheme 41).[54] The

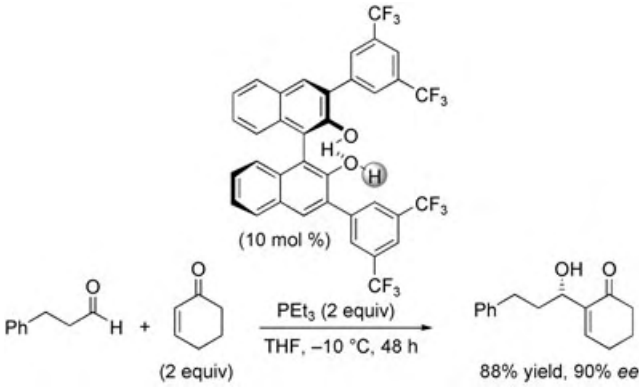

Scheme 41. Asymmetric Baylis–Hillman reaction catalyzed by a chiral binol derivative.

asymmetric MBH reaction requires 2–20 mol% of the chiral Brønsted acid and triethylphosphane as the nucleophilic promoter. The reaction products are obtained in good yields (39–88%) and high enantioselectivities (67–96% *ee*). The Brønsted acid catalyzed reaction is the first example of a highly enantioselective asymmetric MBH reaction of cyclohexenone with aldehydes. Interestingly, the removal of one Brønsted acid equivalent from the binol-derived catalyst to give the corresponding monomethyl ether resulted in a lower catalytic activity and no enantioselectivity. This result also indicates the importance of the *intramolecular* hydrogen-bonding network within the BBA catalyst.[53]

7. Conclusions and Outlook

In recent years, the power of designer acid catalysis has greatly increased as a result of the development of catalytic enantioselective versions described herein. Combined acid catalysis is still very much in a state of infancy, and there is still much more to learn with regard to new reactivity. The ultimate goal is a more reactive, more selective, and more versatile catalyst. We believe the realization of such an objective would be a tremendous benefit for the development of organic synthesis including green chemistry.

It is a great pleasure to thank the many wonderful co-workers who have accompanied me on the scientific journey that is retraced herein. Their names appear in the references cited. However, special mention needs be made to the following talented members of our group: S. Aratake, J. Fujiwara, K. Furuta, Q. Gao, Y. Hiraiwa, K. Inanaga, H. Ishibashi, K. Ishihara, K. Iwanaga, A. Kanematsu, M. Kaneeda, J. Kobayashi, H. Kurihara, K. Maruoka, T. Maruyama, M. Matsumoto, Y. Miwa, M. Miyata, M. Mouri, H. Nakamura, S. Nakamura, D. Nakashima, M. Oishi, and M. Sakurai. I am also grateful to the Japan Science and Technology Corporation for generous financial support over the years.

Received: April 21, 2004

[1] a) *Lewis Acids in Organic Synthesis* (Ed.: H. Yamamoto), Wiley-VCH, Weinheim, **2000**; b) *Lewis Acid Reagents: A Practical Approach* (Ed.: H. Yamamoto), Oxford University Press, Oxford, **1999**.
[2] J. Ren, C. J. Cramer, R. R. Squires, *J. Am. Chem. Soc.* **1999**, *121*, 2633–2634.
[3] J. H. Clark, *Acc. Chem. Res.* **2002**, *35*, 791–797.
[4] E. Negishi, *Chem. Eur. J.* **1999**, *5*, 411–420.
[5] Y. Pocker, K. D. Stevens, J. J. Champoux, *J. Am. Chem. Soc.* **1969**, *91*, 4199–4205; Y. Pocker, K. D. Stevens, *J. Am. Chem. Soc.* **1969**, *91*, 4205–4210.
[6] G. A. Olah, G. K. S. Prakash, J. Sommer, *Science* **1979**, *206*, 13–20.
[7] K. Maruoka, M. Sakurai, J. Fujiwara, H. Yamamoto, *Tetrahedron Lett.* **1986**, *27*, 4895–4898.
[8] a) K. Furuta, Y. Miwa, K. Iwanaga, H. Yamamoto, *J. Am. Chem. Soc.* **1988**, *110*, 6254–6255; b) K. Furuta, S. Shimizu, Y. Miwa, H. Yamamoto, *J. Org. Chem.* **1989**, *54*, 1481–1483; c) K. Furuta, A. Kanematsu, H. Yamamoto, S. Takaoka, *Tetrahedron Lett.* **1989**, *30*, 7231–7232; d) K. Furuta, T. Maruyama, H. Yamamoto, *J. Am. Chem. Soc.* **1991**, *113*, 1041–1042; e) K. Furuta, T. Maruyama, H. Yamamoto, *Synlett* **1991**, 439–440; f) K. Furuta, M. Mouri, H. Yamamoto, *Synlett* **1991**, 561–562; g) K. Ishihara, Q. Gao, H. Yammamoto, *J. Org. Chem.* **1993**, *58*, 6917–6919; h) Q. Gao, T. Maruyama, M. Mouri, H. Yamamoto, *J. Org. Chem.* **1992**, *57*, 1951–1952; i) K. Ishihara, M. Mouri, Q. Gao, T. Maruyama, K. Furuta, H. Yamamoto, *J. Am. Chem. Soc.* **1993**, *115*, 11490–11495; j) K. Ishihara, Q. Gao, H. Yamamoto, *J. Am. Chem. Soc.* **1993**, *115*, 10412–10413.
[9] a) K. Ishihara, H. Yamamoto, *J. Am. Chem. Soc.* **1994**, *116*, 1561–1562; b) K. Ishihara, H. Kurihara, M. Matsumoto, H. Yamamoto, *J. Am. Chem. Soc.* **1998**, *120*, 6920–6930.
[10] K. Ishihara, H. Kurihara, H. Yamamoto, *J. Am. Chem. Soc.* **1996**, *118*, 3049–3050.
[11] K. Ishihara, M. Miyata, K. Hattori, T. Tada, H. Yamamoto, *J. Am. Chem. Soc.* **1994**, *116*, 10520–10524.
[12] Y. S. Kim, S. Matsunaga, J. Das, A. Sekine, T. Ohshima, M. Shibasaki, *J. Am. Chem. Soc.* **2000**, *122*, 6506–6507.
[13] a) S. Kobayashi, M. Murakami, T. Harada, T. Mukaiyama, *Chem. Lett.* **1991**, 1341–1344; b) V. K. Aggarwal, E. Anderson, R. Giles, A. Zaparucha, *Tetrahedron: Asymmetry* **1995**, *6*, 1301–1306.
[14] a) E. J. Corey, T. Shibata, T. W. Lee, *J. Am. Chem. Soc.* **2002**, *124*, 3808–3809; b) D. H. Ryu, T. W. Lee, E. J. Corey, *J. Am. Chem. Soc.* **2002**, *124*, 9992–9993.
[15] a) D. H. Ryu, E. J. Corey, *J. Am. Chem. Soc.* **2003**, *125*, 6388–6390; b) G. Zhou, Q-Y. Hu, E. J. Corey, *Org. Lett.* **2003**, *5*, 3979–3982.

 © 2005 Wiley-VCH Verlag GmbH & Co. KGaA, Weinheim

[16] a) S. Kobayashi, H. Ishitani, *J. Am. Chem. Soc.* **1994**, *116*, 4083 – 4084; b) S. Kobayashi, H. Ishitani, I. Hachiya, M. Araki, *Tetrahedron* **1994**, *50*, 11623 – 11636.
[17] a) S. Kobayashi, H. Ishitani, *J. Am. Chem. Soc.* **1994**, *116*, 4083 – 4084; b) S. Kobayashi, H. Ishitani, I. Hachiya, M. Araki, *Tetrahedron* **1994**, *50*, 11623 – 11636.
[18] H. Ishitani, S. Kobayashi, *Tetrahedron Lett.* **1996**, *37*, 7357 – 7360.
[19] S. Kobayashi, M. Kawamura, *J. Am. Chem. Soc.* **1998**, *120*, 5840 – 5841.
[20] M. Oishi, S. Aratake, H. Yamamoto, *J. Am. Chem. Soc.* **1998**, *120*, 8271 – 8272.
[21] K. Ishihara, J. Kobayashi, K. Inanaga, H. Yamamoto, *Synlett* **2001**, *3*, 394 – 396.
[22] H. Ishitani, S. Komiyama, S. Kobayashi, *Angew. Chem.* **1998**, *110*, 3369 – 3372; *Angew. Chem. Int. Ed.* **1998**, *37*, 3186 – 3188.
[23] a) S. Kobayashi, H. Ishitani, *Chirality* **2000**, *12*, 540 – 543; b) H. Ishitani, S. Komiyama, Y. Hasegawa, S. Kobayashi, *J. Am. Chem. Soc.* **2000**, *122*, 762 – 766.
[24] H. Hanawa, T. Hashimoto, K. Maruoka, *J. Am. Chem. Soc.* **2003**, *125*, 1708 – 1709.
[25] a) R. Mahrwald, *Org. Lett.* **2000**, *2*, 4011 – 4012; b) R. Mahrwald, B. Ziemer, *Tetrahedron Lett.* **2003**, *44*, 4459 – 4461.
[26] a) M. Reilly, T. Oh, *Tetrahedron Lett.* **1994**, *35*, 7209 – 7212; b) M. Reilly, T. Oh, *Tetrahedron Lett.* **1995**, *36*, 217 – 220; c) M. Reilly, T. Oh, *Tetrahedron Lett.* **1995**, *36*, 221 – 224.
[27] a) For a review, see: M. Shibasaki, N. Yoshikawa, *Chem. Rev.* **2002**, *102*, 2187 – 2209; b) recently, a similar heterobimetallic catalyst [YLi_3tris(binaphtoxide)] (YLB) was reported as an effective catalyst for the asymmetric 1,4-addition of *o*-alkyl hydroxylamine to enones: N. Yamagiwa, S. Matsunaga, M. Shibasaki, *J. Am. Chem. Soc.* **2003**, *125*, 16178 – 16179.
[28] N. Yoshikawa, Y. M. Yamada, J. Das, H. Sasai, M. Shibasaki, *J. Am. Chem. Soc.* **1999**, *121*, 4168 – 4178.
[29] N. Yoshikawa, N. Kumagai, S. Matsunaga, G. Moll, T. Ohshima, T. Suzuki, M. Shibasaki, *J. Am. Chem. Soc.* **2001**, *123*, 2466 – 2467.
[30] a) T. Arai, H. Sasai, K. Aoe, K. Okamura, T. Date, M. Shibasaki, *Angew. Chem.* **1996**, *108*, 103 – 105; *Angew. Chem. Int. Ed. Engl.* **1996**, *35*, 104 – 106; b) S. Shimizu, K. Ohori, T. Arai, H. Sasai, M. Shibasaki, *J. Org. Chem.* **1998**, *63*, 7547 – 7551.
[31] Y. Xu, K. Ohori, T. Ohshima, M. Shibasaki, *Tetrahedron* **2002**, *58*, 2585 – 2588.
[32] S. Yamasaki, T. Iida, M. Shibasaki, *Tetrahedron* **1999**, *55*, 8857 – 8867.
[33] S. Matsunaga, J. Das, J. Roels, E. M. Vogl, N. Yamamoto, T. Iida, K. Yamaguchi, M. Shibasaki, *J. Am. Chem. Soc.* **2000**, *122*, 2252 – 2260.
[34] N. Kumagai, S. Matsunaga, T. Kinoshita, S. Harada, S. Okada, S. Sakamoto, K. Yamaguchi, M. Shibasaki, *J. Am. Chem. Soc.* **2003**, *125*, 2169 – 2178.
[35] K. Funabashi, M. Jachmann, M. Kanai, M. Shibasaki, *Angew. Chem.* **2003**, *115*, 5647 – 5650; *Angew. Chem. Int. Ed.* **2003**, *42*, 5489 – 5492.
[36] a) B. M. Trost, H. Ito, *J. Am. Chem. Soc.* **2000**, *122*, 12003 – 12004; b) B. M. Trost, H. Ito, E. R. Silcoff, *J. Am. Chem. Soc.* **2001**, *123*, 3367 – 3368; c) B. M. Trost, E. R. Silcoff, H. Ito, *Org. Lett.* **2001**, *3*, 2497 – 2500; d) B. M. Trost, L. R. Terrell, *J. Am. Chem. Soc.* **2003**, *125*, 338 – 339; e) B. M. Trost, T. Mino, *J. Am. Chem. Soc.* **2003**, *125*, 2410 – 2411.
[37] For the application of MAO as a Lewis acidic reagent in organic synthesis, see: M. Akakura, H. Yamamoto, *Synlett* **1997**, 277 – 278, and references therein.
[38] a) P. Pino, M. Galimberti, P. Prada, G. Consiglio, *Macromol. Chem.* **1990**, *191*, 1677 – 1688; b) P. Pino, P. Cioni, J. Wei, *J. Am. Chem. Soc.* **1987**, *109*, 6189 – 6191; c) for other examples of the use of enantiomerically pure metallocene/MAO catalysts, see: G. W. Coates in *Comprehensive Asymmetric Catalysis*, *Vol. 3* (Eds.: E. N. Jacobsen, A. Pfaltz, H. Yamamoto), Springer, New York, **1999**, pp. 1329 – 1349, and references therein.
[39] D. Y. Kondakov, E. Negishi, *J. Am. Chem. Soc.* **1996**, *118*, 1577 – 1578; E. Negishi, *Chem. Eur. J.* **1999**, *5*, 411 – 420.
[40] T. Ishiyama, T. Ahiko, N. Miyaura, *J. Am. Chem. Soc.* **2002**, *124*, 12414 – 12415.
[41] a) H. Lachance, X. Lu, M. Gravel, D. G. Hall, *J. Am. Chem. Soc.* **2003**, *125*, 10160 – 10161; b) V. Rauniyar, D. G. Hall, *J. Am. Chem. Soc.* **2004**, *126*, 4518 – 4519.
[42] a) E. J. Corey, C. J. Helal, *Angew. Chem.* **1998**, *110*, 2092 – 2118; *Angew. Chem. Int. Ed.* **1998**, *37*, 1986 – 2012, and references therein; b) S. Itsuno in *Comprehensive Asymmetric Catalysis*, *Vol. 1* (Eds.: E. N. Jacobsen, A. Pfaltz, H. Yamamoto), Springer, New York, **1999**, pp. 290 – 315, and references therein.
[43] For examples, see: a) E. J. Corey, K. A. Cimprich, *J. Am. Chem. Soc.* **1994**, *116*, 3151 – 3152; b) N. N. Joshi, M. Srebnik, H. C. Brown, *Tetrahedron Lett.* **1989**, *30*, 5551 – 5554.
[44] a) M. Kitamura, S. Suga, K. Kawai, R. Noyori, *J. Am. Chem. Soc.* **1986**, *108*, 6071 – 6072; b) M. Kitamura, S. Okada, S. Suga, R. Noyori, *J. Am. Chem. Soc.* **1989**, *111*, 4028 – 4036; for an excellent review of this topic, see: K. Soai, T. Shibata in *Comprehensive Asymmetric Catalysis*, *Vol. 2* (Eds.: E. N. Jacobsen, A. Pfaltz, H. Yamamoto), Springer, New York, **1999**, pp. 911 – 922, and references therein.
[45] P. J. Walsh, *Acc. Chem. Res.* **2003**, *36*, 739 – 749, and references therein.
[46] B. L. Pagenkopf, E. M. Carreira, *Tetrahedron Lett.* **1998**, *39*, 9593 – 9596.
[47] For a review, see: H. Ishibashi, K. Ishihara, H. Yamamoto, *Chem. Rec.* **2002**, *2*, 177 – 188.
[48] a) S. Nakamura, M. Kaneeda, K. Ishihara, H. Yamamoto, *J. Am. Chem. Soc.* **2000**, *122*, 8120 – 8130; b) K. Ishihara, M. Kaneeda, H. Yamamoto, *J. Am. Chem. Soc.* **1994**, *116*, 11179 – 11180; c) K. Ishihara, S. Nakamura, M. Kaneeda, H. Yamamoto, *J. Am. Chem. Soc.* **1996**, *118*, 12854 – 12855; d) K. Ishihara, H. Nakamura, S. Nakamura, H. Yamamoto, *J. Org. Chem.* **1998**, *63*, 6444 – 6445; e) K. Ishihara, D. Nakashima, Y. Hiraiwa, H. Yamamoto, *J. Am. Chem. Soc.* **2003**, *125*, 24 – 25.
[49] a) S. Nakamura, K. Ishihara, H. Yamamoto, *J. Am. Chem. Soc.* **2000**, *122*, 8131 – 8140; b) K. Ishihara, S. Nakamura, H. Yamamoto, *J. Am. Chem. Soc.* **1999**, *121*, 4906 – 4907; c) K. Ishihara, H. Ishibashi, H. Yamamoto, *J. Am. Chem. Soc.* **2002**, *124*, 3647 – 3655; d) K. Ishihara, H. Ishibashi, H. Yamamoto, *J. Am. Chem. Soc.* **2001**, *123*, 1505 – 1506.
[50] R. Davydov, T. Matsui, H. Fujii, M. Ikeda-Saito, B. M. Hoffman, *J. Am. Chem. Soc.* **2003**, *125*, 16208 – 16209.
[51] For an excellent review, see: D. Seebach, A. K. Beck, A. Heckel, *Angew. Chem.* **1998**, *110*, 2092 – 2118; *Angew. Chem. Int. Ed.* **2001**, *40*, 92 – 138.
[52] a) Y. Huang, A. K. Unni, A. N. Thadani, V. H. Rawal, *Nature* **2003**, *424*, 146; b) A. N. Thadani, A. R. Stankovic, V. H. Rawal, *Proc. Natl. Acad. Sci. USA* **2004**, *101*, 5846 – 5850.
[53] Alternatively, the activation of carbonyl compounds by double hydrogen bonding was proposed; see: P. M. Pihko, *Angew. Chem.* **2004**, *116*, 2110 – 2113; *Angew. Chem. Int. Ed.* **2004**, *43*, 2062 – 2064.
[54] N. T. McDougal, S. E. Schaus, *J. Am. Chem. Soc.* **2003**, *125*, 12094 – 12095.

 © 2005 Wiley-VCH Verlag GmbH & Co. KGaA, Weinheim

Communications

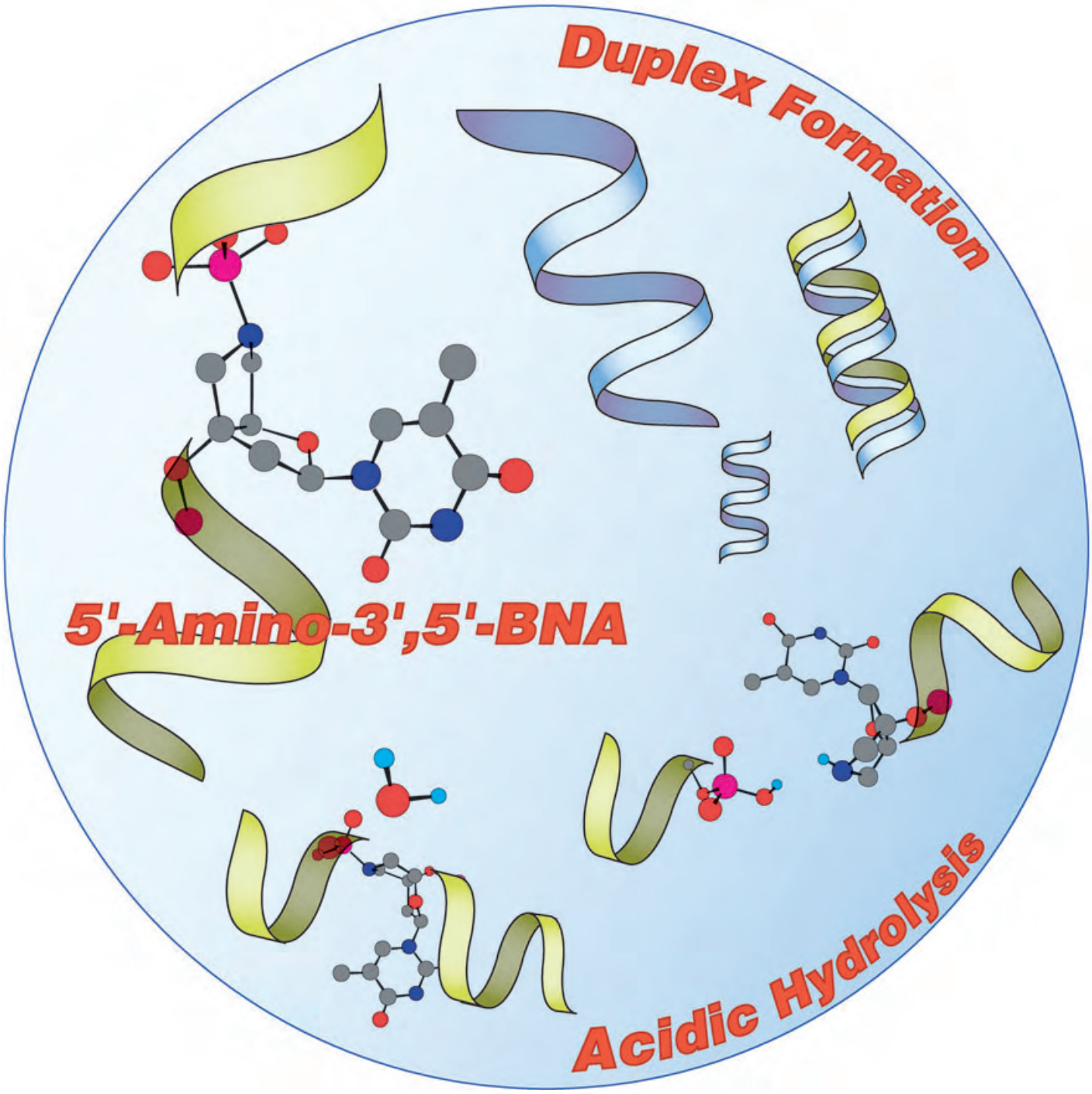

A methylene bridge between the C3′ and N5′ atoms adjusts the γ dihedral angle in 5′-amino-3′,5′-BNA. The bridged structure of this new type of oligonucleotide P3′→N5′ phosphoramidate greatly enhances duplex-forming ability with complementary strands and accelerates cleavage of the phosphoramidate linker under mild acidic conditions.

 © 2005 Wiley-VCH Verlag GmbH & Co. KGaA, Weinheim DOI: 10.1002/anie.200461942

Bridged Nucleic Acids

Adjustment of the γ Dihedral Angle of an Oligonucleotide P3′→N5′ Phosphoramidate Enhances Its Binding Affinity towards Complementary Strands**

*Satoshi Obika, Mitsuaki Sekiguchi, Roongjang Somjing, and Takeshi Imanishi**

Chemical modification of oligodeoxynucleotides (ODNs) has been receiving increasing attention in the fields of gene therapeutics and genetic diagnosis.[1,2] One promising approach is an internucleoside linkage modification of the ODNs. An N3′→P5′-phosphoramidate-linked ODN, in which the 3′-oxygen atom is replaced with a nitrogen atom, forms a stable duplex structure with its DNA or RNA complement.[3] On the other hand, P3′→N5′-phosphoramidate-linked ODNs (5′-amino-DNA, Scheme 1 a), with a 5′-nitrogen atom instead of an oxygen atom, can be hydrolyzed at the phosphoramidate linkage under mild acidic conditions.[4] This property of 5′-amino-DNA has attracted much attention and has been applied to a DNA-sequence determination.[5,6] However, the 5′-amino-DNA modification of ODNs decreases the hybridizing ability with its complementary strand.[7,8] This disadvantage of 5′-amino-DNA may be caused by an inappropriate γ dihedral angle (N5′–C5′–C4′–C3′). ^{1}H NMR analysis of a 5′-amino-DNA dimer revealed that the orientation of the C4′–C5′ bond is predominantly $+ap$ ($\gamma \approx 180°$) or $-sc$ ($\gamma \approx -60°$), which is different from that in a typical DNA/DNA or RNA/RNA duplex ($+sc$, $\gamma \approx 60°$).[9]

One promising strategy for restricting the conformational flexibility of the nucleoside sugar moiety is to increase the binding affinity of the ODNs. We have developed a series of novel nucleic acid analogues bearing a conformationally restricted sugar moiety, bridged nucleic acids (BNAs), and have found that ODNs containing some kinds of BNA acquired extremely high binding affinity for their DNA or RNA complements.[10–12] One such nucleic acid analogue, 5′-amino-2′,4′-BNA (Scheme 1 a), in which the sugar puckering is exactly restricted to the C3′-*endo* conformation (a typical N-type conformation), exhibited high binding affinity with complementary strands, although this nucleic acid analogue has a P3′→N5′ phosphoramidate linkage.[12] Thus, the 5′-amino-2′,4′-BNA may be one example of how to overcome the drawback of 5′-amino-DNA; however, the effect of the γ dihedral angle of 5′-amino-DNA on its hybridizing properties is still unclear.

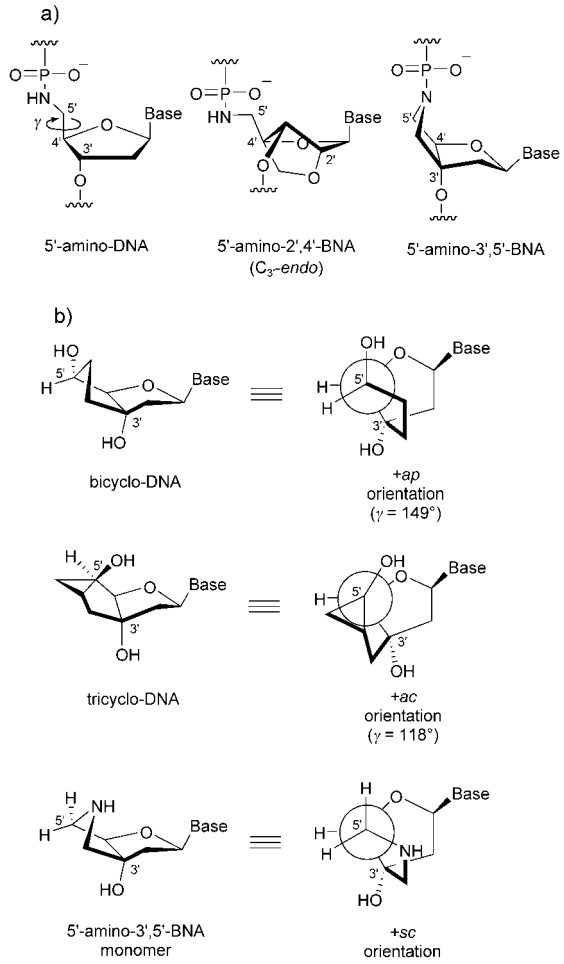

Scheme 1. a) Structures of 5′-amino-DNA, 5′-amino-2′,4′-BNA, and 5′-amino-3′,5′-BNA. b) Structures and γ dihedral angle orientation of bicyclo-DNA, tricyclo-DNA, and the 5′-amino-3′,5′-BNA monomer.

In this study, we have focused on the adjustment of the γ dihedral angle of 5′-amino-DNA. As DNA derivatives having a restricted γ dihedral angle, bicyclo-DNA[13] and tricyclo-DNA,[14] developed by Leumann et al., are well known. These DNA analogues showed interesting duplex- and triplex-forming properties, and the tricyclo-DNA was found to be useful even as an antisense oligonucleotide.[15] However, the γ dihedral angles of bicyclo-DNA and tricyclo-DNA were observed to be 149° and 118°, respectively (Scheme 1 b). These γ angles are beyond the range of those for typical DNA/DNA and RNA/RNA duplexes. To adjust the γ angle of 5′-amino-DNA to an appropriate value for stable duplex formation, we have designed a novel bridged nucleic acid, 5′-amino-3′,5′-BNA, which has a methylene linkage between the 3′-carbon and 5′-nitrogen atoms (Scheme 1 a). The orientation of the C4′–C5′ bond of the 5′-amino-3′,5′-BNA was fully expected to be $+sc$ by comparison with the structure of bicyclo-DNA (Scheme 1 b). Herein we describe the synthesis

[*] Dr. S. Obika, M. Sekiguchi, R. Somjing, Prof. Dr. T. Imanishi
Graduate School of Pharmaceutical Sciences
Osaka University
1-6 Yamadaoka, Suita, Osaka 565–0871 (Japan)
Fax: (+81) 6-6879-8204
E-mail: imanishi@phs.osaka-u.ac.jp

[**] This research was partially supported by a Grant-in-Aid from the Japan Society for the Promotion of Science, a Grant-in-Aid from the Ministry of Education, Culture, Sports, Science, and Technology of Japan, and a SUNBOR Grant from the Suntory Institute for Bioorganic Research. We gratefully acknowledge a JSPS Research Fellowship for Young Scientists (M.S.).

Supporting information for this article is available on the WWW under http://www.angewandte.org or from the author.

 © 2005 Wiley-VCH Verlag GmbH & Co. KGaA, Weinheim

and conformation of the 5′-amino-3′,5′-BNA monomer and some interesting properties of its ODN derivatives.

For the synthesis of the 5′-amino-3′,5′-BNA, we chose 3′-deoxy-3′-*C*-methylene-5′-*O*-triphenylmethylthymidine (**2**)[16] as the starting material (Scheme 2). Stereoselective oxidation

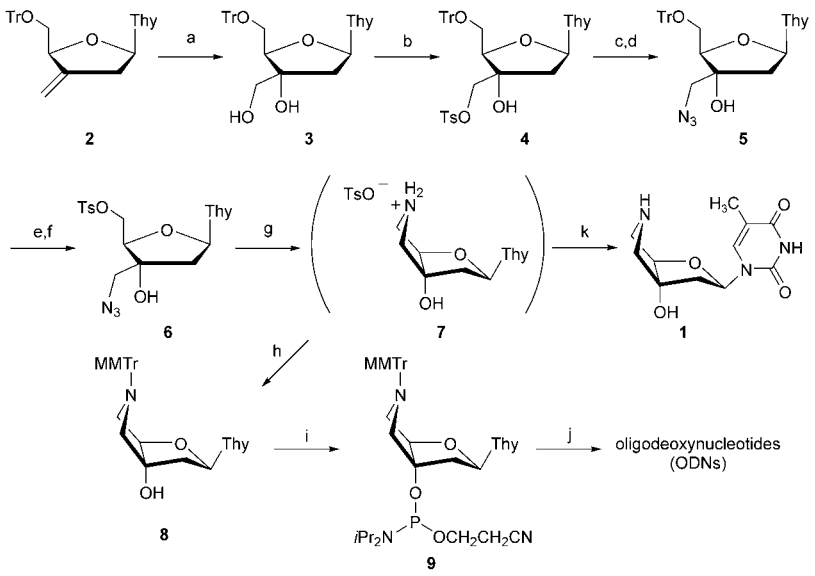

Scheme 2. Synthesis of 5′-amino-3′,5′-BNA-thymine monomer **1** and its phosphoramidite derivative **9**. a) OsO_4 (cat.), NMO, pyridine, H_2O, *t*BuOH, 76 °C, 69 %; b) TsCl, nBu_2SnO, Et_3N, CH_2Cl_2, RT, 72 %; c) K_2CO_3, MeOH, RT; d) NaN_3, DMF, 90 °C, 98 % from **4**; e) CSA, CH_2Cl_2/MeOH, RT; f) TsCl, pyridine, 50 °C, 53 % from **5**; g) 10 % Pd/C (wet), H_2, MeOH, RT; h) MMTrCl, pyridine, RT, 69 % from **6**; i) 2-cyanoethyl *N*,*N*-diisopropylchlorophosphoramidite, iPr_2NEt, CH_2Cl_2, RT, 86 %; j) DNA synthesizer (ABI Expedite 8909); k) Et_3N, MeOH, RT, then purified by reversed-phase HPLC. CSA = (+)-camphorsulfonic acid, DMF = *N*,*N*-dimethylformamide, MMTr = monomethoxytrityl, NMO = 4-methylmorpholine *N*-oxide, Thy = thymin-1-yl, Tr = triphenylmethyl = trityl, Ts = toluene-4-sulfonyl = tosyl.

of **2** by using osmium tetroxide gave diol **3**. A *p*-toluenesulfonyl group was introduced at the primary hydroxy group of **3** to afford **4**. Epoxidation with potassium carbonate and subsequent treatment with sodium azide gave **5**. After removing the 5′-*O*-triphenylmethyl (trityl) group, the obtained diol was treated with *p*-toluenesulfonyl chloride to give **6**. The azide group of **6** was reduced with palladium on carbon under a hydrogen atmosphere and subsequent pyrrolidine ring formation afforded the desired 5′-amino-3′,5′-BNA monomer **7** as a salt of *p*-toluenesulfonic acid. Without any purification at this stage, **7** was treated with monomethoxytrityl chloride to give **8**, and the phosphoramidite building block **9** was obtained by phosphitilation of **8**. Alternatively, the salt **7** was treated with triethylamine and was then purified by reversed-phase HPLC to afford the 5′-amino-3′,5′-BNA monomer **1** in a free form. X-ray crystallograpic analysis of **1** (Figure 1) showed that the γ dihedral angle of **1** is 28.3° (+*sc* orientation).[17] This value is quite different from that found in the 5′-amino-DNA dimer[9] and would be appropriate for stable duplex formation. It was also observed that the furanose ring of **1** has the C1′-*exo*-O4′-*endo* conformation (pseudorotational phase angle $P = 115.4°$), which is neither an N-type nor an S-type conformation, but an in-between conformation.

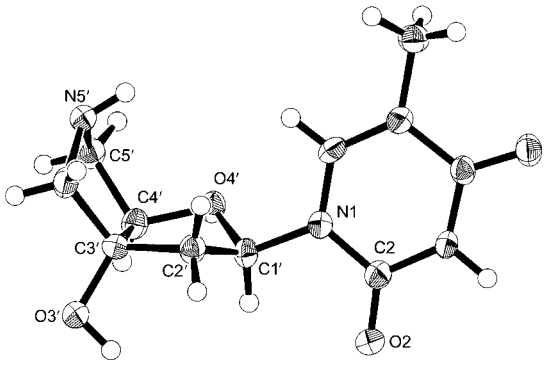

Figure 1. X-ray crystal structure of 5′-amino-3′,5′-BNA monomer **1**.

The phosphoramidite **9** was incorporated into 12-mer DNA strands **11**–**13** by using an automated DNA synthesizer.[18] To improve coupling and oxidizing efficiency, 4,5-dicyanoimidazole[19] and *t*BuOOH[20,21] were used instead of 1*H*-tetrazole and I_2/pyridine/H_2O, respectively. The coupling efficiency for **9**, estimated from monitoring the free trityl groups, was approximately 90 %.

Duplex-forming ability of the ODNs with complementary DNA and RNA was evaluated by means of UV melting experiments. The differences in melting temperatures (ΔT_m values) between the duplexes containing 5′-amino-3′,5′-BNA or 5′-amino-DNA[22] and the natural DNA/DNA or DNA/RNA duplexes are summarized in Figure 2.[23] As previously reported,[7,8] the duplexes comprising the 5′-amino-DNA, **14**–**16**, showed a decrease in T_m value compared with the corresponding DNA/DNA and DNA/RNA duplexes. ODN **16**, in particular, containing six con-

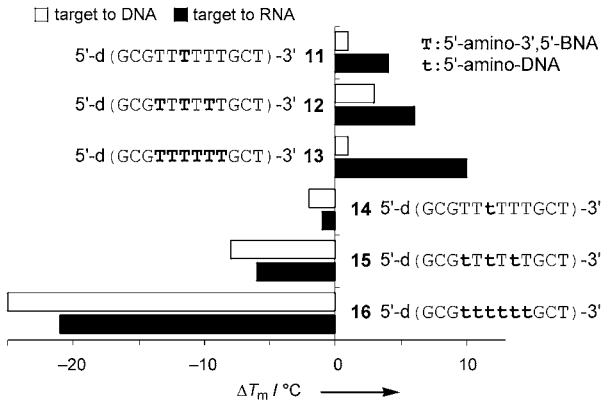

Figure 2. Differences in melting temperatures (ΔT_m values) between the modified oligonucleotides **11**–**16** and the reference oligonucleotide **10**, 5′-d(GCGTTTTTTGCT)-3′. The T_m values of duplexes of **10** with complementary DNA and RNA were 50 °C and 45 °C, respectively. The T_m values obtained from the maxima of the first derivatives of the melting curves (absorbance at 260 nm versus temperature) were recorded in a medium salt buffer (10 mM sodium phosphate, 100 mM NaCl, pH 7.2) with 4 μM complementary strands. The sequence of target DNA and RNA complement is 5′-AGCAAAAAACGC-3′.

 © 2005 Wiley-VCH Verlag GmbH & Co. KGaA, Weinheim

secutive 5′-amino-DNA monomers, displayed a drastically decreased binding affinity with its DNA and RNA complements. On the other hand, the 5′-amino-3′,5′-BNA ODNs **11**–**13** achieved stable duplex formation with complementary strands. An increase in the T_m values by 1–3 °C and 4–10 °C was observed when the ODNs **11**–**13** formed duplexes with complementary DNA and RNA, respectively. It is noteworthy that the difference between the T_m values of **13**/RNA and **16**/RNA hybrids was over 30 °C. Thus, the 5′-amino-3′,5′-BNAs have strong duplex-forming ability. This result indicates that the methylene bridge between the C3′ and N5′ atoms successfully restricts the conformation around the γ dihedral angle in an appropriate form for duplex formation.

Next, we investigated the effect of the methylene bridge on acid-mediated hydrolysis of the P3′→N5′-phosphoramidate linkage. The 5′-amino-3′,5′-BNA ODN **11** was treated with buffer (pH 3.0 or pH 7.0) to be hydrolyzed, and the amount of intact **11** was determined by reversed-phase HPLC analysis (Figure 3). Under pH 3.0 conditions, 50 % of **11** was

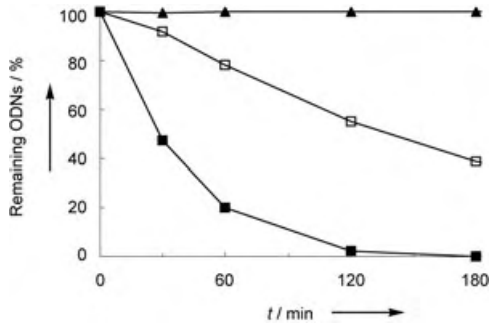

Figure 3. Hydrolytic cleavage of the P3′→N5′-phosphoramidate bond in modified ODNs: ■: 5′-amino-3′,5′-BNA ODN **11** at pH 3.0; ▲: 5′-amino-3′,5′-BNA ODN **11** at pH 7.0; □: 5′-amino-DNA ODN **14** at pH 3.0. The reaction was carried out at 30 °C with 1 nmol of ODN in buffer (100 μL). The sequence of oligonucleotides **11** and **14** is shown in Figure 2.

hydrolyzed at the P3′→N5′-phosphoramidate linkage within 30 min and 95 % was cleaved at 120 min, while no hydrolysis was observed at pH 7.0. The 5′-amino-DNA **16** was also cleaved at pH 3.0; however, hydrolysis is much slower than for 5′-amino-3′,5′-BNA. Thus, the additional methylene bridge between N5′ and C3′ atoms accelerates the hydrolysis of phosphoramidate linkage probably due to its electron-donating property.

We have synthesized a novel 5′-amino-DNA analogue, 5′-amino-3′,5′-BNA, with a γ dihedral angle that is well adjusted by the methylene bridge between the C3′ and N5′ atoms. We have also found that the methylene bridge effectively elicits not only a strong hybridizing ability but also the rapid hydrolysis of the P3′→N5′-phosphoramidate linkage of 5′-amino-3′,5′-BNA. This feature of 5′-amino-3′,5′-BNA would be applicable to a variety of genome technologies, such as a novel sequence determination or single-nucleotide-polymorphism analysis.

Received: September 10, 2004
Published online: January 28, 2005

Keywords: conformation analysis · nucleic acids · nucleosides · oligonucleotides · phosphoramidates

[1] N. Venkatesan, S. J. Kim, B. H. Kim, *Curr. Med. Chem.* **2003**, *10*, 1973 – 1991.
[2] J. Kurreck, *Eur. J. Biochem.* **2003**, *270*, 1628 – 1644.
[3] S. M. Gryaznov, *Biochim. Biophys. Acta* **1999**, *1489*, 131 – 140.
[4] W. Bannwarth, *Helv. Chim. Acta* **1988**, *71*, 1517 – 1527.
[5] M. S. Shchepinov, M. F. Denissenko, K. J. Smylie, R. J. Wörl, A. L. Leppin, C. R. Cantor, C. P. Rodi, *Nucleic Acids Res.* **2001**, *29*, 3864 – 3872.
[6] J. L. Wolfe, B. H. Wang, T. Kawate, V. P. Stanton, Jr., *J. Am. Chem. Soc.* **2003**, *125*, 10500 – 10501.
[7] S. M. Gryaznov, R. L. Letsinger, *Nucleic Acids Res.* **1992**, *20*, 3403 – 3409.
[8] E. Viazovkina, K.-L. Min, A. Galarneau, M. J. Damha, *Nucleosides Nucleotides Nucleic Acids* **2003**, *22*, 1335 – 1338.
[9] E. M. Nottoli, J. B. Lambert, R. L. Letsinger, *J. Am. Chem. Soc.* **1977**, *99*, 3486 – 3491.
[10] T. Imanishi, S. Obika, *Chem. Commun.* **2002**, 1653 – 1659.
[11] a) S. Obika, D. Nanbu, Y. Hari, K. Morio, Y. In, T. Ishida, T. Imanishi, *Tetrahedron Lett.* **1997**, *38*, 8735 – 8738; b) S. Obika, K. Morio, D. Nanbu, T. Imanishi, *Chem. Commun.* **1998**, 1643 – 1644; c) S. Obika, J. Andoh, T. Sugimoto, K. Miyashita, T. Imanishi, *Tetrahedron Lett.* **1999**, *40*, 6465 – 6468; d) S. Obika, J. Andoh, M. Onoda, O. Nakagawa, A. Hiroto, T. Sugimoto, T. Imanishi, *Tetrahedron Lett.* **2003**, *44*, 5267 – 5270.
[12] S. Obika, O. Nakagawa, A. Hiroto, Y. Hari, T. Imanishi, *Chem. Commun.* **2003**, 2202 – 2203.
[13] M. Tarköy, M. Bolli, B. Schweizer, C. Leumann, *Helv. Chim. Acta* **1993**, *76*, 481 – 510.
[14] R. Steffens, C. Leumann, *Helv. Chim. Acta* **1997**, *80*, 2426 – 2439.
[15] a) D. Renneberg, E. Bouliong, U. Reber, D. Schümperli, C. J. Leumann, *Nucleic Acids Res.* **2002**, *30*, 2751 – 2757; b) D. Ittig, S. Liu, D. Renneberg, D. Schümperli, C. J. Leumann, *Nucleic Acids Res.* **2004**, *32*, 346 – 353.
[16] M. Sharma, M. Bobek, *Tetrahedron Lett.* **1990**, *31*, 5839 – 5842.
[17] CCDC-247780 contains the supplementary crystallographic data for this paper. These data can be obtained free of charge from The Cambridge Crystallographic Data Centre via www.ccdc.cam.ac.uk/data_request/cif.
[18] The composition of the oligonucleotides **11**–**13** was confirmed by MALDI-TOF MS in negative-ion mode. A molecular-ion peak $[M-H]^-$ was detected in all cases, except for oligonucleotide **12**. See the Supporting Information.
[19] C. Vargeese, J. Carter, J. Yegge, S. Krivjansky, A. Settle, E. Kropp, K. Peterson, W. Pieken, *Nucleic Acids Res.* **1998**, *26*, 1046 – 1050.
[20] C. Scheuer-Larsen, B. M. Dahl, J. Wengel, O. Dahl, *Tetrahedron Lett.* **1998**, *39*, 8361 – 8364.
[21] Y. Hayakawa, M. Uchiyama, R. Noyori, *Tetrahedron Lett.* **1986**, *27*, 4191 – 4194.
[22] Synthesis of 5′-amino-DNA oligonucleotides **14**–**16** was performed according to ref. [4].
[23] The T_m profiles of duplexes containing the oligonucleotides **11**–**13** can be found in the Supporting Information.

 © 2005 Wiley-VCH Verlag GmbH & Co. KGaA, Weinheim

Liquid Crystals

Finite Enantiomeric Excess Nucleated in an Achiral Banana Mesogen by Chiral Alignment Surfaces**

*Kazuaki Shiromo, Daniel A. Sahade, Takuro Oda, Takayasu Nihira, Yoichi Takanishi, Ken Ishikawa, and Hideo Takezoe**

Controlling the chirality of molecular systems is important from the perspective of science as well as technology, and several methods have been adopted to achieve this. The most direct way is to dope achiral and chiral systems with chiral dopants. For example, the helical pitch of helical liquid crystals, such as cholesteric liquid crystals, can be readily tuned by the amount of dopants.[1] Another interesting and well-established method is irradiation with light of systems consisting of molecules with conformational chirality.[2] Asymmetric photoreactions, such as photoenantiomerization and asymmetric destruction, have been proposed as ways to introduce chirality. Herein we propose another method to control the chirality in a bent-core liquid-crystalline (banana mesogen) system.

The B_4 phase in achiral banana-shaped molecules is known to segregate into two chiral domains with opposite senses.[3–5] Since the two chiral domains are formed in equal probabilities, the B_4 phase has no macroscopic chirality and zero enantiomeric excess (*ee*). To produce an imbalance in the two chiral domains and nucleate a finite *ee* value in the bulk phase, we synthesized polyimides with chiral side chains and succeeded in nucleating an imbalance in the chiral domains in the B_4 phase of achiral P-14-O-PIMB (Scheme 1a) by using cells with chiral polyimide surfaces. Rubbing the surfaces makes the domains larger and enhances the effect of the chiral polyimide and results in an *ee* value of 10%.

The discovery of ferroelectric switching and chirality in liquid-crystalline phases of achiral banana-shaped molecules[6,7] has generated a new era in liquid-crystal science. The classic banana-shaped molecules, the homologous series of 1,3-benzenebis(4-(4-*n*-alkoxyphenyliminomethyl) benzoates (P-*n*-O-PIMB; Scheme 1a), exhibit some of the four phases B_1, B_2, B_3, and B_4. These phases are generated in this order (if all of them appear) with decreasing temperature. Antiferroelectric switching is clearly observed in the B_2 phase of P-*n*-O-PIMB.[6,8–11]

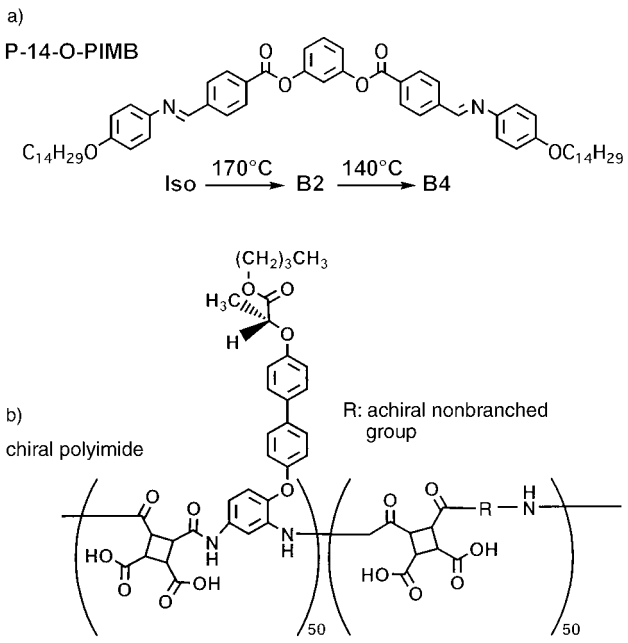

Scheme 1. Chemical structure of a) P-14-O-PIMB and b) a chiral polyimide with chiral side chains.

Herein, we focus on chirality. At least two kinds of chirality are known to exist, layer chirality[12] and conformational chirality,[5,7,13] which are closely related to each other.[5] The layer chirality appears because of a tilt in the bent-core molecules defined by a molecular long axis (*n*) and a bent direction (*b*) with respect to a layer normal (*z*). Since the molecules are achiral, two chiral domains (+ and −) appear in the B_2 phase in which the molecules tilt from the layer normal. The chiral domains are either the size of a layer or are macroscopic. For example, in the former case the layer chirality alternates from layer to layer so that the overall layer chirality is racemic, and in the latter case macroscopic homochiral domains can be observed under a polarizing optical microscope but are formed with equal probability.

Spontaneous chiral segregation also occurs in the B_4 phase, in which no layer chirality exists because of the nontilted phase. A conformational chiral structure is the origin of this type of chiral domain.[5] Some strong chiral conformations which resulted in a helical structure similar to the twist-grain boundary (TGB) phase[15] were suggested by NMR[7,14] and FTIR spectroscopic analysis,[13] and was confirmed by X-ray crystallographic analysis,[7] observation of the texture,[4] atomic force microscopy,[16] and freeze-fracture electron microscopy.[17] The spontaneous chiral segregation in the B_4 phase was easily seen by decrossing the polarizers.[3,4] In this way, local spontaneous deracemization is observed both in the B_2 and B_4 phases. However, the overall *ee* value is zero because the molecular systems are achiral. The banana-shaped molecules can be regarded as racemic mixtures rather than an achiral system because of the

[*] K. Shiromo, Dr. Y. Takanishi, Prof. Dr. K. Ishikawa, Prof. Dr. H. Takezoe
Department of Organic and Polymeric Materials
Tokyo Institute of Technology
O-okayama, Meguro-ku, Tokyo 152-8552 (Japan)
Fax: (+81) 3-5734-2876
E-mail: htakezoe@o.cc.titech.ac.jp
Dr. D. A. Sahade, T. Oda, Dr. T. Nihira
Electronic Materials Research Laboratories
Nissan Chemical Industries, LTD 722-1
Tsuboi-cho, Funabashi, Chiba-ken, 274-8507 (Japan)

[**] This work was partly supported by a Grant-in-Aid for Scientific Research (S) (16105003) from the Ministry of Education, Culture, Sports, Science, and Technology, Japan, and the Asahi Glass Foundation.

 © 2005 Wiley-VCH Verlag GmbH & Co. KGaA, Weinheim DOI: 10.1002/anie.200461881

chirality mentioned above. One remarkable difference between banana-shaped molecules and racemic mixtures of columitic molecules with stereogenic carbon atom(s) is evident: both layer chirality and conformational chirality are not inherent in phases formed from banana-shaped molecules and can switch to the opposite chirality, while chiral *S* and *R* conformers cannot be interchanged. In this sense, it is possible to control the enantioselectivity in banana mesogens.

The most direct way to control the *ee* value is by molecular doping with chiral compounds, and this has been shown to be a viable method.[18,19] Doping an achiral banana mesogen with only a small amount of chiral dopant (a few wt%) nucleates with 100% *ee*. This observation suggests a possibility to control the *ee* value by using chiral surfaces. Therefore, we attempted to nucleate a finite *ee* value in banana mesogens by using a polyimide surface-alignment layer with chiral side chains to nucleate a chiral field within the achiral molecules in the bulk phase.

The alignment layer used in this study is shown in Scheme 1b. We fabricated sandwich cells with four different surfaces: 1) bare glass, 2) glass coated with achiral polyimide, 3) glass coated with chiral polyimide, and 4) glass coated with chiral polyimide and rubbed. Rubbing was carried out by using a commercial rubbing machine (EHC, Japan using velvet under a moderate rubbing strength (depth = 200 μm). Dust and contaminants were blown off the rubbed surface with dry air. We used cells of different thicknesses between 2 and 12 μm. Since no essential difference was observed in the phenomenon, we only show the data for a 2-μm cell. The banana mesogen used was P-14-O-PIMB (Scheme 1a), which was introduced into each cell and then slowly cooled from the isotropic phase to the B_4 phase. A temperature-cycling technique between the B_2 and B_4 phases was adopted to enlarge the domain size, since the chiral nature is preserved during the process.[5]

The imbalance between the two chiral domains was evaluated by means of CD spectroscopic analysis (JASCO J-720WI) and direct observation of the texture under a polarizing microscope (Nikon, OPTIPHOT-POL). The temperature-cycling technique mentioned above is also effective in removing the effect of birefringence in the CD spectra. All experiments were carried out at room temperature and atmospheric pressure.

The B_4 phase is characterized by a blue color under crossed polarizers. The existence of chiral domains was confirmed in the usual way: The two domains become apparent as bright and dark regions when one of the polarizers was rotated clockwise by a small angle (2–3°) with respect to the crossed position. The brightness of the two domains interchanges when the polarizer is rotated counterclockwise. The difference in the texture of the four different cells is shown in Figure 1. The contrast between the domains is high in the cell with rubbed chiral surfaces and the size of domains is large, thus allowing the domain boundaries to be seen clearly (Figure 1d). On the other hand, the B_4 phase exhibits grainy (bare glass, Figure 1a), low contrast (glass coated with achiral polyimide, Figure 1b), and high contrast but fine (glass coated with chiral polyimide, Figure 1c)

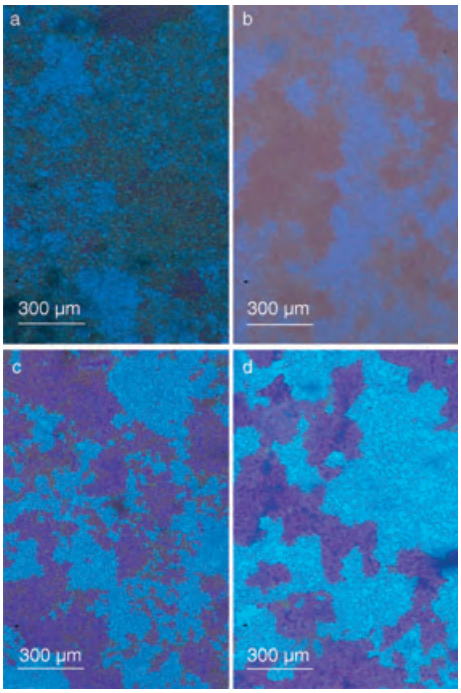

Figure 1. Optical micrographs of the B_4 phase of achiral P-14-O-PIMB under a 2°-clockwise decrossed position using cells with a) bare glass, b) glass coated with achiral polyimide, c) glass coated with chiral polyimide, and d) glass coated with chiral polyimide and rubbed.

textures in the cells with other surfaces. Thus, the rubbed chiral polyimide surface produces distinct large chiral domains in the B_4 phase compared to the other surfaces.

To evaluate the effect of the chiral polyimide surfaces on the enantioselectivity we measured the CD spectra of the cells. First we confirmed that empty cells with chiral surfaces show no CD effect, and that a CD signal emerges by introducing P-14-O-PIMB. The maximum CD intensity was observed at about 400 nm in the B_4 phase (see the inset of Figure 2). Since two chiral domains generally exist within an observation area, both positive and negative signals with a maximum at 400 nm were seen at different points by moving the aperture (diameter: 6 mm) in the cells. Figure 2 shows the spatial distribution of the maximum CD signal in the cells with the four different surfaces. An equal distribution of positive and negative CD signals were found in cells with bare glass surfaces (a) and achiral polyimide surfaces (b). This observation is expected, since the molecules are achiral and form chiral domains with equal probability. Hence, the B_4 phase has no macroscopic chirality and has zero enantioselectivity in cells with these surfaces.

On the other hand, the B_4 phase in cells with chiral surfaces exhibited positive CD intensities on average, despite the molecular systems being achiral. Thus, we succeeded in nucleating an imbalance or finite enantioselectivity in the B_4 phase by using the chiral surfaces. The rubbing treatment enhanced the effect of the chiral polyimide by about a factor of four compared with the unrubbed cells. As mentioned above, rubbing enlarges the domain size. Since the formation of the chiral domain with a finite *ee* value is a sort of crystal

 © 2005 Wiley-VCH Verlag GmbH & Co. KGaA, Weinheim

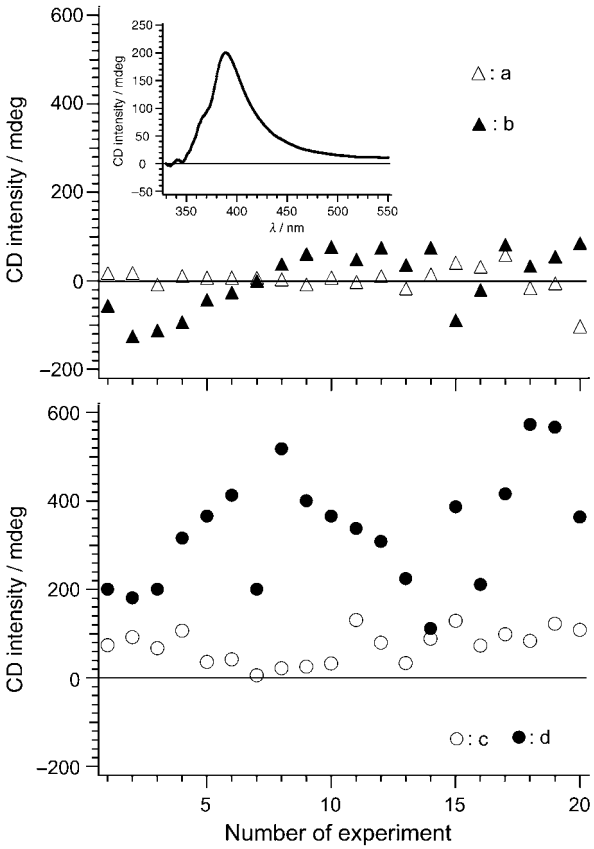

Figure 2. Spatial distribution of the maximum CD intensity in the B_4 phase of P-14-O-PIMB with a) bare glass, b) glass coated with achiral polyimide, c) glass coated with chiral polyimide, and d) glass coated with chiral polyimide and rubbed. The measurements were made by laterally shifting an aperture with a diameter of 6 mm. A typical CD spectrum of the B_4 phase of P-14-O-PIMB is also shown in the inset.

growth, the ability to form larger domains on rubbed chiral surfaces may promote enantioselectivity, although the real reason for the effect of rubbing on the domain size needs to be clarified. We confirmed that the sign of the CD signal in the B_4 phase is the same as that of the chiral polyimide.

On the basis of the results mentioned above we calculated the value of the induced enantioselectivity in the B_4 phase of P-14-O-PIMB in the cell with the rubbed chiral polyimide by two methods: 1) direct observation under a polarizing microscope and 2) measurement of the intensity of the CD signal. In the former method we took microphotographs and analyzed them using computer software packages (Photoshop and Image-J). The ratio of the + and − domains were determined over a large area and found to be 55:45, namely 10% *ee*. The maximum ratio attained if the analysis was made over a small area (1 mm diameter) in which a large imbalance was observed in a particular position was 75:25. CD measurements were made using a 1-mm aperture to enable this value to be compared with the CD signal. The spatial variation of the CD signals was much larger than the previous measurements using a 6-mm aperture. However, the average CD signals for the two aperture sizes were almost the same: 246 mdeg (1 mm) and 254 mdeg (6 mm). The maximum CD signal was 1600 mdeg in the measurement using a 1-mm aperture. If we assume that this value (1600 mdeg) corresponds to the ratio of 75:25 in the direct observation of the texture, the average ratio of 55:45 obtained over a wide area is consistent with the average CD intensity of about 320 mdeg. Thus, we can safely conclude on the basis of the two methods that 10% *ee* is nucleated under the influence of chiral surfaces.

Control of chirality by irradiation with light has only been demonstrated with a few specific molecules.[2] In the majority of molecular systems, however, the induced *ee* value was less than 1%,[20] except for diastereomeric helicenes,[21–23] which showed diastereomeric excess with a magnitude of tens of percent.[22,24] In this respect, the present *ee* value obtained in the B_4 phase of achiral P-14-O-PIMB by using cells with chiral polyimide surfaces is remarkably large and the mechanism is totally different from that ocurring under irradiation with light. The present phenomenon using chiral surfaces has not been reported. However, Jakli et al.,[25] reported macroscopic chiral induction with a nonchiral polymer network. If the polymer network is formed in cholesteric liquid crystals that are then removed after polymerization, the banana mesogen introduced into the cells with the remaining network gives rise to a chiral domain, whereas the polymerization in the isotropic phase does not give such an effect. Since chiral molecules do not exist in the cell, the chirality induced in the banana mesogen originates from polymer fibers with helical structures. Similarities and differences between the study by Jakli et al. and the present work are related to the mechanism.

The present technique is based on the different chiral interactions between the chiral side chain and bent-core molecules that form the + and − domains. These interactions are either at the molecular or macroscopic levels. In the former case, the operating interaction is essentially the same as that responsible for the effect of the chiral dopants. As a latter interaction, the possible formation of helical structures of polyimide main chains resulting as a consequence of the chiral side chains may play a role in the chiral interactions between the surfaces and bent-core molecules. This mechanism is quite similar to the phenomenon reported by Jakli et al.,[25] although the density of the helical fibrils is quite different because of their existence on the surface and in the bulk phase. Since chiral species exist only at the two surfaces in the present method, nucleation, growth, and formation of chiral domains are important factors for enhancing the *ee* value. Therefore, the following two possible ways are suggested to further enhance the enantioselectivity: 1) a chemical method: the design of chiral side chains that strengthen the chiral interactions of the bent-core molecules or by attaching chiral bent-core molecules as side chains, and 2) a physical method: the introduction of a temperature gradient to nucleate liquid-crystalline domains from the chiral surfaces that utilizes the maximum contribution from the chiral surface interactions.In conclusion, we have succeeded in obtaining finite *ee* values in the B_4 phase of an achiral bent-core molecule by using cells with polyimide layers possessing chiral side chains. The obtained *ee* value was 10% in cells with rubbed chiral polyimide surfaces. This technique opens up the

 © 2005 Wiley-VCH Verlag GmbH & Co. KGaA, Weinheim

possibilty for controlling the chirality in chemical and biological systems.

Received: September 3, 2004
Revised: October 18, 2004
Published online: February 21, 2005

Keywords: banana mesogens · chirality · enantioselectivity · liquid crystals · polyimides

[1] S. Chandrasekhar, *Liquid Crystals*, Cambridge University Press, Cambridge, **1992**.
[2] H. Rau, *Chem. Rev.* **1983**, *83*, 535 – 547.
[3] G. Pelzl, S. Diele, W. Weissflog, *Adv. Mater.* **1999**, *11*, 707 – 724.
[4] J. Thisayukta, H. Takezoe, J. Watanabe, *Jpn. J. Appl. Phys.* **2001**, *40*, 3277 – 3287.
[5] H. Niwano, M. Nakata, J. Thisayukta, D. R. Link, H. Takezoe, J. Watanabe, *J. Phys. Chem. B* **2004**, *108*, 14889 – 14896.
[6] T. Niori, T. Sekine, J. Watanabe, T. Furukawa, H. Takezoe: *J. Mater. Chem.* **1996**, *6*, 1231 – 1233
[7] T. Sekine, T. Niori, M. Sone, J. Watanabe, S. W. Choi, Y. Takanishi, H. Takezoe, *Jpn. J. Appl. Phys.* **1997**, *36*, 6455 – 6463.
[8] G. Heppke, D. D. Pargh, H. Sawade, *Liq. Cryst.* **2000**, *27*, 313 – 320.
[9] G. Pelzl, S. Diele, S. Grande, A. Jakli, Ch. Lischka, H. Kresse, H. Schmalfuss, I. Wirth, W. Weissflog, *Liq. Cryst.* **1999**, *26*, 401 – 413.
[10] D. Shen, A. Pegenau, S. Diele, I. Wirth, C. Tschierske, *J. Am. Chem. Soc.* **2000**, *122*, 1593 – 1601.
[11] M. Zennyoji, Y. Takanishi, K. Ishikawa, J. Thisayukta, J. Watanabe, H. Takezoe, *Jpn. J. Appl. Phys.* **2000**, *39*, 3536 – 3541.
[12] D. R. Link, G. Natale, R. Shao, J. E. Maclennan, N. A. Clark, E. Korblova, D. M. Walba, *Science* **1997**, *278*, 1924 – 1927.
[13] M. Zennyoji, Y. Takanishi, K. Ishikawa, J. Thisayukta, J. Watanabe, H. Takezoe, *Mol. Cryst. Liq. Cryst.* **2001**, *366*, 693 – 701.
[14] H. Kurosu, M. Kawasaki, M. Hirose, M. Yamada, S. Kang, J. Thisayukta, M. Sone, H. Takezoe, J. Watanabe, *J. Phys. Chem. A* **2004**, *108*, 4674 – 4678.
[15] J. W. Goodby, M. A. Waugh, S. M. Stein, E. Chin, R. Pindak, J. S. Patel, *Nature* **1989**, *337*, 449 – 452.
[16] H. Kresse, J. Salfetnikova, H. Nadashi, W. Weissflog, A. Hauser, *Liq. Cryst.* **2001**, *28*, 1017 – 1023.
[17] N. A. Clark, private communication.
[18] J. Thisayukta, Y. Nakayama, S. Kawauchi, H. Takezoe, J. Watanabe, *J. Am. Chem. Soc.* **2000**, *122*, 7441 – 7448.
[19] J. Thisayukta, H. Niwano, H. Takezoe, J. Watanabe, *J. Mater. Chem.* **2001**, *11*, 2717 – 2721.
[20] K. S. Burnham, G. B. Schuster, *J. Am. Chem. Soc.* **1999**, *121*, 10245 – 10246.
[21] B. L. Feringa, N. P. M. Huck, H. A. van Doren, *J. Am. Chem. Soc.* **1995**, *117*, 9929 – 9930.
[22] C.-T. Chen, Y.-C. Chou, *J. Am. Chem. Soc.* **2000**, *122*, 7662 – 7672.
[23] N. P. M. Huck, W. F. Jager, B. de Lange, B. L. Feringa, *Science* **1996**, *273*, 1686 – 1688.
[24] B. L. Feringa, N. P. M. Huck, A. M. Schoevaars, *Adv. Mater.* **1996**, *8*, 681 – 684
[25] A. Jakli, G. G. Nair, C. K. Lee, R. Su, L. C. Chien, *Phys. Rev. E* **2001**, *63*, 061710-1-4.

 © 2005 Wiley-VCH Verlag GmbH & Co. KGaA, Weinheim

Polymer–Surfactant Gels

Rapid Swelling/Collapsing Behavior of Thermoresponsive Poly(*N*-isopropylacrylamide) Gel Containing Poly(2-(methacryloyloxy)decyl phosphate) Surfactant**

Hu Yan, Hideki Fujiwara, Keiji Sasaki, and Kaoru Tsujii**

Poly(*N*-isopropylacrylamide) (PNIPA) gel has attracted considerable attention, from both the academic and technological viewpoints.[1–6] PNIPA gel undergoes an abrupt volume change at the phase-transition temperature (ca. 34 °C),[1] which can be utilized in several promising applications such as drug delivery systems and actuators.[4,5] For better performance of these applications, several strategies have been reported to exploit the rapid volume change of PNIPA gels.[7–9] However, PNIPA gel also exhibits salt-tolerant water absorbency through the incorporation of surfactants such as sodium dodecyl sulfate (SDS).[2] The behavior of the PNIPA gel in surfactant solutions has been extensively studied,[10] but little research has been reported on PNIPA gels containing polymeric surfactants. In our studies, poly(2-(methacryloyloxy)decyl phosphate) (PMDP) was chosen as the polymeric surfactant, which was expected to afford a superabsorbent PMDP-containing PNIPA (PNIPA–PMDP) gel in the presence of salts. The PNIPA–PMDP gel did not exhibit superabsorbency in sodium chloride solutions, but interestingly showed a rapid volume change above its phase transition temperature when compared to conventional PNIPA gels. Herein, we report the rapid volume change of PNIPA–PMDP gels as a function of temperature as well as by laser-beam irradiation. Our results clearly demonstrate the PMDP-induced enhancement of the response dynamics for the polymeric network of PNIPA gels.

The PNIPA gels were synthesized by free-radical polymerization under the reaction conditions shown in Table 1 (see Experimental Section). PMDP was readily prepared from 2-(methacryloyloxy)decyl phosphate by free-radical polymerization at about 25 °C (Scheme 1). To determine the phase-transition temperature of the gels, the value of V/V_c was measured, in which V and V_c are the gel volumes at the target and at the highest temperatures of the measurements, respectively. Notably, V_c does not represent the volume of the completely collapsed structure, especially for the PNIPA gel,

[*] Dr. H. Yan, Dr. H. Fujiwara, Prof. Dr. K. Sasaki, Prof. Dr. K. Tsujii
Research Institute for Electronic Science (RIES)
Hokkaido University, Sapporo 001-0021 (Japan)
Fax: (+81) 11-706-9357
E-mail: yanhu@es.hokudai.ac.jp
tsujik@es.hokudai.ac.jp

[**] H.Y. acknowledges fellowship support from the 21st century COE program "Center of Excellence for Advanced Life Science on the Base of Bioscience and Nanotechnology" of Hokkaido University, Japan. The authors thank Prof. T. Akutagawa of RIES, Hokkaido University, for assistance with the infrared spectroscopic measurements.

 DOI: 10.1002/anie.200462288 © 2005 Wiley-VCH Verlag GmbH & Co. KGaA, Weinheim

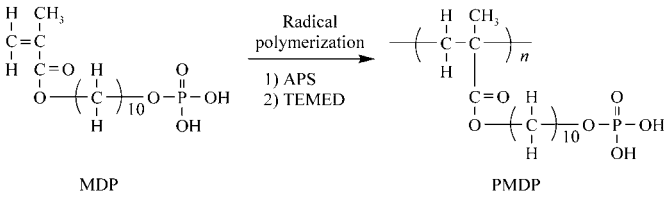

Scheme 1. Synthesis of PMDP. APS = ammonium persulfate, TEMED = tetramethylethylenediamine.

since V and V_c were measured at intervals of 1 h and the gel samples were not in the perfect equilibrated state. This situation, however, had little influence on the determination of the transition temperature. The shrinking kinetics of the gels was determined by measuring $\Delta V\,\%$ at 43 °C as a function of time, in which $\Delta V\,\% = (V_i - V_t)/V_i \times 100\,\%$ (V_i and V_t are the volumes at the initial and the target time, respectively).

As shown in Figure 1, the water absorbencies (V/V_c) of the PNIPA–PMDP gels were five- and fourfold greater than those

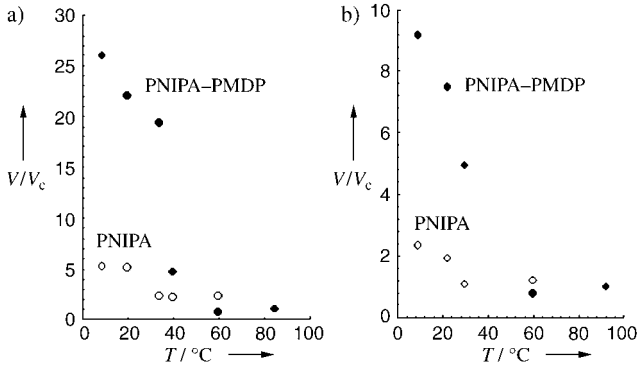

Figure 1. Temperature dependences of normalized gel volumes in pure water (a) and in 0.15 M NaCl solution (b). V_c denotes the gel volume in the collapsed state (but not in a completely collapsed state). Values for V/V_c did not have any significant effect on the estimation of phase-transition temperatures.

of PNIPA in pure water (Figure 1a) and in 0.15 M NaCl solution (Figure 1b), respectively, within the investigated time (1 h). The salt-tolerant superabsorbency behavior, which was observed in the PNIPA–SDS system,[2] was not observed for PNIPA–PMDP gels; in fact, completely different behaviors were observed for PNIPA–PMDP gels as compared to those of the PNIPA–SDS gel. Interestingly, the phase-transition temperature of the PNIPA–PMDP gel was comparable, within experimental error, to that of the conventional PNIPA gel, both in pure water and in 0.15 M NaCl solution, whereas the transition temperature of PNIPA–SDS gel increased to 90 °C in 0.15 M NaCl solution.[2] It is important to note that the PNIPA gel has been extensively studied as a tool of drug delivery systems as its transition temperature is approximately 34 °C, which is comparable to body temperatures.[4]

The time-dependent volume changes ($\Delta V\,\%$) of PNIPA–PMDP and PNIPA gels at 43 °C are shown in Figure 2. The PNIPA–PMDP gel showed a significantly greater volume change than that of the PNIPA gel (Figure 2a). The PNIPA–

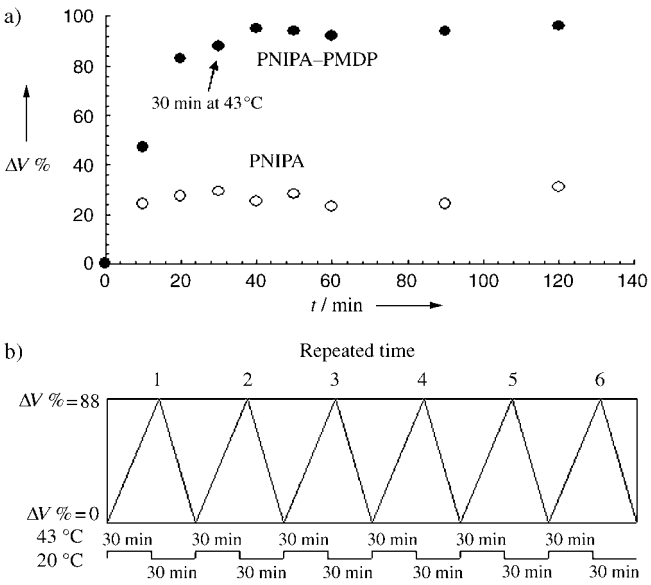

Figure 2. a) Degree of volume change (shrinkage) of PNIPA and PNIPA–PMDP gels at 43 °C after specific times. b) Reproducibility and reversibility of the volume change between 20 and 43 °C. Initial sizes of the gels were 1.7 × 9.2 mm (diameter × length) for PNIPA–PMDP gel and 1.6 × 9.6 mm for PNIPA gel.

PMDP gel had a ΔV value of 88 % within 30 min, and subsequently collapsed within 120 min; in contrast, the PNIPA gel showed a ΔV value of only 24 % within 30 min, and did not attain the completely collapsed state within the experimental time. Figure 2b shows that the $\Delta V\,\%$ values of the PNIPA–PMDP gel are both reproducible and reversible. The PNIPA–PMDP gel contracted to 88 % at 43 °C in 30 min, and swelled back to the initial volume at 20 °C within 30 min. The reversible volume change was repeated at least six times. No escape of PMDP molecules from the PNIPA–PMDP gel system was observed even after repeated reversible volume changes, which was confirmed by ultraviolet absorption spectra. The volume changes of PNIPA–PMDP and PNIPA gels at 43 °C can be visually observed in Figure 3. For the PNIPA–PMDP gel, significant changes in the diameter and the length were observed within 30 min. Specifically, a sample with dimensions of 1.7 × 9.2 mm (diameter × length) contracted to 0.8 × 3.4 mm; in contrast, a PNIPA sample with initial dimensions of 1.6 × 9.6 mm contracted to 1.4 × 8.8 mm.

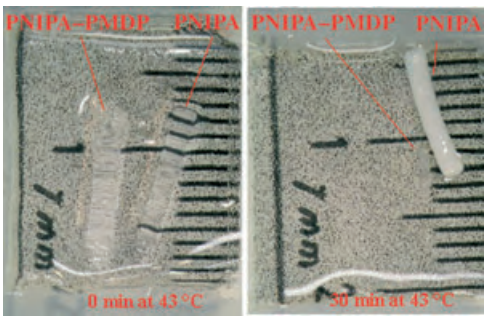

Figure 3. The hydrogels before (left) and after (right) the volume phase-transition under the conditions described.

 © 2005 Wiley-VCH Verlag GmbH & Co. KGaA, Weinheim

Furthermore, the PNIPA–PMDP gel remained almost transparent, even after a large volume change in a short time, whereas the PNIPA gel turned completely turbid. Unlike the conventional PNIPA gel, no skin formed on the surface of the PNIPA–PMDP gel, which could accelerate the phase transition in the PNIPA–PMDP system.

To verify the effects of polymeric surfactant PMDP on the prevention of skin formation and the acceleration of the phase transition of the PNIPA gel, a cylindrical sample of PNIPA gel with a PMDP concentration gradient was utilized for the phase-transition experiments. Images of the PMDP-gradient PNIPA gel below (at 9 °C) and above (at 60 °C) the phase transition temperature are shown in Figure 4. Half of

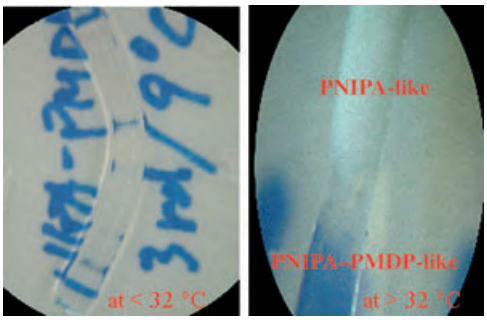

Figure 4. The PMDP-gradient PNIPA gel below (left, at 9 °C) and above (right, at 60 °C) the volume phase-transition temperature.

the PMDP-gradient PNIPA gel was transparent, whereas the other half was turbid. In such gels, the negatively charged PMDP molecules migrated from the turbid to the transparent region by electrophoretic action, thus forming a half-and-half PNIPA–PMDP-like and PNIPA-like gel. Both regions consist of a structurally identical PNIPA polymer network with the same degree of cross-linkage, and differ only in the amounts of PMDP. Therefore, the observed phase transition for the PMDP-gradient PNIPA gel unambiguously demonstrated that the polymeric surfactant PMDP prevents the formation of a skin structure and accelerates the volume change of PNIPA gel above the phase-transition temperature. The PNIPA–PMDP gel solubilized an oil-soluble dye, Yellow AB, which comprises hydrophobic crystals and is insoluble in water. The results indicate that PMDP forms micelles within the PNIPA gel network. It is, however, unclear at this stage how the micelles of PMDP prevent skin formation.

The PNIPA–PMDP gel also responded significantly quickly to the stimulus of a laser beam (Nd:YAG; wavelength, 1064 nm; power, ca. 100 mW) compared with conventional PNIPA gels. Interestingly, upon laser-beam irradiation, the rapid volume change of the PNIPA–PMDP gel resulted in a jet stream of water from the gel (Figure 5). A small block of PNIPA–PMDP gel (0.2 mm diameter, 0.2 mm length) in a glass capillary was used in the laser-irradiation experiments. No water droplets were observed on either side of the gel in the capillary before irradiation by the laser beam. Irradiation for 1 min resulted in the formation of numerous water droplets on the inside wall of the glass tube. The observation of some water droplets relatively far away from the gel on

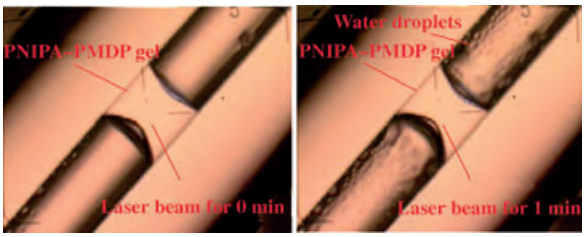

Figure 5. The PNIPA–PMDP gel before (left) and after (right) laser irradiation (Nd^{3+}:YAG; wavelength, 1064 nm; power, 100 mW).

both sides indicated that the abrupt contraction or rapid volume change of the swollen PNIPA–PMDP gel by the stimulus of the laser beam caused a jet stream of water. Juodkazis and co-workers recently reported that PNIPA gels undergo laser-induced volume phase transition under well-controlled conditions, in which D_2O was used as the solvent to avoid any temperature rise as a result of light absorption (wavelength, 1064 nm).[11] However, when laser beams with a power less than 700 mW were used, the PNIPA gel did not exhibit any volume changes.[11] In contrast, the present PNIPA–PMDP gel clearly showed a volume change using a laser beam with a power as weak as $\approx$100 mW. In a comparison experiment in which D_2O was used instead of H_2O solvent, no such rapid volume change was observed. Therefore, it is considered that the volume phase transition was triggered by rising temperatures inside the gel through absorption of near-infrared light (1064 nm) by water.

In conclusion, a PNIPA gel containing the polymeric surfactant PMDP (PNIPA-PMDP gel) has been synthesized and found to show a rapid volume change above its phase-transition temperature (ca. 34 °C). Interestingly, the phase-transition temperature of the PNIPA–PMDP gel is equal to that of the PNIPA gel. A concentration gradient of PMDP within the PNIPA gel can be obtained by applying an electric field to the gel, similar to the gel electrophoresis technique. The PMDP-gradient PNIPA gel clearly demonstrates the prevention of skin formation and acceleration of the phase transition of the PNIPA gel by PMDP, which forms micelles and does not escape from the gel system. Upon laser-beam irradiation (wavelength, 1064 nm; power, 100 mW), which is possibly converted to thermal energy, the PNIPA–PMDP gel undergoes rapid volume change, which can result in expulsion of a stream of water from the gel. Accordingly, this PNIPA–PMDP gel system could be extended to drug delivery systems[4] in which the target drug is exclusively released by laser stimuli on a diseased part, or to microvalves that can finely control fluids in the microchannels of a micro/miniaturized total analysis system (μTAS).[12]

Experimental Section

Sample preparation: PMDP was synthesized from MDP, which was prepared according to a previous report,[13] as follows: MDP (9.2 g) and ammonium persulfate (APS; 0.2 g) were dissolved in deionized water (397 g) at 25 °C. The solution was degassed by N_2 gas bubbling and polymerized for 1 h after addition of tetramethylethylenediamine (TEMED; 240 μL). The resulting precipitate (PMDP) was isolated by

 © 2005 Wiley-VCH Verlag GmbH & Co. KGaA, Weinheim

filtration, washed with pure water, and dried overnight under vacuum at 60 °C. Infrared spectra revealed that the characteristic peaks of the methylene groups at 3034 and 1637 cm^{-1} diminished, whereas those of the alkyl groups at around 2900 cm^{-1} increased after the reaction, which indicated the polymerization of MDP. PMDP showed a strong ultraviolet absorption at 205 nm. No such absorption was observed in the UV spectra of water in which the PNIPA–PMDP gel repeatedly underwent volume phase transition, which indicated that the PMDP did not escape from the gel network, probably because of entanglement of the polymeric surfactant with the network. Attempts to determine the molecular weight (M_w or M_n) of PMDP by gel-permeation chromatography were unsuccessful, probably because the polymeric surfactant forms micelles or aggregated structures in organic solvents. Some experimental and instrumental problems remain, but further investigations to determine the molecular weight of the polymers are currently underway. The PMDP dissolved well in water and its solubility increased with increasing temperature.

The PNIPA-based gels were synthesized by free-radical polymerization as follows (see Table 1): PMDP (0.044 g), PNIPA (0.87 g),

Table 1: Preparation of PNIPA and PNIPA–PMDP gels.[a]

PNIPA-based gel	Concentration [wt%]			Appearance
	PNIPA	MBA	polymeric surfactant	
PNIPA gel	8.6	0.12	–	colorless
PNIPA–PMDP gel[b]	8.2	0.12	0.42	colorless

[a] APS and TEMED as an initiator and accelerator, respectively, at 4 °C. [b] PMDP was neutralized by an aqueous solution of NaOH before addition of TEMED.

N,*N*′-methylenebisacrylamide (MBA; 0.014 g), and APS (0.013 g) were dissolved in deionized water (8.5 g). The solution was adjusted to pH 6 with NaOH solution (0.1M, 0.93 g), then degassed and polymerized at 4 °C by the addition of TEMED (24 μL). Polymerizations were carried out in 1.3-mm capillaries (for measurements of phase-transition temperature, time dependence of volume change at 43 °C, and response to stimulus of laser beam) or in 0.2-mm capillaries (for observations of jet streams of water from the gels upon laser-beam irradiation). The resulting PNIPA–PMDP gels were repeatedly washed by immersion in pure water for several days. The PNIPA gels were similarly synthesized but without PMDP. In addition, a concentration gradient of PMDP inside the PNIPA gel was created by applying a 10-V electric field for 2 h between both ends of the cylinder-shaped PNIPA–PMDP gel within a glass capillary.

Measurements: PNIPA–PMDP and PNIPA gels with initial sizes (diameter × length) of 1.7 × 9.2 and 1.6 × 9.6 mm, respectively, were used for measurements of volume phase transition. The experiments were performed in a temperature-controllable water bath filled with deionized water. The sizes of the gels were measured by optical microscopic observation. The measurements were carried out twice, and the data were in good agreement within a standard deviation of 1%.

The optical stimulus was obtained by introducing a Nd^{3+}:YAG laser (cw mode; wavelength, 1064 nm; power, 100 mW) into an optical microscope (IX-70 Olympus, 10×) and focusing on the gel sample at about 25 °C. Changes in the shape and the occurrence of water jet streams were monitored with a charge-coupled device camera and recorded as moving images. Pictures of the jet streams of water from the PNIPA–PMDP gel were transformed from the moving images.

Received: October 13, 2004

Keywords: gels · phase transitions · polymers · surfactants

[1] Y. Hirokawa, T. Tanaka, *J. Chem. Phys.* **1984**, *81*, 6379–6380.
[2] Y. Zhang, T. Tanaka, M. Shibayama, *Nature* **1992**, *360*, 142–144.
[3] H. G. Schild, *Prog. Polym. Sci.* **1992**, *17*, 163–249.
[4] L. E. Bromberg, E. S. Ron, *Adv. Drug Delivery Rev.* **1998**, *31*, 197–221.
[5] R. Yoshida, K. Uchida, Y. Kaneko, K. Sakai, A. Kikuchi, Y. Sakurai, T. Okano, *Nature* **1995**, *374*, 240–242.
[6] T. Okajima, I. Harada, K. Nishio, S. Hirotsu, *J. Chem. Phys.* **2002**, *116*, 9068–9077.
[7] X. Zhang, R. Zhuo, Y. Yang, *Biomaterials* **2002**, *23*, 1313–1318.
[8] W. Xue, I. W. Hamley, M. B. Huglin, *Polymer* **2002**, *43*, 5181–5186.
[9] T. Matsuura, M. Sugiyama, M. Annaka, Y. Hara, T. Okano, *Polymer* **2003**, *44*, 4405–4409.
[10] Y. Murase, K. Tsujii, T. Tanaka, *Langmuir* **2000**, *16*, 6385–6390.
[11] S. Juodkazis, N. Mukai, R. Wakaki, A. Yamaguchi, S. Matsuo, H. Misawa, *Nature* **2000**, *408*, 178–181.
[12] A. Manz, N. Graber, H. M. Widmer, *Sens. Actuators B* **1990**, *1*, 244–248.
[13] T. Koudate, Y. Nakano, JP patent P2000-26481A, **2000**.

 © 2005 Wiley-VCH Verlag GmbH & Co. KGaA, Weinheim

Molecular Recognition

Molecular Apple Peels**

*Joachim Garric, Jean-Michel Léger, and Ivan Huc**

Molecular encapsulation, defined here as the complete isolation of guest molecules from the solvent within a molecular or supramolecular container, has attracted widespread interest because of the applications it may have, for example, in molecular recognition and catalysis,[1] and because of the new insights it gives on otherwise unstable guest species that are protected from degradation within a secluded environment.[2] Several strategies are available to create a closed shell around a cavity. On the one hand, capsules may be unimolecular and consist of polymacrocyclic structures[1a,3] or of deep bowl-shaped molecules with a bulky rim,[4] while on the other hand, capsules may be formed by self-assembly of several molecular components. Examples of this latter category illustrate the numerous possibilities for

[*] J. Garric, Dr. I. Huc
Institut Européen de Chimie et Biologie
2 rue Robert Escarpit
33607 Pessac (France)
Fax: (+33) 540-00-30-09
E-mail: i.huc@iecb.u-bordeaux.fr
Prof. J.-M. Léger
Laboratoire de Pharmacochimie
146 rue Léo Saignat
33076 Bordeaux (France)

[**] This work was supported by the CNRS, the University of Bordeaux I, the University of Bordeaux II, and by the French Ministry of Research and Education (predoctoral fellowship to J.G.).

Supporting information for this article is available on the WWW under http://www.angewandte.org or from the author.

 © 2005 Wiley-VCH Verlag GmbH & Co. KGaA, Weinheim DOI: 10.1002/anie.200462898

dividing the surface of a sphere[1d,e] (for example, two hemispherical halves,[5] two non-hemispherical sections,[6] four quarters,[7]) or of a polyhedron[1b,c] (for example, tetrahedron,[8] icosahedron,[9] snub cube,[10] triangular prism[11]) into complementary elements. Herein we present a new approach for preparing unimolecular capsules from a molecular strand folded into a helix, the diameter of which is large at the center and reduced at both ends—similar to the shape of the skin of an apple peeled in a helical fashion.[12]

Some helices possess a hollow large enough to channel ions through biological membranes[13] or to host organic guest molecules.[14–18] Helices derived from aromatic oligoamides (AOAs) may prove particularly suitable for the purpose of molecular recognition because their diameter can be tuned at will according to the size of the monomers and the orientation of the amine and acid groups on each aromatic ring.[16–21] Thus, hollows as large as 3 nm[19] and as low as 0.5 nm[17,18] have been reported for AOAs. A refinement of this concept is the design of an oligomeric sequence comprising both monomers that code for helical segments with a hollow and monomers that code for no hollow at all. If the former are introduced at the center of the sequence and the latter are located at both ends, a helix defining a closed shell—a helix with both its extremities capped—may result and allow the encapsulation of guest species (Figure 1). The mechanism of binding a guest

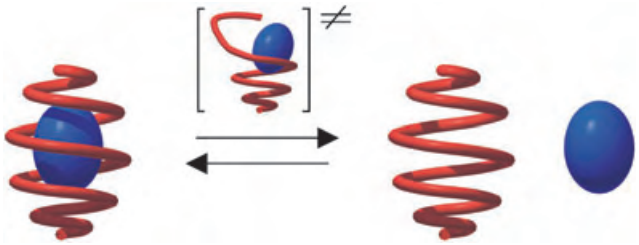

Figure 1. Encapsulation of an egg-shaped guest by partial unfolding of a helix possessing a reduced diameter at both ends.

in a capsule of this kind is expected to differ from the simple binding of a guest in the open hollow of a helix because it requires a partial unfolding of the capsule (Figure 1).[1e] This design also represents a novel way to relate the secondary structure and the chemical function of an oligomer to the primary sequence of its monomers.

To validate this concept we designed the prototypical capsule **1** (Scheme 1) which should be able to accommodate a small but highly relevant guest such as water. The hollow defined by helices of oligoamides of 2,6-diaminopyridine and 2,6-pyridinedicarboxylic acid is highly polar and can bind water in the solid state[18] and in solution.[17] However, oligoamides of 8-amino-2-quinolinecarboxylic acid form very stable helices with a hollow too small to accommodate any guest.[21] Oligomer **1** combines a central trimeric segment of pyridine monomers flanked by two short dimeric segments of quinoline monomers. Preliminary modeling studies showed that the central unit should form a sort of bulge large enough to bind a water molecule whilst the peripheral units should cap the helix hollow and possibly trap the guest.

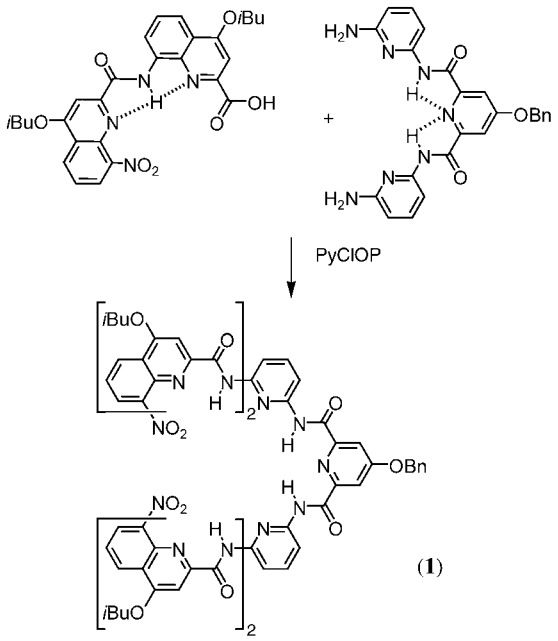

Scheme 1. Structure and synthesis of oligomer **1**. The dashed lines indicate hydrogen bonds that contribute to the stabilization of the helical conformation of **1**. Bn = benzyl, py = pyridyl.

The oligomer was prepared in one step from the previously described central trimeric unit[18a] and peripheral dimeric units[21] (Scheme 1). Evidence that oligomer **1**[22] can indeed encapsulate a small guest came from X-ray diffraction analysis of a single crystal grown from the slow diffusion of heptane into a toluene solution (Figure 2).[23] The solid-state structure reveals the expected helical shape that spans over two full turns. The pitch equals the thickness of one aromatic ring (about 3.45 Å), as found in previous structures of pyridine and quinoline oligomers.[17,18,21] The CPK views show that the terminal quinoline units do cap the hollow defined by the pyridine segment—the inner diameter of the helix is reduced at both ends. Most importantly, the helices all contain one molecule of water despite the low water content of the unpolar crystallization medium. The water oxygen atom is hydrogen bonded to the two amide protons of the central pyridine-2,6-dicarboxamide units (d_{N-O}: 2.84 Å, N-H-O: 150.1°) and sandwiched between the terminal nitro groups. The water molecule is completely surrounded by the helix and not visible from the outside. This observation implies that the binding and release of the water molecule in solution involves a partial unfolding or a springlike extension of the strand[24] (Figure 1). The kinetics of such a process should fundamentally differ from the binding and release of a guest from the open hollow of a normal cylindrical helix.[1e]

The behavior of **1** in solution was studied by NMR spectroscopy to test this hypothesis. The ^{1}H NMR spectrum of **1** in $CDCl_3$ possesses all the characteristic features of folded helices formed from oligomers with only pyridine[17,18] or only quinoline[21] units: sharp lines, spreading of the signals over a wide range of chemical shifts, downfield shifts of the signals of the amide protons involved in intramolecular hydrogen bonding, shielding of the protons involved in intramolecular

 © 2005 Wiley-VCH Verlag GmbH & Co. KGaA, Weinheim

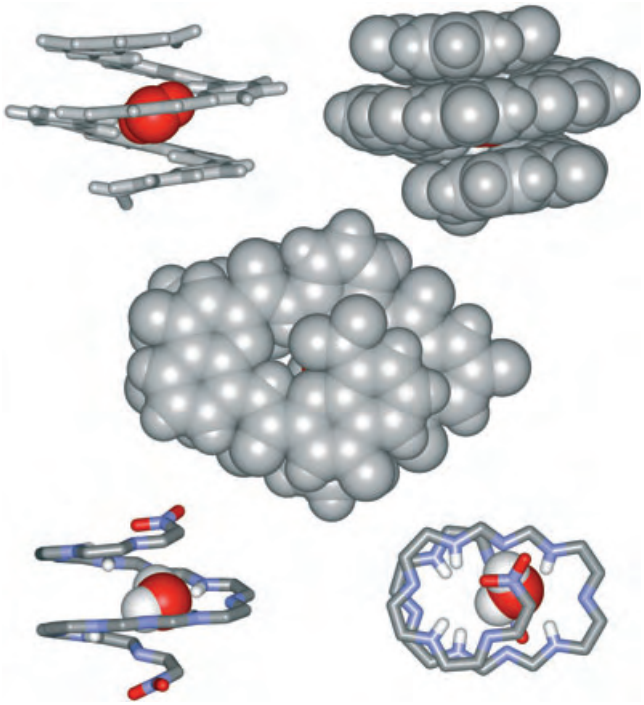

Figure 2. Views of the structure of $H_2O\subset$**1** in the crystal. Isobutyl and benzyl chains as well as included toluene molecules have been omitted for clarity. The hydrogen atoms of the water molecule could not be located and their positions are hypothesized from X-ray structures in which they could be determined.[18] The CPK views clearly show that the water is completely isolated from the surrounding medium. The two bottom structures only show the inner rim of the capsule and its numerous polar functions converging towards the hollow.

π–π stacking (Figures 3 and 4). No diastereotopic patterns of the signals of the methylene protons of the side chains are observed at room temperature, thus indicating that the equilibrium between the right-handed and the left-handed helices is fast on the NMR timescale, and that partial unfolding of the helix does occur. Of note is that the chemical shift of the amide protons appears to be dependent on their positions in the sequence. Whilst the most peripheral amide protons give rise to signals at $\delta = 11.62$ and 10.08 ppm, the amide protons of the central pyridinedicarboxamide monomer are strongly shielded and their signal appears at $\delta =$ 8.62 ppm (Figure 3a). Aromatic stacking is probably responsible for this upfield shift. Indeed, the crystal structure of **1** shows that these amide protons are sandwiched between the two terminal quinoline rings in the helix and should be strongly exposed to ring-current effects (Figure 2).

A first indication that water is bound in the helix hollow not only in the solid state but also in solution came from the variation of the chemical shifts of the NH protons with the water content of the chloroform. Samples were prepared using $CDCl_3$ dried over activated alumina and $CDCl_3$ saturated with H_2O. Drying or wetting the solvent had little effect on the chemical shift of the two signals of the four peripheral amide protons ($\Delta\delta < 0.2$ ppm). However, large variations in the position of the signal of the most central amide protons were observed: this signal shifted upfield to $\delta = 8.08$ ppm upon drying[25] (Figure 3d) but shifted downfield to $\delta = 9.39$ ppm upon wetting the solvent[26] (Figure 3c). This variation of cgemical shift ($\Delta\delta = 1.31$ ppm) is consistent with the hydrogen bonding of these amide protons to the oxygen atom of a water molecule, as seen in the solid state.

Additionally, the three amide protons undergo very different rates of exchange with deuterons in the presence of an excess of D_2O.[26] The amide protons of the central unit protrude into the helix cavity and hydrogen bond to water, and are fully exchanged within 3 h. For comparison, the second amide protons from the center of the sequence are only partially exchanged after 24 h (< 87 %), and the most peripheral amides show no sign of exchange after 4 days.

When a sample of **1** in $CDCl_3$ "from the bottle"—that is not specially dried—is cooled down, the signal of the central amide protons progressively shifts downfield (to $\delta = 9.73$ ppm at −40 °C), similar to the situation when excess water is added to the solution at room temperature (Figure 3b). The binding of water is apparently favored upon cooling. Cooling also causes a broadening of the signal of residual water in the solvent which then separates into two signals at $\delta = 4.44$ ppm and $\delta = 1.81$ ppm (Figure 4). The signal at higher field is intense when the sample is wet and shifts downfield as the temperature decreases, thus suggesting that it corresponds to

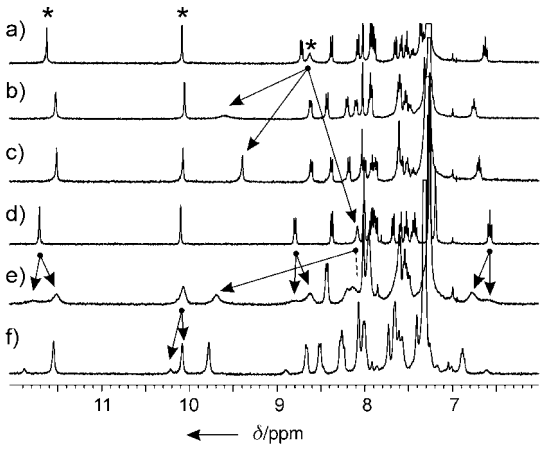

Figure 3. Part of the 400 MHz ^{1}H NMR spectra of **1** showing the amide and aromatic resonances: a) in $CDCl_3$ at 25 °C; b) in $CDCl_3$ at −20 °C; c) in "wet"[26] $CDCl_3$ at 25 °C; d) in "dried"[25] $CDCl_3$ at 25 °C, e) in "dried"[25] $CDCl_3$ at −20 °C; f) in "dried"[25] $CDCl_3$ at −50 °C. The asterisks indicate the resonances of the amide protons. The arrows indicate some corresponding signals.

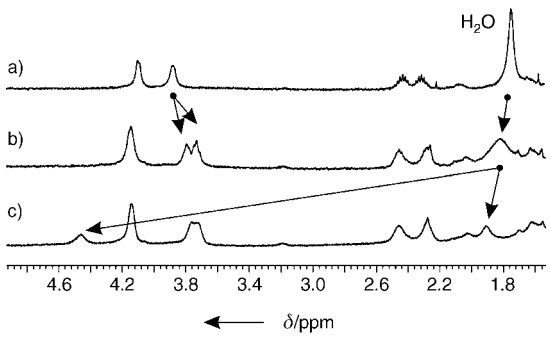

Figure 4. Part of the 400 MHz ^{1}H NMR spectra of **1** in $CDCl_3$ showing alkyl and water resonances: a) at 25 °C; b) at −30 °C; c) at −55 °C. The arrows link corresponding signals.

 © 2005 Wiley-VCH Verlag GmbH & Co. KGaA, Weinheim

free water. The signal at lower field has an integration corresponding to two protons and its position changes very little with temperature. These signals are not seen when the solution is washed with D_2O. A NOESY spectrum recorded at −55 °C shows strong correlations corresponding to exchange phenomena and/or NOE interactions between the central amide NH protons which point towards the capsule cavity and the two signals of water at $\delta = 4.44$ and $\delta = 1.81$ ppm (see the Supporting Information). However, the two other types of amide protons show no such correlations. All these data are consistent with the assignment of the signal at $\delta = 4.44$ ppm to a molecule of water bound inside the helix cavity. Such a water molecule would be surrounded by polar amide groups, nitro groups, and endocyclic pyridine and quinoline nitrogen atoms which would result in a downfield shift of the signal of the bound water protons. As an indication of the polarity of the environment in the capsule, the chemical shift of $H_2O \subset \mathbf{1}$ is similar to the chemical shift of H_2O in D_2O. The binding constant of water by the capsule at room temperature is estimated to be of the order of 150 $L\,mol^{-1}$ from the chemical shift variations of the NMR signals of the amide protons and integration of the water signal.

Slow exchange of the water molecule on the NMR timescale is consistent with the diastereotopic pattern observed at low temperature for the signal of the CH_2 group of one isobutyl sidechain (signals at $\delta = 3.8$ ppm in Figure 4). The equilibrium between the right-handed and the left-handed helices, and thus the opening of the capsule, is slowed down. Such a slow exchange of the water molecule at low temperature is in sharp contrast with the behavior of oligoamides of diaminopyridine and pyridinedicarboxylic acid described previously and which do not bear quinoline end caps.[17] These helical oligomers were also shown to bind water in solution in their hollow,[17,18] but the exchange of water remains fast on the NMR timescale, even at temperatures as low as −55 °C. The quinoline end caps in oligomer **1** seem to be critical in slowing down the binding and release of the water molecule.

We were intrigued by the fact that bound water and free water are in slow exchange on the NMR timescale at low temperature, whereas no splitting of the signals of the capsule occurred; thus the filled capsule appears to be in fast exchange with the empty capsule. We attribute this discrepancy to the presence of a large excess of water in these experiments, which causes the saturation of the capsule at low temperature: most capsules are occupied and the small portion of empty capsules are rapidly filled because of the large excess of water. We thus measured the NMR spectra after having eliminated as much water as possible.[25] Upon cooling the solution we observed a broadening of the amide and of several aromatic signals of the capsule which split into two sets of signals having identical chemical shifts to those of the empty capsule, and to those of the full capsule, respectively (Figure 3 d–f). The signals of the empty and full capsule can thus be distinguished at low water content, although the full capsule remains the major species.

The aim of this study was to illustrate a new concept for creating molecular closed shells around a cavity that can bind to molecular guests. Ongoing research includes the preparation of more stable capsules that would release guests at even lower rates, and of larger capsules that could accommodate larger guests or more than one guest.

Received: December 10, 2004
Published online: February 23, 2005

Keywords: helical structures · host–guest systems · molecular recognition · structure elucidation · supramolecular chemistry

[1] For recent reviews see: a) R. Warmuth, J. Yoon, *Acc. Chem. Res.* **2001**, *34*, 95–105; b) M. Fujita, K. Umemoto, M. Yoshizawa, N. Fujita, T. Kusukawa, K. Biradha, *Chem. Commun.* **2001**, 509–518; c) S. Russel Seidel, P. J. Stang, *Acc. Chem. Res.* **2002**, *35*, 972–983; d) F. Hof, S. L. Craig, C. Nuckolls, J. Rebek, Jr., *Angew. Chem.* **2002**, *114*, 1556–1578, *Angew. Chem. Int. Ed.* **2002**, *41*, 1488–1508; e) L. C. Palmer, J. Rebek, Jr., *Org. Biomol. Chem.* **2004**, 3051–3059.

[2] D. J. Cram, M. E. Tanner, R. Thomas, *Angew. Chem.* **1991**, *103*, 1048–1051; *Angew. Chem. Int. Ed. Engl.* **1991**, *30*, 1024–1027; R. Warmuth, *Angew. Chem.* **1997**, *109*, 1406–1409; *Angew. Chem. Int. Ed. Engl.* **1997**, *36*, 1347–1350; M. Yoshisawa, T. Kusukawa, M. Fujita, K. Yamaguchi, *J. Am. Chem. Soc.* **2000**, *122*, 6311–6312.

[3] D. J. Cram, S. Karbach, Y. H. Kim, L. Baczynskyj, G. W. Kalleymen, *J. Am. Chem. Soc.* **1985**, *107*, 2575–2576; L. Garel, J.-P. Dutasta, A. Collet, *Angew. Chem.* **1993**, *105*, 1249–1251; *Angew. Chem. Int. Ed. Engl.* **1993**, *32*, 1169–1171; P. Timmerman, W. Verboom, F. C. J. M. van Veggel, D. N. Reinhoudt, *Angew. Chem.* **1994**, *106*, 1313–1315; *Angew. Chem. Int. Ed. Engl.* **1994**, *33*, 1292–1295.

[4] D. M. Rudkevich, G. Hilmersson, J. Rebek, Jr., *J. Am. Chem. Soc.* **1998**, *120*, 12216–12225; J. L. Atwood, A. Szumna, *J. Am. Chem. Soc.* **2002**, *124*, 10646–10647.

[5] B. C. Hamann, K. D. Shimizu, J. Rebek, Jr., *Angew. Chem.* **1996**, *108*, 1425–1427; *Angew. Chem. Int. Ed. Engl.* **1996**, *35*, 1326–1329; O. Mogck, V. Böhmer, W. Vogt, *Tetrahedron* **1996**, *52*, 8489–8496; J. J. Gonzàlez, R. Ferdani, E. Albertini, J. M. Blasco, A. Arduini, A. Pochini, P. Prados, J. D. Mendoza, *Chem. Eur. J.* **2000**, *6*, 73–80.

[6] R. Meissner, J. Rebek, Jr., J. de Mendoza, *Science* **1995**, *270*, 1485–1488.

[7] F. Hof, C. Nuckolls, S. L. Craig, T. Martin, J. Rebek, Jr., *J. Am. Chem. Soc.* **2000**, *122*, 10991–10996.

[8] D. L. Caulder, R. E. Powers, T. N. Parac, K. N. Raymond, *Angew. Chem.* **1998**, *110*, 1940–1943; *Angew. Chem. Int. Ed.* **1998**, *37*, 1840–1843.

[9] T. Kusukawa, M. Fujita, *Angew. Chem.* **1998**, *110*, 3327–3329; *Angew. Chem. Int. Ed.* **1998**, *37*, 3142–3144.

[10] L. R. MacGillivray, J. L. Atwood, *Nature* **1997**, *389*, 469–472.

[11] J. M. C. A. Kerckhoffs, F. W. B. van Leeuwen, A. L. Spek, H. Kooijman, M. Crego-Calama, D. N. Reinhoudt, *Angew. Chem.* **2003**, *115*, 5895–5900; *Angew. Chem. Int. Ed.* **2003**, *42*, 5717–5722.

[12] To the best of our knowledge, helical capsules have not yet been reported, but it is interesting to note that helical guests have been encapsulated: A. Scarso, L. Trembleau, J. Rebek, Jr., *Angew. Chem.* **2003**, *115*, 5657–5660; *Angew. Chem. Int. Ed.* **2003**, *42*, 5499–5502.

[13] B. M. Burkhart, N. Li, D. A. Langs, W. A. Pangborn, W. L. Duax, *Proc. Natl. Acad. Sci. USA* **1998**, *95*, 12950–12955; B. M. Burkhart, R. M. Gassman, D. A. Langs, W. A. Pangborn, W. L. Duax, V. Pletnev, *Biopolymers* **1999**, *51*, 129–144.

[14] R. B. Prince, S. A. Barnes, J. S. Moore, *J. Am. Chem. Soc.* **2000**, *122*, 2758–2762; T. Nishinaga, A. Tanatani, O. Keuchan, J. S.

 © 2005 Wiley-VCH Verlag GmbH & Co. KGaA, Weinheim

Moore, *J. Am. Chem. Soc.* **2002**, *124*, 5934 – 5935; A. Tanatani, T. S. Hughes, J. S. Moore, *Angew. Chem.* **2002**, *114*, 335 – 338; *Angew. Chem. Int. Ed.* **2002**, *41*, 325 – 328; M. T. Stone, J. S. Moore, *Org. Lett.* **2004**, *6*, 469 – 472.

[15] M. Inouye, M. Waki, H. Abe, *J. Am. Chem. Soc.* **2004**, *126*, 2022 – 2027.

[16] J.-L. Hou, X.-B. Shao, G.-J. Chen, Y.-X. Zhou, X.-K. Jiang, Z.-T. Li, *J. Am. Chem. Soc.* **2004**, *126*, 12386 – 12394; J.-L. Hou, M.-X. Jia, X.-K. Jiang, Z.-T. Li, G.-J. Chen, *J. Org. Chem.* **2004**, *69*, 6228 – 6237.

[17] V. Berl, I. Huc, R. G Khoury, J.-M. Lehn, *Chem. Eur. J.* **2001**, *7*, 2810 – 2820.

[18] a) I. Huc, V. Maurizot, H. Gornitzka, J.-M. Léger, *Chem. Commun.* **2002**, 578 – 579; b) V. Maurizot, J.-M. Léger, P. Guionneau, *Russ. Chem. Bull. Int. Ed.* **2004**, *53*, 1572 – 1576.

[19] B. Gong, *Chem. Eur. J.* **2001**, *7*, 4336 – 4342; B. Gong, H. Zeng, J. Zhu, L. Yuan, Y. Han, S. Cheng, M. Furukawa, R. D. Parra, A. Y. Kovalevsky, J. L. Mills, E. Skrzypczak-Jankun, S. Martinovic, R. D. Smith, C. Zheng, T. Szyperski, X. C. Zeng, *Proc. Natl. Acad. Sci. USA* **2002**, *99*, 11583 – 11588.

[20] I. Huc, *Eur. J. Org. Chem.* **2004**, 17 – 29.

[21] H. Jiang, J.-M. Léger, I. Huc, *J. Am. Chem. Soc.* **2003**, *125*, 3448 – 3449; H. Jiang, J.-M. Léger, C. Dolain, P. Guionneau, I. Huc, *Tetrahedron* **2003**, *59*, 8365 – 8374.

[22] Physical data for **1**: ^{1}H NMR (400 MHz, $CDCl_3$, 25 °C, solvent as internal reference): $\delta = 11.62$ (s, 2H), 10.08 (s, 2H), 8.72 (d, $^3J(H,H) = 7.4$ Hz, 2H), 8.62 (s, 2H), 8.38 (d, $^3J(H,H) = 7.4$ Hz, 2H), 8.08 (d, $^3J(H,H) = 7.7$ Hz, 2H), 8.02 (s, 2H), 7.94–7.87 (m, 6H), 7.65 (d, $^3J(H,H) = 7.3$ Hz, 2H), 7.58 (d, $^3J(H,H) = 7.3$ Hz, 2H), 7.52 (t, $^3J(H,H) = 7.7$ Hz, 2H), 7.35–7.25 (m, 7H), 6.62 (t, $^3J(H,H) = 7.7$ Hz, 2H), 5.43 (s, 2H), 4.06 (d, $^3J(H,H) = 5.3$ Hz, 4H), 3.84 (s, 4H), 2.39–2.36 (m, 4H), 1.27 (d, $^3J(H,H) = 6.8$ Hz, 12H), 1.17 ppm (d, $^3J(H,H) = 6.8$ Hz, 12H); ^{13}C NMR (100 MHz, $CDCl_3$, 25 °C): $\delta = 162.32$, 161.94,161.36, 160.40, 153.03, 149.52, 148.84, 148.60, 148.49, 144.19, 140.16, 139.72, 137.17, 133.06, 128.64, 128.55, 127.58, 127.48, 127.01, 126.12, 123.49, 123.11, 121.02, 117.61, 116.23, 111.49, 110.26, 109.19, 98.99, 98.81, 74.87, 74.73, 70.58, 29.35, 29.01, 27.98, 27.69, 19.10, 18.97 ppm; IR (KBr): $\tilde{\nu} = 3155$, 2965, 2254, 1794, 1527, 1471, 1383, 1262, 1096, 1013, 908 cm^{-1}; TOF-MS: *m/z:* 1484.44 $[M+H]^+$, 1506.44 $[M+Na]^+$, 1522.44 $[M+K]^+$.

[23] Crystal data: **1:** $C_{80}H_{73}N_{15}O_{15}(C_7H_8)_{1.5}(H_2O)$, $M_r = 1640.75$, crystal size $0.15 \times 0.10 \times 0.10$, monoclinic, space group $P\bar{1}$, $Z = 2$, $a = 16.9588(12)$, $b = 17.2292(10)$, $c = 17.5449(10)$ Å, $\alpha = 114.178(1)$, $\beta = 92.719(1)$, $\gamma = 116.029(1)$°, $V = 4037.7(4)$ Å^3, $\rho_{calcd} = 1.350$ mg m^{-3}, $T = 193(2)$ K, $\theta_{min} = 2.87$, $\theta_{max} = 68.31$, $\lambda = 1.54180$ Å; $Cu_{K\alpha}$, $\mu(Cu_{K\alpha}) = 0.775$ mm^{-1}. Data collected on a Rigaku MM007-Rapid R-AXIS diffractometer. Of 71512 reflections measured, 14143 were unique ($R_{int} = 0.0851$), 8827 with $I > 2\sigma(I)$, 1093 parameters in final refinement. The structure was solved by direct methods and refined by full-matrix least-squares on F^2 (SHEXLTL version 6.12). The final R indices were R_1 ($I > 2\sigma(I)$) = 0.0738, $wR_2(F^2) = 0.2165$ (all data). CCDC 258147 contains the supplementary crystallographic data for this paper. These data can be obtained free of charge from the Cambridge Crystallographic Data Centre via www.ccdc.cam.ac.uk/data_request/cif.

[24] The springlike extension of related oligomers has been characterized in solution upon the formation of double-helical dimers; for a recent report see: H. Jiang, V. Maurizot, I. Huc, *Tetrahedron* **2004**, *60*, 10029 – 10038.

[25] Oligomer **1** was dissolved in dry toluene and water was removed azeotropically by distillation before evaporation under vacuum. $CDCl_3$ was filtered through activated alumina just before sample preparation.

[26] One drop added to 500 μL of $CDCl_3$.

 © 2005 Wiley-VCH Verlag GmbH & Co. KGaA, Weinheim

Porous Materials

Highly Porous, Homochiral Metal–Organic Frameworks: Solvent-Exchange-Induced Single-Crystal to Single-Crystal Transformations**

*Chuan-De Wu and Wenbin Lin**

Porous metal–organic frameworks (MOFs) have recently received much attention owing to their potential applications in several technological areas such as gas storage, separation, and heterogeneous catalysis.[1] The modular nature of MOFs means they are readily tunable and, as a result, the synthesis of ideal, heterogenized single-site catalysts can be envisioned from porous MOFs by a judicious choice of metal-connecting nodes and/or bridging ligands.[2] Homochiral, porous MOFs are particularly attractive candidates as heterogeneous asymmetric catalysts for the economical production of optically active organic compounds due to the lack of chiral, inorganic zeolites.[3] Although we and others have recently provided preliminary evidence for the potential utility of homochiral, porous MOFs in enantioselective separation and catalysis,[4,5] several key issues remain to be addressed before practical applications of such materials can be realized. First, homochiral MOFs with permanent porosity are still extremely rare, even though there are now numerous reported examples of porous, achiral MOFs with extremely high surface areas.[6] Second, as yet there has been no study on the structural integrity of homochiral MOFs under catalytic conditions. Herein we report the design and synthesis of highly porous, homochiral solids based on 1D MOFs and their single-crystal to single-crystal transformations induced by solvent exchange. Our results suggest that the framework integrity of porous, homochiral MOFs can be maintained under typical asymmetric catalytic reaction conditions.

Colorless hexagonal crystals of $[CdL_2(ClO_4)_2]\cdot 11\,EtOH\cdot 6\,H_2O$ (**1**), where L is (*S*)-2,2′-diethoxy-1,1′-binaphthyl-6,6′-bis(4-vinylpyridine), were obtained by heating a mixture of $Cd(ClO_4)_2\cdot 6\,H_2O$ and L in DMF/*o*-$C_6H_4Cl_2$/EtOH at 70 °C for two days.[7] A single-crystal X-ray diffraction study revealed that **1** crystallizes in the chiral hexagonal space group $P6_222$ and adopts a 1D polymeric chain structure (Figure 1).[8] The adjacent Cd^{II} centers are linked by two L ligands to form 46-membered macrocycles with a Cd–Cd distance of 19.333(1) Å. The rhombic macrocycle has an opening of approximately 19.3×19.3 Å^2. Each

[*] Dr. C.-D. Wu, Prof. W. Lin
Department of Chemistry, CB#3290
University of North Carolina
Chapel Hill, NC 27599 (USA)
Fax: (+1) 919-962-2388
E-mail: wlin@unc.edu

[**] We acknowledge financial support from NSF. W.L. is an Alfred P. Sloan Fellow, an Arnold and Mabel Beckman Young Investigator, a Cottrell Scholar of Research Corp, and a Camille Dreyfus Teacher-Scholar.

Supporting information for this article is available on the WWW under http://www.angewandte.org or from the author.

 © 2005 Wiley-VCH Verlag GmbH & Co. KGaA, Weinheim DOI: 10.1002/anie.200462711

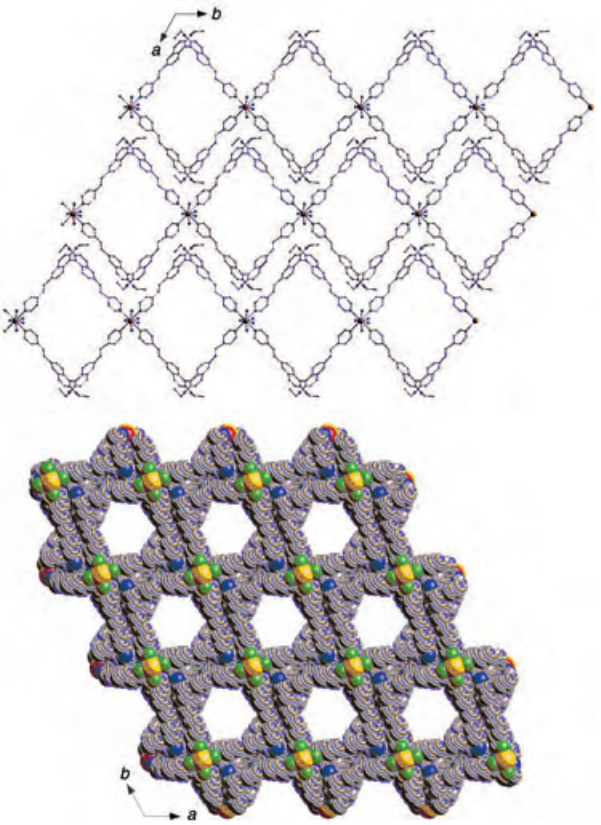

Figure 1. A view of the packing of the 1D polymeric chains in the *ab* plane (top) and a space-filling representation of **1** with chiral, 1D hexagonal channels (bottom).

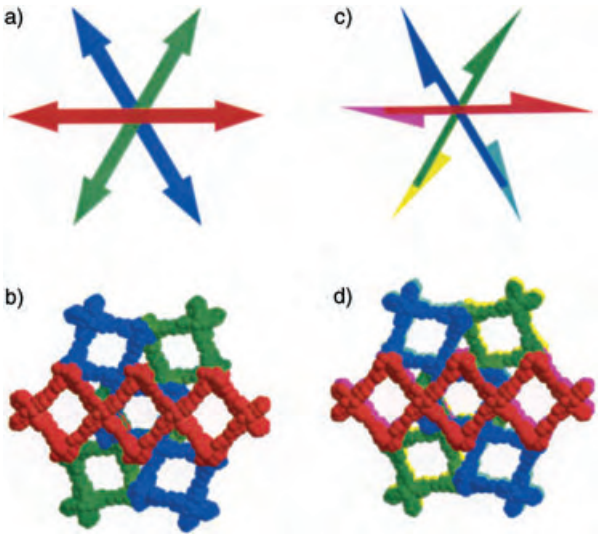

Figure 2. Schematic (a) and space-filling (b) views of the 6_2-helical arrangement of the 1D polymeric chains of **1** along the *c* axis. Schematic (c) and space-filling (d) views of the 6_1-helical arrangement of the 1D polymeric chains of **2a** along the *c* axis.

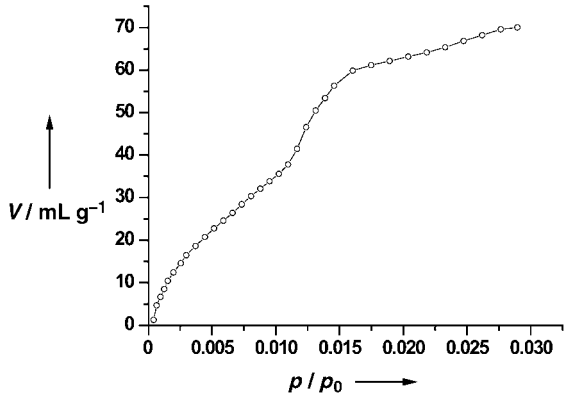

Figure 3. CO_2 gas-adsorption isotherm for an evacuated sample of **1** at 273 K.

Cd^{II} center adopts a slightly distorted octahedral environment by coordinating to four N atoms from four L ligands in the equatorial positions and two O atoms of two crystallographically disordered ClO_4^- ions in the axial positions. All the 1D chains lie parallel to each other in the *ab* plane due to interdigitation (Figure 1). These layer structures of **1** are stabilized by strong π···π stacking interactions (the nearest carbon-to-carbon separation is 3.360 Å between neighboring molecules). The 6_2 operation generates an …ABCABC… stacking pattern for all the 1D chains along the *c* axis, as shown in Figure 2. As expected, the 1D chains in the adjacent layers along the *c* axis are rotated by 120° with respect to each other to create chiral, 1D pseudo-hexagonal channels of 16.77 Å in dimension. There are no significant interactions between adjacent layers. Calculations with PLATON show that the effective volume for the inclusion is 4900.6 $Å^3$ per unit cell, which is 53.6% of the crystal volume.[9] TGA analysis indicated that a weight loss of 30.4% occurs between 20 and 194 °C, which corresponds to the loss of all the ethanol and water molecules (expected 30.4%).

We measured the CO_2 gas-sorption isotherm of **1** at 273 K to evaluate its permanent porosity. A sample of **1** was evacuated at 50 °C for 6 h under vacuum to remove the included solvent molecules before CO_2-adsorption measurements were attempted. As shown in Figure 3, a significant increase in the amount of CO_2 gas adsorbed by **1** was observed as the pressure of CO_2 increased, thus indicating the rapid diffusion of CO_2 molecules into the channels. The microporous surface area was calculated by fitting the adsorption data to the Dubinin–Radushkevich (DR) equation. The microporous surface area of an evacuated sample of **1** is 1096 $m^2 g^{-1}$, while the microporous volume is 0.47 $mL g^{-1}$. This level of porosity is among the highest reported for homochiral MOFs.

Whereas most applications of MOFs require only the presence of permanent porosity, the framework structures of homochiral MOFs need to be maintained in the presence of exchangeable solvents if they are to find applications in heterogeneous asymmetric catalysis. We therefore examined the framework stability of **1** during solvent removal and exchange processes. The X-ray diffraction pattern of **1** disappeared almost completely upon exposing the crystal to air for 30 min at room temperature. Such a distortion of the long-range order of homochiral MOFs upon solvent loss has

 © 2005 Wiley-VCH Verlag GmbH & Co. KGaA, Weinheim

previously been observed in chiral, lamellar metal phosphonates.[10]

Interestingly, however, the X-ray diffraction patterns could be readily regenerated by submerging amorphous evacuated samples of **1** in either EtOH or benzene for 30 min. We also noticed that many crystals of **1** fractured into smaller pieces (while maintaining the same hexagonal morphology) after being submerged in EtOH or benzene for 30 min. In order to rule out the possibility that **1** may have undergone recrystallization due to the dissolution of the building blocks in EtOH or benzene, we carried out the solvent removal and exchange processes by exposing samples of **1** to air, EtOH vapor, or benzene vapor. After exposure of a crystal of **1** to benzene vapor for 12 h, no change in the morphology, size, or transparency of the crystal was observed under a microscope. An X-ray diffraction study, however, revealed that the benzene-exposed crystal (**2a**) has a formula of $[CdL_2(ClO_4)_2]\cdot 2\,C_6H_6\cdot 7\,EtOH\cdot 4\,H_2O$ as a result of the exchange of some of the ethanol and water guest molecules by benzene molecules. The unit-cell size of the crystal doubles as a result of the doubling of the *c*-axis in **2a**, and the space group of **2a** is $P6_122$ instead of $P6_222$ for **1** (Table 1). The most

Table 1: Selected crystallographic data for **1**, **2a**, **2b**, **3**, **2′**, and **1′**.

Compound	Space group	*a* [Å]	*c* [Å]	*V* [Å^3]	Solvent content[a]
1	$P6_222$	19.333	28.252	9145.1	$11\,EtOH\cdot 6\,H_2O$
2a	$P6_122$	19.442	55.939	18312.0	$2\,C_6H_6\cdot 7\,EtOH\cdot 4\,H_2O$
2b	$P6_122$	19.438	55.937	18304.3	$4\,C_6H_6\cdot 3\,EtOH\cdot 4\,H_2O$
3	$P6_222$	19.477	28.277	9289.8	$6\,C_6H_6\cdot H_2O$
2′	$P6_122$	19.431	55.968	18300.7	$2\,C_6H_6\cdot 7\,EtOH\cdot 2\,H_2O$
1′	$P6_222$	19.254	28.326	9094.2	$11\,EtOH\cdot 2\,H_2O$

[a] The solvent content is given per formula unit of $[CdL_2(ClO_4)_2]$.

significant structural difference between **1** and **2a** lies in the relative orientation of the ethoxy groups of the ligands L and the coordinating perchlorate groups, and the relative orientation of the 1D polymeric chains. As a result of these changes, the 1D polymeric chains stack in an …ABCDEFABCDEF… pattern along the *c* axis in **2a** instead of the …ABCABC… pattern in **1** (Figure 2). Unlike **1**, which has all the macrocycle planes parallel to the *ab* plane, the macrocycle planes in **2a** are slightly tilted away (by 0.2°) from the *ab* plane.[11]

Exposure of **2a** to benzene vapor for another 24 h caused more of the ethanol guest molecules to be replaced by benzene molecules, which results in a new crystal of the formula $[CdL_2(ClO_4)_2]\cdot 4\,C_6H_6\cdot 3\,EtOH\cdot 4\,H_2O$ (**2b**). Complex **2b** is structurally very similar to **2a** except that different numbers of solvent molecules are included. Further exposure of **2b** to benzene vapor resulted in complete replacement of EtOH by benzene to afford a new crystal of the formula $[CdL_2(ClO_4)_2]\cdot 6\,C_6H_6\cdot H_2O$ (**3**). Interestingly, the space group of the resulting crystal **3** is now $P6_222$ again and the packing of the 1D polymeric chains in **3** is essentially identical to that of **1**. The only difference between **1** and **3** lies in the inclusion of different solvent molecules. We also prepared samples of **3** by an entirely different route by slow diffusion of a solution of L in benzene into a solution of $Cd(ClO_4)_2$ in methanol.

Because the solvent-exchange processes are carried out in the presence of solvent vapors (with no condensed liquids), we believe that no dissolution of the MOFs occurs. The solvent exchange and accompanying structural transformation is thus a single-crystal to single-crystal process. Although several examples of single-crystal to single-crystal transformations were reported for achiral MOFs very recently,[12] this is the first example where chiral MOFs exhibit a single-crystal to single-crystal structural transformation induced by solvent exchange.

The structural transformation **1**⇔**2**⇔**3** is totally reversible. For example, a crystal of **3** can be transformed into **2′** and then **1′** by exposing **3** to ethanol vapor for varying amounts of time; the corresponding structures were verified by single-crystal X-diffraction studies. To eliminate the ambiguity of the solvent identities from X-ray diffraction studies, we also monitored the solvent-exchange processes by ^{1}H NMR spectroscopy. With an acetone internal standard and CD_2Cl_2 as the solvent, we determined that a freshly prepared sample of **1** contains 11 EtOH molecules per formula unit, which is consistent with the X-ray diffraction results (see Supporting Information). After exposure of **1** to benzene vapor for 12 h, crystals of **2** contain two benzene and 6.4 EtOH molecules, as determined by NMR integrations. Further exposure of **2** to benzene vapor for 48 h resulted in complete exchange of EtOH with benzene guest molecules. The reverse solvent-exchange processes **3**→**2′**→**1′** were also confirmed by ^{1}H NMR spectroscopy.

In summary, we have successfully constructed homochiral MOFs based on 1D polymeric chains. As schematically summarized in Figure 4, removal of the included solvent molecules from these MOFs leads to homchiral solids with permanent porosity and framework integrity. These homochiral MOFs undergo interesting reversible single-crystal to single-crystal structural transformations that are induced by solvent exchange. These results lend support to the notion that the framework structures of homochiral MOFs can be maintained during potential heterogeneous asymmetric catalytic reactions, and that true heterogeneous asymmetric catalysts can therefore be built from homochiral MOFs.

Experimental Section

1: A mixture of $Cd(ClO_4)_2\cdot 6\,H_2O$ (4.2 mg, 0.01 mmol), L (5.5 mg, 0.01 mmol), $CHCl_3$ (2 mL), *o*-$C_6H_4Cl_2$ (1 mL), and EtOH (1 mL) in a small, capped vial was heated at 70 °C for two days. Colorless crystals of **1** were isolated by filtration, washed with EtOH and Et_2O, and dried at room temperature. Yield: 5.8 mg (57.3% based on L). Elemental analysis (%) calcd. for **1**: C 58.2, H 7.07, N 2.77; found: C 60.4, H 4.24, N 3.43 (microanaylsis results are not informative owing to the ease of solvent loss). IR (KBr pellet): $\tilde{\nu}$ = 3462 (m), 3251 (w), 3085 (w), 2978 (w), 1605 (s), 1506 (m), 1468 (m), 1383 (w), 1327 (w), 1244 (m), 1203 (w), 1173 (w), 1108 (s), 1050 (m), 963 (w), 920 (w), 862 (w), 818 (w), 788 (w), 624 (m), 564 (w), 518 cm^{-1} (w).

NMR studies: A freshly prepared sample of **1** was exposed to benzene vapor. After 12 h, 13.2 mg of the benzene-exposed sample (**2**) was loaded into an NMR tube. A defined amount of acetone (ca. 1 μL) was added as the internal standard, followed by the solvent CD_2Cl_2. The absolute amounts of EtOH and benzene were deter-

 © 2005 Wiley-VCH Verlag GmbH & Co. KGaA, Weinheim

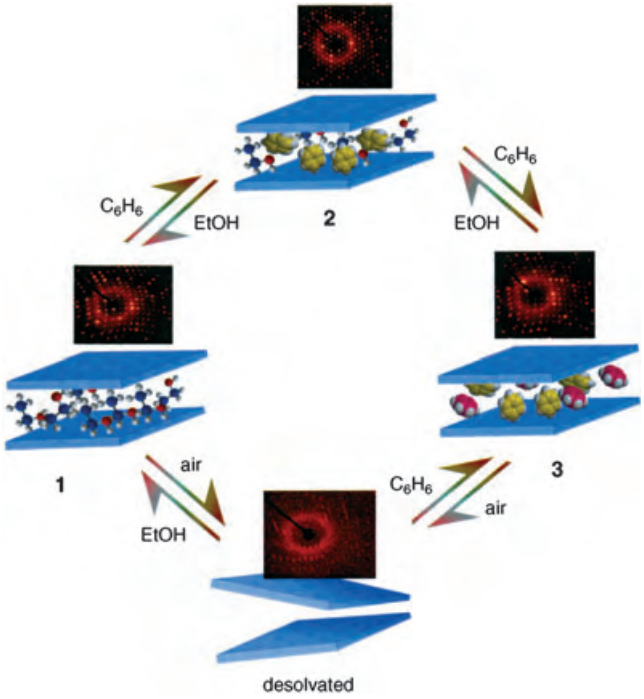

Figure 4. Schematic representation of the reversible single-crystal to single-crystal and single-crystal to amorphous to single-crystal transformation processes between **1**, **2**, and **3**.

mined by integration of the signature peaks. Similar NMR studies were carried out on **3** and samples of **1** and **2** that were prepared by exchanging the benzene guest molecules of **3**.

Received: November 24, 2004
Published online: February 23, 2005

Keywords: chirality · crystal engineering · functional materials · heterogeneous catalysis · metal–organic frameworks

[1] a) S. Kitagawa, R. Kitaura, S.-i. Noro, *Angew. Chem.* **2004**, *116*, 2388 – 2430; *Angew. Chem. Int. Ed.* **2004**, *43*, 2334 – 2375; b) B. Moulton, M. Zaworotko, *Chem. Rev.* **2001**, *101*, 1629 – 1658; c) M. Eddaoudi, D. B. Moler, H. Li, B. Chen, T. M. Reineke, M. O'Keeffe, O. M. Yaghi, *Acc. Chem. Res.* **2001**, *34*, 319 – 330; d) O. R. Evans, W. Lin, *Acc. Chem. Res.* **2002**, *35*, 511 – 522; e) N. G. Pschirer, D. M. Ciurtin, M. D. Smith, U. H. F. Bunz, H. C. zur Loye, *Angew. Chem.* **2002**, *114*, 603 – 605; *Angew. Chem. Int. Ed.* **2002**, *41*, 583 – 585; f) M. Fujita, Y. J. Kwon, S. Washizu, K. Ogura, *J. Am. Chem. Soc.* **1994**, *116*, 1151 – 1152.

[2] a) X. Zhao, B. Xiao, A. J. Fletcher, K. M. Thomas, D. Bradshaw, M. J. Rosseinsky, *Science* **2004**, *306*, 1012 – 1014; b) M. Oh, G. B. Carpenter, D. A. Sweigart, *Acc. Chem. Res.* **2004**, *37*, 1 – 11; c) G. S. Papaefstathiou, L. R. MacGillivray, *Coord. Chem. Rev.* **2003**, *246*, 169 – 184.

[3] B. Kesanli, W. Lin, *Coord. Chem. Rev.* **2003**, *246*, 305 – 326.

[4] a) J. S. Seo, D. Whang, H. Lee, S. I. Jun, J. Oh, Y. J. Jeon, K. Kim, *Nature* **2000**, *404*, 982; b) A. Hu, H. L. Ngo, W. Lin, *J. Am. Chem. Soc.* **2003**, *125*, 11490 – 11491; c) A. Hu, H. L. Ngo, W. Lin, *Angew. Chem.* **2003**, *115*, 6182 – 6185; *Angew. Chem. Int. Ed.* **2003**, *42*, 6000 – 6003; d) D. Bradshaw, T. J. Prior, E. J. Cussen, J. B. Claridge, M. J. Rosseinsky, *J. Am. Chem. Soc.* **2003**, *125*, 6106 – 6114.

[5] Related chiral hydrogen-bonded networks have also been reported: a) R. Custelcean, M. D. Ward, *Angew. Chem.* **2002**, *114*, 1800 – 1804; *Angew. Chem. Int. Ed.* **2002**, *41*, 1724 – 1728; b) P. Grosshans, A. Jouaiti, V. Bulach, J.-M. Planeix, M. W. Hosseini, J.-F. Nicoud, *Chem. Commun.* **2003**, 1336 – 1337.

[6] a) H. K. Chae, D. Y. Siberio-Perez, J. Kim, Y. Go, M. Eddaoudi, A. J. Matzger, M. O'Keeffe, O. M. Yaghi, *Nature* **2004**, *427*, 523 – 527; b) S. L. James, *Chem. Soc. Rev.* **2003**, *32*, 276 – 288; c) C. Janiak, *Dalton Trans.* **2003**, 2781 – 2804.

[7] The synthesis of L has been reported previously: Y. Cui, S. J. Lee, W. Lin, *J. Am. Chem. Soc.* **2003**, *125*, 6014 – 6015.

[8] X-ray single-crystal diffraction data for all the samples were collected on a Siemens SMART CCD diffractometer at 173 K. The data sets were corrected with the SADABS program (G. M. Sheldrick, SADABS, Siemens Analytical X-ray Instrument Division, Madison, WI, **1995**). The structures were solved by direct methods, and refined by full-matrix least-squares methods with the SHELXTL-97 program package (G. M. Sheldrick, SHELXTL-97, Program for Structure Refinement, University of Göttingen, Göttingen (Germany), **1998**). Selected crystallographic data are listed in Table 1; additional crystal data are given here. **1**: $Z=3$, $\rho_{calcd}=1.10\ g\,cm^{-3}$, $\mu(Mo_{K\alpha})=0.288\ mm^{-1}$, $R1=0.128$, $wR2=0.321$, Flack parameter = 0.06(12) and GOF = 1.12. **2a**: $Z=6$, $\rho_{calcd}=1.07\ g\,cm^{-3}$, $\mu(Mo_{K\alpha})=0.282\ mm^{-1}$, $R1=0.182$, $wR2=0.425$, Flack parameter = 0.1(1) and GOF = 1.08. **2b**: $Z=6$, $\rho_{calcd}=1.05\ g\,cm^{-3}$, $\mu(Mo_{K\alpha})=0.279\ mm^{-1}$, $R1=0.191$, $wR2=0.453$, Flack parameter = 0.06(12) and GOF = 1.06. **3**: $Z=3$, $\rho_{calcd}=1.02\ g\,cm^{-3}$, $\mu(Mo_{K\alpha})=0.271\ mm^{-1}$, $R1=0.084$, $wR2=0.201$, Flack parameter = −0.01(6) and GOF = 1.08. **2′**: $Z=6$, $\rho_{calcd}=1.05\ g\,cm^{-3}$, $\mu(Mo_{K\alpha})=0.280\ mm^{-1}$, $R1=0.194$, $wR2=0.442$, Flack parameter = 0.04(12) and GOF = 1.12. **1′**: $Z=3$, $\rho_{calcd}=1.07\ g\,cm^{-3}$, $\mu(Mo_{K\alpha})=0.285\ mm^{-1}$, $R1=0.091$, $wR2=0.229$, Flack parameter = 0.05(8) and GOF = 1.17. The high $R1$ values for **2a**, **2b**, and **2′** are probably a result of their metastable nature, which can lead to less perfect single crystals. CCDC-256708 (**1**), -256709 (**1′**), -256710 (**2′**), -256711 (**2a**), -256712 (**2b**), and -256713 (**3**) contain the supplementary crystallographic data for this paper. These data can be obtained free of charge from The Cambridge Crystallographic Data Centre via www.ccdc.cam.ac.uk/data_request/cif.

[9] A. L. Spek, *PLATON, A Multipurpose Crystallographic Tool*, Utrecht University, Utrecht, The Netherlands, **2001**.

[10] O. R. Evans, H. L. Ngo, W. Lin, *J. Am. Chem. Soc.* **2001**, *123*, 10395 – 10396.

[11] The macrocycle plane is defined by the Cd atoms and the middle of the 1,1′-carbon atoms of the binaphthyl moiety. **2b** and **2′** have a tilt angle of 0.2° and 1.1°, respectively.

[12] a) D. N. Dybtsev, H. Chun, K. Kim, *Angew. Chem.* **2004**, *116*, 5143 – 5146; *Angew. Chem. Int. Ed.* **2004**, *43*, 5033 – 5036; b) C. Y. Su, A. M. Goforth, M. D. Smith, P. J. Pellechia, H. C. zur Loye, *J. Am. Chem. Soc.* **2004**, *126*, 3576 – 3586; c) H. J. Choi, M. P. Suh, *J. Am. Chem. Soc.* **2004**, *126*, 15844 – 15851; d) R. Matsuda, R. Kitaura, S. Kitagawa, Y. Kubota, T. C. Kobayashi, S. Horike, M. Takata, *J. Am. Chem. Soc.* **2004**, *126*, 14063 – 14070; e) E. Y. Lee, M. P. Suh, *Angew. Chem.* **2004**, *116*, 2858 – 2861; *Angew. Chem. Int. Ed.* **2004**, *43*, 2798 – 2801.

 © 2005 Wiley-VCH Verlag GmbH & Co. KGaA, Weinheim

Host–Guest Systems

A Two-in-One Crystal: Uptake of Two Different Guests into Two Distinct Channels of a Biporous Coordination Network

Osamu Ohmori, Masaki Kawano, and Makoto Fujita**

Coordination networks with well-defined microchannels hold great promise for a number of applications owing to guest adsorption, removal, and exchange behaviors in the channels.[1,2] In general, the channels formed in crystals are uniform and therefore inclusion phenomena in all the channels are identical. However, if two (or more) distinct channels exist in a crystal, they may take up two (or more) guests independently. Such biporous materials[3] make, for example, the simultaneous isolation or transportation of two different guests possible. Herein, we report the formation of two distinct large channels within a three-dimensional coordination network. These channels adsorb their own preferred guests from a mixture of two guests to form two independent columnar arrays of guests in the crystal. Since the guest uptake proceeds in a single-crystal-to-single-crystal fashion, we can observe all the processes by X-ray crystallographic analysis.

The coordination network discussed herein is composed of the tris(4-pyridyl)triazine ligand **1** and ZnI_2. Single crystals of $\{[(ZnI_2)_3(\mathbf{1})_2(\mathbf{2})]\cdot x\,(\text{nitrobenzene})\cdot y\,(\text{methanol})\}_z$ –(**3**; $x \approx 4$, $y \approx 2$) were grown from a triple-layered solution with a methanol solution (0.5 mL) of ZnI_2 (0.03 mmol) as the top layer, methanol (0.5 mL) as the middle layer, and a nitrobenzene/methanol solution (4:1, 5 mL) of ligand **1** (0.02 mmol) and triphenylene (**2**, 0.1 mmol) as the bottom layer. The crystals were isolated in 54% yield [Eq. (1)].

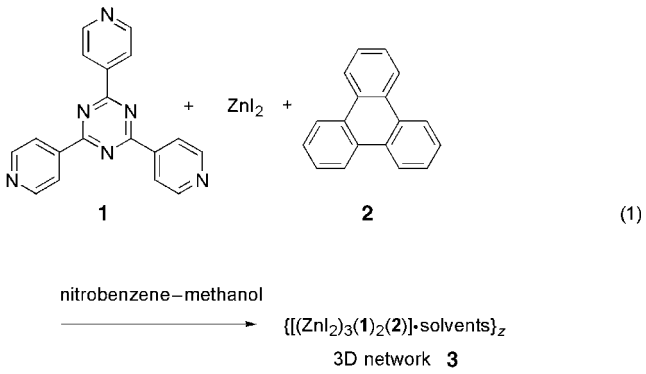

[*] O. Ohmori, Prof. Dr. M. Kawano, Prof. Dr. M. Fujita
Department of Applied Chemistry
School of Engineering
The University of Tokyo and
Genesis Research Institute, Inc.
Hongo, Bunkyo-ku, Tokyo 113-8656 (Japan)
Fax: (+81) 3-5841-7257
E-mail: mkawano@appchem.t.u-tokyo.ac.jp
mfujita@appchem.t.u-tokyo.ac.jp

Supporting information for this article is available on the WWW under http://www.angewandte.org or from the author.

Crystallographic analysis showed that the network has an interpenetrated structure (Figure 1a), in which triphenylene is tightly intercalated between two triazine ligands ($\mathbf{1}_A$ and $\mathbf{1}_B$; Figure 1b). An infinite aromatic stacking is observed, which presumably stabilizes the solid structure.

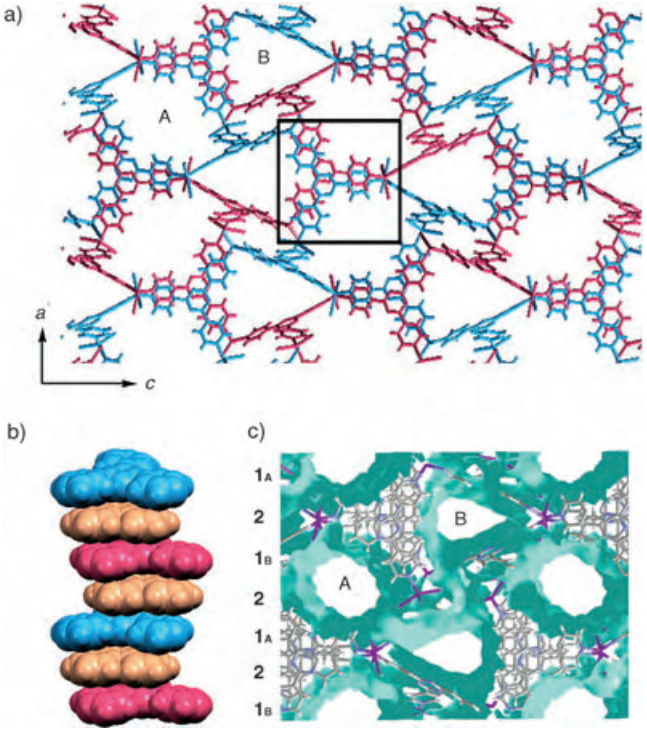

Figure 1. Crystal structure of **3**: a) view of the interpenetrated networks along the *b* axis; b) the infinite aromatic stacking between the ligands ($\mathbf{1}_A$ and $\mathbf{1}_B$) and triphenylene (**2**) at the inserted square in (a); c) a free-volume drawing showing the two distinct channels **A** and **B**.

Intercalated triphenylene is not replaced by common aromatic compounds under guest-exchange conditions because of this strong stacking. Therefore, triphenylene is best regarded as forming part of the host framework rather than being a guest. The strong binding of triphenylene is ascribed to a charge-transfer (CT) interaction between the layers. A broad CT absorption band was observed in the range 400–600 nm in the UV/Vis spectrum. Furthermore, calculations predicted an efficient in-phase overlap between the triphenylene HOMO and ligand LUMO (Figure 2).[4] In the absence of triphenylene, a 3D coordination network with a

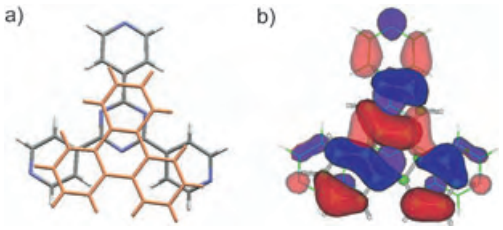

Figure 2. Structures showing a) π-π stacking between ligand **1** and triphenylene (**2**) in **3** (occupancy: 84%); b) superposition of the HOMO and the LUMO.

 © 2005 Wiley-VCH Verlag GmbH & Co. KGaA, Weinheim DOI: 10.1002/anie.200462201

different network topology is obtained,[2c,5] which is not converted to complex **3** under guest-exchange conditions with triphenylene.

The structure of complex **3** contains two distinct channels (**A** and **B**) within the framework. Channel **A** is roughly cylindrical and is mainly surrounded by the hydrogen atoms of infinitely stacked **1** and **2**. Channel **B**, however, is roughly trigonal prismatic, where two of the three walls are the π faces of ligand **1** and the third is the edges of **1** and **2** (Figure 1a,c). The approximate dimensions of the channels are 7.4 × 5.5 Å (channel A) and 7.3 × 5.5 Å (channel B). Their void occupancies are almost identical (ca. 20% for each).[6]

Surprisingly, the two channels take up their own preferred guests from a mixture: channels **A** of as-synthesized **3** are filled with nitrobenzene and methanol, which are considerably disordered and could not be fully located by crystallographic analysis, whereas channels **B** are filled with nitrobenzene (Figure 3a). Dipping crystals of **3** into a saturated cyclohexane solution of naphthalene at room temperature for two days caused channels **A** and **B** to be selectively filled with naphthalene and cyclohexane, respectively, to give guest-exchanged crystals of $\{[(ZnI_2)_3(\mathbf{1})_2(\mathbf{2})]\cdot x\,(\text{cyclohexane})\cdot y\,(\text{naphthalene})\}_z$ (**4**, $x \approx 1.3$ and $y \approx 2.3$; Figure 3b). Even after this guest exchange, high-quality diffraction data could be collected, and the structure converged to a final R_1 value of 0.052. The crystallographic analysis revealed the formation of columnar arrays of naphthalene (100% occupancy) and cyclohexane (82% occupancy) in channels **A** and **B**, respectively (Figure 3b). The geometry of the host framework, including intercalated triphenylene, remained almost unchanged despite the dramatic replacement of large molecules in the channels. The uptake of two different guests by the two channels was also observed for the azulene/cyclohexane pair: channels **A** and **B** selectively adsorbed azulene (100% occupancy) and cyclohexane (100% occupancy), respectively, to give **5** (Figure 3c).

Guest-exchange experiments with each individual guest showed the preference of the two channels for a specific guest: channel **A** prefers naphthalene whereas channel **B** prefers cyclohexane. Channel **A** was 50% filled with naphthalene to form a naphthalene/nitrobenzene 1:1 column when only naphthalene (nitrobenzene solution) was used, whereas channel **B** remained intact (**6**; Figure 3d). In contrast, guest exchange with cyclohexane led to the complete filling of channel **B** with cyclohexane (occupancy 100%) but only partial filling of channel **A** in compound **7** (occupancies: cyclohexane 64% and nitrobenzene 36%; Figure 3e).

Thermogravimetric (TG) analysis of a crystalline sample of **4** showed the release of guest molecules in three steps. The guest molecules, the weight loss observed (%; calcd (%)), and the temperature (°C) are as follows: cyclohexane, 4.55 (4.93), 50–160; naphthalene, 12.87 (13.31), approximately 200; triphenylene, 10.31 (10.31), approximately 420. These results agree with the elemental and crystallographic analyses. Note that crystals of pure triphenylene undergo a weight loss at a much lower temperature (below 330 °C). This fact indicates that the coordination network holds triphenylene strongly.

In conclusion, we have prepared a biporous coordination network where two guests are separately included into two channels by guest exchange. Two compounds which cannot

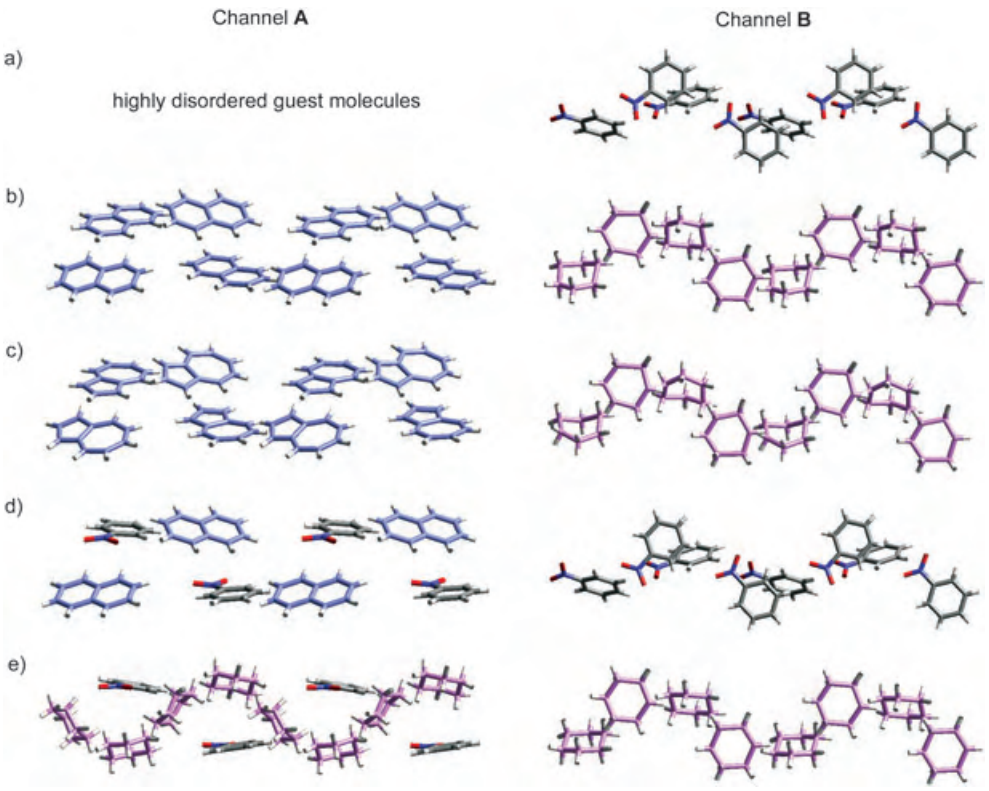

Figure 3. Columnar arrays of guest molecules in channels **A** (left) and **B** (right) in: a) **3** before guest exchange; b) **4**, c) **5**, d) **6**, and e) **7** after guest exchange. Partially disordered molecules have been omitted for clarity. The crystallographic details are given in the Supporting Information.

 © 2005 Wiley-VCH Verlag GmbH & Co. KGaA, Weinheim

coexist can, therefore, be stored within the same crystal (for example, an acid/base or an oxidizing/reducing agent pair) as they are separated from each other by a rigid host framework. A variety of scientific and technological applications are likely to be possible for such a "two-in-one" crystal.

Experimental Section

Elemental analyses for **3**–**7**: $\{[(ZnI_2)_3(\mathbf{1})_2(\mathbf{2})]\cdot 3.9\,(\text{nitrobenzene})\cdot 1.8\,(\text{methanol})\}_z$ (**3**): calcd C 40.51, H 2.69, N 9.48; found C 40.89, H 2.60, N 9.49. $\{[(ZnI_2)_3(\mathbf{1})_2(\mathbf{2})]\cdot 1.3\,(\text{cyclohexane})\cdot 2.3\,(\text{naphthalene})\}_z$ (**4**): calcd C 45.99, H 3.19, N 7.59; found C 45.71, H 2.92, N 7.29. $\{[(ZnI_2)_3(\mathbf{1})_2(\mathbf{2})]\cdot 1.4\,(\text{cyclohexane})\cdot 2\,(\text{azulene})\}_z$ (**5**): calcd C 45.30, H 3.17, N 7.69; found C 45.50, H 2.88, N 7.41. $-\{[(ZnI_2)_3(\mathbf{1})_2(\mathbf{2})]\cdot 2.4\,(\text{nitrobenzene})\cdot(\text{naphthalene})\}_z$ (**6**): calcd C 42.15, H 2.53, N 9.03; found C 41.85, H 2.67, N 8.94. $\{[(ZnI_2)_3(\mathbf{1})_2(\mathbf{2})]\cdot 2.0\,(\text{cyclohexane})\cdot 0.4\,(\text{nitrobenzene})\}_z$ (**7**): calcd C 40.51, H 3.08, N 8.56; found C 40.51, H 3.03, N 8.18. The cyclohexane and nitrobenzene in **7** could be completely removed by heating the crystals at 250 °C under N_2 for 20 min. $[(ZnI_2)_3(\mathbf{1})_2(\mathbf{2})]_z$: calcd C 35.82, H 2.00, N 9.28; found C 36.12, H 2.17, N 9.02. Part of the guest molecules escaped at room temperature.

Crystallographic data for **3**–**7. 3**: $C_{79.33}H_{55.56}I_6N_{15.91}O_{9.68}Zn_3$, $M_r = 2344.00$, orthorhombic, space group *Pbca*, $a = 27.268(3)$, $b = 13.6992(16)$, $c = 45.888(5)$ Å, $V = 17141(3)$ Å^3, $T = 80$ K, $Z = 8$, $\rho_{calcd} = 1.817$ g cm^{-3}, 15876 unique reflections out of 21251 with $I > 2\sigma(I)$, 1025 parameters, $1.72 < \theta < 28.92°$, final R factors $R_1 = 0.0821$ and $wR_2 = 0.1478$; **4**: $C_{85.38}H_{71.07}I_6N_{12}Zn_3$, $M_r = 2222.62$, orthorhombic, space group *Pbca*, $a = 27.6479(19)$, $b = 13.7500(9)$, $c = 45.714(3)$ Å, $V = 17379(2)$ Å^3, $T = 80$ K, $Z = 8$, $\rho_{calcd} = 1.854$ g cm^{-3}, 15905 unique reflections out of 21663 with $I > 2\sigma(I)$, 1057 parameters, $1.72 < \theta < 28.75°$, final R factors $R_1 = 0.0517$ and $wR_2 = 0.1174$; **5**: $C_{86}H_{76}I_6N_{12}Zn_3$, $M_r = 2235.10$, orthorhombic, space group *Pbca*, $a = 27.787(3)$, $b = 13.7247(12)$, $c = 45.881(4)$ Å, $V = 17498(3)$ Å^3, $T = 80$ K, $Z = 8$, $\rho_{calcd} = 1.697$ g cm^{-3}, 14824 unique reflections out of 21598 with $I > 2\sigma(I)$, 904 parameters, $1.71 < \theta < 28.71°$, final R factors $R_1 = 0.0783$ and $wR_2 = 0.1636$; **6**: $C_{82}H_{59}I_6N_{15}O_6Zn_3$, $M_r = 2307.95$, orthorhombic, space group *Pbca*, $a = 27.5680(18)$, $b = 13.7285(9)$, $c = 45.836(3)$ Å, $V = 17347(2)$ Å^3, $T = 80$ K, $Z = 8$, $\rho_{calcd} = 1.767$ g cm^{-3}, 14715 unique reflections out of 21416 with $I > 2\sigma(I)$, 1005 parameters, $1.71 < \theta < 28.84°$, final R factors $R_1 = 0.0776$ and $wR_2 = 0.1678$; **7**: $C_{77.13}H_{77.65}I_6N_{12.66}O_{1.32}Zn_3$, $M_r = 2307.95$, orthorhombic, space group *Pbca*, $a = 27.873(2)$, $b = 13.7073(10)$, $c = 45.852(3)$ Å, $V = 17518(2)$ Å^3, $T = 80$ K, $Z = 8$, $\rho_{calcd} = 1.638$ g cm^{-3}, 15437 unique reflections out of 21619 with $I > 2\sigma(I)$, 1086 parameters, $1.71 < \theta < 28.84°$, final R factors $R_1 = 0.0739$ and $wR_2 = 0.1323$.

CCDC-251671 (**3**), -251672 (**4**), -251675 (**5**), -251673 (**6**), and -251674 (**7**) contain the supplementary crystallographic data for this paper. These data can be obtained free of charge from the Cambridge Crystallographic Data Centre via www.ccdc.cam.ac.uk/data_request/cif.

Received: October 5, 2004
Published online: February 21, 2005

Keywords: coordination networks · crystal engineering · host–guest systems · zeolite analogues · zinc

[1] a) S. Kitagawa, R. Kitaura, S. Noro, *Angew. Chem.* **2004**, *116*, 2388 – 2430; *Angew. Chem. Int. Ed.* **2004**, *43*, 2334 – 2375; b) O. M. Yaghi, M. O'Keeffe, N. W. Ockwig, H. K. Chae, M. Eddaoudi, J. Kim, *Nature* **2003**, *423*, 705 – 714; c) S. L. James, *Chem. Soc. Rev.* **2003**, *32*, 276 – 288; d) C. Janiak, *Dalton Trans.* **2003**, 2781 – 2804; e) D. Braga, F. Grepioni, *Angew. Chem.* **2004**, *116*, 4092 – 4102; *Angew. Chem. Int. Ed.* **2004**, *43*, 4002 – 4011.

[2] a) K. Biradha, Y. Hongo, M. Fujita, *Angew. Chem.* **2000**, *112*, 4001 – 4003; *Angew. Chem. Int. Ed.* **2000**, *39*, 3843 – 3845; b) K. Biradha, Y. Hongo, M. Fujita, *Angew. Chem.* **2002**, *114*, 3545 – 3548; *Angew. Chem. Int. Ed.* **2002**, *41*, 3395 – 3398; c) K. Biradha, M. Fujita, *Angew. Chem.* **2002**, *114*, 3542 – 3545; *Angew. Chem. Int. Ed.* **2002**, *41*, 3392 – 3395; d) M. P. Suh, J. W. Ko, H. J. Choi, *J. Am. Chem. Soc.* **2002**, *124*, 10976 – 10977; e) E. Y. Lee, M. P. Suh, *Angew. Chem.* **2004**, *116*, 2858 – 2861; *Angew. Chem. Int. Ed.* **2004**, *43*, 2798 – 2801; f) B. Rather, M. J. Zaworotko, *Chem. Commun.* **2003**, 830 – 831; g) H. Li, M. Eddaoudi, M. O'Keeffe, O. M. Yaghi, *Nature* **1999**, *402*, 276 – 279; h) T. K. Maji, K. Uemura, H.-C. Chang, R. Matsuda, S. Kitagawa, *Angew. Chem.* **2004**, *116*, 3331 – 3334; *Angew. Chem. Int. Ed.* **2004**, *43*, 3269 – 3272; i) C. J. Kepert, M. J. Rosseinsky, *Chem. Commun.* **1999**, 375 – 376; j) G. J. Halder, C. J. Kepert, B. Moubaraki, K. S. Murray, J. D. Cashion, *Science* **2002**, *298*, 1762 – 1765; k) C.-Y. Su, A. M. Goforth, M. D. Smith, P. J. Pellechia, H.-C. zur Loye, *J. Am. Chem. Soc.* **2004**, *126*, 3576 – 3586; l) S. Takamizawa, E. Nakata, T. Saito, *Angew. Chem.* **2004**, *116*, 1392 – 1395; *Angew. Chem. Int. Ed.* **2004**, *43*, 1368 – 1371; m) S. Takamizawa, E. Nakata, H. Yokoyama, K. Mochizuki, W. Mori, *Angew. Chem.* **2003**, *115*, 4467 – 4470; *Angew. Chem. Int. Ed.* **2003**, *42*, 4331 – 4334; n) D. N. Dybtsev, H. Chun, K. Kim, *Angew. Chem.* **2004**, *116*, 5143 – 5146; *Angew. Chem. Int. Ed.* **2004**, *43*, 5033 – 5036.

[3] For a hydrophilic/hydrophobic biporous complex, see: B. F. Abrahams, M. Moylan, S. D. Orchard, R. Robson, *Angew. Chem.* **2003**, *115*, 1892 – 1895; *Angew. Chem. Int. Ed.* **2003**, *42*, 1848 – 1851.

[4] The simplified model of **3**, $[(ZnI_2)_3(\mathbf{1})(\text{pyridine})_3]$, was optimized at the B3LYP level of theory with the SDD basis set for Zn and I. M. J. Frisch, G. W. Trucks, H. B. Schlegel, G. E. Scuseria, M. A. Robb, J. R. Cheeseman, V. G. Zakrzewski, J. A. Montgomery, R. E. Stratmann, J. C. Burant, S. Dapprich, J. M. Millam, A. D. Daniels, K. N. Kudin, M. C. Strain, O. Farkas, J. Tomasi, V. Barone, M. Cossi, R. Cammi, B. Mennucci, C. Pomelli, C. Adamo, S. Clifford, J. Ochterski, G. A. Petersson, P. Y. Ayala, Q. Cui, K. Morokuma, D. K. Malick, A. D. Rabuck, K. Raghavachari, J. B. Foresman, J. Cioslowski, J. V. Ortiz, A. G. Baboul, B. B. Stefanov, G. Liu, A. Liashenko, P. Piskorz, I. Komaromi, R. Gomperts, R. L. Martin, D. J. Fox, T. Keith, M. A. Al-Laham, C. Y. Peng, A. Nanayakkara, M. Challacombe, P. M. W. Gill, B. Johnson, W. Chen, M. W. Wong, J. L. Andres, C. Gonzalez, M. Head-Gordon, E. S. Replogle, J. A. Pople, GAUSSIAN 98; Gaussian, Pittsburgh PA, **1998**.

[5] S. R. Batten, R. Robson, *Angew. Chem.* **1998**, *110*, 1558 – 1595; *Angew. Chem. Int. Ed.* **1998**, *37*, 1460 – 1494.

[6] A. L. Spek, *PLATON*, Version 1.62, University of Utrecht, **1999**.

 © 2005 Wiley-VCH Verlag GmbH & Co. KGaA, Weinheim

Surface Structures

Adsorption and Self-Assembly of Peptides on Mica Substrates**

Conor Whitehouse, Jiyu Fang, Amalia Aggeli, Mark Bell, Rik Brydson, Colin W. G. Fishwick, Jim R. Henderson, Charles M. Knobler, Robert W. Owens, Neil H. Thomson, D. Alastair Smith, and Neville Boden**

Nature produces a wide variety of biocomposite materials, from merely proteins and inorganic salts, often having remarkable properties not encountered in the "inorganic world".[1] These materials are formed by a precisely controlled templating process, whereby the protein preferentially nucleates a specific crystallographic face of the seed crystals.[2–4] Conversely, inorganic substrates may act as templates to induce large-scale order in protein supramolecular structures.[5,6] An understanding of these processes requires insight into the fundamental nature of the interactions between proteins and inorganic substrates. To this end we have carried out an empirical study of the adsorption and self-assembly behavior of a model peptide, CH_3CO-Q-Q-R-F-Q-W-Q-F-E-Q-Q-$CONH_2$ (P_{11}-2),[8] at solution/mica interfaces, and find that tapes with a cross β-sheet structure, a single molecule in thickness, grow epitaxially to produce a two-dimensional network reflecting the hexagonal symmetry of the substrate. Evaporation of the solvent gives rise to a dramatic reorganization of the tapes to produce a variety of structural morphologies depending on the drying process.

Our earlier work demonstrated how peptides with a propensity to form cross-β structures can, above a particular concentration, the critical tape concentration (ca. 90 μM for P_{11}-2), undergo self-assembly in either water or polar organic solvents to form long helicoidal, tapelike objects.[7–9] At higher concentrations still, ribbons (double tapes), fibrils (stacks of four or more tapes), and fibers (entwined fibrils) are formed successively. This hierarchical self-assembly behavior has been shown to stem from the chirality of the individual peptide molecules.[10]

In the present study our working hypothesis was that, below the critical tape concentration, we can expect planar tapelike structures to self-assemble at solid/solution interfaces, provided the peptide/surface binding energy is more than sufficient to compensate for the elastic distortion energy cost of "flattening" the tape onto the surface. This should make it possible to coat a solid surface with a "self-assembled monolayer" of tapes. Just how these tapes would interact with each other and how this would influence the longer length scale self-organization was less certain.

Working with aqueous solutions at pH 6.7, we were unable to image by atomic force microscopy (AFM) any in situ adsorbed P_{11}-2 structures. We raised the peptide/surface binding energy by lowering the dielectric constant of the solvent. In particular, using a solvent mixture of 10% water in 2-propanol (v/v), dielectric constant 26.1[11] and ${}^{s}_{w}$pH 5.5,[12] we were able to image the spontaneous formation of β-sheet tapes at the surface of the mica substrate in solution (Figure 1). The peak-to-peak distance between two touching tapes was 4.9 nm. (For reference, the calculated length of an 11-residue peptide in an extended β-strand conformation is 3.7 nm.) The tapes are seen to extend across the surface until they make contact. This contact inhibition defines the length of the tapes, and their growth is restricted to the two-dimensional plane of the surface. This peptide "monolayer" has a well-defined hexagonal symmetry, reflecting that of the mica surface lattice.

The orientation of dried films prepared by the immersion method (see Experimental Section) was studied by angle-resolved X-ray photoelectron spectroscopy (XPS) (tabulated results may be found in the Supporting Information). These experiments reveal that the peptide molecules within the adsorbed β-sheet tapes are oriented with the hydrophobic moieties of the amino acid residues at positions 4, 6, and 8 oriented outwards into the solution phase as illustrated in Figure 2. We were unsuccessful in our attempts to use ATR-IR spectroscopy to directly establish how the peptide molecules are packed within the tapes. However, structural studies of P_{11}-2 tapes in solution have established previously that the tapes are packed in an antiparallel cross-β struc-

[*] Dr. C. Whitehouse,[+] Dr. A. Aggeli, Dr. M. Bell, Dr. C. W. G. Fishwick, Prof. Dr. N. Boden
Centre for Self-Organising Molecular Systems
Department of Chemistry
University of Leeds
Leeds, LS2 9JT (UK)
Fax: (+44) 113-343-6452
E-mail: cd-whitehouse@fujirebio.co.jp
n.boden@chem.leeds.ac.uk

Dr. R. Brydson
Institute for Materials Research
School of Process, Environmental and Materials Engineering
University of Leeds
Leeds LS2 9JT (UK)

Dr. J. R. Henderson, Dr. R. W. Owens, Dr. N. H. Thomson, Dr. D. A. Smith
Department of Physics and Astronomy
University of Leeds
Leeds LS2 9JT (UK)

Prof. Dr. J. Fang, Prof. Dr. C. M. Knobler
Department of Chemistry and Biochemistry
University of California
Los Angeles, CA 90095-1569 (USA)

[+] Present address:
Research and Development Division
Fujirebio Inc.
51, Komiya-cho, Hachioji-shi, Tokyo 192-0031 (Japan)
Fax: (+81) 426-468-325

[**] The authors gratefully acknowledge the financial support provided by the UK Engineering and Physical Sciences Research Council, the UK Biotechnology and Biological Sciences Research Council (research studentship to C.W.), the Royal Society (University research fellowship to A.A.), and the U.S. National Science Foundation (Grant CHE 00-7931). We thank Prof. John Watts of the University of Surrey (UK) for his expert advice and for conducting the XPS analysis presented in this communication.

Supporting information for this article is available on the WWW under http://www.angewandte.org or from the author.

 DOI: 10.1002/anie.200462160 © 2005 Wiley-VCH Verlag GmbH & Co. KGaA, Weinheim

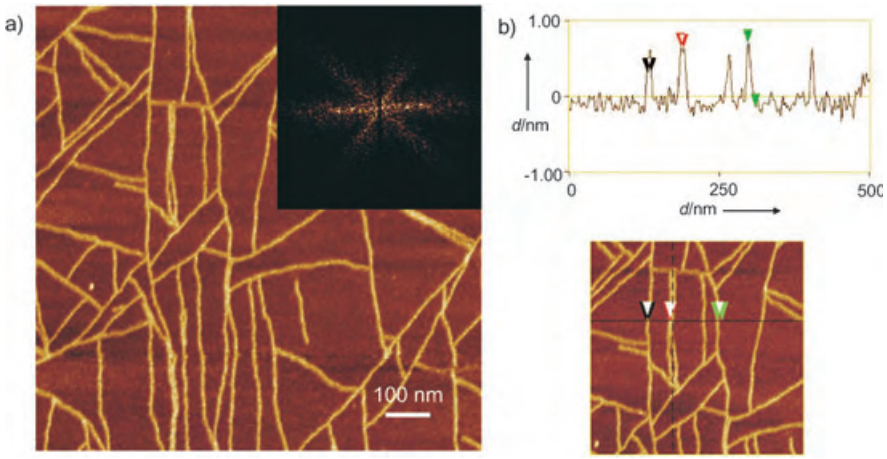

Figure 1. In situ AFM images measured by the tapping mode showing single β-sheet tapes grown on mica from 5 μM P_{11}-2 in 10% H_2O in 2-propanol; height scale 2 nm. a) Tapes aligned with the hexagonal symmetry of the underlying mica lattice with Fourier transform of the image showing hexagonal symmetry (inset, top right corner). b) Section analysis with line graph (top) showing the width (black arrows, convoluted width 6.9 nm) and height (green arrows, 0.8 nm) of the self-assembled tapes. The red arrows show the peak-to-peak distance (4.9 nm) between adjacent tapes.

ture.[7–10] The dimensions of the tapes assembled on the mica surface are very similar to those of the tapes in solution. Furthermore, molecular dynamics simulations[9] of tapes in aqueous solution have established that the antiparallel arrangement of peptide molecules depicted in Figure 2 is more stable than the alternative parallel one. These calculations also revealed how, for P_{11}-2, an intrinsic twist of three degrees per molecule along the tape axis is reduced to one degree in its corresponding dimeric ribbonlike structure. This is due largely to the cross-tape hydrophobic forces between residues at positions 4, 6, and 8. These are relatively modest forces. In the case of P_{11}-2 tapes on mica surfaces, we believe the predominant forces involved are electrostatic in origin. In particular, the positively charged δ-guanidinium of the arginine residues in position 3 displace hexagonally coordinated potassium ions on the basal layer (0001) of muscovite mica,[13] and the negatively charged γ-carboxylate of the glutamate residues at position 9 bind in turn to the K^+ ions. This directs the epitaxial growth of the β-sheet tapes.

We also studied dried films prepared on freshly cleaved mica substrates by the drop and blotting methods (see Experimental Section). In both cases a dramatic restructuring was observed upon drying. Contact-mode AFM images (Figure 3a–d) show that, as successive drops of a 10 μM aqueous solution (pH 6.7) of P_{11}-2 were applied to the surface and allowed to dry, there was a corresponding increase in the surface coverage of adsorbed peptide. The adsorbed peptide took the form of flat elongated aggregates. It appears that these objects are formed during the drying process through a combination of self-assembly and capillary interactions between the mesoscopic self-assembled β-sheet tapes. We have termed these objects, tactoids, meaning organized particles composed of smaller subunits (tapes). The tactoids have a uniform height of approximately 0.8 nm, commensurate with a monomolecular layer. The length and width of the tactoids vary from one area to another. Although generally elongated, some are needlelike and others more sheetlike in form. We believe that the variation in the dimensions of the mesoscopic tapes and consequently the tactoids is related to the drying rate for specific areas on the surface. The images shown in Figure 3 are representative of the needlelike

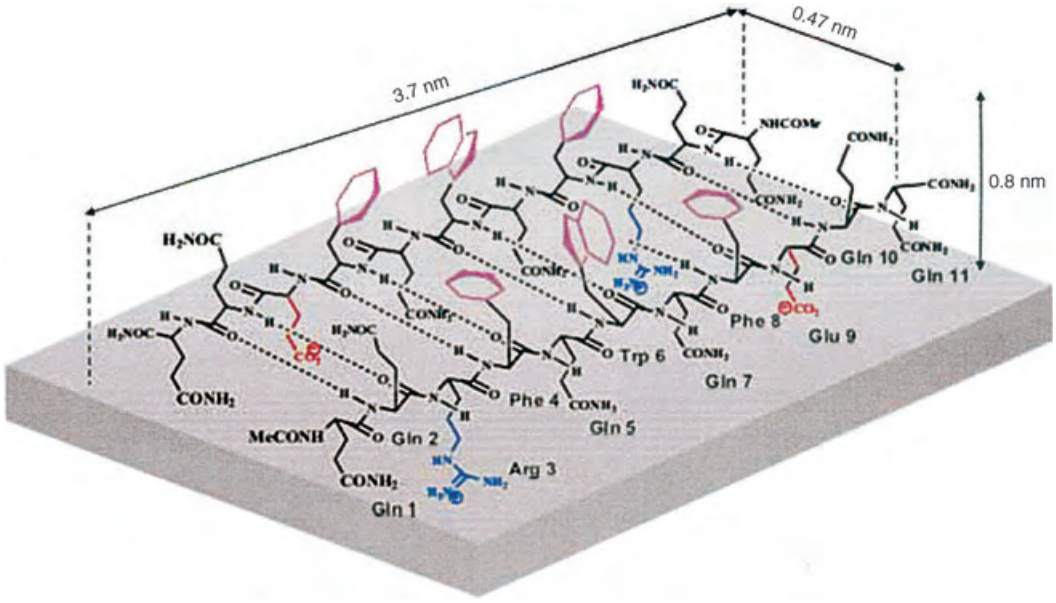

Figure 2. Schematic diagram showing the orientation and dimensions of a dimeric P_{11}-2 peptide tape in an antiparallel cross-β configuration adsorbed at the mica–water interface. XPS measurements show that the hydrophobic side chains in the residues at positions 4, 6, and 8 are directed into solution. The dimensions correspond with those obtained from modeling experiments.[9]

 © 2005 Wiley-VCH Verlag GmbH & Co. KGaA, Weinheim

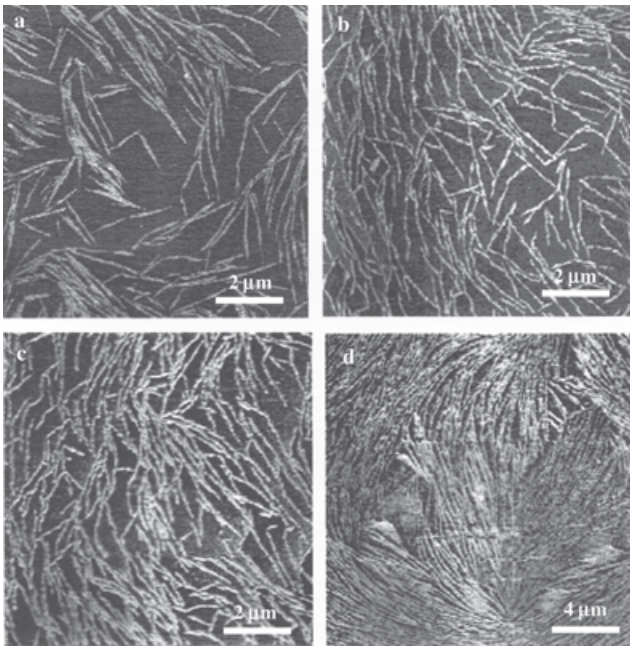

Figure 3. Contact-mode AFM images (a–d) of the tactoid distributions obtained by drying a film produced from sequential drops of 10 μM P_{11}-2 aqueous solution (pH 6.7). Height scale was 5 nm.

morphology. These tactoids were generally 100–200 nm in width and 2–3 μm in length. Interestingly, they are self-avoiding and do not overlap. This gives rise, at the higher surface concentrations, to a nematic-like long-range orientational ordering of tactoids, evident in Figure 3d, with the occurrence of a prominent disclination.[14] The monolayers obtained by the immersion method were similar in appearance to those described above for the drop method. Using this method, we were able to conduct precisely controlled adsorption studies, which will be described in subsequent publications.

In samples prepared by the blotting method it was possible to induce macroscopic uniaxial order in the adsorbed self-assembled tapes. The image in Figure 4 was obtained by allowing a 10 μL drop of 10 μM P_{11}-2 solution in water to flow over the surface of a freshly cleaved mica substrate, blotting excess fluid from the edge, then allowing the film to dry. The flow of the macroscopic drop over the surface produces a shear field that aligns the individual tapes in the direction of the receding interface. The tapes, imaged as regular corrugations, have an average width of 4.4 nm and correspond to single β-sheet tapes. They appear to extend indefinitely, suggesting that it ought to be possible, given a large enough volume of peptide solution and controlled retraction of the substrate through the air/water interface, to produce macroscopically aligned peptide monolayers on solid substrates.

In conclusion, it has been demonstrated that a peptide, P_{11}-2, designed to form twisted tapes and higher order structures in solution, can self-assemble at solution/mica interfaces into planar tapes, a single molecule in thickness, and having a cross-β structure. This is seen to occur at concentrations well below the critical concentration at which self-assembly into tapes occurs in bulk solution. Growth of planar tapes at an interface requires a peptide/surface binding energy sufficient to suppress the intrinsic twist in the tapes stemming from the chirality of the individual peptide molecules.[10] We believe, that in the system alluded to here, the predominant forces involved are electrostatic in origin. In particular, that the δ-guanidinium of Arg in position 3 displaces hexagonally coordinated potassium ions within the basal layer (0001) of the mica substrate, and the γ-carboxylate of Glu at position 9 binds to potassium ions. When the solvent is allowed to evaporate, quite different aggregate morphologies are obtained depending on the method used to prepare the initial film. One of these, a close-packed monolayer of parallel-aligned tapes, may be of practical utility as a functionalized protein-like surface.

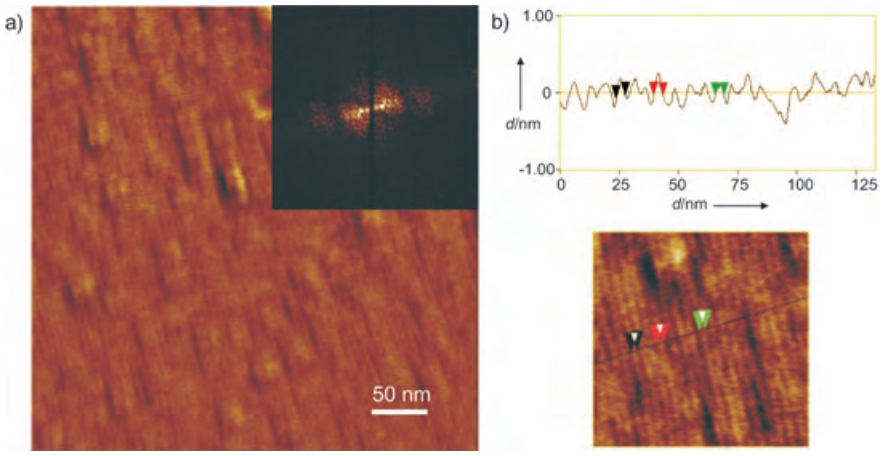

Figure 4. Tapping-mode AFM images showing aligned β-sheet tapes produced by shear flow alignment on a mica surface. a) Aligned tapes at the surface with Fourier transform of the image showing the uniaxial orientation of aligned tapes (inset, top right corner). Height scale: 5 nm. b) Section analysis and line graph (top) showing the measured widths of three single tapes imaged as corrugations within the sheet. The black, red, and green arrows show measured widths of 4.0, 4.0, and 3.8 nm, respectively.

Experimental Section

P_{11}-2 ($M_w = 1593.7$ Da by MS) was synthesized by Neosystems Groupe SNPE, France.[8] Solutions (pH 6.7) were prepared from freeze-dried P_{11}-2 with HPLC-grade water and 10% H_2O in 2-propanol. Circular dichroism (CD) spectroscopy (260–190 nm) confirmed that P_{11}-2 was present in its monomeric, random-coil state. To study the growth of equilibrium structures at solution/mica interfaces, we injected the solution of monomeric peptide into a sealed AFM fluid cell containing a freshly cleaved mica substrate. The peptide was allowed to adsorb, and the spontaneous self-assembly was imaged in solution. In the drying experiments, samples were prepared by one of three methods. Drop method: One or more drops of 10 μM peptide solution were placed onto the center of a freshly cleaved mica sheet and the resulting film allowed to dry. Immersion method: A freshly cleaved mica sheet was placed into a

 © 2005 Wiley-VCH Verlag GmbH & Co. KGaA, Weinheim

flat-bottomed vial containing 10 mL of P_{11}-2 solution. After the allotted time the mica sheet was removed and blotted from the edge to remove any excess solution, and the sample left to dry. Blotting method: A 10 μL drop of peptide solution was placed on the edge of a freshly cleaved mica sheet and allowed to wash over the inclined surface. Excess solution was blotted from the edge of the sheet, and the sample was left to dry in air. Tapping-mode AFM observations were carried out using a Multimode Nanoscope IIIa Scanning Probe Microscope (Veeco, USA). Noncontact silicon probes (NCL, Nanosensors GmbH) were used for imaging in air. In situ imaging was performed using a closed fluid cell with contact-mode oxide-sharpened silicon nitride probes (NP-S, Veeco) driven at a frequency of $\approx$9.2 kHz, within the broad resonance in fluid. Contact-mode AFM observations in air were performed on a Park Scientific Instruments Autoprobe using v-shaped silicon nitride cantilevers (Veeco, USA). High-resolution X-ray photoelectron spectra for both the C 1s/K 2p and N 1s regions were recorded on a VG Scientific Sigma Probe instrument with monochromatic $Al_{K\alpha}$ radiation. XPS spectra were taken from monolayers adsorbed on mica from 22 μM P_{11}-2 solution in water using the immersion method. Additional experimental details for XPS measurements are given in the Supporting Information.

Received: September 30, 2004
Published online: February 23, 2005

Keywords: adsorption · nanostructures · peptides self-assembly · surface chemistry

[1] S. Mann, *Science* **1993**, *261*, 1286 – 1292.
[2] C. A. Orme, A. Noy, A. Wierzbicki, M. T. McBride, M. Grantham, H. H. Teng, P. M. Dove, J. J. DeYoreo, *Nature* **2001**, *411*, 775 – 779.
[3] H. Bekele, J. H. Fendler, J. W. Kelly, *J. Am. Chem. Soc.* **1999**, *121*, 7266 – 7267.
[4] L. Addadi, S. Weiner, *Angew. Chem.* **1992**, *104*, 159 – 176; *Angew. Chem. Int. Ed. Engl.* **1992**, *31*, 153 – 169.
[5] T. Kowalewski, D. M. Holtzman, *Proc. Natl. Acad. Sci. USA* **1999**, *96*, 3688 – 3693.
[6] C. L. Brown, I. A. Aksay, D. A. Saville, M. H. Hecht, *J. Am. Chem. Soc.* **2002**, *124*, 6846 – 6848.
[7] A. Aggeli, M. Bell, N. Boden, J. N. Keen, P. F. Knowles, T. C. B. McLeish, M. Pitkeathly, S. E. Radford, *Nature* **1997**, *386*, 259 – 262.
[8] A. Aggeli, M. Bell, N. Boden, J. N. Keen, T. C. B. McLeish, I. Nyrkova, S. E. Radford, A. Semenov, *J. Mater. Chem.* **1997**, *7*, 1135 – 1145.
[9] C. W. G. Fishwick, A. J. Beevers, L. M. Carrick, C. D. Whitehouse, A. Aggeli, N. Boden, *Nano Lett.* **2003**, *3*, 1475 – 1479.
[10] A. Aggeli, I. A. Nyrkova, M. Bell, R. Harding, L. Carrick, T. C. B. McLeish, A. N. Semenov, N. Boden, *Proc. Natl. Acad. Sci. USA* **2001**, *98*, 11 857 – 11 862.
[11] Calculated using $\varepsilon = \varepsilon_1 V + \varepsilon_2(1-V)$, where $V = 0.9$ = volume fraction of major component, $\varepsilon_1 = 20.1$ for 2-propanol and $\varepsilon_2 =$ 80.18 for water at STP.
[12] M. Rosés, *J. Chromatogr. A* **2004**, *1037*, 283 – 298.
[13] M. A. Osman, U. W. Suter, *J. Colloid Interface Sci.* **2000**, *224*, 112 – 115.
[14] M. A. Bates, D. Frenkel, *J. Chem. Phys.* **2000**, *112*, 10034 – 10040.
[15] J. R. Pels, F. Kapteijn, J. A. Moulijn, Q. Zhu, K. M. Thomas, *Carbon* **1995**, *33*, 1641 – 1653.
[16] J. F. Moulder, W. F. Stickle, P. E. Sobol, K. D. Bomben, *Handbook of XPS*, Physical Electronics Inc., Eden Prairie, Minnesota, **1995**.

 © 2005 Wiley-VCH Verlag GmbH & Co. KGaA, Weinheim

Controlled Fibril Assembly

Controlled Assembly of Macromolecular β-Sheet Fibrils**

*Jurgen M. Smeenk, Matthijs B. J. Otten, Jens Thies, David A. Tirrell, Hendrik G. Stunnenberg, and Jan C. M. van Hest**

Construction of functional molecular devices by directed-assembly processes is one of the main challenges in the field of nanotechnology.[1,2] Many approaches to this challenge use biological assembly as a source of inspiration for the build up of new materials with controlled organization at the nanoscale. In particular, the self-assembly properties of β-sheet peptides have been used in the design of supramolecular materials, such as tapes, nanotubes, and fibrils.[3–6]

The incorporation of self-organizing peptides into synthetic polymeric materials has been investigated by a number of groups, all of whom were working on fully synthetic approaches. Lynn and co-workers studied the dilute-solution properties of a diblock copolymer of the central domain of β-amyloid peptide and poly(ethylene glycol) (PEG).[7–9] Rathore and Sogah synthesized multiblock copolymers of oligopeptide β-sheet silk domains and PEG.[10,11] The work of Klok and co-workers is another interesting example as they reported the solid-state/melt properties of block copolymers of PEG and an amphiphilic β strand peptide.[12] The introduction of protein engineering to the field of materials science means that the structural peptide unit can be extended from peptides to tailor-made, monodisperse, high-molecular-weight macromolecules of controlled amino acid sequence.[13–15] The predetermined composition of these proteins leads to a higher level of control over folding than can be achieved with smaller peptide elements. Furthermore,

[*] J. M. Smeenk, M. B. J. Otten, Prof. J. C. M. van Hest
Organic Chemistry Department
Radboud University Nijmegen
Institute for Molecules and Materials
Toernooiveld 1, 6525 ED Nijmegen (The Netherlands)
Fax: (+31) 24-365-3393
E-mail: j.vanhest@science.ru.nl

J. Thies
DSM Research
P.O. Box 18
6160 MD Geleen (The Netherlands)

Prof. D. A. Tirrell
Division of Chemistry and Chemical Engineering
California Institute of Technology
Pasadena, CA 91125 (USA)

H. G. Stunnenberg
Department of Molecular Biology
University of Nijmegen
NCMLS 191, P.O. Box 9101, 6500 HB Nijmegen (The Netherlands)

[**] J.T. gratefully acknowledges the financial support of DSM Research. D.A.T. acknowledges National Sciences Foundation grant no. DMR-0110437.

Supporting information for this article is available on the WWW under http://www.angewandte.org or from the author.

 © 2005 Wiley-VCH Verlag GmbH & Co. KGaA, Weinheim DOI: 10.1002/anie.200462415

the assembly properties of a block copolymer consisting of a designed, genetically engineered, high-molecular-weight polypeptide and PEG have not been described to the best of our knowledge.

The feasibility of controlling the solid-state structure of polymeric materials through protein engineering was shown by Krejchi et al.[16,17] The observation that alanylglycine (AG) repeating units form extended β strands in a variety of AG-rich polypeptides, including *Bombyx mori* silk fibroin,[18] was the basis for the preparation of polypeptides containing the repetitive sequence $[(AG)_xEG]_n$ ($x = 3$–6). Insertion of the more polar and bulky glutamic acid (E) residue into this sequence resulted in controlled crystallization from formic acid and the formation of needle-shaped lamellar crystals with the glutamic acid residues confined to the crystal surface. Although the folding pattern of the polypeptide chain was well controlled, assembly resulted in extended-plate-like structures. Therefore, some of the information present in the polypeptide design, such as the height and width of the β-sheet elements, was lost during the aggregation process.

Herein, we describe the preparation and assembly of a triblock copolymer consisting of a central β-sheet polypeptide block composed of the repetitive $[(AG)_3EG]_n$ sequence conjugated to PEG end blocks. The rationale behind the attachment of synthetic polymer blocks at the N and C termini was to restrict macroscopic crystallization and allow translation of the β-sheet design characteristics of width, height, and surface functionality into the self-assembled structures.

We first constructed $[(AG)_3EG]_n$ β-sheet polypeptides outfitted with N- and C-terminal cysteine residues by protein engineering. The target sequence of this protein is depicted in Scheme 1a. The presence of a hexahistidine tag enabled purification of the polypeptides from the *Escherichia coli* cell lysates by nickel–nitrilotriacetate (Ni–NTA) affinity chromatography. The thiol functionality of the cysteines was subsequently used for selective alkylation with maleimide-functionalized PEG of $M_n = 750\ g\,mol^{-1}$ (Scheme 1b). Conjugates were prepared by reaction with an excess of maleimide-functionalized PEG, followed by removal of this excess by a second Ni–NTA affinity chromatography step. Furthermore, cyanogen bromide (CNBr) cleavage allowed removal of the residual N- and C-terminal amino acids introduced during the cloning process. The preparation of DNA constructs, protein expression/purification, conjugation reactions, and final characterization by sodium dodecylsulfate (SDS) polyacrylamide gel electrophoresis, ^1H NMR spectroscopic analysis, and MALDI-TOF mass-spectrometric analysis is described in the Supporting Information.

Crystallization experiments were performed both with conjugates still containing the N- and C-terminal amino acids and with conjugates that had been cleaved with CNBr. Crystallization was induced by vapor diffusion of methanol into a solution ($10\ mg\,mL^{-1}$) of the protein in 70% formic acid and resulted, in all cases, in the formation of transparent gels. Attenuated total-reflectance IR and circular dichroism spectroscopic analysis of the conjugates indicated that the antiparallel β-sheet architecture was retained upon conjugation with PEG (see the Supporting Information).

The assembly behavior of the crystallized conjugates was analyzed by transmission electron microscopy (TEM) with samples deposited on carbon-coated grids. This was achieved by either placing the grid with the carbon side down on top of the gel or by diluting the gel tenfold in methanol and then placing the grid on top of this suspension. Both approaches resulted in the same morphology. The TEM grid was covered consistently with fibrillar structures for PEG–$[(AG)_3EG]_{20}$–PEG conjugates. Aligned micrometer-long fibrils with a width of approximately 12 nm were observed for the variant still containing the nonrepetitive amino acids (Figure 1a). A

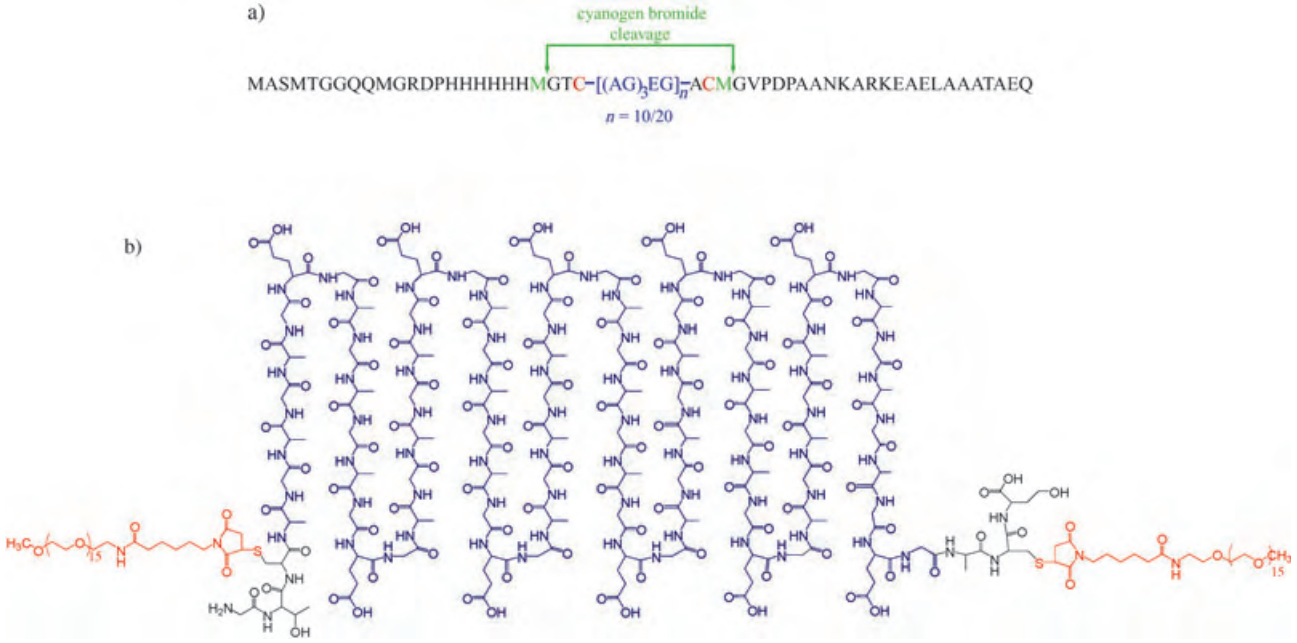

Scheme 1. a) Target protein sequence; b) ABA-type block copolymer formed by reaction of maleimide-functionalized PEG ($M_n = 750\ g\,mol^{-1}$) with the cysteine-flanked $[(AG)_3EG]_n$ β-sheet element.

 © 2005 Wiley-VCH Verlag GmbH & Co. KGaA, Weinheim

network of individual fibrils with the same width was observed when the residual amino acids were cleaved from the conjugate (Figure 1b). Only a few individual aggregated fibrils were found on the grid surface for the proteins without

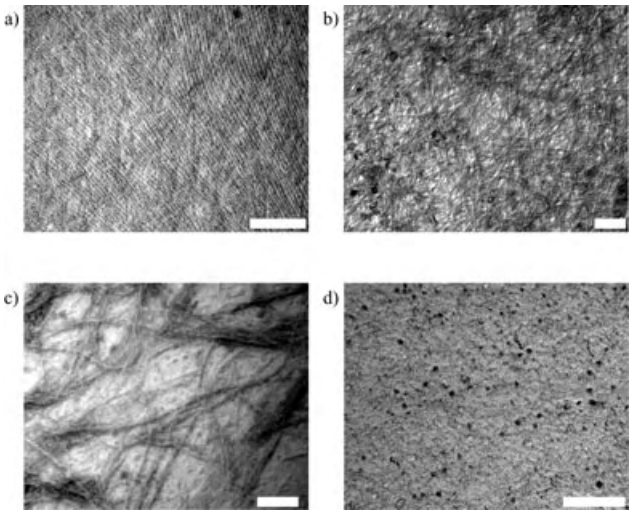

Figure 1. Transmission electron micrographs of crystallized PEG–$[(AG)_3EG]_n$–PEG conjugates: a) PEG–$[(AG)_3EG]_{20}$–PEG before CNBr cleavage; b) PEG–$[(AG)_3EG]_{20}$–PEG after CNBr cleavage; c) PEG–$[(AG)_3EG]_{10}$–PEG before CNBr cleavage; d) PEG–$[(AG)_3EG]_{10}$–PEG after CNBr cleavage. The scale bars represent 200 nm.

conjugated PEG (see the Supporting Information); this effect is most probably the result of the formation of larger aggregated structures because of the increased interaction between the β-sheet polypeptides.

Comparison of this texture with PEG–$[(AG)_3EG]_{10}$–PEG conjugates, in which the β-sheet block was exactly halved, also showed the formation of fibrils for the uncleaved PEG–$[(AG)_3EG]_{10}$–PEG sample (Figure 1c). However, the fibrillar width was clearly smaller than that of the PEG–$[(AG)_3EG]_{20}$–PEG conjugates as it could not be measured because, in this case, the grain size of the platinum particles was too large relative to the fibril width to distinguish single fibrils. Single fibrils were difficult to distinguish because of dense coverage of the grid for the CNBr-cleaved PEG–$[(AG)_3EG]_{10}$–PEG conjugate (Figure 1d).

To investigate further the fibrillar texture and the effect of β-sheet length, we analyzed the fibril dimensions by atomic force microscopy (AFM). Most importantly, the AFM experiments proved the presence of fibrils for samples spincoated on mica surfaces, although no single fibrils could be observed for the CNBr-cleaved PEG–$[(AG)_3EG]_{10}$–PEG conjugate by using TEM (Figure 2a). Individual fibrils were also visualized for the CNBr-cleaved PEG–$[(AG)_3EG]_{20}$–PEG conjugate, the result of which indicates that the fibrils are stable upon dilution (Figure 2b). Furthermore, fibril heights of approximately 2 nm were measured for PEG conjugates of both $[(AG)_3EG]_{10}$ and $[(AG)_3EG]_{20}$.

An organization in which the hydrogen-bond direction is perpendicular to the fibril direction is plausible when these data are taken into consideration. Fibril formation in the β-

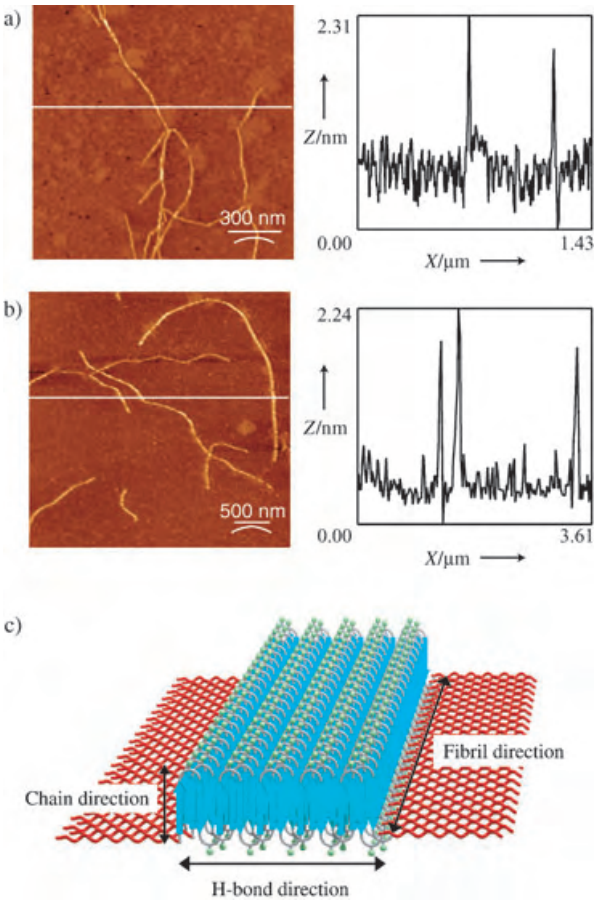

Figure 2. Tapping-mode AFM images of β-sheet fibrils on a mica support: Height image and height profile from single fibrils of a) PEG–$[(AG)_3EG]_{10}$–PEG and b) PEG–$[(AG)_3EG]_{20}$–PEG conjugates. c) Schematic illustration of the proposed organization within the β-sheet fibrils.

sheet stacking direction then results in an assembly in which the hydrophobic β-sheet surfaces are shielded from the polar solvent, whereas the PEG chains are in contact with the environment. This organization is schematically depicted in Figure 2c. The height values of approximately 2 nm measured for both conjugates are supportive for this type of organization. These fibril heights are in reasonable agreement with the calculated height of 2.8 nm, particularly when one takes into account the fact that AFM measurements do not give absolute height values as a result of possible deformation caused by the tip's pressure and the influence of air humidity.[19] The wide-angle X-ray diffraction data from Krejchi et al.[17] shows that the lengths of the crystalline blocks in the hydrogen-bond direction are 4.3 and 8.9 nm for the $[(AG)_3EG]_{10}$ and $[(AG)_3EG]_{20}$ conjugates, respectively. An accurate indication of the β-sheet width of the PEG–$[(AG)_3EG]_{10}$–PEG and PEG–$[(AG)_3EG]_{20}$–PEG conjugates proved to be difficult because of the geometry of the probe tip (it typically has a finite size of 10 nm). A qualitative assessment of the combination of AFM and TEM data, however, showed that the PEG–$[(AG)_3EG]_{20}$–PEG fibrils were consistently broader than the PEG–$[(AG)_3EG]_{10}$–PEG assemblies, whereas no difference in height was observed. X-ray

 © 2005 Wiley-VCH Verlag GmbH & Co. KGaA, Weinheim

measurements were carried out to obtain conclusive evidence for the crystalline organization within the fibrils and the direction of the hydrogen-bonding and hydrophobic interactions, but this turned out not to be trivial and needs to be explored in more detail.

In conclusion, we have shown that the attachment of PEG end blocks to a central poly[$(AG)_3EG$] β-sheet block prevents the macroscopic aggregation of the β-sheet blocks into needle-shaped lamellar crystals. Instead, crystallization results in well-defined fibrils. Microscopy data suggest an organization in which fibrils are formed in the β-sheet stacking direction. Furthermore, absolute control over the amino acid sequence might offer the possibility of introducing specific amino acid residues at the turns of the β-sheets, thereby creating a regular array of functional moieties at the fibril surface. Patterning of the surface with different amino acid combinations might provide a method for positioning different chemical functionalities on the nanometer scale.

Experimental Section

TEM: All samples were prepared on copper specimen grids covered with a carbon support film (CF200-Cu; Electron Microscopy Sciences, Washington, USA). The grids were placed with the carbon film down on top of a 5-μL droplet of protein suspension (1 mg mL^{-1}) in methanol or on a gel (10 mg mL^{-1}) for 30 s. The grids were allowed to dry and were subsequently shadowed with platinum at an elevation angle of 45°. Images were recorded by using a JEOL 1010 electron microscope.

AFM: Protein solutions with concentrations of 10–100 μg mL^{-1} were spincoated onto a freshly cleaved mica surface. The morphologies of the samples were analyzed by means of tapping-mode AFM with a Nanoscope IIIa instrument operating in air at room temperature. Height and phase images were recorded with microfabricated silicon cantilevers (length of 100 mm and width of 35 mm) that had a spring constant of 5.5–22.5 N m^{-1} by using scan rates of 1–2 lines s^{-1} and a resolution of 512 × 512 pixels.

Received: October 25, 2004
Published online: February 21, 2005

Keywords: conjugation · fibers · peptides · polymers · self-assembly

[1] J.-M. Lehn, *Science* **2002**, *295*, 2400.
[2] O. Ikkala, G. ten Brinke, *Science* **2002**, *295*, 2407.
[3] A. Aggeli, M. Bell, N. Boden, J. N. Keen, P. F. Knowles, T. C. B. McLeish, M. Pitkeathly, S. E. Radford, *Nature* **1997**, *386*, 259.
[4] J. D. Hartgerink, J. R. Granja, R. A. Milligan, M. R. Ghadiri, *J. Am. Chem. Soc.* **1996**, *118*, 43.
[5] H. Rapaport, G. Moller, C. M. Knobler, T. R. Jensen, K. Kjaer, L. Leiserowitz, D. A. Tirrell, *J. Am. Chem. Soc.* **2002**, *124*, 9342.
[6] M. W. West, W. X. Wang, J. Patterson, J. D. Mancias, J. R. Beasley, M. H. Hecht, *Proc. Natl. Acad. Sci. USA* **1999**, *96*, 11211.
[7] P. Thiyagarajan, T. S. Burkoth, V. Urban, S. Seifert, T. L. S. Benzinger, D. M. Morgan, D. Gordon, S. C. Meredith, D. G. Lynn, *J. Appl. Crystallogr.* **2000**, *33*, 535.
[8] T. S. Burkoth, T. L. S. Benzinger, D. N. M. Jones, K. Hallenga, S. C. Meredith, D. G. Lynn, *J. Am. Chem. Soc.* **1998**, *120*, 7655.
[9] T. S. Burkoth, T. L. S. Benzinger, V. Urban, D. G. Lynn, S. C. Meredith, P. Thiyagarajan, *J. Am. Chem. Soc.* **1999**, *121*, 7429.
[10] O. Rathore, D. Y. Sogah, *Macromolecules* **2001**, *34*, 1477.
[11] O. Rathore, D. Y. Sogah, *J. Am. Chem. Soc.* **2001**, *123*, 5231.
[12] A. Rosler, H. A. Klok, I. W. Hamley, V. Castelletto, O. O. Mykhaylyk, *Biomacromolecules* **2003**, *4*, 859.
[13] J. Capello, J. Crissman, M. Dorman, M. Mikolajczak, G. Textor, M. Marquet, F. Ferrari, *Biotechnol. Prog.* **1990**, *6*, 198.
[14] J. C. M. van Hest, D. A. Tirrell, *Chem. Commun.* **2001**, 1897.
[15] N. L. Goeden Wood, J. D. Keasling, S. J. Muller, *Macromolecules* **2003**, *36*, 2932.
[16] M. T. Krejchi, E. D. T. Atkins, A. J. Waddon, M. J. Fournier, T. L. Mason, D. A. Tirrell, *Science* **1994**, *265*, 1427.
[17] M. T. Krejchi, S. J. Cooper, Y. Deguchi, E. D. T. Atkins, M. J. Fournier, T. L. Mason, D. A. Tirrell, *Macromolecules* **1997**, *30*, 5012.
[18] R. D. B. Fraser, T. P. MacRae, *Conformation of Fibrous Proteins and Related Synthetic Polypeptides*, Academic Press, New York, **1973**.
[19] *Atomic Force Microscopy: Biomedical Methods and Applications* (Eds.: P. C. Braga, D. Ricci), Humana Press, Totowa, **2004** (*Methods in Molecular Biology*, *Vol. 242*).

 © 2005 Wiley-VCH Verlag GmbH & Co. KGaA, Weinheim

Mixed-Metal Clusters

Metal Clusters as Ligands: Substitution of Fe ions in Fe/Mo/S Clusters by Thiophilic Cu^{I} Ions To Give Clusters with $[Cu_4Mo_2Fe_2S_8]^{4+}$ and $[Cu_5Mo_3Fe_4S_{11}]^{6+}$ Cores**

*Markos Koutmos and Dimitri Coucouvanis**

The edge-fused double cubanes $[(Cl_4\text{-cat})_2(PR_3)_2Mo_2Fe_8S_8(L')_4]$ (**1**; Cl_4-cat = tetrachlorocatecholate dianion) contain the $Mo_2Fe_6S_8$ core and have been obtained with various terminal ligands on the Fe atoms ($L' = PR_3$,[1] BH_4^-,[2] Cl^-,[3] and N^{3-}[3]). More recently analogues of these clusters with tris(pyrazolyl) borate as a molybdenum-bound terminal ligand also have been reported.[4] The exceptional reactivity of **1** and its pronounced tendency to undergo core rearrangement has made possible the synthesis of various derivative clusters that are relevant as partial analogues for the FeMo-cofactor[5] or the P-clusters of nitrogenase.[6]

Herein we report on the reaction of $[(Cl_4\text{-cat})_2Mo_2Fe_8(PnPr_3)_6]$ (**2**; Figure 1), with $[Cu(CH_3CN)_4]^+$ ions and the subsequent substitution of for iron centers by for copper

[*] M. Koutmos, Prof. D. Coucouvanis
930 N. University
Department Of Chemistry
The University Of Michigan
Ann Arbor, MI 48109-1055 (USA)
Fax: (+1) 734-936-2916
E-mail: dcouc@umich.edu

[**] The authors acknowledge the support of this work by a grant from the National Institutes of Health (GM 33080).

Supporting information for this article is available on the WWW under http://www.angewandte.org or from the author.

 DOI: 10.1002/anie.200462596 © 2005 Wiley-VCH Verlag GmbH & Co. KGaA, Weinheim

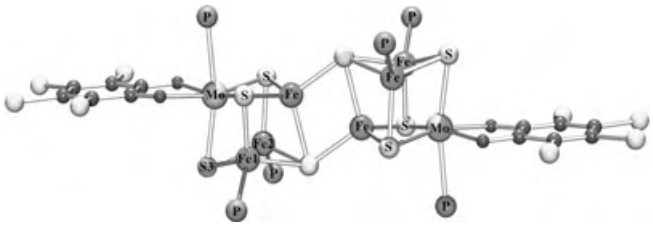

Figure 1. Structure of **2**. The carbon and hydrogen atoms of the propyl groups of the phosphine ligands are omitted for clarity.

centers to give a structure that retains the basic, edge-fused, M_8S_8 cubane structure and contains three different metal ions in three different coordination geometries. The reaction of **2** with $[Cu(CH_3CN)_4]^+$ in a CH_2Cl_2/CH_3CN solution at low temperature (−40 °C) affords the cluster $[(Cl_4\text{-cat})_2Mo_2Cu_4Fe_2S_8(PnPr_3)_4]$ (**3**), in 65 % yield.[7] A byproduct of this reaction has been isolated and crystallographically characterized as a rather complex but unique cluster with the formulation $[(Cl_4\text{-cat})_3Mo_3Cu_4Fe_5S_{11}(PnPr_3)_7(pyr)]$ (**4**; pyr = pyridine). These products are the first two examples of heterotrimetallic-sulfur compounds that have a cubane-like structure. Compounds that contain Mo/Fe/Cu and S atoms are rare and the only two examples known are the linear $(Et_4N)_2[(PPh_3)_2CuS_2MoS_2FeS_2Cl_2]$[8] and a $[CuS_2MoS_2Cu]^{2+}$ complex[9] that coordinates through the copper atoms to a diphenylphosphinoferrocene ligand.

The structure of **3**[10] was determined (Figure 2) and can be described in terms of a ferredoxin-type $[Fe_2S_2]^{2+}$ center bound

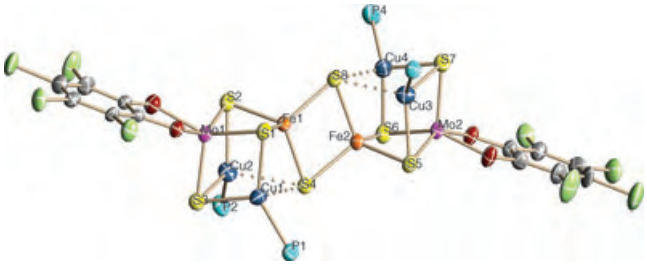

Figure 2. ORTEP diagram of **3** (thermal ellipsoids set at 50 % probability). The carbon and hydrogen atoms of the propyl groups of the phosphine ligands are omitted for clarity.

by two $\{(R_3PCu^I)_2Mo(Cl_4\text{-cat})S_3\}$ units. These units contain MoS_3Cu_2 cores structurally similar to those found in the $[Cu_3Cl_3MoS_3O]^{2-}$[11] and $[Cu_3(NCS)_3MoS_3O]^{2-}$[12] clusters. The Cu^I sites in the $\{(R_3PCu^I)_2Mo(Cl_4\text{-cat})S_3\}$ units are three-coordinate, distorted pyramidal (one of them (Cu1) is almost trigonal planar, deviating from planarity by $\Delta\Phi_{eq} = 4.6°$),[13] and only weakly interact with the μ_2-S ligands in the $[Fe_2S_2]^{2+}$ center. The intercubane Fe1–Fe2 separation in **3**, at 2.630 Å, is not much different than that of **2**, at 2.645 Å. There is a distinct shortening of the Fe–S separations by almost 0.1 Å on average.[14] Specifically, the separations Fe1–S8 (2.198 Å), Fe1–S4 (2.250 Å), Fe2–S8 (2.261 Å), and Fe2–S4 (2.197 Å) in **3** give $Fe–S_{av} = 2.226$ Å. The corresponding separations in cluster **2** (Fe–S4 and Fe–S8) are 2.379 Å, and 2.268 Å and give $Fe–S_{av} = 2.324$ Å. These $Fe–S_{av}$ separation in **3** is comparable albeit slightly longer than that found for the $[Fe_2S_2Cl_4]^{2-}$ dimer[15] at 2.200 Å.

In **3** the molybdenum atoms are five-coordinate rather than six-coordinate as in **2** and the $MoFeCu_2S_4$ cuboidal subunits are "opened-up" in **3** whereas the $MoFe_3S_4$ subunits in **2** are "closed". The axial and mean equatorial Mo–S bonds in **3** at 2.227 Å and 2.325 Å, respectively, are not very similar to those in either the $[(S_4)_2Mo^{IV}S]^{2-}$ complex[16] (2.128(1) Å, 2.359 Å) or the $S{=}Mo^V(S_4)$ unit in the $[Mo_2S_{10}]^{2-}$ ion[17] (2.123 Å, 2.413 Å).

An assignment of the +4 oxidation state to the molybdenum atoms in **3** leads to the unrealistic electronic description $[Mo^{IV}Cu^I{}_4Fe^{IV}{}_2S_8]^{4+}$. With Mo^V, the description $[Mo^V\text{-}Cu^I{}_4Fe^{III}{}_2S_8]^{4+}$ appears more satisfactory. The magnetic properties of **3** (μ_{eff}^{corr}: 4.91 μ_B, 300 K; 1.01 μ_B, 4.2 K (H = 5000 G)) suggest antiferromagnetic coupling between the two Fe^{III} ions. It appears that the substitution of the iron atoms by copper atoms in compound **2** results in the removal of the axial bound phosphine unit of the molybdenum atom with a concomitant oxidation of the molybdenum atom from +3 to +5.

The μ_3-S3–Mo separation in **2** (2.397 Å) is shortened to 2.230 Å when the μ_3-S3 ligand assumes the role of an axial ligand in the square-pyramidal Mo^V in **3**. This change is accompanied by an increase in the Fe1,2–S4 separation in **2** (2.250 Å and 2.267 Å) to separations in **3** (Cu1,2–S4 and Cu3,4? no Cu5,6–S8) that are nearly non-bonding and range from 2.562 Å to 2.726 Å. The Cu1–Cu2 and Cu3–Cu4 separations in **3** at 3.106(1) Å and 3.131(1) Å, respectively, are much longer than the corresponding Fe–Fe separations in **2** (2.631(1) Å).

The THF/hexanes filtrate collected during the isolation of **3** was kept and after removal of the solvents under a N_2 stream part of the resulting black material was extracted with diethyl ether. Slow evaporation of the solvent resulted in the formation of a few milligrams of single crystals that were structurally, characterized as **4**.[18]

The X-Ray crystal structure revealed[19] a cluster with unprecedented features (Figure 3). The structure is best described when it is separated into two fragments. The first fragment exhibits an unusual $[MoCuFe_2S_4]$ "cubane" like core that is depicted in Figure 4. The molybdenum retains its original coordination environment with one phosphine, one Cl_4-catecholate, and three μ_3-S ligands. The copper atom again has an almost trigonal planar coordination environment ($\Delta\Phi_{eq}$ 6.1°, $Cu–S_{ax}$ 2.591 Å) with one phosphine and 2 μ_3-S ligands. The two Fe atoms are distorted tetrahedral and one (Fe1) has only a sulfur coordination environment (with two μ_3-S and μ_4-S ligands (S1, S2, and S4 in Figure 3)) while the other (Fe2) has three S ligands with its coordination completed by a pyridine atom.

The second fragment (with a $[Mo_2Cu_2Fe_3S_6]$ core) is best described as the edge fusion (along an Fe–S edge (Fe3–S5)) of a sulfur voided $[MoCuFe_2S_3]$ cuboidal subunit with a $[MoCuFe_2S_4]$ cubane where the Fe–S edge is shared (Figure 5). The molybdenum atoms have the same coordination environment as the previous fragment. The two copper centers have also almost trigonal planar coordination environments ($\Delta\Phi_{eq}$ 5.4°, $\Delta\Phi_{eq}$ 7.8°, with $Cu–S_{ax}$ of 2.924 Å and 2.723 Å). The two fragments shown in Figure 4 and Figure 5,

 © 2005 Wiley-VCH Verlag GmbH & Co. KGaA, Weinheim

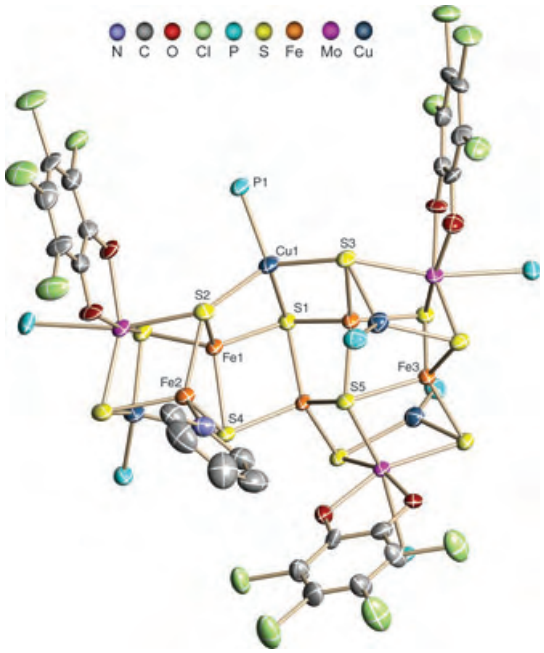

Figure 3. ORTEP diagram of the $[(Cl_4\text{-cat})_3Mo_3Cu_4Fe_5S_{11}(PnPr_3)_7(pyr)]$ cluster **4** (thermal ellipsoids set at 50% probability). The carbon and the hydrogen atoms of the *n*Pr groups of the phosphine ligands are omitted for clarity.

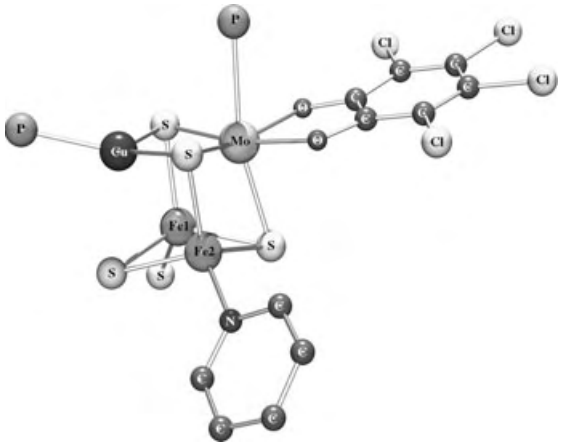

Figure 4. Schematic representation of the $\{MoCuFe_2S_4\}$ fragment of cluster **4**.

are connected through a μ_4-S ligand (S1 in Figure 3) and a $CuPnPr_3$ unit (Cu1,P1). In the $CuPnPr_3$ unit the copper atom has a distorted tetrahedral coordination environment and is coordinated by 3 μ_4-S ligands (S1, S2, S3; Figure 3) however, the Cu–S separations at 2.411, 2.435, and 2.437 Å are unusually long, and indicate weak bonding.

Mo/Fe/S and Mo/Cu/S clusters have been extensively studied over the past years; the Mo/Fe/S clusters, mainly because of their relevance to the FeMo cofactor of nitrogenase,[20] the Mo/Cu/S clusters because of their optical properties and their potential importance in the sequestering and regulation of copper in biological systems.[21] The reactivity of Mo/Fe/S clusters prompt us to the exploration

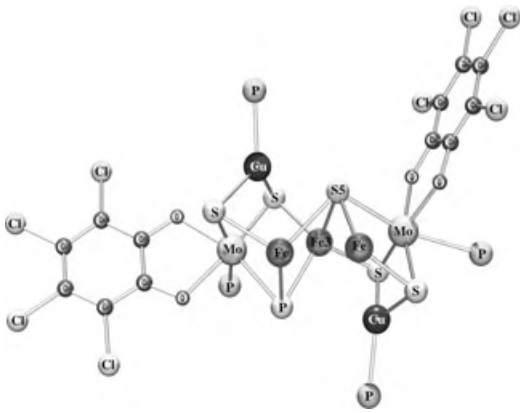

Figure 5. Schematic representation of the $\{Mo_2Cu_2Fe_3S_6\}$ fragment of cluster **4**.

of their reactions with monomeric copper complexes. Our studies have led to the discovery of a new class of trimetallic sulfur compounds.

Received: November 12, 2004
Published online: February 21, 2005

Keywords: cluster compounds · copper · iron · molybdenum · sulfur

[1] a) K. D. Demadis, C. F. Campana, D. Coucouvanis, *J. Am. Chem. Soc.* **1995**, *117*, 7832–7833; b) J. Han, M. Koutmos, S. Al Ahmad, D. Coucouvanis, *Inorg. Chem.* **2001**, *40*, 5985–5999; c) F. Osterloh, B. M. Segal, C. Achim, R. H. Holm, *Inorg. Chem.* **2000**, *39*, 980–989.

[2] M. Koutmos, D. Coucouvanis, *Inorg. Chem.* **2004**, *43*, 6508–6510.

[3] M. Koutmos, I. Georgakaki, D. Coucouvanis, unpublished results.

[4] a) C. Hauser, E. Bill, R. H. Holm, *Inorg. Chem.* **2002**, *41*, 1615–1624; b) D. V. Fomitchev, C. C. McLauchlan, R. H. Holm, *Inorg. Chem.* **2002**, *41*, 958–966.

[5] a) M. A. Tyson, D. Coucouvanis, *Inorg. Chem.* **1997**, *36*, 3808–3809; b) J. H. Han, K. Beck, N. Ockwig, D. Coucouvanis, *J. Am. Chem. Soc.* **1999**, *121*, 10448–10449; c) D. Coucouvanis, J. H. Han, N. Moon, *J. Am. Chem. Soc.* **2002**, *124*, 216–224.

[6] a) Y. G. Zhang, R. H. Holm, *J. Am. Chem. Soc.* **2003**, *125*, 3910–3920; b) Y. Zhang, R. H. Holm, *Inorg. Chem.* **2004**, *43*, 674–682; c) Y. G. Zhang, J. L. Zuo, H. C. Zhou, R. H. Holm, *J. Am. Chem. Soc.* **2002**, *124*, 14292–14293.

[7] For the synthesis of **3** see Supporting Information. Elemental analysis (%) calcd for **3**: C 29.61, H 4.35; found: C 29.82, H 4.42. FT-IR (KBr): $\tilde{\nu}$ = 2958(s), 2928(s), 28699(s), 1419(vs), 989(s), 812(s), 789(s), 575(s), 555(m), 443 cm^{-1} (m). ^1H NMR (CD_2Cl_2): δ = 1.08 (CH_3-CH_2-CH_2-P), 1.64 (CH_3-CH_2-CH_2-P), 2.18 (CH_3-CH_2-CH_2-P). Cyclic voltammetry (CH_2Cl_2) shows two reversible reduction process at −1.07 V and −0.64 V and one irreversible oxidation at 1.15 V (experiments were carried out with Pt working and Ag/AgCl reference electrodes with 0.1 M of nBu_4NPF_6 electrolyte and the redox potentials are reported versus the saturated calomel electrode (SCE). Electron microprobe analysis for both **3** and **4** (The University of Michigan Electron Microbeam Analysis Laboratory) confirmed the ratio of Mo/Fe/Cu/S thus supporting the assignment based on crystallographic and chemical criteria (phosphine should bind preferentially to Cu^I since Cu^I is more electron rich than Fe^{III}).

 © 2005 Wiley-VCH Verlag GmbH & Co. KGaA, Weinheim

[8] T. L. Sheng, S. W. Du, X. T. Wu, *Polyhedron* **1993**, *12*, 111 – 115.
[9] Y. Y. Niu, T. N. Chen, S. X. Liu, Y. L. Song, Y. X. Wang, Z. L. Xue, X. Q. Xin, *J. Chem. Soc. Dalton Trans.* **2002**, 1980 – 1984.
[10] a) Suitable crystals for X-ray structure determination were isolated from THF/hexanes at −23 °C. Diffraction data were collected on a Bruker SMART CCD-based X-ray diffractometer equipped with an LT-2 low-temperature device and normal focus Mo-target X-ray tube ($\lambda = 0.71073$ A) operated at 150(2) K, at the University of Michigan X-ray facility ($2\theta_{max} = 44.22$). The space group ($P2(1)/c$, monoclinic) was determined based on systematic absences and intensity statistics. A successful direct-methods solution was calculated using the software package SHELXTL v.6.1 that revealed the locations of most non-hydrogen atoms. Several full-matrix least-squares refinements followed by difference Fourier calculations were performed using SHELXTL, which located the remainder of the non-hydrogen atoms. All non-hydrogen atoms were refined with anisotropic thermal-displacement parameters unless stated otherwise. All hydrogen atoms were placed in ideal positions and refined as riding atoms with individual isotropic thermal-displacement parameters. From the 51518 reflections that were collected, 9884 were independent while the number of parameters was 746. The data were processed with SADABS for absorption correction. Cell dimensions $a = 20.525(4)$, $b = 19.832(4)$, $c = 19.928(4)$ Å with $\beta = 96.630(4)°$, $V = 8057(3)$ Å^3. Full-matrix least-squares refinement based on F^2 converged to an $R1$ $[I > 2\sigma]$ value of 0.0524 and a wR2 value of 0.1173, GOF 0.999; b) CCDC-255596 (**3**) and CCDC-255597 (**4**) contains the supplementary crystallographic data for this paper. These data can be obtained free of charge from the Cambridge Crystallographic Data Centre via www.ccdc.cam.ac.uk/data_request/cif.
[11] a) A. Muller, U. Schimanski, J. Schimanski, *Inorg. Chim. Acta* **1983**, *76*, L245; b) F. Sécheresse, S. Bernes, F. Robert, Y. Jeannin, *J. Chem. Soc. Dalton Trans.* **1991**, 2875; c) Y. Jeannin, F. Sécheresse, S. Bernes, F. Robert, *Inorg. Chim. Acta* **1992**, *198*, 493.
[12] W. Clegg, A. Beheshti, C. D. Garner, *Acta Crystallogr. Sect. C* **1988**, *44*, 170.
[13] We define $\Delta\Phi_{eq}$ as: $\Delta\Phi_{eq} = 360 - \Sigma\Phi_{eq}$, where $\Sigma\Phi_{eq}$ is the sum of the angles in the triangular base to which the longest Cu–S separation (Cu–S_{ax}) is normal. The $\Delta\Phi_{eq}$ values for the other three atoms are for 9.2° (Cu2), 15.9° (Cu3), and 20.3° (Cu4). These values increase as the Cu–S_{ax} separations for the corresponding copper centers decrease: Cu1–S4 (2.728 Å), Cu2–S4 (2.648 Å), Cu3–S8 (2.565 Å), and Cu4–S8 (2.560 Å).
[14] Owing to the lack of good structural data for compound **2**, [(Cl_4-cat)$_2$$Mo_2Fe_6S_8$(P*n*$Bu_3$)$_6$] has been used for the comparison of the two structures. Compounds [(Cl4-cat)$_2$$Mo_2Fe_6S_8$($PR_3$)$_6$] (were R = Et, *n*Pr, and *n*Bu) have identical core structures and exhibit minimal differences in bond lengths.
[15] M. A. Bobrik, K. O. Hodgson, R. H. Holm, *Inorg. Chem.* **1977**, *16*, 1851.
[16] E. D. Simhon, N. C. Baenziger, M. Kanatzidis, M. Draganjac, D. Coucouvanis, *J. Am. Chem. Soc.* **1981**, *103*, 1218 – 1219.
[17] M. Draganjac, E. Simhon, L. T. Chan, M. Kanatzidis, N. C. Baenziger, D. Coucouvanis, *Inorg. Chem.* **1982**, *21*, 3321 – 3332.
[18] Elemental analysis (%) calcd for **4**·2(CH_3)$_2$O, $C_{91}H_{172}Cl_{12}Cu_4Fe_5Mo_3NO_9P_7S_{11}$: C 33.73, H 5.35, N 0.43; found: C 33.86, H 5.47, N 0.38.
[19] Crystals suitable for X-ray diffraction were grown for compound **3** from a diethyl ether solution at −30 °C. Data were collected at 150 K, ($2\theta_{max} = 48.2$). The space group ($P\bar{1}$, triclinic) was determined based on systematic absences and intensity statistics. From the 52838 reflections that were collected, 23685 were independent while the number of parameters was 1377. Cell dimensions are $a = 15.906(3)$, $b = 19.922(4)$, $c = 24.978(5)$ Å, with $\alpha = 87.11(3)$, $\beta = 71.89(3)$ $\gamma = 89.15(3)°$ and the volume is $V = 7513(3)$ Å^3. Full-matrix least-squares refinement based on F^2 converged to an $R1$ $[I > 2\sigma]$ value of 0.0677 and a $wR2$ value of 0.1776, GOF 0.993.[10b]
[20] a) J. Kim, D. C. Rees, *Science* **1992**, *257*, 1677; b) J. B. Howard, D. C. Rees, *Chem. Rev.* **1996**, *96*, 2965.
[21] H. W. Hou, X. Q. Xin, S. Shi, *Coord. Chem. Rev.* **1996**, *153*, 25 – 56, and references therein.

 © 2005 Wiley-VCH Verlag GmbH & Co. KGaA, Weinheim

Electrochromism

Electrochromism of Titanate-Based Nanotubes**

*Hiromasa Tokudome and Masahiro Miyauchi**

Wide-bandgap semiconductor nanotubes have potential as components in electronic and optical devices because of their transparency and high energies of excited charge-carriers.[1–3] Among the various semiconductor nanotubes with wide bandgaps, titanate-based nanotubes, which have been synthesized and characterized over the last few years,[4–9] have received a lot of attention because of their cheap fabrication and unique one-dimensional nanostructure. Recently, we reported the synthesis of a novel thin film of titanate nanotubes by an alternate adsorption method and its photochemical properties, in particular its photocatalytic oxidation activity and photoinduced hydrophilicity.[10] Thin-film fabrication of titanate nanotubes enables us to develop a new, functional, transparent device.

Herein, we focus on the electrochromic properties of titanate nanotubes. Electrochromism depends on the crystal structure, and cathodic coloration occurs in transition metal oxide semiconductors such as TiO_2, WO_3, MoO_3, MnO_2, and Nb_2O_5 that are constructed from MO_6 octahedra.[11] Recently, several research groups have reported the electrochemical properties of layered materials made from these oxides;[12,13] however, the electrochromic properties of transparent nanotube thin films have yet to be disclosed. A titanate nanotube is composed of a one-dimensional nanostructure generated from nanosheets of TiO_6 octahedra, and therefore unique electrochromic properties are expected. In this study, transparent thin films of titanate nanotubes were deposited on electroconductive substrates by an alternate-layer deposition and their electrochromism was evaluated. The titanate nanotubes were found to exhibit significant electrochromism

[*] H. Tokudome, Dr. M. Miyauchi
Research Institute
TOTO Ltd.
2-8-1 Honson, Chigasaki-shi, Kanagawa, 253-8577 (Japan)
Fax: (+81) 467-54-3469
E-mail: masahiro.miyauchi@toto.co.jp

[**] We thank Ms. A. Iwasawa at TOTO Ltd. for performing the SEM measurements.

Supporting information for this article is available on the WWW under http://www.angewandte.org or from the author.

 © 2005 Wiley-VCH Verlag GmbH & Co. KGaA, Weinheim DOI: 10.1002/anie.200462448

under cathodic polarization in water, and turned brown. This phenomenon arises from the creation of Ti^{3+} centers caused by intercalation of protons in the nanotubes. The color change of these titanate nanotubes is more significant than that of TiO_2 anatase because of their layered nanostructure.

Powders of titanate nanotubes were synthesized by a hydrothermal method.[4] After the hydrothermal reaction, the products were immersed in an aqueous HNO_3 solution to replace the sodium ions with protons, and were subsequently stirred in an aqueous solution of tetra(*n*-butyl)ammonium hydroxide, which resulted in a translucent, colloidal suspension of titanate nanotubes.[10] Subsequent TEM and XRD analysis revealed that the nanotubes were constructed of scrolled titanate nanosheets, similar to the previous reports.[5–7] The inner cavity diameter, the outer diameter, and the length of the nanotubes were approximately 3.5 nm, 9.0 nm, and several hundreds of nanometers, respectively. The interlayer separation corresponds to a 2θ value of around 9.0° in the XRD patterns obtained with $Cu_{K\alpha}$ radiation;[5,6] the estimated interlayer separation is 0.98 nm.

Electrodes of titanate nanotubes were fabricated by an alternate-layer deposition process.[10,14,15] A zeta-potential analysis revealed that the pH value at the zero-charge point of the titanate nanotubes is 5.5. In the present study, the pH value in solution was adjusted to 9.0. Under these conditions the titanate nanotubes act as negatively charged particles, while poly(ethyleneimine) (PEI) or poly(diallyldimethylammonium chloride) (PDDA) are polycations. Alternate adsorption of titanate nanotubes and polycations is a result of the Coulomb force. Transparent electroconductive glass plates (F-doped SnO_2-coated glass: Asahi Glass Co. Ltd.) were used as the substrates and one-third of the SnO_2 area was covered with masking tape to prevent coating. The substrates were dipped into PEI solution and rinsed with pure water (first step), then dipped into a solution of titanate nanotubes and rinsed with water (second step), and finally dipped into PDDA solution and rinsed with water (third step). A multilayered film, substrate/PEI/(nanotube/PDDA)$_5$/nanotube, was created by repeating the second and third steps six times. As in our previous report, the inserted polycations were removed by a photocatalytic oxidation process under UV irradiation using a 200 W Hg–Xe lamp (Hayashi Watch Works Co. Ltd., Japan).[10] This procedure resulted in thin films of polymer-free titanate nanotubes deposited on transparent electroconductive substrates. A copper wire was attached to the uncoated SnO_2 surface with silver paste and the attached part and the uncoated SnO_2 area were then covered with an epoxy resin so that only the surface of the titanate nanotubes was exposed (size of the exposed area: 15×25 mm). TiO_2 anatase electrodes with the same size were also fabricated by a dip coating method with a titanium tetraisopropoxide solution (NDH-510C, Nihon Soda Co. Ltd., Japan). The coated substrates were annealed at 500 °C for 30 min to give a polycrystalline TiO_2 anatase electrode.

Figure 1 shows the SEM images of the electrodes observed from a tilted angle (30°). Titanate nanotubes and TiO_2 anatase films are coated on columnar crystallites of SnO_2. Both films are optically transparent. Their thicknesses were investigated by taking cross-sectional SEM images at several points, and, as a result, the average thicknesses of the titanate nanotube and anatase layers were calculated to be 60 nm and 80 nm, respectively. As for the titanate nanotube thin films, the thickness for each adsorption cycles is about 10 nm, which corresponds to the diameter of the nanotubes. These results demonstrate that the self-assembled alternate absorption method results in the growth of titanate nanotubes layer-by-layer. The diameter of TiO_2 anatase particles ranges from 20 to 30 nm.

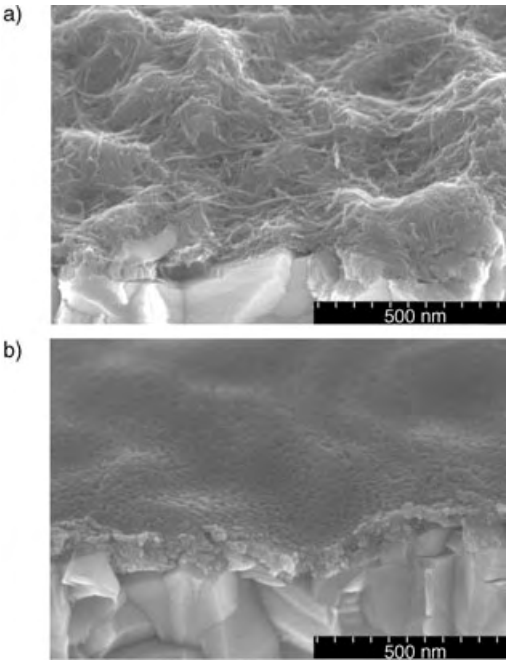

Figure 1. SEM images of the electrodes: a) titanate nanotube; b) TiO_2 (anatase).

Electrochemical measurements were conducted in a standard buffer solution (pH 6.8) containing 0.1 M Na_2SO_4 as an electrolyte, in the dark with a potentiostat (HSV-100, Hokuto Denko Co. Ltd., Japan). The working electrode, the counterelectrode, and the reference electrode were titanate nanotube electrode, platinum wire, and Ag/AgCl/saturated KCl(aq), respectively. Figure 2 shows the cyclic voltammograms for electrodes of the titanate nanotube and the TiO_2 (anatase) at various scan rates. Changes in the current were observed under cathodic polarization for both electrodes, but not under anodic polarization. These results indicate that both titanate nanotubes and TiO_2 anatase are n-type semiconductors. In addition, oxidation waves were observed between -1.0 V and -0.5 V for both electrodes. Previous studies have reported that cathodic polarization causes electrons to accumulate in the semiconductor film; thus, charge compensation is accomplished by proton intercalation [Eq. (1)].[16,17]

$$Ti^{4+} + e^- + H^+ \rightarrow Ti^{3+}H^+ \quad (1)$$

This reaction is reversible; therefore, an oxidation current is observed when the voltage is scanned in a positive mode. The current at the oxidation peaks increases linearly as the square root of the scan rate increases for both films. These

 © 2005 Wiley-VCH Verlag GmbH & Co. KGaA, Weinheim

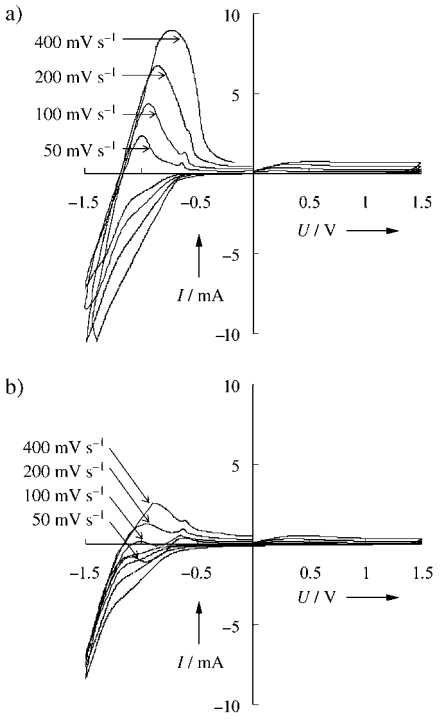

Figure 2. Cyclic voltammograms of the electrodes, at various scan rates, in a standard buffer solution (pH 6.8) containing 0.1 M Na_2SO_4: a) titanate nanotube; b) TiO_2 (anatase).

results are consistent with the Nernst equation, thus indicating that the redox process proceeds with proton diffusion. It is noteworthy that the oxidation peak current of the titanate nanotube is higher than that of TiO_2 (anatase), although the thickness of the titanate nanotube (60 nm) is less than that of TiO_2 (80 nm). These results indicate that proton diffusion in the titanate nanotube is faster than in TiO_2.

Figure 3 shows photographs of the electrodes before and after cathodic polarization at −1.5 V for three minutes. Both films are optically transparent before cathodic polarization,

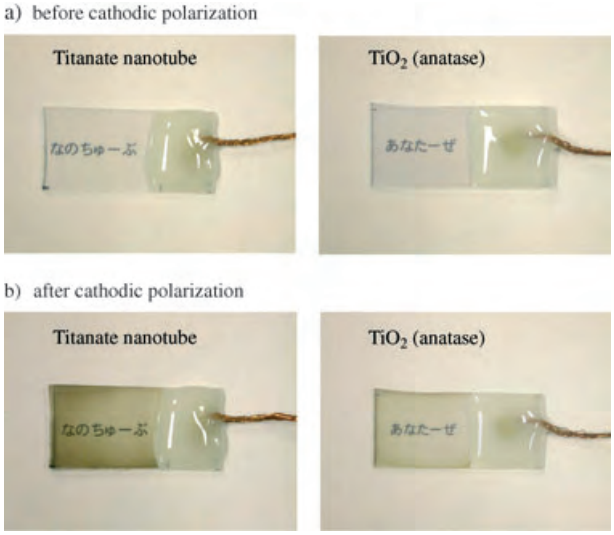

Figure 3. Photographs of the electrodes before (a) and after (b) three minutes of cathodic polarization at −1.5 V.

whereas they are brown after cathodic polarization. The color change of titanate nanotubes is more striking than that of TiO_2 (anatase). We also evaluated electrochromism on the bare electroconductive SnO_2-coated substrate. This bare electrode, however, did not turn brown under cathodic polarization. Thus, the color change originates in the titanate nanotube or TiO_2 anatase films.

Figure 4 shows the UV/Vis spectra for the electrodes. The absorbance value in the visible light region is higher after cathodic polarization. The increase in the absorbance value in the titanate nanotube is more significant than that in TiO_2. As mentioned earlier, cathodic polarization forms Ti^{3+} species by proton intercalation. A previous study has reported that the Ti^{3+} bands are located between 0.75 and 1.18 eV, which is below the minimum conduction-band level of TiO_2.[18] Therefore, the TiO_2 containing Ti^{3+} centers absorbs a broad range of visible light and is generally darker.

In the present study, titanate nanotubes exhibit a faster proton diffusion and higher proton capacity than TiO_2 (anatase). The significant electrochromism of the titanate nanotube is attributed to its layered nanostructure. In an earlier work, the crystal structure of nanotubes was considered to be anatase.[4] However, it was later realized that the crystal structure is not anatase, but contains protonated titanate.[5–7] Chen et al. have reported that the nanotubes are composed of scrolled trititanate ($H_2Ti_3O_7$) sheets.[5,6] On the other hand, Ma et al. have reported that the nanotubes are constructed from lepidocrocite ($H_xTi_{2-x/4}\square_{x/4}O_4$, $x \approx 0.7$, □: vacancy) sheets.[7] The exact crystal structure is therefore still

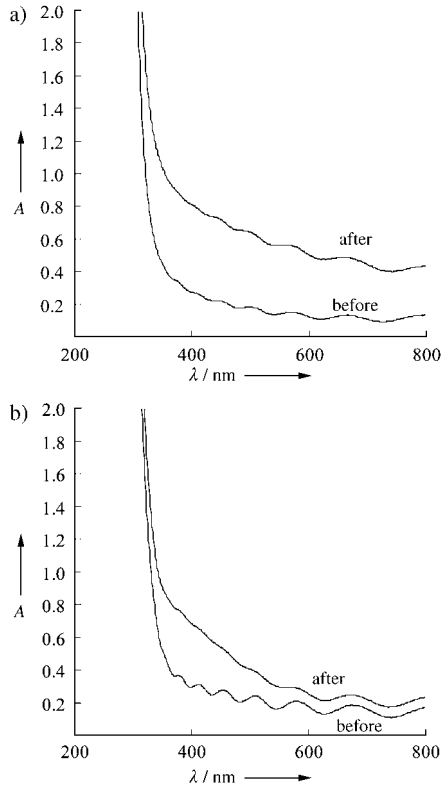

Figure 4. UV/Vis spectra for the electrodes before and after three minutes of cathodic polarization at −1.5 V: a) titanate nanotube; b) TiO_2 (anatase).

 © 2005 Wiley-VCH Verlag GmbH & Co. KGaA, Weinheim

unknown, although both these reports indicate that the titanate nanotubes are composed of scrolled TiO_2 sheets separated by H^+ ions. Our X-ray diffraction pattern for a dried powder formed from the colloidal solution is similar to these reports and indicates that the nanotubes are composed of scrolled nanosheets of protonated titanate. In this arrangement, a large surface area acts as H^+ host as a result of its one-dimensional, open-pore nature. Therefore, it is reasonable to suppose that protons can diffuse more easily into the layered nanostructure than into a densely packed polycrystalline TiO_2 particle.

In summary, new nanotube-based devices can be created from a stable, colloidal solution of titanate nanotubes and a thin film fabricated by an alternate-layer deposition process. The transparent titanate nanotube electrode demonstrates an intriguing electrochromism because of its layered nanostructure. Although the film thickness is only 60 nm, the color change in the titanate nanotubes is significant. An alternate-layer deposition process does not need an annealing step, therefore titanate nanotubes can be coated on various plastic substrates. This unique material has potential applications in various industrial components such as displays, sensor devices, and smart windows.

Received: October 28, 2004
Revised: December 15, 2004
Published online: February 23, 2005

Keywords: electrochromism · layered compounds · nanotubes · thin films · titanium

[1] J. Goldberger, R. He, Y. Zhang, S. Lee, H. Yan, H. J. Choi, P. Yang, *Nature* **2003**, *422*, 599 – 602.
[2] O. K. Varghese, D. Gong, G. M. Paulose, K. G. Ong, E. C. Dickey, C. A. Grimes, *Adv. Mater.* **2003**, *15*, 624 – 627.
[3] Y. Li, Y. Bando, D. Golberg, *Adv. Mater.* **2003**, *15*, 1294 – 1296.
[4] T. Kasuga, M. Hiramatsu, A. Hoson, T. Sekino, K. Niihara, *Langmuir* **1998**, *14*, 3160 – 3163.
[5] Q. Chen, W. Zhou, G. H. Du, L. M. Peng, *Adv. Mater.* **2002**, *14*, 1208 – 1211.
[6] Q. Chen, G. H. Du, S. Zhang, L. M. Peng, *Acta Crystallogr., Sect. A* **2002**, *58*, 587 – 593.
[7] R. Ma, Y. Bando, T. Sasaki, *Chem. Phys. Lett.* **2003**, *380*, 577 – 582.
[8] J. Yang, Z. Jin, X. Wang, W. Li, J. Zhang, S. Zhang, X. Guo, Z. Zhang, *Dalton Trans.* **2003**, *20*, 3898 – 3901.
[9] X. Sun, Y. Li, *Chem. Eur. J.* **2003**, *9*, 2229 – 2238.
[10] H. Tokudome, M. Miyauchi, *Chem. Commun.* **2004**, 958 – 959.
[11] C. G. Granqvist, *Handbook of Inorganic Electrochromic Materials*, Elsevier, Amsterdam, **1995**.
[12] Y. Matsumoto, A. Funatsu, D. Matsuo, U. Unal, *J. Phys. Chem. B* **2001**, *105*, 10893 – 10899.
[13] L. Wang, Y. Omomo, N. Sakai, K. Fukuda, I. Nakai, Y. Ebina, K. Takada, M. Watanabe, T. Sasaki, *Chem. Mater.* **2003**, *15*, 2873 – 2878.
[14] G. Decher, *Science* **1997**, *277*, 1232 – 1237.
[15] Y. Lvov, K. Ariga, I. Ichinose, T. Kunitake, *J. Am. Chem. Soc.* **1995**, *117*, 6117 – 6123.
[16] N. Sakai, A. Fujishima, T. Watanabe, K. Hashimoto, *J. Electrochem. Soc.* **2001**, *148*, E395 – E398.
[17] L. A. Lyon, J. T. Hupp, *J. Phys. Chem. B* **1999**, *103*, 4623 – 4628.
[18] D. D. Cronemeyer, *Phys. Rev.* **1959**, *113*, 1222 – 1225.

 © 2005 Wiley-VCH Verlag GmbH & Co. KGaA, Weinheim

Sensors

An Electroactive Nitrogen-Rich [4.4]Ferrocenophane Displaying Redox-Switchable Behavior: Selective Sensing, Complexation, and Decomplexation of Mg^{2+} ions**

Antonio Caballero, Vega Lloveras, Alberto Tárraga, Arturo Espinosa, María D. Velasco, José Vidal-Gancedo, Concepció Rovira, Klaus Wurst, Pedro Molina, and Jaume Veciana**

Redox-responsive ligands that contain a ferrocene unit as the redox-active group have been one of the most extensively studied groups among the numerous examples of these ligands.[1] These ferrocene-containing ligands have been widely investigated because of their electrochemical response upon complexation of a suitable guest molecule or ion. A positive shift of the Fe^{II}/Fe^{III} redox couple is observed on coordination of a metal ion because the proximity of the metal alters the ability of the ferrocene framework to be oxidized.[1,2] A further exciting challenge that has been less explored is the design of redox-switchable ligands that are not only able to monitor binding (namely, a shift in the $E_{1/2}$ value upon metal complexation is observed) but are also able to act as an actuator through the progressive electrochemical release of the metal cation (that is, the binding constant upon electrochemical oxidation is decreased). In this context, some electroactive tetrathiafulvalene (TTF) derivatives that exist in three different redox stages (as a neutral species, radical cation, and dication) have been described as tunable materials that can bind a metal cation when neutral (TTF) and then expel it upon oxidation (TTF^{2+}).[3] This is an

[*] A. Caballero, Prof. A. Tárraga, Dr. A. Espinosa, Dr. M. D. Velasco, Prof. P. Molina
Universidad de Murcia
Departamento de Química Orgánica, Facultad de Química
Campus de Espinardo, 30100 Murcia (Spain)
Fax: (+34) 968-364-149
E-mail: pmolina@um.es

V. Lloveras, Dr. J. Vidal-Gancedo, Prof. C. Rovira, Prof. J. Veciana
Institut de Ciencia de Materials de Barcelona (CSIC)
Campus Universitari de Bellaterra
08193 Cerdanyola (Spain)
Fax: (+34) 935-805-729
E-mail: vecianaj@icmab.es

Dr. K. Wurst
Institut für Allgemeine, Anorganische und Theoretische Chemie
Universität Innsbruck
Innrain 52a, A-6020 Innsbruck (Austria)

[**] This work was supported by the Dirección General de Investigación (Spain) (projects MAT2003-04699 and BQU 2001-0014), Generalitat de Catalunya (2001SGR00362 and CERMAE), and Fundación Séneca CARM (PB/72/FS/02). We also thank Acción Integrada Hispano-Austríaca HU20020046, and V.L. is grateful to the Ministerio de Educación y Ciencia for a predoctoral grant.

Supporting information for this article is available on the WWW under http://www.angewandte.org or from the author.

 DOI: 10.1002/anie.200462521 © 2005 Wiley-VCH Verlag GmbH & Co. KGaA, Weinheim

unfamiliar area in ferrocene-based ligands and it has been only described in a very few cases: first, in an early report about the abrupt decrease in the binding strength of Na^+ ions by electrochemical oxidation of a pentaoxa[13]ferrocenophane[4] and then, later on, in a few compounds that had only one ferrocenyl redox-active center.[5]

On the basis of this work, we designed a new highly preorganized molecular system that links two ferrocene subunits that have dissimilar electronic environments through a conjugated double bridge, which comprises a putative cation-binding site. This molecular system should show three different oxidation states with different binding abilities so that a metal cation can be bound in its neutral state and then released upon oxidation of the complexed species. Herein, we report the preparation of one such system, the redox-switchable, azaferrocenophane ligand **4**, that fulfils those electronic and structural characteristics. We also report the ability of **4** to selectively recognize Mg^{2+} ions and the unequivocal demonstration of electrochemical-mediated control of successive trapping and expulsion of Mg^{2+} ions. Furthermore, the ability of **4** to transport Mg^{2+} ions through a liquid membrane is described, in which the switchable activation/deactivation of the ligand is carried out electrochemically.

Compound **4** was prepared (Scheme 1) from the readily available diethyl aminomethylphosphonate (**1**),[6] which was

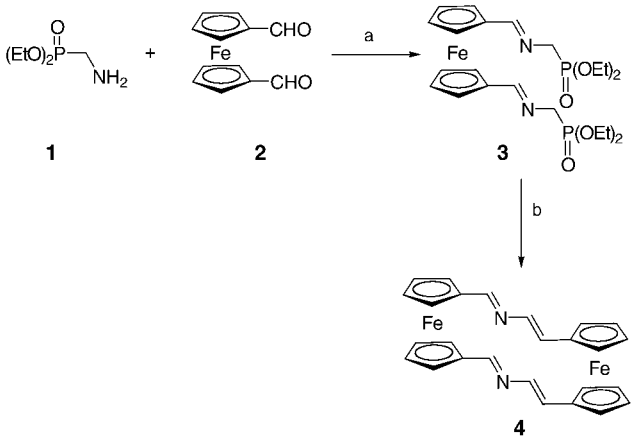

Scheme 1. Synthesis of 2,17-diaza[4,4]ferrocenophane **4**: a) anhydrous Na_2SO_4/CH_2Cl_2, RT, 4 h; b) *n*BuLi/THF, −78 °C, and then **2**, 12 h, RT.

condensed with 1,1′-diformylferrocene[7] (**2**) to give the corresponding *N*-substituted diethyl aminomethylphosphonate **3** in excellent yield (95%). Generation of the metalloenamine by reaction with *n*BuLi at −78 °C and subsequent reaction with one equivalent of 1,1′-diformylferrocene (**2**) provided 2,17-diaza[4,4]ferrocenophane **4** in 31% yield, which was recrystallized from THF and characterized by ^{1}H NMR and ^{13}C NMR spectroscopic, FAB mass-spectrometric, and elemental analysis.

The X-ray crystal structure reveals that the two bridges of compound **4** are in the *E*,*E* form in the solid state (and also in solution as observed by ^{1}H NMR spectroscopy) and that they have an *s-trans* configuration (Figure 1).[8] Consequently, ferrocenophane **4** has two nitrogen atoms that are arranged

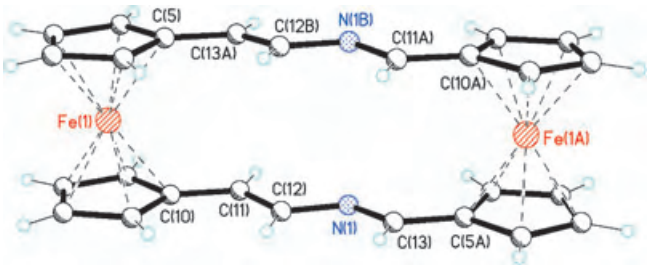

Figure 1. Crystal structure of the ferrocenophane **4**.

in such a way that they can act as a chelating agent for a metal cation: the nitrogen atoms are eclipsed at a distance of 3.48 Å and have their nonbonding pair of electrons on the same side of the molecule.

One of the most interesting attributes of ferrocenophane **4** is the presence of two differentiated redox-active ferrocene moieties close to the cation-binding bisaldimine site. The metal-recognition properties of **4** were evaluated by optical and electrochemical analysis. The cyclic voltammetric (CV) and Osteryoung square-wave voltammetric (OSWV) analyses of **4** (Figure 2) show two well-resolved quasi-reversible one-electron oxidations in a 1:1 ratio at formal potentials of +0.44 and +0.89 V versus decamethylferrocene (DMFc). The first reversible oxidation process arises from the oxidation of the ferrocene unit at the 4-position of the two bridges, while the second is associated with the oxidation of the ferrocene unit at

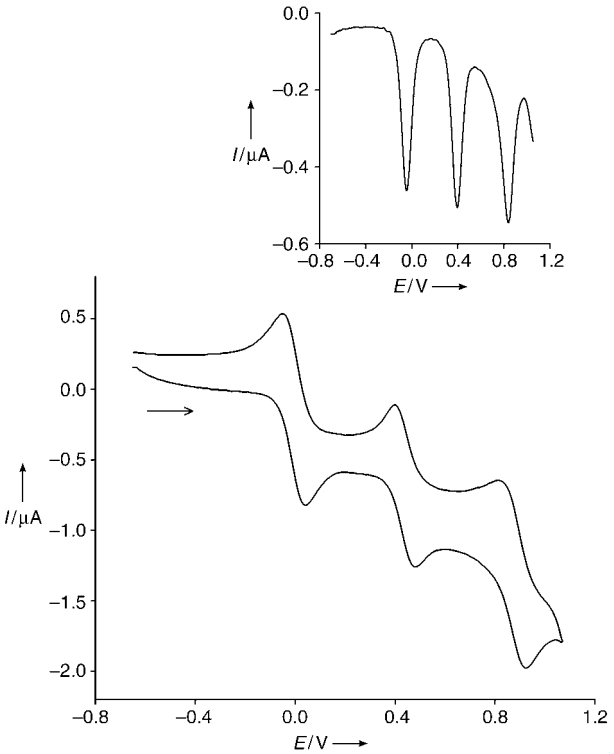

Figure 2. Cyclic voltammogram of **4** in CH_2Cl_2. Conditions: 1 mM of **4** and 0.1 M nBu_4NClO_4, a Pt-disk electrode, and a scan rate of 0.1 Vs^{-1} in the presence of DMFc as the internal standard. Upper inset: square-wave voltammogram of compound **4** (1 mM) in $CH_2Cl_2/(nBu)_4N^+ClO_4^-$ recorded at 0.1 Vs^{-1}.

 © 2005 Wiley-VCH Verlag GmbH & Co. KGaA, Weinheim

the 1-position. Whereas, no perturbation of the voltammograms was observed upon addition of Ca^{2+}, Li^{+}, Na^{+}, and K^{+} ions, even in a large excess, a significant modification was observed for the first oxidation wave upon addition of Mg^{2+} ions (see the Supporting Information). In contrast, the second oxidation wave was apparently not perturbed on the addition of Mg^{2+} ions. This particular behavior is characteristic of a large equilibrium constant for the binding of Mg^{2+} ions by the neutral receptor.[9] The fact that the second oxidation process of complex $[Mg_2(\mathbf{4})]^{4+}$ practically occurs at the same potential as that observed for the free ligand **4** (that is, the $\mathbf{4}^{+}/\mathbf{4}^{2+}$ couple) suggests that the complex is disrupted after the first monoelectronic oxidation of complex $[Mg_2(\mathbf{4})]^{4+}$ and the second oxidation really takes place on the uncomplexed mono-oxidized species $\mathbf{4}^{+}$. Therefore, ligand **4** behaves as a switchable receptor that appears to be a very attractive carrier for the selective transport of Mg^{2+} ions.

The UV/Vis spectrum of the neutral ligand **4** is characterized by a very strong absorption band at 331 nm ($\varepsilon = 17200\,\text{M}^{-1}\,\text{cm}^{-1}$), which is assigned to a high-energy ligand-centred π–π* electronic transition, and a lower-energy weaker band at 500 nm ($\varepsilon = 1600\,\text{M}^{-1}\,\text{cm}^{-1}$), which is attributed to a metal-to-ligand charge-transfer (CT) process (d–π*).[10] Such spectral characteristics confer an orange color to the neutral ferrocenophane **4**. The mono-oxidized species $\mathbf{4}^{+}$ has a remarkable green–brown color and exhibits absorption bands at 355 nm ($\varepsilon = 17000\,\text{M}^{-1}\,\text{cm}^{-1}$) and 528 nm ($\varepsilon = 1900\,\text{M}^{-1}\,\text{cm}^{-1}$) along with a weak CT band at 1353 nm ($\varepsilon = 400\,\text{M}^{-1}\,\text{cm}^{-1}$). The presence of this weak CT band is a clear manifestation of the electronic coupling between the two redox-active ferrocene groups through the conjugated azadiene bridges. The dioxidized species $\mathbf{4}^{2+}$ exhibits a yellowish color and shows absorption bands at 334 nm ($\varepsilon = 17600\,\text{M}^{-1}\,\text{cm}^{-1}$) and 512 nm ($\varepsilon = 1400\,\text{M}^{-1}\,\text{cm}^{-1}$) along with one ligand-to-metal CT band at 1027 nm ($\varepsilon = 290\,\text{M}^{-1}\,\text{cm}^{-1}$).

The addition of increasing amounts of $Mg(ClO_4)_2$ to a solution of **4** in CH_2Cl_2 caused a progressive appearance of a band at 350 nm ($\varepsilon = 19900\,\text{M}^{-1}\,\text{cm}^{-1}$) and a new, more intense band located at $\lambda = 520$ nm ($\varepsilon = 3700\,\text{M}^{-1}\,\text{cm}^{-1}$) as well as the complete disappearance of the initial band at 500 nm. A well-defined isosbestic point at 339 nm indicates that a neat interconversion between the uncomplexed and complexed species occurs (Figure 3). The new band is red-shifted by 20 nm and is responsible for the change of color from orange (neutral ferrocenophane **4**) to deep purple (complexed ferrocenophane $[Mg_2(\mathbf{4})]^{4+}$). This color change can be used for a "naked-eye" detection of Mg^{2+} ions even in the presence of Ca^{2+} ions. The high-energy band of **4** is also red-shifted by 19 nm upon complexation of Mg^{2+} ions. It is important to note that the appearance of an Mg^{2+} ion induced sigmoidal curve in the titrations suggests that a 1:2 host-to-guest complex is formed via the corresponding 1:1 complex. In this case, the binding mode should be estimated on the basis of the following biphasic equilibria:

$$\mathbf{4} + Mg^{2+} \rightleftharpoons [Mg(\mathbf{4})]^{2+};\ K_{11} \quad (1)$$

$$[Mg(\mathbf{4})]^{2+} + Mg^{2+} \rightleftharpoons [Mg_2(\mathbf{4})]^{4+};\ K_{12} \quad (2)$$

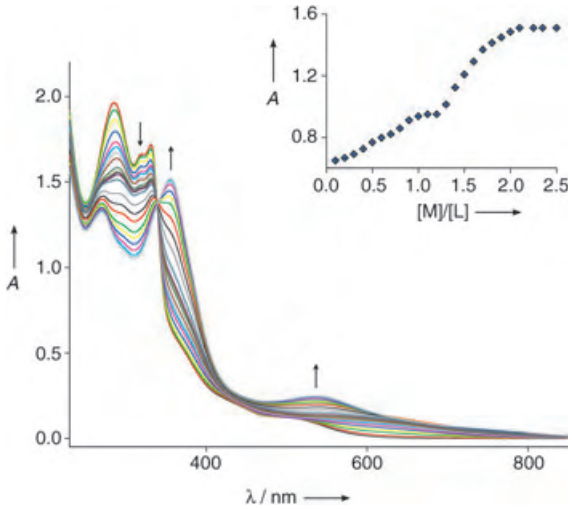

Figure 3. UV/Vis spectra obtained during the titration of **4** with $Mg(ClO_4)_2$ in CH_2Cl_2 ($c = 10^{-4}$ mol dm^{-3}). The initial spectrum is of the neutral species **4** and the final spectrum is of $[Mg_2(\mathbf{4})]^{4+}$. The arrows indicate the absorptions that increased (up) and decreased (down) during the titration experiments. Upper inset: change of absorbance at 537 nm upon addition of $Mg(ClO_4)_2$.

The two association constants, calculated by nonlinear least-squares analysis, were found to be $K_{11} = 9.8 \times 10^5$ and $K_{12} = 6.3 \times 10^5\,\text{M}^{-1}$, respectively.

A spectro–electrochemical study of the electrochemically induced, switchable chemosensor properties of complex $[Mg_2(\mathbf{4})]^{4+}$ was carried out. Thus, two equivalents of $Mg(ClO_4)_2$ were added to a solution of **4** in CH_2Cl_2 with $[n\text{Bu}_4\text{N}]PF_6$ (0.15 M) as the supporting electrolyte to obtain the complexed ferrocenophane $[Mg_2(\mathbf{4})]^{4+}$ species. The complex was oxidized at +1.0 V versus $Ag/AgNO_3$ until complete oxidation was reached and the color of the solution changed from deep purple to yellow (Figure 4). The optical spectrum of the resulting solution was the same as that obtained by the bielectronic oxidation of the free ligand **4** to $\mathbf{4}^{2+}$, thus suggesting that decomplexation of the two Mg^{2+} ions occurs during the electrochemical oxidation. The solution was completely reduced at +0.35 V versus $Ag/AgNO_3$, and the initial spectrum of the complex was fully recovered together with its purple color. Thus, the free dioxidized ligand $\mathbf{4}^{2+}$ is reduced to **4**, which has a large binding affinity for Mg^{2+} ions and nitites the formation of complex $[Mg_2(\mathbf{4})]^{4+}$. Oxidation of complex $[Mg_2(\mathbf{4})]^{4+}$ and its subsequent reduction were carried out over several cycles in a chronoamperometric experiment (Figure 4). The optical spectrum was recorded after each step and found to be fully recovered on completion of the step; thus, demonstrating the reversibility of the complexation/decomplexation process.

A preliminary study of the ability of the ferrocenophane **4** to transport Mg^{2+} ions across a CH_2Cl_2 liquid membrane was also undertaken. The CH_2Cl_2 membrane seperates two aqueous phases, the "source" and "receiving" phases, that are layered at the two branches of an H-type cell with a working electrode in one of the branches (see the Supporting Information). This study measures the time-dependence of the transportation of Mg^{2+} ions by the carrier **4** across the

 © 2005 Wiley-VCH Verlag GmbH & Co. KGaA, Weinheim

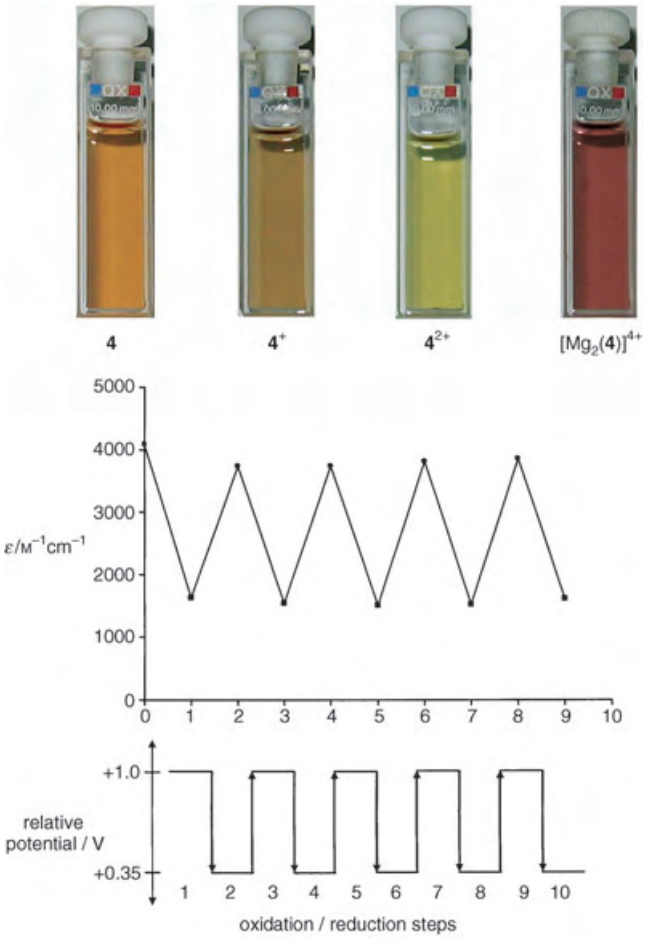

Figure 4. Top: colors shown by the studied species. Bottom: stepwise oxidation and reduction cycles carried out in CH_2Cl_2 by chronoamperometric analysis, which uses fixed potentials at +1.00 and +0.35 V and follows the changes observed by visible spectroscopy at 520 nm.

CH_2Cl_2 liquid membrane. The transport of Mg^{2+} ions was studied in the presence of **4** but in the absence of any applied potential at the working electrode of the H-type cell in a preliminary control experiment. Then, by oxidation of the carrier **4** a controlled potential electrolysis at the working electrode was performed while a constant potential of +0.95 V (versus $Ag/AgNO_3$) was maintained. The transport rate of the Mg^{2+} ions increased abruptly and the stationary state was achieved rapidly after starting the electrolysis (see the Supporting Information). These results are attributed to the decreased ion-binding ability of $\mathbf{4}^{2+}$ with respect to the neutral carrier **4**. A transport rate of Mg^{2+} ion of 3.2×10^{-6} mol h^{-1} was observed in the control experiment with no applied potential but it was increased to 2.1×10^{-5} mol h^{-1} when the controlled potential electrolysis was applied. Thus, electrochemical oxidation leads to a nearly sevenfold increase in the transport rate.

In conclusion, we have reported the first example of a redox-switchable receptor composed of two electronically coupled, electroactive ferrocene subunits that selectively recognizes Mg^{2+} ions through complexation. Transport and release of the Mg^{2+} ions by an external electrochemical stimulus is shown to be possible. The combination of two ferrocene subunits that have dissimilar electronic environments connected by two conjugated bridges with cation-binding sites is shown to be an attractive strategy for preparing new reversible redox-switchable ion carriers.

Received: November 5, 2004
Published online: February 21, 2005

Keywords: electrochemistry · ferrocene · ionophores · magnesium · UV/Vis spectroscopy

[1] a) P. D. Beer, *Adv. Inorg. Chem.* **1992**, *39*, 79–157; b) P. L. Boulas, M. Gomez-Kaifer, L. Echegoyen, *Angew. Chem.* **1998**, *110*, 226–258; *Angew. Chem. Int. Ed. Engl.* **1998**, *37*, 216–247; c) P. D. Beer, *Acc. Chem. Res.* **1998**, *31*, 71–80; d) P. D. Beer, P. A. Gale, *Adv. Phys. Org. Chem.* **1998**, *31*, 1–90; e) A. E. Kaifer, *Acc. Chem. Res.* **1999**, *32*, 62–71; f) P. D. Beer, J. Cadman, *Coord. Chem. Rev.* **2000**, *205*, 131–155; g) P. D. Beer, P. A. Gale, *Angew. Chem.* **2001**, *113*, 502–532; *Angew. Chem. Int. Ed.* **2001**, *40*, 486–516; h) I. E. Philip, A. E. Kaifer, *J. Am. Chem. Soc.* **2002**, *124*, 12678–12679; h) P. V. Bernhardt, E. G. Moore, *Aust. J. Chem.* **2003**, *56*, 239–258.

[2] For recent examples of ferrocene compounds that bind and electrochemically respond to metal cations, see: a) J. L. Lopez, A. Tarraga, A. Espinosa, M. D. Velasco, P. Molina, V. Lloveras, J. Vidal-Gancedo, C. Rovira, J. Veciana, D. J. Evans, K. Wurst, *Chem. Eur. J.* **2004**, *10*, 1815–1826; b) A. Tarraga, P. Molina, J. L. Lopez, M. D. Velasco, *Dalton Trans.* **2004**, 1159–1165; c) M. Li, P. Cai, C. Duan, F. Lu, J. Xie, Q. Meng, *Inorg. Chem.* **2004**, *43*, 5174–5176; d) A. Ion, M. Buda, J.-C. Moutet, E. Saint-Aman, G. Royal, I. Gautier-Luneau, M. Bonin, R. Ziessel, *Eur. J. Inorg. Chem.* **2002**, 1357–1366; e) O. B. Sutcliffe, R. M. Bryce, A. S. Batsanov, *J. Organomet. Chem.* **2002**, *656*, 211–216; f) H. Plenio, C. Aberle, Y. Al Shihaded, J. M. Lloris, R. Martinez-Mañez, T. Pardo, J. Soto, *Chem. Eur. J.* **2001**, *7*, 2848–2861.

[3] F. Le Derf, E. Levillain, G. Trippé, A. Gorgues, M. Sallé, R.-M Sebastian, A.-M. Caminade, J. P. Majoral, *Angew. Chem.* **2001**, *113*, 230–233; *Angew. Chem. Int. Ed.* **2001**, *40*, 224–227; b) F. Le Derf, M. Mazari, N. Mercier, E. Levillain, G. Trippé, A. Riou, P. Richomme, J. Becher, J. Garin, J. Orduna, N. Gallego-Planas, A. Gorgues, M. Sallé, *Chem. Eur. J.* **2001**, *7*, 447–455; c) J. L. Segura, N. Martín, *Angew. Chem.* **2001**, *113*, 1416–1455; *Angew. Chem. Int. Ed.* **2001**, *40*, 1372–1409; d) J. Lyskawa, F. Le Derf, E. Levillain, M. Mazari, M. Sallé, L. Dubois, P. Viel, C. Bureau, S. Palacin, *J. Am. Chem. Soc.* **2004**, *126*, 12194–12195.

[4] T. Saji, I. Kinoshita, *J. Chem. Soc. Chem. Commun.* **1986**, 716–717.

[5] a) A. C. Hall, C. Suarez, A. Hom-Choudhury, A. N. A. Manu, C. D. Hall, G. J. Kirkovits, I. Ghiriviga, *Org. Biomol. Chem.* **2003**, *1*, 2973–2982; b) J. C. Medina, T. T. Goodnow, M. T. Rojas, J. L. Atwood, B. C. Lynn, A. E. Kaifer, G. W. Gokel, *J. Am. Chem. Soc.* **1992**, *114*, 10583–10595.

[6] S. K. Davidsen, G. W. Phillips, S. F. Martin, *Org. Synth.* **1993**, *8*, 451–458.

[7] G. G. A. Balavoine, G. Doisneau, T. Fillebeen-Khan, *J. Organomet. Chem.* **1991**, *412*, 381–382.

[8] X-ray single-crystal diffraction data for **4** was collected on a Nonius KappaCCD diffractometer with an area detector and graphite-monochromized $Mo_{K\alpha}$ radiation ($\lambda = 0.71074$ Å). Crystal data: $C_{26}H_{22}Fe_2N_2$, $M_r = 474.16$, monoclinic, space group $C2/c$ with $a = 20.5134(3)$, $b = 9.9522(2)$, $c = 9.9596(4)$ Å, $\alpha = 90.00$, $\beta = 106.986(2)$, $\gamma = 90.00$, $V = 1944.59(9)$ Å^3, $Z = 4$, $T = 233$ K, $\mu = 15.08$ cm^{-}. Least-squares refinement based on measured reflections with $I > 2\sigma(I)$ led to convergence with a final $R1 =$

 © 2005 Wiley-VCH Verlag GmbH & Co. KGaA, Weinheim

0.0240, *wR*2 = 0.0592, and GOF = 1.063. CCDC-262815 contains the supplementary crystallographic data for this paper. These data can be obtained free of charge from The Cambridge Crystallographic Data Centre via www.ccdc.cam.ac.uk/data_request/cif.

[9] S. R. Miller, D. A. Gustowski, Z. H. Chen, G. W. Gokel, L. Echegoyen, A. E. Kaifer, *Anal. Chem.* **1988**, *60*, 21021 – 21024.

[10] S. Barlow, H. E. Bunting, C. Ringham, J. C. Green, G. V. Bublitz, S. G. Boxer, J. W. Perry, S. R. Marder, *J. Am. Chem. Soc.* **1999**, *121*, 3715 – 3723.

 © 2005 Wiley-VCH Verlag GmbH & Co. KGaA, Weinheim

Fullerenes

Floating Single Hydrogen Molecule in an Open-Cage Fullerene**

Hiroshi Sawa, Yusuke Wakabayashi, Yasujiro Murata, Michihisa Murata, and Koichi Komatsu*

A technique for inserting gaseous or unstable molecules into a molecular cage is a significant problem when researching into molecular capsules for use as hydrogen storage materials or for medicinal applications. We recently succeeded in fully incorporating a H_2 molecule into a derivative of an aza–thia open-cage fullerene (ATOCF). This compound can be regarded as a nanosized container for a single H_2 molecule, with which hydrogen storage can be controlled by pressure and temperature. X-ray diffraction analysis of a single crystal of this fully H_2-encapsulating molecule allowed the successful direct observation of a single H_2 molecule floating inside the hollow cavity of an ATOCF molecule.

Various types of endohedral fullerene complexes are known to date. For example, pure metallofullerenes have been subjected to complete scrutiny as to their structures and properties,[1] but the isolated amounts are generally quite minute. The cages are made of higher fullerenes and the metal atom tends to be located not in the center of the interior space, but close to the carbon cage.[2] These metallofullerenes are generally produced by the arc-discharge method, but the use of such extreme conditions is apparently not suitable for encapsulation of unstable molecules or gases. Rubin et al. reported the synthesis of a fullerene derivative with a 14-membered-ring orifice and succeeded in introducing a He atom and a H_2 molecule inside this fullerene molecule.[3] However, the content of these guest species was so low (1.5 and 5%, respectively) that sufficient information about the encapsulated species could not be obtained, except for NMR data.

We recently succeeded in fully incorporating a H_2 molecule into a derivative of the ATOCF molecule (Figure 1).[4,5] This compound is regarded as a unique model

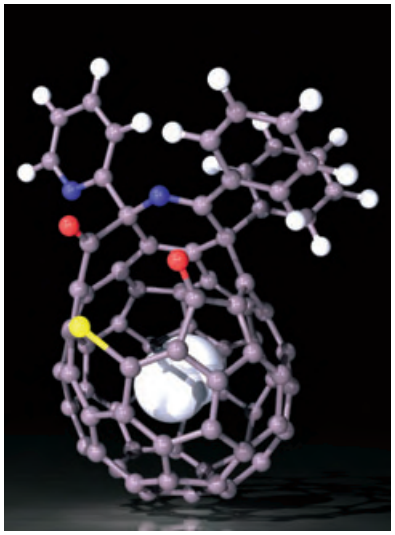

Figure 1. Molecular structure of H_2@ATOCF. The encapsulated H_2 molecule is shown as a space-filling model, and the host molecule is shown as a ball-and-stick model.

that can provide an opportunity to observe a single molecule of H_2 as a completely isolated species. The extraordinary high-field shift ($\delta = -7.25$ ppm) of the ^{1}H NMR signal of the H_2 molecule surely indicates that H_2 is encapsulated *somewhere* inside the fullerene cage. However, we desired more substantial information about the location of the H_2 molecule within the ATOCF cage, hopefully through direct observation of the molecule. X-ray diffraction analysis with synchrotron radiation appeared most suitable for this purpose.

Thus, we conducted an X-ray diffraction study of single crystals of H_2-containing ATOCF (H_2@ATOCF) and of empty-cage ATOCF as a matching reference. Accurate X-ray diffraction data were obtained by synchrotron radiation with a Weissenberg-type imaging-plate detector at BL-1A in the Photon Factory at KEK, Japan.[6] The results showed good agreement with those of a previous report on the crystal structure of ATOCF.[5] According to the results of differential-Fourier calculations, there were clearly observed electron-density peaks with a height of 0.46 electrons Å^{-3} in the cages of H_2@ATOCF in the unit cell, while no such electron density was observed in the case of the empty ATOCF cage. Thus, the direct observation of the H_2 molecule encapsulated in the cage of ATOCF was achieved for the first time.

It is not possible to precisely locate the electron density of a species as small as a H_2 molecule by conventional least-squares refinement. However, we were able to picture an

[*] Prof. Dr. H. Sawa, Dr. Y. Wakabayashi
Institute of Materials Structure Science
High-Energy Accelerator Research Organization
Tsukuba 305-0801 (Japan)
Fax: (+81) 29-864-5623
E-mail: hiroshi.sawa@kek.jp
Dr. Y. Murata, M. Murata, Prof. Dr. K. Komatsu
Institute for Chemical Research, Kyoto University
Uji, Kyoto 611-0011 (Japan)

[**] This work was supported by a Grant-in-Aid for Creative Scientific Research (13NP0201) from the Ministry of Education, Culture, Sports, Science, and Technology of Japan.

 DOI: 10.1002/anie.200462850 © 2005 Wiley-VCH Verlag GmbH & Co. KGaA, Weinheim

image, which enabled us to construct a three-dimensional electron-density map from the diffraction data by using the maximum entropy method (MEM). The MEM analysis was carried out with the Enigma program[7] at a resolution of 128 × 128 × 128 pixels. The *R* factors of the final MEM charge density were 0.028 and 0.024 for H_2@ATOCF and empty ATOCF, respectively. Three-dimensional representations of the final MEM charge densities of H_2@ATOCF and empty ATOCF are shown in Figure 2. The equal-density levels are at

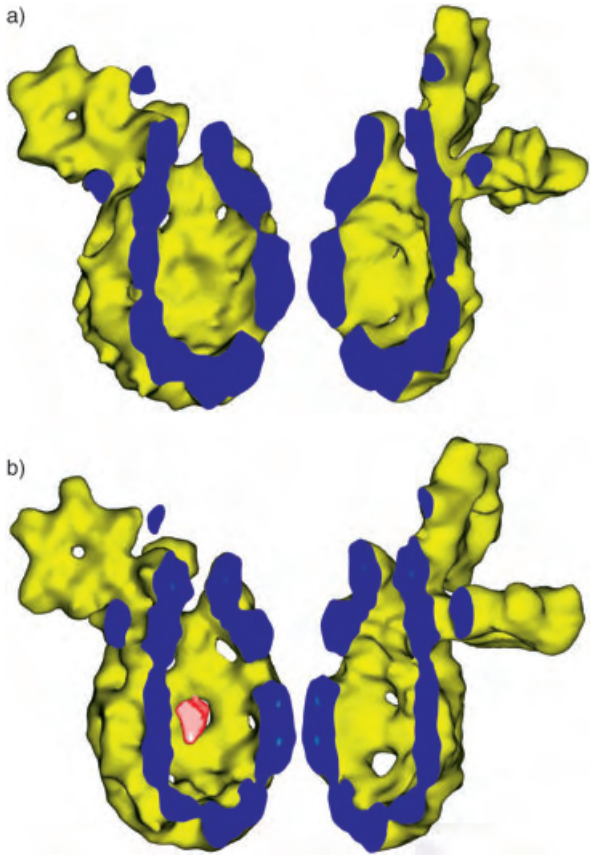

Figure 2. MEM electron densities of a) empty ATOCF and b) H_2@ATOCF as an equal-density contour surface and as a vertical division. The equicontour level is at 0.4 e Å^{-3}. The electron density of the encapsulated H_2 molecule is colored red in (b).

0.4 electrons Å^{-3}. The MEM charge-density maps clearly show an area of electron density, which is colored red in Figure 2, floating at the center of the cage in the H_2@ATOCF molecule. In sharp contrast, no such electron density was observed in the case of the empty ATOCF cage. These characteristic density features are also shown as contour maps in Figure 3.

The main charge density within the fullerene cage is condensed almost at the center of the cage, and a much lower density seems to exist in the area between the center and the inside wall of the cage (Figure 3: vertical division, map 2). However, it is difficult to determine whether the shape of the encapsulated charge density is spherical or elliptical. This ambiguity is most probably caused by the motion of the H_2

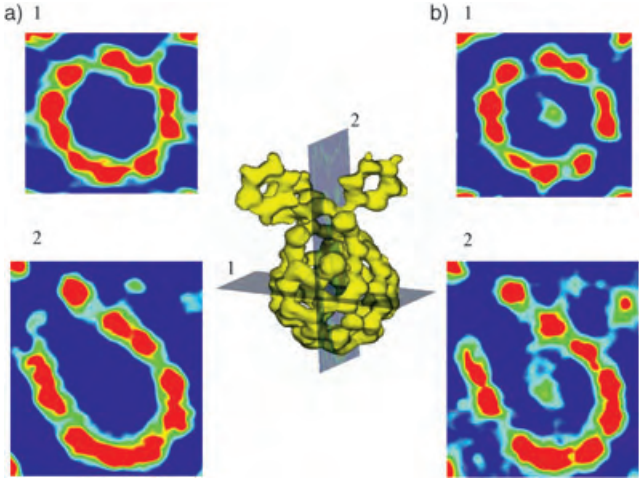

Figure 3. MEM electron-density distributions of a) empty ATOCF and b) H_2@ATOCF for 1) horizontal division and 2) vertical division. The center figure shows the positions of division for (1) and (2). The contour maps are drawn from 0.01 to 0.11 e Å^{-3}.

molecule, because there is no chemical bond between the trapped H_2 and the carbon cage. Very recently, Carravetta et al. investigated the rotational motion of encapsulated H_2 in H_2@ATOCF by low-temperature solid-state NMR measurements.[8] Their results show that the motional anisotropy of the H_2 molecule inside the ATOCF cage is very small, and that the orifice in the ATOCF molecule only slightly perturbs the rotational motion. In the contour vertical division map (Figure 3) there is no electron density along the neck of the ATOCF molecule, which indicates that the H_2 molecule is electronically segregated from the outside of the cage. Therefore, this H_2 molecule is considered to be completely isolated from the outside. In that sense, the environment of the encapsulated H_2 is assumed to be similar to that of the H_2 molecule incorporated in the pristine C_{60} itself, that is, H_2@C_{60}.

Is there any charge-transfer interaction between the encapsulated H_2 molecule and the cage? In the case of metallofullerenes M@C_{82}, the presence of significant charge-transfer interaction between the encapsulated metal and the cage has been reported, which also causes the selection of cage symmetry according to the stability of different isomers.[9,10] In striking contrast, there is no difference in cage structure between H_2@ATOCF and empty ATOCF. Thus, we conclude that there is no appreciable charge transfer between the encapsulated H_2 and the cage.

The precise electron-density profile obtained by the MEM analysis is visualized by the dependence of the electron density on the radius (*r*), or distance from the center of the cage (Figure 4). The filled and open circles represent the profiles for H_2@ATOCF and empty ATOCF, respectively. The maximum peaks at around $r \approx 3.6$ Å apparently correspond to the cage frame of the ATOCF molecule itself. In the case of an empty ATOCF cage, no charge density is observed in the region of $r < 1.8$ Å. In contrast, the electron density of H_2@ATOCF, which appears to show a local maximum at

 © 2005 Wiley-VCH Verlag GmbH & Co. KGaA, Weinheim

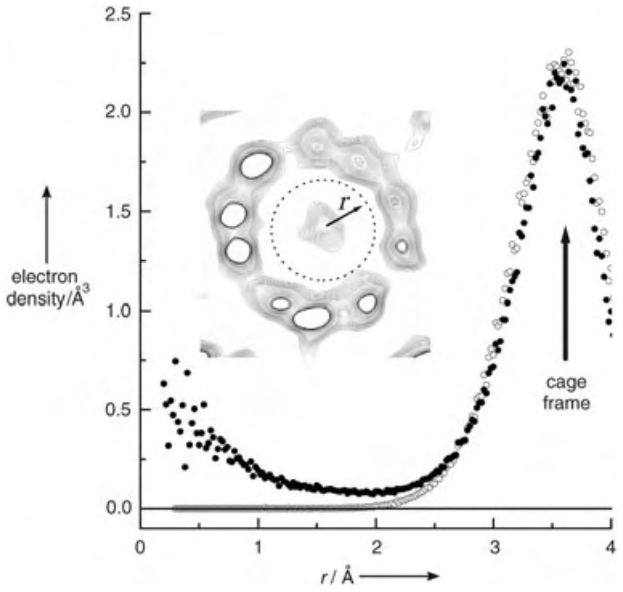

Figure 4. Dependence of electron density on the radius *r* from the center of the cage for endohedral (●) and empty (○) ATOCF molecules. The inset picture demonstrates the determination of the radius (*r*). The electron-density peak for H_2@ATOCF shows a floating H_2 molecule.

the center ($r = 0$ Å), gradually decreases as the distance from the center increases until *r* reaches about 2 Å, but the minimum value for the electron density is not exactly zero. This electron-distribution profile involving nonzero electron density seems to reflect the unsteady motion of the encapsulated H_2. The number of electrons belonging to this H_2 molecule, which was estimated by integration from the center of the cage to the minimum point of electron density, turned out to be 2.0 ± 0.1. This result exactly corresponds to the presence of one H_2 molecule at the center of the hollow cage of the ATOCF molecule, which is in excellent agreement with the ^{1}H NMR result.[4]

The preference of the H_2 molecule to be located at the center of the cage is considered to be the result of van der Waals interaction between the H_2 molecule and the 60 sp^2-hybridized carbon atoms that have an inward curvature in the ATOCF molecule. A preliminary theoretical calculation by density functional theory conducted for H_2@C_{60} revealed that the total energy loss caused by shifting the H_2 molecule from the center of the cage is 0.02, 0.2, and 1.0 eV for a H_2 shift of 0.5, 1, and 1.5 Å from the center, respectively.[11] This result suggests that the encapsulated H_2 molecule is confined to the spherical space at the center of the cage, and strongly supports the results of the MEM analysis.

In summary, we have observed a single H_2 molecule encapsulated in the fullerene cage of ATOCF with synchrotron X-ray diffraction experiments and MEM analysis. The H_2@ATOCF molecule is regarded as an excellent system to examine the important issues characteristic of a single isolated H_2 molecule, for example, *ortho*-H_2 to *para*-H_2 conversion, and the quantum motion of the H_2 molecule at low temperatures in a tiny space. At present H_2@ATOCF is the only molecule which can allow us to discuss the electronic state of a H_2 molecule that is entirely isolated from the atmosphere.

Received: December 8, 2004
Published online: February 23, 2005

Keywords: cage compounds · fullerenes · host–guest systems · hydrogen · X-ray diffraction

[1] a) H. Shinohara, *Rep. Prog. Phys.* **2000**, *63*, 843 – 892; b) *Endofullerenes: A New Family of Carbon Clusters* (Eds.: T. Akasaka, S. Nagase), Kluwer, Dordrecht, **2002**.
[2] For examples, see: a) M. Tanaka, B. Umeda, E. Nishibori, M. Sakata, Y. Saito, M. Ohno, H. Shinohara, *Nature* **1995**, *377*, 46 – 49; b) C.-R. Wang, T. Kai, T. Tomiyama, T. Yoshida, Y. Kobayashi, E. Nishibori, M. Takata, M. Sakata, H. Shinohara, *Nature* **2000**, *408*, 426 – 427.
[3] Y. Rubin, T. Jarrosson, G.-W. Wang, M. D. Bartberger, K. N. Houk, G. Schick, M. Saunders, R. J. Cross, *Angew. Chem.* **2001**, *113*, 1591 – 1594; *Angew. Chem. Int. Ed.* **2001**, *40*, 1543 – 1546.
[4] Y. Murata, M. Murata, K. Komatsu, *J. Am. Chem. Soc.* **2003**, *125*, 7152 – 7153.
[5] Y. Murata, M. Murata, K. Komatsu, *Chem. Eur. J.* **2003**, *9*, 1600 – 1609.
[6] The X-ray wavelength was 1.0 Å. The intensity of the Bragg reflections was measured in a half-sphere of reciprocal space in the range $2\theta < 120°$. The sample was cooled at 200 K by a N_2-gas flow-type refrigerator. The Rapid-Auto program by MSC Corporation was used for two-dimensional image processing; the Sir2002 program was used for the direct method. The number of observed reflections with $I > 5\sigma(I)$ was 9449 for the H_2@ATOCF crystal and 9302 for the empty ATOCF crystal. The Shelx97 program was used for refinements. After full refinement, the *R* factor was 0.09 for the H_2@ATOCF crystal and 0.08 for the empty one.
[7] H. Tanaka, M. Takata, E. Nishibori, K. Kato, T. Iishi, M. Sakata, *J. Appl. Crystallogr.* **2002**, *35*, 282 – 286.
[8] M. Carravetta, Y. Murata, M. Murata, I. Heinmaa, R. Stern, A. Tontcheva, A. Samoson, Y. Rubin, K. Komatsu, M. H. Levitt, *J. Am. Chem. Soc.* **2004**, *126*, 4092 – 4093.
[9] K. Kobayashi, S. Nagase, *Chem. Phys. Lett.* **1998**, *282*, 325 – 329.
[10] S. Nagase, K. Kobayashi, *Chem. Phys. Lett.* **1994**, *231*, 319 – 324.
[11] S. Tsuneyuki, K. Akagi, private communication. The calculation is done within the generalized gradient approximation (PW91) with Gaussian basis functions 6-31G(d,p).

 © 2005 Wiley-VCH Verlag GmbH & Co. KGaA, Weinheim

Enzyme Inhibitors

Switching on a Signaling Pathway with an Organoruthenium Complex**

*Douglas S. Williams, G. Ekin Atilla, Howard Bregman, Arpine Arzoumanian, Peter S. Klein, and Eric Meggers**

Altering cellular function with small synthetic molecules is a general approach for the design of drugs (medicinal chemistry) and molecular probes (chemical genetics). Medicinal chemistry and chemical genetics are focused predominately on the design of organic molecules, whereas inorganic compounds find applications mainly for their reactivity (e.g., cisplatin as DNA-reactive therapeutic) or imaging properties (e.g., gadolinium complexes as MRI diagnostics).[1,2] We are exploring a new direction that aims at utilizing the unique structural opportunities of metal complexes for the design of "organiclike" small-molecule probes and drugs.[3,4] We recently described an organoruthenium compound to be a low-nanomolar inhibitor for the protein kinase glycogen synthase kinase 3 (GSK-3).[4] Here we disclose our success in developing this compound into a molecular probe for cellular signal transduction pathways involving GSK-3.[5]

Our strategy for the design of metal complexes as protein kinase inhibitors uses the class of indolocarbazole alkaloids (e.g., staurosporine) as a lead structure. Accordingly, these metal complexes bear a bidentate ligand which retains the structural features of the indolocarbazole heterocycle. This targets the metal complexes to the ATP-binding site by enabling two hydrogen bonds to the backbone of the hinge between the N-terminal and C-terminal kinase domains, analogous to ATP and conventional organic indolocarbazole inhibitors (Scheme 1).[6] The remaining ligand sphere of the ruthenium atom gives the opportunity to create interactions with other parts of the ATP-binding site. Following this strategy, we recently described ruthenium compound **1-H** as a selective low-nanomolar and ATP-competitive inhibitor of GSK-3.[4] The key component of the design was the novel pyridocarbazole ligand **2-H**, derived from arcyriaflavin A by just replacing one indole moiety with a pyridine residue.

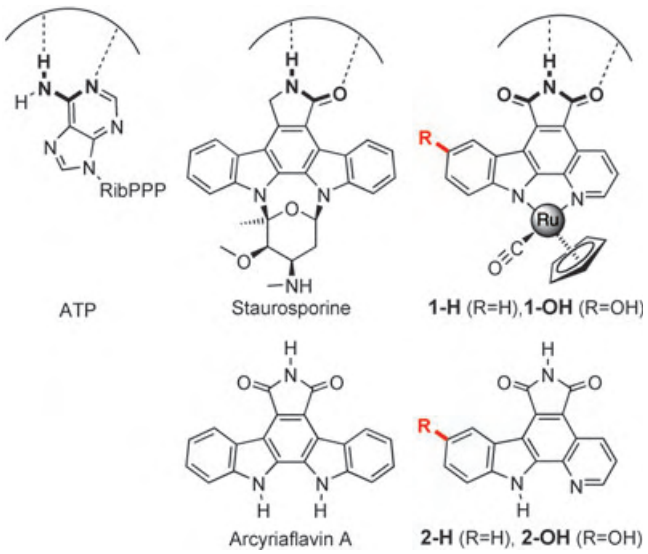

Scheme 1. Designing ruthenium complexes as protein kinase inhibitors by mimicking ATP-competitive indolocarbazoles.

Here we introduce the ruthenium complex **1-OH** (Scheme 1), derived from **1-H** by adding a single hydroxy group to the indole moiety. Molecular modeling suggests that this OH group can occupy a small hydrophilic cavity within the ATP-binding site of GSK-3. Indeed, this modification not only increases the affinity for GSK-3 by an order of magnitude, but at the same time increases water solubility considerably, and thus makes it a promising molecular probe for GSK-3. GSK-3 is a component and negative regulator of the wnt signaling pathway, and we demonstrate in the following that **1-OH** can switch on the wnt signaling pathway by inhibiting GSK-3 inside living cells and in *Xenopus* embryos.

We devised a short and economic synthetic route to this class of metalated pyridocarbazoles (Scheme 2). Starting with aryl hydrazine hydrochloride **3**, Fischer indole synthesis and protecting-group exchange lead to pyridoindole **4**, which is deprotonated and treated with the TBS-protected dibromomaleimide **5** to yield monosubstitution product **6**. The key step of the synthetic scheme is the following smooth anaerobic photocyclization to the TBS-protected pyridocarbazole **7** in 78% yield.[7] Compound **7** can be deprotected with TBAF to give **2-OH** or treated with $[Ru(Cp)(CO)(CH_3CN)_2]PF_6$ in the presence of K_2CO_3 to yield cyclometalated ruthenium complex **8**.[8] Subsequent TBS deprotection with TBAF gives **1-OH**. Complex **1-OH** is stable in aqueous solution, in cell culture medium, under air, and can even withstand a 5 mM solution of 2-mercaptoethanol for 12 h without any sign of decomposition, as determined by 1H NMR spectroscopy. Furthermore, **1-OH** also has favorable solubility in water. For example, it can be dissolved in 3% DMSO/water at a concentration of 1 mM.

We next examined the potency of **1-OH** by determining the concentration required for 50% inhibition (IC_{50}) of GSK-3α (the α isoform) and GSK-3β (the β isoform). The IC_{50} of **1-OH** is 300 pM and 500 pM for GSK-3α and GSK-3β, respec-

[*] D. S. Williams, G. E. Atilla, H. Bregman, Prof. Dr. E. Meggers
Department of Chemistry
University of Pennsylvania
231 South 34th Street, Philadelphia, PA 19104 (USA)
Fax: (+1) 215-746-0348
E-mail: meggers@sas.upenn.edu
A. Arzoumanian, Prof. Dr. P. S. Klein
Department of Medicine
Division of Hematology-Oncology and
Howard Hughes Medical Institute
University of Pennsylvania
415 Curie Blvd, Philadelphia, PA 19104 (USA)

[**] We thank the University of Pennsylvania and the Camille and Henry Dreyfus Foundation for financial support of this research.

Supporting information for this article is available on the WWW under http://www.angewandte.org or from the author.

 © 2005 Wiley-VCH Verlag GmbH & Co. KGaA, Weinheim DOI: 10.1002/anie.200462501

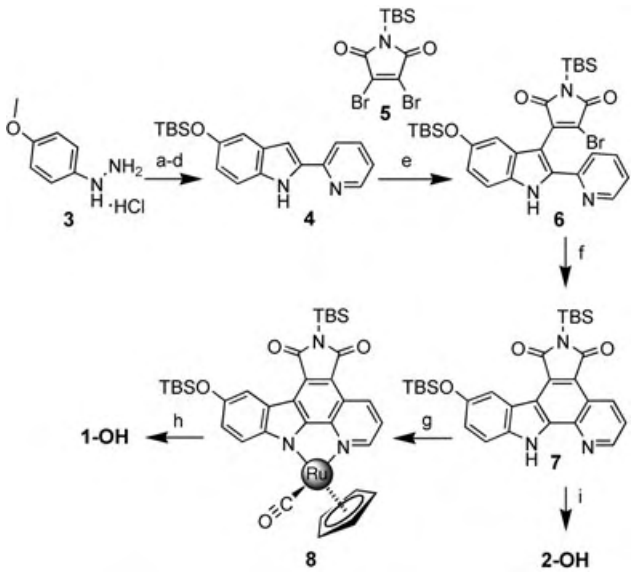

Scheme 2. Synthesis of ruthenium complex **1-OH** and pyridocarbazole **2-OH**. a) 2-Acetylpyridine, *t*BuOH, 4 h reflux (100%). b) Trimethylsilyl polyphosphate, 115°C, overnight (63%). c) BBr_3, CH_2Cl_2, −60°C, then RT overnight (87%). d) DIEA, DMF, 0°C, 40 min, then TBS triflate, 0°C, 1 h (71%). e) Li hexamethyldisilazide, THF, −15°C, 45 min, then **5** in THF, −15°C, 15 min, then RT, 45 min (58%). f) *hν*, Pyrex filter, MeCN, 3 h, (78%). g) $[Ru(Cp)(CH_3CN)_2(CO)]PF_6$, K_2CO_3, MeCN, 55°C, overnight (86%). h) TBAF, CH_2Cl_2, RT, 30 min (87%). i) TBAF, CH_2Cl_2, RT, 30 min (80%). DIEA = *N*,*N*-diisopropylethylamine, TBAF = tetrabutylammonium fluoride, TBS = *tert*-butyldimethylsilyl.

tively, approximately an order of magnitude lower than that of the initial complex **1-H**. For comparison, ruthenium compound **1-OH** is at least 100 times more potent against GSK-3 than staurosporine under our experimental conditions (IC_{50} of 40 nM against GSK-3α).[9–12] Methylation of the imide nitrogen atom (**Me1-OH**) reduces the activity dramatically by almost four orders of magnitude (IC_{50} of 2 μM against GSK-3α), as demonstrated by the IC_{50} curves in Figure 1, which

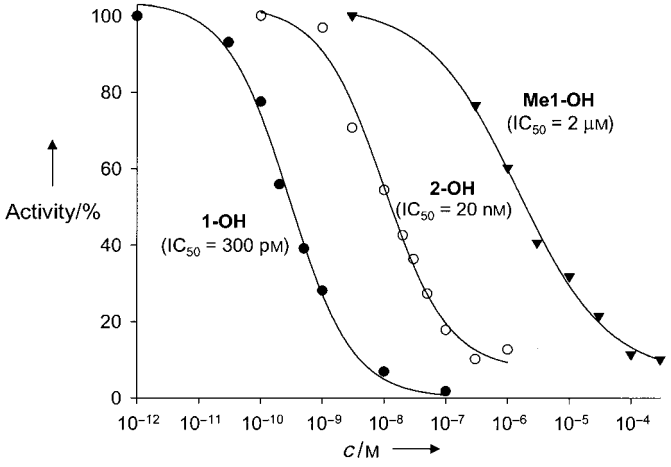

Figure 1. IC_{50} curves with GSK-3α obtained by phosphorylation of phosphoglycogen synthase peptide-2 with [γ-32P]ATP: ruthenium complex **1-OH** (●), ligand **2-OH** (○), and methylated ruthenium complex **Me1-OH** (▼).

reconfirms that the potency of **1-OH** is entirely based on specific recognition. It is also noteworthy that ligand **2-OH** is almost two orders of magnitude less active than the corresponding ruthenium complex **1-OH**, clearly verifying that the entire assembly is necessary for full activity.

Ruthenium complex **1-OH** also shows high selectivity. The protein kinases Abl (IC_{50} = 1 μM), CHK-1 (IC_{50} = 2 μM), Lck (IC_{50} = 500 nM), MAPK-1 (IC_{50} > 3 μM), RSK-1 (25 nM), Src (IC_{50} = 4 μM), and Zap-70 (IC_{50} > 10 μM) are inhibited at concentrations that are 80 to more than 30000 times higher relative to GSK-3α. Even the evolutionarily closely related protein kinase CDK-2 is only inhibited with an IC_{50} of 200 nM.[9–12]

Next, we investigated whether **1-OH** can inhibit GSK-3 inside mammalian cells. GSK-3 is a negative regulator of the wnt signal transduction pathway that phosphorylates β-catenin.[13] Phosphorylated β-catenin is unstable and is degraded rapidly by the proteasome. Wnt signaling inhibits GSK-3, leading to stabilization of β-catenin protein. β-Catenin then accumulates and serves as a transcriptional coactivator through its interaction with the T-cell factor (Tcf) family of transcription factors. Thus inhibition of GSK-3 by pharmacological inhibitors or by wnt signaling leads to increased β-catenin levels and activation of wnt-dependent transcription.

To test for cellular accumulation of β-catenin as a response to inhibition of GSK-3 by ruthenium complex **1-OH**, we used human embryonic kidney cells (HEK293T) that have stably incorporated a Tcf-luciferase transcription reporter (OT-Luc cells). This transcription reporter generates luciferase in response to increased concentrations of β-catenin.[14] Exposure of OT-Luc cells to varying concentrations of **1-OH** over a period of 24 h yields a strong upregulation of luciferase in the concentration window of 3 μM down to 100 nM (Figure 2A). For example, at a **1-OH** concentration of 300 nM, luciferase activity is enhanced by a factor of 1180. Intriguingly, at the same time, methylated control **Me1-OH** and free ligand **2-OH** do not yield any significant increase in luciferase activity at a concentration of 1 μM (1.6- and 2.4-fold, respectively). As a positive control, the established selective GSK-3 inhibitor LiCl leads to an increase of the luminescence signal by a factor of 1190 at a concentration of 30 mM.[14,15]

To verify the accumulation of β-catenin directly, we analyzed the cellular β-catenin concentration by Western blotting after incubation with **1-OH**. Figure 2B demonstrates an increase in β-catenin in the presence of **1-OH**, but not **Me1-OH** or **2-OH**, at 1 μM. These experiments demonstrate that ruthenium complex **1-OH** crosses the cell membrane and activates the wnt pathway at low micromolar and even nanomolar concentrations.

It is also noteworthy that **1-OH** does not show any signs of cytotoxicity at concentrations of 3 μM or less, supporting our assumption that the kinetically inert ruthenium center is only an innocent nonreactive bystander. The integrity of complex **1-OH** inside the cell is also reinforced by the fact that the entire ligand assembly is necessary for the activity inside the cell and that the free ligand **2-OH** does not activate the wnt pathway itself at similar concentrations. This is a remarkable

 © 2005 Wiley-VCH Verlag GmbH & Co. KGaA, Weinheim

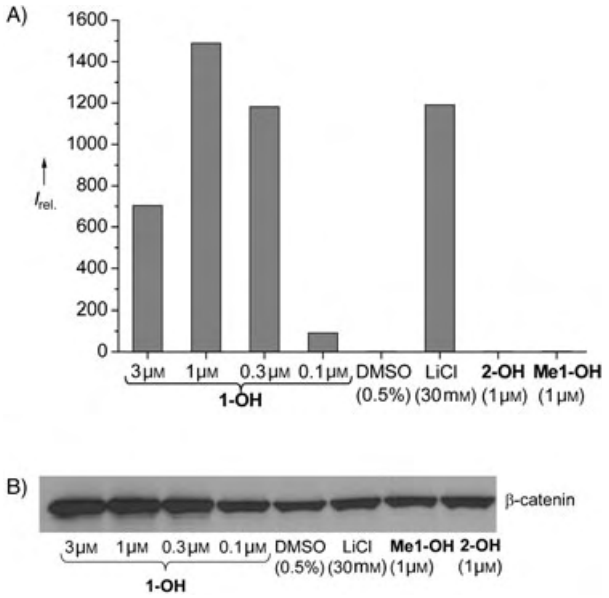

Figure 2. Cells transfected with a β-catenin-responsive luciferase reporter were treated with different concentrations of **1-OH**, ligand **2-OH**, and methylated ruthenium complex **Me1-OH** for 24 h. LiCl served as a positive control, and DMSO as a negative control. A) Relative luciferase activity determined after cell lysis, addition of the substrate luciferin, and luminescence measurement. B) Western blot of the cell lysate qualitatively detecting the amount of β-catenin.

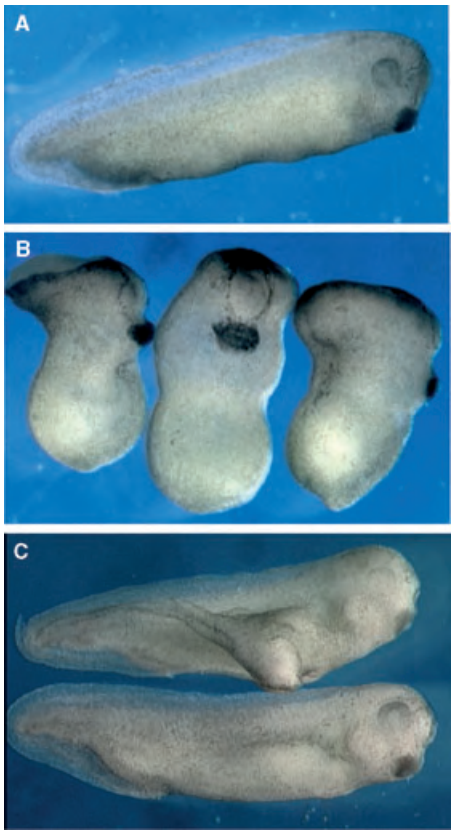

Figure 3. Effect of **1-OH** on dorsal development in *Xenopus laevis*. A) Control tadpole. B) *Xenopus* embryos were treated with **1-OH** (10 μM) added to the culture medium from the 32-cell stage until midblastula stage and then allowed to develop until tadpole stage. 100% of embryos showed this hyperdorsalized phenotype ($n = 29$). A similar effect was observed with **1-OH** at 5 μM ($n = 27$; data not shown). C) **1-OH** (ca. 0.5 mM in 10% DMSO) was injected into a ventral blastomere of 32–64-cell stage *Xenopus* embryos (upper embryo, with twinned dorsal axis). Control injections with water or DMSO did not affect dorsal axis development (lower embryo in C).

observation considering the millimolar concentrations of highly metallophilic thiols such as glutathione, cysteine, and cysteine-containing proteins within the cell.

Finally, we investigated the in vivo effects of **1-OH**. β-Catenin is required for dorsal axis formation in *Xenopus laevis* embryos, while ectopic activation of the wnt pathway, for example, with lithium, induces an ectopic dorsal axis.[16] Thus, we examined the phenotypes of embryos treated with **1-OH**. *Xenopus* embryos were exposed to **1-OH** added to the culture medium from the 32-cell stage until the midblastula stage (stage 8.5), and then were transferred to control medium until the tadpole stage. 100% of embryos ($n = 56$) treated with 5 or 10 μM **1-OH** demonstrated a hyperdorsalized phenotype, with expansion of dorsal and anterior structures and loss of posterior tissues (Figure 3B), highly similar to embryos exposed to lithium or the recently described GSK-3 inhibitor 6-bromoindirubin-3′-oxime.[10] Furthermore, injection of **1-OH** into a ventral blastomere at the 32–64-cell stage caused formation of a complete secondary dorsal axis (Figure 3C), similar to effects observed with injection of LiCl.[15–17] Thus, it can be concluded that ruthenium complex **1-OH** inhibits GSK-3 and activates wnt signaling in vivo in *Xenopus* embryos.

In summary, we have reported a ruthenium complex, **1-OH**, which is a highly potent inhibitor for the protein kinase GSK-3 and demonstrated that **1-OH** can switch on the wnt signal transduction pathway inside living cells and in *Xenopus* embryos. Such properties of an organometallic compound are unprecedented, and this success indicates that our strategy of using kinetically inert metal centers as rigid structural scaffolds for the design of enzyme inhibitors leads to new opportunities for creating highly potent molecular probes and ultimately drugs.

Received: November 2, 2004
Published online: March 2, 2005

Keywords: bioinorganic chemistry · enzymes · medicinal chemistry · ruthenium · signal transduction

[1] Metal based drugs: a) *Chem. Rev.* **1999**, *99*, 2201–2842 (Eds.: C. Orvig, M. J. Abrams); b) Z. Guo, P. Sadler, *Angew. Chem.* **1999**, *111*, 1512–1531; *Angew. Chem. Int. Ed.* **1999**, *38*, 1512–1531; c) *Coord. Chem. Rev.* **2002**, *232*, 1–230 (Ed.: N. Farrell).

[2] For bioorganometallic chemistry, see a) K. Severin, R. Bergs, W. Beck, *Angew. Chem.* **1998**, *110*, 1722–1743; *Angew. Chem. Int. Ed.* **1998**, *37*, 1634–1654; b) D. B. Grotjahn, *Coord. Chem. Rev.* **1999**, *190*, 1125–1141; c) *J. Organomet. Chem.* **1999**, *589*, 1–126 (Ed.: G. Jaouen); d) N. Metzler-Nolte, *Angew. Chem.* **2001**, *113*, 1072–1076; *Angew. Chem. Int. Ed.* **2001**, *40*, 1040–1043; e) R. H. Fish, G. Jaouen, *Organometallics* **2003**, *22*, 2166–2177;

 © 2005 Wiley-VCH Verlag GmbH & Co. KGaA, Weinheim

f) R. Stodt, S. Gencaslan, I. M. Müller, W. S. Sheldrick, *Eur. J. Inorg. Chem.* **2003**, 1873 – 1882.
[3] L. Zhang, P. J. Carroll, E. Meggers, *Org. Lett.* **2004**, *6*, 521 – 523.
[4] H. Bregman, D. S. Williams, G. E. Atilla, P. J. Carroll, E. Meggers, *J. Am. Chem. Soc.* **2004**, *126*, 13594 – 13595.
[5] For pioneering work on using chemically inert ruthenium complexes as bioactive compounds in vivo, see a) F. P. Dwyer, E. C. Gyarfas, W. P. Rogers, J. H. Koch, *Nature* **1952**, *170*, 190 – 191; b) F. P. Dwyer, E. C. Gyarfas, R. D. Wright, A. Shulman, *Nature* **1957**, *179*, 425 – 426.
[6] a) L. M. Toledo, N. B. Lydon, *Structure* **1997**, *5*, 1551 – 1556; b) A. M. Lawrie, M. E. M. Noble, P. Tunnah, N. R. Brown, L. N. Johnson, J. A. Endicott, *Nat. Struct. Biol.* **1997**, *4*, 796 – 801.
[7] A related approach was used to synthesize granulatimides: a) T. Yoshida, M. Nishiyachi, N. Nakashima, M. Murase, E. Kotani, *Chem. Pharm. Bull.* **2002**, *50*, 872 – 876; b) T. Yoshida, M. Nishiyachi, N. Nakashima, M. Murase, E. Kotani, *Chem. Pharm. Bull.* **2003**, *51*, 209 – 214.
[8] A related cyclometalation of 2-pyridylindoles and 2-pyridylpyrroles has been reported: a) R. P. Thummel, V. Hedge, *J. Org. Chem.* **1989**, *54*, 1720 – 1725; b) F. Wu, C. M. Chamchoumis, R. P. Thummel, *Inorg. Chem.* **2000**, *39*, 584 – 590.
[9] For a review on potent small organic inhibitors of GSK-3, see a) A. Martinez, A. Castro, I. Dorronsoro, M. Alonso, *Med. Res. Rev.* **2002**, *22*, 373 – 384.
[10] L. Meijer, A.-L. Skaltsounis, P. Magiatis, P. Polychronopoulos, M. Knockaert, M. Leost, X. P. Ryan, C. A. Vonica, A. Brivanlou, R. Dajani, C. Crovace, C. Tarricone, A. Musacchio, S. M. Roe, L. Pearl, P. Greengard, *Chem. Biol.* **2003**, *10*, 1255 – 1266.
[11] J. Witherington, V. Bordas, A. Gaiba, A. Naylor, A. D. Rawlings, B. P. Slingsby, D. G. Smith, A. K. Takle, R. W. Ward, *Bioorg. Med. Chem. Lett.* **2003**, *13*, 3059 – 3062.
[12] C. Kunick, K. Lauenroth, M. Leost, L. Meijer, T. Lemcke, *Bioorg. Med. Chem. Lett.* **2004**, *14*, 413 – 416.
[13] a) P. J. Morin, *BioEssays* **1999**, *21*, 1021 – 1030; b) P. Cohen, S. Frame, *Nat. Rev. Mol. Cell Biol.* **2001**, *2*, 769 – 776; c) R. S. Jope, G. V. W. Johnson, *Trends Biochem. Sci.* **2004**, *29*, 95 – 102.
[14] F. Zhang, C. J. Phiel, L. Spece, N. Gurvich, P. S. Klein, *J. Biol. Chem.* **2003**, *278*, 33067 – 33077.
[15] P. S. Klein, D. A. Melton, *Proc. Natl. Acad. Sci. USA* **1996**, *93*, 8455 – 8459.
[16] J. Heasman, *Development* **1997**, *124*, 4179 – 4191.
[17] W. B. Busa, R. L. Gimlich, *Dev. Biol.* **1989**, *132*, 315 – 324.

 © 2005 Wiley-VCH Verlag GmbH & Co. KGaA, Weinheim

Cell Signaling

A Small-Molecule Agonist of the Wnt Signaling Pathway**

Jun Liu, Xu Wu, Brian Mitchell, Chris Kintner, Sheng Ding, and Peter G. Schultz**

The Wnt signaling pathway plays an important role in a variety of physiological and pathological processes by regulating genes involved in cellular adhesion, proliferation, and differentiation.[1,2] Many of the key components of the signaling pathway have been elucidated. The Wnt ligand activates downstream signal transduction through interaction with its receptor, Frizzled. This interaction leads to the inhibition of β-catenin phosphorylation by the axin–APC–GSK-3β complex and results in the accumulation of β-catenin in the cytoplasm.[3,4] β-Catenin then translocates to the nucleus and forms a complex with T-cell factor/lymphoid-enhancer factor (TCF/LEF), which drives target gene expression. Because Wnt signaling is essential for many aspects of early embryonic development, genetic alteration of this pathway often results in complicated embryonic defects in animal models, which complicates the interpretation of experimental results.[1] In contrast, small-molecule agonists or antagonists offer greater temporal control over Wnt signaling and provide useful tools for the studies of adult-tissue homeostasis and regeneration, and embryogenesis in animal models.[5] Herein we report the identification and characterization of a small-molecule agonist of Wnt that activates Wnt signaling in cellular assays as well as in a *Xenopus* model.

Combinatorial small-molecule libraries that consist of 100000 heterocyclic compounds (including substituted purines, pyrimidines, indoles, quinazolines, pyrazines, pyrrolopyrimidines, pyrazolopyrimidines, phthalazines, pyridazines, and quinoxalines) were screened for small-molecule modulators of Wnt signaling.[6–9] A reporter-based cellular assay was used to measure the transcriptional activity of β-

[*] Dr. J. Liu, Dr. X. Wu,[+] Dr. S. Ding, Dr. P. G. Schultz
Department of Chemistry and
The Skaggs Institute for Chemical Biology
The Scripps Research Institute
10550 North Torrey Pines Road, SR202, La Jolla, CA 92037 (USA)
Fax.: (+1) 858-784-9440
E-mail: sding@scripps.edu
schultz@scripps.edu
Dr. B. Mitchell,[+] Dr. C. Kintner
The Salk Institute for Biological Studies
P.O. Box 85800, La Jolla, California 92186 (USA)
[+] These authors contributed equally to this paper.

[**] This work was supported by the Novartis Research Foundation and the Skaggs Institute for Chemical Biology (P.G.S.). We thank Dr. Xiang-ju Gu and Dr. Carsten Andersen for various reagents and technical assistance in GSK-3β kinase assays. This is manuscript 16945-CH of the Scripps Research Institute.

Supporting information for this article is available on the WWW under http://www.angewandte.org or from the author.

 DOI: 10.1002/anie.200462552 © 2005 Wiley-VCH Verlag GmbH & Co. KGaA, Weinheim

catenin/TCF in 384-well cell culture plates. β-Catenin/TCF transcriptional activity is dependent on Wnt signaling and can be used to monitor the activity of the Wnt signaling pathway.[1] The reporter construct encodes the luciferase gene driven by β-catenin/TCF-responsive elements.[10] 293T cells were transiently transfected with the reporter construct in T75 cell culture flasks and replated onto 384-well cell culture plates after overnight culture; 24 h later, cells were treated with library compounds at a concentration of 10 μM. After incubation for another 24 h, luciferase activity was measured, and a number of compounds were identified as potent modulators of the Wnt/β-catenin signaling pathway. One such compound, 2-amino-4-[3,4-(methylenedioxy)benzylamino]-6-(3-methoxyphenyl)pyrimidine (**1**; Figure 1a), induces β-catenin- and TCF-dependent transcriptional activity in a dose-dependent manner with an EC_{50} value of 0.7 μM (Figure 1b).

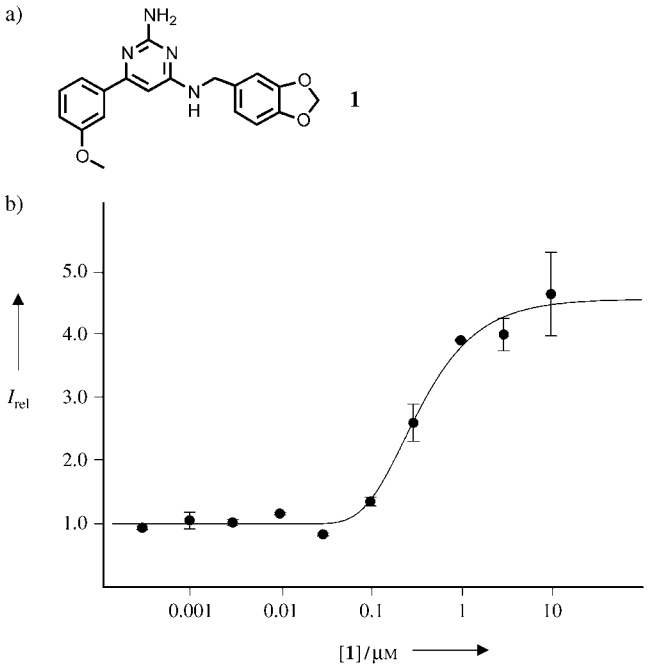

Figure 1. a) Structure of compound **1**; b) compound **1** induces the β-catenin/TCF-dependent reporter in a dose-dependent manner. I_{rel} = relative intensity of the luciferase signal, reflective of the fold activation in reporter gene expression.

zylamino group and the 2-(4-hydroxyphenyl)ethylamino group. Representative active and inactive analogues and their EC_{50} values are provided in the Supporting Information.

The Wnt signal is transduced through its receptor and results in the formation of a heterodimeric complex of β-catenin and TCF that drives downstream target gene expression.[1,3,4] To determine if the active compounds induce reporter gene expression in a TCF-dependent manner, a dominant-negative TCF4 was constructed and transfected into cells in the absence or presence of compound. The dominant negative TCF4 contains a DNA-binding domain but lacks the β-catenin-interaction motif, which leads to the sequestration of TCF-binding sites and subsequent blockage of β-catenin- and TCF-dependent transcriptional activity.[10] The gene encoding the dominant negative TCF4 was generated by PCR and cloned into the eukaryotic expression vector pcDNA3. As shown in Figure 2, β-catenin- and TCF-

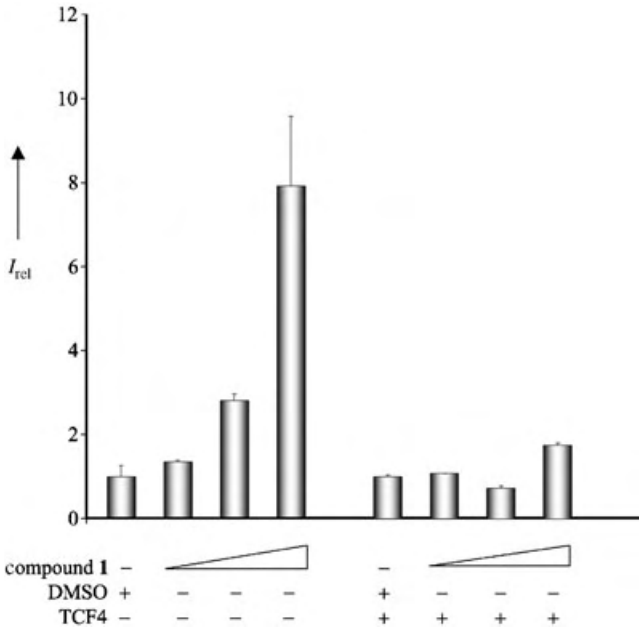

Figure 2. Activity of compound **1** blocked by the presence of a dominant-negative TCF4. 293T cells were treated with DMSO or **1** (0.2–5 μM) in the presence or absence of a dominant negative TCF4. I_{rel} = relative intensity of the luciferase signal, reflective of the fold activation in reporter gene expression.

To further explore the structure–activity relationship, 124 similar compounds bearing the core 4,6-disubstituted 2-aminopyrimidine scaffold were analyzed in the same reporter assay for activation of the Wnt/β-catenin signaling pathway. Only a fraction of these structurally related compounds function as Wnt agonists. The active compounds have small aryl substituents (such as phenyl or methoxyphenyl groups) at position 6 of the pyrimidine ring. Substitution with bulky aryl groups at this position dramatically decreases activity. The introduction of an additional O or NH linkage between the pyrimidine ring and the aryl groups at position 6 also leads to a loss in activity. Only two substituents at position 4 were tolerated in active compounds: the 3,4-(methylenedioxy)ben-

dependent reporter gene expression induced by compound **1** was blocked in the presence of the dominant negative TCF4, thus suggesting that the active compound functions in the canonical Wnt pathway through the TCFs.

A number of known agonists of the Wnt pathway act through inhibition of the activity of the kinase GSK-3β.[7,11,12] As GSK-3β is involved in multiple signaling pathways other than Wnt, a small molecule that blocks GSK-3β could have disparate effects in cellular and organism models. To determine if compound **1** is an inhibitor of GSK-3β, its activity in an in vitro GSK-3β kinase assay was measured. As described previously,[13] purified GSK-3β was incubated with its substrate, a peptide derived from glycogen synthetase, and γ-^{33}P-

 © 2005 Wiley-VCH Verlag GmbH & Co. KGaA, Weinheim

labeled ATP with or without compound **1**. The kinase activity of GSK-3β can be blocked by the known inhibitor, staurosporine (Supporting Information).[11] The pyrimidine analogues have no such effect, which suggests that they act independently of GSK-3β. Although the molecular targets of the active compounds and their mechanism of action are still under investigation, current results indicate that the active compounds activate Wnt without inhibiting GSK-3β.

We next tested the ability of pyrimidine **1** to function in a whole-organism model. During early *Xenopus* development, Wnt antagonism plays an essential role in head specification. The expression of Wnt inhibitors results in enlarged heads and forebrains.[14–20] Conversely, inactivation of Wnt inhibitors, or overexpression of Wnt activators leads to microcephalic embryos.[21] This developmental process provides an excellent experimental means to test the ability of a compound to modulate Wnt signaling in vivo. Embryos were treated with compound **1** (10 μM) or the vehicle, DMSO, at stage 10.5 (gastrulation stage) for 24 h, and allowed to develop until stage 40 (tadpole stage). All the vehicle-treated embryos ($n = 29$) appeared normal (Figure 3). All

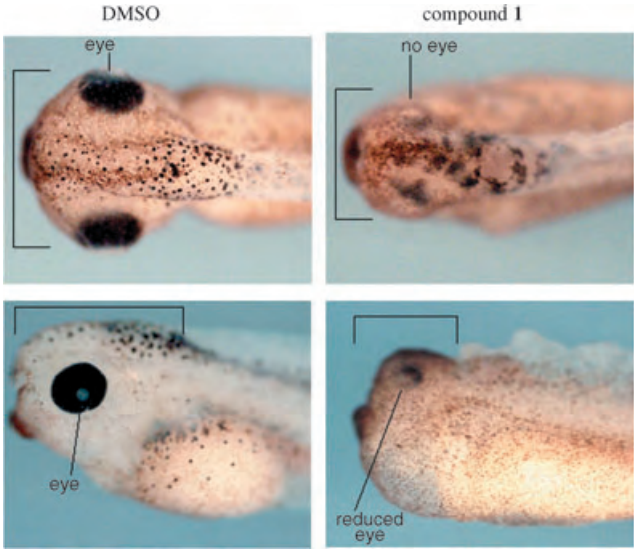

Figure 3. Compound **1** affected *Xenopus* embryonic head specification. Embryos were treated with compound **1** (10 μM) or DMSO from developmental stage 10.5 to stage 40. All DMSO-treated embryos appeared normal ($n = 29$). All drug-treated embryos ($n = 36$) had substantial head defects.

embryos treated with compound **1** ($n = 36$) had substantial head defects that ranged from significantly diminished heads and complete loss of eyes, to reduced eyes and heads; the posterior structures of tadpoles remained largely intact. This phenotype is similar to that which results from Wnt overexpression in head specification during early embryonic development.[21] These results suggest that the small-molecule Wnt agonist indeed mimics the effects of Wnt at the whole-organism level.

In conclusion, the small-molecule Wnt agonist identified in this study functions both in cell culture and a *Xenopus* model. Determination of the molecular mechanism of **1** may reveal novel components of Wnt signaling, including the effects of oscillating pathway activities.[22,23] Furthermore, small-molecule Wnt modulators should be useful tools for studies of biological processes that involve Wnt signaling, such as hematopoietic stem cell renewal, mesenchymal progenitor cell differentiation, and embryonic limb development. They may also reveal new physiological effects of Wnt signaling in model organisms, and might ultimately lead to novel therapeutic targets.[24]

Experimental Section

1: All chemicals were purchased from Aldrich. 2-Amino-4,6-dichloropyrimidine (100 mg, 0.61 mmol) was dissolved in 1-butanol (5 mL). Diisopropylethylamine (117 μL, 0.67 mmol) and piperonylamine (92.2 mg, 0.61 mmol) were then added to the mixture. The reaction mixture was heated at 70 °C for 12 h, and the desired product (2-amino-4-chloro-6-(1,3-benzodioxol-5-ylmethylamino)pyrimidine) was purified by column chromatography (85 % yield). 2-Amino-4-chloro-6-(1,3-benzodioxol-5-ylmethylamino)pyrimidine (10 mg, 0.036 mmol), $[Pd(PPh_3)_4]$ (2.1 mg, 0.0018 mmol), Na_2CO_3 (15.2 mg, 0.144 mmol), acetonitrile/water (1:1, 2 mL), and 3-methoxyphenylboronic acid (11 mg, 0.072 mmol) were mixed together under Ar. The reaction mixture was then heated at 150 °C for 20 min in a microwave reactor. The product was then purified by using reversed-phase HPLC with trifluoroacetic acid (0.1 % in H_2O) and MeCN as solvents. A linear gradient of MeCN (5 %→95 %) over 5 min was used, in which **1** has a retention time of 3.5 min. The corresponding fractions were collected and lyophilized to yield pure **1** as a white powder (80 % yield). ^{1}H NMR (400 MHz, [D$_6$]DMSO): $\delta = 3.84$ (s, 3H), 4.54 (d, 2H, $J = 5.8$ Hz), 6.0 (s, 2H), 6.39 (s, 1H), 6.85 (m, 2H), 6.96 (s, 1H), 7.19 (m, 1H), 7.28 (m, 2H), 7.52 (m, 1H), 9.13 ppm (s, 1H); HRMS (ESI-TOF): $C_{19}H_{19}N_4O_3$ $[M+H]^+$ calcd: 351.1457, found: 351.1455.

Cell culture, transfection, and high-throughput screening: Human embryonic kidney (HEK) 293T cells were cultured in Dulbecco's modified Eagle's medium (Invitrogen) supplemented with fetal bovine serum (10 %) and the antibiotics penicillin (100 IU mL^{-1}) and streptomycin (100 μg mL^{-1}). Cells were cultured in a humidified incubator at 37 °C in CO_2 (5 %). Cells were transiently transfected with FuGene 6 (Roche) at a FuGene/DNA ratio of 3:1 according to the manufacturer's instructions. Luciferase activity was measured with a BrightGlo or DualGlo luciferase kit (Promega). For high-throughput screening, 293T cells were transiently transfected with the reporter construct (Upstate) in T75 cell culture flasks. After overnight culture, cells were harvested and replated onto 384-well plates with 1.5×10^3 cells in each well; 24 h later, compound solution (1 mM, 500 nL) was added to each well. After incubation for another 24 h, luciferase activity was measured with BrightGlo (Promega).

Plasmid construction: A dominant negative TCF4 was generated by PCR with primer F1: GCGCGC GGATCC GCCGCCACC ATG ACGA ATCAAAACAG CTCCTC and primer R1: GGGTTAGG-GATAGGCTTACC TTCTAAAGACTTGGTGACGA. The product was used in a second round of PCR with primer F1 and primer R2 GCCGCC TCTAGA TTA CGTAGAATCGAGACCGAGGA-GAGGGTTAGGGATAGGCTTACC to add a V5 epitope tag at the C terminus. It then was digested with BamH1 and XbaI, inserted into the pcDNA3 vector (Invitrogen), and sequenced.

Received: November 9, 2004
Published online: February 21, 2005

Keywords: cellular adhesion · gene expression · high-throughput screening · pyrimidines · signal transduction

 © 2005 Wiley-VCH Verlag GmbH & Co. KGaA, Weinheim

[1] M. Peifer, P. Polakis, *Science* **2000**, *287*, 1606.
[2] A. Giannis, *Angew. Chem.* **2000**, *112*, 2349; *Angew. Chem. Int. Ed.* **2000**, *39*, 2261.
[3] M. Bienz, H. Clevers, *Cell* **2000**, *103*, 311.
[4] X. He, *Dev. Cell* **2003**, *4*, 791.
[5] C. A. Grimes, R. S. Jope, *Prog. Neurobiol.* **2001**, *65*, 391.
[6] S. Ding, N. S. Gray, X. Wu, Q. Ding, P. G. Schultz, *J. Am. Chem. Soc.* **2002**, *124*, 1594.
[7] S. Ding, T. Y. Wu, A. Brinker, E. C. Peters, W. Hur, N. S. Gray, P. G. Schultz, *Proc. Natl. Acad. Sci. USA* **2003**, *100*, 7632.
[8] X. Wu, S. Ding, Q. Ding, N. S. Gray, P. G. Schultz, *J. Am. Chem. Soc.* **2002**, *124*, 14520.
[9] X. Wu, S. Ding, Q. Ding, N. S. Gray, P. G. Schultz, *J. Am. Chem. Soc.* **2004**, *126*, 1590.
[10] M. Molenaar, M. van de Wetering, M. Oosterwegel, J. Peterson-Maduro, S. Godsave, V. Korinek, J. Roose, O. Destree, H. Clevers, *Cell* **1996**, *86*, 391.
[11] J. A. Bertrand, S. Thieffine, A. Vulpetti, C. Cristiani, B. Valsasina, S. Knapp, H. M. Kalisz, M. Flocco, *J. Mol. Biol.* **2003**, *333*, 393.
[12] L. Meijer, A. L. Skaltsounis, P. Magiatis, P. Polychronopoulos, M. Knockaert, M. Leost, X. P. Ryan, C. A. Vonica, A. Brivanlou, R. Dajani, C. Crovace, C. Tarricone, A. Musacchio, S. M. Roe, L. Pearl, P. Greengard, *Chem. Biol.* **2003**, *10*, 1255.
[13] Y. Wan, W. Hur, C. Y. Cho, Y. Liu, F. J. Adrian, O. Lozach, S. Bach, T. Mayer, D. Fabbro, L. Meijer, N. S. Gray, *Chem. Biol.* **2004**, *11*, 247.
[14] M. A. Deardorff, C. Tan, L. J. Conrad, P. S. Klein, *Development* **1998**, *125*, 2687.
[15] A. Glinka, W. Wu, D. Onichtchouk, C. Blumenstock, C. Niehrs, *Nature* **1997**, *389*, 517.
[16] A. Glinka, W. Wu, H. Delius, A. P. Monaghan, C. Blumenstock, C. Niehrs, *Nature* **1998**, *391*, 357.
[17] S. Hoppler, J. D. Brown, R. T. Moon, *Genes Dev.* **1996**, *10*, 2805.
[18] K. Itoh, T. L. Tang, B. G. Neel, S. Y. Sokol, *Development* **1995**, *121*, 3979.
[19] L. Leyns, T. Bouwmeester, S. H. Kim, S. Piccolo, E. M. De Robertis, *Cell* **1997**, *88*, 747.
[20] S. B. Pierce, D. Kimelman, *Dev. Biol.* **1996**, *175*, 256.
[21] G. Davidson, B. Mao, I. del Barco Barrantes, C. Niehrs, *Development* **2002**, *129*, 5587.
[22] A. Hoffmann, A. Levchenko, M. L. Scott, D. Baltimore, *Science* **2002**, *298*, 1241.
[23] K. Serth, K. Schuster-Gossler, R. Cordes, A. Gossler, *Genes Dev.* **2003**, *17*, 912.
[24] T. Reya, A. W. Duncan, L. Ailles, J. Domen, D. C. Scherer, K. Willert, L. Hintz, R. Nusse, I. L. Weissman, *Nature* **2003**, *423*, 409.

 © 2005 Wiley-VCH Verlag GmbH & Co. KGaA, Weinheim

Polymerization

Acid-Initiated Stereospecific Polymerization of Isocyanopeptides**

Gerald A. Metselaar, Jeroen J. L. M. Cornelissen, Alan E. Rowan,* and Roeland J. M. Nolte*

The occurrence of only one type of chirality in biomolecules is a remarkable fact of life that has piqued the curiosity of numerous research groups in a wide range of scientific disciplines. Most theories concerning the origin of this phenomenon assume that after the initial induction of a chiral bias, a process of chiral amplification has occurred.[1–4] One possible route for chiral amplification is through a process of molecular recognition between diastereomeric oligopeptides, which enables one form to polymerize or aggregate into larger chiral structures while the other form cannot.[4] Herein, we report on the unique acid-initiated polymerization of chiral isocyanodipeptides which occurs with unprecedented stereospecificity.

In the past, we and others have studied in great detail the polymerization of isocyanides by metal complexes, in particular nickel(II) derivatives. It was shown that these monomers yield polymers with a stable approximately 4_1 helical conformation.[5] More recently, we demonstrated that the polymerization of peptide-derived isocyanides results in polymers with a new type of helix structure, that is, a β helix in which the peptide side arms attached to the central helical core form a β-sheet-like architecture.[6,7] During these studies, it was discovered that isocyano-L-alanyl-D-alanine methyl ester (L,D-IAA) rapidly polymerizes even without a nickel(II) catalyst present. The resulting polymer was found to have exactly the same composition and conformation as poly(isocyano-L-alanyl-D-alanine methyl ester) (L,D-PIAA) prepared by using nickel(II) catalysis.[8] Further studies revealed that this polymerization, which occurs in chloroform, is initiated by free protons in this solvent. In stark contrast, when identical polymerization conditions were applied to the diastereomeric L,L-IAA monomer, no polymerization was observed to take place.[9]

To obtain more insight into the stereospecificity of this acid-catalyzed polymerization, kinetic studies were performed with trifluoroacetic acid (TFA) in dichloromethane, and the polymerization reaction was monitored by IR spectroscopy. During polymerization, the isocyanide absorption at $\nu = 2136\ cm^{-1}$ disappeared and the amide I absorption

[*] G. A. Metselaar, Dr. J. J. L. M. Cornelissen, Prof. Dr. A. E. Rowan, Prof. Dr. R. J. M. Nolte
Institute for Molecules and Materials
Department of Organic Chemistry, University of Nijmegen
Toernooiveld, 6525 ED Nijmegen (The Netherlands)
Fax: (+31) 24-365-2929
E-mail: j.cornelissen@science.ru.nl
a.rowan@science.ru.nl

[**] The Council for the Chemical Sciences of the Netherlands Organization for Scientific Research is acknowledged for financial support to J.J.L.M.C. (Veni Grant) and to A.E.R. (Vidi Grant).

 © 2005 Wiley-VCH Verlag GmbH & Co. KGaA, Weinheim DOI: 10.1002/anie.200462417

shifted from $\nu = 1686\ cm^{-1}$ to $\nu = 1656\ cm^{-1}$, thereby indicating the formation of the polymer and its simultaneous folding into a β-helical structure; this was also indicated by the arising Cotton effect at $\lambda = 306$ nm in the CD spectra. When 0.15 equivalents of TFA with respect to monomer were used, a slight induction period was clearly visible, after which the polymerization reaction (route A, Scheme 1) followed first-order kinetics with respect to the monomer. The reaction rate of L,D-IAA (16 mM) with TFA (1 mM) in dichloromethane was studied at different temperatures. Evaluation of the rate data in an Eyring plot revealed that the polymerization reaction displayed a large negative entropy of activation ($\Delta S^{\neq}$) of $-170\ J\,mol^{-1}\,K^{-1}$, which implies a very high degree of organization in the transition state,[10] and an activation enthalpy ($\Delta H^{\neq}$) of 42 kJ mol^{-1}; this gives an overall free energy of activation ($\Delta G^{\neq}_{293\,K}$) of 92 kJ mol^{-1}. At higher acid concentrations (that is, when > 0.15 equivalents of TFA with respect to monomer were used), IR, CD, and ^{1}H NMR spectroscopic studies indicated that a second reaction starts to compete with the polymerization reaction. This reaction is the hydration of the isocyanide through the formation of a cyclic imidazolone to form the corresponding formamide (FAA; route B, Scheme 1).[11] When the formation of polymer, calculated from the intensity of change in the molar circular dichroic absorption at $\lambda = 306$ nm ($\Delta\varepsilon_{306}$), was plotted as a function of the TFA concentration, a sigmoidal curve was obtained (Figure 1). As the polymer formation decreased, the formation of the formamide via the cyclic imidazolone increased concomitantly, as monitored by ^{1}H NMR spectroscopy. This indicates that at high acid concentrations the isocyanide monomers cannot be incorporated into the growing polymer chain and as a result cyclize to give the imidazolone (route B). Interestingly, the transition from polymerization to cyclization is a cooperative process, as highlighted by the S-shaped curve (Figure 1), and takes place in a rather narrow concentration range.

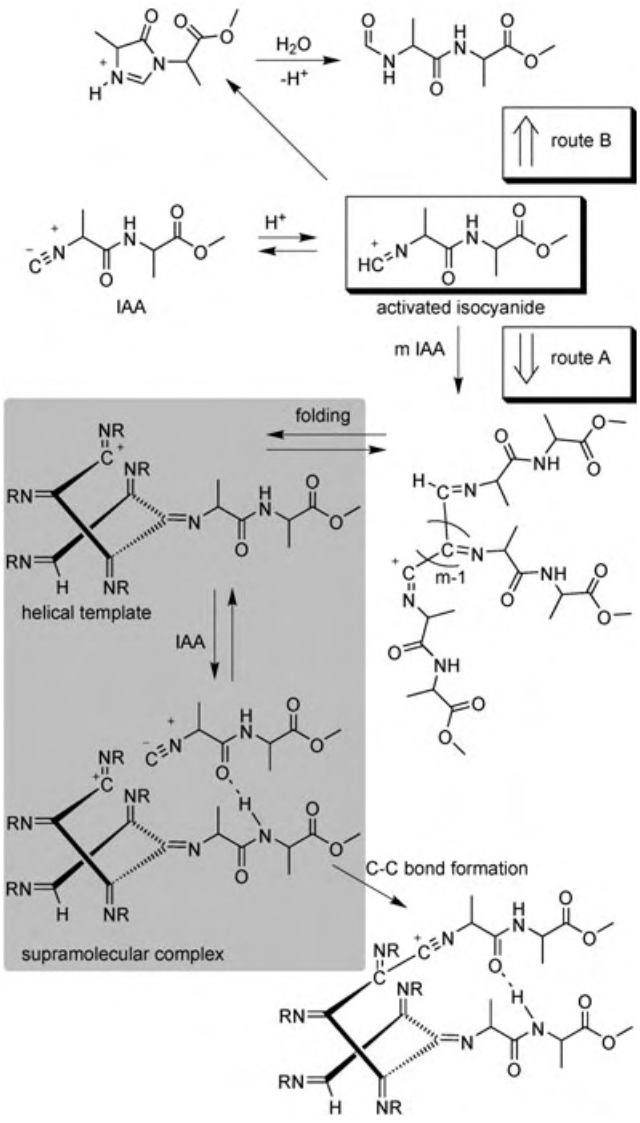

Scheme 1. Proposed initiation and propagation of the acid-initiated polymerization of isocyanopeptides (route A) and a side reaction forming the formamide via a cyclic imidazolone (route B).

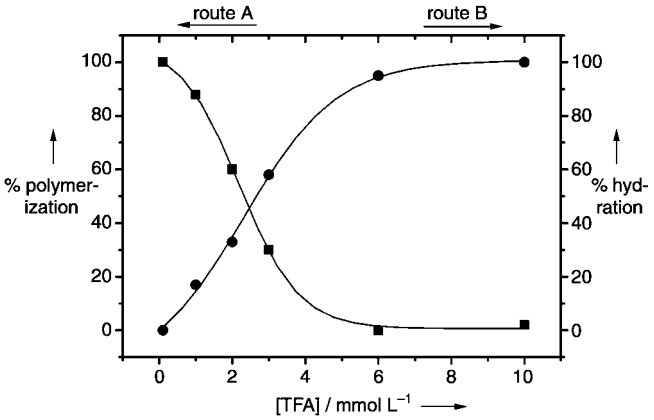

Figure 1. Polymerization (■) and hydration (●) of L,D-IAA as a function of the TFA concentration ([L,D-IAA] = 16 mmol L^{-1} in dichloromethane, $T = 25\,°C$).

The stereochemical nature of the polymerization was studied at a low acid concentration ([TFA]/[IAA] < 0.15) to negate the side reaction. The formation of both block and random copolymers of the different diastereomers (L,L-IAA, L,D-IAA, and D,L-IAA) was measured by CD spectroscopy ($\lambda = 306$ nm) as a function of time. An initial block of L,D-PIAA was grown by using TFA as an initiator. Once all of the L,D-IAA had been consumed, a second equivalent of this monomer was added and the reaction was found to proceed further (Figure 2, curve a). However, when the enantiomeric monomer D,L-IAA was added, no further polymerization took place and the added isocyanide was recovered (curve c). This remarkable observed inhibition is likely caused by the presence of trace residues of the enatiomeric L,D-IAA monomer, which poisons the poymerization reaction of D,L-IAA.[7,12] Remarkably, this stereospecificity was also observed when L,D-IAA and D,L-IAA were randomly copolymerized; the enantiomeric monomers inhibited each other and no

 © 2005 Wiley-VCH Verlag GmbH & Co. KGaA, Weinheim

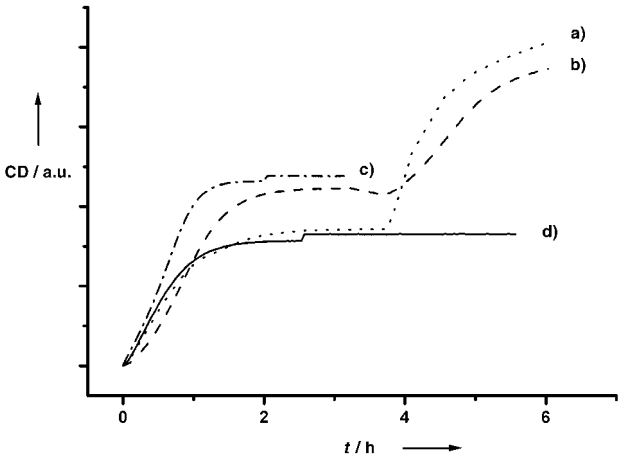

Figure 2. Acid-catalyzed block copolymerizations of L,D-IAA (16 mM) with a) L,D-IAA, b) L,L-IAA, c) D,L-IAA, and d) D,D-IAA, monitored by CD spectroscopy as a function of time at $\lambda = 306$ nm ([IAA] = 16 mmol L^{-1}, [TFA] = 1 mmol L^{-1}, CH_2Cl_2, $T = 25\,^{\circ}C$).

polymerization was observed, even when a monomer ratio of 99:1 was applied.[13] In contrast to the above observation, copolymerization of diastereomeric monomers was found to be possible. When L,L-IAA (which when polymerized with a Ni^{II} catalyst gives polymers with the same right-handed screw sense as L,D-IAA) was used as a second monomer in a block copolymerization with L,D-PIAA, the polymer continued to grow (curve b). However, addition of D,D-IAA, which is the enantiomer of L,L-IAA, did not result in any polymerization (curve d). The molecular weights for the two block copolymers L,D-PIAA/L,D-PIAA and L,D-PIAA/L,L-PIAA were obtained by AFM studies of the molecules deposited on a mica surface.[8] It was observed that the molecular weight for the block homopolymer L,D-PIAA/L,D-PIAA only slightly increased upon addition of the second monomer, a result indicating that mainly new L,D-PIAA polymers are formed. In contrast, for the block copolymer L,D-PIAA/L,L-PIAA, the observed molecular weight was found to almost double; this indicates that the second block grows almost exclusively on from the first. The energetic penalty caused by steric repulsion between the alanine methyl groups, which prevents the acid-initiated homopolymerization of L,L-IAA,[9] can evidently be overcome by the increased hydrogen bonding to the preformed helical L,D-PIAA macroinitiator. This increased hydrogen bonding is the result of polarization of the amides by the cooperative hydrogen-bonding network present in the helix architecture, an observation often observed in α helices.[14] The above results clearly demonstrate the critical effect of the configuration of the first chiral center of the dipeptide monomer on the polymerization reaction and show that the initiation step is crucial. The stereospecificity of the transition state of the acid-initiated polymerization is further highlighted by the fact that all of the above monomer combinations could readily be polymerized when a nickel(II) catalyst was used.[5]

Helix-sense-selective polymerizations, such as those of bulky methacrylates,[15] chloral,[16] and *N*-propargylamides,[17] are well documented, whereas for more dynamic helical polymers, for example, polyisocyanates,[18] polysilanes,[19] and polyacetylenes,[20] copolymerization with optically active monomers is required to obtain a lasting preferred helix sense. However, there are virtually no examples of monomers that are enantioselectively polymerized.[21] This unique stereoselectivity is remarkable in its efficiency, in that even when only 1% of the incorrect monomer is present the polymerization does not proceed. The exhibited stereoselectivity and also the switching of the reaction to a different product, that is, the cyclic imidazolone, can both be explained by the involvement in the reaction of a helical template, which is present at low acid concentrations and destroyed at high acid concentrations.

The formation of a helical template is not only a crucial step in the acid-initiated polymerization but was also found to play an important role in the Ni^{II}-catalyzed polymerization of isocyanopeptides. In a titration experiment in which L,L-IAA was added stepwise to tri(*tert*-pentyl isocyanide)[benzylamino(*tert*-pentylamino)carbene]nickel(II) perchlorate,[22] the formation of the helical polymer was monitored as a function of added monomer by recording the increasing Cotton effect coming from the n–π* transition at $\lambda = 308$ nm (Figure 3). The

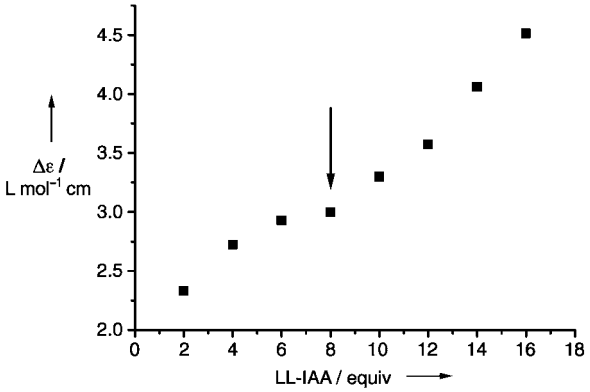

Figure 3. Titration of L,L-IAA to tri(*tert*-pentyl isocyanide)[benzylamino(*tert*-pentylamino)carbene]nickel(II) perchlorate, monitored by CD spectroscopy. The arrow indicates the start of the formation of the helical template. At this point, the signal of a hydrogen-bonded amide appears at $\delta = 9.4$ ppm in the ^{1}H NMR spectrum.

molar circular dichroic absorption ($\Delta\varepsilon_{308}$) increased in a nonlinear fashion with the number of added monomer equivalents. The steep increase after the addition of approximately eight equivalents of isocyanopeptide monomer results from a rearrangement of the secondary polyisocyanide structure from a random conformation when less than eight monomers are incorporated into the growing oligomer to a 4_1 helical conformation when more than eight monomers are built onto the growing polymer. These results were confirmed by monitoring the same titration experiment by ^{1}H NMR spectroscopy. Only when 8–10 molar equivalents of L,L-IAA had been added to a solution of the nickel(II) catalyst in deuterated chloroform, were signals at $\delta = 9.4$ ppm, corresponding to the hydrogen-bonded amide protons of the peptide side chains, observed.

 © 2005 Wiley-VCH Verlag GmbH & Co. KGaA, Weinheim

In summary, for the acid-initiated polymerization of isocyanopeptides, we propose a polymerization mechanism in which an initial helical oligomer is formed, which acts as a template for the incorporation of subsequent monomer units through a supramolecular complex. The formation of this supramolecular complex is in line with the measured activation parameters, which point to a highly organized transition state. This result, in combination with the observed induction time of the polymerization suggests that for the polymerization reaction to occur, a helical template must first be formed (Scheme 1). When the acid concentration is increased, this helical template is destroyed in a cooperative fashion and the reaction switches from route A to route B in Scheme 1. Previous experiments have demonstrated the sensitivity of polyisocyanopeptides to an excess of TFA. In these experiments, the well-defined hydrogen-bonded network was disrupted in a cooperative fashion.[8b] The intermediate supramolecular complex also readily explains the high stereoselectivity observed, as the equilibrium for the complex formation will be predominantly shifted to the uncomplexed state in the case of configurationally incorrect monomers. Hence, no or very limited polymerization will occur. The combination of a peptide segment and a polymerizable isocyanide function give a unique type of monomer, which exhibits unprecedented polymerization properties when initiated with acid. The polymerization process is in competition with the formation of a reactive cyclic imidazolone, which depends on the acid concentration. The polymerization reaction stops in a rather narrow concentration range when the helical template is destroyed. Extreme stereospecificity is also found when diastereomeric isocyanopeptides are copolymerized. This observation is also explained by the formation of a highly organized supramolecular complex, which strongly retards the rate of polymerization when "nonfitting" monomers are present.

Received: October 25, 2004
Published online: February 23, 2005

Keywords: helical structures · isocyanides · polymerization · stereoselectivity · supramolecular chemistry

[1] W. A. Bonner, *Origins Life* **1991**, *21*, 59 – 111.
[2] M. Quack, *Angew. Chem.* **2002**, *114*, 4812 – 4825; *Angew. Chem. Int. Ed.* **2002**, *41*, 4618 – 4630.
[3] P. Cintas, *Angew. Chem.* **2002**, *114*, 1187 – 1193; *Angew. Chem. Int. Ed.* **2002**, *41*, 1139 – 1145.
[4] Z. Takats, S. C. Nanita, R. G. Cooks, *Angew. Chem.* **2003**, *115*, 3645 – 3647; *Angew. Chem. Int. Ed.* **2003**, *42*, 3521 – 3523, and references therein.
[5] a) R. J. M. Nolte, *Chem. Soc. Rev.* **1994**, *23*, 11 – 19; b) J. J. L. M. Cornelissen, R. J. M. Nolte, A. E. Rowan, N. A. J. M. Sommerdijk, *Chem. Rev.* **2001**, *101*, 4039.
[6] J. J. L. M. Cornelissen, J. J. J. M. Donners, R. de Gelder, W. S. Graswinckel, G. A. Metselaar, A. E. Rowan, N. A. J. M. Sommerdijk, R. J. M. Nolte, *Science* **2001**, *239*, 676 – 680.
[7] F. Heitz, G. Détriché, F. Vovelle, G. Spach, *Macromolecules* **1981**, *14*, 47 – 50.
[8] a) P. Samori, C. Ecker, I. Gössl, P. A. J. de Witte, J. J. L. M. Cornelissen, G. A. Metselaar, M. B. J. Otten, A. E. Rowan, R. J. M. Nolte, J. P. Rabe, *Macromolecules* **2002**, *35*, 5290 – 5294; b) J. J. L. M. Cornelissen, W. S. Graswinckel, A. E. Rowan, N. A. J. M. Sommerdijk, R. J. M. Nolte, *J. Polym. Sci. Part A* **2003**, *41*, 1725 – 1736. Here, the molecular weight of the polymers was determined by contour-length measurement and by assuming a length of 4.6 Å ($\equiv 400\,g\,mol^{-1}$ per nm) per 4 repeat units.
[9] Earlier, molecular-modeling studies revealed that the L,L-PIAA polymer has a less favorable conformation than the L,D-PIAA polymer due to unfavorable steric interactions between the side chains n and $n+1$.[6] In the polymerization reaction, a similar unfavorable interaction is probably present, which prevents the polymerization reaction of L,L-IAA from taking place.
[10] The error in the activation enthalpy, $\Delta H^{\neq}$, is $\pm 10\,\%$ and in the entropy of activation, $\Delta S^{\neq}$, is $\pm 20\,\%$. For the nickel(II)-catalyzed polymerization of isocyanides, the activation parameters are $\Delta H^{\neq} = 61.4\,kJ\,mol^{-1}$, $\Delta S^{\neq} = -54\,J\,mol^{-1}\,K^{-1}$, and the free energy of activation, $\Delta G^{\neq}_{293\,K}$ is $77.2\,kJ\,mol^{-1}$ (R. J. M. Nolte, W. Drenth, *Recl. Trav. Chim. Pays-Bas* **1973**, *92*, 788). Note that for the acid-catalyzed polymerization $\Delta S^{\neq}$ is about three times more negative.
[11] Under the reaction conditions, a water content of 0.03 % is sufficient for complete hydration of the isocyanide monomers.
[12] See also: P. Pino, A. Oschwald, F. Ciardelli, C. Carlini, E. Chiellini in *Coordination Polymerization: A Memorial to Karl Ziegler* (Ed.: J. C. W. Chien), Academic, New York, **1975**, p.75.
[13] This is indeed a remarkable result, as statistically some polymer should be formed. IR spectroscopy, however, clearly showed that virtually no monomer is consumed. This subject is currently being studied further.
[14] R. Wieczorek, J. J. Dannenberg, *J. Am. Chem. Soc.* **2003**, *125*, 8124 – 8129.
[15] T. Nakano, Y. Okamoto, *Chem. Rev.* **2001**, *101*, 4013 – 4038.
[16] P. Sikorsi, I. S. Cooper, E. D. T. Atkins, G. D. Jayhox, O. Vogl, *J. Polym. Sci. Part A* **1998**, *36*, 1855 – 1860.
[17] R. Nomura, J. Tabei, S. Nishiura, T. Masuda, *Macromolecules* **2003**, *36*, 561 – 564.
[18] M. M. Green, J.-W. Park, T. Sato, A. Teramoto, S. Lifson, R. L. B. Selinger, J. V. Selinger, *Angew. Chem.* **1999**, *111*, 3328 – 3345; *Angew. Chem. Int. Ed.* **1999**, *38*, 3138 – 3154.
[19] M. Fujiki, *J. Am. Chem. Soc.* **1994**, *116*, 11 976.
[20] G. Gao, F. Sanda, T. Masuda, *Macromolecules* **2003**, *36*, 3938 – 3943, and references therein.
[21] E. Yashima, Y. Okamoto, K. Hatada, *Macromolecules* **1988**, *21*, 854 – 855.
[22] A similar catalyst is described in J. J. L. M. Cornelissen, M. Fisher, N. A. J. M. Sommerdijk, R. J. M. Nolte, *Science* **1998**, *280*, 1477.

 © 2005 Wiley-VCH Verlag GmbH & Co. KGaA, Weinheim

Host–Guest Systems

Fluorophenoxycarbene inside a Hemicarcerand: A Bottled Singlet Carbene**

Xuejun Liu, Gaosheng Chu, Robert A. Moss, Ronald R. Sauers,* and Ralf Warmuth**

The reactivity, selectivity, and stability of singlet carbenes are strongly dependent on the carbenes' substituents.[1] Indeed, the intrinsic stabilization of carbenes by electron donation from their substituents and steric crowding permits "tuning" of the carbenes' chemical properties and life-times. This stabilization enables the generation of the fleeting and voraciously electrophilic singlet methylene (CH_2) species,[2] through the long-lived triplet bis[9-(10-phenyl)anthryl]carbene[3] to such stable and isolable species as the phosphorus-stabilized singlet carbene $(i\text{Pr})_2\text{PCSiMe}_3$[4] and the amine-stabilized Arduengo carbene 1,3-di-(1-adamantyl)imidazol-2-ylidene[5a] or $(i\text{Pr})_2\text{NCN}(i\text{Pr})_2$.[5b] Extrinsic stabilization through confinement inside a molecular container should provide additional stabilization to carbenes.[6] In fact, incarceration in the inner phase of a hemicarcerand is one of the most powerful approaches for the room-temperature stabilization of highly reactive intermediates.[7] The surrounding host protects the guest from dimerization or reaction with bulk-phase species that are too large to enter the inner phase. We report herein the first example of a normally nonisolable, fleeting singlet carbene that is rendered persistent by incarceration. We selected fluorophenoxycarbene (**1**) as our target for three reasons: it is sufficiently stabilized by its substituents (calculated stabilization energy $= 60$ kcal mol^{-1} relative to the singlet methylene species[1c]) that C–H insertion or C=C addition reactions with a hemicarcerand host are unlikely, its size should result in a good fit within host **2**, and it carries a NMR-sensitive fluorine "label".

Treating diol **3**[7c] with $\text{MsO(CH}_2)_4\text{OMs}$ (Ms = SO_2Me), Cs_2CO_3, and excess 3-fluoro-3-phenoxydiazirine (**4**)[8] in hexamethylphosphoramide gave the hemicarceplex **2·4** in 23 % yield. Photolysis of **2·4** in degassed CD_2Cl_2 ($\lambda > 320$ nm, 77 K) produced a new hemicarceplex in 93 % yield on the basis of integration of the ^{1}H NMR spectrum (Figure 1 a,b).[9]

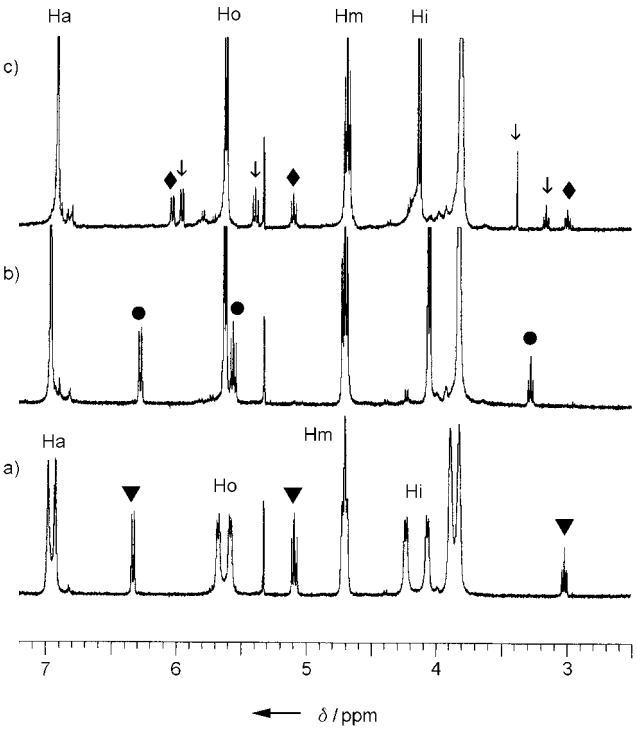

Figure 1. Partial ^{1}H NMR spectra (399.969 MHz, CD_2Cl_2, 25 °C) of the hemicarceplex **2·4**: a) before and b) after photolysis ($\lambda > 320$ nm, 77 K, 4 h). c) Same solution as (b) after complete decomposition. The signals assigned to the protons of the incarcerated **4** (▼), **1** (●), **5** (↓), and **6** (◆) are marked.

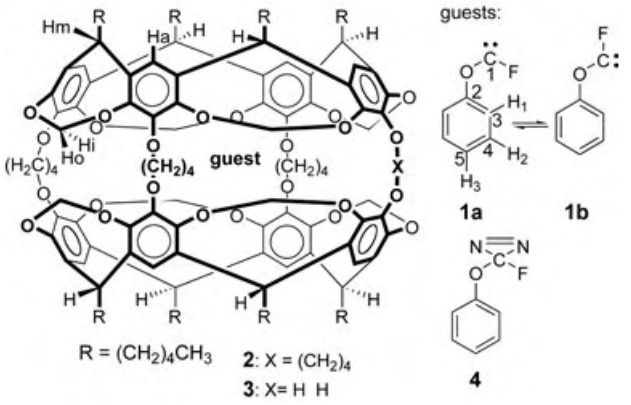

The UV absorption of **2** decreases sharply above 275 nm. Thus, it must be the guest **4** that absorbs light at the wavelengths used in the photolysis experiments ($\lambda >$ 320 nm). We assigned the newly formed hemicarceplex as the fluorophenoxycarbene hemicarceplex **2·1** on the basis of: the photochemistry of free **4**, which quantitatively produces **1**;[8] the ^{1}H NMR spectroscopic properties of this hemicarceplex (see below); and trapping experiments. Trapping experiments at 25 °C in CD_2Cl_2 (containing small amounts of water) showed **2·1** reacted very slowly over several days to form the phenyl formate hemicarceplex **2·5** and the phenyl-(difluoromethyl) ether hemicarceplex **2·6** (Figure 1 b,c). The

[*] X. Liu, Dr. G. Chu, Prof. R. A. Moss, Prof. R. R. Sauers, Prof. R. Warmuth
Department of Chemistry and Chemical Biology
Rutgers, The State University of New Jersey
610 Taylor Road, Piscataway, NJ 08854 (USA)
Fax: (+1) 732-445-5312
E-mail: moss@rutchem.rutgers.edu
sauers@rutchem.rutgers.edu
warmuth@rutchem.rutgers.edu

[**] This research was supported by the NSF (Grants CHE-0431749 to R.W. and CHE-0345240 to R.A.M.) and Rutgers University. We thank Dr. Seho Kim for assistance with NMR spectroscopic experiments and Prof. Karsten Krogh-Jespersen for helpful suggestions.

Supporting information for this article is available on the WWW under http://www.angewandte.org or from the author.

 © 2005 Wiley-VCH Verlag GmbH & Co. KGaA, Weinheim DOI: 10.1002/anie.200462633

hemicarceplex **2·5** was identified by comparison with an authentic sample prepared by heating empty **2** in neat **5**, whereupon **5** enters **2** (150 °C, 48 h, 58 % yield).[7b] The hemicarceplex **2·6** gave FAB-MS, ^{1}H NMR, and ^{19}F NMR spectra that are fully consistent with its structure. For example, the ^{19}F NMR spectrum shows a doublet at $\delta_F = -82.9$ ppm ($^2J_{HF} = 73.3$ Hz) which is almost identical to that of free **6** ($\delta_F = -81.39$ ppm, $^2J_{HF} = 74$ Hz).[10] We rationalize the formation of **2·5** and **2·6** in almost equal amounts as follows: bulk phase water enters the inner phase and reacts with **1** to give the hemiacetal **7**, which subsequently loses HF. The HF is extruded from the inner phase and rapidly enters another hemicarceplex **2·1**, where it reacts with **1** to yield **6** (Scheme 1). The concentrations of HF and **2·7** were below the NMR detection limit, which shows that fragmentation of **7** and addition of HF to **1** are much faster than the acid-catalyzed addition of water to encapsulated **1**.

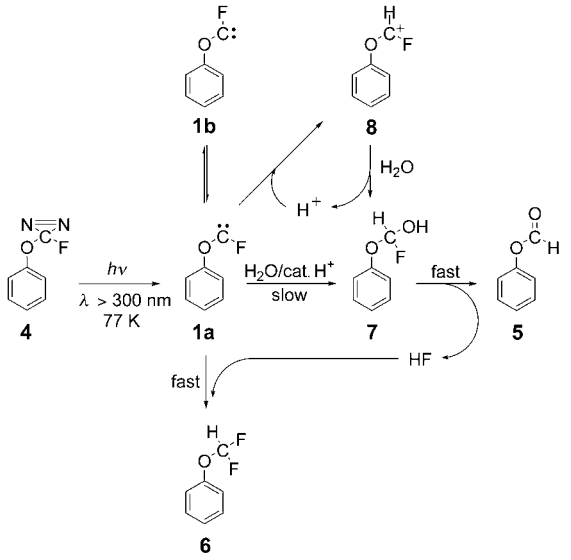

Scheme 1. Photolysis of **4** and reactions of **1** in the inner phase of **2**.

If [D_5]pyridine is added to the sample before photolysis, **2·1** persists for days without any decomposition (Figure 2). This shows that the addition of water is acid-catalyzed (Scheme 1, **1a**→**8**→**7**) and that water is not acidic enough in the hydrophobic inner phase of **2** to trap **1**, presumably because of the high energetic cost of charge separation to form [**8**]$^+$OH$^-$.[7e] It also suggests that **7** does not form from **1** by an ylide pathway, which would not be inhibited by pyridine. Thus, the following factors lead to the remarkable stability of **2·1**: 1) the incarceration of **1** which inhibites dimerization;[11] 2) the hydrophobicity of the inner phase; and, possibly, 3) the stabilization effect of the carbene–π interactions.[6,12] In the absence of a base, trace amounts of DCl in CD_2Cl_2 initiate the catalytic cycle shown in Scheme 1 (**1a**→**8**→**7**). After the H^+ concentration reaches a certain level, the reaction proceeds to completion at a constant rate, which depends on the concentration of bulk water (Figure 2).

The aryl protons H1, H2, and H3 of **2·1** are assigned to a doublet at $\delta = 6.28$ ppm and triplets at $\delta = 5.56$ and 3.28 ppm

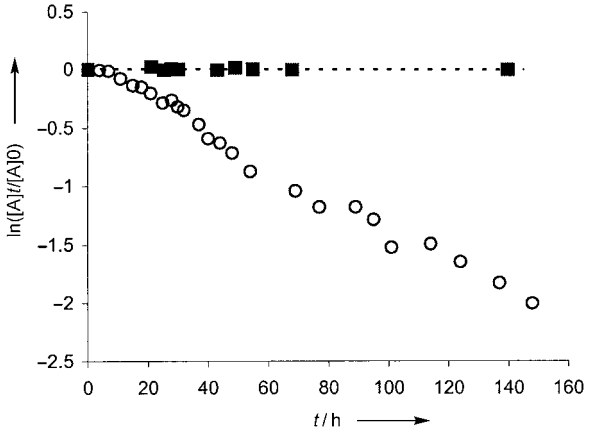

Figure 2. Concentration change of **2·1** versus time (CD_2Cl_2, 25 °C) in the presence (■) and absence (○) of [D_5]pyridine. The amount of **2·1** was estimated from the integral of the guest proton H1.

in the ^{1}H NMR spectrum (Table 1, Figure 1 b). The observation of single multiplets for host protons Ha, Ho, Hm, and Hi indicates fast tumbling of **1** relative to **4**, whose rotation

Table 1: ^{1}H, ^{19}F, and ^{13}C NMR chemical shifts of **1** referenced to trimethylsilane (TMS) or $CFCl_3$.

Nucleus	δ_{exp} [ppm]	δ_{calcd}[a] [ppm]	
		cis	*trans*
H1	6.28	7.13	7.70
H2	5.56	7.57	7.62
H3	3.28	7.47	7.56
F	149.8	179.1	159.4
C1	285.7	297.1	309.0
C2	148.0	158.3	159.6
C3	117.4	125.8	122.6
C4	129.9	133.1	134.1
C5	124.7	131.4	131.6

[a] GIAO chemical shift tensors (PBE1PBE/6-311++G(2d,p) relative to TMS (^{1}H, ^{13}C) or $CFCl_3$ (^{19}F).

around the equatorially located axis of **2** is frozen. This observation is consistent with the difference in size between **1** and **4**. The ^{19}F and ^{13}C NMR spectra of **2·1** provided further interesting insights into the properties of **1**. The ^{19}F atom of **1** resonates at $\delta = 149.8$ ppm, which indicates a fairly electropositive fluorine center (Figure 3).[13] Furthermore, the multiplicity and chemical shift of the ^{19}F signal clearly rules out **7** as the guest.

The guest's aryl carbon atoms are assigned to singlets at $\delta = 148$ (C2), 129.9 (C4), 124.7 (C5), and 117.4 ppm (C3) in the ^{13}C NMR spectrum. The highly electron-deficient carbene C1 resonates at $\delta_C = 285.7$ ppm (d, $^1J_{CF} = 569$ Hz), which is comparable to the δ_C value of other persistent heteroatom-substituted singlet carbenes.[4b] The strongly downfield-shifted fluorine atom, the unusually large C–F coupling constant,[13] and the C2 signal, which is shifted upfield by $\Delta\delta_C = 3.2$ ppm relative to C2 of **4**, are consistent with strong participation of both oxygen and fluorine atoms in carbene stabilization through delocalization of a lone pair into the vacant carbene p orbital (Scheme 2).

 © 2005 Wiley-VCH Verlag GmbH & Co. KGaA, Weinheim

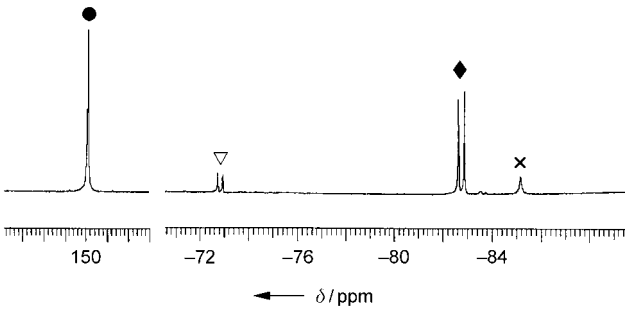

Figure 3. ^{19}F NMR spectrum (282.232 MHz, CD_2Cl_2, 25 °C) of partially decomposed **2**·**1** referenced to $CFCl_3$. Signals assigned to ^{19}F atoms of incarcerated **1** (●), **6** (◆), and two further photoproducts of **2**·**4** (▽,×) are marked.

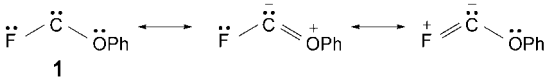

Scheme 2. Resonance stabilization of **1**.

DFT calculations (B3LYP/6-31G*) predict that **1** preferentially adopts the *trans*- (**1b**) rather than the *cis* conformation (**1a**; $\Delta H^{o} = 2.2\ \text{kcal mol}^{-1}$). Does **1** also adopt the intrinsically more stable *trans* conformation in the inner phase of **2**? This is an interesting question in light of recent work by Rebek and co-workers,[14] who found that linear alkanes prefer higher energy conformations when encapsulated inside self-assembled capsules. We addressed this question by comparing the experimental δ_C and δ_F values of **1** with those predicted by gauge-independent atomic orbital (GIAO) chemical-shift calculations at the PBE1PBE/6-311++G(2d,p) level (Table 1).[15] Olah, Prakash, and co-workers compared experimental and computed chemical shifts for several F-substituted carbocations and showed that GIAO calculations slightly overestimate δ_F and δ_C values.[13] More importantly, they observed excellent linear correlations between measured and computed δ_F and δ_C values. We were delighted to find similar correlations when we compared the experimentally derived chemical shifts of C_6H_5F, CH_3F, 1,3-dimethylimidazolidin-2-ylidene,[4b] 1,3-dimethylimidazol-2-ylidene,[4b] 1-fluoro-1-cyclopentyl cation,[13] 1-fluoro-1-cyclopropyl cation,[16] and 2-fluoro-2-propyl cation[16] with those computed at the PBE1PBE/6-311++G(2d,p) level (see the Supporting Information). These experimentally derived values were then used to correct the δ_F and δ_C values reported in Table 1: $\delta_F^{corr}(\mathbf{1a}) = 159.2$, $\delta_F^{corr}(\mathbf{1b}) = 141.1$, $\delta_C^{corr}(\mathbf{1a}) = 290.0$, and $\delta_C^{corr}(\mathbf{1b}) = 301.4$ ppm. If we also take a complexation-induced upfield shift of $\Delta\delta_F \sim 1$–2 and $\Delta\delta_C \sim 1$–2 ppm into consideration, we find that the chemical shifts predicted for **1a** are in better agreement with the experimental values, which suggest that **1a** is the major conformer inside **2**. To further strengthen this conclusion we performed heteronuclear $^1H[^{19}F]$ NOE interaction experiments (Figure 4). The fluorine center in **1** yields positive NOE interactions for H1(s) in **1** and for Hi(m) and Ha(m) in **2** upon irradiation.

A strong NOE interaction between the fluorine atom and H1 is only expected for **1a**. The calculated F–H1 distances are

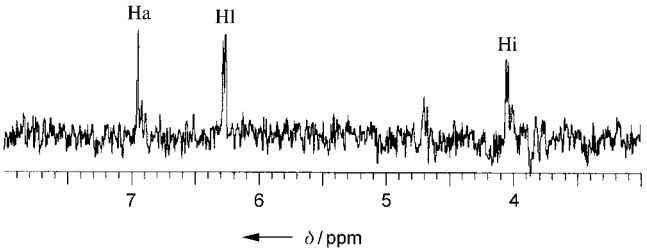

Figure 4. $^1H[^{19}F]$ NOE difference spectrum (399.971 MHz, CD_2Cl_2, 28 °C) of **2**·**1**.

3.021 and 3.716 Å for **1a** and 3.839 and 4.392 Å for **1b**. The steep distance-dependence of the $^1H[^{19}F]$ NOE interaction renders a NOE interaction in the *trans* conformation unlikely. Also consistent with **1a**, is the intermolecular Hi–F NOE interaction. However, our observation of an almost equally strong intermolecular Ha–F NOE interaction is more difficult to rationalize for **1a** and suggests that **1b** is partially populated. From the temperature insensitivity of δ_F (25 to −70 °C, $\Delta\delta_F = 0.2$ ppm) and the failure to detect a second ^{19}F signal at $\delta_F = 150 \pm 30$ ppm at −70 °C, the *cis–trans* isomerization should be frozen at −70 °C ($\Delta H^{\pm}_{calcd} = 13.9\ \text{kcal mol}^{-1}$), which suggests that one conformer is predominately populated at 25 °C and below. On the basis of the NOE interaction experiments and the comparison of the δ_C and δ_F values with the calculated GIAO chemical shifts we conclude that **1a** is the major conformer in the inner phase. The higher population of **1a** must be a consquence of steric interactions between **1b** and **2** (ca. 2–3 kcal mol^{-1}) and is consistent with earlier observations that confinement favors coiled over extended conformations.[14,17]

In summary, free fluorophenoxycarbene is a transient species;[8] however, if incarcerated inside a hemicarcerand, **1** persists for days at room temperature. Incarceration not only prevents dimerization but also slows the reaction of **1** with water by many orders of magnitude and reverses its *cis–trans* equilibrium. We predict that many other singlet carbenes of comparable reactivity will become persistent by this approach.

Received: November 17, 2004
Published online: February 21, 2005

Keywords: carbenes · host–guest systems · NMR spectroscopy · photolysis · reactive intermediates

[1] a) R. A. Moss in *Carbene Chemistry: From Fleeting Intermediates to Powerful Reagents* (Ed.: G. Bertrand), FontisMedia–Marcel Dekker, Lausanne, **2002**, p. 57; b) R. A. Moss, *Acc. Chem. Res.* **1980**, *13*, 58; c) N. G. Rondan, K. N. Houk, R. A. Moss, *J. Am. Chem. Soc.* **1980**, *102*, 1770; d) R. A. Moss, *Acc. Chem. Res.* **1989**, *22*, 15.

[2] W. v. E. Doering, R. G. Buttery, R. G. Laughlin, N. Chaudhuri, *J. Am. Chem. Soc.* **1956**, *78*, 3224.

[3] H. Tomioka, E. Iwamoto, H. Itakura, K. Hirai, *Nature* **2001**, *412*, 626.

 © 2005 Wiley-VCH Verlag GmbH & Co. KGaA, Weinheim

[4] a) S. Goumri-Magnet, T. Kato, H. Gornitzka, A. Baceiredo, G. Bertrand, *J. Am. Chem. Soc.* **2000**, *122*, 4464; b) D. Bourissou, O. Guerret, F. P. Gabbai, G. Bertrand, *Chem. Rev.* **2000**, *100*, 39.
[5] a) A. J. Arduengo III, R. L. Harlow, M. Kline, *J. Am. Chem. Soc.* **1991**, *113*, 361; b) R. W. Alder, P. R. Allen, M. Murray, A. G. Orpen, *Angew. Chem.* **1996**, *108*, 1211; *Angew. Chem. Int. Ed. Engl.* **1996**, *35*, 1121.
[6] C. Kemmis, R. Warmuth, *J. Supramol. Chem.* **2003**, 253.
[7] a) D. J. Cram, M. E. Tanner, R. Thomas, *Angew. Chem.* **1991**, *103*, 1048; *Angew. Chem. Int. Ed. Engl.* **1991**, *30*, 1024; b) R. Warmuth, *Angew. Chem.* **1997**, *109*, 1406; *Angew. Chem. Int. Ed. Engl.* **1997**, *36*, 1347; c) R. Warmuth, M. A. Marvel, *Angew. Chem.* **2000**, *112*, 1168; *Angew. Chem. Int. Ed.* **2000**, *39*, 1117; d) P. Roach, R. Warmuth, *Angew. Chem.* **2003**, *115*, 3; *Angew. Chem. Int. Ed.* **2003**, *42*, 3039; e) D. A. Makeiff, K. Vishnumurthy, J. C. Sherman, *J. Am. Chem. Soc.* **2003**, *125*, 9558.
[8] R. A. Moss, G. Kmiecik-Lawrynowicz, K. Krogh-Jespersen, *J. Org. Chem.* **1986**, *51*, 2168.
[9] Yields are slightly lower at higher temperature as a result of the formation of by-products, possibly by partial reaction of the photochemically excited **4** with the surrounding host at these temperatures.
[10] S. V. Pasenok, Y. L. Yagupolskii, W. Tyrra, D. Naumann, *Z. Anorg. Allg. Chem.* **1999**, *625*, 831.
[11] Free **1** dimerizes quantitatively in pentane solution (determined by GC–MS analysis).
[12] K. Krogh-Jespersen, S. Yan, R. A. Moss, *J. Am. Chem. Soc.* **1999**, *121*, 6269.
[13] G. A. Olah, G. Liang, Y. K. Mo, *J. Org. Chem.* **1974**, *39*, 2394.
[14] A. Scarso, L. Trembleau, J. Rebek, Jr., *Angew. Chem.* **2003**, *115*, 5657; *Angew. Chem. Int. Ed.* **2003**, *42*, 5499.
[15] Gaussian 03 (Revision B.02), M. J. Frisch, G. W. Trucks, H. B. Schlegel, G. E. Scuseria, M. A. Robb, J. R. Cheeseman, J. A. Montgomery, Jr., T. Vreven, K. N. Kudin, J. C. Burant, J. M. Millam, S. S. Iyengar, J. Tomasi, V. Barone, B. Mennucci, M. Cossi, G. Scalmani, N. Rega, G. A. Petersson, H. Nakatsuji, M. Hada, M. Ehara, K. Toyota, R. Fukuda, J. Hasegawa, M. Ishida, T. Nakajima, Y. Honda, O. Kitao, H. Nakai, M. Klene, X. Li, J. E. Knox, H. P. Hratchian, J. B. Cross, C. Adamo, J. Jaramillo, R. Gomperts, R. E. Stratmann, O. Yazyev, A. J. Austin, R. Cammi, C. Pomelli, J. W. Ochterski, P. Y. Ayala, K. Morokuma, G. A. Voth, P. Salvador, J. J. Dannenberg, V. G. Zakrzewski, S. Dapprich, A. D. Daniels, M. C. Strain, O. Farkas, D. K. Malick, A. D. Rabuck, K. Raghavachari, J. B. Foresman, J. V. Ortiz, Q. Cui, A. G. Baboul, S. Clifford, J. Cioslowski, B. B. Stefanov, G. Liu, A. Liashenko, P. Piskorz, I. Komaromi, R. L. Martin, D. J. Fox, T. Keith, M. A. Al-Laham, C. Y. Peng, A. Nanayakkara, M. Challacombe, P. M. W. Gill, B. Johnson, W. Chen, M. W. Wong, C. Gonzalez, J. A. Pople, Gaussian, Inc., Pittsburgh, PA, **2003**.
[16] G. K. S. Prakash, G. Rasul, A. Burrichter, K. K. Laali, G. A. Olah, *J. Org. Chem.* **1996**, *61*, 9253.
[17] a) A. P. Minton, *Biophys. J.* **1992**, *63*, 1090; b) R. W. Peterson, K. Anbalagan, C. Tommos, A. J. Wand, *J. Am. Chem. Soc.* **2004**, *126*, 9498.

 © 2005 Wiley-VCH Verlag GmbH & Co. KGaA, Weinheim

Molecular Magnetism

[GdNi$_6$] and [LaNi$_6$]: High-Field EPR Spectroscopy and Magnetic Studies of Exchange-Coupled Octahedral Clusters**

Yasuhiko Yukawa, Guillem Aromí,* Satoshi Igarashi, Joan Ribas, S. A. Zvyagin, and J. Krzystek*

The preparation of transition-metal clusters with relevance in molecular magnetism has been a very prolific area of coordination chemistry,[1–3] and has become of primary importance since the discovery of single-molecule magnets (SMMs).[4,5] As a result, a high level of understanding has been achieved of the nature and mechanism of the magnetic super exchange between 3d metals.[6–8] Indeed, the vast majority of SMMs known to date are made of manganese,[9] iron,[10] nickel,[11] cobalt,[12] and vanadium.[13] In contrast, the magnetic coupling between 3d and 4f metals is still not understood very well and has therefore not been exploited as a potential entry to a new category of SMMs.[14,15]

Of all open-shell 4f ions, Gd^{III} has been studied the most since it does not show the complicating effect of spin-orbit coupling. The quasi-systematic ferromagnetic nature of the coupling between Cu^{II} and Gd^{III} has been corroborated by a considerable amount of experimental data,[16] and a recent report has established the theoretical grounds of this observation.[17] In contrast, the magnetic exchange between Ni^{II} and Gd^{III}—always found to be ferromagnetic so far[18–23]—has not been explored as extensively. The few systems where this coupling has been analyzed are almost all dinuclear compounds.

As a continuation of our studies on heterometallic 3d–4f clusters,[24–26] we have prepared a series of isostructural and highly symmetric exchange-coupled clusters of the formula

[*] Prof. Dr. Y. Yukawa, Dr. S. Igarashi
Department of Environmental Science
Faculty of Science
Niigata University
8050 Ikarashi Nino-cho, Niigata 950-2181 (Japan)
Fax: (+81) 25-262-6361
E-mail: yukawa@env.sc.niigata-u.ac.jp
Dr. G. Aromí, Prof. Dr. J. Ribas
Departament de Química Inorgànica
Universitat de Barcelona
Diagonal 647, 08028 Barcelona (Spain)
Fax: (+34) 93-490-7725
E-mail: guillem.aromi@qi.ub.es
Dr. S. A. Zvyagin, Dr. J. Krzystek
National High Magnetic Field Laboratory
Florida State University
Tallahassee, FL 32310 (USA)

[**] This work was supported by grants from the Spanish Ministerio de Ciencia y Tecnología, the Japan Society for the Promotion of Science, the National Science Foundation (USA, Cooperative Agreement No. DMR-0084173), and the State of Florida. The authors are thankful to Andrew Ozarowski for invaluable help with EPR simulations.

Supporting information for this article is available on the WWW under http://www.angewandte.org or from the author.

 DOI: 10.1002/anie.200462401 © 2005 Wiley-VCH Verlag GmbH & Co. KGaA, Weinheim

$(NMe_4)[LnNi_6(pro)_{12}](ClO_4)_4$ (Ln = Gd, La; Hpro = proline). Similar compounds with other amino acids (Gly, Ala, Thr) have been recently reported.[27] This family of clusters provides a good opportunity to systematically study the magnetic exchange between 3d and 4f metals. We started by investigating coupling between Ni^{II} and Gd^{III}, the only case in which first-order spin-orbit coupling is absent, in the cluster $(NMe_4)[GdNi_6(pro)_{12}](ClO_4)_4$ (**1**). We were able to single out the contribution of Ni^{II} by comparing **1** with the lanthanum analogue **2** (La^{III} is diamagnetic). We report here the preparation and structures of **1** and **2** along with the first quantitative study of the magnetic properties of this category of compounds through the use of bulk magnetometry and high-frequency and high-field EPR (HF-EPR) spectroscopy.

The heterometallic complexes **1** and **2** were obtained as pure[28] purple precipitates after addition of NMe_4ClO_4 (694 mg, 4 mmol) to mixtures of $Gd(ClO_4)_3$ (911 mg, 2 mmol) or $La(ClO_4)_3$ (875 mg, 2 mmol) and $[Ni(pro)_2]$ (3.47 g, 12 mmol) in acetonitrile (80 mL). The two clusters are isostructural[29] and display the same structure as the Sm^{III} and Eu^{III} analogues.[24–26] The two molecules consist of a Ln^{III}-centered cage of six symmetry-equivalent Ni^{II} ions, which form a perfect octahedron (Figure 1). The nickel centers are

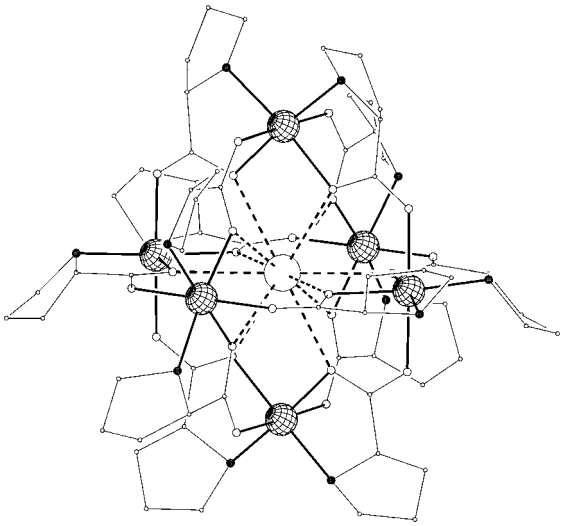

Figure 1. Molecular drawing of the cluster cation of $(NMe_4)[LnNi_6(pro)_{12}](ClO_4)_4$ (Ln = Gd^{III} (**1**), La^{III} (**2**)). Hydrogen atoms are not shown. Code for atoms: Ln: large empty sphere, Ni: large globes, N: medium-sized black spheres, O: medium-sized empty spheres, C: small spheres. Selected average distances [Å] for **1**/**2**: Ln—O 2.681(2)/2.713(2), O···O (within icosahedron) 2.83(3)/2.86(4), Ni—O 2.04(1)/2.05(2), Ni—N 2.059(4)/2.069(4), Ln···Ni 3.6970(6)/3.7114(7), Ni···Ni (*cis*) 5.2283(6)/5.2486(7), Ni···Ni (*trans*) 7.3939(9)/7.4227(9).

equatorially *cis*-chelated by two prolinate ligands. The oxygen donor of the chelate rings is also connected to the central lanthanide, providing dodeca coordination around this ion. The other oxygen donor of each prolinate group occupies one axial position of an adjacent $[Ni(pro)_2]$ unit, forming Ni···Ni carboxylate bridges in a *syn*,*anti* fashion. Replacement of Gd^{III} by La^{III} has very little influence on the metric parameters of the cluster.

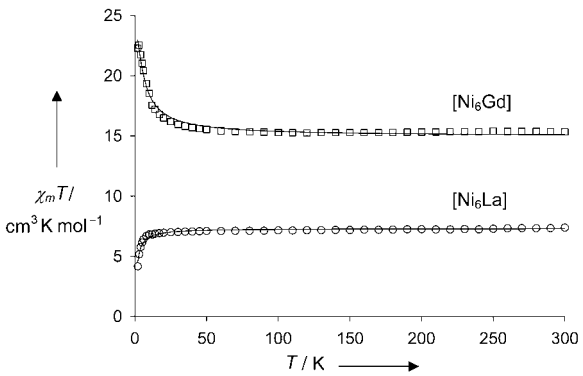

Figure 2. Plots of $\chi_m T$ versus T for compounds **1** and **2**. The solid lines represent fits to the experimental data (see text for details).

In contrast, there is a dramatic influence on the magnetic behavior of the cluster upon replacement of La^{III} in **2** (f^0, diamagnetic) with Gd^{III} in **1** (f^7, paramagnetic). Figure 2 shows the plots of the molar paramagnetic susceptibility $\chi_m T$ (corrected for the diamagnetic contribution) as a function of temperature T. The measurements were made under a constant magnetic field of 0.3 T between 2 and 300 K. The product $\chi_m T$ for **1** is 15.34 $cm^3 K mol^{-1}$ at room temperature, consistent with six independent Ni^{II} centers and one Gd^{III} ion in the molecule, following a Curie law with an average of $g \approx 2.2$. This value remains unchanged with decreasing temperature until about 50 K, where it increases to 22.29 $cm^3 K mol^{-1}$ at 2 K. This shows that the coupling within the cluster is predominantly ferromagnetic in character.

To describe this behavior, the spin Hamiltonian in Equation (1) was used (S_1 to $S_6 = 1$ and $S_7 = 7/2$, see

$$\hat{H} = -2J(\hat{S}_1\hat{S}_2 + \hat{S}_1\hat{S}_3 + \hat{S}_1\hat{S}_4 + \hat{S}_1\hat{S}_5 + \hat{S}_2\hat{S}_3 + \hat{S}_2\hat{S}_5 + \hat{S}_2\hat{S}_6 + \hat{S}_3\hat{S}_4 + \hat{S}_3\hat{S}_6 + \hat{S}_4\hat{S}_5 + \hat{S}_4\hat{S}_6 + \hat{S}_5\hat{S}_6) - 2J'\hat{S}_7\sum_{i=1}^{6}\hat{S}_i \quad (1)$$

Figure 3). This Hamiltonian, which can be solved analytically by using the Kambe vector-coupling approach,[30] incorporates the Ni···Ni coupling (J) and the Ni···Gd exchange (J'), whereas the coupling between nonadjacent Ni^{II} atoms as well as zero-field splitting effects (ZFS) are not included.

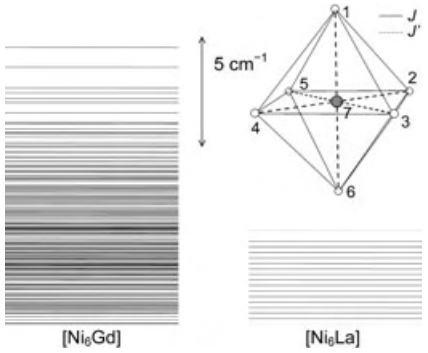

Figure 3. Schematic representations of the spin-level ladders for compounds **1** (left) and **2** (right). The number of spin states are 694 and 141, and the energy ranges spanned by the ladders are 12.70 and 5.67 cm^{-1} for **1** and **2**, respectively. Also shown is the numbering scheme employed for the magnetic models.

 © 2005 Wiley-VCH Verlag GmbH & Co. KGaA, Weinheim

This model affords a total of 694 $|S_T,S_{ABC},S_A,S_B,S_C\rangle$ spin states ranging from $S_T = 1/2$ to 19/2, with a total degeneracy of 5832. Their energies were inserted into a $\chi_m = f(T)$ expression derived from the Van Vleck equation to fit the experimental data. The calculation yielded the fit parameters $J = -0.12\ cm^{-1}$, $J' = 0.13\ cm^{-1}$, and $g = 2.02$. The difference between this g value and that estimated at 300 K with a Curie law underscores the sensitivity to the model used in fitting the data. The calculated coupling constants give rise to a fivefold degenerate spin ground state with $S_T = 13/2$ corresponding to $|13/2,3,2,2,2\rangle$, in an example of spin frustration in the strictest sense of the word.[31] This ground state is close in energy to a threefold degenerate excited state, with $S_T = 15/2$ lying only $0.01\ cm^{-1}$ higher in energy. The energies of the spin states span an energy range of $12.70\ cm^{-1}$ (see spin-level ladder in Figure 3).

The possible influence of a D parameter on the $\chi_m T$ versus T curve was evaluated by means of simulations from full-matrix diagonalization using the program MAGPACK.[32] It was found that reasonable values for this parameter have almost no influence on the curve for this system (see Figure S1 in the Supporting Information). This, and the results from HF-EPR spectroscopy (see below), justify the omission of D from the model used to fit this curve. Variable-temperature isofield-reduced magnetization measurements on **1** (not shown) indicate that at high enough fields, the $|M_s| = 19/2$ level becomes the ground state, since $M/N\mu_B$ reaches a value of 18.41 reduced units, higher than expected for the $S_T = 13/2$ ground state. The AC susceptibility measurements showed that complex **1** does not display slow relaxation of the magnetization (as ascertained by the absence of an out-of-phase component of χ_m). This might be due to the lack of ZFS or by the accumulation of spin states within a very narrow energy range near the ground state. The above results confirm the observations made on the very few cases of Gd···Ni exchange previously studied; all were found to be very weakly ferromagnetic. Furthermore, these findings supplement the limited data on Ni···Ni coupling through only one *syn*,*anti* carboxylate ligand. The reported J values are also very small, two of them antiferromagnetic[33,34] and the third ferromagnetic.[35]

Complex **2** was studied to establish the properties of the Ni_6 moiety without the influence of a paramagnetic ion at the central position. The value of $\chi_m T$ at room temperature is $7.38\ cm^3\,K\,mol^{-1}$, which corresponds to the expected value for a cluster of six isolated Ni^{II} centers ($S = 1$) with $g \approx 2.2$. This value remains essentially constant until approximately 10 K, where it drops suddenly to $4.15\ cm^3\,K\,mol^{-1}$ at 2 K. These results can be explained in terms of very weak antiferromagnetic coupling between Ni^{II} centers within the molecule. This is in contrast with preliminary results for a cluster with the same spin topology.[27] The magnitude of the coupling under this hypothesis was calculated by using a numerical method based on the Heisenberg spin Hamiltonian in Equation (2) ($S_i = 1$, see Figure 3).

$$\hat{H} = -2J(\hat{S}_1\hat{S}_2 + \hat{S}_1\hat{S}_3 + \hat{S}_1\hat{S}_4 + \hat{S}_1\hat{S}_5 + \hat{S}_2\hat{S}_3 + \hat{S}_2\hat{S}_5 + \hat{S}_2\hat{S}_6 + \hat{S}_3\hat{S}_4 + \hat{S}_3\hat{S}_6 + \hat{S}_4\hat{S}_5 + \hat{S}_4\hat{S}_6 + \hat{S}_5\hat{S}_6) \quad (2)$$

This equation gives rise to 141 spin states, with a total degeneracy of 729. The energies of these states can be found by applying the Kambe vector-coupling method, as previously reported for a Mn_6 cluster with the same spin topology.[36] These energies allowed least-squares fitting of the experimental data to the Van Vleck expression of the susceptibility (Figure 2, bottom, solid line), yielding $J = -0.14\ cm^{-1}$ and $g = 2.20$ as best-fit parameters. This value is remarkably close to that obtained with **1** for the Ni···Ni coupling. The spin ground state originated is $S_T = 0$, with three degenerate $S_T = 1$ states lying $0.27\ cm^{-1}$ higher in energy. Accordingly, all 141 spin states would be contained within an energy range $5.67\ cm^{-1}$ wide (see the spin-level ladder in Figure 3). In addition to small antiferromagnetic coupling as assumed by the above analysis, the drop of $\chi_m T$ at low temperatures observed in **2** could also be caused by small magnetic anisotropy, or a combination of both factors. To explore this possibility, the susceptibility data were fit to the corresponding expression for six independent octahedral Ni^{II} ions that included a ZFS parameter D.[37] The best fit (not shown) was obtained for $g = 2.18$ and $D = 4.98\ cm^{-1}$. Since the two factors considered are expected to have the same effect on $\chi_m T$, it is not possible to determine which one is dominating. Comparison with complex **1** suggests that exchange coupling predominates in **2**, since the values obtained for J are almost the same for both complexes. Additional insight into this problem was obtained following HF-EPR measurements.

Complexes **1** and **2** were further characterized by EPR spectroscopy in both the conventional X-band as well as the high-frequency and high-field versions ($\tilde{\nu} \sim 150$–600 GHz; B_0 up to 25 T). Complex **1** produces spectra at any frequency employed, as expected from a Kramers (half-integer) spin state. The best spectra were obtained at low temperatures (5–40 K) and consist of one broad resonance at $g \approx 2$ (not shown). A careful look at this signal reveals that it is asymmetric, and cannot be fitted with a single absorption of any shape. Also, the actual g value is higher than 2.00, and weakly frequency dependent, varying from $g = 2.20(2)$ at 186 GHz to 2.11(2) at 368 GHz. These two features point to the presence of a small ZFS, for which an upper limit of $D \geq 0.02\ cm^{-1}$ could be established by simulation.

In contrast to **1**, complex **2** does not produce EPR spectra at X-band, as expected for a non-Kramers (integer-spin) system of large ZFS. The HF-EPR spectra are totally different from those of **1**, consisting at low temperatures of two broad lines characterized by g_{eff} that strongly vary with frequency. The spectrum at 189.9 GHz contains a transition at or near zero-field (infinite g_{eff}, inset of Figure 4) identified as a typical $\Delta M_s = \pm 2$ transition and a resonance at higher field corresponding to a "double-quantum" transition.[38] No $\Delta M_s = \pm 1$ resonances were observed, presumably due to their low intensity and/or large line width. The dependence of the EPR resonances for **2** on the full field (Figure 4) can be best explained by assuming single-ion anisotropy of Ni^{II} with the spin Hamiltonian parameters $S = 1$, $D = 5.5(1)\ cm^{-1}$, $E = 0.8(3)\ cm^{-1}$, $g_x = 2.06(3)$, $g_y = 2.21(4)$, and $g_z = 2.30(3)$. Thus, the magnetic properties of the six Ni^{II} ions determine the properties of **2**, and the coupling between these ions is clearly of much less magnitude than the single-ion ZFS anisotropy.

 © 2005 Wiley-VCH Verlag GmbH & Co. KGaA, Weinheim

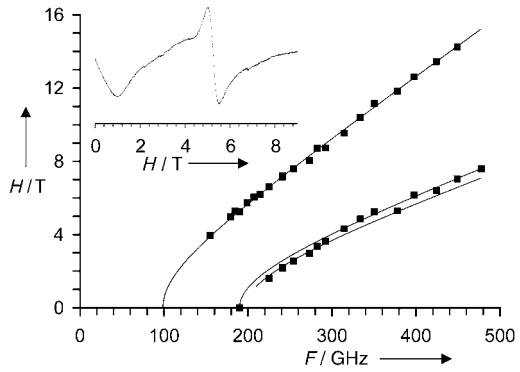

Figure 4. Plot of the magnetic field H versus the operating frequency F for the HFEPR resonances of complex **2**. The squares represent experimental data, while the lines were drawn using best-fitted spin Hamiltonian parameters as described in the text. Inset: The HFEPR spectrum of **2** at 189 GHz and 10 K. See text for details.

This conclusion can only be reconciled with the results from the susceptibility studies in the hypothesis that both, ZFS and weak Ni···Ni antiferromagnetic super-exchange have an influence in the low temperature behavior of complex **2**. The fact that complex **1** is a spin-frustrated system, caused by the presence of such Ni···Ni coupling, suggests that this coupling should not be ruled out in **2**.

In conclusion, two rare heterometallic clusters containing Ni and a lanthanide ion have been prepared and their magnetic properties analyzed with the methods used typically to study SMMs. Synthetic efforts aimed at expanding the small family of heterometallic 3d–4f clusters and understanding their magnetic properties should lead to the development of a new generation of molecular nanomagnets, with potentially new and improved properties.[39]

Received: October 22, 2004

Keywords: cluster compounds · EPR spectroscopy · lanthanides · magnetic properties · nickel

[1] R. E. P. Winpenny, *Adv. Inorg. Chem.* **2001**, *52*, 1.
[2] R. E. P. Winpenny, *J. Chem. Soc. Dalton Trans.* **2002**, 1.
[3] G. Aromí, S. M. J. Aubin, M. A. Bolcar, G. Christou, H. J. Eppley, K. Folting, D. N. Hendrickson, J. C. Huffman, R. C. Squire, H. L. Tsai, S. Wang, M. W. Wemple, *Polyhedron* **1998**, *17*, 3005.
[4] R. Sessoli, H. L. Tsai, A. R. Schake, S. Y. Wang, J. B. Vincent, K. Folting, D. Gatteschi, G. Christou, D. N. Hendrickson, *J. Am. Chem. Soc.* **1993**, *115*, 1804.
[5] G. Christou, D. Gatteschi, D. N. Hendrickson, R. Sessoli, *MRS Bull.* **2000**, *25*, 66.
[6] O. Kahn, *Molecular Magnetism*, VCH, New York, **1993**.
[7] J. Cernak, M. Orendac, I. Potocnak, J. Chomic, A. Orendacova, J. Skorsepa, A. Feher, *Coord. Chem. Rev.* **2002**, *224*, 51.
[8] D. Gatteschi, R. Sessoli, *Angew. Chem.* **2003**, *115*, 278; *Angew. Chem. Int. Ed.* **2003**, *42*, 268.
[9] M. Murugesu, M. Habrych, W. Wernsdorfer, K. A. Abboud, G. Christou, *J. Am. Chem. Soc.* **2004**, *126*, 4766.
[10] D. Gatteschi, R. Sessoli, A. Cornia, *Chem. Commun.* **2000**, 725.
[11] H. Andres, R. Basler, A. J. Blake, C. Cadiou, G. Chaboussant, C. M. Grant, H. U. Gudel, M. Murrie, S. Parsons, C. Paulsen, F. Semadini, V. Villar, W. Wernsdorfer, R. E. P. Winpenny, *Chem. Eur. J.* **2002**, *8*, 4867.
[12] M. Murrie, S. J. Teat, H. Stoeckli-Evans, H. U. Gudel, *Angew. Chem.* **2003**, *115*, 4801; *Angew. Chem. Int. Ed.* **2003**, *42*, 4653.
[13] S. L. Castro, Z. M. Sun, C. M. Grant, J. C. Bollinger, D. N. Hendrickson, G. Christou, *J. Am. Chem. Soc.* **1998**, *120*, 2365.
[14] S. Osa, T. Kido, N. Matsumoto, N. Re, A. Pochaba, J. Mrozinski, *J. Am. Chem. Soc.* **2004**, *126*, 420.
[15] C. M. Zaleski, E. C. Depperman, J. W. Kampf, M. L. Kirk, V. L. Pecoraro, *Angew. Chem.* **2004**, *116*, 4002; *Angew. Chem. Int. Ed.* **2004**, *43*, 3912.
[16] M. Sakamoto, K. Manseki, H. Okawa, *Coord. Chem. Rev.* **2001**, *219*, 379.
[17] J. Paulovic, F. Cimpoesu, M. Ferbinteanu, K. Hirao, *J. Am. Chem. Soc.* **2004**, *126*, 3321.
[18] S. R. Bayly, Z. Q. Xu, B. O. Patrick, S. J. Rettig, M. Pink, R. C. Thompson, C. Orvig, *Inorg. Chem.* **2003**, *42*, 1576.
[19] Q. Y. Chen, Q. H. Luo, L. M. Zheng, Z. L. Wang, J. T. Chen, *Inorg. Chem.* **2002**, *41*, 605.
[20] M. L. Kahn, P. Lecante, M. Verelst, C. Mathoniere, O. Kahn, *Chem. Mater.* **2000**, *12*, 3073.
[21] J. P. Costes, F. Dahan, A. Dupuis, *Inorg. Chem.* **2000**, *39*, 165.
[22] J. P. Costes, F. Dahan, A. Dupuis, J. P. Laurent, *Inorg. Chem.* **1997**, *36*, 4284.
[23] T. Yamaguchi, Y. Sunatsuki, M. Kojima, H. Akashi, M. Tsuchimoto, N. Re, S. Osa, N. Matsumoto, *Chem. Commun.* **2004**, 1048.
[24] Y. Yukawa, S. Igarashi, A. Yamano, S. Sato, *Chem. Commun.* **1997**, 711.
[25] S. Igarashi, Y. Hoshino, Y. Masuda, Y. Yukawa, *Inorg. Chem.* **2000**, *39*, 2509.
[26] S. Igarashi, Y. Yukawa, *Chem. Lett.* **1999**, 1265.
[27] J.-J. Zhang, S.-C. Xiang, S.-M. Hu, S.-Q. Xia, R.-B. Fu, X.-T. Wu, Y.-M. Li, H.-S. Zhang, *Polyhedron* **2004**, *23*, 2265.
[28] Elemental analysis calcd (%) for **1**: C 32.96, H 4.67, N 7.81; found: C 32.53, H 4.75, N 7.81. Calcd (%) for **2**: C 32.70, H 4.63, N 7.75; found: C 32.39, H 4.52, N 7.87.
[29] Crystal data for **1** ($C_{64}H_{108}Cl_4GdN_{13}O_{40}Ni_6$): Data were collected on a purple block-shaped crystal ($0.30\times0.30\times0.32$ mm), cubic, space group $F23$ (no. 196) with $a=21.275(1)$, $b=21.2750$, $c=21.2750$ Å, $V=9629.6(6)$ Å^3, $Z=4$, $\alpha=89$, $\beta=90$, $\gamma=89°$; of 4779 reflections measured, 1564 were independent; $R_{int}=0.028$. Crystal data for **2** ($C_{64}H_{108}Cl_4LaN_{13}O_{40}Ni_6$): Data were collected on a purple block-shaped crystal ($0.30\times0.30\times0.24$ mm), cubic, space group $F23$ (no. 196) with $a=21.305(2)$, $b=21.3052$, $c=21.3052$ Å, $V=9670.7(10)$ Å^3, $Z=4$, $\alpha=89$, $\beta=90$, $\gamma=89°$; of 4736 reflections measured, 1575 were independent; $R_{int}=0.028/0.029$. Measurements were carried out on a Rigaku AFC7R diffractometer ($2\theta_{max}=65°$, $T=296.2$ K, $Mo_{K\alpha}$ radiation, $\lambda=0.7107$ Å) with intensity data corrected for Lorentz and polarization effects. The structures were solved by heavy-atom Patterson methods and expanded using Fourier techniques. The non-hydrogen atoms were refined anisotropically. Hydrogen atoms were included but not refined. All calculations were performed using the teXsan crystallographic software package of Molecular Structure Corporation. Refinement of 98 parameters converged at a final w$R2$ value of 0.1373, $R1=0.0415$ (for 1053 reflections with $I>2\sigma(I)$), $S=1.042$, $-0.70<\Delta\rho<1.20$ e Å^{-3}. CCDC-253529 (**1**) and CCDC-253530 (**2**) contain the supplementary crystallographic data for this paper. These data can be obtained free of charge from the Cambridge Crystallographic Data Centre via www.ccdc.cam.ac.uk/data_request/cif.
[30] K. Kambe, *J. Phys. Soc. Jpn.* **1950**, *5*, 48.
[31] O. Kahn, *Chem. Phys. Lett.* **1997**, *265*, 109.

 © 2005 Wiley-VCH Verlag GmbH & Co. KGaA, Weinheim

[32] J. J. Borras-Almenar, J. M. Clemente-Juan, E. Coronado, B. S. Tsukerblat, *J. Comput. Chem.* **2001**, *22*, 985.
[33] L. M. Zheng, T. Whitfield, X. Q. Wang, A. J. Jacobson, *Angew. Chem.* **2000**, *112*, 4702; *Angew. Chem. Int. Ed.* **2000**, *39*, 4528.
[34] X. Lin, D. M. J. Doble, A. J. Blake, A. Harrison, C. Wilson, M. Schroder, *J. Am. Chem. Soc.* **2003**, *125*, 9476.
[35] M. Du, X. H. Bu, Y. M. Guo, L. Zhang, D. Z. Liao, J. Ribas, *Chem. Commun.* **2002**, 1478.
[36] G. Aromí, J. P. Claude, M. J. Knapp, J. C. Huffman, D. N. Hendrickson, G. Christou, *J. Am. Chem. Soc.* **1998**, *120*, 2977.
[37] O. Kahn, *Molecular Magnetism*, VCH, New York, **1993**, p. 17.
[38] D. Collison, M. Helliwell, V. M. Jones, F. E. Mabbs, E. J. L. McInnes, P. C. Riedi, G. M. Smith, R. G. Pritchard, W. I. Cross, *J. Chem. Soc. Faraday Trans.* **1998**, *94*, 3019.
[39] **Note added in proof** (14.2.2005): After submission of this paper, an important article on the preparation of a new example of a mixed 3d–4f single-molecule magnet appeared: A. Mishra, W. Wernsdorfer, K. A. Abboud, G. Christou, *J. Am. Chem. Soc.* **2004**, *126*, 15648.

 © 2005 Wiley-VCH Verlag GmbH & Co. KGaA, Weinheim

Enzyme Inhibition

The Synthesis of Hybrids of D-Galactose with 1-Deoxynojirimycin Analogues as Glycosidase Inhibitors**

*B. Gopal Reddy and Yashwant D. Vankar**

The synthesis of hybrid molecules, which are made up of two different molecular units, has recently gained importance because many of them exhibit promising physical, chemical, and biological properties as well as being novel architectures.[1] These molecules are derived from either natural products or are a combination of natural products and synthetic compounds that have established or potentially significant properties, for example, compounds that could be used in biological or material science applications. In this context, natural products such as carbohydrates,[2] peptides,[3] steroids,[4] and taxoids[5] have been employed in the preparation of hybrid molecules, and their synthetic counterparts have included anthraquinones,[6] fullerenes,[7] and β-lactams.[8] Combinations are chosen with the expectation that the hybrid molecules will display enhanced or modified properties. Further work on the synthesis of newer hybrid molecules is expected, as is evident from two very important, recent reviews.[1]

The importance of glycobiology in medicinal and biological chemistry is at its height, and there have been several notable contributions in this area from both biologists and chemists.[9] Recent advances in understanding the role of glycosidase inhibitors in treating various diseases, though in their infancy, are significant in the study of glycobiology.[10] Among many glycosidase inhibitors, nojirimycin, 1-deoxynojirimycin, and their analogues have received a large amount of attention.[11] Clearly, hybrid molecules derived from nojirimycin analogues will be of interest from the standpoint of glycosidase inhibition. From the point of view of drug discovery, hybrids of D-glucose and some heterocycles have been designed and synthesized by Smith III, Hirschman, and co-workers.[12] Also, an interesting hybrid molecule that contains carbasugars has recently been found to be a better glycosidase inhibitor than the parent carbasugar.[13] These reports and our interest in the chemistry of glycals[14] and nitroglycals[14f,g] prompted us to explore the synthesis of novel hybrids as possible glycosidase inhibitors.

Herein, we report the synthesis of three novel hybrids of D-galactose with three analogues of 1-deoxynojirimycin: 1-deoxymannonojirimycin, 1-deoxygulonojirimycin, and 1-deoxymannohomonojirimycin, with 3,4,6-tri-*O*-benzyl-2-nitro-D-galactal (**1**) used as the starting point. The importance of 2-nitroglycals in the synthesis of glycopeptides, 2-amino-*O*-glycosides, 2-amino-*C*-glycosides, and other useful molecules has been well demonstrated by Schmidt and co-workers.[14g,15] We have also recently reported the synthesis of D-lividosaminide[14f] from 3-deoxy-2-nitroglucal and 2-amino-*C*-glycosides from 2-nitroglycals.[14g] A general retrosynthetic analysis of the hybrids of D-galactose and analogues of 1-deoxynojirimycin is presented in Scheme 1, which illustrates the importance of 2-nitrogalactal and ring-closing metathesis in our synthetic endeavors. Treatment of 2-nitrogalactal derivative **1**[15] with vinylmagnesium bromide gave a 1:5 mixture of **2a** and **2b** (Scheme 1) in 73% yield, which were readily separated by column chromatography. The minor compound **2a** was found to possess a $^1C_4$ conformation as was revealed by ^{1}H NMR spectroscopic analysis and NOE interaction experiments. The ^{1}H NMR spectrum of the major compound **2b**, on the other hand, indicated that it is a mixture of two inseparable components in a ratio of 1.2:1. However, reduction of this mixture with $LiAlH_4$ followed by protection of the free amine with an *N-tert*-butoxycarboxy (NHBoc) group gave a mixture of three compounds **3a**, **3b**, and **3c** that could be readily separated by chromatography. The structures of compounds **3a** and **3c** were confirmed by ^{1}H NMR spectroscopic analysis, COSY, and NOE interaction experiments as having $^4C_1$ conformations. It was difficult to assign the stereochemical orientations of the vinyl and NHBoc groups on the basis of the ^{1}H NMR spectrum of **3b**; however, the appearance of the *tert*-butyl group as a clean singlet at $\delta = 1.42$ ppm in the spectrum indicated that **3b** is a single isomer, which was also confirmed by its ^{13}C NMR spectrum. However, it was the spectral analysis of the bicyclic compound **7** that provided the basis for the conclusive assignment of the stereochemistry of **3b**.

[*] Dr. B. G. Reddy, Prof. Dr. Y. D. Vankar
Department of Chemistry
Indian Institute of Technology — Kanpur
Kanpur 208 016 (India)
Fax: (+91) 512-259-0007
E-mail: vankar@iitk.ac.in

[**] We thank the Department of Science and Technology, New Delhi, India for financial support (Grant no. SP/S1/G-21/2001). We also thank Dr. D. D. Dhavale, Dr. S. G. Sabharwal, and Mr. Tarun Sharma of the University of Pune for help in carrying out the enzyme inhibition studies.

Supporting information for this article is available on the WWW under http://www.angewandte.org or from the author.

 DOI: 10.1002/anie.200462413 © 2005 Wiley-VCH Verlag GmbH & Co. KGaA, Weinheim

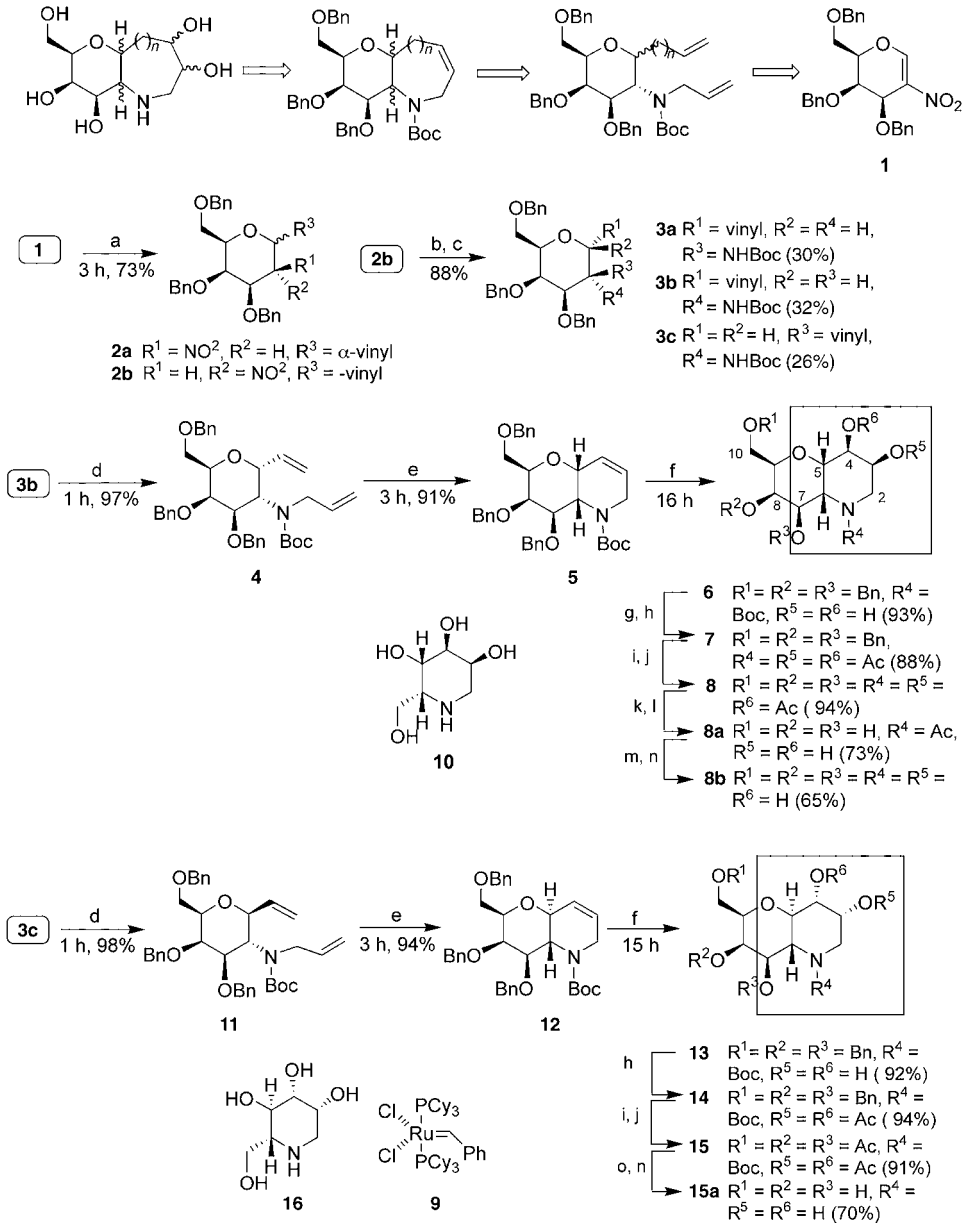

Scheme 1. a) CH_2=CHMgBr, THF, −60 °C–RT; b) $LiAlH_4$, THF, 0 °C–RT, 0.5 h; c) Boc_2O, Et_3N, CH_2Cl_2; d) allylbromide, NaH, DMF, 0 °C–RT; e) Grubbs' catalyst (5 mol %), CH_2Cl_2, reflux; f) OsO_4, NMO, acetone/H_2O/*t*BuOH (1:1:0.4); g) 3 M HCl in EtOAc, RT, 1 h; h) Ac_2O, Et_3N, CH_2Cl_2, RT, 3 h; i) 20 % $Pd(OH)_2$/C, THF, H_2, 8 h; j) Ac_2O, pyridine, 4 h; k) NaOMe, MeOH, RT, 15 min; l) amberlite (H^+) resin (300 mg), MeOH, 10 min; m) 3 M HCl in MeOH, RT, 1 h; n) dowex (OH^-) resin; o) conc. HCl (0.5 mL) in MeOH (3 mL), reflux, 17 h. DMF = *N*,*N*-dimethylformamide, Boc = *tert*-butoxycarbonyl, Bn = benzyl, and Cy = cyclohexyl.

The NHBoc group in **3a** is axially oriented and allylation failed under a variety of conditions possibly because of steric hindrance. However, compound **3b** underwent smooth allylation with allyl bromide in the presence of NaH at 0 °C–room temperature over one hour to give compound **4** in 97 % yield. Ring-closing metathesis of the diene **4** by using the first generation Grubbs' catalyst **9**[16] produced the expected bicyclic compound **5** in 91 % yield. Dihydroxylation of **5** was then performed with OsO_4/*N*-methylmorpholine *N*-oxide (NMO) to form diol **6** in 93 % yield. The *cis*-dihydroxy groups were found to have a β geometry as revealed by ^{1}H NMR spectroscopic analysis and the NOE interaction experiments of the corresponding triacetate **7**. Compound **7** showed significant NOE interaction correlations between H7, H8, and H9; H5 and H6; and H3, H4, and H9 (see the Supporting Information). Hydrogenolysis of the triacetate **7** followed by acetylation was carried out to obtain the hexaacetate **8**, which represents a hybrid molecule of D-galactose and 1-deoxygulonojirimycin (**10**).

Compound **3c** was also transformed into a bicyclic compound **15** (Scheme 1), a hybrid of D-galactose and 1-deoxymannonojirimycin (**16**), by following the same reaction sequence as above. The *cis*-dihydroxy groups of the diol **13** were found to have an α geometry, as confirmed by ^{1}H NMR

 © 2005 Wiley-VCH Verlag GmbH & Co. KGaA, Weinheim

spectroscopic analysis and NOE interaction experiments of the corresponding diacetate **14** (see the Supporting Information). Further hydrogenolysis of the diacetate **14** with Pd-$(OH)_2$/C and hydrogen gas followed by acetylation yielded the pentaacetate **15**, whose structure was determined by X-ray crystallographic studies;[17] thus, the structures assigned to compounds **3c** and **13** were further confirmed.

A hybrid molecule containing a homologue of the 1-deoxynojirimycin analogue was prepared from 2-nitrogalactal (**1**; Scheme 2), which was treated with allylzinc bromide at

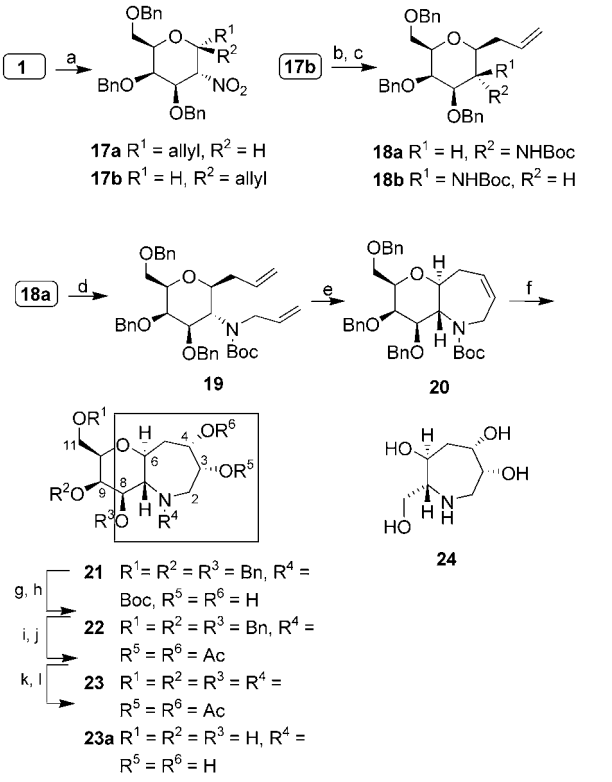

Scheme 2. a) $CH_2{=}CH{-}CH_2ZnBr$, THF, −60 °C–RT, 3.5 h, 82%; b) $LiAlH_4$, THF, 0 °C–RT, 0.5 h; c) Boc_2O, Et_3N, CH_2Cl_2, RT, 2 h, 78% (over two steps); d) allylbromide, NaH, DMF, 0 °C–RT, 1 h, 98%; e) Grubbs' catalyst (5 mol%), CH_2Cl_2, reflux, 6 h, 94%; f) OsO_4, NMO, acetone/H_2O/*t*BuOH (1:1:0.4), 14 h, 85%; g) 3 M HCl in EtOAc, RT, 1 h; h) Ac_2O, Et_3N, CH_2Cl_2, RT, 3 h, 87% (over two steps); i) Pd-$(OH)_2$/C, H_2, RT, overnight; j) Ac_2O, pyridine, RT, overnight, 98%; k) conc. HCl (0.5 mL) in MeOH (3 mL), reflux, 17 h; l) dowex (OH^-) resin, 75%.

−60 °C. The corresponding 2-nitro-*C*-allyl glycoside was produced in 82% yield as a 1:4 mixture of two isomers **17a** and **17b**, which were readily separated by column chromatography. The minor isomer **17a** was assigned the structure as shown; NOE interaction correlation data (see the Supporting Information) indicated it had a $^1C_4$ conformation. The major *trans* isomer **17b** was reduced with $LiAlH_4$ and the free amine protected as a NHBoc group to give a 1:1 mixture of two isomers **18a** and **18b** in 78% yield. Clearly, epimerization of **17b** had occurred even under mild reaction conditions (0 °C to room temperature). The structures of isomers **18a** and **18b** were confirmed by COSY and NOE interaction experiments.

The *trans* isomer **18a** underwent smooth allylation with allyl bromide in the presence of NaH to give diene **19** in 98% yield. An attempted allylation of **18b** under similar conditions was unsuccessful, even with heating. This observation is not surprising as the orientation of the allyl group at C1 and the NHBoc group at C2 is *cis* and so there may be steric hindrance towards allylation. Ring-closing metathesis of the diene **19** with the Grubbs' catalyst **9** gave the expected bicyclic compound **20** in 94% yield, which was then dihydroxylated with OsO_4/NMO to give **21** in 85% yield. The signal of the anomeric hydrogen atom of **17b** appeared in the ^1H NMR spectrum as a quintet at $\delta = 3.72$–3.75 ppm. However, irridation of the signal for the allylic methylene groups in **17b** at $\delta =$ 2.29 ppm in a homonuclear decoupling experiment resulted in the signal for the anomeric hydrogen atom becoming a doublet with $J = 10.0$ Hz. This result indicated that hydrogen atoms H1 and H2 are diaxially oriented. The structure was further confirmed by NOE interaction experiments that established a *cis* relationship between H1, H3, and H5 (see the Supporting Information). Additionally, the structure was also confirmed by single-crystal X-ray diffraction analysis of the triacetate **22**.[17] The triacetate **22** was hydrogenolyzed and acetylated to obtain the hexaacetate **23**, a hybrid of D-galactose and 1-deoxymannohomonojirimycin (**10**).

The hybrid azasugars **8a**, **8b**, **15a**, and **23a** showed selective inhibition activity towards the α-glycosidases[18] at millimolar concentrations (Table 1). 1-Deoxymannonojirimycin[11a,d] and 1-deoxygulonojirimycin have been recently isolated,[11a,d] however, enzyme inhibition activity of these compounds has been studied with only three glycosidases. Thus, the natural 1-deoxymannonojirimycin inhibits α-galactosidase (coffee beans) at a concentration of 420 μM (IC_{50}).[11d] In our studies with the same galactosidase, the hybrid molecule **15a** of D-galactose with 1-deoxymannonojirimycin showed no inhibition even at 7 mM concentrations (entry 1). However, it showed considerable inhibition of α-glucosidase (rice) at a concentration of 2.20 mM (entry 2). Conversely, the hybrid of D-galactose with 1,4-dideoxyhomomannonojirimy-

Table 1: Inhibitory activity of compounds **8a**, **8b**, **15a**, and **23a**.[a]

Entry	Enzymes	IC_{50} [mM]			
		8a	**8b**	**15a**	**23a**
1	α-galactosidase				
	coffee beans	3.73	4.68	NI	2.00
	almonds	NI	6.22	NI	NI
2	α-glucosidase				
	rice	3.70	7.00	2.20	2.19
	yeast	NI	4.86	NI	ND
3	β-glucosidase				
	almonds	NI	NI	NI	NI
4	α-mannosidase				
	jack beans	6.80	5.20	NI	2.66
5	β-galactosidase				
	bovine liver	ND	NI	4.50	NI
	almonds	NI	5.39	NI	NI

[a] Inhibition studies were carried out at millimolar concentrations, optimal pH of the enzymes, and 37 °C. NI = no inhibition at < 7.00 mM concentration of the inhibitor, ND = not determined.

 © 2005 Wiley-VCH Verlag GmbH & Co. KGaA, Weinheim

cin **23a** showed reasonable inhibition of α-galactosidase (coffee beans), α-glucosidase (rice), and α-mannosidase (jack beans; entries 1, 2, and 4) and no inhibition of β-glucosidase and β-galactosidase (entries 3 and 5). This observation indicates that compound **23a** is more specific towards the inhibition of α-glycosidases than β-glycosidases. Likewise, hybrid molecules **8a** and **8b** also moderately inhibit α-glucosidase (rice) and α-galactosidase (coffee beans). These studies indicate that the hybrid molecules **8a**, **8b**, **15a**, and **23a** are indeed moderate inhibitors of various glycosidases. It further suggests that structural variations of these hybrid molecules could promote glycosidase inhibition. We are currently investigating this possibility and will report our results in due course.

In summary, we have synthesized three novel hybrids of D-galactose and 1-deoxynojirimycin analogues that act as glycosidase inhibitors. Furthermore, they represent novel scaffolds for possible use in drug discovery, especially in view of the reports by Smith III, Hirschmann, and co-workers.[12] Also, the presence of five hydroxy groups raises the possibility of generating a library of such hybrid molecules, which enhances the scope of the present syntheses.

Received: October 24, 2004
Published online: February 21, 2005

Keywords: carbohydrates · enzymes · inhibitors · metathesis · ring closure

[1] a) L. F. Tietze, H. P. Bell, S. Chandrasekhar, *Angew. Chem*, **2003**, *115*, 4128; *Angew. Chem. Int. Ed.* **2003**, *42*, 3996; b) G. Mehta, V. Singh, *Chem. Soc. Rev.* **2002**, *31*, 324.

[2] a) L. F. Tietze, T. Feuerstein, A. Fecher, F. Haunert, O. Panknin, U. Borchers, I. Schuberth, F. Alves, *Angew. Chem.* **2002**, *114*, 785; *Angew. Chem. Int. Ed.* **2002**, *41*, 759; b) L. F. Tietze, M. Lieb, T. Herzig, F. Haunert, I. Schuberth, *Bioorg. Med. Chem.* **2001**, *9*, 1929; c) L. F. Tietze, T. Herzig, A. Fecher, F. Haunert, I. Schuberth, *ChemBioChem* **2001**, *2*, 758.

[3] a) W. K. C. Park, M. Auer, H. Jaksche, C.-H. Wong, *J. Am. Chem. Soc.* **1996**, *118*, 10150; b) U. J. Nilsson, E. J.-L. Fournier, O. Hindsgaul, *Bioorg. Med. Chem.* **1998**, *6*, 1563; c) T. D. W. Claridge, D. D. Long, N. L. Hungerford, R. T. Aplin, M. D. Smith, D. G. Marquess, G. W. J. Fleet, *Tetrahedron Lett.* **1999**, *40*, 2199; d) R. M. van Well, H. S. Overkleeft, M. Overhand, E. V. Carstenen, G. A. van der Marel, J. H. van Boom, *Tetrahedron Lett.* **2000**, *41*, 9331.

[4] a) L. F. Tietze, G. Schneider, J. Wolfling, A. Fecher, T. Nobel, S. Petersen, I. Schuberth, C. Wulff, *Chem. Eur. J.* **2000**, *6*, 3755; b) J. J. Masters, D. K. Jung, S. J. Danishefsky, L. B. Snyder, T. K. Park, R. C. A. Issacs, C. A. Alaimo, W. B. Young, *Angew. Chem*, **1995**, *107*, 495; *Angew. Chem. Int. Ed. Engl.* **1995**, *34*, 452; c) J. Wang, P. J. De Clercq, *Angew. Chem*, **1995**, *107*, 1898; *Angew. Chem. Int. Ed. Engl.* **1995**, *34*, 1749; d) S. D. Kuduk, C. R. Harris, F. F. Zheng, L. Sepp-Lorenzino, Q. Ouerfelli, N. Rosen, S. J. Danishefsky, *Bioorg. Med. Chem. Lett.* **2000**, *10*, 1303.

[5] a) I. Ojima, S. Lin, T. Inoue, M. L. Miller, C. P. Borella, X. Geng, J. J. Walsh, *J. Am. Chem. Soc.* **2000**, *122*, 5343; b) B. B. Metaferia, J. Hoch, T. E. Glass, S. L. Bane, S. K. Chatterjee, J. P. Snyder, A. Lakdawala, B. Cornett, D. G. I. Kingston, *Org. Lett.* **2001**, *3*, 2461.

[6] a) F. De Riccardis, I. Izzo, M. Di Filippo, G. Sodano, F. D. Acquisto, R. Carnuccio, *Tetrahedron* **1997**, *53*, 10871; b) F. De Riccardis, D. Meo, I. Izzo, M. Di Filippo, A. Casapullo, *Eur. J. Org. Chem.* **1998**, 1965.

[7] a) S. Boutorine, H. Tokuyama, M. Takasugi, H. Isobe, E. Nakamura, C. Helene, *Angew. Chem.* **1994**, *106*, 2526; *Angew. Chem. Int. Ed. Engl.* **1994**, *33*, 2462; b) E. Nakamura, H. Tokuyama, S. Yamago, T. Shiraki, Y. Sugiura, *Bull. Chem. Soc. Jpn.* **1996**, *69*, 2143; c) M. Bergamin, T. Da Ros, G. Spalluto, A. Boutorine, M. Prato, *Chem. Commun.* **2001**, 17; d) S. MacMahon, R. Fong II, P. S. Baran, I. Safonov, S. R. Wilson, D. I. Schuster, *J. Org. Chem.* **2001**, *66*, 5449.

[8] L. Banfi, G. Guanti, *Angew. Chem*, **1995**, *107*, 2613; *Angew. Chem. Int. Ed. Engl.* **1995**, *34*, 2393.

[9] a) A. Varki, *Glycobiology* **1993**, *3*, 97; b) P. Sears, C.-H. Wong, *Science* **2001**, *291*, 2344; c) C. R. Bertozzi, L. L. Kiessling, *Science* **2001**, *291*, 2357.

[10] a) T. D. Heightman, A. T. Vasella, *Angew. Chem.* **1999**, *111*, 794; *Angew. Chem. Int. Ed.* **1999**, *38*, 750; b) V. H. Lillelund, H. H. Jensen, X. Liang, M. Bols, *Chem. Rev.* **2002**, *102*, 515, and references therein.

[11] a) N. Asano, K. Yasuda, H. Kizu, A. Kato, J.-Q. Fan, R. J. Nash, G. W. J. Fleet, R. J. Molyneux, *Eur. J. Biochem.* **2001**, *268*, 35; b) M. H. Haukaas, G. A. O'Doherty, *Org. Lett.* **2001**, *3*, 401; c) J. L. O'Brien, M. Tosin, P. V. Murphy, *Org. Lett.* **2001**, *3*, 3353; d) N. Asano, S. Ishil, H. Kizu, K. Ikeda, A. Kato, O. R. Martin, J.-Q. Fan, *Eur. J. Biochem.* **2000**, *267*, 4179; e) Y. Ichikawa, Y. Igarashi, M. Ichikawa, Y. Suhara, *J. Am. Chem. Soc.* **1998**, *120*, 3007; f) G. C. Look, C. H. Fotsch, C.-H. Wong, *Acc. Chem. Res.* **1993**, *26*, 182; g) T. Kajimoto, K. K.-C. Liu, R. L. Pederson, Z. Z. Hong, Y. Ichikawa, J. A. Porco, Jr., C.-H. Wong, *J. Am. Chem. Soc.* **1991**, *113*, 6187.

[12] a) L. Abrous, J. Hynes, Jr., S. R. Friedrich, A. B. Smith III, R. Hirschmann, *Org. Lett.* **2001**, *3*, 1089; b) L. Abrous, P. K. Jokiel, S. R. Friedrich, J. Hynes, Jr., A. B. Smith III, R. Hirschmann, *J. Org. Chem.* **2004**, *69*, 280.

[13] G. Mehta, S. S. Ramesh, *Chem. Commun.* **2000**, 2429.

[14] a) B. G. Reddy, K. P. Madhusudanan, Y. D. Vankar, *J. Org. Chem.* **2004**, *69*, 2630; b) A. Agarwal, S. Rani, Y. D. Vankar, *J. Org. Chem.* **2004**, *69*, 6137; c) B. G. Reddy, Y. D. Vankar, *ARKIVOC* **2004**, *8*, 12; d) S. Rani, Y. D. Vankar, *Tetrahedron Lett.* **2003**, *44*, 907; e) S. Rani, A. Agarwal, Y. D. Vankar, *Tetrahedron Lett.* **2003**, *44*, 5001; f) B. G. Reddy, Y. D. Vankar, *Tetrahedron Lett.* **2003**, *44*, 4765; g) K. Pachamuthu, J. Das, A. Gupta, R. R. Schmidt, Y. D. Vankar, *Eur. J. Org. Chem.* **2002**, 1479; h) K. Pachamuthu, Y. D. Vankar, *J. Org. Chem.* **2001**, *66*, 7511; i) A. Gupta, Y. D. Vankar, *Tetrahedron* **2000**, *56*, 8525.

[15] a) N. Barroca, R. R. Schmidt, *Org. Lett.* **2004**, *6*, 1551; b) A. I. Khodair, K. Pachamuthu, R. R. Schmidt, *Synthesis* **2004**, 53; c) K. Pachamuthu, R. R. Schmidt, *Synlett* **2003**, 1351; d) A. I. Khodair, G. A. Winterfeldt, R. R. Schmidt, *Eur. J. Org. Chem.* **2003**, 1847; e) G. A. Winterfeldt, R. R. Schmidt, *Angew. Chem.* **2001**, *113*, 2718; *Angew. Chem. Int. Ed.* **2001**, *40*, 2654; f) G. A. Winterfeldt, J. Das, R. R. Schmidt, *Eur. J. Org. Chem.* **2000**, 3047; g) G. A. Winterfeldt, Y. Ito, T. Ogawa, R. R. Schmidt, *Eur. J. Org. Chem.* **1999**, 1167; h) J. Das, R. R. Schmidt, *Eur. J. Org. Chem.* **1998**, 1609.

[16] R. H. Grubbs, *Handbook of Metathesis*, *Vol. 2*, Wiley-VCH, Weinheim, **2003**, chap. 2.

[17] CCDC-239523 and -239524 contain the supplementary crystallographic data for this paper. These data can be obtained free of charge from The Cambridge Crystallographic Data Centre via http://www.ccdc.cam.ac.uk/data_request/cif..

[18] All the enzymes (except α-galactosidase, β-galactosidase, and β-glucosidase, which were isolated from almond seeds) and the corresponding substrates were purchased from Sigma Chemicals Co. The inhibition potencies of the sugar–azasugar hybrids **8a**, **8b**, **15a**, and **23a** were evaluated using α-glycosidases. The IC_{50} values obtained are summarized in Table 1.

 © 2005 Wiley-VCH Verlag GmbH & Co. KGaA, Weinheim

Metallacycles

Water-Induced Rearrangement of a Platinacyclic Carbene Produces a Platinacyclic Carbaphosphazene with an Intraannular Pt–C Bond in a Pt–N–P–N–P–C Ring**

*Min Fang, Nathan D. Jones, Michael J. Ferguson, Robert McDonald, and Ronald G. Cavell**

The cyclophosphazenes are a key family of inorganic heterocycles. These rings, which contain alternating four-coordinate P^V and two-coordinate N^{III} atoms $(R_2P{=}N)_n$ $(n \geq 3)$, have attracted considerable attention, principally because they are precursors to polyphosphazenes of high molecular weight.[1] These polyphosphazenes constitute the largest and one of the most important classes of inorganic polymers. A large body of synthetic phosphazine chemistry has furnished a wide array of organocyclophosphazenes with exocyclic P–E bonds (E = O, S, N, and C).[2] More recently, the cyclophosphazenes have served as ligands for transition metals,[3,4] and their complexes have found application in catalysis,[5] dendrimers,[6] and cancer therapeutics.[7] Cyclophosphazenes containing metal centers that are covalently bonded in the ring (e.g., **I**–**IV**; Scheme 1)

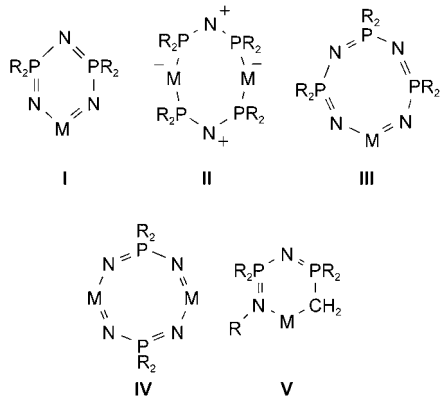

Scheme 1. Known cyclic metallaphosphazene structures (**I**–**IV**) and the metallacarbaphosphazene ring obtained in this work (**V**).

are also well established,[8] but have a shorter history: the first example was reported by Roesky et al. in 1986 (**I**, M = WCl_3, R = Ph).[9] Although a variety of these compounds are now known, to the best of our knowledge, there have been no previous reports of M-N-P-N-P-C ring systems (**V**). Herein, we present an unusual synthetic route to the first example of such a metallacycle, which involves a water-induced rearrangement of our previously reported Pt-N-P-C-P-N carbene [**1**][OTf] (OTf = $CF_3SO_3^-$) into the unique Pt-N-P-N-P-C platinacyclophosphazene [**2**][OTf] (Scheme 2). In the presence of Lewis acids (LA), [**2**][OTf] converts quantitatively to its orthometalated isomer, [**3**][OTf] (Scheme 2; LA = MeOTf, AgOTf). Both metallacarbaphosphazenes **2** and **3**, which contain the $[P{=}N{=}P]^+$ fragment, have been fully characterized spectroscopically and by X-ray crystallography.

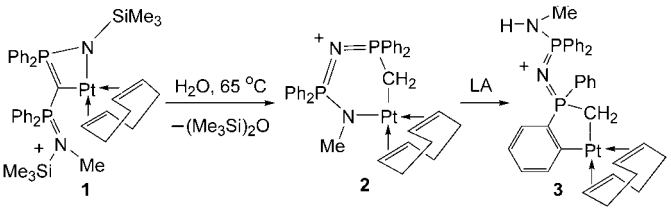

Scheme 2. The syntheses of **2** and **3** (LA = AgOTf and MeOTf, all anions = OTf).

Recently, we reported the synthesis, characterization, and reactivity of the phosphoranimine-stabilized carbene complex **4** (Scheme 3),[10,11] which, when heated to 65 °C in the presence of H_2O, gave the orthometalated methanide **5** quantitatively within minutes. No orthometalation occurred

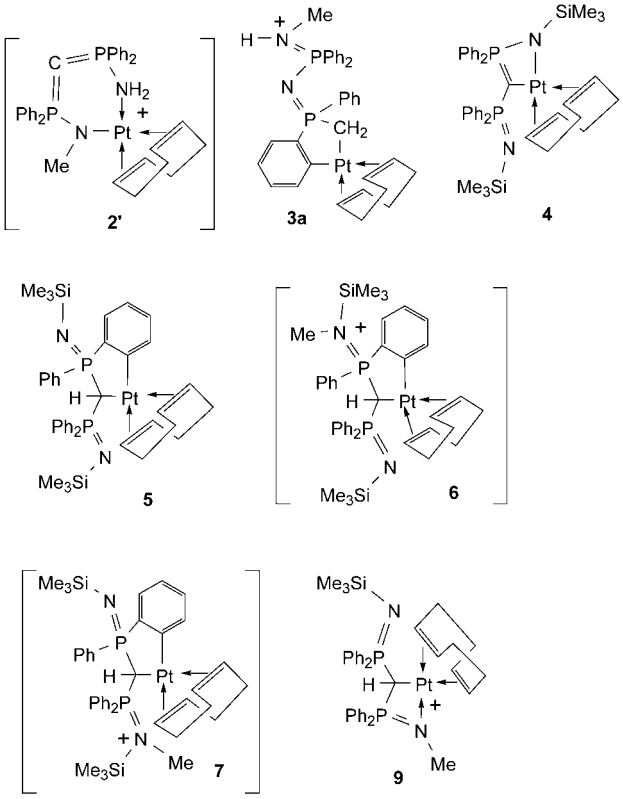

Scheme 3. Structures discussed in the text. The structure **2′** is the unrearranged isomer of the title compound with a carbodiphosphorane structure. The bracketed structures are unobserved species.

[*] Dr. M. Fang, Dr. N. D. Jones, Dr. M. J. Ferguson, Dr. R. McDonald, Prof. Dr. R. G. Cavell
Department of Chemistry, University of Alberta
Edmonton, Alberta T6G 2G2 (Canada)
Fax: (+1) 780-492-8321
E-mail: ron.cavell@ualberta.ca

[**] We thank the Natural Sciences and Engineering Research Council of Canada (NSERC) and the American Chemical Society Petroleum Research Fund (ACS-PRF) for financial support. N.D.J. acknowledges the Killam Trust for a post-doctoral fellowship.

Supporting information for this article is available on the WWW under http://www.angewandte.org or from the author.

 DOI: 10.1002/anie.200461525 © 2005 Wiley-VCH Verlag GmbH & Co. KGaA, Weinheim

over a period of several hours in the absence of H_2O. Methyl triflate (MeOTf) reacted with **4** to give [**1**][OTf]. However, when this complex was heated in the presence of H_2O (1 equiv), neither of the anticipated *N*-methyl analogues of **5** ([**6**][OTf] and [**7**][OTf]—which are shown in brackets to indicate that they are not observed) were formed, but instead the unusual platinacyclophosphazene [**2**][OTf] resulted (Scheme 2). In the absence of H_2O, [**1**][OTf] was stable. To ensure a high yield of [**2**][OTf], a solution of H_2O (1 equiv) in THF was added dropwise to a solution of [**1**][OTf] in THF; when neat H_2O was added, unidentified side products resulted and yields were low.[12] The reaction was complete within 24 h. Typical conversions of [**2**][OTf], as determined in situ by $^{31}P\{^1H\}$ NMR spectroscopy, were 60–70%, with the best conversion being about 90%; yields were approximately 60%. The platinacyclic carbaphosphazene [**2**][OTf] is insensitive to and insoluble in H_2O; heating a THF solution that contained [**2**][OTf] and H_2O to 65°C for several days had no effect. In the solid state, [**2**][OTf] was also stable in air.

The structures of [**2**][OTf] (monoclinic or triclinic polymorph depending on crystal growing methods)[13] were deduced by using a combination of X-ray crystallography and NMR spectroscopy. Although the crystallographic data for the monoclinic form of [**2**][OTf] gave a good fit ($R_1 = 2.3\%$) when it was assumed that there was no rearrangement of the backbone (as the structure of the unrearranged isomer of **2**, **2′**), this structure was not compatible with NMR data. Heteronuclear correlation through multiple quantum coherence (HMQC) NMR studies (see Supporting Information) revealed no NH_2 protons. In addition to the cross signals arising from the CH_2 protons in 1,5-cyclooctanediene (cod) ligand, one additional CH_2 signal was found. Moreover, the putative "P=C=P" group in **2′** would be expected to show a nucleophilic character that is conspicuously absent in the reactivity of **2** (see below). Refinement of the X-ray crystallographic data by assuming [**2**][OTf] gave a slightly better fit ($R_1 = 2.2\%$).[13] A similar result was obtained for the refinement of the triclinic polymorph of [**2**][OTf]. Similarly, the identity of [**3**][OTf] was confirmed by using a combination of X-ray crystallography and NMR spectroscopy.

Bond lengths and angles for **2** in the two determinations of [**2**][OTf] (monoclinic or triclinic polymorph) are very similar. A labeled ORTEP representation of the molecular structure of the monoclinic isomorph of [**2**][OTf][13] is shown in Figure 1 (the structure of **2** in triclinic [**2**][OTf] is included in the Supporting Information). The $CF_3SO_3^-$ ion is not coordinated to the metal center and has only a few close contacts with hydrogen atoms (the separations which are less than the sum of van der Waals radii are for Ph–H: F(2)-H(13) 2.518(2), F(2)-H(14) 2.631(2), O(1)-H(25) 2.683(3), O(2)-H(22) 2.491(3), O(2)-H(43) 2.633(3), and O(3)-H(34) 2.483(3) Å; for the methylene bridge hydrogen atom: O(2)-H(1B) 2.360(3) Å). Within the six-membered ring, C(1), P(1), N(1), and P(2) are essentially coplanar (dihedral angle φ(P(2)-N(1)-P(1)-C(1)) = 2.6(2)°). N–P bond lengths of the P(1)-N(1)-P(2) fragment are virtually identical (1.593(2) and 1.599(2) Å, respectively) and are consistent with the P–N bond lengths determined for other compounds that contain a $[P{=}N{=}P]^+$ fragment,[14–16] for example, 1.57(1) Å in $[Ph_3P{=}N{=}PPh_3]^+$ and 1.572(3) Å in $[Ph_2(NH_2)P{=}N{=}P(CH_3)Ph_2]^+$.[16] Therefore, it can be concluded that **2** contains a $\{P{=}N{=}P\}^+$ fragment. Atoms P(2), N(2), Pt, and C(2) are also nearly coplanar (φ = (P(2)-N(2)-Pt-C(2)) = 177.1(3)°, and the sum of angles around N(2) is 360.0(5)°). The P(2)–N(2) bond length of 1.627(2) Å is between that of a P–N single and double bond, thus indicating that there is electronic delocalization over P(1), N(1), P(2), and N(2), even though N(2) is not coplanar with the P(2)-N(1)-P(1) plane ($\varphi = -45.5(2)°$). The Pt–C(1) bond length (2.072(3) Å) is within the typical range for a Pt–C single bond (2.039–2.085 Å).[17] The Pt–N(2) bond length (2.051(2) Å) is close to those found for Pt–N dative bonds, such as 2.049 Å found in Pt^{II}–NH_3 complexes.[17]

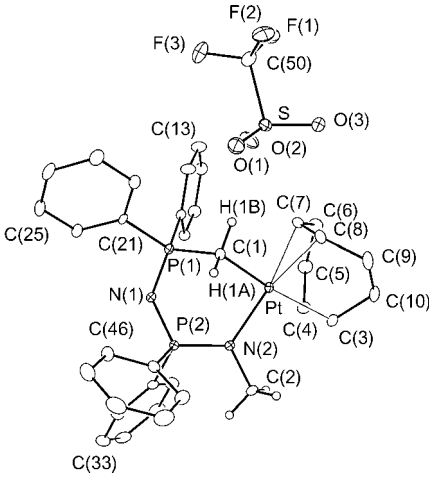

Figure 1. ORTEP diagram of the structure of [**2**][OTf] (monoclinic polymorph). Non-hydrogen atoms are represented by Gaussian ellipsoids at the 50% probability level. Hydrogen atoms on methylene [C(1)] and methyl [C(2)] centers are shown with arbitrarily small thermal parameters, those on the cod and phenyl rings are not shown. Selected bond lengths [Å] and angles [°]: Pt–N(2) 2.051(2), Pt–C(1) 2.072(3), P(1)–N(1) 1.593(2), P(1)–C(1) 1.777(3), P(1)–C(11) 1.807(3), P(1)–C(21) 1.800(3), P(2)–N(1) 1.599(2), P(2)–N(2) 1.627(2), N(2)–C(2) 1.482(4); angles: N(2)-Pt-C(1) 90.92(10), Pt-C(1)-P(1) 108.5(1), C(1)-P(1)-N(1) 112.2(1), P(1)-N(1)-P(2) 123.2(2), N(1)-P(2)-N(2) 114.7(1), P(2)-N(2)-Pt 123.2(1); P(2)-N(2)-C(2) 117.4(2), Pt-N(2)-C(2) 119.4(2); dihedral angles: P(2)-N(1)-P(1)-C(1) 2.6(2), P(2)-N(2)-Pt-C(2) 177.1(3), N(2)-P(2)-N(1)-P(1) −45.5(2), Pt-C(1)-P(1)-N(1) 57.6(2).

The N-P-C-P-N to N-P-N-P-C rearrangement reported herein is unique in that it gives a cyclic product but is not without precedence in giving acyclic compounds. Two previous examples have been reported. $(Me_3SiN{=}PPh_2)_2CH_2$, **8**, was converted to the acyclic cation $[Ph_2(NH_2)PNP(CH_3)Ph_2]^+$ by treatment with aqueous HCl solution[18] or by treatment with Ph_3GeCl or Ph_3SnCl in wet solvents.[16] Possible intermediates for these rearrangements are shown in the Supporting Information. In these systems and in the conversion of **1** into **2** (Scheme 2), hydrolysis of the N–Si bonds is promoted by the formation of an iminium group, which presumably renders the silicon much more electrophilic and susceptible to attack by H_2O. In contrast, complex **4**, which bears no iminium groups, does not undergo N-P-C-P-N to N-P-N-P-C rearrangement in the presence of H_2O. The key rearrangement step is the attack of the basic phosphoranimine nitrogen

 © 2005 Wiley-VCH Verlag GmbH & Co. KGaA, Weinheim

atom on an electrophilic phosphorus atom, which leads to P–C bond cleavage.

We were able to identify an intermediate, **9** (Scheme 3), by means of in situ NMR spectroscopic studies (^{31}P NMR at 25 °C: $\delta = 73.8$ (brs, ^1J(P,Pt) = 393 Hz), −7.2 ppm (brs, ^1J(P,Pt) = 95 Hz)). The formation was further confirmed by electrospray mass spectrometry (*m*/*z* calcd (observed) 802.24697 (802.24722) [M$^+$] with an isotope-match score of 0.9482). The intermediate **9** was the major product formed (calculated by in situ ^{31}P NMR spectroscopy: 80% of P atoms) when only about 0.5 equivalent H_2O was added to [**1**][OTf]. The ^{1}H NMR data for Pt–CH in **9** ($\delta = 4.11$ ppm, dd, J(H,Pt) = 73 Hz, ^2J(H,P) = 7.5 Hz, ^2J(H,P) = 8.4 Hz) is similar to data for the same feature in **5** ($\delta = 4.00$ ppm, dd, ^2J(H,Pt) = 96, ^2J(H,P) = 13, ^2J(H,P) = 16 Hz).[10] Other characterization data for **9** are given in the Supporting Information. We surmise that the initial step is hydrolysis of the N–Si bond of the iminium moiety in **1**, which then undergoes N-to-C proton transfer. Coordination of the methylated N to Pt displaces the other P=N imine center to form **9**. The resultant Me_3SiOH by-product of this reaction condenses to $(Me_3Si)_2O$ (as determined by ^{1}H and ^{29}Si NMR spectroscopies) and H_2O. The liberated silylated phosphimine moiety in **9** further reacts with H_2O to again form Me_3SiOH (which condenses as above) and a P=NH group. Subsequent P–C bond cleavage and proton transfer from the N atom to the C atom completes the rearrangement into **2**.

In the presence of substoichiometric quantities of the electrophiles (AgOTf and MeOTf, about 0.5 equivalent), **2** was quantitatively converted into **3** (Scheme 2); there was no incorporation of the electrophile into the product.[19] Analysis by NMR spectroscopy and mass spectrometry showed that the products of the reactions mediated by either of these Lewis acid catalysts were identical. Without catalyst, the conversion of **2** into **3** occurred but was extremely slow; heating a C_6D_6 solution of **2** to 65 °C for two weeks gave less than 33% conversion. No intermediate was observed by in situ ^{31}P NMR spectroscopy for either the catalyzed or uncatalyzed reactions. The precise role of the catalytic electrophile in this reaction remains poorly understood. It is possible that reversible association between electrophile and the amido N atom in **2** (all the possible resonance forms **2a–d** are given in the Supporting Information) gives rise to a coordinatively unsaturated Pt center, which then undergoes orthometallation.[20]

The Pt-C-C-P-C metallacyclic structure of [**3**][OTf] is shown in Figure 2.[13] As in [**2**][OTf], the $CF_3SO_3^-$ ion does not coordinate to the metal center. The close O–H contact (2.145(2) Å) between $CF_3SO_3^-$ and the HNMe fragment suggests that the NH proton bears a significant positive charge and that the resonance form **3a** is an important contributor to the structure of **3** (see the Supporting Information for the remaining resonance forms).

Related crystal structures of complexes with similar rings have been reported.[10,21,22,23] The C(1), P(1), N(1), and P(2) atoms in **3** are coplanar as they are in **2**. The P–N bond lengths in the {P=N=P}$^+$ fragment (1.607(2) and 1.583(2) Å) and P-N-P angle (128.4(1)°) are similar to those in **2** (1.593(2) and 1.599(2) Å, and 123.2(2)°).

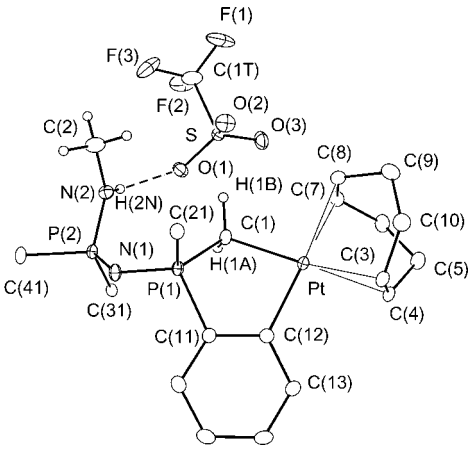

Figure 2. ORTEP diagram of the structure of [**3**][OTf]. Non-hydrogen atoms are represented by Gaussian ellipsoids at the 50% probability level. Hydrogen atoms on methyl, methylene, and N(2) centers are shown with arbitrarily small thermal parameters, those on the cod and phenyl rings are not shown. For all phenyl rings, except that forming the orthometalated center, only the *ipso* carbon atom is shown. The dotted line indicates the interaction of the triflate oxygen atom with the hydrogen atom on N(2). Selected bond lengths [Å] and angles [°]: Pt–C(1) 2.072(2), Pt–C(12) 2.040(2), P(1)–N(1) 1.607(2), P(1)–C(1) 1.775(3), P(1)–C(11) 1.786(3), P(2)–N(1) 1.583(2), P(2)–N(2) 1.635(2), N(2)–C(2) 1.465(4), C(11)–C(12) 1.411(3); angles: P(1)-N(1)-P(2) 128.4(1), C(1)-Pt-C(12) 85.5(1); dihedral angles: C(1)-P(1)-N(1)-P(2) 0.9(2), N(2)-P(2)-N(1)-P(1) 48.1(2), P(1)-C(11)-C(12)-Pt −1.5(3), C(1)-P(1)-C(11)-C(12) −23.0(2).

In summary, the first example of a M-C-P-N-P-N metallaheterocycle, the platinacyclic carbaphosphazene [**2**][OTf] has been synthesized in high yield through a unique four- to six-membered ring expansion and rearrangement induced by water. The synthetic method described herein for [**2**][OTf] may provide routes for synthesizing new metal-containing cyclophosphazenes. The mechanisms through which **2** and **3** were formed are currently under investigation.

Received: August 3, 2004
Revised: November 25, 2004
Published online: February 23, 2005

Keywords: carbenes · metallacycles · phosphorus · platinum · rearrangement

[1] A. R. McWilliams, H. Dorn, I. Manners, *Top. Curr. Chem.* **2002**, *220*, 141 – 167, and references therein.
[2] V. Chandrasekhar, K. R. J. Thomas, *Struct. Bonding (Berlin)* **1993**, *81*, 42 – 113, and references therein.
[3] V. Chandrasekhar, K. R. J. Thomas, *Appl. Organomet. Chem.* **1993**, *7*, 1 – 31, and references therein.
[4] V. Chandrasekhar, S. Nagendran, *Chem. Soc. Rev.* **2001**, *30*, 193 – 203, and references therein.
[5] K. Brandt, I. Porwolik, T. Kupka, A. Olejnik, R. A. Shaw, D. B. Davies, *J. Org. Chem.* **1995**, *60*, 7433 – 7438.
[6] C. Diaz, M. Barbosa, Z. Godoy, *Polyhedron* **2004**, *23*, 1027 – 1035.
[7] H. R. Allcock, F. H. Allen, J. P. O'Brien, *J. Am. Chem. Soc.* **1977**, *99*, 3984 – 3987.

 © 2005 Wiley-VCH Verlag GmbH & Co. KGaA, Weinheim

[8] M. Witt, H. W. Roesky, *Chem. Rev.* **1994**, *94*, 1163 – 1181, and references therein.
[9] H. W. Roesky, K. V. Katti, U. Seseke, M. Witt, E. Egert, R. Herbst, G. M. Sheldrick, *Angew. Chem.* **1986**, *98*, 447 – 449; *Angew. Chem. Int. Ed. Engl.* **1986**, *25*, 477 – 478.
[10] N. D. Jones, G. Lin, R. A. Gossage, R. McDonald, R. G. Cavell, *Organometallics* **2003**, *22*, 2832 – 2841; N. D. Jones, G. Lin, R. A. Gossage, R. McDonald, R. G. Cavell, *Organometallics* **2003**, *22*, 5378.
[11] G. Lin, N. D. Jones, R. A. Gossage, R. McDonald, R. G. Cavell, *Angew. Chem.* **2003**, *115*, 4188 – 4191; *Angew. Chem. Int. Ed.* **2003**, *42*, 4054 – 4057.
[12] Synthesis of [**2**][OTf]: A THF solution containing H_2O (4.94 mL, 0.0245 M, 0.121 mmol) was added dropwise to a stirred solution of [**1**][OTf] (130 mg, 0.127 mmol) in THF (10 mL). The mixture was heated to 65 °C for 24 h. Removal of the solvent and recrystallization from THF gave [**2**][OTf] (73 mg, 65 %). $^{31}P\{^1H\}$ NMR (161.9 MHz, [D_8]THF): $\delta = 33.5$ (d, $^2J(P,P) = 6.1$, $^2J(P,Pt) = 122$ Hz), 25.0 ppm (d, $^2J(P,P) = 6.0$, $^2J(P,Pt) = 124$ Hz); $^{13}C\{^1H\}$ NMR (100.6 MHz, [D_8]THF) for CH_2Pt: $\delta = 15.3$ ppm (dd, $^1J(P,C) = 46$, $^3J(P,C) = 8.4$ Hz, $^1J(C,Pt)$ not observed). Complete synthetic and characterization data are given in the Supporting Information.
[13] CCDC-242499 ([**2**][OTf], monoclinic form), CCDC-2425001 ([**2**][OTf], triclinic form), and CCDC-242451 ([**3**][OTf]) contain the supplementary crystallographic data for this paper. These data can be obtained free of charge from The Cambridge Crystallographic Data Centre via www.ccdc.cam.ac.uk/data_request/cif. The full crystal data and their completely labeled diagrams are included in the Supporting Information.
[14] A. Müller, M. Möhlen, B. Neumüller, N. Faza, W. Massa, K. Dehnicke, *Z. Anorg. Allg. Chem.* **1999**, *625*, 1748 – 1751.
[15] H. R. Allcock in *Phosphorus–Nitrogen Compounds* (Ed.: H. R. Allcock), Academic Press, New York, **1972**, pp. 36 – 93.
[16] K. V. Katti, A. A. Pinkerton, R. G. Cavell, *Inorg. Chem.* **1991**, *30*, 2631 – 2633.
[17] A. G. Orpen, L. Brammer, F. H. Allen, O. Kennard, D. G. Watson, R. Taylor, *J. Chem. Soc. Perkin Trans. 2* **1989**, S1 – S83.
[18] R. Appel, I. Ruppert, *Z. Anorg. Allg. Chem.* **1974**, *406*, 131 – 144.
[19] Synthesis of [**3**][OTf]: A mixture of MeOTf (5.3 μL, 47 μmol), [**2**][OTf] (82 mg, 93 μmol) and C_6H_6 (4 mL) was stirred for 1 day at room temperature and then heated to 68–70 °C for 7 h. Removal of the solvent gave spectroscopically pure [**3**][OTf] quantitatively. $^{31}P\{^1H\}$ NMR (161.9 MHz, C_6D_6): $\delta = 21.7$ (s), 37.7 ppm (s, $^2J(P,Pt) = 217$ Hz); $^{13}C\{^1H\}$ NMR (100.6 MHz, [D_8]THF) for CH_2Pt: $\delta = 26.1$ ppm (dd, $^1J(P,C) = 50$, $^3J(P,C) = 1.2$ Hz, $^1J(C,Pt)$ not observed); Microscope IR: $\tilde{\nu} = 3246$ cm^{-1} (m, ν_{NH}). Complete synthetic and characterization data are given in the Supporting Information.
[20] P. Foley, R. DiCosimo, G. M. Whitesides, *J. Am. Chem. Soc.* **1980**, *102*, 6713 – 6725.
[21] M. W. Avis, K. Vrieze, J. M. Ernsting, C. J. Elsevier, N. Veldman, A. L. Spek, K. V. Katti, C. L. Barnes, *Organometallics* **1996**, *15*, 2376 – 2392.
[22] M. L. Illingsworth, J. A. Teagle, J. L. Burmeister, W. C. Fultz, A. L. Rheingold, *Organometallics* **1983**, *2*, 1364 – 1369.
[23] G. Facchin, L. Zanotto, R. Bertani, G. Nardin, *Inorg. Chim. Acta* **1996**, *245*, 157 – 166.

 © 2005 Wiley-VCH Verlag GmbH & Co. KGaA, Weinheim

Organometallic Chemistry

Stereoselective Transformations of Trihalomethylcarbinols Induced by Chromous Chloride**

Romain Bejot, Steve Tisserand, L. Manmohan Reddy, Deb K. Barma, Rachid Baati, J. R. Falck, and Charles Mioskowski**

Organochromium reagents are gaining greater prominence in organic synthesis owing to their unique reactivities, high stereoselectivities, compatibility with numerous functional groups, and the recent introduction of regeneration systems that only require catalytic chromium.[1–3] As part of our continuing investigations into novel organochromium methodology, we discovered that trihalomethylcarbinol esters and ethers **1** undergo efficient, stereoselective intramolecular rearrangements induced by chromous chloride in THF. The resultant products, (*Z*)-α-haloenol esters **2** and (*Z*)-β-haloenol ethers **3**, respectively, are potentially useful, yet highly elusive synthetic intermediates (Scheme 1).[4] Esters **2** are new, stable acyl halide enolate equivalents. They have only been mentioned briefly in the literature as minor by-products and their synthetic utility remains to be explored.[5] To help

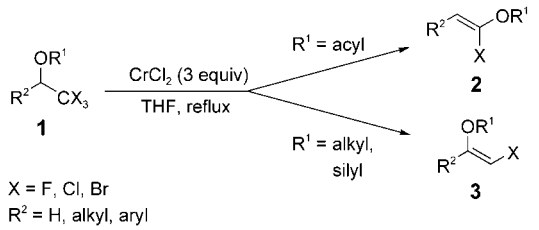

Scheme 1. Reactivity of trihalomethylcarbinols esters and ethers with $CrCl_2$.

[*] Dr. L. M. Reddy, Dr. D. K. Barma, Prof. J. R. Falck
Department of Biochemistry
University of Texas Southwestern Medical Center
5323 Harry Hines Blvd., Dallas, TX 75235-9038 (USA)
Fax: (+) 214-648-6455
E-mail: j.falck@utsouthwestern.edu
R. Bejot, Dr. S. Tisserand, Dr. R. Baati, Dr. C. Mioskowski
Laboratoire de Synthèse Bioorganique, UMR 7514
Faculté de Pharmacie
Université Louis Pasteur
74 Route du Rhin, BP 24, 67401 Illkirch (France)
Fax: (+33) 3-9024-4306
E-mail: mioskow@aspirine.u-strasbg.fr

[**] This work was supported by the Ministère de la Jeunesse, de l'Education Nationale et de la Recherche (to R. Bejot), the CNRS, the Institut de Recherche Pierre Fabre (S.T.), the Robert A. Welch Foundation, and the NIH (GM31278). We thank Euriso-Top SA for $^{18}O_2$-labeled sodium acetate, Dr. T. G. LaCour for suggesting the dyotropic rearrangement, and C. Antheaume and A. Valleix for NMR spectroscopy and mass spectrometry measurements.

Supporting information for this article is available on the WWW under http://www.angewandte.org or from the author.

 © 2005 Wiley-VCH Verlag GmbH & Co. KGaA, Weinheim DOI: 10.1002/anie.200461884

expedite access to these highly functionalized olefins and to better understand their formation, we report herein the results of treating a series of representative trihalomethylcarbinol esters and ethers with $CrCl_2$ as well as insights from mechanistic studies.

When trihalomethylcarbinol ester **1a** was stirred with commercial $CrCl_2$ (3 equiv) for 3 h with heating at reflux in THF under an argon atmosphere, α-haloenol ester **2a** was obtained as the principal product in 76% yield (Table 1, entry 1). Applying Fürstner's catalytic system, which utilizes Mn^0 powder to recycle chromium(III) to chromium(II), also gave rise to **2a**, though in lower but acceptable yield (entry 2).[6] The scope of the reaction was explored by using various esters: cinnamate (entry 3), benzoate (entry 4), and acetate (entry 5); all of these primarily undergo 1,2-migration of the acyloxy group. Likewise, trichloromethylcarbinol and dibromofluoromethylcarbinol esters derived from aliphatic aldehydes (entries 6, 8, and 11), aryl aldehydes (entries 5 and 10), a cyclic ketone (entry 7), and (formally) formaldehyde (entry 9) behaved analogously to furnish good to excellent yields of (*Z*)-α-haloenol esters. In contrast, dichloromethyl- and dichlorofluoromethylcarbinols are refractory under the standard conditions (entries 12 and 14). Addition of TMEDA (*N*,*N*,*N*′,*N*′-tetramethylethylenediamine) as donor ligand, which enhances the reduction power of chromium(II), did not improve this result (entry 13). On the other hand, tribromomethylcarbinols, which are more reactive toward chromous chloride, only furnished complex mixtures of products; for example, 2,2,2-tribromoethyl benzoate gave a mixture of 1-bromoethyl benzoate, 1-chloroethyl benzoate, 2,2-dibromoethyl benzoate, and several unidentified compounds.[7]

The data in Table 1 also indicate that the carbinol substitution pattern influences the stereoselectivity of the rearrangement. For instance, the hydrocinnamyl adducts **1e**,**g**, and **j**, and dibromofluoromethylcarbinol derivative **1i** afforded exclusively the *Z* isomers **2e**,**g**, and **j**, and **2i**, respectively, whereas the *p*-tolyl-trichloromethylcarbinols **1c** and **d** yielded **2c** and **d** as mixtures of *Z* and *E* isomers.[8]

Table 1: Conversion of trihalomethylcarbinol esters into *(Z)*-α-haloenol esters.

Entry	Trihalomethyl carbinol ester **1**	Product(s)	Yield [%][a]
1	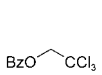 **1a**	**2a**	76
		3a	7[b]
2[c]	**1a**	**2a**	53
		3a	5
		1k	2[b]
3	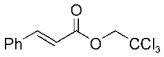 **1b**	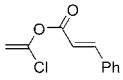 **2b**	85
		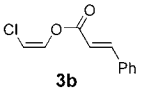 **3b**	4[b]
4	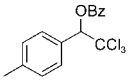 **1c**	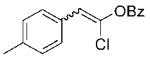 **2c**	84 (*Z*/*E* = 78:22)
5	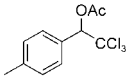 **1d**	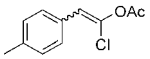 **2d**	75 (*Z*/*E* = 87:13)
6	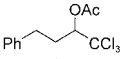 **1e**	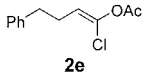 **2e**	80 (*Z*/*E* > 99:1)[d]
7	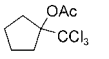 **1f**	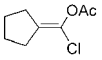 **2f**	82
8	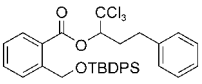 **1g**	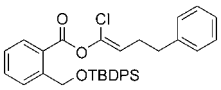 **2g**	84 (*Z*/*E* > 99:1)[d]
9	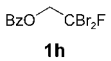 **1h**	**2h**	80[e]
10	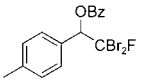 **1i**	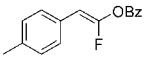 **2i**	98 (*Z*/*E* > 99:1)[d]
11	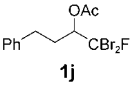 **1j**	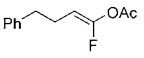 **2j**	98 (*Z*/*E* > 99:1)[d]
12	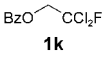 **1k**	[f]	0
13[g]	**1k**	[f]	0
14	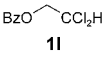 **1l**	[f]	0

[a] Yields for isolated materials after purification by column chromatography, unless otherwise stated. [b] Yields calculated from ^{1}H NMR spectrum of isolated mixture of **2** and **3**. [c] Reaction was conducted using catalytic chromium and excess Mn^0 powder. [d] Only one isomer was detected by ^{1}H NMR and/or GC analysis of crude material. [e] Crude purity greater than 97%; volatile compound not purified by column chromatography. [f] Starting material was recovered in 100% yield. [g] Two equivalents of TMEDA added. Bz = benzoyl, Ac = acetyl, TBDPS = *tert*-butyldiphenylsilyl.

The isolation in some cases of minor amounts of (*Z*)-β-haloenol ester, such as **3a**,**b**, is consistent with the expectation that acyloxy groups have a significantly better migratory aptitude relative to hydrogen. This also prompted an examination of the reactivity of trichloromethylcarbinol ethers.[9] As anticipated, when treated with commercial $CrCl_2$ under the standard conditions these ethers exclusively formed *(Z)*-β-chlorovinyl ethers **3** in good yields and with good stereoselectivities (Table 2, entries 1–5).[10]

 © 2005 Wiley-VCH Verlag GmbH & Co. KGaA, Weinheim

Table 2: Conversion of trichloromethylcarbinol ethers into (*Z*)-β-chloroenol ethers.

Entry	Trichloromethyl ether **1**	Product	Yield [%][a]
1	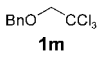 **1m**	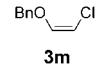 **3m**	89
2	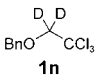 **1n**	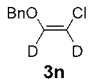 **3n**	77
3	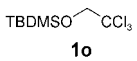 **1o**	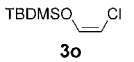 **3o**	76
4	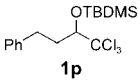 **1p**	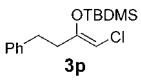 **3p**	75
5	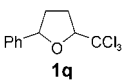 **1q**	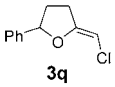 **3q**	75

[a] Yields for isolated materials after purification by column chromatography. Bn = benzyl, TBDMS = *tert*-butyldimethylsilyl.

Mechanistically, the formation of **2** from **1** probably proceeds initially through oxidative addition of chromium into a C–X (X = Cl, Br) bond through two consecutive single-electron transfers (Scheme 2).[11] Next, the dichlorocarbenoid

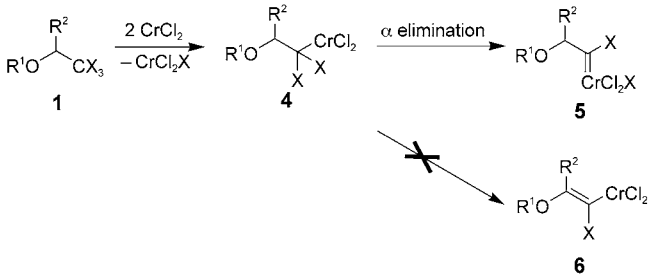

Scheme 2. Proposed mechanism for the rearrangement of trichloromethylcarbinol esters and ethers.

4 species undergoes an α elimination of $CrCl_2X$ through metal-assisted ionization[12] to give the proposed carbene **5**. Then, intramolecular nucleophilic rearrangement involving the nonbonded (n) electrons of the carbonyl group converts this highly reactive intermediate into ester **2**. This suprafacial rearrangement is most likely a concerted 2,3-shift mechanism through a five-center cyclic transition state: $CrCl_2$ reduction of ^{18}O-labeled substrate **1r** indicates a complete exchange of the carbonyl and carboxyl oxygens [Eq. (1)]. This trans-

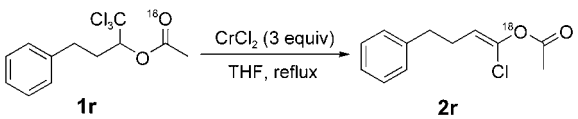

(1)

formation is comparable to the Surzur–Tanner rearrangement, which involves intramolecular 1,2-suprafacial migration of the acyloxy group of β-acyloxyalkyl halides under radical conditions.[4,13] We postulate that this particular reactivity of trihalomethylcarbinol esters with chromium(II) is a result of coordination of the β oxygen atom to the metal which induces rehybridization of the organochromium species **4**, thus precluding oxidative addition of $CrCl_2$ into a second C–X bond.[14]

The observed *Z* stereochemistry of products **2c–e**, **g**, **i**, and **j** may be rationalized if one takes into account the possible conformations of the postulated Fischer carbene **5** (Scheme 3).[15] Of both possible conformations of the

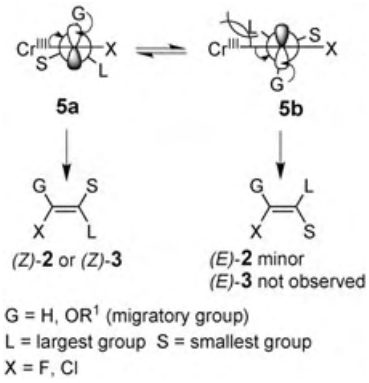

Scheme 3. Stereochemical model for the migration.

chromium(III) carbene complex, conformer **5a** is much more favored than **5b** because of steric interactions between hexacoordinated chromium and the large group L (R^2). Secondary steric repulsion between L and the halogen atom in **5a** might be responsible for the formation of minor amounts of the *E* stereoisomer. Interestingly, when the latter steric interaction is decreased by using less-bulky substituents such as cinnamyl (versus *p*-tolyl) or fluoride (versus chloride), the reaction provides exclusively and stereospecifically the *Z* isomers in good isolated yields (Table 1, entries 6, 8, 10, and 11).

The 1,2-migration of hydride in chlorocarbene **5** (Scheme 2) rationalizes the origin of the ethers in Table 2. A pathway proceeding through the β-oxy-vinylidene carbenoid **6** is disproved.[16] Quenching with D_2O the reduction of **1m** by $CrCl_2$ did not lead to 2-chloro-2-*d*-vinyloxybenzyl: **3m** was obtained instead.[16,17] Moreover, the deuterated compound 2,2,2-trichloro-1,1-d_2-ethoxybenzyl **1n** gives exclusively *(Z)*-2-chloro-1,2-d_2-vinyloxybenzyl **3n**, consistent with a 1,2-migration of a deuterium atom (Table 2, entry 2). As above, the *Z* stereochemistry of ethers **3** can be rationalized if the possible conformations of the proposed Fischer carbene are taken into account (Scheme 3).

This intriguing new reactivity, observed for carboxylic esters and ethers of trihalomethylcarbinols, led us finally to study sulfonic and phosphoric esters. Unfortunately, no rearrangement was observed. Fragmentation occured preferentially to lead to 1,1-dichloroalkenes.[18]

In conclusion, we have demonstrated that (*Z*)-α-haloenol esters **2** and (*Z*)-β-haloenol ethers **3** can be efficiently obtained from trihalomethylcarbinol esters and ethers, respectively, with chromous chloride in THF. A mechanism has been proposed which accounts for both the nature of the

 © 2005 Wiley-VCH Verlag GmbH & Co. KGaA, Weinheim

observed products and their preferred *Z* stereochemistry. This contribution to organochromium chemistry affords new insight into β-oxy-alkylidene carbenoids and chlorochromium(III)–carbene complexes as proposed key intermediates. Finally, we also established a reactivity scale of *gem*-polyhalide compounds with chromous chloride: $CBr_3 > CCl_3$ and $CBr_2F \gg CCl_2F$ and CCl_2H (not reactive). Further extensions are underway in our laboratory, including the use of (*Z*)-α-haloenol esters **2** as unique ketene precursors.

Experimental Section

$CrCl_2$ was purchased from Strem. Tetrahydrofuran (THF) was distilled from Na/benzophenone ketyl before use.

General Procedure: Compound **1** (0.39 mmol)[19] in THF (2 mL) was added to a stirring suspension of chromium(II) chloride (145 mg, 1.17 mmol) in anhydrous THF (3 mL) at RT under argon. The mixture was heated at reflux for 3 h, cooled to RT, quenched with 5% HCl, and diluted with Et_2O. The layers were separated, and the aqueous phase was extracted twice with Et_2O. The combined organic extracts were washed twice with brine, dried over $MgSO_4$, and filtered over Florisil. Alternatively, the reaction mixture can be diluted with Et_2O and filtered through a small pad of SiO_2. After concentration of the organic extract under vacuum, the crude product was purified by chromatography on silica gel to give **2** and/or **3**.

Received: September 3, 2004
Revised: November 26, 2004
Published online: February 23, 2005

Keywords: carbenes · chromium · isotopic labeling · rearrangement · synthetic methods

[1] a) J. R. Falck, D. K. Barma, R. Baati, C. Mioskowski, *Angew. Chem.* **2001**, *113*, 1321; *Angew. Chem. Int. Ed.* **2001**, *40*, 1281; b) D. K. Barma, A. Kundu, H. M. Zhang, C. Mioskowski, J. R. Falck, *J. Am. Chem. Soc.* **2003**, *125*, 3218.

[2] a) A. Fürstner, *Chem. Rev.* **1999**, *99*, 991; b) L. A. Wessjohann, G. Scheid, *Synthesis* **1999**, *1*, 1.

[3] M. Bandini, P. G. Cozzi, A. Umani-Ronchi, *Angew. Chem.* **2000**, *112*, 2417; *Angew. Chem. Int. Ed.* **2000**, *39*, 2327.

[4] 2,2,2-Trichloroethyl esters undergo rearrangement to 1-halovinyl esters through a radical pathway known as a Surzur–Tanner rearrangement with a mixture of CuCl and bipyridine (1:1). See: R. N. Ram, N. K. Meher, *Org. Lett.* **2003**, *5*, 145.

[5] K. Takai, R. Kokumai, T. Nobunaka, *Chem. Commun.* **2001**, 1128.

[6] a) A. Fürstner, N. Shi, *J. Am. Chem. Soc.* **1996**, *118*, 2533; b) A. Fürstner, N. Shi, *J. Am. Chem. Soc.* **1996**, *118*, 12349.

[7] 1-Chloroethyl benzoate probably arises through halide scrambling, see: M. B. Smith, J. March, *March's Advanced Organic Chemistry : Reactions, Mechanisms, and Structure*, *5th ed.*, Wiley, New York, **2001**.

[8] The *Z* stereochemistry of the major isomers of **2c** and **g** was determined by X-ray crystallography. CCDC-234464 and CCDC-254732 contain the supplementary crystallographic data for this paper. These data can be obtained free of charge from The Cambridge Crystallographic Data Centre via www.ccdc.cam.ac.uk/data_request/cif. The *Z* stereochemistry of **2d** was determined by 2D ^{1}H nOe NMR spectroscopy. The *Z* stereochemistry of **2i** and **j** was determined from the coupling constant $^3J_{HF}$ by ^{1}H NMR spectroscopy. The stereochemistry of **2e** could not be determined by spectroscopy, but by analogy with the other compounds it is assumed that *(Z)*-**2e** is obtained.

[9] The reduction of **2** with $CrCl_2$ in aqueous media was reported by Steckhan and gave (*Z*)-chloroalkenes: R. Wolf, E. Steckhan, *J. Chem. Soc. Perkin Trans. 1* **1986**, 733.

[10] The *Z* stereochemistry of **3m**, **p**, and **q** was determined by 2D ^{1}H nOe NMR spectroscopy.

[11] a) J. K. Kochi, D. D. Davis, *J. Am. Chem. Soc.* **1964**, *86*, 5264; b) J. K. Kochi, D. M. Singleton, *J. Am. Chem. Soc.* **1968**, *90*, 1582; c) J. Mulzer, A. R. Strecker, L. Kattner, *Tetrahedron Lett.* **2004**, *45*, 8867.

[12] The organochromium species undergo a rehybridization by placing a positive charge in a p orbital to produce a tight ion pair: a) H. M. Walborsky, M. Duraisamy, *J. Am. Chem. Soc.* **1984**, *106*, 5035; b) H. M. Walborsky, J. Rachon, V. Goedken, *J. Am. Chem. Soc.* **1986**, *108*, 7435.

[13] For a review on this and related reactions, see: A. L. J. Beckwith, D. Crich, P. J. Duggan, Q. Yao, *Chem. Rev.* **1997**, *97*, 3273.

[14] Another possible mechanism would proceed through a dyotropic rearrangement, that is to say a process in which C–Cl and C–OR^1 σ bonds of the dichlorocarbenoid species simultaneously migrate intramolecularly, followed by a β elimination of $CrCl_2X$. However, this mechanism is unlikely as the formation of **2f** (Table 1, entry 7) would require rearrangement to a quaternary center. For a review of the dyotropic rearrangement, see: M. T. Reetz, *Tetrahedron* **1973**, *29*, 2189.

[15] For an example of a postulated chromium(III)–carbene complex, see: M. H. Voges, C. Romming, M. Tilset, *Organometallics* **1999**, *18*, 529.

[16] R. Baati, D. K. Barma, J. R. Falck, C. Mioskowski, *J. Am. Chem. Soc.* **2001**, *123*, 9196.

[17] The non-incorporation of a deuterium atom could be explained by the internal proton return phenomenon, that is, the delivery of a proton from coordinated water triggered by the addition of D_2O. See: a) P. L. Creger, *J. Am. Chem. Soc.* **1970**, *92*, 1396; b) D. Seebach, M. Boes, R. Naef, W. B. Schweizer, *J. Am. Chem. Soc.* **1983**, *105*, 5390.

[18] The fragmentation of β-sulfonate- and β-phosphate-substituted alkyl radicals is known to compete with the Surzur–Tanner rearrangement. See ref. [13].

[19] The starting 2-alkoxy-substituted 1,1,1-trihaloalkanes were prepared according to: a) E. J. Corey, J. O. Link, Y. Shao, *Tetrahedron Lett.* **1992**, *33*, 3435; b) J. Russell, N. Roques, *Tetrahedron* **1998**, *54*, 13771; c) M. Shimizu, N. Yamada, Y. Takebe, T. Hata, M. Kuroboshi, T. Tamejiro Hiyama, *Bull. Chem. Soc. Jpn.* **1998**, *71*, 2903.

 © 2005 Wiley-VCH Verlag GmbH & Co. KGaA, Weinheim

Zeolites

SU-16: A Three-Dimensional Open-Framework Borogermanate with a Novel Zeolite Topology**

*Yafeng Li and Xiaodong Zou**

Microporous materials with tetrahedrally coordinated frameworks, such as zeolites, are important from both industrial and academic points of view due to their shape-selective catalytic properties and ion-exchange behaviors.[1,2] Great efforts have been made to synthesize open frameworks with extra-large pores, and thus very low framework densities. Such compounds often consist of secondary building units (SBUs) of small rings formed by three or four tetrahedrally coordinated T atoms (TO_4).[3] Owing to the large T-O-T angles ($\approx$145°), silicon seldom forms 3-rings alone with oxygen, but sometimes together with Zn[4] and Be,[5] and in a few cases with Al[6] and Li.[7] Recently, germanates have been receiving attention since a number of new zeolite topologies were discovered in germanates and silicogermanates (ASV, BEC, IWR, IWW, UOZ).[8] The major advantage of incorporating germanium into zeolite structures is that the T-O-T angles can be much smaller ($\approx$130°), which is needed to form framework structures with 3- and 4-rings. In fact, germanium can form both 3-rings and 4-rings, and has a tendency to form double 4-rings with oxygen.[8–10] Germanium can also adopt other coordination geometries than tetrahedral with oxygen, and several open frameworks with extra-large pores (24-rings) have been reported.[11]

Attempts have also been made to incorporate elements from the third main group (B, Al, Ga) into the silicate zeolite frameworks to adjust the acid strength of zeolite-based catalysts. Although aluminum and gallium have been introduced into germanate zeolite frameworks,[12] no borogermanates with zeolite topologies have been reported so far. We have successfully incorporated boron into germanates and obtained the first two-dimensional templated borogermanates,[13] where both germanium and boron are tetrahedrally coordinated with oxygen. The 3-rings formed by the GeO_4 tetrahedra are also present in the framework. Now we present the first three-dimensional open-framework borogermanate $[NH_3(CH_2)_2NH(CH_2)_2NH_3]\cdot[(GeO_2)_4(BO_2)_2]$ (SU-16). It has a novel zeolite topology with intersecting 12- and 8-ring channels.

Treatment of a mixture of GeO_2, diethylenetriamine (DETA), H_3BO_3, H_2O, and pyridine under mild hydrothermal conditions provides SU-16 as colorless needlelike crystals. The crystal structure analysis shows that there are four unique Ge and two unique B atoms in the asymmetric unit, all of them tetrahedrally coordinated by oxygen. The framework of SU-16 can be described by using a secondary building unit (SBU) consisting of two edge-sharing 3-rings (B_2Ge) connected to two GeO_4 tetrahedra, one on each side of the 3-rings (Figure 1a and b). The SBUs are connected in the [100] direction to form a ladder, with alternating 3-ring (B_2Ge) and 4-ring (BGe_3) pairs (Figure 1c). All the ladders are parallel, running along the [100] direction in the framework. Six such ladders are connected, producing a three-dimensional framework with 12-ring channels along the [100] direction (Figure 1d). The openings of the 12-rings are built by pure GeO_4

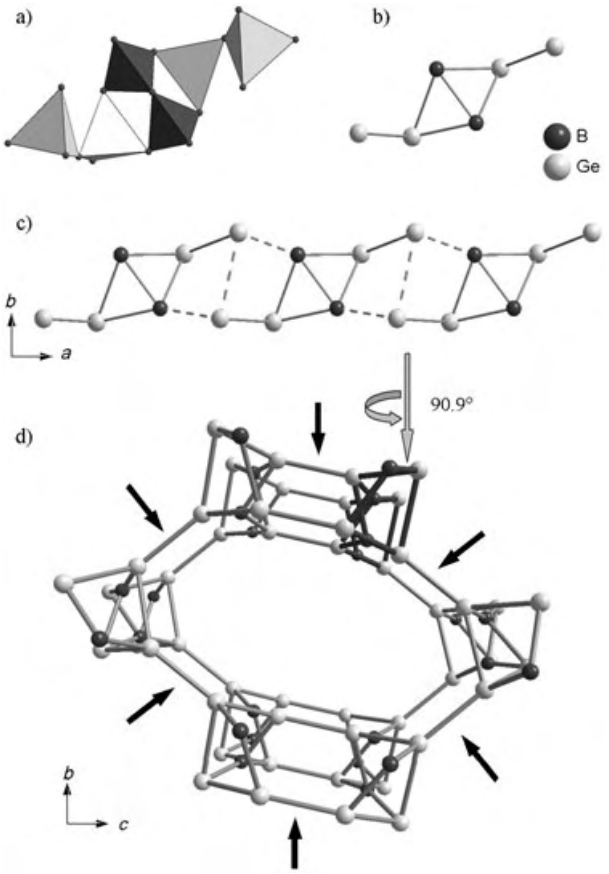

Figure 1. The secondary building unit (SBU) of SU-16 shown a) as tetrahedra (BO_4: dark gray, GeO_4: light gray) and b) in terms of T—T connections. c) The SBUs are connected in the [100] direction to form a ladder. The dashed lines show the T—T connections of different SBUs. d) All the ladders in SU-16 are parallel, running in the [100] directions. Here the structure is shown along these ladders, rotated by 90.9° with respect to the representation in (c); one of the ladders is marked in black. Six such ladders are connected, forming a 12-ring channel. There are six 8-ring windows perpendicular to the 12-ring channel, running in the $\pm$[010], $\pm$[0$\bar{1}$1], and $\pm$[011] directions (indicated by dark arrows). Each 8-ring window connects the 12-channel to the neighboring 12-ring channel.

[*] Dr. Y. Li, Prof. X. D. Zou
Structural Chemistry
Arrhenius Laboratory
Stockholm University
106 91 Stockholm (Sweden)
Fax: (+46) 8-163-118
E-mail: zou@struc.su.se

[**] This research was supported by the Swedish Research Council. X.D.Z. is a senior researcher of the Royal Swedish Academy of Sciences supported by a grant from the Knut and Alice Wallenberg Foundation. Y.F.L. is supported by a grant from the Wenner–Gren Foundation. We thank Prof. Osamu Terasaki, Dr. Lynne McCusker, and Prof. Jihong Yu for valuable discussions and help.

Supporting information for this article is available on the WWW under http://www.angewandte.org or from the author.

 © 2005 Wiley-VCH Verlag GmbH & Co. KGaA, Weinheim DOI: 10.1002/anie.200461911

tetrahedra, and no BO_4 tetrahedra are involved (Figure 2a). The 12-ring channels are elliptical (with a free diameter of 4.7×9.0 Å), which is very unusual in zeolite framework structures. There are six 8-ring windows perpendicular to each

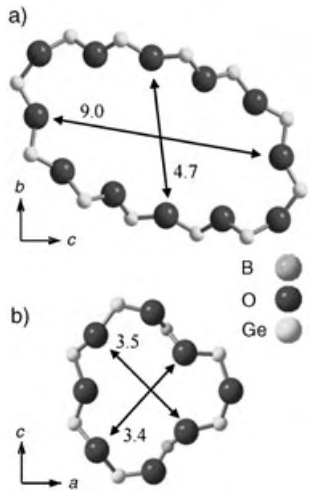

Figure 2. a) The elliptical 12-ring opening with a free diameter of 4.7×9.0 Å and b) the 8-ring opening with a free diameter of 3.4×3.5 Å. The van der Waals diameter of oxygen atoms is assumed to be 2.7 Å.

12-ring channel; each connects the 12-ring channel to a neighboring 12-ring channel (Figure 1d). Although they run along different directions, the atomic arrangements and shape of all the 8-ring windows are the same, built by two BO_4 and six GeO_4 tetrahedra (Figure 2b). The free diameter of the 8-ring openings is 3.4×3.5 Å.

The structure of SU-16 is very open, containing three-dimensional intersecting channel systems. Three 8-ring channels are perpendicular to the 12-ring channels, all intersecting with each other and running along three different directions: [010], [01$\bar{1}$], and [011] (Figure 3).

The B-O-B connection found in SU-16 violates Löwenstein's rule. The Ge–O distances range from 1.72 to 1.76 Å and the B–O distances from 1.45 to 1.51 Å, similar to those reported earlier.[13] The Ge-O-Ge and B-O-B bond angles are 130.0–141.5° and 122.0(3)°, respectively, and thus close to those reported.[13,14] Interestingly, the Ge-O-B angles (115.5–117.8°) are significantly smaller than those in other borogermanates with tetrahedral coordination (121.6–127.8°).[13] The diprotonated DETA cations are located in the 12-ring channels, balancing the charges of the framework (Figure 4). Furthermore, they are strongly hydrogen-bonded to the framework; each DETA cation is hydrogen-bonded to three SBUs (Figure 4). The N–H···O distances are between 2.76 and 3.22 Å.

The borogermanate SU-16 has a novel zeolite framework topology, with coordination sequences different from any existing zeolite frameworks (see the Supporting Information).[15] It is one of the very few zeolite framework structures which contain 3-rings. The two edge-sharing 3-rings of SU-16 have not been observed in other zeolite structures. As a result, two novel configurations of the T atoms are formed (see the

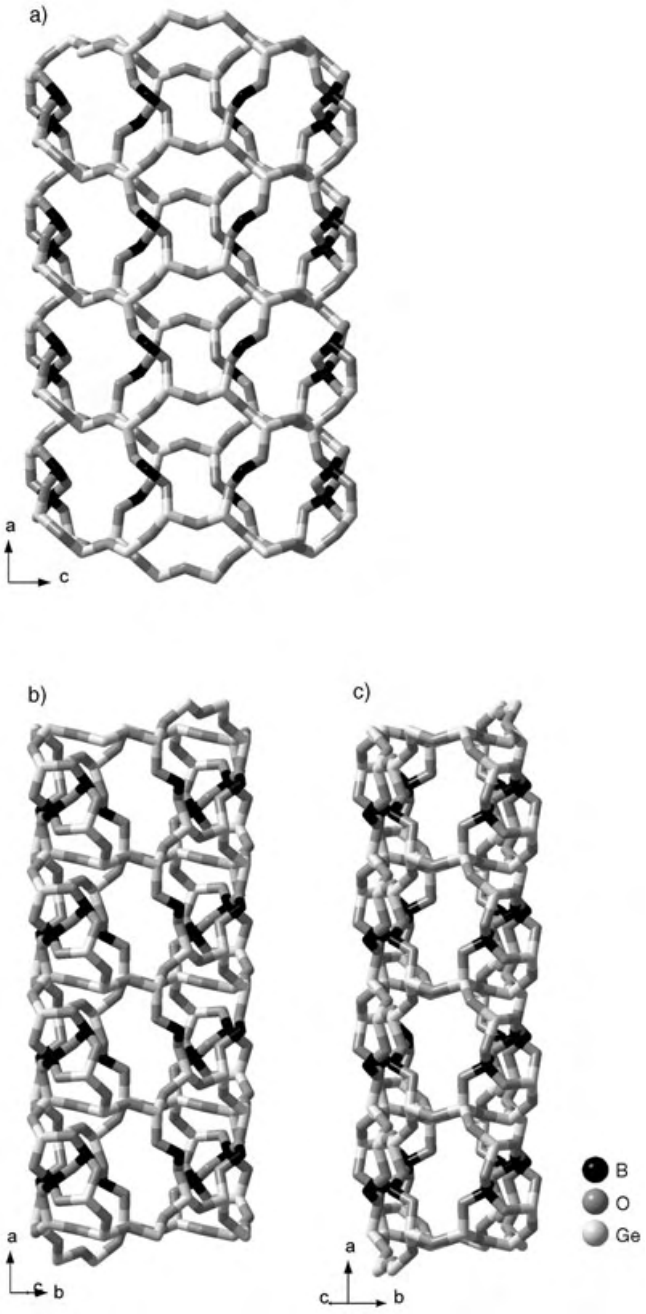

Figure 3. The three-dimensional channel systems in the SU-16 zeolite structure. The 12-ring channel is vertical, along the [100] direction. There are three different 8-ring channels perpendicular to the 12-ring channels, all of them intersecting with each other and with the 12-ring channel. a) The 8-ring channels running along the [010] direction. Here two columns of 8-ring channels (left and right) are shown. b) The 8-ring channels running along the [01$\bar{1}$] direction. c) The 8-ring channels along the [011] direction.

Supporting Information). The framework density of SU-16 is 16.1 T atoms per 1000 Å^3.

The thermogravimetric analysis of SU-16 (in N_2) shows a large weight loss from 370 °C to 465 °C and then a gradual loss from 465 °C to 800 °C. The total weight loss is 16.6%, corresponding to decomposition of the template DETA (calcd 17.2%). The elemental analysis also agrees well with

 © 2005 Wiley-VCH Verlag GmbH & Co. KGaA, Weinheim

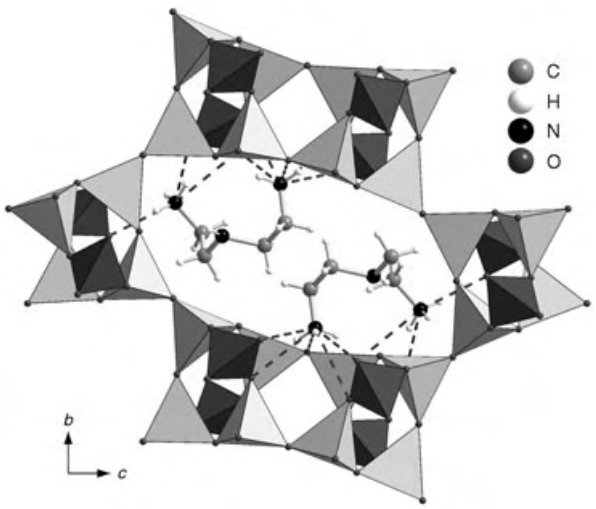

Figure 4. The 12-ring channel of SU-16 running along the [100] direction shown as polyhedra (BO_4: dark gray, GeO_4: light gray). The template cations DETA are located in the 12-ring channels; each is hydrogen bonded to three SBUs of the framework.

that obtained from single crystal X-ray diffraction (found: C 7.9, H 2.5, N 6.8; calcd: C 7.9, H 2.5, N 6.9%). The in situ X-ray powder diffraction in air showed that the crystallinity of SU-16 starts to decrease at 290°C. Attempts to exchange DETA with inorganic cations such as Na^+, K^+, and Ca^{2+} failed, maybe due to the strong interaction resulting from hydrogen bonding between the framework and the DETA cations.

In contrast to the synthesis of most germanates and borogermanates, in which the addition of F^- ions as mineralizers was essential, SU-16 could only be synthesized in the absence of F^-. In the presence of hydrofluoric acid, boron could not be incorporated into the framework. Instead, a layered germanate (SU-17) with the same framework structure as ASU-20[16] was formed.

We have shown for the first time that the two kinds of tetrahedra BO_4 and GeO_4, which differ very much in size (T–O 1.48 and 1.74 Å, respectively), can be connected to form an open framework with three-dimensional intersecting 12- and 8-ring channels. SU-16 is built from a new secondary building unit formed by 3-rings, which has not been reported before. This opens possibilities of designing new zeolite structures with more open frameworks than the existing zeolite structures and novel structure topologies.

Experimental Section

SU-16 was synthesized from a mixture containing GeO_2, H_2O, $[NH_2(CH_2)_2NH(CH_2)_2NH_2]$ (DETA), pyridine, and H_3BO_3 in a molar ratio of 1:20:8:40:2. Typically GeO_2 (0.25 g) was added to H_2O (0.85 mL) under stirring, and then DETA (2.04 mL) was added dropwise to the mixture until the GeO_2 was completely dissolved. Finally, pyridine (7.59 mL) and H_3BO_3 (0.29 g) were added. The reaction mixture ($pH \approx 14$) was stirred for 3 h, sealed in a 38-mL Teflon-lined autoclave and heated at 165°C for eight days. The autoclave was slowly cooled to room temperature, and then the product was filtered, washed with distilled water and acetone, and dried at room temperature. Large colorless needlelike single crystals of SU-16 were obtained in yields up to 70% (based on GeO_2). The X-ray powder diffraction indicated that the product was a single phase and a new structure (see the Supporting Information). The synthesis conditions of SU-16 were not very critical: Crystals of SU-16 could be obtained with molar ratios of GeO_2/DETA ranging from 1:4 to 1:12, GeO_2/H_2O from 1:20 to 1:40, GeO_2/pyridine from 1:20 to 1:60, and GeO_2/H_3BO_3 from 1:1 to 1:2. However, when other polyamines, such as 1,6-diaminohexane, 1,7-diaminoheptane, tetraethylenepentamine (TEPA), and bis(3-aminopropyl)amine were used instead of DETA, no SU-16 was formed.

The in situ X-ray powder diffraction (XRPD) of as-synthesized SU-16 was performed on a Huber Guinier camera 670 equipped with an imaging plate, using synchrotron radiation ($\lambda = 1.2768$ Å) at the Beam line I711, Max-lab, Lund University, Sweden. SU-16 was heated in air from 30°C to 650°C at 20°C/step and an average heating rate of 7°C min^{-1}. Powder diffraction patterns were collected at each step.

Elemental analysis of C, H, and N was performed on a FISON 1108 elemental analyser by Mikro Kemi AB, Uppsala University, Stockholm, Sweden. Thermogravimetric analysis (TGA) was carried out in N_2 gas in the temperature range 20–800°C with a heating rate of 5°C min^{-1}, using a high-resolution TGA 7 thermogravimetric analyzer (PERKIN ELMER).

X-ray diffraction data were collected at 293 K from a single crystal ($0.60 \times 0.10 \times 0.10$ mm^3) on a STOE IPDS diffractometer equipped with an image plate and graphite-monochromatized $Mo_{K\alpha}$ radiation ($\lambda = 0.71073$ Å) from a rotating anode. A total of 9062 reflections, of which 2760 are unique ($R(\text{int}) = 0.0445$), were collected in the region $2.78° < \theta < 26.03°$. The crystal was monoclinic with space group $P2_1/c$ (no. 14) and unit cell dimensions $a = 6.9365(14)$, $b = 10.493(2)$, $c = 20.448(4)$ Å, $\beta = 90.09(3)°$, and $V = 1488.3(5)$ Å^3, $\rho_{calcd} = 2.719$ g cm^{-3}. The structure was solved by the direct-method routine of SHELXS-97 and refined by full-matrix least-squares on F^2 using SHELXL-97.[17] All non-hydrogen atoms were refined anisotropically. Numerical absorption correction was applied with a linear absorption coefficient 8.073 mm^{-1}, using X-red and X-shape;[18] $T_{max}/T_{min} = 0.6202/0.1405$. $R_1 = 0.0337$ for 2483 reflections with $F_0 > 2\sigma(F_0)$ and 0.0377 for all 2760 reflections, $wR_2(F^2) = 0.0990$, GOF = 1.188. Max/min residual electron densities are 0.726/−1.182 e Å^{-3}, respectively. The C atoms bonded to N2 and C4 (C3 and C3′) are disordered, with occupancies of 0.675 and 0.325, respectively. The hydrogen atoms were geometrically idealized and allowed to ride on their parent atoms.

CCDC-243002 contains the supplementary crystallographic data for this paper. These data can be obtained free of charge from The Cambridge Crystallographic Data Centre via www.ccdc.cam.ac.uk/data_request/cif. The FTIR spectroscopy data, the TGA curve, calculated and experimental XRPD patterns, the loop configurations and the coordination sequences of SU-16 are presented in the supporting information.

Received: September 7, 2004
Revised: December 11, 2004
Published online: February 21, 2005

Keywords: boron · germanium · hydrothermal synthesis · zeolite analogues

[1] a) D. W. Breck, *Zeolite Molecular Sieves: Structure, Chemistry, and Use*, Wiley, New York, **1973**; b) N. Y. Chen, W. E. Garfield, F. G. Dwyer, *Shape Selective Catalysis in Industrial Applications*, 2nd rev. ed., Marcel Dekker, New York, **1996**; c) J. C. Jansen, M. Stöcker, H. G. Karge, J. Weitcamp, *Advanced Zeolite Science and Applications*, Elsevier, Amsterdam, **1994**; d) A. Corma, *Chem. Rev.* **1995**, *95*, 559–614, and references therein; e) J. M.

 © 2005 Wiley-VCH Verlag GmbH & Co. KGaA, Weinheim

Thomas, R. Raja, *Chem. Commun.* **2001**, 675 – 687, and references therein.
[2] a) R. M. Barrer, *Hydrothermal Chemistry of Zeolite*, Academic Press, London, **1982**; b) C. S. Cundy, P. A. Cox, *Chem. Rev.* **2003**, *103*, 663 – 701, and references therein; c) J. V. Smith, *Chem. Rev.* **1988**, *88*, 149 – 182.
[3] G. O. Brunner, W. M. Meier, *Nature* **1989**, *337*, 146 – 147.
[4] a) M. J. Annen, M. E. Davis, J. B. Higgins, J. L. Schlenker, *J. Chem. Soc. Chem. Commun.* **1991**, 1715 – 1716; b) C. Röhrig, H. Gies, *Angew. Chem.* **1995**, *107*, 125 – 127; *Angew. Chem. Int. Ed. Engl.* **1995**, *34*, 63 – 65; c) L. B. McCusker, R. W. Grosse-Kunstsleve, C. Baerlocher, M. Yoshikawa, M. E. Davis, *Microporous Mater.* **1996**, *6*, 295 – 309.
[5] a) S. Merlino, *Eur. J. Mineral.* **1990**, *2*, 809 – 817; b) T. Cheetham, H. Fjellvåg, T. E. Gier, K. O. Kongshaug, K. P. Lillerud, G. D. Stucky, *Stud. Surf. Sci. Catal.* **2001**, *135*, 788 – 795, and references therein; c) O. V. Petersen, G. Giester, F. Brandstätter, G. Niedermayr, *Can. Mineral.* **2002**, *40*, 173 – 181.
[6] S. L. Lawton, W. J. Rohrbaugh, *Science* **1990**, *247*, 1319 – 1321.
[7] a) S. H. Park, P. Daniels, H. Gies, *Microporous Mesoporous Mater.* **2000**, *37*, 129 – 143; b) S. H. Park, J. B. Parise, H. Gies, H. Liu, C. P. Grey, B. H. Toby, *J. Am. Chem. Soc.* **2000**, *122*, 11 023 – 11 024.
[8] a) H. Li, O. M. Yaghi, *J. Am. Chem. Soc.* **1998**, *120*, 10 569 – 10 570; b) T. Conradsson, M. S. Dadachov, X. D. Zou, *Microporous Mesoporous Mater.* **2000**, *41*, 183 – 191; c) R. Castaneda, A. Corma, V. Fornes, F. Rey, J. Rius, *J. Am. Chem. Soc.* **2003**, *125*, 7820 – 7821; d) A. Corma, F. Rey, S. Valencia, J. L. Jorda, J. Rius, *Nat. Mater.* **2003**, *2*, 493 – 497; e) Y. Mathieu, J. -L. Paillaud, P. Caullet, N. Bats, *Microporous Mesoporous Mater.* **2004**, submitted.
[9] a) T. Conradsson, X. D. Zou, M. S. Dadachov, *Inorg. Chem.* **2000**, *39*, 1716 – 1720; b) X. Bu, P. Feng, G. D. Stucky, *Chem. Mater.* **1999**, *11*, 3423 – 3424; c) P. Feng, X. Bu, G. D. Stucky, *Chem. Mater.* **1999**, *11*, 3025 – 3027; d) C. Cascales, B. Gomez-Lor, E. Gutierrez-Puebla, M. Iglesias, M. A. Monge, C. Ruiz-Valero, N. Snejko, *Chem. Mater.* **2002**, *14*, 677 – 681; e) C. Cascales, E. Gutierrez-Puebla, M. Iglesias, M. A. Monge, C. Ruiz-Valero, *Angew. Chem.* **1999**, *111*, 2592 – 2595; *Angew. Chem. Int. Ed.* **1999**, *38*, 2436 – 2439; f) C. Cascales, E. Gutierrez-Puebla, M. Iglesias, M. A. Monge, C. Ruiz-Valero, N. Snehko, *Chem. Commun.* **2000**, 2145 – 2146.
[10] a) M. O'Keeffe, O. M. Yaghi, *Chem. Eur. J.* **1999**, *5*, 2796 – 2801; b) A. Corma, M. Puche, F. Rey, G. Sankar, S. J. Teat, *Angew. Chem.* **2003**, *115*, 1188 – 1191; *Angew. Chem. Int. Ed.* **2003**, *42*, 1156 – 1159, and references therein; c) A. Corma, M. J. Diaz-Cabanas, J. Martines-Triguero, F. Re, J. Rius, *Nature* **2002**, *418*, 514 – 517.
[11] a) Y. Zhou, H. Zhu, Z. Chen, M. Chen, Y. Xu, H. Zhang, D. Zhao, *Angew. Chem.* **2001**, *113*, 2224 – 2226; *Angew. Chem. Int. Ed.* **2001**, *40*, 2166 – 2168; b) J. Plevert, T. M. Gentz, A. Laine, H. Li, V. G. Young, O. M. Yaghi, M. O'Keeffe, *J. Am. Chem. Soc.* **2001**, *123*, 12 706 – 12 707.
[12] a) T. E. Gier, X. Bu, P. Feng, G. D. Stucky, *Nature* **1998**, *395*, 154 – 157; b) X. Bu, P. Feng, T. E. Gier, D. Zhao, G. D. Stucky, *J. Am. Chem. Soc.* **1998**, *120*, 13 389 – 13 397; c) X. Bu, P. Feng, G. D. Stucky, *J. Am. Chem. Soc.* **1998**, *120*, 11 204 – 11 205.
[13] a) M. S. Dadachov, K. Sun, T. Conradsson, X. D. Zou, *Angew. Chem.* **2000**, *112*, 3820 – 3822; *Angew. Chem. Int. Ed.* **2000**, *39*, 3674 – 3676; b) X. D. Zou, T. Conradsson, M. S. Dadachov, *Stud. Surf. Sci. Catal.* **2001**, *135*, 1494 – 1501; c) Y. F. Li, X. D. Zou, *Acta Crystallogr. Sect. C* **2003**, *59*, m471 – m472.
[14] A. Choudhury, S. Neeraj, S. Natarajan, C. N. R. Rao, *J. Chem. Soc. Dalton Trans.* **2002**, 1535 – 1538.
[15] C. Baerlocher, W. M. Meier, D. H. Olson, *Atlas of Zeolite Framework Types*, 5th ed., Elsevier, Amsterdam, **2001**.
[16] J. Plevert, T. M. Gentz, T. L. Groy, M. O'Keeffe, O. M. Yaghi, *Chem. Mater.* **2003**, *15*, 714 – 718.
[17] a) G. M. Sheldrick, SHELXS-97, Program for the Solution of Crystal Structures, University of Göttingen, Göttingen (Germany), **1997**; b) G. M. Sheldrick, SHELXL-97, Program for Refinement of Crystal Structures, University of Göttingen, Göttingen (Germany), **1997**.
[18] a) STOE & CIE, X-RED 1.09, Program for Data Reduction, Darmstadt, Germany, **1996**; b) STOE & CIE, X-SHAPE Version 1.01, Crystal Optimization for Numerical Absorption Correction, Darmstadt, Germany, **1996**.

 © 2005 Wiley-VCH Verlag GmbH & Co. KGaA, Weinheim

Functional Materials

Single-Wall Carbon Nanotubes as Integrative Building Blocks for Solar-Energy Conversion**

Dirk M. Guldi, G. M. A. Rahman, Maurizio Prato, Norbert Jux, Shuhui Qin, and Warren Ford*

Abundant clean energy is one of the greatest challenges facing the world in the 21st century. Solar energy conversion is one of the most natural and abundant ways to produce alternative energy to carbon fuels. Over the years, the use of inorganic semiconducting materials has dominated the solar energy conversion market. However, the production of organic or mixed organic/inorganic solar cells has visibly increased the potential of solar energy conversion and made an impact with a broad range of innovative technologies. Most promising approaches include dye-sensitized nanocrystalline solar cells,[1] polymer/fullerene blends,[2] small-molecule thin

[*] Prof. D. M. Guldi
Universität Erlangen
Institute for Physical and Theoretical Chemistry
91058 Erlangen (Germany)
Fax: (+49) 913-1852-8307
E-mail: dirk.guldi@chemie.uni-erlangen.de

Dr. G. M. A. Rahman
Radiation Laboratory, University of Notre Dame
Notre Dame, Indiana 46556 (USA)

Prof. M. Prato
Dipartimento di Scienze Farmaceutiche
Università di Trieste
Piazzale Europa, 1, 34127 Trieste (Italy)

Dr. S. Qin, Prof. W. Ford
Chemistry Department, Oklahoma State University
Stillwater, Oklahoma 74078 (USA)

Dr. N. Jux
Universität Erlangen, Institute for Organic Chemistry
91054 Erlangen (Germany)

[**] This work was carried out with partial support from the EU (RTN networks "WONDERFULL" and "CASSIUSCLAYS"), MIUR (cofin prot. 2004035502), SFB583, the National Science Foundation (grant EPS-0132543), and the Office of Basic Energy Sciences of the U.S. Department of Energy. This is document NDRL-4586 from the Notre Dame Radiation Laboratory.

Supporting information for this article is available on the WWW under http://www.angewandte.org or from the author.

 DOI: 10.1002/anie.200462416 © 2005 Wiley-VCH Verlag GmbH & Co. KGaA, Weinheim

films,[3] and hybrid polymer/nanocrystal devices.[4] Small-area dye-sensitized solar cells have so far reached conversions of about 11%,[5] whereas polymer-fullerene blends have been reported with 3% efficiency.[6] Recently, discotic liquid crystalline materials have been successfully used in the construction of organic solar cells.[7]

Single-wall carbon nanotubes (SWNT), are attractive platforms for photovoltaic applications.[8,9] In principle, these innovative materials, which possess extended π-electron systems, in combination with photoexcitable electron donors, could be useful for novel, ultrahigh efficient photoelectrochemical cells for water splitting and reduction of CO_2 to fuels.[10] In fact, SWNT are good electron acceptors and, at the same time, one-dimensional nanowires.[10d,11,12] Therefore, they are ready to accept electrons, which are then transported with high efficiency. In light of this feature, the combination of SWNT with donor groups signifies an innovative concept to 1) harvest solar energy and 2) convert it into useful electricity. Based on these principles, a SWNT-based solar cell should work efficiently. The role and potential of SWNT photovoltaic hybrids has only been sparingly explored.[13] Herein we focus for the first time on the systematic and molecularly controlled integration/organization of SWNT, together with porphyrin systems, into nanostructured devices. The rich and extensive absorptions, typical of porphyrinoid systems, make an efficient use of light. The new system gives rise to promising monochromatic solar-energy conversion efficiencies—up to 8.5% internal photoconversion efficiencies (IPCE).

The favorable charge-separation features of SWNT–PSS^{n-}/H_2P^{8+}[11] and SWNT/$pyrene^{+}$/ZnP^{8-} nanohybrids[12b] (shown in Scheme 1) are promising for the construction of photoactive electrode surfaces.[14] The combination of the electron-accepting character of SWNT with ZnP, which acts as an excited state electron donor, is a fundamental design consideration.[15]

To test these novel SWNT architectures in photoelectrochemical devices, we take advantage of the electrostatic interactions, which govern the organization of SWNT-PSS^{n-}/ZnP^{8+} and SWNT/$pyrene^{+}$/ZnP^{8-} in solution, to integrate them sequentially onto solid substrates.[11,12b] In particular, points of multiple interactions between poly(diallyl dimethylammonium) chloride ($PDDA^{n+}$) and sodium poly(styrene-4-sulfonate) (PSS^{n-}) base layers and SWNT-PSS^{n-} or SWNT/$pyrene^{+}$ are expected to secure strong and tight binding.[16]

Owing to the absorption features of the polyelectrolytes ($PDDA^{n+}$ and PSS^{n-}), SWNT (SWNT and SWNT-PSS^{n-}), and porphyrins (ZnP^{8+}, ZnP^{8-}), conventional spectrophotometry is a convenient tool to assess the adhesion of the individual building blocks to the surface (Figure 1). For example, on quartz substrates, $PDDA^{n+}$ and PSS^{n-} exhibit transitions that are mainly located in the UV region (mainly below 200 nm for $PDDA^{n+}$ and 260 nm for PSS^{n-}). SWNT, on the other hand, are strong UV/Vis-NIR absorbers, since the van Hove singularities extend up to 1500 nm. Finally, the porphyrin systems exhibit strong Soret- and Q-bands at around 435 nm and in the 550–600 nm region, respectively. Also the strong π–π* transitions of $pyrene^{+}$ can be observed at 235, 290 and 365 nm.

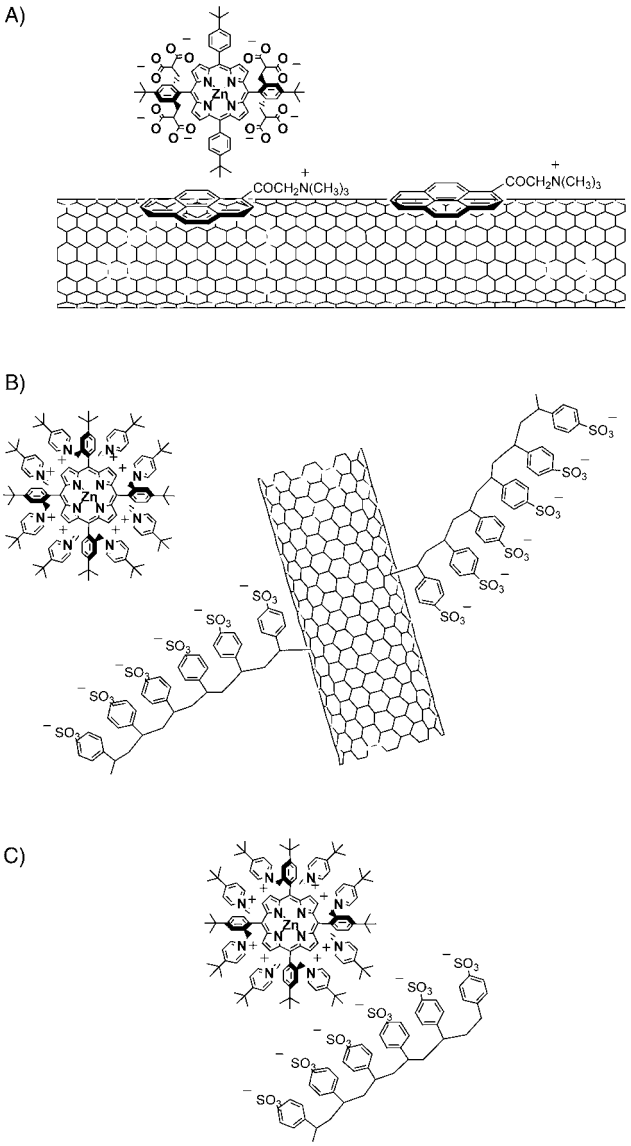

Scheme 1. Structure of A) SWNT/$pyrene^{+}$/ZnP^{8-}, B) SWNT-PSS^{n-}/ZnP^{8+}, and C) PSS^{n-}/ZnP^{8+} used in this work.[12]

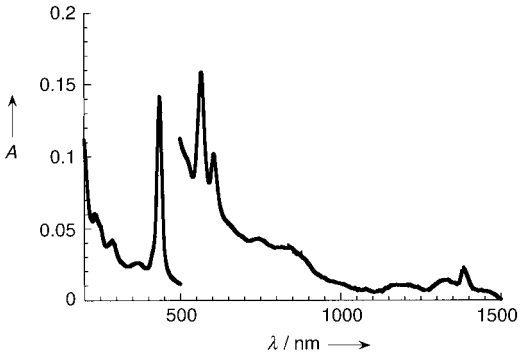

Figure 1. Absorption spectrum of a single SWNT/$pyrene^{+}$/ZnP^{8-} stack on quartz. The 500–1500 nm region is amplified by a factor of 10.

The electrostatically driven deposition of SWNT and porphyrins onto the surface was also monitored by atomic force microscopy (AFM). (Figure S1 in the Supporting

 © 2005 Wiley-VCH Verlag GmbH & Co. KGaA, Weinheim

Information shows randomly organized bundles of SWNT on a pretreated silicon wafer in the case of SWNT/pyrene$^+$. Layers of SWNT-PSS^{n-} behave similarly.)

Photoaction and photocurrent measurements with different sets of electrodes were performed in aqueous solutions containing 0.1 M Na_3PO_4.[17] Photoaction spectra with monochromatic light were measured (see Figure 2) which confirm

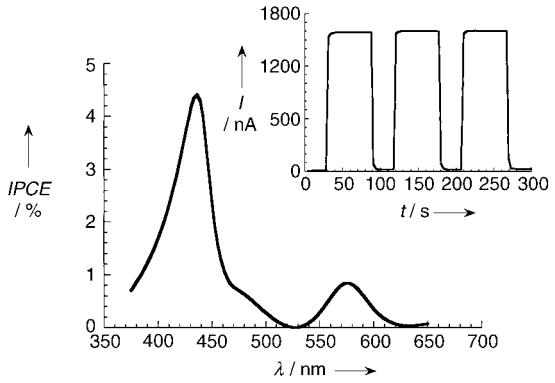

Figure 2. Photoaction spectrum of a single SWNT/pyrene$^+$/ZnP^{8-} stack: 0.1 M Na_3PO_4, 1 mM sodium ascorbate, N_2-purged, electrochemical bias of +200 mV. Insert several on/off cycles for a single SWNT/pyrene$^+$/ZnP^{8-} stack: 0.1 M Na_3PO_4, 1 mM sodium ascorbate, N_2-purged, electrochemical bias of +200 mV.

the photoactivity of the porphyrin chromophores. Through photocurrent measurements, in which the entire solar spectrum was used, we probed mechanistic aspects. Upon addition of sodium ascorbate—an electron donor that restores the oxidized porphyrins—the photocurrents of the system increased markedly. Obviously, regeneration of the initial porphyrin state helps to close the photo-electrochemical circuit. In concentration-dependent assays between 0 and 10 mM sodium ascorbate, a maximum response was observed at 1 mM. At higher quencher concentrations, though, the currents stagnate. When monitoring several back-to-back intervals of light-on and light-off, exceptionally reproducible and stable photocurrents were obtained, which is illustrated in the inset to Figure 2.

Another decisive set of data comes from biasing the indium tin oxide (ITO) electrode through electrochemical charging. With increasingly negative potentials, the photocurrents drop, while an opposite trend is observed in the positive region. In fact, changing the bias from −200 mV to 0 mV and to +200 mV versus Ag/AgCl leads to threefold and sixfold increase of the photocurrent, respectively. It is very likely that, at the minimum value of the bias, we reach equilibrium conditions between the ITO conduction band and the reduction of SWNT.[18]

Considering all the pieces of information together, we reach the following conclusion. Charge separation from the photoexcited porphyrin to SWNT generates electron-hole pairs at the SWNT surface.[10d,12b,19] While the energetic position of the ITO conduction band favors a thermodynamically driven electron transfer from the reduced SWNT, the sacrificial electron-donor sodium ascorbate reduces the oxidized porphyrins (Scheme 2).[20]

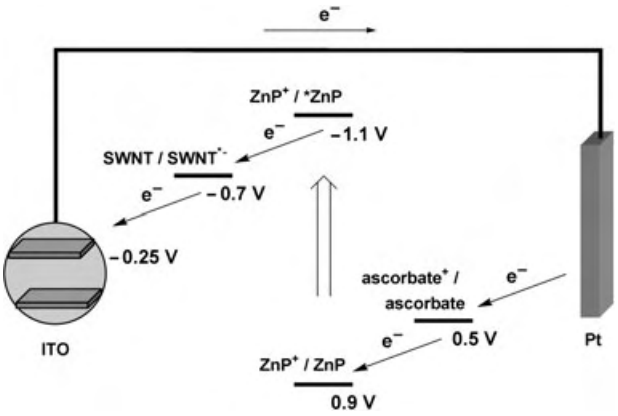

Scheme 2. Schematic illustration of photocurrent generation in ITO electrodes covered with a single SWNT/pyrene$^+$/ZnP^{8-} stack.[17]

The photoaction spectra (Figure 2) were further used to quantify the internal photoconversion efficiency. For SWNT-PSS^{n-}/ZnP^{8+} cells that contain single layers of PDDA^{n+}, SWNT-PSS^{n-}, and ZnP^{8+} monochromatic IPCE values of 0.25 % were determined. A lot more efficient is the SWNT/pyrene$^+$/ZnP^{8-} cell with 1.8 %. Next we replaced the electron-accepting SWNTs with C_{60}. In the corresponding C_{60} cells, namely, PDDA^{n+}/C_{60}^{9-}/ZnP^{8+} moderate IPCE values of 0.15 % were noted.[21] Finally, in the absence of any electron acceptor—neither SWNT nor C_{60} were present—the efficiencies for PSS^{n-}/ZnP^{8+} cells drop dramatically to 0.08 %.[22]

Repetition of the deposition steps allows modifying the PDDA^{n+} or PSS^{n-} baselayers with SWNT-PSS^{n-}/ZnP^{8+} and SWNT/pyrene$^+$/ZnP^{8-} stacks. The repetitive growth is monitored with absorption spectroscopy (a typical example is shown in Figure S2 in the Supporting Information). The transitions of pyrene$^+$ (that is, 235, 290 and 365 nm), ZnP^{8+} (435, 565, and 605 nm), and SWNT (685, 745, 815 and 880 nm) grow linearly up to 10 stacks, that is, 10 alternate layers of SWNT/pyrene$^+$ and ZnP^{8-}. Of note is that we see an overall increase in photocurrent generation up to at least 10 stacks (Figure 3). Greatly enhanced absorption cross-sections favor the photocurrent increase. In addition, strong electronic coupling between the stacks, which is augmented by the

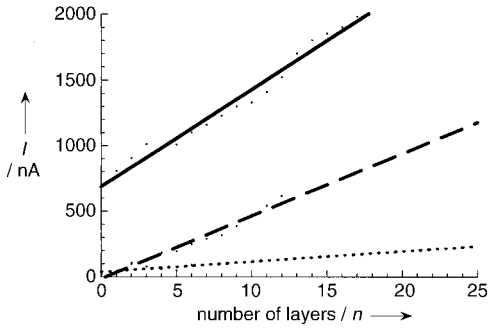

Figure 3. Photocurrent dependence for the different SWNT structures; *n* reflects the number of individual deposited layers: SWNT/pyrene$^+$ and ZnP^{8-} (solid line), SWNT-PSS^{n-} and ZnP^{8+} (dashed line), PSS^{n-} and ZnP^{8+} (dotted line); these three lines are the extrapolated fit of the experimental data (dots).

 © 2005 Wiley-VCH Verlag GmbH & Co. KGaA, Weinheim

intriguing SWNT transport features within the individual layers, is believed to be critical for the observed trend. Translating the currents into IPCEs, maximum values for SWNT/pyrene^{+}/ZnP^{8-} and SWNT-PSS^{n-}/ZnP^{8+} are 4.2% and 1.0%, respectively. With a +200 mV bias the corresponding monochromatic efficiency is approximately 8.5%. In the case of PSS^{n-}/ZnP^{8+} no significant current increase is seen owing to the insulating features of PSS^{n-}.

In conclusion, we have demonstrated that the successful incorporation of SWNT hybrids—noncovalently linked SWNT/pyrene^{+} and covalently linked SWNT-PSS^{n-}—onto semitransparent ITO electrodes leads to solar-energy conversion devices. Considering that a cell containing a single SWNT/pyrene^{+}/ZnP^{8-} stack, namely, a single layer of SWNT/pyrene^{+} and single layer of ZnP^{8-}, leads to monochromatic conversion efficiencies of up to 4.2% (that is, with a +200 mV bias) this is a promising starting point.[23] The strategy illustrated herein is not optimized, but leaves ample room for improvement. Whereas other systems may have shown higher efficiency, the present method offers flexibility and can be considered as a complementary technique to those already existing. Since the problem of solar-energy conversion is so important, we believe that the high photocurrents found in our preliminary experiments deserve much further investigation, including studies of efficient ways of dispersing individual SWNT better into thin films.

Received: October 25, 2004
Revised: December 6, 2004
Published online: February 21, 2005

Keywords: carbon nanotubes · charge separation · porphyrinoids · solar-energy conversion · zinc

[1] a) N. S. Lewis, *Nature* **1983**, *305*, 671; b) B. Oregan, M. Grätzel, *Nature* **1991**, *353*, 737; c) M. Grätzel, *Nature* **2001**, *414*, 338.
[2] a) N. S. Sariciftci, L. Smilowitz, A. J. Heeger, F. Wudl, *Science* **1992**, *258*, 1474; b) G. Yu, J. Gao, J. C. Hummelen, F. Wudl, A. J. Heeger, *Science* **1995**, *270*, 1789; c) C. J. Brabec, N. S. Sariciftci, J. C. Hummelen, *Adv. Funct. Mater.* **2001**, *11*, 15.
[3] a) A. Shah, P. Torres, R. Tscharner, N. Wyrsch, H. Keppner, *Science* **1999**, *285*, 692; b) P. Peumans, S. Uchida, S. R. Forrest, *Nature* **2003**, *425*, 158.
[4] a) J. J. M. Halls, C. A. Walsh, N. C. Greenham, E. A. Marseglia, R. H. Friend, S. C. Moratti, A. B. Holmes, *Nature* **1995**, *376*, 498; b) H. E. Katz, A. J. Lovinger, J. Johnson, C. Kloc, T. Siegrist, W. Li, Y. Y. Lin, A. Dodabalapur, *Nature* **2000**, *404*, 478; c) J. Nelson, *Science* **2001**, *293*, 1059; d) W. U. Huynh, J. J. Dittmer, A. P. Alivisatos, *Science* **2002**, *295*, 2425.
[5] R. Kern, N. Van Der Burg, G. Chmiel, J. Ferber, G. Hasenhindl, A. Hinsch, R. Kinderman, J. Kroon, A. Meyer, T. Meyer, R. Niepmann, J. Van Roosmalen, C. Schill, P. Sommeling, M. Spath, I. Uhlendorf, *Opto-Electron. Rev.* **2000**, *8*, 284.
[6] F. Padinger, R. S. Rittberger, N. S. Sariciftci, *Adv. Funct. Mater.* **2003**, *13*, 85.
[7] L. Schmidt-Mende, A. Fechtenkotter, K. Müllen, E. Moons, R. H. Friend, J. D. MacKenzie, *Science* **2001**, *293*, 1119.
[8] Special issue on Carbon Nanotubes *Acc. Chem. Res.* **2002**, *35*, 997.
[9] a) A. Hirsch, *Angew. Chem.* **2002**, *114*, 1933; *Angew. Chem. Int. Ed.* **2002**, *41*, 1853; b) J. L. Bahr, J. M. Tour, *J. Mater. Chem.* **2002**, *12*, 1952; c) S. Niyogi, M. A. Hamon, H. Hu, B. Zhao, P. Bhomwik, R. Sen, M. E. Itkis, R. C. Haddon, *Acc. Chem. Res.* **2002**, *35*, 1105; d) Y.-P. Sun, K. Fu, Y. Lin, W. Huang, *Acc. Chem. Res.* **2002**, *35*, 1096; e) S. Banerjee, M. G. C. Kahn, S. S. Wang, *Chem. Eur. J.* **2003**, *9*, 1899; f) D. Tasis, N. Tagmatarchis, V. Georgakilas, M. Prato, *Chem. Eur. J.* **2003**, *9*, 4000; g) N. Tagmatarchis, M. Prato, *J. Mater. Chem.* **2004**, *14*, 437.
[10] a) V. Georgakilas, K. Kordatos, M. Prato, D. M. Guldi, M. Holzinger, A. Hirsch, *J. Am. Chem. Soc.* **2002**, *124*, 760; b) H. Murakami, T. Nomura, N. Nakashima, *Chem. Phys. Lett.* **2003**, *378*, 481; c) H. Li, B. Zhou, L. Gu, W. Wang, K. A. Shiral Ferando, S. Kumar, J. F. Allard, Y.-P. Sun, *J. Am. Chem. Soc.* **2004**, *126*, 1014; d) D. M. Guldi, M. Marcaccio, D. Paolucci, F. Paolucci, N. Tagmatarchis, D. Tasis, E. Vázquez, M. Prato, *Angew. Chem.* **2003**, *115*, 4243; *Angew. Chem. Int. Ed.* **2003**, *42*, 4206.
[11] D. M. Guldi, G. M. A. Rahman, J. Ramey, M. Marcaccio, D. Paolucci, F. Paolucci, S. Qin, W. T. Ford, D. Balbinot, N. Jux, N. Tagmatarchis, M. Prato, *Chem. Commun.* **2004**, 2034.
[12] a) N. Nakashima, Y. Tomonari, H. Murakami, *Chem. Lett.* **2002**, 638; b) D. M. Guldi, G. M. A. Rahman, N. Tagmatarchis, M. Prato, *Angew. Chem.* **2004**, *116*, 5642; *Angew. Chem. Int. Ed.* **2004**, *43*, 5526.
[13] A promising approach includes a naphthalocyanine dye (as the main sensitizer) carbon nanotubes (as the electron acceptor), and poly(3-octylthiophene) (as the electron donor): a) E. Kymakis, G. A. J. Amaratunga, *Sol. Energy Mater. Sol. Cells* **2003**, *80*, 465; b) E. Kymakis, G. A. J. Amaratunga, *Appl. Phys. Lett.* **2002**, *80*, 112; c) E. Kymakis, I. Alexandrou, *J. Appl. Phys.* **2003**, *93*, 1764.
[14] SWNT-PSS^{n-}: SWNT grafted with poly(sodium 4-styrenesulfonate), see S. Qin, D. Qin, W. T. Ford, J. E. Herrera, D. E. Resasco, S. M. Bachilo, R. B. Weisman, *Macromolecules* **2004**, *37*, 752; pyrene^{+}: 1-(trimethylammonium acetyl) pyrene; ZnP^{8+}: zinc 5,10,15,20-tetrakis(2′,6′-bis(*N*-methylene-(4″-*tert*-butylpyridinium))-4′-*tert*-butylphenyl)porphyrin octabromide salt; ZnP^{8-}: zinc 5,15-bis[2′,6′-bis{2″,2″-bis(carboxy)ethyl}methyl-4′-*tert*-butylpheny]-10,20-bis(4′-*tert*-butylphenyl)porphyrin octasodium salt.
[15] J. Liu, S. S. Fan, H. J. Dai, *MRS Bull.* **2004**, *29*, 244.
[16] Surprisingly, SWNT/pyrene^{+} adsorbed as well to PDDA^{n+}.
[17] We also tested 0.1 M H_3PO_4, 0.1 M NaH_2PO_4, and 0.1 M Na_2HPO_4.
[18] In the presence of molecular oxygen leads to a moderate amplification of the photocurrent. The overall amplification can be rationalized based on the high mobility of molecular oxygen as an electron carrier.
[19] See for a similar conclusion: M. Alvaro, P. Atienzar, P. de la Cruz, J. L. Delgado, H. Garcia, F. Langa, *J. Phys. Chem. B* **2004**, *108*, 12691.
[20] Energy levels were taken from previous work. See refs [11] and [12b].
[21] D. M. Guldi, I. Zilbermann, G. Anderson, A. Li, D. Balbinot, N. Jux, M. Hatzimarinaki, A. Hirsch, M. Prato, *Chem. Commun.* **2004**, 726.
[22] Following the same procedure, we performed comparative assays with PSS^{n-} alone, that is, without electron-accepting SWNTs interlayered with ZnP^{8+}.
[23] Multilayered cells give rise to power conversion efficiencies of up to 8.5% (with a +200 mV bias).

 © 2005 Wiley-VCH Verlag GmbH & Co. KGaA, Weinheim

Molecular Switches

Photoswitching of Stereoselectivity in Catalysis Using a Copper Dithienylethene Complex**

*David Sud, Tyler B. Norsten, and Neil R. Branda**

Harnessing the changes in molecular structure and function that occur when photoresponsive compounds are reversibly toggled between thermally stable isomers is becoming increasingly important to the development of molecular devices containing switching elements.[1] Compounds that undergo reversible photochemical transformations have been investigated for use in optoelectronic technologies and to a lesser extent, in influencing chemical reactivity. Although the concept of using the geometric changes that accompany a photoreaction to regulate chemical reactivity and catalysis was introduced over 20 years ago, only a few examples have been reported,[2–5] and all rely on azobenzene units as the photoresponsive structure. The large molecular movements that result from the *cis–trans* isomerization were shown to influence ester hydrolysis within modified cyclodextrins[2] or crowns ethers,[3] and amide formation in hydrogen-bonded receptors.[4,5] Although they remain elegant examples of the concept of photocontrolling catalysis, the photoresponsive azobenzene derivatives are plagued by thermal reversibility, which will significantly limit their practical use.

Compounds constructed from the 1,2-dithienylethene backbone represent a significant improvement over most other photoresponsive structures primarily because they undergo thermally irreversible photochemical ring-closing and ring-opening reactions.[6] Our goals include using the structural differences between the two photoisomers to influence the outcome of metal-catalyzed reactions. We prepared the chiral bis(oxazoline) ligand **1** with the expectation that it can only chelate to a metal when the photoswitch is in its flexible ring-open state, **1o** (Scheme 1).[7] This complexation places the metal center within a chiral environment ready to perform stereoselective reactions.[8] Irradiation with UV light will generate the ring-closed form, **1c**, which cannot chelate the metal because the photochemically produced rigid backbone forces the two oxazolines to exist in a divergent relationship to each other.

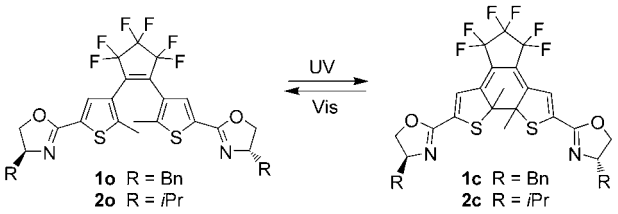

Scheme 1. Interconversion of ring-open (**o**) and ring-closed (**c**) isomers of **1** and **2**.

Our original work proved this anticipated metal-binding mode to be incorrect and instead of forming a chelated complex with copper(I), **1o** forms a double helicate, [Cu_2-(**1o**)$_2$], where two ligands are wrapped around two metals in a stereospecific manner.[7] This result helps to explain why there is no observable stereoselectivity when a metal-catalyzed reaction (cyclopropanation, see entry 1 in Table 1) is carried out using the *iso*-propyl version of bis(oxazoline) **2o** as the ligand (10 to 25 mol%).[9] However, the fact that **2o** may not be conformationally well-defined around the metal center so as to provide an appropriate chiral catalytic environment cannot be ruled out.[10]

Table 1: Results of the cyclopropanation reactions of styrene with ethyl diazoacetate using ligands **2** and **3**, and CuOTf·0.5 C_6H_6 in CH_2Cl_2.[a]

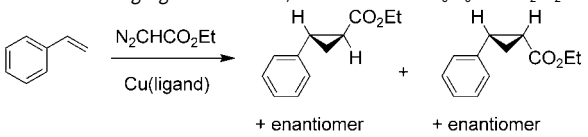

Entry	Ligand	*ee* [%][b]		d.r.[c]
		trans	*cis*	
1	**2o**	0	0	–
2	**3o**	30	50	55:45
3	23% **3c**[d]	11	37	70:30
4	97% **3c**[e]	5	5	63:37

[a] All values are averages of multiple runs using 10 mol% catalyst.[13] [b] Determined by HPLC analysis using a CHIRACEL-OD column. The values for the *cis* isomer are estimates owing to significant peak overlap in the HPLC traces. [c] Determined by ^{1}H NMR spectroscopic analysis of the crude reaction mixture. The *trans* isomer was always found to be the major product. [d] Represents the photostationary state generated by irradiating a solution of the ligand with 313 nm light for 15 min. [e] Isolated from the photostationary state by centrifugal chromatography using 0.5% CH_3OH in CH_2Cl_2. The remaining 3% is **3o**.

One of the appealing features of photoresponsive dithienylethene compounds is the versatility with respect to what can be attached onto the thiophene heterocycles. Relocating the oxazoline groups onto the internal positions (thiophene C2) provides ligand **3o** that, according to computer modeling, cannot form a helicate with metal ions such as copper(I). This ligand is prepared from the known oxazoline **4** (Scheme 2) by taking advantage of the oxazoline to direct the lithiation to the C3 position on the thiophene.[11] Scheme 2 also illustrates the significant differences between the metal-binding pocket in the ring-open **3o** and ring-closed **3c** forms.

[*] D. Sud, Prof. N. R. Branda
Department of Chemistry
Simon Fraser University
8888 University Drive
Burnaby, BC V5A1S6 (Canada)
E-mail: nbranda@sfu.ca
T. B. Norsten
National Research Council of Canada
ICPET-Polymeric Materials Group
1200 Montreal Road, Ottawa, ON K1A0R6 (Canada)

[**] This work was supported by the Natural Sciences and Engineering Research Council of Canada, the Canada Research Chair Program, and Simon Fraser University. We thank Nippon Zeon Corporation for supplying the octafluorocyclopentene needed to prepare the photochromic compound.

 DOI: 10.1002/anie.200462538 © 2005 Wiley-VCH Verlag GmbH & Co. KGaA, Weinheim

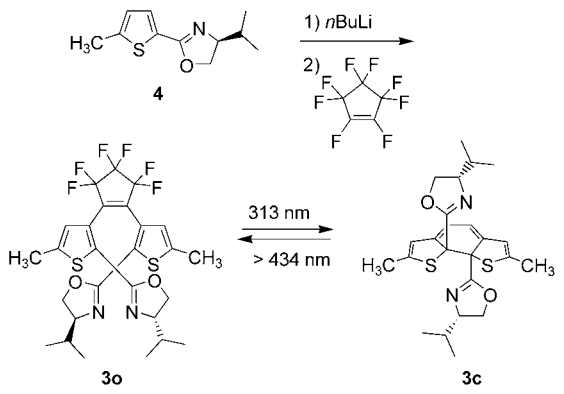

Scheme 2. Synthesis and photochemical cyclization of bis(oxazoline) **3o**.

Bis(oxazoline) **3o** can be toggled between its ring-open and ring-closed isomers by alternate irradiation with appropriate wavelengths of light as is best demonstrated using UV/Vis absorption spectroscopy (Figure 1). Irradiation of a

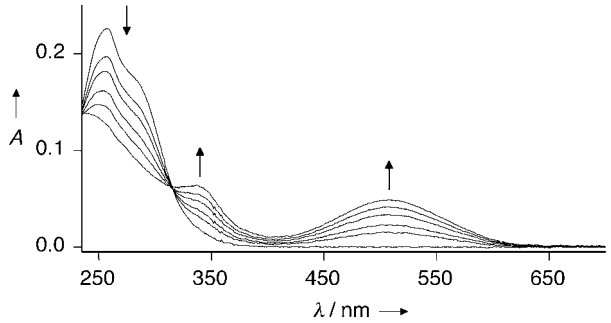

Figure 1. Changes in the UV/Vis absorption spectra of **3o** upon irradiation with 313 nm light. Irradiation periods are 0, 5, 10, 20, 30, and 60 s.

CH_2Cl_2 solution of **3o** with 313 nm light[12] results in the appearance of an absorption band in the visible spectral region ($\lambda_{max} = 510$ nm) and a visual change from colorless to deep red owing to the generation of the ring-closed isomer, **3c**. Irradiation of **3c** at wavelengths greater than 434 nm triggers the ring-opening photoreaction and the regenerates the original absorption spectrum corresponding to **3o**.

One reaction involving bis(oxazolines) as chelating ligands is the copper-catalyzed cyclopropanation of olefins with diazoesters, and is a good reaction to illustrate our concept because is provides a simple model reaction with an easy to analyze and well characterized product distribution. The results from the stereoselective cyclopropanation reactions of styrene with ethyldiazoacetate using bis(oxazolines) **2** and **3** are listed in Table 1.[13]

The low enantioselectivities observed when **3o** is used as the ligand (entry 2) and copper(I) trifluoromethanesulfonate ($CuOTf{\cdot}0.5\,C_6H_6$) as the metal source (10 mol% of each) are a result of the flexibility of the ligand around the metal center and are adequate to evaluate the efficacy of the bis(oxazoline) as a photoresponsive catalyst. When a solution of the **3o** is irradiated with 313 nm light to form the photostationary state[12] and the catalytic reaction is repeated using this solution as the ligand source, the enantioselectivities drop (entry 3). The small magnitude of the changes can be explained by the fact that the photostationary state generated under these conditions consists of 23% of the ring-closed isomer, **3c**, as identified by ^{1}H NMR spectroscopy. Although this low photostationary state is a temporary drawback, future generations of photoswitchable ligands based on the 1,2-dithienylethene scaffold will circumvent this limitation by taking advantage of the electronic tuning that can be tailored into the structure. Photostationary states containing a greater amount of the ring-closed isomer can be expected to display more significant differences in the product distribution when used as ligands in catalytic reactions. This assumption is confirmed when a purified sample of the ring-closed isomer, **3c**, is used as the ligand, in this case the enantioselectivities are insignificant (entry 4). The enantioselectivities can be turned back on by converting the ring-closed isomer back into its ring-open counterpart by irradiating the reaction mixture containing all the ingredients with light of wavelength greater than 434 nm[12] before the cyclopropanation reaction has finished. When this experiment is performed, the original values for the enantio- and diastereoselectivity are regenerated as a result of the photoinduced ring-opening reaction to regenerate **3o**, (**3c**→**3o**). This observation clearly demonstrates the in situ photoswitching of stereoselective catalysis and is the first example of its kind.

The photoinduced ring-closing reaction (**3o**→**3c**), however, is inhibited when the metal is present and irradiation of CH_2Cl_2 solutions of ligand **3o** and $CuOTf{\cdot}0.5\,C_6H_6$ results in no changes in the color or in the observed stereoselectivities. This inhibition is caused by the copper being too tightly bound within the ligand's chelation site to allow for photoswitching. The presence of the copper center prevents the ligand from undergoing the necessary geometric changes during the photoreaction. This problem is overcome by adding a small amount (5%) of the more competitive coordinating solvent CH_3CN to the CH_2Cl_2 solutions. When the cyclopropanation reactions are repeated using this solvent mixture, the outcome of the reaction can be photoregulated. For example, the enantioselectivity of the *trans* isomer of the cyclopropane product can be decreased from 23% to 10% by irradiating the CH_3CN/CH_2Cl_2 reaction mixture containing **3o** and $CuOTf{\cdot}0.5\,C_6H_6$ with 313 nm light to convert the ring-open isomer into the photostationary state.

Herein we have described the first example of photoregulation in metal catalysis using the established 1,2-dithienylethene photoswitch. Future reports will focus on expanding the range of reactions that will benefit from this molecular-level control as well as optimizing the photochemistry to afford more versatile catalysts.

Received: November 6, 2004
Published online: February 23, 2005

Keywords: copper · enantioselectivity · homogeneous catalysis · molecular switches · photochromism

 © 2005 Wiley-VCH Verlag GmbH & Co. KGaA, Weinheim

[1] a) *Molecular Switches* (Ed.: B. L. Feringa), Wiley-VCH, Weinheim, **2001**; b) *Organic Photochromic and Thermochromic Compounds*, *Vol. 1* and *2* (Eds: J. C. Crano, R. J. Gugliemetti), Plenum, New York, **1999**.
[2] A. Ueno, K. Takahashi, T. Osa, *J. Chem. Soc. Chem. Commun.* **1981**, 94 – 96.
[3] R. Cacciapaglia, S. Di Stefano, L. Mandolini, *J. Am. Chem. Soc.* **2003**, *125*, 2224 – 2227.
[4] F. Würthner, J. Rebek, Jr., *Angew. Chem.* **1995**, *107*, 1802 – 1805; *Angew. Chem. Int. Ed. Engl.* **1995**, *34*, 446 – 448.
[5] F. Würthner, J. Rebek,Jr., *J. Chem. Soc. Perkin Trans. 2* **1995**, 1727 – 1734.
[6] a) M. Irie in *Molecular Switches* (Ed.: B. L. Feringa), Wiley-VCH, Weinheim, **2001**, p. 37; b) M. Irie, *Chem. Rev.* **2000**, *100*, 1685 – 1716.
[7] E. Murguly, T. B. Norsten, N. R. Branda, *Angew. Chem.* **2001**, *113*, 1802 – 1805; *Angew. Chem. Int. Ed.* **2001**, *40*, 1752 – 1755.
[8] H. A. McManus, P. J. Guiry, *Chem. Rev.* **2004**, *104*, 4151 – 4202.
[9] It was originally anticipated that the ring-open isomer **2o** would induce a greater amount of stereoselectivity in the cyclopropanation reactions than the ring-closed isomer **2c**. However, when using **2o** resulted in no observable stereoselectivity, **2c** was never tested as a ligand.
[10] A. V. Bedekar, E. B. Koroleva, P. G. Anderson, *J. Org. Chem.* **1997**, *62*, 2518 – 2526.
[11] A. J. Carpenter, D. J. Chadwick, *J. Chem. Soc. Perkin Trans. 1* **1985**, 173 – 181.
[12] Standard lamps used for visualizing thin-layer chromatography (TLC) plates (Spectroline E-series, 470 $\mu W\,cm^{-2}$) were used to carry out the ring-closing reaction of **3o** to **3c** with and without copper(I). The ring-opening reactions were carried out using the light of a 150-W tungsten source that was passed through a 434 nm cutoff filter to eliminate higher energy light.
[13] In a typical reaction, the oxazoline ligand (7.6 mg; 1.1 equiv) was dissolved in CH_2Cl_2 (1 mL) and $CuOTf{\cdot}0.5\,C_6H_6$ (5.5 mg; 1 equiv, 10 mol%; $OTf = [CF_3SO_3]^-$) was added. The solution was cooled to 0 °C in an ice bath and stirred for 30 min at which time an excess of styrene (100 μL) was added. After stirring for an additional 30 min, ethyl diazoacetate (10 μL) in CH_2Cl_2 (1 mL) was added using a syringe pump over 4–6 h while maintaining the solution at 0 °C. The solution was stirred overnight at room temperature, then filtered through a small plug of silica (CH_2Cl_2). The excess styrene was removed by gradient flash chromatography (silica, hexanes to 1:1 hexanes/ethyl acetate). The purity and identity of both diastereoisomers was verified with ^1H NMR spectroscopy. Both the *cis* and *trans* enantiomeric mixtures were analyzed by chiral HPLC using a CHIRACEL-OD chiral column (0.5 $mL\,min^{-1}$, 95:5 hexanes:2-propanol). Detection was adjusted at 220 nm, which is a maximum in the absorption spectrum of the *trans* isomers. A solution of *trans* enantiomers gave two peaks separated in their retention time by 3.7 min. The *cis* isomers were only separated by 0.4 min and were not baseline separated. It was however possible to distinguish both maxima and by deconvoluting the data using the software provided with the HPLC, the separate peak areas were obtained. The amount of catalyst can be lowered to 1 mol% with respect to the ethyl diazoacetate to produce 120 mg (63%) of the cyclopropanated products as a mixture of stereoisomers after workup and isolation by centrifugal chromatography (2% ethyl acetate/hexanes).

 © 2005 Wiley-VCH Verlag GmbH & Co. KGaA, Weinheim

Ruthenium-Catalyzed Reactions

Concomitant Monoreduction and Hydrogenation of Unsaturated Cyclic Imides to Lactams Catalyzed by Ruthenium Compounds**

*Rimane Aoun, Jean-Luc Renaud, Pierre H. Dixneuf, and Christian Bruneau**

Catalytic transformations of multifunctional molecules now offer access to a variety of useful intermediates. However, there are still some important unsolved problems. This is the case of the transformation of cyclic imides into lactams through selective monoreduction of one carbonyl group which is still a challenge in organic synthesis. Strong reducing reagents such as $LiAlH_4$ have been used to perform complete reduction with formation of cyclic amines,[1] and only in the special case of highly substituted cyclic acylureas (hydantoins) was the monoreduction into ureas obtained.[2] The monoreduction of phthalimides into isoindolinone derivatives has been performed in moderate to good yields under acidic conditions in the presence of stoichiometric amounts of reducing metals such as Sn[3] or Zn.[4] Their catalytic reduction in the presence of hydrogen has been carried out with Raney nickel as catalyst, but under drastic conditions (180 °C, 190 bar H_2).[5] In water, under hydrogen pressure at 100 °C, *N*-methylsuccinimide was transformed into 2-pyrrolidinone in the presence of water-soluble ruthenium precatalysts such as $RuCl_3 \cdot 3H_2O$, $[RuCl_2(dmso)_4]$, or $[Ru(dmp)(H_2O)_2](PF_6)_2$ (dmp = 2,9-dimethylphenanthroline), but in modest yields (< 28 %).[6]

Herein we report that the ruthenium precatalysts $[RuCl_2(p\text{-cymene})]_2$ and $[Ru_4H_6(p\text{-cymene})_4]Cl_2$ are efficient catalyst precursors for the monoreduction of cyclic imides in water under hydrogen pressure. Moreover, they make possible the concomitant monoreduction and hydrogenation of unsaturated cyclic imides into saturated lactams (Scheme 1).

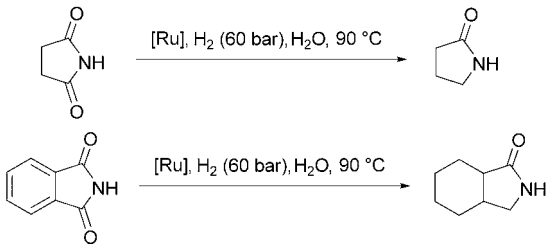

Scheme 1. [Ru] = $[Ru_4H_6(p\text{-cymene})_4]Cl_2$ and $[RuCl_2(p\text{-cymene})]_2$.

[*] Dr. R. Aoun, Dr. J.-L. Renaud, Prof. P. H. Dixneuf, Dr. C. Bruneau
Institut de Chimie de Rennes
UMR 6509: CNRS-Université de Rennes
Organométalliques et Catalyse
Campus de Beaulieu-35042 Rennes Cedex (France)
Fax: (+33) 2-2323-6939
E-mail: christian.bruneau@univ-rennes1.fr

[**] The authors thank ORIL Industrie for financial support.

 DOI: 10.1002/anie.200462996 © 2005 Wiley-VCH Verlag GmbH & Co. KGaA, Weinheim

This represents a new example of a multifunctional catalytic system able to perform two chemical transformations[7] (reduction of carbonyl groups and hydrogenation of double and aromatic bonds) with the same reagent (H_2) and with atom economy, to release only water, which is the solvent of the reaction.

The reaction of succinimide **1** (5 mmol) in distilled water (10 mL) in the presence of $[Ru_4H_6(p\text{-cymene})_4]Cl_2$[8] (1 mol%) under hydrogen (60 bar) for 13 h led to its complete and selective conversion into 2-pyrrolidinone **2**, which was isolated in 87% yield (Table 1, entry 1). No further reduction into the amine was detected. Under similar conditions, the unsaturated maleimide **3** quantitatively provided the same lactam **2** in 86% isolated yield, whereas the unsaturated tetrahydrophtalimide **4** underwent complete conversion into the bicyclic lactam **5** after 22 h of reaction (Table 1, entry 3). These reactions showed that the catalytic system operating in water is able to perform the selective monoreduction of one carbonyl group of a cyclic imide and the hydrogenation of activated and nonactivated olefinic bonds. The concomitant reduction and hydrogenation of aromatic substrates was also attempted and phthalimide **6** was converted into the aliphatic lactam **5**, which was isolated in 78% yield, after 24 h under similar catalytic conditions (Table 1, entry 4). The saturated imide **7** was also detected as a minor reaction product. Furthermore, ^{1}H NMR analyses and chiral gas-chromatography studies showed that the hydrogenation was diastereoselective and that the formed product **5** resulted from a pure *cis* addition of hydrogen to a formal junction C=C bond.

This ruthenium-based catalytic system tolerated the presence of functional groups such as primary amines as it performed the transformation of the 5-aminouracil **8** into the novel 5-amino tetrahydropyrimidin-2-one **9** through selective reduction of the acyl carbonyl group of the starting acylurea structure. The example reported in Table 1, entry 6 revealed that the reduction of the carbonyl group was more difficult to perform than the hydrogenation of the carbon–carbon double bond of uracil **10**, as after complete conversion the tetrahydropyrimidin-2-one **11** was isolated in only 70% yield together with only 30% of the saturated hydantoin **12**.

$[Ru_4H_6(p\text{-cymene})_4]Cl_2$ was prepared by treatment of $[RuCl_2(p\text{-cymene})]_2$ in water at 60 °C under 60 bar of hydrogen pressure,[8] thus under conditions very close to those of the catalytic conditions described above. The hypothesis of a common or closely related intermediates that are active in catalysis in both the previous catalytic system and during the stoichiometric transformation of $[RuCl_2(p\text{-cymene})]_2$ was evaluated. The hydrogenation of the cyclic imides **3**, **4**, **6**, **8**, and **10** in water in the presence of $[RuCl_2(p\text{-cymene})]_2$ (1–2 mol%) as catalyst precursor at 90 °C under hydrogen (60 bar; Table 1) took place even more efficiently than with $[Ru_4H_6(p\text{-cymene})_4]Cl_2$ as precatalyst to give **2**, **5**, **7**, **9**, and **11**. Indeed, with half the amount of potentially active ruthenium sites, complete conversions and transformations into lactams were reached within shorter reaction times. For instance, the complete conversion of the imide **10** into the sole tetrahydropyrimidin-2-one **11** was obtained within 24 h which indicates a more efficient carbonyl-reduction reaction. Note that it had already been shown that the binuclear system was more active than the corresponding hydride cluster for the simple hydrogenation of aromatic hydrocarbons.[9]

With both catalysts, the hydrogenation of N-substituted phthalimides and phthalic anhydride only led to the hydrogenation of the aromatic ring. This shows that the presence of the NH bond of the cyclic imides plays a crucial role in the reduction of one carbonyl group.

A screening of the temperature and H_2 pressure parameters in the presence of $[RuCl_2(p\text{-cymene})]_2$ as catalyst precursor indicated that the hydrogenation of the aromatic ring of phthalimide **6** took place even at low temperature (50 °C) and low pressure (10 bar), whereas the reduction of

Table 1: Monoreduction/hydrogenation of cyclic imides in the presence of $[Ru_4H_6(p\text{-cymene})_4]Cl_2$ and $[RuCl_2(p\text{-cymene})]_2$ as catalyst precursors.[a]

Entry	Substrate	Product	$[Ru_4H_6(p\text{-cymene})_4]Cl_2$		$[RuCl_2(p\text{-cymene})]_2$	
			t [h]	Isolated Yield[b] [%]	t [h]	Conversion [%]
1	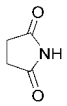 **1**	**2**	13	87	–	–
2	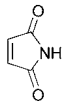 **3**	**2**	13	86	3	100
3	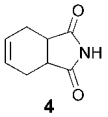 **4**	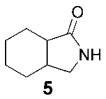 **5**	22	97	15	100
4	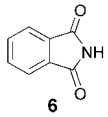 **6**	**5** + 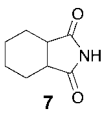 **7**	24	78 (**5**)	15[c]	76 (**5**) 24 (**7**)
5	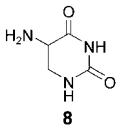 **8**	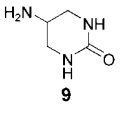 **9**	24	66	13	100
6	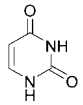 **10**	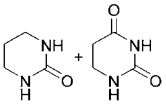 **11** **12**	23	70 (**11**) 30 (**12**)	24	100 (**11**)

[a] General conditions: imide (1 mmol), $[Ru_4H_6(p\text{-cymene})]Cl_2$ (1 mol%), $[RuCl_2(p\text{-cymene})]_2$ (1 mol%), water (5–10 mL), hydrogen (60 bar), 90 °C. [b] Complete conversion. [c] Catalyst (2 mol%).

 © 2005 Wiley-VCH Verlag GmbH & Co. KGaA, Weinheim

the carbonyl group required high temperatures (Table 2). In hydrogenation with molecular metal catalysts, the question of the colloidal or nanoparticle nature relative to the molecular nature of the active species is raised.[10,11] Mercury is known to

Table 2: Reaction of phthalimide **6** in the presence of $[RuCl_2(p\text{-cymene})]_2$ (2 mol%).[a]

$P(H_2)$ [bar]	T [°C]	t [h]	**7/5**
60	90	15	24:76
30	90	23	20:80
10	90	21	25:75
60	50	23	78:22
60	90	15	17:83[b]

[a] **6** (1 mmol), H_2O (5 mL), complete conversion of **6.** [b] Reaction performed in the presence of mercury.

poison heterogeneous catalysts by formation of an amalgam with metals.[11] We have found that the transformation of **6** with a catalytic amount of $[RuCl_2(p\text{-cymene})]_2$ in the presence of mercury under our most severe conditions (90 °C, 60 bar) during 15 h led to quantitative conversion of the phthalimide **6** to form **7** and **5** in the ratio 17:83, which is very close to that observed in the absence of mercury (Table 2). This result tends to corroborate the involvement of molecular catalytic species rather than colloids or nanoparticles in this type of hydrogenation process under the temperature and hydrogen pressure conditions used.

We have revealed a new catalytic activity of easy to prepare or commercially available ruthenium complexes and solved the problem of selective monoreduction of cyclic imides into lactams. Moreover, these complexes generate catalytic systems that are able to promote two catalytic reactions in one pot: the hydrogenation of carbon–carbon double bonds, including aromatic structures, and the monoreduction of cyclic imides. These catalytic systems might be very helpful for selective reduction of imides and desymmetrization transformations.

Received: December 20, 2004
Published online: February 21, 2005

Keywords: hydrogenation · lactams · reduction · ruthenium

[1] a) K. C. Schreiber, V. P. Fernandez, *J. Org. Chem.* **1961**, *26*, 1744; b) H. Okamura, H. Shimizu, Y. Nakamura, T. Iwagawa, M. Nakatani, *Tetrahedron Lett.* **2000**, *41*, 4147.
[2] F. Marshall, *J. Am. Chem. Soc.* **1956**, *78*, 3696.
[3] a) M. H. Norman, D. J. Minick, G. C. Rigdon, *J. Med. Chem.* **1996**, *39*, 149; b) S. Cacchi, G. Fabrizi, L. Moro, *Synlett* **1998**, 741.
[4] a) S. Feng, C. A. Panetta, D. E. Graves, *J. Org. Chem.* **2001**, *66*, 612; b) P. S. Anderson, M. E. Christy, C. D. Colton, W. Halczenco, G. S. Ponticelli, K. L. Shepard, *J. Org. Chem.* **1979**, *44*, 1519.
[5] H. Hennige, R. P. Kreher, M. Konrad, F. Jelitto, *Chem. Ber.* **1988**, *121*, 234.
[6] D. E. Patton, R. S. Drago, *J. Chem. Soc. Perkin Trans. 1* **1993**, 1611.
[7] a) A. Ajamian, J. L. Gleason, *Angew. Chem.* **2004**, *116*, 3842; *Angew. Chem. Int. Ed.* **2004**, *43*, 3754; b) D. E. Fogg, E. N. dos Santos, *Coord. Chem. Rev.* **2004**, *248*, 2365.
[8] L. Plasseraud, G. Süss-Fink, *J. Organomet. Chem.* **1997**, *539*, 163.
[9] E. Garcia Fidalgo, L. Plasseraud, G. Süss-Fink, *J. Mol. Catal. A* **1998**, *132*, 5.
[10] a) G. Süss-Fink, M. Faure, T. R. Ward, *Angew. Chem.* **2002**, *114*, 105; *Angew. Chem. Int. Ed.* **2002**, *41*, 99; b) G. Süss-Fink, B. Therrien, L. Vieille-Petit, M. Tschan, V. B. Romakh, T. R. Ward, M. Dadras, G. Laurenczy, *J. Organomet. Chem.* **2004**, *689*, 1362.
[11] J. A. Widegren, M. A. Bennett, R. G. Finke, *J. Am. Chem. Soc.* **2003**, *125*, 10301.

 © 2005 Wiley-VCH Verlag GmbH & Co. KGaA, Weinheim

Polyoxotungstates

Vicinal Tungsten–Tungsten Coupling Constants in Polyoxotungstates: DFT Calculations Challenge an Empirical Rule

Alessandro Bagno and Marcella Bonchio*

Nuclear magnetic resonance spectroscopy of the ^{183}W nucleus ($I = 1/2$, 14 % natural abundance) is an essential tool for the characterization of tungsten polyoxometalates (POMs). It provides direct information on the electronic environment of each nonequivalent tungsten atom of these compounds, which display a formidable structural diversity and a constantly increasing range of applications.[1,2]

Spin–spin coupling is observed between vicinal tungsten nuclei separated by one oxygen atom ($^2J_{WW}$), and gives rise to satellites having 7 % intensity of the main peak.[3] The analysis of such coupling constants is a traditional mainstay of POM characterization, but has been so far based on a mere empirical approach. The rationale for this is rooted in the two basic structural arrangements that WO_6 octahedra display in the POM cage, that is, edge- or corner-sharing junctions. The two cases differ in W-O-W angle, which lies in typical ranges of 120–130° (edge-sharing) and 140–150° (corner-sharing).[1] There is much empirical evidence that the corresponding values of $^2J_{WW}$ take on values of 5–12 and 15–30 Hz, respectively, and this criterion is extensively applied in the assignment of POM spectra, based on the assumption that the W-O-W angle is the sole factor involved.[4] However, there has been no clear indication of

[*] Prof. A. Bagno
Department of Chemistry, University of Padova
via Marzolo 1, 35131 Padova (Italy)
Fax: (+39) 0498275239
E-mail: alessandro.bagno@unipd.it
Dr. M. Bonchio
CNR Institute for Membrane Technology
Padova Section, via Marzolo 1, 35131 Padova (Italy)

Supporting information for this article is available on the WWW under http://www.angewandte.org or from the author.

 DOI: 10.1002/anie.200462292 © 2005 Wiley-VCH Verlag GmbH & Co. KGaA, Weinheim

whether other structural or electronic factors contribute to the observed $^2J_{WW}$ values, so the scope of this empirical criterion remains somewhat uncertain.

Instances are indeed known where this paradigm has led to ambiguous conclusions: a cogent and timely example is provided by POMs derived from the γ-$[XW_{10}O_{36}]^{n-}$ (X = P, Si) structure, which have promising applications in catalysis and materials science.[5] In aqueous solution, the tungstosilicate anion γ-$[SiW_{10}O_{36}]^{8-}$ exhibits a three-line (2:2:1) ^{183}W spectrum with three $^2J_{WW}$ couplings (Figure 1).[6] The NMR

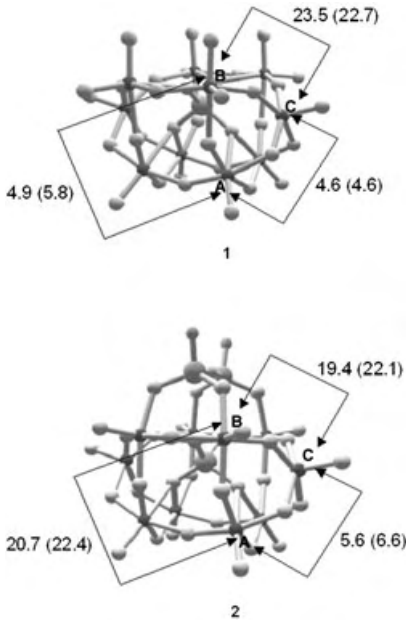

Figure 1. Structures of γ-$[SiW_{10}O_{36}]^{8-}$ (**1**) and γ-$[(HSi)_2OSiW_{10}O_{36}]^{4-}$ (**2**) with experimental and calculated (in parentheses) $^2J_{WW}$ couplings.

parameters were obtained for the Li salt of the nonsymmetric monoprotonated form, but fast exchange on the NMR timescale renders the spectrum still consistent with C_{2v} symmetry (see below).

However, the coupling constants of 23.5 (BC), 4.6 (AC), and 4.9 Hz (AB) contrast with the empirical rule expecting two large corner couplings (BC and AB) and one small edge coupling (AC).[6] Conversely, the hybrid derivatives γ-$[(RSi)_2OSiW_{10}O_{36}]^{4-}$ show the expected corner AB coupling (20.7 Hz for R = H).[7] This evidence speaks against the generally accepted empirical correlation linking the magnitude of $^2J_{WW}$ couplings simply to the W-O-W angle of the junctions, which are preserved along the series of these isostructural complexes. The small $^2J_{WW}$ in the divacant precursor, despite its corner-sharing arrangement, was tentatively ascribed to a concurrent decrease of the W_A-O-W_B angle and an elongation of the W–O bond involving lacunary tungsten atom W_B.[7]

Here we provide a consistent set of computed coupling constants both for model fragments and complete POM systems, and show that 1) the W-O-W angle is the sole important factor *only* when the W–O distance has typical values or remains constant within the series examined, and 2) the electronic structure of the surroundings farther than one bond away does not affect these couplings significantly. Finally, we confirm the proposed structure assignment of the two decatungstates, provide a rationale for the observed anomaly, and address structure equilibria in aqueous solution.

Further pursuing our aim of devise a reliable computational approach to predict ^{183}W NMR parameters,[8] we made use of the ADF DFT code[9] for relativistic calculations of NMR coupling constants[10] by means of the ZORA approximation.[11] Owing to the very high computational cost of such calculations on systems as large as those dealt with here, preliminary calculations were run on a model system consisting of two oxotungstate fragments $[O_4W\text{-}O\text{-}WO_4]^{6-}$ (Figure 2), which allowed the coupling surface to be scanned.[12,13]

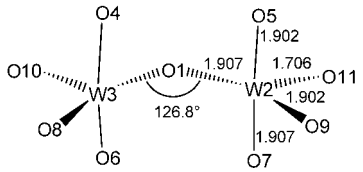

Figure 2. Internal coordinates of the $[O_4W\text{-}O\text{-}WO_4]^{6-}$ system. The W-O-W angle was set to 126.8° for edge-sharing (as in the figure) or 152.4° for corner-sharing, respectively. For the coupling surface scan, the O5-W2-O1-W3 dihedral angle was set to 85.3°. See Supporting Information for other geometrical parameters.

For initial testing, the W2-O1-W3 angle was set to 126.8° (edge) or 152.4° (corner), and the W2–O1 distance to 1.907 Å. Both fragments were optimized at the BP-ZORA scalar/TZ2P level, and coupling constants were calculated at the same level. We thus obtained values of 26.5 and 8.4 Hz for corner and edge couplings, respectively.[14] The corresponding values at the ZORA spin–orbit level (25.7 and 8.2 Hz, respectively) are very similar, as is commonly found.[11]

All further calculations were carried out at the BP-ZORA scalar/TZ2P level.[15] We then scanned the $[O_4W\text{-}O\text{-}WO_4]^{6-}$ coupling surface as a function of the W–O distance (r_{WO} = 1.80–2.20 Å) and the W-O-W angle (α = 120–160°), whereas the O5-W2-O1-W3 dihedral angle was kept constant at 85.3°.[16]

Figure 3 shows that a smooth decrease in $^2J_{WW}$ is predicted with decreasing α and increasing r_{WO}. The calculated angular dependence conforms with the accepted picture. Moreover, a marked dependence on distance is also revealed, especially at large α values.[17] Thus, for α = 150° the dependence on distance is sufficiently pronounced that such couplings encompass a fairly wide range (15–22 Hz) just by varying r_{WO} within reasonable bounds.

Hence, this model allows the magnitude of the sought coupling constants as a function of r_{WO} and α to be predicted. However, the coupling surface was determined for, among others, fixed O5-W2-O1-W3 dihedral angle and O1-W2-O5 angle; these are expected to differ among various tungsten sites, and the two W–O distances are normally not equal. Thus, actual couplings may depend on further geometrical variables. Moreover, electronic effects of other atoms are not

 © 2005 Wiley-VCH Verlag GmbH & Co. KGaA, Weinheim

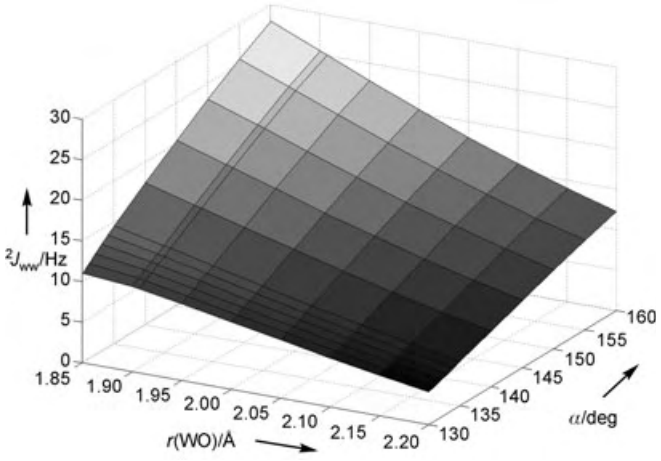

Figure 3. $^2J_{WW}$ coupling surface of the $[O_4W\text{-}O\text{-}WO_4]^{6-}$ system. Numerical data are collected as Supporting Information.

taken into account. However, a key point was provided by the recognition that reducing the basis set of the terminal (O4–O11) or the bridging (O1) oxygen atoms to frozen-core basis sets of DZ or TZ2P quality[18] only slightly affected the calculated coupling.[19] Hence, the typical range of couplings is preserved even when the coupled nuclei are computationally "severed" from the rest of the POM, which implies that its electronic structure is expected to have little if any effect. It is then possible to run a coupling calculation on a complete POM structure, provided that all atoms except the W-O-W triad being investigated are modeled at a relatively low level. In this way, one can include all structural factors in the calculation at a reasonable cost.

We have applied this concept to γ-$[SiW_{10}O_{36}]^{8-}$ and γ-$[(HSi)_2OSiW_{10}O_{36}]^{4-}$ (Figure 1). The speciation of the parent lacunary anion and the counterion effect (H^+ or Li^+) on the NMR parameters was also addressed by considering two limiting forms undergoing fast exchange[6]: monoprotonated γ-$[SiW_{10}O_{36}H]^{7-}$ and the inclusion complex γ-$[Li(H_2O)SiW_{10}O_{36}]^{7-}$ (Scheme 1). The solution structure of

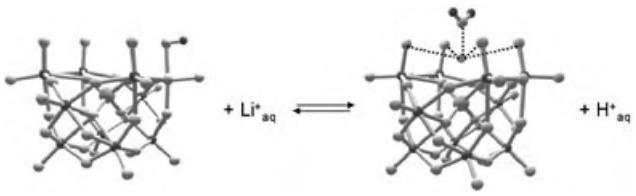

Scheme 1. Proposed speciation[6] of γ-$[SiW_{10}O_{36}]^{8-}$ in aqueous solution, with equilibrium between the monoprotonated form γ-$[SiW_{10}O_{36}H]^{7-}$ (left) and the Li complex γ-$[Li(H_2O)SiW_{10}O_{36}]^{7-}$ (right).

these polyoxoanions is a matter of debate owing to the known influence of the counterion on their spectroscopic properties,[8] stability, and catalytic activity.[5]

After geometry optimization,[8] the relevant W and O atoms were treated at the usual TZ2P level, and all other atoms with small basis sets.[20] The results[21] for γ-$[SiW_{10}O_{36}]^{8-}$ and γ-$[(HSi)_2OSiW_{10}O_{36}]^{4-}$ match very well the experimental values (Figure 1): in the divacant POM, J_{AB} has a value typical of an edge coupling, even though the W-O-W angle (144°) is typical of a corner junction. By comparison with the coupling surface, this is understood as arising from a longer W–O distance in the divacant POM (2.06 Å) than in the hybrid derivative (1.94 Å).

Neither protonation nor inclusion of Li^+ causes a change in W-O-W angles. However, protonation brings about a marked shortening of the average W–O bond (2.06 to 1.96 Å); the other W–O distances are unchanged.[22] Consistent with the shorter distance, J_{AB} is larger (16.7 Hz). Under conditions of fast exchange among all four lacunary oxygen atoms (for which the previous value can still be assumed, since the local geometries are not affected), an average value of about 8.5 Hz can be estimated. Inclusion of $Li(H_2O)^+$ in the lacuna entails opposite effects: the average W–O distance is enlarged to 2.15 Å, and correspondingly J_{AB} decreases to 4.6 Hz. Assuming equal populations at equilibrium, one can estimate an average of 6 Hz, and the net result is very similar to that of the isolated divacant species.

In conclusion, empirical arguments based on the relationship between the magnitude of $^2J_{WW}$ and corner- versus edge-sharing octahedra must be looked upon carefully, since situations may arise in which the W–O distance is an important or even controlling factor. Even though these couplings appear to be a local property of each WOW triad, they may probe longer range interactions (protonation, counterions, etc.) insofar as these reflect changes in the main structural variables (r_{WO} and α).

Received: October 13, 2004
Revised: December 12, 2004
Published online: February 21, 2005

Keywords: density functional calculations · NMR spectroscopy · polyoxometalates · spin–spin coupling · tungsten

[1] *Polyoxometalates* (Ed.: C. L. Hill), thematic issue of *Chem. Rev.* **1998**, *98*, 1–390.
[2] *Polyoxometalate Chemistry for Nano-Composite Design* (Eds.: T.Yamase, M. Pope), Kluwer, Plenum, New York, **2002**, pp. 1–232.
[3] Y.-G. Chen, J. Gong, L.-Y. Qu, *Coord. Chem. Rev.* **2004**, *248*, 245–260.
[4] C. Brevard, R. Schimpf, G. Tourne, C. M. Tourne, *J. Am. Chem. Soc.* **1983**, *105*, 7059–7063.
[5] a) M. Bonchio, M. Carraro, G. Scorrano, A. Bagno, *Adv. Synth. Catal.* **2004**, *346*, 648–654; b) K. Kamata, K. Yonehara, Y. Sumida, K. Yamaguchi, S. Hikichi, N. Mizuno, *Science* **2003**, *300*, 964–966; c) C. R. Mayer, V. Cabuil, T. Lalot, R. Thouvenot, *Angew. Chem.* **1999**, *111*, 3878–3881; *Angew. Chem. Int. Ed.* **1999**, *38*, 3672–3675.
[6] J. Canny, A. Tézé, R. Thouvenot, G. Hervé, *Inorg. Chem.* **1986**, *25*, 2114–2119.
[7] C. R. Mayer, I. Fournier, R. Thouvenot, *Chem. Eur. J.* **2000**, *6*, 105–110. Coupling constants were reported for a similar derivative exhibiting very similar behavior to the POM discussed here.
[8] A. Bagno, M. Bonchio, A. Sartorel, G. Scorrano, *ChemPhysChem* **2003**, *4*, 517–519.

 © 2005 Wiley-VCH Verlag GmbH & Co. KGaA, Weinheim

[9] G. te Velde, F. M. Bickelhaupt, E. J. Baerends, C. Fonseca-Guerra, S. J. A. van Gisbergen, J. G. Snijders, T. Ziegler, *J. Comput. Chem.* **2001**, *22*, 931–967.
[10] a) J. Autschbach, T. Ziegler, *J. Chem. Phys.* **2000**, *113*, 936–947; b) J. Autschbach, T. Ziegler, *J. Chem. Phys.* **2000**, *113*, 9410–9418.
[11] J. Autschbach, T. Ziegler in *Calculation of NMR and EPR Parameters* (Eds.: M. Kaupp, M. Bühl, V. G. Malkin), Wiley-VCH, Weinheim, **2004**.
[12] We employed the Becke88 exchange plus the Perdew86 correlation functional (BP) with basis sets composed of Slater functions optimized for ZORA calculations.[9] We used double-ζ or triple-ζ basis sets, the latter with a single or double set of polarization functions on all atoms (DZ, TZP, and TZ2P, respectively), with frozen core orbitals where appropriate. Relativistic core potentials were generated with the Dirac utility.
[13] This arrangement was obtained by cutting off the relevant fragments from the calculated structure of α-$[PW_{11}O_{39}]^{7-}$.[8]
[14] See the Supporting Information for details. DSO, PSO, FC, and SD denote the diamagnetic and paramagnetic spin–orbit, Fermi contact, and spin–dipole contributions. All couplings are dominated by the FC term, which accounts for 90–95% of the total.
[15] Only the DSO, PSO, and FC terms were calculated; the DSO term never exceeded 2 mHz.
[16] Although most POMs bear remarkably large negative charges (up to −12), solvent effects on coupling constants are hardly known, consistent with their low charge density (q/m ratio; see X. López, C. Bo, J. M. Poblet, *J. Am. Chem. Soc.* **2002**, *124*, 12574–12582 for a discussion of its implications). Thus, isolated-ion modeling is probably suitable, despite the higher q/m of the model system. Work is in progress to address this issue.
[17] At very small r_{WO} and α values large negative values are predicted (see Supporting Information). However, this region is probably incompatible with the cage structures of POMs.
[18] Both basis sets had the 1s shell frozen, that is, not participating in the SCF procedure. Owing to their insufficient flexibility in the critical region near the nucleus, these basis sets are not recommended for these calculations.[9]
[19] At $r_{WO} = 1.907$ Å, $\alpha = 160°$ the calculated coupling decreased from 25 Hz to 23 Hz.
[20] All basis sets of DZ quality. W: 4f shell frozen; O: 1s shell frozen; Si: 2p shell frozen. No core was frozen for H and Li.
[21] The relative contributions of FC and PSO terms (Supporting Information) follow the same trend as the model system.
[22] See the Supporting Information for details of bond lengths.

 © 2005 Wiley-VCH Verlag GmbH & Co. KGaA, Weinheim

Palladium Catalysts

Palladium–(N-Heterocyclic Carbene) Hydrogenation Catalysts**

*Jeroen W. Sprengers, Jeroen Wassenaar, Nicolas D. Clement, Kingsley J. Cavell, and Cornelis J. Elsevier**

N-Heterocyclic carbenes (NHCs) have become valuable ligands in organometallic chemistry and homogeneous catalysis. In particular, palladium–NHC systems have been successfully employed in various reactions such as C–C and C–N coupling reactions, oxidations, polymerization reactions, and telomerizations.[1] However, the important class of hydrogenation reactions has not yet been reported for palladium–NHC catalysts. Transition-metal catalysts with NHC ligands for hydrogenation have been reported for rhodium, iridium, and ruthenium[1,2] which are suitable for hydrogenation of alkenes. It has been observed that catalytic reactions in which hydridopalladium–carbene intermediates are involved can suffer from catalyst deactivation owing to attack of the hydride on the carbene which results in reductive elimination to give the imidazolium salt.[3] Cloke and coworkers reported complete hydrogenation of [Pd(1,3-di(*tert*-butyl)imidazol-2-ylidene)$_2$] upon its exposure to hydrogen to yield metallic palladium and 1,3-bis-*tert*-butylimidazolidine (Scheme 1 a).[4] However, we recently demonstrated for the first time that hydridopalladium–NHC compounds, obtained

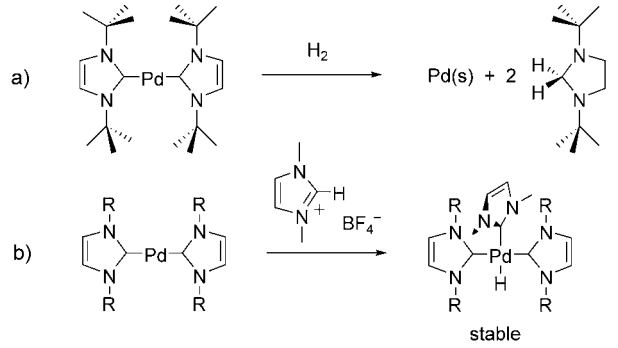

Scheme 1. a) Hydrogenation of [Pd(1,3-di(*tert*-butyl)imidazol-2-ylidene)$_2$];[4] b) oxidative addition of imidazolium salts to [Pd(1,3-dimesitylimidazol-2-ylidene)$_2$].[5] R = 2,4,6-trimethylphenyl.

[*] J. W. Sprengers, J. Wassenaar, Prof. Dr. C. J. Elsevier
Van't Hoff Institute for Molecular Sciences
University of Amsterdam
Nieuwe Achtergracht 166
1018 WV Amsterdam (The Netherlands)
Fax: (+31) 20-525-6456
E-mail: elsevier@science.uva.nl
N. D. Clement, Prof. Dr. K. J. Cavell
Department of Chemistry, Cardiff University
PO Box 912, Cardiff CF11 3TB Wales (UK)

[**] This research was partially funded by the National Research School Combination Catalysis (project no. 2000-14).

 © 2005 Wiley-VCH Verlag GmbH & Co. KGaA, Weinheim DOI: 10.1002/anie.200462930

by oxidative addition of imidazolium salts to [Pd(1,3-dimesitylimidazol-2-ylidene)$_2$] (Scheme 1b),[5] are stable, isolable entities. In that case, the large *N*-mesityl substituents prevent orbital overlap between the hydride and the carbon atom of the carbene and hence preclude the reductive elimination.

Here we report that palladium(0)–NHC catalysts that contain bulky *N*-aryl substituents are very stable under hydrogenation conditions. They catalyze the hydrogenation of 1-phenyl-1-propyne with outstanding efficiency and exquisite selectivity. In this respect, only very few homogeneous palladium catalysts are known to catalyze the desirable, selective semihydrogenation of alkynes to *Z* alkenes (Scheme 2).[6] Problems frequently observed for this reaction include inadvertent isomerization of the *Z* alkene to the *E* isomer, shift of the double bond, overreduction to the alkane, low stability of the catalyst, and low reproducibility. So far, only [Pd(Ar-bian)(η^2-alkene)] (bian = bis(arylimino)acenaphthene) complexes were reported to hydrogenate a variety of alkynes to the *Z* alkenes with reasonable to excellent selectivity. Unfortunately, however, the important class of arylalkynes is hydrogenated only with lower selectivity (87–92%; Scheme 2) with such a catalyst.[6d]

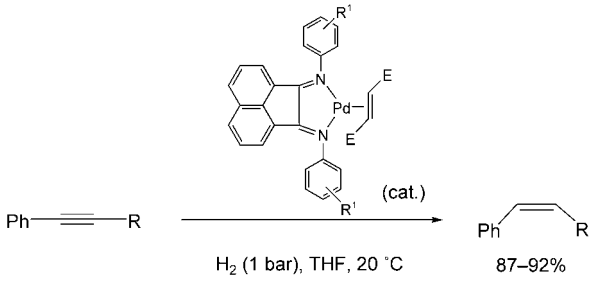

Scheme 2. Hydrogenation of alkynes catalyzed by [Pd^0(Ar-bian)(alkene)]. R = CH_3, Ph.

Our conjecture was that palladium(0)–monocarbene compounds that contain one strongly coordinated and two labile ligands should be good catalysts for this semihydrogenation reaction, as related platinum compounds were found to be active and selective hydrosilylation catalysts.[7] Furthermore, we have shown that platinum–NHC species formed in situ were more-active catalysts in the hydrosilylation reaction than well-defined [Pt(NHC)(η^2-alkene)$_2$] complexes.[7b] Hence, we aimed at the development of effective palladium(0)–NHC catalysts generated in situ for the desired hydrogenation reactions. As [Pd(η^2-ma)(η^4-nbd)] (ma = maleic anhydride, nbd = norbornadiene) was found to be a much more efficient palladium precursor than [Pd(dba)$_2$] (dba = dibenzylideneacetone) in the synthesis of a series of [Pd(L)$_2$(η^2-ma)] complexes,[8] we applied this [Pd(ma)(nbd)] complex as the source of palladium (Scheme 3).

Consequently, imidazolinium chlorides **1a** and **1b** and imidazolium chlorides **2a**–**2d** were stirred with 4 equivalents of *t*BuOK and 1 equivalent of [Pd(ma)(nbd)] in THF for 1 hour. Imidazolium chloride **2d** and the corresponding NHC generated in situ are new compounds. We then synthesized three palladium(0)–NHC complexes **3**, **4**, and **5**, which were also applied as catalysts. The [Pd(NHC)(η^2-alkene)$_2$] complexes **3** and **5** have been reported as precatalysts for other reactions.[9] The new complex **4** was isolated by addition of a second equivalent of maleic anhydride after the generation in situ of the palladium catalyst from **2a** and [Pd(ma)(nbd)]. This proves that palladium(0)–NHC species are indeed formed by the in situ approach according to Scheme 3.

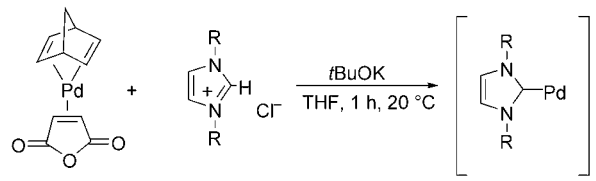

Scheme 3. Generation in situ of palladium(0)–NHC catalysts using [Pd(ma)(nbd)].

The hydrogenation was initiated by addition of the alkyne to the solution of the catalyst and then bubbling H_2 (1 bar) through the solution at 20 °C. The results of the hydrogenation of 1-phenyl-1-propyne are compiled in Table 1. Exhaustive hydrogenation to the alkane is observed when catalysts are not stable, as is nicely demonstrated for [Pd(ma)(nbd)] (Table 1, entry 1). Immediate formation of palladium black was observed when this complex was exposed to hydrogen, and 41.8% of *n*-propylbenzene was obtained after total consumption of 1-phenyl-1-propyne. Significantly better results were obtained when NHC ligands were used. When 1,3-dimesityl-4,5-dihydroimidazolium chlo-

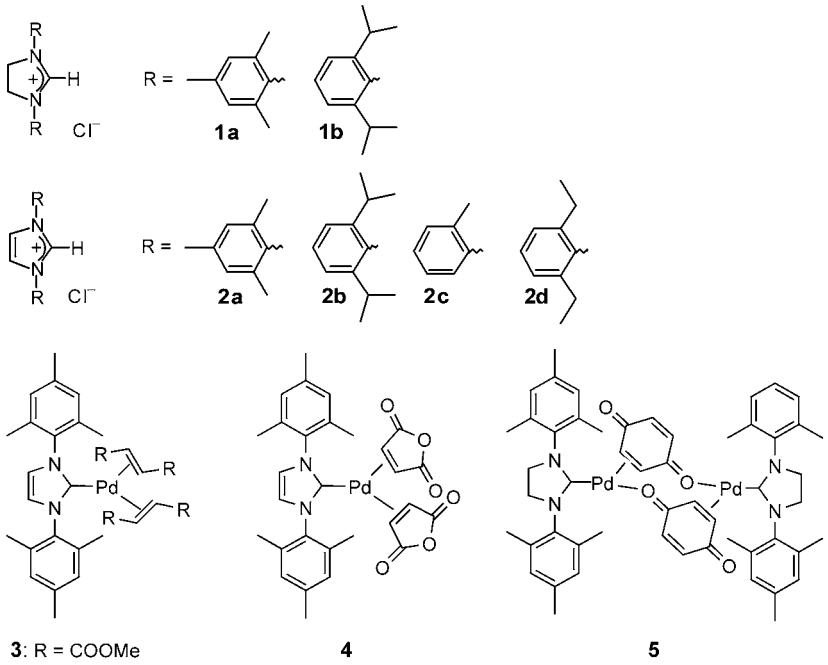

 © 2005 Wiley-VCH Verlag GmbH & Co. KGaA, Weinheim

Table 1: Hydrogenation of 1-phenyl-1-propyne to 1-phenyl-1-propene and *n*-propylbenzene.[a]

Entry	Catalyst	Yield [%][b]	*t* [h]	TOF [h^{-1}][c]	Selectivity [%][d] *Z* alkene:*E* alkene:alkane
1	[Pd(ma)(nbd)]	>99	2	100	57.0:1.2:41.8
2	[Pd(ma)(nbd)] + **1a**[e]	>99	6	18.6	90.1:2.2:7.7
3	[$Pd(dba)_2$] + **1a**[e]	>99	12	18.8	90.9:4.0:5.2
4	[Pd(ma)(nbd)] + **1b**[e]	>99	3.5	29.3	84.9:2.6:12.6
5	[Pd(ma)(nbd)] + **2a**[e]	>99	2.5	45.5	91.6:1.7:6.7
6	[Pd(ma)(nbd)] + **2b**[e]	>99	3.5	52.8	89.4:1.7:8.9
7	[Pd(ma)(nbd)] + **2c**[e]	>99	3.5	29.0	93.6:2.9:3.5
8	[Pd(ma)(nbd)] + **2d**[e]	>99	2.75	49.9	95.0:2.0:3.0
9	**3**	0	–	–	–
10	**4**	>99	2.75	41.5	79.1:4.3:16.6
11	**5**	>99	2.5	46.8	76.0:6.4:17.7

[a] Catalyst (1 mol%), THF, 20°C. [b] Yield determined by GC. [c] Turnover frequency determined at 25% conversion, defined as moles of 1-phenyl-1-propyne converted per mole of catalyst per hour. [d] Selectivity determined at >99% conversion of 1-phenyl-1-propyne. [e] Palladium precursor stirred with the imidazolium salt (1.0 equiv) and *t*BuOK (4 equiv) for 1 h in THF prior to addition of the substrate and initiation of hydrogenation.

ride (**1a**) was added to [Pd(ma)(nbd)] in the presence of *t*BuOK, a stable complex was obtained (entry 2). No formation of palladium black was observed when using this saturated NHC ligand, and the amount of *n*-propylbenzene produced was decreased to 7.7%. A similar selectivity was obtained when [$Pd(dba)_2$] was applied as the precursor (entry 3), however, a very long induction time was observed. Although the turnover frequency (TOF = 18.8 h^{-1}) is almost identical to the case when [Pd(ma)(nbd)] was employed (18.6 h^{-1}), initially five hours are needed to obtain the active catalyst which is much longer than the 30 minutes of induction time for [Pd(ma)(nbd)]. Most likely, the alkene ligands have to dissociate or have to be hydrogenated to create vacant sites for the hydrogenation. [Pd(ma)(nbd)] is a much more labile complex than [$Pd(dba)_2$][8] and is unquestionably a much more suitable palladium(0) precursor for many reactions. Replacement of the mesityl substituents by 2,6-diisopropylphenyl substituents (**1b**) results in a higher activity, but with lower selectivity.

The activity of the catalyst increases remarkably when reverting to unsaturated carbenes **2a** and **2b** (Table 1, entries 5 and 6). Relative to **1a** and **1b**, the high selectivities are maintained, but the TOF values nearly double to 45.5 h^{-1} (**2a**) and 52.8 h^{-1} (**2b**). Interestingly, the reverse has been observed for hydrosilylation reactions catalyzed by platinum(0)–NHC; there the saturated carbenes yield significantly more active catalysts than their unsaturated counterparts.[7b] The two unsaturated carbenes that contain 2-methylphenyl and 2,6-diethylphenyl substituents (**2c** and **2d**, entries 7 and 8) were also tested. For palladium catalysts derived from these NHC ligands, very high selectivities of 93.6% and 95.0%, respectively, towards (*Z*)-1-phenylpropene were observed. These results convey a significant improvement with respect to the selectivity towards *Z*-1-phenyl-1-propene relative to known palladium catalysts such as [Pd(2,2′-bpy)(dmfu)][6d] (bpy = bipyridyl, dmfu = dimethyl fumarate; 73%), [Pd(dppe)(dmfu)][6d] (dppe = 1,2-bis(diphenylphosphino)ethane; 80%), [Pd(2-{*N*-(2-propyl)carbaldimino}-pyridine)(dmfu)][6e] (87%), [Pd(bian)(dmfu)][6d] (92%), and a [$Pd_2(dba)_3${P(*n*Bu)$_3$}] system[6c] (87% *Z*-1-phenyl-1-butene in the hydrogenation of 1-phenyl-1-butyne).

A comparison of the results obtained with the catalysts generated in situ with those for complexes **3**, **4**, and **5** reveals that the latter catalysts show much lower selectivities (Table 1, entries 9–11). Complex **3** does not catalyze the hydrogenation at all: it would appear that the dimethyl fumarate complexes coordinate too strongly to create vacant sites needed for catalysis. It is known that fumarates are stronger alkene ligands in platinum(0) complexes than maleic anhydride and quinones.[10] Indeed, complexes **4** and **5** do enter the catalytic cycle owing to the weaker alkene ligands. However, during hydrogenation, considerable amounts of (*E*)-1-phenylpropene and alkane are observed for these catalysts. A full explanation cannot be given yet. Note that with the [Pd{1,3-(2,6-diethylphenyl)imidazol-2-ylidene}] catalyst generated in situ, complete hydrogenation can also take place, however, this process becomes significant only after all of the alkyne has been consumed.

As the new carbene 1,3-(2,6-diethylphenyl)imidazol-2-ylidene (**2d**) shows the highest selectivity combined with good activity, this carbene ligand was applied in the hydrogenation of diphenyl acetylene and 4-octyne. Surprisingly, 4-octyne could not be hydrogenated under these conditions: less than 1% conversion was observed after 5 h. Diphenylacetylene was hydrogenated to *Z*-stilbene (88%), to its *E* isomer (5%), and 1,2-diphenylethane (7%). For comparison, [Pd(*p*-MeO-bian)(dmfu)][6d] yielded a selectivity of 87% towards the *Z* alkene and 13% towards the alkane. The electron-poor dimethyl butynedioate was selectively hydrogenated using **5** as the catalyst, with >99% conversion to dimethyl maleate (96%), dimethyl fumarate (1%), and dimethyl succinate (3%). In this case, [Pd(*p*-MeO-bian)(dmfu)][6d] induced a selectivity of 99% towards the maleate with >99% conversion.

In conclusion, the [Pd{1,3-(2,6-diethylphenyl)imidazol-2-ylidene}] catalyst generated in situ is completely stable under hydrogenation conditions. The intermediately bulky NHC ligand **2d** effectively stabilizes palladium(0) species and hydridopalladium intermediates. Hence, the [Pd{1,3-(2,6-

 © 2005 Wiley-VCH Verlag GmbH & Co. KGaA, Weinheim

diethylphenyl)imidazol-2-ylidene}] complex generated in situ is a suitable catalyst for the selective semihydrogenation of aryl-substituted alkynes to *Z* alkenes. The procedure for the formation of palladium(0)–NHC catalysts in situ starting from [Pd(ma)(nbd)] is very efficient. This procedure may also prove effective for the generation of catalysts for various other catalytic reactions such as C–C couplings, telomerizations, and additions of elemental hydrogen to unsaturated compounds. Further studies aimed at the elucidation of the reaction mechanism of the palladium–NHC-catalyzed semihydrogenation are in progress.

Experimental Section

All experiments were carried out using standard Schlenk-line techniques under an atmosphere of dry nitrogen. Solvents were dried according to standard procedures and distilled prior to use. **2d**: The compound was prepared in an analogous manner to that described in the literature:[11] (9.54 g, 25.9 mmol, 51%). ^{1}H NMR (300.1 MHz, [D$_6$]DMSO, 20°C): $\delta = 1.11$ (t, ^3J(H,H) = 7.4 Hz, 12H, CH_3), 2.40 (m, 8H, CH_2), 7.44 (d, ^3J(H,H) = 8.0 Hz, 4H, *m*-CH), 7.60 (t, ^3J(H,H) = 8.0 Hz, 2H, *p*-CH), 8.47 (s, 2H, im-H^{4,5}), 10.06 ppm (s, 1H, im-H^2); ^{13}C NMR (75.5 MHz, [D$_6$]DMSO, 20°C): $\delta = 15.8$ (CH_3), 24.5 (CH_2), 126.4 (im-H^{4,5}), 128.2 (*m*-CH), 132.1(*p*-CH), 132.5 (*ipso*-C), 139.5 (im-CH^2), 141.0 ppm (*o*-C).

4: 1,3-Dimesitylimidazolium chloride (172 mg, 0.51 mmol) and *t*BuOK (0.77 mL of 1M solution in THF, 0.77 mmol) were dissolved in THF (8 mL), and the solution was stirred for 30 min at 20°C. [Pd(ma)(nbd)] (150 mg, 0.51 mmol) was added, and the dark purple mixture was stirred at 20°C for 30 min. Maleic anhydride (50.0 mg, 0.51 mmol) was then added. The dark red solution was stirred for 2 h at 20°C and filtered over celite, and the solvent was evaporated. The solid compound was washed with ether (4 × 10 mL) and dried in vacuo to give a red powder (157 mg, 0.26 mmol, 51%). ^{1}H NMR (499.8 MHz, CD_2Cl_2, −50°C): $\delta = 1.72$ (s, 6H, CH_3), 2.28 (s, 6H, CH_3), 2.31 (s, 6H, CH_3), 3.53 (d, ^3J(H,H) = 4.6 Hz, 2H, CH=CH), 4.13 (d, ^3J(H,H) = 4.6 Hz, 2H, CH=CH), 6,89 (s, 2H, (Ar)CH), 7.07 (s, 2H, (Ar)CH), 7.32 ppm (s, 2H, im-H^{4,5}); ^{13}C NMR (125.7 MHz, CD_2Cl_2, −40°C): $\delta = 17.4$ (CH_3), 18.2 (CH_3), 18.4 (CH_3), 64.7 (CH=CH), 68.2 (CH=CH), 124.8 (im-H^{4,5}), 129.3 (*m*-CH), 129.7 (*m*-CH), 134.5 ((Ar)C), 135.0 ((Ar)C), 135.4 ((Ar)C), 139.6 ((Ar)C), 167.6 (C=O), 167.9 (C=O), 193.1 ppm (im-CH^2); IR (KBr): $\tilde{\nu} = 1816$ (C=O), 1761 cm^{-1} (C=O).

Typical procedure for catalytic hydrogenation (in situ experiment): THF (30 mL), imidazolium chloride (0.05 mmol), [Pd(ma)(nbd)] (0.05 mmol), and *t*BuOK (0.20 mmol) were introduced into a two-necked Schlenk tube, equipped with a septum and a stirring bar. After stirring for 1 h, the solution was filtered over Celite to remove traces of palladium black. Then the appropriate alkyne (5.0 mmol) was added through a syringe, and hydrogen gas (1 bar) was bubbled slowly through the solution by using a gas tube. Samples were removed periodically for GC analysis. The crude reaction mixtures were also analyzed by ^{1}H NMR spectroscopy for comparison.

Received: December 14, 2004
Published online: February 23, 2005

Keywords: alkynes · hydrogenation · N-heterocyclic carbenes · palladium

[1] a) W. A. Herrmann, *Angew. Chem.* **2002**, *114*, 1342; *Angew. Chem. Int. Ed.* **2002**, *41*, 1290; b) B. S. Yong, S. P. Nolan, *Chemtracts* **2003**, *16*, 205; c) K. J. Cavell, D. S. McGuinness, *Coord. Chem. Rev.* **2004**, *248*, 671.

[2] For selected examples, see: a) H. M. Lee, D. C. Smith, Jr., Z. He, E. D. Stevens, C. S. Yi, S. P. Nolan, *Organometallics* **2001**, *20*, 794; b) J. R. Miecznikowski, R. H. Crabtree, *Organometallics* **2001**, *20*, 629; c) L. D. Vázquez-Serrano, B. T. Owens, J. M. Buriak, *Chem. Commun.* **2003**, 2518.

[3] D. S. McGuinness, K. J. Cavell, B. W. Skelton, A. H. White, *Organometallics* **1999**, *18*, 1596.

[4] P. L. Arnold, F. G. N. Cloke, T. Geldbach, P. B. Hitchcock, *Organometallics* **1999**, *18*, 3228.

[5] N. D. Clement, K. J. Cavell, C. Jones, C. J. Elsevier, *Angew. Chem.* **2004**, *116*, 1297; *Angew. Chem. Int. Ed.* **2004**, *43*, 1277.

[6] For homogeneous palladium(0)-catalyzed hydrogenations of alkynes, see: a) E. W. Stern, P. K. Maples, *J. Catal.* **1972**, *27*, 120; b) B. M. Trost, R. Braslau, *Tetrahedron Lett.* **1989**, *30*, 4657; c) K. Tani, N. Ono, S. Okamoto, F. Sato, *J. Chem. Soc. Chem. Commun.* **1993**, 386; d) M. W. van Laren, C. J. Elsevier, *Angew. Chem.* **1999**, *111*, 3926; *Angew. Chem. Int. Ed.* **1999**, *38*, 3715; e) M. W. van Laren, M. A. Duin, C. Klerk, M. Naglia, D. Rogolino, P. Pelagatti, A. Bacchi, C. Pelizzi, C. J. Elsevier, *Organometallics*, **2002**, *21*, 1546.

[7] a) E. Markó, S. Stérin, O. Buisine, G. Mignani, P. Branlard, B. Tinant, J.-P. Declercq, *Science* **2002**, *298*, 204; b) J. W. Sprengers, M. J. Mars, M. A. Duin, K. J. Cavell, C. J. Elsevier, *J. Organomet. Chem.* **2003**, *679*, 149; c) I. E. Markó, S. Stérin, O. Buisine, G. Berthon, G. Michaud, B. Tinant, J.-P. Declercq, *Adv. Synth. Catal.* **2004**, *346*, 1429.

[8] A. M. Kluwer, C. J. Elsevier, M. Buhl, M. Lutz, A. L. Spek, *Angew. Chem.* **2003**, *115*, 3625; *Angew. Chem. Int. Ed.* **2003**, *42*, 3501.

[9] a) R. Jackstell, M. Gómez Andreu, A. Frisch, K. Selvakumar, A. Zapf, H. Klein, A. Spannenberg, D. Röttger, O. Briel, R. Karch, M. Beller, *Angew. Chem.* **2002**, *114*, 1028; *Angew. Chem. Int. Ed.* **2002**, *41*, 986; b) K. Selvakumar, A. Zapf, A. Spannenberg, M. Beller, *Chem. Eur. J.* **2002**, *8*, 3901; c) R. Jackstell, S. Harkal, H. Jiao, A. Spannenberg, C. Borgmann, D. Röttger, F. Nierlich, M. Elliot, S. Niven, K. J. Cavell, O. Navarro, M. S. Viciu, S. P. Nolan, M. Beller, *Chem. Eur. J.* **2004**, *10*, 3891; d) N. D. Clement, K. J. Cavell, unpublished results.

[10] J. W. Sprengers, M. J. Agerbeek, C. J. Elsevier, H. Kooijman, A. L. Spek, *Organometallics* **2004**, *23*, 3117.

[11] L. Delaude, M. Szypa, A. Demonceau, A. F. Noels, *Adv. Synth. Catal.* **2002**, *344*, 749.

 © 2005 Wiley-VCH Verlag GmbH & Co. KGaA, Weinheim

Ordered Nanostructures

1D Arrangement of Au Nanoparticles by the Helical Structure of Schizophyllan: A Unique Encounter of a Natural Product with Inorganic Compounds**

*Ah-Hyun Bae, Munenori Numata, Teruaki Hasegawa, Chun Li, Kenji Kaneko, Kazuo Sakurai, and Seiji Shinkai**

Assemblies of inorganic materials on the nanoscale have received considerable attention in recent years owing to their potential use as novel functional materials.[1] Especially, arrangement of metal nanoparticles in desired assemblies may be a new methodology for nanopatterning, which is indispensable for nanotechnologies. However, it is difficult to create assemblies of metal particles in a regulated fashion because of their inability to self-assemble without the aid of organic molecules. One approach to overcome these difficulties includes the immobilization of the metal with organic molecules or polymers to yield two- or three-dimensional organic–metal hybrid nanostructures in which the metal particles are linked by the organic molecules.[2] For example, several research groups have successfully exploited biological macromolecules such as DNA and antibodies to create metal assemblies in which DNA–DNA or antibody–antigen interactions play a crucial role in the self-assembling process of the inorganic nanoparticles.[3]

The preparation of a one-dimensional metal array in the solution state is a fascinating target owing to favorable electronic and magnetic properties which may result from their alignment and allow application of the arrays as nanowires or nanosensors. However, to arrange metal particles into a 1D array requires a sophisticated approach because otherwise the metal surface tends to aggregate into two- or three-dimensional structures. Bioinorganic nanocomposite materials based on metal nanoparticles and 1D biomolecular species, namely DNA[4] and proteins,[5] have recently attracted considerable interest because of the potential to tune the optical, electrical, and even mechanical properties of these materials.[6] For example, Shionoya and coworkers[7] successfully aligned a metal array in one dimension by using a double-stranded skeleton of DNA that contained metal-coordination moieties. However, successful examples of 1D metal arrays in solution are still very limited.

Schizophyllan (SPG) is a natural polysaccharide produced by the fungus *Schizophyllum commune*, and its repeating unit consists of three β-(1–3)-glucoside and one β-(1–6)-glucoside side chain linked at every third main-chain glucoside unit (Figure 1). Interestingly, SPG adopts a triple-helical conformation (t-SPG) in nature which is stabilized by hydrogen-bonding interactions between 2-hydroxy groups, but can be dissociated (reversibly) into a single chain (s-SPG) by dissolving it in dimethylsulfoxide (DMSO);[8] the s-SPG chain can reassume the original triple-helix arrangement by exchanging DMSO for water. In the glucose unit, the 2-hydroxy side of the molecule is a hydrophobic face, whereas the 6-hydroxy side is a hydrophilic face.[9] As the triple-stranded helical structure of SPG is stabilized by the hydrogen-bonding interaction between the 2-hydroxy groups formed inside the helical column, one may presume that the inside hollow is considerably hydrophobic, in a similar fashion to the inside cavity of cyclodextrins.[10] It thus occurred to us that when the renaturating process from s-SPG to t-SPG is carried out in the presence of hydrophobic polymers or assemblies, they would be entrapped in the cavity with the aid of the hydrophobic force to give a novel nanocomposite, which has a unique one-dimensional structure. In this case, the inner cavity of t-SPG may be somewhat enlarged by the inclusion of a guest and as a result several hydrogen bonds may be cleaved, but this destabilization would be sufficiently compensated by the stabilization effect arising from the SPG–guest interaction. Previously, we focused our attention on the inclusion of single-walled carbon nanotubes and found that SPG can include them inside the helical structure through the renaturating process.[11] Herein our attention is focused on extending this novel concept to Au nanoparticles, and we report that owing to its strong helix-forming nature, SPG is capable of assembling Au nanoparticles into a one-dimensional array (Figure 2).

Stock solutions of s-SPG were prepared in DMSO or water. An aliquot of an aqueous solution of dispersed Au nanoparticles (250 μL containing 1250 particles of 5-nm diameter) was mixed with the solution of s-SPG (M_w = 150000) in DMSO (50 mg mL^{-1}, 50 μL). The mixture was centrifuged (9000 rpm) for 1 h, and the supernatant, which contained unconverted s-SPG and Au nanoparticles, was removed with a pipette. The precipitated SPG–Au complexes were separated and then dispersed into fresh water (200 μL). By repeating this process three times, any excess s-SPG was removed and the solvent was replaced by water. We found that both SPG and amylose yield a homogeneous aqueous solution in the presence of Au nanoparticles, whereas other polysaccharide samples (dextran and pullulan) result in a

[*] A.-H. Bae, Dr. M. Numata, Dr. T. Hasegawa, Dr. C. Li, Prof. Dr. S. Shinkai
Department of Chemistry and Biochemistry
Graduate School of Engineering
Kyushu University
Fukuoka 812-8581 (Japan)
Fax: (+81) 92-642-3611
E-mail: seijitcm@mbox.nc.kyushu-u.ac.jp
Prof. Dr. K. Kaneko
HVEM Laboratory
Kyushu University
Fukuoka 812-8581 (Japan)
Prof. Dr. K. Sakurai
Department of Chemical Processes and Environments
Faculty of Environmental Engineering
The University of Kitakyushu
1–1 Hibikino, Wakamatsu-ku, Kitakyushu
Fukuoka 808-0135 (Japan)

[**] We thank Taito Co., Japan, for providing schizophyllan samples. This work was supported by the Japan Science and Technology Corporation, SORST Program.

Supporting information for this article is available on the WWW under http://www.angewandte.org or from the author.

 © 2005 Wiley-VCH Verlag GmbH & Co. KGaA, Weinheim DOI: 10.1002/anie.200462810

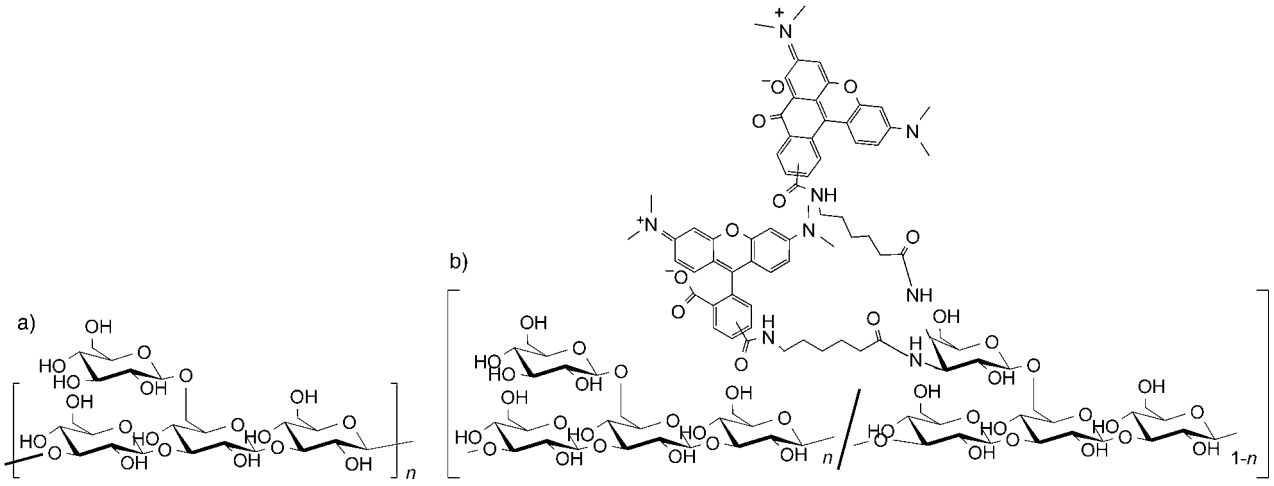

Figure 1. Repeating units of a) schizophyllan (SPG) and b) rhodamine-appended SPG (Rho-SPG).

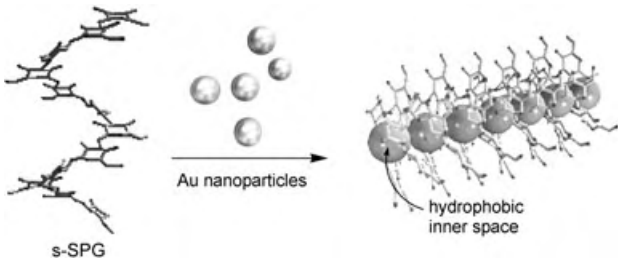

Figure 2. 1D array of Au nanoparticles resulting from their inclusion in the helical structure of SPG.

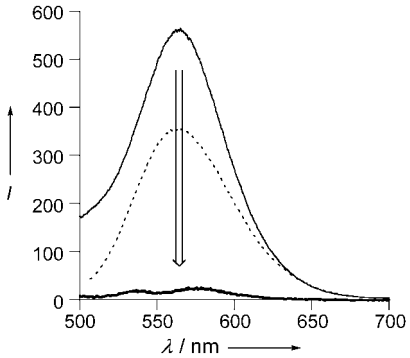

Figure 3. Fluorescence spectra of Rho-SPG (——) and the Rho-SPG–Au complex (——) in aqueous solution at 25 °C (λ_{ex} = 450 nm). Also shown is the reference spectrum of rhodamine dye in the presence of Au nanoparticles (-----).

precipitate. The SPG–Au complex was characterized by UV/Vis absorption spectroscopy. It is well known that Au nanoparticles show a plasmon absorption peak at 525 nm, which is significantly broadened upon aggregation.[12] In the present system, this peak was substantially broadened which indicates that the nanoparticles are assembled by s-SPG (see Supporting Information).

We further confirmed the formation of the composite between SPG and the Au nanoparticles by using rhodamine-appended SPG (Rho-SPG, see Figure 1) instead of s-SPG. The Rho-SPG–Au complex was prepared by an identical procedure to that used for the s-SPG–Au complex and then characterized by fluorescence spectroscopy. The fluorescence spectrum of Rho-SPG shows an emission peak at 565 nm, which is characteristic of rhodamine. However, the intensity of fluorescence of the dye in the Rho-SPG–Au complex was decreased to nearly zero (Figure 3). To examine whether the fluorescence of the dye was quenched by the metal nanoparticles themselves, we mixed Au nanoparticles and rhodamine and observed that there was no significant quenching of the fluorescence of the dye. This result suggests that the interaction of all three components—dye, nanoparticles, and SPG—leads to a decrease in the fluorescence of rhodamine, and supports the view that Au nanoparticles are entrapped by Rho-SPG.[13]

To obtain further evidence that SPG interacts with Au nanoparticles, the morphology of the complex was directly observed by AFM and TEM. By AFM, we observed the presence of fibrous structures of the complex, with diameters of around 6–7 nm, which are wider than that of SPG chains (≈1 nm, see Supporting Information). The Au nanoparticles have an average diameter of 5 nm. The coincidence of the diameter of the complex (≈6–7 nm) with the sum of the diameters of the nanoparticles and SPG (approximately 5 and 1 nm, respectively) supports the view that Au nanoparticles are arranged one-dimensionally through wrapping of SPG chains by hydrophobic force.[14] This unique morphology is probably a result of the inclusion of Au nanoparticles in the SPG helical structure. TEM images of Au nanoparticles on their own as well as in their complex with s-SPG are shown in Figure 4. The TEM pictures were taken without staining: the images shows the spots of Au nanoparticles themselves. From the TEM image shown in Figure 4a, we can see that Au nanoparticles are randomly distributed on the grid. On the other hand, in the presence of s-SPG, Au nanoparticles appear to be one-dimensionally aligned, which suggests that the wrapping by s-SPG enforces Au nanoparticles to adopt a 1D arrangement (Figure 4b). The length of the complex is consistent with that of s-SPG itself (≈200 nm). In reference

 © 2005 Wiley-VCH Verlag GmbH & Co. KGaA, Weinheim

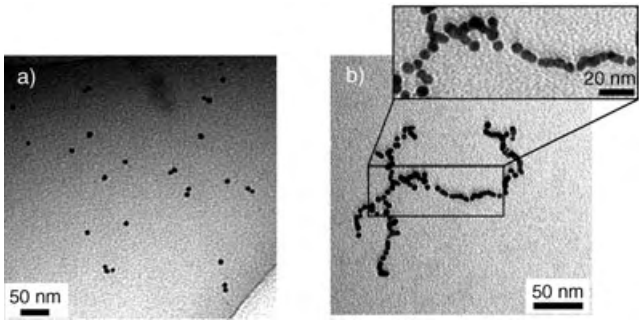

Figure 4. TEM images of a) Au nanoparticles and b) the SPG–Au complex, both in the absence of stain.

experiments, we prepared separate samples of amylose–Au (amylose: $M_w = 15000$) and t-SPG–Au complexes according to the same procedure. However, we could not recognize any significant structure as observed for the s-SPG–Au complex (see Supporting Information). From these TEM images, we can conclude that the difference in the higher-order morphology between SPG (highly ordered triple-helix) and amylose (random coil or disordered helix) determines the final characteristic structure of the complexes: that is, the strong helix-forming nature of SPG is the driving force to arrange Au nanoparticles in one dimension.

The presence of s-SPG in the complex was revealed by energy-dispersive X-ray (EDX) spectroscopy. Figure 5 shows a TEM image of the s-SPG–Au complex and its EDX line-scan profile. As seen in Figure 5, the oxygen component that arises from SPG overlaps the Au

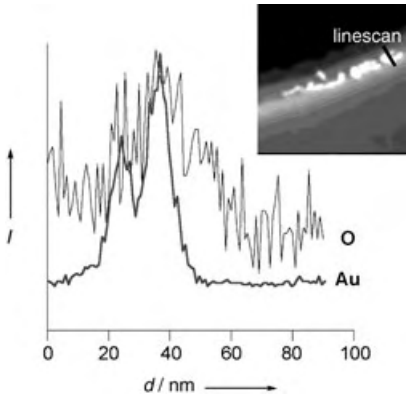

Figure 5. An EDX line-scan profile and TEM image of the SPG–Au complex; d = distance.

component and confirms the coexistence of these two elements. Furthermore, it should be emphasized that broadened distribution of the oxygen element in comparison to that of Au supports our assumption that Au nanoparticles are wrapped by SPG. The findings further confirm that s-SPG works as a "mold" for the one-dimensional arrangement of Au nanoparticles.

Furthermore, we succeeded in taking a three-dimensional image of this picture.[15] The four selected still pictures are shown in Figure 6b–e (see also Supporting Information), and each 3D image corresponds to the clockwise rotation of the structure shown in Figure 6a, with 45°, 135°, 225°, and 315° along a perpendicular axis. In these 3D images, one can see that SPG appears as a thin white layer around the Au

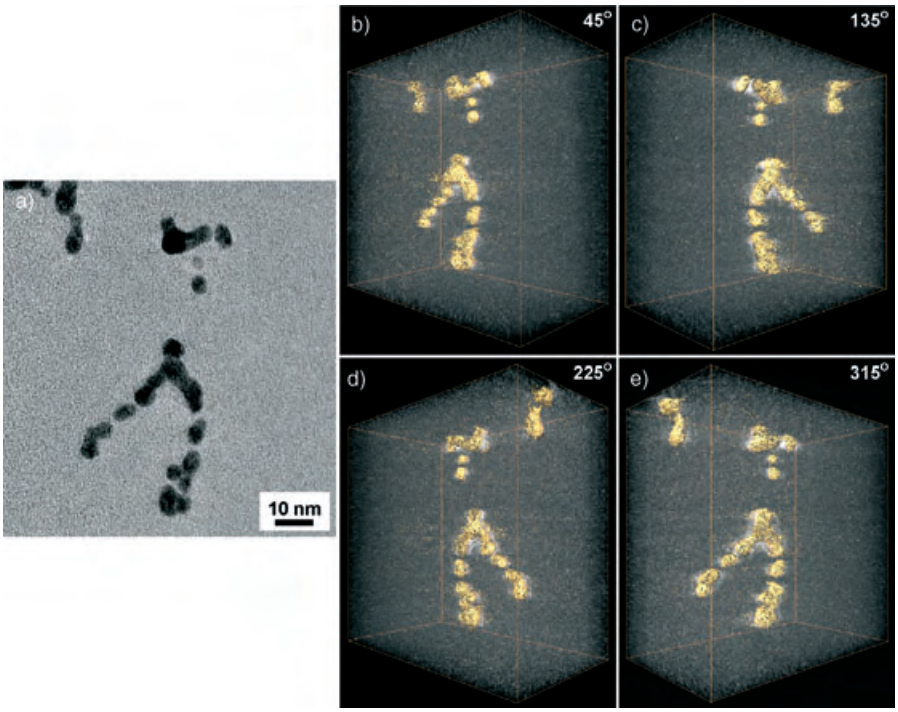

Figure 6. High-resolution 3D TEM images of the s-SPG–Au complex.

nanoparticles. This result strongly supports the fact that s-SPG can enwrap Au nanoparticles without any gaps and arrange them in a one-dimensional array.[16]

In conclusion, we have demonstrated that Au nanoparticles can be aligned in one-dimensional architecture by wrapping them in the helical structure of schizophyllan. The findings clearly show that schizophyllan has potential as an induced-fit-type one-dimensional host and implies many future applications not only to arrange Au nanowires in a desired orientation but also to assemble other hydrophobic building blocks. We believe, therefore, that this system would be readily applicable to the design of new sensors, nanocomposites, nanowires, and nanocircuits.

Experimental Section

Synthesis of rhodamine-appended SPG: Schizophyllan (500 mg, $M_w = 150000$) was suspended in distilled water (500 mL), and the

 © 2005 Wiley-VCH Verlag GmbH & Co. KGaA, Weinheim

mixture was heated at reflux for 12 h until a clear solution was obtained. After cooling to room temperature, $NaIO_4$ (4.0 mg) was added and the mixture was stirred at 4 °C for 3 d protected from light by a shield. To remove inorganic salts, the resultant solution was subjected to dialysis with cellulose membrane (MWCO = 3500) to give an aqueous solution that contained aldehyde-appended SPG. Methylamine (1.0 mL of 40 % aqueous solution) and $NaBH_3CN$ (100 mg) were added to the resultant solution of SPG (500 mg of SPG), and the mixture was stirred at room temperature for 5 days. Dialysis with cellulose membrane followed by freeze–dry treatments gave amine-modified SPG as a white powder. The modification ratio was estimated by elemental analysis.

An excess amount of 6-(tetramethylrhodamine-5-(and 6)-carboamido) hexanoic acid succinimidyl ester (1.0 mg; Molecular Probes) was added to a solution (5.0 mL) in DMSO of methylamine-modified SPG (30 mg), and the mixture was stirred at room temperature in the dark. After one week, the resultant solution was dialyzed against distilled water through a cellulose membrane (MWCO = 3500). This dialysis process was repeated until the color of the tetramethylrhodamine no longer persisted in the distilled water, which indicated complete removal of any unreacted dye. Freeze–dry treatment of the resultant solution gave rhodamine-appended SPG (Rho-SPG) as a purple powder. The percentage of rhodamine introduced was determined by elemental analysis to be 3.0 mol %.

Au nanoparticles (5-nm diameter) were purchased as an aqueous solution of bare gold nanoparticles (without surfactant stabilizer; BB International). TEM and HR-TEM images were acquired using JEOL TEM-2010 (acceleration voltage: 120 kV) and FEI TECNAI-20 (acceleration voltage: 200 kV) apparatus, respectively. A TEM grid was dried under reduced pressure for 6 h before TEM observation. EDX spectra and EDX line-scan profiles were obtained using a FEI TECNAI-20 microscope. AFM images were acquired in air using a Topo METRIX SPM 2100 (noncontact mode). The sample was cast on mica and dried for 6 h under reduced pressure before AFM observation. 3D TEM images were taken using a FEI TECNAI-20 microscope. The TEM parameters were controlled during the acquisition of a tilted series of projections by a cooled slow-scan charge-coupled device (CCD) camera for 3D electron tomography (3D-ET) by fully digitized and automated TEM. A series of tilted projections were acquired for this experiment from −60° to 60°, with an image recorded every 2° to give a total of 60 images. A short exposure time (1.0 sec) was used to reduce the damage of the samples by irradiation. Once the acquisition of a tilt series was complete, the data were transferred to a workstation for fine-tuning of the alignments and for 3D reconstruction. These data were spatially aligned using a cross-correlation algorithm in IMOD software, and a 3D reconstruction was achieved by using a weighted back-projection of consecutive 2D slices by AMIRA 3.0.

Received: December 4, 2004
Published online: February 25, 2005

Keywords: gold · helical structures · nanotechnology · natural products · organic–inorganic hybrid composites

[1] A. Fu, C. M. Micheel, J. Cha, H. Chang, H. Yang, A. P. Alivisatos, *J. Am. Chem. Soc.* **2004**, *126*, 10832 – 10833.

[2] a) S. Yamada, T. Tasaki, T. Akiyama, N. Terasaki, S. Nitahara, *Thin Solid Films* **2003**, *438–439*, 70 – 74; b) S.-J. Park, T. A. Taton, C. A. Mirkin, *Science* **2002**, *295*, 1503 – 1506; c) J.-M. Nam, S.-J. Park, C. A. Mirkin, *J. Am. Chem. Soc.* **2002**, *124*, 3820 – 3821; d) E. Katz, I. Willner, *Angew. Chem.* **2004**, *116*, 6166 – 6235; *Angew. Chem. Int. Ed.* **2004**, *43*, 6042 – 6108; e) C. M. Niemeyer, *Angew. Chem.* **2001**, *113*, 4254 – 4287; *Angew. Chem. Int. Ed.* **2001**, *40*, 4128 – 4158; f) B. Yang, S. Kamiya, K. Yoshida, T. Shimizu, *Chem. Commun.* **2004**, 500 – 501; g) H. Matsune, N. Nakashima, N. Kimizuka, *Polymer Preprints, Jpn.* **2002**, *51*, 2435 – 2436.

[3] a) C. A. Mirkin, R. L. Letsinger, R. C. Mucic, J. J. Storhoff, *Nature* **1996**, *382*, 607 – 609; b) L. Josephson, J. M. Perez, R. Weissleder, *Angew. Chem.* **2001**, *113*, 3304 – 3306; *Angew. Chem. Int. Ed.* **2001**, *40*, 3204 – 3206; c) J.-M. Nam, S. I. Stoeva, C. A. Mirkin, *J. Am. Chem. Soc.* **2004**, *126*, 5932 – 5933.

[4] a) A. P. Alivisatos, K. P. Johnsson, X. Peng, T. E. Wilson, C. J. Loweth, M. P. J. Bruchez, P. G. Schultz, *Nature* **1996**, *382*, 609 – 611; b) J. J. Storhoff, A. A. Lazarides, R. C. Mucic, C. A. Mirkin, R. L. Letsinger, G. C. Schatz, *J. Am. Chem. Soc.* **2000**, *122*, 4640 – 4650.

[5] S. Connolly, S. N. Rao, D. Fitzmaurice, *J. Phys. Chem. B* **2000**, *104*, 4765 – 4776.

[6] a) M. Brust, D. Bethell, C. J. Kiely, D. J. Schiffrin, *Langmuir* **1998**, *14*, 5425 – 5429; b) Y. Kuwahara, T. Akiyama, S. Yamada, *Thin Solid Films* **2001**, *393*, 273 – 277; c) T. Sagara, T. Kato, N. Nakashima, *J. Phys. Chem. B* **2002**, *106*, 1205 – 1212.

[7] a) K. Tanaka, A. Tengeiji, T. Kato, N. Toyama, M. Shionoya, *Science* **2003**, *299*, 1212 – 1213; b) M. Shionoya, *Macromol. Symp.* **2004**, *209*, 41 – 50.

[8] K. Sakurai, S. Shinkai, *J. Am. Chem. Soc.* **2000**, *122*, 4520 – 4521.

[9] K. Miyoshi, K. Uezu, K. Sakurai, S. Shinkai, *Chem. Biodiversity* **2004**, *1*, 916 – 924.

[10] a) H. Okumura, Y. Kawaguchi, A. Harada, *Macromolecules* **2003**, *36*, 6422 – 6429; b) P. N. Taylor, M. J. O'Connell, L. A. McNeill, M. J. Hall, R. T. Aplin, H. L. Anderson, *Angew. Chem.* **2000**, *112*, 3598 – 3602; *Angew. Chem. Int. Ed.* **2000**, *39*, 3456 – 3458; c) A. Harada, *Acc. Chem. Res.* **2001**, *34*, 456 – 464; d) T. Michishita, M. Okada, A. Harada, *Macromol. Rapid Commun.* **2001**, *22*, 763 – 767.

[11] a) M. Numata, M. Asai, K. Kaneko, T. Hasegawa, N. Fujita, Y. Kitada, K. Sakurai, S. Shinkai, *Chem. Lett.* **2004**, 232 – 233; b) T. Hasegawa, T. Fujisawa, M. Numata, M. Umeda, T. Matsumoto, T. Kimura, S. Okumura, K. Sakurai, S. Shinkai, *Chem. Commun.* **2004**, 2150 – 2151; c) M. Numata, T. Hasegawa, T. Fujisawa, K. Sakurai, S. Shinkai, *Org. Lett.* **2004**, *6*, 4447 – 4450.

[12] a) J. J. Storhoff, R. Elghanian, C. Mucic, C. A. Mirkin, R. L. Letsinger, *J. Am. Chem. Soc.* **1998**, *120*, 1959 – 1964; b) M. Brust, D. Bethell, C. J. Kiely, D. J. Schiffrin, *Langmuir* **1998**, *14*, 5425 – 5429.

[13] D. J. Maxwell, J. R. Taylor, S. M. Nie, *J. Am. Chem. Soc.* **2002**, *124*, 9606 – 9612.

[14] R. Takahashi, T. Ishiwatari, *Chem. Commun.* **2004**, 1406 – 1407.

[15] Electron tomography (ET) is a useful technique for reconstructing an object from a series of projections acquired by TEM. Recent development of fully digitized and automated TEM has enabled us to achieve three-dimensional ET images, not only to determine the size and distribution of objects but also to provide information about the morphology of them on the nanometer scale. Three-dimensional structures were reconstructed by processing a series of projections through a combination of IMOD and Amira. See: a) J. Frank, *Three-Dimensional Electron Microscopy of Macromolecular Assemblies*, Academic Press, San Diego, **1996**; b) P. A. Midgley, M. Weyland, *Ultramicroscopy* **2003**, *96*, 413 – 431; c) J. R. Kremer, D. N. Mastronarde, J. R. McIntosh, *J. Struct. Biol.* **1996**, *116*, 71 – 76.

[16] This 1D alignment was reproducibly observed for Au nanoparticles with diameters of 2–20 nm, but not for those with a diameter of 250 nm.

 © 2005 Wiley-VCH Verlag GmbH & Co. KGaA, Weinheim

Cover Picture

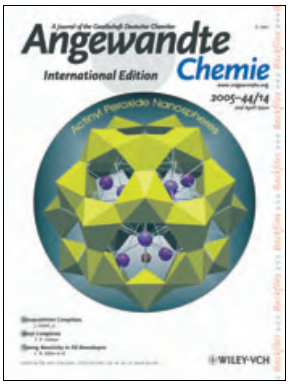

Peter C. Burns,* Karrie-Ann Kubatko, Ginger Sigmon, Brian J. Fryer, Joel E. Gagnon, Mark R. Antonio, and L Soderholm

Structurally tuneable spheroids offer the opportunity to systematically probe electronic, magnetic, and catalytic properties on the nanoscale. In their Communication on page 2135 ff., P. C. Burns et al. describe the self-assembly of nanospheres based on actinyl ions. Furthermore, they report how these nanospheres could form in nuclear waste and so have an impact on the mobility of actinides in the environment. The cover picture shows a polyhedral representation of a spherical actinyl peroxide nanocluster.

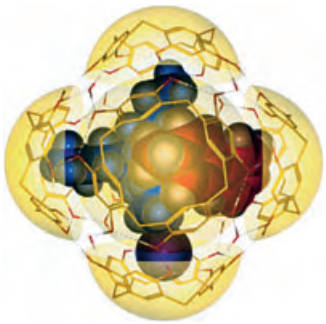

Host–Guest Chemistry
The unique behavior of molecules resulting from their simultaneous inclusion inside molecular capsules, including new forms of stereochemistry, isomerism, and asymmetry within the capsule, are described by J. Rebek, Jr. in his Review on page 2068 ff.

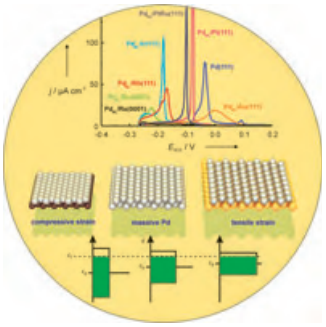

Surface Chemistry
The effects on surface reactivity caused by the lateral deformation of pseudomorphic palladium monolayers deposited on single crystals are described by L. A. Kibler et al. in their Communication on page 2080 ff.

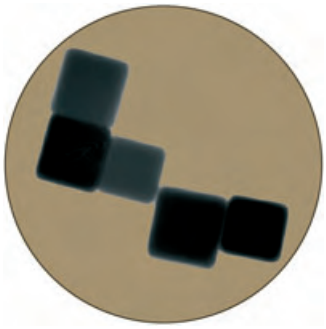

Silver Nanocubes
In their Communication on page 2154 ff. Y. Xia and co-workers report the gram-scale synthesis of single-crystal silver nanocubes and describe how HCl improves the yield and morphology of the sample.

Contents

VIP *The following Communications have been judged by at least two referees to be "very important papers" and will be published online at www.angewandte.org soon:*

*J. Malo, J. C. Mitchell, C. Vénien-Bryan, J. R. Harris, H. Wille, D. J. Sherratt, A. J. Turberfield**
Engineering a 2D Protein–DNA Crystal

*F. López, S. R. Harutyunyan, A. Meetsma, A. J. Minnaard, B. L. Feringa**
Copper-Catalyzed Enantioselective Conjugate Addition of Grignard Reagents to α,β-Unsaturated Esters

*A. Tavassoli, S. J. Benkovic**
Genetically Selected Cyclic Peptide Inhibitors of AICAR Transformylase Homodimerization

*V. Huber, M. Katterle, M. Lysetska, F. Würthner**
Reversible Self-Organization of Semi-Synthetic Zinc Chlorins into Well-Defined Rod Antennae

*N. P. Grimster, Carolyn Gauntlett, C. R. A. Godfrey, M. J. Gaunt**
Intermolecular Palladium-Catalyzed Alkenylation of Indoles through Solvent-Controlled Regioselective C–H Functionalization

*R. Banerjee, P. M. Bhatt, M. T. Kirchner, G. R. Desiraju**
Structural Studies of the System Sodium Saccharinate Hydrate: A Model for Crystallization

News

Mitsui Chemicals Catalysis Science Awards: E. Jacobsen, S. Kobayashi, R. Kuwano, K. Itami ——— **2052**

Books

Modern Aldol Reactions	Rainer Mahrwald	*reviewed by M. Breuning*	**2053**
Amines	Stephen A. Lawrence.	*reviewed by M. North*	**2053**

Highlights

Boryl Complexes

T. P. Fehlner* ——— **2056 – 2058**

Borane Mimics of C_1–M_m Organometallic Complexes

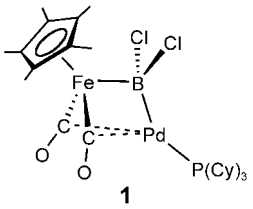

1

Missing link! The boryl-bridged complex $[Cp^*Fe(CO)_2BCl_2Pd(PCy_3)]$ (**1**), which was recently reported by Braunschweig et al. in this journal, fills one of the remaining holes in the edifice of B_1–M_m chemistry. The $\{Pd(Cy_3)\}$ fragment in **1** acts as both a Lewis acid and a Lewis base to coordinate the Fe and B centers, respectively.

Correspondence

Artemisinin Derivatives

S. A.-L. Laurent, A. Robert,*
B. Meunier* ——— **2060 – 2063**

C10-Modified Artemisinin Derivatives: Efficient Heme-Alkylating Agents

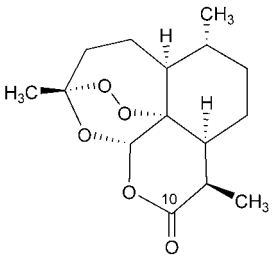

artemisinin

Discussion is reopened regarding C10-substituted derivatives of the peroxide-based antimalarial agent artemisinin (see picture); they are shown to react readily with iron(II)-heme to provide heme–drug adducts in high yields. Substitution or steric hindrance at C10 does not affect the reactivity of the peroxide bond and, thus, does not alter the ability of these powerful antimalarial drugs to alkylate heme.

In light of the discussion on C10-substituted derivatives of the antimalarial agent artemisinin in the preceding correspondence article which relates to his earlier work, R. K. Haynes reiterates here that there is no correlation between the ability of artemisinins to react with heme- or non-heme-Fe^{II} and their antimalarial activity.

Artemisinin Derivatives

R. K. Haynes* ——— **2064 – 2065**

Reply to Comments on "Highly Antimalaria-Active Artemisinin Derivatives: Biological Activity Does Not Correlate with Chemical Reactivity"

Reviews

Snapshots of interacting species are possible with molecules that are reversibly encapsuled together and temporarily isolated from bulk solution. The systems give physical organic chemistry a tool that reveals intermolecular interactions not observable by other methods. Simultaneously encapsulated molecules show new forms of stereoisomerism, asymmetric interactions, and amplified reactivity. The picture shows a single molecule of benzene solvent in contact with each end of *p*-ethyltoluene.

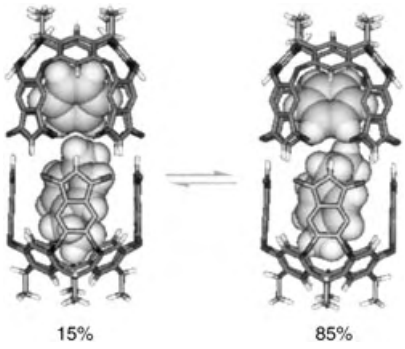

Host—Guest Chemistry

J. Rebek, Jr.* ——— **2068 – 2078**

Simultaneous Encapsulation: Molecules Held at Close Range

Communications

Stretching exercises: The electrochemical behavior of pseudomorphic palladium monolayers (Pd_{ML}) on various single-crystal electrodes is investigated (see picture) to demonstrate the influence of lateral compression and dilation on surface activity. The adsorption behavior and the catalytic activity for formic acid electrooxidation varies dramatically depending on whether the palladium monolayer is compressed or dilated by the single-crystal electrode.

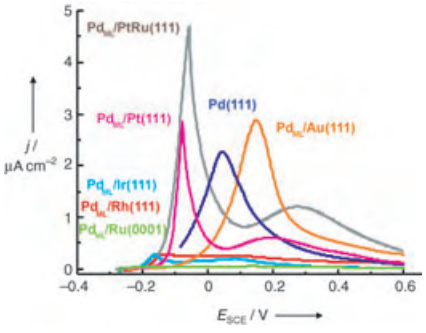

Electrocatalysis

L. A. Kibler,* A. M. El-Aziz, R. Hoyer, D. M. Kolb ——— **2080 – 2084**

Tuning Reaction Rates by Lateral Strain in a Palladium Monolayer

For the USA and Canada:
ANGEWANDTE CHEMIE International Edition (ISSN 1433-7851) is published weekly by Wiley-VCH PO Box 191161, D 69451 Weinheim, Germany. Air freight and mailing in the USA by Publications Expediting Inc. 200 Meacham Ave., Elmont, NY 11003. Periodicals postage paid at Jamaica NY 11431. US POSTMASTER: send address changes to *Angewandte Chemie*, Wiley-VCH, 111 River Street, Hoboken, NJ 07030. Annual subscription price for institutions: US$ 4948.00/4498.00 (valid for print and electronic / print or electronic delivery); for individuals who are personal members of a national chemical society, or whose institution already subscribes, or who are retired or self-employed consultants, print only: US$ 394.00. Postage and handling charges included. All Wiley-VCH prices are exclusive VAT.

 © 2005 Wiley-VCH Verlag GmbH & Co. KGaA, Weinheim

The best in chemistry –

for more than a hundred years

A Journal of the Gesellschaft Deutscher Chemiker

Angewandte
International Edition **Chemie**

www.angewandte.org

1888: ***The beginning of a success story***

Constant Innovations

1962: *First issue of the International Edition*
1976: *Graphical abstracts*
1979: *Cover pictures*
1988: *Centenary of Angewandte*
1989: *Routine use of color*
1991: *New section: Highlights*
1992: *Computerized editorial tracking system*
1995: *Internet service for readers*
1998: *Regular press service; full-text online*
2000: *New section: Essays; EarlyView: Communications available online ahead of the printed version*
2001: *New section: Minireviews*
2002: *Online submission of manuscripts*
2003: *Weekly publication; new section: News; new layout*
2004: *Backfiles (1962-1997); ManuscriptXpress: Online system for authors and referees*

Angewandte's advisors...

Rainer Metternich
Schering AG, Berlin

»***Angewandte Chemie*** *keeps me up to date on the top new developments in chemistry. I am engaged in drug discovery, and this high-quality journal covering breakthrough discoveries in interdisciplinary research, particularly in bioorganic chemistry, is of the highest relevance to me. Each issue of Angewandte provides an outstanding source for innovations.*«

Angewandte Chemie International Edition *is a journal of the German Chemical Society (GDCh)*

GDCh

WILEY InterScience® DISCOVER SOMETHING GREAT

WILEY-VCH

1804502_gu

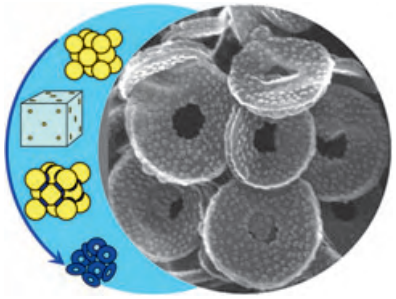

Partially filling a colloidal crystal can give rise to mesoscopic rings (see scheme). The liquid forms rings by capillary forces in the wedges around the contact points between particles. The liquid is solidified, the templating particles are removed, and dispersions of solid rings remain.

Mesoscopic Rings

F. Yan,* W. A. Goedel* ____ **2084 – 2088**

The Preparation of Mesoscopic Rings in Colloidal Crystal Templates

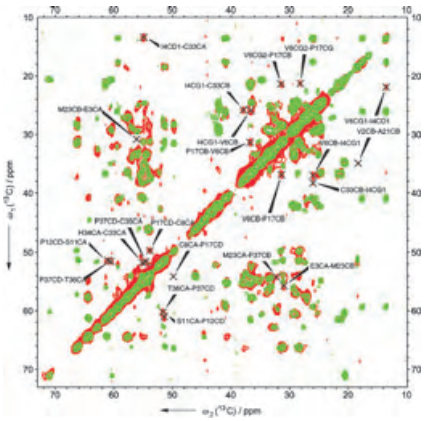

The three-dimensional fold of an immobilized polypeptide is predicted at atomic resolution from solid-state NMR spectroscopic data (see picture) obtained for a single uniformly [^{13}C,^{15}N] isotope labeled sample. The method involves the combined analysis of conformation-dependent NMR frequencies and short ^{1}H–^{1}H distances and may lead to the rapid characterization of three-dimensional protein structures.

Solid-State NMR Spectroscopy

A. Lange, S. Becker,* K. Seidel, K. Giller, O. Pongs, M. Baldus* ____ **2089 – 2092**

A Concept for Rapid Protein-Structure Determination by Solid-State NMR Spectroscopy

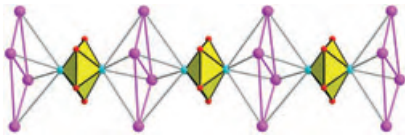

Lead around: The cyclic $[Pb_5]^{4-}$ ion can be stabilized as an organometallic complex with the $\{Mo(CO)_3\}$ fragment. This complex is formed by the reaction of $[Pb_9]^{4-}$ with $[MesMo(CO)_3]$ (Mes = 1,3,5-trimethylbenzene). In the solid state this highly charged anion forms a linear chain with strong interactions between the potassium cations and the carbonyl oxygen atoms (see picture; cyan Mo, purple K, and red Pb; C and O atoms are omitted).

Zintl Anions

L. Yong, S. D. Hoffmann, T. F. Fässler,* S. Riedel, M. Kaupp* ____ **2092 – 2096**

$[Pb_5\{Mo(CO)_3\}_2]^{4-}$: A Complex Containing a Planar Pb_5 Unit

It takes two: Sugar diamino acids which differ from established sugar amino acids by an additional amino group provide access to novel branched oligosaccharide mimetics and a novel class of aminoglycoside mimetics such as **1**. The latter are of great significance as potential ligands for new RNA targets emerging in the post-genome era.

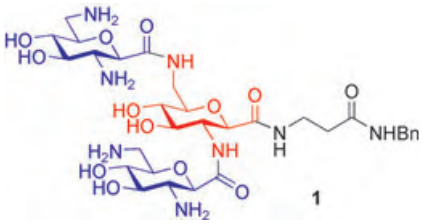

Carbohydrate Mimetics

F. Sicherl, V. Wittmann* ____ **2096 – 2099**

Orthogonally Protected Sugar Diamino Acids as Building Blocks for Linear and Branched Oligosaccharide Mimetics

 © 2005 Wiley-VCH Verlag GmbH & Co. KGaA, Weinheim

Contents

Nanoporous Materials

J. M. Macák, H. Tsuchiya, P. Schmuki* ——— **2100 – 2102**

High-Aspect-Ratio TiO_2 Nanotubes by Anodization of Titanium

Growing holes: With the aid of a new technique highly organized surface layers of TiO_2 nanotubes that are open at one end (see picture) are formed by the anodization of titanium. The pore structure is determined by the pH gradient within the forming pore, this in turn is controlled by the electrochemical sweep rate and the electrolyte concentration.

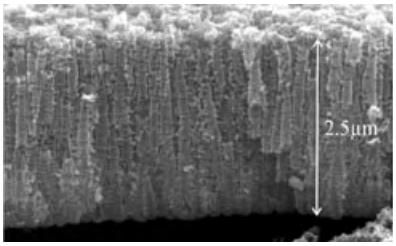

Copper Complexes

S. Ye, B. Sarkar, F. Lissner, T. Schleid, J. van Slageren, J. Fiedler, W. Kaim* ——— **2103 – 2106**

Three-Spin System with a Twist: A Bis(semiquinonato)copper Complex with a Nonplanar Configuration at the Copper(II) Center

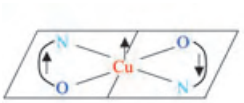

1

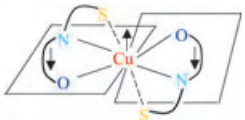

2

A new twist: Structural twisting by about 32° between the semiquinoneiminecopper(II) entities in **2** caused by weak Cu–S interaction results in a different spin arrangement (↑,↓,↑) than for planar **1** (↑,↑,↓). Most revealingly, **2** has an EPR spectrum typical for a radical whereas **1** displays a signal for a Cu^{II} center. Oxidation state distributions for the $\mathbf{2}^{2+,+,0,-,2-}$ forms are assigned on the basis of UV/Vis/NIR spectroelectrochemistry.

Mesoporous Materials

K. Landskron, G. A. Ozin* ——— **2107 – 2109**

Periodic Mesoporous Organosilicas: Self-Assembly from Bridged Cyclic Silsesquioxane Precursors

No holes barred: Trimethylene-bridged **1** can be prepared from $[\{SiCH_2(OEt)_2\}_3]$. Compound **1** can be directed to self-assemble by a tri-block copolymer template to form a periodic mesoporous organosilica with highly ordered and uniform-diameter mesopores in which practically all the building blocks remain intact within the as-synthesized and template-extracted material.

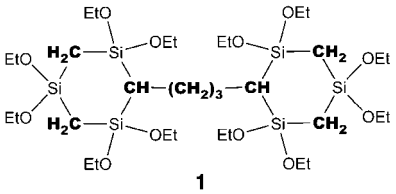

1

Enzyme Engineering

T. Woodhall, G. Williams, A. Berry, A. Nelson* ——— **2109 – 2112**

Creation of a Tailored Aldolase for the Parallel Synthesis of Sialic Acid Mimetics

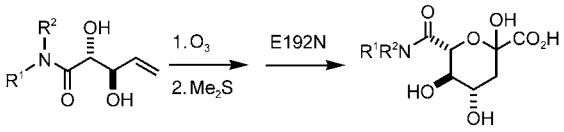

1 2

Broadening substrate specificity: A modified form of sialic acid aldolase (E192N) exhibits a 640-fold switch in substrate specificity relative to the wild-type enzyme. Ozonolysis of the unsaturated amides **1**, followed by an E192N-mediated step, was exploited in the parallel synthesis of 14 different sialic acid mimetics of general structure **2**.

 © 2005 Wiley-VCH Verlag GmbH & Co. KGaA, Weinheim

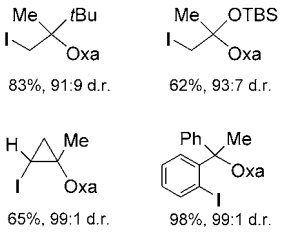

Specific, asymmetric, and mild: Oxazoline (Oxa), a removable chelating chiral auxiliary, assists in the asymmetric activation of C(sp^3)–H bonds at the β position and C(sp^2)–H bonds at the γ position. Pd($OAc)_2$ is an effective catalyst for the selective and asymmetric iodination of methyl, cyclopropyl, and aryl groups at room temperature (see formulae).

Asymmetric Catalysis

R. Giri, X. Chen, J.-Q. Yu* — **2112 – 2115**

Palladium-Catalyzed Asymmetric Iodination of Unactivated C–H Bonds under Mild Conditions

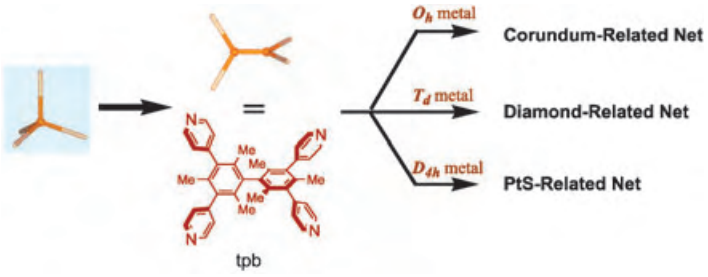

A ligand with a twist: The coordination of distorted-tetrahedral D_{2d}-symmetric tetrapyridylbimesityl (tpb) with O_h, T_d, and D_{4h} metal centers leads to metal–organic frameworks with unprecedented topologies related to those of corundum, diamond, and PtS, respectively (see picture).

Crystal Engineering

R. Natarajan, G. Savitha, P. Dominiak, K. Wozniak, J. N. Moorthy* — **2115 – 2119**

Corundum, Diamond, and PtS Metal–Organic Frameworks with a Difference: Self-Assembly of a Unique Pair of 3-Connecting D_{2d}-Symmetric 3,3′,5,5′-Tetrakis(4-pyridyl)bimesityl

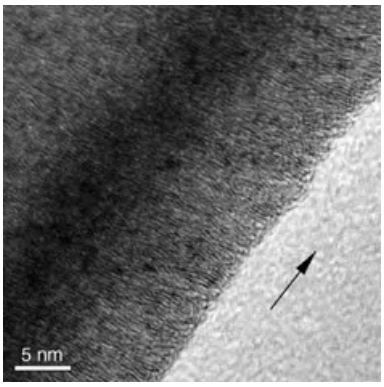

Graphitic carbon nanotubes that comprise graphene layers aligned perpendicular to the tube axis (see image; arrow indicates tube axis) were obtained by stepwise carbonization of preorganized disclike molecules in a porous alumina template. The alignment, size, wall thickness, and shape of the tubes were all controlled by this method.

Nanotube Synthesis

L. Zhi, J. Wu, J. Li, U. Kolb, K. Müllen* — **2120 – 2123**

Carbonization of Disclike Molecules in Porous Alumina Membranes: Toward Carbon Nanotubes with Controlled Graphene-Layer Orientation

Open the gate: Thermoresponsive gating membranes based on interpenetrating polymer networks composed of polyacrylamide (PAAM) and poly(acrylic acid) (PAAC) have inverse gating characteristics, with opening of the membrane pores induced by a decrease rather than an increase in temperature (see picture; UCST = upper critical solution temperature). The membranes provide a new mode of phase-transition behavior for thermoresponsive "smart" membrane actuators.

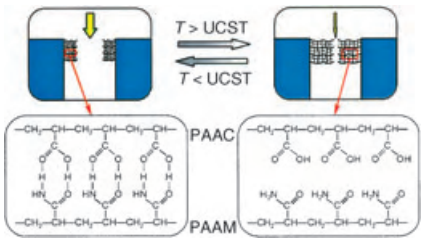

Polymer Membranes

L.-Y. Chu,* Y. Li, J.-H. Zhu, W.-M. Chen — **2124 – 2127**

Negatively Thermoresponsive Membranes with Functional Gates Driven by Zipper-Type Hydrogen-Bonding Interactions

 © 2005 Wiley-VCH Verlag GmbH & Co. KGaA, Weinheim

Contents

Carboranes

L. Deng, H.-S. Chan, Z. Xie* **2128 – 2131**

Synthesis, Reactivity, and Structural Characterization of a 14-Vertex Carborane

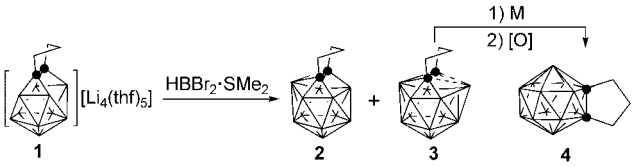

The largest known carborane, which has 14 vertices, was prepared by the reaction of *arachno*-carborane tetraanion **1** with $HBBr_2{\cdot}SMe_2$ (see scheme). The reactivity of both 13- (**2**) and 14-vertex carboranes (**3** and **4**) has also been examined. The key to the successful preparation of supracarboranes is to block the redox reactions between carborane anions and RBX_2 reagents.

Electrocatalysis

J. Zhang, M. B. Vukmirovic, Y. Xu, M. Mavrikakis,* R. R. Adzic* **2132 – 2135**

Controlling the Catalytic Activity of Platinum-Monolayer Electrocatalysts for Oxygen Reduction with Different Substrates

Peak performance: Electrochemical experiments show that the oxygen reduction reaction (ORR) on platinum monolayers supported on various transition metals exhibits a volcano-type behavior (see graph). Calculations reveal that bond-breaking occurs more easily as bond-making becomes harder, and why the Pd-supported Pt monolayer (Pt_{ML}/Pd(111)) has higher ORR activity than pure Pt(111).

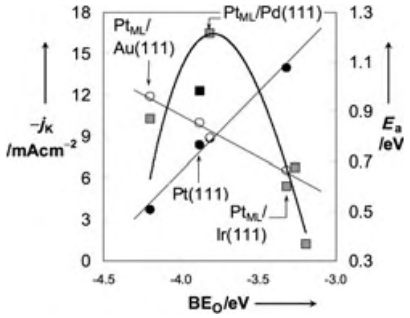

Nanostructures

P. C. Burns,* K.-A. Kubatko, G. Sigmon, B. J. Fryer, J. E. Gagnon, M. R. Antonio, L. Soderholm **2135 – 2139**

Actinyl Peroxide Nanospheres

Waste not: Actinyl nanospheres self-assembled from alkaline solutions have been shown to be composed of 24, 28, and 32 actinyl peroxide polyhedra (for example, see picture of the uranyl peroxide polyhedra (U-28)). The nanospheres represent a new class of polyoxometalates, and their formation in nuclear waste may have an impact on the mobility of actinides in the environment.

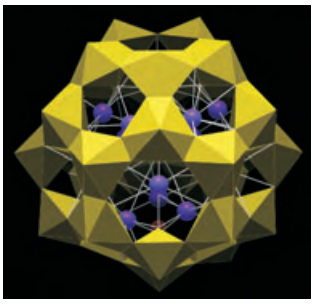

Nanotechnology

J. Zhan,* Y. Bando, J. Hu, Z. Liu, L. Yin, D. Golberg **2140 – 2144**

Fabrication of Metal–Semiconductor Nanowire Heterojunctions

Nanoscale sensors and switches for future electronics may take advantage of metal–semiconductor end-to-end nanowire contacts that can be made by simultaneous evaporation of In and SiO powders. The In and Si subnanowires (indicated) are crystallographically oriented at each junction and are sheathed by silica nanotubes.

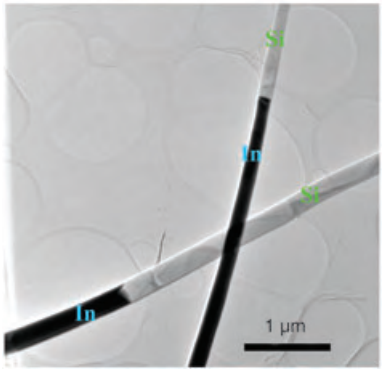

 © 2005 Wiley-VCH Verlag GmbH & Co. KGaA, Weinheim

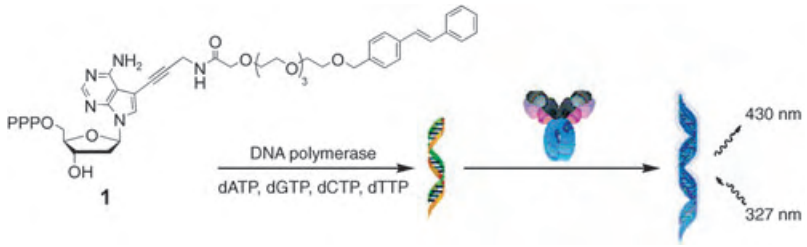

Antibodies as light switches: The deoxynucleotide analogue–stilbene conjugate **1** can be incorporated into nascent DNA by DNA polymerase activity. The blue fluorescence of stilbene is detected only upon binding of an antibody that specifically recognizes the stilbene-modified nucleotide. Therefore, DNA generated through PCR with **1** in the substrate pool can be used for hybridization assays in which detection is triggered by the antibody (see scheme).

Fluorescence Biochemistry

G. F. Kaufmann, M. M. Meijler, C. Sun, D.-W. Chen, D. P. Kujawa, J. M. Mee, T. Z. Hoffman, P. Wirsching, R. A. Lerner,* K. D. Janda* ——— **2144 – 2148**

Enzymatic Incorporation of an Antibody-Activated Blue Fluorophore into DNA

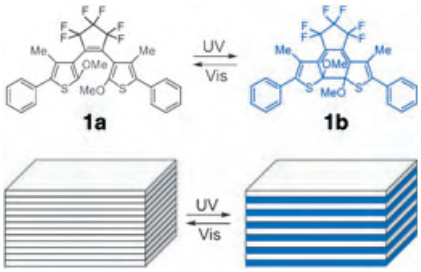

The deck is stacked in favor of future photonic devices. Novel photochromic crystals comprise alternating layers of two conformations of diarylethene **1a**. Irradiation with UV light induces isomerization of only one conformer to the blue-colored, closed-ring form, **1b**. This selective reactivity is ascribed to the difference in distance between the reactive carbon atoms of the two conformers.

Photochemistry

S. Kobatake,* Y. Matsumoto, M. Irie* ——— **2148 – 2151**

Conformational Control of Photochromic Reactivity in a Diarylethene Single Crystal

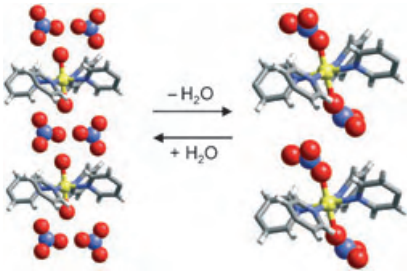

Aqua and nitrate forms of a Co^{II} center are reversibly interconverted within a square-grid complex because of flexible side chains attached to a rodlike ligand (see scheme; Co yellow, N blue, O red). The ligand exchange proceeds in a single-crystal-to-single-crystal fashion despite the drastic structural changes at the metal center. All processes are observed by in situ X-ray crystallography.

Coordination Networks

K. Takaoka, M. Kawano,* M. Tominaga, M. Fujita* ——— **2151 – 2154**

In Situ Observation of a Reversible Single-Crystal-to-Single-Crystal Apical-Ligand-Exchange Reaction in a Hydrogen-Bonded 2D Coordination Network

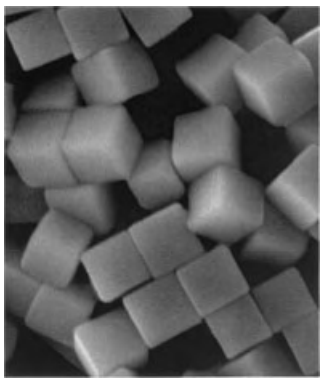

One lump or two! Selective etching of twinned seeds, mediated by HCl and the oxygen in air, resulted in high yields of perfect single-crystal silver nanocubes in a range of sizes (30–130 nm). The chloride ion enhances oxidation and prevents aggregation, while the proton decreases the rate of reduction and facilitates etching through the formation of nitric acid.

Nanocube Synthesis VIP

S. H. Im, Y. T. Lee, B. Wiley, Y. Xia* ——— **2154 – 2157**

Large-Scale Synthesis of Silver Nanocubes: The Role of HCl in Promoting Cube Perfection and Monodispersity

 © 2005 Wiley-VCH Verlag GmbH & Co. KGaA, Weinheim

Contents

Computer Chemistry

S.-D. Li,* J.-C. Guo, C.-Q. Miao, G.-M. Ren ——— **2158 – 2161**

$[(\eta^6\text{-}B_6X)_2M]$ (X = C, N; M = Mn, Fe, Co, Ni): A New Class of Transition-Metal Sandwich-Type Complexes

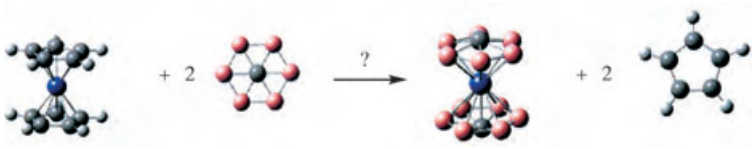

Sandwich maker: A new class of transition-metal sandwich complexes $[(\eta^6\text{-}B_6X)_2M]$ (X = C, N; M = Mn, Fe, Co, Ni) is predicted by density functional calculations. The results suggest that salts of transition-metal complexes containing carbon atoms in a planar hexacoordinate environment might be synthesized and characterized (see picture; B red, C gray, Fe blue, H white).

Sources

Product and Company Directory

You can start the entry for your company in "Sources" in any issue of *Angewandte Chemie*.

If you would like more information, please do not hesitate to contact us.

Wiley-VCH Verlag – Advertising Department
Tel.: 0 62 01 - 60 65 65
Fax: 0 62 01 - 60 65 50
E-Mail: MSchulz@wiley-vch.de

Service

Keywords ——— *2162*

Authors ——— *2163*

Angewandte's Sister Journals ——— *2164*

Preview ——— *2165*

Corrigendum

Chasing Molecules That Were Never There: Misassigned Natural Products and the Role of Chemical Synthesis in Modern Structure Elucidation

K. C. Nicolaou,* S. A. Snyder **1012–1044**

Angew. Chem. Int. Ed. **2005**, *44*

DOI 10.1002/anie.200460864

Irony is the comic relief of life. Either that or we must admit embarrassment about misdrawing structure **1** (the structure proposed by Wieland and Windaus for cholesterol) in this Review. We thank Prof. Dr. R. W. Hoffmann for politely pointing out to us one additional means by which one can chase a molecule that was never there.

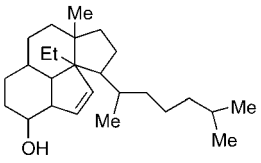

1: misdrawn structure

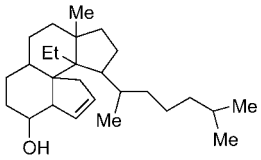

1: structure proposed by Wieland and Windaus

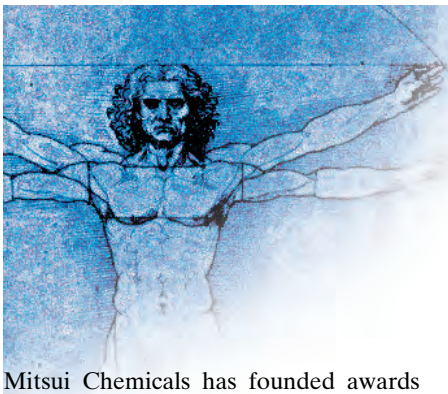

Mitsui Chemicals has founded awards for "the sustainable development of chemistry and the chemical industry" that are to be awarded every two years to researchers at universities and public research institutions who have made important contributions in the field of catalysis research. The awards are being presented during the Mitsui Chemicals International Symposium on Catalysis Science on March 22–23.

Catalysis Science Award to E. N. Jacobsen and S. Kobayashi

The Catalysis Science Award, worth 5 million yen (ca. € 36000), is awarded to researchers under the age of 45. This year, as an exception, two awards will be made.

E. Jacobsen

Eric N. Jacobsen completed his PhD in 1986 at the University of California, Berkeley, under the guidance of R. G. Bergman on dinuclear transition-metal complexes with bridging ligands in heterogeneous catalysis. He then undertook postdoctoral research in the group of K. B. Sharpless at the Massachusetts Institute of Technology. From 1988 to 1993 he was professor at the University of Illinois in Urbana-Champaign, and in 1993 took up a position at Harvard University. The award recognizes his development of asymmetric catalysts with broad applicability for oxidation, hydrolysis, and C–C coupling. His research group also carries out physical organic studies on reactivity and recognition phenomena in homogeneous catalysis. He recently reported in *Angewandte Chemie* on highly enantioselective thiourea-catalyzed nitro-Mannich reactions.[1] Jacobsen is a member of the Editorial Board of *Advanced Synthesis & Catalysis*.

Shū Kobayashi is also a member of the Editorial Board of *Advanced Synthesis & Catalysis*. He studied chemistry at the University of Tokyo and completed his PhD there in 1988 under the guidance of T. Mukaiyama. He took up a position as assistant professor at the Science University of Tokyo as early as 1987. By the time he transferred to the University of Tokyo in 1998, he had already been a visiting professor at the universities of Strasbourg (France), Kyoto (Japan), Nijmegen (The Netherlands), and Marburg (Germany). The award recognizes Kobayashi's development of new catalysts for environmentally benign organic synthesis, including water-stable Lewis acids. He recently reported in *Angewandte Chemie* a dinulear chiral niobium complex that functions as an enantioselective catalyst.[2] His research interests also include the total synthesis of biologically active compounds, microencapsulated catalysts, and organic reactions in microreactors.

S. Kobayashi

Catalysis Science Award of Encouragement to R. Kuwano and K. Itami

Awards of Encouragement worth 1 million yen (ca. € 7000) are awarded every two years to up to two scientists under 35 years of age.

Ryoichi Kuwano is being honored for his work on asymmetric catalysis and transition-metal-catalyzed reactions. For example, he developed a chiral phosphine ligand whose *trans*-chelation properties promote high stereoselectivity. Kuwano studied at Kyoto University and completed his PhD there in 1998 under the guidance of Y. Ito and M. Sawamura. He was assistant professor at Kyoto University from 1995 to 2002. In 2001/2002 he was a guest in the research group of J. F. Hartwig at Yale University (New Haven, CT, USA), where he investigated the activation of aryl halides.[3] Since 2002 he has been associate professor at Kyushu University.

R. Kuwano

The research of **Kenichiro Itami** on removable directing groups in metal catalysis, in particular in palladium-catalyzed reactions, has improved the efficiency of organic synthesis. Itami has been assistant professor since 1998 at Kyoto University, where he develops new reagents and methods for organic synthesis and elucidates their reaction mechanisms. He recently reported a sequence of catalytic carbometalation and cross-coupling for the synthesis of tetrasubstituted olefins.[4] Itami studied at Kyoto University and completed his PhD there in 1998 under the guidance of Y. Ito on the transition-metal-catalyzed cycloaddition of vinyl allenes. In 1997/98 he spent a period as a guest in the research group of J. E. Bäckvall in Stockholm (Sweden).

K. Itami

[1] T. P. Yoon, E. N. Jacobsen, *Angew. Chem.* **2005**, *117*, 470; *Angew. Chem. Int. Ed.* **2005**, *44*, 466.

[2] S. Kobayashi, K. Arai, H. Shimizu, Y. Ihori, H. Ishitani, Y. Yamashita, *Angew. Chem.* **2005**, *117*, 771; *Angew. Chem. Int. Ed.* **2005**, *44*, 761.

[3] J. P. Stambuli, R. Kuwano, J. F. Hartwig, *Angew. Chem.* **2002**, *114*, 4940; *Angew. Chem. Int. Ed.* **2002**, *41*, 4746.

[4] T. Kamei, K. Itami, J.-i. Yoshida, *Adv. Synth. Catal.* **2004**, *346*, 1824.

 © 2005 Wiley-VCH Verlag GmbH & Co. KGaA, Weinheim DOI: 10.1002/anie.200500770

Boryl Complexes

Borane Mimics of C_1–M_m Organometallic Complexes**

*Thomas P. Fehlner**

Keywords:
boranes · boron · boryl complexes · metallaboranes · transition metals

The explosive growth of organometallic chemistry in the second half of the 20th century witnessed the generation of structures with novel metal–ligand geometries containing new electronic interactions. The models of the metal–carbon bonding distilled from the data further accelerated growth. Students of the area are familiar with the landmark molecules and the bonding paradigms they spawned. Some of these models are old enough now to attract comment from a historical perspective, for example, metal–olefin binding on the 50th anniversary of Dewar's landmark publication.[1] A glance at any organometallic textbook will reveal organic ligands with common hapticities ranging from 1 to 6. Of particular relevance to this highlight are alkyl, alkylidene, and alkylidyne complexes represented by CH_3–M_m, $m = 1$, CH_2–M_m, $m = 1$, 2, and CH–M_m, $m = 1$–3 (Scheme 1). These types of C_1–M_m compounds constitute a subarea of organometallic chemistry of relevance to a wide variety of problems ranging from, for example, understanding the radical chemistry generated by homolytic cleavage of the Co–C bond in vitamin B_{12} (metal alkyls) to ring-opening polymerization (metal carbenes).

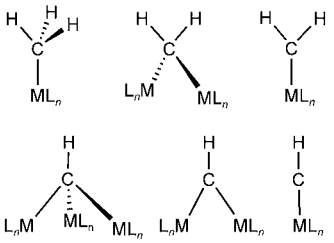

Scheme 1.

Boranes are near-neighbors of hydrocarbons and also possess substantial catenation chemistry. But with their hydridic B-H hydrogen atom, boranes commonly coordinate to metal centers through B-H-M three-center interactions, that is, the early history is predominately that of $[BH_4]^-$ metal complexes. Early examples of compounds with unbridged M–B bonds were considered curiosities in view of the perceived "electron deficiency" of boranes when compared with hydrocarbons of similar composition. But elemental properties are modified in molecules, and bridging hydrogen atoms associated with three-center bonds in polyboranes have protonic character. Hence, they can be removed to generate sites of Lewis basicity (Scheme 2).[2] Alternatively, nucleophilic organometallic complexes provide another route to compounds with M–B bonds, for example, the generation of borane analogues of olefin complexes such as $[Cp(CO)_2Fe(B_2H_5)]$ (Scheme 3).[3] Over time, and in the shadow of organometallic chemistry, a systematic structural chemistry for polyboron–metal compounds developed. The development of polyboron metallaboranes, which were frequently treated as main-group metal clusters rather than metal complexes with polyhaptoborane ligands, benefited from the understanding provided by the cluster electron-counting rules.[4,5]

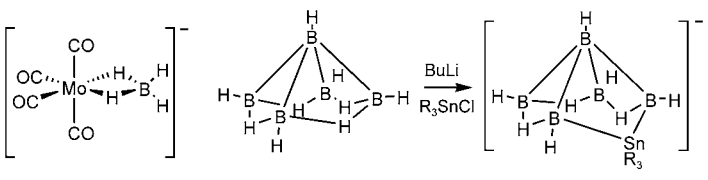

Scheme 2.

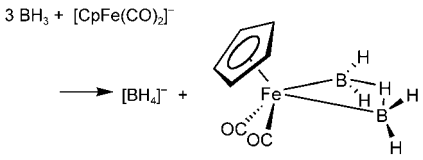

Scheme 3.

Curiously, polyborane mimics of classic organometallic complexes, for example, $[CpCoB_4H_8]$ versus $[CpCo(\eta^4\text{-}C_4H_4)]$ in Scheme 4,[6] were characterized first, and well-defined mimics of C_1–M_m organometallic compounds only appeared from 1990.[7] Compounds with two-center–two-electron classical bonds followed those with nonclassical bonds! Reviews of the area show that it was not for lack of trying, as reactions of metal compounds with monoboranes were reported as early as the 1960s.[8,9] Known derivatives of BH_3–M_m, $m = 1$, BH_2–M_m, $m = 1$, and BH–M_m, $m = 1$–2, com-

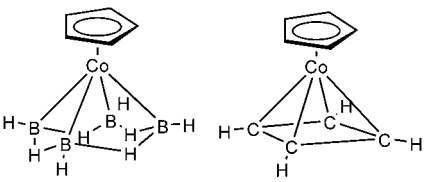

Scheme 4.

[*] Prof. T. P. Fehlner
Department of Chemistry & Biochemistry
University of Notre Dame
Notre Dame, IN 46556 (USA)
Fax: (+1) 504-631-6652
E-mail: fehlner.1@nd.edu

[**] This work was supported by the National Science Foundation (CHE-0304008)

 © 2005 Wiley-VCH Verlag GmbH & Co. KGaA, Weinheim DOI: 10.1002/anie.200500054

plexes, which may be compared to their stoichiometric C_1M_m analogues, are shown in Scheme 5. Although there are

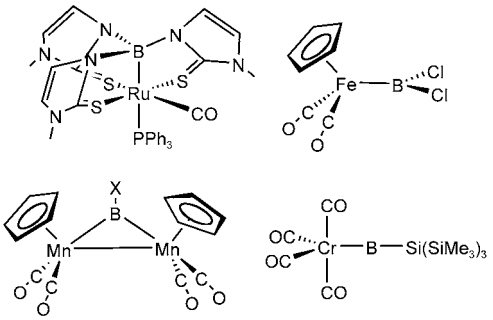

Scheme 5.

now a substantial number of terminal boryl complexes known, examples of the other analogues are scarce or missing, for instance, a boryl-bridged complex. The stage is set for the work highlighted.[10]

To appreciate this chemistry, we must understand the electronic structure of the three-coordinate metal–boryl complex, $[Cp^*Fe(CO)_2BCl_2]$ ($Cp^* = \eta^5$-C_5Me_5) from which the new species is synthesized.[11] Now the $\{Cp^*Fe(CO)_2\}$ fragment can be considered isolobal with NH_2 if we let one of the filled metal "t_{2g}" orbitals mimic the nitrogen lone-pair orbital. $[Cp^*Fe(CO)_2BCl_2]$, then, is isolobal with H_2NBH_2.

There are two limiting ways of formulating H_2NBH_2: one is analogous to ethylene and one is analogous to methyl borane. The former requires a specific geometric relationship between the nitrogen and boron fragments to maximize the π interaction. The same is true with $[Cp^*Fe(CO)_2BCl_2]$. In geometry **1a** (Scheme 6), the Fe–B bond contains both σ and π components with the latter arising from a filled metal "t_{2g}" orbital interacting with the empty out-of-plane B 2p orbital. In **1b**, only a σ component is possible, as the principal donor and

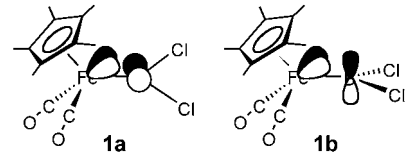

Scheme 6.

acceptor orbitals are orthogonal. The difference in energy between these two configurations constitutes a barrier to rotation about the Fe–B bond. Solid-state structure data and density functional calculations on a variety boryl complexes show that in the competition between the π interactions of the three fragments attached to boron for the empty B 2p orbital, the Fe–B interaction is weak. Thus, the boryl complex is better represented by methyl borane than ethylene. Consequently, $[Cp^*Fe(CO)_2BCl_2]$ is a lightly stabilized tricoordinate boron compound. Indeed a main-group base adduct, $[Cp^*Fe(CO)_2BCl_2]\cdot NC_5H_4$-4-Me (Scheme 7), is known and metal–base adducts should be possible.[12]

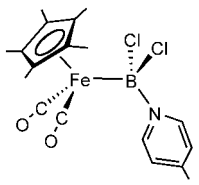

Scheme 7.

To envision a boryl-bridged species, consider first a main-group analogue. A fragment suitable to bridge the B–N bond in H_2NBH_2 needs an acceptor orbital for the N lone pair and a donor orbital to the empty B orbital, that is, a CH_2 fragment would generate a cyclopropane analogue. Switching to a metal system, a Group 10 ML_2 fragment would be suitable and 14-electron and near-linear $Pd(PCy_3)_2$ was the reagent of choice. Interestingly, one phosphine group is lost in the overall reaction, and in the product $[Cp^*Fe(CO)_2BCl_2Pd(PCy_3)]$ (Scheme 8), the $Pd(Cy_3)$ fragment acts as a Lewis acid, accepting a filled iron "t_{2g}" orbital to

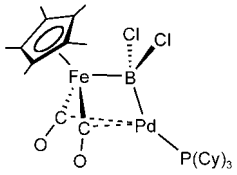

Scheme 8.

generate two semibridging carbonyls in the process. The geometric structure of $[Cp^*Fe(CO)_2BCl_2Pd(PCy_3)]$ suggests that the $Pd(PCy_3)$ fragment must also act as a Lewis base to coordinate to the boron center, thereby providing another example of a complex containing a four-coordinate borane.

The ring analogy highlights another feature of $[Cp^*Fe(CO)_2BCl_2Pd(PCy_3)]$. As pointed out above, 16-electron PdL_2 is isolobal with CH_2, and $[Cp^*Fe(CO)_2BCl_2Pd(PCy_3)_2]$ would be an analogue of a dimetallacyclopropane such as $[Fe_2(CO)_8(\mu\text{-}CH_2)]$. But in fact unsaturated 34-electron $[Cp^*Fe(CO)_2BCl_2Pd(PCy_3)]$ is produced. As with free $Pd(PCy_3)_2$, it must be the steric bulk of the phosphine group plus the metal fragment that supports the 14-electron Pd center.[13] Perhaps it is no surprise, then, that $[Cp^*Fe(CO)_2BCl_2Pd(PCy_3)]$ is extremely air sensitive in solution and slowly decomposes into $[Cp^*Fe(CO)_2BCl_2]$ and Pd metal.

Is this novel borane complex a curious new compound but just a side show to the organometallic C_1–M_m headliners? Recent progress in the boron functionalization of hydrocarbons[14,15] and its flip side, the carbon functionalization of polyhedral boranes,[16] plus metal-promoted hydroboration[17] suggest otherwise. New compounds provide substances with new properties and possible solutions to old problems. Most of them won't be solutions but then the same may be said of organometallic chemistry. It is through the systematic study of an area that compounds of the practical importance of a Wilkinson's catalyst are discovered. The work highlighted fills one of the remaining holes in the edifice of B_1–M_m chemistry and is of fundamental importance. Where it will lead in terms of practical applications remains to be seen. Still, the possibilities generated add to the continuing fascination of chemistry.

[1] D. M. P. Mingos, *J. Organomet. Chem.* **2001**, *635*, 1.

[2] D. F. Gaines in *Boron Chemistry-4* (Eds.: R. W. Parry, G. Kodama), Pergamon, Oxford, **1980**, p. 73.

 © 2005 Wiley-VCH Verlag GmbH & Co. KGaA, Weinheim

[3] T. J. Coffy, G. Medford, J. Plotkin, G. J. Long, J. C. Huffman, S. G. Shore, *Organometallics* **1989**, *8*, 2404.
[4] K. Wade, *Adv. Inorg. Chem. Radiochem.* **1976**, *18*, 1.
[5] D. M. P. Mingos, D. J. Wales, *Introduction to Cluster Chemistry*, Prentice Hall, New York, **1990**.
[6] R. N. Grimes, *Acc. Chem. Res.* **1978**, *11*, 420.
[7] R. T. Baker, D. W. Ovenall, J. C. Calabrese, S. A. Westcott, N. J. Taylor, I. D. Williams, T. B. Marder, *J. Am. Chem. Soc.* **1990**, *112*, 9399.
[8] H. Braunschweig, M. Colling, *Coord. Chem. Rev.* **2001**, *223*, 1.
[9] S. Aldridge, D. L. Coombs, *Coord. Chem. Rev.* **2004**, *248*, 535.
[10] H. Braunschweig, K. Radacki, D. Rais, G. R. Whittell, *Angew. Chem.* **2005**, *117*, 1217; *Angew. Chem. Int. Ed.* **2005**, *44*, 1192.
[11] S. Aldridge, R. J. Calder, R. E. Baghurst, M. E. Light, M. B. Hursthouse, *J. Organomet. Chem.* **2003**, *649*, 9.
[12] H. Braunschweig, K. Radacki, F. Seeler, G. R. Whittell, *Organometallics* **2004**, *23*, 4178.
[13] W. Kuran, A. Musco, *Inorg. Chim. Acta* **1975**, *12*, 1867.
[14] H. Chen, S. Schlecht, T. C. Semple, J. F. Hartwig, *Science* **2000**, *287*, 1995.
[15] M. R. Smith III, *Prog. Inorg. Chem.* **1999**, *48*, 505.
[16] D. E. Kadlecek, P. J. Carroll, L. G. Sneddon, *J. Am. Chem. Soc.* **2000**, *122*, 10686.
[17] I. Beletskaya, A. Pelter, *Tetrahedron* **1997**, *53*, 4957.

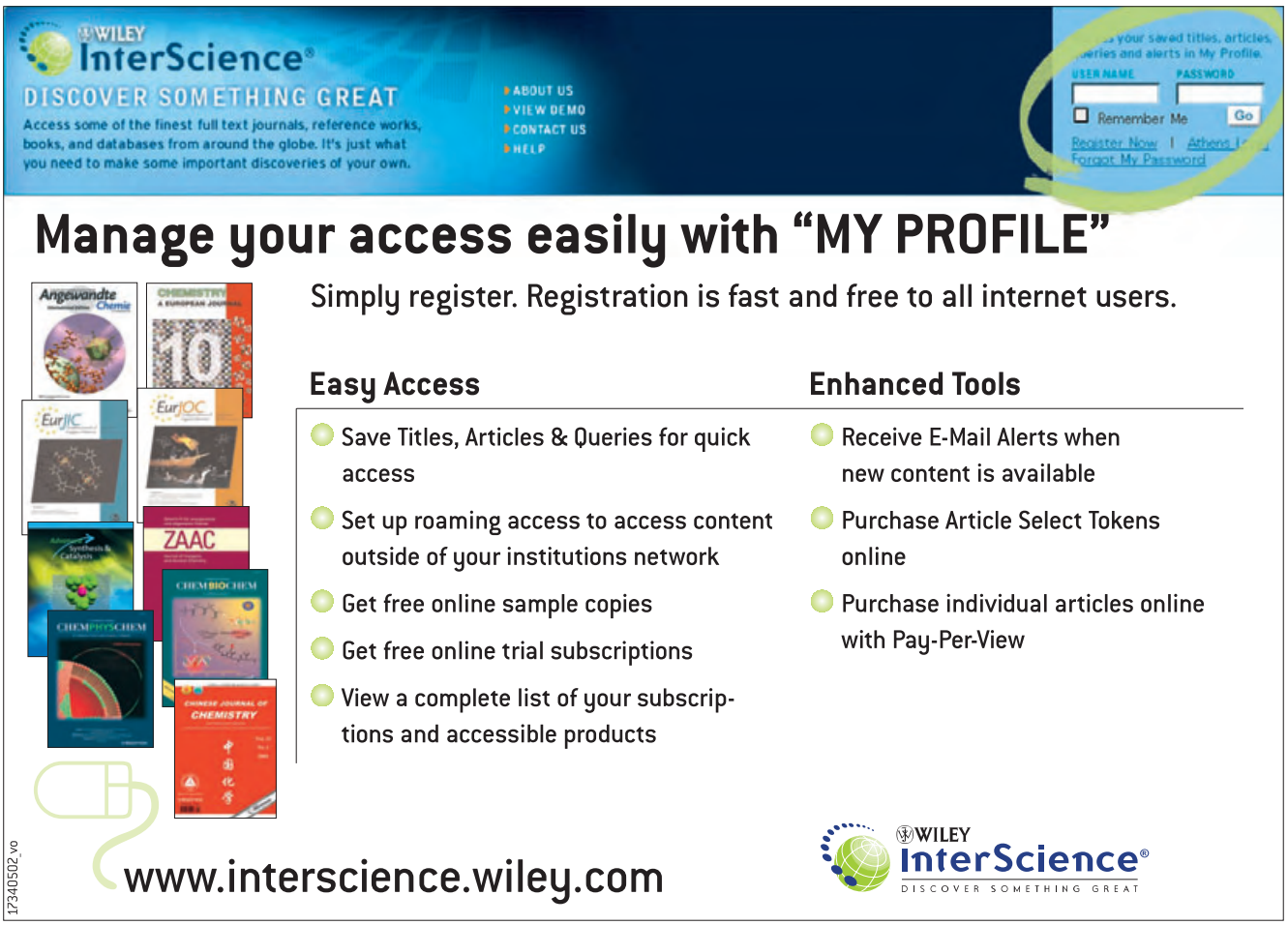

Artemisinin Derivatives

C10-Modified Artemisinin Derivatives: Efficient Heme-Alkylating Agents**

Sophie A.-L. Laurent, Anne Robert, and Bernard Meunier**

Keywords:
alkylation · antiviral agents · heme proteins · iron · porphyrinoids

Artemisinin (**1**, Figure 1) is a sesquiterpene extracted from the leaves of *Artemisia annua* which contains a 1,2,4-trioxane structure that is essential for its activity against malaria-infected erythrocytes. The mechanism of action of artemisinin has been the center of intense debate over the last two decades.[1–4] Among the different possible mechanisms, one suggestion is that reductive activation of its endoperoxide function by the iron(II) center of heme generates a C4-centered radical that alkylates the *meso* positions of protoporphyrin-IX (PPIX).[5] We found that many antimalarial trioxanes related to artemisinin are also able to interact with heme or heme-like models and consequently alkylate the porphyrin ring.[4c,6] We were working on the identification of heme–artesunate and heme–trioxaquine adducts[7] when Haynes et al. reported the preparation and antimalarial activities of several C10-substituted artemisinin derivatives.[8] As all of these compounds are based on different substituents at the C10 position, no structural modification in terms of steric effects or reactivity is expected for the untouched trioxane entity of these derivatives. Consequently, one can expect that the heme-alkylating capacities of these molecules should be very similar to that of artemisinin, artemether, or artesunate. In Table 2 of the article by Haynes et al.,[8] the authors claimed that some of these efficient antimalarial C10-modified derivatives were unable to alkylate free heme. For example, the highly active 10-deoxoartemisinin derivative **2** (labeled **23** in Ref. [8]; see Figure 1) with a methylene group at C10 was totally inert to Fe^{II}-heme. On the other hand, the 10-(4-benzyl)-piperazinyl derivative **3** (labeled **18** in Ref. [8]) reacted with heme, however, the major reaction products, presumably heme–drug adducts, were not characterized.

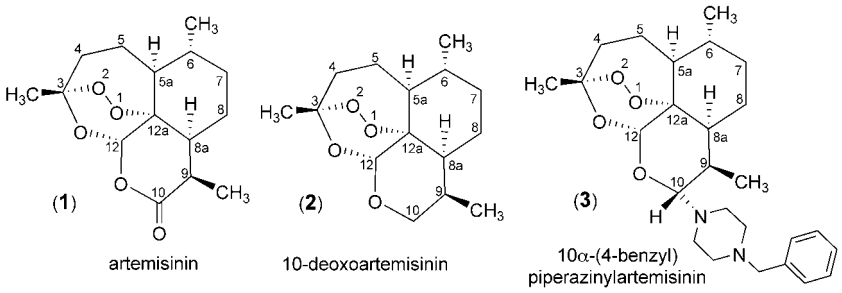

Figure 1. Structures of artemisinin (**1**), 10-deoxoartemisinin (**2**), and 10α-(4-benzyl)piperazinyl-10-deoxoartemisinin (**3**).

Herein we report that both compounds **2** and **3** are indeed potent heme-alkylating agents; both heme–drug adducts have been obtained in high yields. In fact, heme is poorly soluble in the mixture of acetonitrile and phosphate buffer (pH 7.4) used by Haynes et al. The saturation concentration of heme under these conditions at room temperature is not higher than 100 μM, and such a low solubility probably does not allow heme to react with artemisinin. For this reason of solubility, we used a homogeneous solution in dimethylsulfoxide (DMSO) containing 2–4 vol% of water in which heme was significantly more soluble (6 mM). Artemisinin itself and its derivatives **2** and **3** are not very soluble in aqueous solution. However, many drugs are insoluble in water, yet they are highly active, as hydrophobicity is required for them to cross cell membranes (e.g. the anticancer drug taxol is insoluble in water). Furthermore, solutions that contain some volume of DMSO are usually used in biologically relevant studies to evaluate the activity of artemisinin or related compounds in vitro and in vivo.[9,10]

Compound **3** was obtained from the corresponding 10-trimethylsilyl ether

[*] S. A.-L. Laurent, Dr. A. Robert, Dr. B. Meunier
Laboratoire de Chimie de Coordination du CNRS
205 route de Narbonne
31077 Toulouse cedex 4 (France)
Fax: (+33) 5-6155-3003
E-mail: arobert@lcc-toulouse.fr
bmeunier@lcc-toulouse.fr

[**] Comments on "Highly Antimalaria-Active Artemisinin Derivatives: Biological Activity Does Not Correlate with Chemical Reactivity". This work was supported by the CNRS and Palumed, and S.A.-L.L. is indebted to both for a joint fellowship. Dr. Y. Coppel (CNRS, Toulouse) is acknowledged for the measurement of 2D NMR spectra.

Supporting information for this article is available on the WWW under http://www.angewandte.org or from the author.

 © 2005 Wiley-VCH Verlag GmbH & Co. KGaA, Weinheim DOI: 10.1002/anie.200462556

4[11,12] after modification of the procedure published by Haynes et al.[8] In our hands, the original procedure provided essentially the elimination product **5** with a double bond between C9 and C10 (Scheme 1). However, when agents other than dithionite can be used. The use of glutathione (which is a "biological" reductant present at approximately 5-mM concentration in red blood cells) to form heme– or hemoglobin–artemisinin adducts has already

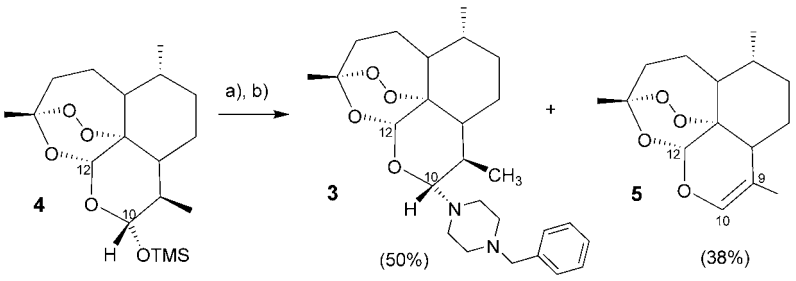

Scheme 1. Synthesis of 10α-(4-benzyl)piperazinyl-10-deoxoartemisinin (**3**): a) TMSBr, 25 min, 0°C; b) 1-benzylpiperazine, HFIP, 45 min, 0°C. TMS = trimethylsilyl.

1,1,1,3,3,3-hexafluoropropan-2-ol (HFIP) was used as an additive[10] in the amination step of the 10-brominated intermediate, the expected compound **3** was obtained in 50% yield (see Supporting Information). Compound **2** was prepared by using a modification of the described procedure,[13] and then the two compounds **2** and **3** were tested for their alkylation of heme.

Alkylation of Heme by 2

Iron(II) protoporphyrin-IX, generated in situ from its iron(III) analogue and sodium dithionite, readily reacted with **2** at room temperature to provide the covalent heme–drug adduct **6**-Fe (1:1:1 molar ratio of [Fe^{III}(PPIX)Cl]/**2**/dithionite; Scheme 2). In fact, several reducing been reported.[5b,c] This confirms that this alkylation process is not dependent on the reductant used, provided that its redox potential is consistent with the reduction of iron(III)-heme to iron(II)-heme. As previously described for artemisinin,[2b,5] the reductive activation of the peroxide bond of 10-deoxoartemisinin leads to an alkoxy radical on O2 which, after β scission, gives a C4-centered radical. This species efficiently alkylates the *meso* carbon atoms of heme and leads to the four regioisomeric covalent adducts **6**-Fe. All of the porphyrinic material was precipitated from the reaction mixture and analyzed by mass spectrometry. The major compound was the adduct **6**-Fe, characterized by its molecular mass peak (m/z = 884.4 [M^+]) with the parent peak (m/z = 824.4 [$M-CH_3COOH]^+$) resulting from the loss of a molecule of acetic acid at C12. A small amount of unconverted heme (m/z = 616.3) was also present. A ratio of 89:11 of **6**-Fe to heme in the crude reaction mixture was indicated by mass spectrometry.

The mixture of heme and **6**-Fe was demetalated to provide the free-base covalent adduct **6**, which was characterized by MS (m/z = 831.3 [MH]$^+$). However, owing to the strongly acidic conditions required for demetalation, the parent peak detected at m/z = 789.5 corresponded to compound **7**, which has a hemiacetal structure. The ratio of **6**/**7** was 3:10. As expected, a small amount of H_2PPIX was detected at m/z = 563.3 (ratio **6**+**7**/H_2PPIX = 81:19).

Owing to the low solubility of heme derivatives, the purification and characterization by NMR spectroscopy of these heme–drug adducts was not possible. We therefore repeated these reactions using heme-dimethylester (heme-DME) instead of heme. In this case, the alkylation reaction was immediately followed by demetalation to afford, as expected, a mixture of adducts **8** and **9**, which are the dimethylester analogues of compounds **6** and **7**. Adducts **8** and **9** were detected at m/z = 859.5 and 817.7, respectively (MH$^+$), with a ratio of **8**/**9** of 34:100, along with H_2PPIX-DME (m/z = 591.3). The yield of alkylation calculated from this analysis was 69% (for a 1:1 molar ratio of heme-DME/drug).

Column chromatography of this mixture yielded pure adduct **9**, which was characterized by 1D and 2D NMR spectroscopy. The ^{1}H NMR spectrum exhibited three signals in the range δ =

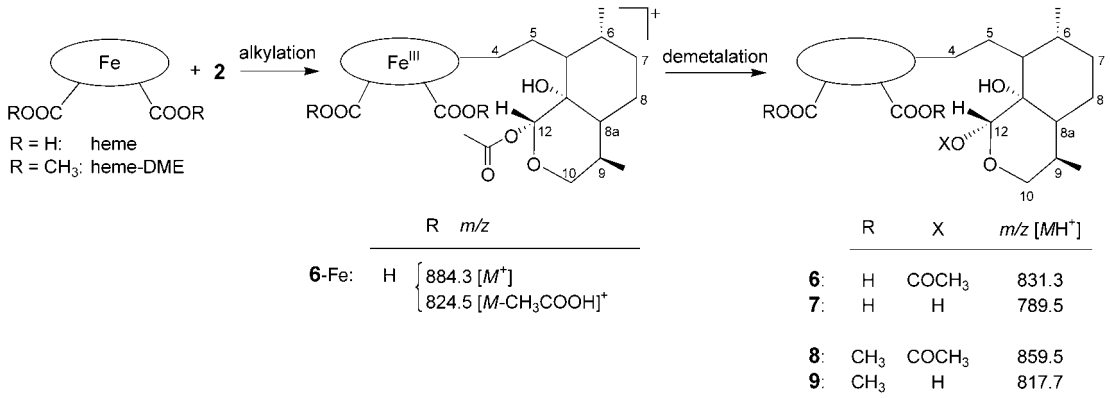

Scheme 2. Alkylation of heme and heme-dimethylester by 10-deoxoartemisinin (**2**), and demetalation of the obtained adducts. The configuration at C12 of adducts **7** and **9** has not been verified.

 © 2005 Wiley-VCH Verlag GmbH & Co. KGaA, Weinheim

10.63–9.76 ppm for the protons in the *meso* positions. The resonance of the methylene group at C4 was detected as a broad pattern at $\delta = 5.42$–5.05 ppm, a proof of the covalent coupling between the porphyrin and drug moieties. The hemiacetal proton H12 gave a signal at $\delta = 4.63$ ppm. The signals for the two methylene protons at C10 at $\delta = 3.68$ and 3.27 ppm overlapped with those of the protons of the β-pyrrolic CH_3 and CH_2COOCH_3 groups, respectively. These assignments were attested by ^1H–^{13}C correlation spectroscopy. Both protons H10 correlated with C10, which was detected at $\delta = 61$ ppm, and proton H12 correlated with the resonance found at $\delta = 93$–95 ppm for C12. These NMR data allow to rule out the possible hydrolysis of the cycle C8a-C10-C12 with formation of an alcohol at C10 and an aldehyde at C12; in fact, such a product is expected to exhibit the same mass spectrum as **9**, but with different NMR characteristics.

Alkylation of Heme by 3

Iron(II) protoporphyrin-IX was also efficiently alkylated by the C10-benzylpiperazinyl-substituted deoxoartemisinin derivative. Mass spectrometry of the crude porphyrinic residue revealed the presence of the adduct **10**-Fe, which corresponds to alkylation of heme at the *meso* positions by the drug **3** ($m/z =$ 998.8, $[M^{III}-CH_3COOH]^+$), along with a minor amount of unconverted heme (7% measured by HPLC; Scheme 3). The structure of **10**-Fe was confirmed by the presence of peaks at $m/z = 999.7$ and 499.9 which could be assigned to $[M^{II}-CH_3COO^-]^+$ and $[M^{III}-CH_3COO^-]^{2+}$, respectively (see Supporting Information). The reduction of iron(III) porphyrins and the loss of acetate at C12 in artemisinin-derived adducts under the analytical conditions of mass spectrometry are well-known phenomena.[15]

Covalent adduct **11**-Fe ($m/z = 840.3$, MH^+) was also produced during the alkylation of heme by **3** by hydrolysis of the C8a-C10-C12 cycle of adduct **10**-Fe, followed by nucleophilic attack of HO-C12a at C10, and loss of 1-benzylpiperazine (Scheme 4). This structure, which contains an exocyclic aldehyde, was confirmed by ^1H–^{13}C NMR correlation spectroscopy after demetalation of the heme-dimethylester derivative (see below). Minor peaks were also detected at $m/z = 858.7$ (hydration of the aldehyde function: +18 amu) and 872.5 (hydration of the aldehyde and methylation of the hydroxyl function: +32 amu). The ratio **10**-Fe/**11**-Fe was 43:57, as determined from mass spectrometry, while the ratio of **10**-Fe + **11**-Fe/[Fe(PPIX)] was 80:20.

Demetalation of the mixture of **10**-Fe and **11**-Fe was performed and gave rise to the respective free-base adducts **10** and **11**. Adduct **11** was characterized by the presence of its molecular peak at $m/z = 787.7$ (MH^+) and a small signal at $m/z = 805.8$ owing to hydration of the aldehyde function. Adduct **10** was characterized by the presence of a peak at $m/z = 829.7$ owing to the loss of the benzylpiperazinyl substituent (see Supporting Information).

The identification of the covalent adducts **10**-Fe and **11**-Fe was confirmed by using heme-dimethylester instead of heme as the starting material. Under these circumstances, the analogous adducts **12**-Fe ($m/z = 1124.9$ $[M-H+K]^+$, 1026.5 $[M-CH_3COOH]^+$) and **13**-Fe ($m/z = 868.5$ $[M^+]$) were observed (Scheme 4; yield = 77% from HPLC analysis). Demetalation of the mixture

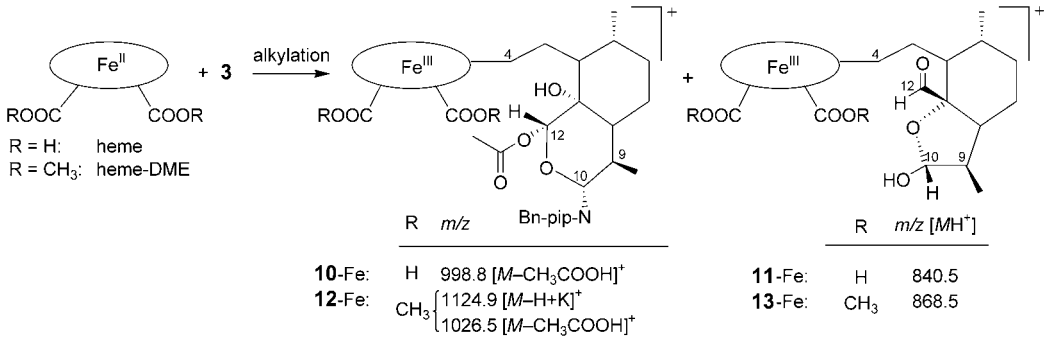

Scheme 3. Alkylation of heme and heme-dimethylester by 10α-(4-benzyl)piperazinylartemisinin (**3**). Bn = benzyl, pip = piperazinyl.

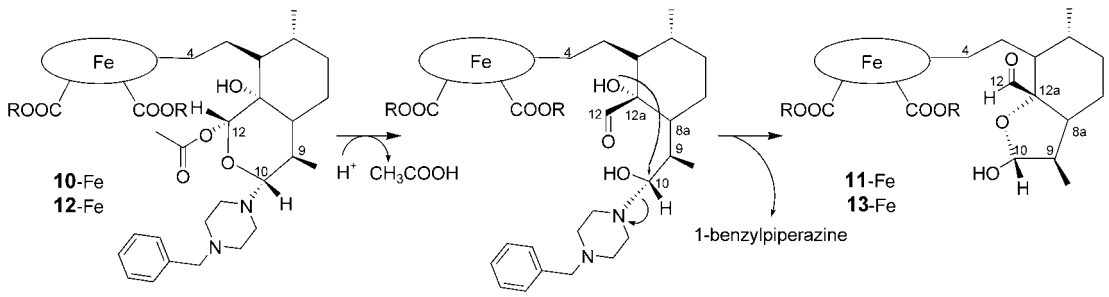

Scheme 4. Modification of the covalent adducts **10**-Fe and **12**-Fe to give **11**-Fe and **13**-Fe, respectively. The configuration at C10 is more probable, but has not been verified.

 © 2005 Wiley-VCH Verlag GmbH & Co. KGaA, Weinheim

of **12**-Fe and **13**-Fe yielded **13** as the main adduct ($m/z = 815.6$ [MH^+]), while a significant peak at $m/z = 857.8$ was also detected that probably corresponds to the molecular ion [M^+] of compound

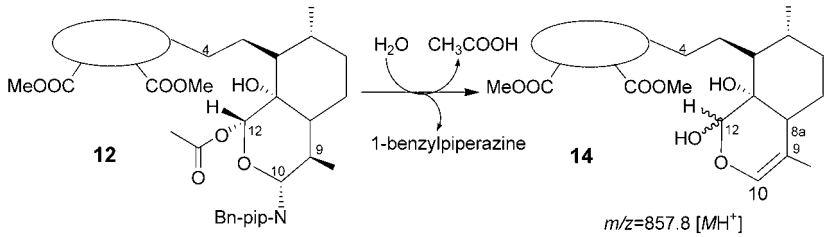

Scheme 5. Structure of adduct **14**.

14 (see Scheme 5). The presence of this adduct, formed by the elimination of 9,10-piperazine from **12**, indicates that the C8a-C10-C12 cycle may withstand to some extent the harsh conditions required for the demetalation step. It also confirms the high propensity of the artemisinin derivatives that are substituted at C10 by an amine to produce the C9-C10 unsaturated derivative, as observed during the synthesis of **3**.

The structure of **13** was unambiguously determined by ^{1}H–^{13}C NMR correlation spectroscopy. The protons of the *meso* positions and the aldehyde (H12) appeared at $\delta = 9.82$–10.24 ppm (4H) and correlated with the *meso* carbon atoms and the carbonyl center C12 at $\delta = 95$–99 and 209 ppm, respectively. A broad pattern at $\delta = 5.10$–5.54 ppm accounted for three protons, namely from H_2C4 and H10, which correlated with C4 and C10 that were detected at $\delta = 31$–33 ppm and 107 ppm, respectively. These data confirm the presence of both the exocyclic aldehyde and the 5-membered cyclic hemiacetal. The NMR spectra were complex owing to the presence of four regioisomeric adducts. The confirmation of the stereochemistry at C10 could therefore not be obtained. However, the intramolecular reaction makes the *S* configuration probable.

Mass spectrometry is not, in principle, a quantitative method. However, heme derivatives are supposed to have similar volatilities under given conditions. Furthermore, the consistency between the results of HPLC and MS analyses confirms that the yields of the alkylation reactions of heme by **2** or **3** ranged from 70 to 90% under the reported conditions.

In conclusion, it is clear that compounds **2** and **3** are very efficient alkylating agents toward iron(II)-heme to provide covalent heme–drug adducts in high yields. The bulky amine substituent in the α position at C10 of compound **3** (on the same side as the peroxide bond) did not prevent the interaction with the iron center of heme that mediates the reductive activation. This is consistent with previous results obtained with model trioxanes which suggest that hindrance at C10 has no influence on the reactivity of the peroxide toward heme (active artesunate has an α configuration at C10). In fact, reduction of the carbonyl function at C10 to give an sp^3-hybridized carbon center renders the C8a-C10-C12 cycle relatively labile, as previously reported for artemether.[16] This feature somewhat complicates the characterization of the heme–drug adducts, but does not change the reactivity of the peroxide bond and, thus, does not alter the alkylating ability of these powerful antimalarial drugs.

[1] S. R. Meshnick, T. E. Taylor, S. Kamchonwongpaisan, *Microbiol. Rev.* **1996**, *60*, 301–315.

[2] a) P. L. Olliaro, R. K. Haynes, B. Meunier, Y. Yuthavong, *Trends Parasitol.* **2001**, *17*, 122–126; b) A. Robert, J. Cazelles, O. Dechy-Cabaret, B. Meunier, *Acc. Chem. Res.* **2002**, *35*, 167–174.

[3] a) U. Eckstein-Ludwig, R. J. Webb, I. D. A. van Goethem, J. M. East, A. G. Lee, M. Kimura, P. M. O'Neill, P. G. Bray, S. A. Ward, S. Krishna, *Nature* **2003**, *424*, 957–961.

[4] P. M. O'Neill, G. H. Posner, *J. Med. Chem.* **2004**, *47*, 2945–2964.

[5] a) A. Robert, J. Cazelles, B. Meunier, *Angew. Chem. Int. Ed.* **2001**, *40*, 1954–1957; b) A. Robert, Y. Coppel, B. Meunier, *Inorg. Chim. Acta* **2002**, *339*, 488–496; c) K. Selmeczi, A. Robert, C. Claparols, B. Meunier, *FEBS Lett.* **2004**, *556*, 245–248.

[6] J. Cazelles, A. Robert, B. Meunier, *J. Org. Chem.* **2002**, *67*, 609–612.

[7] S. A.-L. Laurent, C. Loup, S. Mourgues, A. Robert, B. Meunier, *ChemBioChem*, in press.

[8] R. K. Haynes, W.-Y. Ho, H.-W. Chan, B. Fugmann, J. Stetter, S. L. Croft, L. Vivas, W. Peters, B. L. Robinson, *Angew. Chem.* **2004**, *116*, 1405–1409; *Angew. Chem. Int. Ed.* **2004**, *43*, 1381–1385.

[9] a) P. M. O'Neill, A. Miller, L. P. D. Bishop, S. Hindley, J. L. Maggs, S. A. Ward, S. M. Roberts, F. Scheinmann, A. V. Stachulski, G. H. Posner, B. K. Park, *J. Med. Chem.* **2001**, *44*, 58–68; b) S. Hindley, S. A. Ward, R. C. Storr, N. L. Searle, P. G. Bray, B. K. Park, J. Davies, P. M. O'Neill, *J. Med. Chem.* **2002**, *45*, 1052–1063; c) M. Jung, K. Lee, H. Kendrick, B. L. Robinson, S. L. Croft, *J. Med. Chem.* **2002**, *45*, 4940–4944.

[10] G. Magueur, B. Crousse, S. Charneau, P. Grellier, J.-P. Bégué, D. Bonnet-Delpon, *J. Med. Chem.* **2004**, *47*, 2694–2699.

[11] A. J. Lin, D. L. Klayman, W. K. Milhous, *J. Med. Chem.* **1987**, *30*, 2147–2150.

[12] R. K. Haynes, H.-W. Chan, M.-K. Cheung, W.-L. Lam, M.-K. Soo, H.-W. Tsang, A. Voerste, I. D. Williams, *Eur. J. Org. Chem.* **2002**, 113–132.

[13] M. Jung, X. Li, D. A. Bustos, H. N. ElSohly, J. D. McChesney, W. K. Milhous, *J. Med. Chem.* **1990**, *33*, 1516–1518.

[14] A. J. Lin, M. Lee, D. L. Klayman, *J. Med. Chem.* **1989**, *32*, 1249–1252.

[15] A. Robert, Y. Coppel, B. Meunier, *Chem. Commun.* **2002**, 414–416.

[16] A. Robert, B. Meunier, *Chem. Eur. J.* **1998**, *4*, 1287–1296.

 © 2005 Wiley-VCH Verlag GmbH & Co. KGaA, Weinheim

Artemisinin Derivatives

Reply to Comments on "Highly Antimalaria-Active Artemisinin Derivatives: Biological Activity Does Not Correlate with Chemical Reactivity"

*Richard K. Haynes**

Keywords:
alkylation · antiviral agents · heme proteins · iron · porphyrinoids

Laurent, Robert, and Meunier describe the efficient alkylation of the artemisinin derivatives **18** and **23** (our original numbering;[1a] see Figure 1) by iron(II)

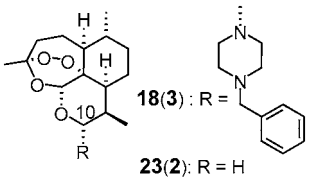

Figure 1. Artemisinin derivatives **18** and **23**, as numbered in our original communication.[1a] In parentheses are the compound numbers (**3** and **2**, respectively) according to Laurent, Robert, and Meunier.[2]

protoporphyrin-IX (Fe^{II}-heme) generated under strong reducing conditions (sodium dithionite in dimethylsulfoxide (DMSO) containing 4% water).[2] Glutathione (GSH) is also used as reductant, although no further details are given. According to an earlier publication,[3] this is likely to be a large excess (10 equiv) in DMSO, hardly conditions which can be said to mimic the biological system. We found previously that compound **18** reacts substantially (82%; see Table 2 in Ref. [1a]) with Fe^{II}-heme, generated from heme by treatment with cysteine (1 equiv) under aqueous conditions (1:1 MeCN/H_2O, pH 7.4 with phosphate buffer), although compound **23** did not.[1a] For compound **18**, besides the organic-soluble product dihydroartemisinin (6%) and non-heme decomposition products (10%), the major organic-insoluble products were heme–artemisinin adducts. However, no attempt was made to isolate or characterize these adducts, and we give credit to Laurent, Robert, and Meunier for their work in this regard.

The authors go on to ascribe the difference in reactivities observed to differences in the solubility of heme in our solvent system and their own. Whether the heme used by the authors contains iron as Fe^{II} or Fe^{III} is not specified, but one may assume that as the "heme" descriptor is used, it is in the Fe^{III} state. Thus, the authors' assumption is tenuous, particularly as compound **18** does react with Fe^{II}-heme under our conditions. They also state that derivatives **18** and **23** are "not very soluble" in aqueous solution. However, **18** reacts with Fe^{II}-heme in a 1:1 mixture of MeCN and H_2O, while **23** is completely decomposed by Fe^{II} sulfate (0.3 or 1.0 equiv) in 1:1 MeCN/H_2O. In contrast, compound **18** is much more resistant to the effect of Fe^{II} sulfate, with only a maximum of 27% undergoing decomposition.[1a] Thus, the contrasting reactivities of compounds **18** and **23** towards Fe^{II} and Fe^{II}-heme is not a result of solubility factors of the compounds.[1b] Furthermore, the comments made by the authors about the stereochemistry at C10 are not alluded to in our paper and are taken out of context. Nevertheless, if one does examine 3D structures of compound **18**, the piperazine ring is disposed such that access of Fe^{II} to the peroxide bridge may be blocked. However, this is speculative—it is not a statement of fact. Our preparative method,[1a] which could not be reproduced in Meunier's laboratory, works on multigram scales for the preparation of both **18** and all other 10-amino derivatives.

For a drug to cross a membrane, in particular from the blood stream as for an antimalarial drug, it must be dissolved in the medium outside the membrane. The use of DMSO as a vehicle for administering drugs, usually in vitro, cannot be taken to justify the authors' use of DMSO as the medium for their reactions. However, it does raise the question of the detailed environment under which heme is generated in the breakdown of hemoglobin in the food vacuole of the parasite. Whatever the environment it cannot be lipophilic, as apparently assumed by the authors. After all, the pH of the food vacuole can be measured, the food vacuole contains free Ca^{2+} ions, and fluorescence indicators,[4] which are hardly lipophilic molecules, can readily enter. Therefore, we submit that our conditions used for the heme reactions are a rather better mimic of the food vacuole than those of Laurent, Robert, and Meunier.

Laurent, Robert, and Meunier subscribe to the idea that generation of "C-centered radicals" by heme is responsible for antimalarial activity, and substantial effort has been vested thereby in the development of their "trioxaquines". As the heme–artemisinin ad-

[*] Prof. Dr. R. K. Haynes
Department of Chemistry
The Hong Kong University of Science and Technology
Clear Water Bay, Kowloon
Hong Kong (China)
Fax: (+852) 2358-1594
E-mail: haynes@ust.hk

 © 2005 Wiley-VCH Verlag GmbH & Co. KGaA, Weinheim DOI: 10.1002/anie.200462723

ducts generated from the carbon-centered radicals are inactive as antimalarials, the ability of artemisinins to generate such adducts is irrelevant. If indeed the artemisinins function as antimalarials by generating radicals, according to the heme-activation idea, this requires 1) encounter of artemisinin with Fe^{II}-heme in the food vacuole, 2) binding of the peroxide to the iron center in Fe^{II}-heme for inner-sphere electron transfer, 3) generation of the C4-centered radical and conversion of Fe^{II}-heme to Fe^{III}-heme, 4) dissociation of the oxygen ligand (arising from cleavage of the peroxide bridge) of the C4-centered radical from the iron center in Fe^{III}-heme, and 5) escape of the resulting "free" C4-centered radical from the environment of the heme, migration, and encounter with a vital parasite protein. The inner-sphere electron transfer requires that Fe is coordinated to the oxygen atom of the peroxide during the decomposition step in which it transforms to an alkoxyl. Therefore, ligand exchange with a putative external ligand (water?) is required to release the C-centered radical from the heme more rapidly than the very fast intramolecular reaction between the radical and the heme.[5] Not surprisingly, it is not possible to trap the C4 radical with cysteine, or indeed glutathione (GSH), when this reagent is used to reduce Fe^{III}-heme. The radical, however, does react with cysteine, and much less effectively with glutathione, when free Fe^{II} is used for reductive cleavage of the peroxide. Not all antimalarial-active peroxides alkylate heme-Fe^{II},[6] although there is no doubt that some artemisinins may be sequestered by heme in a biologically irrelevant process.[7] During P-450-mediated Phase I metabolism of artemisinins, inhibition of the enzyme is not observed and hydroxylation of the artemisinins takes place without affecting the peroxide function by heme within P-450.[8] Furthermore, the food vacuole does not contain the bioactive target of the artemisinins.[9]

The thrust of our original paper (see Reference [1a]) is to show that there is no correlation between the ability of artemisinins to react with either heme or non-heme Fe^{II} and their antimalarial activity. The work described by Laurent, Robert, and Meunier does not provide sufficient evidence to the contrary to force a change of view. The extremely high activities of artemisinins described in Reference [1a] are also consistent with binding to a specific target and not to a heme-mediated process that requires conversion of artemisinins into reactive intermediates—C-centered radicals—whose application as parasiticidal agents has so often been presumed but never demonstrated.

[1] a) R. K. Haynes, W. Y. Ho, H.-W. Chan, B. Fugmann, J. Stetter, S. L. Croft, L. Vivas, W. Peters, B. L. Robinson, *Angew. Chem.* **2004**, *116*, 1405 – 1409; *Angew. Chem. Int. Ed.* **2004**, *43*, 1381 – 1385; b) See reference [46] cited in our original communication (Ref. [1a]).

[2] S. A.-L. Laurent, A. Robert, B. Meunier, *Angew. Chem.* **2005**, *117*, 2096 – 2099; *Angew. Chem. Int. Ed.* **2005**, *44*, 2060 – 2063.

[3] A. Robert, Y. Coppel, B. Meunier, *Chem. Commun.* **2002**, 414 – 415.

[4] G. A. Biagini, P. G. Bray, D. G. Spiller, M. R. H. White, S. A. Ward, *J. Biol. Chem.* **2003**, *278*, 27910 – 27915.

[5] J. Cazelles, A. Robert, B. Meunier, *J. Org. Chem.* **2002**, *67*, 609 – 619.

[6] P. M. O'Neill, G. H. Posner, *J. Med. Chem.* **2004**, *47*, 2945 – 2964.

[7] S. Krishna, S. , A.- C. Uhlemann, R. K. Haynes, *Drug Resist. Updates* **2004**, *7*, 233 – 244, and references therein.

[8] R. K. Haynes, *Curr. Opin. Infect. Dis.* **2001**, *14*, 719 – 726.

[9] U. Eckstein-Ludwig, R. J. Webb, I. D. A. van Goethem, J. M. East, A. G. Lee, M. Kimura, P. M. O'Neill, P. G. Bray, S. A. Ward, S. Krishna, *Nature* **2003**, *424*, 957 – 961.

 © 2005 Wiley-VCH Verlag GmbH & Co. KGaA, Weinheim

Host—Guest Chemistry

Simultaneous Encapsulation: Molecules Held at Close Range

*Julius Rebek, Jr.**

Keywords:
molecular capsules · molecular recognition · self-assembly · stereoisomerism · tautomerism

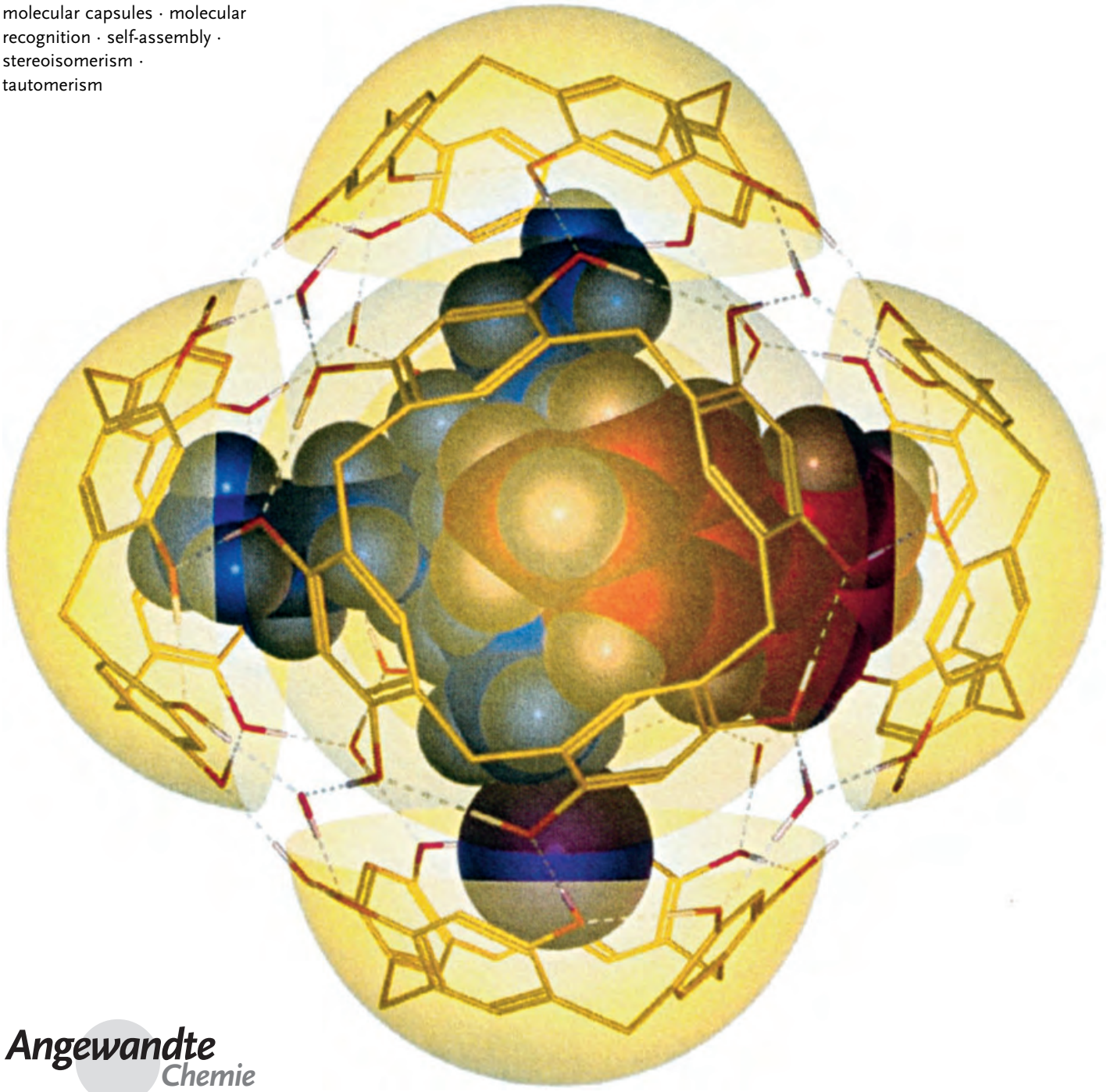

 © 2005 Wiley-VCH Verlag GmbH & Co. KGaA, Weinheim DOI: 10.1002/anie.200462839

Reversible encapsulation creates spaces where molecules are temporarily isolated from others in solution. Molecules are held within the space of the capsule for lifetimes ranging from milliseconds to hours, and conventional NMR spectroscopy can be used to report on the chemical and magnetic environment as well as the arrangement of the molecules in the encapsulation complex. The complexes self-assemble when, and only when, the spaces inside the capsules are appropriately filled. The weak intermolecular forces that hold these self-assemblies together allow equilibration of the encapsulation complexes at ambient temperatures and pressures in the liquid phase. When two or more molecules are simultaneously encapsulated, intermolecular phenomena are revealed in solution that cannot be observed by other methods. We describe here the unique behavior that emerges from molecules that are simultaneously encapsulated and includes new forms of stereochemistry, isomerism, and asymmetry inside capsules.

From the Contents

1. Introduction	2069
2. Identification of Guest Molecules inside the Capsules	2069
3. Forces within Capsules	2072
4. Arrangements in the Encapsulation Space	2073
5. Chiral Spaces	2075
6. Reactivity	2076
7. Conclusion	2077

1. Introduction

During the past two decades, molecular recognition—the science of how molecules fit together—has progressed far beyond the sequestration of ions by macrocyclic polyethers.[1] Synthetic receptors with a variety of shapes have been fashioned for binding their charged or neutral targets. These systems all share one feature: the receptors offer concave surfaces that complement their convex targets. The next generation of receptors were fashioned to cover more of their targets' surfaces, and they became more selective. It therefore appeared to us that an ultimate, if different, form of molecular recognition could involve a receptor that completely surrounded the target, namely, *encapsulated it*. Covalent bonds had already been used to make permanent arrangements of molecules-within-molecules,[2,3] but we pursued and achieved reversible encapsulation by using the weak intermolecular forces of recognition and the principles of self-assembly. Multiple copies of small modules that fit together through self-recognition were used to create a capsule—the superstructure that surrounds the target molecule. The alternative to self-assembly is the synthesis of a single (and necessarily very large) covalent structure.[4] The walls of the capsules provide mechanical barriers that temporarily isolate molecules from the outside medium. The dynamic nature of the system is simultaneously an advantage and a disadvantage. The formation and dissociation of the capsules is reversible since only weak intermolecular interactions such as hydrogen bonds are involved. The systems reach thermodynamic equilibrium rapidly under mild conditions in solution, but they require analytical methods that operate on the same timescale (such as NMR spectroscopy and electrospray mass spectrometry). The inclusion complexes do not survive purification by chromatography and only a few of our encapsulation complexes have been characterized by X-ray crystallography. Associated questions are: "What is it like inside the capsule? Are there rules that govern the filling of the space? What rules are valid for liquids? Which for gases? Is there a best fit? Can the capsule be empty? Can two or more molecules be inside? Can the space be made chiral? Can reactions occur inside?" Relatively stable (that is, longer-lived but still reversibly formed) encapsulation complexes can be accessed by using the stronger forces of metal–ligand interactions. Many examples now exist that utilize these forces; they are described elsewhere.[5–10] They provide parallel applications of the same principles of self-assembly and encapsulation that characterize the hydrogen-bonded capsules described here.

2. Identification of Guest Molecules inside the Capsules

Our initial capsule, an assembly that grew out of a collaborative effort with de Mendoza and co-workers in Madrid, was a semispherical, dimeric structure held together by a seam of eight hydrogen bonds.[11] The cavity size could accommodate only one small molecule (see Figure 1 for the structure of the capsule and its encapsulation of ethane). The assembly was characterized in solution by NMR spectroscopy. The signal for the encapsulated ethane molecule appears far upfield ($\delta = -1$ ppm), shifted there as a result of the anisotropy of the aromatic subunits of the capsule that sandwich the ethane molecule.[12] The separate signals for free and bound ethane allowed integration and the direct determination of equilibrium constants. This slow exchange (typical lifetimes are ca. 1 s) in and out of the capsules and

[*] Prof. J. Rebek, Jr.
The Skaggs Institute for Chemical Biology and
Department of Chemistry
The Scripps Research Institute
10550 North Torrey Pines Road
La Jolla, California 92037 (USA)
Fax: (+1) 858-784-2876
E-mail: jrebek@scripps.edu

 DOI: 10.1002/anie.200462839 © 2005 Wiley-VCH Verlag GmbH & Co. KGaA, Weinheim

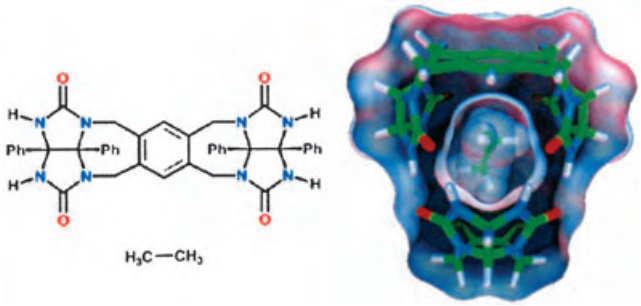

Figure 1. Left: the structure of a self-complementary module capable of forming a dimeric capsule through hydrogen bonding. Right: a view of its solvent-accessible surfaces showing the space remaining in the capsule (visualized with AVN software). The encapsulated molecule is ethane.

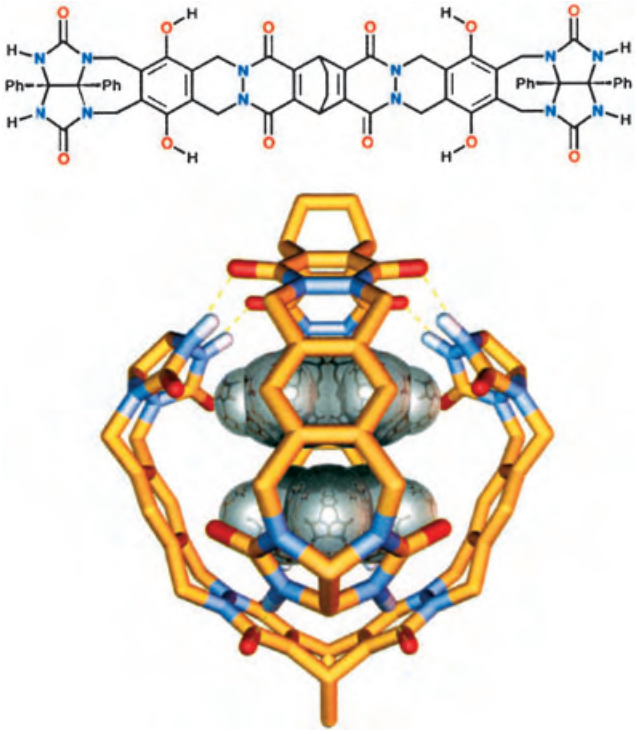

Figure 2. Top: the structure of a module for a large (400 Å^3) capsule. The molecule assembles as a spherical dimer in benzene and encapsulates two solvent molecules.

the large upfield shifts of the protons of molecules inside are characteristic of these assemblies and are common to all the capsules we describe here. The NMR spectrum indicates the magnetic environment experienced by encapsulated molecules, and integration of the spectra reveals the stoichiometry of the entire assembly.

We used a similar array of hydrogen-bond donors and acceptors to synthesize the larger semispherical structure shown in Figure 2.[13] The capsule assembled in either deuterated benzene or deuterated monofluorobenzene, but the NMR spectra gave no hint of how many solvent molecules were detained inside, or the number of subunits that formed the capsule. A third capsule species appeared in the NMR spectrum recorded in a mixture of the two solvents; accordingly, the new capsule must contain both solvents (but only one molecule of each).[14] This indirect method was the first indication of simultaneous encapsulation. This result—namely the inclusion of different solvent molecules inside the capsule—is general for large capsules and leads to the unusual thermodynamic behavior of capsules constructed from large molecules: several solvents are displaced into the bulk solution and encapsulation is entropy driven. In contrast, conventional recognition is enthalpy driven and complexes tend to dissociate at higher temperatures.

It was not until we had a nonspherical (or more specifically, a cylindrical) capsule in hand that we were able to elucidate the additional rules governing the simultaneous encapsulation of molecules. We will use this capsule to explore most of the interactions of molecules at close range. The synthesis and various calculations of the structure of this capsule is shown in Scheme 1. Our initial experiments in filling its space showed the preferential encapsulation of two *different* molecules.[15] Benzene, toluene, and *p*-xylene were all encapsulated under certain conditions, but when all three of these solvents were present, one molecule of benzene and one of *p*-xylene were preferentially encapsulated. Deuterated mesitylene is the solvent of choice for driving molecules into this capsule, as its dimensions exceed those of the cavity. Even so, a capsule forms in the unpurified, commercial solvent and it contains one molecule of deuterated benzene and one molecule of deuterated *p*-xylene, both of which are impurities in the solvent. (Note that impurities of even 0.1 % in the pure solvent represent concentrations in the millimolar range, which is the typical concentrations of the capsule used in typical NMR experiments, and demonstrates the remarkable ability of these capsules to sequester trace impurities.)

The largest of the reversibly formed capsules held together by hydrogen bonds results from the self-assembly of resorcinarenes and the closely related pyrogallolarenes (Scheme 2). They show similar tendencies to assemble, the difference being that the resorcinarenes require water for assembly and the pyrogallols do not. The resorcinarenes hold a special place in the history of encapsulation: they are the most complicated capsules and, ironically, they are the easiest to come by. Their simple synthesis—developed by Hög-

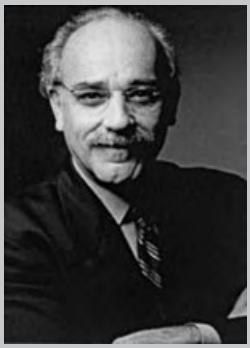

Julius Rebek, Jr. was born in Hungary in 1944. In 1970 he obtained his PhD from the Massachusetts Institute of Technology (MIT) for studies on peptide chemistry with Prof. D. S. Kemp. In the same year he became Assistant Professor at the University of California at Los Angeles and then Professor at the University of Pittsburgh (1976). In 1989 he returned to MIT as the Camille Dreyfus Professor of Chemistry. In July 1996 he moved his research group to The Scripps Research Institute to become the Director of The Skaggs Institute for Chemical Biology. His research focuses on molecular recognition and self-assembling systems.

 © 2005 Wiley-VCH Verlag GmbH & Co. KGaA, Weinheim

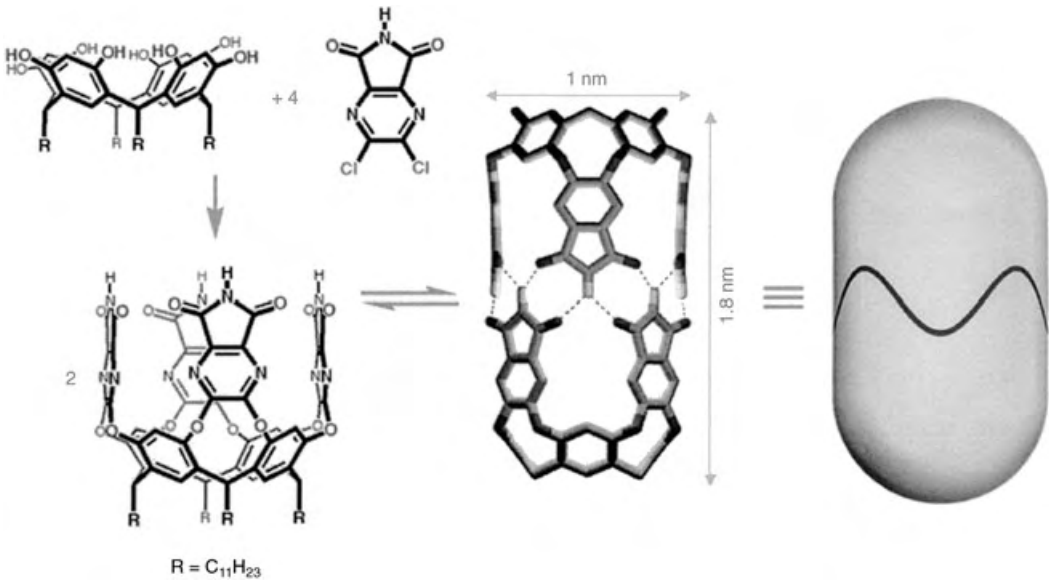

Scheme 1. Left: synthesis and structure of a cylindrical capsule. The peripheral alkyl groups that impart solubility in organic solvents are not shown. Middle: a belt of eight bifurcated hydrogen bonds holds the capsule together and generates a tapered cavity of 420 Å^3. Right: a schematic abbreviation of the capsule, which is used elsewhere in this Review.

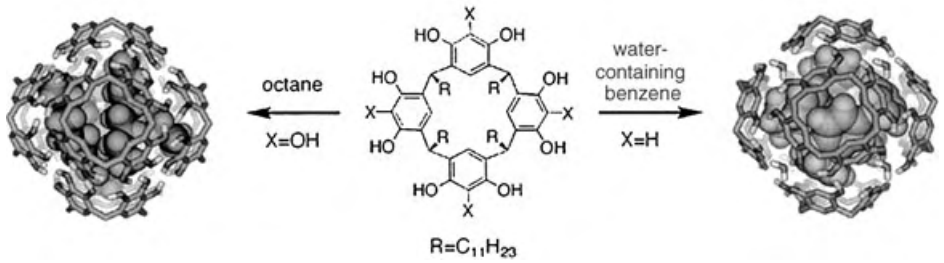

Scheme 2. Hexameric assemblies resembling cubes with one subunit at each face. Left: the pyrogallolarenes self-assemble in dry organic solvents and can encapsulate four octane molecules. Right: the resorcinarenes require eight water molecules, one at each corner of the cube. The encapsulation of eight benzene molecules is shown.

berg[16]—accounts for their active pursuit in laboratories worldwide.[17–26]

Chemical modifications of the resorcinarenes provided the first cavitands[27] and carcerands,[28] and there is now a growing body of evidence that the hexameric assemblies were present some years before, but were not recognized as hydrogen-bonded capsules. These form in wet organic solvents and contain a huge cavity (1375 Å^3) that permits encapsulation of more and ever larger guests, for example, eight benzene molecules, three biphenyl molecules, and even bulky tetraalkylammonium salts. The simultaneous encapsulation of tetrabutylammonium iodide and *p*-phenyltoluene is shown in Figure 3. Neutral molecules such as covalent antimony(v) bromides are encapsulated together with sizable smaller molecules such as naphthalene, biphenyl, anthracene, and azulene,[29] but slightly longer molecules, such as *n*-heptylbenzene, *trans*-stilbene, azobenzene, *p*-terphenyl, are not simulataneously encapsulated. The size, shape, polarity, and polarizability of the aromatic effect influences the simultaneous encapsulation, at least with nBu$_4$SbBr.

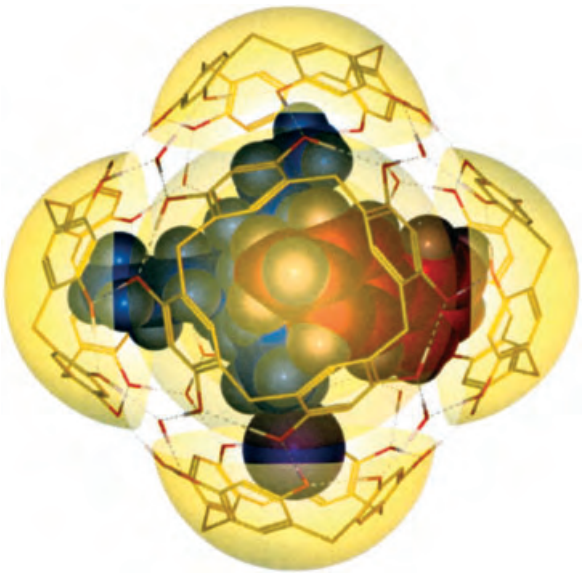

Figure 3. Encapsulation of an ion pair of tetrabutyl ammonium iodide with *p*-phenyltoluene in the hexameric resorcinarene. The hydrogen-bond network is shown as dashed lines.

 © 2005 Wiley-VCH Verlag GmbH & Co. KGaA, Weinheim

3. Forces within Capsules

The cylindrical capsule shown in Scheme 1 offers a gradient of polarity and shape along its length: the four aromatic units at the tapered ends offer a shallow, apolar (but polarizable) surface that is rigidly fixed; the four pyrazine units nearer the center are more polar but less polarizable and capable of slight breathing motions; the seam of imide groups around the center of the cavity is rich in hydrogen-bonding donors and acceptors and is the most mobile section. The entry and exit of the guests occurs through movement here, and this region attracts polar groups of encapsulated molecules.[30,31]

A molecule appears frozen in time and in space while inside a capsule, typically for one to two seconds. Its interactions with other encapsulated molecules are extended and, compared to the random and rapid collisions and exchange of partners that occur in bulk solution, are intensified or amplified in the capsule. It is possible to align the two molecules inside the cylindrical capsule so that only certain areas of their surfaces come into contact. To our knowledge this cannot be achieved by other methods and it provides a means by which subtle, intermolecular forces can be evaluated pairwise, and at the molecular level.

The ideal situation for a planned simultaneous encapsulation of two different molecules is one in which two molecules of the same species do not fill the appropriate amount of space but the combination of the two different molecules do. Fujita and co-workers have referred to this situation as an "and/or gate" and have encountered many such phenomena in metal–ligand capsules.[32] We were able to transfer this principle to the encapsulation of gases. Small molecules such as cyclopropane, methane, or ethane do find their way into the cylindrical capsule alone, nor does naphthalene, anthracene, or azulene. However, when *both* methane and anthracene are present, the NMR spectra are very sharp and illustrate that one molecule of each species is inside (Figure 4).[33] This occurrence allowed us to look at molecules that we had not been able to encapsulate under normal conditions. These studies also led to the (not surprising) conclusion that gases need more space: filling about 55% of the space or a packing coefficient of 55% is optimal for typical liquids,[34] but gases having packing coefficients as low as 30% have been encountered. A good question to ask is: what does a single molecule experience as a phase inside these capsules? Its collisions with the walls are hardly inelastic, particularly as attractive forces exist between the π lining of the capsule and the C–H bonds of small hydrocarbon gases.[35] These molecules are not billiard balls knocking around in a three-dimensional table. The notion of pressure is, accordingly, hard to define under these conditions.

The four walls of the capsule are at right angles and the cross-section generates a square array of aromatic pyrazine surfaces. How are encapsulated aromatic compounds positioned in this cavity? A diagonal arrangement offers the most space and is expected to minimize contacts that lead to steric effects (electron–electron repulsions), but what if the contacts are weakly attractive as in CH–π interactions? Many attempts to find aromatic molecules that would wedge into the corners failed to show the expected loss of symmetry in their NMR spectra, thus indicating that spinning of the encapsulated molecules remained fast—at least on the NMR timescale. We therefore created a situation in which even the spinning of a molecule would be affected by simultaneous encapsulation, with the size of one guest limiting the rotational motions of another.[36] This situation reflects the constant tradeoffs between freedom of movement and the very attractions between molecules that define the liquid state. The cubelike 2,2-paracyclophane fits snugly into one end of the cylindrical capsule, as shown in Figure 5. Any spinning motion of the cyclophane must result in a breathing motion of the capsule walls, and it is the only case we have encountered in which spinning was slow on the NMR timescale. The dimensions of the guest are such that it is too long to tumble while it is within the capsule and is too bulky to move past a simultaneously encapsulated molecule. The flexibility is likely to be greater near the more pliable hydrogen bonds at the center of the capsule than at the covalent bonds at the ends. One end of the cyclophane is forced into the tapered ends of the cavity and we believe that the contact with this narrowing space hinders the rotation of the molecule. Accordingly, simultaneously encapsulated large molecules force the paracyclophane deeper into the tapered ends and slow its rotation further. The largest simultaneously encapsulated guest, cyclohexane, slows the spinning rate the

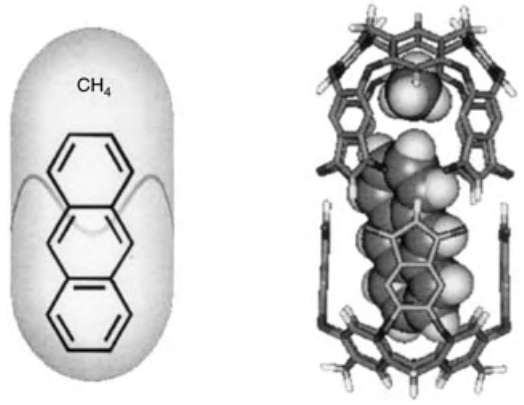

Figure 4. Anthracene and methane are encapsulated together, but neither component alone assembles an encapsulation complex.

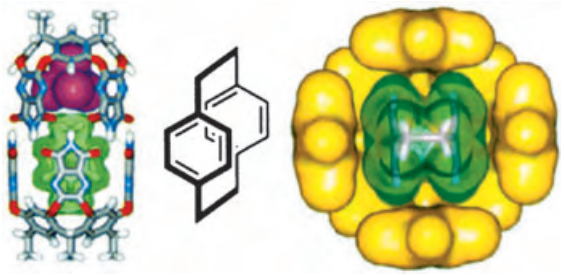

Figure 5. Simultaneously encapsulated molecules affect the spinning of paracyclophane, and is size-dependent. Left: the complex formed between carbon tetrachloride and paracyclophane (middle). Right: the paracyclophane enjoys a snug fit at one end of the capsule.

 © 2005 Wiley-VCH Verlag GmbH & Co. KGaA, Weinheim

most—with a barrier of about 16 kcal mol^{-1}—while the smallest, ethane, shows a barrier for the spinning of a little less than 15 kcal mol^{-1}. This fine-tuning is a subtle and unexpected effect, but it is confirmed by the change in chemical shifts: the furthest upfield cyclophane signal appears in the presence of the largest simultaneously encapsulated molecule.

One question remains, to what extent do the encapsulated molecules respond to events outside the capsule? Since these systems are at equilibrium with the outside their very existence represents a response to the situation in the bulk solution. There is evidence, however, that more subtle influences also exist. Specifically a chiral environment outside an achiral capsule can affect the spectrum of a molecule inside. We investigated the effect of chiral solvents and additives such as lanthanide shift reagents, but found no measurable effects, but when asymmetric centers were covalently attached to the capsule we were able to resolve diastereotopic hydrogen atoms of an encapsulated molecule in the NMR spectra. Thus, the steric effects and magnetic effects can be separated by encapsulation. It appears that the former cannot penetrate the walls of the capsule but the latter can.[37]

4. Arrangements in the Encapsulation Space

4.1. "Social Isomers"

The restrictions on the translational motions of molecules inside capsules can be easily appreciated since the structure of the capsule itself provides mechanical boundaries. However, there are also restrictions on the tumbling and, as we encountered above, spinning motions. Earlier, Reinhoudt and co-workers defined a new form of isomerism—carcero-isomerism—which arose as a result of restricted tumbling of a single molecule in an unsymmetrical capsule.[38] This restricted tumbling is also a necessary, but not sufficient, requirement for the "social isomerism" we encountered.[39]

Two different arrangements—social isomers—are observed by NMR spectroscopy (Figure 6) when one molecule of chloroform and one molecule of *N*-methyl-*p*-toluidine are simultaneously encapsulated within the cylinder. The isomers could, in principle, interconvert through the tumbling of the aromatic molecule. This process is quite slow on the NMR timescale at ambient temperature, although on heating, shorter molecules such as *p*-xylene begin to tumble while still inside the cylindrical capsule. The other means by which the two isomers could interconvert requires that one molecule slides past the other within the capsule. We have evidence of this only for narrow molecules such as short, normal alkanes. These thin, flexible molecules can slither past others of a similar kind inside, but any branching increases the steric barriers to the process.

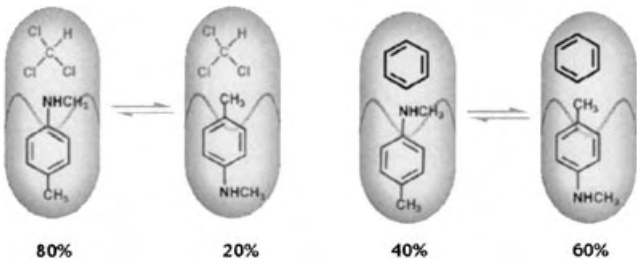

Figure 6. Interactions between single molecules of solvents and solutes. Left: the simultaneous encapsulation of chloroform and *N*-methyl-*p*-toluidine generates two "social isomers", in which the interaction of the chloroform with the *N*-methyl group is favored. Right: simultaneously encapsulated benzene with *N*-methyl-*p*-toluidine; the interaction of benzene with the C-methyl group is slightly favored. These social isomers do not interconvert within the capsule because the molecules cannot squeeze past one another and the *p*-substituted aromatic is too long to tumble freely within the capsule.

4.2. Solvation of a Single Molecule

Social isomerism is a consequence of the dimensions of the cylindrical capsule and those of the molecules inside. We have used social isomerism to assess interactions between specific functional groups of the simultaneously encapsulated molecules. The limitations on motion constrain intermolecular contact between the guests to two areas. Again, the concentrations are amplified—the volume of the capsule (ca. 4×10^{-25} L) translates into molar concentrations of each encapsulated molecule. From another viewpoint, we can observe the interaction of a solute with a single molecule of solvent in equilibrium at ambient temperatures. We tested 3 toluene derivatives (*p*-ethyl-, *p*-*N*-methyl-, and *p*-*O*-methyl) in combination with 12 simultaneously encapsulated solvents.[40] NMR spectroscopic analysis allowed the direct determination as to whether the solvent molecules had a preference for one end of the toluene derivatives or the other. The NMR spectra offer snapshots of short-lived relationships between molecules isolated from the bulk solution. We know of no other method that is capable of this determination in solution, but related studies are available in supersonic jets in the gas phase or through matrix isolation in frozen argon.[41]

4.3. Tautomeric Equilibria

We used the cylindrical capsule as a controlled nanoscale environment to influence the keto–enol equilibria. The equilibrium constants for encapsulated β-ketoesters show values that differ, both larger and smaller, by an order of magnitude from those of the free tautomers in solution. For complexes with a single, large encapsulated guest, the inner surfaces of the capsule and the seam of hydrogen bonds influence the equilibrium between the encapsulated keto and enol forms. For complexes of smaller β-ketoesters, solvents can be simultaneously encapsulated, and the solvent influences the equilibria: the solvent reduces the space available and affects the positioning of the ester in the capsule.[42] Events are no longer stochastic in the capsule and solution-phase descriptions may not be adequate to capture the nature of the events inside.

 © 2005 Wiley-VCH Verlag GmbH & Co. KGaA, Weinheim

4.4. Isotope Effects

One of the most subtle cases of social isomerism was encountered with the isotopic substitution of one of the ends of an encapsulated molecule. Equilibrium isotope effects are somewhat of a rarity in molecular recognition, but are not insignificant.[43,44] Deuterium substitution of C–H bonds tends to make the molecules slightly more polar. Perdeuterated *p*-xylene was found to be preferentially encapsulated with CCl_4 than was undeuterated *p*-xylene. The isotope effect in the competition experiments was about 1.3 in favor of the deuterated material.[45] We were then able to locate the regions of the structure that were susceptible to these subtle changes. Most of the isotope effect was located at the methyl groups of the *p*-xylene molecule; isotope substitutions on the aromatic ring had marginal effects. We next prepared a sample in which one methyl group was deuterated and one was not. This study showed the preferential binding of the deuterated methyl group to the tapered end of the cavity, away from the simultaneously encapsulated CCl_4 molecule (Figure 7). The experimental results were also reproduced by high-level computational analyses.[46]

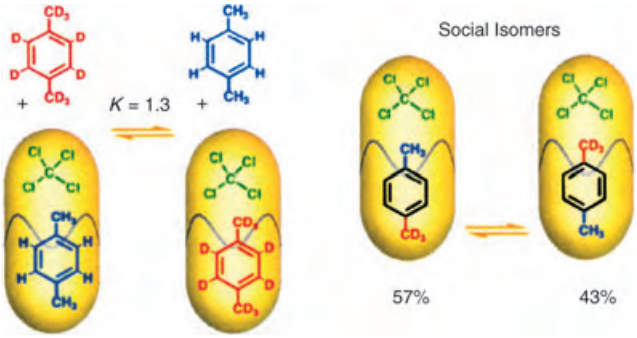

Figure 7. Equilibrium isotope effects through simultaneous encapsulation. Left: the deuterated xylene is preferentially encapsulated over the nondeuterated isotope. Right: the deuterated methyl group is more attracted to the resorcinarene that defines the end of the capsule.

4.5. Constellation Isomers

The cylindrical capsule can contain three molecules each of $CHCl_3$, 1,2-dichloroethane, or isopropyl chloride. The NMR spectrum shows two signals in a 2:1 ratio in each case. This ratio corresponds to molecules at the ends of the capsule and those near its center, respectively. Again, the simultaneously encapsulated molecules do not exchange positions while inside. Any three molecules (73–75 Å^3 each) optimally fill the capsule as they occupy about 52–54% of the space (420 Å^3). When two different guests are encapsulated, the spectra show up to four additional species which correspond to two sets of constellational isomers (Figure 8). The isomers represent molecules held in different arrangements in the space of the capsule, that is, in different *constellations*.[47] All the isomers could be identified in every pairwise combination of the solvents, with the equilibrium distributions of isomers depending on the concentrations of the solvents in the bulk

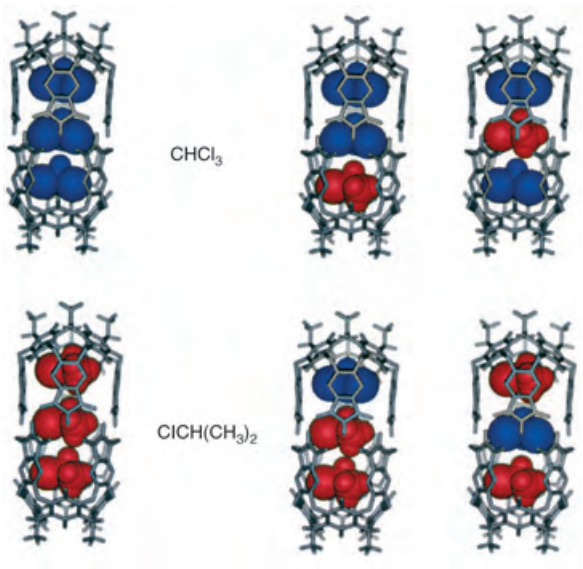

Figure 8. Isomeric constellations. Left: the capsule accommodates three molecules of chloroform (top) or three molecules of isopropyl chloride (bottom). Right: new isomeric arrangements in space can be observed for the capsules having two molecules of one solvent and one of the other when both solvents are present.

solution. The relative stability of the constellational isomers depends on the polarity of the guest molecule and their ability to interact with the capsule. All combinations of the two guests appears to be energetically acceptable and fit well into the capsule. The different arrangements represent different information, and lead to the possibility of their use in data storage.

Two isomeric constellations correspond to a binary system, and the symmetry of the capsule limits the number of states to six.[48] Three different guests offer 18 possibile states, including a constellational triplet with one of each guest inside. It is unlikely that NMR spectoscopy will be able to resolve all 18 combinations of these solvents inside, and alternative spectroscopic techniques must be found. One such assembly exists, but involves the encapsulation of anions and neutral molecules (Figure 9).[49] Unexpectedly, a number of anions are driven into the capsule when dissolved in $CHCl_3$ as

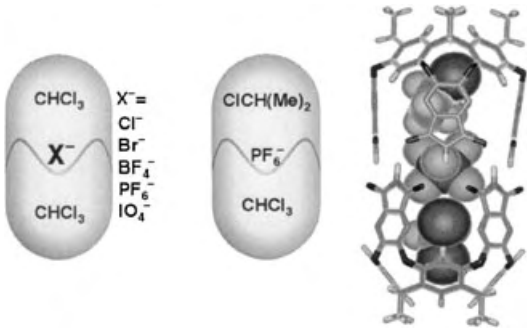

Figure 9. Encapsulation of three molecules. Left: anions are encapsulated simultaneously with chloroform solvent. The anions occupy the center of the capsule and interact with its belt of hydrogen bonds. Right: when both chloroform and isopropyl chloride are present a capsule with three different species is observed.

 © 2005 Wiley-VCH Verlag GmbH & Co. KGaA, Weinheim

their tetrabutylammonium salts. A cavitand of readily accessible size can completely surround an ion pair,[50] but we chose large cations to avoid this. The driving force is believed to be the ability of the ion to interact with the polar groups at the center of the capsule and the relatively weak interactions of the ions with solvent. We found that a PF_6^- ion could be sandwiched between simultaneously encapsulated chloroform and isopropyl chloride molecules, and were able to show the formation of other combinations of three different molecules inside.[51]

4.6. Diastereomers

We have also observed that three small chiral molecules, such as propylene sulfides, can be accommodated inside the cylindrical capsule. The odd number of molecules inside has the inevitable consequence that each capsule is chiral, and the constellational isomerism shown here involves diastereomers (Figure 10).[52] The assignments could be made using an optically pure propylene sulfide and the gradual addition of racemic material. Each isomer could be assigned at 60% *ee*. Accordingly, it is possible to use encapsulation to determine enantiomeric excesses of small molecules inside, but there are many other ways to do this.

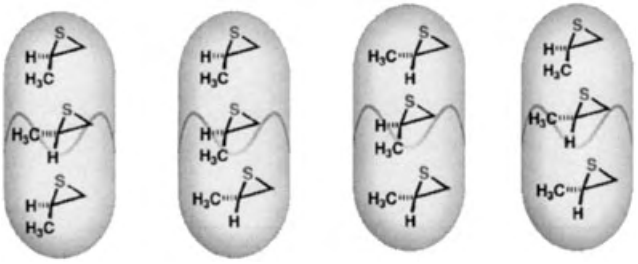

Figure 10. Diastereomeric constellations. Six possible arrangements are possible for the small chiral molecule propylene sulfide in the cylindrical capsule. The four assemblies shown each contain both enantiomers and were identified by NMR spectroscopy. All assemblies are chiral since an odd number of molecules are in each capsule.

5. Chiral Spaces

Asymmetric capsules can be synthesized from assemblies held together with covalent bonds,[53] or, through the principles of self-assembly, with hydrogen bonds[54] and metal–ligand interactions.[55,56] Enantioselection within these systems has, with very few exceptions,[52b] been disappointing, and the syntheses are lengthy and problematic. An alternative method involves the placement of a chiral molecule in an achiral capsule, *because the remaining space is also chiral!* But can that space distinguish between enantiomers of the second molecule? Complexes with simultaneously encapsulated chiral molecules in an achiral cavity is ideally, perhaps uniquely, suited to this situation. Diastereomeric complexes can be formed in a process similar to classical resolution methods. The longer lifetimes and limited inner space of capsules are likely to amplify stereochemical recognition over that in the bulk solution. Every encounter of a molecule with, for example, mandelic acid in bulk solution, involves asymmetry, but contacts are made at random and many of these place the asymmetric centers far apart. Only the average distance is experienced and recorded. Inside the capsule the asymmetric carbon atom of mandelic acid and its its partner molecule point toward the remaining space in the cavity

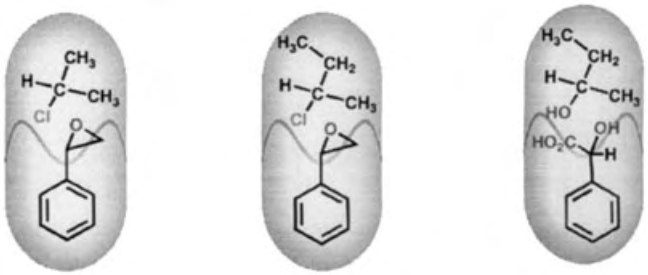

Figure 11. A chiral molecule in an achiral capsule creates a chiral space around it. Left: chiral styrene oxide is encapsulated with isopropyl chloride. The two methyl groups of the latter show different signals in the NMR spectrum. Middle: simultaneous encapsulation of styrene oxide and 2-chlorobutane leads to two diastereomers being observed in the NMR spectrum. Right: mandelic acid is encapsulated with 2-butanol and the two asymmetric centers encounter each other in the center of the capsule. A 65% diastereoselectivity results.

(Figure 11). This effect of a single enantiomer influences the simultaneously encapsulated molecule for a lifetime on the order of one second. The frenzied exchange of partners that occurs in the bulk solution contrasts with the strict pairing and the fixed orientations of the two encapsulated molecules. The effects of the asymmetric environment on molecules such as isopropyl chloride showed that the two methyl groups become diastereotopic. This result means that they experience the steric asymmetry presented by the three different groups of the nearby mandelic acid—hydrogen, hydroxy, and carboxyl. The chiral molecule imparts a magnetic asymmetry as well, which affects the remaining space.[57] The phenyl group is at the end of the capsule, "behind" the asymmetric center and acts as an excellent anchor. The positioning is optimal but we can hardly claim that we can control the process. Rather, each system has its characteristics and things can be made to happen within those constraints by manipulating the sizes, shapes, and functional groups. Molecules such as racemic 2-butanol, which can interact well with mandelic acid, generate some diastereoselectivity. Although the levels of diastereoselectivity are, at best, 60–70% and are low by the standards of modern catalytic asymmetric synthesis, they are quite high for systems held together by only hydrogen bonding.[58]

Unexpected results can emerge even when two related molecules are simultaneously encapsulated. We encountered these initially as "complexes within complexes", as shown in Figure 12. The benzoic acid and pyridone dimers are isolated in the capsule and protected from exchange of partners from the bulk solution. The compounds are held in contact within the capsule by hydrogen bonding. The complexes of *trans*-

 © 2005 Wiley-VCH Verlag GmbH & Co. KGaA, Weinheim

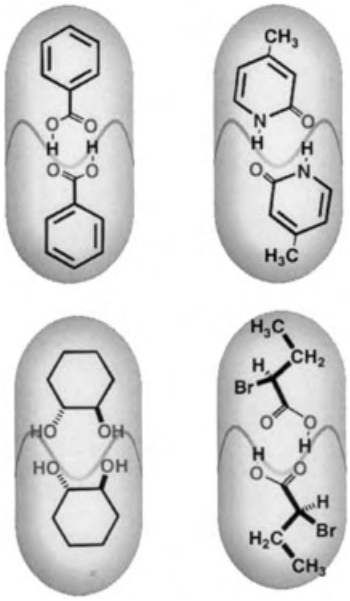

Figure 12. "Complexes inside complexes." Top: Two molecules of benzoic acid or a pyridone are encapsulated as their hydrogen-bonded dimers. Bottom: *trans*-cyclohexane diol is encapsulated as a pair of enantiomers, while 2-bromo-3-methylbutyric acid forms a complex in which two identical molecules are encapsulated.

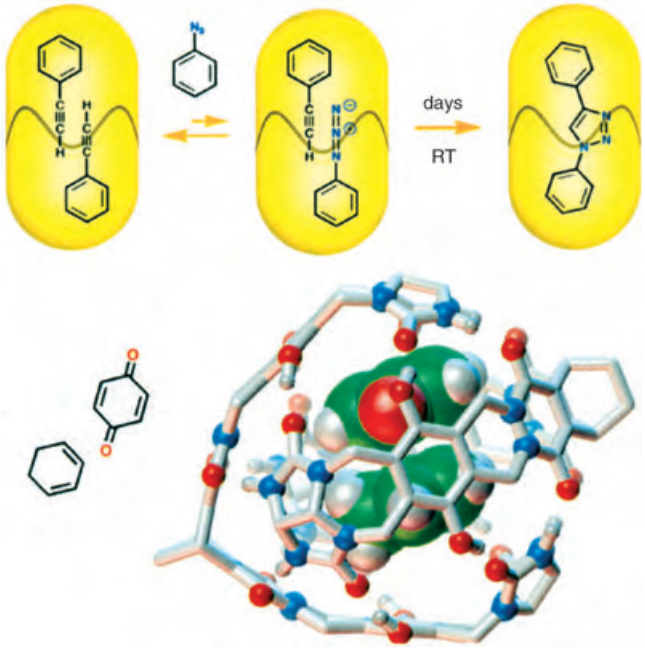

Figure 13. Encapsulated cycloaddition reactions. Top: phenylazide and phenylacetylene are preferentially encapsulated together and are positioned with their functional groups near one another at the center of the capsule. The cycloaddition gives exclusively the encapsulated regioisomer shown. Bottom: simultaneous encapsulation of *p*-benzoquinone and cyclohexadiene, both at a concentration of about 4 M in the semispherical capsule. The complex was calculated with AVN software and illustrates the reagents poised for an encapsulated Diels–Alder reaction. The acceleration in reaction rate is nearly 200-fold in the capsule, but product inhibition prevents catalytic turnover.

cyclohexane diols are more stable when two enantiomers occupy the capsule, rather than two identical molecules. This would come as no surprise to crystallographers, as centrosymmetric arrangements tend to be preferred in the solid state for packing reasons. The bromoacids shown in Figure 12, however, show the opposite preference: the capsule with two identical molecules is favored. The reason for this result is hard to specify, but it is not likely to be the steric effects of the asymmetric centers, as these are more than 6 Å apart and are shielded by the intervening carboxy groups. There appears to be little difference in the packing of the bromoacid diastereomers in the capsule. We suggest that, in addition to the well-appreciated steric effects, electronic effects may play a role in chiral recognition.

6. Reactivity

Simultaneous encapsulation creates an environment in which two molecules might be induced to react, or, if their arrangement is wrong, be prevented from reacting. We investigated a bimolecular Diels–Alder reaction of encapsulated *p*-benzoquinone and cyclohexadiene (Figure 13). The reaction in bulk solution has a half-life of more than one year at millimolar concentrations in deuterated *p*-xylene solution. However, after addition of the capsule to the reactants at these concentrations, the product could be seen inside the capsule by NMR spectroscopy after only one day.[59] Initially, the capsule contains two molecules of the quinone, but gradually fills with the product, which must arise from the encapsulation of a low concentration of the cyclohexadiene. The Diels–Alder adduct is the best guest available to the capsule, and the generation of a catalytic cycle is prevented by product inhibition. Nonetheless an acceleration of about 200-fold results. A truly catalytic system was found when thiophene dioxide was used as the diene: the Diels–Alder adduct with quinone is displaced by further reactant quinone and a catalytic cycle develops.

The cycloaddition of phenylacetylene and phenylazide is also very slow at NMR spectroscopic concentrations and gives roughly equal amounts of two regioisomeric triazoles. The rate of reaction at ambient temperature and molar concentrations in mesitylene is also very slow. However, the encapsulated product can be detected within three days at millimolar concentrations in the presence of the cylindrical capsule. Moreover, the selective formation of the encapsulated 1,4 isomer was observed.

The substrate shows size and shape selectivity, since neither 1-naphthylazide nor 4-biphenylazide show rate accelerations in their cycloadditions with phenyl acetylene when in the presence of the capsule. The naphthylazide is not encapsulated while the biphenyl azide is quickly displaced from the capsule by two phenylacetylene molecules.

The NMR spectra indicate that when both azide and acetylene are present, *the favored species is the capsule containing one molecule of each reactant*.[60] This result is a consequence of the similarity of the two guests, and it allowed the direct observation of the generated "Michaelis' complex"

 © 2005 Wiley-VCH Verlag GmbH & Co. KGaA, Weinheim

(Figure 13). The concentrations inside the capsule are about 4 M each—so viewed this way, there is no acceleration. The capsule merely concentrates the reactants temporarily and apparently in an orientation appropriate for reaction. This arrangement of reactants is a characteristic feature of enzyme catalysis. Compared with the reaction rate outside the capsule (at 25 mM each reactant), the reaction within the capsule is accelerated about 30000-fold. Product inhibition normally occurs in reactions where the products resemble transition states, and this case was no exception. Maximum binding in the transition state is the ideal situation; transition states are moving targets and reactants and products are stationary and more accessible. A recent example of an encapsulated unimolecular rearrangement with catalytic turnover[61] promises additional applications, but overcoming the general problem remains a challenge.

What is the source of the enhanced rate of reaction within the capsule? The volume of the cylindrical capsule is about 400 Å^3, and so each molecule in that space is at a concentration of about 4 M. We prefer to use these "real" concentrations, that is, molecules in a given volume, but this system has also been calculated to exhibit one of the highest known effective molarities.[62] Another approach concerns the time factor: the encapsulated complex has a lifetime on the order of one second, while in bulk solution a diffusion complex of the two reactants lives less than a nanosecond. A third consideration involves solvation: the walls of the capsule correspond to the solvent molecules, and structural changes undergone by the simultaneously encapsulated reactants—from ground state to transition state and products—are not mirrored by changes in solvation. No organization or reorganization of the walls can take place; the arrangement was determined by synthesis. We propose that the combination of well-defined volume, extended timing, and fixed solvation of the encounter in a complex formed by simultaneously encapsulated species is different from earlier inclusion systems. Cyclodextrins, crown ethers, cyclophanes, and conventional macrocyclic receptors have open-ended structures that are exposed to solvents and allow the guests to exit rapidly. Whatever the source or sources of the effect, the potential of complexes formed with simultaneously encapsulated guests to influence chemical reactivity was established with these capsules and has been borne out with many other encapsulation complexes.[63–65]

7. Conclusion

The present research on molecular capsules has its origins in the discovery of cryptophanes by Collet et al.[66] and carcerands by Cram et al.[67] None of the cryptophanes were large enough to surround more than one molecule; typical guests were small molecules, such as methane, or atoms, such as xenon. The larger carcerands (in contrast to the capsules) were sealed off and initially trapped any molecule that happened to be inside at the time the final covalent bond was formed. The encapsulation complexes are also descendants of host–guest chemistry, a term that was introduced, as far as we know, by Fieser and Fieser in their description of choleic acid complexes.[68] They are at the same time examples of molecular self-assembly and the prefix "nano" could be appropriately applied to them. We entered the study of encapsulation phenomena through the side door of physical organic chemistry; that door is still wide open.

I am grateful to the Skaggs Institute for Research and the National Institutes of Health (GM 50174) for financial support and to Professor T. Bartfai for advice. The many co-workers, whose names appear in the reference section, have made this research far more than work.

Received: December 6, 2004

[1] a) D. J. Cram, *Angew. Chem.* **1988**, *100*, 1041 – 1052; *Angew. Chem. Int. Ed. Engl.* **1988**, *27*, 1009 – 1020; b) J.-M. Lehn, *Angew. Chem.* **1988**, *100*, 91 – 116; *Angew. Chem. Int. Ed. Engl.* **1988**, *27*, 90 – 112; c) C. J. Pedersen, *Angew. Chem.* **1988**, *100*, 1053 – 1059; *Angew. Chem. Int. Ed. Engl.* **1988**, *27*, 1021 – 1027.
[2] D. J. Cram, H.-J. Choi, J. A. Bryant, C. B. Knobler, *J. Am. Chem. Soc.* **1992**, *114*, 7765 – 7773.
[3] A. Collet, *Tetrahedron* **1987**, *43*, 5725 – 5759.
[4] N. Chopra, J. C. Sherman, *Angew. Chem.* **1999**, *111*, 2109 – 2111; *Angew. Chem. Int. Ed.* **1999**, *38*, 1955 – 1957.
[5] M. Fujita, K. Umemoto, M. Yoshizawa, N. Fujita, T. Kusukawa, K. Biradha, *Chem. Commun.* **2001**, 509 – 518.
[6] S. Hirakoa, M. Fujita, *J. Am. Chem. Soc.* **1999**, *121*, 10239 – 10240.
[7] T. Kusukawa, M. Fujita, *J. Am. Chem. Soc.* **2002**, *124*, 13576 – 13582.
[8] D. J. Johnson, K. N. Raymond, *Supramol. Chem.* **2001**, *13*, 639 – 659.
[9] A. V. Davis, R. M. Yeh, K. N. Raymond, *Proc. Natl. Acad. Sci. USA* **2002**, *99*, 4793 – 4796.
[10] D. L. Caulder, K. N. Raymond, *Acc. Chem. Res.* **1999**, *32*, 975 – 992.
[11] R. Wyler, J. de Mendoza, J. Rebek, Jr., *Angew. Chem.* **1993**, *105*, 1820 – 1821; *Angew. Chem. Int. Ed. Engl.* **1993**, *32*, 1699 – 1701.
[12] N. Branda, R. Wyler, J. Rebek, Jr., *Science* **1994**, *263*, 1222 – 1223.
[13] R. Meissner, J. Rebek, Jr., J. de Mendoza, *Science* **1995**, *270*, 1485 – 1488.
[14] J. Kang, J. Rebek, Jr., *Nature* **1996**, *382*, 239 – 241.
[15] T. Heinz, D. M. Rudkevich, J. Rebek, Jr., *Nature* **1998**, *394*, 764 – 766.
[16] a) A. G. S. Högberg, *J. Am. Chem. Soc.* **1980**, *102*, 6046 – 6050; b) A. G. S. Högberg, *J. Org. Chem.* **1980**, *45*, 4498 – 4500.
[17] T. Gerkensmeier, W. Iwanek, C. Agena, R. Fröhlich, S. Kotila, C. Näther, J. Mattay, *Eur. J. Org. Chem.* **1999**, 2257 – 2262.
[18] J. L. Atwood, L. J. Babour, A. Jerga, *Chem. Commun.* **2001**, 2376 – 2377.
[19] J. L. Atwood, L. J. Babour, A. Jerga, *Proc. Natl. Acad. Sci. USA* **2002**, *99*, 4837 – 4841.
[20] G. W. V. Cave, J. Antesberger, L. J. Barbour, R. M. McKinlay, J. L. Atwood, *Angew. Chem.* **2004**, *116*, 5375 – 5378; *Angew. Chem. Int. Ed.* **2004**, *43*, 5263 – 5266.
[21] L. Avram, Y. Cohen, *J. Am. Chem. Soc.* **2002**, *124*, 15148 – 15149.
[22] L. Avram, Y. Cohen, *Org. Lett.* **2002**, *4*, 4365 – 4368.
[23] L. Avram, Y. Cohen, *J. Am. Chem. Soc.* **2004**, *126*, 11556 – 11563.
[24] M. Yamanaka, A. Shivanyuk, J. Rebek, Jr., *J. Am. Chem. Soc.* **2004**, *126*, 2939 – 2943.
[25] A. Shivanyuk, J. Rebek, Jr., *Proc. Natl. Acad. Sci. USA* **2001**, *98*, 7662 – 7665.
[26] L. C. Palmer, J. Rebek, Jr., *Chem. Commun.* **2005**, in press.

 © 2005 Wiley-VCH Verlag GmbH & Co. KGaA, Weinheim

[27] J. R. Moran, S. Karbach, D. J. Cram, *J. Am. Chem. Soc.* **1982**, *104*, 5826 – 5828.
[28] J. C. Sherman, C. C. Knobler, D. J. Cram, *J. Am. Chem. Soc.* **1991**, *113*, 2194 – 2204.
[29] A. Shivanyuk, J. Rebek, Jr., *Chem. Commun.* **2001**, 2424 – 2425.
[30] T. Heinz, D. M. Rudkevich, J. Rebek, Jr., *Angew. Chem.* **1999**, *111*, 1206 – 1209; *Angew. Chem. Int. Ed.* **1999**, *38*, 1136 – 1139.
[31] M. H. K. Ebbing, M.-J. Villa, J.-M. Valpuesta, P. Prados, J. de Mendoza, *Proc. Natl. Acad. Sci. USA* **2002**, *99*, 4962 – 4966.
[32] See, for example, M. Yoshizawa, M. Tamura, M. Fujita, *J. Am. Chem. Soc.* **2004**, *126*, 6846 – 6847.
[33] A. Shivanyuk, A. Scarso, J. Rebek, Jr., *Chem. Commun.* **2003**, *11*, 1230 – 1231.
[34] S. Mecozzi, J. Rebek, Jr., *Chem. Eur. J.* **1998**, *4*, 1016 – 1022.
[35] M. Nishio, Y. Umezawa, M. Hirota, Y. Takeuchi, *Tetrahedron* **1995**, *51*, 8665 – 8701.
[36] A. Scarso, H. Onagi, J. Rebek, Jr., *J. Am. Chem. Soc.* **2004**, *126*, 12728 – 12729.
[37] M. M. Spence, S. M. Rubin, I. E. Dimitrov, E. J. Ruiz, D. E. Wemmer, A. Pines, S. Q. Yao, F. Tian, P. G. Schultz, *Proc. Natl. Acad. Sci. USA* **2001**, *98*, 10654 – 10657.
[38] P. Timmerman, W. Verboom, F. C. J. M. van Veggel, J. P. M. van Duynhoven, D. N. Reinhoudt, *Angew. Chem.* **1994**, *106*, 2437 – 2440; *Angew. Chem. Int. Ed. Engl.* **1994**, *33*, 2345 – 2348.
[39] A. Shivanyuk, J. Rebek, Jr., *J. Am. Chem. Soc.* **2002**, *124*, 12074 – 12075.
[40] A. Scarso, A. Shivanyuk, J. Rebek, Jr., *J. Am. Chem. Soc.* **2003**, *125*, 13981 – 13983.
[41] a) K. Sundararajan, K. Sankaran, K. S. Viswanathan, *J. Phys. Chem. A* **2002**, *106*, 1504 – 1510; b) L. George, E. Sanchez-Garcia, W. Sander, *J. Phys. Chem. A* **2003**, *107*, 6850 – 6858; c) J. R. Clarkson, E. Baquero, V. A. Shubert, E. M. Myshakin, K. D. Jordan, T. S. Zwier, *Science*, published online on 3rd February 2005, 10.1126/science.1106977.
[42] A. Scarso, J. Rebek, Jr., *J. Am. Chem. Soc.* **2004**, *126*, 8956 – 8960.
[43] D. Wade, *Chem.-Biol. Interact.* **1999**, *117*, 191 – 217.
[44] M. Turowski, N. Yamakawa, J. Meller, K. Kimata, T. Ikegami, K. Hosoya, N. Tanaka, E. R. Thornton, *J. Am. Chem. Soc.* **2003**, *125*, 13836 – 13849.
[45] D. Rechavi, A. Scarso, J. Rebek, Jr., *J. Am. Chem. Soc.* **2004**, *126*, 7738 – 7739.
[46] Y.-L. Zhao, K. N. Houk, D. Rechavi, A. Scarso, J. Rebek, Jr., *J. Am. Chem. Soc.* **2004**, *126*, 11428 – 11429.
[47] A. Shivanyuk, J. Rebek, Jr., *Angew. Chem.* **2003**, *115*, 708 – 710; *Angew. Chem. Int. Ed.* **2003**, *42*, 684 – 686.
[48] M. Yamanaka, J. Rebek, Jr., *Proc. Natl. Acad. Sci. USA* **2004**, *101*, 2669 – 2672.
[49] O. Hayashida, A. Shivanyuk, J. Rebek, Jr., *Angew. Chem.* **2002**, *114*, 3573 – 3576; *Angew. Chem. Int. Ed.* **2002**, *41*, 3423 – 3426.
[50] J. L. Atwood, A. Szumna, *J. Am. Chem. Soc.* **2002**, *124*, 10646 – 10647.
[51] T. Amaya, J. Rebek, Jr., *Chem. Commun.* **2004**, 1802 – 1803.
[52] M. Yamanaka, J. Rebek, Jr., *Chem. Commun.* **2004**, 1690 – 1691.
[53] a) J. Canceill, L. Lacombe, A. Collet, *J. Am. Chem. Soc.* **1985**, *107*, 6993 – 6996; b) J. Yoon, D. J. Cram, *J. Am. Chem. Soc.* **1997**, *119*, 11796 – 11806; c) J. K. Judice, D. J. Cram, *J. Am. Chem. Soc.* **1991**, *113*, 2790 – 2791.
[54] a) J. M. Rivera, T. Martin, J. Rebek, Jr., *J. Am. Chem. Soc.* **2001**, 123, 5213 – 5220; b) J. Tokunaga, J. Rebek, Jr., *J. Am Chem. Soc.* **1998**, *120*, 66 – 69; c) R. K. Castellano, C. Nuckolls, J. Rebek, Jr., *J. Am. Chem. Soc.* **1999**, 11156 – 11163; d) R. K. Castellano, B. H. Kim, J. Rebek, Jr., *J. Am. Chem. Soc.* **1997**, *119*, 12671 – 12672; e) C. Nuckolls, F. Hof, T. Martin, J. Rebek, Jr., *J. Am. Chem. Soc.* **1999**, *121*, 10281 – 10285.
[55] a) M. Fujita, K. Umemoto, M. Yoshizawa, N. Fujita, T. Kusukawa, K. Biradha, *Chem. Commun.* **2001**, 509 – 518; b) S. Hirakoa, M. Fujita, *J. Am. Chem. Soc.* **1999**, *121*, 10239 – 10240; c) T. Kusukawa, M. Fujita, *J. Am. Chem. Soc.* **2002**, *124*, 13576 – 13582.
[56] D. L. Caulder, K. N. Raymond, *Acc. Chem. Res.* **1999**, *32*, 975 – 982.
[57] A. Scarso, A. Shivanyuk, O. Hayashida, J. Rebek, Jr., *J. Am. Chem. Soc.* **2003**, *125*, 6239 – 6243.
[58] L. R. MacGillivray, J. L. Atwood, *Nature* **1997**, *389*, 469 – 472.
[59] J. Kang, J. Rebek, Jr., *Nature* **1997**, *385*, 50 – 52.
[60] J. Chen, J. Rebek, Jr., *Org. Lett.* **2002**, *4*, 327 – 329.
[61] D. Fiedler, R. G. Bergman, K. N. Raymond, *Angew. Chem.* **2004**, *116*, 6916 – 6919; *Angew. Chem. Int. Ed.* **2004**, *43*, 6748 – 6751.
[62] R. Cacciapaglia, S. Di Stefano, L. Mandolini, *Acc. Chem. Res.* **2004**, *37*, 113 – 122.
[63] For recent examples, see L. S. Kaanumalle, C. L. D. Gibb, B. C. Gibb, V. Ramamurthy, *J. Am. Chem. Soc.* **2004**, *126*, 14366 – 14367; D. H. Leung, D. Fielder, R. G. Bergman, K. N. Raymond, *Angew. Chem.* **2004**, *116*, 981 – 984; *Angew. Chem. Int. Ed.* **2004**, *43*, 963 – 966; M. Yoshizawa, Y. Takeyama, T. Okano, M. Fujita, *J. Am. Chem. Soc.* **2003**, *125*, 3243 – 3247.
[64] M. Ziegler, J. L. Brumaghim, K. N. Raymond, *Angew. Chem.* **2000**, *112*, 4285 – 4287; *Angew. Chem. Int. Ed.* **2000**, *39*, 4119 – 4121.
[65] M. Yoshizawa, T. Kusukawa, M. Fujita, K. Yamaguchi, *J. Am. Chem. Soc.* **2000**, *122*, 6311 – 6312.
[66] a) A. Collet, J.-P. Dutasta, B. Lozach, J. Canceill, *Top. Curr. Chem.* **1993**, *165*, 103 – 129; b) L. Garel, J.-P. Dutasta, A. Collet, *Angew. Chem.* **1993**, *105*, 1048 – 1050; *Angew. Chem. Int. Ed. Engl.* **1993**, *32*, 1169 – 1171.
[67] a) D. J. Cram, S. Karbach, Y. H. Kim, *J. Am. Chem. Soc.* **1985**, *107*, 2575; b) D. J. Cram, J. M. Cram, *Container Molecules and Their Guests*, Royal Society of Chemistry, Cambridge, **1994**.
[68] L. F. Fieser, M. Fieser, *Steroids*, Reinhold, New York, **1959**, p. 58.

 © 2005 Wiley-VCH Verlag GmbH & Co. KGaA, Weinheim

Communications

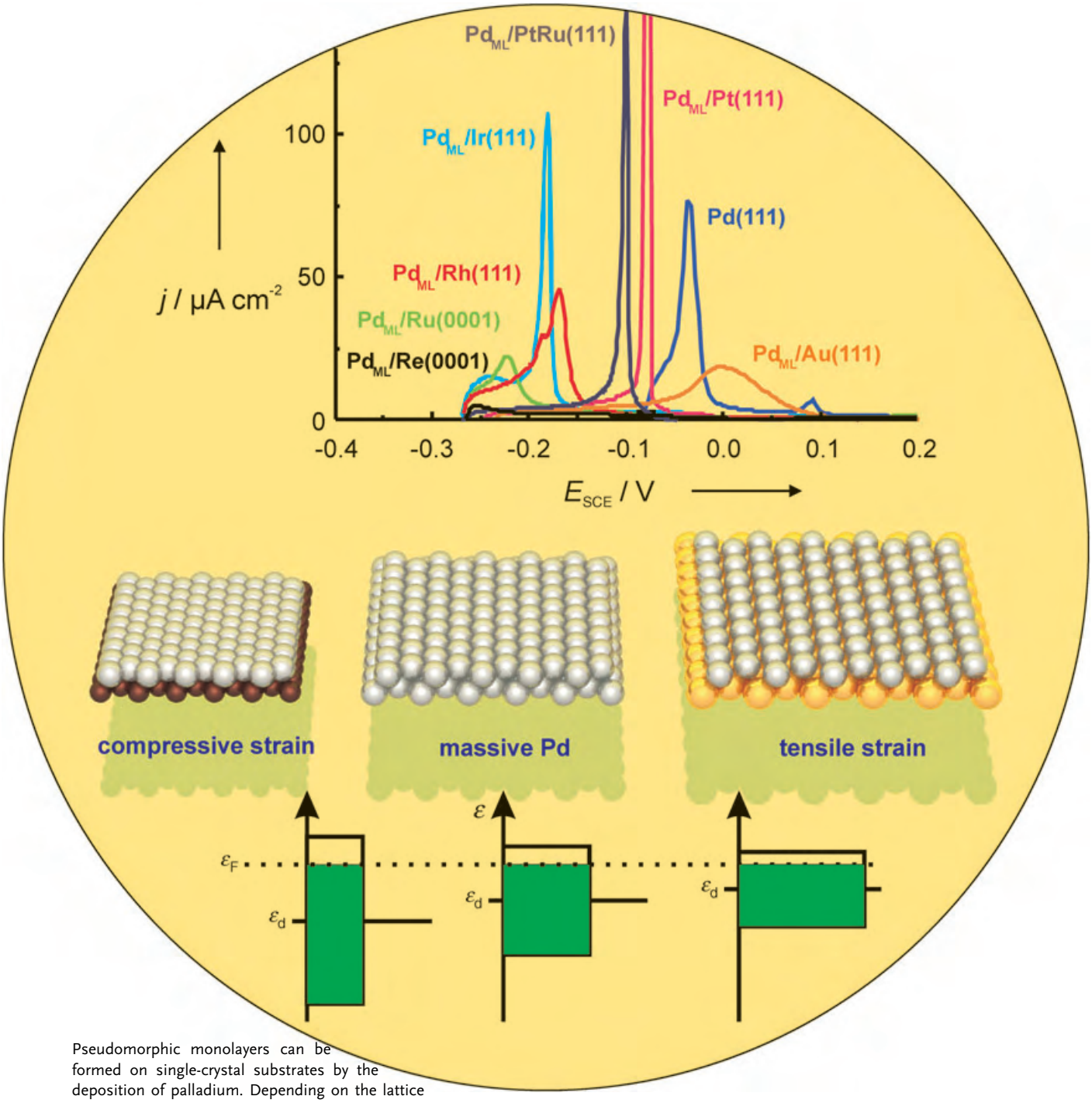

Pseudomorphic monolayers can be formed on single-crystal substrates by the deposition of palladium. Depending on the lattice parameters of the substrate, the palladium monolayer is compressed or dilated, effects which alter its properties, for example, the adsorption of hydrogen or the electrooxidation of formic acid. The changes in these properties can be studied electrochemically. For more information see the Communication by L. A. Kibler et al. on the following pages.

 © 2005 Wiley-VCH Verlag GmbH & Co. KGaA, Weinheim DOI: 10.1002/anie.200462127

Electrocatalysis

Tuning Reaction Rates by Lateral Strain in a Palladium Monolayer**

Ludwig A. Kibler, Ahmed M. El-Aziz, Rüdiger Hoyer, and Dieter M. Kolb*

One main goal of current electrocatalysis studies is to establish the relationship between the surface structure of an electrode material and its catalytic activity for a given reaction.[1] Because of constraints set by most experimental techniques, catalytic phenomena on surfaces are commonly studied with model reactions on well-ordered metal surfaces. Such studies contribute to a general understanding of structure–reactivity relationships. In addition, model surfaces are also used in theory to elucidate basic principles and trends in catalysis, for example, by density functional theory (DFT) calculations.[2]

Commonly employed model surfaces comprise single-crystal electrode surfaces, which are mainly characterized by their chemical composition, their crystallographic orientation, and the amount and the type of defects. These parameters are crucial for the kinetics of electrode reactions that involve adsorption of intermediates.[3,4]

More recently, the role of surface strain in catalysis, particularly as a means of tuning the catalytic activity, has attracted interest.[5–7] Such strained surfaces can be realized by the deposition of a metal onto a single-crystal substrate that has different lattice constants. In the case of palladium (1×1) commensurates are formed, that is, pseudomorphic monolayers, this topic is reported herein.

Palladium overlayers on early-transition-metal surfaces can have altered physical and chemical properties.[8–10] However, there was not always consensus concerning the origin of such changes.[11] A rehybridization of the d-band without considerable charge transfer from one metal to the other seems to be the key to understanding this phenomenon.[11]

Recently, it has been shown by DFT calculations that the electronic properties of a surface can be modified considerably by changing nearest-neighbor separations, such as in pseudomorphic overlayers.[12–18] This effect is related to a shift in the d-band center, the energetic position of which is crucial for determining the physical and chemical properties of the surface.[13] Accordingly, a change in the geometry of the surface lattice will influence the bond strength of an adsorbate. However, most of the calculated structures cannot easily be fabricated or are not stable under real conditions. As an extreme case, Koper et al. calculated the effect of changing the atomic separations in an unsupported(!) platinum monolayer on its adsorption properties.[19] In this way, the effect of pure lateral strain has been computed, since substrate effects are excluded, and valuable physical trends are obtained.

The effect of local strain, which is induced by subsurface argon bubbles, on the adsorption strength of oxygen atoms has been examined by scanning tunneling microscopy (STM).[20] Other methods, such as photoelectron[10] and vibrational spectroscopy,[21] have been used to reveal the altered properties of pseudomorphic overlayers. However, these methods give only indirect information about adsorption strengths.

Although of practical importance, the consequences of lateral strain within metal overlayers on electrocatalytic reactions have to date not been studied systematically. Only in a few investigations, was the influence of pseudomorphic growth on the catalytic activity considered.[5,7,22] Recent electrochemical studies with epitaxially grown palladium overlayers on Au(111) surfaces involved adsorption and absorption of hydrogen,[23] formic acid oxidation,[5,22] oxygen reduction,[24] as well as formaldehyde[25] and CO oxidation.[4] In all these cases, systematic changes in the activity with palladium overlayer thickness were reported.

Herein, we present an electrochemistry study with pseudomorphic palladium monolayers on seven different single-crystal electrode surfaces of hexagonal orientation. We give clear experimental evidence for a change in electrochemical properties of the (1×1) palladium monolayer with the lattice parameter, in full accord with theory.[13] The processes studied are hydrogen adsorption and the electrooxidation of formic acid.

The electrochemical behavior of a freshly prepared,[4,26] massive Pd(111) electrode in 0.1 M H_2SO_4 is most conveniently characterized by a cyclic voltammogram (Figure 1). Positive of 0.6 V (all potentials are measured and quoted against the

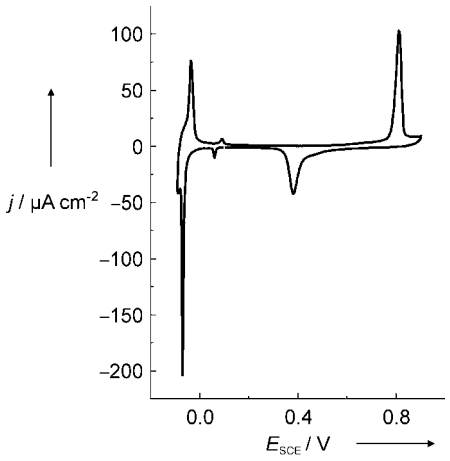

Figure 1. Cyclic voltammogram for a clean and well-ordered Pd(111) electrode in 0.1 M H_2SO_4. Scan rate $\nu = 10\ mV s^{-1}$. The curve shows the first scan, starting at 0.1 V versus SCE in negative direction.

[*] Dr. L. A. Kibler, Dr. R. Hoyer, Prof. Dr. D. M. Kolb
Abteilung Elektrochemie
Universität Ulm
89069 Ulm (Germany)
Fax: (+49) 731-50-25409
E-mail: ludwig.kibler@chemie.uni-ulm.de
Dr. A. M. El-Aziz
National Research Center, Physical Chemistry Department
El-Tahrir Street 12622 Dokki, Cairo (Egypt)

[**] Financial support by the Fonds der Chemischen Industrie is greatly acknowledged.

 © 2005 Wiley-VCH Verlag GmbH & Co. KGaA, Weinheim

saturated calomel electrode SCE) surface oxidation starts, with an anodic current peak at 0.8 V. This potential region is usually avoided in our experiments, since irreversible surface defects are generated during reduction of the oxide at 0.4 V.[27] Negative of 0 V, the electrochemical behavior of palladium is dominated by absorption of hydrogen into the bulk metal. However, with well-ordered Pd(111) surfaces a sharp peak around −0.07 V emerges for concomitant hydrogen adsorption and sulfate desorption.[28,29] An ordered sulfate adlayer is formed on the Pd(111) surface at +0.09 V[29] giving rise to a small voltammetric peak (Figure 1).

While the surface preparation for massive palladium single-crystal electrodes needs careful control of annealing and cooling conditions, the preparation of pseudomorphic palladium monolayers can easily be done by electrochemical deposition. This process has been thoroughly studied for palladium on Au(111)[23,30,31] and Pt(111),[5,27,32,33] and recently also for Rh(111),[34] Ru(0001),[35,36] Ir(111), Re(0001) and PtRu(111).[36] Palladium is deposited onto these single-crystal surfaces from $PdCl_2$ or $PdSO_4$ containing acidic solutions. A palladium monolayer can be formed either by underpotential deposition (upd) as in the case of Au, Pt, or Rh surfaces, or by controlled dissolution of multilayers (Ru, Ir, Re). A transition to a rather three-dimensional growth is observed after the formation of one monolayer in all cases except for Au(111), where two complete monolayers can be obtained.[31]

Figure 2 shows a series of STM images for the growth of the first pseudomorphic palladium monolayer on Au(111).[31] The topography of the substrate is nicely reproduced by the monoatomic high-palladium layer (Figure 2d). Note that there are no signs of alloy formation for all the systems under study. The pseudomorphy of palladium monolayers on Au(111)[37] and Pt(111)[38] was verified by in situ surface X-ray diffraction measurements. For the other systems, the formation of a pseudomorphic monolayer is inferred from in situ STM measurements, which reveal two-dimensional growth, and from cyclic voltammetry.

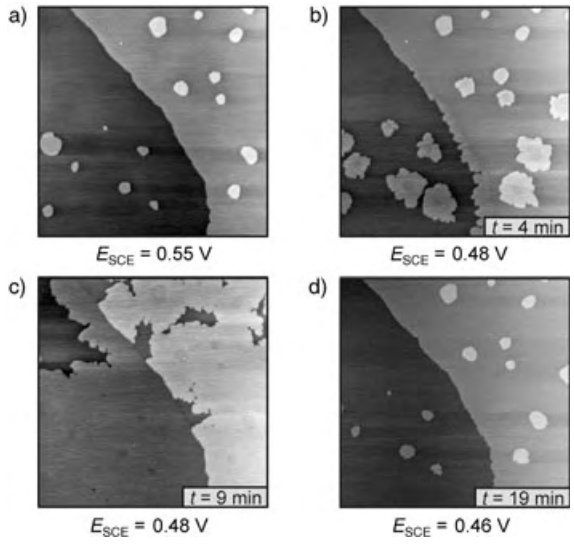

Figure 2. Series of STM images (500 nm × 500 nm) for palladium deposition onto Au(111) from 0.1 M H_2SO_4 + 0.1 mM $[PdCl_4]^{2-}$.[31] A monoatomic high step and several monoatomic high islands are seen on the bare gold surface (a) at 0.55 V. Starting from these defects palladium islands grow on the surface (b, c). The full pseudomorphic palladium monolayer reproduces exactly the topography of the substrate (d).

While the electrochemical behavior of the pseudomorphic palladium layers is markedly different from that of a massive Pd(111) electrode, bulk properties are approached for thicker overlayers in all cases. Thin Pd overlayers show a high overpotential for the absorption of hydrogen.[23] As a consequence, characteristic voltammetric peaks arising from hydrogen adsorption can be readily observed, which are usually masked by the large currents for hydrogen absorption into bulk palladium.

Figure 3 shows the positive-potential scans of cyclic voltammograms for pseudomorphic palladium monolayers on Au(111), Pt(111), PtRu(111), Rh(111), Ir(111), Ru(0001),

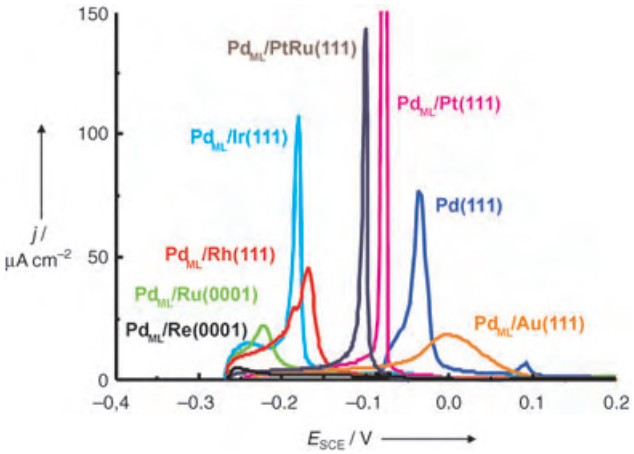

Figure 3. Positive voltammetric sweeps for Pd(111) and pseudomorphic palladium monolayers (Pd_{ML}) on seven different single-crystal substrates in 0.1 M H_2SO_4, revealing a spectrum for hydrogen desorption. Scan rate $\nu = 10\ mV s^{-1}$.

and Re(0001) together with the corresponding curve for bulk Pd(111). Sulfuric acid was used instead of perchloric acid as electrolyte owing to the possibility of chloride formation by electrocatalytic perchlorate reduction. The so-called CO displacement method has shown that (bi)sulfate is adsorbed on the palladium surface at potentials positive of the characteristic peaks in Figure 3, and hydrogen at potentials negative of them.[4,39] Though influenced by anion adsorption, the peak potentials serve as a measure for the hydrogen-adsorption strength (the free enthalpy of adsorption can be derived directly from them) in such a solution. We assume that hydrogen adsorbs much stronger than sulfate, since the hydrogen peak potentials for sulfuric acid are more positive than the potentials of zero charge.[40]

Nørskov et al. have shown recently that d-band centers for pseudomorphic overlayers, shift in energy with nearest-neighbor separations, an effect which has a direct influence on binding energies.[12,13] Their model is reproduced in simplified form in Figure 4a. In Figure 4b, the electrode potentials for hydrogen desorption on the various Pd(111) surfaces are plotted versus the d-band shift, taken from

 © 2005 Wiley-VCH Verlag GmbH & Co. KGaA, Weinheim

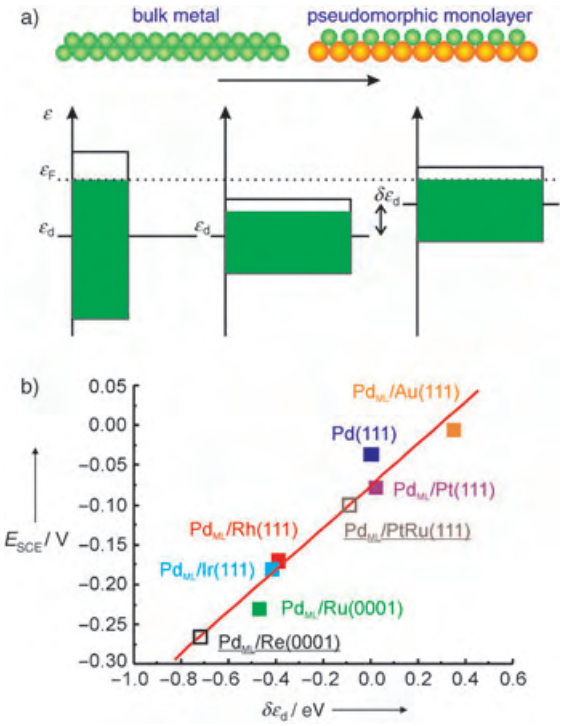

Figure 4. a) The main origin of a shift in the d-band center ε_d is a change in the interatomic distances within an overlayer. If the d-band of a metal is more than half-filled, an expanded pseudomorphic monolayer will lead to an up-shift of ε_d owing to band narrowing and energy conservation.[13] b) A plot of the hydrogen-desorption potentials versus the shift of the d-band center, $\delta\varepsilon_d$, shows a linear correlation as theoretically predicted.[13] For palladium on the Re(0001) substrate, no hydrogen peak was measured (see text). The hydrogen peak at −0.1 V for palladium on PtRu(111) suggests a shift of the d-band center $\delta\varepsilon_d$ of about −0.1 eV, which has not yet been calculated.

The altered adsorption behavior of hydrogen on the different palladium surfaces, suggests that reactions involving adsorbed intermediates will also have different kinetic parameters for the various palladium surfaces. We chose formic acid oxidation as a test reaction.

Although platinum as the most prominent electrocatalyst for many oxidation reactions, it is easily poisoned during the oxidation of formic acid by intermediate carbon monoxide, this undesired side reaction is strongly suppressed on palladium electrodes. Figure 5 shows current–potential

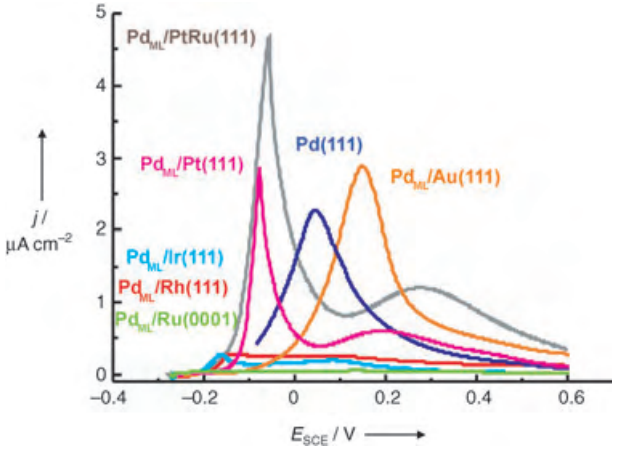

Figure 5. Current–potential curves (positive sweeps) showing the oxidation of formic acid on Pd(111) and on pseudomorphic palladium monolayers in 0.1 M H_2SO_4 + 0.2 M HCOOH. Scan rate $\nu = 20$ mV s^{-1}. The curve for palladium on Re(0001) is not shown, since the activity of that surface is practically zero as in the case of palladium on Ru(0001).

ref. [13]. The linear correlation between both quantities is clearly seen.

Cyclic voltammograms performed with palladium monolayers on Re(0001) revealed that there is no hydrogen adsorption on such a surface in sulfuric acid solutions. An explanation for this observation is also given in Figure 4b: From the calculation of the corresponding d-band shift (−0.72 eV[41]), it is concluded that hydrogen is only weakly bound to this surface and the hydrogen adsorption peak is shifted into the hydrogen-evolution region and hence, escapes detection. This example shows that the electronic modification of a palladium monolayer has essentially two contributions. 1) If the lattice parameter of the overlayer is different from that of the surface of the bulk metal, the extent of metal–metal bonding within the surface is changed and accompanied by a shift in the d-band center (geometric effect). 2) If the electronic interaction between the surface layer and the substrate is large, the location of the d-band center is also influenced by the so-called ligand effect. Since the d-band center shifts systematically with the lattice (the Pd–Pd separation) the geometric effect is dominant for all the systems shown in Figure 4 except for palladium on Re(0001), where the ligand effect seems to be more important.

curves for the anodic oxidation of formic acid on seven different palladium monolayers and on a massive Pd(111) electrode in acidic media. Comparison with the results in Figure 3, shows that the onset of formic acid oxidation follows the same trend as the hydrogen-desorption peak potential. This result means that, starting with palladium on Au(111), the catalytic activity of a palladium monolayer can be substantially increased by shifting center of the d-band down by means of lateral compression (see Figure 4b). However, if the position of the d-band center becomes too low, as in the case of Pd on Rh, Ir, Ru, and Re, the oxidation currents decrease owing to a weaker binding of adsorbates which reduces their coverage. This situation leads to a maximum in catalytic activity when the ability of the palladium surface to bind adsorbates is not too weak and not too strong. The difference between the two classes of palladium surfaces is eye-catching: While the more open palladium monolayers show an overall high catalytic activity, compression reduces the oxidation currents significantly.

For the first time, a systematic electrochemical study is presented, which is in full agreement with the so-called d-band model from Nørskov et al.[12,13] The adsorption behavior and the catalytic activity for formic acid electrooxidation of a pseudomorphic palladium monolayer on various single-crystal electrodes—Au(111), Pt(111), PtRu(111), Rh(111),

 © 2005 Wiley-VCH Verlag GmbH & Co. KGaA, Weinheim

Ir(111), Ru(0001), Re(0001), and Pd(111)—vary dramatically with lateral compression or dilatation. Characteristic voltammetric peaks have been taken as a measure for the hydrogen-binding energy on the pseudomorphic palladium monolayers. There is a linear relation between the hydrogen-desorption peak potential and the calculated shift in the d-band center. The consequences for the electrooxidation of formic acid on these surfaces are highlighted. Although at present we cannot make any quantitative correlation with calculated d-band shifts because of lack of knowledge about the actual reaction paths, our systematic studies clearly show the great importance of nearest-neighbor separations in heterogeneous catalysis. They also emphasize the ease of tuning reaction rates by the electrochemical modification of catalysts.

Received: September 27, 2004
Revised: October 28, 2004
Published online: February 11, 2005

Keywords: adsorption · electrochemistry · heterogeneous catalysis · monolayers · oxidation · surface chemistry

[1] N. M. Markovic, P. N. Ross, *Surf. Sci. Rep.* **2002**, *45*, 117.
[2] J. P. Perdew, J. A. Chevary, S. H. Vosko, K. A. Jackson, M. R. Pederson, D. J. Singh and C. Fiolhais, *Phys. Rev. B* **1992**, *46*, 6671.
[3] R. R. Adzic, A. V. Tripkovic, W. E. O'Grady, *Nature* **1982**, *296*, 137.
[4] A. M. El-Aziz, L. A. Kibler, *J. Electroanal. Chem.* **2002**, *534*, 107.
[5] M. Baldauf, D. M. Kolb, *J. Phys. Chem.* **1996**, *100*, 11375.
[6] C. Xu, D. W. Goodman, *J. Phys. Chem.* **1996**, *100*, 245.
[7] L. A. Kibler, D. M. Kolb, *Z. Phys. Chem.* **2003**, *217*, 1265.
[8] J. A. Rodriguez, D. W. Goodman, *J. Phys. Chem.* **1991**, *95*, 4196.
[9] M. W. Ruckman, M. Strongin, *Acc. Chem. Res.* **1994**, *27*, 250.
[10] J. A. Rodriguez, *Surf. Sci. Rep.* **1996**, *24*, 223.
[11] J. A. Rodriguez, D. W. Goodman, *Acc. Chem. Res.* **1995**, *28*, 477.
[12] B. Hammer, J. K. Nørskov, *Surf. Sci.* **1995**, *343*, 211.
[13] A. Ruban, B. Hammer, P. Stoltze, H. L. Skriver, J. K. Nørskov, *J. Mol. Catal. A* **1997**, *115*, 421.
[14] M. Mavrikakis, B. Hammer, J. K. Nørskov, *Phys. Rev. Lett.* **1998**, *81*, 2819.
[15] P. Liu, J. K. Nørskov, *Fuel Cells* **2001**, *1*, 192.
[16] A. Roudgar, A. Groß, *Phys. Rev. B* **2003**, *67*, 033409.
[17] A. Schlapka, M. Lischka, A. Groß, U. Käsberger, P. Jakob, *Phys. Rev. Lett.* **2003**, *91*, 016101.
[18] A. Roudgar, A. Groß, *J. Electroanal. Chem.* **2003**, *548*, 121.
[19] T. E. Shubina, M. T. M. Koper, *Electrochim. Acta* **2002**, *47*, 3621.
[20] M. Gsell, P. Jakob, D. Menzel, *Science* **1998**, *280*, 717.
[21] E. Kampshoff, E. Hahn, K. Kern, *Phys. Rev. Lett.* **1994**, *73*, 704.
[22] L. A. Kibler, A. M. El-Aziz, D. M. Kolb, *J. Mol. Catal. A* **2003**, *199*, 57.
[23] M. Baldauf, D. M. Kolb, *Electrochim. Acta* **1993**, *38*, 2145.
[24] H. Naohara, S. Ye, K. Uosaki, *Electrochim. Acta* **2000**, *45*, 3305.
[25] H. Naohara, S. Ye, K. Uosaki, *J. Electroanal. Chem.* **2001**, *500*, 435.
[26] A. Cuesta, L. A. Kibler, D. M. Kolb, *J. Electroanal. Chem.* **1999**, *466*, 165.
[27] R. Hoyer, L. A. Kibler, D. M. Kolb, *Electrochim. Acta* **2003**, *49*, 63.
[28] N. Hoshi, K. Kagaya, Y. Hori, *J. Electroanal. Chem.* **2000**, *485*, 55.
[29] L.-J. Wan, T. Suzuki, K. Sashikata, J. Okada, J. Inukai, K. Itaya, *J. Electroanal. Chem.* **2000**, *484*, 189.
[30] H. Naohara, S. Ye, K. Uosaki, *J. Phys. Chem. B* **1998**, *102*, 4366.
[31] L. A. Kibler, M. Kleinert, R. Randler, D. M. Kolb, *Surf. Sci.* **1999**, *443*, 19.
[32] G. A. Attard, A. Bannister, *J. Electroanal. Chem.* **1991**, *300*, 467.
[33] J. Inukai, M. Ito, *J. Electroanal. Chem.* **1993**, *358*, 307.
[34] R. Hoyer, L. A. Kibler, D. M. Kolb, *Surf. Sci.* **2004**, *562*, 275.
[35] S. R. Brankovic, J. McBreen, R. R. Adzic, *Surf. Sci.* **2001**, *479*, L363.
[36] L. A. Kibler, A. M. El-Aziz, unpublished results. The PtRu(111) electrode had a 1:1 composition and has been prepared to yield a presumably pseudomorphic platinum overlayer on the bulk alloy.[7]
[37] M. Takahasi, Y. Hayashi, J. Mizuki, K. Tamura, T. Kondo, H. Naohara, K. Uosaki, *Surf. Sci.* **2001**, *461*, 213.
[38] M. J. Ball, C. A. Lucas, N. M. Markovic, V. Stamenkovic, P. N. Ross, *Surf. Sci.* **2002**, *518*, 201.
[39] B. Álvarez, V. Climent, A. Rodes, J. M. Feliu, *Phys. Chem. Chem. Phys.* **2001**, *3*, 3269.
[40] A. M. El-Aziz, L. A. Kibler, D. M. Kolb, *Electrochem. Commun.* **2002**, *4*, 535.
[41] V. Pallassana, M. Neurock, L. B. Hansen, B. Hammer, J. K. Nørskov, *Phys. Rev. B* **1999**, *60*, 6146.

 © 2005 Wiley-VCH Verlag GmbH & Co. KGaA, Weinheim

Mesoscopic Rings

The Preparation of Mesoscopic Rings in Colloidal Crystal Templates**

*Feng Yan and Werner A. Goedel**

Ringlike structures have several features that set them apart from compact objects of the same size: magnetic fields can induce persistent currents in conducting rings,[1] plasmon resonances can give rise to enhancement and polarization of

[*] Prof. Dr. W. A. Goedel
Polymerphysik, Polymerforschung
BASF Aktiengesellschaft (Germany)
and
Anorganische Chemie – Materialien und Katalyse, AC II
Universität Ulm (Germany)
and
Physikalische Chemie
Technische Universität Chemnitz
Straße der Nationen 62
09111 Chemnitz (Germany)
Fax: (+49) 371-531-1371
E-mail: werner.goedel@chemie.tu-chemnitz.de

F. Yan, Prof. Dr. W. A. Goedel
Organische und Makromolekulare Chemie, OC III
Universität Ulm (Germany)

[**] We thank Prof. Dr. M. Möller, Prof. Dr. B. Rieger, and Prof. Dr. K. Landfester (Universität Ulm), and Dr. H. Auweter and Prof. Dr. R. Iden (BASF) for their support, and Prof. Dr. P. Walther for his help with the SEM measurements. This work was funded by the Deutsche Forschungsgemeinschaft (SFB 569, SPP 1052).

Supporting information for this article (experimental details and theoretical calculations) is available on the WWW under http://www.angewandte.org or from the author.

 © 2005 Wiley-VCH Verlag GmbH & Co. KGaA, Weinheim DOI: 10.1002/anie.200460584

electrical fields in the ring cavity,[2] and arrays of rods and split rings can give rise to materials of negative refractive index.[3] These effects are size dependent. It is therefore desirable to optimize the ring size to suit the intended investigation. Especially if the ringlike structures have to interact with visible light, dimensions down to the submicrometer range are necessary. In principle, rings of that size can be made by advanced lithographic techniques, but these methods are often expensive and limited in resolution or speed. As an alternative, various nonlithographic methods to prepare mesoscopic rings from semiconductors, metals, polymers, and other materials have been reported.[4–11] Most of these preparation methods are based on the selective deposition of materials on two-dimensionally structured substrates. For example, gold rings have been prepared by a suitable combination of nanostructured templates (such as two-dimensional arrays of spherical particles[2] or thin slices of perforated glass[8]), metal deposition, and subsequent removal of unwanted metal by ion-beam etching. Metal, ceramic, and organic rings have been prepared by selective wetting of colloidal monolayers,[6] porous membranes,[7] or water droplets[9] on planar substrates. Due to capillary forces, liquid precursors assembled around these objects in the form of rings. These rings were then solidified and the templates removed. However, it is not always possible to separate the rings from the underlying substrates. In addition, upscaling of these two-dimensional techniques for the preparation of rings in larger quantities inherently requires the preparation of comparatively large substrates bearing the templates. For example, the preparation of rings by selective wetting of the contact points between a planar substrate and a monolayer of spheres 1 μm in diameter yields approximately 10^{12} rings per square meter. If the rings were assembled instead at the mutual contact points of the same spheres in a close-packed structure (fcc or hcp), even 1 mL of this three-dimensional template would suffice to generate the eightfold number of rings.[12] It is thus desirable to extend the concept of assembly by capillary forces into the third dimension.

Here, we report that the concept of ring preparation by means of capillary forces can indeed be extended to simple three-dimensional structures. The preparation is based on the partial filling of colloidal crystals with a liquid, the assembly of the liquid in the wedges around the contact points between the particles, the solidification of the resulting liquid rings, and the subsequent removal of the templating particles (Figure 1). This approach is related to previous work in which complete filling of colloidal crystals or complete coverage of the internal interfaces was used to general three-dimensional porous material.[13–19] However, due to the confinement of the liquid in the wedges between particles we obtain isolated rings instead of a three-dimensional macroscopic body.

Silica spheres of uniform size were synthesized according to Stöber's method[20] and hydrophobized by coating them with 3-(trimethoxysilyl)propyl methacrylate (TPM).[21] The particles initially suspended in ethanol were packed into a three-dimensional colloidal crystal by centrifugation. After the ethanol was removed by evaporation at room temperature, the crystals were filled with a solution of a nonvolatile

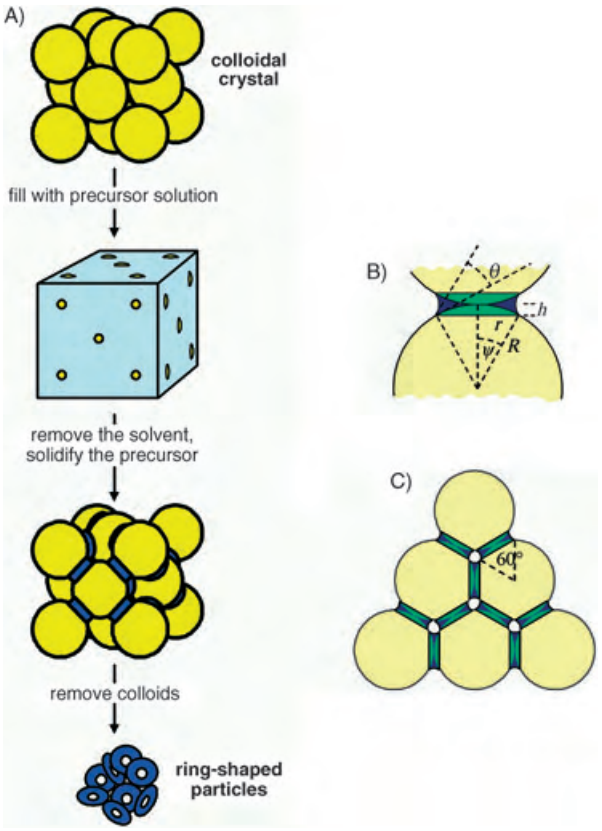

Figure 1. A) Schematic outline of the experimental procedure. B) Details of one ring including the geometrical parameters discussed in the text. C) View of the 111 plane of a unit cell to illustrate the maximum achievable ring radius of $r/R = 1/2$ at $2\psi = 60°$.

polymer or a nonvolatile precursor in a volatile solvent. The filled samples were then dried overnight in air at room temperature followed by additional drying under vacuum. The liquid precursor was solidified, and the silica particles were removed by exposure to hydrofluoric acid vapor in a sealed plastic container. The resulting rings were dispersed in ethanol by sonication.

In our first experiment we used a colloidal crystal composed of 1100-nm diameter silica particles as the template and filled it with a solution of polystyrene (0.2 wt%, $M_n \approx 115000\ g\,mol^{-1}$) in $CHCl_3$. In this case removal of the volatile solvent (see Figure 1) resulted immediately in a solid residue, and no additional chemical reactions were required. Figure 2A shows a scanning electron microscopy (SEM) image of the colloidal crystal that already contains solidified polystyrene rings. One observes domains of face-centered cubic packed particles, indicating that the original arrangement of the silica particles in the crystal is not disrupted during the infiltration and drying process. At the wedges around the contact points between spheres, one observes rings of polystyrene (Figure 2B, indicated by white arrows) that presumably were formed due to capillary forces occurring during and after the evaporation of the solvent and gradual concentration of the polymer solution. These rings are isolated from each other, and an unfilled triangular space between the rings can be clearly seen. Figure 2C shows a pile

 © 2005 Wiley-VCH Verlag GmbH & Co. KGaA, Weinheim

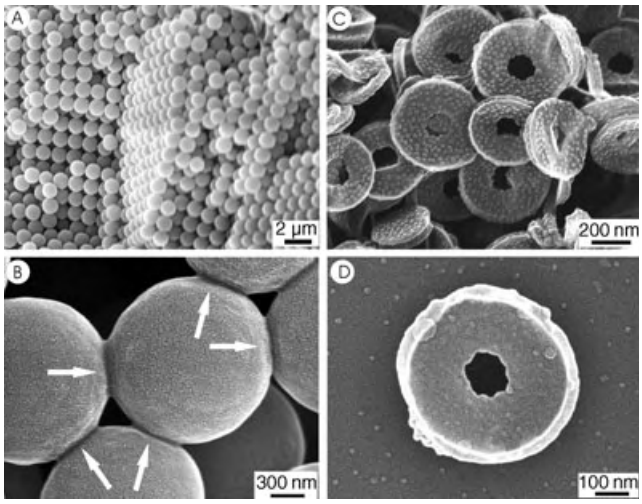

Figure 2. SEM images of A) a colloidal crystal template made from SiO_2 particles 1100 nm in diameter, which contains polymer rings made of polystyrene; B) the positions of the rings; C) rings obtained after the removal of the SiO_2 particles; and D) an isolated ring after redispersion in ethanol and deposition onto a silicon wafer.

of polystyrene rings obtained after the removal of the particles by dry etching with hydrofluoric acid vapor. These rings have a uniform size with an outer diameter of approximately 430 nm and an inner diameter of approximately 160 nm, and they can be redispersed in ethanol. Figure 2D shows an isolated polystyrene ring after redispersion in ethanol and deposition onto a silicon wafer. After the dry etching, the rings are covered with small particles a few nanometers in diameter. These small particles do not adhere to the rings but are separated from the rings when they are redispersed in a liquid (see Figure 2D). These small particles are residues of the organic coating of the spheres and are also observed as well when the silica spheres alone are etched with hydrofluoric acid.

The method can also be extended for the synthesis of mesoscopic rings made from other materials and for processes involving chemical reactions for solidification of the nonvolatile components. Figure 3A shows an isolated ring made from poly(methyl methacrylate) ($M_n \approx 53\,100\ g\,mol^{-1}$) in a process similar to the one discussed above. TiO_2 rings prepared by filling the colloidal crystal with a solution of $Ti(OEt)_4$ (0.1 wt%) in $CHCl_3$ are shown in Figure 2B. After evaporation of the solvent, the liquid $Ti(OEt)_4$ remained; the partially filled template was exposed to humid air to hydrolyze and condense the $Ti(OEt)_4$ into TiO_2.

Rings also can be prepared by filling the templates with solutions of a polymerizable organic liquid instead of preformed polymers. In this case, the colloidal crystal was filled with a 0.35-wt% solution of the nonvolatile organic monomer trimethylolpropane trimethacrylate (TMPTMA) as a liquid precursor in $CHCl_3$/EtOH (9:1 v:v). After the solvent was removed by evaporation at room temperature, the liquid precursor was cross-linked by exposure to UV light. Figure 3C shows an isolated ring on a silicon wafer.

In the four cases described above, we used identical colloidal crystals as templates and obtained rings of compa-

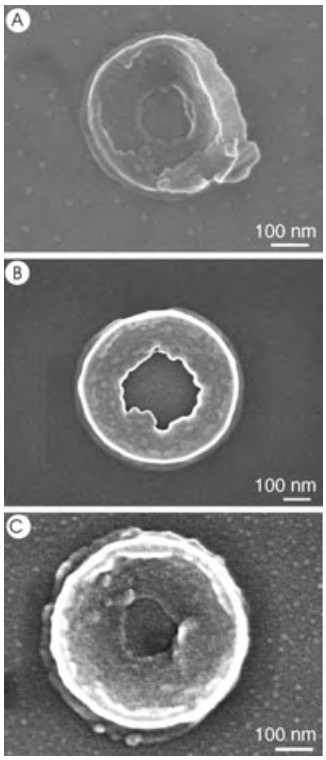

Figure 3. SEM images of isolated rings of A) poly(methyl methacrylate), B) TiO_2, and C) poly(trimethylolpropane trimethacrylate). All of the rings were prepared with a colloidal crystal composed of silica particles 1100 nm in diameter.

rable sizes. Through variations in the colloidal crystals, the size of the prepared rings can be fine-tuned. For example, Figure 4A shows an SEM image of a template made from

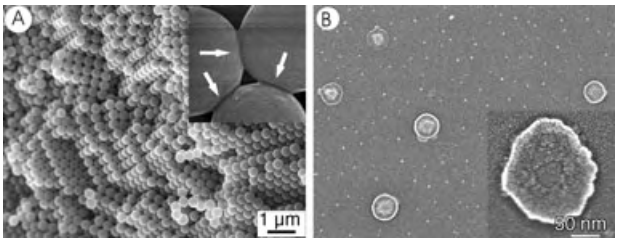

Figure 4. SEM images of A) a colloidal crystal template made from SiO_2 particles 330 nm in diameter that contains polymer rings made of cross-linked TMPTMA (the inset shows the positions of the rings); B) isolated rings obtained from the structure shown in A after removal of the SiO_2 particles and redispersion in ethanol.

particles 330 nm in diameter that already contains cross-linked TMPTMA rings. As in the example in Figure 2, the arrangement of the silica particles in the colloidal crystal is not disrupted during the infiltration, drying, and cross-linking process, and one observes again the unfilled triangular space between the rings (see inset in Figure 4A). Figure 4B shows SEM images of the cross-linked polymer rings obtained after the removal of the particles, redispersion in ethanol, and deposition onto a silicon wafer. As expected, the dimensions

 © 2005 Wiley-VCH Verlag GmbH & Co. KGaA, Weinheim

of these rings (outer diameter ≈ 155 nm, inner diameter ≈ 50 nm) are approximately one-third of that in the previous case.

The assembly of liquid around the contact points between particles through capillary forces has already been investigated in detail mainly in the context of wet soil. It thus seems straightforward to solidify these liquid rings to obtain unusual particles. However, two ideal incompressible spheres are in contact with each other at only one point of zero lateral extension. One might be puzzled why the rings obtained here have a considerably wide inner opening. First of all, one must note that the silica particles are imperfect spheres and may be deformed further by the attractive forces between them. Thus the contact sites between spheres will be wider than just points of zero lateral extension. Secondly, similar openings appear as well in three-dimensional porous solids that are generated by completely filling the free volume of a colloidal crystal with a liquid, solidification of that liquid, and subsequent removal of the colloids. The well-accepted explanation for the formation of openings in this context is incomplete penetration of the liquid into the wedges between the spheres and the fact that the liquid shrinks during its solidification and thus retracts from the wedges at an intermediate, gellike stage.[16] We are convinced that similar processes occur in our experiments, too. It is further instructive to compare the dimensions of the rings with the values estimated assuming ideal spherical geometry. If two spheres touch each other and a liquid bridge encircles the contact point, the radius of this ring and its height at the outer perimeter increase with an increasing volume of the ring. For simplicity one might assume that the perimeter is a cylinder with straight walls or has cross-section in the form of an arc, but in the general case the azimuthal and the meridional curvature of the perimeter are non-zero and the profile of the perimeter of the ring has the shape of a nodoid. For any given volume and contact angle the height and radius of the ring (and its detailed shape) can be calculated numerically by using procedures given in ref. [22] By using these procedures we calculate the theoretical radius of the rings, r, and their height, h, as a function of the ratio of the volume of the rings to the volume not occupied by the spheres with radius R. The latter quantity is the equivalent of the fraction of the nonvolatile compounds in the solution used for infiltration of the crystal. The corresponding relations are shown in Figure 5 for the numerical solution of the nodoid surface as well as for the simplified geometries of uniform curvature (cross-section of the perimeter is assumed to be a circular segment) and zero meridional curvature (perimeter is assumed to be cylindrical). At a volume fraction of 0.003 of nonvolatile material in the infiltration solution (the equivalent of the 0.2-wt% polystyrene in chloroform used above) and a sphere diameter of 1100 nm, we expect to obtain rings of approximately 190 nm radius and 16 nm height—considerably smaller than those obtained experimentally. Thus, the material "missing" in the center of the ring is found at the perimeter. We believe that during the evaporation of the volatile components, the liquid/vapor interface moves through the colloidal crystal, leaving behind rings of liquid at each contact point between two spheres.[24] These rings still

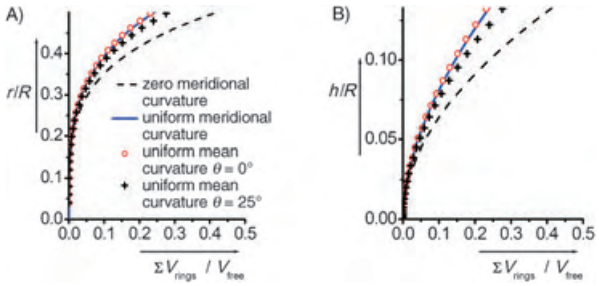

Figure 5. Theoretical values for the ratio of the radius r and height h of the rings to the radius R of the spheres as a function of the ratio of the total volume of the rings ΣV_{rings} to the volume not occupied by the spheres V_{free}. (If nonideality of the partial mixing volumes is negligible $\Sigma V_{rings}/V_{free}$ is equal to the volume fraction of nonvolatile material in the infiltration solution; for a definition of the geometrical parameters r and h see Figure 1; for details of the calculation see the Supporting Information.) +,○: cross-section of the perimeter has the shape of a nodoid;[22] ——: cross-section of the perimeter has the shape of an arc;[23] -----: perimeter is assumed to be cylindrical.

contain a considerable amount of volatile solvent and shrink further until finally solidification occurs. At some stage in this process before all the solvent is evaporated, either the three-phase contact line is pinned, or a solid skin is formed on the perimeter of the ring, or the whole ring forms a gel. Further shrinking and final solidification then draws the interior of the ring outward rather than moving the perimeter inward.

This pinning or solidification of the receding liquid interface is further visible if the volume fraction of the nonvolatile material is increased. If we assume that the liquid left behind by the receding interface can only assume the shape of rings, we expect that isolated rings of a diameter up to the radius of the spheres can form (max value of $r/R = 1/2$, see Figure 1C). If these rings would form at equilibrium conditions, they would comprise a volume fraction of the free space of approximately 0.25 (see Figure 5A). Experimentally, however, we observe that already at volume fractions exceeding 0.005 one obtains—besides isolated rings—structures consisting of fused rings. Most of them are connected by lamellae that result from filling the triangular space between three neighboring spheres. For example, Figure 6A shows a silica colloidal template filled with 0.5 wt% TMPTMA in chloroform. One can compare this with the result shown in Figure 4A, in which the colloidal template was filled with 0.2 wt% TMPTA. Now, the triangular space between the rings has been filled with polymer (Figure 6A, indicated by white arrows). Figure 6B shows the resulting connected rings obtained after the removal of the particles. Similarly, if a silica colloidal template is filled with a 0.5-wt% solution of polystyrene, connected polystyrene rings are obtained (Figure 6C), which can be separated only partially by sonication (Figure 6D). Obviously, in this case the pinning or solidification of the receding liquid already takes place before the liquid in the triangular space can rupture even though the concentration of nonvolatile components is still below the theoretical maximum. This observation indicates that the dimensions of the rings produced most likely always have to

 © 2005 Wiley-VCH Verlag GmbH & Co. KGaA, Weinheim

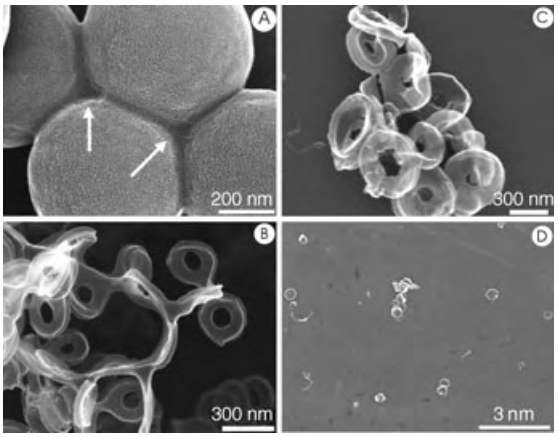

Figure 6. SEM images of A) a colloidal crystal template (made from SiO_2 particles 550 nm in diameter) that contains polymer rings made of cross-linked TMPTMA; B) connected polymer rings obtained from the structure shown in A after the removal of the SiO_2 particles; C) connected polystyrene rings (prepared with 1100-nm silica templates); D) connected polystyrene ring from C) after redispersion in ethanol.

be chosen significantly smaller than the particles used for their preparation.

In summary, we have developed a simple and effective technique for the preparation of dispersions of isolated mesoscopic rings. The diameter of the rings can be controlled by the size of the templating particles and one has significant flexibility in choosing the material with which to form the rings.

Received: May 7, 2004
Revised: December 17, 2004
Published online: March 2, 2005

Keywords: capillary forces · colloids · mesoscopic structures · silica gel · template synthesis

[1] a) D. Mailly, C. Chapelier, A. Benoit, *Phys. Rev. Lett.* **1993**, *70*, 2020; K. A. Matveev, A. I. Larkin, L. I. Glazman, *Phys. Rev. Lett.* **2002**, *89*, 096802; b) W. Rabaud, L. Saminadayar, D. Mailly, K. Hasselbach, A. Benoit, B. Etienne, *Phys. Rev. Lett.* **2001**, *86*, 3124.
[2] J. Aizpurua, P. Hanarp, D. S. Sutherland, M. Käll, G. W. Bryant, F. J. Garcia de Abajo, *Phys. Rev. Lett.* **2003**, *90*, 057401.
[3] D. R. Smith, W. J. Padilla, D. C. Vier, S. C. Nemat-Nasser, S. Schultz, *Phys. Rev. Lett.* **2000**, *84*, 4184.
[4] A. Lorke, R. J. Luyken, A. O. Govorov, J. P. Kotthaus, J. M. Garcia, P. M. Petroff, *Phys. Rev. Lett.* **2000**, *84*, 2223.
[5] a) J. M. Garcia, G. Medeiros-Ribeiro, K. Schmidt, T. Ngo, J. L. Feng, A. Lorke, J. Kotthaus, P. M. Petroff, *Appl. Phys. Lett.* **1997**, *71*, 2014; b) R. J. Warburton, C. Schäflein, D. Haft, F. Bickel, A. Lorke, K. Karrai, J. M. Garcia, W. Schoenfeld, P. M. Petroff, *Nature* **2000**, *405*, 926; c) T. Raz, D. Ritter, G. Bahir, *Appl. Phys. Lett.* **2003**, *82*, 1706.
[6] a) M. Winzer, M. Kleiber, N. Dix, R. Wiesendanger, *Appl. Phys. A* **1996**, *63*, 617; b) J. Boneberg, F. Burmeister, C. Schäfle, P. Leiderer, D. Reim, A. Fery, S. Herminghaus, *Langmuir* **1997**, *13*, 7080; c) P. M. Tessier, O. D. Velev, A. T. Kalambur, A. M. Lenhoff, J. F. Rabolt, E. W. Kaler, *Adv. Mater.* **2001**, *13*, 396.
[7] a) D. K. Yi, D. Y. Kim, *Nano Lett.* **2003**, *3*, 207; b) H. Xu, W. A. Goedel, *Angew. Chem.* **2003**, *115*, 4845; *Angew. Chem. Int. Ed.* **2003**, *42*, 4696; c) F. Yan, W. A. Goedel, *Nano Lett.* **2004**, *4*, 1193.
[8] D. H. Pearson, R. J. Tonucci, K. M. Bussmann, E. A. Bolden, *Adv. Mater.* **1999**, *11*, 769.
[9] G. Lu, W. Li, J. Yao, G. Zhang, B. Yang, J. Shen, *Adv. Mater.* **2002**, *14*, 1049.
[10] M. Sano, A. Kamino, J. Okamura, S. Shinkai, *Science* **2001**, *293*, 1299.
[11] M. Steinhart, J. H. Wendorff, A. Greiner, R. B. Wehrspohn, K. Nielsch, J. Schilling, J. Choi, U. Gösele, *Science* **2002**, *296*, 1997.
[12] In the case of a two-dimensional hexagonal dense layer on a substrate, the number of spheres of diameter D per unit area is $1/(D\,D\sin 30°) = 2/(\sqrt{3}D^2) \approx 1.15/D^2$, and there is one ring generated per sphere. For three-dimensional hexagonal close packing and for face-centered cubic packing, the number of spheres per unit volume is given by $4/(\sqrt{2}\,D^2)^3 = \sqrt{2}/D^3 \approx 1.41/D^3$; the number of contact points between spheres is six times that number, and thus the number density of rings that can be generated at these positions is given by $24/(\sqrt{2}\,D^2)^3 = 6\sqrt{2}/D^3 \approx 8.5/D^3$.
[13] O. D. Velev, A. M. Lenhoff, *Curr. Opin. Colloid Interface Sci.* **2000**, *5*, 56.
[14] H. Yan, C. F. Blanford, J. C. Lytle, C. B. Carter, W. H. Smyrl, A. Stein, *Chem. Mater.* **2001**, *13*, 4314.
[15] S. H. Park, Y. Xia, *Adv. Mater.* **1998**, *10*, 1045.
[16] P. Jiang, K. S. Hwang, D. M. Mittleman, J. F. Bertone, V. L. Colvin, *J. Am. Chem. Soc.* **1999**, *121*, 11630.
[17] P. Jiang, J. F. Bertone, V. L. Colvin, *Science* **2001**, *291*, 453.
[18] Z. Zhong, Y. Yin, B. Gates, Y. Xia, *Adv. Mater.* **2000**, *12*, 206.
[19] P. M. Tessier, O. V. Velev, A. T. Kalambur, A. M. Lenhoff, J. F. Rabolt, E. W. Kaler, *Adv. Mater.* **2001**, *13*, 396.
[20] W. Stöber, A. Fink, E. Bohn, *J. Colloid Interface Sci.* **1968**, *26*, 62.
[21] P. Philipse, A. Vrij, *J. Colloid Interface Sci.* **1989**, *128*, 121.
[22] J. C. Melrose, *AIChE J.* **1966**, *12*, 986–994.
[23] R. A. Fisher, *J. Agric. Sci.* **1926**, *16*, 492.
[24] W. O. Smith, P. D. Foote, P. F. Busang, *Phys. Rev.* **1930**, *36*, 524.

 © 2005 Wiley-VCH Verlag GmbH & Co. KGaA, Weinheim

Solid-State NMR Spectroscopy

A Concept for Rapid Protein-Structure Determination by Solid-State NMR Spectroscopy**

Adam Lange, Stefan Becker, Karsten Seidel, Karin Giller, Olaf Pongs, and Marc Baldus**

Despite its enormous pharmacological relevance, no general concept for studying three-dimensional (3D) biomolecular structures and interactions in noncrystalline and insoluble systems is currently available. Examples of such structures and interactions include ligands bound with high affinity to G-protein-coupled receptors or ion channels, protein fibrils, and biopolymers. In these cases, the application of the two principal experimental methods for 3D-structure determination, X-ray crystallography and solution-state NMR spectroscopy, can be challenging. Alternatively, NMR spectroscopic techniques specifically designed for the study of immobilized, possibly membrane-associated, systems (solid-state NMR spectroscopy) can be used to infer structural or dynamic parameters (see, for example, references [1,2]).

3D molecular structures of small peptides have been probed by using solid-state NMR spectroscopic methods based on the determination of specific ^{13}C–^{13}C or ^{13}C–^{15}N distances.[3,4] These techniques can require a high degree of spectral dispersion and the recording of a large number of NMR spectra. The extension of such methods to larger polypeptides may therefore be difficult. Instead, newer methods are based on the spectral analysis of several polypeptide variants containing isotope labels at well-defined atomic positions or amino acid residue types.[5–7] Such approaches were successful for membrane-embedded proteins oriented macroscopically on glass plates,[1,5] as well as for peptides,[4] amyloid fibrils,[6] and a solid-phase protein[7] studied under the conditions of magic-angle spinning (MAS).[8] Since these methods require the synthesis of several isotope-labeled protein variants, they are of limited use if a rapid 3D structural characterization is desired. Their application may be further complicated by difficulties in producing adequate quantities of isotope-labeled samples of a protein or (possibly nonpeptidic) ligand.

Herein we present a solid-state NMR spectroscopic approach that permits the rapid determination of 3D molecular structure with a single uniformly isotope labeled sample. For analogous NMR spectroscopic investigations in the solution state, the detection of short distances between hydrogen atoms provides the principal source of information about through-space distances and hence about the 3D fold of the protein.[9] Because of the restricted spectral resolution, two-dimensional (2D) ^{1}H,^{1}H-correlation methods are of limited use for solid-state NMR spectroscopy. Instead we rely in the following on the indirect detection and structural analysis of ^{1}H–^{1}H interactions by using ^{13}C,^{13}C-correlation spectroscopy.[10] Combined with dihedral-angle constraints, which can be derived from conformation-dependent chemical shifts, the characterization of the 3D molecular structure from a single protein sample becomes possible. Our approach is demonstrated on kaliotoxin (KTX), a 38-residue peptide found in the venom of the scorpion *Androctonus mauretanicus mauretanicus*.[11] KTX has been shown to block voltage-dependent eukaryotic potassium channels (e.g., Shaker and Kv1.3) with high affinity and a 1:1 stoichiometry.[12]

First, a series of two-dimensional ^{13}C,^{13}C- and ^{15}N,^{13}C-correlation experiments were conducted on a uniformly [^{13}C,^{15}N] labeled sample of KTX under MAS conditions to establish sequential ^{13}C/^{15}N resonance assignments. For example, Figure 1 contains the results of a ^{13}C,^{13}C spin-diffusion experiment[13] (green), which reveals a variety of intraresidue side-chain correlations with typical ^{13}C line widths well below 1 ppm. The combination of N,C and C,C 2D correlation methods resulted in de novo ^{13}C/^{15}N resonance assignments for 87 % of all peptide residues (deposited in the BioMagResBank under accession number 6351). Spectral assignments derived from MAS-based solid-state NMR spectroscopic experiments can be analyzed for selectively[14] or uniformly[15,16] isotope labeled polypeptides with regard to the conformation of the protein backbone by using solution-state NMR spectroscopic data as a reference. Thus, the ^{13}C/^{15}N resonance assignments obtained for U-[^{13}C,^{15}N]-labeled KTX (U = uniformly) served as input parameters for the program TALOS[17] and resulted in a total set of 2×27 constraints on the dihedral angles of the peptide backbone. As shown in Figure 2 (top), the resulting parameters are indicative of β-strand arrangements comprising residues 2–9, 24, 28, 29, and 32–37, and suggest the existence of an α helix containing residues 11–21.

Sequential medium- and long-range ^{1}H–^{1}H-distance constraints were determined subsequently from the analysis of three ^{13}C,^{13}C-encoded ^{1}H,^{1}H mixing experiments (CHHC[18,19]). With mixing times of 250–400 μs and an MAS rate of 12.5 kHz ($B_0 = 18.8$ T), the spectra are dominated by ^{1}H–^{1}H interactions corresponding to distances of 1.8–3.5 Å in a uniformly ^{13}C labeled sample.[19] Figure 1 shows the experimental results of a CHHC correlation experiment for a (^{1}H,^{1}H) mixing time of 250 μs (red), whereby ^{13}C,^{13}C-cross-peak intensities reflect ^{1}H–^{1}H interactions. Correlations assigned in Figure 1 include long-range contacts along the

[*] A. Lange, Dr. S. Becker, K. Seidel, K. Giller, Dr. M. Baldus
Max-Planck-Institut für Biophysikalische Chemie
Abteilung für NMR-Basierte Strukturbiologie
37077 Göttingen (Germany)
Fax: (+49) 551-201-2202
E-mail: sabe@nmr.mpibpc.mpg.de
maba@mpibpc.mpg.de
Prof. Dr. O. Pongs
Institut für Neurale Signalverarbeitung
Zentrum für Molekulare Neurobiologie der Universität Hamburg
20246 Hamburg (Germany)

[**] Presented at the EENC/AMPERE conference in Lille (France), September 6–11, 2004. We thank C. Legros for providing the KTX clone and C. Griesinger for scientific discussions and continuous support of this project. A.L. acknowledges the Fonds der Chemischen Industrie for a PhD fellowship.

Supporting information for this article is available on the WWW under http://www.angewandte.org or from the author.

 DOI: 10.1002/anie.200462516 © 2005 Wiley-VCH Verlag GmbH & Co. KGaA, Weinheim

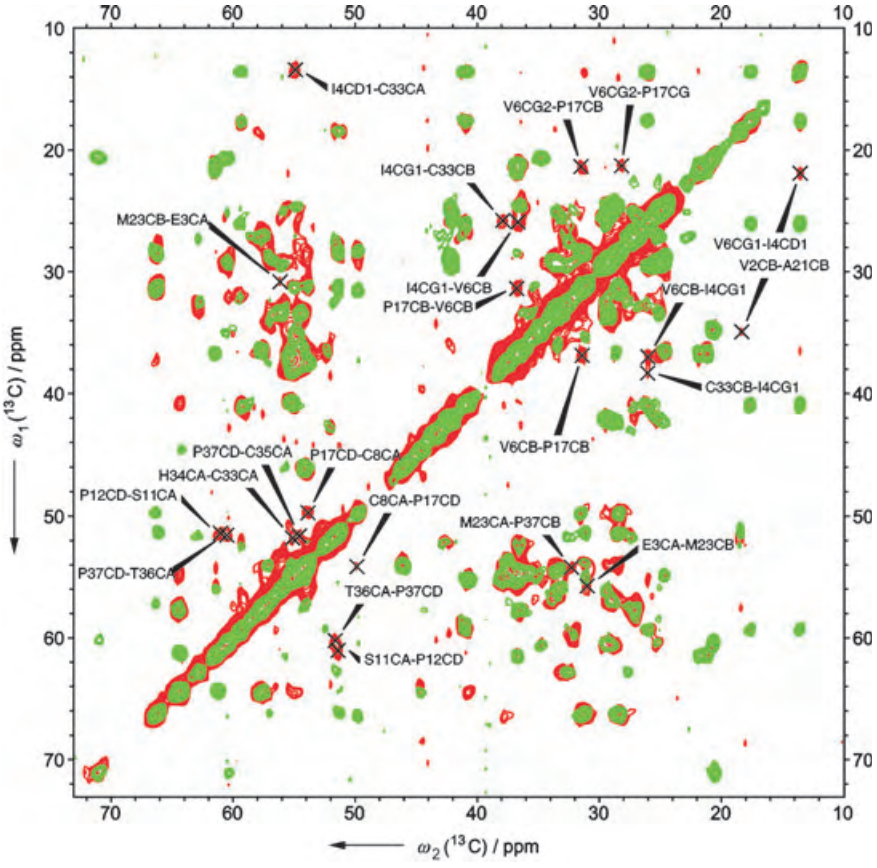

Figure 1. Comparison of a 2D C,C spin-diffusion spectrum (green, mixing time: 50 ms) and a CHHC spectrum (red, ^{1}H,^{1}H mixing time: 250 μs) of U-[^{13}C,^{15}N]-labeled KTX recorded on an 800-MHz NMR spectrometer (Bruker Biospin). Assigned correlations reflect interresidue CHHC constraints.

polypeptide chain and connect protein segments of different secondary structure (Figure 2, bottom). Additional distance restraints were deduced from the analysis of CHHC spectra with mixing times of 325 and 400 μs (see also Supporting Information).

To construct the 3D structure of KTX, solution-state NMR spectroscopic methods[20] were adapted as follows: In a first round of molecular-dynamics-based structure calculations in CNS,[21] dihedral-angle restraints, as given in Figure 2 (top), information about the covalent structure (three disulfide bonds), and eight unambiguously assigned CHHC constraints were used (see Supporting Information). Because ^{1}H–^{1}H interactions are detected indirectly through the spins of bonded ^{13}C atoms, the assignment of methylene and methyl hydrogen atoms remains ambiguous. Following solution-state NMR spectroscopic approaches,[22] this aspect was accounted for during the calculation by using an r^{-6} summation involving all possible ^{1}H–^{1}H contacts (see also reference [19]). In principle, incorrect or missing assignments and intermolecular interactions can affect the reliability of the CHHC-detected constraints. A systematic analysis reveals that such influences characterize one of the CHHC-detected distance constraints, which leads to a significant increase in overall energy in the structure calculation. This constraint was therefore removed for the later stages of structure refinement. Notably, this CHHC correlation was also not observed for a U-[^{13}C,^{15}N]-labeled sample diluted in unlabeled KTX (data not shown).

Next, we calculated an ensemble of structures, which were used to assign ambiguous CHHC correlations (see Supporting Information and reference [20]). Finally, 54 dihedral-angle constraints and 28 distance constraints (6 sequential, 7 medium-range, and 15 long-range) were employed to calculate 200 structures. As in the model study in reference [19], these ^{1}H–^{1}H contacts (see Supporting Information) also involve methyl–methyl interactions. The 10 conformers with the lowest energy (Figure 3; PDB entry: 1XSW) exhibit a good covalent structure and a converging fold with an average backbone root-mean-square deviation (RMSD) of 0.81 Å (see Supporting Information). Structures with a different fold display significantly higher overall energies (see Supporting Information).

The backbone RMSD (residues 4–38) between the mean solid-state and solution-state structures (PDB entry: 2KTX based on ^{1}H NMR spectroscopy[23]) is 1.9 Å. Solution- and solid-state NMR spectroscopic structures are described by the same characteristic α/β fold. Further evidence for the validity of the derived solid-state NMR spectroscopic structure comes from PROCHECK NMR analysis (see Supporting Information), which yields 81% of all peptide residues in most favored regions. A back calculation of CHHC and additionally recorded NHHC[19] 2D spectra, which not only provide tertiary contacts but also reflect backbone conformation, confirmed the 3D structure shown in Figure 3.[18,19] These results demonstrate the general validity of our proposed concept.

The determination of the 3D structure of fully or partially immobilized biomolecules, such as membrane or fibrous proteins and their ligands, can be a significant challenge for conventional biophysical methods. The use of established solution-state NMR spectroscopic methods for the direct (NOESY-type[9]) detection of ^{1}H–^{1}H contacts in the solid state is usually prohibited by spectral dispersion and line width. For this reason, ^{13}C,^{15}N-correlation spectroscopy must generally be used for high-resolution solid-state NMR spectroscopic applications, and the collection of a sufficient number of long-range constraints until now required a high degree of spectral dispersion or the study of differently isotope-labeled samples. We have shown that it is possible to construct a 3D molecular structure from a single uniformly labeled solid-phase sample. Our approach relies on the encoding of short ^{1}H–^{1}H distances in high-resolution ^{13}C,^{15}N evolution and detection dimensions and exploits the high sensitivity of chemical shifts detected by solid-state NMR spectroscopy to the conformation of the protein backbone.

In close analogy to NOESY-type experiments on soluble molecules, the general applicability of the concept discussed

 © 2005 Wiley-VCH Verlag GmbH & Co. KGaA, Weinheim

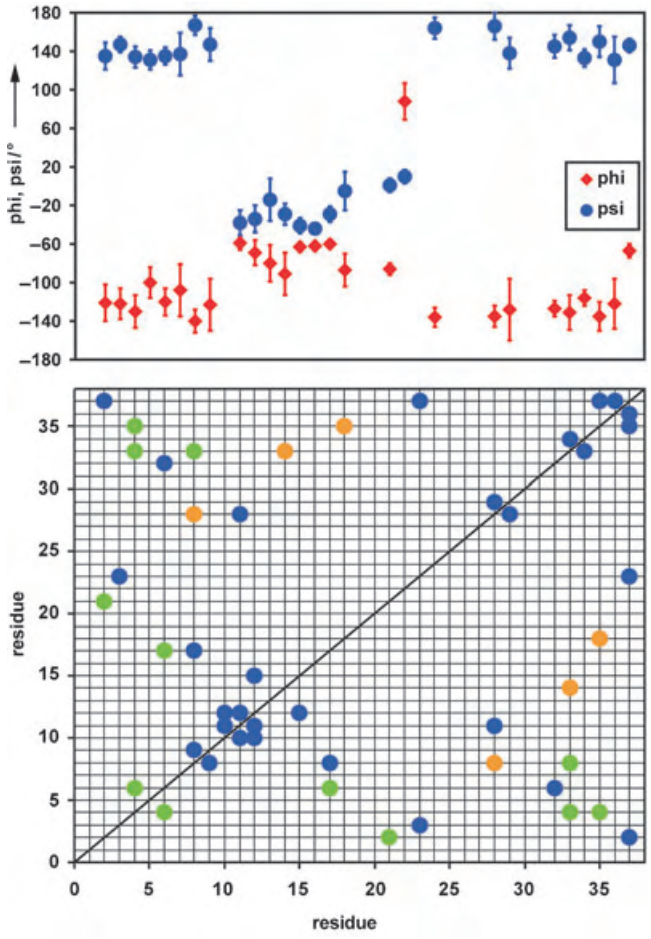

Figure 2. Top: Dihedral-angle constraints derived from de novo $^{13}C/^{15}N$ resonance assignments with TALOS. Bottom: Interresidue distance restraints based on unambiguous (green) and ambiguous (blue) CHHC interactions. Disulfide bonds are depicted in orange.

Figure 3. Ribbon diagram of the ten conformers determined by solid-state MAS NMR spectroscopy with the lowest energy (PDB entry: 1XSW). The conformers were aligned along the backbone by using MOLMOL.[28]

herein and the accuracy of the derived structures are predominantly determined by spectral resolution. As ^{1}H–^{1}H correlations are detected indirectly, the sensitivity of the experiment is lower than that of standard ^{13}C,^{15}N-correlation methods. Unless prohibited by dynamic or structural disorder, the accuracy of the derived structure can be further improved by including intraresidue structural constraints obtained from side-chain resonances, by employing three-dimensional NMR spectroscopy,[24] or by improving the structural homogeneity of the sample under study. In the case of KTX, such conditions could be established by preparing microcrystals or by complexing the ligand with KcsA-Kv1.3 potassium channels.[27]

Restriction of the mixing time of the N/CHHC experiments to the initial rate regime not only increases the structural reliability of the detected distance restraints but also reduces spectral overlap. NMR spectroscopic data obtained with longer mixing times can be incorporated into the structural analysis to increase the number of ^{1}H–^{1}H distance restraints, but at the cost of reduced structural accuracy. In the case of KTX, two-dimensional spectroscopy was sufficient to determine the 3D conformation by using a set of dihedral-angle constraints, ^{1}H–^{1}H distance constraints, and three disulfide bridges. Additional structure calculations (without the inclusion of disulfide bonds) show that the latter parameters are not critical for the general validity of this approach.

The concept presented herein is also amenable to the study of nonpeptidic biomolecules, whereby a combination of ^{1}H–^{1}H and selective ^{13}C–^{13}C distance restraints may be measured, again for one uniformly labeled sample. As in the case of KTX, which blocks Kv channels with high affinity, ligand–receptor interactions, which are of great pharmacological relevance, may thus be probed readily. Moreover, the technique can be applied to structural studies of membrane proteins and protein fibrils. Depending on the molecule under investigation, the presented approach can be combined with other solid-state NMR spectroscopic methods. For example, in the case of membrane-embedded proteins, additional structural constraints could be obtained from a macroscopically aligned specimen. Applications to larger (membrane) proteins may benefit from the use of block[7,25] or modular[26] isotope labeling.

Received: November 4, 2004
Revised: December 20, 2004
Published online: March 2, 2005

Keywords: isotope labeling · kaliotoxin · magic-angle spinning · NMR spectroscopy · protein structures

[1] T. A. Cross, S. J. Opella, *Curr. Opin. Struct. Biol.* **1994**, *4*, 574–581.
[2] R. G. Griffin, *Nat. Struct. Biol.* **1998**, *5*, 508–512.
[3] K. Nomura, K. Takegoshi, T. Terao, K. Uchida, M. Kainosho, *J. Am. Chem. Soc.* **1999**, *121*, 4064–4065.
[4] C. M. Rienstra, L. Tucker-Kellogg, C. P. Jaroniec, M. Hohwy, B. Reif, M. T. McMahon, B. Tidor, T. Lozano-Perez, R. G. Griffin, *Proc. Natl. Acad. Sci. USA* **2002**, *99*, 10260–10265.

 © 2005 Wiley-VCH Verlag GmbH & Co. KGaA, Weinheim

[5] S. J. Opella, F. M. Marassi, *Chem. Rev.* **2004**, *104*, 3587 – 3606.
[6] A. T. Petkova, Y. Ishii, J. J. Balbach, O. N. Antzutkin, R. D. Leapman, F. Delaglio, R. Tycko, *Proc. Natl. Acad. Sci. USA* **2002**, *99*, 16742 – 16747; C. P. Jaroniec, C. E. MacPhee, V. S. Bajaj, M. T. McMahon, C. M. Dobson, R. G. Griffin, *Proc. Natl. Acad. Sci. USA* **2004**, *101*, 711 – 716.
[7] F. Castellani, B. van Rossum, A. Diehl, M. Schubert, K. Rehbein, H. Oschkinat, *Nature* **2002**, *420*, 98 – 102.
[8] E. R. Andrew, A. Bradbury, R. G. Eades, *Nature* **1958**, *182*, 1659.
[9] K. Wüthrich, *NMR of Proteins and Nucleic Acids*, Wiley Interscience, New York, **1986**.
[10] X. L. Wu, S. M. Zhang, X. W. Wu, *Phys. Rev. B* **1988**, *37*, 9827 – 9829.
[11] M. Crest, G. Jacquet, M. Gola, H. Zerrouk, A. Benslimane, H. Rochat, P. Mansuelle, M. F. Martin-Eauclaire, *J. Biol. Chem.* **1992**, *267*, 1640 – 1647.
[12] S. Grissmer, A. N. Nguyen, J. Aiyar, D. C. Hanson, R. J. Mather, G. A. Gutman, M. J. Karmilowicz, D. D. Auperin, K. G. Chandy, *Mol. Pharmacol.* **1994**, *45*, 1227 – 1234.
[13] N. Bloembergen, *Physica* **1949**, *15*, 386 – 426.
[14] H. Saito, *Magn. Reson. Chem.* **1986**, *24*, 835 – 852.
[15] S. Luca, D. V. Filippov, J. H. van Boom, H. Oschkinat, H. J. M. de Groot, M. Baldus, *J. Biomol. NMR* **2001**, *20*, 325 – 331.
[16] S. Luca, J. F. White, A. K. Sohal, D. V. Filippov, J. H. van Boom, R. Grisshammer, M. Baldus, *Proc. Natl. Acad. Sci. USA* **2003**, *100*, 10706 – 10711.
[17] G. Cornilescu, F. Delaglio, A. Bax, *J. Biomol. NMR* **1999**, *13*, 289 – 302.
[18] A. Lange, S. Luca, M. Baldus, *J. Am. Chem. Soc.* **2002**, *124*, 9704 – 9705.
[19] A. Lange, K. Seidel, L. Verdier, S. Luca, M. Baldus, *J. Am. Chem. Soc.* **2003**, *125*, 12640 – 12648.
[20] M. Nilges, *Curr. Opin. Struct. Biol.* **1996**, *6*, 617 – 623.
[21] A. T. Brunger, P. D. Adams, G. M. Clore, W. L. DeLano, P. Gros, R. W. Grosse-Kunstleve, J. S. Jiang, J. Kuszewski, M. Nilges, N. S. Pannu, R. J. Read, L. M. Rice, T. Simonson, G. L. Warren, *Acta Crystallogr. Sect. D* **1998**, *54*, 905 – 921.
[22] C. M. Fletcher, D. N. M. Jones, R. Diamond, D. Neuhaus, *J. Biomol. NMR* **1996**, *8*, 292 – 310.
[23] M. Gairi, R. Romi, I. Fernandez, H. Rochat, M. F. Martin-Eauclaire, J. Van Rietschoten, M. Pons, E. Giralt, *J. Pept. Sci.* **1997**, *3*, 314 – 319.
[24] H. Heise, K. Seidel, M. Etzkorn, S. Becker, M. Baldus, *J. Magn. Reson.* **2004**, *173*, 64 – 74.
[25] D. M. LeMaster, D. M. Kushlan, *J. Am. Chem. Soc.* **1996**, *118*, 9255 – 9264.
[26] A. R. Pickford, I. D. Campbell, *Chem. Rev.* **2004**, *104*, 3557 – 3565.
[27] C. Legros, V. Pollmann, H. G. Knaus, A. M. Farrell, H. Darbon, P. E. Bougis, M. F. Martin-Eauclaire, O. Pongs, *J. Biol. Chem.* **2000**, *275*, 16918 – 16924.
[28] R. Koradi, M. Billeter, K. Wüthrich, *J. Mol. Graphics* **1996**, *14*, 51 – 60.

 © 2005 Wiley-VCH Verlag GmbH & Co. KGaA, Weinheim

Zintl Anions

$[Pb_5\{Mo(CO)_3\}_2]^{4-}$: A Complex Containing a Planar Pb_5 Unit**

Li Yong, Stephan D. Hoffmann, Thomas F. Fässler, Sebastian Riedel, and Martin Kaupp**

Dedicated to Professor Arndt Simon on the occasion of his 65th birthday

Homoatomic polyhedra E_n^{x-} of the heavier Group 14 elements are known as Zintl ions. Even though the synthesis, isolation, and characterization of Zintl ions in solution dates back to the 19th century,[1] only few homoatomic Zintl ions have been isolated from solutions.[2a] This number is very small when compared to the larger variety of main-group clusters observed in Zintl phases.[2b,c] In solution chemistry, generally there are two adopted approaches towards the isolation of polyanions, either by extraction of pre-formed alloys[3a] or by direct reaction of main-group metals in a suitable solvent.[3b–e] Through these two approaches homoatomic polyhedra of tetrahedral structure $[Sn_4]^{4-}$,[4] of trigonal-bipyramidal structure $[E_5]^{2-}$ (E = Ge, Sn, Pb),[5] and of monocapped square-antiprismatic or tricapped trigonal-prismatic structure $[E_9]^{x-}$ (E = Si, Ge, Sn, Pb; $x = 2, 3, 4$)[2a,3,6] have been isolated and structurally characterized. Among these homoatomic polyanions, the nine-atom polyhedra $[E_9]^{x-}$ have drawn much attention[7] owing to their high abundance, relatively easy access, and potential utility in preparing ligand-free nanomaterials. In recent years, few Group 14 Zintl clusters with other atom aggregations have been reported in form of transition-metal-stabilized species. Octahedral clusters $[E_6]^{2-}$ (E = Ge, Sn) occur in $[E_6\{M(CO)_5\}_6]^{2-}$ (M = Cr, Mo, W) and are formed by the reaction of $K_2[M(CO)_5]$ with GeI_2 and $SnCl_2$.[8] A *cyclo*-$[Sn_6]^{12-}$ Zintl ion is observed in the $[Sn_6\{Nb(\eta\text{-}C_6H_5Me)\}_2]^{2-}$ ion in which the chair-conformation Sn_6 ring takes the role of an η^3 ligand to each of the two niobium atoms above and below the ring.[9] The remarkable formation of the $[Pt@Pb_{12}]^{2-}$ ion which contains a platinum atom centering the *closo*-icosahedral $[Pb_{12}]^{2-}$ cluster[10] shows that clusters of other sizes are formed from solutions of $[Pb_9]^{4-}$ ions. Herein we report the formation of a novel planar *cyclo*-$[Pb_5]^{4-}$ unit in the

[*] Dr. L. Yong, Dr. S. D. Hoffmann, Prof. Dr. T. F. Fässler
Department Chemie
Technische Universität München
Lichtenbergstrasse 4, 85747 Garching (Germany)
Fax: (+49) 89-2891-3186
E-mail: thomas.faessler@lrz.tum.de
S. Riedel, Prof. Dr. M. Kaupp
Institut für Anorganische Chemie
Universität Würzburg
Am Hubland, 97074 Würzburg (Germany)
Fax: (+49) 931-888-7135
E-mail: kaupp@mail.uni-wuerzburg.de

[**] We thank the Deutsche Forschungsgemeinschaft (SPP 1072) for financial support.

 © 2005 Wiley-VCH Verlag GmbH & Co. KGaA, Weinheim DOI: 10.1002/anie.200462342

$[\{(OC)_3Mo\}Pb_5\{Mo(CO)_3\}]^{4-}$ ion (**1**), where the *cyclo*-$[Pb_5]^{4-}$ acts in an unique way as an η^5 ligand to each $\{Mo(CO)_3\}$ fragment.

In the presence of [2.2.2]-crypt[11] the reaction of ethylenediamine (en) solutions of K_4Pb_9 with $[MesMo(CO)_3]$ (Mes = 1,3,5-trimethylbenzene) leads to the addition products $[\eta^4\text{-}Pb_9Mo(CO)_3]^{4-}$[12] and $[\eta^5\text{-}Pb_9Mo(CO)_3]^{4-}$.[13] Using [2.2]-crypt (diazo[18]crown-6) instead of the more frequently used [2.2.2]-crypt, we found the formation of $K_2[K([2.2]\text{-crypt})]_2[Pb_5\{Mo(CO)_3\}_2](en)_3$ in moderate and reproducible yield (ca. 40%). The black, air-sensitive crystals suitable for single-crystal X-ray diffraction studies[14] are obtained by careful layering of the reaction mixture with toluene. Four K^+ ions per cluster unit assign formally the charge (−4) to the cluster anion. Remarkably, there are two uncrowned K^+ ions in the crystal (Figure 1) in spite of the four equivalents of

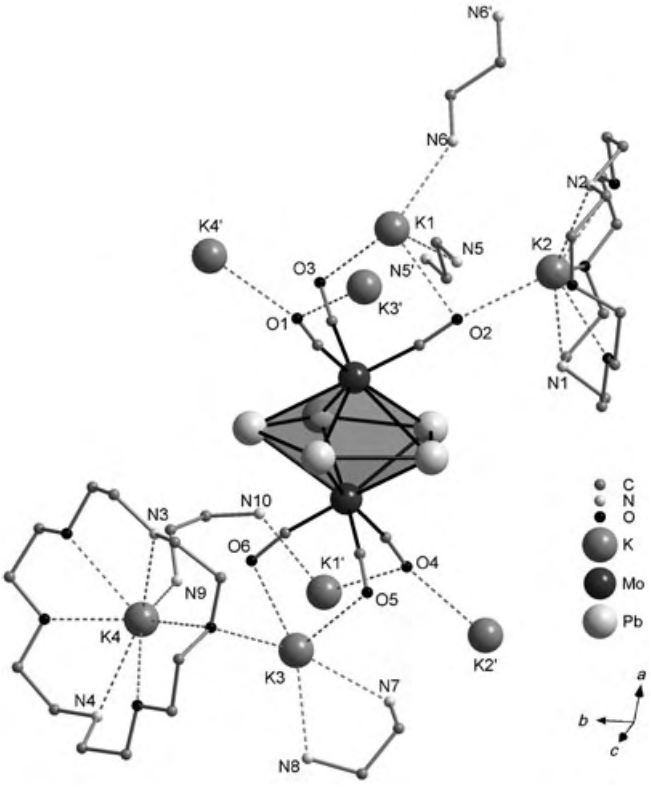

Figure 1. Structure detail showing the atom connectivity of the complex $K_2[K([2.2]\text{-crypt})]_2[Pb_5\{Mo(CO)_3\}_2](en)_3$. For the K–N or K–O separations see ref. [22].

[2.2]-cryptand used in the reaction. These two K^+ ions are coordinated to the N atoms of en and [2.2]-cryptand molecules as well as to oxygen atoms of carbonyl ligands. The crystals are insoluble in most solvents (en, DMF, THF, DMSO, and toluene).

The structure of **1** (Figure 2) contains a five-membered ring of lead atoms in a planar conformation. The anion has a virtual C_{5v} symmetry if the CO groups are ignored. The five angles in the Pb_5 ring are very close to the ideal 108° and their sum 540° fits perfectly for a planar pentagon. The five lead–

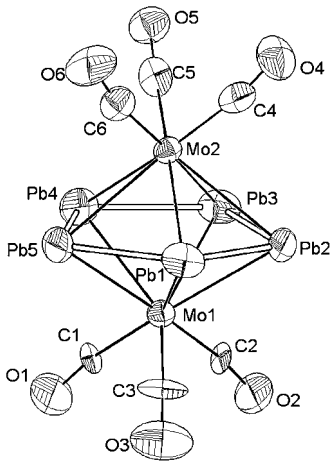

Figure 2. Molecular structure of *closo*-$[Pb_5\{Mo(CO)_3\}_2]^{4-}$ ion in compound **1** (Thermal ellipsoids set at 90% probability). Selected interatomic distances [Å] and angles [°]: Pb1-Pb2 3.0186(4), Pb1-Pb5 3.0138(4), Pb2-Pb3 3.0647(4), Pb3-Pb4 3.0569(4), Pb4-Pb5 3.0507(4), Mo1-Pb1 3.0762(6), Mo1-Pb2 3.0133(6), Mo1-Pb3 3.0646(6), Mo1-Pb4 3.0393(6), Mo1-Pb5 3.0012(6), Mo2-Pb1 3.0402(6), Mo2-Pb2 3.0582(6), Mo2-Pb3 3.0343(6), Mo2-Pb4 3.0320(6), Mo2-Pb5 3.0929(7); Pb1-Pb2-Pb3, 108.57(1) Pb2-Pb3-Pb4 106.84(1), Pb3-Pb4-Pb5 107.95(1), Pb4-Pb5-Pb1 108.25(1), Pb5-Pb1-Pb2 108.15(1). For further separations and angles, see text and ref. [22].

lead separations in the ring are in the narrow range of 3.014–3.065 Å and are significantly shorter than those in other homoatomic Zintl ions (e.g. $[Pb_9]^{4-}$ 3.076–3.544 Å,[3e,15] $[Pb_9]^{3-}$ 3.022–3.259 Å,[16] $[Pb_5]^{2-}$ 3.075–3.319 Å.[5]) and transition-metal-stabilized Zintl ions (e.g. $[\eta^4\text{-}Pb_9Cr(CO)_3]^{4-}$ 3.031–3.403 Å,[17] $[\eta^4\text{-}Pb_9Mo(CO)_3]^{4-}$ 3.033–3.329 Å,[12] $[\eta^5\text{-}Pb_9Mo(CO)_3]^{4-}$ 3.055–3.416 Å[13]). With an average value of 3.041 Å, the lead–lead contacts in this *cyclo*-$[Pb_5]^{4-}$ are longer than those in a typical diplumbane, such as $Ph_3Pb{-}PbPh_3$ with 2.844(4) Å.[18] This bond elongation is expected for such a highly charged anion. On the other hand, the Pb–Pb bonds in **1** are short compared to those of neutral diplumbylene RPb=PbR (3.188 Å)[19] or hexaarylcyclotriplumbane $(PbR_2)_3$ (3.184 Å).[20] It is worth noting that the highly charged *cyclo*-$[Sb_5]^{5-}$ ion stabilized in $[Li[NH_3]_4]_3[Li_2(NH_3)_2Sb_5]\cdot 2NH_3$ is in an envelope (cyclopentane-like) conformation.[21]

As shown in Figure 2, the Pb_5 ring in **1** binds to two $\{Mo(CO)_3\}$ fragments in η^5 fashion. Unlike the bicapped square-antiprismatic *closo*-$[\eta^5\text{-}Pb_9Mo(CO)_3]^{4-}$ ion, where the Mo atom occupies a waist vertex and the resulting Mo–Pb bonds are quite different from each other (2.962–3.241 Å),[13] the Mo–Pb bonds in **1** are in a relatively narrow range (3.001–3.093 Å) quite similar to that in $[\eta^4\text{-}Pb_9Mo(CO)_3]^{4-}$ (2.985–3.084 Å).[12] The Mo–C bonds in anion **1** are somewhat longer (1.917(7)–1.961(7) Å) than those in $[\eta^5\text{-}Pb_9Mo(CO)_3]^{4-}$ (1.874–1.934 Å), and are again close to those in $[\eta^4\text{-}Pb_9Mo(CO)_3]^{4-}$ (1.926–1.950 Å). The mean C–O bond length in **1** (1.195 Å) is in the middle of those of $[\eta^4\text{-}Pb_9Mo(CO)_3]^{4-}$ (1.184 Å) and $[\eta^5\text{-}Pb_9Mo(CO)_3]^{4-}$ (1.225 Å). The Mo-C-O angles in **1** deviate from linearity and range from 169.8(7)° to 172.1(6)°.

 © 2005 Wiley-VCH Verlag GmbH & Co. KGaA, Weinheim

The $\{Pb_5Mo_2\}$ core of **1** can also be described as a pentagonal bipyramid with the two Mo atoms occupying the apexes and the Mo–Mo vector crossing the center of the Pb_5 ring. The Mo–Mo separation is 3.2156(8) Å, much longer than in the organometallic compound $[Mo_2(CO)_{10}]^{2-}$ (3.123 Å)[23a] or in $[(C_5H_5)Mo(\eta^5\text{-}As_5)Mo(C_5H_5)]$ (2.764 Å).[23b]

According to Wade's rule, the *closo*-$\{Pb_5Mo_2\}^{4-}$ ion should be a 7-vertex 16-electron polyhedron. Based on the isolobal analogy $\{Mo(CO)_3\}$ acts as a zero-electron fragment and fulfills the electron-counting rules for *closo*-$[\eta^4\text{-}Pb_9Mo(CO)_3]^{4-}$ and *closo*-$[\eta^5\text{-}Pb_9Mo(CO)_3]^{4-}$. Counting the lead atoms as vertices which donate two electrons per atom to the polyhedral skeleton, then according to Wade rules, cluster **1** is a 14 $(5\times2+4)$ instead of the expected 16 $(7\times2+2)$ electron polyhedron. Assuming the Pb_5 ring as π ligand bound to a neutral $\{Mo(CO)_3\}$ fragment, then the $[Pb_5]^{4-}$ ion is an antiaromatic system and **1** can be view as an analogue to other complexes of 4π systems, such as $[(C_4H_4)Fe(CO)_3]$.[24]

B3LYP density-functional calculations (DFT)[25] on the $[Pb_5\{Mo(CO)_3\}_2]^{4-}$ ion employing the solid-state structural parameters, and calculations with point charges of $+0.5$ added at the nearest eight K^+ ion positions in the solid-state structure, provide a relatively low but still notable HOMO–LUMO gap of approximately 0.81 eV (free anion) and approximately 0.45 eV (with point charges). The frontier orbitals are consistent with appreciable backbonding from the tetraanionic Pb_5 fragment to the low-lying empty orbitals of a neutral $\{Mo(CO)_3\}$ fragment. The highest occupied molecular orbitals (MOs) of a planar $[Pb_5]^{4-}$ ion are either of in-plane (mixed Pb–Pb σ bonding and lone-pair) or of out-of-plane (π Pb–Pb bonding) character. In the complex, both in-plane and out-of-plane MOs are engaged heavily in π backbonding to the two $\{Mo(CO)_3\}$ fragments. One example of each type is shown in Figure 3. While the HOMO-1 (and its almost degenerate partner, the HOMO) involves mainly orbitals which originally had σ character within the Pb_5 ring, the HOMO-3 (and the almost degenerate HOMO-2) is a more genuine π orbital, both with respect to Pb–Pb bonding and with respect to ligand–metal bonding. Both transfer charge into π-type MOs on the $\{Mo(CO)_3\}$ fragments. Indeed, the highest five occupied MOs of the complex are of $[Pb_5]^{4-}\rightarrow Mo(CO)_3$ π-bonding character and only the HOMO-6 exhibits σ bonding between the fragments. The LUMO has mainly carbonyl oxygen atom character.

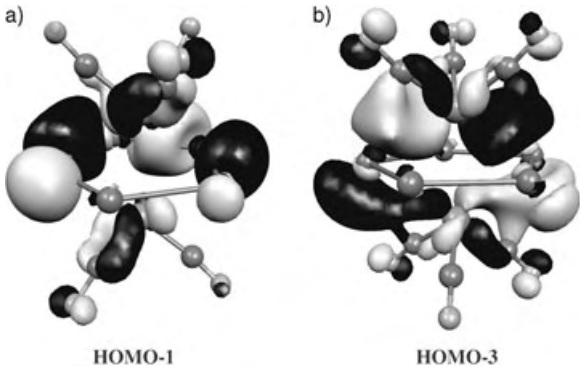

Figure 3. Isosurface plot (+/−0.03 a.u.) of two representative frontier MOs of the $[Pb_5\{Mo(CO)_3\}_2]^{4-}$ ion. a) HOMO-1 (together with the HOMO, this forms a nearly degenerate set); note the Pb–Pb σ-bonding, the lead lone pair, and Pb–Mo π-bonding character. b) HOMO-3 (together with the HOMO-2, this forms a nearly degenerate set), note the Pb–Pb π-bonding and Pb–Mo π-bonding character.

Natural population analyses[25g] of the free tetraanion place an average charge of approximately -1.43 on each $\{Mo(CO)_3\}$ fragment and leave approximately 1.13 extra electrons on the Pb_5 unit. Upon adding the point charges, the charge transfer is enhanced to -1.8 per $Mo(CO)_3$ fragment with -0.4 left on the Pb_5 unit. Wiberg and natural atomic orbital (NAO) overlap-weighted bond orders (data not given), as well as natural-bond-orbital (NBO) analyses, are consistent with essentially single bonds between the lead atoms and partial bonding between lead and molybdenum. Moreover, the π backbonding strengthens the Mo–C bonds (with partial multiple-bonding character) and weakens the C–O bonds, as expected. Generally, addition of the cation charges enhances these effects of backbonding. The appreciable charge transfer into the $\{Mo(CO)_3\}$ moieties is consistent with the relatively long C–O and relatively short Mo–C bonds. Analyses of the electron localization function (ELF; not shown) are also consistent with relatively large donation of charge from the central five-ring towards the $\{Mo(CO)_3\}$ moieties. Formal transfer of one electron from the $[Pb_5]^{4-}$ unit to each of the $\{Mo(CO)_3\}$ fragments would leave an aromatic 2π-$[Pb_5]^{2-}$ unit. Alternatively, three-dimensional aromaticity of the $[Pb_5\{Mo(CO)_3\}_2]^{4-}$ ion may be envisioned.

Although a few tetrel pentarings have been discovered in Zintl phases, such as $Li_{12}Si_7$,[26] Li_8MgSi_6,[27] Na_8BaPb_6, and Na_8EuSn_6,[28] the anion **1** is the first compound with a planar Pb_5 ring that has been isolated in solution. In contrast to Zintl phases where the charge transfer from the electropositive to the electronegative component is only formal, it can be assumed that Zintl ions isolated from solution possess fully ionic character.

The formation of anion **1** shows that in $[Pb_9]^{4-}$ solutions various species exist in equilibrium and that redox processes may take place between these species. Since ^{207}Pb NMR spectroscopy investigations of $[Pb_9]^{4-}$ Zintl anions in NH_3 solution showed only one signal, fragmentation of the nine-atom cluster and cluster growth might occur through activation from transition metals.

Experimental Section

The synthesis of compound **1** was carried out under an Argon atmosphere using a glove-box or Schlenk line. Toluene (Merck) and ethylenediamine (Merck) were dried over K/CaH_2 (Fluka), freshly distilled, and degassed. The binary phase of the formal composition "K_4Pb_9" was prepared by high-temperature reaction (350 °C) from the elements K and Pb in the ratio of 4:9. $[MesMo(CO)_3]$ was prepared by heating $[Mo(CO)_6]$ (Alfa Inorganics) in an excess of mesitylene under reflux in a nitrogen atmosphere.[29]

K_4Pb_9 (100 mg, 0.049 mmol) and [2.2]-crypt (52 mg, 0.196 mmol) were dissolved in en (ca. 1 mL) in Schlenk tube A and stirred for 5 min to yield a dark brown solution. In Schlenk tube B, $[MesMo(CO)_3]$ (15 mg, 0.049 mmol) was dissolved in toluene (ca. 2 mL) to yield a yellow solution. The solution in Schlenk tube B was added dropwise to Schlenk tube A at room temperature. The resulting mixture was stirred for another 2 h at room temperature to yield a reddish-brown solution. After filtration the filtrate was layered with

 © 2005 Wiley-VCH Verlag GmbH & Co. KGaA, Weinheim

toluene (2 mL). After 48 h, dark brown crystals of $[K([2.2]\text{-crypt}]_2K_2[Pb_5\{Mo(CO)_3\}_2](en)_3$ precipitated with a yield of 46 mg, (ca. 41 % with respect to K_4Pb_9).

The IR spectrum (KBr) of compound **1** shows that the characteristic CO stretching vibrations are red-shifted with respect to $[MesMo(CO)_3]$ to $\tilde{\nu} = 1889$ (vw, sh), 1878 (w), 1737 cm^{-1} (vs, broad). The quantitative energy-dispersive X-ray spectroscopy (EDX) analysis of the crystals shows the presence of elements K, Mo, and Pb, with roughly the expected ratios.

Received: October 18, 2004
Published online: March 2, 2005

Keywords: cluster compound · crown ether compound · lead · molybdenum · zintl anions

[1] a) A. Joannis, *C. R. Hebd. Seances Acad. Sci.* **1891**, *113*, 795; b) for an overview of organometallic substituted clusters, see: A. Schnepf, *Angew. Chem.* **2004**, *116*, 680; *Angew. Chem. Int. Ed.* **2004**, *43*, 664; c) S. Yao, Y. Xiong, K. W. Klinkhammer, *Angew. Chem.* **2004**, *116*, 6328; *Angew. Chem. Int. Ed.* **2004**, *43*, 6202.

[2] a) For a recent review see: T. F. Fässler, *Coord. Chem. Rev.* **2001**, *215*, 347; b) for the polyhedral group 14 clusters occurring in Zintl phases, see: H. Schäfer, B. Eisenmann, *Rev. Inorg. Chem.* **1981**, *3*, 29; c) S. M. Kauzlarich, *Chemisty, Structure, and Bonding of Zintl Phases and Ions*, VCH Publishers, New York, **1996**.

[3] a) E. Zintl, J. Goubeau, W. Dullenkopf, *Z. Phys. Chem. Abt. A* **1931**, *154*, 1; b) C. A. Kraus, *J. Am. Chem. Soc.* **1907**, *29*, 1557; c) F. H. Smyth, *J. Am. Chem. Soc.* **1917**, *39*, 1299; d) T. F. Fässler, R. Hoffmann, *Angew. Chem.* **1999**, *111*, 526; *Angew. Chem. Int. Ed.* **1999**, *38*, 543; e) T. F. Fässler, R. Hoffmann, *J. Chem. Soc. Dalton Trans.* **1999**, 3339.

[4] N. Korber, A. Fleischmann, *J. Chem. Soc. Dalton Trans.* **2001**, 383.

[5] a) P. A. Edwards, J. D. Corbett, *Inorg. Chem.* **1977**, *16*, 903; b) J. Campbell, G. J. Schrobilgen, *Inorg. Chem.* **1997**, *36*, 4078; c) M. Somer, W. Carrillo-Cabrera, E. M. Peters, K. Peters, M. Kaupp, H. G. von Schnering, *Z. Anorg. Allg. Chem.* **1999**, *625*, 37.

[6] J. M. Goicoechea, S. C. Sevov, *J. Am. Chem. Soc.* **2004**, *126*, 6860.

[7] a) H. G. von Schnering, M. Somer, M. Kaupp, W. Carrillo-Cabrera, M. Baitinger, A. Schmeding, Y. J. Grin, *Angew. Chem.* **1998**, *110*, 2507; *Angew. Chem. Int. Ed.* **1998**, *37*, 2359; b) L. Xu, S. C. Sevov, *J. Am. Chem. Soc.* **1999**, *121*, 9245; c) C. Downie, Z. Tang, A. M. Guloy, *Angew. Chem.* **2000**, *112*, 346; *Angew. Chem. Int. Ed.* **2000**, *39*, 338; d) T. F. Fässler, *Angew. Chem.* **2001**, *113*, 4289; *Angew. Chem. Int. Ed.* **2001**, *40*, 4161; e) A. Nienhaus, R. Hauptmann, T. F. Fässler, *Angew. Chem.* **2002**, *114*, 3352; *Angew. Chem. Int. Ed.* **2002**, *41*, 3213; f) A. Ugrinov, S. C. Sevov, *Inorg. Chem.* **2003**, *42*, 5789; g) C. Downie, J.-G. Mao, H. Parmar, A. M. Guloy, *Inorg. Chem.* **2004**, *43*, 1992; h) L. Yong, S. D. Hoffmann, T. F. Fässler, *Z. Anorg. Allg. Chem.* **2004**, *630*, 1977.

[8] a) P. Kircher, G. Huttner, K. Heinze, G. Renner, *Angew. Chem.* **1998**, *110*, 1754; *Angew. Chem. Int. Ed.* **1998**, *37*, 1664; b) G. Renner, P. Kircher, G. Huttner, P. Rutsch, K. Heinze, *Eur. J. Inorg. Chem.* **2001**, 973.

[9] B. Kesanli, J. Fettinger, B. Eichhorn, *Angew. Chem.* **2001**, *113*, 2364; *Angew. Chem. Int. Ed.* **2001**, *40*, 2300.

[10] a) E. N. Esenturk, J. Fettinger, Y.-F. Lam, B. Eichhorn, *Angew. Chem.* **2004**, *116*, 2184; *Angew. Chem. Int. Ed.* **2004**, *43*, 2132; b) T. F. Fässler, S. D. Hoffmann, *Angew. Chem.* **2004**, *116*, 6400; *Angew. Chem. Int. Ed.* **2004**, *43*, 6242.

[11] [2.2.2]-crypt = 4,7,13,16,21,24-hexaoxa-1,10-diazabicyclo[8.8.8]-hexacosane, [2.2]-crypt = 4,13-Diaza[18]crown-6 = 1,7,10,16-tetraoxa-4,13-diazacyclooctadecane.

[12] J. Campbell, H. P. A. Mercier, H. Franke, D. P. Santry, D. A. Dixon, G. J. Schrobilgen, *Inorg. Chem.* **2002**, *41*, 86.

[13] L. Yong, S. D. Hoffmann, T. F. Fässler, submitted for publication.

[14] Crystals of **1** were mounted on glass capillaries. Structure solution (SHELXS-97) and refinement (SHELXL-97) was carried out with direct methods and full-matrix least-square methods based on F^2 for all non-hydrogen atoms, with anisotropic displacement parameters. Crystal dimensions: $0.5 \times 0.4 \times 0.2$ mm. Lattice constants at 120 K: $a = 10.662(1)$, $b = 13.639(1)$, $c = 22.598(1)$ Å, $\alpha = 95.573(1)$, $\beta = 96.283(1)$, $\gamma = 108.553(1)°$, $V = 3066.0(1)$ Å^3; space group $P\bar{1}$ (No. 2); $Z = 2$, $\rho_{calcd} = 2.445$ g cm^{-1}, $\mu = 14.404$ mm^{-1}; Data collection: Nonius Kappa CCD device at the window of a rotating anode X-ray generator; $Mo_{K\alpha}$ radiation, $2\theta_{max} = 25.42$; 61472 total reflections, 11222 were independent reflections. ($R_{int} = 0.063$), $R_1 = 0.033$, and $wR_2 = 0.085$ with $I > 2\sigma(I)$, $R_1 = 0.039$ and $wR_2 = 0.089$ for all data, respectively. CCDC-252717 (**1**) contains the supplementary crystallographic data for this paper. These data can be obtained free of charge from The Cambridge Crystallographic Data Centre via www.ccdc.cam.ac.uk/data_request/cif.

[15] J. Campbell, D. A. Dixon, H. P. A. Mercier, G. J. Schrobilgen, *Inorg. Chem.* **1995**, *34*, 5798.

[16] T. F. Fässler, M. Hunziker, *Inorg. Chem.* **1994**, *33*, 5380.

[17] B. W. Eichhorn, R. C. Haushalter, *J. Chem. Soc. Chem. Commun.* **1990**, 937.

[18] H. Preut, F. Huber, *Z. Anorg. Allg. Chem.* **1976**, *419*, 92.

[19] L. Pu, B. Twamley, P. P. Power, *J. Am. Chem. Soc.* **2000**, *122*, 3524.

[20] F. Stabenow, W. Saak, H. Marsmann, M. Weidenbruch, *J. Am. Chem. Soc.* **2003**, *125*, 10172.

[21] N. Korber, F. Richter, *Angew. Chem.* **1997**, *109*, 1575; *Angew. Chem. Int. Ed. Engl.* **1997**, *36*, 1512.

[22] Bond lengths [Å] and angles [°] in *closo*-$[Pb_5\{Mo(CO)_3\}_2]^{4-}$ ion (**1**): Mo1-C1 1.929(6), Mo1-C2 1.920(6), Mo1-C3 1.961(7), C1-O1 1.193(8), C2-O2 1.220(8), C3-O3 1.168(9), Mo2-4 1.917(8), Mo2-C5 1.928(7), Mo2-C6 1.925(7), C4-O4 1.202(9), C5-O5 1.195(9), C6-O6 1.194(9), Mo1-Mo2 3.215(1), K1-N5 2.923(8), K1-N6 2.890(6), K1-O2 2.912(6), K1-O3 3.048(6), K1-O'4 2.813(6), K2-N1 2.948(7), K2-N2 2.927(6), K2-O2 2.766(1), K2-O7 2.958(5), K2-O8 2.981(5), K2-O9 2.985(6), K2-O10 2.817(5), K2-O'4 2.903(6), K3-N7 2.776(8), K3-N8 2.948(7), K3-O5 2.879(6), K3-O6 2.913(6), K3-O11 2.756(6), K3-O' 1 2.769(1), K4-N3 2.942(7), K4-N4 2.907(8), K4-N9 2.880(7), K4-O11 3.210(6), K4-O12 2.831(5), K4-O13 2.912(6), K4-O14 2.931(6), K4-O' 1 2.912(6); separation ranges: $d(K\text{-}N_{en})$ 2.776(8)–2.948(7), $d(K\text{-}N_{Crypt})$ 2.907(8)–2.948(7), $d(K\text{-}O_{Crypt})$ 2.756(6)–2.985(6), $d(K\text{-}O_{CO})$ 2.766(5)–3.048(6); O1-C1-Mo1 170.6(6), O3-C3-Mo1 169.8(7), O2-C2-Mo1 172.1(6), Mo2-C4-O4 172.0(6), Mo2-C5-O5 171.1(6), Mo2-C6-O6 170.0(6). All K-O separations are in the range of other observed $K\text{–}O_{CO}$ contacts in compounds with [K(crown ether)] as a complex.[30]

[23] a) L. B. Handy, J. K. Ruff, L. F. Dahl, *J. Am. Chem. Soc.* **1970**, *92*, 7312; b) A. L. Rheingold, M. J. Foley, P. J. Sulliven, *J. Am. Chem. Soc.* **1982**, *104*, 4727; c) for a review on cyclic group 15 element ligands, see: O. J. Scherer, *Angew. Chem.* **1990**, *102*, 1137; *Angew. Chem. Int. Ed.* **1990**, *29*, 1104.

[24] a) G. F. Emerson, L. Watts, R. Pettit, *J. Am. Chem. Soc.* **1965**, *87*, 131; b) for a recent article about (cyclobutadiene)iron tricarbonyl, see: D. Seyferth, *Organometallics* **2003**, *22*, 2.

[25] The Gaussian98 program[25b] and the B3LYP functional[25c] were used for calculations. The Mo[25d] and Pb[25e] atoms were described by small-core quasirelativistic pseudopotentials with 6s5p3d and 6s6p4d valence basis sets, respectively. Dunning's DZP basis set[25f] was used for C and O. Natural population analyses (NPA)[25g] used the built-in routines of Gaussian98, and orbitals are visualized with the Molekel program.[25h] b) Gaussian 98 (Revision A.7), M. J. Frisch, G. W. Trucks, H. B. Schlegel,

 © 2005 Wiley-VCH Verlag GmbH & Co. KGaA, Weinheim

G. E. Scuseria, M. A. Robb, J. R. Cheeseman, V. G. Zakrzewski, J. A. Montgomery, R. E. Stratmann, J. C. Burant, S. Dapprich, J. M. Millam, A. D. Daniels, K. N. Kudin, M. C. Strain, O. Farkas, J. Tomasi, V. Barone, M. Cossi, R. Cammi, B. Mennucci, C. Pomelli, C. Adamo, S. Clifford, J. Ochterski, G. A. Petersson, P. Y. Ayala, Q. Cui, K. Morokuma, D. K. Malick, A. D. Rabuck, K. Raghavachari, J. B. Foresman, J. Cioslowski, J. V. Ortiz, B. B. Stefanov, G. Liu, A. Liashenko, P. Piskorz, I. Komaromi, R. Gomperts, R. L. Martin, D. J. Fox, T. Keith, M. A. Al-Laham, C. Y. Peng, A. Nanayakkara, C. Gonzalez, M. Challacombe, P. M. W. Gill, B. G. Johnson, W. Chen, M. W. Wong, J. L. Andres, M. Head-Gordon, E. S. Replogle, J. A. Pople, Gaussian, Inc., Pittsburgh, PA, **1998**; c) A. D. Becke, *J. Chem. Phys.* **1993**, *98*, 5648–5652; C. Lee, W. Yang, R. G. Parr, *Phys. Rev. B* **1988**, *37*, 785; B. Miehlich, A. Savin, H. Stoll, H. Preuss, *Chem. Phys. Lett.* **1989**, *157*, 200; d) D. Andrae, U. Häußermann, M. Dolg, H. Stoll, H. Preuß, *Theor. Chim. Acta* **1990**, *77*, 123; e) B. Metz, H. Stoll, M. Dolg, *J. Chem. Phys.* **2000**, *113*, 2563; f) T. H. Dunning, P. J. Hay in *Methods of Electronic Structure Theory*, *Modern Theoretical Chemistry*, *Vol. 3* (Ed.: H. F. Schaefer III), Plenum, New York, **1977**; g) A. E. Reed, F. Weinhold, *J. Chem. Phys.* **1985**, *83*, 735; h) see, for example, S. Portmann, H. P. Lüthi, *Chimia* **2000**, *54*, 766.

[26] a) R. Nesper, H. G. von Schnering, J. Curda, *Chem. Ber.* **1986**, *119*, 3576; b) H. G. von Schnering, R. Nesper, J. Curda, K.-F. Tebbe, J. Curda, *Angew. Chem.* **1980**, *92*, 1070; *Angew. Chem. Int. Ed. Engl.* **1980**, *19*, 1033.

[27] R. Nesper, J. Curda, H. G. von Schnering, *J. Solid State Chem.* **1986**, *62*, 199.

[28] I. Todorov, S. C. Sevov, *Inorg. Chem.* **2004**, *43*, 6490.

[29] E. L. Muetterities, J. R. Bleeke, A. C. Sievert, *J. Organomet. Chem.* **1979**, *178*, 197.

[30] a) C. Borgmann, C. Limberg, L. Zsolnai, K. Heinze, *Z. Naturforsch. B* **1999**, *54*, 473; b) J. W. Freeman, A. M. Arif, R. D. Ernst, *Inorg. Chim. Acta* **1995**, *240*, 33; c) C. P. Horwitz, E. M. Holt, C. P. Brock, D. F. Shriver, *J. Am. Chem. Soc.* **1985**, *107*, 8136; d) G. Tripepi, V. G. Young, Jr., J. E. Ellis, *J. Organomet. Chem.* **2000**, *593*, 354; e) C. Borgmann, C. Limberg, S. Cunskis, P. Kircher, *Eur. J. Inorg. Chem.* **2001**, 349; f) D. G. Gusev, A. J. Lough, R. H. Morris, *J. Am. Chem. Soc.* **1998**, *120*, 13138.

 © 2005 Wiley-VCH Verlag GmbH & Co. KGaA, Weinheim

Carbohydrate Mimetics

Orthogonally Protected Sugar Diamino Acids as Building Blocks for Linear and Branched Oligosaccharide Mimetics**

*Frank Sicherl and Valentin Wittmann**

Sugar amino acids (SAAs),[1] which are carbohydrate derivatives with both an amino group and a carboxyl group connected to the carbohydrate frame, have found wide application as building blocks for oligosaccharide[2,3] and peptide mimetics,[4,5] as secondary-structure inducing elements, and as pharmacophore-presenting scaffolds[6] for the generation of combinatorial libraries.[7] Used as monomers with a rigid pyran ring, functional pharmacophoric groups attached to the hydroxy, amino, and carboxyl groups can be presented in a distinct spatial arrangement as was demonstrated in seminal studies by Hirschmann et al.[8] Linear and cyclic oligomers of SAAs have been synthesized, taking advantage of well-established peptide chemistry, and in certain cases they adopt defined secondary structures.[3,5] Sugar amino acids with an additional amino group, that is, sugar diamino acids, would be an attractive extension of this concept, giving access to novel branched oligomeric structures.[9] However, their synthesis has not been reported until now.

Here we introduce the protected derivatives **1** and **2** of 2,6-diamino-2,6-dideoxy-β-D-glucopyranosyl carboxylic acid,

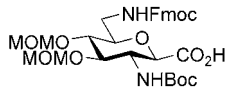

1

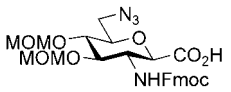

2

the first examples of sugar diamino acids (SDAs) that are amenable to peptide synthesis following standard Fmoc strategy (Fmoc = 9-fluorenylmethoxycarbonyl) in solution and on solid phase. The additional amino group in SDAs can be used to form branched amide-linked oligosaccharide mimetics. Besides that, oligomeric SDAs with unprotected amino groups represent a new class of potential aminoglycoside mimetics.[10] Such structures are of great significance as potential ligands for the new RNA targets emerging in the post-genome era.[11]

[*] Dipl.-Chem. F. Sicherl, Prof. Dr. V. Wittmann
Fachbereich Chemie
Universität Konstanz
Fach M 709, 78457 Konstanz (Germany)
Fax: (+49) 7531-88-4573
E-mail: mail@valentin-wittmann.de

[**] This work was supported by the Deutsche Forschungsgemeinschaft (SFB 579 "RNA–Ligand Interactions"). We thank the coordinator of the SFB 579, Prof. Joachim W. Engels, for his support and Aventis AG for providing an HPLC system.

Supporting information for this article is available on the WWW under http://www.angewandte.org or from the author.

 © 2005 Wiley-VCH Verlag GmbH & Co. KGaA, Weinheim DOI: 10.1002/anie.200462595

Whereas the protecting-group pattern of SDA **1** was conceived for the construction of linear oligomers through the amino group in the 6-position[12] following Fmoc strategy, SDA **2** can be employed for the synthesis of branched structures since the two amino groups are orthogonally protected with the Fmoc group and as an azide, respectively. We decided to use methoxymethyl (MOM) groups for hydroxy protection, because they are small and easily removable together with Boc (*tert*-butyloxycarbonyl) groups under acidic conditions, and they do not deactivate adjacent nucleophiles as it is known from electron-withdrawing acyl or sterically demanding benzyl protecting groups.[3] Finally, since **2** has protected hydroxy groups, a large excess of the activated amino acid can be used during peptide-bond formation typically employed during solid-phase peptide synthesis.

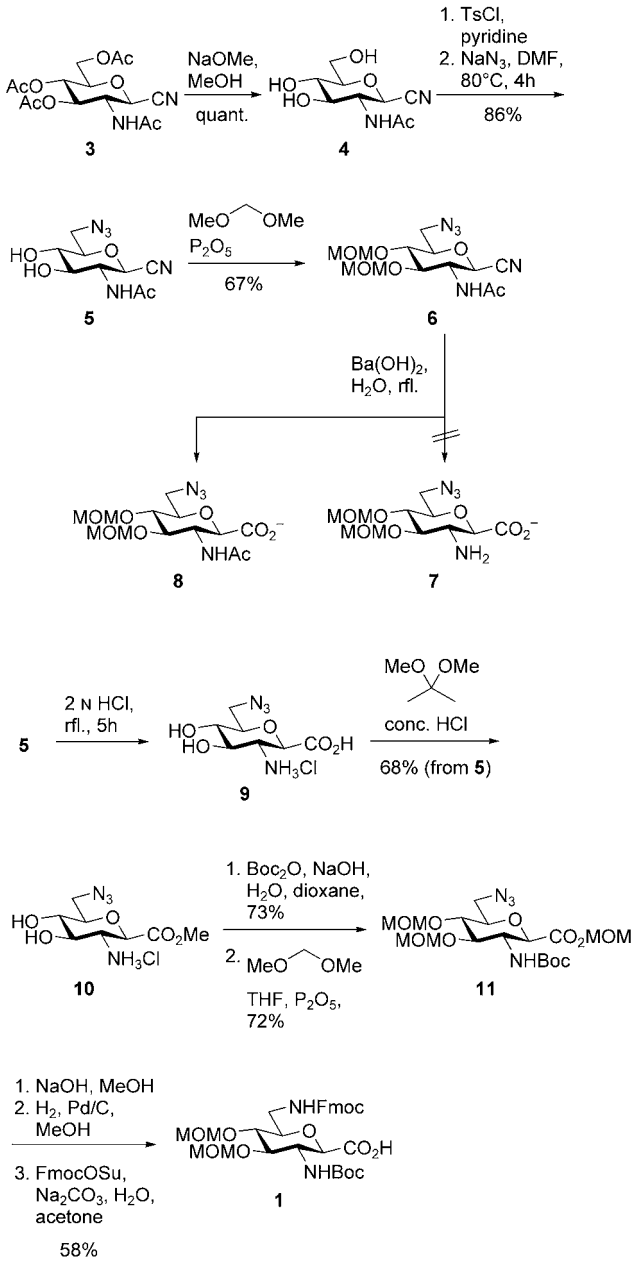

Scheme 1. Synthesis of SDA **1**; rfl. = reflux.

SDA **1** was synthesized from the known glycosyl cyanide **3**[13] (Scheme 1). After *O*-deacetylation, triol **4** was tosylated regioselectively at the 6-position. Nucleophilic substitution with sodium azide gave **5** in 86% yield over three steps. MOM groups were introduced by treatment with dimethoxymethane and P_2O_5[14] (in order to circumvent toxic MOM-Cl) leading to **6**. Initial attempts to hydrolyze the nitrile and acetamide simultaneously under basic conditions with aqueous $Ba(OH)_2$, however, failed. Under these conditions the reaction stopped at the acetamidocarboxylate stage (**8**). Other bases such as methanolic KOH and aqueous NaOH either led to the same result or to complete decomposition. Finally, heating **5** in 2 N aqueous HCl at reflux successfully effected amide and nitrile hydrolysis to give the free amino acid **9**. To facilitate its purification, methyl ester **10** was formed by treatment with dimethoxypropane and HCl. The amino group of **10** was protected by the Boc group with concomitant cleavage of the methyl ester. Compound **11** was obtained by MOM protection using the procedure mentioned earlier. The MOM ester in **11** was cleaved with NaOH. Finally, hydrogenation of the azide and subsequent Fmoc protection of the amine gave SDA building block **1** (Table 1).

SDA **2** was synthesized commencing with methyl ester **10** (Scheme 2). The 2-amino function was masked temporarily,

Table 1: Selected physical properties of compounds **1**, **2**, **19**, and **20**.

1: White amorphous solid; $R_f = 0.24$ (silica, MeOH/CH_2Cl_2 9/1); ^{1}H NMR (600 MHz, DMSO, 300 K, TMS) (major conformation): $\delta = 7.87$ (d, $J = 7.4$ Hz, 2H, arenes), 7.68 (m, 2H, arenes), 7.38–7.40 (m, 3H, arenes, NH-Fmoc), 7.29–7.32 (m, 2H, arenes), 6.86 (br s, 1H, NH-Boc), 4.75 (d, $J = 6.4$ Hz, 1H, O-CH_2-O), 4.62–4.65 (m, 3H, O-CH_2-O), 4.11–4.24 (m, 3H, H-9^{Fmoc}, CH_2^{Fmoc}), 3.64 (m, 1H, H-1), 3.55 (m, 1H, H-2), 3.55 (m, 1H, H-3), 3.51 (m, 1H, H-6), 3.30 (s, 3H, O-CH_3), 3.26 (s, 3H, O-CH_3), 3.24 (m, 1H, H-5), 3.23 (m, 1H, H-4), 3.00 (m, 1H, H-6′), 1.33 ppm (s, 9H, $C(CH_3)_3$); ^{13}C NMR (150 MHz, DMSO, 300 K, TMS): $\delta = 171.1$ (COOH), 156.4 (C=O), 155.0 (C=O), 143.9, 140.8, 127.7, 127.2, 125.3, 120.2 (arenes), 97.9 (O-CH_2-O), 97.3 (O-CH_2-O), 81.3 (C-3), 79.2 (CMe_3), 78.3 (C-1), 77.8 (C-5), 77.1 (C-4), 65.6 (CH_2^{Fmoc}), 56.0 (O-CH_3), 55.5 (O-CH_3), 53.8 (C-2), 46.7 (CH^{Fmoc}), 42.0 (C-6), 28.3 ppm ($C(CH_3)_3$); MS (MALDI-TOF), calcd for $C_{31}H_{40}N_2NaO_{11}$ [M+Na$^+$]: 639.25, found: 639.5.

2: White amorphous solid; $R_f = 0.63$ (silica, H_2O/MeCN 1/4); ^{1}H NMR (600 MHz, DMSO, 300 K, TMS): $\delta = 7.86$ (m, 2H, arenes), 7.69 (d, $J = 7.4$ Hz, 1H, arenes), 7.66 (d, $J = 7.4$ Hz, 1H, arenes), 7.46 (d, 1H, NH), 7.39 (m, 2H, arenes), 7.30 (m, 2H, arenes), 4.72 (d, $J = 6.5$ Hz, 1H, O-CH_2-O), 4.59 (d, $J = 6.5$ Hz, 1H, O-CH_2-O), 4.57 (d, $J = 6.5$ Hz, 1H, O-CH_2-O), 4.53 (d, $J = 6.5$ Hz, 1H, O-CH_2-O), 4.29 a. 4.20 (2 m, 2H, CH_2^{Fmoc}), 4.15 (m, 1H, H-9^{Fmoc}), 3.73 (d, $J = 10.0$ Hz, 1H, H-1), 3.61 (m, 1H, H-2), 3.55 (m, 1H, H-3), 3.54 a. 3.45 (2 m, 2H, 2 H-6), 3.38 (m, 1H, H-4), 3.33 (m, 1H, H-5), 3.27 (s, 3H, O-CH_3), 3.09 ppm (s, 3H, O-CH_3); ^{13}C NMR (150 MHz, DMSO, 300 K, TMS): $\delta = 170.9$ (COOH), 155.8 (C=O^{Fmoc}), 144.0, 143.8, 140.8, 127.6, 127.1, 125.3, 120.1 (arenes), 97.9 (O-CH_2-O), 97.3 (O-CH_2-O), 81.3 (C-3), 79.2 (C-1), 77.5 (C-5), 76.9 (C-4), 65.4 (CH_2^{Fmoc}), 55.9 (O-CH_3), 55.4 (O-CH_3), 54.2 (C-2), 51.0 (C-6), 46.7 ppm (CH^{Fmoc}); MS (MALDI-TOF), calcd for $C_{26}H_{30}N_4NaO_9$ [M+Na$^+$]: 565.19, found: 565.4.

19: HRMS (MALDI-FTICR), calcd for $C_{83}H_{110}N_8O_{27}$: 1673.73730 [M+Na$^+$], found: 1673.73587, $\Delta m = 0.8$ ppm.

20: HRMS (ESI-FTICR, MeCN/H_2O), calcd for $C_{31}H_{50}N_8O_{13}$: 743.35696 [M+H$^+$], found: 743.35563, $\Delta m = 1.8$ ppm.

 © 2005 Wiley-VCH Verlag GmbH & Co. KGaA, Weinheim

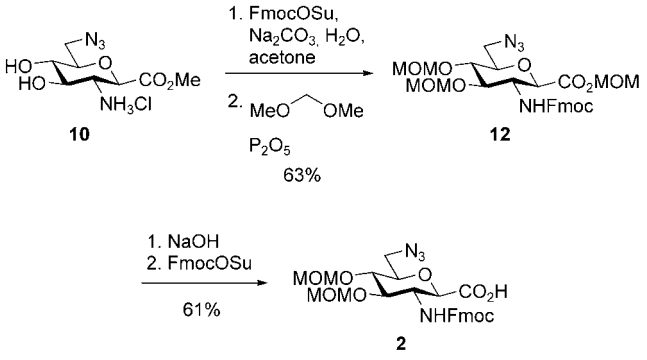

Scheme 2. Synthesis of SDA **2**.

and introduction of MOM groups gave **12**, which was treated with NaOH. Reprotection of the amino group at the 2-position gave building block **2**.

Scheme 3 illustrates the application of SDA building block **1** in the peptide synthesis of aminoglycoside mimetic **16** following the standard Fmoc protocol. We carried out the synthesis in solution to be able to follow the outcome of each step. Starting with β-alanine amide **13**, stepwise coupling of **1** using 2-(1*H*-benzotriazol-1-yl)-1,1,3,3-tetramethyluronium hexafluorophosphate (HBTU) and 1-hydroxy-1*H*-benzotriazole (HOBt) as coupling reagents led to linear pseudotrisaccharide **16** in six steps. When SDA building block **1** was applied in excess, peptide couplings proceeded smoothly with no side products detectable by TLC and yields up to 95% after column chromatography. The integrity of the chirality at the α-carbon of the sugar diamino acids was verified by ^{1}H NMR spectroscopy (e.g. **14**: $\delta_{H\text{-}1} = 3.56$ ppm, $^3J_{H\text{-}1,H\text{-}2} = 9.8$ Hz).

The utilization of the orthogonally protected SDA **2** for the preparation of the branched oligomer **20** is demonstrated in Scheme 4. After coupling of **2** to β-alanine amide **13**, the amine at the 2-position was deprotected by treatment with piperidine. Coupling of SDA **1** to this sterically hindered amine proceeded in a yield of 79% after column chromatography on silica gel to give **18**. In this case *O*-(7-azabenzotriazol-1-yl)-1,1,3,3-tetramethyluronium hexafluorophosphate (HATU) and 1-hydroxy-7-aza-1*H*-benzotriazole (HOAt) were used as coupling reagents. Reduction of the

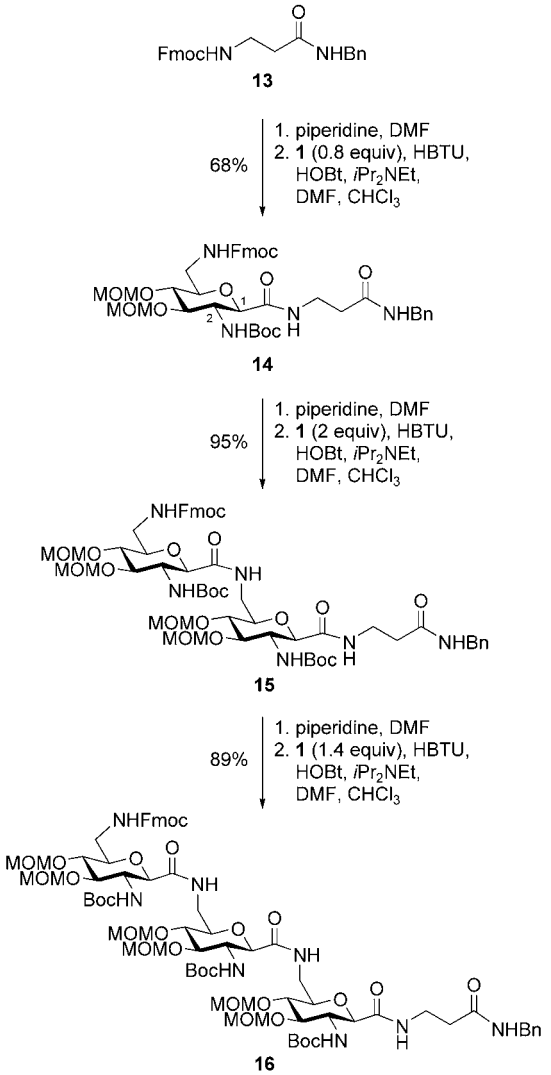

Scheme 3. Synthesis of linear oligomer **16**; Bn = benzyl.

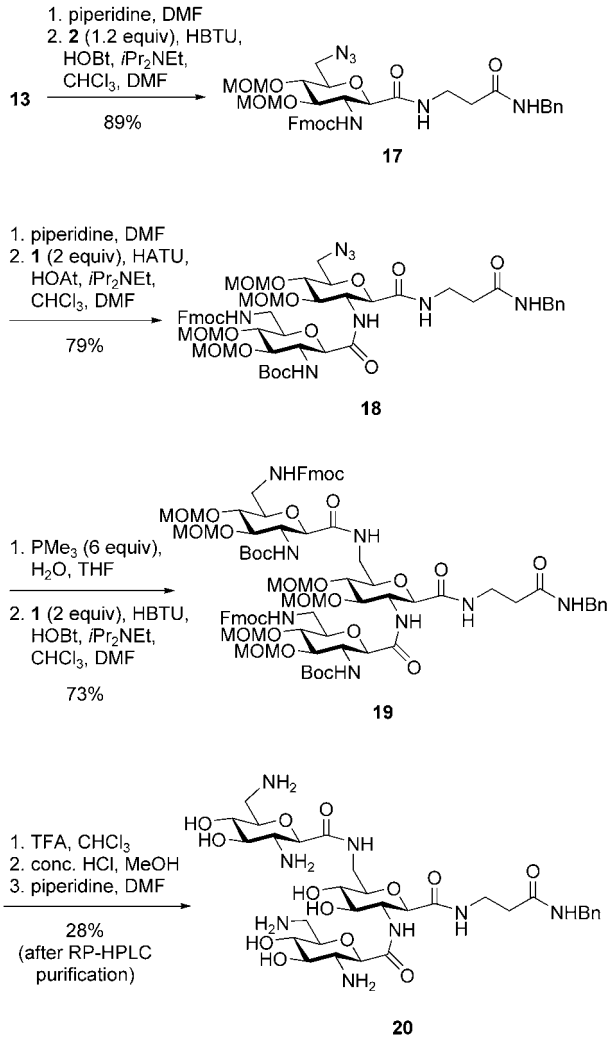

Scheme 4. Synthesis of branched oligomer **20**.

 © 2005 Wiley-VCH Verlag GmbH & Co. KGaA, Weinheim

azide in presence of the hydrogenolytically labile Fmoc group was accomplished under Staudinger conditions.[15] Subsequent coupling with **1** provided the branched oligomer **19** in a yield of 73 % over two steps. Complete deprotection of **19** was carried out by a three-step procedure. Treatment with TFA/$CHCl_3$ (1:1) led to complete Boc removal and partial cleavage of the MOM groups. The latter could be completed by addition of a small amount of water. A cleaner product, however, was obtained removing the MOM groups with conc. HCl in methanol. Finally, Fmoc groups were cleaved by treatment with piperidine in DMF to yield **20**, which was purified by RP-HPLC with added ion-pairing reagent pentafluoropropionic acid.[16] Compound **20** is the first sugar amino acid oligomer in which branching is achieved through two amide linkages.

In conclusion, we have presented a divergent synthesis of the SDA building blocks **1** and **2** and their application in the efficient assembly of oligosaccharide mimetics **16** and **20**, which are the first examples of a new class of aminoglycoside mimetics. The protecting-group scheme of **1** and **2** is compatible with conventional Fmoc solid-phase peptide synthesis and includes the option of generating branched structures. Future applications include the utilization of SDA building blocks in the preparation of combinatorial libraries of aminoglycoside mimetics. Due to the various possibilities with which SDAs can be connected to each other, a high degree of diversity can be achieved by employing only a small set of different sugar diamino acids.

Received: November 12, 2004
Published online: February 25, 2005

Keywords: amino acids · aminoglycosides · carbohydrates · C-glycosides · peptides

[1] Reviews: a) T. K. Chakraborty, P. Srinivasu, S. Tapadar, B. K. Mohan, *J. Chem. Sci.* **2004**, *116*, 187 – 207; b) E. Gräfin von Roedern, M. A. Born, M. Stöckle, H. Kessler in *Methods of Organic Chemistry (Houben-Weyl)*, *Vol. E22c* (Eds.: M. Goodman, A. Felix, L. Moroder, C. Toniolo), Thieme, Stuttgart, **2003**, p. 807 – 821; c) S. A. W. Gruner, E. Locardi, E. Lohof, H. Kessler, *Chem. Rev.* **2002**, *102*, 491 – 514; d) F. Schweizer, *Angew. Chem.* **2002**, *114*, 240 – 264; *Angew. Chem. Int. Ed.* **2002**, *41*, 230 – 253.

[2] a) T. Q. Gregar, J. Gervay-Hague, *J. Org. Chem.* **2004**, *69*, 1001 – 1009; b) S. Sabesan, *Tetrahedron Lett.* **1997**, *38*, 3127 – 3130; c) H. P. Wessel, C. Mitchell, C. M. Lobato, G. Schmid, *Angew. Chem.* **1995**, *107*, 2920 – 2921; *Angew. Chem. Int. Ed. Engl.* **1995**, *34*, 2712 – 2713.

[3] Y. Suhara, Y. Yamaguchi, B. Collins, R. L. Schnaar, M. Yanagishita, J. E. K. Hildreth, I. Shimada, Y. Ichikawa, *Bioorg. Med. Chem.* **2002**, *10*, 1999 – 2013.

[4] a) M. Raunkjær, F. El Oualid, G. A. van der Marel, H. S. Overkleeft, M. Overhand, *Org. Lett.* **2004**, *6*, 3167 – 3170; b) E. Lohof, E. Planker, C. Mang, F. Burkhart, M. A. Dechantsreiter, R. Haubner, H.-J. Wester, M. Schwaiger, G. Hölzemann, S. L. Goodman, H. Kessler, *Angew. Chem.* **2000**, *112*, 2868 – 2871; *Angew. Chem. Int. Ed.* **2000**, *39*, 2761 – 2764; c) A. B. Smith III, S. Sasho, B. A. Barwis, P. Sprengeler, J. Barbosa, R. Hirschmann, B. S. Cooperman, *Bioorg. Med. Chem. Lett.* **1998**, *8*, 3133 – 3136.

[5] a) T. K. Chakraborty, V. Ramakrishna Reddy, G. Sudhakar, S. Uday Kumar, T. Jagadeshwar Reddy, S. Kiran Kumar, A. C. Kunwar, A. Mathur, R. Sharma, N. Gupta, S. Prasad, *Tetrahedron* **2004**, *60*, 8329 – 8339; b) S. Chandrasekhar, M. S. Reddy, B. Jagadeesh, A. Prabhakar, M. H. V. R. Rao, B. Jagannadh, *J. Am. Chem. Soc.* **2004**, *126*, 13586 – 13587; c) R. M. van Well, L. Marinelli, C. Altona, K. Erkelens, G. Siegal, M. van Raaij, A. L. Llamas-Saiz, H. Kessler, E. Novellino, A. Lavecchia, J. H. van Boom, M. Overhand, *J. Am. Chem. Soc.* **2003**, *125*, 10822 – 10829; d) S. A. W. Gruner, V. Truffault, G. Voll, E. Locardi, M. Stöckle, H. Kessler, *Chem. Eur. J.* **2002**, *8*, 4365 – 4376; e) N. L. Hungerford, T. D. W. Claridge, M. P. Watterson, R. T. Aplin, A. Moreno, G. W. J. Fleet, *Perkin 1* **2000**, 3666 – 3679.

[6] M. Ghosh, R. G. Dulina, R. Kakarla, M. J. Sofia, *J. Org. Chem.* **2000**, *65*, 8387 – 8390.

[7] a) A. A. Edwards, O. Ichihara, S. Murfin, R. Wilkes, M. Whittaker, D. J. Watkin, G. W. J. Fleet, *J. Comb. Chem.* **2004**, *6*, 230 – 238; b) M. J. Sofia, N. Allanson, N. T. Hatzenbuhler, R. Jain, R. Kakarla, N. Kogan, R. Liang, D. Liu, D. J. Silva, H. Wang, D. Gange, J. Anderson, A. Chen, F. Chi, R. Dulina, B. Huang, M. Kamau, C. Wang, E. Baizman, A. Branstrom, N. Bristol, R. Goldman, K. Han, C. Longley, S. Midha, H. R. Axelrod, *J. Med. Chem.* **1999**, *42*, 3193 – 3198.

[8] a) R. Hirschmann, K. C. Nicolaou, S. Pietranico, J. Salvino, E. M. Leahy, P. A. Sprengeler, G. Furst, A. B. Smith III, C. D. Strader, M. A. Cascieri, M. R. Candelore, C. Donaldson, W. Vale, L. Maechler, *J. Am. Chem. Soc.* **1992**, *114*, 9217 – 9218. b) For recent reports on the use of carbohydrates as multifunctional scaffolds, see: U. Hünger, J. Ohnsmann, H. Kunz, *Angew. Chem.* **2004**, *116*, 1125 – 1128; *Angew. Chem. Int. Ed.* **2004**, *43*, 1104 – 1107; c) C.-H. Wong, X.-S. Ye, Z. Zhang, *J. Am. Chem. Soc.* **1998**, *120*, 7137 – 7138.

[9] For the synthesis of a branched oligomer employing a glycosylated sugar amino acid, see: C. M. Timmers, J. J. Turner, C. M. Ward, G. A. van der Marel, M. L. C. E. Kouwijzer, P. D. J. Grootenhuis, J. H. van Boom, *Chem. Eur. J.* **1997**, *3*, 920 – 929.

[10] 2,6-Diamino-2,6-dideoxyglucose is a substructure of the aminoglycoside antibiotic neomycin B. For the use of disaccharide-based diamino acid derivatives as inhibitors of bacterial cell-wall biosynthesis, see ref. [7b].

[11] a) Q. Vicens, E. Westhof, *ChemBioChem* **2003**, *4*, 1018 – 1023; b) Y. Tor, *ChemBioChem* **2003**, *4*, 998 – 1007.

[12] Numbering according to the parent compound glucosamine is used throughout this communication.

[13] D. Carrière, S. J. Meunier, F. D. Tropper, S. Cao, R. Roy, *J. Mol. Catal. A* **2000**, *154*, 9 – 22.

[14] K. Fuji, S. Nakano, E. Fujita, *Synthesis* **1975**, 276 – 277.

[15] J. T. Lundquist IV, J. C. Pelletier, *Org. Lett.* **2002**, *4*, 3219 – 3221.

[16] M. McCroskey, V. E. Groppi, J. D. Pearson, *Anal. Biochem.* **1987**, *163*, 427 – 432.

 © 2005 Wiley-VCH Verlag GmbH & Co. KGaA, Weinheim

Nanoporous Materials

High-Aspect-Ratio TiO_2 Nanotubes by Anodization of Titanium**

*Jan M. Macák, Hiroaki Tsuchiya, and Patrik Schmuki**

Nanotubular material surfaces produced by the electrochemical formation of self-organized porous structures on materials such as aluminum[1,2] and silicon[3,4] have attracted significant interest in recent years. While scientific thrust is often directed towards the elucidation of the principles of the self-organization phenomena, technological efforts target applications based on the direct use of the high surface area, for example, for sensing[5,6] or controlled catalysis,[7] exploit the optical properties in photonic crystals,[8] waveguides,[9] or in 3D arranged Bragg-stack type of reflectors.[10] The highly organized structures may be used indirectly as templates[11] for the deposition of other materials such as metals,[12] semiconductors,[13] or polymers.[14] Over the past few years, nanoporous TiO_2 structures have also been formed by electrochemical anodization of titanium.[15–17] Although several applications have been proposed,[18,19] a wider impact of these structures has been hampered by the fact that the layers could only been grown to a limiting thickness of a few hundreds of nanometers.

Herein we demonstrate for the first time how high-aspect-ratio, self-organized, TiO_2 films can be grown by tailoring the electrochemical conditions during titanium anodization.

Figure 1 shows scanning electron microscope (SEM) images of self-organized porous titanium oxide formed to a thickness of approximately 2.5 μm in 1M $(NH_4)_2SO_4$ electrolyte containing 0.5 wt.% NH_4F. From the SEM images it is evident that the self-organized regular porous structure consists of pore arrays with a uniform pore diameter of approximately 100 nm and an average spacing of 150 nm. It is also clear that pore mouths are open on the top of the layer while on the bottom of the structure the tubes are closed by presence of an about 50-nm thick barrier layer of TiO_2.

The key to achieve high-aspect-ratio growth is to adjust the dissolution rate of TiO_2 by localized acidification at the pore bottom while a protective environment is maintained along the pore walls and at the pore mouth. In our previous work in HF and NaF solutions[15,20] it was established that the thickness of the porous layer is essentially the result of an equilibrium between electrochemical formation of TiO_2 at the pore bottom and the chemical dissolution of this TiO_2 in an F^- ion containing solution (Figure 2). The solubility of TiO_2 in HF, forming $[TiF_6]^{2-}$, is essential for pore formation, however, it is also the reason that previous attempts to form porous layers in HF electrolytes always resulted in layer thicknesses in the range of some 100 nm.

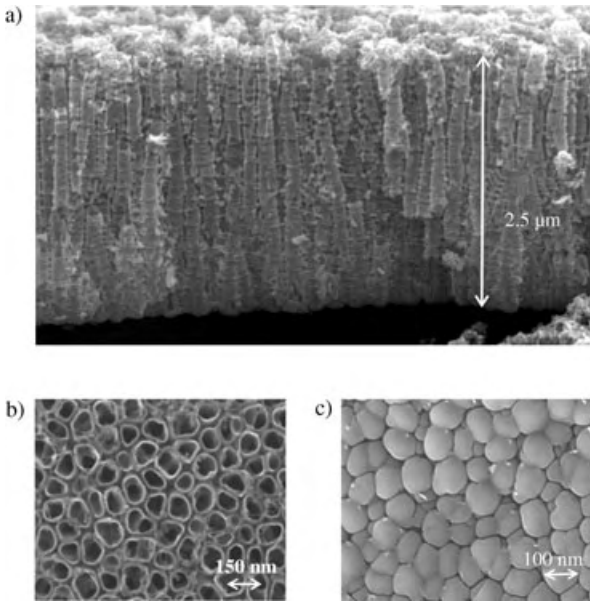

Figure 1. SEM images of porous titanium oxide nanotubes. The cross-sectional (a), top (b), and bottom (c) views of a 2.5-μm thick self-organized porous layer. The titanium sample was anodized up to 20 V in 1 M $(NH_4)_2SO_4$ + 0.5 wt.% NH_4F using a potential sweep from open-circuit potential to 20 V with sweep rate 0.1 Vs^{-1}. The average pore diameter is approximately 100 nm and the average pore spacing is approximately 150 nm.

We tackled the problem by controlling the self-induced acidification of the pore bottom that is caused by the electrochemical dissolution of the metal (Figure 2a–c). Main reason for the localized acidification is the oxidation and hydrolysis of elemental titanium [Eq. (1), in Figure 2]. The chemical dissolution rate of TiO_2 is highly dependent on the pH value (see Figure 2d). Using a numerical simulation of the relevant ion fluxes we can construct the pH profile in the pore (such as in Figure 2b), in other words, the ideal ion flux for the desired pH profile can then be determined. Furthermore we can tune the dissolution rate by the dissolution current. In other words, using a buffered neutral solution as electrolyte and adjusting the anodic current flow to an ideal value, acid can be created where it is needed, that is, at the pore bottom, while higher pH values are established at the pore mouth as a result of migration and diffusion effects of the pH buffer species (NH_4F, $(NH_4)_2SO_4$). Assuming equilibrium, the flux of dissolving species (leading to acidification at the pore bottom) and the flux of buffering species are equal. The calculations show that for the experimental conditions given in Figure 1 the pH value at the pore bottom is around 2 and increase to about 5 at the pore mouth, this corresponds to a drop in the local chemical etch rate of about 20 times.

We used a voltage-sweep technique to achieve a steady-state current and to establish the desired pH profile. The reason to use a voltage-sweep technique rather than a

[*] J. M. Macák, Dr. H. Tsuchiya, Prof. Dr. P. Schmuki
Department of Materials Science, WW4-LKO
University of Erlangen-Nuremberg
Martensstrasse 7, 91058 Erlangen (Germany)
Fax: (+49) 9131-852-7582
E-mail: schmuki@ww.uni-erlangen.de

[**] The authors would like to acknowledge A. Friedrich and H. Hildebrand for SEM and XPS investigations and L. Taveria for valuable help with the experiments.

 © 2005 Wiley-VCH Verlag GmbH & Co. KGaA, Weinheim DOI: 10.1002/anie.200462459

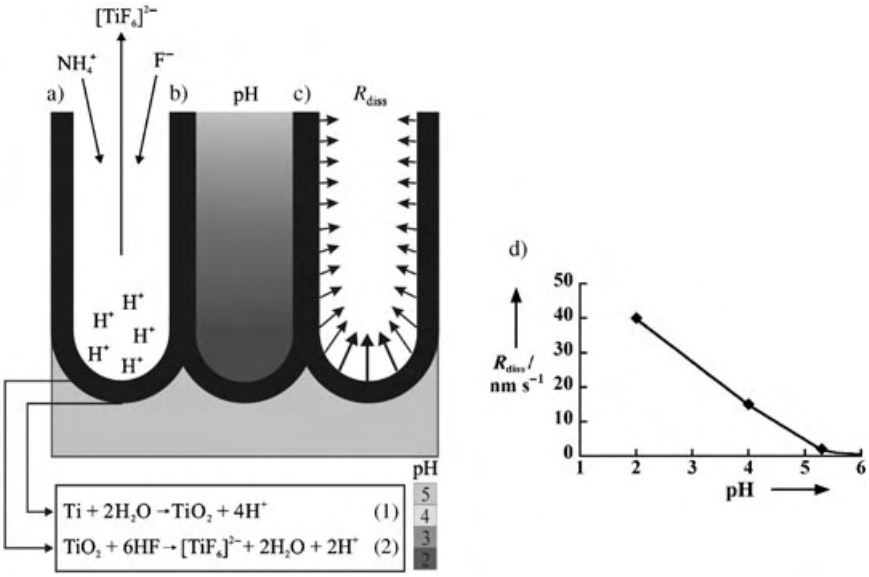

Figure 2. Tuning the electrochemical conditions to achieve high-aspect-ratio structures. Schematic representation of the dissolution reactions and mechanisms (a), the pH profile within a pore (b), the dissolution-rate profile within a pore wall (c). Experimental determination of the dissolution rate, R_{diss}, of the anodic TiO_2 depending on the pH value (d), results are taken from XPS sputter profiles of 20 V anodic oxide immersed for different times in 1 M $(NH_4)_2SO_4$ + 0.5 wt.% NH_4F solution with different pH values.

galvanostatic approach is that the system in galvanostatic mode has a tendency to oscillate, which leads to a destabilization of the steady-state situation within the pore.[21]

X-ray photoelectron spectroscopy (XPS) analysis revealed that the porous layer shown in Figure 1 consists of approximately 62 ± 5 atom% of oxygen and 38 ± 5 atom% of titanium. The Ti $2p_{3/2}$ peak was found to be at $458.5\,eV \pm 0.5\,eV$ (TiO_2 reference 458.8 eV). So evidently the porous layer consists of TiO_2. Only negligible traces of F from the electrolyte could be detected throughout the film. Depending on the applied voltage the structure of the TiO_2 film is typically reported to be either amorphous (below 20 V) or crystalline (higher voltages), where the presence of anatase, a mixture of anatase and rutile, or rutile can be observed.[22,23] X-ray diffraction analysis[21] of our structures indicated an amorphous structure that can be converted, for example, into anatase upon annealing.

Figure 3 demonstrates that the pore-formation process is indeed sensitive to the electrochemical parameters used. For example, for anodization in electrolyte containing a significantly higher NH_4F concentration (5 wt.%) and using a low sweep rate only short pores (nanotubes) are obtained (Figure 3a). Using a fast sweep rate leads to the growth of thick porous layer (Figure 3b). However, the surface in this thick porous layer is very rough and not regular and the structure itself is loosely cross-linked and not tubular.

In general, using a lower NH_4F concentration leads to the growth of regular self-organized porous tube-like structures, whereas in concentrated electrolytes the structure is rough and cross-linked. For the electrolyte used (1M $(NH_4)_2SO_4$ + 0.5 wt.% NH_4F) the diameter is slightly influenced by the sweep rate. The pore diameter changes in range of 90–110 nm and the higher the sweep rate the wider the pores. In the light of our simulations these morphological effects can be associated with the degree of acidification of the pore electrolyte during anodization, this leads to an enhanced or retarded etching of the side walls of the pores. The results thus imply that the mechanism of pore formation in this system is significantly different from the relatively well investigated aluminum case. While in aluminum, electric-field-aided ion transport through the pore bottom is the dominant mechanism (chemical oxide dissolution plays a minor role) it is evident that the chemical effects in the case of TiO_2 pore growth can become dominant.

The self-organized porous TiO_2 layers have various potential applications. For example, TiO_2 nanoparticles are extremely efficient for solar energy conversion[24] when used in dye-sensitized solar cells. These cells consist typically of a 5–10-μm thick layer of TiO_2 nanoparticles. Ordered TiO_2 nanotubes with tube lengths in this

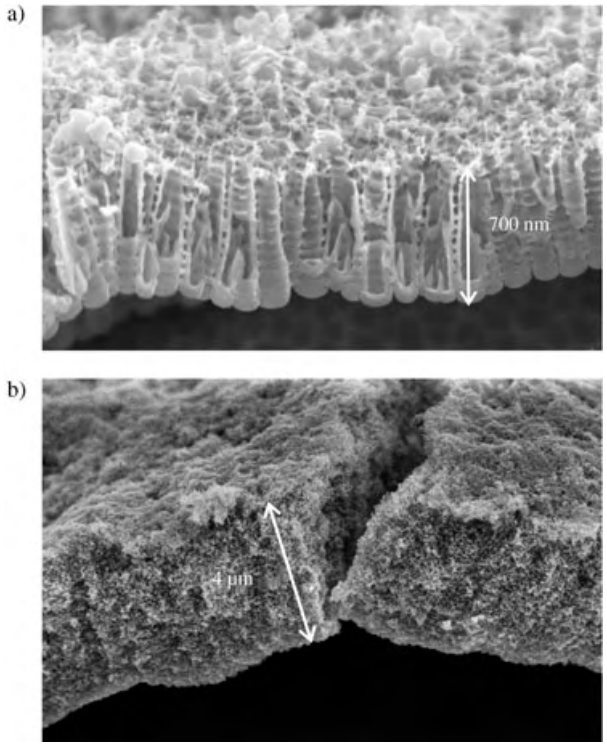

Figure 3. Anodization parameter dependence of the morphology of porous titanium oxide. Both samples were anodized in 1 M $(NH_4)_2SO_4$ + 5 wt.% NH_4F to 20 V with a low ramp speed of $10\,mV\,s^{-1}$ (a), and with a high ramp speed of $20\,V\,s^{-1}$ (b). In both cases a distinctly different thickness and morphology from that shown in Figure 1 is obtained as a result of the strongly different pH profiles in the pores.

 © 2005 Wiley-VCH Verlag GmbH & Co. KGaA, Weinheim

range may give higher conversion efficiency as losses owing to grain boundaries (in the sintered nanoparticles) can be avoided. Additionally, TiO_2 shows self-cleaning properties,[25] a controllable wettability,[26] and a high degree of biocompatibility in biomedical applications,[27] for instance as a dental or hip implant (high osseointegration). It can be used for controlled catalysis of organic reactions[7] or for sensing (e.g. hydrogen[18] and oxygen[28]). Owing to its high refractive index (about 60% higher than porous alumina), the self-organized porous TiO_2 structures may be suitable for the construction of photonic crystals[29] or waveguides.[9]

In all these applications the nanotubular structures herein offer advantages: unspecified nanoparticles can be replaced by highly ordered tubes. A key advantage is that essentially any form of a titanium surface (sheets, foils, sputtered layers) can be treated in a quick and low-cost approach with a TiO_2 nanotube layer coating. However, for some applications a separation of the tube array into isolated tubes may be essential—this will be subjected to future work.

Experimental Section

Surface treatment: Titanium samples (0.1-mm thick foils, 99.6% purity, Goodfellow) were degreased by sonicating in acetone, isopropanol, and methanol, then rinsed with deionized water and dried in a nitrogen stream.

Electrochemical treatment: Titanium samples were contacted and then pressed against an O-ring in an electrochemical cell, leaving 1 cm^2 exposed to the electrolyte. The electrochemical setup consisted of a conventional three-electrode configuration with a platinum gauze as a counter electrode and a Haber–Luggin capillary with Ag/AgCl (1M KCl) reference. Electrochemical experiments were carried out at room temperature using a high-voltage potentiostat Jaissle IMP 88. The electrolyte was 1M $(NH_4)_2SO_4$ with the addition of small amounts of NH_4F (0.5–5 wt.%). All electrolytes were prepared from reagent grade chemicals and deionized water. The electrochemical treatment consisted of a potential ramp from the open-circuit potential (OCP) to 20 V with a different sweep rate followed by holding the applied potential at 20 V for different times. After the electrochemical treatment the samples were rinsed with deionized water and dried with nitrogen stream.

Numerical calculations: Finite element based calculations of the pH profiles in the tubes were performed using the approach given by Kelly et al.[30]

Surface characterization: Scanning electron microscopy using a Hitachi SEM FE 4800 was employed for the structural and morphological characterization of the porous titanium oxide. In order to gain information on thickness of the porous layer, direct SEM cross-sectional thickness measurements were carried out on mechanically bent samples, while bending the porous layer cracked into many parts and in some cases a partial lift-off of the porous layer occurred. In this way the bottom-view images of the porous layer pieces were obtained.

XPS (PHI 5600 XPS) depth profiles (by Ar^+ ion sputtering at 3.2 kV using the Ti peak at 459 eV, the O peak at 528 eV, and the F peak at 685 eV) were acquired on samples with a TiO_2 layer formed anodically at 20 V (this layer has a thickness of 50 nm) The anodic oxide layer was immersed for different times in the fluoride-containing etching solution to determine the dissolution rate of the oxide at the different pH values.

Received: October 28, 2004
Published online: February 25, 2005

Keywords: electrochemistry · nanoporous materials · nanotubes · self-organization · titanium

[1] H. Masuda, K. Fukuda, *Science* **1995**, *268*, 1466.
[2] H. Masuda, K. Fukuda, *Appl. Phys. Lett.* **1997**, *71*, 2770.
[3] L. T. Canham, *Appl. Phys. Lett.* **1990**, *57*, 1046.
[4] V. Lehmann, U. Gösele, *Adv. Mater.* **1992**, *4*, 116.
[5] M. A. Brusatori, P. R. Van Tassel, *Biosens. Bioelectron.* **2003**, *18*, 1269.
[6] O. K. Varghese, D. Gong, K. G. Ong, C. A. Grimes, *Sens. Actuators B* **2003**, *93*, 338.
[7] J. Clarke, R. Hill, D. R. Roberts, *J. Chem. Technol. Biotechnol.* **1997**, *68*, 397.
[8] A. Birner, R. Wehrspohn, U. Gösele, K. Busch, *Adv. Mater.* **2001**, *13*, 377.
[9] C. Haginoya, M. Ishibashi, K. Koike, *Appl. Phys. Lett.* **1997**, *71*, 2934.
[10] H. Masuda, M. Yotsuya, M. Asano, K. Nishio, M. Nakano, A. Yokoo, T. Tamamura, *Appl. Phys. Lett.* **2001**, *78*, 828.
[11] H. Masuda, T. Mizuno, N. Baba, T. Ohmori, *J. Electroanal. Chem.* **1994**, *368*, 333.
[12] M. Wirtz, C. R. Martin, *Adv. Mater.* **2003**, *15*, 455.
[13] D. Al Mawiawi, N. Coombs, M. Moskovits, *Jpn. J. Appl. Phys.* **1991**, *70*, 4421.
[14] M. Steinhart, J. H. Wendorff, A. Greiner, R. B. Wehrspohn, K. Nielsch, J. Schilling, J. Choi, U. Gösele, *Science* **2002**, *296*, 1997.
[15] R. Beranek, H. Hildebrand, P. Schmuki, *Electrochem. Solid-State Lett.* **2003**, *6*, B12.
[16] D. Gong, C. A. Grimes, O. K. Varghese, W. Hu, R. S. Singh, Z. Chen, E. C. Dickey, *J. Mater. Res.* **2001**, *16*, 3331.
[17] V. Zwilling, E. Darque-Ceretti, A. Boutry-Forveille, *Electrochim. Acta* **1999**, *44*, 921.
[18] O. K. Varghese, D. Gong, M. Paulose, K. G. Ong, E. C. Dickey, C. A. Grimes, *Adv. Mater.* **2003**, *15*, 624.
[19] N. Savage, B. Chwieroth, A. Ginwalla, B. R. Patton, *Sens. Actuators B* **2001**, *79*, 17.
[20] J. M. Macak, K. Sirotna, P. Schmuki, *Electrochim. Acta*, in press.
[21] J. M. Macak, P. Schmuki, unpublished results.
[22] J. B. Cotton, B. H. Hanson in *Corrosion*, *Vol. 1* (Eds.: L. L. Sheir, R. A. Jarman, G. T. Burstien), Butterworth-Heinemann, Oxford, **1994**, pp. 5–36.
[23] J. W. Schultze, M. M. Lohrengel, D. Ross, *Electrochim. Acta* **1983**, *28*, 973.
[24] M. Grätzel, *J. Photochem. Photobiol. C* **2003**, *4*, 145.
[25] A. Fujishima, K. Honda, *Nature* **1972**, *238*, 37.
[26] R. Wang, K. Hashimoto, A. Fujishima, M. Chikuni, E. Kojima, A. Kitamura, *Nature* **1997**, *388*, 431.
[27] *Titanium in Medicine* (Eds.: D. M. Brunette, P. Tengvall, M. Textor, P. Thomsen) , Springer, Berlin, **2001**, p. 1.
[28] A. Rothschild, F. Edelman, Y. Komem, F. Cosandey, *Sens. Actuators B* **2000**, *67*, 282.
[29] K. Busch, R. Wehrspohn, *Phys. Status Solidi A* **2003**, *197*, 593.
[30] J. S. Lee, M. I. Reed, R. G. Kelly, *J. Electrochem. Soc.* **2004**, *151*, B423.

 © 2005 Wiley-VCH Verlag GmbH & Co. KGaA, Weinheim

Copper Complexes

Three-Spin System with a Twist: A Bis(semiquinonato)copper Complex with a Nonplanar Configuration at the Copper(II) Center**

*Shengfa Ye, Biprajit Sarkar, Falk Lissner, Thomas Schleid, Joris van Slageren, Jan Fiedler, and Wolfgang Kaim**

Complexes with a significantly nonplanar environment around tetracoordinate copper(II) centers are comparatively rare and were often investigated in connection with copper enzyme modeling[1] or with the highly distorted type 1 copper centers in blue copper proteins.[2] These centers exhibit partial sulfur coordination and act as electron-transfer sites, shuttling between the Cu^{II} and Cu^{I} states. The $Cu^{II,I}$ couple can also be active in the electron-transfer interaction with one[3,4] or two[5,6] non-innocent quinone ligands (Q). While a biochemically relevant valence tautomer equilibrium $Cu^{II}(Q^{2-}) \rightleftarrows Cu^{I}(Q^{\bullet-})$ has been observed within[7] and outside[4] oxidase enzymes, the focus with $Cu(Q)_2$ compounds has been on the study of spin–spin interaction in stable three-spin systems $(Q^{\bullet-})Cu^{II}(Q^{\bullet-})$.[5,6] Using sterically protected *o*-benzosemiquinonemonoimines, such as $Q_x^{\bullet-}$, Chaudhuri et al. have described a planar such complex $[(Q_x^{\bullet-})Cu^{II}(Q_x^{\bullet-})]$ (**1**), with a $(\uparrow,\uparrow,\downarrow)$ ground state containing two antiferromagnetically coupled radical ligands.[6]

Herein we describe how a minor modification, the introduction of a potentially coordinating methylthio substituent in the *o*-position of the N-aryl group to form $Q_y^{\bullet-}$, can considerably change the structure and the properties of this three-spin system.

The new ligand system was synthesized in the reduced form H_2Q_y.[8] Its reaction with CuCl produced an air-stable complex $[(Q_y)Cu(Q_y)]$ (**2**) which could be crystallographically characterized (Figure 1).[9] A significantly twisted arrangement is found about the copper center which has a N1CuO1/N2CuO2 dihedral angle of 32.20(9)° and is coordinated by two ligands through the N and O donors. However, there is also a weak additional interaction from S1 to the copper atom (Cu–S1 3.198(1) Å; Cu–S2 3.475(1) Å). Very long Cu^{II}–S(thioether) separations have also been reported for certain type 1 copper centers in proteins, especially azurin.[2] The structural data show unambiguously that the ligands are in the semiquinone state,[10] which implies the +II oxidation state for the copper center in its highly twisted coordination environment. The sum of bond angles at the copper is 685.8°, about halfway between the values for square planar (720°) and tetrahedral geometry (ca. 657°). Although the Cu–O and Cu–N bonds are comparable, the N1-Cu-N2 angle is closer to linearity at 171.85° than the O1-Cu-O2 angle (149.70°)—possibly a result of steric repulsion between the aryl substituents.

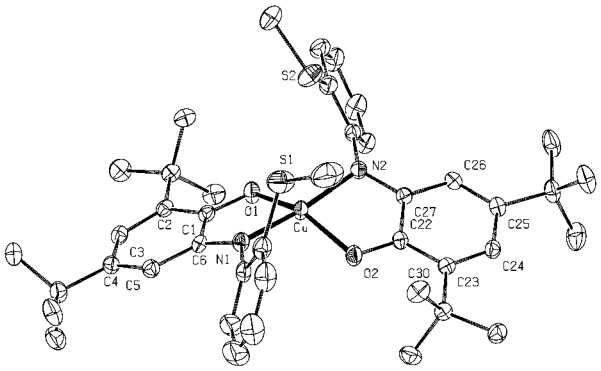

Figure 1. Molecular structure of complex **2**. Selected bond lengths [Å] and angles [°]: Cu-O1 1.9173(15), Cu-O2 1.9290(16), Cu-N1 1.9372(19), Cu-N2 1.9368(18), O1-C1 1.296(3), O2-C22 1.292(3), N1-C6 1.355(3), N2-C27 1.352(3), C1-C2 1.430(3), C22-C23 1.430(3), C2-C3 1.380(3), C23-C24 1.373(3), C3-C4 1.433(3), C24-C25 1.433(3), C4-C5 1.371(3), C25-C26 1.368(3), C5-C6 1.419(3), C26-C27 1.421(3), C6-C1 1.453(3), C27-C22 1.455(3); O1-Cu-O2 149.81(8), O1-Cu-N2 97.00(7), O2-Cu-N1 98.30(7), N2-Cu-N1 171.95(8), O1-Cu-N1 84.51(7), O2-Cu-N2 84.40(7).

Figure 2 shows the dependence of χT on T for the three-spin compound $[(Q_y^{\bullet-})Cu^{II}(Q_y^{\bullet-})]$.[11a] The room temperature χT value of 0.46 $cm^3 K mol^{-1}$ is much lower than expected (1.125 $cm^3 K mol^{-1}$) for three uncoupled $S = 1/2$ spins with $g \approx 2$, which indicates predominantly antiferromagnetic exchange interactions in the system. At lower temperatures, the χT value reaches a plateau at $\chi T = 0.365$ $cm^3 K mol^{-1}$, in agreement with an $S = 1/2$ ground state. At the lowest temperatures the χT value decreases again. This system of three exchange-coupled spins can be described by the

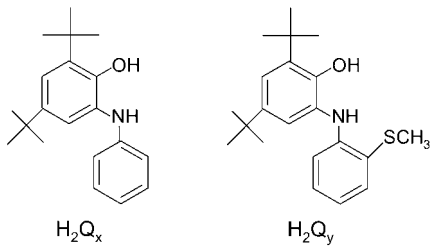

[*] S. Ye, B. Sarkar, Dr. F. Lissner, Prof. Dr. T. Schleid, Prof. Dr. W. Kaim
Institut für Anorganische Chemie
Universität Stuttgart
Pfaffenwaldring 55, 70550 Stuttgart (Germany)
Fax: (+49) 711-685-4165
E-mail: kaim@iac.uni-stuttgart.de
Dr. J. van Slageren
1. Physikalisches Institut, Universität Stuttgart
Pfaffenwaldring 57, 70550 Stuttgart (Germany)
Dr. J. Fiedler
J. Heyrovský Institute of Physical Chemistry
Academy of Sciences of the Czech Republic
Dolejškova 3, 18223 Prague (Czech Republic)

[**] Support from the Deutsche Forschungsgemeinschaft, the Fonds der Chemischen Industrie, the Grant Agency of the Czech Republic (Grant No. 203/03/0821), and the Ministry of Education of the Czech Republic (Grant COST OC D15.10) is gratefully acknowledged.

 DOI: 10.1002/anie.200462339 © 2005 Wiley-VCH Verlag GmbH & Co. KGaA, Weinheim

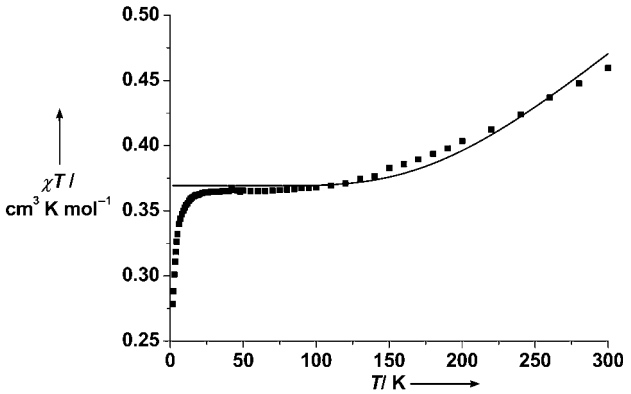

Figure 2. Magnetic susceptibility–temperature product for **2** as a function of temperature (■) at 1 T and fit (——) using the parameters $g = 2.00$, $J = -414\ cm^{-1}$, and $J' = -114\ cm^{-1}$.

isotropic exchange Hamiltonian [Eq. (1)] where spins S_1 and S_3 refer to the two $Q_y^{\bullet -}$ radicals and spin S_2 is the Cu^{II} center.

$$\mathscr{H} = -J\,(S_1 \cdot S_2 + S_2 \cdot S_3) - J'\,S_1 \cdot S_3 \qquad (1)$$

The exchange coupling in such a system leads to three spin states, two with $S = 1/2$ and one with $S = 3/2$, the energies of which depend on the sign and magnitude of the two exchange interactions.[6] The two $S = 1/2$ states differ in the relative orientation of the magnetic moments of spin S_1 and S_3 which can be described by $S^* = S_1 + S_3$. The spin functions are fully described by the total and intermediate spins as $|S_T S^*\rangle = |{}^1/_2\,0\rangle$, $|{}^1/_2\,1\rangle$, and $|{}^3/_2\,1\rangle$, or in symbolic fashion (↓,↑,↓), (↑,↑,↓), and (↑,↑,↑). Their energies are given by $E(\uparrow,\uparrow,\downarrow) = -J + J'$, $E(\downarrow,\uparrow,\downarrow) = 0$, and $E(\uparrow,\uparrow,\uparrow) = -{}^3/_2 J$, taking the (↓,↑,↓) state as the energy origin. The χT product as a function of temperature is then given by Equation (2).

$$\chi T = \frac{N_A\,\mu_B^2}{4k}\,\frac{g_{z,1}^2 + g_{z,0}^2 \exp[(J-J')/kT] + 10\exp[3J/2kT]}{1 + \exp[(J-J')/kT] + 2\exp[3J/2kT]} \qquad (2)$$

The $S = 1/2$ ground state can have either (↑,↑,↓) or (↓,↑,↓) character, depending on whether the antiferromagnetic interaction between the two radicals or between the radical and metal are dominating. Electron paramagnetic resonance (EPR) results indicate that the lowest spin state has predominant radical character (see below), from which it can be concluded that this lowest spin state is best described as (↓,↑,↓). Thus the antiferromagnetic metal–radical interaction must be stronger than that between the two radicals ($|J| > |J'|$). Since EPR shows no evidence for excited spin states between 110 K and room temperature in the form of extra signals or shifting signals (in the case of fast spin-state interconversion), the excited $S = 1/2$ state must lie at high energy, meaning that $|J| - |J'|$ is large.

Fitting a susceptibility curve using the Equation (2) is problematic since the parameters are interdependent and there is no unique solution.[11b] However, the results suggest that the metal–radical interaction is strongly antiferromagnetic with a magnitude of $J = -414\ cm^{-1}$, while the radical–radical interaction is also antiferromagnetic, but probably weaker. For more definitive conclusions to be drawn the excited $S = 1/2$ (↑,↑,↓) state needs to be determined exactly.

The EPR results for **2** differ significantly from those of **1** (with planar configuration at the metal):[6] Instead of a signal for copper(II) with $g > 2$[6] we observe a partially resolved radical-type spectrum at $g = 2.0012$ in CH_2Cl_2 solution (Figure 3). In the frozen state at 110 K or 4 K the g components were found at $g_1 = 2.050$, $g_2 = 1.9937$ ($A_2 = 2.0$ mT), and $g_3 = 1.957$, $g_{av} = 2.0006$. The g value and hyperfine data are fully compatible with a copper-coordinated 3,5-di-*tert*-butyl-*o*-semiquinoneimine radical anion,[3a,4] the slightly lower g value signifies the presence of low-lying excited states with non-zero orbital angular momentum.[12]

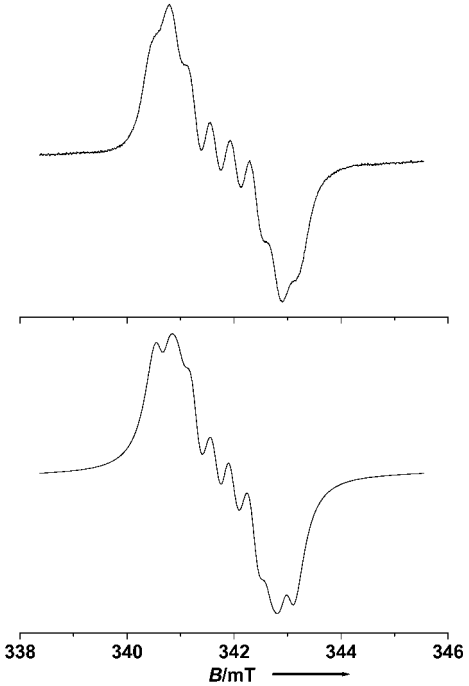

Figure 3. EPR spectrum of complex **2** in dichloromethane at 210 K (top) with computer simulation (bottom): $a(^{63,65}Cu) = 0.22$ mT, $a(^{14}N) = 0.70$ mT, $a(^1H) = 0.36$ mT (1 H,H^3).

The EPR result in particular points to a (↑,↓,↑) ground state for $[(Q_y^{\bullet -})Cu^{II}(Q_y^{\bullet -})]$ with a dominant antiferromagnetic metal–ligand (and not ligand–ligand[6]) interaction. Clearly the interligand spin–spin interaction between the two semiquinone ligands is diminished as a consequence of the nonplanar coordination arrangement.

In the absence of detailed structural and magnetic results, the appearance of a radical-type EPR signal could suggest an alternative oxidation state combination of $(Q_y^{\bullet -})Cu^{I}(Q_y)$ for **2** which would also be in agreement with a nonplanar metal configuration. However, the susceptibility behavior and the bond lengths within the two very similar ligands clearly demonstrate the presence of $[(Q_y^{\bullet -})Cu^{II}(Q_y^{\bullet -})]$ with a (↑,↓,↑) ground state.

Like the planar analogue **1**[6] with $Q_x^{\bullet -}$, the compound **2** described herein undergoes four reversible one-electron steps, two oxidations at $+0.37$ and -0.38 V, and two

 © 2005 Wiley-VCH Verlag GmbH & Co. KGaA, Weinheim

reductions at −1.07 and −1.49 V (versus $Fc^{+/0}$ (Fc = ferrocene) in CH_2Cl_2/0.1 M Bu_4NPF_6). The results of spectroelectrochemistry investigations in the UV/Vis-NIR regions are summarized in Figure 4, Table 1, [Eq. (3)]: On oxidation to $\mathbf{2}^+$ the long-wavelength bands attributed to intraligand (IL) and ligand-to-metal charge transfer (LMCT) transitions are diminished and a strong band emerges at 515 nm, possibly associated with the formation of a quinone ligand in

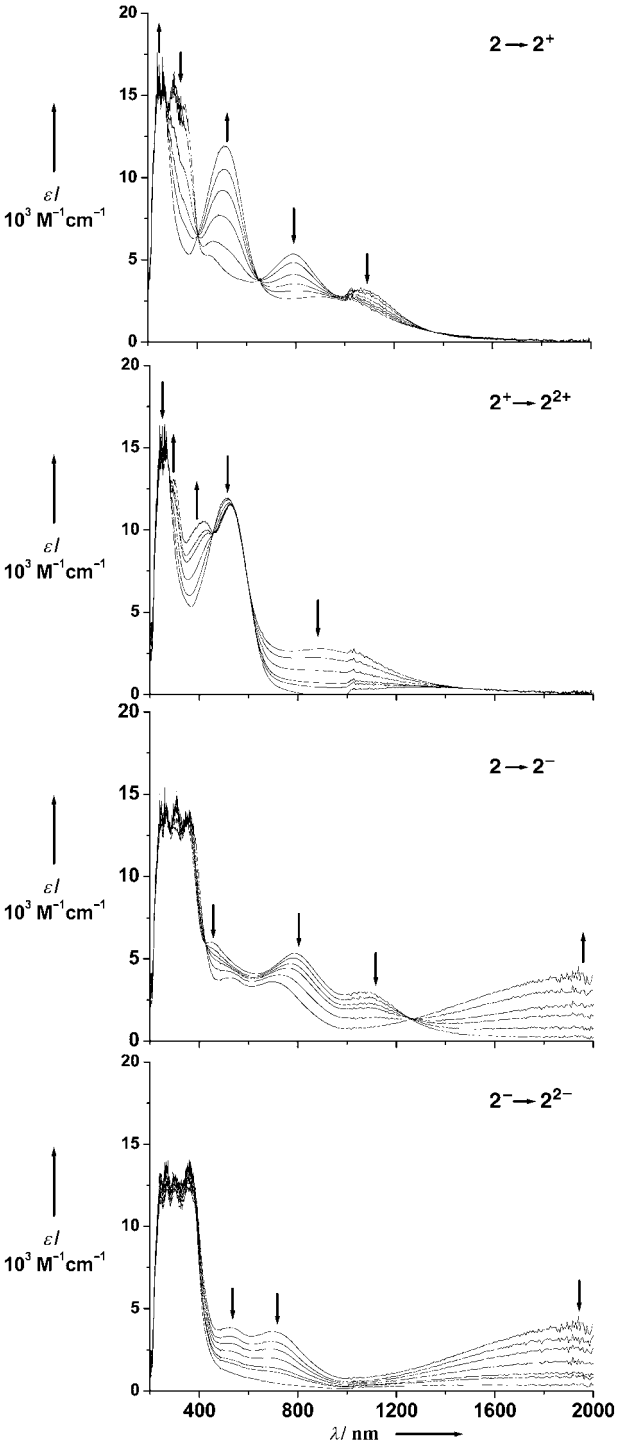

Figure 4. Spectroelectrochemistry study of complex **2** in CH_2Cl_2/0.1 M Bu_4NPF_6.

$$[(Q_y)Cu^{II}(Q_y)]^{2+} \underset{-e^-}{\overset{+e^-}{\rightleftharpoons}} [(Q_y)Cu^{II}(Q_y^{\bullet-})]^{+} \underset{-e^-}{\overset{+e^-}{\rightleftharpoons}} [(Q_y^{\bullet-})Cu^{II}(Q_y^{\bullet-})] \underset{-e^-}{\overset{+e^-}{\rightleftharpoons}}$$
$$\mathbf{2^{2+}} \qquad\qquad \mathbf{2^{+}} \qquad\qquad \mathbf{2}$$
$$[(Q_y^{\bullet-})Cu^{II}(Q_y^{2-})]^{-} \underset{-e^-}{\overset{+e^-}{\rightleftharpoons}} [(Q_y^{\bullet-})Cu^{I}(Q_y^{2-})]^{2-} \text{ or } [(Q_y^{2-})Cu^{II}(Q_y^{2-})]^{2-} \quad (3)$$
$$\mathbf{2^{-}} \qquad\qquad \mathbf{2^{2-}}$$

$[(Q_y)Cu^{II}(Q_y^{\bullet-})]^+$. The second oxidation to $[(Q_y)Cu^{II}(Q_y)]^{2+}$ leaves only the band arising from quinone, shifted to 528 nm. One-electron reduction could lead to either $[(Q_y^{\bullet-})Cu^{II}(Q_y^{2-})]^-$ or $[(Q_y^{\bullet-})Cu^{I}(Q_y^{\bullet-})]^-$. Spectroelectrochemical reduction gives rise to a strong, broad ($\Delta\nu_{1/2} = 2600\ cm^{-1}$) band at 1940 nm (5150 cm^{-1}, Figure 4, Table 1) in addition to absorptions at 526 and 695 nm. The intense band (oscillator strength $f = 5.4 \times 10^{-2}$) in the near infrared is more compatible with the ligand-to-ligand intervalence charge-transfer transition[13] for a $[(Q_y^{\bullet-})Cu^{II}(Q_y^{2-})]^-$ formulation, however, the structure of this species is not known. The second reduction to either $[(Q_y^{\bullet-})Cu^{I}(Q_y^{2-})]^{2-}$ or $[(Q_y^{2-})Cu^{II}(Q_y^{2-})]^{2-}$ does not produce intense absorptions above 450 nm. More detailed assignments of oxidation state combinations and electronic transitions will require high-quality excited-state TD-DFT calculations.

Table 1: Absorption data of complexes.[a]

Compound	λ_{max} [nm] ($10^3\ \varepsilon$ [$M^{-1}\,cm^{-1}$])
2	316(15.7), 345(16.5), 446 sh(5.3), 790(5.4), 1062(3.0)
$\mathbf{2}^+$	259(16.5), 242(15.8), 515(11.9), 930(2.7)
$\mathbf{2}^{2+}$	238(14.2), 270(14.7), 300 sh(13.1), 424(10.5), 528(11.6)
$\mathbf{2}^-$	245 sh(13.2), 273(14.0), 358(14.1), 526(3.8), 695(3.6), 1940(4.5)
$\mathbf{2}^{2-}$	247 sh(11.6), 270(12.3), 307(12.2), 364(12.4)

[a] In CH_2Cl_2 solution, charged species were electrochemically generated in CH_2Cl_2/0.1 M Bu_4NPF_6.

Summarizing, we have found an additional factor in determining the oxidation and spin state for the already complicated interaction[3–6] between the copper(II,I) couple and quinonoid ligands, that is, the possible structural distortion caused by secondary coordination. While radical anion ligands[12] already yield unusual complexes with transition metals in "normal" configurations,[3b,6,14,15] the geometrical distortion can add, literally, another twist to this remarkable class of compounds, allowing for a striking switch of spin combinations. The behavior of the $Q_y^{0,\bullet-,2-}$ redox system as a ligand towards other transition metals is currently being investigated.

Received: October 18, 2004
Published online: February 21, 2005

Keywords: copper · electrochemistry · EPR spectroscopy · radical ligands · spin–spin interactions

[1] Y. Wang, J. L. DuBois, B. Hedman, K. O. Hodgson, T. D. P. Stack, *Science* **1998**, *279*, 537.
[2] a) W. Kaim, J. Rall, *Angew. Chem.* **1996**, *108*, 47; *Angew. Chem. Int. Ed. Engl.* **1996**, *35*, 43; b) A. Messerschmidt, *Struct. Bonding (Berlin)* **1998**, *90*, 37; c) A. J. Vila, C. O. Fernandez in *Handbook*

 © 2005 Wiley-VCH Verlag GmbH & Co. KGaA, Weinheim

on Metalloproteins (Eds.: A. Bertini, A. Sigel, H. Sigel), Marcel Dekker, New York, **2001**, p. 813; d) M. D. Harrison, C. Dennison, *ChemBioChem* **2004**, *5*, 1579.

[3] a) J. Rall, W. Kaim, *J. Chem. Soc. Faraday Trans.* **1994**, *90*, 2905; b) C. G. Pierpont, C. W. Lange, *Prog. Inorg. Chem.* **1994**, *41*, 331; c) C. G. Pierpont, *Coord. Chem. Rev.* **2001**, *99*, 216; d) D. A. Shultz, *Comments Inorg. Chem.* **2002**, *23*, 1.

[4] a) J. Rall, M. Wanner, M. Albrecht, F. M. Hornung, W. Kaim, *Chem. Eur. J.* **1999**, *5*, 2802; b) W. Kaim, M. Wanner, A. Knödler, S. Zalis, *Inorg. Chim. Acta* **2002**, *337*, 163; c) G. A. Abakumov, V. K. Cherkasov, V. I. Nevodchikov, V. A. Kuropatov, G. T. Yee, C. G. Pierpont, *Inorg. Chem.* **2001**, *40*, 2434; d) G. Speier, Z. Tyeklár, P. Tóth, E. Speier, S. Tisza, A. Rockenbauer, A. M. Whalen, N. Alkire, C. G. Pierpont, *Inorg. Chem.* **2001**, *40*, 5653.

[5] a) G. A. Abakumov, V. K. Cherkasov, M. P. Bubnov, O. G. Ellert, Yu. V. Rakitin, L. N. Zakharov, Yu. T. Struchkov, Yu. N. Saf'yanov, *Izv. Akad. Nauk Ser. Khim.* **1992**, *10*, 2315; b) A. Dei, D. Gatteschi, C. Sangregorio, L. Sorace, *Acc. Chem. Res.* **2004**, *37*, 827.

[6] P. Chaudhuri, C. N. Verani, E. Bill, E. Bothe, T. Weyhermüller, K. Wieghardt, *J. Am. Chem. Soc.* **2001**, *123*, 2213.

[7] a) D. M. Dooley, M. A. McGuirl, D. E. Brown, P. N. Turowski, W. S. McIntire, P. F. Knowles, *Nature* **1991**, *349*, 262; b) M. A. McGuirl, D. E. Brown, D. M. Dooley, *J. Biol. Inorg. Chem.* **1997**, *2*, 336.

[8] Preparation of Q_y: A solution of 2-(methylthio)aniline (1.44 mL, 11.5 mmol) in *n*-heptane (4 mL) was added dropwise to a suspension of 3,5-di-*tert*-butylcatechol (2.56 g, 11.5 mmol) and triethylamine (0.15 mL) in *n*-heptane (10 mL). The solution was heated to reflux for 3 h, the solvent then evaporated to dryness, and the residue washed with cold *n*-heptane to yield a colorless solid. Yield 2.37 g (60%). ^{1}H NMR (250 MHz, 300 K, $CDCl_3$): $\delta = 6.35$–7.48 (m, 6H, arom), 2.45 (s, 3H, SCH_3), 1.44 (s, 9H, $C(CH_3)_3$), 1.26 ppm (s, 9H, $C(CH_3)_3$). Elemental analysis (%) calcd for $C_{21}H_{29}NOS$: C 73.42, H 8.51, N 4.08; found: C 73.49, H 8.42, N 4.07.

[9] Synthesis of **2**: A solution of Q_y (736 mg 2.14 mmol), NEt_3 (0.5 mL), and CuCl (106 mg, 1.07 mmol) was heated to reflux in acetonitrile (25 mL) for 4 h in the presence of air. The dark precipitate was collected by filtration, then washed with cold acetonitrile. A dark green microcrystalline material was obtained. Yield 520 mg (65%). Elemental analysis (%) calcd for $C_{42}H_{54}CuN_2O_2S_2$: C 67.57, H 7.29 N 3.75; found: C 67.30, H 7.31, N 3.73. Single crystals were obtained from a dichloromethane solution of **2** layered with *n*-hexane. Crystal data: $C_{42}H_{54}CuN_2O_2S_2$ (746.53); monoclinic $P2_1/n$; $a = 16.3439(2)$, $b = 14.5226(2)$, $c = 16.9358(3)$ Å; $\beta = 90.140(1)°$; $V = 4019.8(1)$ Å^3; $Z = 4$; $\rho_{calcd} = 1.234$ g cm^{-3}; $\mu = 0.683$ mm^{-1}; $T = 100(2)$ K; number of unique reflections 9142, number of parameters 498; $R1 = 0.0475$, $wR2 = 0.1143$ ($I > 2\sigma(I)$); $R1 = 0.0570$, $wR2 = 0.1203$ (all data); GOOF = 1.044. The structure was solved by direct methods and refined using the SHELXS-97/SHELXL-97 program package (G. M. Sheldrick, SHELXS-97, Program for the Solution of Crystal Structures, University of Göttingen, Germany, **1997**, G. M. Sheldrick, SHELXL-97, Program for the Refinement of Crystal Structures, University of Göttingen, Germany, **1997**). The scattering factors for the neutral atoms were those incorporated in the programs. CCDC-251450 contains the supplementary crystallographic data for this paper. These data can be obtained free of charge from the Cambridge Crystallographic Data Centre via www.ccdc.cam.ac.uk/data_request/cif.

[10] a) S. Bhattacharya, P. Gupta, F. Basuli, C. G. Pierpont, *Inorg. Chem.* **2002**, *41*, 5810; b) K. S. Min, T. Weyhermüller, E. Bothe, K. Wieghardt, *Inorg. Chem.* **2004**, *43*, 2922.

[11] a) The magnetic susceptibility measurements were performed on a powder sample of **2** using a Quantum Design MPMS XL7 SQUID magnetometer. The data were corrected for the diamagnetic contributions to the molar magnetic susceptibility using Pascal's constants and for temperature-independent paramagnetism ($TIP = 120 \times 10^{-6}$ cm^3 mol^{-1}); b) The following constraints were used: The *g* values of the radicals and the Cu^{II} center were taken to be 2.00 (see EPR discussion). Furthermore, the difference between the two exchange interaction parameters was not allowed to decrease below 300 cm^{-1} in order to keep the excited $S = 1/2$ state at high energies. From the fit ($T > 50$ K), the following parameters are obtained: $J = -414$ cm^{-1}, and $J' = -114$ cm^{-1} (± 6 cm^{-1}). If not constrained, the radical–radical exchange interaction tends to increase, leading to similar values for both exchange parameters, $J = -367$ cm^{-1}, and $J' = -357$ cm^{-1}, without significantly improving the fit.

[12] W. Kaim, *Coord. Chem. Rev.* **1987**, *76*, 187.

[13] a) D. Herebian, E. Bothe, F. Neese, T. Weyhermüller, K. Wieghardt, *J. Am. Chem. Soc.* **2003**, *125*, 9116; b) A. Dogan, B. Sarkar, A. Klein, F. Lissner, T. Schleid, J. Fiedler, S. Zalis, V. K. Jain, W. Kaim, *Inorg. Chem.* **2004**, *43*, 5973.

[14] W. Kaim, *Dalton Trans.* **2003**, 761.

[15] P. Chaudhuri, K. Wieghardt, *Prog. Inorg. Chem.* **2001**, *50*, 151.

 © 2005 Wiley-VCH Verlag GmbH & Co. KGaA, Weinheim

Mesoporous Materials

Periodic Mesoporous Organosilicas: Self-Assembly from Bridged Cyclic Silsesquioxane Precursors**

*Kai Landskron and Geoffrey A. Ozin**

Synthetic materials with a hierarchically ordered structure spanning multiple length scales from the molecular up to the macroscopic level, akin to nature's biological systems, are currently of considerable interest for a future nanotechnology that uses "bottom-up" approaches.[1] In this context periodic mesoporous organosilicas (PMOs) are a promising class of compounds.[2–4] They exhibit crystalline mesopores with walls comprising tetrahedrally coordinated silicon[4] centers bridged by oxygen atoms[2] and organic groups (R)[2]. This arrangement represents a fusion of inorganic and organic components at the subnanometer length scale within an ordered nanoscopic material. Because they can be made with powder or film morphologies, their macroscopic shape can also be designed.[5–7] The first PMOs synthesized from silsesquioxanes of the type $(EtO)_3Si\text{-}R\text{-}Si(OEt)_3$ contain one organic bridging group R, such as methene, ethene, or ethylene, bound to each Si atom and consist exclusively of SiO_3R tetrahedra[5–7] leading to an approximate composition of $SiO_{1.5}R_{0.5}$. Recently we have shown that by using cyclic silsesquioxanes of the type $[\{SiR(OEt)_2\}_3]$ a far higher organic load can be achieved in a PMO because each silicon tetrahedral center is bound to two organic bridging groups and an approximate composition of SiOR is reached.[7] We call this class of compounds "high organic group content PMOs". Higher organic content can lead to significantly improved materials properties, such as very low dielectric constants, a high elastic modulus, excellent thermal stability, and hydrophobicity, which make the PMOs interesting as a packaging material for microelectronic applications.[7] Furthermore hierarchical order within the channel walls is achieved owing to the material's exclusive construction from Si_3R_3 3-ring building blocks rather than acyclic building blocks that give a three-dimensional framework with a random distribution of condensed $Si_nO_{n-m}R_m$ rings ($n>1$; $0<m<n$).

To drive the complexity and the hierarchical order of the channel walls in high organic group content PMOs to the next level we have aimed to synthesize silsesquioxane precursors in which two cyclic building blocks are bridged by an organic group. Recently we showed that the CH_2 groups of the 3-ring molecule $[\{SiCH_2(OEt)_2\}_3]$ can be lithiated with *t*BuLi and then treated with an electrophile E, such as ethyl iodide, Br_2, or I_2, to yield E-substituted cyclic silsesquioxanes of the type $[\{SiCH_2(OEt)_2\}_2\{SiCHE(OEt)\}]$.[7] This chemistry suggested the use of reagents with two electrophilic ends of the type Hal-R-Hal (Hal = halogen) to achieve ring linkage and then self-assembly of the resulting precursor of the type $[\{[(EtO)_2SiCH_2]_2[(EtO)_2SiCH]\}_2R]$ into a PMO.

We chose 1,2-dibromoethane and 1,3-dibromopropane as electrophiles. While reactions with dibromoethane failed to give the expected ethene-bridged ring silsesquioxane, we successfully obtained the target molecule $[\{[(EtO)_2SiCH_2]_2[(EtO)_2SiCH]\}_2\{(CH_2)_3\}]$ (**1**) with trimethylene-bridged 3-rings (Scheme 1).

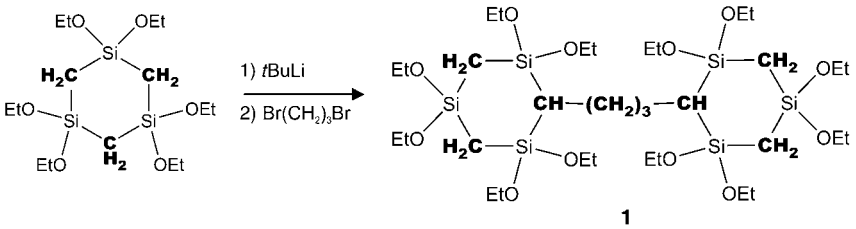

1

Scheme 1. Preparation of $[\{[(EtO)_2SiCH_2]_2[(EtO)_2SiCH]\}_2\{(CH_2)_3\}]$ (**1**).

After purification by distillation under high vacuum, **1** was obtained in pure form according to ^1H, ^{13}C, and ^{29}Si NMR spectroscopy data as well as electrospray mass spectrometry. In the case of dibromoethane surprisingly we obtained $[\{SiCH_2(OEt)_2\}_2\{SiCHBr(OEt)\}]$ as the main product. The explanation may be that the dibromoethane reacts with the lithiated intermediate through transfer of Br^+ to the ring and elimination of ethene (C_2H_4) and Br^-.

The PMO self-assembled from **1** by using NaCl-assisted acid-catalyzed self-assembly with the tri-block copolyether P123 as templating agent. The as-synthesized material was extracted with a HCl/acetone mixture to remove the template. The resulting PMO showed periodic mesopores with a *d* spacing of 11.5 nm according to powder X-ray diffraction (PXRD) studies (Figure 1 A), a pore diameter of approximately 6 nm, and a channel wall thickness of also approximately 6 nm determined by scanning electron microscopy (SEM; Figure 1 B) and transmission electron microscopy (TEM; Figure 1 D). N_2 adsorption experiments revealed a type IV isotherm with minor hysteresis indicating the existence of highly uniform mesopores (Figure 1 C). A BJH analysis of the adsorption branch showed a narrow pore size distribution with an average pore size of 6.9 nm consistent with the TEM data (Figure 1 C, inset). The BET surface area was determined to be 967 m^2g^{-1}. The PMO material displayed excellent thermal stability with no mass loss up to 400 °C in a N_2 atmosphere (determined by thermal gravimetric analysis (TGA)).

^{29}Si magic-angle spinning (MAS) NMR spectroscopy data for both the as-synthesized (Figure 2 A) and the extracted PMO (Figure 2 B) showed a broad signal between $\delta = 0$ and -30 ppm that can be assigned to D sites of the SiC_2O_2

[*] Dr. K. Landskron, Prof. G. A. Ozin
Materials Chemistry Research Group
Department of Chemistry
University of Toronto
80 St. George Street, Toronto, Ontario M5S 3H6 (Canada)
Fax: (+1) 416-971-0091
E-mail: gozin@alchemy.chem.utoronto.ca

[**] G.A.O. is Government of Canada Research Chair in Materials Chemistry. He is indebted to the Natural Sciences and Engineering Research Council (NSERC) of Canada for support of this work.

 DOI: 10.1002/anie.200462279 © 2005 Wiley-VCH Verlag GmbH & Co. KGaA, Weinheim

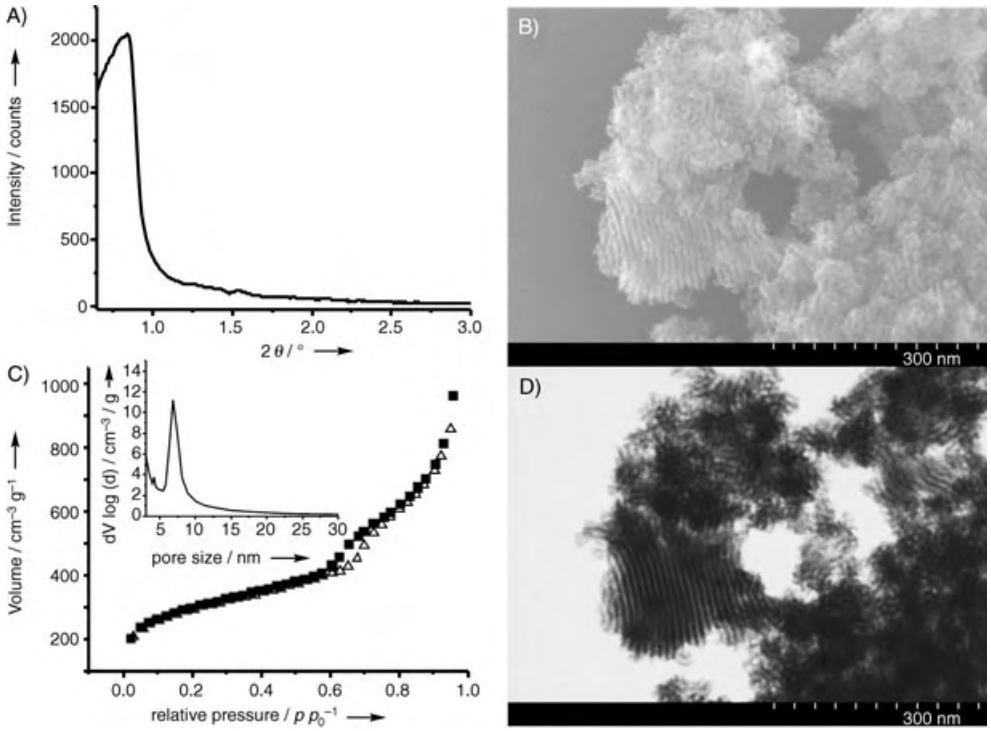

Figure 1. A) PXRD of the extracted PMO, B) SEM image, D) TEM image of the PMO with trimethylene-bridged 3-ring building units, C) N_2 isotherm of the PMO. Inset: pore size distribution.

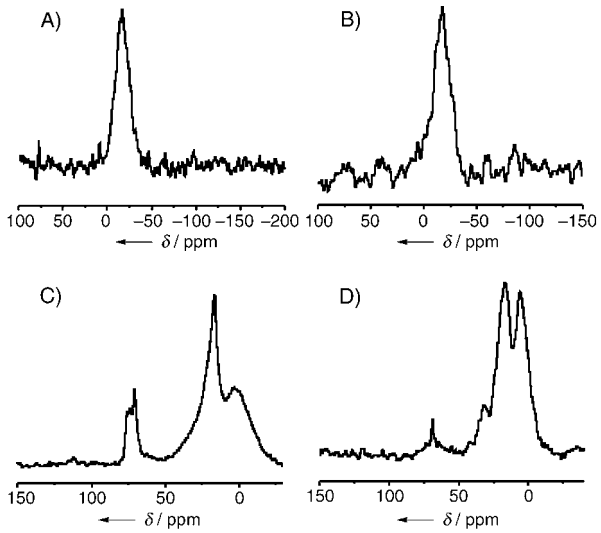

Figure 2. ^{29}Si MAS-NMR spectrum of the as-synthesized PMO (A) and the corresponding spectrum for the extracted PMO (B), the ^{13}C CP-MAS-NMR spectrum of the as-synthesized material (C) and the corresponding spectrum for the extracted PMO (D).

tetrahedra, which correspond well to the chemical shift of the ^{29}Si signals ($\delta = -8.1$ and -9.0 ppm) of the precursor molecule. The presence of the organic groups is confirmed by ^{13}C cross-polarization (CP)-MAS-NMR spectra of the as-synthesized (Figure 2C) and the extracted (Figure 2D) samples. In the spectrum of the extracted material, three overlapping signals around $\delta = 5$, 17, and 32 ppm can be seen, which can be assigned to the trimethylene group as well as the CH and CH_2 groups of the trimethylene-bridged 3-ring units. The peaks correspond well with the ^{13}C signals at $\delta = 36.4$, 23.9 ppm (CH_2 groups of the trimethylene bridge), 14.3, and -1.6 ppm (CH and CH_2 groups of the ring) of the precursor molecule. The weak signal at 69 ppm indicates that small amounts of P123 template remained after the extraction of the material (Figure 2D). In the ^{13}C NMR spectrum of the as-synthesized PMO (Figure 2C) the presence of the P123 template is indicated by intense peaks at $\delta = 70$, 73, and 75 ppm for the carbon atoms bound to oxygen in the polyether. The CH_3 groups of the 1,2-dioxopropene $OCH_2CH(CH_3)O$ groups of P123 that have a chemical shift around $\delta = 20$ ppm overlap with the signals of the organic bridging groups in the channel walls of the PMO which accounts for the difference between the spectra of the as-synthesized and the extracted PMO. The NMR spectroscopic data indicate that practically no Si–C bond cleavage has occurred in the PMO during the self-assembly or the extraction processes. Thus, the integrity of the trimethylene-bridged 3-ring building block is maintained intact in the channel walls of the PMO.

Note that all previous attempts to self-assemble conventional $(EtO)_3SiRSi(OEt)_3$ silsesquioxane precursors that have alkene bridging groups with more than two CH_2 groups between silicon have failed to give PMOs with long range mesostructural order. Hence, the successful self-assembly of the trimethylene-bridged cyclic silsesquioxane precursor **1** to yield the well-ordered trimethylene-bridged 3-ring PMO described herein opens a myriad of opportunities for integrating a far wider range of organic bridging groups into PMOs than previously deemed possible.

 © 2005 Wiley-VCH Verlag GmbH & Co. KGaA, Weinheim

Experimental Section

1: [{$(EtO)_2SiCH_2$}$_3$] (7.5 mmol, 3 g) was dissolved in THF (200 mL; dried over Na/benzophenone) in a 1-l 3-necked flask under nitrogen and cooled to −78 °C in a dry ice/acetone bath. A 1.7 M solution of *t*BuLi (8.25 mmol, 4.8 mL; Aldrich) was added dropwise and the mixture was stirred for 30 min. Then 1,3-dibromopropane (3.75 mmol, 0.38 mL; Aldrich) was added dropwise. The solution was slowly warmed to room temperature and stirred for 2 days, then the solvent was removed in a rotary evaporator. Pentane (200 mL; anhydrous, 99 + %; Aldrich) was added, and the mixture was filtered. The pentane was evaporated from the filtrate and the residue was distilled under high vacuum. The third fraction gave the desired pure product [{[$(EtO)_2SiCH_2$]$_2$[$(EtO)_2SiCH$]}$_2${$(CH_2)_3$}] (30%, b.p. 145 °C at 20 mTorr). ^{13}C NMR (300 MHz, $CDCl_3$): $\delta = 58.36$ (s, CH_2), 58.21 (s, CH_2), 58.17 (s, CH_2), 58.13 (s, CH_2), 18.41–18.48 (m, CH_3), 36.44 (s, CH_2), 23.93 (s, CH_2), 14.27 (s, CH), −1.61 ppm (s, CH_2); ^{1}H NMR (300 MHz, $CDCl_3$): $\delta = 3.65$–3.85 (24 H, m), 1.45–1.6 (2 H, m), 1.1–1.25 (38 H, m), 0.15–0.3 (2 H, m), 0–0.1 ppm (8 H, m); ^{29}Si NMR (400 MHz, $CDCl_3$): $\delta = -8.1$ (s), −9.0 ppm (s); MS (ESI): *m*/*z*: 832 (100%).

Synthesis of trimethylene-bridged 3-ring periodic mesoporous organosilica (PMO): NaCl (25.8 mmol, 1.85 g) and Pluronic 123 (0.336 g; BASF) were dissolved in 2 N HCl (8.4 g) and H_2O (155 mmol, 2.8 g). Compound **1** (0.84 mmol, 0.7 g) was added to this solution with vigorous stirring at room temperature. The mixture was stirred at room temperature for 24 h and a white precipitate formed. The mixture was kept under static conditions for another 48 h at 80 °C. After filtration the PMO was obtained as a white powder. The extraction was carried out by stirring the as-synthesized PMOs in a mixture of acetone (250 mL) and 2 N HCl (10 mL) for 2 days.

PXRD patterns were measured with a Siemens D5000 diffractometer using $Cu_{K\alpha}$ radiation ($\lambda = 154.18$ pm). TEM and SEM images were recorded on a Hitachi S5200 microscope at an accelerating voltage of 30 kV (film fragments on carbon-film-coated Cu grids) at the University of Toronto nanoimaging facilities. All solid-state NMR experiments were performed with a Bruker Avance DSX 400 NMR spectrometer. ^{29}Si MAS-NMR spectra were recorded at a spin rate of 5 kHz and a pulse delay of 5 s. ^{13}C CP-MAS-NMR experiments were performed at a spin rate of 5 kHz, a contact time of 5 ms, and a pulse delay of 3 s. Sorption experiments were performed by a Quantachrome Autosorb-1C machine with N_2 as sorption gas at 77 K starting at a relative pressure $p/p_0 = 10^{-5}$. Seven data points were selected for BET analysis from a relative pressure of 0.1.

Received: October 12, 2004
Published online: March 2, 2005

Keywords: mesoporous materials · organosilica · self-assembly · silicon · soft matter

[1] I. W. Hamley, *Angew. Chem.* **2003**, *115*, 1730; *Angew. Chem. Int. Ed.* **2003**, *42*, 1692.
[2] T. Asefa, M. J. MacLachlan, N. Coombs, G. A. Ozin, *Nature* **1999**, *402*, 867.
[3] B. J. Melde, B. T. Holland, C. F. Blanford, A. Stein, *Chem. Mater.* **1999**, *11*, 3302.
[4] S. Inagaki, S. Guan, Y. Fukushima, T. Ohsuna, O. Terasaki, *J. Am. Chem. Soc.* **1999**, *121*, 9611.
[5] S. Park, C.-S. Ha, *Chem. Commun.* **2004**, 1986.
[6] O. Dag, C. Yoshina-Ishii, T. Asefa, M. J. MacLachlan, H. Grondey, N. Coombs, G. A. Ozin, *Adv. Funct. Mater.* **2001**, *11*, 213.
[7] K. Landskron, B. D. Hatton, D. D. Perovic, G. A. Ozin, *Science* **2003**, *302*, 266.

 © 2005 Wiley-VCH Verlag GmbH & Co. KGaA, Weinheim

Enzyme Engineering

Creation of a Tailored Aldolase for the Parallel Synthesis of Sialic Acid Mimetics

*Thomas Woodhall, Gavin Williams, Alan Berry, and Adam Nelson**

The exquisite selectivity and efficiency of enzymes has served as an inspiration to chemists for many years.[1] These remarkable properties enable enzymes to guide the assembly of complex products from mixtures of reactants present in low concentrations (in the nM–μM range).[2] Indeed, high levels of substrate specificity, and stereo- and chemoselectivity are hallmarks of enzymatic catalysis.

The most useful catalysts to the synthetic chemist, however, are those that are broadly applicable. Indeed, Sharpless has commented on the synthetic virtues of asymmetric dihydroxylation in terms of its remarkable scope: "It [OsO_4] reacts *only* with olefins and it reacts with *all* olefins (slight poetic license here)".[3] The substrate ranges of many enzymes are rather more restricted which limits their utility in chemical synthesis. The power of directed evolution has been brought to bear on this problem[4] and has, for example, been used to create an amine oxidase with broad substrate specificity and high enantioselectivity[5] and aldolases that modify the stereochemical course of C–C bond formation.[6,7]

Our challenging objective was to broaden the substrate specificity of the carbon–carbon bond-forming enzyme, sialic acid aldolase (*N*-acetylneuraminic acid aldolase), in a manner sufficient for application in the parallel synthesis of sialic acid mimetics. Sialic acid aldolase catalyses the reversible aldol condensation between pyruvate and *N*-acetylmannosamine **3** to give sialic acid **4** (Scheme 1). Although a number of hexoses, pentoses, and their analogues are substrates for this enzyme, condensations that involve shorter aldehydes are less promising: L- and D-erythrose and threose react at between 0.3 and 5% of the rate of *N*-acetylmannosamine, and two- and three-carbon aldehydes are not substrates.[8] The substituted dihydropyran **2** is an influenza A sialidase inhibitor[9] whose activity was optimized from the first potent inhibitor of influenza sialidases, zanamivir (**1**).[10] We decided, therefore, to engineer an aldolase with sufficiently broad substrate specificity to convert four-carbon aldehydes of general structure **5** into the corresponding sialic acid mimetics **6** (Scheme 1).

[*] T. Woodhall, Dr. A. Nelson
School of Chemistry
University of Leeds, Leeds, LS2 9JT (UK)
Fax: (+44) 113-233-6565
E-mail: a.s.nelson@leeds.ac.uk

T. Woodhall, Dr. G. Williams, Dr. A. Berry, Dr. A. Nelson
Astbury Centre for Structural Molecular Biology
University of Leeds, Leeds, LS2 9JT (UK)

Dr. G. Williams, Dr. A. Berry
School of Biochemistry and Microbiology
University of Leeds, Leeds, LS2 9JT (UK)

 DOI: 10.1002/anie.200462733 © 2005 Wiley-VCH Verlag GmbH & Co. KGaA, Weinheim

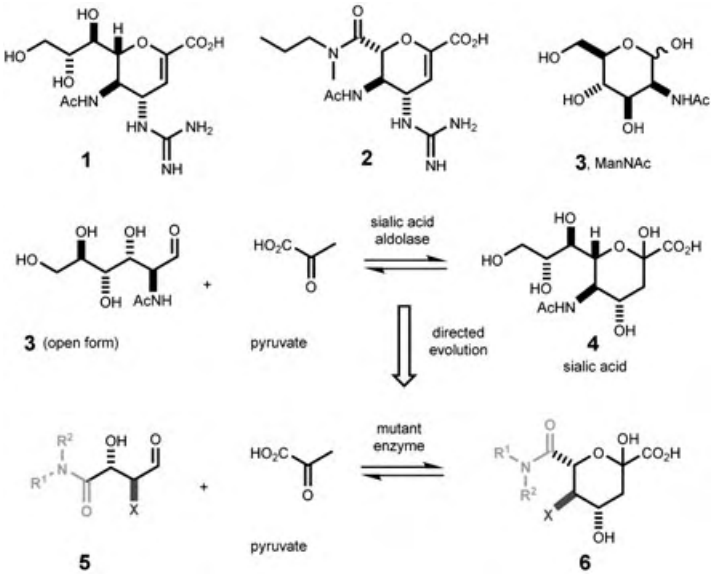

Scheme 1. Directed evolution of an aldolase for application in the parallel synthesis of sialic acid mimetics.

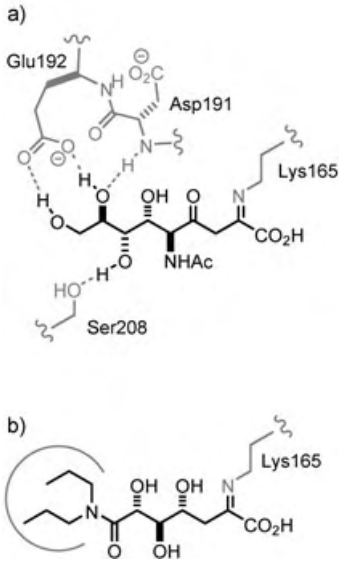

Figure 1. Schematic diagrams of the active sites of sialic acid aldolases: a) residues which have been shown by X-ray crystallography to interact with C7-C9 of 4-oxosialic acid; b) representation of the active site of an evolved enzyme in which a hydrophobic pocket has been sculpted to accommodate the dipropylaminocarbonyl group of the screening substrate.

We used a semirational approach, starting with the structure of the sialic acid aldolase from *Haemophilus influenzae*, which has 35% identity and 59% similarity to the corresponding *E. coli* protein. Analysis of the X-ray crystallographic structure[11] of the aldolase in complex with the inhibitor 4-oxosialic acid revealed three residues in contact with the C7–C9 side chain. The corresponding residues in the *E. coli* protein, Asp191, Glu192, and Ser208 were targeted separately by using saturation mutagenesis (Figure 1a). As the aim of this investigation was to evolve an aldolase with broad substrate specificity, we designed a screening substrate **12** with relatively large R^1 and R^2 groups (*n*Pr); it was hypothesized that an active site able to accommodate this rather bulky substrate would also be able to accept a wide range of smaller substrates. Furthermore, the tolerance of the wild-type enzyme toward a wide range of C2-substituted aldehydes[8] was expected to be preserved, as this substituent (NHAc in *N*-acetylmannosamine) is solvent-exposed.[11] A schematic diagram of the designed screening substrate in complex with the mutant enzyme is shown in Figure 1b.

The screening substrate **12** was prepared with the synthetic sequence outlined in Scheme 2. The lactone **7**, readily available by oxidative cleavage of isoascorbic acid,[12] was opened with dipropylamine to give the γ-hydroxyamide **8**. Swern oxidation of **8** and indium-mediated coupling with ethyl α-bromomethylacrylate (**13**)[13] gave the γ-hydroxyamides **9** (*anti*/*syn* 77:33), an outcome consistent with Felkin–Anh-controlled[14] attack on the intermediate aldehyde. Cleavage of the acetonide and hydrolysis of the ester gave the screening substrate **12**.

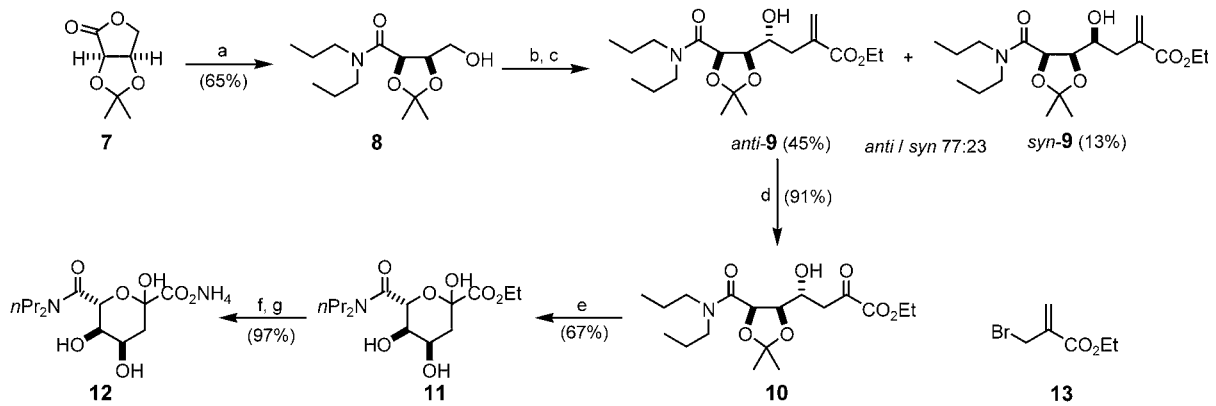

Scheme 2. Synthesis of the screening substrate **12**. Reagents and conditions: a) $n Pr_2NH$, MeOH; b) DMSO, $(COCl)_2$, Et_3N, CH_2Cl_2; c) In, **13**, THF/H_2O (1:1); d) O_3, MeOH, −78 °C then Me_2S; e) TFA/H_2O (1:1); f) $Ba(OH)_2$, EtOH/H_2O; g) $(NH_4)_2SO_4$, H_2O. DMSO = dimethyl sulfoxide; TFA = trifluoroacetic acid.

 © 2005 Wiley-VCH Verlag GmbH & Co. KGaA, Weinheim

The library of enzymes produced by saturation mutagenesis of residues 191, 192, and 208, in turn, were screened for useful synthetic activity on the premise that mutant enzymes able to cleave the screening substrate **12** would also be able to catalyze the forward reaction.[6] Libraries of proteins were screened in 96-well plates by analysis of thermally treated crude-cell lysates in which His-tagged mutant proteins had been overexpressed to ≈40% of the total protein content. A coupled enzyme assay was used in which the cleavage of the screening substrate to generate pyruvate was detected spectroscopically at 340 nm by the lactate dehydrogenase catalyzed reduction of pyruvate, with concomitant oxidation of NADH. In this way, a mutant enzyme was identified that contains the Glu192→Asn mutation (E192N), for which substrate specificity [(k_{cat}/$K_{M(12)}$)/(k_{cat}/$K_{M(sialic\ acid)}$)] had been switched 640-fold (Table 1). The k_{cat}/K_M value of the E192N mutant toward the screening substrate **12** is 50-fold higher than that of the wild-type enzyme; indeed, cleavage of substrate **12** by the mutant enzyme was six times more efficient than the wild-type enzyme-catalyzed cleavage of sialic acid!

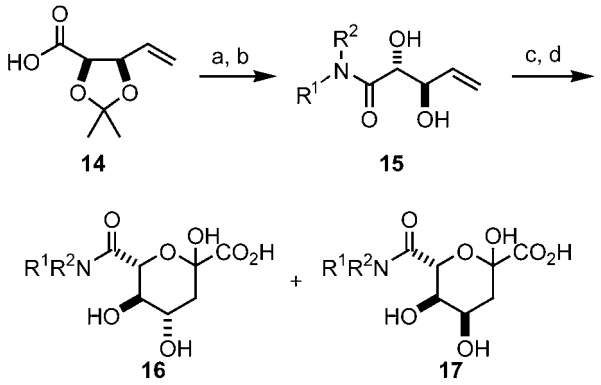

Scheme 3. Parallel synthesis of the sialic acid mimetics **16**/**17** (see Table 2). Reagents and conditions: a) EDC, HOBt, R^1R^2NH, CH_2Cl_2; b) TFA/H_2O (9:1); c) O_3, MeOH, −78 °C then Me_2S; d) E192N (2×10^{-2} mol%), pyruvate, buffer, (pH 7.4). EDC = 1-(3-dimethylaminopropyl)-3-ethylcarbodiimide hydrochloride; HOBt = 1-hydroxybenzotriazole hydrate.

Table 1: Characterization of the kinetics of the wild-type and E192N aldolases.

	Sialic Acid			**12**			
	k_{cat} [min^{-1}]	K_M [mM]	k_{cat}/K_M [min^{-1} mM^{-1}]	k_{cat} [min^{-1}]	K_M [mM]	k_{cat}/K_M [min^{-1} mM^{-1}]	$\frac{k_{cat}/K_{M(12)}}{k_{cat}/K_{M(sialic\ acid)}}$
WT	260 ± 6	4.4 ± 0.3	59 ± 4	74 ± 4	11 ± 1	6.9 ± 1.0	0.12
E192N	170 ± 10	38 ± 5	4.4 ± 0.6	130 ± 3	0.39 ± 0.04	340 ± 30	77

The synthetic utility of the evolved E192N enzyme was investigated with the crude aldehydes **18** generated by ozonolysis of the corresponding γ,δ-unsaturated amides **15**, prepared in parallel from the known γ,δ-unsaturated acid **14**[15] (Scheme 3 and Table 2). With the tertiary amide-containing aldehydes **18a–g** (Table 2, entries 1–7), the enzymatic reactions reached completion well within 3 days, and, after purification by ion-exchange chromatography, the sialic acid mimetics **16**/**17a–g** were obtained in 37–66% yield over the two steps from the corresponding γ,δ-unsaturated amides **15a–g**. In each case, the products **16**/**17** were obtained as ≈80:20 mixtures of epimers (**16**/**17**) which is consistent with thermodynamic stereochemical control.[16]

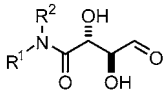

18

The enzymatic reactions of the secondary amide substrates **15h–m** were less efficient (Table 2, entries 8–13). In each case, the required products were observed after 14 days by analysis of crude reaction mixtures by MS and ^{1}H NMR spectroscopy at 500 MHz. The yields of the products **16**/**17h–m**, determined by ^{1}H NMR spectroscopy, were low (19–55%). After purification, the *tert*-butyl amide **16h**/**17h** was obtained in 35% yield over two steps from **15h** as a 45:55 mixture of epimers.

Remarkably, the enantiomeric aldehyde *ent*-**15c**, prepared analogously from D-lyxose,[17] was also a substrate for the evolved aldolase (Table 2, entry 14). After 7 days, the enzymatic reaction was worked up, and the enantiomeric mimetic *ent*-**16c**/*ent*-**17c** was obtained in 32% yield. The catalysis of the aldol reaction was not as efficient in

Table 2: Synthetic utility of the mutant sialic acid aldolase E192N.

Entry	Alkene **15**	R^1	R^2	Yield[a] **15** [%]	Products	*t* [days]	**16**:**17**[b]	Yield **16**/**17**[c,d] [%]
1	**15a**	Et	Et	61	**16**/**17a**	3	82:18	37
2	**15b**	*n*Pr	Me	73[e]	**16**/**17b**	3	82:18	42
3	**15c**	*n*Pr	*n*Pr	78	**16**/**17c**	3	82:18	42
4	**15d**	*n*Bu	*n*Bu	88	**16**/**17d**	3	82:18	66
5	**15e**	$-(CH_2)_4-$		66	**16**/**17e**	3	82:18	48
6	**15f**	$-(CH_2)_5-$		59	**16**/**17f**	3	79:21	55
7	**15g**	$-(CH_2)_2O(CH_2)_2-$		68	**16**/**17g**	3	82:18	47
8	**15h**	*t*Bu	H	79	**16**/**17h**	14	45:55	35 (55)
9	**15i**	*n*Pent	H	81	**16**/**17i**	14	70:30	(13)[f]
10	**15j**	*c*Hex	H	90	**16**/**17j**	14	60:40	(29)[f]
11	**15k**	Ph	H	67	**16**/**17k**	14	60:40	(19)[f]
12	**15l**	(*R*)-CHMeBn	H	74	**16**/**17l**	14	60:40	(30)[f]
13	**15m**	(*S*)-CHMeBn	H	68	**16**/**17m**	14	60:40	(35)[f]
14	*ent*-**15c**	*n*Pr	*n*Pr	78[g]	*ent*-**16c**/*ent*-**17c**	7	64:36	32[h]

[a] Yield of purified product over two steps from the acid **14**. [b] Determined by integration of the ^{1}H NMR spectrum (500 MHz). [c] Yield of purified product over two steps from the corresponding alkene **15**; (yields in parentheses were determined by integration of the ^{1}H NMR spectrum (500 MHz) of the crude reaction mixture). [d] Products were obtained as mixtures of the two pyranose and the two furanose forms: for **16**, ≈75:8:8:7 and for **17**, ≈13:7:44:36. [e] 53:47 mixture of rotomers. [f] The ratio of the two pyranose and two furanose forms was not determined. [g] The enantiomeric acid *ent*-**14** was used. [h] The enantiomeric starting material *ent*-**15c** ($R^1 = R^2 = n$Pr) was used.

 © 2005 Wiley-VCH Verlag GmbH & Co. KGaA, Weinheim

this case, however, as thermodynamic equilibration between the epimeric products was not complete (Table 2, compare the 82:18 ratio of epimers, entry 3, with the 64:36 ratio of epimers, entry 14).

In summary, we have engineered an aldolase that was exploited in the parallel synthesis of sialic acid mimetics. The mutant enzyme was most efficient in catalysis of the synthesis of the tertiary amides **16a–g**/**17a–g**, presumably a consequence of the screening assay used; it is well known that "you get what you screen for"[18] and our assay would have selected for enzymes able to accept a range of sterically varied *tertiary* amides. The novel enzyme might be used to catalyze the interconversion of dynamic combinatorial libraries,[19] for example, in the discovery of functional sialic acid mimetics such as paramyxovirus sialidase inhibitors.[20]

Received: November 26, 2004
Published online: March 2, 2005

Keywords: aldol reactions · biotransformations · enzyme catalysis · mutagenesis · protein engineering

[1] For example, see: W. J. Albery, J. R. Knowles, *Angew. Chem.* **1977**, *89*, 295–304; *Angew. Chem. Int. Ed. Engl.* **1977**, *16*, 285–293.
[2] X. Li, D. R. Liu, *Angew. Chem.* **2004**, *116*, 4956–4979; *Angew. Chem. Int. Ed.* **2004**, *43*, 4848–4870.
[3] For a transcript of his Nobel lecture, see: K. B. Sharpless, *Angew. Chem.* **2002**, *114*, 2126–2135; *Angew. Chem. Int. Ed.* **2002**, *41*, 2024–2032.
[4] a) M. Alexeeva, R. Carr, N. J. Turner, *Org. Biomol. Chem.* **2003**, *1*, 4133–4137; b) K. A. Powell, S. W. Ramer, S. B. del Cardayre, W. P. C. Stemmer, M. B. Tobin, P. F. Longchamp, G. W. Huisman, *Angew. Chem.* **2001**, *113*, 4068–4080; *Angew. Chem. Int. Ed.* **2001**, *40*, 3948–3959; c) M. T. Reetz, K.-E. Jaeger, *Top. Curr. Chem.* **1999**, *200*, 31–57; d) K.-E. Jaeger, T. Eggert, *Curr. Opin. Biotechnol.* **2004**, *15*, 305–313.
[5] R. Carr, M. Alexeeva, A. Enright, T. S. C. Eve, M. J. Dawson, N. J. Turner, *Angew. Chem.* **2003**, *115*, 4955–4958; *Angew. Chem. Int. Ed.* **2003**, *42*, 4807–4810.
[6] G. J. Williams, S. Domann, A. Nelson, A. Berry, *Proc. Natl. Acad. Sci. USA* **2003**, *100*, 3143–3148.
[7] M. Wada, C.-C. Hsu, D. Franke, M. Mitchell, A. Heine, I. Wilson, C.-H. Wong, *Bioorg. Med. Chem.* **2003**, *11*, 2091–2098.
[8] C.-H. Wong, G. M. Whitesides, *Enzymes in Synthetic Organic Chemistry*, Pergamon, Oxford, **1994**.
[9] a) P. W. Smith, S. L. Sollis, P. D. Howes, P. C. Cherry, I. D. Starkey, K. N. Cobley, H. Weston, J. Scicinski, A. Merritt, A. Whittington, P. Wyatt, N. Taylor, D. Green, R. Bethell, S. Madar, R. J. Fenton, P. J. Morley, T. Pateman, A. Beresford, *J. Med. Chem.* **1998**, *41*, 787–797; b) N. R. Taylor, A. Cleasby, O. Singh, T. Skarzynski, A. J. Wonacott, P. W. Smith, S. L. Sollis, P. D. Howes, P. C. Cherry, R. Bethell, P. Colman, J. Varghese, *J. Med. Chem.* **1998**, *41*, 798–807.
[10] M. von Itzstein, W.-Y. Wu, G. B. Kok, M. S. Pegg, J. C. Dyason, B. Jin, T. van Phan, M. L. Smythe, H. F. White, S. W. Oliver, P. M. Colman, J. N. Varghese, D. M. Ryan, J. M. Woods, R. C. Bethell, V. J. Hotham, J. M. Cameron, C. R. Penn, *Nature* **1993**, *363*, 418–423.
[11] J. A. R. G. Barbosa, B. J. Smith, R. DeGori, H. C. Ooi, S. M. Macuccio, E. M. Campi, W. R. Jackson, R. Brossmer, M. Sommer, M. C. Lawrence, *J. Mol. Biol.* **2000**, *303*, 405–421.
[12] N. Cohen, B. L. Banner, A. J. Laurenzano, L. Carozza, *Org. Synth.* **1985**, *63*, 127–135.
[13] a) T. H. Chan, C. J. Li, *J. Chem. Soc. Chem. Commun.* **1992**, 747–748; b) M. D. Chappell, R. L. Halcomb, *Org. Lett.* **2000**, *2*, 2003–2005; c) C.-J. Li, T.-H. Chan, *Tetrahedron* **1999**, *55*, 11149–11176.
[14] a) M. Chérest, H. Felkin, N. Prudent, *Tetrahedron Lett.* **1968**, 2199–2204; b) N. T. Anh, *Top. Curr. Chem.* **1980**, *88*, 145–162.
[15] V. Jaeger, B. Haefele, *Synthesis* **1987**, 801–806.
[16] C. H. Lin, T. Sugai, R. L. Halcomb, Y. Ichikawa, C. H. Wong, *J. Am. Chem. Soc.* **1992**, *114*, 10138–10145.
[17] B. V. Lao, S. Lahiri, *J. Carbohydr. Chem.* **1996**, *15*, 975–984.
[18] F. H. Arnold, *Acc. Chem. Res.* **1998**, *31*, 125–131.
[19] a) R. J. Lins, S. L. Flitsch, N. J. Turner, E. Irving, S. A. Brown, *Angew. Chem.* **2002**, *114*, 3555–3557; *Angew. Chem. Int. Ed.* **2002**, *41*, 3405–3407; b) R. J. Lins, S. L. Flitsch, N. J. Turner, E. Irving, S. A. Brown, *Tetrahedron* **2004**, *60*, 771–780.
[20] For the application of dihydropyran carboxamides similar to **2** in the inhibition of paramyxovirus sialidase, see: P. Chand, Y. S. Babu, S. R. Rowland, T.-H. Lin, *PCT Int. Appl.* **2002**, WO 2002076971.

 © 2005 Wiley-VCH Verlag GmbH & Co. KGaA, Weinheim

Asymmetric Catalysis

Palladium-Catalyzed Asymmetric Iodination of Unactivated C–H Bonds under Mild Conditions**

*Ramesh Giri, Xiao Chen, and Jin-Quan Yu**

Dedicated to Professor E. J. Corey

The catalytic activation of $C(sp^3)$–H and $C(sp^2)$–H bonds in readily available, inexpensive starting materials would provide a valuable array of new transformations for organic chemistry research and the fine chemical industry.[1] Activation of $C(sp^2)$–H bonds in benzene and *ortho*-substituted arenes has been successfully exploited in the development of catalytic C–C bond-forming reactions by coupling to olefins.[2,3] The selective activation of $C(sp^3)$–H bonds under mild conditions could be an attractive strategy for the development of catalytic reactions with wide applicability. Despite extensive efforts that have focused mainly on carbene and nitrene insertions, metathesis, Shilov chemistry, and biomimetic approaches, the catalytic and asymmetric functionalization of $C(sp^3)$–H bonds remains a significant challenge.[4]

We report herein an auxiliary approach for the chemoselective and asymmetric room-temperature iodination of

[*] R. Giri, Dr. X. Chen, Prof. Dr. J.-Q. Yu
Department of Chemistry, Brandeis University
Waltham, MA 02454-9110 (USA)
Fax: (+1) 781-736-2516
E-mail: yu200@brandeis.edu

[**] We thank Brandeis University for financial support, and the Camille and Henry Dreyfus Foundation for a New Faculty Award.

Supporting information for this article is available on the WWW under http://www.angewandte.org or from the author.

 © 2005 Wiley-VCH Verlag GmbH & Co. KGaA, Weinheim DOI: 10.1002/anie.200462884

methyl groups located at the α position of saturated aliphatic acids.[5] This protocol also applies to the activation of cyclopropanes (C–H bond β to the carboxy group) and arenes (C–H bond γ to the carboxy group). Our strategy involves the installation of a σ-chelating auxiliary, such as oxazoline,[6] to facilitate the assembly of the pre-transition state for cyclometallation through a square-planar complex as illustrated by compound **1** (Scheme 1). One of the earliest observed

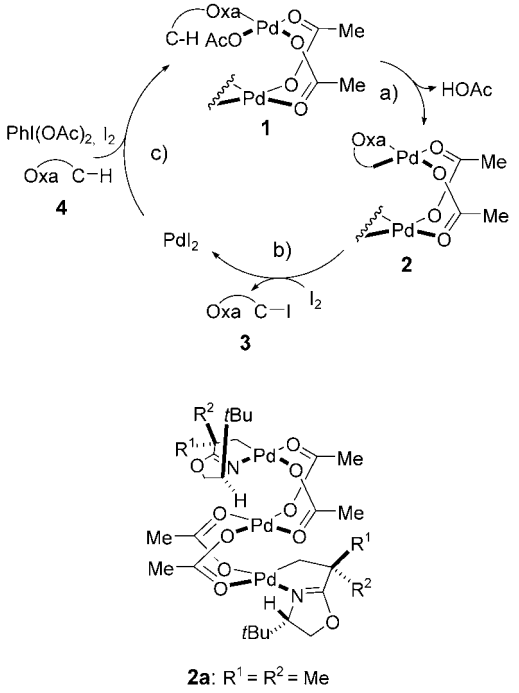

2a: $R^1 = R^2 = Me$

Scheme 1. Proposed catalytic cycle of C–H-bond activation.

examples of C–H bond activation was cyclometallation promoted by agostic interactions or sigma chelation.[7] The activation of *ortho* aryl C–H bonds to give cyclopalladation by the pre-coordination of a nitrogen atom has been reviewed extensively.[8] Inspired by the remarkable discovery of, and recent progress in the Shilov oxidation cycle,[9] we searched for an oxidation system that would render the cyclopalladation reaction catalytic in a similar manner. Notably, Sanford and co-workers recently reported an efficient Pd^{II}-catalyzed acetoxylation reaction with *O*-methyl oxime as a directing group at the time our work was in progress.[10]

Trimethylacetic acid was selected for an initial test, owing to its structural simplicity. Oxazoline **5a** and other substrates were readily prepared from their corresponding carboxylic acids and (*S*)-*tert*-leucinol (Table 1). We found that $Pd(OAc)_2$/I_2 was an effective stoichiometric reagent for the iodination of a methyl group in **5a**. Stirring **5a** with $Pd(OAc)_2$ and I_2 (1 equivalent each) in CH_2Cl_2 at 24 °C for 24 h gave exclusive iodination of the methyl group to provide the monoiodide in 80% yield. Reactions of other oxazolines that were prepared from trimethylacetic acid and ethanolamine, 2-methyl-2-aminopropanol, or valinol were either very slow or did not proceed under the same conditions.

Table 1: Monoiodination of methyl groups catalyzed by $Pd(OAc)_2$.[a]

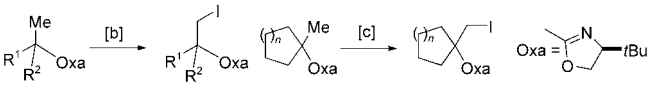

5a–7a **5b–7b** **8a–10a** **8b–10b**

Entry		Substrate	Yield [%]
1	**5a**	$R^1 = R^2 = Me$	92
2	**6a**	$R^1 = Me$; $R^2 = Et$	91[d]
3	**7a**	$R^1 = R^2 = Et$	88[e]
4	**8a**	$n = 1$	90[e]
5	**9a**	$n = 2$	97[e]
6	**10a**	$n = 3$	81
7	**11a**	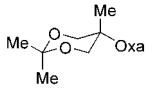	67[f]
8	**12a**	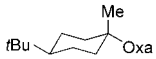	98
9	**13a**	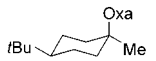	32

[a] Reaction conditions: $Pd(OAc)_2$ (10 mol%), I_2 (1 equiv), $PhI(OAc)_2$ (1 equiv), CH_2Cl_2, 24 °C, 48–72 h. [b] Entries 1–3. [c] Entries 4–6. [d] 63:37 d.r. (NMR spectroscopy). [e] PdI_2 precipitated at 36–48 h, $PhI(OAc)_2$ (1 equiv) was added, and stirring continued for another 48 h. [f] $PhI(OAc)_2$ (2 equiv), 50 °C, 48 h.

A single isomer of the trinuclear palladium alkyl species **2a** (Scheme 1) was obtained in 60% yield (determined by Pd recovery) by simply stirring substrate **5a** with $Pd(OAc)_2$ (1 equiv) in CH_2Cl_2 at 24 °C for 36 h (Supporting Information).[11] The *syn* geometry of **2a** was tentatively assigned by a steric argument: the bulky *tert*-butyl group must avoid the concave face. This complex was instantly converted into the iodinated product **5b** when I_2 was added.

Following these experimental observations, we proposed a stoichiometric C–H bond-activation pathway that involves steps a) and b) shown in Scheme 1. From the known structure of the cyclic trimer $Pd_3(OAc)_6$ crystallized from CH_2Cl_2[12] and the isolated complex **2a**, we assumed the trinuclear bis-μ-acetatopalladium complex **1** is formed as the reactive precursor. First, electrophilic cleavage of the C–H bond occurs to give the trinuclear square-planar Pd^{II} complex **2**. Next, I_2 reacts with complex **2**, presumably by oxidative addition[13] and reductive elimination, to form the iodinated product **3** and PdI_2 (isolated as a powder in quantitative yield and characterized by X-ray powder diffraction).[14] The kinetic isotope effect (KIE) of the iodination reaction of substrate **9a** into **9b**, in which the methyl group was deuterated ($k_H/k_D = 4.7$), is also consistent with C–H bond cleavage as the rate-limiting step.[15]

PdI_2 was unreactive with substrate **5a**. Therefore, IOAc generated[16] in situ from AgOAc and I_2 was used to convert PdI_2 into $Pd(OAc)_2$ to close the catalytic cycle, as shown in step c) (Scheme 1). $PhI(OAc)_2$ was more effective for this catalytic reaction.[17] Control experiments showed that $PhI(OAc)_2$ alone does not react directly with PdI_2. However, PdI_2 was converted into $Pd(OAc)_2$ by stirring with $PhI(OAc)_2$ and I_2 (1 equiv each) in CH_2Cl_2 at 24 °C for 1 h (Supporting Information). Thus, substrate **5a** was stirred with I_2, $PhI(OAc)_2$ (1 equiv each), and $Pd(OAc)_2$ (10 mol%) in CH_2Cl_2 at

 © 2005 Wiley-VCH Verlag GmbH & Co. KGaA, Weinheim

24 °C for 64 h to afford the iodination product in 92 % yield (Table 1).

The highly selective activation of primary over secondary C–H bonds was conclusively demonstrated with substrates **6a** and **7a**. The oxazoline prepared from triethylacetic acid does not react under the same conditions. These observations are consistent with the unfavorable steric interactions between coordinated ligands and branched alkyl groups in a cyclometalation step. Cyclic substrates (**8a**–**10a**) were also examined, and the methyl C–H bonds were consistently selectively iodinated in high yields. Substrate **11a**, which bears a polar ketal group, was also iodinated in 67 % yield at 50 °C (Table 1). The striking rate difference ($k_{trans}/k_{cis} = 5.7$) between isomeric substrates **12a** and **13a** is particularly intriguing. A detailed understanding of this observation requires further mechanistic exploration of the C–H bond-cleavage processes.

The moderate diastereoselectivity (63:37 d.r.) observed with substrate **6a** prompted us to test asymmetric iodination with various prochiral substrates. Iodination of substrate **14a** exhibited drastically improved diastereoselectivity relative to the reaction of **6a**. The two diastereomers were isolated as a mixture (d.r. = 91:9) (Table 2). We were pleased to find that the reaction conditions were also compatible with a TBS-protected hydroxy group in substrate **15a**.

Table 2: Asymmetric iodination.[a]

Entry	Substrate		Product		Yield [%]	d.r.
1	**14a**		**14b**	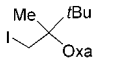	83[b]	91:9
2	**15a**		**15b**	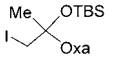	62[c]	93:7
3	**16a**		**16b**	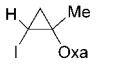	65[d]	99:1
4	**17a**		**17b**	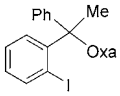	98[e]	99:1

[a] Reaction conditions: $Pd(OAc)_2$ (10 mol %), I_2 (1 equiv), $PhI(OAc)_2$ (1 equiv), CH_2Cl_2. [b] 24 °C, 30 h. [c] 50 °C, 48 h. [d] 24 °C, 96 h. [e] 24 °C, 13 h. TBS = *tert*-butyldimethylsilyl.

The well-documented amide-directed lithiation reactions of cyclopropanes[18] prompted us to determine if this newly developed catalytic system could functionalize the secondary cyclopropyl C–H bond in the presence of a methyl group. Cyclopropane substrate **16a** was subjected to the same conditions as described. Indeed, the selectivity was completely reversed from primary to secondary C–H bonds. Of particular importance is the excellent stereochemical control in the exclusive iodination of the cyclopropyl C–H bond. Reaction of **16a** afforded iodinated product **16b** as a single isomer in 65 % yield. The *cis* geometry of **16b** was established by NOE experiments. The enantiomer of **16b** was also obtained with oxazoline substrate prepared from (*R*)-*tert*-leucinol. Both **16b** and its enantiomer were hydrolyzed by treatment with H_2SO_4/dioxane (1:1, 4 M) at reflux for 8 h to give the corresponding carboxylic acids with > 99 % *ee* as determined by HPLC analysis.

The scope of this C–H bond-activation reaction was further examined with the arene-containing substrate **17a**. Interestingly, the arene C–H bond was iodinated with high selectivity in the presence of a methyl group. The monoiodinated product **17b** was isolated in 98 % yield (> 99:1 d.r.; NMR spectroscopy, GC–MS, Table 2).[19] We reasoned that if the reaction proceeds by cyclometallation of the trinuclear complex **1**, the hydrogen atom cleaved from the methyl group is the one that affords **2** with the larger group on the convex face (R^2) (Scheme 1*)*. This model explains the high diastereoselectivity attained, even though the stereogenic center in the oxazoline ring is far removed from the reaction site. Unfortunately, confirmation of this model through the assignment of the absolute configuration of the products has proven difficult, and is still in progress.

A clear advantage of this catalytic system is the ease with which the palladium catalyst can be recycled (Table 3). As

Table 3: Catalyst recycling experiments with substrate **17a**.[a]

Run	1	2	3	4	5
Yield [%]	98	97	93	88	84

[a] Reaction conditions: $Pd(OAc)_2$ (10 mol %), I_2 (1 equiv), $PhI(OAc)_2$ (1 equiv), CH_2Cl_2, 24 °C, 13–20 h.

PdI_2 precipitates from solution toward the completion of the reaction, it can be isolated by centrifugation. After decanting the supernatant, PdI_2 is recycled with a fresh supply of I_2 and $PhI(OAc)_2$. With **17a**, five reaction cycles starting with only 22.4 mg (0.1 mmol) of $Pd(OAc)_2$ produced 1.99 g (4.6 mmol) of the iodinated product **17b** with high diastereoselectivity (> 99:1 d.r.).

In summary, the combination of a hindered oxazoline auxiliary, $Pd(OAc)_2$, I_2, and $PhI(OAc)_2$ was shown to be a powerful protocol for the catalytic and asymmetric iodination of inactivated C–H bonds of methyl, cyclopropyl and aryl groups under mild conditions.

Received: December 10, 2004
Published online: February 23, 2005

Keywords: asymmetric catalysis · C-H activation · chiral auxiliaries · iodine · palladium

[1] a) N. Chatani, T. Asaumi, S. Yorimitsu, Y. Ishii, F. Kakiuchi, S. Murai, *J. Am. Chem. Soc.* **2000**, *122*, 12882; b) G. Dyker, *Angew. Chem.* **1999**, *111*, 1808; *Angew. Chem. Int. Ed.* **1999**, *38*, 1699; c) H. Chen, S. Schlecht, T. C. Semple, J. F. Hartwig, *Science* **2000**, *287*, 1995; d) J. Y. Cho, M. K. Tse, D. Holmes, R. E. Maleczka, Jr., M. R. Smith III, *Science* **2002**, *295*, 305; e) R. H. Crabtree, *J. Chem. Soc. Dalton Trans.* **2001**, 2437.

[2] a) C. Jia, T. Kitamura, Y. Fujiwara, *Acc. Chem. Res.* **2001**, *34*, 633; b) F. Kakiuchi, M. Yamauchi, N. Chatani, S. Murai, *Chem. Lett.* **1996**, *2*, 111; c) C. P. Lenges, M. Brookhart, *J. Am. Chem. Soc.* **1999**, *121*, 6616; d) Y. G. Lim, Y. H. Kim, J. B. Kang, *J. Chem. Soc. Chem. Commun.* **1994**, 2267; e) R. K. Thalji, K. A. Ahrendt, R. G. Bergman, J. A. Ellman, *J. Am. Chem. Soc.* **2001**, *123*, 9692; f) C. H. Jun, C. W. Moon, J. B. Hong, S. G. Lim, K. Y. Chung, Y. H. Kim, *Chem. Eur. J.* **2002**, *8*, 485.

 © 2005 Wiley-VCH Verlag GmbH & Co. KGaA, Weinheim

[3] For enantioselective aromatic C–H coupling to olefins, see: a) R. K. Thalji, J. A. Ellman, R. G. Bergman, *J. Am. Chem. Soc.* **2004**, *126*, 7192; b) K. Mikami, M. Hatano, M. Terada, *Chem. Lett.* **1999**, *1*, 55.
[4] a) H. M. L. Davies, R. E. J. Beckwith, *Chem. Rev.* **2003**, *103*, 2861; b) P. Muller, C. Fruit, *Chem. Rev.* **2003**, *103*, 2905; c) C. G. Espino, J. D. Bois, *Angew. Chem.* **2001**, *113*, 618; *Angew. Chem. Int. Ed.* **2001**, *40*, 598; d) A. E. Shilov, G. B. Shul'pin, *Chem. Rev.* **1997**, *97*, 2879; e) J. T. Groves, P. J. Viski, *J. Am. Chem. Soc.* **1989**, 111, 8537; f) R. Breslow, A. B. Brown, R. D. McCullough, P. W. White, *J. Am. Chem. Soc.* **1989**, *111*, 4517.
[5] For a recent example of a chiral auxiliary in the dehydrogenation of an ethyl group involving stoichiometric amounts of $PtMe_2L_2$, see: J. A. Johnson, N. Li, D. Sames, *J. Am. Chem. Soc.* **2002**, *124*, 6900.
[6] A. I. Meyers, *Acc. Chem. Res.* **1978**, *11*, 375.
[7] a) M. A. Bennett, D. L. Milner, *J. Am. Chem. Soc.* **1969**, *91*, 6983; b) J. A. Ibers, R. Dicosimo, G. M. Whitesides, *Organometallics* **1982**, *1*, 13; c) for various examples of stoichiometric cyclopalladation reactions, see: A. J. Canty *in Comprehensive Organometallic Chemistry II: A Review of the Literature 1982–1994* (Eds.: E. W. Abel, F. G. A. Stone, G. Wilkinson), Pergamon, New York, **1995**.
[8] a) A. D. Ryabov, *Synthesis* **1985**, 233; b) K. Carr, J. K. Sutherland, *J. Chem. Soc. Chem. Commun.* **1984**, 1227; c) J. E. Baldwin, R. H. Jones, C. Najera, M. Yus, *Tetrahedron* **1985**, *41*, 699.
[9] a) N. F. Gol'dshleger, M. B. Tyabin, A. E. Shilov, A. A. Shteinman, *Zh. Fiz. Khim. (Engl. Transl.)* **1969**, *43*, 1222; b) S. S. Stahl, J. A. Labinger, J. E. Bercaw, *J. Am. Chem. Soc.* **1996**, *118*, 5961; c) U. Fekl, K. I. Goldberg, *J. Am. Chem. Soc.* **2002**, *124*, 6804; d) R. A. Periana, D. J. Taube, S. Gamble, H. Taube, T. Satoh, H. Fujii, *Science* **1998**, *280*, 560; e) B. D. Dangel, J. A. Johnson, D. Sames, *J. Am. Chem. Soc.* **2001**, *123*, 8149.
[10] a) A. R. Dick, K. L. Hull, M. S. Sanford, *J. Am. Chem. Soc.* **2004**, *126*, 2300; b) L. V. Desai, K. L. Hull, M. S. Sanford, *J. Am. Chem. Soc.* **2004**, *126*, 9542.
[11] The predominant formation of a dimeric complex by combining $Pd(OAc)_2$ and 2-*tert*-butyl-4,5-dihydro-4,4-dimethyloxazole in HOAc at reflux was previously reported. Trinuclear Pd alkyl species at a *syn*/*anti* ratio of 2:3 were also observed as minor products, and determined by crystallographic analysis to be stacked in a head-to-tail orientation: G. Balavoine, J. C. Clinet, *J. Organomet. Chem.* **1990**, *390*, C84.
[12] For the crystallographic structure of the trinuclear Pd acetate obtained from CH_2Cl_2, see: F. A. Cotton, S. Han, *Rev. Chim. Miner.* **1985**, *22*, 277.
[13] For the oxidative addition of I_2 to organoplatinum(II) complexes, see: J. C. Muijsers, J. W. Niemantsverdriet, I. C. M. Wehman-Ooyevaar, D. M. Grove, G. van Koten, *Inorg. Chem.* **1992**, *31*, 2655.
[14] Acetoxylation product from the reductive elimination of acetate was not observed under our reaction conditions.
[15] For the measurement of KIE in stoichiometric oxime-directed palladation, see: A. P. Wells, W. Kitching, *Organometallics* **1992**, *11*, 2750.
[16] G. M. Rubottom, R. C. Mott, *J. Org. Chem.* **1979**, *44*, 1731.
[17] For the early use of $PhI(OAc)_2$ as an oxidant for the acetoxylation of benzene, see: T. Yoneyama, R. H. Crabtree, *J. Mol. Catal. A* **1996**, *108*, 35; for activation of alkanes upon reaction with $PhI(OAc)_2/I_2$, see: J. Barluenga, F. Gonzales-Bobes, J. M. Gonzalez, *Angew. Chem.* **2002**, *114*, 2668; *Angew. Chem. Int. Ed.* **2002**, *41*, 2556; for recent work with $PhI(OAc)_2$ as an oxidant for C–H bond activation, see reference [10].
[18] P. E. Eaton, R. G. Daniels, D. Casucci, G. T. Cunkle, *J. Org. Chem.* **1987**, *52*, 2100.
[19] Oxazoline **17b** was also hydrolyzed to give the iodo acid in >99% *ee*.

 © 2005 Wiley-VCH Verlag GmbH & Co. KGaA, Weinheim

Crystal Engineering

Corundum, Diamond, and PtS Metal–Organic Frameworks with a Difference: Self-Assembly of a Unique Pair of 3-Connecting D_{2d}-Symmetric 3,3′,5,5′-Tetrakis(4-pyridyl)bimesityl**

*Ramalingam Natarajan, Govardhan Savitha, Paulina Dominiak, Krzysztof Wozniak, and J. Narasimha Moorthy**

There is an upsurge of interest in the synthesis of coordination polymers in contemporary supramolecular chemistry, as coordination polymerization may lead to materials with controllable functions such as porosity, sensing, nonlinear optical (NLO) activity, and chirality.[1] Crystal engineering based on predesigned organic linkers and metal centers (building blocks) with specific coordination geometries is an important approach in the preparation of coordination materials with desired functions.[2] Based on the knowledge of the structures of the ligands and the coordination geometries of a variety of metal centers, diverse 2D and 3D nets—several of which are analogous to structures of inorganic materials—have been engineered in the field of metal–organic frameworks (MOFs). Thus, the syntheses of 3-connected nets corresponding to the topologies of $SrSi_2$/-(10,3)-a,[3] $ThSi_2$/(10,3)-b,[4] (12,3),[5] (3,4)-connected nets with the topologies of boracite,[6] $Cu_{15}Si_4$,[7] $(5,^3_{\ 4})$,[8] and (3,6)-connected nets corresponding to the topologies of rutile[9] and pyrite[10] have been accomplished. Insofar as the 4-connected nets are concerned, the syntheses of MOFs with unusual topologies[11] and with topologies corresponding to those of diamond,[1c,d,12] NbO,[13] quartz,[14] and PtS[15] have been reported. Similarly, the (4,8)- and 6-connected metal–organic frameworks with fluorite[16] and cubic[17] topologies, respectively, have been designed and synthesized. In view of the success of such building-block approaches to realize metal–organic frameworks with specific topologies, the multidentate ligands with novel structural features offer the possibility to construct new and unique coordination poly-

[*] R. Natarajan, Dr. G. Savitha, Dr. J. N. Moorthy
Department of Chemistry
Indian Institute of Technology
Kanpur 208 016 (India)
Fax: (+91) 512-259-7436
E-mail: moorthy@iitk.ac.in

P. Dominiak, Prof. K. Wozniak
Department of Chemistry
Warsaw University
Passteura 1, 02-093 Warszawa (Poland)

[**] We gratefully acknowledge financial support from the Department of Science and Technology, India. We thank Prof. V. Chandrasekhar and P. Sasikumar (IIT, Kanpur) for their help with TGA analysis, and Prof. T. N. Guru Row (IISc., Bangalore) and Prof. P. K. Bharadwaj (IIT, Kanpur) for useful discussions. We also thank the referees for invaluable suggestions.

Supporting information for this article is available on the WWW under http://www.angewandte.org or from the author.

 DOI: 10.1002/anie.200461625 © 2005 Wiley-VCH Verlag GmbH & Co. KGaA, Weinheim

mers.[18] In continuation of our recent studies on the self-assembly of acids,[19] we conceived a unique tetradentate ligand with D_{2d}-symmetry to explore the construction of 3D coordination networks by metal-directed self-assembly with O_h, T_d, and D_{4h} metal centers (Figure 1).

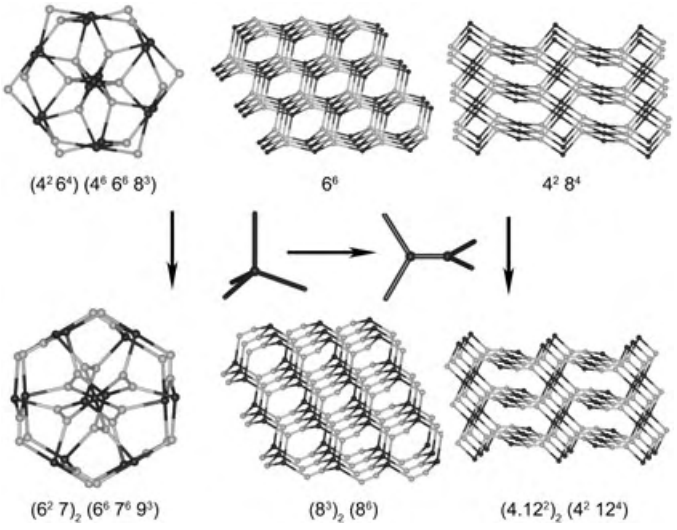

Figure 1. Top: Representation of the ideal corundum, diamond, and PtS networks. Bottom: The nets resulting from replacement of tetrahedral nodes by pairs of 3-connecting nodes. The Schläfli notations for the networks, shown below the structures, signify the changes in the network topologies.

Construction of a network by combining T_d ligands and O_h metal centers has been regarded as being very difficult.[20] The best compromise between a 4-connecting ligand and an octahedral metal center turns out to be that of the corundum form of Al_2O_3, in which both Al^{3+} and O^{2-} ions are distorted from their ideal octahedral and tetrahedral geometries, respectively.[21] Thus, by considering the D_{2d}-symmetric ligand as a distorted-tetrahedral building block, one can envisage the synthesis of metal–organic equivalents of the corundum net as shown in Figure 1. Similarly, the combination of D_{2d}-symmetric ligands and T_d metal centers should yield an analogue of the diamond net, the difference being that each ring in the resultant net is eight-membered as opposed to a six-membered ring in the ideal diamond net. Indeed, Wells pointed out that (10,3)-a and (10,3)-b nets derive from the replacement of tetrahedral nodes of a diamond net by pairs of 3-connecting nodes.[22] He also showed that the $(8,^3_4)$-b net results from replacement of alternate tetrahedral nodes in a diamond net by pairs of 3-connecting nodes. Furthermore, the combination of a D_{2d}-symmetric tetratopic ligand with a square-planar D_{4h} metal center should be expected to afford a PtS network, the difference being that the resulting network would be constituted by four- and twelve-membered rings instead of four- and eight-membered rings in the ideal PtS net. The metal–organic corundum-, diamond-, and PtS-related nets arising from the replacement of a T_d ligand by a D_{2d} ligand as shown in Figure 1 are also unprecedented. Herein, we document the engineering of these three distinct 3D metal–organic networks shown in Figure 1 based on a rationally designed and synthesized unique D_{2d}-symmetric 3,3′,5,5′-tetrakis(4-pyridyl)bimesityl (tpb) ligand.[23]

The reaction of tpb with $Zn(ClO_4)_2{\cdot}6H_2O$, $Cd(ClO_4)_2{\cdot}6H_2O$, $AgNO_3$, and $MnCl_2{\cdot}4H_2O$ led to corresponding complexes **1**–**4**, whose compositions were formulated

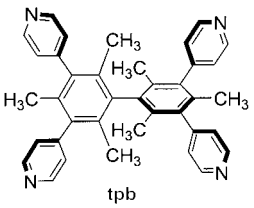

1: $\{Zn(tpb)_{1.5}(ClO_4)_2{\cdot}(H_2O)_n\}_\infty$
2: $\{Cd(tpb)_{1.5}(ClO_4)_2{\cdot}(H_2O)_n\}_\infty$
3: $\{Ag(tpb)(NO_3)(CH_3OH)\}_\infty$
4: $\{Mn(tpb)(Cl)_2(CH_3OH)(H_2O)_n\}_\infty$

based on microanalytical and single-crystal X-ray crystal structure determinations. Compound **1** was obtained as colorless cubic crystals by slow diffusion over two days of the ethanolic solution of $Zn(ClO_4)_2{\cdot}6H_2O$ into a solution of tpb in dichloromethane that was contained in a vial. A similar diffusion of $Cd(ClO_4)_2{\cdot}6H_2O$ in ethanol into a solution of tpb in dichloroethane yielded hexagonal colorless crystals of **2**. Both **1** and **2** were isolated in $>60\,\%$ yield from preparative experiments. The crystals of compound **2** were found to be stable, while those of **1** were fragile and degraded upon removal from the mother liquor. X-ray single-crystal structure determinations[24] revealed that both compounds are isostructural, with a cubic space group of $Ia\bar{3}d$.

The metal ions in both **1** and **2** reside on the crystallographic threefold inversion center and are perfectly octahedral. Each of the metal ions is surrounded by six pyridyl rings of independent tpb ligands. The two mesityl rings of the tpb ligand are absolutely orthogonal and each of the pyridyl rings is tilted by about 80° with respect to the mesitylene core. Figure 2b shows the crystal-packing diagram of **1**; the packing for compound **2** is virtually indistinguishable. The interatomic distances associated with the coordination bonds that involve the metal ion and the pyridyl nitrogen atom in **1** and **2** are 2.183(1) and 2.359(1) Å, respectively. The networks are not interpenetrated in both complexes and the perchlorate counterions and water molecules occupy the void space.

The seemingly complex structure of the coordination polymer can be best understood by simplification of the ligand structure to that of the D_{2d}-symmetric allene (Figure 2a) and by representing the metal as a 6-connecting octahedral node. Figure 2c shows the crystal packing based on this simplification. Decorating ligand **1** by connecting the carbon atoms of the bimesityl rings (to which the angularly disposed pyridyl rings are attached) as shown in Figure 2a leads to further simplification of the ligand structure to a distorted tetrahedron. Thus, by depicting the metal center as well as the ligand tpb as 6- and 4-connecting polyhedra, the structure of the coordination polymer is reduced to that shown in Figure 2d. This network may be readily compared to that of the corundum modification of Al_2O_3, in which each octahedral Al^{3+} ion is surrounded by six O^{2-} ions, while each oxygen center is surrounded by four Al^{3+} ions arranged in a distorted tetrahedral configuration. Although the analogy

 © 2005 Wiley-VCH Verlag GmbH & Co. KGaA, Weinheim

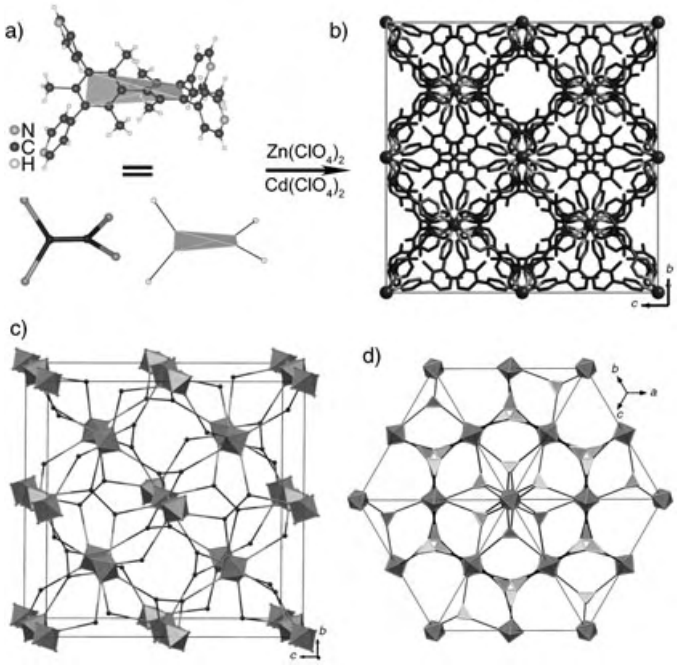

Figure 2. a) Illustration of the formal equivalence of the ligand tpb to that of the D_{2d}-symmetric allene; b) the crystal packing of compounds **1** and **2**; c) the crystal packing by depicting the ligand tpb as a pair of 3-connecting topological equivalents of allene and the metal as a 6-connecting octahedron; d) the crystal packing shown again by depicting the ligand as a distorted 4-connecting tetrahedron and the metal as a 6-connecting octahedron, which is similar to that of the corundum. Hydrogen atoms, solvent molecules, and counterions have been removed for clarity.

between Zn/Cd-coordination polymers of the ligand tpb and the corundum form of Al_2O_3 is established by simplification of the structure of the ligand to a distorted tetrahedral 4-connecting node (Figure 2 d), the tetradentate tpb is in reality a pair of 3-connected nodes that are linked together. Accordingly, the Schläfli notation for the topology of the coordination polymer based on a 4-connecting tetrahedral ligand is similar to that of the corundum and is given by $(4^26^4)(4^66^68^3)$. However, tpb is best described as a pair of 3-connecting nodes and thus the Schläfli topological description for the Zn/Cd-coordination polymers of tpb takes the form $(6^27)_2(6^67^69^3)$.

The colorless crystals of compound **3** were obtained by slow diffusion of a methanolic solution of $AgNO_3$ into a solution of tpb in methanol followed by keeping the resultant solution at room temperature in the dark for 2–3 days. The crystals were found to decay as soon as they were removed from the mother liquor. Single-crystal X-ray diffraction analysis[24] revealed that the complex crystallizes in the monoclinic space group $C2/c$. The geometry of the metal ion is found to be tetrahedral as it is coordinated by the pyridyl groups of four distinct molecules. The bond lengths associated with the metal ion and pyridyl nitrogen atoms are 2.326(5) and 2.330(1) Å. The metal ion and the tpb ligand assemble into a diamond network with the incorporation of solvent molecules. A typical adamantanoid unit formed by the unique assembly of six molecules of tpb (only two pyridyl rings contribute to the construction of adamantanoid unit, the other two are used for 3D propagation) and four Ag^I ions that act as nodes is shown in Figure 3; the assembly involves two of the tpb ligands coordinating to the metal through two of their

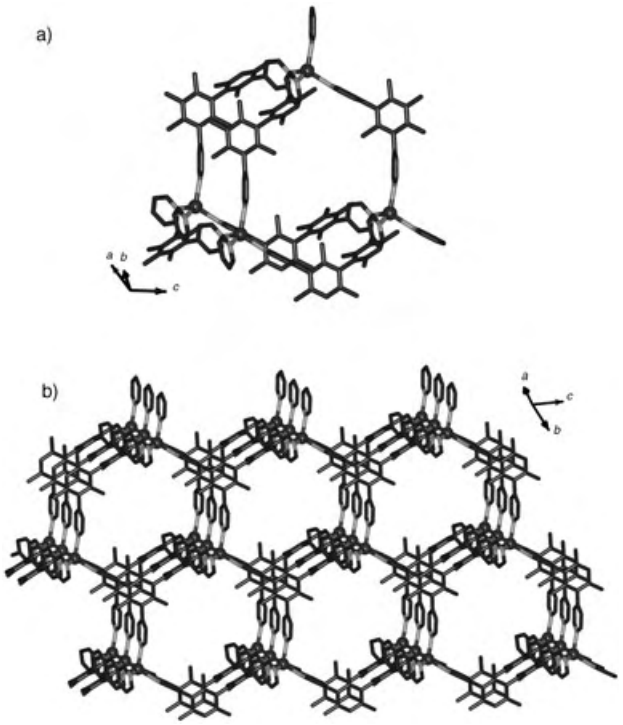

Figure 3. a) The core adamantanoid unit of compound **3**. Notice that the shortest circuit of the unit is an eight-membered ring. b) The diamond-related net of **3**, which undergoes interpenetration. Hydrogen atoms, solvent molecules, and counteranions have been removed for clarity. The solid spheres represent metal cations.

pyridyl rings linked to two mesitylene rings of the bimesityl core, while the remaining four use two pyridyl rings linked to the same mesitylene ring for coordinative covalent bonding. The 3D propagation of these adamantanoid units leads to a porous network as shown in Figure 3. Unfortunately, the porosity is destroyed by interpenetration of an independent second diamondoid network. The overall network is topologically equivalent to that resulting from the replacement of alternative tetrahedral nodes of an adamantanoid unit by D_{2d}-symmetric pairs of 3-connecting nodes as shown in Figure 1. When alternative tetrahedral nodes of an adamantanoid unit are replaced by pairs of 3-connecting nodes as those represented by the tpb ligands, the shortest circuit of the resultant (3,4)-connected net is an eight-membered ring leading to the topology of $(8,^3_4)$-b. Indeed, this net was predicted by Wells 25 years ago and has surprisingly not been realized so far in metal-coordination chemistry.[22] The Schläfli symbol for the network of **3** is $(8^3)_2(8^6)$, which illustrates that the shortest circuits meeting at both 3- and 4-connected points are eight-membered. This network is thus different from that of the ideal diamond net for which the Schläfli notation is 6^6.

 © 2005 Wiley-VCH Verlag GmbH & Co. KGaA, Weinheim

Compound **4** was obtained by slow diffusion of the methanolic solution of $MnCl_2{\cdot}4H_2O$ into a solution of tpb in CH_2Cl_2. Single-crystal X-ray analysis[24] of **4** revealed a coordination polymer in which the geometry of the metal ion is octahedral. Whereas the two Cl^- ions coordinate axially to the metal ion, the pyridyl rings of four distinct tpb ligands are found to occupy the equatorial positions about the metal center (Figure 4); the four metal-ion–pyridine-nitrogen bond

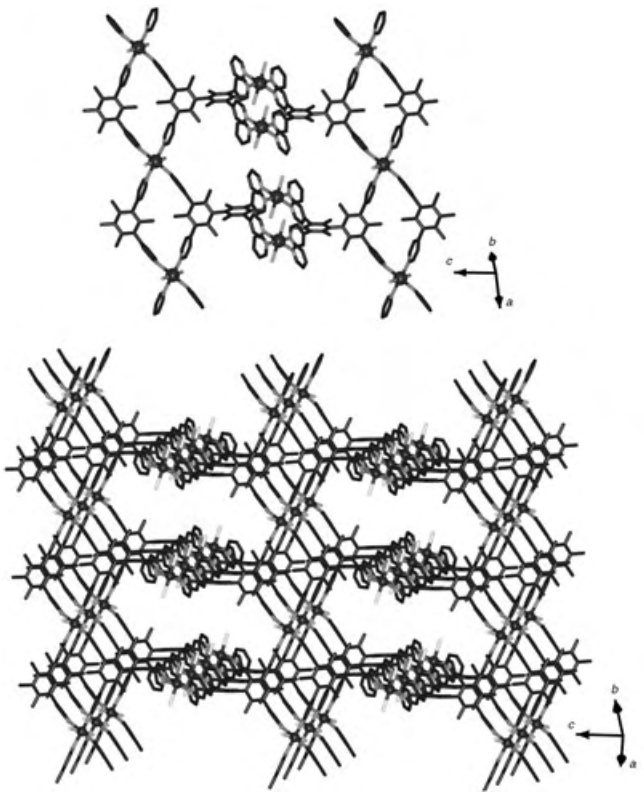

Figure 4. The PtS-related net of compound **4**, which undergoes interpenetration. The top picture is a basic unit of the network. Hydrogen atoms and the solvent molecules have been removed for clarity. The solid spheres represent metal cations.

lengths (d_{Mn-N}) are 2.318(1), 2.285(1), 2.257(1), and 2.332(1) Å. From the point of view of structural description of the coordination polymer, the metal ion may be considered equivalent to a 4-connecting square-planar node, as the Cl^- ions merely serve to fill the coordination sphere. Thus, the coordination polymer built up of 4-connecting D_{4h}-symmetric metal ions (by considering only pyridyl ligands) and a pair of 3-connecting tpb ligands shown in Figure 4 is precisely equivalent to the PtS network in which the tetrahedral ligand is replaced by a pair of 3-connecting ligand as exemplified in Figure 1. While the Schläfli notation for the ideal PtS network is 4^28^4, that of the network of compound **4** is $(4.12^2)_2(4^2.12^4)$, which illustrates that the eight-membered ring in PtS net is replaced by a twelve-membered ring. Thus, the PtS-related net observed with **4** is unique and unknown. The network is twofold interpenetrated with solvent water molecules incorporated in the pores of the crystal lattice.

According to thermogravimetric analyses, the compounds **1**, **2**, and **4** lose their included solvent molecules upon heating. The complexes are stable after the initial loss of the solvent molecules up to about 340, 395, and 388 °C for **1**, **2**, and **4**, respectively (see Supporting Information). The porosity coupled with stability promises potential for their usage as storage devices.[1a] The variation in the network topologies in going from Ag^I to Mn^{II} to Zn^{II}/Cd^{II} centers must be due to the coordination preferences of the metal ions and the choice of the counteranions. While the preferred coordination geometry for an Ag^I center is tetrahedral, as is observed, the square-planar connectivity with the pyridyl ligands in the case of Mn^{II} complex is dictated by the two Cl^- ions that occupy the axial positions about the metal. The observed octahedral geometry about the Zn^{II}/Cd^{II} ions must be connected with the ability of the perchlorate anions to reside away from the metal centers. We wish to point out that well-characterized hexapyridinate metal complexes are rare. We are aware of only one instance of a coordination polymer in which six pyridine ligands are octahedrally coordinated to the metal center.[10a]

In summary, we have designed and synthesized a unique D_{2d}-symmetric tetratopic tetrapyridylbimesityl ligand, tpb, which can be readily used as a pair of 3-connecting nodes in coordination polymerization. Thus, it is shown that the combination of a D_{2d}-symmetric ligand with O_h, T_d, and D_{4h} metal centers leads to MOFs with the topologies related to those of corundum, diamond, and PtS, which have not previously been realized.

Experimental Section

1: A solution of $Zn(ClO_4)_2{\cdot}6H_2O$ (0.0341 g, 0.0915 mmol) in 10 mL of MeOH was layered over a solution of tpb (0.05 g, 0.0915 mmol) in 10 mL of CH_2Cl_2, and the resultant solution was kept at room temperature. Colorless cubic crystals formed in 2 days (yield 60%). Elemental analysis (%) calcd for $Zn(tpb)_{1.5}(ClO_4)_2{\cdot}(H_2O)_{12}$: C 52.72, H 5.82, N 6.47; found: C 52.65, H 5.16, N 6.20.

2: A similar procedure to that described above was applied with dichloroethane in place of CH_2Cl_2 to obtain colorless hexagonal crystals in 2 days. Elemental analysis (%) calcd for $Cd(tpb)_{1.5}(ClO_4)_2{\cdot}(H_2O)_{13}$: C 50.13, H 5.68, N 6.15; found: C 49.85 H 5.71 N 6.12.

3: A methanolic solution of $AgNO_3$ (0.031 g, 0.183 mmol in 10 mL) was added slowly to a solution of tpb (0.05 g, 0.0915 mmol) in 10 mL of MeOH. The container was closed tightly and kept in the dark. Colorless crystals were observed after 2–3 days and were isolated in about 55% yield in three independent experiments. These crystals turned brown when exposed to light and air.

4: A solution of $MnCl_2{\cdot}4H_2O$ (0.0217 g, 0.0109 mmol) in 15 mL of MeOH was layered over a solution of tpb (0.03 g, 0.0549 mmol) in 10 mL of CH_2Cl_2 and the resultant solution was allowed to evaporate slowly over 10 days. Colorless crystals were obtained in 55% yield. Elemental analysis (%) calcd for $Mn(tpb)(Cl)_2(CH_3OH)(H_2O)_8$: C 55.72, H 5.52, N 6.66; found C 55.01, H 5.42, N 6.45.

Received: August 12, 2004
Revised: December 12, 2004
Published online: February 23, 2005

Keywords: coordination modes · crystal engineering · N ligands · self-assembly · supramolecular chemistry

 © 2005 Wiley-VCH Verlag GmbH & Co. KGaA, Weinheim

[1] a) S. Kitagawa, R. Kitaura, S.-i. Noro, *Angew. Chem.* **2004**, *116*, 2388 – 2430; *Angew. Chem. Int. Ed.* **2004**, *43*, 2334 – 2375; b) C. Janiak, *Dalton Trans.* **2003**, 2781 – 2804; c) O. R. Evans, W. Lin, *Acc. Chem. Res.* **2002**, *35*, 511 – 522; d) S. R. Batten, R. Robson, *Angew. Chem.* **1998**, *110*, 1558 – 1595; *Angew. Chem. Int. Ed.* **1998**, *37*, 1460 – 1494.

[2] a) B. J. Holliday, C. A. Mirkin, *Angew. Chem.* **2001**, *113*, 2076 – 2097; *Angew. Chem. Int. Ed.* **2001**, *40*, 2022 – 2043; b) B. Moulton, M. J. Zaworotko, *Chem. Rev.* **2001**, *101*, 1629 – 1658; c) R. Robson, *J. Chem. Soc. Dalton Trans.* **2000**, 3735 – 3744.

[3] a) C. J. Kepert, T. J. Proir, M. J. Roessiensky, *J. Am. Chem. Soc.* **2000**, *122*, 5158 – 5168; b) B. F. Abrahams, P. A. Jackson, R. Robson, *Angew. Chem.* **1998**, *110*, 2801 – 2804; *Angew. Chem. Int. Ed.* **1998**, *37*, 2656 – 2659.

[4] K. Biradha, M. Fujita, *Angew. Chem.* **2002**, *114*, 3542 – 3545; *Angew. Chem. Int. Ed.* **2002**, *41*, 3392 – 3395.

[5] B. F. Abrahams, S. R. Batten, M. J. Grannas, H. Hamit, B. F. Hoskins, R. Robson, *Angew. Chem.* **1999**, *111*, 1538 – 1540; *Angew. Chem. Int. Ed.* **1999**, *38*, 1475 – 1477.

[6] B. F. Abrahams, S. R. Batten, H. Hamit, B. F. Hoskins, R. Robson, *Angew. Chem.* **1996**, *108*, 1794 – 1796; *Angew. Chem. Int. Ed. Engl.* **1996**, *35*, 1690 – 1692.

[7] D. N. Dyebtsev, H. Chun, K. Kim, *Chem. Commun.* **2004**, 1594 – 1595.

[8] B. Moulton, J. Lu, M. J. Zaworotko, *J. Am. Chem. Soc*, **2001**, *123*, 9224 – 9225.

[9] S. R. Batten, B. F. Hoskins, B. Moubaraki, K. S. Murray, R. Robson, *J. Chem. Soc. Dalton Trans.* **1999**, 2977 – 2986.

[10] a) S. R. Batten, B. F. Hoskins, R. Robson, *Angew. Chem.* **1995**, *107*, 884 – 886; *Angew. Chem. Int. Ed. Engl.* **1995**, *34*, 820 – 822; b) H. K. Chae, J. Kim, O. D. Friedrichs, M. O'Keeffe, O. M. Yaghi, *Angew. Chem.* **2003**, *115*, 4037 – 4039; *Angew. Chem. Int. Ed.* **2003**, *42*, 3907 – 3909.

[11] a) L. Carlucci, N. Cozzi, G. Ciani, M. Moret, D. M. Proserpio, S. Rizzato, *Chem. Commun.* **2002**, 1354 – 1355; b) B. Rather, B. Moulton, R. D. B. Walsh, M. J. Zaworotko, *Chem. Commun.* **2002**, 694 – 695.

[12] Y.-H. Liu, H.-C. Wu, H.-M. Lin, W.-H. Hou, K.-L. Lu, *Chem. Commun.* **2003**, 60 – 61, and references therein.

[13] a) M. Eddaoudi, J. Kim, M. O'Keeffe, O. M. Yaghi, *J. Am. Chem. Soc.* **2002**, *124*, 376 – 377; b) X.-H. Bu, M.-L. Tong, H.-C. Chang, S. Kitagawa, S. R. Batten, *Angew. Chem.* **2004**, *116*, 194 – 197; *Angew. Chem. Int. Ed.* **2004**, *43*, 192 – 195.

[14] J. Sun, L. Weng, Y. Zhou, J. Chen, Z. Chen, Z. Liu, D. Zhao, *Angew. Chem.* **2002**, *114*, 4561 – 4563; *Angew. Chem. Int. Ed.* **2002**, *41*, 4471 – 4473.

[15] a) B. F. Abrahams, B. F. Hoskins, D. M. Michail, R. Robson, *Nature* **1994**, *369*, 727 – 729; b) B. Chen, M. Eddaoudi, T. M. Reineke, J. W. Kampf, M. O'Keeffe, O. M. Yaghi, *J. Am. Chem. Soc.* **2000**, *122*, 11559 – 11560.

[16] H. Chun, D. Kim, D. N. Dybtsev, K. Kim, *Angew. Chem.* **2004**, *116*, 989 – 992; *Angew. Chem. Int. Ed.* **2004**, *43*, 971 – 974.

[17] a) B. F. Hoskins, R. Robson, D. A. Slizys, *Angew. Chem.* **1997**, *109*, 2861 – 2863; *Angew. Chem. Int. Ed. Engl.* **1997**, *36*, 2752 – 2755; b) M. Eddaoudi, J. Kim, N. Rosi, D. Vodak, J. Wachter, M. O'Keeffe, O. M. Yaghi, *Science* **2002**, *295*, 469 – 472.

[18] a) J.-P. Zhang, S.-L. Zheng, X.-C. Huang, X.-X. Chen, *Angew. Chem.* **2004**, *116*, 208 – 211; *Angew. Chem. Int. Ed.* **2004**, *43*, 206 – 209; b) D.-L. Long, R. J. Hill, A. J. Blake, N. R. Champness, P. Hubberstey, D. M. Proserpio, C. Wilson, M. Schröder, *Angew. Chem.* **2004**, *116*, 1887 – 1890; *Angew. Chem. Int. Ed.* **2004**, *43*, 1851 – 1854; c) O. V. Dolomanov, D. B. Cordes, N. R. Champness, A. J. Blake, L. R. Hanton, G. B. Jameson, M. Schröder, C. Wilson, *Chem. Commun.* **2004**, 642 – 643.

[19] J. N. Moorthy, R. Natarajan, P. Mal, P. Venugopalan, *J. Am. Chem. Soc.* **2002**, *124*, 6530 – 6531; b) J. N. Moorthy, R. Natarajan, P. Venugopalan, *Angew. Chem.* **2002**, *114*, 3567 – 3570; *Angew. Chem. Int. Ed.* **2002**, *41*, 3417 – 3420.

[20] M. O'Keeffe, M. Eddaoudi, H. Li, T. Reineke, O. M. Yaghi, *J. Solid State Chem.* **2000**, *152*, 3 – 20.

[21] E. N. Maslen, V. A. Streltsov, N. R. Streltsova, *Acta Crystallogr. Sect. B* **1993**, *49*, 973 – 980.

[22] A. F. Wells, *Three-Dimensional Nets and Polyhedra*, Wiley, New York, **1977**.

[23] The synthesis of tetrapyridylbimesityl ligand, tpb, was accomplished starting from the readily synthesized bimesityl (P. Kovacic, C. Wu, *J. Org. Chem.* **1961**, *26*, 759 – 762). Tetraiodination of bimesityl by using iodine/H_2SO_4/HNO_3 yielded 3,3′,5,5′-tetraiodobimesityl in 86 % yield. Suzuki coupling of this compound with the 4-pyridineboronate ester 2-(4-pyridyl)-4,4,5,5-tetramethyl-1,3-dioxaborolane (6 equiv) in the presence of $[Pd(PPh_3)_4]$ (5 mol %) and K_3PO_4 afforded **1** in 57 % yield.

[24] Crystal data for **1**: Moiety formula $C_{57}H_{51}N_6Cl_2O_{9.5}Zn$, cubic, space group $Ia\bar{3}d$ (no. 230); $a = 32.198(4)$ Å, $V = 33380.03(7)$ Å^3, $Z = 16$; $T = 100$ K, $\mu = 0.358$ mm^{-1}; $R_1 = 0.0709$, $wR_2 = 0.1802$ ($I > 2\sigma(I)$), $S = 0.831$, data/restraints/parameter = 1467/54/101. Crystal data for **2**: Moiety formula $C_{57}H_{51}N_6Cl_2O_{9.5}Cd$, cubic, space group $Ia\bar{3}d$ (no. 230); $a = 32.727(4)$ Å, $V = 35052.82(7)$ Å^3, $Z = 16$; $T = 100$ K, $\mu = 0.310$ mm^{-1}; $R_1 = 0.0728$, $wR_2 = 0.1741$ ($I > 2\sigma(I)$), $S = 0.670$, data/restraints/parameter = 1525/54/89. Out of the expected 32 perchlorate ions in the unit cell of each of the Zn and Cd compounds (**1** and **2**), only 16 could be located. The solvent molecules and the remaining counteranions that reside in the regions of diffuse electron density were treated by the Platon/Squeeze procedure (A. L. Spek, *J. Appl. Crystallogr.* **2003**, *36*, 7 – 13), which suggested, after accounting for the missing counteranions, a solvent accessible volume of about 44 % and 46 % in the case of **1** and **2**, respectively. Crystal data for **3**: Moiety formula $C_{39}H_{38}N_5O_4Ag$, monoclinic, space group $C2/c$ (no. 15); $a = 21.169(4)$, $b = 17.027(3)$, $c = 16.501$ Å(3), $V = 4580.79(1)$ Å^3, $Z = 4$; $T = 100$ K, $\mu = 0.463$ mm^{-1}; $R_1 = 0.1296$, $wR_2 = 0.2126$ ($I > 2\sigma(I)$), $S = 1.160$, data/restraints/parameter = 2216/0/223. Crystal data for **4**: Moiety formula $C_{39}H_{34}N_4Cl_2O_6Mn$, monoclinic, space group $C2/c$ (no. 15); $a = 20.9751(1)$, $b = 15.3662(1)$, $c = 25.8748(1)$ Å, $V = 8196.9(1)$ Å^3, $Z = 8$; $T = 100$ K; $R_1 = 0.0919$, $wR_2 = 0.2668$ ($I > 2\sigma(I)$), $S = 1.062$, data/restraints/parameter = 10056/0/420. Structure solutions were done by direct methods and refinements on F^2 with Shelxtl. Non-hydrogen atoms were refined anisotropically and H-atoms were generated at idealized geometries and refined isotropically. The hydrogen atoms for the solvent molecules were not fixed. CCDC-216293 and CCDC-247028–247030 contain the supplementary crystallographic data for this paper. These data can be obtained free of charge from The Cambridge Crystallographic Data Centre via www.ccdc.cam.ac.uk/data_request/cif.

 © 2005 Wiley-VCH Verlag GmbH & Co. KGaA, Weinheim

Nanotube Synthesis

Carbonization of Disclike Molecules in Porous Alumina Membranes: Toward Carbon Nanotubes with Controlled Graphene-Layer Orientation**

*Linjie Zhi, Jishan Wu, Jixue Li, Ute Kolb, and Klaus Müllen**

Graphitic carbon nanotubes have attracted great attention since their discovery[1] because of their unique electronic properties and many potential applications.[2] Pyrolysis of organic precursors is a commonly used chemical method for carbon-nanotube preparation[3] in which metal catalysts are believed to play a key role in the incorporation of carbon atoms into graphitic (not amorphous) carbon structures at high temperatures.[2a,4] One serious problem is the separation of catalysts from the nanotube products, as typically most of the catalyst particles are encapsulated into the nanotubes.[2i,4c,5] Template methods have also been used to conduct the formation of carbon tubes.[3c,h,6] However, without metal catalysts, even with the help of templates, it is difficult to form graphite-structured carbon nanotubes.[3c,6b,6e,7] This graphitic structure yields materials with excellent properties for which many potential applications have been proposed.

To form ordered graphite structures without metal catalysts, one possible approach is carbonization within a liquid-crystalline mesophase. By this method, large aromatic molecules preorganize into ordered columnar superstructures before carbonization and maintain this architecture during carbonization under a controlled heating process. Experiments showed that disclike polycyclic aromatic hydrocarbons (PAHs) in pitch can be preorganized on many kinds of substrates such as glass, quartz, polytetrafluoroethene (PTFE), aluminum, and alumina by an edge-on orientation, with the main axis of the discs approximately parallel to the substrate surface.[8a] Recently, carbon nanofibers with ordered graphene architectures have been fabricated by carbonization of pitch in a mesophase by using an alumina template method.[8b] However, to create a well-defined supramolecular order of the graphene sheets, especially for nanoscale carbon tubes, is still a challenge. It is well known that disclike PAHs such as alkyl- and alkylphenyl-substituted hexa-*peri*-hexabenzocoronenes (HBC) show exceptional mesomorphic properties and form highly ordered columnar architectures in the liquid-crystalline phase owing to the strong π–π interactions between the HBC discs. These discotic liquid crystals usually display an edge-on orientation in thin films on different substrates such as glass, PTFE and highly oriented pyrolyzed graphite (HOPG).[9] Our recent studies showed that in the absence of a catalyst, pyrolysis of this kind of disclike graphite-structured molecules in the bulk state resulted in different types of carbon nano- and microobjects with graphitic structures.[10] Herein, we report a novel synthetic approach to fabricate graphite-structured carbon nanotubes by carbonization of the preorganized disclike molecules in porous alumina membranes (Scheme 1). The

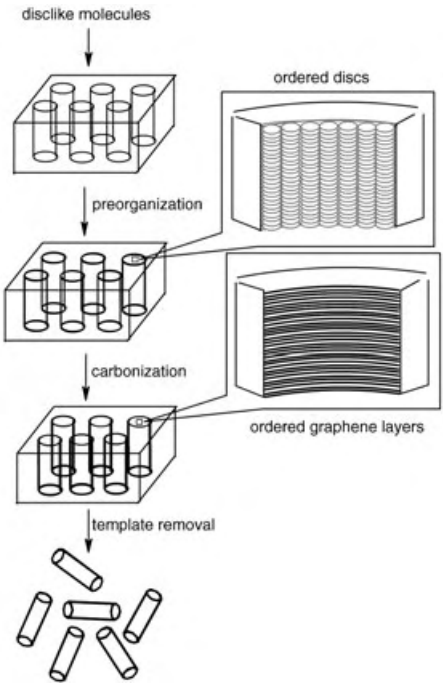

Scheme 1. The formation of carbon nanotubes with controlled orientation of graphene layers.

molecules were preorganized by π–π stacking into highly ordered columnar architectures that were maintained to form ordered graphene sheets after carbonization at high temperatures. By removal of the template, carbon nanotubes with ordered graphene layers that lie perpendicular to the tube axis were obtained.

Commercially available anodic alumina membranes were chosen as a template because of their relatively narrow pore size distribution and as they comprise mostly open and separated straight channels. Hexa(4-dodecylphenyl)-*peri*-hexabenzocoronene (HBC-PhC_{12}, **1**; Scheme 2) was chosen as a carbon precursor in this work because of its good solubility and as it forms stable columnar liquid-crystalline phases.[11] A solution of **1** in dichloromethane was added dropwise onto the surface of the alumina template. The

[*] Dr. L. Zhi, Dr. J. Wu, Prof. K. Müllen
Max Planck Institute for Polymer Research
Ackermannweg 10, 55128 Mainz (Germany)
Fax: (+49) 6131-379-350
E-mail: muellen@mpip-mainz.mpg.de
Dr. J. Li, Dr. U. Kolb
Institute of Physical Chemistry
Johannes Gutenberg Universität
55128 Mainz (Germany)

[**] This work was financially supported by the EU projects MAC-MES (Grd2-2000-30242), DISCEL (G5RD-CT-2000-00321), Deutsche Forschungsgemeinschaft (Schwerpunkt Feldeffekttransistoren), as well as the Zentrum für Multifunktionelle Werkstoffe und Miniaturisierte Funktionseinheiten (BMBF 03N 6500). We thank G. Glasser for SEM measurements.

Supporting information for this article is available on the WWW under http://www.angewandte.org or from the author.

 © 2005 Wiley-VCH Verlag GmbH & Co. KGaA, Weinheim DOI: 10.1002/anie.200460986

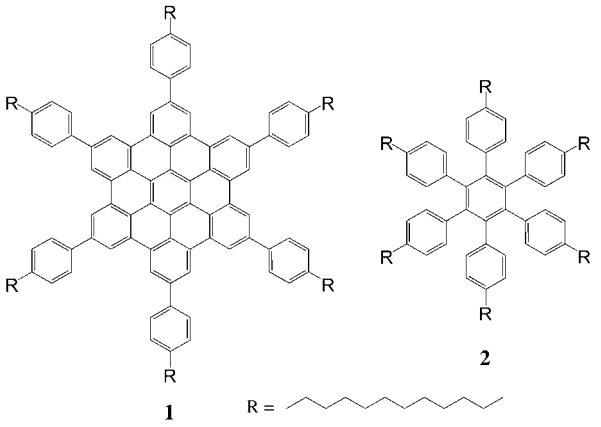

Scheme 2. The discotic molecules used in the carbonization process. R is a C_{12} alkyl chain.

solution spread along the inner surfaces of the nanoscale channels of the template and completely filled the pore. As a result, the alumina film became transparent. When the solvent was evaporated, the film became opaque again which indicated that HBC-PhC_{12} (**1**) had coated the surface of the channel to form a tube instead of a fiber. Tubes are formed because the cohesive driving forces for complete filling are much weaker than the adhesive forces, as explained by Steinhart et al.[12] After heating the HBC-PhC_{12}-loaded template at 400 °C for 5 h, then at 600 °C for 5 h, and finally at 900 °C for 5 h, with a rate of increase in temperature of 2 °C min^{-1}, completely carbonized and uniformly sized carbon nanotubes formed in the channels of the alumina membrane.

Figure 1 shows an image obtained by scanning electronic microscopy (SEM) of the aligned carbon nanotubes that formed in the channels of the template, which was partially etched with an aqueous solution of sodium hydroxide. The shape and size of the tubes are in agreement with the dimensions of the template channels. Most of the tubes are cylindrically shaped with open ends. Tubes with a closed end were occasionally observed, as shown in Figure 1 b, and were produced in a channel with one closed end. After complete removal of the template, single carbon nanotubes with lengths of several to tens of micrometers were obtained. The average outer diameter is about 100 nm and the wall thickness is around 20 nm. High resolution transmission electronic microscopy (HR-TEM) measurements showed that graphitic structured walls were formed and highly ordered graphene layers with a layer-to-layer distance of about 0.34 nm were aligned, as expected, perpendicular to the tube axis (Figure 2). The same architecture was found at every tube and at every position studied by HR-TEM. Raman spectra of the nanotubes also confirmed the graphitic structure of the tube walls (see Supporting Information). Because of the special graphene sheet orientation, we predict that this kind of carbon nanotube will display quite different properties relative to catalytically prepared carbon nanotubes. For example, the tubes here should have a relatively higher density of active sites on the surface,[8b] and the tube walls will be more reactive toward functionalization by chemical or physical methods. Electron transport along the tube wall should also be quite different from that of normal carbon tubes, and this difference will be interesting from the standpoint of microelectronic devices.

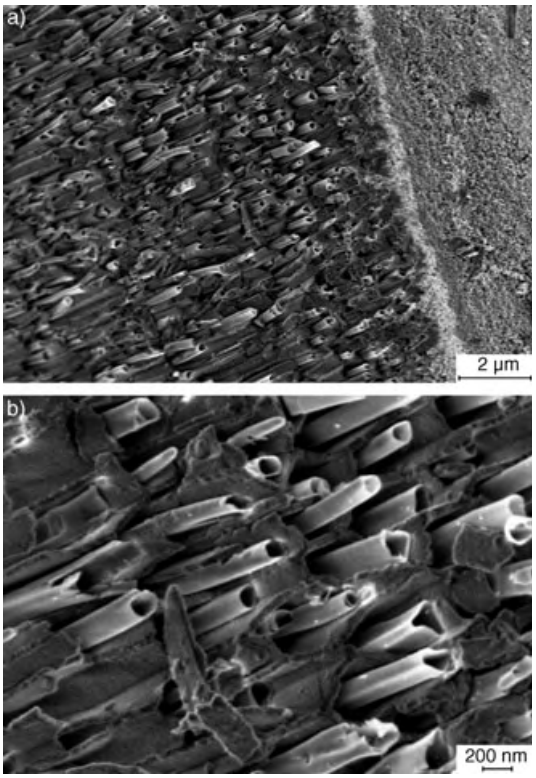

Figure 1. Aligned carbon nanotubes formed in the template channels. Most of the tubes are cylindrically shaped with open ends. Tubes with a closed end or special shapes can be seen occasionally.

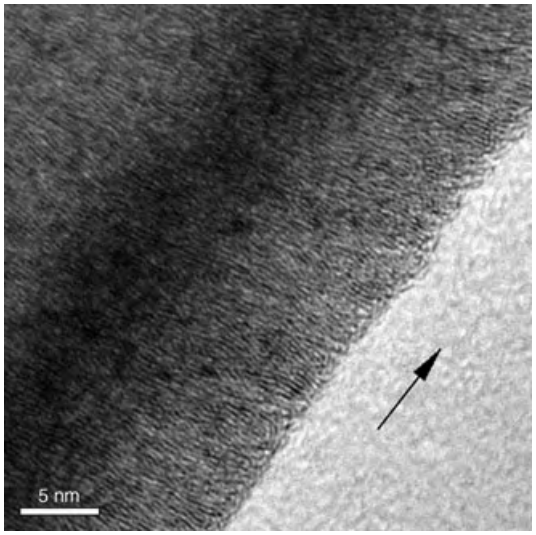

Figure 2. HR-TEM image of as-prepared carbon nanotubes with highly ordered graphene layers oriented perpendicularly to the tube axis. The arrow indicates the tube axis.

The ordered preorganization of the HBC molecules at the inner surface is thought to play an important role in the final unique graphene wall structures. Previously, we reported that

 © 2005 Wiley-VCH Verlag GmbH & Co. KGaA, Weinheim

HBC molecules substituted with alkyl chains formed uniaxially oriented columnar architectures on a glass surface by a "zone-casting" technique.[9a] Given the similar hydrophilic properties of alumina and the glass surface, the HBC molecules in the alumina pores could also adopt an edge-on stacking and orient along the channel during the diffusion and evaporation processes of the solution. This prediction is supported by the TEM measurements of the samples after heat treatment at the relatively "low" temperature of 400 °C for 5 h. After removal of the template, formation of carbon-like nanotubes was observed, and the HR-TEM measurement of the tubes revealed that the ordered columnar superstructures with the graphene layer aligned perpendicular to the tube axis had been formed at this stage, although the alignment was not perfect (see Supporting Information). According to thermogravimetric analysis (TGA), HBC-PhC_{12} (**1**) loses its alkyl chains at 400 °C and cross-linking reactions take place at this stage. This process was confirmed to be effective for cross-linking the graphitic disc units together and preserving the discotic mesophase.[10] After this stage, a stabilized ordered supercolumnar architecture formed which could be preserved at higher carbonization temperatures. Instead of using the three-step heat treatment, we also performed the carbonization by heating the HBC-PhC_{12}-loaded template from 25 °C to 900 °C with a heating rate of 10 °C min^{-1} and holding the temperature at 900 °C for 5 h. Graphitic carbon nanotubes were also formed, however, the graphene layers of thus-formed carbon tubes were not as highly ordered as those of carbon tubes prepared by the stepwise carbonization, although most of the graphene layers were still oriented perpendicular to the tube axis (Figure 3). This experiment further reinforced the importance of the stepwise heat treatment of the HBC discs in the mesophase.

Similar carbon nanotubes were also formed by this method from another discotic molecule, hexa(4-dodecylphenyl)benzene (HPB-C_{12}, **2**; Scheme 2), by the same procedure as used for HBC-PhC_{12} (**1**). However, the carbon nanotubes that formed did not have an ordered graphitic architecture and the graphene layers did not orient fully perpendicularly to the tube axis, as shown in Figure 4. In this case, we did not observe the ordered columnar structures after treatment at 400 °C because this temperature is much higher than the melting point of HPB-C_{12}; that is, the order is disrupted before the intermolecular cross-linking reactions take place. Other disclike molecules such as HBCs substituted with oxygen-containing alkyl chains, and the alkylated larger graphite disc C96-C_{12},[13] which has a core of 96 carbon atoms, were also chosen as carbon precursors in our work and detailed investigations are ongoing. It is clear that the stabilized preorganization of the discs is essential for effective control of the orientation of the graphene layers in carbon nanotubes.

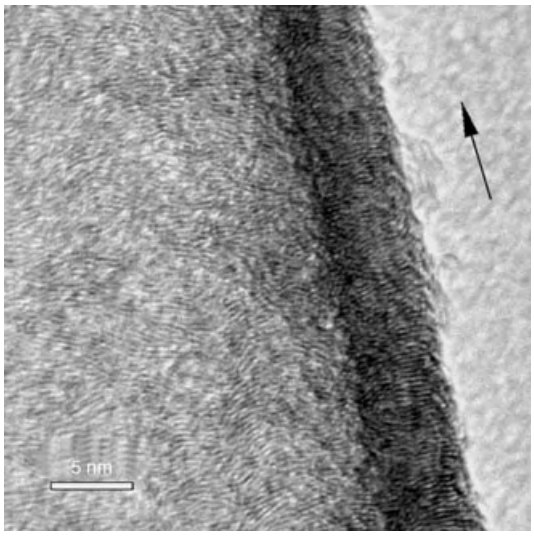

Figure 3. HR-TEM image of carbon nanotubes prepared from HBC-PhC_{12} (**1**) by rapid heating to 900 °C with a heating rate of 10 °C min^{-1}. The arrow indicates the tube axis. The graphene layers are not as highly ordered as those shown in Figure 2.

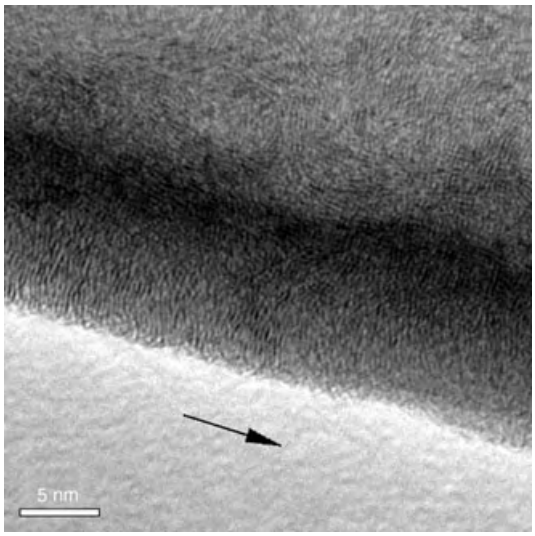

Figure 4. HR-TEM image of carbon nanotube prepared from HPB-C_{12} (**2**). The graphene layers do not orient fully perpendicular to the tube axis. The arrow indicates the tube axis.

Different types of carbon nanotubes were observed in our products, for example, the tubes with triangular and quadrate shapes as shown in Figure 1 b. Some Y-shaped tubes were also observed after complete removal of the template. These special types of carbon nanotubes were formed following the types of channels within the template. In fact, different shapes of carbon tubes have been prepared from different types of template by chemical vapor deposition (CVD) methods.[14] Thus, by using differently shaped template channels,[14,15] different types of carbon nanotubes with controlled orientation of graphene sheets can be synthesized following our method.

In conclusion, a novel molecular engineering approach has been developed to prepare carbon nanotubes with controlled orientation of graphene layers from graphitic molecules preorganized in a porous template. Graphitic carbon nanotubes were synthesized successfully in the absence of metal catalysts, and the graphene layers of the as-formed carbon nanotubes were orderly stacked and

 © 2005 Wiley-VCH Verlag GmbH & Co. KGaA, Weinheim

oriented perpendicular to the tube axis. The orthogonally oriented carbon nanotubes are of interest for use as chemical or biological sensors, absorbants, catalyst supports, nanoreactors, battery electrodes, and many other microscale investigations. Because of the controllable orientation of graphene layers and alignment, shape, and size of the tubes, our process should also allow fabrication of special carbon materials for microelectronic devices.

Experimental Section

Anodic alumina membranes were purchased from Whatman International Ltd. The average pore size of the membrane was around 100 nm (evaluated by SEM) and the thickness was 60 μm. The membranes were washed in ethanol with sonication for 10 min and then dried under vacuum. Compounds **1** and **2** were synthesized according to procedures described elsewhere[16] and then dissolved separately in dichloromethane (10–30 mg mL^{-1}). The solution of **1** or **2** was then added dropwise onto the membrane surface. The amount of substance loaded in the membrane can be controlled by the concentration of the solution and by the volume of solution applied to the membrane. All heat treatments of the samples were carried out in quartz ampoules sealed under high vacuum in an electric furnace. Alumina templates were removed by dissolving the templates in a solution of NaOH (3 M). The template-free samples were washed with water and ethanol, dried under vacuum, and submitted for SEM and TEM measurements. SEM measurements were performed on a LEO 1530 field emission scanning electron microscope. High resolution TEM studies were conducted on an EM420 electron microscope at an operating voltage of 120 kV. The sample was dispersed in ethanol under ultrasonication, and the suspension was dropped onto a copper grid. TGA measurements were performed on a Mettler TG50 thermobalance. Raman spectra were recorded with a Bruker RFS100/S spectrometer.

Received: June 16, 2004
Revised: January 19, 2005
Published online: February 25, 2005

Keywords: aluminum · carbon · mesoporous materials · nanostructures · template synthesis

[1] S. Iijima, *Nature* **1991**, *354*, 56.
[2] For recent reviews, see: a) S. Subramoney, *Adv. Mater.* **1998**, *10*, 1157; b) P. M. Ajayan, *Chem. Rev.* **1999**, *99*, 1787; c) F. T. Edelmann, *Angew. Chem.* **1999**, *111*, 1473; *Angew. Chem. Int. Ed.* **1999**, *38*, 1381; d) L. Dai, A. W. H. Mau, *Adv. Mater.* **2001**, *13*, 899; e) R. Andrews, D. Jacques, D. Qian, T. Rantell, *Acc. Chem. Res.* **2002**, *35*, 1008; f) P. Avouris, *Acc. Chem. Res.* **2002**, *35*, 1026; g) Y. Sun, K. Fu, Y. Lin, W. Huang, *Acc. Chem. Res.* **2002**, *35*, 1096; h) M. Terrones, *Annu. Rev. Mater. Res.* **2003**, *33*, 419; i) R. H. Baughman, A. A. Zakhidov, W. A. Heer, *Science* **2002**, *297*, 787; j) H. Dai, *Acc. Chem. Res.* **2002**, *35*, 1035; k) O. Zhou, H. Shimoda, B. Gao, S. Oh, L. Fleming, G. Yue, *Acc. Chem. Res.* **2002**, *35*, 1045; l) A. Hirsch, *Angew. Chem.* **2002**, *114*, 1933; *Angew. Chem. Int. Ed.* **2002**, *41*, 1853.
[3] a) M. Endo, K. Takeuchi, K. Kobori, K. Takahashi, H. W. Kroto, A. Sarkar, *Carbon* **1995**, *33*, 873; b) R. V. Parthasarathy, K. L. N. Phani, C. R. Martin, *Adv. Mater.* **1995**, *7*, 896; c) T. Kyotani, L. Tsai, A. Tomita, *Chem. Mater.* **1996**, *8*, 2109; d) C. N. R. Rao, A. Govindaraj, *Acc. Chem. Res.* **2002**, *35*, 998; e) V. S. Iyer, P. C. Vollhardt, R. Wilhelm, *Angew. Chem.* **2003**, *115*, 4515; *Angew. Chem. Int. Ed.* **2003**, *42*, 4379; f) B. Rajesh, K. R. Thampi, J. M. Bonard, N. Xanthopoulos, H. J. Mathieu, B. Viswanathan, *J. Phys. Chem. B* **2003**, *107*, 2701; g) S. Rahman, H. Yang, *Nano. Lett.* **2003**, *3*, 439; h) A. Amma, B. Razavi, S. K. St. Angelo, T. S. Mayer, T. E. Mallouk, *Adv. Funct. Mater.* **2003**, *13*, 365.
[4] a) A. Chambers, N. M. Rodriguez, R. T. K. Baker, *J. Phys. Chem.* **1995**, *99*, 10581; b) N. M. Rodriguez, A. Chambers, R. T. K. Baker, *Langmuir* **1995**, *11*, 3862; c) J. M. Bonard, H. Kind, T. Stöckli, L. O. Nilsson, *J. Solid State Electrochem.* **2001**, *45*, 893.
[5] a) R. Andrews, D. Jacques, D. Qian, E. C. Dickey, *Carbon* **2001**, *39*, 1681; b) R. C. Haddon, *Acc. Chem. Res.* **2002**, *35*, 997; c) R. G. Ding, G. Q. Lu, Z. F. Yan, M. A. Wilson, *J. Nanosci. Nanotechnol.* **2001**, *1*, 7.
[6] a) S. Jeong, O. Lee, K. Lee, *Chem. Mater.* **2002**, *14*, 1859; b) G. Che, B. B. Lakshmi, C. R. Martin, E. R. Fisher, *Chem. Mater.* **1998**, *10*, 260; c) J. S. Suh, J. S. Lee, *Appl. Phys. Lett.* **1999**, 75, 2047; d) J. Li, M. Moskovits, T. L. Haslett, *Chem. Mater.* **1998**, *10*, 1963; e) E. J. Bae, W. B. Choi, K. S. Jeong, J. U. Chu, G. S. Park, S. Song, I. K. Yoo, *Adv. Mater.* **2002**, *14*, 277; f) F. Zheng, L. Liang, Y. Gao, J. H. Sukamto, C. L. Aardahl, *Nano Lett.* **2002**, *2*, 729; g) H. Hou, D. H. Reneker, *Adv. Mater.* **2004**, *16*, 69.
[7] a) Y. C. Sui, D. R. Acosta, J. A. Gonzalez-Leon, A. Bermudez, J. Feuchtwanger, B. Z. Cui, J. O. Flores, J. M. Saniger, *J. Phys. Chem. B* **2001**, *105*, 1523; b) G. L. Hornyak, A. C. Dillon, P. A. Parilla, J. J. Schneider, N. Czap, K. M. Jones, F. S. Fasoon, A. Mason, M. J. Heben, *Nanostruct. Mater.* **1999**, *12*, 83; c) G. Che, B. B. Lakshmi, E. R. Fisher, C. R. Martin, *Nature* **1998**, *393*, 346.
[8] a) R. Hurt, G. Krammer, G. Crawford, K. Jian, C. Rulison, *Chem. Mater.* **2002**, *14*, 4558; b) K. Jian, H. Shim, A. Schwartzman, G. P. Crawford, R. H. Hurt, *Adv. Mater.* **2003**, *15*, 164.
[9] a) A. Tracz, J. K. Jeszka, M. D. Watson, W. Pisula, K. Müllen, T. Pakula, *J. Am. Chem. Soc.* **2003**, *125*, 1682; b) A. M. van de Craats, N. Stutzmann, O. Bunk, M. M. Nielsen, M. D. Watson, K. Müllen, H. D. Chanzy, H. Sirringhaus, R. H. Friend, *Adv. Mater.* **2003**, *15*, 495; c) J. Wu, M. D. Watson, L. Zhang, Z. Wang, K. Müllen, *J. Am. Chem. Soc.* **2004**, *126*, 177; d) C. D. Simpson, J. Wu, M. D. Watson, K. Müllen, *J. Mater. Chem.* **2004**, *14*, 494.
[10] L. Gherghel, C. Kübel, G. Lieser, H. J. Räder, K. Müllen, *J. Am. Chem. Soc.* **2002**, *124*, 13130.
[11] I. Fischbach, T. Pakula, P. Minkin, A. Fechtenkötter, K. Müllen, H. W. Spiess, *J. Phys. Chem. B* **2002**, *106*, 6408.
[12] a) M. Steinhart, J. H. Wendorff, A. Greiner, R. B. Wehrspohn, K. Nielsch, J. Schilling, J. Choi, U. Gösele, *Science* **2002**, *296*, 1997; b) M. Steinhart, R. B. Wehrspohn, U. Gösele, J. H. Wendorff, *Angew. Chem.* **2004**, *116*, 1356; *Angew. Chem. Int. Ed.* **2004**, *43*, 1334.
[13] Z. Tomovic, M. D. Watson, K. Müllen, *Angew. Chem.* **2004**, *116*, 773; *Angew. Chem. Int. Ed.* **2004**, *43*, 755.
[14] a) J. Li, C. Papadopoulos, J. Xu, *Nature* **1999**, *402*, 253; b) T. Yanagishita, M. Sasaki, K. Nishio, H. Masuda, *Adv. Mater.* **2004**, *16*, 429.
[15] a) S. Rahman, H. Yang, *Nano Lett.* **2003**, *3*, 439; b) J. S. Lee, G. H. Gu, H. Kim, K. S. Jeong, J. Bae, J. S. Suh, *Chem. Mater.* **2001**, *13*, 2387.
[16] A. Fechtenkötter, K. Saalwächter, M. A. Harbison, K. Müllen, H. W. Spiess, *Angew. Chem.* **1999**, *111*, 3224; *Angew. Chem. Int. Ed.* **1999**, *38*, 3039.

 © 2005 Wiley-VCH Verlag GmbH & Co. KGaA, Weinheim

Polymer Membranes

Negatively Thermoresponsive Membranes with Functional Gates Driven by Zipper-Type Hydrogen-Bonding Interactions**

Liang-Yin Chu, Yan Li, Jia-Hua Zhu, and Wen-Mei Chen*

Membranes with porous substrates and functional gates that are responsive to environmental stimuli are attracting increasing interest from various fields. Their permeation properties can be controlled or adjusted by the gates according to the external chemical and/or physical environment, and they may find various applications e.g. in controlled drug delivery, bioseparation, chemical separation, water treatment, tissue engineering, and as chemical sensors. The functional gates for stimuli-responsive membranes serve as chemical valves, and have been reported to act in response to changes in environmental temperature,[1–5] pH,[5–10] ionic strength,[11] glucose concentration,[12,13] electric field,[14] light,[15] redox properties,[16] or different molecules.[17–19] There are many cases in which environmental temperature fluctuations occur naturally, and in which the temperature stimuli can be easily designed and artificially controlled; therefore much attention has recently been focused on thermoresponsive membranes.[2–5] Up to now, almost all of the thermoresponsive gating membranes have featured positively thermoresponsive characteristics, that is, the membrane permeability increases with increasing environmental temperature, because all of the thermoresponsive functional gates were constructed from poly(*N*-isopropylacrylamide) (PNIPAM).[1–5] In these cases, the membrane pores change from a "closed" to an "open" state when the environmental temperature increases from below the lower critical solution temperature (LCST) of PNIPAM to above the LCST, as a result of the swelling/shrinking conformational change of the polymer. In certain applications, however, an inverse mode of the thermoresponsive gating behavior of the membranes is preferred. Here we report a novel family of thermoresponsive gating membranes with negatively thermoresponsive gating characteristics, that is, "opening" of the membrane pores is induced by a decrease rather than an increase in temperature.

The concept of the proposed negatively thermoresponsive gating membrane and the fabrication procedure are schematically illustrated in Figure 1. The functional gates of the membrane are constructed from thermoresponsive interpenetrating polymer networks (IPNs) composed of polyacrylamide (PAAM) and poly(acrylic acid) (PAAC). It is known that PAAM and PAAC form complexes in solution through hydrogen-bonding interactions.[20] The resultant cooperative "zipping" interactions between the polymer chains indicate that the PAAM/PAAC-based IPN hydrogels have a thermoresponsive volume phase transition characteristic that is the reverse of that of PNIPAM, that is, the hydrogel swelling is induced by an increase rather than a decrease in temperature.[21–23] PAAC forms intermolecular hydrogen bonds with PAAM when the environmental temperature is lower than the upper critical solution temperature (UCST) of the

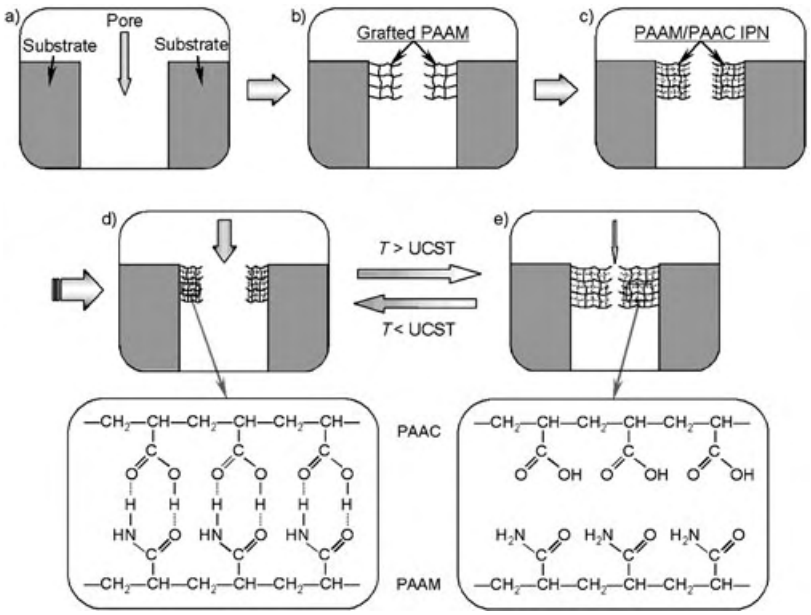

Figure 1. Schematic illustration of the concept of the proposed negatively thermoresponsive gating membrane and the fabrication procedure. The functional gates of the membrane are thermoresponsive interpenetrating polymer networks (IPNs) composed of polyacrylamide (PAAM) and poly(acrylic acid) (PAAC), in which the volume phase transition is driven by the cooperative "zipping" interactions between the molecules that result from hydrogen-bonding interactions. a) Porous membrane substrates. b) Membranes with grafted PAAM gates prepared by a plasma-graft pore-filling polymerization method. c) Membranes with PAAM/PAAC-based IPN gates prepared by sequential IPN synthesis. d) The pores of the membranes "open" because the functional gates are in their shrunken state at temperatures below the upper critical solution temperature (UCST) as a result of PAAM/PAAC complex formation by hydrogen-bonding interactions. e) The membrane pores "close" because the PAAM/PAAC-based IPN gates are in their swollen state at temperatures above the UCST as a result of complex dissociation by the breakage of hydrogen bonds.

[*] Prof. L.-Y. Chu, Dr. Y. Li, Prof. J.-H. Zhu, Prof. W.-M. Chen
School of Chemical Engineering, Sichuan University
Chengdu, Sichuan 610065 (China)
Fax: (+86) 28-8540-4976
E-mail: chuly@scu.edu.cn

[**] The National Natural Science Foundation of China (20206019, 50373029), the Trans-Century Training Program Foundation for the Talents by the Ministry of Education of China (2002-48), and Sichuan Youth Science and Technology Foundation for Distinguished Young Scholars (03ZQ026-41) are acknowledged for supporting this research.

Supporting information for this article is available on the WWW under http://www.angewandte.org or from the author.

 © 2005 Wiley-VCH Verlag GmbH & Co. KGaA, Weinheim DOI: 10.1002/anie.200462687

PAAM/PAAC-based IPN gel, and the IPN hydrogels have a shrunken state as a result of the interaction between two polymer chains, which is the so-called chain–chain zipper effect. However, when the environmental temperature is higher than the UCST of the IPN gel, intermolecular PAAM–PAAC hydrogen bonds are disrupted and the IPN hydrogels become swollen. Therefore, the proposed membrane gates shrink at temperatures below the UCST as a result of PAAM–PAAC complex formation by hydrogen-bonding interactions, and swell at temperatures above the UCST as a result of PAAM–PAAC complex dissociation. Consequently, the membrane pores change from an "open" gate to a "closed" gate when the temperature increases from below the UCST above the UCST.

Thermoresponsive membranes with PAAM/PAAC-based IPN gates were prepared by a method of sequential IPN synthesis, in which cross-linked PAAM grafted in the pores of porous nylon 6 (N6) membranes and PAAC gels were synthesized as an initial gel matrix and as secondary gels, respectively (see Supporting Information). Briefly, plasma-graft pore-filling polymerization was employed to graft cross-linked PAAM gates in the pores of the substrates according to the method described previously.[3,10,13,17] The PAAM-grafted N6 membranes were swollen, immersed in aqueous acrylic acid (AAC) solution containing initiator and cross-linker, and the AAC monomer was polymerized and cross-linked within the grafted PAAM matrix gels in the pores to form PAAM/PAAC-based IPN gates. Scanning electron microscope (SEM) images and X-ray photoelectron spectroscopy (XPS) were used to confirm the structure of the membrane and the IPN synthesis. Pressure-driven filtration experiments were carried out to determine the temperature dependence of the hydraulic permeability of membranes with PAAM/PAAC-based IPN gates.

Figure 2 shows SEM images of the cross-sectional views of the virgin porous N6 substrate and membranes with grafted PAAM gates and PAAM/PAAC-based IPN gates. The parameters Y_{PAAM} and Y_{PAAC} are the mass increase ratios of the membrane after PAAM grafting and PAAC synthesis, respectively. It can be seen from the cross sections of the virgin (Figure 2a), PAAM-grafted (Figure 2b), and PAAM/PAAC-based IPN-gated (Figure 2c) membranes that the structures are quite different. After grafting of PAAM onto the inner pore surfaces of the porous N6 membrane, a significant gating layer with a thickness of about 2 μm was formed near the membrane surface. On synthesis of the PAAM/PAAC-based IPN, the gating layer under the membrane surface clearly became denser than that of the PAAM-grafted membrane, while the thickness of the gating layer was almost the same. These microstructures indicate that the PAAM/PAAC-based IPNs were only synthesized in the initial PAAM gel matrix.

Figure 3 shows the XPS O_{1s} core-level spectra of the virgin N6 membrane, the membrane with grafted PAAM gates, and the membrane with PAAM/PAAC-based IPN gates. The spectrum of the N6 membrane can be curve-fitted with a single peak of binding energy (BE) of 531.7 eV for the C=O species. For the membrane with grafted PAAM gates, the peak area of the C=O species is larger than that of the N6 substrate, as a result of the contribution of C=O groups of the

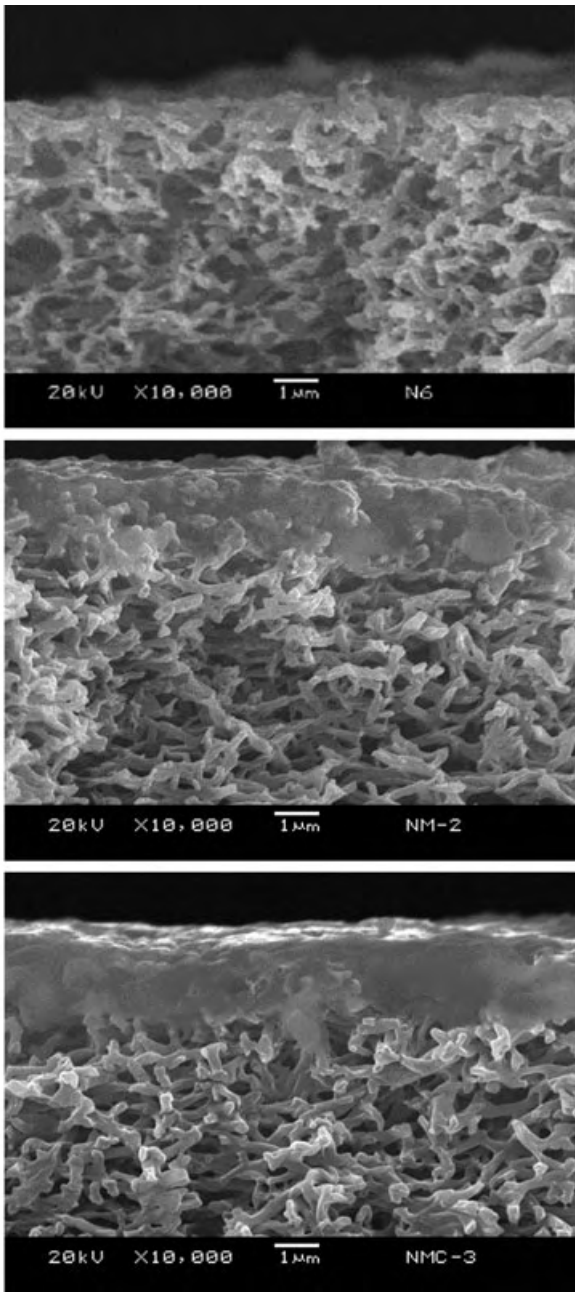

Figure 2. SEM images of the cross sections of a) virgin nylon 6 (N6) substrate membrane, b) membrane with grafted PAAM gates ($Y_{PAAM} = 4.61\%$), and c) membrane with PAAM/PAAC-based IPN gates ($Y_{PAAM} = 4.25\%$ and $Y_{PAAC} = 2.20\%$). Scale bar 1 μm.

grafted PAAM. The O_{1s} core-level spectrum of the membrane with PAAM/PAAC-based IPN gates can be curve-fitted by using two peak components with BEs of 531.8 eV for the C=O species and 533.2 eV for the O–H species. The new peak component at BE 533.2 eV is assigned to the O–H species of the synthesized PAAC polymers in the PAAM/PAAC-based IPN. These experimental observations confirm that the prepared gates of the porous membranes have the expected PAAM/PAAC-based IPN architecture.

Figure 4a–c shows the temperature dependence of hydraulic permeability through the virgin N6 substrate

 © 2005 Wiley-VCH Verlag GmbH & Co. KGaA, Weinheim

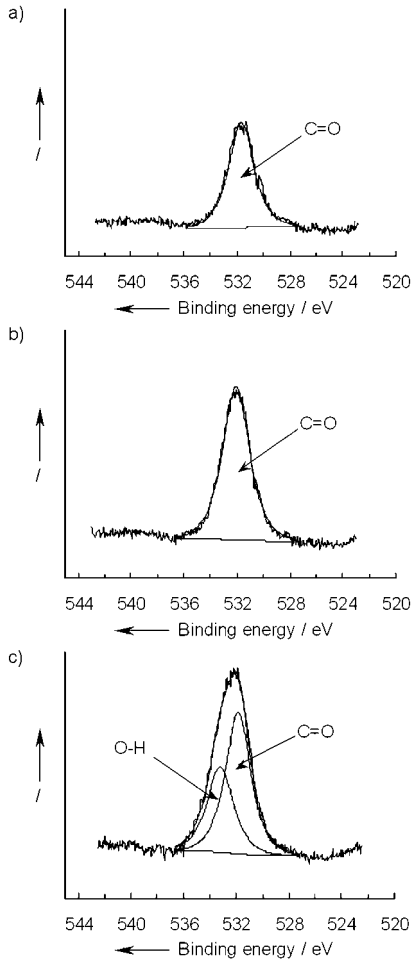

Figure 3. XPS O_{1s} core-level spectra of a) virgin N6 membrane, b) membrane with grafted PAAM gates ($Y_{PAAM} = 7.57\%$), and c) membrane with PAAM/PAAC-based IPN gates ($Y_{PAAM} = 6.94\%$ and $Y_{PAAC} = 7.53\%$).

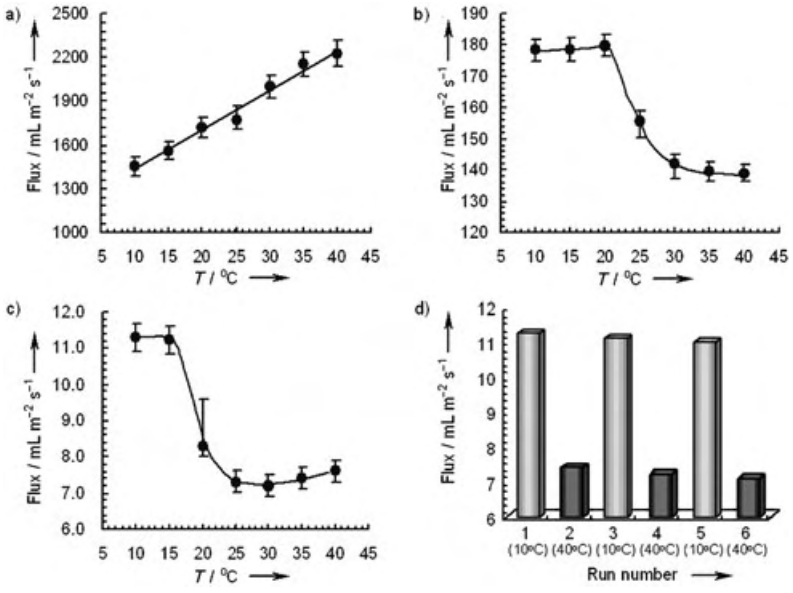

Figure 4. Temperature dependence and reversible thermoresponsive gating characteristics of hydraulic permeability through membranes with PAAM/PAAC-based IPN gates. a) Virgin N6 membrane and b–d) membranes with PAAM/PAAC-based IPN gates. b) $Y_{PAAM} = 2.94\%$ and $Y_{PAAC} = 4.12\%$; c, d) $Y_{PAAM} = 5.01\%$ and $Y_{PAAC} = 4.64\%$.

membrane and the membranes prepared with PAAM/PAAC-based IPN gates. The water flux of the virgin N6 substrate simply increased with increasing environmental temperature, as a consequence of the decreasing viscosity of water with increasing temperature. However, under the same experimental conditions, the temperature-dependent water flux curves of membranes with PAAM/PAAC-based IPN gates were quite different. These membranes exhibited negatively thermoresponsive characteristics, such that the membrane permeability decreased with increasing environmental temperature. The water flux in the temperature range from 10 to 15 °C was much larger than that in the range from 30 to 40 °C. A sharp transition of the hydraulic permeability occurred on going from 20 to 25 °C, which corresponded to the UCST of PAAM/PAAC-based IPN hydrogels.[21–23] The water flux of the membrane dropped rapidly with formation of PAAM/PAAC-based IPN gates in the pores or with increasing Y_{PAAM} and Y_{PAAC} values in the synthesis of IPN gates, which arose from the decrease of the effective mean diameter of the membrane pores. According to Hagen–Poiseuille's law, the water flux of a porous membrane is governed by the fourth power of the pore diameter.[3e,13a] Thus, the conformational change of PAAM/PAAC-based IPN gates constructed on the inner surfaces of membrane pores greatly affects the water flux. Below the UCST, PAAM/PAAC intermolecular complexes are formed by hydrogen-bonding interactions and the chain–chain zipper effect leads to collapse of the IPN and opening of the membrane pores; as a result the hydraulic permeability was large. In contrast, the IPN was in its swollen state at temperatures above the UCST because of PAAM–PAAC complex dissociation due to disruption of hydrogen bonds; therefore, the pores in the membrane were closed by the IPN gates, which resulted in a smaller hydraulic permeability (Figure 1). The thermoresponsive gating characteristics of the prepared membranes were complementary to those of membranes constructed with PNIPAM gates.[1–5]

To verify the reversibility of the IPN gates, pressure-driven filtration experiments were carried out by changing the environmental temperature across the UCST; the temperature was alternately kept at 10 and 40 °C. The reversible thermoresponsive gating characteristics of the membrane with PAAM/PAAC-based IPN gates are shown in Figure 4 d. The thermoresponsive permeability of the membrane was satisfactorily reproducible, which suggests that the IPN gates retained their thermal swelling/shrinking properties intact, even though they underwent repeated temperature changes across the UCST. Thus, reversible thermoresponsive permeation was effectively achieved.

In summary, a novel family of thermoresponsive gating membranes composed of a porous substrate membrane and PAAM/PAAC-based IPN polymers in the pores, which act as thermoresponsive gates, has been successfully developed. The hydraulic perme-

 © 2005 Wiley-VCH Verlag GmbH & Co. KGaA, Weinheim

ability of the membranes exhibits significant negative gating characteristics, that is, the "opening" of the membrane pores is induced by a decrease rather than an increase in the environmental temperature. The membranes with PAAM/PAAC-based IPN gates show satisfactorily reversible and reproducible thermoresponsive permeation characteristics. These gating membranes provide a new mode of behavior for thermoresponsive "smart" or "intelligent" membrane actuators, which is highly attractive for targeting drug delivery systems, chemical separations, and sensors.

Received: November 22, 2004
Published online: February 25, 2005

Keywords: hydrogen bonds · membranes · phase transitions · polymers

[1] a) Y. Okahata, H.-J. Lim, G. Nakamura, S. Hachiya, *J. Am. Chem. Soc.* **1983**, *105*, 4855; b) Y. Okahata, H. Noguchi, T. Seki, *Macromolecules* **1986**, *19*, 493; c) H. Iwata, M. Oodate, Y. Uyama, H. Amemiya, Y. Ikada, *J. Membr. Sci.* **1991**, *55*, 119; d) H. Kubota, N. Nagaoka, R. Katakai, M. Yoshida, H. Omichi, Y. Hata, *J. Appl. Polym. Sci.* **1994**, *51*, 925; e) T. Peng, Y.-L. Cheng, *J. Appl. Polym. Sci.* **1998**, *70*, 2133; f) Y. S. Park, Y. Ito, Y. Imanishi, *Langmuir* **1998**, *14*, 910; g) L. Liang, X. Feng, L. Peurrung, V. Viswanathan, *J. Membr. Sci.* **1999**, *162*, 235.

[2] a) Y.-J. Choi, T. Yamaguchi, S. Nakao, *Ind. Eng. Chem. Res.* **2000**, *39*, 2491; b) N. I. Shtanko, V. Ya. Kabanov, P. Yu. Apel, M. Yoshida, A. I. Vilenskii, *J. Membr. Sci.* **2000**, *179*, 155; c) B. Yang, W. Yang, *J. Membr. Sci.* **2003**, *218*, 247.

[3] a) L.-Y. Chu, S.-H. Park, T. Yamaguchi, S. Nakao, *J. Membr. Sci.* **2001**, *192*, 27; b) L.-Y. Chu, S.-H. Park, T. Yamaguchi, S. Nakao, *Langmuir* **2002**, *18*, 1856; c) L.-Y. Chu, T. Niitsuma, T. Yamaguchi, S. Nakao, *AIChE J.* **2003**, *49*, 896; d) L.-Y. Chu, J.-H. Zhu, W.-M. Chen, T. Niitsuma, T. Yamaguchi, S. Nakao, *Chin. J. Chem. Eng.* **2003**, *11*, 269; e) Y. Li, L.-Y. Chu, J.-H. Zhu, H.-D. Wang, S.-L. Xia, W.-M. Chen, *Ind. Eng. Chem. Res.* **2004**, *43*, 2643.

[4] a) L. Ying, E. T. Kang, K. G. Neoh, *Langmuir* **2002**, *18*, 6416; b) L. Ying, E. T. Kang, K. G. Neoh, K. Kato, H. Iwata, *Macromol. Mater. Eng.* **2003**, *288*, 11.

[5] a) K. Zhang, H. Huang, G. Yang, J. Shaw, C. Yip, X. Y. Wu, *Biomacromolecules* **2004**, *5*, 1248; b) K. Zhang, X. Y. Wu, *Biomaterials* **2004**, *25*, 5281.

[6] a) Y. Osada, K. Honda, M. Ohta, *J. Membr. Sci.* **1986**, *27*, 327; b) Y. Okahata, H. Noguchi, T. Seki, *Macromolecules* **1987**, *20*, 15; c) H. Iwata, T. Matsuda, *J. Membr. Sci.* **1988**, *38*, 185; d) M. A. Islam, A. Dimov, A. L. Malinova, *J. Membr. Sci.* **1992**, *66*, 69; e) R. Israels, D. Gersappe, M. Fasolka, V. A. Roberts, A. C. Balazs, *Macromolecules* **1994**, *27*, 6679; f) M. Ulbricht, *React. Funct. Polym.* **1996**, *31*, 165; g) J. Hautojarvi, K. Kontturi, J. H. Nasman, B. L. Svarfvar, P. Viinikka, M. Vuoristo, *Ind. Eng. Chem. Res.* **1996**, *35*, 450.

[7] a) Y. Ito, S. Kotera, M. Inaba, K. Kono, Y. Imanishi, *Polymer* **1990**, *31*, 2157; b) Y. Ito, M. Inaba, D.-J. Chung, Y. Imanishi, *Macromolecules* **1992**, *25*, 7313; c) Y. Ito, Y. Ochiai, Y. S. Park, Y. Imanishi, *J. Am. Chem. Soc.* **1997**, *119*, 1619; d) Y. Ito, Y. S. Park, Y. Imanishi, *J. Am. Chem. Soc.* **1997**, *119*, 2739.

[8] a) Y. M. Lee, S. Y. Ihm, J. K. Shim, J. H. Kim, C. S. Cho, Y. K. Sung, *Polymer* **1995**, *36*, 81; b) Y. M. Lee, J. K. Shim, *J. Appl. Polym. Sci.* **1996**, *61*, 1245; c) Y. M. Lee, J. K. Shim, *Polymer* **1997**, *38*, 1227; d) J. K. Shim, Y. B. Lee, Y. M. Lee, *J. Appl. Polym. Sci.* **1999**, *74*, 75.

[9] a) M. Nishino, J. Gong, Y. Osada, *Bioseparation* **1999**, *7*, 269; b) T. Peng, Y.-L. Cheng, *J. Appl. Polym. Sci.* **2000**, *76*, 778; c) A. M. Mika, R. F. Childs, J. M. Dickson, *J. Membr. Sci.* **2002**, *206*, 19; d) G. S. Irwan, S. Kuroda, H. Kubota, T. Kondo, *Eur. Polym. J.* **2002**, *38*, 1145; e) V. Smuleac, D. A. Butterfield, D. Bhattacharyya, *Chem. Mater.* **2004**, *16*, 2762; f) Y. Wang, Z. Liu, B. Han, Z. Dong, J. Wang, D. Sun, Y. Huang, G. Chen, *Polymer* **2004**, *45*, 855.

[10] L.-Y. Chu, Y. Li, H.-D. Wang, J.-H. Zhu, W.-M. Chen in *Frontiers on Separation Science and Technology* (Eds.: Z. Tong, S. H. Kim), World Scientific Publishing, Singapore, **2004**, p. 541.

[11] a) J. T. Kim, J. L. Anderson, *J. Membr. Sci.* **1989**, *47*, 163; b) A. M. Mika, R. F. Childs, J. M. Dickson, B. E. McCarry, D. R. Gagnon, *J. Membr. Sci.* **1995**, *108*, 37.

[12] a) Y. Ito, M. Casolaro, K. Kono, Y. Imanishi, *J. Controlled Release* **1989**, *10*, 195; b) S. Cartier, T. A. Horbett, B. D. Ratner, *J. Membr. Sci.* **1995**, *106*, 17.

[13] a) L.-Y. Chu, Y. Li, J.-H. Zhu, H.-D. Wang, Y.-J. Liang, *J. Controlled Release* **2004**, *97*, 43; b) L.-Y. Chu, Y.-J. Liang, W.-M. Chen, X.-J. Ju, H.-D. Wang, *Colloids Surf. B* **2004**, *37*, 9.

[14] a) R. K. Bhaskar, R. V. Sparer, K. J. Himmelstein, *J. Membr. Sci.* **1985**, *24*, 83; b) Y. Ly, Y.-L. Cheng, *J. Membr. Sci.* **1993**, *77*, 99.

[15] D.-J. Chung, Y. Ito, Y. Imanishi, *J. Appl. Polym. Sci.* **1994**, *51*, 2027.

[16] Y. Ito, S. Nishi, Y. S. Park, Y. Imanishi, *Macromolecules* **1997**, *30*, 5856.

[17] L.-Y. Chu, T. Yamaguchi, S. Nakao, *Adv. Mater.* **2002**, *14*, 386.

[18] a) T. Yamaguchi, T. Ito, T. Sato, T. Shinbo, S. Nakao, *J. Am. Chem. Soc.* **1999**, *121*, 4078; b) T. Ito, T. Hioki, T. Yamaguchi, T. Shinbo, S. Nakao, S. Kimura, *J. Am. Chem. Soc.* **2002**, *124*, 7840; c) T. Ito, T. Yamaguchi, *J. Am. Chem. Soc.* **2004**, *126*, 6202; d) T. Ito, Y. Sato, T. Yamaguchi, S. Nakao, *Macromolecules* **2004**, *37*, 3407.

[19] a) B. B. Lakshmi, C. R. Martin, *Nature* **1997**, *388*, 758; b) S. B. Lee, D. T. Mitchell, L. Trofin, T. K. Nevanen, H. Soderlund, C. R. Martin, *Science* **2002**, *296*, 2198.

[20] D. J. Eustace, D. B. Siano, E. N. Drake, *J. Appl. Polym. Sci.* **1988**, *35*, 707.

[21] F. Ilmain, T. Tanaka, E. Kokufuta, *Nature* **1991**, *349*, 400.

[22] a) H. Katono, A. Maruyama, K. Sanui, N. Ogata, T. Okano, Y. Sakurai, *J. Controlled Release* **1991**, *16*, 215; b) H. Katono, K. Sanui, N. Ogata, T. Okano, Y. Sakurai, *Polym. J.* **1991**, *23*, 1179; c) H. Sasase, T. Aoki, K. Katona, K. Sanui, N. Ogata, R. Ohta, T. Kondo, T. Okano, Y. Sakurai, *Makromol. Chem. Rapid Commun.* **1992**, *13*, 577; d) T. Aoki, M. Kawashima, H. Katono, K. Sanui, N. Ogata, T. Okano, Y. Sakurai, *Macromolecules* **1994**, *27*, 947; e) N. Endo, H. Shirota, K. Horie, *Macromol. Rapid Commun.* **2001**, *22*, 593.

[23] a) X.-C. Xiao, L.-Y. Chu, W.-M. Chen, S. Wang, Y. Li, *Adv. Funct. Mater.* **2003**, *13*, 847; b) P. Bouillot, B. Vincent, *Colloid Polym. Sci.* **2000**, *278*, 74; c) J. Chen, L. Yang, M. Wu, Q. Xi, S. He, Y. Li, Y. C. Nho, *Radiat. Phys. Chem.* **2000**, *59*, 313.

 © 2005 Wiley-VCH Verlag GmbH & Co. KGaA, Weinheim

Carboranes

Synthesis, Reactivity, and Structural Characterization of a 14-Vertex Carborane**

*Liang Deng, Hoi-Shan Chan, and Zuowei Xie**

closo-Boranes and carboranes, which have received much attention, are among the simplest cluster systems; their chemistry is dominated by icosahedral molecules with 12 vertices.[1] Carboranes with 13 vertices were unknown until 2003[2] although a series of metallacarboranes of s-, p-, d-, and f-block elements with 13 vertices have been prepared and structurally characterized[3] since the first one was reported in 1971.[4] A few metallacarboranes with 14 vertices are also known.[5] Thus, the question arises as to why the development of supracarborane chemistry is well behind that of the metallacarboranes. One may attribute this fact to the thermodynamic difficulties that arise in building up large carboranes beyond the icosahedron, as suggested by the theoretical calculations on $[B_nH_n]^{2-}$ systems.[6] We believe, on the basis of our own work, that the energies of BH (BR) group additions are not the major issue, rather, the reducing power of the parent *nido*-carborane dianions (*nido*-$[R_2C_2B_{10}H_{10}]^{2-}$) is the key factor for the successful preparation of $C_2B_nH_{n+2}$ when $n > 10$.

It has been well documented that "carbon-atoms-apart" (CAp) *nido*-$[R_2C_2B_{10}H_{10}]^{2-}$ ions are very strong reducing agents that can reduce M^{4+} (M = Group 4 metal atom) and Ln^{3+} (Ln = Sm, Eu, Yb) to the corresponding divalent species,[7,8] but are inert toward Group 1 metals.[9] Conversely, "carbon-atoms-adjacent" (CAd) *nido*-$[R_2C_2B_{10}H_{10}]^{2-}$ ions do react with lithium metal to generate CAd *arachno*-$[R_2C_2B_{10}H_{10}]^{4-}$ ions,[10] which suggests that CAp *nido*-$[R_2C_2B_{10}H_{10}]^{2-}$ ions are more powerful reducing agents than their CAd counterparts. In fact, there are two competitive reactions between *nido*-$[R_2C_2B_{10}H_{10}]^{2-}$ ions and $R'BX_2$ (R′ = H, aryl; X = halide): redox and capping reactions. Lowering the reducing power of *nido*-$[R_2C_2B_{10}H_{10}]^{2-}$ ions and the oxidizing ability of $R'BX_2$ is critical for the preparation of supracarboranes. In this regard, we suggest that the isolation of the first carborane with 13 vertices[2a] should be attributed to the relatively weaker reducing power of CAd *nido*-[1,2-{*o*-$C_6H_4(CH_2)_2$}-1,2-$C_2B_{10}H_{10}]^{2-}$.[10] We wondered if such a cage-opening and boron-insertion would be applicable to the CAd *arachno*-carborane tetraanions bearing both six- and five-membered bonding faces that were prepared recently in our laboratory.[10] Such a methodology may lead to the formation of carboranes with 14 vertices in one reaction. Herein we report the synthesis, reactivity, and structural characterization of carboranes with 13 and 14 vertices.

Treatment of 1,2-$(CH_2)_3$-1,2-$C_2B_{10}H_{10}$ (**1**)[11] with excess lithium metal in THF at room temperature gave $\{[(CH_2)_3C_2B_{10}H_{10}][Li_4(thf)_5]\}_2$ (**2**) in 85% yield (Scheme 1).

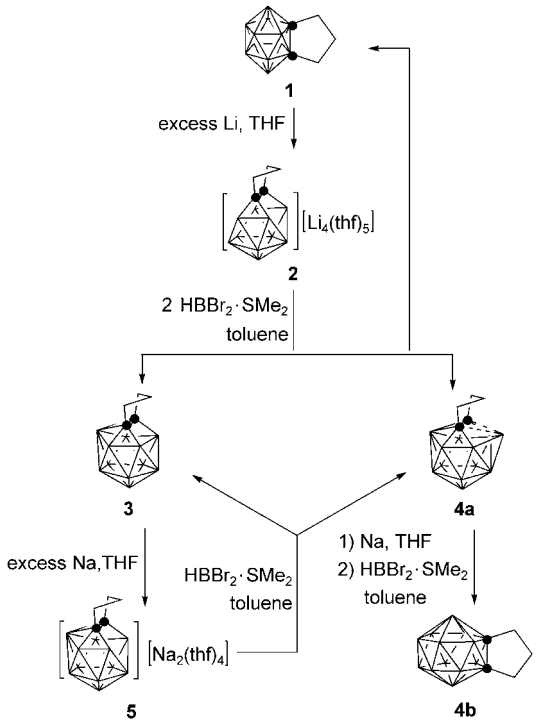

Scheme 1. Synthesis of *closo*-, *nido*-, and *arachno*-carboranes.

This reaction was closely monitored by the ^{11}B NMR spectroscopy as **1** and **2** had distinct splitting patterns. A single-crystal X-ray analysis showed that **2** is a centrosymmetric dimer in which each CAd *arachno*-carborane tetraanion contains both hexagonal and pentagonal bonding faces (Figure 1).[12] The structural motif is the same as in $\{[1,2-\{o-C_6H_4(CH_2)_2\}-1,2-C_2B_{10}H_{10}][Li_4(thf)_6]\}_2$[10] except for the bridging unit, which offers the possibility of adding two new vertices.

The reaction of **2** with 2.5 equivalents of $HBBr_2{\cdot}SMe_2$ in toluene at −78 to 25 °C gave, after chromatographic separation, a 13-vertex carborane $(CH_2)_3C_2B_{11}H_{11}$ (**3**; 32%), a 14-vertex carborane $(CH_2)_3C_2B_{12}H_{12}$ (**4a**; 7%) and a 12-vertex species (**1**; 2%; Scheme 1). Both **3** and **4a** were characterized by ^1H, ^{13}C, and ^{11}B NMR spectroscopies as well as high-resolution mass spectrometry. The ^{11}B NMR spectrum of **3** displayed a 1:5:5 splitting pattern whereas that of **4a** showed a 1:2:2:1:2:1:2:1 splitting pattern in the range 7.8 to −24.7 ppm. The unique resonance at −24.7 ppm could be attributed to the newly added BH vertex, which is less connected. The isolation of **1** and **3** indicated that $HBBr_2{\cdot}SMe_2$ can oxidize **2** to *nido*-$[(CH_2)_3C_2B_{10}H_{10}]^{2-}$ and finally to *closo*-$(CH_2)_3C_2B_{10}H_{10}$ (**1**). The resulting *nido*-$[(CH_2)_3C_2B_{10}H_{10}]^{2-}$ reacts with

[*] L. Deng, H.-S. Chan, Prof. Dr. Z. Xie
Department of Chemistry
The Chinese University of Hong Kong
Shatin, NT, Hong Kong (China)
Fax: (+852) 2603-5057
E-mail: zxie@cuhk.edu.hk

[**] This work was supported by grants from the Research Grants Council of the Hong Kong Special Administration Region (Project No. 4026/02P), Direct Grant (CUHK 2060266) and an anonymous donor who made the donation to the Department of Chemistry at the Chinese University of Hong Kong.

 © 2005 Wiley-VCH Verlag GmbH & Co. KGaA, Weinheim DOI: 10.1002/anie.200462708

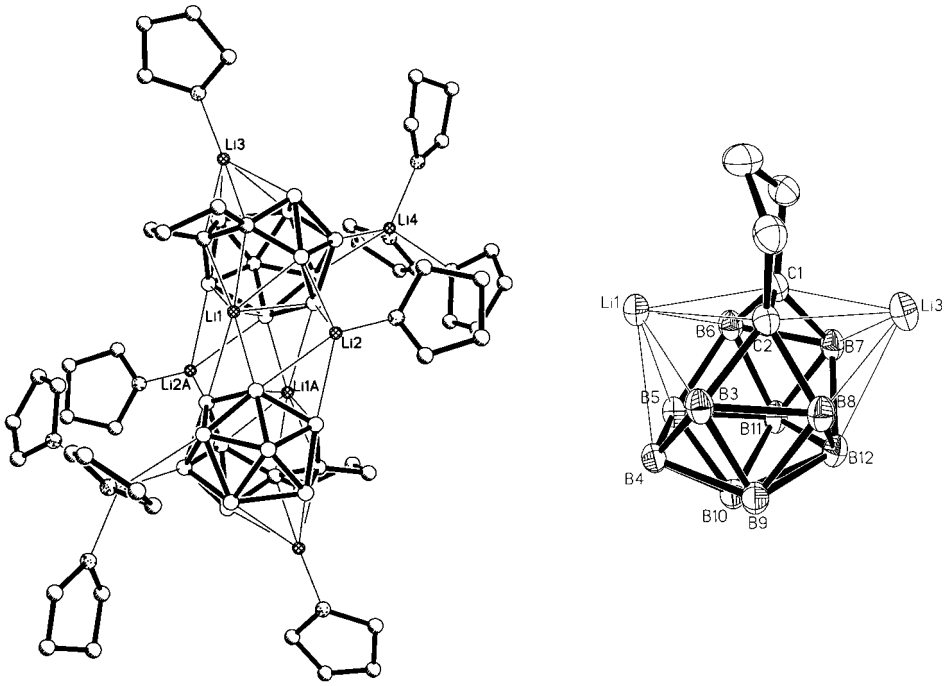

Figure 1. Left: molecular structure of **2**. Right: bonding interactions between Li^+ ions and the open faces of **2**. Selected bond lengths [Å]: C1–C2 1.560(4), B12–B7 1.898(5), B12–B8 1.888(5), B7–C1 1.625(4), B8–C2 1.619(4), C1–B6 1.640(4), B6–B5 1.761(5), B5–B4 1.768(5), B4–B3 1.753(5), B3–C2 1.635(4), av Li3–cage atom 2.257(6), av Li1–cage atom 2.298(6).

$HBBr_2{\cdot}SMe_2$ to form a new 13-vertex carborane *closo*-$(CH_2)_3C_2B_{11}H_{11}$ (**3**).

These results also clearly showed that CAd *arachno*-carborane tetraanions can react with $HBBr_2{\cdot}SMe_2$ to afford carboranes with 14 vertices. We are uncertain, however, if the two BH vertexes are added simultaneously or sequentially. It is assumed that the addition of the first BH vertex to **2** results in the formation of *nido*-$[(CH_2)_3C_2B_{11}H_{11}]^{2-}$ ion, which can either host the second BH vertex to form **4a** or be oxidized by $HBBr_2{\cdot}SMe_2$ to generate *closo*-carborane **3**. Such an assumption prompted us to examine the property of new 13- and 14-vertex carboranes.

Both **3** and **4a** are stable in air, in moisture, and in refluxing toluene as indicated by the ^{11}B NMR spectroscopy, which suggests that they are thermodynamic products. Compounds **3** and **4a** react readily with excess sodium metal at room temperature to give the corresponding *nido*-carborane dianions, $\{nido\text{-}[(CH_2)_3C_2B_{11}H_{11}][Na_2(thf)_4]\}_n$ (**5**) and presumably *nido*-$[(CH_2)_3C_2B_{12}H_{12}][Na_2(thf)_x]$, respectively. Treatment of **5** with 1.5 equivalents of $HBBr_2{\cdot}SMe_2$ produced **4a** and **3** in 30% and 12% yield, respectively. The resulting *nido*-$[(CH_2)_3C_2B_{12}H_{12}][Na_2(thf)_x]$ reacted with $HBBr_2{\cdot}SMe_2$ to afford a new 14-vertex carborane [*closo*-1,2-$(CH_2)_3$-1,2-$C_2B_{12}H_{12}$] (**4b**) in 37% yield, which indicates that the redox reaction was favored (Scheme 1). These results show that **4a** and **4b** are not thermally interchangeable but **4a** can be converted into **4b** through a redox reaction. Compounds **4a** and **4b** have identical molecular masses but the splitting pattern of the ^{11}B NMR spectrum of **4b** is much simpler than that of **4a**, which suggests that they are isomers and **4b** has a much higher symmetry than **4a**.

X-ray analyses revealed that **5** is a coordination polymer in which $[Na(thf)_2]^+$ ions link *nido*-carborane cages to form zigzag polymeric chains (Figure 2).[12] After careful examination of the cage structures in **2** and **5**, we conclude that if the formation of **4a** proceeds by a stepwise mechanism, the first BH vertex adds to the open six-membered bonding face and the second BH vertex then adds to the five-membered bonding face to form **4a**, which has a long B–C bond as depicted in Figure 3. The molecular structure of **3** is similar to that of the anion in **5**, but the B2–B2A bond length of **3** is within the expected range for a normal B–B bond and is the same as that previously reported for a carborane with 13 vertices.[2] Compound **3** accepts two electrons from Na metal to break the B2–B2A bond to form **5**

Single-crystal X-ray analyses showed that **4b** is a bicapped hexagonal antiprism (Figure 4),[12] with a geometry similar to that predicted for $[B_{14}H_{14}]^{2-}$ by computation.[6c] All twenty-four faces are triangulated, with B4 and B4A being seven-coordinated. The average separation of B4 from its connecting vertexes is 1.902(3) Å, the apical B4 is 0.84 Å above the hexagonal plane formed by C1, B3, B6, B7, B5A, and B2A, which is less than the corresponding distance of 0.94 Å observed in icosahedral *o*-carborane.[13] The distance between the two hexagonal planes (1.51 Å) is comparable with that found in icosahedral *o*-carborane (1.50 Å).[13]

In conclusion, we have demonstrated that two BH vertexes can be added to CAd *arachno*-carborane tetraanions in one reaction to give the first 14-vertex *closo*-carborane, the largest carborane presently known. The reactivity of the 13- and 14-vertex *closo*-carboranes has also been examined for the first time. This work suggests that the energies of BH

 © 2005 Wiley-VCH Verlag GmbH & Co. KGaA, Weinheim

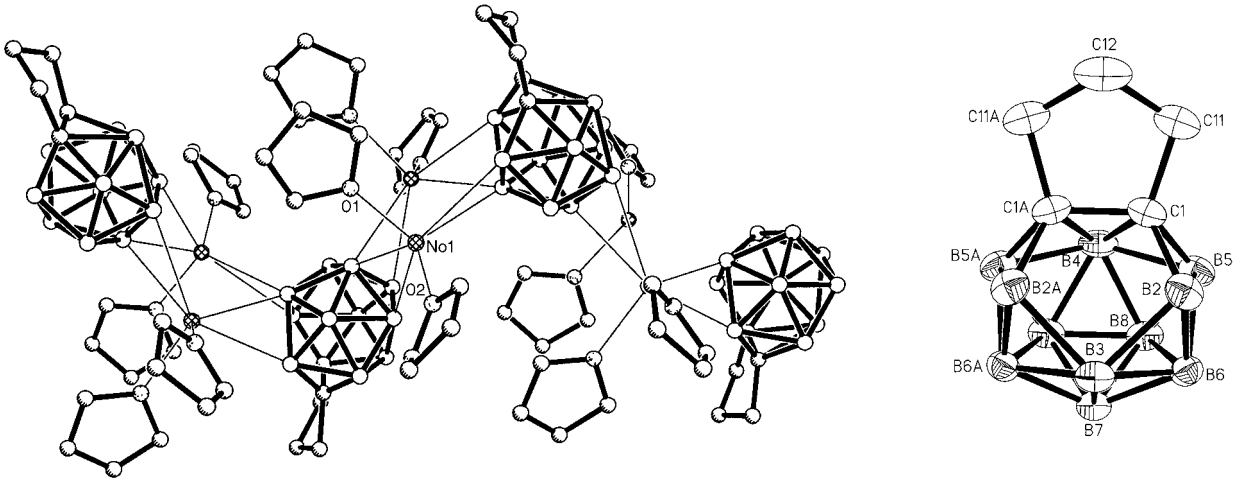

Figure 2. Left: a portion of the infinite polymeric chains in **5**. Right: structure of the anion in **5**. Selected bond lengths [Å]: C1–C1A 1.529(8), C1–B2 1.557(6), B3–B2 1.903(6), B3–B2A 1.903(6), B2A–C1A 1.557(6), B2···B2A 2.677(6).

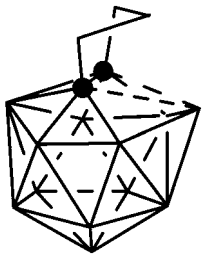

Figure 3. Proposed molecular structure of **4a**.

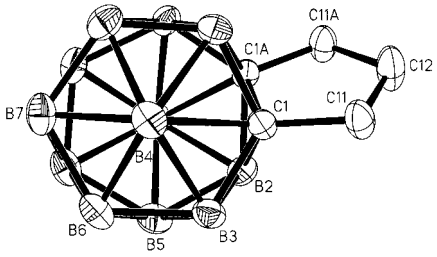

Figure 4. Molecular structure of **4b**. Selected bond lengths [Å]: C1–C1A 1.599(3), B4–C1 1.963(2), B4–B3 1.911(3), B4–B6 1.852(3), B4–B7 1.910(3).

group additions are overstated, and the key issue for the synthesis of supracarboranes is how to block the redox reactions between carborane anions and RBX_2 reagents. It is anticipated that carboranes $C_2B_nH_{n+2}$ with $n > 12$ may be prepared as long as these redox reactions can be suppressed.

Experimental Section

2: Finely cut Li metal (1.80 g, 200 mmol) was added to a solution of **1** (5.52 g, 30.0 mmol) in THF (100 mL)[11], and the mixture was stirred at room temperature for one day to give a red solution. Removal of excess Li and THF yielded a pale-yellow solid. Recrystallization from THF afforded **2** as colorless crystals (14.6 g, 85%). ^{1}H NMR (300 MHz, [D$_5$]pyridine): $\delta = 3.64$ (m, 20H), 1.62 (m, 20H, THF), 2.99 (m, 2H), 2.84 (m, 2H, $CH_2CH_2CH_2$), 1.94 ppm (m, 2H, $CH_2CH_2CH_2$); ^{13}C NMR (75 MHz, [D$_5$]pyridine): $\delta = 67.19$, 25.15 (THF), 45.05 ($CH_2CH_2CH_2$), 28.98 ppm ($CH_2CH_2CH_2$), the cage carbons were not observed; ^{11}B NMR (128 MHz, [D$_5$]pyridine): $\delta =$ 7.71 (2), 3.15 (2), −1.63 (3), −12.93 (1), −16.54 (1), −18.00 ppm (1); IR (KBr): $\tilde{\nu} = 2510$ (vs), 2427 (vs), 2355 cm^{-1} (s) (BH) ; elemental analysis calcd (%) for $C_{21}H_{48}B_{10}Li_4O_4$ (**2**–THF): C 50.40, H 9.67; found: C 50.01, H 9.86.

3 and **4a**: $HBBr_2{\cdot}SMe_2$ (1.0 M in dichloromethane, 75.0 mL, 75.0 mmol) at −78 °C was slowly added to a suspension of **2** (17.2 g, 30.0 mmol) in toluene (100 mL), and the mixture was stirred at this temperature for 1 h and at room temperature for a further 6 h. Removal of the precipitate by filtration and solvents by evaporation gave a brown sticky solid. Chromatographic separation (SiO_2, 300–400 mesh, *n*-hexane) afforded **1** (0.12 g, 2%), **3** (1.88 g, 32%), and **4a** (0.44 g, 7%) as white solids. **3**: ^{1}H NMR (300 MHz, $CDCl_3$): $\delta = 3.26$ (t, $J = 7.5$ Hz, 4H, $CH_2CH_2CH_2$), 2.18 ppm (m, 2H, $CH_2CH_2CH_2$); ^{13}C NMR (100 MHz, $CDCl_3$): $\delta = 49.11$ ($CH_2CH_2CH_2$), 25.55 ppm ($CH_2CH_2CH_2$), resonances from the cage carbon atoms were not observed; ^{11}B NMR (128 MHz, $CDCl_3$): $\delta = 3.52$ (1), 0.96 (5), −1.19 ppm (5); IR (KBr): $\tilde{\nu} = 2570$ cm^{-1} (vs) (BH); HRMS: calcd for $[C_5H_{17}B_{11}]^+$, *m*/*z*: 195.2457; found: 195.2455. For **4a**: ^{1}H NMR (300 MHz, $CDCl_3$): $\delta = 3.15$ (m, 4H, $CH_2CH_2CH_2$), 2.31 ppm (m, 2H, $CH_2CH_2CH_2$); ^{13}C NMR (100 MHz, $CDCl_3$): $\delta = 40.73$ ($CH_2CH_2CH_2$), 25.88 ppm ($CH_2CH_2CH_2$), resonances from the cage carbon atoms were not observed; ^{11}B NMR (128 MHz, $CDCl_3$): $\delta =$ 7.80 (1), 5.64 (2), 2.87 (2), −4.23 (1), −6.39 (2), −9.29 (1), −12.34 (2), −24.73 ppm (1); IR (KBr): $\tilde{\nu} = 2566$ cm^{-1} (vs) (BH) ; HRMS: calcd for $[C_5H_{18}B_{12}]^+$, *m*/*z*: 208.2592; found: 208.2583.

Treatment of **5** (3.20 g, 4.0 mmol) with $HBBr_2{\cdot}SMe_2$ (6.0 mL of 1.0 M in dichloromethane, 6.0 mmol) in toluene (20 mL) by using the above procedure gave **3** (0.09 g, 12%) and **4a** (0.26 g, 30%).

4b: Finely cut Na metal (0.20 g, 8.70 mmol) was added to a solution of **4a** (0.30 g, 1.44 mmol) in THF (10 mL) and the mixture was stirred at room temperature for one day to give a yellow solution. Removal of excess Na metal by filtration and THF by evaporation afforded a pale yellow solid, presumably *nido*-$[(CH_2)_3C_2B_{12}H_{12}][Na_2(thf)_x]$. Toluene (10 mL) was then added to this solid to give a yellow suspension. $HBBr_2{\cdot}SMe_2$ (3.0 mL of 1.0 M in dichloromethane, 3.0 mmol) was slowly added to the suspension at −78 °C, and the mixture was stirred at this temperature for 1 h, and then at room temperature for 6 h. Chromatographic separation gave **4b** as a white solid (0.11 g, 37%). Single crystals suitable for X-ray analysis were obtained by recrystallization from *n*-hexane. ^{1}H NMR (300 MHz, $CDCl_3$): $\delta = 2.89$ (br, 4H, $CH_2CH_2CH_2$), 2.25 ppm (br, 2H,

 © 2005 Wiley-VCH Verlag GmbH & Co. KGaA, Weinheim

$CH_2CH_2CH_2$); ^{13}C NMR (75 MHz, $CDCl_3$): $\delta = 42.96$ ($CH_2CH_2CH_2$), 28.86 ppm ($CH_2CH_2CH_2$), the cage carbons were not observed; ^{11}B NMR (128 MHz, $CDCl_3$): $\delta = 4.48$ (2), 0.14 (2), −2.85 (4), −4.17 (2), −16.78 ppm (2); IR (KBr): $\tilde{\nu} = 2555\ cm^{-1}$ (vs) (BH); HRMS: calcd for $[C_5H_{18}B_{12}]^+$, m/z: 207.2629; found: 207.2636.

5: Finely cut Na metal (0.40 g, 17.4 mmol) was added to a solution of **3** (1.00 g, 5.10 mmol) in THF (10 mL) and the mixture was stirred at room temperature for one day to give a clear yellow solution. After removal of excess Na metal by filtration, the resulting yellow solution was concentrated to about 5 mL, to which 4 mL of toluene was added. **5** was obtained as colorless crystals from this solution after one week at room temperature (2.17 g, 80%). ^1H NMR (300 MHz, [D$_5$]pyridine): $\delta = 3.63$ (m, 16H), 1.59 (m, 16H, THF), 2.46 (t, $J = 6.3$ Hz, 4H, $CH_2CH_2CH_2$), 2.25 ppm (m, 2H) ($CH_2CH_2CH_2$); ^{13}C NMR (100 MHz, [D$_5$]pyridine): $\delta = 67.15$, 25.11 (THF), 42.93 ($CH_2CH_2CH_2$), 29.24 ppm ($CH_2CH_2CH_2$), the cage carbons were not observed; ^{11}B NMR (128 MHz, [D$_5$]pyridine): $\delta = 9.01$ (1), −14.67 (5), −24.64 ppm (5); IR (KBr): $\tilde{\nu} = 2501\ cm^{-1}$ (vs) (BH); elemental analysis calcd (%) for $C_{17}H_{41}B_{11}Na_2O_3$ (**5**−THF): C 44.54, H 9.02; found: C 44.20, H 9.03.

Received: November 24, 2004
Published online: February 23, 2005

Keywords: boron · cage compounds · carbon · carboranes · cluster compounds

[1] a) R. N. Grimes, *Advanced Inorganic Chemistry, 6th ed.* (Eds.: F. A. Cotton, G. Wilkinson, C. A. Murillo, M. Bochmann), Wiley-Interscience, New York, **1999**, chap. 5; b) C. A. Reed, *Acc. Chem. Res.* **1998**, *31*, 133; c) M. F. Hawthorne, *Angew. Chem.* **1993**, *105*, 779; *Angew. Chem. Int. Ed. Engl.* **1993**, *32*, 950.

[2] a) A. Burke, D. Ellis, B. T. Giles, B. E. Hodson, S. A. Macgregor, G. M. Rosair, A. J. Welch, *Angew. Chem.* **2003**, *115*, 235; *Angew. Chem. Int. Ed.* **2003**, *42*, 225; b) R. N. Grimes, *Angew. Chem.* **2003**, *115*, 1232; *Angew. Chem. Int. Ed.* **2003**, *42*, 1198.

[3] a) A. K. Saxena, N. S. Hosmane, *Chem. Rev.* **1993**, *93*, 1081; b) R. N. Grimes in *Comprehensive Organometallic Chemistry II*, *Vol. 1* (Eds.: E. W. Abel, F. A. G. Stone, G. Wilkinson), Pergamon, Oxford, **1995**, p. 373; c) R. N. Grimes, *Coord. Chem. Rev.* **2000**, *200/202*, 773; d) Z. Xie, *Coord. Chem. Rev.* **2002**, *231*, 23; e) Z. Xie, *Acc. Chem. Res.* **2003**, *36*, 1; f) N. M. M. Wilson, D. Ellis, A. S. F. Buoyd, B. T. Giles, S. A. Macgregor, G. M. Rosair, A. J. Welch, *Chem. Commun.* **2002**, 464; g) K.-H. Wong, H.-S. Chan, Z. Xie, *Organometallics* **2003**, *22*, 1175.

[4] G. B. Dunks, M. M. McKown, M. F. Hawthorne, *J. Am. Chem. Soc.* **1971**, *93*, 2541.

[5] a) W. J. Evans, M. F. Hawthorne, *J. Chem. Soc. Chem. Commun.* **1974**, 38; b) W. M. Maxwell, R. F. Bryan, E. Sinn, R. N. Grimes, *J. Am. Chem. Soc.* **1977**, *99*, 4016; c) J. R. Pipal, R. N. Grimes, *Inorg. Chem.* **1978**, *17*, 6.

[6] a) L. D. Brown, W. N. Lipscomb, *Inorg. Chem.* **1977**, *16*, 2989; b) J. Bicerano, D. S. Marynick, W. N. Lipscomb, *Inorg. Chem.* **1978**, *17*, 2041; c) J. Bicerano, D. S. Marynick, W. N. Lipscomb, *Inorg. Chem.* **1978**, *17*, 3443; d) P. v. R. Schleyer, K. Najafian, A. M. Mebel, *Inorg. Chem.* **1998**, *37*, 6765.

[7] a) F. Y. Lo, C. E. Strouse, K. P. Callahan, C. B. Knobler, M. F. Hawthorne, *J. Am. Chem. Soc.* **1975**, *97*, 428; b) C. G. Salentine, M. F. Hawthorne, *Inorg. Chem.* **1976**, *15*, 2872; c) W.-C. Kwong, H.-S. Chan, Y. Tang, Z. Xie, *Organometallics* **2004**, *23*, 3098.

[8] a) R. Khattar, M. J. Manning, C. B. Knobler, S. E. Johnson, M. F. Hawthorne, *Inorg. Chem.* **1992**, *31*, 268; b) Z. Xie, S. Wang, Z.-Y. Zhou, T. C. W. Mak, *Organometallics* **1999**, *18*, 1641; c) Z. Xie, Z. Liu, Q. Yang, T. C. W. Mak, *Organometallics* **1999**, *18*, 3603.

[9] K. Chui, H.-W. Li, Z. Xie, *Organometallics* **2000**, *19*, 5447.

[10] a) G. Zi, H.-W. Li, Z. Xie, *Organometallics* **2001**, *20*, 3836; b) G. Zi, H.-W. Li, Z. Xie, *Organometallics* **2002**, *21*, 15415.

[11] T. E. Paxson, M. K. Kaloustian, G. M. Tom, R. J. Wiersema, M. F. Hawthorne, *J. Am. Chem. Soc.* **1972**, *94*, 4882.

[12] Crystal data for **2**: $C_{25}H_{56}B_{10}Li_4O_5$, $M_r = 572.6$, triclinic, space group $P\bar{1}$, $a = 10.788(1)$, $b = 13.079(1)$, $c = 14.710(2)$ Å, $\alpha = 114.82(1)$, $\beta = 102.68(1)$, $\gamma = 97.49(1)°$, $V = 1779(1)$ Å^3, $T = 293$ K, $Z = 2$, $\rho_{calcd} = 1.069\ g\,cm^{-3}$, $2\theta_{max} = 50°$, $\mu(Mo_{K\alpha}) = 0.71073$ Å, absorption corrections applied by using SADABS,[14] relative transmission factors in the range 0.963–0.981. A total of 7950 reflections were collected and led to 4633 unique reflections, 4633 of which with $I > 2\sigma(I)$ were considered as observed, $R_1 = 0.0805$, $wR_2\ (F^2) = 0.2350$. Crystal data for **4b**: $C_5H_{18}B_{12}$, $M_r = 207.9$, orthorhombic, space group $Pnna$, $a = 15.519(1)$, $b = 10.858(1)$, $c = 7.544(1)$ Å, $V = 1271(1)$ Å^3, $T = 293$ K, $Z = 4$, $\rho_{calcd} = 1.086\ g\,cm^{-3}$, $2\theta_{max} = 50°$, $\mu(Mo_{K\alpha}) = 0.71073$ Å, absorption corrections applied by using SADABS,[14] relative transmission factors in the range 0.390–1.000. A total of 6431 reflections were collected and led to 1122 unique reflections, 1122 of which with $I > 2\sigma(I)$ were considered as observed, $R_1 = 0.0602$, $wR_2\ (F^2) = 0.1553$. Crystal data for **5**: $C_{21}H_{49}B_{11}Na_2O_4$, $M_r = 530.5$, orthorhombic, space group $Cmc2_1$, $a = 16.717(1)$, $b = 16.997(1)$, $c = 11.377(1)$ Å, $V = 3233(1)$ Å^3, $T = 293$ K, $Z = 4$, $\rho_{calcd} = 1.090\ g\,cm^{-3}$, $2\theta_{max} = 50°$, $\mu(Mo_{K\alpha}) = 0.71073$ Å, absorption corrections applied by using SADABS,[14] relative transmission factors in the range 0.966–0.983. A total of 8657 reflections were collected and led to 2912 unique reflections, 2912 of which with $I > 2\sigma(I)$ were considered as observed, $R_1 = 0.0694$, $wR_2\ (F^2) = 0.1802$. These structures were solved by direct methods and refined by full-matrix least squares on F^2 by using the SHELXTL/PC crystallographic program.[15] All non-hydrogen atoms were refined anisotropically and all hydrogen atoms were geometrically fixed by using the riding model. CCDC-256419–2564121 contain the supplementary crystallographic data for this paper. These data can be obtained free of charge from the Cambridge Crystallographic Data Centre via www.ccdc.cam.ac.uk/data_request/cif.

[13] R. K. Bohn, M. D. Bohn, *Inorg. Chem.* **1971**, *10*, 2.

[14] G. M. Sheldrick, SADABS: Program for Empirical Absorption Correction of Area Detector Data, University of Göttingen, Germany, **1996**.

[15] G. M. Sheldrick, SHELXTL 5.10 for Windows NT: Structure Determination Software Programs, Bruker Analytical X-ray Systems, Inc., Madison, Wisconsin, USA, **1997**.

 © 2005 Wiley-VCH Verlag GmbH & Co. KGaA, Weinheim

Electrocatalysis

Controlling the Catalytic Activity of Platinum-Monolayer Electrocatalysts for Oxygen Reduction with Different Substrates**

Junliang Zhang, Miomir B. Vukmirovic, Ye Xu, Manos Mavrikakis, and Radoslav R. Adzic**

As the interest for "hydrogen-based economy" grows, the research on its major elements, that is, hydrogen production and storage[1–3] and energy conversion in fuel cells is expanding.[4,5] Electrocatalytic oxygen reduction, the reaction at fuel-cell cathodes, has been the focus of attention because of its slow kinetics and because of the need for better electrocatalysts with decreased platinum content.[6–8] Herein we report the results of a study on the electrocatalytic activity for the oxygen reduction reaction (ORR) of platinum monolayers supported on Au(111), Rh(111), Pd(111), Ru(0001), and Ir(111) surfaces in a 0.1 M $HClO_4$ solution. The experimentally measured electrocatalytic activity of platinum monolayers for the ORR shows a volcano-type dependence on the center of their d-bands as determined by density functional theory (DFT) calculations. The platinum monolayer supported on Pd(111) (denoted by Pt_{ML}/Pd(111)) is at the top of the volcano curve and shows improved ORR activity over pure Pt(111). We demonstrate that this behavior is determined by two opposite trends: while a higher lying d-band center tends to facilitate O–O bond breaking, a lower lying one tends to facilitate bond formation (e.g.: hydrogen addition). Our results suggest that improvement in the overall fuel-cell efficiency can be combined with substantial cost savings that result from using less platinum at the cathode.

The catalytic properties of bimetallic surfaces consisting of metal monolayers on single-crystal metal surfaces have been extensively studied in ultrahigh vacuum[9] and, to a lesser extent, in electrochemical systems.[10–13] In many cases, the formation of a surface metal–metal bond produced significant changes in the electronic properties of the metal overlayer, and pronounced differences were observed in the reactivity of some transition-metal monolayers on various substrates.[9] A description of the activity of metal monolayers has been proposed by Nørskov and co-workers.[14,15] According to these authors, the characteristics of the surface metal d-bands, particularly the weighted center of the d-band (ε_d), play a decisive role in determining surface reactivity. DFT calculations have shown that the binding energies and reactivity of small adsorbates correlate well with the position of ε_d on strained surfaces and metal overlayers,[3,16] in accord with data from numerous experimental studies.[17–20] The framework of that description is implemented herein to elucidate trends governing the behavior of platinum monolayers on other transition-metal surfaces.

Figure 1 shows the rotating disk measurements for O_2 reduction on platinum monolayers on the five different

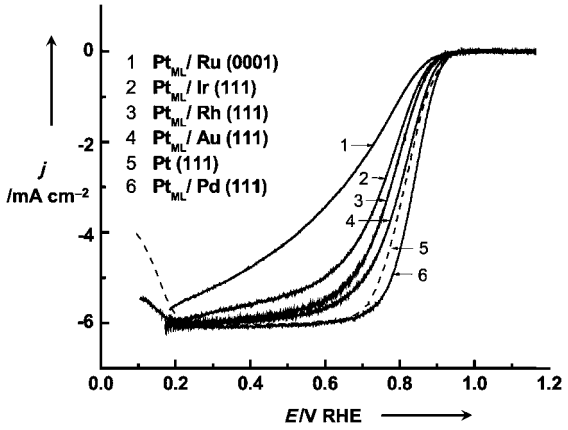

Figure 1. Polarization curves for O_2 reduction on platinum monolayers (Pt_{ML}) on Ru(0001), Ir(111), Rh(111), Au(111), and Pd(111) in a 0.1 M $HClO_4$ solution on a disk electrode. The curve for Pt(111) is taken from ref. [21] and included for comparison. The rotation rate is 1600 rpm, and the sweep rate is 20 $mV s^{-1}$ (50 $mV s^{-1}$ for Pt(111)); j = current density, RHE = reverible hydrogen electrode.

single-crystal surfaces and, for comparison, on a Pt(111) surface.[21] The most active of all surfaces is Pt_{ML}/Pd(111), and the least active is Pt_{ML}/Ru(0001). When the kinetic currents obtained from Koutecky–Levich plots (not shown) for O_2 reduction on the platinum monolayers on various substrates at 0.8 V are plotted as a function of the calculated ε_d (Figure 2), a volcano-like curve is generated, with Pt_{ML}/Pd(111) showing the maximum activity. The use of kinetic current instead of the exchange current density in this plot is preferred because there is no reliable method for determining the exchange current density for the ORR. Other authors have used the same approach.[22] The increase in the O_2 reduction kinetics on Pt_{ML}/Pd(111) compared with that on Pt(111) is surprising since Pt(111) and Pt(110) are the most active electrocatalysts for ORR in $HClO_4$ solutions known to date. In addition, to our knowledge, the finding of this volcano-type dependence of monolayer catalytic activity on the substrate is novel both in the field of electrocatalysis and in catalysis in general. For a number of catalytic reactions, it has been shown that the activity of catalysts exhibits volcano-type dependence on some variable and that the best of the

[*] Y. Xu, Prof. M. Mavrikakis
Department of Chemical and Biological Engineering
University of Wisconsin-Madison
1415 Engineering Drive, Madison, WI 53706 (USA)
Fax: (+1) 608-262-5434
E-mail: manos@engr.wisc.edu
J. Zhang, Dr. M. B. Vukmirovic, Dr. R. R. Adzic
Materials Science Department, Building 555
Brookhaven National Laboratory
Upton, NY 11973 (USA)
Fax: (+1) 631-344-5815
E-mail: adzic@bnl.gov

[**] Work at BNL was supported by the Divisions of Chemical and Material Sciences, U.S. Department of Energy (Contract No. DE-AC02-98CH10886). Work at UW-Madison was supported by NSF-CTS and DOE-BES and used CPU time at NPACI, DOE-NERSC, and PNNL supercomputing centers. Y.X. and M.M. thank Denise Ford, Amit Gokhale, and Shampa Kandoi for their valuable help.

 © 2005 Wiley-VCH Verlag GmbH & Co. KGaA, Weinheim DOI: 10.1002/anie.200462335

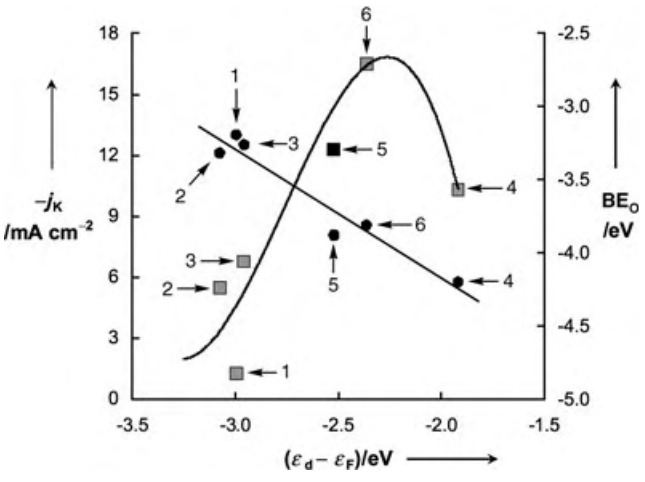

Figure 2. Kinetic currents (j_K; square symbols) at 0.8 V for O_2 reduction on the platinum monolayers supported on different single-crystal surfaces in a 0.1 M $HClO_4$ solution and calculated binding energies of atomic oxygen (BE_O; filled circles) as functions of calculated d-band center ($\varepsilon_d - \varepsilon_F$; relative to the Fermi level) of the respective clean platinum monolayers. The current data for Pt(111) is taken from ref. [21] and included for comparison. Labels: 1. Pt_{ML}/Ru(0001), 2. Pt_{ML}/Ir(111), 3. Pt_{ML}/Rh(111), 4. Pt_{ML}/Au(111), 5. Pt(111), 6. Pt_{ML}/Pd(111).

catalysts strikes a balance between two competing influences.[23–25] To ascertain the competing influences in the present case, it is necessary to have an understanding of the ORR mechanism, which, however, is still the subject of extensive discussions.[7,26–28] Evidence suggests that the first charge-transfer step, or O_2 adsorption with simultaneous charge and proton transfer, appears to be the rate-determining step on pure platinum.[7] The exchange of a second electron with the addition of another proton forms two OH species or hydrogen peroxide (H_2O_2). H_2O_2 can escape into the solution phase, which terminates the reaction in a two-electron process. An additional exchange of two electrons and two protons in reactions with OH or H_2O_2 completes the four-electron reduction of O_2 to H_2O.

Despite the lack of consensus in regard to this mechanism, the four-electron O_2 reduction reaction must involve both the breaking of the O–O bond (whether in O_2, O_2H, or H_2O_2) and the formation of an O–H bond. As has been demonstrated,[16] a more reactive surface, such as one characterized by a higher-lying ε_d, tends to bind adsorbates more strongly, thereby enhancing the kinetics of dissociation reactions producing these adsorbates. On the other hand, a surface with a lower-lying ε_d tends to bind adsorbates more weakly and facilitates the formation of bonds amongst them. Thus, it may be expected that the most active platinum monolayer should have an ε_d with an intermediate value.

DFT studies have shown that compressive strain tends to down-shift ε_d in energy, whereas tensile strain has the opposite effect.[29] The platinum monolayers on Ru(0001), Rh(111), and Ir(111) are compressed compared with Pt(111), whereas Pt_{ML}/Au(111) is stretched by more than 4%. Indeed their ε_d are calculated to be accordingly either lower or higher in energy than that of Pt(111) (see Figure 2). The positions of the ε_d of the platinum monolayers do not correlate strictly with the amount of strain present because the position of the ε_d for the platinum monolayers depends both on the strain (geometric effects) and on the electronic interaction between the platinum monolayer and its substrate (ligand effect).[30]

When the binding energy of atomic oxygen on the six surfaces considered herein is plotted against the corresponding ε_d in Figure 2, a nearly linear correlation results. Pt_{ML}/Au(111) lies at the high ε_d end of the plot and binds oxygen much more strongly than Pt(111), whereas Pt_{ML}/Ru(0001), Pt_{ML}/Rh(111), and Pt_{ML}/Ir(111) lie at the other end and bind oxygen considerably less strongly than Pt(111). If Pt(111) is taken to be close to the optimum balance described above, then the position of the ε_d would suggest that Pt_{ML}/Ru(0001), Pt_{ML}/Ir(111), and Pt_{ML}/Rh(111) are less active for O_2 reduction than platinum because breaking the O–O bond is more difficult on these surfaces than on Pt(111). This situation would facilitate H_2O_2 formation at the expense of the complete reduction of oxygen to water. On the other hand, Pt_{ML}/Au(111) may suffer from hindered oxygen atom or OH hydrogenation kinetics owing to the stronger binding of oxygen atoms or oxygen-containing fragments and is therefore less active than Pt(111) as well. Slow O or OH hydrogenation rates may also cause surface O or OH coverage to build up and block O_2 adsorption, dissociation, or hydrogenation sites. Pt_{ML}/Pd(111) is most similar to pure Pt(111) and should possess greater activity than the other platinum monolayers. Indeed, the ORR kinetics on Pt_{ML}/Pd(111) is measured to be higher than even that on Pt(111). In addition, the production of H_2O_2 is higher on Pt_{ML}/Ru(0001) and Pt_{ML}/Ir(111) than on the rest of the platinum monolayers (Figure 3). Both of these experimental findings are in line with our predictions, which are based on the premise that the optimal ORR catalyst should strike a balance between O–O bond breaking and O–H bond-making activity.

To interpret the experimental data for the ORR activity of the platinum monolayers, additional DFT calculations have been performed to study the thermochemistry and kinetics of two representative elementary reaction steps [Eq. (1)] and [Eq. (2)] on Pt_{ML}/Au(111) (stretched platinum monolayer),

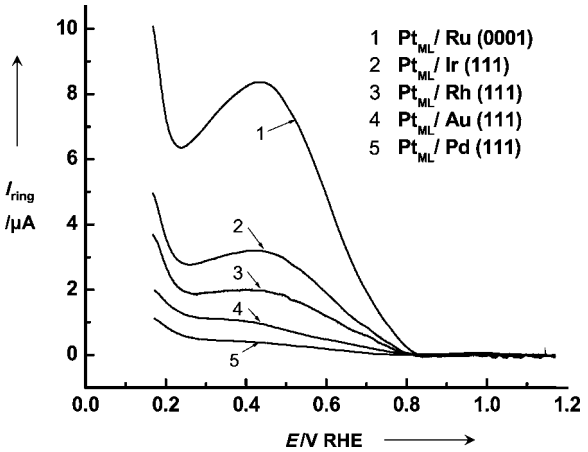

Figure 3. The currents for H_2O_2 oxidation on a ring electrode (I_{ring}) as a function of the disk potential corresponding to the polarization curves for O_2 reduction shown in Figure 1. The ring potential is 1.1 V, and the collection efficiency is 0.20.

 © 2005 Wiley-VCH Verlag GmbH & Co. KGaA, Weinheim

Pt(111) (normal platinum surface), and Pt_{ML}/Pd(111) and Pt_{ML}/Ir(111) (compressed platinum monolayers).

$$O_2 \rightarrow O + O \quad (1)$$

$$O + H \rightarrow OH \quad (2)$$

These two reactions are chosen because O_2 dissociation can be viewed as a representative O–O bond-breaking step, whereas the hydrogenation of O can be viewed as a representative O–H bond-forming step, both of which are relevant types of elementary step in the ORR regardless of the detailed mechanism. We note here that Equation (2) does not necessarily imply that H is adsorbed on the surface before adding to O, under ORR conditions. We use this step only to trace the energy needed for activating adsorbed O to accomplish a hydrogen addition to O, since the largest component of the OH formation energy barrier is the activation of O.

The experimentally measured kinetic currents shown in Figure 2, along with the calculated activation energies (E_a) of the elementary steps [Eq. (1) and (2)], are re-plotted against the binding energy of O on each of the platinum monolayers (Figure 4). The binding energy of O is used as a descriptor of surface reactivity both for simplicity and for the fact that atomic oxygen probably interacts more strongly with the surface than any other intermediate in the ORR mechanism and is, therefore, most sensitive to changes in surface properties. The E_a for O_2 dissociation is smallest on Pt_{ML}/Au(111) and largest on Pt_{ML}/Ir(111). The trend is just the opposite for the hydrogenation of O, which has the highest barrier on Pt_{ML}/Au(111) and the lowest on Pt_{ML}/Ir(111). Pt(111) lies close to the crossing of the two E_a trend lines, suggesting that it is close to where the optimum compromise lies. Although the crossing point may depend on factors including coverage, field, and solvent, it appears to be a good indicator of the ORR activity of these surfaces. The only platinum monolayer in this study that falls in the vicinity of the crossing is Pt_{ML}/Pd(111), which also turns out to be the only one whose experimentally measured activity is comparable to that of pure Pt(111).

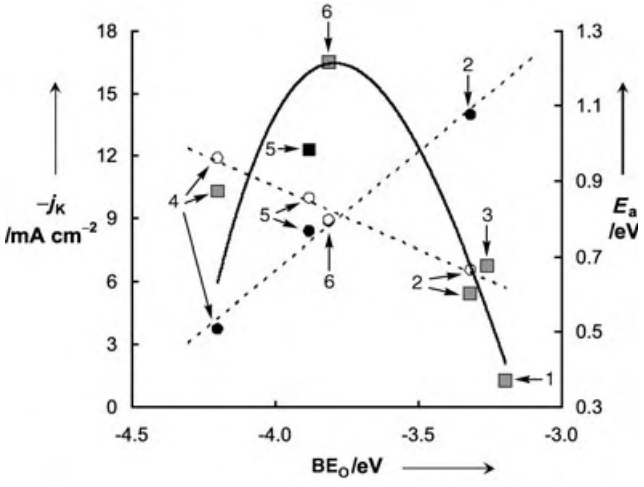

Figure 4. Kinetic currents (j_K; square symbols) at 0.8 V for O_2 reduction on the platinum monolayers in a 0.1 M $HClO_4$ solution and the activation energies for O_2 dissociation (filled circles) and for OH formation (open circles) on Pt_{ML}/Au(111), Pt(111), Pt_{ML}/Pd(111), and Pt_{ML}/Ir(111), as functions of the calculated binding energy of atomic oxygen (BE_O). The current data for Pt(111) is obtained from ref. [21]. Labels: 1. Pt_{ML}/Ru(0001), 2. Pt_{ML}/Ir(111), 3. Pt_{ML}/Rh(111), 4. Pt_{ML}/Au(111), 5. Pt(111), 6. Pt_{ML}/Pd(111).

Experimentally, we found that the superior ORR catalytic activity of Pt_{ML}/Pd(111) is associated with a reduced OH coverage,[31] which may be explained, in view of our DFT findings, as the result of enhanced OH hydrogenation rates, which should follow a trend similar to that of O hydrogenation rates. Furthermore, voltammetry and X-ray absorption near-edge structure spectroscopy (XANES)[31] have identified a shift of OH adsorption on Pt_{ML}/Pd(111) to potentials more positive than those on Pt(111), which can be attributed to an enhanced repulsive interaction of OH groups on the Pt_{ML}/Pd(111) compared to on pure Pt(111). Pd-OH, on the other hand, forms at less positive potentials than Pt-OH. This result is also in agreement with our DFT findings that the binding energy of OH is weaker on Pt_{ML}/Pd(111) than on Pt(111), which, in turn, binds OH weaker than Pd(111).

In conclusion, the ORR electrocatalytic activity of platinum monolayers supported on Au(111), Ir(111), Pd(111), Rh(111), and Ru(0001) surfaces show a volcano-type dependence on the d-band center of the platinum monolayer structures. Our results elucidate, for the first time, that for a good ORR electrocatalyst the kinetics of both the O–O bond breaking and the hydrogenation of reactive intermediates have to be facile at the cathode. More importantly and from a practical perspective, we show that it is possible to devise an ORR electrocatalyst that contains only a fractional amount of platinum but can surpass the activity of pure platinum (e.g.: Pt monolayer on Pd(111)). Therefore, platinum monolayers supported on appropriate metal substrates represent a viable way to reduce platinum loadings and the associated cost of fuel-cell electrodes. Our results also point to the fundamentally important possibility of fine-tuning the electrocatalytic activity of transition metals.

Experimental Section

The working electrodes were (111)-oriented Au, Pd, Ir, Rh, and Ru(0001) single crystals of 6 mm (used in rotating electrode) and 8 mm (used for the STM measurements) in diameter (obtained from Metal Crystals and Oxides). The surface preparation followed a standard procedure.[31] The electrochemical measurements were taken at room temperature using an interchangeable rotating disk-ring electrode (Pine Instruments). A platinum monolayer was deposited using the galvanic displacement of a Cu adlayer deposited at underpotentials by platinum from a K_2PtCl_4 solution.[32] The deposits were characterized using STM and the charge associated with hydrogen adsorption on platinum. A lack of significant change of the platinum deposit by ORR was verified by comparing the charges for H adsorption measured before and after the kinetic measurements, and by the stability of the catalytic activity.

Theoretical Methods: The spin-polarized DFT calculations were performed in the generalized gradient approximation (GGA-PW91) using ultrasoft pseudopotentials[33] as implemented in the DACAPO code.[15,34] The parameters of our calculations were identical to those used in previous studies.[16] Convergence of the results with respect to calculation parameters has been verified in all cases. The platinum monolayer surfaces were modeled by a single layer of platinum placed on top of Au(111), Pd(111), Ir(111), Rh(111), and Ru(0001), at the

 © 2005 Wiley-VCH Verlag GmbH & Co. KGaA, Weinheim

substrate's lattice constants. Each surface was constructed from a (2 × 2) surface unit cell and modeled by a slab consisting of four layers of metal atoms. The top two layers, that is, the platinum monolayer and the first layer of the substrate metal, were relaxed. The binding energies ($E_b = E_{total} - E_{substrate} - E_{gas\text{-}phase\ adsorbate}$) and geometries of adsorbed O, O_2, and OH, as well as O_2 dissociation and O hydrogenation, were studied on the relaxed surfaces. Minimum-energy reaction paths were calculated using the climbing-image nudged elastic band method.[35] The equilibrium PW91 lattice constants for bulk metals were calculated to be 4.18 (Au), 4.00 (Pt), 3.99 (Pd), 3.86 (Ir), 3.85 (Rh), and 2.74 Å (Ru), in good agreement with the experimental values[36] (4.08 (Au) 3.92 (Pt), 3.89 (Pd), 3.84 (Ir), 3.80(Rh), and 2.70 Å (Ru)).

Received: October 17, 2004
Published online: February 16, 2005

Keywords: density functional calculations · electrochemistry · heterogeneous catalysis · oxygen reduction · surface chemistry

[1] L. Schlapbach, A. Züttel, *Nature* **2001**, *414*, 353.
[2] R. D. Cortright, R. R. Davda, J. A. Dumesic, *Nature* **2002**, *418*, 964.
[3] J. Greeley, M. Mavrikakis, *Nat. Mater.* **2004**, *3*, 810.
[4] W. B. Kim, T. Voitl, G. J. Rodriguez-Rivera, J. A. Dumesic, *Science* **2004**, *305*, 1280.
[5] Handbook of Fuel Cells: Fundamentals, Technology, Applications (Eds.: W. Vielstich, A. Lamm, H. A. Gasteiger), Wiley, West Sussex, **2003**.
[6] M. R. Tarasevich, Sadkowski, E. Yeager, Comprehensive Treatise of Electrochemistry, *Vol. 7* (Eds.: B. E. Conway, J. O. M. Bockris, E. Yeager, S. U. M. Khan, R. E. White), Plenum, New York, **1983**, p. 301.
[7] R. R. Adzic in *Electrocatalysis*, *Vol. 5* (Eds.: J. Lipkowski, P. N. Ross), VCH, New York, **1998**, p. 197.
[8] S. Gottesfeld, T. A. Zawodzinski, Advances in Electrochemical Science and Engineering, *Vol. 5* (Eds.: R. C. Alkire, D. M. Kolb), Wiley-VCH, Weinheim, **1997**.
[9] J. A. Rodriguez, *Surf. Sci. Rep.* **1996**, *24*, 225.
[10] M. Baldauf, D. M. Kolb, *J. Phys. Chem.* **1996**, *100*, 11375.
[11] H. Naohara, S. Ye, K. Uosaki, *Electrochim. Acta* **2000**, *45*, 3305.
[12] R. R. Adzic in *Encyclopedia of Electrochemistry*, *Vol. 1* (Eds.: A. Bard, M. Stratmann), Wiley-VCH, New York, **2002**.
[13] T. J. Schmidt, V. Stamenkovic, M. Arenz, N. M. Markovic, P. N. Ross, *Electrochim. Acta* **2002**, *47*, 3765.
[14] B. Hammer, J. K. Nørskov, *Adv. Catal.* **2000**, *45*, 71.
[15] J. Greeley, J. K. Nørskov, M. Mavrikakis, *Annu. Rev. Phys. Chem.* **2002**, *53*, 319.
[16] Y. Xu, A. V. Ruban, M. Mavrikakis, *J. Am. Chem. Soc.* **2004**, *126*, 4717.
[17] J. A. Rodriguez, D. W. Goodman, *Science* **1992**, *257*, 897.
[18] F. B. de Mongeot, M. Scherer, B. Gleich, E. Kopatzki, R. J. Behm, *Surf. Sci.* **1998**, *411*, 249.
[19] E. Christoffersen, P. Liu, A. Ruban, H. L. Skiver, J. K. Nørskov, *J. Catal.* **2001**, *199*, 123.
[20] K. Sasaki, Y. Mo, J. X. Wang, M. Balasubramanian, F. Uribe, J. McBreen, R. R. Adzic, *Electrochim. Acta* **2003**, *48*, 3841.
[21] N. M. Markovic, H. A. Gasteiger, B. N. Grgur, P. N. Ross, *J. Electroanal. Chem.* **1999**, *467*, 157.
[22] S. Mukerjee, S. Srinivasan, M. Soriaga, J. McBreen, *J. Electrochem. Soc.* **1995**, *142*, 1409.
[23] G. A. Somorjai, *Introduction to Surface Chemistry and Catalysis*, Wiley, New York, **1994**.
[24] I. Chorkendorff, J. W. Niemantsverdriet, *Concepts of Modern Catalysis and Kinetics*, Wiley-VCH, Weinheim, **2003**.
[25] J. K. Nørskov, T. Bligaard, A. Logadottir, S. Bahn, L. B. Hansen, M. Bollinger, H. Bengaard, B. Hammer, Z. Sljivancanin, M. Mavrikakis, Y. Xu, S. Dahl, C. J. H. Jacobsen, *J. Catal.* **2002**, *209*, 275.
[26] S. J. Clouser, J. C. Huang, E. Yeager, *J. Appl. Electrochem.* **1993**, *23*, 597.
[27] E. Yeager, M. Razaq, D. Gervasio, A. Razaq, D. Tryk, *J. Serb. Chem. Soc.* **1992**, *57*, 819.
[28] R. A. Sidik, A. B. Anderson, *J. Electroanal. Chem.* **2002**, *528*, 69.
[29] M. Mavrikakis, B. Hammer, J. K. Nørskov, *Phys. Rev. Lett.* **1998**, *81*, 2819.
[30] J. R. Kitchin, J. K. Nørskov, M. A. Barteau, J. G. Chen, *J. Chem. Phys.* **2004**, *120*, 10240.
[31] J. Zhang, Y. Mo, M. B. Vukmirovic, R. Klie, K. Sasaki, R. R. Adzic, *J. Phys. Chem. B* **2004**, *108*, 10955.
[32] S. R. Brankovic, J. X. Wang, R. R. Adzic, *Surf. Sci.* **2001**, *474*, L173.
[33] D. Vanderbilt, *Phys. Rev. B* **1990**, *41*, 7892.
[34] B. Hammer, L. B. Hansen, J. K. Nørskov, *Phys. Rev. B* **1999**, *59*, 7413.
[35] G. Henkelman, B. P. Uberuaga, H. Jónsson, *J. Chem. Phys.* **2000**, *113*, 9901.
[36] N. W. Ashcroft, N. D. Mermin, *Solid State Physics*, Saunders College, Orlando, FL, **1976**.

 © 2005 Wiley-VCH Verlag GmbH & Co. KGaA, Weinheim

Nanostructures

Actinyl Peroxide Nanospheres**

Peter C. Burns, Karrie-Ann Kubatko, Ginger Sigmon, Brian J. Fryer, Joel E. Gagnon, Mark R. Antonio, and L Soderholm*

Self-assembling small clusters provide an ideal venue for the study of fundamental structure–property relationships. The monodispersed nanoaggregates that have been reported to

[*] Prof. P. C. Burns, K.-A. Kubatko, G. Sigmon
Department of Civil Engineering and Geological Sciences
University of Notre Dame
156 Fitzpatrick Hall, Notre Dame, IN 46556 (USA)
Fax: (+1) 574-631-9236
E-mail: pburns@nd.edu

Prof.Dr. B. J. Fryer, J. E. Gagnon
Great Lakes Institute for Environmental Research
University of Windsor
Windsor, Ontario N9B 3P4 (Canada)

Dr. M. R. Antonio, Dr. L. Soderholm
Chemistry Division
Argonne National Laboratory
Argonne, IL 60439 (USA)

[**] This research was supported at the University of Notre Dame by the Environmental Management Science Program of the Office of Science, US Department of Energy (DE-FG07-97ER14820), and the National Science Foundation Environmental Molecular Science Institute at the University of Notre Dame (EAR02-21966). This research was supported at Argonne National Laboratory by the US Department of Energy Office of Basic Energy Sciences (DOE/BES) – Chemical Sciences Division and by the Material Sciences Division for the Advanced Photon Source studies under contract number W-31-109-ENG-38.

 DOI: 10.1002/anie.200462445 © 2005 Wiley-VCH Verlag GmbH & Co. KGaA, Weinheim

date are based on main-group elements, most notably C_{60} (buckminsterfullerene)[1] and transition-metal oxide clusters, including a wide variety of polyoxometalates built on WO, MoO, and NbO frameworks.[2] Studies based on these systems have resulted in new insight into electronic, magnetic, and structural properties at the nanoscale and provide numerous examples of novel materials with important applications.[3,4] Nanoparticles are also of considerable importance in many environmental systems as they often form at low temperatures, can impact the transport of heavy metals and radionuclides in geologic fluids, and are small enough that their properties are often particle-size dependent.[5] Herein, we report the synthesis and characterization of a new family of self-assembling nanospheres from actinide ions (*Ac*) and their persistence as stable entities in alkaline solutions. These nanospheres have compositions such as $[K_{16}(H_2O)_2(UO_2)(O_2)_2(H_2O)_2\{(UO_2)(O_2)_{1.5}\}_{28}]^{14-}$ and $[Li_6(H_2O)_8NpO_2(H_2O)_4\{(NpO_2)(O_2)(OH)\}_{24}]^{20-}$ and are comprised of linear actinyl peroxide building blocks.

The uranyl and neptunyl members of this new family of actinyl peroxide compounds precipitated from alkaline peroxide solutions of U^{VI} and Np^{V} ions at 25 °C after approximately seven days or longer. Figure 1 a–c shows the structures of four exemplary actinyl peroxide nanospheres that are the focus herein. Their molecular units are composed of 24, 28, or 32 uranyl peroxide polyhedra (U-24, U-28, and U-32) or 24 neptunyl peroxide polyhedra (Np-24).[6] The nanospheres are approximately 16.4, 17.7, and 18.6 Å in diameter (as measured between the centers of bonding oxygen atoms).

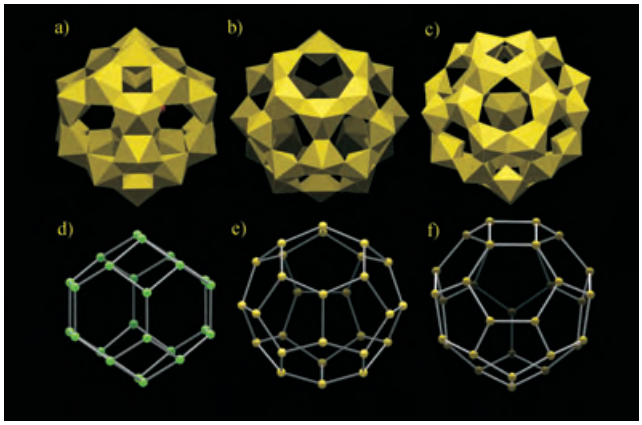

Figure 1. Polyhedral representations of spherical actinyl peroxide nanoclusters found in a) U-24 and Np-24, b) U-28, and c) U-32 and *Ac–Ac* connectivity diagrams for d) Np-24, e) U-28, and f) U-32.

The nanospheres are composed of two types of actinyl peroxide polyhedra: U-24, U-32, and Np-24 contain topologically identical $[(AcO_2)(O_2^{2-})_2(OH)_2]$ hexagonal bipyramids, in which the oxygen atoms of the actinyl ions constitute the apices of the bipyramids and the peroxide groups form two of the equatorial edges of the polyhedra (Figure 1 a,c). U-28 contains only $[(AcO_2)(O_2^{2-})_3]$ hexagonal bipyramids, in which three equatorial edges of the polyhedra are peroxide groups (Figure 1 b). In all cases, the hexagonal bipyramids are linked by sharing three of their equatorial edges with adjacent polyhedra. Two of the shared edges in U-24, Np-24, and U-32 correspond to peroxide groups and the third edge consists of two hydroxy groups, whereas all three shared edges in U-28 are peroxide groups. The outer surfaces of the nanospheres are the oxygen atoms of the actinyl ions and each Ac^{VI}–O bond corresponds to approximately 1.7 valence units;[7] therefore, these oxygen atoms can form only weak bonds.

The shortening of the polyhedra edges associated with peroxide groups favors formation of nanospheres over the normal linkage into sheets or chains. Figure 2 illustrates the linkage of the polyhedra into four-membered rings in U-24, U-32, and Np-24. Each shared edge within the four-membered ring is a peroxide group with approximate lengths of 1.45 Å, whereas the edge defined by one oxygen atom of each of the two peroxide groups has a length of approximately 2.8 Å. The linkage of four polyhedra into a ring requires a tilting of the polyhedra with the actinyl ions directed towards a common point located approximately 3.5 Å below the four coplanar Ac^{VI} cations (Figure 2 c). The nanospheres found in U-24 and Np-24 result from the linkage of eight topologically and chemically identical four-membered rings of polyhedra (Figure 2 d).

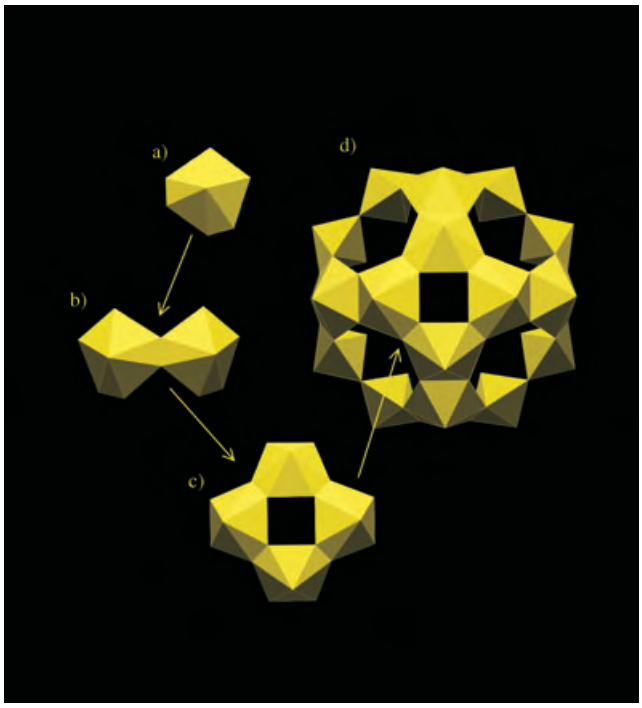

Figure 2. Polyhedral representations of linkages in the U-24 and Np-24 nanoclusters: a) hexagonal bipyramid with composition $[(AcO_2)(O_2)_2(OH)_2]$, b) linkages of two hexagonal bipyramids by the sharing of a peroxide edge, c) linkage of four hexagonal bipyramids into a four-membered ring by the sharing of four peroxide edges, and d) the U-24 cluster.

U-28 contains 28 uranyl triperoxide polyhedra that form the nanosphere, and there is a partially occupied $[(UO_2)(O_2)_2(H_2O)_2]$ polyhedron at its center (Figure 3 b). There are 16 K-ion sites within the cluster that bond to as many as ten ligands, which are mostly at the vertices of the uranyl

 © 2005 Wiley-VCH Verlag GmbH & Co. KGaA, Weinheim

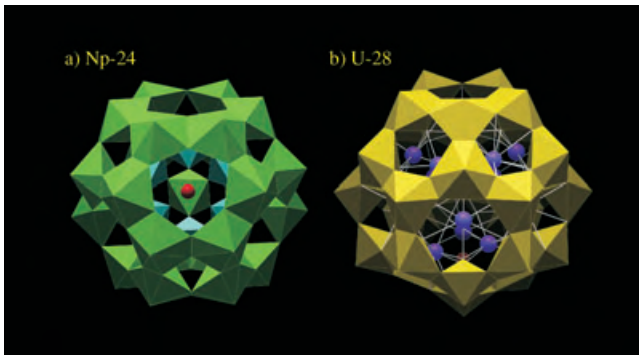

Figure 3. Polyhedral representations of the details of the a) Np-24 and b) U-28 clusters. $[NpO_2(O_2)_2(OH)_2]$ polyhedra are green, $[UO_2(O_2)_3]$ polyhedra are yellow, LiO_5 polyhedra are blue, K cations are shown as purple spheres, and O atoms of the H_2O groups are shown as red spheres in (b).

polyhedra. In the case of occupancy of the U position at the center of the cluster, the composition is $[K_{16}(H_2O)_2(UO_2)(O_2)_2(H_2O)_2\{(UO_2)(O_2)_{1.5}\}_{28}]^{14-}$. The charge of the nanosphere in each structure is balanced by Li or K ions in the intercluster regions. The Li-ion content was confirmed for U-24 by laser-ablation inductively coupled plasma mass-spectrometry (ICPMS) and was 1.90 ± 0.15 wt%, which is comparable to the theoretical value of 1.77 wt%, which was derived from the U/Li ion ratio of 1:1 required for charge balance.

Np-24 and U-28 also contain an actinyl ion at the center of the nanosphere, although these sites are occupied in approximately 50% of the clusters and are not necessary for their stability. U-24, Np-24, and U-32 contain Li ions and H_2O, while U-28 contains K ions and H_2O. The actinyl ion at the center of Np-24 is in square bipyramidal coordination with four equatorial H_2O groups, and each of the ligands are shared with LiO_5 square pyramids (Figure 3a). The framework of Np-24 contains four symmetrically independent Np sites: each center has a neptunyl ion with Np–O bond lengths of 1.792(11) and 1.809(9) Å for Np1, 1.802(10) and 1.839(10) Å for Np2, 1.784(7) and 1.811(7) for Np3, and 1.788(7) and 1.796(7) Å for Np4. The equatorial Np–O bond lengths range from 2.344 to 2.455 Å for all polyhedra, and the average equatorial Np–O bond lengths are 2.407, 2.433, 2.389, and 2.382 Å for Np1, Np2, Np3, and Np4, respectively. The neptunyl ion geometry and the equatorial Np–O bond lengths indicate that Np1, Np3, and Np4 are hexavalent, whereas the longer neptunyl and equatorial bond lengths for Np2 strongly suggest it is pentavalent. The valence of the Np5 ion at the center of the nanosphere is ambiguous, but it is present as an actinyl ion and is considered hexavalent for the purpose of counting charges. Np-24 also contains eight H_2O groups, which are only held in place by hydrogen-bonding interactions. Where the Np site at the center of Np-24 is occupied, its composition is $[Li_6(H_2O)_8NpO_2(H_2O)_4\{(NpO_2)(O_2)(OH)\}_{24}]^{20-}$.

The crystals of all of the U-based nanospheres are yellow, which is consistent with the $(UO_2)^{2+}$ ion and its unoccupied valence f states.[8] Most cluster anions based on W–O, Mo–O, and Nb–O units are white and have unoccupied valence d states. In contrast, the crystals of the neptunyl nanospheres are close to black and are composed primarily of Np^{VI}, which are f^1 ions. Np2 is of further interest as the Np–O bond lengths indicate it is an Np^{V} ion. The slight difference in the coordination environment of this site relative to the other Np^{VI} sites in the framework suggests that Np-24 may be electroactive under a minimal applied potential, which is similar to the behavior exhibited by several polyoxometalates based on W–O groups.[9–11]

Small angle X-ray scattering (SAXS) data for solutions of H_2O_2, LiOH, and $[UO_2(NO_3)_2(H_2O)_6]$ in H_2O recorded 2, 28, and 180 days following their initial preparation are shown together with the fitted response in Figure 4. The time

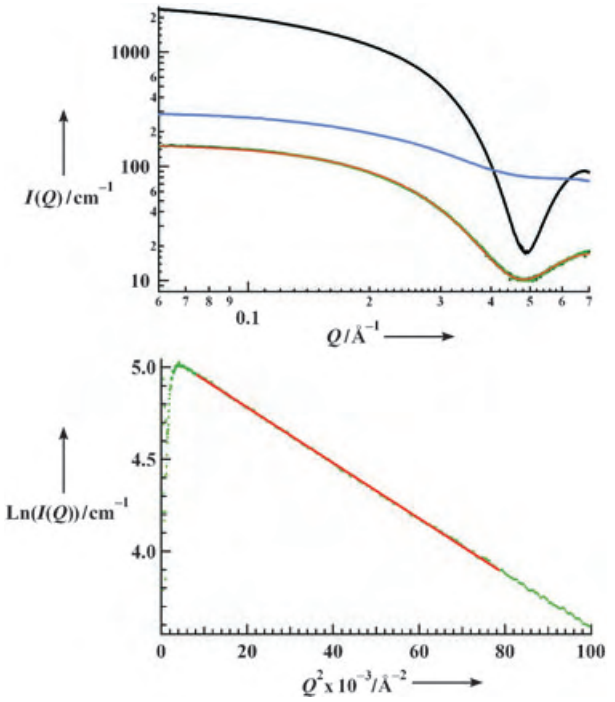

Figure 4. SAXS data from the mother liquor (H_2O, H_2O_2, LiOH, and $[UO_2(NO_3)_2(H_2O)_6]$) 2 (blue line), 28 (black line), and 180 days (green line) old. Top: change in the shape of the curves with solution age demonstrates evolving aggregation of the uranyl species. Data for the solutions after 2 and 28 days indicate the presence of multiple aggregates. Data for the solutions after 180 days are consistent with a spherical-shell model (red line), thus indicating a monodisperse cluster in solution. Bottom: Guinier plot of data for the solution after 180 days, which is linear over a wide Q range and so is a representative fit (red line, ca. 0.01–0.03 $Å^{-2}$).

progression of the scattering data, particularly for the high Q data that deepen and broaden with sample age, are attributed to an evolving distribution both in terms of size and morphology of uranyl peroxo aggregates in solution. The data obtained from the solution aged for 180 days, which produced U-24 crystals, corresponds to spherically ripened monodisperse nanospheres. There are indications of cluster anion polydispersity in the SAXS data for the two younger solutions. A spherical-shell model provided the best fit of the $I(Q)$ versus Q data from the solution recorded after 180 days

 © 2005 Wiley-VCH Verlag GmbH & Co. KGaA, Weinheim

and was in excellent agreement with the solid-state structural data. The central cavity radius determined by the spherical-shell model was 1.7 ± 0.2 Å and the shell radius was 6.2 ± 0.2 Å, which represents an overall diameter of 16.2 Å. Confirmation for the presence of well-formed U-24 nanospheres in solution was obtained from a Guinier analysis of the low-Q SAXS data. A radius of gyration ($R_g = 6.7 \pm 0.1$ Å), determined from the fit to the low-Q data (Figure 4), was the same (within error) as the R_g value determined from the U-24 single-crystal structural parameters.

The SAXS data reveal an evolving structural organization in solution with well-defined clusters present as early as two days after preparation. The overall change in SAXS data with time indicates a ripening of the solution and is consistent with a self-assembly process that yields the initial nanospheres in solution, which subsequently precipitated. This mechanism is consistent with the lag time of several days between the initial preparation of the solution and precipitation of the nanospheres. Verification of the existence and solubility of U-24 in solution as a stable anionic species suggests a variety of further synthetic, structural, magnetic, electrochemical, and reactivity studies.

The actinyl peroxide nanospheres described herein represent a new class of polyoxometalates. The largest reported actinide polyoxometalate ion to date contains only six U^V ions.[12] Only 41 out of over 325 inorganic structures known to contain essential U^{VI} ions have finite clusters of polyhedra composed of high-valence cations,[13] and none contain more than four uranyl polyhedra. Peroxopolyoxometalates that contain Mo, W, and V form in aqueous solutions in the presence of small quantities of H_2O_2 and some catalyze the oxidation of a variety of organic substrates with H_2O_2 as the cooxidant.[14–16] Several such peroxopolyoxometalates have been isolated and structurally characterized.[17] The peroxide group typically defines an outer edge of a polyhedron in such clusters, although one or both of the oxygen atoms of the peroxide group form a bridge between metal centers in some cases.[18] Peroxo groups occur along the shared edges of the uranyl polyhedra in the nanospheres isolated in the current study and are, therefore, integral elements of the structure connectivity.

The formation of actinyl peroxide nanospheres is important from a practical standpoint, as they may form in alkaline mixtures of nuclear waste containing various salts and organic solvents by incorporating peroxides created by the alpha-radiolysis of water. The synthesis conditions reported herein are broadly similar to those in high-level waste storage tanks (for example, alkaline solution, ambient temperature),[19,20] as well as soils and sediments contaminated by the leakage of such waste. The formation of actinyl peroxide nanospheres in such systems is probable and could have a profound impact on the mobility of actinides in the environment given their persistence in solution.

This new class of actinyl peroxide clusters is a rare example of self-assembling nanospheres. The potential for the further preparation of novel structure types through the metered addition of actinyl peroxide units is suggested by solution SAXS data and is demonstrated by the variety of structures synthesized. A series of structurally tuneable spheroids would afford an unprecedented opportunity to study size/structure–function relationships. Furthermore, variability in the valence electron count associated with the actinyl ions, coupled with 5 f-bonding behavior that is intermediate between localized and itinerant, offers the control to systematically probe electronic, magnetic, and catalytical properties on the nanoscale. The broad potential generated by the tunability of the actinyl peroxides and their likely presence in natural and contaminated environmental samples provides impetus for further study of this unusual family of nanospheres.

Experimental Section

Crystals of U-24, U-28, U-32, and Np-24 were obtained from alkaline solutions left to stand at 298 K in air for 7–14 days. The solutions contained the following: U-24: 30% H_2O_2 (5 mL), H_2O (1 mL), LiOH (1 g), 3 M $[UO_2(NO_3)_2(H_2O)_6]$ solution in H_2O (1 mL); U-28: aqueous solution of tartaric acid (0.1 mL), 4 M KOH in H_2O (0.25 mL), 30% H_2O_2 (0.15 mL), 3 M $[UO_2(NO_3)_2(H_2O)_6]$ solution in H_2O (0.25 mL); U-32: 30% H_2O_2 (1 mL), H_2O (1 mL), LiOH (1 g), 3 M solution of $[UO_2(NO_3)_2(H_2O)_6]$ in H_2O (1 mL); Np-24: 87 mM Np^V ions in 1 M HCl (1 mL), 30% H_2O_2 (0.04 mL), 2 M LiOH solution in H_2O (1.38 mL). The syntheses for U-24, U-32, and Np-24 each provided several dozen crystals as well as fine-grained precipitates. The yields were estimated to be 20–40%. The synthesis of U-28 provided only one identifiable crystal.

The laser-ablation ICPMS analysis of U-24 crystals was conducted at the Great Lakes Institute for Environmental Research, University of Windsor with a nonhomogenized, solid-state, 266 nm Nd-doped Y–Al garnet (Nd/YAG) laser. Sample ablation was done in a sampling cell filled with argon gas on a modified polarizing microscope. Ablated material was transported in an argon carrier gas from the ablation cell to the ICPMS equipment. The U-24 crystals were mounted on double-sided tape attached to precleaned glass microscope slides and were traversed into the laserbeam using a computer-controlled X-Y-Z stage. The normal high sensitivity (ppb to low ppm) of the analytical system was reduced by positioning a 2.5 × beam expander in front of a 1.0 mm pinhole in the laser path prior to focusing the laser energy on the sample. The vastly different elemental concentrations of the calibration standard and U-24 were compensated for by decreasing the laser power between the NIST glass (1.30 kV) and U-24 (1.20 kV) ablations.

The Li content was analyzed on a ThermoElemental X-7 ICP mass spectrometer. NIST glass standard 610 was used for calibration with elemental uranium as the internal standard (NIST 610 = 457 ppm and U-24 = 60.64 wt % U, respectively). The absolute sensitivity of the Li content (relative to elemental uranium) was increased by addition of ultrapure nitrogen gas at a flow rate of 3.0 mL min^{-1} to the nebulizer gas flow downstream of the laser cell. The LAMTRACE program[21] was used to convert the ICPMS output data (integrated counts/second) into concentration units.

The SAXS data were collected with the facilities at beam-line 12-BM-B at the Advanced Photon Source.[22] An incident photon energy of 16 keV was chosen to eliminate X-ray fluorescence that is excited by higher-energy incident photons at (and above) the U L_3-edge threshold of 17.166 keV. Approximately 20 μL of the cluster-containing solutions were contained in purpose-built polychlorotrifluoroethylene (PCTFE), thin-layer cells with 0.010″ PCTFE windows and a 1.7 mm pathlength. Data reduction to obtain $I(Q)$ versus Q (Å^{-1}), where $Q = 4\pi\sin\theta/\lambda$ and 2θ is the scattering angle and λ is the wavelength of the X-rays, was performed following standard procedures, and Guinier analysis in the low Q region was carried out using

 © 2005 Wiley-VCH Verlag GmbH & Co. KGaA, Weinheim

standard methods to obtain the radius of gyration R_g of the particles.[23,24]

Received: October 27, 2004

Keywords: actinides · peroxides · polyoxometalates · self-assembly · uranium

[1] H. W. Kroto, J. R. Heath, S. C. O'Brien, R. F. Curl, R. E. Smalley, *Nature* **1985**, *318*, 162.
[2] A. Muller, F. Peters, M. T. Pope, D. Gatteschi, *Chem. Rev.* **1998**, *98*, 239.
[3] A. F. Hebard, M. J. Rosseinsky, R. C. Haddon, D. W. Murphy, S. H. Glarum, T. T. M. Palstra, A. P. Ramirez, A. R. Kortan, *Nature* **1991**, *350*, 600.
[4] "Comprehensive Coordination Chemistry-II: From Biology to Nanotechnology": C. L. Hill in *Applications of Coordination Chemistry*, *Vol. 4* (Ed.: M. Ward), Elsevier, Oxford, **2003**, pp. 679–759.
[5] J. F. Banfield, H. Zhang, *Rev. Mineral. Geochem.* **2001**, *44*, 1.
[6] X-ray diffraction data for U-24, U-28, and U-32 were collected at 100 K using a Bruker SMART APEX diffractometer at the University of Notre Dame ($\lambda = 0.71073$ Å). X-ray diffraction data for Np-24 was collected at 298 K using a Bruker SMART APEX II diffractometer at Argonne National Laboratory ($\lambda = 0.71073$ Å). A sphere of data was collected for each crystal using frame-widths of 0.3° in ω. Data were corrected for Lorentz and polarization using the Bruker program SAINT, absorption corrections were performed using the Bruker program XPREP (version 5.1, 1997), and the structures were solved by direct methods and refined on the basis of F^2 for all unique reflections using the Bruker SHELXTL system of programs (version 5.10, 1997). Refinement of the structure of Np-24 was straightforward. The Np5 site, located at the center of the nanosphere, and its associated ligands were assigned 50% occupancy following refinement of their corresponding site occupancies. Refinement of the structure of U-24 was challenging because of the very large number of atoms in the asymmetric unit and the contrast of scattering efficiencies between the Li and U atoms. Soft constraints of Li–O distances were added to the refinement, and the positions of the Li atoms are tentative. Refinement of the structure of U-28 was reasonably straightforward: Following refinement of their scattering site, the occupancies of U18, which is located at the center of the nanosphere, and its associated oxygen atoms were set at 50%. The K atoms in the structure were assigned full occupancy, but some may be partially occupied by K atoms or a combination of K atoms and H_2O. Solution of U-32 and refinement of its structure was extremely difficult because of the large number of atoms in the asymmetric unit and positional disorder of some constituents. Soft constraints for U–O(uranyl) distances were added to the refinement to improve the uranyl ion geometries. It was not possible to locate any Li atoms in the structure, and the positions and identities of oxygen atoms not bonded to U atoms are considered to be tentative. U-24: 315223 total reflections, 75761 unique reflections, 75761 reflections used in the refinement, 26.6° maximum theta, $R1 = 0.080$, $wR2 = 0.186$, GOF = 0.80, space group $P\bar{1}$, triclinic, $a = 19.2111(11)$, $b = 31.003(2)$, $c = 32.252(2)$ Å, $\alpha = 102.404(4)$, $\beta = 99.506(4)$, $\gamma = 95.362(4)°$, $V = 18336.8(19)$ Å^3. Np-24: 46131 total reflections, 5606 unique reflections, 5606 reflections used in the refinement, 28.3° maximum theta, $R1 = 0.044$, $wR2 = 0.122$, GOF = 1.04, space group $I4/m$, tetragonal, $a = 18.1554(4)$, $c = 26.6926(14)$, $V = 8798.4(5)$ Å^3. U-28: 140070 total reflections, 12294 unique reflections, 12294 reflections used in the refinement, 22.5° maximum theta, $R1 = 0.058$, $wR2 = 0.141$, GOF = 0.75, space group *Pbcm*, orthorhombic, $a = 19.2609(13)$, $b = 33.813(2)$, $c = 28.1628(19)$ Å, $V = 18341(2)$ Å^3. U-32: 275074 total reflections, 74664 unique reflections, 74664 reflections used in the refinement, 22.5° maximum theta, $R1 = 0.085$, $wR2 = 0.153$, GOF = 0.52, space group $P2_1/c$, monoclinic, $a = 38.84(3)$ Å, $b = 36.52(3)$ Å, $c = 41.30(3)$ Å, $\beta = 102.863(13)°$, $V = 57098(69)$ Å^3. Further details on the crystal structure investigations may be obtained from the Fachinformationszentrum Karlsruhe, 76344 Eggenstein-Leopoldshafen, Germany (fax: (+49) 7247-808-666; e-mail: crysdata@fiz-karlsruhe.de) on quoting the depository number CSD-414640 (U-24), -414641 (Np-24), -414642 (U-28), and -414643 (U-32).
[7] P. C. Burns, R. C. Ewing, F. C. Hawthorne, *Can. Mineral.* **1997**, *35*, 1551.
[8] R. G. Denning, *Struct. Bonding (Berlin)* **1992**, *79*, 215.
[9] D. C. Duncan, C. L. Hill, *Inorg. Chem.* **1996**, *35*, 5828.
[10] B. Keita, Y. Jean, B. Levy, L. Nadjo, R. Contant, *New J. Chem.* **2002**, *26*, 1314.
[11] M.-H. Chiang, M. R. Antonio, L. Soderholm, *Dalton Trans.* **2004**, 3562.
[12] P. B. Duval, C. J. Burns, D. L. Clark, D. E. Morris, B. L. Scott, J. D. Thompson, E. L. Werkema, L. Jia, R. A. Andersen, *Angew. Chem.* **2001**, *113*, 3461; *Angew. Chem. Int. Ed.* **2001**, *40*, 3358.
[13] P. C. Burns, *Mater. Res. Soc. Symp. Proc.* **2004** *802*, 89.
[14] P. Gouzerh, A. Proust, *Chem. Rev.* **1998**, *98*, 77.
[15] D. C. Duncan, R. C. Chambers, E. Hecht, C. L. Hill, *J. Am. Chem. Soc.* **1995**, *117*, 681.
[16] M. V. Vasylyev, R. Neumann, *J. Am. Chem. Soc.* **2004**, *126*, 884.
[17] D. Sloboda-Rozner, P. L. Alsters, R. Neumann, *J. Am. Chem. Soc.* **2003**, *125*, 5280.
[18] M. H. Dickman, M. T. Pope, *Chem. Rev.* **1994**, *94*, 569.
[19] B. Wakoff, K. L. Nagy, *Environ. Sci. Technol.* **2004**, *38*, 1765.
[20] B. O. Hansen, P. Kwan, M. M. Benjamin, C.-W. Li, G. V. Korshin, *Environ. Sci. Technol.* **2001**, *35*, 4905.
[21] E. Van Achterbergh, C. G. Ryan, S. E. Jackson, W. L. Griffin in *Laser-Ablation-ICP-MS in the Earth Sciences*, Mineralogical Association of Canada, Shortcourse, **2001**, p. 239.
[22] S. Seifert, R. E. Winans, D. M. Tiede, P. Thiyagarajan, *J. Appl. Crystallogr.* **2000**, *33*, 782.
[23] P. Thiyagarajan, F. Zeng, C. Y. Ku, S. C. Zimmerman, *J. Mater. Chem.* **1997**, *7*, 1221.
[24] P. Thiyagarajan, *J. Appl. Crystallogr.* **2003**, *36*, 373.

 © 2005 Wiley-VCH Verlag GmbH & Co. KGaA, Weinheim

Nanotechnology

Fabrication of Metal–Semiconductor Nanowire Heterojunctions

Jinhua Zhan, Yoshio Bando, Junqing Hu, Zongwen Liu, Longwei Yin, and Dmitri Golberg*

One-dimensional nanostructures play an important role in nanotechnology for their use as building blocks in nanoscale circuits, and in optoelectronic, electrochemical, and electromechanical devices.[1] Nanotubes, nanobelts, nanorods, and semiconducting nanowires have been fabricated through a number of advanced nanolithographic techniques, thermal evaporation, and solution-based methods.[2] For the development of a wide selection of nanoscale building blocks for nanometer-sized electrical and optical lines with new properties, it is important that the potential barrier between adjacent constituents has the appropriate current–voltage characteristics. This can be realized by the creation of various heterostructures including p–n junctions, metal–oxide–semiconductor junctions, or metal–semiconductor contacts that allow reliable signal processing.[3] Diverse heterostructures assembled in either radial or axial directions within a single nanometer-scale building block have been fabricated.[4–9] These include the axial block-by-block groups III-V (GaAs/GaP, InAs/InP) and group IV (Si/Ge) semiconductor nanowires, epitaxial Si/Ge core–shell nanowire heterostructures, heterojunctions of carbon nanotubes and silicon nanowires, and NiSi/Si nanowire heterostructures.

Silicon has long been considered the prime material for information-technology electronics.[10] It has recently been found valuable for photonics as well.[11] Silicon nanowires are particularly important for the miniaturization of Si-integrated circuits (IC). Various approaches including vapor-liquid-solid (VLS) growth, solution-liquid-solid (SLS) growth, and oxide-assisted (OA) growth, have been used for the synthesis of Si nanowires.[12] Metallic nanowires that display novel magnetic or electrical properties have been extensively studied.[13–16]

Upon connection of a metallic nanowire to a semiconducting Si nanowire, a unique metal–semiconductor nanoscale contact can be prepared as a fundamental component of a novel miniaturized semiconductor device. The metal–semiconductor nanowire junctions are sheathed with insulating silicon oxide. Herein, we demonstrate the fabrication of In–Si end-to-end nanowire contacts and present a thorough analysis of their morphological and structural characteristics.

Thermal evaporation of an In/SiO powder mixture in an induction furnace results in the generation of a gray-colored product in the outlet of a graphite induction-heated cylinder. A powder XRD pattern (Figure 1) of the product initially

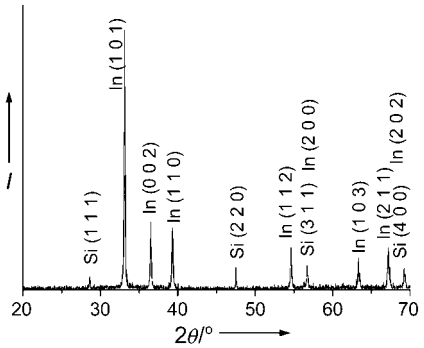

Figure 1. XRD pattern of the product of thermal evaporation of an In/SiO powder mixture in an induction furnace.

suggested the coexistence of diamond-cubic silicon (JCPDS file 27-1402) and tetragonal indium (JCPDS file 05-0642). Detailed structural and chemical analyses of the products were further carried out with TEM, high-resolution TEM (HRTEM), electron diffraction (ED), and energy-dispersive X-ray spectroscopy (EDS). Figure 2a shows a TEM micrograph of a typical nanowire junction. The nanostructure is composed of two distinct end-to-end segments. The bottom gray-contrast portion is several micrometers in length. The length of the upper black-contrast portion reaches dozens of micrometers (it is only partially shown in Figure 2a). The diameter of the 1D nanostructure is $\approx$200 nm. EDS spectra generated with an electron nanoprobe ($\approx$20 nm) were collected from three spots along the nanostructure: the upper tubelike segment, the black-contrast segment, and the gray-contrast segment as indicated by the corresponding circles in Figure 2a. The respective results are shown in Figure 2b–d. The tube is silicon oxide with a composition of 68.6% oxygen and 31.4% silicon. The dark-contrast branch is composed of indium; the gray-contrast branch is made of silicon. The O peaks in Figure 2c and d may originate from a Si oxide sheath on the In and Si nanowires, respectively, whereas the C and Cu signals come from a C-coated Cu TEM grid. EDS elemental mapping sheds additional light on the nanowire-junction chemistry. Figure 3a is a scanning transmission electron microscopy (STEM) image of an In–Si end-to-end nanowire heterojunction. This reveals a clear interface between the two domains. The respective In, Si, and O elemental maps are shown in Figures 3b–d. They demonstrate well-defined composition variations and the sharp interface between the In and Si segments. The uniform oxygen scattering originates from the amorphous silicon oxide that sheaths the entire nanowire. Notably, nearly all Si nanowires observed during extensive TEM studies were connected with In nanowires to display the In–Si heterojunction morphology.

[*] Dr. J. Zhan, Prof. Y. Bando, Dr. Z. Liu, Dr. L. Yin, Prof. D. Golberg
Advanced Materials Laboratory and Nanomaterials Laboratory
National Institute for Materials Science
Namiki 1-1, Tsukuba, Ibaraki 305-0044 (Japan)
Fax: (+81) 29-851-6280
E-mail: zhan.jinhua@nims.go.jp
Dr. J. Hu
International Center for Young Scientists (ICYS)
National Institute for Materials Science (NIMS)
Namiki 1-1, Tsukuba, Ibaraki 305-0044 (Japan)

Supporting information for this article is available on the WWW under http://www.angewandte.org or from the author.

 © 2005 Wiley-VCH Verlag GmbH & Co. KGaA, Weinheim DOI: 10.1002/anie.200462813

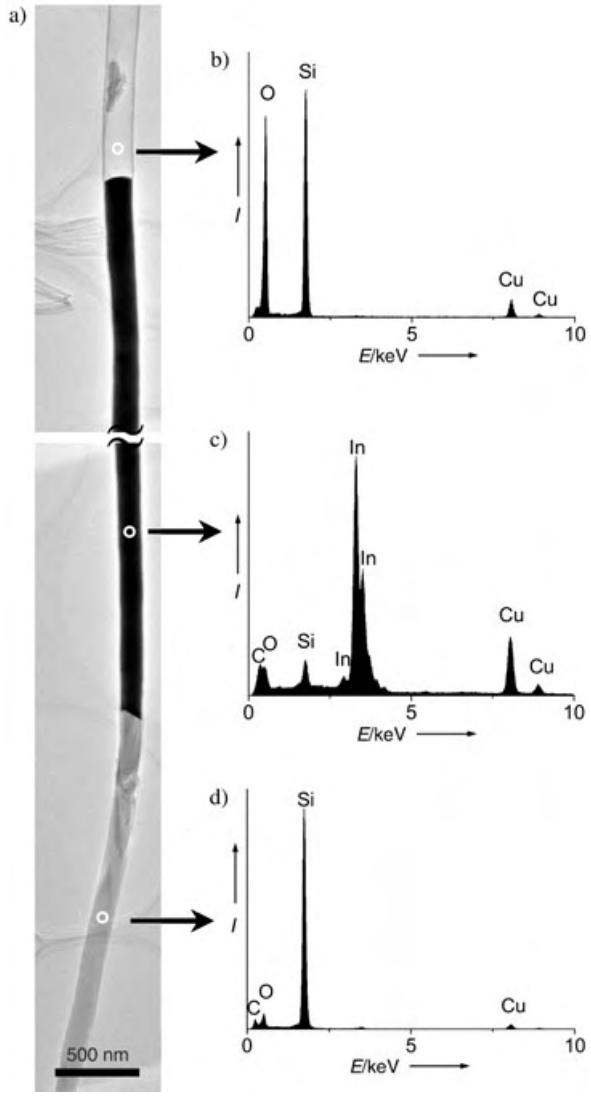

Figure 2. a) TEM image of a typical In–Si nanowire heterojunction; b)–d) respective EDS spectra taken from the regions indicated with the white circles on the nanowire image of part a).

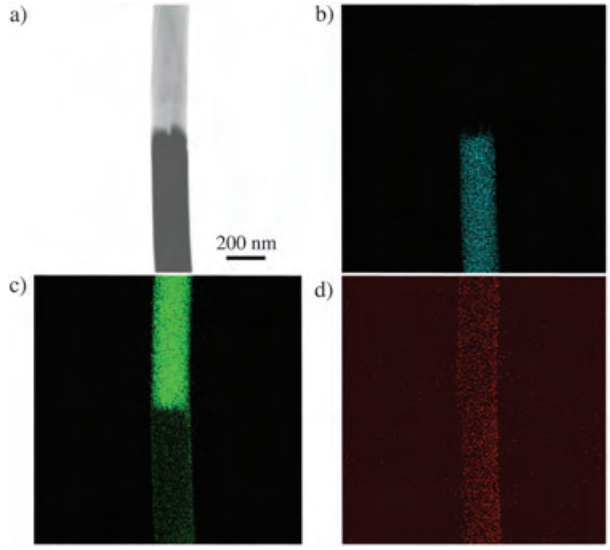

Figure 3. a) STEM image depicting Si (light) and In (dark) domains within an In–Si nanowire junction; b) In; c) Si; and d) O elemental maps demonstrating the elemental-spatial distribution.

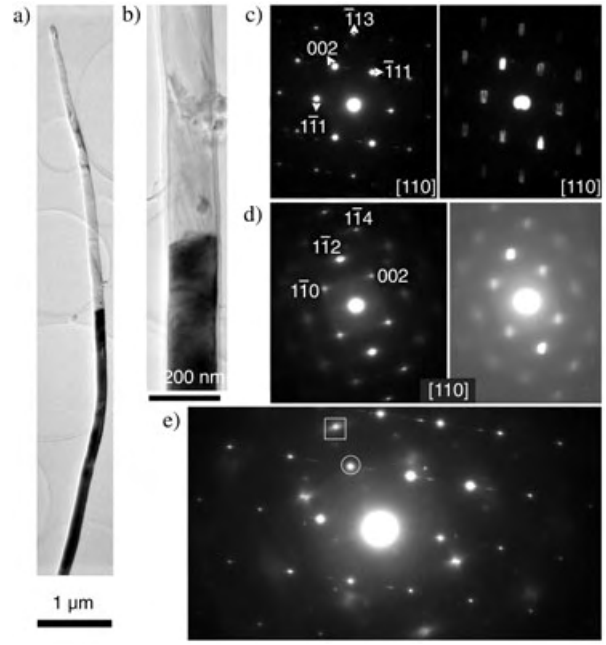

Figure 4. a) TEM image of a single In–Si nanowire junction; b) magnified TEM image that shows the In–Si nanowire junction is uniformly sheathed with silica; c)–e) respective SAED patterns taken from the selected Si, In, and In–Si boundary regions.

Detailed TEM investigations provided further insight into the heterojunction microstructure. Figure 4a depicts a representative In–Si nanowire heterojunction. Figure 4b shows its magnified view. It is apparent that the entire nanowire junction is uniformly coated with an 8-nm-thick silicon oxide sheath. Selected area electron diffractions (SAED) were taken from a Si nanowire segment (light contrast), an In nanowire segment (dark contrast), and the boundary between the two. The respective SAED patterns are shown in Figures 4c–e,. All diffraction spots in Figures 4c and d can be indexed to those of the [110] zone axes of diamondlike Si and tetragonal In, respectively. Streaking of the reflections in the underfocused electron diffraction patterns shown on the right-hand panels of Figures 4c,d implies that the preferred growth directions of the Si and In nanowires are close to the $[\bar{1}13]$ and $[1\bar{1}4]$ orientations, respectively. A HRTEM image taken from the Si domain is depicted in Figure 5a. This indicates the clearly resolved interplanar fringes (3.10 Å) that correspond to the {111} lattice distances. The inset in Figure 5a is the [110] projection of a diamondlike Si crystal lattice. Furthermore, HRTEM analysis reveals that the crystalline Si nanowire is free from planar defects and is coated with an amorphous silica sheath. The pattern taken from the boundary region between the Si and In segments shown in Figure 4e implies that the (002) plane of Si (marked with a circle) is nearly parallel to the $(1\bar{1}2)$ plane of In

 © 2005 Wiley-VCH Verlag GmbH & Co. KGaA, Weinheim

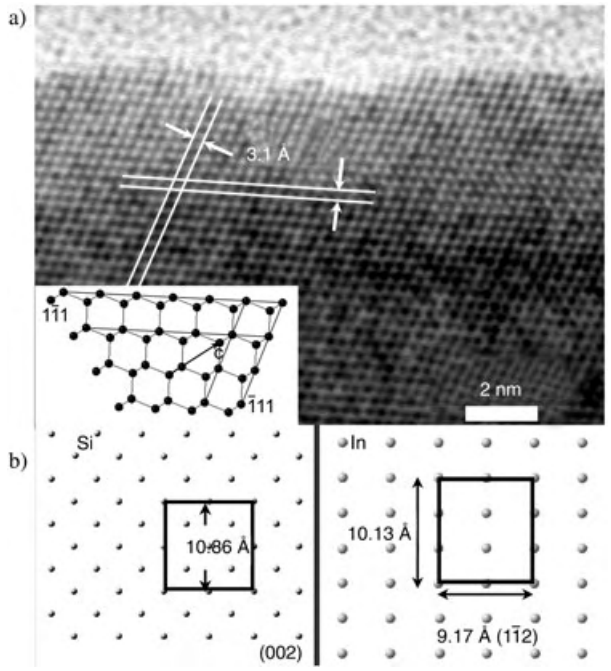

Figure 5. a) High-resolution TEM image of a Si subnanowire in which sets of {111} ($d_{111} = 3.135$ Å) planes are marked with double lines; the inset shows the scheme of a diamondlike Si crystal structure viewed along the [110] direction; b) structural model showing the (002) plane of diamondlike Si and the (1$\bar{1}$2) plane of tetragonal In.

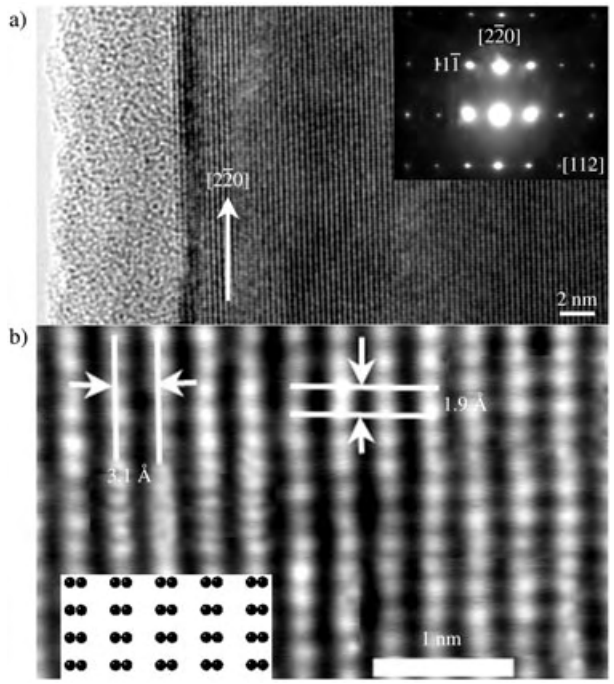

Figure 6. a) TEM image of a Si subnanowire in which the inset shows the corresponding SAED pattern; b) HRTEM image of Si subnanowire growth along the [1$\bar{1}$0] direction ($d_{11\bar{1}} = 3.13$ Å, $d_{2\bar{2}0} = 1.92$ Å, indicated by double lines) in which the inset shows the scheme of the diamondlike Si crystal structure viewed along the [112] direction.

(marked with a square). Figure 5b shows the structural model of diamondlike Si on the (002) plane and that of tetragonal In on the (1$\bar{1}$2) plane. The square dimensions on the Si (002) plane are close to those of the rectangle on the In (1$\bar{1}$2) plane. Thus it is reasonable to suggest that the growth of Si and In nanowires is crystallographically related.

The HRTEM image of a Si branch in Figure 6a clearly shows that a Si crystalline core is sheathed by an $\approx$8-nm thick amorphous silica shell. The spots on the corresponding SAED pattern (Figure 6a, inset) can be indexed to the [112]-zone axis of a diamondlike Si crystal. The clearly resolved interplanar fringes of 3.10 Å and 1.90 Å are observed in the HRTEM image (Figure 6b). These coincide with the (111) and (220) lattice spacings, respectively, of a diamondlike Si crystal. The HRTEM image is consistent with the projection of the diamondlike Si crystal along the [112] orientation, as shown in the inset of Figure 6b. The [2$\bar{2}$0] preferential growth orientation is also confirmed by the SAED pattern and the HRTEM image. Some other preferential growth orientations such as [1$\bar{1}$1] and [3$\bar{3}$1] are illustrated in the Supporting Information.

VLS or OA growth mechanisms are generally attributed to the anisotropic growth of Si nanowires. During the VLS-growth process,[17,18] a metal nanoparticle acts as a preferential site for vapor absorption to form a liquid alloy. Once an absorbed reactant is supersaturated within a liquid alloy at a given temperature, it nucleates from the supersaturated liquid droplet. Further condensation of the reactant vapors on the alloy droplets may result in the continuous axial growth of Si nanowires. It is crucial for VLS growth that one end of the Si nanowire is capped with an alloy droplet. Si nanowires generated by the VLS process are generally oriented along the [111] axis. In contrast, Si atom supersaturation during OA growth ranges from negligible to moderate.[19–22]

The Si nanowires presented herein are sheathed with amorphous silica along their entire lengths. The presence of oxygen leads to the formation of amorphous silica and has a significant effect on the surface stability of crystalline Si. This may promote the anisotropic growth of Si nanowires. Various growth directions have been documented for Si nanowires generated by OA growth.[21,22] Given that various orientations are possible for the anisotropic growth of Si nanowires sheathed with amorphous silica, it is assumed that their growth is determined by an OA-growth process. Silicon oxide clusters are stable in the gas phase at high temperatures.[23] They facilitate the nucleation and growth of Si nanostructures.[20] Disproportionation of SiO to Si and SiO_2 can result in the growth of Si nanowires.[19–22] During the synthesis process, SiO powder may sublime to generate a SiO vapor. At 1400 °C, the equilibrium pressure of metallic In is as high as $\approx$1000 Pa. If brought by an Ar gas flow to a lower-temperature region ($\approx$900 °C), In vapor condenses to produce liquid In droplets. Gaseous SiO deposits on the In droplets and subsequently disproportionates to generate Si nanocrystals and an amorphous silica sheath. Anisotropic growth of Si nanocrystals by the OA process results in the formation of Si nanowires sheathed with amorphous silica. At $\approx$900 °C, atomic mobility is high enough to allow self-assembly of newly arrived atoms within the growing edges and to promote the fast growth of silica nanotubes on the In droplets.[24] During the growth of Si

 © 2005 Wiley-VCH Verlag GmbH & Co. KGaA, Weinheim

nanowires, silica nanotubes may grow in the opposite direction. Meanwhile, a condensed In vapor is drawn into the nanometer-sized cavity of silica nanotubes through capillarity.[25] No indium oxide is observed, as the bonding energy of Si–O (798.8 kJ mol^{-1}) is much higher than that of In–O (360.21 kJ mol^{-1}).[26] Consequently, a uniform SiO_2 sheath is formed along an entire In–Si contact. When the furnace temperature is lower than the melting point of metallic In (156.6 °C), columns of liquid In confined within silica nanotubes transform into solid In nanowires. The crystalline Si nanowires may have a certain impact on the crystallization of In nanowires, as both materials have closely related crystallographic features, as demonstrated in Figure 4. Owing to a volume decrease of an In column upon crystallization, an empty amorphous silica nanotube may remain above an In–Si heterojunction as shown in Figure 2a.

Finally, the thermal expansion of an In column confined within a silica nanotube and adjacent to a Si segment was investigated by means of a Gatan heating holder attached to the TEM. Figure 7 shows consecutive TEM images of an In column under heating. Initially the In column jumps abruptly upon melting (m.p. 156.6 °C), a consequence of the significant density difference between the solid and liquid In phases. Next the In column expands linearly with increasing temperature, in accord with the thermal-expansion behavior of bulk metallic In (or Ga).[27,28] The expansion of a liquid In column as a part of an In–Si 1D heterojunction sheathed with silica may permit the smart design of a temperature-driven switch and/or sensor within an electronic device.

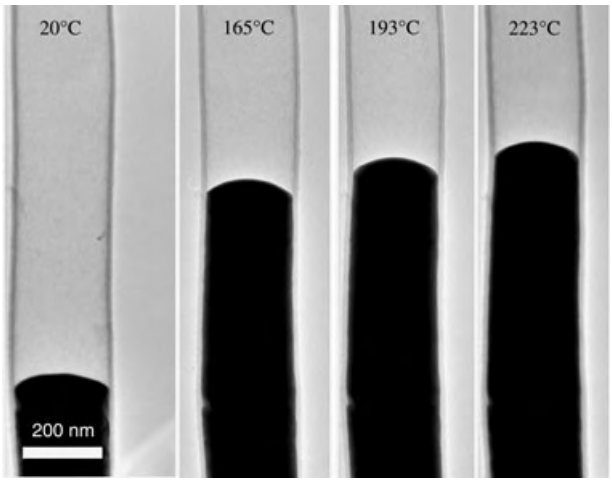

Figure 7. Consecutive TEM images of melting and thermal expansion of an In column (the part of an In–Si heterojunction) confined within a silica tube during TEM heating in situ.

In conclusion, simultaneous thermal evaporation of In and SiO powders has been shown to generate end-to-end In–Si nanowire contacts that are uniformly sheathed with amorphous silica. Within a junction, the In and Si fragments are crystallographically oriented with respect to each other. The In branch of a given junction, confined within the silica nanotube, displays a thermal expansion similar to that of bulk metallic In which opens prospects for the design of a unique temperature-driven switch and/or sensor within a metal–semiconductor electronic device.

Experimental Section

The In–Si nanowire heterojunctions were synthesized in a vertical induction furnace equipped with a fused-quartz tube and an induction-heated cylinder made of high-purity graphite coated with a carbon fiber thermoinsulating layer. The furnace was equipped with an inlet C pipe on top, and an outlet C pipe at the base. A graphite crucible that contained a ground mixture of In (1.15 g) and SiO (0.44 g) was placed in the center cylinder zone. After evacuation of the quartz tube to $\approx 10^{-3}$ Pa, a pure Ar flow was set within the carbon cylinder at a constant rate of 1000 std cm^3 min^{-1}. The furnace was heated to and kept at 1400 °C for 1 h. After the reaction was terminated and the furnace cooled to room temperature, a gray-colored product was collected from the cylinder outlet. The product was characterized by powder XRD (RINT 2200) with $Cu_{K\alpha}$ radiation ($\lambda = 1.5418$ Å), SEM (JSM-6700F), and by means of HRTEM (JEM-3000F) on a field-emission (300 kV) energy-filtered (Omega Filter) electron microscope (JEM-3100F; JEOL) equipped with an energy-dispersive X-ray spectrometer.

Received: December 5, 2004
Published online: February 23, 2005

Keywords: indium · nanostructures · nanotubes · semiconductors · silicon

[1] a) X. F. Duan, Y. Huang, R. Agarwal, C. M. Lieber, *Nature* **2003**, *421*, 241–245; b) Y. Cui, C. M. Lieber, *Science* **2001**, *291*, 851–853; c) M. Law, D. Sirbuly, J. Johnson, J. Goldberger, R. Saykally, P. Yang, *Science* **2004**, *305*, 1269–1273.

[2] a) Y. Xia, G. M. Whitesides, *Angew. Chem.* **1998**, *110*, 568–594; *Angew. Chem. Int. Ed.* **1998**, *37*, 550–575; b) Y. Xia, P. Yang, Y. Sun, Y. Wu, B. Mayers, B. Gates, Y. Yin, F. Kim, Y. Yan, *Adv. Mater.* **2003**, *15*, 353–389; c) D. Wang, H. Dai, *Angew. Chem.* **2002**, *114*, 4977–4980; *Angew. Chem. Int. Ed.* **2002**, *41*, 4783–4786; d) J. Zhan, X. Yang, D. Wang, S. Li, Y. Xia, Y. Qian, *Adv. Mater.* **2000**, *12*, 1348–1351; e) G. R. Patzke, F. Krumeich, R. Nesper, *Angew. Chem.* **2002**, *114*, 2554–2571; *Angew. Chem. Int. Ed.* **2002**, *41*, 2446–2461; f) C. N. R. Rao, F. L. Deepak, G. Gundiah, A. Govindaraj, *Prog. Solid State Chem.* **2003**, *31*, 5–147; g) R. Q. Zhang, Y. Lifshitz, S. T. Lee, *Adv. Mater.* **2003**, *15*, 635–640; h) B. Liu, S. Yu, L. Li, Q. Zhang, F. Zhang, K. Jiang, *Angew. Chem.* **2004**, *116*, 4849–4854; *Angew. Chem. Int. Ed.* **2004**, *43*, 4745–4750; i) J. Liu, Q. Li, T. Wang, D. Yu, Y. Li, *Angew. Chem.* **2004**, *116*, 5158–5162; *Angew. Chem. Int. Ed.* **2004**, *43*, 5048–5052; j) A. R. Armstrong, G. Armstrong, J. Canales, P. G. Bruce, *Angew. Chem.* **2004**, *116*, 2336–2338; *Angew. Chem. Int. Ed.* **2004**, *43*, 2286–2288.

[3] S. M. Sze, *Physics of Semiconductor Devices*, Wiley, New York, **1981**.

[4] M. S. Gudiksen, L. J. Lauhon, J. Wang, D. C. Smith, C. M. Lieber, *Nature* **2002**, *415*, 617–620.

[5] Y. Wu, R. Fan, P. Yang, *Nano Lett.* **2002**, *2*, 83–86.

[6] M. T. Bjork, B. J. Ohlsson, T. Sass, A. I. Persson, C. Thelander, M. H. Magnusson, K. Deppert, L. R. Wallenberg, L. Samuelson, *Nano Lett.* **2002**, *2*, 87–89.

[7] L. J. Lauhon, M. S. Gudiksen, D. Wang, C. M. Lieber, *Nature* **2002**, *420*, 57–61.

[8] J. Hu, M. Ouyang, P. Yang, C. M. Lieber, *Nature* **1999**, *399*, 48–51.

 © 2005 Wiley-VCH Verlag GmbH & Co. KGaA, Weinheim

[9] Y. Wu, J. Xiang, C. Yang, W. Lu, C. M. Lieber, *Nature* **2004**, *430*, 61 – 65.
[10] *Future Trends in Microelectronics: The Road Ahead* (Eds: S. Luryi, J. M. Xu, A. Zaslavsky), Wiley, New York, **1999**.
[11] a) A. Liu, R. Jones, L. Liao, D. Samara-Rubio, D. Rubin, O. Cohen, R. Nicolaescu, M. Paniccia, *Nature* **2004**, *427*, 615 – 618; b) N. Mathur, *Nature* **2002**, *419*, 573 – 575.
[12] a) Y. Wu, Y. Cui, L. Huynh, C. J. Barrelet, D. C. Bell, C. M. Lieber, *Nano Lett.* **2004**, *4*, 433 – 436; b) J. D. Holmes, K. P. Johnston, R. C. Doty, B. Korgel, *Science* **2000**, *287*, 1471 – 1473; c) S. T. Lee, Y. F. Zhang, N. Wang, Y. H. Tang, I. Bello, C. S. Lee, *J. Mater. Res.* **1999**, *14*, 4503 – 4507; d) G. Gundiah, F. L. Deepak, A. Govindaraj, C. N. R. Rao, *Chem. Phys. Lett.* **2003**, *381*, 579 – 583.
[13] K. Soulantica, A. Maisonnat, F. Senocq, M. C. Fromen, M. J. Casanove, B. Chaudret, *Angew. Chem.* **2001**, *113*, 3071 – 3074; *Angew. Chem. Int. Ed.* **2001**, *40*, 2984 – 2986.
[14] Y. Li, X. Li, Z. Deng, B. Zhou, S. Fan, J. Wang, X. Sun, *Angew. Chem.* **2002**, *114*, 343 – 345; *Angew. Chem. Int. Ed.* **2002**, *41*, 333 – 335.
[15] A. Rogachev, A. Bezryadin, *Appl. Phys. Lett.* **2003**, *83*, 512 – 514.
[16] P. Schwerdtfeger, *Angew. Chem.* **2003**, *115*, 1936 – 1939; *Angew. Chem. Int. Ed.* **2003**, *42*, 1892 – 1895.
[17] A. M. Morales, C. M. Lieber, *Science* **1998**, *279*, 208 – 211.
[18] Y. Wu, P. Yang, *J. Am. Chem. Soc.* **2001**, *123*, 3165 – 3166.
[19] D. D. D. Ma, C. S. Lee, F. C. K. Au, S. Y. Tong, S. T. Lee, *Science* **2003**, *299*, 1874 – 1877.
[20] R. Q. Zhang, M. W. Zhao, S. T. Lee, *Phys. Rev. Lett.* **2004**, *93*, 095503-1–095503-4.
[21] T. Y. Tan, S. T. Lee, U. Gösele, *Appl. Phys. A* **2002**, *74*, 423 – 432.
[22] C. P. Li, C. S. Lee, X. L. Ma, N. Wang, R. Q. Zhang, S. T. Lee, *Adv. Mater.* **2003**, *15*, 607 – 609.
[23] L. Brewer, *Chem. Rev.* **1953**, *53*, 1 – 75.
[24] Z. R. Dai, Z. W. Pan, Z. L. Wang, *Adv. Funct. Mater.* **2003**, *13*, 9 – 24.
[25] P. M. Ajayan, S. Iijima, *Nature* **1993**, *361*, 333 – 334.
[26] *Lange's Handbook of Chemistry*, 15th ed. (Ed.: J. A. Dean), McGraw-Hill, New York, **1999**, section 4.
[27] Y. Li, Y. Bando, D. Golberg, *Adv. Mater.* **2004**, *16*, 37 – 40.
[28] Y. Gao, Y. Bando, *Nature* **2002**, *415*, 599 – 599.

 © 2005 Wiley-VCH Verlag GmbH & Co. KGaA, Weinheim

Fluorescence Biochemistry

Enzymatic Incorporation of an Antibody-Activated Blue Fluorophore into DNA**

Gunnar F. Kaufmann, Michael M. Meijler, Chengzao Sun, Da-Wei Chen, David P. Kujawa, Jenny M. Mee, Timothy Z. Hoffman, Peter Wirsching, Richard A. Lerner, and Kim D. Janda**

Fluorescently labeled DNA polymers are valuable molecular probes that are widely used in fundamental science and medicine. A variety of methods for the generation of fluorescently labeled DNA have been reported over the past 10 years. These include the enzymatic incorporation of fluorophore-conjugated deoxynucleotide triphosphates into nucleic acids by such techniques as random priming, nick translation, and PCR.[1,2] High-throughput genomic analyses such as DNA arrays rely on the availability of fluorescent probes that have exceptional hybridization characteristics, minimal cross-reactivity, and low background fluorescence. Significant progress continues in the discovery of new hybridization assays and in the improvement of those already in use.[3] However, further investigations of new fluorescent nucleic acid probes are required to sustain the current level of success in this field.

In this context we recently reported the generation of antibodies that bind with stilbene to perturb its excited state potential energy surface; upon irradiation with UV light the antibody–stilbene complexes emit a bright blue fluorescence with high quantum yield.[4–6] We have termed such complexes blue-fluorescent antibodies. Aside from their benefit to studies of the dynamics of protein–ligand interactions, these antibodies can be envisioned in a number of practical applications. One such potential application involves modified C-nucleoside–stilbene conjugates designed to probe native and non-natural DNA polymers; we have reported a series of first-generation stilbene-tethered C-nucleosides that have the capacity to combine with monoclonal antibodies (mAbs) that specifically bind *trans*-stilbene. UV irradiation of the resulting complexes produces a powder-blue fluorescence.[5]

Another major potential of blue-fluorescent antibodies lies in the generation of DNA molecules that are essentially

[*] G. F. Kaufmann, Dr. M. M. Meijler, Dr. C. Sun, Dr. D.-W. Chen, D. P. Kujawa, J. M. Mee, T. Z. Hoffman, Prof. Dr. P. Wirsching, Prof. Dr. R. A. Lerner, Prof. Dr. K. D. Janda
Department of Chemistry and
The Skaggs Institute for Chemical Biology
The Scripps Research Institute
10550 N. Torrey Pines Road, La Jolla, CA 92037 (USA)
Fax: (+1) 858-784-2595
E-mail: rlerner@scripps.edu
kdjanda@scripps.edu

[**] This work was supported by The Skaggs Institute for Chemical Biology. We thank Dr. Malcolm Wood for technical assistance.

Supporting information for this article is available on the WWW under http://www.angewandte.org or from the author.

 © 2005 Wiley-VCH Verlag GmbH & Co. KGaA, Weinheim DOI: 10.1002/anie.200461143

"profluorescent"—they can be activated at will to generate a tunable and long-lived emission. Herein we describe the synthesis of a stilbene-tethered deoxyadenosine triphosphate analogue, its enzymatic incorporation into DNA to yield an antibody-activated blue fluorescent DNA polymer, and hybridization studies of the modified DNA polymer with chromosomal DNA.

To increase the chances of successful enzymatic incorporation into DNA, the stilbene moiety was conjugated to deazaadenosine with a polyethylene glycol (PEG) linker. Deazaadenosine was used for this second-generation conjugate as it is a better mimic of a natural DNA base than is the first-generation substituted benzene C-nucleoside which facilitates its recognition and incorporation by promiscuous DNA polymerases. X-ray crystallographic data from the first-generation stilbene-modified C-nucleoside–antibody EP2-19G2 complex were used for the strategic design of the second-generation linker between the stilbene group and the nucleotide analogue, as it was important to ensure sufficient linker length to allow stilbene protrusion from the DNA helix. These structural data had shown an antibody-binding-pocket depth of 7.5 Å,[6] and a completely buried stilbene molecule. This information in conjunction with the known DNA-major-groove depth of 8.5 Å[5] led to our selection of a PEG linker of four ethylene glycol units. This provides the necessary 16-Å length and is sufficiently hydrophilic to ensure solvent exposure of the stilbene moiety. We therefore anticipated that the PEG linker would permit efficient incorporation by DNA polymerases and facilitate unhindered antibody binding.

Deaza-ATP–PEG–stilbene **9** was synthesized in a convergent fashion as presented in Scheme 1. The stilbene–PEG linker **5** was prepared by coupling chloromethylstilbene with mono(tetrahydropyranyl)-protected tetraethylene glycol **2,** followed by deprotection and addition of bromoacetic acid. With compound **5** in hand, attachment of the deazaadenosine base was the next task. We envisioned the use of **7** to meet our needs as it could be readily prepared from 7-deaza-2′-deoxy-7-[ω-(trifluoroacetamido)propynyl]-adenosine **6**.[7] Conjugation of **5** and **7** through EDC coupling generated **8** as the main product, albeit in moderate yield (Scheme 1B). The stilbene-tethered nucleoside **8** was converted into the final product triphosphate form **9** by a three-step one-pot procedure developed by Kovacs and Otvos.[8] The product **9** in its TEA salt form was purified by DEAE column chromatography and characterized by ^{1}H, ^{13}C, and ^{31}P NMR spectroscopy and FTMS.

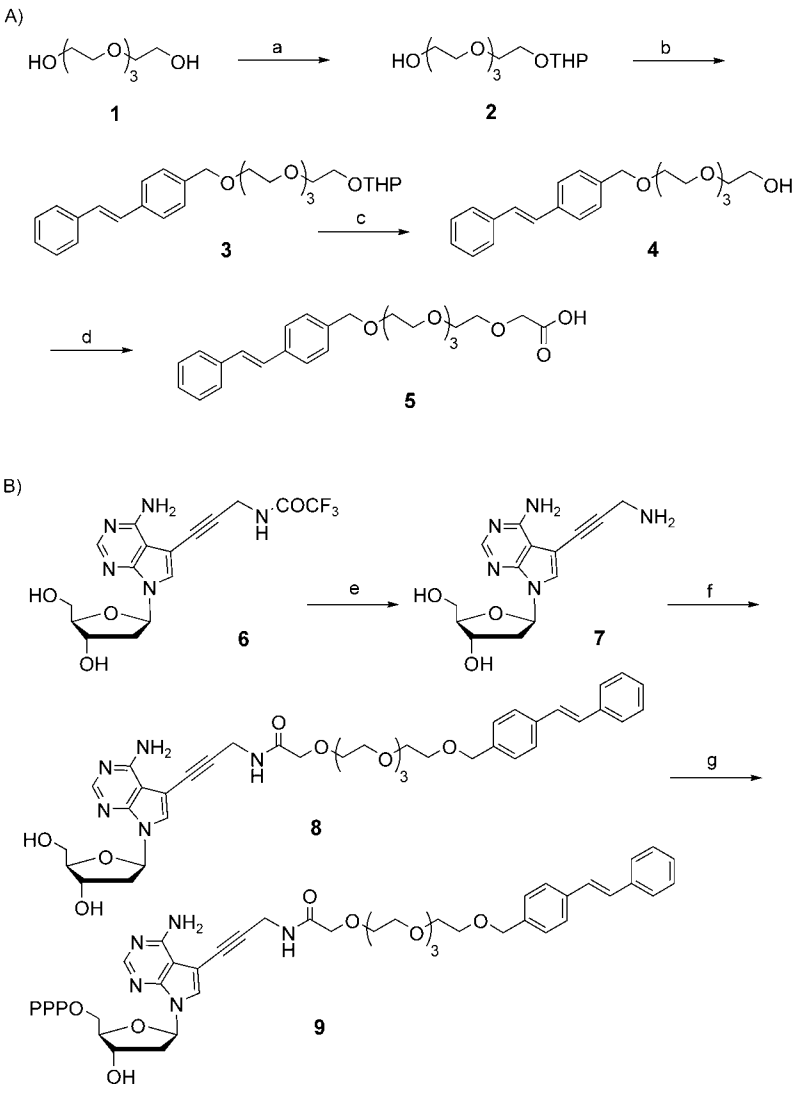

Scheme 1. Synthesis of deaza-ATP–PEG–stilbene **9**: A) Synthesis of PEG-modified stilbene: a) dihydropyran, PPTS, CH_2Cl_2, 38%; b) chloromethylstilbene, NaH, THF, 61%; c) *p*TsOH, MeOH, 86%; d) bromoacetic acid, NaH, THF, 67%; B) Conjugation of the PEG–stilbene group to deazaadenosine and phosphorylation: e) NH_4OH, MeOH, 90%; f) **5**, EDC, NHS, CH_2Cl_2/DMF, 36%; g) $POCl_3$, proton sponge, $PO(OMe)_3$; then bis(tri-*n*-butylammonium) pyrophosphate, Bu_3N, DMF; then TEA/H_2CO_3, 52%; DMF = *N*,*N*-dimethylformamide; EDC = 3-(3-dimethylaminopropyl)-1-ethylcarbodiimide; NHS = *N*-hydroxysuccinimide; PPTS = pyridinium 4-toluenesulfonate; TEA = triethylamine; THP = tetrahydropyranyl; Ts = 4-toluenesulfonyl; see Supporting Information for details.

As detailed above, a key prerequisite for the success in the general applicability of compound **9** is for it to be recognized as a viable substrate by thermophilic DNA polymerases. The efficiency of enzymatic incorporation of modified nucleotides into nascent DNA varies widely; it depends on the DNA polymerase used, and the size, charge, and hydrophobicity of the nucleobase modification. It is assumed that the hydrophobic nature of most fluorescent modifications, steric congestion, as well as intra- and intermolecular interactions play an important role in the enzyme-directed incorporation of modified nucleotides into a DNA polymer. Four commercially available thermophilic DNA polymerases were evaluated for their ability to incorporate **9** into a DNA polymer. Based on amino acid sequence similarities to *E. coli* DNA polymerases I, II, III, and IV/V, other DNA polymerases can be classified into families A, B, C, and Y, respectively.[9] From the family of A-type DNA polymerases, Red*Taq* DNA polymerase was chosen; *Vent* DNA polymerase represented the family of B-type DNA polymerases. Critical importance was also placed on the influence of polymerase proofreading (3′→5′ exonuclease activity) on the ability of the enzymes to

 © 2005 Wiley-VCH Verlag GmbH & Co. KGaA, Weinheim

recognize compound **9** as substrate. Therefore, *Pfu* DNA polymerase, known for its efficient proofreading ability was investigated along with an enzyme that lacks proofreading activity, the exonuclease-deficient form of *Vent* DNA polymerase, *Vent* exo$^-$.

The gene encoding the anti-cocaine single-chain antibody (scFv) GNC92H2 was chosen as template DNA.[10] It provides an excellent test, as the gene consists of 801 base pairs with 372 adenosine residues, including the flanking primer sequences. In the standard PCR reactions all four natural nucleotides were used at concentrations of 200 μM each, yet the ratio between dATP and **9** was varied (Table 1). The PCR products were purified and subsequently analyzed on an agarose gel (1%) after electrophoretic separation. The results that indicate whether full-length gene products were obtained and the relative yields are summarized in Table 1, and can be summarized as follows: 1) all four commercially-available DNA polymerases are able to incorporate **9** into a DNA polymer; 2) the extent to which these DNA polymerases are able to process compound **9** as substrate depends on the proofreading activity of the enzyme; 3) the proofreading activity appears to interfere minimally with the incorporation of **9**, which suggests that in the case of the *Vent* and *Pfu* DNA polymerases, compound **9** is recognized as a substrate for 3′→5′ exonuclease activity; 4) *Vent* exo$^-$ is the most efficient in the incorporation of **9**, and up to 40% of the available ATP in the reaction medium consisted of **9** (although, as measured by UV/Vis and fluorescence spectroscopy (discussed below) the yield of incorporation was lower: roughly 3% of the DNA consisted of **9**). This is consistent with other reports that describe the ability of *Vent* exo$^-$ DNA polymerase to incorporate nucleotide analogues.

Table 1: Summary of PCR experiments with different DNA polymerases.

dATP/**9** ratio	98:2	96:4	94:6	92:8	9:1	8:2	7:3	6:4	5:5
[**9**] [μM]	4	8	12	16	20	40	60	80	100
Pfu	√	√	√	√	√	(√)	(√)	–	–
Red*Taq*	√	√	√	√	√	√	(√)	–	–
Vent	√	√	√	√	√	(√)	(√)	–	–
Vent exo$^-$	√	√	√	√	√	√	√	√	(√)

√ = PCR product clearly visible; (√) = PCR product visible as faint band; – = no PCR product visible.

It has been shown that *Vent* exo$^-$ DNA polymerase has a higher binding affinity for nucleotides and a faster phosphoryl-transfer rate than the *Vent* DNA polymerase.[11] Notably, the overall fidelity of *Vent* exo$^-$ DNA polymerase is still twofold higher than that of *Taq* DNA polymerase. To underscore the significance of our findings, we sought to compare the incorporation data of compound **9** with pyrene-8-dATP, a structurally related, commercially available, non-natural fluorescent nucleotide in its role as substrate for the four DNA polymerases tested. Pyrene-8-dATP was also a good candidate for the determination of any potential differences in fluorescence intensity relative to that of **9**; this point is especially pertinent as the fluorescence excitation and emission maxima of pyrene-8-dATP ($\lambda_{excitation} = 340$ nm, $\lambda_{emission} = 376, 395$ nm) are relatively close to those of **9**. Quite unexpectedly, the same four DNA polymerases that incorporated compound **9** successfully, did not produce any observable incorporation of pyrene-8-dATP into nascent DNA along the same DNA template under a wide variety of conditions (Supporting Information).

To further elucidate the properties of the stilbene-modified nucleotide **9** and its corresponding DNA polymer, gel shift mobility assays and sandwich enzyme-linked immunosorbent assays (ELISA) were used to scrutinize purified full-length PCR products containing stilbene residues (Supporting Information). The fluorescence emission characteristics of stilbene-bearing DNA upon binding to mAb EP2-19G2 were measured by fluorescence spectroscopy (Figure 1). The fluorescence quantum yield of the EP2-19G2–**9** complex is lower ($\Phi_f = 0.21$) than the quantum yield of the complex with the nonconjugated stilbene hapten ($\Phi_f = 0.78$). Notably, however, this quantum yield is comparable to that of other fluorescent nucleotides.[2] Furthermore, this fluorescent nucleotide–antibody complex is less prone to bleaching than many other fluorescent nucleotides.

As can be deduced from Figure 1, out of the four polymerases analyzed the *Vent* exo$^-$ DNA polymerase was the most efficient in incorporating **9** into DNA. Under the assumption that fluorescence quenching by the DNA polymer is minimal, these results indicate that up to 10

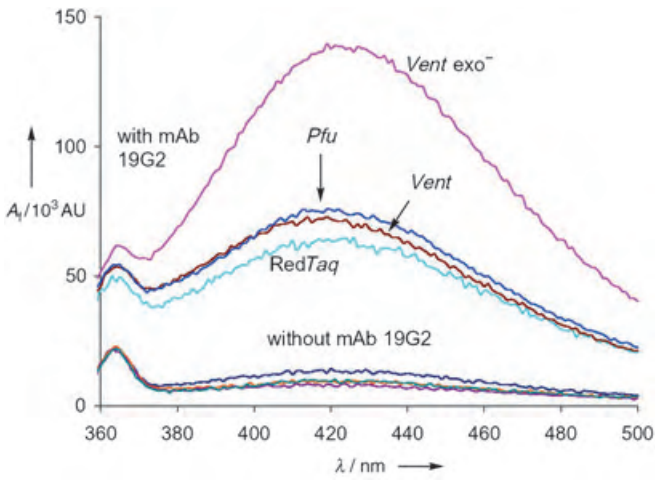

Figure 1. Fluorescence spectra of DNA containing **9** (sDNA). sDNA was obtained by PCR with four different DNA polymerases and a mixture of dATP and **9**, with the template plasmid, pCGMT-92H2. Fluorescence spectra of the purified reaction products (0.1 μM) were measured in the presence (upper four traces) or absence (lower four traces) of excess (10 μM) mAb EP2-19G2. The complex of mAb EP2-19G2 and the stilbene-containing DNA emits blue fluorescence upon UV irradiation ($\lambda_{excitation} = 327$ nm, $\lambda_{emission} = 425$ nm). The signal intensity (with mAb) for the DNA generated by reaction with the *Vent* exo$^-$ DNA polymerase roughly corresponds to that of a solution of **9** (1 μM, with mAb) which indicates complex formation of about 10 antibody molecules per stilbene-containing DNA polymer (2.7% of the total number of deoxyadenosine residues present). UV and fluorescence measurements on the sample without added mAb indicated a slightly higher incorporation yield (≈13–14 units of **9** per DNA molecule). Incubation of unmodified DNA with mAb EP2-19G2 showed only background fluorescence.

 © 2005 Wiley-VCH Verlag GmbH & Co. KGaA, Weinheim

stilbene moieties are bound by mAb EP2-19G2. A slightly higher incorporation yield for **9** was observed by spectroscopic analysis of the modified DNA in the absence of antibody (based on the absorption of stilbene at 320 nm); we believe that steric hindrance prevents recognition of some of the neighboring stilbene moieties.

Having established the spectral and enzymatic incorporation properties of compound **9**, the next step was to test the applicability of this technique for hybridization studies. Our initial study was designed to assess the ability of the stilbene-modified DNA to hybridize with isolated chromosomal DNA without loss of its ability to be recognized and activated by an antibody. Isolated genomic DNA from the ovary cancer cell line NIH:OVCAR-3 was used to generate DNA probes specific for the X-chromosomal centromeric alpha satellite DNA, locus DXZ1. NIH:OVCAR-3 cells were grown in culture and harvested at a density of 10^6 mL^{-1}. The cells were then fixed, and hybridization experiments were conducted according to standard literature protocols (Supporting Information). An excess of mAb EP2-19G2 was added, and after an incubation time of 1 h the outcome of the hybridization experiment was analyzed with deconvolution fluorescence microscopy (Figure 2). Figure 2A provides a differential interference contrast (DIC) image, Figure 2B shows the fluorescence image of the same view, and Figure 2C is a merged image of both. The combination of these three images provides strong evidence of hybridization between probes that consist of compound **9** and chromosomal DNA.

We have reported herein the chemical synthesis and biological evaluation of a nucleotide analogue modified with an antibody-activated blue fluorophore. The labeled nucleotide alone is essentially nonfluorescent, and only upon addition of the antibody is fluorescence generated. Thus, the antibody may be envisioned as a secondary affinity reagent that specifically induces a signal. The importance of this is that one can visualize, in real time, the presence or absence of a given strand of DNA by the simple augmentation of a reagent (antibody). This provides an "encoded" response, in which the antibody serves as a means of decoding. This method has the advantage that a fluorescent complex can be generated without the need for a secondary label or antibody that has inherent fluorescence (for example, digoxigenin–fluorescent-antidigoxigenin antibody complexes). All other methods, including continual DNA tagging, present fluorescence properties all of the time.

As a further advantage, the highly specific and strong interaction between the antibody and the stilbene-modified nucleotide should be amenable to DNA affinity purification and enrichment strategies. We anticipate that the preparation of additional non-natural bases tethered to modified stilbenes should allow the generation of a variety of "profluorescent" DNA molecules. In this context we note that very few fluorescent nucleotides fluoresce at 420 nm. This, combined with the ability to change the intensity of the emission, adds variability to the repertoire of techniques available for DNA staining in genomic applications. DNA molecules modified with compound **9** and related bases have envisioned uses in a variety of experimental settings such as investigations of protein–DNA interactions, gene arrays (DNA chips), detection of single nucleotide polymorphisms (SNPs), and in situ fluorescence hybridization (FISH).

Experimental Section

Synthesis. ^{1}H and ^{13}C NMR spectra were measured on a Bruker AMX-400 or Bruker AMX-500 spectrometer as indicated. Chemical shifts (ppm) are reported relative to internal $CDCl_3$ (^{1}H, 7.26 ppm and ^{13}C, 77.0 ppm); CD_3OD (^{1}H, 3.30 ppm and ^{13}C, 49.2 ppm), and [D_6]DMSO (^{1}H, 2.49 ppm and ^{13}C, 39.0 ppm). HRMS data were collected with ESI or MALDI techniques. Glassware and solvents were dried by standard methods. Flash chromatography was performed on silica gel 60 (230–400 mesh), and thin-layer chromatography, on glass plates coated with a layer (0.02 mm) of silica gel 60 F-254. All chemical reagents and solvents were obtained from Aldrich unless otherwise noted, and used without further purification.

8: EDC-HCl was added to a solution of **5** (27.5 mg, 0.062 mmol) and NHS (8.8 mg, 0.074 mmol) in CH_2Cl_2 (1.5 mL) and DMF (0.2 mL), and stirred for 6 h at room temperature under N_2. A solution of **7** (15 mg, 0.05 mmol) in DMF (0.6 mL) was added. The suspension was stirred overnight. After concentration, the residue was purified by PTLC (CH_2Cl_2/MeOH, 10:1) to give **8** (13 mg, 36%) as a colorless syrup. ^{1}H NMR (400 MHz, CD_3OD): $\delta = 8.05$ (s, 1H), 7.53–7.46 (m, 5H), 7.33–7.27 (m, 4H), 7.23–7.19 (m, 1H), 7.11 (s, 2H), 6.43 (dd, $J = 7.9$, 5.8 Hz, 1H), 4.49–4.46 (m, 3H), 4.24 (s, 2H), 4.01 (s, 2H), 3.99–3.97 (m, 2H), 3.76 (dd, $J = 12.3$, 3.2 Hz, 1H), 3.71–3.58 (m, 17H), 2.62–2.54 (m, 1H), 2.27 ppm (ddd, $J = 13.2$, 5.9, 2.6 Hz, 1H); ^{13}C NMR (100 MHz, CD_3OD): $\delta = 173.2$, 159.2, 155.5, 153.2, 150.0,

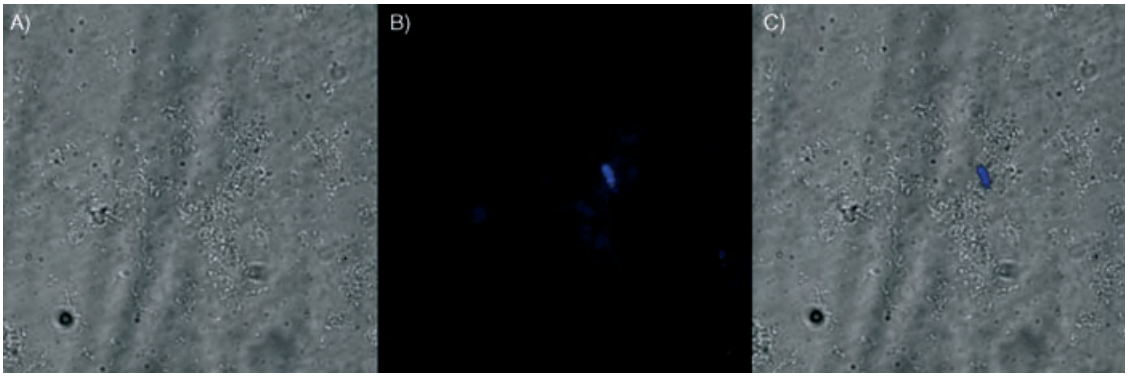

Figure 2. Examples of deconvolution microscopy images showing the hybridization of DXZ1-specific, stilbene-labeled DNA probes to chromosomal DNA. A) Differential interference contrast (DIC) image; B) fluorescence image of the same experiment; C) merged view of images from parts A) and B). Note that a fluorescence image of the sample without added antibody is completely dark.

 © 2005 Wiley-VCH Verlag GmbH & Co. KGaA, Weinheim

139.0, 138.8, 138.2, 130.0, 129.7, 129.3, 129.2, 128.6, 128.0, 127.5, 104.8, 96.9, 89.4, 89.2, 86.7, 76.1, 73.8, 73.0, 72.0, 71.5, 71.4, 71.3, 71.2, 70.6, 63.6, 41.6, 30.2 ppm; FTMS: calcd for $C_{39}H_{47}N_5NaO_9$ $[M+Na]^+$: 752.3266; found: 752.3291.

9: A solution of **8** (13 mg, 0.018 mmol) and proton sponge (5.6 mg, 0.027 mmol) in $PO(OMe)_3$ (0.18 mL) was stirred for 10 min at 0 °C under N_2. $POCl_3$ (3.3 μL, 0.036 mmol) was added, and the mixture was stirred for 2 h at 0 °C. A mixture of Bu_3N (25 μL, 0.11 mmol) and anhydrous bis(tri-*n*-butylammonium) pyrophosphate (40 mg, 0.089 mmol) in DMF (0.18 mL) was added at once. After 1 min, triethylammonium bicarbonate buffer (1.0 M, 4 mL) was added, and the clear solution was stirred at room temperature for 30 min and lyophilized overnight. The crude material was separated by reversed-phase HPLC with a DEAE column (0.1 M TEAB/MeCN) to give **9** (9.0 mg, 52%) as a white solid. ^{31}P NMR (140 MHz, Tris (50 mM), EDTA (2 mM), pH 7.5 in D_2O): $\delta = -5.6$ (d, $J = 15.8$ Hz), -10.5 (d, $J = 15.8$ Hz), -21.6 ppm (t, $J = 15.8$ Hz); MALDI-FTMS: calcd for $C_{39}H_{50}N_5O_{18}P_3$ $[M+H]^+$: 970.2436; found: 970.2477; TEAB = tetraethylammonium bromide.

Additional experimental details for the synthesis of reported compounds, and ^1H and ^{13}C NMR spectra of compounds **7** and **8** can be found in the Supporting Information.

Fluorescence spectroscopy: Stilbene-containing DNA was generated by using PCR methodology with a dATP/**9** ratio of 7:3 and *Vent* exo$^-$ DNA polymerase. The PCR product was purified, and the product DNA concentration was spectrophotometrically determined to be 0.55 μM. This DNA was used in spectrofluorometric assays to estimate the actual concentration of the stilbene fluorophore. The fluorescence ($\lambda_{excitation} = 327$ nm, $\lambda_{emission} = 425$ nm) of **9** was measured at various concentrations before and after complex formation with mAb EP2–19G2 in PBS (pH 7.4). Compound **9** by itself displayed only negligible fluorescence at the concentrations used (1 μM–50 μM), whereas complex formation with mAb EP2-19G2 resulted in strong blue fluorescence comparable to that measured for the original stilbene hapten complexed with the same antibody.[6] Stilbene-modified DNA (0.1 μM) was incubated with excess (10 μM) mAb EP2-19G2 for 30 min and its fluorescence was measured with an SLM-AMINCO 8100 spectrofluorometer equipped with a 450 W xenon lamp.

Fluorescence microscopy: Fluorescence images were taken with a DeltaVision deconvolution microscope (API, Issaquah WA) equipped with a Photometrics CH350 L liquid-cooled CCD camera attached to an Olympus IX70 inverted microscope. These data were collected with either a 60× (1.4 NA) or a 100× (1.35 NA) oil immersion objective lens, and a DAPI 360/40 nm (excitation), 457/50 nm (emission) filter set. All images were deconvoluted with constrained iterative algorithms (10 iterations) of DeltaVision software (softWoRx, v2.5). The deconvoluted images were subsequently converted into tiff format using softWoRx, v2.5.

Received: July 1, 2004
Revised: November 22, 2004
Published online: March 2, 2005

Keywords: antibodies · DNA recognition · fluorescent probes · nucleotides · polymerase chain reaction

[1] a) M. Mehedi Masud, A. Ozaki-Nakamura, M. Kuwahara, H. Ozaki, H. Sawai, *ChemBioChem* **2003**, *4*, 584–588; b) S. Brakmann, S. Lobermann, *Angew. Chem.* **2001**, *113*, 1473–1476; *Angew. Chem. Int. Ed.* **2001**, *40*, 1427–1429; c) S. Brakmann, P. Nieckchen, *ChemBioChem* **2001**, *2*, 773–777.

[2] T. Tasara, B. Angerer, M. Damond, H. Winter, S. Dorhofer, U. Hubscher, M. Amacker, *Nucleic Acids Res.* **2003**, *31*, 2636–2646.

[3] a) I. Braslavsky, B. Hebert, E. Kartalov, S. R. Quake, *Proc. Natl. Acad. Sci. USA* **2003**, *100*, 3960–3964; b) D. Summerer, A. Marx, *Angew. Chem.* **2002**, *114*, 3778–3780; *Angew. Chem. Int. Ed.* **2002**, *41*, 3620–3622; c) S. Brakmann, S. Lobermann, *Angew. Chem.* **2002**, *114*, 3350–3352; *Angew. Chem. Int. Ed.* **2002**, *41*, 3215–3217.

[4] a) M. Matsushita, K. Yoshida, N. Yamamoto, P. Wirsching, R. A. Lerner, K. D. Janda, *Angew. Chem.* **2003**, *115*, 6166–6169; *Angew. Chem. Int. Ed.* **2003**, *42*, 5984–5987; b) Q. Wang, K. S. Raja, K. D. Janda, T. W. Lin, M. G. Finn, *Bioconjugate Chem.* **2003**, *14*, 38–43.

[5] D. W. Chen, A. E. Beuscher, R. C. Stevens, P. Wirsching, R. A. Lerner, K. D. Janda, *J. Org. Chem.* **2001**, *66*, 1725–1732.

[6] A. Simeonov, M. Matsushita, E. A. Juban, E. H. Z. Thompson, T. Z. Hoffman, A. E. Beuscher, M. J. Taylor, P. Wirsching, W. Rettig, J. K. McCusker, R. C. Stevens, D. P. Millar, P. G. Schultz, R. A. Lerner, K. D. Janda, *Science* **2000**, *290*, 307–313.

[7] F. Seela, M. Zulauf, *Helv. Chim. Acta* **1999**, *82*, 1878–1898.

[8] T. Kovacs, L. Otvos, *Tetrahedron Lett.* **1988**, *29*, 4525–4528.

[9] a) D. K. Braithwaite, J. Ito, *Nucleic Acids Res.* **1993**, *21*, 787–802; b) J. Filee, P. Forterre, T. Sen-Lin, J. Laurent, *J. Mol. Evol.* **2002**, *54*, 763–773.

[10] J. A. Moss, A. R. Coyle, J. M. Ahn, M. M. Meijler, J. Offer, K. D. Janda, *J. Immunol. Methods* **2003**, *281*, 143–148.

[11] a) A. F. Gardner, C. M. Joyce, W. E. Jack, *J. Biol. Chem.* **2004**, *279*, 11834–11842; b) A. F. Gardner, W. E. Jack, *Nucleic Acids Res.* **2002**, *30*, 605–613.

 © 2005 Wiley-VCH Verlag GmbH & Co. KGaA, Weinheim

Photochemistry

Conformational Control of Photochromic Reactivity in a Diarylethene Single Crystal**

Seiya Kobatake, Yoshimichi Matsumoto, and Masahiro Irie**

Photochromism is the result of reversible photoisomerization between two isomers that have distinct absorption spectra.[1,2] The two isomers differ from one another not only in their absorption spectra but also in various physical and chemical

[*] Dr. S. Kobatake
Department of Applied and Bioapplied Chemistry
Graduate School of Engineering, Osaka City University
Sugimoto 3-3-138, Sumiyoshi-ku, Osaka 558-8585 (Japan)
Fax: (+81) 6-6605-2797
E-mail: kobatake@a-chem.eng.osaka-cu.ac.jp
Y. Matsumoto, Prof. M. Irie
Department of Chemistry and Biochemistry
Graduate School of Engineering, Kyushu University
Hakozaki 6-10-1, Higashi-ku, Fukuoka, 812-8581 (Japan)
Fax: (+81) 92-642-3568
E-mail: irie@cstf.kyushu-u.ac.jp

[**] This work was supported in part by Grants-in-Aid for Scientific Research on Priority Area (417) (15033252), Young Scientists (A) (16685014), Scientific Research (S) (15105006), and the 21st Century COE Program from the Ministry of Education, Culture, Sports, Science, and Technology of Japan. We thank NIPPON ZEON CO., Ltd. for the supply of octafluorocyclopentene.

Supporting information for this article is available on the WWW under http://www.angewandte.org or from the author.

 © 2005 Wiley-VCH Verlag GmbH & Co. KGaA, Weinheim DOI: 10.1002/anie.200462426

properties, such as refractive index, dielectric constant, oxidation–reduction potential, and geometric structure. Among a number of photochromic compounds, diarylethenes with heterocyclic aryl groups such as thiophene or benzothiophene are the most promising candidates for applications in optical memories and switches, owing to their *thermally irreversible* and fatigue-resistant photochromic performance.[3,4]

Photochemical reactions in the crystalline state have been intensively investigated since the pioneering work of Schmidt and co-workers in the early 1960s.[5–11] Although many photochromic compounds have been reported already, compounds that exhibit photochromism in the crystalline state are rare.[12,13] Typical photochromic compounds such as spiropyran and azobenzene are not photochromic in the crystalline phase, as large geometric structural changes are prohibited in crystals. However, some diarylethene derivatives can exhibit photochromism even in the single-crystalline phase.[14–16] Depending on the particular structure, diarylethene crystals turn yellow, red, blue, or green upon irradiation with UV light. The color of the crystal is thermally stable, and never returns to the initial colorless state in the dark. Diarylethene derivatives are the only photochromic chromophores that exhibit *thermally irreversible* photochromism in the single-crystalline phase.[17]

Recently, our group prepared alternating nanolayered or mosaic structures composed of two kinds of diarylethene derivatives and examined their photochromic performance.[18] When the cocrystals were irradiated with UV light, only one of the derivatives underwent photochromism. As a result, the irradiated co-crystals consisted of an alternating layered structure of open- and closed-ring isomers, or of a three-dimensional alternating alignment structure of open- and closed-ring isomers. During the course of our studies into single-crystalline photochromism, we found that crystals of 1,2-bis(2-methoxy-4-methyl-5-phenyl-3-thienyl)perfluorocyclopentene (**1a**) have a novel molecular-packing structure in which two different conformations are alternately packed. Herein we report single-crystalline photochromism and the important role that conformation plays in photochromic reactivity.

Single crystals of **1a** were obtained by recrystallization from acetone. The crystals have well-developed (001), ($\bar{1}$01), (00$\bar{1}$), and (10$\bar{1}$) surfaces. Other surfaces are not well-developed and were not determined. The crystals of **1a** turned blue upon irradiation at a wavelength of 366 nm (Scheme 1). To confirm that the blue color is a result of the closed-ring isomer **1b**, the blue-colored crystal was dissolved in hexane. The solution in hexane showed a visible absorption maximum at 617 nm, which is the same as that of the isolated closed-ring isomer **1b**. The blue color of the crystal disappeared upon irradiation with visible light ($\lambda > 500$ nm). The crystal of **1a** underwent photochromism.

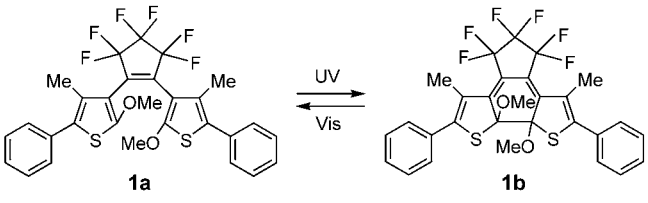

Scheme 1. Photochromic isomerization of diarylethene **1a** to the closed-ring structure **1b**.

The color of the crystal was observed with a polarizing microscope in which the polarizer and analyzer were set in parallel with each other. The UV-irradiated, colored crystal was placed on the sample stage and rotated. Viewed from the (001) surface at a given starting angle, the crystal showed a strong blue color. Upon rotation by 90°, the color of the crystal disappeared; the blue color reappeared at a rotation of 180°. The clear dichroism indicates that the photogenerated closed-ring isomers are regularly oriented in the crystal and that the photochromic reaction takes place in the crystal lattice.[14]

The crystal and molecular structures of **1a** were determined by X-ray crystallographic analysis. The crystal belongs to a monoclinic system with space group $P2_1/c$, and $Z = 8$ (Experimental Section). The two diarylethene conformers A and B are independent in the crystal. Figure 1 shows ORTEP renderings of the two conformers. The two geometric structures are different from each other, but in either case the molecules are arranged in an antiparallel orientation. Figure 2 shows the molecular packing diagrams viewed from the *b* and *c* axes. Blue- and red-rendered structures represent conformers A and B, respectively. In the crystal, the two conformations are alternately packed in layered structures with a layer thickness of ≈ 1 nm.

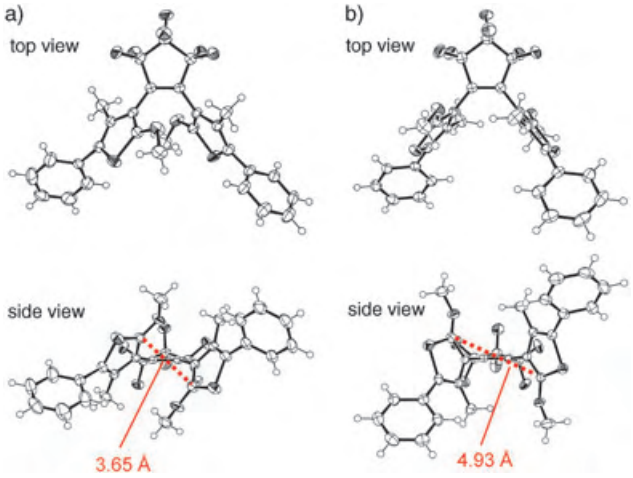

Figure 1. ORTEP renderings of a) conformer A, and b) conformer B in crystals of **1a** with 50% probability displacement ellipsoids. Distances between reactive carbon atoms are indicated, and highlighted with dashed lines.

Our group previously reported that the photocyclization reactivity of diarylethenes in the single-crystalline phase is controlled by the distance between the reactive carbon atoms in the antiparallel orientation.[19] If the distance exceeds 4.2 Å, the photocyclization reaction does not take place. However, if distance is shorter than 4.0 Å, the diarylethenes can undergo an efficient photocyclization reaction. The

 © 2005 Wiley-VCH Verlag GmbH & Co. KGaA, Weinheim

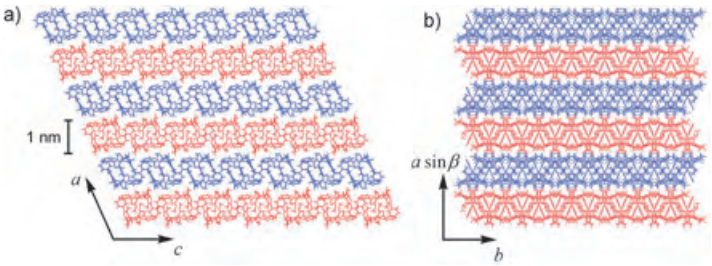

Figure 2. Molecular-packing diagrams of **1a** viewed from a) the *b* axis and b) the *c* axis. Blue- and red-colored molecules show photoactive and photoinactive diarylethene conformers A and B, respectively.

distance dependence of photochromic reactivity is similar to the observation of photochemical C–C bond formation in the crystalline phase reported by Schmidt and co-workers.[5] As shown in Figure 1, conformer A has a distance of 3.65 Å between the reactive carbon atoms, whereas the analogous distance in conformer B is 4.93 Å.

Thin microcrystals of diarylethene **1a** were prepared by sublimation on a thin glass plate by heating at 104 °C. The typical crystal size was $\approx 10 \times 10 \times 5\ \mu m^3$. Crystal shapes and reversible color changes were similar to those of crystals obtained from a solution in acetone. Microcrystals were irradiated at 366 nm ($\approx 26\ mW\,cm^{-2}$). The molar ratio of open- to closed-ring isomers (**1a**/**1b**) after irradiation with UV light was determined by HPLC (silica gel column, hexane/ethyl acetate (98:2) as eluent). Figure 3 shows the

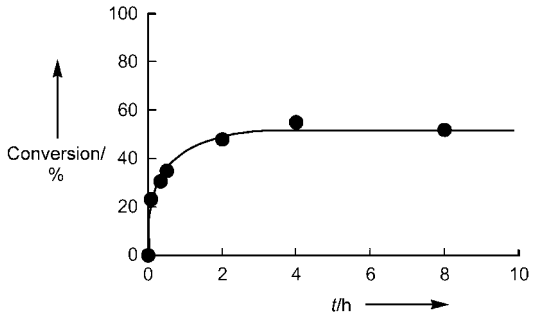

Figure 3. The progress of the photocyclization reaction over time in the diarylethene microcrystal of **1a** by irradiation at $\lambda = 366$ nm.

time dependence of the conversion ratio for the photocyclization reaction in the crystal. Upon irradiation at 366 nm, **1a** was efficiently converted into closed-ring isomer **1b** by as much as 50 % after irradiation for 4 h. This indicates that half the molecules packed in the crystal undergo the photochromic reaction.

Single crystals of **1a** were prepared by recrystallization from acetone, and were used for X-ray crystallography in situ. An appropriate size for crystallographic analysis was obtained by cutting the crystals to final dimensions of $\approx 0.3 \times 0.2 \times 0.05\ mm^3$. A single crystal was then irradiated with UV light. A high conversion ratio for such a thick crystal cannot be expected, owing to the inner-filter effect of absorption.[20] After irradiation at 366 nm ($\approx 5\ mW\,cm^{-2}$) for 5 h, the closed-ring isomer **1b** was detected by X-ray diffractometry. The space group was not changed, and the unit-cell dimensions were similar to those initially determined (Experimental Section). The molecular structure is shown in Figure 4. The

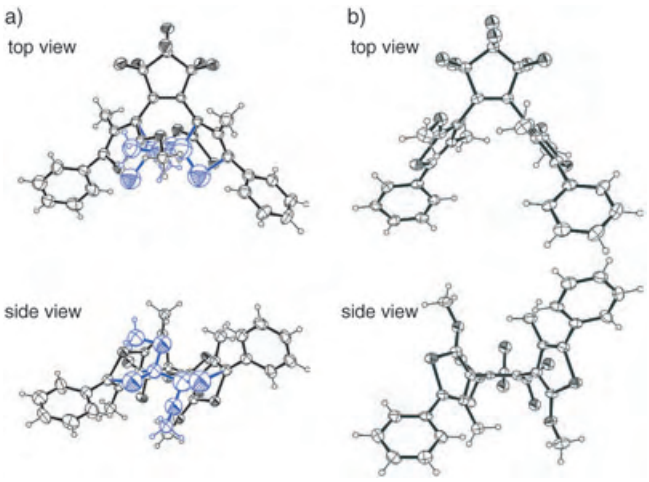

Figure 4. ORTEP renderings of a) conformer A and b) conformer B in photoirradiated crystals of **1a** with 30 % probability displacement ellipsoids. The photogenerated closed-ring isomer **1b** is indicated in blue. The conversion ratio obtained by X-ray crystallographic analysis was 8 %.

positions of the sulfur atoms, the reactive carbon atoms, and the methoxy groups in the closed-ring isomer were obtained only from conformer A. No peak that corresponds to the closed-ring isomer of conformer B was observed. This result indicates that only conformer A underwent the photochromic reaction upon irradiation with UV light, and that conformer B remained inactive. The difference in the distance between the reactive carbon atoms explains the different reactivity of the two conformers. The conversion saturation at 50 % shown in Figure 3 is also explained by the selective photoreaction. The conformational difference controls the reactivity, as observed for chiral organic salts.[21]

In conclusion, diarylethene **1a** is packed in two different conformations in the crystalline state, and the two conformers exhibit different photochemical reactivities. The periodic refractive index change in the crystal structure could be potentially useful in future photonic devices, such as one-dimensionally periodic photonic crystals and three-dimensional optical memory.[22]

Experimental Section

Single crystals were observed with a Nikon E600POL polarizing microscope. Polarizer and analyzer were set in parallel with each other. Photoirradiation was carried out with a mercury short arc lamp (100 W). The wavelength ($\lambda = 366$ nm) was selected by passing the light through a band-pass filter. X-ray crystallographic analysis of single crystals was performed with a Bruker SMART CCD X-ray diffractometer or a Rigaku RAXIS X-ray diffractometer with $Mo_{K\alpha}$ radiation ($\lambda = 0.71073$ Å) and a graphite monochromator. Crystal cell constants were calculated by global refinement. The structure was

 © 2005 Wiley-VCH Verlag GmbH & Co. KGaA, Weinheim

solved by direct methods with SHELXS86[23] and refined by full least-squares on F^2 with SHELXL97.[24]

1a (Synthesis details in the Supporting Information): m.p. 117.5–118.5 °C; UV/Vis (*n*-hexane): λ_{max} (ε) = 288 nm (28600 $M^{-1}cm^{-1}$); ^{1}H NMR (200 MHz, $CDCl_3$/TMS): δ = 2.10 (s, 6H; Me), 3.78 (s, 6H; MeO), 7.2–7.5 ppm (m, 10H; Ph); ^{13}C NMR (100 MHz, $CDCl_3$): δ = 14.1 (Me), 61.3 (MeO), 110.2 (3-thienyl), 111.5 (CF_2), 116.0 (CF_2), 124.4 (5-thienyl), 127.1 (Ph), 128.6 (Ph), 129.1 (Ph), 130.5 (4-thienyl), 134.1 (Ph), 139.5 (C=C), 163.4 ppm (2-thienyl); FAB-HRMS: *m*/*z*: calcd for $C_{29}H_{22}F_6O_2S_2$ $[M]^+$: 580.0965; found: 580.0966.

Crystal data for **1a**: $C_{29}H_{22}F_6S_2O_2$; monoclinic; space group $P2_1/c$; a = 24.036(5), b = 10.017(2), c = 24.141(6) Å, β = 114.104(4)°, V = 5306(2) Å^3; Z = 8; T = 123(2) K; M = 580.61; $\mu(Mo_{K\alpha})$ = 0.269 mm^{-1}, 30557 reflections measured, 11264 independent reflections. Final R_1 [$I > 2\sigma(I)$] = 0.0456, wR_2 (all data) = 0.1202.

Crystal data for **1a**/**1b** (photoirradiated crystal): $C_{29}H_{22}F_6S_2O_2$; monoclinic; space group $P2_1/c$; a = 24.040(7), b = 9.929(3), c = 24.191(7) Å, β = 113.897(7)°, V = 5279(3) Å^3; Z = 8; T = 123(2) K; M = 580.61; $\mu(Mo_{K\alpha})$ = 0.271 mm^{-1}, 38733 reflections measured, 12116 independent reflections. Final R_1 [$I > 2\sigma(I)$] = 0.0794, wR_2 (all data) = 0.1690.

CCDC-253671 (**1a**) and -253672 (**1a**/**1b**) contain the supplementary crystallographic data for this paper. These data can be obtained free of charge from The Cambridge Crystallographic Data Centre via www.ccdc.cam.ac.uk/data_request/cif.

Received: October 26, 2004
Published online: February 23, 2005

Keywords: chromophores · crystal engineering · isomerization · photochromism · X-ray diffraction

[1] G. H. Brown, *Photochromism*, Wiley-Interscience, New York, **1971**.
[2] H. Dürr, H. Bouas-Laurent, *Photochromism: Molecules and Systems*, Elsevier, Amsterdam, **1990**.
[3] a) M. Irie, K. Uchida, *Bull. Chem. Soc. Jpn.* **1998**, *71*, 985; b) M. Irie, *Chem. Rev.* **2000**, *100*, 1685, and references therein.
[4] A. J. Myles, N. R. Branda, *Adv. Funct. Mater.* **2002**, *12*, 167, and references therein.
[5] a) M. D. Cohen, G. M. J. Schmidt, *J. Chem. Soc.* **1964**, 1996; b) M. D. Cohen, G. M. J. Schmidt, F. I. Sonntag, *J. Chem. Soc.* **1964**, 2000; c) G. M. J. Schmidt, *J. Chem. Soc.* **1964**, 2014; d) G. M. J. Schmidt, *Pure Appl. Chem.* **1971**, *27*, 647.
[6] V. Ramamurthy, K. Venkatesan, *Chem. Rev.* **1987**, *87*, 433.
[7] G. R. Desiraju, *Crystal Engineering: The Design of Organic Solids*, Elsevier, Amsterdam, **1989**.
[8] a) G. Kaupp, *Angew. Chem.* **1992**, *104*, 606; *Angew. Chem. Int. Ed. Engl.* **1992**, *31*, 592; b) G. Kaupp, *Angew. Chem.* **1992**, *104*, 609; *Angew. Chem. Int. Ed. Engl.* **1992**, *31*, 595.
[9] K. Novak, V. Enkelmann, G. Wegner, K. B. Wagener, *Angew. Chem.* **1993**, *105*, 1678; *Angew. Chem. Int. Ed. Engl.* **1993**, *32*, 1614.
[10] X. Gao, T. Rriscic, L. R. MacGillivray, *Angew. Chem.* **2004**, *116*, 234; *Angew. Chem. Int. Ed.* **2004**, *43*, 232.
[11] D. Braga, F. Grepioni, *Angew. Chem.* **2004**, *116*, 4092; *Angew. Chem. Int. Ed.* **2004**, *43*, 4002.
[12] J. R. Scheffer, P. R. Pokkuluri, *Photochemistry in Organized & Constrained Media*, (Ed.: V. Ramamurthy), VCH, New York, **1990**, p. 185.
[13] G. Kaupp, *Justus Liebigs Ann. Chem.* **1973**, 844.
[14] a) S. Kobatake, T. Yamada, K. Uchida, N. Kato, M. Irie, *J. Am. Chem. Soc.* **1999**, *121*, 2380; b) S. Kobatake, M. Yamada, T. Yamada, M. Irie, *J. Am. Chem. Soc.* **1999**, *121*, 8450; c) S. Kobatake, K. Shibata, K. Uchida, M. Irie, *J. Am. Chem. Soc.* **2000**, *122*, 12135; d) M. Morimoto, S. Kobatake, M. Irie, *Chem. Eur. J.* **2003**, *9*, 621; e) M. Morimoto, S. Kobatake, M. Irie, *J. Am. Chem. Soc.* **2003**, *125*, 11080.
[15] a) T. Kodani, K. Matsuda, T. Yamada, S. Kobatake, M. Irie, *J. Am. Chem. Soc.* **2000**, *122*, 9631; b) K. Matsuda, S. Yamamoto, M. Irie, *Tetrahedron Lett.* **2001**, *42*, 7291; c) S. Yamamoto, K. Matsuda, M. Irie, *Org. Lett.* **2003**, *5*, 1769; d) S. Yamamoto, K. Matsuda, M. Irie, *Angew. Chem.* **2003**, *115*, 1636; *Angew. Chem. Int. Ed.* **2003**, *42*, 1589.
[16] M. Irie, S. Kobatake, M. Hoichi, *Science* **2001**, *291*, 1769.
[17] a) S. Kobatake, M. Irie, *Bull. Chem. Soc. Jpn.* **2004**, *77*, 195, and references therein.
[18] a) M. Morimoto, S. Kobatake, M. Irie, *Chem. Rec.* **2004**, *4*, 23; b) M. Morimoto, S. Kobatake, M. Irie, *Photochem. Photobiol. Sci.* **2003**, *2*, 1088.
[19] a) S. Kobatake, K. Uchida, E. Tsuchida, M. Irie, *Chem. Commun.* **2002**, 2804; b) K. Shibata, K. Muto, S. Kobatake, M. Irie, *J. Phys. Chem. A* **2002**, *106*, 209.
[20] T. Yamada, S. Kobatake, M. Irie, *Bull. Chem. Soc. Jpn.* **2000**, *73*, 2179.
[21] E. Cheung, T. Kang, M. R. Netherton, J. R. Scheffer, J. Trotter, *J. Am. Chem. Soc.* **2000**, *122*, 11753.
[22] a) J. D. Joannopoulos, R. D. Meade, J. N. Winn, *Photonic Crystals*, Princeton University Press, Princeton, **1995**; b) J. D. Joannopoulos, P. R. Villeneuve, S. Fan, *Nature* **1997**, *386*, 143.
[23] G. M. Sheldrick, *Acta Crystallogr. Sect. A* **1990**, *46*, 467.
[24] G. M. Sheldrick, SHELXL-97, Program for Crystal Structure Refinement, Universität Göttingen, Göttingen, 1997.

 © 2005 Wiley-VCH Verlag GmbH & Co. KGaA, Weinheim

Coordination Networks

In Situ Observation of a Reversible Single-Crystal-to-Single-Crystal Apical-Ligand-Exchange Reaction in a Hydrogen-Bonded 2D Coordination Network

Kanji Takaoka, Masaki Kawano, Masahide Tominaga, and Makoto Fujita**

Functionalization of coordination networks is a crucial step for their application.[1] One of the salient features of coordination networks is that they often contain substitution-active metal sites in their framework. Ligand exchange will considerably affect their d-orbital configuration and lead to the electronic and spin control of coordination networks. Cobalt is a classical example that shows chromism upon ligand exchange in the solid state, as commonly observed in

[*] K. Takaoka, Prof. Dr. M. Kawano, Dr. M. Tominaga, Prof. Dr. M. Fujita
Department of Applied Chemistry
School of Engineering
The University of Tokyo
and Genesis Research Institute, Inc.
7-3-1 Hongo, Bunkyo-ku, Tokyo 113-8656 (Japan)
Fax: (+81) 3-5841-7257
E-mail: mkawano@appchem.t.u-tokyo.ac.jp
mfujita@appchem.t.u-tokyo.ac.jp

Supporting information for this article is available on the WWW under http://www.angewandte.org or from the author.

 DOI: 10.1002/anie.200462214 © 2005 Wiley-VCH Verlag GmbH & Co. KGaA, Weinheim

the hydration-induced color change of silica gel. Such a ligand-exchange process is, however, seldom observable by single-crystal X-ray diffraction studies because the drastic structural changes during the process readily cause loss of crystallinity. Here we report the crystallographic observation of reversible apical-ligand exchange at a cobalt center in situ. The metal center is incorporated in a square-grid coordination network that provides a relatively fluid cavity within the solid. We show that aqua and nitrate ligands can be reversibly coordinated to the cobalt center in a single-crystal-to-single-crystal fashion.[2–4]

We designed a 4-pyridyl-terminated, rodlike ligand containing ethylene glycol side chains (**1**).[5] Slow complexation of $Co(NO_3)_2 \cdot 6H_2O$ in MeOH over a solution of **1** in toluene produced orange-yellow single crystals of $\{[Co(\mathbf{1})_2(H_2O)_2](NO_3)_2 \cdot 1.5H_2O\}_n$ (**2**) in 76% yield [Eq. (1)].

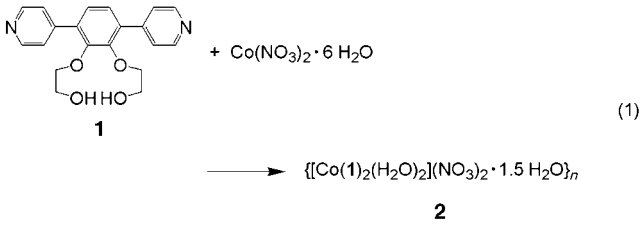

(1)

X-ray crystallographic analysis revealed the square-grid network structure of **2** (Figure 1a). The grid sheet layers are stacked above each other in an offset fashion on both edges (Figure 1b). The ethylene glycol chains play two important roles: they add considerable stabilization to the crystal due to hydrogen-bond formation and they also introduce moderate flexibility inside the cavity by allowing guest molecules to behave as in solution. As regards the stabilization effect, we assume that the crystal is stabilized by infinite 1D hydrogen-bond (O–H···O) arrays that interpenetrate the layers (Figure 1c).[6] In fact, a similar square-grid coordination network that does not contain an ethylene glycol chain on the ligand is much less stable than **2**:[7] a crystal of the coordination network with no substituent gradually deteriorated above room temperature due to the loss of guest molecules.

The stability and flexibility of **2** enabled us to directly observe a reversible apical-ligand-exchange reaction at the hinge metals by X-ray crystallography. Two water molecules are coordinated to the cobalt(II) center at the apical positions (aqua form) with four pyridyl groups at the equatorial positions (Figure 2a). Upon heating at 150 °C for 24 h the yellow crystal turned red, with no loss of crystallinity. The crystallographic analysis revealed that the apical water molecules had been substituted by two nitrate ions and extruded from the crystal to give the nitrate complex $[Co^{II}(\mathbf{1})_2(NO_3)_2]_n$ (**3**; Figure 2b). Upon exposure of **3** to air at room temperature, it changed back to the initial aqua form. The color of the crystal returned to yellow within a few minutes and the crystallinity was again retained. Crystallographic and elemental analysis showed that the newly obtained aqua form $\{[Co(\mathbf{1})_2(H_2O)_2](NO_3)_2 \cdot 1.5H_2O\}_n$ (**2′**) is almost superimposable on the original structure of **2** (Figure 2c).

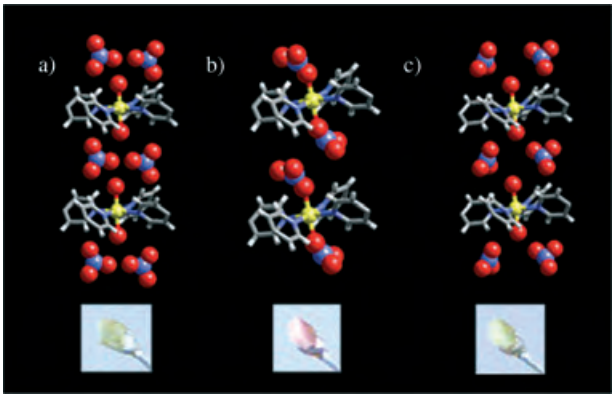

Figure 2. Photographs and crystal views around the cobalt ion: a) original crystal **2**, b) the crystal after heating at 150 °C for 24 h (**3**), and c) the crystal after exposure of **3** to air (**2′**). Two other disordered nitrate ions have been omitted for clarity.

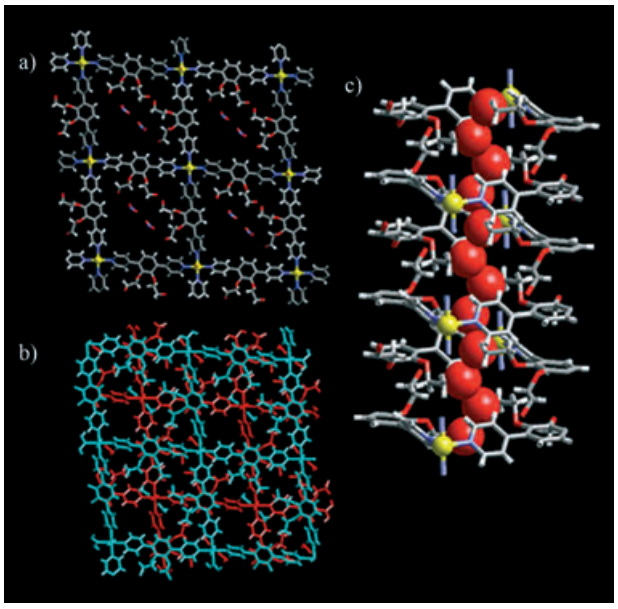

Figure 1. a) The square-grid network of **2**. Guest molecules (H_2O) have been omitted for clarity. b) The two-layer stack of **2**. c) The infinite 1D hydrogen bond (O–H···O) array in **2**. The oxygen atoms of the OH groups are represented by a space-filling model.

The chromism of the crystal is principally ascribed to the energy-level change of the d orbitals of cobalt induced by apical-ligand exchange. The nitrate anion, which has a weaker crystal-field-splitting ability than water, decreases the HOMO–LUMO energy gap in the complex, which causes a red shift of the absorption bands. The energy-level change also influences the geometrical parameters of the cobalt center.[8]

The void present after removal of the water molecules is mainly offset by framework distortion. The grid framework is slightly compressed, which causes a decrease of cell volume from 4263.9(7) to 4036.0(16) $Å^3$. Interestingly, the void is also

 © 2005 Wiley-VCH Verlag GmbH & Co. KGaA, Weinheim

offset by dynamic disordering of the flexible ethylene glycol chains. The mobility of the carbon and oxygen atoms in the side chains significantly increases in the absence of guest molecules, as shown by the ORTEP drawing of the square-grid cavity in Figure 3.

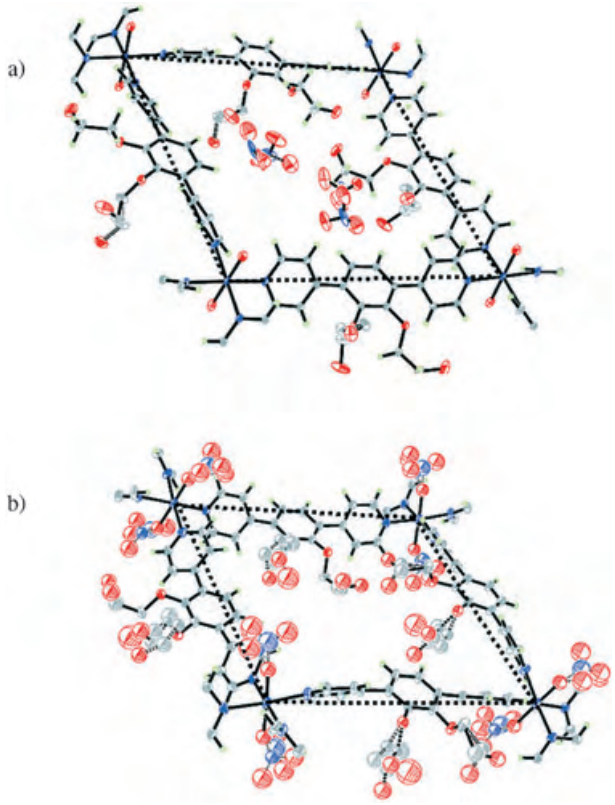

Figure 3. ORTEP drawing (30% probability) of a square-grid unit of **2** (a) and **3** (b). The bridging ligand of **3** shows considerable distortion compared to that of **2**. The disordered guest water molecules in (a) have been omitted for clarity.

Thermogravimetric analysis of the crystal of **2** showed loss of all water molecules in the range 25–90 °C. The number of water molecules removed (weight loss of 6.47%) agrees well with that determined by X-ray analysis (6.6%). DSC analysis of a crystal of **2** showed two endothermic peaks at 93.8 °C and 77.4 °C, which are attributed to the release of coordinated water from the cobalt ion and noncoordinated water from the cavity, respectively.

In summary, we have succeeded in the crystallographic observation of an apical-ligand-exchange reaction at a cobalt ion within a square-grid coordination network. Since ligand exchange at a metal is a bimolecular reaction, the process can only rarely be observed by X-ray crystallography. We have realized the in situ crystallographic observation of this dynamic process, which involves drastic structural changes around the reaction center, by utilizing functionalized bridging ligands. The in situ observation of various chemical processes in the fluid cavity is our next challenge, and the results will be reported in due course.

Experimental Section

Single crystals of **2** were grown by layering a methanol solution of $Co(NO_3)_2 \cdot 6H_2O$ (5.8 mg in 1 mL) onto a toluene solution of **1** (15.0 mg in 2 mL). After allowing the solution to stand for 4 d, the crystals were isolated in 76% yield by filtration. Elemental analysis (%) calculated: C 50.53, H 4.98, N 8.84; found: C 50.34, H 4.86, N 8.72. Crystal data for **2**: orthorhombic, *Pbcn*, $a = 20.580(6)$, $b = 23.717(7)$, $c = 8.820(3)$ Å, $V = 4263.9(7)$ Å^3, $Z = 4$, $T = 80$ K, $\rho_{calcd} = 1.434$ g cm^{-3}, $\mu = 0.483$ mm^{-1}, final R_1 ($I > 2\sigma(I)$) = 0.0762, wR_2 (all data) = 0.2062, GOF = 1.044.

Crystal data for **3**: orthorhombic, *Pbcn*, $a = 20.572(5)$, $b = 23.092(5)$, $c = 8.496(2)$ Å, $V = 4036.0(16)$ Å^3, $Z = 4$, $T = 423$ K, $\rho_{calcd} = 1.441$ g cm^{-3}, $\mu = 0.506$ mm^{-1}, final R_1 ($I > 2\sigma(I)$) = 0.1039, wR_2 (all data) = 0.2384, GOF = 1.039.

2′: Elemental analysis (%) calculated: C 50.53, H 4.98, N 8.84; found: C 50.60, H 4.89, N 8.73. Crystal data for **2′**: orthorhombic, *Pbcn*, $a = 20.576(2)$, $b = 23.677(3)$, $c = 8.7155(9)$ Å, $V = 4246.0(8)$ Å^3, $Z = 4$, $T = 80$ K, $\rho_{calcd} = 1.304$ g cm^{-3}, $\mu = 0.466$ mm^{-1}, final R_1 ($I > 2\sigma(I)$) = 0.0948, wR_2 (all data) = 0.2206, GOF = 1.025.

All the diffraction data were measured on a Siemens SMART/CCD diffractometer ($Mo_{K\alpha}$ radiation, $\lambda = 0.71073$ Å). Non-hydrogen atoms were refined anisotropically and hydrogen atoms were fixed at calculated positions and refined using a riding model. CCDC-250540 (**2**), -250541 (**3**), and -250542 (**2′**) contain the supplementary crystallographic data for this paper. These data can be obtained free of charge from the Cambridge Crystallographic Data Center via www.ccdc.cam.ac.uk/data_request/cif.

Received: October 6, 2004
Published online: February 25, 2005

Keywords: cobalt · coordination polymers · host–guest systems · hydrogen bonds · ligand design

[1] For pertinent reviews, see: a) S. Kitagawa, R. Kitaura, S. Noro, *Angew. Chem.* **2004**, *116*, 2388–2430; *Angew. Chem. Int. Ed.* **2004**, *43*, 2334–2375; b) C. Janiak, *Dalton Trans.* **2003**, 2781–2804.

[2] Single-crystal-to-single-crystal guest inclusion/removal in coordination networks is a topic of current interest: a) H. Li, M. Eddaoudi, M. O'Keeffe, O. M. Yaghi, *Nature* **1999**, *402*, 276–279; b) S. S.-Y. Chui, S. M.-F. Lo, J. P. H. Charmant, A. G. Orpen, I. D. Williams, *Science* **1999**, *283*, 1148–1150; c) C. J. Kepert, M. J. Rosseinsky, *Chem. Commun.* **1999**, 375–376; d) K. Biradha, Y. Hongo, M. Fujita, *Angew. Chem.* **2000**, *112*, 4001–4003; *Angew. Chem. Int. Ed.* **2000**, *39*, 3843–3845.

[3] For the dynamic behavior of coordination networks in a single-crystal-to-single-crystal fashion, see: a) K. Biradha, M. Fujita, *Angew. Chem.* **2002**, *114*, 3542–3545; *Angew. Chem. Int. Ed.* **2002**, *41*, 3392–3395; b) K. Biradha, Y. Hongo, M. Fujita, *Angew. Chem.* **2002**, *114*, 3545–3548; *Angew. Chem. Int. Ed.* **2002**, *41*, 3395–3398; c) M. P. Suh, W. J. Ko, H. J. Choi, *J. Am. Chem. Soc.* **2002**, *124*, 10976–10977; d) S. Takamizawa, E. Nakata, T. Saito, *Angew. Chem.* **2004**, *116*, 1392–1395; *Angew. Chem. Int. Ed.* **2004**, *43*, 1368–1371; e) B. F. Abrahams, M. Moylan, S. D. Orchard, R. Robson, *Angew. Chem.* **2003**, *115*, 1892–1895; *Angew. Chem. Int. Ed.* **2003**, *42*, 1848–1851; f) T. K. Maji, K. Uemura, H.-C. Chang, R. Matsuda, S. Kitagawa, *Angew. Chem.* **2004**, *116*, 3331–3334; *Angew. Chem. Int. Ed.* **2004**, *43*, 3269–3272; g) D. N. Dybtsev, H. Chun, K. Kim, *Angew. Chem.* **2004**, *116*, 5143–5146; *Angew. Chem. Int. Ed.* **2004**, *43*, 5033–5036.

[4] For reversible single-crystal-to-single-crystal transformation of coordination networks, see: a) B. Rather, M. J. Zaworotko, *Chem. Commun.* **2003**, 830–831; b) E. Y. Lee, M. P. Suh, *Angew. Chem.* **2004**, *116*, 2858–2861; *Angew. Chem. Int. Ed.* **2004**, *43*, 2798–

 © 2005 Wiley-VCH Verlag GmbH & Co. KGaA, Weinheim

2801; c) S. Takamizawa, E. Nakata, H. Yokoyama, K. Mochizuki, W. Mori, *Angew. Chem.* **2003**, *115*, 4467 – 4470; *Angew. Chem. Int. Ed.* **2003**, *42*, 4331 – 4334; d) K. Hanson, N. Calin, D. Bugaris, M. Scancella, S. C. Sevov, *J. Am. Chem. Soc.* **2004**, *126*, 10502 – 10503.

[5] For the synthesis of **1**, see the Supporting Information.

[6] The hydrogen-bond length (average O···O distance is 2.60 Å) is particularly short despite the absence of charged species: B. G. Hong, J. Y. Lee, C.-W. Lee, J. C. Kim, S. C. Bae, K. S. Kim, *J. Am. Chem. Soc.* **2001**, *123*, 10748 – 10749.

[7] For the square-grid coordination network that does not contain an ethylene glycol chain on the ligand, see the Supporting Information.

[8] The change of the geometrical parameters of cobalt: Co–O_{H_2O} 2.095(4) Å to Co–O_{NO_3} 2.129(8) Å; Co–N_{Py1} from 2.160(3) to 2.144(5) Å; Co–N_{Py2} from 2.142(3) to 2.129(5) Å. These values are typical of Co^{II}–pyridyl aqua complexes: a) M. Felloni, A. J. Blake, N. R. Champness, P. Hubberstey, C. Wilson, M. Schröder, *J. Supramol. Chem.* **2002**, 163 – 174; b) S. Banfi, L. Carlucci, E. Caruso, G. Ciani, D. Proserpio, *J. Chem. Soc. Dalton Trans.* **2002**, 2714 – 2721.

 © 2005 Wiley-VCH Verlag GmbH & Co. KGaA, Weinheim

Nanocube Synthesis

Large-Scale Synthesis of Silver Nanocubes: The Role of HCl in Promoting Cube Perfection and Monodispersity**

*Sang Hyuk Im, Yun Tack Lee, Benjamin Wiley, and Younan Xia**

Shape control of metal nanoparticles has received considerable attention in recent years because of the strong correlation between the shape and the chemical, physical, electronic, optical, magnetic, and catalytic properties of a nanoparticle.[1] Silver and gold, in particular, have been intensively studied owing to their numerous applications that include surface plasmonics, surface-enhanced Raman scattering (SERS), as well as chemical and biological sensing.[2] A wealth of chemical methods have been developed for the synthesis of silver and gold nanostructures that have well-controlled shapes, including triangular plates,[3] cubes,[4] belts,[5] wires,[6] rods,[7] and branched multipods.[8] Most of these methods, however, still require improvement in terms of yield, purity, monodispersity, and scale of synthesis before they will find use in commercial applications. We and other groups have established the polyol process as a means to synthesize silver and gold nanoparticles with controllable shapes in relatively large quantities.[4–6] Furthermore, we discovered that single-crystal cubes and tetrahedrons of silver with truncated corners/edges could be prepared in high yields through the selective etching and dissolution of twinned seeds by chloride ions and oxygen (from air).[9] Herein, we report another highly effective mediator—hydrochloric acid—for the production of single-crystal nanocubes. The yield, perfection of the cube, and monodispersity of the sample are all greatly improved by employing HCl. More importantly, the robustness of this reaction even allows it to be carried out in a disposable vial submerged in an oil bath and heated on a hotplate. The dependence of morphology on the concentration of hydrochloric acid was also investigated, and the synthesis was successfully scaled up to produce silver nanocubes on the gram scale.

In a typical polyol synthesis, silver atoms are obtained by reducing $AgNO_3$ with ethylene glycol (EG) through reactions (1) and (2).[10]

$$2\,HOCH_2CH_2OH \rightarrow 2\,CH_3CHO + 2\,H_2O \quad (1)$$

$$2\,Ag^+ + 2\,CH_3CHO \rightarrow CH_3CHO{-}OHCCH_3 + 2\,Ag + 2\,H^+ \quad (2)$$

Once the concentration of silver atoms has reached the supersaturation value, they will start to nucleate and grow into nanoparticles. At the same time, nitric acid generated in situ activates a backward reaction that dissolves the solid silver that is initially formed [Eq. (3)].[11] Through the introduction of HCl, reaction (3) could be driven further to the right owing to the formation of more HNO_3 from HCl and $AgNO_3$.

$$4\,HNO_3 + 3\,Ag \rightarrow 3\,AgNO_3 + NO + 2\,H_2O \quad (3)$$

On the basis of these reactions and experimental observations, we can explain why and how perfect single-crystal silver nanocubes were formed in high yields. First, upon addition of silver nitrate and PVP (poly(vinyl pyrrolidone)) to the hot solution of EG, both twinned and single-crystal seeds of silver are formed through homogeneous nucleation, with the twinned particles being the most abundant morphology as a result of their relatively lower surface energies.[12] These initially formed nanoparticles are dissolved owing to the relatively high concentration of HNO_3 present in the early stages of the reaction. As the reaction continues, HNO_3 is gradually consumed and a second round of nucleation occurs. At very small sizes, it is expected that the crystal structure of these nuclei fluctuates, as has been observed in several TEM

[*] Dr. S. H. Im, Y. T. Lee, Prof. Y. Xia
Department of Chemistry
University of Washington
Seattle, WA 98195 (USA)
Fax: (+1) 206-685-8665
E-mail: xia@chem.washington.edu
B. Wiley
Department of Chemical Engineering
University of Washington
Seattle, WA 98195 (USA)

[**] This work was supported in part by ONR (N-00014-01-1-0976) and a fellowship from the David and Lucile Packard Foundation. Y.X. is an Alfred P. Sloan Research Fellow and a Camille Dreyfus Teacher Scholar. Both S.H.I. and Y.T.L. have been partially supported by the Postdoctoral Fellowship Program of the Korean Science and Engineering Foundation (KOSEF). B.W. thanks the Center for Nanotechnology at the University of Washington for an IGERT Fellowship Award supported by the NSF (DGE-9987620).

Supporting information for this article is available on the WWW under http://www.angewandte.org or from the author.

 © 2005 Wiley-VCH Verlag GmbH & Co. KGaA, Weinheim DOI: 10.1002/anie.200462208

studies.[13] When the nanoparticles grow in dimension, they will be locked into either a single-crystalline or twinned morphology. While the twinned particles have a lower overall surface energy, this comes at the expense of significant lattice distortion and surface defects. Thus, twinned particles are expected to exhibit a stronger reactivity and susceptibility towards etching. As no lattice distortion is required to form a single crystal, these seeds should be relatively more stable in this environment and can continue to grow. Consequently, through the selective etching of twinned seeds by HNO_3, high yields of single-crystal nanocubes result (see Supporting Information for a schematic of this mechanism).

While selective etching is the dominant mechanism for producing nanocubes, there are additional elements that contribute to its success. In the present study, both the proton and the chloride ion of HCl play a significant role. As well as its function in increasing the concentration of HNO_3, the proton can greatly reduce the net reaction rate according to Le Chatelier's principle. At the same time, chloride ions likely adsorb onto the surfaces of silver seeds and thereby prevent agglomeration through electrostatic stabilization.[14] We also lowered the reaction temperature from 160 to 140 °C to further slow down the net reaction rate in an effort to increase the efficiency of selective etching by nitric acid. This combination of factors allies to promote the production of silver nanocubes with high yields and monodispersed sizes.

The primary stages of the reaction can be recognized by their distinctive colors. As illustrated in Figure 1 a, the solution turned milky white after the injection of the solutions of $AgNO_3$ and PVP. This color suggests the presence of AgCl precipitate caused by the relatively high concentration of chloride ions in the reaction mixture (0.25 mM). Figure 1 e shows a TEM image of a sample taken from the suspension at this stage. The chemical composition of these particles was AgCl, as confirmed by both X-ray diffraction (XRD) and energy dispersive X-ray (EDX) analyses. At $t = 45$ min, the solution turned light yellow in color (Figure 1 b) which indicates that the AgCl particles had dissolved and only Ag nanoparticles remained in the reaction mixture. As shown by TEM (Figure 1 f), Ag nanoparticles of two different sizes (diameter, $d \approx 20$ and ≈ 5 nm) coexist in the solution at this time. The light yellow color gradually faded, and the solution appeared transparent and colorless at around $t = 105$ min (Figure 1 c) which suggests the complete dissolution of all large Ag nanoparticles. This picture is also consistent with TEM observations (Figure 1 g) in which only very few Ag nanoparticles of very small size ($d \approx 6$ nm) could be found. This transparent state lasted for approximately one hour, after which time the solution acquired a reddish tint whose intensity increased over a period of several hours. By $t = 15$ h, the solution had become red (as shown in Figure 1 d), implying the formation of small Ag nanocubes. A typical TEM image (Figure 1 h) of these Ag nanocubes shows that they were perfect in shape and approximately 30 nm in edge length. These Ag nanocubes could further grow into cubes of larger sizes if the reaction was allowed to continue. Finally, the solution became ocher in color at approximately $t = 26$ h. The Ag nanocubes contained in this solution were also perfect in shape with their edge length increased to around 130 nm.

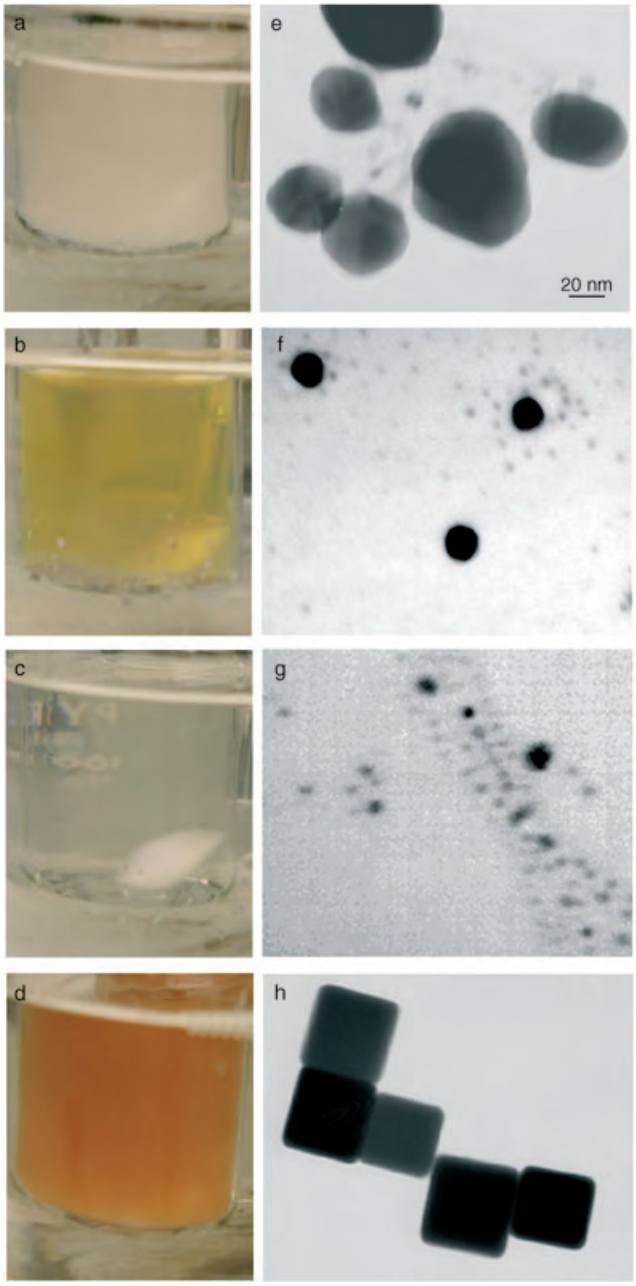

Figure 1. Morphological revolution with reaction time. a)–d) Photographs of the reaction solution at $t = 4$, 46, and 103 min, and 15 h, respectively. e)–h) TEM images of silver nanoparticles contained in the corresponding reaction solution shown on the left (a–d).

This observation implies that it will be possible to control the size and therefore the optical properties of Ag nanocubes simply by varying the reaction time. Figure 2 demonstrates the size-dependent absorption spectra of the cubes. The number of peaks and relative positions are consistent with theoretical calculations.[15]

The dependence of morphology on the concentration of HCl was also examined. Figure 3 a shows the SEM image of a product obtained at $t = 25$ h when the concentration of HCl was 0.125 mM in the final mixture. This sample contained a mixture of polydisperse silver nanocubes, tetrahedrons, and

 © 2005 Wiley-VCH Verlag GmbH & Co. KGaA, Weinheim

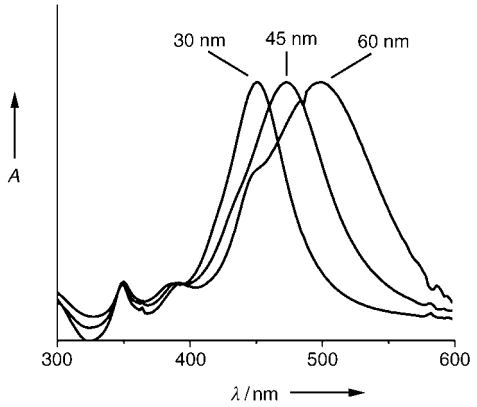

Figure 2. UV/Vis absorption spectra of aqueous solutions that contain silver nanocubes with different edge lengths (30, 45, and 60 nm).

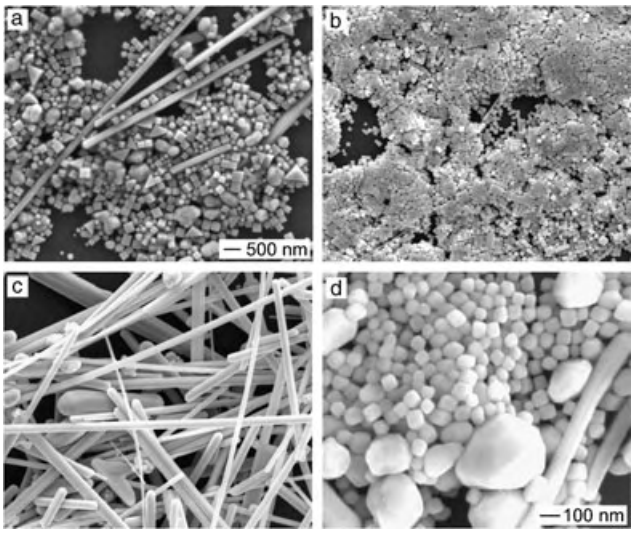

Figure 3. SEM images of silver nanoparticles synthesized at different concentrations of HCl (scale bar: 500 nm): a) 0.125, b) 0.25, and c) 0.375 mM, respectively. The reaction solution contained $AgNO_3$ (23.5 mM) and PVP (36.7 mM, calculated in terms of the repeating unit) and was heated in an oil bath held at 140 °C. d) Silver nanoparticles obtained under the same conditions except that HNO_3 (0.25 mM) was used instead of HCl (0.25 mM).

nanowires. It is believed that the wires and irregular particles form as a result of the incomplete etching of twinned seeds by the lower concentration of HNO_3. Figure 3b shows an SEM image of the final product obtained at $t = 26$ h when the concentration of HCl was increased to 0.25 mM (namely, the synthesis described in Figure 1). The solution contained only monodisperse silver nanocubes of about 130 nm in edge length. As the concentration of HCl was further increased to 0.375 mM, a different morphology was observed (Figure 3c). This product, obtained at $t = 22$ h, was characterized by a mixture of relatively thick wires and irregular particles. The mechanism behind this morphological variant is yet to be understood. In this case, it was found that the reaction mixture did not become transparent which indicates that the twinned seeds were not dissolved to cut short their growth into nanowires and irregular particles. It is assumed that chloride ions could slow down the etching of twinned seeds by selectively blocking the twin sites through surface adsorption. Alternatively, it is possible that an increase in the concentration of HCl may result in the formation of more AgCl precipitate at the initial stage of the synthesis and that some of these AgCl colloids may survive and serve as seeds for the subsequent growth of twinned particles. On the basis of the results of these experiments, it is concluded that 0.25 mM represents an ideal concentration of HCl for the synthesis of silver nanocubes.

To separate the roles played by the proton and chloride, we also replaced HCl (0.25 mM) with HNO_3 (0.25 mM). The NO_3^- ions from HNO_3 should have a negligible effect on the synthesis because the concentration of HNO_3 was extremely low as compared to the concentration of $AgNO_3$. Figure 3d shows a typical SEM image of the product at $t = 30$ h that comprised a mixture of small silver nanocubes (edge length ≈ 40 nm) and some irregular particles. This observation implies that HNO_3 alone is able to induce the etching and dissolution of twinned seeds and thus channel the product into single-crystal nanocubes. However, owing to the absence of Cl^- ions in the solution, the single-crystal seeds could not be stabilized and therefore might agglomerate into larger, irregularly shaped particles. It is also expected that a combination of Cl^- ions and O_2 will facilitate the etching and dissolution of twinned seeds to further decrease the percentage of twinned particles in the final product.

It is an important issue to scale up the synthesis from the viewpoint of commercial usage. To this end, we increased the volumes of all solutions by a factor of five. In this case, the synthesis followed the same pattern of color changes which suggests that the nucleation and growth mechanisms did not change as the reaction volume was increased. Figure 4a shows

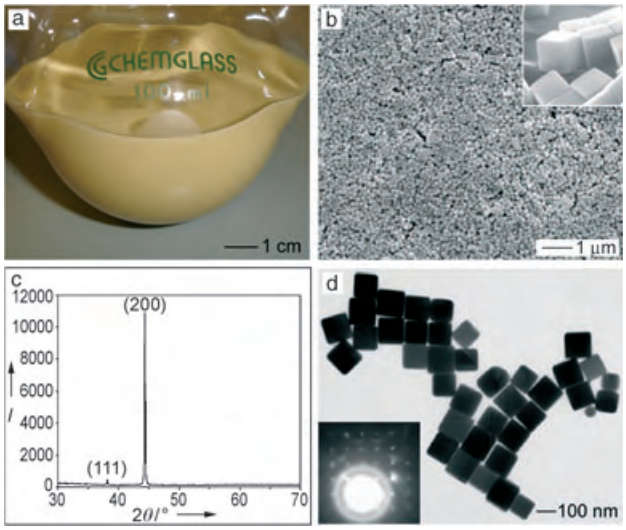

Figure 4. a) Photograph of the reaction mixture in a scale-up (×5) synthesis. b) Typical SEM images of the as-synthesized silver nanocubes. The inset shows a magnified SEM image that illustrates the sharp corners and edges of these nanocubes. c) An XRD pattern of the same batch of silver nanocubes. d) TEM image of the silver nanocubes. The inset shows an electron diffraction pattern recorded by directing the electron beam perpendicular to the (100) facet of a silver nanocube.

 © 2005 Wiley-VCH Verlag GmbH & Co. KGaA, Weinheim

a photograph of the final product, which displayed an ocher color similar to that seen for the smaller reaction volume. Figure 4b shows a typical SEM image of this sample and indicates that all particles were cubic in shape with an average edge length of 125 nm. The inset shows a tilted SEM image at higher magnification that clearly displays the sharp corners and edges of these nanocubes. Figure 4c shows an XRD pattern recorded from the same batch of silver nanocubes. The abnormal intensity of the (200) peak suggests that the sample exclusively comprises nanocubes that were preferentially oriented with their (100) planes parallel to the supporting substrate. Figure 4d shows a typical TEM image of the silver nanocubes. Again, it is clear that these silver nanocubes are single crystals with sharp corners and edges. The inset shows an electron diffraction pattern recorded by directing the electron beam perpendicular to the (100) facet of an individual nanocube and confirms that the particles are single crystals.

In summary, monodispersed nanocubes of silver have been synthesized in large quantities by introducing a small amount of hydrochloric acid to the conventional polyol synthesis. From the color changes involved and electron microscopy studies, it is believed that hydrochloric acid plays an important role in selectively etching and dissolving twinned silver nanoparticles. In contrast to our previous work based on the mediation of NaCl, the current process is more robust as it involves two different types of etchants: HNO_3 and Cl^-/O_2. Furthermore, the presence of protons greatly slows down the reduction reaction and thereby facilitates the formation of single-crystal seeds. Under the optimized conditions, we have been able to scale up the synthesis to 0.25 grams (or 1.2×10^{21} 130-nm-wide cubes).

Experimental Section

In a typical synthesis, ethylene glycol (EG; 5 mL, J. T. Baker, 9300-01) was placed in a 20-mL vial, capped, and heated with stirring in an oil bath at 140 °C for 1 h. HCl (1 mL of a 3 mM solution in EG) was then quickly added, and the vial was recapped. After 10 min, $AgNO_3$ (3 mL of a 94 mM solution in EG; Aldrich, 209139–100G) and poly(vinyl pyrrolidone) (PVP; 3 mL of a solution in EG (147 mM in terms of the repeating unit); $M_r \approx 55000$, Aldrich, 856568-100G) were simultaneously added with a two-channel syringe pump (KDS-200, Stoelting, Wood Dale, IL) at a rate of 45 mL per hour to the stirring solution. The vial was then capped and heated at 140 °C. Upon injection of the solution of $AgNO_3$, the reaction mixture went through a series of color changes that included milky white, light yellow, transparent, red, and ocher. To separate the roles of the proton and chloride, we performed a synthesis under the same conditions except for the replacement of HCl by HNO_3. For the scale-up synthesis, the vial was replaced with a 100-mL flask, and the volumes of all solutions were increased by a factor of five.

All samples for morphology and structure analysis were washed with acetone and then with water to remove excess EG and PVP. SEM images were taken using a field emission scanning electron microscope (FEI, Sirion XL) operated at an accelerating voltage of 10–20 kV. The transmission electron microscopy (TEM) images and diffraction patterns were obtained using a JEOL microscope (1200EX II) operating at 80 kV. X-ray diffraction (XRD) studies were performed on a Philips 1820 diffractometer with a scan rate of 0.2 degrees per minute in the range 20–90°. UV/Vis absorption spectra were taken at room temperature on a Hewlett Packard 8452 spectrometer (Palo Alto, CA) using a quartz cuvette with an optical path of 1 cm.

Received: October 5, 2004
Published online: February 28, 2005

Keywords: aggregation · crystal growth · nanostructures · polyol synthesis · silver

[1] a) Y. Xia, P. Yang, Y. Sun, Y. Wu, B. Gate, Y. Yin, F. Kim, H. Yan, *Adv. Mater.* **2003**, *15*, 353; b) Y. Wu, B. Messer, P. Yang, *Adv. Mater.* **2001**, *13*, 1487; c) N. I. Kovtyukhova, T. E. Mallouk, *Chem. Eur. J.* **2002**, *8*, 4354; d) C. Salzemann, I. Lisiecki, A. Brioude, J. Urban, M.-P. Pileni, *J. Phys. Chem. B* **2004**, *108*, 13243; e) N. R. Jana, L. Gearheart, S. O. Obare, C. J. Murphy, *Langmuir* **2002**, *18*, 922; f) A. T. Ngo, M. P. Pileni, *Colloids Surf. A* **2003**, *228*, 107; g) V. F. Puntes, K. M. Krishnan, A. P. Alivisatos, *Science* **2001**, *291*, 2115; h) Z. L. Wang, T. S. Ahmad, M. A. El-Sayed, *Surf. Sci.* **1997**, *380*, 302.

[2] a) D. Roy, J. Fendler, *Adv. Mater.* **2004**, *16*, 479; b) J. R. Krenn, *Nat. Mater.* **2003**, *2*, 210; c) K. Kneipp, Y. Wang, H. Kneipp, L. T. Perelman, I. Itzkan, R. R. Dasari, M. S. Feld, *Phys. Rev. Lett.* **1997**, *78*, 1667; d) J. P. Kottmann, O. J. F. Martin, D. R. Smith, S. Schultz, *Phys. Rev. B* **2001**, *64*, 235402; e) A. J. Haes, R. P. Van Duyne, *J. Am. Chem. Soc.* **2002**, *124*, 10596; f) B. D. Moore, L. Stevenson, A. Watt, S. Flitsch, N. H. Turner, C. Cassidy, D. Graham, *Nat. Biotechnol.* **2004**, *22*, 1133; g) Y. Cao, R. Jin, C. Mirkin, *Science* **2002**, *297*, 1536.

[3] a) R. Jin, Y. Cao, C. A. Mirkin, K. L. Kelly, G. G. Schatz, J. G. Zheng, *Science* **2001**, *294*, 1901.

[4] a) Y. Sun, Y. Xia, *Science* **2002**, *298*, 2176; b) R. Jin, S. Egusa, N. F. Scherer, *J. Am. Chem. Soc.* **2004**, *126*, 9900; c) T. K. Sau, C. J. Murphy, *J. Am. Chem. Soc.* **2004**, *126*, 8648; d) F. Kim, S. Connor, H. Song, T. Kuykendall, P. Yang, *Angew. Chem.* **2004**, *43*, 3759; *Angew. Chem. Int. Ed.* **2004**, *43*, 3673.

[5] Y. Sun, B. Mayers, Y. Xia, *Nano. Lett.* **2003**, *5*, 675.

[6] a) Y. Sun, B. Mayers, T. Herricks, Y. Xia, *Nano Lett.* **2003**, *3*, 955; b) Y. Sun, Y. Yin, B. Mayers, T. Herricks, Y. Xia, *Chem. Mater.* **2002**, *14*, 4736; c) Y. Sun, B. Mayers, Y. Xia, *Adv. Mater.* **2003**, *15*, 641.

[7] a) N. R. Jana, L. Gearheart, C. J. Murphy, *J. Phys. Chem. B* **2001**, *105*, 4065; b) C. J. Murphy, N. R. Jana, *Adv. Mater.* **2002**, *14*, 80; c) F. Kim, J. H. Song, P. Yang, *J. Am. Chem. Soc.* **2002**, *124*, 14316.

[8] a) E. Hao, R. C. Bailey, G. C. Schartz, J. T. Hupp, S. Li, *Nano Lett.* **2004**, *4*, 327; b) S. Chen, Z. L. Wang, J. Ballato, S. H. Foulger, D. L. Carroll, *J. Am. Chem. Soc.* **2003**, *125*, 16186.

[9] B. Wiley, T. Herricks, Y. Sun, Y. Xia, *Nano Lett.* **2004**, *4*, 1733.

[10] a) C. Özmetin, M. Çopur, A. Yartasi, M. M. Kocakerim, *Chem. Eng. Technol.* **2003**, *23*, 707; b) B. Blin, F. Fievet, D. Beaupère, M. Figlarz, *Nouv. J. Chim.* **1989**, *13*, 67.

[11] F. Fievet, J. P. Lagier, M. Figlarz, *MRS Bull.* **1989**, *14*, 29.

[12] Z. L. Wang, *J. Phys. Chem. B* **2000**, *104*, 1153; b) C. Cleveland, U. Landman, *J. Chem. Phys.* **1991**, *94*, 7376; c) P. M. Ajayan, L. D. Marks, *Phys. Rev. Lett.* **1988**, *60*, 585.

[13] a) S. Iijima, T. Ichihashi, *Phys. Rev. Lett.* **1986**, *56*, 616; b) D. J. Smith, A. K. Petford Long, L. R. Wallenberg, J. O. Bovin, *Science* **1986**, *233*, 872; c) N. Doraiswamy, L. Marks, *Surf. Sci.* **1996**, *348*, L67.

[14] a) C. A. Mirkin, *Inorg. Chem.* **2000**, *39*, 2258; b) S. Lin, Y. Tsai, C. Chen, C. Lin, C. Chen, *J. Phys. Chem. B* **2004**, *108*, 2134.

[15] I. O. Sosa, C. Noguez, R. G. Barrera, *J. Phys. Chem. B 107*, 6269.

 © 2005 Wiley-VCH Verlag GmbH & Co. KGaA, Weinheim

Computer Chemistry

$[(\eta^6\text{-}B_6X)_2M]$ (X = C, N; M = Mn, Fe, Co, Ni): A New Class of Transition-Metal Sandwich-Type Complexes**

Si-Dian Li, Jin-Chang Guo, Chang-Qing Miao, and Guang-Ming Ren*

Metallocenes, including ferrocene, $[(\eta^5\text{-}C_5H_5)_2Fe]$, and its 18-electron analogues $[(\eta^5\text{-}E_5)_2M]$ (E = P, N, As, Sb, and Bi; M = transition-metal atom), have found important applications in both fundamental research and materials science.[1–8] Planar aromatic D_{6h} C_6H_6 and D_{4h} $[N_4]^{2-}$ and $[Al_4]^{2-}$ can also be utilized as ligands to coordinate transition metals and form similar $[(\eta^n\text{-}E_n)_2M]$ complexes ($n = 4, 6$).[9–11] In these sandwich-type structures, the transition-metal center, M, is coordinated between two aromatic $\eta^n\text{-}E_n$ monocycles ($n = 4$–6), each of which has 6-π electrons. The π–d interactions between the delocalized π molecular orbitals (MOs) of the ligands and the partially occupied d orbitals of the transition-metal center play a crucial role in stabilizing the systems. Designing new forms of metallocenes and their sandwich-type analogues requires the right match between the monocyclic ligands and transition-metal centers, both geometrically and electronically. Inspired by the proposed 6-π electron aromatic D_{6h} B_6C^{2-} ion featuring a carbon atom in a planar hexacoordinate environment (denoted phC) at the center of a perfect B_6 hexagon,[12] we present herein an investigation by density functional theory (DFT) of a new class of sandwich-type complexes, D_{6d} $[(\eta^6\text{-}B_6X)_2M]$ (X = C, N; M = Mn, Fe, Co, Ni). These complexes are unique in that they contain two parallel $\eta^6\text{-}B_6X$ hexagons centered with two nearly planar hexacoordinate carbon or nitrogen atoms (phN) located along the sixfold molecular axis. The results obtained in this work provide an important extension to the traditional concept of sandwich-type complexes by incorporating hexacoordinate carbon or nitrogen atoms in the systems and present a viable possibility to stabilize and characterize phC or phN atoms in future experiments. To the best of our knowledge, there have been no investigations reported to date on B_6C^{2-} ligands in metallocene-like complexes.

[*] Prof. S.-D. Li, Dr. J.-C. Guo, C.-Q. Miao, G.-M. Ren
Institute of Materials Sciences and
Department of Chemistry
Xinzhou Teachers' University
Xinzhou 034000, Shanxi (P. R. China)
and
Institute of Molecular Science
Shanxi University
Taiyuan 030001, Shanxi (P. R. China)
Fax: (+86) 350-303-1845
E-mail: lisidian@yahoo.com

[**] This work was financially supported by the Shanxi Natural Science Foundation. The authors thank Dr. Hai-Jun Jiao for inspiring discussions.

Supporting information for this article is available on the WWW under http://www.angewandte.org or from the author.

DFT structural optimizations at the B3LYP/6-311 + G-(3df) level[13–15] were performed on the sandwich complexes under investigation and imaginary frequencies and DFT wavefunction instabilities checked at the same theoretical level. Natural bond orbital (NBO)[16] analyses were implemented to gain insight into the bonding pattern of the complexes. Figure 1 and Figure 2 depict the optimized

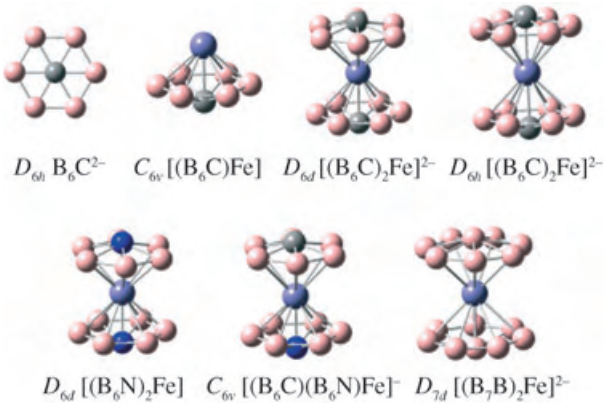

Figure 1. Optimized structures of D_{6h} B_6C^{2-}, C_{6v} $[(B_6C)Fe]$, D_{6d} $[(B_6C)_2Fe]^{2-}$, D_{6h} $[(B_6C)_2Fe]^{2-}$, D_{6d} $[(B_6N)_2Fe]$, C_{6v} $[(B_6C)(B_6N)Fe]^-$, and D_{7d} $[(B_7C)_2Fe]^{2-}$.

structures of Fe-containing complexes, and Figure 3 shows the MO pictures of the top 13 occupied energy levels of D_{6d} $[(\eta^6\text{-}B_6C)_2Fe]^{2-}$ (with one orbital shown for two degenerate MOs). These optimum structures are well-maintained when symmetry constraints are removed. Co-, Ni-, and Mn-centered complexes have the same geometries and similar MOs but have different energy levels. Table 1 tabulates the calculated bond lengths, natural atomic charges, lowest vibrational frequencies ($\tilde{\nu}_{min}$), highest occupied molecular orbital (HOMO) energies, and total Wiberg bond indices (WBIs)[12,17] of the constituent atoms for the complexes under investigation. Detailed geometrical and electronic properties of 28 neutral and charged complex ions that contain B_6X^{2-} (X = C, N) and B_7B^{2-} ligands are tabulated in the Supporting Information. All the calculations in this work were carried out by using the Gaussian 03 program.[17]

When a transition-metal center M (M = Mn, Fe, Co) coordinates one $\eta^6\text{-}B_6C^{2-}$ ligand along the sixfold axis, a hexagonal-bipyramidal C_{6v} $[(\eta^6\text{-}B_6C)M]$ complex is formed (see Figure 1). The 12-electron C_{6v} $[(\eta^6\text{-}B_6C)Mn]^-$, $[(\eta^6\text{-}B_6C)Fe]$, and $[(\eta^6\text{-}B_6C)Co]^+$ species are all found to be true minima with the lowest vibrational frequencies greater than 280 cm^{-1}. Adding one more $\eta^6\text{-}B_6C^{2-}$ ligand to a C_{6v} $[(\eta^6\text{-}B_6C)M]$ complex from the opposite direction along the sixfold axis results in a staggered D_{6d} $[(\eta^6\text{-}B_6C)_2M]$ complex, which contains two parallel C_{6v} B_6C^{2-} ligands around the transition-metal center. D_{6d} $[(\eta^6\text{-}B_6C)_2M]$ complexes have practically the same B–B bond lengths as C_{6v} $[(B_6C)M]$ but have slightly shorter B–C bonds and longer B–Fe separations as indicated in Table 1. The DFT Fe–B bond lengths in D_{6d} $[(\eta^6\text{-}B_6C)_2Fe]^{2-}$ are about 0.194 Å longer than the Fe–C separation (2.064 Å) observed in $[(\eta^5\text{-}C_5H_5)_2Fe]$.[9] The C atoms in D_{6d} $[(\eta^6\text{-}$

 © 2005 Wiley-VCH Verlag GmbH & Co. KGaA, Weinheim DOI: 10.1002/anie.200462476

Table 1: Optimized bond lengths, r [Å]; natural atomic charges, q [$|e|$]; lowest vibrational frequencies, $\tilde{\nu}_{min}$ [cm^{-1}]; HOMO energies [eV]; total Wiberg bond indices (WBIs) of the constituent atoms of D_{6h} B_6C^{2-}, D_{6h} B_6N^-, and D_{7h} B_7B^{2-} ligands and their sandwich complexes.

	r_{B-B}	r_{B-X}	r_{B-M}	r_{X-M}	q_B	q_X	q_M	$\tilde{\nu}_{min}$	WBI_B	WBI_X	WBI_M	HOMO
D_{6h} B_6C^{2-}	1.588	1.588			−0.21	−0.76		270	3.65	3.84		+4.18
C_{6v} $[Li(B_6C)]^-$	1.579	1.594	2.360	1.968	−0.19	−0.78	+0.92	291	3.64	3.87	0.02	−0.67
C_{6v} $[(B_6C)Mn]^-$	1.579	1.676	2.100	1.946	−0.12	−0.56	+0.31	312	3.63	3.93	3.67	+0.09
C_{6v} $[(B_6C)Fe]$	1.570	1.660	2.108	1.947	+0.02	−0.59	+0.48	282	3.53	3.93	3.21	−5.09
C_{6v} $[(B_6C)Co]^+$	1.574	1.665	2.135	1.982	+0.17	−0.67	+0.67	309	3.38	3.90	2.63	−12.40
D_{6d} $[(B_6C)_2Fe]^{2-}$	1.578	1.626	2.258	2.003	−0.01	−0.74	−0.42	43	3.54	3.86	3.03	+2.09
D_{6d} $[(B_6C)_2Co]^-$	1.580	1.619	2.265	1.974	+0.05	−0.79	+0.03	45	3.50	3.86	2.38	−2.46
D_{6d} $[(B_6C)_2Ni]$	1.588	1.616	2.302	1.964	+0.11	−0.89	+0.51	39	3.44	3.83	1.70	−6.75
D_{6h} B_6N^-	1.579	1.579			−0.02	−0.91		282i	3.45	3.17		−0.41
D_{6d} $[(B_6N)_2Fe]$	1.594	1.648	2.205	1.942	+0.20	−0.99	−0.40	58	3.30	3.06	3.11	−6.65
C_{6v} $[(B_6C)(B_6N)Fe]^-$	N 1.594	1.672	2.141	1.935	+0.13	−0.96	−0.38	55	3.35	3.05	3.17	−2.29
	C 1.578	1.617	2.300	2.026	+0.05	−0.76			3.49	3.86		
D_{6d} $[(B_6N)_2Mn]^-$	1.593	1.673	2.190	2.015	+0.14	−0.96	−0.78	63	3.34	3.05	3.69	−1.58
D_{7h} B_7B^{2-}	1.546	1.781			−0.30	+0.08		328	3.77	3.73		+3.44
D_{7d} $[(B_7B)_2Fe]^{2-}$	1.533	1.814	2.419	2.067	−0.12	−0.04	−0.427	37	3.68	3.76	2.98	+1.55
D_{7d} $[(B_7B)_2Co]^-$	1.534	1.813	2.408	2.040	−0.07	−0.004	−0.01	39	3.63	3.78	2.38	−2.91
D_{7d} $(B_7B)Ni$	1.542	1.815	2.427	2.027	−0.018	−0.101	+0.45	37	3.58	3.84	1.68	−6.98

$B_6C)_2Fe]^{2-}$, $[(\eta^6\text{-}B_6C)_2Co]^-$, and $[(\eta^6\text{-}B_6C)_2Ni]$ are only 0.39, 0.35, and 0.30 Å above the B_6 planes and can be approximately treated as quasi-phC atoms.

Although the energy differences between the staggered (D_{6d}) and the eclipsed (D_{6h}) conformations are very small and both structures have similar MOs, the eclipsed $[(\eta^6\text{-}B_6C)_2M]$ complexes all turn out to be transition states with one imaginary frequency. For example, for $[(\eta^6\text{-}B_6C)_2Fe]^{2-}$, $[(\eta^6\text{-}B_6C)_2Co]^-$, and $[(\eta^6\text{-}B_6C)_2Ni]$, the calculated energy differences between the eclipsed and staggered conformations are only 2.80, 2.88, and 2.41 kJ mol^{-1}, respectively, and their eclipsed structures are found to have one imaginary vibrational frequency located at 38i (b_{2g}), 39i (a_{1u}), and 32i (b_{2g}) cm^{-1}, respectively. This situation is different from the eclipsed D_{5h} $[(\eta^5\text{-}C_5H_5)_2Fe]$ observed in the gas phase[9] and D_{5h} $[(\eta^5\text{-}P_5)_2Ti]^{2-}$ in solids.[5] As the transition states are on rotational paths, the eclipsed D_{6h} $[(\eta^6\text{-}B_6C)_2M]$ complexes are automatically transferred to the staggered conformation when relaxed in the modes with the imaginary frequencies mentioned above. Thus, the complexes have very low rotational-energy barriers between D_{6d} and D_{6h} $[(\eta^6\text{-}B_6C)_2M]$, which is similar to the situation for D_5 ferrocene[9] (a slight distortion from a perfect D_{5h} $[(\eta^5\text{-}C_5H_5)_2Fe]$ as revealed by DFT). The contribution of the transition-metal centers in stabilizing these sandwich complexes is best illustrated in the cases of D_{6d} $[(\eta^6\text{-}B_6N)_2Fe]$, C_{6v} $[(\eta^6\text{-}B_6C)(\eta^6\text{-}B_6N)Fe]^-$, and D_{6d} $[(\eta^6\text{-}B_6N)_2Mn]^-$, in which the unstable phN centers in D_{6h} B_6N^- (which has an imaginary frequency at 282i cm^{-1} in e_{1u} mode) have been stabilized when incorporated in sandwich complexes. As indicated in Figure 1 and Table 1, the sandwich-type D_{7d} $[(\eta^7\text{-}B_7B)_2M]$ complexes (M = Fe, Co, Ni), which contain two 6-π-electron heptagons (D_{7h} B_7B^{2-}) centered with two B atoms,[18] are also true minima of the systems.

It is interesting to study reaction (1) of D_{6h} B_6C^{2-} with D_5 $[(C_5H_5)_2Fe]$ to produce D_{6d} $[(B_6C)_2Fe]^{2-}$ and D_{5h} $C_5H_5^-$. With zero-point corrections included, the reaction (1) is highly exothermic as calculated by DFT and has an enthalpy change of $\Delta H^0 = -530.9$ kJ mol^{-1} and a Gibbs free energy change of $\Delta G^0 = -533.6$ kJ mol^{-1}, which indicates that the replacement of $C_5H_5^-$ in D_5 $[(\eta^5\text{-}C_5H_5)_2Fe]$ with B_6C^{2-} is strongly favored thermodynamically. Based upon this observation, we propose to synthesize stable and characterizable salts of $[(B_6C)_2Fe]^{2-}$ containing phC atoms as outlined in Equation (1). Further investigation on the reaction kinetics is currently in progress.

$$[(C_5H_5)_2Fe] + 2\,B_6C^{2-} \rightarrow [(B_6C)_2Fe]^{2-} + 2\,C_5H_5^- \quad (1)$$

Why are these sandwich-type structures stable? NBO analyses help to answer this question. D_{6d} $[(B_6C)_2Fe]^{2-}$ has the natural atomic electronic configurations of C, [He]$2s^{1.04}2p^{3.60}$ ($2s^{1.04}2p_x^{1.27}2p_y^{1.27}2p_z^{1.05}$); Fe, [Ar]$4s^{0.16}3d^{8.18}$ ($4s^{0.16}3d_{xy}^{1.88}3d_{xz}^{1.38}3d_{yz}^{1.38}3d_{x^2-y^2}^{1.88}3d_{z^2}^{1.66}$); and B, [He] $2s^{0.86}2p^{2.12}$ ($2s^{0.86}2p_x^{0.99}2p_y^{0.55}2p_z^{0.58}$), which are in agreement with the natural atomic charges tabulated in Table 1. The $4s^2$ electrons of the neutral Fe have been almost completely stripped away in $[(B_6C)_2Fe]^{2-}$, with the occupancy of the 4s orbital of the Fe atom decreased to $4s^{0.16}$. The negative charge of the Fe atom (−0.42 $|e|$) results from the π→d back-bonding from the B_6C^{2-} ligands to the Fe center. Similar to the situation in D_{6h} B_6C^{2-}, a C center provides three sp^2-hybridized orbitals to form six partial bonds with the surrounding B atoms and provides one singly occupied p_z orbital to participate in the formation of the delocalized MOs within the complex (HOMO-9 and HOMO-12 shown in Figure 2). The electron-deficient peripheral B atoms each

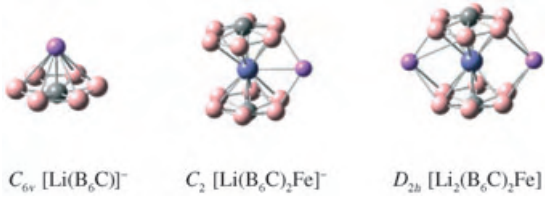

Figure 2. Optimized structures of C_{6v} $[LiB_6C]^-$, C_2 $Li[(B_6C)_2Fe]^-$, and D_{2h} $Li_2[(B_6C)_2Fe]$.

 © 2005 Wiley-VCH Verlag GmbH & Co. KGaA, Weinheim

contribute three partially occupied sp^2-hybridized orbitals to form three in-plane bonds and provide one partially filled p_z orbital to participate in the π–d interaction with the metal center.

Orbital analyses indicate that all the occupied MOs of $[(B_6C)_2Fe]^{2-}$ can be unambiguously assigned to different combinations of the frontier MOs of the two D_{6h} B_6C^{2-} ligands and the 3d orbitals of the Fe center (Figure 3). The

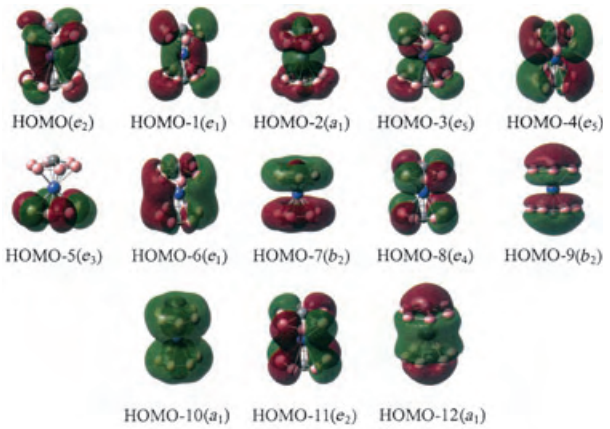

Figure 3. Molecular orbital pictures of the top 13 energy levels of D_{6d} $[(B_6C)_2Fe]^{2-}$.

degenerate HOMOs (e_2) originate from the nearly fully occupied Fe $3d_{xy}^{1.88}$ and Fe $3d_{x^2-y^2}^{1.88}$ orbitals. The degenerate HOMO-1(e_1) mainly represent the in-phase overlaps between the two delocalized π HOMOs (e_{1g}) of the two B_6C^{2-} ligands,[12] whereas HOMO-3(e_5) reflects the interactions between the two π HOMOs (e_{1g}) of the two B_6C^{2-} ligands with opposite orbital signs and the $3d_{xz}^{1.38}$ and $3d_{yz}^{1.38}$ orbitals of the Fe center, which match the ligands in orbital signs and geometries. Interestingly, it is mainly the in-phase participation of the Fe 3d orbitals in HOMO-3(e_5) that makes the two degenerate HOMO-3(e_5) MOs lie lower in energy than HOMO-1(e_1). HOMO-2(a_1) and HOMO-10(a_1), which form the weak Fe–C interactions (as indicated by the Wiberg bond index detailed below) along the sixfold axis, mainly correspond to out-of-phase and in-phase overlaps of Fe $3d_{z^2}$ and C 2s orbitals, respectively. HOMO-4(e_5) and HOMO-6(e_1) clearly originate from the four degenerate HOMO-1(e_{1u}) orbitals of the two B_6C^{2-} ligands. HOMO-5(e_3) and HOMO-7(b_2) are directly inherited from the HOMO-2(b_{2u}) and HOMO-3(a_{1g}) of the B_6C^{2-} ion, while HOMO-8(e_4) and HOMO-11(e_2) result from different combinations of the degenerate HOMO-4(e_{2g}) of the two ligands. Finally, HOMO-9(b_2) and HOMO-12(a_1) correspond to the out-of-phase and in-phase combinations of the two totally delocalized π HOMO-5(a_{2u}) of the two ligands, respectively.

The calculated total Wiberg bond indices (WBIs) of the constituent atoms with $WBI_C = 3.83–3.93$, $WBI_N = 3.05–3.17$, $WBI_B = 3.30–3.68$, and $WBI_M = 1.68–3.69$ indicate that these complexes follow the octet role in bonding nature, similar to the situation observed in the D_{6h} B_6C^{2-} ion.[12] The introduction of a transition-metal center, M, leads to two additional C–M interactions and twelve additional B–M interactions, whereas the C–B and B–B bonds in B_6C^{2-} ligands are well maintained. For example, the Wiberg bond orders of D_{6d} $[(B_6C)_2Fe]^{2-}$ are $WBI_{C-B} = 0.60$, $WBI_{B-B} = 1.17$, $WBI_{Fe-C} = 0.19$, and $WBI_{Fe-B} = 0.22$, of which, WBI_{C-B} and WBI_{B-B} are practically the same as the corresponding values of 0.64 and 1.26 in a perfect D_{6h} B_6C^{2-} hexagon calculated at the same DFT level.

It should be pointed out that, as expected, D_{6d} $[(\eta^6\text{-}B_6C)_2Fe]^{2-}$ is unstable towards electron dissociation: its top nine occupied MOs have positive eigenvalues when calculated by DFT. Similar situations are met in other dianions such as D_{6h} B_6C^{2-}[12] and D_{4h} $[Al_4]^{2-}$ and D_{4d} $[Al_4TiAl_4]^{2-}$,[11] all of which have positive HOMO energies. However, these aromatic dianions can be effectively stabilized by introducing alkali-metal counterions into the systems while keeping the basic structures of the dianions unchanged, as shown in the cases of C_{4v} $[MAl_4]^-$ (M = Li, Na, Cu) and $[NaAl_4TiAl_4]^-$.[11] C_{6v} $[LiB_6C]^-$, C_2 $[Li(\eta^6\text{-}B_6C)_2Fe]^-$, and D_{2h} $[Li_2(\eta^6\text{-}B_6C)_2Fe]$ studied in this work (see Figure 2) are confirmed to have the negative HOMO energies of −0.67, −1.82 ,and −5.68 eV, respectively. The structures of B_6C^{2-} ligands are well maintained in these complexes and the staggered→eclipsed structural change is completed in D_{2h} $[Li_2(\eta^6\text{-}B_6C)_2Fe]$, in which the relatively strong Coulomb attractions between the two Li^+ ions and their neighboring B atoms with partial negative charges determine the structure of the neutral complex. All the occupied MOs of other neutral and monoanionic sandwich complexes tabulated in Table 1 are confirmed to have negative energies. According to Koopman's theorem, the negative values of the HOMO energies listed in Table 1 approximately represent the first-electron-detachment energies of the corresponding complexes.

In summary, we have predicted by DFT a new class of sandwich-type complexes D_{6d} $[(B_6X)_2M]$ with two nearly planar hexacoordinate carbon or nitrogen atoms located at the centers of two parallel B_6 hexagons about the transition-metal center M. The proposal of replacing C_5H_5- in $[(\eta^5\text{-}C_5H_5)_2Fe]$ with B_6C^{2-} to form D_{6d} $[(\eta^6\text{-}B_6C)_2Fe]^{2-}$ may represent a step forward towards the synthesis and characterization of phC centers incorporated in transition-metal complex salts in future experiments. The sandwich structural pattern developed in this work may be extended along the sixfold molecular axis (or in its perpendicular direction) to form $[(B_6C)M]_n$ chains ($n \geq 3$) linked with alkali-metal cations and the hexagonal B_6 centered with C or N may be modified to form various heterocyclic ligands.

Received: October 30, 2004
Revised: December 17, 2004
Published online: March 2, 2005

Keywords: boron · computer chemistry · density functional calculations · electronic structures · hexacoordinate carbon

[1] T. J. Kealy, P. L. Pauson, *Nature* **1951**, *168*, 1039.
[2] N. J. Long, *Metallocenes*, Blackwell, Oxford, UK, **1998**.
[3] A. D. Garnovskii, A. P. Sadimenko, M. I. Sadimenko, D. A. Garnovskii, *Coord. Chem. Rev.* **1998**, *173*, 31.

 © 2005 Wiley-VCH Verlag GmbH & Co. KGaA, Weinheim

[4] P. v. R. Schleyer, B. Kiran, D. V. Simion, T. S. Sorensen, *J. Am. Chem. Soc.* **2000**, *122*, 510.
[5] E. Urnezius, W. W. Brennessel, C. J. Cramer, J. E. Ellis, P. v. R. Schleyer, *Science* **2002**, *295*, 832.
[6] A. C. Tsipis, A. T. Chaviara, *Inorg. Chem.* **2004**, *43*, 1273.
[7] M. Lein, J. Frunzke, G. Frenking, *Angew. Chem.* **2003**, *115*, 1341; *Angew. Chem. Int. Ed.* **2003**, *42*, 1303.
[8] M. Lein, J. Frunzke, A. Timoshkin, G. Frenking, *Chem. Eur. J.* **2001**, *7*, 4155.
[9] A. Haaland, *Acc. Chem. Res.* **1979**, *12*, 415.
[10] J. M. Mercero, J. M. Matxain, J. M. Ugalde, *Angew. Chem.* **2004**, *116*, 5601; *Angew. Chem. Int. Ed.* **2004**, *43*, 5485.
[11] X. Li, A. E. Kuznetsov, H. F. Zhang, A. I. Boldyrev, L.-S. Wang, *Science* **2001**, *291*, 859; J. M. Mercero, J. M. Ugalde, *J. Am. Chem. Soc.* **2004**, *126*, 3380.
[12] K. Exner, P. v. R. Schleyer, *Science* **2000**, *290*, 1937.
[13] A. D. Becke, *J. Chem. Phys.* **1993**, *98*, 5648.
[14] C. Lee, W. Yang, R. G. Parr, *Phys. Rev. B* **1988**, *37*, 785.
[15] S. H. Vosko, L. Wilk, M. Nusair, *Can. J. Phys.* **1980**, *58*, 1200.
[16] J. E. Carpenter, F. Weinhold, *J. Mol. Struct.* **1988**, *169*, 41.
[17] Gaussian 03 (Revision A.1), M. J. Frisch, G. W. Trucks, H. B. Schlegel, G. E. Scuseria, M. A. Robb, J. R. Cheeseman, J. A. Montgomery, Jr., T. Vreven, K. N. Kudin, J. C. Burant, J. M. Millam, S. S. Iyengar, J. Tomasi, V. Barone, B. Mennucci, M. Cossi, G. Scalmani, N. Rega, G. A. Petersson, H. Nakatsuji, M. Hada, M. Ehara, K. Toyota, R. Fukuda, J. Hasegawa, M. Ishida, T. Nakajima, Y. Honda, O. Kitao, H. Nakai, M. Klene, X. Li, J. E. Knox, H. P. Hratchian, J. B. Cross, C. Adamo, J. Jaramillo, R. Gomperts, R. E. Stratmann, O. Yazyev, A. J. Austin, R. Cammi, C. Pomelli, J. W. Ochterski, P. Y. Ayala, K. Morokuma, G. A. Voth, P. Salvador, J. J. Dannenberg, V. G. Zakrzewski, S. Dapprich, A. D. Daniels, M. C. Strain, O. Farkas, D. K. Malick, A. D. Rabuck, K. Raghavachari, J. B. Foresman, J. V. Ortiz, Q. Cui, A. G. Baboul, S. Clifford, J. Cioslowski, B. B. Stefanov, G. Liu, A. Liashenko, P. Piskorz, I. Komaromi, R. L. Martin, D. J. Fox, T. Keith, M. A. Al-Laham, C. Y. Peng, A. Nanayakkara, M. Challacombe, P. M. W. Gill, B. Johnson, W. Chen, M. W. Wong, C. Gonzalez, J. A. Pople, Gaussian, Inc., Pittsburgh, PA, **2003**..
[18] H. J. Zhai, A. N. Alexandrova, K. A. Birch, A. I. Boldyrev, L. S. Wang, *Angew. Chem.* **2003**, *115*, 6186; *Angew. Chem. Int. Ed.* **2003**, *42*, 6004.

 © 2005 Wiley-VCH Verlag GmbH & Co. KGaA, Weinheim

Cover Picture

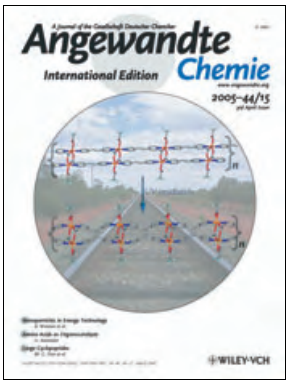

Ni Lian Toh, Mangayarkarasi Nagarathinam, and Jagadese J. Vittal*

Railroad polymers are one-dimensional metal coordination polymers that form a molecular ladder structure. The cover picture shows such a structure, comprised of Zn–(4,4′-bipyridylethylene) units, which undergoes [2+2] photochemical cycloaddition across the rails to form another 1D coordination polymeric structure accompanied by quantitative single-crystal to single-crystal transformation. For more details see the Communication by J. J. Vittal and co-workers on page 2237 ff. (The cover picture was designed by Bellam Sreenivasulu.)

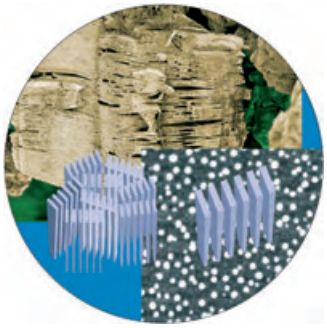

Nanotechnology
Nanoparticles are key components in heterogeneous catalysis and future energy technologies. In their Review on page 2190 ff., A. Wokaun et al. discuss how electronic and morphological factors affect the properties of metal nanoparticles.

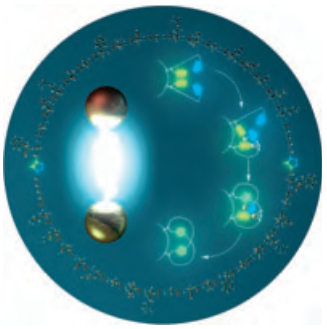

Large Cyclopeptides
Two copper centers catalyze the cycloaddition reaction between an azide and an alkyne. In their Communications on pages 2210 ff. and 2215 ff., M. G. Finn and co-workers show how this reaction can be used for the selective production of large cyclic dimers from resin-
tethered peptides.

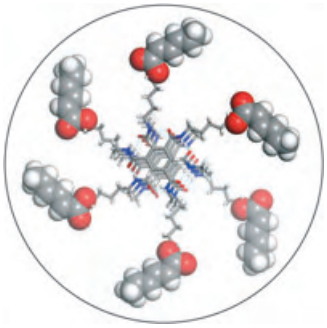

Helical Polymers
In their Communication on page 2275 ff., E. W. Meijer and co-workers discuss how a chiral supramolecular “sergeant” affects the backbone stereochemistry during the polymerization of achiral “soldier” monomers.

Contents

VIP *The following Communications have been judged by at least two referees to be "very important papers" and will be published online at www.angewandte.org soon:*

*J. Malo, J. C. Mitchell, C. Vénien-Bryan, J. R. Harris, H. Wille, D. J. Sherratt, A. J. Turberfield**
Engineering a 2D Protein–DNA Crystal

*F. López, S. R. Harutyunyan, A. Meetsma, A. J. Minnaard, B. L. Feringa**
Copper-Catalyzed Enantioselective Conjugate Addition of Grignard Reagents to α,β-Unsaturated Esters

*A. Tavassoli, S. J. Benkovic**
Genetically Selected Cyclic-Peptide Inhibitors of AICAR Transformylase Homodimerization

*V. Huber, M. Katterle, M. Lysetska, F. Würthner**
Reversible Self-Organization of Semisynthetic Zinc Chlorins into Well-Defined Rod Antennae

*N. P. Grimster, Carolyn Gauntlett, C. R. A. Godfrey, M. J. Gaunt**
Intermolecular Palladium-Catalyzed Alkenylation of Indoles through Solvent-Controlled Regioselective C–H Functionalization

*R. Banerjee, P. M. Bhatt, M. T. Kirchner, G. R. Desiraju**
Structural Studies of the System Sodium Saccharinate Hydrate: A Model for Crystallization

News

Awards of the Chemical Society of Japan 2004 ____ **2180**

Books

Protein Synthesis and Ribosome Structure — Knud H. Nierhaus, Daniel N. Wilson — *reviewed by M. Sprinzl* ____ ***2182***

High-Throughput Screening in Chemical Catalysis — Alfred Hagemeyer, Peter Strasser, Anthony F. Volpe, Jr. — *reviewed by C. Markert* ____ ***2183***

Highlights

Carbohydrate Synthesis

U. Kazmaier* ____ **2186 – 2188**

Amino Acids—Valuable Organocatalysts in Carbohydrate Synthesis

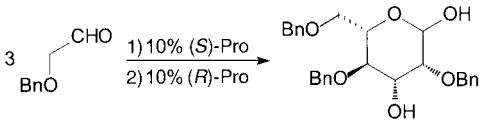

Sweet developments: Proline-catalyzed aldol reactions readily allow access to complex carbohydrates from simple glycolaldehydes in a highly stereoselective fashion (see scheme; Bn = benzyl).

Reviews

Nanotechnology

F. Raimondi, G. G. Scherer, R. Kötz, A. Wokaun* ____ **2190 – 2209**

Nanoparticles in Energy Technology: Examples from Electrochemistry and Catalysis

Made to measure: Nanostructuring of surfaces is important for the activity of catalysts in the conversion of fuels and in electrochemistry. Particular care must be taken to ensure the optimal particle size in the nanometer range. The picture shows a new method for the colloidal synthesis of platinum and platinum-alloy nanoparticles of defined dimensions.

Communications

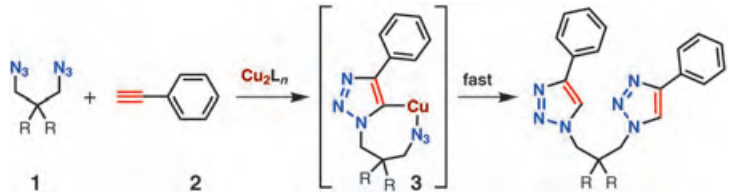

A powerful engine: The Cu-catalyzed azide–alkyne cycloaddition depends on rapid formation of Cu^{I}–acetylide complexes from terminal alkynes **2** and their ability to activate organic azides **1**. A kinetics study uncovered a bimolecular dependence on the metal and an unusually fast intramolecular variant of the process. The results suggest the importance of **3** as a reactive intermediate.

Azide–Alkyne Cycloadditions

V. O. Rodionov, V. V. Fokin,*
M. G. Finn* ——— **2210 – 2215**

Mechanism of the Ligand-Free Cu^{I}-Catalyzed Azide–Alkyne Cycloaddition Reaction

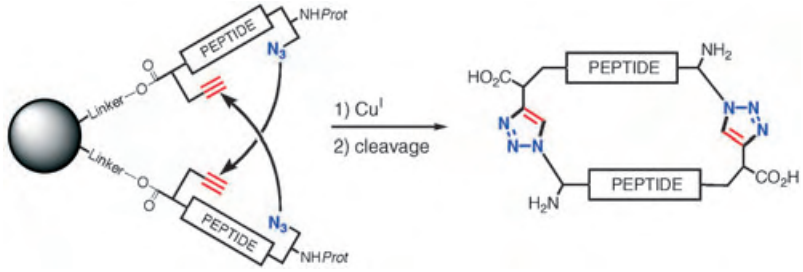

Rings forged with copper: Oligopeptide cyclodimerization occurs selectively when precursors containing azide and alkyne groups are exposed to copper(I) ions on polystyrene supports (see picture; *Prot* = protecting group).

Azide–Alkyne Cycloadditions

S. Punna, J. Kuzelka, Q. Wang,
M. G. Finn* ——— **2215 – 2220**

Head-to-Tail Peptide Cyclodimerization by Copper-Catalyzed Azide–Alkyne Cycloaddition

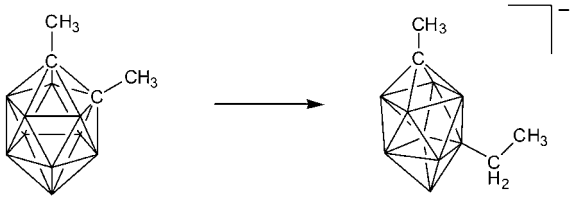

A nonclassical carbon atom of a dicarbaborane is converted into a classical carbon atom, and the substituent increases in length by one CH_2 group (see scheme). This is the path followed to form [1-Me-6-Et-1-*closo*-CB_9H_8]$^-$ regioselectively from [1,2-Me_2-1,2-*closo*-$C_2B_{10}H_{10}$]. First, the *o*-carborane derivative is reduced to [7-Me-μ-(9,10-HMeC)-7-*nido*-$CB_{10}H_{11}$]$^-$, and then a carbon-atom extrusion followed by selective deboronation takes place.

Monocarboranes

A. Laromaine, F. Teixidor,
C. Viñas* ——— **2220 – 2222**

Carbon Extrusion in 1,2-Dicarba-*closo*-dodecaboranes: Regioselective Boron Substitution in Ten-Vertex *closo*-Monocarbaborane Anions

For the USA and Canada:
ANGEWANDTE CHEMIE International Edition (ISSN 1433-7851) is published weekly by Wiley-VCH PO Box 191161, D 69451 Weinheim, Germany. Air freight and mailing in the USA by Publications Expediting Inc. 200 Meacham Ave., Elmont, NY 11003. Periodicals postage paid at Jamaica NY 11431. US POSTMASTER: send address changes to *Angewandte Chemie*, Wiley-VCH, 111 River Street, Hoboken, NJ 07030. Annual subscription price for institutions: US$ 4948.00/4498.00 (valid for print and electronic / print or electronic delivery); for individuals who are personal members of a national chemical society, or whose institution already subscribes, or who are retired or self-employed consultants, print only: US$ 394.00. Postage and handling charges included. All Wiley-VCH prices are exclusive VAT.

 © 2005 Wiley-VCH Verlag GmbH & Co. KGaA, Weinheim

The best in chemistry –

for more than a hundred years

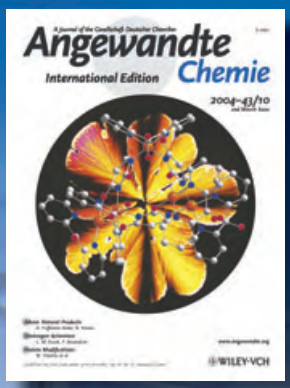

A Journal of the Gesellschaft Deutscher Chemiker

Angewandte
International Edition **Chemie**

www.angewandte.org

1888: ***The beginning of a success story***

Constant Innovations

1962: *First issue of the International Edition*
1976: *Graphical abstracts*
1979: *Cover pictures*
1988: *Centenary of Angewandte*
1989: *Routine use of color*
1991: *New section: Highlights*
1992: *Computerized editorial tracking system*
1995: *Internet service for readers*
1998: *Regular press service; full-text online*
2000: *New section: Essays; EarlyView: Communications available online ahead of the printed version*
2001: *New section: Minireviews*
2002: *Online submission of manuscripts*
2003: *Weekly publication; new section: News; new layout*
2004: *Backfiles (1962-1997); ManuscriptXpress: Online system for authors and referees*

Angewandte's advisors...

E. W. "Bert" Meijer
Technische Universiteit Eindhoven

» ***Angewandte Chemie,*** *in its way of publishing, is as original as the chemistry described in the journal. It serves our society in a superb and attractive way. Many leading communications and comprehensive reviews have been published through the years and many of them are used in my teaching and cited in my own papers. It is a privilege to publish in and to be connected to a journal that is the trendsetter in chemistry of the highest standards.* «

Angewandte Chemie International Edition *is a journal of the German Chemical Society (GDCh)*

GDCh

WILEY InterScience® DISCOVER SOMETHING GREAT

WILEY-VCH

12001404_gu

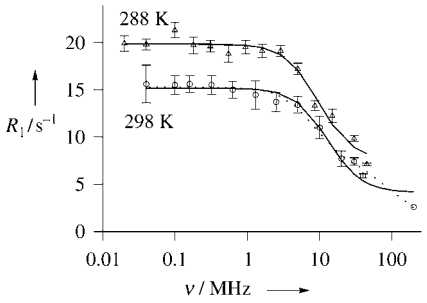

Relaxation time: Direct profiles of protein ^{1}H relaxation in D_2O at mM concentrations were generated by NMR spectroscopy at 0.01–50 MHz (see picture). The study of lysozyme at pH 3.5 (monomeric) and pH 9.0 (dimeric), and of α-synuclein (unfolded), provides direct information on aggregation through estimates of the realignment correlation time and on the overall compactness of the protein.

Protein Dynamics

I. Bertini,* Y. K. Gupta, C. Luchinat, G. Parigi, C. Schlörb, H. Schwalbe _____ **2223 – 2225**

NMR Spectroscopic Detection of Protein Protons and Longitudinal Relaxation Rates between 0.01 and 50 MHz

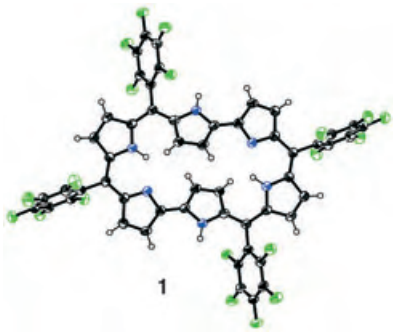

Acid-specific conformational changes: Protonation of *meso*-aryl-substituted rubyrin **1** with HCl or CF_3CO_2H causes different conformational changes, as revealed by specific shifts in the UV/Vis absorption bands relative to those of the free-base form (Cl^-: blue shift; $CF_3CO_2^-$: red shift). The distinct counteranion-dependent color changes upon addition of the acids to the "anion sensor" **1** are easily detected.

Expanded Porphyrins

S. Shimizu, R. Taniguchi, A. Osuka* _____ **2225 – 2229**

meso-Aryl-Substituted [26]Hexaphyrin(1.1.0.1.1.0) and [38]Nonaphyrin(1.1.0.1.1.0.1.1.0) from Oxidative Coupling of a Tripyrrane

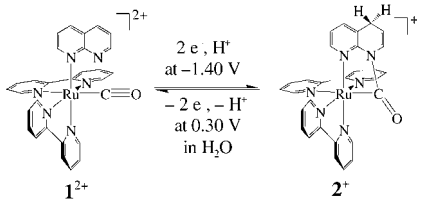

A five-membered metallacycle ($\mathbf{2}^+$) hydrogenated at the 4-position of the naphthyridine ligand results from the reduction of $[Ru(bpy)_2(napy\text{-}\kappa N)(CO)]^{2+}$ ($\mathbf{1}^{2+}$; bpy = 2,2′-bipyridine, napy = 1,8-naphthyridine) at −1.40 V in H_2O. Chemical or electrochemical oxidation of $\mathbf{2}^+$ regenerates $\mathbf{1}^{2+}$ in almost quantitative yield.

Redox Chemistry

T. Tomon, T.-a. Koizumi, K. Tanaka* _____ **2229 – 2232**

Electrochemical Hydrogenation of $[Ru(bpy)_2(napy\text{-}\kappa N)(CO)]^{2+}$: Inhibition of Reductive Ru–CO Bond Cleavage by a Ruthenacycle

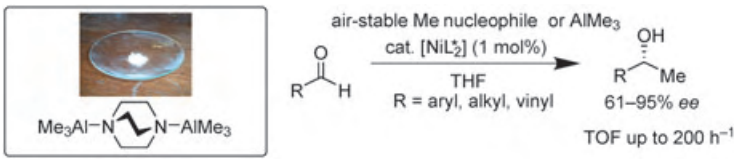

Weigh it out in air! The DABAL reagent $(Me_3Al)_2{\cdot}$(DABCO) (DABCO = 1,4-diazabicyclo[2.2.2]octane) can be easily handled under normal laboratory conditions. Furthermore, chiral secondary alcohols can be efficiently prepared from prochiral aldehydes (see scheme; TOF = turnover frequency) by using either DABAL or AlR_3 reagents (R = Me, Et). Thus, DABAL can be used as an efficient, convenient alternative to the Schumann–Blum reagent.

Asymmetric Synthesis

K. Biswas, O. Prieto, P. J. Goldsmith, S. Woodward* _____ **2232 – 2234**

Remarkably Stable $(Me_3Al)_2{\cdot}$DABCO and Stereoselective Nickel-Catalyzed AlR_3 (R = Me, Et) Additions to Aldehydes

 © 2005 Wiley-VCH Verlag GmbH & Co. KGaA, Weinheim

Contents

Asymmetric Synthesis

P. J. Goldsmith, S. J. Teat, S. Woodward* ——— 2235 – 2237

Enantioselective Preparation of β,β-Disubstituted α-Methylenepropionates by MAO Promotion of the Zinc Schlenk Equilibrium

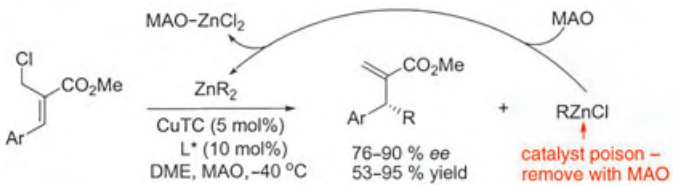

The zinc Schlenk equilibrium, little used since it was first described in 1966, has been promoted through the addition of methylaluminoxane (MAO) to maximize the yield of ZnR_2 from deleterious RZnCl by-products. This process allows an S_N2'-addition approach to the preparation of chiral β,β-disubstituted α-methylenepropionates with high enantioselectivity (see scheme).

Supramolecular Chemistry

N. L. Toh, M. Nagarathinam, J. J. Vittal* ——— 2237 – 2241

Topochemical Photodimerization in the Coordination Polymer $[\{(CF_3CO_2)(\mu\text{-}O_2CCH_3)Zn\}_2(\mu\text{-bpe})_2]_n$ through Single-Crystal to Single-Crystal Transformation

The molecular-ladder-structured, one-dimensional Zn–(4,4′-bipyridylethylene) coordination polymer **1** undergoes [2+2] photochemical cycloaddition across the rails to form **2** in up to 100% yield, accompanied by a single-crystal to single-crystal transformation.

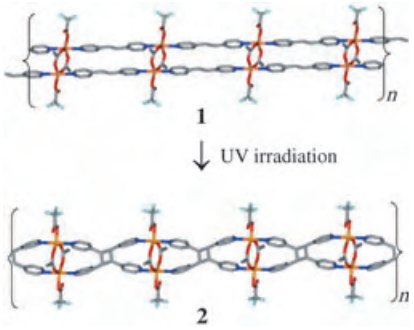

Supported Catalysts

S. Carrettin, J. Guzman, A. Corma* ——— 2242 – 2245

Supported Gold Catalyzes the Homocoupling of Phenylboronic Acid with High Conversion and Selectivity

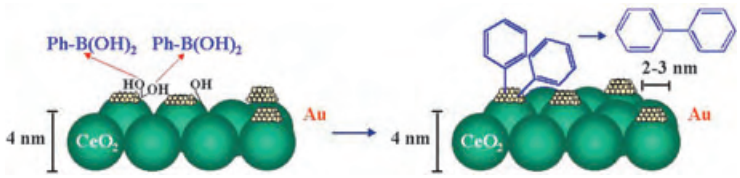

Gold on nanocrystalline cerium oxide is a highly active and selective catalyst for the homocoupling of phenylboronic acid derivatives in the presence of K_2CO_3 as a base (see picture). Au^{3+} species are thought to be the active sites for the reaction, and water is required to activate the boronic acid through the participation of surface hydroxy groups.

β-Selective Glycosidation

R. Arihara, S. Nakamura, S. Hashimoto* ——— 2245 – 2249

Direct and Stereoselective Synthesis of 2-Acetamido-2-deoxy-β-D-glycopyranosides by Using the Phosphite Method

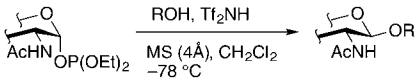

Avoiding the intermediate: The β-selective glycosidation of 2-acetamido-2-deoxyglycosyl diethyl phosphites promoted by bis(trifluoromethanesulfonyl)imide (Tf_2NH) proceeds in a direct manner and does not afford an oxazolinium ion as an intermediate (see scheme; MS (4Å) = 4-Å molecular sieves).

 © 2005 Wiley-VCH Verlag GmbH & Co. KGaA, Weinheim

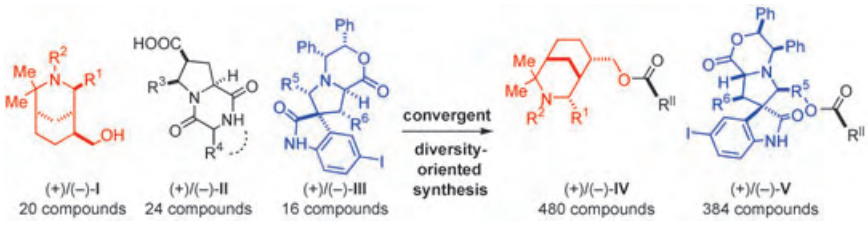

Complex small-molecule libraries were constructed by a convergent approach with a short linear sequence: a 480-membered bridged-piperidine/fused-pyrrolidine hybrid library **IV** and a 384-membered spirocyclic-oxindole/fused-pyrrolidine hybrid library **V** from the sublibrary **II** and the sublibraries **I** and **III**, respectively. **II** = R^{II}—COOH.

Library Synthesis

C. Chen, X. Li, C. S. Neumann, M. M.-C. Lo, S. L. Schreiber* ____ **2249 – 2252**

Convergent Diversity-Oriented Synthesis of Small-Molecule Hybrids

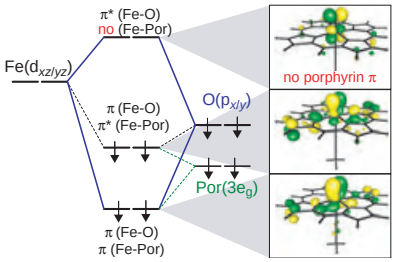

Extremely similar electronic structures and Fe—O bonding characterize Fe^{IV}=O $S=1$ heme and non-heme species as a result of a decoupling of the oxoiron unit from the porphyrin (Por) π system in the heme complex (see scheme). However, along the reaction coordinate towards an Fe^{III}—OH product, the Por π system interacts with the iron d orbitals, thus resulting in different reactivities for heme and non-heme complexes.

Oxoiron(IV) Complexes

A. Decker, E. I. Solomon* ____ **2252 – 2255**

Comparison of Fe^{IV}=O Heme and Non-heme Species: Electronic Structures, Bonding, and Reactivities

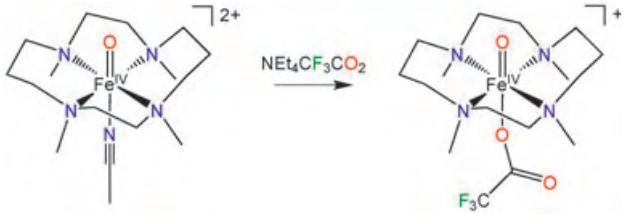

Enhancing reactivity: A common feature of non-heme iron enzymes is the presence of carboxylate groups. An axial carboxylate group has been introduced *trans* to the oxo group of a non-heme oxoiron(IV) complex (see scheme). The coordination of carboxylate destabilizes the Fe^{IV}=O unit and activates it towards reaction with dihydroanthracene.

Oxoiron(IV) Complexes

J.-U. Rohde, L. Que, Jr.* ____ **2255 – 2258**

Axial Coordination of Carboxylate Activates the Non-heme Fe^{IV}=O Unit

Unusual substrates for cascade reactions: Racemic β-ketoesters with all-carbon quaternary centers were used as starting materials in a dynamic kinetic resolution process to produce complex polycycles in high enantio- and diastereoselectivities (see scheme; TBS = *tert*-butyldimethylsilyl). The cascade reactions involved epimerization in the second step through the formation and cleavage of multiple C—C bonds in a retro-aldol/aldol equilibrium.

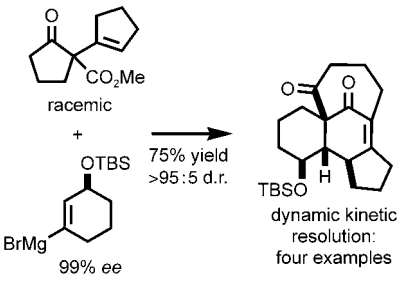

Asymmetric Synthesis

K. Xu, G. Lalic, S. M. Sheehan, M. D. Shair* ____ **2259 – 2261**

Dynamic Kinetic Resolution during a Cascade Reaction on Substrates with Chiral All-Carbon Quaternary Centers

 © 2005 Wiley-VCH Verlag GmbH & Co. KGaA, Weinheim

Contents

Chiral Fullerene Adducts

S. Kuwahara, K. Obata, K. Yoshida, T. Matsumoto, N. Harada,* N. Yasuda, Y. Ozawa, K. Toriumi ——— **2262 – 2265**

Conclusive Determination of the Absolute Configuration of Chiral C_{60}-Fullerene *cis*-3 Bisadducts by X-ray Crystallography and Circular Dichroism

Ultrathin red plate crystals of a chiral C_{60}-fullerene *cis*-3 bisadduct were subjected to X-ray crystallographic analysis to finally determine the absolute configuration of such an adduct conclusively (see picture; C gray, O red, H blue). A comparison of its circular-dichroism spectrum with those of similar compounds suggested that the absolute configurations reported for some compounds may require revision.

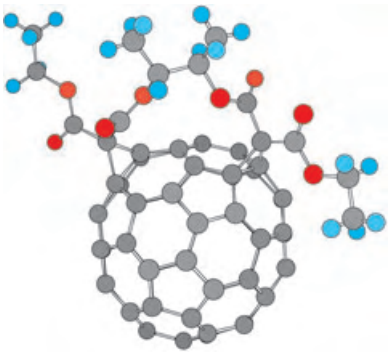

Colorimetric Sensors

M. Maue, T. Schrader* ——— **2265 – 2270**

A Color Sensor for Catecholamines

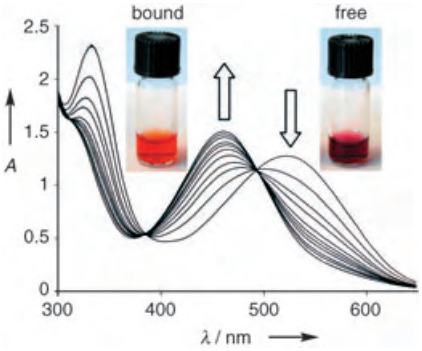

Right in front of your eyes: Upon addition of a catecholamine to a catechol-containing receptor precomplexed with a dye, a change in color from orange to deep red signals the release of the dye and capture of the guest (see picture). This simple competition experiment allows exact quantitative determination of the concentration of catecholamines in complex mixtures, such as that of adrenaline in urine samples.

Nucleic Acid Structure

R. Otero, M. Schöck, L. M. Molina, E. Lægsgaard, I. Stensgaard, B. Hammer, F. Besenbacher* ——— **2270 – 2275**

Guanine Quartet Networks Stabilized by Cooperative Hydrogen Bonds

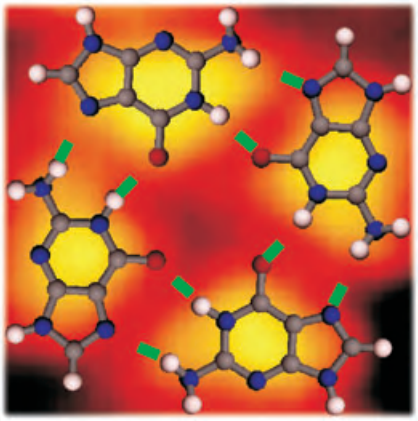

String quartets: Guanine molecules self-assemble into a hydrogen-bonded network of G quartets upon deposition under ultrahigh vacuum conditions onto Au(111) surfaces as shown by STM (see picture). The resilience of the H-bonded network (stable up to 400 K) is explained through a cooperative increase in the strength of H-bonds between guanine molecules in a quartet.

Helical Structures

A. J. Wilson, M. Masuda, R. P. Sijbesma,* E. W. Meijer* ——— **2275 – 2279**

Chiral Amplification in the Transcription of Supramolecular Helicity into a Polymer Backbone

A chiral supramolecular "sergeant" as the structure-directing agent affects the backbone stereochemistry during polymerization of the achiral "soldier" monomers. The polymer obtained shows preferred helical folding despite its mixed microstructure.

 © 2005 Wiley-VCH Verlag GmbH & Co. KGaA, Weinheim

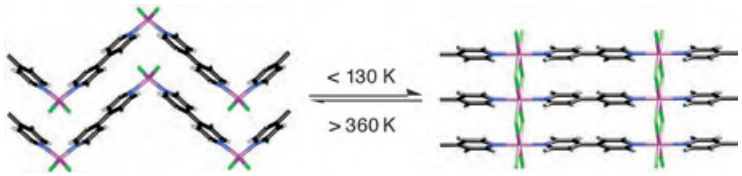

Zipping in an extra dimension: In the coordination polymer $[ZnCl_2(\mu\text{-bipy})]_\infty$ one-dimensional chains (left) switch into a two-dimensional network (right) in the solid at a surprisingly low temperature of 130 K. At temperatures above 360 K the reverse transformation takes place. The reaction occurs in single crystals as well as in powders. bipy = 4,4′-bipyridine.

Solid-State Reactions

C. Hu, U. Englert* ——— **2281 – 2283**

Crystal-to-Crystal Transformation from a Chain Polymer to a Two-Dimensional Network at Low Temperatures

---

A vitamin that switches states: The appended nucleotide base B assists in the constitutional switch from the base-on form of the B_{12} conjugate (blue, with a coordinated 5,6-dimethylbenzimidazole (DMB) unit) to the base-off form (red, with a free DMB unit). The process is strongly temperature dependent.

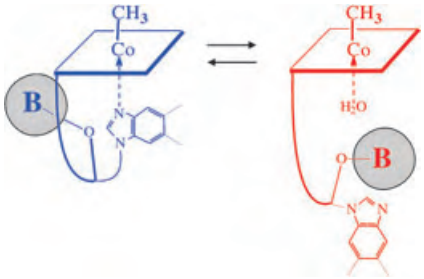

Molecular Switches

S. Gschösser, K. Gruber, C. Kratky,* C. Eichmüller, B. Kräutler* _ **2284 – 2288**

B_{12}-*retro*-Riboswitches: Constitutional Switching of B_{12} Coenzymes Induced by Nucleotides

---

Molecular lamps: Analogously to a lamp with a light bulb, a switch, and a plug, the fluorescent ON state of dyad **1** can be blocked by other means besides the light switch ("removing the plug"). By using flavin as a redox unit and thermal or UV-activated thiol/disulfide redox chemistry, one can switch between the oxidized and reduced forms of the dyad (see picture). The reaction is reminiscent of the LOV domains of blue-light photoreceptors such as the phototropins.

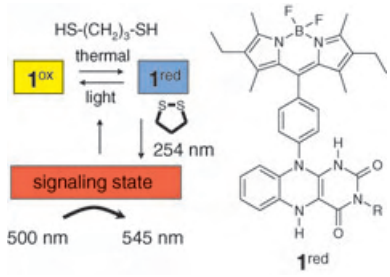

Photoreceptor Mimetics

C. Trieflinger, K. Rurack,* J. Daub* ——— **2288 – 2291**

"Turn ON/OFF your LOV light": Borondipyrromethene–Flavin Dyads as Biomimetic Switches Derived from the LOV Domain

---

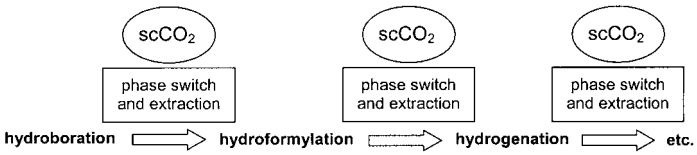

A judicious combination of an organometallic catalyst and workup with supercritical CO_2 resulted in a recyclable system for mediating a variety of transformations. Between reactions the catalyst is "switched off" and recovered as a precipitate from the reaction mixture when $scCO_2$ is introduced. Simultaneously the product is isolated by extraction with $scCO_2$. The key is the unique solubility properties of the Rh catalyst arising from the poly(ethyleneglycol) chains in the phosphine ligands (see scheme).

Green Chemistry

M. Solinas, J. Jiang, O. Stelzer, W. Leitner* ——— **2291 – 2295**

A Cartridge System for Organometallic Catalysis: Sequential Catalysis and Separation Using Supercritical Carbon Dioxide to Switch Phases

 © 2005 Wiley-VCH Verlag GmbH & Co. KGaA, Weinheim

Contents

Natural Product Synthesis

D. E. N. Jacquot, M. Zöllinger, T. Lindel* ——— **2295 – 2298**

Total Synthesis of the Marine Natural Product *rac*-Dibromophakellstatin

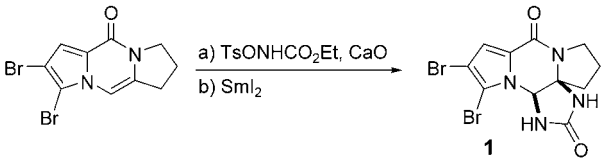

1

The pyrrole-imidazole alkaloid dibromophakellstatin (**1**) from the marine sponge *Phakellia mauritiana* was synthesized in only five steps starting from L-prolinol. The key step of the synthesis is the direct annulation of the imidazolinone ring to a pyrrolopyrazinone precursor by employing an ethoxycarbonylnitrene generated in situ. Samarium diiodide proved to be the best choice for the chemoselective, stepwise deprotection of the resulting tetracycle. Ts = toluenesulfonyl.

Sources

Product and Company Directory

You can start the entry for your company in "Sources" in any issue of *Angewandte Chemie*.

If you would like more information, please do not hesitate to contact us.

Wiley-VCH Verlag – Advertising Department
Tel.: 0 62 01 - 60 65 65
Fax: 0 62 01 - 60 65 50
E-Mail: MSchulz@wiley-vch.de

Service

Keywords ——— **2300**

Authors ——— **2301**

Preview ——— **2303**

Corrigendum

Halide Recognition through Diagnostic "Anion–π" Interactions: Molecular Complexes of Cl^-, Br^-, and I^- with Olefinic and Aromatic π Receptors

Y. S. Rosokha, S. V. Lindeman, S. V. Rosokha, J. K. Kochi ——— **4650–4652**

Angew. Chem. Int. Ed. **2004**, *43*

DOI 10.1002/anie.200460337

In this Communication, the authors inadvertedly omitted an acknowledgement. It should read: "We thank D. K. Kim for providing the crystal of the charge-transfer complex *o*-chloranil/tetra-*n*-propylammonium bromide in Table 1 as well as spectral data relating to the *o*-chloranil acceptor in Figure 1. We are also grateful to M. G. Davlieva for providing the crystal of the tetracyanopyrazine/tetra-*n*-butylammonium iodide complex. We thank the R. A. Welch Foundation and the National Science Foundation for financial support."

© 2005 Wiley-VCH Verlag GmbH & Co. KGaA, Weinheim

The Chemical Society of Japan (CSJ) presents a number of awards annually, including the six CSJ Awards for important contributions to chemistry in terms of both fundamental research and applications. In the following we introduce briefly the award winners for 2004 with their award-winning research.

S. Fukuzumi: Electron Transfer

Shunichi Fukuzumi (Osaka University) has received a CSJ Award for his research on electron-transfer reactions and their applications. His research includes the redox chemistry of coenzyme analogues, organometallic chemistry, and photochemistry. He described recently in *Angewandte Chemie* the production of a particularly persistent charge-separated state in a zinc chlorine–C_{60} dyad through electron transfer in a single step.[1] Fukuzumi completed his PhD in 1978 at Tokyo Institute of Technology under the guidance of T. Keii and Y. Ono, and then undertook postdoctoral research at Indiana University (USA). In 1981 he took up a position as assistant professor at Osaka University, where he is currently professor in the Department of Materials and Life Sciences.

S. Fukuzumi

K. Hirao: Quantum Chemistry

Kimihiko Hirao's research at the University of Tokyo on the development of molecular theories in quantum chemistry has a particular focus on the development of ab initio methods (Møller–Plesset calculations), density functional methods,[2a] and relativistic theories.[2b] Hirao completed his studies at Kyoto University in 1974 with a PhD. As a postdoctoral fellow he spent time at the universities of Alberta, in the research group of S. Huzinaga, and Sheffield, with R. McWeeny. He became professor at Nagoya University in 1988, and moved to the University of Tokyo in 1993. Hirao is a member of the Editorial Advisory Board of the *Journal of Computational Chemistry*.

K. Hirao

T. Imanaka: Biochemistry

Tadayuki Imanaka has been recognized for his research on the molecular mechanisms involved in the adaptation of thermophilic bacteria to high temperatures of up to 100 °C. He is particularly interested in the chemical foundations for the stability of the proteins and the DNA.[3] Imanaka completed his PhD in 1973 at Osaka University and then carried out postdoctoral research at the Massachusetts Institute of Technology (USA) in the groups of C. L. Cooney and D. I. C. Wang. In 1981 he became associate professor in Osaka, in 1989 full professor. He transferred to Kyoto University in 1996. Imanaka is Executive Editor of the journal *The Chemical Record*.

T. Imanaka

M. Irie: Materials Science

Masahiro Irie began his studies at Kyoto University and completed his PhD in 1973 in radiation chemistry at Osaka University. From 1975 to 1976 he undertook postdoctoral research with G. Smets at the Catholic University Leuven (Belgium). He was made associate professor at Osaka University in 1978, and in 1988 moved as Professor of Advanced Materials to Kyushu University, where he became Professor of Chemistry in 1996. Irie's research focuses on the development of photoactive polymers and photochromic materials. His discovery that diaryl ethene derivatives undergo fatigue-resistant and thermally irreversible photochromic reactions has led to their widespread use as photoswitching elements of molecular switches. Irie's research interests also include single-molecule photochemistry and near-field optics. His Communication on the conformation control of photochromic reactivity in a diaryl ethene single crystal has just appeared in *Angewandte Chemie*.[4]

M. Irie

K. Itaya: Electrochemistry

Kingo Itaya (Tohoku University) has been recognized for his research on atomic and molecular processes in electrochemical surface reactions. He investigates these processes by scanning tunneling microscopy. His most recent Communication in *Angewandte Chemie* deals with the control of molecular orientation in an adlayer of a supramolecular assembly consisting of an open-cage C_{60} derivative and zinc(II) octaethylporphyrin on gold.[5]

K. Itaya

Mitsuo Kira: Silicon Chemistry

Mitsuo Kira (Tohoku University) has received a CSJ Award for his contributions to the chemistry of silicon and other Group 14 elements. He has a particular interest in dialkyl silylenes, disilenes, 1,3-disilabicyclo-

Mitsuo Kira

 © 2005 Wiley-VCH Verlag GmbH & Co. KGaA, Weinheim DOI: 10.1002/anie.200500861

[1.1.0]butanes, and transition-metal complexes of disilenes. He described recently in *Angewandte Chemie* the role of the singlet excited state of a stable dialkyl silylene on the photochemistry of the compound.[6]

[1] a) K. Ohkubo, H. Kotani, J. Shao, Z. Ou, K. M. Kadish, G. Li, R. K. Pandey, M. Fujitsuka, O. Ito, H. Imahori, S. Fukuzumi, *Angew. Chem.* **2004**, *116*, 871; *Angew. Chem. Int. Ed.* **2004**, *43*, 853, b) A. Harriman, *Angew. Chem.* **2004**, *116*, 5093; *Angew. Chem. Int. Ed.* **2004**, *43*, 4985.

[2] a) T. Nakajima, T. Yanai, K. Hirao, *J. Comput. Chem.* **2002**, *23*, 847 , b) T. Tsuneda, M. Kamiya, K. Hirao, *J. Comput. Chem.* **2003**, *24*, 1592.

[3] T. i. Imanaka, H. Atomi, *Chem. Rec.* **2002**, *2*, 149.

[4] S. Kobatake, Y. Matsumoto, M. Irie, *Angew. Chem.* **2005**, *117*, 2186, *Angew. Chem. Int. Ed.* **2005**, *44*, 2148.

[5] S. Yoshimoto, E. Tsutsumi, Y. Honda, Y. Murata, M. Murata, K. Komatsu, O. Ito, K. Itaya, *Angew. Chem.* **2004**, *116*, 3106; *Angew. Chem. Int. Ed.* **2004**, *43*, 3044.

[6] M. Kira, S. Ishida, T. Iwamoto, A. de Meijere, M. Fujitsuka, O. Ito, *Angew. Chem.* **2004**, *116*, 4610; *Angew. Chem. Int. Ed.* **2004**, *43*, 4510.

The Latest from Ullmann's

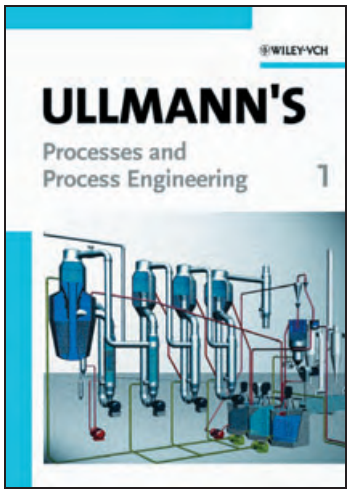

2004. 2301 pp., 1975 figs., 294 tabs. Hardcover.
ISBN 3-527-31096-7
€ 549.- /£415.- /US$ 699.-

WILEY-VCH (ed.)
Ullmann's Processes and Process Engineering

3-Volume Set

Ullmann's Processes and Process Engineering is tailor-made for anyone interested in industrial chemical processes, unit operations, process engineering, reactor design and optimization. Based on the very latest edition of the 40-volume Ullmann's Encyclopedia of Industrial Chemistry, the contents represent an up-to-date source of information. The detailed and thoroughly edited articles are written by renowned experts from industry and academia.

The three volumes provide coverage on all aspects of processes an process engineering.

The major headings are:

Separation Processes; Separation and Classification; Mixing; Particle Technology: Heat Generation; Processes under Special Conditions; Principles of Process Engineering: Reactor Types.

This 3-volume handbook is an invaluable and convenient source of information for chemical engineers, chemists, patent attorneys, marketing manager and all those involved in the chemical process industry.

10760402_kn

Register now for the free
WILEY-VCH Newsletter!
www.wiley-vch.de/home/pas

WILEY-VCH • P.O. Box 10 11 61 • D-69451 Weinheim, Germany
Fax: +49 (0) 62 01 - 60 61 84
e-mail: service@wiley-vch.de • http://www.wiley-vch.de

WILEY-VCH

 © 2005 Wiley-VCH Verlag GmbH & Co. KGaA, Weinheim

Carbohydrate Synthesis

Amino Acids—Valuable Organocatalysts in Carbohydrate Synthesis

*Uli Kazmaier**

Keywords:
aldol reactions · amino acids · carbohydrates · organocatalysis

Carbohydrates are an important class of natural products. Besides their occurrence as biological scaffolds and energy reservoirs in the living cell, they are also significant from a pharmaceutical point of view owing to their involvement in cell–cell recognition processes and signal transduction.[1] For chemists they are interesting as chiral-pool materials[2] and as building blocks for the synthesis of natural products and drugs.[3] Especially with respect to the latter issue, the de novo synthesis of carbohydrate-type structures is a challenging issue. Although many approaches concerning this topic have been reported in the literature, many protocols are rather lengthy and require sophisticated protecting-group strategies.[4] Aldol reactions, which give rise directly to β-hydroxycarbonyl compounds, are an especially important tool in the preparation of carbohydrate scaffolds.[5]

Nature uses the same strategy for carbohydrate synthesis, for example, dihydroxyacetone phosphate (DHAP) is involved in enzyme-catalyzed aldol reactions.[6] Several synthetic applications of aldolases have been reported that allow access to more- or less-protected carbohydrates.[7] Recently, these biological methods have been facing serious competition, mainly as a result of the blooming of organocatalysis.[8] Since the early days of the Hajos–Parrish–Eder–Sauer–Wichert reaction,[9] proline-catalyzed reactions have developed at a dramatic pace.[10] Enolizable achiral aldehydes and ketones, for example, can be converted with proline (derivatives) into the corresponding enamines, which can then react with less-enolizable carbonyl compounds, even in one-pot protocols and often with high selectivities.[11] List and Notz used hydroxyacetone **1** as a precursor to an enamine, which underwent addition to several aldehydes such as **2** with excellent *ee* values (Scheme 1).[12] The regioselectivity and diastereoselectivity were also significant.

A closer look at aldol product **3** reveals a certain relationship to the carbohydrates that cannot be neglected. Therefore, carbohydrate-type structures such as **C** should be accessible in two steps from α-substituted aldehydes according to the retrosynthesis shown in Scheme 1.

As simple as this retrosynthetic analysis might seem, its synthetic transformation is far from trivial and requires the selective introduction of several stereogenic centers. Furthermore, aldehydes **A** have to react both as donors and acceptors and the aldol products **B** should be inert to further aldol reaction. Alternatively, **B** should not be enolizable so that it can only react as an acceptor with further aldehyde **A′**.

MacMillan and co-workers recently reported the first practical application of this concept.[13] They showed that O-protected glycol aldehydes **4** could be converted in the presence of (*S*)-proline into the corresponding aldol products **5** with high *ee* values (Scheme 2). In general, the reactions were run in *N*,*N*-

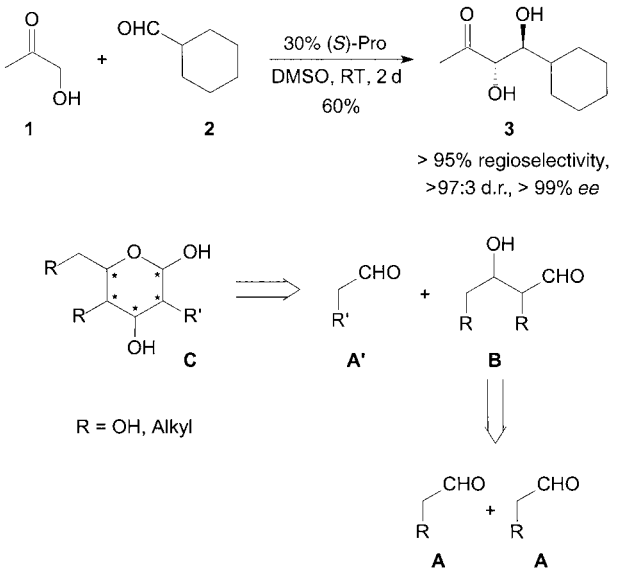

Scheme 1. Proline-catalyzed aldol reactions and retrosynthesis of a carbohydrate framework. DMSO = dimethyl sulfoxide.

[*] Prof. Dr. U. Kazmaier
Institut für organische Chemie
Universität des Saarlandes
Im Stadtwald, Geb. 23.2
66123 Saarbrücken (Germany)
Fax: (+49) 681-302-2409
E-mail: u.kazmaier@mx.uni-saarland.de

 © 2005 Wiley-VCH Verlag GmbH & Co. KGaA, Weinheim DOI: 10.1002/anie.200462873

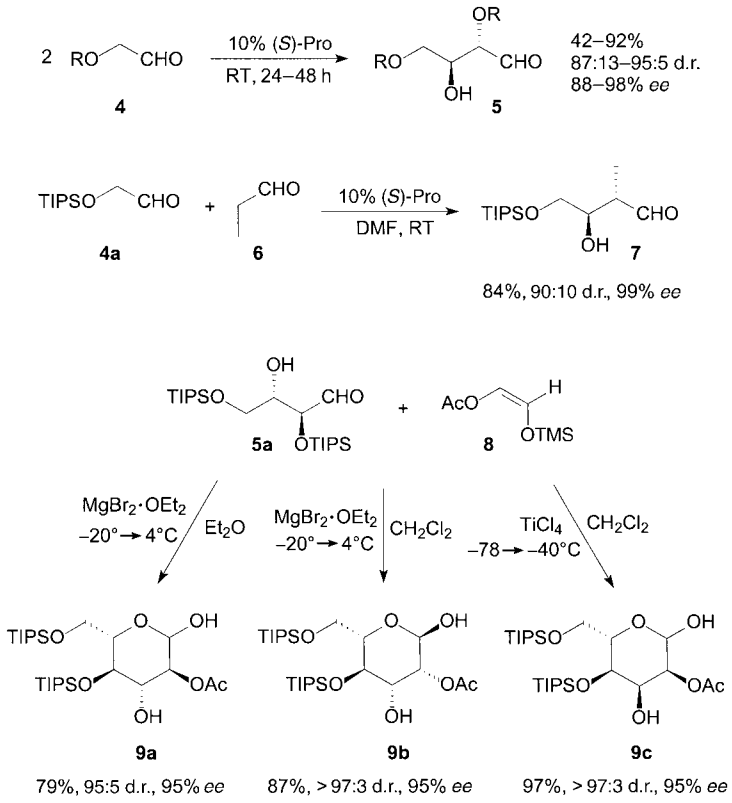

Scheme 2. Proline-catalyzed carbohydrate synthesis according to MacMillan and co-workers. TIPS = triisopropylsilyl, TMS = trimethylsilyl.

dimethylformamide (DMF), and the best results were obtained with silyl-protected aldehyde derivatives. However, other electron-rich O-alkylated derivatives could be converted with good results, whereas electron-withdrawing protecting groups (such as acetyl) suppressed the aldol reaction. The diastereoselectivities attained varied in the range 87:13–95:5 d.r. in favor of the *anti* product. Interestingly, this concept is also suitable for cross-aldol reactions, in which the protected glycol aldehyde reacts as the acceptor component. For example, propionaldehyde (**6**) reacts with silylated glycol aldehyde **4a** to give the β-hydroxyaldehyde **7** with comparable selectivity.

A subsequent reaction of the aldol products **5** and **7** was not observed. Therefore these could be subjected to a second aldol reaction, for example, under Mukaiyama conditions.[14] The partially protected carbohydrate **9** was obtained from the reaction of **5a** with silyl enol ether **8** (Scheme 2). Under consideration of the anomeric centre, three new stereogenic centers are formed in one step. MacMillan and co-workers rationalized that the stereochemical outcome of the reaction can be controlled well under the reaction conditions used. Thus, $MgBr_2$ as a Lewis acid led to the glucose derivative **9a** in ether, whereas the corresponding mannose derivative **9b** was formed in CH_2Cl_2. In the presence of $TiCl_4$, the corresponding allose **9c** is obtained. Similar results were obtained with other aldehydes **5** and silyl enol ethers.

Enders and Grondal were able to use the proline-catalyzed aldol addition also for the synthesis of pentoses (Scheme 3).[15] Taking an example from nature, they used the dihydroxyacetone derivative **10** as a methylene component. This biomimetic C_3+C_n strategy allows the direct synthesis of selectively protected carbohydrates in one step. The best results were obtained when using 30% proline in DMF at 2°C. Besides the high enantioselectivities, excellent diastereoselectivities were attained. The yields varied depending on the aldehyde used. In general, the best results were observed with α-branched aldehydes; both yield and selectivity were worse in the case of linear unbranched aldehydes such as **11**. The latter results could be attributed to the fact that these aldehydes can react both as donor and acceptor, thus giving rise to side products from homoaldol additions. When chiral aldehydes such as **13** and **15** are applied, a matched/mismatched situation arises. Whereas in the reactions of **13** the best results are observed with (*S*)-proline, (*R*)-proline is the catalyst of choice for reactions of glycerinaldehyde **15**. As illustrated with **13**, the "wrong" catalyst merely has a negative influence

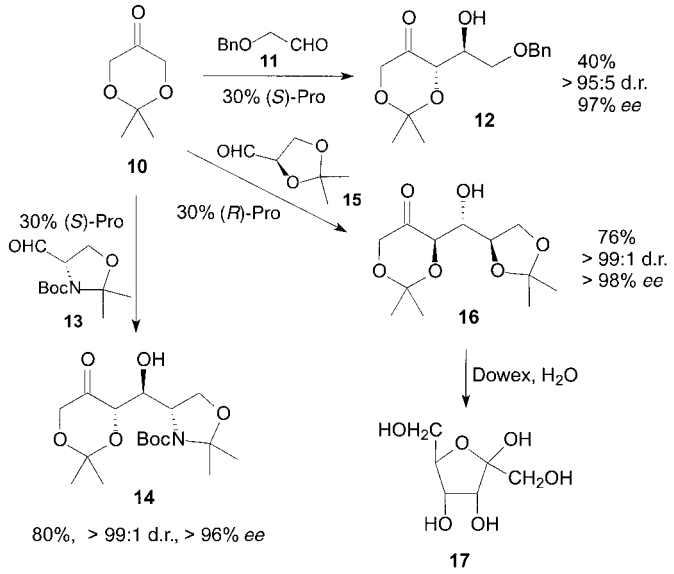

Scheme 3. Proline-catalyzed carbohydrate synthesis according to Enders and Grondal. Boc = *tert*-butoxycarbonyl.

 © 2005 Wiley-VCH Verlag GmbH & Co. KGaA, Weinheim

on the yield, but not on the stereochemical outcome of the reaction. This example illustrates that this protocol is also suitable for the synthesis of aminosugars. Acidic cleavage of the protecting groups in **16** gave rise to ketose D-psicose **17**.

Very recently, Cordova and coworkers realized the two-step concept of MacMillan under complete proline catalysis.[16] They showed that aldol product **18** obtained in an (*S*)-proline-catalyzed reaction can react in a second aldol reaction, this time catalyzed by (*R*)-proline, to give rise to carbohydrate **19** (Scheme 4). Independent of the aldehydes used, the enantioselectivities were consistently excellent (≥99% *ee*), and the overall yields ranged from 15 to 42%. For example, the 2,4,6-tri-*O*-benzylmannose **21** was obtained as a single stereoisomer from α-benzyloxyacetaldehyde (**20**). When the organocatalysts were used in the alternative sequence, the enantiomeric products were formed. (*S*)-Proline can be replaced by (*S*)-hydroxyproline without significant changes.

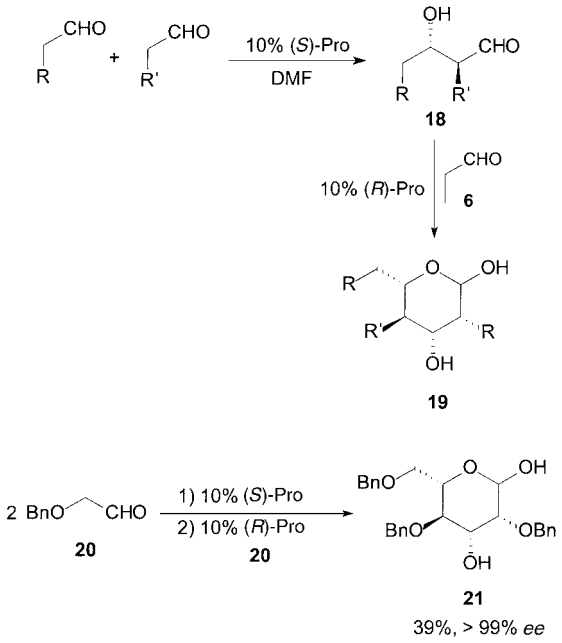

Scheme 4. Proline-catalyzed carbohydrate synthesis according to Córdova and co-workers.

The examples described herein indicate the impressive potential of amino acid catalyzed reactions, and the chemistry community can expect further exciting developments from proline-catalyzed reactions in the near future.

[1] K. C. Nicolaou, H. J. Mitchell, *Angew. Chem.* **2001**, *113*, 1624–1672; *Angew. Chem. Int. Ed.* **2001**, *40*, 1576–1624.

[2] *Carbohydrate Building Blocks* (Eds.: M. Bols), Wiley-VCH, Weinheim, **1996**.

[3] *Carbohydrate-based Drug Discovery* (Eds.: C. H. Wong), Wiley-VCH, Weinheim, **2003**.

[4] For reviews, see: a) T. Ogawa, *Chem. Soc. Rev.* **1994**, *23*, 397–407; b) S. J. Danishefsky, M. T. Bilodeau, *Angew. Chem.* **1996**, *108*, 1482–1522; *Angew. Chem. Int. Ed. Engl.* **1996**, *35*, 1380–1419; c) S. Hanessian, *Preparative Carbohydrate Chemistry*, Marcel Dekker, New York, **1997**; d) T. Hudlicky, D. A. Entwistle, K. K. Pitzer, A. J. Thorpe, *Chem. Rev.* **1996**, *96*, 1195–1220, and references therein.

[5] For reviews, see: a) D. A. Evans, J. V. Nelson, T. Taber in *Topics in Stereochemistry*, *Vol. 13*, Wiley, New York, **1982**, pp. 1–115; b) R. Mahrwald, *Chem. Rev.* **1999**, *99*, 1095–1120; c) C. Palomo, M. Oiarbide, J. M. Garcia, *Chem. Eur. J.* **2002**, *8*, 37–44, and references therein.

[6] M. Calvin, *Angew. Chem.* **1962**, *74*, 165–175; *Angew. Chem. Int. Ed. Engl.* **1962**, *1*, 65–75.

[7] a) T. D. Machajewski, C. H. Wong, *Angew. Chem.* **2000**, *112*, 1406–1430; *Angew. Chem. Int. Ed.* **2000**, *39*, 1352–1375; b) "Enolates, Organocatalysis, Biocatalysis and Natural Product Synthesis": W. D. Fessner in *Modern Aldol Reactions*, *Vol. 1* (Eds.: R. Mahrwald), Wiley-VCH, Weinheim, **2004**; c) W. D. Fessner, C. Walter, *Top. Curr. Chem.* **1996**, *184*, 97–194; d) S. Takayama, G. J. McGarvey, C. H. Wong, *Chem. Soc. Rev.* **1997**, *26*, 407–415, and references therein.

[8] For recent reviews, see: a) P. I. Dalko, L. Moisan, *Angew. Chem.* **2001**, *113*, 3840–3864; *Angew. Chem. Int. Ed.* **2001**, *40*, 3726–3748; b) E. R. Jarvo, S. J. Miller, *Tetrahedron* **2002**, *58*, 2481–2495; c) R. O. Duthaler, *Angew. Chem.* **2003**, *115*, 1005–1008; *Angew. Chem. Int. Ed.* **2003**, *42*, 975–978; d) P. I. Dalko, L. Moisan, *Angew. Chem.* **2004**, *116*, 5248–5286; *Angew. Chem. Int. Ed.* **2004**, *43*, 5138–5175.

[9] a) U. Eder, G. Sauer, R. Wiechert, *Angew. Chem.* **1971**, *83*, 492–493; *Angew. Chem. Int. Ed. Engl.* **1971**, *10*, 496–497; b) Z. H. Hajos, D. R. Parrish, *J. Org. Chem.* **1974**, *39*, 1612–1615.

[10] For a review, see: B. List, *Tetrahedron* **2002**, *58*, 5573–5590.

[11] a) B. List, R. A. Lerner, C. F. Barbas III, *J. Am. Chem. Soc.* **2000**, *122*, 2395–2396; b) K. Sakthivel, W. Notz, T. Bui, C. F. Barbas III, *J. Am. Chem. Soc.* **2001**, *123*, 5260–5267.

[12] W. Notz, B. List, *J. Am. Chem. Soc.* **2000**, *122*, 7386–7387.

[13] A. B. Northrup, I. K. Mangion, F. Hettche, D. W. C. MacMillan, *Angew. Chem.* **2004**, *116*, 2204–2206; *Angew. Chem. Int. Ed.* **2004**, *43*, 2152–2154.

[14] A. B. Northrup, D. W. C. MacMillan, *Science* **2004**, *305*, 1752–1755.

[15] D. Enders, C. Grondal, *Angew. Chem.* **2005**, *117*, 1235–1238; *Angew. Chem. Int. Ed.* **2005**, *44*, 1210–1212.

[16] J. Casas, M. Engqvist, I. Ibrahem, B. Kognak, A. Córdova, *Angew. Chem.* **2005**, *117*, 1367–1369; *Angew. Chem. Int. Ed.* **2005**, *44*, 1343–1345.

 © 2005 Wiley-VCH Verlag GmbH & Co. KGaA, Weinheim

Nanotechnology

Nanoparticles in Energy Technology: Examples from Electrochemistry and Catalysis

*Fabio Raimondi, Günther G. Scherer, Rüdiger Kötz, and Alexander Wokaun**

Keywords:
electrochemistry · energy technology · heterogeneous catalysis · nanoparticles · surface chemistry

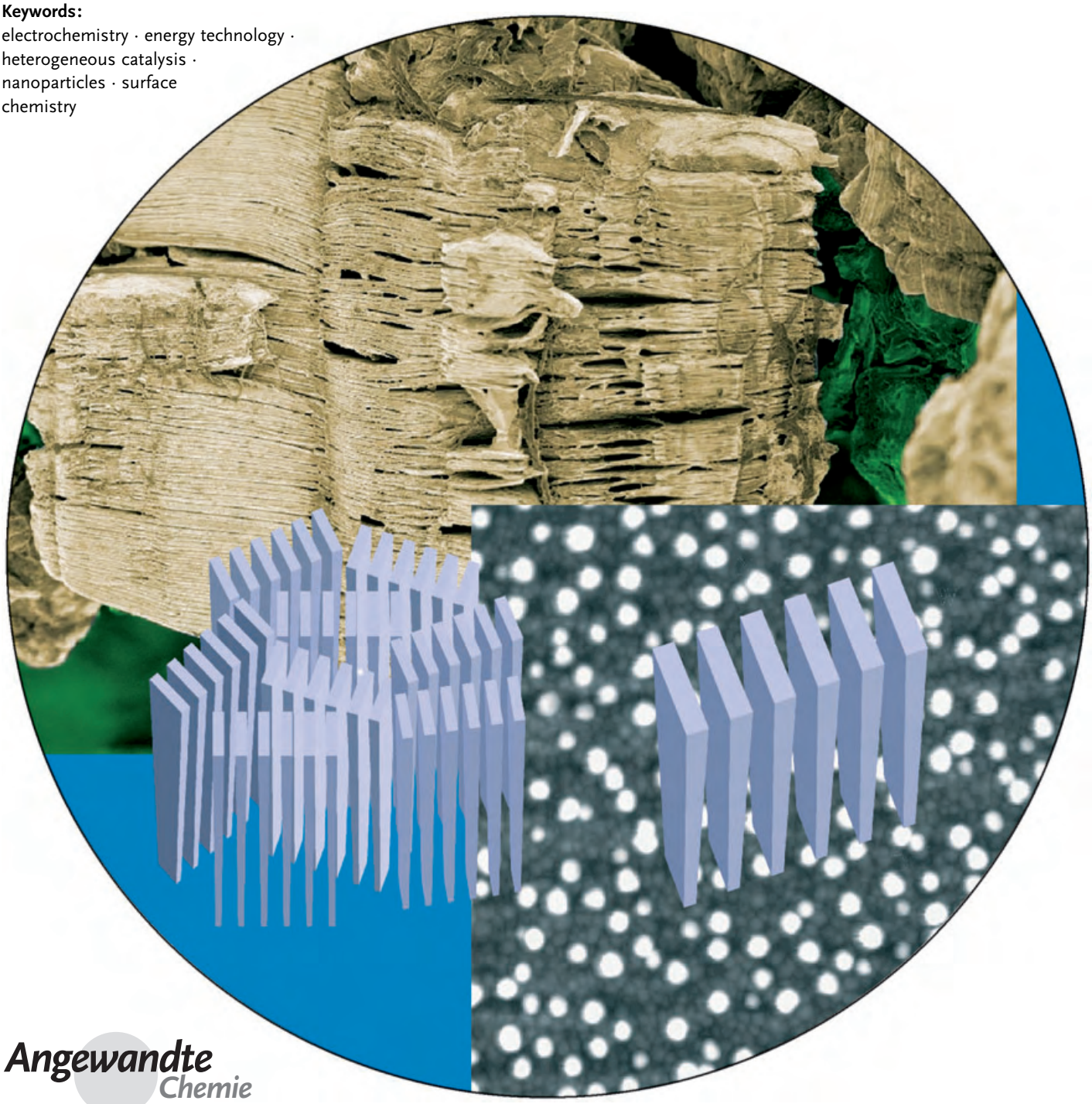

© 2005 Wiley-VCH Verlag GmbH & Co. KGaA, Weinheim

DOI: 10.1002/anie.200460466

Angewandte Chemie

Nanoparticles are key components in the advancement of future energy technologies, thus, strategies for preparing nanoparticles in large volume by techniques that are cost-effective are required. In the substitution of fossil-fuels by renewable energy resources, nanometer-sized particles play a key role for synthesizing energy vectors from varying and heterogeneous biomass feedstocks. They are extensively used in reformers for the production of hydrogen from solid, liquid, or gaseous energy carriers. Catalyst activities depend critically on their size-dependent properties. Nanoparticles are further indispensable as electrocatalysts in fuel cells and other electrochemical converters. The desire to increase the activity per unit area, and decrease the necessary amount of the expensive catalytic standard, platinum, has spurred innovative approaches for the synthesis of platinum-alloy nanoparticles by wet chemistry, colloidal routes, or physical techniques such as sputtering.

From the Contents

1. Introduction	2191
2. Catalyst Nanoparticles	2193
3. Precious-Metal Nanoparticles as Fuel-Cell Catalysts	2198
4. Carbon Nanoparticles in Electrochemistry	2203
5. Conclusions and Outlook	2207

1. Introduction

Surface processes are of key importance in energy technology. There are applications where a surface-to-volume ratio as low as possible is desired—for example, for the avoidance of heat losses in thermal energy converters, or for the reduction of frictional losses. Herein we shall focus on another class of processes where a high surface-to-volume ratio is desired. This is the case whenever the surface plays an active role in the phenomenon itself. Examples include catalytic processes where the overall rate is (among many other factors) proportional to the available catalytically active surface, electron-transfer reactions where the current density is proportional to the total electrode or electrocatalyst area, and capacitive charge storage where again the stored charge is dependent on the electrode surface.

1.1. Nanoparticle Fundamentals

High surface areas (relative to the volume or mass of the active component) are achieved by dispersion, that is, by the production of small particles or structured surfaces. The fraction of atomic constituents exposed on the surface of a particle is given by simple and well-known geometrical considerations. Taking a metal with a face-centered cubic unit cell as an example, the fraction of surface atoms on a cube with an edge length of 1, 2, 5, 10, and 20 lattice constants, corresponds to 100, 79, 45, 31, and 14% of the total number of atoms present, respectively. If we assume a lattice constant of 0.2 nm, the edge lengths of those cubes will be 0.2, 0.4, 1, 2, and 4 nm, respectively. From this elementary consideration we see that a surface fraction (dispersion) of over 15% is realized only for particles smaller than 4 nm. If the metal happened to be expensive, such as platinum, the use of metal particles any larger than 4 nm would only be a waste of resources and would not contribute significantly to a higher catalytic activity. This simple fact shows the importance of nanoparticles in energy technology.

A second aspect emerges from the above example: metal atoms at the edges and corners of the mentioned cubes have a smaller coordination number than those on the planar faces. These low-coordination sites are higher in energy and generally give rise to stronger metal–adsorbate bonds. In reality, nanoparticles are not cubes but often irregularly shaped objects, and hence there are additional defect sites, such as steps that separate planar atomic terraces, or kinks where a step advances or recedes, exposing corner or edge atoms on a plane. The enhancement of the reactivity of low-coordination defect sites can be so large that their presence determines to a very large extent the catalytic activity of a material, in spite of their very low concentration. This is, for example, the case for the dissociation of N_2 on Ru(0001) single crystals. Essentially, this reaction takes place only at step sites, which exhibit a reactivity approximately 10^9 times larger than terrace sites, although they make up less that 1% of all the exposed ruthenium atoms.[1] A general survey on the influence of particle morphology on the number and type of different surface sites has been given by Henry.[2]

At this point it must be emphasized that the presence of low-coordination, high-energy sites is not beneficial for all catalytic reactions. As a matter of fact, the influence of defects and surface sites presenting special geometric configurations (such as corners, edges, steps, kinks, and adatoms) on a catalytic process depends intrinsically on the elementary steps composing it. For some processes high-energy sites are favorable, for example, in the case of the activation of inert molecules, such as N_2 and CH_4. However, strong interaction of the adsorbate with the catalytic surface may represent a strong disadvantage, since it very often implies that the products desorb only very slowly from the surface, blocking the catalytic sites, which become unavailable for the catalytic

[*] Dr. F. Raimondi, Dr. G. G. Scherer, Dr. R. Kötz, Prof. Dr. A. Wokaun
Paul Scherrer Institut
5232 Villigen PSI (Switzerland)
Fax: (+41) 56-310-4416
E-mail: alexander.wokaun@psi.ch

 DOI: 10.1002/anie.200460466 © 2005 Wiley-VCH Verlag GmbH & Co. KGaA, Weinheim

process. This delicate balance, involving the capability of a catalyst of activating the reactants without being irreversibly poisoned by the reaction products, has been emphasized throughout the fascinating and successful development of heterogeneous catalysis (see, for example, refs. [3,4]).

The binding of a substrate to a catalyst surface exhibits all the diversity of chemistry itself. The specific role that nanosized metal clusters play in a catalytic process depends on the preferred binding geometry of the adsorbate(s) on the catalyst surface and on the surface electronic properties that are most advantageous for the whole catalytic cycle. As an example, the catalytic rate of the hydrogenolysis of cyclopropane on platinum, which requires a single atomic site, scales directly with the dispersion of platinum and does not show a significant variation with the size of the platinum clusters.[5] In contrast, the hydrogenation of aromatic rings often requires planar surfaces onto which the π-electron system can bind.[6,7] Similarly, the selective catalytic reduction of nitrogen oxides over V_2O_5 depends on the presence of extended planar structures,[8] with the consequence that very small V_2O_5 aggregates do not present a good catalytic activity. Hence, chemists must differentiate and cannot propose "nano" as the magic bullet that serves every purpose.

1.2. Outline

In Section 2, the consequences of the limited size of metal nanoclusters on their electronic and morphological properties will be illustrated and a few selected examples. The influence of the cluster size on the metal–support interactions will also be presented, focusing mainly on the production of hydrogen from methanol on Cu/ZnO-based catalysts.

Particle size effects are similarly important for electrocatalysts. Fuels cells offer the advantages of high efficiency and zero local emissions. The electrocatalyst is a decisive element determining the performance of the membrane–electrode assembly. In Section 3 we show that the interaction of the noble-metal nanoparticles with the carbon support and their contact with the solid polymer electrolyte greatly influence the utilization of the active metal surface.

Microstructured bipolar plates are used as models for studying electrocatalyst utilization, and have a high potential for micro-fuel-cell applications. Two laser-based methods for microstructuring of glassy carbon substrates are compared, that is, direct laser ablation and a mask process combining ablation with reactive ion etching. Options for the deposition of the electrocatalyst onto these substrates are discussed.

Recently the introduction of "ultracapacitors" has revolutionized electrochemical energy storage. Modules of the size of a beverage can exhibit capacitance values of several hundred up to >1000 Farad, rather than the milli- to pico-Farad values familiar from electronic circuitry. This increase by a factor of 10^6 is achieved by charge storage in the electrochemical double layer. This charge is directly proportional to the active area. As a consequence, highly porous materials with specific surface areas up to 1000 $m^2 g^{-1}$ are used to manufacture the electrodes.

Alexander Wokaun studied chemistry at the ETH in Zurich. In 1978, he received his PhD in the area of magnetic resonance with Richard R. Ernst. During the subsequent three years at IBM and Bell Laboratories he focused on surface studies by laser spectroscopic techniques. From 1982 to 1985, he directed a program on surface energy-transfer processes at ETH Zurich. In 1986, he became full professor of physical chemistry at the University of Bayreuth. Since 1994, he is head of the Research Department General Energy of the Paul Scherrer Institut, and teaches at the ETH in Zurich.

Rüdiger Kötz received his PhD in Physics from the Technical University in Berlin in 1979. After postdoctoral years at the Case Western Reserve University in Cleveland, Ohio, and at the Fritz Haber Institut of the Max Planck Society in Berlin he joined the ABB Corporate Research Center in Baden, Switzerland. Since 1989 he heads the capacitor and interface analysis group of the Electrochemistry Laboratory at the Paul Scherrer Institut. Throughout his career his research has been aimed at the characterization of the solid–electrolyte interphase and the understanding of electroactive materials.

Günther G. Scherer studied chemistry at the Technical University Munich and received his PhD in 1976 from the Technical University of Berlin. As a postdoc he joined the IBM Research Laboratory in San Jose, California. Later on he joined the Battelle Institut in Frankfurt/Main, the BBC Research center Baden/Switzerland, and Ingold Messtechnik in Urdorf. In 1989 he became leader of the Fuel Cell research group at the Paul Scherrer Institut, and since 2002 he heads the Electrochemistry Laboratory there. He conducts international as well as national projects on material und structural aspects of polymer electrolyte fuel cells.

Fabio Raimondi studied chemistry at the University of Palermo including an exchange year at University College London. From 1999 to 2002 he worked at the Paul Scherrer Institut on his thesis on the structure elucidation of Cu/ZnO reforming catalysts and obtained a PhD from the ETH Zurich. From 2003 to 2004 he spent another year at the Paul Scherrer Institut and carried out XPS surface studies on catalysts. Since the middle of 2004 he has been working as a project manager in an industrial research laboratory.

 © 2005 Wiley-VCH Verlag GmbH & Co. KGaA, Weinheim

These materials, typically active carbons, again exhibit nanostructured surfaces (Section 4). The electrochemical behavior will be related to the structural properties of the active carbon materials, and compared to the performance of electrodes prepared from glassy carbon or hard carbon precursors.

The second example from the field of electrochemical energy storage concerns graphites that are widely used as negative electrodes in rechargeable lithium ion batteries. The high power and energy densities achievable with this battery class are related to the reversible intercalation of lithium ions into the graphite structure. The charge storage capacity in these layered structures is compared with lithium storage in carbon nanotubes.

2. Catalyst Nanoparticles

To survey the importance of nanoparticles in catalysis would require a compendium (see for example ref. [9]), rather than a small chapter. For this reason, we shall restrict ourselves to recent illustrative examples, rather than aiming at any extensive coverage of the subject. To guide the reader through the multiplicity of phenomena from which the special catalytic properties of nanosized metal clusters originate, we will distinguish in the following between electronic and geometric effects of the small cluster size. A separate section (Section 2.3) will be dedicated to so-called support effects, which are responsible for the unusual properties of small clusters supported on certain oxides. Electronic effects are defined as size-dependent changes of the local electronic structure of the surface. Geometric effects involve the presence of sites presenting special geometric arrangements. The different spatial configuration of some surface atoms in small metal clusters affects the surface–adsorbate interaction and enables chemisorption geometries that are typically not accessible on metal surfaces presenting other morphologies. Clearly, electronic and geometric effects are not always distinct, since a change of the surrounding of a surface atom cannot occur without a simultaneous influence on its electronic structure. In the following we will classify the special catalytic behavior of nanosized metal particles under the category "electronic effects" or "geometric effects", depending on which of these appear to be the most important for the given process.

2.1. Electronic Effects

Photoemission spectroscopy investigations have shown that the electronic structure of metal clusters smaller than approximately 5 nm is different from that of the bulk metal. The small number of atoms involved in the formation of the electron bands results in a greater localization of the valence electrons, and in a smaller width of the valence band.[10,11] The altered electronic structure and the pressure towards the center generated by the surface curvature of small metal clusters give rise to a significant contraction of the lattice constant with respect to the bulk material.[2] In turn, the smaller lattice constant is responsible for a shift of the center of the d-band to higher energies, which generally enhances the reactivity of the surface towards adsorbates.[12] The availability of valence electrons for the formation of surface–adsorbate bonds is further increased by a drop of the work function typically observed with increasing surface curvature.[13]

2.1.1. Catalytic reduction of NO

The effects of the change of the electronic properties with the size of small metal clusters is appropriately illustrated by the reaction of CO and NO on palladium surfaces,[14,15] which is an essential step of the removal of NO from exhaust gases [Eq. (1)].

$$CO + NO \rightarrow CO_2 + 0.5\,N_2 \quad (1)$$

This process proceeds by dissociative adsorption of NO on the catalyst surface, and subsequent associative desorption of N_2. Figure 1 shows the turnover frequency (TOF) relative to

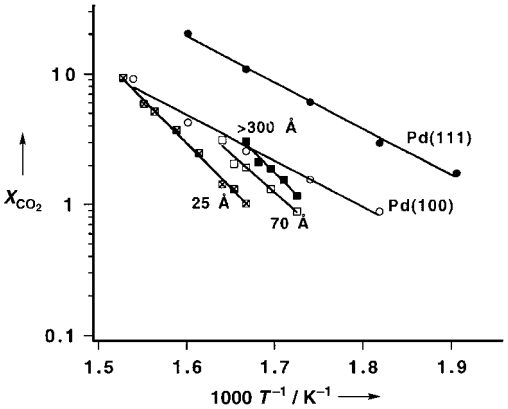

Figure 1. Arrhenius plots of the turnover frequency X_{CO_2} of CO_2 formation from NO and CO on selected palladium single-crystalline surfaces and on $Pd/Al_2O_3/Ta(110)$ model catalysts with various average palladium-cluster sizes. Adapted from ref. [14].

the production of CO_2 on selected palladium single-crystalline surfaces and on $Pd/Al_2O_3/Ta(110)$ model catalysts with various average sizes of the supported palladium clusters. The TOF data measured for the $Pd/Al_2O_3/Ta(110)$ model catalysts indicate that the catalytic activity decreases with decreasing average palladium-cluster size. Temperature-programmed desorption (TPD) and X-ray photoelectron spectroscopy (XPS) allow it to be concluded that this decrease is due to poisoning of the small clusters by strongly adsorbed, catalytically inactive N atoms formed by dissociative chemisorption of NO.[15] Owing to size-dependent changes in the electronic structure of the palladium clusters, the chemisorption energy of N atoms on the palladium surface decreases with increasing cluster size. This fact results in larger palladium clusters having a smaller surface coverage of unreactive N atoms and therefore a higher TOF for the production of CO_2. An additional consequence of the smaller adsorption energy of N atoms on the surface of large palladium clusters is that the

 © 2005 Wiley-VCH Verlag GmbH & Co. KGaA, Weinheim

fraction of molecularly adsorbed NO increases with increasing palladium-cluster size.[15] The larger coverage of undissociated NO on large palladium clusters causes an increase in the yield of N_2O from CO/NO mixtures with increasing palladium-cluster size.

Figure 1 also shows that the Pd(111) and Pd(100) surfaces have a different catalytic activities, with the more open (100) surface being more active. This observation suggests that the relative fraction of (111) and (100) facets on the surface of the supported clusters also has an influence on the catalytic activity. The increase of catalytic activity observed by increasing the average palladium-cluster size from 70 to > 300, that is, in a size range where the electronic structure of the clusters resembles very closely that of the bulk metal, can thus be rationalized. It is a common qualitative observation that small metal clusters behave more similarly to open (100) and (110) surfaces, rather than to close-packed (111) planes.[4] This effect is mainly because both the open single-crystalline surfaces and the small metal clusters have a larger number of coordinatively unsaturated surface atoms present on their surfaces.[16]

2.1.2. *Selective Redox Processes on VO_x-Based Catalysts*

Vanadium oxide based catalysts are the established materials for several selective redox processes. The most active catalysts present two-dimensional oligomeric domains of polyvanadate species dispersed on a support, where vanadium is in the oxidation state +v and is surrounded by O-ligands in a tetrahedral geometry.[17] The reaction mechanisms typically imply the reduction of V^V centers to V^{IV} as the rate-limiting step. A well-understood example of this class of reactions is the oxidative dehydrogenation (ODH) of propane [Eq. (2)].

$$CH_3{-}CH_2{-}CH_3 + 0.5\,O_2 \rightarrow CH_3{-}CH{=}CH_2 + H_2O \qquad (2)$$

The widely accepted mechanism of this reaction is shown in Scheme 1.[18] The rate-determining step is the extraction of a hydrogen atom from the methylene group of the propane molecule, with concomitant reduction of two V^V centers to the +IV oxidation state. The transition state is essentially product-like, and the electron transfer from the propane molecule to the vanadium centers is in an advanced state

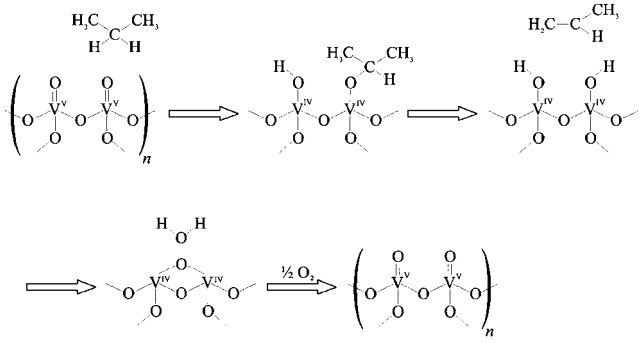

Scheme 1. Schematic representation of the mechanism of the oxidative dehydrogenation of propane.

when the activated complex is reached along the reaction coordinate. It is therefore predictable that any structural property of the VO_x domains that stabilizes the V^{IV}-like centers in the transition state will have a positive effect on the overall reaction rate.[18] The facility of reduction of the vanadium centers is related to the energy of the lowest unoccupied molecular orbital (LUMO) of the V^V species. The energy of the LUMO is accessible experimentally from the absorption-edge energy of a ligand-to-metal charge-transfer transition, which involves the transfer of an electron from the highest occupied molecular orbital (HOMO) of a lattice oxygen atom to the LUMO of the V^V centers:[19] the lower the energy of the ligand-to-metal charge-transfer transition the lower the position of the LUMO on the energy scale. The adsorption-edge of the ligand-to-metal charge transfer-transition has been shown to shift to lower energy with increasing size of the two-dimensional polyvanadate domains, indicating a decrease of the energy of the V^V LUMO and therefore an increase of the reducibility of the V^V centers. This change in the electronic properties of the V^V centers with the increasing size of the polyvanadate domains results in an increased TOF for the conversion of propane.[18]

A similar electronic size effect is observed for the selective catalytic reduction (SCR) of NO by ammonia on TiO_2 (titania) supported VO_x-based catalysts [Eq. (3)].

$$4\,NH_3 + 4\,NO + O_2 \rightarrow 4\,N_2 + 6\,H_2O \qquad (3)$$

The widely accepted reaction mechanism of the SCR process (see Scheme 2) presents some analogies with that

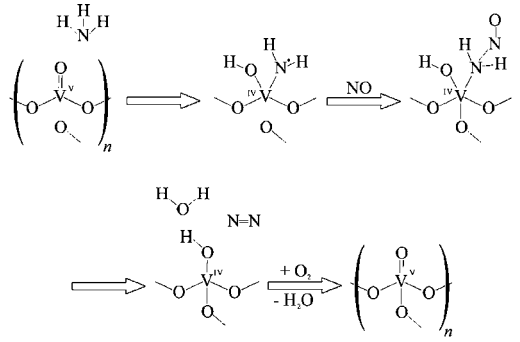

Scheme 2. Schematic representation of the mechanism of the selective catalytic reduction of NO, as proposed in ref. [20].

discussed above for the ODH of propane.[20] The reaction proceeds by the addition of ammonia to a V^V species, which is concomitantly reduced to the +IV oxidation state. The resulting amide complex reacts with NO to form a nitrosamide species, which eventually decomposes with formation of N_2 and water. As in the case of the ODH process, the catalytic cycle is closed by the re-oxidation of the V^{IV} centers by molecular oxygen. Although there is no general agreement on which of the steps composing the reaction mechanism is rate limiting,[21] the similarity of the size effects observed for the ODH and SCR processes suggests that the same structural properties of the VO_x phase steer the catalytic activity in both

 © 2005 Wiley-VCH Verlag GmbH & Co. KGaA, Weinheim

processes. Similarly to the ODH case, characterization of VO_x/TiO_2 catalysts with various VO_x coverages by Raman spectroscopy and XPS has shown that the formation of extended two-dimensional domains of VO_x has a beneficial effect on the SCR catalytic activity.[22] It appears that the stabilization of V^{IV} centers in larger VO_x islands is a general phenomenon that determines to a large extent the effectiveness of VO_x-based catalysts in several selective redox processes.

The same study also showed that the size of the VO_x islands on the support surface has a strong influence on the extent of the transformation of the two-dimensional VO_x domains into three-dimensional VO_x clusters during the SCR process.[22] This structural modification represents the main deactivation pathway for VO_x/TiO_2 catalysts during exposure to high temperatures. An optimum coverage of VO_x could be found, at which high catalytic activity is achieved with only minimal formation of three-dimensional VO_x clusters during operation at high temperature.

2.2. Geometric Effects

In a different way, the size of the nanoclusters used as catalysts influences many processes in new energy cycles that are based on renewable energy sources. For these reactions, the variation of the electronic properties of the surface with cluster size does not have a direct influence on the reaction rate. Instead, the structural changes in the catalyst that are responsible for a variation of the catalytic activity during the process are strongly affected by specific morphological features of the nanoclusters. Since the morphological properties of small clusters (average coordination number of the surface atoms, abundance of defects, concentration of sites with a specific spatial configuration of the metal atoms) change with size, a size effect is observed in this case too.

2.2.1. Methanation of CO

The overall efficiency of the hydrogenation of CO to methane on nickel-based catalysts [Eq. (4)] is influenced through a variety of mechanisms by the size of the catalytically active nickel clusters.

$$CO + 3\,H_2 \rightarrow CH_4 + H_2O \qquad (4)$$

This process has recently awakened renewed interest as part of the search for renewable energy sources as replacements for fossil fuel energy carriers. Gas mixtures mainly consisting of carbon oxides and hydrogen can be effectively produced by the gasification of biomass, which is a prime resource in several locations in the world. The results of studies estimating the fraction of human energy needs that could be covered by biomass vary widely depending on assumptions, but values of 25 % are typically obtained.[23] For the climate conditions of the Northern hemisphere and of Europe in particular, analyses show that biomass, after hydroelectricity, is the second most important and most competitive renewable energy resource.

Biomass can be used as raw material for the production of heat and electricity, or for the synthesis of fuels. The ecological balance shows that the direct use of, for example, logwood for heating is hampered by high particle and NO_x emissions.[24] As a consequence, it is attractive to first convert biomass into a standardized gaseous fuel, for example, substitute natural gas, which can subsequently be used in gas burners, gas turbines, solid-oxide fuel cells, or gas engines propelling cars.[25]

The hydrogenation of CO to methane has been shown to be insensitive to the size of the nickel clusters of average dimensions, that is, from 15 to 80 Å.[26,27] This situation is in contrast with the marked dependence of the adsorption of CO on the size of the nickel clusters, as found by TPD investigations on mass-selected nickel clusters. This work has shown that the fraction of dissociatively chemisorbed CO increases markedly with cluster size.[28] Since the methanation of CO occurs by the stepwise hydrogenation of carbon formed by dissociative chemisorption of CO,[29] it would be expected that the rate of the overall process is affected by the extent of CO dissociation on the nickel surface. A possible explanation for why the CO methanation is in fact size independent is that the rate-determining step of the methanation process [Eq. (5); (a) = adsorbed][29] is catalyzed by a single nickel atom and that the rate of this step is only weakly dependent on the electronic structure of the metal surface.

$$CH_{(a)} + H_{(a)} \rightarrow CH_{2(a)} \qquad (5)$$

In this case an increase of the surface coverage of atomic C resulting from a faster dissociation of CO on the nickel surface would not be beneficial to the methanation process, the overall rate being determined only by the rate of the hydrogenation step in Equation (5).[26]

Although the intrinsic rate of the hydrogenation of CO is not dependent on the nickel-cluster size, the catalyst deactivation mechanisms, which eventually determine how effectively a catalyst can be used in an industrial-scale process, are. The most important deactivation pathways for nickel catalysts under CO methanation conditions are the formation of graphitic carbon that physically blocks the metal surface (coking) and the loss of nickel surface area owing to sintering of the nickel clusters.

Polymerization of atomic carbon resulting in the formation of graphite occurs predominantly at steps separating atomic terraces with a (111) geometry.[30] The graphite sheets grow epitaxially on the Ni(111) terraces extending away from the step that initiated their formation. The prerequisite for the growth of stable graphite crystallite is the formation of graphite nuclei exceeding a critical size of approximately 25 Å.[30] Below this critical size the graphite sheets are unstable and can be eventually hydrogenated, leading to their disappearance. This fact implies that only nickel clusters with (111) terraces longer than about 25 Å can allow the growth of stable graphite crystallites. This indirect effect of the morphology of the nickel clusters on the stability of the graphite crystallites formed results in an increase in the extent of coking of the nickel catalysts with increasing nickel-cluster size. It has been experimentally demonstrated that clusters

 © 2005 Wiley-VCH Verlag GmbH & Co. KGaA, Weinheim

smaller than around 100 Å do not undergo significant coking at 773 K.[31]

The second deactivation pathway under CO methanation conditions, namely the loss of nickel surface area by sintering, also shows a marked dependence on the initial size of the supported nickel clusters. This process is especially active at temperatures around 500 K and involves the net migration of $Ni(CO)_x$ ($x = 2$ or 3) surface complexes from small to large nickel clusters (Figure 2).[32] After migrating to a large nickel

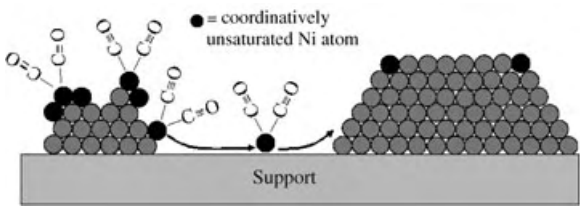

Figure 2. Schematic representation of the low-temperature sintering mechanism operating under CO methanation conditions.

cluster the complexes decompose at its surface and the transported nickel atoms are incorporated in a close-packed terrace. Since the formation of polycarbonyl complexes requires the presence of coordinatively unsaturated surface nickel atoms, extended close-packed terraces are the most stable structures under methanation conditions and their size grows irreversibly. Because of the larger number of coordinatively unsaturated surface atoms in smaller clusters, the formation of polycarbonyl complexes becomes more pronounced with decreasing average cluster size (as observed by IR spectroscopy).[33] Thus, with small nickel clusters, the greater formation of polycarbonyl complexes results in a more rapid loss of surface area by sintering and in a more rapid deactivation during CO methanation. The atomic migration of nickel via formation of polycarbonyl complexes is suppressed entirely at temperatures above 700 K, because nickel carbonyl species are not stable at high temperatures.[34]

2.3. Support Effects

The interaction of the catalytically active clusters with the support often results in a change in the electronic properties of the atoms close to the cluster–support interface.[16] For large aggregates most of the surface is so far away from the cluster–support interface that only minor effects on the catalytic behavior result from the interaction with the support. When the size of the clusters is reduced, the electronic structure of the surface becomes increasingly affected by the changes occurring at the cluster–support interface. These effects can be so extreme that they result in a dramatic variation of the catalytic activity. This is for example the case for nanometer-sized gold clusters supported on TiO_2. The partial oxidation of the gold atoms promoted by their vicinity to the TiO_2 support makes the small gold clusters active catalysts for the oxidation of CO by oxygen at room temperature.[35] The catalytic activity decreases rapidly with increasing size and essentially disappears for clusters larger than approximately 5 nm.

2.3.1. Example: Methanol Reforming on Cu/ZnO/Si Model Catalysts

Clear size effects, related to the interaction of the catalytically active copper clusters with the ZnO support have recently been observed during the production of hydrogen from methanol on Cu/ZnO-based catalysts. This process, often referred to as methanol reforming, is the key step for the use of methanol as the primary fuel in fuel-cell-powered vehicles. The most convenient process for the on-board production of hydrogen-rich gas mixtures is methanol autothermal reforming [Eq. (6)].[36]

$$4\,CH_3OH + 3\,H_2O + 0.5\,O_2 \rightarrow 4\,CO_2 + 11\,H_2 \qquad (6)$$

However, the actual partial pressures of water and oxygen in the reactant mixture are expected to vary during operation, according to the power requirements of the fuel cell. This implies that the conditions to which the catalyst is exposed change frequently during its lifetime and that a wide range of methanol-reforming reaction conditions have to be considered to assess the suitability of a catalyst for this process.

Cu/ZnO-based materials are effective catalysts for methanol reforming between 200 and 300 °C. The chemical and structural properties of the catalyst surface are strongly affected by the specific reaction conditions.[37] In particular, the oxidation state of copper is very sensitive to the partial pressure of oxygen and water in the reactant mixture. Changes of the oxidation state of copper significantly affect the activity of the catalyst and the selectivity for the production of hydrogen.[38,39]

The effect of the size of the copper clusters on the structural changes accompanying the exposure of Cu/ZnO-based catalysts to methanol-reforming conditions was investigated using Cu/ZnO/Si model catalysts with various copper coverages. These catalysts, consisting of a silicon(111) wafer covered by a 100-nm thick ZnO layer onto which copper nanoclusters were deposited by thermal evaporation, were prepared and characterized by a combination of spectroscopic and microscopic techniques.[40,41] Catalytic tests were carried out for 16 h at 550 K in the absence of water.

Figure 3 shows the $Cu\,2p_{3/2}/Zn\,2p_{3/2}$ ratio determined by XPS as well as the oxidation state of copper after exposure to methanol-reforming conditions with various O_2/CH_3OH molar ratios in the reactant mixture. For the two Cu/ZnO/Si model catalysts which differ in the amount of copper on their surfaces and in the average size of the supported copper clusters, a progressive change of the copper oxidation state from 0 to +1 is observed with increasing oxygen partial pressure. The oxygen partial pressure at which the oxidation of copper takes place is clearly dependent on the size of the copper clusters on the ZnO surface (Figure 3). An O_2/CH_3OH molar ratio of 0.33 is sufficient to completely oxidize the copper in the high-copper-coverage catalyst (left axis; average copper-cluster height 5.2 nm, as determined by AFM). On the other hand, an O_2/CH_3OH molar ratio > 0.4 is necessary

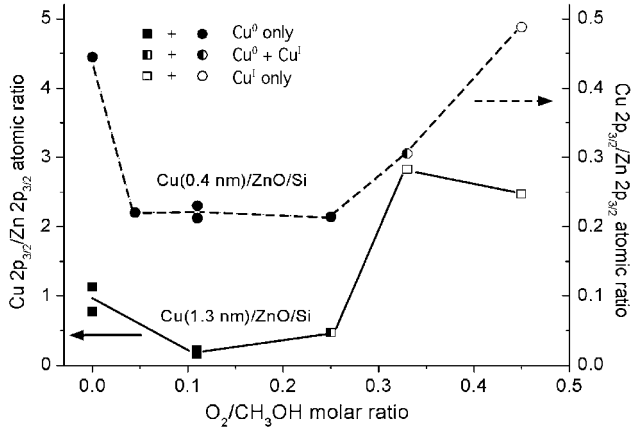

Figure 3. XPS determined $Cu\,2p_{3/2}/Zn\,2p_{3/2}$ ratio after exposure of Cu(0.4 nm)/ZnO/Si (right axis) and Cu(1.3 nm)/ZnO/Si (left axis) model catalysts to methanol-reforming conditions with various O_2/CH_3OH molar ratios in the feed. In all cases $T = 550$ K and $p_{H_2O} = 0$ bar. The numbers in parenthesis indicate the nominal thickness of the copper coverage calculated from the intensity of the $Cu\,2p_{3/2}$ and $Zn\,2p_{3/2}$ XPS peaks assuming a layer-by-layer growth of the copper layer.

to completely oxidize copper in the low-coverage case (right axis; average copper-cluster height 2.2 nm). The lower reactivity towards oxidation observed for the small copper clusters on the surface of the low-coverage Cu/ZnO/Si model catalysts contradicts the general statement that small metal clusters exhibit a higher reactivity than large metal aggregates (cf. Sections 1 and 2.1) and shows how important support effects can be for the behavior of supported nanoclusters. Stabilization of the copper surface against oxidation has also been observed for very thin copper islands on $ZnO(000\bar{1})$ single-crystalline surfaces.[42] The reduced reactivity of the small metal clusters with oxygen is very likely to be the result of electron donation from the copper surface to the underlying ZnO layer.

The data in Figure 3 show that the partial pressure of oxygen also influences the $Cu\,2p_{3/2}/Zn\,2p_{3/2}$ ratio measured by XPS after the catalytic tests. Again, a significant size effect is observed: the high-copper-coverage samples (left axis) have a larger relative decrease of the $Cu\,2p_{3/2}/Zn\,2p_{3/2}$ ratio at intermediate O_2/CH_3OH molar ratios than the low-copper-coverage catalysts (right axis).

Changes in the copper-cluster morphology upon exposure to methanol-reforming conditions were monitored for both the low- and high-copper-coverage model catalysts. Comparison of the AFM images in Figure 4 reveals that the average lateral size of the copper clusters is essentially the same for each model catalyst after both catalytic tests (O_2/CH_3OH molar ratios of 0 and 0.11). This result indicates that the decrease of the $Cu\,2p_{3/2}/Zn\,2p_{3/2}$ ratio mentioned above is not due to more extensive agglomeration of the copper clusters in the presence of oxygen in the reactant mixture. However, the average height of the copper clusters in the high-copper-coverage model catalyst increases from 14 to 19 nm upon increasing the O_2/CH_3OH molar ratio from 0 to 0.11. The increase in cluster height is smaller for the low-copper-coverage model catalyst, in which the increase is only from 4 to 6 nm.

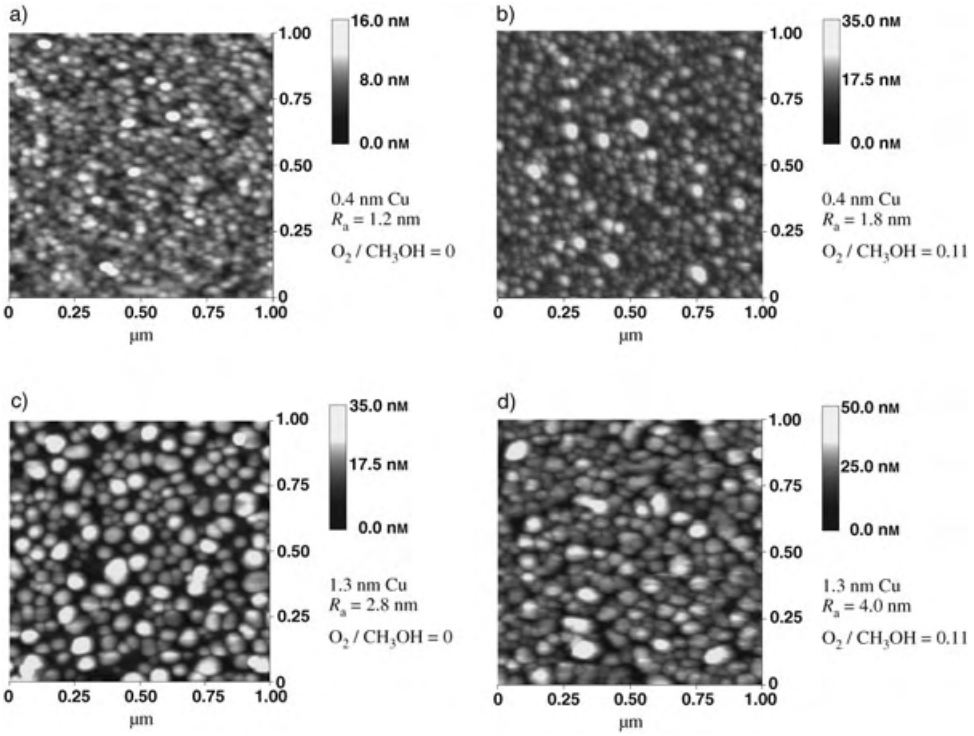

Figure 4. AFM images ($1 \times 1\,\mu m^2$). a) and b) Cu(0.4 nm)/ZnO/Si model catalysts; c) and d) Cu(1.3 nm)/ZnO/Si model catalysts. All samples were exposed to methanol-reforming conditions at 550 K prior to AFM analysis. The O_2/CH_3OH molar ratio for each treatment is indicated in the corresponding image, together with the measured average surface roughness (R_a). For all treatments no water was included in the reaction mixtures.

 © 2005 Wiley-VCH Verlag GmbH & Co. KGaA, Weinheim

Argon-ion XPS depth-profiling experiments (Figure 5) strongly indicate that the reason for the smaller values of the $Cu\,2p_{3/2}/Zn\,2p_{3/2}$ ratio and for the larger average height of the copper clusters observed in the presence of oxygen in the

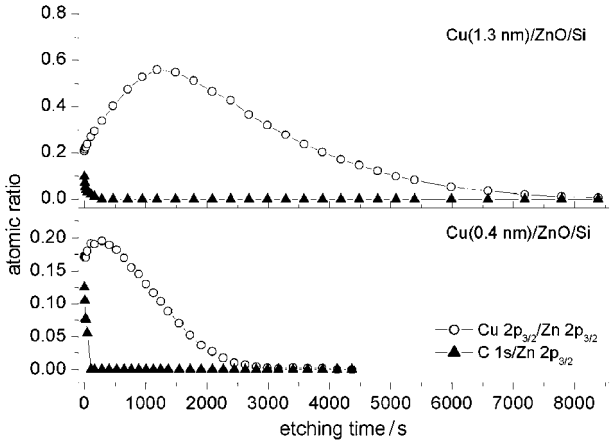

Figure 5. XPS depth profiles of Cu(0.4 nm)/ZnO/Si (bottom panel) and Cu(1.3 nm)/ZnO/Si (top panel) after methanol reforming at 550 K with an O_2/CH_3OH molar ratio of 0.11 and no water in the reaction mixture. The kinetic energy of the incoming argon ions was 1.0 keV.

reactant mixture is the partial coverage of the copper-cluster surface by a thin ZnO_x layer. The depth profiles obtained for the two model catalysts are qualitatively similar, and indicate removal of a ZnO_x layer covering the copper surface. The position of the maximum $Cu\,2p_{3/2}/Zn\,2p_{3/2}$ ratio (as a function of etching time) depends on the copper coverage, which suggests an influence of the cluster size on the migration of ZnO over the copper surface. The maximum ratio is reached earlier for the Cu(0.4 nm)/ZnO/Si model catalyst than for the Cu(1.3 nm)/ZnO/Si model catalyst. This result indicates that the ZnO_x layer covering the small copper clusters on the low-copper-coverage model catalyst is significantly thinner than for the larger copper clusters. This conclusion is supported by the smaller increase of the average height of the copper clusters observed by AFM for the low-copper-coverage model catalyst upon varying the O_2/CH_3OH molar ratio from 0 to 0.11 (see Figure 4). It appears likely that a relation between the size-dependence of the oxidation of copper and of the migration of ZnO during methanol reforming exists. In both cases small copper clusters appear less reactive and exhibit a greater resistance to structural change. It can be speculated that the migration of ZnO onto the copper clusters is accelerated by coverage of the copper surface by adsorbed atomic oxygen. The coverage of the active copper surface by ZnO has been observed to contribute significantly to the deactivation of commercial Cu/ZnO-based catalysts during methanol reforming.[37,43] The observed size-dependence of this surface modification opens up new ways of designing Cu/ZnO-based catalysts exhibiting superior stability during the methanol-reforming process.

3. Precious-Metal Nanoparticles as Fuel-Cell Catalysts

Polymer electrolyte fuel cells (PEFCs) and phosphoric acid fuel cells (PAFCs) operate below 100 °C and at around 200 °C, respectively. They are low-voltage, high-current-density devices; the current is generated by the electrochemical reactions at the electrodes. At these operating temperatures a catalyst with high dispersion and a high active surface area is needed even for the hydrogen oxidation reaction (HOR) and for the oxygen reduction reaction (ORR). Platinum and platinum alloys are the electrode materials of choice, owing to their favorable electrocatalytic properties and their corrosion stability in an acidic environment at the operating temperatures.

Platinum blacks were commonly used in the past as electrodes. They are prepared by reduction of a platinum salt and typical surface areas of 25 to 30 $m^2 g^{-1}$ could be obtained, with particle sizes of around 10 nm.[44] In a fuel-cell electrode the platinum particles together with polytetrafluoroethene (PTFE) as a binder are incorporated into the active layer of a gas-diffusion electrode, this results in the formation of a kind of interpenetrating network. The typical platinum loadings, which could be obtained with blacks, are in the range of several $mg\,cm^{-2}$. Further, the electrode consists of a "second" porous structure, for example, a carbon cloth or carbon paper impregnated with a PTFE suspension, which is responsible for the reactant (H_2, O_2) transport to and product (H_2O) transport away from the electrochemically active interface. At the same time these porous structures serve as current collectors which conduct the current from the electrochemical interface to the cell housing (bipolar plate).[45]

For further commercialization of the fuel-cell technology, the cost stemming from among other factors, the precious-metal content in the cells, is still a major challenge. Hence, creating higher active surfaces at lower precious-metal content, that is, smaller particles, is a research topic of utmost importance in fuel-cell related electrocatalysis of today.

3.1. Carbon-Supported Nanoparticles as Precursors for Fuel-Cell Gas-Diffusion Electrodes

3.1.1. Platinum and Platinum-Alloy Nanoparticles for ORR

Even 30 years ago, platinum and platinum-alloy nanoparticles were employed as electrocatalysts in the first prototype phosphoric acid fuel cells (PAFCs).[46] For the commercialization of fuel cells, these catalysts had to meet three requirements: high performance (high surface), low cost (small particles, thin layers), longevity (corrosion resistant in the acidic environment). Owing to the fact that only platinum (being a precious metal) can survive the corrosive environment of the PAFC, the challenge was to synthesize high-surface-area platinum catalysts to utilize as many platinum surface atoms as possible. Other than for gas-phase reactions, where oxidic substrates are used, the electrochemical application requires a conducting substrate. Carbon black in many variations is the material of choice.[47] To control the size of

 © 2005 Wiley-VCH Verlag GmbH & Co. KGaA, Weinheim

the latent platinum particles better, the deposition from sols was introduced. As could be shown, the overall platinum crystallite surface area depends on the BET surface area of the carbon.[48] Over the past years, platinum deposited onto a high-surface-area carbon (XC-72; Cabot) with a BET surface area of approximately 250 $m^2 g^{-1}$, has become a standard in the fuel-cell community, with platinum surface areas up to 180 m^2 per g Pt depending on the platinum loading (mg Pt per mg C) being achieved.

Around 1980, the first supported platinum-alloy nanoparticles, namely PtV/C were synthesized, which showed somewhat higher specific activity than pure platinum for ORR.[49] In the following years, many other binary and even ternary alloy nanoparticles supported on carbon were synthesized with higher specific activities than platinum. The reason for the higher specific activity is still under discussion (see the end of this Section).

In an "Electrocatalyst by Design" approach[50] binary Pt_xCo_y and Pt_xNi_y alloys were investigated with respect to their oxygen-reduction activity.[51,52] This approach starts from well-defined and characterized bulk alloy surfaces, continues with the characterization of catalyst powders PtM/C, and ends with the test of real (commercial products) gas-diffusion electrodes in fuel cells (Figure 6).

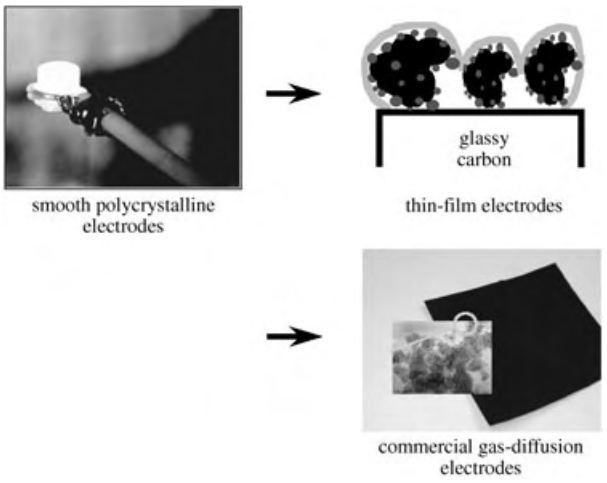

Figure 6. Approach for "designing" an optimized gas-diffusion electrode.

Polycrystalline planar alloy electrodes were prepared, cleaned by sputtering and annealing cycles, and their surface composition characterized by Auger spectroscopy and low-energy ion scattering. For the compositions PtM (M = Co, Ni) and Pt_3M well-defined surfaces were obtained and their electrochemical behavior was studied as a reference case for the PtM nanoparticles supported on XC-72. Commercial PtM/C catalysts were obtained (E-TEK) and their electrochemical oxygen-reduction activity was tested with the thin-film rotating ring-disk electrode (RRDE) (thin-film electrode, Figure 6, middle).[53] All the experiments were carried out in 0.1M $HClO_4$ between room temperature and 60 °C. As an example, a low-magnification HREM micrograph of PtCo/C and in comparison Pt/C is shown in Figure 7 and the particle size distributions for the four catalysts are given in Figure 8.

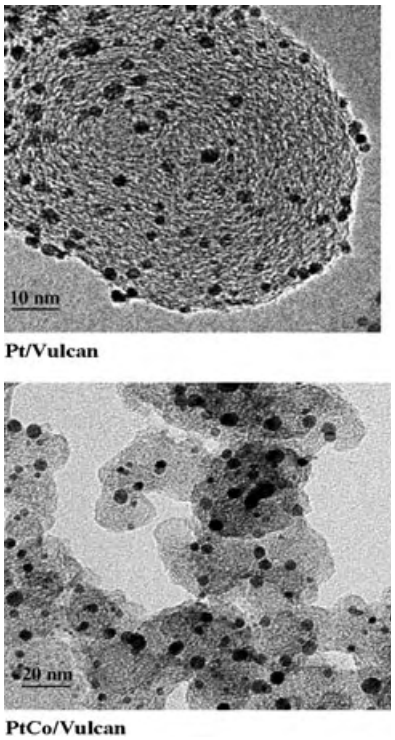

Figure 7. Low-magnification HREM micrograph of Pt/Vulcan and PtCo/Vulcan (Vulcan XC-72 is a nongraphitized carbon support (Cabot) with a BET surface area of 220 $m^2 g^{-1}$).

The commercial catalyst PtCo/C was further employed as the "active layer" in a commercially available gas-diffusion electrode (Figure 6, right) and tested in H_2/O_2 polymer electrolyte fuel cells. Kinetic analysis on the model electrodes revealed a small but reproducible activity enhancement. This enhancement amounts to roughly a factor of 1.5 per unit electrode area in the case of the bulk electrodes, a factor of 1.5 to 2 for the supported 75% platinum catalysts, and a more significant factor of 2 to 3 for the 50% PtCo/Vulcan catalyst (per mg of Pt; see Figure 9). Peroxide yields, Tafel slopes, and apparent activation enthalpies were found to be very similar on the electrodes and catalysts (with the exception of the 50% PtNi/Vulcan catalyst). These findings lead to the conclusion that the reaction pathway and rate-determining step is identical on all the electrodes and catalysts investigated.

It was proposed that the kinetic enhancement affects the pre-exponential factor of the conventional transition-state-theory rate expression. It can, however, only be speculated why alloying with Ni or Co produces these changes.

Investigating the commercially available PtCo gas-diffusion electrode (E-TEK) in a fuel cell. Its activity as a PEFC cathode was found to be slightly inferior to that of the platinum gas-diffusion electrode (in terms of geometric current densities) with the same precious-metal loading ($mg\,cm^{-2}$).[54] This behavior is not yet conclusively understood. Different wetting properties of the catalyst or modified surface compositions may contribute to this unexpected and undesired behavior. In addition, possible deviations in the metal loadings must be taken into account. The metal loading could be completely different from the data supplied by the

 © 2005 Wiley-VCH Verlag GmbH & Co. KGaA, Weinheim

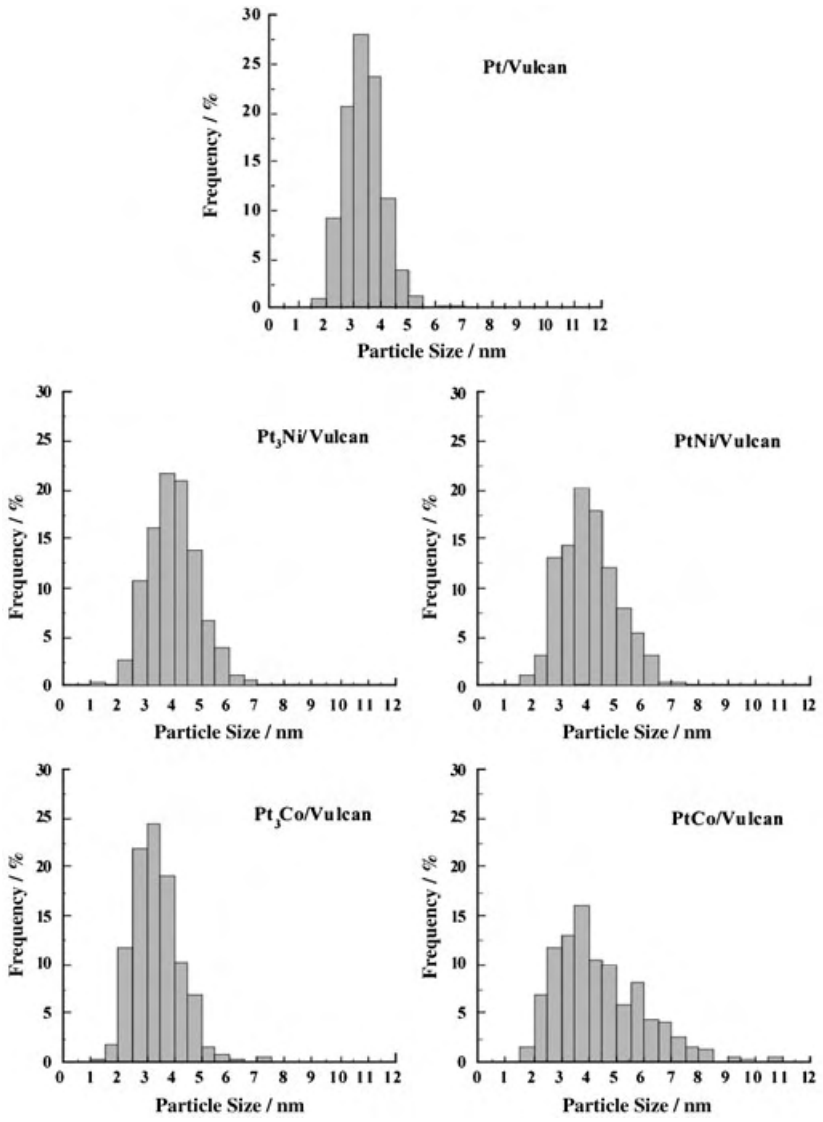

Figure 8. Histograms illustrating the particle size distribution for Pt/Vulcan and the four binary alloy catalysts, determined from HREM micrographs.

manufacturers or deviations could be found within the electrode. A further reason for lower catalytic activity may be the ripening of the PtCo-particles during the electrode manufacturing process, as indicated by TEM particle-size analysis.[54]

The question still remains why these alloy nanoparticles are more active than the pure platinum particles. Several factors, which are difficult to separate, may contribute to an activity enhancement. The alloying component may change the distribution of islands of a given metal (ensemble effect). It may change the local binding geometry (structural effect) or it may directly modify the reactivity of the platinum surface atoms (electronic effect). Some of these effects were already invoked in previous studies,[48,49,55] to explain the enhanced activity of the platinum alloys. The idea of modifying the activity of platinum surface atoms was further put forward recently within the concept of "platinum-group-metal (PGM) skin with base-metal core" particles.[56] The goal of this work is a unified concept for both anode and cathode catalysts utilizing PGM-based bimetallic nanoparticles with "grape" structure, whereby skin and core metal are different for anode and cathode. Under current discussion are nanoparticles with Rhenium as metal core and platinum and palladium as PGMs.

3.1.2. *Platinum-Alloy Nanoparticles for the Hydrogen Oxidation Reaction in the Presence CO*

Platinum-alloy nanoparticles, again supported on carbon, are also employed as anode catalysts in the hydrogen oxidation reaction (HOR), in particular to achieve CO tolerance for fuels generated by a reforming process (methanol, gasoline). In these cases, metals, for example, ruthenium, tin, molybdenum, are co-alloyed to platinum to yield oxygen-containing species (e.g. RuO_x) (at low overpotentials versus the dynamic hydrogen electrode (DHE)) to oxidize CO adsorbed on platinum. In terms of CO tolerance in fuel-cell experiments anode electrodes with the same precious-metal loading (approximately. 0.6 mg cm^{-2} geometric area) and formally the similar composition (Type A: $Pt_{50}Ru_{50}$, type B: $Pt_{40}Ru_{60}$) yield a very different behavior with respect to their "practical" CO tolerance (see Figure 10). Type A electrode (E-TEK) contains PtRu and RuOx nanoparticles supported on Vulcan XC-72,[57] while Type B electrodes (Tanaka Kikinzoku) contains hydrous PtRu-oxides, as characterized by XPS-analysis, supported on high area surface carbon (HASC, ca. 800 m^2).[58,59] The dependence of the CO adsorption by platinum (mL per g Pt (mL = milli-Langmuir)) on the carbon surface area is displayed in Figure 11, which demonstrates the advantage of a HASC material as a substrate for the nanoparticles. Further differences in the anode electrodes are the metal:carbon ratio: 20 wt % for type A and 54 wt % for type B (see electron micrograph in Figure 12). The difference in the impedance spectra between these two catalysts (see Figure 13) is explained in terms of CO adsorption on the platinum component of the alloys.[59–61]

3.1.3. *Novel Nanoparticle Preparation Approaches through the use of Colloids*

Recently, a novel approach to synthesize platinum and platinum-alloy nanoparticles for fuel-cell applications of defined size was demonstrated by synthesis of stabilized colloids from organometallic species (Figure 14).[62,63] Colloid precursors that are stabilized with NR_4X- or organoaluminum shells and that have defined particle size distribution can be prepared. The precursors, still containing the stabilizer shell, are mixed with a carbon support and heat treated at around 250 °C, first in an O_2 and subsequently in a H_2 atmosphere. This process removes the shell so that the nanoparticles adhere to the support afterwards. Bimetallic colloids of

 © 2005 Wiley-VCH Verlag GmbH & Co. KGaA, Weinheim

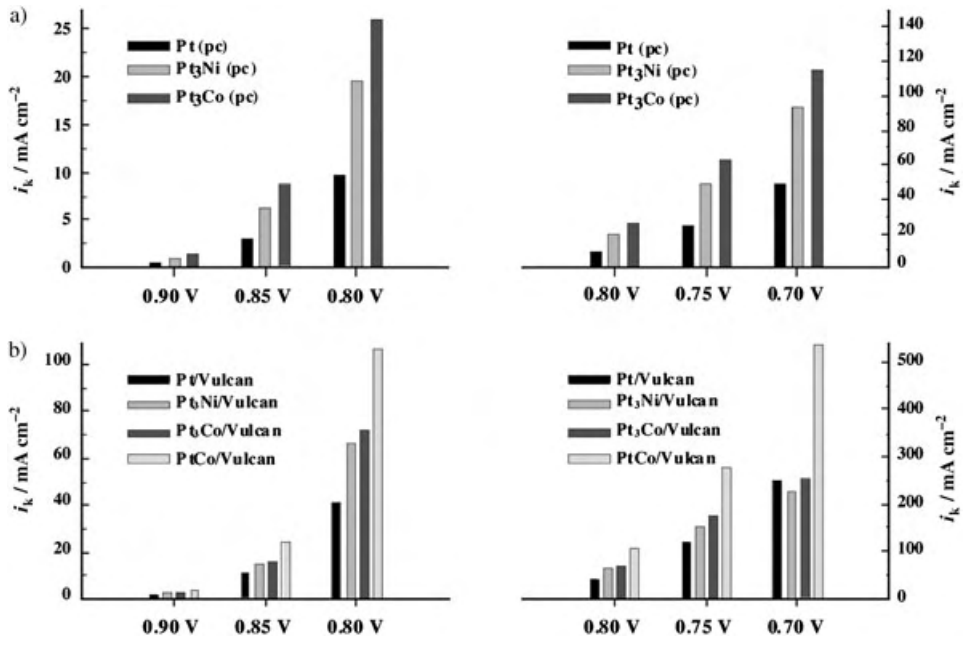

Figure 9. Histograms showing the kinetic current densities at different potentials for a) polycrystalline (pc) electrodes and b) thin-film electrodes at 60 °C and 1600 rpm in the anodic sweep direction normalized to the geometric electrode area (0.283 cm^2); potentials versus the reversible hydrogen electrode (RHE).

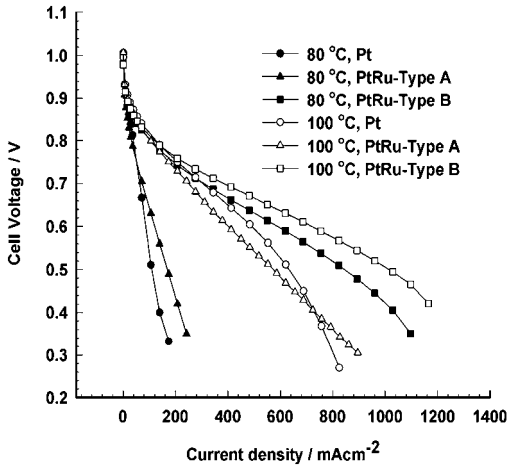

Figure 10. Comparison of the cell current–voltage curves for the three anodes containing nanoparticles of platinum and PtRu in the active layer at 80 °C and 100 °C.

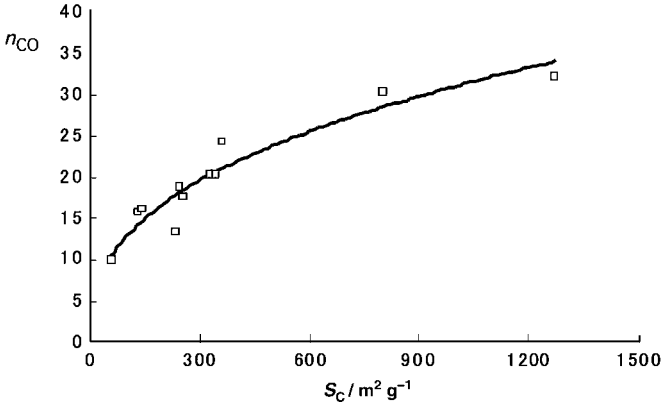

Figure 11. Relationship between quantity of CO adsorbed on catalyst, n_{CO} (in mL g^{-1} Pt (mL = milliLangmuir)), and surface area of carbon support S_C (data from Tanaka Corp.).

different compositions, for example, PtRu, PtSn, PtMo, as well as ternary colloids, such as, PtRuMOx (M = W, Mo, V) were synthesized and tested for their CO tolerance as HOR catalysts as well as for the direct oxidation of MeOH.[64] For the ternary alloy, it was reported that the surface area occupied by MeO_x and the electrochemical active noble-metal surface compete for the oxidation of MeOH.[64]

3.1.4. Platiunm Nanoparticles Supported by Carbon Nanohorns

Recently, the development of platinum nanoparticles supported on carbon nanohorns (nanotubes with irregular hornlike shape) and their use in active layers of fuel-cell electrodes was described.[65] It was claimed that platinum particles less than half the size of those supported on activated carbons, for example, Vulcan XC-72, could be obtained and stabilized under fuel-cell operating conditions.

3.2. Nanoparticle Ensemble in an Active Layer of a Fuel-Cell Gas-Diffusion Electrode

3.2.1. Characterization of Active Layers

Fuel cells contain an ensemble of platinum and platinum-alloy nanoparticles in a mixture with a binder (normally PTFE-particles), which together act as an electrocatalytic layer in contact with the electrolyte, that is, the proton-conducting polymer membrane in polymer electrolyte fuel

 © 2005 Wiley-VCH Verlag GmbH & Co. KGaA, Weinheim

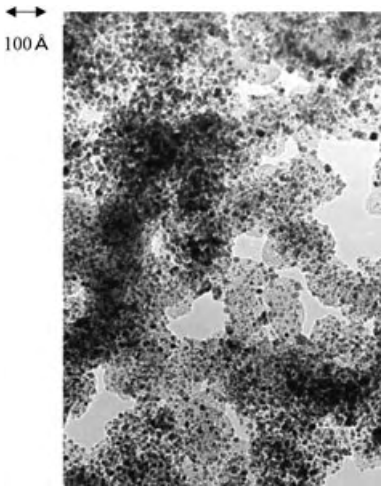

Figure 12. Electron micrograph of a PtRu catalyst with a metal loading [Pt/(Pt+C)] of 54 wt%.

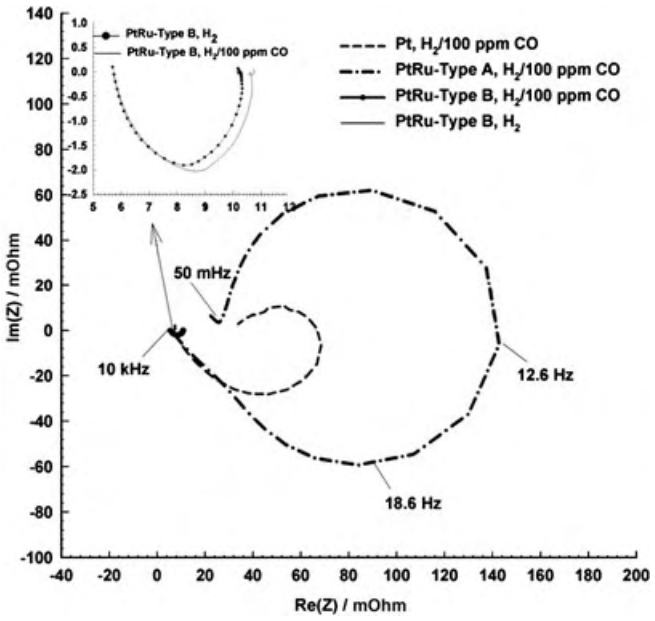

Figure 13. Nyquist plots of the measured cell impedance at 100 °C, 500 mA cm^{-2}, for different anodes. Pure H_2 or H_2/100 ppm CO was used as fuel.

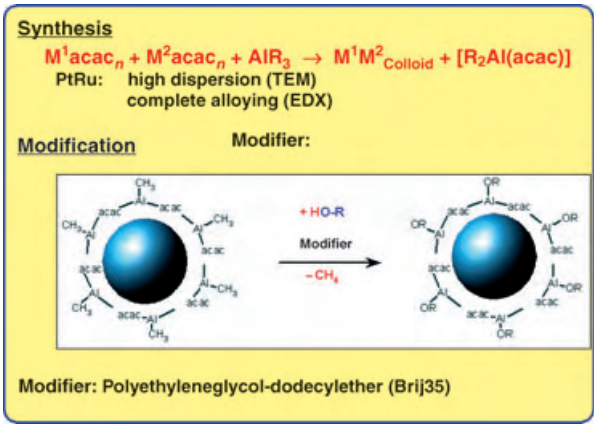

Figure 14. Synthesis of nanoparticles from metal–organic precursors; acac = 2,4-pentanedione.[62,63]

cells.[45] As has been discussed widely, an optimal performance of the fuel cell requires an optimized three-phase boundary of the electronic (electrocatalyst), ionic (electrolyte), and gas (reactants, products) phase.

Practice has shown that active layers of platinum-black particles, attached to a membrane electrolyte, work reasonably well under fuel-cell conditions. However, the electrolyte phase has to be actively incorporated into an active layer consisting of platinum particles supported on carbon. Initially, a "crude" approach was used by hot-pressing the active layer of these electrodes into the membrane surface.[66] Later on, as a result of the availability of solubilized membrane material (liquid Nafion; DuPont), the impregnation of already formed active layers (network of Pt/C-particles and sintered PTFE-particles as a binder) with the liquid ionomer was possible. It could be clearly demonstrated that the impregnation improved the electrochemical coupling between platinum nanoparticles and the electrolyte, leading to improved fuel-cell performance.[67] In all this work the active layer was prepared on the porous gas-diffusion layer (carbon substrate, cloth or paper) before impregnation with the liquid ionomer.

Further progress was made with the "decal" technique developed at Los Alamos Laboratory:[68] An ink is prepared consisting of the ionic phase (liquid Nafion), a binder (PTFE), and the Pt/C particles, and then poured onto an inert substrate (decal), and dried. The dried layer is subsequently transferred and hot-pressed onto the membrane. Thinner active layers (approximately 5 μm thick versus 30 to 40 μm thick for the old method) could be prepared by this technique. As a consequence, active layers with lower platinum loadings (mg cm^{-2}) and even better transport properties could be prepared. This development was taken up by several commercial producers, which nowadays sell so called catalyst-coated membranes (CCMs).

The problem then remains, how to characterize the electrochemical coupling between the three-dimensional network of platinum particles supported on carbon, interpenetrated with ionic phase and binder phase, in contact to a "solid" polymer electrolyte. A model system based on defined, microstructured carbon surfaces (glassy carbon) was developed, which allows the microstructured surface to be covered with platinum in different ways (Figure 15).[69]

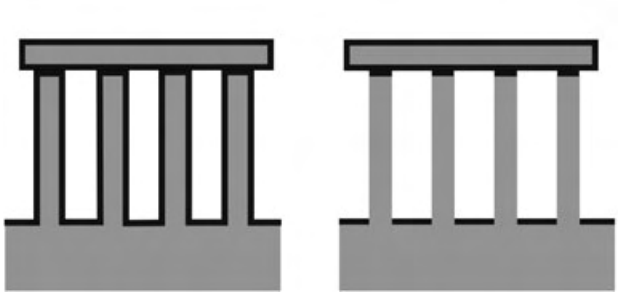

Figure 15. Model system to characterize the electrocatalytic effects at the interface between the active layer and the proton-conducting membrane. The structures (50-μm channel width) have been prepared by microsawing; a continuous (left) or discontinuous platinum layer (right) was deposited by sputtering.[69]

 © 2005 Wiley-VCH Verlag GmbH & Co. KGaA, Weinheim

Model systems can be established, which correspond to active layers consisting of platinum black or platinum–carbon particles. Striking similarities between the model systems and real gas-diffusion electrodes (E-TEK, platinum black ($4\,mg\,cm^{-2}$), E-TEK, Pt/C ($0.6\,mg\,cm^{-2}$), 20% Pt/C) have been found in cyclic voltammetry analysis. This model system allows further characterization of this particular interface by other electrochemical techniques, for example, ac-impedance spectroscopy. In addition, new structuring techniques for the planar carbon support are being developed, adding more freedom to the geometric arrangement of the microstructures.[70]

3.2.2. Novel Approaches to Active-Layer Preparation

A novel approach for nanostructured platinum and PtRu particles at the interface to the solid-polymer electrolyte was described recently.[71] A non-traditional catalyst-support system and catalyst-deposition process were employed, which allow both lower loadings and simpler dry processing to be used to fabricate so called roll-good catalyst coated membranes (CCMs). The catalyst-support system is a non-structured thin film consisting of a single layer of a dense distribution of oriented crystalline whiskers of an organic pigment material (perylene red (PR): *N*,*N*-di(3,5-xylyl)perylene-3,4:9,10-bis(dicarboximide)). This material is insoluble in any common solvent, acid, or base and shows greater electrochemical stability against dissolution than platinum in the potential range of interest for H_2/O_2 fuel-cell application. PR was vacuum deposited and converted into the oriented whisker phase by thermal annealing. These nanostructured support elements have number densities on the order of 3–5 billion cm^{-2} and aspect ratios of length to widths on the order of 10. The nanostructured film is generated by dry vacuum processing on a temporary substrate web, coated with multi-element catalysts, and transferred to a proton-conducting membrane to form the CCM. The nanostructured thin-film electrode on the CCM contains no carbon and has submicron thickness (Figure 16). The catalyst ORR activity per unit platinum electrochemical surface area is several times that of carbon-supported dispersed electrodes. It is also been stated that this approach might have advantages in other aspects of fuel-cell design, such as fuel utilization and humidification.

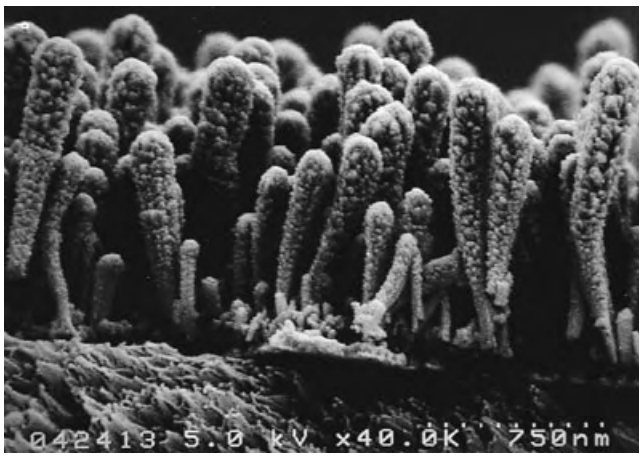

Figure 16. Nanostructured thin-film electrode containing platinum particles on perylene red whiskers (from ref. [71]).

A quite different approach to obtain nanostructured platinum particles, supported in a carbon matrix is being developed by us.[72] We studied the co-sputtering of platinum and carbon onto flat as well as porous gas-diffusion-media-like substrates.[58,73,74] At film thicknesses ranging from 1–2 μm, typical loadings were in the range of 0.2 to $1.2\,mg\,Pt\,cm^{-2}$, with Pt/(Pt+C) ratios ranging from 43 to around 90%. Specific platinum surface areas of around $100\,cm^2_{real}/cm^2_{geometric}$ were obtained, as determined electrochemically by hydrogen underpotential desorption H_{upd}.

X-ray absorption spectroscopy (XAS), anomalous small-angle X-ray scattering (ASAXS), and electron microscopy (HRTEM, SEM) gave insight into the nanostructured morphology of platinum within the carbon matrix. The scattering curves can be interpreted according to a "zone model",[75] in which the influence of substrate temperature and sputter-gas pressure on the layer morphology is described. The data can be modeled according to a columnar structure, built up of several arrangements of perfectly aligned columns, each consisting of $N_s = 6$ single column like structure elements (Figure 17). Typical values obtained from a fit to the scattering curves are $W = 0.2$ nm, $T = 0.1$ nm, $L = 0.2$ to 1 μm, $D = 0$ to 3 nm. From these geometric values specific active-surface roughness values can be calculated for different Pt/C ratios, which agree well with the values determined by cyclic voltammetry.

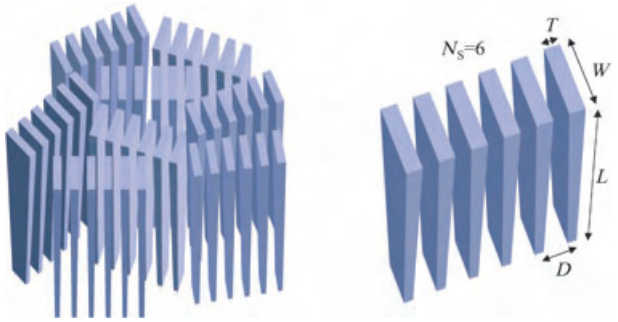

Figure 17. Part of a model columnar structure (left) built up by several arrangements of perfectly aligned columns, each consisting of $N_s = 6$ single columnar structure elements (right). In a real columnar structure, these arrangements are in addition tilted against each other.

4. Carbon Nanoparticles in Electrochemistry

Carbon in its various modifications plays an important role in almost any kind of electrochemical storage device.[76] The good electrical and thermal conductivity, low density, sufficient corrosion resistance, and the relative low activity for electrochemical oxidation or reduction makes carbon an interesting material for passive as well as electroactive components in electrochemical devices. In addition, carbon materials can be produced in a variety of modifications such as powders, fibers, and solid or porous sheets.[76,77] Moreover,

 © 2005 Wiley-VCH Verlag GmbH & Co. KGaA, Weinheim

the cost and availability of carbon is highly advantageous. Consequently, carbon is used in batteries, low-temperature fuel cells, electrochemical capacitors as well as in electrochemical synthesis and electroanalysis.

Carbon is used as the support for noble metals and other electrocatalysts in electrodes for batteries and fuel cells. The diffusion layer in gas-consuming electrodes for metal–air batteries or fuel cells is made from carbon in the form of powder, cloth, or paper. As mentioned in Section 3, carbon may be used as a composite material for the bipolar plate in low-temperature fuel cells. Microstructured bipolar plates were also made from glassy carbon to investigate catalyst utilization in fuel cells. Carbon, typically in the form of graphite powders or graphite fibers, is often used as conductive additive in electrodes for electrochemical devices, such as Leclanché-type cells, to improve MnO_2 cathode performance. The extensive surface area available with carbon electrodes, and the double-layer capacitance of such electrodes, are utilized in commercial electrochemical capacitors.

Furthermore, carbon may also be used as an electroactive electrode material in electrochemical devices. The ability of carbon to intercalate anions as well as cations facilitates the charge-storage process in intercalation batteries. In lithium ion batteries, for example, carbon is used in the form of graphite as the negative electrode that functions as a lithium intercalation host. Last but not least, carbon may be used as an oxygen-reduction catalyst for the electrochemical generation of hydrogen peroxide.

For the above-mentioned applications carbon powders are utilized with particle sizes typically in the micrometer regime. Carbon nanoparticles or nanotubes, however, have not yet found their way into industrial electrochemical energy storage and conversion devices in a major way. On the research level, however, the potential use of carbon nanoparticles or carbon nanotubes in electrochemical devices is being investigated with increasing effort. In particular, the template technique has gained increasing attention in recent years for the preparation of well-defined nanomaterials for electrochemistry.[78]

4.1. Activated Carbons

Activated carbon (AC) is a widely used carbon material in various filter and purification applications where the huge surface area of AC promotes adsorption of various molecules. Close inspection of AC reveals that this high-surface-area carbon can be considered as a nano material. AC consists of a network of nanosize carbon walls separating nanosize pores. Such nanoscale characteristics of activated carbon are often ignored. In recent years template processes were also used to synthesize carbon nanomaterials with a pore structure and surface area resembling those of activated carbons. Such materials have the advantage of a well-defined pore size distribution and the possibility to tailor the structure by tuning process parameters.[79,80]

Recently carbon in the form of high-surface-area activated carbon has evolved into a key material for an electrochemical storage device called electrochemical double-layer capacitor (EDLC).[81] Activated carbons are the material of choice for carbon-based EDLCs using aqueous or non-aqueous electrolytes.

EDLCs, also called supercapacitors or ultracapacitors, store the electric energy in the field of the electrochemical double layer (Helmholtz layer) formed at any interface between an electronically conducting electrode and an ionically conducting electrolyte. The specific capacitance of this double layer is typically in the order of 10–30 $\mu F\,cm^{-2}$ for concentrated electrolytes and good conducting electrodes. The area of the electrochemical interface and thus the overall capacitance can be significantly increased by the use of high-surface-area AC with a typical surface area of 1000–2000 $m^2\,g^{-1}$. Such an electrode would have a capacitance of some 100 $F\,g^{-1}$.

Simple calculation assuming spherical carbon particles shows that such a high gravimetric surface area can only be achieved when the diameter of the carbon spheres is in the order of only a few nm.

The assumption of slit-like pores is a much more realistic picture of the microscopic structure of AC. Based on this rather simple approach it becomes clear that the thickness of carbon particles separating the pores is only 1–3 nm for a material with a gravimetric surface area of 1000 $m^2\,g^{-1}$. The relation between wall thickness and gravimetric surface area (carbon density 2.2 $g\,cm^{-3}$) is shown in Figure 18. For a surface area of 2500 $m^2\,g^{-1}$, which is often claimed for carbons in EDLC electrodes, the carbon walls between pores approach the thickness of one graphene layer only.

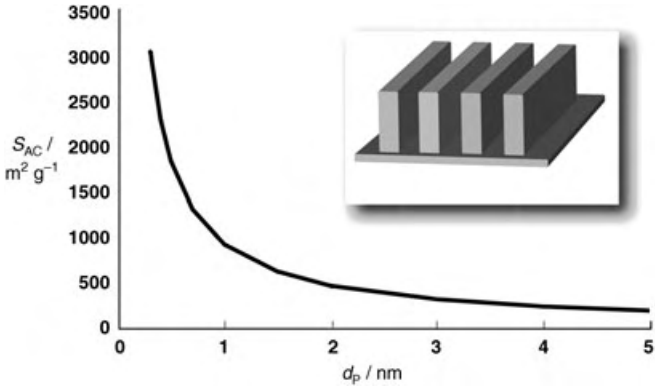

Figure 18. Gravimetric surface area of amorphous carbon S_{AC} with slit-like pores (shown schematically in the inset) as a function of the thickness of the carbon walls d_p separating the pores.

For a industrial application, not only the gravimetric but also the volumetric surface area of the active material is important, and it is clear that a surface area of 1000 $m^2\,cm^{-3}$ requires the diameter of the pores to be also in the range of some nm only.

In a first approximation, the measured capacitance of an EDLC electrode made of AC is expected to be proportional to the surface area of the AC, provided all of the surface area can be accessed by the electrolyte. In an extensive study of more than 40 different types of carbon we have observed (see

 © 2005 Wiley-VCH Verlag GmbH & Co. KGaA, Weinheim

Figure 19), that a linear increase of the capacitance with surface area is valid for surface area smaller than about 1000 $m^2 g^{-1}$. However, the slope obtained for the linear part is about 6 $\mu F cm^{-2}$ instead of the above-mentioned 20–

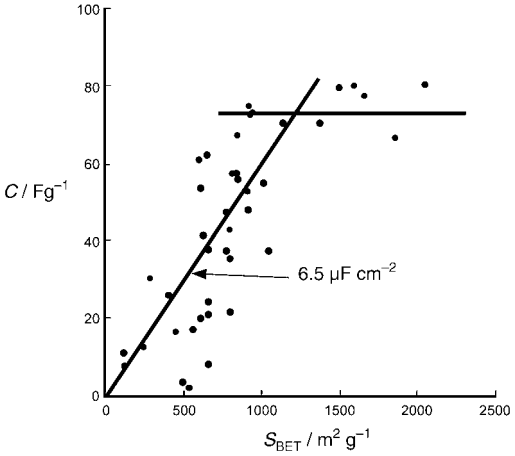

Figure 19. Correlation between the specific surface (S_{BET}) and the gravimetric capacitance C_g for 40 different carbon materials. Capacitance of the carbons was measured at the potential of zero charge.

30 $\mu F cm^{-2}$. For higher surface area the specific capacitance tends to level off.

We have demonstrated that such a decrease of specific capacitance at high surface area may be correlated with a "size effect".[82] Simultaneous in situ measurement of the electrochemical capacitance and electronic conductance of AC with a surface area of 1500 $m^2 g^{-1}$ allows the calculation of the density of states (DOS) in the carbon. It turns out that the DOS is much smaller than for a metal. Therefore, a significant part of the potential drop at the carbon–electrolyte interface occurs within the graphite. The respective screening length (δ_{SC}; Thomas–Fermi length) can be written as Equation (7) where ε is the dielectric constant in the direction normal to the graphene layers, ε_0 is the vacuum permittivity, e_0 is the absolute value of the electronic charge and $D(E_F)$ the density of states at the Fermi level. For activated carbon the screening length can be estimated to 8.5 Å.[82]

$$\delta_{SC} = \sqrt{\frac{\varepsilon\varepsilon_0}{e_0^2 D(E_F)}} \tag{7}$$

As a consequence, the interface capacitance is significantly smaller than expected from the capacitance of the Helmholtz layer. For a carbon particle with a thickness under 2 nm separating two pores and a screening length in the order of 1 nm the available volume is too small for a complete screening of the charges accumulated at the surface. This situation is illustrated in Figure 20 and results in capacitance limitations for very-high-surface-area carbons in electrochemical double-layer capacitors. This effect may at least in part explain the leveling off of the curve plotted in Figure 19.

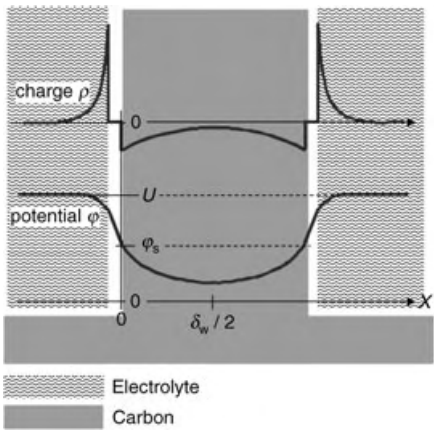

Figure 20. Sketch of charge and potential distribution across the pore wall (gray) and the adjacent solution phase inside the pores.

4.2. Hard or Glassy Carbon

Glassy-carbon (GC) electrodes are applied in electroanalytic chemistry and often replace mercury electrodes in electroanalytical studies. GC, also called hard carbon, has also been investigated as electrode material for supercapacitors and lithium ion batteries. GC is made from polymeric precursors, particularly from phenolic resins, by pyrolysis at temperatures above 800 °C.[83] GC is rather inert against chemical corrosion and impermeable to gases. Nevertheless its structure is porous, as shown by the low density of about 1.4 $g cm^{-3}$ to 1.53 $g cm^{-3}$, depending on the pyrolysis temperature. The dimensions of the closed pores can be determined by small-angle X-ray scattering (SAXS), and it was found that the diameter is about 1 nm only.[84] The pores at the surface of GC can be opened by a chemical or electrochemical[85] oxidation process (Figure 21) to form a surface layer with a thickness of several micrometers having an internal surface area of more than 1000 $m^2 cm^{-3}$.[84,86]

The formation process of this surface layer and its utilization for EDLC applications was extensively investigated at our institute. A growth model for the porous surface film was established assuming two moving reaction fronts; one arising from the shrinking unreacted core, and one from

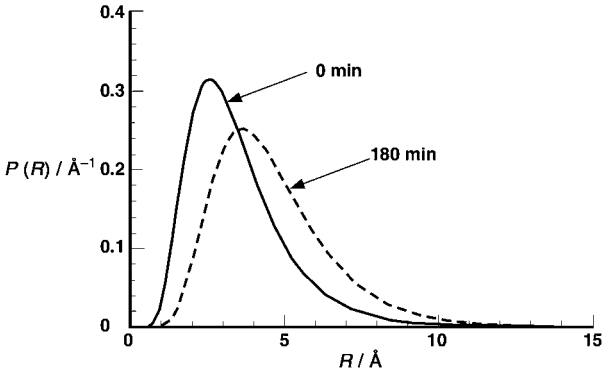

Figure 21. Pore radius distribution for non-activated glassy carbon (0 min), and for glassy carbon activated for 180 min. Adapted from ref. [80].

 © 2005 Wiley-VCH Verlag GmbH & Co. KGaA, Weinheim

the changing thickness of the samples as a result of combustion.[86] In good agreement with experiments the model showed that the film saturation thickness depends on the reaction temperature as well as on sample structure.

The increase in pore diameter and the simultaneous decrease in surface area during film formation could be explained with the so-called falling-cards model.[87] In this model, the porous material is envisaged as a "house" of graphene platelets ("cards") with nanometer dimensions and a thickness of a few graphene layers only. Chemical or electrochemical attack results in burning off and collapse of some of the carbon structures, resulting in pore opening and widening. Although the total surface area is reduced during this process, an increase in electrochemical capacitance of the activated GC is observed (Figure 22). This effect could be explained by improved electrolyte access to the surface through the wider pores.

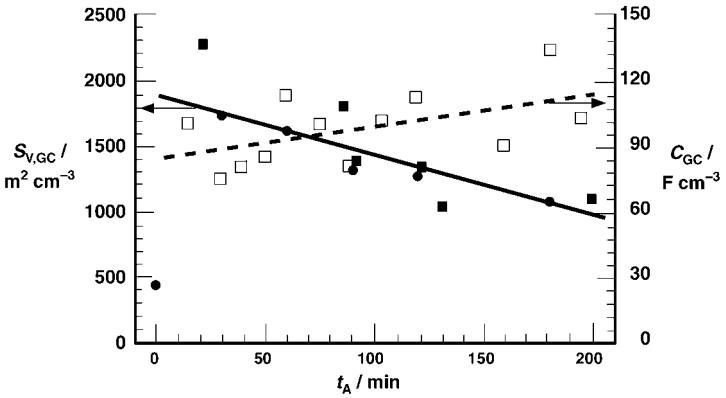

Figure 22. Volumetric surface area of activated GC, as measured with BET gas adsorption (●) and SAXS (■) and volumetric capacitance of activated GC (□) versus activation time t_A. The straight solid line denotes the average of both BET and SAXS measurements, and the dashed line is the average fit to the capacitance data. Adapted from ref. [80].

We also investigated GC as an electrode material for lithium ion batteries.[88] The advantage of GC is a relatively high charge capacitance of above 372 Ah kg^{-1}, which is the theoretical limit for the formation of LiC_6. It turned out, however, that irreversible losses during the first charging cycle are too high compared to other available materials. The losses are caused by Li trapping in the nanopores of the GC in addition to the electrolyte decomposition.

4.3. Graphites

Graphites are used in the classical alkaline battery as additive in the cathode mix for the MnO_2 electrode. More recently graphite turned out to be one of the key materials for the negative electrode in lithium ion batteries. The crystallite size of typical graphites utilized for lithium ion batteries depends on the graphitization temperature and ranges from about 10 nm to several hundred nm. These crystals agglomerate into graphite particles with a size of several micrometers.

In general it can be stated that nanoparticles for lithium ion batteries have the advantage of fast lithium diffusion kinetics within the host. On the other hand, as a result of the huge surface area, irreversible losses become rather considerable. The correlation between particle size and lithium ion battery performance was extensively studied for graphites.[89] It was demonstrated that there is a linear relation between surface area and irreversible capacitance of the battery (Figure 23). In agreement with the above argument, the

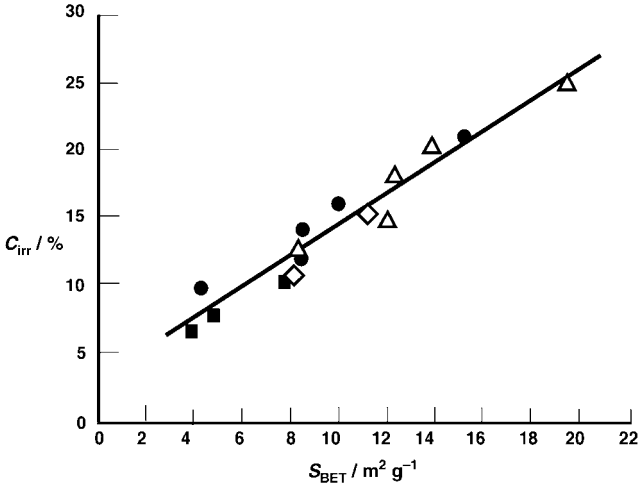

Figure 23. Irreversible capacitance C_{irr} of the first electrochemical Li^+ ion intercalation into different synthetic and natural TIMREX graphites (indicated by the different symbols) as a function of the specific surface area measured at 10 mAg^{-1} in 1 M $LiPF_6$ ethylene carbonate:dimethyl carbonate (1:1) electrolyte. Adapted from ref. [85].

irreversible losses during formation of the protective surface layer on the negative electrode are larger for smaller particles, that is, for higher surface area. A comprehensive overview of graphite and other intercalation materials for rechargeable lithium batteries is given in ref. [90]

According to the simple model calculation mentioned in the context of Figure 18, the particle sizes corresponding to BET surface areas between 4 m^{2}g^{-1} and 20 m^{2}g^{-1}, are between 300 nm and 50 nm, respectively. Consequently, the graphite particles for lithium ion intercalation should be small to facilitate fast intercalation kinetics, but not too small to prevent extensive irreversible losses owing to electrolyte decomposition.

Graphite exfoliation is another undesired process, which may occur for certain electrolytes and lowers the battery performance. The group of Novak in our institute has shown[91,92] that the texture of the graphite and its surface chemistry significantly effect the exfoliation process. In case of a low surface reactivity the formation of the protective surface layer on the negative electrode in the lithium ion battery may be too slow compared to the intercalation process. As a consequence solvent intercalation and decomposition may occur during the first charging cycle resulting in exfoliation.

 © 2005 Wiley-VCH Verlag GmbH & Co. KGaA, Weinheim

4.4. Nanotubes

About six years after the first observation of carbon nanotubes (CNT) by Iijima, carbon nanotubes were considered for electrochemical double-layer capacitors by Niu et al.[93] in 1997.. The surface area of the CNT electrodes was only between 250 and 430 $m^2 g^{-1}$. However, it was demonstrated, that almost all of the available surface area of CNT could be used for double-layer capacitance. Thus a rather high value for the gravimetric capacitance of 117 $F g^{-1}$ resulted in aqueous electrolyte. Interest in CNT has increased since then, but a significant breakthrough with respect to the application of CNT in real devices has not occurred.

In a recent study[94] the performance of CNT electrodes and electrodes based on activated carbons (ACs) were compared. In an electrochemical double-layer capacitor with organic electrolyte the gravimetric capacitances of CNT and AC were comparable (about 70 $F g^{-1}$) while the volumetric capacitance of the CNT was significantly lower than that of the AC electrode with a comparable gravimetric surface area of around 1000 $m^2 g^{-1}$.

Promising results for EDLC electrodes were obtained recently with CNTs deposited directly on aluminum foils.[95] Surprisingly, the CNTs form brushlike bundles and stand upright on the metal support (Figure 24).

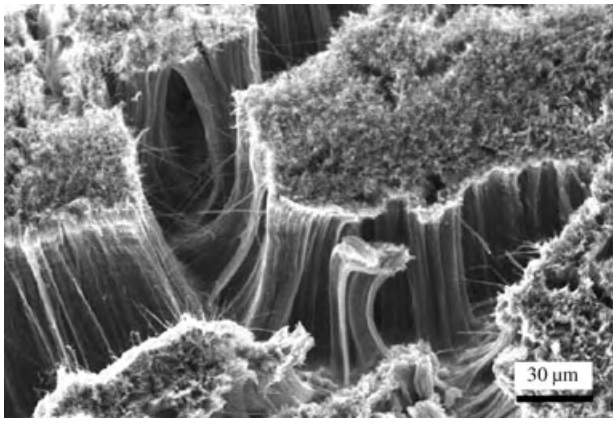

Figure 24. SEM picture of carbon nanotubes directly deposited on an aluminum substrate. Adapted from C. Emmenegger, P. Mauron, A. Züttel, University of Fribourg, Switzerland (unpublished).

We found that CNTs have a similar potential dependence of the double-layer capacitance as AC electrodes, however, the specific double-layer capacitance is only about 3 $\mu F cm^{-2}$, which is about half of the capacitance determined for AC.[82] Thus, the relative low specific double-layer capacitance may counteract the advantages of CNT for EDLC applications.

Composite materials from CNTs and ABO_3 type perovskites were produced by a catalytic hydrocarbon dissociation reaction for application in Zn–air batteries.[96] In this application the perovskite serves as the electrocatalyst for oxygen-reduction and the CNT as a stable support. Gas-diffusion electrodes made from this material exhibit a performance comparable to electrodes made from the same perovskite supported on conventional carbon.

CNTs were also investigated for use in lithium ion batteries. CNTs had a charge capacity larger than graphite because, owing to the special geometry of the CNT, more than one Li^+ ion per six carbon ions could be intercalated. Unfortunately, as mentioned above in the context of graphite, the large surface area responsible for the good capacitance resulted again in very high irreversible losses.

5. Conclusions and Outlook

The examples presented herein demonstrate convincingly that particles and structures in the size range of 2–10 nm are particularly attractive for applications in energy technologies. Access to these nanometer-sized structures has been opened by a variety of chemical and physical preparation techniques. The advantages of nanoparticles reside, among other factors, in their high specific surface area, high dispersion of the active component, as well as the presence of specific energetic surface sites.

For the example of copper particles supported on ZnO, we have seen that smaller particles are better stabilized against surface oxidation and overlayer formation, thanks to their more intense interaction with the ZnO support.

It is also evident that decreasing the size below a few nanometers must not always be beneficial for the envisaged application because:

- the electronic properties of metallic particles change as the particle size becomes less than approximately 2 nm
- electronic repulsion within the particle limits the maximum available surface charge
- pores with diameters of less than approximately 2 nm (micropores) are generally considered to be inaccessible to reactants in catalysis
- small particles become reactive themselves towards reagents such as oxygen
- nanoparticles are often unstable against sintering or dissolution.

Even single-wall carbon nanotubes, which have recently attracted much attention in search for convincing applications, exhibit a typical diameter of approximately 2 nm. Whereas these observations appear to suggest that the chemist's nanoworld starts at 2 nm, recent advances in preparation methods may pave the way towards even smaller entities. Examples of the new methods include template-directed syntheses, the formation of whiskers, or of particle substructures at the one-nanometer scale. However new problems are also encountered in working with objects on this scale, for example, let us mention the effort of synthesizing catalyst particles that consist of a base-metal core, covered by only one or two atomic layers of a noble metal, such as platinum. One prerequisite for their entry into applications might be the need for advanced methods of characterization: single-nanometer-sized objects appear amorphous to many spectroscopic techniques, and they are difficult to image with transmission electron microscopy. Even for techniques with

 © 2005 Wiley-VCH Verlag GmbH & Co. KGaA, Weinheim

atomic resolution, such as AFM or STM, the nanometer particle needs to be found first before it can be imaged.

Received: April 27, 2004

[1] A. Logadottir, R. C. Egeberg, J. H. Larsen, I. Chorkendorff, E. Törnqvist, J. K. Nørskov, *Phys. Rev. Lett.* **1999**, *8*, 1814.
[2] C. R. Henry, *Surf. Sci. Rep.* **1998**, *31*, 231.
[3] M. Boudart in *Handbook of Heterogeneous Catalysis*, *Vol. 1* (Eds.: G. Ertl, H. Knözinger, J. Weitkamp), Wiley-VCH, Weinheim, **1997**, p. 1.
[4] G. A. Somorjai, *Introduction to Surface Chemistry and Catalysis*, Wiley, New York, **1994**.
[5] M. Boudart, G. Djéga-Mariadassou, *Kinetics of Heterogeneous Catalytic Reactions*, Princeton University Press, Princeton, **1984**, p. 156.
[6] D. R. Huntley, S. L. Jordan, F. A. Grimm, *J. Phys. Chem.* **1992**, *96*, 1409.
[7] G. A. Martin, J. A. Delmon, *J. Catal.* **1982**, *75*, 233.
[8] G. T. Went, L.-J. Leu, R. R. Rosin, A. T. Bell, *J. Catal.* **1992**, *134*, 492.
[9] *Handbook of Heterogeneous Catalysis* (Eds.: G. Ertl, H. Knözinger, J. Weitkamp), Wiley-VCH, Weinheim, **1997**.
[10] V. de Gouveia, B. Bellamy, Y. Hadj Romdhane, A. Masson, *Z. Phys. D* **1989**, *12*, 587.
[11] A. Sandell, J. Libuda, P. Brühwiler, S. Andersson, A. Maxwell, M. Bäumer, N. Mårtensson, H.-J. Freund, *J. Electron Spectrosc. Relat. Phenom.* **1995**, *76*, 301.
[12] B. Hammer, J. K. Nørskov, *Adv. Catal.* **2000**, *45*, 71.
[13] H. Poppa, *Vacuum* **1984**, *34*, 1081.
[14] D. R. Rainer, S. M. Vesecky, M. Koranne, W. S. Oh, D. W. Goodman, *J. Catal.* **1997**, *167*, 234.
[15] D. R. Rainer, C. Xu, D. W. Goodman, *J. Mol. Catal. A* **1997**, *119*, 307.
[16] M. Bäumer, H.-J. Freund, *Prog. Surf. Sci.* **1999**, *61*, 127.
[17] G. Busca, L. Lietti, G. Ramis, F. Berti, *Appl. Catal. B* **1998**, *18*, 1.
[18] K. Chen, A. T. Bell, E. Iglesias, *J. Catal.* **2002**, *209*, 35.
[19] R. S. Weber, *J. Catal.* **1995**, *151*, 470.
[20] G. Ramis, G. Busca, F. Bregani, P. Forzatti, *Appl. Catal.* **1990**, *64*, 259.
[21] M. Koebel, G. Madia, F. Raimondi, A. Wokaun, *J. Catal.* **2002**, *209*, 159.
[22] G. Madia, M. Elsener, M. Koebel, F. Raimondi, A. Wokaun, *Appl. Catal. B* **2002** *39*, 181.
[23] "The Biofuels Directive: Potential for Climate Protection?": *Proceedings of the 3rd Autumn Conference of the European Climate Forum*, Norwich, September 2003, www.european-climate-forum.net.
[24] F. M. Kessler, N. Knechtle, R. Frischknecht, *Heizenergie aus Heizöl, Erdgas oder Holz?*, Bundesamt für Umwelt, Wald und Landschaft, Bern, **2002**.
[25] a) M. Mozzafarian, R. W. R. Zwart, *Feasibility of Biomass/Waste-Related SNG Production Technologies*, Report ECN-CX-02-119, Energy Research Center of the Netherlands, **2003**; b) S. Biollaz, S. Stucki in *PSI Scientific Report 2003*, *Vol. V*, **2004**, S. 22.
[26] K. Coulter, X. P. Xu, D. W. Goodman, *J. Phys. Chem.* **1994**, *98*, 1245.
[27] S. D. Bischke, D. W. Goodman, *Surf. Sci.* **1985**, *150*, 351.
[28] U. Heiz, *Appl. Phys. A* **1998**, *67*, 621.
[29] I. Alstrup, *J. Catal.* **1995**, *151*, 216.
[30] H. S. Bengaard, J. K. Nørskov, J. Sehested, B. S. Clausen, L. P. Nielsen, A. M. Molenbroek, J. R. Rostrup-Nielsen, *J. Catal.* **2002**, *209*, 365.
[31] T. Borowiecki, *Appl. Catal.* **1982**, *4*, 223.
[32] M. Agnelli, M. Kolb, C. Mirodatos, *J. Catal.* **1994**, *148*, 9.
[33] G. Martra, H. M. Swaan, C. Mirodatos, M. Kermarec, C. Louis in *Catalyst Deactivation 1997* (Eds.: C. H. Bartholomew, G. A. Fuentes), Elsevier, Amsterdam, **1997**, p. 617.
[34] M. Agnelli, C. Mirodatos, *J. Catal.* **2000**, *192*, 204.
[35] M. Valden, X. Lai, D. W. Goodman, *Science* **1998**, *281*, 1647.
[36] T. J. Huang, S. W. Wang, *Appl. Catal.* **1986**, *24*, 28.
[37] F. Raimondi, K. Geissler, J. Wambach, A. Wokaun, *Appl. Surf. Sci.* **2002**, *189*, 59.
[38] T. Reitz, M. Ahmed, R. Kumar, H. Kung, *Stud. Surf. Sci. Catal.* **2000**, *130*, 3645.
[39] L. Alejo, R. Lago, M. A. Peña, J. L. G. Fierro, *Appl. Catal. A* **1997**, *162*, 281.
[40] F. Raimondi, B. Schnyder, R. Kötz, R. Schelldorfer, T. Jung, J. Wambach, A. Wokaun, *Surf. Sci.* **2003**, *532–535*, 383.
[41] F. Raimondi, J. Wambach, A. Wokaun, *Phys. Chem. Chem. Phys.* **2003**, *5*, 4015.
[42] S. V. Didziulis, K. D. Butcher, S. L. Cohen, E. I. Solomon, *J. Am. Chem. Soc.* **1989**, *111*, 7110.
[43] F. Raimondi, Ph.D. Thesis No. 14963, Swiss Federal Institute of Technology, Zürich, **2003**.
[44] D. A. Landsman, F. J. Luczak in *Handbook of Fuel Cells*, *Vol. 4* (Eds.: W. Vielstich, H. A. Gasteiger, A. Lamm), Wiley, New York, **2003**, p. 821.
[45] G. G. Scherer, *Solid State Ionics* **1997**, *94*, 249.
[46] H. R. Kunz, G. A. Grover, *J. Electrochem. Soc.* **1975**, *122*, 1279.
[47] H. G. Petrow, R. J. Allen, US Patent 3.992.331, US Patent 3.992.512.
[48] P. Stonehart, *Ber. Bunsenges. Phys. Chem.* **1990**, *94*, 913.
[49] V. M. Jalan, US Patent 4.202.934.
[50] N. M. Markovic, P. N. Ross, *Electrochim. Acta* **2000**, *45*, 4101.
[51] U. A. Paulus, G. G. Scherer, A. Wokaun, T. J. Schmidt, V. Stamenkovic, V. Radmilovic, N. M. Markovic, P. N. Ross, *J. Phys. Chem. B* **2002**, *106*, 4181.
[52] U. A. Paulus, A. Wokaun, G. G. Scherer, T. J. Schmidt, V. Stamenkovic, N. M. Markovic, P. N. Ross, *Electrochim. Acta* **2002**, *47*, 3787.
[53] T. J. Schmidt, Diploma Thesis, Universität Ulm, **1996**.
[54] U. A. Paulus, Ph.D. Thesis No. 14795, Swiss Federal Institute of Technology, Zürich, **2002**.
[55] S. Mukerjee, S. Srinivasan, M. P. Soriaga, J. McBreen, *J. Electrochem. Soc.* **1995**, *142*, 1409.
[56] N. M. Markovic, P. N. Ross, CATTECH **2000**, *4*, 2; N. M. Markovic, P. N. Ross, *Electrochim. Acta* **2000**, *45*, 4101.
[57] C. Roth, N. Martz, F. Hahn, J.-M. Leger, C. Lamy, H. Fuess, *J. Electrochem. Soc.* **2002**, *149*, 433.
[58] F. Hajbolouri, Ph.D. Thesis, Swiss Federal Institute of Technology Zürich, **2004**.
[59] F. Hajbolouri, B. Andreaus, G. G. Scherer, A. Wokaun in *2003 Fuel Cell Seminar*, *Extended Abstracts*, November 3–7, Miami Beach, Florida, **2003**, p. 53.
[60] F. Hajbolouri, B. Andreaus, G. G. Scherer, A. Wokaun, *Fuel Cells* **2004**, *4*, 160.
[61] B. Andreaus, Ph.D. Thesis No. 2598, Swiss Federal Institute of Technology Lausanne, **2002**.
[62] H. Bönnemann, R. Richards in *Synthetic Methods of Organometallic and Inorganic Chemistry*, *Vol. 10* (Eds.: W. A. Herrmann, G. Brauer), Thieme, Stuttgart, **2002**, p. 209.
[63] H. Bönnemann, R. Brinkmann, P. Britz, U. Endruschat, R. Mörtel, U. A. Paulus, G. J. Feldmeyer, T. J. Schmidt, H. A. Gasteiger, R. J. Behm, *J. New Mater. Electrochem. Sys.* **2000**, *3*, 199.
[64] Z. Jusys, T. J. Schmidt, L. Dubau, K. Lasch, L. Jörissen, J. Garche, R. J. Behm, *J. Power Sources*, **2002**, *105*, 297.
[65] T. Yoshitake, Y. Shimakawa, S. Kuroshima, H. Kimura, T. Ichihashi, Y. Kubo, D. Kasuya, K. Takahashi, F. Kokai, M. Yudasaka, S. Iijima, *Phys. B* **2002**, *323*, 124.

 © 2005 Wiley-VCH Verlag GmbH & Co. KGaA, Weinheim

[66] S. Srinivasan, E. A. Ticianelli, C. R. Derouin, A. Redondo, *J. Power Sources* **1988**, *22*, 359.
[67] I. D. Raistrick, US Patent 4.876.115.
[68] M. S. Wilson, US Patent 5.234.777.
[69] U. A. Paulus, Z. Veziridis, B. Schnyder, M. Kuhnke, G. G. Scherer, A. Wokaun, *J. Electroanal. Chem.* **2003**, *541*, 77.
[70] M. Kuhnke, T. Lippert, E. Ortelli, G. G. Scherer, A. Wokaun, *Thin Solid Films* **2004**, *453–454*, 36.
[71] M. K. Debe in *Handbook of Fuel Cells*, *Vol. 3* (Eds.: W. Vielstich, H. A. Gasteiger, A. Lamm), Wiley, New York, **2003**, p. 576.
[72] Paul Scherrer Institut, patent applied.
[73] L. Gubler, Ph.D. Thesis No. 13954, Swiss Federal Institute of Technology Zürich, **2001**.
[74] F. Hajbolouri, G. G. Scherer, A. Wokaun, unpublished results.
[75] T. Vad, F. Hajbolouri, H. G. Haubold, G. G. Scherer, A. Wokaun, *J. Phys. Chem. B.* **2004**, 108, 12442.
[76] K. Kinoshita, *Carbon. Electrochemical and Physicochemical Properties*, Wiley, New York, **1988**.
[77] "Supercarbon: Synthesis, Properties and Applications": *Springer Ser. Mater. Sci.* **1998**, *33*, 1.
[78] C. R. Martin, D. T. Mitchell, *Electroanal. Chem.* **1999**, *21*, 1.
[79] A. B. Fuertes, D. M. Nevskaia, *Microporous Mesoporous Mater.* **2003**, *62*, 177.
[80] A. B. Fuertes, F. Pico, J. M. Rojo, *J. Power Sources* **2004**, *133*, 329.
[81] R. Kötz, M. Carlen, *Electrochim. Acta* **2000**, *45*, 2483.
[82] M. Hahn, M. Bärtschi, O. Barbieri, J.-C. Sauter, R. Kötz, R. Gallay, *Electrochem. Solid-State Lett.* **2004**, *7*, A33.
[83] G. M. Jenkins, K. Kawamura, *Polymeric Carbons – Carbon Fibre, Glass and Char*, 1st ed., Cambridge University Press, Cambridge, **1976**.
[84] A. Braun, M. Bärtsch, B. Schnyder, R. Kötz, O. Haas, H.-G. Haubold, G. Goerigk, *J. Non-Cryst. Solids* **1999**, *260*, 1.
[85] M. G. Sullivan, B. Schnyder, M. Bärtsch, D. Alliata, C. Barbero, R. Imhof, R. Kötz, *J. Electrochem. Soc.* **2000**, *147*, 2636.
[86] A. Braun, M. Bärtsch, B. Schnyder, R. Kötz, *Chem. Eng. Sci.* **2000**, *55*, 5273.
[87] W. Xing, J. S. Xue, T. Zheng, A. Gibaud, J. R. Dahn, *J. Electrochem. Soc.* **1996**, *143*, 3482.
[88] M. C. Bärtsch, P. Novak in *PSI Scientific Report 2003*, *Vol. V*, **2004**, p. 79.
[89] F. Joho, B. Rykhart, A. Blome, P. Novák, H. Wilhelm, M. E. Spahr, *J. Power Sources* **2001**, *97–98*, 78.
[90] M. Winter, J. O. Besenhard, M. E. Spahr, P. Novak, *Adv. Mater.* **1998**, *10*, 725.
[91] M. E. Spahr, H. Wilhelm, T. Palladino, N. Dupont-Pavlovsky, D. Goers, F. Joho, P. Novák, *J. Power Sources* **2003**, *119–121*, 543.
[92] H. Buqa, D. Goers, M. E. Spahr, P. Novák, *J. Solid State Electrochem.* **2003**, *8*, 79.
[93] C. Niu, E. K. Sichel, R. Hoch, D. Moy, H. Tennent, *Appl. Phys. Lett.* **1997**, *70*, 1480.
[94] C. Emmenegger, P. Mauron, P. Sudan, P. Wenger, V. Hermann, R. Gallay, A. Züttel, *J. Power Sources* **2003**, *124*, 321.
[95] C. Emmenegger, J.-M. Bonard, P. Mauron, P. Sudan, A. Lepora, B. Grobety, A. Züttel, L. Schlapbach, *Carbon* **2003**, *41*, 539.
[96] A. Weidenkaff, S. G. Ebbinghaus, T. Lippert, *Chem. Mater.* **2002**, *14*, 1797.

 © 2005 Wiley-VCH Verlag GmbH & Co. KGaA, Weinheim

Communications

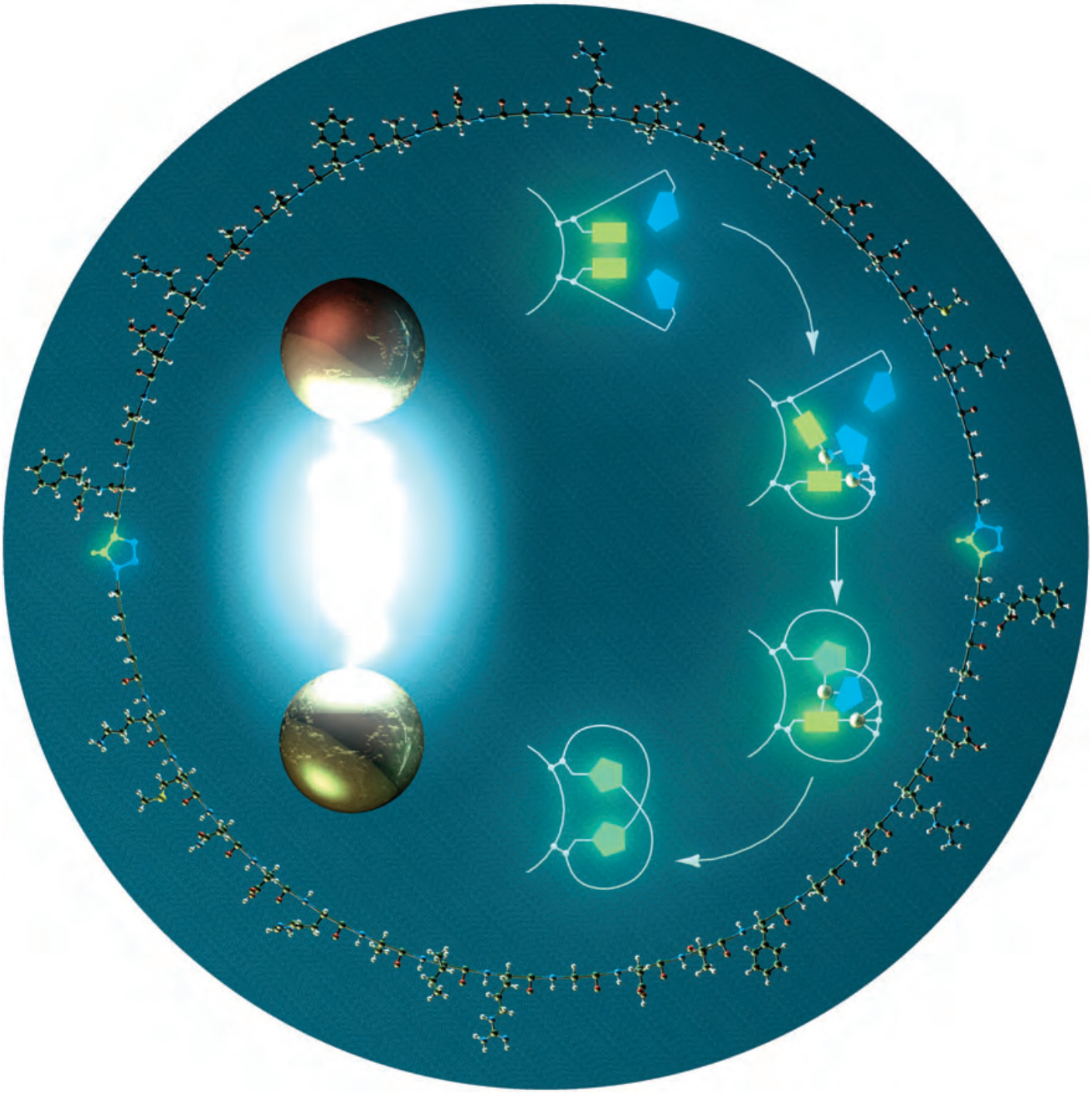

Two copper centers acting in concert are required for azide–alkyne cycloaddition at high rates. When applied to solid-phase oligopeptides bearing azide and alkyne units at opposite ends of each chain, dimeric cyclic structures of unprecedented ring size are produced selectively. For more information, see the Communications by M. G. Finn and co-workers on the following pages.

 © 2005 Wiley-VCH Verlag GmbH & Co. KGaA, Weinheim DOI: 10.1002/anie.200461496

Azide–Alkyne Cycloadditions

Mechanism of the Ligand-Free Cu^{I}-Catalyzed Azide–Alkyne Cycloaddition Reaction**

Valentin O. Rodionov, Valery V. Fokin, and M. G. Finn**

The 1,3-dipolar cycloaddition of azides and alkynes[1] is an effective way to make connections between structures that bear a wide variety of functional groups.[2] The process is strongly favored in thermodynamic terms, yet both azide and alkyne units are highly selective in their reactivity; they are inert to most chemical functionalities and are stable in wide ranges of solvents, temperatures, and pH values. The discovery of copper(I) catalysis of this process[3] has opened a myriad of applications in bioconjugation,[4] organic synthesis,[5] materials and surface science,[6] and combinatorial chemistry.[7] Herein we report the results of the first experimental investigation of the mechanism of the fundamental reaction catalyzed by copper(I) species generated in situ from copper(II) and ascorbate.[8] This "ligand-free" process, which lacks the heterocyclic chelates that have been found to accelerate the reaction,[9] has been used in many situations and represents a good starting target for mechanistic study.

Pseudo-first-order (initial rate) kinetics experiments were performed on the reaction of benzyl azide (**1**) and phenylacetylene (**2**). Aliquots taken at intervals from the reactions by an automated liquid handler under inert atmosphere were quenched with H_2O_2. Quantitative LC–MS analysis of the resulting samples (Agilent Zorbax C18 column, MS detection in single-ion mode) allowed the collection of reliable kinetic data for reactions with concentrations of organic starting materials ranging from 0.4 to 100 mM. Examples of the data are shown in Figure 1, and the results are summarized in Table 1.[10]

Under conditions of excess Cu^{I} (Table 1, entries 1, 4, 7), the experimental rate law was:

$$\text{rate} = k[\text{alkyne}]^{1.3\pm0.2}[\text{azide}]^{1\pm0.2}[\text{Cu}]^{0}.$$

With catalytic Cu^{I} under saturating conditions (Table 1, entries 2, 3, 5, 9; rate independent of [alkyne]), the reaction was second order in metal. A small amount of deuterated triazole product [D_7]**3**, prepared from perdeuterobenzyl azide, was added as an internal standard in some cases. The presence or absence of [D_7]**3** made no difference in the observed rate law, except in the cases of catalytic copper. In the absence of supplemental triazole, the reaction rate increased more slowly than expected with increasing [Cu] (Figure 1c), suggesting that less-reactive species—presumably higher aggregates—accumulate at higher metal concentrations. The addition of 30 μM [D_7]**3** prevents this phenomenon, which permits the observation of a clean second-order dependence on [Cu] (Figure 1b). Benzyl azide was found to be slightly inhibitory when present in large excess over copper (Figure 1d–f and Table 1, entry 6), which reveals the presence of an unproductive Cu–azide association.

Table 1: Observed rate orders in the variable component derived from kinetics measurements.[a]

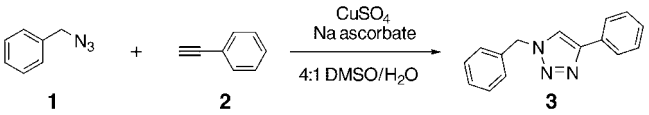

1 + **2** → **3**

Entry	Component[b]	[PhC≡CH] [mM]	[BnN_3] [mM]	[Cu] [mM]	Rate order
1	PhC≡CH[c]	0.4–1.0	0.04	10	1.3 ± 0.2
2	PhC≡CH	1–2.5	100	5	0
3	PhC≡CH[c]	10–25	1	0.1	0
4	BnN_3[c]	0.04	0.4–1	10	1.0 ± 0.2
5	BnN_3	1	1–25	10	0
6	BnN_3[c]	1	1–25	0.1	-0.25 ± 0.1
7	Cu	1	1	1–10	0.1 ± 0.1
8	Cu	10	10	0.5–2	0.6 ± 0.2
9	Cu[c]	0.4	0.4	0.04–0.16	2.0 ± 0.1

[a] Reactions were performed at 20 ± 2°C in DMSO/H_2O (4:1), [Na ascorbate] = 20 or 40 mM. Addition of organic reagents did not change the pH value of the solution. [b] Reaction component with varied initial concentration. [c] Performed with the addition of [D_7]**3** as internal standard.

The kinetics results are consistent with a stepwise mechanism that involves a dynamically exchanging family of Cu–acetylide complexes.[11] We propose the broad outline shown in Scheme 1. In the presence of excess copper, no catalyst turnover is required and all of the organic components are engaged with the metal, making the reaction zero order in Cu^{I}. Under these conditions, the reaction was found to be first order in azide, and between first and second order in alkyne. We have not yet determined if two pathways are operative (requiring one and two alkynes, respectively) or if the preferred catalytic mechanism involves two alkynes but is inhibited by excess alkyne, giving rise to the intermediate observed rate order. (While σ-acetylide–Cu complexes are shown in Scheme 1 and are proposed to be the active form,[12] π complexes of alkynes may also play a role. Commercially available copper acetylides have so far proven to be ineffective in this reaction.)

It is envisioned that azide is activated by the appropriate Cu–acetylide; compound **4** represents one of many possible structures consistent with density functional theory calculations performed earlier.[12] Formation of the resulting Cu–C bond-containing (triazole) species is then followed by proteolysis of the Cu–C bond to regenerate the catalyst.[13] When the amount of azide and alkyne was increased to stoichiometric levels with respect to metal (Table 1, entry 5), the rate

[*] V. O. Rodionov, Prof. V. V. Fokin, Prof. M. G. Finn
Department of Chemistry
The Scripps Research Institute
10550 N. Torrey Pines Rd., La Jolla, CA 92037 (USA)
Fax: (+1) 858-784-8850
E-mail: fokin@scripps.edu
mgfinn@scripps.edu

[**] We thank the Skaggs Institute for Chemical Biology for support of this work.

Supporting information for this article is available on the WWW under http://www.angewandte.org or from the author.

 © 2005 Wiley-VCH Verlag GmbH & Co. KGaA, Weinheim

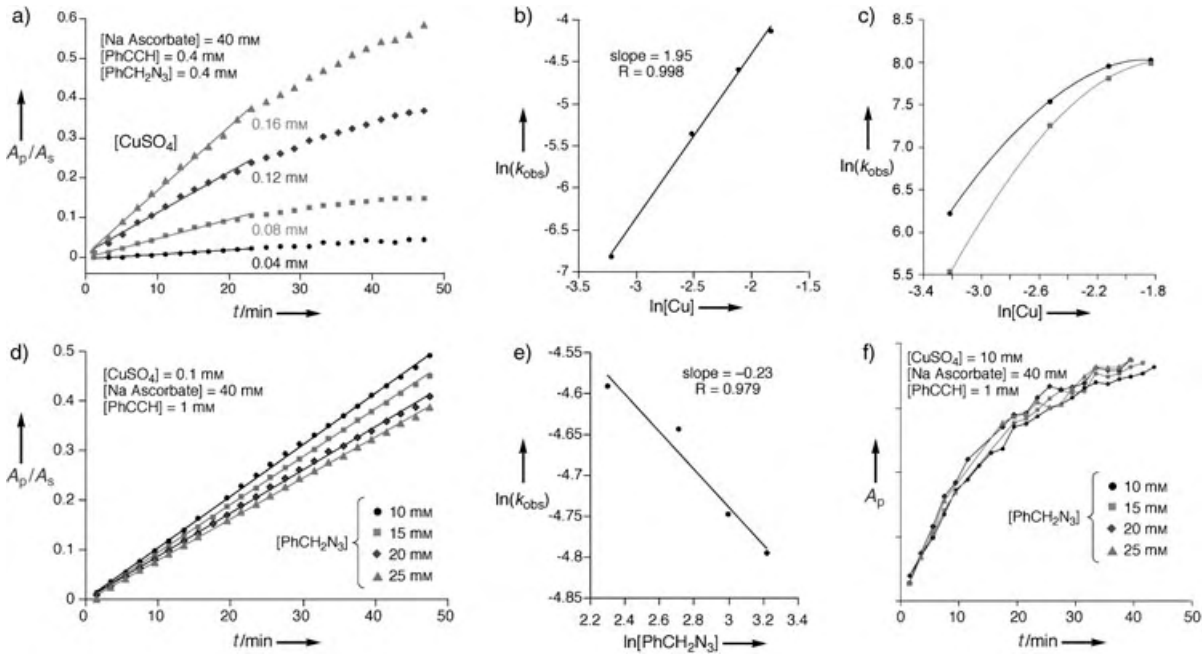

Figure 1. Examples of initial-rate kinetics measurements: a) data and b) rate-order plots showing second-order dependence on [Cu] under catalytic conditions; c) analogous to b), except that the two sets of reactions shown were performed without the deuterated product as internal standard; d) data and e) rate-order plots showing the inhibitory effect of large amounts of azide under catalytic conditions; f) data showing zero-order dependence on azide under noncatalytic conditions. A_P/A_S = peak area ratio of product/standard; A_P = peak area of product determined by single-ion mode LC–MS.

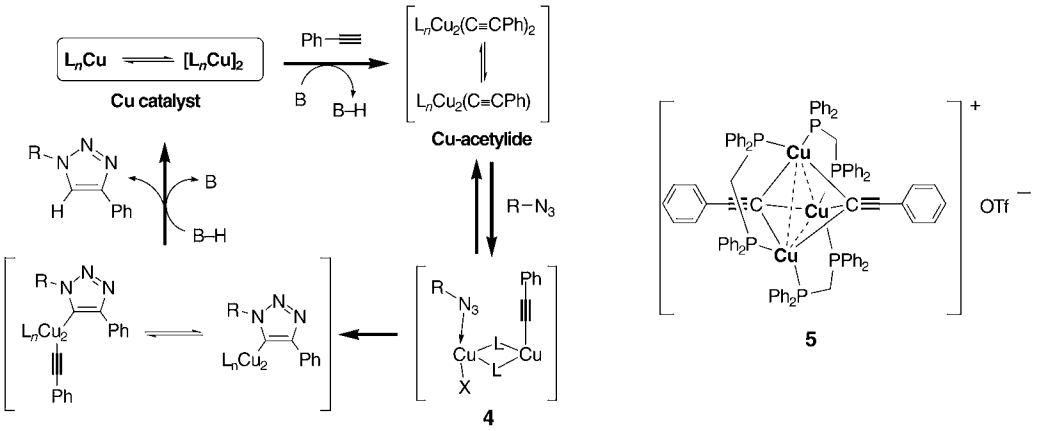

Scheme 1. Outline of species involved in the copper catalytic cycle, and the known trinuclear Cu–acetylide complex **5**.

order in azide was zero, consistent with an increase in the rate of capture by azide and a concomitant change in the rate-determining step to the formation of activated acetylide.

Under catalytic conditions at saturating levels (rates independent of [azide] and [alkyne]), the reaction was second order in copper,[13] consistent with parallel observations for a highly active Cu–phenanthroline catalyst.[9b] There are several possible explanations; perhaps the simplest is the activation of azide and alkyne by different metal centers as suggested in **4**. However, multinuclear Cu–acetylide species are common. One example, the known[14] phenylacetylide cation $[Cu_3(\mu_3\text{-}\eta^1\text{-}C{\equiv}CPh)_2(\mu\text{-dppm})_3]^+$ (**5**, prepared as the triflate salt, Scheme 1), was found to react with excess benzyl azide at room temperature to give clean **3** in 50% yield with respect to total alkyne. *p*-Tolylacetylene was also incorporated into its respective 1,4-disubstituted triazole, but catalytic activity (>100% yield with respect to Cu) was not observed. The reactivities of other model Cu–acetylide complexes are currently being explored to test various mechanistic hypotheses. The details of the interaction of organic azide with monomeric Cu–acetylide have been explored by computational methods.[12]

Further insight was gained by examination of the reactivities of diazides and dialkynes (Scheme 2). Compound **6** provided ditriazole **8** as the major product, even when 10 equivalents of diazide over alkyne were used, whereas the analogous dialkyne **9** gave statistically expected quantities of **10** and **11**. Of the six additional diazides shown in

 © 2005 Wiley-VCH Verlag GmbH & Co. KGaA, Weinheim

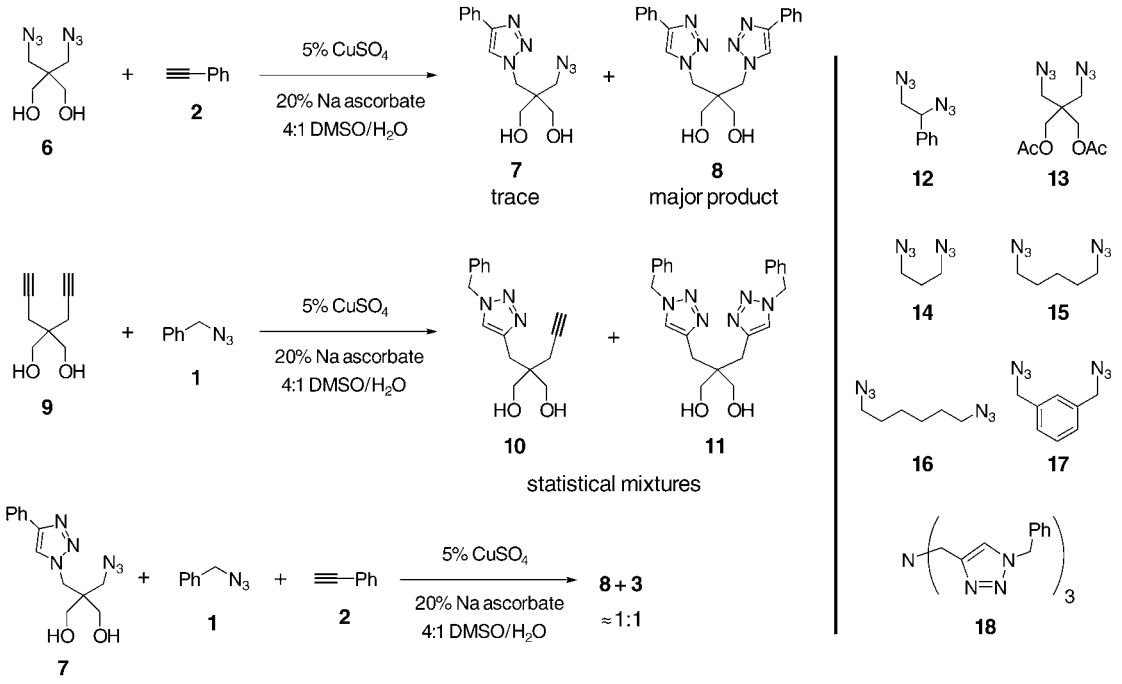

Scheme 2. Comparison of diazide and dialkyne reactivity.

Scheme 2, only the 1,2 compound **12** and the 1,3 compound **13** (but not **14**) exhibited the same strong preference as **6** for the formation of ditriazole products.[15] Therefore, the first triazole formed, and not a pendant hydroxy group, is the critical accelerating element. Conformational constraints present in **6** and **13**, but not **14**, are required to hold the triazole and the second azide in close proximity. The rates of reactions between **1** and **2** were not affected by the addition of **8**. Furthermore, cycloaddition reactions of **6** did not exhibit any features of autocatalysis. Thus, Cu·**8** complexes do not catalyze the process. When the accelerating ligand **18**[4a] was added, the overall rate of disappearance of **6** was increased (reactions were complete within 20 min), but the ratio of **8** to **7** remained unchanged.

Reactions of **9** and **1** were carefully monitored. Product **10** initially built up, and then diminished to give **11** in a manner expected for sequential reactions of approximately the same rate. In contrast, the reaction of **6** with **2** was found to generate a small amount (< 3 mol %) of **7**, which persisted throughout the reaction. Compound **7** was prepared independently, and the rate of its disappearance in reaction with phenylacetylene was found to be significantly faster than that of **6** (complete reaction in 30 min for **7**, versus 30–40 % completion in the same time for **6**). However, the rate difference was not large enough to account for the predominant formation of ditriazole **8** from diazide **6**, especially in the presence of a large excess of **6** relative to alkyne. Moreover, reactions of **2** with a mixture of **1** and **7** were found to proceed with consumption of the two azides at an approximately equal rate, and much more slowly than reactions of **2** and **7** in the absence of **1**. In other words, the reaction of azide **7** was inhibited by benzyl azide, but no increase in the amount of **7** was detected when benzyl azide was added to reactions of **6**. Therefore, free **7** is unlikely to be an intermediate in the conversion of **6** into **8**. Rather, we suggest that the Cu–triazole organometallic precursor to **7** may be the active structure.

The conversion of **7** into **8** was slowed neither by toluene, nor when benzyl azide was used in the presence of a large excess of alkyne (a better ligand for Cu^I than the azide). These observations, along with the inhibitory behavior of benzyl azide under catalytic conditions in metal (Table 1, entry 6), suggest that benzyl azide binds reversibly to Cu^I centers through interactions with both the aromatic ring[16] and azide group.[12] This model is supported by a recent report of an inorganic Ru–N_3 moiety that participates in a cycloaddition reaction with alkynes.[17]

A proposed series of steps consistent with the data obtained thus far is shown in Scheme 3. Diazide **6** is converted into the Cu–C bond-containing triazole intermediate **19**, from which free **7** can be obtained by proteolysis of the Cu–C bond.[13] However, **19**, a Cu^I complex, can also bind alkyne[18] to give a system of the form **20** or Cu–acetylide[18a,19] to give **21**, with subsequent rapid intramolecular capture of the remaining azide to afford **8** without the intermediacy of free **7**, when conformational factors permit. The fact that the triazole unit of **7** can direct Cu–acetylide to the pendant azide (structure **22**) also serves to accelerate the reactions of **7** relative to **6**. The observed inhibition of the **7**→**8** conversion by added benzyl azide is proposed to result from competitive binding of active Cu–acetylide in a chelate such as structure **23**. Finally, the necessary intermediate **24** from dialkyne **9** cannot easily recruit a reaction partner, as Cu–azide coordination alone is too weak. The binding of Cu^I by the triazole moiety of **10** offers little advantage, as the Cu–alkyne interaction is rapid even without pendant-group assistance.

In summary, a mechanistic outline that requires the ordered interaction of two copper centers, with one or two

 © 2005 Wiley-VCH Verlag GmbH & Co. KGaA, Weinheim

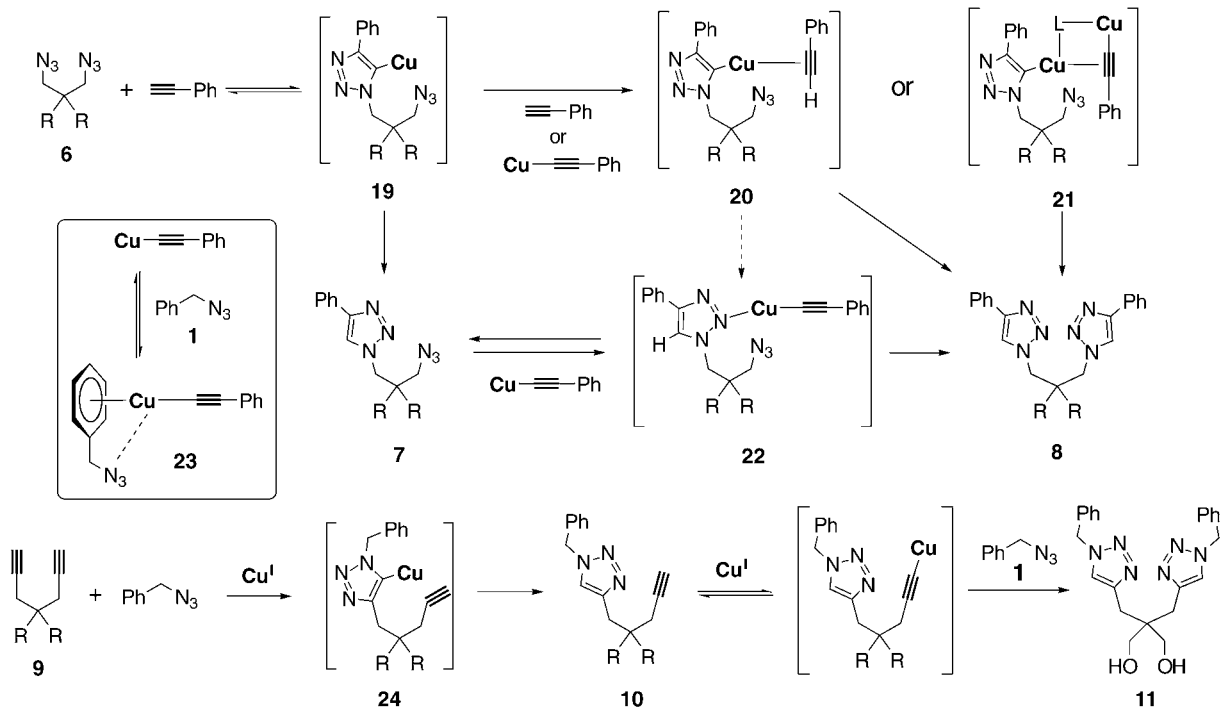

Scheme 3. Proposed steps in the transformations of **6** and **9** into mono- and ditriazoles.

alkyne/acetylide units and one azide, has been uncovered by kinetics measurements. For certain 1,2- and 1,3-diazides, the formation of the second triazole ring was found to be much faster than the first. An unusual inhibitory effect of benzyl azide was also observed, which suggests the presence of two pathways to ditriazole, one via free monotriazole and the other via a copper(I) organometallic intermediate. Much, of course, remains to be explained. For example, in addition to employing only one of its two acetylide fragments in cycloaddition, complex **5** was found to mediate the exclusive transformation of **6** into **7**, in remarkable contrast to all other systems examined so far. The most important unresolved issue is the precise nature of the putative binuclear copper system responsible for efficient catalysis—a question we are addressing with copper-chelating ligands. Preliminary measurements with ligand-accelerated catalysts are currently underway and show kinetic parameters similar to those described above. The requirement for two copper centers and the advantages of intramolecular positioning of azide groups are highlighted in the selective synthesis of cyclic peptide dimers, described in the accompanying paper.[20] These principles also provide guidance for ongoing efforts in our laboratories to develop new ligands and self-accelerating (autocatalytic) systems.

Received: July 31, 2004
Revised: October 18, 2004
Published online: February 3, 2005

Keywords: alkynes · azides · click chemistry · copper · cycloaddition

[1] R. Huisgen in *1,3-Dipolar Cycloaddition Chemistry, Vol. 1* (Ed.: A. Padwa), Wiley, New York, **1984**, pp. 1–176.

[2] a) W. G. Lewis, L. G. Green, F. Grynszpan, Z. Radic, P. R. Carlier, P. Taylor, M. G. Finn, K. B. Sharpless, *Angew. Chem.* **2002**, *114*, 1095–1099; *Angew. Chem. Int. Ed.* **2002**, *41*, 1053–1057; b) H. C. Kolb, K. B. Sharpless, *Drug Discovery Today* **2003**, *8*, 1128–1137.

[3] a) C. W. Tornøe, C. Christensen, M. Meldal, *J. Org. Chem.* **2002**, *67*, 3057–3062; b) V. V. Rostovtsev, L. G. Green, V. V. Fokin, K. B. Sharpless, *Angew. Chem.* **2002**, *114*, 2708–2711; *Angew. Chem. Int. Ed.* **2002**, *41*, 2596–2599.

[4] a) Q. Wang, T. R. Chan, R. Hilgraf, V. V. Fokin, K. B. Sharpless, M. G. Finn, *J. Am. Chem. Soc.* **2003**, *125*, 3192–3193; b) A. J. Link, D. A. Tirrell, *J. Am. Chem. Soc.* **2003**, *125*, 11164–11165; c) A. E. Speers, B. F. Cravatt, *Chem. Biol.* **2004**, *11*, 535–546; d) A. E. Speers, G. C. Adam, B. F. Cravatt, *J. Am. Chem. Soc.* **2003**, *125*, 4686–4687; e) L. V. Lee, M. L. Mitchell, S.-J. Huang, V. V. Fokin, K. B. Sharpless, C.-H. Wong, *J. Am. Chem. Soc.* **2003**, *125*, 9588–9589; f) A. Deiters, T. A. Cropp, M. Mukherji, J. W. Chin, J. C. Anderson, P. G. Schultz, *J. Am. Chem. Soc.* **2003**, *125*, 11782–11783; g) R. Breinbauer, M. Köhn, *ChemBioChem* **2003**, *4*, 1147–1149.

[5] a) F. Fazio, M. C. Bryan, O. Blixt, J. C. Paulson, C.-H. Wong, *J. Am. Chem. Soc.* **2002**, *124*, 14397–14402; b) K. D. Bodine, D. Y. Gin, M. S. Gin, *J. Am. Chem. Soc.* **2004**, *126*, 1638–1639; c) T. S. Seo, Z. Li, H. Ruparel, J. Ju, *J. Org. Chem.* **2003**, *68*, 609–612; d) Z. Zhou, C. J. Fahrni, *J. Am. Chem. Soc.* **2004**, *126*, 8862–8863; e) T. Jin, S. Kamijo, Y. Yamamoto, *Eur. J. Org. Chem.* **2004**, 3789–3791.

[6] a) P. Wu, A. K. Feldman, A. K. Nugent, C. J. Hawker, A. Scheel, B. Voit, J. Pyun, J. M. J. Fréchet, K. B. Sharpless, V. V. Fokin, *Angew. Chem.* **2004**, *116*, 4018–4022; *Angew. Chem. Int. Ed.* **2004**, *43*, 3928–3932; b) D. D. Díaz, S. Punna, P. Holzer, A. K. McPherson, K. B. Sharpless, V. V. Fokin, M. G. Finn, *J. Polym. Sci. Part A* **2004**, *42*, 4392–4403; c) J. P. Collman, N. K. Devaraj,

 © 2005 Wiley-VCH Verlag GmbH & Co. KGaA, Weinheim

C. E. D. Chidsey, *Langmuir* **2004**, *20*, 1051 – 1053; d) T. Lummerstorfer, H. Hoffmann, *J. Phys. Chem. B* **2004**, *108*, 39663 – 33966; e) J. K. Lee, Y. S. Chi, I. S. Choi, *Langmuir* **2004**, *20*, 3844 – 3847.

[7] S. Löber, P. Rodriguez-Loaiza, P. Gmeiner, *Org. Lett.* **2003**, *5*, 1753 – 1755.

[8] a) C. Creutz, *Inorg. Chem.* **1981**, *20*, 4449 – 4452; b) M. B. Davies, *Polyhedron* **1992**, *11*, 285 – 321.

[9] a) T. R. Chan, R. Hilgraf, K. B. Sharpless, V. V. Fokin, *Org. Lett.* **2004**, *6*, 2853 – 2855; b) W. G. Lewis, F. G. Magallon, V. V. Fokin, M. G. Finn, *J. Am. Chem. Soc.* **2004**, *126*, 9152 – 9153.

[10] For details, see Supporting Information.

[11] B. M. Mykhalichko, O. N. Temkin, M. G. Mys'kiv, *Russ. Chem. Rev.* **2001**, *69*, 957 – 984.

[12] F. Himo, T. Lovell, R. Hilgraf, V. V. Rostovtsev, V. V. Fokin, L. Noodleman, K. B. Sharpless, *J. Am. Chem. Soc.* **2005**, *127*, 210 – 216.

[13] The use of PhC≡CD in protic solvent gave no deuterium incorporation in the triazole product, whereas reactions in D_2O or MeOD provided high levels of deuteration at the C5 triazole position.

[14] J. Diez, M. P. Gamasa, J. Gimeno, E. Lastra, A. Aguirre, S. Garcia-Granda, *Organometallics* **1993**, *12*, 2213 – 2220.

[15] Geminal diazides also show this behavior. This chemistry will be described separately in a report on asymmetric induction with chiral ligands.

[16] a) F.-B. Xu, Q.-S. Li, L.-Z. Wu, X.-B. Leng, Z.-C. Li, X.-S. Zeng, Y. L. Chow, Z.-Z. Zhang, *Organometallics* **2003**, *22*, 633 – 640; b) M. Mascal, J.-L. Kerdelhué, A. J. Blake, P. A. Cooke, *Angew. Chem.* **1999**, *111*, 2094 – 2096; *Angew. Chem. Int. Ed.* **1999**, *38*, 1968 – 1971; c) S. M. Hubig, S. V. Lindeman, J. K. Kochi, *Coord. Chem. Rev.* **2000**, *200*, 831 – 873; d) T. Osako, Y. Tachi, M. Taki, S. Fukuzumi, S. Itoh, *Inorg. Chem.* **2001**, *40*, 6604 – 6609; e) H. Schmidbaur, W. Bublak, B. Huber, G. Reber, G. Mueller, *Angew. Chem.* **1986**, *98*, 1108 – 1109; *Angew. Chem. Int. Ed. Engl.* **1986**, *25*, 1089 – 1090; f) R. W. Turner, E. L. Amma, *J. Am. Chem. Soc.* **1966**, *88*, 1877 – 1882.

[17] C.-W. Chang, G.-H. Lee, *Organometallics* **2003**, *22*, 3107 – 3116.

[18] a) F. Olbrich, U. Behrens, E. Weiss, *J. Organomet. Chem.* **1994**, *472*, 365 – 370; b) W. Frosch, S. Back, G. Rheinwald, K. Köhler, H. Pritzkow, H. Lang, *Organometallics* **2000**, *19*, 4016 – 4024; c) K. Köhler, H. Pritzkow, H. Lang, *J. Organomet. Chem.* **1998**, *553*, 31 – 38.

[19] V. W.-W. Yam, S. W.-K. Choi, C.-L. Chan, K.-K. Cheung, *Chem. Commun.* **1996**, 2067 – 2068.

[20] See the following Communication in this issue: S. Punna, J. Kuzelka, Q. Wang, M. G. Finn, *Angew. Chem.* **2005**, *117*, 2255; *Angew. Chem. Int. Ed.* **2005**, *44*, 2215 (DOI: 10.1002/anie.200461656).

 © 2005 Wiley-VCH Verlag GmbH & Co. KGaA, Weinheim

Azide–Alkyne Cycloadditions

Head-to-Tail Peptide Cyclodimerization by Copper-Catalyzed Azide–Alkyne Cycloaddition**

*Sreenivas Punna, Jane Kuzelka, Qian Wang, and M. G. Finn**

Cyclic peptides and related structures have received attention in a variety of fields pertinent to drug discovery and biochemistry.[1] Peptide cyclization[2] has been managed most commonly by the formation of amide,[3] ester,[4] disulfide,[3b,5] olefin,[6] and C–C[7] bonds. Most methods include cyclization as part of solid-phase peptide synthesis, with ring closure performed on the resin support.[8] Olefin metathesis is particularly attractive for ring closure, because terminal alkenes and the transition-metal catalysts used to manipulate them are generally unreactive with protein functional groups.[6] Thus, the "handles" for cyclization can be installed and ignored until the time comes for their connection. We report herein a conceptually similar approach with different chemistry—the copper(I)-catalyzed azide–alkyne cycloaddition reaction[9]—and describe the propensity of this process to give selective dimerization in the ring-closure step.

In the course of constructing linear and cyclic versions of the same peptide sequence for display on supramolecular protein scaffolds, we needed a cyclization method compatible with the requirements of side-chain protection/deprotection and with the installation of a reactive group to enable subsequent bioconjugation. The 11-mer and 19-mer Arg-Gly-Asp (RGD)-containing peptides **1** and **2** (Scheme 1) contain sequences taken from an adenovirus serotype that binds several α_v integrins.[10] They were synthesized by standard 9-fluorenylmethyloxycarbonyl (Fmoc) methods, starting with Fmoc-Phe-Wang resin and L-propargylglycine as the second residue installed. The end of each chain was terminated with side-chain Boc-protected Fmoc-lysine (Boc = *tert*-butoxycarbonyl), followed by Fmoc deprotection and capping of the N terminus with 5-azidopentanoic acid. The syntheses were also performed with a standard Boc-based protocol, starting

[*] Dr. S. Punna, Dr. J. Kuzelka, Dr. Q. Wang,[+] Prof. M. G. Finn
Department of Chemistry
The Scripps Research Institute
10550 N. Torrey Pines Rd., La Jolla, CA 92037 (USA)
Fax: (+1) 858-784-8850
E-mail: mgfinn@scripps.edu

[+] Present address:
Department of Chemistry & Biochemistry
University of South Carolina (USA)

[**] We thank the Skaggs Institute for Chemical Biology and the NIH (N01-CO-27181) for support of this work, and Dr. Manoj P. Samant, Dr. Sayam Sen Gupta, Mr. Warren G. Lewis, Prof. Gary Siuzdak, Prof. Valery Fokin, and Prof. K. Barry Sharpless for helpful discussions. We are especially grateful to Prof. Philip Dawson and his group for guidance regarding peptide synthesis.

Supporting information for this article is available on the WWW under http://www.angewandte.org or from the author.

 DOI: 10.1002/anie.200461656 © 2005 Wiley-VCH Verlag GmbH & Co. KGaA, Weinheim

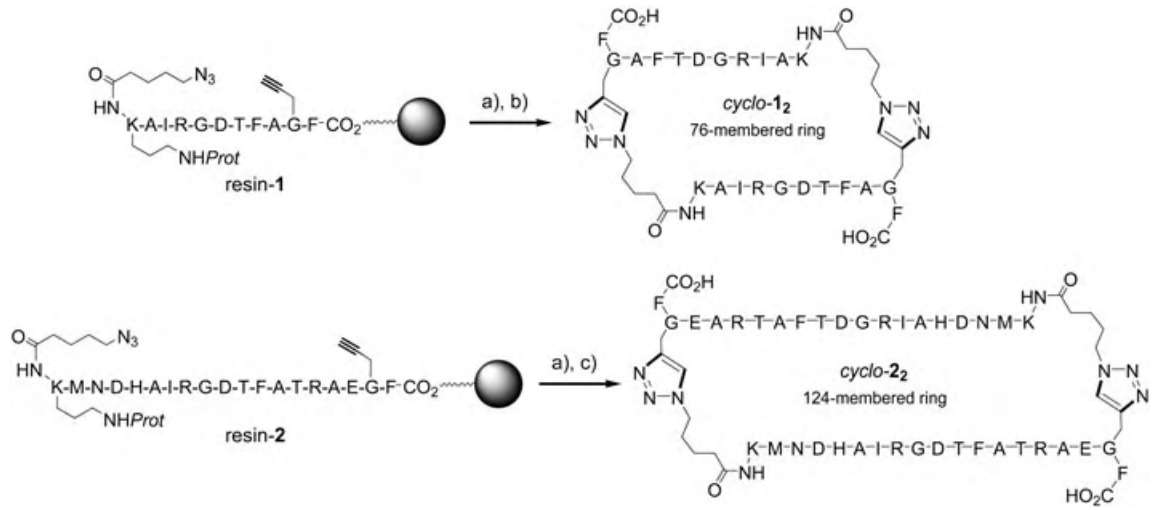

Scheme 1. Peptide cyclization by azide–alkyne cycloaddition: a) CuI (0.5 equiv), Na ascorbate (1 equiv), 2,6-lutidine (2 equiv), $CH_3CN/DMSO/H_2O$ (8:2:1), room temperature, 16 h; b) $CF_3CO_2H/H_2O/SiH(iPr)_3$ (95:2.5:2.5), room temperature, 3 h; c) CF_3CO_2H/H_2O/1,2-ethanedithiol/$SiH(iPr)_3$ (94:2.5:2.5:1), room temperature, 3 h. Initial substitution for both resins **1** and **2** was 0.77 mmol g^{-1}. *Prot* = protecting group.

with a Boc-Phe-PAM (4-hydroxymethylphenylacetamidomethyl) resin, terminated with Z- (benzyloxycarbonyl) or Fmoc-protected lysine, and finished with the appropriate capping step to install the azide group.[11]

Cyclization was carried out by exposure of each resin to 0.5 equivalents of Cu^I (with respect to the maximum possible amount of alkyne) for 16 h at room temperature. The complete consumption of azide groups was verified by a modified ninhydrin test developed for the detection of resin-bound azides,[12] which is more sensitive than IR spectroscopy. In the absence of Cu^I, no reaction occurred even upon heating to 100 °C. Cleavage from the solid support and HPLC analysis showed the complete disappearance of the linear oligopeptides and the production of a single dominant species in each case, which proved to be cyclic dimers rather than monomers (Scheme 1). The yields of isolated purified linear and cyclic peptides (linear-**1**, 25–30 %; linear-**2**, 15–20 %; *cyclo*-$\mathbf{1_2}$, 15–20 %; *cyclo*-$\mathbf{2_2}$, 10–15 %, all relative to the starting resin) reflect 90–95 % yields for peptide coupling and cleavage steps, and approximately 60 % yield for cyclodimerization, including loss during purification by HPLC.

MALDI MS analyses under a variety of conditions showed *cyclo*-$\mathbf{1_2}$ and *cyclo*-$\mathbf{2_2}$ to be of dimeric molecular mass, m/z $[M+H]^+ = 2690$ and 4602, respectively. Further support for the assignment of cyclic dimers was supplied by the following four observations, details of which are provided in the Supporting Information:

1) Peptides cleaved from the resin before cyclization, but not the cyclized products, were reactive with phosphine, which confirms the consumption of the azide groups in the cyclization step.
2) High-resolution ESI MS showed strong peaks at m/z values that correspond to the addition of odd numbers of protons to the dimers and that could not arise from monomers.
3) The use of a mixture of two amino acids in one of the chain-building steps toward resin-**1** provided a mixture of two sequences on the resin, which gave the three cyclized products expected from cyclodimerization.
4) Trypsin digestion of *cyclo*-$\mathbf{1_2}$ was monitored as a function of time, showing one and two cleavage events to give products of greater than monomeric molecular weight, ruling out the existence of a catenated structure.

Whereas cyclic peptide dimers have been previously prepared and shown to have interesting functional properties,[13] the selective production of such large rings as *cyclo*-$\mathbf{1_2}$ and *cyclo*-$\mathbf{2_2}$ is unprecedented. The following experiments were performed to probe the mechanism of the process:

a) Cyclization reactions of analogous resins that have a lower density of peptide chains were found to be much slower. Thus, resin-**1** and resin-**2** were prepared from Fmoc-Phe-Wang resin with an initial loading of 0.12 mmol g^{-1} (1.2 derivatized styrene units per 100) instead of 0.77 mmol g^{-1} (9 functionalized monomers per 100). With the same ratio of copper to alkyne (and therefore much more dilute in both), a substantial amount of unconverted peptide remained after 24 h, but cyclic dimers were still the only products detected. This suggests that a threshold density of azides or alkynes is required on the solid support, and that the dimeric pathway is favored even when two chains are difficult to bring together.
b) Cyclodimerization was neither favored by the peptide sequence itself nor by the presence of copper ions, as shown by the attempted ring closure with amide bond formation shown in Scheme 2. HBTU-mediated cyclization of resin-**3**, incorporating orthogonally-protected aspartic acid in place of propargyl glycine, gave poor results, and no compounds of dimeric molecular weight were observed.[14] The expected monocyclic peptide *cyclo*-**3** was detected by mass spectrometry, but the material was impossible to isolate by HPLC owing to the presence of many impurities. Added copper(I) iodide did not induce dimer formation in this process.

 © 2005 Wiley-VCH Verlag GmbH & Co. KGaA, Weinheim

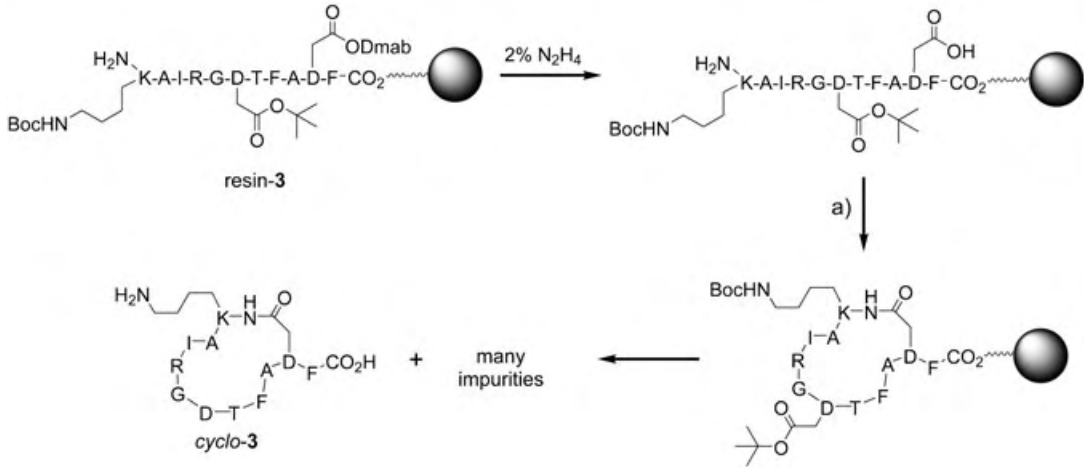

Scheme 2. Peptide cyclization by amide bond formation: a) Performed with and without Cu^{I} (0.5 equiv); HBTU (5 equiv), iPr_2NEt, DMF, room temperature. DMF = dimethylformamide; HBTU = *O*-(1*H*-benzotriazoyl-1-yl)-*N*,*N*,*N*′,*N*,′-tetramethyluronium hexafluorophosphate.

c) The use of more than 0.5 equivalents of Cu with respect to the maximum number of alkyne groups was deleterious. For example, when 10 equivalents of Cu were employed with resin-**1**, many peaks were observed by HPLC, none of them representing *cyclo*-$\mathbf{1_2}$ or linear-**1**. With 1.5 equivalents of Cu, cyclic dimer was recovered in lower yield than before, along with some of the linear unconverted peptide. Small peaks in the chromatogram suggested peptide decomposition in the presence of excess copper.[15] The addition of the copper-binding ligand 4,4′-dimethylbipyridine to the latter process (1.5 equiv Cu to alkyne; 2 equiv ligand to Cu)[16] suppressed much of the reaction, giving unaltered linear peptide as the major recovered material.

d) The cyclization of resin-**1** performed in the presence of added benzyl azide provided *cyclo*-$\mathbf{1_2}$ and the azide-trapped monomer **4** as major products (Scheme 3). In contrast, the addition of phenylacetylene completely suppressed cyclization, giving rise to the alkyne-trapped monomer **5** as the major product, with a trace of the linear dimer **6**, detected by MS. The different outcomes correlate with the much greater affinity of Cu^{I} for alkyne over azide, as discussed below.

e) Switching the positions of the azide and alkyne fragments allowed some monocyclization to occur. Resin-**7** was constructed with a side-chain-derivatized glutamic azide in the second amino acid position and propargyl glycine at the end of the chain (Scheme 4). Subjection of this material to the standard cyclization conditions gave an approximate 2:1 mixture of cyclic dimer *cyclo*-$\mathbf{7_2}$ and cyclic monomer *cyclo*-**7**, along with a greater amount of impurities than were produced from the analogous resin-**1**.

The kinetic parameters of the reaction provide the basis for understanding the factors that cause cyclization to involve two peptide chains rather than one. In the previous paper in this issue,[17] we showed that the solution-phase reaction between benzyl azide and phenylacetylene exhibits a second-order dependence on Cu^{I}. Peptide cyclodimerization occurs cleanly only when less than 1 equivalent of copper per alkyne unit is present—when most or all of the metal is tied up in the

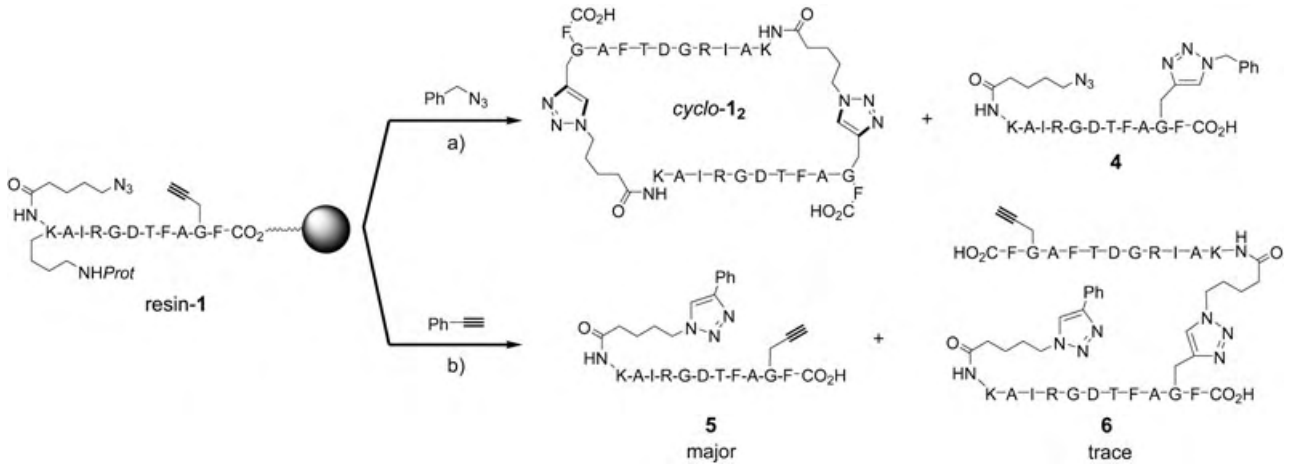

Scheme 3. Cu^{I}-mediated peptide cyclization in the presence of added azide and alkyne: a) Cu^{I} (0.5 equiv), benzyl azide (0.5 equiv), then cleavage from resin; b) Cu^{I} (0.5 equiv), phenylacetylene (0.5 equiv), then cleavage from resin.

 © 2005 Wiley-VCH Verlag GmbH & Co. KGaA, Weinheim

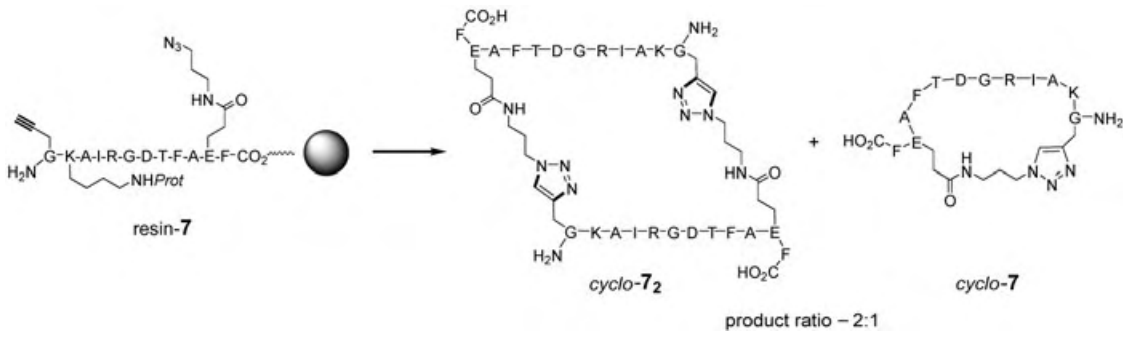

Scheme 4. Cyclization of peptide bearing azide and alkyne in "switched" positions.

form of Cu–acetylide on the resin. If the reaction of these resin-bound species also requires the participation of two copper centers, then only adjacent chains that happen to have copper bound to their alkyne residues will engage in the cycloaddition reaction. (The 1% cross-linked polystyrene used herein is a highly flexible material,[18] so the term "adjacent" refers simply to those chains for which the alkyne groups can reach each other without too great an energetic cost.) In other words, the mechanism of the copper-mediated reaction demands the interaction of two peptide chains.

As the peptides used in this case are long and flexible, there must be some additional factor(s) that induce the azide of one chain to engage the alkyne of its neighbor rather than its own. We suggest at least three potential contributing interactions (Figure 1):

1) As the solution-phase reaction showed a rate order in PhC≡CH of between 1 and 2, a second-order pathway in alkyne is possible, with one alkyne playing a structural role. If, for example, one Cu–acetylide of associated chains undergoes π complexation to the other, as shown in structure **8**, the reactivities of the two acetylides toward azide will be different.
2) An interaction of a Cu^I center with the peptide chain may fold the oligopeptide in such a way as to make it more difficult for the azide at the terminus to interact with the Cu–acetylide at its base, also represented in structure **8**. Since no clear Cu^I-binding side chains (His, Trp, Cys, Met) were present in structure **1** (one Met residue exists in **2**), we believe that Cu binding to the peptide may occur at the backbone amide groups.[19] Other possibilities that derive from conformational bias imposed by the peptide sequence are being explored, but we do not see how such factors could generally favor dimeric cyclization.
3) Once the directed cycloaddition occurs to make one triazole connection, the organometallic Cu–triazole intermediate **9** may bind and direct the second azide to engage the remaining acetylide and complete the macrocyclization. A similar phenomenon is proposed in the accompanying article to explain the anomalously fast second cycloaddition process in the conversion of tethered diazides into ditriazoles. Although this does not bear on the question of monomeric versus dimeric cyclization, it may help explain why linear dimers are not observed.

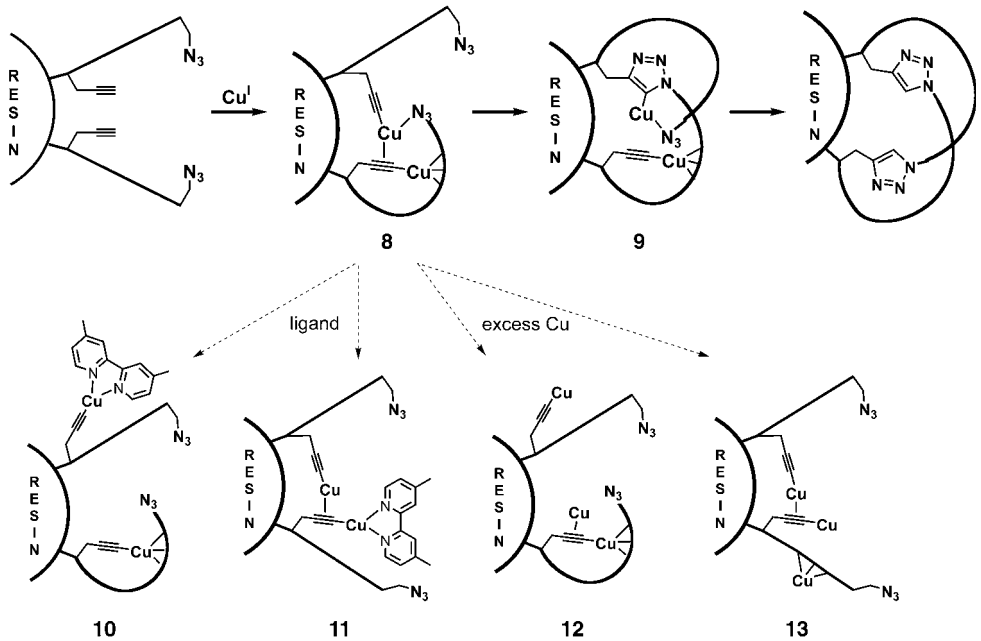

Figure 1. Schematic illustration of potential interactions leading to selective cyclodimerization.

 © 2005 Wiley-VCH Verlag GmbH & Co. KGaA, Weinheim

The experimental observations are accommodated by this mechanistic scheme as follows: the slow rate of reaction on a lightly loaded resin (observation (a), above) can be ascribed to a dramatic decrease in the concentration of adjacent Cu-bearing sites. The deleterious effects of bidentate ligand or excess Cu^{I} (observation c)) are similarly consistent with the loss of the required binuclear Cu–alkyne–peptide ensemble, either by disrupting Cu–alkyne–Cu binding (**10** and **12**, Figure 1) or Cu–peptide interaction (**11** and **13**). Added alkyne can also block cyclodimerization (observation d)) by competing with the resin-bound alkyne for Cu^{I}, resulting in capture of peptide azide by [Cu−C≡CPh] to afford linear monotriazole **5** (Scheme 3). Benzyl azide does not bind copper with sufficient affinity to take the metal away from the oligopeptide alkyne, so the putative $[Cu_2(alkyne)_2]$ species is either trapped by pendant azide to give the usual cyclic dimer or intercepted by free azide to give linear monomer **4** (Scheme 3). The opening of a competitive monocyclization pathway by placing the alkyne away from the polystyrene backbone (observation e)) suggests that such adjacent Cu–acetylide centers can come together with greater conformational flexibility, allowing the reactive ensemble to find either azide residue of its component chains.

The selective production of large cyclic dimers from resin-tethered peptides containing azide and alkyne residues is a striking consequence of the mechanistic constraints of the copper-catalyzed cycloaddition reaction. The process has clear utility in the construction of large and highly functional molecules if the presence of the triazole moiety can be tolerated.[20] Indeed, a solution-phase synthesis of head-to-tail cyclic dimers of trisaccharides to make ditriazole-containing cyclodextrin analogues has been recently reported.[21] The on-resin phenomena described herein and related future studies of the reaction in solution provide a versatile forum for the continued exploration of the reaction mechanism. The potential for interplay between peptide length, flexibility, secondary structure, and copper–acetylide interactions is especially interesting. We are also exploring the preparation of peptide libraries, catenanes, and nonpeptide cyclic structures.

Received: August 15, 2004
Revised: October 18, 2004
Published online: February 3, 2005

Keywords: alkynes · azides · cycloaddition · dimerization · peptides

[1] a) J. S. Davies in *Cyclic Polymers*, 2nd ed. (Ed.: J. A. Semlyen), Kluwer Academic Publishers, Dordrecht, **2000**, pp. 85–124; b) H. Kessler, *Angew. Chem.* **1982**, *94*, 509–520; *Angew. Chem. Int. Ed. Engl.* **1982**, *21*, 512–523; c) J. S. Davies, *Amino Acides Pept. Proteines* **2002**, *33*, 238–294; d) F. Sarabia, S. Chammaa, A. S. Ruiz, L. M. Ortiz, F. J. L. Herrera, *Curr. Med. Chem.* **2004**, *11*, 1309–1332; e) E. Lohof, E. Planker, C. Mang, F. Burkhart, M. A. Dechantsreiter, R. Haubner, H.-J. Wester, M. Schwaiger, G. Holzemann, S. L. Goodman, H. Kessler, *Angew. Chem.* **2000**, *112*, 2868–2871; *Angew. Chem. Int. Ed.* **2000**, *39*, 2761–2764; f) Y.-Q. Tang, J. Yuan, G. Osapay, K. Osapay, D. Tran, C. J. Miller, A. J. Ouellette, M. E. Selsted, *Science* **1999**, *286*, 498–502; g) B. W. Matthews, C. S. Craik, H. Neurath, *Proc. Natl. Acad. Sci. USA* **1994**, *91*, 4103–4105.

[2] a) P. Li, P. P. Roller, J. Xu, *Curr. Org. Chem.* **2002**, *6*, 411–440; b) J. N. Lambert, J. P. Mitchell, K. D. Roberts, *J. Chem. Soc. Perkin Trans. 1* **2001**, 471–484.

[3] a) J. T. Lundquist IV, J. C. Pelletier, *Org. Lett.* **2002**, *4*, 3219–3221; b) E. Falb, Y. Salitra, T. Yechezkel, M. Bracha, P. Litman, R. Olender, R. Rosenfeld, H. Senderowitz, S. Jiang, M. Goodman, *Bioorg. Med. Chem.* **2001**, *9*, 3255–3265; c) Y. Shao, W. Lu, S. B. H. Kent, *Tetrahedron Lett.* **1998**, *39*, 3911–3914.

[4] a) D. Ranganathan, V. Haridas, S. Kurur, R. Nagaraj, E. Bikshapathy, A. C. Kunwar, A. V. S. Sarma, M. Vairamani, *J. Org. Chem.* **2000**, *65*, 365–374; b) W. D. F. Meutermans, S. W. Golding, G. T. Bourne, L. P. Miranda, M. J. Dooley, P. F. Alewood, M. L. Smythe, *J. Am. Chem. Soc.* **1999**, *121*, 9790–9796.

[5] a) B. A. Katz, *Biochemistry* **1995**, *34*, 15421–15429; b) D. Ranganathan, V. Haridas, R. Nagaraj, I. L. Karle, *J. Org. Chem.* **2000**, *65*, 4415–4422.

[6] a) S. J. Miller, R. H. Grubbs, *J. Am. Chem. Soc.* **1995**, *117*, 5855–5856; b) S. J. Miller, H. E. Blackwell, R. H. Grubbs, *J. Am. Chem. Soc.* **1996**, *118*, 9606–9614; c) T. D. Clark, M. R. Ghadiri, *J. Am. Chem. Soc.* **1995**, *117*, 12364–12365; d) J. Pernerstorfer, M. Schuster, S. Blechert, *Chem. Commun.* **1997**, 1949–1951; e) A. S. Ripka, R. S. Bohacek, D. H. Rich, *Bioorg. Med. Chem. Lett.* **1998**, *8*, 357–360; f) H. E. Blackwell, R. H. Grubbs, *Angew. Chem.* **1998**, *110*, 3469–3472; *Angew. Chem. Int. Ed.* **1998**, *37*, 3281–3284; g) N. Schmiedeberg, H. Kessler, *Org. Lett.* **2002**, *4*, 59–62.

[7] M. Hiroshige, J. R. Hauske, P. Zhou, *J. Am. Chem. Soc.* **1995**, *117*, 11590–11591.

[8] S. A. Kates, N. A. Sole, F. Albericio, G. Barany in *Peptides* (Eds.: C. Basava, G. N. Anantharamaiah), Birkhaeuser, Boston, **1994**, pp. 39–58.

[9] a) C. W. Tornøe, C. Christensen, M. Meldal, *J. Org. Chem.* **2002**, *67*, 3057–3062; b) V. V. Rostovtsev, L. G. Green, V. V. Fokin, K. B. Sharpless, *Angew. Chem.* **2002**, *114*, 2708–2711; *Angew. Chem. Int. Ed.* **2002**, *41*, 2596–2599.

[10] G. R. Nemerow, P. L. Stewart, *Virology* **2001**, *288*, 189–191.

[11] For details, see Supporting Information.

[12] S. Punna, M. G. Finn, *Synlett* **2004**, 99–100.

[13] a) B. P. England, P. Balasubramanian, I. Uings, S. Bethell, M.-J. Chen, P. J. Schatz, Q. Yin, Y.-F. Chen, E. A. Whitehorn, A. Tsavaler, C. L. Martens, R. W. Barrett, M. McKinnon, *Proc. Natl. Acad. Sci. USA* **2000**, *97*, 6862–6867; b) Z. Szewczuk, P. Buczek, P. Stefanowicz, K. Krajewski, Z. Wieczorek, I. Z. Siemion, *Acta Biochim. Pol.* **2001**, *48*, 121–130.

[14] The use of azide and alkyne connecting groups avoids certain protecting group problems commonly encountered in solid phase peptide synthesis. For example, orthogonal protection was required for an aspartate residue of resin-**3** to prepare for cyclization by amide bond formation. The 4-(*N*-(1-(4,4-dimethyl-2,6-dioxocyclohexylidene)-3-methylbutyl)amino)benzyl ester (Dmab) group, most commonly used in such situations, is expensive, bulky, and chemically sensitive: T. Johnson, M. Liley, T. J. Cheeseright, F. Begum, *J. Chem. Soc. Perkin Trans. 1* **2000**, 2811–2820. The introduction and manipulation of aspartate can give rise to undesired aspartamide cyclization with neighboring residues during both Fmoc and Boc synthetic approaches and piperidide formation during Fmoc manipulations; deprotection is often relatively difficult. The standard solutions to these difficulties (such as protecting the preceding residue as *N*-Hmb; Hmb = 2-hydroxy-4-methoxybenzyl) are also somewhat cumbersome. Each of these problems were encountered in the synthesis and isolation of *cyclo*-**3**, but did not occur in the preparation and reactions of the analogous sequence **1**.

[15] J. T. Groves, R. R. Chambers, Jr, *J. Am. Chem. Soc.* **1984**, *106*, 630–638.

 © 2005 Wiley-VCH Verlag GmbH & Co. KGaA, Weinheim

[16] W. G. Lewis, F. G. Magallon, V. V. Fokin, M. G. Finn, *J. Am. Chem. Soc.* **2004**, *126*, 9152 – 9153.
[17] See the preceding Communication in this issue: V. O. Rodionov, V. V. Fokin, M. G. Finn, *Angew. Chem.* **2005**, *117*, 2250; *Angew. Chem. Int. Ed.* **2005**, *44*, 2210 (DOI: 10.1002/anie.200461496).
[18] a) J. I. Crowley, T. B. Harvey, III, H. Rapoport, *J. Macromol. Sci. Part A* **1973**, *7*, 1117 – 1126; b) S. L. Regen, D. P. Lee, *J. Am. Chem. Soc.* **1974**, *96*, 294 – 296; c) J. Rebek, Jr., J. E. Trend, *J. Am. Chem. Soc.* **1979**, *101*, 737.
[19] The formation of peptide dimers with copper(II) by interaction with backbone amide nitrogen atoms has been described: H. Yokoi, A. Hanaki, *Chem. Lett.* **1983**, *8*, 1319 – 1322. This is, of course, different from copper(I), for which many protein interactions are known, but all involve anchoring to at least one "soft" side-chain ligand.
[20] Q. Su, A. B. Beeler, E. Lobkovsky, J. A. Porco, Jr., J. S. Panek, *Org. Lett.* **2003**, *5*, 2149 – 2152.
[21] K. D. Bodine, D. Y. Gin, M. S. Gin, *J. Am. Chem. Soc.* **2004**, *126*, 1638 – 1639.

 © 2005 Wiley-VCH Verlag GmbH & Co. KGaA, Weinheim

Monocarboranes

Carbon Extrusion in 1,2-Dicarba-*closo*-dodecaboranes: Regioselective Boron Substitution in Ten-Vertex *closo*-Monocarbaborane Anions**

*Anna Laromaine, Francesc Teixidor, and Clara Viñas**

Dedicated to Dr. Raikko Kivekäs on the occasion of his 60th birthday

While dicarba-*closo*-dodecaboranes are the most investigated of polyhedral boron-containing clusters,[1,2] *closo*-monocarbaboranes have been less examined,[1] probably because of the absence of suitable protocols of synthesis. Currently, the monocarbaboranes $[1\text{-}closo\text{-}CB_9H_{10}]^-$ and $[1\text{-}closo\text{-}CB_{11}H_{12}]^-$ along with their derivatives are attracting much attention.[3,4] This has stimulated the search for new methods of synthesis; $[1\text{-}closo\text{-}CB_9H_{10}]^-$ was originally obtained from $B_{10}H_{14}$ and CN^- but is now more conveniently produced from $[6\text{-}(NMe_3)\text{-}nido\text{-}6\text{-}CB_9H_{11}]$ by dehydrogenation.[5] The method of Brellochs,[6] based on the reaction of RCHO with *arachno*-$B_{10}H_{14}$, is gaining importance for the synthesis of phenyl derivatives of $[1\text{-}closo\text{-}CB_9H_{10}]^-$.[4,7] Ultimately all these methods are based on a single carbon insertion into a $B_{10}H_{14}$ cluster followed by a deboronation step. In theory, an alternative way to the $[1\text{-}closo\text{-}CB_9H_{10}]^-$ cluster would be from the highly stable and widely studied 1,2-dicarba-*closo*-dodecaboranes, namely, carbon extrusion with subsequent boron elimination. This is the objective of this work.

Taking the well-known benzyl cation–tropylium ion rearrangement as a model (Scheme 1 a),[8] Jemmis and Jayasree have carried out theoretical calculations on the rearrangement of the dicarbaboranyl methyl cation to generate tricarbaborane cations.[9] We considered that a monocarbaborane could be produced from a dicarbaborane by a similar extrusion of one cluster carbon atom. The analogy between the system in boron chemistry and the benzyl cation–tropylium equilibrium is shown in Scheme 1 b.

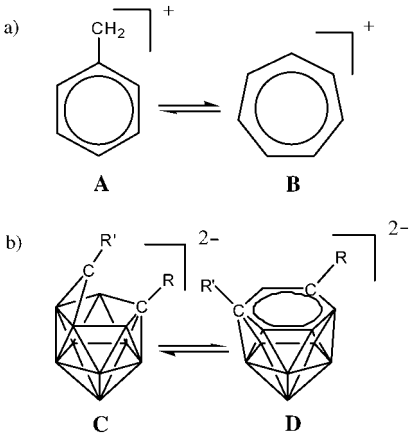

Scheme 1. Schematic representations of a) the benzyl cation–tropylium rearrangement and b) the rearrangement of the 12-vertex dicarba-*nido*-dodecaborate(-2).

Although there is no experimental proof for the expected rearrangement, support comes from the fact that isomer **E** (Scheme 2), which is structurally similar to **C** (Scheme 1), is produced on treatment of **D** with water. A second isomer **F** (less stable than **E** by 6.7 kcal mol^{-1}) is also produced.[10] Indeed **F** was considered to be the only reactive isomer,[11,12] and pioneering work for carbon extrusion from **F** has been reported[11c,13] in which a mixture of non-*closo* compounds forms depending on the nucleophile. To our understanding, the reactive nature of **F** as well as its easily accessible C_2B_4 open face facilitated formation of a range of products. It was

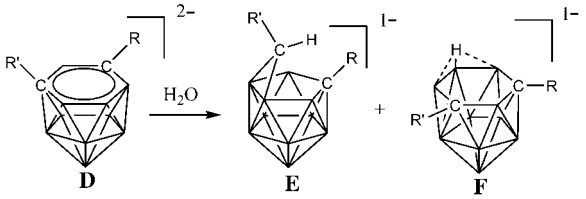

Scheme 2. Protonation of $[C_2B_{10}RR'H_{10}]^{2-}$ produces the two isomers [7-R-μ-(9,10-HR′C)-7-*nido*-$CB_{10}H_{11}]^-$ (**E**) and [7-R-9-R′-7,9-*nido*-$C_2B_{10}H_{11}]^-$ (**F**).

[*] A. Laromaine, Prof. F. Teixidor, Dr. C. Viñas
Institut de Ciència de Materials de Barcelona (CSIC)
Campus UAB
08193 Bellaterra (Spain)
Fax: (+34) 93-580-57-29
E-mail: clara@icmab.es

[**] The authors thank the CICYT (MAT01-1575) and the Generalitat de Catalunya (2001/SGR/00337) for financial support.

Supporting information for this article is available on the WWW under http://www.angewandte.org or from the author.

 © 2005 Wiley-VCH Verlag GmbH & Co. KGaA, Weinheim DOI: 10.1002/anie.200462209

anticipated that the more rigid structure of **E** would be more likely to undergo a regioselective reaction.

Two drawbacks were apparent: Isomer **E** had been synthesized in low yield, around 20%,[11b] and had been considered to be unreactive.[11,12] Recently a convenient route to **E** with Mg as a reducing agent has been described with yields close to 95% for R = H, Me, Ph.[14] As far as the low reactivity of **E** was concerned, we have recently shown that it can be forced to react with $[PdCl_2(PPh_3)_2]$ to generate a mixture of compounds, mostly obtained in low yield.[15] Although some products were generated by carbon extrusion, no [1-*closo*-CB_9H_{10}]$^-$ derivatives were found. In order to generate the latter, a regioselective cluster deboronation on **E** was of utmost importance, and we found K[NC_4H_4] and K[$NC_4Me_2H_2$] to be the most suitable nucleophiles for this task.[16a]

In a typical experiment, [NMe_4][μ-(9,10-H_2C)-7-*nido*-$CB_{10}H_{11}$] (**E**, R = H; 0.12 mmol) in 20 mL of THF was added to freshly prepared K[NC_4H_4] (0.48 mmol) under N_2. The mixture was heated at reflux for 72 h. The reaction was monitored by $^{11}B\{^1H\}$ NMR spectroscopy to examine the appearance of a resonance near +30 ppm. Following workup of the products, [NMe_4][6-Me-1-*closo*-CB_9H_9] was obtained in 55% yield.

This product was characterized by ^{11}B, $^{11}B\{^1H\}$, $^{13}C\{^1H\}$, and $^1H\{^{11}B\}$ NMR spectroscopy and MALDI-TOF analysis. A pattern 1(d):1(s):2(d):2(d):2(d):1(d) at δ = 30.3, −16.2, −17.1, −18.2, −22.2, and −26.5 ppm, respectively, in agreement with a six-substituted bicapped square antiprism,[17] was observed in the $^{11}B\{^1H\}$ NMR spectrum. Comparison with resonances for [1-*closo*-CB_9H_{10}]$^-$, application of ^{11}B NMR rules[18] for *closo* species, and the position of the singlet at δ = −16.2 ppm indicated that a regioselective alkyl substitution at the 6-position in [1-*closo*-CB_9H_{10}]$^-$ had taken place from the readily available 1,2-*closo*-$C_2B_{10}H_{12}$ neutral compounds. The assignments indicated on the $^{11}B\{^1H\}$–$^{11}B\{^1H\}$ 2D COSY NMR spectrum in Figure 1 are consistent with the structure of [6-Me-1-*closo*-CB_9H_9]$^-$: B10 is correlated with B6, B{7,9}, and B8; B8 is correlated with B10, B{7,9}, and B{4,5}; B{7,9} is correlated with B10, B8, B6, B{4,5}, and B{2,3}. The MALDI-TOF mass spectrum of [6-Me-1-*closo*-CB_9H_9]$^-$ (Figure 2) displays a signal group centered at *m*/*z* 133.2 corresponding to the anionic fragment. All this data prove that [1-R-6-CH_2R′-1-*closo*-CB_9H_8]$^-$ derivatives can be generated in only two steps. [6-Me-1-*closo*-CB_9H_9]$^-$ is the first example of a monoalkyl substitution on B in [1-*closo*-CB_9H_{10}]$^-$ derivatives.

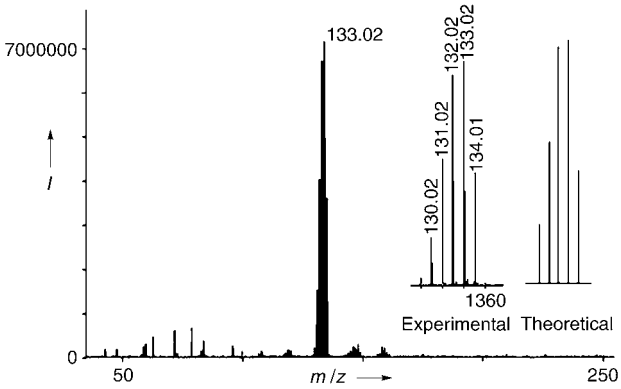

Figure 2. The MALDI-TOF mass spectrum of [NMe_4]-**1** with a comparison of the theoretical and experimental distribution for the molecular peak. *I* = intensity.

To demonstrate the versatility of this reaction, it was also applied to 1-Me-1,2-*closo*-$C_2B_{10}H_{11}$, 1,2-Me_2-1,2-*closo*-$C_2B_{10}H_{10}$, and 1-Ph-1,2-*closo*-$C_2B_{10}H_{11}$. In all cases anions corresponding to [1-R-6-CH_2R′-1-*closo*-CB_9H_8]$^-$ were obtained (Table 1).

Table 1: Nonoptimized yields for the synthesis of [1-R-6-CH_2R′-1-*closo*-CB_9H_8]$^-$.

Compound	[1-R-6-CH_2R′-1-*closo*-CB_9H_8]$^-$		
	R	R′	Yield [%]
[NMe_4]-**1**	H	H	55
[NBu_4]-**2**	H	Me	30
[NBu_4]-**3**	Me	Me	47
[NBu_4]-**4**	H	Ph	45

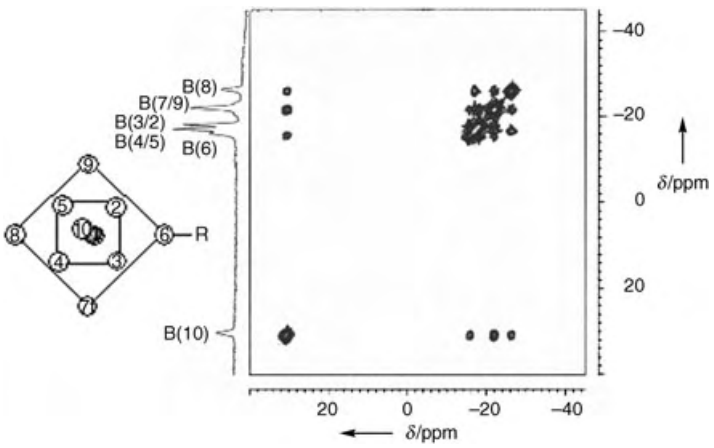

Figure 1. The $^{11}B\{^1H\}$–$^{11}B\{^1H\}$ 2D COSY NMR spectrum of [NMe_4]-**1** with the assignments deduced from the off-diagonal resonances.

In Scheme 3 the transformation from the neutral dicarbaborane to the anionic monocarbaborane cluster is exemplified for [1-Me-6-Et-1-*closo*-CB_9H_8]$^-$. Considering that carbon extrusion takes place, the alkyl group at the 6-position must have one more carbon atom than in the precursor dicarbaborane. As an

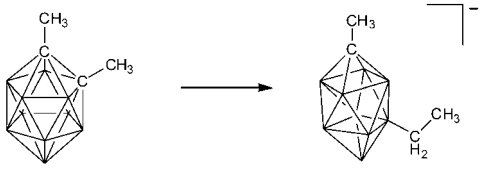

Scheme 3. Schematic representation of the carbon extrusion for regioselective synthesis of [1-Me-6-Et-1-*closo*-CB_9H_9]$^-$ from [1,2-Me_2-1,2-*closo*-$C_2B_{10}H_{10}$] species.

 © 2005 Wiley-VCH Verlag GmbH & Co. KGaA, Weinheim

example, if [6-Pr-1-*closo*-CB_9H_9]$^-$ were sought, 1-Et-1,2-*closo*-$C_2B_{10}H_{11}$ would be required as the starting compound.

A plausible pathway for the synthesis of **3**$^-$ is shown in Scheme 4. A B^{3+} unit is formally removed from [7-Me-μ-(9,10-HMeC)-7-*nido*-$CB_{10}H_{11}$]$^-$ by using [NC_4H_4]$^-$. At this stage the nonclassical bridging carbon atom of μ-(9,10-HMeC) is converted into a classical one. The boron atom removed is B(9) or B(10), generating a six-membered open face. Dehydrogenation leads to the *closo* monocarbaborane anion. The deboronation step is very important in this synthetic process. In previous work,[15] a neutral nucleophile (PPh_3) was shown to attack the bridging μ-(9,10-HMeC) group to generate the CH(Me)PPh_3 moiety. The result was a nucleophilic addition. The negative [NC_4H_4]$^-$ removes B(9) or B(10) to produce a *closo* {CB_9} anionic cluster and $(H_4C_4N)_3$B-THF.[16b] As the deboronation succeeded with an anionic nucleophile, experiments were also carried out with CN^- and F^- on [7-Me-μ-(9,10-HMeC)-7-*nido*-$CB_{10}H_{11}$]$^-$. For CN^-, [1-Me-6-Et-1-*closo*-CB_9H_8]$^-$ was formed in yields of less than 3%, and with F^- the starting material was fully recovered. The effect of enhanced nucleophilicity was monitored by ^{11}B NMR spectroscopy using [$NC_4Me_2H_2$]$^-$. Interestingly the same conversion as for [NC_4H_4]$^-$ (55%) was obtained in 24 h (72 h for [NC_4H_4]$^-$).

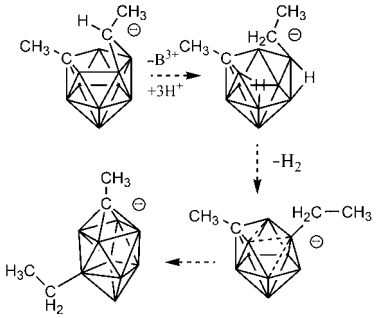

Scheme 4. Suggested pathway for deboronation and carbon extrusion in the [7-Me-μ-(9,10-HMeC)-7-*nido*-$CB_{10}H_{11}$]$^-$.

The inadequacy of isomer **F** (Scheme 2) for this reaction was demonstrated by attempting to produce **1**$^-$ under the same conditions and with K[$NC_4Me_2H_2$] as a nucleophile. In this case **1**$^-$ was produced in only 2% yield, along with [NMe_4][7,8-*nido*-$C_2B_9H_{11}$] (21%) and 1,2-*closo*-$C_2B_{10}H_{12}$ (58%). Even the low yield of **1**$^-$ cannot be claimed to originate from the use of **F** because the latter slowly isomerizes under the reaction conditions to yield **E**, which in turn may generate the [6-Me-1-*closo*-CB_9H_9]$^-$ cluster.

With these results we have shown that [1-H-6-CH_2R′-1-*closo*-CB_9H_8]$^-$ (R′ = H, Me, Ph) or [1-Me-6-CH_2Me-1-*closo*-CB_9H_8]$^-$ derivatives can be produced in a regioselective way from 1-H-2-R′-1,2-*closo*-$C_2B_{10}H_{10}$ (R′ = H, Me, Ph) or 1,2-Me_2-1,2-*closo*-$C_2B_{10}H_{10}$. Work is now underway for the case of unsymmetrical alkyl/aryl substitution on both cluster carbon atoms in the dicarbaboranes, to discern which group will occupy the 6-position in the resulting [1-*closo*-CB_9H_{10}]$^-$ derivatives, and which functional groups are compatible with such rearrangements.

Received: October 5, 2004
Revised: December 20, 2004
Published online: March 10, 2005

Keywords: boron · carboranes · rearrangement · regioselectivity · synthetic methods

[1] B. Stíbr, *Chem. Rev.* **1992**, *92*, 225.
[2] V. I. Bregadze, *Chem. Rev.* **1992**, *92*, 209.
[3] a) Z. Xie, T. Jelinek, R. Bau, C. Reed, *J. Am. Chem. Soc.* **1994**, *116*, 1907; b) C. Reed, *Acc. Chem. Res.* **1998**, *31*, 133; c) S. Strauss, *Chem. Rev.* **1993**, *93*, 927; d) B. T. King, Z. Janousek, B. Grüner, M. Trammell, B. C. Noll, J. Michl, *J. Am. Chem. Soc.* **1996**, *118*, 3313.
[4] P. Kaszynski, *Collect. Czech. Chem. Commun.* **1999**, *64*, 895, and references therein.
[5] a) K. Nestor, B. Stíbr, J. D. Kennedy, M. Thornton-Pett, T. Jelinek, *Collect. Czech. Chem. Commun.* **1992**, *57*, 1262; b) T. Jelinek, B. Stíbr, J. Plesek, M. Thornton-Pett, J. D. Kennedy, *J. Chem. Soc. Dalton Trans.* **1997**, 4231.
[6] B. Brellochs in *Contemporary Boron Chemistry* (Eds.: M. G. Davidson, A. K. Hughes, T. B. Marder, K. Wade), Royal Society of Chemistry, Cambridge, **2000**, pp. 212.
[7] a) J. Plesek, T. Jelinek, B. Stíbr, S. Hemánek, *J. Chem. Soc. Chem. Commun.* **1988**, 348; b) T. Jelinek, B. Stíbr, J. Plesek, J. D. Kennedy, M. Thornton-Pett, *J. Chem. Soc. Dalton Trans.* **1995**, 431.
[8] a) A. Nicolaides, L. Radom, *J. Am. Chem. Soc.* **1994**, *116*, 9769; b) S. K. Shin, *Chem. Phys. Lett.* **1997**, *280*, 260; c) C. Lifshitz, *Acc. Chem. Res.* **1994**, *27*, 138; d) C.-H. Shin, K-C. Park, S.-J. Kim, B. Kim, *Bull. Korean Chem. Soc.* **2002**, *23*, 337.
[9] E. D. Jemmis, E. G. Jayasree, *Inorg. Chem.* **2003**, *42*, 7725.
[10] M. L. McKee, M. Bühl, P. von R. Schleyer, *Inorg. Chem.* **1993**, *32*, 1712.
[11] a) G. B. Dunks, R. J. Wiersema, M. F. Hawthorne, *J. Chem. Soc. Chem. Commun.* **1972**, 899; b) G. B. Dunks, R. J. Wiersema, M. F. Hawthorne, *J. Am. Chem. Soc.* **1973**, *95*, 3174; c) J. Plesek, T. Jelinek, B. Stíbr, S. Hermánek, *J. Chem. Soc. Chem. Commun.* **1988**, 348.
[12] a) D. Grafstein, J. Dvorak, *Inorg. Chem.* **1963**, *2*, 1128; b) L. Zakharkin, V. Kalinin, L. Podvisotskaya, *Izv. Akad. Nauk SSSR Ser. Khim.* **1967**, *10*, 2310; c) Y. Stanko, V. Goltypin, V. Brattsev, *Zh. Obshch. Khim.* **1969**, *39*, 1175.
[13] J. Plesek, B. Stíbr, X. L. R. Fontaine, T. Jelinek, M. Thornton-Pett, S. Hermánek, J. D. Kennedy, *Inorg. Chem.* **1994**, *33*, 2994.
[14] C. Viñas, G. Barberà, F. Teixidor, *J. Organomet. Chem.* **2002**, *642*, 16.
[15] J. Bould, A. Laromaine, C. Viñas, F. Teixidor, L. Barton, N. P. Rath, R. E. K. Winter, R. Kivekäs, R. Sillanpää, *Organometallics* **2004**, *23*, 3335.
[16] a) M. Lamrani, S. Gómez, C. Viñas, F. Teixidor, R. Sillanpää, R. Kivekäs, *New J. Chem.* **1996**, *20*, 909; b) F. Teixidor, S. Gómez, M. Lamrani, C. Viñas, R. Sillanpää, R. Kivekäs, *Organometallics* **1997**, *16*, 1278.
[17] a) S. V. Ivanov, J. J. Rockwell, S. M. Miller, O. P. Anderson, K. A. Solntsev, S. H. Strauss, *Inorg. Chem.* **1996**, *35*, 7882; b) N. J. Bullen, A. Franken, C. A. Kilner, J. D. Kennedy, *Chem. Commun.* **2003**, 1684.
[18] F. Teixidor, C. Viñas, R. W. Rudolph, *Inorg. Chem.* **1986**, *25*, 3339.

 © 2005 Wiley-VCH Verlag GmbH & Co. KGaA, Weinheim

Protein Dynamics

NMR Spectroscopic Detection of Protein Protons and Longitudinal Relaxation Rates between 0.01 and 50 MHz**

Ivano Bertini, Yogesh K. Gupta, Claudio Luchinat, Giacomo Parigi, Christian Schlörb, and Harald Schwalbe*

Nuclear magnetic relaxation data of water nuclei at variable fields provide valuable information on the dynamics of water–solute interactions.[1–3] However, information can be collected only within certain field ranges in which the nuclear relaxation rates are field-dependent owing to the dispersion of the spectral density, $J(\omega,\tau)$. The dispersion depends on the type of motion and on the observed nucleus. The most informative ^{1}H NMR spectroscopic frequency range for rotational motions is centered around 10 MHz for small proteins ($M_W \approx 10^4$ Da) and smaller frequencies for larger proteins and protein aggregates. Of course, resolution is low at these fields and in practice only one signal (or an unresolved signal envelope) can be detected. Furthermore, only the abundant water protons can be conveniently studied under such low sensitivity.

Relaxation of the isotopes ^{17}O and ^{2}H in enriched water can also be studied;[1] in these cases the centers of the informative field ranges increase by a factor ≈ 7 with respect to ^{1}H as a result of the magnetogyric ratios of ^{17}O and ^{2}H. Because water interacts with proteins, such relaxation studies provide direct information on the nature of water–protein dynamics, but give only indirect information on the protein itself.[4–6] It would be highly desirable to have complementary information directly from the protons of the protein, but this has been impractical so far owing to the low sensitivity of the available instrumentation. Protein ^{1}H relaxation data have been reported only on protein solutions of concentrations $\geq 35\%$ by mass,[7,8] far from physiological conditions. Improvements in field-cycling technology[9–12] have led to the production of instrumentation[13] with a $\approx$10-fold increase in the signal-to-noise ratio,[14] with which direct protein ^{1}H detection can be attempted for protein concen-

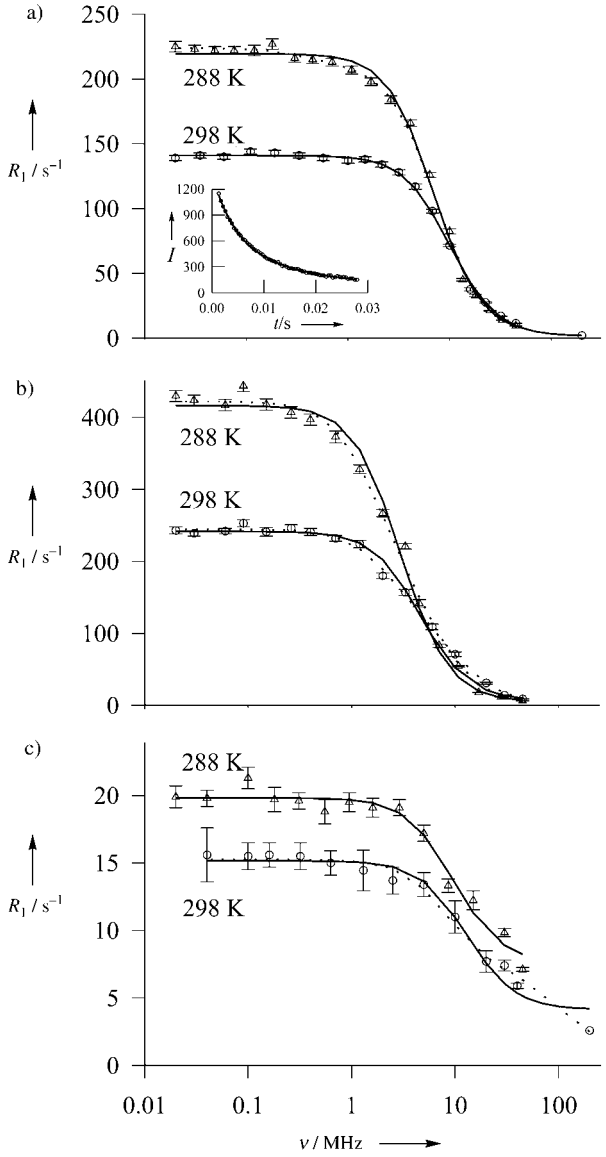

Figure 1. Protein ^{1}H relaxation dispersions for lysozyme solutions (2.8 mM in D_2O) at a) pH* 3.5, and b) pH* 9.0 (pH=pH-meter reading in D20 solution). The time decay of the collective protein ^{1}H magnetization at 0.1 MHz and its single-exponential fit are shown in the inset of part a). Theoretical relaxation rates were obtained through single-exponential fits of time decays of collective protein ^{1}H magnetization calculated from the known protein structure of lysozyme[17] and a complete relaxation matrix (CORMA) analysis.[18] Only exchangeable NH protons from secondary structure elements ($\approx$50% of total) were included, whereas all other exchangeable proton positions were assumed to be deuterated. Inclusion of either all or none of the NH protons affected the calculated rates by $\pm$2%. The theoretical low-field $\langle E^2 \rangle$ values obtained in this way were used to fit Equation (1) to the data (solid lines). The dotted lines represent data fits with two $J(\omega,\tau)$ terms in Equation (1) (Table 1). Panel c) shows the protein ^{1}H relaxation dispersion for a solution of α-synuclein in D_2O (1.4 mM, pH* 7.1). The solid and dotted lines represent fits with one or two $J(\omega,\tau)$ terms in Equation (1), respectively (Table 1). Points at 200 MHz were obtained from inversion-recovery experiments performed on a standard spectrometer.

[*] Prof. I. Bertini
Magnetic Resonance Center and Department of Chemistry
University of Florence
Via Luigi Sacconi 6, 50019 Sesto Fiorentino (Italy)
Fax: (+39) 055-457-4271
E-mail: bertini@cerm.unifi.it
Y. K. Gupta, Prof. C. Luchinat, Dr. G. Parigi
Magnetic Resonance Center and
Department of Agricultural Biotechnology
University of Florence
P. le delle Cascine 28, 50144 Florence (Italy)
C. Schlörb, Prof. H. Schwalbe
Center for Biomolecular Magnetic Resonance and
Institute for Organic Chemistry and Chemical Biology
Johann Wolfgang Goethe University Frankfurt
Marie-Curie-Strasse 11, 60439 Frankfurt (Germany)

[**] This work was supported by the European Union (contract HPRI-CT-2001-50028), by MIUR-FIRB, and by Ente Cassa di Risparmio di Firenze.

 DOI: 10.1002/anie.200462344 © 2005 Wiley-VCH Verlag GmbH & Co. KGaA, Weinheim

trations of ≈ 1 mM. Notably, the field-shuttling technique cannot be applied for these purposes, as it is limited by the time of sample transfer which does not permit detection of relaxation rates greater than $\approx 20\ s^{-1}$.[15,16]

The inset in Figure 1a shows the collective proton-magnetization decay at 0.1 MHz for a solution of lysozyme (2.8 mM, pH* 3.5 in D_2O; pH* = pH-meter reading in D_2O solution) previously treated with D_2O for deuteration at exchangeable-proton positions. For a rigid protein, at all frequencies of interest herein, CH_2 protons relax approximately two to three times faster than CH and nonexchanged NH protons; internal rotation causes CH_3 protons to relax as slowly as CH protons.[18] The magnetization decay should therefore be nonexponential, as it is a superposition of different decays. In practice, however, the decay can be fit with a single relaxation rate, R_1, in the time range from 1 ms to five times the value of R_1^{-1}. The root-mean-square deviation from the calculated decay is always below 1% of the maximum intensity of the signal. Residual water protons (estimated always to be fewer in number than protein protons by the peak amplitudes observed at 200 MHz) do not contribute appreciably to the observed decay in magnetization, as the polarization field was applied for a duration much shorter than the proton-relaxation time of water. Figure 1a shows the relaxation dispersion of lysozyme in D_2O. Note that the R_1 values at low field are on the order of $10^2\ s^{-1}$, whereas they decrease to essentially zero at high field. Relaxation can be interpreted with an equation of the type[1,6]

$$R_1 = S^2\langle E^2\rangle J(\omega,\tau_R) \qquad (1)$$

in which $J(\omega,\tau_R) = \frac{0.8\tau_R}{1+4\omega^2\tau_R^2} + \frac{0.2\tau_R}{1+\omega^2\tau_R^2}$, τ_R is the rotational correlation time, S^2 is an effective order parameter, and $\langle E^2\rangle$ is the squared average interaction energy among protein protons, whose theoretical value can be predicted (Figure 1) if the protein structure is known.

The best-fit τ_R and S^2 values are shown in Table 1. The τ_R values are as expected for monomeric lysozyme[19] and are in agreement with ^{15}N-relaxation measurements.[20] The S^2 parameter accounts for local motions that occur at times shorter than τ_R. The S^2 values are somewhat smaller than those found at high field according to the model-free approach for NH protons,[20] as for the measurements reported herein, the side chains contribute to the sub-τ_R mobility. Side-chain order parameters were estimated earlier to range between 0.05 and 0.9, depending on their position.[20] This effective S^2 parameter can be viewed as a measure of the overall rigidity of the protein.

Lysozyme is known to aggregate at high pH values, and is proposed[19] to be dimeric at pH 9.0. Measurements at pH* 9.0 (Figure 1b) demonstrate the sensitivity of this technique to aggregation. The R_1 values are markedly higher than those at low pH values; this results primarily from an increase in τ_R (Table 1).

Confirmation that this technique is also sensitive to the effective S^2 parameter comes from the dispersion of α-synuclein in its native, largely unfolded state[21] (Figure 1c). The low-field R_1 values of α-synuclein are only about 10% of those of lysozyme. A dispersion is observed with a correlation time similar to the τ_R of lysozyme (Table 1). As the two proteins have similar molar masses, the observed correlation time would correspond roughly to the τ_R value of hypothetically folded α-synuclein. As the $\langle E^2\rangle$ value is dominated by short-range interactions and is therefore modestly sensitive to the extent of protein folding, the small R_1 value essentially originates from a small S^2 value [Eq. (1)].

Information regarding protein rigidity (S^2) and aggregation (τ_R) can thus be easily obtained from the direct relaxation dispersion of protein protons. With respect to water nuclei dispersions, the analysis is neither complicated by the unknown number of long-lived water molecules and exchangeable protein protons, nor by the presence of water protons that exchange faster than τ_R (Table 1, footnote [a]).

Expected improvements in sensitivity will allow an increased complexity in analysis; for example, the detection of equilibria between different protein aggregates should be possible as well as the determination of protein folding in more quantitative terms. The quality of the present data may already permit further semiquantitative considerations. Inspection of Figure 1a and 1b reveals that a fit with a single $J(\omega,\tau)$ term in Equation (1) is satisfactory at low pH values at 298 K, reasonably good at low pH values at 288 K and at high pH values at 298 K, and definitely less satisfactory at high pH values at 288 K. A fit with two $J(\omega,\tau)$ terms in Equation (1) was thus attempted (Table 1). Largely aggregated protein at 0.3% is sufficient for the dramatic improvement of the data fit for low pH values at 288 K, whereas at high pH values a mixture of monomers and higher aggregates would fit the data much better and would yield more reasonable S^2 values. The fit with a single $J(\omega,\tau)$ term is good for α-synuclein, but tends to overestimate the height of the high-field-relaxation plateau. A much better fit of the data

Table 1: Fitting parameters for the relaxation dispersions of the protons of lysozyme and α-synuclein.

			One spectral density			Two spectral densities					
	pH*	T [K]	τ_R [ns]	S^2	α [%][a]	τ_R [ns]	%	τ'_R [ns]	%	S^2	α [%][a]
lysozyme	3.5	298	9.0 ± 0.4	0.77 ± 0.04	1.2 ± 2.5						
	3.5	288	12.9 ± 1.5	0.85 ± 0.09	1.2 ± 4.1	12.4 ± 0.1	99.7 ± 0.9	231 ± 447	0.3	0.85[b]	1.5 ± 1.8
	9.0	298	21.0 ± 3.7	0.53 ± 0.10	7.1 ± 6.7	9.0[b]	75 ± 7	35 ± 7	25	0.77[b]	2.2 ± 2.7
	9.0	288	31.7 ± 5.4	0.64 ± 0.12	3.3 ± 6.0	12.9[b]	64 ± 13	47 ± 13	36	0.85[b]	0.2 ± 3.5
α-synuclein	7.1	298	7.0 ± 1.8	0.08 ± 0.02	28 ± 10	10 ± 3		0.6 ± 0.2		0.08[b]	0 ± 6
	7.1	288	9.5 ± 2.5	0.06 ± 0.02	38 ± 10						

[a] Percent value of the high-field plateau, related only to fast local motions. Note that in nuclear magnetic relaxation dispersion for water nuclei, this term is dominated by the relaxation contribution from an unknown number of water molecules exchanging rapidly with respect to τ_R. [b] Fixed at the monomer value.

 © 2005 Wiley-VCH Verlag GmbH & Co. KGaA, Weinheim

at 298 K is obtained by using a model-free approach under the assumption of segmental motions[22] of the unfolded protein to account for the missing $(1-S^2)$ term. An inflection with a τ value of 10 ns and a second inflection with a τ value of 0.6 ns is in good agreement with the experimental data (Figure 1c and Table 1).

In conclusion, we have shown that data from direct protein ^{1}H relaxation dispersion yield information on: 1) the lack of rigidity through S^2, which is directly related to the range of folded states of the protein (from fully folded to the extreme state of complete unfolding) and 2) protein aggregation through a safe estimate of τ_R.

Received: October 18, 2004
Published online: March 4, 2005

Keywords: aggregation · deuterium · protein folding · protein structures · protonation

[1] B. Halle, V. P. Denisov, *Methods Enzymol.* **2001**, *338*, 178–201.
[2] J. A. Butterwick, J. P. Loria, N. S. Astrof, C. D. Kroenke, R. Cole, M. Rance, A. G. Palmer III, *J. Mol. Biol.* **2004**, *339*, 855–871.
[3] D. M. Korzhnev, X. Salvatella, M. Vendruscolo, A. A. Di Nardo, A. R. Davidson, C. M. Dobson, L. E. Kay, *Nature* **2004**, *430*, 586–590.
[4] V. P. Denisov, B.-H. Jonsson, B. Halle, *Nat. Struct. Biol.* **1999**, *6*, 253–260.
[5] B. Halle, M. Davidovic, *Proc. Natl. Acad. Sci. USA* **2003**, *100*, 12135–12140.
[6] A. Van-Quynh, S. Willson, R. G. Bryant, *Biophys. J.* **2003**, *84*, 558–563.
[7] W. Nusser, R. Kimmich, *J. Phys. Chem.* **1990**, *94*, 5637–5639.
[8] J.-P. Korb, R. G. Bryant, *J. Chem. Phys.* **2001**, *115*, 10964–10974.
[9] F. Noack, *Prog. Nucl. Magn. Reson. Spectrosc.* **1986**, *18*, 171–276.
[10] S. H. Koenig, R. D. Brown III, *Prog. Nucl. Magn. Reson. Spectrosc.* **1991**, *22*, 487–567.
[11] R. Kimmich, E. Anoardo, *Prog. Nucl. Magn. Reson. Spectrosc.* **2004**, *44*, 257–320.
[12] I. Bertini, C. Luchinat, G. Parigi, *Solution NMR of Paramagnetic Molecules*, Elsevier, Amsterdam, **2001**.
[13] G. Ferrante, S. Sykora, *Adv. Inorg. Chem.* **2005**, in press.
[14] G. Ferrante, personal communication.
[15] M. F. Roberts, A. G. Redfield, *J. Am. Chem. Soc.* **2004**, *126*, 13765–13777.
[16] S. Wagner, T. R. J. Dinesen, T. Rayner, R. G. Bryant, *J. Magn. Reson.* **1999**, *140*, 172–178.
[17] M. S. Weiss, G. J. Palm, R. Hilgenfeld, *Acta Crystallogr. D* **2000**, *56*, 952–958.
[18] B. Borgias, M. Gochin, D. J. Kerwood, T. L. James, *Prog. Nucl. Magn. Reson. Spectrosc.* **1990**, *22*, 83–100.
[19] M. Gottschalk, B. Halle, *J. Phys. Chem. B* **2003**, *107*, 7914–7922.
[20] M. Buck, J. Boyd, C. Redfield, D. A. MacKenzie, D. J. Jeenes, D. B. Archer, C. M. Dobson, *Biochemistry* **1995**, *34*, 4041–4055.
[21] C. Bertoncini, C. O. Fernandez, W. Hoyer, C. Griesinger, T. M. Jovin, M. Zweckstetter, *Proceedings of the EENC-Ampere*, Lille, Sept. **2004**; C. O. Fernandez, W. Hoyer, M. Zweckstetter, E. A. Jares-Erijman, V. Subramaniam, C. Griesinger, T. M. Jovin, *EMBO J.* **2004**, *23*, 2039–2046; R. Bussell, Jr., D. Eliezer, *J. Biol. Chem.* **2001**, *276*, 45996–46003; D. Eliezer, E. Kutluay, R. Bussell, Jr., G. Browne *J. Mol. Biol.* **2001**, *307*, 1061–1073.
[22] G. Lipari, A. Szabo, *J. Am. Chem. Soc.* **1982**, *104*, 4546–4559.

 © 2005 Wiley-VCH Verlag GmbH & Co. KGaA, Weinheim

Expanded Porphyrins

meso-Aryl-Substituted [26]Hexaphyrin(1.1.0.1.1.0) and [38]Nonaphyrin(1.1.0.1.1.0.1.1.0) from Oxidative Coupling of a Tripyrrane**

*Soji Shimizu, Ryuichiro Taniguchi, and Atsuhiro Osuka**

In recent years, there has been a surge in the development of expanded porphyrins which has been boosted by their unique optical, electrochemical, and coordination properties, as well as their potential uses as receptors of anionic or neutral substrates.[1] Rubyrin, which represents a class of [26]hexaphyrin(1.1.0.1.1.0) macrocycles, was first synthesized and characterized by Sessler et al. as a dication of a β-dodeca-(alkyl)-substituted molecule.[2,3] A range of core-modified rubyrins that bear *meso*-aryl substituents have also been explored by Chandrashekar and co-workers.[4] The rubyrins prepared so far all exhibit a strong diatropic ring current in line with their 26-π-aromatic circuit. Furthermore, dicationic rubyrins have been shown to serve as a good receptor for anions,[2,4] but structural details of resultant complexes have been only poorly studied except for the case of the parent rubyrin. Herein we report the concise synthesis of *meso*-aryl-substituted rubyrin **2** and interesting anion-recognition behavior of its dication. To the best of our knowledge, an all-aza isomer of a *meso*-aryl-substituted rubyrin has not been reported, despite its importance in the chemistry of expanded porphyrins. Besides the rubyrin derivative, its higher homologue nonaphyrin(1.1.0.1.1.0.1.1.0) was also obtained, and its structural characterization is also described here.

Following the method reported by Chandrashekar and co-workers,[4b,c] a solution of *meso*-pentafluorophenyl-substituted tripyrrane **1**[5] in CH_2Cl_2 was treated with 0.5 equivalents of trifluoroacetic acid (TFA) in CH_2Cl_2 for 90 minutes at room temperature, then 3 equivalents of chloranil (tetrachloro-1,4-benzoquinone) was added, and the mixture was subsequently heated at reflux for 90 minutes. Sequential separations by column chromatography provided the rubyrin 5,10,19,24-tetrakis(pentafluorophenyl)-[26]hexaphyrin-(1.1.0.1.1.0) (**2**) as a stable violet solid in 24% yield, and 5,10,19,24,33,38-hexakis(pentafluorophenyl)-[38]nonaphyrin

[*] S. Shimizu, R. Taniguchi, Prof. A. Osuka
Department of Chemistry
Graduate School of Science, Kyoto University and
Core Research for Evolutional Science and Technology (CREST)
Japan Science and Technology Agency
Sakyo-ku, Kyoto 606-8502 (Japan)
Fax: (+81) 75-753-4007
E-mail: osuka@kuchem.kyoto-u.ac.jp

[**] This work was partly supported by a grant-in-aid (no. 15350022) from the Ministry of Education, Culture, Sports, Science, and Technology, Japan. S.S. thanks JSPS for a Research Fellowship for Young Scientists.

Supporting information for this article is available on the WWW under http://www.angewandte.org or from the author.

 DOI: 10.1002/anie.200463054 © 2005 Wiley-VCH Verlag GmbH & Co. KGaA, Weinheim

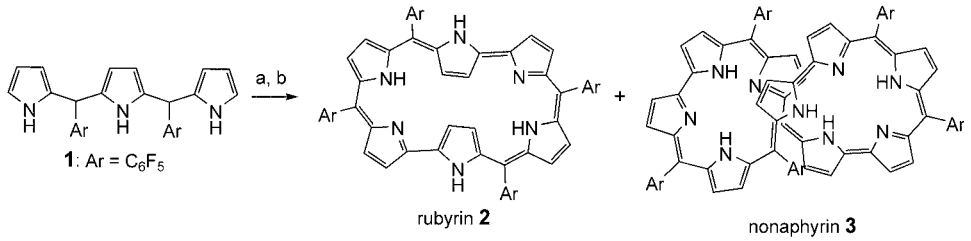

Scheme 1. Oxidative coupling reaction of *meso*-pentafluorophenyl-substituted tripyrrane **1** to form the rubyrin [26]hexaphyrin(1.1.0.1.1.0) (**2**) and [38]nonaphyrin(1.1.0.1.1.0.1.1.0) (**3**): a) TFA, CH_2Cl_2; b) chloranil, reflux.

(1.1.0.1.1.0.1.1.0) (**3**) as a green solid in 9% yield (Scheme 1).[6] Interestingly, MALDI-TOF-MS analysis of the reaction mixture revealed the formation of higher homologues such as dodecaphyrin and pentadecaphyrin, but macrocycles that may have formed through acidolysis of **1** were not detected.

The rubyrin **2** exhibited its parent-ion peak at $m/z = 1105$ ($[M+H]^+$). Its ^{1}H NMR spectrum taken in $CDCl_3$ revealed the inner β-CH protons at $\delta = -2.11$ and -2.18 ppm as a pair of doublets ($J = 3.4$ Hz), the outer β-CH protons at $\delta = 9.16$ (2H, doublet, $J = 4.1$ Hz), 8.74 (4H), and 8.66 ppm (2H, doublet, $J = 4.1$ Hz), and the outer NH protons at $\delta =$ 11.5 ppm. The inner NH protons appeared at $\delta = 1.63$ ppm as a singlet. These data indicate a diatropic ring current for **2**. The structure of **2** was confirmed by X-ray crystallographic analysis[7] and adopts a parallelogram shape in which the pyrrole rings C and F of the bipyrrolic subunits are inverted and canted by 30° from the mean plane defined by the other pyrrole rings (Figure 1, type I conformation as shown in Scheme 2). This type of conformation was proposed for a dioxarubyrin macrocycle on the basis of the ^{1}H NMR spectroscopic data,[4e] but has now been revealed for the first time for a free-base *meso*-aryl-substituted rubyrin. In line with the 26-π-electron aromaticity, the bond lengths of bridging C–C bonds are rather similar. There are two intramolecular hydrogen-bonding interactions at the dipyrromethene moieties with a N–H···N distance of 1.99 Å and an angle of 125°. This shorter hydrogen-bonding distance accounts for the rather downfield shift of the inner NH protons that appear in a strongly shielding region.

The absorption spectrum of free-base **2** exhibited a sharp Soret-like band at 537 nm ($\varepsilon = 1.70 \times 10^5\,\text{M}^{-1}\,\text{cm}^{-1}$) and a weak broad Q-like band with peaks at 802, 832, and 919 nm (Figure 2), similar to the absorption spectra of other rubyrins.[2,4,8] Protonation of **2** upon addition of an excess amount of TFA in CH_2Cl_2 led to a red shift and intensification of the Soret-like band to 555 nm ($\varepsilon = 3.3 \times 10^5\,\text{M}^{-1}\,\text{cm}^{-1}$). Curiously, the protonation of **2** with HCl caused intensification of its Soret-like band ($\varepsilon = 3.4 \times 10^5\,\text{M}^{-1}\,\text{cm}^{-1}$) at 518 nm, which was distinctly blue-shifted relative to the free-base **2**. These results suggest that the resultant rubyrin dication salts **2**·2TFA and **2**·2HCl may have different conformations and thus different electronic structures.

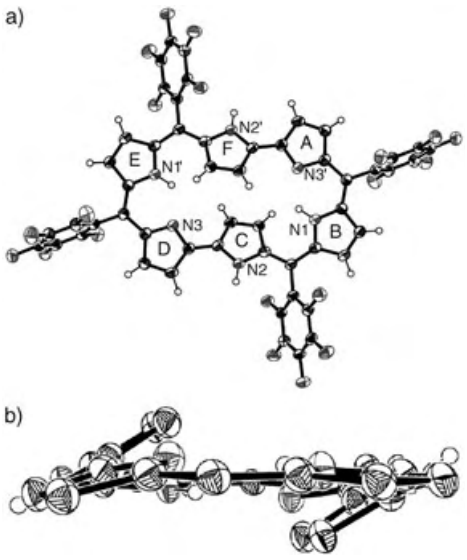

Figure 1. X-ray crystal structure of **2**: a) top view and b) side view. The thermal ellipsoids were scaled to the 50% probability level. The solvent molecule was omitted in the top view, and *meso*-pentafluorophenyl substituents and hydrogen atoms at the β position were omitted in the side view for clarity.

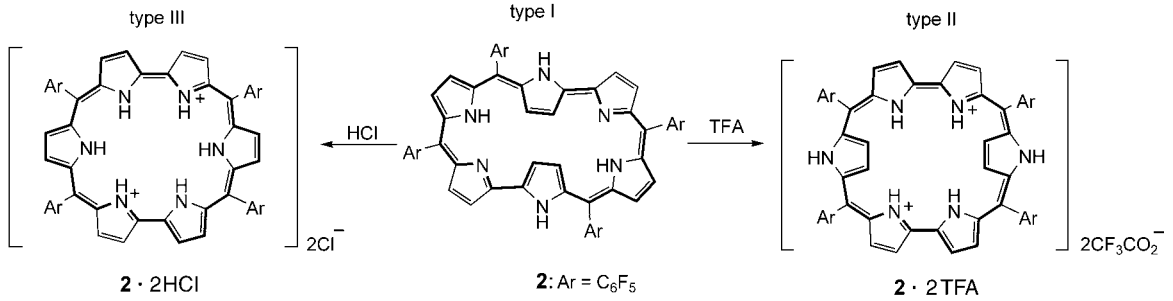

Scheme 2. Conformational changes in **2** upon protonation with HCl and trifluoroacetic acid (TFA).

 © 2005 Wiley-VCH Verlag GmbH & Co. KGaA, Weinheim

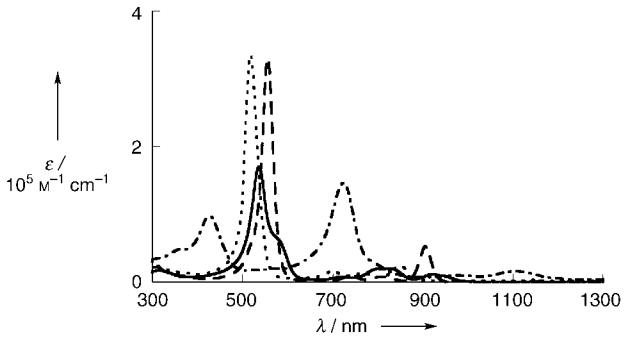

Figure 2. UV/Vis absorption spectra of **2** (——), **2**·2TFA (– – –), **2**·2HCl (-----), and **3** (–•–•) recorded in CH_2Cl_2.

The ^{1}H NMR spectrum of salt **2**·2TFA in [D_8]THF showed D_2O-exchangeable broad peaks at $\delta = -3.86$ and 16.5 ppm in a 2:1 ratio that have been assigned to the inner and outer NH protons. In [D_8]THF containing a small amount of D_2O, the spectrum showed a sharp singlet at $\delta = -3.30$ ppm and two signals at $\delta = 10.9$ and 10.2 ppm in a 1:1:1 ratio which have been assigned to the inner and outer β-CH protons, respectively. These data suggest a symmetric structure, with two bipyrrolic moieties pointing inward and two pyrroles pointing outward (type II conformation in Scheme 2). In contrast, the ^{1}H NMR spectrum of salt **2**·2HCl in $CDCl_3$ revealed the β-CH protons at $\delta = 10.6$, 9.75, and 8.95 ppm in a 1:1:1 ratio, and the NH protons at $\delta = -3.05$ and -3.26 ppm in a 1:2 ratio, which indicates a different symmetric structure with all the pyrrole rings pointing inward (type III conformation in Scheme 2).

Both the structures of **2**·2TFA and **2**·2HCl were explicitly determined by single-crystal X-ray diffraction analysis (Figure 3 and Figure 4, respectively).[9,10] The salt **2**·2TFA displays a rectangular conformation with the pyrrole rings B and E inverted and canted by 35° with respect to the mean plane defined by the other four pyrrolic rings (Figure 3).

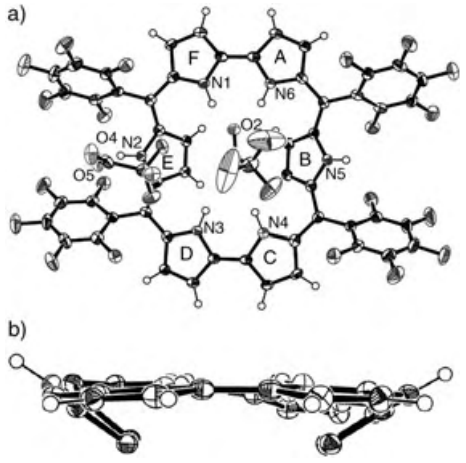

Figure 3. X-ray crystal structure of **2**·2TFA: a) top view and b) side view. The thermal ellipsoids were scaled to the 50% probability level. Solvent molecules were omitted in the top view, and *meso*-pentafluorophenyl substituents, hydrogen atoms at the β position, and counteranions were omitted in the side view for clarity.

meso-Pentafluorophenyl substituents are canted by about 50° in a V-shape to establish a channel above the molecular plane along which two trifluoroacetate anions, one molecule of TFA, and one solvent molecule (THF) are aligned. One trifluoroacetate anion lies just above the center of the macrocycle and is bound by the four bipyrrolic amine groups through hydrogen-bonding interactions, with N–H···O distances of about 1.9 Å, while the other trifluoroacetate anion resides at the edge of the macrocyclic ring, hydrogen-bonded with the amine group of the inverted pyrrole E (N–H···O: 1.94 Å, 140°). On the other hand, the salt **2**·2HCl exhibits a domelike ruffled structure in which all the pyrrole rings take inward orientation to interact with two chloride anions (Figure 4). One chloride anion is positioned

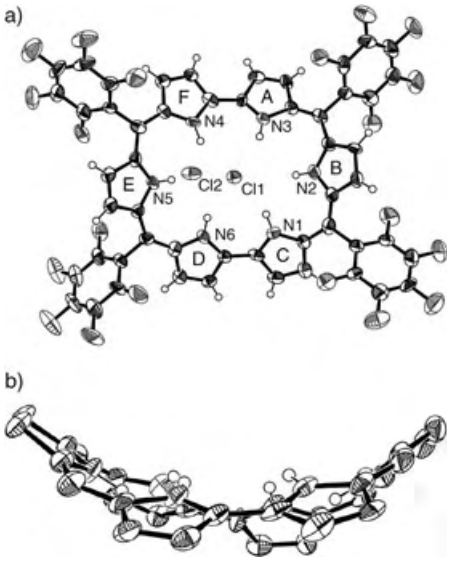

Figure 4. X-ray crystal structure of **2**·2HCl: a) top view and b) side view. The thermal ellipsoids were scaled to the 50% probability level. Solvent molecules were omitted in the top view, and *meso*-pentafluorophenyl substituents, hydrogen atoms at the β positions, and counteranions were omitted in the side view for clarity.

1.2 Å above the macrocycle mean plane and is bound by the four bipyrrolic NH protons with distances of 2.34, 2.33, 2.39, and 2.42 Å, while the other chloride ion lies near to the NH of pyrrole E through hydrogen-bonding interaction (N–H···Cl: 2.42 Å, 142°), thus lying slightly off-center. Furthermore, a molecule of acetic acid, which results from hydrolysis of ethyl acetate (the solvent used in crystallization), lies next to the second chloride anion and is held by the macrocycle through hydrogen-bonding interactions between the acid C=O moiety and the NH group of pyrrole B, and between the acid OH group and the chloride counteranion bound by the NH of pyrrole E (see Supporting Information).

The type III structure of **2**·2HCl is essentially the same as that of the β-dodeca(alkyl)-substituted-rubyrin–HCl salt reported by Sessler et al. which exhibited a blue-shifted Soret-like band at $\lambda = 505$ nm.[2] These results clearly indicate that the dication of rubyrin **2** can change its conformation in response to added acids, through interactions with counteranions.[11] This comes from conformational flexibility, partic-

 © 2005 Wiley-VCH Verlag GmbH & Co. KGaA, Weinheim

ularly rotational freedom about the bipyrrolic bonds. Interestingly, the structural changes among types I, II, and III are linked, through changes in the conjugated electronic network, to the spectral changes, which can be detected easily. Preliminary measurements have shown that methanesulfonic acid behaves in essentially the same manner as TFA towards **2**, but the addition of H_2SO_4 or H_3PO_4 leads to two sharp Soret-like bands around 515 and 555 nm, which suggests the presence of both type II and type III structures. Conformational flexibility of **2** has been examined by variable-temperature ^{1}H NMR measurements. The spectrum did not change up to 60 °C, but became broader at 80 °C and converged to a signal at $\delta = 8.68$ ppm for the β protons and a broad signal at $\delta = -1.82$ ppm for the NH protons at 120 °C, probably indicating rapid flipping of the bipyrrolic moieties (see Supporting Information).

Nonaphyrin **3** exhibited its parent-ion peak at $m/z = 1655$ (M^+) in its FAB mass spectrum. Its ^{1}H NMR spectrum displayed eighteen different signals for the peripheral β protons, among which seven β protons resonated in a slightly upfield region at $\delta = 6.30$, 6.08, 5.67, 5.54, 4.73, and 4.64 ppm relative to the others. Two D_2O-exchangeable singlets at $\delta =$ 11.3 and 11.0 ppm were assigned to two NH protons, while the rest of the NH proton signals were not detected probably on account of broadening of the peaks owing to hydrogen-bonding interactions. The structure of **3** has been also confirmed by X-ray crystallographic analysis (Figure 5),[12] which reveals a twisted figure-of-eight conformation without any planes of symmetry and is consistent with the ^{1}H and ^{19}F NMR spectroscopic data. The macrocyclic structure consists of two semihelical planes of four and five pyrrole rings aided by hydrogen-bonding interactions between amine NH groups and imine N atoms of the pyrrole rings (the N–H···N distances are 2.86 (A to B), 2.59 (B to C), 2.24 (C to D), 2.63 (D to E), 2.02 (F to G), 2.66 (G to H), and 2.02 Å (H to I), respectively). The dihedral angles between the neighboring pyrrole rings are 2.0, 21.2, 10.4, 7.5, 35.9, 14.3, 11.9, 10.0, and 26.9° clockwise from pyrrole A, and the pyrrole-linking C–C bond lengths are in the range of 1.38–1.41 Å and feature only modest bond-length alternation. The UV/Vis absorption spectrum of **3** exhibited two sharp Soret-like bands at $\lambda =$ 427 ($\varepsilon = 1.00 \times 10^5$) and 724 nm ($\varepsilon = 1.46 \times 10^5\,\text{M}^{-1}\text{cm}^{-1}$) and Q-like bands at $\lambda = 970$ and 1107 nm (Figure 1), which reflect a larger 38-π-conjugated electronic system.

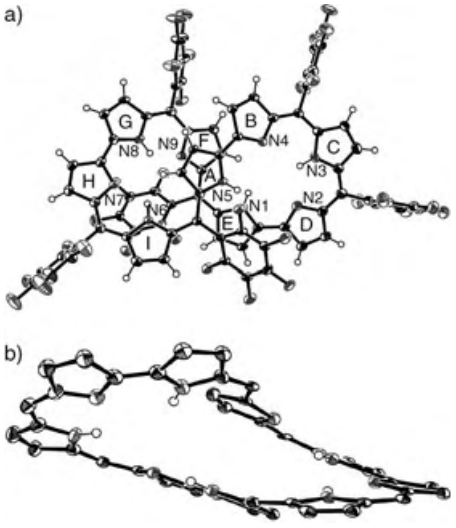

Figure 5. X-ray crystal structure of **3**: a) top view and b) side view. The thermal ellipsoids were scaled to the 50% probability level. Solvent molecules were omitted in the top view, and *meso*-pentafluorophenyl substituents and hydrogen atoms at the β positions were omitted in the side view for clarity.

In summary, rubyrin **2** and nonaphyrin **3** were simply prepared from the acid-catalyzed oxidative coupling reaction of the tripyrrane **1**. Rubyrin **2** is an aromatic macrocycle that exhibits a diatropic ring current and displays clear spectral changes upon the addition of acid, as a result of conformational changes through interaction with the counteranion, thus encouraging its dication as a potential anion-recognition reagent. The structural changes of expanded porphyrins induced by outer stimuli are being further investigated in our laboratory.

Experimental Section

Rubyrin **2** and nonaphyrin **3**: TFA (30.6 μL, 0.4 mmol) was added to a solution of **1** (450 mg, 0.81 mmol) in CH_2Cl_2 (90 mL), and the resulting solution was stirred for 90 min at RT under N_2. Then chloranil (594 mg, 2.63 mmol) was added, and the mixture was heated at reflux for a further 90 min. The reaction was quenched with an aqueous solution of $NaHCO_3$, and the organic layer was separated, washed once with water, and dried over anhydrous Na_2SO_4. After removal of solvent, the crude product was purified over a neutral-alumina column using a mixture of CH_2Cl_2/hexane as eluent. After elution of deeply colored fractions, a purple fraction was eluted with

Table 1: Selected physical data for **2**, **2**·2TFA, **2**·2HCl, and **3**.

2: ^{1}H NMR ($CDCl_3$, 600 MHz 298 K): $\delta = 11.49$ (s, 2H; NH), 9.16 (d, $J = 4.1$ Hz, 2H; β-CH), 8.74 (m, 4H; β-CH), 8.66 (d, $J = 4.1$ Hz, 2H; β-CH), 1.63 (s, 2H; NH), −2.11 (d, $J = 3.4$ Hz, 2H; β-CH), −2.18 ppm (d, $J = 3.4$ Hz, 2H; β-CH); UV/Vis (CH_2Cl_2): λ_{max} (ε): 537 (1.70), 802 (0.18), 832 (0.19), 919 nm ($0.11 \times 10^5\,\text{M}^{-1}\text{cm}^{-1}$); HRMS (ESI-TOF): m/z calcd for $C_{52}N_6F_{20}H_{17}$: 1105.1190; found: 1105.1186 (100%) $[M+H]^+$.

2·2TFA: ^{1}H NMR ([D_8]THF, 600 MHz 298 K): $\delta = 16.47$ (br s, 2H; NH), 10.91 (br s, 4H; β-CH), 10.16 (br s, 4H; β-CH), −3.29 (s, 4H; β-CH), −3.86 ppm (s, 4H; NH); UV/Vis (CH_2Cl_2): λ_{max} (ε): 555 (3.30), 737 (0.10), 808 (0.08), 904 nm ($0.52 \times 10^5\,\text{M}^{-1}\text{cm}^{-1}$).

2·2HCl: ^{1}H NMR ($CDCl_3$, 600 MHz 298 K): $\delta = 10.57$ (d, $J = 3.5$ Hz, 4H; β-CH), 9.75 (d, $J = 3.4$ Hz, 4H; β-CH), 8.95 (s, 4H; β-CH), −3.05 (s, 2H; NH), −3.26 ppm (s, 4H; NH); UV/Vis (CH_2Cl_2): λ_{max} (ε): 518 (3.35), 700 (0.16), 764 (0.12), 848 nm ($0.24 \times 10^5\,\text{M}^{-1}\text{cm}^{-1}$).

3: ^{1}H NMR ($CDCl_3$, 600 MHz 298 K): $\delta = 11.28$ (br s, 1H; NH), 10.98 (br s, 1H; NH), 8.00 (d, $J = 4.8$ Hz, 1H; β-CH), 7.82 (d, $J = 4.8$ Hz, 1H; β-CH), 7.60 (d, $J = 4.8$ Hz, 1H; β-CH), 7.53 (d, $J = 4.1$ Hz, 1H; β-CH), 7.16 (d, $J = 4.8$ Hz, 1H; β-CH), 7.09 (d, $J = 4.8$ Hz, 1H; β-CH), 6.98 (d, $J = 4.9$ Hz, 1H; β-CH), 6.91 (d, $J = 4.8$ Hz, 1H; β-CH), 6.85 (d, $J = 4.8$ Hz, 1H; β-CH), 6.78 (2H; β-CH), 6.30 (m, 2H; β-CH), 6.08 (d, $J = 4.8$ Hz, 1H; β-CH), 5.67 (d, $J = 4.1$ Hz, 1H; β-CH), 5.54 (d, $J = 4.1$ Hz, 1H; β-CH), 4.73 (d, $J = 4.1$ Hz, 1H; β-CH), 4.64 ppm (d, $J = 4.8$ Hz, 1H; β-CH); UV/Vis (CH_2Cl_2): λ_{max} (ε): 427 (1.00), 724(1.46), 970 (0.10), 1107 nm ($0.16 \times 10^5\,\text{M}^{-1}\text{cm}^{-1}$); HRMS (ESI-TOF): m/z calcd for $C_{78}N_9F_{30}H_{24}$: 1656.1670; found: 1656.1699 (100%) $[M+H]^+$.

 © 2005 Wiley-VCH Verlag GmbH & Co. KGaA, Weinheim

CH_2Cl_2 which contained **2** (107 mg, 24%). The first eluted fraction from the alumina column was further purified by column chromatography on silica gel using a mixture of CH_2Cl_2/hexane as eluent to give a green fraction of **3** (38 mg, 8.5%; see Table 1).

Received: December 24, 2004
Published online: March 10, 2005

Keywords: aromaticity · hydrogen bonds · macrocycles · porphyrinoids · protonation

[1] a) A. Jasat, D. Dolphin, *Chem. Rev.* **1997**, *97*, 2267; b) T. D. Lash, *Angew. Chem.* **2000**, *112*, 1833; *Angew. Chem. Int. Ed.* **2000**, *39*, 1763; c) H. Furuta, H. Maeda, A. Osuka, *Chem. Commun.* **2002**, 1795; d) J. L. Sessler, D. Seidel, *Angew. Chem.* **2003**, *115*, 5292; *Angew. Chem. Int. Ed.* **2003**, *42*, 5134; e) A. Ghosh, *Angew. Chem.* **2004**, *116*, 1952; *Angew. Chem. Int. Ed.* **2004**, *43*, 1918; f) T. K. Chandrashekar, S. Venkatraman, *Acc. Chem. Res.* **2003**, *36*, 676.

[2] J. L. Sessler, T. Morishima, V. Lynch, *Angew. Chem.* **1991**, *103*, 1018; *Angew. Chem. Int. Ed. Engl.* **1991**, *30*, 977.

[3] Sessler et al. noted that efforts to obtain the free-base form of β-dodeca(alkyl)-substituted rubyrin had so far been unsuccessful, but the free-base β-deca(alkyl)-substituted rubyrin, which may have some rotational freedom, was stable in contrast to fully β-dodeca(alkyl)-substituted rubyrin, which implies the importance of rotational freedom about the bipyrrolic bonds for the stability of free-base rubyrin.[2]

[4] a) A. Srinivasan, V. M. Reddy, S. J. Narayanan, B. Sridevi, S. K. Pushpan, M. Ravikumar, T. K. Chandrashekar, *Angew. Chem.* **1997**, *109*, 2710; *Angew. Chem. Int. Ed. Engl.* **1997**, *36*, 2598; b) S. J. Narayanan, B. Sridevi, T. K. Chandrashekar, A. Vij, R. Roy, *Angew. Chem.* **1998**, *110*, 3582; *Angew. Chem. Int. Ed.* **1998**, *37*, 3394; c) S. J. Narayanan, B. Sridevi, T. K. Chandrashekar, A. Vij, R. Roy. *J. Am. Chem. Soc.* **1999**, *121*, 9053; d) A. Srinivasan, S. K. Pushpan, M. Ravikumar, T. K. Chandrashekar, R. Roy, *Tetrahedron* **1999**, *55*, 6671; e) S. J. Narayanan, A. Srinivasan, B. Sridevi, T. K. Chandrashekar, M. O. Senge, K. Sugiura, Y. Sakata, *Eur. J. Org. Chem.* **2000**, 2357.

[5] a) P. D. Rao, S. Dhanalekshmi, B. J. Littler, J. S. Lindsey, *J. Org. Chem.* **2000**, *65*, 7323; b) B. J. Littler, M. A. Miller, C.-H. Hung, R. W. Wagner, D. F. O'Shea, P. D. Boyle, J. S. Lindsey, *J. Org. Chem.* **1999**, *64*, 1391.

[6] Similar acid-promoted oxidative coupling of pyrroles has been shown to be quite effective in the synthesis of expanded porphyrins. See: a) J. L. Sessler, D. Seidel, V. Lynch, *J. Am. Chem. Soc.* **1999**, *121*, 11257; b) D. Seidel, V. Lynch, J. L. Sessler, *Angew. Chem.* **2002**, *114*, 1480; *Angew. Chem. Int. Ed.* **2002**, *41*, 1422; c) T. Köhler, D. Seidel, V. Lynch, F. O. Arp, Z. Ou, K. M. Kadish, J. L. Sessler, *J. Am. Chem. Soc.* **2003**, *125*, 6872.

[7] Crystallographic data for *meso*-pentafluorophenyl-substituted rubyrin **2**: $C_{60}H_{32}F_{20}N_6O_4$, $M_W = 1280.92$, monoclinic, space group $P2_1/a$ (no. 14), $a = 10.422(5)$, $b = 15.731(7)$, $c = 17.097(8)$ Å, $\beta = 103.03(4)°$, $V = 2730(2)$ Å^3, $Z = 2$, $\rho_{calcd} = 1.558\ g\,cm^{-3}$, $T = -150\,°C$, 19549 measured reflections, 6201 unique reflections ($R_{int} = 0.073$), 2932 with $I \geq 3\sigma(I)$ used in refinement, $R = 0.062$, $R_w = 0.067$, GOF = 1.275.

[8] A stable β-deca(alkyl)rubyrin was reported to exhibit its Soret-like band at $\lambda = 513$ nm in its free-base form.[2]

[9] Crystallographic data for rubyrin–TFA complex **2**·2TFA: $C_{62}H_{26}F_{29}N_6O_7$, $M_W = 1517.88$, monoclinic, space group $P2_1/a$ (no. 14), $a = 17.51(1)$, $b = 18.18(1)$ $c = 18.87(1)$ Å, $\beta = 90.47(6)°$, $V = 6006(6)$ Å^3, $Z = 4$, $\rho_{calcd} = 1.678\ g\,cm^{-3}$, $T = -150\,°C$, 105844 measured reflections, 13695 unique reflections ($R_{int} = 0.057$), 7364 with $I \geq 3\sigma(I)$ used in refinement, $R = 0.071$, $R_w = 0.087$, GOF = 1.266.

[10] Crystallographic data of rubyrin–HCl complex **2**·2HCl: $C_{62}H_{30}F_{20}N_6O_6Cl_2$, $M_W = 1405.83$, triclinic, space group $P\bar{1}$ (no. 2), $a = 14.62(1)$, $b = 15.07(1)$ $c = 15.87(1)$ Å, $\alpha = 82.74(7)$, $\beta = 73.73(6)$, $\gamma = 74.35(6)°$, $V = 3227(4)$ Å^3, $Z = 2$, $\rho_{calcd} = 1.446\ g\,cm^{-3}$, $T = -150\,°C$, 29837 measured reflections, 29837 unique reflections ($R_{int} = 0.100$), 8804 with $I \geq 3\sigma(I)$ used in refinement, $R = 0.097$, $R_w = 0.125$, GOF = 1.045.

[11] Anion-binding behavior with conformational changes through interactions with anions are one of well-known and promising properties in the area of pyrrole-based macrocycles, such as calixpyrroles. See: P. A. Gale, J. L. Sessler, V. Kral, *Chem. Commun.* **1998**, 1. In the case of expanded porphyrins, sapphyrins are the first example of anion-binding agents, see: J. L. Sessler, J. M. Davis, *Acc. Chem. Res.* **2001**, *34*, 989. Similar counteranion-dependent spectral changes were reported for a dication of dithiarubyrin.[4a]

[12] Crystallographic data for *meso*-pentafluorophenyl-substituted [38]nonaphyrin(1.1.0.1.1.0.1.1.0) **3**: $C_{79}H_{23}F_{30}N_9O_2Cl_2$, $M_W = 1770.96$, triclinic, space group $P\bar{1}$ (no. 2), $a = 11.9440(19)$, $b = 17.319(3)$, $c = 17.915(3)$ Å, $\alpha = 82.739(4)$, $\beta = 71.418(3)$, $\gamma = 77.792(3)°$, $V = 3426.4(10)$ Å^3, $Z = 2$, $\rho_{calcd} = 1.717\ g\,cm^{-3}$, $T = -153\,°C$, 12100 measured reflections, 9720 unique reflections ($R_{int} = 0.0241$). $R = 0.0847$, R_w (all data) = 0.2538, GOF = 1.041. CCDC 258963 (**2**), 258964 (**2**·2TFA), 258965 (**2**·2HCl), and 258966 (**3**) contain the supplementary crystallographic data for this paper. These data can be obtained free of charge from the Cambridge Crystallographic Data Centre via www.ccdc.cam.ac.uk/data_request/cif.

 © 2005 Wiley-VCH Verlag GmbH & Co. KGaA, Weinheim

Redox Chemistry

Electrochemical Hydrogenation of $[Ru(bpy)_2(napy\text{-}\kappa N)(CO)]^{2+}$: Inhibition of Reductive Ru–CO Bond Cleavage by a Ruthenacycle**

*Takashi Tomon, Take-aki Koizumi, and Koji Tanaka**

Multielectron reduction of CO_2 and CO to afford highly reduced organic molecules has a fundamental importance in the utilization of C_1 resources. A number of metal complexes have been proven to work as catalyst precursors in photo-[1] and electrochemical[2] reduction of CO_2, although the reduction products are limited to CO and HCOOH as two-electron-reduced products. The generation of CO occurs by reductive cleavage of metal–CO bonds derived from M-η^1-CO_2 and M-η^1-CO(O)H complexes in protic media. The

[*] Dr. T. Tomon, Dr. T.-a. Koizumi, Prof. K. Tanaka
Institute for Molecular Science and CREST
Japan Science and Technology Agency
5-1 Higashiyama, Myodaiji, Okazaki, Aichi 444-8787 (Japan)
Fax: (+81) 564-59-5582
E-mail: ktanaka@ims.ac.jp

[**] bpy = 2,2′-bipyridine, napy = 1,8-naphthyridine.

Supporting information for this article is available on the WWW under http://www.angewandte.org or from the author.

 DOI: 10.1002/anie.200462486 © 2005 Wiley-VCH Verlag GmbH & Co. KGaA, Weinheim

requisites for multielectron reduction of CO_2 and CO catalyzed by metal complexes, therefore, are electrochemical hydrogenation of CO in aqueous media without accompanying reductive cleavage of the M–CO bonds. We have been studying electro- and photochemical reduction of CO_2 using polypyridyl ruthenium carbonyl complexes,[3] in which ligand-based redox reactions supply the electrons required for the reduction of CO_2. A Ru–CO complex with monodentate 1,8-naphthyridine (napy) appears to be a suitable candidate to satisfy the contradicting requisites for suppression of the reductive cleavage of Ru–CO bonds and reductive activation of the carbonyl ligands in aqueous media, since the napy-localized redox reaction that enhances the nucleophilicity of the nonbonded nitrogen atom may trigger an intramolecular attack at the α-carbon atom of a neighboring ligand to form a metallacycle.[4] Therefore, we examined the possibility of metallacyclization of $[Ru(bpy)_2(napy\text{-}\kappa N)(CO)]^{2+}$ ($\mathbf{1}^{2+}$; napy = 1,8-naphthylidine) driven by the napy-based redox reaction with the aim of inhibiting the reductive cleavage of the Ru–CO bond and reductive activation of the carbonyl group in H_2O.

The cyclic voltammogram (CV) of the monocarbonylruthenium(II) complex $\mathbf{1}(BF_4)_2$ exhibits one irreversible cathodic wave at $E_{p,c} = -1.40$ V and two reversible redox couples at $E_{1/2} = -1.85$ and -2.09 V (versus Ag/Ag^+ in CH_3CN; Figure 1). The former and the latter two couples can be

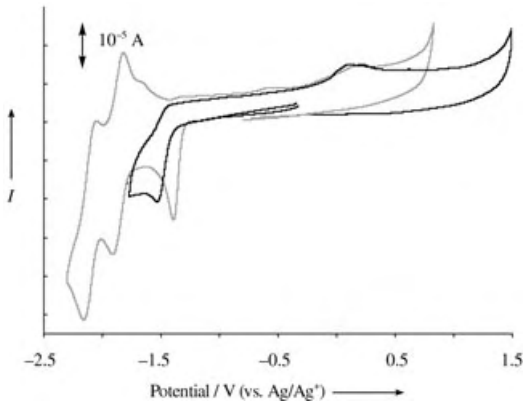

Figure 1. Cyclic voltammograms of $\mathbf{1}(BF_4)_2 \cdot H_2O$ in CH_3CN (light gray) and H_2O (dark gray).

assigned to the napy- and bpy-localized reductions, respectively, based on the redox potentials of $[Ru(bpy)_2(napy\text{-}\kappa N)(CH_3CN)]^{2+}$.[5] The exhaustive electrolysis of $\mathbf{1}(BF_4)_2$ at -1.40 V in CD_3CN consumed just 1.0 F mol^{-1} of electricity. The IR spectrum of $\mathbf{1}(BF_4)_2$ shows a strong ν(CO) band at $\tilde{\nu} = 2000$ cm^{-1} in CD_3CN. Electrochemical reduction of $\mathbf{1}^{2+}$ at -1.40 V resulted in complete disappearance of the bands between 2000 and 1700 cm^{-1}, and a new band emerged at 1587 cm^{-1}.[4b] The original IR spectrum of $\mathbf{1}^{2+}$ in CD_3CN could be regenerated by electrochemical oxidation of the resulting solution at 0 V. Attempts to isolate the one-electron-reduced form of $\mathbf{1}^{2+}$ were unsuccessful; however, exposure of the solution of the reduced complex $\mathbf{2}^+$ in CH_3CN to air regenerated $\mathbf{1}^{2+}$. The unusually large shift of the ν(CO) band ($|\Delta\tilde{\nu}| = 413$ cm^{-1}) of $\mathbf{1}^{2+}$ during the one-electron reduction/oxidation cycle in CH_3CN can be reasonably explained by a nucleophilic attack of the free nitrogen atom of napy at the carbonyl carbon [Eq. (1)].

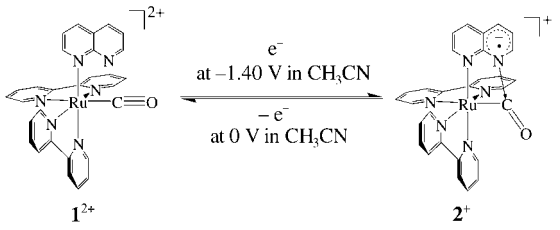

(1)

In H_2O, $\mathbf{1}^{2+}$ also displays one irreversible cathodic wave for the napy-based reduction, at -1.54 V. The bpy-localized redox couples were not detected as a consequence of the strong irreversible cathodic currents arising from the reduction of protons on a glassy carbon electrode at potentials more negative than -1.60 V in H_2O (Figure 1). In sharp contrast with the electrolysis of $\mathbf{1}(BF_4)_2$ at -1.40 V in CH_3CN, 2.0 F mol^{-1} of electricity flowed during the exhaustive electrolysis of the complex in H_2O under otherwise similar electrolysis conditions. Addition of a large excess of NH_4PF_6 to the resulting electrolyte solution precipitated $\mathbf{3}(PF_6)$ as a red powder. Diffusion of diethyl ether vapor into a solution of the crude products in CH_3CN afforded single crystals of $\mathbf{3}(PF_6)$.

The molecular structures of $\mathbf{1}^{2+}$ and $\mathbf{3}^+$ determined by X-ray crystallography[6] are shown in Figures 2 and 3, respectively. The ruthenium centers of $\mathbf{1}^{2+}$ and $\mathbf{3}^+$ have a distorted octahedral N_5C coordination sphere consisting of four nitrogens of two bpy ligands, one nitrogen of napy, and one carbon of CO. The Ru1–C29 and C29–O1 bond lengths in $\mathbf{1}^{2+}$ are 1.870(5) and 1.143(7) Å, respectively, and are similar to those of $[Ru(bpy)_2(X)(CO)]^{n+}$ (Ru–C = 1.861 Å for X = Cl,[7] and 1.865 and 1.906 Å for X = CO;[8] C–O = 1.122 Å for X = Cl

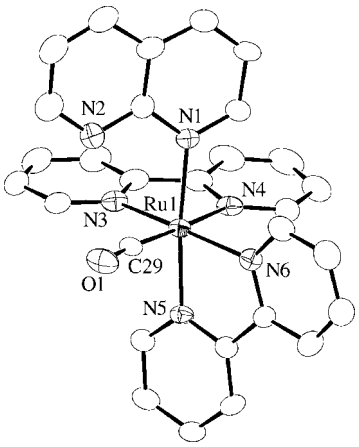

Figure 2. An ORTEP view of $\mathbf{1}^{2+}$. The hydrogen atoms have been omitted. Selected bond lengths [Å] and angles [°]: Ru1-N1 2.139(4), Ru1-N3 2.096(5), Ru1-N4 2.136(4), Ru1-N5 2.071(4), Ru1-6 2.077(4), Ru1-C29 1870(5), O1-C29 1.143(7); N1-Ru1-C29, 93.2(2), N3-Ru1-N4 78.3(2), N5-Ru1-N6 78.5(2), Ru1-C29-O1 175.6(5).

 © 2005 Wiley-VCH Verlag GmbH & Co. KGaA, Weinheim

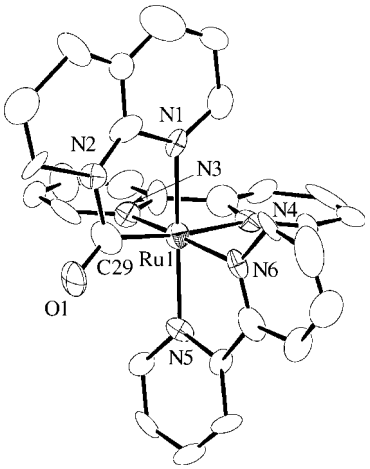

Figure 3. An ORTEP view of $\mathbf{3}^{+}$. The hydrogen atoms have been omitted.

and 1.144 and 1.125 Å for X = CO). The N1-Ru1-C29 and Ru1-C29-O1 bond angles are 93.2(2)° and 175.6(5)°, respectively. The aromatic ring of the napy ligand of $\mathbf{1}^{2+}$ is located above the CO ligand with a torsion angle C7-N1-Ru1-C29 of 35.6(4)°. However, the atomic distance between N2 and C29 of $\mathbf{1}^{2+}$ (2.765(7) Å) is apparently too long for a dative bond to form between the uncoordinated nitrogen atom of napy and the carbonyl carbon atom of $\mathbf{1}^{2+}$. The Ru1–N1 bond length (2.139(4) Å) is close to that in the analogous complex $[Ru(bpy)_2(napy\text{-}\kappa N)(CH_3CN)]^{2+}$ (2.137 Å),[5] although the napy plane of the latter is located on the opposite side to the CH_3CN ligand, and is situated in the space between the two bpy ligands of the axial and equatorial planes. Although the quality of the crystals of $\mathbf{3}(PF_6)\cdot 2\,CH_3CN$ was not good enough for a detailed analysis of the bond angles and lengths ($R_1 = 0.17$, $R_w = 0.226$), it is clear that $\mathbf{3}^{+}$ has a ruthenacycle structure which results from bond formation between the free nitrogen atom of napy and the carbonyl carbon atom of $\mathbf{1}^{2+}$. The almost planar napy ring of $\mathbf{3}^{+}$ is coplanar with the C29-Ru1-N4 axis and the C29-Ru1-N5 plane. Moreover, the O1-C29-Ru1 angle deviates significantly from the 180° expected for the sp-hybridized C29.

The ESI mass spectra of a CH_3CN solution of $\mathbf{3}(PF_6)$ prepared in H_2O and D_2O exhibit signals at *m*/*z* 573 and *m*/*z* 574, respectively, for the monocationic parent complexes thus indicating that $\mathbf{3}^{+}$ is produced by a proton-coupled one-electron reduction of $\mathbf{2}^{+}$. The ^{1}H NMR spectrum of $\mathbf{3}(PF_6)$ prepared in H_2O shows a new multiplet signal at $\delta = 3.66$ ppm with an intensity of two protons. The NOE spectrum indicates that this new CH_2 signal arises from the addition of a proton at the 4-position of napy [Eq. (2)]; the chemical shift of the signal is very close to that of the CH_2 group of 4-dihydro-*N*-methyl quinoline ($\delta = 3.52$ ppm). [9] Furthermore, electrochemical oxidation of $\mathbf{3}^{+}$ at +0.4 V in H_2O and treatment of $\mathbf{3}^{+}$ with an equivalent amount of chloranil in CH_3CN regenerates $\mathbf{1}^{2+}$ almost quantitatively.[10] Such an unprecedented reversible ring-closing and -opening coupled with hydrogenation and dehydrogenation of napy can be explained as follows: the napy-localized reduction of $\mathbf{1}^{2+}$ at −1.40 V results in a substantial increase in the basicity of the uncoordinated nitrogen atom, which leads to a nucleophilic attack of this atom at the carbonyl carbon atom to give the metallacyclic complex $\mathbf{2}^{+}$. Protonation of the 4-position of napy in $\mathbf{2}^{+}$ in H_2O induces a further one-electron reduction of the ligand, which changes the dative C–N in $\mathbf{2}^{+}$ to the covalent one in $\mathbf{3}^{+}$.

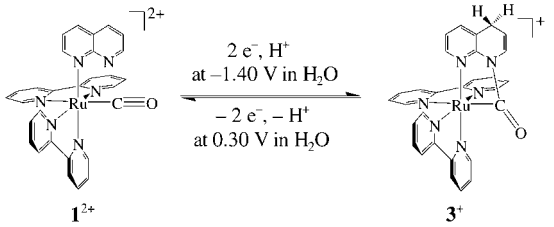

(2)

Further electrolysis of $\mathbf{3}^{+}$ at −1.80 V at an Hg electrode in H_2O caused the disappearance of the parent peak of $\mathbf{3}^{+}$ (*m*/*z* 573) and the emergence of two peaks at *m*/*z* 443 and 575 for monocationic species in the electrospray mass spectra of the electrolyte solution. Addition of NH_4PF_6 to the electrolyte solution precipitated a mixture of orange and red powders (ca. 3:1 based on ^{1}H NMR analysis). The ^{1}H NMR spectrum of the orange powder (*m*/*z* = 443) in CD_3CN is consistent with $[Ru(bpy)_2(CO)H](PF_6)$ (δ(Ru–H) = −11.45 ppm). The ^{1}H NMR spectrum of the red powder ($\mathbf{4}^{+}$: *m*/*z* = 575) shows three methylene proton signals at δ = 1.88, 2.83, and 3.82 ppm, while the ^{13}C NMR spectrum shows a signal corresponding to a carbamoyl group $\delta = 222$ ppm. The fact that these chemical shifts are similar to those of *N*-alkyl-1,2,3,4-tetrahydroquinoline derivatives[11] indicates that the carbamoyl moiety of $\mathbf{3}^{+}$ is not reduced even at −1.80 V in H_2O. Instead, the 2- and 3-positions of the napy moiety are hydrogenated, and about 75% of $\mathbf{3}^{+}$ is converted into $[Ru(bpy)_2(CO)H]^{+}$ [Eq. (3)].

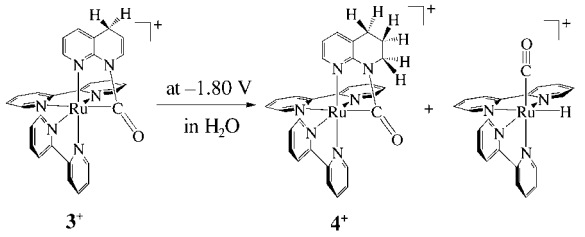

(3)

The present study reveals that the napy-localized reduction of $[Ru(bpy)_2(napy\text{-}\kappa N)(CO)]^{2+}$ ($\mathbf{1}^{2+}$) forms a metallacycle. Electrochemical reduction of $\mathbf{1}^{2+}$ in H_2O at −1.40 V causes an attack of the free nitrogen atom of napy at the carbonyl carbon atom, followed by hydrogenation at the 4-position of napy to produce the ruthenacyclic complex $\mathbf{3}^{+}$. The resultant metallacycle ring effectively inhibits reductive cleavage of the Ru–CO bond, and hydrogenation takes place on the napy ligand rather than on the CO group ($\mathbf{3}^{+}$) in H_2O. Both electrochemical oxidation of $\mathbf{3}^{+}$ in H_2O and treatment of the complex with chloranil in CH_3CN can be used to regenerate $\mathbf{1}^{2+}$ almost quantitatively. Such an unpre-

 © 2005 Wiley-VCH Verlag GmbH & Co. KGaA, Weinheim

cedented intramolecular reversible formation and cleavage of a C–N bondcoupled with hydrogenation and dehydrogenation of napy is ascribed to the drastic change of nucleophilicity of the nonbonded nitrogen atom of monodentate napy in a ligand-localized redox reaction.

Received: November 1, 2004
Published online: March 4, 2005

Keywords: carbonyl ligands · metallacycles · redox electrochemistry · reduction · ruthenium

[1] a) S. Matsuoka, K. Yamamoto, T. Ogura, M. Kusaba, N. Nakashima, E. Fujita, S. Yanagida, *J. Am. Chem. Soc.* **1993**, *115*, 601; b) J.-M. Lehn, R. Ziessel, *J. Organomet. Chem.* **1990**, *382*, 157; c) A. Craig, L. O. Spreer, J. W. Otvos, M. Calvin, *J. Phys. Chem.* **1990**, *94*, 7957; d) T. J. Meyer, *J. Chem. Soc. Chem. Commun.* **1985**, 1416.

[2] a) P. Paul, B. Tyagi, A. K. Bilakhiya, M. M. Bhadbhade, E. Suresh, G. Ramachandraiah, *Inorg. Chem.* **1998**, *37*, 5733; b) A. G. M. Mostafa Hossain, T. Nagaoka, K. Ogura, *Electrochim. Acta* **1997**, *42*, 2577; c) I. Bhugun, D. Lexa, J.-M. Saveant, *J. Am. Chem. Soc.* **1996**, *118*, 1769.

[3] a) H. Nakajima, Y. Kushi, H. Nagao, K. Tanaka, *Organometallics* **1995**, *14*, 5093; b) H. Nagao, T. Mizukawa, K. Tanaka, *Inorg. Chem.* **1994**, *33*, 3415; c) H. Ishida, T. Terada, K. Tanaka, T. Tanaka, *Inorg. Chem.* **1990**, *29*, 905; d) H. Ishida, K. Tanaka, T. Tanaka, *Chem. Lett.* **1988**, 339; e) H. Ishida, K. Tanaka, T. Tanaka, *Chem. Lett.* **1987**, 1035.

[4] a) T. Tomon, D. Ooyama, T. Wada, K. Shiren, K. Tanaka, *Chem. Commun.* **2001**, 1100; b) H. Nakajima, T. Tanaka, *Chem. Lett.* **1995**, 891.

[5] H. Nakajima, H. Nagao, K. Tanaka, *J. Chem. Soc. Dalton Trans.* **1996**, 1405.

[6] Crystal data for $\mathbf{1}(BF_4)_2{\cdot}H_2O$: $C_{29}H_{24}B_2F_8N_6O_2Ru$, $M_r = 763.22$, orthorhombic, space group $P2_12_12_1$ (no. 19), $a = 12.6480(8)$, $b = 12.8137(7)$, $c = 18.815(1)$ Å, $V = 3049.2(3)$ Å^3, $Z = 4$, $\rho_{calcd} = 1.662\ g\,cm^{-3}$, $\mu = 0.603\ mm^{-1}$, $F(000) = 1528.00$, 3865 unique reflections, 3865 independent reflections, ($R_{int} = 0.033$), $R1 = 0.047$, $wR2 = 0.123$ (all data); $\mathbf{3}(PF_6){\cdot}MeCN$: $C_{31}H_{26}F_6N_7OPRu$, $M_r = 758.63$, monoclinic, space group $P2_1/c$ (no. 14), $a = 13.342(8)$, $b = 15.718(9)$, $c = 29.49(2)$ Å, $V = 6020(6)$ Å^3, $Z = 8$, $\rho_{calcd} = 1.674\ g\,cm^{-3}$, $\mu = 0.615\ mm^{-1}$, $F(000) = 3056.00$, 14164 unique reflections, 6898 reflections with $I > 3.00\sigma(I)$, $R1 = 0.169$, $wR2 = 0.226$ (all data). Crystals for X-ray analyses of the complexes were obtained as described in the text for $\mathbf{1}(BF_4)_2{\cdot}H_2O$ and by vapor diffusion of diethyl ether into a CH_3CN solution for $\mathbf{3}(PF_6){\cdot}CH_3CN$. A suitable single crystal for the measurement was mounted on a glass fiber for $\mathbf{1}(BF_4)_2{\cdot}H_2O$ and in a capillary for $\mathbf{3}(PF_6){\cdot}CH_3CN$. Data were collected at −100 °C on a Rigaku/MSC Mercury CCD diffractometer equipped with graphite-monochromated $Mo_{K\alpha}$ radiation ($\lambda = 0.71070$ Å). All data were collected and processed using the Crystal Clear program (Rigaku). All the calculations were carried out with the teXsan software package.[12] All structures were solved by direct methods and expanded using Fourier techniques. Refinements were performed anisotropically for all non-hydrogen atoms by the full-matrix least-squares method. Hydrogen atoms were placed at their calculated positions and were included in the structure calculation without further refinement of the parameters. CCDC-254155 ($\mathbf{1}(BF_4)_2{\cdot}H_2O$) contains the supplementary crystallographic data for this paper. These data can be obtained free of charge from the Cambridge Crystallographic Data Centre via www.ccdc.cam.ac.uk/data_request/cif.

[7] J. M. Clear, J. M. Kelly, C. M. O'Connell, J. G. Vos, C. J. Cardin, S. R. Costa, *J. Chem. Soc. Chem. Commun.* **1980**, 750.

[8] H. Tanaka, B.-C. Tzeng, H. Nagao, S.-M. Peng, K. Tanaka, *Inorg. Chem.* **1993**, *32*, 1508.

[9] R. M. Coates, E. F. Johnson, *J. Am. Chem. Soc.* **1971**, *93*, 4016.

[10] The CV of complex $\mathbf{3}^+$ also displays an irreversible anodic wave at 0.3 V; no other waves are detected in MeCN.

[11] a) K. A. Zachariasse, S. I. Druzhinin, W. Bosch, R. Machinek, *J. Am. Chem. Soc.* **2004**, *126*, 1705; b) B. Alcaide, P. Almendros, J. M. Alonso, M. F. Aly, *Org. Lett.* **2001**, *3*, 3781.

[12] teXane version 1.11, 2000: Crystal Structure Analysis Package, Molecular Structure Corporation / Rigaku Corporation.

 © 2005 Wiley-VCH Verlag GmbH & Co. KGaA, Weinheim

Asymmetric Synthesis

Remarkably Stable $(Me_3Al)_2$·DABCO and Stereoselective Nickel-Catalyzed AlR_3 (R = Me, Et) Additions to Aldehydes**

*Kallolmay Biswas, Oscar Prieto, Paul J. Goldsmith, and Simon Woodward**

The attainment of a largely air-stable, low-molecular-weight equivalent of "chiral Me^-" for addition to prochiral aldehydes is reported herein together with complementary additions of AlR_3 (R = Me, Et). Although there has been considerable interest recently in air-stable boron, silicon, and tin reagents for the catalytic delivery of $C(sp^2)$ nucleophiles,[1,2] the equivalent alkyl ($C(sp^3)$) chemistry, including methyl transfer, remains quite underdeveloped; however, a notable exception is the stabilization of a methylaluminum species by formation of a Lewis acid/base pair, whose use has been pioneered by Blum, Schumann, and co-workers.[3] Despite this development, asymmetric addition to carbonyl compounds using such reagents has not been realized.

The reports of X-ray crystallographic studies of several $Me_3Al{\cdot}NR_3$ species encouraged us to test their synthetic utility. Although Me_3Al·pyridine and $(Me_3Al)_2$·TMEDA (TMEDA = tetramethylethylenediamine) proved far too reactive to handle under normal laboratory conditions, we were astonished to find that $(Me_3Al)_2$·DABCO (DABCO = 1,4-diazabicyclo[2.2.2]octane; **1a**),[5] which we call DABAL-Me_3, is surprisingly robust and can be readily used in the

[*] Dr. K. Biswas, Dr. O. Prieto, P. J. Goldsmith, Dr. S. Woodward
School of Chemistry
The University of Nottingham
Nottingham NG7 2RD (UK)
Fax: (+44) 115-951-3564
E-mail: simon.woodward@nottingham.ac.uk

[**] This work was supported in part by the European Union Framework 6 Programme (project FP6-505267-1; LIGBANK). P.J.G. is also grateful for the support of the Grundy Educational Trust.
DABCO = 1,4-diazabicyclo[2.2.2]octane.

Supporting information for this article is available on the WWW under http://www.angewandte.org or from the author.

 © 2005 Wiley-VCH Verlag GmbH & Co. KGaA, Weinheim DOI: 10.1002/anie.200462569

laboratory. Compound **1a** has a hydrolytic stability comparable to $LiBH_4$ as it is moisture sensitive but can be weighed out easily on the bench without the need for an inert air atmosphere and stored in standard glassware. DABAL-Me_3 (**1a**), unlike the Schumann–Blum reagent **2**, is prepared in a single step from commercially available materials and is obtained directly from the reaction mixture as a free-flowing, white powder. The analogous DABAL-Et_3 species (**1b**) proved too reactive to isolate (possibly because of weaker Al–C bonds) but it can be generated and used in situ.

We initially concentrated on the addition DABAL-Me_3 to prochiral aldehydes to fashion secondary alcohols to demonstrate the utility of this reaction. Approaches based on [L*$AlMe_n$] (L* = chiral ligand) Lewis acids seemed unlikely to be very successful as the Lewis acidity of the aluminum center in **1** is rather compromised by the coordination of DABCO to it, and so an alternative strategy based on transmetalation was sought. In 1997, Fujisawa and coworkers demonstrated that phosphanes cause dramatic rate acceleration in the nickel-catalyzed additions of (neat) $AlMe_3$ to aldehydes.[6] To the best of our knowledge, no asymmetric version of this reaction has appeared despite the enormous recent interest in selective nickel catalysis.[7] Pleasingly, when DABAL-Me_3 (**1a**; 1.0–1.5 equiv) is added to PhCHO in THF in the presence of [$Ni(acac)_2$] (acac = acetylacetone; 1 mol%) and (R_{ax},*S*,*S*)-Feringa ligand **3** (2 mol%) at 5°C, the resulting alcohol **4** (R = Ph) is isolated in high yield and enantiomeric excess (Scheme 1). We were further gratified to find that the range of substrates for this reaction using DABAL-Me_3 **1** was rather wider than that of the original Fujisawa reaction (Table 1), which had a rather narrow substrate range as only electron-rich aldehydes reacted quickly. Furthermore, the scope of the reaction could be extended by the use of DABAL-Et_3 (**1b**). Remarkably, byproduct formation arising from β elimination of any [$L_nNi(Et)$] intermediate amounted to less than 1 mol%, which is in accordance with the findings of Fujisawa and coworkers.[6]

Electron-deficient aromatic aldehydes gave the highest enantioselectivities in our reaction, while the electron-rich substrate 4-MePh gave the poorest (compare entries 15 versus 5, 7–12, and 14). Control reactions showed that electronic effects do not contribute to any competing reactions (4-XPhCHO (X = MeO, H, NO_2) did not react with **1a** alone within 3 h at 5°C). The enantioselectivity and reactivity of the reaction is also influenced significantly by steric factors (compare entries 1 and 2 versus 8–10; 1, 2 versus 18 and 21; 15 versus 17; and 21 versus 23). The activities displayed outperform other reported data given for addition reactions of AlR_3 to an aldehyde, which normally require catalyst

Table 1: Alkylation of aldehydes (RCHO) with A) DABAL-R_3 **1** or B) AlR_3 reagents.

Entry	R in RCHO	Method (R)	*t* [h]	Yield [%][a]	Product *ee* (antipode) [%][b]
1	Ph (**a**)	A (Me)	1	92	91 (*R*)-(+)-**4a**
2	Ph (**a**)	B (Me)	3	60	85 (*R*)-(+)-**4a**
3	Ph (**a**)	A (Et)	5	95	86 (*R*)-(+)-**5a**
4	Ph (**a**)	B (Et)	5	95	83 (*R*)-(+)-**5a**
5	4-BrC_6H_4 (**b**)	A (Me)	1	98	93 (*R*)-(+)-**4b**
6	4-BrC_6H_4 (**b**)	A (Et)	1	91	89 (*R*)-(+)-**5d**
7	4-ClC_6H_4 (**c**)	A (Me)	1	79	93 (*R*)-(+)-**4c**
8	4-FC_6H_4 (**d**)	A (Me)	3	84	94 (*R*)-(+)-**4d**
9	3-FC_6H_4 (**e**)	A (Me)	1	77	94 (*R*)-(+)-**4e**
10	2-FC_6H_4 (**f**)	A (Me)	1	81	87 (*R*)-(+)-**4f**
11	4-$(CN)C_6H_4$ (**g**)	A (Me)	1	69	94 (*R*)-(+)-**4g**
12	4-$(CF_3)C_6H_4$ (**h**)	A (Me)	1	58	94 (*R*)-(+)-**4h**
13	4-$(CF_3)C_6H_4$ (**h**)	A (Et)	1	90	95 (*R*)-(+)-**5h**
14	3-$(CF_3)C_6H_4$ (**i**)	A (Me)	1	93	93 (*R*)-(+)-**4i**
15	4-MeC_6H_4 (**j**)	A (Me)	3	90	81 (*R*)-(+)-**4j**
16	3-MeC_6H_4 (**k**)	A (Me)	1	82	93 (*R*)-(+)-**4k**
17	2-MeC_6H_4 (**l**)	A (Me)	1	78	90 (*R*)-(+)-**4l**
18	*c*-C_6H_{11}[c] (**m**)	A (Me)	1	80	94 (*R*)-(−)-**4m**
19	*c*-C_6H_{11}[c] (**m**)	A (Et)	10	60[d]	91 (*R*)-(+)-**5m**
20	*c*-C_6H_{11}[c] (**m**)	B (Et)	1.5	55	7 (*R*)-(+)-**5m**
21	*i*Bu (**n**)	B (Me)	6	60	95 (*R*)-(−)-**4n**
22	*i*Bu (**n**)	B (Et)	6	72	48 (*R*)-(−)-**5n**
23	*t*$BuCH_2$ (**o**)	B (Me)	7	95	67 (*R*)-(−)-**4o**
24	*n*-C_6H_{13} (**p**)	B (Me)	6	91	61 (*R*)-(−)-**4p**
25	$PhCH_2CH_2$ (**q**)	B (Me)	6	94	77 (*R*)-(−)-**4q**
26	(*E*)-PhCH=CH (**r**)	A (Me)	1	94	66 (*R*)-(+)-**4r**

[a] Yield determined from isolated product or by GC analysis: GC versus the internal standard on 0.25 mmol (RCHO) scale reaction and yields of isolated product were within 2–5% of these obtained on 1.0 mmol scale duplicate reactions. Compounds **4** and **5** were authenticated against genuine samples prepared either by reactions catalyzed with achiral Ph_3P (2 mol%)/[$Ni(acac)_2$] (1 mol%) and **1** and/or $NaBH_4$ reduction of the parent ketones. [b] Determined by GC analysis on a cyclodex-B column in all cases except **4a** and **5a** (GC analysis on lipodex-A); **4q** and **4r** (GC analysis on 2,6-me-3-pe-γ-CD[9]); and **4m**–**p**, **5m**, and **5n** (determined by GC analysis of the acetate of isolated secondary alcohol as described before).[8] Stereochemical correlations were assigned on the basis of the sign of the optical rotation or by comparison with the GC data of authentic samples of known configuration. [c] 1.0 equivalents of DABAL-R_3 **1** were used. [d] Mass balance was accounted for from by-products derived from α deprotonation.

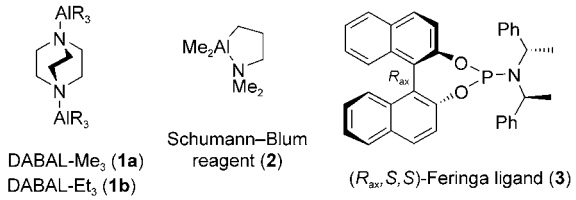

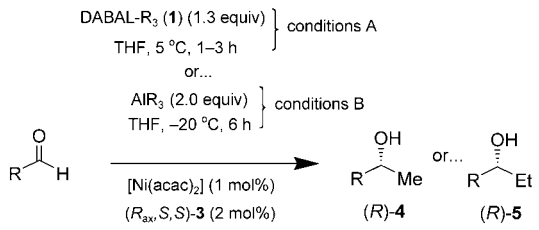

Scheme 1. The asymmetric synthesis of chiral secondary alcohols from benzaldehyde using either A) DABAL-R_3 or B) AlR_3 reagents (R = Me, Et).

 © 2005 Wiley-VCH Verlag GmbH & Co. KGaA, Weinheim

loadings of 10–15 mol%.[8] Further lowering of the ligand loading was possible: methylation of PhCHO with 1 mol% of **3** proceeded in identical enantiomeric excess but in a slightly lower yield (78%). PhCHO was converted into **4a** even when undried THF was used as the solvent (89% *ee*, 96% yield). An enal also participated in the reaction with **1a** but at lower selectivity (**4r**, entry 26). In two cases, the use of **1a** and **1b** allowed the isolation of secondary alcohols that are not available from classical Noyori-type transfer hydrogenations (**4m** and **5m**).[10] However, reagents **1a** and **1b** can cause the α deprotonation of some aliphatic aldehydes, thus resulting in aldol/Knovenagel derived by-products. This problem can be overcome by carrying out the reaction with these substrates at −20°C in the absence of DABCO.

The enantioselectivities attained in reactions using AlR_3 reagents are low to excellent (entries 4 and 20–25), thus indicating that the structure of **3** requires modification for each substrate.[11] Again β elimination by-products are only present at trace levels in all addition reactions using the $AlEt_3$ reagent under DABCO-free conditions. The use of DABCO is critical with some substrates, for example, **5m** is attained in only 7% *ee* in its absence (entry 20).[12] Although detailed discussion of the mechanism of the catalytic cycle is premature at this point, we strongly suspect that Lewis acid activation of an nickel/η^2-aldehyde complex by the aluminum reagent, in a manner related to the work of Ogoshi et al., is involved.[13] Extensive work to further delineate the reactivity of other DABAL-reagents and to explore their substrate range, both in the present reaction and other metal-catalyzed processes, is underway.

Experimental Section

1a: Neat $AlMe_3$ (4.5 g, 62.5 mmol) was added to a solution of freshly sublimed DABCO (3.4 g, 34.7 mmol) in toluene (30 mL) at 0°C. The resulting white precipitate was allowed to settle, and the supernatant toluene was removed by cannula. Dry diethyl ether (20 mL) was added and swirled with the solid. The solid was again allowed to settle and the supernatant liquid removed by cannula. Washing with diethyl ether was repeated four times before the residual slurry was evaporated to dryness under vacuum to obtain **1a** directly (4.5–6.1 g; 60–81%); its spectroscopic properties were as described previously.[5] DABAL-Me_3 (**1a**) that had been stored in screw-top vials under an argon blanket was still active after at least 4 months. (**Warning**: while we have encountered no problems using this reagent on scales of up to 25 g, we recommend caution on its initial handling. For example, if washing with diethyl ether, as outlined above, is not carried out properly traces of free $AlMe_3$ can lead to very reactive samples of **1a**. Deliberate addition of water to **1a** causes a strong exothermic reaction and methane liberation. Furthermore, **1a** ignites on tissue paper especially on "damp" days.)

Catalytic addition to aldehydes: $[Ni(acac)_2]$ (0.6 mg, 2.33 μmol, 1 mol%) and (R_{ax},*S*,*S*)-**3** (2.7 mg, 0.005 mmol, 2 mol%) were stirred in dry THF (2 mL) under an argon atmosphere at 5°C for 10–30 min. Neat aldehyde (0.25 mmol) was then added and DABAL-Me_3 (**1a**) (84 mg, 0.325 mmol, 1.3 equiv) was added after a further 10 min. The yellow reaction mixture was stirred (1–3 h) before being quenched with aqueous NH_4Cl. The yields of the obtained secondary alcohols were determined either by isolation or by GC analysis after addition of dodecane as the internal standard. DABAL-Et_3 (**1b**) was prepared by mixing 2:1 molar quantities of $AlEt_3$ and DABCO in THF. The use of **1b** or an uncoordinated AlR_3 species was carried out in an equivalent manner to that for **1a**. Screening reactions using AlR_3 (R = Me, Et) were carried out in 2.0 M hexanes solutions.

Received: November 10, 2004
Published online: March 14, 2005

Keywords: aluminum · asymmetric catalysis · Lewis bases · nickel · phosphoramidites

[1] Selected uses of RBX_n (R = C(sp^2), n = 2 or 3) reagents in selective catalysis: a) C. Bolm, J. Rudolph, *J. Am. Chem. Soc.* **2002**, *124*, 14850–14851 (activation with $ZnEt_2$ is required); b) A. Takezawa, K. Yamaguchi, T. Ohmura, Y. Yamamoto, N. Miyaura, *Synlett* **2002**, 1733–1735; c) M. Ueda, N. Miyaura, *J. Org. Chem.* **2000**, *65*, 4450–4452; d) R. A. Batey, A. N. Thadani, D. V. Smil, *Org. Lett.* **1999**, *1*, 1683–1686.

[2] Selected uses of $RSiX_3$ and $RSnX_3$ (R = C(sp^2)) reagents in selective catalysis: a) J. Ichikawa, H. Fukui, Y. Ishibashi, *J. Org. Chem.* **2003**, *68*, 7800–7805; b) S. Oi, Shuichi, M. Moro, H. Fukuhara, T. Kawanishi, Y. Inoue, *Tetrahedron* **2003**, *59*, 4351–4361; c) M. Murata, R Shimazaki, M. Ishikura, S. Watanabe, Y. Masuda, *Synthesis* **2002**, 717–719.

[3] a) H. Schumann, B. C. Wassermann, S. Schutte, B. Heymer, S. Nickel, T. D. Seuß, S. Wernik, J. Demtschuk, F. Girgsdies, R. Weimann, *Z. Anorg. Allg. Chem.* **2000**, *626*, 2081–2095; b) W. Baidossi, A. Rosenfeld, B. C. Wasswemann, S. Schutte, H. Schumann, J. Blum, *Synthesis* **1996**, 1127–1130. Alternative reagents based on {$[Me_2AlYCH_2CH_2NMe_2]_2$} (Y = O, NR) can be of superior reactivity in some cases: c) D. Gelman, S. Dechert, H. Schumann, J. Blum, *Inorg. Chim. Acta* **2002**, *334*, 149–158; d) H. Schumann, M. Frick, B. Heymer, F. Girgsdies, *J. Organomet. Chem.* **1996**, *512*, 117–126.

[4] CSD structure reference codes: $Me_3Al{\cdot}NMe_3$ (DOCQOB), $(Me_3Al)_2{\cdot}$DABCO (JOMBOC), $(Me_3Al)_2{\cdot}$TMEDA (JUBHAP), and $Me_3Al{\cdot}$(quinuclidine) (TMQUAL). These data can be obtained free of charge from The Cambridge Crystallographic Data Centre via www.ccdc.cam.ac.uk/data_request/cif.

[5] A. M. Bradford, D. C. Bradley, M. B. Hursthouse, M. Moteiralli, *Organometallics* **1992**, *11*, 111–115.

[6] T. Ichiyanagi, S. Kuniyama, M. Shimizu, T. Fujisawa, *Chem. Lett.* **1998**, 1033–1034.

[7] Key overview: a) J. Montgomery, *Angew. Chem.* **2004**, *116*, 3980–3998; *Angew. Chem. Int. Ed.* **2004**, *43*, 3890–3908; the following articles, in particular, should also be highlighted: b) K. M. Miller, W.-S. Huang, T. J. Jamison, *J. Am. Chem. Soc.* **2003**, *125*, 3442–3443; c) E. A. Colby, J. T. Jamison, *J. Org. Chem.* **2003**, *68*, 156–166.

[8] a) B. L. Pagenkopf, E. M. Carreira, *Tetrahedron Lett.* **1998**, *39*, 9593–9596; b) J.-S. You, S.-H. Hsieh, H.-M. Gau, *Chem. Commun.* **2001**, 1546–1547.

[9] A. J. Blake, A. Cunningham, A. Ford, S. J. Teat, S. Woodward, *Chem. Eur. J.* **2000**, *6*, 3586–3594; C. Börner, M. R. Denis, E. Sinn, S. Woodward, *Eur. J. Org. Chem.* **2001**, 2435–2446.

[10] T. Ohkuma, R. Noyori in *Comprehensive Asymmetric Catalysis*, *Vol. 1* (Eds.: E. N. Jacobsen, A. Pfaltz, H. Yamamoto), Springer, Berlin, **1999**, pp. 199–246.

[11] Individual ligand optimization is underway in our laboratory for both alkyl aldehyde and enal substrates (on the basis of PM3 studies of the selective step in the reaction).

[12] The presence of *c*-$C_6H_{11}C(=O)Et$ (c = cyclo) can be detected, which indicates product racemization by Meerwin–Pondorf–Varley–Oppenauer reactions. Related ketones were not detected in the products **4**.

[13] S. Ogoshi, M. Oka, H. Kurasawa, *J. Am. Chem. Soc.* **2004**, *126*, 11802–11803.

 © 2005 Wiley-VCH Verlag GmbH & Co. KGaA, Weinheim

Asymmetric Synthesis

Enantioselective Preparation of β,β-Disubstituted α-Methylenepropionates by MAO Promotion of the Zinc Schlenk Equilibrium**

*Paul J. Goldsmith, Simon J. Teat, and Simon Woodward**

Dedicated to Dr. John M. Brown, FRS on the occasion of his 65th birthday

In the copper-catalyzed reactions of organometallic nucleophiles (RM) with allylic halides $R^1CH{=}CR^2CH_2X$, two reaction pathways are possible: either direct S_N2 displacement at the α carbon or S_N2' displacement γ to the leaving group. Recently, considerable progress has been made towards the development of asymmetric processes that result from copper-catalyzed S_N2' addition of organozinc or Grignard reagents.[1] These studies have generally used allylic halides that lack functional groups and have focused largely on (*E*)-cinnamyl halides or equivalent phosphate esters ($R^1 = Ph$, $R^2 = H$). Reactions with ester-functionalized electron-deficient allylic halides ($R^2 = CO_2R$, $R^1 =$ various, **1**) would offer rapid access to highly useful chiral β,β-disubstituted α-methylenepropionates **2** (see Table 1). Highly selective additions of ZnR_2 to the regioisomers of **1** have been demonstrated,[2] but the former substrates themselves have proved highly resistant to effective asymmetric catalysis.[3]

Stoichiometric groundwork by Xu and Kündig showed the viability of addition of organozinc reagents to halides of type **1**.[4] Using Baylis–Hillman chemistry (to obtain suitable allylic halides **1**), we developed a first-generation catalytic system for the addition of ZnR_2 to allylic chloride **1a** by employing a chiral thioether ligand.[5] However, only low levels of enantioselectivity were observed, and the system was resistant to further optimization. With high-throughput screening, the chiral secondary amines **3** were identified as alternative ligands for the transformation of **1a** to **2a** in the presence of $Cu^{I}I$ (Table 2). A number of the other 80 species tried produced significant ligand-accelerated catalysis (LAC)[6]

Table 1: Synthesis of chiral β,β-disubstituted α-methylenepropionates **2**.

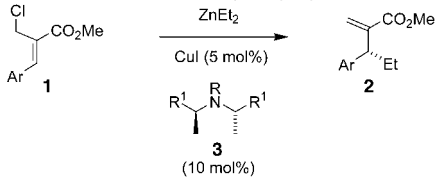

1	Ar	3	R^1	R	2	Ar
a	Ph	**a**	Ph	H	**a**	Ph
b	4-(MeO)C_6H_4	**b**	Ph	Me	**b**	4-(MeO)C_6H_4
c	4-MeC_6H_4	**c**	Ph	CHO	**c**	4-MeC_6H_4
d	1-Naphthyl	**d**	*c*-C_6H_{11}	H	**d**	1-Naphthyl
e	2-BrC_6H_4	**e**	1-Naphthyl	H	**e**	2-BrC_6H_4
f	4-FC_6H_4	**f**	4-FC_6H_4	H	**f**	4-FC_6H_4
g	4-(CF_3)C_6H_4	**g**	4-MeC_6H_4	H	**g**	4-(CF_3)C_6H_4
h	4-(NO_2)C_6H_4	**h**	4-(MeO)C_6H_4	H	**h**	4-(NO_2)C_6H_4
		i	3-(MeO)C_6H_4	H		
		j	2-(MeO)C_6H_4	H		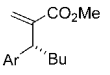

2aa

Table 2: Addition of $ZnEt_2$ to allylic chloride **1a** using CuI and (*S*,*S*)-**3**.[a]

Entry	Ligand	R^1	R	Yield **2a** [%]	*ee* **2a** [%]
1	**3a**	Ph	H	50	65
2	**3a**·HCl	Ph	H	50	51
3	**3b**·HCl	Ph	Me	10	<5
4	**3c**·HCl	Ph	CHO	18	<5
5	**3d**·HCl	*c*-C_6H_{11}	H	41	<5
6	**3e**·HCl	1-Naphthyl	H	18	15
7	**3f**·HCl	4-FC_6H_4	H	28	47
8	**3g**·HCl	4-MeC_6H_4	H	60	72
9	**3h**	4-(MeO)C_6H_4	H	70	78
10	**3h**·HCl	4-(MeO)C_6H_4	H	69	74
11	**3i**·HCl	3-(MeO)C_6H_4	H	56	53
12	**3j**	2-(MeO)C_6H_4	H	53	6

[a] Addition of $ZnEt_2$ (0.7 mL of a solution in toluene (1.1 M), 0.77 mmol) to **1a** (0.5 mmol) in THF (1 mL) at −20 °C in the presence of (*S*,*S*)-**3** (10 mol%) and CuI (5 mol%). Yield and *ee* values determined after 1 h by chiral-GC analysis (see Supporting Information).

effects (see Supporting Information), but only compound **3** gave *ee* values over 35%. Subsequent investigation revealed that the presence of C_2 symmetry is vital for efficient stereoselection; for example, use of (*S*)-PhCH(Me)NHBn gave **2a** in high yield, but with less than 20% *ee*. The presence of the secondary amino group is also crucial as either its alkylation or formylation (Table 2, entries 3 and 4, respectively) dramatically reduced the activity and selectivity of the catalyst. Finally, it was noted that the presence of an aryl function in the ligand **3** was also vital as **3d**·HCl showed no enantioselectivity and poor conversion of **1a** (entry 5). The

[*] P. J. Goldsmith, Dr. S. Woodward
School of Chemistry
The University of Nottingham
Nottingham NG72RD (UK)
Fax: (+44) 115-951-3564
E-mail: simon.woodward@nottingham.ac.uk
Dr. S. J. Teat
Diamond Light Source Ltd.
Rutherford Appleton Laboratory
Chilton, Didcot
Oxfordshire OX110QX (UK)

[**] This work was supported in part by the European Union COST-D24 Program (W6-D24-0003) and by the EPSRC (Grant GR/S56054). P.J.G. is also grateful for the support of the Grundy Educational Trust. MAO = methylaluminoxane.

Supporting information for this article is available on the WWW under http://www.angewandte.org or from the author.

 DOI: 10.1002/anie.200463028 © 2005 Wiley-VCH Verlag GmbH & Co. KGaA, Weinheim

role of the ligand aryl group was further investigated by increasing the range of substituents in **3** (Table 2). These were mostly screened as their HCl salts as these are more convenient to handle than the free amines. A strong detrimental steric effect was noted for ligands with a 2-substituent (entries 6 and 12), but a favorable electronic effect (either +I or +M) existed at the 4-position (entries 8–10). Through these studies the 4-methoxy ligand **3h** was determined to be optimal (Table 2, entry 9).

These studies also highlighted that the free amines **3** outperformed their corresponding salts **3**·HCl in terms of product stereoselectivity (compare entries 1 and 9 versus 2 and 10, respectively; Table 2). Alongside this, kinetic studies had shown that the enantioselectivity of the reaction in THF was time-dependent: When substrate **1a** was treated with $ZnEt_2$ using ligand **3h**·HCl, the *ee* value fell from 80% at the onset of the reaction to 74% after one hour (69% yield, the mass balance being **1a**). Coupled together these facts indicated that EtZnCl, whose concentration increases as the reaction evolves, impairs the selective transition state. This could be confirmed by deliberate addition of EtZnCl (prepared from a 1:1 mixture of $ZnEt_2$ and $ZnCl_2$) [7] which led to an immediate and catastrophic collapse in the catalyst selectivity (30% *ee*, 12% yield at 1 h,). We therefore reasoned that if we could promote the forward reaction (k_1) of the zinc Schlenk equilibrium [Eq. (1)], the enantioselectivity of the reaction should improve with the lower concentration of EtZnCl. Conditions under which $ZnCl_2$ is scavenged from the reaction mixture should fulfil this requirement. After screening several additives, including crown ethers, we found that the addition of methylaluminoxane (MAO; [-Al(Me)O-]$_n$) which is known to strongly scavenge halides[8] led to the desired effect (83% *ee*, 48% yield of **2a** at 1 h, −20 °C). It has been speculated that MAO can act as a "latent Lewis acid" and sequester chlorides as shown in structure **4**. $ZnMe_2$

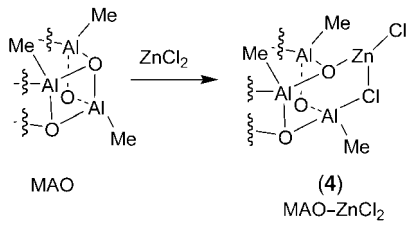

showed similar benefit, presumably through formation of unreactive MeZnCl, though catalyst turnover was reduced (84% *ee*, 35% yield of **2a** at 1 h, −20 °C).[9]

$$2\,EtZnCl \underset{k_{-1}}{\overset{k_1}{\rightleftharpoons}} ZnEt_2 + ZnCl_2 \qquad (1)$$

To the best of our knowledge, attempted manipulation of the zinc Schlenk equilibrium as a synthetic route to alkyl ZnR_2 species has not been reported before.[10] Alongside these additive trials, stronger coordinating solvents were screened, and we found that DME (1,2-dimethoxyethane) as solvent (with no additive) leads to a significant increase in enantioselectivity (88% *ee*, 47% yield of **2a** at 1 h, −20 °C). A combination of the use of MAO and DME and lowering the temperature led to the attainment of synthetically useful levels of enantioselectivity in the preparation of **2a**. Use of excess MAO led to *ee* values greater than 95%, but with low yields of **2a**. These results could be generalized across the range of substrates **1** (Table 3), with optimal results attained when CuTC (copper(I) thiophene-2-carboxylate)[11] was used as the source of copper(I). The origin of the enantioselectivity attained in this reaction unusually depends critically on electronic effects. Electron-rich substrates give products with higher enantioselectivities than electron-poor substrates (compare entry 3 versus 9, Table 3), which implicates a π-stacking interaction in the transition state.

Table 3: CuTC/(*S*,*S*)-**3h**-catalyzed addition of ZnR_2 (R = Et, Bu) to allylic chlorides **1** under conditions that promote Schlenk equilibration.[a]

Entry	Product	Ar	Yield [%]	$[\alpha]_D^{23}$[b]	*ee* [%] (stereoisomer)[b]
1	**2a**	Ph	92	−92.8	87 (*R*)
2	**2aa**	Ph	81	−76.2	78 (*R*)[c]
3	**2b**	4-(MeO)C_6H_4	80	−96.4	90 (*R*)
4	**2c**	4-MeC_6H_4	95	−94.4	89 (*R*)
5	**2d**	1-Naphthyl	53	−63.3	86 (*R*)
6	**2e**	2-BrC_6H_4	95	−82.7	80 (*S*)[d]
7	**2f**	4-FC_6H_4	95	−90.0	87 (*R*)
8	**2g**	4-(CF_3)C_6H_4	93	−80.3	83 (*R*)
9	**2h**	4-(NO_2)C_6H_4	95	−97.0	76 (*R*)

[a] Addition of $ZnEt_2$ (1.0 mL of a solution in toluene (1.1 M), 1.1 mmol) to **1** (0.5 mmol) in DME (1 mL) at −40 °C in the presence of (*S*,*S*)-**3h** (10 mol%), CuTC (5 mol%), and MAO (0.5 mL, 15 wt% solution in toluene). Yields of isolated products quoted. [b] (*c* 1.0, $CHCl_3$) for $[\alpha]_D^{23}$ in all cases. The absolute configuration of (−)-**2a** was confirmed crystallographically as *R*, and the products **2aa–h** were assumed to show the same sense of stereoinduction. [c] The reaction was performed using Zn(*n*Bu)$_2$ (1.0 mL of a solution in heptane (1 M), 1.0 mmol). [d] Yield from NMR spectroscopic studies based on isolation of a mixture of **1e** and **2e**. The absolute configuration has changed owing to a change in assignment priority of the aryl substituent.

The sense of the enantioselectivity in the addition of $ZnEt_2$ to the halide **1a** could be determined by X-ray crystallographic analysis of the carboxylic acid **2ab**, which resulted from the hydrolysis of **2a**, when crystallized as its (*R*)-α-methylbenzylamine salt (Scheme 1). Single recrystallizations of the acids derived from **2** and further derivatization with α-methylbenzylamine improved the enantioselectivity to >99% *ee* for the catalytic addition. This enrichment was considerably easier and more efficient than direct resolution of racemic **2ab**. The product **2ab** of the S_N2' reaction is of

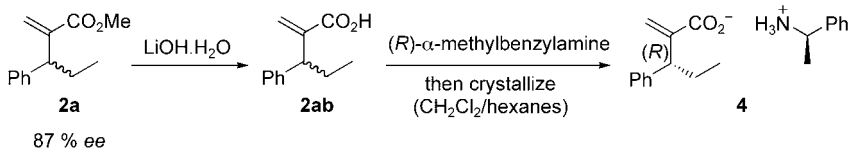

Scheme 1.

 © 2005 Wiley-VCH Verlag GmbH & Co. KGaA, Weinheim

direct use in the preparation of combined ACE–NEP (angiotensin-converting enzyme and neutral endopeptidase) inhibitors.[12]

In conclusion, we have described the first method for the copper-catalyzed enantioselective alkylation of Baylis–Hillman-derived electron-deficient allylic chlorides with organozinc reagents thorough the use of a simple chiral secondary amine and promotion by MAO of the zinc Schlenk equilibrium. Further intensive studies are underway to identify the nature of the π-stacking interactions responsible for the ordered transition state.

Experimental Section

General procedure for the CuTC-catalyzed alkylation of allylic chlorides **1**: A dried Schlenk tube was charged with chloride **1** (0.50 mmol), CuTC (4.8 mg, 0.025 mmol), and (*S*,*S*)-**3h** (14.3 mg, 0.05 mmol). Dry DME (1 mL) was introduced, the stirred mixture was cooled to −40 °C, and MAO (0.5 mL of a 15 wt % solution in toluene; Aldrich) was added. The yellow reaction mixture was stirred for 5 min at −40 °C, and then ZnR_2 (for R = Et: 1 mL of a 1.1 M solution in toluene, 1.1 mmol; for R = *n*Bu: 1 mL of a 1 M solution in heptane, 1.0 mmol) was added. Stirring was continued for 45 h at −40 °C, then the reaction was quenched by cautious addition of 2 M HCl (2 mL). The aqueous layer was extracted with Et_2O (2 × 5 mL), then the organic extracts were dried ($MgSO_4$), and the solvent was evaporated. The products were isolated by flash chromatography using mixtures of Et_2O/hexanes as eluent.

Received: December 22, 2004
Published online: March 10, 2005

Keywords: allylation · asymmetric catalysis · copper · zinc

[1] a) K. Tissot-Croset, D. Polet, A. Alexakis, *Angew. Chem.* **2004**, *116*, 2480 – 2482; *Angew. Chem. Int. Ed.* **2004**, *43*, 2426 – 2428; b) A. O. Larsen, W. Leu, C. N. Oberhuber, J. E. Campbell, A. H. Hoveyda, *J. Am. Chem. Soc.* **2004**, *126*, 11130 – 11131; c) U. Piarulli, P. Daubos, C. Claveric, M. Roux, C. Genari, *Angew. Chem.* **2003**, *115*, 244 – 246; *Angew. Chem. Int. Ed.* **2003**, *42*, 234 – 236; d) W.-J. Shi, L.-X. Wang, Y. Fu, S.-F. Zhou, Q.-L. Zhou, *Tetrahedron: Asymmetry* **2003**, *14*, 3867 – 3872; e) H. Malde, A. W. van Zijl, L. A. Arnold, B. L. Feringa, *Org. Lett.* **2001**, *3*, 1169 – 1171; f) F. Dubner, P. Knochel, *Tetrahedron Lett.* **2000**, *41*, 9233 – 9237.

[2] a) K. E. Murphy, A. H. Hoveyda, *J. Am. Chem. Soc.* **2003**, *125*, 4690 – 4691; b) M. A. Kacrpzynski, A. H. Hoveyda, *J. Am. Chem. Soc.* **2004**, *126*, 10676 – 10681.

[3] The addition of $Zn(CH_2tBu)_2$ to **1a** (62 % yield, 12 % *ee*, 6.8:1 S_N2'/S_N2) has been reported in a patent: P. Knochel, F. Dübner (Avecia Ltd., UK), PCT Int. Appl. WO2000012449, **2000** [*Chem. Abstr.* **2000**, *132*, 22 2063].

[4] L.-H. Xu, E. P. Kündig, *Helv. Chim. Acta* **1994**, *77*, 1480 – 1484.

[5] C. Börner, P. J. Goldsmith, S. Woodward, J. Gimeno, S. Gladiali, D. Ramazzotti, *Chem. Commun.* **2000**, 2433 – 2434.

[6] D. J. Berrisford, C. Bolm, K. B. Sharpless, *Angew. Chem.* **1995**, *107*, 1159 – 1171; *Angew. Chem. Int. Ed. Engl.* **1995**, *34*, 1059 – 1070.

[7] a) J. Boersma, J. G. Noltes, *Tetrahedron Lett.* **1966**, 1521 – 1525; The limited data that exists suggests that under MAO-free conditions $k_1/k_{-1} < 0.01$, see: b) D. F. Evans, I. Wharf, *J. Chem. Soc. A* **1968**, *4*, 783 – 787.

[8] The structure of MAO is not known (linear, ring, and cage structures have all been proposed). Structure **4** is given for conceptual purposes only. For lead overviews, see: a) E. Zurek, T. Ziegler, *Prog. Polym. Sci.* **2004**, *29*, 107 – 148; b) P. L. Bryant, C. R. Harwell, A. A. Mrse, E. F. Emery, Z. Gan, T. Caldwell, A. P. Reyes, P. Kuhns, D. W. Hoyt, L. S. Simeral, R. W. Hall, L. G. Butler, *J. Am. Chem. Soc.* **2001**, *123*, 12009 – 12017; c) H. Hanawa, N. Abe, K. Marouka, *Tetrahedron Lett.* **1999**, *40*, 5365 – 5368.

[9] The preparation of PhZnEt (from $ZnPh_2$ and $ZnEt_2$) has been reported by the groups of Fu and others, see: a) M. Fontes, X. Verdaguer, L. Solà, M. A. Pericàs, A. Riera, *J. Org. Chem.* **2004**, *69*, 2532 – 2543; b) J. Rudolph, N. Hermanns, C. Bolm, *J. Org. Chem.* **2004**, *69*, 3997 – 4000; c) P. I. Dosa, G. C. Fu, *J. Am. Chem. Soc.* **1998**, *120*, 445 – 446; d) P. I. Dosa, J. C. Ruble, G. C. Fu, *J. Org. Chem.* **1997**, *62*, 444 – 445. We are unaware of any work on the equivalent halide equilibrium.

[10] a) NMR spectroscopic evidence indicates a value of $k_1/k_{-1} < 0.002$ under unpromoted conditions: D. F. Evans, G. V. Fazakerley, *J. Chem. Soc. A* **1971**, 182 – 183; b) Very recently, Knochel has demonstrated exchange of ArZnI species: F. F. Kneisel, M. Dochnahl, P. Knochel, *Angew. Chem.* **2004**, *116*, 1032 – 1036; *Angew. Chem. Int. Ed.* **2004**, *43*, 1017 – 1021.

[11] G. D. Allred, L. S. Liebeskind, *J. Am. Chem. Soc.* **1996**, *118*, 2748 – 2749.

[12] N. Inguimbert, P. Coric, H. Poras, H. Meudal, F. Teffot, M.-C. Fournie-Zaluski, B. P. Roques, *J. Med. Chem.* **2002**, *45*, 1477 – 1486.

 © 2005 Wiley-VCH Verlag GmbH & Co. KGaA, Weinheim

Supramolecular Chemistry

Topochemical Photodimerization in the Coordination Polymer $[\{(CF_3CO_2)(\mu\text{-}O_2CCH_3)Zn\}_2(\mu\text{-bpe})_2]_n$ through Single-Crystal to Single-Crystal Transformation**

*Ni Lian Toh, Mangayarkarasi Nagarathinam, and Jagadese J. Vittal**

Solid-state photochemical [2+2] cycloadditions of organic molecules have been very well studied in the past.[1] Although the geometric criteria for such topochemical dimerizations are well established, it has been a challenge to organize the two double bonds in the solid state.[2] MacGillivray and co-workers had considerable success in aligning the double bonds in small organic molecules by using the strength and directionality of the hydrogen bonds.[3] Serendipitous single-

[*] N. L. Toh, Dr. M. Nagarathinam, Prof. J. J. Vittal
Department of Chemistry
National University of Singapore
Science Drive 3
Singapore 117543 (Singapore)
Fax: (+65) 6779-1691
E-mail: chmjjv@nus.edu.sg

[**] We thank the National University of Singapore for financial support (Grant No. R143-000-153-112) and Professor Wai Yip Fan for the Xe lamp and his interest in this project. bpe = 4,4′-bipyridylethylene.

Supporting information for this article is available on the WWW under http://www.angewandte.org or from the author.

 DOI: 10.1002/anie.200462673 © 2005 Wiley-VCH Verlag GmbH & Co. KGaA, Weinheim

crystal to single-crystal (SCSC) polymerization of 1,6-triacetylene has been reported to occur, assisted by π–π stacking.[4] Metal complexes have also been successfully used for dimerization, oligomerization, and polymerization of olefins and acetylenes.[5,6] This includes solid-state polymerization of the monomeric metal complex, aquabis(3-butenoato)calcium by ^{60}Co γ irradiation.[5a]

Compared to the solid-state photochemical reactions involving mostly two molecules, the transformations of one coordination polymeric structure to another are very rare in solid-state supramolecular reactions as the breaking and forming of bonds should occur in more than one direction simultaneously. Most of the reversible topotactic solid-state reactions involve the removal of guest solvent molecules from cavities.[7] Iordanidis and Kanatzidis reported SCSC structural transformations based on the redox-induced zipper action of selenium atoms by iodine.[8] A few more interesting solid-state supramolecular transformations including SCSC have been reported recently.[9]

One dimensional metal coordination polymers with molecular ladder structures can easily be prepared by self-assembly.[10] Hence these structures provide another interesting possibility to align photoreactive double bonds in the solid state as the distance between the vertical strands can be manipulated by a judicious choice of the bridging ligands or metallophilic interactions. Such metal coordination polymeric structures have not been exploited for this purpose before. Here, we report the topochemical transformation of a 1D metal coordination polymer, $[\{(F_3CCO_2)(\mu\text{-}O_2CCH_3)Zn\}_2(\mu\text{-bpe})_2]_n$ (bpe = 4,4′-bipyridylethylene), which has a molecular ladder structure, through [2+2] photochemical cycloaddition across the vertical strands into $[\{(F_3CCO_2)(\mu\text{-}O_2CCH_3)Zn\}_2(\mu\text{-tpcb})_2]_n$ (tpcb = tetrakis(4-pyridyl)-cyclobutane) in up to 100% yield. This cycloaddition is accompanied by SCSC transformation.

When $Zn(O_2CCH_3)_2\cdot 2H_2O$ was treated with an equimolar amount of bpe, compounds $[\{(\mu\text{-}O_2CCH_3)_4Zn_2\}(\mu\text{-bpe})]_n$ (**1**), $[\{Zn(O_2CCH_3)_2\}(\mu\text{-bpe})]_n\cdot n H_2O$ (**2**), and $[\{(H_3CCO_2)(\mu\text{-}O_2CCH_3)Zn\}_2(\mu\text{-bpe})_2]_n$ (**3**) were isolated. Their composition and solid-state structures depend on the way in which the crystals were grown as illustrated in Scheme 1. Compound **1** forms a linear 1D coordination polymer and has a zinc/bpe-ligand stoichiometry of 2:1, whereas **2** and **3** are supramolecular isomers that have a 1:1 ratio of metal to linear spacer ligand.[11] Light-yellow hexagonal crystals of **1** were obtained by diffusion of a solution of bpe in THF into Zn-

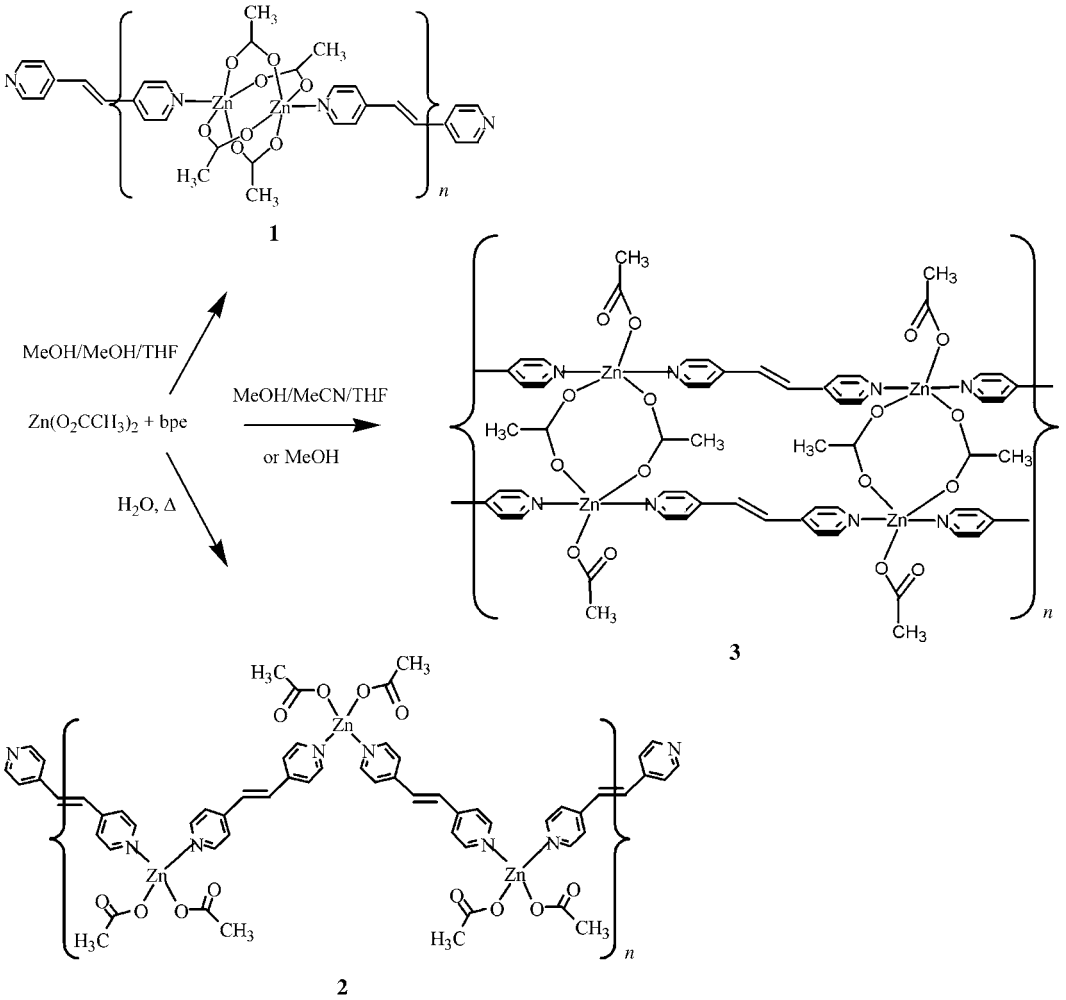

Scheme 1. The formation of different products upon reaction of $Zn(O_2CCH_3)_2$ with bpe in various solvents and under various conditions.

 © 2005 Wiley-VCH Verlag GmbH & Co. KGaA, Weinheim

$(O_2CCH_3)_2{\cdot}2H_2O$ in solution in MeOH at room temperature. A buffer layer of MeOH was added between these two solutions to avoid instant precipitation. When a layer of MeCN was used as the buffer, colorless rodlike crystals of **3** were isolated from the solvent junction in a day. A mixture of **1** and **3** were furnished in a ratio of approximately 60:40 if the crystals were allowed to grow for 4 days. The colorless long, thin, platelet crystals of **3** were separated by hand-picking from the clusters of **1** under a microscope. Compound **2** was formed as colorless distorted cubic crystals by cooling a clear filtered solution of boiled aqueous solution containing an equimolar ratio of $Zn(O_2CCH_3)_2{\cdot}2H_2O$ and bpe.

Compound **2** forms a zigzag polymer in which Zn^{II} has tetrahedral geometry. On the other hand, the Zn^{II} ions present in the two linear infinite polymers $[\{(O_2CCH_3)Zn\}(bpe)]_n$ in **3** are bridged by two acetate ligands to provide a molecular ladder polymeric structure. The Zn^{II} ion has, therefore, distorted trigonal bipyramidal geometry with the two pyridyl nitrogen atoms occupying the axial positions. The Zn···Zn distance in **3** (3.82 Å) is longer than that found in **1** (2.900(1) Å). This may be caused by the fact that four acetate ligands bridging the two Zn^{II} ions provide a paddle-wheel structure in **1** with *trans* O-Zn-O angles of 158.4(3) and 162.0(3)°. A crystallographic center of inversion is present in all of the structures. The two bpe ligands in the adjacent chains in **3** are aligned parallel, but are slightly slip-stacked. The nonbonding distances between the double bonds of the two bpe ligands in the parallel chains (C···C distance 3.63 Å, and C-C···C angles 74.0 and 106.0°) are congenial for the [2+2] cycloaddition to take place in the solid state.[2,3]

The powdered crystalline compound **3** was subjected to UV irradiation using a xenon lamp for a period of 14 hours. The cycloaddition was accompanied by a color change from colorless to pale yellow. The quantitative photoreactivity of the molecular ladder polymer **3** is evident from the ^1H and ^{13}C NMR spectra of the irradiated product in $[D_6]$DMSO. The ^1H NMR spectrum shows complete disappearance of the signals for the olefinic protons at $\delta = 7.56$ ppm, the appearance of signals for cyclobutane protons at $\delta = 4.68$ ppm, and a shift in the resonances of the bipyridyl protons from $\delta = 8.61$ and 7.63 ppm to $\delta = 8.35$ and 7.26 ppm. However, single crystals of **3** after irradiation were found to split into two, and the much anticipated SCSC structural transition was not successful.

Long rodlike colorless crystals of $[\{(F_3CCO_2)(\mu\text{-}O_2CCH_3)Zn\}_2(\mu\text{-bpe})_2]_n$, **4** were obtained exclusively from a solution containing an equimolar ratio of $Zn(O_2CCH_3)_2{\cdot}2H_2O$, bpe, and CF_3CO_2H in DMF (*N*,*N*-dimethylformamide). A perspective view of a portion of the molecular ladder polymer as determined by X-ray crystallography is shown in Figure 1. Two acetato ligands bridge a pair of Zn^{II} ions in $[Zn_2(\mu\text{-bpe})_2]_n$ with a Zn···Zn distance of 3.848(1) Å to form a molecular ladder polymer. A trifluoroacetate anion chelates each Zn^{II} center to complete the distorted octahedral geometry at the metal center. A crystallographic inversion center is present in the middle of the $[Zn_2(\mu\text{-}O_2CCH_3)_2]$ ring, and the polymer propagates in the [011] direction. As in **3**, the linear spacer ligands are disposed facing each other, but are slightly slip-stacked. This is evident

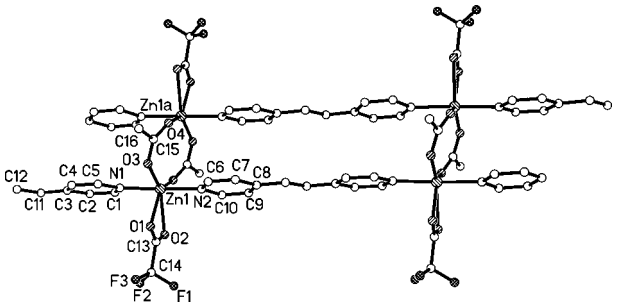

Figure 1. A perspective view of a portion of the 1D molecular ladder polymeric structure of **4**. The hydrogen atoms and disordered; fluorine atoms have been omitted for clarity. Selected bond parameters [Å, °]: Zn(1)–N(1) 2.143(3), Zn(1)–N(2) 2.146(3), Zn(1)–O(1) 2.234(4), Zn(1)–O(2) 2.431(5), Zn(1)–O(3) 2.013(3), Zn(1)–O(4a) 2.019(3), C(3)–C(11) 1.458(5), C(8)–C(12b) 1.463(5), C(11)–C(12) 1.321(6), Zn(1)···Zn(1a) 3.848(1), N(1)-Zn(1)-N(2) 178.6(1), O(3)-Zn(1)-O(4a) 129.5(1), O(1)-Zn(1)-O(2) 53.9(1), O(1)-Zn-O(4a) 138.0(1), O(3)-Zn(1)-O(2) 146.2(1). The symmetry operators are: $a = 1-x, 1-y, 1-z$; $b = x, y-1, z-1$; $c = x, y+1, z+1$.

from the deviation from 90° of Zn-Zn-N angles (i.e. 78.8 and 100.0°). The C···C nonbonding distance between the two ethylene carbon atoms of the bpe ligands in the parallel chains is 3.747 Å and the C-C···C angles are 78.9 and 101.1°. In the crystal structure of **4**, the bpe ligands are free from disorder, unlike **3**, and are employed for SCSC transformation studies. The adjacent ladders are also slip-stacked such that the pyridyl rings are close to the ethylene carbon atoms while the closest C···C distance between ethylenic carbon atoms is 7.10 Å.

UV irradiation of single crystals of **4** for about 3 hours did not change its single-crystal nature, morphology, transparency, or its diffracting power of X-rays. Hence, an irradiated single crystal of **4** ($[\{(F_3CCO_2)(\mu\text{-}O_2CCH_3)Zn\}_2(\mu\text{-tpcb})_2]_n$ (**5**) was selected for structure determination by single-crystal X-ray diffraction experiments. The X-ray crystallographic analysis confirmed the formation of new bonds across the vertical strands shown in Figure 2. The two pyridyl rings are bent towards each other with an interplanar angle of 27.4°. As a result, the Zn···Zn distance increased from 3.747 Å in **4** to 4.162 Å in **5**, and other bond parameters in **5** have also changed to accommodate the formation of new single bonds across the ethylene bonds. The formation of tpcb from two bpe ligands in the bulk of **5** was also confirmed by ^1H NMR spectroscopy.

Recently bpe ligands have been successfully oriented in parallel to form an infinite 1D ribbonlike polymer by utilizing the N···I interactions with an iodo derivative of pentaerythritol ether, and photochemical dimerization has also been accomplished through SCSC transformation.[12] While this work was in progress, a [2+2] cycloaddition reaction in cadmium fumarate dehydrate, which has a square-grid 2D structure, was reported;[13] however, it appears that neither complete photoconversion nor SCSC were observed. A discrete metal complex has been employed previously to orient the molecules for cycloaddition to take place in the solid state.[5b] In this present work, $Zn(O_2CCH_3)_2$ has been used to align the bpe ligands in a parallel fashion in a metal

 © 2005 Wiley-VCH Verlag GmbH & Co. KGaA, Weinheim

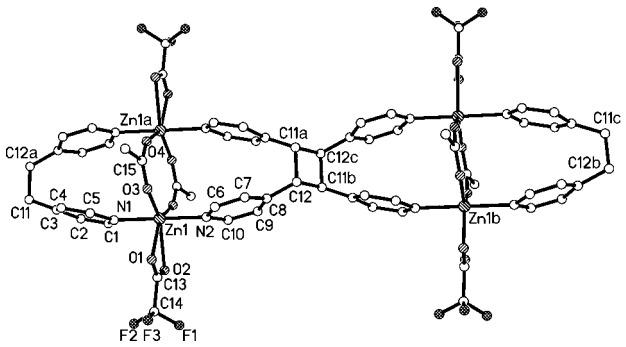

Figure 2. A view showing a part of the 1D polymeric structure of **5**. The hydrogen atoms have been omitted for clarity. Selected bond parameters [Å, °]: Zn(1)–N(1) 2.138(4), Zn(1)–N(2) 2.127(4), Zn(1)–O(1) 2.157(4), Zn(1)–O(2) 2.500(4), Zn(1)–O(3) 2.018(5), Zn(1)–O(4a) 2.030(5), C(3)–C(11) 1.497(7), C(8)–C(12) 1.505(7), C(11)–C(12b) 1.536(7), Zn(1)···Zn(1a) 4.162(1), N(1)-Zn(1)-N(2) 178.3(2), O(3)-Zn(1)-O(4a) 122.8(2), O(1)-Zn(1)-O(2) 55.2(2), O(1)-Zn-O(4a) 141.7(2), C(3)-C(11)-C(12b) 119.4(4), C(3)-C(11)-C(12a) 114.3(4), C(8)-C(12)-(C11c) 120.1(4), C(8)-C(12)-C(11a) 114.3(4), C(11c)-C(12)-C(11a) 89.6(4). The symmetry operators are: $a=1-x$, $1-y$, $1-z$; $b=x$, $1+y$, $1+z$; $c=x$, $y-1$, $z-1$.

coordination polymer, and expectedly, the coordination polymer has been found to exhibit photochemical reactivity. Furthermore, solid-state supramolecular transformation of one type of coordination polymer into another has been accompanied by photodimerization across the strands. The SCSC transformation has been successfully accomplished by partially replacing the acetate anion with trifluoroacetate ions to eliminate the problem of disorder in bpe.

In summary, the use of coordination polymers in topochemical photodimerization reactions has been illustrated. A number of other metal coordination network structures may also be used to preorganize the double bonds in the spacer ligands. Further new interesting network structures can be synthesized from a number of metal coordination polymeric structures in the SCSC structural transformation. Such new exciting coordination polymers are waiting to be explored.

Experimental Section

1: A solution of $Zn(O_2CCH_3)_2{\cdot}2H_2O$ (0.110 g, 0.5 mmol) in methanol (2 mL) was layered over a solution of bpe (0.090 g, 0.5 mmol) in THF (2 mL), with methanol (8 mL) as a middle buffer layer. Hexagonal crystals were obtained after 2 days (0.07 g, 26%). IR (KBr): $\tilde{\nu}=$ 1611(s), 1506(m), 1400(s), 1226(w), 1071(w), 1026(s), 830(s), 675(m), 621(m) cm^{-1}; ^1H NMR ([D_6]DMSO, 300 MHz, 298 K): $\delta=$ 8.61 (d, 4H, Py-H), 7.63 (d, 4H, Py-H), 7.56 (s, 4H, CH=CH), 1.81 ppm (s, 6H, CH_3COO); Elemental analysis (%) calcd. for $C_{20}H_{22}N_2O_8Zn_2$: C, 43.74; H, 4.03; N, 5.10; found: C, 44.07; H, 4.34; N, 5.06.

2: Bpe (0.182 g, 1 mmol) in DMF (2 mL) was added to $Zn(O_2CCH_3)_2{\cdot}2H_2O$ (0.220 g, 1 mmol) in DMF (4 mL), and the white precipitate which immediately separated out was filtered and redissolved in hot water. The clear solution was filtered and allowed to slowly evaporate; yellow cubic crystals separated out after a week and were collected, washed with ether, and dried under vacuum (0.140 g, 36%). IR (KBr): $\tilde{\nu}=$1637(s), 1504(m), 1420(s), 1064(m), 1031(w), 830(m), 719(s) cm^{-1}; Elemental analysis (%) calcd. for $C_{16}H_{18}N_2O_5Zn$: C, 50.08; H, 4.73; N, 7.30; found: C, 50.38; H, 4.65; N, 7.23. A NMR spectrum was not recorded owing to the insolubility of the complex in common deuterated solvents.

3: A solution of $Zn(O_2CCH_3)_2{\cdot}2H_2O$ (0.11 g, 0.5 mmol) in methanol (2 mL) was layered over a solution of bpe (0.09 g, 0.5 mmol) in THF (2 mL), with CH_3CN (4 mL) as a middle buffer layer. Colorless rodlike crystals that formed in the junction were separated out the next day (0.12 g, 38%). In another method, equimolar amounts of $Zn(CH_3COO)_2{\cdot}2H_2O$ (0.22 g) and bpe (0.18 g) in CH_3OH (4 mL and 2 mL, respectively) were mixed, and after stirring for a minute at room temperature, the clear solution was filtered and allowed to evaporate slowly. Colorless rodlike crystals separated out after two days; these were collected, washed with ether, and dried under vacuum (75%). IR (KBr): $\tilde{\nu}=$1610.6(vs), 1429.3(vs), 1251.8 (vw), 1209.0(vw), 1070.5(w), 1026.1(m), 929.7(vw), 839.0(s, bpeth), 686.7(w), 553.7(m) cm^{-1}; ^1H NMR ([D_6]DMSO, 300 MHz, 298 K): $\delta=$ 8.61 (d, 4H, Py-H), 7.64 (d, 4H, Py-H), 7.56 (s, 4H, CH=CH), 1.83 ppm (s, 6H, CH_3COO); ^{13}C NMR: ([D_6]DMSO, 300 MHz, 298 K): $\delta=$ 176 (O=CO), 150.05 (C-Py), 143.55 (C-Py), 130.63 (C=C), 121.30 (C-Py), 22.30 ppm (CH_3); Elemental analysis (%) calcd. for $C_{32}H_{32}N_4O_8Zn_2$: C, 52.55; H, 4.41; N, 7.66; found: C, 51.45; H, 4.35; N, 7.23%.

UV Irradiation of **3:** A powdered sample of **3** (30 mg) was placed between two glass slides and was irradiated using a Xe lamp (60 W) for approximately 18 h. IR (KBr): $\tilde{\nu}=$1622(s), 1590(s), 1508(m), 1410(m), 1381(m), 1232(w), 1060(m), 1026(m), 825(m), 675(m) cm^{-1}; ^1H NMR ([D_6]DMSO, 300 MHz, 298 K): $\delta=$ 8.35 (d, 4H, Py-H), 7.24 (d, 4H, Py-H), 4.68 (s, 4H, CH-CH), 1.81 ppm (s, 6H, CH_3COO); ^{13}C NMR: ([D_6]DMSO, 300 MHz, 298 K): $\delta=$ 176.48 (O=CO), 149.14 (C-Py), 148.24 (C-Py), 123.26 (C-Py), 44.31 (CH-CH), 22.31 ppm (CH_3).

4: Trifluoroacetic acid (0.1 mL, 1.2 mmol) and bpe (0.186 g, 1 mmol) in DMF (2 mL) were added consecutively to a solution of $Zn(O_2CCH_3)_2{\cdot}2H_2O$ (0.220 g, 1 mmol) in DMF (4 mL). After stirring for 1 min at RT, the clear solution was filtered and allowed to evaporate slowly. Colorless rodlike crystals separated out after two days; these were collected, washed with ether, and dried under vacuum (0.21 g, 53%). IR (KBr): $\tilde{\nu}=$1690.3(m), 1610.6(vs,), 1430.9(m), 1205.5(m), 1126.4(m), 1070.1(vw), 1018.3(w), 979.8(vw), 832.8(s), 726.0(w), 617.6(vw), 552.9(m) cm^{-1}; ^1H NMR ([D_6]DMSO, 300 MHz, 298 K): $\delta=$ 8.60 (d, 4H, Py-H), 7.63 (d, 4H, Py-H), 7.56 (s, 4H, CH=CH), 1.85 ppm (s, 3H, CH_3COO); Elemental analysis (%) calcd. for $C_{32}H_{26}N_4O_8F_6Zn_2$: C, 45.79; H, 3.12; N, 6.07; found: C, 45.63; H, 3.32; N, 6.07.

5: A powdered sample of **4** (10 mg) placed between two glass slides was irradiated using a Xe lamp for approximately 12 h. IR (KBr): $\tilde{\nu}=$1686(s), 1613(s), 1502(m), 1430(m), 1205(m), 1129(m), 1068(m), 1018(m), 832(m), 725(m) cm^{-1}; ^1H NMR ([D_6]DMSO, 300 MHz, 298 K): $\delta=$ 8.35 (d, 4H, Py-H), 7.26 (d, 4H, Py-H), 4.69 (s, 4H, CH–CH), 1.85 ppm (s, 3H, CH_3COO).

Crystal data for **1**: Monoclinic space group $C2/c$, $a=$ 10.530(3) Å, $b=$ 16.345(3) Å, $c=$ 12.901(2) Å, $\beta=$ 101.140(5)°, $V=$ 2178.5(7) $Å^3$, $Z=4$, $\rho_{calcd}=$ 1.674 $g\,cm^{-3}$. In the final least-squares refinement cycles on $|F|^2$, the model converged at $R_1=$ 0.0678, $wR2=$ 0.1650, and GOF = 1.168 for 1451 reflections with $F_o>4\sigma(F_o)$ and 151 parameters. Crystal data for **2**: Monoclinic space group $P2/n$, $a=$ 9.5526(6) Å, $b=$ 5.6572(3) Å, $c=$ 16.034(1) Å, $\beta=$ 98.492(1), $V=$ 857.00(9) $Å^3$, $Z=$ 2, $\rho_{calcd}=$ 1.487 $g\,cm^{-3}$. In the final least-squares refinement cycles on $|F|^2$, the model converged at $R_1=$ 0.0293, $wR2=$ 0.0802, and GOF = 1.086 for 1463 reflections with $F_o>4\sigma(F_o)$ and 120 parameters. Crystal data for **3**: Triclinic space group $P\bar{1}$, $a=$ 7.9853(7) Å, $b=$ 9.3552(9) Å, $c=$ 11.099(1) Å, $\alpha=$ 95.792(2), $\beta=$ 99.325(2), $\gamma=$ 105.797(2)°, $V=$ 778.0(1) $Å^3$, $Z=1$, $\rho_{calcd}=$ 1.561 $g\,cm^{-3}$. In the final least-squares refinement cycles on $|F|^2$, the model converged at $R_1=$ 0.0404, $wR2=$ 0.1042, and GOF = 1.039 for 2459 reflections with $F_o>4\sigma(F_o)$ and 233 parameters. Crystal data for **4**: Triclinic space group $P\bar{1}$, $a=$ 8.179(1) Å, $b=$ 9.528(1) Å, $c=$ 11.373(1) Å, $\alpha=$ 98.922(3), $\beta=$ 97.602(3), $\gamma=$ 103.846(3)°, $V=$ 836.8(2) $Å^3$, $Z=2$, $\rho_{calcd}=$

 © 2005 Wiley-VCH Verlag GmbH & Co. KGaA, Weinheim

1.665 g cm^{-3}. In the final least-squares refinement cycles on $|F|^2$, the model converged at $R_1 = 0.0526$, $wR2 = 0.1382$, and GOF = 1.058 for 2508 reflections with $F_o > 4\sigma(F_o)$ and 263 parameters. Crystal data for **5**: Triclinic space group $P\bar{1}$, $a = 8.4414(9)$ Å, $b = 9.806(1)$ Å, $c = 10.799(1)$ Å, $\alpha = 99.066(2)$, $\beta = 99.101(2)$, $\gamma = 105.796(2)°$, $V = 830.1(2)$ Å^3, $Z = 2$, $\rho_{calcd} = 1.679$ g cm^{-3}. In the final least-squares refinement cycles on $|F|^2$, the model converged at $R_1 = 0.0534$, $wR2 = 0.1415$, and GOF = 1.037 for 2456 reflections with $F_o > 4\sigma(F_o)$ and 236 parameters.

Crystal data for **1**–**5** were collected on a Bruker APEX diffractometer attached with a CCD detector and graphite-monochromated $Mo_{K\alpha}$ radiation (2.4 kW) using a sealed tube at 223(2) K. Absorption corrections were made with the program SADABS,[14] and the crystallographic package SHELXTL[15] was used for all calculations. CCDC-255233–255237 contain the supplementary crystallographic data for this paper. These data can be obtained free of charge from the Cambridge Crystallographic Data Centre via www.ccdc.cam.ac.uk/data_request/cif.

Received: November 19, 2004
Published online: February 11, 2005

Keywords: cycloaddition · photochemistry · self-assembly · topochemistry · zinc

[1] a) G. M. J. Schmidt, *Pure Appl. Chem.* **1971**, *27*, 647–678; b) C. R. Theocharis, W. Jones in *Organic Solid State Chemistry* (Ed.: G. R. Desiraju), Elsevier, **1987**, chap. 2, pp. 47–68; c) D. Braga, F. Grepioni, *Angew. Chem.* **2004**, *116*, 4092–4102; *Angew. Chem. Int. Ed.* **2004**, *43*, 4002–4011.

[2] a) V. Ramamurthy, K. Venkatesan, *Chem. Rev.* **1987**, *87*, 433–481; b) P. Wagner, B.-S. Park in *Organic Photochemistry*, *Vol. 11* (Ed.: A. Padwa), Marcel Dekker, New York, **1991**, chap. 4; c) W. Jones, *Organic Molecular Solids: Properties and Applications*, CRC, Boca Raton, FL, **1997**; d) B. S. Green, R. M. Lahav, D. Rabinovich, *Acc. Chem. Res.* **1979**, *12*, 191–197; e) F. Toda, *Acc. Chem. Res.* **1995**, *28*, 480–486; f) A. E. Keating, M. A. Garcia-Garibay in *Organic and Inorganic Photochemistry* (Eds.: V. Ramamurthy, K. S. Schanze), Marcel Dekker, New York, **1998**, pp. 195–248; g) K. Tanaka, F. Toda, *Chem. Rev.* **2000**, *100*, 1025–1074.

[3] a) X. Gao, T. Friščič, L. R. MacGillivray, *Angew. Chem.* **2004**, *116*, 234–238; *Angew. Chem. Int. Ed.* **2004**, *43*, 232; b) T. Friščič, L. R. MacGillivray, *Chem. Commun.* **2003**, 306–307; c) B. Dushyant, G. Papaefstathiou, L. R. MacGillivray, *Chem. Commun.* **2002**, 1964–1965; d) L. R. MacGillivray, J. L. Reid, J. A. Ripmeester, *J. Am. Chem. Soc.* **2000**, *122*, 7817–7818; e) L. R. MacGillivray, *CrystEngComm* **2002**, *4*, 37–47.

[4] T. Hoang, J. W. Lauher, F. W. Fowler, *J. Am. Chem. Soc.* **2002**, *124*, 10656–10657.

[5] a) M. J. Vela, B. B. Snider, B. M. Foxman, *Chem. Mater.* **1998**, *10*, 3167–3171; b) G. S. Papaefsthathiou, Z. Zhong, L. Geng, L. R. MacGillivray, *J. Am. Chem. Soc.* **2004**, *126*, 9158–9159; c) F. D. Lewis, S. L. Quillen, P. D. Hale, J. D. Oxman, *J. Am. Chem. Soc.* **1988**, *110*, 1261–1267; d) M. J. Vela, V. Buchholz, V. Enkelmann, B. B. Snider, B. M. Foxman, *Chem. Commun.* **2000**, 2225–2226; e) N. W. Alcock, P. de Meester, T. J. Kemp, *J. Chem. Soc. Perkin Trans. 2* **1979**, 921–926; f) G. Cao, T. E. Mallouk, *J. Solid State Chem.* **1991**, *94*, 59–71; g) C. R. Theocharis, A. M. Clark, S. E. Hopkin, P. Jones, *Mol. Cryst. Liq. Cryst.* **1988**, *156 (Pt.A)*, 85–91.

[6] For polymerization without metals, see: a) V. Enkelmann, *Adv. Polym. Sci.* **1984**, *63*, 92–136; b) G. W. Coats, A. R. Dunn, L. M. Henling, J. W. Ziller, E. B. Lobkovsky, R. H. Grubbs, *J. Am. Chem. Soc.* **1998**, *120*, 3641–3649; c) W. L. Dilling, *Chem. Rev.* **1983**, *83*, 3–47; d) M. Hasegawa, *Chem. Rev.* **1983**, *83*, 507–518.

[7] For example, see: a) S. Rabe, U. Müller, *Z. Anorg. Allg. Chem.* **1999**, *625*, 1367–1370; b) U. Englert, B. Ganter, B, T. Wagner, W. Kläui, *Z. Anorg. Allg. Chem.* **1998**, *624*, 970–974; c) C. J. Kepert, M. J. Rosseinsky, *Chem. Commun.* **1999**, 375–376; d) H. Li, M. Eddaoudi, M. O'Keefe, O. M. Yaghi, *Nature* **1999**, *402*, 276–279; e) D. V. Soldatov, E. V. Grachev, J. A. Ripmeester, *Cryst. Growth Des.* **2002**, *2*, 401–408; f) C. J. Kepert, T. J. Prior, M. J. Rosseinsky, *J. Am. Chem. Soc.* **2000**, *122*, 5158–5168; g) E. Y. Lee, M. P. Suh, *Angew. Chem.* **2004**, *116*, 2858–2861; *Angew. Chem. Int. Ed.* **2004**, *43*, 2798–2801.

[8] a) L. Iordanidis, M. G. Kanatzidis, *Angew. Chem.* **2000**, *112*, 2004–2006; *Angew. Chem. Int. Ed.* **2000**, *39*, 1928–1930; b) L. Iordanidis, M. G. Kanatzidis, *J. Am. Chem. Soc.* **2000**, *122*, 8319–8320.

[9] a) D. M. Shin, I. S. Lee, D. Cho, Y. K. Chung, *Inorg. Chem.* **2003**, *42*, 7722–7724; b) O. S. Jung, S. H. Park, K. M. Kim, H. G. Jang, *Inorg. Chem.* **1998**, *37*, 5781–5785; c) X. Xue, X.-S. Wang, R.-G. Xiong, X.-Z. You, B. F. Abrahams, C.-M. Che, H.-X. Ju, *Angew. Chem.* **2002**, *114*, 3068–3070; *Angew. Chem. Int. Ed.* **2002**, *41*, 2944–2946; d) B. Rather, B. Moulton, R. D. B. Walsh, M. J. Zaworotko, *Chem. Commun.* **2002**, 694–695; e) B. Rather, M. J. Zaworotko, *Chem. Commun.* **2003**, 830–831; f) M.-H. Zeng, X.-L. Feng, X.-M. Chen, *Dalton Trans.* **2004**, 2217–2223; g) K. Biradha, Y. Hongo, M. Fujita, *Angew. Chem.* **2002**, *114*, 3545–3548; *Angew. Chem. Int. Ed.* **2002**, *41*, 3395–3398; h) K. Biradha, M. Fujita, *Angew. Chem.* **2002**, *114*, 3542–3545; *Angew. Chem. Int. Ed.* **2002**, *41*, 3392–3395; i) J. D. Ranford, J. J. Vittal, D. Wu, *Angew. Chem.* **1998**, *110*, 1159–1162; *Angew. Chem. Int. Ed.* **1998**, *37*, 1114–1116; j) J. D. Ranford, J. J. Vittal, D. Wu, X. Yang, *Angew. Chem.* **1999**, *111*, 3707–3710; *Angew. Chem. Int. Ed.* **1999**, *38*, 3498–3501.

[10] a) B. Moulton, M. J. Zaworotko, *Chem. Rev.* **2001**, *101*, 1629–1658; b) M. J. Zaworotko, *Chem. Commun.* **2001**, 1–10; c) M. J. Zaworotko in *Crystal Engineering: The Design and Application of Functional Solids, NATO ASI Ser. C-539* (Eds.: M. J. Zaworotko, K. R. Seddon), Kluwer, Dordrecht, **1999**, pp. 383–408; d) A. N. Khlobystov, A. J. Blake, N. R. Champness, D. A. Lemenovskii, A. G. Majouga, N. V. Zyk, M. Schröder, *Coord. Chem. Rev.* **2001**, *222*, 155–192; e) N. R. Champness, M. Schröder, *Curr. Opin. Solid State Mater. Sci.* **1998**, *3*, 419–424.

[11] Compound **3** is strictly a pseudosupramolecular isomer of **2** as it has one lattice water molecule in the asymmetric unit. For the definition of supramolecular isomer, see Ref. [10a].

[12] T. Caronna, R. Liantonio, T. A. Logothetis, P. Metrangolo, T. Pilati, G. Resnati, *J. Am. Chem. Soc.* **2004**, *126*, 4500–4501.

[13] A. Michaelides, S. Skoulika, M. G. Siskos, *Chem. Commun.* **2004**, 2418–2419.

[14] G. M. Sheldrick, SADABS, Software for Empirical Absorption Corrections, University of Göttingen (Germany), **2000**.

[15] SHELXTL Reference Manual, version 5.1, Bruker AXS, Analytical X-Ray Systems, Madison, WI, USA, **1997**.

 © 2005 Wiley-VCH Verlag GmbH & Co. KGaA, Weinheim

Supported Catalysts

Supported Gold Catalyzes the Homocoupling of Phenylboronic Acid with High Conversion and Selectivity**

*Silvio Carrettin, Javier Guzman, and Avelino Corma**

Coupling reactions are largely dominated by the use of palladium catalysts and are a powerful and versatile tool in synthetic organic chemistry for the formation of carbon–carbon bonds.[1,2] Among the different coupling reactions, the Suzuki reaction plays an important role and it is already used in some industrial processes.[3] The possible products include biaryls which are interesting because of their presence in many natural products and biologically active compounds.[4] This class of compounds can be prepared by two different types of reactions: homocoupling or cross-coupling.

The general mechanism for the Suzuki cross-coupling reaction involves the transmetalation of a boronic acid by Pd^{2+} ions. Various examples have recently been reported for the homocoupling of boronic acids by different metals.[5] One of these[5a] shows that homocoupling of boronic acids occurs by a double transmetalation at Pd^{2+} centers formed by oxidative addition of an α-halocarbonyl compound to an initial Pd^0 complex. The authors found that there was no reaction in the absence of the α-halocarbonyl compound, thus confirming that the transmetalation of the boronic acid occurs at Pd^{2+} species. Taking this into account, we thought that as Au^{3+} is isoelectronic with Pd^{2+} and able to undergo the redox cycle $Au^{3+} \rightleftarrows Au^{+}$, it may be possible for a solid catalyst containing Au^{3+} species to be active in the cross-coupling as well as the homocoupling reaction (Scheme 1). To the best of our knowledge the only examples of C–C bond formation catalyzed by gold have been performed using homogeneous catalytic systems.[6,7]

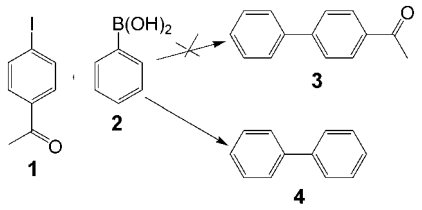

Scheme 1. Possible Suzuki and homocoupling reactions catalyzed by gold; reaction conditions: 2.25 wt% Au/CeO_2, toluene, K_2CO_3, $T = 333$ K.

[*] Dr. S. Carrettin, Dr. J. Guzman, Prof. A. Corma
Instituto de Tecnología Química
UPV-CSIC
Universidad Politécnica de Valencia
Avda. de los Naranjos s/n, 46022 Valencia (Spain)
Fax: (+34) 96-387-7809
E-mail: acorma@itq.upv.es

[**] The authors thank MAT 2003-07945-C02-01 and the Auricat EU-Network (HPRN-CT-2002-00174) for financial support.

Supporting information for this article is available on the WWW under http://www.angewandte.org or from the author.

To investigate our hypothesis, we prepared a supported gold catalyst containing cationic gold species. The support consists of nanocrystalline ceria particles, which are able to stabilize ionic states of gold because of their electron-withdrawing properties.[8] Indeed, the IR spectrum of CO adsorbed on an Au/CeO_2 catalyst[9] shows a band at 2148 cm^{-1} that confirms the presence of Au^{3+} ions. This result was supported by XPS data, which display a peak at 86.2 eV corresponding to the binding energy ($4f_{7/2}$) of Au^{3+} (Supporting Information).

To test the reactivity of gold supported on nanocrystalline CeO_2 for Suzuki cross-coupling, reactions were carried out between *p*-iodobenzophenone and phenylboronic acid (Experimental Section, Reaction a). We observed that all the boronic acid was transformed into biphenyl, thus indicating that the homocoupling reaction occurs with practically 100% conversion and selectivity (Supporting Information). The product of Suzuki cross-coupling condensation was detected in very small amounts (< 0.5%).

Interestingly, the reaction also proceeds with the same conversion and selectivity in the absence of the α-halocarbonyl compound and K_2CO_3. When the reaction is carried out without K_2CO_3, the only difference observed is the degradation of the catalyst. The base is known to activate phenylboronic acid;[1] however, our results indicate that with our catalytic system base is not needed for the activation of phenylboronic acid, and its only role is to neutralize the boric acid. Furthermore, the turnover number (TON) of 20 (calculated as the moles of boronic acid converted divided by two and by the moles of gold in the catalyst per hour) indicates that the process is catalytic. It should be noted that because not all the gold atoms are available for the reaction, the real TON is likely to be much higher than 20.

Blank experiments without catalyst or using gold-free nanocrystalline ceria gave no conversion, thus showing that the catalytically active sites are associated with gold. Possible Au leaching during the reaction was checked by analyzing gold in the supernatant liquid by AAS; 0.3 ± 0.1 ppm of gold was detected (Supporting Information). The activity of the leached gold was found to be negligible by carrying out an experiment in which 3 ppm of gold (ten times the amount of leached gold) in the form of $HAuCl_4$ was introduced as catalyst. After 6 h at 333 K the conversion was 1.1%. Under the same conditions using our gold catalyst the conversion was 100%.

From a stoichiometric point of view, the formation of boric acid from boronic acid requires the participation of either a surface hydroxy group (associated to gold[10] and/or to the cerium oxide[11]) or molecular water that will dissociate and subsequently hydrolyze the boronic acid to boric acid. For either case, it is clear that hydroxy groups participate in the catalytic reaction, and regeneration of such species requires dissociation of molecular water on the surface of the support to restore the surface hydroxy groups and generate molecular hydrogen.[11] The overall homocoupling reaction is therefore as described in [Eq. (1)].

$$2\,(HO)_2BPh + 2\,H_2O + Au^{3+} \rightarrow 2\,B(OH)_3 + PhPh + Au^{+} + H_2 \quad (1)$$

 © 2005 Wiley-VCH Verlag GmbH & Co. KGaA, Weinheim DOI: 10.1002/anie.200462560

To prove experimentally that this reaction is taking place we monitored the homocoupling reaction by Raman spectroscopy to detect H_2 formation. The results presented in Figure 1 clearly show the presence of molecular hydrogen, as indicated by the band at 4104 cm^{-1}.[12]

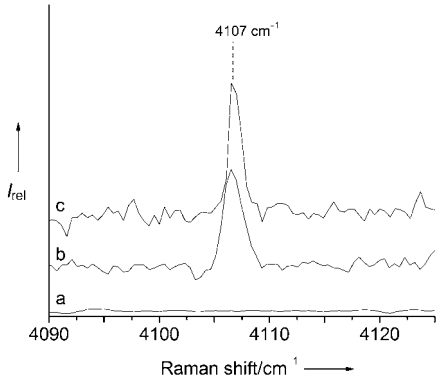

Figure 1. Raman spectra of a) toluene; b) H_2 in toluene; and c) homocoupling reaction in toluene.

The presence of H_2O is required for this reaction. To confirm this we performed a set of experiments using anhydrous materials (Experimental Section, Reaction b) which lead to only 17% conversion after 7 h. At this point 30 μL of H_2O was added, and the conversion increased to 47.5% after another 7 h. Furthermore, when 50 μL of H_2O was added to the dried catalyst and reactants the conversion increased to 61%. These results clearly support the importance of H_2O in the catalytic reaction, and suggest the participation of hydroxy groups in hydrolyzing the boronic acid.

Raman spectroscopy was used to characterize the addition of water to the gold catalyst and the support alone. The spectrum of the Au/CeO_2 catalyst treated with water shows the formation of hydroxy groups on the support, as evidenced by new bands at 3427 and 3594 cm^{-1} (Supporting Information). These hydroxy groups disappeared after addition of phenylboronic acid, thereby indicating the participation of OH species in the activation of the phenylboronic acid. In contrast, when the same experiment was carried out with the CeO_2 support, the Raman bands representing the hydroxy groups showed no variation after addition of boronic acid. These results indicate that gold is required to enhance the interaction between OH species and the boronic acid. It has been shown previously that the presence of gold weakens the surface oxygen species of ceria.[13]

When boronic acid was mixed with water or with water and cerium oxide at the reaction temperature in the absence of gold, neither product formation nor substrate decomposition were observed. We can therefore conclude that the OH groups on the surface of the CeO_2 support interact with the boronic acid to form boric acid, while two phenyl species interact with Au^{3+} to form a carbon–metal bond. Thus, homocoupling occurs and Au^{3+} is reduced to Au^{+}.

To regenerate the active species and to close the catalytic cycle, Au^{+} has to be reoxidized to Au^{3+}. This oxidation can occur by three different routes: by air, by H^{+} generated in the media, or by Ce^{4+} present in the support. We have seen that the reaction proceeds in the absence of oxygen with the same activity, therefore the first possibility can be rejected. To investigate the second option—oxidation of Au^{+} by H^{+} to give Au^{3+} and H_2—we monitored the homocoupling reaction by Raman spectroscopy; formation of H_2 was observed.[12] However, it would appear that the redox potential for the whole reaction ($2H^{+}$ to H_2 and Au^{+} to Au^{3+}) is not high enough to cause a spontaneous electron transfer. Nevertheless, it should be taken into account that in the case of nanoparticles, as the number of atoms n per particle decreases, a nonlinear relationship exists between n, the redox potential (E_0), and the lattice stabilization energy of the atoms involved. As a consequence, E_0 decreases drastically with decreasing n.[14] Therefore, considering the formation of H_2 and the effect of small particle sizes on the oxidation potential of gold, it is possible that Au^{+} present as a gold nanoparticle could be reoxidized to Au^{3+} by H^{+}.

Looking into the third possibility—Ce^{4+} acting as an oxidant for Au^{+}—it has been reported[11] that water dissociates on the surface of cerium oxide to form OH groups and oxidize Ce^{3+} to Ce^{4+}. This reaction produces the H_2 that was detected by Raman spectroscopy.[12] In this case the redox potential for the reduction of Ce^{4+} to Ce^{3+} is high enough to oxidize Au^{+} to Au^{3+}, therefore this is also a promising candidate for the process that closes the catalytic cycle. Consistent with this hypothesis, XPS data characterizing the gold catalyst support the presence of Ce^{4+} and Ce^{3+} species (Supporting information).

We can therefore postulate two possible mechanisms for the homocoupling of phenylboronic acid on Au/CeO_2 catalysts (Scheme 2). For both catalytic mechanisms we infer that Au^{3+} is present at the active sites. To confirm this we investigated a series of Au/CeO_2 catalysts with different Au^{3+}/Au^{0} and Au^{+}/Au^{0} ratios, as determined by IR spectroscopy using CO as a probe molecule. The results presented in Figure 2 clearly show a direct correlation between the

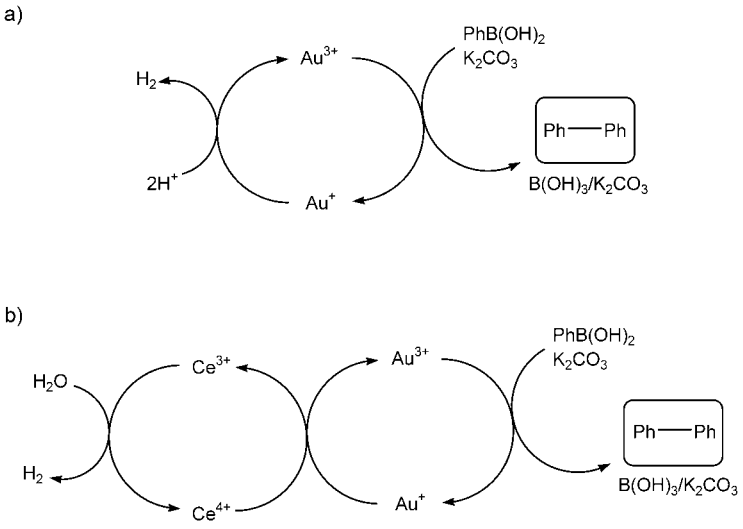

Scheme 2. Catalytic cycle for the homocoupling reaction catalyzed by Au^{3+} species: a) Au^{+} reoxidation to Au^{3+} by H^{+}; b) Au^{+} reoxidation to Au^{3+} by Ce^{4+}.

 © 2005 Wiley-VCH Verlag GmbH & Co. KGaA, Weinheim

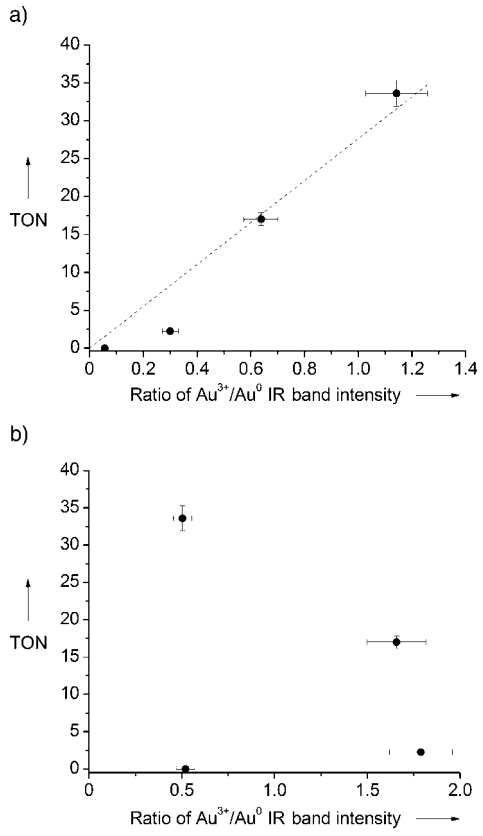

Figure 2. a) Correlation between Au^{3+} and Au^0 species and TON for the homocoupling reaction catalyzed by gold; b) correlation between Au^+ and Au^0 species and TON for the homocoupling reaction catalyzed by gold. The frequency and intensity of the IR band of CO adsorbed on gold catalysts were used to identify Au^{3+} (band at 2148 cm^{-1} representing Au^{3+}-bound CO), Au^+ (2130 cm^{-1}, Au^+-bound CO) and Au^0 (2104 cm^{-1}, Au^0-bound CO).

concentration of Au^{3+} species and catalytic activity; no correlation was found between catalytic activity and the concentration of Au^+ or Au^0.

Gold on nanocrystalline CeO_2 is a much more active catalyst than gold on precipitated CeO_2 for the homocoupling reaction. Consistent with these results, our group has recently demonstrated that the characteristics of the cerium oxide surface are extremely important for CO oxidation on an Au/CeO_2 catalyst.[9] We found that nanocrystalline CeO_2 (nanoparticles of about 4 nm in size with fluorite structure) increases the activity of gold for CO oxidation by two orders of magnitude with respect to a precipitated CeO_2 support. The results obtained for gold on different metal-oxide catalysts tested for CO oxidation and for homocoupling show a direct correlation between the activities (Supporting Information).

We also studied the homocoupling of other aryl boronic acids to determine the possible influence of substituents on the aromatic ring. The Au/CeO_2 catalyst gave practically 100% conversion and selectivity in all cases (Table 1).

In conclusion, we have found that gold supported on nanocrystalline cerium oxide catalyzes the homocoupling reaction of phenylboronic acid with very high activity and selectivity in the absence of an α-halocarbonyl compound and presence of a base. Au^{3+} species are the active sites for the reaction and water is required to hydrolize the boronic acid through surface hydroxy groups.

Table 1: Homocoupling of phenylboronic acids.[a]

Reaction	Yield [%]
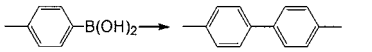	100
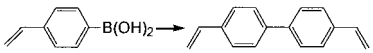	100
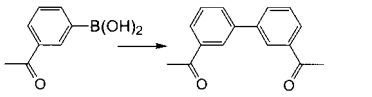	97[b]

[a] Reaction conditions: 5 mL toluene, 0.3 mmol of phenylboronic acid, 5 mol% of Au, $T = 333$ K, 15 h; yield determined by GC-MS with *n*-decane as internal standard. [b] 3% Acetophenone was formed as byproduct.

Experimental Section

Au/CeO_2 catalysts were prepared by precipitation of $HAuCl_4$ with NaOH following a procedure described elsewhere.[9] The total Au content of the final catalyst was determined by chemical analysis to be 2.25 wt%.

The solvent (5 mL) and the catalyst (the amount depends on the mol percent of gold required) were added to a 10-mL round-bottomed flask containing phenylboronic acid (0.3 mmol) and K_2CO_3 (0.4 mmol). The reactions were carried out at 333 K (unless otherwise specified) for 15 h with vigorous stirring. The yields and conversions were determined by GC-MS analysis using decane as internal standard.

Reaction a (Suzuki cross-coupling): The catalyst (100 mg; 5 mol% of Au per mol of $PhB(OH)_2$) was added to a round-bottomed flask together with DMF (5 mL), *p*-iodobenzophenone (0.2 mmol), and phenylboronic acid (0.3 mmol). The reaction was carried out at 433 K.

Reaction b: The catalyst and reactants were dried at 333 K and 10^{-3} Torr and anhydrous solvent was used; the reaction was carried out at 333 K under nitrgoen.

Received: November 9, 2004
Revised: January 10, 2005
Published online: March 10, 2005

Keywords: C–C coupling · gold · heterogeneous catalysis · nanostructures · supported catalysts

[1] a) A. de Meijere, F. Diederich, *Metal-Catalyzed Cross-Coupling Reactions*, *Vol. 1–2*, Wiley-VCH, Weinheim, **2004**; b) G. C. Fu, A. F. Littke, *Angew. Chem.* **2002**, *114*, 4350–4386; *Angew. Chem. Int. Ed.* **2002**, *41*, 4176–4211.
[2] K. C. Nicolaou, E. I. Sorensen, *Classics in Total Synthesis*, VCH, New York, **1996**.
[3] G. B. Smith, G. C. Dezeny, D. L. Hughes, A. O. King, T. R. Verhoeven, *J. Org. Chem.* **1994**, *59*, 8151–8156.
[4] J. Hassan, V. Penalva, L. Lavenot, C. Gozzi, M. Lamaire, *Tetrahedron* **1998**, *54*, 13793–13804.

 © 2005 Wiley-VCH Verlag GmbH & Co. KGaA, Weinheim

[5] a) A. Lei, X. Zhang, *Tetrahedron Lett.* **2002**, *43*, 2525 – 2528, and references cited therein; b) J. R. Falck, S. Mohapatra, M. Bondlela, S. K. Venkataraman, *Tetrahedron Lett.* **2002**, *43*, 8149 – 8151; c) A. S. Demir, Ö. Reis, M. Emrullahoglu, *J. Org. Chem.* **2003**, *68*, 578 – 580; d) J. P. Parrish, Y. C. Jung, R. J. Floyd, K. W. Jung, *Tetrahedron Lett.* **2002**, *43*, 7899 – 7902; e) A. Demir, Ö. Reis, M. Emrullahoglu, *J. Org. Chem.* **2003**, *68*, 10130 – 10134; f) C. J. Li, *Angew. Chem.* **2003**, *115*, 5004 – 5006; *Angew. Chem. Int. Ed.* **2003**, *42*, 4856 – 4858.

[6] a) G. Dyker, *Angew. Chem.* **2000**, *112*, 4407 – 4409; *Angew. Chem. Int. Ed.* **2000**, *39*, 4237 – 4239, and references cited therein; b) A. S. K. Hashmi, L. Ding, J. W. Bats, P. Fisher, W. Frey, *Chem. Eur. J.* **2003**, *9*, 4339 – 4345.

[7] One of the referees pointed out an ASAP publication where colloidal gold is used as a catalyst for the homocoupling of phenylboronic acids. However, the activity is low and, more importantly, the selectivity is always below 80 %: H. Tsunoyama, H. Sakurai, N. Ichikuni, Y. Negishi, T. Tsukuda, *Langmuir* **2004**, *20*, 11293 – 11296.

[8] a) Q. Fu, H. Saltsburg, M. Flytzani-Stephanopoulos, *Science* **2003**, *301*, 935 – 938; b) F. Zhang, S. W. Chan, J. E. Spanier, E. Apak, Q. Jin, R. D. Robinson, I. P. Herman, *Appl. Phys. Lett.* **2002**, *80*, 127 – 129; c) A. N. Pestryakov, V. V. Lunin, A. N. Kharlanov, N. E. Bogdanchikova, I. V. Tuzovskaya, *Eur. Phys. J. D* **2003**, *24*, 307 – 309; d) A. N. Pestryakov, V. V. Lunin, *J. Mol. Catal. A* **2000**, *158*, 325 – 329.

[9] S. Carrettin, P. Concepción, A. Corma, J. M. López-Nieto, V. F. Puntes, *Angew. Chem.* **2004**, *116*, 2592 – 2594; *Angew. Chem. Int. Ed.* **2004**, *43*, 2538 – 2540.

[10] E. D. Park, J. S. Lee, *J. Catal.* **1999**, *186*, 1 – 11.

[11] a) T. Tabakova, F. Boccuzzi, M. Manzoli, D. Andreeva, *Appl. Catal. A* **2003**, *252*, 385 – 397; b) Lj. Kundakovic, D. R. Mullins, S. H. Overbury, *Surf. Sci.* **2000**, *457*, 51 – 62.

[12] a) D. Gracin, I. Bogdanovic, V. Bojanovic, M. Jaksic, Z. Pastuovic, J. M. Dutta, V. Vlahovic, R. J. Nemanich, *Vacuum* **2001**, *61*, 303 – 308; b) A. W. R. Leitch, J. Weber, V. Alex, *Mater. Sci. Eng. B* **1999**, *58*, 6 – 12.

[13] D. Andreeva, V. Idakiev, T. Tabakova, L. Ilieva, P. Falaras, A. Bourlinos, A. Travlos, *Catal. Today* **2002**, *72*, 51.

[14] L. D. Burke, A. J. Ahern, A. P. O'Mullane, *Gold Bull.* **2002**, *35*, 3 – 10.

 © 2005 Wiley-VCH Verlag GmbH & Co. KGaA, Weinheim

β-Selective Glycosidation

Direct and Stereoselective Synthesis of 2-Acetamido-2-deoxy-β-D-glycopyranosides by Using the Phosphite Method**

*Ryoichi Arihara, Seiichi Nakamura, and Shunichi Hashimoto**

2-Acetamido-2-deoxy-D-glycopyranosides occur as common and important structural units in oligosaccharides and glycoconjugates, such as glycolipids, glycoproteins, proteoglycans, and peptidoglycans, and are associated with a wide range of biological processes.[1] Whereas 2-acetamido-2-deoxy-α-D-galactopyranose residues are linked through a glycoside bond to the side-chain hydroxy groups of serine and threonine, the majority of 2-acetamido-2-deoxy-D-glycopyranosides are found as β-linked glycosides.

The most general and extensively developed strategy for the synthesis of 1,2-*trans*-β-glycosides of 2-amino-2-deoxysugars utilizes donors containing a participating group as the amino-protecting functionality, which is replaced by an acetyl group after the glycosidation event.[2,3] 2-Azido-2-deoxyglycosyl donors have also been used for this purpose.[4,5] Clearly, a direct glycosidation method by using donors with the natural *N*-acetyl function would constitute an ideal procedure in terms of efficiency and practicality. In practice, however, the reaction of these donors, **1**, generally leads to the predominant formation of oxazoline derivatives **3** through neighboring-group participation and the subsequent abstraction of a proton from the NH group (Scheme 1).[6,7] Although oxazolines can react with acceptor alcohols in the presence of Brønsted or Lewis acids to afford 2-acetamido-2-deoxy-β-glycosides **4** via oxazolinium ion intermediates **2** or **5** (that is, oxazoline method[8]), the harsh reaction conditions required for this conversion have precluded its wide application in the synthesis of complex oligosaccharides. As part of a program to extend the recently developed glycosidation method that capitalizes on diethyl phosphite as a leaving group,[9,10] we wish to report the stereoselective synthesis of 2-acetamido-2-deoxy-β-glycosides by a direct glycosidation that does not proceed via an oxazolinium ion intermediate.

At the outset of this study, we explored the trimethylsilyl trifluoromethanesulfonate (TMSOTf) promoted glycosidation of 2-acetamido-3,4,6-tri-*O*-benzyl-2-deoxy-α-D-glucopyr-

[*] R. Arihara, Dr. S. Nakamura, Prof. Dr. S. Hashimoto
Graduate School of Pharmaceutical Sciences
Hokkaido University
Sapporo 060–0812 (Japan)
Fax: (+81) 11-706-3236
E-mail: hsmt@pharm.hokudai.ac.jp

[**] This research was supported in part by a Grant-in-Aid for Scientific Research on Priority Areas (A) "Exploitation of Multi-Element Cyclic Molecules" from the Ministry of Education, Culture, Sports, Science, and Technology, Japan. We thank H. Matsumoto, A. Maeda, S. Oka, and M. Kiuchi of the Center for Instrumental Analysis, Hokkaido University, for technical assistance with MS and elemental analysis.

 DOI: 10.1002/anie.200461988 © 2005 Wiley-VCH Verlag GmbH & Co. KGaA, Weinheim

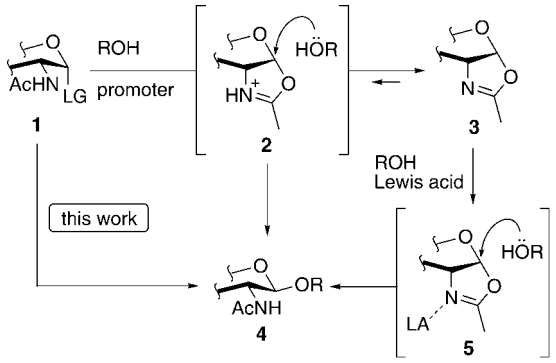

Scheme 1. Glycosidation of 2-acetamido-2-deoxyglycosyl donors. Ac = acetyl, LA = Lewis acid, LG = leaving group.

anosyl diethyl phosphite (**6**)[11] with 6-*O*-unprotected glycoside **7** (1.1 equiv; Table 1). An initial experiment revealed that the donor **6** was completely consumed within 5 min at 0 °C, thereby affording a mixture of disaccharide **8** and oxazoline **9** in the ratio of 0.3:1 (Table 1, entry 1). To our surprise, an examination of the temperature profile of the reaction revealed a trend for the yield of disaccharide **8** to increase with descending temperature (entries 1–3). The temperature limit for a smooth reaction was −60 °C, at which disaccharide **8** was produced in 36 % yield (entry 3).[12] A number of other promoters were then examined for the reaction of diethyl phosphite **6** and alcohol **7**. Among a variety of Lewis acids that were screened (entries 3–6), $Hf(OTf)_4$[13] proved to be superior to TMSOTf; however, disaccharide **8** was still obtained in only 66 % yield (entry 6). Our interest was then directed to the use of promoters with Brønsted acidity.[10b,14] We found that the coupling of donor **6** with **7** in CH_2Cl_2 in the presence of TfOH proceeded even at −78 °C to give disaccharide **8** in 75 % yield (entry 7). It is interesting to note that the sulfonic acids with greater Brønsted acidity[15] resulted in higher yields of **8** (entries 7–9). The use of $HClO_4$ prepared from *t*BuBr and $AgClO_4$[16] also promoted the reaction at −78 °C, but a significantly longer time was required to reach completion (entry 10). Finally, we were gratified to find that a simple change in the counterion in super Brønsted acids from trifluoromethanesulfonate (triflate) to bis(trifluoromethanesulfonyl)imide (triflimide)[17] dramatically enhanced the reaction rate, without compromising product yield. Although the reason for this difference in reactivity is currently unclear, the use of Tf_2NH provided disaccharide **8** rapidly (1 h) in 73 % yield (entry 11).[18] Eventually, the use of 2 equivalents of acceptor alcohol **7** led to an additional increase in the yield (84 %) of **8** (entry 12). When the reaction was carried out using 2 equivalents of donor **6**, disaccharide **8** was obtained in comparable (93 %) yield (entry 13).

Table 1: Effect of temperature and promoter on the glycosidation of **6** with **7**.[a]

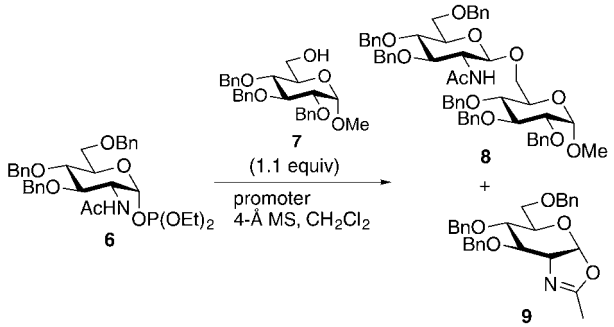

Entry	Promoter	*T* [°C]	*t* [h]	**8**:**9**[b]	Yield of **8** [%]
1[c,d]	TMSOTf	0	0.1	0.3:1	18
2[c,d]	TMSOTf	−23	0.1	0.4:1	24
3[c,d]	TMSOTf	−60	0.5	0.7:1	36
4	$BF_3{\cdot}OEt_2$	−60	4	2.0:1	39
5	$Sn(OTf)_2$	−60	1	1.6:1	46
6	$Hf(OTf)_4$	−60	1	2.9:1	66
7	TfOH	−78	5	4.2:1	75
8	TsOH	−78	1	1.8:1	51
9	MsOH	−78	1	0.8:1	38
10	$HClO_4$[e]	−78	12	2.2:1	59
11[d]	Tf_2NH	−78	1	4.1:1	73
12[d,f]	Tf_2NH	−78	1	7.8:1	84
13[g]	Tf_2NH	−78	1	–	93

[a] The reaction was carried out on a 0.1 mmol scale with 1.1 equivalents of acceptor **7** and 1.5 equivalents of promoter in the presence of pulverized 4-Å molecular sieves (4-Å MS) in CH_2Cl_2, unless otherwise noted. Ts = *p*-toluenesulfonyl, MS = methanesulfonyl. [b] The ratio was determined by 500-MHz ^{1}H NMR spectroscopic analysis of the crude mixture. [c] The reaction was performed in the absence of 4-Å MS. [d] The reaction was performed with 1.1 equivalents of promoter. [e] Prepared from *t*BuBr and $AgClO_4$. See ref. [16]. [f] The reaction was carried out by using 2.0 equivalents of **7**. [g] Donor/acceptor/Tf_2NH molar ratio = 2.0:1.0:2.2. Bn = benzyl.

With the reaction conditions optimized, we then explored the glycosidation of **6** and **10**–**12**[11] for both the D-gluco and D-galacto series with a range of acceptor alcohols with different reactivities (Scheme 2, Table 2). The examples highlighted in Table 2 deserve some comments. In all cases, $-Tf_2NH$-promoted glycosidations in CH_2Cl_2 at −78 °C were found to offer a facile, efficient, and stereoselective route to 1,2-*trans*-β-linked glycosides. Under these conditions, secondary as well

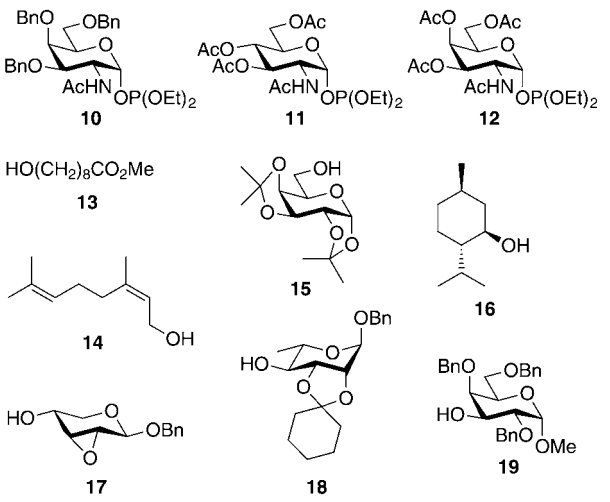

Scheme 2. Glycosyl donors and acceptor alcohols used for the reactions described in Table 2.

 © 2005 Wiley-VCH Verlag GmbH & Co. KGaA, Weinheim

Table 2: Glycosidation of **6**, **10**–**12**.[a]

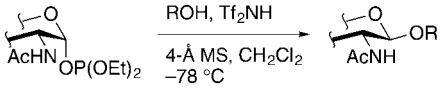

Entry	Donor	Acceptor	*t* [h]	Yield [%][b]
1[c]	**6**	**13**	1	80 (83)
2	**6**	**15**	1	89 (92)
3	**6**	**17**	1	79 (78)
4	**6**	**18**	1	57 (44)
5	**6**	**19**	1	65 (64)
6	**10**	**7**	1	83 (87)
7[d]	**10**	**14**	1	81 (79)
8[c]	**10**	**16**	1	74 (71)
9	**11**	**7**	24	70 (72)
10	**12**	**15**	24	67 (70)
11	**12**	**17**	24	59 (59)

[a] Donor/acceptor/Tf_2NH molar ratio = 1.0:2.0:1.1 unless otherwise noted. [b] Yields in parentheses were obtained when a donor/acceptor/Tf_2NH molar ratio of 2.0:1.0:2.2 was used. [c] The reaction was carried out by using 1.5 equivalents of acceptor alcohol or, for the results in parentheses, 1.5 equivalents of donor. [d] The reaction was carried out by using 1.1 equivalents of acceptor alcohol or, for the results in parentheses, 1.1 equivalents of donor.

as primary alcohols could be employed and β-glycosides were obtained in good to high yields. It is also noteworthy that the alcohols bearing acid-sensitive acetal or epoxy groups could be safely glycosylated (entries 2–4, 10, and 11). The *O*-acetyl protective groups in **11** and **12** lowered the reactivities of these compounds relative to those with the fully benzylated donors **6** and **10** in a consistent and general trend,[19] but the β-glycosides were still produced in moderate to good yields (entries 9–11).[20]

To gain an insight into the mechanism of this glycosidation reaction, further experiments were performed to determine whether the glycosidation proceeded via an oxazolinium ion intermediate. The reaction of oxazoline **9** with **7** did not occur under the optimized conditions described above (Scheme 3).[21,22] This result, together with the finding that a prolonged reaction time (20 h) had no effect on the yield of disaccharide **8** in the reaction of **6** with **7**, suggests that the present reaction does not proceed via the intermediacy of an oxazolinium ion. In this context, it is interesting to note that Crich and Sun identified an anomeric mixture of glycosyl triflates as intermediates in the sulfoxide glycosidation reaction of Kahne et al.[23] when a participating acetyl group was present on the oxygen atom at position 2.[24,25] Based on this remarkable observation, a proposed reaction mechanism is outlined in Scheme 4. Diethyl phosphite **21** is activated by

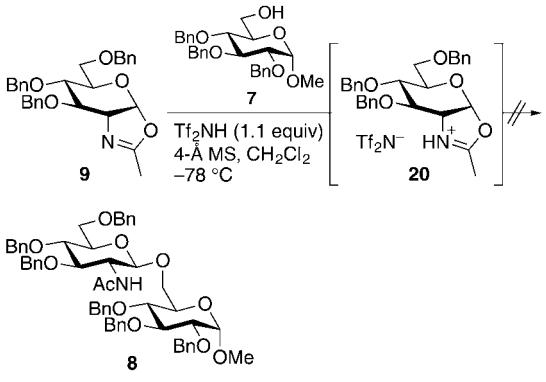

Scheme 3. Glycosidation of oxazoline **9** with **7** did not proceed via an oxazolinium ion intermediate **20** under the optimized conditions.

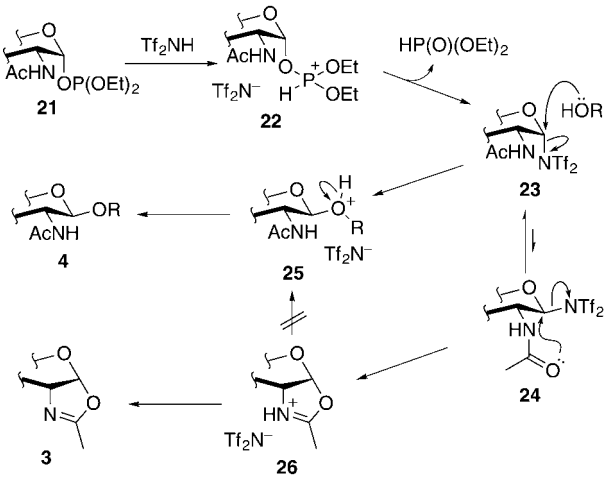

Scheme 4. Plausible mechanism of the glycosidation of 2-acetamido-2-deoxyglycosyl diethyl phosphites.

protonation of the phosphorus atom[26] and the phosphite group cleaves to produce an equilibrium mixture of α- and β-glycosyl triflimide intermediates **23** and **24**. An S_N2-like displacement by the acceptor alcohol at the anomeric carbon atom of the α-glycosyl triflimide **23** affords β-glycoside **4** via intermediate **25**. On the other hand, the β-glycosyl triflimide **24** undergoes an intramolecular attack by the acetamido group, thereby generating the oxazolinium ion **26**,[27] from which the oxazoline **3** is formed by the elimination of a proton from the NH group.

In conclusion, we have demonstrated herein that Tf_2NH-promoted glycosidations of 2-acetamido-2-deoxyglycopyranosyl diethyl phosphites with a variety of acceptor alcohols in CH_2Cl_2 at −78 °C give 1,2-*trans*-β-linked glycosides in good to high yields with perfect stereoselectivity. This protocol represents the first example of the direct glycosidation of 2-acetamido-2-deoxyglycosyl donors that does not proceed via an oxazolinium ion intermediate. Spectroscopic investigations to support the proposed mechanism, as well as further studies aimed at expanding the synthetic utility of this protocol, are in progress.

Experimental Section

A representative procedure for glycosidation of 2-acetamido-2-deoxyglycopyranosyl diethyl phosphite (entry 12 in Table 1): A 1M solution of Tf_2NH in EtCN (0.11 mL, 0.11 mmol) was added to a mixture of donor **6** (61.2 mg, 0.1 mmol), acceptor **7** (92.9 mg, 0.2 mmol), and pulverized 4-Å molecular sieves (61.2 mg) in

 © 2005 Wiley-VCH Verlag GmbH & Co. KGaA, Weinheim

CH_2Cl_2 (1 mL) at −78 °C. After stirring at this temperature for 1 h, the reaction was quenched by addition of Et_3N (0.15 mL), and the whole mixture was partitioned between EtOAc and saturated aqueous $NaHCO_3$. The organic extract was washed with brine and dried over anhydrous Na_2SO_4. Filtration and evaporation in vacuo furnished the crude products, whose ratio was determined to be 7.8:1 by 500-MHz ^1H NMR spectroscopic analysis. For easy purification, a solution of the crude mixture in EtOAc (12 mL) and CH_2Cl_2 (2 mL) was vigorously stirred with 10% aqueous HCl (2 mL) for 10 min, during which time the oxazoline **9** was completely hydrolyzed to form the corresponding glycopyranose. The whole mixture was extracted with EtOAc, and the organic extract was washed successively with saturated aqueous $NaHCO_3$ and brine, then dried over anhydrous Na_2SO_4. Filtration and evaporation in vacuo followed by flash column chromatography (silica gel, toluene/acetone 7:1) afforded disaccharide **8** (77.2 mg, 84%) as a white solid.

Received: September 14, 2004
Revised: December 6, 2004
Published online: March 3, 2005

Keywords: glycosidation · glycosides · neighboring-group effects · phosphites · synthetic methods

[1] For reviews, see: a) R. A. Dwek, *Chem. Rev.* **1996**, *96*, 683–720; b) N. E. Zachara, G. W. Hart, *Chem. Rev.* **2002**, *102*, 431–438.

[2] For reviews, see: a) J. Banoub, P. Boullanger, D. Lafont, *Chem. Rev.* **1992**, *92*, 1167–1195; b) J. Debenham, R. Rodebaugh, B. Fraser-Reid, *Liebigs Ann./Recueil* **1997**, 791–802.

[3] a) Phthaloyl group: R. U. Lemieux, T. Takeda, B. Y. Chung, *ACS Symp. Ser.* **1976**, *39*, 90–115; b) 2,2,2-trichloroethoxycarbonyl group: M. Imoto, H. Yoshimura, T. Shimamoto, N. Sakaguchi, S. Kusumoto, T. Shiba, *Bull. Chem. Soc. Jpn.* **1987**, *60*, 2205–2214; c) allyloxycarbonyl and benzyloxycarbonyl groups: P. Boullanger, M. Jouineau, B. Bouammali, D. Lafont, G. Descotes, *Carbohydr. Res.* **1990**, *202*, 151–164; d) trichloroacetyl group: G. Blatter, J. Beau, J. Jacquinet, *Carbohydr. Res.* **1994**, *260*, 189–202; e) tetrachlorophthaloyl group: J. S. Debenham, R. Madsen, C. Roberts, B. Fraser-Reid, *J. Am. Chem. Soc.* **1995**, *117*, 3302–3303; f) dithiasuccinoyl group: E. Meinjohanns, M. Meldal, H. Paulsen, K. Bock, *J. Chem. Soc. Perkin Trans. 1* **1995**, 405–415; g) *N*,*N*-diacetyl group: J. C. Castro-Palomino, R. R. Schmidt, *Tetrahedron Lett.* **1995**, *36*, 6871–6874; h) 4,5-dichlorophthaloyl group: H. Shimizu, Y. Ito, Y. Matsuzaki, H. Iijima, T. Ogawa, *Biosci. Biotechnol. Biochem.* **1996**, *60*, 73–76; i) dimethylmaleoyl group: M. R. E. Aly, J. C. Castro-Palomino, E.-S. I. Ibrahim, E.-S. H. El-Ashry, R. R. Schmidt, *Eur. J. Org. Chem.* **1998**, 2305–2316; j) *N*,*N*-dibenzyl group: H. Jiao, O. Hindsgaul, *Angew. Chem.* **1999**, *111*, 421–424; *Angew. Chem. Int. Ed.* **1999**, *38*, 346–348; k) thiodiglycoloyl group: J. C. Castro-Palomino, R. R. Schmidt, *Tetrahedron Lett.* **2000**, *41*, 629–632.

[4] a) W. Kinzy, R. R. Schmidt, *Liebigs Ann. Chem.* **1985**, 1537–1545; b) R. R. Schmidt, M. Behrendt, A. Toepfer, *Synlett* **1990**, 694–696; c) T. Tsuda, S. Nakamura, S. Hashimoto, *Tetrahedron Lett.* **2003**, *44*, 6453–6457, and references therein.

[5] For methods involving azaglycosidation of glycals, see: a) D. A. Griffith, S. J. Danishefsky, *J. Am. Chem. Soc.* **1990**, *112*, 5811–5819; b) V. Di Bussolo, J. Liu, L. G. Huffman, Jr., D. Y. Gin, *Angew. Chem.* **2000**, *112*, 210–213; *Angew. Chem. Int. Ed.* **2000**, *39*, 204–207; c) J. Liu, D. Y. Gin, *J. Am. Chem. Soc.* **2002**, *124*, 9789–9797.

[6] Although 2-acetamido-2-deoxyglycosyl donors have been used for the construction of β-glycosides, the reactions are assumed to proceed via oxazolinium ion intermediates. For recent examples, see: a) G. Arsequell, L. Krippner, R. A. Dwek, S. Y. C. Wong, *J. Chem. Soc. Chem. Commun.* **1994**, 2383–2384; b) E. R. Kumar, H.-S. Byun, S. Wang, R. Bittman, *Tetrahedron Lett.* **1994**, *35*, 505–508; c) J. Sun, X. Han, B. Yu, *Carbohydr. Res.* **2003**, *338*, 827–833; d) I. Carvalho, S. L. Scheuerl, K. P. R. Kartha, R. A. Field, *Carbohydr. Res.* **2003**, *338*, 1039–1043.

[7] Lubineau and co-workers reported that the $Sn(OTf)_2$-mediated glycosidation of 2-acetamido-2-deoxy-α-D-glucosyl chloride with a range of alcohols afforded β-glycosides in good yields. They suggested that the corresponding oxazoline is not an intermediate in the reaction since the rate and yield of the glycosidations were considerably lowered when the oxazoline was used as a starting donor: A. Lubineau, J. Le Gallic, A. Malleron, *Tetrahedron Lett.* **1987**, *28*, 5041–5044. However, our experiments revealed that the glucosyl chloride was quantitatively converted into the oxazoline within 30 min under the reported conditions and the desired disaccharide was formed at the expense of the oxazoline. We speculate that hydrogen chloride generated in situ would act as a promoter for oxazoline activation.

[8] a) S. E. Zurabyan, T. P. Volosyuk, A. J. Khorlin, *Carbohydr. Res.* **1969**, *9*, 215–220; b) S. E. Zurabyan, T. S. Antonenko, A. Y. Khorlin, *Carbohydr. Res.* **1970**, *15*, 21–27; c) M. Kiso, L. Anderson, *Carbohydr. Res.* **1979**, *72*, C12–C14; d) M. Kiso, L. Anderson, *Carbohydr. Res.* **1979**, *72*, C15–C17; e) T. Ogawa, K. Beppu, S. Nakabayashi, *Carbohydr. Res.* **1981**, *93*, C6–C9; f) M. Kiso, L. Anderson, *Carbohydr. Res.* **1985**, *136*, 309–323; g) V. Wittmann, D. Lennartz, *Eur. J. Org. Chem.* **2002**, 1363–1367; h) C. F. Crasto, G. B. Jones, *Tetrahedron Lett.* **2004**, *45*, 4891–4894.

[9] The effectiveness of glycosyl phosphites as glycosyl donors was originally demonstrated by the Wong and Schmidt groups in 1992: a) H. Kondo, Y. Ichikawa, C.-H. Wong, *J. Am. Chem. Soc.* **1992**, *114*, 8748–8750; b) T. J. Martin, R. R. Schmidt, *Tetrahedron Lett.* **1992**, *33*, 6123–6126.

[10] a) S. Hashimoto, K. Umeo, A. Sano, N. Watanabe, M. Nakajima, S. Ikegami, *Tetrahedron Lett.* **1995**, *36*, 2251–2254; b) H. Tanaka, H. Sakamoto, A. Sano, S. Nakamura, M. Nakajima, S. Hashimoto, *Chem. Commun.* **1999**, 1259–1260, and references therein. See also: http://www.glycoforum.gr.jp/science/word/glycotechnology/GT-A01E.html.

[11] 2-Acetamido-2-deoxy-D-glycopyranosyl diethyl phosphites were readily prepared from the corresponding glycopyranoses by using a previously reported procedure[10a] ($ClP(OEt)_2$, Et_3N, CH_2Cl_2, 0 °C).

[12] With the lone exception of THF, where oxazoline **9** was exclusively produced, the product ratio (**8**:**9** = 0.7:1) was nearly the same in the other solvents tested (EtCN/CH_2Cl_2 (1:1) and toluene/CH_2Cl_2 (1:1)), although the low solubility of donor **6** in EtCN and toluene precluded a direct comparison.

[13] I. Azumaya, M. Kotani, S. Ikegami, *Synlett* **2004**, 959–962.

[14] a) H. Kondo, S. Aoki, Y. Ichikawa, R. L. Halcomb, H. Ritzen, C.-H. Wong, *J. Org. Chem.* **1994**, *59*, 864–877; b) H. Sakamoto, S. Nakamura, T. Tsuda, S. Hashimoto, *Tetrahedron Lett.* **2000**, *41*, 7691–7695.

[15] The pK_a values for TfOH, TsOH, and MsOH are −14, −6.5, and −2.6, respectively: a) F. G. Bordwell, *Acc. Chem. Res.* **1988**, *21*, 456–463; b) E. N. Krylov, O. G. Tokareva, *Russ. J. Gen. Chem.* **1997**, *67*, 1–4; c) http://www.chem.wisc.edu/areas/reich/pkatable/ka-water.gif.

[16] H. Jona, H. Mandai, W. Chavasiri, K. Takeuchi, T. Mukaiyama, *Bull. Chem. Soc. Jpn.* **2002**, *75*, 291–309.

[17] a) J. Foropoulos, Jr., D. D. DesMarteau, *Inorg. Chem.* **1984**, *23*, 3720–3723; b) K. Ishihara, M. Kubota, H. Yamamoto, *Synlett* **1996**, 1045–1046; c) B. Mathieu, L. Ghosez, *Tetrahedron Lett.* **1997**, *38*, 5497–5500; d) B. Mathieu, L. Ghosez, *Tetrahedron* **2002**, *58*, 8219–8226; e) A. Hasegawa, K. Ishihara, H. Yamamoto, *Angew. Chem.* **2003**, *115*, 5909–5911; *Angew. Chem. Int. Ed.* **2003**, *42*, 5731–5733.

 © 2005 Wiley-VCH Verlag GmbH & Co. KGaA, Weinheim

[18] The $TMSNTf_2$-promoted glycosidation of **6** with **7** proceeded at −60 °C to give **8** in 35% yield (reaction time 1 h, **8**/**9** = 0.7:1).
[19] a) B. Fraser-Reid, Z. Wu, C. W. Andrews, E. Skowronski, J. P. Bowen, *J. Am. Chem. Soc.* **1991**, *113*, 1434–1435; b) B. Fraser-Reid, U. E. Udodong, Z. Wu, H. Ottosson, J. R. Merritt, C. S. Rao, C. Roberts, R. Madsen, *Synlett* **1992**, 927–942; c) N. L. Douglas, S. V. Ley, U. Lücking, S. L. Warriner, *J. Chem. Soc. Perkin Trans. 1* **1998**, 51–65; d) Z. Zhang, I. R. Ollmann, X.-S. Ye, R. Wischnat, T. Baasov, C.-H. Wong, *J. Am. Chem. Soc.* **1999**, *121*, 734–753.
[20] The limitation of the present method was encountered with unreactive acceptor alcohols, such as 4- or 2-*O*-unprotected glucosides.
[21] ^{1}H NMR spectral data (400 MHz) clearly revealed that oxazoline **9** was protonated upon treatment with Tf_2NH in CD_2Cl_2 at −78 °C to form oxazolinium ion **20** (**9**, $\delta = 5.91$ (d, $J = 7.2$ Hz, H1), 4.20 (m, H2), 1.95 ppm (s, CH_3); **20**, $\delta = 6.63$ (d, $J = 8.0$ Hz, H1), 4.51 (m, H2), 2.39 ppm (s, CH_3)).
[22] The reaction of glycosyl diethyl phosphites with alcohols is accompanied by the formation of $HP(O)(OEt)_2$. However, the addition of $HP(O)(OEt)_2$ was not effective for the Tf_2NH-promoted reaction of oxazoline **9** with alcohol **7**, which proceeded at temperatures above approximately 5 °C.
[23] a) D. Kahne, S. Walker, Y. Cheng, D. Van Engen, *J. Am. Chem. Soc.* **1989**, *111*, 6881–6882; b) J. Gildersleeve, R. A. Pascal, Jr., D. Kahne, *J. Am. Chem. Soc.* **1998**, *120*, 5961–5969.
[24] D. Crich, S. Sun, *J. Am. Chem. Soc.* **1997**, *119*, 11217–11223.
[25] Very recently, Yamago and co-workers observed two 2-deoxy-2-phthalimido-β-glucosyl triflimide intermediates, tentatively assigned as rotamers of the carbon–nitrogen bond, as well as the corresponding α-glucosyl triflate: S. Yamago, T. Yamada, T. Maruyama, J. Yoshida, *Angew. Chem.* **2004**, *116*, 2197–2200; *Angew. Chem. Int. Ed.* **2004**, *43*, 2145–2148.
[26] G. A. Olah, C. W. McFarland, *J. Org. Chem.* **1971**, *36*, 1374–1378.
[27] A β-oriented anomeric leaving group of a 2-acetamido-2-deoxyglycosyl donor is known to be readily eliminated to form the corresponding oxazoline derivative: a) R. U. Lemieux, H. Driguez, *J. Am. Chem. Soc.* **1975**, *97*, 4063–4069; b) G. Kretzschmar, W. Stahl, *Tetrahedron* **1998**, *54*, 6341–6358.

 © 2005 Wiley-VCH Verlag GmbH & Co. KGaA, Weinheim

Library Synthesis

Convergent Diversity-Oriented Synthesis of Small-Molecule Hybrids**

*Chuo Chen, Xiaodong Li, Christopher S. Neumann, Michael M.-C. Lo, and Stuart L. Schreiber**

Nature uses convergent biosynthesis to yield natural product hybrids whose special properties derive from their enhanced protein-interacting capabilities; two examples are the vinca dimers and the cephalostatins (Scheme 1).[1]

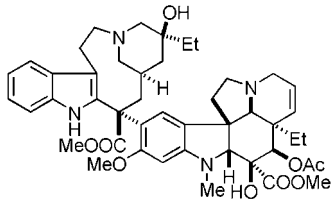

vinblastine

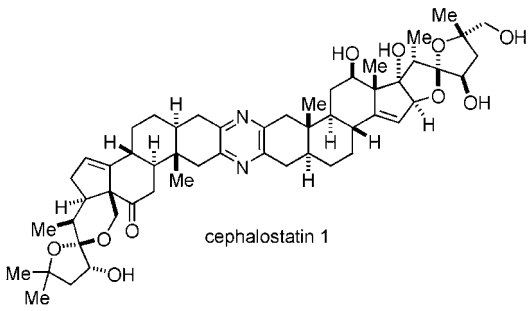

Scheme 1. Structures of naturally occurring small-molecule hybrids.

We wish to determine whether non-natural small molecules comprising two elements, each of which has structural features reminiscent of those of natural products, might also have special properties when used in small-molecule screens. As a first step to address this question, we describe a synthesis that results in examples of "hybrid" synthetic small molecules.

[*] Dr. C. Chen,[+] X. Li,[+] C. S. Neumann, Dr. M. M.-C. Lo, Prof. S. L. Schreiber
Howard Hughes Medical Institute
Department of Chemistry and Chemical Biology
Harvard University and
The Broad Institute of Harvard and MIT
12 Oxford Street, Cambridge, MA 02138 (USA)
Fax: (+1) 617-495-0751
E-mail: stuart_schreiber@harvard.edu

[+] These authors contributed equally to this work.

[**] We thank the NIGMS for support of this research. C.C. is a research associate and S.L.S is an investigator with the Howard Hughes Medical Institute at the Department of Chemistry and Chemical Biology, Harvard University. C.S.N. acknowledges an NSF predoctoral fellowship.

Supporting information for this article is available on the WWW under http://www.angewandte.org or from the author.

 DOI: 10.1002/anie.200462798 © 2005 Wiley-VCH Verlag GmbH & Co. KGaA, Weinheim

We use a convergent diversity-oriented synthesis (DOS)[2,3] strategy with synthetic fragments common to natural products[4] and both solution-phase/solid-phase and solid-phase/solid-phase coupling methods (Figure 1).[5] The strategy should enable other such hybrids to be made in the future so that the above hypothesis can be tested.

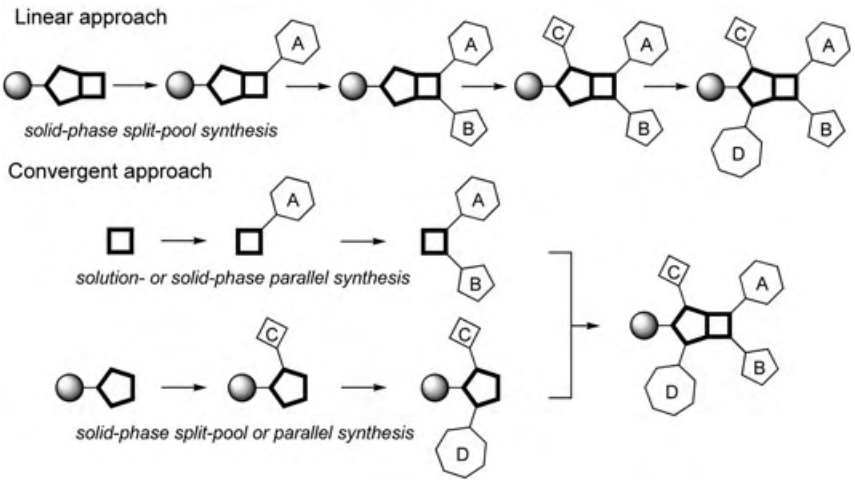

Figure 1. Linear and convergent approaches in diversity-oriented synthesis.

Three natural product subunits, based upon bridged piperidines, fused pyrrolidines, and spirocyclic oxindoles, were selected for two different hybrid-library syntheses. The key sublibrary-coupling steps are outlined in Scheme 2. The bridged-piperidine sublibrary **I** synthesized in solution was coupled to the fused-pyrrolidine sublibrary **II** immobilized on a macrobead solid support to provide the bridged-piperidine/fused-pyrrolidine hybrid library **IV**. The spirocyclic-oxindole sublibrary **III**[6] was released from a macrobead solid support and coupled to the fused-pyrrolidine sublibrary **II** to afford the spirocyclic-oxindole/fused-pyrrolidine hybrid library **V**. Sublibraries **I**, **II**, and **III** were synthesized in both enantiomeric forms by using chiral-pool, chiral-catalysis, and chiral-auxiliary approaches, respectively, to provide libraries **IV** and **V** in four diastereomeric forms.[7]

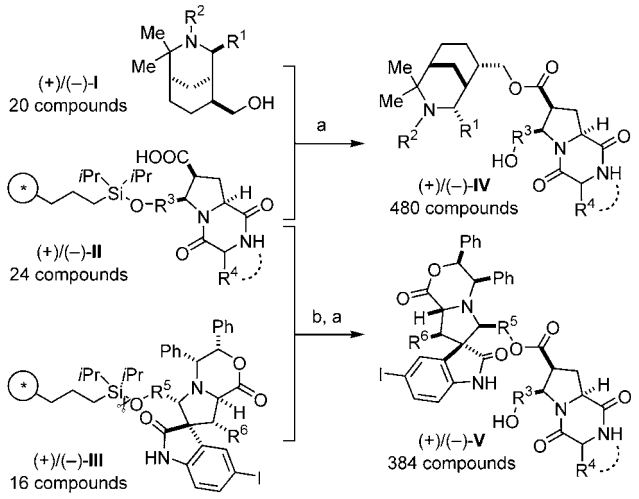

Scheme 2. Synthesis of libraries **IV** and **V** from sublibraries **I**, **II** and **II**, **III**. Only one diastereomer is shown for libraries **IV** and **V**. a) 1. PyBOP, DMAP, CH_2Cl_2, 23 °C, 16 h; 2. HF–py, THF, 23 °C, 2 h, then TMSOEt; b) **III**, HF–py, THF, 23 °C, 2 h, then TMSOEt. DMAP = 4-dimethylaminopyridine, py = pyridine, PyBOP = (1*H*-benzotriazol-1-yloxy)tripyrrolidinophosphonium hexafluorophosphate, TMS = trimethylsilyl.

The synthesis of sublibraries **I**–**III** is depicted in Scheme 3. The monoterpene (+)/(−)-β-pinene was chosen as the starting material for sublibrary **I** to introduce chirality, complexity, and rigidity (Scheme 3 A). The bicyclic skeleton of pinene was used to construct a chiral, nonracemic, structurally complex sublibrary with well-defined topography. The synthesis of sublibrary **I** started with a mercury(II)-mediated Ritter reaction of pinene, originally developed by Delpech and Khuong-Huu,[8] under modified conditions.[9] Analytically pure products were obtained after simple acid–base extractions. The bicyclic amines obtained after reduction with boron hydride were subjected to a diversification step comprising two processes to add an appending group (triazene formation and reductive methylation) and one skeleton-transforming reaction (Pictet–Spengler cyclization). A hydroxy group was then installed as a handle for the subsquent sublibrary-coupling reaction. A 20-membered bridged-piperidine sublibrary **I** with three different skeletons was synthesized in four steps in solution without recourse to column chromatography.

The parallel synthesis of the fused-pyrrolidine sublibrary **II** features a catalytic, asymmetric cycloaddition reaction of an azomethine ylide (Scheme 3 B) that was developed in the course of these studies.[10] Three phenolic aldehydes were loaded onto 500–600 μm polystyrene macrobeads,[11] condensed with methyl glycinate, and treated with *tert*-butyl acrylate in the presence of silver(I) acetate–(*R*)/(*S*)-quinap as the chiral catalyst. Amide coupling of the resulting pyrrolidines with *N*-Boc-protected amino acids (Gly, D-Leu, L-Phe, and D-Pro), followed by removal of both the *tert*-butyl and *N*-Boc protecting groups, provided the 24-membered fused-pyrrolidine sublibrary **II** on macrobeads in five steps.

The spirocyclic-oxindole sublibrary **III** was also synthesized in parallel on macrobeads by a Lewis acid catalyzed variant[6] of the Williams three-component coupling reaction[12] (Scheme 3 C). This 16-membered spirocyclic-oxindole sublibrary contains four different hydrogen-bond-acceptor appendages and two differently oriented "handles" for coupling to sublibrary **II**.

The final sublibrary-coupling step (**I**–**II** and **II**–**III**) involved a PyBOP/DMAP-promoted esterification (Scheme 2).[13] This convergent step provided a 480-membered bridged-piperidine/fused-pyrrolidine hybrid library **IV** and a 384-membered spirocyclic-oxindole/fused-pyrrolidine hybrid library **V**. For quality analysis, four representative compounds from **IV** and four representative compounds from **V**, which contain all building blocks, were analyzed by ^{1}H NMR spectroscopy. In all cases, good levels of purity were observed.[14] With the exception of the subset of

 © 2005 Wiley-VCH Verlag GmbH & Co. KGaA, Weinheim

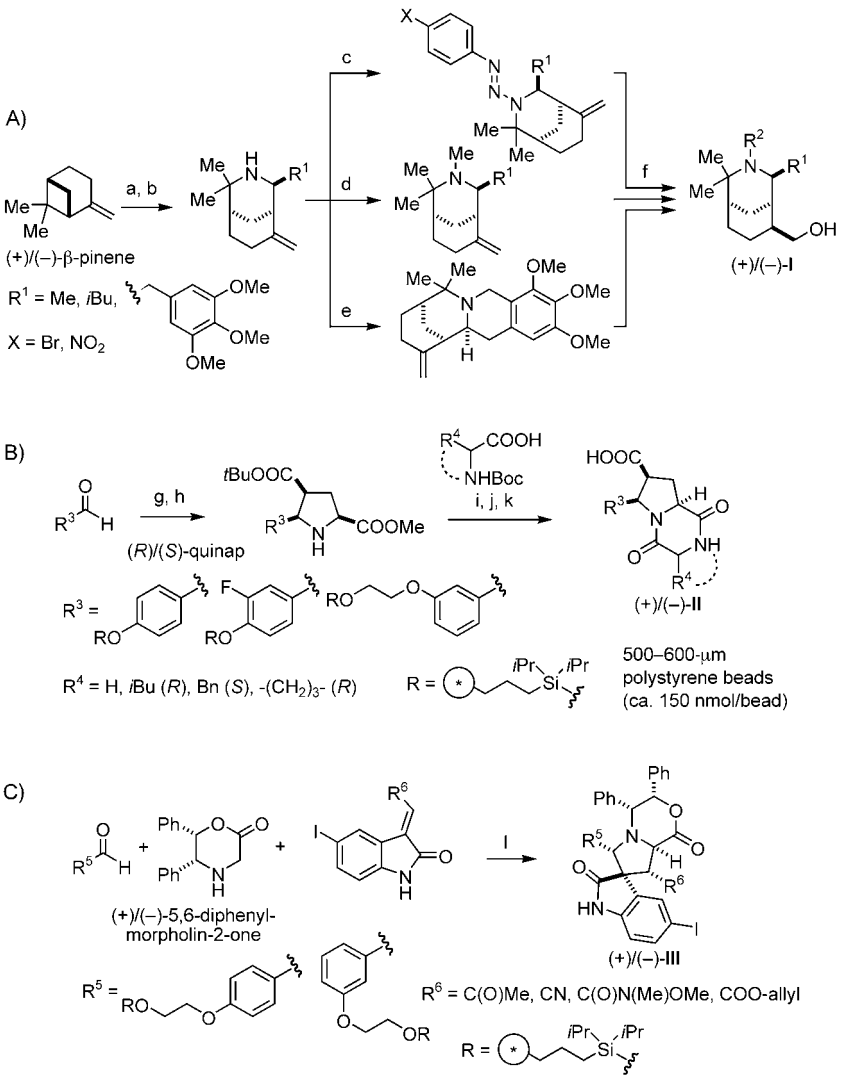

Scheme 3. Synthesis of sublibraries **I**, **II**, and **III**. a) $Hg(OTf)_2$, R^1CN (see Supporting Information for details); b) $NaBH(OAc)_3$, CH_2Cl_2, 23 °C, 3 h; c) ArN_2BF_4, pyridine, $MeOH/CH_2Cl_2$, 4 °C, 30 min, then KOH, 4–23 °C, 5 min; d) HCHO(aq), $NaBH(OAc)_3$, CH_3CN, 23 °C, 3 h; e) HCHO(aq), Ac_2O, CH_3CN, 60 °C, 18 h; f) BH_3·THF, THF, 23 °C, 3.5 h, then NaOH, H_2O_2, H_2O, 23 °C, 2 h; g) H_2NCH_2COOMe, benzene/DMF/MeOH, 90 °C, 16 h; h) AgOAc–(*R*)/(*S*)-quinap, iPr_2NEt, *t*BuOOCCH=CH_2, THF, −45 °C, 72 h; i) R^4(BocNH)CHCOOH, EDC, DMF/CH_2Cl_2, 23 °C, 16 h; j) TMSOTf, 2,6-lutidine, CH_2Cl_2, 40 °C, 4 h; k) NEt_3, MeOH, DMF/CH_2Cl_2, 23 °C, 24 h; l) $Mg(ClO_4)_2$, $HC(OMe)_3$, pyridine, toluene, 23 °C, 72 h. Boc = *tert*-butoxycarbonyl, DMF = *N*,*N*-dimethylformamide, EDC = 1-ethyl-3-(3′-dimethylaminopropyl)carbodiimide hydrochloride, Tf = trifluoromethanesulfonyl.

compounds containing the *p*-bromoaryl triazene functionality, standard conditions for cleavage from the macrobeads yielded 37 of 43 compounds with >80% purity by LCMS.[15]

The convergent strategy described herein allows the synthesis of complex small molecules through a short linear sequence on solid supports. The small-molecule products enable us to begin to determine whether the joining of fragments imparts special protein-binding and/or protein-modulating properties on the products in a manner reminiscent of natural product hybrids. The results of such experiments with the small molecules described herein and others synthesized in the future by other applications of this convergent strategy will be made available on the public database ChemBank.[16]

Received: December 3, 2004
Published online: March 3, 2005

Keywords: convergent synthesis · diversity-oriented synthesis · polycycles · small-molecule hybrids · solid-phase synthesis

[1] For reviews of small-molecule hybrids, see: a) L. F. Tietze, H. P. Bell, S. Chandrasekhar, *Angew. Chem.* **2003**, *115*, 4128–4160; *Angew. Chem. Int. Ed.* **2003**, *42*, 3996–4028; b) G. Mehta, V. Singh, *Chem. Soc. Rev.* **2002**, *31*, 324–334.

[2] M. D. Burke, S. L. Schreiber, *Angew. Chem.* **2004**, *116*, 48–60; *Angew. Chem. Int. Ed.* **2004**, *43*, 46–58.

[3] For a discussion of the use of DOS to explore biology, see: S. L. Schreiber, *Chem. Eng. News* **2003**, *81*(9), 51–61.

[4] For a Review, see: R. Breinbauer, I. R. Vetter, H. Waldmann, *Angew. Chem.* **2002**, *114*, 3002–3015; *Angew. Chem. Int. Ed.* **2002**, *41*, 2878–2890.

[5] We are aware of only two reports of solution-phase convergent combinatorial parallel library synthesis: a) a 1600-membered library was made by an automated system: C. M. Baldino, D. S. Casebier, J. Caserta, G. Slobodkin, C. Tu, D. L. Coffen, *Synlett* **1997**, 488–490; b) an approximately 40-membered convergent library of HUN-7293 analogues was also reported: Y. Chen, M. Bilban, C. A. Foster, D. L. Boger, *J. Am. Chem. Soc.* **2002**, *124*, 5431–5440; c) for a discussion of solution-phase convergent library synthesis, see: D. L. Boger, J. Desharnais, K. Capps, *Angew. Chem.* **2003**, *115*, 4270–4309; *Angew. Chem. Int. Ed.* **2003**, *42*, 4138–4176.

[6] M. M.-C. Lo, C. S. Neumann, S. Nagayama, E. O. Perlstein, S. L. Schreiber, *J. Am. Chem. Soc.* **2004**, *126*, 16077–16086.

[7] Although ester functionalities can be vulnerable to cellular enzymatic cleavage, these two libraries possess highly hindered ester linkages that are not expected to suffer hydrolysis in cells.

[8] B. Delpech, Q. Khuong-Huu, *J. Org. Chem.* **1978**, *43*, 4898–4900.

[9] a) R. V. Stevens, P. M. Kenney, *J. Chem. Soc. Chem. Commun.* **1983**, 384–386; for improved procedures, see: b) D. Stoermer, C. H. Heathcock, *J. Org. Chem.* **1993**, *58*, 564–568; c) M. Dobler, H.-J. Borschberg, *Tetrahedron: Asymmetry* **1994**, *5*, 2025–2032.

[10] C. Chen, X. Li, S. L. Schreiber, *J. Am. Chem. Soc.* **2003**, *125*, 10174–10175.

[11] H. E. Blackwell, L. Pérez, R. A. Stavenger, J. A. Tallarico, E. C. Eatough, M. A. Foley, S. L. Schreiber, *Chem. Biol.* **2001**, *8*, 1167–1182; P. A. Clemons, A. N. Koehler, B. K. Wagner, T. G. Sprigings, D. R. Spring, R. W. King, S. L. Schreiber, M. A. Foley, *Chem. Biol.* **2001**, *8*, 1183–1195.

 © 2005 Wiley-VCH Verlag GmbH & Co. KGaA, Weinheim

[12] P. R. Sebahar, R. M. Williams, *J. Am. Chem. Soc.* **2000**, *122*, 5666 – 5667.
[13] HPLC and ^{1}H NMR analyses, performed on eight products of the esterification reaction, revealed that minor stereoisomers made up 15–25 % of the product mixtures.
[14] For the structures of these eight compounds as well as their ^{1}H NMR spectra (of the crude and purified material), see Supporting Information.
[15] The *p*-bromoaryl triazene functionality proved problematic when subjected to our standard macrobead-cleavage reaction, which resulted in cleavage of the remote N–N bond. This undesired process can be prevented by the addition of Et_3N: In the case of IV-211121, cleavage with HF–py and Et_3N yielded the crude product with good purity by ^{1}H NMR spectroscopy.
[16] http://chembank.med.harvard.edu; R. L. Strausberg, S. L. Schreiber, *Science* **2003**, *300*, 294 – 295.

 © 2005 Wiley-VCH Verlag GmbH & Co. KGaA, Weinheim

Oxoiron (IV) Complexes

Comparison of Fe^{IV}=O Heme and Non-heme Species: Electronic Structures, Bonding, and Reactivities**

*Andrea Decker and Edward I. Solomon**

Mononuclear non-heme iron enzymes catalyze a variety of essential biological reactions that require the binding and activation of dioxygen;[1,2] their reactivity is as extensive as that of heme enzymes.[3] In both heme and non-heme enzymatic cycles, a high-valent oxoiron species is often invoked as the key active oxidizing species.

In many heme systems and biomimetic porphyrin model complexes oxoiron(IV) porphyrin cation radical (the so-called compound I in biological systems) and oxoiron(IV) porphyrin (compound II in biological systems) species, both with an Fe–O $S=1$ unit, are found to be important intermediates and are well studied and characterized by experimental and theoretical techniques.[4–7]

In mononuclear non-heme enzymes, a high-valent oxoiron(IV) ($S=2$) intermediate is often evoked, but has only recently been reported[8] and initially characterized.[9,10] There are also numerous theoretical studies on putative mononuclear non-heme Fe^{IV}=O ($S=2$) enzyme intermediates.[11–13] However, the coordination environment of these enzyme intermediates is not known and thus a direct correlation to calculations is not accessible.

The only structurally characterized mononuclear non-heme Fe^{IV}=O species are biomimetic model complexes with an $S=1$ ground state,[14,15] some of which exhibit C–H bond cleavage and oxidation reactivity similar to mononuclear non-heme iron enzymes.[16] Spectroscopic studies and experimentally calibrated density functional theory (DFT) calculations on the structurally defined complex provide a detailed description of the electronic structure and Fe–O bonding.[17]

While the oxoiron intermediates in heme and mononuclear non-heme enzymes and model complexes have been characterized experimentally and theoretically, we present herein the first comparison between oxoiron(IV) species in heme and non-heme environments. We will a) show that the electronic structures and Fe–O bonding in Fe^{IV}=O ($S=1$) heme and non-heme complexes are in fact very similar, b) provide an explanation for this, focusing on the effects of the Fe–O bond on the porphyrin π system, and c) evaluate the relative reactivities of the heme and non-heme oxoiron(IV) complexes for hydrogen-atom abstraction reactions.

Unrestricted DFT calculations using the Amsterdam density functional (ADF)[18] program package (see Supporting Information for detailed computational methodology) were carried out on an $[Fe^{IV}(O)(Por)(NCMe)]$ (Por = unsubstituted porphyrin ring) $S=1$ complex. Acetonitrile was chosen as the axial ligand[19] to correspond with the $[Fe^{IV}(O)(TMC)(NCMe)]^{2+}$ (TMC = 1,4,8,11-tetramethyl-1,4,8,11-tetraazacyclotetradecane) non-heme model complex.

The geometric and electronic structure description of the heme Fe^{IV}=O (Figure 1a) agrees well with other results on heme Fe^{IV}=O species.[20–23] The Fe–O bond is short (1.65 Å, Table 1) and the $(d_{xy})^2(d_{xz}/d_{yz})^2$ electronic configuration is as expected. The two unpaired electrons are distributed across the Fe–O unit with little delocalization onto the porphyrin ring. The strong Fe–O π bonds are formed by overlap of the $Fe(d_{xz}/d_{yz})$ and $O(p_x/p_y)$ orbitals (Figure 1b) with a large contribution from the oxygen p orbitals (43%, Table 1).

This Fe^{IV}=O heme complex is compared to the well-characterized non-heme $[Fe^{IV}(O)(TMC)(NCMe)]^{2+}$ model complex[14,17] (Figure 1c), using the same computational methodology. A comparison of the key parameters describing the electronic structure and bonding (Table 1) shows that the heme and non-heme complexes are very similar, with almost identical Fe–O bond lengths and bond strengths (reflected by the vibrational frequencies) and comparable frontier molecular orbitals (FMOs).[24] According to these calculations, both heme and non-heme Fe^{IV}=O systems have very similar electronic structures and strong and very covalent oxo-to-iron π-donor and σ-donor bonds.

Key experimental parameters of heme and non-heme Fe^{IV}=O complexes are also similar (Table 2). The Fe–O bond lengths of compound II of horseradish peroxidase, measured by extended X-ray absorption fine structure spectroscopy (EXAFS), are comparable to the X-ray structure bond length of the non-heme $[Fe^{IV}(O)(TMC)(NCMe)]^{2+}$ model complex, despite having different *trans* axial ligands. The Fe–O vibrational frequencies, a measure of bond strength, are somewhat dependent on the nature of the *trans* axial ligand, but very

[*] A. Decker, Prof. Dr. E. I. Solomon
Department of Chemistry
Stanford University
Stanford, California, 94305 (USA)
Fax: (+1) 650-723-0553
E-mail: Edward.Solomon@stanford.edu

[**] This research was supported by the National Institutes of Health (GM-40392). A.D. was supported by an Evelyn Laing McBain Stanford Graduate Fellowship.

Supporting information for this article is available on the WWW under http://www.angewandte.org or from the author.

 © 2005 Wiley-VCH Verlag GmbH & Co. KGaA, Weinheim DOI: 10.1002/anie.200462182

Table 1: Key computational results of heme and non-heme Fe^{IV}=O and Fe^{III}–OH complexes.[a]

System	r(Fe–O) [Å]	ν(Fe–O) [cm^{-1}][b]	Spin density Fe	Spin density O	β d_{yz}(π*) [%] Fe(d)	β d_{yz}(π*) [%] O(p)	β d_{yz}(π*) [%] L(eq)	β d_{xz}(π*) [%] Fe(d)	β d_{xz}(π*) [%] O(p)	β d_{xz}(π*) [%] L(eq)	β d_{z^2}(σ*) [%] Fe(d)	β d_{z^2}(σ*) [%] O(p)	β d_{z^2}(σ*) [%] L(eq)
Fe^{IV}=O													
L(eq) = Por	1.65	849	1.13	0.90	49	43	4	49	43	4	55	24	13
L(eq) = TMC	1.65	846	1.31	0.77	53	37	5	54	36	5	56	22	15
Fe^{III}–OH													
L(eq) = Por	1.81	633	0.83	0.23	74	4	18	55	22	17	–[c]	15[c]	–[c]
L(eq) = TMC	1.82	615	0.93	0.16	85	4	3	72	17	3	66	11	15

[a] All structures fully optimized in adf/tzp, all with NCMe axial ligation. [b] From g98/BP86/lanl2dz calculation, for details see Supporting Information. [c] Weaker Fe–O bond causes d_{z^2} and $d_{x^2-y^2}$ to mix, Fe and Por contributions cannot be separated.

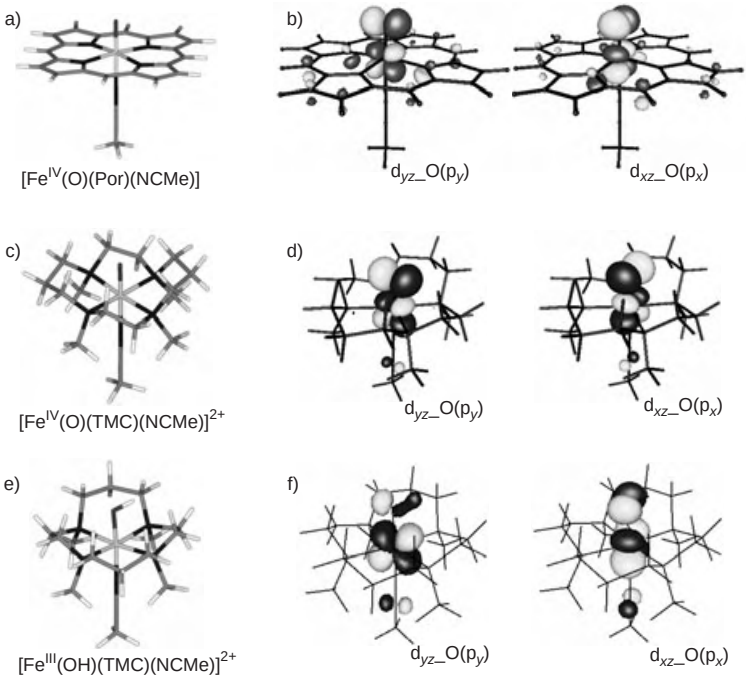

Figure 1. Optimized structures (a, c, e) and isosurfaces (b, d, f) of the Fe–O π* orbitals of Fe^{IV}=O and Fe^{III}–OH complexes.

Table 2: Comparison of experimental and theoretical parameters of non-heme and heme Fe^{IV}=O enzyme intermediates and model complexes.

	r(Fe-O) [Å] heme	r(Fe-O) [Å] non-heme[a]	ν(Fe-O) [cm^{-1}] heme	ν(Fe-O) [cm^{-1}] non-heme[a]
experimental data[b]	1.64(3)[d] [35] 1.704(10)[d] [37] 1.69[d] [39]	1.646(3)[e] [14]	807[f] [36] 814[d] [38] 843[g] [25]	834[e] [14]
calculations[c]	1.66[d] 1.65[e]	1.65[d] 1.65[e]	803[d] 849[e]	819[d] 846[e]

[a] TMC as equatorial ligand. [b] No structural data (X-ray or EXAFS) available on heme model complexes (compound II), EXAFS data of enzyme intermediates shown. [c] All theoretical values from this study. [d] Imidazole as axial ligand. [e] NCMe as axial ligand. [f] 1-Me-imidazole as axial ligand. [g] No axial ligand (five coordinate).

similar for heme and non-heme systems with the same axial ligands.[7,25] Mössbauer studies have shown a positive, large zero-field splitting ($D \approx 30\ cm^{-1}$) for both heme and non-heme Fe^{IV}=O complexes.[14,26,27] Importantly, the calculated geometric and electronic-structure descriptions for the heme and non-heme Fe^{IV}=O species correlate well with experimental data (Table 2).

This comparison of theoretical and experimental data of heme and non-heme Fe^{IV}=O ($S = 1$) complexes demonstrates that the aromatic porphyrin system in the equatorial plane does not significantly change the electronic structure and Fe–O bonding when compared to "innocent", only σ-donating amine-based equatorial ligands, such as the TMC-macrocycle. These Fe^{IV}=O ($S = 1$) heme and non-heme complexes have very similar electronic structures and Fe–O bonding.

This similarity is remarkable, since the e_g set of the porphyrin π system (in idealized D_{4h} symmetry) can interact with the Fe d_{xz}/d_{yz} orbitals (Figure 2, left) and thus affect the Fe–O π bonds, while the amines of the TMC ligand do not have any equivalent orbitals (Figure 2, right).

However, a fragment analysis (see Supporting Information) shows that there is no net π bonding between the porphyrin ring and the iron center.

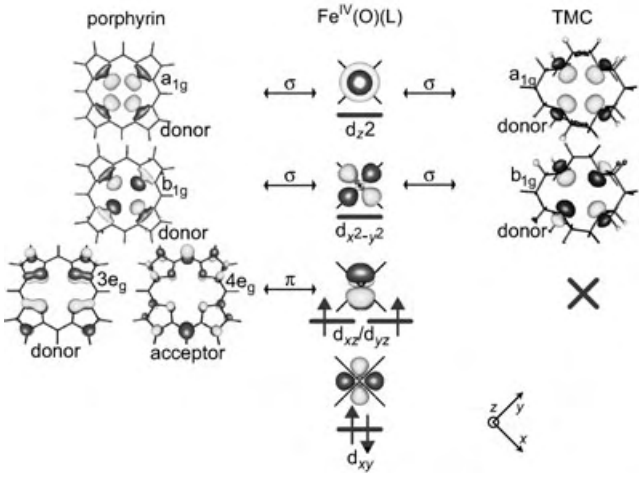

Figure 2. Schematic energy-level diagram for Fe^{IV}=O(L) and possible interactions with the equatorial ligands (labels according to idealized D_{4h} symmetry).

 © 2005 Wiley-VCH Verlag GmbH & Co. KGaA, Weinheim

Figure 3 shows an interaction diagram for the three important fragment orbitals in the β-spin manifold. The occupied porphyrin $3e_g$ fragment orbitals only mix into the Fe–O π-bonding orbitals, forming Fe–Por bonding and antibonding

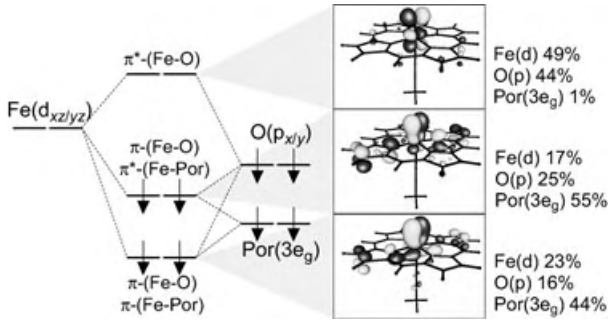

Figure 3. Interactions between β-spin Fe(d_{xz}/d_{yz}), O(p_x/p_y), and Por-($3e_g$) orbitals.

combinations. There is no mixing into the Fe–O π-antibonding orbitals.[28] The very strong and covalent π bond between the close lying iron and oxygen atoms (1.65 Å) dominates the overall bonding and decouples the Fe^{IV}=O unit from the porphyrin π system. NMR spectroscopy studies which show that there is no spin delocalization onto the porphyrin ring support this model.[29,30]

With its conjugated π system in the equatorial plane decoupled from the metal center, the porphyrin system is similar to an "innocent" nitrogen-based σ-donating macrocycle. This situation leads to the similar electronic structures of Fe^{IV}=O ($S=1$) heme and non-heme systems.[31]

The reactivity of these Fe^{IV}=O complexes requires consideration of the electronic structures and FMOs of not only the Fe^{IV}=O reactant, but of the reaction products as well. Herein we consider the hydrogen-atom abstraction reaction of the Fe^{IV}=O ($S=1$) species in heme and non-heme environments resulting in a low-spin Fe^{III}–OH species.[32] As one would expect, both heme and non-heme Fe^{III}–OH (Table 1, Figure 1e and f) have much longer Fe–O bonds than the Fe^{IV}=O complexes. Weakening the Fe–O bond allows the porphyrin π system to interact and covalently mix with the Fe(d_{xz}/d_{yz}) orbitals. As the coefficients in Table 1 show, the porphyrin contribution to these molecular orbitals increases from 4% (Fe^{IV}=O) to approximately 18% in the Fe^{III}–OH heme complex, while in the non-heme complex the contribution of the equatorial TMC ligand, which does not have π interactions, remains low (3–5%). The one-electron reduction and protonation weakens the Fe=O bond and allows the porphyrin π system to couple to the iron center. This delocalization of electron density onto the ligand is observed experimentally in low-spin ferric hemes.[33,34] In contrast to Fe^{IV}=O, for low-spin Fe^{III}–OH, the electronic structures and bonding differ greatly between heme and non-heme complexes.

This difference in the electronic structures of the products will contribute significantly to differences in reactivity between heme and non-heme Fe^{IV}=O complexes. Consequently, for the thermodynamics of the hydrogen-atom abstraction reaction, the greater stability of the Fe^{III}–OH reaction product in a heme environment leads to a less positive reaction free energy (ΔG) by about 10 kcal mol^{-1} (Table 3).

Table 3: Thermodynamics for the hydrogen-atom abstraction reaction by Fe^{IV}=O heme and non-heme complexes.

Ligation	ΔE	+Solvent	ZPCE[b]	$-T\Delta S$[c]	ΔG
TMC_NCCH_3	24.2	−2.7	−1.6	−2.3	17.6
por_NCCH_3	15.4	−3.6	−1.2	−4.4	6.1

[a] All values in kcal mol^{-1}; hydrogen at the tertiary carbon center of 2,3-dimethylbutane abstracted. [b] Zero-point correction energy. [c] Entropy term; for computational details see Supporting Information.

Thus, the electronic structures of the Fe^{IV}=O complexes are dominated by the very strong Fe–O bonding, which decouples the porphyrin π system, leading to similar bonding in heme and non-heme complexes. A weakening of the Fe–O bond in Fe^{III}–OH products of a hydrogen-atom abstraction reaction, however, allows the porphyrin π system to interact with the iron center, stabilizing the heme relative to the non-heme complex and leading to different reactivities.

Received: October 2, 2004
Revised: December 1, 2004
Published online: February 18, 2005

Keywords: bioinorganic chemistry · density functional calculations · electronic structure · high-valent compounds · iron

[1] E. I. Solomon, T. C. Brunold, M. I. Davis, J. N. Kemsley, S. K. Lee, N. Lehnert, F. Neese, A. J. Skulan, Y. S. Yang, J. Zhou, *Chem. Rev.* **2000**, *100*, 235–349.
[2] M. Costas, M. P. Mehn, M. P. Jensen, L. Que, Jr., *Chem. Rev.* **2004**, *104*, 939–986.
[3] M. Sono, M. P. Roach, E. D. Coulter, J. H. Dawson, *Chem. Rev.* **1996**, *96*, 2841–2887.
[4] B. Meunier, J. Bernadou, *Met.-Oxo Met.-Peroxo Species Catal. Oxid.* **2000**, *97*, 1–35.
[5] Y. Watanabe, H. Fujii, *Met.-Oxo Met.-Peroxo Species Catal. Oxid.* **2000**, *97*, 61–89.
[6] D. L. Harris, *Curr. Opin. Chem. Biol.* **2001**, *5*, 724–735.
[7] H. Fujii, *Coord. Chem. Rev.* **2002**, *226*, 51–60.
[8] J. C. Price, E. W. Barr, B. Tirupati, J. M. Bollinger, C. Krebs, *Biochemistry* **2003**, *42*, 7497–7508.
[9] D. A. Proshlyakov, T. F. Henshaw, G. R. Monterosso, M. J. Ryle, R. P. Hausinger, *J. Am. Chem. Soc.* **2004**, *126*, 1022–1023.
[10] P. J. Riggs-Gelasco, J. C. Price, R. B. Guyer, J. H. Brehm, E. W. Barr, J. M. Bollinger, C. Krebs, *J. Am. Chem. Soc.* **2004**, *126*, 8108–8109.
[11] A. Bassan, M. R. A. Blomberg, P. E. M. Siegbahn, *Chem. Eur. J.* **2003**, *9*, 106–115.
[12] A. Bassan, M. R. A. Blomberg, P. E. M. Siegbahn, *Chem. Eur. J.* **2003**, *9*, 4055–4067.
[13] T. Borowski, A. Bassan, P. E. M. Siegbahn, *Chem. Eur. J.* **2004**, *10*, 1031–1041.
[14] J.-U. Rohde, J.-H. In, M. H. Lim, W. W. Brennessel, M. R. Bukowski, A. Stubna, E. Munck, W. Nam, L. Que, Jr., *Science* **2003**, *299*, 1037–1039.
[15] M. H. Lim, J. U. Rohde, A. Stubna, M. R. Bukowski, M. Costas, R. Y. N. Ho, E. Munck, W. Nam, L. Que, Jr. *Proc. Natl. Acad. Sci. USA* **2003**, *100*, 3665–3670.

 © 2005 Wiley-VCH Verlag GmbH & Co. KGaA, Weinheim

[16] J. Kaizer, E. J. Klinker, N. Y. Oh, J.-U. Rohde, W. J. Song, A. Stubna, J. Kim, E. Munck, W. Nam, L. Que, Jr., *J. Am. Chem. Soc.* **2004**, *126*, 472 – 473.

[17] A. Decker, J.-U. Rohde, L. Que, Jr., E. I. Solomon, *J. Am. Chem. Soc.* **2004**, *126*, 5378 – 5379.

[18] ADF 2003_01, *SCM, Theoretical Chemistry*, Vrije Universiteit, Amsterdam, The Netherlands, http://www.scm.com.

[19] A correlation to [Fe^{IV}(O)(Por)(imidazole)], a model of horseradish peroxidase compound II, shows both complexes are very similar (see Supporting Information).

[20] G. H. Loew, Z. S. Herman, *J. Am. Chem. Soc.* **1980**, *102*, 6173 – 6174.

[21] S. Yamamoto, J. Teraoka, H. Kashiwagi, *J. Chem. Phys.* **1988**, *88*, 303 – 312.

[22] H. Kuramochi, L. Noodleman, D. A. Case, *J. Am. Chem. Soc.* **1997**, *119*, 11442 – 11451.

[23] A. Dey, A. Ghosh, *J. Am. Chem. Soc.* **2002**, *124*, 3206 – 3207.

[24] The spin densities and orbital contributions in the Fe–O π* MOs vary somewhat between the heme and the TMC species. However, calibration calculations for a series of σ-donor amine complexes (see Supporting Information) with different donor strengths ($NH_3 < NH_2Me < NR_3$) establish a range of spin densities and π-delocalization values consistent with the heme results.

[25] S. Hashimoto, Y. Mizutani, Y. Tatsuno, T. Kitagawa, *J. Am. Chem. Soc.* **1991**, *113*, 6542 – 6549.

[26] G. Simonneaux, W. F. Scholz, C. A. Reed, G. Lang, *Biochim. Biophys. Acta* **1982**, *716*, 1 – 7.

[27] C. E. Schulz, R. Rutter, J. T. Sage, P. G. Debrunner, L. P. Hager, *Biochemistry* **1984**, *23*, 4743 – 4754.

[28] Likewise, in the α-spin manifold, there is no interaction between the unoccupied Por($4e_g$) orbitals and the occupied Fe(d_{xz}/d_{yz}) orbitals (see Supporting Information).

[29] G. N. Lamar, J. S. Deropp, L. Latosgrazynski, A. L. Balch, R. B. Johnson, K. M. Smith, D. W. Parish, R. J. Cheng, *J. Am. Chem. Soc.* **1983**, *105*, 782 – 787.

[30] A. L. Balch, Y. W. Chan, R. J. Cheng, G. N. Lamar, L. Latosgrazynski, M. W. Renner, *J. Am. Chem. Soc.* **1984**, *106*, 7779 – 7785.

[31] Calculation on the $S = 2$ state were also included (see computational details and Tables in the Supporting Inforamtion), showing very similar Fe–O bonding properties compared to the $S = 1$ ground state. As analyzed for the TMC complex,[17] the spin change affects electron occupations in orbitals in the equatorial plane (d_{xy} and $d_{x^2-y^2}$); the orbitals involved in Fe–O bonding (d_{xz}/d_{yz} and d_{z^2}) are not affected.

[32] Most heme enzymes utilize a Fe^{IV}=O-porphyrin-radical (compound I) to achieve hydrogen-atom abstraction, while mononuclear non-heme iron enzymes utilize a high-spin ($S = 2$) oxo intermediate. In this study we focus on the relative reactivities of heme and non-heme Fe^{IV}=O ($S = 1$) complexes in the same redox and spin states.

[33] G. N. Lamar, F. A. Walker, *J. Am. Chem. Soc.* **1973**, *95*, 1782 – 1790.

[34] E. C. Wasinger, E. I. Solomon, unpublished results.

[35] J. E. Penner-Hahn, K. S. Eble, T. J. McMurry, M. Renner, A. L. Balch, J. T. Groves, J. H. Dawson, K. O. Hodgson, *J. Am. Chem. Soc.* **1986**, *108*, 7819 – 7825.

[36] M. Schappacher, G. Chottard, R. Weiss, *J. Chem. Soc. Chem. Commun.* **1986**, 93 – 94.

[37] M. T. Green, J. H. Dawson, H. B. Gray, *Science* **2004**, *304*, 1653 – 1656.

[38] K. Czarnecki, J. R. Kincaid, H. Fujii, *J. Am. Chem. Soc.* **1999**, *121*, 7953 – 7954.

[39] M. Chance, L. Powers, C. Kumar, B. Chance, *Biochemistry* **1986**, *25*, 1259 – 1265.

 © 2005 Wiley-VCH Verlag GmbH & Co. KGaA, Weinheim

Oxoiron(IV) Complexes

Axial Coordination of Carboxylate Activates the Non-heme Fe^{IV}=O Unit**

*Jan-Uwe Rohde and Lawrence Que, Jr.**

High-valent oxoiron intermediates have been implicated in the dioxygen activation mechanisms of many mononuclear non-heme iron enzymes as the oxidizing species in metabolically important transformations.[1] Recently, the first such species was directly observed in the catalytic cycle of TauD, a member of the superfamily of enzymes with a common 2-His-1-carboxylate facial triad motif that binds the active-site iron center.[2–4] This short-lived intermediate has a high-spin iron(IV) center and the Fe–O bond is 1.62 Å long (determined by extended X-ray absorption fine structure spectroscopy (EXAFS)).[5] Within the same time frame, we reported the first synthetic examples of mononuclear non-heme oxoiron(IV) complexes supported by tetradentate N4 (TMC and TPA) and pentadentate N5 (N4Py and Bn-TPEN) ligands.[6–10] In the case of the TMC complex, $[Fe^{IV}(O)(TMC)(NCMe)](OTf)_2$ was sufficiently stable at −40 °C to be crystallized and characterized by X-ray diffraction.[6] The synthetic complexes, in contrast to the TauD intermediate, have low-spin iron(IV) centers.[6–9] The difference in spin states may arise from the nitrogen-rich nature of the iron coordination environment in the model complexes and the involvement of carboxylate ligands in TauD. This comparison prompted us to investigate whether a carboxylate ligand can be introduced into the iron coordination sphere of a synthetic oxoiron(IV) complex by ligand exchange and thus to assess how such a ligand substitution may affect the spectroscopic properties of the oxoiron(IV) center and its reactivity. We report herein on the reaction of $[Fe^{IV}(O)(TMC)(NCMe)]^{2+}$ (**2**-NCMe) with $NEt_4CF_3CO_2$ and describe the properties of the new intermediate $[Fe^{IV}(O)(TMC)\{OC(O)CF_3\}]^+$ (**2**-O_2CCF_3).

The reaction of $[Fe^{IV}(O)(TMC)(NCMe)]^{2+}$ (**2**-NCMe, $\lambda_{max} = 824$ nm, $\varepsilon = 400\,M^{-1}\,cm^{-1}$) with 10 equivalents of $NEt_4CF_3CO_2$ in MeCN at −20 °C affords a new species designated **2**-O_2CCF_3 within 20 minutes, as indicated by the shift of the absorption maximum to 836 nm with a concomitant loss in intensity ($\varepsilon = 250\,M^{-1}\,cm^{-1}$; Figure 1a). Additional features are also observed to grow at around 940 and 990 nm. This conversion is marked by an isosbestic point, which suggests that **2**-O_2CCF_3 is produced directly from **2**-NCMe (Figure 1a, Scheme 1). Complex **2**-O_2CCF_3 can also be generated by oxygen-atom transfer from PhIO to

[*] Dr. J.-U. Rohde, Prof. Dr. L. Que, Jr.
Department of Chemistry and
Center for Metals in Biocatalysis
University of Minnesota
207 Pleasant Street SE, Minneapolis, MN 55455 (USA)
Fax: (+1) 612-624-7029
E-mail: que@chem.umn.edu

[**] This research was supported by the National Institutes of Health (GM-33162). J.-U.R. acknowledges support by the Deutsche Forschungsgemeinschaft.

 DOI: 10.1002/anie.200462631 © 2005 Wiley-VCH Verlag GmbH & Co. KGaA, Weinheim

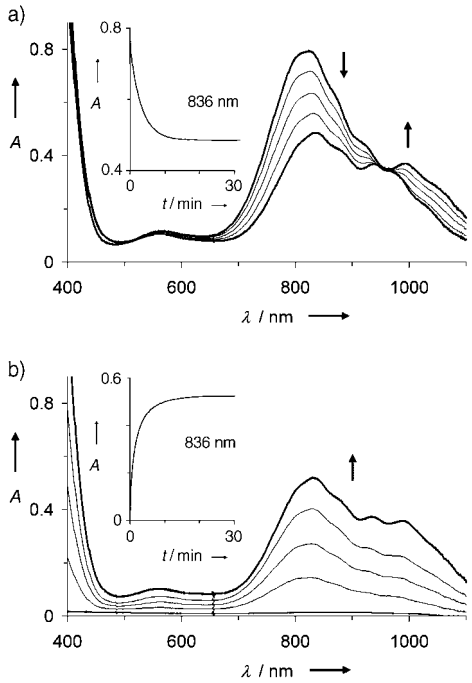

Figure 1. Generation of **2**-O_2CCF_3 by a) addition of $NEt_4CF_3CO_2$ (10 equiv) to **2**-NCMe, and b) addition of PhIO (1 equiv) to **1**-O_2CCF_3 as monitored by UV/Vis/NIR spectroscopy. Reaction conditions: 2 mM iron complex in MeCN at −20 °C. Insets: Corresponding time courses of the reactions monitored at 836 nm.

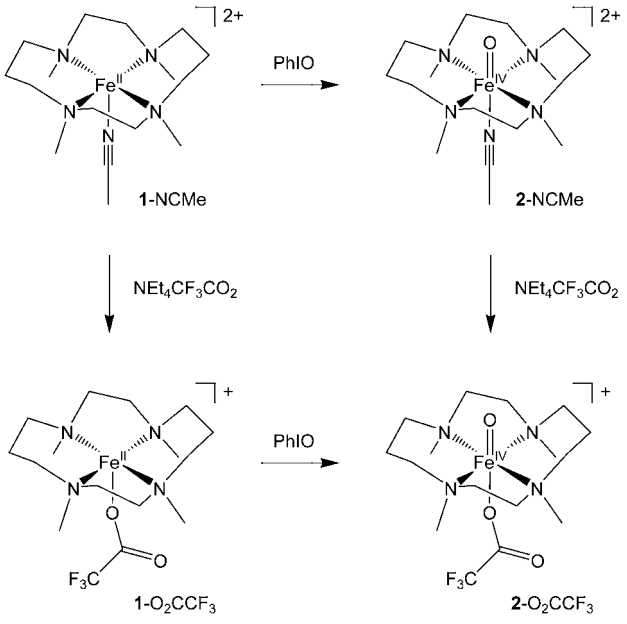

Scheme 1. Ligand-substitution and oxygen-atom-transfer reactions of Fe(TMC) complexes.

$[Fe^{II}(TMC)\{OC(O)CF_3\}]^+$ (**1**-O_2CCF_3; Figure 1b). Complex **1**-O_2CCF_3 is formed in situ by treatment of $[Fe^{II}(TMC)(NCMe)]^{2+}$ (**1**-NCMe) with 1 equivalent of $NEt_4CF_3CO_2$ as indicated by the shift of the very weak ligand-field band at $\lambda \approx 780$ nm to $\lambda \approx 890$ nm. Thus, **2**-O_2CCF_3 can be formed from **1**-NCMe by two pathways, both involving ligand exchange and oxygen-atom transfer but in different order (Scheme 1).

Direct evidence for the binding of trifluoroacetate to the metal centers in **1**-O_2CCF_3 and **2**-O_2CCF_3 is provided by ^{19}F NMR spectroscopy. In CD_2Cl_2, the starting material $[Fe^{II}(TMC)(OTf)]OTf$ has two equally intense ^{19}F resonance signals at $\delta = 15.6$ ppm and −85.2 ppm (−20 °C); the signal at $\delta = -85.2$ ppm corresponds to free triflate ion in CD_2Cl_2 indicating that the signal at $\delta = 15.6$ ppm arises from triflate that is coordinated to the paramagnetic high-spin iron(II) center, $[Fe^{II}(TMC)(OTf)]OTf$ (Figure 2a). In CD_3CN, only

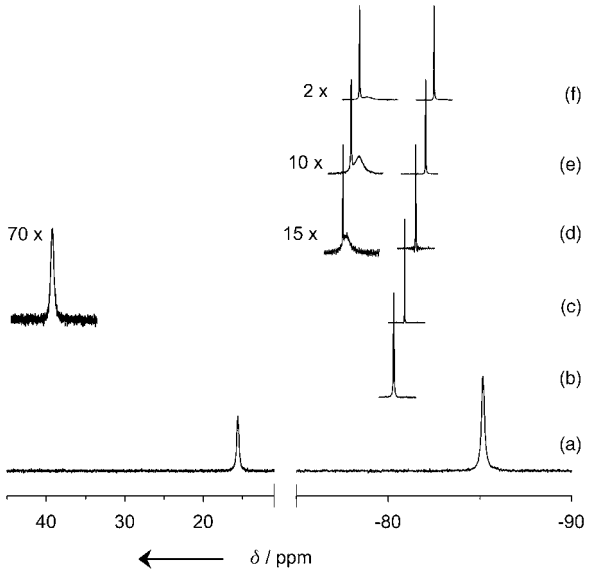

Figure 2. ^{19}F NMR spectra: a) $[Fe^{II}(TMC)(OTf)]OTf$ in CD_2Cl_2 (**1**-OTf) and b) in CD_3CN (**1**-$NCCD_3$), −20 °C; c) equimolar amounts of $[Fe^{II}(TMC)(OTf)]OTf$ and $NEt_4CF_3CO_2$ in CD_3CN (**1**-O_2CCF_3), −20 °C; d) $[Fe^{IV}(O)(TMC)\{OC(O)CF_3\}]OTf$ in CD_3CN (**2**-O_2CCF_3) at −20 °C and e) at −40 °C; and f) after addition of 1 equivalent of $NEt_4CF_3CO_2$ to **2**-O_2CCF_3 in CD_3CN, −40 °C.

one peak at $\delta = -79.9$ ppm is observed, which is attributed to the free triflate counterions (Figure 2b). Addition of 1 equivalent of $NEt_4CF_3CO_2$ to this solution results in the appearance of a resonance at $\delta = 40.3$ ppm, which corresponds to $CF_3CO_2^-$ ligated to high-spin Fe^{II}, with half the intensity of the peak at $\delta = -80.0$ ppm arising from the free triflate counterions (Figure 2c). Addition of a second equivalent of $NEt_4CF_3CO_2$ affords a new peak at $\delta = -76.0$ ppm arising from free $CF_3CO_2^-$ ions (not shown), indicating that the iron center can only bind one trifluoroacetate. Upon addition of PhIO to **1**-O_2CCF_3 at −20 °C, the resonance of bound $CF_3CO_2^-$ disappeared and two new features could be observed close to $\delta = -76$ ppm (Figure 2d). The broader peak is assigned to the $CF_3CO_2^-$ ligated to the paramagnetic Fe^{IV} center ($\delta = -76.3$ ppm, 80%), while the sharper peak corresponds to residual free $CF_3CO_2^-$ ($\delta = -76.1$ ppm, 20%). In support, addition of another equivalent of $NEt_4CF_3CO_2$ results in an increased intensity for the sharper peak (Figure 2f). Thus trifluoroacetate can displace the axial MeCN ligand in **2**-NCMe to form **2**-O_2CCF_3.

 © 2005 Wiley-VCH Verlag GmbH & Co. KGaA, Weinheim

Interestingly, the binding of trifluoroacetate affects the stability and reactivity of the oxoiron(IV) unit (Table 1). As previously reported, **2**-NCMe is unexpectedly rather stable and quite unreactive, persisting for at least a month at −40 °C,

Table 1: Properties of **2**-NCMe and **2**-O_2CCF_3.

	2-NCMe	**2**-O_2CCF_3
λ_{max} [nm] (ε [$M^{-1}cm^{-1}$])	824 (400)	836 (250)
$k_{subst.}$ [s^{-1}] (−20 °C)[a]	–	0.0053(2)
for **2**-NCMe→**2**-O_2CCF_3		
k_{decay} [s^{-1}] (25 °C)[b]	$1.8(2)\times10^{-5}$	$2.2(4)\times10^{-4}$
$t_{1/2}$ (25 °C)		
in the absence of substrates[b]	10 h	1 h
+ 1 PPh_3[c]	≈20 s	≈20 s
+ 10 $C_{14}H_{12}$[d]	1 min	<5 s

Reaction conditions: [a] Addition of $NEt_4CF_3CO_2$ (10 equiv) to 2 mM **2**-NCMe in MeCN at −20 °C. [b] Addition of $NEt_4CF_3CO_2$ (1 equiv) to 2 mM **2**-NCMe in MeCN at 25 °C. [c] Addition of PPh_3 (1 equiv) to 2 mM $[Fe^{IV}(O)(TMC)(L)]^{n+}$ (**2**-L) in MeCN at 25 °C. [d] Addition of dihydroanthracene (10 equiv) to 2 mM **2**-L in MeCN at 25 °C.

thereby allowing crystals to be obtained.[6] PPh_3 is the only substrate reported to date to be oxidized at −40 °C by **2**-NCMe[7] and the oxo transfer to one equivalent of substrate occurs over the course of an hour. Raising the temperature to 25 °C shortens its half-life to 10 h and to 20 s in the presence of one equivalent PPh_3. Furthermore, **2**-NCMe reacts with 10 equivalents of dihydroanthracene to form anthracene (half-life of 1 min), so **2**-NCMe appears capable of hydrogen-atom abstraction from weak C–H bonds at room temperature. The yield of anthracene is 45%, the same as that observed for the much more reactive $[Fe^{IV}(O)(N4Py)]^{2+}$,[11] suggesting that both oxoiron(IV) units act as one-electron oxidants in this transformation.

In contrast, **2**-O_2CCF_3 has a half-life at 25 °C an order of magnitude shorter ($t_{1/2}\approx1$ h; Table 1) than **2**-NCMe. Furthermore, **2**-O_2CCF_3 reacts much faster than **2**-NCMe with 10 equivalents of dihydroanthracene ($t_{1/2}\approx5$ s) to produce approximately 0.4 equivalents of anthracene. However, the reaction of **2**-O_2CCF_3 with one equivalent of PPh_3 to afford $OPPh_3$ and regenerate **1**-O_2CCF_3, as monitored by ^{31}P and ^{19}F NMR spectroscopy, occurs on the same time scale as that of **2**-NCMe. So axial coordination of carboxylate to the Fe^{IV}=O unit appears to convert **2**-NCMe into a more reactive oxidant for one-electron oxidations, but not for oxygen atom transfer onto a phosphorus, formally a two-electron process.

The observed lower thermal stability and greater reactivity of **2**-O_2CCF_3 towards dihydroanthracene may at first glance appear counterintuitive, as the replacement of neutral MeCN with a monoanionic $[CF_3CO_2]^-$ ligand might be expected to stabilize the iron(IV) oxidation state by reducing its high effective charge. Indeed Collins has used this principle in his design of tetraanionic macrocyclic tetraamidate ligands that led to the isolation and crystallization of novel iron(IV) complexes.[12] On the other hand, Borovik and co-workers have reported the first example of an iron(III) complex with a terminal oxo ligand, $[Fe^{III}(O)(L)]^{2-}$, where L is a tripodal trianionic tris(ureaylato)amine ligand, which is derived from the reaction of O_2 with the iron(II) precursor. They have invoked the involvement of an oxoiron(IV) species that is too reactive to be detected as the precursor to the oxoiron(III) complex.[13,14] Also, Wieghardt and co-workers have observed the formation of a rather unstable oxoiron(IV) complex containing a cyclam ligand with a carboxymethyl tether from the reaction of its iron(III) precursor with O_3.[15,16] Our results, together with the latter two observations above, suggest that introducing anionic ligands can in fact destabilize the oxoiron(IV) center. In the case of **2**, replacing the nitrile with a carboxylate results in the weakening of the ligand field, as indicated by the red shift observed for the near-IR d–d transitions associated with the $S=1$ oxoiron(IV) unit of **2**-O_2CCF_3 relative to those of **2**-NCMe,[17] and a consequent decrease in the low-spin/high-spin energy gap. The higher reactivity observed for **2**-O_2CCF_3 may thus be associated with enhanced access to a more reactive high-spin $S=2$ reaction surface, although the current limited information available on oxoiron(IV) centers indicates that the strength of the Fe=O bond is comparable for low-spin and high-spin complexes.[4–6,9,17] Nevertheless, there has been considerable discussion on the spin-state-dependent reactivity of oxoiron(IV) species in heme systems to rationalize some of the conflicting observations that have been made for the nature of the active oxidant;[18,19] similar considerations may apply to non-heme oxoiron(IV) oxidations.

In summary, we have introduced a carboxylate ligand *trans* to an oxo group in an iron(IV) complex and, in so doing, have enhanced the reactivity of the $S=1$ oxoiron(IV) unit in **2**.[20] We hypothesize that the higher reactivity may be due to a weakening of the ligand field that provides greater access to a more reactive $S=2$ surface. We note that such $S=2$ iron(IV) centers are utilized by non-heme iron enzymes, such as methane monooxygenase, ribonucleotide reductase, and TauD, to carry out their respective oxidative reactions, and the common feature among these enzymes is the presence of histidine and carboxylate ligands.[1,21,22]

Experimental Section

Physical Methods: UV/Vis spectra were recorded on an HP 8453 A diode array spectrometer with samples maintained at low temperature by using a cryostat from Unisoku Scientific Instruments, Japan. ^{19}F and ^{31}P NMR spectra were recorded on a Varian Inova VXR-300 or Varian Inova VI-300 spectrometer at ambient temperature, unless noted otherwise. Chemical shifts (ppm) are reported referenced to an external standard, $CFCl_3$ ($\delta=0$ ppm) for ^{19}F NMR spectra and H_3PO_4 (85%, 0 ppm) for ^{31}P NMR spectra. GC analyses were performed on a Perkin-Elmer Sigma 3 gas chromatograph (AT-1701 column, 30 m) with flame-ionization detection. The products were identified by comparing their retention times to those of authentic samples.

Generation of [Fe(O)(TMC){OC(O)CF_3}]OTf (**2**-O_2CCF_3(OTf)) via [Fe(O)(TMC)(NCMe)]$(OTf)_2$ (**2**-NCMe$(OTf)_2$). A 2 mM solution of $[Fe^{II}$(TMC)(OTf)]OTf[6] in MeCN (2.5 mL, 0.005 mmol Fe) in a 1-cm UV/Vis cuvette was pre-cooled to −20 °C. (Note: Dissolution of $[Fe^{II}$(TMC)(OTf)]OTf in MeCN readily afforded [Fe(TMC)-(NCMe)]$(OTf)_2$ (**1**-NCMe$(OTf)_2$), as indicated by the ^{19}F resonance of the free triflate ion in its NMR spectrum.) Addition of PhIO[23] (1 equiv, 0.005 mmol) in MeOH (0.05 mL) afforded **2**-NCMe$(OTf)_2$. Subsequent addition of $NEt_4CF_3CO_2$ (10 equiv, 0.050 mmol) in MeCN (0.05 mL) afforded **2**-O_2CCF_3(OTf). ^{19}F NMR for **1**-OTf(OTf)

 © 2005 Wiley-VCH Verlag GmbH & Co. KGaA, Weinheim

(CD_2Cl_2, 282.4 MHz, −20 °C): $\delta = 15.6$ (s, [Fe(TMC){OS(O)$_2$CF_3}]$^+$) and −85.2 ppm (s, CF_3SO$_3^-$); **1**-NCCD$_3$(OTf)$_2$ (CD_3CN, 282.4 MHz, −20 °C): $\delta = -79.9$ ppm (s, CF_3SO$_3^-$). ^{19}F NMR for **2**-O$_2$CCF$_3$(OTf) + NEt_4OTf (CD_3CN, 282.4 MHz, −20 °C): $\delta = -76.1$ (s, CF_3CO$_2^-$), −76.3 (s, [Fe(O)(TMC){OC(O)CF_3}]$^+$), and −80.0 ppm (s, CF_3SO$_3^-$). ^{19}F NMR for $NEt_4CF_3CO_2$ (CD_2Cl_2, 282.4 MHz): $\delta = -75.9$ ppm (s, CF_3CO$_2^-$); $NEt_4CF_3CO_2$ (CD_3CN, 282.4 MHz): $\delta = -75.8$ ppm (s, CF_3CO$_2^-$).

Generation of **2**-O$_2$CCF$_3$(OTf) via [Fe(TMC){OC(O)CF$_3$}]OTf (**1**-O$_2$CCF$_3$(OTf)). A 2 mM solution of [Fe^{II}(TMC)(OTf)]OTf in MeCN (2.5 mL, 0.005 mmol Fe) in a 1-cm UV/Vis cuvette was converted into **1**-O$_2$CCF$_3$(OTf) by addition of $NEt_4CF_3CO_2$ (1 equiv, 0.005 mmol) in MeCN (0.05 mL). This solution was then cooled to −20 °C. **2**-O$_2$CCF$_3$(OTf) was generated by addition of PhIO (1 equiv, 0.005 mmol) in MeOH (0.05 mL). ^{19}F NMR for **1**-O$_2$CCF$_3$(OTf) + NEt_4OTf (CD_3CN, 282.4 MHz, −20 °C): $\delta = 40.3$ (s, [Fe(TMC){OC(O)CF_3}]$^+$) and −80.0 ppm (s, CF_3SO$_3^-$).

Reaction of **2**-L with PPh_3. A 2 mM solution of **2**-NCMe(OTf)$_2$ or **2**-O$_2$CCF$_3$(OTf) in MeCN (2 mL), generated from **1**-NCMe(OTf)$_2$ or **1**-O$_2$CCF$_3$(OTf) and PhIO (1 equiv) at 25 °C, was treated with PPh_3 (1 equiv, 0.004 mmol) in a solvent mixture of MeCN and CH_2Cl_2 (1:1; 0.04 mL). Products were analyzed by ^{31}P NMR (CD_3CN, 121.4 MHz): $\delta = 27.9$ ppm (s, OPPh$_3$), and ^{19}F NMR (CD_3CN, 282.4 MHz): $\delta = 21.4$ (s, [Fe(TMC){OC(O)CF_3}]$^+$) and −80.0 ppm (s, CF_3SO$_3^-$).

Reaction of **2**-L with dihydroanthracene: A 2 mM solution of **2**-NCMe(OTf)$_2$ or **2**-O$_2$CCF$_3$(OTf) in MeCN (2 mL), generated by addition of PhIO (1 equiv) to **1**-NCMe(OTf)$_2$ or **1**-O$_2$CCF$_3$(OTf) at 25 °C, was treated with dihydroanthracene (10 equiv, 0.040 mmol; recrystallized from EtOH)[24] in a solvent mixture of MeCN and CH_2Cl_2 (1:1; 0.08 mL). Products were analyzed by GC: Reaction with **2**-NCMe(OTf)$_2$ yielded 0.0018 mmol anthracene (45% based on equivalents of Fe complex) and reaction with **2**-O$_2$CCF$_3$(OTf) gave 0.0016 mmol anthracene (40%).

Received: November 16, 2004
Published online: February 28, 2005

Keywords: bioinorganic chemistry · carboxylate ligands · high-valent compounds · iron · oxo ligands

[1] M. Costas, M. P. Mehn, M. P. Jensen, L. Que, Jr., *Chem. Rev.* **2004**, *104*, 939.
[2] J. C. Price, E. W. Barr, B. Tirupati, J. M. Bollinger, Jr., C. Krebs, *Biochemistry* **2003**, *42*, 7497.
[3] J. C. Price, E. W. Barr, T. E. Glass, C. Krebs, J. M. Bollinger, Jr., *J. Am. Chem. Soc.* **2003**, *125*, 13008.
[4] D. A. Proshlyakov, T. F. Henshaw, G. R. Monterosso, M. J. Ryle, R. P. Hausinger, *J. Am. Chem. Soc.* **2004**, *126*, 1022.
[5] P. J. Riggs-Gelasco, J. C. Price, R. B. Guyer, J. H. Brehm, E. W. Barr, J. M. Bollinger, Jr., C. Krebs, *J. Am. Chem. Soc.* **2004**, *126*, 8108.
[6] J.-U. Rohde, J.-H. In, M. H. Lim, W. W. Brennessel, M. R. Bukowski, A. Stubna, E. Münck, W. Nam, L. Que, Jr., *Science* **2003**, *299*, 1037.
[7] M. H. Lim, J.-U. Rohde, A. Stubna, M. R. Bukowski, M. Costas, R. Y. N. Ho, E. Münck, W. Nam, L. Que, Jr., *Proc. Natl. Acad. Sci. USA* **2003**, *100*, 3665.
[8] J. Kaizer, E. J. Klinker, N. Y. Oh, J.-U. Rohde, W. J. Song, A. Stubna, J. Kim, E. Münck, W. Nam, L. Que, Jr., *J. Am. Chem. Soc.* **2004**, *126*, 472.
[9] J.-U. Rohde, S. Torelli, X. Shan, M. H. Lim, E. J. Klinker, J. Kaizer, K. Chen, W. Nam, L. Que, Jr., *J. Am. Chem. Soc.* **2004**, *126*, 16750.
[10] Abbreviations used: Bn-TPEN = *N*-benzyl-*N*,*N*′,*N*′-tris(2-pyridylmethyl)-1,2-diaminoethane, N4Py = *N*,*N*-bis(2-pyridylmethyl)-*N*-bis(2-pyridyl)methylamine, OTf = trifluoromethylsulfonate (or triflate) anion, TMC = 1,4,8,11-tetramethyl-1,4,8,11-tetraazacyclotetradecane (or tetra(*N*-methyl)cyclam), TPA = *N*,*N*,*N*-tris(2-pyridylmethyl)amine.
[11] E. J. Klinker, L. Que, Jr., University of Minnesota, unpublished results.
[12] T. J. Collins, *Acc. Chem. Res.* **1994**, *27*, 279.
[13] C. E. MacBeth, A. P. Golombek, V. G. Young, Jr., C. Yang, K. Kuczera, M. P. Hendrich, A. S. Borovik, *Science* **2000**, *289*, 938.
[14] C. E. MacBeth, R. Gupta, K. R. Mitchell-Koch, V. G. Young, Jr., G. H. Lushington, W. H. Thompson, M. P. Hendrich, A. S. Borovik, *J. Am. Chem. Soc.* **2004**, *126*, 2556.
[15] C. A. Grapperhaus, B. Mienert, E. Bill, T. Weyhermüller, K. Wieghardt, *Inorg. Chem.* **2000**, *39*, 5306.
[16] Wieghardt's putative oxoiron(IV) complex with a pentadentate ligand consisting of the macrocyclic cyclam ligand with a pendent acetate from one of the nitrogen atoms is a rather unstable species that was generated from the reaction of [Fe^{III}(cyclam-acetate)(OTf)]$^+$ and O_3 at −80 °C in less than 25% yield and thus difficult to characterize.[15] The proposed oxoiron(IV) formulation was made on the basis of a Mössbauer analysis, a hypothesis that was subsequently supported by the synthesis and characterization of more stable oxoiron(IV) complexes.[6–9] The instability of this complex might be ascribed to the presumed ligation of the pendent carboxylate, consistent with the results reported herein, but might also derive from the presence of secondary amine ligands (versus tertiary amine ligands in **2**-NCMe and **2**-O$_2$CCF$_3$) that are more susceptible to ligand oxidation.[25] The lack of more detailed structural information on this interesting complex however makes it difficult to draw firm conclusions about its properties.
[17] A. Decker, J.-U. Rohde, L. Que, Jr., E. I. Solomon, *J. Am. Chem. Soc.* **2004**, *126*, 5378.
[18] J. C. Schoeneboom, S. Cohen, H. Lin, S. Shaik, W. Thiel, *J. Am. Chem. Soc.* **2004**, *126*, 4017.
[19] S. Shaik, S. P. de Visser, D. Kumar, *J. Biol. Inorg. Chem.* **2004**, *9*, 661.
[20] Gross and co-workers have also reported that coordination of an axial carboxylate to an oxoiron(IV) porphyrin cation radical complexes similarly enhances its reactivity:Z. Gross, S. Nimri, C. M. Barzilay, L. Simkhovich, *J. Biol. Inorg. Chem.* **1997**, *2*, 492.
[21] B. J. Wallar, J. D. Lipscomb, *Chem. Rev.* **1996**, *96*, 2625.
[22] M. Merkx, D. A. Kopp, M. H. Sazinsky, J. L. Blazyk, J. Müller, S. J. Lippard, *Angew. Chem. Int. Ed.* **2001**, *40*, 2782.
[23] H. Saltzman, J. G. Sharefkin, *Organic Syntheses*, Coll. Vol. *V*, Wiley, New York, **1973**, p. 658.
[24] W. L. F. Armarego, D. D. Perrin, *Purification of Laboratory Chemicals*, Butterworth-Heinemann, Oxford, **1997**.
[25] D. H. Busch, N. W. Alcock, *Chem. Rev.* **1994**, *94*, 585.

 © 2005 Wiley-VCH Verlag GmbH & Co. KGaA, Weinheim

Asymmetric Synthesis

Dynamic Kinetic Resolution during a Cascade Reaction on Substrates with Chiral All-Carbon Quaternary Centers**

*Kaichen Xu, Gojko Lalic, Scott M. Sheehan, and Matthew D. Shair**

Dynamic kinetic resolution has become a useful method for the diastereoselective and enantioselective synthesis of organic compounds.[1] Dynamic kinetic resolution, presented in Equation (1) (Scheme 1), in its most common form results in greater than 50% conversion of a mixture of stereoisomers into products enriched in one enantiomer or diastereoisomer.[2]

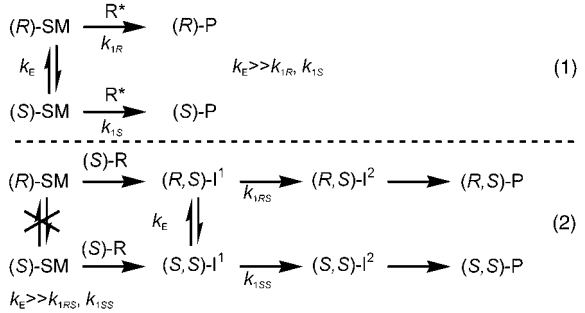

Scheme 1. Dynamic kinetic resolution with enantiomerization of the starting materials (SM; Eq. (1)). Dynamic kinetic resolution with epimerization in the second step (Eq. (2)). I^1 = first intermediate, I^2 = second intermediate, P = product.

Most dynamic kinetic resolutions require rapidly equilibrating enantiomeric starting materials that undergo a slower second step, in which the enantiomers react with enantiomerically enriched reagents at different rates ($k_{1R} \neq k_{1S}$; Scheme 1, Eq. (1)). Conceptually, it is difficult to imagine how starting materials that are not directly susceptible to enantiomerization, such as molecules where the only chirality present is in all-carbon quaternary stereocenters, could take part in dynamic kinetic resolutions. However, if a molecule incapable of direct enantiomerization were to undergo a cascade reaction (a reaction comprising one or more intermediates) and if any one of the intermediates in the reaction was capable of epimerization or enantiomerization (I^1, Scheme 1, Eq. (2)), then dynamic kinetic resolution could be achieved. Furthermore, equilibration of stereoisomers in dynamic kinetic resolutions is most often achieved by proton transfer,[3] addition–elimination reactions,[4] oxidation–reduction reactions,[5] or isomerization of configurationally labile carbanions,[6] whereas equilibration between stereoisomers containing all-carbon quaternary stereocenters can only be achieved through reversible C–C bond-forming reactions, which have rarely been used so far in dynamic kinetic resolutions.

Therefore, it may be possible to generate complex structures as single stereoisomers from a racemic starting material and an enantiopure reagent by developing cascade reactions with dynamic kinetic resolutions. Despite the potential of this concept, there are few examples of cascade reactions that incorporate dynamic kinetic resolution, especially ones involving the formation of multiple C–C bonds.[7] Herein, we report on dyanmic-kinetic-resolution cascade reactions that occur with racemic starting materials that contain all-carbon quaternary stereocenters.

During our synthesis of CP-263,114, we developed a diastereoselective cascade reaction comprising an alkylation, an anion-accelerated oxy-Cope rearrangement, and a transannular Dieckmann-like cyclization.[8] Using this latter reaction, we synthesized a wide range of complex polycyclic bridgehead enone compounds (Scheme 2).[9] The possible

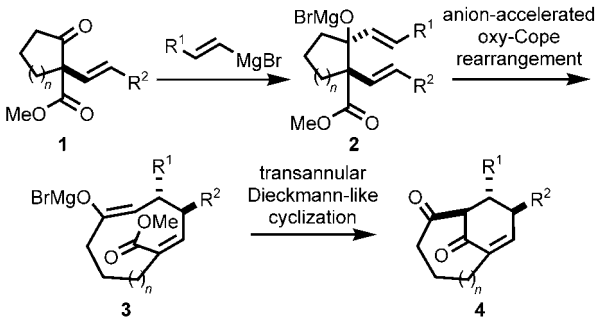

Scheme 2. A cascade reaction for the synthesis of polycyclic bridgehead enone compounds.

participation of intermediate **2** in a retro-aldol/aldol equilibrium and the consequences of this equilibrium on the transfer of stereochemistry from C2 of **1** to the product **4** was of particular interest to us (Scheme 3).[10]

The occurance of the retro-aldol/aldol equilibration during the cascade reaction was tested with β-ketoester **5**, which was prepared in 99% *ee* by the enantioselective reduction of the corresponding racemate with the Corey–Bakshi–Shibata (CBS) catalyst and catecholborane[11] followed by separation and oxidation of the resulting diastereomers. Compound **5** was subjected to the conditions previously developed for the cascade reaction (see above), and the bicyclic product **6** was isolated as a racemate in 67% yield. The reaction was stopped after 15 minutes at 0 °C by the addition of AcOH and addition product **7** was isolated in

[*] K. Xu, G. Lalic, S. M. Sheehan, Prof. M. D. Shair
Department of Chemistry and Chemical Biology
Harvard University
12 Oxford Street, Cambridge, MA 02138 (USA)
Fax: (+1) 617-495-5008
E-mail: shair@chemistry.harvard.edu

[**] We gratefully acknowledge NIGMS R01 GM59403-01A1, Bristol–Myers Squibb, Novartis, Eli Lilly, Merck Research Laboratories, the Alfred P. Sloan Foundation, GlaxoSmithKline, and the Arthur C. Cope Fund for support. We also thank Brian Goess for assistance with the preparation of this manuscript.

Supporting information for this article is available on the WWW under http://www.angewandte.org or from the author.

 DOI: 10.1002/anie.200462039 © 2005 Wiley-VCH Verlag GmbH & Co. KGaA, Weinheim

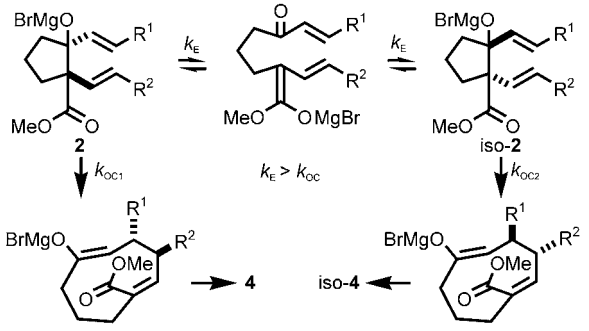

Scheme 3. Racemization in the cascade reaction. k_E = rate of the equilibration, k_{OC1} and k_{OC2} = rates of the anion-accelerated oxy-Cope rearrangements.

99% ee and in 82% yield (Scheme 4). The results of these experiments indicate that there was a retro-aldol/aldol equilibrium between the two enantiomers of the addition

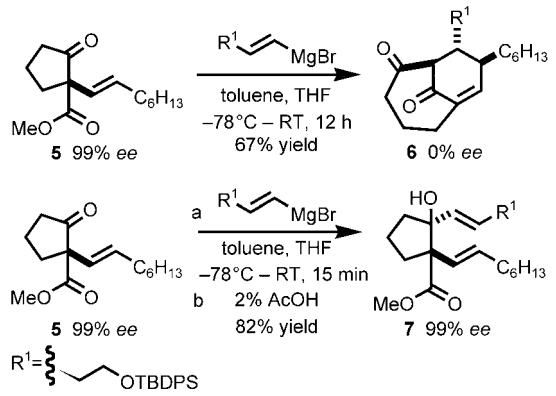

Scheme 4. Mechanism of racemization. TBDPS = *tert*-butyldiphenylsilyl.

product **2** and iso-**2** and that the rate of the equilibration (k_E) was significantly higher than the rate of the anion-accelerated oxy-Cope rearrangements (k_{OC1} and k_{OC2}; see Scheme 3). These results also establish that epimerization of the quaternary stereocenter of **1** occurred only after addition of the Grignard reagent.

The rapid enantiomerization between **2** and iso-**2** provided an intriguing opportunity for the dynamic kinetic resolution of **1**. A single enantiomer of a chiral vinyl Grignard reagent added to a racemic β-ketoester should result in two diastereomeric products (Scheme 3, **2** and iso-**2**, chiral R^1).

The fast retro-aldol/aldol reactions would result in equilibration of **2** and iso-**2** (with chiral R^1) at a rate higher than the rate of the ensuing anion-accelerated oxy-Cope rearrangements ($k_E \gg k_{OC1}$ and $k_E \gg k_{OC2}$). Considering a highly organized transition state of the anion-accelerated oxy-Cope rearrangement, with appropriately substituted chiral vinyl Grignard reagents, we anticipated that the two diastereomers would react at different rates ($k_{OC1} \neq k_{OC2}$), thus leading to dynamic kinetic resolution.

We assumed that the transition state for the anion-accelerated oxy-Cope rearrangement had a chairlike structure and so anticipated that 3-silyloxy-substituted cyclopentenyl and cyclohexenyl Grignard reagents would lead to different rates of the anion-accelerated oxy-Cope rearrangements (Scheme 5). Specifically, a nonbonded interaction

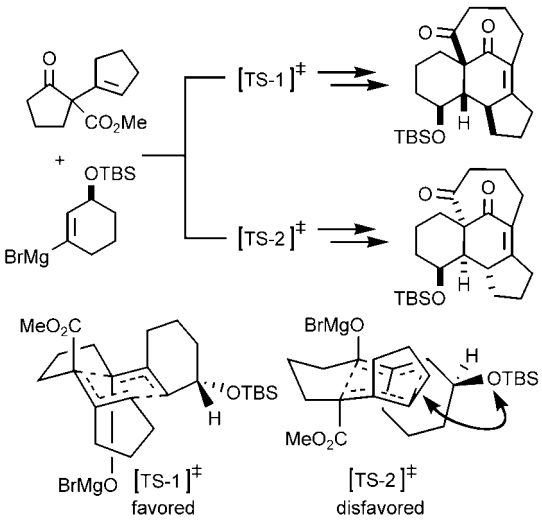

Scheme 5. Dynamic kinetic resolution of the polycyclic products. TBS = *tert*-butyldimethylsilyl.

between the silyloxy group and the cyclopentene that would exist in the second transition state (TS-2) but not the first transition state (TS-1) would differentiate between these two transition states, thus leading to the formation of the diastereomer derived from TS-1.

Indeed, treatment of racemic β-ketoester **8** with a single enantiomer of a Grignard reagent derived from vinyl stannane **9** (Scheme 6, Eq. (3)) afforded the product **10** of the expected cascade reaction as a single diastereomer in 75% yield, which is indicative of dynamic kinetic resolution. The product would have been generated as a 1:1 mixture of diastereomers in 99% *ee* if dynamic kinetic resolution had not occurred. However, the products would have been formed in 99% *ee* as a single diastereomer but in a maximum yield of 50% if only a kinetic resolution had occurred.

The diastereoselectivity of these reactions are, predictably, sensitive to the degree of nonbonded interactions between the silyloxy group and the olefin substituent on the β-ketoester. For example, the lowest diastereoselectivity was obtained in the reaction of **8** with **12** [Eq. (5)], in which both five-membered rings diminish the nonbonded interaction between the silyloxy group and the olefin substituent. The diastereoselectivity was high (≥95% d.r.) as long as one of the olefin substituents is part of a six-membered ring [Eqs. (3)–(5)]. The stereochemistry of the cascade reaction product **10** was confirmed by X-ray crystallographic studies (Figure 1).

The cascade reactions reported here are unique because they involve dynamic kinetic resolutions that required the formation and cleavage of multiple C–C bonds. Although

 © 2005 Wiley-VCH Verlag GmbH & Co. KGaA, Weinheim

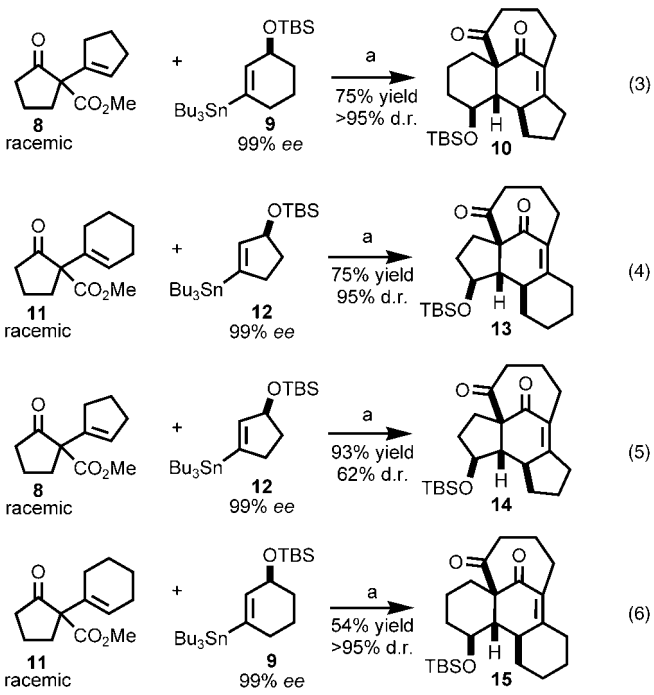

Scheme 6. Dynamic kinetic resolution during the cascade reaction. Conditions: a) *n*BuLi, THF, −78 °C,; $MgBr_2$, Et_2O/benzene, O °C; THF/toluene, 23 °C, 18 h.

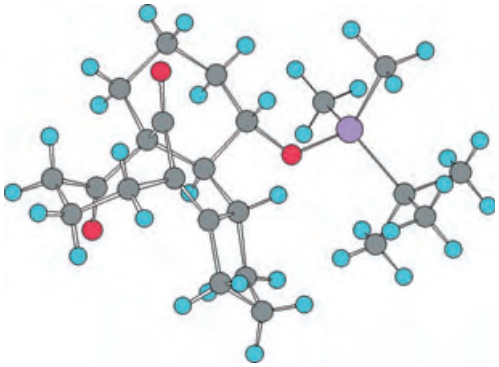

Figure 1. X-ray structure of **10**.

dynamic kinetic resolution is used more often in organic synthesis, this process is still rare for substrates with chiral all-carbon quaternary centers. The reactions reported in Scheme 6 demonstrate the necessity of reversible C–C bond-forming reactions in the dynamic kinetic resolution of starting materials with all-carbon quaternary stereocenters. Furthermore, the products generated in these reactions are among the most complex prepared to date involving dynamic kinetic resolution, which suggests that cascade reactions that comprise dynamic kinetic resolution may be useful for the stereoselective synthesis of complex molecules.

Received: September 19, 2004
Revised: December 12, 2004
Published online: March 4, 2005

Keywords: asymmetric synthesis · diastereoselectivity · dynamic kinetic resolution · pericyclic reactions · polycycles

[1] a) R. Noyori, T. Ikeda, T. Chkuma, M. Widhalm, M. Kitamura, H. Takaya, S. Akutagawa, N. Sayo, T. Saito, T. Taketomi, H. Kumobayashi, *J. Am. Chem. Soc.* **1989**, *111*, 9134–9135; b) R. Noyori, M. Tokunaga, M. Kitamura, *Bull. Chem. Soc. Jpn.* **1995**, *68*, 36–56; c) H. Pellissier, *Tetrahedron* **2003**, *59*, 8291–8327; d) R. S. Ward, *Tetrahedron: Asymmetry* **1995**, *6*, 1475–1490.
[2] The definition of dynamic kinetic resolution adopted by some researchers requires the equilibrium in the first step to be between enantiomers; however, some researchers have adopted a broader, more inclusive definition, in which equilibrating diastereomers can also be part of a dynamic kinetic resolution (see Refs. [1c] and [1d]).
[3] a) L. Tang, L. Deng, *J. Am. Chem. Soc.* **2002**, *124*, 2870–2871; b) V. Jurkauskas, S. L. Buchwald, *J. Am. Chem. Soc.* **2002**, *124*, 2892–2893; c) K.-i. Nunami, H. Kubota, A. Kubo, *Tetrahedron Lett.* **1994**, *35*, 8639–8642.
[4] a) M. Node, K. Nishide, Y. Shigeta, H. Shiraki, K. Obata, *J. Am. Chem. Soc.* **2000**, *122*, 1927–1936; b) S. Brand, M. F. Jones, C. M. Rayner, *Tetrahedron Lett.* **1995**, *36*, 8493–8496.
[5] a) M. Kitamura, M. Tokunaga, R. J. Noyori, *J. Am. Chem. Soc.* **1993**, *115*, 144–152; a) J. V. Allen, J. M. J. Williams, *Tetrahedron Lett.* **1996**, *37*, 1859–1862; b) B. A. Persson, A. L. E. Larsson, M. Le Ray, J.-E. Baeckvall, *J. Am. Chem. Soc.* **1999**, *121*, 1645–1650; c) O. Pamies, J.-E. Baeckvall, *Chem. Rev.* **2003**, *103*, 3247–3261.
[6] a) T. Hayashi, M. Konishi, M. Fukushima, T. Mise, M. Kagotani, M. Tajika, M. Kumada, *J. Am. Chem. Soc.* **1982**, *104*, 180–186; b) K. Mikami, A. Yoshida, *Tetrahedron* **2001**, *57*, 889–898.
[7] S. Akai, K. Tanimoto, Y. Kita, *Angew. Chem.* **2004**, *116*, 1431–1434; *Angew. Chem. Int. Ed.* **2004**, *43*, 1407–1410.
[8] a) C. Chen, M. E. Layton, M. D. Shair, *J. Am. Chem. Soc.* **1998**, *120*, 10784–10785; b) C. Chen, M. E. Layton, S. M. Sheehan, M. D. Shair, *J. Am. Chem. Soc.* **2000**, *122*, 7424–7425.
[9] S. M. Sheehan, G. Lalic, J. S. Chen, M. D. Shair, *Angew. Chem.* **2000**, *112*, 2826–2827; *Angew. Chem. Int. Ed.* **2000**, *39*, 2714–2715.
[10] For an example of an anion-accelerated oxy-Cope rearrangement that involves a retro-aldol/aldol equilibrium, see: C. H. Heathcock, C. M. Tice, *J. Org. Chem.* **1981**, *46*, 9–13.
[11] E. J. Corey, R. K. Bakshi, S. Shibata, *J. Am. Chem. Soc.* **1987**, *109*, 5551–5553.

 © 2005 Wiley-VCH Verlag GmbH & Co. KGaA, Weinheim

Chiral Fullerene Adducts

Conclusive Determination of the Absolute Configuration of Chiral C_{60}-Fullerene *cis*-3 Bisadducts by X-ray Crystallography and Circular Dichroism**

Shunsuke Kuwahara, Kazuhiro Obata, Kazuhiro Yoshida, Takatoshi Matsumoto, Nobuyuki Harada, Nobuhiro Yasuda, Yoshiki Ozawa, and Koshiro Toriumi*

The fullerene C_{60} is a symmetrical and achiral molecule. However, an addition reaction at two chiral positions of the C_{60} skeleton, for example, a *cis*-3 addition,[1] makes the π-electron system of fullerene chiral in the resulting bisadduct. Synthetic and configurational studies of such chiral fullerene bisadducts have been carried out by many research groups (Scheme 1). For example, Nakamura et al. first synthesized the chiral bisadduct **1** by using a chiral tether and tentatively assigned its absolute configuration as *R*,*R*,^{f,s}*A*[1] (≡*R*,*R*,^{f}*C*[1]) on the basis of MM2/Monte Carlo calculations.[2] Diederich and co-workers synthesized the chiral bisadduct **2** as the sole product of a double Bingel reaction. The absolute stereochemistry of [CD(+)281]-**2** was determined to be *S*,*S*,^{f,s}*A* (≡*S*,*S*,^{f}*C*), because the results of molecular-mechanics calculations indicated that of the two possible diastereomeric bisadducts, diastereomer (*S*,*S*,^{f,s}*A*)-**2** is much more stable than the other diastereomer (*S*,*S*,^{f,s}*C*)-**2**.[3] The same absolute configuration was assigned by the theoretical calculation of circular-dichroism (CD) spectra of chiral bisadducts and related compounds based on the π-electron SCF-CI-DV MO method, as reported by the Harada and Diederich groups.[4] Later, Diederich and co-workers applied the CD exciton chirality method to related compounds and confirmed their previous assignment.[5] Nishimura and co-workers synthesized the chiral bisadduct **3** by using a chiral tether prepared from 2,3-butanediol,[6] and tentatively assigned its absolute configuration as shown in Scheme 1 on the basis of the results of molecular-mechanics calculations. Shinkai and co-workers reported the synthesis of the boron-containing chiral bisadduct **4**, the absolute configuration of which was assigned by the comparison of its CD spectrum with that of **2**.[7] As shown in Scheme 1, however, those assignments of absolute configuration disagreed with one another: Compound (^{f,s}*A*)-**1** (≡(^{f}*C*)-**1**) showed a negative CD Cotton effect at 288 nm, whereas (^{f,s}*A*)-**2** (≡(^{f}*C*)-**2**) exhibited a positive Cotton effect at 281 nm. The CD spectra of (^{f,s}*A*)-**1** and (^{f,s}*A*)-**2** were thus opposite in sign despite their identical chiral π-electron systems in the C_{60} skeleton. The bisadduct (^{f,s}*C*)-**3** (≡(^{f}*A*)-**3**) showed a positive Cotton effect at 284 nm, in disagreement with the assignment of (^{f,s}*A*)-**2**, which exhibits a positive

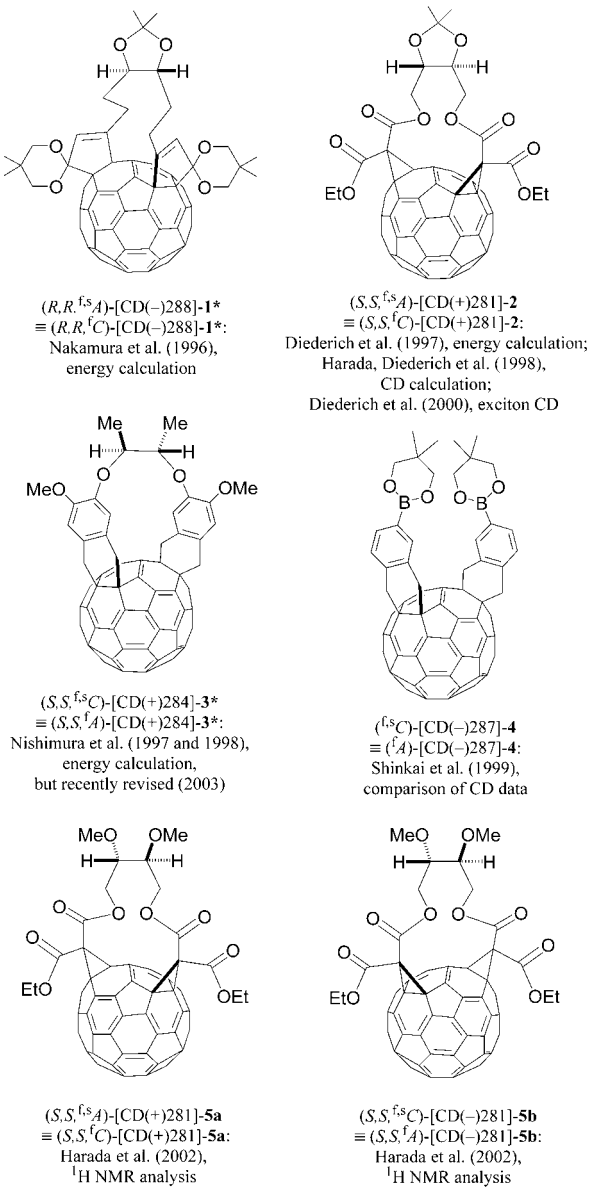

Scheme 1. Previously reported chiral C_{60}-fullerene *cis*-3 bisadducts together with their CD data and absolute configurations, which are designated by the new systematic nomenclature (^{f,s}*C* and ^{f,s}*A*) as well as by the old nomenclature (^{f}*C* and ^{f}*A*). The present study suggests that the absolute configuration should be revised in the case of compounds marked with the symbol *.

[*] S. Kuwahara, K. Obata, Dr. K. Yoshida, Dr. T. Matsumoto, Prof. Dr. N. Harada
Institute of Multidisciplinary Research for Advanced Materials
Tohoku University
2-1-1 Katahira, Aoba, Sendai 980-8577 (Japan)
Fax: (+81) 22-217-5667
E-mail: n-harada@tagen.tohoku.ac.jp
Dr. N. Yasuda
SPring-8/Japan Synchrotron Radiation Research Institute (JASRI)
1-1-1 Kouto, Mikazuki-cho, Hyogo 679-5198 (Japan)
Dr. Y. Ozawa, Prof. Dr. K. Toriumi
Graduate School of Material Science
University of Hyogo
3-2-1 Kouto, Kamigori-cho, Hyogo 678-1297 (Japan)

[**] This work was supported in part by grants from the Japan Society for the Promotion of Science: Scientific Research (B) No. 16350069 (to N.H.) and Young Scientists Research (B) No. 15710073 (to S.K.).

Supporting information for this article is available on the WWW under http://www.angewandte.org or from the author.

 © 2005 Wiley-VCH Verlag GmbH & Co. KGaA, Weinheim DOI: 10.1002/anie.200462811

Cotton effect at 281 nm. These results clearly indicated that some configurational assignments were erroneous.

What is the main reason for such disagreement? In most cases of the preparation of *cis*-3 bisadducts by using a chiral tether, only one of two possible diastereomers had been isolated, and its configuration had been assigned based on the assumption that the isolated diastereomer should be more stable than the other diastereomer. To judge which of the diastereomers was more stable, their relative steric energies were calculated by empirical MM (molecular mechanics) methods. Thus, there were two problems of ambiguity in these studies. The first is that the major product isolated is not necessarily the most stable compound if the reaction is kinetically controlled. The second is that the MM method used for the calculation of steric energy is empirical, and therefore the results might not always be correct.

To overcome the drawbacks of previous studies for the assignment of absolute configuration, we employed a different strategy: If a loose and more flexible chiral tether with known absolute configuration was used, two possible diastereomers would be obtained, and therefore it should be relatively straightforward to determine their absolute stereostructures by comparing ^{1}H NMR spectroscopic data for two diastereomers. Thus, the double Bingel reaction of C_{60} with (2*S*,3*S*)-(−)-2,3-dimethoxybutane-1,4-diyl bis(ethyl malonate) yielded the chiral bisadducts [CD(+)281]-**5a** and [CD(−)281]-**5b** as expected; their CD spectra were almost mirror images of one another, thus reflecting the opposite chirality of the π-electron systems in the two C_{60} skeletons (Scheme 1).[8] The analyses of ^{1}H NMR spectroscopic chemical-shift and coupling-constant data led to the absolute-configuration assignments (*S*,*S*,^{f,s}*A*)-[CD(+)281]-**5a** (≡(*S*,*S*,^{f}*C*)-[CD(+)281]-**5a**) and (*S*,*S*,^{f,s}*C*)-[CD(−)281]-**5b** (≡(*S*,*S*,^{f}*A*)-[CD(−)281]-**5b**), respectively; the results were consistent with those reported by Diederich, and co-workers[3,5] as well as by Harada, Diederich, and co-workers.[4] Although these assignments by ^{1}H NMR spectroscopic analysis were more reliable than the previous assignments, we wanted to confirm our results by X-ray crystallography, the most unambiguous and conclusive method for the determination of absolute configuration. Recently, we succeeded in obtaining single crystals of a chiral C_{60}-fullerene bisadduct of the *cis*-3 type, and we report herein the first X-ray crystallographic determination of its absolute configuration.

It was known that chiral fullerene derivatives hardly ever crystallized as single crystals suitable for X-ray diffraction experiments. To our knowledge, no one had succeeded in determining the absolute configuration of chiral C_{60}-fullerene bisadducts of the *cis*-3 type by X-ray crystallography, and this situation prompted us to take up the challenge of crystallizing derivatives. To obtain single crystals, we prepared the chiral C_{60}-fullerene bisadducts **6**–**12** of the *cis*-3 type from (2*R*,3*R*)-(−)-2,3-butanediol, the absolute configuration of which would be useful as an internal reference for determining the absolute stereostructures of the adducts (Scheme 2). The ethyl ester [CD(+)280]-**6** had been prepared previously by Diederich and co-workers (see Supporting Information).[5,9] Besides the bisadducts **7** and **12** with aliphatic side chains, derivatives **8**–**11** with aromatic side chains were synthesized in

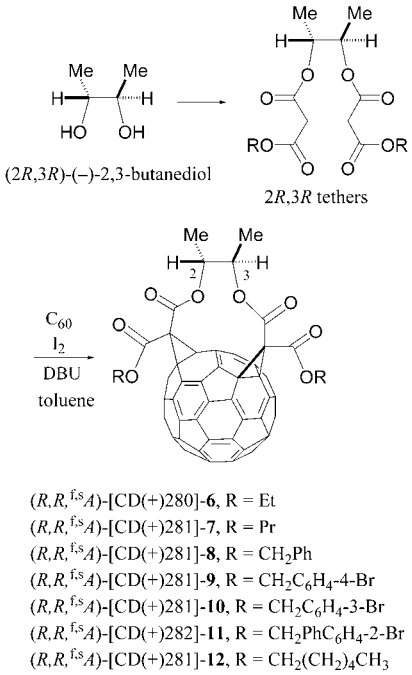

(*R*,*R*,^{f,s}*A*)-[CD(+)280]-**6**, R = Et
(*R*,*R*,^{f,s}*A*)-[CD(+)281]-**7**, R = Pr
(*R*,*R*,^{f,s}*A*)-[CD(+)281]-**8**, R = CH_2Ph
(*R*,*R*,^{f,s}*A*)-[CD(+)281]-**9**, R = $CH_2C_6H_4$-4-Br
(*R*,*R*,^{f,s}*A*)-[CD(+)281]-**10**, R = $CH_2C_6H_4$-3-Br
(*R*,*R*,^{f,s}*A*)-[CD(+)282]-**11**, R = $CH_2PhC_6H_4$-2-Br
(*R*,*R*,^{f,s}*A*)-[CD(+)281]-**12**, R = $CH_2(CH_2)_4CH_3$

Scheme 2. Synthesis of chiral fullerene *cis*-3 bisadducts by the Bingel reaction.

the expectation that π–π stacking between neighboring molecules would promote the molecular packing in the crystal lattice.

We attempted the crystallization of these compounds **6**–**12** many times from various solvents and solvent mixtures. However, in all cases but one, amorphous solids were obtained. When the ethyl ester [CD(+)280]-**6** was recrystallized from chloroform/hexane (1:1), extremely thin, red plate crystals were obtained (see Supporting Information). The crystals formed had a thickness of just 1–2 μm, which is too thin for conventional X-ray diffractometers. Therefore, the extremely strong synchrotron X-ray radiation at the SPring-8 in Hyogo (Japan) was required for the X-ray diffraction experiment: X-ray 22.00 keV, $\lambda = 0.5633$ Å, data collected at 100 K, red thin plate, $0.100 \times 0.075 \times 0.002$ mm, monoclinic, space group $P2_1$ (#4), $Z = 2$, $a = 9.9890(11)$, $b = 9.984(2)$, $c = 21.047(5)$ Å, $\beta = 102.193(12)°$, $V = 2051.7(7)$ Å^3, 4375 unique reflections.[11] The structure was solved by direct methods and refined by full-matrix least-squares analysis, whereby all non-hydrogen atoms were refined isotropically, whereas all hydrogen atoms were placed at their idealized positions: $R = 0.180$ for 3110 reflections with $I > 2\sigma(I)$ and 329 parameters (Figure 1). Although the final R value remained large, the absolute configuration of the bisadduct [CD(+)280]-**6** was clearly determined as $^{f,s}A$ (≡^{f}C) by using the 2*R*,3*R* absolute configuration of the tether moiety as an internal reference.

The molecular packing in the unit lattice is shown in Figure 1. The tether moieties of two molecules are in contact with one another, thus leading to the non-C_2-symmetrical conformation of the two ethyl ester groups on each fullerene. In contrast, the compound has a C_2-symmetric structure in the solution state, as proved by ^{1}H and ^{13}C NMR spectroscopy (see Supporting Information). The X-ray crystallographic

 © 2005 Wiley-VCH Verlag GmbH & Co. KGaA, Weinheim

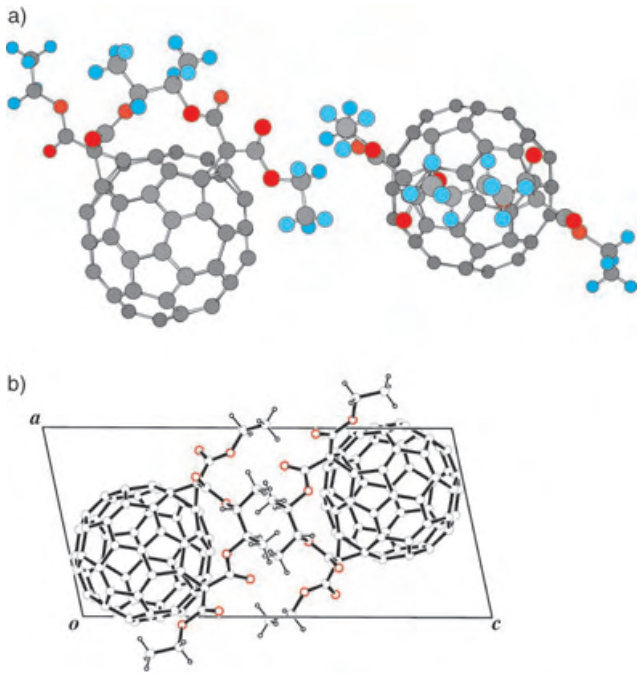

Figure 1. a) Absolute stereostructure of the C_{60}-fullerene bisadduct ($R,R,^{f,s}A$)-[CD(+)280]-**6**, as determined by X-ray crystallography. b) Projection of the X-ray crystal structure of ($R,R,^{f,s}A$)-[CD(+)280]-**6** along the *b* axis.

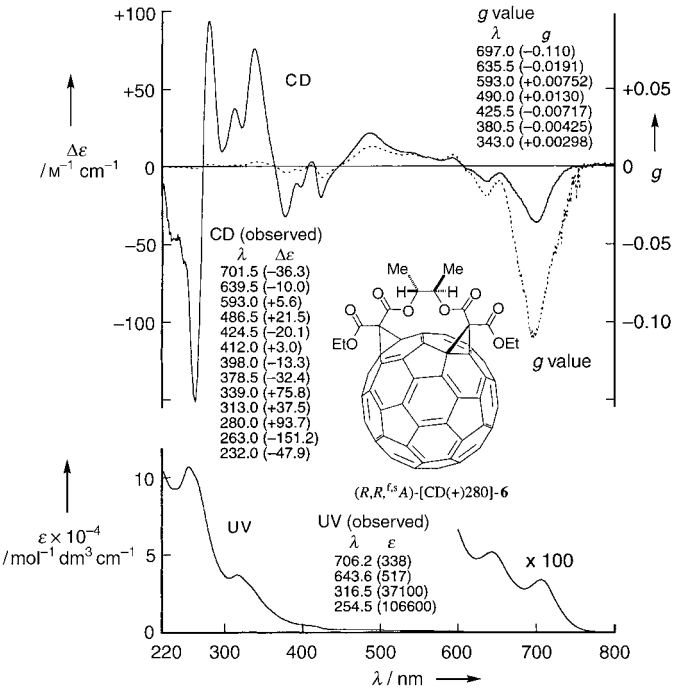

Figure 2. CD and UV spectra and *g*-value curve of the bisadduct ($R,R,^{f,s}A$)-[CD(+)280]-**6** in $ClCH_2CH_2Cl$: CD and UV, solid lines; *g* value ($g = \Delta\varepsilon/\varepsilon$), dotted line.

analysis revealed that the *c* axis is perpendicular to the main plane of the extremely thin plate crystal. These data explain the reason why compound **6** crystallizes as extremely thin plate crystals: When the compound packs along the *c* axis, two bare spherical regions of the C_{60} skeleton have to come into contact with one another, and no effective interaction suitable for fixing two molecules is expected. Therefore, the crystal hardly grows along the *c* axis at all. On the other hand, when the crystal grows along the *a* and *b* axes, parts of the tether come into contact with one another to favor the molecular packing. This is the mechanism of formation of extremely thin plate crystals.

The bisadduct ($R,R,^{f,s}A$)-**6** ($\equiv$($R,R,^{f}C$)-**6**) exhibits the CD and UV spectra shown in Figure 2. The CD spectrum shows an intense positive Cotton effect ($\Delta\varepsilon = +93.7$) at 280 nm. Therefore, the absolute configuration of the bisadduct was designated as ($R,R,^{f,s}A$)-[CD(+)280]-**6** ($\equiv$($R,R,^{f}C$)-[CD(+)280]-**6**). As the CD spectra of chiral C_{60}-fullerene *cis*-3 bisadducts, including derivatives **1**–**6**, are similar to one another in shape (Table 1), the results obtained in this study clearly indicate that the compounds that exhibit a positive Cotton effect at around 280 nm should have the $^{f,s}A$ ($\equiv {}^{f}C$) absolute configuration, whereas the opposite enantiomers with a negative Cotton effect at around 280 nm should have the $^{f,s}C$ ($\equiv {}^{f}A$) absolute configuration. Therefore, our previous assignments of ($S,S,^{f,s}A$)-[CD(+)281]-**5a** and ($S,S,^{f,s}C$)-[CD(−)281]-**5b** by ^{1}H NMR spectroscopic analysis were corroborated by this study (Table 1). The assignment of ($S,S,^{f,s}A$)-[CD(+)281]-**2** by Diederich and co-workers was also confirmed. On the other hand, the results of this study suggest that the absolute configuration of the bisadduct [CD(−)288]-**1** should be revised as $R,R,^{f,s}C$ (Table 1). Similarly, we propose the absolute configuration $S,S,^{f,s}A$ for [CD(+)284]-**3** (Table 1).

Table 1: CD spectral data and correct absolute configurations of chiral C_{60}-fullerene bisadducts of the *cis*-3 type.

	This study	Ref. [8]	Ref. [2]	Ref. [3]	Ref. [6]	Ref. [7]
compound	**6**	**5a**	**1**	**2**	**3**	**4**
absolute configuration	$R,R,^{f,s}A$	$S,S,^{f,s}A$	$R,R,^{f,s}C$[a]	$S,S,^{f,s}A$	$S,S,^{f,s}A$[a]	$^{f,s}C$
CD $\Delta\varepsilon$	−36.3	−38.9	+4.69[b]	−37.0	−36.3	+26.7
λ_{ext} [nm]	701.5	696.5	720.0	706.0	737.0	726.0
CD $\Delta\varepsilon$	+93.7	+99.3	−75.0[b]	+89.0	+60.6	−73.2
λ_{ext} [nm]	280.0	280.5	288.0	281.0	284.0	287.0

[a] Revised absolute configuration as suggested by this study. [b] Values are 1/1000 of the $\Delta\varepsilon$ values reported in reference [2], which are too large.

We observed unique phenomena in the CD and UV spectra of C_{60}-fullerene bisadducts of the *cis*-3 type. For example, ($R,R,^{f,s}A$)-[CD(+)280]-**6** exhibits a very weak UV band at 706.2 nm ($\varepsilon = 338$), as shown in Figure 2; this band is due to the forbidden π–π* transition as a result of the small ε value. In the corresponding region, the CD spectrum shows an intense negative Cotton effect at 701.5 nm ($\Delta\varepsilon = -36.3$). The curve of the dissymmetry ratio, *g* ($g = \Delta\varepsilon/\varepsilon$), was calculated as illustrated in Figure 2: the maximum value found is $g = -0.110$ at 697.0 nm. This *g* value is much larger than that of the n–π* forbidden transition of chiral ketones and that of the π–π* allowed transition of other compounds with strong CD absorption: n–π*, (*R*)-(+)-3-methylcyclohex-

 © 2005 Wiley-VCH Verlag GmbH & Co. KGaA, Weinheim

anone, $g = +0.03$ at 298 nm;[12] π–π*, (+)-hexahelicene, $g = +0.007$ at 325 nm; π–π*, exciton-coupling CD of (2*S*,3*S*)-butanediyl bis(4-bromobenzoate), $g = +0.00035$ at 252 nm. A similar large *g* value was also observed for the bisadduct (*S*,*S*,^{f,s}*A*)-[CD(+)281]-**5a**: $g = -0.126$ at 696 nm. To our knowledge, these *g* values for chiral C_{60}-fullerene *cis*-3 bisadducts are the largest found for chiral organic compounds. Why does this transition in chiral fullerenes give rise to such a large *g* value? The phenomenon can be interpreted as follows: This π–π* transition is electronically forbidden as described above, but is magnetically allowed, because the molecular orbitals occupied by the π electrons are spherical, as they reflect the shape of the fullerene. Therefore, the transition contains a lot of angular momentum, thus yielding a large magnetic moment and generating an intense CD Cotton effect, with the result that this transition has a very large *g* value.

In conclusion, we have determined the absolute configuration of a chiral C_{60}-fullerene bisadduct of the *cis*-3 type by X-ray crystallography. We could establish the general rule that chiral C_{60}-fullerene bisadducts with a *cis*-3 relationship that show a positive Cotton effect in their CD spectrum at around 280 nm have the ^{f,s}*A* configuration, whereas those that show a negative Cotton effect have the ^{f,s}*C* configuration.

Received: December 4, 2004
Published online: March 2, 2005

Keywords: chirality · circular dichroism · dissymmetry ratio · fullerenes · X-ray diffraction

[1] For the nomenclature of regioisomeric fullerene derivatives, see: a) A. Hirsch, I. Lamparth, H. R. Karfunkel, *Angew. Chem.* **1994**, *106*, 453 – 455; *Angew. Chem. Int. Ed. Engl.* **1994**, *33*, 437 – 438; b) for the nomenclature of chiral fullerene derivatives, see: C. Thilgen, A. Herrmann, F. Diederich, *Helv. Chim. Acta* **1997**, *80*, 183 – 199; c) for a new and systematic nomenclature for fullerenes (IUPAC Recommendations 2002), see: W. H. Powell, F. Cozzi, G. P. Moss, C. Thilgen, R. J.-R. Hwu, A. Yerin, *Pure Appl. Chem.* **2002**, *74*, 629 – 695.

[2] E. Nakamura, H. Isobe, H. Tokuyama, M. Sawamura, *Chem. Commun.* **1996**, 1747 – 1748.

[3] J.-F. Nierengarten, T. Habicher, R. Kessinger, F. Cardullo, F. Diederich, V. Gramlich, J.-P. Gisselbrecht, C. Boudon, M. Gross, *Helv. Chim. Acta* **1997**, *80*, 2238 – 2276.

[4] H. Goto, N. Harada, J. Crassous, F. Diederich, *J. Chem. Soc. Perkin Trans. 2* **1998**, 1719 – 1723.

[5] R. Kessinger, C. Thilgen, T. Mordasini, F. Diederich, *Helv. Chim. Acta* **2000**, *83*, 3069 – 3096.

[6] a) M. Taki, S. Sugita, Y. Nakamura, E. Kawashima, E. Yashima, Y. Okamoto, J. Nishimura, *J. Am. Chem. Soc.* **1997**, *119*, 926 – 932; b) N. Taki, Y. Nakamura, H. Uehara, M. Sato, J. Nishimura, *Enantiomer* **1998**, *3*, 231 – 239; c) revised assignment: Y. Nakamura, K. O-kawa, J. Nishimura, *Bull. Chem. Soc. Jpn.* **2003**, *76*, 865 – 882.

[7] T. Ishi-i, K. Nakashima, S. Shinkai, A. Ikeda, *J. Org. Chem.* **1999**, *64*, 984 – 990.

[8] K. Yoshida, S. Osawa, K. Monde, M. Watanabe, N. Harada, *Enantiomer* **2002**, *7*, 23 – 32.

[9] (*R*,*R*,^{f,s}*A*)-[CD(+)280]-**6**: red thin plates recrystallized from hexane/$CHCl_3$ (1:1); m.p. > 360 °C; $[\alpha]_D^{28} + 3950$ ($c = 0.0214$, $CHCl_3$). The physical data obtained (see Supporting Information) almost agree with those reported by Diederich and coworkers.[5] However, in the case of the ^{1}H NMR coupling constant between the two equivalent hydrogen atoms at the 2- and 3-positions, our value of $J_{2,3} = 9.1$ Hz, which was obtained by the ^{13}C satellite band method,[8,10] is consistent with the antiperiplanar conformation of 2-H and 3-H observed in the crystalline state (Scheme 2).

[10] N. Harada, H.-Y. Li, N. Koumura, T. Abe, M. Watanabe, M. Hagiwara, *Enantiomer* **1997**, *2*, 349 – 352.

[11] CCDC 258268 contains the supplementary crystallographic data for this paper. These data can be obtained free of charge from the Cambridge Crystallographic Data Centre via www.ccdc.cam.ac.uk/data_request/cif.

[12] S. F. Mason, *Molecular Optical Activity and the Chiral Discriminations*, Cambridge University Press, Cambridge (UK), **1982**.

 © 2005 Wiley-VCH Verlag GmbH & Co. KGaA, Weinheim

Colorimetric Sensors

A Color Sensor for Catecholamines**

*Michael Maue and Thomas Schrader**

Dedicated to Professor Christian Reichardt on the occasion of his 70th birthday

Catecholamines are characterized by their phenylethylamine skeleton, which carry two phenolic *ortho*-hydroxy groups. The level of these and related compounds in blood and urine reflects the biodegradation efficiency of aromatic amino acids, especially tyrosine, and plays an important role in diagnostic purposes. Patients suffering from phaeochromocytoma display a critically elevated concentration of the catecholamine adrenaline in their blood which inevitably leads to heart failure and death.[1] Malfunction of the catecholamine dopamine-responsive neurons is a key feature for Parkinson's disease.[2] Usually, noradrenaline and adrenaline are determined in blood and urine samples through HPLC analyses with electrochemical or neurochemical detection.[3] In recent years, a large number of catecholamine-receptor structures have been designed for organic solvents, some as ditopic host molecules with recognition sites

[*] M. Maue, Prof. T. Schrader
Fachbereich Chemie
Universität Marburg
Hans-Meerwein-Strasse
35032 Marburg (Germany)
Fax: (+49) 6421-28-25544
E-mail: schradet@staff.uni-marburg.de

[**] The authors are indebted to Dr. Uwe Linne for ESI-HRMS measurements. We gratefully acknowledge Martin Münzel for his preparative work. M.M. thanks the Fonds der Chemischen Industrie for a Ph.D. grant. The coupling reagent T3P[a] (1-propylphosphonic acid cyclic anhydride) was generously provided by Clariant GmbH, Frankfurt-Hoechst.

Supporting information for this article is available on the WWW under http://www.angewandte.org or from the author.

 DOI: 10.1002/anie.200462702 © 2005 Wiley-VCH Verlag GmbH & Co. KGaA, Weinheim

for both parts of the guest.[4] However, only very few of these receptors operate in pure aqueous solution.[5] To this end, receptors have been embedded in membranes[6] or sol-gel films.[7] RNA aptamers[8] represent a bioorganic solution to the problem of dopamine recognition. A less selective alternative is the fabrication of immobilized monotopic receptor structures with simple functional groups on electrodes, for example, in a polymer matrix,[9] on silica particles or other solids,[10] or on biofilms containing polyphenolases.[11] Recently a certain shape-selectivity has been achieved for the slim dopamine skeleton with designed cyclophanes.[12] However, almost none of the preceding examples are selective for catecholamines in complex mixtures that contain other amines, amino acids, and neurotransmitters. Herein we present a receptor that combines our bisphosphonate recognition motif, which is selective for amino alcohols,[13] with a boronic acid, which is highly selective for catechols. In a simple competition experiment with a catechol-containing dye, a color signal is induced that indicates the presence of catecholamines and allows an exact quantitative determination of the concentration of catecholamines in complex mixtures, for example, in urine samples.

The groups of Shinkai and Czarnik have used multiple boronic acid moieties extensively for the covalent recognition of *cis*-glycol units in sugars.[14,15] Numerous examples of derivatives with a secondary or tertiary benzylic amine functionality *ortho* to a phenylboronic acid have been reported,[16] and even in aqueous solution, the thermodynamically stable tetrahedral zwitterionic intermediate is formed almost quantitatively.[17] However, much less is known about the related formation of boronic acid esters with catechols, although the flat 1,2-arrangement of both acidic hydroxy groups should facilitate this condensation even more. Early investigations by Smith and co-workers described transport agents based on arylboronic acids for catecholamines.[18] Other groups combined the boronic acid moiety with binding motifs for other functionalities to synthesize ditopic receptor molecules with a high selectivity for the corresponding guests.[19] For example, Cooper and James covalently attached a phenylboronic acid to a crown ether through an anthracene spacer and obtained a fluorescent sensor for D-glucosamine hydrochloride.[19a,c]

In our rational design, we bridged a xylylene bisphosphonate unit for aminoalcohol recognition and a toluneboronic acid moiety for binding to catecholamine with a non-proteinogenic amino acid of appropriate length in the aim of using the amine group as an internal base. To this end, the *N*-acyl-protected amino acid was coupled to the readily available *m*-aminoxylylene bisphosphonate,[20] and the coupled product was then deprotected and monodealkylated at its phosphonate ester groups. In the final step, the dilithium salt was subjected to a reductive amination sequence with *o*-formylphenylboronic acid.[21] The resulting benzylamine, the desired receptor molecule, was obtained as a water-soluble, colorless solid (Scheme 1). Three different spacer groups were chosen: *m*-aminomethylbenzoic acid acts as a semirigid building block in **1**, whereas GABA (γ-aminobutyric acid) as the secondary and tertiary amine in **2** and **3,** respectively, provides a flexible alkyl chain.

Upon equilibration of the ditopic receptors with noradrenaline, a second set of signals were observed in the ^{1}H NMR spectrum which correspond to the catechol-boronate zwitterion (Figure 1). In our case, formation of the catechol-borane is slow on the NMR timescale. Distinct signals appeared for both the host (amino alcohol) and guest (catechol) parts. This effect was examined in buffered aqueous solution (NaH_2PO_4 (100 mM), pH 7.0). Recently a weak phosphate–boronic acid interaction was described which could also interfere in our system.[22] To verify this, a "model" NMR titration between a boronic acid derivative and catechol was carried out in the presence and absence of phosphate buffer. The corresponding binding constant was not affected by the presence of phosphate anions, so we conclude that the influence of coordination of the boronic

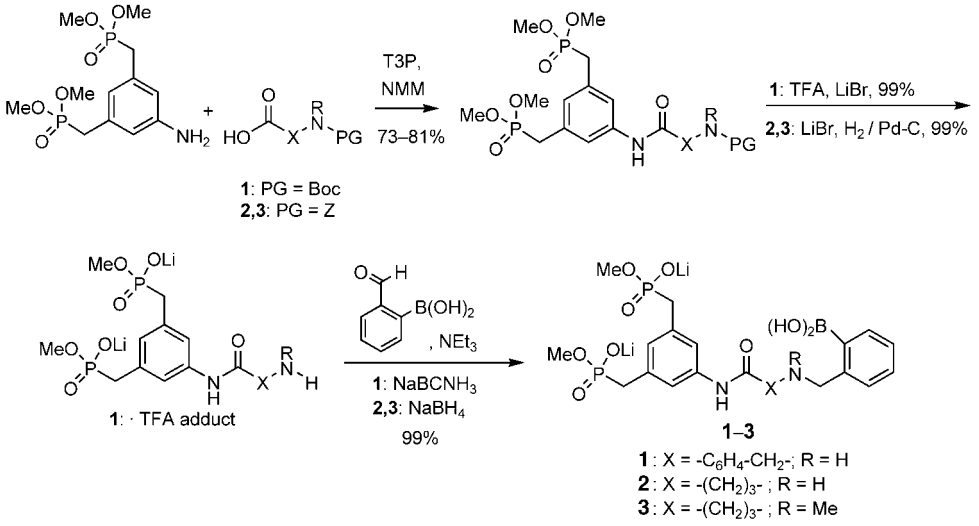

Scheme 1. Synthetic route with reductive amination as the key step to the ditopic adrenaline receptors **1**–**3**, which carry a boronate and a bisphosphonate group bridged by non-proteinogenic amino acids. PG = protecting group, Boc = *tert*-butyloxycarbonyl, Z = benzyloxycarbonyl, T3P = 1-propylphosphonic acid cyclic anhydride, NMM = *N*-methylmorpholine, TFA = trifluoroacetic acid.

 © 2005 Wiley-VCH Verlag GmbH & Co. KGaA, Weinheim

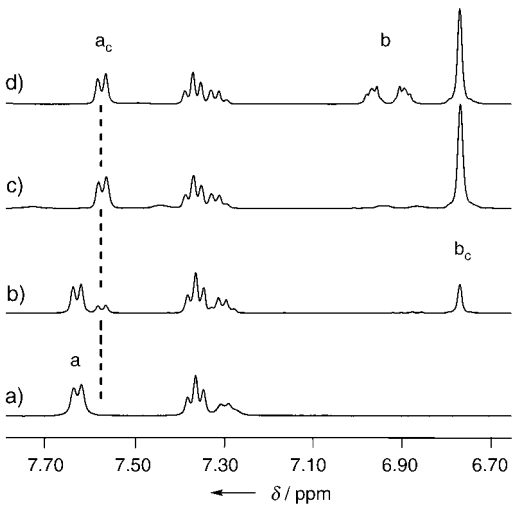

Figure 1. Model binding ^{1}H NMR experiment for the quantitative determination of the K_a value between phenylboronic acid (host), precomplexed with piperidine, and catechol. a) Free host, b)–d) host in the presence of 0.6 (b), 1.0 (c), and 1.6 equivalents (d) of catechol. A new set of signals appear for the protons of the host ($\delta > 7$ ppm) and the guest ($\delta < 7$ ppm). Binding constants (K_a) can be calculated from the ratio of free:complexed host (b) or free:complexed guest (d).

Table 1: Association constants between amines and/or diols and ditopic receptors **1**–**3**.[a]

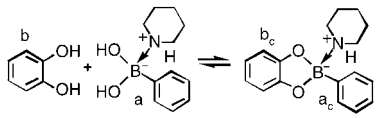

Guest	**1** K_a [M^{-1}][b]	**2** K_a [M^{-1}][b]	**3** K_a [M^{-1}][b]
catechol	50	150	350
adrenaline	190	200	550
DOPA[c]	–	–	590
dopamine	180	230	630
noradrenaline	190	340	690
tyrosine ester	<10	<10	<10
phenylalanine ester	<10	<10	<10

[a] Determined from ^{1}H NMR titrations in buffered aqueous solution (Na_2HPO_4/NaH_2PO_4 (100 mM)) at 20 °C. [b] Error values were calculated as standard deviations from three independent measurements; all values were between 4% and 12%. [c] DOPA = 3,4-dihydroxyphenylalanine.

acid to phosphate ions is negligible. Analysis of the ratio between free host, guest, and complex revealed binding constants (K_a) in the order of 200–700 M^{-1} for adrenaline derivatives, but significantly smaller values for catechol itself ($K_a \approx 50$–300 M^{-1}).[23] Together with distinct changes in the chemical shifts in the bisphosphonate and amino alcohol region, these findings indicate a simultaneous cooperative participation of the ammonium-boronate and the bisphosphonate in the binding of catecholamine. Relative to conventional NMR titrations, this is a very economic and convenient procedure for the accurate determination of K_a values: by variation of the host:guest stoichiometry, each mixture gives an association constant with very small deviations (see Table 1).

Probably owing to its C-4 linker, the rigid benzoic acid spacer in **1** produced only a relatively weak adrenaline receptor and gave a K_a value of 190 M^{-1} upon association with noradrenaline. A little more effective was the flexible C-3 alkyl chain of the GABA spacer in **2** with a K_a value of 340 M^{-1}, which was further improved by introduction of a second *N*-alkyl group to produce a superior electron-pair donor in the form of the tertiary amine bridge in **3**. The resulting association constant of **3** with noradrenaline almost reached 700 M^{-1}, while with its *N*-isopropyl derivative isoproterenol, K_a reached almost 800 M^{-1}.[24] Although the affinities towards adrenaline derivatives in buffered aqueous solution are still moderate, the new receptor family is extremely selective for catecholamines. Simple biogenic amines such as phenylethylamine are not bound at all, and aliphatic diols such as glucose are likewise rejected. Even more impressive is the phenylalanine, tyrosine, and DOPA series, which shows exclusive interaction between the ditopic receptors and the dihydroxy amino acid. Other neurotransmitters are also neglected, such as glycine, glutamate, GABA, and acetylcholine.

The high selectivity of our new receptor molecules for catecholamines prompted us to develop a color assay for their detection in complex mixtures. Recently a simple dopamine sensor which comprised a boronic acid tethered to a fluorescent reporter group was reported.[5] Secor and Glass very recently reported a related system that featured a coumarin aldehyde for chromophoric response.[25] Our approach relies on precomplexation of alizarin complexone ((3,4-dihydroxy-2-anthraquinonylmethyl)iminodiacetic acid) by the receptor and its subsequent displacement by the guest of choice. This concept has been introduced in several elegant contributions by Anslyn and co-workers who used competition experiments for citrate and tartrate ion sensing.[26] The dye compound carries a relatively acidic catechol moiety incorporated into its anthraquinone chromophore, and—in its zwitterionic form—also an ammonium ion.[27] In a similar approach, the groups of Wang and James established a fluorometric and colorimetric system using the alizarine red S–boronic acid interaction.[28] ^{1}H NMR titrations of a mixture of alizarin complexone and increasing amounts of **2** reveal a rather high binding constant of $K_a \approx 1700$ M^{-1}. Formation of the complex was also accompanied by a strong bathochromic shift in the absorption maximum of the dye. Figure 2 illustrates the resulting UV/Vis absorption curves obtained, as well as a clear isosbestic point and the concomitant color change from deep red (bordeaux) to orange.[29] As soon as a competing catecholamine is added, the dye is successively replaced and released into the free solution, and the color change is reverted. A large excess of the guest finally restores the original spectrum of the dye.

From the quantitative evaluation of the decrease in intensity at the new absorption maximum at 460 nm, binding constants were calculated for the guest molecules discussed above and lie in exactly the same relative order as those determined by NMR titrations, but remain somewhat lower (Figure 3a, Table 2).[30] Upon changing the solvent from pure

 © 2005 Wiley-VCH Verlag GmbH & Co. KGaA, Weinheim

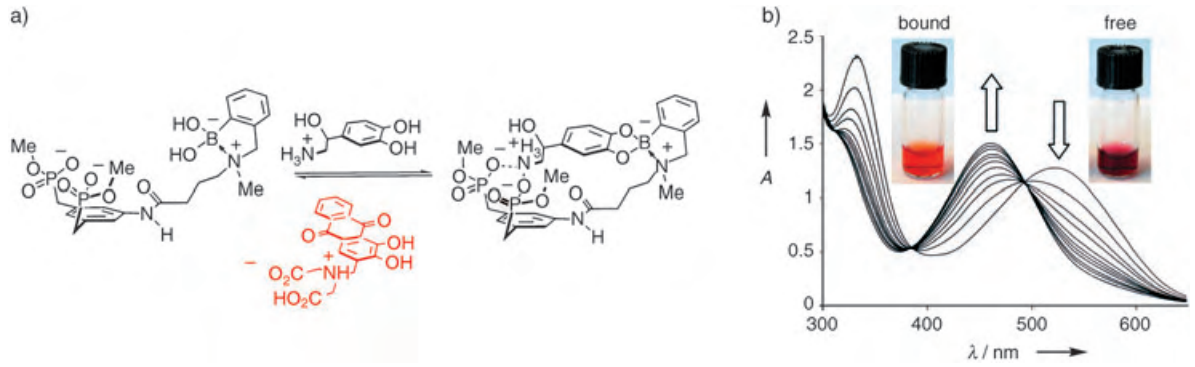

Figure 2. Competitive color assay that relies on the displacement of precomplexed alizarin complexone with concomitant color change. a) Lewis acidic/basic structures of the host **3**. b) Corresponding UV/Vis absorption curves of alizarin complexone with **2**, with deep red (bordeaux) and orange colors indicating the free and complexed states, respectively, of the alizarin dye. The isosbestic points indicate the direct interconversion of both states.

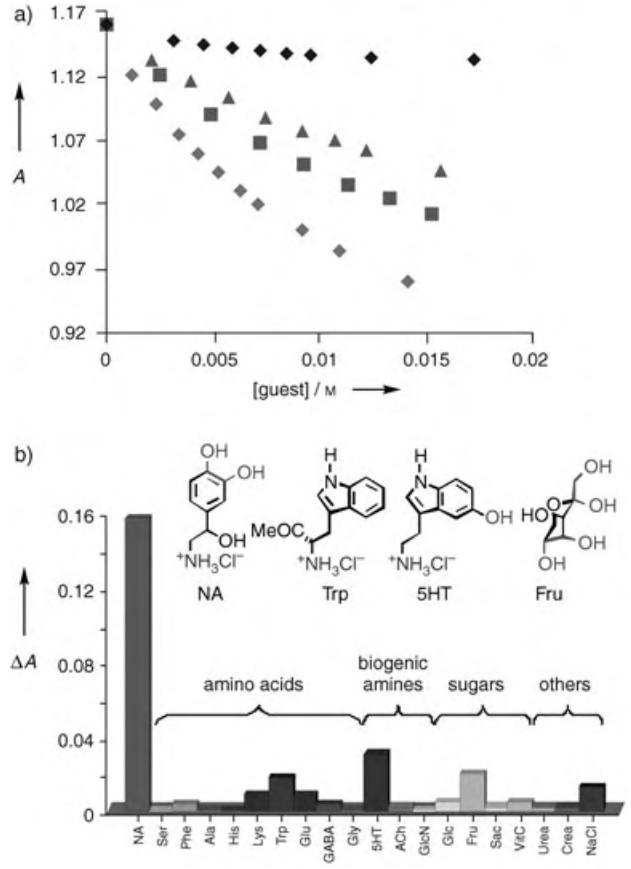

Figure 3. a) Binding curves obtained from the UV/Vis titrations of receptor **3** (1 mM) with various analytes by indirect visualization of their affinities through the respective decrease in the absorbance at $\lambda = 460$ nm (A_{460}) of the receptor-precomplexed alizarin dye (1 mM). Methoxytyrosine hydrochloride (black rhombus); fructose (gray triangle); catechol (gray square); noradrenaline (light-gray rhombus). b) Selectivity of the new ditopic receptor **3** for catecholamines as illustrated by changes in absorption ΔA_{460} at the absorption maximum of the dye–**3** complex (1 mM each) after the addition of 5 equivalents of guest in the color assay. NA = noradrenaline, Ser = serine, Phe = phenylalanine, Ala = alanine, His = histidine, Lys = lysine, Trp = tryptophan, Glu = glutamate, GABA = γ-aminobutyric acid, Gly = glycine, 5HT = serotonin, ACh = acetylcholine, GlcN = glucosamine, Glc = glucose, Fru = fructose, Sac = saccharose, VitC = vitamin C, Crea = creatinine.

Table 2: Association constants between amines and/or diols and ditopic receptors **1**–**3**.[a]

Guest	**1** K_a [M^{-1}][b]	**2** K_a [M^{-1}][b]	**3** K_a [M^{-1}][b]
catechol	60	150	100
adrenaline	160	210	310
DOPA	–	–	270
dopamine	170	220	280
noradrenaline	180	250	350
alizarin complexone	2050	1620	3440

[a] Determined by UV/Vis spectroscopy from competition experiments in buffered aqueous solution (NaH_2PO_4 (100 mM)) at 20 °C. [b] Error values were calculated as standard deviations from three independent measurements; all values were between 4% and 10%.

water to a 3:1 mixture of methanol/water (HEPES (*N*-(2-hydroxyethyl)-piperazine-*N*′-2-ethanesulfonic acid) buffer (150 mM), pH 7.0), the K_a value for alizarin complexone increases from 3300 M^{-1} to 7000 M^{-1}. However, the expected rise in noradrenaline binding could not be confirmed: the determined association constant remained at 330 M^{-1} in this system. In general, catecholamines are again bound in the range of 300–400 M^{-1}, catechol somewhat less tightly with 200 M^{-1} and simple amines such as phenylethylamine are not bound at all. With the latter, no color change whatsoever could be detected which underlies the extreme selectivity of the receptor for catecholamines. Again a large number of other potential guests were examined, with the satisfying result that only catecholamines and no other amino acids, sugars,[31] neurotransmitters, or biogenic amines produced any positive responses (Figure 3b).

Consequently, we measured the decrease in absorption, brought about by noradrenaline during the competition experiment, at varying concentrations of analyte in the linear range of the Beer–Lambert law, between 10^{-4} M and 10^{-2} M, and obtained a straight calibration line. Extrapolation of the ΔA values measured from unknown samples of this neurotransmitter led to concentrations which were in excellent agreement with the amounts weighed (Figure 4). These values were exactly reproduced (less than 15% difference) in complex mixtures with up to 10 different competing amines or

 © 2005 Wiley-VCH Verlag GmbH & Co. KGaA, Weinheim

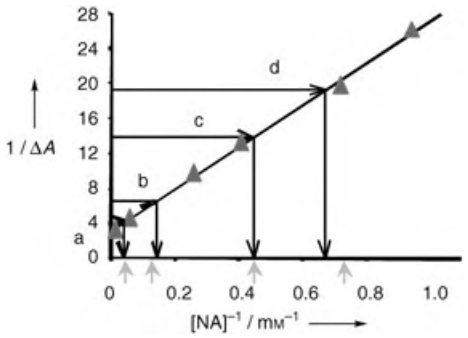

Figure 4. Benesi–Hildebrandt plot of the linear relationship between reciprocal absorption and reciprocal concentration of noradrenaline (NA).[32] a–d) Analytical samples of unknown concentration of noradrenaline which were determined by extrapolation from the observed $1/\Delta A_{460}$ value to the 1/[NA] axis. Such calibration curves were used for all subsequent adrenaline determinations.

Table 3: Quantitative detection of noradrenaline (NA) in a complex mixture of 11 different analytes in approximately equimolar concentrations, as well as detection in the millimolar regime of noradrenaline and total catecholamine (Cat) in a sample of human urine.

11-compound mixture		Urine			
$[NA]_{calcd}$ [mM]	$[NA]_{found}$ [mM]	$[NA]_{calcd}$ [mM]	$[NA]_{found}$ [mM]	$[Cat]_{calcd}$ [mM]	$[Cat]_{found}$ [mM]
1.3	1.5	2.7	3.3	6.4	7.6
2.2	2.5	7.5	7.9	9.5	11.3
7.9	6.7	8.8	9.8	13.0	14.6
23.2	22.5	14.9	17.6	–	–

diols in fivefold molar excess (Table 3). Human urine contains large amounts of urea, uric acid, creatinine, amino acids, organic acids, and various salts, as well as the yellow dye urobilin. Remarkably, even in this highly competitive environment, our color assay works and gives reliable results (less than 20% difference) with the simple calibration curve taken from the initial competition experiment with pure noradrenaline (Table 3). As all catecholamines give comparable quantitative effects, the total catecholamine concentration can be calculated from microliter quantities of such a sample, which contains dopamine, noradrenaline, adrenaline, and DOPA (Table 3), for example. Together with the simple competition measurement by UV/Vis spectroscopy, these features characterize the new method as a highly economic and fast assay for the determination of catecholamines in urine samples.[33] The selectivity of our new ditopic receptor molecules for catecholamines in highly competitive environments renders them useful in situations normally reserved for antibodies. There is only one drawback: the average level of catecholamine in human urine is much lower, in the micromolar concentration range. We are currently increasing the sensitivity of our assay, on one hand, by optimizing the receptor affinity for catecholamines and, on the other hand, by transferring the experiment to fluorescence techniques.

Experimental Section

General Procedure for Colorimetric Titrations: *Determination of the complexation constant of alizarin complexone with hosts **1–3***: A solution of alizarin complexone (1 mM) was prepared in phosphate buffer (150 mM, pH 6.9). Solutions of hosts **1–3** (≈20 mM) were prepared from this buffered solution of alizarin complexone to avoid dilution of the dye during the titration. An aliquot of the solution of alizarin complexone (400 μL) was taken in a cuvette (2-mm inner diameter) and treated stepwise with the hosts **1–3** (0–6 equiv). The reference cuvette was filled with phosphate buffer (150 mM; 400 μL). After every addition of host, the mixture was equilibrated for 30 s before the corresponding spectrum was measured. The binding constant was determined by nonlinear regression of the curve of ΔA versus [host] at a specific wavelength. In all cases, the absorption at 460 nm (λ_{max} of the alizarin complexone–host complex) was used as the maximum changes in the absorption were observed at this specific wavelength.

*Determination of the complexation constants for the guests catechol, adrenaline, dopamine, and noradrenaline with hosts **1–3** by competitive UV/Vis titration*: The solution of alizarin complexone (1 mM in phosphate buffer (150 mM)) prepared above was treated with host **1–3**, such that a 1:1 mixture was obtained. The stock solutions of guests were prepared using the solution of alizarin complexone–host complex, again to avoid dilution of the dye during the titration. An aliquot of the solution of alizarin complexone–host (1 mM each in phosphate buffer (150 mM)) complex (400 μL) was filled in a cuvette (2-mm inner diameter; reference: phosphate buffer) and treated stepwise with the guests (0–33 equiv). The ΔA_{460} values were used in the calculation of the corresponding binding constants (see Supporting Information for the detailed procedure).

Received: November 23, 2004
Published online: March 4, 2005

Keywords: host–guest systems · NMR spectroscopy · sensors · UV/Vis spectroscopy

[1] E. L. Bravo, R. C. Tarazi, *N. Engl. J. Med.* **1979**, *301*, 682–686.
[2] J. A. Gingrich, M. G. Caron, *Annu. Rev. Neurosci.* **1993**, *16*, 299–321.
[3] a) M. Ackenheil, M. Fröhler, G. Goldig, G. Rall, D. Welter, *Arzneim.-Forsch./Drug Res.* **1982**, *32*, 893; b) C. Holmes, G. Eisenhofer, D. S. Goldstein, *J. Chromatogr. Biomed. Appl.* **1994**, *653*, 131–138.
[4] a) K. Hayakawa, K. Kido, K. Kanematsu, *J. Chem. Soc. Perkin Trans. 1* **1988**, 511–519; b) T. Ishizu, J. Hirayama, S. Noguchi, *Chem. Pharm. Bull.* **1994**, *42*, 1146–1148; c) T. Schrader, *Angew. Chem.* **1996**, *108*, 2816–2818; *Angew. Chem. Int. Ed. Engl.* **1996**, *35*, 2649–2651; d) L. Campayo, J. M. Bueno, C. Ochoa, P. Navarro, J. Jimenez-Barbero, G. Pepe, A. Samat, *J. Org. Chem.* **1997**, *62*, 2684; e) J. A. Gavin, M. E. Garcia, A. J. Benesi, T. E. Mallouk, *J. Org. Chem.* **1998**, *63*, 7663–7669; f) O. Molt, D. Rübeling, T. Schrader, *J. Am. Chem. Soc.* **2003**, *125*, 12086–12087.
[5] A. Coskun, E. U. Akkaya, *Org. Lett.* **2004**, *6*, 3107–3109.
[6] a) A. R. Bernardo, J. F. Stoddart, A. Kaifer, *J. Am. Chem. Soc.* **1992**, *114*, 10624–10631; b) K. Odashima, K. Yagi, K. Tohda, Y. Umezawa, *Bioorg. Med. Chem. Lett.* **1999**, *9*, 2375; c) O. Molt, T. Schrader, *Angew. Chem.* **2003**, *115*, 5667–5671; *Angew. Chem. Int. Ed.* **2003**, *42*, 5509–5513.
[7] R. R. Makote, M. M. Collinson, *Chem. Mater.* **1998**, *10*, 2440–2445.

 © 2005 Wiley-VCH Verlag GmbH & Co. KGaA, Weinheim

[8] C. Mannironi, A. Di Nardo, P. Fruscoloni, G. P. Tocchini-Valentini, *Biochemistry* **1997**, *36*, 9726 – 9734.

[9] B. Fabre, L. Taillebois, *Chem. Commun.* **2003**, 2982 – 2983. Other electrochemical techniques employ the redox potential of the catechol, see: E. Kimura, A. Watanabe, M. Kodama, *J. Am. Chem. Soc.* **1983**, *105*, 2063 – 2066; S. M. Strawbridge, S. J. Green, J. H. R. Tucker, *Chem. Commun.* **2000**, 2393 – 2394.

[10] a) F. M. Raymo, M. A. Cejas, *Org. Lett.* **2002**, *4*, 3183 – 3185; b) V. S.-Y. Lin, C.-Y. Lai, J. Huang, S.-A. Song, S. Zu, *J. Am. Chem. Soc.* **2001**, *123*, 11510 – 11511; c) D. Radu, C.-Y. Lai, J. Wiench, M. Pruski, V. S.-Y. Lin, *J. Am. Chem. Soc.* **2004**, *126*, 1640 – 1641.

[11] Y. Chen, T. C. Tan, *Talanta* **1995**, *42*, 1181 – 1188.

[12] a) M. B. Inoue, E. F. Velazquez, M. Inoue, Q. Fernando, *J. Chem. Soc. Perkin Trans. 2* **1997**, 2113 – 2118; b) M. Herm, O. Molt, T. Schrader, *Chem. Eur. J.* **2002**, *8*, 1485 – 1499.

[13] T. Schrader, *J. Org. Chem.* **1998**, *63*, 264 – 272.

[14] a) K. Tsukagoshi, S. Shinkai, *J. Org. Chem.* **1991**, *56*, 4089 – 4091; b) K. R. A. S. Sandanayake, S. Shinkai, *J. Chem. Soc. Chem. Commun.* **1994**, 477 – 478; c) K. R. A. S. Sandanayake, S. Shinkai, *J. Chem. Soc. Chem. Commun.* **1994**, 1083 – 1084; d) A. Robertson, S. Shinkai, *Coord. Chem. Rev.* **2000**, *205*, 157 – 199; e) T. D. James, S. Shinkai, *Top. Curr. Chem.* **2002**, *218*, 159 – 200.

[15] a) J. Yoon, A. W. Czarnik, *J. Am. Chem. Soc.* **1992**, *114*, 5874 – 5875; b) J. Yoon, A. W. Czarnik, *Bioorg. Med. Chem.* **1993**, *1*, 267 – 271.

[16] a) T. D. James, K. R. A. S. Sandanayake, R. Iguchi, S. Shinkai, *J. Am. Chem. Soc.* **1995**, *117*, 8982 – 8987; b) T. D. James, K. R. A. S. Sandanayake, S. Shinkai, *Angew. Chem.* **1996**, *108*, 2038 – 2050; *Angew. Chem. Int. Ed. Engl.* **1996**, *35*, 1910 – 1922.

[17] M. Lauer, H. Böhnke, R. Grotstollen, M. Salehnia, G. Wulff, *Chem. Ber.* **1985**, *118*, 246 – 260. It has recently been proposed that this intermediate does not contain a direct B–N bond, but instead contains a protonated amine and a hydroxylated boronate ester, see: N. Wi, G. Kaur, B. Wang, S. Franzen, *Bioorg. Chem.* **2004**, *33*, 571 – 581.

[18] a) M.-F. Paugam, L. S. Valencia, B. Boggess, B. D. Smith, *J. Am. Chem. Soc.* **1994**, *116*, 11203 – 11204; b) M.-F. Paugam, J. T. Bien, B. D. Smith, L. A. J. Christoffels, F. de Jong, D. A. Reinhoudt, *J. Am. Chem. Soc.* **1996**, *118*, 9820 – 9825.

[19] a) C. R. Cooper, T. D. James, *Chem. Commun.* **1997**, 1419 – 1420; b) M. J. Deetz, B. D. Smith, *Tetrahedron Lett.* **1998**, *39*, 6841 – 6844; c) C. R. Cooper, T. D. James, *J. Chem. Soc. Perkin Trans. 1* **2000**, 963 – 969; d) W. Yang, J. Yan, H. Fang, B. Wang, *Chem. Commun.* **2003**, 792 – 793.

[20] S. Rensing, T. Schrader, *Org. Lett.* **2002**, *4*, 2161 – 2164.

[21] a) E. Anslyn, J. J. Lavigne, E. V. Anslyn, *Angew. Chem.* **1999**, *111*, 3903 – 3906; *Angew. Chem. Int. Ed.* **1999**, *38*, 3666 – 3669; b) C. W. Gray, Jr., T. A. Houston, *J. Org. Chem.* **2002**, *67*, 5426 – 5428.

[22] L. I. Bosch, T. M. Fyles, T. D. James, *Tetrahedron* **2004**, *60*, 11175 – 11190.

[23] a) H. J. Schneider, R. Kramer, S. Simova, U. Schneider, *J. Am. Chem. Soc.* **1988**, *110*, 6442; b) C. S. Wilcox in *Frontiers in Supramolecular Chemistry* (Ed.: H. J. Schneider), VCH, Weinheim, **1991**, p. 123.

[24] It has already been observed that the efficiency of the formation of a zwitterion depends on the Lewis basicity of the internal amine substituent. See Reference [17].

[25] K. E. Secor, T. E. Glass, *Org. Lett.* **2004**, *6*, 3727 – 3730.

[26] a) A. Metzger, E. V. Anslyn, *Angew. Chem.* **1998**, *110*, 682 – 684; *Angew. Chem. Int. Ed.* **1998**, *37*, 649 – 652; b) J. J. Lavigne, E. V. Anslyn, *Angew. Chem.* **1999**, *111*, 3903 – 3906; *Angew. Chem. Int. Ed.* **1999**, *38*, 3666 – 3669.

[27] Alizarine complexone has hitherto been used as a sensor for pH, as well as lanthanide and fluoride ions. See: a) M. A. Leonard, T. S. West, *J. Chem. Soc.* **1960**, 4477 – 4485; b) R. Belcher, M. A. Leonard, T. S. West, *J. Chem. Soc.* **1958**, 2390 – 2393.

[28] a) G. Springsteen, B. Wang, *Chem. Commun.* **2001**, 1608 – 1609; b) G. Springsteen, B. Wang, *Tetrahedron* **2002**, *58*, 5291 – 5300; c) S. Arimori, C. J. Ward, T. D. James, *Tetrahedron Lett.* **2002**, *43*, 303 – 305.

[29] This color change cannot be brought about by a change in pH owing to the presence of a large excess of phosphate buffer, which maintains the pH at 7.0 throughout the entire titration.

[30] For algorithms for competitive equilibria, see: K. A. Connors, *Binding Constants, The Measurement of Molecular Complex Stability*, Wiley, New York, **1987**.

[31] An exception is fructose, which is a *cis*-diol and binds to the receptor **3** with $K_a = 170\,\text{M}^{-1}$.[16a]

[32] H. A. Benesi, J. H. Hildebrandt, *J. Am. Chem. Soc.* **1949**, *71*, 2703.

[33] Earlier examples of indicators in competition with the desired analyte were mainly focused on biological systems, see: a) M. A. Roberts, R. A. Durst, *Anal. Chem.* **1995**, *67*, 482 – 491; b) C. Beyer, I. H. Alting, *Clin. Chem.* **1996**, *42*, 313 – 318.

 © 2005 Wiley-VCH Verlag GmbH & Co. KGaA, Weinheim

Nucleic Acid Structure

Guanine Quartet Networks Stabilized by Cooperative Hydrogen Bonds**

*Roberto Otero, Maya Schöck, Luis M. Molina, Erik Lægsgaard, Ivan Stensgaard, Bjørk Hammer, and Flemming Besenbacher**

Hydrogen bonding between DNA or RNA bases is one of the main interactions that determines the conformation and biochemical activity of nucleic acids.[1,2] Apart from Watson–Crick base pairing,[1] which predominates in the double-helical structure of DNA, nucleobases can form other H-bonded aggregates that lead to different DNA structures such as guanine quadruplexes[3,4] and i-motifs.[5] Despite increasing evidence for the presence and function of these structures

[*] Dr. R. Otero,[+] Dr. M. Schöck,[+] Dr. L. M. Molina, Prof. E. Lægsgaard, Prof. I. Stensgaard, Prof. B. Hammer, Prof. Dr. F. Besenbacher
Interdisciplinary Nanoscience Center (iNANO) and
Department of Physics and Astronomy, University of Aarhus
Ny Munkegade, 8000 Aarhus C (Denmark)
Fax: (+45) 8612-0740
E-mail: fbe@inano.dk

[+] These authors contributed equally to this work.

[**] We acknowledge financial support from the Danish National Research Foundation through the Center for Atomic-Scale Materials Physics (CAMP), the VELUX foundation, the EU network 'Atomic and Molecular Manipulations (AMMIST)', the Danish Ministry for Science, Technology and Innovation through the iNANO Center, and the Danish Research Councils. Computational resources were supplied by the Danish Center for Scientific Computing. R.O. and M.S. acknowledge the financial support from the EU through a Marie Curie Individual Fellowship. We thank J. Kjems and L. Kantorovitch for fruitful discussions.

 © 2005 Wiley-VCH Verlag GmbH & Co. KGaA, Weinheim DOI: 10.1002/anie.200461586

in vivo,[6] the exact physiochemical nature of the hydrogen bonds and the importance of charge-transfer contributions to the stabilization energy attributed to hydrogen bonding[7] in these structures is still under debate.[8] Semiclassical molecular dynamics (MD) simulations based on empirical potentials have generally been used to explain the observed nucleic acid structures and conformations.[9] Assessing the accuracy of these simulations requires a thorough study of charge-transfer effects on hydrogen bonds and their chemical nature. The MD calculations rely heavily on a number of assumptions, such as mutual cancellation of polarization effects between solute and solvent, whose validity can be determined only by comparison with experimental data.[9,10] Therefore, results of experiments carried out under controlled conditions may be used as benchmarks to test the predictions of MD simulations and the accuracy of the force fields in use. Herein we show, by high-resolution variable-temperature STM, that guanine deposited under ultraclean conditions onto an inert Au(111) substrate self-assembles into a H-bonded network of G quartets with the same structure as that found in quadruplex telomeric DNA.[3,4] Comparison with our DFT calculations shows that the strong preference of guanine to form quartets arises from a cooperative effect that strengthens the hydrogen bonds within the G-quartet network relative to those in isolated G dimers. These findings provide a framework to evaluate the accuracy of the different assumptions that are commonly used in MD simulations of nucleic acids.[9]

To study the H-bond interactions between nucleic acid bases in the absence of any other perturbing interactions, we deposited guanine onto inert Au(111) substrates under well-controlled ultrahigh-vacuum (UHV) conditions at room temperature. Ultraclean deposition ensures that no other chemical species affect the interactions between guanine molecules. The noble-metal close-packed Au(111) substrate was chosen to minimize surface interference with guanine; in this way, assembly was mainly determined by the intermolecular H-bond interactions of guanine, as discussed below.

Scanning probe microscopy is the technique of choice to investigate the assembly of organic and biological molecules at surfaces with atomic precision.[11] STM images recorded at 150–170 K show that guanine molecules, upon deposition onto Au(111) at room temperature, self-assemble into well-ordered islands with irregular shapes (Figure 1a). The adsorption of guanine does not reconstruct the gold surface, as the well-known herringbone reconstruction characteristic of clean Au(111) surfaces can still be observed as modulations of the corrugation of guanine islands (Figure 1b). Figure 1c shows a closer view of the self-assembled G-network structure, the lattice parameter of which is 1.5 ± 0.1 nm. Despite the hexagonal symmetry of the substrate, the G networks depict an almost square symmetry with a unit-cell composition of four molecules.

In high-resolution STM images, guanine molecules are imaged as triangular protrusions. The same signature is found if the Tersoff–Hamann[12] approach is used to calculate STM images of guanine molecules adsorbed flat against the Au surface (Figure 1d). This geometry, which has been generally found for purine molecules adsorbed onto metal surfaces,[13,14] arises from the interaction between the delocalized π-molecular orbitals and the metallic electronic density of the substrate.[15] First-principles DFT calculations of a single adsorbed guanine molecule on Au(111) demonstrate that the molecule–substrate interaction is rather weak. The calculated adsorption energy of a single guanine molecule is only 0.25 eV, with a rather large equilibrium distance of 0.375 nm between the molecule and the substrate. By placing the molecule at several different positions and orientations with respect to the surface, we found a very small corrugation of the potential energy surface in which energy differences do not exceed 0.05 eV from the minimum energy adsorption configuration (Figure 1d). In contrast, the calculated formation energy of the freestanding G-quartet network (in the absence of substrate) is 4.73 eV per unit cell which corresponds to a binding energy of 1.18 eV per guanine molecule.[16] This shows that the H-bonding interaction among guanine molecules completely determines the features of the observed G network, whereas the role of the Au(111) surface is minor; the surface serves primarily as a template to accommodate the molecules in a planar geometry.

The STM results show that each unit cell is composed of four molecules.[17] From the arrangement of the triangles the chirality of the structure can be observed.[18] (Figure 1d) Thus, the unit cell is reminiscent of the G-quartet Hoogsteen-

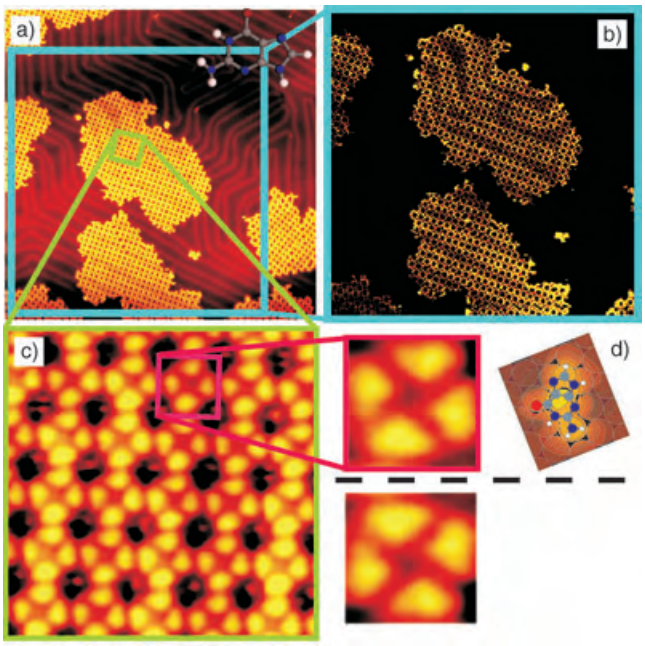

Figure 1. a) STM image (100×100 nm^2) of several self-assembled G islands on Au(111); b) higher magnification (80×80 nm^2) of the previous image, in which the color scale has been adjusted so that the herringbone reconstruction can be recognized on top of the G islands; c) STM image (8×8 nm^2) showing that the G network has an almost square geometry in which the lattice parameter is ≈ 1.5 nm, and the unit cell is composed of four guanine molecules; d) higher magnification (1.5×1.5 nm^2) of image c) showing a high-resolution image of the unit cell. guanine molecules appear as triangular protrusions, in good agreement with theoretical calculations for guanine adsorbed flat onto Au(111) terraces. The unit cell can be recognized as a chiral structure from the geometry of the guanine molecules within; a mirror image is shown below the dashed line.

 © 2005 Wiley-VCH Verlag GmbH & Co. KGaA, Weinheim

bonded structures known to hold up to four G-rich DNA strands together under suitable solution conditions.[2,3] Indeed, by superimposing the G-quartet structure determined by X-ray crystallography on G-quadruplex DNA crystals[19] and the STM images reported herein (Figure 2a), a good correspondence is observed between the former and the unit cell of our G network. Furthermore, the lateral interaction between different unit cells consisting of G quartets can be explained by the formation of eight new hydrogen bonds between the N3 and N9 atoms of adjacent guanine molecules (Figure 2b). We therefore conclude that guanine, upon deposition onto Au(111) under ultraclean conditions, spontaneously self-assembles into a H-bonded network of G quartets with structures similar to those found in telomeric DNA, even in the absence of the DNA backbone and metal ions in solution. Other examples of guanosine derivatives that can self-assemble into G-quartet structures in the absence of templating metal ions have been previously reported.[20]

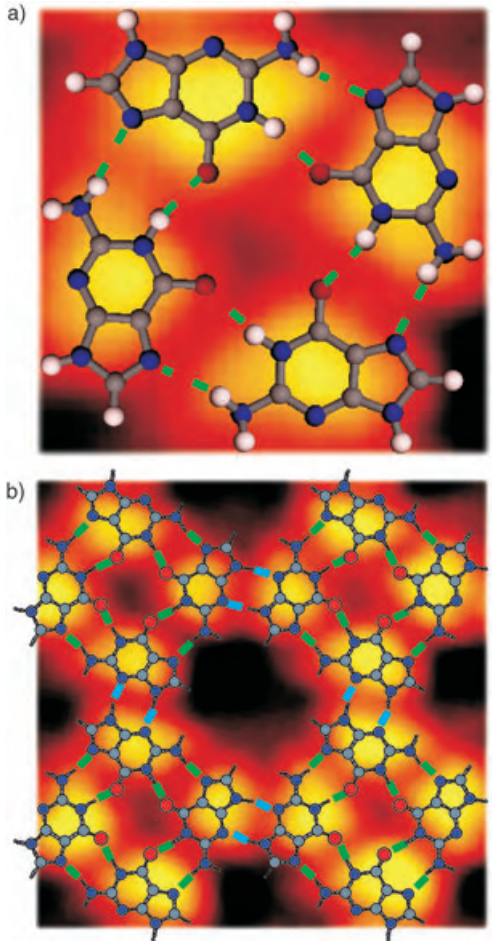

Figure 2. a) Comparison of a high-resolution STM image of the G-quartet unit cell with the Hoogsteen-bonded G-quartet structure determined by X-ray crystallography; b) comparison of an STM image of several G-quartet unit cells with the relaxed structure obtained by DFT calculations. The lateral interaction between G quartets occurs by eight new hydrogen bonds between the peripheral N3 and N9 atoms of neighboring guanine molecules. Intraquartet hydrogen bonds are shown in green; interquartet hydrogen bonds, in blue.

The G-quartet network is not the only H-bonded network that guanine adopts when deposited onto Au(111). By annealing the sample at 400 K, the G network changes irreversibly to another structure, depicted in Figure 3, and no trace of the G-quartet structure is found after annealing.

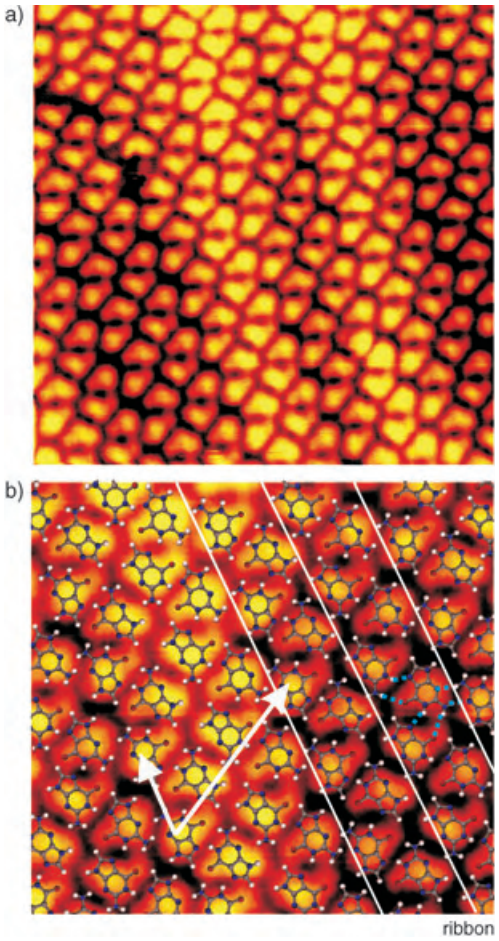

Figure 3. a) STM image (10×10 nm^2) of the high-temperature phase of guanine on Au(111); b) model for the H-bonded network that corresponds to the high-temperature phase of guanine on Au(111) with unit vectors displayed. The local environment of each guanine molecule within this network is similar to that within the G-quartet network, in that each molecule is coordinated by six hydrogen bonds to three nearest neighbors. Ribbon patterns are indicated.

The STM images (recorded at 150–170 K) of the high-temperature structure correspond perfectly to earlier results of self-assembled monolayers of guanine molecules on highly oriented pyrolytic graphite (HOPG) or MoS_2 formed from solution.[14] The high-temperature network is composed of antiparallel molecular "ribbons" (Figure 3b), which are also well-known motifs for self-assemblies of guanosine derivatives in solution.[4,21] The local environment of a guanine molecule in a ribbon network is similar to that in a G-quartet network; each molecule is doubly hydrogen bonded to three nearest neighbors. The entropy penalty for assembly formation is similar in both networks, but the molecular density is about 30% higher in the ribbon network (1.6 and 2.1 mol nm^{-2} for the G-quartet and ribbon networks, respec-

 © 2005 Wiley-VCH Verlag GmbH & Co. KGaA, Weinheim

tively), which probably explains its increased stability. Therefore, although the G-quartet network is stable at room temperature, it does not correspond to the most stable arrangement of guanine molecules on the Au(111) surface. This suggests that the preference for the G-quartet network for depositions carried out at room temperature is a phenomenon governed by kinetics rather than thermodynamics. Our findings therefore raise the question: why do guanine molecules assemble *exclusively* into the G-quartet structure when deposited at room temperature, and what is the reason behind the stability of the metastable G-quartet network?

To understand the basis of the stability of the G-quartet network, we have calculated the formation energy of isolated G quartets and their constituent dimers and trimers as shown in Figure 4a. Our calculations show that the formation energy of the dimer, trimer, and quartet structures does not scale with the number of hydrogen bonds between guanine molecules. The average energy per hydrogen bond increases from 0.22 eV in the dimer to 0.31 eV in the trimer and 0.42 eV in the quartet. Previous MD calculations gave a value of $\approx$2.21 eV for the H-bonding energy of the G quartet[22] which corresponds to $\approx$0.27 eV per hydrogen bond. This value is much closer to our result for the dimer than for the quartet. This means that this cooperative effect, as expected, is not well-described by MD simulations. On the other hand, quantum mechanical (QM) approaches (particularly Hartree–Fock and DFT) have been used to estimate the binding energy of the G quartets, and these results (2.86 eV for the quartet, 0.36 eV per hydrogen bond) are in better agreement with our values.[8,23] Figures 4c and d depict the charge-density-perturbation plots for a G dimer and a G quartet, and illustrate the basis of these cooperative hydrogen bonds. The formation of a dimer leads to a rearrangement of the electron density of the guanine molecules to allow some electron charge to be transferred to the oxygen atom that is not involved in hydrogen bonding, thus helping the formation of a new hydrogen bond at this position (arrow in Figure 4c). The intramolecular charge perturbation ascribed to hydrogen bonding is about one order of magnitude greater than that associated with the adsorption of a single guanine molecule on the Au(111) substrate, as shown in Figure 4b. As a consequence of the charge transfer associated with hydrogen bonding, the perturbation of the charge density of guanine involved in a quartet (Figure 4d) is more pronounced (the maximum contour line is 30% larger) than the perturbation in the charge density of guanine in a dimer. This explains why the hydrogen bonds within a quartet are calculated to be about twice as strong as they are in a dimer. This phenomenon, referred to as resonance-assisted hydrogen bonding (RAHB), has been suggested to contribute to the stabilization energy of Watson–Crick base pairs in DNA[24] and G quartets.[8]

Our calculated energy values in combination with an assumed attempt frequency of 10^{13}–10^{14} s^{-1} (consistent with previous studies on the diffusion of organic molecules onto noble metal surfaces,[25]) gives an estimate of $\approx 10^{14}$–10^{15} s for the average lifetime of a guanine molecule within a G quartet at room temperature before its four hydrogen bonds are broken. For comparison, the average lifetimes of a guanine molecule within a dimer or a trimer before the hydrogen bonds are broken are as short as $\approx 5\times10^{-7}$ and 5×10^{-4} s, respectively. We thus conclude that G quartets are the smallest stable structures at room temperature. Once four guanine molecules meet to form a quartet, the structure they form will not break apart before the arrival of another

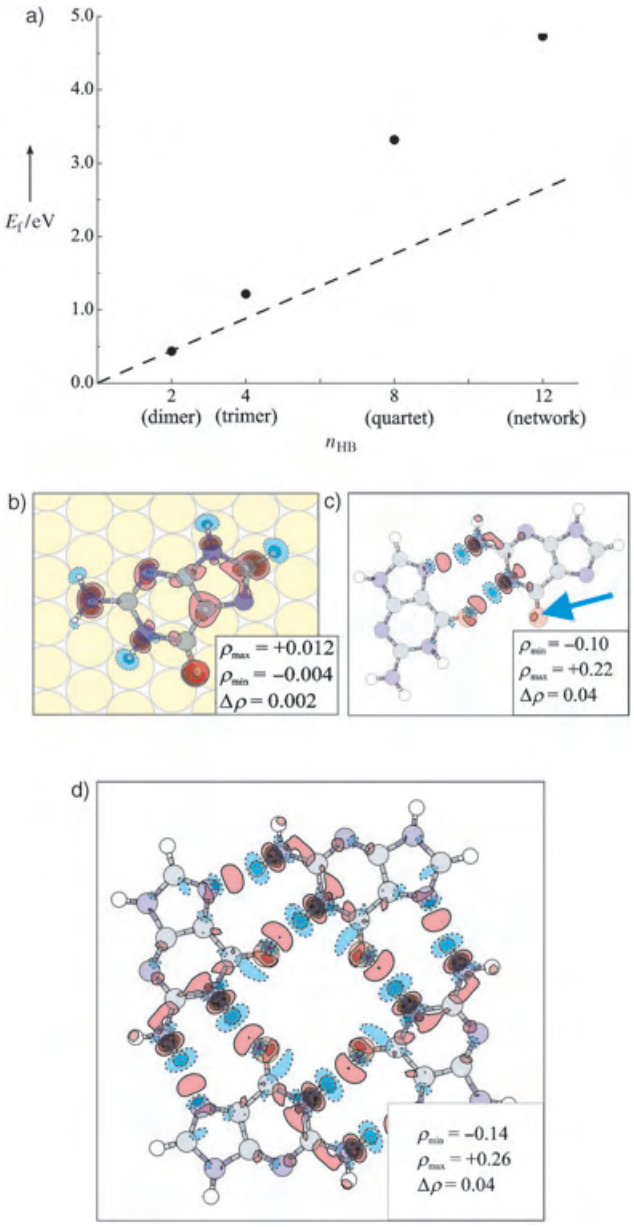

Figure 4. a) Formation energy (E_f) as a function of the number of hydrogen bonds (n_{HB}) in dimer, trimer, quartet, and network structures (as indicated). The dashed line represents the expected result if the hydrogen bonds were mutually independent and thus, if E_f scaled with n_{HB}. Charge-density perturbations determined by DFT calculations for b) adsorption of a molecule onto Au(111); c) the formation of a H-bonded dimer; and d) the formation of a H-bonded quartet. Insets show the values for the maximum and minimum contours and the interval between consecutive contours in eÅ^{-3}. Results shown in parts c) and d) are from calculations performed in the absence of the Au substrate.

 © 2005 Wiley-VCH Verlag GmbH & Co. KGaA, Weinheim

guanine molecule, thus directing the assembly of a G-quartet network, which precludes the formation of a more stable ribbon structure (Figure 3). In the absence of the RAHB effect, the energy required to break up a G quartet would be only $0.22\ \text{eV} \times 4 = 0.88\ \text{eV}$, which corresponds to an average lifetime of about 5–50 s at room temperature. With the deposition rate in our experiments (1.5×10^{-6} molecules per unit cell s^{-1}), only one to ten molecules would be deposited in an area of $100 \times 100\ \text{nm}^2$ during this time interval. In this case, the quartet structure would not be sufficiently stable at room temperature to direct the growth of the G-quartet network, and there would be nothing to prevent the molecules from assembly into the minimum-energy configuration. The fact that our STM results show formation of the G-quartet network after room-temperature deposition constitutes the first experimental evidence that charge-transfer effects, like the RAHB effect, decisively affect the strength of the hydrogen bonds among nucleobases.

According to the results of previous theoretical work, hydrogen bonding contributes between 30% (for MD simulations)[22] and 60% (for QM calculations)[23,26] of the total binding energy of G-quadruplex DNA in the gas phase, that is, in the absence of solvent. In solution, the remaining binding energy of G quadruplexes arises from complex formation with metal ions (mainly Na^+ and K^+).[27] New experiments are underway to explore the possibility of complex formation with these ions for adsorbed G-quartet networks under UHV conditions. In any case, we have demonstrated that a significant contribution of the H-bonding energy of the G quartets within G quadruplexes can be attributed to the RAHB effect, as previous DFT calculations have also shown.[28] The RAHB strengthening of the hydrogen bonds must therefore be included in any calculation of the structure of G quadruplexes.

In summary, we have demonstrated that by a careful choice of substrate it is possible to observe the geometry of molecular assembly governed by intermolecular interactions while minimizing surface-derived perturbations in such a way that structures known from biology or solution studies can be reproduced on solid surfaces. Exploitation of the RAHB-mediated increase of intermolecular H-bond energies can lead to a more efficient design of the molecular building blocks for 2D self-assembled architectures. The stabilizing effect of RAHB may therefore play an important role in the rational design of drugs, as G quartets have been proposed as targets for drug design in cancer therapeutics.[29]

Experimental Section

All experiments were performed in a UHV chamber (base pressure 10^{-10} Torr) equipped with a variable-temperature, fast-scanning STM (Aarhus type),[30] a homemade molecular evaporator, and facilities for preparing single-crystal surfaces. Au(111) substrates were prepared by repeated cycles of Ar^+-ion sputtering followed by annealing at 800 K. Guanine in powder form was purchased from Sigma-Aldrich (2-Amino-6-hydroxypurine, MFCD 00071533), and loaded into glass crucibles in the molecular evaporator. After thorough degassing, guanine was deposited onto the Au(111) surface by thermal evaporation (crucible temperature 450–470 K, substrate held at room temperature) at a rate of 1.5×10^{-6} molecules per unit cell s^{-1}. The STM experiments were carried out at 150–170 K to prevent tip interaction with the adsorbed guanine molecules. Typical tunneling parameters in our STM images were 0.5–2 V for the bias voltage and 0.2–0.7 nA for the tunneling current. Attempts to bring the tip in closer proximity to the surface usually resulted in an increased interaction between the tip and adsorbed molecules which led to manipulation events.

The first-principles DFT simulations were performed with a plane-wave basis set (expanded up to 35 Rydbergs) together with ultrasoft pseudopotentials,[31] with the exchange-correlation effects treated in the GGA-PW91 approximation.[32]

Received: August 9, 2004
Revised: January 15, 2005
Published online: March 10, 2005

Keywords: hydrogen bonds · nucleic acids · nucleobases · scanning probe microscopy · self-assembly

[1] J. D. Watson, F. H. C. Crick, *Nature* **1953**, *171*, 737–738.
[2] R. R. Sinden, *DNA Structure and Function*, 1st ed., Academic Press, San Diego, **1994**.
[3] W. I. Sundquist, A. Klug, *Nature* **1989**, *342*, 825–829.
[4] J. T. Davis, *Angew. Chem.* **2004**, *116*, 684–716; *Angew. Chem. Int. Ed.* **2004**, *43*, 668–698.
[5] K. Gehring, J.-L. Leroy, M. Guéron, *Nature* **1993**, *363*, 561–565.
[6] a) D. Kipling, *The Telomere*, 1st ed., Oxford University Press, Oxford, **2002**; b) J. C. Darnell, K. B. Jensen, P. Jin, V. Brown, S. T. Warren, R. B. Darnell, *Cell* **2001**, *107*, 489–499.
[7] T. Steiner, *Angew. Chem.* **2002**, *114*, 50–80; *Angew. Chem. Int. Ed.* **2002**, *41*, 48–76.
[8] G. Louit, A. Hocquet, M. Ghomi, M. Meyer, J. Sühnel, *PhysChemComm* **2002**, *5*, 94–98.
[9] T. E. Cheatham III, P. A. Kollman, *Annu. Rev. Phys. Chem.* **2000**, *51*, 435–471.
[10] C. F. Guerra, F. M. Bickelhaupt, *Angew. Chem.* **2002**, *114*, 2194–2197; *Angew. Chem. Int. Ed.* **2002**, *41*, 2092–2095.
[11] a) J. V. Barth, J. Weckesser, C. Cai, P. Günter, L. Bürgi, O. Jeandupeux, K. Kern, *Angew. Chem.* **2000**, *112*, 1285–1288; *Angew. Chem. Int. Ed.* **2000**, *39*, 1230–1234; b) F. Oesterhelt, D. Oesterhelt, M. Pfeiffer, A. Engel, H. E. Gaub, D. J. Müller, *Science* **2000**, *288*, 143–146; c) A. Kühnle, T. R. Linderoth, B. Hammer, F. Besenbacher, *Nature* **2002**, *415*, 891–893.
[12] a) J. Tersoff, D. R. Hamann, *Phys. Rev. Lett.* **1983**, *50*, 1998–2001; b) J. Tersoff, D. R. Hamann, *Phys. Rev. B* **1985**, *31*, 805–813.
[13] a) Q. Chen, D. J. Frankel, N. V. Richardson, *Langmuir* **2002**, *18*, 3219–3225; b) M. Furukawa, H. Tanaka, T. Kawai, *J. Chem. Phys.* **2001**, *115*, 3419–3423.
[14] a) S. J. Sowerby, M. Edelwirth, W. M. Heckl, *J. Phys. Chem. B* **1998**, *102*, 5914–5922; b) W. M. Heckl, D. P. E. Smith, G. Binnig, H. Klagges, T. W. Hänsch, J. Maddocks, *Proc. Natl. Acad. Sci. USA* **1991**, *88*, 8003–8005.
[15] This π interaction contains an important contribution from van der Waals attraction between the surface and the molecule; it therefore scales with the number of atoms in the molecule, and can be very important for large molecules: F. Rosei, M. Schunack, P. Jiang, A. Gourdon, E. Lægsgaard, I. Stensgaard, C. Joachim, F. Besenbacher, *Science* **2002**, *296*, 328–331; R. Otero, F. Rosei, Y. Naitoh, P. Jiang, P. Thostrup, A. Gourdon, E. Lægsgaard, I. Stensgaard, C. Joachim, F. Besenbacher, *Nano Lett.* **2004**, *4*, 75–78; N. Katsonis, A. Marchenko, D. Fichou, *Adv. Mater.* **2004**, *16*, 309–312.
[16] This number is a lower bound, as DFT largely ignores van der Waals interactions. However, some van der Waals interaction has been reported with the same exchange-correlation

 © 2005 Wiley-VCH Verlag GmbH & Co. KGaA, Weinheim

function that we employed (S. Grimme, *J. Comput. Chem.* **2004**, *25*, 1463 – 1473).
[17] We are confident that under our current conditions, most of the quartets are indeed empty. At the base pressure at which we work, the flux of molecules from the residual gas on the surface is estimated to be $< 2.4 \times 10^{14}$ molecules $m^{-2} s^{-1}$. To fill in all quartets in a full monolayer of G-quartet structures with molecules from the residual gas, a period longer than 1 day would be needed.
[18] Each guanine island is enantiomerically pure, but different islands can have different configurations, giving rise to an overall racemic mixture.
[19] G. Laughlan, A. I. H. Murchie, D. G. Norman, M. H. Moore, P. C. E. Moody, D. M. J. Lilley, B. Luisi, *Science* **1994**, *265*, 520 – 524.
[20] J. L. Sessler, M. Sathiosatham, K. Doerr, V. Lynch, K. A. Abboud, *Angew. Chem.* **2000**, *112*, 1356 – 1359; *Angew. Chem. Int. Ed.* **2000**, *39*, 1300 – 1303.
[21] T. Giorgi, F. Grepioni, I. Manet, P. Mariani, S. Masiero, E. Mezzina, S. Pieraccini, L. Saturni, G. P. Spada, G. Gottarelli, *Chem. Eur. J.* **2002**, *8*, 2143 – 2152.
[22] N. Spackova, I. Berger, J. Sponer, *J. Am. Chem. Soc.* **2001**, *123*, 3295 – 3307.
[23] J. Gu, J. Leszczynski, M. Bansal, *Chem. Phys. Lett.* **1999**, *311*, 209 – 214.
[24] G. Gilli, F. Bellucci, V. Ferretti, V. Bertolasi, *J. Am. Chem. Soc.* **1989**, *111*, 1023 – 1028. Evidence is mounting against a significant role for cooperative effects on the hydrogen bonds of Watson–Crick base pairs; see: J. Sponer, P. Jurecka, P. Hobza, *J. Am. Chem. Soc.* **2004**, *126*, 10142 – 10151 and reference [10]).
[25] M. Schunack, T. R. Linderoth, F. Rosei, E. Lægsgaard, I. Stensgaard, F. Besenbacher, *Phys. Rev. Lett.* **2002**, *88*, 156102.
[26] J. Gu, J. Leszczynski, *J. Phys. Chem. A* **2000**, *104*, 6308 – 6313.
[27] C. C. Hardin, A. G. Perry, K. White, *Biopolymers* **2000**, *56*, 147 – 194.
[28] M. Meyer, T. Steinke, M. Brandl, J. Sühnel, *J. Comput. Chem.* **2001**, *22*, 109 – 124.
[29] J.-L. Mergny, C. Hélène, *Nat. Med.* **1998**, *4*, 1366 – 1367.
[30] E. Lægsgaard, L. Österlund, P. Thostrup, P. B. Rasmussen, I. Stensgaard, F. Besenbacher, *Rev. Sci. Instrum.* **2001**, *72*, 3537 – 3542.
[31] D. Vanderbilt, *Phys. Rev. B* **1990**, *41*, 7892 – 7895.
[32] J. P. Perdew, J. A. Chevary, S. H. Vosko, K. A. Jackson, M. R. Pederson, D. J. Singh, *Phys. Rev. B* **1992**, *46*, 6671 – 6687.

 © 2005 Wiley-VCH Verlag GmbH & Co. KGaA, Weinheim

Helical Structures

Chiral Amplification in the Transcription of Supramolecular Helicity into a Polymer Backbone**

Andrew J. Wilson, Mitsutoshi Masuda, Rint P. Sijbesma, and E. W. Meijer**

Dedicated to Professor Roeland Nolte on the occasion of his 60th birthday

Herein, we describe the expression of chirality into a polymer backbone during the photopolymerization of achiral monomers. The monomers are brought into a chiral self-organized supramolecular structure by using an enantiomerically pure structure-directing agent. The polymer obtained, despite incomplete tacticity, holds enough chiral information to fold itself into an almost homochiral, helical structure. In reporting this system we outline the first example of a chiral supramolecular "sergeant"[1] that affects backbone stereochemistry during a polymerization process by controlling the intrinsic helicity of self-assembled achiral monomers. It implies that self-organization[2–5] can play a critical role in amplifying the enantiomeric purity of the monomeric constituents of polymers.[6]

Cooperative expression and amplification of chirality present in the monomeric components of biopolymers is central to biological function, particularly with respect to folding and hierarchical self-assembly of large functional nanoscale ensembles. For synthetic chiral polymers, asymmetric synthesis of the polymer backbone with chiral monomers, catalysts, initiators, and solvents is well established.[7,8] However, in investigating why biopolymers are composed of enantiomerically pure monomers, it is useful to consider mechanisms[9,10] through which small unbalances in enantiomeric excess[11] are amplified.[12] In synthetic polymers without stereocenters, the latent helical conformation of polyisocyanates,[13] polyisocyanides,[14,15] and polysilanes[16] can be expressed by using small quantities of chiral monomer, chiral

[*] Dr. A. J. Wilson,[++] Dr. M. Masuda,[+] Dr. R. P. Sijbesma, Prof. Dr. E. W. Meijer
Laboratory of Macromolecular and Organic Chemistry
Eindhoven University of Technology
PO Box 513, 5600 MB, Eindhoven (The Netherlands)
Fax: (+31) 402-474-706
E-mail: r.p.sijbesma@tue.nl
e.w.meijer@tue.nl

[+] Present address: National Institute of Advanced Industrial Science and Technology (AIST)
Tsukuba (Japan)

[++] Present address:
Department of Chemistry, University of Leeds (UK)

[**] We acknowledge Dr. Jef Vekemans for stimulating discussions and the Council for Chemical Sciences of the Netherlands Organization for Scientific Research for financial support.

Supporting information for this article is available on the WWW under http://www.angewandte.org or from the author.

 DOI: 10.1002/anie.200462347 © 2005 Wiley-VCH Verlag GmbH & Co. KGaA, Weinheim

catalysts, and/or chiral solvents during polymerization. Similarly, noncovalent interaction of chiral molecules with the backbone of an achiral polymer can bias and express a preferred helical conformation,[17] while subsequent exchange for achiral guests results in a chiral memory effect.[18] Wholly self-organizing systems take advantage of cooperative noncovalent interactions to elicit so-called supramolecular induction of chirality[1,19] and supramolecular memory of chirality.[20] However, the kinetic lability of self-assembled architectures renders them subject to environmental stress. Recently, Feringa and co-workers used labile supramolecular chirality to enhance significantly the asymmetric induction in a photochemical ring closure.[21]

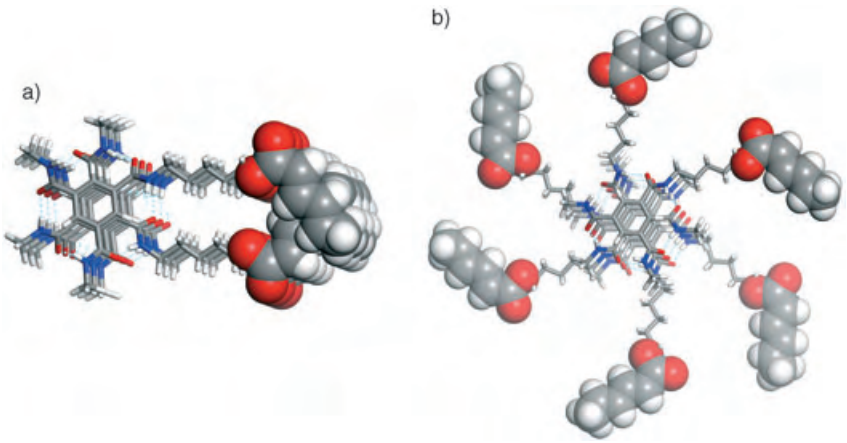

Figure 1. Representation of regular conformations of polymerizable self-assembled columns of **1**, based on the crystal structure of a benzene tricarboxamide.[24] Octyl side chains have been omitted for clarity. a) "Zigzag" conformation of sorbyl-containing side chains to give an achiral polysorbyl backbone. b) Helical conformation of sorbyl-containing side chains to give a chiral polysorbyl backbone.

We propose herein the use of covalent fixation after self-assembly[22] as a means of obtaining kinetically robust chiral nanoscale architectures, as an extension of our previously described self-assembly and polymerization of achiral discotic **1** in apolar solvents (Scheme 1 and Figure 1).[23] By introducing an enantiomerically pure structure-directing agent, we found one handedness of the helix only. After polymerization and removal of the structure-directing agent, the polymer obtained from achiral monomers is chiral and folds into a preferred helical superstructure. Surprisingly, the folding process is more directed by the supramolecular interactions than by the tacticity of the polymer backbone.

Self-assembly of **1** in cyclohexane (10^{-5}–10^{-2} M) occurs through cooperative hydrogen bonding, aromatic stacking, and van der Waals interactions as proposed in Figure 1. The proposed mode of assembly results in the cooperative formation of a triple helical seam of hydrogen bonds down the axis of the column[1,24–28] with equal probabilities of left- and right-handed helices in the absence of further sources of chirality. This proposal for the structure of **1** is based on the single-crystal structure of another substituted benzene-1,3,5-tricarboxamide.[24] It is therefore important to explore the effect of the supramolecular sergeants-and-soldiers experiment[1,25] during polymerization because it results in the formation of two new chiral centers per discotic **1**. As has been observed in several other systems,[1,25,27,28] in the absence of any chiral additives equal quantities of left- and right-handed helices composed of discotic **1** are present in solution (0.8×10^{-3} M, cyclohexane). However, in the presence of chiral discotic **2a** a large negative circular dichroism (CD) effect is observed (Figure 2). The CD effect is induced by a supramolecular sergeant-and-soldiers effect as the spectrum reflects the absorption spectrum of monomer **1**, while its

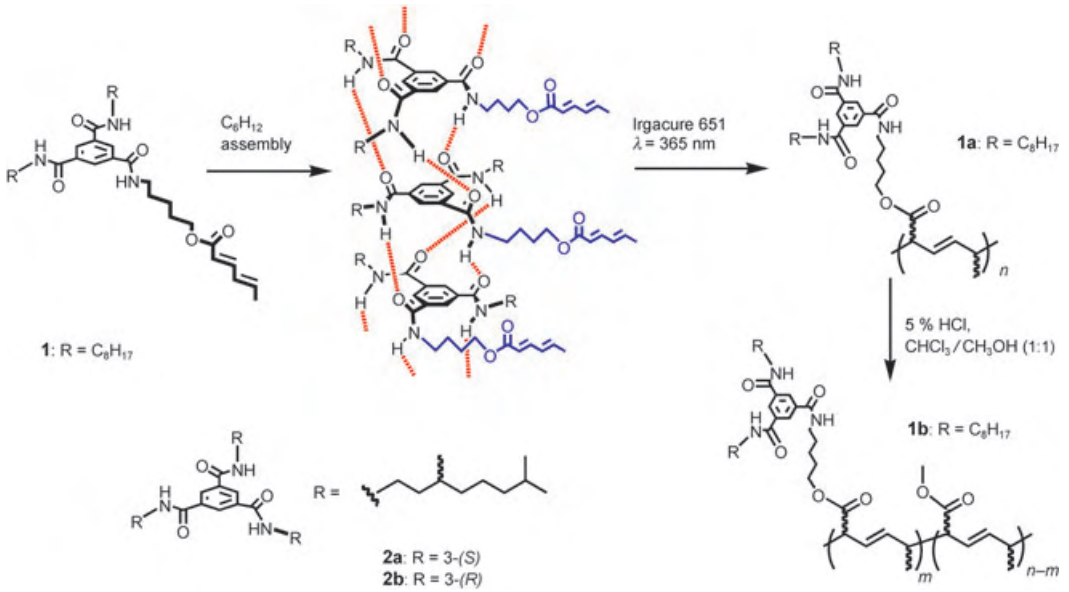

Scheme 1. Self-assembly and polymerization of discotic **1**.

 © 2005 Wiley-VCH Verlag GmbH & Co. KGaA, Weinheim

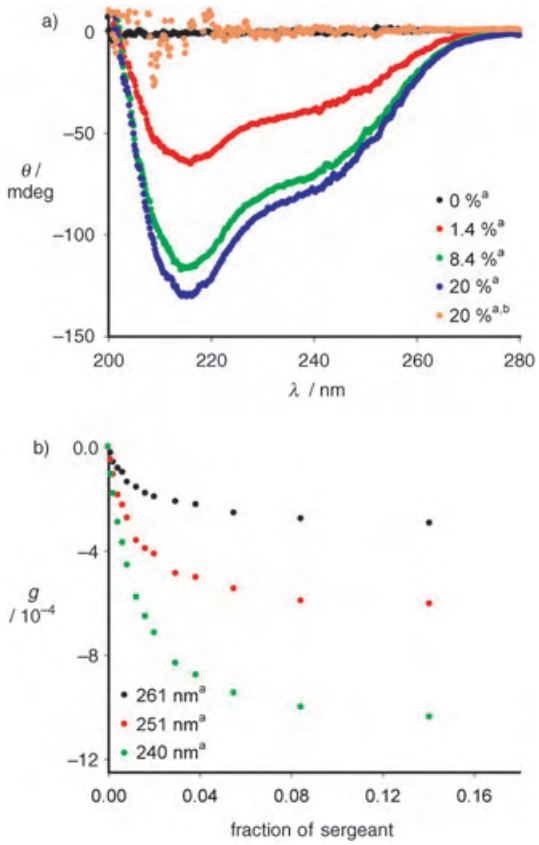

Figure 2. a) CD spectra of monomer **1** in the presence of different amounts of sergeant **2a** and b) anisotropy factor of monomer **1** as a function of added sergeant **2a**. [a] [**1**] = 8.1×10^{-4} M, cyclohexane, 0.1 cm pathlength. [b] [**1**] = 8.1×10^{-4} M, 95:4.5:0.5 $C_6H_{12}/CHCl_3/CH_3OH$, 0.1 cm path length.

magnitude increases nonlinearly with the quantity of added "sergeant" **2a** (leveling off at around 10%). The effect is completely lost upon increasing the solvent polarity (C_6H_{12}/$CHCl_3$/CH_3OH 95:4.5:0.5). Gratifyingly, the use of a mirror image "sergeant" **2b** with opposite chirality results in an induced CD signal of opposite and similar magnitude (see ESI).

We next investigated whether the chirality induced by sergeant **2a** was retained upon polymerization of monomer **1** in the presence of varying amounts of sergeant **2a**. As reported previously by us,[23] 1,4-polymerization of the sorbyl moiety in **1** provides sufficient distance to bridge stacked aromatics. Photoinitiated polymerization (365 nm) of the self-assembled stacks (1×10^{-2} M solution in cyclohexane) of **1**, in the presence of 2,2-dimethoxyphenylacetophenone as initiator, furnishes columnar polymers **1a**. Full analysis of the polymers requires careful removal of monomer **1** and structure-directing agent **2a** by Soxhlet extraction followed by methanolysis of the polymer formed[29] to detach most of the trimesic amide moieties from the polysorbyl backbone. The highly soluble and non-aggregating polymethyl sorbate **1b** can be analyzed by ^{1}H NMR, ^{13}C NMR, and size-exclusion chromatography (SEC). The latter analysis shows that the photopolymerization results in polymers with DPs of 50–130 and polydispersities of $\approx$1.7, while no signals of remaining **1** or **2a**, nor products thereof are detected. Importantly, the presence of varying amounts of **2a** does not significantly affect these parameters through radical C–H abstraction mechanisms, that is, the sergeant does not act as a chain stopper. (Table 1)

Table 1: Conversion, degree of polymerization (DP), and polydispersity index (PDI) of photoinitiated polymerization of **1** in the presence of varying amounts of sergeant **2a**.

2a [%]	Conversion [%]	DP	PDI
0	58	58	1.76
0	51	110	2.1
0	50	103	1.53
10	56	130	1.68
10	47	63	1.2
15	50	100	1.7
20	50	54	1.57
20	45	77	1.6

Induced chirality was studied by CD spectroscopy on **1a** after careful removal of unconverted monomer and sergeant **2a** by exhaustive Soxhlet extraction with diethyl ether. ^{13}C NMR spectroscopy of a methanolyzed sample demonstrated the absence of any sergeant (incorporation at a level below 0.3 molecules of **2a** per polymer chain, see ESI). CD spectra were recorded in $C_6H_{12}/CHCl_3/CH_3OH$ (95:4.5:0.5), a solvent combination in which the polymer has sufficient solubility and in which monomer and sergeant **2a** do not form columnar stacks as outlined above. Remarkably, the polymers still display optical activity in the CD spectrum (Figure 3) despite the complete removal of chiral sergeant **2a** from the product. The CD spectra were concentration independent between 10^{-3} and 10^{-4} M (see ESI) which suggests that the signal is a consequence of intramolecular organization within molecularly dissolved polymers. If the variation in the magnitude of the CD spectrum is plotted against the fraction of sergeant **2a** present during the polymerization, almost complete induction of helicity is observed at around 10% of added sergeant **2a** (once again the use of sergeant **2b** produces an opposite response of equal intensity, see ESI). The shape of the curve matches that observed during the self-assembling sergeants-and-soldiers experiment and the anisotropy value is of similar magnitude, suggesting that the helical bias present before polymerization is almost completely (>80%) retained in the polymer. The Cotton effect completely disappears when the methanol content is increased to 1.5%. Removal of all solvent and redissolution in the original solvent mixture leads to complete recovery of the original Cotton effect. The process can be repeated several times without significant loss of CD signal. The process amounts to an unfolding–refolding cycle of the polymer and indicates that the helical bias induced by sergeant **2a** in self-assembled stacks of monomer **1** is locked in the polymer and that the chiral information is encoded in the stereochemistry of the sorbyl main chain. The complete sequence of assembly, fixation, sergeant removal, and reversible unfolding is summarized in Figure 4.

 © 2005 Wiley-VCH Verlag GmbH & Co. KGaA, Weinheim

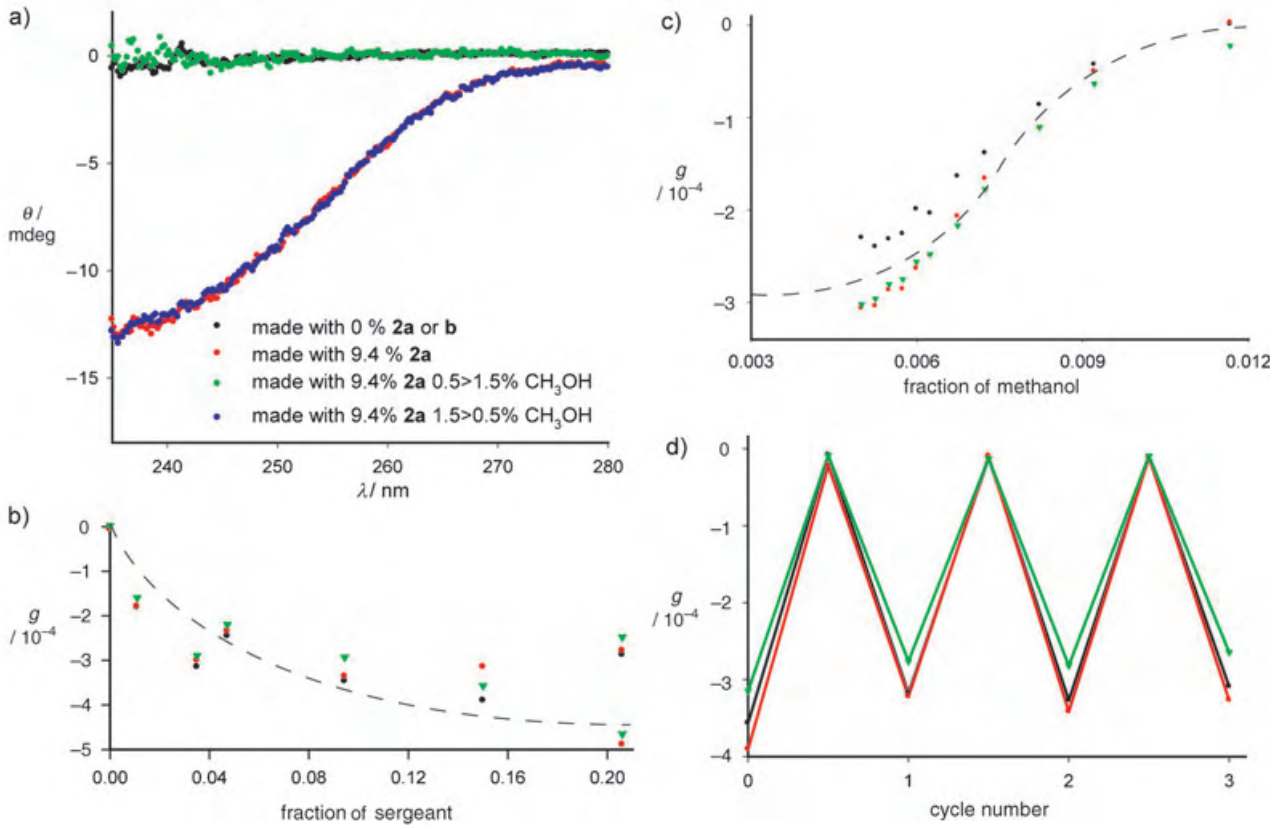

Figure 3. CD spectroscopy of polymer **1a** made in the presence and absence of sergeant **2a** (0.1 cm path length, 95:4.5:0.5 $C_6H_{12}/CHCl_3/CH_3OH$). a) CD spectra of polymer **1a** (9.5×10^{-4} M). b) Variation in the anisotropy factor *g* of the polymer **1a** as a function of sergeant **2a** present during polymerization. c) Variation in the anisotropy factor *g* as a function of added methanol (polymer **1a** with 9.4% sergeant **2a** present during the polymerization). d) Folding and unfolding behavior (as shown by *g* value) upon addition and removal of methanol (polymer **1b** made with 15% sergeant **2a** present during the polymerization).

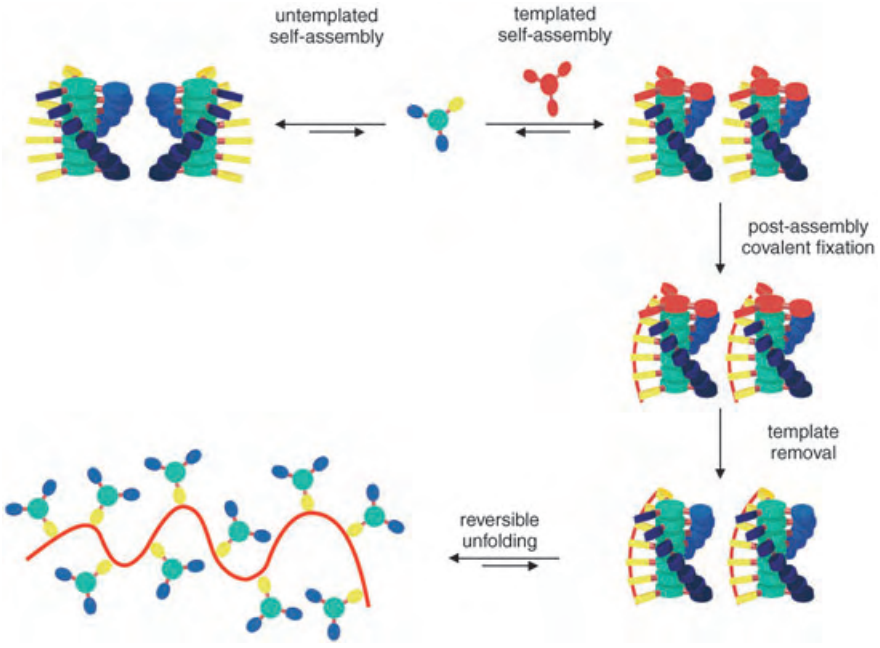

Figure 4. Sequence of events leading to locking of supramolecular chirality into columnar self-assemblies of **1**.

Deeper understanding of the structural details responsible for the chiral amplification effect required a more detailed analysis of the polymer backbone. This was achieved with transesterified polymer **1b**, which has higher mobility relative to **1a** resulting in higher-quality ^{13}C- and ^{1}H-correlated spectra. $^{1}H,^{1}H$ COSY of **1b** reveals the interconnection along the backbone and is entirely consistent with a 1,4-*trans* polymerization (confirmed with ^{13}C NMR spectroscopy) in which both *erythro* and *threo* stereocoupled centers are formed.[30,31] The addition of sergeant **2a** or **2b** to a solution of the self-assembled stack prior to polymerization has very little effect on the NMR spectrum of the polymer. However, the unfolding–refolding experiments show that the helical bias is strongly retained in the backbone of the polymer. This implies that despite the fact that the polymer has a mixed microstructure, at least part of the polysorbyl backbone has been formed with asymmetric preference. It is highly surprising that the mixed microstructure results in a very high stereoselectivity in the folding process. It can

 © 2005 Wiley-VCH Verlag GmbH & Co. KGaA, Weinheim

be rationalized with the notion that the polymer backbone is formed in a perfect helical assembly and that the backbone, despite its mixed microstructure, fits perfectly into the refolded helical polymer. Notably, order in polymer backbones lowers chirality, and disorder enhances chirality, as beautifully shown by Green and Garetz for polystyrene.[32]

We made several models to rationalize these observations further. The *trans*-1,4-polymerization of (*E*,*E*)-sorbyl esters in the preferred transoid conformation fixes the relative stereochemistry of methyl and ester groups on each side of the double bond to *rel-(R,S)*. But the relative stereochemistry of adjacent methyl and ester groups in the polymer is determined by the relative orientation of the sorbyl groups during polymerization (see ESI). In all cases in which the polymerization proceeds in a zig-zag fashion down the column from sorbyl-containing side chains alternating in orientation by +30° and −30° (Figure 2a), no net chirality results. When sorbyl-containing side chains follow the seam of hydrogen bonds, a chiral polymer results, but the increased distance between consecutive monomeric units results in the accumulation of strain in the polymer (Figure 2b). Therefore, a mixed microstructure, resulting from polymerization switching between zig-zag and helical propagation is in line with both NMR and CD spectral evidence. In the presence of **2a** or **2b** there is no change in tacticity of the polymerization;[33,34] rather it introduces a bias of the absolute stereochemistry with which the helical propagation proceeds. Therefore it resembles in many aspects the "majority rules" principle pioneered by Green.[13]

In summary, we have shown that it is possible to exploit noncovalent interactions to first assemble and then transfer chiral information to a well-defined, kinetically inert, columnar architecture by using a chiral structure-directing agent. Even though the polysorbate backbone is not completely stereoregular, it is capable of storing complete stereochemical information. The observation of the remarkable chiral memory effect opens up the possibility of using noncovalent interactions to amplify and transfer chiral information to structurally robust nanoscale architectures.

Received: October 18, 2004
Revised: January 26, 2005

Keywords: helical structures · polymerization · polymers · self-assembly · supramolecular chemistry

[1] A. R. A. Palmans, J. A. J. M. Vekemans, E. E. Havinga, E. W. Meijer, *Angew. Chem.* **1997**, *109*, 2763–2765; *Angew. Chem. Int. Ed. Engl.* **1997**, *36*, 2648–2651.
[2] D. Philp, J. F. Stoddart, *Angew. Chem.* **1996**, *108*, 1242–1286; *Angew. Chem. Int. Ed. Engl.* **1996**, *35*, 1155–1196.
[3] J.-M. Lehn, *Science* **2002**, *295*, 2400–2403.
[4] D. N. Reinhoudt, M. Crego-Calama, *Science* **2002**, *295*, 2403–2407.
[5] G. M. Whitesides, B. Grzybowski, *Science* **2002**, *295*, 2418–2421.
[6] L. Brunsveld, J. Vekemans, J. Hirschberg, R. P. Sijbesma, E. W. Meijer, *Proc. Natl. Acad. Sci. USA* **2002**, *99*, 4977–4982.
[7] "Materials Chirality": G. Guerra, L. Cavallo, P. Corradini in *Topics in Stereochemistry, Vol. 24* (Eds.: M. M. Green, R. J. M. Nolte, E. W. Meijer), Wiley-Interscience, New York, **2003**.
[8] G. Wulff, P. K. Dhal, *Macromolecules* **1990**, *23*, 4525–4527.
[9] K. Mislow, *Collect. Czech. Chem. Commun.* **2003**, *68*, 849–864.
[10] D. G. Blackmond, *Proc. Natl. Acad. Sci. USA* **2004**, *101*, 5732–5836.
[11] F. C. Frank, *Biochim. Biophys. Acta* **1953**, *11*, 459–463.
[12] K. Soai, T. Shibata, H. Morioka, K. Choji, *Nature* **1995**, *378*, 767–768.
[13] M. M. Green, J.-W. Park, T. Sato, A. Teramoto, S. Lifson, R. L. B. Selinger, J. V. Selinger, *Angew. Chem.* **1999**, *111*, 3328–3345; *Angew. Chem. Int. Ed.* **1999**, *38*, 3138–3154; .
[14] J. J. L. M. Cornelissen, M. Fischer, N. A. J. M. Sommerdijk, R. J. M. Nolte, *Science* **1998**, *280*, 1427–1430.
[15] J. J. L. M. Cornelissen, J. J. J. M. Donners, R. d. Gelder, W. S. Graswinckel, G. A. Metselaar, A. E. Rowan, N. A. J. M. Sommerdijk, R. J. M. Nolte, *Science* **2001**, *293*, 676–680.
[16] M. Fujiki, J. R. Koe, K. Terao, T. Sato, A. Teramoto, J. Watanabe, *Polym. J.* **2003**, *35*, 297–344.
[17] E. Yashima, T. Matsushima, Y. Okamoto, *J. Am. Chem. Soc.* **1997**, *119*, 6345–6359.
[18] E. Yashima, K. Maeda, Y. Okamoto, *Nature* **1999**, *399*, 449–451.
[19] L. J. Prins, J. Huskens, F. d. Jong, P. Timmermann, D. N. Reinhoudt, *Nature* **1999**, *398*, 498–502.
[20] L. J. Prins, F. d. Jong, P. Timmermann, D. N. Reinhoudt, *Nature* **2000**, *408*, 181–184.
[21] J. J. D. d. Jong, L. N. Lucas, R. M. Kellog, J. H. v. Esch, B. L. Feringa, *Science* **2004**, *304*, 278–281.
[22] S. J. Rowan, S. J. Cantrill, G. R. L. Cousins, J. K. M. Sanders, J. F. Stoddart, *Angew. Chem.* **2002**, *114*, 938–993; *Angew. Chem. Int. Ed.* **2002**, *41*, 898–952; .
[23] M. Masuda, P. Jonkheijm, R. P. Sijbesma, E. W. Meijer, *J. Am. Chem. Soc.* **2003**, *125*, 15935–15940.
[24] M. P. Lightfoot, F. S. Mair, R. G. Pritchard, J. E. Warren, *Chem. Commun.* **1999**, 1945–1946.
[25] L. Brunsveld, A. Schenning, M. A. C. Broeren, H. M. Janssen, J. Vekemans, E. W. Meijer, *Chem. Lett.* **2000**, 292–293.
[26] M. L. Bushey, A. Hwang, P. W. Stephens, C. Nuckolls, *J. Am. Chem. Soc.* **2001**, *123*, 8157–8158.
[27] M. L. Bushey, A. Hwang, P. W. Stephens, C. Nuckolls, *Angew. Chem.* **2002**, *114*, 2952–2955; *Angew. Chem. Int. Ed.* **2002**, *41*, 2828–2831; .
[28] J. J. van Gorp, J. Vekemans, E. W. Meijer, *J. Am. Chem. Soc.* **2002**, *124*, 14759–14769.
[29] H. Lamparski, D. F. O'Brien, *Macromolecules* **1995**, *28*, 1786–1794.
[30] M. Farina, M. Grassi, G. D. Silvestro, L. Zetta, *Eur. Polym. J.* **1985**, *21*, 71–74.
[31] W. R. Hertler, T. V. RajanBabu, D. W. Ovenall, G. S. Reddy, D. Y. Sogah, *J. Am. Chem. Soc.* **1988**, *110*, 5841–5853.
[32] M. M. Green, B. A. Garetz, *Tetrahedron Lett.* **1984**, *25*, 2831–2832.
[33] A. Matsumoto, T. Chiba, K. Oka, *Macromolecules* **2003**, *36*, 2573–2575.
[34] S. Nagahama, T. Tanaka, A. Matsumoto, *Angew. Chem.* **2004**, *116*, 3899–3902; *Angew. Chem. Int. Ed.* **2004**, *43*, 3811–3814.

 © 2005 Wiley-VCH Verlag GmbH & Co. KGaA, Weinheim

Solid-State Reactions

Crystal-to-Crystal Transformation from a Chain Polymer to a Two-Dimensional Network at Low Temperatures**

*Chunhua Hu and Ulli Englert**

Single-crystal to single-crystal transformations involve cooperative movement of atoms in the solid state. Classical studies by Schmidt et al.[1,2] on the solid-state reactivity of different polymorphs of cinnamic acid paved the way to understanding topochemical reactions in molecular crystals. In this early work as well as in numerous later examples for dimerization,[3–6] cyclization,[7,8] polymerization,[9,10] and racemization[11–14] photochemical excitation was required to bring about the transformations. Examples of thermally induced topotactic reactions are relatively rare.[15–20] In this contribution we report on an unprecedented change in network topology that occurs at surprisingly low temperatures.

The solid-state transformation starts from the one-dimensional polymer $[ZnCl_2(\mu\text{-bipy})]_\infty$ (**1**): zinc(II) centers are linked by 4,4′-bipyridine (bipy) ligands to form infinite zigzag chains. Terminal chloro groups complete the distorted tetrahedral coordination around each metal atom. The halogen ligands are oriented towards the neighboring polymer chains. A schematic representation of this topology is shown in Figure 1 (left). Dashed lines indicate the shortest nonbonding contacts between the halogen substituents of one polymer and the zinc atoms of its neighbor; this interatomic distance amounts to 4.6 Å. One may intuitively assume that these contacts shorten in the course of the solid-state reaction and turn into bonds. This approach between the chains is accompanied by variations in the metal-centered angles and by expansion of the originally terminal zinc–chlorine bonds from 2.2 to 2.5 Å. The rearrangement product $[Zn(\mu\text{-}Cl)_2(\mu\text{-bipy})]_\infty$ (**2**, Figure 1) represents a two-dimensional network in which the chloro ligands symmetrically bridge metal cations in a direction perpendicular to the bipy linkers. The additional Zn–Cl bonds increase the coordination number of the cations from 4 to 6, leading to a distorted octahedral coordination.

This change in network topology from one- to two-dimensional connectivity is triggered when solid **1** is cooled to temperatures below 130 K: The atomic movement underlying the rearrangement apparently occurs under very mild conditions. The reaction is reversible, albeit with a very large hysteresis: Polymer **2** may be converted back to **1** at temperatures above 360 K.

It is important to note that our starting material shows concomitant polymorphism:[21] In addition to the modification **1α** described in the literature,[22] a second polymorph, **β**, forms under the same conditions of preparation (see Experimental Section for the characterization of **1β**). A section of the polymer chain in this hitherto unknown polymorph is shown in Figure 2. In principle, **1α** and **1β** can differ in their solid-state properties. Individual crystals cannot be distinguished readily by their morphology but must be sorted out based on their diffraction pattern. Neither IR spectra (KBr pellets, 400–4000 cm^{-1}) on small samples nor UV/Vis (200–1000 nm) or Raman microscopic (150–4000 cm^{-1}) studies on individual crystals result in significant differences that might be used for a reliable phase assignment.

Solid **1**, single crystals of either modification as well as crystalline powder composed of both concomitant phases, undergoes conversion to **2**. Strictly speaking, the above-mentioned crosslinking of neighboring 1D polymer chains to a 2D net must therefore be related to two different solid-state reactions rather than to a single one! In view of their common reactivity and spectroscopic properties, it is no surprise that the modifications **1α** and **1β** show close structural similarity. In both phases the arrangement of adjacent polymers in principle matches the simplified picture of Figure 1 (left). Closest intermetal distances between 1D chains correspond to translation along the shortest lattice parameters and hence amount to very similar values around 5.11 Å in both polymorphs, and the resulting layers satisfy the crystal-chemical requirements for the rearrangement. Figure 3 shows how the polymorphs differ slightly in the stacking sequence of these layers.

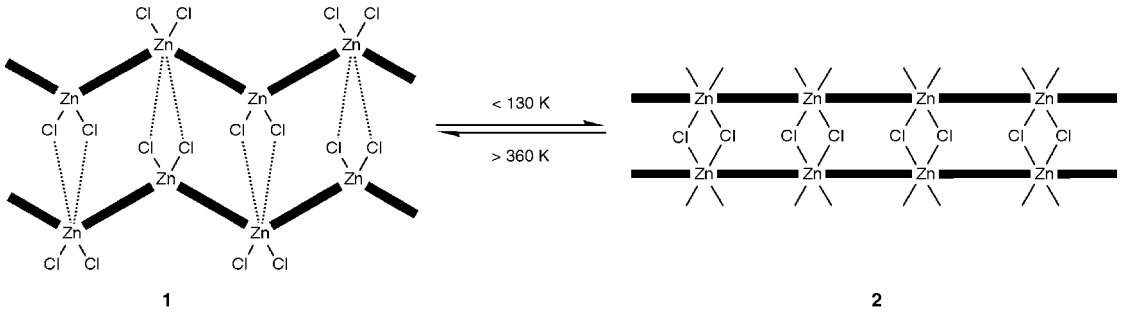

Figure 1. Schematic representation of the solid-state conversion of two neighboring chains in **1** to form the two-dimensional network in **2**.

[*] Dr. C. Hu, Prof. Dr. U. Englert
Institut für Anorganische Chemie
RWTH Aachen
Professor-Pirlet-Strasse 1, 52074 Aachen (Germany)
Fax: (+49) 241-8092288
E-mail: ullrich.englert@ac.rwth-aachen.de

[**] This article is dedicated to Fudan University on the occasion of its centenary celebration and to Prof. Lidun Ma on the occasion of his 70th birthday. We thank Dr. A. Fischer and D. Lischke, Grünenthal GmbH, Aachen, for DSC measurements, temperature-dependent powder diffraction, and Raman microscopy. We thank M. Noyong and I. Kalf for their help with UV/Vis microscopy and IR spectroscopy.

 DOI: 10.1002/anie.200462100 © 2005 Wiley-VCH Verlag GmbH & Co. KGaA, Weinheim

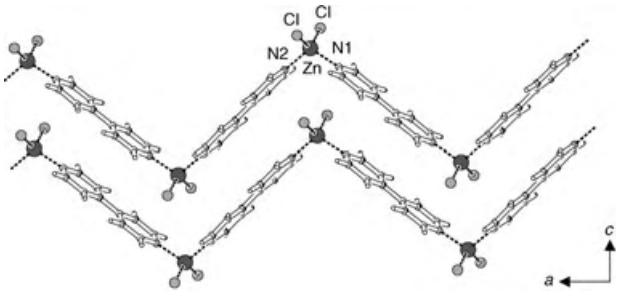

Figure 2. PLATON representation of two neighboring chains in **1β**; the view direction is slightly tilted toward *b*. Selected distances: Zn–Cl 2.2038(12), Zn–N1 2.047(4), Zn–N2 2.054(4) Å.

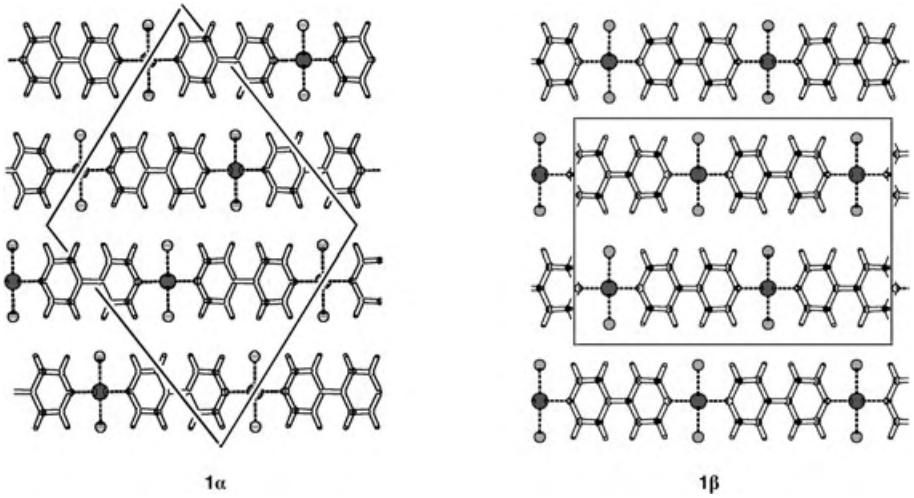

Figure 3. PLATON projection of the layer stacking in the two polymorphs of **1**; view directions are along short interchain distances, that is, along *b* in **1α** (left) and along *c* in **1β** (right).

Large single crystals of either polymorph of **1** on the diffractometer fragmented when exposed to a stream of cold (120 K) nitrogen; single crystals of **2** with dimensions of up to 0.3 mm can be found among the resulting fragments. A layer of the two-dimensional network structure **2** is shown in Figure 4.

Once formed, the transformation product is stable over a wide temperature range. Both the crystal that had formed at 120 K on the diffractometer as well as a second crystal were studied at ambient temperature. A DSC experiment indicated an endothermal effect at ca. 350 K. When single crystals of **2** were heated to 360 K on the diffractometer, the 2D network reverted to the 1D coordination polymer. Numerous experiments on individual crystals of **2** showed unambiguously that both polymorphs, **1α** and **1β**, can be formed as products of these conversions.

Not only single crystals can be subjected to the solid-state reaction: A Schlenk tube containing a macroscopic sample of 100 mg of crude crystalline **1**—a mixture of the polymorphs, according to the powder pattern—was immerged for fractions of a minute into liquid nitrogen and quantitatively converted into the 2D polymer **2**; the phase purity of the reaction product was proven by powder diffraction. When the sample was heated to 393 K in an oven, it converted back to the polymorphic mixture of the starting material; the powder pattern again showed the presence of both **1α** and **1β**, albeit with much lower crystallinity.

We note that crystallinity plays an important role for the degree of conversion: Samples of **1** made up from large crystals or coarse crystalline powder are completely transformed to **2**, whereas samples of very small crystallites undergo only partial conversion. Similarly, the reverse reaction (**2**→**1**) requires more elevated temperatures for complete conversion if the starting material is a powder with small grain size. All macroscopic crystals of the chain polymer **1** and the network structure **2** tested in our experiments underwent conversion reproducibly as indicated in Figure 1.

The solid-state transformation and its reaction conditions, namely the conversion of the coordination polymer **1** to the network structure **2** at surprisingly low temperatures, are without precedent. Solid-state reactions with changes in network topology have been described for other types of systems: Ranford, Vittal, and co-workers[17,18] showed that hydrogen-bonded networks can be transformed into coordination polymers by irreversible dehydration. In the thermochromic compounds studied by Yalpani et al.[19,20] the reversible transition between individual molecules and polymers is associated with a change in the coordination number of the boron atoms.[19,20] Our reaction does not represent just another example but differs from both above mentioned systems in two important aspects: It involves major rearrangement of the whole structure, and, despite this fact, the transformation occurs at clearly lower temperatures.

The tetrahedral coordination of the zinc atoms in the chains of **1** is unexceptional.[22] The reaction product **2**, however, belongs to a structure type rarely encountered for zinc[23] but quite common for larger divalent metals.[24–26] The combination of chloro and bipyridine ligands with the

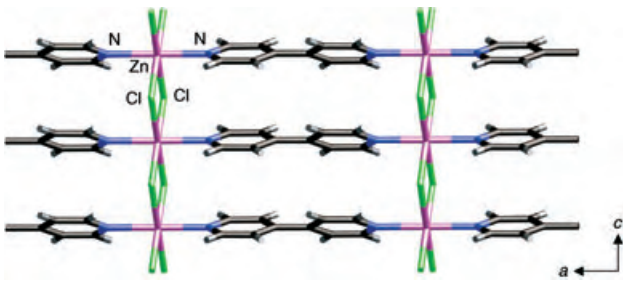

Figure 4. View of a section of the 2D network in **2**; the view direction is slightly tilted away from *b*. Selected interatomic distances: Zn–Cl 2.5035(4), Zn–N 2.1456(17) Å.

 © 2005 Wiley-VCH Verlag GmbH & Co. KGaA, Weinheim

relatively small Zn^{II} cations provides a fascinating meeting ground for two competing construction principles in the solid state.

Experimental Section

Single-crystal X-ray structure determinations: Data were collected with a Bruker Smart APEX CCD detector ($Mo_{K\alpha}$ radiation, $\lambda = 0.71073$ Å, graphite monochromator) on a D8 goniometer. Temperature was controlled with an Oxford Cryosystems Series 800 instrument. Intensities were integrated with SAINT[27] and corrected for absorption with SADABS.[28] Structures were solved by direct methods (SHELXS-97)[29] and refined on F^2 with SHELXL-97.[30]

Crystal data for **1α**: Monoclinic space group $C2/c$, $a = 15.830(2)$, $b = 5.1132(6)$, $c = 14.5963(18)$ Å, $\beta = 110.265(2)°$, $V = 1108.3(2)$ Å^3, $Z = 4$; $T = 293$ K; for refinement results see ref. [17].

Crystal data for **1β**: Orthorhombic space group *Pnma*, $a = 17.319(4)$, $b = 12.389(3)$, $c = 5.1116(11)$ Å, $V = 1096.8(4)$ Å^3, $Z = 4$; $T = 293$ K; refinement of 76 parameters based on 1428 independent out of totally 10577 reflections converged at $R1 = 0.0432$, $wR2 = 0.1264$, and $GOF = 1.097$.

We note that 2D networks of the type $[M(\mu\text{-}X)_2(\mu\text{-bpy})]_\infty$ show an interesting space-group ambiguity.[31,26] The correct space group for compound **2** both at 120 and 293 K is *Pban*.

Crystal data (data collected at room temperature in square brackets) for **2**: Orthorhombic space group *Pban*, $a = 11.380(2)$ [11.368(2)], $b = 11.922(2)$ [11.974(2)], $c = 3.6199(6)$ [3.6433(7)] Å, $V = 491.16(15)$ [495.93(17)] Å^3, $Z = 4$; $T = 120$[293] K; refinement of 37 parameters based on 618 [622] independent out of totally 4424 [4424] reflections converged at $R1 = 0.0189$ [0.0221], $wR2 = 0.0526$ [0.0610], and $GOF = 1.068$ [1.091].

CCDC-250863 (**1β**), CCDC-250864 (**2** at 120 K), and CCDC-250865 (**2** at 293 K) contain the supplementary crystallographic data for this paper. These data can be obtained free of charge from The Cambridge Crystallographic Data Centre via www.ccdc.cam.ac.uk/data_request/cif. The alternative polymorph of the chain polymer, **1α**,[17] corresponds to CCDC-162051.

Received: September 24, 2004
Revised: December 10, 2004
Published online: March 2, 2005

Keywords: coordination polymers · crystal engineering · solid-state reactions · topochemistry · zinc

[1] M. D. Cohen, G. M. J. Schmidt, *J. Chem. Soc.* **1964**, 1996.
[2] M. D. Cohen, G. M. J. Schmidt, F. I. Sonntag, *J. Chem. Soc.* **1964**, 2000.
[3] H. Nakanishi, W. Jones, J. M. Thomas, *Chem. Phys. Lett.* **1980**, *71*, 44.
[4] H. Nakanishi, W. Jones, J. M. Thomas, M. B. Hursthouse, M. Motevalli, *J. Phys. Chem.* **1981**, *85*, 3636.
[5] K. Tanaka, F. Toda, E. Mochizuki, N. Yasui, K. Yasushi, I. Miyahara, K. Hirotsu, *Angew. Chem.* **1999**, *111*, 3733; *Angew. Chem. Int. Ed.* **1999**, *38*, 3523.
[6] G. S. Papaefstathiou, Z. Zhong, L. Geng, L. R. MacGillivray, *J. Am. Chem. Soc.* **2004**, *126*, 9158.
[7] H. Koshima, D. Matsushige, M. Miyauchi, *CrystEngComm* **2001**, *33*, 1.
[8] M. Irie, S. Kobatake, M. Horichi, *Science* **2001**, *291*, 1769.
[9] J. Xiao, M. Yang, J. W. Lauher, F. W. Fowler, *Angew. Chem.* **2000**, *112*, 2216; *Angew. Chem. Int. Ed.* **2000**, *39*, 2132.
[10] X. Ouyang, F. W. Fowler, J. W. Lauher, *J. Am. Chem. Soc.* **2003**, *125*, 12400.
[11] Y. Ohashi, K. Yanagi, T. Kurihara, Y. Sasada, Y. Ohgo, *J. Am. Chem. Soc.* **1982**, *104*, 6353.
[12] A. Uchida, J. D. Dunitz, *Acta Crystallogr. Sect. B* **1990**, *46*, 45.
[13] Y. Takenaka, Y. Ohashi, T. Tamura, A. Uchida, Y. Sasada, Y. Ohgo, S. Baba, *Acta Crystallogr. Sect. B* **1993**, *49*, 272.
[14] Y. Ohashi, Y. Sakai, A. Sekine, A. Arai, Y. Ohgo, N. Kamiya, H. Iwasaki, *Bull. Chem. Soc. Jpn.* **1995**, *68*, 2517.
[15] J. H. Kim, S. M. Hubig, S. V. Lindeman, J. K. Kochi, *J. Am. Chem. Soc.* **2001**, *123*, 87.
[16] B. Lotsch, J. Senker, W. Schnick, *Inorg. Chem.* **2004**, *43*, 895.
[17] J. D. Ranford, J. J. Vittal, D. Wu, *Angew. Chem.* **1998**, *110*, 1159; *Angew. Chem. Int. Ed.* **1998**, *37*, 1114.
[18] J. D. Ranford, J. J. Vittal, D. Wu, X. Yang, *Angew. Chem.* **1999**, *111*, 3707; *Angew. Chem. Int. Ed.* **1999**, *38*, 3498.
[19] M. Yalpani, R. Boese, D. Bläser, *Chem. Ber.* **1983**, *116*, 3338.
[20] M. Yalpani, W. Scheidt, K. Seevogel, *J. Am. Chem. Soc.* **1985**, *107*, 1684.
[21] J. Bernstein, R. J. Davey, J.-O. Henck, *Angew. Chem.* **1999**, *111*, 3646; *Angew. Chem. Int. Ed.* **1999**, *38*, 3440.
[22] C. Hu, U. Englert, *CrystEngComm* **2001**, *3*, 91.
[23] J. Pickardt, B. Staub, *Z. Naturforsch. B* **1996**, *51*, 947.
[24] T. R. Musgrave, C. E. Mattson, *Inorg. Chem.* **1968**, *7*, 1433.
[25] M. A. Lawandy, X. Huang, R.-J. Wang, J. Li, J. Y. Lu, T. Yuen, C. L. Lin, *Inorg. Chem.* **1999**, *38*, 5410.
[26] C. Hu, Q. Li, U. Englert, *CrystEngComm* **2003**, *5*, 519.
[27] SAINT+ (version 6.02), Program for Reduction of Data Collected on Bruker CCD Area Detector Diffractometer, Bruker AXS Inc., Madison, WI, **1999**.
[28] G. M. Sheldrick, SADABS, Program for Empirical Absorption Correction of Area Detector Data, University of Göttingen, Germany, **1996**.
[29] G. M. Sheldrick, SHELXS-97, Program for Solution of Crystal Structures, University of Göttingen, Germany, **1997**.
[30] G. M. Sheldrick, SHELXL-97, Program for Refinement of Crystal Structures, University of Göttingen, Germany, **1997**.
[31] A. M. Chippindale, A. R. Cowley, K. J. Peacock, *Acta Crystallogr. Sect. C* **2000**, *56*, 651.

 © 2005 Wiley-VCH Verlag GmbH & Co. KGaA, Weinheim

Molecular Switches

B_{12}-*retro*-Riboswitches: Constitutional Switching of B_{12} Coenzymes Induced by Nucleotides**

Sigrid Gschösser, Karl Gruber, Christoph Kratky, Christian Eichmüller, and Bernhard Kräutler**

Dedicated to Professor Karl Schlögl on the occasion of his 80th birthday

The recent discovery of "B_{12}-riboswitches" revealed a new mechanism of genetic control and established the biological relevance of the direct interaction between RNA and B_{12} coenzymes.[1,2] B_{12}-riboswitches are natural messenger RNAs (mRNAs) which bind coenzyme B_{12} (**1**) and then undergo a change in conformation ("switch"), suggested to lead to inhibition of the expression of proteins relevant in B_{12} biosynthesis or B_{12} transport.[1,3] Artificial RNA sequences with the ability to bind small molecules tightly, including vitamin B_{12},[4] have been prepared earlier by chemical in vitro evolution experiments.[4a,5] Such studies have served to expand our knowledge recently on the intriguing functional diversity of RNA.[6]

The possible structural changes in a bound B_{12} cofactor induced by an RNA environment pose an interesting problem, which has become even more relevant since the discovery of B_{12}-riboswitches. Indeed, the "complete" B_{12} derivatives can be considered to be molecular switches[7] themselves, in which the nucleotide base is either coordinated (base-on) or not coordinated (base-off; see Figure 1).[8,9]

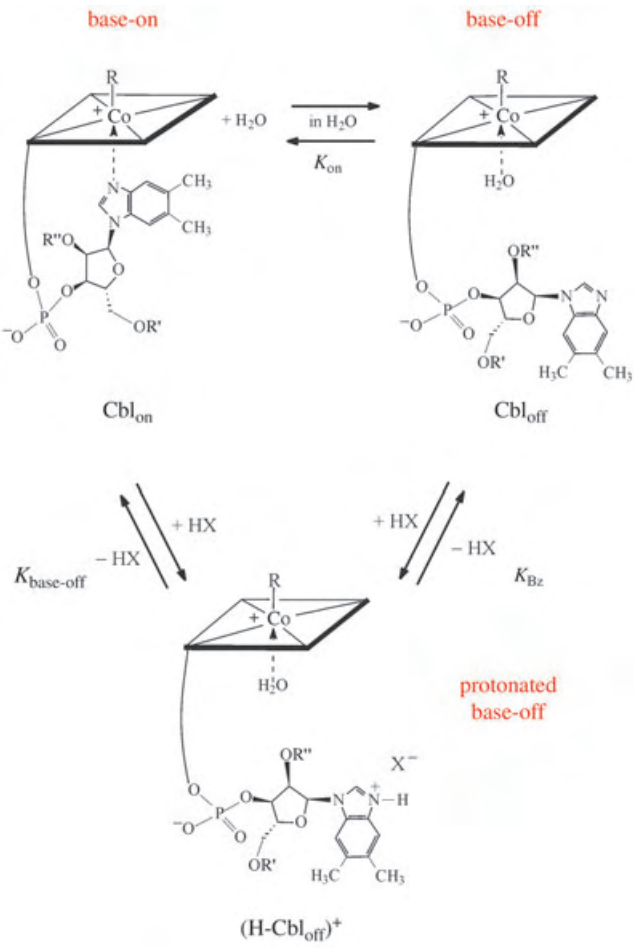

Figure 1. The B_{12} "molecular switch": The dimethylbenzimidazole (DMB) nucleotide base in coenzyme B_{12} (**1**) and other cobalamins (Cbl) is coordinated (base-on form Cbl_{on}) or noncoordinated (base-off form Cbl_{off}); protonation of DMB results in $(H-Cbl_{off})^+$ and release of the base from the cobalt center ($K_{on} = [Cbl_{on}]/[Cbl_{off}]$; $K_{Bz} = [Cbl_{off}]\text{-}[H^+]/[(H-Cbl_{off})^+]$; $K_{base\text{-}off} = (1 + K_{on})\,K_{Bz}$).

Coenzyme B_{12} (**1**)[10] and methylcobalamin (**2**) contain a 5,6-dimethylbenzimidazole (DMB) nucleotide, which harbors the known structural variability of the natural "complete" cobamides.[8,9] The nucleotide unit in B_{12} may be seen potentially as a remnant of interactions of corrinoids with a nucleotide environment.

To explore the chemical consequences of the interaction of B_{12} derivatives with a nucleotide environment in covalent models, we used vitamin B_{12} (**3**) to prepare conjugates of the organometallic B_{12} cofactors **1** and of **2** with (deoxy)nucleotides. Here we report on two covalent organometallic B_{12} nucleotides, Na-**4** (an RNA conjugate of **1**) and Na-**5** (a DNA conjugate of **2**; see Figure 2). These organometallic B_{12} nucleotides were designed as "B_{12}-*retro*-riboswitches", in which the appended (deoxy)nucleotide would assist in giving the base-off form (see Figure 1).

The synthesis of Na-**4** and Na-**5** proceeded via the cyanocorrinoids Na-**6** and Na-**7**, which were prepared by incorporation of DNA and RNA moieties, respectively, at O2R of **3**. This required the corresponding phosphoramidites[11] and reversible covalent attachment of the B_{12}

[*] Mag. S. Gschösser, Dr. C. Eichmüller,[+] Prof. Dr. B. Kräutler
Institut für Organische Chemie
Innrain 52a
and
Zentrum für molekulare Biowissenschaften
Leopold-Franzens-Universität Innsbruck
6020 Innsbruck (Austria)
Fax: (+43) 512-507-2892
E-mail: bernhard.kraeutler@uibk.ac.at
Dr. K. Gruber, Prof. Dr. C. Kratky
Institut für Chemie
Karl-Franzens-Universität Graz
Heinrichstrasse 28, 8010 Graz (Austria)
Fax: (+43) 316-380-9850
E-mail: christoph.kratky@kfunigraz.ac.at
[+] Present address:
Purdue University
West Lafayette (USA)

[**] We would like to thank Prof. K.-H. Ongania for mass spectrometric analyses, Mag. Tea Pavkov for assistance in X-ray data collection, Dr. M. Fasching, Prof. R. Micura, and Dr. C. Höbartner for helpful discussions, and F. Hoffmann-La Roche & Co., Basel, for a generous gift of vitamin B_{12}. We are also grateful to the Austrian National Science Foundation (FWF, project P13595), and the European Union (project EU-HPRN-CT-2002-00195) for support of our work.

Supporting information for this article is available on the WWW under http://www.angewandte.org or from the author.

 © 2005 Wiley-VCH Verlag GmbH & Co. KGaA, Weinheim DOI: 10.1002/anie.200462085

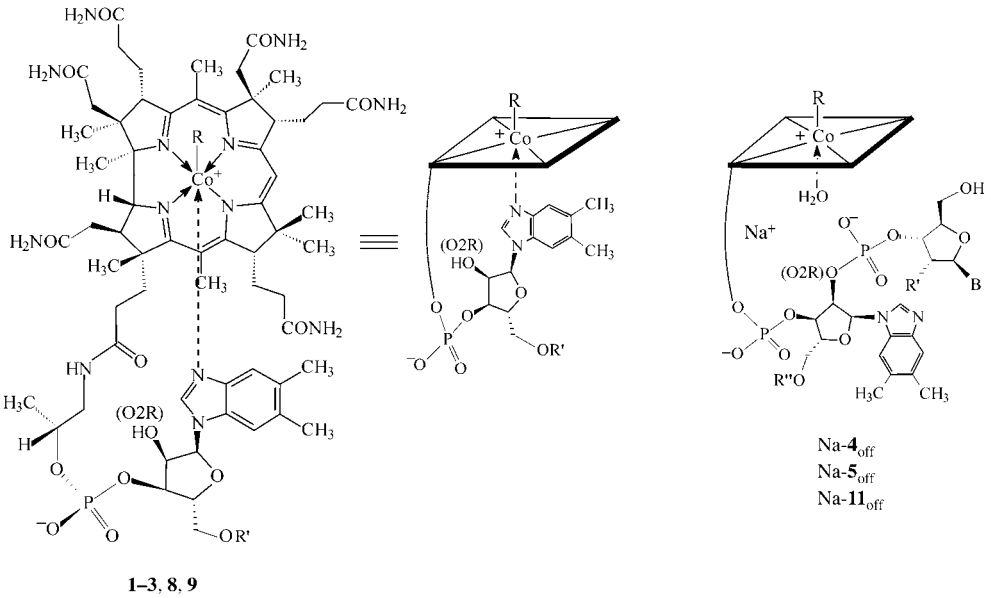

Figure 2. Left: coenzyme B_{12} (**1**, adenosylcobalamin, R = 5′-adenosyl, R′ = H), methylcobalamin (**2**, R = CH_3, R′ = H), vitamin B_{12} (**3**, cyanocobalamin, R = CN, R′ = H,), Co_β-cyano-5′-acetylcobalamin (**8**, R = CN, R′ = acetyl), Co_β-(3-carboxypropyl)-5′-acetylcobalamin (**9**, R = $(CH_2)_3CO_2H$, R′ = acetyl); right: Na-**4** (R = 5′-adenosyl, R′ = OCH_3, R″ = H, B = guanine), Na-**5** (R = CH_3, R′ = H, R″ = acetyl, B = thymine), and Na-**11** (R = CH_3, R′ = R″ = H, B = thymine) in their base-off forms Na-$\mathbf{4}_{off}$, Na-$\mathbf{5}_{off}$, and Na-$\mathbf{11}_{off}$.

substrate to a suitable solid support (Scheme 1).[12]. The essential intermediate Co_β-(3-carboxypropyl)-*O5R*-acetylcobalamin (**9**), made from Co_β-cyano-*O5R*-acetyl-cobalamin

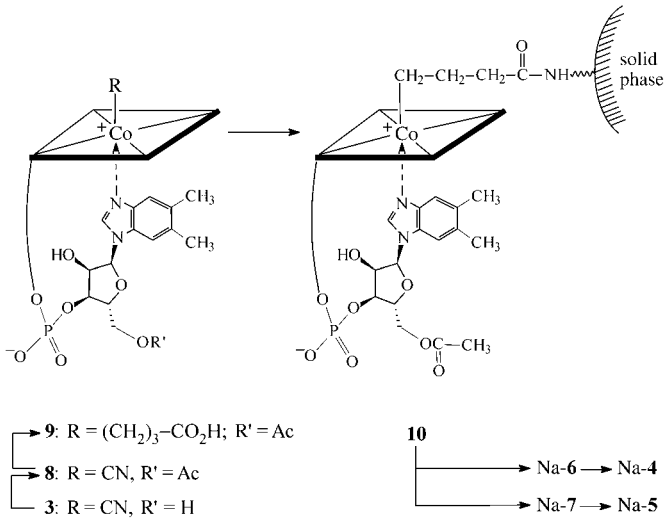

Scheme 1. Synthesis of the organometallic B_{12} nucleotides Na-**4** and Na-**5** via the solid-phase-bound B_{12} derivative **10**.

(**8**), was attached to an amino-functionalized Tentagel resin[11] to give the red solid **10**, which was coupled with *5′O*-dimethoxytrityl-*2′O*-methyl-*N2*-(4-isopropylphenyl)oxyacetyl-guanosyl-*3′O*-(β-cyanoethyl-*N*,*N*-diisopropyl)phosphoramidite (DMT-mGi^{Pr-PAC}) at room temperature. This step was followed by a modified oxidation/deprotection protocol including photo-induced cleavage from the solid support[12] to give Co_β-cyanocobalamin-(3″→*O2R*)-guanyl-3″-ate (Na-**6**). A corresponding protocol with *5′O*-dimethoxytrityl-2′-deoxythymidyl-*3′O*-(β-cyanoethyl-*N*,*N*-diisopropyl)phosphoramidite (DMT-T) and using triethylamine in pyridine in the deprotection step[12] gave the cyanocorrinoid Na-**7**.

For the preparation of Na-**4**, a solution of Na-**6** in methanol was reduced electrochemically to a cob(I)alamin-(3″→*O2R*)-guanyl-3″-ate,[13] which was treated with 5′-deoxy-5′-chloroadenosine to give Co_β-(5′-deoxyadenosyl)cobalamin-(3″→*O2R*)-guanyl-3″-ate (Na-**4**) in 74% yield. Crystalline red sodium Co_β-methyl-*O5R*-acetyl-cobalamin-(3″→*O2R*)-2″-deoxythymidyl-3″-ate (Na-**5**) was obtained similarly in 81% yield from the electrochemical reduction of Na-**7** and methylation at cobalt by methyl iodide.[12]

The molecular formulae of all new compounds were confirmed by mass spectrometry. The spectroscopic properties of Na-**6** and Na-**7** confirmed their structures and the suggested base-on constitution of these cyanocorrinoids (see the Supporting Information). In contrast, the UV/Vis spectra of Na-**4** and Na-**5** at room temperature feature absorbance maxima in the visible range which are shifted hypsochromically compared to those of the organometallic reference compounds **1** and **2**. The UV/Vis spectrum of Na-**4** in aqueous solution (pH 7) exhibits an absorption maximum at 473.5 nm, corresponding to a shift by about 50 nm to shorter wavelengths relative to the spectrum of **1** (Figure 3a). Using the absorbance coefficients at 523 nm of **1** and of the protonated base-off form H-$\mathbf{1}^+$, we estimated the spectrum of the RNA conjugate Na-**4** to correspond to 38% of the base-off form (Na-$\mathbf{4}_{off}$) and 62% of the base-on form (Na-$\mathbf{4}_{on}$) at room temperature. For the base-off/base-on equilibrium of Na-**4**, the data indicate $\Delta G_o = -1.2\ kJ\,mol^{-1}$ at 25°C. The base-on form Na-$\mathbf{4}_{on}$ is stabilized significantly less in Na-**4** than in coenzyme B_{12} (**1**), where the base-on form predominates strongly.[14]

 © 2005 Wiley-VCH Verlag GmbH & Co. KGaA, Weinheim

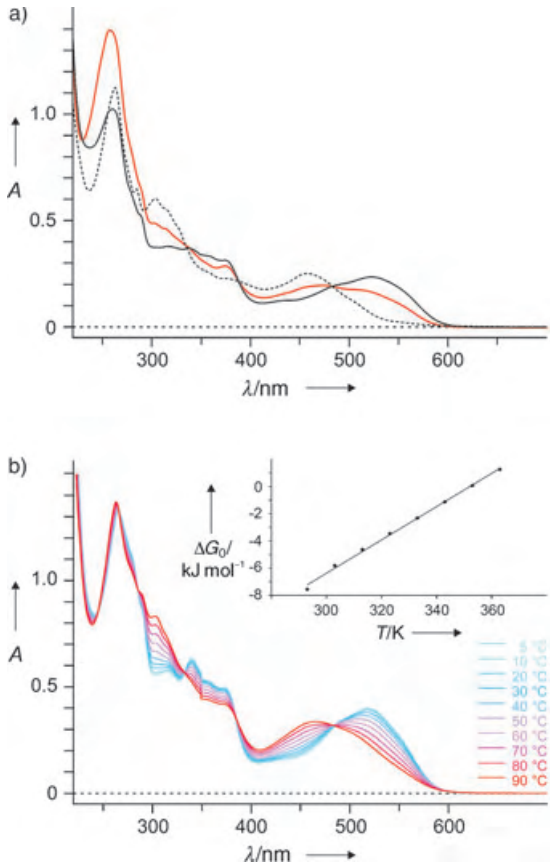

Figure 3. a) UV/Vis spectra at 26 °C of Na-**4** (red line) and base-on **1** (black line) ($c = 0.00034$ M, phosphate buffer, 1 mM, pH 7.0) and base-off **1** (dashed line, $c = 0.00034$ M, 0.1 M HCl, pH 1). b) UV/Vis spectra of Na-**5** at different temperatures ($c = 0.00049$ M, phosphate buffer, 10 mM, pH 7.0). Insert: Plot of ΔG_0 vs. T for the base-off/base-on equilibrium of Na-**5** (for details see the Supporting Information).

Likewise, by comparison with the UV/Vis spectrum of methylcobalamin (**2**) the spectrum of Co_β-methyl-cobalaminate Na-**5** exhibits a hypsochromic shift by about 13 nm (absorption maximum at 515 nm). In contrast to observations with **2**, the spectrum of the organometallic DNA conjugate Na-**5** shows a pronounced temperature dependence (see Figure 3b and the Supporting Information). The absorbance maximum in the spectrum of Na-**5** shifts from roughly 518 nm at low temperature to 466 nm at elevated temperatures (Figure 3b), indicative of a switch to a predominant base-off form. The temperature dependence of the UV/Vis spectra of Na-**5** was analyzed by using the extinction coefficients of the UV/Vis spectra of **2** in aqueous solution at pH 7 and of (H-**2**)$^+$ at pH 1. The spectra of Na-**5** fit a two-state model, for which $\Delta H_o = -40(\pm 3)$ kJ mol^{-1} and $\Delta S_o = -115(\pm 7)$ J K^{-1} mol^{-1} can be estimated (from the ratio of base-on and base-off forms, see the Supporting Information). Under similar experimental conditions the analogous values that were found earlier for **2** were $\Delta H_o = -31.6(\pm 1.6)$ kJ mol^{-1} and $\Delta S_o = -55.2(\pm 5.3)$ J K^{-1} mol^{-1} (see also ref.[15]).

Both the enthalpy and entropy values of the DNA conjugate Na-**5** are thus more negative than the data for **2**. However, the entropic contribution is more than twice as large in Na-**5**, and the temperature dependence of the base-on/base-off switch is more pronounced in the conjugate Na-**5**. Accordingly, the equilibrium constant K_{on}(Na-**5**) decreases from about 10 at 25 °C to 0.8 at 80 °C.[16] In contrast, the analogous base-off/base-on equilibrium of **2** favors the base-on form strongly throughout the whole temperature range (K_{on}(**2**) = 93 at 25 °C, 62 at 80 °C).[15] These values are about 10 and 80 times, respectively, larger than those of Na-**5**, indicating ΔG_o of the equilibrium in Na-**5** to be shifted by roughly $-9(-13)$ kJ mol^{-1} towards the base-off form Na-$\mathbf{5}_{off}$.

Protonation of the DMB base in cobalamins leads to decoordination from the cobalt center and to the base-off form (Figure 1).[15,17] The basicity of "complete" corrinoids thus is a measure of their stabilization by formation of the base-on form. The pH-dependent UV/Vis and CD spectra of Na-**5** (see the Supporting Information) were used to determined a pK_a(H-**5**) value of 3.78($\pm$0.02), which is about 0.9 units higher than than pK_a(H-**2**)$^+$.[15] This indicates the **5**$^-$ ion to be about six times more basic than **2**, in line with a less strongly coordinated DMB base in Na-**5**.

Crystals of the B_{12} nucleotide Na-**5** obtained from aqueous acetone did not diffract well; however, crystals that formed from water at 5 °C over 18 months proved suitable for X-ray analysis at a crystallographic resolution of 1.02 Å.[18] The crystals contained Na-**11**, the sodium complex in the base-on constitution of adventitiously deacetylated Na-**5** (Figure 4). This type of deacetylation in aqueous solution has precedence in other O5R-acylated B_{12} derivatives.

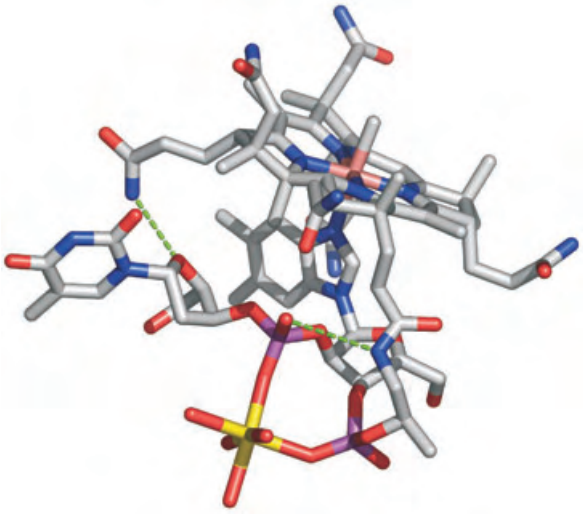

Figure 4. Crystal structure of the base-on DNA conjugate Na-**11**. The hydrogen bonds are indicated by dashed lines. C gray, N blue, O red, Na yellow, P violet.

The crystal structure of Na-**11** features the base-on form of a "complete" Co_β-methylcorrinoid, in which the DMB base is coordinated to cobalt with an axial Co–N3N bond length of 2.15 Å; this is slightly shorter than that in methylcobalamin (**2**).[19] Otherwise, the geometric characteristics of cobalamin segment in Na-**11** are similar to those in **2**. The mutual arrangement of the 2″-deoxythymidyl-3″-ate group and the cobamide moiety is well defined by two hydrogen bonds

 © 2005 Wiley-VCH Verlag GmbH & Co. KGaA, Weinheim

(Figure 4). A nonbonding contact exists between the interconnecting O atom O3R1 of the 2″-deoxythymidyl-3′-ate and the methyl group $H_3C(1A)$ (see the Supporting Information for the atom numbering). The sodium counterion is bound in a remarkable bidentate, bridging fashion to $OP1_R$ (of the 2″-deoxythymidyl-3′-ate phosphate and to OP_R (of the B_{12} nucleotide loop), forming an unprecedented sodium-containing nine-membered ring. The electron density of four water molecules indicates the metal ion to be coordinated by (overall) six ligands in a pseudooctahedral fashion and with bond lengths characteristic for a sodium ion. The finding of a well-structured, sodium-bridged base-on form in the crystal is compatible with an NMR study[16] of Na-**5** in aqueous solution at low temperatures. In contrast, the base-off form (Na-$\mathbf{5}_{off}$) is less well-defined; $\mathbf{5}_{off}^-$ is likely to be more flexible than $\mathbf{5}_{on}^-$ and not to bind a sodium ion as tightly.

In the organometallic B_{12} nucleotides Na-**4** and Na-**5** the attached nucleotide moiety induces the base-on form to rearrange to the base-off form (Figure 3b). This temperature-dependent switch is driven by large entropic effects. In contrast to the situation of the "B_{12}-riboswitches", where the result of B_{12} binding on the structure of an mRNA[2,20] was of concern, the focus of our work centered on the B_{12} moieties. The B_{12} nucleotides Na-**4** and Na-**5** represent covalent models of "B_{12}-*retro*-riboswitches", as it is their cobalamin moieties that are observed to undergo a switch under the influence of the appended (deoxy)nucleotide. "*Retro*-switching" by a nucleotide environment may be a common phenomenon in metabolite binding riboswitches.[21] It may be seen, in particular, in "B_{12}-riboswitches", as the "complete" corrinoids themselves can be switched between the base-on and the base-off forms. B_{12}-binding proteins[22,23] and a B_{12}-binding antibody[24] are B_{12}-specific examples for similar effects by protein environments. As observed in the latter case,[24] the resulting change of the structure of bound B_{12} cofactors affects their reactivity[25] and may increase their potency as catalysts in chemical and enzymatic reactions.[8] Indeed, the base-off form is a specific characteristic of corrinoid methyl transferases, such as methionine synthase.[22,26,27] However, in this multimodular enzyme, the B_{12} cofactor appears also to have a remarkable second role as a conformational "switch" in order to control selective methyl-group transfer reactions.[29]

Corrinoids extend the scope of biological catalysis and are essential in basic metabolic processes in archea and other microorganisms.[30] The corrin structure has been suggested to be of "pre-enzymatic" origin[31] and coenzyme B_{12} (or a simpler molecular progenitor of it) may have played a detrimental role in the appearance of DNA by reduction of ribonucleotides.[32] The reactivity of corrinoids thus may be of particular interest in the context of the hypothesis of an early RNA-based form of life.[6,33]

"Complete" corrinoids have evolved not only to be unique (organometallic) cofactors but also as biological "molecular switches". "B_{12}-*retro*-riboswitching", introduced here, may not only be relevant for coenzyme B_{12} binding mRNAs ("B_{12}-riboswitches"),[1–3] which highlight the genetic importance of the direct interaction between B_{12} derivatives and RNA, but also in the context of the question of how the catalytic functions of corrinoids could have arisen in a controlled way in a nucleotide environment. These aspects invite further studies on the hypothetical role of B_{12} in pre-enzymatic "life processes" in designed or evolved nucleotide environments. Investigations along these lines[12] are underway in our laboratories.

Received: September 23, 2004
Revised: November 9, 2004
Published online: February 11, 2005

Keywords: bioorganometallic chemistry · DNA · molecular switches · RNA · vitamin B_{12}

[1] a) A. Nahvi, N. Sudarsan, M. S. Ebert, X. Zou, K. L. Brown, R. R. Breaker, *Chem. Biol.* **2002**, *9*, 1043–1049; b) A. Nahvi, J. E. Barrick, R. R. Breaker, *Nucleic Acids Res.* **2004**, *32*, 143–150.

[2] W. C. Winkler, A. Nahvi, A. Roth, J. A. Collins, R. R. Breaker, *Nature* **2004**, *428*, 281–286.

[3] A. G. Vitreschak, D. A. Rodionov, A. A. Mironov, M. S. Gelfand, *RNA* **2003**, *9*, 1084–1097.

[4] a) J. R. Lorsch, J. W. Szostak, *Biochemistry* **1994**, *33*, 973–982; b) D. Sussman, J. C. Nix, C. Wilson, *Nat. Struct. Biol.* **2000**, *7*, 53–57.

[5] a) S. E. Osborne, A. D. Ellington, *Chem. Rev.* **1997**, *97*,349–370; b) M. Famulok, A. Jenne, *Curr. Opin. Chem. Biol.* **1998**, *2*, 320–327.

[6] *The RNA World* (Eds.: R. F. Gesteland, T. R. Cech, J. F. Atkins), Cold Spring Harbor Laboratory Press, Cold Spring Harbor, **1999**.

[7] *Molecular Switches* (Ed.: B. Feringa), Wiley-VCH, Weinheim, **2001**.

[8] B. Kräutler, S. Ostermann in *The Porphyrin Handbook*, *Vol. 11* (Eds.: K. M. Kadish, K. M. Smith, R. Guilard), Elsevier Science, Dordrecht, **2003**, pp. 229–276.

[9] W. Fieber, B. Hoffmann, W. Schmidt, E. Stupperich, R. Konrat, B. Kräutler, *Helv. Chim. Acta* **2002**, *85*, 927–944.

[10] P. G. Lenhert, D. C. Hodgkin, *Nature* **1961**, *192*, 937–938.

[11] *Nucleic Acids in Chemistry and Biology* (Eds.: G. M. Blackburn, M. J. Gait), Oxford University Press, Oxford, UK, **1996**.

[12] M. Fasching, H. Perschinka, C. Eichmüller, S. Gschösser, B. Kräutler, *Chem. Biodiversity*, in press.

[13] B. Kräutler in *Chemistry and Biochemistry of B_{12}* (Ed.: R. Banerjee), Wiley, New York, **1999**, pp. 315–339.

[14] K. L. Brown, J. M. Hakimi, *J. Am. Chem. Soc.* **1986**, *108*, 496–503.

[15] K. L. Brown, S. Peck-Siler, *Inorg. Chem.* **1988**, *27*, 3548–3555.

[16] In the 500-MHz ^{1}H NMR spectra of Na-**5** recorded between 4 °C and 62 °C the position of diagnostic signals (such as of HC(10), $H_3C(1A)$, HC2N, HC4N) confirmed the switch of Na-**5** from a predominant base-on form at low temperatures to a base-off form at higher temperatures.

[17] a) K. L. Brown, J. M. Hakimi, D. M. Nuss, Y. D. Montejano, D. W. Jacobsen, *Inorg. Chem.* **1984**, *23*, 1463–1471; b) J. M. Pratt in *B_{12}, Vol. I* (Ed.: D. Dolphin), Wiley, New York, **1982**, pp. 325–392.

[18] Structure determination of Na-**11** (crystals grew from water): $C_{74}H_{103}N_{15}O_{21}P_2CoNa\cdot(H2o)22$, $M_r = 2078.9$, space group $P4_3$, $a = 17.699$ Å, $c = 61.906$ Å, $R_{sym} = 0.041$. Diffraction data to a maximum resolution of 1.02 Å were collected at 103 K using synchrotron radiation ($\lambda = 0.8126$ Å) on beamline X11 at EMBL/DESY in Hamburg. Refinement on F^2 (9540 unique reflections, 2497 parameters and 3072 restraints) converged at residuals of $R1 = 0.1018$ and $wR2 = 0.2799$ for all reflections.

 © 2005 Wiley-VCH Verlag GmbH & Co. KGaA, Weinheim

Details are given in the Supporting Information. CCDC 249566 contains the supplementary crystallographic data for this paper. These data can be obtained free of charge from the Cambridge Crystallographic Data Centre via www.ccdc.cam.ac.uk/data_request/cif.

[19] C. Kratky, B. Kräutler in *Chemistry and Biochemistry of B_{12}* (Ed.: R. Banerjee), Wiley, New York, **1999**, pp. 9 – 41.

[20] a) E. Nudler, A. Mironov, *Trends Biochem. Sci.* **2004**, *29*, 11 – 17; b) S. Müller, *ChemBioChem* **2002**, *3*, 817 – 819.

[21] The binding of large cofactors to a biomacromolecular matrix often is associated with a mutual structural adaptation, see, for example, T. Hermann, D. J. Patel, *Science* **2000**, *287*, 820 – 826.

[22] a) C. L. Drennan, S. Huang, J. T. Drummond, R. G. Matthews, M. L. Ludwig, *Science* **1994**, *266*, 1669 – 1674; b) M. L. Ludwig, P. R. Evans in *Chemistry and Biochemistry of B_{12}* (Ed.: R. Banerjee), Wiley, New York, **1999**, pp. 595 – 632.

[23] E. Nexø in *Vitamin B_{12} and B_{12}-Proteins* (Eds.: B. Kräutler, D. Arigoni, B. T. Golding), Wiley-VCH, Weinheim, **1998**, pp. 461 – 471.

[24] R. B. Hannak, R. Konrat, W. Schüler, B. Kräutler, M.-T. M. Auditor, D. Hilvert, *Angew. Chem.* **2002**, *114*, 3765 – 3768; *Angew. Chem. Int. Ed.* **2002**, *41*, 3613 – 3616.

[25] B. Kräutler, *Helv. Chim. Acta* **1987**, *70*, 1268 – 1278.

[26] R. G. Matthews, *Acc. Chem. Res.* **2001**, *34*, 681 – 689.

[27] The base-off form is also found in many, though not all, of the other known B_{12}-dependent enzymes.[8,22,28]

[28] A. Abend, R. Nitsche, V. Bandarian, E. Stupperich, J. Rétey, *Angew. Chem.* **1998**, *110*, 643 – 645; *Angew. Chem. Int. Ed. Engl.* **1998**, *37*, 625 – 627.

[29] V. Bandarian, M. L. Ludwig, R. G. Matthews, *Proc. Natl. Acad. Sci. USA* **2003**, *100*, 8156 – 8163.

[30] K. Sauer, R. K. Thauer in *Chemistry and Biochemistry of B_{12}* (Ed.: R. Banerjee), Wiley, New York, **1999**, pp. 655 – 679.

[31] A. Eschenmoser, *Angew. Chem.* **1988**, *100*, 5 – 40; *Angew. Chem. Int. Ed. Engl.* **1988**, *27*, 5 – 40.

[32] J. Stubbe, J. Ge, C. S. Yee, *Trends Biochem. Sci.* **2001**, *26*, 93 – 99.

[33] a) T. R. Cech, *Biochem. Soc. Trans.* **2002**, *30*, 1162 – 1166; b) F. Joyce, *Nature* **2002**, *418*, 214 – 221; c) A. Schwögler, T. Carell, *Org. Lett.* **2000**, *2*, 1415 – 1418; d) S. Tsukiji, S. B. Pattnaik, H. Suga, *Nat. Struct. Biol.* **2003**, *10*, 713 – 717.

 © 2005 Wiley-VCH Verlag GmbH & Co. KGaA, Weinheim

Photoreceptor Mimetics

"Turn ON/OFF your LOV light": Boron-dipyrromethene–Flavin Dyads as Biomimetic Switches Derived from the LOV Domain**

Christian Trieflinger, Knut Rurack, and Jörg Daub**

The induction and control of many important biological processes rely on light signals. Chromophores participate in actions such as charge separation, ion pumping, neural responses, or photostimulated movement as photoreceptors or photosensors.[1] In the course of evolution, Nature has created rather complex biochemical processes that are photoregulated or -mediated, for example, the visual process or light-activated plant defense. As light is a very convenient tool to be used as a trigger or control signal, chemists have been attracted by the potential that lies in photobiological systems to be adopted for the design of artificial supramolecular ensembles that show addressable photochemical activity. Primary research areas here include photoresponsive membranes, light-controlled host–guest chemistry, and photochemical switching.[2] Among the latter, however, biologically inspired systems are still scarce, and the examples reported so far have been mainly accomplished in conjunction with polymeric structures.[3]

Distinct molecular systems are even less abundant.[4] This is surprising as particular biochemical moieties are very attractive candidates for multimode supramolecular photoswitches, a field of research in which we have become increasingly interested over the years.[5] One such example is the functionalized isoalloxazine chromophore. Flavins are among the most important biological redox-active dye units, and their rich photo, redox, and (inter)molecular chemistry distinguish them as ideal composites for sophisticated chemical switches.[6] Furthermore, a flavin residue is at the heart of the active site of one of the most exciting photorecepting proteins, the LOV (light-, oxygen-, or voltage-sensing)

[*] Dr. C. Trieflinger, Prof. J. Daub
Institut für Organische Chemie
Universität Regensburg
Universitätsstrasse 31, 93053 Regensburg (Germany)
Fax: (+49) 941-943-4984
E-mail: joerg.daub@chemie.uni-regensburg.de
Dr. K. Rurack
Div. I.3
Bundesanstalt für Materialforschung und -prüfung (BAM)
Richard-Willstätter-Strasse 11, 12489 Berlin (Germany)
Fax: (+49) 30-8104-5005
E-mail: knut.rurack@bam.de

[**] From the song by D. Malone and J. W. Scott (1961). LOV = light-, oxygen-, or voltage-sensing domain (*Science* **1997**, *278*, 2120). Financial support by the Deutsche Forschungsgemeinschaft (DFG) and the Studienstiftung des Deutschen Volkes is highly appreciated. This work is part of the Graduate College "Sensory Photoreceptors in Natural and Artificial Systems" granted by DFG (GRK 640).

Supporting information for this article is available on the WWW under http://www.angewandte.org or from the author.

 © 2005 Wiley-VCH Verlag GmbH & Co. KGaA, Weinheim DOI: 10.1002/anie.200462377

domains of phototropin.[7,8] Based on this background and owing to the exceptional complementarity of flavin and the borondipyrromethene (BDP) fluorophore, which itself exhibits several important features of efficient photoswitching,[9] we designed the BDP–flavin dyads **1–3** to realize our idea of a distinctly controllable and reversible fluorescent switch (for synthetic details, see Supporting Information).

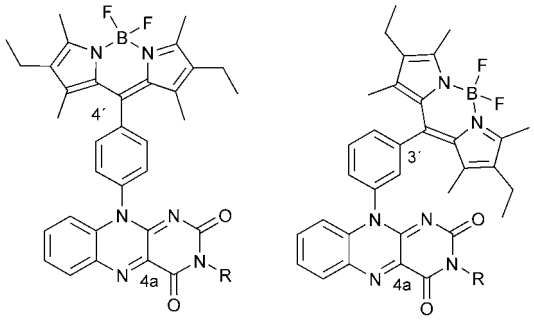

1: 4′-BDP, R = CH_3
2: 3′-BDP, R = CH_3
3: 4′-BDP, R = H

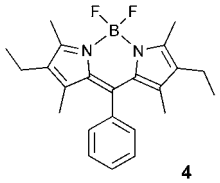

4
(reference compound)

The data in Table 1 and Figure 1 clearly reveal the composite nature of the dyads as the absorption spectra of **1–3** are a linear combination of the bands of the subchromophores, the main maxima being centered at 530 nm (BDP) and 449 nm (flavin). This indication of electronically decoupled ground states is further supported by cyclic voltammetry, in which the reversible reduction of flavin (−1.1 V vs. Fc^+/Fc) and the quasi-reversible oxidation and reduction of BDP (0.65 V, −1.6 V vs. Fc^+/Fc) are found at the expected potentials. The different electrochemical behavior of **3** compared with **1** and **2**, deducible from the additional reoxidation peak at −0.92 V vs. Fc^+/Fc (Table 1), is ascribed to the well-known ECE (electron transfer–chemical step–electron transfer) mechanism of flavin which involves an intermolecular proton-assisted redox reaction.[10] The results obtained for the ground-state properties of **1–3** presented so far suggest that one important prerequisite for the facile control of a switch is fulfilled, that is, both switching modules are independent. However, to generate ON/OFF behavior as expressed by strong signal changes in light output, a well-defined OFF state is necessary, especially when a switch is constructed from two strongly emitting fluorophores such as flavin and BDP. In this respect, the suitability of our design rationale is evident from Table 2 (see also the theoretical considerations detailed in the Supporting Information).

Table 1: Absorption (in $CHCl_3$) and redox data (in MeCN) of **1–3** ($E_{1/2}$ in V vs. Fc^+/Fc).

	λ_{abs} [nm] ([lg ε]/[lg ($M^{-1}cm^{-1}$)])	$E^{red}_{1/2}$ [V]	$E^{c,red}_{p}$ [V]	$E^{red}_{1/2}$ [V]	$E^{ox}_{1/2}$ [V]
1	529 (4.86), 448 (4.15)	−1.11	–	−1.60	0.65
2	531 (4.81), 449 (4.12)	−1.11	–	−1.63	0.66
3	531 (4.81), 448 (4.10)	−1.10	−0.92	−1.63	0.65

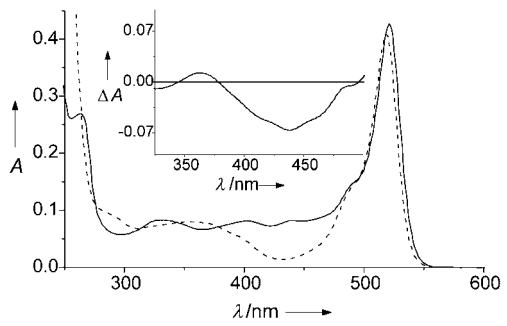

Figure 1. Absorption spectra of **1** (solid line) and twofold reduced $\mathbf{1}^{red}$ ($c = 5\times10^{-6}$ M; dashed line) in MeCN/MeOH (1:1). Inset: Difference spectrum of the flavin region.

Table 2: Fluorescence properties of **1–3**.

	Solvent	$\Phi_f \times 10^{-3}$ [a]	τ_f [ps][b]	τ_f [ns][c]
1	MeCN/toluene[d]	1.3/2.3	10/17	–
	EtOH	1.6	13	5.33
2	MeCN/toluene[d]	0.7/1.3	6/11	–
	EtOH	1.0	8	5.54
3	MeCN/toluene[d]	0.8/1.5	6/10	–
$\mathbf{3}^{-}$ [e]	MeCN	8.8	96	–

[a] Relative to fluorescein 27 in NaOH (0.1 N; 0.90 ± 0.03),[15] ±15%. [b] At 298 K, ±3 ps. [c] At 77 K, ±0.003 ns. [d] First value in MeCN, second in toluene. [e] Deprotonated with 1,8-diazabicyclo[5.4.0]undec-7-ene (DBU).

All three dyads show only a weak fluorescence with typical BDP features, regardless of solvent polarity and proticity. No isoalloxazine emission could be detected, even with excitation at 449 nm. The fluorescence also decays rapidly, stressing the fact that an efficient nonradiative deactivation path exists in the title compounds. Furthermore, **1** and **2** show a very similar behavior, excluding any influence of a "meta" effect.[11] The important role of the directly fused phenylene spacer becomes apparent, especially from the emission data. This moiety acts simultaneously as an orbital insulator (by preventing a mixing of states that is often found in connection with the "meta" effect) and as an electronic mediator (by enabling efficient fluorescence quenching). At 77 K, the fluorescence increases dramatically, and decay times that are typical for BDP dyes and close to the value of the reference compound **4** (6.27 ns) are measured. Again, after excitation of the flavin, only BDP emission can be detected, thus suggesting that efficient energy transfer to the BDP occurs. At room temperature, photoinduced electron transfer (PET) from the BDP to the electron-poor flavin most probably accounts for the strong quenching of the fluorescence.

 © 2005 Wiley-VCH Verlag GmbH & Co. KGaA, Weinheim

In glassy ethanol at 77 K, PET is inhibited as a result of the freezing out of solvent reorganization and intramolecular movement. This interpretation is supported by the results obtained upon deprotonation of **3** at N3. Such an increase in electron density at the flavin entails a >10-fold enhancement of the BDP emission (Table 2). Dyads **1** and **2**, which are methylated at N3, do not show any spectroscopic changes upon base addition.

Once the conventional OFF state of the switch was defined, the next step was to install a control function that allows this state to be "unlocked". The versatile redox chemistry of flavin[6] allows such an activation to be performed chemically. In this experiment and in analogy to thiol-based natural systems, the spectroscopic changes were monitored in situ during the chemical reduction of the flavin moiety with 1,3-propanedithiol[12] and DBU in MeCN/MeOH (1:1) under an argon atmosphere. The products were the twofold reduced dyads $\mathbf{1}^{red}$ and $\mathbf{2}^{red}$ and [1,2]dithiolane. As can be seen in Figure 1, the flavin absorption at 440 nm decreases, whereas the BDP absorption is not affected, which clearly indicates that the redox process occurs in the flavin. However, both $\mathbf{1}^{red}$ and $\mathbf{2}^{red}$ are still weakly fluorescent, with fluorescence lifetimes within the resolution of the instrument ($\tau_f = 3$–5 ps). These observations now mark the chemically controlled OFF state and can be explained by a reversal of the ET process (Supporting Information). In the reduced dyads, the electron density at the flavin is so high that excitation of the BDP triggers a PET from the flavin to the BDP, reductive PET processes being well-known for donor-substituted BDPs (Figure 2).[9b]

Now that we were able to switch between an inactive and an activated OFF state, the last requirement concerned the input that allows reversible OFF/ON switching. Keeping in mind the discourse in the introductory paragraph, at this stage the photomediated reaction cycle of the LOV domain comes into play. If a solution with the chemically activated ensemble is irradiated with UV light of 254 nm, a strong increase in BDP fluorescence is noticed. The high efficiency of the switching process is strikingly evident from a several-100-fold enhancement of BDP emission and is manifested in τ_f values of 4.96 and 5.27 ns for the systems based on **1** and **2**. The two reduced dyads are fully and rapidly converted, and after turning off the UV-light source, the fluorescence decreases again to its initial value.

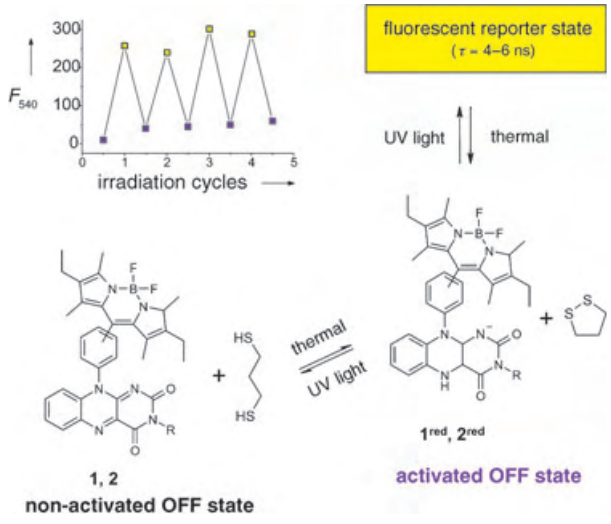

Figure 2. Reaction scheme of the thermal and photochemical switching between the non-activated OFF states (**1**, **2**), the activated OFF states ($\mathbf{1}^{red}$, $\mathbf{2}^{red}$), and the ON state (reporter state). Inset: Reversible switching between the activated OFF (mauve) and the ON state (yellow) of $\mathbf{1}^{red}$ as reflected by the change in emission intensity in MeCN/MeOH (1:1) during several irradiation cycles with cycle times of 30 s irradiation and 300 s thermal reverse reaction ($c_1 = 1 \times 10^{-6}$ M).

The reversibility of this reaction is shown in Figure 2, which indicates that irreversible side reactions do not play a major role. Most probably, UV irradiation initiates the formation of a thermally unstable but highly emissive species, which is accumulated upon continuous irradiation. Dyads $\mathbf{1}^{red}$ and $\mathbf{2}^{red}$ are then regenerated in a thermal reverse reaction. Although the real nature of the emitting species could not yet be analytically determined with methods available to us, the results strongly suggest that the electron density of the flavin is considerably lower than in the oxidized state, but higher than in the fully reduced state. A mono-reduced state can be excluded as such radicals would also quench the emission.

Thus, we tentatively assume that the light-induced formation of an emissive flavin–thiol adduct in analogy to the LOV domain photocycle occurs under the prevailing reaction conditions. The thermal recovery rates reported for LOV domains are commonly in the range of 0.02 to 0.003 s^{-1}, depending on its type, the medium, and possible protein assistance.[7,13] These properties suggest that a C4a adduct or a C4a–C10a cycloadduct might be involved under the present, more-extreme conditions. Further experiments are currently underway to elucidate the mechanism in more detail.

In conclusion we have presented novel BDP–flavin dyads with distinctive electrochemical and optical properties, including energy- and electron-transfer-modulated emission. The direction and efficiency of the ET process can be influenced by various input signals, such as the addition of base, redox processes, and irradiation with light. These features distinguish **1** and **2** as potent biomimetic photochemical switches[14] in which the activation state can be independently controlled and the output emission reversibly switched.

Received: October 20, 2004
Published online: March 8, 2005

Keywords: boron · flavin · fluorescence · molecular switches · photoreceptors

[1] M. A. van der Horst, K. J. Hellingwerf, *Acc. Chem. Res.* **2004**, *37*, 13–20.
[2] a) T. Kinoshita, *J. Photochem. Photobiol. B* **1998**, *42*, 12–19; b) I. Willner, B. Willner in *Molecular Switches* (Ed.: B. L. Feringa), Wiley-VCH, Weinheim, **2001**, pp. 165–218.
[3] a) O. Pieroni, A. Fissi, N. Angelini, F. Lenci, *Acc. Chem. Res.* **2001**, *34*, 9–17; b) I. Willner, S. Rubin, *React. Polym.* **1993**, *21*, 177–186.

 © 2005 Wiley-VCH Verlag GmbH & Co. KGaA, Weinheim

[4] a) A. Niemz, V. M. Rotello, *Acc. Chem. Res.* **1999**, *32*, 44 – 52; b) Z. Shen, R. Prochazka, J. Daub, N. Fritz, N. Acar, S. Schneider, *Phys. Chem. Chem. Phys.* **2003**, *5*, 3257 – 3269.
[5] a) H. Spreitzer, J. Daub, *Chem. Eur. J.* **1996**, *2*, 1150 – 1158; b) K. Rurack, M. Kollmannsberger, J. Daub, *Angew. Chem.* **2001**, *113*, 396 – 399; *Angew. Chem. Int. Ed.* **2001**, *40*, 385 – 387; c) K. Rurack, A. Koval'chuck, J. L. Bricks, J. L. Slominskii, *J. Am. Chem. Soc.* **2001**, *123*, 6205 – 6206.
[6] *Chemistry and Biochemistry of Flavoenzymes*, *Vol. 1* (Ed.: F. Müller), CRC, Boca Raton, FL, **1991**.
[7] a) T. E. Swartz, S. B. Corchnoy, J. M. Christie, J. W. Lewis, I. Szundi, W. R. Briggs, R. A. Bogomolni, *J. Biol. Chem.* **2001**, *276*, 36493 – 36500; b) E. Schleicher, R. M. Kowalczyk, C. W. M. Kay, P. Hegemann, A. Bacher, M. Fischer, R. Bittl, G. Richter, S. Weber, *J. Am. Chem. Soc.* **2004**, *126*, 11067 – 11076.
[8] LOV domains are the primary signaling subunits of blue-light photoreceptors and sense light, oxygen, or voltage. They transfer the information to serine/threonine kinases. In the primary step, a C4a-thiol adduct of flavin mononucleotide is formed.
[9] a) R. A. Wagner, J. S. Lindsey, *J. Am. Chem. Soc.* **1994**, *116*, 9759 – 9760; b) M. Kollmannsberger, T. Gareis, S. Heinl, J. Breu, J. Daub, *Angew. Chem.* **1997**, *109*, 1391 – 1393; *Angew. Chem. Int. Ed. Engl.* **1997**, *36*, 1333 – 1335; c) M. Kollmannsberger, K. Rurack, U. Resch-Genger, W. Rettig, J. Daub, *Chem. Phys. Lett.* **2000**, *329*, 363 – 369.
[10] A. Niemz, J. Imbriglio, V. M. Rotello, *J. Am. Chem. Soc.* **1997**, *119*, 887 – 892.
[11] F. D. Lewis, J.-S. Yang, *J. Am. Chem. Soc.* ***1997***, *119*, 3834 – 3835.
[12] E. L. Loechler, T. C. Hollocher, *J. Am. Chem. Soc.* **1980**, *102*, 7312 – 7321.
[13] M. Salomon, J. M. Christie, E. Knieb, U. Lempert, W. R. Briggs, *Biochemistry* **2000**, *39*, 9401 – 9410.
[14] For a native LOV domain as a photochromic switch, see: J. T. M. Kennis, I. H. M. van Stokkum, S. Crosson, M. Gauden, K. Moffat, R. van Grondelle, *J. Am. Chem. Soc.* **2004**, *126*, 4512 – 4513.
[15] J. Olmsted III, *J. Phys. Chem.* **1979**, *83*, 2581 – 2584.

 © 2005 Wiley-VCH Verlag GmbH & Co. KGaA, Weinheim

Green Chemistry

A Cartridge System for Organometallic Catalysis: Sequential Catalysis and Separation Using Supercritical Carbon Dioxide to Switch Phases**

*Maurizio Solinas, Jingyang Jiang, Othmar Stelzer†, and Walter Leitner**

There is continued interest in homogeneous organometallic catalysis[1] as an important synthetic tool in the research and production of fine chemicals and pharmaceuticals. As a consequence, effective separation techniques are needed increasingly for the clean isolation of products and catalyst recycling.[2,3] A promising approach toward this goal is provided by regulated systems in which a defined substitution pattern in the periphery of the metal's coordination sphere affects the catalyst's solubility, making it possible to switch between two states: the catalyst is homogeneously dissolved during the reaction and precipitates quantitatively in the separation stage.[4] The most commonly used parameters to induce the precipitation are temperature,[5] solvent polarity,[6] and pH of the solution.[7] It has been shown also that compressed and in particular supercritical carbon dioxide[8] ($scCO_2$, $T_c = 31.0\,°C$, $p_c = 73.75$ bar) can be used to control the solubility of transition-metal catalysts, such that one can switch from the reaction mode to the separation stage in certain cases.[9,10]

Ideally, in a regulated system all reaction components are removed from the precipitated catalyst quantitatively under mild conditions to ensure that the catalyst remains available for repeated application in homogenous form after redissolving. In particular, it would be attractive to devise a "catalyst cartridge" with a single catalyst batch for a range of transition-metal-catalyzed conversions utilizing different substrates or even different reaction types in the same apparatus

[*] Dr. M. Solinas, Dr. J. Jiang, Prof. Dr. W. Leitner
Institut für Technische und Makromolekulare Chemie
RWTH Aachen
Worringer Weg 1, 52074 Aachen (Germany)
Fax: (+49) 241-8022177
E-mail: leitner@itmc.rwth-aachen.de
Prof. Dr. W. Leitner
Max-Planck-Institut für Kohlenforschung
Kaiser-Wilhelm-Platz 1, 45472 Mülheim an der Ruhr (Germany)
Dr. J. Jiang, Prof. Dr. O. Stelzer†+
FB 9, Anorganische Chemie
Universität Wuppertal
Gaussstrasse 20, 42097 (Germany)
Dr. J. Jiang
Permanent address:
Dalian Institute of Technology, Dalian 116023 (P.R. China)
[†] Deceased on January 27, 2002.
[**] This work was supported by the German Ministry of Research and Education (BMBF) under the ConNeCat program as part of the project "Regulated Systems for Multiphase Catalysis—smart solvents/smart ligands", the Deutsche Forschungsgemeinschaft, and the Fonds der Chemischen Industrie.

 DOI: 10.1002/anie.200461768 © 2005 Wiley-VCH Verlag GmbH & Co. KGaA, Weinheim

with an integrated separation technique.[11] Several limitations hamper the development of efficient systems for cartridge catalysts based on the more conventional regulated systems:

1) Thermal and/or chemical stress can lead to deactivation of the organometallic catalyst.
2) Additives used to induce precipitation may accumulate in the catalyst compartment or require additional operations for purification of the product stream.
3) Reaction and separation are difficult to integrate if pressurized gases are used as reagents.
4) As the catalyst must be soluble in a broad range of reaction mixtures of different polarities, it can be difficult or even impossible to find a suitable solvent for separation without cross-contamination and catalyst leaching.

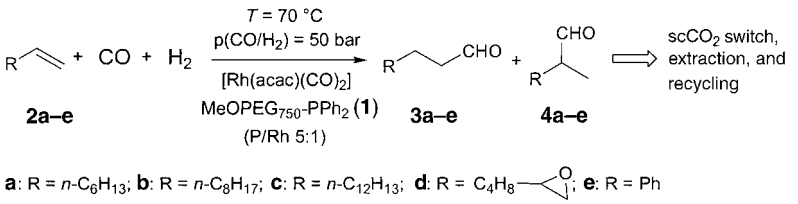

Scheme 1. Hydroformylation as a benchmark reaction to validate the cartridge catalyst system **1**/[Rh(acac)(CO)$_2$]/scCO$_2$.

We report here on the design and application of a system approaching the cartridge-catalyst ideal based on the use of a poly(ethyleneglycol) (PEG) modified phosphine ligand in a CO$_2$-regulated reaction/separation sequence (Figure 1).

In contrast to liquid solvent systems, separation with scCO$_2$ can be regulated through a combination of polarity and volatility.[12] The design of ligand **1**[13] reflects this principle. A PEG chain of moderate length ($M_w = 750$, $n = 16$) was used having a medium polarity compatible with a broad range of chemical environments and an almost negligible vapor pressure considerably below that of typical reaction products in fine-chemical applications. This substitution pattern makes catalysts based on ligand **1** soluble in a variety of organic substrates without the need for additional solvents; at the same time they are expected to be completely insoluble in scCO$_2$ even at high density.

We chose the hydroformylation of 1-octene (**2a**) initially as our benchmark reaction to validate these considerations (Scheme 1). In a first set of experiments we found that the hydroformylation of **2a** catalyzed by a catalyst formed in situ from **1** and [Rh(acac)(CO)$_2$] (acac = acetylacetonate; P/Rh = 5:1) could be "switched off" completely by the introduction of CO$_2$ into the reactor. Thus, conversion achieved within two hours' reaction time ($T = 70\,°C$, $p(H_2/CO) = 50$ bar) dropped from 99% in the absence of CO$_2$ to 66.4% at a density $d(CO_2) = 0.35\ g\,mL^{-1}$ to 0% at $d(CO_2) = 0.57\ g\,mL^{-1}$. Visual inspection revealed that this complete stop of the reaction was accompanied by precipitation of a yellow-orange solid, demonstrating the perfect separation of the catalyst and substrate **2a**.[14] When CO$_2$ was introduced after the two-hour reaction time, the same efficient separation was induced in the product mixture (Figure 2). A mixture of **3a** and **4a**

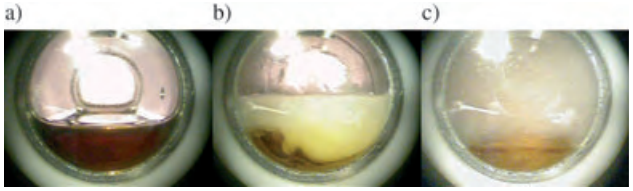

Figure 2. CO$_2$-induced quantitative precipitation of the rhodium catalyst formed from **1** and [Rh(acac)(CO)$_2$] during hydroformylation of **2a**. a) Reaction mixture without CO$_2$, b) during addition of CO$_2$, and c) after introduction of CO$_2$ at a density of approximately 0.5 g mL^{-1}.

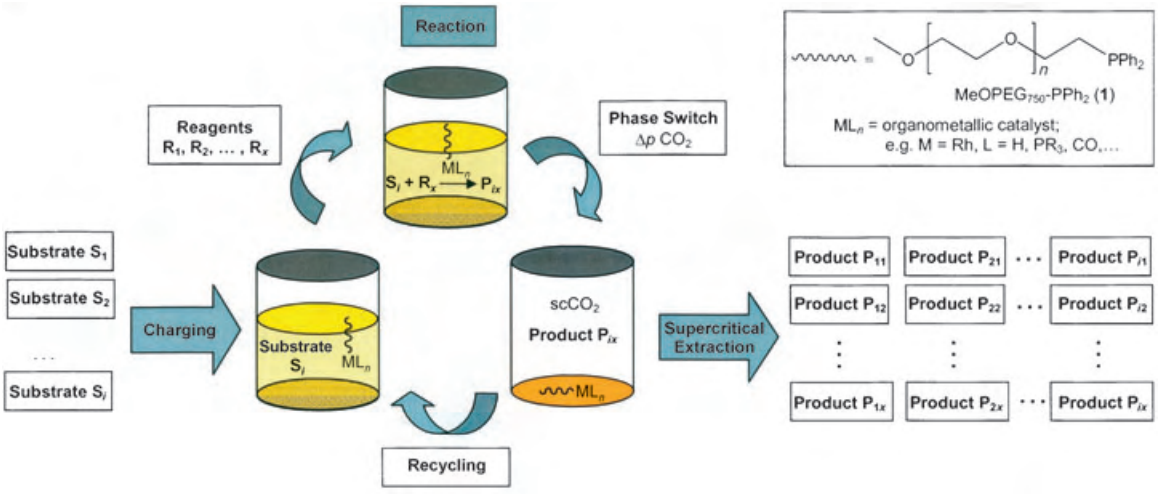

Figure 1. The cartridge catalyst system should be flexible enough such that any of a variety of transition-metal-catalyzed conversions of substrates S$_i$ with different reagents R$_x$ can give the desired product P$_{ix}$ by means of one single catalyst batch with the same apparatus and separation techniques. In the present case, a PEG-modified phosphine ligand defines the solubility properties of a rhodium catalyst, and scCO$_2$ is used to switch from the reaction stage (homogeneously dissolved catalyst) to the separation/extraction stage (precipitated catalyst).

 © 2005 Wiley-VCH Verlag GmbH & Co. KGaA, Weinheim

(*n*/*iso* = 2.5:1) was isolated quantitatively in solvent-free form with low levels of metal contamination (ca. 5 ppm, vide infra) by extraction with $scCO_2$. The reaction/separation sequence was repeated successfully six times with no significant changes in conversion or selectivity (conversion: 99.3–99.7%, *n*/*iso*: 2.3:1–2.5:1, isomerization: 1.6–2.5%, recovery of organic material: 91–103%).

Based on these findings, a catalyst cartridge based on **1**/[Rh(acac)$(CO)_2$] (P/Rh = 5:1) was successfully implemented for the hydroformylation of a set of structurally diverse olefins **2a**–**e** using $scCO_2$ to induce a phase switch and mass separation (Table 1).[11] After a recycling experiment with **2a** as described above, the substrate was changed to **2b**, which was equally well converted and isolated in two subsequent runs. The same was shown for styrene (**2e**) and the functionalized olefin **2d**. In cycle 9 substrate **2a** was employed again; the results demonstrated that the catalyst had largely preserved its high activity and selectivity throughout the procedure. This was further confirmed by an additional run in which the **2a**/Rh ratio was increased to 3000:1; the resulting turnover frequency was 852 h^{-1} and the selectivity for **3a** was 72.2%.

Table 1: Hydroformylation of **2a**–**e** using MeOPEG$_{750}$-PPh_2 (**1**)/[Rh(acac)$(CO)_2$]/$scCO_2$.

Cycle[a]	Substr.	Substr./Rh	Conv. [%]	Prod., sel. [%]	$scCO_2$ extraction[b] *T* [°C]/*p* [bar]/*V* [L]	Recov. [%]
1	**2a**	984	>99	**3a**, 73.7	45–50/80–96/130	87.0
2	**2a**	1010	>99	**3a**, 72.2	45–50/85–95/140	92.7
3	**2c**	1018	>99	**3c**, 70.6	45–50/120–130/188	99.8
4	**2c**	1003	>99	**3c**, 70.6	45–50/120–140/200	100
5	**2d**	997	>99	**3d**, 68.8	45–50/90–100/120	100
6	**2d**	1010	>99	**3d**, 68.9	45–50/95–105/130	100
7	**2e**	1039	>99	**4e**, 90.0	45–50/86–95/115	91.0
8	**2e**	1015	>99	**4e**, 89.8	45–50/88–100/120	91.0
9	**2a**	1056	94.1	**3a**, 73.0	45–50/80–100/100	86.2

[a] For details see the Experimental Section. [b] The exit flow was maintained at 0.5–0.7 L min^{-1}; the total volume of CO_2 is given as a liter of gas at standard conditions.

The conditions of the extraction step were not optimized in detail, albeit slightly higher pressures and longer extraction times were applied for the less volatile products. The products were collected from the CO_2 stream upon depressurization in two sequential cold traps kept at −60 °C. Small amounts of the more volatile products **3a** and **4e** were lost by evaporation in this simple setup, but in general the recovery of organic material was good to excellent. Most importantly, the products of the individual reactions were obtained without any significant cross-contamination of material from the previous runs (< 0.5% according to GC analysis). A total turnover number of almost 11 000 was achieved over the nine consecutive reactions. Rhodium and phosphorous contamination in all samples was determined by ICP MS (inductively coupled plasma mass spectrometry), and the total loss of the original catalyst amounted to 1.2% for rhodium and 2.4% of phosphorous over the entire sequence. It is important to note that none of the products **3a**–**e**/**4a**–**e** would be amenable to isolation by distillation without thermal decomposition of the catalyst. Furthermore, it would be very difficult, if not impossible, to achieve a comparable efficient separation by standard solvent extraction owing to the similarities in polarity between catalyst and some of the substrates.

Encouraged by the promising performance of the cartridge system **1**/[Rh(acac)$(CO)_2$]/$scCO_2$ for hydroformylation, we wanted to extend our approach to a series of different reaction types. It is now necessary that the precipitated catalyst is able to enter different catalytic cycles independent of its previous history. The hydrogenation, hydroformylation, and hydroboration of styrene **2e** were chosen as test reactions for our catalyst cartridge (Scheme 2). All three reactions involve phosphine rhodium hydride fragments as part of the active intermediates, providing a reasonable chance of linking the different catalytic cycles.

We were very pleased to find that the reaction sequence shown in Scheme 2 can be indeed realized with the cartridge system **1**/[Rh(acac)$(CO)_2$]/$scCO_2$. Excellent results were obtained over extended periods of time independent of the starting point and the order of the subsequent reactions. Figure 3 shows the results of a representative series starting with hydroboration and following the reaction/separation sequence of Scheme 2 in a clockwise manner

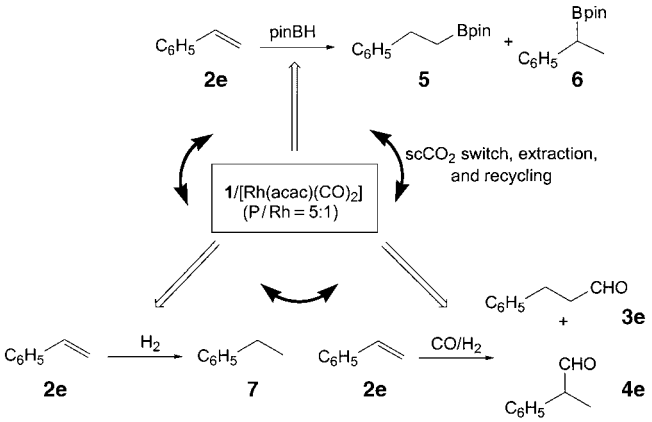

Scheme 2. A series of different catalytic reactions carried out sequentially with the cartridge catalyst system **1**/[Rh(acac)$(CO)_2$]/$scCO_2$; pinBH = pinacolborane.

The series of reactions was carried out in a 24-mL stainless steel reactor equipped with a window. The substrate-to-metal ratio **2e**/Rh was adjusted to approximately 1000:1 in all cases, and no additional solvent was used. The catalyst was formed in situ in the first run from **1** and [Rh(acac)$(CO)_2$] (P/Rh = 5:1). As the initial reaction a hydroboration of **2e** was carried out with pinacol borane at room temperature for (3 h)

 © 2005 Wiley-VCH Verlag GmbH & Co. KGaA, Weinheim

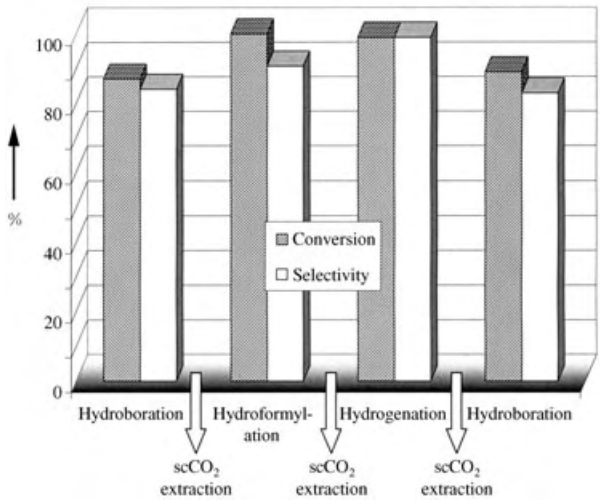

Figure 3. Representative example for a series of different catalytic reactions linked sequentially with the cartridge system **1**/[Rh(acac)(CO)$_2$]/scCO$_2$ (see Scheme 2 and text for details).

followed by extraction of all organic material with scCO$_2$ (45 °C/60–100 bar). The conversion of **2e** was 87 %, the two regioisomeric borane adducts **5** and **6** were the only significant products (**7** was formed in 1 % yield), and the selectivity for the branched product **5** was 84 %. A new batch of **2e** was added to the material remaining in the reactor, and a hydroformylation was carried out and worked up as described above (see Table 1, entry 8). Complete conversion with a selectivity of 90 % for **4e** was achieved. In the third catalytic process, hydrogenation of **2e** ($T = 50$ °C, $p(H_2) = 50$ bar, $t = 2$ h) and subsequent extraction with scCO$_2$ (45 °C/80 bar) gave ethylbenzene (**7**) in practically quantitative yield. Finally, the sequence was completed with a hydroboration, which gave results identical to those from the initial run (89 % conversion, 83 % selectivity for **5**). All samples were analyzed for their rhodium and phosphorous content; the total loss over all four reactions was only 0.16 and 1.3 %, respectively.

In summary, we have demonstrated for a series of rhodium-catalyzed reactions that the combination of a PEG-modified phosphine ligand and scCO$_2$ as phase switch provides an efficient cartridge system for organometallic catalysis. As all reactions examined here were carried out neat and proceeded as 100 % atom-efficient addition reactions, no solvent waste or by-products were generated and the products were isolated directly in high purity. The equipment required for handling the supercritical fluid is largely identical to that established in supercritical extraction or chromatography. Thus it would be possible to retrofit a commercially available technology platform to accommodate this reaction–separation system. The method is readily scalable to small- or medium-size production, and can be automated and even parallelized for the generation of libraries of structural diversity on a laboratory scale. This seems particularly intriguing for reactions involving pressurized gases, for which the integration of reaction and separation in one operation unit is notoriously difficult in the context of conventional homogeneous catalysis.

Although the metal contamination (ca. 5 ppm) achieved under the nonoptimized conditions reported here would be too high for larger scale production in many cases, it may be acceptable in synthetic laboratory-scale applications. Further reduction of the catalyst leaching seems possible by improved engineering and optimization of the extraction conditions. Another limitation of the system at its current stage of development is imposed by the range of catalytic transformations that can be achieved with the ligand type **1**. However, the synthetically straightforward modification of achiral or chiral ligands with PEG chains together with the significant solubility of a large body of organic compounds in scCO$_2$ suggest that this strategy can be extended also to other broadly applicable catalytic systems. Side chains other than PEG may also be envisaged to provide similar solubility properties, for example, ionic groups such as those reported recently for continuous-flow hydroformylation of propene.[10e]

Experimental Section

Safety warning: Experiments using compressed gases must be carried out only with appropriate equipment and under rigorous safety precautions.

Typical procedure for the catalysis/separation sequence, exemplified by the hydroformylation of **2a**–**e**. A window-equipped stainless steel reactor ($V = 24$ mL) was charged under argon atmosphere with [Rh(acac)(CO)$_2$] (0.01 mmol) and ligand **1**[13] (0.05 mmol). Substrate **2a** (10 mmol) was added under argon to give a clear orange solution, and the reactor was heated to 70 °C. The reaction was started by introduction of synthesis gas (H_2/CO = 1:1, 50 bar) and allowed to proceed for two hours during which the color of the reaction mixture changed to dark red. At the end of the reaction, the autoclave was cooled to 50 °C, and carbon dioxide was added to reach a density of approximately 0.5–0.6 g mL^{-1}. An orange solid precipitated and most of the liquid product dissolved. The extraction was performed by flushing CO$_2$ through the reactor at a flow rate of approximately 0.5–0.7 mL min^{-1} (STP); the reactor was maintained at a temperature between 45 and 50 °C and a pressure between 80 and 100 bar. After exiting the reactor, the CO$_2$ stream was vented to ambient pressure through a series of two cold traps (−60 °C). The extraction process was monitored visually through the windows of the reactor and continued for twice the time after which no liquid product was visible in the reactor. The contents of the cold traps were combined and collected for off-line analysis, and the reactor was charged again with a new batch of substrate for the next cycle.

Received: August 23, 2004
Revised: November 16, 2004
Published online: March 10, 2005

Keywords: green chemistry · homogeneous catalysis · phosphine ligands · rhodium · supercritical fluids

[1] a) *Transition Metals for Organic Synthesis* (Eds.: M. Beller, C. Bolm), Wiley-VCH, Weinheim, **1998**; b) *Applied Homogeneous Catalysis with Organometallic Compounds* (Eds.: B. Cornils, W. A. Herrmann), 2nd ed., Wiley-VCH, Weinheim, **2000**.
[2] a) *Green Chemistry: Theory and Practice* (Eds.: P. T. Anastas, J. Warner), Oxford University Press, Oxford, **1998**; b) R. A. Sheldon, *Pure Appl. Chem.* **2000**, *72*, 1233–1246; c) P. T. Anastas, M. M. Kirchhoff, *Acc. Chem. Res.* **2002**, *35*, 686–694.
[3] a) R. T. Baker, W. Tumas, *Science* **1999**, *284*, 1477–1479; b) D. J. Cole-Hamilton, *Science* **2003**, *299*, 1702–1706; c) *Aqueous-*

 © 2005 Wiley-VCH Verlag GmbH & Co. KGaA, Weinheim

Phase Organometallic Catalysis (Eds.: B. Cornils, W. A. Herrmann), 2nd ed., Wiley-VCH, Weinheim, **2004**.

[4] a) D. E. Bergbreiter, *Chem. Rev.* **2002**, *102*, 3345 – 3384; b) Z. Jin, Y. Wang, X. Zheng in *Aqueous-Phase Organometallic Catalysis* (Eds.: B. Cornils, W. A. Herrmann), 2nd ed., Wiley-VCH, Weinheim, **2004**, pp. 301 – 311.

[5] a) D. E. Bergbreiter, R. Chandran, *J. Am. Chem. Soc.* **1987**, *109*, 174 – 179; b) D. E. Bergbreiter, L. Zhang, V. M. Mariagnanam, *J. Am. Chem. Soc.* **1993**, *115*, 9295 – 9296; c) E. A. Karakhanov, E. A. Runova, G. V. Berezkin, E. B. Neimerovets, *Macromol. Symp.* **1994**, *80*, 231 – 240.

[6] a) M. Wende, J. A. Gladysz, *J. Am. Chem. Soc.* **2003**, *125*, 5861 – 5872; b) V. K. Dioumaev, R. M. Bullock, *Nature* **2004**, *434*, 530 – 532.

[7] a) T. Malmström, C. Andersson, *J. Mol. Catal. A* **1997**, *116*, 237 – 245; b) D. E. Bergbreiter, Y.-S. Liu, *Tetrahedron Lett.* **1997**, *38*, 3703 – 3706.

[8] a) *Chemical Synthesis Using Supercritical Fluids* (Eds.: P. G. Jessop, W. Leitner), Wiley-VCH, Weinheim, **1999**; b) W. Leitner, *Acc. Chem. Res.* **2002**, *35*, 746 – 756.

[9] a) D. Koch, W. Leitner, *J. Am. Chem. Soc.* **1998**, *120*, 13398 – 13404; b) S. Kainz, A. Brinkmann, W. Leitner, A. Pfaltz, *J. Am. Chem. Soc.* **1999**, *121*, 6421 – 6429; c) G. Franciò, K. Wittmann, W. Leitner, *J. Organomet. Chem.* **2001**, *621*, 130 – 142; d) W. Leitner, A. M. Scurto in *Aqueous-Phase Organometallic Catalysis* (Eds.: B. Cornils, W. A. Herrmann), 2nd ed., Wiley-VCH, Weinheim, **2004**, pp. 665 – 685.

[10] a) M. F. Sellin, D. J. Cole-Hamilton, *J. Chem. Soc. Dalton Trans.* **2000**, *11*, 1681 – 1683; b) C. D. Ablan, J. P. Hallett, K. N. West, R. S. Jones, C. A. Eckert, C. L. Liotta, P. G. Jessop, *Chem. Commun.* **2003**, 2972 – 2973; c) M. Wei, G. T. Musie, D. H. Busch, B. Subramaniam, *J. Am. Chem. Soc.* **2002**, *124*, 2513 – 2517; d) G. B. Combes, F. Dehghani, F. P. Lucien, A. K. Dillow, N. R. Foster in *Reaction Engineering for Pollution Prevention* (Eds.: M. A. Abraham, R. P. Hesketh), Elsevier Science, Dordrecht, **2000**, pp. 173 – 181; e) P. B. Webb, D. J. Cole-Hamilton, *Chem. Commun.* **2004**, 612 – 613.

[11] For examples of sequential catalytic reactions of different olefins on polymer-bound heterogenized rhodium catalysts, see: a) A. J. Sandee, J. N. H. Reek, P. C. J. Kamer, P. van Leeuwen, *J. Am. Chem. Soc.* **2001**, *123*, 8468 – 8476; b) F. Shibahara, K. Nozaki, T. Hiyama, *J. Am. Chem. Soc.* **2003**, *125*, 8555 – 8560.

[12] For this reason in his pioneering work on natural product extraction, Kurt Zosel referred to supercritical-fluid extraction as "Destraktion", an artificial word composed from Latin "destillare" and "extrahere". K. Zosel, *Angew. Chem.* **1978**, *90*, 748; *Angew. Chem. Int. Ed. Engl.* **1978**, *17*, 702.

[13] Ligand **1** was obtained as a colorless solid in 81 % yield on a 30-g scale from the reaction of $MeOPEG_{750}$-$OS(O)_2Me$ with $LiPPh_2$ in THF. ^1H NMR (CD_3OD): $\delta = 2.40$ (t, 2H), 3.38 (s, 3H), 3.54–3.65 (m, 71H), 7.35–7.48 ppm (m, 10H); $^{13}C\{^1H\}$ NMR $\delta = 30.0$ (d, $J_{CP} = 13$ Hz), 69.7 (d, $J_{CP} = 23$ Hz), 59.2 (s), 71.3–71.7 (m), 129.7 (s), 129.9 (d, $J_{CP} = 12$ Hz), 133.9 (d, $J_{CP} = 19$ Hz), 139.9 ppm (d, $J_{CP} = 13$ Hz); $^{31}P\{^1H\}$ NMR $\delta = -21.1$ ppm.

[14] It is important to note that rhodium catalysts based on other very poorly CO_2-soluble ligands tend to give some background reaction under similar conditions either through formation of liquid phases[10a] or through small amounts of unmodified soluble rhodium carbonyl complexes.[9c] These ligands cannot be recycled with the high efficiency required for cartridge catalysts as experimentally verified for the hydroformylation of **2a** with the system PPh_3/[$Rh(acac)(CO)_2$]/$scCO_2$, where the selectivity and activity were found to decrease significantly upon recycling.

 © 2005 Wiley-VCH Verlag GmbH & Co. KGaA, Weinheim

Natural Product Synthesis

Total Synthesis of the Marine Natural Product *rac*-Dibromophakellstatin**

*Delphine E. N. Jacquot, Michael Zöllinger, and Thomas Lindel**

Dedicated to Professor Rolf Huisgen

Pyrrole-imidazole alkaloids from marine sponges constitute a family of over 100 natural products.[1] Some of them have an important ecological function in the chemical defense against fish,[2] bacteria, and corals.[3] Moreover, a number of interesting pharmacological activities of the pyrrole-imidazole alkaloids have been reported. Among them, the cytotoxicity of dibromophakellstatin (**1**) and the immunosuppressive activity of palau'amine (**2**) are remarkable (Figure 1).

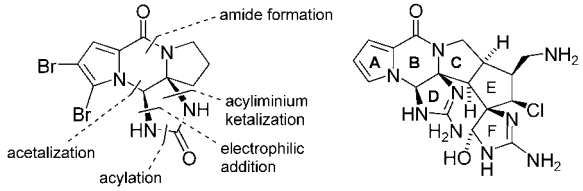

Figure 1. Outline of the total synthesis of the marine natural product dibromophakellstatin (**1**).

Thus far, pyrrole-imidazole alkaloids have been detected in the sponge cells but not in associated microorganisms.[3] Their total synthesis[4] is necessary for further biological evaluation. This is especially true for dibromophakellstatin (**1**), of which only 31 mg has been isolated from 170 kg of *Phakellia mauritiana*.[5] Both compound **1** and palau'amine (**2**) have ABCD tetracycles.[6] In a pioneering paper Büchi and Foley disclosed a biomimetic synthesis of the guanidine analogue *rac*-dibromophakellin.[7] A very similar biomimetic synthesis of *rac*-dibromophakellstatin (*rac*-**1**) was achieved 20 years later by Horne et al.[8] Recently, Romo et al. described the first enantioselective synthesis of *ent*-**1**, which required more than 15 steps.[9]

[*] Dr. D. E. N. Jacquot,[+] Dipl.-Chem. M. Zöllinger, Prof. Dr. T. Lindel
Department Chemie und Biochemie
Ludwig-Maximilians-Universität München
Butenandtstrasse 5–13, 81377 Munich (Germany)
Fax: (+49) 89-2180-77734
E-mail: thomas.lindel@cup.uni-muenchen.de

[+] Present address:
Department of Chemistry
University of Pennsylvania
Philadelphia, PA 19104 (USA)

[**] We thank Dr. Kurt Polborn and Dr. Peter Mayer for crystal structure determinations.

Supporting information for this article is available on the WWW under http://www.angewandte.org or from the author.

 DOI: 10.1002/anie.200462252 © 2005 Wiley-VCH Verlag GmbH & Co. KGaA, Weinheim

Herein, we describe a novel five-step synthesis of *rac*-dibromophakellstatin (*rac*-**1**) starting from L-prolinol. The key step in the synthesis is the direct assembly of ring D from the readily available, unsymmetrical dipyrrolopyrazinone **3** (Figure 2) by reaction with ethoxycarbonylnitrene generated in situ.

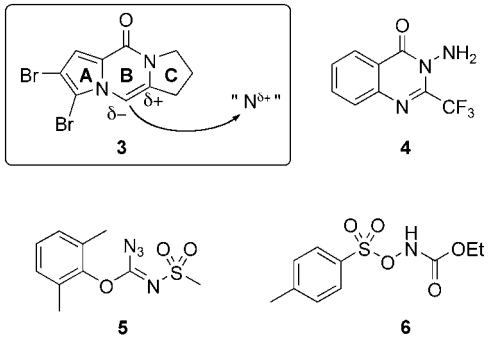

Figure 2. Functionalization of tricycle **3** with N electrophiles.

Tricycle **3**[10] features an electron-rich enamine double bond between C10 and C10a that is prone to react with nitrogen electrophiles. In a model study we investigated the reaction of **3** with *N*-aminoquinazolinone **4**[11] in the presence of $Pb(OAc)_4$, which provided the trisubstituted hydrazide **7** (Scheme 1). The *trans* configuration of hydroxy analogue **8** obtained in the presence of traces of water was secured by X-ray analysis.[12] However, attempts to reduce the trisubstituted hydrazide unit of **7** with samarium diiodide or sodium in ammonia failed. When we tried to acylate hydrazide **7** in the presence of NaH in order to facilitate reduction of the N–N bond,[13] the dipyrroloimidazolone **9** was formed by contraction of ring B (Scheme 1).

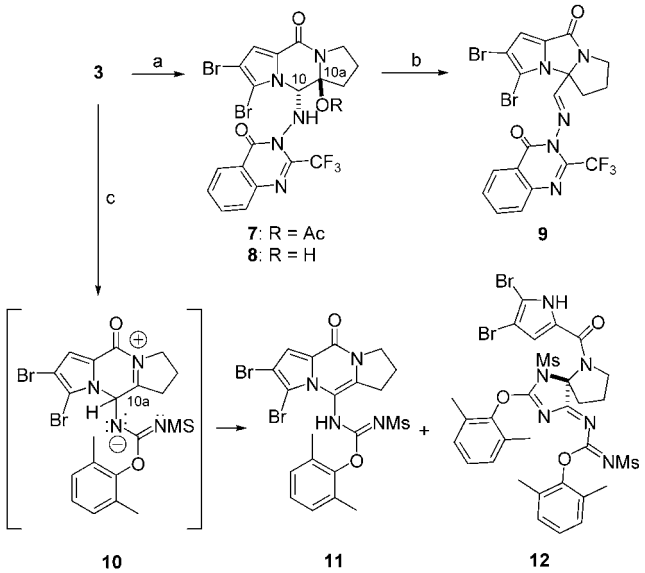

Scheme 1. Study of the electrophilic attack at the C10–C10a double bond of **3**. a) **4**, $Pb(OAc)_4$, CH_2Cl_2, 0→23 °C, 24 h, 58%; b) NaH, THF, 23 °C, then reflux, 48 h, 35%; c) **5**, dioxane, reflux, 8 h. **11**: 35%; **12**: 10%. Ms = methanesulfonyl.

We then analyzed the reactivity of the nitrenes generated from the sources **5** and **6** (Figure 2) towards the tricyclic acylenamine **3**.[14,15] Compound **5** would provide an isourea-derived nitrene, which could first add electrophilically to C10. The second nitrogen atom would act as a nucleophile in the subsequent ring closure to give the tetracycle. Thermolysis of the azide **5** in dioxane for 8 h in the presence of **3** led mainly to the formation of the alkenyl isourea **11**, which arose presumably via intermediate **10** (Scheme 1).

Compound **11** was accompanied by a less polar product which was identified conclusively by X-ray analysis as **12** (Figure 3).[12] Two equivalents of the nitrene had been

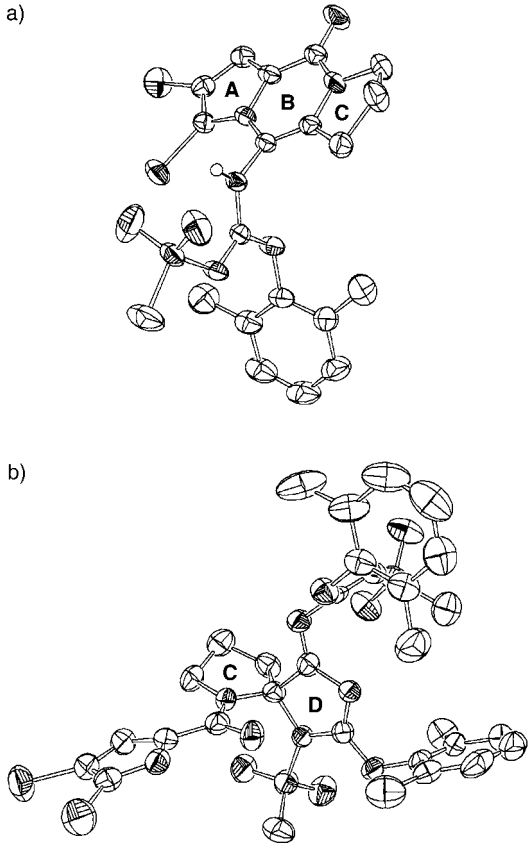

Figure 3. ORTEP drawings of **11** (a) and **12** (b) in the crystal (50% probability level). Hydrogen atoms are omitted for clarity.[12]

incorporated, and the imidazolinone ring had closed, but at the cost of ring B opening. The resulting spirocycle **12** possesses an ACD ring system. An orthoamide involving the pyrrole nitrogen can be discussed as an intermediate, which undergoes ring-opening to yield the amidine partial structure of **12** with release of strain energy. We had already obtained a similar ACD *spiro*-hydantoin by cyclization of an open-chain precursor.[16]

The goal of assembling the ABCD tetracycle was achieved by reaction of the tricycle **3** with ethyl *N*-tosyloxycarbamate (**6**) in the presence of calcium oxide.[17] In the first step deprotonation of the urethane **6** at room temperature generates the corresponding nitrene by α-elimination of tosylate.[14] One of the compounds in the product mixture

 © 2005 Wiley-VCH Verlag GmbH & Co. KGaA, Weinheim

turned out to be the alkenyl carbamate **13**, the structure of which was confirmed by X-ray analysis (Scheme 2, Figure 4).[12] Upon heating of the alkenyl carbamate **13** and aqueous ammonia in methanol in a sealed tube at 120 °C for

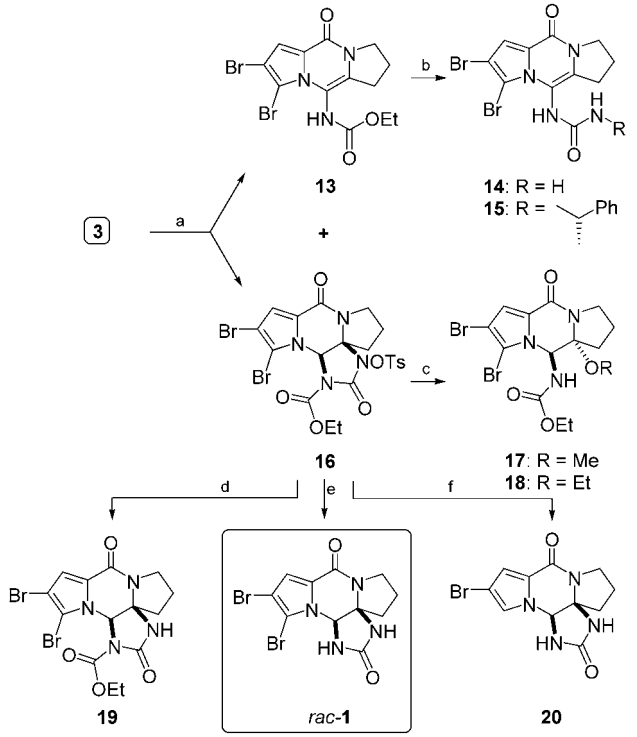

Scheme 2. Two-step synthesis of *rac*-dibromophakellstatin (*rac*-**1**) from the tricycle **3**. a) **6** (7 equiv), CaO (7 equiv), CH_2Cl_2, 23 °C, 24 h, after chromatography: **13** (20%) and **16** (25%); b) **14**: 25% NH_3, MeOH, 120 °C, 12 h, 46%; **15**: (*S*)-(−)-1-phenylethylamine, *N*-methyl-2-pyrrolidinone, 150 °C, 2 h, 51%; c) 5 N NaOH, EtOH, 23 °C, 16 h, then chromatography with RP-18, MeOH, H_2O: **17** (34%) and **18** (15%); d) SmI_2 (2.5 equiv), THF, 23 °C, 15 min, 95%; e) SmI_2 (5 equiv), THF, 23 °C, 36 h, then MeOH, 23 °C, 12 h, 76%; f) i. SmI_2 (7.5 equiv), THF, 23 °C, 36 h, then MeOH, 23 °C, 12 h, 50%. Ts = toluenesulfonyl.

12 h, the alkenyl urea **14** was readily obtained (Scheme 2). The chiral analogue **15** was obtained from (*S*)-(−)-1-phenylethylamine in a similar manner, and we hoped to be able to cyclize ring D under acidic conditions. Kishi et al. had reported the related construction of the imidazoline ring of saxitoxin from an alkenyl urea.[18] However, in our case neither cyclization of **14** nor of **15** to the corresponding tetracycle could be achieved.

Importantly, further analysis of the reaction mixture (Scheme 2) led to the isolation of a product (25% yield) containing the desired tetracycle. The configuration of the cyclic urea **16** was deduced from an HMBC correlation between the hemiaminal proton 10-H and the ethoxycarbonyl carbon, and X-ray analysis of **16** confirmed our conclusions (Figure 4). The tosyloxy group is attached to 10a-N. The alkenyl carbamate **13** and the tetracycle **16** possibly arise from a common acyliminium intermediate formed on electrophilic attack of a nitrene at C10. Deprotonation of that intermediate could provide **13** directly, while incorporation of a second

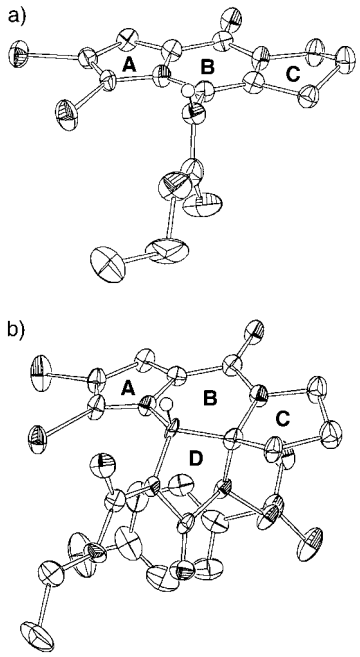

Figure 4. ORTEP drawings of **13** (a) and **16** (b) in the crystal (50% probability level). Hydrogen atoms are omitted for clarity.[12]

tosyloxycarbamoyl group and elimination of ethanol are necessary for the formation of **16.** The attack at C10a appears to occur from the same side of the ABC system as the initial attack at C10, but currently the mechanism is unclear.[19]

Simultaneous to and independent of our work, Pellacani and co-workers reported direct formation of different cyclic ureas with the *tert*-butyl analogue of the urethane **6**.[20] Interestingly, they obtained a cyclic urea that did not contain a tosyloxy but rather butoxy group, probably due to a Lossen-type rearrangment forming *tert*-butoxyisocyanate.[21]

In an initial attempt, alkaline hydrolysis (NaOEt) of the carbamate moiety led to the open-chain carbamates **17** and **18** after workup with methanol. Samarium diiodide[22] proved to be the key to the clean deprotection of **16** to furnish *rac*-dibromophakellstatin (*rac*-**1**). Selective removal of the tosyloxy moiety of **16** with complete retention of the two bromine substituents proceeded with 2.5 equiv of SmI_2, affording **19** (Scheme 2). To our satisfaction, the use of 5.0 equiv of SmI_2 smoothly led to the additional deprotection of the imidazolone ring and provided the natural product *rac*-dibromophakellstatin (*rac*-**1**). Treatment of **16** with 7.5 equiv of SmI_2 yielded monobromophakellstatin (**20**). Reduction of carbamates with SmI_2 has rarely been reported.[23]

In summary, the total synthesis of *rac*-dibromophakellstatin (*rac*-**1**) was accomplished in only five steps and with 8% overall yield starting from L-prolinol.[24] Key steps of the synthesis are the direct annulation of imidazolinone ring from the dipyrrolopyrazinone **3** using nitrene chemistry and the simultaneous deprotection of the nitrogen atoms of the tetracycle **16** with SmI_2.

Received: October 8, 2004
Revised: December 3, 2004
Published online: March 4, 2005

 © 2005 Wiley-VCH Verlag GmbH & Co. KGaA, Weinheim

Keywords: alkaloids · imidazolinones · nitrenes · samarium diiodide · total synthesis

[1] For a review, see A. Al-Mourabit, P. Potier, *Eur. J. Org. Chem.* **2001**, 237 – 243.
[2] a) B. Chanas, J. R. Pawlik, T. Lindel, W. Fenical, *J. Exp. Mar. Biol. Ecol.* **1997**, *208*, 185 – 196; b) T. Lindel, H. Hoffmann, M. Hochgürtel, J. R. Pawlik, *J. Chem. Ecol.* **2000**, *26*, 1477 – 1496.
[3] E. Richelle-Maurer, M. J. De Kluijver, S. Feio, S. Gaudêncio, H. Gaspar, R. Gomez, R. Tavares, G. Van de Vyver, R. W. M. Van Soest, *Biochem. Syst. Ecol.* **2003**, *31*, 1073 – 1091.
[4] For a review, see H. Hoffmann, T. Lindel, *Synthesis* **2003**, 1753 – 1783.
[5] G. R. Pettit, J. McNulty, D. L. Herald, D. L. Doubek, J. C. Chapuis, J. M. Schmidt, L. P. Tackett, M. R. Boyd, *J. Nat. Prod.* **1997**, *60*, 180 – 183.
[6] a) R. B. Kinnel, H.-P. Gehrken, P. J. Scheuer, *J. Am. Chem. Soc.* **1993**, *115*, 3376 – 3377; b) R. B. Kinnel, H.-P. Gehrken, R. Swali, G. Skoropowski, P. J. Scheuer, *J. Org. Chem.* **1998**, *63*, 3281 – 3286.
[7] L. H. Foley, G. Büchi, *J. Am. Chem. Soc.* **1982**, *104*, 1776 – 1777.
[8] K. J. Wiese, K. Yakushijin, D. A. Horne, *Tetrahedron Lett.* **2002**, *43*, 5135 – 5136.
[9] K. G. Poullennec, D. Romo, *J. Am. Chem. Soc.* **2003**, *125*, 6344 – 6345.
[10] D. E. N. Jacquot, H. Hoffmann, K. Polborn, T. Lindel, *Tetrahedron Lett.* **2002**, *43*, 3699 – 3702.
[11] a) R. S. Atkinson, M. P. Coogan, C. L. Cornell, *J. Chem. Soc. Perkin Trans. 1* **1996**, 157 – 166; b) R. S. Atkinson, M. J. Grimshire, B. J. Kelly, *Tetrahedron* **1989**, *45*, 2875 – 2886.
[12] CCDC-252068 (**8**), CCDC-252066 (**11**), CCDC-252067 (**12**), CCDC-252090 (**13**), and CCDC-252091 (**16**) contain the supplementary crystallographic data for this paper. These data can be obtained free of charge from the Cambridge Crystallographic Data Centre via www.ccdc.cam.ac.uk/data_request/cif.
[13] L. Horner, M. Jordan, *Justus Liebigs Ann. Chem.* **1978**, 1505 – 1517.
[14] W. Lwowski, T. J. Maricich, *J. Am. Chem. Soc.* **1963**, *85*, 1200 – 1202.
[15] A. Subbaraj, S. Rao, W. Lwowski, *J. Org. Chem.* **1989**, *54*, 3945 – 3952.
[16] T. Lindel, H. Hoffmann, *Liebigs Ann./Recl.* **1997**, 1525 – 1528.
[17] M. Barani, S. Fioravanti, L. Pellacani, P. A. Tardella, *Tetrahedron* **1994**, *50*, 3829 – 3834.
[18] H. Tanino, T. Nakata, T. Kaneko, Y. Kishi, *J. Am. Chem. Soc.* **1977**, *99*, 2818 – 2819.
[19] We have evidence for an additional product with two ethoxycarbonylamino groups at C10 which is formed by reaction of **13** with another equivalent of the tosyloxycarbamate.
[20] S. Fioravanti, F. Marchetti, A. Morreale, L. Pellacani, P. A. Tardella, *Org. Lett.* **2003**, *5*, 1019 – 1021.
[21] S. Hanessian, S. Johnstone, *J. Org. Chem.* **1999**, *64*, 5896 – 5903.
[22] For recent reviews, see a) H. B. Kagan, *Tetrahedron* **2003**, *59*, 10351 – 10372; b) D. J. Edmonds, D. Johnston, D. J. Procter, *Chem. Rev.* **2004**, *104*, 3371 – 3403.
[23] For an example, see C. Exon, T. Gallagher, P. Magnus, *J. Am. Chem. Soc.* **1983**, *105*, 4739 – 4749.
[24] While this manuscript was under review, an alternative total synthesis of *rac*-dibromophakellstatin appeared (8 steps, 2% overall yield): R. Chung, E. Yu, C. D. Incarvito, D. J. Austin, *Org. Lett.* **2004**, *6*, 3881 – 3884.

 © 2005 Wiley-VCH Verlag GmbH & Co. KGaA, Weinheim

Cover Picture

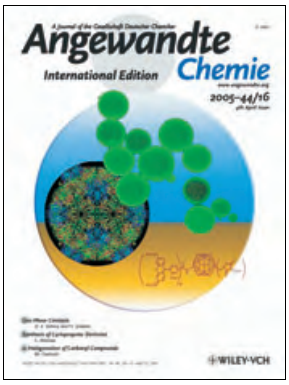

Justin T. Russell, Yao Lin, Alexander Böker, Long Su, Philippe Carl, Heiko Zettl, Jinbo He, Kevin Sill, Ravisubhash Tangirala, Todd Emrick, Kenneth Littrell, Pappannan Thiyagarajan, David Cookson, Andreas Fery, Qian Wang,* and Thomas P. Russell*

Interfacial activities of the cowpea mosaic virus (CPMV) between two immiscible liquids are examined by fluorescent labeling. The cover picture shows a ribbon diagram of CPMV, fluorescence laser scanning confocal microscopy images of perfluorodecalin droplets in water encapsulated by a layer of CPMV, and the structure of a CPMV particle labeled with a fluorescent dye and biotin. In their Communication on page 2420 ff., T. P. Russell, Q. Wang, and co-workers describe the formation of robust membranes by the self-assembly of CPMV bionanoparticles at liquid–liquid interfaces.

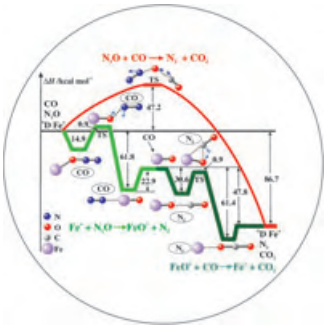

Gas-Phase Catalysis

Kinetics, thermodynamics, and mechanisms of catalysis by metal ions in the gas phase can be uncovered by mass spectrometry. D. K. Böhme and H. Schwarz report on this in their Review on page 2336 ff.

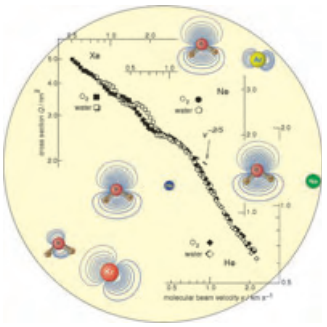

Hydrogen Bonding

In their Communication on page 2356 ff., D. Cappelletti and co-workers describe theoretical calculations as well as molecular-beam-scattering experiments on the interaction of water with noble-gas molecules.

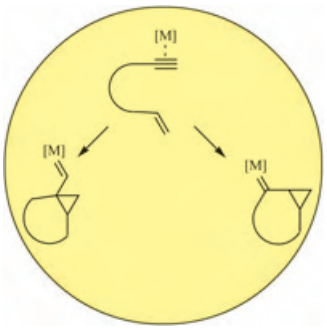

Cyclopropane Derivatives

In the Minireview on page 2328 ff., C. Bruneau discusses recent developments in the electrophilic activation of enynes catalyzed by gold, platinum, and ruthenium derivatives to produce fused cyclopropane derivatives.

Reviews in *Angewandte Chemie*: Influence, Language, Competition

*François Diederich**

F. Diederich

When I joined the German Chemical Society (GDCh, Gesellschaft Deutscher Chemiker) as a student member in the fall of 1974, I took out a personal subscription to *Angewandte Chemie*, as did many of my fellow students at the University of Heidelberg. I received the first issue at the beginning of October, and in the second October issue I already found a review that influenced me significantly in the orientation of my research interests and which I still often cite and recommend today, namely, the progress report by R. H. Martin on "The Helicenes", elegantly translated into German by F. Vögtle, who was a young professor in Würzburg at the time. I am sure that many share my experience, and that reviews in *Angewandte Chemie* have fascinated them and shaped their development to an unusual extent since the beginning of their academic careers.

Angewandte Chemie is not only the flagship of the GDCh journals, but of chemistry journals worldwide. In the more than thirty years that I have been reading the journal, its appearance has been transformed significantly; a number of changes, such as the introduction of the coveted cover picture and the tantalizing graphical table-of-contents entries, led the way for many other journals. Despite the changes and adjustments to the details, the highly successful combination of Reviews and Communications, which is unique among chemistry journals, has been preserved in essence. The need for the rapid communication of information has been met through weekly publication, and the popular "Highlights" have joined the Reviews and Minireviews. In a broader sense, the Essays also fall into this category, so that the status of the reviews in *Angewandte Chemie* has, if anything, increased.

... the status of the Reviews is increasing ...

Indeed, reviews are of particular importance in our highly interdisciplinary, rapidly developing scientific world. Besides high scientific quality, one of the main requirements of a review for *Angewandte Chemie* is that the content can be "digested" by as many readers as possible and doesn't only interest specialists. If these criteria are fulfilled, a review is almost unbeatable in the function of the rapid transmission of knowledge beyond subject boundaries.

The reviews in *Angewandte Chemie* are also unique in that they appear in both German and English. Admittedly the task of translating a review takes time, if one undertakes it oneself, and can be somewhat laborious. However, other authors of reviews certainly share my experience that *both* versions benefit significantly from this exercise. The act of translating forces one to reconsider definitions and formulations in the original version (whether English or German) in terms of clarity and precision, which leads to the revision and improvement of the language and content of both versions. In this way, the result is a better review in both German and English.

It is discussed every year in Editorial Board meetings of *Angewandte Chemie* whether the German Edition should be maintained alongside the International Edition. The recommendation is a clear "yes" each time, as the German edition makes a valuable contribution to the preservation and further development of the German language in chemical research and teaching. Another reason for its importance is that it is one of the few remaining places where it is possible to publish in German; even funding applications are often submitted in English. This influence of the German Edition, and in particular of the reviews, is not only of importance for the academic and industrial world, but also helps make it possible to teach modern chemistry in German at high schools and other educational establishments. From my own experience, I know that it is easier for students from German-speaking countries to first use the German version to become accustomed to reading *Angewandte Chemie* and the general chemical literature regularly.

... a valuable contribution to the scientific German language ...

Therefore, it was an apt and useful initiative taken in 2003 for the first time by the GDCh to ask about 200 people from the German-speaking readership of *Angewandte Chemie* to act as a jury and select the best reviews of the year. Everyone benefits from this initiative: the authors, whose reviews are recognized, the GDCh, who with *Angewandte Chemie* delivers the forum for the reviews, and the readers, who via the selected jury play an active part in the scientific publication process with their judgment. Furthermore, the jurors par-

[*] Prof. Dr. F. Diederich
Laboratorium für Organische Chemie
ETH-Hönggerberg, HCI
8093 Zürich (Switzerland)
Fax: (+41) 01-632-1109
E-mail: diederich@org.chem.ethz.ch

Figure 1. The cover pictures of the most popular Reviews of 2004 ...

 © 2005 Wiley-VCH Verlag GmbH & Co. KGaA, Weinheim DOI: 10.1002/anie.200500233

ticipate in a draw with attractive prizes to the value of almost 13000 Euro. The main winners are the student members of the GDCh, who are given a complementary copy of the special issue of *Angewandte Chemie* with the twelve reviews that received the most votes.

Those allowed to vote in the review selection in 2004 were: a) lecturers at four German tertiary institutions with full chemistry programs selected at random (the universities of Bremen, Frankfurt, Jena, and Karlsruhe); b) 40 principal authors of scientific publications in the previous 12 months; these authors from Germany, Austria, and Switzerland were selected at random, with authors of reviews excluded; and c) 20 chemists in industry, who were selected at random from the referee database of *Angewandte Chemie*. As the reviews are directed above all at students, the jurors were encouraged in the invitation letter to involve their research group (university jurors) and young colleagues (industry jurors) in the nomination.

... everyone benefits from the competition ...

The results are shown in Table 1. The selection is representative of the diversity of the topics covered in *Angewandte Chemie*: The theoretical treatments of gold clusters described by P. Pyykkö and physical chemical models for enzyme–ligand interactions of D. H. Williams et al. appear next to I. Krossing and I. Raabe's description of salts with noncoordinating anions and reviews with a focus on preparative organic chemistry by T. Mukaiyama as well as P. I. Dalko and L. Moisan. Natural products are represented with the story of the total synthesis of colchicine by H.-G. Schmalz and T. Graening, and the review by B. Hauer and colleagues offers insight into modern industrial synthetic processes. The popularity of instrumental methods is recognizable from the fact that C. O. Kappe's review on heating with microwaves occupies first place, and S. W. Homans's report on the application of NMR spectroscopy in drug design is likewise high on the list. D. R. Liu and X. Li build a bridge to biochemistry with their description of DNA-supported organic syntheses, and as is the case in the articles by I. Willner and E. Katz on hybrids formed from biomolecules and nanoparticles and by N. Budisa on the engineering of the genetic code, two conceivably distinct subdisciplines are covered. It is precisely these interdisciplinary topics that show that chemistry is no longer limited to core fields—themselves far from exhausted—such as inorganic and organic synthesis, but is developing in cooperation with neighboring disciplines. The review selection presented in Table 1 reflects this development, as such reviews with topical themes deliver new stimuli and are particularly valued by readers.

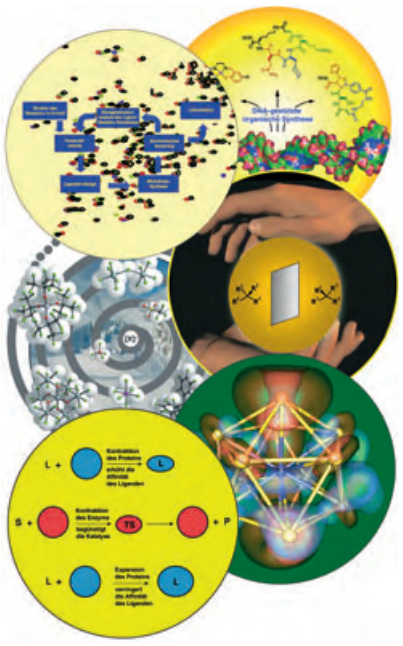

Figure 2. ... express the diversity of the topics.

Table 1: The twelve "best reviews of 2004"; correspondence authors are marked with a star.

Rank	Authors	Title
1	C. O. Kappe*	Controlled Microwave Heating in Modern Organic Synthesis
2	T. Mukaiyama*	Explorations into New Reaction Chemistry
3	E. Katz, I. Willner*	Integrated Nanoparticle–Biomolecule Hybrid Systems: Synthesis, Properties, and Applications
4	P. I. Dalko*, L. Moisan	In the Golden Age of Organocatalysis
	T. Graening, H.-G. Schmalz*	Total Syntheses of Colchicine in Comparison: A Journey through 50 Years of Synthetic Organic Chemistry
6	N. Budisa*	Prolegomena to Future Experimental Efforts on Genetic Code Engineering by Expanding Its Amino Acid Repertoire
7	S. W. Homans*	NMR Spectroscopy Tools for Structure-Aided Drug Design
	X. Li, D. R. Liu*	DNA-Templated Organic Synthesis: Nature's Strategy for Controlling Chemical Reactivity Applied to Synthetic Molecules
	I. Krossing*, I. Raabe	Noncoordinating Anions—Fact or Fiction? A Survey of Likely Candidates
10	M. Breuer, K. Ditrich, T. Habicher, B. Hauer*, M. Keßeler, R. Stürmer, T. Zelinski	Industrial Methods for the Production of Optically Active Intermediates
	P. Pyykkö*	Theoretical Chemistry of Gold
	D. H. Williams*, E. Stephens, D. P. O'Brien, M. Zhou	Understanding Noncovalent Interactions: Ligand Binding Energy and Catalytic Efficiency from Ligand-Induced Reductions in Motion within Receptors and Enzymes

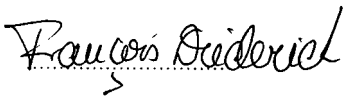

Prof. F. Diederich, Chairman of the Editorial Board of *Angewandte Chemie*

 © 2005 Wiley-VCH Verlag GmbH & Co. KGaA, Weinheim

Contents

VIP ***The following Communications have been judged by at least two referees to be "very important papers" and will be published online at www.angewandte.org soon:***

*J. Malo, J. C. Mitchell, C. Vénien-Bryan, J. R. Harris, H. Wille, D. J. Sherratt, A. J. Turberfield**
Engineering a 2D Protein–DNA Crystal

*F. López, S. R. Harutyunyan, A. Meetsma, A. J. Minnaard, B. L. Feringa**
Copper-Catalyzed Enantioselective Conjugate Addition of Grignard Reagents to α,β-Unsaturated Esters

*A. Tavassoli, S. J. Benkovic**
Genetically Selected Cyclic Peptide Inhibitors of AICAR Transformylase Homodimerization

*V. Huber, M. Katterle, M. Lysetska, F. Würthner**
Reversible Self-Organization of Semi-Synthetic Zinc Chlorins into Well-Defined Rod Antennae

*N. P. Grimster, Carolyn Gauntlett, C. R. A. Godfrey, Matthew J. Gaunt**
Intermolecular Palladium-Catalyzed Alkenylation of Indoles through Solvent-Controlled Regioselective C–H Functionalization

*R. Banerjee, P. M. Bhatt, M. T. Kirchner, G. R. Desiraju**
Structural Studies of the System Sodium Saccharinate Hydrate: A Model for Crystallization

News

N. Turro Gives Theodor Förster Memorial Lecture — **2320**

D. Klemm Receives Anselme Payen Award — **2320**

S. Buchwald Receives Bristol-Myers Squibb Award — **2320**

Books

Modern Oxidation Methods — Jan-Erling Bäckvall — *reviewed by F. Recupero* — ***2321***

Fluorine in Organic Chemistry — Richard D. Chambers — *reviewed by G. K. S. Prakash* — ***2322***

Concepts of Modern Catalysis and Kinetics — I. Chorkendorff, J. W. Niemantsverdriet — *reviewed by P. A. Sermon* — ***2323***

Highlights

Synthetic Methods

M. Oestreich* — **2324 – 2327**

Strategies for Catalytic Asymmetric Electrophilic α Halogenation of Carbonyl Compounds

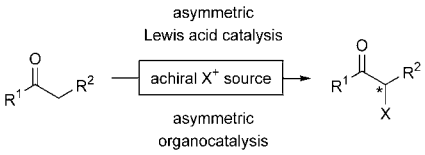

Mission possible: Today, catalytic asymmetric variants of nearly all fundamental bond-forming reactions are known, yet catalyst-controlled enantioselective construction of carbon–halogen bonds (see scheme; X = F, Cl, Br) was still missing. This gap has now been filled by a cornucopia of conceptually diverse approaches that provide a novel tool for asymmetric organic synthesis.

Minireviews

Cyclopropane Derivatives

C. Bruneau* — **2328 – 2334**

Electrophilic Activation and Cycloisomerization of Enynes: A New Route to Functional Cyclopropanes

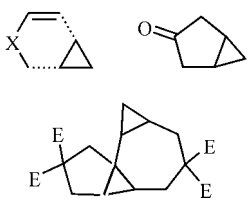

The chemistry of triangles: Various types of functional cyclopropane structures (see picture) can be prepared through efficient and selective activation of the triple bond of enynes with electrophilic metal (Au, Pt, and Ru) derivatives. Nucleophilic addition of the double bond then generates metal–cyclopropylcarbenoid intermediates, which undergo skeleton rearrangements and formation of fused rings that contain at least one cyclopropane subunit.

Reviews

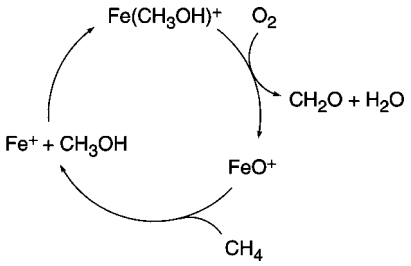

Not just hot air: Complete catalytic cycles under strictly thermal conditions can be studied by means of modern mass spectrometry, and the underlying elementary processes have been uncovered (see picture for the Fe^+-mediated oxidation of methane by molecular oxygen, with methanol as a catalytic co-reductant). Examples cover aspects of catalysis pertinent to areas as diverse as atmospheric chemistry and surface chemistry.

Gas-Phase Reactions

D. K. Böhme,* H. Schwarz* **2336 – 2354**

Gas-Phase Catalysis by Atomic and Cluster Metal Ions: The Ultimate Single-Site Catalysts

Communications

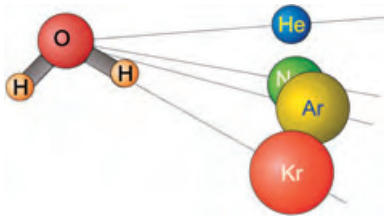

Incipient hydrogen bonds in water–noble gas complexes, which increase in strength from He to Xe, are manifested by progressive alignment along the O–H bond (see picture) according to ab initio calculations. The strength of the interaction in excess of that expected for pure van der Waals forces was assessed experimentally by molecular beam scattering.

Hydrogen Bonds

V. Aquilanti, E. Cornicchi, M. Moix Teixidor, N. Saendig, F. Pirani, D. Cappelletti* **2356 – 2360**

Glory-Scattering Measurement of Water–Noble-Gas Interactions: The Birth of the Hydrogen Bond

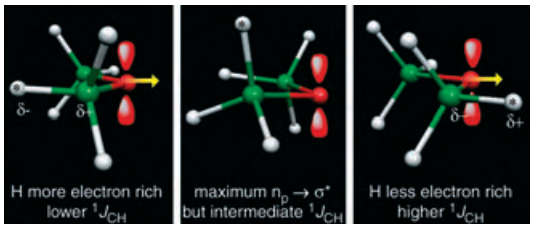

Conforming couples: Coupling constants $^1J_{CH}$ and C–H bond lengths were calculated for various conformations of tetrahydropyran, ethyl methyl ether, and dimethyl ether. The dependence of $^1J_{CH}$ on the H-C-O-C dihedral angle does not parallel the $n_O \rightarrow \sigma^*_{CH}$ delocalization (see picture). Dipolar interactions that affect electron densities are proposed to be responsible.

Coupling Constants

G. Cuevas,* K. Martínez-Mayorga, M. C. Fernández-Alonso, J. Jiménez-Barbero, C. L. Perrin,* E. Juaristi, N. López-Mora **2360 – 2364**

The Origin of One-Bond C–H Coupling Constants in OCH Fragments: Not Primarily $n_O \rightarrow \sigma^*_{CH}$ Delocalization

For the USA and Canada:
ANGEWANDTE CHEMIE International Edition (ISSN 1433-7851) is published weekly by Wiley-VCH PO Box 191161, D 69451 Weinheim, Germany. Air freight and mailing in the USA by Publications Expediting Inc. 200 Meacham Ave., Elmont, NY 11003. Periodicals postage paid at Jamaica NY 11431. US POSTMASTER: send address changes to *Angewandte Chemie*, Wiley-VCH, 111 River Street, Hoboken, NJ 07030. Annual subscription price for institutions: US$ 4948.00/4498.00 (valid for print and electronic / print or electronic delivery); for individuals who are personal members of a national chemical society, or whose institution already subscribes, or who are retired or self-employed consultants, print only: US$ 394.00. Postage and handling charges included. All Wiley-VCH prices are exclusive VAT.

 © 2005 Wiley-VCH Verlag GmbH & Co. KGaA, Weinheim

The best in chemistry –

for more than a hundred years

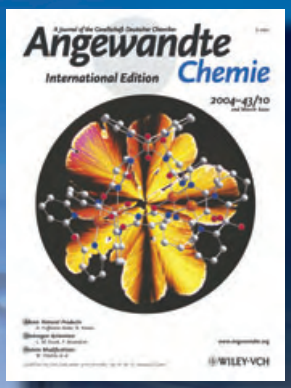

A Journal of the Gesellschaft Deutscher Chemiker

Angewandte
International Edition **Chemie**

www.angewandte.org

1888: ***The beginning of a success story***

Constant Innovations

1962: *First issue of the International Edition*
1976: *Graphical abstracts*
1979: *Cover pictures*
1988: *Centenary of Angewandte*
1989: *Routine use of color*
1991: *New section: Highlights*
1992: *Computerized editorial tracking system*
1995: *Internet service for readers*
1998: *Regular press service; full-text online*
2000: *New section: Essays; EarlyView: Communications available online ahead of the printed version*
2001: *New section: Minireviews*
2002: *Online submission of manuscripts*
2003: *Weekly publication; new section: News; new layout*
2004: *Backfiles (1962-1997); ManuscriptXpress: Online system for authors and referees*

Angewandte's advisors...

Martin Quack
Physical Chemistry,
ETH Zürich

»**Angewandte Chemie** *is my favourite journal covering all aspects of chemistry, from theoretical and physical chemistry to inorganic, organic, and biochemistry. It is by far the best journal worldwide for an overview of current research in chemistry as a whole. Beyond just publishing the best research in chemistry, it also helps us to fight the trend of too narrow specialization.*«

Angewandte Chemie International Edition *is a journal of the German Chemical Society (GDCh)*

GDCh

WILEY InterScience® DISCOVER SOMETHING GREAT

WILEY-VCH

11971404_gu

A limited number and variety of polyphosphorus cations exist in comparison to their neutral (polyphosphines) and anionic (polyphosphides) counterparts. A general and facile method has now been developed for the preparation of phosphinophosphonium, diphosphinophosphonium, and cyclotetraphosphinophosphonium cations from polyphosphines. Furthermore, the stability of the cyclopentaphosphorus ring is emphasized (see crystal structure of $[Ph_6P_5]^+$).

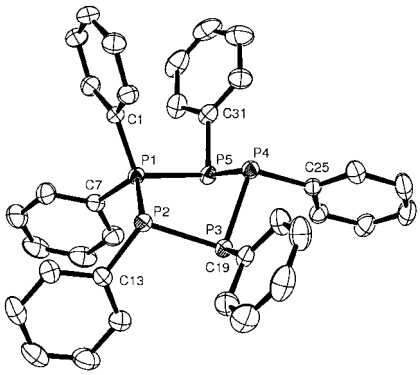

Phosphorus Chemistry

N. Burford,* C. A. Dyker, A. Decken ——— **2364 – 2367**

Facile Synthetic Methods for the Diversification of Catena-Polyphosphorus Cations

---

Treatment of terminal and internal alkynes with diphenylphosphane in the presence of catalytic amounts of a base and cobalt(II) acetylacetonate affords, with perfect and universal *syn* selectivity, the (*E*)-alkenyldiphenylphosphane derivatives in good yield (see scheme, acac = acetylacetonate).

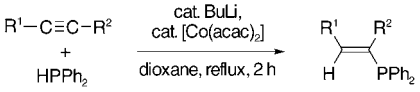

Synthetic Methods

H. Ohmiya, H. Yorimitsu, K. Oshima* ——— **2368 – 2370**

Cobalt-Catalyzed *syn* Hydrophosphination of Alkynes

At least two possible pathways were found for the Beckmann rearrangement of acetophenone oxime to acetanilide over zeolite catalysts. In the first step, the N atom of the oxime is protonated over the Brønsted acid sites of an aluminum siliceous zeolite (see picture), but not over the silanol groups of a pure siliceous zeolite.

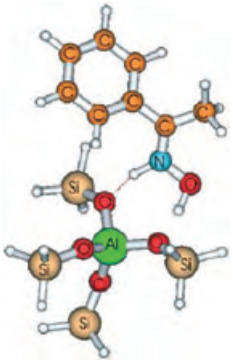

Reaction Mechanisms

A. B. Fernández, M. Boronat, T. Blasco,* A. Corma ——— **2370 – 2373**

Establishing a Molecular Mechanism for the Beckmann Rearrangement of Oximes over Microporous Molecular Sieves

---

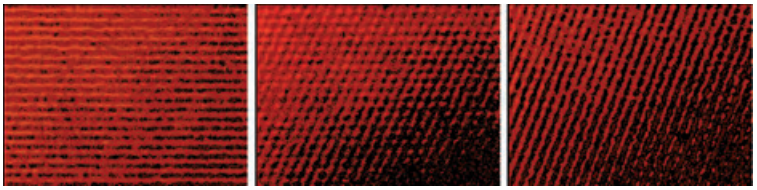

Molecular Devices

J. J. D. de Jong, P. R. Hania, A. Pugžlys, L. N. Lucas, M. de Loos, R. M. Kellogg, B. L. Feringa,* K. Duppen,* J. H. van Esch* ——— **2373 – 2376**

Light-Driven Dynamic Pattern Formation

The reversible photoconversion of self-assembling dithienylcyclopentene photochromic switches between an aggregated and nonaggregated state is manifest at the macroscopic level by a fully reversible sol–gel phase transition and results in spatially confined structure formation in an inhomogeneous optical field. The reversibility of aggregation is exploited in dynamic pattern formation (see images).

 © 2005 Wiley-VCH Verlag GmbH & Co. KGaA, Weinheim

Contents

Asymmetric Synthesis

M. R. Nahm, X. Linghu, J. R. Potnick, C. M. Yates, P. S. White, J. S. Johnson* ——— **2377 – 2379**

Metallophosphite-Induced Nucleophilic Acylation of α,β-Unsaturated Amides: Facilitated Catalysis by a Diastereoselective Retro [1,4] Brook Rearrangement

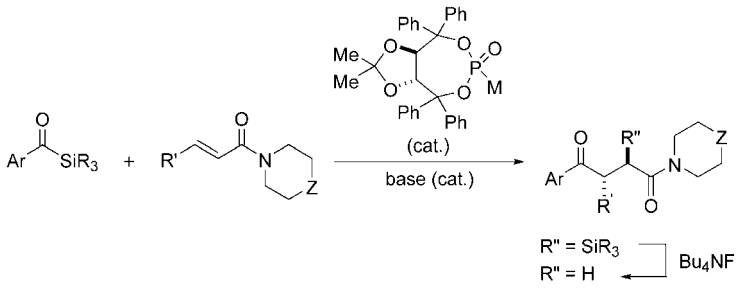

Intermolecular alkene acylation reactions between acyl silanes and α,β-unsaturated amides with metallophosphite catalysis afford α-silyl-γ-ketoamides with high diastereoselectivities (see scheme). These can be converted into the corresponding γ-ketoamides and α-bromo-γ-ketoamides. Asymmetric catalysis of the acylation delivers the γ-ketoamide in the highest enantioselectivity yet reported for an intermolecular Stetter-type reaction.

Cyanoboration

M. Suginome,* A. Yamamoto, M. Murakami* ——— **2380 – 2382**

Palladium-Catalyzed Addition of Cyanoboranes to Alkynes: Regio- and Stereoselective Synthesis of α,β-Unsaturated β-Boryl Nitriles

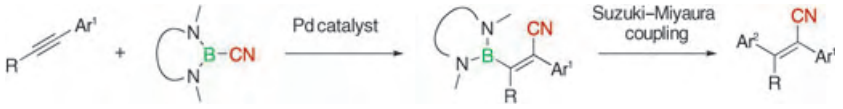

Highly versatile intermediates are formed through the Pd-catalyzed cyanoboration of alkynes, which proceeds in a *cis* fashion. When 1-aryl alkynes are used, the corresponding α,β-unsaturated β-boryl nitriles are obtained regioselectively in good yields with the cyano group α to the aryl group. Suzuki–Miyaura coupling of the products leads to highly substituted α,β-unsaturated nitriles (see scheme).

Reaction Mechanisms

H. A. Bechtel, J. P. Camden, D. J. A. Brown, M. R. Martin, R. N. Zare,* K. Vodopyanov ——— **2382 – 2385**

Effects of Bending Excitation on the Reaction of Chlorine Atoms with Methane

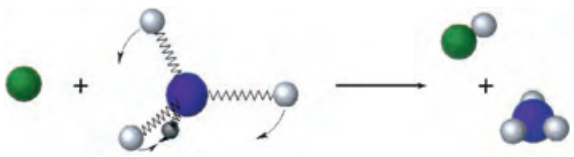

Bent up energy: Contrary to intuitive expectations, excitation of the low-frequency $CH_4(\nu_4=1)$ bending motion enhances the cross section for reaction with Cl atoms by a factor of two or more. This enhancement, which is constant over the collision energy range 0.12 eV to 0.26 eV, implies that shearing motion, in addition to stretching motion, can facilitate C–H bond cleavage in this direct abstraction reaction (see scheme; green Cl, purple C, gray H).

Crystal Growth

Y.-J. Han, L. M. Wysocki, M. S. Thanawala, T. Siegrist, J. Aizenberg* ——— **2386 – 2390**

Template-Dependent Morphogenesis of Oriented Calcite Crystals in the Presence of Magnesium Ions

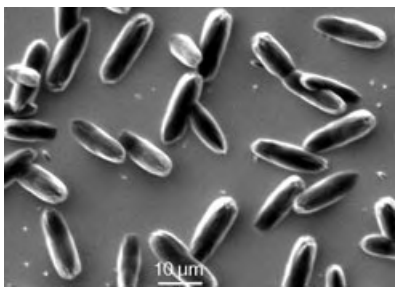

A potent crystallization strategy for the synthesis of homogeneous calcite crystals in a variety of morphological forms (see picture) from solutions containing Mg ions and using self-assembled monolayers as nucleation templates is reported. The approach is based on a new phenomenon – template-dependant crystal morphogenesis.

 © 2005 Wiley-VCH Verlag GmbH & Co. KGaA, Weinheim

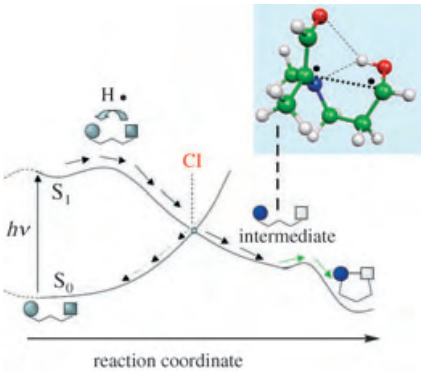

Remember how it was ...? A mechanistic explanation for the chiral-memory effect in Norrish–Yang photoreactions has been obtained by computing the reaction pathway (see figure) at the ab initio level. The results show that both the ultrafast excited-state decay, which occurs at a conical intersection (CI), and the specific hydrogen-bonded structure of the primary diradical intermediate determine the high stereoselectivity of the reaction.

Reaction Mechanisms

A. Sinicropi, F. Barbosa, R. Basosi, B. Giese,* M. Olivucci* ____ **2390 – 2393**

Mechanism of the Norrish–Yang Photocyclization Reaction of an Alanine Derivative in the Singlet State: Origin of the Chiral-Memory Effect

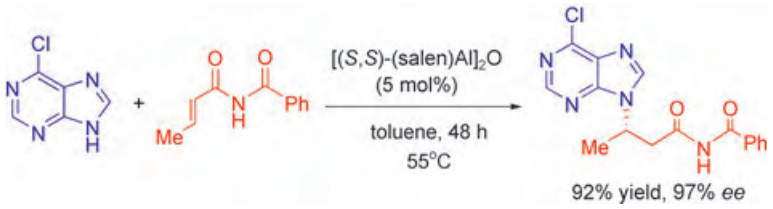

New nucleophiles in the arena of asymmetric catalysis, fused and nonfused N-heterocycles undergo conjugate addition to unsaturated imides and enones in the presence of a chiral [(salen)Al^{III}] complex with generally high enantioselectivities (see scheme; salen=*N*,*N*′-bis(salicylaldehydo)ethylenediamine).

Conjugate Addition

M. Gandelman, E. N. Jacobsen* ____ **2393 – 2397**

Highly Enantioselective Catalytic Conjugate Addition of N-Heterocycles to α,β-Unsaturated Ketones and Imides

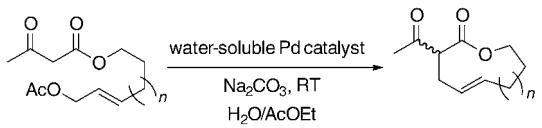

Saving solvent: An aqueous–ethyl acetate biphasic system allows an efficient synthesis of medium- and large-sized lactones by an intramolecular Tsuji–Trost reaction (see scheme, $n = 1$–5). The macrocyclization protocol does not require a large quantity of solvents or a slow-addition technique.

Biphasic Synthesis

H. Kinoshita, H. Shinokubo,* K. Oshima* ____ **2397 – 2400**

Synthesis of Medium- and Large-Sized Lactones in an Aqueous–Organic Biphasic System

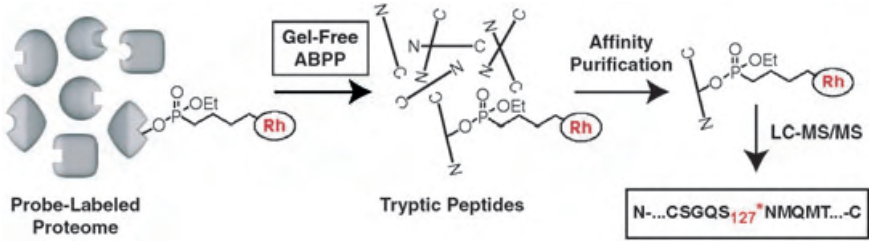

No longer in a class of its own: By using a gel-free platform for activity-based protein profiling (ABPP; see figure), it was shown that the enzyme sialic acid 9-*O*-acetylesterase (SAE), which shares no sequence homology with other enzymes, is a member of the serine hydrolase superfamily. The site of fluorophosphonate labeling in SAE was identified as serine 127; this residue is essential for catalytic activity.

Enzyme Classification

N. Jessani, J. A. Young, S. L. Diaz, M. P. Patricelli, A. Varki, B. F. Cravatt* ____ **2400 – 2403**

Class Assignment of Sequence-Unrelated Members of Enzyme Superfamilies by Activity-Based Protein Profiling

 © 2005 Wiley-VCH Verlag GmbH & Co. KGaA, Weinheim

Contents

Bioinorganic Chemistry

T. S. Keizer, B. L. Scott, N. N. Sauer, T. M. McCleskey* ——— **2403 – 2406**

Stable, Soluble Beryllium Aluminum Citrate Complexes Inspired by the Emerald Mineral Structure

A gem of a structure: A mixed-metal species with a structure very similar to the beryl structure found in nature is the 1:1:2 title complex (see structure). Its core structure contains a ring of alternating Al and Be atoms bridged by the aliphatic hydroxy group of the citric acid. A 1:1:1 complex isolated from phosphate buffer has a larger cluster structure consisting of six Al–Be–citrate species linked by bridging phosphate groups.

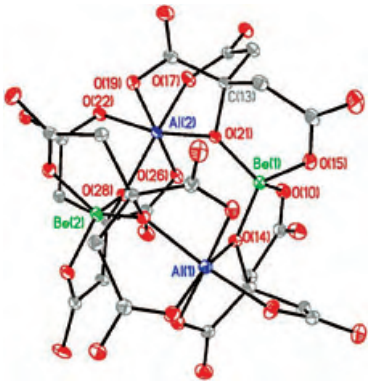

Oxidation of Bridging Phosphanides

J. Forniés,* C. Fortuño, S. Ibáñez, A. Martín, A. C. Tsipis, C. A. Tsipis* ——— **2407 – 2410**

Reversible Transformation of Two Diphenylphosphanido Ligands into the Neutral Tetraphenyldiphosphane Ligand

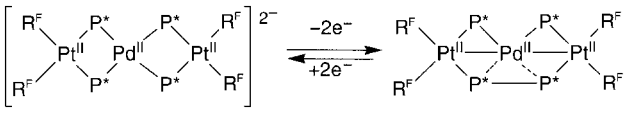

From a theoretical prediction to an experimental finding: Oxidation of two bridging diphenylphosphanido ligands to a neutral tetraphenyldiphosphane is predicted theoretically and achieved experimentally in a trinuclear Pt_2Pd complex (see scheme, $R^F = C_6F_5$, $P^* = PPh_2$).

Electrical Devices

T. Fukushima, K. Asaka, A. Kosaka, T. Aida* ——— **2410 – 2413**

Fully Plastic Actuator through Layer-by-Layer Casting with Ionic-Liquid-Based Bucky Gel

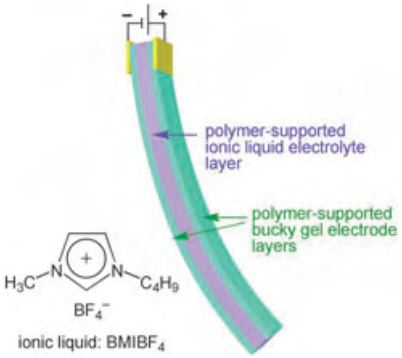

Liquid films: Ionic liquids containing dispersed single-walled carbon nanotubes (bucky gels), allow the first layer-by-layer casting fabrication of a fully plastic actuator. This actuator adopts a simple three-layered configuration of soft electrodes and electrolyte layers (see picture) and can operate in air at low voltages.

Microreactors

T. Kawaguchi, H. Miyata, K. Ataka, K. Mae, J.-i. Yoshida* ——— **2413 – 2416**

Room-Temperature Swern Oxidations by Using a Microscale Flow System

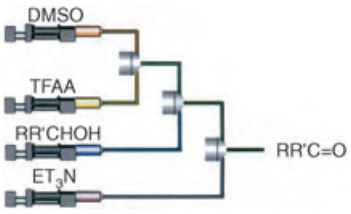

Residence time controlled reaction: The Swern oxidation of alcohols has been accomplished by using a microscale flow system, consisting of micromixers and microscale tube reactors (see schematic representation; DMSO = dimethylsulfoxide, TFAA = trifluoroacetic anhydride), at higher temperatures (−20 to 20 °C) than those for conventional macroscale batch systems (−50 °C or below).

 © 2005 Wiley-VCH Verlag GmbH & Co. KGaA, Weinheim

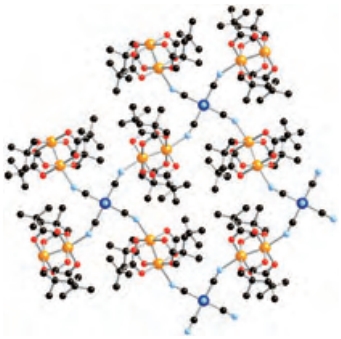

Networking: In contrast to 3D structured $[Ru_2(O_2CR)_4]_3[M^{III}(CN)_6]$ (M = Cr, Fe, Co) in which R = Me, 2D layered network structures form when R = *t*Bu (see structure orange Ru, dark blue Cr, light blue N, red O, black C). The magnetic properties of 2D materials are investigated to further understand the magnetostructural relationship of 2D extended networks, and why the 2D material magnetically orders at higher temperatures than the 3D structured magnets.

Magnetic Properties

T. E. Vos, J. S. Miller* ——— **2416 – 2419**

Building Blocks for 2D Molecule-Based Magnets: The Diruthenium Tetrapivalate Monocation $[Ru^{II/III}_2(O_2CtBu)_4]^+$

Bionanoparticles, such as the cowpea mosaic virus, can stabilize oil droplets in aqueous solutions by self-assembly at liquid interfaces. Subsequent cross-linking of the bionanoparticles transforms the assemblies into robust membranes that have covalent inter-bionanoparticle connections. The resulting membranes are nanoscopically thin sheets (see SANS image (SANS = small-angle neutron scattering)), which were examined by fluorescent labeling.

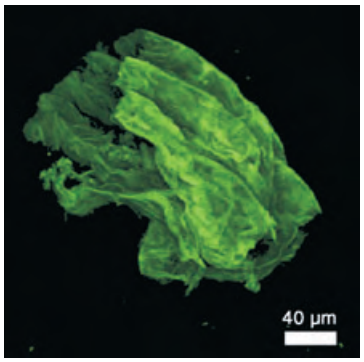

Nanotechnology

J. T. Russell, Y. Lin, A. Böker, L. Su, P. Carl, H. Zettl, J. He, K. Sill, R. Tangirala, T. Emrick, K. Littrell, P. Thiyagarajan, D. Cookson, A. Fery, Q. Wang,* T. P. Russell* ——— **2420 – 2426**

Self-Assembly and Cross-Linking of Bionanoparticles at Liquid–Liquid Interfaces

---

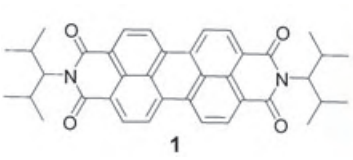

1

A refrigerator when the light is on. In leaflets of **1** ($0.1 \times 50 \times 50\ \mu m^3$) the large planes display a strong, anisotropic solid-state fluorescence. Owing to its small Stokes shift, this perylene dye may have potential for cooling with light.

Solid-State Fluorescence

H. Langhals,* O. Krotz, K. Polborn, P. Mayer ——— **2427 – 2428**

A Novel Fluorescent Dye with Strong, Anisotropic Solid-State Fluorescence, Small Stokes Shift, and High Photostability

---

The key to the cells: The N-terminal organometallic complex shown greatly improves cellular uptake of a bioconjugate containing the NLS peptide (NLS = nuclear localization sequence) and cobaltocenium carboxylic acid. Nuclear localization of this novel organometallic bioconjugate in HepG2 cells is demonstrated by live-cell fluorescence microscopy (see picture). FITC = fluorescein isothiocyanate.

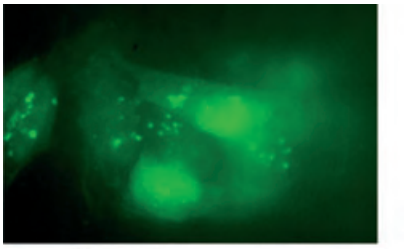

1

Bioorganometallic Chemistry

F. Noor, A. Wüstholz, R. Kinscherf, N. Metzler-Nolte* ——— **2429 – 2432**

A Cobaltocenium–Peptide Bioconjugate Shows Enhanced Cellular Uptake and Directed Nuclear Delivery

 © 2005 Wiley-VCH Verlag GmbH & Co. KGaA, Weinheim

Contents

Homoaromatic Molecules

J. Geier,* H. Grützmacher, K. Exner, H. Prinzbach* ——— **2433 – 2437**

In-Plane Bishomoaromaticity in Tetranitrogen Dianions: Solid-State, Solution, and Electronic Structures

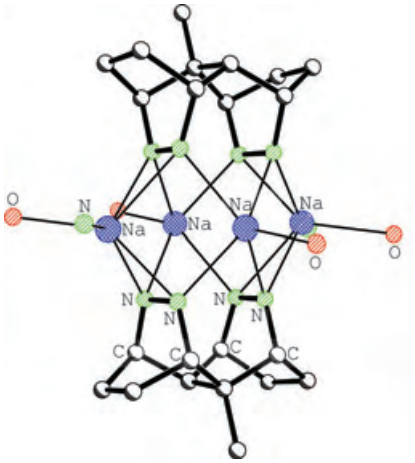

Na_4N_8 cuboctahedra containing nearly planar N_4 polygons make up, in the solid state as well as in solution, the core of the dimer structures of remarkably persistent bishomoaromatic dianions, which are generated by reduction of preoriented bisdiazenes by sodium. As to the nature of the transannular N–N interactions ($d_{N\text{-}N}$ = 2.5–2.8 Å) quantum chemical calculations disclose long bonds.

Fluorescent Nanocrystals

I. Potapova, R. Mruk, C. Hübner, R. Zentel, T. Basché, A. Mews* ——— **2437 – 2440**

CdSe/ZnS Nanocrystals with Dye-Functionalized Polymer Ligands Containing Many Anchor Groups

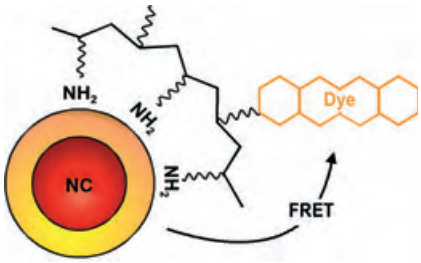

Something to fret about: Luminescent semiconductor nanocrystals are covered with polymeric ligands which form many bonds to the nanocrystal (NC) and increase their solubility. The ligands are decorated with an organic dye molecule (see picture) so that the electronic interaction in individual nanocrystal–dye complexes can be investigated by fluorescence resonance energy transfer (FRET) experiments. The results show many factors influence the FRET results.

Protein Structures

A. B. Siemer, C. Ritter, M. Ernst, R. Riek, B. H. Meier* ——— **2441 – 2444**

High-Resolution Solid-State NMR Spectroscopy of the Prion Protein HET-s in Its Amyloid Conformation

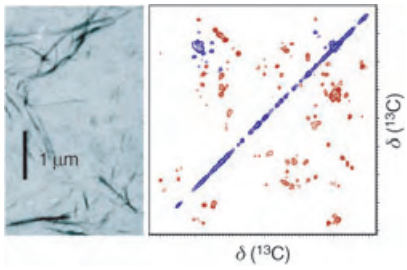

Partly present, partly absent: The solid-state NMR spectra (figure, right side) of the amyloid form of the HET-s prion protein (EM image at left) show the resonances for 43 residues with high resolution, whereas 29 residues give no observable NMR signals. A possible explanation could be that the protein structure consists of both highly ordered and strongly disordered domains.

Catalyzed Cross-Couplings

L. Ackermann,* R. Born ——— **2444 – 2447**

Modular Diamino- and Dioxophosphine Oxides and Chlorides as Ligands for Transition-Metal-Catalyzed C–C and C–N Couplings with Aryl Chlorides

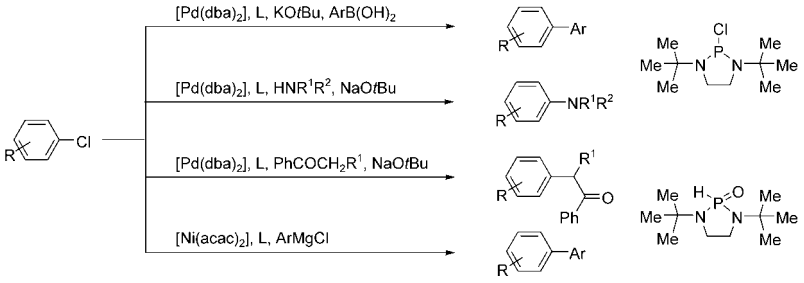

Air-stable diamino- and dioxophosphine oxides were used as ligands in palladium-catalyzed Suzuki reactions of aryl chlorides. Additionally, a diaminophosphine chloride was applied to palladium- and nickel-catalyzed C–C and C–N bond-forming reactions.

© 2005 Wiley-VCH Verlag GmbH & Co. KGaA, Weinheim

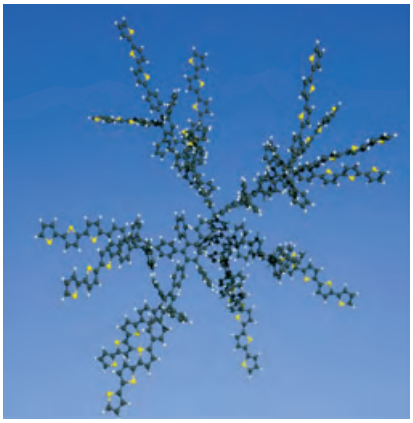

Unusual conductivity effects: Suitably functionalized dendrimers (see picture) are capable of forming truly covalent three-dimensional networks with remarkably high conductivity on electrochemical doping. Depending on the charging level of the electroactive components used as building blocks for the dendrimer core and the perimeter, two separated regimes of electrical conductivity can be observed.

Organic Conductors

H. John, R. Bauer, P. Espindola, P. Sonar, J. Heinze,* K. Müllen* ____ **2447 – 2451**

3D-Hybrid Networks with Controllable Electrical Conductivity from the Electrochemical Deposition of Terthiophene-Functionalized Polyphenylene Dendrimers

WILEY InterScience®
DISCOVER SOMETHING GREAT

"Hot Papers" are chosen by the Editors for their importance in a rapidly evolving field of high current interest. A preview with the graphical abstracts of these articles can be found on the *Angewandte Chemie* homepage in Wiley InterScience at www.angewandte.org.

"VIPs" are Communications which are identified by two referees as being very important. They are published online up to several weeks ahead of print. A preview with short summaries of these articles can also be found on the journal's homepage.

Service

Keywords ____ *2452*

Authors ____ *2453*

Angewandte's Sister Journals ____ *2454 – 2455*

Preview ____ *2457*

 © 2005 Wiley-VCH Verlag GmbH & Co. KGaA, Weinheim

N. Turro Gives Theodor Förster Memorial Lecture

N. Turro

Nicholas J. Turro (Columbia University, New York) has been honored as a pioneer of photochemistry by the Gesellschaft Deutscher Chemiker (GDCh, German Chemical Society) and the Deutsche Bunsen-Gesellschaft für Physikalische Chemie with the Theodor Förster Memorial Lecture. Turro has made central and highly innovative contributions to molecular and supramolecular photochemistry, spectroscopy, and physical organic chemistry. The central topic of his research for the last four decades has been the photon, whether as a "reagent" for the initiation of photoreactions or as a "product" in the deactivation of electronically excited states. The award lecture at the meeting of the GDCh Photochemistry Section in Jena at the end of March was entitled "Making Covalent Bonds through Noncovalent Interactions: Supramolecular and Magnetic Effects on the Selectivity of Radical–Radical Combination". The physicist T. Förster (1910–1974) investigated fluorescence and energy transfer (Förster mechanism).

Turro studied chemistry at Wesleyan University in Middletown, CT (USA) and completed his PhD in 1963 under the guidance of G. Hammond at the California Institute of Technology in Pasadena. After a postdoctoral period at Harvard University (Cambridge, MA), he moved as a lecturer to Columbia University, where he now teaches as both Professor of Chemical Engineering and Applied Chemistry and Professor of Earth and Environmental Engineering and carries out research in the field of photochemistry and electron spin resonance spectroscopy.[1a] His interest in the philosophy of science led to an Essay in *Angewandte Chemie* on revolutionary and pathological science.[1a]

D. Klemm Receives Anselme Payen Award

The American Chemical Society (ACS) has awarded the Anselme Payen Award to a German scientist for the first time: to Dieter Klemm of Friedrich-Schiller-Universität Jena. The award recognizes Klemm's exceptional achievements in the development of new materials based on cellulose. The award was presented during the ACS Meeting in San Diego, where Klemm gave a lecture on selective syntheses, new products, and custom-made biomaterials in cellulose chemistry. The French chemist A. Payen was the first to isolate cellulose from wood in 1838.

D. Klemm

Klemm completed his PhD in 1968 under the supervision of G. Drefahl at the Universität Jena on nitrogen-containing steroids and completed his habilitation there in 1976 on the chemistry and photochemistry of low-molecular-weight and polymeric *o*-nitrobenzene compounds. He then worked for a number of years in the optical and pharmaceutical industries, before returning as a lecturer in 1983 to the Universität Jena, where he was made professor in 1987. He is co-editor of the book "Comprehensive Cellulose Chemistry",[2] and his Review on cellulose as a fascinating biopolymer and sustainable raw material will appear soon in *Angewandte Chemie*.

S. Buchwald Receives Bristol-Myers Squibb Award

Stephen L. Buchwald (Massachusetts Institute of Technology, Cambridge, MA; MIT) is the recipient of the Distinguished Achievement Award in Organic Synthesis of the New York pharmaceutical concern Bristol-Myers Squibb Company. The award recognizes his important contributions to the development of transition-metal-catalyzed coupling methods.

S. Buchwald

Buchwald studied chemistry at Brown University (Providence, RI, USA) and Columbia University, and completed his PhD in 1982 at Harvard University under the guidance of J. R. Knowles on the mechanism of phosphoryl transfer in chemistry and biochemistry. He then carried out postdoctoral research in the group of R. H. Grubbs at the California Institute of Technology on titanocene reagents and the mechanism of Ziegler–Natta catalysis. In 1984 he became assistant professor at MIT, and he has been Camille Dreyfus Professor of Chemistry since 1997. His research includes new methods of C–C, C–N, and C–O bond formation, as well as the asymmetric reduction of prochiral compounds. He reported recently in *Angewandte Chemie* a universal catalyst for Suzuki–Miyaura coupling.[3]

[1] a) N. J. Turro, M. H. Kleinman, E. Karatekin, *Angew. Chem.* **2000**, *112*, 4608; *Angew. Chem. Int. Ed.* **2000**, *39*, 4436; b) N. J. Turro, *Angew. Chem.* **2000**, *112*, 2343; *Angew. Chem. Int. Ed.* **2000**, *39*, 2255.

[2] D. Klemm, B. Philipp, T. Heinze, U. Heinze, W. Wagenknecht, *Comprehensive Cellulose Chemistry*, Wiley-VCH, Weinheim, **1998**.

[3] S. D. Walker, T. E. Barder, J. R. Martinelli, S. L. Buchwald, *Angew. Chem.* **2004**, *116*, 1907; *Angew. Chem. Int. Ed.* **2004**, *43*, 1871.

 © 2005 Wiley-VCH Verlag GmbH & Co. KGaA, Weinheim DOI: 10.1002/anie.200500969

Synthetic Methods

Strategies for Catalytic Asymmetric Electrophilic α Halogenation of Carbonyl Compounds**

*Martin Oestreich**

Keywords:
asymmetric catalysis · carbonyl compounds · halogenation · homogeneous catalysis · Lewis acids

Modern enantioselective synthesis provides a wide selection of catalytic asymmetric carbon–carbon, carbon–heteroatom, and carbon–hydrogen bond-forming processes. In comparison, efficient methods for stereoselective construction of carbon–halogen bonds catalytic in chiral auxiliaries have been remarkably scarce, although these functional groups serve as linchpins for further stereospecific manipulations and are increasingly important structural motifs in medicinal chemistry and material sciences. The quest for such catalytic asymmetric carbon–halogen bond-forming reactions has gained considerable momentum in recent years, and several conceptually attractive strategies have been discovered.[1]

Until half a decade ago, stereoselective carbon–halogen bond formation had been achieved by either diastereoselective substrate-controlled[2,3] or enantioselective reagent-controlled[1,4] procedures.[1–4] These are commonly hinged on the electrophilic halogenation of silicon and metallo enolates, respectively. This approach appears to be predestined for catalytic asymmetric variants, as Lewis acid catalysis is at least conceivable.

In two landmark papers,[5,6] Hintermann and Togni reported the first catalytic asymmetric α-halogenation of carbonyl compounds by chiral Lewis acid catalysis (Scheme 1). Both α-fluorination (**1**→**2**)[5] and α-chlorination (**1**→**3**)[6] proceeded with excellent levels of enantioselectivity in the presence of titanium-based Lewis acids **10**. The related α-bromination (**1**→**4**)[6] was somewhat less successful under identical reaction conditions.

As depicted in Scheme 2, Lewis acid **10** coordinates substrate **1** (**10**→**11**) thereby promoting its enolization (**11**→**12**). The key intermediate **12** is then preferentially approached from the *Si*-face by the electrophilic halogen source **5**, **7**, or **8** (**12**→**13**). The bidentate nature of substrate **1** is undoubtedly beneficial for high facial selectivity in the electrophilic halogenation step. Furthermore, Togni also investigated the origins of the observed enantioselectivity by computational methods.[7]

Recently, late-transition-metal-based Lewis acids coordinated by chiral, nonracemic ligands have also been found to be efficient catalysts.[1,8,9] These related catalytic systems also exploit the concept of two-point binding of 1,3-dicarbonyl compounds and led to improved enantiomeric excesses for selected substrates.

A promising organocatalytic strategy for catalytic enantioselective α-fluorination was presented by Kim and Park (**14**→**15**, Scheme 3).[10] This ap-

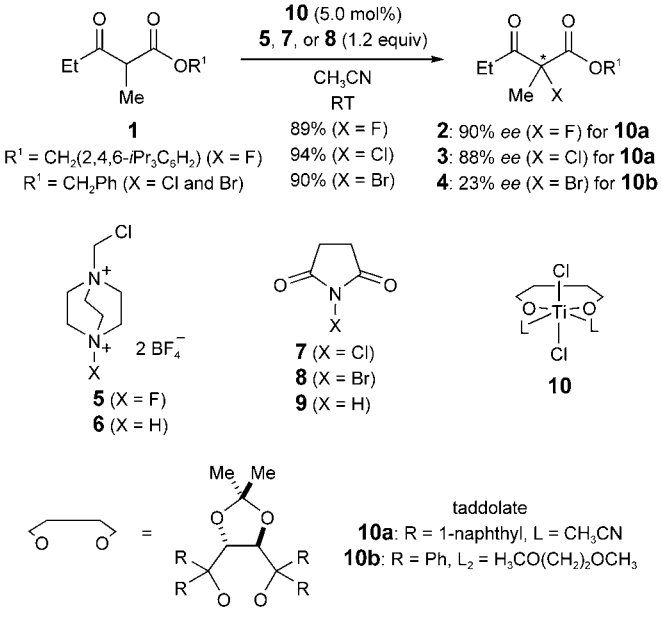

Scheme 1. Lewis acid catalyzed asymmetric α-halogenation.

[*] Dr. M. Oestreich
Institut für Organische Chemie und Biochemie
Albert-Ludwigs-Universität
Albertstrasse 21
79104 Freiburg (Germany)
Fax: (+49) 761-203-6100
E-mail: martin.oestreich@orgmail.chemie.uni-freiburg.de

[**] M.O. is indebted to the Deutsche Forschungsgemeinschaft for an Emmy Noether fellowship (2001–2005) and to Professor Reinhard Brückner for his continuous encouragement.

 © 2005 Wiley-VCH Verlag GmbH & Co. KGaA, Weinheim DOI: 10.1002/anie.200500478

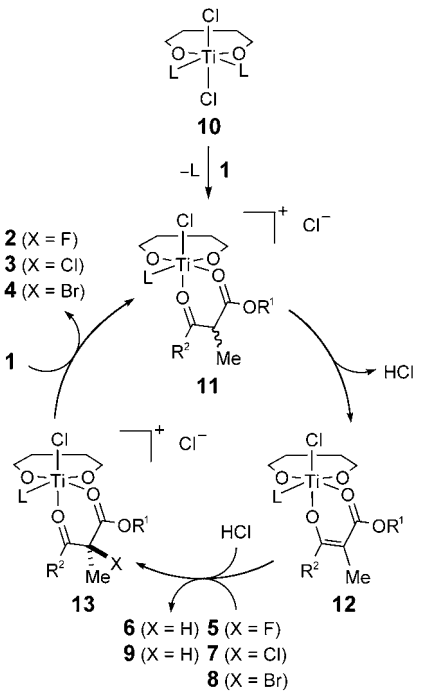

Scheme 2. Lewis acid catalysis.

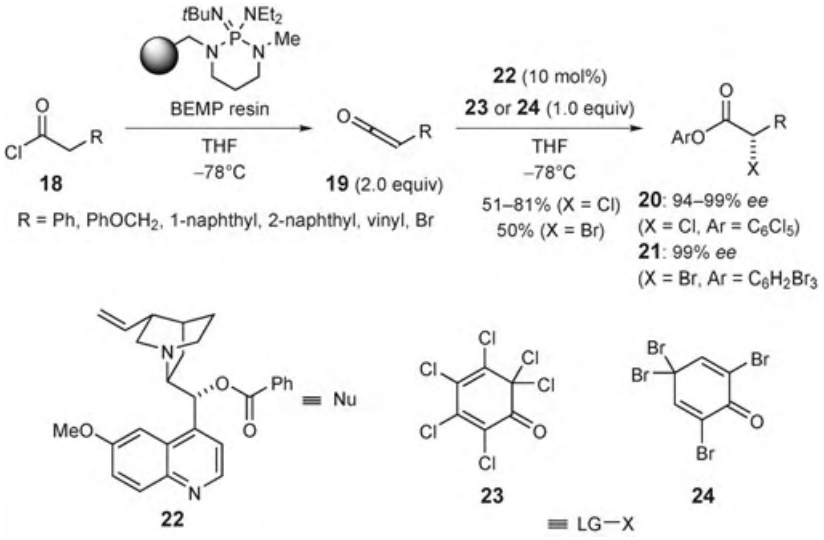

Scheme 4. Cinchona alkaloid catalyzed α-chlorination and α-bromination. LG = leaving group.

proach is based on chiral quaternary ammonium salts as phase-transfer catalysts. A screening of several structurally altered catalysts derived from cinchona alkaloids identified **16** as a suitable catalyst for the electrophilic fluorination of the intermediate enolate generated from readily enolizable 1,3-dicarbonyl **14**.

Lectka and co-workers have elaborated an ingenious reaction sequence that provides a general entry into highly optically enriched α-chloro- as well as α-bromoesters (Scheme 4).[11] The actual starting material of this procedure are ketenes **19**, which are accessed from acyl chlorides **18** by using a resin-bound phosphazene base (BEMP); a solution of pure **19** is obtained after removal of the base by simple filtration. Subsequent treatment of **19** with an electrophilic chlorine (**23**) or bromine (**24**) source in the presence of nucleophilic organocatalyst **22** (Nu) affords α-haloesters **20** and **21**, respectively with very high levels of enantioselectivity.

The mechanism of this process is outlined in Scheme 5.[11] The nucleophilic nitrogen center in **22** attacks the electron-poor ketene carbon atom, thus generating a chirally modified, zwitterionic enolate (**19**→**25**), which undergoes a standard diastereoselective electrophilic halogenation (**25**→**26**). Chlorination and bromination with polyhalogenated quinones **23** and **24** produces phenoxides as leaving groups, which, in turn, are sufficiently nucleophilic to displace the chiral auxiliary in **26**, thus regenerating organocatalyst **22** and forming esters **20** and **21**, respectively. These quinone-derived electrophilic halogen sources **23** and **24** are particularly appealing because the role of the normally useless leaving group as a nucleophile is a pivotal feature of the catalytic cycle.

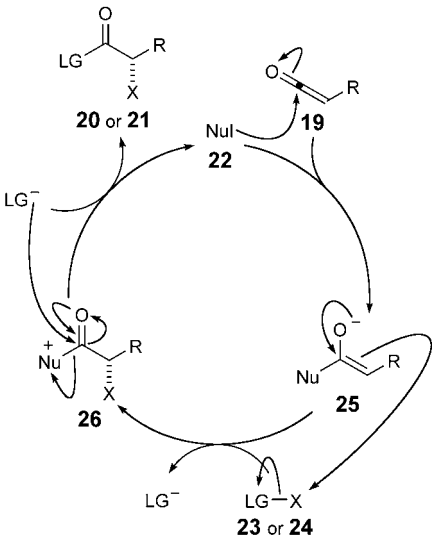

Scheme 5. Tandem halogenation/esterification process.

Recently, MacMillan and co-workers[12] as well as Jørgensen and co-workers[13] independently described the first direct and organocatalytic α-chlorination of aldehydes (**27**→**28**, Scheme 6). This enamine catalysis was initially understood to operate in analogy to related proline-catalyzed α-oxidation and α-amination reactions, yet proline emerged as a particularly poor chiral catalyst for the electrophilic chlorination of electron-rich enamines (low enantiomeric excess at quantitative conversion). MacMillan and co-workers[12] succeeded by using organocatalyst (*S*)-**29** and the chlorine source **23** developed by Lectka, whereas a combination of amine **30** and chlorine source **7** was

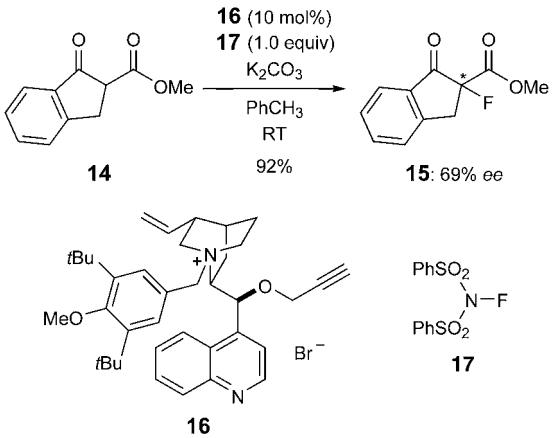

Scheme 3. Phase-transfer-catalyzed α-fluorination.

 © 2005 Wiley-VCH Verlag GmbH & Co. KGaA, Weinheim

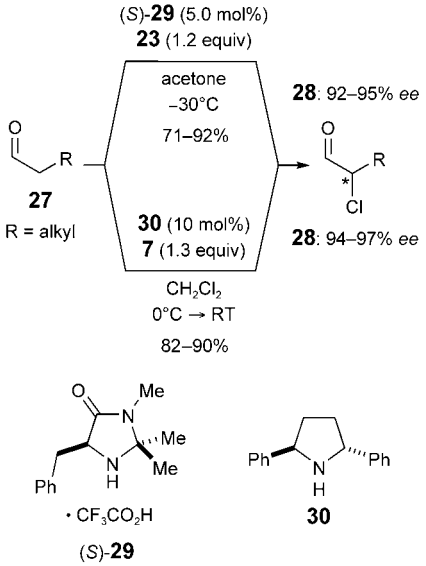

Scheme 6. Organocatalytic α-chlorination of aldehydes (R = primary, secondary, or tertiary alkyl) by enamine catalysis.

found to be effective by Jørgensen and co-workers.[13] Both methods display broad substrate scope. MacMillan and co-workers also probed the chemoselectivity of aldehyde **27**, which contains a methyl ketone moiety (78%, 87% *ee*).[12] Interestingly, however, α-chiral aldehydes **28** proved to be configurationally stable under the reaction conditions, and purification on specific beads[12,13] merely resulted in marginal decrease in enantiomeric purity.

Furthermore, excellent catalytic ((*S*)-**29**) asymmetric induction was verified in the α-chlorination of β-chiral aldehyde (*S*)-**31** (Scheme 7).[12] Internal induction was almost completely overcompensated, as substantiated by the matched case ((*S*)-**31**→*syn*-**32**) with (*S*)-**29** and the mismatched case ((*S*)-**31**→*anti*-**32**) with antipode (*R*)-**29**.

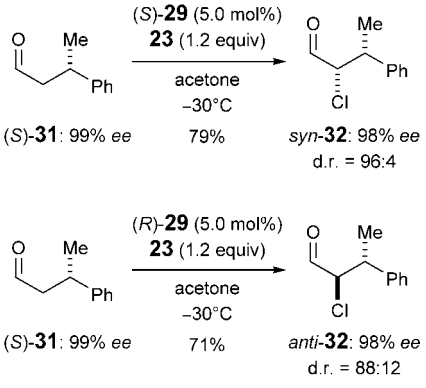

Scheme 7. Catalyst versus substrate control.

Shortly thereafter, Jørgensen and co-workers disclosed the direct organocatalytic α-chlorination of ketones (**33**→**34**, Scheme 8).[14] This investigation impressively demonstrates that the α-chlorination of ketones is not a simple extension of the related transformation of aldehydes! Neither proline nor the optimal catalyst scaffolds **29** and **30** for aldehyde chlorination (**27**→**28**, Scheme 6) promoted this reaction efficiently (**33**→**34**, Scheme 8).

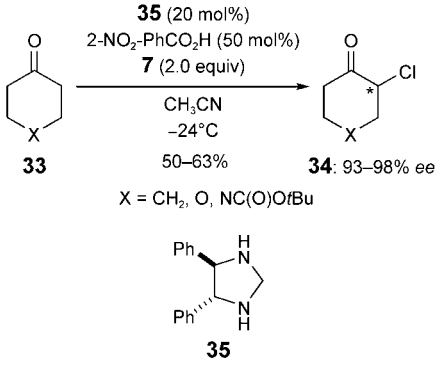

Scheme 8. Organocatalytic α-chlorination of ketones by enamine catalysis.

A thorough survey of a number of organocatalysts under different reaction conditions finally led to imidazolidine **35** as the catalyst of choice and 2-nitrobenzoic acid as an essential, rate-accelerating additive. The authors believe that the presence of protons has two beneficial effects: 1) promotion of enamine formation[15] and 2) suppression of catalyst chlorination. The exact mechanism has not yet been fully understood. Enantiomeric excesses measured for **34** were generally high, whereas the yields have only been moderate so far, which is likely to be attributed to multiple chlorination.

All these diverse strategies for catalytic asymmetric α-halogenation have been developed within an extraordinarily short period of time (2000–2004).[6,8–14] In particular, the (in the broadest sense) organocatalytic methodolgies elaborated by the groups of Lectka[11] as well as of MacMillan[12] and Jørgensen[13,14] are quite general for individual classes of substrates. These authors have already indicated the synthetic usefulness of the α-halogenated carbonyl compounds as versatile chiral building blocks.

Undoubtedly, modern asymmetric chemistry strives for catalyst-controlled processes, which are designed to supersede reagent- and substrate-controlled reactions. However, reagent control can sometimes be a competitive alternative![2,4,16] Apart from several successful reagent-controlled asymmetric α-fluorinations,[2,4] a powerful α-chlorination was recently reported by Yamamoto and co-workers.[16] They showed that the chiral 2,2-dichloro-1,3-dicarbonyl "controller unit" **38** stereoselectively transfers electrophilic chlorine onto silicon enolates upon activitation by a Lewis acid (**36**→**37**, Scheme 9).[16] Activation of **38** is uniquely realized with zirconium tetrachloride, which coordinates bidentate **38** thereby facilitating chlorine transfer to **36** with high enantiofacial selectivity (**40**, Figure 1). Not surprisingly, the enantioselectivity depends on the steric bulk of the silicon group. Acyclic substrates worked equally well.

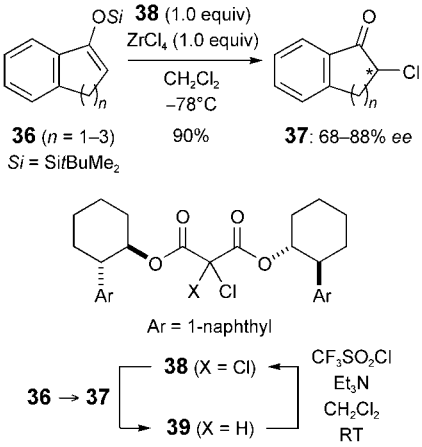

Scheme 9. Reagent-controlled α-chlorination of silicon enolates.

The novel reagent **38** releases only one cationic chlorine atom (**38**→**39**). The resulting 2-chloro-1,3-dicarbonyl compound **39** can be easily recovered during the purification procedure and can be re-used after straightforward chlorination (**39**→**38**, Scheme 9). As claimed by the authors, this novel concept might be extended to catalytic asymmetric variants in the near future.

 © 2005 Wiley-VCH Verlag GmbH & Co. KGaA, Weinheim

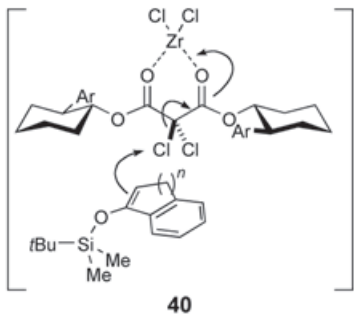

40

Figure 1. Plausible mechanistic rationale for chlorination of **36**.

In conclusion, enantioselective electrophilic α-halogenation of carbonyl compounds belongs to the topical areas of current asymmetric catalysis. The past five years have witnessed significant progress starting from the initial Lewis acid catalyzed enantioselective α-halogenations by Togni and co-workers[5,6] to several highly efficient organocatalytic approaches.[10–14] With the commercial availability of the reagents and catalysts employed (Scheme 4 and 6), a new tool has presented itself to synthetic organic chemistry!

[1] For an excellent account, see: H. Ibrahim, A. Togni, *Chem. Commun.* **2004**, 1147–1155.

[2] For reviews of noncatalytic stereoselective carbon–fluorine bond formation, see: a) S. D. Taylor, C. C. Kotoris, G. Hum, *Tetrahedron* **1999**, *55*, 12431–12477; b) K. Muñiz, *Angew. Chem.* **2001**, *113*, 1701–1704; *Angew. Chem. Int. Ed.* **2001**, *40*, 1653–1656.

[3] For substrate-controlled, diastereoselective α-chlorination and α-bromination with **7** and **8**, respectively, see: a) W. Oppolzer, P. Dudfield, *Tetrahedron Lett.* **1985**, *26*, 5037–5040; b) D. A. Evans, J. A. Ellman, R. L. Dorow, *Tetrahedron Lett.* **1987**, *28*, 1123–1126; c) P. Duhamel, P. Angibaud, J. R. Desmurs, J. Y. Valnot, *Synlett* **1991**, 807–808.

[4] For reagent-controlled, enantioselective α-fluorination of carbonyl compounds, see: a) E. Differding, R. W. Lang, *Tetrahedron Lett.* **1988**, *29*, 6087–6090; b) F. A. Davis, P. Zhou, C. K. Murphy, G. Sundarababu, H. Qi, W. Han, R. M. Przeslawski, B.-C. Chen, P. J. Carroll, *J. Org. Chem.* **1998**, *63*, 2273–2280; c) Z. Liu, N. Shibata, Y. Takeuchi, *J. Org. Chem.* **2000**, *65*, 7583–7587; d) N. Shibata, E. Suzuki, T. Asahi, M. Shiro, *J. Am. Chem. Soc.* **2001**, *123*, 7001–7009; e) P. Mohar, J. Baudoux, J.-C. Plaquevent, D. Cahard, *Angew. Chem.* **2001**, *113*, 4339–4341; *Angew. Chem. Int. Ed.* **2001**, *40*, 4214–4216.

[5] L. Hintermann, A. Togni, *Angew. Chem.* **2000**, *112*, 4530–4533; *Angew. Chem. Int. Ed.* **2000**, *39*, 4359–4362.

[6] a) L. Hintermann, A. Togni, *Helv. Chim. Acta* **2000**, *83*, 2425–2435; b) H. Ibrahim, F. Kleinbeck, A. Togni, *Helv. Chim. Acta* **2004**, *87*, 605–610.

[7] S. Piana, I. Devillers, A. Togni, U. Rothlisberger, *Angew. Chem.* **2002**, *114*, 1021–1024; *Angew. Chem. Int. Ed.* **2002**, *41*, 979–982.

[8] For related Lewis acid catalysis in α-fluorination, see: a) Y. Hamashima, K. Yagi, H. Takano, L. Tomás, M. Sodeoka, *J. Am. Chem. Soc.* **2002**, *124*, 14530–14531; b) J.-A. Ma, D. Cahard, *Tetrahedron: Asymmetry* **2004**, *15*, 1007–1011; c) N. Shibata, T. Ishimaru, T. Nagai, J. Kohno, T. Toru, *Synlett* **2004**, 1703–1706.

[9] For related Lewis acid catalysis in α-chlorination and α-bromination, see: a) M. Marigo, N. Kumaragurubaran, K. A. Jørgensen, *Chem. Eur. J.* **2004**, *10*, 2133–2137; b) L. Bernardi, K. A. Jørgensen, *Chem. Commun.* **2005**, 1324–1326.

[10] D. Y. Kim, E. J. Park, *Org. Lett.* **2002**, *4*, 545–547.

[11] a) For a current account, see: S. France, A. Weatherwax, T. Lectka, *Eur. J. Org. Chem.* **2005**, 475–479; b) H. Wack, A. E. Taggi, A. M. Hafez, W. J. Drury III, T. Lectka, *J. Am. Chem. Soc.* **2001**, *123*, 1531–1532; c) A. M. Hafez, A. E. Taggi, H. Wack, J. Esterbrook, T. Lectka, *Org. Lett.* **2001**, *3*, 2049–2051; d) S. France, H. Wack, A. E. Taggi, A. M. Hafez, T. R. Wagerle, M. H. Shah, C. L. Dusich, T. Lectka, *J. Am. Chem. Soc.* **2004**, *126*, 4245–4255.

[12] a) M. P. Brochu, S. P. Brown, D. W. C. MacMillan, *J. Am. Chem. Soc.* **2004**, *126*, 4108–4109.

[13] N. Halland, A. Braunton, S. Bachmann, M. Marigo, K. A. Jørgensen, *J. Am. Chem. Soc.* **2004**, *126*, 4790–4791.

[14] M. Marigo, S. Bachmann, N. Halland, A. Braunton, K. A. Jørgensen, *Angew. Chem.* **2004**, *116*, 5623–5626; *Angew. Chem. Int. Ed.* **2004**, *43*, 5507–5510.

[15] For acid-promoted aldol reactions via enamine intermediates, see: N. Mase, F. Tanaka, C. F. Barbas III, *Angew. Chem.* **2004**, *116*, 2474–2477; *Angew. Chem. Int. Ed.* **2004**, *43*, 2420–2423.

[16] Y. Zhang, K. Shibatomi, H. Yamamoto, *J. Am. Chem. Soc.* **2004**, *126*, 15038–15039.

 © 2005 Wiley-VCH Verlag GmbH & Co. KGaA, Weinheim

Cyclopropane Derivatives

Electrophilic Activation and Cycloisomerization of Enynes: A New Route to Functional Cyclopropanes

*Christian Bruneau**

Keywords:
carbocycles · cyclization · enynes · isomerization · transition metals

Transformations of enynes in the presence of transition-metal catalysts have played an important role in the preparation of a variety of cyclic compounds. Recent developments in the activation of triple carbon–carbon bonds by electrophilic metal centers have provided a new entry to the selective synthesis of cyclopropane derivatives from enynes. The mechanisms of these reactions involve catalytic species with both ionic and cyclopropylcarbenoid character. This type of activation will undoubtedly be further developed for application to other unsaturated hydrocarbons and inspire new catalytic cascade reaction sequences. This Minireview discusses the recent developments in electrophilic activation of enynes and shows that simple catalysts such as $[Ru_3(CO)_{12}]$, $PtCl_2$, and cationic gold complexes are efficient precursors to promote the formation of functional polyclic compounds.

Introduction

The cyclopropane ring is a quite common subunit of natural products isolated from plants, fungi, and microorganisms.[1] Many of these natural products show biological activity, and some of them have found applications as drugs or insecticides.[1,2] The most common biosynthesis processes are based on cationic intermediates in interaction with carbon–carbon double bonds, as illustrated in the production of terpene from isoprenoid allylic pyrophosphates.[1,3] Classical chemical syntheses of cyclopropane derivatives include the halomethyl–metal-mediated cyclopropanation of olefins, the transition-metal-catalyzed carbene-transfer reaction from diazo compounds, and the nucleophilic-addition/ring-closing sequence.[4] Recently, the very rich chemistry of enynes has made possible the preparation of a variety of carbocycles, depending on both the nature of the enyne and the metal catalyst.[5–7] Various transformations of enynes through metal-catalyzed cycloisomerization have been reported which involve several pathways (Scheme 1):

- the metathesis reaction usually performed with metal–carbene active species which leads to conjugated vinylcycloalkene derivatives **A**,[8,9]
- oxidative cyclometalation followed by β elimination, which provides cycloalkanes that bear an *exo*-1,3- or -1,4-diene motif, **B** and **C**, respectively,[10]

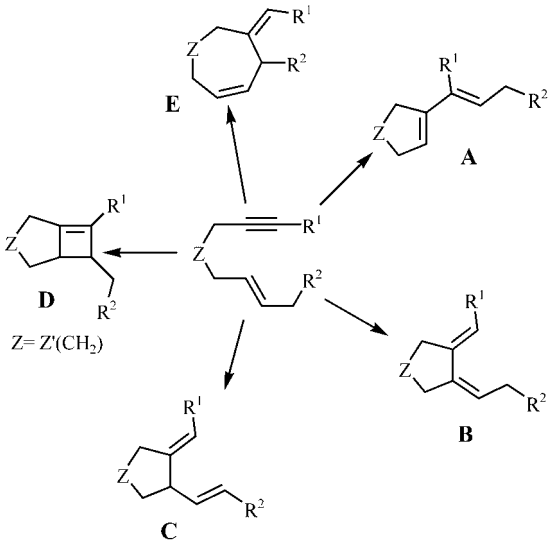

Scheme 1. Z = CH_2, heteroatom; R^1,R^2 = alkyl.

[*] Dr. C. Bruneau
Institut de Chimie
UMR 6509: CNRS-Université de Rennes 1
Organométalliques et Catalyse
Campus de Beaulieu-35042 Rennes Cedex (France)
Fax: (+33) 2-2323-6939
E-mail: christian.bruneau@univ-rennes1.fr

© 2005 Wiley-VCH Verlag GmbH & Co. KGaA, Weinheim
DOI: 10.1002/anie.200462568

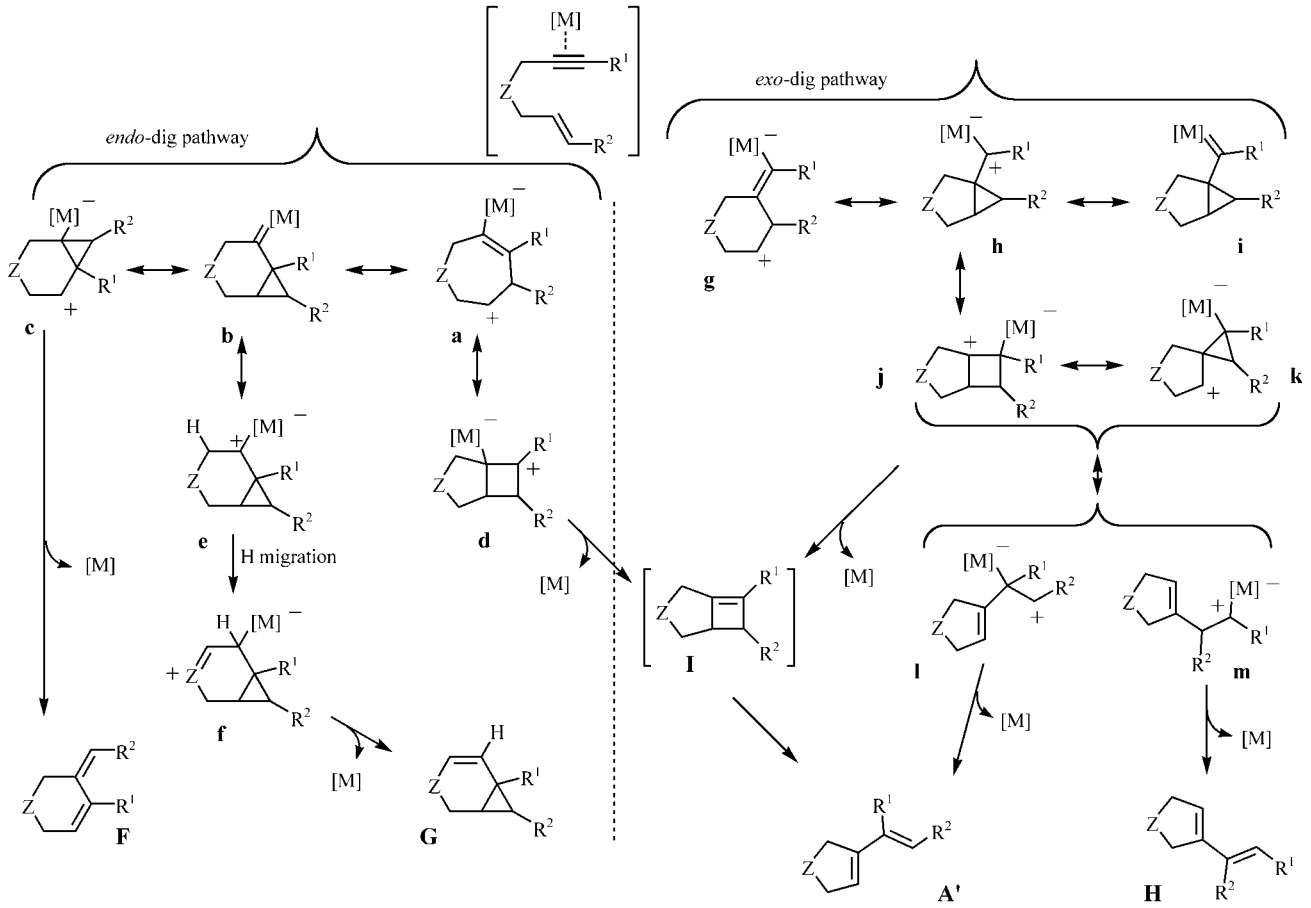

Scheme 2. [M] = transition-metal catalyst. Z = CH_2, heteroatom; R^1,R^2 = alkyl.

- oxidative coupling followed by reductive elimination to give cyclobutene derivatives **D**,[11]
- coupling involving π-allyl–metal intermediates to form nonconjugated dienes **E**.[12]

More recently, another mechanism based on the activation of enynes by electrophilic transition-metal derivatives was suggested to rationalize the catalytic isomerization of 1,6- and 1,5-enynes, and polyene-ynes not only into dienic compounds such as **A′**, **F**, and **H** but also into cyclopropane derivatives **G** (Scheme 2). To date, the most appropriate metal derivatives that efficiently perform this type of cycloisomerization are based on electrophilic ruthenium, platinum, and gold complexes or salts. Recent developments of the electrophilic activation of enynes to produce fused cyclopropane derivatives are presented herein.

Dr. Christian Bruneau graduated in Chemistry from the Institut National Supérieur de Chimie Industrielle de Rouen (1974) and obtained his Doctorate degree at the University of Rennes (1979). He then took up a CNRS position in environmental organic chemistry, and since 1986 he has studied molecular catalysis at the Institute of Chemistry in Rennes. His research interests include ruthenium-catalyzed selective transformations of alkynes, alkenes, and enynes, and transition-metal-catalyzed enantioselective hydrogenation and allylic substitution reactions. Since 2000, he is head of the Organometallics and Catalysis research group at the CNRS-University of Rennes.

Electrophilic Activation: Mechanistic Considerations and Model Calculations

The activation of the triple bond of enynes by a metal center generates highly electrophilic species and triggers the nucleophilic attack of a double bond to the activated triple bond by an *endo*- or *exo*-dig pathway. As illustrated in Scheme 2, a large number of resonance structures result from these two possible pathways. The carbon skeleton can adopt the canonical cationic homoallyl, cyclopropylmethyl, or cyclobutyl forms, all of them in resonance with a neutral cyclopropylmethylidene form. As already underlined by Fürstner and co-workers,[13] the congruence between ionic and carbenoid species is obvious in these activation processes. It is thus pertinent to suggest that the reactivity of enynes activated by electrophilic metals is governed by the formation of cyclopropylcarbene–metal intermediates (Scheme 3).[13–15]

DFT calculations based on $PtCl_2 \cdot H_2O$/6-octen-1-yne models suggest that the triple bond is η^2-coordinated to the metal

 © 2005 Wiley-VCH Verlag GmbH & Co. KGaA, Weinheim

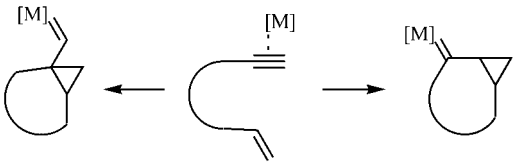

Scheme 3.

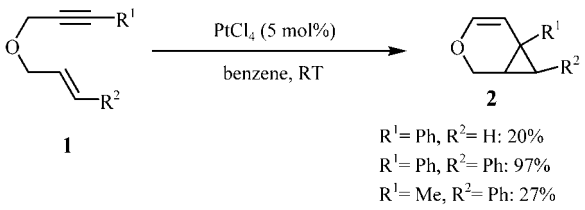

Scheme 4.

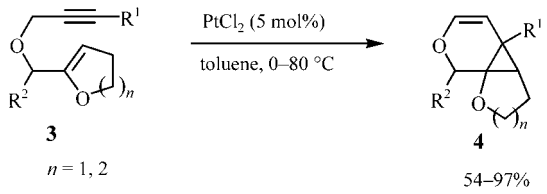

Scheme 5. R^1 = Me, Et, Ph; R^2 = Ph, 1-naphthyl, *i*Pr, *t*Bu, *p*-tolyl, CH=CHMe, CH=CHPh.

center and that the slippage toward an η^1-coordinated vinyl cation is not favored.[16] Furthermore, bicyclic cyclopropane intermediates of type **b** and **i** are expected to be formed directly in a single step by nucleophilic attack of the double bond to the activated triple bond.[16] With the same model, it was also found that the six-membered intermediate **b** (Scheme 2, Z = CH_2, R^1 = H, R^2 = Me) was more stable than the *exo*-dig intermediate **i** by 8.1 kcal mol^{-1}, but a higher activation energy of about 1 kcal mol^{-1} was required.[15,16] When an oxygen atom was introduced in the tether between the triple and the double bonds ((*E*)-HC≡CCH_2OCH_2CH=CHMe; Scheme 2, Z = O), the *endo*-dig pathway leading to **b** was both kinetically and thermodynamically favored.[17] With $[Au(PH_3)]^+$/6-octen-1-yne as a model, calculations show a highly polarized activated triple bond that easily reacts with the double bond with a low activation energy (0.1 kcal mol^{-1}) to give the *exo*-dig cyclization form **g**. However, depending on the nature of the starting enyne, the *endo*-dig cyclization, which requires a higher activation energy (6.1 kcal mol^{-1}), but generates a more stable gold carbene intermediate **b**, can also take place.[18]

Echavarren and co-workers have shown that in the presence of external nucleophiles such as water or alcohols, which are able to intercept cationic intermediate species, cyclic homoallylic alcohols and ethers can be obtained.[19] In the absence of external nucleophiles, catalytic transformations that involve 1,2-hydrogen migration and release of the metal catalyst are observed. From 1,6-enynes (Scheme 2), the only pathway that leads to the formation of cyclopropane compounds involves as the first step the *endo*-dig cyclization to form bicyclic [4.1.0] heteroheptenes. This reactivity is mainly driven by the presence of a heteroatom at the propargylic position which facilitates the 1,2-hydrogen migration and implies the presence of at least one hydrogen atom at the propargylic position.

Cycloisomerization of 1,6- and 1,5-Enynes Catalyzed by Electrophilic Metal Centers

The first examples of cycloisomerization of 1,6 and 1,5-enynes were reported by Blum et al. in 1995.[20] $PtCl_4$ was used as catalyst to promote the selective formation of 3-oxabicyclo-[4.1.0]hept-4-enes **2** from allyl propargyl ethers **1** (Scheme 4). Other reactions of this type were further reported in which $PtCl_2$ was used as catalyst[21] and the reaction was extended to enol ethers as starting compounds (Scheme 5).[22] The presence of a protected nitrogen atom at the propargyl position in 1,6-enynes **5** also orientates the rearrangement of the skeleton of these compounds into 3-azabicyclo[4.1.0]hept-4-ene derivatives **6** in the presence of $PtCl_2$ as catalyst at 60–80 °C in toluene (Scheme 6).[21,23]

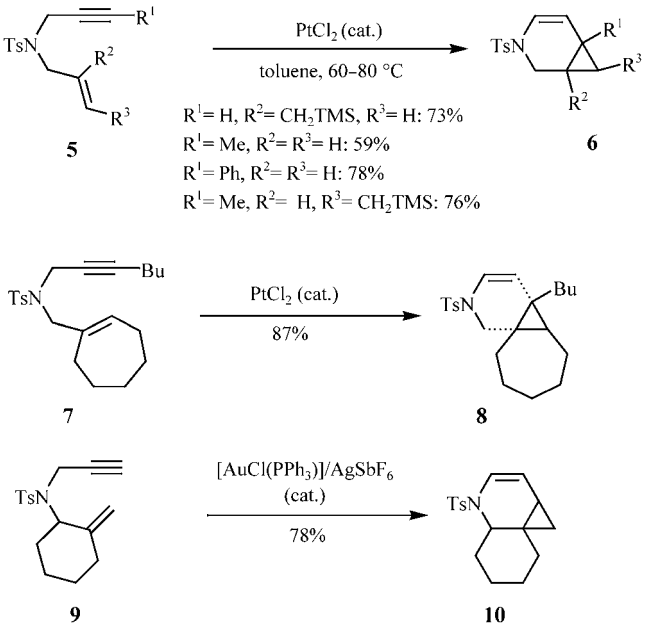

Scheme 6. Ts = *p*-toluenesulfonyl, TMS = trimethylsilyl.

Tricyclic structures such as **8** and **10** are also obtained from allyl propargyl tosylamides, such as **7** and **9**, which respectively contain an endo- or exocyclic double bond. In this context, catalytic systems based on gold complexes such as $[AuCl(PPh_3)]/AgSbF_6$ were more active under milder conditions and these reactions could be performed in dichloromethane at room temperature with very short reaction times.[18] In the absence of a heteroatom in the bridge between the triple and the double bonds of 1,6-enynes, a skeletal rearrangement leading to 1,3-dienes such as **A′** and **H** is observed (Scheme 2),[13,14,18] but cyclopropanation usually does not take place. However, when a carbene intermediate

 © 2005 Wiley-VCH Verlag GmbH & Co. KGaA, Weinheim

can be intramolecularly transferred to another double bond, the generation of polycyclic compounds that contain two cyclopropane structures is possible from the *exo*-dig intermediates that feature the less hindered metal–carbene moieties **i** (Scheme 2). This type of cascade reaction was first observed by Murai and co-workers with the skeleton rearrangement of **11** into **12**, when the starting compound was heated at 80 °C in the presence of catalytic amounts of $[\{RuCl_2(CO)_3\}_2]$, $PtCl_2$, or $[\{Rh(O_2CCF_3)_2\}_2]$ (Scheme 7).[24]

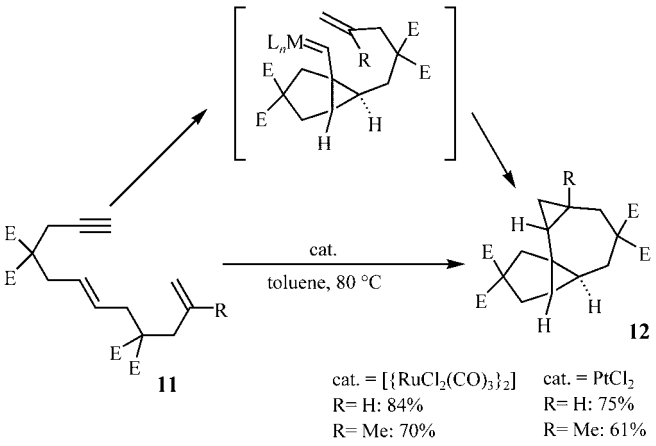

Scheme 7. L = ligand, E = CO_2Et.

In this case, the *exo*-dig cyclization is probably the first step followed by cyclopropanation with the pendant terminal olefin. Note that the corresponding oxygen-tethered dienyne, which in principle favors the *endo*-dig cyclization, is much less reactive. Recently, less activated substrates **13** which contain diene-yne substructures connected by only one $C(CO_2Me)_2$, $C(SO_2Ph)_2$, or NTs group were efficiently isomerized into tetracyclic derivatives **14** in the presence of cationic gold catalysts in dichloromethane at −30 to 23 °C (Scheme 8).[18]

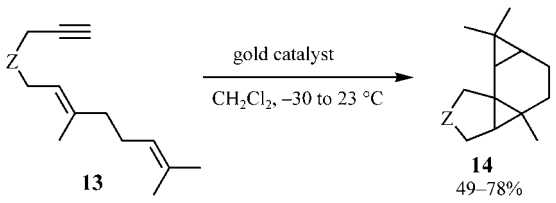

Scheme 8. Z = $C(CO_2Me)_2$, $C(SO_2Ph)_2$, NTs.

Upon treatment of tertiary propargylic alcohols or ethers **15** that bear two unsaturated chains at the propargylic position with $PtCl_2$ (5 mol%) at 80 °C, tetracyclic compounds **16** that result from electrophilic activation of the triple bond, *exo*-dig cyclization, and cyclopropanation were also formed (Scheme 9).[25] However, when a propargylic ester is submitted to similar reaction conditions (Y = MeCO, *p*-$NO_2C_6H_4$-CO), the formation of a metal–cyclopropylcarbene such as **i** is inhibited, as the metal-stabilized vinyl cation intermediate is trapped by the ester functionality, as shown from a more simple enyne in Scheme 11.[25–27] This mechanism leads to the

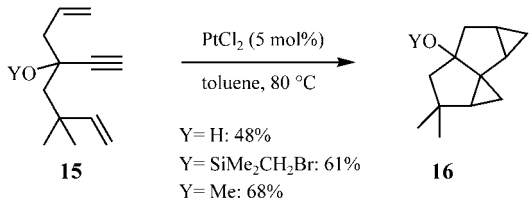

Scheme 9.

migration of the ester group and the formation of a metal–vinylcarbene species, which transfers the carbene to one of the two double bonds of **17** depending on the configuration of the intermediate, as illustrated in the formation of **18** and **19** (Scheme 10).[25]

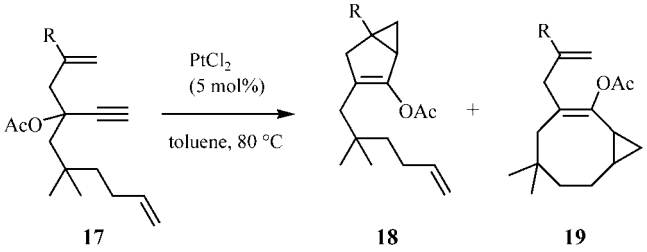

Scheme 10.

When the starting compound is a simple 1,*n*-enyne that contains only one olefinic bond, isomerization takes place at room temperature in the presence of $PtCl_2$[25] or $[AuCl(PPh_3)]/AgSbF_6$[26] as catalyst and provides bicyclic enol esters in good yields (Scheme 11). The stereoselectivity of this reaction is especially interesting from a synthetic point of view. The formation of the sole diastereoisomer **21** with control of three asymmetric centers during the cycloisomerization of a diastereomeric mixture of **20** is a representative example (Scheme 12).[25]

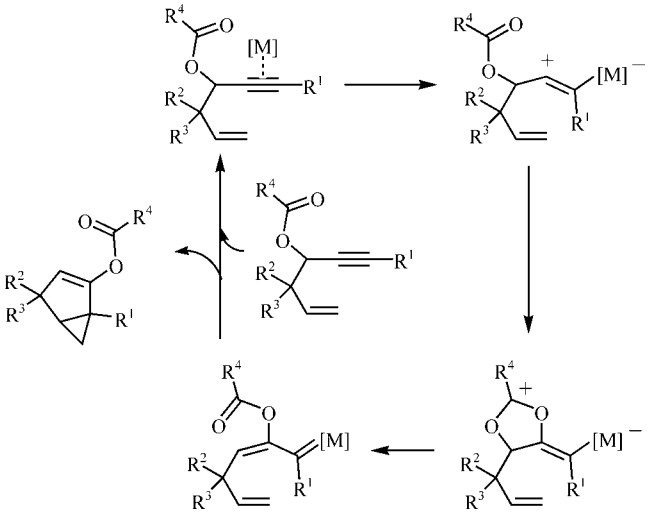

Scheme 11. [M] = Pt or Au complexes.

 © 2005 Wiley-VCH Verlag GmbH & Co. KGaA, Weinheim

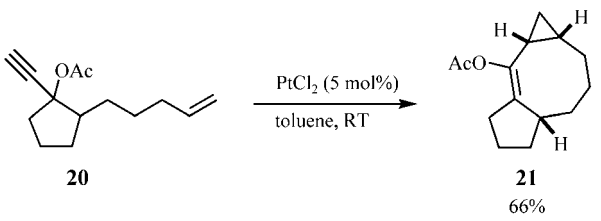

Scheme 12.

Note that the intermolecular coupling of propargylic acetates with styrene and other olefins (1,2-diphenylethene, 1,2-diethylethene, 3-trimethylsilylprop-1-ene, *tert*-butoxyethene, vinyl acetate) which takes place in the presence of $[\{RuCl_2(CO)_3\}_2]$, $PtCl_2$, or $AuCl_3$ as catalyst and leads to 1-cyclopropylvinyl acetate derivatives **22** is reminiscent of this general mechanism (Scheme 13).[28]

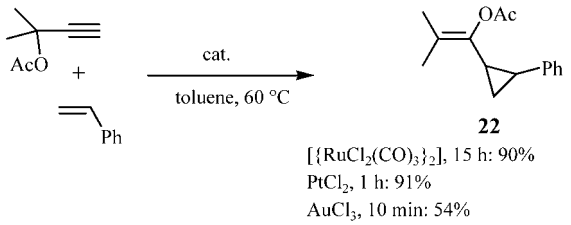

Scheme 13.

The cycloisomerization of 1,5-enynes into bicyclo-[3.1.0]hexane derivatives has recently been performed by using a gold catalyst.[29] In the presence of a cationic gold precursor such as $[Au(PPh_3)]SbF_6$ or $[AuCl(PPh_3)]/AgBF_4$, a very efficient *endo*-dig cyclization takes place with a variety of substrates even if they do not contain a heteroatom in the tether between the two unsaturated bonds. This observation confirms that the catalytic activity of cationic gold catalysts is superior to that of platinum catalysts. This transformation includes terminal as well as substituted triple- and double-bond-containing enynes, and substitution at the allylic or propargylic position does not constitute a drawback. Note that the very electrophilic gold center tolerates oxygen functionalities such as ethers, esters, and silyl ethers. The stereochemistry of this reaction is also very well controlled as exemplified by the transformation of **23** into **24** (Scheme 14).

Very recently, fused polycyclic cyclopropanes have been obtained by sequential one-pot catalytic reactions that involve first, the formation of a 1,5-enyne through intramolecular carbon–carbon bond formation from a propargylic moiety and an olefinic group catalyzed by [Cp*RuCl(μ^2-S*i*Pr)$_2$RuCp*Cl] (Cp* = pentamethylcyclopentadienyl), followed by a 1,5-enyne cycloisomerization catalyzed by $PtCl_2$.[30] Among the other 1,5-enynes which have been investigated, 3-hydroxy-1,5-enynes that bear propargyl and allyl motifs represent an interesting class of compounds. Indeed, the hydrogen migration that occurs for the formation of the final organic compound directly provides cyclic ketones. Terminal as well as substituted triple and double bonds provide bicyclo[3.1.0]hexan-3-ones in good yields. The stereochemical implication of this reaction is also very valuable and can be rationalized and predicted on the basis of the mechanism and structure of the starting enyne. Indeed, excellent results have been obtained upon catalysis with $PtCl_2$ in toluene at 60–80 °C (Scheme 15).[26,31]

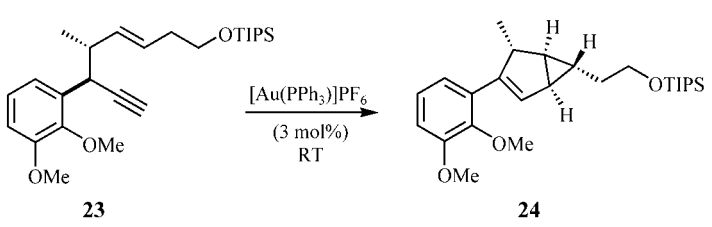

Scheme 14. TIPS = triisopropylsilyl.

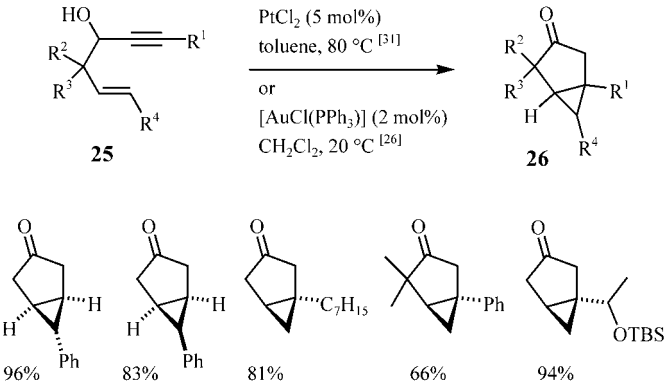

Scheme 15. TBS = *tert*-butyldimethylsilyl.

Formation of Cyclopropanes from Enynes through Tandem Reactions

Other transformations that are not purely isomerizations but also involve activation of enynes and lead to cyclopropane derivatives have been recently reported and deserve to be discussed here. The formation of cyclopropane derivatives from enynes through tandem cyclopropanation and metathesis can compete with the formation of the products expected from pure electrophilic activation. This is the case when a ruthenium carbene, such as $[RuCl_2(PCy_3)(MesH_2Im)(=CHPh)]$ (Cy = cyclohexyl, $MesH_2Im$ = bis(mesityl)-imidazolinylidene) or the system generated in situ from $[\{RuCl_2(p\text{-cymene})\}_2]$, $MesH_2Im$, and PCy_3, is used as catalyst to promote the tandem cyclopropanation and ring-closing metathesis reactions of the dienyne **27** into **28** as the major compound (Scheme 16).[32] Indeed, compound **28** does not result from isomerization of the starting enyne, as a CH_2 group is transferred to the ruthenium center to generate a metathesis catalyst. This result contrasts with the expected formation of 1,3-dienes and polycyclic compounds as obtained with $RuCl_3$ and $PtCl_2$ as electrophilic catalyst precursors.[32] From a more simple enyne such as **29**, the quantitative formation of the dimer **30** which contains two cyclopropane

 © 2005 Wiley-VCH Verlag GmbH & Co. KGaA, Weinheim

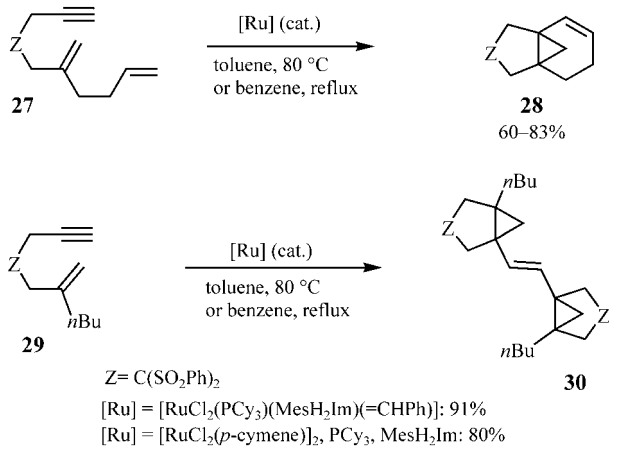

Scheme 16. Cy = cyclohexyl, Mes = mesityl (2,4,6-trimethylphenyl), Im = imidazole, *p*-cymene = 4-isopropyltoluene.

rings is observed from a cyclopropanation and cross-metathesis sequence.

The transformation of 1,6-enynes derived from propargylic alcohols into alkenylcyclopropane derivatives **32** promoted by [RuCl(Cp*)(cod)] (cod = cyclooctadiene) in the presence of a carbene source such as trimethylsilyldiazomethane or ethyl diazoacetate proceeds with skeleton rearrangement and addition of the carbene moiety to the initial enyne through a tandem alkenylation/cyclopropanation reaction (Scheme 17).[33] Unexpectedly, the metal carbene generated in situ is not involved in the cyclopropanation reaction but in the alkenylation reaction.

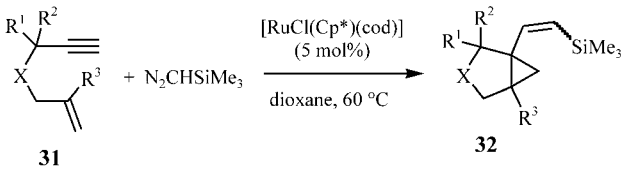

Scheme 17. X = O, NTs. Cp* = pentamethylcyclopentadienyl.

Another catalytic system based on tetrakis(methoxycarbonyl)palladacyclopentadiene has demonstrated a high efficiency to promote the dimerization of 1,6-enynes to form a cyclopropane ring. This reaction results from the intermediate formation of a palladium–cyclopropyl vinyl carbene which is trapped by [4+2] cycloaddition with an external double bond.[34] In the absence of any other olefin, the dimerization product **34** is obtained from **33**, whereas in the presence of a second olefinic substrate such as a conjugated diene or enyne, cyclopropane-containing cycloaddition products are obtained (Scheme 18).[34,35]

Conclusions and Outlook

The activation of the triple bond of enynes with electrophilic metal derivatives, especially cationic gold complexes, platinum salts such as $PtCl_2$, and ruthenium derivatives, makes possible the nucleophilic addition of the double bond to generate metal–cyclopropylcarbenoid intermediates. These species are very reactive and key intermediates to promote skeleton rearrangements and the formation of fused rings that contain at least one cyclopropane subunit. Reactivity strongly depends on the nature and geometry of the starting compounds, and both exo- and endocyclization modes provide atom-economical skeleton rearrangements and cycloisomerizations. Most of these transformations take place under stereochemical control and provide good routes to prepare optically active compounds. At the dawn of this chemistry, there is no doubt that further development will soon appear for the stereocontrolled construction of functional cyclopropane derivatives.

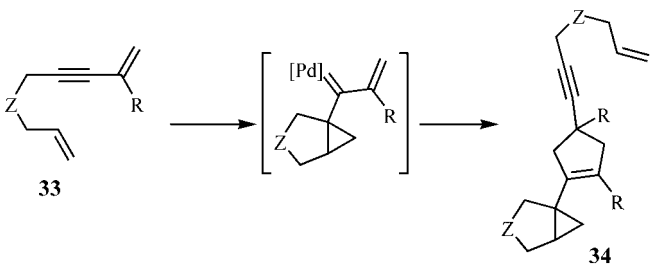

Scheme 18. Z = $C(CO_2Me)_2$.

Received: November 10, 2004
Published online: March 10, 2005

[1] L. A. Wessjohann, W. Brandt, T. Thiemann, *Chem. Rev.* **2003**, *103*, 1625.
[2] A. de Meijere, *Chem. Rev.* **2003**, *103*, 931.
[3] C. D. Poulter, F. Muscio, R. J. Goodfellow, *Biochemistry* **1974**, *13*, 1530.
[4] H. Lebel, J.-F. Marcoux, C. Molinaro, A. B. Charette, *Chem. Rev.* **2003**, *103*, 977.
[5] G. C. Lloyd-Jones, *Org. Biomol. Chem.* **2003**, *1*, 215.
[6] I. J. S. Fairlamb, *Angew. Chem.* **2004**, *116*, 1066; *Angew. Chem. Int. Ed.* **2004**, *43*, 1048.
[7] C. Aubert, O. Buisine, M. Malacria, *Chem. Rev.* **2002**, *102*, 813.
[8] M. Mori in *Topics in Organometallic Chemistry*, *Vol. 1* (Ed.: A. Fürstner), Springer, Berlin, **1998**, pp. 133–154.
[9] C. Storm Poulsen, R. Madsen, *Synthesis* **2003**, 1.
[10] B. M. Trost, M. J. Krische, *Synlett* **1998**, 1.
[11] B. M. Trost, M. Yanai, K. Hoogsteen, *J. Am. Chem. Soc.* **1993**, *115*, 5294.
[12] B. M. Trost, F. D. Toste, *J. Am. Chem. Soc.* **2002**, *124*, 5025.
[13] M. Mendez, V. Mamane, A. Fürstner, *Chemtracts: Org. Chem.* **2003**, *16*, 397.
[14] S. Oi, I. Tsukamoto, S. Miyano, Y. Inoue, *Organometallics* **2001**, *20*, 3704.
[15] A. M. Echavarren, C. Nevado, *Chem. Soc. Rev.* **2004**, *33*, 431.
[16] M. Mendez, M. Paz Munoz, C. Nevado, D. J. Cardenas, A. M. Echavarren, *J. Am. Chem. Soc.* **2001**, *123*, 10511.
[17] C. Nevado, D. J. Cardenas, A. M. Echavarren, *Chem. Eur. J.* **2003**, *9*, 2627.
[18] C. Nieto-Oberhuber, M. Paz Munoz, E. Bunuel, C. Nevado, D. J. Cardenas, A. M. Echavarren, *Angew. Chem.* **2004**, *116*, 2456; *Angew. Chem. Int. Ed.* **2004**, *43*, 2402.

 © 2005 Wiley-VCH Verlag GmbH & Co. KGaA, Weinheim

[19] a) M. Paz Munoz, M. Mendez, C. Nevado, D. J. Cardenas, A. M. Echavarren, *Synthesis* **2003**, 2898; b) B. Martin-Matute, C. Nevado, D. J. Cardenas, A. M. Echavarren, *J. Am. Chem. Soc.* **2003**, *125*, 5757; c) M. Mendez, M. P. Munoz, A. M. Echavarren, *J. Am. Chem. Soc.* **2000**, *122*, 11549; d) C. Nevado, L. Charruault, V. Michelet, C. Nieto-Oberhuber, M. P. Munoz, M. Mendez, M.-N. Rager, J.-P. Genêt, A. M. Echavarren, *Eur. J. Org. Chem.* **2003**, 706; e) L. Charruault, V. Michelet, R. Taras, S. Gladiali, J.-P. Genêt, *Chem. Commun.* **2004**, 850.

[20] J. Blum, H. Beer-Kraft, Y. Badrieh, *J. Org. Chem.* **1995**, *60*, 5567.

[21] A. Fürstner, F. Stelzer, H. Szillat, *J. Am. Chem. Soc.* **2001**, *123*, 11863.

[22] C. Nevado, C. Ferrer, A. M. Echavarren, *Org. Lett.* **2004**, *6*, 3191.

[23] A. Fürstner, H. Szillat, F. Stelzer, *J. Am. Chem. Soc.* **2000**, *122*, 6785.

[24] N. Chatani, K. Kataoka, S. Murai, *J. Am. Chem. Soc.* **1998**, *120*, 9104.

[25] E. Mainetti, V. Mouriès, L. Fensterbank, M. Malacria, J. Marco-Contelles, *Angew. Chem.* **2002**, *114*, 2236; *Angew. Chem. Int. Ed.* **2002**, *41*, 2132.

[26] V. Mamane, T. Gress, H. Krause, A. Fürstner, *J. Am. Chem. Soc.* **2004**, *126*, 8654.

[27] V. Rautenstrauch, *J. Org. Chem.* **1984**, *49*, 950.

[28] a) K. Miki, K. Ohe, S. Uemura, *Tetrahedron Lett.* **2003**, *44*, 2019; b) K. Miki, K. Ohe, S. Uemura, *J. Org. Chem.* **2003**, *68*, 8505.

[29] M. R. Luzung, J. P. Markham, F. D. Toste, *J. Am. Chem. Soc.* **2004**, *126*, 10858.

[30] Y. Nishibayashi, M. Yoshikawa, Y. Inada, M. Hidai, S. Uemura, *J. Am. Chem. Soc.* **2004**, *126*, 16066.

[31] Y. Harrak, C. Blaszykowski, M. Bernard, K. Cariou, E. Mainetti, V. Mouriès, A.-L. Dhimane, L. Fensterbank, M. Malacria, *J. Am. Chem. Soc.* **2004**, *126*, 8656.

[32] B. P. Peppers, S. T. Diver, *J. Am. Chem. Soc.* **2004**, *126*, 9524.

[33] F. Monnier, D. Castillo, S. Dérien, L. Toupet, P. H. Dixneuf, *Angew. Chem.* **2003**, *115*, 5632; *Angew. Chem. Int. Ed.* **2003**, *42*, 5474.

[34] B. M. Trost, A. S. K. Hashmi, R. G. Ball, *Adv. Synth. Catal.* **2001**, *343*, 490.

[35] B. M. Trost, A. S. K. Hashmi, *J. Am. Chem. Soc.* **1994**, *116*, 2183.

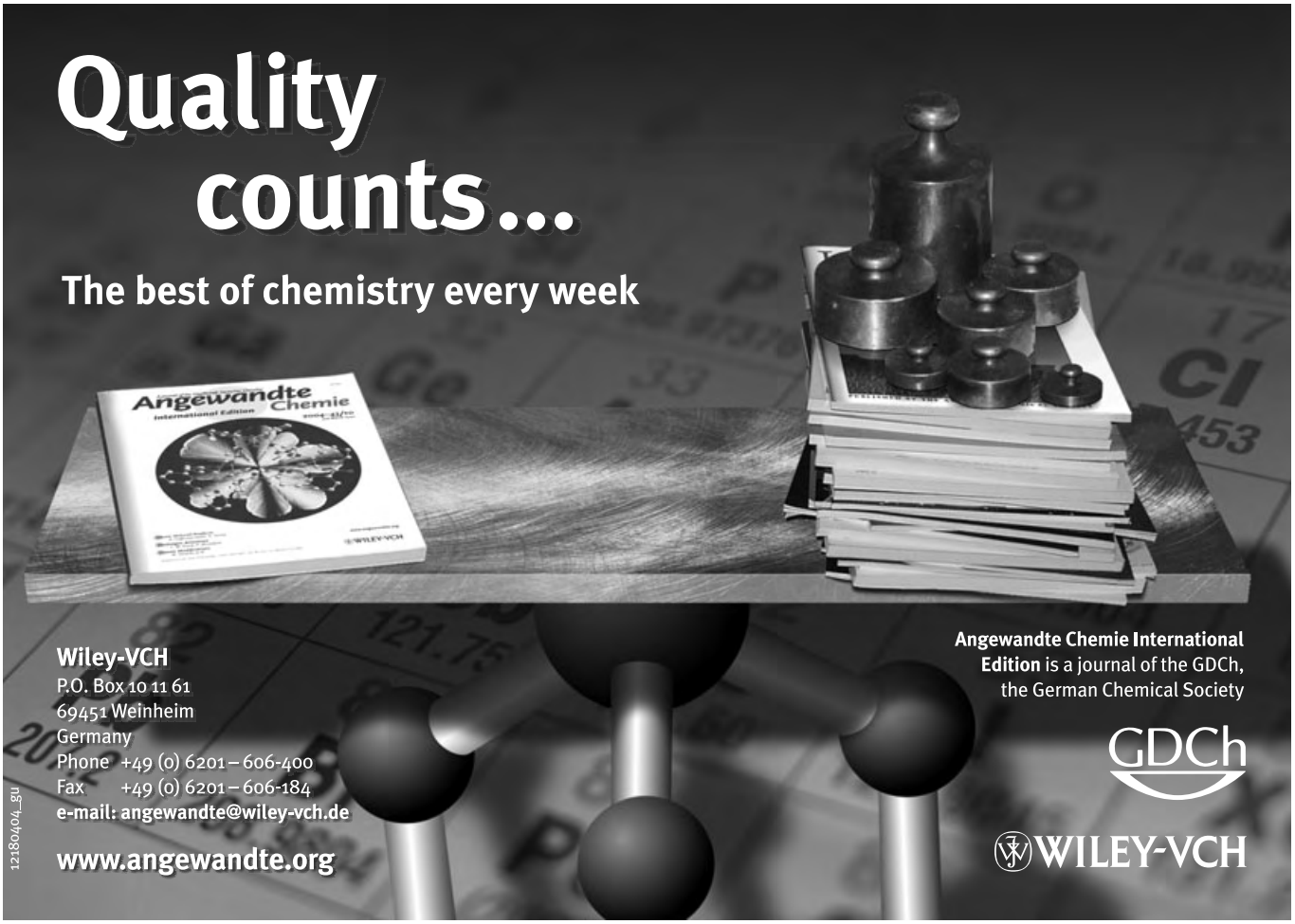

 © 2005 Wiley-VCH Verlag GmbH & Co. KGaA, Weinheim

Gas-Phase Reactions

Gas-Phase Catalysis by Atomic and Cluster Metal Ions: The Ultimate Single-Site Catalysts

Diethard K. Böhme and Helmut Schwarz**

Keywords:
bond activation · catalysis · cluster compounds · elementary processesmass spectrometry

Dedicated to Professor Gerhard Ertl

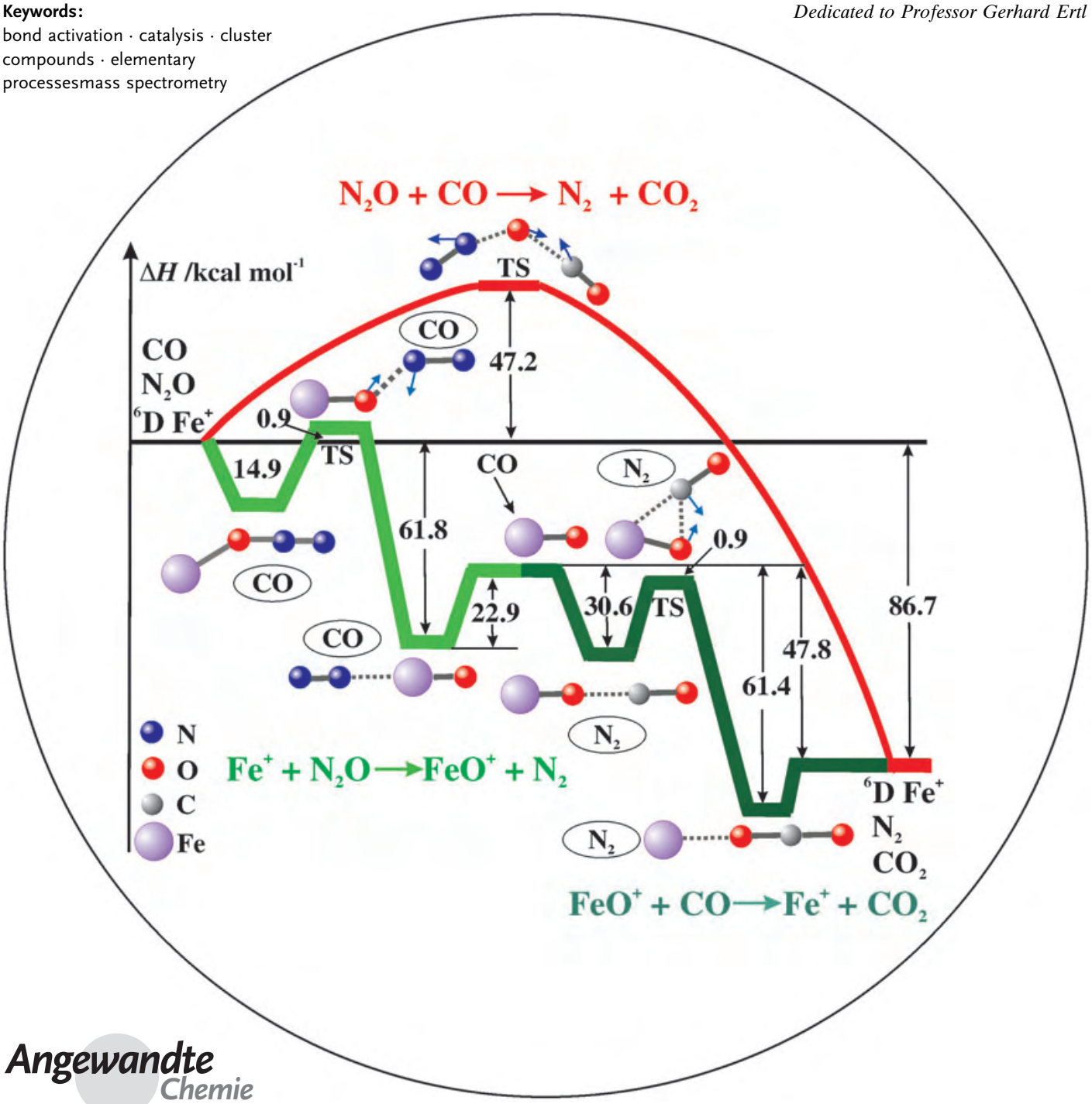

© 2005 Wiley-VCH Verlag GmbH & Co. KGaA, Weinheim
DOI: 10.1002/anie.200461698

Gas-phase experiments with state-of-the-art techniques of mass spectrometry provide detailed insights into numerous elementary processes. The focus of this Review is on elementary reactions of ions that achieve complete catalytic cycles under thermal conditions. The examples chosen cover aspects of catalysis pertinent to areas as diverse as atmospheric chemistry and surface chemistry. We describe how transfer of oxygen atoms, bond activation, and coupling of fragments can be mediated by atomic or cluster metal ions. In some cases truly unexpected analogies of the idealized gas-phase ion catalysis can be drawn with related chemical transformations in solution or the solid state, and so improve our understanding of the intrinsic operation of a practical catalyst at a strictly molecular level.

From the Contents

1. Introduction 2337
2. Catalysis of Oxygen-Atom Transport 2338
3. Bond-Activation Catalysis 2344
4. Metal-Mediated Coupling Processes 2346
5. Toward Heterogeneous Catalysis: Gas-Phase Catalysis with Cluster Ions 2348
6. Processes Mediated by Metal-Oxide Clusters: Redox versus Nonredox Reactivities 2350
7. Conclusions 2351

> *"... die Chemie der Gase ist seit einigen Jahren in eine neue Epoche, in das Zeichen der Katalyse getreten. Mit Hilfe von Katalysatoren gelingen die wundersamsten Umwandlungen durch Wasserstoff, Sauerstoff, Stickstoff, Kohlenoxid bei Temperaturen, die viele hundert Grad niedriger sind als diejenigen, bei denen man früher diese Gase reagieren sah. Dieses Kapitel der Katalyse ist schier unbegrenzt ..."*[+]
> Emil Fischer[1]

1. Introduction

Man-made catalysts contribute substantially to the value of all manufactured goods in industrialized countries;[2] consequently, there are huge efforts to understand and advance the performance of catalysts by uncovering the elementary steps of a catalytic reaction, be it homogeneous (including enzymatic) or heterogeneous. Improving existing catalysts has been identified as one of the three top challenges in contemporary chemistry.[3] However, a tunable catalyst does not exist even for the deceptively simple problem of selective activation and functionalization of an alkane, and resolving mechanistic problems associated with these transformations has proved particularly difficult.[4] This deplorable situation is not really surprising given the enormous complexity of the "real-life situation" in which solvents, counterions, aggregates, or surface inhomogeneities obscure the intrinsic features of a reaction center or the reactive intermediates, the understanding of which is paramount to improving catalysts.

Gas-phase studies on "isolated" reactants provide an ideal arena for detailed experiments of the energetics and kinetics of any bond-making and bond-breaking process at a strictly molecular level. In the last decade mass-spectrometric experiments with advanced techniques have been exploited to provide useful insight into the elementary steps of various catalytic reactions and to characterize reactive intermediates that have previously not been within reach of condensed-phase techniques.[5] Clearly, as a result of the net coulombic charge of the ions studied in a mass spectrometer as well as the absence of counterions and solvation, these coordinatively unsaturated ("naked") species will, in general, be much more reactive than their condensed-phase analogues.[6] Thus, gas-phase studies will, in principle, never account for the precise mechanisms, energetics, and kinetics operating in applied catalysis. However, such experimental studies, complemented by computational investigations, are not at all without meaning, for they provide a conceptual framework and an efficient means to obtain direct insight into reactivity patterns, the role of differential ligation, the importance of aspects of electronic structure, and the nature of crucial intermediates. Furthermore, as these gas-phase studies can be performed under well-defined conditions, they play a key role in the evolution of approaches aimed at a more comprehensive understanding of elementary steps, knowledge of which is mandatory for the design of tailor-made catalysts.[5,7]

[+] "... the chemistry of gases has entered into a new era in which catalysis has a presence. With help from catalysts, the wonderous transformations involving hydrogen, oxygen, nitrogen, and carbon monoxide can be achieved at temperatures many hundred degrees lower than those at which these gases were observed previously to react. This chapter in catalysis is almost unlimited ..."

[*] Prof. D. K. Böhme
Department of Chemistry
York University
4700 Keele Street, Toronto, ON, M3J1P3 (Canada)
Fax: (+1) 416-736-5936
E-mail: dkbohme@yorku.ca
Prof. Dr. H. Schwarz
Institut für Chemie
Technische Universität Berlin
Strasse des 17. Juni 135, 10623 Berlin (Germany)
Fax: (+49) 30-314-21102
E-mail: helmut.schwarz@mail.chem.tu-berlin.de

 DOI: 10.1002/anie.200461698 © 2005 Wiley-VCH Verlag GmbH & Co. KGaA, Weinheim

In this Review we focus on selected aspects of genuine gas-phase catalytic reactions mediated by atomic metal ions, metal oxide cations, and cluster ions under *thermal conditions*. The emphasis will be on "full thermal catalytic cycles", that is, reaction cycles which start with a bare or a partially ligated, mass-selected metal ion (which can be atomic or a cluster) which adsorbs a neutral reactant molecule, interacts with the other neutral reactant molecule, and then releases product molecules and regenerates the intact precursor metal ion which can start a second cycle—with all events occurring thermally. For the sake of completeness and also to relate to both homogeneous and heterogeneous catalysis, a few systems will be included in which at least one step of the catalytic cycle, for example, the product release, requires supply of external energy which is often provided by collisional activation in the gas-phase experiments.[8] In this Review we will discuss the chemistry of the following three topics: 1) catalysis of oxygen-atom transport, 2) molecular activation with an emphasis on bond-forming reactions, and 3) gas-phase processes which mimic aspects of surface catalysis. We refrain from describing the various experimental techniques, and the interested reader is referred to the original references and leading review articles.[5,6,8]

2. Catalysis of Oxygen-Atom Transport

Many of the catalytic cycles that have been reported to date involve the simple transfer of an oxygen atom from an O-atom donor O–X to an O-atom acceptor Y mediated by an ion $Z^{+/-}$ according to Equations (1) and (2), which result in the overall neutral chemical Reaction (3). Here, X and Y may be inorganic or organic entities. The thermodynamic requirement that must be met by the ionic catalyst $Z^{+/-}$ can be expressed in terms of a "thermodynamic window of opportunity"[9] framed by the oxygen-atom affinities (OA) of the three species involved in Reactions (1) and (2), namely, $OA(X) < OA(Z^{+/-}) < OA(Y)$. This necessary condition results from the fact that only exothermic (or thermoneutral) reactions take place with measurable rate coefficients under thermal conditions in gas-phase processes, provided that no chemical or spin barriers exist beyond the thermochemistry.[10]

$$OX + Z^{+/-} \rightarrow X + OZ^{+/-} \quad (1)$$

$$OZ^{+/-} + Y \rightarrow Z^{+/-} + OY \quad (2)$$

$$OX + Y \rightarrow X + OY \quad (3)$$

The first example of gas-phase catalysis of O-atom transport of which we are aware, although not recognized as such at the time, is the magnesium-mediated destruction of ozone by atomic oxygen, which was reported in 1968 during the study of some fundamental aspects of the chemistry of the earth's ionosphere (E-region):[11] both ion–molecule reactions were measured with the early flowing-afterglow technique and are known to be fast at ambient temperature, with $k_4 = 2.3 \times 10^{-10}$ and $k_5 = 1 \times 10^{-10}$ cm^3 molecule^{-1} s^{-1}.[11] Overall, the atomic Mg^+ ion acts as a catalyst in the reduction of ozone by atomic oxygen [Equation (6)], which proceeds with the much smaller rate coefficient $k_6 = 9.1 \times 10^{-15}$ cm^3 molecule^{-1} s^{-1} at room temperature.[12] The origin of this catalytic effect is straightforward: the substantial increase often observed in the rate coefficients of ion–molecule reactions, such as (4) and (5), in contrast to neutral–neutral reactions, such as (6), is a consequence of the electrostatic attraction between ions and molecules that acts to reduce activation energies and thus increase reaction rates.[13]

$$O_3 + Mg^+ \rightarrow O_2 + MgO^+ \quad (4)$$

$$MgO^+ + O \rightarrow Mg^+ + O_2 \quad (5)$$

$$O_3 + O \rightarrow 2\,O_2 \quad (6)$$

Of interest in terms of atmospheric chemistry at the time was that Reaction (5) keeps the concentrations of Mg^+ and MgO^+ high in the E-region of the ionosphere where it competes with electron–ion recombination.[11] A variation involving the inefficient direct recombination of oxygen atoms [Equation (10)] has been proposed for the chemistry of Na^+ and Fe^+ ions at an altitude between 75 and 110 km.[14] The slow, direct attachment of oxygen atoms to the metal ions M^+ is circumvented by first coordinating a larger ligand L in a more favorable termolecular fashion [Eq. (7); L = N_2, O_2, CO_2, or H_2O]; next, L is exchanged with atomic oxygen in an efficient bimolecular process according to Equation (8). In

Diethard K. Böhme was born in 1941 in Boston and studied chemistry at McGill University (Montreal) where he received his PhD in 1965. In 1969 he moved to York University (Canada), where he has been Distinguished Research Professor since 1994. From 1974–1976 he was an A. P. Sloan Fellow, 1990–1991 a Humboldt Research Awardee, and 1991–1993 a Killam Research Fellow. Since 1975 he has been a Fellow of the Chemical Institute of Canada and since 1994 a member of the Royal Society of Canada. In 2001 he was awarded a Canada Research Chair in Physical Chemistry.

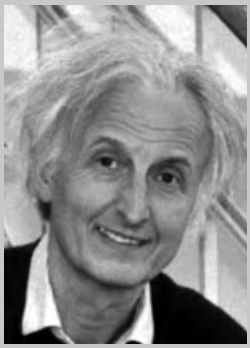

Helmut Schwarz, born in 1943 in Nickenich, has been a professor in Chemistry at the Technische Universität Berlin since 1978. His research interests concern experimental and computational aspects of gas-phase chemistry and physics in their broadest sense and cover chemical systems as diverse as small organic molecules and actinoid polycations. He is the author of more than 800 publications and has given about 700 invited lectures. In 2003 he received the "Otto Hahn Preis für Chemie and Physik". He is a member of several Academies and currently serves as Vice President of the German Research Foundation (DFG).

 © 2005 Wiley-VCH Verlag GmbH & Co. KGaA, Weinheim

the final step [Eq. (9)], the metal cation M^+ is regenerated reductively, with the overall consequence that the inefficient direct oxygen–oxygen recombination [Eq. (10)] is by-passed by a set of kinetically more favorable ion–molecule reactions. However, this appealing model and its generalization as yet lack experimental confirmation with measurements of the individual rate coefficients.

$$M^+ + L \rightarrow ML^+ \quad (7)$$

$$ML^+ + O \rightarrow MO^+ + L \quad (8)$$

$$MO^+ + O \rightarrow M^+ + O_2 \quad (9)$$

$$O + O \rightarrow O_2 \quad (10)$$

2.1. Reduction of Nitrogen Oxides

Catalytic conversion of harmful gases, such as the oxides of nitrogen produced in fossil-fuel combustion into nitrogen and carbon dioxide, is of utmost importance, both environmentally and economically.[15] CO was one of the first gases investigated for eliminating NO from automobile exhaust gas. While this and other reactions of CO with NO_n ($n = 1, 2$) or N_2O are quite exothermic, they do not occur directly to any measurable extent in the gas phase at either room or elevated temperatures. Catalytic converters are required to remove these undesirable pollutants, and metal oxides, mixed metal-oxide compounds, supported metal catalysts, metal zeolites, and alloys have all been investigated as heterogeneous catalysts.

The first example of homogeneous catalysis in the gas phase in which atomic transition-metal cations bring about exothermic reduction of N_2O by CO ($\Delta_r H = -87.3$ kcal mol^{-1}) was reported in a landmark experiment by Kappes and Staley in 1981.[16] These authors observed the occurrence, in an ion cyclotron resonance (ICR) mass spectrometer, of Reactions (11) and (12), in which the Fe^+ ion transports an oxygen atom from N_2O to CO in the overall transformation given by Equation (13). The reported rate coefficients are $k_{11} = 7 \times 10^{-11}$ and $k_{12} = 9 \times 10^{-10}$ cm^3 molecule^{-1} s^{-1}. The oxides of five other transition-metal cations (Ti^+, Zr^+, V^+, Nb^+, and Cr^+) formed from the bare metal ions and N_2O in analogy to Equation (11) were observed not to oxidize CO with a measurable rate, and the findings were ascribed to unfavorable thermochemical features, that is, $D(M^+\text{-}O) > OA(CO)$. Refinement of the rate constants of this remarkably simple system were provided in 1995 by selected ion flow tube (SIFT) experiments with $k_{11} = 3.1 \times 10^{-11}$ and $k_{12} = 2.1 \times 10^{-10}$ cm^3 molecule^{-1} s^{-1}, and this study also demonstrated that the cycle defined by Equations (11)–(13) is not poisoned by N_2O, since $FeO(N_2O)_n^+$ ($n = 0$–3) remains reactive at least up to $n = 3$.[17]

$$N_2O + Fe^+ \rightarrow FeO^+ + N_2 \quad (11)$$

$$FeO^+ + CO \rightarrow Fe^+ + CO_2 \quad (12)$$

$$N_2O + CO \rightarrow N_2 + CO_2 \quad (13)$$

The potential energy curve recently computed for the metal-cation-catalyzed reduction of N_2O by CO according to Equations (11)–(13), is shown in Figure 1 for Fe^+ (^{6}D).[9] The uncatalyzed process has a computed energy barrier of

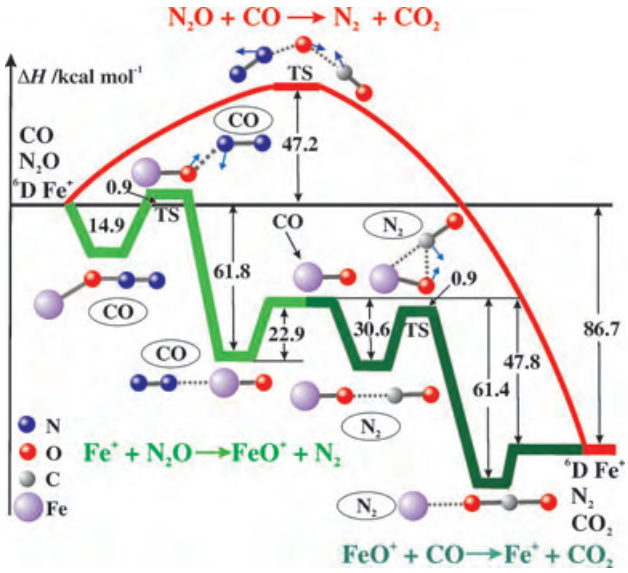

Figure 1. Potential energy curve for the reduction of N_2O by CO in the absence and presence of atomic Fe^+(^{6}D) computed using DFT with hybrid B3LYP functional and a 6-311+G(d) triple-ζ basis set augmented with one set of diffuse and polarization functions (adapted from ref. [9]).

47.2 kcal mol^{-1}, thus preventing any conversion at elevated temperature despite the process being very exothermic. However, the first step of the much faster ion-catalyzed sequence lowers the energy barrier by more than a factor of 50 to a mere 0.9 kcal mol^{-1}. Both ionic steps in this pathway are described by double-minimum potential-energy profiles that are typical for ion–molecule reactions.[13] The reported differences in the rate coefficients[16,17] arise to a large extent from the energetic features associated with the transition states for the making and breaking of the Fe–O bond.[18]

Atomic Pt^+ has also been shown to mediate the reaction of N_2O and CO efficiently, with $k = 7 \times 10^{-11}$ for the reduction of N_2O and 6.7×10^{-10} cm^3 molecule^{-1} s^{-1} for the oxidation of CO.[19] Recently,[20] the use of inductively coupled plasma/selected-ion flow tube (ICP/SIFT) tandem mass spectrometry[21] has added Os^+ and Ir^+ ions to the list of catalysts active in the reduction of N_2O by CO. This technique has also provided insight into the much more general case,[9] which will be discussed further below. The thermal reactions for the formation of diatomic metal oxides with N_2O as an oxidant have been investigated for 59 atomic cations including the fourth-row atomic cations from K^+ to Se^+, fifth-row cations from Rb^+ to Te^+ (excluding Tc^+), sixth-row atomic ions from Cs^+ to Bi^+, and the lanthanide cations (excluding Pm^+).[22] Primary reactions were observed corresponding to O- and N-atom transfer as well as simple N_2O addition. Interestingly, periodicities were noticed in reaction efficiency and these were scrutinized in terms of overall exothermicity, the

© 2005 Wiley-VCH Verlag GmbH & Co. KGaA, Weinheim

presence of a chemical activation barrier in the reaction coordinate, the conservation of spin, and, in the case of lanthanide cations, the energy associated with the promotion of a chemically inert 4f electron to enable formation of a double bond with atomic oxygen (Figure 2). From all the

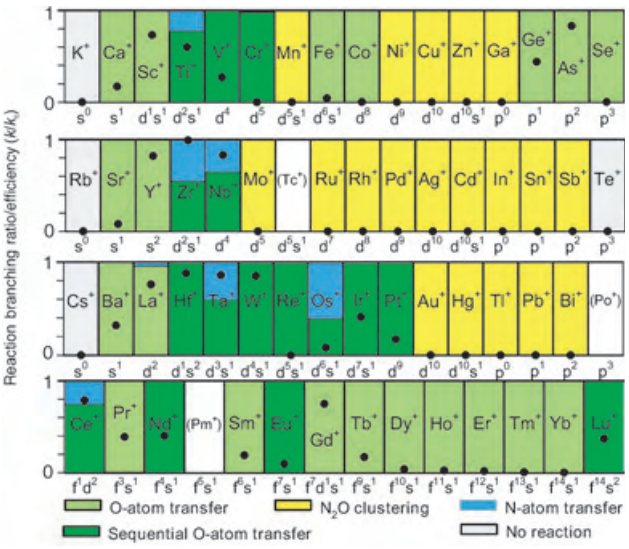

Figure 2. Periodic variations observed in the efficiencies k/k_c (represented as solid circles), for reactions of atomic cations with N_2O. k represents the measured reaction-rate coefficient and k_c is the calculated collision rate coefficient.[23] Also indicated are the observed reaction channels and the ground-state electronic configurations of the atomic cations (adapted from ref. [22a].

cations investigated, 26 atomic systems were shown for the catalysis of O-atom transport to lie within the "thermodynamics window of opportunity" formed by the oxygen affinities of N_2 and CO, with $OA(N_2) = 40$ and $OA(CO) = 127$ kcal mol^{-1}. Catalytic activity was observed with only 10 of these 26 atomic cations, namely Ca^+, Fe^+, Ge^+, Sr^+, Ba^+, Os^+, Ir^+, Pt^+, Eu^+, and Y^+. The remaining 16 cations, which meet the thermodynamic criteria for the catalysis of oxygen-atom transport (Cr^+, Mn^+, Co^+, Ni^+, Cu^+, Se^+, Mo^+, Ru^+, Rh^+, Sn^+, Te^+, Re^+, Pb^+, Bi^+, Tm^+, and Lu^+), reacted too slowly during either the formation of MO^+ or its reduction by CO. As shown earlier,[24] the failure of quite exothermic groundstate O-atom transfer reactions to proceed to a measurable extent at room temperature can often be ascribed in terms of a kinetic barrier resulting from a curve crossing that is required for the change in multiplicity which is necessary for the overall spin to be conserved.[25]

Studies on the role of atomic metal cations in the catalysis of O-atom transport have recently been extended to the oxidation of CO by two other nitrogen oxides, NO and NO_2 [see Eqs. (14) and (15)].[20] These processes, together with the reduction of the intermediary diatomic MO^+ ions by CO, constitute rare examples of metal-cation-catalyzed reduction of NO_2, NO, and N_2O coupled with the formation of N–N bonds during the termolecular reductive dimerization of NO [Eq. (15)]; overall, NO_2 is reduced to N_2 [Eq. (16)]. Scheme 1

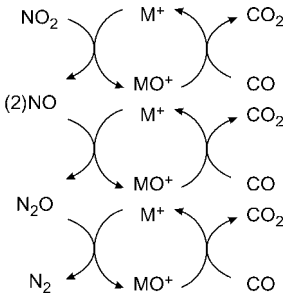

Scheme 1. Reduction with CO and coupling of nitrogen oxides catalyzed by atomic metal cations M^+ (M = Fe, Os, Ir; adapted from ref. [20]).

depicts the various cycles involved in this conversion, which has been demonstrated for $M^+ = Fe^+$, Os^+, and Ir^+.[20] Most of the reactions measured correspond to single-channel processes so that the proposed specific catalytic cycles, in principal, have a turnover number of infinity, and thus constitute a "perfect" catalytic cycle. This aspect will be referred to in more detail below.

$$NO_2 + M^+ \rightarrow MO^+ + NO \quad (14)$$

$$2\,NO + M^+ \rightarrow MO^+ + N_2O \quad (15)$$

$$2\,NO_2 + 4\,CO \rightarrow N_2 + 4\,CO_2 \quad (16)$$

Atomic metal cations have also been invoked as catalysts for the reduction of N_2O by molecular hydrogen, an exothermic process ($\Delta_r H = -77$ kcal mol^{-1}) which does not occur at ambient temperature in the absence of a catalyst. The thermodynamic window of opportunity in this case is still quite large, $40 < OA(M^+) < 117$ kcal mol^{-1}, and includes 25 atomic cations.[8] The perhaps best studied couple, both experimentally and computationally, concerns the oxidation of H_2 by diatomic FeO^+ [Eq. (17)].[16,26] This reaction, in conjunction with the formation of FeO^+ from bare Fe^+ and N_2O [Eq. (11)], is remarkable in itself, and among the many salient features the following are worthy of note:

$$H_2 + FeO^+(^6\textstyle\sum^+) \rightarrow Fe^+(^6D) + H_2O \quad (17)$$

1) Since ground-state atomic Fe^+ is inert towards H_2 and H_2O, and N_2O does not react with FeO^+ nor with H_2 and H_2O, the catalytic cycle defined by the combination of Reactions (11) and (17) proceeds with an infinite turnover number; in practice, however, side reactions with background hydrocarbons limit this number to about 100.[5a]
2) The process depicted in Equation (17) is very exothermic ($\Delta_r H = -37$ kcal mol^{-1}), even when excited $Fe^+(^4F)$ is formed, which is orbitally unrestricted and spin-allowed. Yet, the reaction efficiency $k/k_c < 1\,\%$,[26e] which is almost 100 times slower than the reduction of FeO^+ with CO [Eq. (12)].
3) The reaction efficiencies for the oxidation of molecular hydrogen by FeO^+ show very small intra- and intermolecular kinetic isotope effects for H_2, HD, and D_2.[16,26a]

 © 2005 Wiley-VCH Verlag GmbH & Co. KGaA, Weinheim

4) The most intriguing finding is that the cross-section of Reaction (17) in the vicinity of the threshold slightly diminishes with increasing kinetic energy of the FeO^+ projectile.[26a,e]

Although the small reaction efficiency (< 1 %) could be interpreted in terms of a classical Arrhenius activation barrier,[17] this assumption perhaps does not seem justified in view of the results of the guided ion beam experiments,[26a,e] which show that the reaction cross-section monotonically decreases with increasing collision energy below 0.2 eV on the center-of-mass scale. Hence, the vanishingly low reactivity of FeO^+ toward molecular hydrogen may well be related to the inefficiency associated with switches between surfaces of different spin, and this scenario is in line with extensive computational studies conducted by Shaik, Schwarz, and coworkers.[26c,d,f,g] The scenario depicted in Figure 3 emerged as

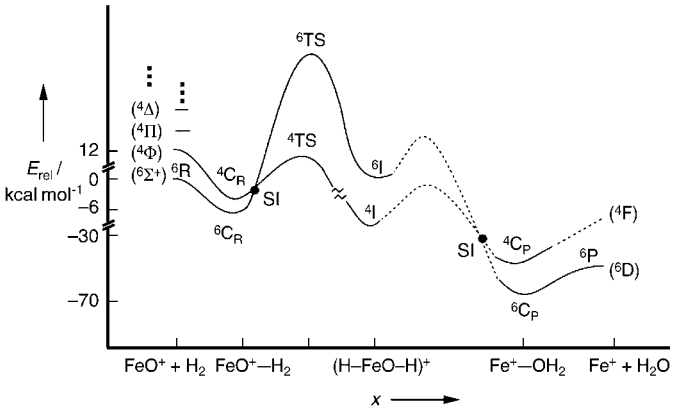

Figure 3. Schematic potential energy profile for Reaction (17). The dashed lines indicate areas not explored computationally. Some energies were taken from refs. [26c, 29]. C_R = reactant complex, SI = spin inversion, I = insertion intermediate, and C_p = product complex (adapted from ref. [26f]).

the most likely description. Two spin-inversion (SI) junctions between the sextet and quartet states occur, one near the FeO^+/H_2 cluster at the entrance channel and one near the Fe^+/H_2O complex at the exit. Calculations of the spin-orbit coupling (SOC) indicate a continuous decrease in the SOC value from significant at the entrance to negligibly small at the product exit. The results further show that while the quartet surface provides a low-energy path, the SI junctions reduce the probability of the reaction significantly, and the suggested interplay between spin inversion and chemical barrier height in the FeO^+-mediated oxidation of molecular hydrogen is confirmed by the pleasing agreement of the experimentally determined (with HD and D_2) kinetic isotope effects of Reaction (17) with the computed data.[26e] Clearly, Reaction (17) should not take place at all without the intervention of spin inversion at thermal condition, and the observation of it (although quite inefficient) is both a convincing example for the concept of a "spin-accelerated" transformation[27] as well as a prototype of a two-state reactivity for a thermal process.[25,28,29]

2.2. Oxidation of Hydrocarbons

The principles outlined above for the metal-catalyzed reduction of nitrogen oxides, coupled with the oxidation of CO or H_2 by the intermediary MO^+ ions, can also be applied to mediate the oxidation of a hydrocarbon. Equations (18) and (19) show a generalized catalytic cycle for this oxygen-atom transfer, and Equation (20) illustrates how the cycle achieves the oxidation of the hydrocarbon RH. Again, although this oxidation is quite exothermic, no measurable reaction occurs at ambient temperature without the intervention of a catalyst. Mass spectrometric measurements of the kinetics of Reactions (18) and (19) have become straightforward, even when the oxidation of the hydrocarbon [Eq. (19)] produces more than one product and the identification of (ROH) is problematic, if not impossible, by mass-spectrometric means alone. However, in certain cases thermodynamic and mechanistic arguments can be used in the identification of (ROH), particularly in the case of small hydrocarbons. Yet, important alternatives, such as the formation of isomers or the release of water and concomitant dehydrogenation of RH, as shown in Reaction (21), often cannot be excluded.

$$M^+ + N_2O \rightarrow MO^+ + N_2 \quad (18)$$

$$MO^+ + RH \rightarrow (ROH) + M^+ \quad (19)$$

$$N_2O + RH \rightarrow (ROH) + N_2 \quad (20)$$

$$MO^+ + RH \rightarrow M^+ + H_2O + [RH{-}H_2] \quad (21)$$

Extensive literature is now available on C–H and C–C bond activation by transition-metal oxide cations in the gas phase.[5a,e,i,29,30] Most of these measurements, at least until recently, have involved Fourier transform ICR mass spectrometry, and the emphasis has been on reactions of MO^+ with M = Fe, as well as a few other metals such as Sc, Ti, V, Cr, Mn, Co, Ni, Os, and Pt. Many of these diatomic metal oxides have been shown to react with a variety of hydrocarbons RH to regenerate M^+, at least in a fraction of the reactive collisions, thus closing the catalytic cycle defined by Equations (18)–(20). This situation has been documented for the following systems:

1) FeO^+/CH_4,[26e,31] FeO^+/C_2H_6–*n*-C_6H_{14},[32,33] and FeO^+/C_2H_2;[16]
2) reactions of CrO^+,[33] MnO^+,[34] FeO^+,[34,35] CoO^+,[34] NiO^+,[34] and OsO^+[36] with ethane to apparently form acetaldehyde in gas-phase processes which often bridge the gap between heterogeneous metal oxide catalysts and solution-phase oxometal reagents;
3) the fundamentally and industrially important benzene oxidation[37] modeled by reaction of C_6H_6 with the late transition metal oxide cations CrO^+, MnO^+, FeO^+, CoO^+, and NiO^+ to apparently produce phenol with high efficiencies (> 56 %).[38] The thermochemical constraints ($D(M^+\text{-}O) > OA(C_6H_6)$) means that the early transition metal oxide cations ScO^+, TiO^+, and VO^+ do not effect oxidation of benzene; rather, they simply add to the hydrocarbon.[38]

 © 2005 Wiley-VCH Verlag GmbH & Co. KGaA, Weinheim

In the following we present in some more detail a few specific examples pertinent to the catalysis of O-atom transfer in the context of hydrocarbon oxidation. Although the conversion of methane into methanol by FeO^+[31] [Eq. (22)], has in common with the FeO^+-mediated oxidation of H_2, the feature of two-state reactivity,[25,28,39] competitive formation of $FeOH^+$ is substantial [Eq. (23)]. As this ion is unreactive towards methane on thermochemical grounds,[40] the turnover number is limited to the disappointingly small value of 1.6. However, put into a more general perspective, the release of a methyl radical in the course of forming $Fe(OH)^+$ can also be viewed as a model for oxidative coupling of methane.[41] There is a pronounced energy dependence of the branching ratios of Reactions (22) and (23)[26a,b] which deserves a brief mention: Starting from a ratio of 0.4/1 at the lowest kinetic energy, the $Fe^+/Fe(OH)^+$ ratio drops to about 0.03/1 between 0.5 and 1.0 eV, and then increases again, and reaches 1/1 above 5 eV center-of-mass energy.

$$CH_4 + FeO^+ \xrightarrow{57\%} Fe^+ + CH_3OH \quad (22)$$

$$CH_4 + FeO^+ \xrightarrow{41\%} Fe(OH)^+ + CH_3 \quad (23)$$

As discussed in detail elsewhere,[25,26d,28,39] formation of CH_3OH is a two-bond process and thus requires the operation of two-state reactivity (TSR). The reactants FeO^+ and CH_4 pass slowly through the crossing region at low kinetic energy, thus allowing the electrons to adjust to a more favorable electronic configuration along the reaction coordinate. Spin inversion from the ground-state sextet entrance channel to a quartet state can take place under such conditions. The latter state provides a low-energy pathway for the formation of Fe^+/CH_3OH in Reaction (22). This reaction declines with increasing kinetic energy since surface crossing becomes less likely at shorter lifetimes of the reactant complexes. The release of a CH_3 radical in Reaction (23) can, however, occur by TSR as well as in a spin-allowed homolytic C–H bond cleavage, which obeys an Arrhenius-type energy dependence and hence dominates at elevated energies. The reaction of FeO^+ with CH_4 has a measured rate coefficient of 2×10^{-10} cm^3 molecule^{-1} s^{-1}, and the kinetic isotope effect analysis favors the insertion species $Fe(CH_3)(OH)^+$ as the intermediate of Reaction (22).[31]

The catalysis of ethane oxidation by Fe^+/N_2O, as illustrated by Reactions (11a) and (24)–(27), is analogous to that of methane except that the channel represented by the formation of C_2H_5OH is now less competitive: rather, the thermochemically favored elimination of H_2O to produce $Fe(C_2H_4)^+$ now comprises 70%,[32] (67%[33]) with Fe^+ formation accounting for only 10%[32] (12%[33]) with $k_{24} = 1 \times 10^{-10}$ cm^3 molecule^{-1} s^{-1}.[33]

$$2\,N_2O + 2\,Fe^+ \rightarrow 2\,FeO^+ + 2\,N_2 \quad (11a)$$

$$FeO^+ + C_2H_6 \rightarrow Fe^+ + C_2H_5OH \quad (24)$$

$$FeO^+ + C_2H_6 \rightarrow Fe(C_2H_4)^+ + H_2O \quad (25)$$

$$Fe(C_2H_4)^+ + N_2O \rightarrow Fe^+ + CH_3CHO + N_2 \quad (26)$$

$$2\,C_2H_6 + 3\,N_2O \rightarrow C_2H_5OH + CH_3CHO + H_2O + 3\,N_2 \quad (27)$$

$Fe(C_2H_4)^+$, which is formed as a major product in Reaction (25), is not lost for catalysis since it reacts further with N_2O to regenerate Fe^+ in 72% of its reactive collisions [Eq. (26)] and so becomes part of the parallel three-step catalytic cycle shown in Scheme 2.[35] The turnover number of

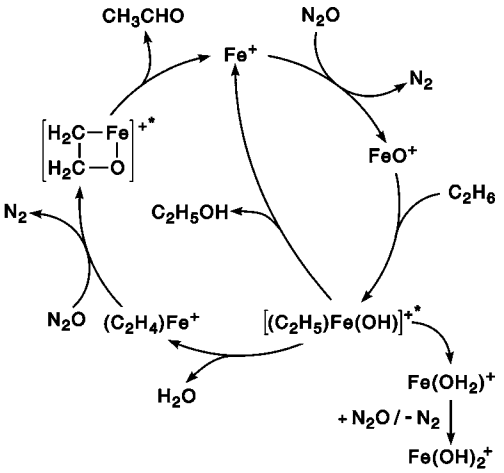

Scheme 2. Catalytic cycle for the Fe^+-mediated oxidation of C_2H_6 by N_2O (adapted from ref. [35]).

the Fe^+-mediated oxidation of C_2H_6 is about 2.5, and the inefficiency in the catalytic cycle is caused by the irreversible formation of $Fe(OH)_2^+$ as a side product. The nonreactivity of this Fe^{III} ion towards ethane emphasizes the essential function of the metal-oxide moiety in FeO^+, rather than the formal iron(III) oxidation state. However, as $Fe(OH)_2^+$ can be converted into $FeO(H_2O)^+$, the reactive species might be regenerated by loss of water upon "heating", that is, collisional activation. This finding actually illustrates, to some extent, an analogy to applied catalytic processes in which desorption of the product (in this case, loss of the water ligand) is often rate-limiting; in practice, dehydration is achieved by performing the oxidation at elevated temperatures. We will return to this aspect of regenerating the active site in a catalytic gas-phase cycle by collisional activation below.

Parallel three-step catalytic cycles may also occur in the catalytic oxidation of alcohols in which production of Fe^+ [Equation (28d)] is a relatively minor channel in the reaction with FeO^+, but which often produces significant amounts of carbonyl-Fe^+ and other Fe^+ complexes.[42] Reaction (28) illustrates the products formed from the oxidation of methanol as an example.

The branching ratio for Reaction (28) is (a)/(b)/(c)/(d) = 0.35/0.35/0.10/0.20, and hence only 20% of the products regenerate the Fe^+ catalyst directly. However, in channels 28b and 28c the Fe^+ complexes $Fe(CH_2O)^+$ and $Fe(H_2O)^+$ are formed and if these both react with N_2O, upon release of the ligands CH_2O and H_2O, the "catalyst" FeO^+ is

 © 2005 Wiley-VCH Verlag GmbH & Co. KGaA, Weinheim

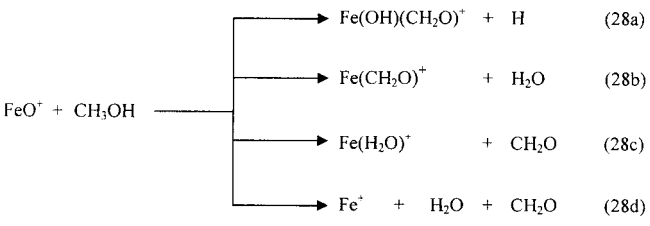

recovered in 45% yield and ready to enter a parallel three-step catalytic chain, in analogy to the $Fe^+/N_2O/C_2H_6$ system discussed above.

An attractive variant has been reported for the Fe^+-catalyzed oxidation of methane that involves the conversion of methane into formaldehyde by O_2 in the presence of methanol as a co-catalyst,[43,44] Oxygen-atom transport may proceed both with the formation of formaldehyde from methanol with O_2 as the O-atom donor for Fe^+ and in the oxidation of methane to methanol with FeO^+ [Eqs. (29)–(31)].

$$CH_4 + \langle O \rangle \rightarrow CH_3OH \quad (29)$$

$$CH_3OH + O_2 \rightarrow CH_2O + H_2O + \langle O \rangle \quad (30)$$

$$CH_4 + O_2 \rightarrow CH_2O + H_2O \quad (31)$$

The key gas-phase experiments that mimic the overall Reaction (31) are summarized in Equations (22a) and (32)–(34). The $\langle O \rangle$ equivalent of Reaction (29) is provided by FeO^+. Since FeO^+ cannot be generated directly from the Fe^+/O_2 couple on thermochemical grounds,[45] the decisive experiment is a methanol-mediated activation of dioxygen in which the alcohol serves as a co-reductant [Eq. (33)]. While this process is quite exothermic ($\Delta_r H = -24$ kcal mol^{-1}), the rate efficiency is only about 10%, as a result of spin barriers.[25,42,46]

$$CH_4 + FeO^+ \rightarrow Fe^+ + CH_3OH \quad (22a)$$
$$\Delta_r H = -7\,\text{kcal mol}^{-1};\ k = 0.4 \times 10^{-10}\,\text{cm}^3\,\text{molecule}^{-1}\,\text{s}^{-1}$$

$$Fe^+ + O_2 \rightarrow FeO^+ + O \quad (32)$$
$$\Delta_r H = 39\,\text{kcal mol}^{-1};\ k \ll 10^{-13}\,\text{cm}^3\,\text{molecule}^{-1}\,\text{s}^{-1}$$

$$Fe(CH_3OH) + O_2 \rightarrow FeO^+ + CH_2O + H_2O \quad (33)$$
$$\Delta_r H = -24\,\text{kcal mol}^{-1};\ k = 0.6 \times 10^{-10}\,\text{cm}^3\,\text{molecule}^{-1}\,\text{s}^{-1}$$

$$Fe^+ + CH_3OH \rightarrow Fe(CH_3OH)^+ \quad (34)$$
$$\Delta_r H = -34\,\text{kcal mol}^{-1};\ k \leqq 10^{-13}\,\text{cm}^3\,\text{molecule}^{-1}\,\text{s}^{-1}$$

Combination of these steps leads to a viable sequence for the Fe^+-mediated oxidation of CH_4 to CH_2O according to Reaction (31). Here, the CH_3OH molecule coordinated to the metal plays a central role both as a precursor for the oxidation product CH_2O as well as a crucial intermediate in the activation of O_2 (Scheme 3). Furthermore, the formation of FeO^+ in Reaction (33) is quite remarkable in that over-oxidation (namely, the formation of Fe^+ and HCOOH) does not occur in this experiment, even though bare FeO^+ rapidly reacts with formaldehyde.[47] The seemingly most simple step in Scheme 3, that is, the mere complexation of methanol by the iron cation [Eq. (34)], however, does not occur in the low pressure regime (typically below 10^{-7} mbar). However, the magnitude of k_{34} will be enhanced with increasing pressure since ligand association often proceeds by termolecular collisions.

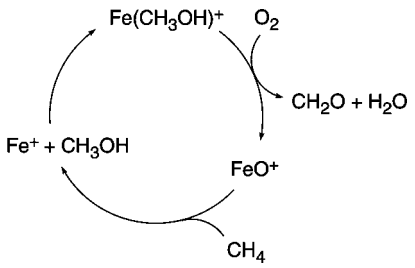

Scheme 3. Catalytic sequence for the Fe^+-mediated oxidation of methane by molecular oxygen with methanol as a catalytic co-reductant. The side reaction of the FeO^+/CH_4 couple, which leads to $FeOH^+/CH_3$ [Eq. (23)] is omitted for clarity (adapted from ref. [43]).

2.3. Ligand Effects

The influence of ligation of a metal-ion catalyst on the rates and products of oxygen-atom-transfer catalysis is also of interest.[5a] FTICR experiments have noted that ligation of a metal cation with an appropriate ligand can "enhance the selectivity at the expense of reactivity",[48] and the gas-phase chemistry of FeO^+ may serve as a good example: although "naked" FeO^+ behaves as a powerful reagent for the activation of C–C and C–H bonds[5a] and also effects product isomerization, that is, olefin→epoxide→aldehyde conversion, during the course of an oxidation, ligated species $Fe(L)O^+$ (L = ligand) are entirely unreactive towards bond activation.[48] In contrast, oxygen transfer from $Fe(L)O^+$ to olefins [Eq. (35)] occurs at the collision rate with less than 10% formation of by-products, and indirect evidence suggests that epoxides rather than ketones or aldehydes are formed. The $Fe(L)O^+$ catalyst itself can be conveniently regenerated by treating $Fe(L)^+$ with N_2O [Eq. (36)], with an efficiency ranging from 40–86% depending on L. Thus, Reactions (35) and (36) can be combined in a catalytic cycle (Scheme 4); in the case of L = benzene, turnover numbers of up to 6 are obtained.[48] Related ligand effects were also reported recently for the oxidation of the unsaturated hydrocarbons

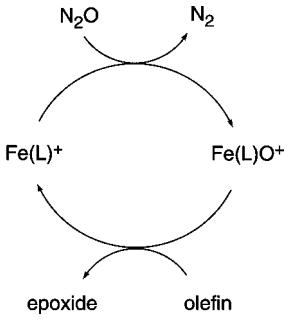

Scheme 4. Catalytic epoxidation of olefins by $Fe(L)O^+$ complexes (adapted from ref. [48]).

 © 2005 Wiley-VCH Verlag GmbH & Co. KGaA, Weinheim

ethene, propene, and benzene by [(phenanthroline)CuO]$^+$ which, in contrast to "naked" CuO^+, brings about almost exclusive transfer of an oxygen atom.[49]

$$Fe(L)O^+ + \text{olefin} \rightarrow Fe(L)^+ + \text{epoxide} \quad (35)$$

$$Fe(L)^+ + N_2O \rightarrow Fe(L)O^+ + N_2 \quad (36)$$

2.4. Catalysis of O-Atom Transport with Metal Oxide Cations

Dioxide and higher oxide cations with appropriate O-atom affinities may also possess the thermodynamic potential to catalyze O-atom transport. Equations (37) and (38) illustrate the MO_n^+-catalyzed ($n = 1, 2$) reduction of N_2O by CO.

$$N_2O + MO_n^+ \rightarrow MO_{n+1}^+ + N_2 \quad (37)$$

$$MO_{n+1}^+ + CO \rightarrow MO_n^+ + CO_2 \quad (38)$$

The "thermodynamic window of opportunity" now becomes $OA(N_2) < OA(MO_n^+) < OA(CO)$ and has been shown to contain a number of metal oxide cations. For example, atomic Pt^+ is readily oxidized sequentially to form PtO^+ and $Pt(O)_2^+$ [Eqs. (39) and (40)], and both oxides are efficiently reduced by CO [Eqs. (41) and (42)],[19,22a] with oxygen affinities $OA(Pt^+) = 75$ kcal mol^{-1} [50] and $OA(PtO^+) = 71$ kcal mol^{-1} [51] which lie almost in the middle of the thermodynamic window.

$$N_2O + Pt^+ \rightarrow PtO^+ + N_2$$
$$k = 0.7 \times 10^{-10}\ cm^3\ molecule^{-1}\ s^{-1}\ [19]$$
$$k = 1.2 \times 10^{-10}\ cm^3\ molecule^{-1}\ s^{-1}\ [22a] \quad (39)$$

$$PtO^+ + N_2O \rightarrow Pt(O)_2^+ + N_2$$
$$k = 1.9 \times 10^{-10}\ cm^3\ molecule^{-1}\ s^{-1}\ [19]$$
$$k = 6.6 \times 10^{-10}\ cm^3\ molecule^{-1}\ s^{-1}\ [22a] \quad (40)$$

$$Pt(O)_2^+ + CO \rightarrow PtO^+ + CO_2$$
$$k = 6.6 \times 10^{-10}\ cm^3\ molecule^{-1}\ s^{-1}\ [19] \quad (41)$$

$$PtO^+ + CO \rightarrow Pt^+ + CO_2$$
$$k = 6.4 \times 10^{-10}\ cm^3\ molecule^{-1}\ s^{-1}\ [19] \quad (42)$$

Clearly, both Pt^+ and PtO^+ can serve as catalysts in the reduction of N_2O by CO. The data given in Figure 4 convincingly demonstrate that the two cycles are coupled: quasistationary intensities of Pt^+, PtO^+, and $Pt(O)_2^+$ are obtained upon treating $Pt(O)_2^+$ with a mixture of CO and N_2O; within experimental error, identical stationary intensities of these ions evolve when starting from Pt^+ and PtO^+, respectively. Hence, the combination of Equations (39)–(42) generates a sequence in which gaseous platinum species effectively catalyze the oxidation of CO by N_2O [Eq. (43)]. Although this reaction is very exothermic, $\Delta_r H = -82.3$ kcal mol^{-1}, it does not proceed at all at ambient and elevated temperatures without a catalyst. Turnover numbers for the Pt^+-mediated gas-phase oxidation of CO range from 80 to

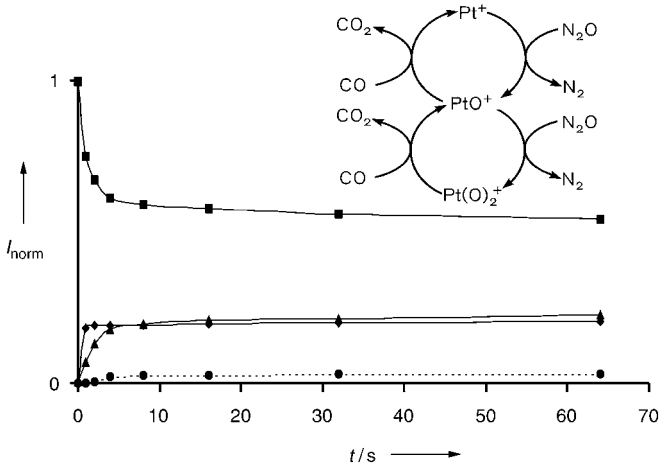

Figure 4. Temporal intensity profiles of $Pt(O)_2^+$ (■), PtO^+ (◆), Pt^+ (▲), and the sum of all side reaction products (●) when treating mass-selected $Pt(O)_2^+$ with a ca. 10:1 mixture of N_2O and CO (total pressure in the FTICR experiment 10^{-7} mbar). The inset shows the coupled catalytic cycles involved (adapted from ref. [19]).

300, and they are basically only limited by side reactions of the powerful oxidants PtO_n^+ ($n = 1, 2$) when they come into contact with residual hydrocarbon gas.[19]

$$2\,CO + 2\,N_2O \rightarrow 2\,CO_2 + 2\,N_2 \quad (43)$$

Recent ICP/SIFT experiments have shown that a series of metal dioxide and higher metal oxide cations can be generated at room temperature from N_2O. For example, a second O-atom transfer was observed with the Group 4–6 transition-metal ions (except Mo^+) as well as the third period ions Re^+, Os^+, Ir^+, and Pt^+. The atomic ions W^+, Os^+, and Ir^+ form trioxides in sequential processes, and even the tetroxide OsO_4^+ can be generated from Os^+ and N_2O.[22a] Only the higher oxides of Ir^+ and Os^+ have so far been treated with CO in the ICP/SIFT experiments, and these are sequentially reduced and revert back to the bare metal cation.[9,21] The reaction efficiencies of many of these O-atom transfer processes do not often correlate with the thermochemistry of the respective transformations, and quite likely this is because of the existence of spin barriers.[21,24,25]

3. Bond-Activation Catalysis

The concept of catalysis through bond activation in gas-phase processes refers to situations in which the ion catalyst in, for example, oxidation reactions, does not completely abstract an oxygen atom from the terminal oxidant; rather, the catalyst simply activates a relevant part of the reagent sufficiently and transfers the reactive fragment to a second molecule trapped in the coordination sphere of the metal ion. As a consequence, significant rate enhancement often results. Three examples from different areas will be used to illustrate this concept.

The first such catalysis was demonstrated for atomic alkali-metal ions in a flowing afterglow apparatus over a large

 © 2005 Wiley-VCH Verlag GmbH & Co. KGaA, Weinheim

temperature region.[52] To this end, the mass-selected cation M^+ (Li^+, Na^+, K^+) is solvated with O_3 upstream of the flow tube and allowed to react with the reductant (NO, CO, SO_2) downstream over the temperature range (125–280 K) determined by the bond energy of the alkali-metal–ozone cluster formed according to Equation (44). Although the rate constants for the association of O_3 and the reactions of the $M(O_3)^+$ complex with the substrates NO, CO, and SO_2 [Eq. (45) for the reductant NO] are not faster than 10% of the gas kinetic collision value, the measured rate constants are orders of magnitude larger than the *direct* gas-phase reaction between these neutral species [Eq. (46)] in the absence of the ions. Clearly, the alkali-metal cations M^+ act as genuine catalysts even though no covalent bond is formed between them and the two neutral molecules at any stage of the reaction.

$$O_3 + M^+ \rightarrow M(O_3)^+ \quad (44)$$

$$M(O_3)^+ + NO \rightarrow M^+ + O_2 + NO_2 \quad (45)$$

$$O_3 + NO \rightarrow O_2 + NO_2 \quad (46)$$

Metal ions have also been found to activate larger molecules so that they undergo chemical reactions. Thus, the gas-phase catalytic oxidation of benzene through Reactions (47) and (48) has been observed by FTICR to be catalyzed by $M^+ = Co^+$, Cr^+, and Mn^+.[38] This process is particularly interesting in the sense that it mimics heterogeneous catalysis (this will be discussed in more detail in Sections 5 and 6 for cluster-mediated reactions): In the first step, benzene coordinates to a bare M^+ ion to afford the corresponding $M(C_6H_6)^+$ species, which in the case of $M^+ = Co^+$ is formed at the collision rate; in the next step [Eq. (48)], the oxidant N_2O also coordinates to and gets activated by the metal ion to yield $M(N_2)(C_6H_6O)^+$. The high exothermicity of Reaction (49) ($\Delta_r H = -62.4$ kcal mol^{-1}) leads to evaporation of the two ligands and thus regenerates the active catalyst. The turnover number for the Co^+-catalyzed hydroxylation of benzene is 18, and is limited mostly by the formation of sandwich complexes $M(C_6H_6)_2^+$.[38]

$$C_6H_6 + M^+ \rightarrow M(C_6H_6)^+ \quad (47)$$

$$M(C_6H_6)^+ + N_2O \rightarrow [M(C_6H_6)(N_2O)]^+ \rightarrow M^+ + C_6H_6O + N_2 \quad (48)$$

$$C_6H_6 + N_2O \rightarrow C_6H_5OH + N_2 \quad (49)$$

The metal-cation mediated oxidation of benzene by molecular oxygen[53–55] has also been investigated in the gas phase, in this case by using ICP/SIFT mass spectrometry.[56] Attachment of the benzene molecule to certain metal cations activates it[57–59] sufficiently to bring about the spin-forbidden oxidation by O_2.[25] The catalytic sequence given by Reactions (47), (50), and (51) was observed for the transition-metal ions $M^+ = Cr^+$, Fe^+, and Co^+, with the crucial oxidation in Equation (50) proceeding at 30, 15, and 20% of the collision rate. While the neutral product of the oxidation is not known, it has been suggested to be catechol, the formation of which corresponds to the most exothermic reaction pathway ($\Delta_r H = -84.8$ kcal mol^{-1}).[55h] It is interesting to recall that catechol is a major metabolite generated by the catalytic oxidation of benzene by an iron-containing dioxygenase metalloenzyme.[60]

$$M(C_6H_6)^+ + O_2 \rightarrow M^+ + C_6H_6O_2 \quad (50)$$

$$C_6H_6 + O_2 \rightarrow C_6H_4(OH)_2 \quad (51)$$

When one of the neutral products remains attached to the ion catalyst, a third reaction is needed to complete the cycle, as illustrated by Reactions (52)–(55) for the oxidation of molecular hydrogen to water by oxygen. For $M^+ = Pt^+$, the reaction sequence constitutes a gas-phase variant of the famous Döbereiner lighter.[61]

$$O_2 + M^+ \rightarrow M(O)_2^+ \quad (52)$$

$$M(O)_2^+ + H_2 \rightarrow MO^+ + H_2O \quad (53)$$

$$MO^+ + H_2 \rightarrow M^+ + H_2O \quad (54)$$

$$2\,H_2 + O_2 \rightarrow 2\,H_2O \quad (55)$$

Kinetic[19,55h] and thermochemical[50,51] data for the reactions of $M^+ = Pt^+$ have been determined by using various techniques. The effective bimolecular rate coefficient for the reaction between Pt^+ and O_2 to generate a high-valent Pt^V dioxide $Pt(O)_2^+$ has been measured at room temperature by ICP/SIFT tandem mass spectrometry to be $k_{52} = 1.6 \times 10^{-13}$ cm^3 molecule^{-1} s^{-1} in He at 0.35 Torr.[55h] The reaction of $Pt(O)_2^+$ with hydrogen proceeds with $k_{53} = 9.1 \times 10^{-11}$ cm^3 molecule^{-1} s^{-1}, and the final O-atom transfer which regenerates the Pt catalyst has a rate coefficient of $k_{54} = 5.0 \times 10^{-10}$ cm^3 molecule^{-1} s^{-1}; both values were determined by FTICR measurements.[19] A similar sequence is observed when D_2 is used instead of H_2, and the intermolecular kinetic isotope effect is minor (ca. 1.3). Thus, factors other than the mere activation of the hydrogen–hydrogen bond contribute to the rate determining step of the catalytic cycle depicted in Scheme 5.

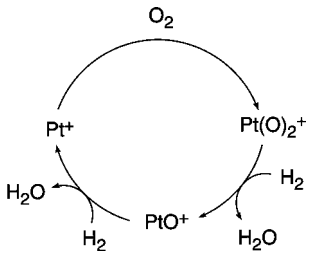

Scheme 5. Catalytic oxidation of H_2 by molecular oxygen, mediated by atomic Pt^+.

 © 2005 Wiley-VCH Verlag GmbH & Co. KGaA, Weinheim

4. Metal-Mediated Coupling Processes

4.1. Formation of Carbon–Carbon Bonds

Cyclooligomerizations of unsaturated hydrocarbons are versatile reactions for the synthesis of organic systems, in particular aromatic compounds.[62] Although these reactions are quite exothermic, they are usually hampered by large kinetic barriers if non-activated hydrocarbons are involved.[62f] Transition metals have been found to facilitate these reactions in the condensed phase,[62a–d] and mass-spectrometric studies have revealed that certain "bare" transition-metal cations M^+ also affect the cyclization reactions of unsaturated hydrocarbons in the gas phase.[63] The cyclization is often coupled with activation of the C–H bond, and as a consequence M^+-mediated cyclization reactions in the gas phase are accompanied by dehydrogenation steps to eventually form quite stable aromatic complexes with M^+. The most classical example of the stepwise route[64] is the gas-phase trimerization of ethene by atomic W^+,[65] U^+,[66] or the Fe_4^+ cluster.[67]

As depicted in Scheme 6, the sequence commences with the formation of a cationic metal–ethyne complex by dehydrogenation of C_2H_4. In the next, and often rate-

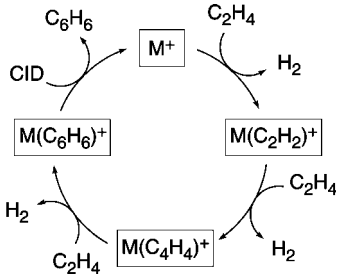

Scheme 6. Dehydrogenative oligomerization of C_2H_4 and formation of benzene by consecutive gas-phase ion–molecule reactions (adapted from ref. [67]).

determining step, the ethyne complex undergoes dehydrogenation of a further ethene molecule to yield $M(C_4H_4)^+$; for some metal cations, for example, U^+, there is experimental evidence that this complex already contains a C_4 unit rather than two separate C_2H_2 ligands.[66] The third addition of C_2H_4 results in the formation of benzene complexes through loss of molecular hydrogen. Although the latter reaction step is very exothermic, the heat of reaction liberated is usually not sufficient to overcome the large bond dissociation energy of M^+-C_6H_6 to release benzene;[58,68] as a consequence, regeneration of the active catalyst M^+ is not observed under thermal conditions. This is only achieved by detaching the benzene ligand from the metal center by, for example, collision-induced dissociation;[65–67] for $M^+ = Fe_4^+$, this requires approximately 75 kcal mol^{-1}.[67] Of course, in a "perfect" catalytic system the catalyst should be regenerated in the reaction system without additional supply of energy. This is conveniently achieved in gas-phase experiments by employing "high-energy" reactants.[64,69a] For example, substituting ethyne for ethene as a reactant increases the exothermicity of the final step [Eq. (56)] by approximately the heat of dehydrogenation of ethene to ethyne, that is, 42 kcal mol^{-1}. As this additional reaction energy is stored completely in the reactive complex, detachment is possible, and has been observed for $M^+ = Ru^+$, Rh^+, and Fe^+, with modest turnover numbers. The metal ions $M^+ = Os^+$, Ir^+, and Pt^+ use the extra energy to activate C–H bonds in the benzene ring and to release H_2 [Eq. (57)] rather than detach C_6H_4. The C_4H_4 complexes of Co^+ and Ni^+ were not found to react efficiently with C_2H_2 at a measurable rate.[64,69b]

$$M(C_4H_4)^+ + C_2H_2 \rightarrow M^+ + C_6H_6 \quad M = Ru, Rh, Fe \tag{56}$$

$$M(C_4H_4)^+ + C_2H_2 \rightarrow M(C_6H_4)^+ + H_2 \quad M = Os, Ir, Pt \tag{57}$$

4.2. Formation of Carbon–Heteroatom Bonds

Bond activation and reaction coupling play a key role in the partial oxidation of methane by molecular oxygen and can be catalyzed by either Pt^+ or PtO^+.[70] The Pt^+-catalyzed part of the cycle involves the combination of bond activation and O-atom transport [Eqs. (58)–(61)], and leads to formaldehyde and methanol.

$$CH_4 + Pt^+ \rightarrow Pt(CH_2)^+ + H_2 \tag{58}$$

$$Pt(CH_2)^+ + O_2 \rightarrow PtO^+ + CH_2O \tag{59}$$

$$PtO^+ + CH_4 \rightarrow Pt^+ + CH_3OH \tag{60}$$

$$2\,CH_4 + O_2 \rightarrow CH_2O + CH_3OH + H_2 \tag{61}$$

However, Reaction (59) regenerates 70% of the atomic Pt^+ immediately along with CH_2O_2 (possibly formic acid), and Reaction (60) leads to 30% of the by-product $Pt(CH_2)^+$, which reacts further with O_2 to regenerate PtO^+. A catalytic cycle with a turnover number of about six results, which actually involves a coupling of two catalytic cycles that form an integral part of the third cycle given by Equations (58)–(60) (Scheme 7). All these reaction pathways have been

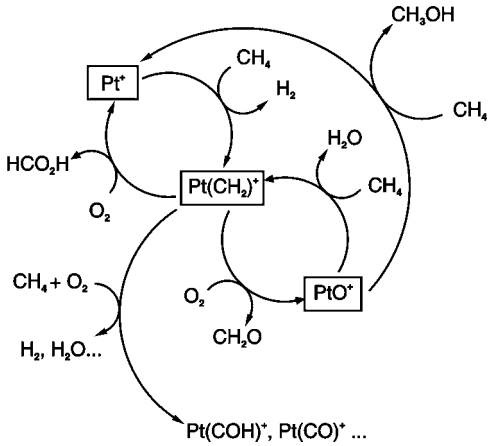

Scheme 7. Pt^+-catalyzed oxidation of methane by molecular oxygen (adapted from ref. [70]).

 © 2005 Wiley-VCH Verlag GmbH & Co. KGaA, Weinheim

followed in detail by FTICR measurements of the various reaction kinetics, and insight into the intriguing mechanistic aspects of this complex reaction sequence was provided by electronic structure calculations which included scalar relativistic and spin-orbit effects.[71]

The platinum–carbene cation produced from methane [Eq. (58)] can also bring about the conversion of CH_4 into CO in a sequence of exothermic dehydrogenation reactions with H_2O, thus conceptually constituting a gas-phase model for a Pt^+-mediated water-gas reaction [Eq. (62)].[72] However, closing the catalytic cycle depicted in Scheme 8 by detaching

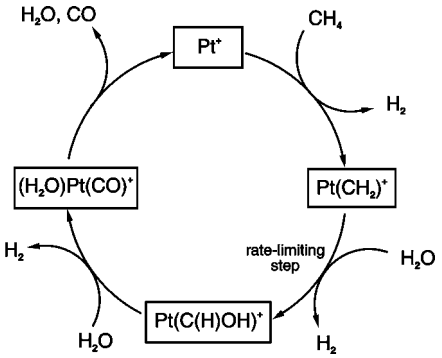

Scheme 8. Gas-phase model for a Pt^+-mediated water-gas reaction [Equation (62); adapted from ref. [72]].

the final ligands CO and H_2O from the Pt^+ catalysts requires about 102 kcal mol^{-1}. This situation is, therefore, analogous to many systems in heterogeneous catalysis, where product release from the catalytic center and regeneration of the latter is achieved by heating.

$$CH_4 + H_2O \rightarrow CO + 3\,H_2 \quad (62)$$

An interesting example of the combination of two- and three-step catalysis is the Fe^+-mediated oxidation of acetylene by N_2O.[16] The O-atom transport in Reaction (11b) first generates FeO^+, which acts as a "monooxygenase" for the oxidation of the hydrocarbon and the positive charge of the intermediate FeO^+ leads to rate enhancement. The oxidation of acetylene itself occurs by two pathways (Reactions (63) and (64)), with an estimated branching ratio of 1/1. The production of Fe^+, according to Equation (63) and from the reaction of $Fe(CH_2)^+$ with N_2O, Equation (65), completes the three-step catalytic cycle in which formaldehyde and CO are formed according to Equation (66).

$$2\,N_2O + 2\,Fe^+ \rightarrow 2\,FeO^+ + 2\,N_2 \quad (11b)$$

$$FeO^+ + C_2H_2 \rightarrow Fe^+ + C_2H_2O \quad (63)$$

$$FeO^+ + C_2H_2 \rightarrow Fe(CH_2)^+ + CO \quad (64)$$

$$Fe(CH_2)^+ + N_2O \rightarrow Fe^+ + N_2 + CH_2O \quad (65)$$

$$2\,C_2H_2 + 3\,N_2O \rightarrow C_2H_2O + CH_2O + CO + 3\,N_2 \quad (66)$$

Catalytic formation of a C–N bond in the gas phase can occur by transfer of a NH group from a metal center to hydrocarbon substrates. Scheme 9 shows an example of the

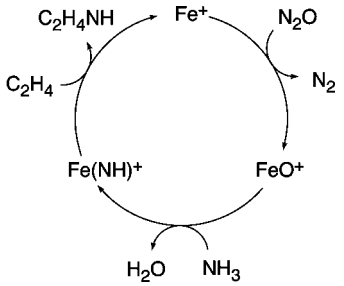

Scheme 9. Catalytic cycle illustrating the dehydrogenative C–N coupling between C_2H_4 and NH_3 (adapted from ref. [73]).

Fe^+-mediated C–N coupling reaction with ammonia and ethene [Eq. (67)]. Here bond activation is preceded by O-atom transport and followed by NH delivery to result in the formation of a C–N bond. However, in this crucial step only 38% of the reactive collisions between $Fe(NH)^+$ and C_2H_4 regenerate the Fe^+ catalyst.[73] Other ionic products are often formed, such as $Fe(NH_3)^+$ (16%) and $Fe(HNC)^+$ (15%); both may, however, also perpetuate the catalytic cycle if they react with N_2O to produce FeO^+. These scenarios have not yet been tested. Equation (68) is another product pathway (19%) that also leads to formation of a C–N bond, but it is not catalytic since the active catalyst (or a precatalyst) is not directly regenerated.[73]

$$NH_3 + C_2H_4 + N_2O \rightarrow C_2H_4NH + H_2O + N_2 \quad (67)$$

$$Fe(NH)^+ + C_2H_4 \rightarrow Fe(CH_2)^+ + CH_2NH \quad (68)$$

The physical properties and the chemistry of $Fe(NH)^+$ have since been studied in considerable detail by both theory and experiment.[74] The relatively low affinity of the "naked" imine NH group for Fe^+ of about 70 kcal mol^{-1} makes $Fe(NH)^+$ a strong imine donor. Indeed, gas-phase experiments have shown a propensity for $Fe(NH)^+$ to react with H_2 to form NH_3, with O_2 to produce HNO_2, with alkanes to form alkyl amines, with benzene to form aniline, and with toluene to produce benzylidenamine. All of these transformations become catalytic when coupled to the production of $Fe(NH)^+$ by Reactions (11c), (69), and (70), since they regenerate Fe^+. This has been demonstrated for the catalytic oxidation of NH_3 to HNO_2 [Eq. (71)].

$$N_2O + Fe^+ \rightarrow FeO^+ + N_2 \quad (11c)$$

$$FeO^+ + NH_3 \rightarrow Fe(NH)^+ + H_2O \quad (69)$$

$$Fe(NH)^+ + O_2 \rightarrow Fe^+ + HNO_2 \quad (70)$$

$$NH_3 + O_2 + N_2O \rightarrow HNO_2 + H_2O + N_2 \quad (71)$$

The ability to transfer NH groups can be extended to other cationic $M(NH)^+$ complexes, but may be more limited

 © 2005 Wiley-VCH Verlag GmbH & Co. KGaA, Weinheim

depending on the magnitude of the M^+–NH binding energy $D(M^+–NH)$. For example, $D(Y^+–NH)$ has a reported lower limit of 101 kcal mol^{-1}, and this is reflected in its chemistry with alkenes, for example, which does not show any reaction pathways that regenerate Y^+ under thermal conditions.[75]

5. Toward Heterogeneous Catalysis: Gas-Phase Catalysis with Cluster Ions

The adsorption of CO on gold has been cited[76a] as the most extensively investigated chemisorption process involving gold. In spite of the inertness of metallic gold,[76] there has been recent interest worldwide in the unique activity of gold-based catalysts that facilitate numerous oxygen-atom transfer reactions at reduced temperatures and with moisture tolerance because of the observation that the activity depends critically on the size of the deposited clusters (as well as the nature of the support).[76a,77] Among these processes are a class of C_1 transformations which are of particular scientific and technical importance [Eq. (72)–(75)].

$$CO + 1/2\,O_2 \rightarrow CO_2 \ \text{(combustion)} \quad (72)$$

$$CO + NO_n \rightarrow CO_2 + NO_{n-1} \ (NO_n \text{ reduction}) \quad (73)$$

$$CO + H_2O \rightarrow CO_2 + H_2 \ \text{(CO conversion)} \quad (74)$$

$$CO + 2\,H_2 \rightarrow CH_3OH \ \text{(methanol synthesis)} \quad (75)$$

Since the catalytic activity correlates with the degree of dispersion, experiments to determine the size-dependence of finite, mass-selected gas-phase clusters were carried out.[5d,i,78,79] It was concluded on the basis of numerous studies[80] that the interplay between cluster physics and surface chemistry is a promising strategy to uncover "mechanisms of elementary steps in nanocatalysis".[81] In this Review we focus on those systems in which a full thermal catalytic cycle involving gas-phase metal clusters has been demonstrated. In these cases a "full thermal catalytic cycle" means a reaction in which one starts with a bare, mass-selected metal cluster, reactant molecules are adsorbed, then the reaction product is released to regenerate the intact cluster—all at thermal energies. Two systems will be described in detail, and both deal with the catalysis of Reaction (72) by *anionic* Pt and Au clusters. The emphasis is on negatively charged clusters, as it transpired that the metallic clusters are immobilized at surface oxide vacancies in surface reactions. These defects comprise localized electrons that can be transferred to the highly electronegative clusters bound at those sites,[77d] thus permitting electron-transfer processes with adsorbed reactants, for example, with the formation of highly reactive O_2 species.

Guided ion beam mass spectrometry has been used to demonstrate that platinum cluster anions Pt_n^- ($n = 3$–7) efficiently catalyze the oxidation of CO to CO_2 by N_2O or O_2. The reactions are exothermic and occur at approximately room temperature with no appreciable activation barrier (< 1 kcal mol^{-1} at 300 K).[5d,82a] Two catalytic cycles (a and b) were identified (Scheme 10).

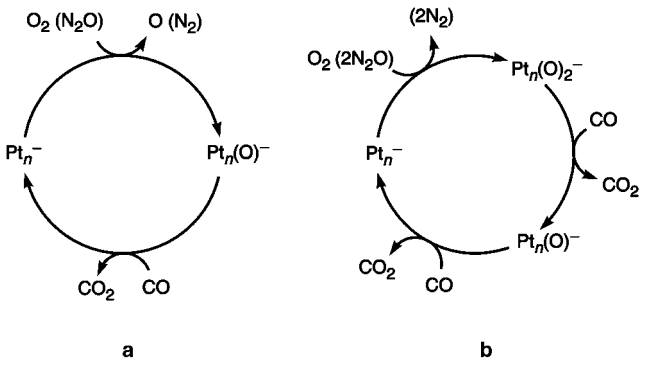

Scheme 10. Catalytic cycles observed for the oxidation of CO to CO_2 by N_2O or O_2 using Pt_n^- cluster anions (adapted from ref. [5d]).

The reaction efficiencies for the CO→CO_2 conversion exceed 40% for $n \geqq 4$, so only a few collisions would be required for complete conversion. These high efficiencies at near room temperatures imply that the gas-phase Pt clusters are better catalysts than the supported catalysts used in current technology for automobile catalytic converters, which need to be heated to high temperatures;[83] temperatures of 400–500 K are typically required for the oxidation of CO on platinum surfaces.[84] The high reactivity of the gas-phase clusters may be attributable to their small size, which ensures that the metal atoms are all exposed on the surface of the cluster and are coordinatively unsaturated ("dangling bonds"). In addition, the negative charge certainly helps in the activation of molecular oxygen; the sequential oxygen-atom transfer shown in Scheme 10b evidences the presence of adsorbed atomic oxygen on the cluster surface.

The extraordinary role that supported gold clusters play in the oxidation of CO[76,77,80,81] has recently stimulated a number of computational and experimental gas-phase studies of reactions catalyzed by Au_n^-.[85] For example, efficient generation of CO_2 from CO and O_2 at room temperature has been achieved with anionic gold clusters serving as catalysts, and remarkable cooperative effects as well as size-dependent even/odd reactivity patterns were observed.[85b] O_2 adsorbs as a one-electron acceptor on Au_n clusters ($n = 4$–20),[80c,85b] with even-numbered clusters showing varying reactivity toward the adsorption of O_2, while odd-numbered clusters are unreactive. CO exhibits a highly size-dependent reactivity for $n = 4$–19, but no adsorption occurs at room temperature for $n = 2,3$. Remarkable effects have been noted when the gold clusters are exposed to both reactants, either simultaneously or sequentially. Although the same rules pertaining to individual O_2 or CO adsorption continue to apply, the preadsorption of one reactant on a cluster may lead to the increased reactivity of the cluster to the other reactant. Thus, rather than competitive coadsorption, the rare phenomenon of cooperative coadsorption is operative here. Experiments with mass-selected Au_6^- have demonstrated that this "cooperative coadsorption" gives rise to the evaporation of CO_2, thus closing the catalytic cycles by regenerating Au_6^- (Scheme 11).[85b]

A possible explanation for this enhancement of coadsorption activity is that the first adsorbate affects the

 © 2005 Wiley-VCH Verlag GmbH & Co. KGaA, Weinheim

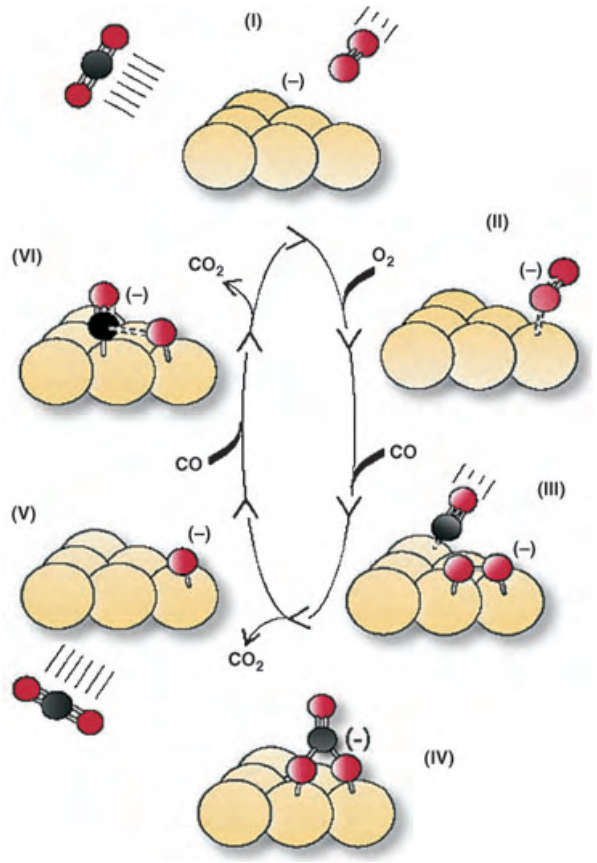

Scheme 11. Catalytic oxidations of CO to CO_2 in the presence of O_2 catalyzed by the cluster anion Au_6^- (Au yellow, C black, O red). The free Au_6^- ion in its calculated equilibrium structure (I) adsorbs O_2 in its superoxide form (II); subsequent coadsorption of CO may initially form an $Au_6CO_3^-$ species (III), which rearranges to the stable CO_3^- adsorbate (IV); elimination of CO_2 yields the Au_6O^- form (V); adsorption of a second CO yields the $Au_6CO_2^-$ species (VI), from which a second CO_2 molecule may be released and return the Au_6^- catalyst—for the sake of clarity, the Au_6^- structure is depicted as retaining the same structure throughout (adapted from ref. [85b]).

electronic structure of the cluster, thus causing it to appear electronically different to the second approaching molecule. This proposal was suggested in a recent theoretical study[85a] for the $Au_2^-/CO/O_2$ system. Accordingly, CO binds much more tightly to neutral Au_2 than to Au_2^- (1.60 versus 0.96 eV). Consequently, an Au cluster anion with a preadsorbed O_2 molecule will appear to be neutral to the approaching CO molecule because of the charge transfer that takes place from the Au_n^- cluster to the O_2 adsorbate. The analogy to the surface-catalyzed oxidation of CO becomes clear in that the excess electron (in the anionic cluster) is necessary for the reaction to occur, and the *neutral* supported clusters acquire the electron by charge transfer from the surface. A turnover frequency of approximately 100 CO_2 per Au atom per second has been estimated[85b] for the reaction catalyzed by Au_n^-, for $n = 10$. This efficiency is two(!) orders of magnitude greater than that seen for commercial gold catalysts.

A full catalytic cycle for Reaction (72) had been predicted theoretically for the free Au_2^- cluster,[85a] and this has been verified recently by experiments.[85c] Temperature-dependent ion-trap mass spectrometry in combination with ab initio simulations has revealed many details of this process. Remarkably, a metastable intermediate with the elemental composition $Au_2CO_3^-$ was observed at low temperatures. For this intermediate, theory proposes two alternative structures, which correspond to digold carbonate or peroxyformate; both of these structures may serve as precursors for the formation of CO_2. Detailed kinetic studies revealed that O_2 adsorption precedes the adsorption of CO in the catalytic cycle. Furthermore, for the kinetic cycle defined by Equations (76)–(78), the steps (76) and (77) proceed without an energy barrier; in contrast, reaction (78) is associated with a small barrier. The turnover frequency amounts to 0.5 CO_2 molecules per gold cluster per second at room temperature. This value is on the same order of magnitude as that for the catalytic activity of oxide-supported gold cluster particles with a size of a few nanometers.[77b,c]

$$Au_2^- + O_2 \rightarrow Au_2O_2^- \quad (76)$$

$$Au_2O_2^- + CO \rightleftharpoons Au_2(CO)O_2^- \quad (77)$$

$$Au_2(CO)O_2^- + CO \rightarrow Au_2^- + 2\,CO_2 \quad (78)$$

Two basic mechanistic scenarios were explored for the formation of intermediate $Au_2CO_3^-$ (structure A in Figure 5

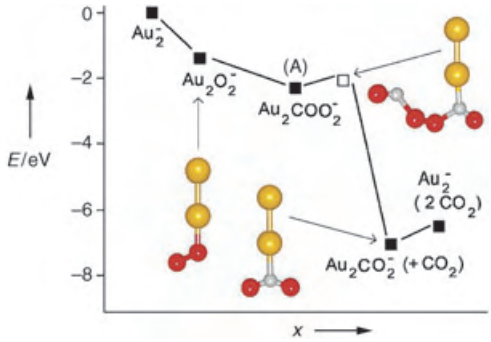

Figure 5. Energetics of the ER mechanism of the reaction, where the peroxyformate-like species $Au_2COO_2^-$ (configuration A, Au yellow, C gray, O red) is the metastable intermediate state. □ denotes the reaction barrier connecting the peroxyformate-like state with the $Au_2CO_2^- + CO_2$ products, and the corresponding transition-state configuration is shown at the top right. The last step of the reaction is desorption of CO_2. The initial energy level at zero corresponds to the sum of the total energies of all the reactants: $Au_2^- + O_2 + 2\,CO$ (adapted from ref. [85c]).

and structure B in Figure 6), that is, the Langmuir–Hinshelwood (LH) and the Eley–Rideal (ER) mechanisms, and it is only the latter pathway which is compatible with the experimental findings. As demonstrated by Figures 5 and 6, all intermediates and transition structures pertinent to the Au_2^--mediated oxidation of CO to CO_2 by molecular oxygen are located energetically well below the entrance channel. Consequently, a full catalytic cycle—even at low temperature—is possible, and this is born out experimentally.[85c]

Even *atomic* Au^- is capable of bringing about efficient catalytic oxidation of CO by O_2, as demonstrated very

 © 2005 Wiley-VCH Verlag GmbH & Co. KGaA, Weinheim

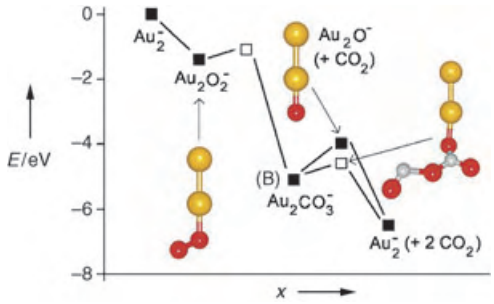

Figure 6. Energetics of the ER mechanism of the reaction in which the carbonate species $Au_2CO_3^-$ (configuration B; Au yellow, C gray, O red) is the metastable intermediate state. □ denotes the reaction barriers. The first reaction barrier is associated with the insertion of CO into the O–O bond of $Au_2O_2^-$, thus leading to the formation of $Au_2CO_3^-$. Two reaction paths are shown on the right: One path involves thermal dissociation of the carbonate to produce Au_2O^- which then reacts with CO(g) to release another CO_2 molecule, while the other path proceeds through an ER reaction of the carbonate with CO(g) and results in the formation of two CO_2 molecules. The latter route involves a barrier of 0.5 eV, and the corresponding transition-state configuration is shown on the right (adapted from ref. [85c]).

recently in a combined experimental/computational study.[85d] Although both AuO^- and AuO_3^- (generated from Au^- and O_2 in a fast-flow reactor) bring about the oxidation of CO, the reaction of AuO_2^- with CO proceeds at an extremely low rate as a result of a relatively high energy barrier involved in the formation of the complex and the existence of spin barriers arising from the inefficient crossings between the singlet and triplet potential energy surfaces. In contrast, the reaction of the two other much more reactive AuO_n^- oxides ($n = 1, 3$) with CO is not impeded by spin restrictions.[85d]

6. Processes Mediated by Metal-Oxide Clusters: Redox versus Nonredox Reactivities

Metal oxides are able to catalyze numerous processes in both the condensed[7c,j,k,30c,86] and the gas phase.[5a,e,43] Here, we will briefly discuss three examples which may serve to define the scope and limitations of a gas-phase approach in the context of cluster-mediated oxidation catalysis. Two gas-phase cycles (Scheme 12a and b) were detected by multistage mass-spectrometry experiments[87] for the two-electron oxidation of primary and secondary alcohols, and a binuclear anionic dimolybdate center $[Mo_2O_6(OCHR_2)]^-$ acts as the central intermediate in both these cycles. Three steps have been characterized: 1) condensation of $[Mo_2O_6(OH)]^-$ with the alcohol R_2CHOH and elimination of water to produce the alkoxo-bound cluster; 2) oxidation of the alkoxo ligand and its liberation as an aldehyde or a ketone in a step which is rate-limiting and requires the supply of external energy through collisional activation; 3) regeneration of the catalyst is achieved by oxidation with nitromethane. The second cycle is similar, but differs in the order of the reaction with the alcohol and the terminal oxidant nitromethane (see Scheme 12 for $R_2CHOH{=}CH_3OH$).[87]

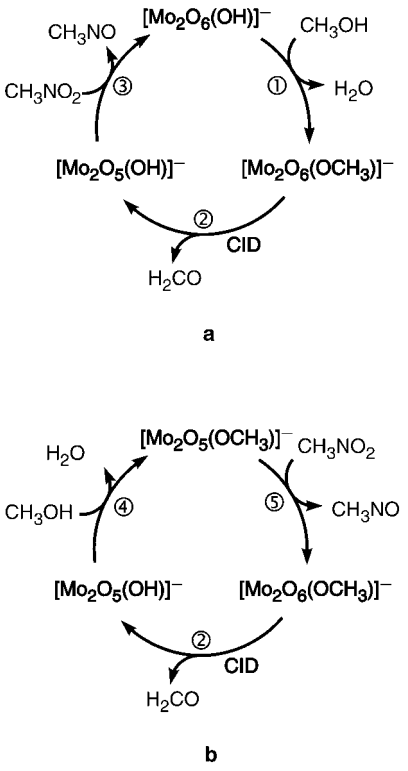

Scheme 12. Gas-phase catalytic cycles for the oxidation of methanol to formaldehyde. The second reaction step links $[Mo_2O_6(OCH_3)]^-$ and $[Mo_2O_5(OH)]^-$ and appears in both cycles. The two cycles a and b differ in the sequence of reaction with CH_3NO_2 and CH_3OH (adapted from ref. [87]).

The role of the binuclear metal center was assessed by examination of the relative reactivities of the mononuclear $[MO_3(OH)]^-$ and binuclear $[M_2O_6(OH)]^-$ complexes (M = Cr, Mo, W). The molybdenum and tungsten binuclear centers (M = Mo, W) were reactive toward alcohol but the chromium complex was not; this finding is consistent with the order of basicity of the hydroxo ligand in these anionic complexes. However, the tungsten center $[W_2O_6(OCHR_2)]^-$ prefers a nonredox elimination of an alkene rather than oxidation of the alkoxo ligand to form an aldehyde or a ketone. This observation is consistent with the oxidizing power of the anions. Interestingly, each of the mononuclear anions $[MO_3(OH)]^-$ (M = Cr, Mo, W) was inert to reaction with methanol and this highlights the importance of the second MO_3 unit in the catalytic cycles. Clearly, only the bimolybdate center has the appropriate mix of electronic properties that allow it to participate in each of the three steps, which corresponds to the unique role of Mo^{VI} trioxide in the industrial oxidation of methanol to formaldehyde at 300–400 °C.[88]

The dinuclear manganese oxide cations $Mn_2O_2^+$ and Mn_2O^+ were generated for gas-phase dioxygen activation studies[89] and found to be potentially active as catalysts in the oxidation of alcohols and aldehydes as well as in the oxidative coupling of unsaturated hydrocarbons.[89] However, the input of external energy is essential to close the catalytic cycle for

 © 2005 Wiley-VCH Verlag GmbH & Co. KGaA, Weinheim

the $Mn_2O_n^+$ ($n = 1, 2$) reactions for at least one of the steps. This can be achieved by product release by collisional activation or, preferably, by a ligand-exchange process.

Finally, a two-step gas-phase catalytic cycle for the dehydration of acetic acid to ketene was realized for mononuclear and dinuclear oxo anions $[MO_3(OH)]^-$ and $[M_2O_6(OH)]^-$ (M = Mo, W).[90a] Some of the mechanistic features of this metal-mediated nonredox process resemble those suggested for the dehydration of acetic acid over metal oxide and silica surfaces.[91]

7. Conclusions

This Review has demonstrated that the application of mass-spectrometric techniques to the study of elementary ion reactions has led to remarkable progress in a relatively short time in the characterization of detailed aspects of the kinetics, thermodynamics, and mechanisms of molecular transformations catalyzed by gas-phase ions. Of course, there are few natural environments, other than the earth's atmosphere, in which gas-phase ion catalysis plays a chemically important role, and practical applications of gas-phase ion catalysis are yet to be exploited (for example, perhaps in future catalytic converters).

However, there can be no doubt that what has so far been learned about ion catalysis in the gas phase is most instructive in the understanding of important fundamental aspects of practical catalysis in the condensed phase. Although the intrinsic catalytic properties of atomic ions are beginning to be well understood, much remains to be learned from future mass-spectrometric investigations about the catalytic properties of ligated ions and cluster ions. The latter will provide the necessary insights that will bridge the gap in our understanding between gas-phase reactions catalyzed by atomic ions and heterogeneous catalysis in the condensed phase—after all, ions in the gas phase provide the "single sites" that are active in surface catalysis.[62g,92]

The research conducted in the authors' laboratories was financially supported by generous grants from the Deutsche Forschungsgemeinschaft (Leibniz Forschungsprogramm), the Fonds der Chemischen Industrie, the Natural Sciences and Engineering Research Council, and the National Research Council of Canada. As holder of a Canada Research Chair in Physical Chemistry (Chemical Mass Spectrometry), D. K. Bohme thanks the contributions of the Canada Research Chair Program to this research. Practical, conceptual, and intellectual contributions of past and present members of our research groups are acknowledged, and technical assistance in the preparation of the article by Andrea Beck is appreciated.

Received: August 18, 2004
Published online: March 18, 2005

[1] E. Fischer, *Stahl Eisen* **1912**, *32*, 1898.
[2] D. F. Shriver, P. W. Atkins, C. H. Langford, *Inorganic Chemistry*, Oxford University Press, Oxford, **1994**, chap. 17.
[3] *Opportunities in Chemistry*, National Academy Press, Washington, DC, **1985**.
[4] a) G. A. Olah, A. Molnar, *Hydrocarbon Chemistry*, Wiley, New York, **1995**; b) A. E. Shilov, G. B. Shul'pin, *Chem. Rev.* **1997**, *97*, 2879; c) A. Sen, *Acc. Chem. Res.* **1998**, *31*, 550; d) W. D. Jones, *Science* **2000**, *287*, 1942; e) J. R. Rostrup-Nielsen, *Catal. Today* **2000**, *63*, 159; f) J. H. Lunsford, *Catal. Today* **2000**, *63*, 165; g) R. H. Crabtree, *J. Chem. Soc. Dalton Trans.* **2001**, 2437; h) A. A. Fokin, P. R. Schreiner, *Chem. Rev.* **2002**, *102*, 1551; i) J. A. Labinger, J. E. Bercaw, *Nature* **2002**, *417*, 507; j) U. Fekl, K. I. Goldberg, *Adv. Inorg. Chem.* **2003**, *54*, 259; k) C. J. Jones, D. Taube, V. R. Ziatdinov, R. A. Periana, R. J. Nielsen, J. Oxgaard, W. A. Goddard III, *Angew. Chem.* **2004**, *116*, 4726; *Angew. Chem. Int. Ed.* **2004**, *43*, 4626, and references therein; l) D. Milstein, *Pure Appl. Chem.* **2003**, *75*, 445; m) M. E. Van der-Boom, D. Milstein, *Chem. Rev.* **2003**, *103*, 1759; n) U. Fekl, K. I. Goldberg, *Adv. Inorg. Chem.* **2003**, *54*, 2590.
[5] For recent reviews, see: a) D. Schröder, H. Schwarz, *Angew. Chem.* **1995**, *107*, 2126; *Angew. Chem. Int. Ed. Engl.* **1995**, *34*, 1973; b) H. Schwarz, D. Schröder, *Pure Appl. Chem.* **2000**, *72*, 2319; c) D. A. Plattner, *Int. J. Mass Spectrom.* **2001**, *207*, 125; d) K. M. Ervin, *Int. Rev. Phys. Chem.* **2001**, *20*, 127; e) K. A. Zemski, D. R. Jurtes, A. W. Castleman, Jr., *J. Phys. Chem. B* **2002**, *106*, 6136; f) U. Mazurek, H. Schwarz, *J. Chem. Soc. Chem. Commun.* **2003**, 1321; g) H. Schwarz, *Angew. Chem.* **2003**, *115*, 4580; *Angew. Chem. Int. Ed.* **2003**, *42*, 4442; h) R. A. J. O'Hair, G. N. Khairallah, *J. Cluster Sci.* **2004**, *15*, 331; i) T. Waters, R. A. J. O'Hair, *Encylopedia of Mass Spectrometry*, (Ed.: N. M. M. Nibbering), Vol. *4*, Elsevier, New York, **2005**, 604; j) P. Chen, *Angew. Chem*, **2003**, *115*, 2938; *Angew. Chem. Int. Ed.* **2003**, *42*, 2832.
[6] a) *Gaseous Ion Chemistry and Mass Spectrometry* (Ed.: J. H. Futrell), Wiley, New York, **1986**; b) K. Eller, H. Schwarz, *Chem. Rev.* **1991**, *91*, 1121; c) "Modern Mass Spectrometry": *Top. Curr. Chem.* **2003**, *225*, Springer, Berlin, **2003**; d) J. H. Gross, *Mass Spectrometry*, Springer, Berlin, **2004**.
[7] For a selection of leading references, see: a) G. Ertl in *Elementary Steps in Ammonia Synthesis. The Surface Science Approach* (Ed.: J. R. Jennings), Plenum, New. York, **1991**, p. 109; b) J. M. Thomas, R. Schlögl, *Angew. Chem.* **1994**, *106*, 316; *Angew. Chem. Int. Ed. Engl.* **1994**, *33*, 308; c) *Applied Homogeneous Catalysis with Organometallic Compounds*, Vol. *1*,2 (Eds.: B. Cornils, W. A. Herrmann), VCH, Weinheim, **1996**; d) J. M. Thomas, *Chem. Eur. J.* **1997**, *3*, 1557; e) G. Ertl, H. J. Freund, *Phys. Today* **1999**, *52*, 32; f) G. A. Somorjai, K. McKrea, *Appl. Catal. A* **2001**, *222*, 3; g) R. Noyori, T. Ohkuma, *Angew. Chem.* **2001**, *113*, 40; *Angew. Chem. Int. Ed.* **2001**, *40*, 41; h) T. M. Tonka, R. H. Grubbs, *Acc. Chem. Res.* **2001**, *34*, 18; i) G. Ertl, *J. Mol. Catal. A* **2002**, *182*/183, 5; j) A. T. Bell, *Science* **2003**, *299*, 1688; k) R. Schlögl, S. B. A. Hamid, *Angew. Chem.* **2004**, *116*, 1656; *Angew. Chem. Int. Ed.* **2004**, *43*, 1628; l) X. Zhang, X. Chen, P. Chen, *Organometallics* **2004**, *23*, 3437; m) S. S. Stahl, *Angew. Chem.* **2004**, *116*, 3480; *Angew. Chem. Int. Ed.* **2004**, *43*, 3400; n) A. Ajamian, J. L. Gleason, *Angew. Chem.* **2004**, *116*, 3842; *Angew. Chem. Int. Ed.* **2004**, *43*, 3754; for reviews with an emphasis on heterogeneous catalysis on the atomic scale, see: o) M. Boudart, *Catal. Lett.* **2000**, *65*, 1; p) G. Ertl, *Chem. Rec.* **2000**, 33; q) G. Ertl, *J. Mol. Catal. A* **2002**, *182/183*, 5; r) J. M. Thomas, C. R. A. Catlow, G. Sankar, *Chem. Commun.* **2002**, 2921; s) B. de Bruin, P. H. M. Budzelaar, A. G. Wal, *Angew. Chem.* **2004**, *116*, 4236; *Angew. Chem. Int. Ed.* **2004**, *43*, 4142; t) C. Copéret, M. Chabanas, R. P. Saint-Arromant, J.-M. Basset, *Angew. Chem.* **2003**, *115*, 164; *Angew. Chem. Int. Ed.* **2003**, *42*, 156; u) C. Hahn, *Chem. Eur. J.* **2004**, *10*, 5888; v) K. Reuter, D. Frenkel, M. Scheffler, *Phys. Rev. Lett.* **2004**, *93*, 116105-1; w) G. W. Coates, D. R. Moore, *Angew. Chem.* **2004**, *116*, 6784; *Angew. Chem. Int. Ed.* **2004**, *43*, 6618.

 © 2005 Wiley-VCH Verlag GmbH & Co. KGaA, Weinheim

[8] a) *Collision Spectroscopy* (Ed.: R. G. Cooks), Plenum Press, New York, **1978**; b) K. L. Busch, G. L. Glish, S. A. McLuckey, *Mass Spectrometry/Mass Spectrometry: Techniques and Applications of Tandem Mass Spectrometry*, VCH, Weinheim, **1988**.

[9] V. Blagojevic, G. Orlova, D. K. Bohme, *J. Am. Chem. Soc.* **2005**, *127*, 3345.

[10] a) G. Bouchoux, J.-Y. Salpin, D. Leblanc, *Int. J. Mass Spectrom. Ion Processes* **1996**, *153*, 37; b) G. Bouchoux, J.-Y. Salpin, *J. Phys. Chem.* **1996**, *100*, 16555; c) M. Moomann, S. Bashir, P. J. Derrick, D. Kuck, *J. Am. Soc. Mass Spectrom.* **2000**, *11*, 544; d) G. Bouchoux, D. Leblanc, M. Sabbier, *Int. J. Mass Spectrom.* **2001**, *210*/211, 189.

[11] E. E. Ferguson, F. C. Fehsenfeld, *J. Geophys. Res.* **1968**, *73*, 6215.

[12] F. Kaufman, *Defense Nuclear Agency Reaction Rate Handbook*, DASIAC, General Electric, TEMPO, Santa Barbara, CA, **1972**, chap. 19.

[13] a) *Ion Molecule Reactions: Kinetics and Dynamics* (Ed.: J. L. Franklin), Dowden, Hutchinson and Ross, Strondsburg, PA, **1979**; b) *Gas Phase Ion Chemistry*, Vol. *1–3* (Ed.: M. T. Bowers), Academic Press, New York, **1979**; c) *Techniques for the Study of Ion-Molecule Reactions* (Eds.: J. M. Farrar, W. H. Saunders, Jr.), Wiley, New York, **1988**; d) R. Zahradnik, *Acc. Chem. Res.* **1995**, *28*, 306.

[14] J. M. C. Plane, *Chem. Rev.* **2003**, *103*, 4963, and references therein.

[15] a) V. I. Parvulescu, P. Grange, B. Oelmon, *Catal. Today* **1998**, *46*, 233, and references therein; b) R. Burch, J. P. Breen, C. F. Meunier, *Appl. Catal. B* **2002**, *39*, 283; c) for a recent review on *biological* reduction of N_2O, see: P. Chen, S. I. Gorelsky, S. Ghosh, E. I. Solomon, *Angew. Chem.* **2004**, *116*, 4224; *Angew. Chem. Int. Ed.* **2004**, *43*, 4132; d) for an ab initio analysis of catalytic NO reduction, see: Z.-P. Liu, S. J. Denkins, D. A. King, *J. Am. Chem. Soc.* **2004**, *126*, 10746; e) for first principles calculations on the oxidation of alkali metal atoms with N_2O, see: O. Tishchenko, C. Vinckier, M. T. Nguyen, *J. Phys. Chem. A* **2004**, *108*, 1268.

[16] M. M. Kappes, R. H. Staley, *J. Am. Chem. Soc.* **1981**, *103*, 1286.

[17] V. Baranov, G. Javahery, A. C. Hopkinson, D. K. Bohme, *J. Am. Chem. Soc.* **1995**, *117*, 12801.

[18] For a theoretical study of the dissociation of N_2O in reactions catalyzed by transition-metal ions, see: A. Martinez, A. Goursot, R. Castañeda, A. Corma, *J. Phys. Chem. B* **2004**, *108*, 8823.

[19] M. Brönstrup, D. Schröder, I. Kretzschmar, H. Schwarz, J. N. Harvey, *J. Am. Chem. Soc.* **2001**, *123*, 142.

[20] V. Blagojevic, M. J. Y. Jarvis, E. Flaim, G. K. Koyanagi, V. V. Lavrov, D. K. Bohme, *Angew. Chem.* **2003**, *115*, 5073; *Angew. Chem. Int. Ed.* **2003**, *42*, 4923.

[21] a) G. K. Koyanagi, V. V. Lavrov, V. I. Baranov, D. Bandura, S. D. Tanner, J. W. McLaren, D. K. Bohme, *Int. J. Mass Spectrom.* **2000**, *194*, L1; b) G. K. Koyanagi, V. I. Baranov, S. T. Tanner, D. K. Bohme, *J. Anal. At. Spectrom.* **2000**, *15*, 1207.

[22] a) V. V. Lavrov, V. Blagojevic, G. K. Koyanagi, G. Orlova, D. K. Bohme, *J. Phys. Chem. A* **2004**, *108*, 5610; b) G. K. Koyanagi, D. K. Bohme, *J. Phys. Chem. A* **2001**, *105*, 8964.

[23] T. Su, W. J. Chesnawich, *J. Chem. Phys.* **1982**, *76*, 5183.

[24] I. Kretzschmar, A. Fiedler, J. N. Harvey, D. Schröder, H. Schwarz, *J. Phys. Chem. A* **1997**, *101*, 6252.

[25] For a recent exhaustive review on the topic of "spin-forbiddeness" in ion-molecule reactions, see: H. Schwarz, *Int. J. Mass Spectrom.* **2004**, *237*, 75.

[26] a) D. E. Clemmer, Y.-M. Chen, F. A. Khan, P. B. Armentrout, *J. Phys. Chem.* **1994**, *98*, 6522; b) D. Schröder, A. Fiedler, M. F. Ryan, H. Schwarz, *J. Phys. Chem.* **1994**, *98*, 68; c) A. Fiedler, D. Schröder, S. Shaik, H. Schwarz, *J. Am. Chem. Soc.* **1994**, *116*, 19734; d) S. Shaik, D. Danovich, A. Fiedler, D. Schröder, H. Schwarz, *Helv. Chim. Acta* **1995**, *78*, 1393; e) D. Schröder, H. Schwarz, D. E. Clemmer, Y. Chen, P. B. Armentrout, V. I. Baranov, D. K. Bohme, *Int. J. Mass Spectrom. Ion Processes* **1997**, *161*, 175; f) D. Danovich, S. Shaik, *J. Am. Chem. Soc.* **1997**, *119*, 1773; g) M. Filatov, S. Shaik, *J. Phys. Chem. A* **1998**, *102*, 3835.

[27] a) R. Poli, J. N. Harvey, *Chem. Soc. Rev.* **2003**, *32*, 1; b) R. Poli, *J. Organomet. Chem.* **2004**, 689, 4291.

[28] For a review, see: D. Schröder, S. Shaik, H. Schwarz, *Acc. Chem. Res.* **2000**, *33*, 139.

[29] A. Fiedler, J. Hrušák, W. Koch, H. Schwarz, *Chem. Phys. Lett.* **1993**, *211*, 242.

[30] a) D. Schröder, H. Schwarz, S. Shaik, *Struct. Bonding (Berlin)* **2000**, *97*, 91; b) for reviews on metal-mediated oxygen-atom transfer catalysis in solution, see: *Catalytic Asymmetric Synthesis*, 2nd ed. (Ed.: I. Ojima), Wiley-VCH, New York, **2000**; c) *Oxygenases and Model Systems* (Ed.: T. Fumabiki), Kluwer, Boston, **1997**; d) *Comprehensive Organometallic Chemistry II*, Vol. *12* (Eds.: G. Wilkinson, F. G. A. Stone, E. W. Abel, L. S. Hegedus), Pergamon, New York, **1995**.

[31] D. Schröder, H. Schwarz, *Angew. Chem.* **1990**, *102*, 1468; *Angew. Chem. Int. Ed. Engl.* **1990**, *29*, 1433.

[32] T. C. Jackson, D. B. Jacobson, B. S. Freiser, *J. Am. Chem. Soc.* **1984**, *106*, 1252.

[33] H. Kang, J. L. Beauchamp, *J. Am. Chem. Soc.* **1986**, *108*, 5663.

[34] a) A. E. Stevens, J. L. Beauchamp, *J. Am. Chem. Soc.* **1971**, *93*, 6449; b) P. B. Armentrout, J. L. Beauchamp, *J. Chem. Phys.* **1981**, *74*, 2819; c) R. Georgiadis, P. B. Armentrout, *Int. J. Mass Spectrom. Ion Processes* **1989**, *89*, 227; d) S. K. Loh, E. R. Fisher, L. Lian, R. H. Schultz, P. B. Armentrout, *J. Phys. Chem.* **1989**, *93*, 3159; e) E. R. Fisher, P. B. Armentrout, *J. Phys. Chem.* **1990**, *94*, 1674.

[35] D. Schröder, H. Schwarz, *Angew. Chem.* **1990**, *102*, 1466; *Angew. Chem. Int. Ed. Engl.* **1990**, *29*, 1431.

[36] K. K. Irikura, J. L. Beauchamp, *J. Am. Chem. Soc.* **1989**, *111*, 75.

[37] N. Ktiajsma, M. Ito, H. Fukui, Y. Moro-Oka, *J. Chem. Soc. Chem. Commun.* **1991**, *102*, and references therein.

[38] M. F. Ryan, D. Stöckigt, H. Schwarz, *J. Am. Chem. Soc.* **1994**, *116*, 9565.

[39] Y. Shiota, K. Yoshizawa, *J. Chem. Phys.* **2003**, *118*, 5872, and references therein.

[40] At thermal energies the reverse reaction $Fe(OH)^+ + CH_3 \rightarrow FeO^+ + CH_4$ takes place instead: O. Blum, D. Stöckigt, D. Schröder, H. Schwarz, *Angew. Chem.* **1992**, *104*, 637; *Angew. Chem. Int. Ed. Engl.* **1992**, *31*, 603.

[41] a) S. T. Ceyer, *Science* **1990**, *249*, 133; b) J. C. Mackie, *Catal. Rev. Sci. Eng.* **1991**, *33*, 169; c) H. Schwarz, *Angew. Chem.* **1991**, *103*, 837; *Angew. Chem. Int. Ed. Engl.* **1991**, *30*, 820; d) J. Kiwi, K. R. Thampi, M. Grätzel, P. Albers, K. Seibold, *J. Phys. Chem.* **1992**, *96*, 1344; e) Z. Zhang, X. E. Verykios, M. Baerns, *Catal. Rev. Sci. Eng.* **1993**, *35*, 169.

[42] D. Schröder, R. Wesendrup, C. A. Schalley, W. Zummack, H. Schwarz, *Helv. Chim. Acta* **1996**, *79*, 123.

[43] D. Schröder, H. Schwarz in *Essays in Contemporary Chemistry: From Molecular Structure towards Biology* (Eds.: G. Quinkert, M. V. Kisakürek), Verlag Helvetica Chimica Acta, Zürich, **2001**, p. 131.

[44] For enhancement effects of added methanol on selective CH_4 oxidations, see: Y. Teng, Y. Yamaguchi, T. Takemoto, K. Tabata, E. Suzuki, *Phys. Chem. Chem. Phys.* **2000**, *2*, 3429.

[45] a) *Organometallic Ion Chemistry* (Ed.: B. S. Freiser), Kluwer, Dordrecht, **1996**, p. 283; b) S. G. Lias, J. E. Bartmess, J. F. Liebman, J. L. Holmes, R. D. Levin, W. G. Mallard, *J. Phys. Chem. Ref. Data Suppl. 1* **1988**, *17*.

[46] A. Fiedler, D. Schröder, H. Schwarz, B. L. Tjelta, P. B. Armentrout, *J. Am. Chem. Soc.* **1996**, *118*, 5047.

[47] I. Kretzschmar, D. Schröder, H. Schwarz, unpublished results.

[48] D. Stöckigt, H. Schwarz, *Liebigs Ann.* **1995**, 429.

 © 2005 Wiley-VCH Verlag GmbH & Co. KGaA, Weinheim

[49] D. Schröder, M. C. Holthausen, H. Schwarz, *J. Phys. Chem. B* **2004**, *108*, 14407.
[50] X.-G. Zhang, P. B. Armentrout, *J. Phys. Chem. A* **2003**, *107*, 8904.
[51] X.-G. Zhang, P. B. Armentrout, *J. Phys. Chem. A* **2003**, *107*, 8915.
[52] B. R. Rowe, A. A. Viggiano, F. C. Fehsenfeld, D. W. Fakey, E. E. Ferguson, *J. Chem. Phys.* **1982**, *76*, 742.
[53] The fundamental aspects associated with the activation of molecular oxygen as well as the "stoichiometry problem" will not be addressed in detail here. For general introductions, see ref. [54], and for some examples pertinent to the content of the present review, see refs. [11, 30, 43, 50, 51, 55].
[54] a) E. F. Elstner, *Der Sauerstoff*, Wissenschaftsverlag, Mannheim, **1990**; b) D. T. Sawyer, *Oxygen Chemistry*, Oxford University Press, New York, **1991**.
[55] a) R. Johnson, F. R. Castell, M. A. Biondi, *J. Chem. Phys.* **1974**, *61*, 5404; b) M. M. Kappes, R. H. Staley, *J. Phys. Chem.* ***1981***, *85*, 942; c) S. Dheandhanoo, B. K. Chatterjee, R. Johnson, *J. Chem. Phys.* **1985**, *83*, 3327; d) E. R. Fisher, J. L. Elkind, D. E. Clemmer, R. Georgiadis, S. K. Loh, N. Aristov, L. S. Sunderlin, P. B. Armentrout, *J. Chem. Phys.* **1990**, *93*, 942; e) A. Fiedler, I. Kretzschmar, D. Schröder, H. Schwarz, *J. Am. Chem. Soc.* **1996**, *118*, 9941; f) R. J. Rollason, J. M. C. Plane, *J. Chem. Soc. Faraday Trans.* **1998**, *94*, 3067; g) M. K. Beyer, C. B. Berg, U. Achatz, S. Joos, G. Niedner-Schatteburg, V. E. Bondybey, *Mol. Phys.* **2001**, *99*, 699; h) G. K. Koyanagi, D. Caraiman, V. Blagojevic, D. K. Bohme, *J. Phys. Chem. A* **2002**, *106*, 4581.
[56] We note in passing that it is this very feature that has caused some interest in the role of metal-ion interactions with benzene in interstellar chemistry, in which benzene can contribute to the depletion of atomic ions and can act as a platform for catalytic gas-phase chemistry. For leading references, see ref. [57]. For a recent computational study on various aspects of the M^+/C_6H_6 interactions, see: ref. [58], and for a review on the role of π interactions with metal cations in biological systems, see: ref. [59].
[57] a) D. K. Bohme, *Chem. Rev.* **1992**, *92*, 1487; b) P. Boissel, *Astron. Astrophys.* **1994**, *285*, L33; c) F. Pirani, D. Coppelletti, M. Bartolomei, V. Aquilanti, M. Scotoni, M. Vescovi, D. Ascenzi, D, Bassi, *Phys. Rev. Lett.* **2001**, *86*, 5035.
[58] M. Diefenbach, H. Schwarz, *Encycl. Comput. Chem.* **2004**, DOI: 10.1002/0470845015.cn0091 (Aug 15, 2004)..
[59] a) D. A. Dougherty, *Science*, **1996**, *271*, 163; b) J. C. Ma, D. A. Dougherty, *Chem. Rev.* **1997**, *97*, 1303.
[60] S. Mallier-Soulier, V. Ducrocq, N. Truffant, *Can. J. Microbiol.* **1999**, *45*, 898.
[61] For a superb discussion on the intricacies in the oxidation of hydrogen on Pt(111), see: a) S. Völkening, K. Bedürftig, K. Jacobi, J. Wintterlin, G. Ertl, *Phys. Rev. Lett.* **1999**, *83*, 2672; b) C. Sachs, M. Hildebrand, S. Völkening, J. Wintterlin, G. Ertl, *Science* **2001**, *293*, 1635; c) C. Sachs, M. Hildebrand, S. Völkening, J. Wintterlin, G. Ertl, *J. Chem. Phys.* **2002**, *116*, 5759, and references therein; d) the discovery of the platinum-catalyzed oxidation of hydrogen in 1823 by Döbereiner (J. W. Döbereiner, *Schweigg. J.* **1823**, *39*, 1) prompted Berzelius to coin the term "catalysis" (J. J. Berzelius, *Iber. Chem.* **1837**, *15*, 237). For a historical account, entitled "Katalyse: Vom Stein der Weisen zu Wilhelm Ostwald", see: G. Ertl, T. Gloyna, *Z. Phys. Chem.* **2003**, *217*, 1207; e) the catalytic oxidation of hydrogen on free *neutral* platinum clusters has been reported by: M. Andersson, A. Rosén, *J. Chem. Phys.* **2002**, *117*, 7051.
[62] a) K. P. C. Vollhardt, *Angew. Chem.* **1984**, *96*, 525; *Angew. Chem. Int. Ed. Engl.* **1984**, *23*, 539; b) N. E. Shore, *Chem. Rev.* **1988**, *88*, 1081; c) M. Lautens, W. Klute, W. Tam, *Chem. Rev.* **1996**, *96*, 49; d) I. Ojima, M. Tzamaviondaki, Z. Li, R. J. Donovan, *Chem. Rev.* **1996**, *96*, 635; e) for a discussion of electron-transfer catalysis using transition-metal complexes, see: S. Hintz, A. Heidbreider, J. Mattay, *Top. Curr. Chem.* **1996**, *177*, 78; f) a survey as well as a detailed computational analysis of the noncatalyzed trimerization of, for example, $3C_2H_2 \rightarrow C_6H_6$, can be found in: R. D. Bach, G. J. Wolber, H. B. Schlegel, *J. Am. Chem. Soc.* **1985**, *107*, 2837; g) for a recent example for C_2H_2 trimerization on single Ag, Rh, and Pd atoms supported on the MgO(001) surface, see: A. S. Wörz, K. Judai, S. Abbet, J.-M. Antonietti, U. Heiz, A. DelVitto, L. Giordano, G. Pacchioni, *Chem. Phys. Lett.* **2004**, *399*, 266; h) for ethylene polymerization mediated by oxygenated chromium cluster ions and the relationship between gas-phase reactivities of isolated clusters versus solid-state behavior, see: T. Hanmura, M. Ichihashi, T. Monoi, K. Matsuura, T. Kondow, *J. Phys. Chem. A*, **2004**, *108*, 10434.
[63] a) S. W. Buckner, T. J. MacMahon, G. D. Byrd, B. S. Freiser, *Inorg. Chem.* **1989**, *28*, 3511; b) R. Bakhtiar, J. J. Drader, D. B. Jacobson, *J. Am. Chem. Soc.* **1992** *114*, 8304.
[64] R. Wesendrup, H. Schwarz, *Organometallics* **1997**, *16*, 461
[65] C. Berg, S. Kaiser, T. Schindler, C. Kronseder, G. Niedner-Schatteburg, V. E. Bondybey, *Chem. Phys. Lett.* **1994**, *231*, 139.
[66] C. Heinemann, H. H. Cornehl, H. Schwarz, *J. Organomet. Chem.* **1995**, *501*, 201.
[67] a) P. Schnabel, M. P. Irion, K. G. Weil, *J. Phys. Chem.* **1991**, *95*, 9688; b) P. Schnabel, K. G. Weil, M. P. Irion, *Angew. Chem.* **1992**, *104*, 633; *Angew. Chem. Int. Ed. Engl.* **1992**, *31*, 636; c) O. Gehret, M. P. Irion, *Chem. Phys. Lett.* **1996**, *254*, 379..
[68] a) V. Ryzhov, R. C. Dunbar, *J. Am. Chem. Soc.* **1999**, *121*, 2259; b) for a recent review, see: L. Operti, R. Rabezzana, *Mass Spectrom. Rev.* **2003**, *22*, 407.
[69] a) For details of the gas-phase oligomerization of C_2H_2 mediated by atomic Fe^+ see: D. Schröder, D. Sülzle, J. Hrušák, D. K. Bohme, H. Schwarz, *Int. J. Mass Spectrom. Ion Processes* **1991**, *110*, 145; b) for an infrared spectroscopic characterization of gaseous $Ni(C_2H_2)_n^+$ ($n = 3$–6) complexes that provide evidence for intracluster cyclization reactions, see: R. S. Walters, T. D. Draeger, M. A. Duncan, *J. Phys. Chem. A* **2002**, *106*, 10482; c) M. A. Duncan, *Int. Rev. Phys. Chem.* **2003**, *22*, 407.
[70] R. Wesendrup, D. Schröder, H. Schwarz, *Angew. Chem.* **1994**, *106*, 1232; *Angew. Chem. Int. Ed. Engl.* **1994**, *33*, 1174.
[71] M. Pavlov, M. R. A. Blomberg, P. E. M. Siegbahn, R. Wesendrup, C. Heinemann, H. Schwarz, *J. Phys. Chem. A* **1997**, *101*, 1567, and references therein.
[72] M. Brönstrup, D. Schröder, H. Schwarz, *Organometallics* **1999**, *18*, 1939.
[73] S. W. Buckner, J. R. Gord, B. S. Freiser, *J. Am. Chem. Soc.* **1988**, *110*, 6606.
[74] a) M. Brönstrup, I. Kretzschmar, D. Schröder, H. Schwarz, *Helv. Chim. Acta* **1998**, *81*, 2348; b) R. Liyange, P. B. Armentrout, *Int. J. Mass Spectrom.* **2005**, *241*, 243.
[75] D. R. A. Ranatunga, Y. D. Hill, B. S. Freiser, *Organometallics* **1996**, *15*, 1242,
[76] a) G. C. Bond, D. J. Thompson, *Catal. Rev. Sci. Eng.* **1999**, *41*, 319, and references therein; b) for the role of gold catalysts in organic *synthesis*, see: G. Dyker, *Angew. Chem.* **2000**, *112*, 4407; *Angew. Chem. Int. Ed.* **2000**, *39*, 4237; c) A. S. K. Hashmi, *Gold Bull.* **2004**, *37*, 51.
[77] a) M. Haruta, N. Yamada, T. Kobayashi, S. Iijima, *J. Catal.* **1989**, *115*, 301; b) M. Haruta, *Catal. Today* **1997**, *36*, 153; c) M. Valden, X. Lai, D. W. Goodman, *Science* **1998**, *281*, 1647; d) A. Sanchez, S. Abbet, U. Heiz, W.-D. Schneider, H. Häkkinen, R. N. Barnett, U. Landman, *J. Phys. Chem. A* **1999**, *103*, 9573; e) U. Heiz, A. Sanchez, S. Abbet, W.-D. Schneider, *Eur. Phys. J. D* **1999**, *9*, 35; f) N. Lopez, J. K. Nørskov, *J. Am. Chem. Soc.* **2002**, *124*, 11262; g) M. S. Chen, D. W. Goodman, *Science*, **2004**, *306*, 252; h) for an essay on this topic, see: A. Cho, *Science* **2003**, *299*, 1684.
[78] For reviews, see: a) D. M. P. Mingos, T. Slee, L. Zhenyang, *Chem. Rev.* **1990**, *90*, 383; b) M. P. Irion, *Int. J. Mass Spectrom. Ion Processes* **1992**, *121*, 1; c) M. B. Knickelbein, *Annu. Rev. Phys. Chem.* **1999**, *50*, 79; d) J. A. Alonso, *Chem. Rev.* **2000**, *100*,

 © 2005 Wiley-VCH Verlag GmbH & Co. KGaA, Weinheim

637; e) P. B. Armentrout, *Annu. Rev. Phys. Chem.* **2001**, *52*, 423; f) V. E. Bondybey, M. K. Beyer, *J. Phys. Chem. A* **2001**, *105*, 951; g) Y. D. Kim, *Int. J. Mass Spectrom.* **2004**, *238*, 17; h) T. M. Bernhardt, *Int. J. Mass Spectrom.*, in press.

[79] a) For an exhaustive collection of experimental/theoretical studies on metal clusters in general, see: *Metal Clusters in Chemistry* (Eds.: P. Braunstein, L. A. Oro, P. R. Raithby), Wiley, New York, **1999**; b) for a recent survey that contains 794 references on the chemistry of gold, see: P. Pyykkö, *Angew. Chem.* **2004**, *116*, 4512; *Angew. Chem. Int. Ed.* **2004**, *43*, 4412.

[80] For a selection of more recent studies, see: a) W. T. Wallace, R. L. Whetten, *J. Phys. Chem. B* **2000**, *104*, 10964; b) X. Wu, L. Senapati, S. K. Nayak, A. Selloni, M. Hajaligol, *J. Chem. Phys.* **2002**, *117*, 4010; c) J. Hagen, L. D. Socaciu, M. Elijazyfer, T. M. Bernhardt, L. Wöste, *Phys. Chem. Chem. Phys.* **2002**, *4*, 1707; d) I. Balteanu, O. P. Balaj, B. S. Fox, M. K. Beyer, Z. Bastl, V. E. Bondybey, *Phys. Chem. Chem. Phys.* **2003**, *5*, 1213; e) D. Stokic, M. Fischer, G. Ganteför, Y. D. Kim, Q. Sun, P. Jena, *J. Am. Chem. Soc.* **2003**, *125*, 2848; f) for the role of the charge of supported gold clusters in the low-temperature oxidation of CO, see: B. Yoon, H. Häkkinen, U. Landman, A. S. Wörz, J.-M. Antonietti, S. Abbot, K. Judai, U. Heiz, *Science* **2005**, *307*, 403.

[81] Y. D. Kim, M. Fischer, G. Ganteför, *Chem. Phys. Lett.* **2003**, *377*, 170.

[82] a) Y. Shi, K. M. Ervin, *J. Chem. Phys.* **1998**, *108*, 1575; b) a full catalytic cycle of CO oxidation with N_2O on cationic platinum clusters for Pt_n^+ ($n = 5$–10), including aspects of catalyst's poisoning by CO, has been reported recently: O. P. Bolaj, I. Balteanu, T. T. J. Roßteunscher, M. K. Beyer, V. E. Bondybey, *Angew. Chem.* **2004**, *116*, 6681; *Angew. Chem. Int. Ed.* **2004**, *43*, 6519; c) for the cluster-size-dependent reaction behavior of CO with O_2 on free, negatively charged silver anions, see: L. D. Socacin, J. Hagen, J. LeRoux, D. Popolan, T. M. Bernhardt, L. Wöste, and S. Vajda, *J. Chem. Phys.* **2004**, *120*, 2078, and references therein; d) in contrast to $Fe_2O_2^+$ which does not oxidize CO (O. Gehret, M. P. Irion, *Chem. Eur. J.* **1996**, *2*, 598; P. Jackson, J. N. Harvey, D. Schröder, H. Schwarz, *Int. J. Mass Spectrom.* **2001**, *204*, 233), $Ni_2O_2^+$ brings about efficient oxidation of CO. $Ni_2O_2^+$ can be conveniently generated by reaction of Ni_2^+ with N_2O, and hence this is another example of cluster-mediated oxygen-atom transport catalysis in the N_2O/CO system. For details, see: K. Koszinowski, M. Schlangen, D. Schröder, H. Schwarz, *Eur. J. Inorg. Chem.*, in press.

[83] R. M. Heck, R. J. Farranto, *Catalytic Air Pollution Control: Commercial Technology*, Van Nortrand Reinhold, New York, **1995**.

[84] a) A. G. Sault, D. W. Goodman, *Adv. Chem. Phys.* **1989**, *76*, 153; b) S. L. Bernasek, *Heterogeneous Reaction Dynamics*, VCH, New York, **1995**.

[85] a) H. Häkkinen, U. Landman, *J. Am. Chem. Soc.* **2001**, *123*, 9704; b) W. T. Wallace, R. L. Whetten, *J. Am. Chem. Soc.* **2002**, *124*, 7499; c) L. D. Socaciu, J. Hagen, T. M. Bernhardt, L. Wöste, U. Heiz, H. Häkkinen, U. Landman, *J. Am. Chem. Soc.* **2003**, *125*, 10437; d) M. L. Kimble, A. W. Castleman, Jr., R. Mitrić, C. Bürgel, V. Bonačic-Koutecký, *J. Am. Chem. Soc.* **2004**, *126*, 2526; e) N. Lopez, J. K. Nørskov, *J. Am. Chem. Soc.* **2002**, *124*, 11262.

[86] G. Centi, F. Cavani, F. Trifiro, *Selective Oxidation by Heterogeneous Catalysis*, Kluwer Academic/Plenum Publishers, New York, **2001**.

[87] T. Waters, R. A. J. O'Hair, A. G. Wedd, *J. Am. Chem. Soc.* **2003**, *125*, 3384.

[88] W. E. Farneth, R. H. Staley, A. W. Sleight, *J. Am. Chem. Soc.* **1986**, *108*, 2327.

[89] B. Chiavarino, M. E. Crestoni, S. Fornarini, *Chem. Eur. J.* **2002**, *8*, 2740.

[90] a) T. Waters, R. A. J. O'Hair, A. G. Wedd, *Int. J. Mass Spectrom.* **2003**, *228*, 599; b) for an example of a catalytic cycle for the gas-phase decarboxylation of acetic acid by organomagnesates, see: R. A. J. O'Hair, A. K. Vrkic, P. F. James, *J. Am. Chem. Soc.* **2004**, *126*, 12173.

[91] M. A. Barteau, *Chem. Rev.* **1996**, *96*, 1413, and references therein.

[92] a) H. S. Taylor, *Proc. R. Soc. London A* **1925**, *108*, 105; b) G. M. Schwab, E. Pletsch, *Z. Phys. Chem.* **1929**, *131*, 385; c) R. J. Davis, *Science* **2003**, *301*, 926; d) Q. Fu, H. Saltsburg, M. Flytzani-Stephanopoulos, *Science* **2003**, *301*, 935; e) K. Horn, *Science* **2004**, *305*, 483.

 © 2005 Wiley-VCH Verlag GmbH & Co. KGaA, Weinheim

Communications

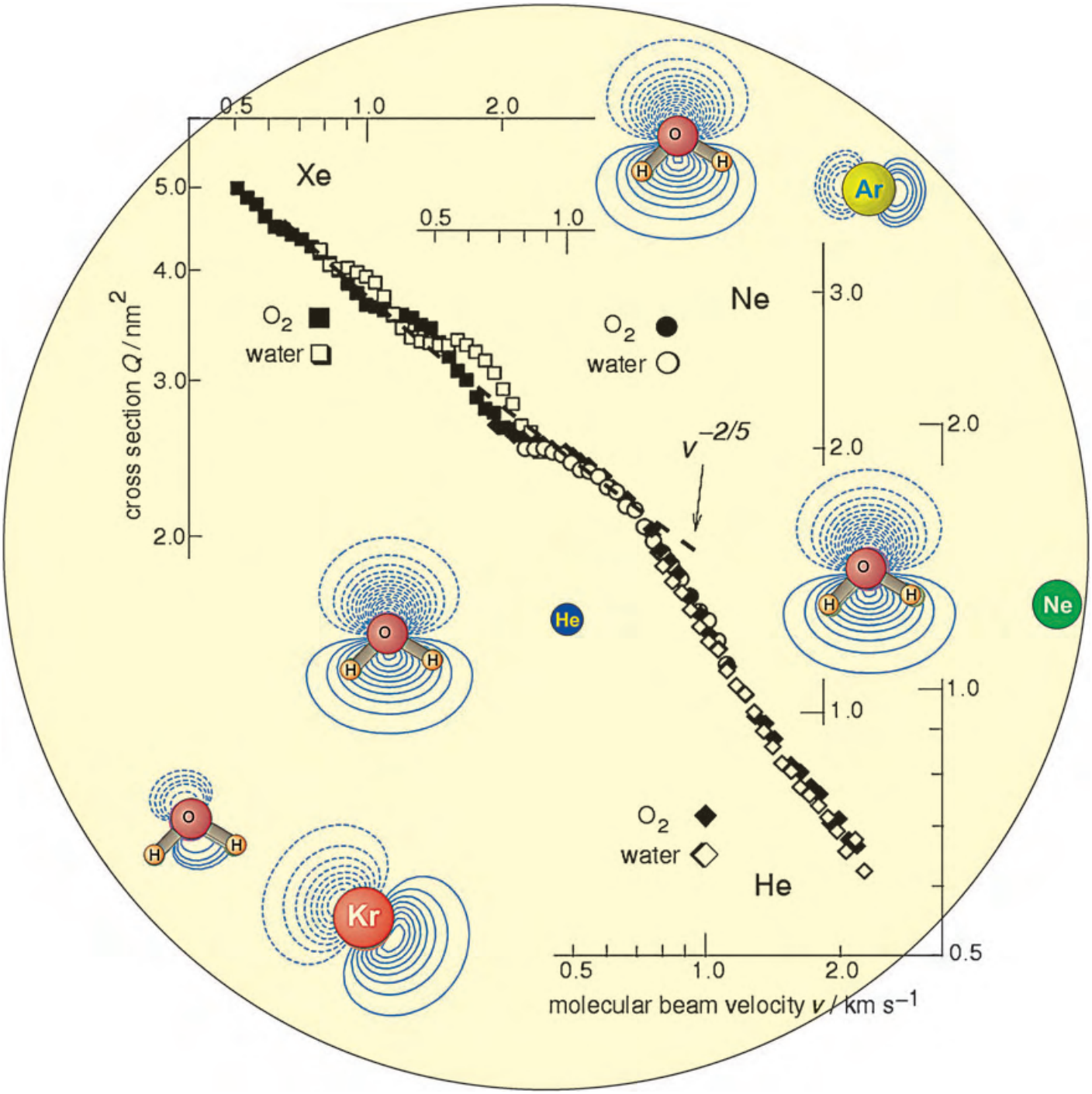

Scattering cross sections for collisions of water and oxygen with the five noble gases reveal the onset of hydrogen bonds in water–noble-gas complexes, which increase in strength from He to Xe. Details on the determination of the strength of the interaction in excess of that expected for pure van der Waals forces are given by D. Cappelletti and co-workers on the following pages.

 © 2005 Wiley-VCH Verlag GmbH & Co. KGaA, Weinheim DOI: 10.1002/anie.200462704

Hydrogen Bonds

Glory-Scattering Measurement of Water–Noble-Gas Interactions: The Birth of the Hydrogen Bond**

*Vincenzo Aquilanti, Elena Cornicchi, Marc Moix Teixidor, Nadja Saendig, Fernando Pirani, and David Cappelletti**

Herein we describe molecular-beam scattering experiments probing the interactions of water with He, Ne, Ar, Kr, and Xe, the observation of the quantum mechanical "glory" interference effect, and the determination of well depths, well positions, and strengths of long-range attraction. Comparisons with expectations from features of typical van der Waals (vdW) dimers indicate how a trend develops along the series for water to bind more strongly than for pure vdW, by means of state-of-the-art ab initio calculations, in which a proton is protruded as a binding bridge towards the heavier noble gases. These precise measurements of the manifestation of an embryonic hydrogen bond contribute to the understanding of this ubiquitous phenomenon and offer important insight for its modeling.

Intermolecular noncovalent interactions control myriad phenomena.[1] They arise from the critical balance of several components, such as electrostatics, induction, and dispersion, which operate at long range, and overlap (size repulsion and charge-transfer), which act at short range.[2] Among intermolecular noncovalent interactions those involving water[3] are of paramount relevance as the archetype of polar hydrogen-containing molecules. They are crucial for the description of its liquid state, its properties as a solvent, and its aggregates. Manifestations and properties of the hydrogen bond have been intensively studied over three quarters of a century, and are currently under more scrutiny than ever, as the list of basic open questions is still impressive.[3,4] Characterizing the relative importance of the various components of the overall noncovalent interaction and understanding how their features modify as different systems are considered are important tasks: the modeling of the diverse components in terms of monomer properties requires appropriate combinations and extensions of experimental and theoretical information on prototypical aggregates. The paradigmatic example is again the most studied liquid, that is, water,[3] which has been simulated by a variety of interaction potential models, often involving only descriptions of electrostatic and size-repulsion components: when calibrated on the gas-phase dimer, that is, on the water–water interaction, the success of these models in accounting for properties of the liquid is only partial.

Herein we focus on the simplest aggregates, those of water with the five noble gases, for which contributions to the interaction from the electrostatic component are absent, and the remaining ones are hopefully amenable to proper testing and modeling. The question is whether the simple vdW picture[2] suffices, or whether there is more to it. The lighter systems, particularly that of He, have been the target of numerous theoretical investigations;[5–7] the heavier ones (that of Kr and Xe) are practically unknown. Except for He[8] and Ar,[9] accurate experimental characterizations are missing. We show that the systematic investigation of the five water–noble-gas systems, the study of variations of our observables along the series, and comparison with the behavior of analogous systems, prototypical of vdW, provide unique information on the strength and range of intermolecular forces and cast light on the nature and role of interaction components which add to the vdW forces.

This series of collisional experiments was carried out in an apparatus (see Figure 1 and details in references [10,11]) in

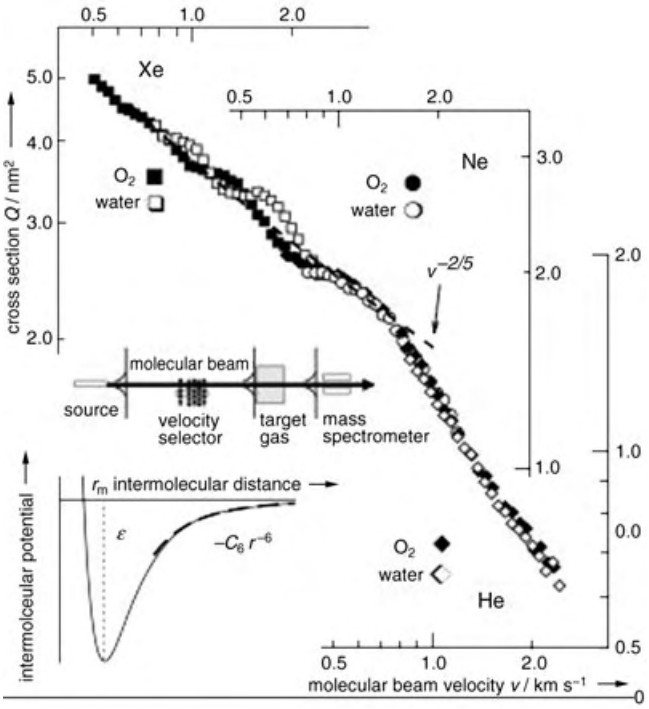

Figure 1. Direct probe of intermolecular interactions. For details, see the Experimental Section. The measurement of the beam attenuation provides $Q(v)$, which is a direct probe of the intermolecular potential features r_m, ε, and C_6 (see text). Typical data can be displayed against molecular beam velocity v on a universal log–log plot, which allows proper scaling to exhibit the coincidence in $Q(v)$ for the Ne and He data, in contrast with the nearly antiphase "glory" behavior for Xe, which is the notable difference visible here between water and oxygen systems (see Figure 2).

[*] D. Cappelletti
Dipartimento di Ingegneria Civile ed Ambientale
Università di Perugia
Perugia (Italy)
and
INFM
Fax: (+39) 05-585-3864
E-mail: prometeo@dyn.unipg.it
V. Aquilanti, E. Cornicchi, M. Moix Teixidor, N. Saendig, F. Pirani
Dipartimento di Chimica
Università di Perugia
Perugia (Italy)
and
INFM

[**] This work was supported by MIUR grants.

 © 2005 Wiley-VCH Verlag GmbH & Co. KGaA, Weinheim

which a well-collimated and velocity-selected "hot" molecular beam of water[12] is scattered by a noble-gas target. The combined use of high angular and velocity resolution permits the total quantum cross section Q to be measured over an ample range of the beam velocity v.[12] The $Q(v)$ results show:

1) The characteristic average decrease as $v^{-2/5}$ (see Figure 1, Figure 2), which provides information on the coefficient C_6 of the leading term of the attraction at long range.

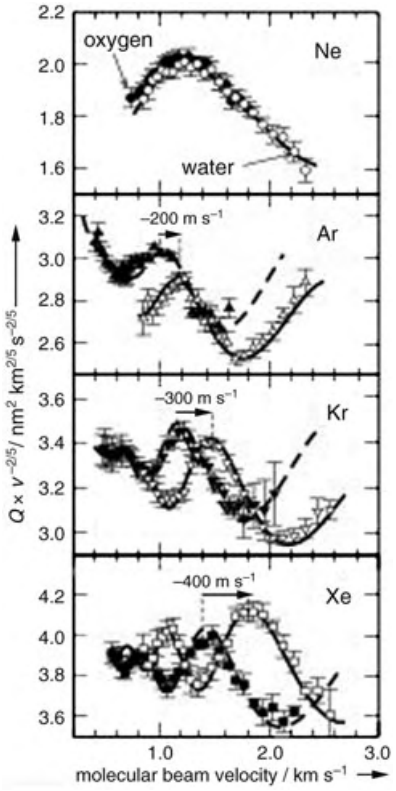

Figure 2. Cross sections (multiplied by $v^{2/5}$ to emphasize the glory oscillations) as a function of v for collisions of water and O_2 with Ne, Ar, Kr, and Xe (filled and open symbols, respectively); continuous and dashed curves are corresponding fits with the potential parameters ε, r_m, and C_6 of Table 1; glory shifts are indicated by arrows.

2) The manifestation of an oscillatory pattern, the "glory" interference effect, superimposed on the smooth component, whose frequency and amplitude correlate with depth ε and position r_m of the potential well.
3) The steeper falloff of Q as a function of v in water–He, which suggests that attraction and repulsion simultaneously influence the scattering in the energy probed by the present experiments.[12]

Illuminating is the direct comparison in Figures 1 and 2 with results from analogous experiments on molecular-oxygen–noble-gas-atom systems: in such well-established series of partners (prototypical vdW interactions[2]), both the long- and medium-range behaviors can be compared with those of the water systems in view of the similarity of oxygen and water in terms of molecular polarizability—the basic property for scaling vdW forces in the full distance range.[13–15] Characteristic potential parameters extracted from the analysis are listed in Table 1.

We have thus provided an accurate determination of the spherically averaged interaction, the leading term in its multipolar expansion. For water–He and water–Ar systems, there is full agreement with previous differential scattering[8] and spectroscopic determination,[9] respectively. In detail: 1) For the lighter gases, He and Ne, the coincidence of cross sections for the water and the oxygen systems suggests that a vdW interaction is also operative in the water case; indeed, the involved components[2] (repulsion, dispersion, induction) can be modeled on the polarizabilities of the partners.[13–15] 2) As we move to the heavier members of the series, the average components of the water cross sections still coincide with those of the oxygen systems and continue to be in accord with polarizability-based models of vdW interactions,[13–15] but this is not so for the "glory" features, which are very sensitive to the depth and position of the wells. The progressive glory shift towards higher velocities on going towards Xe (see Figure 2) is thus a precise measure of an increasing binding strength, larger than expected for pure vdW forces (see Table 1).

Table 1: Potential parameters of the isotropic interaction for water–noble-gas and for molecular oxygen–noble-gas systems. vdW predictions, obtained by combining[14,15] size repulsion with dispersion plus induction attraction, are also reported. The equilibrium distance is defined with respect to the center of mass of the water molecule.

	ε [kJ mol^{-1}]	r_m [nm]	C_6 [10^{-4} kJ nm^6 mol^{-1}]	Refs.
water–He	0.265	0.345	6.3	this work
	0.273	0.342	6.1	predicted
oxygen–He	0.241	0.350	7.4	[17,18]
water–Ne	0.550	0.350	13.7	this work
	0.546	0.346	13.0	predicted
oxygen–Ne	0.557	0.350	14.5	[17]
water–Ar	1.39	0.363	42.9	this work
	1.13	0.374	42.5	predicted
oxygen–Ar	1.11	0.372	48.8	[17,19]
water–Kr	1.65	0.375	63.7	this work
	1.37	0.386	62.9	predicted
oxygen–Kr	1.29	0.388	68.0	[10]
water–Xe	1.92	0.393	102	this work
	1.55	0.404	93.7	predicted
oxygen–Xe	1.47	0.405	98.4	[10]

We believe that such an increase in well depths is the manifestation of a short-range reinforcing attractive component to the bond and its role amplifies as distance decreases (as typical of a covalent or charge-transfer contribution): moving towards Xe along the series of noble gases, ionization potentials decrease, proton affinities increase, and there is circumstantial evidence for sharing of external electrons between the partners in the complexes. We looked for confirmation of such a picture and for further insight by extensive state-of-the-art quantum chemical calculations.[16]

 © 2005 Wiley-VCH Verlag GmbH & Co. KGaA, Weinheim

They are in a sense complementary here, because although quantum chemistry encounters well-known difficulties with absolute estimations of the bond energies of intermolecular forces, its use is of value in searching for the geometries of most stable structures, while our experiments probe absolute orientational averages. The search was made as the noble gas moves in the plane of the water molecule, and Figure 3 shows

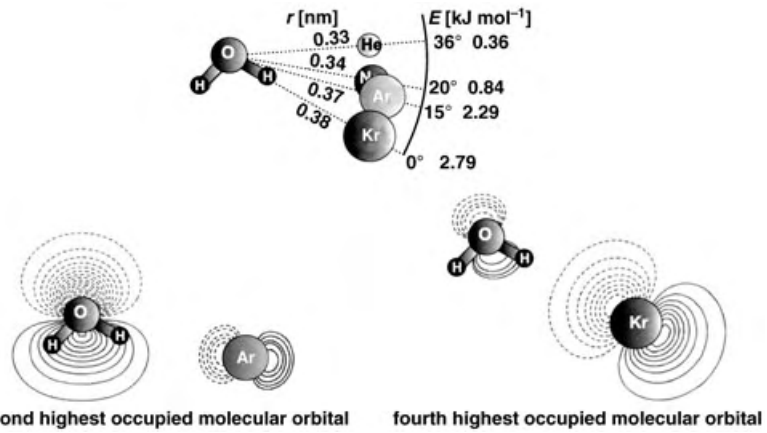

Figure 3. Picture of water–noble gas interactions from ab initio (MRCI) calculations.[16] Oxygen-atom–noble-gas distances *r*, bond angles, and binding energies *E* are given for the most stable configuration of each water–noble-gas complex. The analysis of orbitals corresponding to all structures gave complete separations between those of water and those of the noble gas for He and Ne, although geometries vary. For Ar and Kr, orbitals showing incipient covalence due to charge-sharing appear: for Ar, the hybrid of the figure involves a π_y orbital of the noble gas (coplanar with water) and the bond orbital of OH (σ, π_x, π_y of O and σ of H); it is the second highest occupied molecular orbital. Also in Kr–water an orbital which contains contributions of the noble gas and water is found; it is the fourth highest occupied molecular orbital, which is formed by the π_y orbital of krypton and the σ orbital of hydrogen. In this case the noble gas appears to preferentially interact with just one of the hydrogen atoms of water, as confirmed by the geometry of the complex.

that progressive alignment along the O–H bond is found when heavier noble gases are considered. Such an alignment is known as one of the signatures of the hydrogen bond,[20] while vdW considerations predict a sideways approach, that is, along the direction of minimum electron density in water (see the helium case). An insurgence of covalence is observed in the density maps of hybrid orbitals in the cases of Ar and Kr (Figure 3; the Xe case is currently too hard to study, as it requires a relativistic treatment).

The relevance of the effect can be discussed quantitatively: Taking Kr as the study case for comparison of theory and experiment, we see that the binding energy (Figure 3) is about 1 kJ mol^{-1} higher than $\varepsilon = 1.65$ kJ mol^{-1}, which can be compared with the expected value of 1.37 kJ mol^{-1} for pure vdW interactions (Table 1). The magnitude of the binding energy for Kr and Xe is therefore in the range of the so-called weak hydrogen bonds[21,22] (strong hydrogen bonds can be up to an order of magnitude stronger), and it is important to stress that only a fraction (ca. 50 % for Kr) is accounted for by vdW forces.

This conclusion establishes how components of different nature contribute to a noncovalent interaction, specifically to a simple case study of noncovalent interactions. This type of information is of interest for modeling these interactions to understand the structure and assist in the formulation of the molecular dynamics for the enormous variety of phenomena in which the hydrogen bond plays a major role. Extensions of these measurements to systems consisting of water and simple molecules are in progress.

The two systems water–helium and water–argon can be considered as best characterized, also with regard to potential anisotropies. This information opens perspectives for producing and analyzing collisional alignment phenomena in supersonic seeded molecular beams of water. This should be in line with our previous work with diatomic molecules,[23–25] benzene,[26,27] and C_2 hydrocarbons,[28] and would provide the ground for extending this type of measurements[10] to also probe anisotropy effects in the interactions of water.

Experimental Section

In the experimental apparatus for the measurement of total scattering cross sections Q (see Figure 1), the water (or molecular oxygen) beam emerging from a nearly effusive source is detected by a quadrupole mass spectrometer.[12] Along a path of about 2 m the beam is collimated by a series of skimmers and defining slits, velocity-selected by a set of rotating slotted disks with a resolution of about 5 % (fwhm), and "attenuated" by the noble-gas target, which is confined in a scattering chamber, cooled to about 90 K to minimize effects of gas random motion.

Received: November 24, 2004
Published online: April 1, 2005

Keywords: ab initio calculations · charge transfer · hydrogen bonds · molecular beam scattering · water

[1] K. Müller-Dethlefs, P. Hobza, *Chem. Rev.* **2000**, *100*, 143–168.
[2] The standard picture—size repulsion and induction plus dispersion attraction—is commonly referred to as the van der Waals interaction (vdW).
[3] B. Guillot, *J. Mol. Liq.* **2002**, *101*, 219–260.
[4] I. V. Alabugin, M. Manoharan, S. Peabody, F. Weinhold, *J. Am. Chem. Soc.* **2003**, *125*, 5973–5987.
[5] M. P. Hodges, R. J. Wheatley, A. H. Harvey, *J. Chem. Phys.* **2002**, *116*, 1397–1405.
[6] K. Patkowski, T. Korona, R. Moszynski, B. Jeziorski, K. Szalewicz, *J. Mol. Struct. (Theochem)* **2002**, *591*, 231–243.
[7] G. Calderoni, F. Cargnoni, M. Raimondi, *Chem. Phys. Lett.* **2003**, *370*, 233–239.
[8] J. Brudermann, C. Steinbach, U. Buck, K. Patkowski, R. Moszynski, *J. Chem. Phys.* **2002**, *117*, 11166–11174.
[9] R. C. Cohen, R. J. Saykally, *J. Chem. Phys.* **1993**, *98*, 6007–6030.
[10] V. Aquilanti, D. Ascenzi, D. Cappelletti, M. de Castro, F. Pirani, *J. Chem. Phys.* **1998**, *109*, 3898–3910.
[11] D. Cappelletti, M. Bartolomei, F. Pirani, V. Aquilanti, *J. Phys. Chem. A* **2002**, *106*, 10764–10772.

 © 2005 Wiley-VCH Verlag GmbH & Co. KGaA, Weinheim

[12] The source nozzle is heated to about 600 K to avoid cluster formation[8] and to ensure that rotational excitation is large enough that spherically averaged water interactions are probed. In most experiments, heavy water (100 % isotopically pure D_2O) was used to take advantage of the much lower background noise at mass 20 rather than at 18 in the detector. The experimental range of beam velocities (0.8–2.5 km s^{-1}) corresponds to collision energy ranges of 6–56 kJ mol^{-1} for water and 10–70 kJ mol^{-1} for molecular oxygen.
[13] R. Cambi, D. Cappelletti, G. Liuti, F. Pirani, *J. Chem. Phys.* **1991**, *95*, 1852 – 1861.
[14] V. Aquilanti, D. Cappelletti, F. Pirani, *Chem. Phys.* **1996**, *209*, 299 – 311.
[15] Semiempirical evaluation[13,14] using atomic and molecular polarizabilities and the permanent dipole moment of water suggests that under the present experimental conditions, which involve water at high rotational temperature, the C_6 coefficient is accounted for to more than 90 % by dispersion forces (induced dipole/induced dipole), while induction contributions (included in the present analysis and due to permanent dipole/induced dipole) play a minor role.
[16] CCSD(T) and MRCI calculations were carried out to determine both energy and structure of the water–noble-gas systems (from He to Kr) in the neighborhood of the absolute minimum in the intermolecular interaction potential energy. The ab initio CCSD(T) method was used with several basis sets: cc-VDZ, cc-VTZ, and their augmented versions aug-cc-VDZ and aug-cc-VTZ. All geometries were optimized by using analytical gradient procedures. All structures reported correspond to fully converged geometries with gradients and displacements below the standard thresholds implemented in Gaussian 98. The multireference method MRCI was used with the aug-cc-VTZ basis set. An ample set of about 600 single potential-energy points on each surface was analyzed. Partial charges and orbital occupations, based on the natural bond orbital (NBO) scheme and partly on Mulliken analysis, have been also taken into account to cast light on the nature of the water–noble-gas interactions.
[17] E. Luzzatti, F. Pirani, F. Vecchiocattivi, *Mol. Phys.* **1977**, *34*, 1279.
[18] L. Beneventi, P. Casavecchia, G. G. Volpi, *J. Chem. Phys.* **1986**, *85*, 7011 – 7029.
[19] F. Pirani, F. Vecchiocattivi, *Chem. Phys.* **1981**, *59*, 387.
[20] A. E. Reed, L. A. Curtiss, F. Weinhold, *Chem. Rev.* **1988**, *88*, 899 – 926.
[21] Y. Tatamitani, B. Liu, J. Shimada, T. Ogata, P. Ottaviani, A. Maris, W. Caminati, J.L. Alonso, *J. Am. Chem. Soc.* **2002**, *124*, 2739 – 2743.
[22] J. L. Alonso, S. Antolinez, S. Bianco, A. Lesarri, J.C. Lopez, W. Caminati, *J. Am. Chem. Soc.* **2004**, *126*, 3244 – 3249.
[23] V. Aquilanti, D. Ascenzi, D. Cappelletti, F. Pirani, *Nature* **1994**, *371*, 399 – 402.
[24] V. Aquilanti, D. Ascenzi, D. Cappelletti, S. Franceschini, F. Pirani, *Phys. Rev. Lett.* **1995**, *74*, 2929 – 2932.
[25] V. Aquilanti, D. Ascenzi, D. Cappelletti, R. Fedeli, F. Pirani, *J. Phys. Chem. A* **1997**, *101*, 7648 – 7656.
[26] F. Pirani, M. Bartolomei, V. Aquilanti, M. Scotoni, M. Vescovi, D. Ascenzi, D. Bassi, D. Cappelletti, *Phys. Rev. Lett.* **2001**, *86*, 5035 – 5038. F. Pirani,
[27] F. Pirani, M. Bartolomei, V. Aquilanti, M. Scotoni, M. Vescovi, D. Ascenzi, D. Bassi, D. Cappelletti, *J. Chem. Phys.* **2003**, *119*, 265 – 276.
[28] V. Aquilanti, M. Bartolomei, F. Pirani, D. Cappelletti, F. Vecchiocattivi, Y. Shimizu, T. Kasai, *Phys. Chem. Chem. Phys.* **2005**, *7*, 291 – 300.

 © 2005 Wiley-VCH Verlag GmbH & Co. KGaA, Weinheim

Coupling Constants

The Origin of One-Bond C–H Coupling Constants in OCH Fragments: Not Primarily $n_O \rightarrow \sigma^*_{CH}$ Delocalization**

Gabriel Cuevas, Karina Martínez-Mayorga, María del Carmen Fernández-Alonso, Jesús Jiménez-Barbero, Charles L. Perrin,* Eusebio Juaristi, and Néstor López-Mora*

One-bond coupling constants $^1J_{CH}$ for axial bonds adjacent to oxygen or nitrogen atoms in molecules with chair conformers are smaller than for equatorial bonds. This is known as the Perlin effect[1] and is useful for assigning the stereochemistry of carbohydrates. It is generally interpreted in terms of $n_O \rightarrow \sigma^*_{CH}$ delocalization.[2] In tetrahydropyran (**1**) this corresponds to a resonance form (Figure 1) that weakens the axial C–H

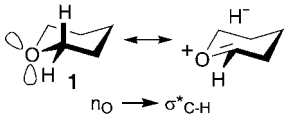

Figure 1. $n_O \rightarrow \sigma^*_{CH}$ delocalization and double bond–no bond resonance in tetrahydropyran.

[*] Dr. G. Cuevas, K. Martínez-Mayorga, N. López-Mora
Instituto de Química
Universidad Nacional Autónoma de México
Cd. Universitaria
Apdo. Postal 70213, 04510, México, D.F. (Mexico)
Fax: (+52) 55-5616-2217

Dr. C. L. Perrin
Department of Chemistry
University of California-San Diego
La Jolla, CA 92093-0358 (USA)
Fax: (+1) 858-534-2164
E-mail: cperrin@ucsd.edu

M. C. Fernández-Alonso, Dr. J. Jiménez-Barbero
Centro de Investigaciones Biológicas
Consejo Superior de Investigaciones Científicas
c/Ramiro Maetzu 9, 28040, Madrid (Spain)

Dr. E. Juaristi
Departamento de Química
Centro de Investigación y de Estudios Avanzados
del Instituto Politécnico Nacional
Apdo. Postal 14-740, 07000 México, D.F. (Mexico)
E-mail: gecgb@servidor.unam.mx

[**] K.M.M. acknowledges Conacyt for financial support. M.C.F.A. thanks the MECD for a fellowship. This work was supported by Conacyt grant 40390-Q. Financial support by the DGICYT is acknowledged (Grant BQU2000-1501-C01). We are grateful to the DGSCA and the CESGA for supercomputing time support. The cooperative program between the CSIC and the UNAM is also gratefully acknowledged. C.L.P. acknowledges the NSF for Grant CHE03-53091.

Supporting information for this article (separation of $^1J_{CH}$ values into Fermi contact, paramagnetic spin-orbit, and diamagnetic spin-orbit contributions; variation of d_{CH} with HCOC dihedral angle; coordinates of tetrahydropyran conformers) is available on the WWW under http://www.angewandte.org or from the author.

 © 2005 Wiley-VCH Verlag GmbH & Co. KGaA, Weinheim DOI: 10.1002/anie.200461583

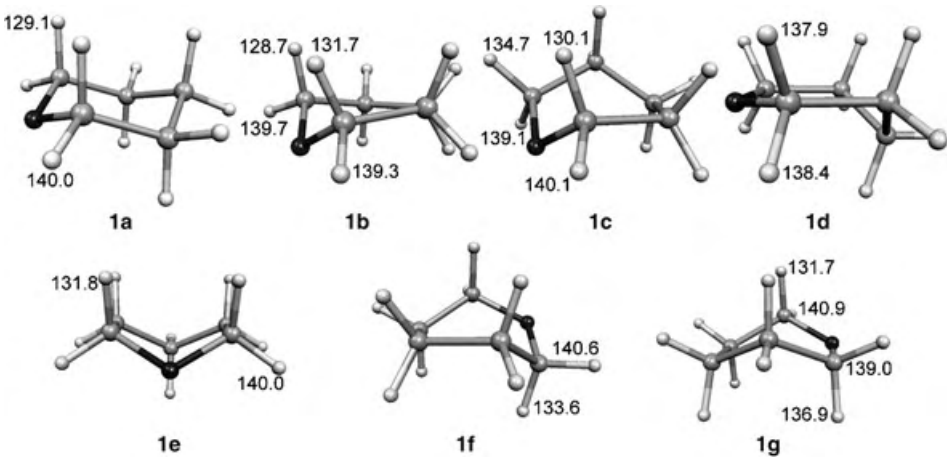

Figure 2. $^1J_{CH}$ in the conformations related by inversion of **1**.

bond and decreases the J value. Through computational analysis we have now probed the conformational dependence of ^1J values. However, we found that delocalization is not the origin of this lower J value, and we propose an alternative explanation.

Recently, the conformational inversion of **1** was monitored through a series of stationary states with different orientations of 2-H relative to the lone pairs of electrons.[3] Figure 2 shows these structures, including transition states **1b** and **1d**, derived from the chair **1a**, as well as transition states **1e** and **1g** for topomerization of skewed boats **1c** and **1f**. These allow the calculation of CH coupling constants and C–H bond lengths at C2 and the determination of how these depend on the 2-H–C2–O1–C6 dihedral angle τ. Calculations were also performed on ethyl methyl ether (**2**) and dimethyl ether (**3**).

Conformations were optimized and characterized at the B3LYP/6-311++G(*2d,2p*) level with Gaussian 94,[4] which includes NBO analyses.[5] The density-functional calculation of coupling constants was performed by using the approach of Malkin et al.[6] at the BP/IGLO-III//B3LYP/6-311++G(*2d,2p*) level.[7]

We had fully expected that $^1J_{CH}$ would be minimum at $\tau = 60$ or 90°. Instead, we found that $^1J_{CH}$ decreases continually from its maximum near 180° and approaches a minimum near 0°. The variations in the coupling constants and C–H bond lengths of **1** with dihedral angle are reported in Table 1. The

Table 1: Coupling constants and C–H bond lengths in tetrahydropyran conformations.

Conf.	τ_{HCOC} [°]	$^1J_{CH}$ [Hz]	d_{CH} [Å]	Conf.	τ_{HCOC} [°]	$^1J_{CH}$ [Hz]	d_{CH} [Å]
1a	62.5	129.1	1.100	**1d**	112.5	137.8	1.094
1a	178.6	140.0	1.089	**1d**	133.2	138.4	1.092
1b	63.9	131.7	1.098	**1e**	63.7	131.8	1.097
1b	179.1	139.3	1.088	**1e**	170.2	140.0	1.088
1b	49.0	128.7	1.099	**1f**	152.2	140.5	1.090
1b	165.3	139.7	1.089	**1f**	92.3	133.6	1.097
1c	86.1	134.7	1.097	**1g**	172.7	140.8	1.089
1c	158.2	139.1	1.090	**1g**	71.9	131.7	1.097
1c	53.3	130.1	1.097	**1g**	119.0	136.9	1.095
1c	169.1	140.1	1.088	**1g**	125.5	139.0	1.093

dominant contribution to $^1J_{CH}$ is the Fermi contact term, and the spin-orbit contributions are not only negligible but hardly depend on τ (Supporting Information). Figure 3a shows the variation of $^1J_{CH}$ with τ. Three-term Fourier analysis gives Equation (1) (correlation coefficient $r = 0.984$), which is superimposed on the figure.

$$^1J_{CH} = 133.63 - 7.321\cos\tau - 0.880\cos 2\tau \quad (1)$$

The dependence of $^1J_{CH}$ for the pro-*R* and pro-*S* hydrogen atoms of **2** is reported in Table 2

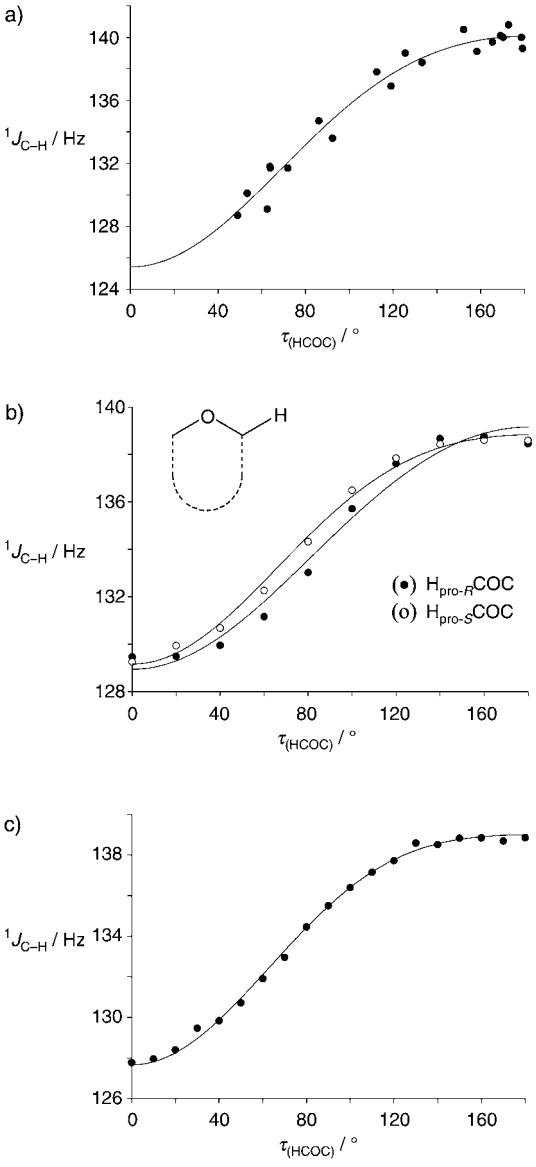

Figure 3. Variation of $^1J_{CH}$ (Hz) with dihedral angle: a) **1**; b) ethyl methyl ether; c) dimethyl ether.

 © 2005 Wiley-VCH Verlag GmbH & Co. KGaA, Weinheim

Table 2: Coupling constants and C–H bond lengths for the pro-*R* and pro-*S* hydrogen atoms in ethyl methyl ether. The dihedral angle restricted was $H_{pro\text{-}S}COC$ or $H_{pro\text{-}R}COC$, respectively.

τ_{HCOC} [°]	$^1J_{CH}$ [Hz][a]	$^1J_{CH}$ [Hz][b]	d_{CH} [Å][a]	d_{CH} [Å][b]
0	129.46	129.25	1.0992	1.0992
20	129.49	129.94	1.1000	1.1007
40	129.95	130.68	1.1023	1.1029
60	131.16	132.26	1.1039	1.1040
80	133.02	134.32	1.1039	1.1020
100	135.71	136.49	1.1026	1.1015
120	137.61	137.84	1.0998	1.0991
140	138.67	138.43	1.0967	1.0969
160	138.75	138.60	1.0951	1.0947
180	138.46	138.59	1.0947	1.0954

[a] Pro-*R* hydrogen atom. [b] Pro-*S* hydrogen atom.

and shown in Figure 3b. Fitting gave Equation (2) ($r = 0.991$), which is superimposed on the figure. Table 3, Figure 3c, and Equation (3) ($r = 0.998$) show $^1J_{CH}$ for **3**. All of these are very

$$^1J_{CH} = 134.48 - 4.969\cos\tau - 0.459\cos 2\tau \quad (2)$$

$$^1J_{CH} = 134.41 - 5.657\cos\tau - 1.070\cos 2\tau \quad (3)$$

similar, but the last two give rise to J values at dihedral angles τ near 0°.

Deletion energies obtained by NBO (natural bond orbital) analysis can identify stereoelectronic interactions.[8] The lone pairs of electrons on the oxygen atom do not occupy sp^3 hybrid orbitals, but n_p and n_s orbitals. Figure 4 shows the separate and total dependence of $n_p \rightarrow \sigma^*_{CH}$ and $n_s \rightarrow \sigma^*_{CH}$ delocalizations on τ in **1** and **2**. Since electrons in the n_s orbital are held more tightly, $n_p \rightarrow \sigma^*_{CH}$ delocalization is stronger. Fourier analysis is given for **1** in Equations (4)–(6)

$$E_p = 4.28 + 0.22\cos\tau - 4.18\cos 2\tau \quad (4)$$

$$E_s = 1.50 - 0.26\cos\tau + 0.86\cos 2\tau \quad (5)$$

$$E_{total} = 6.12 + 0.70\cos\tau - 2.54\cos 2\tau \quad (6)$$

($r = 0.997$, 0.70, 0.996, respectively). For **2** the coefficients are similar. The fittings are superimposed on the figures.

The largest angle-dependent coefficient is 4.18 for n_p, consistent with the above assertion that n_p is more delocalized. Moreover, this is for the $\cos 2\tau$ term. This is exactly the behavior expected from n_p since either lobe can overlap with σ*.

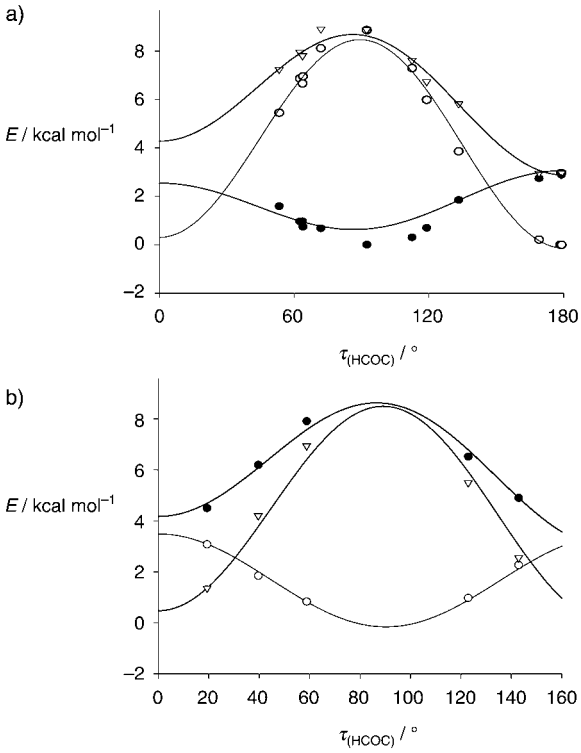

Figure 4. Dependence on dihedral angle of strength of $n_p \rightarrow \sigma^*_{CH}$ (○), $n_s \rightarrow \sigma^*_{CH}$ (●), and $n_s + n_p \rightarrow \sigma^*_{CH}$ ∗ (△) delocalizations in a) **1**, b) ethyl methyl ether.

The variations in C–H bond lengths in **1**, **2** (pro-*R* and pro-*S*), and **3** with τ can be fit to Equations (7)–(9) ($r = 0.982$, 0.971, 0.986, respectively; see Supporting Information). As reported previously[7] there is no correlation between d and J.

$$d_{CH} = 1.095 + 0.0044\cos\tau - 0.0020\cos 2\tau \quad (7)$$

$$d_{CH} = 1.100 + 0.0029\cos\tau - 0.0029\cos 2\tau \quad (8)$$

$$d_{CH} = 1.098 + 0.0032\cos\tau - 0.0030\cos 2\tau \quad (9)$$

All the data are scattered because energy minimization is imperfect (as demonstrated by different results in Table 3 from identical structures) and because J and d do not depend only on the dihedral angle (as demonstrated by different results in Table 2 from pro-*R* and pro-*S* hydrogen atoms and by differences among **1**–**3** arising from steric or torsional effects on the COC angle).

In chair conformer **1a** the dihedral angles are 62.5° and 178.6°. The $C–H_{ax}$ bond is antiperiplanar to a lone pair, permitting $n_O \rightarrow \sigma^*_{CH}$ delocalization and a decrease in J. Indeed, the calculated $^1J_{CH_{ax}}$ (129.1 Hz) is lower than the $^1J_{CH_{eq}} =$ 140.0 Hz. Thus the Perlin effect can be

Table 3: Coupling constants and C–H bond lengths in dimethyl ether.

$\lvert\tau_{HCOC}\rvert$ [°]	$^1J_{CH}$ [Hz][a]	$^1J_{CH}$ [Hz][b]	d_{CH} [Å]	$\lvert\tau_{HCOC}\rvert$ [°]	$^1J_{CH}$ [Hz][a]	$^1J_{CH}$ [Hz][b]	d_{CH} [Å]
0	127.78	127.78	1.0975	100	136.40	136.56	1.1000
10	127.96	127.89	1.0978	110	137.15	137.30	1.0988
20	128.40	128.19	1.0986	120	137.72	137.87	1.0975
30	129.47	128.91	1.0997	130	138.59	139.25	1.0962
40	129.84	129.73	1.1008	140	138.51	138.60	1.0950
50	130.72	130.77	1.1017	150	138.83	138.90	1.0940
60	131.91	132.13	1.1021	160	138.85	138.75	1.0932
70	132.96	133.00	1.1020	170	138.69	138.61	1.0927
80	134.46	134.28	1.1016	180	138.86	138.86	1.0926
90	135.50	135.34	1.1009				

[a] $\tau > 0$. [b] $\tau < 0$.

 © 2005 Wiley-VCH Verlag GmbH & Co. KGaA, Weinheim

reproduced computationally. Moreover, in transition state **1d** τ increases to 112.5° or 133.3°, neither of which is favorable to delocalization, and J increases. In conformer **1c** the hydrogen atom that is antiperiplanar to a lone pair of electrons shows $J = 130.1$ Hz, whereas the hydrogen atoms on the other methylene group show higher a J value. Similar analyses would appear to explain the other coupling constants.

Although $^1J_{CH}$ in **1a** is lower at 60° than at 180°, consistent with delocalization of an antiperiplanar lone pair of electrons, that lone pair occupies an sp^3 hybrid, whereas the strongest $n_O \rightarrow \sigma^*_{CH}$ delocalization, according to Equation (4), is with the p orbital. Figure 5 shows the overlap between that orbital and

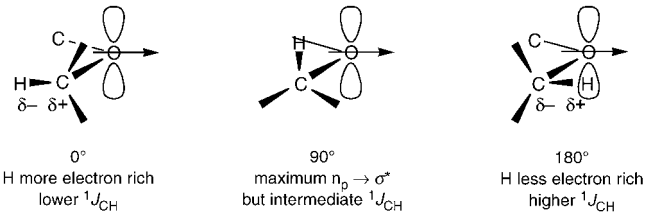

Figure 5. Variation with dihedral angle of the overlap between the n_p orbital and the C–H bond and of the C–H dipole induced by electrostatic interaction with the oxygen dipole.

the C–H at dihedral angles of 0, 90, and 180°. It follows that delocalization should be maximum at 90°, and J should be minimum at this angle. Instead the data in Figure 3a are monotonic, with intermediate J at intermediate τ, including $J = 134.7$ Hz and 133.6 at $\tau = 86°$ or 92°.

Tables 2 and 3 show further contradictions, apparent in acyclic ethers. Although the maximum $n_O \rightarrow \sigma^*_{CH}$ delocalization and minimum $^1J_{CH}$ ought to be at $\tau = 90°$, again the data are monotonic. The minimum $^1J_{CH}$ value occurs at an angle near 0°, when the C–H bond is not antiperiplanar to any lone pair of electrons. (In agreement, $^1J_{CC}$ in ethanol was calculated to be minimum at $\tau_{CCOH} = 0°$.[9]) The minimum $n_O \rightarrow \sigma^*_{CH}$ delocalizations are at $\tau = 0°$ and 180°, where σ* is orthogonal to the n_p lone pair of electrons, as in Figure 5. At these torsion angles τ, $^1J_{CH}$ should be maximum and nearly the same at both. These expectations are very different from what is calculated!

The fittings of Equation (1)–(3) are informative. If $^1J_{CH}$ were determined by $n_O \rightarrow \sigma^*_{CH}$ delocalization, it would have paralleled E_p [Eq. (4)], with the $\cos 2\tau$ term larger. Instead the coefficients of $\cos\tau$ are the larger values. Therefore $^1J_{CH}$ is not determined predominantly by delocalization! *This is an astounding result.*

What then determines the value of $^1J_{CH}$? What parameter follows $\cos\tau$, rather than $\cos 2\tau$? We suggest a dipolar interaction. If the C–H bond interacts with the dipole moment of the lone pairs of electrons and the C–O bonds (Figure 5), the interactions at $\tau = 0°$ and 180° are opposite. This then accounts for why J at 0° and 180° are so different, and why J takes intermediate values between 60° and 120°, where delocalization would be maximum.

It would seem that a dipolar interaction cannot be significant, because the C–H bond is nonpolar. Nevertheless, the electric field of the oxygen dipole might polarize the electron distribution in the C–H bond. Indeed, the calculated electron density at H decreases from $\tau = 0°$ to $\tau = 180°$ (with a corresponding increase at O). For example, the charge at the pro-*R* H atom of **2** can be fit to $q_H = 0.207 - 0.015\cos\tau + 0.006\cos 2\tau$. Furthermore, this means that the charge at H is determined somewhat more by the dipolar interaction than by $n_O \rightarrow \sigma^*_{CH}$ delocalization.

We cannot specify how the electron-density changes affect the ^1J value. It is not through the hybridization, according to our calculations. However, an electric field is known to affect both electron density and coupling constants.[10]

The C–H bond lengths are more complicated. The lengthening of a C–H or C–O bond antiperiplanar to a lone pair of electrons is generally attributed to $n_O \rightarrow \sigma^*_{CH}$ delocalization.[11] Yet Equations (7)–(9) have nearly equal $\cos 2\tau$ and $\cos\tau$ terms. Therefore, dipolar interactions also affect the lengthening of the C–H or C–O bond, as had been suggested.[12] However, it may also be indirect, through the electron population.

In summary, the $^1J_{CH}$ value in HCOC fragments is definitely not a consequence of $n_O \rightarrow \sigma^*_{CH}$ delocalization, despite expectations, although a small contribution cannot be excluded. Instead, $^1J_{CH}$ is found to follow a $\cos\tau$ dependence, which is proposed to arise from dipolar interactions. This conclusion is not necessarily general, and further calculations are in progress on N and S analogues, along with experimental tests of $^1J_{CC}$ in ethers.

Received: August 9, 2004
Revised: December 17, 2004
Published online: March 10, 2005

Keywords: conformation analysis · coupling constants · density functional calculations · dipolar interactions · stereoelectronic effects

[1] A. S. Perlin, B. Casu, *Tetrahedron Lett.* **1969**, *10*, 2921–2924.
[2] E. Juaristi, G. Cuevas, *Tetrahedron* **1992**, *48*, 5019–5087; E. Juaristi, G. Cuevas, *The Anomeric Effect*, CRC, Boca Raton, FL, **1994**.
[3] M. C. Fernández-Alonso, J. L. Asensio, F. J. Cañada, J. Jiménez-Barbero, G. Cuevas, *ChemPhysChem* **2003**, 4, 754–757.
[4] Gaussian 94 (Revision D.4), M. J. Frisch, G. W. Trucks, M. Head-Gordon, P. M. W. Gill, M. W. Wong, J. B. Foresman, B. G. Johnson, H. B. Schlegel, M. A. Robb, E. S. Replogle, R. Gomperts, J. L. Andres, K. Raghavachari, J. S. Binkley, C. Gonzalez, R. L. Martin, D. J. Fox, D. J. Defrees, J. Baker, J. J. P. Stewart, J. A. Pople, Gaussian 94, Gaussian, Inc., Pittsburgh, PA, **1995**.
[5] E. D. Glendening, J. K. Badenhoop, A. E. Reed, J. E. Carpenter, F. Weinhold, *NBO 3.1*, Theoretical Chemistry Institute, University of Wisconsin, Madison, WI, **1994**.
[6] G. G. Malkin, O. L. Malkina, L. A. Eriksson, D. R. Salahub in *Modern Density Functional Theory. A Tool for Chemistry* (Eds.: J. M. Seminario, P. Politzer), Elsevier, Amsterdam, **1995**.
[7] G. Cuevas, A. Vela, E. Juaristi, *J. Phys. Chem. A* **1999**, *103*, 932–937.
[8] A. E. Reed, L. A. Curtiss, F. Weinhold, *Chem. Rev.* **1988**, *88*, 899; U. Salzner, *J. Org. Chem.* **1995**, *60*, 986–995; I. V. Alabugin, M.

 © 2005 Wiley-VCH Verlag GmbH & Co. KGaA, Weinheim

Manoharan, S. Peabody, F. Weinhold, *J. Am. Chem. Soc.* **2003**, *125*, 5973 – 5987.
[9] I. Carmichael, D. M. Chipman, C. A. Podlasek, A. S. Serianni, *J. Am. Chem. Soc.* **1993**, *115*, 10863 – 10870.
[10] R. J. Bartlett, J. E. Del Bene, S. A. Perera, *ACS Symp. Ser.* **2002**, *827*, 150 – 164.
[11] A. J. Briggs, R. Glenn, P. G. Jones, A. J. Kirby, P. Ramaswamy, *J. Am. Chem. Soc.* **1984**, *106*, 6200 – 6206.
[12] C. L. Perrin, K. B. Armstrong, M. A. Fabian, *J. Am. Chem. Soc.* **1994**, *116*, 715 – 722.

 © 2005 Wiley-VCH Verlag GmbH & Co. KGaA, Weinheim

Phosphorus Chemistry

Facile Synthetic Methods for the Diversification of Catena-Polyphosphorus Cations**

Neil Burford, C. Adam Dyker, and Andreas Decken*

The propensity for phosphorus to form catenated compounds is evidenced by the extensive arrays of structurally characterized polyphosphines[1,2] and homopolyatomic anions reported.[3] In contrast, comprehensively characterized polyphosphorus cations are limited to phosphinophosphonium **1**,[4–9] phosphinodiphosphonium **2**,[10] diphosphiranodiphosphonium **3**,[11] and phosphidodiphosphonium **4**[12,13] ions (Scheme 1). Nevertheless, recent and unique examples of cations **5**,[7,14] **6**,[15] **7**,[8,14,16] and **8**[17] illustrate the potential for diversification and highlight catena-polyphosphorus cations as an underexplored avenue in phosphorus chemistry. In this context, we have exploited facile reactions of polyphosphines (di, tetra, and penta species) to prepare a series of new organosubstituted diphosphinophosphonium **9** and cyclotetraphosphinophosphonium cations **10**.

The ^{31}P NMR spectra for reaction mixtures of tetramethyldiphosphane or tetraphenyldiphosphane with Me_2PCl or Ph_2PCl in the presence of $Me_3SiOSO_2CF_3$ (TMSOTf)[18] show rapid, quantitative formation of the corresponding organo-substituted catena-diphosphanophosphonium cations **9a**, **9b**, **9c**, and **9f** (Scheme 2). Derivatives of **9** can be envisaged as diphosphine ligands on phosphenium Lewis acceptors (analogous to **1**, thus representing complexes of R_3P on R'_2P^+),[7] and are structural isomers of **4**.[12] Cation **9f** is a rearrangement product of **9d** or the product of Me_2P^+ insertion into the P–P bond of Ph_2P–PPh_2. The formation of derivative **9e** was not observed. The preferred formation of **9f** over **9d** and **9c** over **9e** is likely to be a result of the steric interactions between the substituents and the relative donor (PMe_2 versus PPh_2)/acceptor (PMe_2^+ versus PPh_2^+) properties of the PR_2 units.

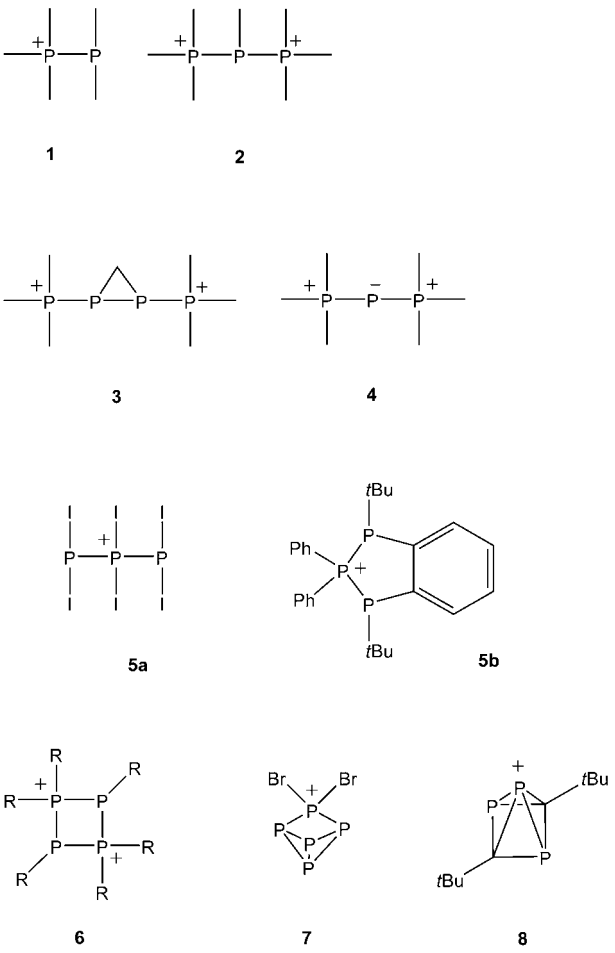

Scheme 1. Previously characterized polyphosphorus cations. ——= alkyl or aryl substituent; R = 2,6-$(OMe)_2C_6H_3$.

An unusual eclipsed/staggered (C_s) conformation is observed for the cation of **9a**-OTf (OTf = trifluoromethanesulfonate) in the solid state (Figure 1). Retention of this nonsymmetric arrangement in solution is evidenced by the slight nonequivalence ($\Delta\delta < 0.1$ ppm, $\Delta J = 11$–35 Hz) of the terminal phosphorus centers in the ^{31}P NMR spectra of **9a**, **9b**, and **9f** at 193 K (Table 1; Figure 2 shows the ^{31}P NMR spectrum of **9b**-OTf as an example). The ^{31}P NMR spectra of all derivatives of **9** at RT show broad, poorly defined triplets and doublets, thus indicating dynamic behavior that may enable rearrangement of **9d** to **9f** by dissociation to Ph_2P–PMe_2 and Ph_2P^+ (Scheme 2).

[*] Prof. N. Burford, C. A. Dyker
Department of Chemistry
Dalhousie University
Halifax, NS B3H 4J3 (Canada)
Fax: (+1) 902-494-1310
E-mail: neil.burford@dal.ca
Dr. A. Decken
Department of Chemistry
University of New Brunswick
Fredericton, NB E3B 6E2 (Canada)

[**] We thank the Natural Sciences and Engineering Research Council of Canada, the Killam Foundation, the Canada Research Chairs Program, the Canada Foundation for Innovation, the Nova Scotia Research and Innovation Trust Fund, and the Walter C. Sumner Memorial Fellowship for funding; the Atlantic Region Magnetic Resonance Centre for use of instrumentation; Dr. M. Lumsden for assistance with the NMR spectroscopic data; and Dr. P. J. Ragogna and D. E. Herbert for preliminary experimental observations.

 © 2005 Wiley-VCH Verlag GmbH & Co. KGaA, Weinheim DOI: 10.1002/anie.200462997

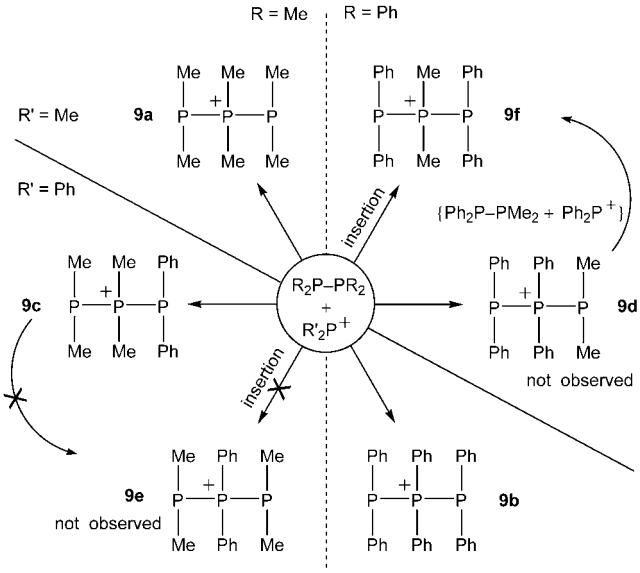

Scheme 2. Derivatives of **9** generated from the reaction of diphosphine ligands with phosphenium Lewis acceptors in the presence of R'_2PCl, TMSOTf, and $R_2P{-}PR_2$.

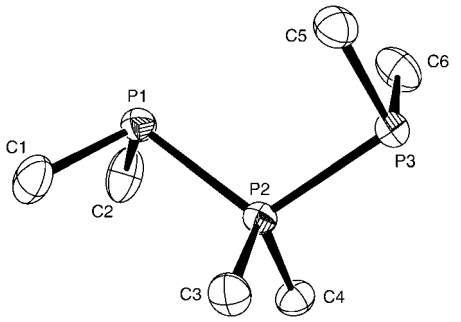

Figure 1. The solid-state structure of the cation **9a**, with thermal ellipsoids at the 50% probability level (hydrogen atoms and OTf anion are omitted). P1–P2 221.60(6), P2–P3 218.83(6) pm; P-P-P 111.56(3)°.

The ^{31}P NMR spectra for equimolar mixtures of R_2PCl and TMSOTf with $(PhP)_4$ or $(PhP)_5$ [Eqs. (1) and (2);

$$(PhP)_4 + R_2PCl + TMSOTf \rightarrow \mathbf{10a,b}\text{-OTf} + TMSCl \quad (1)$$

$$4\,(PhP)_5 + 5\,R_2PCl + 5\,TMSOTf \rightarrow 5\,\mathbf{10a,b}\text{-OTf} + 5\,TMSCl \quad (2)$$

TMS = trimethylsilyl; **10a**: R = R′Ph, **10b**: R = R′ = Me] demonstrate quantitative formation of the corresponding cyclotetraphosphanophosphonium triflate salts **10a**-OTf or **10b**-OTf (Figure 3). The solid-state structure of the cation **10a** is shown in Figure 4. Although complicated, the ^{31}P NMR solution spectra for the derivatives of **10** exhibit a low-field tripletlike signal that is assigned to a phosphonium center and is distinct from a multiplet that corresponds to the four phosphine centers (Figure 3a, b). The exclusive formation of **10a** and **10b** from either $(PhP)_4$ or $(PhP)_5$ demonstrates a thermodynamic preference for the five-membered framework over the hexaphosphorus or pentaphosphorus alternatives **11** and **12** (Scheme 3) and is consistent with the prominence of the cyclopentaphosphorus unit in Hittorf's phosphorus,[19] polyphosphines, and polyphosphorus anions.[3]

Pentaphosphorus cations of type **10** were first proposed on the basis of elemental analysis data for the alkylation products of cyclopentaphosphines.[20,21] This prompted us to exploit the methylation of penta-, tetra-, and diphosphines as an alternative and facile route to phosphinophosphonium cations. New derivatives of **1** were readily observed by ^{31}P NMR spectroscopic analysis as quantitative products (see, **1a**-OTf

Table 1: ^{31}P NMR data for polyphosphines and derivatives of **1**, **2**, **4**, **5**, **9**, and **10**. P_A refers to the phosphonium center(s) and P_B refers to the phosphine center(s) (phosphide center for **4**). New compounds were observed in CH_2Cl_2, and salts contain OTf anions unless otherwise stated.

Compound	$^{31}P_A$ [δ]	$^{31}P_B$ [δ]	$J_{P,P}$ [Hz]	Ref.
$(PhP)_5$		−3[b]	[b]	[22]
$(PhP)_4$		−48	N/A	[24]
$Ph_2P{-}PPh_2$		−14	N/A	[25]
1a $(Me_3P{-}PMe_2)^+$	18	−60	275	[i]
1b $(MePh_2P{-}PPh_2)^+$	15	−18	375	[i]
1c $(Ph_3P{-}PPh_2)^+$	15	−10	340	[7]
1d $(Me_3P{-}PPh_2)^+$	15	−23	289	[7]
1e $(I_3P{-}PI_2)$ (A)[a]	−156	126	[c]	[8]
2 $(Ph_3P{-}PH{-}PPh_3)(AlCl_4)_2$	23	−120	286	[10]
4 $(Ph_3P{-}P{-}PPh_3)(AlCl_4)$	30	−174	502	[12]
5a $(I_2P{-}PI_2{-}PI_2)$ (A)[a]	−5	89	386	[14]
9a $(Me_2P{-}PMe_2{-}PMe_2)^+$[d]	12	−58[f]	303, 292	[i]
9b $(Ph_2P{-}PPh_2{-}PPh_2)^+$[e]	18	−22[f]	365, 335	[i]
9c $(Me_2P{-}PMe_2{-}PPh_2)^+$[e]	8	−52[g], −28[h]	331[g], 296[h]	[i]
9f $(Ph_2P{-}PMe_2{-}PPh_2)^+$[d]	5	−20	357, 313	[i]
10a $(Ph_6P_5)^+$	22[b]	−38[b]	[b]	[i]
10b $(Ph_4Me_2P_5)^+$	26[b]	−29[b]	[b]	[i]
10c $(Ph_5MeP_5)^+$	21[b]	−30[b]	[b]	[i]

[a] [A] = $[((F_3C)_3CO)_3AlFAl(OC(CF_3)_3)_3]$; measured at 183 K. [b] Complex multiplet. [c] Not observed at 183 K. [d] Measured at 220 K, $CDCl_3$. [e] Measured at 193 K. [f] Two signals with $\Delta\delta < 0.1$ ppm. [g] PPh_2 group. [h] PMe_2 group. [i] This work.

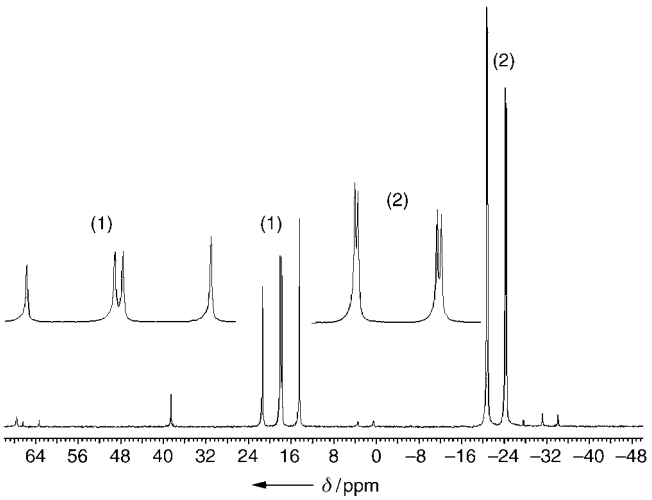

Figure 2. The ^{31}P NMR spectrum for the reaction mixture of Ph_4P_2, Ph_2PCl, and TMSOTf (formation of **9b**-OTf) at 193 K. Signal (1) corresponds to the central P atom, which is coupled to the two nonequivalent terminal P centers responsible for the two doublets labeled (2).

 © 2005 Wiley-VCH Verlag GmbH & Co. KGaA, Weinheim

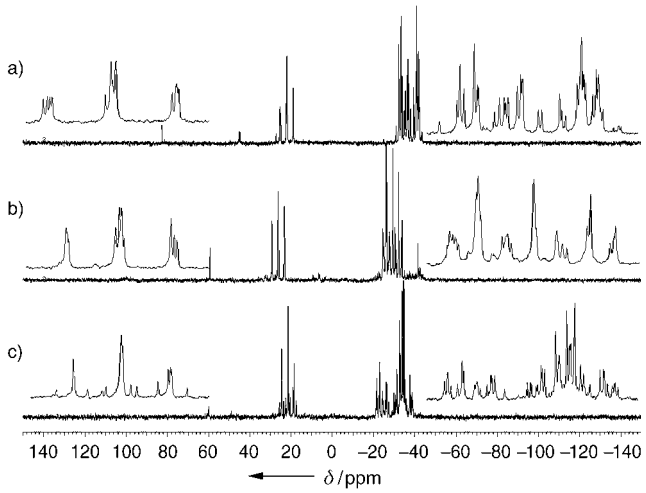

Figure 3. The ^{31}P NMR spectra (RT) for the reaction mixtures of: a) $(PhP)_5$, Ph_2PCl, and TMSOTf (quantitative formation of **10a**-OTf); b) $(PhP)_5$, Me_2PCl, and TMSOTf (quantitative formation of **10b**-OTf); c) $(PhP)_5$ and MeOTf (quantitative formation of **10c**-OTf; see Experimental Section for stoichiometry). Essentially identical spectra were observed for analogous reactions of $(PhP)_4$.

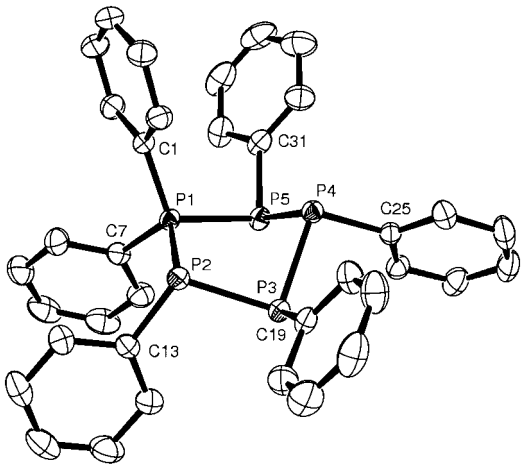

Figure 4. The solid-state structure of the cation **10a**, with thermal ellipsoids at the 50% probability level (hydrogen atoms and OTf anion are omitted). P–P bond lengths range from 220.72(6) to 223.92(6) pm, P-P-P angles range from 89.56(2) to 96.52(2)°.

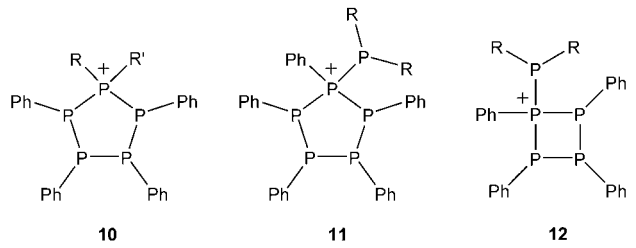

Scheme 3. Cyclotetraphosphinophosphonium triflate salts **10** and the hexaphosphorus or pentaphosphorus alternatives **11** and **12**. **10a**: R = R′ = Ph, **10b**: R = R′ = Me, **10c**: R = Me, R′ = Ph; **11**,**12**: R = Me or Ph.

and **1b**-OTf [Eq. (3)] compared to $(Ph_3P–PPh_2)$OTf (**1c**-OTf) and $(Me_3P–PPh_2)$OTf (**1d**-OTf);[7] Table 1) in equimolar

1a R = Me
b R = Ph

mixtures of Me_2PPMe_2 or Ph_2PPPh_2 with methyltrifluoromethanesulfonate (MeOTf). Both the cyclophosphines $(PhP)_4$ and $(PhP)_5$ react rapidly with an excess of MeOTf according to Equations (4) and (5), respectively, to give **10c**, as shown by

$$5\,(PhP)_4 + 4\,TMSOTf \rightarrow 4\,\mathbf{10c}\text{-OTf} \quad (4)$$

$$(PhP)_5 + 4\,MeOTf \rightarrow \mathbf{10c}\text{-OTf} \quad (5)$$

^{31}P NMR spectroscopic analysis of the reaction mixtures (Figure 3c), which further highlights the thermodynamic preference for the framework of **10**.

In summary, facile association of diphosphines with phosphenium ions represents a general and versatile synthetic method for new organodiphosphinophosphonium cations **9**, which are isomers of phosphidodiphosphonium **4**. Similar reactions involving cyclotetra- or cyclopentaphosphines result in the exclusive formation of cyclotetraphosphinophosphonium cations **10**. We anticipate further application of these synthetic methods will result in the efficient and diverse development of catena-polyphosphorus cations.

Experimental Section

All operations were carried out in an N_2 atmosphere. Caution: Phosphine reagents have a pungent odor and $Me_2P–PMe_2$ is pyrophoric. The ^{31}P NMR data presented in Table 1 were obtained within 40 min of mixing the colorless reaction mixtures and show quantitative formation of: **1a**-OTf and **1b**-OTf from equimolar quantities of MeOTf (0.10 mmol) and $R_2P–PR_2$ (0.10 mmol); **9f**-OTf from PMe_2Cl (0.37 mmol), TMSOTf (0.44 mmol), and $Ph_2P–PPh_2$ (0.37 mmol); **10c**-OTf from MeOTf (0.46 mmol) and $(PPh)_5$[26] (0.093 mmol). **9c**-OTf was observed in high yield from Ph_2PCl (0.093 mmol), TMSOTf (0.11 mmol), and Me_2PPMe_2 (0.093 mmol) with **9a**-OTf as a minor product. Spectra for other derivatives were obtained from the samples described below. Spectra for reactions of $(PPh)_4$[24] with PPh_2Cl/TMSOTf, PMe_2Cl/TMSOTf, or MeOTf were obtained from samples containing tetraphosphine as the limiting reagent.

9a-OTf: Me_2PCl (0.37 mmol) was added to TMSOTf (0.44 mmol) in CH_2Cl_2 (6 mL) followed by $Me_2P–PMe_2$ (0.37 mmol). Vapor diffusion of diethyl ether into the reaction mixture at −28 °C caused crystallization; yield = 0.076 g (0.23 mmol, 62%). Decomp. 44–65 °C; elemental analysis (%) for $C_7H_{18}F_3O_3P_3S$: C 25.3, H 5.5; found: C 25.2, H 5.2; ^{1}H NMR (250.1 MHz, $CDCl_3$, 220 K): δ = 2.0 (d, J(P,H) = 13 Hz, 1H), 1.5 ppm (d, J(P,H) = 18 Hz, 2H); FTIR (nujol (ranked intensities)): $\tilde{\nu}$ = 1314 (8), 1302 (7), 1260 (1), 1224 (3), 1154 (4), 1031 (2), 977 (11), 934 (12), 892 (6), 638 (5), 573 (10), 517 (9) cm^{-1}.

9b-OTf: Ph_2PCl (0.28 mmol) was added to TMSOTf (0.33 mmol) in C_6H_5F (1 mL) followed by $Ph_2P–PPh_2$ (0.28 mmol) in C_6H_5F (1 mL). Slow diffusion of diethyl ether into the filtered solution at −28 °C afforded a white solid, which was washed with diethyl ether

 © 2005 Wiley-VCH Verlag GmbH & Co. KGaA, Weinheim

(2 × 3 mL); yield = 0.127 g (0.18 mmol, 64 %). M.p. 138–142 °C; elemental analysis (%) calcd for $C_{37}H_{30}F_3O_3P_3S$: C 63.1, H 4.3; found: C 62.2, H 4.2; FTIR (nujol, (ranked intensities)): $\tilde{\nu}$ = 1264 (1), 1223 (2), 1149 (7), 1090 (11), 1030 (6), 742 (4), 691 (3), 636 (5), 570 (10), 515 (9), 450 (8) cm^{-1}.

10a-OTf: Ph_2PCl (0.25 mmol) was added to TMSOTf (0.30 mmol) in CH_2Cl_2 (2 mL) followed by $(PhP)_5$[26] (0.185 mmol) in CH_2Cl_2 (2 mL). The solvent was removed in vacuo and the solid washed with hexane (2 × 4 mL); yield = 0.123 g (0.16 mmol, 87 %). Decomp. 65–75 °C; elemental analysis (%) calcd for $C_{37}H_{30}F_3O_3P_5S$: C 58.0, H 3.9, P 20.2; found: C 57.4, H 3.9, P 20.4; ^{1}H NMR (250.1 MHz, $CDCl_3$, 298 K): complex multiplets δ = 7.2–7.9 ppm; FTIR (nujol (ranked intensities)): $\tilde{\nu}$ = 1312 (11), 1263 (1), 1146 (6), 1093 (8), 1029 (2), 997 (9), 843 (7), 740 (3), 687 (5), 635 (4), 570 (12), 517 (10) cm^{-1}.

10b-OTf: Me_2PCl (0.185 mmol) was added to TMSOTf (0.22 mmol) in CH_2Cl_2 (2 mL), and this solution was added to $(PhP)_5$[26] (0.093 mmol). Filtration and slow diffusion of diethyl ether vapor into the solution at −28 °C caused precipitation; yield = 0.027 g (0.042 mmol, 45 %). M.p. 142–145 °C; elemental analysis (%) calcd for $C_{27}H_{26}F_3O_3P_5S$: C 50.5, H 4.1; found: C 49.4, H 3.6; ^{1}H NMR (250.1 MHz, $CDCl_3$, 298 K): complex multiplets δ = 1.8–1.9 ppm, 7.4–7.9 ppm; FTIR (nujol (ranked intensities)): $\tilde{\nu}$ = 1304 (8), 1288 (1), 1247 (2), 1150 (7), 1032 (3), 958 (10), 918 (9), 733 (4), 691 (5), 638 (6), 572 (13), 516 (12), 465 (11) cm^{-1}.

X-ray crystallography: Data collection on Bruker AXS P4/SMART 1000 diffractometer by using ω and θ scans with a width of 0.3° and 10 s (**9a**-OTf) or 30 s (**10a**-OTf) exposure times with a detector distance of 5 cm. The data were reduced (SAINT)[27] and corrected for absorption (SADABS).[28] Structures were solved by direct methods and refined by full-matrix least squares on F^2-(SHELXL).[29] All nonhydrogen atoms were refined anisotropically. **9a**-OTf: $C_7H_{18}F_3O_3P_3S$; colorless, irregular, crystal size 0.60 × 0.15 × 0.15 mm; monoclinic, space group $P2_1/c$, a = 11.9395(8), b = 11.3475(7), c = 12.3165(8) pm, β = 115.818(1)°, V = 1502.1(2), Z = 4, μ = 0.561 mm^{-1}; $\lambda(Mo_{K\alpha})$ = 0.71073 Å, T = 173 K, $2\theta_{max}$ = 53.5°, collected (independent) reflections = 10152 (3362), R_{int} = 0.0210; 226 refined parameters, R_1 = 0.0323, wR_2 = 0.0796 for reflections with $I > 2\sigma(I)$, max/min residual electron density = 0.543/−0.455 e $Å^{-3}$. **10a**-OTf: $C_{37}H_{30}F_3O_3P_5S$; colorless rod, crystal size 0.60 × 0.20 × 0.10 mm; monoclinic, space group $P2_1/c$, a = 10.6004(6), b = 16.7110(8), c = 20.601(1) pm, β = 92.255(1)°, V = 3550.8(3), Z = 4, μ = 0.369 mm^{-1}; $\lambda(Mo_{K\alpha})$ = 0.71073 Å, T = 198 K, $2\theta_{max}$ = 53.4°, collected (independent) reflections = 23629 (7915), R_{int} = 0.0232; 562 refined parameters, R_1 = 0.0343, wR_2 = 0.0861 for reflections with $I > 2\sigma(I)$, max/min residual electron density = 0.432/−0.421 e $Å^{-3}$.

Received: December 20, 2004
Revised: January 14, 2005
Published online: March 10, 2005

Keywords: cations · donor–acceptor systems · phosphines · phosphorus

[1] M. Baudler, K. Glinka, *Chem. Rev.* **1994**, *94*, 1273 – 1297.
[2] M. Baudler, K. Glinka, *Chem. Rev.* **1993**, *93*, 1623 – 1667.
[3] M. Baudler, *Angew. Chem.* **1987**, *99*, 429 – 451; *Angew. Chem. Int. Ed.* **1987**, *26*, 419 – 441.
[4] C. W. Schultz, R. W. Parry, *Inorg. Chem.* **1976**, *15* 3046 – 3050.
[5] N. Burford, T. S. Cameron, P. J. Ragogna, E. Ocando-Mavarez, M. Gee, R. McDonald, R. E. Wasylishen, *J. Am. Chem. Soc.* **2001**, *123,* 7947 – 7948.
[6] N. Burford, T. S. Cameron, D. J. LeBlanc, P. Losier, S. Sereda, G. Wu, *Organometallics* **1997**, *16*, 4712 – 4717.
[7] N. Burford, P. J. Ragogna, R. McDonald, M. Ferguson, *J. Am. Chem. Soc.* **2003**, *125*, 14404 – 14410.
[8] M. Gonsior, I. Krossing, L. Mueller, I. Raabe, M. Jansen, L. van Wuellen, *Chem. Eur. J.* **2002**, *8*, 4475 – 4492.
[9] F. Sh. Shagvaleev, T. V. Zykova, R. I. Tarasova, T. Sh. Sitdikova, V. V. Moskva, *Zh. Obshch. Khim.* **1990**, *60*, 1775 – 1779.
[10] A. Schmidpeter, S. Lochschmidt, K. Karaghiosoff, W. S. Sheldrick, *J. Chem. Soc. Chem. Commun.* **1985**, 1447 – 1448.
[11] S. Lochschmidt, G. Muller, B. Huber, A. Schmidpeter, *Z. Naturforsch. B* **1986**, *41*, 444 – 454.
[12] A. Schmidpeter, S. Lochschmidt, W. S. Sheldrick, *Angew. Chem.* **1985**, *97*, 214 – 215; *Angew. Chem. Int. Ed.* **1985**, *24*, 226 – 227.
[13] A. Schmidpeter, S. Lochschmidt, *Angew. Chem.* **1986**, *98*, 271 – 273; *Angew. Chem. Int. Ed.* **1986**, *25*, 253 – 254.
[14] I. Krossing, *J. Chem. Soc. Dalton Trans.* **2002**, 500 – 512.
[15] L. Heuer, L. Ernst, R. Schmutzler, D. Schomburg, *Angew. Chem.* **1989**, *101*, 1549 – 1550; *Angew. Chem. Int. Ed.* **1989**, *28*, 1507 – 1509.
[16] I. Krossing, I. Raabe, *Angew. Chem.* **2001**, *113*, 4544 – 4547; *Angew. Chem. Int. Ed.* **2001**, *40*, 4406 – 4409.
[17] J. M. Lynam, M. C. Copsey, M. Green, J. C. Jeffrey, J. E. McGrady, C. A. Russell, J. M. Slattery, A. C. Swain, *Angew. Chem.* **2003**, *115*, 2884 – 2888; *Angew. Chem. Int. Ed.* **2003**, *42*, 2778 – 2782.
[18] Equimolar combinations of R'_2PCl with TMSOTf show (^{31}P NMR) only the presence of R'_2PCl; complexes of R'_2P^+ are only observed in the presence of a halide abstactor (for example, TMSOTf) and a Lewis base.
[19] H. Thurn, H. Krebs, *Acta Crystallogr. Sect. B* **1969**, *25*, 125 – 134.
[20] R. Appel, R. Milker, *Z. Anorg. Allg. Chem.* **1975**, *417*, 161 – 170.
[21] K. Issleib, C. Rockstroh, I. Duchek, E. Fluck, *Z. Anorg. Allg. Chem.* **1968**, *360*, 77 – 87.
[22] P. R. Hoffman, K. G. Caulton, *Inorg. Chem.* **1975**, *14*, 1997 – 1999.
[23] T. L. Breen, D. W. Stephan, *Organometallics* **1997**, *16*, 365 – 369.
[24] A. Dashti-Mommertz, B. Neumüller, *Z. Anorg. Allg. Chem.* **1999**, *625*, 954 – 960.
[25] H. Grutzmacher, J. Geier, H. Schönberg, M. Scherer, D. Stein, S. Boulmaaz, International Patent No. 050668, **2004**, .
[26] SAINT 6.02, Bruker AXS, Inc., Madison, Wisconsin, USA, **1997–1999**.
[27] SADABS George Sheldrick, Bruker AXS, Inc., Madison, Wisconsin, USA, **1999**.
[28] SHELXTL 6.14, Bruker AXS, Inc., Madison, Wisconsin, USA, **2000–2003**.

 © 2005 Wiley-VCH Verlag GmbH & Co. KGaA, Weinheim

Synthetic Methods

Cobalt-Catalyzed *syn* Hydrophosphination of Alkynes**

*Hirohisa Ohmiya, Hideki Yorimitsu, and Koichiro Oshima**

Organophosphorus compounds play vital roles in various fields of chemistry, for example, as synthetic reagents, ligands for transition-metal complexes, biologically active substances, advanced materials, and building blocks of supramolecular assemblies. Hydrophosphination, the addition of trivalent phosphine compounds to carbon–carbon multiple bonds, is a straightforward method for the synthesis of organophosphorus compounds.[1] In contrast to the ready availability of hydrophosphonylation reactions wherein pentavalent phosphorus compounds are involved,[2] hydrophosphination by metal catalysis often encounters difficulties. Lanthanide complexes catalyze hydrophosphinations with superb efficiency.[3] However, the catalytic system requires synthetic organic chemists to prepare intricate and highly air- and moisture-sensitive metal complexes. Although palladium- and nickel-catalyzed reactions have been reported, the scope of the alkynes available for use is limited.[4–6] Moreover, the stereoselectivity of reactions catalyzed by lanthanide and Group 10 reagents are highly substrate-dependent. The development of a facile, efficient, and general hydrophosphination reaction has been awaited. Herein, we report such a hydrophosphination reaction in the presence of a cobalt salt.[7] The reaction proceeded in a completely *syn* fashion, which is therefore complementary to *anti* selective radical hydrophosphination reactions.[8]

Treatment of diphenylphosphane (1.0 mmol) in THF (1.0 mL) with butyllithium (0.20 mmol) yielded an orange mixture of lithium diphenylphosphide and diphenylphosphane. $[Co(acac)_2]$ (acac = acetylacetonate; 0.10 mmol), dioxane (3 mL), and 6-dodecyne (**1a**; 1.0 mmol) were added to the mixture. The resulting black mixture was heated at reflux for two hours to provide the corresponding *syn* adduct **2a** quantitatively after sulfidation[9] (Table 1, entry 1). The free alkenyldiphenylphosphane is relatively insensitive to oxygen so we could isolate 1-pentyl-1-heptenyldiphenylphosphane (**4**) in 80% yield on a 10-mmol scale without special care being required in its isolation and subsequent handling (Scheme 1).

Table 1: Cobalt-catalyzed *syn* hydrophosphination of alkynes.

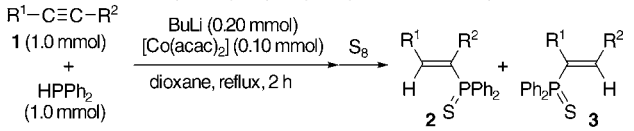

Entry	R^1	R^2	**1a–m**	Yield [%][a]	**2a–m**/**3a–m**[a]
1	C_5H_{11}	C_5H_{11}	**1a**	100 (89)	–
2	C_5H_{11}	Me	**1b**	100 (82)	66:34
3	Ph	Me	**1c**	85 (74)	82:18
4	*p*-$MeOC_6H_4$	Me	**1d**	82 (79)	82:18
5	*p*-FC_6H_4	Me	**1e**	85 (82)	80:20
6[b]	*o*-$MeOC_6H_4$	Me	**1f**	49 (41)	80:20
7	$C_{10}H_{21}$	H	**1g**	93 (83)	71:29
8	tC_4H_9	H	**1h**	87 (81)	100:0
9[b]	$(PhCH_2)_2NCH_2$	H	**1i**	54 (42)	100:0
10[c]	Ph	H	**1j**	72 (70)	89:11
11[c]	*p*-$MeOC_6H_4$	H	**1k**	76 (72)	90:10
12	*p*-$H_2NC_6H_4$	H	**1l**	53 (49)	95:5
13[c]	Et_3Si	H	**1m**	69 (62)	94:6

[a] Yields were determined by ^1H NMR spectroscopic analysis with dibenzyl ether as an internal standard. Yields of isolated product are given in parentheses. [b] Reaction was carried out over 12 h. [c] Diphenylphosphane (1.5 mmol) was used.

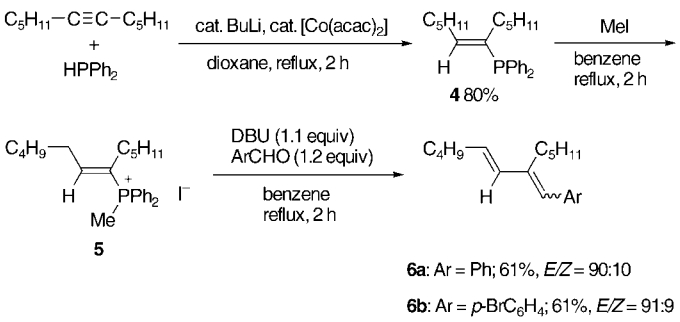

Scheme 1. The hydrophosphination reaction and further treatment of reaction product **4** to obtain a precusor of phosphorus ylides.

The reaction resulted in no or little conversion in the absence of either $[Co(acac)_2]$ or butyllithium. Furthermore, butylmagnesium bromide, diethylzinc, and potassium *tert*-butoxide could not be used in place of butyllithium. The use of $CoCl_2$, $[Co(acac)_3]$, or CoF_2 slightly lowered the yields by approximately 20% under reaction conditions that were otherwise the same. We examined $[Rh(acac)_2]$, $[Ru(acac)_3]$, $[Pd(acac)_2]$, $[Ni(acac)_2]$, $[Mn(acac)_2]$, $[Fe(acac)_3]$, CuI, $ReCl_5$, $[Cp_2TiCl_2]$, and $[Cp_2ZrCl_2]$ (Cp = cyclopentadienyl) as catalysts and none of them showed any catalytic activity. The reaction did not take place at ambient temperature, and dioxane proved to be the best solvent; others, such as heptane (63%), diethylene glycol dimethyl ether (diglyme; 53%), xylene (64%), and THF (29%) were shown to be less effective. Dicyclohexylphosphane, diphenylphosphane oxide, and dialkyl phosphite did not add to alkynes under similar conditions. The reaction was rendered slower as the amount of butyllithium or the cobalt catalyst was lowered; however, a longer reaction time resulted in high product yields, for example, a quantitative yield of **2a** was obtained after the

[*] H. Ohmiya, Dr. H. Yorimitsu, Prof. Dr. K. Oshima
Department of Material Chemistry
Graduate School of Engineering, Kyoto University
Kyoto-daigaku Katsura, Nishikyo-ku, Kyoto 615-8510 (Japan)
Fax: (+81) 75-383-2438
E-mail: oshima@orgrxn.mbox.media.kyoto-u.ac.jp

[**] This work was supported by Grants-in-Aid for Scientific Research, Young Scientists, and COE Research from the Ministry of Education, Culture, Sports, Science, and Technology, Japan.

Supporting information for this article is available on the WWW under http://www.angewandte.org or from the author.

 © 2005 Wiley-VCH Verlag GmbH & Co. KGaA, Weinheim DOI: 10.1002/anie.200500255

mixture was heated for 12 hours in the presence of 0.05 mmol of [Co(acac)$_2$] and 0.20 mmol of butyllithium.

A variety of alkynes were subjected to hydrophosphination (Table 1), and all reactions afforded the corresponding *syn* adducts exclusively irrespective of the substrates. The regioselectivity was governed by the steric interactions of the two alkyne substituents and was generally high in the reactions of **1**. The two resulting regioisomers could be readily separated from each other by chromatographic purification on silica gel or fractional crystallization from acetonitrile. The use of 1-aryl-1-propynes as the substrates provided 1-aryl-2-diphenylthiophosphinyl-1-propenes predominantly (entries 3–6). The methoxy substituent at the *ortho* position hindered the reaction, although no change in regioselectivity was observed (entry 6). Hydrophosphination of terminal alkynes was facile (entries 7–13), and addition across *tert*-butylacetylene led to the exclusive formation of **2h** (entry 8). Propargylamine **1i** underwent hydrophosphination with perfect *anti*-Markovnikov selectivity although the reaction rate was slow (entry 9). The reaction of aryl acetylenes afforded modest yields of the alkenylphosphine derivatives (entries 10–12). Interestingly, an amino moiety did not interfere with the reaction as much as would be expected (entry 12). Triethylsilylacetylene participated in the hydrophosphination to yield primarily a 1-silyl-2-thiophosphanylethene derivative (entry 13). The use of 1,6-heptadiyne as a substrate resulted in a complex mixture, and addition to conjugated diyne and diene compounds, such as 4,6-decadiyne and 1,3-undecadiene, led to slow conversion rates, thus giving the corresponding adducts in no more than 20% yield. The exact mechanism of this reaction, including the role of the acac ligand, is not clear at this stage. Further investigation is necessary to clarify the reaction pathway.

We investigated the utility of the products of the hydrophosphination reaction (Scheme 1). The isolated free phosphane **4** was treated with iodomethane to produce phosphonium salt **5** and then benzaldehyde and 1,8-diazabicyclo-[5.4.0]undec-7-ene (DBU) were added to the salt. The reaction mixture was heated for two hours to provide the conjugated diene **6a** in good yield with concomitant production of styrene (30%).[10] The preparation of ylides from 1-alkenylphosphines and their application to the Wittig reaction are rather difficult processes and have not been established so far.[11] The present strategy offers a simple synthesis of conjugated dienes and related π-electron systems.

In summary, we have developed a universally stereoselective hydrophosphination reaction of alkynes with diphenylphosphane that is mediated by a cobalt catalyst and butyllithium. The procedure is simple and scaleable; thus, it is applicable to the practical synthesis of new ligands and advanced materials.

Experimental Section

A typical procedure for the cobalt-catalyzed hydrophosphination of alkynes **1a**: A solution of diphenylphosphane (186 mg, 1.0 mmol) in anhydrous THF (1 mL) was placed in a 30-mL flask and butyllithium (1.6 M hexane solution, 0.13 mL, 0.20 mmol) was then added under argon. The mixture turned orange and was stirred for 30 min at 0 °C. Anhydrous [Co(acac)$_2$] (26 mg, 0.10 mmol), dioxane (3 mL), and 6-dodecyne (**1a**, 166 mg, 1.0 mmol) were added successively. The resulting black mixture was heated at reflux for 2 h. The reaction was quenched with distilled water (1 mL) after the mixture was cooled to room temperature and S_8 (32 mg, 0.10 mmol) was then added. The reaction mixture was stirred for 15 min at ambient temperature and then poured into water. The product was extracted with ethyl acetate (2 × 20 mL), the combined organic layers were dried over sodium sulfate, and the solvent was removed. ^{1}H NMR spectroscopic analysis with dibenzyl ether as an internal standard revealed quantitative formation of the corresponding product **2a**. Only one signal was detected by ^{31}P NMR spectroscopic analysis. Purification of the crude oil by column chromatography on silica gel (hexane/ethyl acetate, 20:1) provided **2a** (341 mg, 0.89 mmol) in 89% yield.

Received: January 22, 2005
Published online: March 14, 2005

Keywords: alkenes · alkynes · cobalt · phosphines · regioselectivity

[1] a) D. K. Wicht, D. S. Glueck in *Catalytic Heterofunctionalization* (Eds.: A. Togni, H. Grützmacher), Wiley-VCH, Weinheim, **2001**, chap. 5; b) F. Alonso, I. P. Beletskaya, M. Yus, *Chem. Rev.* **2004**, *104*, 3079–3159.

[2] a) L.-B. Han, M. Tanaka, *Chem. Commun.* **1999**, 395–402; b) M. Tanaka, *Top. Curr. Chem.* **2004**, *232*, 25–54.

[3] a) M. R. Douglass, T. J. Marks, *J. Am. Chem. Soc.* **2000**, *122*, 1824–1825; b) M. R. Douglass, C. L. Stern, T. J. Marks, *J. Am. Chem. Soc.* **2001**, *123*, 10221–10238; c) A. M. Kawaoka, M. R. Douglass, T. J. Marks, *Organometallics* **2003**, *22*, 4630–4632; d) K. Takaki, M. Takeda, G. Koshoji, T. Shishido, K. Takehira, *Tetrahedron Lett.* **2001**, *42*, 6357–6360; e) K. Takaki, G. Koshoji, K. Komeyama, M. Takeda, T. Shishido, A. Kitani, K. Takehira, *J. Org. Chem.* **2003**, *68*, 6554–6565; f) K. Takaki, K. Komeyama, K. Takehira, *Tetrahedron* **2003**, *59*, 10381–10395.

[4] M. A. Kazankova, I. V. Efimova, A. N. Kochetkov, V. V. Afanas'ev, I. P. Beletskaya, P. H. Dixneuf, *Synlett* **2001**, 497–500.

[5] Uncatalyzed addition of lithium diphenylphosphide to phenylacetylene: a) A. M. Aguiar, T. G. Archibald, *Tetrahedron Lett.* **1966**, 5471–5475; addition of phosphane–borane under thermal and palladium-catalyzed conditions wherein under the former conditions *anti* addition resulted and under the latter conditions Markovnikov adducts resulted: b) D. Mimeau, A.-C. Gaumont, *J. Org. Chem.* **2003**, *68*, 7016–7022; transition-metal-catalyzed addition of tertiary phosphines to alkynes: c) M. Arisawa, M. Yamaguchi, *J. Am. Chem. Soc.* **2000**, *122*, 2387–2388.

[6] Base or transition-metal-catalyzed hydrophosphination of activated alkenes: a) T. Bunlaksananusorn, P. Knochel, *Tetrahedron Lett.* **2002**, *43*, 5817–5819; b) M. O. Shulyupin, M. A. Kazankova, I. P. Beletskaya, *Org. Lett.* **2002**, *4*, 761–763; c) Y. Hayashi, Y. Matsuura, Y. Watanabe, *Tetrahedron Lett.* **2004**, *45*, 9167–9169; d) A. D. Sadow, I. Haller, L. Fadini, A. Togni, *J. Am. Chem. Soc.* **2004**, *126*, 14704–14705, and references therein.

[7] We have been exploring the catalytic activity of cobalt salts: a) K. Wakabayashi, H. Yorimitsu, K. Oshima, *J. Am. Chem. Soc.* **2001**, *123*, 5374–5375; b) Y. Ikeda, T. Nakamura, H. Yorimitsu, K. Oshima, *J. Am. Chem. Soc.* **2002**, *124*, 6514–6515; c) T. Tsuji, H. Yorimitsu, K. Oshima, *Angew. Chem.* **2002**, *114*, 4311–4313; *Angew. Chem. Int. Ed.* **2002**, *41*, 4137–4139; ; d) T. Fujioka, T. Nakamura, H. Yorimitsu, K. Oshima, *Org. Lett.* **2002**, *4*, 2257–2259; e) K. Mizutani, H. Shinokubo, K. Oshima, *Org. Lett.* **2003**, *5*, 3959–3961; f) K. Mizutani, H. Yorimitsu, K. Oshima, *Chem. Lett.* **2004**, *33*, 832–833; g) T. Nishikawa, H. Yorimitsu, K.

 © 2005 Wiley-VCH Verlag GmbH & Co. KGaA, Weinheim

Oshima, *Synlett* **2004**, 1573 – 1574; h) H. Ohmiya, H. Yorimitsu, K. Oshima, *Chem. Lett.* **2004**, *33*, 1240 – 1241; i) H. Ohmiya, T. Tsuji, H. Yorimitsu, K. Oshima, *Chem. Eur. J.* **2004**, *10*, 5640 – 5648; j) Y. Ikeda, H. Yorimitsu, H. Shinokubo, K. Oshima, *Adv. Synth. Catal.* **2004**, *346*, 1631 – 1634.

[8] T. N. Mitchell, K. Heesche, *J. Organomet. Chem.* **1991**, *409*, 163 – 170.

[9] An 80 % yield of 1-pentyl-1-heptenyldiphenylphosphane (**4**) was isolated without oxidation by the addition of sulfur. The yield for this compound is lower than that obtained after sulfidation (89 %), which results from slow oxidation of **4** by molecular oxygen. We isolated adducts as phosphane sulfides to clarify the efficiency of the hydrophosphination reaction (Table 1).

[10] The reaction with alphatic aldehydes suffered from low yields.

[11] a) E. Vedejs, J. P. Bershas, P. L. Fuchs, *J. Org. Chem.* **1973**, *38*, 3625 – 3627; b) E. Vedejs, K. A. J. Snoble, P. L. Fuchs, *J. Org. Chem.* **1973**, *38*, 1178 – 1183.

 © 2005 Wiley-VCH Verlag GmbH & Co. KGaA, Weinheim

Reaction Mechanisms

Establishing a Molecular Mechanism for the Beckmann Rearrangement of Oximes over Microporous Molecular Sieves**

Ana B. Fernández, Mercedes Boronat, Teresa Blasco, and Avelino Corma*

The Beckmann rearrangement constitutes a common route employed in organic chemistry to transform ketoximes into amides. One of the main industrial applications is the transformation of cyclohexanone oxime into ε-caprolactam, a raw material in the production of nylon 6. The conventional liquid-phase industrial process uses sulfuric acid or oleum as catalysts and is accompanied by the coproduction of large amounts of undesired ammonium sulfate.[1] To solve the problems derived from the use of concentrated sulfuric acid and the generation of this by-product, many solid-acid catalysts have been tested, including zeolites and zeotypes, mesoporous materials, and oxides.[2,3] Recently, Sumitomo Chemical Co. commercialized an environmentally friendly gas-phase heterogeneous process with a high-silica zeolite as the catalyst. The process has been in operation in a new production plant in Japan since 2003.[4]

Though catalytic performance over solids with acidity of a different nature and strength has been tested, the nature of the active sites in the catalysts for the Beckmann rearrangement is still a matter of controversy. In previous publications, strong Brønsted acid sites in zeolites were reported to catalyze the rearrangement.[5,6] Later, it was shown that these sites favor the formation of by-products, and that both the activity and selectivity of the amide is improved in the presence of high-silica zeolites with intermedium or weak Brønsted acid sites.[2,3,7] Finally, it has been suggested that weakly acidic or neutral silanol groups or silanol nests are active catalysts of the rearrangement reaction.[2,3,7,8] Discrepancies are also found in the location of the active sites, which have been proposed to be inside the micropores,[9,10] just at the aperture,[11] or at the zeolite surface.[2,3,7,8]

The reaction mechanism commonly assumed for the Beckmann rearrangement is described in Scheme 1.[5] This

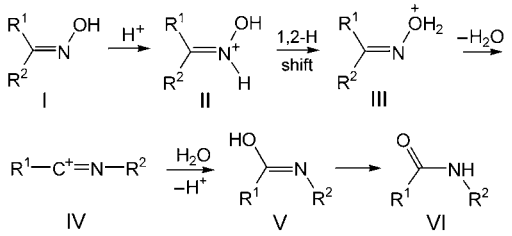

Scheme 1. Generally accepted reaction mechanism for the Beckmann rearrangement.

pathway initially involves the protonation of the oxime at the oxygen atom to give an oxonium cation III, followed by the migration of the alkyl group *anti* to the hydroxy group, the liberation of water, and the formation of a nitrilium cation IV. Cation IV is then hydrolyzed to give V, which finally tautomerizes to the corresponding amide VI. Ab initio molecular-orbital calculations on the isolated gas-phase system suggest that the first step is the N protonation of the oxime to give II, and that the rate-determining step is the 1,2-H shift to give the *O*-protonated oxime III.[12] More recently, quantum-chemical investigations suggested that the transfer of the alkyl group and simultaneous elimination of water to form the nitrilium ion IV is the rate-determining step when the gas-phase reaction occurs over oxide catalysts.[13] Nevertheless, despite numerous investigations, at present there is no experimental proof, and the Beckmann rearrangement reaction pathway is not yet well established.

Herein, we present experimental evidence on the identity of the intermediates formed in the initial stages of the Beckmann rearrangement, through a combination of solid-state NMR spectroscopy and theoretical calculations. For this investigation we chose acetophenone oxime as the reactant (which is transformed into acetanilide) and two beta zeolites as catalysts: pure siliceous beta-D, and Al-containing H-beta-D with Brønsted acid sites. Zeolite beta has a three-dimensional 12-ring channel system with a pore aperture of 0.7 nm,[14] which is able to host acetophenone oxime. We show that the *N*-protonated oxime is formed over Brønsted acid centers, but not over weakly acidic silanol groups.

Scheme 2 shows the models that result from the interaction of a molecule of acetophenone oxime with the $Si(OSiH_3)_3OH$ and $Al(OSiH_3)_3(OH)SiH_3$ clusters, as models

[*] A. B. Fernández, Dr. M. Boronat, Dr. T. Blasco, Prof. A. Corma
Instituto de Tecnología Química (UPV-CSIC)
Avda. de los Naranjos s/n, 46022-Valencia (Spain)
Fax: (+34) 963-877-809
E-mail: tblasco@itq.upv.es

[**] We thank the Spanish CICYT (projects PPQ2003-03946 and MAT 2003-07945-C02-01) and Generalitat Valenciana (project GV04B-272) for financial support. A.B.F thanks the CSIC for a fellowship (Ref. I3P-BP62004)

 © 2005 Wiley-VCH Verlag GmbH & Co. KGaA, Weinheim DOI: 10.1002/anie.200462737

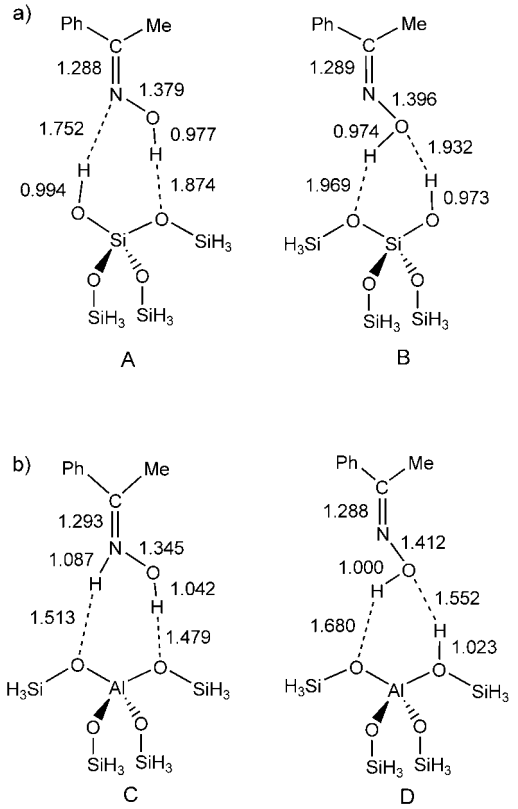

Scheme 2. Optimized structures of acetophenone oxime adsorbed on a) beta-D and b) H-beta-D cluster models. The oxime interacts with the zeolite hydrogen atoms through its nitrogen atom in A and C and through its oxygen atom in B and D. Interatomic distances are expressed in angstroms.

of the silanol-group and Brønsted acid sites, respectively, in the beta zeolites. Silanol defect groups are present in zeolites beta-D and H-beta-D, whereas Brønsted acid sites only exist in the Al-containing H-beta-D. The complexes in Scheme 2 are obtained by assuming that the hydrogen atom of the silanol (A, B) or Brønsted acid centers (C, D) of zeolite beta interacts with the nitrogen (A, C) or oxygen atom (B, D) of the acetophenone oxime molecule. The main distances obtained from the optimization of the geometry of the clusters by using the density functional B3PW91/6-31G(d,p) method are also indicated in Scheme 2. When silanol groups are considered (Scheme 2a), the distances between the H atom of the oxime hydroxy group and the oxygen atom of the zeolite framework are characteristic of hydrogen bonds. The same is true for the distances between the H atom of the zeolite Si–OH group and the nitrogen and oxygen atoms of the oxime in models A and B, respectively (Scheme 2a). Therefore, according to these calculations, no hydrogen-atom transfer occurs from the zeolite hydroxy group, and consequently the acetophenone oxime is not protonated at the N or O atoms. Table 1 summarizes the adsorption energies and the isotropic chemical shifts of the C=N group calculated for the oxime in both its isolated form and in complexes A and B (Scheme 2a). Only a small difference is observed in the energies of the two complexes: Model A, in which the zeolite hydroxy group forms a hydrogen bond with the N atom of the

Table 1: Adsorption energies calculated for models A–D (Scheme 2) along with ^{13}C and ^{15}N NMR isotropic chemical shifts, $\delta(^{13}C)$ and $\delta(^{15}N)$, of the C=N group of acetophenone oxime, both isolated and in models A–D.

	E_{ads} [kcal mol^{-1}]	$\delta(^{15}N)_{calcd}$ [ppm][a],[b]	$\delta(^{13}C)_{calcd}$ [ppm][a],[c]	$\delta(^{15}N)_{exp}$ [ppm][b],[d]	$\delta(^{13}C)_{exp}$ [ppm][c],[d]
oxime		−36.7	157.8	−36.8	155.8
model A	−11.9	−51.9	160.3	−37.8	158.0
model B	−7.8	−26.2	160.4	−29.3	164.2
model C	−27.7	−138.6	165.7	−150.6	166.0
model D	−17.2	−31.2	166.9		

[a] Chemical shifts derived from theoretical calculations. [b] Chemical shifts are expressed in ppm relative to nitromethane. [c] Chemical shifts are expressed in ppm relative to tetramethylsilane. [d] Chemical shifts observed experimentally.

oxime, is slightly more stable. The calculated ^{13}C chemical shift of the carbon atom in the C=N bond is similar in both complexes, and shifted slightly downfield with respect to that of the free oxime. The ^{15}N chemical shift is displaced upfield in model A and downfield in model B relative to that of the oxime.

A different situation appears when acetophenone oxime is adsorbed over the Brønsted acid sites in zeolite beta (Scheme 2b). The complex resulting from the interaction of the oxime oxygen atom with the zeolite acid center (Scheme 2D) is similar to the equivalent complex with the zeolite silanol center (Scheme 2B), but with stronger, shorter hydrogen bonds and thus larger displacements of the ^{15}N and ^{13}C chemical shifts relative to those of the isolated oxime. However, a different result is obtained when the oxime interacts through the nitrogen atom (Scheme 2C). In this case, a very short distance to the acidic hydrogen atom of the zeolite emerges, typical of a N–H bond, thus indicating the complete transfer of the proton and formation of the *N*-protonated oxime. Inspection of the energies calculated for complexes C and D (Table 1) indicates that the former is more stable, and that the formation of the *N*-protonated oxime over the Brønsted acid sites is favored. According to theoretical calculations, the protonation results in a large upfield displacement of the ^{15}N chemical shift, whereas the ^{13}C resonance is shifted slightly downfield.

Figure 1 shows the ^{1}H-to-^{13}C ($^{1}H/^{13}C$) and ^{1}H-to-^{15}N ($^{1}H/^{15}C$) cross-polarization magic-angle spinning (CP MAS) NMR spectra of free acetophenone oxime, and acetophenone oxime on zeolites beta-D and H-beta-D. The ^{13}C and ^{15}N NMR spectra of the solid oxime (Figure 1a,a′) contain a peak at $\delta = 155.8$ and -36.8 ppm, respectively; these values are very close to those calculated theoretically (see Table 1). When acetophenone oxime is mixed with zeolite beta-D, the signals in the ^{13}C and ^{15}N NMR spectra become broader, and are displaced slightly, thus indicating that acetophenone oxime interacts effectively with the zeolite (Figure 1b,b′). After the system has been heated at 473 K, the spectra change considerably, with new signals appearing at $\delta = 172$ and -246 ppm in the ^{13}C and ^{15}N NMR spectra, respectively (Figure 1d,d′). The new signals are attributed to acetanilide, which is the product of the Beckmann rearrangement. Although the spectra are poorly resolved, at least two main

 © 2005 Wiley-VCH Verlag GmbH & Co. KGaA, Weinheim

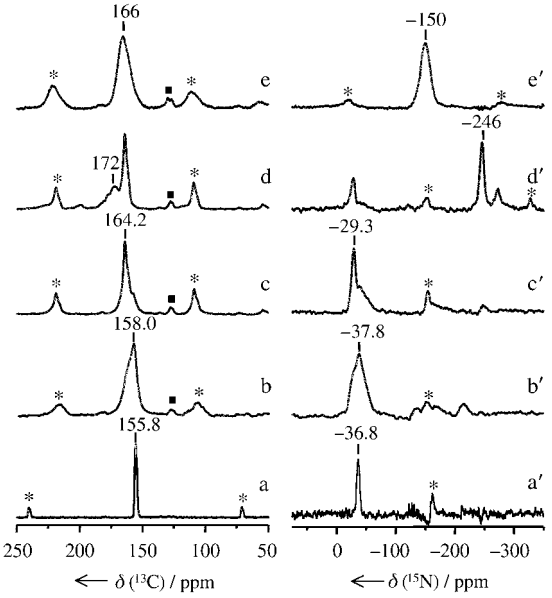

Figure 1. $^{1}H/^{13}C$ (a–d) and $^{1}H/^{15}N$ (a′–d′) CP MAS NMR spectra recorded at room temperature of (α-^{13}C,^{15}N)acetophenone oxime: pure (a, a′); over zeolite beta-D before (b, b′) and after heating the system at 423 K (c, c′) and 473 K (d, d′); over zeolite H-beta-D (e, e′). The asterisks indicate the spinning sidebands, and the squares the resonance of the aromatic carbon atoms.

components are apparent in the ^{13}C and ^{15}N spectra recorded both before (Figure 1 b,b′) and after (Figure 1 c,c′) heating the system at 423 K. The maximum of the main signal appears at $\delta = 158.0$ ppm in the ^{13}C NMR spectrum and $\delta = -37.8$ ppm in ^{15}N NMR spectrum recorded before treatment, and is displaced to $\delta = 164.2$ and -29.3 ppm, respectively, after the mixture has been heated at 423 K. The evolution of the signals in the spectra b,b′ and c,c′ in Figure 1, and comparison with the ^{13}C and ^{15}N chemical shifts calculated for complexes A and B (see Table 1), allows the assignment of the signals as given in Table 1. This assignment is mainly based on the variation of the ^{13}C, and in particular the ^{15}N, chemical shifts calculated for the acetophenone oxime in complexes A and B relative to those of the isolated oxime. The formation of oxime complexes hydrogen bonded through N has also been suggested previously on the basis of ^{15}N NMR spectroscopy for silicalite-1.[15]

The experimental spectra shown in Figure 1 a,a′,b,b′ can be interpreted as follows: The silanol hydroxy groups of the zeolite form hydrogen bonds with the nitrogen and oxygen atom of the acetophenone oxime to give complexes A and B (Scheme 2 a). Whereas the H bonding with the oxime occurs mainly through the nitrogen atom before treatment, interaction with the oxygen atom is preferred after heating. This interpretation is also consistent with the slightly higher stability calculated for the adsorption model A.

When acetophenone oxime is mixed with zeolite H-beta-D, the spectra in Figure 1 e,e′ are obtained. A dramatic upfield shift of the ^{15}N NMR signal relative to that of the free oxime is observed. The position of the signal is consistent with protonation of the oxime at the N atom.[15] This interpretation is further supported by the chemical shift calculated for complex C (see Table 1). Thus, the *N*-protonated oxime is formed immediately at the Brønsted acid sites at room temperature. This result is also coherent with the higher stability of complex C. No other species are observed in the NMR spectra of this system until the rearrangement starts at 373 K.

The results reported herein shed light on the reaction mechanism of the Beckmann rearrangement of oximes to amides on solid catalysts. As in the liquid phase, the *O*- and/or *N*-protonated oxime is usually assumed to be the initial reaction intermediate, whereby protonation at N is very favorable according to quantum-chemical calculations.[12] The theoretical calculations and the experimental results presented herein indicate that the silanol groups in zeolites are not acidic enough to protonate the oxime before its transformation into acetanilide (at 473 K), whereas the N protonation occurs readily over Brønsted acid sites at room temperature. As both sites are catalytically active, there are at least two possible reaction pathways for the Beckmann rearrangement, depending on the acid strength of the active center. We recognized the formation of the intermediates depicted in Scheme 2: complexes A and B over silanol groups and complex C over Brønsted acid sites in zeolites, and no other intermediate species were detected by NMR spectroscopy. Further investigations are now required to complete our understanding of the reaction pathways and to identify the rate-determining step of the Beckmann rearrangement over different active sites.

Experimental Section

Computational details: The structures of pure-silica zeolite beta and the nine different Al-substituted systems, obtained by introducing one Al atom at each of the nine crystallographically different T positions of beta zeolites, were optimized by molecular-mechanics techniques by using the GULP code[16] and the force field derived by Schröder and Sauer.[17] Two clusters of atoms were then cut out of the optimized structures of the pure-silica and T9-Al-substituted beta zeolites (the T9 site was found to be the most favorable substitution site); each cluster contained the T9 atom and two coordination spheres around it. The bonds that connected the clusters with the rest of the solid were saturated with H atoms at 1.49 Å from the Si atoms, and orientated toward the O atoms that occupied the next coordination sphere in the crystal. A silanol defect was created by substituting one siloxy ($OSiH_3$) group in the pure-silica cluster by one hydroxy (OH) group. The resulting $Si(OSiH_3)_3OH$ cluster is denoted as model beta-D. In a similar way, a Brønsted acid site was created by introducing one H atom into the Al-containing cluster. The resulting $Al(OSiH_3)_3(OH)SiH_3$ system is denoted as model H-beta-D. The geometries of the beta-D and H-beta-D clusters, of acetophenone oxime, and of the complexes formed by adsorption of the oxime on each cluster (structures A–D, Scheme 2) were optimized by using the density functional method B3PW91[18] and the standard 6-31G(d,p) basis set.[19] In these calculations, the coordinates of all atoms except the H atoms of the SiH_3 groups were fully optimized.

Isotropic absolute chemical-shielding constants σ were calculated with the B3PW91/6-31G(d,p) method on geometries optimized at the same level by using the gauge including atomic orbitals (GIAO) approach.[20,21] ^{15}N and ^{13}C NMR chemical shifts were calculated as $\delta = \sigma_{ref} - \sigma$ and corrected with the equations obtained from a preliminary study of the performance of B3PW91 functional. In this preliminary study, a least-squares fit of calculated against experimental chemical shifts for a set of 23 N-containing and a set of 30 C-

 © 2005 Wiley-VCH Verlag GmbH & Co. KGaA, Weinheim

containing molecules was performed. The root-mean-square errors obtained were 4.6 and 0.7 ppm for $\delta(^{15}N)$ and $\delta(^{13}C)$, respectively. For comparison with the experimental data, the references chosen were nitromethane for the ^{15}N NMR and tetramethylsilane for the ^{13}C NMR spectra; the calculated absolute chemical-shielding constants are $\sigma(^{15}N) = -108.381$ ppm and $\sigma(^{13}C) = 194.893$ ppm.

All calculations in this work were performed by using the Gaussian98 computer program.[22]

Solid-state NMR spectroscopy: Zeolite H-beta-D with Si/Al = 12.5 is commercially available (zeolyst CP811); zeolite beta-D was synthesized hydrothermally by the procedure described previously.[10] Acetophenone oxime was synthesized from (α-^{13}C)acetophenone (99%) and hydroxyl(^{15}N)amine hydrochloride (98%; both from Cambridge Isotope Laboratories) in a mixture of ethanol and sodium acetate at 368 K. The oxime was recrystallized from ethanol before use and identified by NMR spectroscopy. The zeolite (300 mg) was degassed at 723 K and mixed with acetophenone oxime CH_3-$(C_6H_5)^{13}C{=}^{15}N{-}OH$ (25 mg), a solid at room temperature, under an inert atmosphere. A portion of the mixture was introduced into a glass insert, which was sealed after a second degasification at room temperature. The NMR spectra were recorded at room temperature on a Bruker AV 400 WB spectrometer with a BL7 probe, with the samples spinning (MAS) at a rate of approximately 5 kHz. The ^1H-to-^{13}C ($^1H/^{13}C$) cross-polarization spectra were acquired by using a 90° pulse for ^1H of 5 μs, a contact time of 5 ms, and a recycle delay of 3 s. The ^1H-to-^{15}N ($^1H/^{15}N$) cross-polarization spectra were recorded with a 90° pulse for ^1H of 5 μs, a contact time of 5 ms and a recycle delay of 3 s.

Received: November 26, 2004
Published online: March 10, 2005

Keywords: density functional calculations · heterogeneous catalysis · NMR spectroscopy · reaction mechanisms · zeolites

[1] *Encyclopedia of Chemical Technology*, 4th ed., Wiley, New York, **1992**, 827–838.
[2] G. Dalhhoff, J. P. M. Niederer, W. F. Hölderich, *Catal. Rev.-Sci. Eng.* **2001**, *43*, 381–441.
[3] T. Tatsumi in *Fine Chemicals through Heterogeneous Catalysis* (Eds.: R. A. Sheldon, H. van Bekkum), Wiley-VCH, **2001**, 185–204.
[4] H. Ichihashi, M. Kitamura, *Catal. Today* **2002**, *73*, 23–28.
[5] P. S. Landis, P. B. Venuto, *J. Catal.* **1966**, *6*, 245–252.
[6] A. Aucejo, M. C. Burguet, A. Corma, V. Fornés, *Appl. Catal.* **1986**, *22*, 187–200.
[7] H. Sato, *Catal. Rev.-Sci. Eng.* **1997**, *39*, 395–424.
[8] W. F. Hölderich, *Stud. Surf. Sci. Catal.* **1989**, *46*, 193–209.
[9] H. Kath, R. Gläser, J. Weitkamp, *Chem. Eng. Technol.* **2001**, *24*, 150–153.
[10] M. A. Camblor, A. Corma, H. García, V. Semmer-Herlédan, S. Valencia, *J. Catal.* **1998**, *177*, 267–272.
[11] H. Ichihashi, M. Ishida, A. Shiga, M. Kitamura, T. Suzuki, K. Suenobu, K. Sugita, *Catal. Surv. Asia* **2003**, *7*, 261–269.
[12] M. T. Nguyen, G. Raspoet, L. G. Vanquickenborne, *J. Am. Chem. Soc.* **1997**, *119*, 2552–2562.
[13] Y. Shinohara, S. Mae, D. Shouro, T. Nakajima, *J. Mol. Struct.* **2000**, *497*, 1–9.
[14] M. Newsam, M. M. J. Treacy, W. T. Koetsier, C. B. de Gruyter, *Proc. R. Soc. London A* **1988**, *420*, 375–405.
[15] W. O. N. Parker, *Magn. Reson. Chem.* **1999**, *37*, 433–436.
[16] J. D. Gale, *J. Chem. Soc. Faraday Trans.* **1997**, *93*, 629–637.
[17] K. P. Schröder, J. Sauer, *J. Phys. Chem.* **1996**, *100*, 11043–11049.
[18] a) A. D. Becke, *J. Chem. Phys.* **1993**, *98*, 5648–5652; b) J. P. Perdew, Y. Wang, *Phys. Rev. B* **1992**, *45*, 13244–13249.
[19] P. C. Hariharan, J. A. Pople, *Theor. Chim. Acta* **1973**, *28*, 213–222.
[20] R. Ditchfield, *Mol. Phys.* **1974**, *27*, 789–807.
[21] K. Wolinski, J. F. Hinton, P. Pulay, *J. Am. Chem. Soc.* **1990**, *112*, 8251–8260.
[22] Gaussian 98 (Revision A.7), M. J. Frisch, G. W. Trucks, H. B. Schlegel, G. E. Scuseria, M. A. Robb, J. R. Cheeseman, V. G. Zakrzewski, J. A. Montgomery, R. E. Stratmann, J. C. Burant, S. Dapprich, J. M. Millam, A. D. Daniels, K. N. Kudin, M. C. Strain, O. Farkas, J. Tomasi, V. Barone, M. Cossi, R. Cammi, B. Mennucci, C. Pomelli, C. Adamo, S. Clifford, J. Ochterski, G. A. Petersson, P. Y. Ayala, Q. Cui, K. Morokuma, D. K. Malick, A. D. Rabuck, K. Raghavachari, J. B. Foresman, J. Cioslowski, J. V. Ortiz, B. B. Stefanov, G. Liu, A. Liashenko, P. Piskorz, I. Komaromi, R. Gomperts, R. L. Martin, D. J. Fox, T. Keith, M. A. Al-Laham, C. Y. Peng, A. Nanayakkara, C. Gonzalez, M. Challacombe, P. M. W. Gill, B. G. Johnson, W. Chen, M. W. Wong, J. L. Andres, M. Head-Gordon, E. S. Replogle, J. A. Pople, Gaussian, Inc., Pittsburgh, PA, **1998**..

 © 2005 Wiley-VCH Verlag GmbH & Co. KGaA, Weinheim

Molecular Devices

Light-Driven Dynamic Pattern Formation**

Jaap J. D. de Jong, P. Ralph Hania, Audrius Pugžlys, Linda N. Lucas, Maaike de Loos, Richard M. Kellogg, Ben L. Feringa, Koos Duppen,* and Jan H. van Esch**

Dynamic self-assembly processes are essential for organization and various phenomena in nature,[1] and mimicking of such processes in artificial systems offers fascinating opportunities for the construction of smart materials.[2] However, a major challenge in the design of nonbiological systems is the temporal and spatial control of fully reversible self-assembly processes.[3] Here, we report the incorporation of an address-

[*] J. J. D. de Jong, M. de Loos, Prof. Dr. B. L. Feringa, Dr. J. H. van Esch
Department of Organic and Inorganic Chemistry
Stratingh Institute, University of Groningen
Nijenborgh 4, 9747 AG Groningen (The Netherlands)
Fax: (+31) 50-363-4296
E-mail: b.l.feringa@rug.nl
j.h.van.esch@rug.nl

P. R. Hania, Dr. A. Pugžlys, Prof. Dr. K. Duppen
Ultrafast Laser and Spectroscopy Laboratory
University of Groningen
Nijenborgh 4, 9747 AG Groningen (The Netherlands)
Fax: (+31) 50-363-4441
E-mail: k.duppen@rug.nl

Dr. L. N. Lucas, Prof. Dr. R. M. Kellogg
Syncom
Kadijk 3, 9747 AT Groningen (The Netherlands)

[**] We would like to thank the MSC+ for financial support, H. Nijland for the SEM measurements, and M. Popinciuc for useful discussions and help.

 DOI: 10.1002/anie.200462500 © 2005 Wiley-VCH Verlag GmbH & Co. KGaA, Weinheim

able functionality into a supramolecular building block which allows control over the spatial and temporal self-organization of the molecular material. Light-induced reversible switching of a molecular system between an aggregated and non-aggregated state is manifested at the macroscopic level by a fully reversible sol–gel phase transition[4] and results in spatially confined structure formation in an inhomogeneous optical field. The reversibility of aggregation and the unique photochemically induced, spatially confined self-assembly that leads to light-induced mass transfer is exploited in dynamic pattern formation. These results clearly demonstrate the feasibility of dynamic self-assembly in simple artificial systems and will open new opportunities for smart materials and nanodevices.

Photochromic switches[5] have been exploited successfully in the control of host–guest systems, chiral aggregates, polymers, and gels, and particularly promising in this field are responsive self-assembling molecules in which an addressable function is incorporated.[6] We have designed a diarylethene switch that combines excellent photochromic properties with the ability to undergo self-assembly.[7] A reversible light-induced interconversion between an open form **1** and a closed form **2** (Figure 1a) occurs,[8] and pronounced self-assembly of **1** and **2** in nonpolar solvents (e.g. aliphatic and aromatic hydrocarbons) takes place as a result of hydrogen bonding between the amide groups to result in the formation of gels above a critical gelation concentration.[4] Transmission electron microscopy (TEM) of gels (5.4 mM) in toluene revealed that gelation of the solvent is caused by the formation of entangled fibrous networks by aggregation of **1** or **2**. Fibers formed by **1** are very thin, with diameters as small as 20–25 nm, and the regular elongated shape of the fibers must arise from a strong anisotropic process, which indicates that the fibers are well-ordered with respect to the molecular packing.

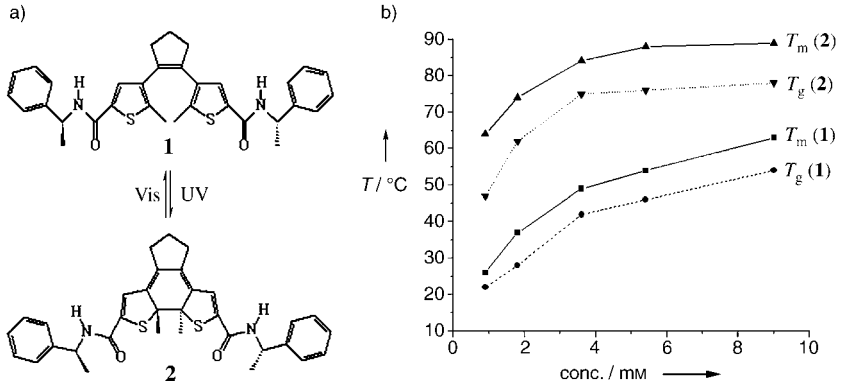

Figure 1. a) Dithienylcyclopentene switch with amide moieties for hydrogen bonding: the open form **1** can be converted into the closed form **2** by UV light, a process which can be reversed upon irradiation with visible light. b) Phase diagrams for **1** and **2** in toluene as measured by CD spectroscopy. The melting temperatures (T_m, ——) were obtained by heating the sample slowly until no CD absorption was observed, whereas the gelation temperatures (T_g) were obtained upon cooling the sample. The difference in T_m and T_g is a characteristic feature of low-molecular-weight gelators.[4] Note that T_m and T_g are independent of the rates of heating or cooling in the range 0.25–2 °C min^{-1}.

Regular fibers are also formed by **2**, but their diameters appear much larger than that for **1**. The different morphologies of **1** and **2** already indicate that the intermolecular interactions which lead to the formation of fibers are different. This difference in morphology of fibers between **1** and **2** is also reflected by the difference in the thermal stability of their gels, which is characterized by the concentration-dependent gel–sol phase-transition temperature. Phase diagrams (Figure 1b) were measured for **1** and **2** by circular dichroism (CD) spectroscopy at concentrations between 1 and 10 mM.[9] Gels that contain **2** are much more thermally robust, presumably owing to the increased rigidity of the monomer.

Above the melting temperature (T_m) of gel **2** in solution the expected photochemical conversion between **1** and **2** occurs (Figure 1b), and below the gelation temperature (T_g) of a gel of **1** the previously reported stereoselective gel-to-gel switching takes place.[7] In the region between T_g(**1**) and T_g(**2**), it is possible to induce a sol-to-gel phase transition (and vice versa) by photochemical conversion between **1** and **2**. Indeed, irradiation ($\lambda = 313$ nm) of a solution of **1** (1.5 mM) in toluene at room temperature results in a transition to a gel of **2**, whereas subsequent irradiation of this gel with visible light ($\lambda > 420$ nm) causes it to dissolve to give a solution of **1**. These observations prompted us to investigate whether it would be possible to generate spatially confined gel objects embedded in a solution. The formation of such objects, by irradiation through an optical mask or by holographic imaging,[10] requires that self-assembly followed by immobilization in the gel state takes place faster than diffusion of molecules of **2** to nonilluminated regions. To the best of our knowledge, no artificial molecular systems are yet known that can be reversibly assembled, on command, into spatially confined macroscopic objects.

A solution of **1** (1.5 mM) in toluene contained in a 1-mm cell was irradiated with crossed UV beams ($\lambda \approx 330$ nm)[10] at room temperature which resulted in the formation of transparent red-colored gel patterns that resist gravitational flow, whereas the nonirradiated surroundings remained in the liquid state. UV irradiation of a solution of **1** with a nonuniform optical field results in the localized photochemical conversion to **2**, which self-assembles to form a gel before diffusion of **2** to the nonirradiated areas can take place. The grating patterns obtained by this process had line spacings in the range of 75 to 5 μm, below which point the contrast of the pattern formed becomes blurred owing to diffusion of **2** out of the irradiated area. Application of more-intense irradiation accelerates the pattern formation and gives rise to smaller structures, although with reduced contrast. Typical macroscopic dimensions of the gel structures that formed in the solution were 10 μm × 5 mm × 1 mm. The large aspect ratio of these objects clearly demonstrates the excellent mechanical stability of the self-assembled gels in a liquid environment and persisting concentration gradients. The patterns could be erased by irradiation with visible light, and this whole cycle of pattern formation and erasing could be repeated several times. Note that this photoinduced self-

 © 2005 Wiley-VCH Verlag GmbH & Co. KGaA, Weinheim

assembly generates diapositive gel patterns, as opposed to dianegative patterns, which have been obtained by the irreversible photochemical decomposition of dye aggregates.[11–13]

A graphical representation of the competing processes is given in Figure 2a. Initially, only **1** is present, and upon irradiation with UV light the concentration of **2** increases at the expense of **1** to create a relatively open fiberlike network. Nonaggregated molecules of **1** are capable of diffusing through the network into the irradiated areas, whereas the outward diffusion of **2** is greatly decreased because of its immobilization into the network structure. This implies that the monomers in the system can be captured in the irradiated area to create not only spatially confined gel objects but also to generate concentration gradients of **1** and **2**. Indeed, uniform irradiation of the sample with UV light below T_g(**2**) after pattern formation from solution did not result in a homogeneously colored sample. It was observed that the existing lines appear much brighter than the previously nonirradiated areas, in agreement with our model.[14] As a control experiment, we repeated this sequence with a sample that contained **1** in the gel state, and here (nondynamic) pattern formation followed by uniform irradiation resulted in a homogeneously colored sample. Scanning electron microscopy (SEM) of the patterned samples revealed sharp boundaries between areas with a fibrous network and almost empty areas with minor amounts of deposited amorphous material (Figure 2b).[15] These observations were further confirmed by real-time dynamics measurements, which trace the optical density (OD) of the sample at $\lambda =$ 650 nm where **2** absorbs while the system is irradiated with UV light within the absorption band of **1**.[16] In the diffusion-free case, which is obtained by uniform irradiation of the whole sample (Figure 2c, dashed line), the OD reaches a maximum value which is determined by the equilibrium ratio between **1** and **2**. The solid line shows the OD trace of a sample that is only locally irradiated by using a narrow laser beam ($\approx$1-mm diameter). The OD at the irradiated spot (e.g. the local concentration of **2**) reaches higher values. An increase in the local concentration by a factor of 20 was observed upon irradiation of small areas of a sample and shows that a considerable fraction of the switch molecules can be fixed at the irradiated spot. The magnitude of the increase in concentration further depends on the ratio between the rates of diffusion of **1** and **2**, which itself is dependent on the concentration and temperature of the sample as well as on the irradiation density.

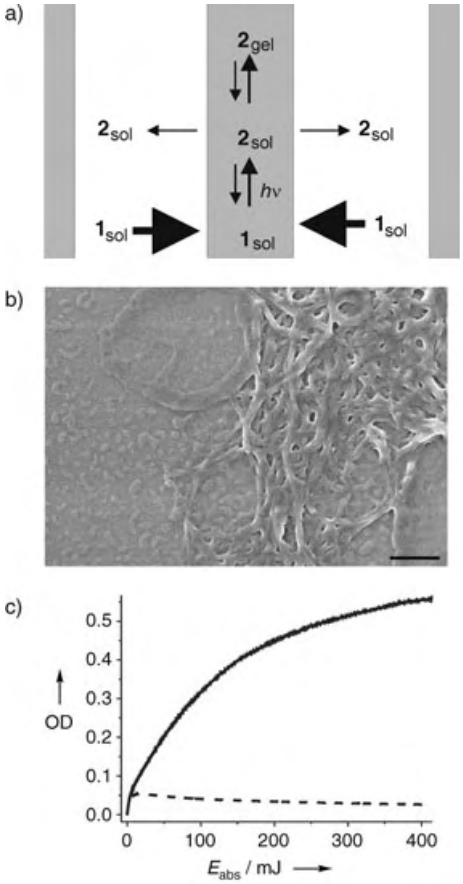

Figure 2. Mass-transfer during photoinduced gel formation in inhomogeneous optical fields. a) Kinetic scheme for the diffusion mechanism in the grating. White areas indicate positions of low UV irradiation intensity in the sample, while darker areas represent areas of high irradiation intensity. The thickness of the arrow indicates the dominance of the process. b) SEM image at the transition area between solution and gel (scale bar = 1 μm). c) Optical density (OD) at $\lambda = 650$ nm of a solution at 1.5 mM as a function of the absorbed energy in the UV region ($\lambda = 330$ nm). The solid line (——) shows the evolution of the optical density for irradiation using a single UV beam with a Gaussian beam profile (FWHM $\approx$ 3 mm) and 30 μW power. The dashed line (- - - -) shows the evolution of a uniformly irradiated sample for which no diffusion effects are present. FWHM = full-width at half maximum.

The reversibility and low degradation of the photochromic system suggest the possibility of dynamic self-assembly and pattern formation. This feature was exploited by irradiation of the sample with a second irradiation beam at a wavelength in the absorption region of the closed form ($\lambda =$ 500–600 nm). This beam provides a pathway for exploitation of the dynamic nature of the system by disassembling patterns that are no longer being formed by the grating setup. Repeating the experiments previously described, but now with homogeneous visible irradiation, resulted in clear patterns and shows that simultaneous writing and erasing does not create difficulties during pattern formation. As shown in Figure 3, the initially created horizontal grating pattern (a) is overlapped (b), and subsequently replaced (c) by a second grating pattern built up at a different angle. This shows clearly that patterns can be created dynamically; that is, the patterns can be changed or replaced after formation. Note that patterns formed from a gel are stable for weeks, whereas those starting from solution are stable for only 1–2 days owing to diffusion of **2**. This diffusion can be inhibited either by freezing the sample or by removal of the solvent to create permanent stable patterns.

The dynamic and reversible pattern formation as reported here offers attractive prospects for future applications in nanotechnology. By manipulation of the delicate balance between solution and aggregation properties of materials at

 © 2005 Wiley-VCH Verlag GmbH & Co. KGaA, Weinheim

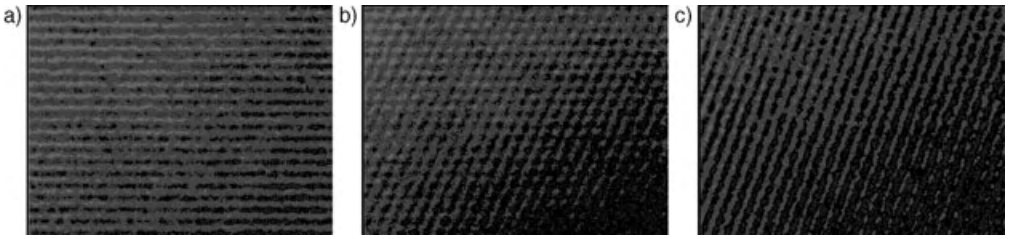

Figure 3. Dynamic spatially controlled self-assembly in time. Micrographs (20× magnification) of a solution of **1** (1.5 mM) in toluene in a 1-mm cell after simultaneous irradiation of the sample with a diffraction grating at $\lambda = 330$ nm (290 μW) and a homogeneous beam at $\lambda = 500$–600 nm (1 mW). Images taken a) after writing a horizontal grating pattern (irradiation: 10 min), b) after recording a second grating pattern following rotation of the sample (irradiation: 10 min), and c) as for (b), but after irradiation for 90 minutes.

the molecular level, stable addressable inhomogeneous micropatterns can be formed by dynamic self-assembly of molecular components in a fully reversible way. Self-assembling systems that can dynamically respond to external stimuli by a clear and appropriate response will be crucial for the development of artificial systems in the fields of smart materials, nanomachines, microfluidics, and molecular transport.

Received: November 2, 2004
Published online: March 10, 2005

Keywords: aggregation · gels · phase transitions · photochromism · self-assembly

[1] B. L. Goode, D. G. Drubin, G. Barnes, *Curr. Opin. Cell Biol.* **2000**, *12*, 63.
[2] a) C. Papaseit, N. Pochon, J. Tabony, *Proc. Natl. Acad. Sci. USA* **2000**, *97*, 8364; b) J. H. Holtz, S. A. Asher, *Nature* **1997**, *389*, 829; c) J. Lahann, S. Mitragotri, T.-N. Tran, H. Kaido, J. Sundaram, I. S. Choi, S. Hoffer, G. A. Somorjai, R. Langer, *Science* **2003**, *299*, 371.
[3] a) G. M. Whitesides, B. Grzybowski, *Science* **2002**, *295*, 2418; b) S. Zhang, *Nat. Biotechnol.* **2003**, *21*, 1171.
[4] P. Terech, R. G. Weiss, *Chem. Rev.* **1997**, *97*, 3133.
[5] a) *Photochroism: Memories and Switches* (Ed.: M. Irie), *Chem. Rev.* **2000**, 100, 1683; b) *Molecular Switches* (Ed.: B. L. Feringa), Wiley-VCH, Weinheim, **2001**; c) H. Tian, S. J. Yang, *Chem. Soc. Rev.* **2004**, *33*, 85.
[6] a) M. Irie, R. Iga, *Macromolecules* **1986**, *19*, 2480; b) J.-P. Desvergne, F. Fages, H. Bouas-Laurent, P. Marsau, *Pure Appl. Chem.* **1992**, 1231; c) K. Murata, M. Aoki, T. Suzuki, T. Harada, H. Kawabata, T. Komori, F. Ohseto, K. Ueda, S. Shinkai, *J. Am. Chem. Soc.* **1994**, *116*, 6664; d) L. Frkanec, M. Jokic, J. Makarevic, K. Wolsperger, M. Zinic, *J. Am. Chem. Soc.* **2002**, *124*, 33, 9716; e) M. S. Vollmer, T. D. Clark, C. Steinem, M. R. Ghadiri, *Angew. Chem.* **1999**, *111*, 1703; *Angew. Chem. Int. Ed.* **1999**, *38*, 1598; f) S. A. Ahmed, X. Sallenave, F. Fages, G. Mieden-Gundert, W. M. Muller, U. Muller, F. Vogtle, J.-L. Pozzo, *Langmuir* **2002**, *18*, 19, 7096; g) M. Ayabe, T. Kishida, N. Fujita, K. Sada, S. Shinkai, *Org. Biomol. Chem.* **2003**, *1*, 2744; h) M. Moriyama, N. Mizoshita, T. Yokota, K. Kishimoto, T. Kato, *Adv. Mater.* **2003**, *15*, 1335; i) N. Koumura, M. Kudo, N. Tamaoki, *Langmuir* **2004**, *20*, 9897; j) J. Eastoe, M. Sanchez-Dominguez, P. Wyatt, R. K. Heenan, *Chem. Commun.* **2004**, 2608.
[7] J. J. D. de Jong, L. N. Lucas, R. M. Kellogg, J. H. van Esch, B. L. Feringa, *Science* **2004**, *304*, 278.
[8] Throughout the text, **2** refers to the photostationary state of the closed form, which consists of 40% of **2** with 60% of **1** still present. Initial experiments with only **2** showed no gelation, which indicates that the presence of both **1** and **2** is essential.
[9] N. Harada, K. Nakanishi, *Circular Dichroic Spectroscopy: Exciton Coupling in Organic Stereochemistry*, University Science Books, Mill Valley, CA, **1983**.
[10] P. R. Hania, A. Pugzlys, L. N. Lucas, J. J. D. de Jong, J. H. van Esch, B. L. Feringa, K. Duppen, *Solid State Phenomena* **2004**, *97–98*, 207.
[11] M. Moriyama, N. Mizoshita, T. Yokota, K. Kishimoto, T. Kato, *Adv. Mater.* **2003**, *15*, 1335.
[12] Y. Zhao, X. Tong, *Adv. Mater.* **2003**, *15*, 1431.
[13] R. Penterman, S. I. Klink, H. de Koning, G. Nisato, D. J. Broer, *Nature* **2002**, *417*, 55.
[14] This was apparent from the different intensity distributions for the red, green, and blue channels on a three-color CCD camera and has been checked with homogeneously irradiated samples and UV/Vis spectroscopy.
[15] Control experiments by SEM at lower concentration showed that in the empty areas too little monomer is present to form fibers.
[16] P. R. Hania, R. Telesca, L. N. Lucas, A. Pugzlys, J. van Esch, B. L. Feringa, J. G. Snijders, K. Duppen, *J. Phys. Chem. A* **2002**, *106*, 8498.

 © 2005 Wiley-VCH Verlag GmbH & Co. KGaA, Weinheim

Asymmetric Synthesis

Metallophosphite-Induced Nucleophilic Acylation of α,β-Unsaturated Amides: Facilitated Catalysis by a Diastereoselective Retro [1,4] Brook Rearrangement**

*Mary R. Nahm, Xin Linghu, Justin R. Potnick, Christopher M. Yates, Peter S. White, and Jeffrey S. Johnson**

Nucleophilic acylation of enones and enoates catalyzed by cyanide ions or heterazolium carbenes, commonly known as the Stetter reaction, is a useful method for the synthesis of 1,4-dicarbonyl compounds.[1] The key feature of this reaction is the carbonyl-polarity reversal initiated by the addition of a cyanide ion or a heterazolium carbene to an aldehyde facilitating subsequent 1,4-addition to an α,β-unsaturated carbonyl compound. Although this reaction has proven fruitful with a variety of acceptors, its success has been largely limited to aryl or unsubstituted[2] substrates. Acceptors bearing a β-alkyl group normally give the 1,4-addition product in 30–40% yield,[3] and achieving enantioselectivity in the intermolecular Stetter reaction has also proven to be difficult.[4] Herein, we provide a strategy to address both of these issues through metallophosphite-catalyzed acylations of α,β-unsaturated amides. These reactions are enabled by an unusual [1,2] Brook rearrangement/conjugate addition/retro [1,4] Brook rearrangement sequence that proceeds with good *anti* diastereoselectivity and allows access to a range of stable α-silyl-γ-ketoamides (Scheme 1).

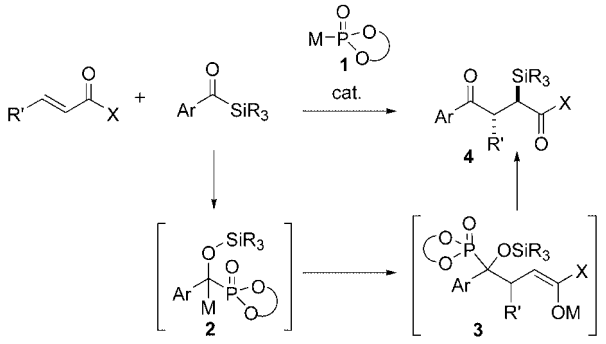

Scheme 1. Metallophosphite-catalyzed alkene acylation. X = OR, NR_2.

[*] M. R. Nahm, X. Linghu, J. R. Potnick, C. M. Yates, P. S. White, Prof. J. S. Johnson
Department of Chemistry
University of North Carolina, Chapel Hill
Chapel Hill, NC 27599-3290 (USA)
Fax: (+1) 919-962-2388
E-mail: jsj@unc.edu

[**] We thank the National Institutes of Health (National Institute of General Medical Sciences (GM068443)) for support of this research. J.S.J. is an Eli Lilly Grantee and a 3 M Nontenured Faculty Awardee.

Supporting information for this article is available on the WWW under http://www.angewandte.org or from the author.

Acyl silanes are effective aldehyde surrogates that confer unique advantages in umpolung reactions. The acyl anion equivalent formed on nucleophilic addition and subsequent [1,2] Brook rearrangement[5,6] undergoes addition to a number of electrophiles. Degl'Innocenti et al. found that the 1,4-addition of benzoyl trimethylsilane to cyclohexenone can be catalyzed by cyanide ions,[7] whereas Scheidt and co-workers recently described the successful conjugate addition of acyl silanes to unsaturated esters and ketones by using thiazolium carbene catalysis.[8,9] The substrate scope of the latter process mirrors the classic Stetter reaction, and conjugate acceptors bearing a β-alkyl substituent have not been reported. Metallophosphites[10,11] can be considered as an alternative to cyanide ions and thiazolium carbenes, and they have recently been described as carbonyl-umpolung catalysts in the context of a new enantioselective cross-benzoin reaction.[12] We projected that this catalysis concept might be applicable to alkene electrophiles as well.

The conjugate addition of acyl silanes (benzoyl trimethylsilane, benzoyl triethylsilane, and benzoyl dimethylphenylsilane) to Michael acceptors (ethyl crotonate, methyl cinnamate, and cyclohexenone) catalyzed by the Enders phosphite **5** was initially examined. Potassium hydride gave the best reactivity of the bases screened in these reactions; however, few reactions provided appreciable quantities of the desired acylation product. The ^{1}H NMR spectra of the reactions typically revealed incorporation of the phosphite in the acyl silane/acceptor adduct, thus indicating that the proposed cycle was initiated but not completed. Exposure of the reaction mixture to tetrabutylammonium fluoride (TBAF) afforded the desired γ-ketoester. Ethyl crotonate provided the best yields of the acceptors screened, but even under optimized conditions these were unacceptably low [≤37% of **6**, Eq. (1)].

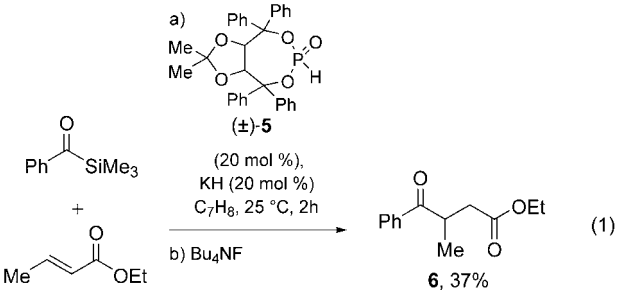

The low turnover and aforementioned observations suggested that enolate **3** did not undergo efficient silyl transfer. We hoped that replacement of the unsaturated ester (X = OR) with an amide (X = NR_2) would enhance the nucleophilicity of the derived enolate, promote the desired silyl transfer, and regenerate the metallophosphite catalyst.

Evaluation of this hypothesis revealed that amides did indeed facilitate catalyst turnover (Table 1). We had expected that O→O 1,6 transfer of the silyl group to form a silylketene aminal might be energetically feasible but were surprised to find that the O→C 1,4 silyl transfer was dominant to the exclusion of the former. Furthermore, the derived α-silyl-

 DOI: 10.1002/anie.200462795 © 2005 Wiley-VCH Verlag GmbH & Co. KGaA, Weinheim

Table 1: Catalytic conjugate addition of acyl silanes to unsaturated amides.[a]

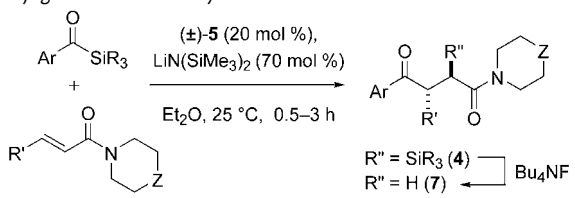

Entry	Ar	SiR_3	R′	Z	d.r.[b] of **4**	*t* [h]	Yield [%][c]
1[d]	Ph	$SiMe_2Ph$	Me	CH_2	7:1 (**4a**)	2	73 (**7a**)
2	Ph	$SiMe_2Ph$	Me	O	4:1 (**4b**)	0.5	81 (**7b**)
3	Ph	$SiMe_2Ph$	Et	CH_2	1.3:1 (**4c**)	0.75	74 (**7c**)
4[e]	Ph	$SiMe_2Ph$	Ph	O	10:1 (**4d**)[f]	0.5[g]	81 (**7d**)
5[e]	Ph	$SiMe_2Ph$	4-MeOPh	O	11:1 (**4e**)	0.5[g]	57 (**7e**)
6[e]	Ph	$SiMe_2Ph$	4-ClPh	O	8:1 (**4f**)	0.5[g]	80 (**7f**)
7	Ph	$SiMe_3$	Me	CH_2	10:1 (**4g**)	3	80 (**7a**)
8	Ph	$SiEt_3$	Me	CH_2	4:1 (**4h**)	2.5	91 (**7a**)
9	4-MeOPh	$SiEt_3$	Me	CH_2	3.5:1 (**4i**)	1	87 (**7i**)
10	4-ClPh	$SiEt_3$	Me	CH_2	3:1 (**4j**)	2	62 (**7j**)

[a] $ArC(O)SiR_3$ (1.0 equiv), $R'CH{=}CHC(O)NC_4H_8Z$ (1.1 equiv) unless otherwise stated. [b] *anti*/*syn* isomers as determined by ^1H NMR spectroscopic analysis unless otherwise stated. [c] Yield of the isolated, analytically pure **7**; average of at least two experiments. [d] Phosphite catalyst loading = 10 mol%. [e] $R'CH{=}CHC(O)NC_4H_8O$ (1.5 equiv). [f] As determined by yield of isolated product. [g] Including slow addition of acyl silane to other reagents.

amide was unexpectedly delivered with good diastereoselectivity in a number of cases. Acceptors bearing a β-alkyl substituent for these metallophosphite-catalyzed reactions[13] are now synthetically useful substrates that generate alkene acylation products in moderate to high yields (62–91%, entries 1–3 and 7–10). A number of acyl silanes are competent in the addition and show only subtle changes in reactivity upon variation of the silyl group (entries 1, 7, and 8) but exhibit more significant differences in reactivity between the electron-rich and electron-poor acyl silanes (entries 9 and 10).

The α-silyl-γ-ketoamides **4** were stable and could be easily isolated by column chromatography. We were naturally attracted to the stereospecific transformation of the functionalized silane to its derived secondary alcohol through the Tamao–Fleming oxidation,[14,15] but were aware of only two reported examples of such oxidations of α-silylcarbonyl compounds.[16,17] Attempts to activate the $C(sp^2)$–Si bond by a variety of protocols led to either desilylation, which yielded **7**, or bromination through cleavage of the C_α–Si bond. The α-bromo-γ-ketoamides **8d** and **8f** were obtained in 75 and 87% yields, respectively, with a diastereomeric ratio of 3:1 in each case (Scheme 2). An X-ray diffraction study of **8d** revealed that the major diastereomer exhibits *syn* stereochemistry.[18] Interestingly, the addition of bromine to **4d** in the absence of $AcOH/AcO_2H$ induces elimination to give the (*Z*)-α,β-unsaturated ketoamide **9** exclusively in 96% yield (Scheme 2). The olefin geometry was determined by NOESY analysis.

Finally, we found that this new catalyzed acylation provides an attractive platform for enantioselective catalysis. The enantiopure Enders phosphite (*R*,*R*)-**5** was employed and the major *anti* diastereomer was delivered in 60% *ee*, whereas the minor *syn* isomer was obtained in 74% *ee* (Scheme 3). Desilylation gave γ-ketoamide (2*R*)-**7d** in 67% yield and 50% *ee*.[19] Although the enantioselectivity is moderate, it already eclipses the highest enantioselectivity of which we are aware for intermolecular Stetter-type reactions (4% yield, 39% *ee*).[20] We further note that the structure of 1,1,4,4-tetraphenyl-2,3-*O*-isopropylidene-L-threitol (TADDOL) phosphite is readily amenable to modifications that we project will deliver more highly enantioselective catalysts.

The proposed catalytic cycle is depicted in Scheme 4 and is initiated by phosphite addition and the [1,2] Brook rearrangement.[21] Catalyst release is apparently triggered after conjugate addition by an unusual diastereoselective retro [1,4] Brook rearrangement (**3**→**10**).[22] The fact that the major enantiomer possesses the same C3 configuration in both the *syn* and *anti* diastereomers (Scheme 3) suggests that the chiral phosphite may be the dominant diastereocontrol element rather than a preferred transition-state topology.

A metallophosphite-catalyzed intermolecular alkene acylation has been achieved employing the Enders TADDOL phosphite, thus giving γ-ketoamides in generally good yields. These reactions allow access to synthetically interesting α-silyl-γ-ketoamides and provide an attractive platform for enantioselective variants. Ongoing work in our laboratory is directed toward the

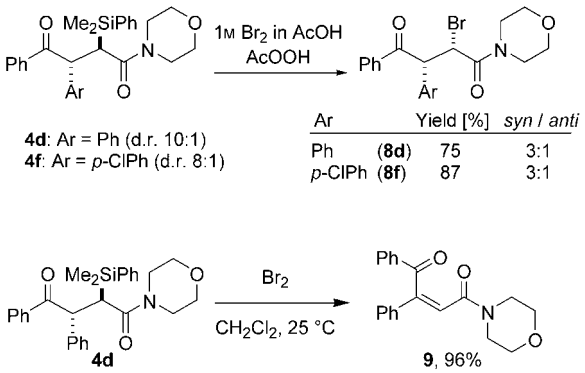

Scheme 2. Functionalization of α-silyl-γ-ketoamides.

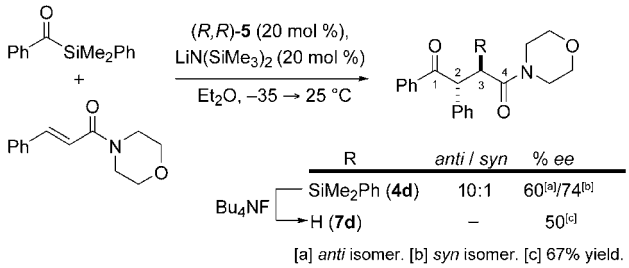

Scheme 3. Enantioselective metallophosphite-catalyzed alkene acylation.

 © 2005 Wiley-VCH Verlag GmbH & Co. KGaA, Weinheim

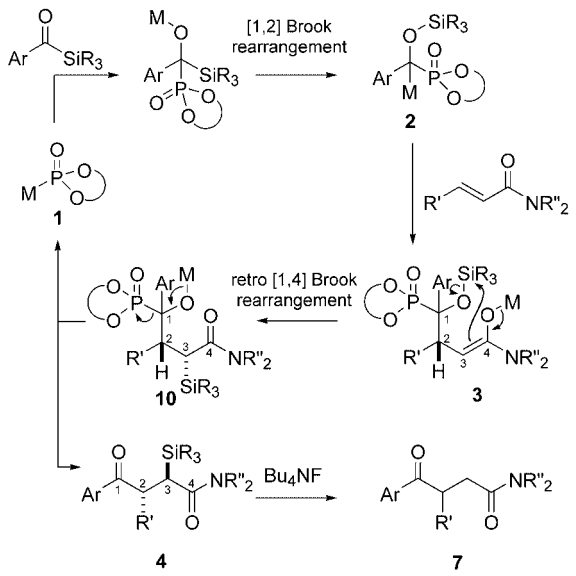

Scheme 4. Proposed catalytic cycle.

development of 1) those strategies that take advantage of the high diastereoselectivity of the retro [1,4] Brook rearrangement and 2) phosphite catalysts that deliver more highly enantioenriched products.

Experimental Section

7a (entry 1, representative procedure): The acyl silane (0.42 mmol) and amide (0.46 mmol, 1.1 equiv) were added to a dry pear-shaped flask in the glovebox, while the TADDOL phosphite (0.084 mmol, 0.2 equiv) and lithium hexamethyldisilazide (LHMDS; 0.29 mmol, 0.7 equiv) were added to a dry round-bottom flask with a magnetic stirring bar. The flasks were removed from the glovebox and Et_2O (3.0 mL) was added to the metallophosphite and stirred in an N_2 atmosphere. The acyl silane/amide mixture was added to the metallophosphite by cannula and the delivery flask was rinsed with Et_2O (7 mL). The resulting mixture was stirred in an N_2 atmosphere at room temperature until the starting material was consumed (TLC analysis). The solvent was removed in vacuo and an aliquot was taken to determine the diastereoselectivity by ^{1}H NMR spectroscopic analysis. The residue was redissolved in THF. The reaction mixture was treated with a solution of tetrabutylammonium fluoride in THF (TBAF; 1M, 0.84 mmol, 2.0 equiv) and immediately quenched with several milliliters of a saturated aqueous solution of NH_4Cl. The product was then extracted with Et_2O, washed with water (2×10 mL), and washed with a saturated aqueous solution of $NaHCO_3$ (2×10 mL). The organic extracts were combined and dried over Na_2SO_4, filtered, and concentrated. The product then was purified by flash chromatography with ethyl acetate/hexanes (30:70) as the eluent to afford the pure 1,4-dicarbonyl compound in 76% yield. Analytical data for **7a**: IR (thin film): $\tilde{\nu}=3061, 2933, 2856, 1684, 1639, 1444, 1369, 1223, 1196, 1122, 1016, 978, 706\ cm^{-1}$; ^{1}H NMR (400 MHz, $CDCl_3$): $\delta=8.07$–7.98 (m, 2H), 7.54–7.47 (m, 1H), 7.47–7.39 (m, 2H), 4.10–4.00 (m, 1H), 3.53–3.36 (m, 4H), 3.02 (dd, $J=16.0$, 8.8 Hz, 1H), 2.40 (dd, $J=16.4$, 4.8 Hz, 1H), 1.66–1.49 (m, 6H), 1.17 ppm (d, $J=7.2$ Hz, 3H); ^{13}C NMR (100 MHz, $CDCl_3$): $\delta=203.9$, 169.3, 136.1, 132.6, 128.41, 128.40, 46.4, 42.6, 37.0, 36.9, 26.2, 25.4, 24.4, 17.8 ppm; TLC (ethyl acetate/hexanes, 40:60) $R_f=0.32$; elemental analysis (%) calcd for $C_{16}H_{21}NO_2$: C 74.10, H 8.16, N 5.40; found: C 74.21, H 8.27, N 5.29.

Received: December 3, 2004
Published online: March 10, 2005

Keywords: acylation · asymmetric catalysis · rearrangement · umpolung

[1] a) H. Stetter, M. Schreckenberg, *Angew. Chem.* **1973**, *85*, 89; *Angew. Chem. Int. Ed.* **1973**, *12*, 81; b) H. Stetter, H. Kuhlmann, *Org. React.* **1991**, *40*, 407–496.
[2] J. H. Gong, Y. J. Im, K. Y. Lee, J. N. Kim, *Tetrahedron Lett.* **2002**, *43*, 1247–1251.
[3] a) H. Stetter, *Angew. Chem.* **1976**, *88*, 695–736; *Angew. Chem. Int. Ed.* **1976**, *15*, 639–647; b) H. Stetter, H. Kuhlmann, *Chem. Ber.* **1976**, *109*, 2890–2896; c) H. Stetter, M. Schreckenberg, K. Wiemann, *Chem. Ber.* **1976**, *109*, 541–545; d) H. Stetter, H. J. Bender, *Chem. Ber.* **1981**, *114*, 1226–1233; e) H. Stetter, L. Simons, *Chem. Ber.* **1985**, *118*, 3172–3187; f) H. Stetter, H. Skobel, *Chem. Ber.* **1987**, *120*, 643–645.
[4] a) D. Enders, K. Breuer in *Comprehensive Asymmetric Catalysis*, *Vol. 3* (Eds.: E. N. Jacobsen, A. Pfaltz, H. Yamamoto), Springer, New York, **1999**, pp. 1093–1102; for examples of enantioselective intramolecular Stetter reactions, see: b) D. Enders, K. Breuer, J. Runsink, J. H. Teles, *Helv. Chim. Acta* **1996**, *79*, 1899–1902; c) M. S. Kerr, J. Read de Alaniz, T. Rovis, *J. Am. Chem. Soc.* **2002**, *124*, 10298–10299; d) M. S. Kerr, T. Rovis, *J. Am. Chem. Soc.* **2004**, *126*, 8876–8877; e) S. M. Mennen, J. T. Blank, M. B. Tran-Dubé, J. E. Imbriglio, S. J. Miller, *Chem. Commun.* **2005**, 195–197.
[5] A. G. Brook, *Acc. Chem. Res.* **1974**, *7*, 77–84.
[6] W. H. Moser, *Tetrahedron* **2001**, *57*, 2065–2084.
[7] A. Degl'Innocenti, A. Ricci, A. Mordini, G. Reginato, V. Colotta, *Gazz. Chim. Ital.* **1987**, *117*, 645–648.
[8] A. E. Mattson, A. R. Bharadwaj, K. A. Scheidt, *J. Am. Chem. Soc.* **2004**, *126*, 2314–2315.
[9] A. R. Bharadwaj, K. A. Scheidt, *Org. Lett.* **2004**, *6*, 2465–2468.
[10] K. Takeda, T. Tanaka, *Synlett* **1999**, 705–708.
[11] D. Enders, L. Tedeschi, J. W. Bats, *Angew. Chem.* **2000**, *112*, 4774–4776; *Angew. Chem. Int. Ed.* **2000**, *39*, 4605–4607.
[12] X. Linghu, J. R. Potnick, J. S. Johnson, *J. Am. Chem. Soc.* **2004**, *126*, 3070–3071.
[13] The racemic TADDOL phosphite **5** regularly provided higher yields than simpler phosphites, for example, diethyl phosphite.
[14] G. R. Jones, Y. Landais, *Tetrahedron* **1996**, *52*, 7599–7662.
[15] I. Fleming, *Chemtracts: Org. Chem.* **1996**, *9*, 1–64.
[16] M. M. Mader, J. C. Edel, *J. Org. Chem.* **1998**, *63*, 2761–2764.
[17] L. A. Dakin, S. E. Schaus, E. N. Jacobsen, J. S. Panek, *Tetrahedron Lett.* **1998**, *39*, 8947–8950.
[18] CCDC-253985 (**4d**) and -253984 (**8d**) contain the supplementary crystallographic data for this paper. These data can be obtained free of charge from the Cambridge Crystallographic Data Centre via www.ccdc.cam.ac.uk/data_request/cif.
[19] The 2*R* configuration of **7d** was assigned through chemical correlation (see the Supporting Information).
[20] D. Enders, T. Balensiefer, *Acc. Chem. Res.* **2004**, *37*, 534–541.
[21] (Silyloxy)phosphonate anion **2** has been previously prepared stoichiometrically: R. E. Koenigkramer, H. Zimmer, *Tetrahedron Lett.* **1980**, *21*, 1017–1020.
[22] C. Gibson, T. Buck, M. Noltemeyer, R. Brückner, *Tetrahedron Lett.* **1997**, *38*, 2933–2936, and references therein.

 © 2005 Wiley-VCH Verlag GmbH & Co. KGaA, Weinheim

Cyanoboration

Palladium-Catalyzed Addition of Cyanoboranes to Alkynes: Regio- and Stereoselective Synthesis of α,β-Unsaturated β-Boryl Nitriles

Michinori Suginome, Akihiko Yamamoto, and Masahiro Murakami**

Much attention has been focused on the development of efficient syntheses of organoboron compounds because of their increasing use in the materials and pharmaceutical sciences.[1] The addition of boron-containing molecules to carbon–carbon multiple bonds is one of the most powerful strategies for the synthesis of organoboron compounds.[2] The process allows the simultaneous introduction into organic molecules of a boryl group and a functional group β to the boryl group regio- and stereoselectively.[3–5]

We have been involved in the development of catalytic addition reactions of boron- and silicon-containing molecules to unsaturated organic compounds.[4,6,7] Our recent interest has focused particularly on the addition of cyanoboranes with a B–CN bond across a carbon–carbon multiple bond to form a C–CN bond and a B–C bond. Although we succeeded recently in the catalytic activation of a B–CN bond in an intramolecular cyanoboration of alkynes, we faced significant difficulties in finding the appropriate reaction conditions for its intermolecular variant with cyanoborane derivatives that had been used in previous studies.[8] It seemed likely that the development of an intermolecular cyanoboration would lead to the efficient synthesis of a wide range of highly substituted α,β-unsaturated nitriles. We report, herein, the intermolecular cyanoboration of alkynes, in which the structure of the cyanoborane has the primary influence on the reactivity and selectivity of the addition.[9]

As reported previously,[8] our attempts at the cyanoboration of alkynes with the bis(dialkylamino) cyanoboranes **1a** and **1b** were unsuccessful. We then turned our attention to cyclic cyanoborane derivatives, such as **1c**–**g**,[10,11] whose reactivities had never been investigated. Representative results of the reactions of **1c**–**g** with 4-octyne (**2a**) are shown in Table 1. We were pleased to find that reactions of the ethylenediamine-derived cyanoboranes **1c** and **1d** afforded the cyanoboration products in moderate yields (Table 1, entries 1 and 2). Only the product of *cis* addition

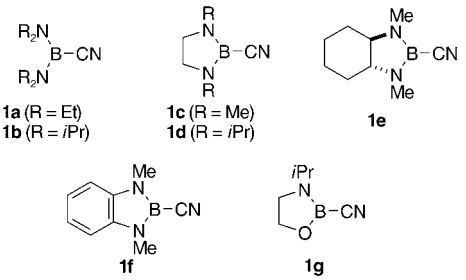

Table 1: Palladium-catalyzed reaction of symmetrical alkynes with cyanoboranes.[a]

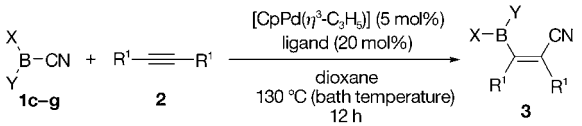

Entry	1	Alkyne (R^1)	Ligand	Yield [%]
1	**1c**	**2a** (Pr)	PMe_3	47[b]
2	**1d**	**2a** (Pr)	PMe_3	49[c]
3	**1e**	**2a** (Pr)	PMe_3	81[b]
4	**1e**	**2a** (Pr)	PCy_3	66[b]
5	**1e**	**2a** (Pr)	PMe_2Ph	8[b]
6	**1e**	**2a** (Pr)	PPh_3	0
7	**1f**	**2a** (Pr)	PMe_3	97[b] (87[d])
8	**1g**	**2a** (Pr)	PMe_3	0
9	**1f**	**2b** (Ph)	PMe_3	99[c] (82[d])

[a] The corresponding cyanoborane **1** (0.5 mmol) and alkyne **2** (0.6 mmol) were heated in dioxane (0.5 mL) in the presence of [CpPd(η³-C_3H_5)] (0.025 mmol; Cp is cyclopentadiene) and PMe_3 (0.1 mmol). [b] Yield determined by GC. [c] Yield determined by NMR spectroscopy. [d] Yield of isolated product.

was formed in the cyanoboration reactions. Interestingly, the use of **1e**, which differs from **1c** only in that it has a fused cyclohexane ring, led to the corresponding cyanoboration products in better yields (compare entry 3 with entry 1 of Table 1). A comparison of different phosphine ligands on palladium indicated that trialkylphosphines were more effective than aryl-substituted phosphines (Table 1, entries 4–6). Remarkably, the reaction of the phenylenediamine-derived cyanoborane **1f** afforded the corresponding cyanoboration product almost quantitatively (Table 1, entry 7); the product was isolated by bulb-to-bulb distillation. In contrast, cyanoborane **1g**—derived from an amino alcohol—completely failed to give any addition product (Table 1, entry 8). Under optimal conditions, the reaction of **1f** with diphenylacetylene (**2b**) afforded the corresponding product in high yield (Table 1, entry 9).

We then examined unsymmetrical alkynes that bear both an aryl and an alkyl group at their sp-hybridized carbon atoms. The reaction of **1c** with 1-phenylpropyne (**4a**) resulted in the formation of the cyanoboration products with moderate regioselectivity (Table 2, entry 1). The regioselectivity was improved significantly to 95:5 with **1d**, which has bulky isopropyl groups on the nitrogen atoms (Table 2, entry 2). The major product was assigned as the isomer in which the cyano

[*] Prof. Dr. M. Suginome, A. Yamamoto, Prof. Dr. M. Murakami
Kyoto University
Department of Synthetic Chemistry and Biological Chemistry
Graduate School of Engineering
Katsura, Nishikyo-ku, Kyoto 615-8510 (Japan)
Fax: (+81) 75-383-2722
E-mail: suginome@sbchem.kyoto-u.ac.jp
murakami@sbchem.kyoto-u.ac.jp
Prof. Dr. M. Suginome
PRESTO, Japan Science and Technology Corporation
Katsura, Nishikyo-ku, Kyoto 615-8510 (Japan)

Supporting information for this article is available on the WWW under http://www.angewandte.org or from the author.

 © 2005 Wiley-VCH Verlag GmbH & Co. KGaA, Weinheim DOI: 10.1002/anie.200462961

group is attached to the carbon atom α to the aryl group. The reactions of **4a** with the other methyl-substituted cyanoboranes **1e** and **1f** were moderately regioselective (Table 2, entries 3 and 4). High regioselectivities were observed for the cyanoboration of other aryl–alkyl acetylenes with **1d** (Table 2, entries 5–11). There may be a tendency for alkynes that bear a bulky aryl group to give rise to particularly high regioselectivities (Table 2, entries 8–10).

The reaction of 1-octyne with **1d** in the presence of a PMe_3/Pd^0 catalyst afforded the corresponding product **7d** in 74% yield as an

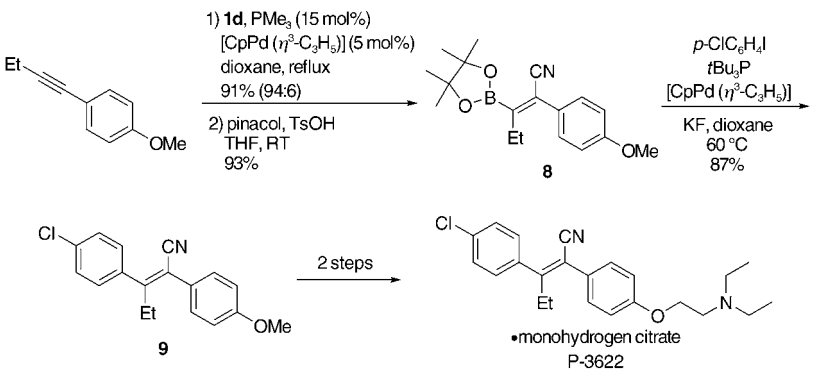

Scheme 1. Formal synthesis of the potential squalene synthetase inhibitor P-3622. Ts = *p*-toluenesulfonyl.

Table 2: Palladium-catalyzed cyanoboration of unsymmetrical alkynes.[a]

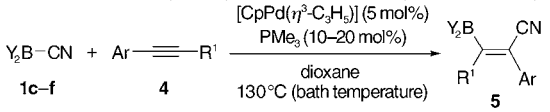

1c–f 4 5

Entry	1	Alkyne (Ar, R^1)	Yield [%][b]	Product ratio[c]
1	**1c**	**4a** (Ph, Me)	77	85:15
2	**1d**	**4a** (Ph, Me)	94	95:5
3	**1e**	**4a** (Ph, Me)	97	83:17
4	**1f**	**4a** (Ph, Me)	96	83:17
5	**1d**	**4b** (Ph, Bu)	89	95:5
6	**1d**	**4c** (*p*-$EtO_2CC_6H_4$, Bu)	72	88:12
7	**1d**	**4d** (*p*-$CF_3C_6H_4$, Me)	81	93:7
8	**1d**	**4e** (*o*-$CH_3C_6H_4$, Bu)	59	98:2
9	**1d**	**4f** (*o*-$MOMOC_6H_4$, Bu)	80	99:1
10	**1d**	**4g** (1-Naph, Me)	72	99:1
11	**1d**	**4h** (2-Naph, Bu)	61	91:9

[a] The corresponding cyanoborane **1** (0.5 mmol) and alkyne **4** (0.6 mmol) were heated in dioxane (0.1–0.5 mL) in the presence of [CpPd(η³-C_3H_5)] (5 mol%) and PMe_3 (0.05–0.1 mmol) unless otherwise noted. [b] Yield of isolated product. [c] Regioisomeric ratio determined by GC and ^{1}H NMR spectroscopy. MOM = methoxymethyl, Naph = naphthyl.

84:16 mixture of regioisomers [Eq. (1)]. The regioselectivity of the reaction was critically affected by the bulkiness of the cyanoborane: The use of **1c** instead of **1d** resulted in a 6:4 ratio of product regioisomers.

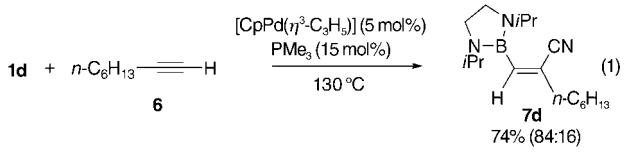

This new cyanation protocol offers a route to fully substituted α,β-unsaturated nitriles, whose regio- and stereoselective synthesis has often proved difficult. We have completed a convenient synthesis of the potential squalene synthetase (SQS) inhibitor P-3622[12] by applying a palladium-catalyzed intermolecular cyanoboration as a key step (Scheme 1). Cyanoboration of 1-(4-methoxyphenyl)-1-butyne with cyanoborane **1d**, followed by exchange of the diamine ligand on the boron atom for a pinacol ligand, afforded the corresponding 2-boryl-1-cyanoalkene **8** with good regioselectivity. Suzuki–Miyaura coupling of **8** with *p*-chloroiodobenzene gave **9**, which was converted into the SQS inhibitor P-3622 and some related compounds.[13,14]

Further optimization of the catalytic system, the synthetic application of the products, and the expansion of the scope of the cyanoboration reaction are now being investigated in our laboratory.

Received: December 16, 2004
Published online: March 10, 2005

Keywords: alkynes · boron · cyanides · palladium · regioselectivity

[1] A. Suzuki, H. C. Brown, *Organic Synthesis via Boranes*, *Vol. 3*, Aldrich, Milwaukee, **2003**.
[2] I. Beletskaya, C. Moberg, *Chem. Rev.* **1999**, *99*, 3435.
[3] For additions of B–B bonds, see: a) T. Ishiyama, K.-i. Nishijima, N. Miyaura, A. Suzuki, *J. Am. Chem. Soc.* **1993**, *115*, 7219; b) for a review, see: T. B. Marder, N. C. Norman, *Top. Catal.* **1998**, *5*, 63.
[4] For additions of B–Si bonds, see: a) M. Suginome, H. Nakamura, Y. Ito, *Chem. Commun.* **1996**, 2777; b) M. Suginome, T. Ohmura, Y. Miyake, S. Mitani, Y. Ito, M. Murakami, *J. Am. Chem. Soc.* **2003**, *125*, 11174; c) M. Suginome, Y. Ito, *J. Organomet. Chem.* **2003**, *680*, 43, and references therein.
[5] For additions of B–Sn bonds, see: S. Onozawa, Y. Hatanaka, T. Sakakura, S. Shimada, M. Tanaka, *Organometallics* **1996**, *15*, 5450.
[6] a) M. Suginome, T. Iwanami, Y. Ito, *J. Am. Chem. Soc.* **2001**, *123*, 4357; b) M. Suginome, Y. Ito, *J. Organomet. Chem.* **2003**, *685*, 218.
[7] M. Suginome, Y. Ito, *Chem. Rev.* **2000**, *100*, 3221.
[8] M. Suginome, A. Yamamoto, M. Murakami, *J. Am. Chem. Soc.* **2003**, *125*, 6358.
[9] For related additions of cyanide-containing σ bonds to alkynes, see: a) hydrocyanation: R. Jackson, C. G. Lovel, *J. Chem. Soc. Chem. Commun.* **1982**, 1231; b) cyanosilylation: N. Chatani, T. Hanafusa, *J. Chem. Soc. Chem. Commun.* **1985**, 838; c) N. Chatani, T. Takeyasu, N. Horiuchi, T. Hanafusa, *J. Org. Chem.* **1988**, *53*, 3539; d) M. Suginome, H. Kinugasa, Y. Ito, *Tetrahedron Lett.* **1994**, *35*, 8635; e) cyanostannation: Y. Obora, A. S. Baleta, M. Tokunaga, Y. Tsuji, *J. Organomet. Chem.* **2002**, *660*, 173; f) acyl cyanation: K. Nozaki, N. Sato, H. Takaya, *J. Org. Chem.*

 © 2005 Wiley-VCH Verlag GmbH & Co. KGaA, Weinheim

1994, *59*, 2679; g) aryl cyanation: Y. Nakao, S. Oda, T. Hiyama, *J. Am. Chem. Soc.* **2004**, *126*, 13904.

[10] **Caution!** The handling cyanoboranes requires special care to avoid inhalation of hydrogen cyanide, which may be generated by the hydrolysis of the cyanoboranes. Although the cyanoboranes can be handled in air for short periods, for example, to be weighed out, all operations should be carried out in a fume hood.

[11] For the synthesis and reactions of amino-substituted cyanoboranes, see: a) A. Meller, W. Maringgele, U. Sicker, *J. Organomet. Chem.* **1977**, *141*, 249; b) M. Suginome, A. Yamamoto, Y. Ito, *Chem. Commun.* **2002**, 1392. The diamine-derived cyanoboranes are readily prepared from the corresponding chloroboranes by Cl–CN exchange with TMSCN (TMS is trimethylsilyl). The chloroboranes are prepared from the reaction of BCl_3 with the corresponding diamines in the presence of a base.

[12] a) H. J. Harwood, Jr., E. G. Barbacci-Tobin, S. F. Petras, S. Lindsey, L. D. Pellarin, *Biochem. Pharmacol.* **1997**, *53*, 839; b) S. K. Figdor, E. C. Schreiber, R. B. Stebbins, P. F. Moore, R. Pinson, Jr., *J. Med. Chem.* **1964**, *7*, 508.

[13] G. M. K. Hughes, P. F. Moore, R. B. Stebbins, *J. Med. Chem.* **1964**, *7*, 511.

[14] N. Miyaura, A. Suzuki, *Chem. Rev.* **1995**, *95*, 2457; for the use of the tBu$_3$P-based catalyst system, see: A. F. Littke, C. Dai, G. C. Fu, *J. Am. Chem. Soc.* **2000**, *122*, 4020.

 © 2005 Wiley-VCH Verlag GmbH & Co. KGaA, Weinheim

Reaction Mechanisms

Effects of Bending Excitation on the Reaction of Chlorine Atoms with Methane**

Hans A. Bechtel, Jon P. Camden, Davida J. Ankeny Brown, Marion R. Martin, Richard N. Zare, and Konstantin Vodopyanov*

Many chemical reactions are accelerated by heating the reagents. This effect is caused by more energy being partitioned into the reagents' electronic, translational, vibrational, and rotational degrees of freedom that ultimately becomes available for overcoming the reaction barrier. Which degrees of freedom are most effective at driving chemical reactions? For endoergic reactions involving an atom and a diatom, Polanyi[1] showed that vibrational excitation of the reagent diatom is the most effective means of overcoming the reaction barrier because the stretching motion along the diatomic internuclear axis efficiently couples to the reaction coordinate, that is, the set of motions that transforms the reagents into the products. For reactions involving polyatomic reagents, the simple concepts associated with atom + diatom reactions become complicated by the $3N-6$ extra degrees of freedom available for internal motions of a nonlinear N-atom polyatomic molecule. Intuitively, stretching vibrations of polyatomic molecules are expected to have the largest effects on abstraction reactions because energy is placed directly into the breaking bond and they most resemble the stretching vibration of diatomic molecules. This notion is confirmed for the Cl + CH_4 reaction, where one quantum of antisymmetric stretch excitation enhances the reaction by a factor of approximately 30.[2]

The effects of reagent bending vibrations on chemical reactions, on the other hand, are less intuitive because they require the concerted motion of three or more atoms in the reagent. Is the energy in these modes available for overcoming the reaction barrier? Unlike the stretching vibrations, the bending vibrations are low-frequency and consequently have less energy. They do not obviously map onto the reaction coordinate. Moreover, it is known from previous studies of the Cl + CH_4 reaction[3] that internal energy placed in more than one C–H stretch of methane remains localized in the methyl product, that is, all the internal energy is not available to appear in internal motion of HCl or in translational motion of the escaping product pair. The effects of bending vibrations have been largely unexplored experimentally despite the fact that these low-frequency vibrations are more easily populated at thermal temperatures. To date, the influence of bending vibrations on chemical reactions remains ambiguous, and many theoretical studies of direct polyatomic reactions treat the system in reduced dimensionality, simply assuming that these low-frequency modes play little or no role.[4]

Herein we present direct measurements of the effects of bend-excitation on an atom + polyatom reaction system under single collision conditions. We have chosen the Cl + CH_4 reaction [Eq. (1)] both as a prototype and for its practical importance to combustion and atmospheric chemistry. This reaction is thought to be responsible for the removal of chlorine in the stratosphere, and kinetic studies have shown a nonlinear variation of the logarithm of the rate constant versus the reciprocal of the temperature (Arrhenius plot).[5]

$$Cl + CH_4\,(\nu_4 = 1) \rightarrow HCl + CH_3 \qquad (1)$$

Contrary to intuitive expectations, we find that excitation of the low-frequency $CH_4(\nu_4{=}1)$ and $CH_3D(\nu_3{=}1)$ bending vibrations enhances the cross section for reaction with Cl atoms by a factor of two or more. This enhancement, which is constant over the collision-energy range 0.12 eV to 0.26 eV, implies that shearing motions, in addition to stretching

[*] Dr. H. A. Bechtel,[+] J. P. Camden, D. J. A. Brown, M. R. Martin, Prof. Dr. R. N. Zare
Department of Chemistry
Stanford University
Stanford CA 94305-5080 (USA)
Fax: (+1) 650-723-9262
E-mail: zare@stanford.edu
Dr. K. Vodopyanov
Ginzton Laboratory
Stanford University, Stanford, CA 94305-4088 (USA)
[+] Present Address:
Department of Chemistry, Massachusetts Institute of Technology
77 Massachusetts Ave., 6–022, Cambridge, MA 02139 (USA)

[**] This material is based upon work supported by the National Science Foundation under Grant No. CHE-0242103. H.A.B, J.P.C., and M.R.M. thank the National Science Foundation for graduate fellowships. H.A.B. also acknowledges Stanford University for the award of a Stanford Graduate Fellowship.

Supporting information for this article is available on the WWW under http://www.angewandte.org or from the author.

 © 2005 Wiley-VCH Verlag GmbH & Co. KGaA, Weinheim DOI: 10.1002/anie.200462837

motions, can facilitate C–H bond cleavage in this direct reaction. Moreover, the nonlocalized motion in the methane reagent is transferred almost exclusively to translational motion of the escaping products, which is in sharp contrast to theoretical calculations[6–9] that predict formation of methyl radicals predominantly excited into the umbrella bending mode. We also observe both H-atom and D-atom abstraction products from the Cl + $CH_3D(\nu_3{=}1)$ reaction, indicating that the reaction is not bond selective although the C–H and C–D motions are different in bend-excited CH_3D.

The Cl + CH_4 reaction is slightly endoergic, $\Delta H = 7.2\ kJ\,mol^{-1}$ (0.07 eV),[10] and has an estimated activation barrier of $32.8\ kJ\,mol^{-1}$ (0.34 eV).[11] The best estimate of the vibrationally adiabatic ground-state barrier, which is a better predictor of threshold energies neglecting tunneling, is $16.4\ kJ\,mol^{-1}$ (0.17 eV).[8,11] Theoretical calculations[6–9] have predicted that the umbrella bending mode should enhance the reaction rate by lowering the barrier. Experimental verification has been lacking in part because selective preparation of low-frequency modes has proven difficult. The few experimental measurements[12–16] that probe the effects of bend excitation on the Cl + CH_4 reaction have been performed using indirect methods, leading to disparate results. Early studies[12] showed no enhancement from the bending mode, whereas more recent measurements[14,15] estimate the enhancement factor to be approximately 200 or approximately 3, respectively, based on studies of residual bend-excited methane present in their molecular beam. We have examined the Cl + $CH_4(\nu_2{+}\nu_4)$ reaction and showed the $\nu_2+\nu_4$ mode to be at least 15% as reactive as the ν_3 (antisymmetric stretch) mode.[16] None of these more recent measurements, however, unambiguously distinguishes the effects of the ν_2 and ν_4 bending modes, although Zhou et al.[15] suggest that the ν_4 mode is the more reactive. Herein, we use a novel IR source to excite directly the $\nu_4 = 1$ mode, which permits us to demonstrate explicitly that bend excitation of methane enhances the Cl + CH_4 reaction.

Figure 1 shows an action spectrum obtained by monitoring the CH_3 reaction signal on the Q branch bandhead of the 2 + 1 resonance-enhanced multiphoton ionization (REMPI) 0_0^0 band while scanning the IR light over the CH_4 4_0^1 bending band. The action spectrum successfully reproduces the absorption spectrum, albeit at a significantly lower temperature (ca. 80 K). This result demonstrates that the umbrella bending vibration (ν_4) enhances the Cl + CH_4 reaction. To determine the enhancement factor, we position the IR laser on the 4_0^1 Q branch bandhead, scan the probe laser over the CH_3 0_0^0 Q branch, and measure the ratio of the IR-on signal (S_{ON}) to the IR-off signal (S_{OFF}). We note that S_{ON} has contributions from both the IR-enhanced reaction and the ground-state reaction, that is, $S_{ON} = \sigma_{GS}(1-f) + \sigma_{IR}f$, where σ_{GS} and σ_{IR} are the cross sections of the ground and vibrationally excited reactions, respectively, and f is the fraction of methane molecules pumped to the vibrationally excited state. In contrast, S_{OFF} arises purely from reaction with ground-state methane, $S_{OFF} = \sigma_{GS}$. Solving for the enhancement factor $F = \sigma_{IR}/\sigma_{GS}$ gives $F = (S_{ON}/S_{OFF} + f - 1)/f$. Assuming $f = 0.5$ (complete saturation of the transition), we find that although the action spectrum in Figure 1b suggests that

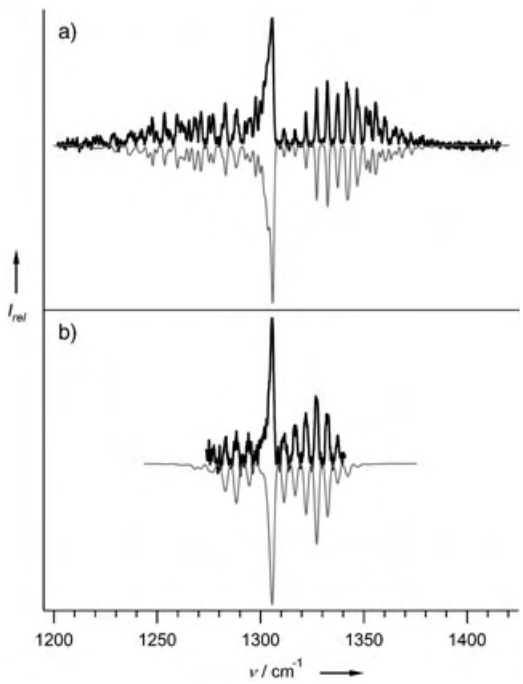

Figure 1. IR spectra of the CH_4 4_0^1 infrared band. a) The upper trace (black, thick line) is the room temperature photoacoustic absorption spectrum, and the lower trace (gray, thin line) is the simulated absorption spectrum at 300 K from the HITRAN database[21] convoluted with a Gaussian line width (1.2 cm^{-1}). b) The upper trace (black, thick line) is the action spectrum (0.16 eV) obtained by monitoring the $CH_3(\nu{=}0)$ reaction products while scanning the vibrational excitation laser wavelength. The lower trace (gray, thin line) is the simulated absorption spectrum at 80 K convoluted with a Gaussian line width of 2.0 cm^{-1}; the larger line width is most likely due to power broadening.

individual rotational lines are power broadened, the power dependence of the 4_0^1 Q branch is nearly linear, indicating that all the Q-branch lines are not saturated. Thus, a factor of two is strictly a lower bound for the enhancement. Using a more realistic estimate of the fraction pumped, $0.1 < f < 0.3$, the enhancement of bend excitation is $F(0.16\ eV) = 3 \pm 1$, which is in excellent agreement with the value Zhou et al. determined by more indirect means at a collision energy of 0.20 eV.[15]

We have measured the enhancement factor over a range of center-of-mass (CM) collision energies (0.12–0.25 eV) and found it to be constant within our experimental uncertainty (Figure 2). This result is particularly surprising for the lowest collision energies because we expect a larger enhancement near the threshold, which is estimated to lie in the middle of the experimental energy range.[8,11] Theoretical calculations[6–9] have predicted the umbrella bending vibration to lower the barrier and thus significantly enhance the reaction rate. In particular, Corchado et al.[8] have calculated that excitation of the ν_4 vibration lowers the barrier by approximately 0.02 eV, which should have a significant effect near the energy threshold. Their calculations, however, do not provide a quantitative estimate of the enhancement nor do they predict the lack of energy dependence. In light of these results, we believe that the energy of the bending vibration is

 © 2005 Wiley-VCH Verlag GmbH & Co. KGaA, Weinheim

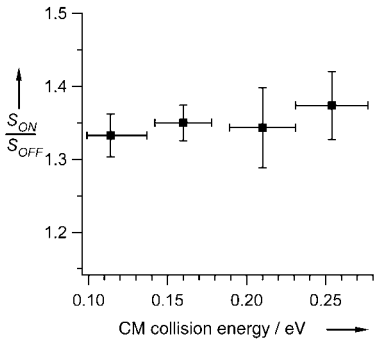

Figure 2. Ratio of S_{ON} to S_{OFF} as a function of center-of-mass (CM) collision energy. This ratio is the direct experimental measurement and makes no assumptions about the fraction of molecules pumped to $CH_4(\nu_4)$. The vertical uncertainty is the 95% confidence interval of replicate measurements, and the horizontal uncertainty represents the full width at half maximum height (FWHM) of the collision energy distributions[22] assuming a translational temperature of 10 K.

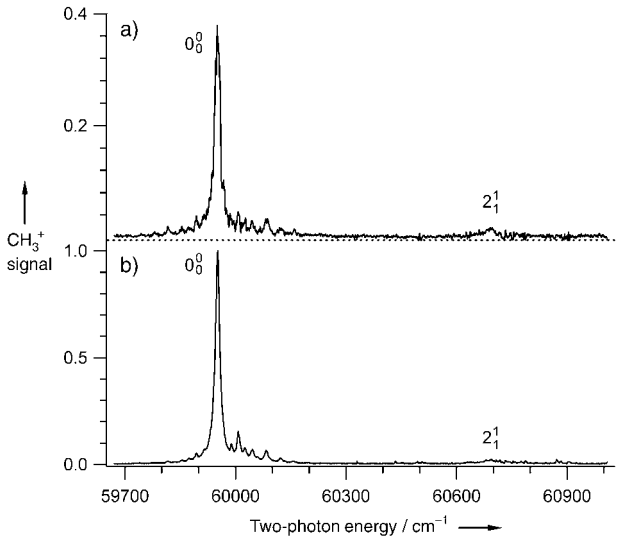

Figure 3. (2+1) REMPI spectra of the methyl radical products from the Cl + CH_4 reaction at a collision energy of 0.16 eV. a) the spectrum from the bend-excited reaction (obtained by subtracting S_{OFF} from S_{ON}) and b) the spectrum from the ground-state reaction (S_{OFF}). The signals have been normalized such that the maximum ground-state reaction signal is 1.

not available to overcome the reaction barrier without a minimal amount of translational energy.

Theoretical calculations[7] also predict forward-scattered CH_3 products, which is in agreement with our results (Figure S1 in the Supporting Information). Both the CH_3 vibrational distributions and angular distributions from the bend-excited reaction are essentially identical to those of the ground-state reaction, indicating that the energy of the bending vibration is transferred into translation and the new HCl bond. Although this result might be unexpected considering the nonlocalized motion of the bending vibration, Corchado et al.[8] have shown theoretically that the internal motion of the methane reagent can be rearranged upon approach of the Cl atom and thus couple energy into the new HCl bond. The same calculations,[6–8] however, have also predicted the $CH_4(\nu_4)$ umbrella bend to promote umbrella-bend-excited $CH_3(\nu_2)$ products, in contrast to our observations (Figure 3) that most of the products are formed in the vibrationless ground state with only a small fraction of the products formed with umbrella bend excitation ($\nu_2 = 1$).

Although the umbrella bending motion does not obviously participate in the bond breaking or forming process, the coupling of the umbrella bend mode to the reaction coordinate might be expected because the methyl radical must change from pyramidal to planar geometry as the reaction proceeds. On the other hand, the enhancement may arise simply because more energy is available for the reaction. To investigate these possibilities, we examine the effects of umbrella bend excitation on the Cl + $CH_3D(\nu_3{=}1)$ reaction, where the predominant motion arises from the three C–H oscillators with little movement of the C–D oscillator. If the reaction is enhanced by facilitating the methyl radical geometry change, then the D-atom abstraction channel (CH_3) should dominate because the CH_3 fragment motion more closely maps onto the product state geometry. If the reaction is enhanced by placing extra energy into the system, then the H-atom abstraction channel (CH_2D) should dominate because the energy is localized into the C–H bonds. Figure 4 shows that both product channels are enhanced by

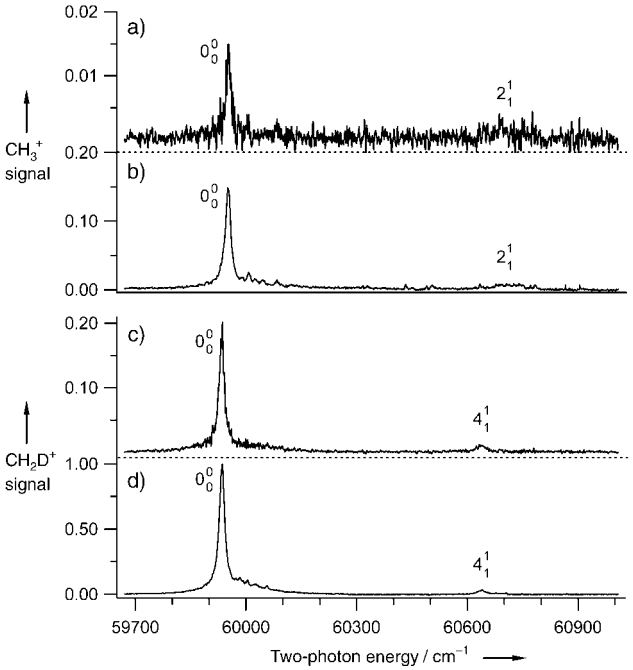

Figure 4. (2+1) REMPI spectra of the methyl radical products from the Cl + CH_3D reaction at a collision energy of 0.16 eV. a) and b) show the D-abstraction channel, c) and d) show the H-abstraction channel. Panels (a) and (c) show the spectra from the bend-excited reaction and panels (b) and (d) show the spectra from the ground-state reactions. The signal intensities have been normalized such that the maximum ground-state signal of the CH_2D product is 1.

bend-excitation, with only a slight preference for the H-atom abstraction channel. Thus, we conclude that neither mechanism alone accounts for what is observed. Furthermore, these

 © 2005 Wiley-VCH Verlag GmbH & Co. KGaA, Weinheim

results also suggest that the approach of the Cl atom rearranges the initial vibrational motion of the methane reagent. The lack of bond selectivity is in striking contrast to the bond selectivity observed in the stretch-excited reactions, where excitation of a C–H stretching motion in methane leads almost exclusively to H-atom abstraction by the Cl atom.[2,17] As expected, the bending motions are not nearly as efficient at providing chemical control because the vibrations are not as localized. These results help to explain why the optimum pulse shapes for laser control of chemical reactions are often so complex in form.[18]

We have demonstrated that excitation of the ν_4 vibration significantly enhances the cross section of the $Cl + CH_4$ reaction. As a result, we might expect the CH_4 ν_2 vibration to have similar effects. Theoretical calculations[8] and indirect experimental measurements[15] have suggested, however, that the ν_2 vibration is less effective at promoting reaction. Clearly, more work is needed to understand the effects of low-frequency bending motions on polyatomic chemical reactions.

Experimental Section

We supersonically expand a 1:4:7 mixture of molecular chlorine, methane (CH_4 or CH_3D), and helium into the extraction region of a Wiley-McLaren time-of-flight (TOF) spectrometer.[19] The vibrational state of methane is prepared by an IR laser that is generated using BBO and GaSe nonlinear crystals. The reaction is initiated by photolysis of Cl_2 with linearly polarized light (303 nm–386 nm), which produces monoenergetic Cl atoms primarily in their ground electronic state ($^2P_{3/2}$).[20] After a delay of 80 ns, the products are state selectively ionized by $2+1$ resonance-enhanced multiphoton ionization (REMPI), separated by mass, and detected by microchannel plates. The reactive signal from vibrationally excited methane is separated from the ground-state reactive signal by turning the IR light off and on and subtracting the resultant signals on a shot-by-shot basis.

The IR radiation required to prepare the vibrational state of methane is generated in a two-step process involving difference-frequency generation (DFG, see Supporting Information). Near-IR light at $\lambda = 1.24$ μm is first generated by DFG by combining the 1.064 μm fundamental of a Nd^{3+}:YAG laser with the output of a dye laser (Exciton R590/R610 mix) in a BBO crystal. The near-IR radiation is then combined with another 1.064 μm beam in a GaSe crystal to produce approximately 150 μJ of tunable light between 7–10 μm. The photolysis wavelengths are generated by mixing a dye laser output (Exciton R610) with 1.064 μm light in a BBO crystal, by doubling the output of a dye laser (Exciton R610, DCM, or LDS698), or by using the third harmonic of a Nd^{3+}:YAG laser. The probe laser light is generated by doubling the output of a dye laser (Exciton DCM/LDS698 mix). The IR light is focused into the chamber using an $f = 15$ cm BaF_2 lens, and the photolysis and probe lasers are focused using separate $f = 25$ cm fused silica lenses.

Received: December 6, 2004
Published online: March 14, 2005

Keywords: gas-phase reactions · kinetics · molecular dynamics · reaction mechanisms · vibrational spectroscopy

[1] J. C. Polanyi, *Acc. Chem. Res.* **1972**, *5*, 161.
[2] W. R. Simpson, T. P. Rakitzis, S. A. Kandel, A. J. Orr-Ewing, R. N. Zare, *J. Chem. Phys.* **1995**, *103*, 7313.
[3] Z. H. Kim, H. A. Bechtel, R. N. Zare, *J. Chem. Phys.* **2002**, *117*, 3232.
[4] S. Yoon, S. Henton, A. N. Zivkovic, F. F. Crim, *J. Chem. Phys.* **2002**, *116*, 10744.
[5] H. A. Michelsen, *Acc. Chem. Res.* **2001**, *34*, 331.
[6] W. T. Duncan, T. N. Truong, *J. Chem. Phys.* **1995**, *103*, 9642.
[7] H.-G. Yu, G. Nyman, *Phys. Chem. Chem. Phys.* **1999**, *1*, 1181.
[8] J. C. Corchado, D. G. Truhlar, J. Espinosa-Garcia, *J. Chem. Phys.* **2000**, *112*, 9375.
[9] S. Skokov, J. M. Bowman, *J. Chem. Phys.* **2000**, *113*, 4495.
[10] R. Atkinson, D. L. Baulch, R. A. Cox, J. R. F. Hampson, J. A. Kerr, J. Troe, *J. Phys. Chem. Ref. Data* **1992**, *21*, 1125.
[11] Y. Zhao, B. J. Lynch, D. G. Truhlar, *J. Phys. Chem. A* **2004**, *108*, 4786.
[12] a) V. V. Vijin, A. N. Mikheev, A. K. Petrov, Y. N. Molin, *React. Kinet. Catal. Lett.* **1975**, *3*, 79; b) E. N. Chesnokov, V. P. Strunin, N. K. Serdyuk, V. N. Panfilov, *React. Kinet. Catal. Lett.* **1975**, *3*, 131.
[13] D. S. Y. Hsu, T. J. Manuccia, *Appl. Phys. Lett.* **1978**, *33*, 915.
[14] S. A. Kandel, R. N. Zare, *J. Chem. Phys.* **1998**, *109*, 9719.
[15] J. Zhou, J. J. Lin, B. Zhang, K. Liu, *J. Phys. Chem. A* **2004**, *108*, 7832.
[16] Z. H. Kim, H. A. Bechtel, J. P. Camden, R. N. Zare, *J. Chem. Phys.* **2005**, *122*, 084303.
[17] a) Z. H. Kim, H. A. Bechtel, R. N. Zare, *J. Am. Chem. Soc.* **2001**, *123*, 12714; b) S. Yoon, R. J. Holiday, F. F. Crim, *J. Chem. Phys.* **2003**, *119*, 4755; c) H. A. Bechtel, Z. H. Kim, J. P. Camden, R. N. Zare, *J. Chem. Phys.* **2004**, *120*, 791.
[18] M. Shapiro, P. Brumer, *Rep. Prog. Phys.* **2003**, *66*, 859.
[19] W. R. Simpson, A. J. Orr-Ewing, T. P. Rakitzis, S. A. Kandel, R. N. Zare, *J. Chem. Phys.* **1995**, *103*, 7299.
[20] P. C. Samartzis, B. Bakker, T. P. Rakitzis, D. H. Parker, T. N. Kitsopoulos, *J. Chem. Phys.* **1999**, *110*, 5201.
[21] L. S. Rothman, A. Barbe, D. C. Benner, L. R. Brown, C. Camy-Peyret, M. R. Carleer, K. Chance, C. Clerbaux, V. Dana, V. M. Devi, A. Fayt, J.-M. Flaud, R. R. Gamache, A. Goldman, D. Jacquemart, K. W. Jucks, W. J. Lafferty, J.-Y. Mandin, S. T. Massie, V. Nemtchinov, D. A. Newnham, A. Perrin, C. P. Rinsland, J. Schroeder, K. M. Smith, M. A. H. Smith, K. Tang, R. A. Toth, J. Vander Auwera, P. Varanasi, K. Yoshino, *J. Quant. Spectrosc. Radiat. Transfer* **2003**, *82*, 5.
[22] W. J. van der Zande, R. Zhang, R. N. Zare, K. G. McKendrick, J. J. Valentini, *J. Phys. Chem.* **1991**, *95*, 8205.

 © 2005 Wiley-VCH Verlag GmbH & Co. KGaA, Weinheim

Crystal Growth

Template-Dependent Morphogenesis of Oriented Calcite Crystals in the Presence of Magnesium Ions**

*Yong-Jin Han, Laura M. Wysocki, Monica S. Thanawala, Theo Siegrist, and Joanna Aizenberg**

The ability of biological systems to exert precise control over the shape, size, orientation, and hierarchical ordering of inorganic materials is of great interest to chemists and material scientists.[1,2] Potential applications of this biological level of control to the development of new synthetic pathways and to the improvement of existing materials is beginning to be recognized. Biogenic calcium carbonate, one of the most abundant minerals formed by organisms, is a wonderful example of nature's precision. The elaborate and unique morphologies of biogenic calcium carbonates, which in the course of evolution are cleverly refined to accommodate diverse survival functions,[1–5] have prompted extensive studies into the mechanism by which they form.[6,7] The development of biogenic calcium carbonates was shown to be closely associated with proteins rich in acidic/hydroxy residues[1,2,4,8] and with divalent cations, such as magnesium ions.[9–11] The formation of crystals with diverse morphologies has been reported by numerous in vitro studies, in which calcite growth was modified by the interaction with various organic and inorganic additives in solution.[4,12–20] Although these experiments demonstrated successfully that the morphology of calcite could be altered from its regular {104} cleavage rhombohedron form, the modified crystals were, in general, heterogeneous in their shapes, sizes, and orientations.

In particular, calcite growth in the presence of Mg ions, in both synthetic and sedimentary environments, was shown to result in the formation of elongated crystals that express new pseudofacets that are roughly parallel to the *c*-axis.[9,13,21–24] This habit modification was traditionally explained by a face-specific mechanism involving interaction between the Mg ions and calcite surfaces parallel to the *c*-axis[24] and recently by a step-specific mechanism involving differential incorporation of Mg ions into nonequivalent steps.[21] It has been shown that such interactions between Mg ions and calcite lead to calcite rhombohedra developing characteristic, elongated, roughened seedlike shapes that depend on the ratio of Mg/Ca ions.[19,21] The experimental data showed, however, that the sizes of Mg-ion-treated crystals, the extent of the elongation along the *c*-axis, the ratio between the {104} plane and the new Mg-ion-induced facets, and their precise {*hkl*} indices were nonuniform, even within the same experiment and under the same conditions. Herein, we report an approach to synthesize arrays of homogeneous calcite crystals in a variety of morphological forms. Crystal growth in the presence of an additive (Mg ions) is coupled with control over the oriented nucleation achieved by using functionalized self-assembled monolayers (SAMs) as nucleation templates.[25–27] Experiments performed with a range of template/additive combinations demonstrated the formation of arrays of calcite crystals with highly uniform features (namely, size, shape, orientation, composition, and dynamics of growth), which are characteristic for each surface. We discuss possible mechanisms for this intriguing new phenomenon, which we have termed template-dependent crystal morphogenesis.

The four surfaces used to control the oriented nucleation were Au films functionalized with thiols containing carboxylic acids of odd chain length (C_{15}–CO_2H), carboxylic acids of even chain length (C_{10}–CO_2H), alcohols (C_{11}–OH), and sulfonic acids (C_{11}–SO_3H). These species were chosen to correspond to the functional residues of biomolecules commonly associated with biominerals. Although ordered functional groups on surfaces alone do not mimic biomolecules, they do provide insight into the importance of ordered arrays of functional groups that are often displayed on proteins repsonsible for the regulation of biomineral formation.

Calcite crystals grown on the surfaces of SAMs in the absence of additives were normal {104} rhombohedra that selectively nucleated from different planes induced by the SAM/metal combination.[26,27] More than 90% of the crystals grown from the surface functionalized with C_{10}–CO_2H species nucleated from the (11*l*) crystallographic planes of calcite (l = 3–4) and more than 95% of crystals templated by the surface functionalized with C_{15}–CO_2H species nucleated from the (01*l*) planes (l = 2–5), as shown by X-ray diffraction and morphological analyses (Figure 1a,b). Interestingly, the surface functionalized with C_{11}–SO_3H species provided a mixture of crystals with the (106) and (1.0.12) nucleating planes in a ratio of 70:30 (Figure 1c). This latter observation suggests that the interfacial SO_3H groups apparently conform to two different orientations/structures upon coordinating with the Ca ions (a possibility that is currently being investigated). More than 98% of the calcite crystals grown on the surfaces functionalized with C_{11}–OH species selectively nucleated from the (104) plane (Figure 1d). The size and nucleation densities of the crystals grown on different templates are summarized in Table 1.

Dramatic changes in the crystallization characteristics were observed upon addition of Mg ions to the solution. Small amounts of Mg ions ($n \leq 0.5$, n = Mg/Ca ions (mol/mol)) induced significant homogenization of crystal sizes for three acid-terminated surfaces with no morphological changes (Table 1). The addition of Mg ions ($n \leq 0.5$) to the crystallizing solution of the SAMs terminated by sulfonic acid groups favored the formation of crystals nucleating from the (106) crystallographic planes and the number of crystals nucleating from the (1.0.12) planes decreased dramatically. This result suggests that Mg ions are involved in the nucleation process,

[*] Dr. Y.-J. Han, L. M. Wysocki, M. S. Thanawala, Dr. T. Siegrist, Dr. J. Aizenberg
Bell Laboratories
Lucent Technologies, 600 Mountain Avenue
Murray Hill, NJ 07974 (USA)
Fax: (+1) 908-582-4868
E-mail: jaizenberg@lucent.com

[**] We thank J. J. DeYoreo, E. DiMasi, and C. Orme for constructive discussions.

 © 2005 Wiley-VCH Verlag GmbH & Co. KGaA, Weinheim DOI: 10.1002/anie.200462296

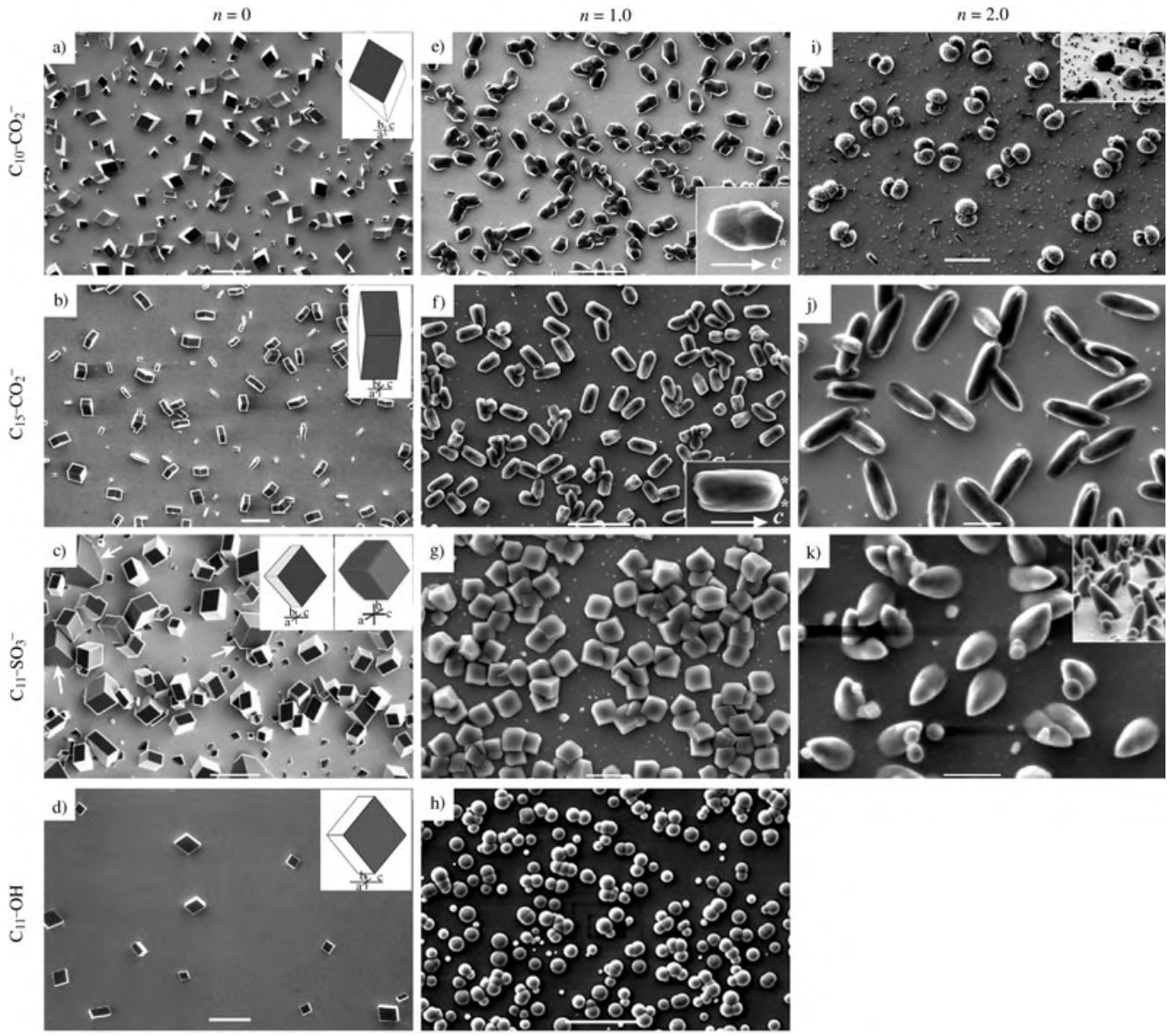

Figure 1. SEM images of oriented calcite crystals grown on different organic templates in the presence or absence of Mg ions. The micrographs were recorded on a JEOL JSM-5600 LV system. The SAMs and the ratios of Mg and Ca ions in solution n are indicated. a) C_{10}–CO_2H functionalization, $n=0$, scale bar = 50 μm, inset: computer simulation of the {104} rhombohedron nucleated from the (113) plane. b) C_{15}–CO_2H functionalization, $n=0$, scale bar = 50 μm, inset: computer simulation of the {104} rhombohedron nucleated from the ($\bar{1}$03) plane. c) C_{11}–SO_3H functionalization, $n=0$, scale bar = 20 μm, insets: computer simulation of the {104} rhombohedron nucleated from the (106) plane (left) and the (1.0.12) plane (right). Crystals in the (1.0.12) orientation are indicated by arrows. d) C_{11}–OH functionalization, $n=0$, scale bar = 100 μm, inset: computer simulation of the {104} rhombohedron nucleated from the (104) plane. e) C_{10}–CO_2H functionalization, $n=1.0$, scale bar = 50 μm, inset: high-magnification SEM analysis showing the morphology of an individual crystal. Although the normal {104} cleavage planes of calcite were still clearly visible (indicated by *), the crystals develop striated facets roughly parallel to the c-axis with a narrow center. f) C_{15}–CO_2H functionalization, $n=1.0$, scale bar = 50 μm, inset: high-magnification of an individual, morphologically modified cylindrical crystal. g) C_{11}–SO_3H functionalization, $n=1.0$, scale bar = 10 μm. Only crystals nucleated from the (106) plane remain. The crystals show no morphological changes. h) C_{11}–OH functionalization, $n=1.0$, scale bar = 10 μm. Total inhibition of crystallization and the formation of ACC. i) C_{10}–CO_2H functionalization, $n=2.0$, scale bar = 20 μm, inset: edge-on view showing the asymmetric orientation of the dumb-bells on the surface. Crystals uniformly develop a dumb-bell shape and ACC spheres start to form. j) C_{15}–CO_2H functionalization, $n=2.0$, scale bar = 10 μm. Crystals uniformly develop a cylindrical shape. k) C_{11}–SO_3H functionalization, $n=2.0$, scale bar = 5 μm, inset: edge-on view showing that the crystals form a high angle with the surface. Crystals uniformly develop a conical shape.

possibly in two ways: by promoting the preferential alignment of the SO_3H groups at the SAM interface in the configuration which induces the nucleation of calcite crystals from the (106) plane, and/or by inhibition of the alternative alignment that would favor nucleation from the (1.0.12) plane. Interestingly, total inhibition of crystallization was observed on the surfaces terminated by C_{11}–OH species upon the addition of Mg ions ($n \leq 0.5$) and a thin layer of amorphous calcium carbonate (ACC) spheres covered the surface of the SAM. This observation is further evidence that Mg ions do not only act as growth modifiers but are also involved at the nucleation stage as surface reconstruction agents, thus promoting/

 © 2005 Wiley-VCH Verlag GmbH & Co. KGaA, Weinheim

Table 1: Crystal size, nucleation density, Mg content, and elongation along the *c*-axis for calcite crystals grown on different SAMs in the presence of Mg ions.

SAM	*n* (Mg/Ca [mol/mol])	Crystal size [μm]		Elongation ratio ($r=l_c/l_{a,b}$)	Nucleation density [mm^{-2}]	Mg content in $CaCO_3$ [mol%]
		along the *c*-axis (l_c)	in the *a*,*b* plane ($l_{a,b}$)			
C_{10}–CO_2^-	0:1	23.7 ± 9.2	31.2 ± 8.9	0.7 ± 0.3	1200	0
	0.5:1	19.3 ± 4.1	20.8 ± 3.7	0.9 ± 0.3	1500	6.54
	1.0:1	21.7 ± 2.2	12.1 ± 1.0	1.8 ± 0.2	1600	8.39
	2.0:1	13.1 ± 1.1	5.5 ± 1.0	2.4 ± 0.4	1300	8.8
C_{15}–CO_2^-	0:1	20.6 ± 8.0	43.8 ± 7.2	0.5 ± 0.2	600	0
	0.5:1	21.7 ± 3.9	19.6 ± 2.1	1.1 ± 0.4	1900	5.96
	1.0:1	25.5 ± 3.6	11.1 ± 0.8	2.3 ± 0.3	3200	9.21
	2.0:1	19.5 ± 2.2	5.8 ± 0.8	3.4 ± 0.6	4400	9.21
C_{11}–SO_3^-	0:1	$6.7 \pm 3.9_{(106)}$	$7.3 \pm 4.1_{(106)}$	0.9 ± 0.2	$10000_{(106)}$	0
		$15.0 \pm 2.1_{(1.0.12)}$	14.2 ± 3.2	1.1 ± 0.1	$500_{(1.0.12)}$	
	0.5:1	5.9 ± 1.9	6.0 ± 1.7	1.0 ± 0.2	25000	5.96
	1.0:1	6.3 ± 0.6	6.4 ± 0.5	1.1 ± 0.1	30000	7.61
	2.0:1	8.3 ± 1.0	2.7 ± 0.3	3.1 ± 0.4	50000	8.99
C_{11}–OH	0:1	40.1 ± 10.6	52.0 ± 7.7	0.7 ± 1.2	25	0
	1.0:1		$1.7 \pm 0.4_{(ACC)}$	1	150000	12.8

inhibiting the crystallization process. The formation of the ACC film is consistent with recent studies in which proteins rich in hydroxy residues (namely, serine and threonine) were reported to stabilize ACC in the presence of Mg ions in biological systems.[10,11,28,29]

A steady increase in the concentration of Mg ions beyond $n = 0.5$ further improved the uniformity of the size and shape of the calcite crystals (Table 1). We also observed morphological changes in the regular {104} rhombohedra, in which there were general elongations of the calcite crystals along the *c*-axis (Figure 1 e–k). Although the results were highly reproducible and characteristic for each surface type and a given *n* value, we detected clear differences in the morphogenesis of calcite crystals grown on the SAMs terminated by C_{10}–CO_2H, C_{15}–CO_2H, and C_{11}–SO_3H species, with the final modified morphologies and crystal shapes being distinctive for each surface type. In particular, progressive asymmetric development and morphological modification of calcites that had been treated with Mg ions yielded arrays of uniform "dumb-bell"-shaped crystals[30,31] on the surfaces terminated by the C_{10}–CO_2H species (Figure 1 e, i), tapered cylinder-shaped crystals on the surfaces terminated by the C_{15}–CO_2H species (Figure 1 f, j), and conical-shaped crystals on the surfaces terminated by the C_{11}–SO_3H species (Figure 1 g, k).

Moreover, each surface type exhibited differences in the following parameters of the morphogenesis: 1) the ratio n_0 of Mg and Ca ions in the crystallizing solution at which the appearance of the new faces was detected; 2) the extent of the elongation along the *c*-axis ($r = l_c/l_{ab}$) and the ratio between the {104} plane and new faces induced by Mg ions for a given *n* value; 3) the ratio n_{Mg} of Mg and Ca ions at which the {104} habit disappears and the crystals exhibit only new facets induced by Mg ions, 4) the ratio $n_{Mg,ACC}$ of Mg and Ca ions at which the ACC phase starts to form and coexists with the calcite crystals; 5) the ratio n_{ACC} of Mg and Ca ions at which total inhibition of crystallization and the formation of ACC occurs. These parameters are summarized schematically in Figure 2.

We observed a gradual increase in the incorporation of Mg ions into the calcite crystals as the amount of Mg ions in the crystallizing solution increased (Table 1). This incorporation followed a near-linear trend in the crystalline material and, generally, increased abruptly in the ACC phase.

Our results show unequivocally that the same growth modifier imposes different morphological changes on crystals nucleated from different organic templates even at the same supersaturation levels and impurity concentrations. Two mechanisms may account for this new observation: 1) The desorption of organic molecules from the SAMs would result in their cooperative interaction with the Mg ions and the growing crystals. Each surface would then produce a specific additive combination that may have a distinct effect on crystal morphogenesis. 2) The interaction between the crystal and the additive, and therefore the resulting morphology, may depend on the orientation of the crystal on the surface.

The first hypothesis was verified by control experiments to test in which trace amounts of one thiol were added together with Mg ions ($n = 2.0$) to a reaction vessel that contained a substrate functionalized with the SAM of a different thiol. Such an addition should change the morphology of the

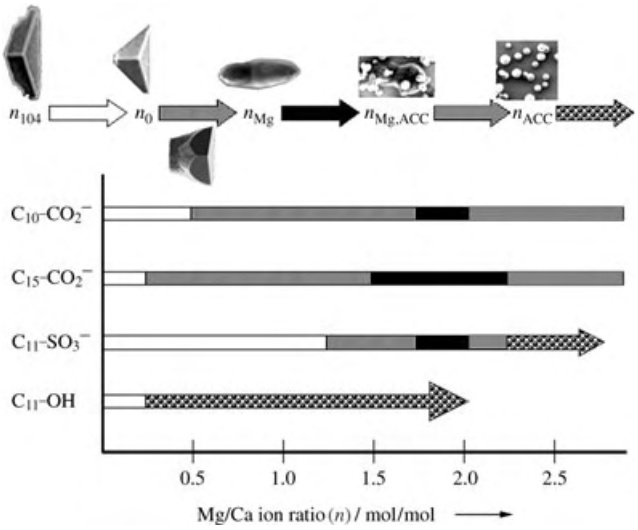

Figure 2. Schematic representation that shows the morphogenetic stages of calcite crystals as a function of *n* values for different SAMs. The range of *n* values from n_{104} to n_0 indicates the stage at which no morphological changes in calcite crystals were detected. The range from n_0 to n_{Mg} indicates the stage for which both {104} and the new Mg-modified faces coexist. The range from n_{Mg} to $n_{Mg,ACC}$ indicates the stage for which only fully developed Mg-affected crystals form. The range from $n_{Mg,ACC}$ to n_{ACC} indicates the stage in which the ACC phase coexists with the treated crystals. Only the ACC phase is observed after n_{ACC}.

 © 2005 Wiley-VCH Verlag GmbH & Co. KGaA, Weinheim

resulting crystals if the first mechanism was correct; for example, the pointed conical shape should change to the dumb-bell shape on addition of the $HS{-}(CH_2)_{10}{-}CO_2H$ thiol to the solution if a SAM of the $HS{-}(CH_2)_{11}{-}SO_3H$ thiol is used as a template. However, no apparent changes in the resulting morphologies were observed.

The second hypothesis was verified by two different experiments: First, we precipitated calcium carbonate in the presence of Mg ions ($n = 1.25$) on a methyl-terminated SAM (a monolayer that does not induce the oriented nucleation and produces an array of randomly oriented calcite crystals).[27] The concentration of Mg ions was chosen to correspond to the interval that resulted in the most pronounced differences in crystal morphogenesis (see Figure 2). We observed that the extent of the morphological modification differed significantly between differently oriented crystals, although the same organic molecule may have leaked into their vicinity. We also noticed that the crystal shapes had a tendency to change from conical to cylindrical as the orientation of their *c*-axes changed from being perpendicular to being parallel to the substrate. This observation is consistent with the different shapes of the crystals that had been grown on the surface terminated with sulfonic acid groups and the surface terminated with carboxylic acid groups, where the angle between the *c*-axis and the SAM is approximately 57 and 23°, respectively (Figure 1j,k). In the second experiment, calcite crystals were grown epitaxially on a biogenic calcite crystal[13,32] (echinoderm skeletal elements) in the presence of Mg ions. The surfaces of the echinoderm crystals are round and, therefore, are oriented differently at different locations with respect to the *c*-axis of the constituent calcite. In this experiment, the combined morphological effect of the Mg ions and macromolecules bleaching from the biogenic substrate was studied. Indeed, different morphologies were observed for differently oriented crystals: crystals nucleated at surfaces that were roughly perpendicular to the *c*-axis were conical, while crystals nucleated at surfaces that were parallel to the *c*-axis were cylindrical (Figure 3).

These control experiments confirm that morphological changes induced by a growth modifier depend primarily on the orientation of the crystal on the surface. For randomly oriented crystals, differences in the relative orientation of the crystal surfaces or steps that are specifically recognized by an additive will cause variations in the availability/reactivity of these sites for interaction as well as the difference in the diffusion of an additive toward these sites and, therefore, variations in the concentration of an additive necessary to promote morphological change. These possible variations would lead ultimately to distinct orientation-dependent morphological changes. The same mechanism can be applied successfully to explain the observed uniformity of similarly oriented crystals. In the latter case, the availability of the interacting planes to the additive and, thus, the modification of crystal growth is identical for all crystals, and so homogeneous, characteristic changes in crystal size and morphology will result.

Although we do not exclude the possible, additional effect of the desorbed organic molecules, we believe that they play a secondary role in the observed shape changes when present in low concentrations (such as in the case of SAMs). Our results suggest that the effect of the organic substrate, as well as inducing the orientated nucleation, may include sequestering of Mg ions from the solution. The extent of complexation depends on the chemistry of the organic substrate[33] and would be manifested in the differences in the threshold values n_0 required for morphological changes to occur, as was indeed demonstrated in our experiments (Figure 2).

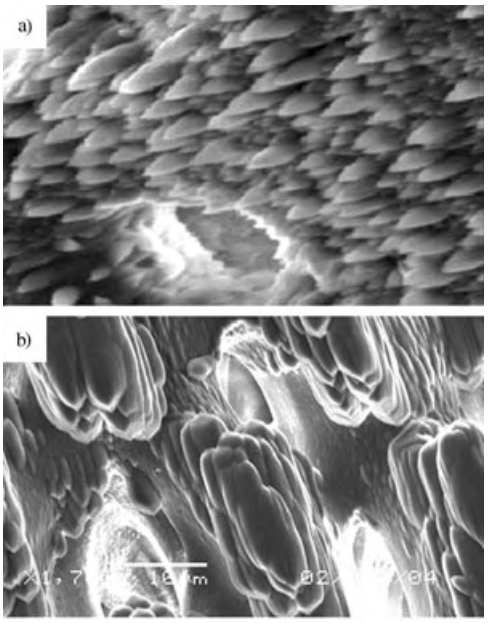

Figure 3. Epitaxial overgrowth of synthetic calcite crystals on the surface of biogenic calcite (lateral arm plate of a brittle star) in the presence of Mg ions. Note that a) the crystals grown on surfaces roughly perpendicular to the *c*-axis have a highly tapered, conical shape, while b) the crystals grown on surfaces roughly parallel to the *c*-axis have a cylindrical shape.

In conclusion, we have described the new phenomenon of template-dependent crystal morphogenesis. We have shown that the effect of a solution growth modifier on crystal shape and size depends on the orientation of the crystals on the surface. The resulting crystal arrays grown from a specific organic template that induces oriented nucleation of the crystals from the same plane are highly uniform in size, morphology, and orientation, which is characteristic of the template/additive combination. We have also presented interesting evidence that Mg ions are involved in the nucleation process and that surfaces functionalized with hydroxy groups can stabilize the formation of amorphous calcium carbonates with few Mg ions present. The impressive crystal homogeneity that is achieved when the addition of a specific crystal growth modifier is coupled with oriented nucleation suggests that the above approach can be used as a powerful synthetic route to crystalline materials with finely tailored morphologies.

Experimental Section

SAMs were prepared by soaking a 50-nm gold film, which had been prepared by evaporation with an E-beam onto a Si(100) wafer primed

 © 2005 Wiley-VCH Verlag GmbH & Co. KGaA, Weinheim

with a 2-nm Ti layer, in 5 mM solutions of $HS-(CH_2)_{11}-OH$, $HS-(CH_2)_{10}-CO_2H$, $HS-(CH_2)_{15}-CO_2H$, or $HS-(CH_2)_{11}-SO_3H$ in alcohol for a minimum of 6 h.[27] Calcium carbonate was precipitated on the SAMs by using stock solutions of $CaCl_2$ (25 mM), $MgCl_2$ (25 mM, 150 mM), and $(NH_4)HCO_{3(s)}$, as described in our previous reports.[25–27] Experiments were carried out in a cell-culture multidish containing 24 reaction vessels. Every reaction vessel was filled with 2 mL of $CaCl_2$ (25 mM stock solution) with an appropriate amount of $MgCl_2$ (25 or 150 mM stock solution) and H_2O to give a total volume of 4 mL.

The magnesium to calcium ratios n (n = Mg/Ca ions (mol/mol)) were varied from 0 to 4 with increments of 0.25. Crystallization was carried out simultaneously for all the SAMs and at six different values of n in the same culture dish to ensure identical experimental conditions for a reliable comparison between different substrates and various n values. The substrates were always completely submerged beneath the solution/air interface for consistency in crystallization. The crystallization took place inside a desiccator at room temperature over 2 h. Each substrate was then rinsed with H_2O and dried with compressed nitrogen gas. The crystals were characterized by scanning electron microscopy (SEM) with energy dispersion X-ray attachment (EDX), X-ray diffraction (XRD) using $Cu_{K\alpha}$ radiation, and computer simulation of the morphology by using a SHAPE 6.0 program. The Mg content in the precipitate was measured using EDX over a large area that represented a statistical number of crystals and/or ACC particles.

Received: October 13, 2004
Published online: February 28, 2005

Keywords: crystal growth · magnesium calcite · morphogenesis · template synthesis

[1] H. A. Lowenstam, S. Weiner, *On Biomineralization*, Oxford University Press, Oxford, **1989**.
[2] S. Mann, *Biomineralization: Principles and Concepts in Bioinorganic Materials Chemistry*, Oxford University Press, Oxford, **2001**.
[3] J. Aizenberg, A. Tkachenko, S. Weiner, L. Addadi, G. Hendler, *Nature* **2001**, *412*, 819.
[4] L. Addadi, S. Weiner, *Proc. Natl. Acad. Sci. USA* **1985**, *82*, 4110.
[5] S. A. Wainwright, W. D. Biggs, J. D. Currey, J. M. Gosline, *Mechanical Design in Organisms*, Wiley, New York, **1976**.
[6] F. C. Meldrum, *Int. Mater. Rev.* **2003**, *48*, 187.
[7] K. J. Davis, P. M. Dove, J. J. De Yoreo, *Science* **2000**, *290*, 1134.
[8] G. Falini, S. Albeck, S. Weiner, L. Addadi, *Science* **1996**, *271*, 67.
[9] S. Raz, S. Weiner, L. Addadi, *Adv. Mater.* **2000**, *12*, 38.
[10] S. Raz, P. C. Hamilton, F. H. Wilt, S. Weiner, L. Addadi, *Adv. Funct. Mater.* **2003**, *13*, 480.
[11] J. Aizenberg, G. Lambert, S. Weiner, L. Addadi, *J. Am. Chem. Soc.* **2002**, *124*, 32.
[12] J. Aizenberg, J. Hanson, T. F. Koetzle, S. Weiner, L. Addadi, *J. Am. Chem. Soc.* **1997**, *119*, 881.
[13] S. Albeck, J. Aizenberg, L. Addadi, S. Weiner, *J. Am. Chem. Soc.* **1993**, *115*, 11691.
[14] C. A. Orme, A. Noy, A. Wierzbicki, M. T. McBride, M. Grantham, H. H. Teng, P. M. Dove, J. J. DeYoreo, *Nature* **2001**, *411*, 775.
[15] D. B. DeOliveira, R. A. Laursen, *J. Am. Chem. Soc.* **1997**, *119*, 10627.
[16] J. Donners, R. J. M. Nolte, N. Sommerdijk, *J. Am. Chem. Soc.* **2002**, *124*, 9700.
[17] M. J. Olszta, S. Gajjeraman, M. Kaufman, L. B. Gower, *Chem. Mater.* **2004**, *16*, 2355.
[18] H. Colfen, M. Antonietti, *Langmuir* **1998**, *14*, 582.
[19] J. J. De Yoreo, P. M. Dove, *Science* **2004**, *306*, 1301.
[20] S. H. Yu, H. Colfen, M. Antonietti, *J. Phys. Chem. B* **2003**, *107*, 7396.
[21] K. J. Davis, P. M. Dove, L. E. Wasylenki, J. J. De Yoreo, *Am. Mineral.* **2004**, *89*, 714.
[22] F. Lippmann, *Sedimentary Carbonate Minerals*, Springer, New York, **1973**.
[23] J. Paquette, R. J. Reeder, *Geology* **1990**, *18*, 1244.
[24] R. L. Folk, *J. Sediment. Petrol.* **1974**, *44*, 40.
[25] Y. J. Han, J. Aizenberg, *J. Am. Chem. Soc.* **2003**, *125*, 4032.
[26] Y. J. Han, J. Aizenberg, *Angew. Chem.* **2003**, *115*, 3796; *Angew. Chem. Int. Ed.* **2003**, *42*, 3668.
[27] J. Aizenberg, A. J. Black, G. H. Whitesides, *J. Am. Chem. Soc.* **1999**, *121*, 4500.
[28] L. Addadi, S. Raz, S. Weiner, *Adv. Mater.* **2003**, *15*, 959.
[29] J. Aizenberg, G. Lambert, L. Addadi, S. Weiner, *Adv. Mater.* **1996**, *8*, 222.
[30] H. Colfen, L. M. Qi, *Chem. Eur. J.* **2001**, *7*, 106.
[31] D. Kralj, J. Kontrec, L. Brecevic, G. Falini, V. Nothig-Laslo, *Chem. Eur. J.* **2004**, *10*, 1647.
[32] J. Aizenberg, S. Albeck, S. Weiner, L. Addadi, *J. Cryst. Growth* **1994**, *142*, 156.
[33] The relative distribution of Ca and Mg ions between the organic surface and the crystallization solution for different SAMs will be reported elsewhere.

 © 2005 Wiley-VCH Verlag GmbH & Co. KGaA, Weinheim

Reaction Mechanisms

Mechanism of the Norrish–Yang Photocyclization Reaction of an Alanine Derivative in the Singlet State: Origin of the Chiral-Memory Effect**

Adalgisa Sinicropi, Frédérique Barbosa, Riccardo Basosi, Bernd Giese, and Massimo Olivucci**

The asymmetric synthesis of enantiomerically pure α-amino acids is a major topic of modern peptide chemistry.[1–8] For the development of new peptidomimetics, proline derivatives are

[*] Dr. F. Barbosa,[+] Prof. Dr. B. Giese
Department of Chemistry
St. Johanns-Ring 19, 4056 Basel (Switzerland)
Fax: (+41) 61-267-1105
E-mail: bernd.giese@unibas.ch
Dr. A. Sinicropi, Prof. Dr. R. Basosi, Prof. Dr. M. Olivucci
Dipartimento di Chimica
Università degli Studi di Siena
via Aldo Moro, 53100 Siena (Italy)
Fax: (+39) 0577-234-278
E-mail: olivucci@unisi.it
[+] Current address:
Cerep
128 rue Danton, 92500 Rueil Malmaison (France)

[**] This work was supported by the HFSP (RG 0229/2000M), the Università di Siena (Progetto di Ateneo A.A. 00/04), FIRB project no. RBAU01EPMR, and the Swiss National Science Foundation.

Supporting information for this article (coordinates and energies of all optimized structures) is available on the WWW under http://www.angewandte.org or from the author.

 © 2005 Wiley-VCH Verlag GmbH & Co. KGaA, Weinheim DOI: 10.1002/anie.200461898

of particular importance.[9] Recently, Giese et al.[10] reported a stereospecific photochemical route to proline derivatives by a singlet Norrish–Yang photocyclization reaction of the alanine derivative **1**, which leads to the diastereoisomers **2**, ent-**2**, **3**, and ent-**3** ("ent" denotes the enantiomer of the compound indicated; Scheme 1). In the presence of the triplet quencher and singlet sensitizer naphthalene, with benzene as the solvent, the photocyclization yielded isomer **2** (92% *ee*) with the *cis* configuration as the major product, with retention of configuration at the α carbon atom. The minor *trans* isomer **3** (*cis*/*trans* 85:15) was also formed with 88% *ee*. This reaction is one of the few remarkable examples of the photochemical "chiral-memory effect".[11] Furthermore, it represents an example of the exploitation of light energy to drive asymmetric synthesis.

To understand this memory effect we carried out ab initio CASPT2//CASSCF[10,8][12–17] computations to map the photochemical reaction pathway of the alanine-derivative model **4**. The results of the calculations are shown in Figure 1. Upon photoexcitation, one electron of the oxygen lone pair is

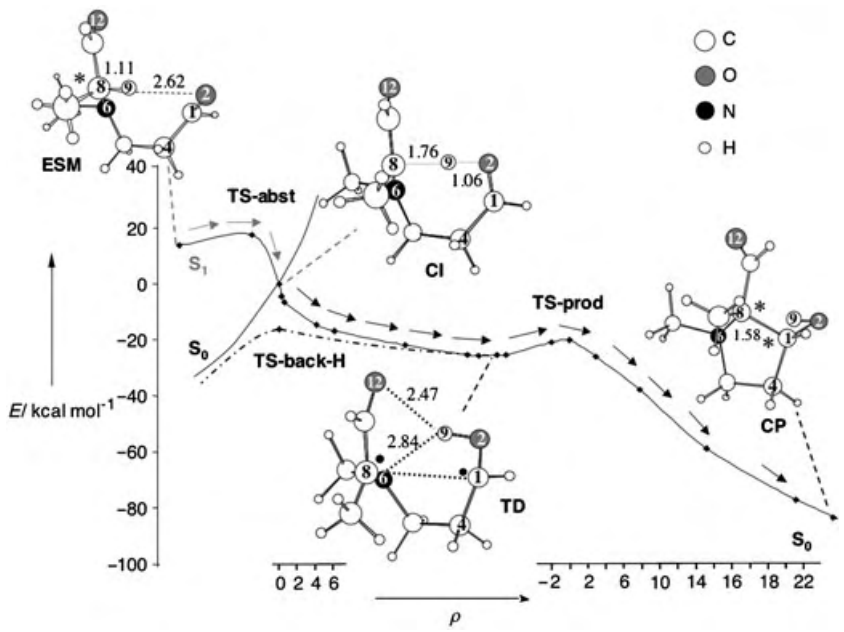

Figure 1. Energy profiles along the S_1 and S_0 reaction coordinate for the intramolecular hydrogen-atom abstraction, hydrogen-atom back transfer (dashed–dotted line), and the cyclization of compound **4**. The chiral centers are labeled with an asterisk.

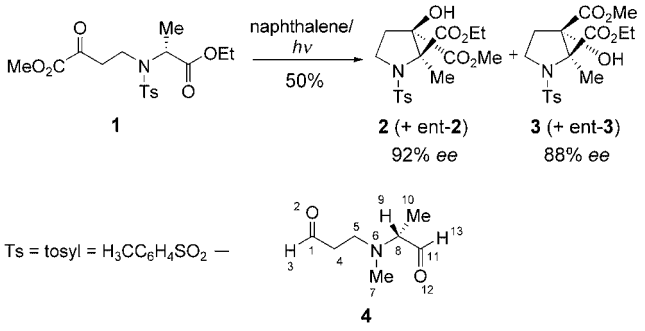

Scheme 1. Singlet Norrish–Yang photocyclization reaction of the alanine derivative **1**; alanine-derivative model **4**.

promoted to the π* orbital of the C1=O2 bond. The computed excitation energy for the singlet n–π* excitation is 98.1 kcal mol^{-1}. After photoexcitation, the molecule relaxes to the stable excited-state (S_1) conformation **ESM** (Figure 1) with an O2–H9 distance of 2.62 Å, which is comparable to the distance of 2.69 Å observed in the 1,5-hydrogen-atom abstraction of solid-state compounds by Ihmels and Scheffer[18] and to the average value of 2.61 ± 0.07 Å observed for 14 ketones whose crystal structures were determined.[19]

The hydrogen-atom transfer from C8 to O2 is controlled by the transition-state structure **TS-abst** (Figure 1), which is located 6.8 kcal mol^{-1} in energy above **ESM** and which connects this intermediate to a conical intersection **CI** between the excited-state S_1 and ground-state S_0 potential-energy surfaces. At the transition state of the H abstraction the distance between the oxygen atom O2 and the hydrogen atom H9 is 1.24 Å, and the distance between the carbon atom C8 and the hydrogen atom H9 is 1.33 Å.

It is generally accepted that in photochemical reactions conical-intersection structures play a role similar to that of transition states in thermal reactions.[20,21] Indeed, these structures provide extremely efficient channels for the decay of the excited-state species to the ground state.

The molecular motion that prompts the $S_1 \rightarrow S_0$ decay occurs along the so-called "branching" plane, which is defined by the coordinates $\mathbf{X_1}$ and $\mathbf{X_2}$ (Figure 2). Any molecular deformation along this plane lifts the S_1/S_0 degeneracy at the intersection. Thus, the analysis of $\mathbf{X_1}$ and $\mathbf{X_2}$ provides useful information about the chemical event mediated by the conical-intersection structure. It is apparent that at the conical intersection **CI** (Figure 1) the hydrogen-atom transfer is almost complete and that an sp^2 radical center has been generated at C8. The plot of the $\mathbf{X_1}$ and $\mathbf{X_2}$ vectors (Figure 2) clearly indicates that the decay leads exclusively to a diradical intermediate or to the original reactant. Indeed, it can be seen that there are no torsional components to prompt twisting about the N6–C8 or C1–C4 bonds accompanied by loss of stereoselectivity at C8 or lack of facial selectivity during the attack at C1.

Consistent with this analysis, the computed paths indicate that the evolution following the decay occurs according to two routes. One of these routes leads back to the starting material, as back transfer of the hydrogen atom may occur after a small degree of rotation around the N6–C8 bond (as required to realign the O2–H9 bond with the C8 radical center). The other pathway on the S_0 potential-energy surface leads to the diradical intermediate **TD**, which is located 25.4 kcal mol^{-1} in energy below the **CI** point and features a distance of 3.97 Å between the radical centers at C1 and C8. (The relative population of such routes can only be estimated by non-adiabatic dynamics computations that are currently impractical for the model **4**). As mentioned above, free rotation about the N6–C8 and C1–C4 bonds would lead to loss of stereoselectivity. However, as shown in Figure 1, the diradical

 © 2005 Wiley-VCH Verlag GmbH & Co. KGaA, Weinheim

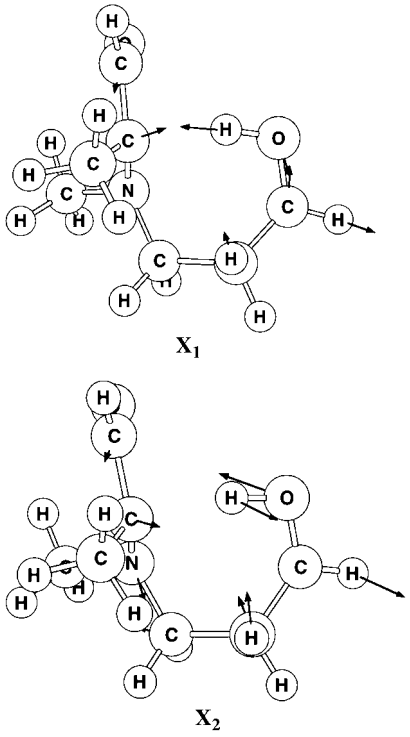

Figure 2. Coordinates X_1 and X_2 that define the "branching" plane along which $S_1 \rightarrow S_0$ decay occurs.

TD is stabilized by a three-center hydrogen bond involving the O12, H9, and N6 atoms, which restrains the conformational freedom of the diradical. Furthermore, diradical disproportionation through the back transfer of the H atom is also restrained by a 9.2 kcal mol^{-1} energy barrier at the transition state **TS-back-H**. This energy barrier results from the large distance (3.19 Å) and unfavorable orientation between the abstracted hydrogen atom and the radical center at C8 imposed by the hydrogen bonds. On the other hand, the orientation of the two carbon-centered radicals at C8 and C1 in the diradical intermediate **TD** is such that cyclization to the product **CP** has a low activation barrier of 5.2 kcal mol^{-1} (**TS-prod**, see Figure 1). Because of the hydrogen-bond network the rotation about N6–C8 required for inversion (or racemization) is slower than the radical coupling, and the original configuration at C8 is thus preserved. The same hydrogen bonds prevent rotation about the C1–C4 bond, so that the *cis* configuration of the hydroxy and aldehyde substituents is favored in the cyclic product. By calculating the energy of nine structures generated by a 20° rotational scan about the C1–O2 bond, the hydrogen-bond strength was estimated to be −5.9 kcal mol^{-1}.[22]

The conclusion that a specific hydrogen-bond network on the S_0 energy surface controls the stereoselectivity of the reaction is supported by reaction-pathway computations for a different, less stable **TD** conformer (6.5 kcal mol^{-1}), indicated as $\mathbf{TD_{conf2}}$, which is not stabilized by two hydrogen bonds (note the long H9–O12 distance of 4.09 Å) as a result of a 180° twisting about C8–C11. The scheme at the bottom of Figure 3 demonstrates that the reaction of this alternative conformer

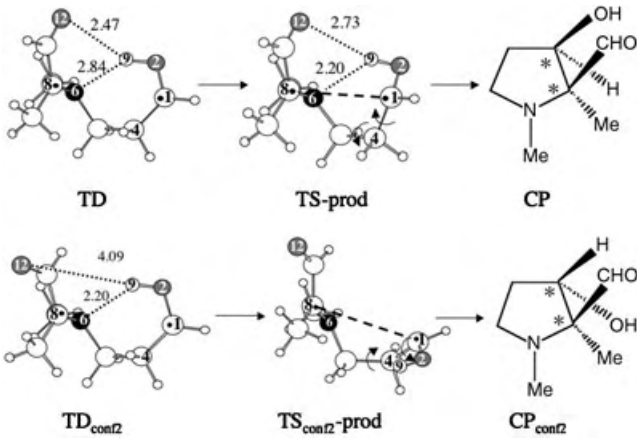

Figure 3. Ground-state reaction routes for two different **TD** conformers of **4** which lead to the *cis* (top) and *trans* (bottom) diastereoisomer of the product; see Figure 1 for atom labels.

generates a $\mathbf{TS_{conf2}}$**-prod** structure, in which the formation of the H9–O12 and H9–N6 hydrogen bonds is impossible. This pathway leads to the minor isomer **3**.

For photoinduced reactions, both the excited- and ground-state branches of the reaction pathway determine the stereoselectivity. Our calculations demonstrate that loss of configuration, through rotation about N6–C8 or C1–C4, can not occur in the excited state. In fact, the transition structure **TS-abst** is cyclic, and the conical intersection **CI** decays to the ground state on a timescale much faster than that of rotation. With regard to the ground-state branch of the reaction, the calculations indicate that the stereoselectivity is determined by the specific structure of the diradical **TD**. In fact, the hydrogen-bond network in **TD** hinders torsional motion about N6–C8 and C1–C4; this torsional motion thus competes inefficiently with cyclization.

Received: September 4, 2004
Revised: January 11, 2005
Published online: March 10, 2005

Keywords: ab initio calculations · chiral memory · conical intersections · photocyclization · reaction mechanisms

[1] A. Córdova, W. Notz, G. Zhong, J. M. Betancort, C. F. Barbas III, *J. Am. Chem. Soc.* **2002**, *124*, 1842.
[2] P. Wessig, P. Wettstein, B. Giese, M. Neuburger, M. Zehnder, *Helv. Chim. Acta* **1994**, *77*, 829.
[3] W. Weigel, S. Schiller, G. Reck, H.-G. Henning, *Tetrahedron Lett.* **1993**, *34*, 6737.
[4] C. Wyss, R. Batra, C. Lehmann, S. Sauer, B. Giese, *Angew. Chem.* **1996**, *108*, 2660; *Angew. Chem. Int. Ed. Engl.* **1996**, *35*, 2529.
[5] K. Nagasawa, A. Georgieva, T. Nakata, *Tetrahedron* **2000**, *56*, 187.
[6] R. Kawecki, *Tetrahedron* **2001**, *57*, 8385.
[7] C. Grison, S. Genève, E. Halbin, P. Coutrot, *Tetrahedron* **2001**, *57*, 4903.
[8] F. Benedetti, M. Magnan, S. Miertus, S. Norbedo, D. Parat, A. Tossi, *Bioorg. Med. Chem. Lett.* **1999**, *9*, 3027.
[9] D. Voet, J. G. Voet, *Biochemie*, VCH, Weinheim, **1992**.

 © 2005 Wiley-VCH Verlag GmbH & Co. KGaA, Weinheim

[10] B. Giese, P. Wettstein, C. Stähelin, F. Barbosa, M. Neuburger, M. Zehnder, P. Wessig, *Angew. Chem.* **1999**, *111*, 2722; *Angew. Chem. Int. Ed.* **1999**, *38*, 2586.
[11] A. G. Griesbeck, *Synlett* **2003**, *4*, 451.
[12] P. Celani, M. A. Robb, M. Garavelli, F. Bernardi, M. Olivucci, *Chem. Phys. Lett.* **1995**, *243*, 1.
[13] K. Andersson, M. R. A. Blomberg, M. P. Fülscher, G. Karlström, R. Lundh, P.-A. Malmqvist, P. Neogrády, J. Olsen, B. O. Roos, A. J. Sadlej, M. Schütz, L. Seijo, L. Serrano-Andrés, P. E. M. Siegbahn, P.-O. Widmark, MOLCAS, Version 4, University of Lund, Lund, Sweden, **1997**.
[14] Gaussian 98 (Revision A.7), M. J. Frisch, G. W. Trucks, H. B. Schlegel, G. E. Scuseria, M. A. Robb, J. R. Cheeseman, V. G. Zakrzewski, J. A. Montgomery, R. E. Stratmann, J. C. Burant, S. Dapprich, J. M. Millam, A. D. Daniels, K. N. Kudin, M. C. Strain, O. Farkas, J. Tomasi, V. Barone, M. Cossi, R. Cammi, B. Mennucci, C. Pomelli, C. Adamo, S. Clifford, J. Ochterski, G. A. Petersson, P. Y. Ayala, Q. Cui, K. Morokuma, D. K. Malick, A. D. Rabuck, K. Raghavachari, J. B. Foresman, J. Cioslowski, J. V. Ortiz, B. B. Stefanov, G. Liu, A. Liashenko, P. Piskorz, I. Komaromi, R. Gomperts, R. L. Martin, D. J. Fox, T. Keith, M. A. Al-Laham, C. Y. Peng, A. Nanayakkara, C. Gonzalez, M. Challacombe, P. M. W. Gill, B. G. Johnson, W. Chen, M. W. Wong, J. L. Andres, M. Head-Gordon, E. S. Replogle, J. A. Pople, Gaussian, Inc., Pittsburgh, PA, **1998**.
[15] "Ab initio Methods in Quantum Chemistry-II": B. O. Roos, *Adv. Chem. Phys.* **1987**, *69*, 399.
[16] B. O. Roos, *Acc. Chem. Res.* **1999**, *32*, 137.
[17] Geometry optimization and reaction-path computations were carried out at the CASSCF level of theory with a complete active space including ten electrons in eight orbitals, and the 6-31G* basis set available in Gaussian 98.[13] The orbitals comprise the two σ and σ* C8–H9 orbitals, the four π and π* orbitals of the C1–O2 and C11–012 bonds, and the N6 and O2 lone-pair orbitals. Because of wavefunction instability, the S_0 transition state **TS-back-H** was optimized by using state-average CASSCF with a S_0 and S_1 weight of 0.5. The relaxation coordinates were computed according to the following procedure: 1) The **CI** between the excited state (S_1) and the ground state (S_0) was optimized by using the methodology available in Gaussian 98; 2) the S_0 relaxation pathways were computed starting from the optimized **CI** point by the IRD method, as described in reference [11], and the IRC method available in Gaussian 98. To obtain more-accurate reaction energetics we reevaluated the energy along selected points of the relaxation coordinate at the CASPT2 level by using the program package MOLCAS-4.[12]
[18] H. Ihmels, J. R. Scheffer, *Tetrahedron* **1999**, *55*, 885.
[19] M. Leibovitch, G. Olovsson, J. R. Scheffer, J. Trotter, *J. Am. Chem. Soc.* **1998**, *120*, 12755.
[20] F. Bernardi, M. Olivucci, M. A. Robb, *Chem. Soc. Rev.* **1996**, *25*, 321.
[21] A. Migani, M. Olivucci in *Conical Intersections: Electronic Structure, Dynamics and Spectroscopy* (Eds.: W. Domcke, D. R. Yarkony, H. Köppel), World Scientific, Singapore, **2004**.
[22] If the thermal equilibration of **TD**, kinetic control, and a parallel reaction scheme are assumed, a simple Arrhenius treatment leads to a ratio **2**/**3** of $\exp(E_3-E_2)/RT$, in which E_3 is the barrier to the production of **3** and E_2 is the barrier to the production of **2**. According to this equation, a ratio of 85:15 requires an E_3-E_2 value of approximately 1 kcal mol^{-1}. Thus, if the errors in our computational model are taken into account, the computed value of 0.7 kcal mol^{-1} is consistent with the expected value and with the observed dominance of isomer **2**. Note also that the error associated with the computation of the energy barriers is expected to be close to the value of E_3-E_2.

 © 2005 Wiley-VCH Verlag GmbH & Co. KGaA, Weinheim

Conjugate Addition

Highly Enantioselective Catalytic Conjugate Addition of N-Heterocycles to α,β-Unsaturated Ketones and Imides**

*Mark Gandelman and Eric N. Jacobsen**

Nitrogen-containing heterocycles and their derivatives have broad application in synthetic, materials, and biological chemistry, and as a result their synthesis and reactivity are subjects of considerable interest.[1] Generation of chiral N-heteroaromatic derivatives in optically active form is a challenging facet of this research area that has seen important, but somewhat uneven progress.[2] For example, neither stoichiometric nor catalytic asymmetric conjugate additions of nitrogen-centered nucleophiles based on N-heterocyclic structures has been developed, despite the impressive recent advances in the general area of 1,4-addition chemistry and the utility that the resulting products might hold.[3,4] Potential applications might include preparation of novel non-natural nucleosides (NNNs),[5] a class of compounds with a broad range of important biological applications.[6,7] Our group demonstrated recently that [(salen)Al] complexes efficiently catalyze the highly enantioselective conjugate addition of HN_3,[8a,e] HCN,[8b] electron-deficient nitrile derivatives,[8c,e] and oximes[8d] to α,β-unsaturated imides and ketones in the absence of added base. As each of these nucleophiles includes a relatively acidic X–H (X = N, C, O) bond (pK_a 5–17), we hypothesized that heterocyclic compounds bearing similarly acidic N–H bonds might be suitable reaction partners in [(salen)Al]-catalyzed conjugate additions. Herein, we report the successful development of catalytic asymmetric conjugate additions of aromatic N-heterocycles to α,β-unsaturated carbonyl compounds. Both α,β-unsaturated imides and ketones undergo efficient and highly regio- and enantioselective additions with a variety of both fused and nonfused aromatic heterocyclic compounds. This methodology introduces a new, versatile synthetic method for the preparation of interesting chiral building blocks, including NNNs.

Purine, the structural core of the nucleobases in the most promising antiviral agents,[7a] was chosen as a model substrate. It contains a relatively acidic N–H bond (pK_a 8.6) and is known to exist in two (N7-H and N9-H) tautomeric forms.[9a] The oxo-bridged dimeric catalyst **1**[8c] was found to promote the addition of purine to 3-hepten-2-one (**2b**) in the absence of external base. The reaction resulted in full conversion into

[*] M. Gandelman, Prof. E. N. Jacobsen
Department of Chemistry and Chemical Biology
Harvard University
12 Oxford St., Cambridge, MA 02138 (USA)
Fax: (+1) 617-496-1880
E-mail: jacobsen@chemistry.harvard.edu

[**] This work was supported by the NIH through GM-43214 and a postdoctoral fellowship from the Rothschild Foundation to M.G.

Supporting information for this article is available on the WWW under http://www.angewandte.org or from the author.

 DOI: 10.1002/anie.200463058 © 2005 Wiley-VCH Verlag GmbH & Co. KGaA, Weinheim

a mixture of the N9 and N7 regioisomers (**3b** and **4b**) within 36 h in THF. The products were obtained in a 3:1 ratio favoring the N9 derivative and with encouraging enantioselectivity (88% *ee*) in the major regioisomer. Optimization studies revealed that reactions carried out in nonpolar solvents led to increased regio- and enantioselectivity, consistent with observations made in other conjugate additions mediated by [Al–salen] catalysts.[8] Reactions carried out in toluene provided the best results, with product **3b** generated in excellent regioselectivity (**3b**/**4b** = 20:1, 80% yield of isolated **3b**) and with 95% *ee*. Generally good reactivity as well as high regio- and enantioselectivity were attained with α,β-unsaturated ketones bearing aliphatic β-substituents (Table 1).[10]

Table 1: Conjugate addition of purine to enones **2a–e**.

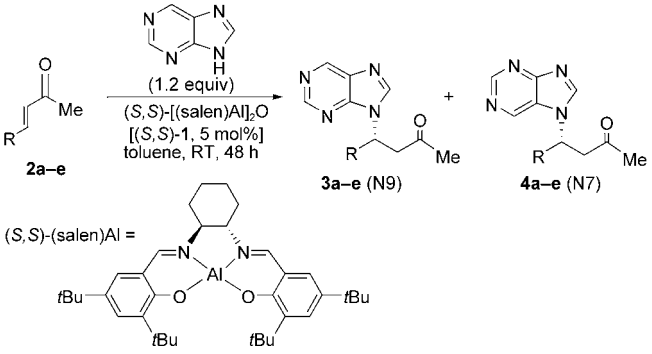

Product	R	Yield [%][a]	**3**/**4**[b]	*ee* [%][c]
3a	Me	78	14:1	90
3b	Pr	80	20:1	95
3c	Bu	76	17:1	93
3d	*i*Pr	86	>99:1	91
3e	CH_2CH_2OBn	74	>99:1	93

[a] Yield of isolated **3**, after chromatography, from reactions carried out on a 0.5-mmol scale. [b] Determined by ^{1}H NMR spectroscopy. [c] Determined by HPLC through commercial columns with chiral stationary phases (see Supporting Information).

α,β-Unsaturated imides were also found to be useful substrates, although lower reaction rates were observed with these electrophiles. Thus, 10 mol% of catalyst **1** was required for the reaction of purine with crotyl imide **5a** to allow complete substrate conversion within 48 h (Table 2). More-hindered imides **5b–e** proved even less reactive; however, useful rates were achieved at slightly elevated temperatures with minimal compromise in enantioselectivity (products **6b–e**). Lower regioselectivities were obtained with imides than with the corresponding enones, but *N*9-alkylated products could still be isolated in pure form and in synthetically useful yields.

Table 2: Conjugate addition of purine to imides **5a–e**.

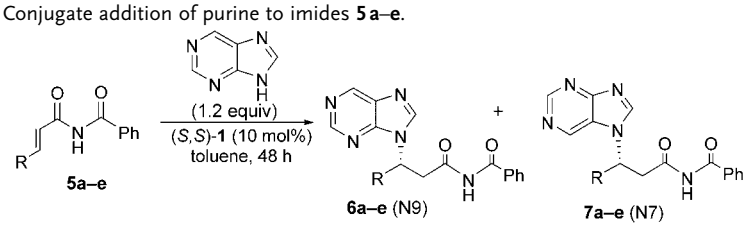

Product	R	Yield [%][a]	**6**/**7**[b]	*ee* [%][c]
6a	Me[d]	74	5:1	95
6b	Pr[e]	69	3:1	95
6c	*i*Pr[e]	64	10:1	98
6d	CH_2Ph[e]	63	3:1	96
6e	CH_2OTBS[e]	65	3:1	94

[a] Yield of isolated **6**, after chromatography, from reactions carried out on a 0.5-mmol scale. [b] Determined by ^{1}H NMR spectroscopy. [c] Determined by HPLC through commercial columns with chiral stationary phases (see Supporting Information). [d] The reaction was carried out at 23 °C. [e] The reaction was carried out at 65 °C. TBS = *tert*-butyldimethylsilyl.

Substituted purines also proved to be interesting substrates in conjugate addition reactions catalyzed by **1**. Although adenine, the parent 6-amino derivative, displayed no reactivity, the *N*-Boc-protected analogue[11] underwent addition to 3-hepten-2-one in the presence of **1** (5 mol%) at 23 °C to afford **8a** in 58% yield with 82% *ee* after 48 h. In the specific case of *N*-Boc-adenine, incorporation of *tert*-butyl alcohol as an additive[12] led to significant rate accelerations and generally good results in additions of this nucleophile to enones bearing aliphatic β substituents (products **8a–c**, Table 3). Extremely high regioselectivity for *N*9-substituted products was observed in these [(salen)Al^{III}]-catalyzed reactions, in marked contrast to racemic 1,4-conjugate additions of adenine and related compounds catalyzed by Brønsted bases, which invariably afford mixtures of N9 and N7 regioisomers.[4b,d,e]

Other 6-substituted purine derivatives, such as 6-benzyloxypurine, 6-chloropurine, and 6-methylsulfanylpurine, displayed excellent reactivity and enantioselectivity in conjugate additions to α,β-unsaturated ketones (products **9–11**, Table 3). Again, exclusive formation of the N9 regioisomers was observed in all cases. The utilization of chloropurine in this method may prove especially noteworthy, as relatively facile nucleophilic substitution of chloride should enable preparation of a wide range of derivatives.[9a]

Reactions of α,β-unsaturated imides with 6-substituted purine derivatives proved substantially slower, although again useful results could be obtained at elevated reaction temperatures (Table 4).[13] The N9 adduct was generated exclusively in good yields and enantioselectivities. Thus, all conjugate additions of 6-substituted purine derivatives to α,β-unsaturated ketones and imides were found to afford the N9 regioisomers with very high selectivity.

Other fused aromatic heterocyclic compounds also proved useful as substrates in this conjugate-addition chemistry. Benzotriazole bears a relatively acidic N–H bond (pK_a 8.6) and exists in solution in two tautomeric forms (N1-H and N2-H).[9b] This nucleophile underwent reaction with various α,β-unsaturated ketones, resulting in two regioisomeric products (N1 and N2), each generated in high

 © 2005 Wiley-VCH Verlag GmbH & Co. KGaA, Weinheim

Table 3: Conjugate addition of 6-substituted purines to α,β-unsaturated enones.

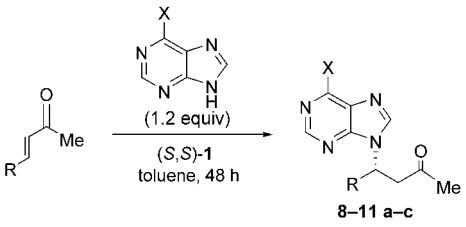

Product	X	R	Yield [%][a]	*ee* [%][b]
8a		Pr	67	95
8b	NHBoc[c]	*i*Pr	60	98
8c		CH_2CH_2OBn	61	99
9a		Pr	93	97
9b	OBn[d]	*i*Pr	89	96
9c		CH_2CH_2OBn	75	95
10a		Pr	95	91
10b	Cl[e]	*i*Pr	85	93.5
10c		CH_2CH_2OBn	82	96
11a		Pr	91	97
11b	SMe[e]	*i*Pr	88	98
11c		CH_2CH_2OBn	79	96

[a] Yield of isolated product, after chromatography, from reactions carried out on a 0.5-mmol scale. [b] Determined by HPLC through commercial columns with chiral stationary phases (see Supporting Information). [c] The reaction was carried out with **1** (10 mol%) and *tert*-butyl alcohol (0.6 equiv) at 0°C. [d] The reaction was carried out with **1** (10 mol%) at 23°C. [e] The reaction was carried out with **1** (5 mol%) at 23°C. Bn = benzyl, Boc = *tert*-butoxycarbonyl.

Table 4: Conjugate addition of 6-substituted purines to α,β-unsaturated imides.

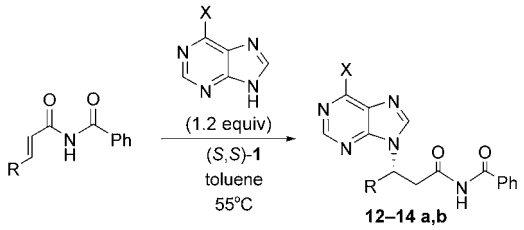

Product	X	R	*t* [h]	Yield [%][a]	*ee* [%][b]
12a	OBn[c]	Me	48	81	91
12b		CH_2OTBS	48	77	95
13a	Cl[d]	Me	18	92	97
13b		CH_2OTBS	24	93	97
14a	SMe[d]	Me	48	90	95.5
14b		CH_2OTBS	48	79	96.5

[a] Yield of isolated product, after chromatography, from reactions carried out on a 0.5-mmol scale. [b] Determined by HPLC through commercial columns with chiral stationary phases (see Supporting Information). [c] The reaction was carried out with **1** (10 mol%). [d] The reaction was carried out with **1** (5 mol%).

enantioselectivity (Table 5). Additions to β-aryl substituted enones also proceeded with high enantioselectivity, although prolonged reaction times were needed to obtain useful yields

Table 5: Conjugate addition of benzotriazole to enones **2a–f**.

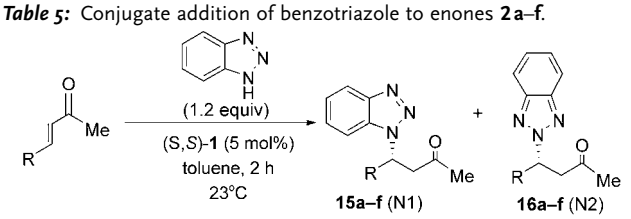

Product	R	Yield [%][a] **15**	**15/16**[b]	*ee* [%][c] **15**	**16**
a	Me	72	3:1	92	92
b	Pr	75	3:1	94	98
c	*i*Pr	67	3:1	98	98
d	CH_2CH_2OBn	65	2.6:1	91	93
e	Ph[d]	53	2:1	90	88
f[e]	*p*-BrPh	60	2.5:1	70 (98)[f]	–

[a] Yield of isolated product **15**, after chromatography, from reactions carried out on a 0.5-mmol scale. [b] Determined by ^{1}H NMR spectroscopy. [c] Determined by HPLC through commercial columns with chiral stationary phases (see Supporting Information). [d] Reaction time: 48 h. [e] Absolute configuration determined by X-ray crystallography (Supporting Information). [f] Number in parentheses is the *ee* value after recrystallization.

(**15e,f** and **16e,f**). X-ray crystallographic analysis of product **15f** served to confirm that the absolute stereochemistry of the products was consistent with that seen in all previous [(salen)Al]-catalyzed conjugate addition reactions.[8,14]

Reactions of benzotriazole with α,β-unsaturated imides also led efficiently to mixtures of N1 and N2 adducts, although the major regioisomeric products were reversed in comparison to those obtained in enone additions (Table 6). Again, both regioisomers were generated with high enantioselectivity, and aliphatic as well as aromatic β-substituted α,β-unsaturated imides were useful substrates.

The scope of useful nucleophiles is not limited to fused aromatic heterocyclic compounds, and any heterocycle that bears appropriately acidic N–H groups may be suitable substrates in these [(salen)Al]-catalyzed conjugate addition

Table 6: Conjugate addition of benzotriazole to α,β-unsaturated imides.

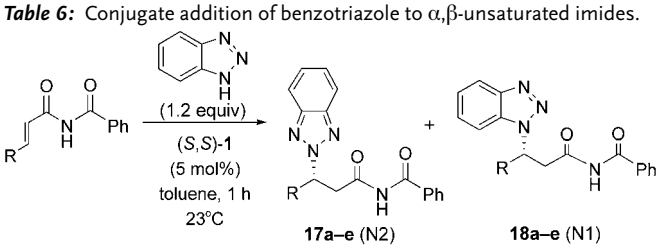

Product	R	Yield [%][a] **17**	**17/18**[b]	*ee* [%][c] **17**	**18**
a	Pr	69	3:1	99	98
b	*i*Pr	65	2.5:1	>99	>99
c	CH_2Ph	67	2:1	96	96
d	CH_2OBn	64	2:1	99	98
e	Ph	55	1.4:1	99	95

[a] Yield of isolated product, after chromatography, from reactions carried out on a 0.5-mmol scale. [b] Determined by ^{1}H NMR spectroscopy. [c] Determined by HPLC through commercial columns with chiral stationary phases (see Supporting Information).

 © 2005 Wiley-VCH Verlag GmbH & Co. KGaA, Weinheim

reactions. We were particularly interested in 1,2,3-triazole (pK_a 9.3) and tetrazole (pK_a 4.76), as these ring frameworks have found increasingly important applications in materials and pharmaceutical sciences.[9b,c] Substituted triazole derivates may be accessed efficiently by sequential catalytic asymmetric conjugate addition of HN_3 to α,β-unsaturated carbonyl compounds[8a,e] followed by [2+3] cycloaddition with alkynes catalyzed by $CuSO_4$.[8e,15] However, the analogous route to substituted tetrazoles is less straightforward owing to the fact that intermolecular 1,3-dipolar cycloaddition of organic azides and nitriles remains a difficult transformation that is limited in scope.[16] Therefore, we explored the direct synthesis of substituted tetrazoles by 1,4-conjugate addition of tetrazole to α,β-unsaturated carbonyl compounds.

Tetrazole itself proved not to be a competent substrate in the [(salen)Al]-catalyzed reactions, promoting instead precipitation of the aluminum complex as an intractable polymer. We assumed that tetrazole was acting as a polycoordinating ligand to form oligomeric Al^{III} species,[17] and examined more sterically encumbered, substituted tetrazoles in the reaction. Gratifyingly, 5-methyl tetrazole displayed the desired reactivity with both α,β-unsaturated ketones and imides. Mixtures of 1,5- and 2,5- substituted regioisomers were formed with high enantioselectivity under the optimal reaction conditions (Table 7).

Table 7: Conjugate addition of 5-methyltetrazole to α,β-unsaturated ketones and imides.

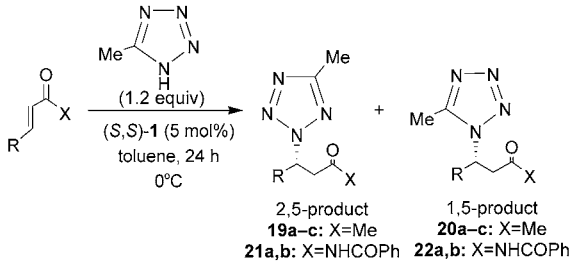

Products	R	Yield [%][a] 2,5-product	Yield [%][a] 1,5-product	*ee* [%][b] 2,5-product	*ee* [%][b] 1,5-product
19a, **20a**	Pr	42	40	94	94.5
19b, **20b**	*i*Pr	64	27	95	96
19c, **20c**	CH_2CH_2OBn	63	30	87.5	87
21a, **22a**	CH_3	61	35	93	92
21b, **22b**	CH_2OTBS	56	35	96	94.5

[a] Yield of isolated pure regioisomer, after chromatography, from reactions carried out on a 0.5-mmol scale. [b] Determined by HPLC through commercial columns with chiral stationary phases (see Supporting Information).

When 5-phenyl tetrazole was used as a nucleophile, the 2,5-substituted regioisomer was obtained as the *only product* in high yield and enantioselectivity (Table 8). Similarly high reactivity and enantioselectivity and exclusive regioselectivity were attained in the reactions of tetrazole with unsaturated imides. The electronic effect of tetrazole *C*-aryl substituents in promoting nucleophilic reactions at N2 is precedented.[9c]

Table 8: Conjugate addition of 5-phenyltetrazole to α,β-unsaturated ketones and imides.

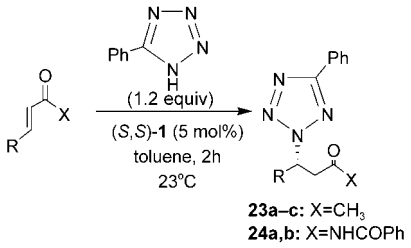

Product	R	Yield [%][a]	*ee* [%][b]
23a	Pr	94	99
23b	*i*Pr	93	95.5
23c	CH_2CH_2OBn	90	94
24a	CH_3	93	95.5
24b	CH_2OTBS	94	97

[a] Yield of isolated product, after chromatography, from reactions carried out on a 0.5-mmol scale. [b] Determined by HPLC through commercial columns with chiral stationary phases (see Supporting Information).

Although this methodology is mostly applicable to relatively acidic heterocycles of $pK_a(N\text{-}H) < 10$, useful reactivity could be achieved for less-acidic compounds. For example, benzimidazole (pK_a 12.75) underwent reaction with 3-hepten-2-one at 23 °C to afford 1,4-addition product **25** in 20 % yield with 90 % *ee* after 48 h (Scheme 1). The reactivity was improved by carrying out the reaction at 60 °C for 2 days (yield of isolated product is 73 %), although this was accompanied by a significant decrease in enantioselectivity (81 % *ee*).

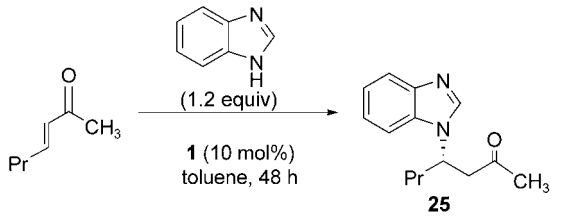

Scheme 1. 1,4-Addition of benzimidazole (pK_a 12.75) to 3-hepten-2-one.

In summary, catalytic asymmetric conjugate addition of N–H- containing heterocycles to α,β-unsaturated ketones and imides has been developed successfully. A wide range of fused and nonfused heterocyclic compounds are useful substrates, generally demonstrating good reactivity and enantioselectivity. This methodology opens a new entry to the synthesis of non-natural nucleosides. Mechanistic studies of these reactions are underway.

Received: December 24, 2004
Published online: March 10, 2005

 © 2005 Wiley-VCH Verlag GmbH & Co. KGaA, Weinheim

Keywords: aluminum · asymmetric catalysis · heterocycles · nucleobases · synthetic methods

[1] A. R. Katritzky, A. F. Pozharskii, *Handbook of Heterocyclic Chemistry*, 2nd ed., Pergamon, Oxford, **2002**.

[2] For discussions on the importance of chiral N-heterocycles, see: a) A. F. Pozharskii, A. T. Soldatenkov, A. R. Katritzky, *Heterocycles in Life and Society*, Wiley, New York, **1997**; b) M. Shipman, *Contemp. Org. Synth.* **1995**, *2*, 1.

[3] a) K. Tomioka, Y. Nagaoka, M. Yamaguchi in *Comprehensive Asymmetric Catalysis*, *Vol. 3* (Eds.: E. N. Jacobsen, A. Pfaltz, H. Yamamoto), Springer, Berlin, **1999**, and *Supplement I and II* to this book (Eds.: E. N. Jacobsen, A. Pfaltz, H. Yamamoto), Springer, Berlin, **2004**; b) N. Krause, A. Hoffmann-Röder, *Synthesis* **2001**, 171.

[4] Conjugate additions of indoles at C3 have been developed: a) J. F. Austin, D. W. C. MacMillan, *J. Am. Chem. Soc.* **2002**, *124*, 1172; the only reported conjugate additions of nitrogen-centered nucleophiles have afforded racemic products, usually as mixtures of regioisomers: b) S. Guillarme, S. Legoupy, A.-M. Aubertin, C. Olicard, N. Bourgougnon, F. Huet, *Tetrahedron* **2003**, *59*, 2177; c) A. Esposito, M. G. Perino, M. Taddei, *Eur. J. Org. Chem.* **1999**, 931; d) G. R. Geen, P. M. Kincey, *Tetrahedron Lett.* **1992**, *33*, 4609; e) E.-S. M. A. Yakout, E. B. Pedersen, *Chem. Scr.* **1989**, *29*, 185; f) E. P. Lira, C. W. Huffman, *J. Org. Chem.* **1966**, *31*, 2188; g) R. H. Wiley, N. R. Smith, D. M. Johnson, J. Moffat, *J. Am. Chem. Soc.* **1954**, *76*, 4933.

[5] C. Simons, *Nucleoside Mimetics. Their Chemistry and Biological Properties*, Gordon and Breach, Australia, **2001**.

[6] For a review on the application of NNNs to structure–activity relationship studies of DNA and RNA and specific recognition of DNA sequences, see: M. G. M. Purwanto, K. Weisz, *Curr. Org. Chem.* **2003**, *7*, 427, and references therein.

[7] For applications as promising anticancer and antiviral chemotherapeutic agents, see: a) R. T. Walker, M. J. Gait in *Nucleic Acids in Chemistry and Biochemistry* (Eds.: G. M. Blackburn, M. J. Gait), IRL, Oxford, **1990**, chap. 4, and references therein; b) L. A. Agrofoglio, S. R. Challand, *Acyclic, Carbocyclic and L-Nucleosides*, Kluwer Academic, Dordrecht, **1998**; c) E. De Clercq, *J. Med. Chem.* **1995**, *38*, 2491.

[8] a) J. K. Myers, E. N. Jacobsen, *J. Am. Chem. Soc.* **1999**, *121*, 8959; b) G. M. Sammis, E. N. Jacobsen, *J. Am. Chem. Soc.* **2003**, *125*, 4442; c) M. S. Taylor, E. N. Jacobsen, *J. Am. Chem. Soc.* **2003**, *125*, 11204; d) C. D. Vanderwal, E. N. Jacobsen, *J. Am. Chem. Soc.* **2004**, *126*, 14724; e) addition of nitrile derivatives and hydrazoic acid to α,β-unsaturated ketones: M. S. Taylor, D. Zalatan, A. M. Lerchner, E. N. Jacobsen, *J. Am. Chem. Soc.* **2005**, *127*, 1313; see also: f) S. C. Jha, N. N. Joshi, *Tetrahedron: Asymmetry* **2001**, *12*, 2463.

[9] For detailed reviews of the properties, reactivity, and applications of studied heterocycles, see: a) purines: G. Shaw, H. Wamhoff, R. N. Butler in *Comprehensive Heterocyclic Chemistry*, *Vol. 5* (Eds.: A. L. Katritzky, C. W. Rees, K. T. Potts), Pergamon, Oxford, **1984**, chap. 4.09; b) benzotriazole and 1,2,3-triazole: G. Shaw, H. Wamhoff, R. N. Butler in *Comprehensive Heterocyclic Chemistry*, *Vol. 5* (Eds.: A. L. Katritzky, C. W. Rees, K. T. Potts), Pergamon, Oxford, **1984**, chap. 4.11; c) tetrazole: G. Shaw, H. Wamhoff, R. N. Butler in *Comprehensive Heterocyclic Chemistry*, *Vol. 5* (Eds.: A. L. Katritzky, C. W. Rees, K. T. Potts), Pergamon, Oxford, **1984**, chap. 4.13.

[10] Enones that bear aromatic β-substituents exhibited low reactivity, even under forcing conditions. Cyclic enones such as 2-cyclopentenone and 2-cyclohexenone underwent conjugate addition with only moderate enantioselectivity (30% *ee* with 2-cyclohexenone under the conditions outlined in Table 1).

[11] Prepared according to the literature procedure: S. Dey, P. Garner, *J. Org. Chem.* **2000**, *65*, 7697.

[12] Rate accelerations by addition of *tert*-butyl alcohol were also achieved in [(salen)Al]-catalyzed addition of nitrile derivatives to α,β-unsaturated imides.[8c] For a discussion on the use of alcohols and other additives in asymmetric catalysis, see: E. M. Vogl, H. Groger, M. Shibasaki, *Angew. Chem.* **1999**, *111*, 1672; *Angew. Chem. Int. Ed.* **1999**, *38*, 1570.

[13] *N*-Boc-protected adenine exhibited poor reactivity with α,β-unsaturated imides even at elevated temperatures.

[14] CCDC-259667 contains the supplementary crystallographic data for this paper. These data can be obtained free of charge from the Cambridge Crystallographic Data Centre via www.ccdc.cam.ac.uk/data_request/cif.

[15] V. V. Rostovtsev, L. G. Green, V. V. Fokin, K. B. Sharpless, *Angew. Chem.* **2002**, *114*, 2708; *Angew. Chem. Int. Ed.* **2002**, *41*, 2596; , and references therein.

[16] a) Z. P. Demko, K. B. Sharpless, *Angew. Chem.* **2002**, *114*, 2214; *Angew. Chem. Int. Ed.* **2002**, *41*, 2110; ; b) Z. P. Demko, K. B. Sharpless, *Angew. Chem.* **2002**, *114*, 2217; *Angew. Chem. Int. Ed.* **2002**, *41*, 2113; , and references therein.

[17] Polymeric Al^{III} complexes bearing polyligating heterocyclic compounds are known: a) C. M. Mikulski, R. De Prince, G. W. Madison, M. Gaul, N. M. Karayannis, *Inorg. Chim. Acta* **1987**, *138*, 55; b) C. M. Mikulski, S. Cocco, L. Mattucci, N. Defranco, L. Weiss, N. M. Karayannis, *Inorg. Chim. Acta* **1982**, *67*, 173.

 © 2005 Wiley-VCH Verlag GmbH & Co. KGaA, Weinheim

Biphasic Synthesis

Synthesis of Medium- and Large-Sized Lactones in an Aqueous–Organic Biphasic System**

Hidenori Kinoshita, Hiroshi Shinokubo, and Koichiro Oshima**

Numerous natural products and biologically active compounds have various types of ring moieties.[1] Cyclization reactions have been investigated extensively, and the devel-

[*] Prof. Dr. H. Shinokubo
Department of Chemistry, Graduate School of Science
Kyoto University
Sakyo-ku, Kyoto 606-8502 (Japan)
PRESTO, Japan Science and Technology Agency (JST)
Fax: (+81) 75-753-3970
E-mail: hshino@kuchem.kyoto-u.ac.jp
H. Kinoshita, Prof. Dr. K. Oshima
Department of Material Chemistry, Graduate School of Engineering
Kyoto University
Nishikyo-ku, Kyoto 615-8510 (Japan)
Fax: (+81) 75-383-2438
E-mail: oshima@orgrxn.mbox.media.kyoto-u.ac.jp

[**] This work was partly supported by a Grant-in-Aid for Scientific Research (No. 14703026) from the Ministry of Education, Culture, Sports, Science, and Technology, Japan. H.K. received a Research Fellowship for Young Scientists from the JSPS.

Supporting information for this article is available on the WWW under http://www.angewandte.org or from the author.

 DOI: 10.1002/anie.200462677 © 2005 Wiley-VCH Verlag GmbH & Co. KGaA, Weinheim

opment of efficient methods to construct cyclic structures has been a central field in organic synthesis.

The formation of medium-sized ring compounds is still problematic even today. The reaction forming the medium-sized ring often proceeds sluggishly, due to the unfavorable transannular interaction and negative activation entropy for the cyclization.[2] In addition, the preparation of macrocycles is not always trivial, since the two reaction sites in a molecule cannot interact with each other efficiently in some cases. In these cases, intermolecular reactions compete with the desired intramolecular reaction. To retard the intermolecular process, high-dilution conditions with large amounts of solvent combined with a slow-addition technique have been adopted in the construction of medium- and large-sized ring compounds. However, the use of large quantities of solvent is uneconomical and inconvenient, and the process of slow addition is a laborious operation. Recently, we have proposed the use of an aqueous–organic biphasic system to circumvent such drawbacks.[3] The biphasic system controls the concentration of the organic hydrophobic substrate in the aqueous phase (Figure 1). The distribution of the substrate retains the high-dilution conditions in the aqueous reaction phase. The applicability of the system has been demonstrated in rhodium-catalyzed [2+2+2] annulation reactions of triynes.

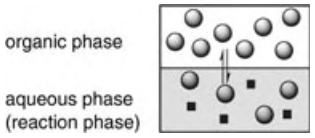

Figure 1. Concept of biphasic control of the concentrations in an aqueous phase. Circles: hydrophobic substrate, squares: water-soluble catalyst.

The formation of medium-sized lactones is still a challenging cyclization. There are few examples of effective medium-sized-lactone formation.[4,5] Herein we wish to report the preparation of a series of medium- and large-sized lactones by an intramolecular Tsuji–Trost reaction without high-dilution conditions.

We investigated the aqueous Tsuji–Trost reaction for the synthesis of medium-sized lactones in the biphasic system for the following reasons: 1) A conformational change of the substrate, which would facilitate ring formation, is expected due to the hydrophobic effect in water. 2) π-Allylpalladium species can be readily formed from allylic esters in aqueous media.[6] 3) Macrocyclization by the Tsuji–Trost reaction has served as a pivotal step in a number of total syntheses of natural products,[7] and it is therefore highly desirable to develop a related efficient procedure without high dilution. The starting materials were synthesized as shown in Scheme 1.

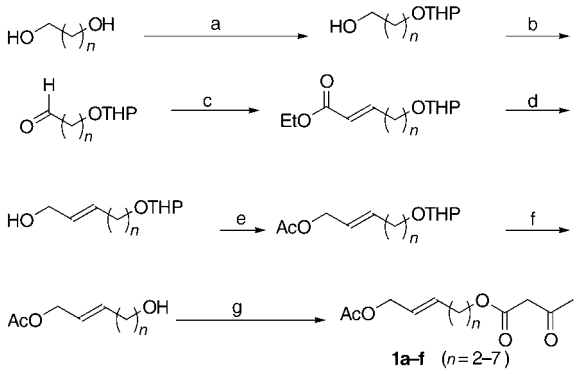

Scheme 1. Preparation of the starting materials. a) 3,4-Dihydro-2*H*-pyran, TsOH (cat.), THF; b) Swern oxidation, c) $(EtO)_2P(O)CH_2C(O)OEt$, NaH, THF, 0 °C→RT; d) DIBAL-H (2 equiv), hexane, 0 °C→RT; e) Ac_2O, pyridine; f) TsOH (cat.), CH_3OH; g) diketene, THF, AcONa, reflux. DIBAL-H = diisobutylaluminum hydride, THP = tetrahydropyranyl, Ts = toluene-4-sulfonyl.

The macrocyclization of **1b** ($n = 3$, 0.5 mmol) to the nine-membered lactone with a water-soluble palladium complex prepared from $[PdCl(\eta^3\text{-}C_3H_5)]_2$ (2.5 mmol %) and the trisodium salt of tris(*m*-sulfonatophenyl)phosphine (tppts; 22 mol %) in water (5 mL) at room temperature for 24 h led to the desired lactone in only 1 % yield. After several trials, we found that an efficient macrocyclization reaction was accomplished in a water–ethyl acetate biphasic system. The results are shown in Table 1. In the biphasic system, an isomeric mixture of lactones **2** and **3** (2:1) was obtained in 63 % combined yield after 12 h (entry 2). Lactone **2** consists of two diastereomers as a consequence of the planar chirality of its *trans* olefinic linkage. With a methoxycarbonate group instead of the acetate group as the leaving group, the yield was slightly improved but the selectivity was decreased (entry 3).[8] The amount of water and ethyl acetate is crucial:

Table 1: Optimization of the reaction conditions for the synthesis of nine-membered lactones.[a]

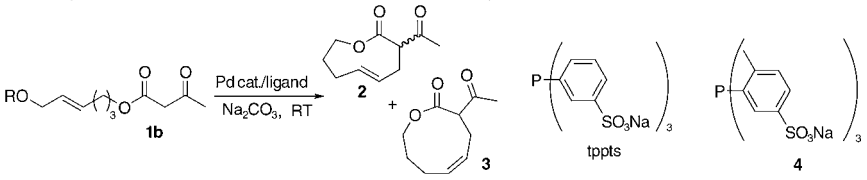

Entry	RO	Ligand	System	*t* [h]	Yield [%][b]	Ratio **2**:**3**[c]
1	AcO	tppts	H_2O[d]	24	trace	
2	AcO	tppts	H_2O/AcOEt	12	63	2:1
3	ZO[e]	tppts	H_2O/AcOEt	24	66	1:1
4	AcO	tppts	H_2O/AcOEt[f]	24	n.r.[g]	
5	HO	tppts	H_2O/AcOEt	24	trace	
6	AcO	**4**	H_2O/AcOEt	12	74	13:1
7	AcO	PPh_3	THF[h]	12	36	1:1

[a] If not otherwise stated, $[PdCl(\eta^3\text{-}C_3H_5)]_2$ (2.5 mol %), water-soluble ligand (22 mol %), Na_2CO_3 (1.2 mmol), **1b** (0.5 mmol), H_2O (5 mL), and AcOEt (5 mL) were employed. [b] Yield of isolated product. [c] Determined by NMR spectroscopy. [d] H_2O (5 mL) was employed. [e] Z: methoxycarbonyl. [f] H_2O (50 mL)/AcOEt (10 mL). [g] Not recorded. [h] THF (10 mL, 0.05 M) was employed.

 © 2005 Wiley-VCH Verlag GmbH & Co. KGaA, Weinheim

in a biphasic system with 50 mL of water and 10 mL of ethyl acetate, the lactone was not obtained even after a prolonged reaction period (24 h, entry 4). Using the water-soluble ligand **4**,[9] prepared by sulfonation of tri(*o*-tolyl)phosphine with oleum, instead of tppts greatly enhanced the yield and selectivity (**2**:**3**, entry 6). Obviously, ligand **4** can suppress the isomerization of the π-allylpalladium intermediate, an isomerization that results in the formation of the more stable *cis*-configured nine-membered ring structure **3**. The reaction in THF also provided lactones **2** and **3**, but yield and selectivity were far less than those observed in the biphasic system (entry 7).[10] Since we have recently reported that π-allylpalladium species can be prepared from allylic alcohols in an aqueous system,[11] we attempted the direct use of an allylic alcohol as the substrate. Disappointingly, the desired lactone was not obtained (entry 5).[12]

Under the optimized reaction conditions, we conducted the synthesis of medium- and large-sized lactones with the substrates that have longer methylene chains, **1c–f** (Scheme 2). These substrates afforded the desired lactones

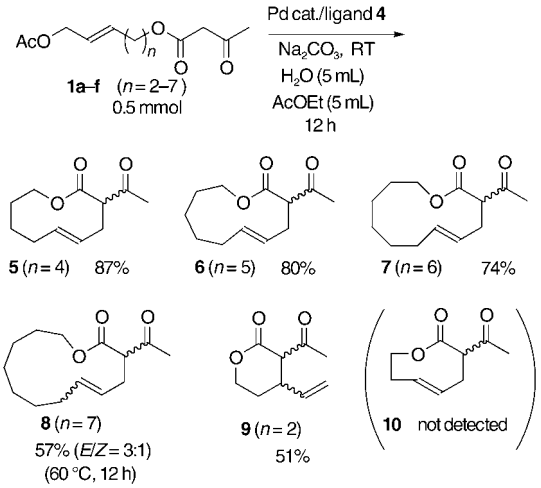

Scheme 2. Synthesis of medium- and large-sized lactones in the biphasic system. The product formed by **1b** ($n = 3$) is shown in Table 1.

in high yields without any byproducts, as in the case with **1b**, R = OAc. In contrast, the reaction of **1e** in *N*,*N*-dimethylformamide (DMF, 0.05 M) provided the 12-membered lactone **7** in only 28% yield. Formation of the 13-membered lactone from **1f** proceeded slowly to provide the product **8** in 17% yield (with 51% recovered starting material) under the biphasic conditions at room temperature for 12 h. However, the yield of **8** was improved to 57% when an elevated reaction temperature was used (60 °C for 12 h), although the stereoselectivity was decreased ($E/Z = 3:1$). Substrate **1a** afforded only **9** in 51% yield by 6-*exo* cyclization. The eight-membered lactone **10** was not detected.

To elucidate the configuration of the olefin moiety in the lactones, we conducted methanolysis of the products. The configuration of the double bond was assigned as *E* in all cases on the basis of ^{1}H NMR spectroscopy analysis and comparison with authentic samples. Interestingly, the configuration of the substrates is retained in the products under the aqueous biphasic conditions with ligand **4**. As shown in Scheme 3, the substrate **11** that has a *Z* olefin moiety afforded the *Z*-configured lactone **12** in excellent yield and with high selectivity.

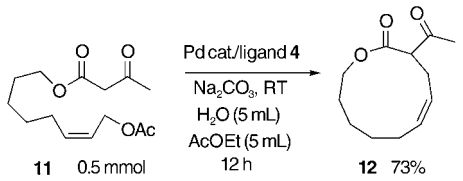

Scheme 3. Cyclization of a *cis* isomer in the biphasic system.

In conclusion, we have succeeded in synthesizing medium- and large-sized lactones in high yields in an aqueous–ethyl acetate biphasic system without the use of large amounts of solvent. These lactones retain the original configuration of the olefin moiety in their rings. We propose that the biphasic cyclization protocol is a useful tool for the preparation of medium- and large-sized ring compounds.

Experimental Section

Representative standard procedure: $[PdCl(\eta^3\text{-}C_3H_5)]_2$ (4.6 mg, 0.0125 mmol) and **4** (67.5 mg, 0.11 mmol) were placed in a 20-mL flask under an argon atmosphere. Degassed water (5 mL) was introduced, and the mixture was stirred vigorously at 75 °C for 15 min. Na_2CO_3 (127.2 mg, 1.2 mmol) and ethyl acetate (3 mL) were added to the homogeneous clear yellow solution at room temperature. A solution of **1c** (128.1 mg, 0.5 mmol) in ethyl acetate (2 mL) was added to the ethyl acetate phase. After stirring for 12 h, the mixture was extracted with ethyl acetate. The organic extracts were dried and concentrated. Purification of the residual oil afforded 3-acetyl-3,4,7,8,9,10-hexahydrooxecin-2-one (**5**, 85.7 mg, 0.44 mmol) in 87% yield.

Received: November 20, 2004
Published online: March 16, 2005

Keywords: allylation · biphasic catalysis · lactones · palladium · solvent effects

[1] a) *Recent Progress in the Chemical Synthesis of Antibiotics* (Eds.: G. Lukacs, M. Ohno), Springer, Berlin, **1990**; b) S. Masamune, G. S. Gates, J. W. Corcoran, *Angew. Chem.* **1977**, *89*, 602; *Angew. Chem. Int. Ed. Engl.* **1977**, *16*, 585.

[2] a) G. Rousseau, *Tetrahedron* **1995**, *51*, 2777; b) L. Yet, *Chem. Rev.* **2000**, *100*, 2963.

[3] H. Kinoshita, H. Shinokubo, K. Oshima, *J. Am. Chem. Soc.* **2003**, *125*, 7784.

[4] a) E. J. Corey, D. J. Brunelle, K. C. Nicolaou, *J. Am. Chem. Soc.* **1977**, *99*, 7359; b) W. H. Kurizinga, R. Kingma, L. Leegstra, E. Rokaszewski, G. Gruppen, R. M. Kellog, *J. Chem. Soc. Chem. Commun.* **1990**, 1647; c) T. Mukaiyama, J. Izumi, M. Miyashita, I. Shuna, *Chem. Lett.* **1993**, 907; d) K. Ishihara, M. Kubota, H. Kurihara, H. Yamamoto, *J. Org. Chem.* **1996**, *61*, 4560.

[5] a) C. Galli, L. Mandolini, *Org. Synth.* **1978**, *58*, 98; b) B. M. Trost, T. R. Verhoeven, *J. Am. Chem. Soc.* **1979**, *101*, 1595; c) J. Christoffers, H. Oertling, P. Fischer, W. Frey, *Synlett* **2002**, *6*, 957; d) B. L. Ashfeld, K. A. Miller, S. F. Martin, *Org. Lett.* **2004**, *6*, 1321; e) R. Munakata, H. Katakai, T. Ueki, J. Kurosawa, K.

 © 2005 Wiley-VCH Verlag GmbH & Co. KGaA, Weinheim

Takao, K. Tadano, *J. Am. Chem. Soc.* **2003**, *125*, 14722; f) G. A. Molander, F. Dehmel, *J. Am. Chem. Soc.* **2004**, *126*, 10313.

[6] The aqueous Tsuji–Trost reaction has been extensively investigated. For selected examples, see: a) M. Safi, D. Sinou, *Tetrahedron Lett.* **1991**, *32*, 2025; b) J. P. Genêt, E. Blart, M. Savignac, *Synlett* **1992**, 715; c) E. Blart, J. P. Genêt, M. Safi, M. Savignac, D. Sinou, *Tetrahedron* **1994**, *50*, 505; d) S. Kobayashi, W. W.-L. Lam, K. Manabe, *Tetrahedron Lett.* **2000**, *41*, 6115; e) H. Danjo, D. Tanaka, T. Hayashi, Y. Uozumi, *Tetrahedron* **1999**, *55*, 14341; f) Y. Uozumi, K. Shibatomi, *J. Am. Chem. Soc.* **2001**, *123*, 2919; g) D. E. Bergbreiter, Y.-S. Liu, *Tetrahedron Lett.* **1997**, *38*, 7843; h) K. Manabe, S. Kobayashi, *Org. Lett.* **2003**, *5*, 3241. See also V. Michelet, M. Savignac, J. P. Genê, *Electronic Encyclopedia of Reagents for Organic Synthesis*, (Eds.: L. Paquette, P. Fuchs, D. Crich, P. Wipf), Wiley, New York, **2004**.

[7] For the use of the Tsuji–Trost reaction for macrocyclization, see: a) B. M. Trost, *Angew. Chem.* **1989**, *101*, 1199; *Angew. Chem. Int. Ed. Engl.* **1989**, *28*, 1173; b) A. Fürstner, H. Weintritt, *J. Am. Chem. Soc.* **1998**, *120*, 2817; c) R. Munakata, H. Katakai, T. Ueki, J. Kurosaka, K. Takao, K. Tadano, *J. Am. Chem. Soc.* **2003**, *125*, 14722; d) R. Munakata, H. Katakai, T. Ueki, J. Kurosaka, K. Takao, K. Tadano, *J. Am. Chem. Soc.* **2004**, *126*, 11254; e) J. Pohlmann, C. Sabater, H. M. R. Hoffmann, *Angew. Chem.* **1998**, *110*, 656; *Angew. Chem. Int. Ed.* **1998**, *37*, 633.

[8] The reaction did not proceed in the absence of Na_2CO_3 at room temperature and the starting material was recovered completely.

[9] W. A. Herrmann, G. P. Albanese, R. B. Manetsberger, P. Lappe, H. Bahrmann, *Angew. Chem.* **1995**, *107*, 893; *Angew. Chem. Int. Ed. Engl.* **1995**, *34*, 811.

[10] The reaction in DMF with tri(*o*-tolyl)phosphine as the ligand provided none of the desired products **2** and **3**.

[11] a) H. Kinoshita, H. Shinokubo, K. Oshima, *Org. Lett.* **2004**, *6*, 4085; b) N. Komine, A. Sako, S. Hirahara, M. Hirano, S. Komiya, *Chem. Lett.* **2005**, *34*, 246.

[12] This allylic alcohol is quite soluble in water. We confirmed that more than 70% of it existed in the water phase. We suppose that the β-dicarbonyl moiety of the substrate affects the activity of the water-soluble palladium catalyst. On the other hand, the concentration of **1c** ($n=4$) in the aqueous phase was measured to be roughly 1.7×10^{-3} mol L^{-1}. This value equals 1.7% of the introduced substrate.

 © 2005 Wiley-VCH Verlag GmbH & Co. KGaA, Weinheim

Enzyme Classification

Class Assignment of Sequence-Unrelated Members of Enzyme Superfamilies by Activity-Based Protein Profiling**

*Nadim Jessani, Jason A. Young, Sandra L. Diaz, Matthew P. Patricelli, Ajit Varki, and Benjamin F. Cravatt**

Enzyme superfamilies are composed of members that share a common catalytic mechanism, but not necessarily sequence or structural homology.[1] The characterization of sequence-unrelated members of enzyme classes is an experimentally challenging endeavor which often requires extensive biochemical studies on purified preparations of enzymes.[2,3] Given these issues, in conjunction with the abundance of unannotated proteins provided by recent genome-sequencing projects, it is likely that cryptic members of many enzyme classes still exist in eukaryotic and prokaryotic proteomes. Herein, we demonstrate that a chemical proteomics method referred to as activity-based protein profiling (ABPP)[4,5] can be used to identify sequence-unrelated members of enzyme superfamilies on the basis of their reactivity with "mechanism-based" probes.

In previous studies, we analyzed a panel of human cancer cell lines with a set of fluorophosphonate (FP) based ABPP probes, [6] which target the serine hydrolase (SH) superfamily of enzymes.[7] FPs are well-characterized affinity labels for SHs; they phosphonylate irreversibly the active-site serine nucleophile in these enzymes.[8] Numerous FP-labeled enzymes were identified in these experiments, including proteases, lipases, and esterases. Most of these enzymes were readily assigned to the SH superfamily on the basis of database (BLAST) searches, which identified conserved sequence elements shared by members of this enzyme class. Notably, however, one FP target, sialic acid 9-*O*-acetylesterase (SAE), which was selectively expressed in melanoma cell lines (Figure 1 a), eluded such classification, as this enzyme shared no sequence homology with SHs or, for that matter, any other enzyme class. SAE was originally characterized by

[*] N. Jessani, J. A. Young, Prof. B. F. Cravatt
The Skaggs Institute for Chemical Biology and
Departments of Cell Biology and Chemistry
The Scripps Research Institute
La Jolla, CA 92037 (USA)
Fax: (+1) 858-784-8023
E-mail: cravatt@scripps.edu

S. L. Diaz, Prof. A. Varki
Departments of Medicine and Cellular & Molecular Medicine
Glycobiology Research and Training Center
University of California, San Diego
La Jolla, CA 92093-0687 (USA)

M. P. Patricelli
Activx Biosciences
11025 N. Torrey Pines Rd, Suite 120, La Jolla, CA 92038 (USA)

[**] This research was supported by the NIH (CA087660 and GM32373) and the Skaggs Institute for Chemical Biology.

 © 2005 Wiley-VCH Verlag GmbH & Co. KGaA, Weinheim DOI: 10.1002/anie.200463098

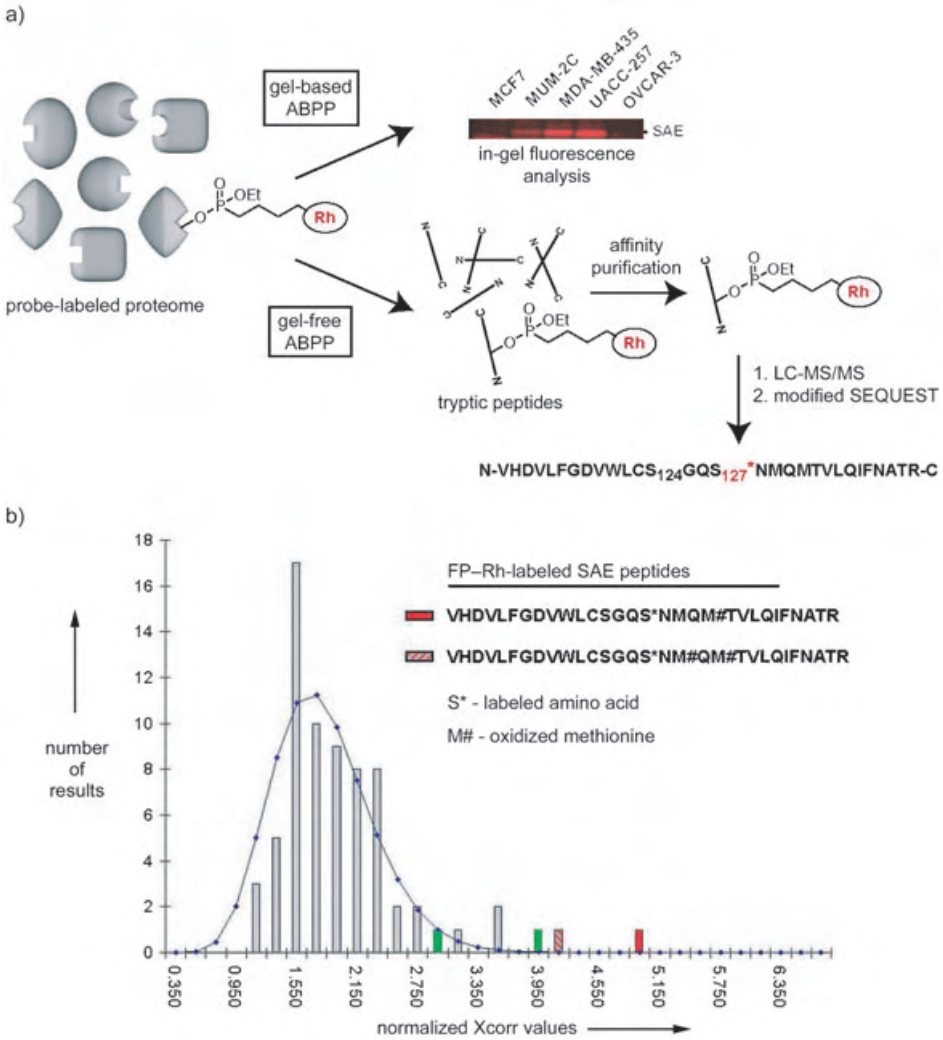

Figure 1. Identification of the site of FP–Rh labeling in SAE by gel-free ABPP. a) General strategy for gel-free ABPP as compared to gel-based ABPP. With gel-based ABPP, probe-labeled proteomes are analyzed by in-gel fluorescence scanning (shown is a representative analysis of FP–Rh-labeled SAE signals in the secreted proteomes of breast (MCF7), ovarian (OVCAR3), and melanoma (MUM-2C, MDA-MB-435, UACC-257) cancer cell lines). With gel-free ABPP, probe-labeled proteomes are denatured and, after reduction and alkylation of their thiol groups, digested with trypsin. Probe-modified peptides are then affinity isolated from the resulting mixture of tryptic peptides by bead-conjugated anti-rhodamine monoclonal antibodies (Activx Biosciences)[12,13] and analyzed by LC-MS/MS and the SEQUEST search algorithm to identify concurrently the protein targets of ABPP probes and the specific residues labeled by these probes. General experimental conditions for gel-free ABPP of SAE: Conditioned-media proteome (2 mL, 1 mg protein mL^{-1}) from COS-7 cells that recombinantly express human SAE was treated with FP–Rh (4 μM) for 1 h. The sample was then processed and analyzed as described above to produce MS/MS spectra of FP–Rh-labeled peptides. The spectra were searched against a human-protein database by using SEQUEST, and the resulting data were filtered and analyzed as described.[12,13] The normalized Xcorr values from the SEQUEST results (shown as bars in the graph in (b)) were plotted against the predicted distribution of false positive results in the same data set (stippled blue line). Red filled and red hatched bars indicate results that represent an SAE peptide, residues 112–141, with S127 as the predicted probe-modified residue. This peptide was identified in both singly methionine-oxidized and doubly methionine-oxidized forms (red filled and red hatched bars, respectively). The combined probability of the random occurrence of the SAE peptides with the indicated scores was calculated at less than 0.0001 %. Green bars indicate results that represent other SHs in the proteome with probe modifications on their active-site serine nucleophile.

Varki and colleagues as an enzyme that removes *O*-acetyl esters from the 9-position of naturally occurring sialic acids[9,10] and has been shown to be inhibited by diisopropyl fluorophosphate and the arginine-modifying reagents 2,3-butandione and phenylglyoxal.[11] Nonetheless, to date the specific residues involved in SAE catalysis have remained obscure, and, as a consequence, so too has the mechanistic classification of this enzyme. To determine whether SAE might represent a novel member of the SH superfamily, we set out to identify and characterize the site of FP labeling in this enzyme.

To further characterize the SAE–FP interaction, we employed a gel-free version of ABPP that enables sites of probe labeling to be determined directly for enzymes in complex proteomes (Figure 1a).[12,13] In this method, probe-treated proteomes are digested with trypsin, and the probe-labeled peptides are captured by affinity chromatography and identified by liquid chromatography–tandem mass spectrom-

 © 2005 Wiley-VCH Verlag GmbH & Co. KGaA, Weinheim

etry (LC-MS/MS). COS-7 cells were transfected transiently with a cDNA that encodes human SAE, and the secreted proteome from these cells was treated with a rhodamine-tagged FP probe (FP–Rh[14]). Following trypsin digestion, FP–Rh-labeled peptides were captured by using anti-Rh antibody beads[12,13] and analyzed by LC-MS/MS. SEQUEST searches of the resulting LC-MS/MS data set identified a single FP-labeled SAE peptide (amino acids 112–141) with a predicted site of probe modification at serine 127 (S127; Figure 1b). Confidence in this assignment was bolstered by the detection of multiple forms of this probe-labeled peptide that differed in the degree of methionine oxidation (Figure 1b). In each case, the site of probe modification was designated as S127.

The mutagenesis of S127 to alanine produced an SAE variant (indicated as S127A) that expressed at wild-type levels in COS-7 cells, but failed to undergo labeling with FP–Rh (Figure 2a). In contrast, the mutagenesis of the neighboring serine residue S124 to alanine generated an enzyme S124A that reacted strongly with FP–Rh (Figure 2a). We next compared the catalytic activity of wild-type SAE (WT SAE) with that of the S124A and S127A mutants by using a radiolabeled-substrate assay. The WT and S124A SAE enzymes hydrolyzed the substrate 9-*O*-[*acetyl*-^{3}H]acetyl-*N*-acetylneuraminic acid ([^{3}H]Neu5,9Ac$_2$)[9] to similar extents (Figure 2b). In contrast, the S127A SAE mutant showed negligible catalytic activity (Figure 2b). Collectively, these data indicate that S127 fulfills two of the major requirements expected of a SH catalytic nucleophile: the residue is 1) specifically labeled by FP inhibitors and 2) essential for catalysis.

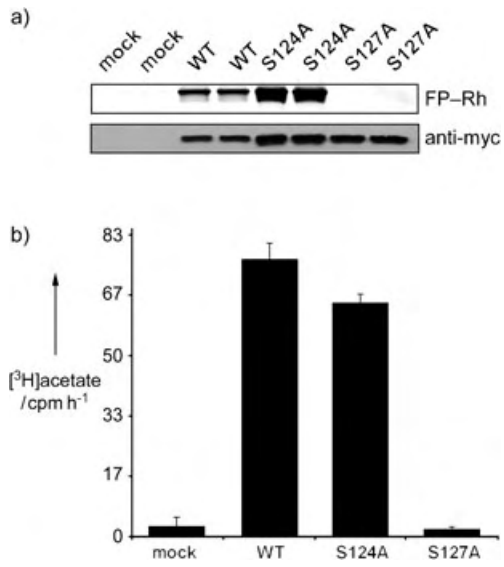

Figure 2. Comparative characterization of WT SAE and the S124A and S127A SAE mutants. SAE proteins were recombinantly expressed in COS-7 cells by transient transfection as myc-epitope-tagged fusion proteins (myc epitope: EQKLISEEDL) and affinity purified by using anti-myc agarose beads (sigma; 50-μL beads with 0.75 mL of proteome in 50 mM tris(hydroxymethyl)aminomethane (Tris), pH 7.5 (1 mg protein mL^{-1})). Following thorough washing of the beads with Tris (50 mM, pH 7.5, 2x0.5 mL), an aliquot of each SAE variant was treated with FP–Rh (4 μM) for 1 h. The reactions were then quenched with standard SDS-PAGE (sodium dodecylsulfate–polyacrylamide gel electrophoresis) loading buffer and analyzed by in-gel fluorescence scanning (a, upper panel) and western blotting with anti-myc antibodies (a, lower panel). The FP–Rh probe labeled both WT and S124A SAE, but not S127A SAE. Anti-myc blotting confirmed that each SAE protein was expressed at high levels in COS-7 cells. b) Comparison of the catalytic activity of WT SAE and the S124A and S127A SAE mutants. SAE variants were assayed on beads with a radiolabeled-substrate assay that follows the cleavage of [^{3}H]acetate from [^{3}H]Neu5,9Ac$_2$ (10000 cpm/reaction; cpm = counts per minute). This assay[11] and the biosynthetic preparation of [^{3}H]Neu5,9Ac$_2$[26] have been described previously. Results represent the averages of two independent trials and have been normalized to account for the relative quantity of enzyme present in each reaction (as estimated by western blotting). Mock cells were transfected with empty vector (pcDNA3mycHis) and served as a background control for all experiments.

If S127 serves as the catalytic nucleophile in SAE, this residue should be conserved among sequence-related homologues of this enzyme. BLAST searches identified over 30 enzymes in public databases that show sequence homology with SAE. Alignment of these sequences revealed that S127 is a conserved residue, even in the most distantly related homologues (which share less than 25% sequence identity; Figure 3). No other conserved serine residues were identified

SAE family members	S127
human	TLRVHD**V**LFG**D**V**W**LC**S**G**Q**S**N**MQMTVLQI
mouse	TLRVHD**V**LFG**D**V**W**LC**S**G**Q**S**N**MQMTVSQI
bact. theta	LLTLQN**V**LIG**E**V**W**FC**S**G**Q**S**N**MEMPMGGF
rhod. baltica	TKTFTD**V**LVG**E**V**W**IC**S**G**Q**S**N**MAWAVQSA
bact. frag.	----NN**V**LAG**E**V**W**LC**S**G**Q**S**N**MEFYLSWS
xanth. axon.	ELQVRD**V**LVG**D**V**W**LAG**G**Q**S**N**N**MEWPLAQA
pedio. pent.	--LLKK**V**RFG**R**V**I**LMAG**G**Q**S**N**N**VGFRMVQD

Figure 3. Sequence comparisons of SAE and representative bacterial homologues. Shown is the region surrounding S127 (red), the predicted serine nucleophile of SAE. S127 is completely conserved among all SAE sequence homologues present in public databases. Additional conserved residues are shown in bold. S124, which is mostly, but not completely, conserved, is shown in blue. SAE enzymes (Genbank accession number): human (NP_733746), mouse (CAA67214), *Bact. theta.* (*Bacteroides thetaiotaomicron*, AA078230), *Rhod. baltica* (*Rhodopirellula baltica*, CAD76603), *Bact. frag.* (*Bacteroides fragilis*, BAC48479), *Xanth. axon.* (*Xanthomonas axonopodis*, AAM36635), *Pedio. pent.* (*Pediococcus pentosaceus*, ZP_00323591).

in this group of proteins. These findings suggest that all SAE-related enzymes, which can be found in both higher eukaryotes and bacteria, are members of the SH superfamily.

SHs also possess a catalytic base to activate the serine nucleophile. Most commonly, this catalytic base is a histidine residue which bridges the serine nucleophile and an aspartate residue to form the classic Ser-His-Asp catalytic triad.[8] However, other arrangements of catalytic residues are also possible, including Ser-Asp[15] and Ser-Lys dyads,[16] as well as a Ser-Ser-Lys triad.[17,18] Sequence comparisons suggest that the SAE subfamily does not employ a Ser-His-Asp catalytic triad, as this group of enzymes lacks a conserved aspartate residue. In contrast, single conserved histidine and lysine residues (H377 and K381), as well as two conserved arginine residues (R301 and R387), are present in the SAE family. The sensitivity of SAE to 2,3-butandione and phenylglyoxal[11] suggests that one or both of the arginine residues may be important for substrate binding and/or catalysis. Future

 © 2005 Wiley-VCH Verlag GmbH & Co. KGaA, Weinheim

studies should clarify the roles that these arginine residues, as well as H377 and K381, play in the SAE catalytic mechanism.

In summary, the results reported herein indicate that SAE and its sequence homologues constitute a novel branch of the SH superfamily. This discovery may enable the design of specific inhibitors of SAE enzymes that incorporate functional groups, such as α-keto heterocycles and trifluoromethyl ketones,[19] that show strong affinity for SH active sites. Such inhibitors would be of value for testing the functional significance of the 9-O acetylation of sialic acids, a modification that is expressed selectively on gangliosides in human melanoma cells.[20] More generally, it is interesting to consider whether the assignment of unannotated enzymes to other mechanistic classes may also be facilitated by ABPP probes. On the one hand, the extrapolation of mechanistic information with active-site-directed probes that target multiple classes of enzymes may prove challenging.[21,22] On the other hand, several ABPP probes do show preferential reactivity with a single class of enzymes (e.g., hydroxamate probes for metalloproteases,[23,24] E-64-based probes for cysteine proteases[25]). In these cases, like with the FP probes, ABPP may provide a useful method to uncover cryptic members of enzyme superfamilies that have resisted classification based on sequence comparisons.

Received: December 29, 2004
Published online: March 14, 2005

Keywords: activity-based protein profiling · enzymes · proteomics · serine hydrolases

[1] J. A. Gerlt, P. C. Babbitt, *Annu. Rev. Biochem.* **2001**, *70*, 209–246.
[2] M. P. Patricelli, M. A. Lovato, B. F. Cravatt, *Biochemistry* **1999**, *38*, 9804–9812.
[3] W. R. Tschantz, M. Sung, V. M. Delgado-Partin, R. E. Dalbey, *J. Biol. Chem.* **1993**, *268*, 27349–27354.
[4] N. Jessani, B. F. Cravatt, *Curr. Opin. Chem. Biol.* **2004**, *8*, 54–59.
[5] A. E. Speers, B. F. Cravatt, *ChemBioChem* **2004**, *5*, 41–47.
[6] N. Jessani, Y. Liu, M. Humphrey, B. F. Cravatt, *Proc. Natl. Acad. Sci. USA* **2002**, *99*, 10335–10340.
[7] Y. Liu, M. P. Patricelli, B. F. Cravatt, *Proc. Natl. Acad. Sci. USA* **1999**, *96*, 14694–14699.
[8] C. T. Walsh, *Enzymatic Reaction Mechanisms*, W. H. Freeman and Company, New York, **1979**.
[9] H. H. Higa, A. Manzi, S. Diaz, A. Varki, *Methods Enzymol.* **1989**, *179*, 409–415.
[10] M. J. Guimaraes, J. F. Bazan, J. Castagnola, S. Diaz, N. G. Copeland, D. J. Gilbert, N. A. Jenkins, A. Varki, A. Zlotnik, *J. Biol. Chem.* **1996**, *271*, 13697–13705.
[11] B. K. Hayes, A. Varki, *J. Biol. Chem.* **1989**, *264*, 19443–19448.
[12] G. C. Adam, J. J. Burbaum, J. W. Kozarich, M. P. Patricelli, B. F. Cravatt, *J. Am. Chem. Soc.* **2004**, *126*, 1363–1368.
[13] E. S. Okerberg, J. Wu, B. Zhang, B. Samii, K. Blackford, D. T. Winn, K. R. Shreder, J. J. Burbaum, M. P. Patricelli, *Proc. Natl. Acad. Sci. USA* **2005**, in press.
[14] M. P. Patricelli, D. K. Giang, L. M. Stamp, J. J. Burbaum, *Proteomics* **2001**, *1*, 1067–1071.
[15] A. Dessen, J. Tang, H. Schmidt, M. Stahl, J. D. Clark, J. Seehra, W. S. Somers, *Cell* **1999**, *97*, 349–360.
[16] M. Paetzel, R. E. Dalbey, N. C. Strynadka, *Nature* **1998**, *396*, 186–190.
[17] M. H. Bracey, M. A. Hanson, K. R. Masuda, R. C. Stevens, B. F. Cravatt, *Science* **2002**, *298*, 1793–1796.
[18] S. Shin, T. H. Lee, N. C. Ha, H. M. Koo, S. Y. Kim, H. S. Lee, Y. S. Kim, B. H. Oh, *EMBO J.* **2002**, *21*, 2509–2516.
[19] D. Leung, C. Hardouin, D. L. Boger, B. F. Cravatt, *Nat. Biotechnol.* **2003**, *21*, 687–691.
[20] D. A. Cheresh, R. A. Reisfeld, A. Varki, *Science* **1984**, *225*, 844–846.
[21] G. C. Adam, E. J. Sorensen, B. F. Cravatt, *Nat. Biotechnol.* **2002**, *20*, 805–809.
[22] K. T. Barglow, B. F. Cravatt, *Chem. Biol.* **2004**, *11*, 1523–1531.
[23] A. Saghatelian, N. Jessani, A. Joseph, M. Humphrey, B. F. Cravatt, *Proc. Natl. Acad. Sci. USA* **2004**, *101*, 10000–10005.
[24] E. W. Chan, S. Chattopadhaya, R. C. Panicker, X. Huang, S. Q. Yao, *J. Am. Chem. Soc.* **2004**, *126*, 14435–14446.
[25] D. Greenbaum, K. F. Medzihradszky, A. Burlingame, M. Bogyo, *Chem. Biol.* **2000**, *7*, 569–581.
[26] H. H. Higa, A. Manzi, A. Varki, *J. Biol. Chem.* **1989**, *264*, 19435–19442.

 © 2005 Wiley-VCH Verlag GmbH & Co. KGaA, Weinheim

Bioinorganic Chemistry

Stable, Soluble Beryllium Aluminum Citrate Complexes Inspired by the Emerald Mineral Structure**

*Timothy S. Keizer, Brian L. Scott, Nancy N. Sauer, and T. Mark McCleskey**

Despite its high toxicity, beryllium is widely used because of its unique properties. Beryllium is toxic both as a carcinogen and as the agent that initiates chronic beryllium disease (CBD). CBD, a granulomatous lung disease, is a cell-mediated immune response to inhaled beryllium in 6–20% of exposed individuals. Considerable invesitagations into the nature and effects of CBD have been conducted[1] but the role of beryllium in triggering CBD is still not well understood.[2,3] Most research has focused on the biological[4] and environmental[5] effects of beryllium with far less emphasis on the speciation and interactions of beryllium under physiological conditions.[6–8] The natural forms of beryllium, beryl and emerald, have not been reported to cause CBD unlike processed forms of beryllium metal and BeO.[9] The beryl structure $[Be_3Al_2(SiO_3)_6]$ (Figure 1) is interesting in two

[*] Dr. T. S. Keizer, Dr. B. L. Scott, Dr. N. N. Sauer, Dr. T. M. McCleskey
Chemistry Division (C-SIC, Mail Stop J514)
Los Alamos National Laboratory
Los Alamos, NM 87545 (USA)
Fax: (+1) 505-667-9905
E-mail: tmark@lanl.gov

[**] This work was supported by the Laboratory Directed Research and Development program (LDRD) at the Los Alamos National Laboratory.

Supporting information for this article is available on the WWW under http://www.angewandte.org or from the author.

 DOI: 10.1002/anie.200462531 © 2005 Wiley-VCH Verlag GmbH & Co. KGaA, Weinheim

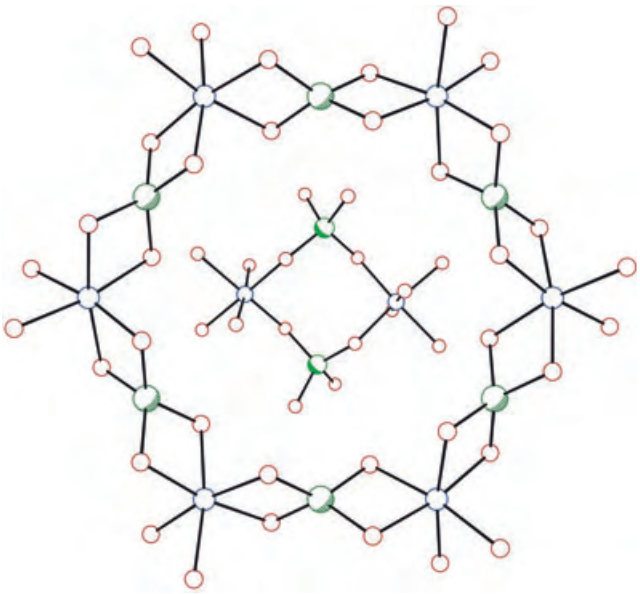

Figure 1. Overlay of the core $(Al\text{-}O\text{-}Be\text{-}O)_n$ structures of beryl $[Be_3Al_2(SiO_3)_6]$ and **1**. The outer ring is beryl and the inner ring is **1**: Be = green, Al = blue, and O = Red.

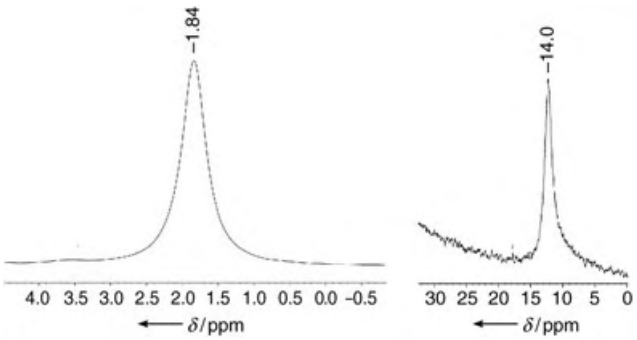

Figure 2. Left: ^{9}Be NMR spectrum of **1**. Right: ^{27}Al NMR spectrum of **1**.

aspects: it has no Be-O-Be linkage despite the propensity of beryllium to form clusters and all of the beryllium-bound oxygen atoms are Si–O units that bridge the aluminum and beryllium atoms. Although this mineral structure occurs in nature, there are no organic-based structures containing aluminum and beryllium. A few citrate-type aqueous complexes containing C–O units bridging two beryllium atoms are known[10,11] and very stable complexes with Be-O-Be linkages with phenolic species acting as bridging oxygen atoms have been recently reported.[12] We report here on the synthesis of a new stable citrate complex containing beryllium and aluminum atoms with a Be-O-Al linkage similar to that of beryl and a related aluminum beryllium citrate structure with bridging phosphate units that is highly soluble (1 M) in aqueous phosphate solution (0.5 M). The mixed-metal citrate complex in both cases is the single dominant species in solution with no evidence of dissociation or rearrangement to Al citrate and Be citrate species.

The complex $(NH_4)_6[Be_2Al_2(citrate)_4]$ (**1**) was formed in quantitative yield by neutralizing an acidic solution containing $Al(NO_3)_3$, $Be(NO_3)_2$, and citric acid with aqueous NH_3. Complex **1** is highly soluble in water (approximately 3 M) between pH 3.5 and 10.5. There is one signal at $\delta = 1.84$ ppm in the ^{9}Be NMR spectrum, thus indicating that the Be center resides in the six-membered citrate chelate ring (Figure 2). The ^{9}Be NMR spectrum of the 2:1 Be citrate complex in solution has been previously reported as having two signals at $\delta = 3.5$ and 1.9 ppm, which have been assigned to Be atoms in five- and six-membered rings of citric acid, respectively.[10,12] A broad singlet at $\delta = 14.0$ ppm in the ^{27}Al NMR spectrum is in stark contrast to the ^{27}Al NMR spectrum of the 1:1 aluminum citrate complex, which comprises four peaks that suggest the presence of many different species in solution.[13] The ^{13}C NMR spectrum has only one resonance for each carbon atom from citric acid, and the pH value of the solution (pH 4–9) does not significantly affect the chemical shift of the signals in the NMR spectra, although the line broadening is influenced slightly. The NMR spectroscopic analysis indicates that there is one dominant species in solution: a Be Al citric acid complex in a ratio of 1:1:2 with beryllium in a six-membered ring.

An X-ray diffraction study of **1** confirms the observations from the NMR spectroscopic analysis of **1** in solution and reveals an interesting four-metal species with a core of two Al atoms and two Be atoms with four bridging O atoms in an eight-membered ring (Figure 3). This core structure is similar to the larger core of the beryl structure that contains six Al and six Be atoms in an alternating pattern bridged by O atoms from Si–O units in the mineral. The four bridging O atoms in the core structure of **1** come from the α-hydroxy group of the four bound citrate ligands. The deprotonation of the α-hydroxy group of citric acid is unusual but has been previously reported for Al citrate complexes.[11,14] The bridging hydroxy group has been shown to be vital for the stability of beryllium citrate type complexes[10,12] but has not been characterized by X-ray diffraction studies to date. Aluminum citrate complexes have been shown to bridge through the α-hydroxy group; however, bridging hydroxy groups or water molecules were also bound to the Al atom in all but one of these cases.[13–16] The aluminum atom is encased by the citrate ligand in complex **1** with two bridging R–O units and two carboxylate groups from each of the two bound citrate ligands. The Al–O (1.864(2)–1.922(3) Å) and Be–O (1.610(4)–1.646(4) Å) bond lengths are within the expected values for octahedral Al centers and tetrahedral Be centers.

One complication of studying the speciation of beryllium in the body is its low solubility in a phosphate media above pH 3. Beryllium precipitates in the presence of a phosphate buffer even in the presence of excellent chelating ligands, such as 2,3-dihydroxybenzoic acid ($k = 18.3$).[12] No stable beryllium complexes have been isolated from a phosphate medium to our knowledge. Although, a few structures of hydrothermally synthesized beryllophosphates[17,18] and beryllium phosphinate complexes[6] are known. Herein, we also report the isolation of a unique beryllium phosphate complex, $(NH_4)_{18}[Al_6Be_6(citrate)_6(PO_4)_8]$ (**2**), which was prepared from a combination of beryllium, aluminum, and citric acid compounds in the presence of phosphate. Complex **2** is highly

 © 2005 Wiley-VCH Verlag GmbH & Co. KGaA, Weinheim

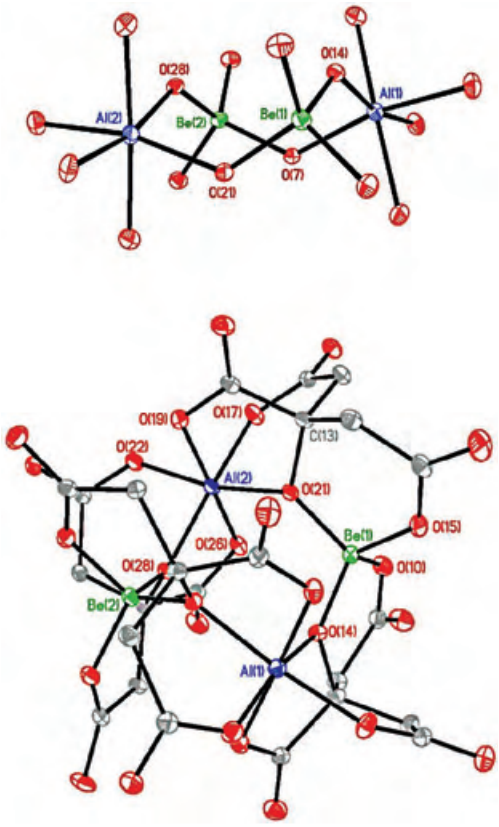

Figure 3. The crystal structure of **1**. Top: ORTEP diagram drawn at the 30% probability level. Bottom: core structure with aluminum, beryllium, and bound-oxygen atoms only. Selected bond lengths [Å] and bond angles [°]: Al(1)-O(12) 1.864(2), Al(1)-O(5) 1.886(3), Al(1)-O(8) 1.887(2), Al(1)-O(14) 1.890(3), Al(1)-O(7) 1.898(2), Al(1)-O(1) 1.922(3), Al(2)-O(26) 1.882(3), Al(2)-O(21) 1.889(2), Al(2)-O(28) 1.893(2), Al(2)-O(19) 1.896(3), Al(2)-O(22) 1.903(2), Al(2)-O(17) 1.908(3), Be(1)-O(14) 1.614(5), Be(1)-O(15) 1.618(5), Be(1)-O(21) 1.624(4), Be(1)-O(10) 1.628(5), Be(2)-O(24) 1.610(4), Be(2)-O(28) 1.622(5), Be(2)-O(7) 1.631(4), Be(2)-O(3) 1.646(4), C(13)-O(21) 1.425(4); O(14)-Al(1)-O(7) 96.75(11), O(21)-Al(2)-O(28) 97.67(10), O(14)-Be(1)-O(21) 108.7(3), O(28)-Be(2)-O(7) 109.5(2), Be(2)-O(7)-Al(1) 130.56(19), Be(1)-O(14)-Al(1) 131.6(2), Be(1)-O(21)-Al(2) 130.2(2), Be(2)-O(28)-Al(2) 132.12(19).

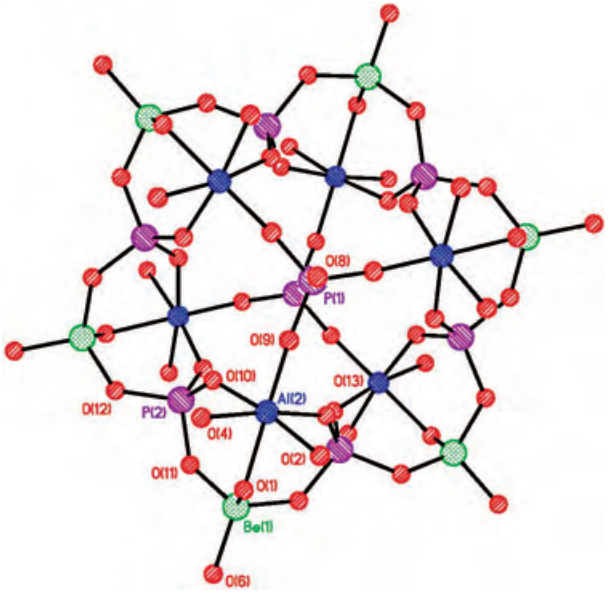

Figure 4. The crystal structure of **2** (ball and stick representation with ellipsoids set at 30% probability; citrates have been omitted for clarity with the exception of the aluminum- and beryllium-bound oxygen atoms). Selected bond lengths [Å] and bond angles [°]: Al(2)-O(9) 1.766(6), Al(2)-O(10) 1.837(6), Al(2)-O(1) 1.850(5), Al(2)-O(13) 1.880(5), Al(2)-O(2) 1.960(6), Al(2)-O(4) 1.985(6), P(1)-O(9) 1.460(6), P(1)-O(8) 1.527(8), P(2)-O(13)′ 1.513(5), P(2)-O(10) 1.520(6), P(2)-O(11) 1.542(5), P(2)-O(12) 1.543(5), Be(1)-O(1) 1.603(11), Be(1)-O(6) 1.624(10), Be(1)-O(11) 1.595(10), Be(1)-O(12)′ 1.630(11); O(9)-Al(2)-O(10) 94.6(4), O(9)-Al(2)-O(1) 169.9(3), O(10)-Al(2)-O(13) 93.8(3), O(9)-Al(2)-O(2) 90.3(4), O(9)-P(1)-O(9)′ 109.6(3), O(9)-P(1)-O(8) 109.3(3), O(10)-P(2)-O(11) 109.7(3), O(10)-P(2)-O(12) 109.9(3), O(11)-P(2)-O(12) 107.3(3), Be(1)-O(1)-Al(2) 120.0(4), P(1)-O(9)-Al(2) 174.8(7), P(2)-O(10)-Al(2) 137.3(3), P(2)-O(11)-Be(1) 127.2(5), O(11)-Be(1)-O(1) 109.3(6), O(11)-Be(1)-O(6) 109.9(6), O(1)-Be(2)-O(6) 107.1(6).

soluble at pH 7 (>1 M) and stable in the presence of a phosphate media (0.5 M).

Complex **2** was characterized by X-ray diffraction studies, and it was seen that the α-hydroxy groups from the citrate ligands bridge the aluminum and beryllium atoms in a similar manner to that observed in structure **1** (Figure 4). The structure of **2** reveals a large cluster with six Be-O-Al units linked by phosphate groups, which is in contrast to the core structure of **1** where two Be-O-Al units are linked by α-hydroxy groups in a ring structure. The structure is templated by two additional phosphate groups in the center of the molecule with each phosphate group binding three aluminum atoms with one unbound $P{-}O_{free}$ bond aligned on the c_3 axis of the molecule. The Al–O bond lengths (1.766(6)–1.985(6) Å) in **2** have a wider range than complex **1**: The $Al{-}O_{citrate}$ bonds are longer by 0.08 Å(avg), the $Al{-}O_{Be}$ bonds are marginally shorter by about 0.04 Å, and the $Al{-}O_{P1}$ bond is the shortest at 1.766(6) Å. The Be–O bond lengths (1.595(10)–1.630(11) Å) are similar to the expected values for the Be–O bonds and show no significant changes. The center P(1) atom has shorter $P(1){-}O_{Al}$ bonds (1.460(6) Å) than the bridging $P(2){-}O_{metal}$ bonds (1.513(5)–1.542(5) Å). The shortening of the P–O bond is presumably because the P(1) center is bonded to three aluminum atoms instead of four aluminum atoms as in the P(2) center, thus providing more electron density at the P(1) center. The ^{27}Al NMR spectrum of **2** in solution shows a relatively narrow signal at $\delta = 12.2$ ppm, which indicates that the structure around the aluminum center is symmetric and stable in solution. There are two signals in the ^{9}Be NMR spectrum of **2** in solution at $\delta = 1.01$ and 2.19 ppm in an approximate 1:3 ratio, respectively. Presumably, one of the oxygen atoms bound to the beryllium center is laible in solution, thus causing the two resonances to appear in the ^{9}Be NMR spectrum. The strong thermodynamic stability of the complex is demonstrated by the aluminum citrate solubilizing the precipitated beryllium phosphate and forming the same species as that of **2** in solution. The addition of aluminum citrate (pH 7) to a solution containing precipitated beryllium phosphate (pH 7) dissolves 74% (149 mM Be) of the precipitated beryllium

 © 2005 Wiley-VCH Verlag GmbH & Co. KGaA, Weinheim

phosphate (initially, 200 mM), which is relative to beryllium phosphate at pH 7 having a solubility of 19 μM Be.

We have structurally characterized a new class of beryllium aluminum compounds based on a Be-O-Al motif similar to beryl where the bridging R–O unit comes from the α-hydroxy group of citric acid. These complexes are remarkably stable, are highly soluble in aqueous solution, and do not appear to dissociate to any appreciable degree in solution. These results suggest a potentially rich new area of beryllium solution chemistry based on a Be-O-Al species that is highly stable and soluble in a phosphate media. Current investigations are underway to determine if the stability and high solubility of the mixed-metal species is driven by electronic factors or geometric considerations (namely, the presence of tetrahedral and octahedral metal sites). Such complexes could offer significant insight into how beryllium becomes mobile in a physiological, phosphate-rich medium and how it interacts within the human body.

Experimental Section

1: Citric acid (432 mg) was dissolved in $Al(NO_3)_3$ (2.25 mL, 1M) and $Be(NO_3)_2$ (2.03 mL, 1.11M) in a 20-mL vial. The pH value was increased to 7 by the addition of NH_4OH. Diffusion of ethanol into the aqueous solution afforded crystals suitable for X-ray diffraction studies. ^{13}C NMR (100.6 MHz, D_2O, 25 °C): $\delta = 40.47$ (CH_2), 43.08 (CH_2), 74.27 (CH), 176.33 (COO), 176.89 (COO), 182.26 ppm (COO); ^{9}Be NMR (56.2 MHz, D_2O, 25 °C, $Be(H_2O)_4^{3+}$): $\delta = 1.84$ ppm ($w_{1/2} = 26$ Hz); ^{27}Al NMR (104.2 MHz, D_2O, 25 °C, $Al(H_2O)_6^{3+}$): $\delta = 14.0$ ppm ($w_{1/2=}$1560 Hz).

2: Citric acid (216 mg) was dissolved in $Al(NO_3)_3$ (1.125 mL 1M) and $Be(NO_3)_2$ (1.015 mL, 1.11M) in a 20-mL vial. The pH value was increased to 7 by the addition of NH_4OH and then ammonium phosphate buffer (2.5 mL, 0.5M, pH 7) was added. Slow diffusion of ethanol into the aqueous solution afforded crystals of suitable quality for X-ray diffraction studies. ^{9}Be NMR (56.2 MHz, D_2O, 25 °C, $Be(H_2O)_4^{2+}$): $\delta = 1.01$ ($w_{1/2=}$48 Hz), 2.19 ppm ($w_{1/2=}$35 Hz); ^{27}Al NMR (104.2 MHz, D_2O, 25 °C, $Al(H_2O)_6^{3+}$): $\delta = 12.2$ ppm ($w_{1/2} = 156$ Hz).

Solubilization of beryllium phosphate with aluminum citrate: $Be(NO_3)_2$ (1.015 mL, 1.11M) was added to ammonium phosphate (2.5 mL, 0.5M) in a 20-mL vial. The pH value was increased to 7 by addition of NH_4OH, and beryllium phosphate began to precipitate above pH 2.7. Citric acid (432 mg) and $Al(NO_3)_3$ (1.125 mL, 1M) were added to H_2O (1 mL) in a separate 20-mL vial. The pH value was increased to 7 by addition of NH_4OH, and then the aluminum citrate solution was added to the beryllium phosphate solution. The mixture was stirred for 3 days, and then filtered (0.45-μm frit). Inductively coupled plasma analysis indicated that 74% of the beryllium had dissolved in the aluminum citrate solution (149 mM Be). A solution of beryllium phosphate (pH 7) was filtered and 0.1% (19 μM Be) of the beryllium was retained.

Crystal data for **1**·7H_2O: $C_{24}H_{54}Al_2Be_2N_6O_{35}$, $M_r = 1058.74$, triclinic, space group $P\bar{1}$, $a = 10.734(2)$, $b = 11.857(2)$, $c = 17.443(4)$ Å, $\alpha = 86.554(4)$, $\beta = 81.216(4)$, $\chi = 76.273(3)°$, $V = 2130.7(7)$ Å^3, $Z = 2$, $\rho_{calcd} = 1.650$ g cm^{-3}, $0.46 \times 0.42 \times 0.40$ mm^3, $2\theta = 56.1°$, $F(000) = 1108$, $\mu(Mo_{K\alpha}) = 0.191$ mm^{-1}, 203(2) K, 8176 unique reflections ($R_{int} = 0.0789$), R (on F) 0.0694, wR (on F^2) 0.2366 ($I > 2\sigma(I)$). Crystal data for **2**·15H_2O: $C_{36}H_{126}Al_6Be_6N_{18}O_{89}P_8$, $M_r = 2699.25$, hexagonal, $R\bar{3}$, $a = 19.5096(19)$, $c = 23.774(5)$ Å, $V = 7836.6(19)$ Å^3, $Z = 3$, $\rho_{calcd} = 1.716$ g cm^{-3}, $0.20 \times 0.12 \times 0.10$ mm^3, $2\theta = 50.68°$, $F(000) = 4206$, $\mu(Mo_{K\alpha}) = 0.322$ mm^{-1}, 203(2) K, 3197 unique reflections ($R_{int} = 0.1598$), R (on F) 0.0883, wR (on F^2) 0.2407 ($I > 2\sigma(I)$). CCDC 253433 and -253432 contain the supplementary crystallographic data for this paper. These data can be obtained free of charge from the Cambridge Crystallographic Data Centre via www.ccdc.cam.ac.uk/data_request/cif.

Received: November 5, 2004
Published online: March 10, 2005

Keywords: aluminum · beryllium · bioinorganic chemistry · citrate · phosphates

[1] C. Saltini, M. Amicosante, *Am. J. Med. Sci.* **2001**, *321*, 89–98.
[2] M. Eisenbud, *Appl. Occup. Environ. Hyg.* **1998**, *13*, 25–31.
[3] C. Saltini, M. Amicosante, A. Franchi, G. Lombardi, L. Richeldi, *Eur. Respir. J.* **1998**, *12*, 1463–1475.
[4] M. D. Rossman, O. P. Preuss, M. B. Powers, *Beryllium: Biomedical and Environmental Aspects*, Williams and Wilkens, Baltimore, **1991**.
[5] T. P. Taylor, M. Ding, D. S. Ehler, T. M. Foreman, J. P. Kaszuba, N. N. Sauer, *J. Environ. Sci. Health* **2003**, *38*, 439–469.
[6] L. Alderighi, P. Gans, S. Midollini, A. Vacca in *Advances in Inorganic Chemistry: Main Group Chemistry, Vol. 50* (Ed.: A. G. Sykes, A. H. Cowley), Academic Press, New York, **2000**, pp. 109–172.
[7] H. Schmidbaur, *Coord. Chem. Rev.* **2001**, *215*, 223–242.
[8] C. Y. Wong, J. D. Woolins, *Coord. Chem. Rev.* **1994**, *130*, 243–273.
[9] D. C. Deubner, M. Kelsh, L. Shum, M. Maier, E. Lau, *Appl. Occup. Environ. Hyg.* **2001**, *16*, 579–592.
[10] T. S. Keizer, N. N. Sauer, T. M. McCleskey, *J. Inorg. Biochem.* **2005**, submitted.
[11] O. Kumberger, J. Riede, H. Schmidbaur, *Z. Naturforsch. B* **1992**, *47*, 1717–1720.
[12] T. S. Keizer, N. N. Sauer, T. M. McCleskey, *J. Am. Chem. Soc.* **2004**, *126*, 9484–9485.
[13] M. Matzapetakis, C. P. Ratopoulou, A. Terzis, A. Lakatos, T. Kiss, A. Salifoglou, *Inorg. Chem.* **1999**, *38*, 618–619.
[14] T. L. Feng, P. L. Gurian, M. D. Healy, A. R. Barron, *Inorg. Chem.* **1990**, *29*, 408–411 .
[15] M. Dakanali, C. P. Ratopoulou, A. Terzis, A. Lakatos, I. Banyai, T. Kiss, A. Salifoglou, *Inorg. Chem.* **2003**, *42*, 252–254.
[16] S. A. Malone, P. Cooper, S. L. Heath, *Dalton Trans.* **2003**, 4572–4573.
[17] T. E. Gier, G. D. Stucky, *Nature* **1991**, *349*, 508–510.
[18] H. Zhang, M. Chen, Z. Shi, X. Bu, Y. Zhou, X. Xu, D. Zhao, *Chem. Mater.* **2001**, *13*, 2042–2048.

 © 2005 Wiley-VCH Verlag GmbH & Co. KGaA, Weinheim

Oxidation of Bridging Phosphanides

Reversible Transformation of Two Diphenylphosphanido Ligands into the Neutral Tetraphenyldiphosphane Ligand**

Juan Forniés, Consuelo Fortuño, Susana Ibáñez, Antonio Martín, Athanasios C. Tsipis, and Constantinos A. Tsipis**

We have recently established that oxidation of the anionic trinuclear Pt^{II} complex $(NBu_4)_2[R^F_2Pt^{II}(\mu\text{-}PPh_2)_2Pt^{II}(\mu\text{-}PPh_2)_2Pt^{II}R^F_2]$ (**1a**; $R^F = C_6F_5$, Scheme 1) by Ag^+ ions yields the neutral Pt^{III} species $[R^F_2Pt^{III}(\mu\text{-}PPh_2)_2Pt^{III}(\mu\text{-}PPh_2)_2Pt^{II}R^F_2]$ (**2a**),[1], which contains a total of 46 valence electrons and hence a Pt–Pt bond. To our surprise, when the starting compound comprises at least one palladium center the analogous Pd^{III}-containing derivatives cannot be isolated from, or identified in, the reaction mixtures.[1]

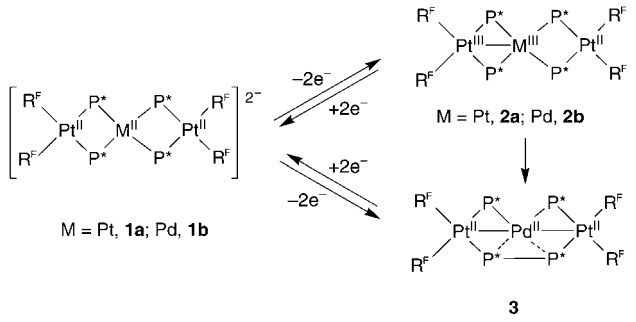

Scheme 1. $R^F = C_6F_5$; $P^* = PPh_2$.

To understand the different response of the heteronuclear species towards oxidation by Ag^+ ions, and guide our experimental efforts towards identifying and finally isolating the reaction products, we searched the potential energy surface (PES) of a model reaction system with electronic structure calculation methods at the B3LYP level of theory[2,3] using the LANL2DZ basis set, as implemented in the Gaussian 03 series of programs.[4] To obtain a computationally convenient size we used a model reaction system where the phenyl groups of the phosphanide ligands are substituted by H atoms and the C_6F_5 ligands by CN ligands. The decision to substitute the C_6F_5 ligands by CN is based on electronic structure calculations of the coordinating ability (σ-donor and π-acceptor capacity) of the ligands and has been described previously.[5] The geometric and energetic profile of the oxidation reaction of **M1b**, along with the HOMO of all stationary points, computed at the B3LYP/LANL2DZ level of theory is depicted schematically in Figure 1.

One-electron oxidation of complex **M1b** yields the intermediate open-shell (doublet) anionic species **M1b1**, which is a symmetric (D_{2h} point group), trinuclear PtPdPt complex without any intermetallic interaction. This one-electron oxidation step requires about 49.3 kcal mol^{-1} at the B3LYP/LANL2DZ level, which is provided by the reduction of the Ag^+ ions used as the oxidant (the electron affinity of the Ag^+ ions was predicted to be 178.7 kcal mol^{-1}). Interestingly, the one-electron oxidation involves a strong coordination of the Ag^+ ion to Pd and one terminal Pt atom to afford complex **M1bAg**, which adopts a chairlike structure (see Supporting Information) with a binding energy predicted to be 171.9 kcal mol^{-1}, thus illustrating that the Pd···Ag^+ and Pt···Ag^+ intermetallic bonds are relatively strong. These strong intermetallic interactions are also mirrored in the short Pd···Ag^+ and Pt···Ag^+ bond distances of 2.756 and 2.746 Å, respectively. Phosphanido Pt/Pd/Ag complexes of this type have recently been isolated by us.[6] It should be noted that the transfer of one electron is a favorable process because the LUMO of **M1bAg** is localized purely on the coordinated Ag^+ ion.

The salient feature of the structure of **M1b1** is the remarkable shortening of the P···P distance by about 0.29 Å with respect to the starting **M1b** species. The localization of the spin density on the P atoms of the bridging phosphanido ligands (Figure 1) is also noteworthy as it indicates that P···P interactions should start to evolve during the course of the oxidation process. Further one-electron oxidation of **M1b1** leads to a second-order saddle point (probably an effective monkey–saddle-type transition state[7] possessing a doubly degenerate zero eigenvalue of the Hessian) **M2b** at 170.5 kcal mol^{-1}, which is higher in energy than **M1b** and has two imaginary frequencies at 65 and 50 cm^{-1}. **M2b** adopts a symmetric structure with D_{2h} symmetry. All attempts to locate a true transition state, even by using larger basis sets, were unsuccessful, which suggests that the saddle point is probably on a quite shallow PES. Correcting the two imaginary frequencies and optimizing the new geometry afforded a local minimum at 5.5 kcal mol^{-1}. This is lower in

[*] Prof. J. Forniés, Dr. C. Fortuño, S. Ibáñez, Dr. A. Martín
Departamento de Química Inorgánica and
Instituto de Ciencia de Materiales de Aragón
Universidad de Zaragoza—CSIC
50009 Zaragoza (Spain)
Fax: (+34) 976-761-187
E-mail: juan.fornies@unizar.es
Prof. C. A. Tsipis
Laboratory of Applied Quantum Chemistry
Faculty of Chemistry
Aristotle University of Thessaloniki
54006 Thessaloniki (Greece)
Fax: (+30) 2310-99-7851
E-mail: tsipis@chem.auth.gr
Dr. A. C. Tsipis
Section of Inorganic and Analytical Chemistry
Department of Chemistry
University of Ioannina
451 10 Ioannina (Greece)

[**] Polynuclear Homo- or Heterometallic Palladium(II)-Platinum(II) Pentafluorophenyl Complexes Containing Bridging Diphenylphosphido Ligands, Part 16. Part 15: I. Ara, N. Chaouche, J. Forniés, C. Fortuño, A. Kribii, A. C. Tsipis, C. A. Tsipis, *Inorg. Chim. Acta* DOI: 10.1016/j.ica.2004.04.006. This work was supported by the Ministerio de Ciencia y Tecnología y Fondos FEDER (Project BQU2002-03997-C02-02) and the Diputación General de Aragón. S.I. thanks the Ministerio de Ciencia y Tecnología for a grant.

Supporting information for this article is available on the WWW under http://www.angewandte.org or from the author.

 DOI: 10.1002/anie.200462498 © 2005 Wiley-VCH Verlag GmbH & Co. KGaA, Weinheim

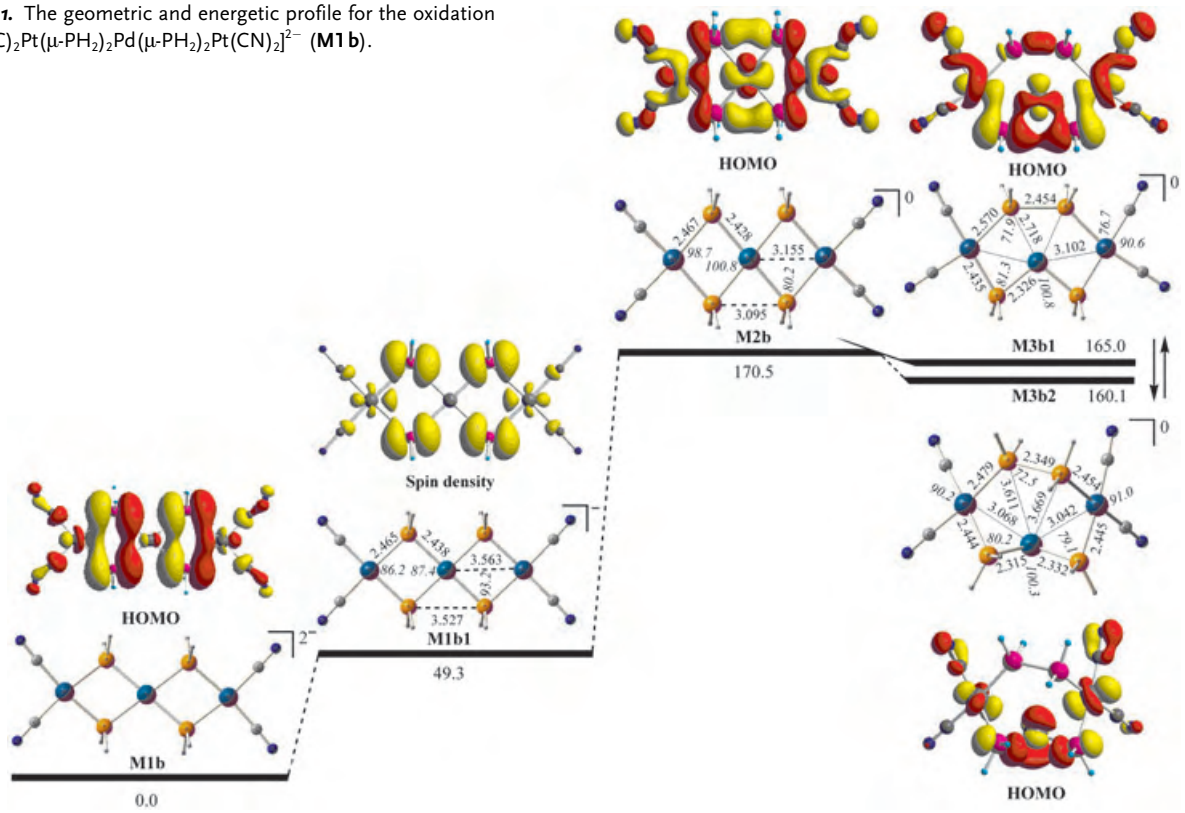

Figure 1. The geometric and energetic profile for the oxidation of $[(NC)_2Pt(\mu\text{-}PH_2)_2Pd(\mu\text{-}PH_2)_2Pt(CN)_2]^{2-}$ (**M1b**).

energy and corresponds to the planar complex **M3b1**, which contains a bridging diphosphane (H_2PPH_2) ligand.

Searching the PES further also allowed us to locate another minimum corresponding to the nonplanar complex **M3b2**, which is stabilized by 4.9 kcal mol^{-1} with respect to the planar conformer. The complexes **M3b1** and **M3b2** contain an angular Pt–Pd–Pt array with angles of 157.4° and 114.7°, respectively. Moreover, in **M3b2** the PPPP dihedral angle is 144.7°. It is important to note that the HOMO of **M2b** involves significant P···P orbital interactions that are responsible for the formation of the P–P bond in complexes **M3b1** and **M3b2**. Moreover, the nature of the HOMOs of **M3b1** and **M3b2** (Figure 1) strongly supports a fluxional behavior of the complexes that involves an easy interconversion of the P···P interactions in an almost barrierless process (activation barrier less than 10.4 kcal mol^{-1}) probably through a symmetric (D_{2h}) transition state similar to **M2b**. However, all attempts to locate the true transition state were unsuccessful.

In light of these theoretical predictions we studied the reaction of $[R^F_2Pt(\mu\text{-}PPh_2)_2Pd(\mu\text{-}PPh_2)_2PtR^F_2]^{2-}$ (**1b**) with Ag^+ in greater detail and we were ultimately able to isolate $[R^F_2Pt(\mu\text{-}PPh_2)Pd(\mu\text{-}PPh_2)(\mu\text{-}Ph_2PPPh_2)PtR^F_2]$ (**3**), a neutral platinum(II) and palladium(II) complex that contains a tetraphenyldiphosphane ligand. The process is reversible and the reduction of **3** with NBu_4BH_4 (1:2 molar ratio) yields **1b** (Scheme 1).

The structure of complex **3** is shown in Figure 2. The trinuclear complex contains an angular Pt–Pd–Pt array (137.23(2)°). The Pd atom is bonded to the platinum atoms

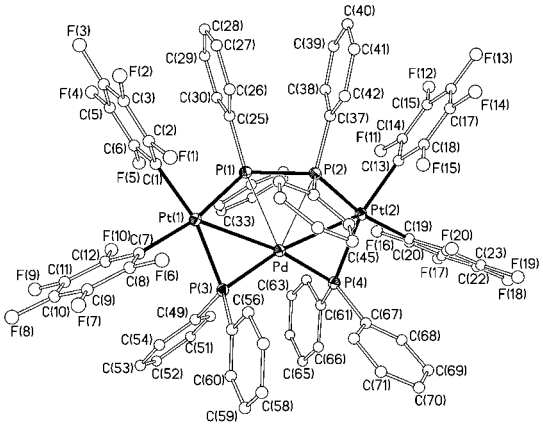

Figure 2. Molecular structure of complex **3**.

through intermetallic bonds (Pt(1)–Pd 2.887(1) Å; Pt(2)–Pd 2.910(1) Å). In addition, there are two PPh_2 bridging ligands linking the Pd atom with each Pt center. All the metal atoms and the phosphanido P(3) and P(4) atoms lie in the same plane. A noteworthy structural feature is that the tetraphenyldiphosphane ligand formed bridges the two external atoms (Pt) of the array, in keeping with the theoretical predictions. P(1) and P(2) do not lie in the plane defined by the metal centers, although the midpoint of the P(1)–P(2) bond is included in this plane. The four Pt–P distances are very similar regardless of whether the P forms part of a phosphanide or the diphosphane ligand. The P(1)–P(2) distance is

 © 2005 Wiley-VCH Verlag GmbH & Co. KGaA, Weinheim

2.261(1) Å, which is similar to the distance found in other complexes containing μ-Ph_2P-PPh_2,[8–11] while the distance between P(3) and P(4) is 3.730(1) Å, thereby excluding any P···P interaction. The Pd–P(3) and Pd–P(4) distances are 2.180(1) Å and 2.177(1) Å, respectively, and are the shortest Pd–P distances reported so far for bridging diphenylphosphanido ligands bonded to Pd. These short distances are probably related to the peculiar coordination sphere of the Pd center, which, apparently, apart from these Pd–P bonds, only establishes the intermetallic interactions and weak interactions,[12] if any, with the P atoms of the tetraphenyldiphosphane ligand (Pd–P(1) and Pd–P(2) are 2.656(1) Å and 2.675(1) Å, respectively). The Pd–P(diphosphane) distance in **M3b1** (2.718 Å) is very close to the experimental value for the "real" **3**. The coordination sphere of the platinum atoms is more conventional: each lies in the center of a square plane. The total valence-electron count in **3** is 44, in agreement with the presence of two M–M′ bonds.

The formation of free P_2R_4 has been observed from early transition metal and lanthanide complexes containing terminal phosphanido ligands,[13–16] and recently an interesting catalytic formation of free tetraphenyldiphosphane has been proposed to take place through an unusual Rh^V intermediate containing two *terminal* phosphanido ligands.[17] In the complex $[(ON)_2Fe(\mu\text{-}CH_2)(\mu\text{-}Ph_2PPPh_2)Fe(NO)_2]$ the η^2-*P,P′*-tetraphenyldiphosphane ligand is formed by coupling of a *bridging* phosphanido with a terminal secondary phosphane ligand.[18,19] Nevertheless, P–P bond formation from the oxidation of *two bridging* phosphanido ligands, as far as we know, has never been observed. However, the reverse process—the reaction of P_2R_4 with transition-metal complexes—is an easy entry into phosphanido complexes of transition metals.[20–23]

The formation of **3** could be regarded as a consequence of the oxidation of two metal centers in **1b** to afford **2b** (an intermediate that has not been observed or even theoretically predicted), analogous to the homotrinuclear complex **2a**, which evolves quickly through a reductive coupling of two bridging PPh_2 ligands to form tetraphenyldiphosphane and the M^{II} trinuclear derivative with 44 valence electrons. This result is in agreement with the greater lability of palladium derivatives than those of platinum and can be related to the faster reductive coupling between the PPh_2 and C_6F_5 groups observed in the palladium(III) intermediates than in the platinum(III) ones.[5]

The $^{31}P\{^1H\}$ NMR spectrum of **3** (CD_2Cl_2 solution) at 183 K shows two broad singlets at $\delta = 123.6$ and -80.0 ppm due to the phosphanido (P3, P4) and phosphane (P1, P2) ligands, respectively. The chemical shift of the equivalent PPh_2 phosphanido groups lies in the expected range for a single PPh_2 ligand bridging two metal centers that are joined by a metal–metal bond.[24–26] Both signals appear as broad singlets and, consequently, the couplings between the P atoms cannot be calculated. Each signal shows a pair of platinum satellites ($^1J_{Pt1,P3} = 1580$ Hz and $^1J_{Pt1,P1} = 1728$ Hz). Platinum satellites are also observed for the PPh_2 phosphanido signal due to $^2J_{Pt,P}$ coupling. However, these satellites are not well separated from the broad central signal and the $^2J_{Pt1,P4}$ value cannot be calculated accurately. This phosphorus–platinum coupling is in agreement with the presence of Pt–Pd bonds in an almost linear P–Pd–Pt arrangement. At 293 K only one very broad signal centered at about $\delta = 27$ ppm is observed, thus indicating that, at room temperature, a dynamic process renders the P atoms of the PPh_2 and P_2Ph_4 ligands equivalent. The ^{19}F NMR spectrum of **3** (CD_2Cl_2 solution) at 183 K shows four signals of equal intensity in the *o*-F region. At higher field two well-separated signals due to *p*-F atoms and overlapped signals due to *m*-F atoms are observed. This pattern indicates the presence of two inequivalent C_6F_5 rings and the inequivalence of both halves within each ring, and is in full agreement with the structure of **3** in the solid state. The spectrum at 293 K shows only three signals (2:1:2 intensity ratio) due to *o*-F, *p*-F, and *m*-F atoms respectively, i.e. all *o*-F atoms are equivalent, as are the *p*-F and *m*-F atoms. The dynamic process shown in Scheme 2, which follows from the NMR spectroscopic data, is in excellent agreement with the theoretically predicted fluxionality of the analogous **M3b** complexes.

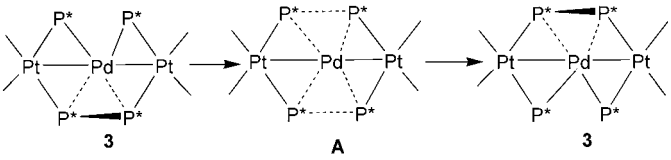

Scheme 2. P* = PPh_2.

In summary, an unprecedented formation of tetraphenyldiphosphane from the coupling of two bridging phosphanido ligands, presumably via a Pd^{III} intermediate, has been predicted theoretically and achieved experimentally. Moreover, the behavior of **3** in solution at room temperature is very striking: the bridging diphosphane and two bridging phosphanido ligands become equivalent, thereby indicating that the Pd–P and P–P bonds are highly delocalized, in line with the electronic structure calculation results.

Experimental Section

3: $AgClO_4$ (0.110 g, 0.510 mmol) was added to an orange solution of **1b** (0.600 g, 0.251 mmol) in acetonitrile (20 mL). A dark-violet suspension and a silver mirror on the walls of the flask formed immediately. After stirring for 15 min at room temperature the mixture was filtered. The resultant dark-purple solid was washed with CH_2Cl_2 (40 mL) and filtered through Celite. The solution was evaporated to about 8 mL and **3** crystallized as an orange-red solid. This was filtered off and washed with 2×0.5 mL of cold CH_2Cl_2 (0.270 g, 58% yield). ^{19}F NMR (282 MHz, CD_2Cl_2, 183 K, $CFCl_3$): $\delta =$ -113.5 ($^3J_{Pt,F} = 342$ Hz, $2 \times o$-F), -115.4 ($^3J_{Pt,F} = 251$ Hz, $2 \times o$-F), -116.8 ($^3J_{Pt,F} = 364$ Hz, $2 \times o$-F), -121.0 ($^3J_{Pt,F} = 261$ Hz, $2 \times o$-F), -160.7 ($2 \times p$-F), -161.3 ($2 \times p$-F), -162.8 ($2 \times m$-F), -163.6 ($4 \times m$-F), -163.9 ppm ($2 \times m$-F). ^{19}F NMR (282 MHz, CD_2Cl_2, 293 K, $CFCl_3$): $\delta = -116.5$ ($^3J_{Pt,F} = 304$ Hz, $8 \times o$-F), -161.7 ($4 \times p$-F), -163.9 ppm ($8 \times m$-F). C,H analysis for $C_{72}H_{40}F_{20}P_4PdPt_2$ (1905.6): calcd: C 45.38, H 2.11; found: C 45.18, H 1.99.

Reaction of **3** with NBu_4BH_4: A solution of NBu_4BH_4 (0.028 g, 0.110 mmol) in 2 mL of MeOH was added to a violet solution of **3** (0.100 g, 0.052 mmol) in $CHCl_3$ (8 mL). Yellow crystals of **1b** appeared immediately. After the mixture had been stirred for

 © 2005 Wiley-VCH Verlag GmbH & Co. KGaA, Weinheim

15 min at room temperature, the resulting **1b** was filtered off and washed with MeOH (2 × 0.5 mL) (0.094 g, 75 % yield).

Received: November 2, 2004
Revised: January 10, 2005
Published online: March 10, 2005

Keywords: cluster compounds · density functional calculations · P ligands · palladium · platinum

[1] E. Alonso, J. M. Casas, J. Forniés, C. Fortuño, A. Martín, A. G. Orpen, C. A. Tsipis, A. C. Tsipis, *Organometallics* **2001**, *20*, 5571.
[2] A. D. Becke, *J. Chem. Phys.* **1992**, *96*, 2125.
[3] A. D. Becke, *J. Chem. Phys.* **1993**, *98*, 907.
[4] Gaussian 03 (Revision B.02), M. J. Frisch, G. W. Trucks, H. B. Schlegel, G. E. Scuseria, M. A. Robb, J. R. Cheeseman, J. A. Montgomery, Jr., T. Vreven, K. N. Kudin, J. C. Burant, J. M. Millam, S. S. Iyengar, J. Tomasi, V. Barone, B. Mennucci, M. Cossi, G. Scalmani, N. Rega, G. A. Petersson, H. Nakatsuji, M. Hada, M. Ehara, K. Toyota, R. Fukuda, J. Hasegawa, M. Ishida, T. Nakajima, Y. Honda, O. Kitao, H. Nakai, M. Klene, X. Li, J. E. Knox, H. P. Hratchian, J. B. Cross, C. Adamo, J. Jaramillo, R. Gomperts, R. E. Stratmann, O. Yazyev, A. J. Austin, R. Cammi, C. Pomelli, J. W. Ochterski, P. Y. Ayala, K. Morokuma, G. A. Voth, P. Salvador, J. J. Dannenberg, V. G. Zakrzewski, S. Dapprich, A. D. Daniels, M. C. Strain, O. Farkas, D. K. Malick, A. D. Rabuck, K. Raghavachari, J. B. Foresman, J. V. Ortiz, Q. Cui, A. G. Baboul, S. Clifford, J. Cioslowski, B. B. Stefanov, G. Liu, A. Liashenko, P. Piskorz, I. Komaromi, R. L. Martin, D. J. Fox, T. Keith, M. A. Al-Laham, C. Y. Peng, A. Nanayakkara, M. Challacombe, P. M. W. Gill, B. Johnson, W. Chen, M. W. Wong, C. Gonzalez, J. A. Pople, Gaussian, Inc., Pittsburgh, PA, **2003**.
[5] N. Chaouche, J. Forniés, C. Fortuño, A. Kribii, A. Martín, P. Karipidis, A. C. Tsipis, C. A. Tsipis, *Organometallics* **2004**, *23*, 1797.
[6] E. Alonso, J. Forniés, C. Fortuño, A. Martín, A. G. Orpen, *Organometallics* **2003**, *22*, 5011.
[7] M. Mauksch, P. v. R. Schleyer, *Inorg. Chem.* **2001**, *40*, 1756, and references cited therein.
[8] J. L. Atwood, J. K. Newell, W. E. Hunter, I. Bernal, F. Calderazzo, I. P. Mavani, D. Vitali, *J. Chem. Soc. Dalton Trans.* **1978**, 1189.
[9] F. Calderazzo, R. P. Poli, D. Vitali, J. D. Korp, I. Bernal, G. Pellizzi, J. L. Atwood, W. E. Hunter, *Gazz. Chim. Ital.* **1983**, *113*, 761.
[10] O. Kühl, S. Blaurock, E. Hey-Hawkins, *Z. Anorg. Allg. Chem.* **1999**, *625*, 1517.
[11] L. J. Arnold, L. Main, B. K. Nicholson, *Appl. Organomet. Chem.* **1990**, *4*, 503.
[12] P. Braunstein, N. M. Boag, *Angew. Chem.* **2001**, *113*, 2493; *Angew. Chem. Int. Ed.* **2001**, *40*, 2427.
[13] D. Neculai, A. M. Neculai, H. W. Roesky, R. Herbst-Irmer, B. Walfort, D. Stalke, *Dalton Trans.* **2003**, 2831.
[14] G. W. Rabe, J. Riede, A. Schier, *Inorg. Chem.* **1996**, *35*, 2680.
[15] G. W. Rabe, G. P. A. Yap, A. L. Rheingold, *Inorg. Chem.* **1995**, *34*, 4521.
[16] P. Y. Zheng, T. T. Nadasdi, D. W. Stephan, *Organometallics* **1989**, *8*, 1393.
[17] V. P. W. Bohm, M. Brookhart, *Angew. Chem.* **2001**, *113*, 4832; *Angew. Chem. Int. Ed.* **2001**, *40*, 4694.
[18] Y. F. Yu, C. N. Chau, A. Wojcicki, M. Calligaris, G. Nardin, G. Balducci, *J. Am. Chem. Soc.* **1984**, *106*, 3704.
[19] C. N. Chau, Y. F. Yu, A. Wojcicki, M. Calligaris, G. Nardin, G. Balducci, *Organometallics* **1987**, *6*, 308.
[20] M. Basato, E. Brescacin, E. Tondello, G. Valle, *Inorg. Chim. Acta* **2001**, *323*, 147.
[21] A. J. M. Caffyn, M. J. Mays, G. A. Solan, D. Braga, P. Sabatino, G. Conole, M. McPartlin, H. R. Powell, *J. Chem. Soc. Dalton Trans.* **1991**, 3103.
[22] A. Adatia, M. McPartlin, M. J. Mays, M. J. Morris, P. R. Raithby, *J. Chem. Soc. Dalton Trans.* **1989**, 1555.
[23] J. C. Stichburg, M. J. Mays, J. E. Davies, P. R. Raithby, G. P. Shields, A. G. Finch, *Inorg. Chim. Acta* **1997**, *262*, 9.
[24] L. R. Falvello, J. Forniés, C. Fortuño, A. Martín, A. P. Martínez-Sariñena, *Organometallics* **1997**, *16*, 5849.
[25] E. Alonso, J. Forniés, C. Fortuño, A. Martín, A. G. Orpen, *Organometallics* **2001**, *20*, 850.
[26] E. Alonso, J. Forniés, C. Fortuño, A. Martín, A. G. Orpen, *Organometallics* **2000**, *19*, 2690.

 © 2005 Wiley-VCH Verlag GmbH & Co. KGaA, Weinheim

Electrical Devices

Fully Plastic Actuator through Layer-by-Layer Casting with Ionic-Liquid-Based Bucky Gel

*Takanori Fukushima, Kinji Asaka, Atsuko Kosaka, and Takuzo Aida**

Printable electrical devices[1,2] are attractive for the development of microelectromechanical systems (MEMS) including sensors, switches, and micromachines. In particular, printable actuators that can infinitely operate in air at low voltages would give a breakthrough in the design of miniaturized mechanical devices. Conjugated polymers can be regarded as potential materials for the fabrication of such soft actuators.[3–7] Although a few examples of conjugated polymer actuators that can work in air have been reported,[8] their complicated configurations require multistage processing that involve, for example, sputter deposition of metallic layer electrodes and electrochemical deposition of polymer layers. Herein we report the first dry actuator that can be fabricated simply through layer-by-layer casting with "bucky gel", a

[*] Prof. T. Aida
Department of Chemistry and Biotechnology
School of Engineering, The University of Tokyo
7-3-1 Hongo, Bunkyo-ku, Tokyo 113-8656 (Japan)
Fax: (+81) 3-5841-7310
E-mail: aida@macro.t.u-tokyo.ac.jp

Dr. T. Fukushima, A. Kosaka, Prof. T. Aida
Aida Nanospace Project
Exploratory Research for Advanced Technology (ERATO)
Japan Science and Technology Agency (JST)
National Museum of Emerging Science and Innovation
2-41 Aomi, Koto-ku, Tokyo 135-0064 (Japan)

Dr. K. Asaka
Artificial Cell Research Group, Research Institute for Cell Engineering
National Institute of Advanced Industrial Science and Technology (AIST)
1-8-31 Midorigaoka, Ikeda, Osaka 563-8577 (Japan)

Supporting information for this article is available on the WWW under http://www.angewandte.org or from the author.

 © 2005 Wiley-VCH Verlag GmbH & Co. KGaA, Weinheim DOI: 10.1002/anie.200462318

gelatinous room-temperature ionic liquid that contains single-walled carbon nanotubes (SWNTs).[9] Our actuator adopts a bimorph configuration with a polymer-supported internal ionic liquid electrolyte layer sandwiched by bucky-gel electrode layers which allows quick and long-lived operation in air at low applied voltages.

Baughman et al. reported that SWNT sheets, laminated together with double-sided Scotch tape, show an electrochemical actuation in aqueous electrolyte solutions, where the SWNT sheets not only serve as electrodes but also undergo elongation/contraction upon charge injection into the nanotubes.[10] We were motivated to apply bucky gels to the fabrication of soft actuators with the expectation that such actuators with built-in ionic-liquid components can operate in air without external electrolytes. Bucky gels can be readily prepared by grinding SWNTs in imidazolium ion-based ionic liquids; the heavily entangled nanotube bundles are exfoliated by a possible cation–π interaction[11] on the SWNT surfaces to give much finer bundles. Ionic liquids are nonvolatile and characterized by their high ionic conductivities and wide potential windows, which are advantageous for rapid responses in actuation and high electrochemical stabilities of the components, respectively.[12]

The configuration of our bucky-gel actuator is illustrated in Figure 1 a. The actuator film was fabricated through layer-by-layer casting of the electrode (SWNTs) and the electrolyte (ionic liquid) components in a gelatinous mixture of poly (vinylidene fluoride-co-hexafluoropropylene) (PVdF(HFP); Figure 1 b) as a polymer support and 4-methyl-2-pentanone (MP). In a typical example, the bucky-gel electrode layers include 13 wt % of SWNTs, 54 wt % of 1-butyl-3-methylimidazolium tetrafluoroborate ($BMIBF_4$; Figure 1 b) and 33 wt % of PVdF(HFP), whereas the internal ionic-liquid electrolyte layer[13] contains 67 wt % of $BMIBF_4$ and 33 wt % of PVdF(HFP). In sharp contrast with previous conjugated polymer actuators, the fabrication process includes neither deposition of metallic layers nor electrochemical polymerization. Scanning electron micrograph of a cross-section of the actuator strip showed that the electrode and electrolyte layers are seamlessly connected with one another (Figure 2), thereby facilitating intra- and interlayer ion transport, which is essential for quick response.

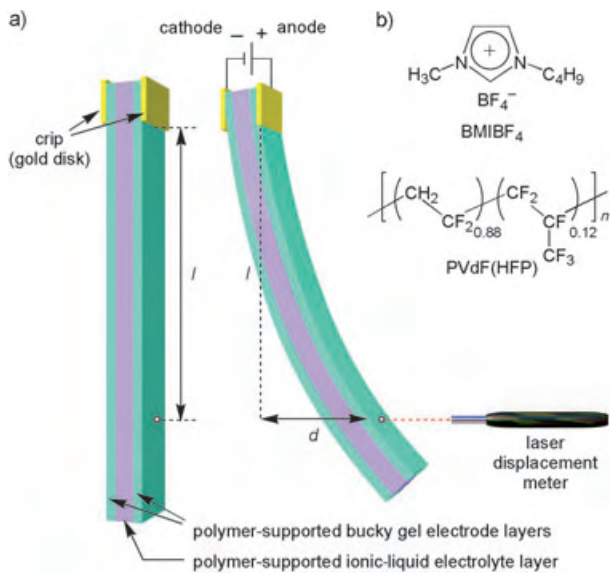

Figure 1. Bucky-gel-based bimorph actuator fabricated through layer-by-layer casting. a) Schematic structure of the actuator strip composed of a polymer-supported ionic-liquid electrolyte layer sandwiched by bucky-gel electrode layers, and experimental setup for cantilever oscillation. The displacements (δ) at a point 10 mm ($=l$) away from the fixed position were continuously measured by a laser displacement meter. b) Molecular structures of $BMIBF_4$ and PVdF(HFP).

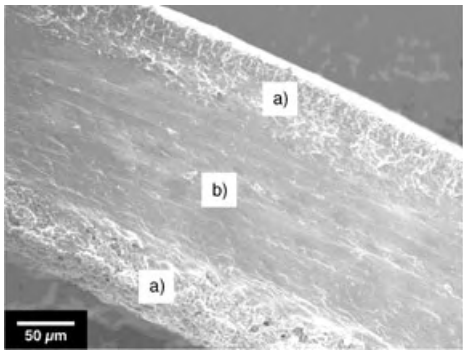

Figure 2. Scanning electron micrograph of a cross section of a bucky-gel actuator strip (0.25 mm in thickness); a) and b) represent the polymer-supported bucky-gel electrode and the ionic-liquid electrolyte layers, respectively.

We confirmed that the bucky-gel actuator with such a simple three-layered configuration indeed operates quickly in air in response to low applied voltages. The actuation experiments were conducted by applying alternating square-wave voltages to a $15 \times 1\text{-mm}^2$-sized actuator strip (0.28 mm in thickness) clipped by working/counter gold disk electrodes; the displacement at a point 10 mm away from the fixed position was continuously monitored from one side of the actuator strip by using a laser displacement meter (Figure 1 a). For example, when an electric potential of ± 3.5 V was applied with a frequency of 0.01 Hz, an actuator strip underwent a bending motion toward the anode side (Figure 3 a) with a maximum displacement of 5 mm. Upon increment of the frequency of an applied voltage of ± 3.0 V from 0.01 to 0.1 Hz, 1.0–10 Hz (Figure 4), and 30 Hz, a perfect response of the actuator strip resulted. As the applied voltage was changed from ± 1.0 to ± 2.0 and then ± 3.0 V (0.1 Hz), the displacement of the actuator strip was increased from 0.36 to 0.76 and 1.8 mm, respectively. The electric current profile of the actuation (Figure 3 b) displayed only charging and discharging, thus indicating that the bucky-gel electrodes act as an electric double-layer capacitor. We found that the double-layer capacitance of the bucky-gel electrode has a value of 48 F (g of SWNTs)$^{-1}$, which is more than twice as large as those of a SWNT sheet dipped in ionic liquids (18–24 F g^{-1}).[14] Such a large double-layer capacitance of the bucky-gel electrode is believed to originate from highly dispersed carbon nanotubes. The strain and stress generated in the bucky-gel electrode layer, when estimated from the displacement (Figure 3 a) at an applied voltage of ± 3.5 V

 © 2005 Wiley-VCH Verlag GmbH & Co. KGaA, Weinheim

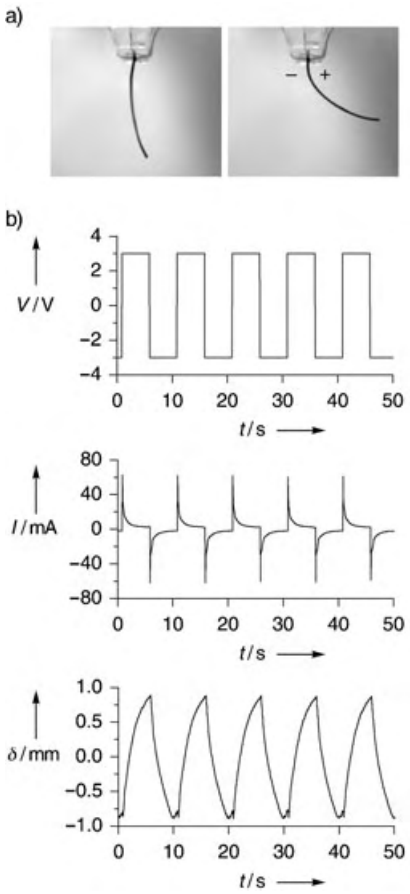

Figure 3. Performances of a bucky gel actuator (15 mm in length, 1 mm in width, 0.28 mm in thickness) in response to alternating square-wave electric potentials. a) Bending motion of the actuator strip at an applied voltage of ±3.5 V with a frequency of 0.01 Hz. b) Input signals (*V*), currents (*I*), and displacements (δ) of the actuator strip at an applied voltage of ±3.0 V with a frequency of 0.1 Hz.

(0.01 Hz), were 0.9% and 0.1 MPa, respectively. Of interest, the observed strain is comparable to or even larger than that of the SWNT sheet-based actuator,[10] in spite of the fact that the SWNT content in the bucky-gel electrodes is only 13 wt%. We consider that the bending motion of our actuator takes place by dimensional changes of the soft electrode layers in response to alternating voltages. When an electric potential is applied to the actuator, imidazolium (BMI^+) and BF_4^- ions of the built-in ionic liquid are thought to be transported to the cathodic and anodic sides, respectively, and form electric double layers with negatively and positively charged nanotubes. These ion transports most likely result in swelling of the cathode layer and shrinkage of the anode layer, as the former ion is larger than the latter. Consequently, the actuator bends toward the anode side (Figure 3a). Such a reversible change in the electrode dimensions takes advantage of the flexibility of the soft component materials. The SWNT-sheet-based actuator has been reported to bend toward the same direction, as it is operative by elongation and contraction of the nanotube bundles upon injection of negative and positive charges, respectively. Thus, these macroscopic and nanoscopic dimensional changes in the actuator strip do not compensate but can be synchronous with one another and may generate a large bending motion.

Our bucky-gel-based actuator is long-lived upon operation in air. Figure 5 shows the cycle life in air under

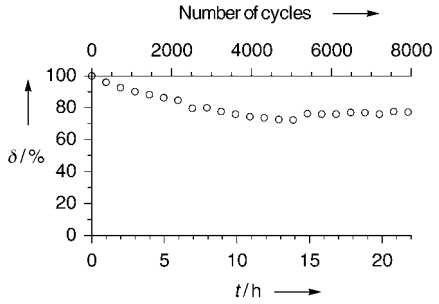

Figure 5. Cycle life of a bucky-gel actuator strip (15 mm in length, 1 mm in width, 0.28 mm in thickness) under continuous operation in air at an alternating square-wave electric potential of ±2.0 V with a frequency of 0.1 Hz.

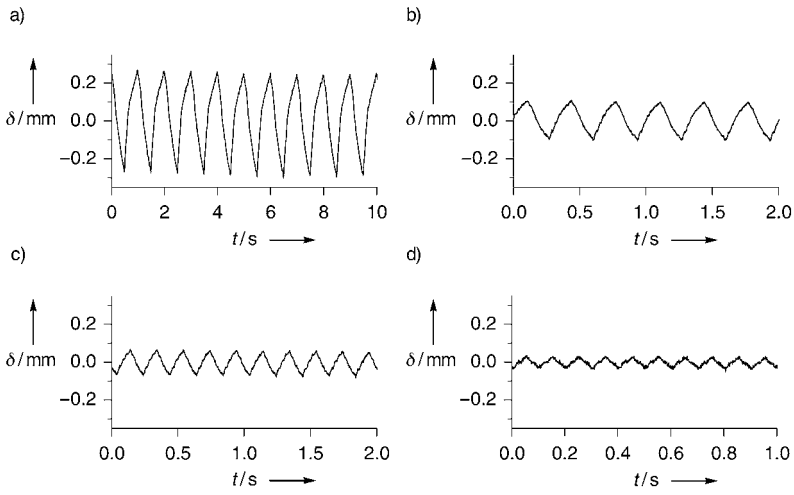

Figure 4. Performances of a bucky gel actuator (15 mm in length, 1 mm in width, 0.28 mm in thickness). Time-dependent displacements (δ) of the actuator strip at an applied square-wave electric potential of ±3.0 V with frequencies of a) 1.0; b) 3.0; c) 5.0; d) 10 Hz.

continuous operation in response to ±2.0 V square-wave input signals at a frequency of 0.1 Hz; the actuation could be repeated at least 8000 cycles, only with a 20% initial decrease in the actuator stroke, possibly as a result of the annealing of the material. We also confirmed that the actuator is usable periodically over a period of two months without any loss of performance.

The actuator reported herein has several advantages. First, the fabrication does not require any special apparatus but only an agate mortar and a hot plate. Such a simple layer-by-layer casting process can readily be extended to printing-based processing essential for miniaturization of machinery. Whereas the quick-responding actuators reported thus far require electro-

 © 2005 Wiley-VCH Verlag GmbH & Co. KGaA, Weinheim

lyte solutions for operation, our bucky-gel-based actuator quickly operates in air for a long time owing to the built-in ionic-liquid component. The observed performance and durability are one of the highest among those reported for low-voltage driven, dry electromechanical actuators and may be further tuned simply by varying the ionic-liquid and supporting-polymer components. The present development provides an important step toward the realization of printing-based fabrication of miniaturized mechanical devices.

Experimental Section

Fabrication of actuator films by layer-by-layer casting: Typically, a suspension of SWNTs (high-purity HiPco SWNTs) (50 mg) in $BMIBF_4$ (205 mg) was ground for 15 min with an agate mortar. The bucky gel thus obtained was transferred to a mixture of PVdF(HFP) (126 mg) and 4-methyl-2-pentanone (MP) (2.5 mL). The mixture was heated at 80 °C for 20 min on a hot plate, and the resultant gelatinous material was then cast on an aluminum mold (4 cm in length, 1 cm in width, 0.17 mm in depth) and allowed to cool to room temperature, affording the first layer. Subsequently, a hot gelatinous mixture[13] of $BMIBF_4$ (253 mg), PVdF(HFP) (127 mg), and MP (0.8 mL) was cast onto the first layer. The resultant double-layered film was allowed to cool to room temperature after the thickness was adjusted by a 0.34-mm-thick spacer. The aforementioned hot gelatinous material derived from bucky gel was again cast onto the second layer and processed with a 0.17-mm-thick spacer. Finally, the three-layered (bimorph) film thus obtained was allowed to stand in air overnight and then dried under reduced pressure to remove the volatile fraction (MP), thus affording an actuator film with a thickness of 0.25–0.3 mm.

Received: October 15, 2004
Published online: March 10, 2005

Keywords: actuators · ionic liquids · materials science · nanotechnology · nanotubes

[1] P. Calvert, *Chem. Mater.* **2001**, *13*, 3299 – 3305.
[2] B.-J. de Gans, P. C. Duineveld, U. S. Schubert, *Adv. Mater.* **2004**, *16*, 203 – 213.
[3] *Electroactive Polymer (EAP) Actuators as Artificial Muscles, Reality, Potential, and Challenges* (Ed.: Y. Bar-Cohen), 2nd ed., SPIE Press, Washington, DC, **2004**.
[4] *Polymer Sensors and Actuators* (Eds.: Y. Osada, D. E. De Rossi), Springer, Berlin, **2000**.
[5] R. H. Baughman, *Synth. Met.* **1996**, *78*, 339 – 353.
[6] E. W. H. Jager, E. Smela, O. Inganäs, *Science* **2000**, *290*, 1540 – 1545.
[7] E. Smela, *Adv. Mater.* **2003**, *15*, 481 – 494.
[8] a) J. M. Sansiñena, V. Olazábal, T. F. Otero, C. N. Polo da Fonseca, Marco-A. De Paoli, *Chem. Commun.* **1997**, 2217 – 2218; b) D. Zhou, G. M. Spinks, G. G. Wallace, C. Tiyapiboonchaiya, D. R. MacFarlane, M. Forsyth, J. Sun, *Electrochim. Acta* **2003**, *48*, 2355 – 2359.
[9] T. Fukushima, A. Kosaka, Y. Ishimura, T. Yamamoto, T. Takigawa, N. Ishii, T. Aida, *Science* **2003**, *300*, 2072 – 2074.
[10] R. H. Baughman, C. Cui, A. A. Zakhidov, Z. Iqbal, J. N. Barisci, G. M. Spinks, G. G. Wallace, A. Mazzoldi, D. De Rossi, A. G. Rinzler, O. Jaschinski, S. Roth, M. Kertesz, *Science* **1999**, *284*, 1340 – 1344.
[11] J. C. Ma, D. A. Dougherty, *Chem. Rev.* **1997**, *97*, 1303 – 1324.
[12] a) W. Lu, A. G. Fadeev, B. Qi, E. Smela, B. R. Mattes, J. Ding, G. M. Spinks, J. Mazurkiewicz, D. Zhou, G. G. Wallace, D. R. MacFarlane, S. A. Forsyth, M. Forsyth, *Science* **2002**, *297*, 983 – 987; b) J. Ding, D. Zhou, G. M. Spinks, G. G. Wallace, S. A. Forsyth, M. Forsyth, D. R. MacFarlane, *Chem. Mater.* **2003**, *15*, 2392 – 2398.
[13] a) J. Fuller, A. C. Breda, R. T. Carlin, *J. Electrochem. Soc.* **1997**, *144*, L67 – L70; b) J. Fuller, A. C. Breda, R. T. Carlin, *J. Electroanal. Chem.* **1998**, *459*, 29 – 34.
[14] J. N. Barisci, G. G. Wallace, D. R. MacFarlane, R. H. Baughman, *Electrochem. Commun.* **2004**, *6*, 22 – 27.

 © 2005 Wiley-VCH Verlag GmbH & Co. KGaA, Weinheim

Microreactors

Room-Temperature Swern Oxidations by Using a Microscale Flow System**

*Tatsuya Kawaguchi, Hiroyuki Miyata, Kikuo Ataka, Kazuhiro Mae, and Jun-ichi Yoshida**

Microreactors (microstructured chemical reactors)[1] are expected to make a revolutionary change in chemical synthesis[2] from both the academic and industrial viewpoints.[3] Microreactors exhibit numerous practical advantages, including safety, easy modulation, and easy scale-up for industrial production, when compared with conventional macroscale batch reactors.[4] It is also advantageous that highly exothermic reactions can be conducted on the basis of efficient mass and heat transfer.[5] Microreactors also enable the precise control of reactive intermediates and thereby facilitate highly selective reactions that are difficult to achieve in conventional reactors.[6] Herein, we report that the Swern oxidation can be accomplished by using a microreactor at temperatures between −20 and 20 °C, much higher temperatures than those required for conventional macroscale batch reactors (−50 °C or below).

[*] Prof. J.-i. Yoshida
Department of Synthetic Chemistry and Biological Chemistry
Graduate School of Engineering
Kyoto University, Kyoto 615-8510 (Japan)
Fax: (+81) 75-383-2727
E-mail: yoshida@sbchem.kyoto-u.ac.jp

Dr. T. Kawaguchi
Micro Chemical Process Technology Research Association (MCPT) in Kyoto
Kyoto University, Kyoto 615-8510 (Japan)

H. Miyata, Dr. K. Ataka
Corporate Research and Development
Ube Industries, Ltd., Ube, Yamaguchi, 755-8633 (Japan)

Prof. K. Mae
Department of Chemical Engineering
Graduate School of Engineering
Kyoto University, Kyoto 615-8510 (Japan)

[**] We thank Technology Japan and the Project of Micro-Chemical Technology for Production, Analysis, and Measurement Systems of NEDO, Japan, for financial support.

Supporting information for this article is available on the WWW under http://www.angewandte.org or from the author.

 DOI: 10.1002/anie.200462466 © 2005 Wiley-VCH Verlag GmbH & Co. KGaA, Weinheim

The oxidation with dimethyl sulfoxide (DMSO), known as the Moffatt–Swern type oxidation, is one of the most versatile and reliable methods for the oxidation of alcohols into carbonyl compounds and is widely utilized in organic synthesis.[7] Various methods for the activation of DMSO have been developed so far, and activation with trifluoroacetic anhydride (TFAA) is frequently employed in modern organic synthesis.[8] It is well known that activation of DMSO leads to an inevitable side reaction, the Pummerer rearrangement. Therefore, the reaction is usually carried out at low temperatures (−50 °C or below) at which the side reaction is very slow. However, the requirement for such low temperatures causes severe limitations in the industrial use of this highly useful reaction.

The Swern oxidation with TFAA generally proceeds as depicted in Scheme 1. In the first step, DMSO (usually in

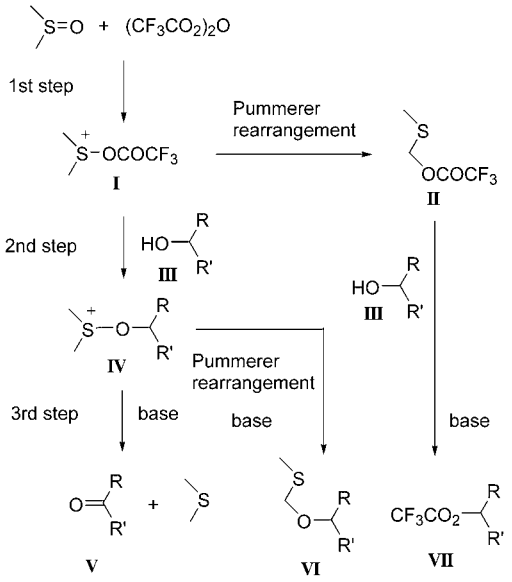

Scheme 1. The proposed mechanism of the Swern oxidation with TFAA.

excess) reacts with TFAA to form cationic intermediate **I**, which is known to be stable only below −30 °C.[9] Therefore, the first step is usually carried out below −50 °C. At higher temperatures, the rearrangement of **I** takes place to give **II**. Therefore, **I** is immediately allowed to react with an alcohol **III** at or below −50 °C to obtain intermediate **IV** (the second step).

In the third step, **IV** is treated with a base (usually triethylamine) to obtain the corresponding carbonyl compound **V** and dimethyl sulfide. However, upon treatment with a base, **IV** may also undergo the Pummerer rearrangement to give a methylthiomethyl ether (MTM ether) **VI**. Another important byproduct is the trifluoroacetate (TFA ester) **VII**, which is formed by the reaction of **II** with an alcohol **III** upon treatment with a base. In fact, the reaction of DMSO with TFAA at or above −30 °C mainly led to the formation the Pummerer rearrangement product **II**, and a significant amount of **VII** is therefore eventually formed in the final stage.

We examined the Swern oxidation by using a microscale flow system consisting of multilamination-type micromixers[10] and stainless tube reactors, as represented in Figure 1. A solution of DMSO (4.0 M) in CH_2Cl_2 (flow rate: 1 mL min^{-1},

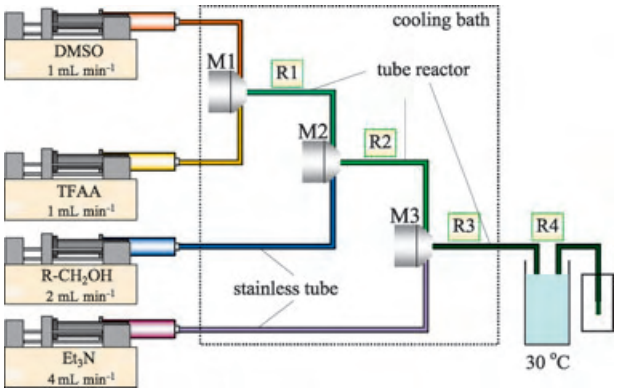

Figure 1. Schematic diagram of the microscale flow system for the Swern oxidation.

4 mmol min^{-1}) and a solution of TFAA (2.4 M) in CH_2Cl_2 (flow rate: 1 mL min^{-1}, 2.4 mmol min^{-1}) were introduced to the first micromixer (M1) by using syringe pumps.[11] The resulting solution was passed through reactor R1 and was mixed with a solution of the alcohol (1.0 M) in CH_2Cl_2 (flow rate: 2 mL min^{-1}, 2 mmol min^{-1}) in the second micromixer (M2). The resulting solution was passed through reactor R2 and was mixed with a solution of triethylamine (1.45 M) in CH_2Cl_2 (flow rate 4 mL min^{-1}, 5.8 mmol min^{-1}) in the third micromixer (M3). The solution was then introduced to tube reactor R3 before being passed through reactor R4. The three mixers (M1–3) and three of the reactors (R1–R3) were dipped in a cooling bath. Reactor R4 was dipped in a bath maintained at 30 °C. The outlet solution was collected and was analyzed by GC with an internal standard. The residence time in each reactor was as follows: R1: 0.01–2.4 s, R2: 1.2 s, R3: 1.2 s, R4: 5.9 s. After a steady state was reached, an aliquot of the product solution was taken over a period of 1.0 min and analyzed by GC.

As indicated in Table 1, the oxidation of primary, secondary, cyclic, and benzylic alcohols took place smoothly to give the corresponding carbonyl compounds in good yields and with good selectivity at −20 °C (R1: 2.4 s). It is noteworthy that the reactions with a conventional macroscale batch reactor (a 30 mL flask with magnetic stirring) at the same temperature led to the formation of significant amounts of trifluoroacetates **VII** and the yields of the carbonyl compounds **V** were low. Significant amounts of substrate alcohols **III** also remained unchanged in the macroscale batch system. The dramatic effect of the microscale flow system seems to be attributable to precise temperature control (small local deviation of temperature in the reactor) and extremely fast and efficient mixing by virtue of a short diffusion path in the micromixer. Short residence time also seems to play a crucial role because fast transfer of the reactive intermediate to the next reactor seems to be essential for the present transformation.

 © 2005 Wiley-VCH Verlag GmbH & Co. KGaA, Weinheim

Table 1: Swern oxidation of alcohols by using the microscale flow system and macroscale batch system.[a]

Alcohol **III**	System	Residence time in R1 [s]	*T* [°C]	Conversion [%]	Yield of **V** [%]	Yield of **VI** [%]	Yield of **VII** [%]
1-decanol	microscale flow	2.4	−20	95	75	8	19
		0.01	0	94	70	6	22
		0.01	20	96	71	6	22
	macroscale batch		−20	73	11	1	90
2-octanol	microscale flow	2.4	−20	92	95	5	2
		0.01	0	91	86	4	3
		0.01	20	88	89	3	2
	macroscale batch		−20	51	20	2	75
cyclohexanol	microscale flow	2.4	−20	88	88	6	5
		0.01	0	90	89	7	1
		0.01	20	81	88	5	2
	macroscale batch		−20	86	19	2	70
			−70	88	83	10	5
benzyl alcohol	microscale flow	2.4	−20	97	91	n.d.[b]	8
		0.01	0	100	78	n.d.[b]	14
		0.01	20	100	75	n.d.[b]	16
	macroscale batch		−20	80	49	n.d.[b]	50

[a] Yields were determined by GC withan internal standard and are based upon the amount of the alcohol consumed. [b] n.d. = not determined.

The success of the Swern oxidation by using the microscale flow system at −20 °C prompted us to examine further increases in the reaction temperature. The reaction at 0 °C resulted in a significant decrease in the yield of carbonyl compounds **V** (32 % for cyclohexanol; results not shown). Presumably Pummerer rearrangement of intermediate **I** took place to give **II** at this temperature. However, we found that by shortening the residence time (R1: 0.01 s) the desired carbonyl compounds **V** were obtained in good yields even at 0 °C. More outstanding is the fact that the reaction can be conducted even at room temperature (20 °C) to obtain **V** in good yields. This success of the Swern oxidation at room temperature seems to be attributable to the extremely short residence time, which ensures very fast transfer of the highly unstable intermediate **I** to the next reactor before decomposition.

It is important to check the durability of the process for scale-up. So, we ran the reaction of cyclohexanol for 3 h (0.36 mol scale) at 20 °C and found that the alcohol conversion and product selectivity did not change (Table 2).

Table 2: Continuous Swern oxidation of cyclohexanol by using the microscale flow system at 20 °C.[a]

t [h]	Conversion [%]	Yield of **V** [%]	Yield of **VI** [%]	Yield of **VII** [%]
0	83	92	5	4
0.5	84	92	5	4
1.0	85	89	5	4
1.5	81	89	4	4
2.0	86	91	5	3
2.5	87	91	5	3
3.0	85	91	5	4

[a] Yields were determined by GC with an internal standard and are based upon the amount of the alcohol consumed.

Another important point is that microsystems serve as a quick means for scale-up, because the quality of the product does not change during the course of scale-up, although batch methods suffer from such a problem.

In conclusion, the present observations demonstrate a striking example of the effectiveness of the microscale flow system for a reaction involving highly unstable intermediates. Further improvement of the reaction system and applications to the synthesis of various carbonyl compounds are in progress.

Received: October 29, 2004
Published online: March 10, 2005

Keywords: alcohols · microreactors · oxidation · Swern oxidation · synthetic methods

[1] a) *Microreaction Technology* (Ed.: W. Ehrfeld), Springer, Berlin, **1998**; b) W. Ehrfeld, V. Hessel, H. Löwe, *Microreactors*, Wiley-VCH, Weinheim, **2000**; c) *Microsystem Technology in Chemistry and Life Sciences* (Eds.: A. Manz, H. Becker), Springer, Berlin, **1999**; d) V. Hessel, S. Hardt, H. Löwe, *Chemical Micro Process Engineering*, Wiley-VCH, Weinheim, **2004**.

[2] a) H. Salimi-Moosavi, T. Tang, D. J. Harrison, *J. Am. Chem. Soc.* **1997**, *119*, 8716 – 8717; b) C. de Bellefon, N. Tanchoux, S. Caravieilhes, P. Grenouillet, V. Hessel, *Angew. Chem.* **2000**, *112*, 3584 – 3587; *Angew. Chem. Int. Ed.* **2000**, *39*, 3442 – 3445; c) H. Hisamoto, T. Saito, M. Tokeshi, A. Hibara, T. Kitamori, *Chem. Commun.* **2001**, 2662 – 2663; d) C. Wiles, P. Watts, S. J. Haswell, E. Pombo-Villar, *Chem. Commun.* **2002**, 1034 – 1035; e) T. Fukuyama, M. Shinmen, S. Nishitani, M. Sato, I. Ryu, *Org. Lett.* **2002**, *4*, 1691 – 1694; f) E. Garcia-Egido, V. Spikmans, S. Y. F. Wong, B. H. Warrington, *Lab Chip* **2003**, *3*, 73 – 76; g) M. Ueno, H. Hisamoto, T. Kitamori, S. Kobayashi, *Chem. Commun.* **2003**, 936 – 937; h) S. M. Lai, R. Martin-Aranda, K. L. Yeung, *Chem. Commun.* **2003**, 218 – 219; i) J. Kobayashi, Y. Mori, K. Okamoto, R. Akiyama, M. Ueno, T. Kitamori, S. Kobayashi, *Science* **2004**, *304*, 1305 – 1308; j) T. Wu, Y. Mei, J. T. Cabral, C. Xu, K. L. Beers, *J. Am. Chem. Soc.* **2004**, *126*, 9880 – 9881.

[3] Example reviews: a) S. H. DeWitt, *Curr. Opin. Chem. Biol.* **1999**, *3*, 350 – 356; b) H. Okamoto, *J. Syn. Org. Chem. Jpn.* **1999**, *57*, 805 – 812; c) T. Sugawara, *Pharmacia* **2000**, *36*, 34 – 38; d) O. Wörz, K. P. Jäckel, T. Richter, A. Wolf, *Chem. Eng. Sci.* **2001**, *56*, 1029 – 1033; e) S. J. Haswell, R. J. Middleton, B. O'Sullivan, V. Skelton, P. Watts, P. Styring, *Chem. Commun.* **2001**, 391 – 398; f) K. F. Jensen, *Chem. Eng. Sci.* **2001**, *56*, 293 – 303; g) A. de Mello, R. Wootton, *Lab Chip* **2002**, *2*, 7N – 13N; h) K. Jähnisch, V. Hessel, H. Löwe, M. Baerns, *Angew. Chem.* **2004**, *116*, 410 – 451; *Angew. Chem. Int. Ed.* **2004**, *43*, 406 – 446. .

[4] S. Taghavi-Moghadam, A. Kleemann, K. G. Golbig, *Org. Process Res. Dev.* **2001**, *5*, 652 – 658.

[5] a) R. D. Chambers, R. C. H. Spink, *Chem. Commun.* **1999**, 883 – 884; b) M. T. Janicke, H. Kestenbaum, U. Hagendorf, F. Schüth, M. Fichtner, K. Schubert, *J. Catal.* **2000**, *191*, 282 – 293; c) M. W.

 © 2005 Wiley-VCH Verlag GmbH & Co. KGaA, Weinheim

Losey, M. A. Schmidt, K. F. Jensen, *Ind. Eng. Chem. Res.* **2001**, *40*, 2555 – 2562.
[6] For example, a) S. Suga, M. Okajima, K. Fujiwara, J. Yoshida, *J. Am. Chem. Soc.* **2001**, *123*, 7941 – 7942; b) J. Yoshida, S. Suga, *Chem. Eur. J.* **2002**, *8*, 2651 – 2658; c) S. Suga, A. Nagaki, J. Yoshida, *Chem. Commun.* **2003**, 354 – 355; d) S. Suga, A. Nagaki, Y. Tsutsui, J. Yoshida, *Org. Lett.* **2003**, *5*, 945 – 947; e) A. Nagaki, K. Kawamura, S. Suga, T. Ando, M. Sawamoto, J. Yoshida, *J. Am. Chem. Soc.* **2004**, *126*, 14702 – 14703.
[7] For example, T. T. Tidwell, *Org. React.* **1990**, *39*, 297 – 572.
[8] a) K. Omura, A. K. Sharma, D. Swern, *J. Org. Chem.* **1976**, *41*, 957 – 962; b) K. Omura, D. Swern, *Tetrahedron* **1978**, *34*, 1651 – 1660.
[9] a) A. K. Sharma, D. Swern, *Tetrahedron Lett.* **1974**, 1503 – 1506; b) A. K. Sharma, T. Ku, A. D. Dawson, D. Swern, *J. Org. Chem.* **1975**, *40*, 2758 – 2764.
[10] The IMM (Institut für Mikrotechnik Mainz GmbH) single mixer, version 2, (http://www.imm-mainz.de/) was used. The inlay is made of silver and the channel width is 40 μm.
[11] The Harvard PHD2000 Programmable syringe pump, Harvard Pump11 (http://www.harvardapparatus.com/), and kdScientific model 100 syringe pump (http://www.kdscientific.com/) were used.

 © 2005 Wiley-VCH Verlag GmbH & Co. KGaA, Weinheim

Magnetic Properties

Building Blocks for 2D Molecule-Based Magnets: The Diruthenium Tetrapivalate Monocation $[Ru^{II/III}_2(O_2CtBu)_4]^+$**

*Thomas E. Vos and Joel S. Miller**

The development of molecule-based magnets has made significant progress with a variety of spin-bearing organic as well as inorganic building blocks.[1] One building block that has garnered attention in molecule-based magnets is the diruthenium tetracarboxylate cation, $[Ru_2(O_2CMe)_4]^+$ (**1**).[2–4] Ion **1** has an $S = 3/2$ ground state with the $\sigma^2\pi^4\delta^2\delta^{*1}\pi^{*2}$ valence electronic configuration, owing to near degeneracy of the π^* and δ^* orbitals.[5] Besides the unusually high spin state for a second-row coordination complex, diruthenium tetracarboxylate species have large zero-field splittings, $D = +63 \pm 11$ cm^{-1},[6,7] and are able to coordinate up to two axial ligands a property that is essential for building extended network structures. Many 1D extended structures based on diruthenium tetracarboxylate compounds have been explored by using organic bridging ligands,[2] such as nitroxide radicals, TCNQ (7,7,8,8-tetracyano-*p*-quinodimethane), quinone, phenazine, $[N(CN)_2]^-$, and $[C(CN)_3]^-$. These extended network structures exhibit weak antiferromagnetic interactions between spin sites, but not long-range magnetic ordering.

$[Ru_2(O_2CMe)_4]^+$ has been incorporated into cubic 3D networks with metal hexacyanometallate(III), $[M(CN)_6]^{3-}$ (M = Co, Fe, Mn, Cr). $[Ru_2(O_2CMe)_4]_3[M^{III}(CN)_6]$ (M = Co (**2**), Fe (**3**), Cr (**4**)) have a 3D body-centered, interpenetrating network structure (Figure 1) that magnetically orders at 2.1 K for **3** and 33 K for **4**.[3] Using pivalate, Yoshioka et al. obtained $[Ru_2(O_2CtBu)_4]_3[M^{III}(CN)_6]\cdot 2H_2O$ (M = Co (**5**), Fe(**6**)), which formed a 2D layered network (Figure 2).[4] Tris(oxalato)metallate(III) species also form 2D and 3D extended networks depending on synthetic conditions and have been studied to understand the magnetostructural relationship of these materials.[8] While the temperature dependence of the magnetic susceptibilities, $\chi(T)$, of **5** and **6** were reported, ferrimagnetic behavior was suggested for **6**, but not established. Owing to the high T_c observed for **4**, we sought to prepare $[Ru_2(O_2CtBu)_4]_3[Cr^{III}(CN)_6]\cdot 2H_2O$ (**7**), for which modeling suggests should form a non-interpenetrating, primitive cubic lattice.[9] Herein we report its magnetic behavior as well as our detailed investigation of the magnetic properties of $[Ru_2(O_2CtBu)_4]_3[M^{III}(CN)_6]\cdot 2H_2O$ [M = Co (**5**), Fe (**6**), Cr (**7**)].

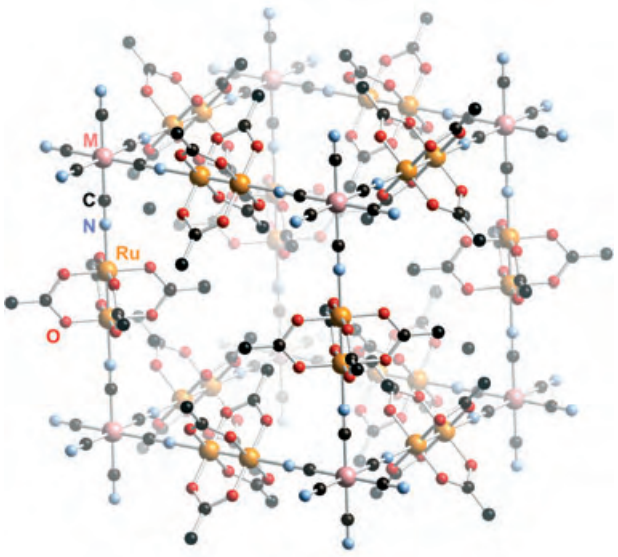

Figure 1. 3D network structure of $[Ru_2(O_2CMe)_4]_3[M^{III}(CN)_6]$ (M = Cr (**2**), Co (**3**), Fe(**4**)).[3] The hydrogen atoms are omitted for clarity. A second network structure interpenetrates this lattice, but it is omitted for clarity.

Orange-brown **5**,[4] **6**,[4] and **7**[10] were synthesized in a similar manner to the published procedure. Compounds **5** and **6** were verified by X-ray powder diffraction[11] and IR data.[4] The X-ray powder diffraction data of **7** was indexed to a

[*] Dr. T. E. Vos, Prof. J. S. Miller
Department of Chemistry
University of Utah
Salt Lake City, UT 84112-0850 (USA)
Fax: (+1) 801-581-8433
E-mail: jsmiller@chem.utah.edu

[**] The authors gratefully acknowledge the partial support from the U.S. National Science Foundation (No. CHE0110685), U.S. Department of Energy (No. DE FG 03-93ER45504), and the Army Research Office (Grant No. DAAD19-01-1-0562).

 © 2005 Wiley-VCH Verlag GmbH & Co. KGaA, Weinheim DOI: 10.1002/anie.200462546

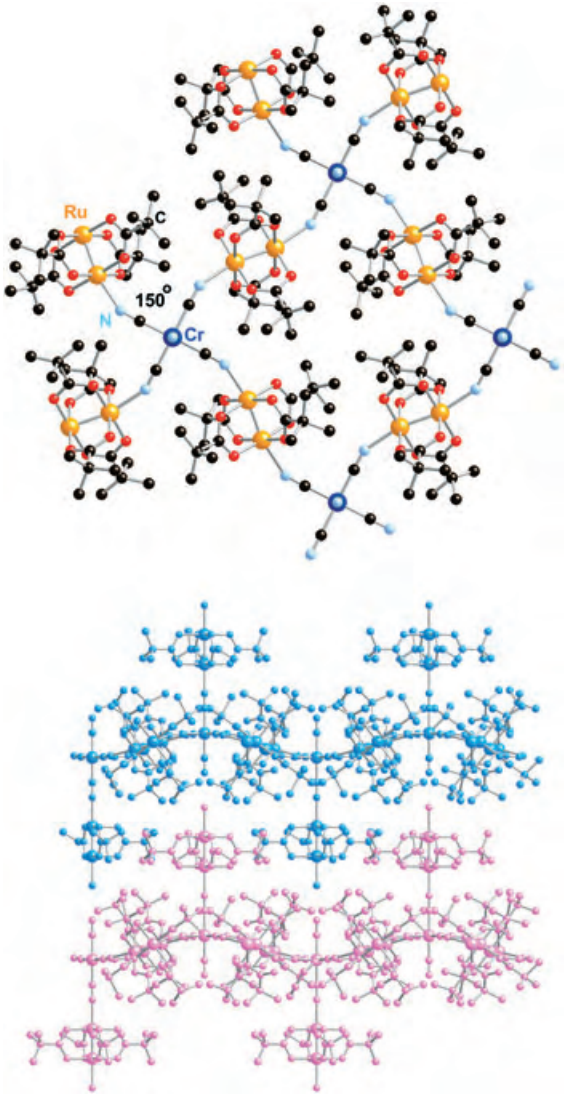

Figure 2. 2D layer structure of $[Ru_2(O_2CtBu)_4]_3[M^{III}(CN)_6]$ (M = Cr (**7**), Co (**5**),[4] Fe (**6**)[4]) viewed from the *c* axis to show the 2D layer connectivity (top) and viewed from the *b* axis to show the stacking of the 2D layers (bottom).

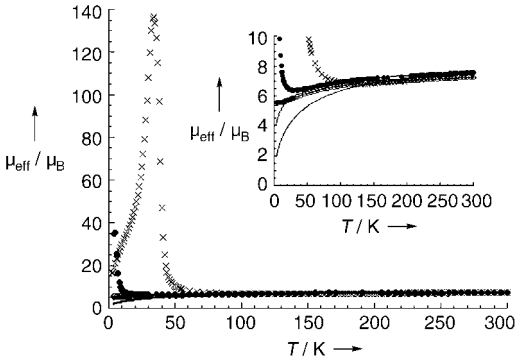

Figure 3. $\mu_{eff}(T)$ for **5** (○), **6** (●), and **7** (×) and the fits to the high-temperature data with Equation (2) as the solid black lines. The insert highlights the region below 10 μ_B.

tetragonal unit cell[10,11] and found to be isomorphous to **6** indicating that **7** was a 2D layered compound similar to **6**.

The 4 to 300 K magnetic susceptibilities, χ, of **5**–**7** were determined on a Quantum Design MPMS-5XL magnetometer at 50 Oe (Figure 3).[12] The 298 K effective moments, μ_{eff} $[=(8\chi T)^{1/2}]$, 7.35 μ_B for **5**, 7.57 μ_B for **6**, and 7.51 μ_B for **7**. The $\mu_{eff}(T)$ for **5** decreases slightly to 5.49 μ_B at 4 K while for **6** it decreases until around 25 K where upon μ_{eff} abruptly increases to a maximum of 36 μ_B at 5 K. The $\mu_{eff}(T)$ for **7** also decreases with lowering of the temperature until around 125 K where upon μ_{eff} increases to a maximum of 137 μ_B at 34 K and then abruptly decreases to 17 μ_B at 4 K. The abrupt peaks in $\mu_{eff}(T)$ plots suggests that **6** and **7** magnetically ordered.

Since the diruthenium tetracarboxylate dimer has a large zero-field splitting (D) and a temperature-independent paramagnetic (TIP) component, fitting the $\chi(T)$ to a simple Curie–Weiss model would not be appropriate; therefore, their contributions were incorporated into Equation (1).[13] The $\mu_{eff}(T)$ for **5**–**7** were modeled with Equation (2) which accounts for D and in addition incorporates the contribution of the paramagnetic metal hexacyanide.[3]

$$\chi_{Ru_2} = \frac{N g_{Ru_2}^2 \mu_B^2}{k_B(T-\theta)}\left[\frac{1}{3}\frac{1+9e^{\frac{-2D}{k_BT}}}{4(1+e^{\frac{-2D}{k_BT}})}+\frac{2}{3}\frac{1+\frac{3k_BT}{4D}(1-e^{\frac{-2D}{k_BT}})}{1+e^{\frac{-2D}{k_BT}}}\right]+\text{TIP for } T>\theta \quad (1)$$

$$\chi_{Tot} = 3\chi_{Ru_2}+\chi_M \text{ where } \chi_M = \frac{N g_M^2 \mu_B^2}{3k_B(T-\theta)}[S(S+1)] \quad (2)$$

The $\mu_{eff}(T)$ for **5** was fitted with $\theta = 0$ K, $g_{Ru_2} = 2.04$, $TIP_{Ru_2} = 800\times10^{-6}$ emu mol^{-1}, and the same D value, 69.4 cm^{-1} as was used for fitting **2**–**4**,[3] (χ^2 agreement factor $= \Sigma(\mu_{obs}-\mu_{calcd})^2\ \mu_{obs}^{-1}$ [14] $= 2.6\times10^{-3}$). The D value and g_{Ru_2} were kept constant in fitting **6** and **7**. The $\mu_{eff}(T)$ for **6** was fitted above 50 K with $\theta = -5$ K, $g_{Ru_2} = 2.04$, $g_{Fe} = 3.0$,[15] $TIP_{Ru_2} = 600\times10^{-6}$ emu mol^{-1} ($\chi^2 = 1.5\times10^{-3}$). The fitting parameters for **6** indicate some antiferromagnetic coupling between adjacent spin sites. This situation is in contrast to **3**, which needed no antiferromagnetic coupling between adjacent spin sites to fit the observed data.[3] Similarly, the $\mu_{eff}(T)$ was fitted above 150 K for **7** with $D = 69.4$ cm^{-1}, $\theta = -45$ K, $g_{Ru_2} = 2.04$, $g_{Cr} = 2.0$, $TIP_{Ru_2} = 300\times10^{-6}$ emu mol^{-1} ($\chi^2 = 2.9\times10^{-3}$). The -40 K θ value obtained for **4** to fit the observed data,[3] is similar to $\theta = -45$ K found for **7**, and the trend of having a stronger magnetic coupling between adjacent spin sites for **6** and **7** than in **3** and **4** correlates with their higher T_cs.

As a result of deviation from Equation (2) at lower temperature, **6** and **7** warranted further study to ascertain evidence of magnetic ordering. Zero-field/field cooled (ZFC/FC) $M(T)$ (M = magnetization) studies revealed bifurcation temperatures, T_b, at 6.5 K for **6** and 39.5 K for **7** (Figure 4) indicative of magnetic ordering.

Magnetic ordering of **6** and **7** was confirmed from the presence of absorptions in both the real (χ') and imaginary (χ'') alternating current (ac) susceptibilities (Figure 5). Compound **6** has a slight frequency dependence for both $\chi'(T)$ and $\chi''(T)$ peaks. The peak in $\chi'(T)$ shifts from 4.8 K at 10 Hz to

 © 2005 Wiley-VCH Verlag GmbH & Co. KGaA, Weinheim

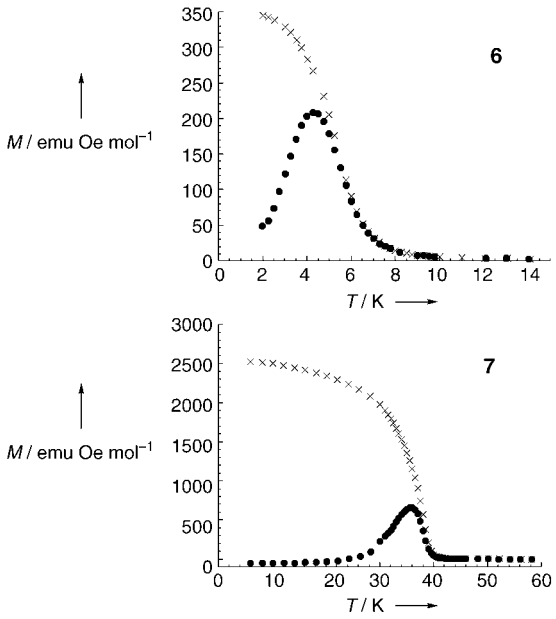

Figure 4. Field cooled (FC, ×) and zero field cooled (ZFC, ●) $M(T)$ data for **6** and **7**.

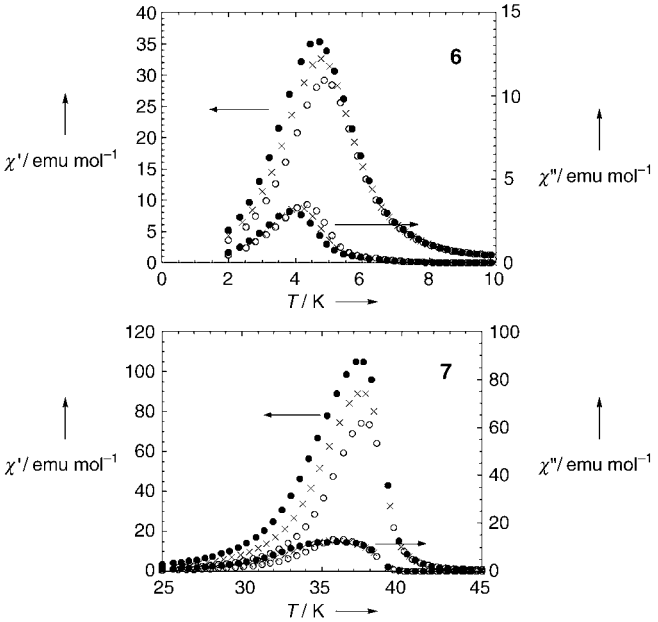

Figure 5. $\chi'(T)$ (left axis) and $\chi''(T)$ (right axis) at 10 (●), 100 (×), and 1000 (○) Hz for **6** and **7**.

4.7 K at 1000 Hz. Compound **7** has nearly frequency independent peaks for both $\chi'(T)$ at 37.5 K and $\chi''(T)$ at 36.5 K.

The 2 K field dependence of the magnetization, $M(H)$, for **6** and **7** exhibit hysteresis (Figure 6). The coercive fields of **6**

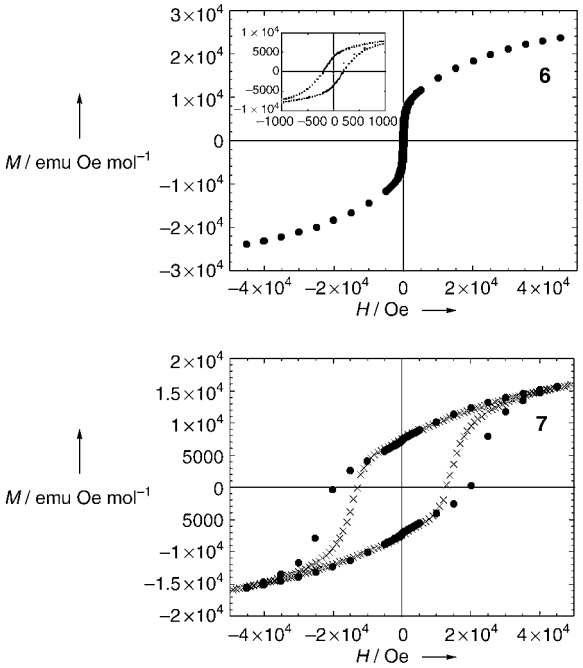

Figure 6. $M(H)$ of **6** at 2 K (●) and **7** at 2 K (●) and 5 K (×) taken from ±50000 Oe. Insert for **6** is an expansion of the region between ±1000 Oe.

was 190 Oe and **7** 20000 Oe, which are larger coercive fields (H_{cr}) than the analogous acetate 3D structures, **3** (10 Oe) and **4** (470 Oe). The large coercive fields are probably related to the 2D layer structure and the large anisotropy of the diruthenium cations. Enormous coercivity of approximately 27000 Oe were reported for [Mn^{III}(porphyrin)][TCNE] family of molecule-based magnets at 2 K, but they are only about 2% of that value at 5 K,[16] Hence, although raising the temperature for **7** to 5 K reduces H_{cr} to 13000 Oe, this value is still substantially greater than observed for the [Mn^{III}(porphyrin)][TCNE] family of magnets and the genesis is under investigation.

The T_c values for **6** and **7** exceed those of their 3D analogous **3** and **4** (Table 1). This result is contrast to 2D

Table 1: Summary of the ν_{CN} IR absorptions and magnetic properties for $[Ru_2(O_2CMe)_4]_3[M^{III}(CN)_6]$[3] and $[Ru_2(O_2CtBu)_4]_3[M^{III}(CN)_6]\cdot 2H_2O$ (M = Cr, Fe, Co).

	M	ν_{CN} [cm^{-1}]	μ_{eff} [μ_B]	T_b [K]	T_c [K][a]	M_s [emu Oe mol^{-1}][b]	M_r [emu Oe mol^{-1}]	H_{cr} [Oe]
2[3]	Co	2125	7.26	–	–	–	–	–
5	Co	2126	7.35	–	–	–	–	–
3[3]	Fe	2116	7.30	3.0	2.1	22700[c]	40[c]	10[c]
6	Fe	2115	7.57	6.5	4.8	24400[c]	3600[c]	190[c]
4[3]	Cr	2138	7.72	32.0	33.0	20800[c]	3840[c]	470[c]
7	Cr	2133	7.57	39.5	37.5	16200[c]	7500[c]	20000[c]
						15800[d]	7500[d]	13000[d]

[a] T_c determined from the peak in $\chi'(T)$ at 10 Hz. [b] M_s is the magnetization at 5 T. [c] Value at 2 K. [d] Value at 5 K.

 © 2005 Wiley-VCH Verlag GmbH & Co. KGaA, Weinheim

(racemic) and 3D (chiral) network structured (cation)M^{II}-$[M^{III}ox_3]$ (ox = oxalato) materials that have similar T_c values.[8] In addition to having a differing dimensionality (2D layer and 3D cubic structures), the angle between CN and diruthenium dimer was 150.5(10)° in the 2D layer structure and 180° in the cubic 3D structure (compare Figure 1 and Figure 2 top). Also, the 3D cubic structure has an interpenetrating lattice not found in the 2D layer. In addition, pivalate is more electron donating into the diruthenium core than the acetate ligand, which might enhance the magnetic coupling between the diruthenium dimer and the metal hexacyanide unit. The structural and/or electronic reasons why **6** and **7** have a higher T_c than **3** and **4** are still under investigation.

Understanding the magnetostructural relationship of this new class of materials incorporating a relatively large zero-field-splitting ligand and metal hexacyanides would provide important information for molecule-based materials. These compounds highlight the importance of determining magnetostructural relationships for rationally design molecule-based magnets with desired physical properties.

Received: November 8, 2004
Revised: January 7, 2005
Published online: March 10, 2005

Keywords: chromium · cyanide ligands · magnetic anisotropy · magnetic properties · ruthenium

[1] a) V. I. Ovcharenko, R. Z. Sagdeev, *Russ. Chem. Rev.* **1999**, *68*, 345; b) P. J. Day, *J. Chem. Soc. Dalton Trans.* **1997**, 701; c) J. S. Miller, A. J. Epstein, *Chem. Eng. News* **1995**, *73*(40), 30; J. S. Miller, A. J. Epstein, *Adv. Chem. Ser.* **1995**, *245*, 161; d) J. S. Miller, A. J. Epstein, *Chem. Commun.* **1998**, 1319; e) J. S. Miller, A. J. Epstein, *Angew. Chem.* **1994**, *106*, 399; *Angew. Chem. Int. Ed. Engl.* **1994**, *33*, 385; f) J. A. Crayson, J. N. Devine, J. C. Walton, *Tetrahedron* **2000**, *56*, 7829; S. J. Blundell, F. L. Pratt, *J. Phys. Condens. Matter* **2004**, *16*, R771.

[2] a) M. A. S. Aquino, *Coord. Chem. Rev.* **1998**, *170*, 141; b) T. M. Buslaeva, S. N. Redkina, O. V. Rudnitskaya, *Russ. J. Coord. Chem.* **1999**, *25*, 3; c) M. A. S. Aquino, *Coord. Chem. Rev.* **2004**, *248*, 1025.

[3] a) T. E. Vos, Y. Liao, W. W. Shum, J.-H. Her, P. W. Stephens, W. M. Reiff, J. S. Miller, *J. Am. Chem. Soc.* **2004**, *126*, 11630; b) Y. Liao, W. W. Shum, J. S. Miller, *J. Am. Chem. Soc.* **2002**, *124*, 9336.

[4] D. Yoshioka, M. Mikuriya, M. Handa, *Chem. Lett.* **2002**, *31*, 1044.

[5] a) F. A. Cotton, R. A. Walton in *Multiple Bonds between Metal Atoms*, 2nd ed., Clarendon Press, Oxford, UK, **1993**, p. 18; b) V. M. Miskowiski, M. D. Hopkins, J. R. Winkler, H. B. Gray in *Inorganic Electronic Structure and Spectroscopy*, *Vol. 2* (Eds.: E. I. Solomon, A. B. P. Lever), Wiley, New York, **1999**, chap. 6; c) J. G. Norman, Jr., G. E. Renzoni, D. A. Case, *J. Am. Chem. Soc.* **1979**, *101*, 5256.

[6] W. W. Shum, Y. Liao, J. S. Miller, *J. Phys. Chem. A* **2004**, *108*, 7460.

[7] a) J. Telser, R. S. Drago, *Inorg. Chem.* **1985**, *24*, 4765; b) J. Telser, R. S. Drago, *Inorg. Chem.* **1984**, *23*, 3114; c) F. D. Cukiernik, A. M. Giroud-Godquin, P. Maldivi, J. C. Marchon, *Inorg. Chim. Acta* **1994**, *215*, 203; d) M. Handa, Y. Sayama, M. Mikuriya, R. Nukada, I. Hiromitsu, K. Kasuga, *Bull. Chem. Soc. Jpn.* **1998**, *71*, 119; e) R. Jimenez-Aparicio, F. A. Urbanos, J. M. Arrieta, *Inorg. Chem.* **2001**, *40*, 613; f) F. D. Cukiernik, D. Luneau, J. C. Marchon, P. Maldivi, *Inorg. Chem.* **1998**, *37*, 3698.

[8] M. Pilkington, S. Decurtins in *Magnetism: Molecules to Materials II* (Eds.: J. S. Miller, M. Drillon), Wiley-VCH, New York, **2001**, p. 339.

[9] W. W. Shum, T. E. Vos, J. L. Dye, J. S. Miller, unpublished results using the void and molecule isosurface method [T. F. Nagy, S. D. Mahanti, J. L. Dye, *Zeolites* **1997**, *19*, 57].

[10] $K_3[Cr(CN)_6]$ (18 mg, 55 mmol) was dissolved in water (5 mL) and was added to a stirred methanol solution (10 mL) of $[Ru_2(O_2CtBu)_4]Cl$ (100 mg, 156 mmol). After 1 h, an orange brown precipitate was isolated by centrifugation, washed with water, then dried in vacuo (Yield 78%; 84 mg). IR (KBr): 2133 cm^{-1} (ν_{CN}). Elemental analysis (%) calcd for $C_{66}H_{112}CrN_6O_{26}Ru_6$: C 38.41, H 5.47, N 4.07; found: C 38.14, H 5.49, N 4.07. The powder diffraction data was indexed to a tetragonal space group: $a = b = 17.39(6)$ Å; $c = 15.67(6)$ Å; $V = 4739(40)$ Å^3.

[11] The powder diffraction data was indexed with the program Treor, see: P.-E. Werner, L. Eriksson, M. Westdahl, *J. Appl. Crystallogr.* **1985**, *18*, 367.

[12] The magnetic data of $[Ru_2(O_2CtBu)_4]_3[Fe(CN)_6]\cdot 2H_2O$ reported in ref. [4] was reproduced at 5000 Oe.

[13] a) C. J. O'Connor, *Prog. Inorg. Chem.* **1982**, *29*, 203; b) J. Telser, R. S. Drago, *Inorg. Chem.* **1985**, *24*, 4765.

[14] J. Taylor, *An Introduction to Error Analysis*: University Science Books, Mill Valley, CA, **1982**, pp. 218–223.

[15] a) R. L. Carlin, *Magnetochemistry*, Springer, New York, **1986**, pp. 28–68; b) B. Bleaney, M. C. M. O'Brien, *Proc. Phys. Soc. London Sect. B* **1956**, *69*, 1216; c) B. C. Guha, *Proc. R. Soc. London Ser. A* **1951**, *206*, 353.

[16] D. K. Rittenberg, K.-i. Sugiura, Y. Sakata, S. Mikami, A. J. Epstein, J. S. Miller, *Adv. Mater.* **2000**, *12*, 126.

 © 2005 Wiley-VCH Verlag GmbH & Co. KGaA, Weinheim

Nanotechnology

Self-Assembly and Cross-Linking of Bionanoparticles at Liquid–Liquid Interfaces**

Justin T. Russell, Yao Lin, Alexander Böker, Long Su, Philippe Carl, Heiko Zettl, Jinbo He, Kevin Sill, Ravisubhash Tangirala, Todd Emrick, Kenneth Littrell, Pappannan Thiyagarajan, David Cookson, Andreas Fery, Qian Wang, and Thomas P. Russell**

The self-assembly of nanoscale materials to form hierarchically ordered structures promises new opportunities in optical, acoustic, electronic, as well as magnetic materials and devices.[1–4] Herein, we apply our recent findings on the self-assembly of nanoparticles at liquid interfaces,[5,6] based on Pickering emulsions,[7,8] to naturally occurring nanometer-scale structures. Bionanoparticles, such as viruses and other biological materials, are truly monodisperse in size and can be functionalized in a robust, well-defined manner.[9–12] These attributes afford a unique platform to investigate the mechanism and kinetics of self-assembly at the liquid–liquid interface quantitatively.

Numerous studies have focused on ordered 2D arrays of protein particles[13] by spreading and adsorbing proteins on surfaces[14,15] or at interfaces.[15–19] However, simple routes to direct and assemble bioparticles into 2D or 3D constructs with hierarchical ordering are still required. Herein, we use the interface between two immiscible liquids (that is, on the surface of droplets), which has been shown to be ideal for the assembly of colloidal and nanoscopic particles,[5–8,20–24] and chose the cowpea mosaic virus (CPMV) as a prototype. The CPMV is a non-enveloped plant virus that is approximately 30 nm in diameter and is isolated from infected black eye pea plants in yields of 1–2 g kg^{-1} of wet leaves.[25] The physical, biological, and genetic properties of the CPMV have been well characterized.[26–28] It consists of an icosahedral protein shell, or capsid, composed of 60 copies of the two different types of protein subunits.[29] CPMV particles are remarkably stable: they maintain their integrity for at least one hour at 50 °C (pH 7) and indefinitely at room temperature (pH 3.5–9). The CPMV was the first virus to be used in organic reactions and bioconjugation and has been studied extensively as a model system.[30–35] Multiple orthogonal reactive sites on the CPMV particles can be selectively functionalized under mild conditions, which is crucial for our self-assembly studies.

Wild-type CPMV (wt-CPMV) was labeled covalently with the fluorescent dye Oregon Green 488 or *N*,*N*,*N*′,*N*′-tetramethylrhodamine (Scheme 1), as described previously.[31] Perfluorodecalin droplets with diameters of 10–100 μm were obtained by dispersing perfluorodecalin in an aqueous buffer solution of fluorescently labeled CPMV particles. The CPMV particles segregated at the perfluorodecalin–water interface, thus stabilizing the dispersion of the oil droplets. Figure 1a shows a fluorescence confocal microscope image of perfluorodecalin droplets in a buffer solution containing 0.25 mg mL^{-1} of wt-CPMV. The particle assemblies of wt-CPMV at the droplet interface are clearly seen by the intense fluorescence at the droplet boundaries. The fluorescent background in the aqueous phase arises from excess virus particles in the buffer. The adsorption kinetics of the assembly process were monitored with a pendant-drop tensiometer. The particles assemble at the oil–water interface, thus leading to a reduction in the interfacial energy between the two phases and stabilization of the oil–water dispersion (Figure 1b). Tensiometric measurements under different bionanoparticle concentrations in the aqueous buffer phase suggest a characteristic timeframe for the assembly to reach monolayer adsorption.

Small-angle neutron scattering (SANS) was carried out using a stock solution of the CPMV (1.80 mg mL^{-1}) in a 100 mM potassium phosphate/D_2O buffer at pH 7.0. The SANS data from the dispersed CPMV bioparticles, the fitting

[*] L. Su, Professor Q. Wang
Department of Chemistry and Biochemistry
University of South Carolina
Columbia, SC 29208 (USA)
Fax: (+1) 803-777-9521
E-mail: wang@mail.chem.sc.edu
Y. Lin,[+] J. He, K. Sill, R. Tangirala, Professor T. Emrick, Professor T. P. Russell
Department of Polymer Science and Engineering
University of Massachusetts
Amherst, MA 01003 (USA)
Fax: (+1) 413-577-1510
E-mail: russell@mail.pse.umass.edu
J. T. Russell
Williston Northampton School
Easthampton, MA 01027 (USA)
Dr. A. Böker,[+] H. Zettl
Lehrstuhl für Physikalische Chemie II
Universität Bayreuth
95440 Bayreuth (Germany)
Dr. P. Carl, Dr. A. Fery
MPI für Kolloid und Grenzflächenforschung
Am Mühlenberg, 14424 Potsdam (Germany)
Dr. K. Littrell, Dr. P. Thiyagarajan
Argonne National Laboratory
IPNS-360, Argonne, IL 60439 (USA)
Dr. D. Cookson
Australian Synchrotron Research Program
Building 434
Argonne, IL 60439 (USA)
[+] equal contribution.

[**] This work was supported by the DOE (DE-FG-02-96ER45 and DE-FG02-04ER46126), the NSF for MRSEC at UMass Amherst (DMR 9400488), the Army Research Laboratory through the MURI program, the Max Planck Society, the DFG within the French–German Network on Complex Fluids, and the MAX KADE Foundation. This work benefited from Argonne's Advanced Photon Source (15-ID) and Intense Pulsed Neutron Source supported by the US Department of Energy, Basic Energy Sciences, Office of Science, under contract no. W-31-109-Eng-38. ChemMatCARS Sector 15 is principally supported by the National Science Foundation/Department of Energy under grant no. CHE0087817 and by the Illinois Board of Higher Education. Q.W. thanks the University of South Carolina and USC Nanocenter for financial support. A.F. and P.C. thank Helmuth Möhwald for stimulating discussions.

 © 2005 Wiley-VCH Verlag GmbH & Co. KGaA, Weinheim DOI: 10.1002/anie.200462653

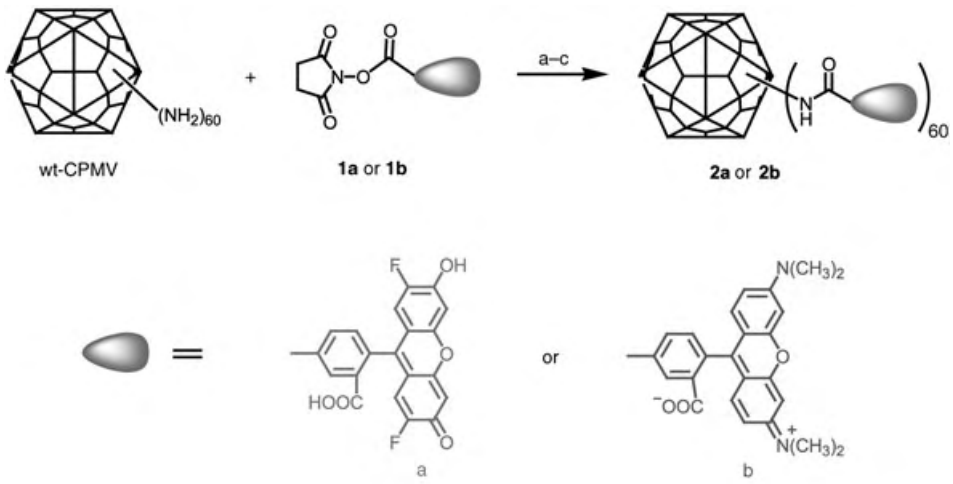

Scheme 1. Covalent labeling of wt-CPMV with fluorescent Oregon Green 488 or *N*,*N*,*N*′,*N*′-tetramethylrhodamine. a) 20% dimethyl sulfoxide (DMSO) in buffer, pH 7.0, 4 °C, 24 h; b) ultracentrifugation; c) dialysis.

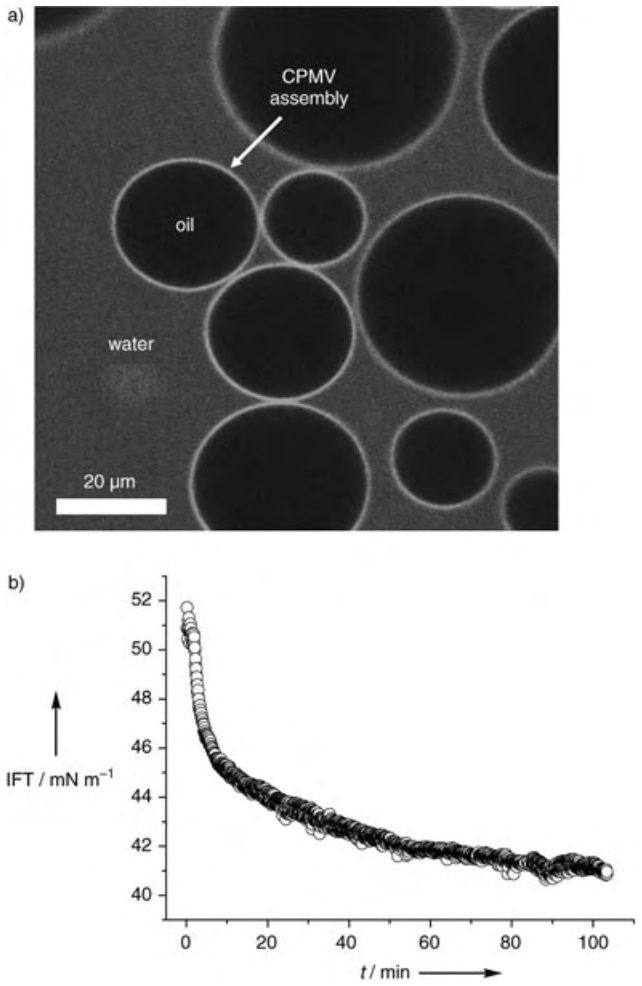

Figure 1. a) Confocal fluorescence microscope image of CPMV–particle assembly at perfluorodecalin droplets in water. b) Pendant-drop tensiometric data (interfacial tension (IFT) versus time) for the adsorption of CPMV particles from a buffered water phase (0.5 mg mL^{-1} CPMV in potassium phosphate buffer) to the perfluordecalin-drop interface.

with the spherical-shell form factor, and the resolution function for the small-angle neutron diffractometer (SAND) instrument are shown in Figure 2a. It is clear that the data are well described by a monodisperse system of spherical shells with an inner radius of 10.7 ± 0.1 nm and a wall thickness of 2.9 ± 0.1 nm; such a system is consistent with the structure of CPMV previously studied by Johnson and co-workers.[29]

The CPMV–particle assemblies were formed at interfaces by addition of perfluorodecalin (10 vol% in water) to the bioparticle in the buffer solutions (prepared by fivefold dilution of the stock solutions with the buffer) in a D_2O/H_2O mixture and shaken vigorously by hand to generate a microemulsion to contrast with the scattering from the perfluorodecalin. The composition of the D_2O/H_2O mixture was 0.313:0.687 (v/v (%)) and was chosen on the basis of the scattering length density of perfluorodecalin (4.18×10^{10} cm^{-2}), which was calculated by using the neutron scattering lengths of its atomic composition and a density of 1.908 g cm^{-3}.

The microemulsion samples were freshly prepared and kept at 6 °C for four hours for the interfacial assembly to attain equilibrium. The bionanoparticle-coated droplets were then accumulated and loaded into 2-mm sample cells. The SANS data were collected at 8 °C over 24 hours. The background-corrected SANS data for the CPMV–particle assemblies exhibit a power-law dependence of the form $I(q) \propto Q^{-2.5(\pm 0.3)}$, as shown by the solid line at low values of Q, where Q is related to the neutron wavelength λ and the scattering angle 2θ by the equation $Q = 4\pi \sin\theta/\lambda$ (Figure 2b). The average thickness t of the bionanoparticle assembly at the interfaces can be measured by using a modified Guinier approximation for sheetlike structures[36,37] [Eq. (1)].

$$I(Q) = Q^{-2} I_T \exp(-Q^2 R_t^2) \quad (1)$$

The thickness factor R_t can be determined from the slope of $\ln(Q^2 I(Q))$ versus Q^2 in an appropriate Q region where $Q_{max} R_t < 0.6$ and the thickness t can be derived from

 © 2005 Wiley-VCH Verlag GmbH & Co. KGaA, Weinheim

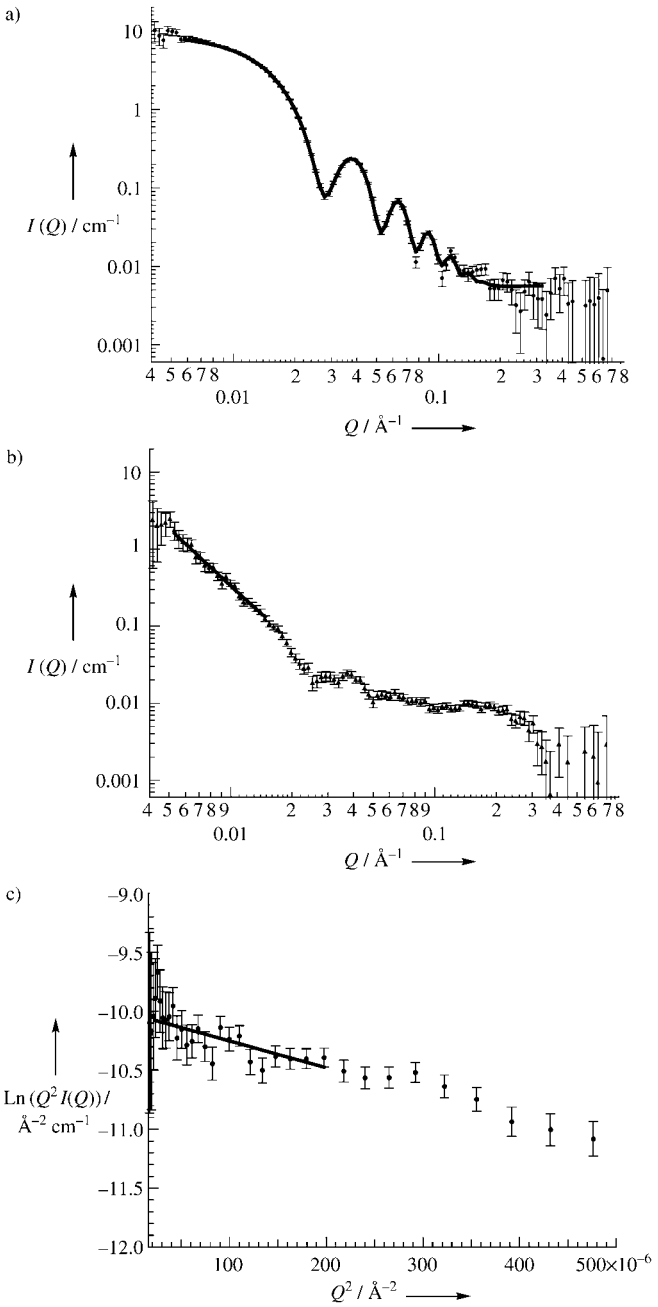

Figure 2. SANS data of a) CPMV particles in D_2O buffer along with a spherical-shell fit and b) CPMV–particle assemblies at the interfaces between the perfluorodecalin and buffer solutions (the H_2O/D_2O ratio is 0.313:0.687 (v/v)) to contrast match the perfluorodecalin. c) Modified Guinier analysis of scattering data from the CPMV–particle assemblies at the interfaces. The linear fit to the slope is shown in the Q region where $Q_{max} R_t < 0.6$ provides the thickness factor R_t from which the thickness t of the shell was derived using $t = \sqrt{12}\, R_t$.

$t = \sqrt{12}\, R_t$. The modified Guinier analysis of the SANS data for the CPMV assemblies demonstrates that the bioparticle assemblies at the interfaces between perfluorodecalin and H_2O/D_2O are sheetlike with $t = 16.5 \pm 1.8$ nm (Figure 2c). This analysis suggests that the CPMV forms a monolayer at the interfaces, thus assuming a uniform scattering length density for the sheets. It should be noted that no pronounced interparticle correlations were seen. At the loading of virus particles used, a low coverage of the CPMV particles at the oil and water interface is indicated by the small average thickness of the monolayer and the absence of a peak.

The wt-CPMV particles were cross-linked at the water–oil interface at 4 °C for 3 hours to lock the assembly into place by adding glutaraldehyde (ca. 2.5 wt %) into the water phase. Figure 3a shows a fluorescence confocal microscope image of a 3D reconstruction of perfluorodecalin droplets coated with wt-CPMV after cross-linking and removal of excess CPMV particles in the buffer phase by washing with water. It can be inferred from the image that the integrity of the assembly is preserved following cross-linking and the resulting capsules are not distorted in shape (see inset). Complete removal of the water and perfluorodecalin disrupts the cross-linked virus shell. Crumpled shells are observed on rehydration with the buffer solution (Figure 3b). It is likely that the perfluorodecalin evaporation and the resulting vapor pressure crushed the capsule; nevertheless, these images show that cross-linking occurred. Figure 3c depicts a spherical cap generated by the assembly and subsequent cross-linking of wt-CPMV particles around a perfluorodecalin droplet sitting on a glass slide. The cap folded backwards after complete evaporation of the solvents and washing with buffer and water, thus revealing distinct wrinkles on the surface. Several scanning force microscopy (SFM) images were taken at the edge of the back-folded cap to determine the thickness of the cross-linked virus–particle assembly. The inset of Figure 3c shows the site where the SFM image in Figure 3d was taken. Cross-sectional analysis, averaged over 256 scan lines, yields a step height of 29 ± 2 nm, which is consistent with a monolayer formed by virus particles 28–32 nm in diameter. The concentration of CPMV particles adsorbed at the interface is much larger than the concentration of residual particles in solution, even though the cross-linking is initiated from the buffer phase, thus leading to preferential cross-linking at the water–oil interface. The low reaction temperature and slow rate of reaction provides further control over the process. The SFM image in Figure 3d shows that closely packed individual CPMV particles can be distinguished, even after cross-linking. Thus, the glutaraldehyde reaction has been shown to induce cross-linking and produce well-defined, robust, and cross-linked virus–particles assemblies.

An even higher level of control over the cross-linking reaction can be achieved with biotin/avidin binding. A CPMV mutant with an inserted cysteine residue was employed to provide orthogonal reactive sites, which were amino groups of the native lysines and thiol groups of the inserted cysteines.[33,34] Doubly labeled virus particles were afforded by attaching biocytin maleimide (**3**) to the surface cysteine units of the virus and then carrying out fluorescent labeling at the lysine moieties (Scheme 2). Avidin has four binding sites for biotin, which allows well-controlled cross-linking of the biotin-modified CPMV particles at interfaces. Figure 4a shows a 3D reconstruction of a series of fluorescence confocal microscope images of the CPMV/biotin assembly around perfluorodecalin droplets cross-linked with avidin for 3 hours at 4 °C. Relative to the glutaraldehyde cross-linking, no desorption of the virus particles is observed after removal of

 © 2005 Wiley-VCH Verlag GmbH & Co. KGaA, Weinheim

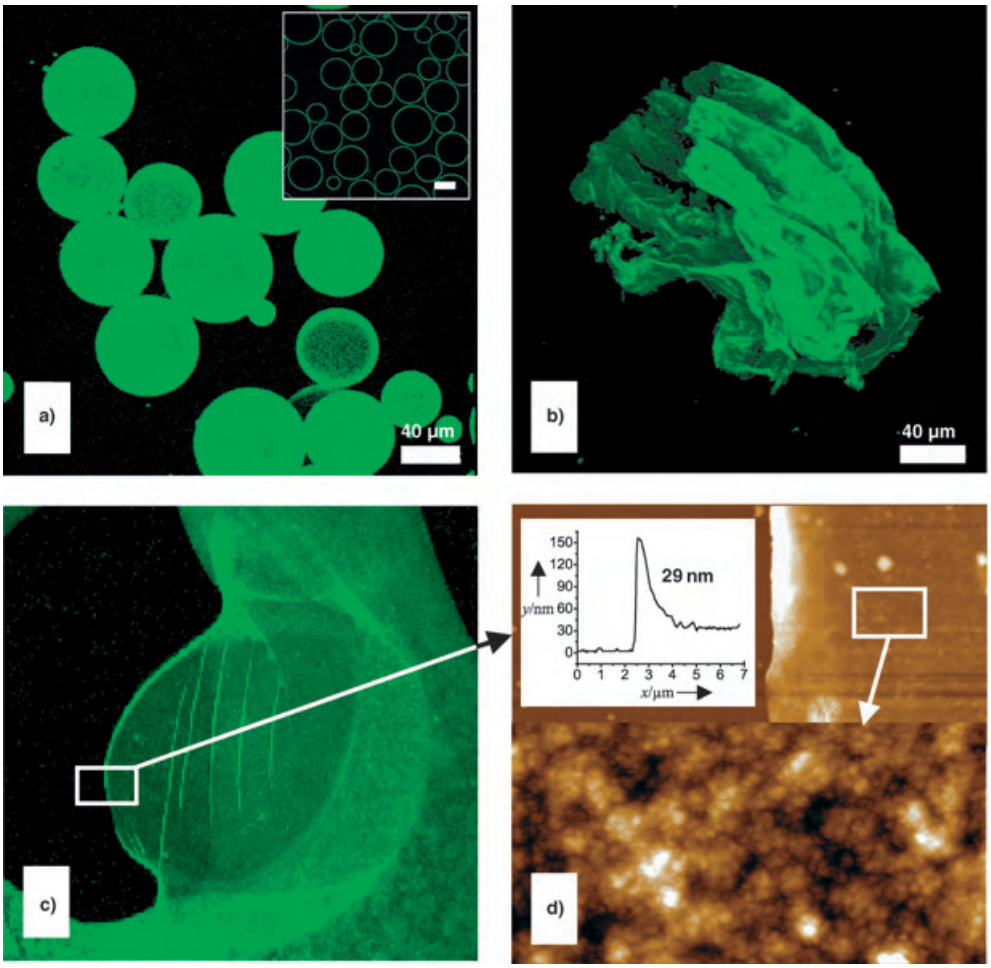

Figure 3. Confocal fluorescence microscope image of CPMV–particle assembly after cross-linking with glutaraldehyde. a) Three-dimensional reconstruction of perfluorodecalin droplets in water that are coated with the virus (inset: cross-sectional view). Excess particles were removed by successive washing with water. b) Crumpled droplet after complete drying and rehydration with water. c) Capsule cap after complete drying. d) The white box shows the area at which the SFM scan was taken, and the lower part shows the height profile on top of the collapsed capsule (image width = 2 µm, *z* range = 30 nm).

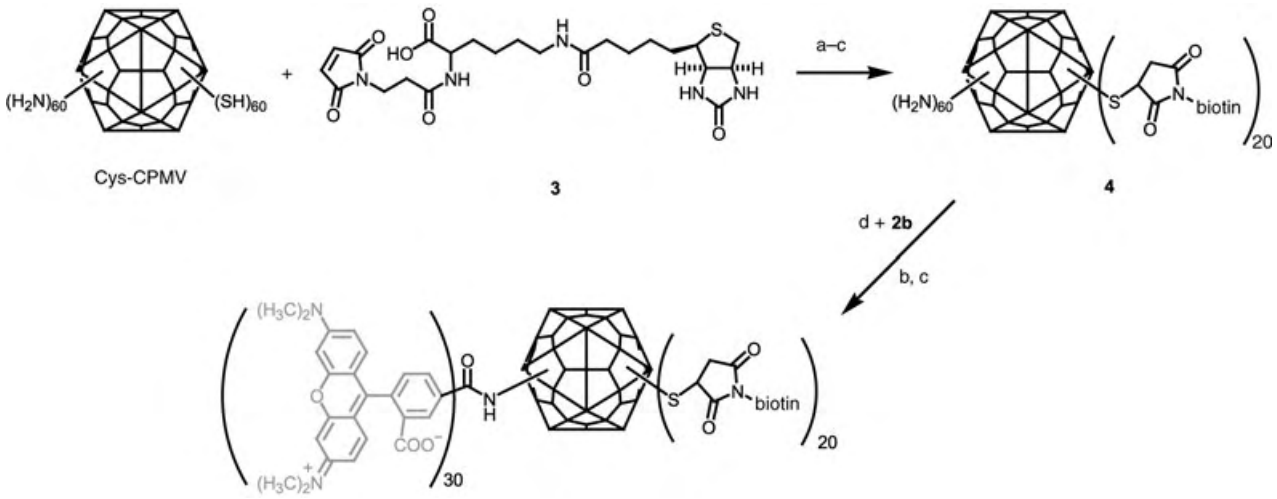

Scheme 2. The formation of doubly labeled Cys-CPMV particles. a) 20% DMSO in buffer, pH 6.0, 4 °C, 24 h; b) ultracentrifugation; c) dialysis; d) 20% DMSO in buffer, pH 7.0, 4 °C, 24 h.

 © 2005 Wiley-VCH Verlag GmbH & Co. KGaA, Weinheim

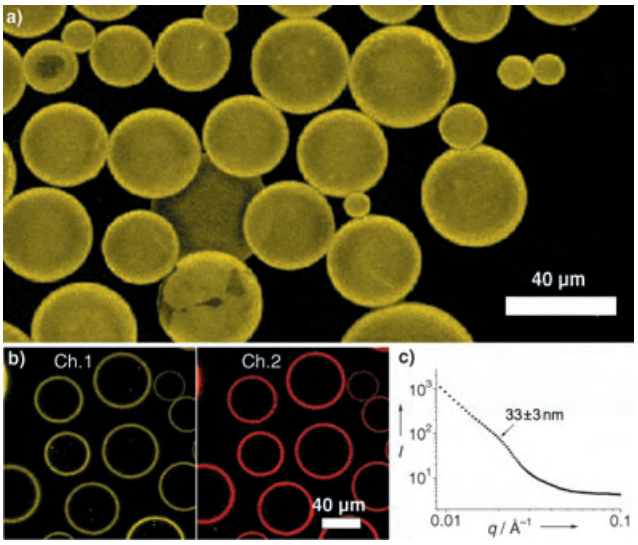

Figure 4. a) A 3D reconstruction of a confocal fluorescence microscope image of perfluorodecalin droplets that are coated with CPMV/biotin after being cross-linked with avidin for 3 h at 4 °C. Excess particles were removed by successive washing with water. b) A two-channel confocal fluorescence microscope image of particle assemblies after cross-linking with fluorescently tagged streptavidin: Channel 1 (yellow, left side) shows the CPMV/biotin fluorescence and channel 2 (red, right side) shows the ATTO-655-streptavidin fluorescence. c) SAXS data of the cross-linked CPMV/biotin shell around the perfluodecalin droplets.

the excess particles by successive washing with water; moreover, the integrity of the capsule shell is retained after the reaction. Nevertheless, evidence for cracks and holes can be found in some of the shells, but the crack characteristics of the capsules in the lower left corner are typical for a solid shell. Figure 4b shows a two-channel confocal fluorescence microscope image of particle assemblies after cross-linking with fluorescently tagged streptavidin. The labeled fluorescence from the particles is seen as yellow and the fluorescence from Atto-655-Streptavidin is seen at the interface as red. Small-angle X-ray scattering (SAXS) data of the cross-linked CPMV/biotin shell around the perfluorodecalin droplets exhibit a weak first order shoulder that corresponds to a *d*-spacing of 33 ± 3 nm (Figure 4c); however, a second order could not be resolved. This interparticle correlation distance is in agreement with the virus–particle diameter of 28–32 nm. We note that the SFM experiments, identical to those performed when the cross-linking was carried out with glutaraldehyde, yielded values for the shell thicknesses that were in agreement with the expected CPMV–monolayer dimension.

The mechanical properties of these cross-linked bionanoparticle assemblies were investigated by atomic force microscopy (AFM). An AFM molecular-force probe mounted on an inverted Olympus IX71 microscope was used, as described in detail previously.[38] For the effective application of AFM force-spectroscopic anaylsis to oil droplets in a water matrix, the droplets were allowed to settle to the bottom of the observation chamber and attach to the polyallylamine-coated glass substrate. The high density of perfluoroctane relative to water promotes rapid sedimentation, and the polyallylamine coating promotes droplet adhesion. Force-deformation measurements were performed on the droplets with particle assemblies that were both non-cross-linked and cross-linked using glutaraldehyde. A typical set of force-deformation data is shown in Figure 5a, along with the statistics of the droplet-

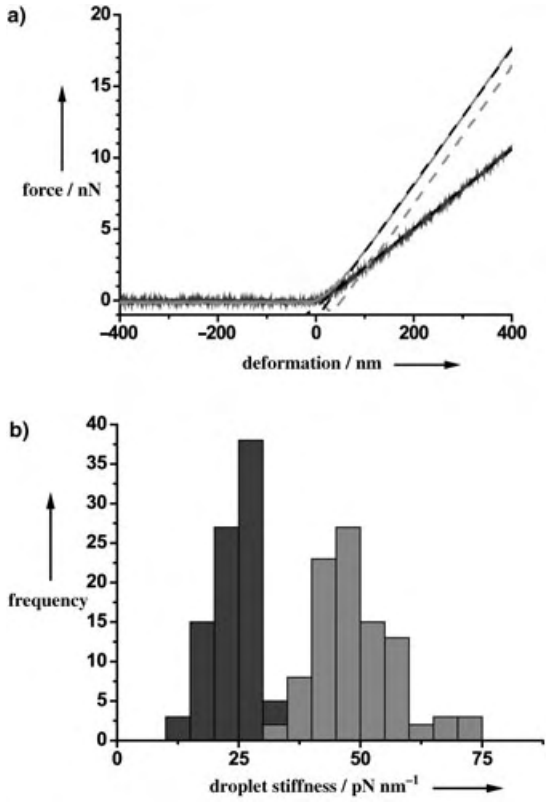

Figure 5. a) A typical force-deformation curve for a droplet of similar size without cross-linking (left) and with cross-linking (right) of virus–particle assemblies. The slope of the linear fit of the force-deformation curves in the linear regime (broken black line) corresponds to the droplet stiffness. b) Statistics of the droplet stiffness for a large number of measurements. Left: non-cross-linked; right: cross-linked.

stiffness measurements for a large number of droplets (Figure 5b). These data clearly indicate that cross-linking of the bionanoparticle assemblies on the surface of the droplets results in an increase in the droplet stiffness. The droplet stiffness is determined by measuring the slope of the force-deformation curves in the linear regime. We note that the deformation behavior of the nanoparticle assemblies is not only determined by membrane bending and stretching, but also by the surface tension of the particle-covered interface. A model that quantifies the force-deformation data in terms of effective surface tension and membrane stiffness will be published separately.

In summary, it has been shown that CPMV nanoparticles self-assemble as a monolayer at perfluorodecalin–water interfaces. These close-packed assemblies were successfully cross-linked by using two different well-defined cross-linking approaches. These reactions did not disrupt the integrity of the virus–particle assemblies, but rather strengthened the

 © 2005 Wiley-VCH Verlag GmbH & Co. KGaA, Weinheim

assembly by formation of a robust membrane with covalent inter-bionanoparticle connectivity. The crumpling of the capsules points to the formation of mechanically robust membranes of CPMV particles that are cross-linked. The assembly of these particles at fluid–fluid interfaces provides opportunities for their use in different applications while further chemical functionalization can be performed.

Experimental Section

Generation of CPMV: wt-CPMV and Cys-CPMV mutants were generated as reported previously.[31–33] Virus concentrations were determined by measuring the absorbance at 260 nm (a concentration of 1.0 mg mL^{-1} gives a standard absorbance of 0.8). The average molecular weight of the wt-CPMV virion is 5.6×10^6 Da.

2a and **2b**: A solution of *N*-hydroxysuccinimide ester (**1a** or **1b**, 5 μmol) in DMSO (2 mL) was introduced into a solution of wt-CPMV (10 mg) in potassium phosphate buffer (8 mL, pH 7.0). The reaction mixture was purified after incubation at 4 °C for 24 h by ultracentrifugation at 42000 rpm over a 1.0-cm-high sucrose cushion, followed by resuspension in potassium phosphate buffer (2 mL, pH 7.0). The recovery of derivatized viruses was typically 60–80 %, and all such samples were composed of > 95 % intact particles. Dialysis over the buffer (4 L) was performed with a 10-kD cut-off membrane (Pierce) to remove any remaining organic reagent. Dye loadings were obtained by measuring the absorbance at λ_{max} and using known molar absorptivities. On average, 60 dye molecules were loaded onto one viral particle.

5: A solution of biocytin maleimide (**3**, 5 μmol) in DMSO (2 mL) was added to a solution of Cys-CPMV mutant[33] (10 mg) in potassium phosphate buffer (8 mL, pH 6.0). The reaction mixture was purified after incubation at 4 °C for 24 h by ultracentrifugation at 42000 rpm over a 1.0-cm-high sucrose cushion. The pellet was dissolved in potassium phosphate buffer (2 mL, pH 7.0) to afford **4**, which was then treated with *N*,*N*,*N*′,*N*′-tetramethylrhodamine (**2b**) in a similar fashion to wt-CPMV. The recovery of derivatized viruses was typically 45–60 %, and all such samples were composed of > 95 % intact particles. Dialysis over the buffer (4 L) was performed with a 10-kD snake-skin dialysis membrane (Pierce) to remove any remaining organic reagent. Dye loading was determined by measurement of the absorbance at λ_{max} and using known molar absorptivities. The loading of biotin was determined by a parallel reaction with 5-maleimidofluorescein. About 20 biotin and 30 dye molecules could be loaded in a typical reaction to one viral particle.

Assembly and cross-linking: The assembly experiments were conducted with fluorescently tagged wt-CPMV particles. The CPMV stock solution (ca. 5 mg mL^{-1}) was diluted 20 times with potassium phosphate buffer (0.1 M, pH 7.0) to give a 0.25 mg mL^{-1} solution. Perfluorodecalin (0.03 mL) was added to the CPMV solution (0.3 mL) and the particles were allowed to assemble for 2–3 h at 4 °C. Glutaraldehyde (15 μL, 50 % in water (v/v)) was then added to cross-link the virus–particle assembly. The addition was carried out at 4 °C and the reaction mixture incubated for 3 h. The CPMV/biotin assemblies were prepared in the same way and cross-linked with avidin (30 μL of a 2 mg mL^{-1} stock solution) with incubation at 4 °C for 3 h. Excess particles in the buffer phase were removed after cross-linking by subsequent washing with water.

Laser scanning confocal microscopy (LSCM) analysis: The LSCM images were taken on a Leica TCS SP2 LSCM with excitation by an Ar laser and HeNe laser. The fluorescence from the virus nanoparticles or the fluorescently tagged streptavidin is shown by a color scale, in which brightness represents intensity.

Tensiometer measurements: The changes in the interfacial tension between the bionanoparticle solution and the oil phase were determined at room temperature with an OCA 20 Dataphysics pendant-drop tensiometer with video camera for drop-image processing, which allows rapid drop-image acquisition, edge detection, and fitting of the Young–Laplace equation.

SFM analysis: SFM images were taken on a Digital Instruments Dimension 3100 microscope operated in the tapping mode (the free amplitude of the cantilever was approximately 20 nm and the amplitude set point was approximately 0.98). The standard silicon nitride probes were driven at 3 % offset below their resonance frequencies in the range of 250–350 kHz. Height and phase images were taken at scanning speeds of around 6 μm s^{-1}.

SANS analysis: SANS experiments were carried out by time-of-flight small-angle neutron diffractometry (SAND)[39,40] at the Intense Pulsed Neutron Source (Argonne National Laboratory, Argonne, IL) using neutrons with wavelengths of 0.9–14 Å at a sample-to-detector distance of 2.0 m. SAND provides data in the Q range of 0.0035–1.0 Å^{-1} in a single measurement, in which the Q value is related to the neutron wavelength λ and the scattering angle 2θ by $Q = 4\pi \sin\theta/\lambda$. The samples were measured in suprasil sample cells with a path length of 2 mm. The data for each sample were corrected for the instrumental background, solvent scattering (for dispersed bioparticles only and not for the bioparticle-coated microemulsions), and detector nonlinearity. The data were then placed on an absolute scale.

Synchrotron SAXS analysis: Synchrotron SAXS measurements were performed with the ID15 beamline equipment at the Advanced Photon Source (Argonne National Laboratory, Argonne, IL). The operating beam energy was 12.5 keV, which corresponds to a peak wavelength of 0.1 nm, and the beam size was 300×300 μm^2. A Bruker CCD detector, housed in a 2-m evacuated flight tube, was used to acquire 1024×1024 pixels images with typical exposure times of around 1 s.

Force spectroscopic analysis: The AFM studies were performed with a Molecular-Force Probe (Asylum Research, Santa Barbara, CA) mounted on an inverted optical microscope (Zeiss Axiomat 200, Zeiss, Oberkochen, Germany). This combination enabled us to position the AFM tip on the area of interest of our sample, which in our case was directly on the top of the emulsion droplets, as well as perform simultaneous quantitative microinterferometry (RICM) experiments.[38] We used the colloidal probe technique[41,42] instead of using a sharp tip for probing the droplets, which has the advantage of providing a defined and reproducible contact geometry and avoids membrane failure because of penetration by a sharp tip. We used some tipless cantilevers (Micromash, Estonia) with a nominal spring constant of 0.08 N m^{-1} on which glass beads of 30–50 μm (Polysciences, Warrington, PA) were fixed using epoxy glue (UHU Plus endfest 300). The cantilevers were plasma-cleaned (PDC-32G, Harrick Scientific Corporation, NY) before mounting on the AFM head for 1 min at a pressure lower than 1 mbar. The force constant for each cantilever was calibrated by using the method of Sader[43,44] and measuring the thermally induced motion of the unloaded cantilever.[45,46] Experiments (at ca. 23 °C) were typically done at imposed displacement rates of 300 nm s^{-1}.

Received: November 17, 2004
Published online: April 1, 2005

Keywords: bionanoparticles · interfaces · membranes · self-assembly · viruses

[1] X. Duan, Y. Huang, Y. Cui, J. Wang, C. M. Lieber, *Nature* **2001**, *409*, 66.
[2] Y. Huang, X. Duan, Q. Wei, C. M. Lieber, *Science* **2001**, *291*, 630.
[3] G. M. Whitesides, B. Grzybowski, *Science* **2002**, *295*, 2418.
[4] S. Paul, C. Pearson, A. Molloy, M. A. Cousins, M. Green, S. Kolliopoulou, P. Dimitrakis, P. Normand, D. Tsoukalas, M. C. Petty, *Nano Lett.* **2003**, *3*, 533.
[5] Y. Lin, H. Skaff, T. Emrick, A. D. Dinsmore, T. P. Russell, *Science* **2003**, *299*, 226.

 © 2005 Wiley-VCH Verlag GmbH & Co. KGaA, Weinheim

[6] Y. Lin, H. Skaff, A. Böker, A. D. Dinsmore, T. Emrick, T. P. Russell, *J. Am. Chem. Soc.* **2003**, *125*, 12690.
[7] S. U. Pickering, *J. Chem. Soc.* **1907**, 2001.
[8] R. Aveyard, B. P. Binks, J. H. Clint, *Adv. Colloid Interface Sci.* **2003**, *100*, 503.
[9] F. H. C. Crick, J. D. Watson, *Nature* **1956**, *177*, 473.
[10] L. Liljas, *Curr. Opin. Struct. Biol.* **1999**, *9*, 129.
[11] J. E. Johnson, V. Chiu, *Curr. Opin. Struct. Biol.* **2000**, *10*, 229.
[12] K. S. Raja, Q. Wang in *Encyclopedia of Nanoscience and Nanotechnology* (Ed.: K. Puryera), Marcel Dekker, New York, **2004**, p. 321.
[13] B. K. Jap, M. Zulauf, T. Scheybani, A. Hefti, W. Baumeister, U. Aebi, A. Engel, *Ultramicroscopy* **1992**, *46*, 45.
[14] P. Fromherz, *Nature* **1971**, *231*, 267.
[15] K. Aoyama, K. Ogawa, Y. Kimura, Y. Fujiyoshi, *Ultramicroscopy* **1995**, *57*, 345.
[16] E. E. Uzgiris, R. D. Kornberg, *Nature* **1983**, *301*, 125.
[17] T. Scheybani, H. Yoshimura, W. Baumeister, K. Nagayama, *Langmuir* **1996**, *12*, 431.
[18] I. Yamashita, *Thin Solid Films* **2001**, *393*, 12.
[19] H. Yoshimura, T. Scheybani, W. Baumeister, K. Nagayama, *Langmuir* **1994**, *10*, 3290.
[20] P. Pieranski, *Phys. Rev. Lett.* **1980**, *45*, 569.
[21] O. D. Velev, K. Furusawa, K. Nagayama, *Langmuir* **1996**, *12*, 2374.
[22] X. Zhai, S. Efrima, *J. Phys. Chem.* **1996**, *100*, 11019.
[23] B. P. Binks, J. H. Clint, *Langmuir* **2002**, *18*, 1270.
[24] A. D. Dinsmore, M. F. Hsu, M. G. Nikolaides, M. Marquez, A. R. Bausch, D. A. Weitz, *Science* **2002**, *298*, 1006.
[25] D. J. Siler, J. Babcock, G. Bruening, *Virology* **1976**, *71*, 560.
[26] G. P. Lomonossoff, J. E. Johnson, *Prog. Biophys. Mol. Biol.* **1991**, *55*, 107.
[27] G. P. Lomonossoff, J. E. Johnson, *Curr. Opin. Struct. Biol.* **1996**, *6*, 176.
[28] G. P. Lomonossoff, M. Shanks, C. L. Holness, A. J. Maule, D. Evans, Z. Chen, C. Stauffacher, J. Johnson in "Comovirus Capsid Proteins: Synthesis, Structure, and Evolutionary Implications" in *Biochem. Mol. Biol. Plant-Pathog. Interact.*, *Vol. 32* (Ed.: C. J. Smith), Clarendon, Oxford, **1991**, pp. 76.
[29] T. W. Lin, Z. G. Chen, R. Usha, C. V. Stauffacher, J. B. Dai, T. Schmidt, J. E. Johnson, *Virology* **1999**, *265*, 20.
[30] Q. Wang, T. R. Chan, R. Hilgraf, V. V. Fokin, K. B. Sharpless, M. G. Finn, *J. Am. Chem. Soc.* **2003**, *125*, 3192.
[31] Q. Wang, E. Kaltgrad, T. W. Lin, J. E. Johnson, M. G. Finn, *Chem. Biol.* **2002**, *9*, 805.
[32] Q. Wang, T. Lin, L. Tang, J. E. Johnson, M. G. Finn, *Angew. Chem.* **2002**, *114*, 477; *Angew. Chem. Int. Ed.* **2002**, *41*, 459.
[33] Q. Wang, T. W. Lin, J. E. Johnson, M. G. Finn, *Chem. Biol.* **2002**, *9*, 813.
[34] Q. Wang, K. S. Raja, K. D. Janda, T. Lin, M. G. Finn, *Bioconjugate Chem.* **2003**, *14*, 38.
[35] S. Meunier, E. Strable, M. G. Finn, *Chem. Biol.* **2004**, *11*, 319.
[36] G. Porod, *Small Angle X-Ray Scattering*, Academic Press, London, **1982**, pp. 17.
[37] J. M. Gallas, K. C. Littrell, S. Seifert, G. W. Zajac, P. Thiyagarajan, *Biophys. J.* **1999**, *77*, 1135.
[38] F. Dubreuil, N. Elsner, A. Fery, *Europhys. J. E* **2003**, *12*, 215.
[39] P. Thiyagarajan, V. Urban, K. Littrell, C. Ku, D. G. Wozniak, H. Belch, R. Vitt, J. Toeller, D. Leach, J. R. Haumann, G. E. Ostrowski, L. I. Donley J. Hammonds, J. M. Carpenter, R. K. Crawford, in *ICANS-XIV, 14th Meeting of the International Collaboration on Advanced Neutron Sources*, *Vol. XIV*, Starved Rock Lodge, Utica, IL, **1998**, Vol. 2, p. 864.
[40] P. Thiyagarajan, J. E. Epperson, R. K. Crawford, J. M. Carpenter, T. E. Klippert, D. G. Wozniak, *J. Appl. Crystallogr.* **1997**, *30*, 280.
[41] W. A. Ducker, T. J. Senden, R. M. Pashley, *Nature* **1991**, *353*, 239.
[42] H. J. Butt, *Biophys. J.* **1991**, *60*, 1438.
[43] J. E. Sader, *J. Appl. Phys.* **1998**, *84*, 64.
[44] J. E. Sader, J. W. M. Chon, P. Mulvaney, *Rev. Sci. Instrum.* **1999**, *70*, 3967.
[45] H. J. Butt, M. Jaschke, *Nanotechnology* **1995**, *6*, 1.
[46] J. L. Hutter, J. Bechhoefer, *Rev. Sci. Instrum.* **1993**, *64*, 1868.

 © 2005 Wiley-VCH Verlag GmbH & Co. KGaA, Weinheim

Solid-State Fluorescence

A Novel Fluorescent Dye with Strong, Anisotropic Solid-State Fluorescence, Small Stokes Shift, and High Photostability**

Heinz Langhals, Oswald Krotz, Kurt Polborn, and Peter Mayer*

There is continuing interest in the technical applications of fluorescent dyes.[1] Whereas many dyes are strongly fluorescent in solution, there are only a few dyes with a strong solid-state fluorescence. We have shown that aggregation, the most important process for fluorescence quenching, can be prevented by steric inhibition.[2] To further test this concept, the novel dye **1** with bulky terminal groups was synthesized in one step from the technical bisanhydride **2** [Eq. (1)]. Compound **2**

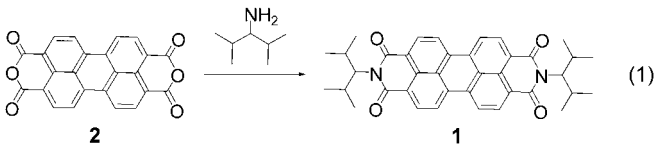

2 **1** (1)

exhibits strong fluorescence not only in concentrated solution but also in the solid state. The dye was obtained as very thin leaflets (typically $0.1 \times 50 \times 50\ \mu m^3$) under typical crystallization conditions. These planes of the leaflets exhibit a remarkably strong fluorescence, whereas that of the edges is much weaker (Figure 1). An X-ray crystal structure analysis

Figure 1. Fluorescence of the crystalline dye **1**.

of **1** resulted in uncertainties in the location of the mobile terminal groups like that observed for other perylene dyes because of disorder; however, the arene atoms and therefore the chromophore could be located with precision (Figure 2).

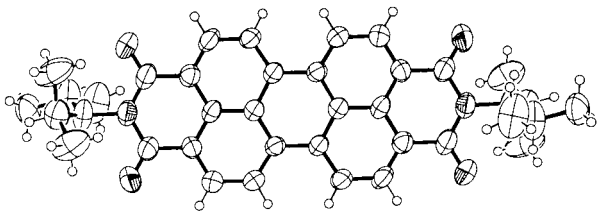

Figure 2. X-ray crystal structure of **1**.

Moreover, the fluorescent plane of the leaflets could be assigned crystallographically[3] to the indices $h,k,l = 100$ or $\bar{1}00$. The stereoview in Figure 3 gives a direct look at the

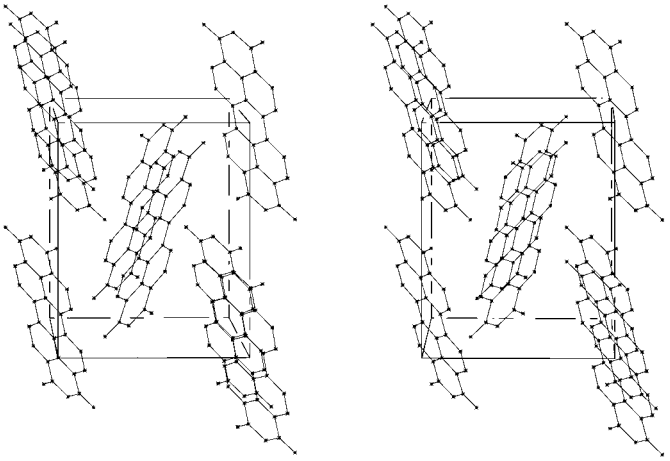

Figure 3. Stereoplot of the unit cell of **1** with the view on the plane with $hkl = 100$; the substituents at the nitrogen atoms are omitted for clarity.

fluorescent arrangement of the chromophores. The long axes of the molecules along the line of connection between the nitrogen atoms are nearly parallel; this arrangement is especially suitable for the emission of fluorescent light. This forms a further experimental basis for the theory of propagation and emission of excitons in crystalline solids.

The UV/Vis absorption and fluorescence spectra of **1** in solution correspond to the spectra of other known perylene dyes.[4] The fluorescence quantum yield reaches nearly 100%; however, the Stokes shift of the solid is unusually small (Figure 4). In principle this implies the possibility of cooling with light,[5–10] and the spectra were therefore examined. The corrected fluorescence spectrum was recorded linearly in wavenumber (linear in energy) and the point of gravity calculated (Figure 4). This spectrum and the point of gravity were transposed to wavelengths for convenience. As the exact recording of the fluorescence excitation spectrum at low intensities is difficult, the excitation spectrum (linear in energy) was split into Gaussian functions[11,12] (R value 0.029, see Table 1). The fluorescence excitation spectrum was simulated on this basis and extrapolated beyond the point of gravity (thin line in the spectrum in Figure 4). An intensity of the fluorescence excitation spectrum of more than 3% with respect to the maximum was found at the point of gravity. Even 5 nm more bathochromic, appreciably beyond the point

[*] Prof. Dr. H. Langhals, Dipl.-Chem. O. Krotz, Dr. K. Polborn,[+] Dr. P. Mayer[+]
Department Chemie, Universität München
Butenandtstrasse 13, 81377 Munich (Germany)
Fax: (+49) 89-2180-77640
E-mail: langhals@lrz.uni-muenchen.de

[+] X-ray crystal structure analysis

[**] This work was supported by the Deutsche Forschungsgemeinschaft and the Fonds der Chemischen Industrie.

 DOI: 10.1002/anie.200461610 © 2005 Wiley-VCH Verlag GmbH & Co. KGaA, Weinheim

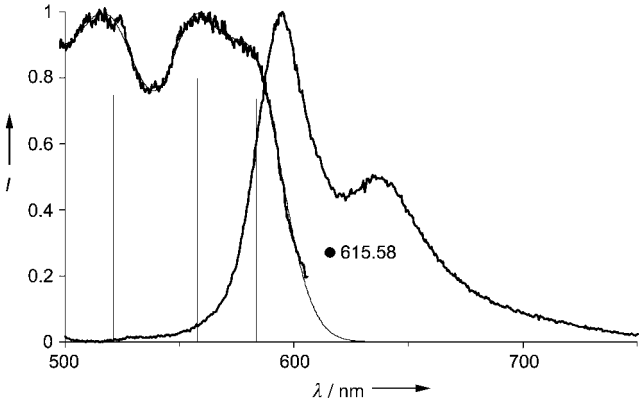

Figure 4. Solid-state fluorescence spectrum (right line) and fluorescence exciton spectrum (left line) of **1**. The point of gravity of the fluorescence spectrum is at 615.6 nm (calculated from the spectrum recorded linearly in energy). The simulated fluorescence excitation spectrum (thin line) based on a Gaussian analysis is superimposed on the experimental spectrum. Bars: positions and intensities of the single Gaussian functions.

Table 1: Gaussian bands[11] of the fluorescence excitation spectrum of **1** with $\lambda > 400$ nm. ε is relative to the maximum in the visible with $\varepsilon = 1$.

No.	λ_{max} [nm]	$2\sigma^2$ [10000 cm^{-2}]	ε_{max}
1	583.4	0.255	0.736
2	557.8	0.310	0.799
3	521.0	0.768	0.747
4	482.3	0.582	0.287
5	461.9	4.421	0.851
6	400.3	3.877	0.950

of gravity, the intensity of the fluorescence excitation spectrum remains more than 1%. Additionally, it was proven experimentally that the fluorescence spectrum exists in the region of short wavelengths even for such a bathochromic excitation.

The values found for intensity can be taken as a lower limit for the anti-Stokes fluorescence. Thus, a bathochromic excitation can result in more hypsochromic fluorescence as an average; losses should be low because of the strong solid-state fluorescence. Since the additional energy for such a process must be taken from the surroundings, the dye can be used, in principle, for cooling with light; for a review concerning the process of cooling with the use of anti-Stokes emission see ref. [13]. The entropy thus required is taken from the spread of the oriented radiation into diffuse radiation of the fluorescence light. Passively working solar cooling systems without any movable parts can be developed by the use of light radiation. The broad fluorescence excitation spectrum extends far into the fluorescence spectrum. This is of special interest because no monochromatic radiation is required for excitation, and a simple edge filter for radiation with short wavelengths is sufficient.

Experimental Section

N,N′-Bis(2,4-dimethylpent-3-yl)perylene-3,4:9,10-tetracarboxylic bisimide (**1**): A solution of 2,4-dimethylpent-3-ylamine (100 mg, 868 μmol) and **2** (145 mg, 369 μmol) in imidazole (2 g) was heated at 140 °C for 4 h and diluted with ethanol before complete cooling in order to dissolve the crystallizing imidazole. The reaction mixture was treated with added 2 M hydrochloric acid and allowed to sit for 1 h. The precipitate that formed was collected by vacuum filtration, washed with distilled water, dried at 120 °C, and purified by column chromatography (chloroform, silica gel). Yield 170 mg (79%) of orange fluorescent crystals. R_f (silica gel, chloroform) = 0.74. IR (KBr): $\tilde{\nu} = 3436.1$ (m), 2963.0 (m), 2924.3 (w), 2867.4 (w), 1697.4 (s), 1656.4 (s), 1593.0 (s), 1577.8 (m), 1507.1 (w), 1462.1 (w), 1435.3 (w), 1405.7 (m), 1382.5 (w), 1336.9 (s), 1261.1 (s), 1200.0 (w), 1167.9 (w), 1100.3 (s), 1022.0 (m), 963.2 (w), 934.1 (w), 853.9 (w), 810.8 (s), 799.9 (sh), 749.9 (m), 714.2 (w), 660.2 (w), 593.8 (w), 476.9 (w), 431.7 cm^{-1} (w); ^{1}H NMR (400 MHz, $CDCl_3$, 25 °C): $\delta = 0.95$ (d, $^3J = 6.8$ Hz, 12H, $4CH_3$), 1.12 (d, $^3J = 6.7$ Hz, 12H, $4CH_3$), 2.66–2.78 (m, 4H, 4CH), 4.76 (t, $^3J = 8.1$ Hz, 2H, 2CH), 8.61–8.71 ppm (m, 8H, arom. CH); ^{13}C NMR (101 MHz, $CDCl_3$, 25 °C): $\delta = 19.6$, 20.8, 28.2, 64.2, 122.1, 125.5, 130.3, 131.0, 133.6, 163.0, 164.2; UV/Vis ($CHCl_3$): λ_{max} (ε) = 458 (18300), 489 (50400), 525 (83900). Fluorescence ($CHCl_3$): $\lambda_{max} = 533$, 575. Fluorescence quantum yield ($CHCl_3$, $\lambda_{ex} = 488$ nm, $E_{488\,nm} = 0.306$ cm^{-1}, reference: *N,N′*-bis(1-tridec-7-yl)perylene-3,4:9,10-tetracarboxylic bisimide with $\Phi = 1.00$.): 1.00. MS (DEI$^+$/70 eV): *m/z* (%): 586 (4) [M^+], 543 (16) [$M^+ - C_3H_7$], 489 (26) [$M^+ - C_7H_{13}$], 390 (135) [$M^+ - 2C_7H_{14}$]. Elemental analysis for $C_{38}H_{38}N_2O_4$ (586.7): calcd. C 77.79, H 6.53, N 4.77; found C 77.67, H 6.56, N 4.72.

Received: August 11, 2004
Published online: March 16, 2005

Keywords: cooling by light · dyes/pigments · perylenes · solid-state fluorescence

[1] H. Zollinger, *Color Chemistry, Synthesis, Properties, and Applications of Organic Dyes and Pigments*, 3rd ed., Wiley-VCH, Zürich, **2003**.
[2] H. Langhals, R. Ismael, O. Yürük, *Tetrahedron* **2000**, *56*, 5435–5441.
[3] Formed crystal plates from toluene/methanol (monoclinic $a = 11.0$ Å, $b = 10.6756$ Å, $c = 13.0427$ Å, $\alpha = 90.0°$, $\beta = 98.650°$, $\gamma = 90.0°$) *h,k,l*: 1,0,0; −1,0,0; −1,−1,1; 1,1,−1; 0,−1,1; 0,1,−1; 0,1,1; 0,−1,−1; 0,4,−9; 0,1,0.
[4] H. Langhals, *Heterocycles* **1995**, *40*, 477–500.
[5] P. Pringsheim, *Z. Phys.* **1929**, *57*, 739–746.
[6] C. Zander, K. H. Drexhage, *Adv. Photochem.* **1995**, *20*, 59–78.
[7] J. L. Bartholomew, P. A. DeBarber, B. Heeg, G. Rumbles, *Mater. Res. Soc. Symp. Proc.* **2001**, 667 [*Chem. Abstr.* **2002**, *136*, 361218].
[8] J. L. Clark, P. F. Miller, G. Rumbles, *J. Phys. Chem. A* **1998**, *102*, 4428–4437.
[9] J. L. Clark, G. Rumbles, *Phys. Rev. Lett.* **1996**, *76*, 2037–2040.
[10] W. Qin, S. Wang, E. Shulin, S. Lu, B. Chen, W. Xu, J. Zhang, S. Huang, *Faguang Xuebao* **1999**, *20*, 123–125 [*Chem. Abstr.* **2000**, *133*, 111763].
[11] H. Langhals, *Spectrochim. Acta Part A* **2000**, *56*, 2207–2210.
[12] H. Langhals, *Anal. Bioanal. Chem.* **2002**, *374*, 573–578.
[13] A. Rayner, N. R. Heckenberg, H. Rubinsztein-Dunlop, *J. Opt. Soc. Am. B* **2003**, *20*, 1037–1053.

 © 2005 Wiley-VCH Verlag GmbH & Co. KGaA, Weinheim

Bioorganometallic Chemistry

A Cobaltocenium–Peptide Bioconjugate Shows Enhanced Cellular Uptake and Directed Nuclear Delivery

*Fozia Noor, Annette Wüstholz, Ralf Kinscherf, and Nils Metzler-Nolte**

Targeted delivery of diagnostic probes and therapeutics into specific compartments inside a cell is of utmost importance in the improvement of disease detection and treatment, especially as the biological target of such compounds is generally strictly localized (for instance DNA in the cell nucleus).

Lately, the field of bioorganometallic chemistry[1–3] has received considerable attention because a number of novel organometallic compounds have been reported as very promising antitumor agents. Schmalz and co-workers reported that nucleoside analogues with a {$Fe(CO)_3$(butadiene)} substructure are cytotoxic by induction of apoptosis.[4] Ferrocifen, a ferrocene derivative of the drug tamoxifen shows activity even on hormone-independent cell lines for which tamoxifen is inactive.[5,6] Further examples include {Ru(arene)} complexes,[7] several {$Co(CO)_2$(alkyne)} derivatives[8–11] in addition to the well-studied titanocene dichloride which has been in clinical trials.[12–15]

DNA interaction has been suggested as the mode of action, at least for some of the organometallic antitumor agents. However, the question of nuclear localization, although a prerequisite for this mode of action, has usually been taken for granted without ever being investigated in detail. This assumption is indeed rather questionable because transport of any compound into the nucleus of an intact cell is limited by at least three major membrane barriers, namely the cell membrane, the endosomal membrane (in the case of active uptake), and the nuclear membrane. Transport across the nuclear membrane has been studied intensely in recent years,[16–19] with a focus on mechanistic details as well as for medicinal applications.[20,21] In general, the delivery of any compound across a given membrane is a challenge. Low-molecular-weight compounds, including many drugs, may enter cells by passive diffusion. However, P-glycoproteins usually pump them out of the cells before they gain access to the nucleus. Enhanced cellular, but not nuclear, uptake of radioactive metals has been achieved by their conjugation to peptides for receptor-mediated uptake.[22–25] Almost nothing is known about the subcellular localization of nonradioactive organometallic compounds.

We report herein the design of a nonradioactive organometallic–peptide conjugate that will specifically deliver the organometallic species into the nucleus of a cell. For this work we have chosen the SV-40 T antigen nuclear localization signal (NLS; primary sequence H-Pro-Lys-Lys-Lys-Arg-Lys-Val-OH).[26,27] This heptapeptide serves as an "address label" for proteins, and indicates their destination as being the cell nucleus. In addition, this heptapeptide enables the active transport of a variety of substrates through the nuclear pore complex.[18] To function properly, the NLS conjugate has to be located in the cytoplasm.[28,17] NLS conjugates, however, are not readily incorporated into cells. Following endosomal uptake, the conjugates are not normally released into the cytoplasm[29] and eventually the endosomes are excluded from the cells again. More complicated conjugates have been devised to circumvent the problem of cellular uptake, for example NLS conjugates with lipophilic membrane-anchoring peptide domains or gold clusters.[29,30]

Herein, we present the first example of the directed nuclear delivery of an organometallic compound, namely the cobaltocenium cation, by conjugation to the NLS peptide. Most of the metallocene bioconjugates prepared to date contain ferrocene (Fc) as the organometallic moiety.[31] In comparison, the isostructural cobaltocenium cation has a much higher redox potential and chemical stability. Therefore, we reasoned that it would be at least equally well suited for physiological studies, which is indeed the case. Live-cell fluorescence microscopy shows that the conjugate is incorporated by endosomes into the cells and rapidly released into the cytoplasm. Control experiments show that the ease of cellular uptake is a property that is particular to the presence of the cobaltocenium moiety in the conjugate.

The cobaltocenium–NLS conjugate **1** (Cc-Lys-NLS, Scheme 1) was prepared by solid-phase peptide synthesis (SPPS) on Wang resin. An additional lysine residue was introduced at the N-terminus. After peptide assembly, the N-terminal Fmoc (Fmoc = 9-fluorenylmethyloxycarbonyl) protecting group was cleaved and cobaltocenium carboxylic acid was coupled by use of 2-(1*H*-benzotriazole-1-yl)-1,3,3-tetramethyluronium tetrafluoroborate (TBTU). Cleavage from the resin was accomplished by concentrated trifluoroacetic acid (TFA) with concurrent deprotection of all amino acid side chains. HPLC analysis showed one major product which could be purified and was fully characterized (see Supporting Information). Compound **1** is completely stable in air and water and was stored for days at room temperature without decomposition (monitored by HPLC).

The MALDI-TOF mass spectrum of **1** shows a peak at m/z 1225.5 for the $[M^+]$ ion as the most intense signal, along with signals for the $[M+K]^+$ and $[M+K+Na-H]^+$ ions. Characteristic signals are also seen in the ^1H NMR spectrum of **1** (Figure 1). In particular, a typical pattern for the monosubstituted cobaltocenium group is observed around $\delta = 6$ ppm (intensity ratio 5:2:1:1). The cyclic voltammogram of **1** shows a reversible wave at -1.38 V versus Fc/Fc^+ in acetonitrile, which can be attributed to reduction of the cobaltocenium moiety. The NLS peptide alone is electrochemically inactive.

[*] F. Noor, A. Wüstholz, Prof. Dr. N. Metzler-Nolte
Institut für Pharmazie und Molekulare Biotechnologie
Universität Heidelberg
Im Neuenheimer Feld 364, 69120 Heidelberg (Germany)
Fax: (+49) 6221-54-64-41
E-mail: Nils.Metzler-Nolte@urz.uni-heidelberg.de
Priv.-Doz. Dr. R. Kinscherf
Institut für Anatomie und Zellbiologie
Universität Heidelberg
Im Neuenheimer Feld 307, 69120 Heidelberg (Germany)

Supporting information for this article is available on the WWW under http://www.angewandte.org or from the author.

 DOI: 10.1002/anie.200462519 © 2005 Wiley-VCH Verlag GmbH & Co. KGaA, Weinheim

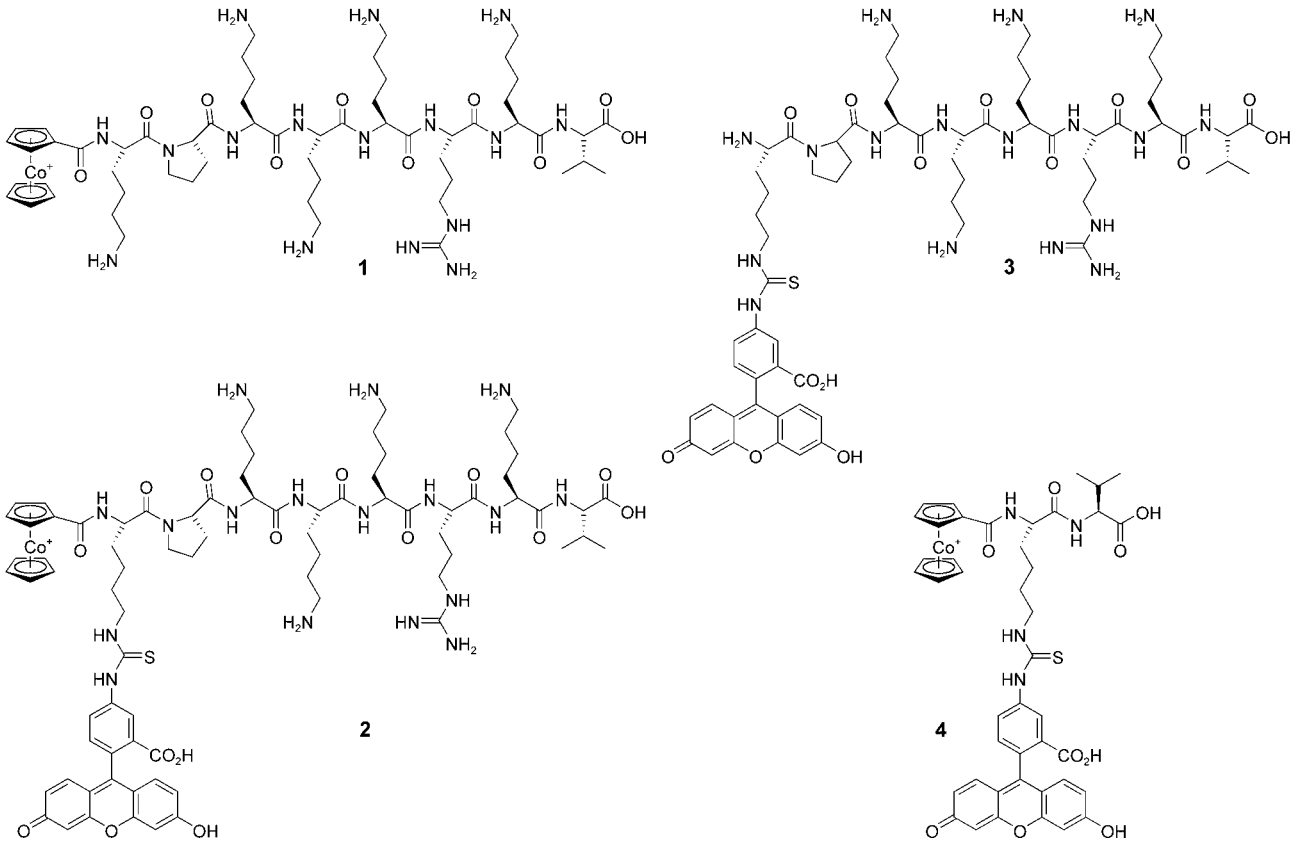

Scheme 1. Compounds prepared and used in this study (see Experimental Section and Supporting Information for synthetic details and analytical data).

To visualize the metal conjugate inside the cells, fluorescein isothiocyanate (FITC) was introduced as a label. For this purpose, the N-terminal lysine residue was introduced with a 4-methyl trityl (Mtt) protecting group. After coupling of the cobaltocenium moiety to the peptide as for **1**, the lysine side chain was deprotected by removal of its Mtt group using dilute TFA. Reaction with FITC yielded the bright orange-red Cc-Lys(FITC)-NLS conjugate **2** on the solid support. After cleavage and HPLC purification, the ^{1}H NMR spectra clearly confirm the expected composition of the conjugates (Figure 1). In addition to the signals from the NLS peptide, the spectra of **1** and **2** show the metallocene cyclopentadiene (Cp) signals around $\delta = 6$ ppm (Figure 1). Only the FITC conjugate **2** exhibits signals in the arene region corresponding to the fluorescein dye. It can be argued that the fluorescein tag will influence the biological properties of the conjugates, thus overriding the influence of the metallocene tag. Therefore, a fluorescent NLS conjugate without the organometallic group (H-Lys(FITC)-NLS) **3** as well as the truncated peptide, Cc-Lys(FITC)-Val-OH (**4**), were also prepared by solid-phase synthesis as controls for the biological experiments. All compounds were synthesized in amounts sufficient for cell-uptake experiments. They were characterized by HPLC, MALDI-TOF mass spectrometry, and ^{1}H NMR spectroscopy (see Supporting Information). Owing to the light sensitivity of the fluorescein tag they were stored in the dark and used shortly after their preparation.

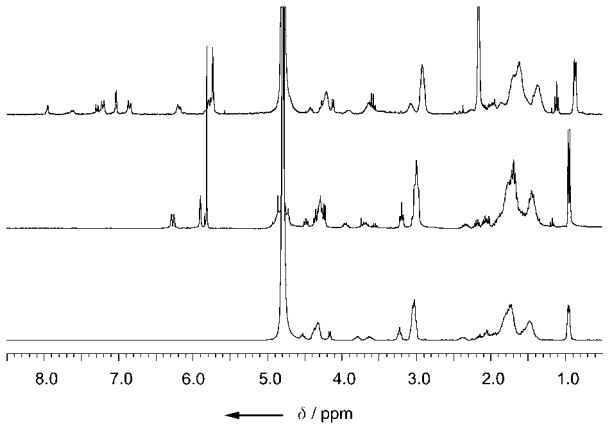

Figure 1. ^{1}H NMR spectra of Cc-Lys(FITC)-NLS (**2**; top), Cc-Lys-NLS (**1**; middle), and H-Lys-NLS (bottom) in D_2O.

An immortalized human liver cancer cell line (HepG2) was used for cellular uptake studies. HepG2 cells were chosen, because they have relatively large nuclei. In addition, membrane translocation in this cell line is known to be rather difficult.[29] HepG2 cells were incubated with compounds **2**–**4** (1 mM) for 24 h at 37 °C. The cells were washed once with RPMI (Roswell Park Memorial Institute) medium containing 10% FBS (fetal bovine serum) to remove any adhering metal–peptide bioconjugate. The cells were then washed twice with PBS (phosphate buffered saline) treated with Hoechst 33342 dye for nuclear staining, and subsequently washed three times with PBS. Finally, the cells were incubated

 © 2005 Wiley-VCH Verlag GmbH & Co. KGaA, Weinheim

with the endosome marker, FM 4–64, and washed again three times prior to their observation under a fluorescence and light microscope. Recent investigations on other cationic peptides, such as Arg-rich or Tat sequences, demonstrate that fixation of the cells may cause artificial redistribution of those peptides into the nucleus, leading to false-positive nuclear localization results.[32,33] Therefore, live-cell microscopic imaging was used to follow the cellular uptake and nuclear localization of the cobaltocenium–NLS conjugate (Figure 2). The integrity of the cell membrane was confirmed throughout our experimental procedure by verifying that the cells excluded propidium iodide (data not shown).

Cells incubated with **2** showed three kinds of fluorescence; weak homogenous green fluorescence in the cytoplasm, intense pointlike fluorescence in the cytoplasm, and homogenous intense green fluorescence in the nuclei (Figure 2 A). Figure 2 B depicts the localization of the endosomes and C the nucleus in the same cells, while Figure 2 D and E are merged images to indicate the intracellular localization of the compound in different compartments of the cells. Our data show that the compound **2** is readily taken up by the cells. Compound **2** is co-localized with the marker FM 4–64 in the endosomes, suggesting an active uptake mechanism by endocytosis. After release into the cytoplasm, **2** then accumulates in the nucleus owing to the presence of the NLS peptide.

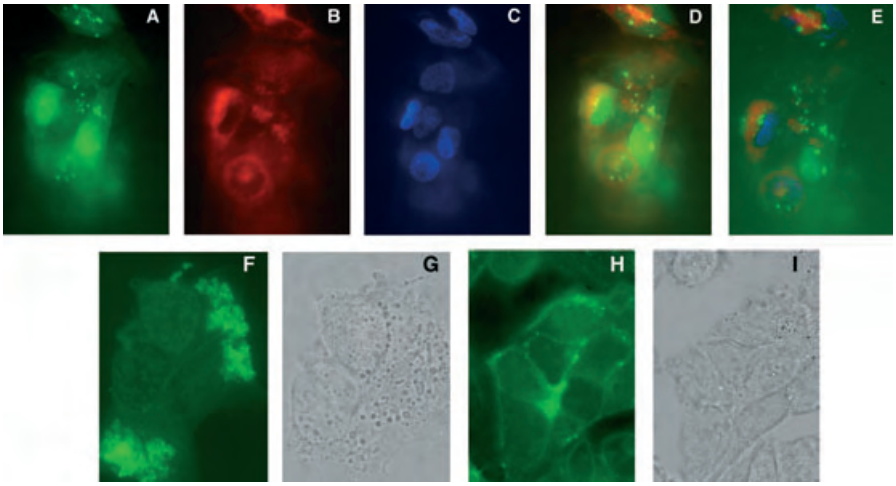

Figure 2. Localization of fluorescent-labeled cobaltocenium–NLS **2** in living HepG2 cells (A–E), and distribution of conjugates **3** and **4** in living HepG2 cells (F–I). HepG2 cells were incubated with bioconjugates **2**–**4** (all 1 mM), with Hoechst 3342 dye (25 $\mu g\,ml^{-1}$) for 5 min for nuclear staining, and with the endosomal marker FM 4–64 (10 μM) for 15 min. A) Bioconjugate **2** in unfixed cells (green fluorescence). B) FM 4–64 in unfixed cells (red flourescence). C) Nuclear staining by Hoechst 3342 dye (blue fluorescence). D) Co-localization of bioconjugate **2** and FM 4–64 (merged images (A) and (B)). Yellow spots indicate localization of **2** in endosomes. E) Co-localization of bioconjugate **2**, FM 4–64, and Hoechst 33342 dye (merged images (A), (B), and (C)). F) Conjugate **3** in unfixed HepG2 cells. G) Light microscopy image of cells in (F). H) Conjugate **4** in unfixed HepG2 cells. I) Light microscopy image of cells in (H). (Magnification: 630×, see text and Supporting Information for discussion and details).

In contrast to **2**, for both compounds **3** and **4**, an overall low and scattered fluorescence in the cytoplasm is observed with no fluorescence in the nucleus. For cells incubated with the metal-free conjugate **3** (Figure 2 F and G), we found that the peptide is mostly trapped in endosomes and, thus, very low fluorescence is seen in the cytoplasm and more in the nucleus. On the other hand, the truncated peptide **4** seems to enter the cells in low concentrations probably by passive diffusion but it is not able to enter the nuclei of cells (Figure 2 H and I).

For all three compounds, some spot-like fluorescence is observed extracellularly and on the outer membrane, although to a varying degree (most for **3** and **4**, much less for **2**). It seems that the compounds attach to the cell surface, a characteristic of cationic cell-penetrating peptides and the first step in cell uptake. However, only the metal conjugate **2** is internalized, whereas the cell membrane indeed presents a strong barrier to compound **4** and to some extent compound **3**. In addition, compound **3** seems not to be able to escape the endosomes. This result is consistent with earlier reports that the cell-penetrating peptides, although taken up into cells by endocytosis, are trapped in the endosomes,[29,33–37] limiting their transport into the nucleus. According to the known mode of action of NLS conjugates, NLS-assisted nuclear delivery is only possible from the cytoplasm. Therefore, the escape of the compound from the endosomes, possibly by late endosomes and lysosomes,[38,39] is essential for subsequent translocation of any NLS bioconjugate into the nucleus.

In conclusion, we report the successful synthesis of the first cobaltocenium conjugate of a nuclear localization signal peptide by SPPS. The cobaltocenium group is exceedingly stable under physiological conditions making it ideally suitable for the study of bioconjugates. The cobaltocenium–NLS conjugate significantly accumulates in the nucleus of HepG2 cells. To our knowledge, this is the first investigation on the subcellular localization of an organometallic bioconjugate with nonradioactive metals.[25] Dilworth and co-workers reported the intracellular distibution of a zinc bis(thiosemicarbazone) complex.[40] Moreover, the organometallic moiety in our conjugate is essential for active endocytosis of the conjugate and release of the conjugate into the cytoplasm. The organometallic bioconjugate **2** undergoes a sequence of metal-enhanced cellular uptake and peptide-mediated nuclear delivery steps. The use of an organometallic species for enhancing cellular uptake of bioconjugates is a novel observation in bioorganometallic chemistry. It is potentially highly useful because the cobaltocenium moiety is relatively small, robust, and easy to handle. We are currently working to expand this finding to other metallocenes and further applications in biology.

 © 2005 Wiley-VCH Verlag GmbH & Co. KGaA, Weinheim

Experimental Section

The bioconjugate was synthesized using standard SPPS methods and Fmoc strategy. Valine-preloaded Wang resin (Fmoc-Val, 300 mg, 0.51 mmol g^{-1}) was used. The resin was swelled in DMF for 1 h. Peptide assembly was performed with threefold excess of the amino acids (Fmoc-Lys(Boc)-OH (Boc = *tert*-butoxycarbonyl), Fmoc-Arg-(Pbf)-OH (Pbf = 2,2,4,6,7-pentamethyldihydrobenzofurane-5-sulfonyl), and Fmoc-Pro-OH) and 1 min preactivation with TBTU and HOBt. Fmoc groups were cleaved using 20% piperidine in DMF. After the completion of the NLS (PKKKRKV) sequence, Fmoc-Lys(Mtt)-OH was added to the sequence as a linker and carrier of the fluorescent label in compounds **2**, **3**, and **4**. Coupling of cobaltocenium carboxylic acid to the terminal amino group was carried out by the same method as for amino acids above, but with a longer coupling time. Upon successful coupling of the metal complex to the peptide, the resin changed color from off white to yellow. The resin was washed repeatedly with DMF, CH_2Cl_2,and shrunk with MeOH. The resin was thoroughly dried over KOH under vacuum overnight prior to cleavage of the bioconjugate. Cleavage was with 95% TFA containing 2.5% triisopropylsilane (TIS) and 2.5% H_2O (3 h). The bioconjugate was precipitated with cold diethyl ether, dried, and lyophilized. Crude yield of **1**: 120 mg. Purification was by preparative HPLC. Compound **1** is a pale yellow solid, soluble in water and ethanol. MALDI-TOF MS: *m*/*z* 1225.5 [M^+]; calcd for $C_{57}H_{98}CoN_{16}O_{10}$: *m*/*z* 1225.7 [$M^+$]. Square-wave voltammetry (MeCN, 0.1 M Bu_4NPF_6): $E_{1/2} = -1.38$ V vs. Fc/Fc^+. ^1H NMR (D_2O, 300 MHz, 25 °C): $\delta = 6.29$ (s, 1H, Cp), 6.25 (s, 1H, Cp), 5.89 (pseudo-t, 2H, Cp), 5.81 (s, 5H, unsubstituted Cp), 4.5–4.1 (overlapping m, 8H, all H_α), 3.96 (m, 1H, $H_{\delta,Pro}$), 3.62 (m, 1H, $H_{\delta,Pro}$), 3.19 (pseudo-t, 2H, $H_{\delta,Arg}$), 2.95–2.85 (m, 10H, $H_{\varepsilon,Lys}$), 2.4–2.0 (m, 5H, $H_{\beta,Pro}$, $H_{\gamma,Pro}$, $H_{\beta,Val}$), 1.96–1.34 (m, 34H, H_β, H_γ, H_δ, all Lys, $H_{\beta,Arg}$, $H_{\gamma,Arg}$), 0.93 ppm (d, J = 7 Hz, 6H, $CH_{3,Val}$).

Supporting Information available: Synthetic and analytical details for compounds **1**–**4**, HPLC and MS. Details for cell culture and microscopy.

Received: November 4, 2004
Published online: March 3, 2005

Keywords: bioinorganic chemistry · bioorganometallic chemistry · cobalt · fluorescence microscopy · metallocenes · peptides

[1] G. Jaouen, A. Vessières, I. S. Butler, *Acc. Chem. Res.* **1993**, *26*, 361–369.
[2] N. Metzler-Nolte, *Angew. Chem.* **2001**, *113*, 1072–1076; *Angew. Chem. Int. Ed.* **2001**, *40*, 1040–1044.
[3] D. R. van Staveren, N. Metzler-Nolte, *J. Chem. Soc. Chem. Commun.* **2002**, 1406–1407.
[4] D. Schlawe, A. Majdalani, J. Velcicky, E. Heßler, T. Wieder, A. Prokop, H.-G. Schmalz, *Angew. Chem.* **2004**, *116*, 1763–1766; *Angew. Chem. Int. Ed.* **2004**, *43*, 1731–1734.
[5] G. Jaouen, S. Top, A. Vessières, G. Leclercq, J. Quivy, L. Jin, A. Croisy, *C. R. Acad. Sci. Ser. IIc* **2000**, *3*, 89–93.
[6] a) S. Top, A. Vessières, G. Leclercq, J. Quivy, J. Tang, J. Vaissermann, M. Huché, G. Jaouen, *Chem. Eur. J.* **2003**, *9*, 5223–5236; b) G. Jaouen, S. Top, A. Vessières, G. Leclercq, M. J. McGlinchey, *Curr. Med. Chem.* **2004**, *11*, 2505–2517.
[7] R. E. Morris, R. E. Aird, P. del Socorro Murdoch, H. Chen, J. Cummings, N. D. Hughes, S. Parsons, A. Parkin, G. Boyd, D. I. Jodrell, P. J. Sadler, *J. Med. Chem.* **2001**, *44*, 3616–3621.
[8] M. Jung, D. E. Kerr, P. D. Senter, *Arch. Pharm.* **1997**, *330*, 173–176.
[9] K. Schmidt, M. Jung, R. Keilitz, B. Schnurr, R. Gust, *Inorg. Chim. Acta* **2000**, *306*, 6–16.
[10] T. Roth, C. Eckert, H.-H. Fiebig, M. Jung, *Anticancer Res.* **2002**, *22*, 2281–2284.
[11] I. Ott, B. Kircher, R. Gust, *J. Inorg. Biochem.* **2004**, *98*, 485–489.
[12] H. Köpf, P. Köpf-Maier, *Angew. Chem.* **1979**, *91*, 509; *Angew. Chem. Int. Ed. Engl.* **1979**, *18*, 477–478.
[13] P. Köpf-Maier, B. Hesse, R. Voigtländer, H. Köpf, *J. Cancer Res. Clin. Oncol.* **1980**, *97*, 31–39.
[14] A. Harstrick, H.-J. Schmoll, G. Sass, H. Poliwoda, Y. Rustum, *Eur. J. Cancer* **1993**, *29A*, 1000–1002.
[15] J. R. Boyles, M. C. Baird, B. G. Campling, N. Jain, *J. Inorg. Biochem.* **2001**, *84*, 159–162.
[16] D. Görlich, I. W. Mattaj, *Science* **1996**, *271*, 1513–1518.
[17] Y. Yoneda, A. Kametaka, T. Sekimoto, *Acta Histochem. Cytochem.* **2002**, *35*, 435–440.
[18] S. Nakielny, G. Dreyfuss, *Cell* **1999**, *99*, 677–690.
[19] D. Görlich, U. Kutay, *Annu. Rev. Cell Dev. Biol.* **1999**, *15*, 607–660.
[20] R. Cartier, R. Reszka, *Gene Ther.* **2002**, *9*, 157–167.
[21] D. A. Jans, C. K. Chan, S. Huebner, *Med. Res. Rev.* **1998**, *18*, 189–223.
[22] S. Liu, D. S. Edwards, J. A. Barrett, *Bioconjugate Chem.* **1997**, *8*, 621–636.
[23] a) M. Langer, R. La Bella, E. Garcia-Garayoa, A. G. Beck-Sickinger, *Bioconjugate Chem.* **2001**, *12*, 1028–1034; b) P. Bläuenstein, E. G. Garayoa, D. Rüegg, A. Blanc, D. Tourwé, A. G. Beck-Sickinger, P. A. Schubiger, *Cancer Biother. Radiopharm.* **2004**, *19*, 181–188.
[24] M. Henze, J. Schuhmacher, A. Dimitrakopoulou-Strauss, L. G. Strauss, H. R. Macke, M. Eisenhut, U. Haberkorn, *Eur. J. Nucl. Med. Mol. Imaging* **2004**, *31*, 466-.
[25] K. E. Bullok, M. Dyszlewski, J. L. Prior, C. M. Pica, V. Sharma, D. Piwnica-Worms, *Bioconjugate Chem.* **2002**, *13*, 1226–1237.
[26] C. M. Feldherr, R. E. Lanford, D. Akin, *Proc. Natl. Acad. Sci. USA* **1992**, *89*, 11002–11005.
[27] E. Conti, M. Uy, L. Leighton, G. Blobel, J. Kuriyan, *Cell* **1998**, *94*, 193–204.
[28] Y. Yoneda, M. Hieda, E. Nagoshi, Y. Miyamoto, *Cell Struct. Funct.* **1999**, *24*, 425–433.
[29] A. G. Tkachenko, H. Xie, D. Coleman, W. Glomm, J. Ryan, M. F. Anderson, S. Franzen, D. L. Feldheim, *J. Am. Chem. Soc.* **2003**, *125*, 4700–4701.
[30] L. Chaloin, P. Vidal, P. Lory, J. Méry, N. Lautredou, G. Divita, F. Heitz, *Biochem. Biophys. Res. Commun.* **1998**, *243*, 601–608.
[31] D. R. van Staveren, N. Metzler-Nolte, *Chem. Rev.* **2004**, *104*, 5931–5985.
[32] M. Lundberg, M. Johansson, *Biochem. Biophys. Res. Commun.* **2002**, *291*, 367–371.
[33] J. P. Richard, K. Melikov, E. Vives, C. Ramos, B. Verbeure, M. J. Gait, L. V. Chernomordik, B. Lebleu, *J. Biol. Chem.* **2003**, *278*, 585–590.
[34] M. Lundberg, S. Wikström, M. Johansson, *Mol. Ther.* **2003**, *8*, 143–150.
[35] S. Console, C. Marty, C. Garcia-Echevarria, R. Schwendener, K. Ballmer-Hofer, *J. Biol. Chem.* **2003**, *278*, 35109–35114.
[36] S. D. Kramer, H. Wunderli-Allenspach, *Biochim. Biophys. Acta* **2003**, *1609*, 161–169.
[37] G. Drin, S. Cootin, E. Blanc, A. R. Rees, J. Temsamani, *J. Biol. Chem.* **2003**, *278*, 31192–31201.
[38] M. Sachse, G. Ramm, G. Strous, J. Klumperman, *Histochem. Cell Biol.* **2002**, *117*, 91–104.
[39] J. Gruenberg, H. Stenmark, *Nat. Rev. Mol. Cell Biol.* **2004**, *5*, 317–323.
[40] A. R. Cowley, J. Davis, J. R. Dilworth, P. S. Donnelly, R. Dobson, A. Nightingale, J. M. Peach, B. Shore, D. Kerr, L. Seymour, *Chem. Commun.* **2005**, 845–847.

 © 2005 Wiley-VCH Verlag GmbH & Co. KGaA, Weinheim

Homoaromatic Molecules

In-Plane Bishomoaromaticity in Tetranitrogen Dianions: Solid-State, Solution, and Electronic Structures**

Jens Geier, Hansjörg Grützmacher, Kai Exner, and Horst Prinzbach**

Dedicated to Professor Emanuel Vogel on the occasion of his 77th birthday

The rigid tetracyclic molecule **1** represents a series of specifically preoriented bisdiazenes, which have been readily reduced by alkali metals to give red, diamagnetic, and thermally stable compounds with the stoichiometry $(M^+)_2$-$\mathbf{1}^{2-}$ (Scheme 1).[1] Spectroscopic data (UV/Vis, ^{1}H, ^{13}C, and ^{7}Li NMR) and DFT calculations indicate that six electrons are cyclically delocalized in the plane made up by the four nitrogen atoms (4N/6e, in-plane (σ) bishomoaromaticity).[2] Calculations, however, show that the S_0 singlet states for the counterion-free dianions are unstable with respect to the T_0 triplet states, which have a significantly greater transannular N···N separation.[1]

The solid-state and solution structures of the sodium compound of $\mathbf{1}^{2-}$ and a topological analysis of its DFT electron density are the major subjects of this communication.

Single crystals of pure $[Na_2(\mathbf{1})(THF/DME)_x]_y$ could not be obtained by reduction of **1** on a sodium mirror in tetrahydrofuran (THF) or dimethoxyethane (DME). However, crystals suitable for a X-ray structure analysis were obtained as a 2:1 mixture of $[Na_2(\mathbf{1})]$ and bishydrazine **2**[1c] (Scheme 1) from a THF solution kept in contact with sodium metal for several weeks. The proton source for the formation of **2** by a Birch-type reduction of **1** is likely the solvent THF. The red crystals obtained contain the chain polymer $[Na_4(\mathbf{1})_2(\mathbf{2})(THF)_4]_\infty$ (Figure 1).[3] The centrosymmetric $[Na_4(\mathbf{1})_2]$ clusters

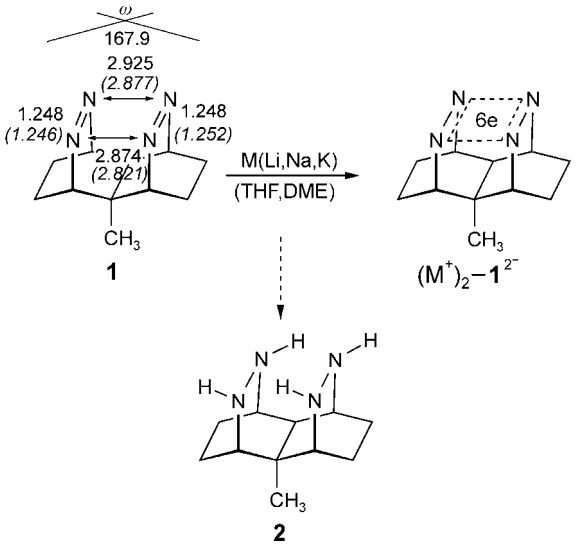

Scheme 1. Generation of $(M^+)_2$-$\mathbf{1}^{2-}$, calculated [B3LYP/6-31+G(d,p)] and experimental N=N bond lengths [Å], transannular N···N distances [Å], and interorbital angle ω [°] of **1**.[1]

(two crystallographically independent but structurally very similar clusters are observed) can be viewed as dimers of $[Na_2(\mathbf{1})]$ units. Each is linked to a bridging molecule of **2** such that an alternating chain results (Figure 1a). The core of the $[Na_4(\mathbf{1})_2]$ unit is a distorted Na_4N_8 cuboctahedron, which is a unique structural motif (Figure 1b). The four nitrogen atoms (N1, N2, N3, N4) of the dianion $\mathbf{1}^{2-}$ have an almost planar trapezoidal arrangement (mean deviation from planarity: 0.006 Å [*0.006*]; values in italics refer to the second dimer). The four sodium cations (Na1, Na2, Na1A, Na2A) are located at the corners of a parallelogram, which is inserted in an almost parallel fashion between two N_4 planes (deviation from coplanarity: 2.8° [*3.5*]). In that arrangement, each sodium cation binds to two nitrogen atoms of each dianion and to one molecule of THF. Furthermore, two Na^+ ions (Na2 and Na2A) in opposite positions of the $(Na_4)^{4+}$ unit bind additionally to a nitrogen atom of the neutral bishydrazine **2**. The Na–N bond lengths vary within the usual range [2.354(3) to 2.572(3) Å] and are not significantly different for the formally neutral and the negatively charged nitrogen atoms. Compared to the bonds in precursor **1**, the N=N bonds are lengthened by 9.8% (mean) to 1.377(4)/1.374(4) Å [*1.376(4)/1.366(4)*], while the transannular N···N distances are shortened by (mean) 9.4% (N1–N4) and 5.2% (N2–N3) to 2.564(4) Å [*2.549(4)*] and 2.721(4) Å [*2.730(4)*].[4]

The N_4 plane is almost orthogonal to the C_α-N-N-C_α planes (the atoms in the latter have a mean deviation of 0.021/0.020 Å [*0.024/0.022*] from their common plane): the angles between the plane normals are 87.5° [*92.2*] (C2-N1-N2-C5) and 91.9° [*87.5*] (C7-N3-N4-C10). The difference (0.16 Å [0.18]) between the two transannular N–N distances (N1–N4, N2–N3) is already observed in the precursor **1** and is caused by the interaction between the methyl group and the hydrogen atoms on C3 and C9 in *anti* position (Figure 1b).

What is the structure of pure $[Na_2(\mathbf{1})(THF)_x]_y$ in solution? Well-resolved ^{1}H NMR spectra measured in [D_8]THF at room

[*] Dr. J. Geier,[+] Prof. Dr. H. Grützmacher
Department of Chemistry and Applied Biosciences, HCI
ETH Hönggerberg, 8093 Zürich (Switzerland)
Fax: (+41) 1-633-1032
E-mail: jgeier@staff.chem.tsukuba.ac.jp
Dr. K. Exner, Prof. Dr. H. Prinzbach
Institut für Organische Chemie und Biochemie
Albert-Ludwigs-Universität Freiburg
79104 Freiburg (Germany)
Fax: (+49) 761-203-6048
E-mail: hprinz@orgmail.chemie.uni-freiburg.de
[+] Present address:
Department of Chemistry
University of Tsukuba
Tsukuba, Ibaraki, 305-8571 (Japan)

[**] This work was supported by the ETH Zürich, the Deutsche Forschungsgemeinschaft, and the Fonds der Chemischen Industrie. We thank Prof. E. Vogel for generous gifts of 1,6-methano[10]annulene and Dr. H. Rüegger for assistance with NMR measurements.

Supporting information for this article is available on the WWW under http://www.angewandte.org or from the author.

 DOI: 10.1002/anie.200462126 © 2005 Wiley-VCH Verlag GmbH & Co. KGaA, Weinheim

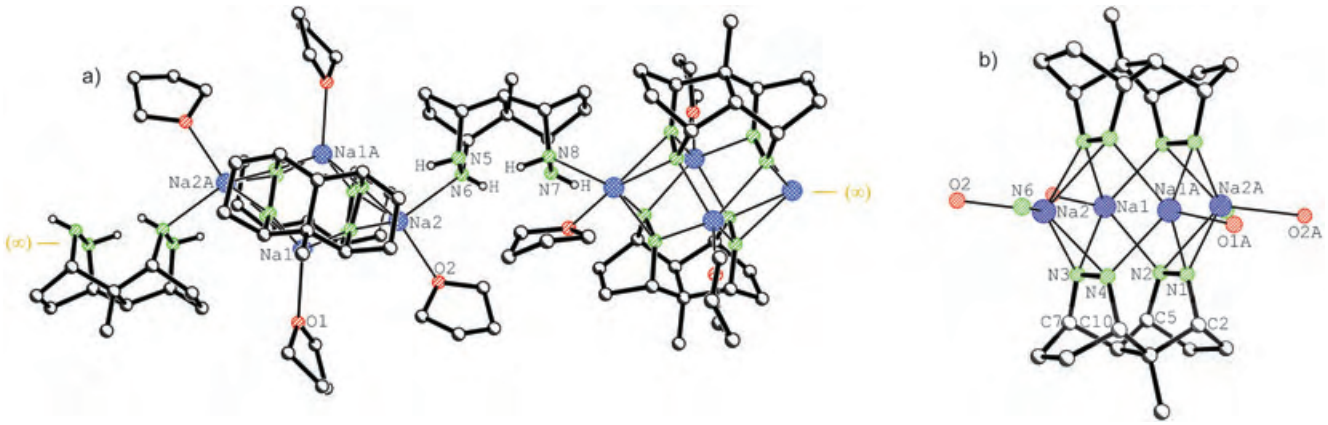

Figure 1. Solid-state structure of $[Na_4(\mathbf{1})_2(\mathbf{2})(THF)_4]_\infty$. Hydrogen atoms are omitted except for the NH protons. a) Part of the chain structure of $[Na_4(\mathbf{1})_2(\mathbf{2})(THF)_4]_\infty$. The asymmetric unit contains one molecule of bishydrazine **2** and two half-molecules of each of two independent centrosymmetric dimer units $[Na_4(\mathbf{1})(THF)_4]$. Only one orientation is shown for the disordered bridging bishydrazine **2** (in the alternative orientation the methyl group is located on the opposite side). Selected distances [Å], values in italics are for the second dimer unit: Na1-O1 2.342(3) [*2.331(3)*], Na2-O2 2.358(3) [*2.357(3)*], Na2-N6 2.533(3) [*2.475(3)*], N5-N6 1.492(4), N7-N8 1.489(4), mean of N5-N8 and N6-N7: 2.849. b) One of the two crystallographically independent dimer units in $[Na_4(\mathbf{1})_2(\mathbf{2})(THF)]_\infty$. Only the oxygen and nitrogen atoms of the coordinating THF and bishydrazine molecules are shown. Selected distances [Å] and angles [°], values in italics are for the second dimer unit: Na1-N2 2.432(3) [*2.373(3)*], Na1-N3 2.354(3) [*2.381(3)*], Na2-N3 2.430(3) [*2.572(3)*], Na2-N4 2.399(3) [*2.376(3)*], Na1A-N4 2.383(3) [*2.428(3)*], Na1A-N1 2.442(3) [*2.417(3)*], Na2A-N1 2.427(3) [*2.404(3)*], Na2A-N2 2.531(2) [*2.466(3)*], N1-N2 1.377(4) [*1.376(4)*], N3-N4 1.374(4) [*1.366(4)*], N1-N4 2.564(4) [*2.549(4)*], N2-N3 2.721(4) [*2.730(4)*], N1-C2 1.458(4) [*1.460(4)*], N2-C5 1.470(4) [*1.458(4)*], N3-C7 1.457(4) [*1.465(4)*], N4-C10 1.459(4) [*1.458(4)*], N1-N2-N3 86.6(2) [*86.6(2)*], N2-N3-N4 86.9(2) [*85.8(2)*], N3-N4-N1 93.2(2) [*94.4(2)*], N4-N1-N2 93.3(2) [*93.2(2)*], C2-N1-N2 112.3(2) [*112.2(3)*], N1-N2-C5 111.8(3) [*111.7(3)*], C7-N3-N4 111.8(3) [*111.9(3)*], N3-N4-C10 112.6(2) [*112.5(3)*], C2-N1-N2-C5 5.3(3) [*6.2(3)*], C7-N3-N4-C10 −5.2(3) [*−5.6(3)*].

temperature indicate that the dianion $\mathbf{1}^{2-}$ has C_s symmetry. The molecular volume calculated from the diffusion coefficient as determined by PGSE experiments[5] amounts to 860 Å^3, which is close to the estimated volume of the $[Na_4(\mathbf{1})_2]$ cluster in the chain polymer $[Na_4(\mathbf{1})_2(\mathbf{2})(THF)_4]_\infty$. Therefore we assume this cluster also to be present in solution, with the bishydrazine **2** as ligand being replaced by THF, that is, $[Na_4(\mathbf{1})_2(THF)_x]$ ($x = 4$–6). Furthermore, a splitting of the ^{1}H NMR signals of the α-hydrogen atoms and the methyl group each into two resonances is observed upon cooling to −30 °C. We interpret this to indicate a fluxional process, whereby the dimer with the methyl groups in *anti* position (Figure 1 b) interconverts with the corresponding *syn* conformer.

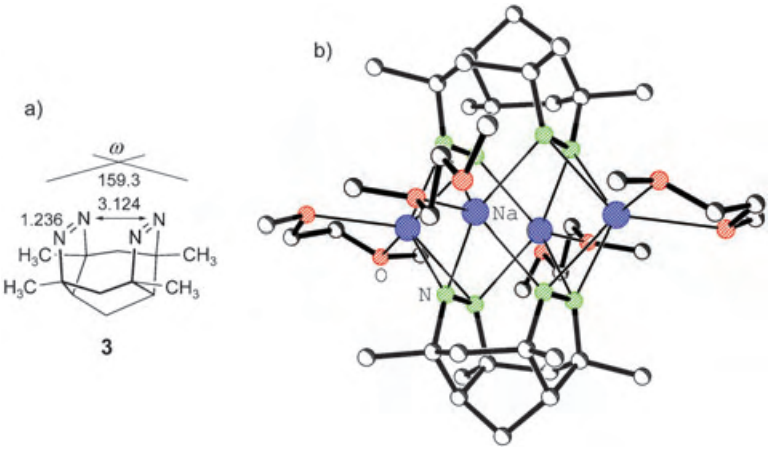

Figure 2. a) Calculated [B3LYP/6-31+G(d,p)] N=N bond lengths [Å], transannular N···N distances [Å], and interorbital angle ω [°] of **3**.[1] b) Solid-state structure of $[Na_4(\mathbf{3})_2(DME)_4]$. The hydrogen atoms are omitted.

Bisdiazene **3** (Figure 2 a) is more flexible, and the transannular distances are significantly greater than in **1** ($d_{N\cdots N} = 3.124$ Å, $\omega = 159.3°$).[1b,d] Still, the bridgehead methyl groups provide kinetic stabilization, and $(Li^+)_2\mathbf{3}^{2-}$ was found to be highly persistent.[1b] The disodium compound could now be crystallized from DME solution as $[Na_4(\mathbf{3})_2(DME)_4]$; it showed a dimeric structure analogous to the $[Na_4(\mathbf{1})_2]$ unit (Figure 2 b).[3] Unfortunately, since this structure could not be refined satisfactorily, no precise structural data are available (crudely estimated transannular N–N distance of 2.7–2.8 Å).

For quantum chemical calculations we chose $[Na_4(\mathbf{1})F_2]$ as a model compound (Figure 3 a). The countercations are included, since most dianions as isolated entities are not stable against spontaneous electron detachment.[6] Two fluoride ions were used in calculating a charge-neutral, physically realistic model. This structure was optimized[7] at the B3LYP/6-31+G(d,p) level;[8] the resulting dianion geometry is in good agreement with the solid-state structure. The bond lengths of the reduced diazene groups are correctly reproduced (1.378/1.378 Å [N1–N2/N3–N4]), while both transannular distances (N1–N4 2.499 Å; N2–N3 2.605 Å) are shorter than the experimental values (Δ(N1–N4) 0.058 Å; Δ(N2-N3) 0.121 Å). The calculated[9] ^{15}N chemical shifts of the dianion in the model compound $[Na_4(\mathbf{1})F_2]$ (N1, N4: 268; N2, N3: 242 ppm)] agree satisfactorily with the corresponding experimental values of $[Na_4(\mathbf{1})_2(THF)_x]$ (244 and 218 ppm)

 © 2005 Wiley-VCH Verlag GmbH & Co. KGaA, Weinheim

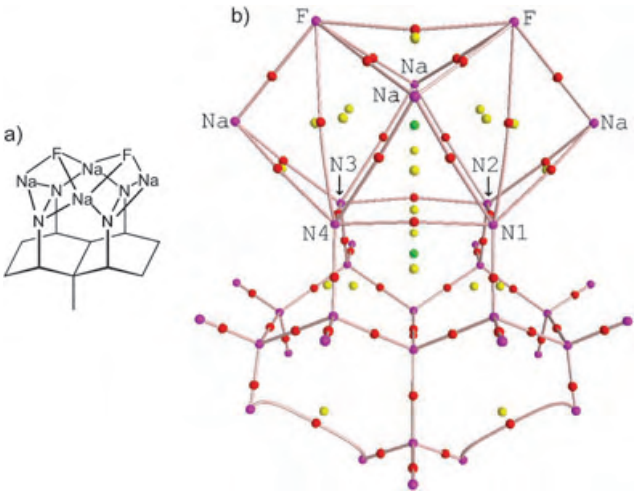

Figure 3. a) Diagram of the calculated model structure $[Na_4(\mathbf{1})F_2]$. b) Molecular graph of $[Na_4(\mathbf{1})F_2]$. Purple spheres correspond to the locations of (3,−3) critical points (maxima) in the electron density, red spheres to (3,−1) (=bond) critical points, yellow spheres to (3,+1) (=ring) critical points, and green spheres to (3,+3) (=cage) critical points (minima); the gray lines are the bond paths.

within the usual range of standard deviations (6–12 ppm)[10]; the experimental values were determined by ^1H–^{15}N-correlated NMR spectroscopy at room temperature in $[D_8]$THF, vs. $\delta[NH_3]=0$. A broken-symmetry UB3LYP/6-31+G(d,p) single-point calculation for this structure gives $\langle S^2\rangle = 0.31$ and occupation numbers of 1.83 and 0.17 for the natural orbitals corresponding to the HOMO and the LUMO.[11] The $\langle S^2\rangle$ value and the occupation numbers are taken as empirical evidence that—at this level of theory—the model structure is still reasonably described by a closed-shell singlet state, as its diradicaloid character is small. A singlet diradical would ideally have two nearly singly occupied natural orbitals and $\langle S^2\rangle \approx 1$.[12] Optimization [UB3LYP/6-31+G(d,p)] in the triplet state[13] results in rather long transannular N–N distances of 2.920 Å (N1–N4) and 3.010 Å (N2–N3), while the lengths of the reduced diazene bonds remain essentially unchanged (1.386/1.386 Å [N1–N2/N3–N4]). The shortening of these transannular distances in the singlet state is indeed caused by chemical bonds linking the formal two adjacent radical anions, as can be shown by a topological analysis[14] of the B3LYP electron density of the model structure.

Clearly, bond paths[14a] are observed that correspond to the transannular N1–N4 and N2–N3 interactions (Figure 3b). Several quantum mechanical properties (in atomic units, a.u.) evaluated at the associated bond critical points (r_b) are given in Table 1. The kinetic energy per electron $[G(r_b)/\rho(r_b)]$ is in the range for shared[14] interactions, that is, well below unity. But due to the low value of the electron density $[\rho(r_b)]$ the magnitude of the potential energy density $[v(r_b)]$ is likewise low. This results in slightly positive values for the Laplacian of the electron density $\nabla^2\rho(r_b)$ [by the relation $(\hbar^2/4m)\nabla^2\rho(r_b) = 2G(r_b)+v(r_b)$][14] and in near-zero values for the sum of potential and kinetic energy densities $[H(r_b)=G(r_b)+v(r_b)]$. The transannular N–N bond paths hence show characteristics between those of typical shared and closed-shell[14] interactions.

The four nitrogen atomic basins have electron populations of 7.70–7.72 each (Table 2).[15] As determined by the pair density,[16] and here exemplified for N1, 5.96 electrons $[\lambda(\Omega_{N1})]$[16a] of its total population (7.70) are localized within the atomic basin (N1). Of the remaining electrons, 0.70 $[{}^1/_2\delta(\Omega_{N1},\Omega_{N2})]$[16a] are shared with the directly bonded nitrogen atom N2 and 0.14 electrons are shared with the transannular nitrogen atom N4.

The delocalization indices $\delta(\Omega_i,\Omega_j)$, when applied to homopolar interactions, give the number of shared Lewis electron pairs; hence, bond orders of 1.40/1.38 (N1–N2/N3–N4) are assigned to the reduced diazene moieties and of 0.28/0.22 (N1–N4/N2–N3) to the transannular bonds. The homotropylium cation, the archetype of compounds showing cyclic homoconjugation, has a $\delta(\Omega_i,\Omega_j)=0.28$ between its transannularly interacting carbon basins.[17] This, in combination with the calculated strongly negative nucleus independent chemical shift (NICS)[18] of −18.4 ppm at the N_4 ring centroid, leads us to conclude that the model structure $[Na_4(\mathbf{1})F_2]$ is a bishomoaromatic system at this level of theory.[19]

In conclusion, in the solid state and (most probably) in solution $(Na^+)_2$-$\mathbf{1}^{2-}$ and $(Na^+)_2$-$\mathbf{3}^{2-}$ exist as dimers ($[Na_4(\mathbf{1})_2]$, $[Na_4(\mathbf{3})_2]$) featuring an unprecedented Na_4N_8 cuboctahedron as core unit; the polygons formed by the four nitrogen atoms of the dianions $\mathbf{1}^{2-}$ and $\mathbf{3}^{2-}$ are almost perfectly planar. The

Table 1: Properties in atomic units (a.u.) evaluated at selected bond [(3,−1)] and ring [(3,+1)] critical points r_b[14c] in the electron density of $[Na_4(\mathbf{1})F_2]$.[a]

	$\rho(r_b)$	$\nabla^2\rho(r_b)$	$G(r_b)/\rho(r_b)$	$H(r_b)$	$v(r_b)$	ε
(3,−1): N1/N4	0.033	0.080	0.576	0.002	−0.017	0.164
(3,−1): N2/N3	0.027	0.064	0.556	0.001	−0.014	0.144
(3,−1): N1/N2	0.345	−0.584	0.548	−0.335	−0.524	0.153
(3,−1): N3/N4	0.345	−0.584	0.548	−0.335	−0.524	0.153
(3,+1): N1/N2/N3/N4	0.017	0.084	1.059	0.002	−0.016	–

[a] $\rho(r_b)$: electron density; $\nabla^2\rho(r_b)$: Laplacian of the electron density; $G(r_b)/\rho(r_b)$: kinetic energy per electron; $H(r_b)$: sum of kinetic and potential energy densities; $v(r_b)$: potential energy density; ε: ellipticity.

Table 2: Electron population $[N(\Omega_i)]$, with variance,[15] of the nitrogen atomic basins and localization indices $\lambda(\Omega_i)$/delocalization indices $\delta(\Omega_i,\Omega_j)$.[16]

	$N(\Omega_i)$	Variance	$\lambda(\Omega_i)$		$\delta(\Omega_i,\Omega_j)$
N1	7.70	1.73	5.96	N1-N2	1.40
N2	7.72	1.71	6.01	N3-N4	1.38
N3	7.72	1.72	6.00	N1-N4	0.28
N4	7.70	1.74	6.00	N2-N3	0.22
				N1-N3	0.18
				N2-N4	0.18

 © 2005 Wiley-VCH Verlag GmbH & Co. KGaA, Weinheim

single-determinant calculations used here provide upper[16] boundaries for the electron delocalization as determined by $\delta(\Omega_i,\Omega_j)$ and for the degree of covalent transannular N–N bonding. Given the experimentally observed significant shortening of the transannular N–N distances in the highly rigid cage of **1** upon reduction, hardly any doubts can remain that the compounds described here, which represent the series of 4N/6e dianions,[1] contain molecules with four cyclically bonded nitrogen atoms[1d] in form of the bishomotetrazete dianion substructure (Figure 4).

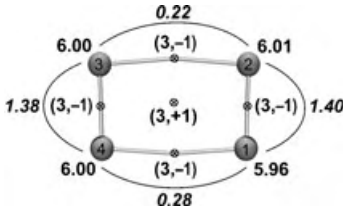

Figure 4. Schematic summary of the quantum chemical investigation of the bishomotetrazete dianion substructure in $[Na_4(\mathbf{1})F_2]$; locations of critical points in $\rho(r)$ (black crosses), localization indices $\lambda(\Omega_i)$, and delocalization indices $\delta(\Omega_i,\Omega_j)$ (italics).

Experimental Section

The solvents THF and DME were stored as violet $[Na_2(Ph_2CO)]$ solutions and were transferred by condensation techniques in a vacuum line (oil-diffusion pump). Compound **1** (40 mg, 0.20 mmol) was reduced on a sodium mirror (excess) in DME solution (4 mL) at room temperature until the initially formed emerald-green color had changed to deep red (30 min). The solvent was removed in vacuo and replaced by THF (1.5 mL). Storage of the resulting clear red solution at room temperature for three weeks under prolonged contact with the sodium mirror gave reproducibly extremely air-sensitive red parallelepiped-shaped crystals (≈10%) of $[Na_4(\mathbf{1})_2(\mathbf{2})(THF)_4]_\infty$. $[Na_4(\mathbf{3})_2(DME)_4]$ was prepared analogously by reducing **3** (10 mg, 0.04 mmol) in DME (0.5 mL) and storing the deep red solution at 0°C for one week, without prolonged contact with sodium metal; deep red crystals (≈15%) were obtained. NMR samples of $[Na_4(\mathbf{1})_2(THF)_x]$ were prepared in vacuo by in situ reduction of **1** in a flame-sealed glass NMR tube on a sodium mirror in $[D_8]$THF (dried over liquid Na/K alloy), ^{1}H NMR (300.13 MHz, 20°C): $\delta = 2.98$ (s, 2H; α-H), 2.52 (s, 2H; α′-H), 1.85–1.40 (m, 9H), 0.73 ppm (s, 3H; CH_3); ^{1}H NMR (−20°C): $\delta = 2.99/2.95$ (2×s, 2H; α-H), 2.54/2.49 (2×s, 2H; α′-H), 1.83–1.30 (m, 9H), 0.72 ppm (s, 3H; CH_3); ^{1}H NMR (−30°C): $\delta = 3.05/2.97$ (br+s, 2H; α-H), 2.58/2.51 (br+s, 2H; α′-H), 1.87–1.35 (m, 9H), 0.76/0.72 ppm (2×s, 3H; CH_3).

Received: September 27, 2004
Revised: December 9, 2004
Published online: March 14, 2005

Keywords: bisdiazenes · dianions · heterocycles · homoaromaticity · quantum chemical calculations

[1] a) K. Exner, D. Hunkler, G. Gescheidt, H. Prinzbach, *Angew. Chem.* **1998**, *110*, 2013; *Angew. Chem. Int. Ed.* **1998**, *37*, 1910; b) K. Exner, O. Cullmann, M. Vögtle, H. Prinzbach, B. Grossmann, J. Heinze, L. Liesum, R. Bachmann, A. Schweiger, G. Gescheidt, *J. Am. Chem. Soc.* **2000**, *122*, 10650; c) J. Geier, K. Exner, M. Vögtle, M. Kegel, F. Yang, D. Hunkler, O. Cullmann, H. Prinzbach, *Tetrahedron* **2002**, *58*, 1137; d) E. Beckmann, N. Bahr, O. Cullmann, F. Yang, M. Kegel, M. Vögtle, K. Exner, M. Keller, L. Knothe, H. Prinzbach, *Eur. J. Org. Chem.* **2003**, 4248; e) H. Prinzbach, G. Fischer, G. Rihs, *Tetrahedron Lett.* **1982**, *23*, 1251.

[2] Review: R. V. Williams, *Chem. Rev.* **2001**, *101*, 1185.

[3] The data were collected on a Bruker AXS APEX CCD diffractometer (100 K) and were corrected by the program Sadabs Version 2.05 (Bruker AXS). The structure was solved by direct methods, all non-hydrogen atoms were refined anisotropically. The hydrogen atoms were treated by a riding model with exception of the four NH protons of the bishydrazine, where the coordinates were refined without restraints (SHELX-97, G. M. Sheldrick, Göttingen, **1997**). Two positions with occupancies of 0.46 and 0.54 were refined for the methyl group of the disordered bishydrazine (C22). $[Na_4(\mathbf{1})_2(\mathbf{2})(THF)_4]_\infty$: $C_{49}H_{84}N_{12}Na_4O_4$; red parallelepiped, crystal size $0.59\times0.40\times0.20$ mm; triclinic, space group $P\bar{1}$, $a = 11.038(2)$, $b = 11.596(3)$, $c = 20.577(4)$ Å, $\alpha = 76.164(4)$, $\beta = 82.759(5)$, $\gamma = 88.104(5)$°, $V = 2536.8(9)$ Å^3, $Z = 2$, $\mu = 0.11$ mm^{-1}; $\lambda(Mo_{K\alpha}) = 0.71073$ Å, $T = 100$ K, $2\theta_{max} = 52.74$°, collected (independent) reflections = 22684 (10324), $R_{int} = 0.0670$; 649 refined parameters, $R_1 = 0.0668$ for 6162 reflections with $I > 2\sigma$, $wR_2 = 0.1930$ for all data, GOF on $F^2 = 1.017$, max./min. residual electron density = 0.53/−0.37 e Å^{-3}. CCDC 247150 contains the supplementary crystallographic data for this paper. These data can be obtained free of charge from the Cambridge Crystallographic Data Centre via www.ccdc.cam.ac.uk/data_request/cif. $[Na_4(\mathbf{3})_2(DME)_4]$: $C_{42}H_{80}N_8Na_4O_8$; red, irregular shape, crystal size $0.11\times0.09\times0.09$ mm; triclinic, space group $P\bar{1}$, $a = 11.027(4)$, $b = 11.391(5)$, $c = 12.607(4)$ Å, $\alpha = 96.44(1)$, $\beta = 115.31(1)$, $\gamma = 112.23(1)$°, $V = 1252.1(7)$ Å^3, $Z = 1$. The structure could be solved unequivocally but due to the low scattering power of the crystals no satisfying refinement was possible.

[4] Cf. the N=N bond lengths/N···N distances of 1.358/2.463 (2.530) Å for monomeric $(Li^+)_2$-$\mathbf{1}^2$ [B3LYP/6-31+G(d,p)]. Attempts to crystallize the latter have not been successful (J. Geier, unpublished).

[5] M. Valentini, H. Rüegger, P. S. Pregosin, *Helv. Chim. Acta* **2001**, *84*, 2833.

[6] T. Sommerfeld, *J. Am. Chem. Soc.* **2002**, *124*, 1119.

[7] Program package: Gaussian 03 (Revision B.04), M. J. Frisch, G. W. Trucks, H. B. Schlegel, G. E. Scuseria, M. A. Robb, J. R. Cheeseman, J. A. Montgomery, Jr., T. Vreven, K. N. Kudin, J. C. Burant, J. M. Millam, S. S. Iyengar, J. Tomasi, V. Barone, B. Mennucci, M. Cossi, G. Scalmani, N. Rega, G. A. Petersson, H. Nakatsuji, M. Hada, M. Ehara, K. Toyota, R. Fukuda, J. Hasegawa, M. Ishida, T. Nakajima, Y. Honda, O. Kitao, H. Nakai, M. Klene, X. Li, J. E. Knox, H. P. Hratchian, J. B. Cross, C. Adamo, J. Jaramillo, R. Gomperts, R. E. Stratmann, O. Yazyev, A. J. Austin, R. Cammi, C. Pomelli, J. W. Ochterski, P. Y. Ayala, K. Morokuma, G. A. Voth, P. Salvador, J. J. Dannenberg, V. G. Zakrzewski, S. Dapprich, A. D. Daniels, M. C. Strain, O. Farkas, D. K. Malick, A. D. Rabuck, K. Raghavachari, J. B. Foresman, J. V. Ortiz, Q. Cui, A. G. Baboul, S. Clifford, J. Cioslowski, B. B. Stefanov, G. Liu, A. Liashenko, P. Piskorz, I. Komaromi, R. L. Martin, D. J. Fox, T. Keith, M. A. Al-Laham, C. Y. Peng, A. Nanayakkara, M. Challacombe, P. M. W. Gill, B. Johnson, W. Chen, M. W. Wong, C. Gonzalez, J. A. Pople, Gaussian, Inc., Pittsburgh, PA, **2003**.

[8] a) A. D. Becke, *J. Chem. Phys.* **1993**, *98*, 5648; b) C. Lee, W. Yang, R. G. Parr, *Phys. Rev. B* **1988**, *37*, 785. Other density functionals (B3PW91, BLYP, BPW91) produced significantly larger deviations from the solid-state structure.

[9] GIAO-B3LYP/6-31+G(d,p). a) R. Ditchfield, *Mol. Phys.* **1974**, *27*, 789; b) K. Wolinski, J. F. Hilton, P. Pulay, *J. Am. Chem. Soc.* **1990**, *112*, 8251.

 © 2005 Wiley-VCH Verlag GmbH & Co. KGaA, Weinheim

[10] A. Dokalik, H. Kalchhauser, W. Mikenda, G. Schweng, *Magn. Reson. Chem.* **1999**, *37*, 895.
[11] D. T. Crawford, E. Kraka, J. F. Stanton, D. Cremer, *J. Chem. Phys.* **2001**, *114*, 10638.
[12] a) Y. Jung, M. Head-Gordon, *J. Phys. Chem. A* **2003**, *107*, 7475; b) Y. Jung, T. Heine, P. von R. Schleyer, M. Head-Gordon, *J. Am. Chem. Soc.* **2004**, *126*, 3132.
[13] $\langle S^2 \rangle = 2.01$. The structure is higher in energy than the closed-shell singlet structure by 5.8 kcal mol^{-1}.
[14] a) R. F. W. Bader, *J. Phys. Chem. A* **1998**, *102*, 7314; b) J. Hernández-Trujillo, R. F. W. Bader, *J. Phys. Chem. A* **2000**, *104*, 1779; c) Review: R. F. W. Bader, *Chem. Rev.* **1991**, *91*, 893. The calculations were performed with the program AIM2000, version 2.0: F. Biegler-König, J. Schönbohm, D. Bayles, *J. Comput. Chem.* **2001**, *22*, 545; http://gauss.fh-bielefeld.de/aim2000.
[15] The atomic populations and the localization/delocalization indices were calculated (AIM covariances) with the program package ToPMoD: a) S. Noury, X. Krokidis, F. Fuster, B. Silvi, Université Pierre et Marie Curie, Paris, **1997**; b) S. Noury, X. Krokidis, F. Fuster, B. Silvi, *Comput. Chem.* **1999**, *23*, 597; The largest deviation from the relation $N(\Omega_i) = \lambda(\Omega_i) + \Sigma_{j,j\neq i}[\delta(\Omega_i,\Omega_j)/2]$ was smaller than 0.5%. Intervalls of 0.1 a.u. were used in the grid calculation.
[16] a) X. Fradera, M. A. Austen, R. F. W. Bader, *J. Phys. Chem. A* **1999**, *103*, 304; b) Y.-G. Wang, C. Matta, N. H. Werstiuk, *J. Comput. Chem.* **2003**, *24*, 1720.
[17] Cycloocta-2,4,6-trien-1-yl cation; it was optimized at the B3LYP/6-31+G(d,p) level; the distance between the homoconjugated carbon atoms was calculated to 2.132 Å.[7,8,14,15] This species does not have a bond critical point between these particular carbon atoms, a phenomenon that was termed "no bond homoaromaticity": a) K. J. Szabo, E. Kraka, D. Cremer, *J. Org. Chem.* **1996**, *61*, 2788. Other applications of the topological analysis of the electron density to potentially homoconjugated systems are described in: b) N. H. Werstiuk, Y.-G. Wang, *J. Phys. Chem. A* **2003**, *107*, 9434. For the application of the electron localization function see: c) C. Lepetit, B. Silvi, R. Chauvin, *J. Phys. Chem. A* **2003**, *107*, 464.
[18] P. von R. Schleyer, C. Maerker, A. Dransfeld, H. Jiao, N. J. R. van Eikema Hommes, *J. Am. Chem. Soc.* **1996**, *118*, 6317.
[19] For the cyclic dimer of the tetracyanoethylene radical anion (4C/6e) chemical bonds over C–C distances of 2.9 Å were formulated: a) J. J. Novoa, P. Lafuente, E. Del Sesto, J. S. Miller, *Angew. Chem.* **2001**, *113*, 2608; *Angew. Chem. Int. Ed.* **2001**, *40*, 2540; b) R. E. Del Sesto, J. S. Miller, P. Lafuente, J. J. Novoa, *Chem. Eur. J.* **2002**, *8*, 4894; c) J.-M. Lü, S. V. Rosokha, J. K. Koch, *J. Am. Chem. Soc.* **2003**, *125*, 12161; d) Y. Jung, M. Head-Gordon, *Phys. Chem. Chem. Phys.* **2004**, *6*, 2008.

 © 2005 Wiley-VCH Verlag GmbH & Co. KGaA, Weinheim

Fluorescent Nanocrystals

CdSe/ZnS Nanocrystals with Dye-Functionalized Polymer Ligands Containing Many Anchor Groups**

*Inga Potapova, Ralf Mruk, Christian Hübner, Rudolf Zentel, Thomas Basché, and Alf Mews**

Colloidal semiconductor nanocrystals (NCs) are color tunable inorganic fluorophores, which consist of an inorganic core and an outer shell of molecular ligands.[1] While the optical properties can be adjusted by the composition[2] and the size of the core,[3] the ease with which the NCs can be chemically processed is mainly governed by the molecular structure of the ligands. In this context we define a ligand as consisting of three parts: a functional anchor group that attaches to the inorganic NC surface, an outer functional group, and a spacer in between. The architecture of the ligand is of major importance for assembling the NCs into larger supramolecular structures[4] or conjugating them to biological samples where they serve as fluorescence labels.[5] For these purposes it is essential that both the anchor and outer functionality can form strong chemical bonds. We will address this problem by introducing a novel type of polymer ligand, where the bond strength is increased by the presence of multiple anchor groups. Since our model ligands are decorated with dye molecules, we can employ fluorescence resonance energy transfer (FRET) to study the formation and stability of the NC–dye couples, where the NCs are the donors and the dyes the acceptors[6,7]. Based on the ensemble absorption and fluorescence spectra, the amount of dye attached to a given NC[6] and the average distance between the NC and the dye molecules can be estimated.[8] However, since the relative orientation and structure of the FRET couples can differ significantly from one complex to the next, we extend our measurements to single NC–dye complexes. Our experiments clearly show that static and dynamic heterogeneities occur in the ensemble of NC–dye couples, a result which is of importance for a FRET-based analysis of intermolecular distances.

The CdSe/ZnS core–shell NCs are synthesized by an established method[3,9] in the presence of phosphonic acids[10] and trioctylphosphine oxide (TOPO) as ligands. The surface molecules can be subsequently cross linked to form multianchor ligands to stabilize the ligand shell.[11,12] Herein we follow a different strategy by prefabricating a multianchor

[*] Dr. I. Potapova, Dr. C. Hübner, Prof. Dr. T. Basché, Dr. A. Mews
Institute for Physical Chemistry
University of Mainz
55099 Mainz (Germany)
Fax: (+49) 6131-39-23953
E-mail: alf.mews@uni-siegen.de
Dr. R. Mruk, Prof. Dr. R. Zentel
Institute for Organic Chemistry
University of Mainz, 55099 Mainz (Germany)

[**] This work was supported by a grant from the SFB 625 (A10 and B7).

 DOI: 10.1002/anie.200462236 © 2005 Wiley-VCH Verlag GmbH & Co. KGaA, Weinheim

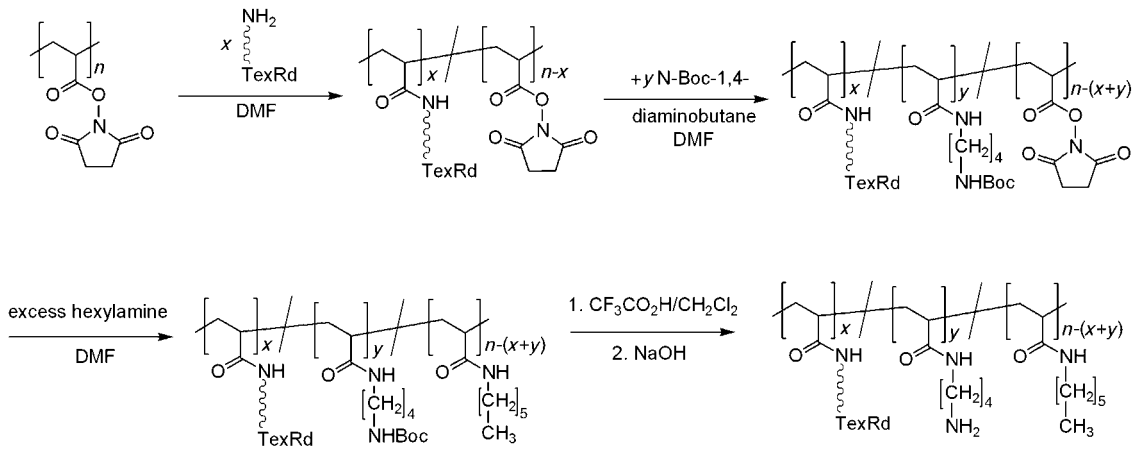

Scheme 1. Stepwise build-up of a dye-labeled multianchor ligand. The reactive ester groups of the polymer chain ($n \approx 200$) are successively exchanged by ($x \approx 1$) Texas Red molecules (TexRd), and ($y \approx 100$) Boc-protected butyldiamine and hexylamine groups. After deprotection the functional ligand carries amino groups as anchors for the NCs, alkyl chains for solubility, and on average one dye molecule. DMF = *N*,*N*-dimethylformamide.

ligand, which is based on a statistical copolymer. The synthesis (Scheme 1) starts from a polymer chain of reactive esters ($n \approx 200$),[13] which is labeled with one dye molecule on average by reaction with the amino group of Texas Red cadaverine.[14] The next step is the replacement of approximately 50% of the reactive esters within each polymer molecule with mono-Boc (Boc = *tert*-butoxycarbonyl) protected diamine groups, subsequently the remaining ester groups are substituted by mono-amines. After deprotection, the polymer ligands have amine groups as anchors for the NC surface, long alkyl chains to provide solubility in hydrophobic solvents, and about one dye molecule for optical tracing and energy-transfer experiments.

Although we had evidence that the functionalized ligands can also bind to the TOPO covered NCs (see below), we performed experiments where the attachment can be monitored directly by a solubility change. In these experiments we stripped most of the TOPO molecules from the NC surface by several cycles of successive precipitation and dissolution of the particles in pyridine.[15] These particles could only be dissolved in chloroform upon addition of the dye-labeled polymer. This behavior is direct evidence for the attachment of the polymer to NCs, because the alkyl chains of the polymer provide solubility in chloroform and not in pyridine.

Another indication for the formation of the NC–dye complexes comes from the spectroscopic observation of FRET between the NCs and the dyes. The FRET process, which is operative on a length scale of several nanometers, leads to a decrease of the donor (NC) fluorescence F_D to a fluorescence intensity F_{DA} in the presence of an acceptor, and an increase of the acceptor (dye) fluorescence. From the spectral overlap between the emission spectrum of the NCs and the absorption spectrum of the dyes (gray shaded area in Figure 1a) a Förster radius of $R_0 = 4.6$ nm can be calculated at which the transfer efficiency should be $E = 1 - F_{DA}/F_D$, as described in detail in ref. [6] This calculation has assumed a dipole orientation factor between the dyes and the NCs of $\kappa^2 = {}^2/_3$,[16,17] which is not justified in advance.

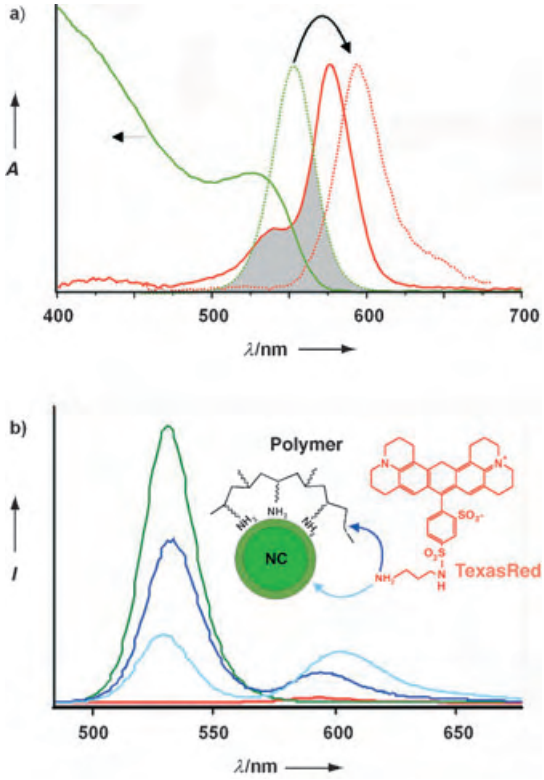

Figure 1. a) Absorption (solid lines) and fluorescence (dotted lines) spectra of the NC (green) and the dye (red) in solution. The spectral overlap of the NC fluorescence (dotted, green) and the dye absorption (solid, red) is shaded in gray. b) Fluorescence spectra of the NCs (green), dye (red), NC–polymer–dye (dark blue), and NC–dye (light blue), respectively, upon excitation at $\lambda = 488$ nm. Dye fluorescence can only be observed upon energy transfer within the NC–dye and NC–polymer–dye complexes.

Whereas the absorption spectra of NC–dye and NC–polymer–dye are just superpositions of the spectra of the respective compounds, the corresponding fluorescence spectra shown in Figure 1b change by complex formation. In

 © 2005 Wiley-VCH Verlag GmbH & Co. KGaA, Weinheim

Figure 1b the fluorescence spectra of the pure NCs (green) and dyes (red) are compared to those of an NC–polymer–dye (dark blue) and an additional composite of NCs and Texas Red without the polymer linker (NC–dye, light blue). Without the polymer linker the dye either binds to the NC surface through its amino group or by nonspecific binding.[18] The NC–dye composites were prepared by mixing the TOPO–NCs and the dye ligands in chloroform with NC:dye concentration ratios of 1:1. These ratios were judged from the UV/Vis spectra of the isolated compounds.[19,20] The fluorescence spectra were taken at an excitation wavelength of 488 nm, where the absorption is strong for the donor (NC, green) and weak for the acceptor (dye, red), as can be seen in Figure 1a. This approach leads to a strong NC fluorescence and a weak dye fluorescence for the isolated compounds. In contrast, the NC–dye composites show enhanced dye fluorescence and reduced NC fluorescence, which is a signature of electronic excitation-energy transfer from the NCs to the acceptor dye(s).

Although the spectra presented in Figure 1b serve as a clear indication for a FRET-type process, quantitative information is difficult to extract. Besides uncertainties in the calculation of the Förster radius R_0, the transfer efficiencies, as estimated from the spectra, depend on an accurate determination of the respective NC:dye ratios,[6] on the specificity of the anchor group,[7,18] and even on the reaction time.[21] We found that the measured transfer efficiency increases within the first minutes, probably owing to the diffusion-limited reaction between the dyes and the NCs. This increase is followed by a decrease over the next few hours. Because the dye absorption also decreases over this time, this change is most likely a result of a time-dependent degradation of the dyes. As a general trend, the NC–polymer–dye composite was much more stable than the NC–dye composite against dye degradation. The decomposition of the dye is thought to be induced by charge (hole)-transfer process from the NCs to the dyes,[19] which should strongly depend on the NC–dye separation. Thus the polymer backbone that increases the NC–dye separation, leads to a spatial and energetic barrier to the charge transfer. In the same way the polymer spacer also leads to a reduced FRET efficiency which can be seen in the spectra in Figure 1.

In addition to the complications mentioned above, there could be several sources of inhomogeneity within the ensemble of FRET pairs, which can only be addressed by investigating individual luminescing complexes.[22] We therefore performed fluorescence measurements with a scanning confocal optical microscope on single NC–dye and NC–polymer–dye structures blended in thin polymer films.[23] The image shown in Figure 2a represents the total fluorescence of individual NC-dye complexes without the polymer spacer. To visualize the energy-transfer efficiency, we plotted the dichroic ratio ($D=(I_{NC}-I_{dye})/(I_{NC}+I_{dye})$) of the same area (Figure 2b), that is, emission predominantly from the NCs appears in green, whereas red spots reflect emission of the dyes. The red spots in this image are attributed to dye molecules, that were excited by energy transfer from the NCs, because samples of the dye molecules alone showed no detectable fluorescence signal under the same experimental conditions.

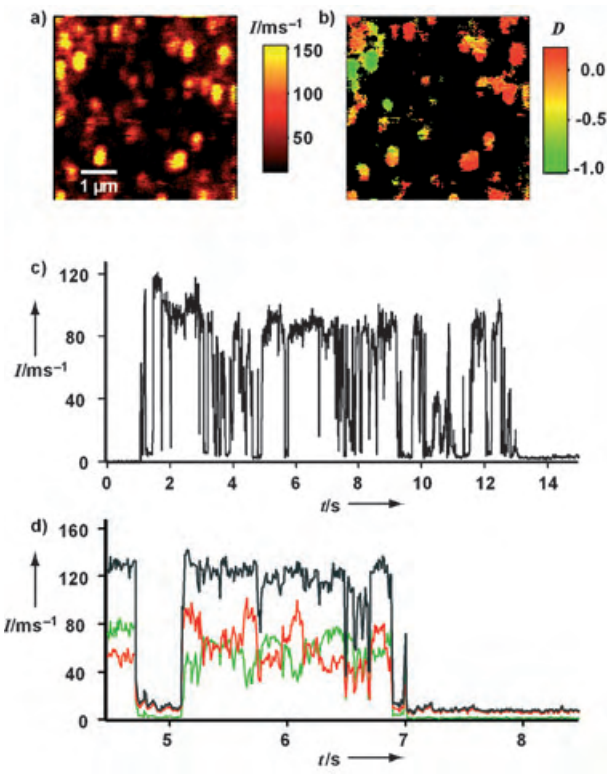

Figure 2. a) Fluorescence image and b) dichroic ratio of the NC–dye complexes upon excitation with $\lambda = 488$ nm (red: high-intensity dye fluorescence; green: high-intensity NC fluorescence). The transfer efficiency can vary greatly between single complexes. c) Integral transient fluorescence intensity of a single NC–polymer–dye complex and d) comparison of the transient total intensity (black), dye fluorescence (red), and NC fluorescence (green). The off periods of the NCs and dyes occur simultaneously and the transfer efficiency fluctuates during the on time.

Clearly there are several complexes where energy transfer cannot be observed at all, which is most likely due to the stochastic labeling process. Following Poisson statistics about 37% of the particles contain no dye molecule at all and about 8% are labeled with more than two dye-molecules and therefore show a higher transfer efficiency.[6] The variation of transfer efficiency can also be attributed to the formation of small aggregates, variations in ligand geometries,[24] or the random distribution of transition dipole alignments between the NCs and dyes.[25] Further it can be seen in Figure 2b that sometimes the lower part of the spots is red and the upper part is green, which is due to dye degradation during the scan (the image is built up line-by-line from bottom to top). This behavior could not be seen for the NC–polymer–dye complexes, highlighting again the higher photostability of this compound. Otherwise, the fluorescence images of the NC–polymer–dye composites were almost identical to those in Figure 2b and are not shown.

Only the confocal fluorescence microscopy experiments on single fluorescing complexes allowed the temporal fluctuations of the FRET efficiencies to be investigated. These experiments were only performed with NC–polymer–dyes, owing to their higher photostability. The transient total emission intensity shown in Figure 2c exhibits the typical

 © 2005 Wiley-VCH Verlag GmbH & Co. KGaA, Weinheim

fluorescence on–off blinking behavior, which can also be observed for isolated NCs not interacting with dye molecules.[26] The off periods of the fluorescence of isolated NCs are explained by a very fast quenching process of the excited state, possibly a result of temporary charging of the NCs.[26] Since this quenching process ($\tau_{nr} \approx 100$ ps)[27] is much faster than the estimated energy-transfer time, which is in the range of the NC fluorescence lifetime ($\tau_{fl} \approx 10$–30 ns),[28,29] the off states of NC and dye in a complex appear simultaneously. In addition it can be seen from Figure 2d that even within the on state of an individual NC–polymer–dye donor–acceptor pair the transfer efficiency is fluctuating in time. Although such fluctuations can be readily observed by studying single complexes, it is difficult to determine their origin because a number of parameters (e.g. separation, orientation, spectral overlap) can influence the energy-transfer efficiency.

In summary we have introduced a versatile ligand which can be modified by a large number of anchors and functional groups. Decoration of the ligand with dye molecules allowed us to investigate electronic excitation energy transfer between the NCs and the attached chromophores. NC–polymer–dye composites were found to be of higher photostability than NC–dye composites which allowed FRET experiments on single composites to be performed. These experiments revealed substantial inhomogeneities within the ensemble of NC–polymer–dye complexes and even dynamic fluctuations of the electronic interactions for single NC–polymer–dye composites, which must be taken into account when interpreting FRET results for separation determinations.

Experimental Section

Synthesis of aminopolymers: Poly(*N*-acryloyloxysuccinimide) (245 mg; 1.45 mmol repeating units) was solved in DMF (12 mL). A solution of Texas-red cadaverine (5.0 mg; 0.007 mmol) in DMF (4 mL) was added. The resulting solution was stirred for 5 h at 50 °C. After that a solution of 1-Boc-1,4-diaminobutane (136.5 mg; 0.725 mmol) in DMF (4 mL) was added and the solution again stirred for 5 h at 50 °C. After addition of hexylamine (2.0 mL) the solution was stirred for further 16 h at 50 °C. The solution was concentrated to about 5 mL in vacuum and poured onto water. After the precipitation of the polymer the mixture was centrifuged and the solvent was decanted. After drying, 286 mg of a red solid was obtained. ^{1}H NMR ($CDCl_3$, 200 MHz): $\delta = 3.07$ (CH_2 α to NH), 2.48 (CH, main chain), 1.47 (CH_2, main chain), 1.40 (CH_3, Boc group), 1.25 (CH_2, side chain), 0.85 ppm (CH_3, hexyl chain).

Cleavage of the Boc group: The polymer was dissolved in CH_2Cl_2 (30 mL). After that trifluoroacetic acid (2.0 mL) was added. The mixture was stirred at room temperature for 2 h. After that 2 N HCl (40 mL) was added and the phases separated. The organic phase was extracted with 2 N HCl (2 × 20 mL). The combined aqueous phases were adjusted to pH 13 by addition of 4 N NaOH solution. After heating, the polymer precipitated as a red solid that was purified by repeated stirring in hot water. The reaction yields 102 mg of the polymer. ^{1}H NMR ($CDCl_3$, 200 MHz): $\delta = 3.11$ (CH_2 α to NH), 2.69 (CH, main chain), 1.49 (CH_2, main chain), 1.26 (CH_2, side chain), 0.86 ppm (CH_3, hexyl chain).

Optical Characterization: Confocal fluorescence images and spectra were obtained at room temperature using a home-built microscope equipped with a piezo scanner (Physical Instruments) and a high NA microscope objective (100×, NA = 1.4). Circularly polarized laser light ($\lambda = 488$ nm) was focused down to a diffraction-limited spot size corresponding to an excitation intensity of 200 W cm^{-2}. To obtain the images, the sample was raster-scanned through the objective and the fluorescence light was guided to EG&G avalanche photo diodes with optical filters being used to eliminate the scattered light. The images are of size 256 × 256 pixels obtained with an integration time of 10 ms/pixel.

Received: October 7, 2004
Published online: March 17, 2005

Keywords: cadmium selenide · dye labeling · energy transfer · nanocrystals · polymer ligands

[1] A. P. Alivisatos, *J. Phys. Chem.* **1996**, *100*, 13226.
[2] H. Weller, *Angew. Chem.* **1993**, *105*, 43; *Angew. Chem. Int. Ed. Engl.* **1993**, *32*, 41.
[3] C. B. Murray, D. J. Norris, M. G. Bawendi, *J. Am. Chem. Soc.* **1993**, *115*, 8706.
[4] X. G. Peng, T. E. Wilson, A. P. Alivisatos, P. G. Schultz, *Angew. Chem.* **1997**, *109*, 113; *Angew. Chem. Int. Ed. Engl.* **1997**, *36*, 145.
[5] M. Bruchez, M. Moronne, P. Gin, S. Weiss, A. P. Alivisatos, *Science* **1998**, *281*, 2013.
[6] A. R. Clapp, I. L. Medintz, J. M. Mauro, B. R. Fisher, M. G. Bawendi, H. Mattoussi, *J. Am. Chem. Soc.* **2004**, *126*, 301.
[7] Y. Ebenstein, T. Mokari, U. Banin, *J. Phys. Chem. B* **2004**, *108*, 93.
[8] D. M. Willard, L. L. Carillo, J. Jung, A. Van Orden, *Nano Lett.* **2001**, *1*, 469.
[9] M. A. Hines, P. Guyot-Sionnest, *J. Phys. Chem.* **1996**, *100*, 468.
[10] X. G. Peng, L. Manna, W. D. Yang, J. Wickham, E. Scher, A. Kadavanich, A. P. Alivisatos, *Nature* **2000**, *404*, 59.
[11] W. Guo, J. J. Li, Y. A. Wang, X. Peng, *J. Am. Chem. Soc.* **2003**, *125*, 3901.
[12] S. Kim, M. G. Bawendi, *J. Am. Chem. Soc.* **2003**, *125*, 14652.
[13] I. Potapova, R. Mruk, S. Prehl, R. Zentel, T. Basche, A. Mews, *J. Am. Chem. Soc.* **2003**, *125*, 320.
[14] http://www.probes.com/servlets/product?item = 2425.
[15] J. E. B. Katari, V. L. Colvin, A. P. Alivisatos, *J. Phys. Chem.* **1994**, *98*, 4109.
[16] S. A. Empedocles, R. Neuhauser, M. G. Bawendi, *Nature* **1999**, *399*, 126.
[17] J. Matensson, *Chem. Phys. Lett.* **1994**, *229*, 449.
[18] F. Patolsky, R. Gill, Y. Weizmann, T. Mokari, U. Banin, I. Willner, *J. Am. Chem. Soc.* **2003**, *125*, 13918.
[19] O. Schmelz, A. Mews, T. Basche, A. Herrmann, K. Müllen, *Langmuir* **2001**, *17*, 2861.
[20] W. Yu, L. Qu, W. Guo, X. Peng, *J. Phys. Chem.* **2003**, *107*, 2854.
[21] P. L. T. M. Frederix, E. L. de Beer, W. Hamelink, H. C. Gerritsen, *J. Phys. Chem. B* **2002**, *106*, 6793.
[22] S. A. Empedocles, R. Neuhauser, K. Shimizu, M. G. Bawendi, *Adv. Mater.* **1999**, *11*, 1243.
[23] C. G. Hübner, G. Zumofen, A. Renn, A. Herrmann, K. Müllen, T. Basche, *Phys. Rev. Lett.* **2003**, *91*, 093903.
[24] S. F. Wuister, A. van Houselt, C. D. M. Donega, D. Vanmaekelbergh, A. Meijerink, *Angew. Chem.* **2004**, *116*, 3091; *Angew. Chem. Int. Ed.* **2004**, *43*, 3029.
[25] T. Vosch, M. Cotlet, J. Hofkens, K. van der Biest, M. Lor, K. Weston, P. Tinnefeld, M. Sauer, L. Latterini, K. Müllen, F. C. De Schryver, *J. Phys. Chem. A* **2003**, *107*, 6920.
[26] M. Nirmal, B. O. Dabbousi, M. G. Bawendi, J. J. Macklin, J. K. Trautman, T. D. Harris, L. E. Brus, *Nature* **1996**, *383*, 802.
[27] P. Roussignol, D. Ricard, J. Lukasik, C. Flyzanis, *J. Opt. Soc. Am. B* **1987**, *4*, 5.
[28] G. Schlegel, J. Bohnenberger, I. Potapova, A. Mews, *Phys. Rev. Lett.* **2002**, *88*, 137401.
[29] B. R. Fisher, H. J. Eisler, N. E. Stott, M. G. Bawendi, *J. Phys. Chem. B* **2004**, *108*, 143.

 © 2005 Wiley-VCH Verlag GmbH & Co. KGaA, Weinheim

Protein Structures

High-Resolution Solid-State NMR Spectroscopy of the Prion Protein HET-s in Its Amyloid Conformation**

*Ansgar B. Siemer, Christiane Ritter, Matthias Ernst, Roland Riek, and Beat H. Meier**

High-resolution solid-state NMR spectroscopy is being established as a technique to enable the determination of biological macromolecular structure with atomic-level resolution. The main focus is on microcrystalline and noncrystalline solids with particular emphasis on the latter for which there are presently no suitable structure-determination methods available. For nanocrystalline compounds, the potential of solid-state NMR spectroscopy has been clearly demonstrated by the complete resonance assignment of several proteins and peptides with sizes of up to 100 residues[1–5] and by the structure determination of an SH3 domain with 62 amino acids.[6] Herein we demonstrate the applicability of high-resolution solid-state NMR-spectroscopic techniques to the structure determination of amyloid fibrils of a prion protein.

The aforementioned pilot applications of solid-state NMR spectroscopy to structure determination were made possible by considerable technical progress over the past few years and through new developments in pulse-sequence methods.[7] In particular, the line width in the ^{13}C and ^{15}N NMR spectra of uniformly labeled microcrystalline compounds has been decreased to 0.5–0.8 ppm.[5,8] These line widths are partially limited by homonuclear *J* couplings, and in samples that lack directly bound ^{13}C atoms, line widths as small as 0.2 ppm have been observed.[8] Herein we demonstrate that approximately the same resolution (up to 0.25 ppm for resonances with resolved *J* couplings or 0.5 ppm for those without resolved *J* couplings) can also be obtained in spectra of amyloid fibrils, in our case the amyloidogenic fragment 218–289 of the HET-s prion protein from the fungus *Podospora anserina.*

The HET-s protein is involved in a genetically controlled programmed-cell-death phenomenon termed heterokaryon incompatibility.[9,10] It is encoded by the *het-s* gene, one of at least nine *het* loci that are involved in heterokaryon incompatibility, and exists in two different forms: a nonprion form and a prion form. The prion form aggregates in vivo to generate amyloid fibrils.[11] Recombinant HET-s can also aggregate in vitro to form amyloid fibrils,[12] in which the C-terminal fragment that consists of residues 218–289 (HET-s(218–289)) forms the protease-resistant part of the fibrils. This fragment has the sequence KI DAIVGRNSAK DIRT-EERARV QLGNVVTAAA LHGGIRISDQ TTNSVE-TVVG KGESRVLIGN EYGGKGFWDN and alone forms amyloid fibrils in vitro.[13] Strains that express HET-s in the nonprion form ([Het-s*]) can undergo a transition to the prion-expressing state ([Het-s]) through contact with [Het-s] strains, by introduction of HET-s fibrils composed of full-length recombinant HET-s,[14] or fibrils formed by the fragment HET-s(218–289).[13] Therefore this fragment is thought to be not only the amyloid-forming part, but also the prion-propagating portion of the HET-s protein.

To our knowledge, there are as yet no published solid-state NMR spectra of prions with sufficient resolution to permit the assignment of resonances in a uniformly labeled sample. In contrast, similarly well-resolved spectra have been recorded for other amyloid fibrils such as the A-β-peptide[15,16] and transthyretin(105–115),[17] in which line widths of 1–2 ppm were found as well as even narrower lines for certain methyl groups.[16] Solid-state NMR spectra of fibrils from a fragment of the mammalian prion protein (PrP) have been obtained[18,19] and show a lower spectral resolution.

Figure 1 shows the homonuclear ^{13}C,^{13}C-correlation spectra of fibrils derived from HET-s(218–289) with a C-terminal His tag collected by using a DREAM polarization transfer (DREAM = dipolar recoupling enhanced by amplitude modulation)[20,21] at a MAS frequency of 40 kHz (MAS = magic-angle spinning). The C'–C^{α} and C'– C^{α}–C^{β} correlations in Figure 1a were recorded in two separate experiments in which the tangential amplitude ramp in the DREAM pulse sequence was taken from low to high amplitude in one case and from high to low amplitude in the other. The labels given in Figure 1 correspond to the tentative assignment of the resonance frequencies as listed in Table 1. The assignment was obtained from 2D and 3D heteronuclear ^{15}N,^{13}C,^{13}C-correlation spectra with adiabatic polarization-transfer techniques.[1,22] This correlation identifies two separate but contiguous segments of the peptide, namely the 23 residues of positions 226–248 and the 20 residues of positions 262–282 (see also Table 1), in which amino acid 274 of the second segment is missing. These resonances explain almost all the signals in the spectra, except for some unassigned cross-peak intensities in the aromatic region and very few unassigned cross-peaks in other regions, leaving 29 residues whose signals cannot be detected. The resonances from the six residues in the His tag are also unassigned. The missing resonances are not a consequence of inefficient cross-polarization. Proton-driven spin-diffusion (PDSD) correlation spectra without cross-polarization (direct excitation of carbon coherence by a 90° pulse) showed additional diagonal peak intensity in the aromatic region, but no new cross-peaks that could lead to the assignment of the backbone atoms of the missing 29 residues. Interestingly, NOE presaturation provided significant signal enhancement for our samples, but no additional resonances were observed.

The line width of the observed resonances is astonishingly narrow. Figure 2 is an extracted portion of Figure 1 which

[*] A. B. Siemer, Dr. M. Ernst, Prof. Dr. B. H. Meier
Laboratory of Physical Chemistry, ETH Zurich
ETH-Hönggerberg, 8093 Zurich (Switzerland)
Fax: (+41) 1632-1621
E-mail: beme@ethz.ch
Dr. C. Ritter, Prof. Dr. R. Riek
Structural Biology Laboratory, The Salk Institute
La Jolla, 92037 CA (USA)

[**] We are grateful to Andreas Hunkeler and Urban Meier for their technical support, to Dr. René Verel and Rochus Keller for scientific advice, and to Dr. Thorsten Luehrs for the EM pictures. This work was supported by the Swiss National Science Foundation (SNF) and the ETH Zurich.

 DOI: 10.1002/anie.200462952 © 2005 Wiley-VCH Verlag GmbH & Co. KGaA, Weinheim

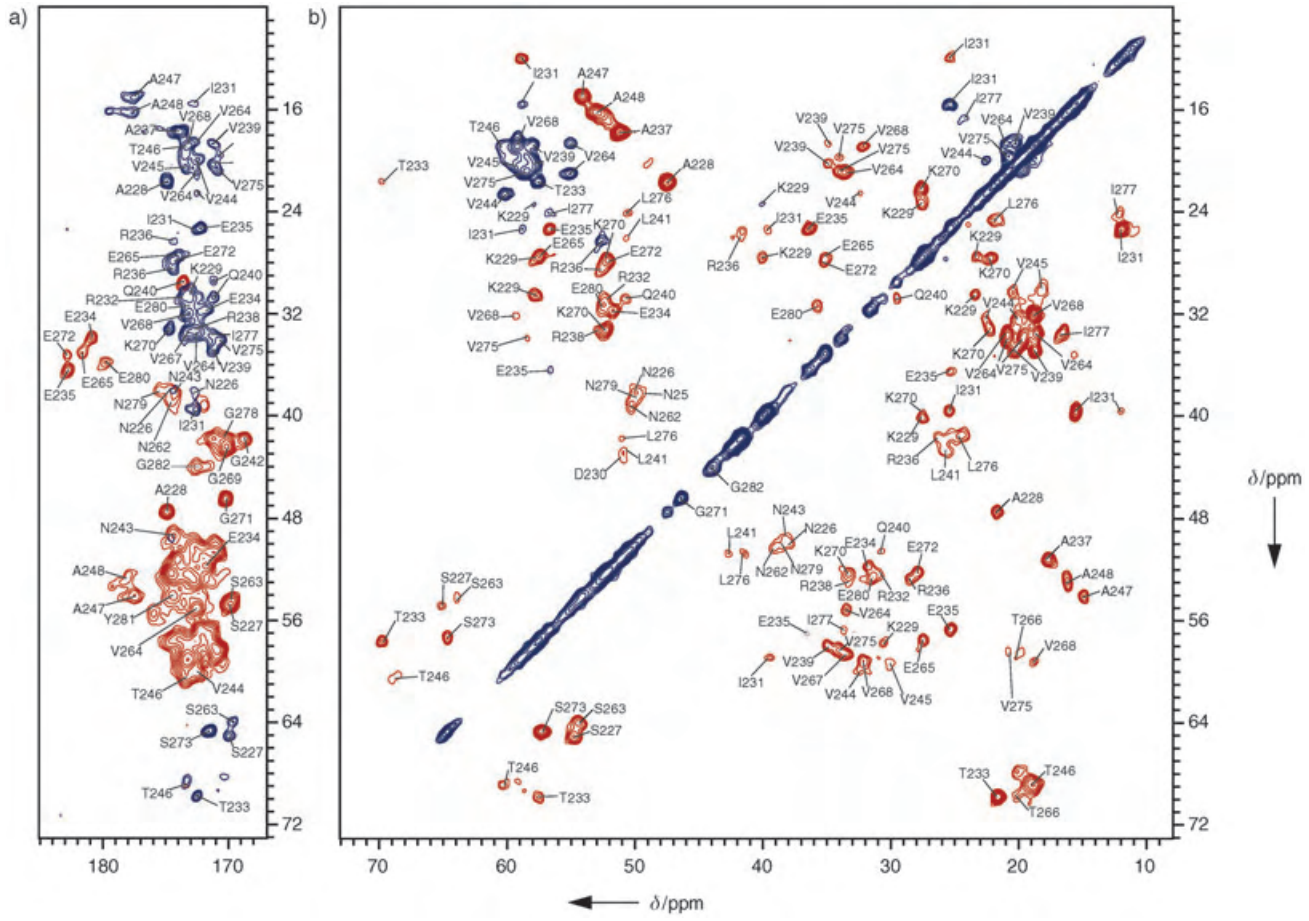

Figure 1. Homonuclear ^{13}C DREAM correlation spectra of fibrillized HET-s(218–289) recorded at 40 kHz MAS. The lower level of the contours was chosen just above the noise level (5% of the maximal intensity); adjacent contour levels differ by a factor of 1.4. Positive contours are shown in blue, negative contours in red. Spectra underwent Fourier transformation with a shifted $\sin^2$ window function with zero filling to 2048 data points. a) Carbonyl region of the DREAM spectra. Positive contours were taken from a spectrum recorded with a tangential DREAM sweep from high- to low-amplitude modulation; negative contours were taken from a similar spectrum but with a sweep from low- to high-amplitude modulation. b) Aliphatic region of the DREAM spectrum recorded with a tangential DREAM sweep from low- to high-amplitude modulation.

shows the well-isolated cross-peaks of Gly271 and Ala228 and a 1D cut through their centers. In the δ_2 dimension, the *J*-split doublet is clearly visible, and several other carbonyl resonances are also resolved sufficiently to show the *J* splitting. The line shape of Gly271, for example, can be fitted by two Gaussian lines with a full width at half height of 30 Hz or 0.2 ppm (left multiplet line) and 37 Hz or 0.24 ppm (right multiplet line) with a splitting of 54 Hz. This line is as narrow as corresponding resonances from microcrystalline samples which indicates that the fibrils in HET-s are highly ordered on a molecular scale.

This observation of high molecular order for part of the molecule stands in striking contrast to the absence of signals from more than one third of the residues from the spectrum which, almost certainly, must be explained by pronounced molecular disorder. This disorder can either be of static or dynamic origin and the spectra measured so far do not permit an unequivocal distinction. The disorder affects only parts of the molecule and must be distinguished from the helical pitch variation observed, for example, by cryoelectron microscopy.[23] Static disorder can lead to line widths of up to 10 ppm in proteins, which is the range of resonance frequencies for the backbone carbon resonances when the two backbone torsion angles vary over the entire range.[24] For such an extreme disorder, the line width would increase by a factor of 20 in a 1D spectrum and up to 20^2 in 2D spectra; such lines may escape detection. Dynamic disorder can also lead to very broad lines if the molecular motion has spectral components in the kHz range, and interferes with the averaging by MAS or with the decoupling. We can exclude $T_{1\rho}$ effects as the cause of the missing signals of the 29 residues, owing to the absence of additional cross-peaks in the PDSD spectra as discussed above.

An attempt was made to freeze out the dynamics of the missing residues. The resulting 1D variable-temperature ^{13}C CP-MAS spectra (CP = cross-polarization) of HET-s(218–289) fibrils are shown in Figure 3. Significant line broadening is observed below −20 °C, but the number of observed resonances seems to be independent of temper-

 © 2005 Wiley-VCH Verlag GmbH & Co. KGaA, Weinheim

Table 1: Chemical shifts (^{13}C and ^{15}N) of the peptide backbone of the assigned regions of HET-s(218–289).[a]

Residue	N	C′	C^{α}	Residue	N	C′	C^{α}
Asn226	125.5	–	49.9	Asn262	128.2	–	50.3
Ser227	119.2	169.9	54.7	Ser263	117.6	169.8	54.3
Ala228	122.7	174.9	47.4	Val264	125.6	172.5	55.0
Lys229	123.6	–	57.7	Glu265	127.3	174.0	57.4
Asp230	117.7	–	51.1	Thr266	112.8	171.0	58.9
Ile231	122.7	172.6	58.9	Val267	124.1	–	58.5
Arg232	129.8	–	52.1	Val268	128.6	173.2	59.2
Thr233	113.5	172.5	57.6	Gly269	113.4	170.0	42.5
Glu234	120.0	171.8	51.7	Lys270	121.5	174.7	52.3
Glu235	117.3	172.2	56.6	Gly271	115.6	170.1	46.4
Arg236	122.8	174.3	52.6	Glu272	128.6	174.3	52.1
Ala237	126.0	173.9	51.1	Ser273	116.3	171.5	57.2
Arg238	117.9	172.7	52.9				
Vla239	122.7	171.1	58.0	Val275	122.9	170.7	58.2
Gln240	126.7	171.1	50.7	Leu276	130.6	–	50.6
Leu241	131.4	–	50.6	Ile277	130.3	171.3	56.6
Gly242	113.7	168.7	41.8	Gly278	111.3	170.0	41.9
Asn243	109.9	174.3	49.2	Asn279	114.5	171.0	49.8
Val244	122.8	172.5	60.0	Glu280	120.4	–	52.6
Val245	129.3	–	59.2	Tyr281	128.9	174.4	54.0
Thr246	116.7	173.3	60.4	Gly282	109.9	172.3	44.0
Ala247	121.1	177.4	54.1				
Ala248	119.3	177.6	53.0				

[a] ^{13}C NMR chemical shifts were referenced to tetramethylsilane, ^{15}N NMR chemical shifts to liquid ammonia.

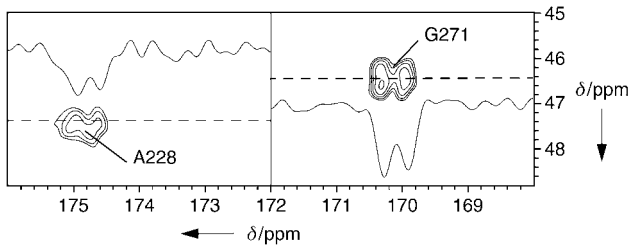

Figure 2. Detail of Figure 1 showing the C^{α}—C′ cross-peaks of Ala228 and Gly271 and 1D cuts through these signals. To get maximal resolution, no window function was applied before the Fourier transformation. The *J*-split doublet of Gly271 is best fit with a pair of Gaussian lines of line width = 30 Hz (left multiplet line), 37 Hz (right multiplet line), and a *J* coupling of 54 Hz. Such differences in line width of a *J*-split doublet have also been observed in simple model compounds but is, to our knowledge, not yet understood.

ature. The changes in spectra with temperature were found to be reversible.

We have shown that the HET-s(218–289) prion protein fibrils are highly ordered for approximately two-thirds of the structure and have found strong evidence for pronounced disorder in the remaining region. The ordered and disordered parts of the protein can be assigned to different protein segments (Table 1). The observation of narrow lines in the NMR spectra and the assignment of the resonances demonstrate the potential of solid-state NMR spectroscopy to elucidate the structures of these molecules in the amyloid form. The collection of structural-constraint information from solid-state NMR spectroscopy is currently in progress.

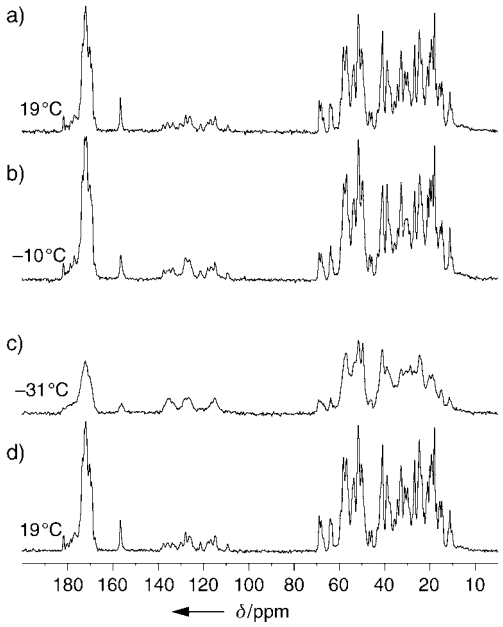

Figure 3. Variable-temperature ^{13}C-CP spectra of HET-s(218–289) recorded at 25 kHz MAS: a) 19°C, 256 scans; b) −10°C, 256 scans; c) −31°C, 256 scans; d) 19°C (after cooling down to −31°C), 430 scans.

Experimental Section

All spectra were recorded with a Bruker AV600 spectrometer (^{1}H-resonance frequency = 600.13 MHz) at a static field of 14.09 T. The 1D CP-MAS spectra were recorded with a Varian probe (2.5 mm) at a MAS frequency of 25 kHz. The initial cross-polarization was done for 1.5 ms with RF-field amplitudes of 70 and 95 kHz on the ^{13}C and ^{1}H channels, respectively. Decoupling was performed at an RF-field amplitude of 130 kHz by using the XiX decoupling Scheme (τ_p = 74 μs, XiX = X inverse X).[25] ^{13}C,^{13}C-correlation spectra were recorded with a 1.8-mm probe[26] at a MAS frequency of 40 kHz and a probe temperature of 15°C. The initial cross-polarization was done for 1 ms with RF-field amplitudes of 90 and 130 kHz on the ^{13}C and ^{1}H channels, respectively. During the DREAM[20,21] recoupling period of 7 ms the RF-field amplitude was tangentially swept between 15 and 26 kHz under the following parameters:[21] $\Delta_{RF}/2\pi = 4.5$ kHz, $d_{est} = 1.5$ kHz and $\bar{\omega}_1/2\pi = 20$ kHz. Continuous-wave decoupling was applied during the DREAM recoupling, and XiX decoupling (τ_p = 70 μs) was applied during t_1 and t_2, both with a RF-field amplitude of 150 kHz. The spectral width was 40 kHz and 62 scans were added together for each of the 1024 t_1 increments which led to a total acquisition time of 55 h. Data were processed with XWINMR (Bruker Biospin) and analyzed with CARA.[27]

Received: December 15, 2004
Published online: March 16, 2005

Keywords: fibrils · NMR spectroscopy · prions · protein structures · structure elucidation

[1] A. Detken, E. H. Hardy, M. Ernst, M. Kainosho, T. Kawakami, S. Aimoto, B. H. Meier, *J. Biomol. NMR* **2001**, *20*, 203.
[2] A. McDermott, T. Polenova, A. Böckmann, K. W. Zilm, E. K. Paulsen, R. W. Martin, G. T. Montelione, *J. Biomol. NMR* **2000**, *16*, 209.

 © 2005 Wiley-VCH Verlag GmbH & Co. KGaA, Weinheim

[3] A. Böckmann, A. Lange, A. Galinier, S. Luca, N. Giraud, M. Juy, H. Heise, R. Montserret, F. Penin, M. Baldus, *J. Biomol. NMR* **2003**, *27*, 323.
[4] J. Pauli, M. Baldus, B. van Rossum, H. de Groot, H. Oschkinat, *ChemBioChem* **2001**, *2*, 272.
[5] T. I. Igumenova, A. E. McDermott, K. W. Zilm, R. W. Martin, E. K. Paulson, A. J. Wand, *J. Am. Chem. Soc.* **2004**, *126*, 6720.
[6] F. Castellani, B. van Rossum, A. Diehl, M. Schubert, K. Rehbein, H. Oschkinat, *Nature* **2002**, *420*, 98.
[7] S. Dusold, A. Sebald, *Annu. Rep. NMR Spectrosc.* **2000**, *41*, 185.
[8] F. Castellani, B. J. van Rossum, A. Diehl, K. Rehbein, H. Oschkinat, *Biochemistry* **2003**, *42*, 11476.
[9] N. L. Glass, I. Kaneko, *Eukaryotic Cell* **2003**, *2*, 1.
[10] S. J. Saupe, *Microbiol. Mol. Biol. Rev.* **2000**, *64*, 489.
[11] V. Coustou-Linares, M.-L. Maddelein, J. Begueret, S. J. Saupe, *Mol. Microbiol.* **2001**, *42*, 1325.
[12] S. Dos Reis, B. Coulary-Salin, V. Forge, I. Lascu, J. Begueret, S. J. Saupe, *J. Biol. Chem.* **2002**, *277*, 5703.
[13] A. Balguerie, S. Dos Reis, C. Ritter, S. Chaignepain, B. Coulary-Salin, V. Forge, K. Bathany, I. Lascu, J.-M. Schmitter, R. Riek, S. J. Saupe, *EMBO J.* **2003**, *22*, 2071.
[14] M. L. Maddelein, S. Dos Reis, S. Duvezin-Caubet, B. Coulary-Salin, S. J. Saupe, *Proc. Natl. Acad. Sci. USA* **2002**, *99*, 7402.
[15] R. Tycko, *Curr. Opin. Struct. Biol.* **2004**, *14*, 96.
[16] A. T. Petkova, G. Buntkowsky, F. Dyda, R. D. Leapman, W. M. Yau, R. Tycko, *J. Mol. Biol.* **2004**, *335*, 247.
[17] C. P. Jaroniec, C. E. MacPhee, V. S. Bajaj, M. T. McMahon, C. M. Dobson, R. G. Griffin, *Proc. Natl. Acad. Sci. USA* **2004**, *101*, 711.
[18] J. Heller, A. C. Kolbert, R. Larsen, M. Ernst, T. Bekker, M. Baldwin, S. B. Prusiner, A. Pines, D. E. Wemmer, *Protein Sci.* **1996**, *5*, 1655.
[19] D. D. Laws, H. M. L. Bitter, K. Liu, H. L. Ball, K. Kaneko, H. Wille, F. E. Cohen, S. B. Prusiner, A. Pines, D. E. Wemmer, *Proc. Natl. Acad. Sci. USA* **2001**, *98*, 11686.
[20] R. Verel, M. Baldus, M. Ernst, B. H. Meier, *Chem. Phys. Lett.* **1998**, *287*, 421.
[21] R. Verel, M. Ernst, B. H. Meier, *J. Magn. Reson.* **2001**, *150*, 81.
[22] M. Ernst, B. H. Meier in *Encyclopedia of Nuclear Magnetic Resonance*, *Vol. 9* (Eds.: D. M. Grant, R. K. Harris), Wiley, Chichester, **2002**, pp. 23.
[23] J. L. Jimenez, J. I. Guijarro, E. Orlova, J. Zurdo, C. M. Dobson, M. Sunde, H. R. Saibil, *EMBO J.* **1999**, *18*, 815.
[24] A. C. Dedios, J. G. Pearson, E. Oldfield, *Science* **1993**, *260*, 1491.
[25] A. Detken, E. H. Hardy, M. Ernst, B. H. Meier, *Chem. Phys. Lett.* **2002**, *356*, 298.
[26] A. Samoson, T. Tuherm, J. Past, *Chem. Phys. Lett.* **2002**, *365*, 292.
[27] R. L. J. Keller, *The Computer Aided Resonance Assignment Tutorial*, Cantina, Goldau, **2004**.

 © 2005 Wiley-VCH Verlag GmbH & Co. KGaA, Weinheim

Catalyzed Cross-Couplings

Modular Diamino- and Dioxophosphine Oxides and Chlorides as Ligands for Transition-Metal-Catalyzed C–C and C–N Couplings with Aryl Chlorides**

Lutz Ackermann and Robert Born*

Transition-metal-catalyzed cross-coupling reactions[1] such as the Suzuki coupling[2] and the Buchwald–Hartwig amination[3] provide reliable tools in synthetic organic chemistry. Aryl iodides and activated aryl bromides can be transformed successfully using simple palladium salts. In contrast, analogous reactions of the more readily available aryl chlorides require recently developed stabilizing ligands.[4] While the ligand design focused primarily on electron-rich alkyl-substituted tertiary phosphines,[1,4,5] Li presented an alternative strategy that employs alkyl-substituted secondary phosphine oxides.[6,7] Their synthesis generally relies on the use of the corresponding metalated species,[6,8] thereby limiting the flexibility of this approach. On the other hand, heteroatom-substituted phosphine oxides are easily accessible from diamines, diols, and amino alcohols.[9,10] Hence, we wondered if phosphine oxides derived from diamines or diols could be utilized as ligands for the cross-coupling of aryl chlorides.[11,12] Herein, we present the first use of inexpensive air-stable diaminophosphine oxides in palladium-catalyzed Suzuki-type reactions of aryl chlorides. Furthermore, unprecedented applications of a diaminophosphine chloride[13] to palladium- and nickel-catalyzed C–C and C–N bond-forming reactions are reported.

We synthesized three sterically encumbered, air-stable phosphine oxides **3** directly from PCl_3 and the corresponding diamine in a one-pot procedure (Scheme 1). The reactivity of

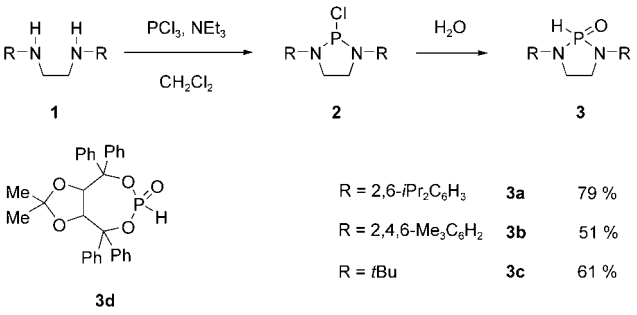

Scheme 1. Synthesis of novel diaminophosphine oxides **3**.

[*] Dr. L. Ackermann, R. Born
Ludwig-Maximilians-Universität München
Department Chemie und Biochemie
Butenandtstrasse 5–13, Haus F, 81377 München (Germany)
Fax: (+49) 89-2180-77425
E-mail: lutz.ackermann@cup.uni-muenchen.de

[**] We thank Prof. Paul Knochel, the DFG (Emmy Noether-Programm), and the Ludwig-Maximilians-Universität for support.

Supporting information for this article is available on the WWW under http://www.angewandte.org or from the author.

 © 2005 Wiley-VCH Verlag GmbH & Co. KGaA, Weinheim DOI: 10.1002/anie.200462371

the complexes generated from diaminophosphine oxides **3a–c** as well as from taddol derivative **3d** was probed in the palladium-catalyzed Suzuki reaction of 4-chlorobenzotrifluoride (**4a**) with phenylboronic acid (**5a**) (Table 1). Preliminary experiments showed THF and KO*t*Bu to be the best solvent and bases, respectively, when the di(isopropyl)phenyl-substituted ligand **3a** was used. Although the reaction proceeded well at ambient temperature (entry 2), quantitative conversion of aryl chloride **4a** was achieved only with 5 mol% of the palladium catalyst (entries 3 and 4). Changing the substituents on nitrogen to mesityl groups resulted in decreased conversion (entry 5). A significant improvement of catalytic performance was accomplished with the sterically hindered ligand **3c** (entry 6) or the taddol derivative **3d** (entry 7).

The optimized catalyst system facilitated the efficient conversion of a representative set of electron-rich aryl chlorides (Table 2). In addition, the catalyst enabled the synthesis of *ortho*-substituted biaryls (entries 3–5) and the functionalization of heteroaromatic aryl chlorides (entries 8 and 9) with good to excellent yields of isolated product.

Application of diaminophosphine oxide **3c** to palladium-catalyzed Buchwald–Hartwig amination reactions led to unsatisfactory results, yielding predominantly the corresponding hydrodehalogenated arenes. However, during studies directed towards an in situ preparation of ligands we found that a complex generated from phosphine chloride **2c** and $[Pd(dba)_2]$[14] resulted in efficient amination of aryl chlorides (Table 3). The protocol is applicable to various amines **7** (entries 1–4 and 12) and diversely substituted aryl chlorides **4** (entries 1 and 5–8), including deactivated 4-chloroanisole (**4h**) (entry 8). Analogous aryl bromides **4m** and **4n** were converted quantitatively but provided only slightly improved yields of isolated product due to reduction of the aryl halide (entries 10 and 11). It is worth noting that the use of chloride **2c** enabled efficient conversion of deactivated chloroanisole **4h** in a representative set of palladium- and nickel-catalyzed reactions such as Suzuki reaction (entry 14), Buchwald arylation of ketone **8** (entry 16), and nickel-catalyzed Kumada cross-coupling with Grignard reagent **9** (entry 17). While pyridine **6i** was obtained in excellent yield (entry 15), the synthesis of tetra-*ortho*-substituted biaryls was not viable.[5a,15]

Table 2: Scope of the Suzuki cross-coupling reaction employing phosphine oxide **3c**.[a]

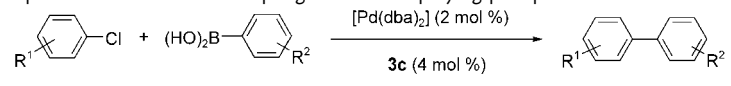

4 **5** **6**

Entry	Aryl chloride	Boronic acid	Product	Yield [%][b]
1	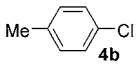 **4b**	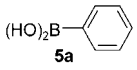 **5a**	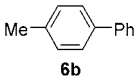 **6b**	75
2	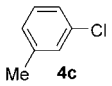 **4c**	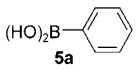 **5a**	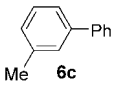 **6c**	78
3	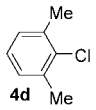 **4d**	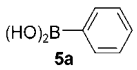 **5a**	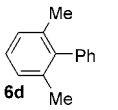 **6d**	70
4	**4e**	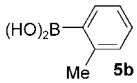 **5b**	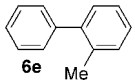 **6e**	93
5	**4f**	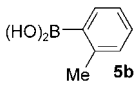 **5b**	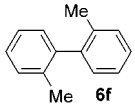 **6f**	95
6	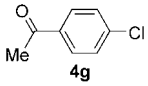 **4g**	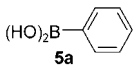 **5a**	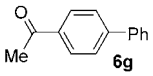 **6g**	81
7	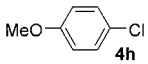 **4h**	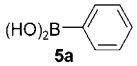 **5a**	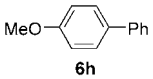 **6h**	70
8	**4i**	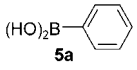 **5a**	**6i**	88
9	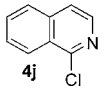 **4j**	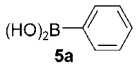 **5a**	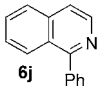 **6j**	94

[a] Reaction conditions: **4** (1.00 mmol), **5** (1.50 mmol), KO*t*Bu (3.00 mmol), $[Pd(dba)_2]$ (2 mol%), **3c** (4 mol%), THF (5 mL). [b] Yield of isolated product.

Table 1: Air-stable phosphine oxides **3** in Suzuki cross-coupling reactions.[a]

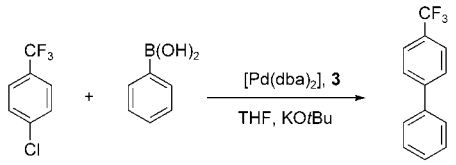

4a **5a** **6a**

Entry	Ligand	$[Pd(dba)]_2$ [mol%]	*t* [h]	*T* [°C]	Yield [%][b]
1	–	2.0	12	60	<2
2	**3a**	5.0	14	20	83
3	**3a**	5.0	2	60	97
4	**3a**	2.0	18	60	68
5	**3b**	5.0	16	60	(12)[c]
6	**3c**	2.0	3	60	94
7	**3d**	2.0	11	60	92

[a] Reaction conditions: **4a** (1.00 mmol), **5a** (1.50 mmol), KO*t*Bu (3.00 mmol), $[Pd(dba)_2]$/**3** = 1:2, THF (5 mL); dba = dibenzylideneacetone. [b] Yield of isolated product. [c] Determined by GC analysis.

 © 2005 Wiley-VCH Verlag GmbH & Co. KGaA, Weinheim

Table 3: Transition-metal-catalyzed coupling reactions of aryl chlorides **4** using phosphine chloride **2c** (see Scheme 1; R = *t*Bu).[a]

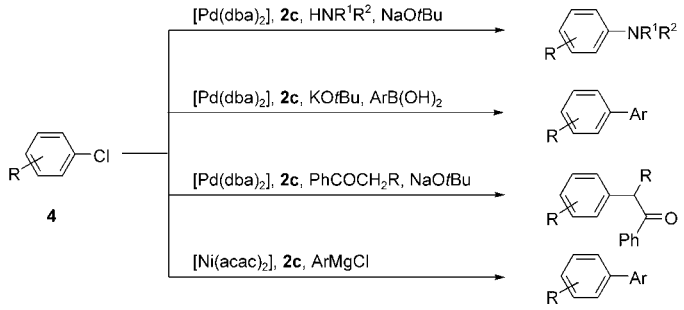

Entry	Aryl halide	Pronucleophile	*t* [h]	Product	Yield [%][b]	Entry	Aryl halide	Pronucleophile	*t* [h]	Product	Yield [%][b]
1	**4a**	**7a**	3	**10a**	82	10	**4m**	**7a**	1	**10f**	83
2	**4a**	**7b**	3	**10b**	81	11	**4n**	**7a**	1	**10h**	68
3	**4a**	PhNHMe **7c**	2	**10c**	80	12	**4e**	**7e**	20	**10i**	62[d]
4	**4a**	Ph_2NH **7d**	12	**10d**	59	13	**4a**	**5a**	15	**6a**	89
5	**4e**	**7a**	5	**10e**	81	14	**4h**	**5a**	20	**6h**	62
6	**4b**	**7a**	16	**10f**	75	15	**4i**	**5a**	2	**6i**	91
7	**4c**	**7a**	5	**10g**	81	16	**4h**	**8**	24	**11**	60
8	**4h**	**7a**	6	**10h**	63	17	**4h**	PhMgCl **9**	24	**6h**	64
9	**4h**	**7a**	8	**10h**	62[c]						

[a] General reaction conditions: Amination: **4** (1.00 mmol), **7** (1.20 mmol), NaO*t*Bu (1.30 mmol), $[Pd(dba)_2]$ (5 mol%), **2c** (10 mol%), toluene (2.5 mL), 105°C. Ketone arylation: **4** (1.00 mmol), **8** (1.20 mmol), NaO*t*Bu (1.30 mmol), $[Pd(dba)_2]$ (2 mol%), **2c** (4 mol%), toluene (2.5 mL), 105°C. Kumada reaction: **4** (1.00 mmol), **9** (1.50 mmol), $[Ni(acac)_2]$ (3 mol%), **2c** (3 mol%) in THF (5 mL), 20°C. Suzuki reaction: **4** (1.00 mmol), **5** (1.50 mmol), KO*t*Bu (3.00 mmol), $[Pd(dba)_2]$ (5 mol%), **2c** (10 mol%), THF (5 mL), 60°C. [b] Yield of isolated product. [c] Using **12** (10 mol%) instead of **2c**. [d] Conversion, determined by GC analysis.

NMR studies directed towards elucidating the catalyst's mode of action in amination reactions were performed. Addition of phosphine chloride **2c** to a solution of $[Pd(dba)_2]$ in toluene gave rise to a compound displaying a singlet low-field resonance at $\delta = 308.7$ ppm in the ^{31}P NMR spectrum, suggesting the formation of a phosphenium species.[14] Upon addition of an excess NaO*t*Bu to this mixture, phosphine **12** ($\delta = 110.3$ ppm) was formed along with a compound exhibiting a resonance at $\delta = 115.2$ ppm, which was also selectively generated by reaction of phosphine **12** with $[Pd(dba)_2]$.

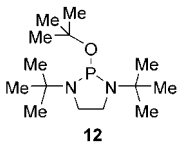
12

In the amination reaction of aryl chloride **4h** the system **12**/$[Pd(dba)_2]$ exhibited catalytic activity comparable to that observed with **2c**/$[Pd(dba)_2]$ (Table 3, entries 8 and 9). To the best of our knowledge, this is an unprecedented example for the use of a highly modular, diaminooxophosphine (daop) ligand in palladium-catalyzed amination reactions of deactivated aryl chlorides.[11]

In summary, we have presented the use of air-stable diamino- and dioxophosphine oxides as ligands in palladium-catalyzed Suzuki reactions of aryl chlorides. The unprecedented use of a diaminophosphine chloride as a ligand precursor in palladium- and nickel-catalyzed C–C and C–N bond-forming reactions of aryl chlorides has also been demonstrated. Further studies are directed towards an improvement of the present systems.

 © 2005 Wiley-VCH Verlag GmbH & Co. KGaA, Weinheim

Experimental Section

Representative procedure for palladium-catalyzed amination using phosphine chloride **2c** (Table 3, entry 8): A solution of [Pd(dba)$_2$] (29 mg, 0.05 mmol, 5 mol%) and phosphine chloride **2c** (23 mg, 0.10 mmol, 10 mol%) in toluene (2.5 mL) was stirred for 10 min at ambient temperature under N_2. NaO*t*Bu (125 mg, 1.3 mmol), morpholine (**7a**) (105 mg, 1.2 mmol), and 4-chloroanisole (**4h**) (142 mg, 1.00 mmol) were added, and the resulting mixture was stirred at 105 °C for 6 h. Et_2O (50 mL) and brine (50 mL) were added to the cold reaction mixture. The separated aqueous phase was extracted with Et_2O (2 × 50 mL). The combined organic layers were dried over $MgSO_4$ and concentrated in vacuo. The remaining residue was purified by column chromatography on silica gel (*n*-pentane/Et_2O, 4:1→2:1) to yield **10h** as a white solid (121 mg, 63%).

Received: October 20, 2004
Published online: March 16, 2005

Keywords: cross-coupling · nickel · P ligands · palladium · phosphorus trichloride

[1] a) *Metal-catalyzed Cross-Coupling Reactions* (Eds.: A. de Meijere, F. Diederich), Wiley-VCH, Weinheim, **2004**; b) J. Tsuji, *Palladium Reagents and Catalysts*, 2nd ed., Wiley, Chichester, **2004**.

[2] a) M. Miura, *Angew. Chem.* **2004**, *116*, 2251 – 2253; *Angew. Chem. Int. Ed.* **2004**, *43*, 2201 – 2203; b) A. Suzuki in *Modern Arene Chemistry* (Ed.: D. Astruc), Wiley-VCH, Weinheim, **2002**, pp. 53 – 106.

[3] a) J. F. Hartwig in *Modern Arene Chemistry* (Ed.: D. Astruc), Wiley-VCH, Weinheim, **2002**, pp. 107 – 168; b) B. H. Yang, S. L. Buchwald, *J. Organomet. Chem.* **1999**, *576*, 125 – 146.

[4] A. F. Littke, G. C. Fu, *Angew. Chem.* **2002**, *114*, 4350 – 4386; *Angew. Chem. Int. Ed.* **2002**, *41*, 4176 – 4211.

[5] For representative examples, see: a) S. D. Walker, T. E. Barder, J. R. Marinelli, S. L. Buchwald, *Angew. Chem.* **2004**, *116*, 1907 – 1912; *Angew. Chem. Int. Ed.* **2004**, *43*, 1871 – 1876; b) J. P. Stambuli, R. Kuwano, J. F. Hartwig, *Angew. Chem.* **2002**, *114*, 4940 – 4942; *Angew. Chem. Int. Ed.* **2002**, *41*, 4746 – 4748; c) F. Rataboul, A. Zapf, R. Jackstell, S. Harkal, T. Riermeier, A. Monsees, U. Dingerdissen, M. Beller, *Chem. Eur. J.* **2004**, *10*, 2983 – 2990; d) M. Nishiyama, T. Yamamoto, Y. Koie, *Tetrahedron Lett.* **1998**, *39*, 617 – 620, and references therein; e) for the use of *N*-heterocyclic carbenes, see: W. A. Herrmann, *Angew. Chem.* **2002**, *114*, 1342 – 1363; *Angew. Chem. Int. Ed.* **2002**, *41*, 1290 – 1309.

[6] a) G. Y. Li, *Angew. Chem.* **2001**, *113*, 1561 – 1564; *Angew. Chem. Int. Ed.* **2001**, *40*, 1513 – 1516; b) G. Y. Li, US patent 6124462, **2000**.

[7] Selected applications: a) C. Wolf, R. Lerebours, *Org. Lett.* **2004**, *6*, 1147 – 1150; b) W. Yang, Y. Wang, J. R. Corte, *Org. Lett.* **2003**, *5*, 3131 – 3134; c) J. W. Han, J. C. Castro, K. Burgess, *Tetrahedron Lett.* **2003**, *44*, 9359 – 9362; d) G. Y. Li, *J. Organomet. Chem.* **2002**, *653*, 63 – 68; e) G. Y. Li, W. J. Marshall, *Organometallics* **2002**, *21*, 590 – 591; f) G. Y. Li, *J. Org. Chem.* **2002**, *67*, 3643 – 3650; g) G. Y. Li, G. Zheng, A. F. Noonan, *J. Org. Chem.* **2001**, *66*, 8677 – 8681.

[8] For a combinatorial approach, see: G. Y. Li, P. J. Fagan, P. L. Watson, *Angew. Chem.* **2001**, *113*, 1140 – 1143; *Angew. Chem. Int. Ed.* **2001**, *40*, 1106 – 1109.

[9] A representative example: A. de la Cruz, K. J. Koeller, N. P. Rath, C. D. Spilling, I. C. F. Vasconcelos, *Tetrahedron* **1998**, *54*, 10513 – 10524.

[10] Recent examples for the use in homogenous catalysis: a) T. Nemoto, T. Matsumoto, T. Masuda, T. Hitomi, K. Hatano, Y. Hamada, *J. Am. Chem. Soc.* **2004**, *126*, 3690 – 3691; b) X. Linghu, J. R. Potnick, J. S. Johnson, *J. Am. Chem. Soc.* **2004**, *126*, 3070 – 3071.

[11] Verkade recently disclosed successful palladium-catalyzed cross-coupling reactions of aryl chlorides using a triaminophosphine with a bicyclic framework: a) J. You, J. G. Verkade, *Angew. Chem.* **2003**, *115*, 5205 – 5207; *Angew. Chem. Int. Ed.* **2003**, *42*, 5051 – 5053; b) J. G. Verkade, *Top. Curr. Chem.* **2003**, *233*, 1 – 44; c) for a discussion of the σ-donor abilities of diamino phosphines, see: M. L. Clarke, D. L. Cole-Hamilton, A. M. Z. Slawin, J. D. Woollins, *Chem. Commun.* **2000**, 2065 – 2066.

[12] For a single account on the use in palladium-catalyzed cross-coupling reactions on aryl bromides, see: R. B. Bedford, S. L. Hazelwood, M. E. Limmert, J. M. Brown, S. Ramdeehul, A. R. Cowley, S. J. Coles, M. B. Hursthouse, *Organometallics* **2003**, *22*, 1364 – 1371.

[13] Recently, a patent was filed describing the use of a dialkyl-substituted phosphine chloride in amination and Suzuki reactions: G. Y. Li, US patent application 20040147392, July 29, **2004**.

[14] a) An example of oxidative addition of a chlorodiazaphospholene to yield a phosphenium complex: D. Gudat, A. Haghverdi, M. Nieger, *J. Organomet. Chem.* **2001**, *617–618*, 383 – 394; See, also: b) H. Nakazawa, *Adv. Organomet. Chem.* **2004**, *50*, 107 – 143; c) D. Gudat, *Coord. Chem. Rev.* **1997**, *163*, 71 – 106.

[15] G. Altenhoff, R. Goddard, C. W. Lehmann, F. Glorius, *J. Am. Chem. Soc.* **2004**, *126*, 15195 – 15201, and references therein.

 © 2005 Wiley-VCH Verlag GmbH & Co. KGaA, Weinheim

Organic Conductors

3D-Hybrid Networks with Controllable Electrical Conductivity from the Electrochemical Deposition of Terthiophene-Functionalized Polyphenylene Dendrimers**

Hermann John, Roland Bauer, Pamela Espindola, Prashant Sonar, Jürgen Heinze, and Klaus Müllen**

One of the striking properties of organic conjugated polymers, such as polypyrrole or polythiophene, is their electrical conductivity, which develops during doping of their π systems.[1–3] Normally, semiconducting behavior is observed, but

[*] Dipl.-Chem. H. John, Lic. en Qca. P. Espindola, Prof. Dr. J. Heinze
Institute of Physical Chemistry
University of Freiburg
Albertstrasse 21, 79104 Freiburg (Germany)
Fax: (+49) 761-2036237
E-mail: juergen.heinze@physchem.uni-freiburg.de
Dipl.-Chem. R. Bauer, Dipl.-Chem. P. Sonar, Prof. Dr. K. Müllen
Max-Planck-Institute for Polymer Research
Ackermannweg 10, 55128 Mainz (Germany)
Fax: (+49) 6131-379350
E-mail: muellen@mpip-mainz.mpg.de

[**] Financial support by the Deutsche Forschungsgemeinschaft through SFB428 (Freiburg) and SFB625 (Mainz) is gratefully acknowledged.

Supporting information for this article is available on the WWW under http://www.angewandte.org or from the author.

 DOI: 10.1002/anie.200462378 © 2005 Wiley-VCH Verlag GmbH & Co. KGaA, Weinheim

at high doping levels the metallic regime may be reached. It has been assumed that the charge-carrier transport proceeds along a polymer chain and depends on the chain length of the so-called one-dimensional conductors.[4,5] The effective conjugation length and even the real length of conjugated polymers does in general not exceed 16–30 units.[6,7] Further findings indicate the formation of networks during the electropolymerization.[8] Consequently, new concepts have been developed which involve, among others, interchain charge-hopping processes.[9] Nevertheless, clear evidence for such intrinsic 2D or even 3D conductivities on a molecular level in conjugated polymers is elusive owing to the lack of suitable molecular structures.

A new class of monodisperse macromolecules which opens the way to the synthesis of complex three-dimensional (3D) systems are dendrimers.[10–13] They represent a key stage in the ongoing evolution of macromolecular and polymer chemistry. Along with a wide range of flexible-backbone dendrimers, rigid shape-persistent species, such as phenylacetylene,[14] phenylenevinylene,[15] thiophene dendrimers,[16] and the herein presented polyphenylene dendrimers[17] have been developed in recent years. These shape-persistent, nanometer-sized macromolecules exhibit unique self-assembly properties; spherical oligomeric aggregates, nanofibers,[18] and extended layers with parallel rods[19] have been observed.

We have now synthesized new polyphenylene dendrimers built around a tetraphenylmethane core and decorated with terthiophene units at the periphery (**7a** and **7b**, Scheme 1). Owing to the stiffness and shape-persistence of the dendrimers the π-conjugated terthiophene units are exposed in a radial fashion on the surface, thus maximizing the possibilities for intermolecular interactions. And indeed, upon electrochemical or chemical oxidation the "hedgehog-like" core–shell system **7a** formed a network. Analogous syntheses of 3D systems using thiophene bridges have been reported.[13,20] Moreover, the possibility to partially planarize the four

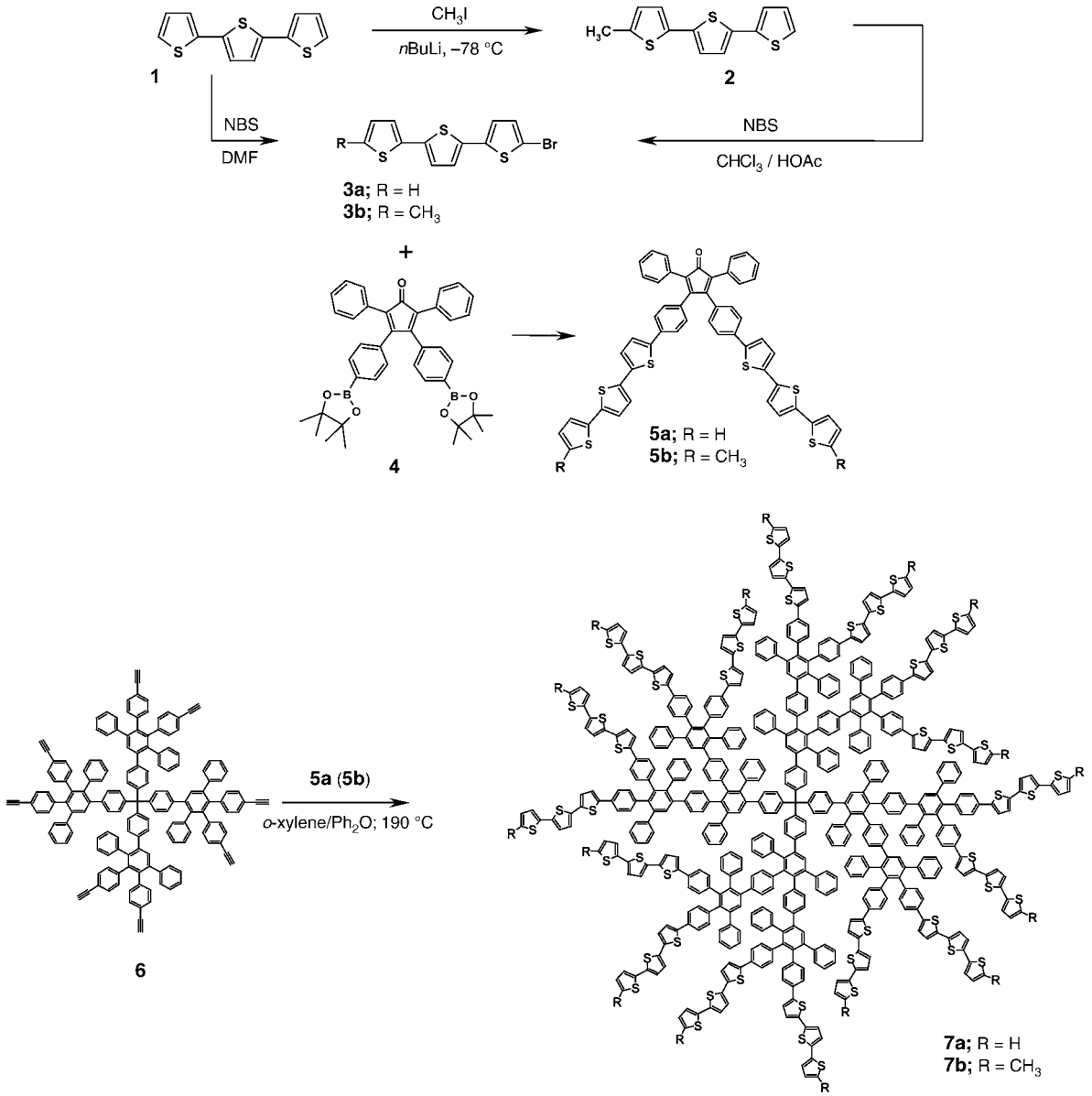

Scheme 1. Synthesis of terhiophene-functionalized polyphenylene dendrimers **7a** and **7b**. NBS = *N*-bromosuccinimide.

 © 2005 Wiley-VCH Verlag GmbH & Co. KGaA, Weinheim

oligophenylene wings of the dendrimer by anodic cyclodehydrogenation and, thus, to generate four conductive 2D layers that are almost isotropically tetrahedrally arranged make **7a** and **7b** suitable as the building blocks of a 3D network.

Herein, we show that 3D hybrid networks formed by the electrochemical oxidation of **7a** exhibit remarkable conducting properties. One key point is that a maximum conductivity is observed when the conjugated systems are embedded in a 3D network, the other point is that in this special network there are two independent regimes of conductivity.

The synthesis of dendrimer **7a** is carried out as outlined in Scheme 1 according to the divergent synthetic method for polyphenylene dendrimers.[17] The build-up of the terthiophene-substituted cyclopentadienones **5** requires the unsymmetrical terthiophene derivatives **3** which are available from established procedures.[21]

The Suzuki cross-coupling reaction of **3a** and **3b** with the dioxaborolane-functionalized cyclopentadienone **4** results in the desired cyclopentadienone building blocks **5a** and **5b** in acceptable yields (64% and 61%). The subsequent Diels–Alder cycloaddition of **5a** and **5b** with the octaethinyl-functionalized first-generation polyphenylene dendrimer **6** in *o*-xylene/diphenyl ether provides the final dendrimers **7**. They are purified by repetitive washing with a dichloromethane/methanol mixture and isolated as yellow powders with low solubility in common organic solvents. Their structure is confirmed by means of NMR spectroscopy and MALDI-TOF mass spectrometry, with special attention being paid to the complete Diels–Alder reactions. All MALDI-TOF mass spectra show peaks that can clearly be correlated with the structure of the terthiophene-functionalized dendrimers: mass of **7a** (8827 g mol^{-1}) and **7b** (9606 g mol^{-1}). The UV/Vis and emission spectra of **7a**, **7b**, and of some precursor molecules, as well as their detailed analytical data are presented as Supporting Information.

The electrochemical oxidation of the terthiophene-substituted dendrimer **7a** in methylene chloride commences at a potential of +0.81 V and during continuous potentiodynamic cycling between 0 and 1.2 V an electroactive film is deposited on the electrode (see Supporting Information). This film is redoxactive between 0.4 and 1.1 V. At higher potentials of up to 1.2 V the current almost drops to zero (Figure 1). The resulting film is extremely stable and can be charged and discharged without any degradation. In accordance with these data, UV/Vis measurements show that the stepwise chemical oxidation of **7a**, the dendrimer carrying the unsubstituted terthiophene units, leads to a gradual decrease of the π–π* absorption at 390 nm while two new transitions develop around 600 and 1200 nm (Figure 2a). During discharging a new band appears in the deposited material at 475 nm (Figure 2b). The presence of this band can be rationalized by the irreversible intermolecular coupling of a part of the terthiophene units to give sexithiophene moieties. Within several charging/discharging cycles the absorption band at 475 nm intensifies indicating that the number of sexithiophene bridges in the film increases. The absorption band at 407 nm corresponds to the absorption of the remaining phenyl-substituted terthiophene units. After coupling, an

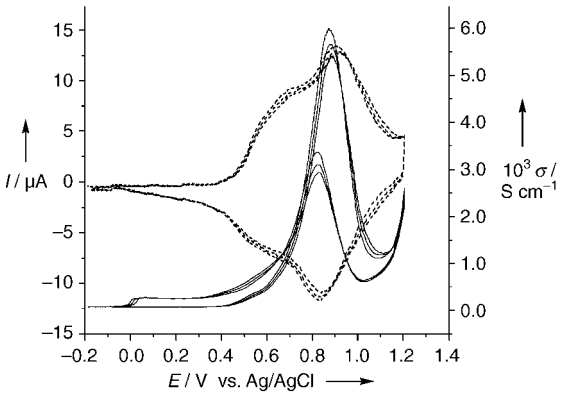

Figure 1. In situ conductivity measurement in the potential range between 0.0 and 1.2 V. The film was generated in a solution of **7a** and measured in a monomer-free cell. Polymerization: two potentiodynamic cycles between 0.0 and 1.5 V, 50 mV s^{-1}, $c = 10^{-3}$ mol L^{-1} in CH_2Cl_2/Bu_4NPF_6. Measurement: $\nu = 5$ mV s^{-1}, CH_2Cl_2/Bu_4NPF_6, room temperature; ----- current, —— conductivity.

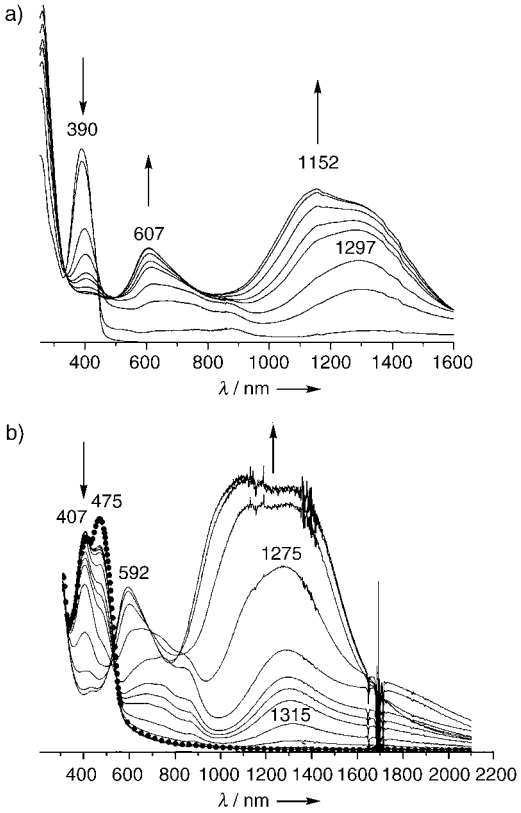

Figure 2. a) Sequential UV/Vis spectra recorded during chemical oxidation of dendrimer **7a** in $CHCl_3$ solution with thianthrenium perchlorate. b) Sequential UV/Vis spectra recorded during electrochemical oxidation (—— between 0.0 and 0.725 V) and after discharging (••••• 0.0 V) of a polymer film of **7a**.

analysis of the terthiophene and sexithiophene absorption bands indicated the approximately 8 out of a possible 16 linkages had formed. All this data indicates that a 3D network has formed with oligomeric thiophene bridges between the dendrimeric cores. When the α position of the terthiophene units is blocked, such as in **7b**, the chemical and the

 © 2005 Wiley-VCH Verlag GmbH & Co. KGaA, Weinheim

electrochemical oxidation process at +0.87 V are fully reversible (see Supporting Information) and the starting species is regenerated thus demonstrating that the irreversible oxidative coupling of the terthiophene units in **7a** occurs at its free α position.

The in situ conductivity measurements of the coupling product of **7a** show an increase in the conductivity during voltammetric charging of the thiophene chains in the deposited material. However, this conductivity passes a maximum approximately at the half-charged level and drops to low values at higher potentials when all the dicationic states in the sexithiophene chains are occupied (Figure 1). In view of the bipolaron model this finding is surprising, since the occupied bipolaron states should exhibit a maximum of conductivity.[4,22] A better understanding results when hopping processes are assumed that are similar to those observed in organic radical-ion salts.[23,24] All the experimental data obtained from conductivity measurements with radical-ion salts reveal that a conductivity maximum will be reached when only half of the redox states are charged, because the number of mobile charge carriers hopping intermolecularly between isoenergetic states approaches its highest value.

Our oligomers and radical-ion stacks show a striking similarity in the increase and decrease of conductivity as a function of the charging level, a result that suggests that identical conductivity mechanisms are operating in both systems. The only obvious difference is that radical-ion salts are well-ordered crystalline materials in which the hopping processes of charges preferably take place along the stacks while the dendritic networks are amorphous leading to a 3D charge transport.

Applying higher potentials than 1.2 V induces new oxidation processes (Figure 3a) which affect the dendritic core and slowly produces planarized "propeller blades" by cyclodehydrogenation reactions. Such oxidation processes can be carried out with chemical oxidants, such as $FeCl_3$,[25] and the oxidation of **8** which has a purely dendrimer core (see below) supports this conclusion. In the voltammetric response, this new additional electrochemical oxidation can be recognized by a steep increase of the current which, on the one hand, is consumed for the cyclodehydrogenation reaction, and on the other, leads to the charging of the slowly forming planarized propeller structures. The most important observation is that the conductivity in this new material increases up to a value of 0.13 $S\,cm^{-1}$ despite the fact that the redox charges do not exceed a value of 5×10^{-4} C. This result in combination with the experimental data of **8** (see below) shows that charge transport takes place between dendritic core units and, moreover, that the formation of the network structure drastically increases conductivity.

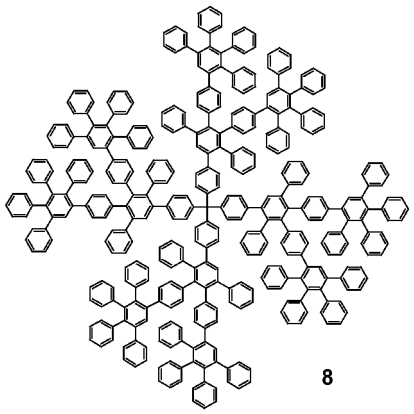

8

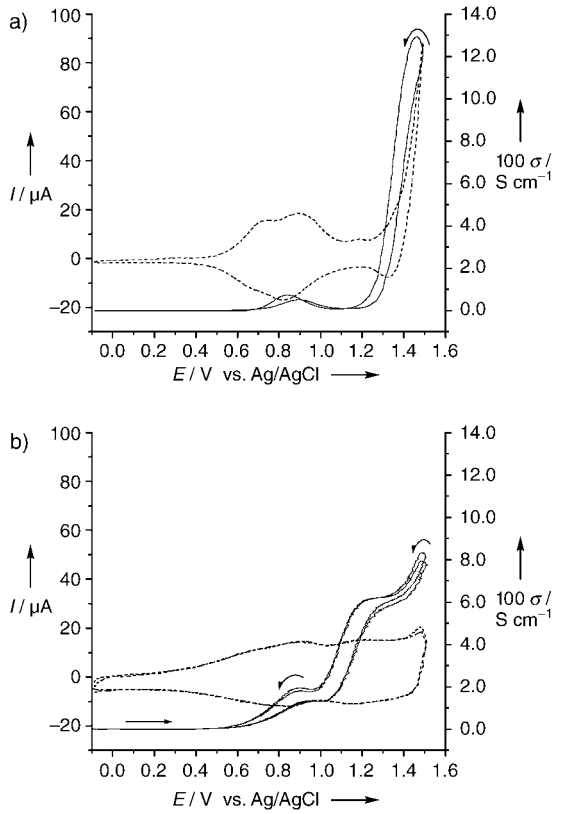

Figure 3. In situ conductivity measurements in the potential range between 0.0 and 1.5 V. a) The film was generated in solution of **7a** by polymerization (two potentiodynamic cycles between 0.0 and 1.5 V, 50 $mV\,s^{-1}$, $c=10^{-3}$ $mol\,L^{-1}$ in CH_2Cl_2/Bu_4NPF_6). b) The film was generated in solution of **8** by electrochemical deposition (300 potentiodynamic cycles between 0.0 and 1.5 V, 50 $mV\,s^{-1}$, $c=10^{-4}$ $mol\,L^{-1}$ in CH_2Cl_2/Bu_4NPF_6). Both films of the same amount of dendrimer were measured in a monomer-free cell (CH_2Cl_2/Bu_4NPF_6, $\nu=5$ $mV\,s^{-1}$, room temperature).

By using suitable precursor molecules a cross-linked material can be generated in which there are two separate regimes of electrical conductivities. There is a low-conductivity regime that can be reached by the redox charging of the thiophene system in the potential range between 0.5 and 0.9 V and subsequently a high-conductivity regime linked to the graphene core between 1.3 and 1.6 V. To our knowledge, this is the first example of an organic conducting polymer in which two separated regimes of conductivity have been detected. These regimes can be addressed by appropriate charging of the polymer in a suitable potential range.

The anodic oxidation of **8**, the hydrocarbon dendrimer without terthiophene units, starts at potentials above 1.35 V ($E_{pa}=+1.7$ V) vs. Ag/AgCl and leads to a deposition of a black material on the working electrode. Multisweep voltammetry in the potential range between 0 and 1.8 V shows that the growing film is electroactive and can be reversibly charged and discharged at potentials higher than +0.2 V.

 © 2005 Wiley-VCH Verlag GmbH & Co. KGaA, Weinheim

The broad potential range in which the charging occurs reveals that anodic oxidation produces multicationic states of **8**, which initiates intramolecular coupling processes between the phenyl rings of the dendrimeric segments. This coupling results in the elimination of protons and the planarization of the four independent dendritic arms around the tetraphenylmethane core.

The resulting graphene-type nanoparticles form weakly interacting aggregates which are partially deposited on the electrode but mainly diffuse into the solution giving rise to dark brownish streaks. This finding excludes the formation of a network. In situ conductivity measurements on films of these materials carried out simultaneously with voltammetric measurements in an electrochemical cell[26] show that during charging the conductivity drastically increases reaching a maximum value of $8.3 \times 10^{-2}\,S\,cm^{-1}$ at a potential of $+1.5$ V (Figure 3b). During discharging the conductivity decreases and returns to its starting value again. The conductivity maximum has approximately two-thirds of the value of that of **7a**. However, the redox charge incorporated into the film during charging amounts to 3×10^{-3} C which is by a factor of six higher than in the case of the polymeric material of **7a**. Note that the films of **8** and **7a** contained the same amount of dendrimer.

These results clearly demonstrate that the charge-carrier mobility in the 3D network generated from **7a** is extraordinarily high while that in the weakly interacting aggregates of **8** is comparatively low. As the core structure in both materials is similar the only difference between the films obtained from **7a** and **8** is that the distance between the conducting dendritic cores is small in the polymeric 3D network, but "large" in the weakly interacting aggregates of **8**. Clearly, the hopping processes of charge carriers are facilitated in the 3D network as a result of the small distances between the planarized wings of different dendritic cores. These results show that charge transport, and as a consequence conductivity, are phenomena which are not only related to linear chain-like conductors but also to 3D networks.

Our investigations of materials forming 3D networks on a molecular level have offered new insights into conductivity mechanisms of polymers. The use of different electroactive components as building blocks in such systems opens new perspectives in creating materials with tailor-made properties.

Experimental Section

In situ conductivity measurements were carried out on a microarray working electrode (5 μm gap). The working electrode was separated from the potentiostat by two 1 kΩ resistors. A bias of $E = 10$ mV was applied to the microarray electrode and a third 1 kΩ resistor at which the potential was measured. The conductivities of the polymers on the microarray electrode were calculated according to the ohmic rules. This set-up was controlled by an AMEL 553 potentiostat and the potential scans were performed with an EG&G PARC model 175 scan generator. All values described as conductivity were calculated from the area and thickness of the films. The film thickness was determined with the help of a profilometer. To compare the films of **7a** and **8** probes of the same area and thickness were used.

UV/Vis data were obtained on a Perkin-Elmer Lambda 9 spectrometer.

For all further experimental details see the Supporting Information.

Received: November 20, 2004
Published online: March 10, 2005

Keywords: conducting polymers · cyclic voltammetry · dendrimers · networks · polymers

[1] a) *Handbook of Conducting Polymers* (Eds.: T. A. Skotheim, R. L. Elsenbaumer, J. R. Reynolds), 2. Ed., Dekker, New York, **1998**; b) M. G. Kanatzidis, *Chem. Eng. News* **1990**, *68*(49), 36–54; c) A. G. MacDiarmid, *Angew. Chem.* **2001**, *113*, 2649–2659; *Angew. Chem. Int. Ed.* **2001**, *40*, 2581–2590.
[2] J. Heinze in *Encyclopedia of Electrochemistry*, *Vol. 8* (Eds.: A. J. Bard, M. Stratmann, H. J. Schäfer), Wiley-VCH, Weinheim, **2004**, pp. 605–644.
[3] J. Roncali, *Chem. Rev.* **1992**, *92*, 711–738.
[4] J. L. Brédas, B. Thémans, J. G. Fripiat, J. M. André, R. R. Chance, *Phys. Rev. B* **1984**, *29*, 6761–6773.
[5] A. N. Samukhin, V. N. Prigodin, L. Jastrabík, *Phys. Rev. Lett.* **1997**, *78*, 326–329.
[6] J. Grimme, M. Kreyenschmidt, F. Eckert, K. Müllen, U. Scherf, *Adv. Mater.* **1995**, *7*, 292–295.
[7] a) J. Kowalski, J. Płoszyńska, A. Sobkowiak, *Synth. Met.* **2002**, *130*, 149–153; b) L. M. Goldenberg, S. Aeiyach, P. C. Lacaze, *J. Electroanal. Chem.* **1992**, *335*, 151–161.
[8] a) K. Meerholz, J. Heinze, *Synth. Met.* **1993**, *55–57*, 5040–5045; b) J. Heinze, P. Tschuncky in *Electronic Materials: The Oligomer Approach* (Eds.: K. Müllen, G. Wegner), Wiley-VCH, Weinheim, **1998**, pp. 479–513.
[9] L. Zuppiroli, M. N. Bussac, S. Paschen, O. Chauvet, L. Forro, *Phys. Rev. B* **1994**, *50*, 5196–5203.
[10] D. A. Tomalia, A. M. Naylor, W. A. Goddard, *Angew. Chem.* **1990**, *102*, 119–157; *Angew. Chem. Int. Ed. Engl.* **1990**, *29*, 138–175.
[11] G. R. Newkome, C. N. Moorefield, F. Vögtle, *Dendritic Molecules—Concepts, Syntheses, Perspectives*, VCH, Weinheim, **1996**.
[12] J. M. J. Fréchet, *Science* **1994**, *263*, 1710–1715.
[13] R.-M. Sebastian, A.-M. Caminade, J.-P. Majoral, E. Levillain, L. Huchet, J. Roncali, *Chem. Commun.* **2000**, 507–508.
[14] Z. F. Xu, J. S. Moore, *Angew. Chem.* **1993**, *105*, 1394–1396; *Angew. Chem. Int. Ed. Engl.* **1993**, *32*, 1354–1357.
[15] S. K. Deb, T. M. Maddux, L. P. Yu, *J. Am. Chem. Soc.* **1997**, *119*, 9079–9080.
[16] C. Xia, X. Fan, J. Locklin, R. C. Advincula, A. Gies, W. Nonidez, *J. Am. Chem. Soc.* **2004**, *126*, 8735–8743.
[17] U. M. Wiesler, T. Weil, K. Müllen, *Dendrimers III* **2001**, *212*, 1–40.
[18] D. J. Liu, S. De Feyter, P. C. M. Grim, T. Vosch, D. Grebel-Koehler, U. M. Wiesler, A. J. Berresheim, K. Müllen, F. C. De Schryver, *Langmuir* **2002**, *18*, 8223–8230.
[19] S. Loi, H. J. Butt, C. Hampel, R. Bauer, U. M. Wiesler, K. Müllen, *Langmuir* **2002**, *18*, 2398–2405.
[20] J. Roncali, C. Thobie-Gautier, H. Brisset, J.-F. Favart, A. Guy, *J. Electroanal. Chem.* **1995**, *381*, 257–260.
[21] P. Bäuerle, F. Wuerthner, G. Goetz, F. Effenberger, *Synthesis* **1993**, 1099–1103.
[22] J. Brédas, G. Street, *Acc. Chem. Res.* **1985**, *18*, 309–315.
[23] G. Wegner, *Angew. Chem.* **1981**, *93*, 352–371; *Angew. Chem. Int. Ed. Engl.* **1981**, *20*, 361–381.
[24] J. B. Torrance, *Acc. Chem. Res.* **1979**, *12*, 79–86.
[25] C. D. Simpson, G. Mattersteig, K. Martin, L. Gherghel, R. E. Bauer, H. J. Räder, K. Müllen, *J. Am. Chem. Soc.* **2004**, *126*, 3139–3147.
[26] A. Smie, A. Synowczyk, J. Heinze, R. Alle, P. Tschuncky, G. Götz, P. Bäuerle, *J. Electroanal. Chem.* **1998**, *452*, 87–95.

 © 2005 Wiley-VCH Verlag GmbH & Co. KGaA, Weinheim

Cover Picture

Radu Custelcean, Lætitia H. Delmau, Bruce A. Moyer,* Jonathan L. Sessler,* Won-Seob Cho, Dustin Gross, Gareth W. Bates, Simon J. Brooks, Mark E. Light, and Philip A. Gale*

Ion-pair complexation properties of the calix[4]pyrroles could open up a new chapter in their chemistry, with potential applications in salt extraction and crystal engineering. In their Communication on page 2537 ff., B. A. Moyer, J. L. Sessler, P. A. Gale, and co-workers examine the binding properties of this macrocycle, which was first synthesized almost 120 years ago and continues to provide surprises. The cover picture shows various representations of the calix[4]pyrrole unit binding with large diffuse cations, such as the cesium and imidazolium ions, and various halide and oxo-anions.

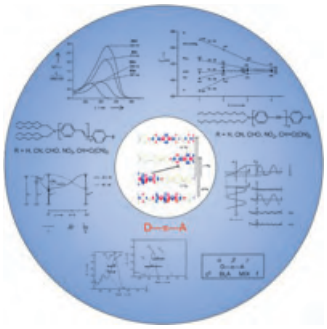

Conjugated Oligomers
Push-pull substituted conjugated oligomers have special optical and electronic properties. H. Meier describes in his Review on page 2482 ff. the strategies for the synthesis and the linear and nonlinear optical properties of these compounds.

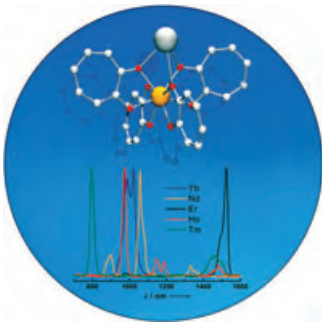

Lanthanide Complexes
The luminescence of lanthanide (Ln) cations is sensitized through bidentate coordination with tropolonate ligands. The structures of several such complexes with various Ln ions are discussed in the Communication by S. Petoud and co-workers on page 2508 ff.

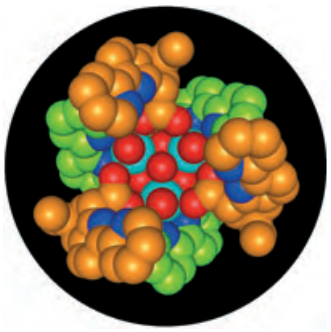

Supramolecular Chemistry
A trinuclear Eu^{III} helix with six chiral bipyridine-carboxylate ligands self-assembles with complete diastereoselectivity (Eu = green, O = red, N = blue). In their Communication on page 2527 ff., O. Mamula and co-workers discuss the chiroptical properties of this complex.

Contents

VIP *The following Communications have been judged by at least two referees to be "very important papers" and will be published online at www.angewandte.org soon:*

*R. Schiffmann, A. Heine, G. Klebe, C. D. P. Klein**
Metal Ions as Cofactors for Ligand Binding at Methionine Aminopeptidase: A Critical View on the Relevance of In Vitro Metalloenzyme Assays

*R. Shintani, A. Tsurusaki, K. Okamoto, T. Hayashi**
Rhodium–Chiral Diene Catalyzed Highly Chemo- and Enantioselective Arylative Cyclization of Alkyne-Tethered Electron-Deficient Olefins

E. Ruiz, G. Rajaraman, S. Alvarez, B. Gillon, J. Stride, R. Clérac, J. Larionova, S. Decurtins*
Symmetry and Topology Determine the Mo^{V}–CN–Mn^{II} Exchange Interactions in High-Spin Molecules

A. Fürstner, L. Turet*
Concise and Practical Synthesis of Latrunculin A by Ring-Closing Enyne–Yne Metathesis

*D. Wan, R. Tu, L. Zhang, H. Dai**
Deterministic One-to-One Synthesis of Germanium Nanowires and Individual Gold Nanoseed Patterning for Aligned Nanowire Arrays

*D. Cappel, S. Tüllmann, A. Krapp, G. Frenking**
Direct Estimate of the Conjugative and Hyperconjugative Stabilization in Diynes, Dienes, and Related Compounds

News

Chemical Societies Honor J.-M. Lehn

S. Ma Receives Awards ——— **2472**

Books

One-Dimensional Metals — Sigmar Roth, David Carroll — *reviewed by T. M. Swager* ——— **2473**

Introduction to Solid-State NMR Spectroscopy — Melinda J. Duer — *reviewed by M. Baldus* ——— **2473**

Highlights

Carbene Chemistry

W. Kirmse* ——— **2476 – 2479**

Incarcerated Carbenes

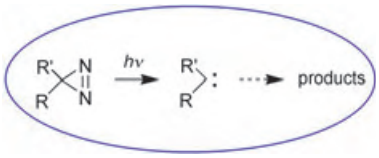

Parole denied: Fluoro(phenoxy)carbene persists for days if generated inside the cavity of a hemicarcerand. Elusive products of carbene rearrangements, such as cycloheptatetraenes and bridgehead alkenes, have also been stabilized by incarceration. Carbenes attack hemicarcerand hosts less readily than cyclodextrins whose hydroxy groups are the preferred sites of reaction.

Reviews

Conjugated Oligomers

H. Meier* ——— **2482 – 2506**

Conjugated Oligomers with Terminal Donor–Acceptor Substitution

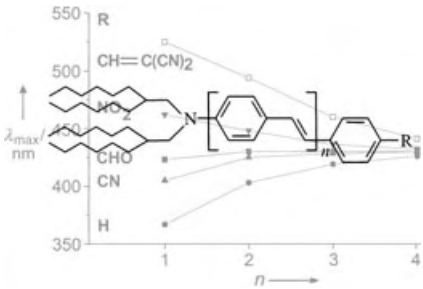

When push comes to shove: Push-pull substituted conjugated oligomers (see scheme) are distinguished by special optical and electronic properties. The general synthetic strategies for such oligomers are described together with their linear and nonlinear optical properties to obtain an interdisciplinary image of this class of compounds.

© 2005 Wiley-VCH Verlag GmbH & Co. KGaA, Weinheim

Communications

One ligand, five NIR-emitting complexes: Tropolonate (trp) ligands sensitize the near-infrared emission of several lanthanide (Ln^{III}) ions upon formation of $[Ln(trp)_4]^-$ complexes (Ln = Nd, Ho, Er, Tm, and Yb; see emission spectra). The solid-state structures and solution-state photophysical properties of the $[Ln(trp)_4]^-$ complexes have been characterized.

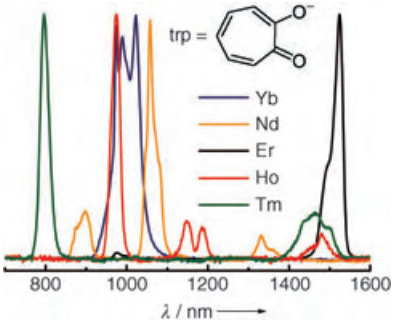

Luminescent Lanthanide Complexes

J. Zhang, P. D. Badger, S. J. Geib, S. Petoud* ——— 2508 – 2512

Sensitization of Near-Infrared-Emitting Lanthanide Cations in Solution by Tropolonate Ligands

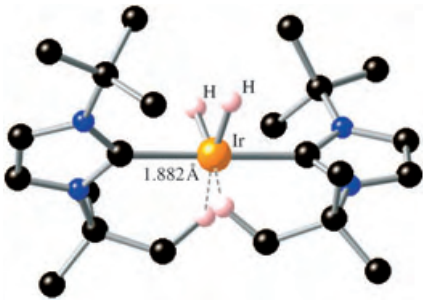

Double take: A remarkable electron-deficient cationic dihydride complex $[Ir(ItBu)_2(H)_2](PF_6)$ (see crystal structure), prepared in high yield from the reaction of 14-electron complex $[Ir(ItBu')_2](PF_6)$ and H_2 gas, shows a rare agostic interaction. The reaction illustrates the reversibility of a double, intramolecular C–H activation process and provides a rare example of a "proposed" intermediate. ItBu: *N*,*N*′-di(*tert*-butyl)imidazol-2-ylidene.

Carbene Ligands

N. M. Scott, V. Pons, E. D. Stevens, D. M. Heinekey, S. P. Nolan* ——— 2512 – 2515

An Electron-Deficient Iridium(III) Dihydride Complex Capable of Intramolecular C–H Activation

Not far from a crystal nucleus? The complex crystal structure of sodium saccharin "dihydrate" could be a good model for nucleation (see graphic). The asymmetric unit contains 362 atoms and much water, and the crystal contains ordered and disordered regions. Amazingly, the crystal structure of this metastable compound was not determined for 125 years following its isolation, although it is manufactured in bulk.

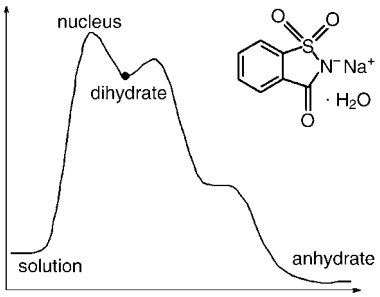

Structure Elucidation

R. Banerjee, P. M. Bhatt, M. T. Kirchner, G. R. Desiraju* ——— 2515 – 2520

Structural Studies of the System Na(saccharinate)·*n* H_2O: A Model for Crystallization

Plugging a gap in screening: Arrays of nanoliter-sized plugs of different compositions can be preformed in a three-phase liquid/liquid/gas flow. The arrays can be transported into a microfluidic channel to test against a target (see schematic representation), as demonstrated in protein crystallization and an enzymatic assay.

Miniaturization in Screening

B. Zheng, R. F. Ismagilov* 2520 – 2523

A Microfluidic Approach for Screening Submicroliter Volumes against Multiple Reagents by Using Preformed Arrays of Nanoliter Plugs in a Three-Phase Liquid/Liquid/Gas Flow

For the USA and Canada:
ANGEWANDTE CHEMIE International Edition (ISSN 1433-7851) is published weekly by Wiley-VCH PO Box 191161, D 69451 Weinheim, Germany. Air freight and mailing in the USA by Publications Expediting Inc. 200 Meacham Ave., Elmont, NY 11003. Periodicals postage paid at Jamaica NY 11431. US POSTMASTER: send address changes to *Angewandte Chemie*, Wiley-VCH, 111 River Street, Hoboken, NJ 07030. Annual subscription price for institutions: US$ 4948.00/4498.00 (valid for print and electronic / print or electronic delivery); for individuals who are personal members of a national chemical society, or whose institution already subscribes, or who are retired or self-employed consultants, print only: US$ 394.00. Postage and handling charges included. All Wiley-VCH prices are exclusive VAT.

 © 2005 Wiley-VCH Verlag GmbH & Co. KGaA, Weinheim

The best in chemistry –

for more than a hundred years

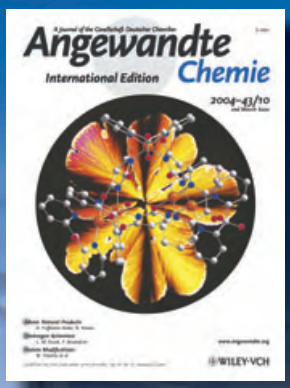

A Journal of the Gesellschaft Deutscher Chemiker

Angewandte International Edition **Chemie**

www.angewandte.org

1888: ***The beginning of a success story***

Constant Innovations

1962: *First issue of the International Edition*
1976: *Graphical abstracts*
1979: *Cover pictures*
1988: *Centenary of Angewandte*
1989: *Routine use of color*
1991: *New section: Highlights*
1992: *Computerized editorial tracking system*
1995: *Internet service for readers*
1998: *Regular press service; full-text online*
2000: *New section: Essays; EarlyView: Communications available online ahead of the printed version*
2001: *New section: Minireviews*
2002: *Online submission of manuscripts*
2003: *Weekly publication; new section: News; new layout*
2004: *Backfiles (1962-1997); ManuscriptXpress: Online system for authors and referees*

Angewandte's advisors...

Richard R. Ernst
ETH Zürich

» I support ***Angewandte Chemie*** *because it is a first rank international journal of European origin. More than many other renowned journals, it implements a pioneering spirit, being ready for innovating its form and contents. Its bilingual mode of appearance is another plus. I am looking forward to an equally prosperous future for* ***Angewandte Chemie.*** *«*

Angewandte Chemie International Edition *is a journal of the German Chemical Society (GDCh)*

GDCh

WILEY InterScience® DISCOVER SOMETHING GREAT

WILEY-VCH

1821404_gu

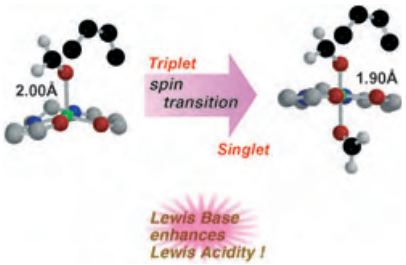

Density functional calculations on the hetero-Diels–Alder reaction catalyzed by 3-oxobutylideneaminatocobalt(II) and -cobalt(III) complexes revealed that axial coordination of an aldehyde as a Lewis base induces a spin transition in the Co^{III} catalytic cycle. The Lewis acidity of the complex is increased, the $Co{-}O_{aldehyde}$ distance shortened (see picture; Co green, N blue, O red), and the enantioselectivity improved.

Mechanistic Models

I. Iwakura, T. Ikeno,
T. Yamada* ——— **2524 – 2527**

A DFT Study on Hetero-Diels–Alder Reactions Catalyzed by Cobalt Complexes: Lewis Acidity Enhancement as a Consequence of Spin Transition Caused by Lewis Base Coordination

---

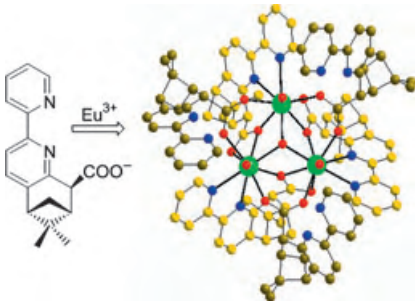

A supramolecular propeller: A trinuclear Eu^{III} helix with six chiral bipyridine-carboxylate ligands self-assembles with complete diastereoselectivity (see graphic; Eu green, O red, N blue). Ground- and excited-state chiroptical properties of this red-emissive complex reflect the helical arrangement of the ligands around the metallic core.

Supramolecular Chemistry

VIP

O. Mamula,* M. Lama, S. G. Telfer,
A. Nakamura, R. Kuroda,
H. Stoeckli-Evans,
R. Scopelitti ——— **2527 – 2531**

A Trinuclear Eu^{III} Array within a Diastereoselectively Self-Assembled Helix Formed by Chiral Bipyridine-Carboxylate Ligands

---

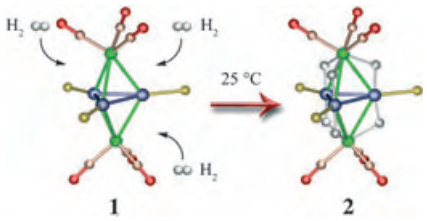

Where have all the electrons gone? The complex $[Pt_3Re_2(CO)_6(PtBu_3)_3]$ (**1**) containing a trigonal bipyramidal metal cluster is unsaturated by the amount of 10 valence electrons. Compound **1** reacts with hydrogen by adding three equivalents to form the hexahydrido complex **2**. The metal cluster in **2** is similar to that of **1**, but contains one bridging hydrido ligand on each of the Re–Pt bonds. Pt blue, Re green.

Cluster Compounds

R. D. Adams,* B. Captain ——— **2531 – 2533**

A Highly Unsaturated Platinum–Rhenium Cluster Complex that Adds an Unusually Large Amount of Hydrogen

---

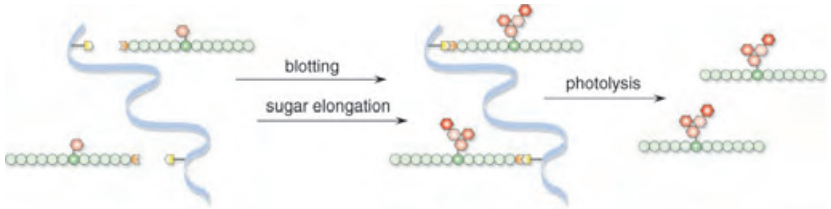

The molecule standing at platform one ...: Rapid glycopeptide synthesis is achieved with a heterobifunctional "molecular transporter" (see scheme), which interfaces two types of polymer platforms for combined chemical and enzymatic synthesis. This linker allows both chemoselective blotting and photoselective cleavage of the glycopeptides. Red: sugar residues; green: amino acid residues.

Glycopeptide Synthesis

M. Fumoto
H. Hinou, T. Matsushita, M. Kurogochi,
T. Ohta, T. Ito, K. Yamada, A. Takimoto,
H. Kondo, T. Inazu,
S.-I. Nishimura* ——— **2534 – 2537**

Molecular Transporter Between Polymer Platforms: Highly Efficient Chemoenzymatic Glycopeptide Synthesis by the Combined Use of Solid-Phase and Water-Soluble Polymer Supports

 © 2005 Wiley-VCH Verlag GmbH & Co. KGaA, Weinheim

Contents

Supramolecular Chemistry

R. Custelcean, L. H. Delmau, B. A. Moyer*
J. L. Sessler,* W.-S. Cho, D. Gross,
G. W. Bates, S. J. Brooks, M. E. Light,
P. A. Gale* _____ **2537 – 2542**

Calix[4]pyrrole: An Old yet New Ion-Pair Receptor

Ditopic cation–anion binding is revealed by solid-state studies of the anion-recognition behavior of the calix[4]pyrrole unit. Anion binding causes an electron-rich conelike cavity to be formed that can then bind large polarizable cations. Furthermore, complexation of calix[4]pyrrole with cesium carbonate results in dimerization, in which a single anion bridges two calix[4]pyrroles (see the crystal structure of the Cs_2CO_3 complex).

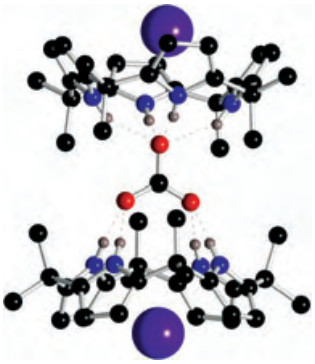

Bioconjugate Chemistry

L. M. Wittenhagen, J. R. Carreon,
E. G. Prestwich,
S. O. Kelley* _____ **2542 – 2546**

Phototoxicity of Peptidoconjugates Modulated by a Single Amino Acid

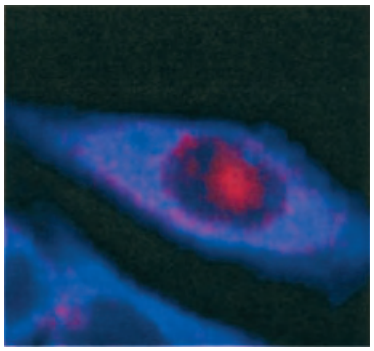

Working under oxidative stress: The DNA photocleavage activity of cell-permeable peptide conjugates depends on the nature of the amino acid side chains present. The cellular localization of these peptide-based compounds (see fluorescence image of a conjugate in a living cell) and their phototoxicity were studied in human cells, and the results demonstrate that the activity can be engineered through the manipulation of sequence composition.

Cluster Compounds

A. F. Richards, B. E. Eichler, M. Brynda,
M. M. Olmstead,
P. P. Power* _____ **2546 – 2549**

Metal-Rich, Neutral and Cationic Organotin Clusters

Tin can form examples of rare organically substituted clusters whose structures are related to Zintl salts. The two new types of metal-rich organotin clusters, a neutral Sn_9Ar_3 (see picture) and two ionic $[Sn_{10}Ar'_3]^+$ species, were structurally characterized and their bonding situation investigated by density functional calculations.

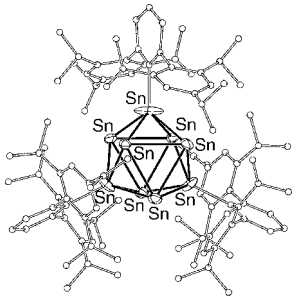

Cluster Compounds

E. J. Welch, C. L. Yu, N. R. M. Crawford,
J. R. Long* _____ **2549 – 2553**

Synthesis and Characterization of the Nitrogen-Centered Trigonal Prismatic Clusters $[W_6NCl_{18}]^{n-}$ ($n = 1$–3)

Central effects: Molecular salts, including $Na[W_6NCl_{18}]$, $(Bu_4N)[(Ph_3P)_2N][W_6NCl_{18}]$, and $(Bu_4N)_3[W_6NCl_{18}]\cdot MeCN$, were prepared that contain $[W_6NCl_{18}]^{n-}$ ($n = 1$–3) clusters (for an example, see picture of $[W_6NCl_{18}]^-$), reminiscent of a fragment of WN. Cyclic-voltammetric studies indicate the accessibility of species possessing 24–27 $\{W_6N\}$-based valence electrons.

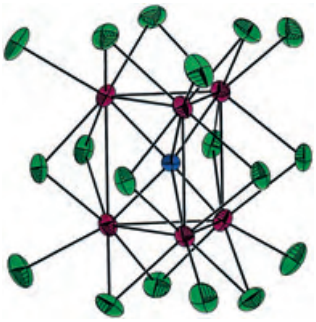

© 2005 Wiley-VCH Verlag GmbH & Co. KGaA, Weinheim

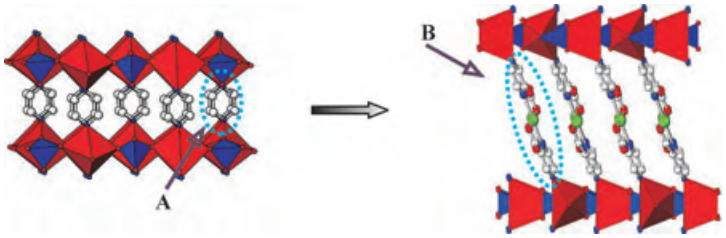

A layered effect: Replacement of pyrazine (**A**) with Co- or Ni-coordinated 2-pyrazinecarboxylate (pzc; **B**) between neutral $AgReO_4$ layers (red and blue polyhedra) yields $M(pzc)_2(H_2O)_2AgReO_4$ (M = Co (shown) or Ni). This novel strategy is aimed at pillared solids with coordinated H_2O that can be reversibly removed without causing structural collapse to give coordinatively unsaturated Ni and Co sites.

Solid-State Chemistry

P. A. Maggard,* B. Yan, J. Luo ——— 2553 – 2556

Pillared Hybrid Solids with Access to Coordinatively Unsaturated Metal Sites: An Alternative Strategy

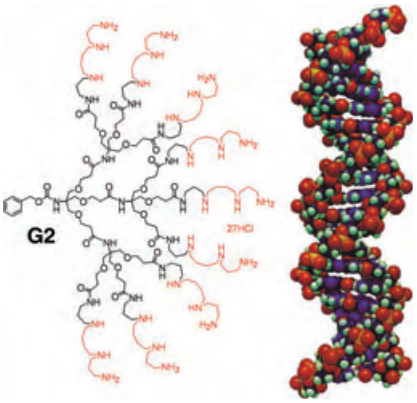

Nine spermines are better than one: Compound **G2** exhibits high-affinity, salt-independent DNA binding as a consequence of the spermine array on its surface. Comparison with smaller dendrons and model compounds indicates a clear multivalency effect on binding.

Multivalent DNA Binding

M. A. Kostiainen, J. G. Hardy, D. K. Smith* ——— 2556 – 2559

High-Affinity Multivalent DNA Binding by Using Low-Molecular-Weight Dendrons

Dinitrogen connects molybdenum and phosphorus: The diazo(triorgano)-phosphorane ligand Ph_2MePN_2 is multiply bonded through its N-terminus to molybdenum in the depicted cationic complex. The Ph_2MePN_2 ligand was synthesized within molybdenum's coordination sphere by rational assembly from a precursor N_2 complex. Computational studies reveal the N–N bond to be highly activated in the complex, which nonetheless readily fragments (with N_2 loss) upon one-electron reduction.

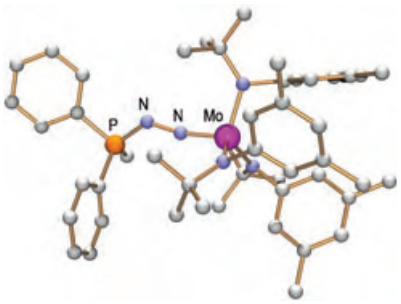

N,P Ligands

T. Murahashi, C. R. Clough, J. S. Figueroa, C. C. Cummins* ——— 2560 – 2563

A Ligand Composed of Dinitrogen and Methyldiphenylphosphane in a Cationic Molybdenum Complex

Synthesis in confined spaces: A simple route for designing and controlling the size of uniform zeolite nanocrystals (60–500 nm) uses the voids between monodisperse polymer spheres in an aqueous medium as nanoreactors. The crystal size is controlled by the content and diameter of the recyclable polymer spheres. The picture shows zeolite β nanocrystals (60 nm) with their X-ray diffraction (XRD) pattern (inset).

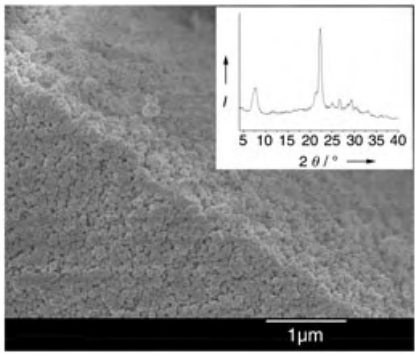

Zeolite Nanocrystals

X. Yang, Y. Feng, G. Tian, Y. Du, X. Ge, Y. Di, Y. Zhang, B. Sun, F.-S. Xiao* 2563 – 2568

Design and Size Control of Uniform Zeolite Nanocrystals Synthesized in Adjustable Confined Voids Formed by Recyclable Monodisperse Polymer Spheres

 © 2005 Wiley-VCH Verlag GmbH & Co. KGaA, Weinheim

Contents

Bridging N,P Ligands

C. Lidrissi, A. Romerosa,* M. Saoud, M. Serrano-Ruiz, L. Gonsalvi, M. Peruzzini* ——— **2568 – 2572**

Stable, Water-Soluble Pta-Based Ru–Ag Organometallic Polymers

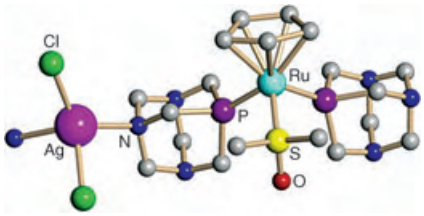

The cagelike 1,3,5-triaza-7-phosphaadamantane ligand bridges $[CpRu]^+$ and $[AgCl_2]^-$ moieties by an unprecedented N,P-coordinating mode (see picture) to yield water-soluble, air-stable heterobimetallic polymeric structures. The products have been structurally characterized, and dynamic light-scattering measurements confirm the polymeric nature of the complex in water.

Amplifying Fluorescent Polymers

C. J. Yang, M. Pinto, K. Schanze, W. Tan* ——— **2572 – 2576**

Direct Synthesis of an Oligonucleotide–Poly(phenylene ethynylene) Conjugate with a Precise One-to-One Molecular Ratio

Polymer probes light up: Amplifying fluorescent polymers conjugated with biomolecules have excellent light-harvesting and superquenching properties (see scheme). A novel synthetic method is reported for the highly efficient, simple, fast, and readily controllable conjugation of a water-soluble poly(phenylene ethynylene) with an oligonucleotide.

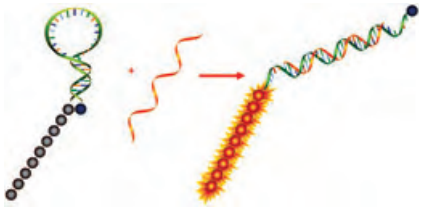

Metathesis Catalysts

R. Castarlenas, M. Eckert, P. H. Dixneuf* ——— **2576 – 2579**

Alkenylcarbene Ruthenium Arene Complexes as Initiators of Alkene Metathesis: An Enyne Creates a Catalyst that Promotes Its Selective Transformation

A molecule makes its own catalyst: $[RuCl(arene)(PCy_3)]OTf$ (e.g. **1**) with allyl or propyl propargyl ethers gives alkenylcarbene derivatives **2** by a metallo-retro-ene reaction. The latter species are efficient initiators for catalytic ring-closing metathesis of allyl propargyl ethers into alkenylcycloalkenes and of dienes into cyclic alkenes (see scheme).

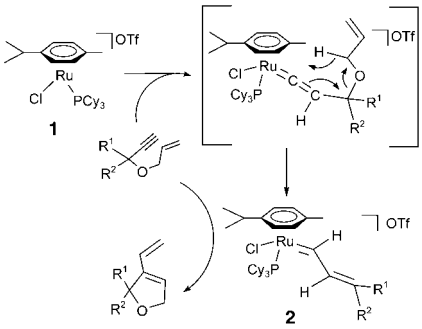

Chelating Ligands

M. Apostol, P. Baret, G. Serratrice, J. Desbrières, J.-L. Putaux, M.-J. Stébé, D. Expert, J.-L. Pierre* ——— **2580 – 2582**

Self-Assembly of an Amphiphilic Iron(III) Chelator: Mimicking Iron Acquisition in Marine Bacteria

Iron rations: Amphiphilic catechol-based chelators and their iron complexes self-assemble in solution at physiological pH values to form spherical particles (see cryo-TEM image). In terms of iron nutrition properties these abiotic chelators mimic siderophores from marine bacteria.

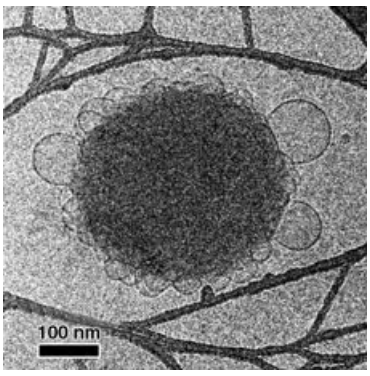

 © 2005 Wiley-VCH Verlag GmbH & Co. KGaA, Weinheim

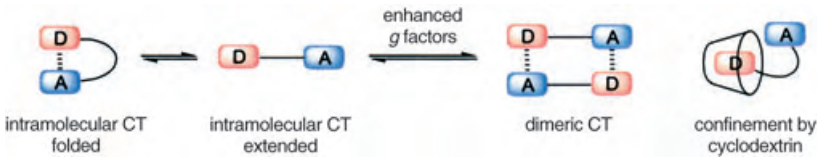

At the end of its tether: A charge-transfer (CT) dyad with a trimethylene tether forms a folded or extended monomer or a dimer depending on the conditions (see picture). Both dimer formation at low temperatures and monomer confinement by inclusion in a cyclodextrin cavity greatly enhance the anisotropy (*g*) factor of the CT transition of the complex.

Donor–Acceptor Systems

T. Mori,* Y. Inoue* ——— **2582 – 2585**

Circular Dichroism of a Chiral Tethered Donor–Acceptor System: Enhanced Anisotropy Factors in Charge-Transfer Transitions by Dimer Formation and by Confinement

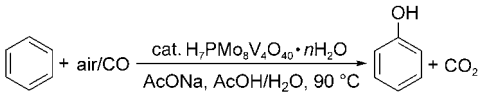

The simpler, the better: Phenol is synthesized by the direct oxidation of benzene under air (15 atm) and CO (10 atm) with molybdovanadophosphoric acid as the catalyst (see scheme). Activated molecular oxygen serves as the oxidant and phenol is produced in 28% yield. The catalyst can be recovered and reused.

Phenol Synthesis

M. Tani, T. Sakamoto, S. Mita, S. Sakaguchi, Y. Ishii* ——— **2586 – 2588**

Hydroxylation of Benzene to Phenol under Air and Carbon Monoxide Catalyzed by Molybdovanadophosphoric Acid

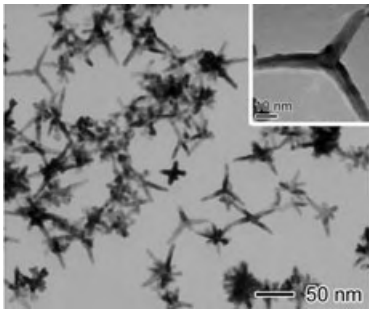

Getting into shape: The shape of Pt^0 nanostructures obtained by polyol synthesis can be altered by controlling the rate of reduction of the Pt^{II} precursor. Kinetic control is achieved by coupling the reduction with an Fe^{II}/Fe^{III} redox reaction and/or by blocking the self-catalytic sites of the Pt particles with oxygen. The shapes of the nanoparticles (see picture for an example) are different from that of the thermodynamic product.

Nanostructures

J. Chen, T. Herricks, Y. Xia* **2589 – 2592**

Polyol Synthesis of Platinum Nanostructures: Control of Morphology through the Manipulation of Reduction Kinetics

A new route to poly(ethylene-*alt*-butadiene) uses a homogeneous neodymocene/dialkylmagnesium catalyst which exhibits high activity and allows the polymerization to be easily controlled, both in terms of molecular weight and microstructure of the product. The *s-trans*-η^4-butadiene complex shown in the picture is thought to be an essential intermediate of this reaction.

$[Me_2Si(C_5H_4)(C_{13}H_8)NdCl]$ / MgRR'
cat.

Ethylene–Butadiene Copolymers

J. Thuilliez, V. Monteil, R. Spitz, C. Boisson* ——— **2593 – 2596**

Alternating Copolymerization of Ethylene and Butadiene with a Neodymocene Catalyst

Spin doctored: In reactions with phenolate anions, the (tetraisopropylcyclopentadienyl)iron fragment forms low-spin or high-spin iron(II) complexes with different coordination geometries. The lithium complex **1** allows a direct comparison of low-spin and high-spin cyclopentadienyliron fragments within one molecule.

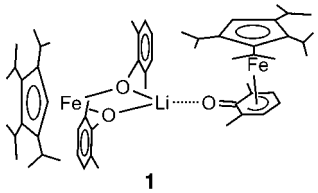

1

Organometallic Chemistry

M. Wallasch, G. Wolmershäuser, H. Sitzmann* ——— **2597 – 2599**

Phenolate Complexes of Iron(II) in Different Spin States

 © 2005 Wiley-VCH Verlag GmbH & Co. KGaA, Weinheim

Contents

Oligonucleotide Folding

P. Wenter, B. Fürtig, A. Hainard, H. Schwalbe,* S. Pitsch* — **2600 – 2603**

Kinetics of Photoinduced RNA Refolding by Real-Time NMR Spectroscopy

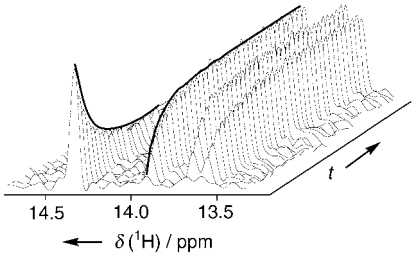

By introducing a photolabile group in the Watson–Crick base-pairing site of a guanosine residue, a bistable 20-base RNA sequence was forced into a less stable conformation. A single laser pulse released the native sequence, and the subsequent refolding equilibration was monitored with time-resolved NMR spectroscopy (see spectra). This permitted a quantitative description of the refolding process.

DNA–Enzyme Conjugates

L. Fruk, C. M. Niemeyer* — **2603 – 2606**

Covalent Hemin–DNA Adducts for Generating a Novel Class of Artificial Heme Enzymes

Well-defined conjugates between DNA and heme enzymes are accessible by the reconstitution of apo-enzymes with covalent hemin-DNA adducts (see picture). This concept allows access to novel redox catalysts with programmable binding properties that may be applied as biocatalysts, sensors, and biomaterials.

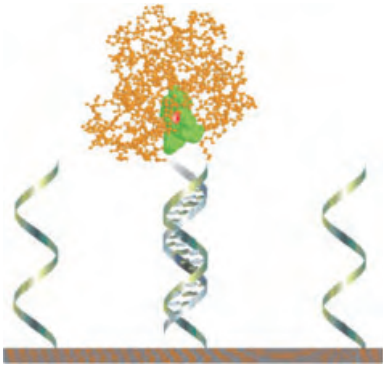

The issues for April 2005 appeared online on the following dates:
Issue 13: March 16. · Issue 14: March 22. · Issue 15: April 6. · Issue 16: April 13.

Sources

Product and Company Directory

You can start the entry for your company in "Sources" in any issue of *Angewandte Chemie*.

If you would like more information, please do not hesitate to contact us.

Wiley-VCH Verlag – Advertising Department
Tel.: 0 62 01 - 60 65 65
Fax: 0 62 01 - 60 65 50
E-Mail: MSchulz@wiley-vch.de

Service

Keywords — *2608*

Authors — *2609*

Angewandte's Sister Journals — *2610*

Preview — *2611*

Corrigendum

The authors inadvertently omitted to reference important work on ellagitannin synthesis. Ref. [7] should read:

[7] For reviews of ellagitannins, see: a) K. Khanbabaee, T. van Ree, *Synthesis* **2001**, 1585; b) S. Quideau, K. S. Feldman, *Chem. Rev.* **1996**, *96*, 475; c) total synthesis through intermolecular oxazoline-mediated asymmetric Ullmann coupling: T. D. Nelson, A. I. Meyers, *J. Org. Chem.* **1994**, *59*, 2577; d) total synthesis through organocuprate oxidation using a (*S*,*S*)-biphenyl tether: B. H. Lipshutz, Z.-P. Liu, F. Kayser, *Tetrahedron Lett.* **1994**, *35*, 5567; e) total synthesis of sanguiin H-5 through biomimetic oxidative coupling: K. S. Feldman, A. Sambandam, *J. Org. Chem.* **1995**, *60*, 8171.

The first sentence of ref. [17] in this communication contains a mistake. It should read: "A 1:1 mixture of **6a** and **8a**: colorless solid, m.p. 132–133 °C (decomp), yield 85 %."

Synthesis of Medium-Ring and Iodinated Biaryl Compounds by Organocuprate Oxidation

D. S. Surry, X. Su, D. J. Fox, V. Franckevicius, S. J. F. Macdonald, D. R. Spring* ——— **1870–1873**

Angew. Chem. Int. Ed. **2005**, *44*

DOI 10.1002/anie.200462642

Derivatives of the Simplest Polyhedral Carborane Anion: Structures at the Borderline between Two- and Three-Dimensional Aromatic Compounds**

Y. Sahin, C. Präsang, M. Hofmann, G. Geiseler, W. Massa, A. Berndt* ——— **1643–1646**

Angew. Chem. Int. Ed. **2005**, *44*

DOI 10.1002/anie.200462397

 © 2005 Wiley-VCH Verlag GmbH & Co. KGaA, Weinheim

Chemical Societies Honor J.-M. Lehn

During the symposium in celebration of the 10th anniversary of *Chemistry—A European Journal*, Jean-Marie Lehn (Université Louis Pasteur, Strasbourg (France) and Collège de France, Paris) received the "Award for Service" of the European Association for Chemical and Molecular Sciences (EuCheMS).

J.-M. Lehn

About 50 chemical societies and organizations from all over Europe are in the EuCheMS. The award honors Lehn for his numerous initiatives towards cooperation in Europe in the field of chemistry, including the creation of *Chemistry—A European Journal*.[1] He was recognized previously for his European initiatives in publishing by the Gesellschaft Deutscher Chemiker (German Chemical Society) in 1998 with honorary membership. Lehn presides over the Scientific Advisory Committee for the 1st European Chemistry Congress, which will take place in Budapest from August 27 to 31, 2006. Together with A. R. Fersht, he is chairman of the Editorial Advisory Board of *ChemBioChem*.

Lehn studied chemistry in Strasbourg and completed his PhD there in 1963 under the guidance of G. Ourisson on the conformations and physical chemical properties of triterpenes. He then undertook postdoctoral research with R. B. Woodward (Harvard University) on the synthesis of vitamin B_{12}. In 1966 he returned as a lecturer to the University of Strasbourg, where he was made associate professor in 1970. In 1979 he was offered a position at the Collège de France, and since then he has shared his time between Paris and Strasbourg. His research interests initially encompassed physical organic chemistry, neurochemistry, and artificial photosynthesis. These topics finally led him to the field that would earn him the Nobel Prize in Chemistry in 1987: molecular recognition and supramolecular chemistry with the long-term goal of creating molecules that can process signals and information.[2a] Lehn is regarded as a pioneer of supramolecular chemistry.[2b] He directed the establishment and construction of the Institut des Sciences et d'Ingénierie Supramoléculaires (ISIS) of the University of Strasbourg, which was opened in December 2002, and has since been director of the Supramolecular Chemistry Laboratory there. He recently reported in *Angewandte Chemie* the "Generation of Dynamic Constitutional Diversity and Driven Evolution in Helical Molecular Strands under Lewis Acid Catalyzed Component Exchange".[2c]

S. Ma Receives Awards

Shengming Ma (Shanghai Institute of Organic Chemistry (SIOC) of the Chinese Academy of Sciences) is the recipient of the 2004 Mr. and Mrs. Sun Chan Memorial Award in Organic Chemistry. At the award presentation in December at an international symposium in Hong Kong he gave a lecture on transition-metal-catalyzed reactions of functionalized allenes. In July he will receive the OMCOS Award during the International Symposium on Organometallic Chemistry Directed Towards Organic Synthesis (OMCOS) in Geneva. The award is given to young scientists (under the age of 40) who have made important contributions to this field.

S. Ma

Ma completed his master's degree in 1988 and PhD in 1990 at the SIOC under the guidance of Xiyan Lu. He remained at the SIOC and took up a position there in 1992 as Research Associate Professor of Chemistry. In 1992/1993 he was a visiting scientist in the research group of L. M. Venanzi at the ETH Zürich (Switzerland), before spending several years (1993–1997) at Purdue University in West Lafayette, IN (USA) with E. Negishi. In 1997 he returned to Shanghai, where he became Research Professor of Chemistry and director of the State Key Laboratory of Organometallic Chemistry. Since 2003 he has also been professor at Zhejiang University in Hangzhou (180 km southwest of Shanghai). Ma is deputy editor-in-chief of the *Chinese Journal of Chemistry*. In *Chemistry—A European Journal* he recently described a Pd^{II}-catalyzed oxidative cyclization–coupling reaction of 2,3-allenoic acids and in a microreview in the *European Journal of Organic Chemistry* discussed Pd-catalyzed coupling reactions of propargyl and allenyl compounds.[3]

[1] N. Compton, *Chem. Eur. J.* **2005**, *11*, 4.

[2] a) J.-M. Lehn, *Angew. Chem.* **1988**, *100*, 91; *Angew. Chem. Int. Ed. Engl.* **1988**, *27*, 89; b) J.-M. Lehn, *Supramolecular Chemistry*, Wiley-VCH, Weinheim, **1995**; c) N. Giuseppone, J.-L. Schmitt, J.-M. Lehn, *Angew. Chem.* **2004**, *116*, 5010; *Angew. Chem. Int. Ed.* **2004**, *43*, 4902.

[3] a) S. Ma, Z. Yu, Z. Gu, *Chem. Eur. J.* **2005**, *11*, 2351; b) S. Ma, *Eur. J. Org. Chem.* **2004**, 1175.

 © 2005 Wiley-VCH Verlag GmbH & Co. KGaA, Weinheim DOI: 10.1002/anie.200501072

Carbene Chemistry

Incarcerated Carbenes

*Wolfgang Kirmse**

Keywords:
carbenes · cyclodextrins · hemicarcerands · host–guest systems · supramolecular chemistry

Carbenes (divalent derivatives of carbon) are, for the most part, fleeting intermediates.[1] The search for persistent carbenes has only recently been successful. *Intrinsic stabilization* by amino groups (Arduengo, Alder)[2] and phosphanyl groups (Bertrand)[3] provided "bottleable" singlet carbenes such as **1** and **2** (Scheme 1). Steric protection,

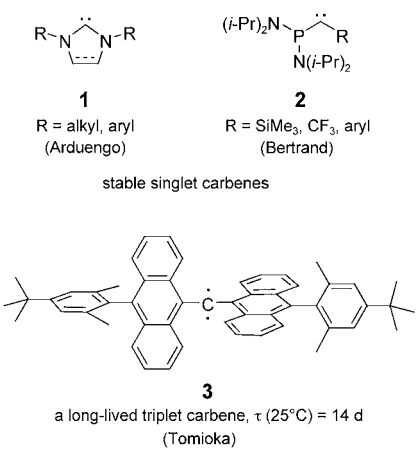

Scheme 1. Persistent carbenes.

together with electron delocalization, led to long-lived triplet carbenes (Tomioka).[4] The success of this approach is illustrated by carbene **3**, which currently holds the record in lifetime (14 days at 25 °C).[5]

The isolation of carbenes in a rigid matrix under cryogenic conditions is an efficient method of *extrinsic stabilization*.[6] At 8–15 K the thermal energy is insufficient to induce carbene rearrangements (with the exception of H shifts which proceed by quantum mechanical tunneling). Diffusion of the carbenes to give dimers is suppressed by the rigid medium, although intermolecular processes can be studied by "doping" the matrix with a reactant. UV/Vis, ESR, and IR spectroscopy have been employed to identify the embedded carbenes. However, the most powerful tool for structural elucidation, NMR spectroscopy, is not applicable.

Encapsulation can serve to immobilize carbenes at ambient temperatures. To that end, the carbene precursor (most often a diazirine) is introduced into a suitable host (see below), and the host–guest complex is then irradiated. The carbenes thus generated are protected from dimerization, from reaction with diazirine (formation of azine), and from reaction with bulk-phase molecules that are too large to enter the inner phase. However, reactive carbenes will attack X–H bonds, C=C bonds, and heteroatoms of the host. Host–guest reactions are termed *innermolecular* to distinguish them from *intermolecular* reactions of the guest with outer-phase molecules and *intramolecular* reactions that involve only the guest. Rearrangements of encapsulated carbenes do occur, but they may be affected by restrictions in space. Processes with small volumes of activation should be favored.

The enclosure of diazirines in cyclodextrins and/or zeolites has been studied by Brinker and his associates.[7] Cyclodextrins (CyDs, **4**) are cyclic oligomers of α-D-glucose (Scheme 2). The dimensions of their toroidal-shaped cavities depend on the ring size. Zeolites are microporous aluminosilicate materials whose free volume is influenced by the Si/Al ratio and the counterion. Both types of hosts have been widely employed in supramolecular chemistry. Aziadamantane (**6**) and α-cyclodextrin were found to give the complex (6-CyD)$_2$·**6**, for which structure **7** was proposed on the basis of induced circular dichroism (ICD) analyses.[7b]

The photochemistry of **7** is dominated by innermolecular reactions of adamantylidene.[7c,f] Insertion into the 2′- and 3′-OH groups of the host gave the 6-

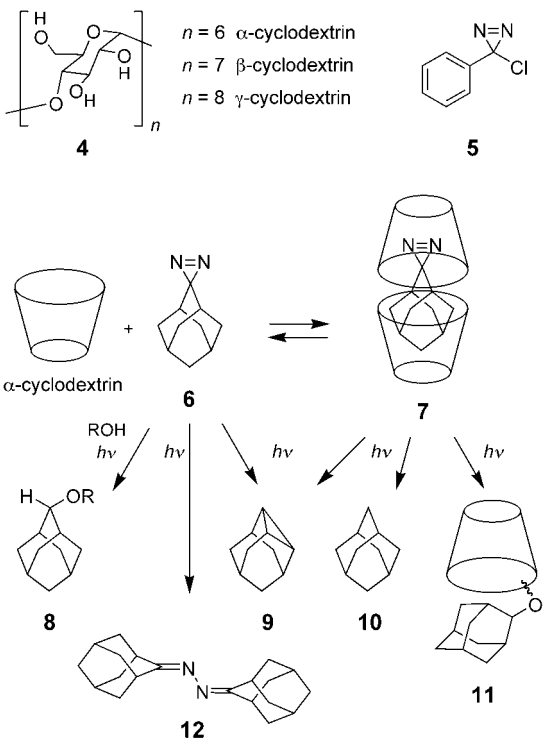

Scheme 2. Chemistry of cyclodextrin-entrapped carbenes.

[*] Prof. Dr. W. Kirmse
Fakultät für Chemie
Ruhr-Universität Bochum
Universitätsstrasse 150
44780 Bochum (Germany)
Fax: (+49) 234-3214-353
E-mail:
wolfgang.kirmse@ruhr-uni-bochum.de

 © 2005 Wiley-VCH Verlag GmbH & Co. KGaA, Weinheim DOI: 10.1002/anie.200500546

CyD derivatives **11**, which account for ca. 50% of the entrapped diazirine **6**. These products are analogues of the ethers **8** that arise from adamantylidene in alcohol solutions. The 2′- and 3′-OH groups are located on or close to the wider aperture of 6-CyD. Insertion into the 6′-OH groups, located on the opposite face, was not observed. A second major product was adamantane (**10**, ca. 30%), formed by reduction of **6** and concomitant oxidation of the host. The intramolecular C–H insertion leading to **9** was not significantly enhanced relative to that observed in photolyses of **6** in solution. While **7** did not produce the azine **12**, substantial amounts of **12** were formed from 7-CyD·**6** and 8-CyD·**6**.[7f] These data indicate that **6** is effectively isolated in the 1:2 complex with 6-CyD but rather poorly in the 1:1 complexes with 7-CyD and 8-CyD. Complexes of 3-chloro-3-phenyldiazirine (**5**) with CyDs gave similar results although the structure of the innermolecular products was not fully elucidated.[7c]

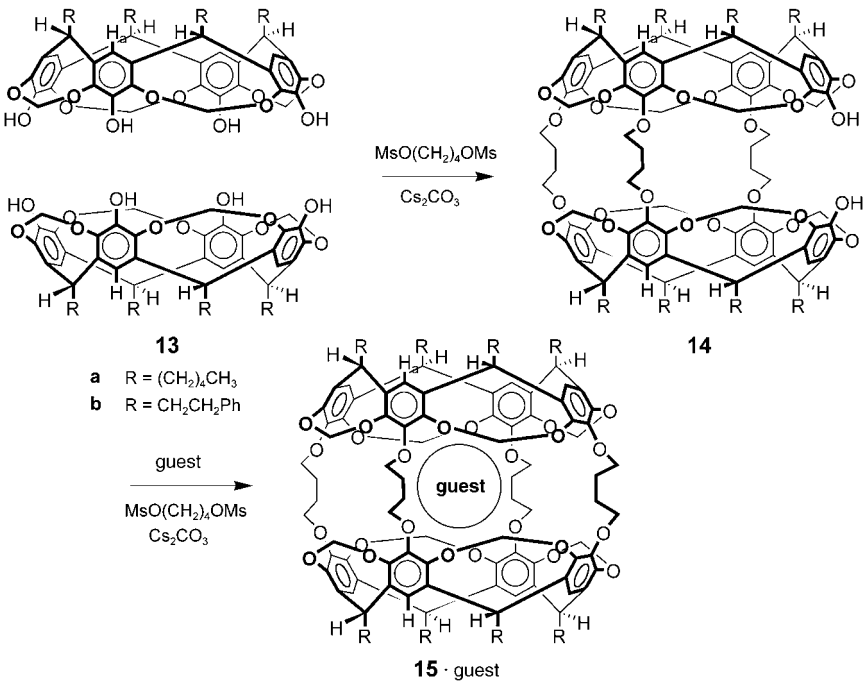

Scheme 3. Formation of hemicarcerands and hemicarceplexes. Ms = methanesulfonyl.

The study of zeolite-entrapped carbenes is hampered by the inevitable presence of water. Thus **6** produced large amounts of adamantan-2-ol,[7a] and benzaldehyde was the major product obtained from **5**.[8] Recently, chloro(phenyl)carbene was directly observed, by means of nanosecond diffuse reflectance spectroscopy, within the cavities of Y zeolites.[8] The decay rates ($k \approx 10^5\ s^{-1}$) were comparable to those observed in isooctane or acetonitrile.

The formation of host–guest complexes of cyclodextrins and other "prefabricated" hosts is a reversible process. To avoid dissociation, the complexes must be processed as solids, with a limited choice of photochemical and spectroscopic methods. These drawbacks can be overcome by assembling the host in the presence of the guest. *Hemicarcerands*, a class of host molecules developed by Cram's group in the early 1990s,[9] are made by connecting two bowl-shaped *cavitands* (resorcin[4]arenes, **13**) with appropriate linkers (Scheme 3). Short linkers provide rigid *carcerands*, which incarcerate (small) guest molecules permanently. With increasing length of the linker, the flexibility and permeability of the host is enhanced. Hemicarcerands incarcerate and liberate guests at elevated temperatures; the *hemicarciplexes* thus produced are stable at ambient temperature. However, this route to **15**·guest is not applicable to thermally labile diazirines. The decay of some diazirines was even found to be accelerated by incarceration.[10] Fortunately, **14** can be isolated as an intermediate en route to **15**. Introduction of the guest at this stage, followed by closing of the "open door", provides **15**·guest under mild conditions. The solubility of the complexes can be adjusted by the choice of the substituents R.

Hemicarcerands have served to stabilize a series of elusive intermediates.[11] The success story started with Cram's report on incarcerated cyclobutadiene.[12] Somewhat later, Warmuth's group added *o*-benzyne,[13] cycloheptatetraene (**18a**),[14] bridgehead alkenes (**19, 20**),[15] and 1-azacyclohepta-1,2,4,6-tetraene (**21**)[16] to the list of guests (Scheme 4). Compounds **18**–**20** were made by way of carbene rearrangements.

The case of phenylcarbene (**17**) is particularly instructive.[14] When incarcerated phenyldiazirine (**15**·**16**) was photolyzed at ambient temperature, **17** was found to insert into the C–H bonds and aryl units of **15**. The undesired innermolecular reactions were suppressed by deuteration of the CH_2 groups of **15**, lower temperatures, and triplet excitation transfer through the walls of the hemicarcerand. The incarcerated cycloheptatetraenes (**15**·**18**) thus obtained in up to 67% yield are stable at 25°C in the absence of oxygen but regenerate **17** at 70–100°C. NMR studies of **15**·**18** confirmed the twisted, nonplanar structure of **18**. The enantiomerization barrier of **18b** was estimated as $82 \pm 1\ kJ\ mol^{-1}$.[14c] (To that end, a chiral analogue of **15** was prepared from **14** and (*S*,*S*)-1,4-di-*O*-tosyl-2,3-*O*-isopropylene-L-threitol).

Most recently, the incarceration of a singlet carbene has been accomplished. Fluoro(phenoxy)carbene (**23**) is a fleeting though relatively selective species. Aside from addition reactions with alkenes,[17] only dimerization has been observed. Therefore, **23** is unlikely to attack the wall of hemicarcerands. The photolysis of **15**·**22** in degassed CH_2Cl_2 at 77 K afforded almost quantitatively a new hemicarceplex, **15**·**23**, which persisted for days at 25°C.[18] The ^{13}C chemical shift of the divalent carbon of **15**·**23** is $\delta = 285.7$ ppm, intermediate to those of diaminocarbenes ($\delta = 235$–255 ppm) and amino(aryl)carbenes

 © 2005 Wiley-VCH Verlag GmbH & Co. KGaA, Weinheim

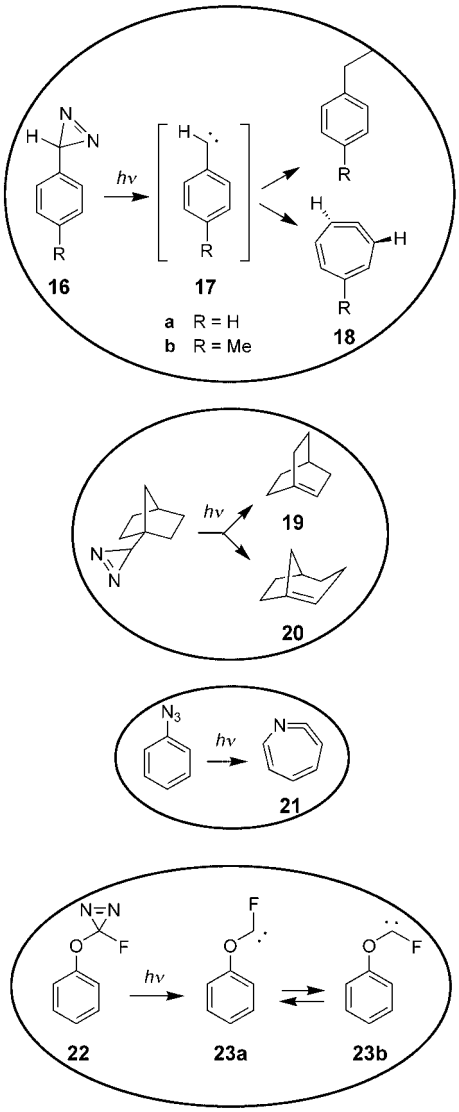

Scheme 4. Reactive intermediates generated inside hemicarcerands.

($\delta = 300$–310 ppm). The ^{13}C and ^{19}F NMR data point to strong electron donation from fluorine and oxygen to the divalent carbon. NOE experiments indicate that the incarcerated carbene prefers the *cis* conformation **23b**. For the free carbene, the *trans* conformation **23a** should be more favorable according to DFT calculations. The only chemical transformation of **15**·**23** observed so far was a slow, acid-catalyzed reaction with water [Eq. (1)]. (Both H_2O and HF molecules can enter the inner phase of **15**.)

$$2\,\mathbf{15}\cdot\mathbf{23} + H_2O \rightarrow \mathbf{15}\cdot PhOCHO + \mathbf{15}\cdot PhOCHF_2 \quad (1)$$

Incarceration holds much promise for the investigation of other carbenes. The method is particularly suited for singlet carbenes that do not persist in solution but are reluctant to undergo intramolecular and/or innermolecular reactions. Incarceration could also grant longevity to triplet carbenes that decay mainly by dimerization. Taking carbene incarceration to its limits will be a fascinating endeavor.

[1] Reviews: a) *Reactive Intermediate Chemistry* (Eds.: R. A. Moss, M. S. Platz, M. Jones, Jr.), Wiley, Hoboken, NJ, **2004**, Chap. 7–9, 12; b) *Carbene Chemistry* (Ed.: G. Bertrand), Marcel Dekker, New York, **2002**; c) *Carben-(oide), Carbine*, *Vol. E19b* (Ed.: M. Regitz), Houben-Weyl, Thieme, Stuttgart, **1989**; d) R. A. Moss, M. Jones, Jr., *Carbenes*, Wiley, New York, **1973** (Vol. I), **1975** (Vol. II); e) W. Kirmse, *Carbene Chemistry*, 2nd ed., Academic Press, New York, **1971**.

[2] Reviews: a) R. W. Alder in *Carbene Chemistry* (Ed.: G. Bertrand), Marcel Dekker, New York, **2002**, pp. 153–176; b) A. J. Arduengo, *Acc. Chem. Res.* **1999**, *32*, 913–921; c) W. A. Herrmann, C. Köcher, *Angew. Chem.* **1997**, *109*, 2256–2282; *Angew. Chem. Int. Ed. Engl.* **1997**, *36*, 2162–2187.

[3] Reviews: a) G. Bertrand in *Reactive Intermediate Chemistry* (Eds.: R. A. Moss, M. S. Platz, M. Jones, Jr.), Wiley, Hoboken, NJ, **2004**, pp. 329–373; b) W. Kirmse, *Angew. Chem.* **2004**, *116*, 1799–1801; *Angew. Chem. Int. Ed.* **2004**, *43*, 1767–1769; c) G. Bertrand in *Carbene Chemistry* (Ed.: G. Bertrand), Marcel Dekker, New York, **2002**, pp. 177–203; d) D. Bourissou, O. Guerret, F. P. Gabbai, G. Bertrand, *Chem. Rev.* **2000**, *100*, 39–91.

[4] Reviews: a) H. Tomioka in *Reactive Intermediate Chemistry* (Eds.: R. A. Moss, M. S. Platz, M. Jones, Jr.), Wiley, Hoboken, NJ, **2004**, pp. 375–461; b) W. Kirmse, *Angew. Chem.* **2003**, *115*, 2165–2167; *Angew. Chem. Int. Ed.* **2003**, *42*, 2117–2119; c) H. Tomioka in *Carbene Chemistry* (Ed.: G. Bertrand), Marcel Dekker, New York, **2002**, pp. 103–152; d) H. Tomioka in *Advances in Carbene Chemistry*, *Vol. 2* (Ed.: U. H. Brinker), Jai, London, **1998**, pp. 175–214; e) H. Tomioka, *Acc. Chem. Res.* **1997**, *30*, 315–321.

[5] E. Iwamoto, K. Hirai, H. Tomioka, *J. Am. Chem. Soc.* **2003**, *125*, 14664–14665.

[6] Reviews: a) W. Sander in *Carbene Chemistry* (Ed.: G. Bertrand), Marcel Dekker, New York, **2002**, pp. 1–25; b) G. Maier in *Advances in Carbene Chemistry*, *Vol. 3* (Ed.: U. H. Brinker), Elsevier, Amsterdam, **2001**, pp. 115–157; c) H. Tomioka, *Bull. Chem. Soc. Jpn.* **1998**, *71*, 1501–1524; d) W. Sander, *Chem. Rev.* **1993**, *93*, 1583–1621.

[7] a) U. H. Brinker, M. Rosenberg in *Advances in Carbene Chemistry*, *Vol. 2* (Ed.: U. H. Brinker), Jai, London, **1998**, pp. 29–44 (review of earlier work); b) D. Krois, U. H. Brinker, *J. Am. Chem. Soc.* **1998**, *120*, 11627–11632; c) D. Krois, M. M. Bobek, A, Werner, H. Kählig, U. H. Brinker, *Org. Lett.* **2000**, *2*, 315–318; d) M. G. Rosenberg, U. H. Brinker, *J. Org. Chem.* **2001**, *66*, 1517–1522; e) M. G. Rosenberg, U. H. Brinker, *J. Org. Chem.* **2003**, *68*, 4819–4832; f) D. Krois, L. Becker, A. Werner, U. H. Brinker, *Adv. Synth. Catal.* **2004**, *346*, 1367–1374.

[8] R. Moya-Barrios, F. L. Cozens, *Org. Lett.* **2004**, *6*, 881–884.

[9] Reviews: a) R. Warmuth, J. Yoon, *Acc. Chem. Res.* **2001**, *34*, 95–105; b) A. Jasat, J. C. Sherman, *Chem. Rev.* **1999**, *99*, 931–967; c) E. Maverick, D. J. Cram in *Comprehensive Supramolecular Chemistry*, *Vol. 2* (Ed.: F. Vögtle), Elsevier, Oxford, **1996**, pp. 367–418; d) J. C. Sherman, *Tetrahedron* **1995**, *51*, 3395–3422; e) D. J. Cram, J. M. Cram in *Container Molecules and their Guests* (Ed.: J. F. Stoddart), The Royal Society of Chemistry, Cambridge, **1994**, pp. 131–216; f) D. J. Cram, *Nature* **1992**, *356*, 29–36.

[10] R. Warmuth, J.-L. Kerdelhué, S. Sánchez Carrera, K. J. Langenwalter, N. Brown, *Angew. Chem.* **2002**, *114*, 102–105; *Angew. Chem. Int. Ed.* **2002**, *41*, 96–99.

[11] Reviews: a) R. Warmuth, *Eur. J. Org. Chem.* **2001**, 423–437; b) R. Warmuth, *J. Inclusion Phenom.* **2000**, *37*, 1–38.

[12] D. J. Cram, M. E. Tanner, R. Thomas, *Angew. Chem.* **1991**, *103*, 1048–1051; *Angew. Chem. Int. Ed. Engl.* **1991**, *30*, 1024–1027.

[13] a) R. Warmuth, *Angew. Chem.* **1997**, *109*, 1406–1409; *Angew. Chem. Int. Ed. Engl.* **1997**, *36*, 1347–1350; b) R. Warmuth, *Chem. Commun.* **1998**, 59–60.

[14] a) R. Warmuth, M. A. Marvel, *Angew. Chem.* **2000**, *112*, 1168–1171; *Angew. Chem. Int. Ed.* **2000**, *39*, 1117–1119; b) R. Warmuth, M. A. Marvel, *Chem. Eur. J.* **2001**, *7*, 1209–1220; c) R. Warmuth, *J. Am. Chem. Soc.* **2001**, *123*, 6955–6956; d) J.-L. Kerdelhué, K. J. Langenwalter, R. Warmuth, *J. Am. Chem. Soc.* **2003**, *125*, 973–986.

[15] P. Roach, R. Warmuth, *Angew. Chem.* **2003**, *115*, 3147–3150; *Angew. Chem. Int. Ed.* **2003**, *42*, 3039–3042.

 © 2005 Wiley-VCH Verlag GmbH & Co. KGaA, Weinheim

[16] R. Warmuth, S. Makowiec, *J. Am. Chem. Soc.* **2005**, *127*, 1084 – 1085.

[17] R. A. Moss, G. Kmiecik-Lawrynowicz, K. Krogh-Jespersen, *J. Org. Chem.* **1986**, *51*, 2168 – 2172.

[18] X. Liu, G. Chu, R. A. Moss, R. R. Sauers, R. Warmuth, *Angew. Chem.* **2005**, *117*, 2030 – 2033; *Angew. Chem. Int. Ed.* **2005**, *44*, 1994 – 1997.

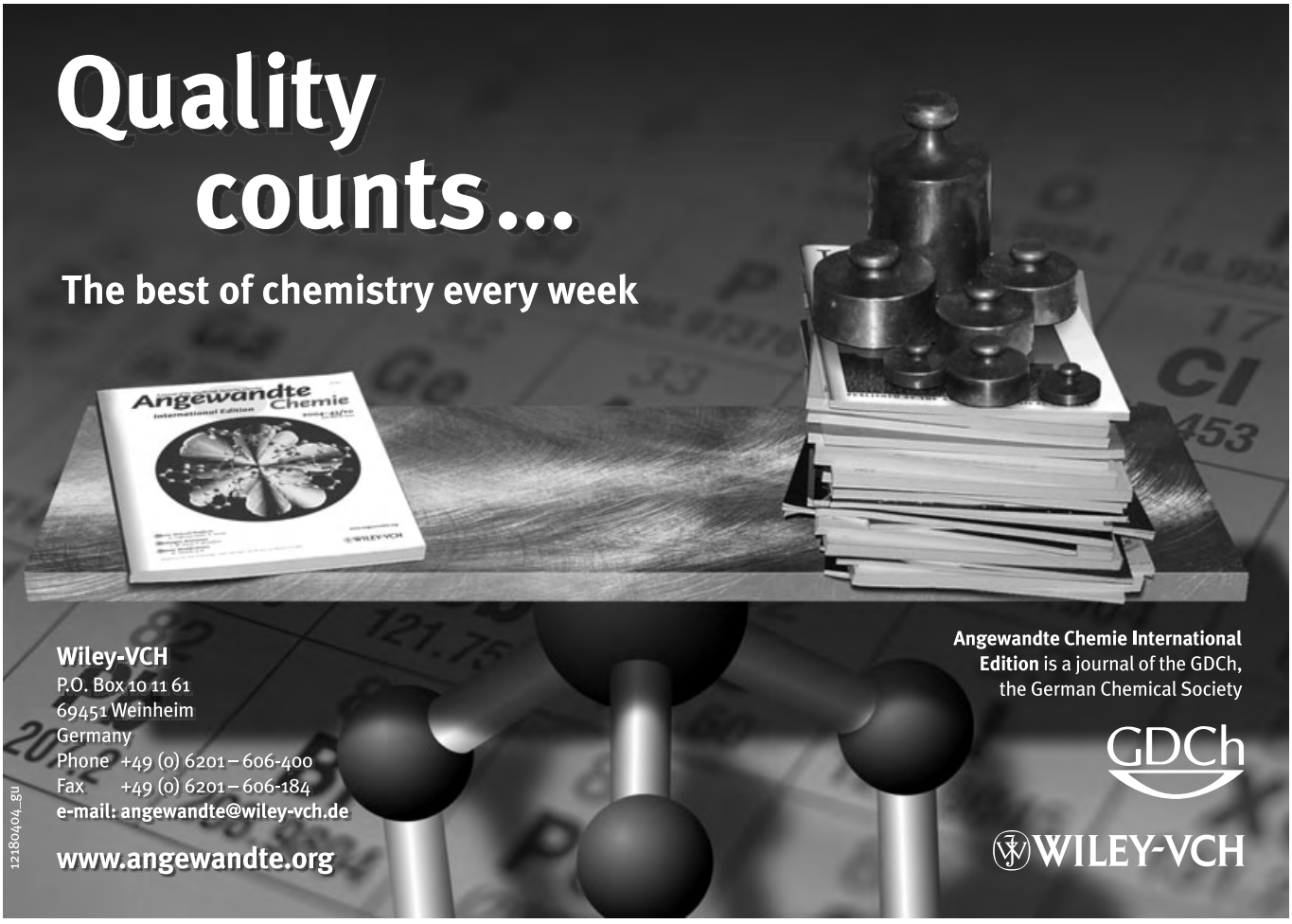

 © 2005 Wiley-VCH Verlag GmbH & Co. KGaA, Weinheim

Conjugated Oligomers

Conjugated Oligomers with Terminal Donor–Acceptor Substitution

*Herbert Meier**

Keywords:
absorption · conjugation · intramolecular charge transfer · nonlinear optics · oligomers

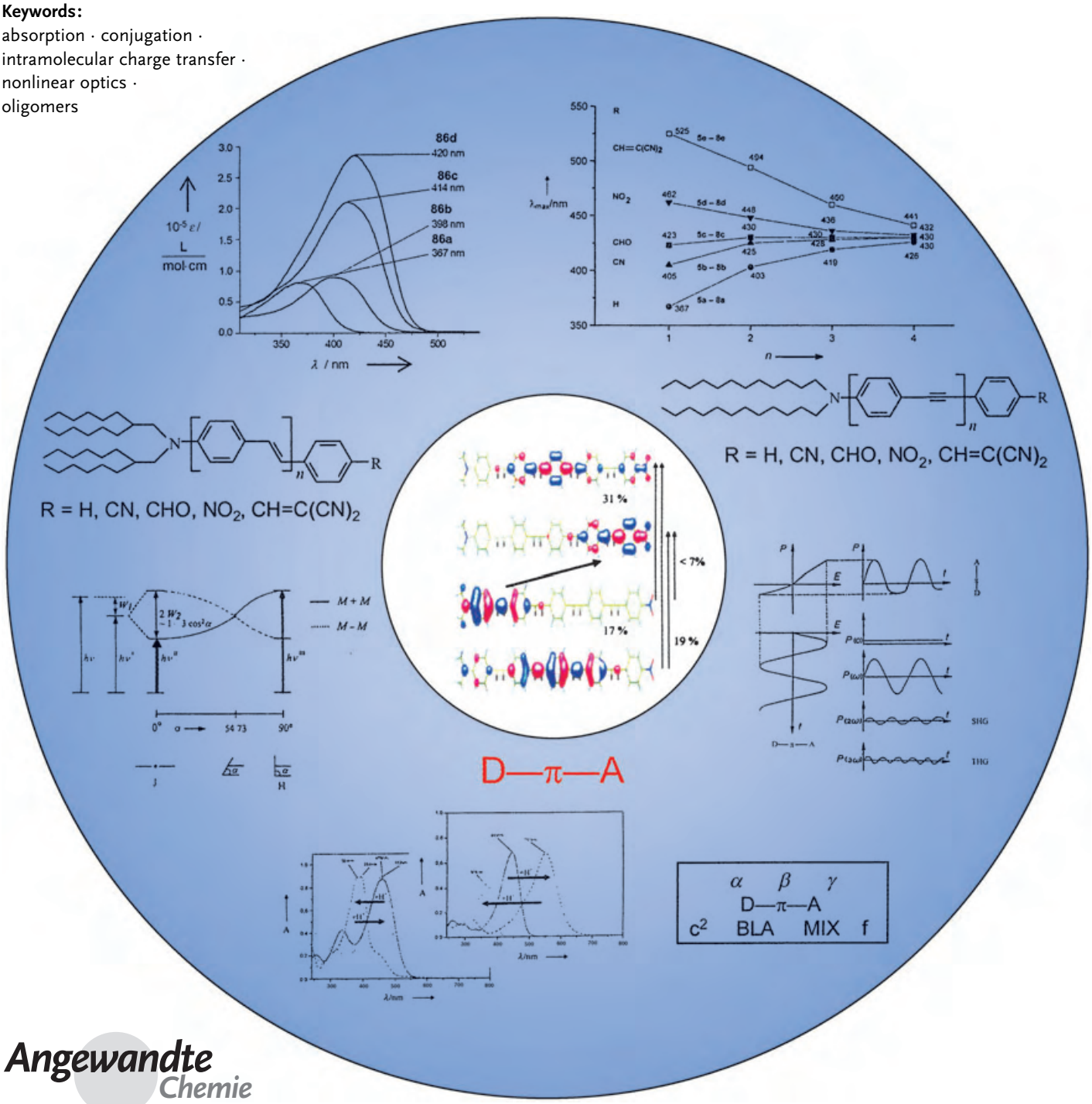

© 2005 Wiley-VCH Verlag GmbH & Co. KGaA, Weinheim
DOI: 10.1002/anie.200461146

Conjugated oligomers represent a prominent class of compounds from a viewpoint of their theory, synthesis, and applications in materials science. Push-pull substitution with an electron donor D at one end of the conjugation and an electron acceptor A at the other end results in them having outstanding optical and electronical properties. This Review highlights fundamental synthetic strategies for the preparation of such oligomers with n *repeat units* (n = *1, 2, 3, 4, …) and the rules that govern their linear and nonlinear optical properties (absorption, frequency doubling and tripling). The unification of chemical, physical, and theoretical aspects with an interdisciplinary image of this class of compounds is attempted herein.*

From the Contents

1. Introduction 2483
2. Long-Wavelength Electron Transitions in Conjugated Oligomers 2484
3. Push-Pull-Substituted Oligomers: Synthetic Concepts and Absorption Behavior 2486
4. Nonlinear Optics in Series of Oligomers with Donor–Acceptor Substitution 2496
5. VB and MO Models of D-π-A Systems 2499
6. Summary and Outlook 2502

1. Introduction

Conjugated oligomers are target compounds for numerous applications in materials science because of their interesting electrical, optical, and optoelectronic properties and they are also model compounds for the corresponding conjugated polymers.[1] A topic of high topicality in terms of nonlinear optics and electroluminescence concerns π systems substituted with donor and acceptor groups in which conjugated oligomers form the π-electron linker. The compounds can have a linear or a star-shaped architecture. Scheme 1 provides an overview of the most important structural types.

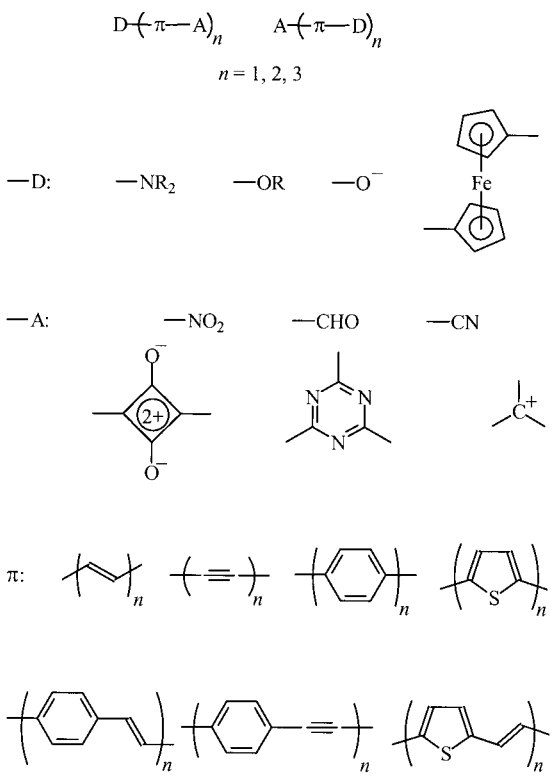

Scheme 1. Construction of donor–acceptor-substituted conjugated oligomers consisting of donor groups D, a π-electron linker, and acceptor groups A; selected examples are shown.

The push-pull effect of this class of compounds depends on the strength of the donor and acceptor groups; however, it also depends on the conjugated π system, to which a zwitterionic resonance structure should contribute (Scheme 2). The energy of the dipolar resonance structure is

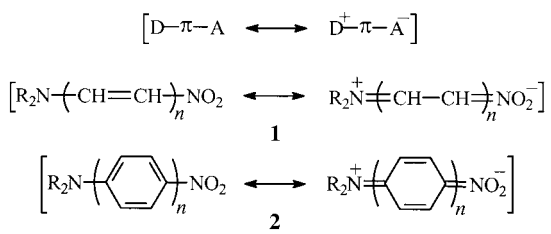

Scheme 2. Participation of zwitterionic resonance structures for the illustration of the push-pull effect in conjugated oligomers.

determined by the charge separation as well as the change in the π system. The latter influence is certainly smaller for an oligoene chain (**1**) than for repeat units consisting of aromatic rings (**2**), whose zwitterionic resonance structures have *p*-quinoid character.

Several parameters, such as BLA,[2–5] MIX,[6] and c^2,[7–9] have been suggested for quantification of the contribution of zwitterionic resonance structures. This will be discussed further in Section 5. However, it should be noted here that the "weight" of resonance structures depends on external factors such as the solvent or an applied electrical field.

[*] Prof. Dr. H. Meier
Johannes Gutenberg-Universität
Duesbergweg 10–14
55099 Mainz (Germany)
Fax: (+49) 6131-392-5396
E-mail: hmeier@mail.uni-mainz.de

 DOI: 10.1002/anie.200461146 © 2005 Wiley-VCH Verlag GmbH & Co. KGaA, Weinheim

A special case, which is occasionally referred to in this article, is represented by the symmetrical, charged, all-*E*-configured polymethines **3a** and **3b** (Scheme 3). At larger values of *n* (beyond the so-called cyanine limit) it needs to be

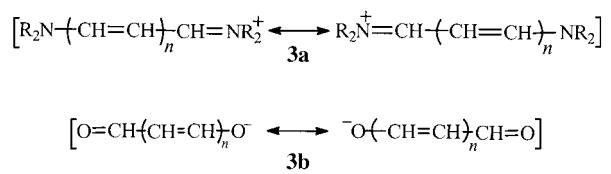

Scheme 3. Symmetrical charged polymethines (cyanines).

considered[10] whether the resonance should be substituted by a fast equilibration (automerization) as soon as the C_{2v} symmetry is abandoned in favor of a C_s symmetry.[10–16]

A special aspect of series of conjugated oligomers is given by the expectance that certain properties P(n) converge towards a limiting value P_∞ for increasing numbers n of repeat units, or at least their derivatives dP(n)/dn converge towards P'_∞. The long-wavelength electron transition $S_0 \rightarrow S_1$ provides an example of the first case [$\lambda_{max}(n) \rightarrow \lambda_\infty$],[17–22] while the hyperpolarizability of second order γ is an example of the latter case [d$\gamma(n)$/d$n \rightarrow \gamma'_\infty$].[23] In most cases $\lambda_{max}(n)$ increases monotonously with n and reaches the limiting value λ_∞ at the so-called effective conjugation length n_{ECL}.[1a,18] In contrast, the slope of the curves $\gamma(n)$ and log$\gamma(n)$, respectively, decreases with increasing n.[23,24]

Recently it was found that certain conjugated oligomers with terminal donor–acceptor substitution can exhibit a monotonously decreasing value for λ_{max} with increasing numbers n of repeat units;[25] the behavior of the hyperpolarizabilities β and γ of such series is currently unknown. Both effects will be discussed in Sections 3 and 4, while quantum mechanical models for D-π-A systems will be discussed in Section 5.

2. Long-Wavelength Electron Transitions in Conjugated Oligomers

As already expressed in the Introduction, one expects the lowest electron excitation energies $E(n)$ for conjugated oligomers to converge towards a certain limiting value E_∞ for $n \rightarrow \infty$. The hyperbolic function described by Equation (1)

$$E(n) = c + f\left(\frac{1}{n+1}\right) \quad (1)$$

seems to be adequate for polyenes. However, simple HMO theory [Eq. (2)] supplies the limiting value (zero). Only the

$$\lim_{n\rightarrow\infty} E(n) = c = 0 \quad (2)$$

consideration of perturbation theory of first or second order results in a limiting value which is different from zero [Eq. (3)].[26] $\Delta\beta$ is the difference in the resonance integrals of

$$\lim_{n\rightarrow\infty} E(n) = \frac{4}{\pi}\Delta\beta > 0 \quad (3)$$

neighboring bonds. The perturbation is based on the fact that polyenes have alternating single and double bonds of different lengths and consequently different β values.

Wenz, Wegner et al. derived a function on the basis of the electron gas theory[27,28] as Equation (4) with a limiting value

$$E(n) = c + f\left(\frac{1}{n+0.5}\right) \quad (4)$$

of $c \neq 0$.[29] Root laws, such as Equation (5) used by Drefahl

$$\lambda_{max}(n) = c + b\sqrt{n} \quad (5)$$

and Plötner[30] for the long-wavelength absorption maxima, and the corresponding functions for λ^2 suggested by Lewis and Calvin[31] on the basis of coupled oscillator models were modified by Hirayama[32,33] to Equation (6) and revised by

$$\lambda^2_{max}(n) = c + b\ a^n \quad (6)$$

Dähne und Radeglia.[34] Since $a < 1$, Equation (6) yields a finite limiting value as shown by Equation (7). Equation (5)[30]

$$\lim_{n\rightarrow\infty} \lambda_{max} = \sqrt{c} \quad (7)$$

and the related Equation (8)[23] are in principle suited for an

$$E(n) = E(1)\, n^{-\nu} \quad (8)$$

interpolation but not for the extrapolation ($n \rightarrow \infty$). Finally, the matrix method, conceived by Pade,[35] could also succeed [Eq. (9)].

$$E_\infty = \frac{\begin{vmatrix} E(1)-E(2) & E(1) \\ E(2)-E(n) & E(2) \end{vmatrix}}{\begin{vmatrix} E(1)-E(2) & 1 \\ E(2)-E(n) & 1 \end{vmatrix}} \quad (9)$$

However, it turned out that none of these procedures correctly reflect the "saturation phenomenon" for series of oligomers having high numbers (n) of repeat units. The OPV

Herbert Meier was born 1939 in Prague. He studied chemistry and mathematics at the University of Tübingen and the Free University in Berlin and in 1968 he completed his doctoral thesis in organic chemistry with Prof. E. Müller in Tübingen. After a habilitation in organic chemistry and photochemistry he became a docent in 1972 and a full Professor in 1975. In 1982 he accepted the chair of Prof. L. Horner at Mainz University. His research focuses on organic compounds with interesting properties for materials science and on heterocycles with a possible activity spectrum. He is co-author of the textbook "Spectroscopic Methods in Organic Chemistry".

 © 2005 Wiley-VCH Verlag GmbH & Co. KGaA, Weinheim

series **4**[18,19,36] will be used here as an example. Figure 1 demonstrates that a linear function of type (1) fits for the first members ($n = 1$–8) of the series, but it is not suitable for the higher oligomers ($n = 11, 15$) or for the extrapolation to the

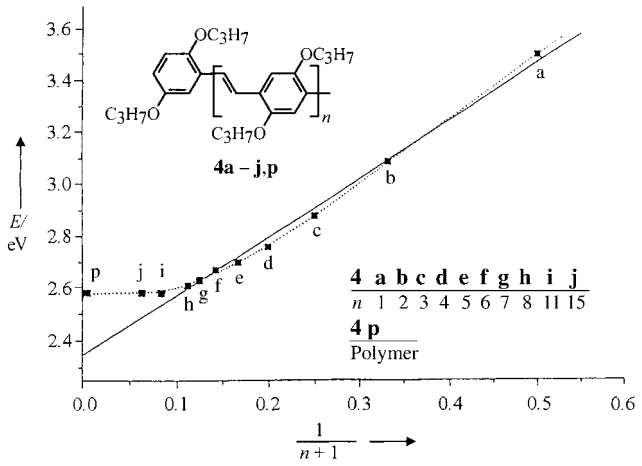

Figure 1. Energies of the long-wavelength absorption maxima of **4a–j** and **4p** in chloroform and their exponential fit function (dotted line), which approaches the value of the corresponding polymer **4p**. The linear function of $(n+1)^{-1}$ furnishes an erroneous limiting value.

(infinitely long) polymer chain. Exponential functions $E(n)$ and $\lambda_{max}(n)$ can be used here according to Equations (10) and (11) as natural growth functions for such a case.[18,19] The effective conjugation length amounts to Equation (12).

$$E(n) = E_\infty + (E_1 - E_\infty)e^{-a(n-1)} \quad (10)$$

$$\lambda_{max}(n) = \lambda_\infty - (\lambda_\infty - \lambda_1)e^{-b(n-1)} \quad (11)$$

$$n_{ECL} = \frac{\ln(\lambda_\infty - \lambda_1)}{6} + 1 \quad (12)$$

Aggregation has to be avoided, especially for UV/Vis measurements of higher oligomers, which means that series of decreasing concentrations need to be measured in a good solvent. Comparative measurements with a constant product of molar concentration and cell thickness, namely, $c\,d = (10^{-1}c)(10\,d) = (10^{-2}c)(100\,d)$, proved to be particularly successful. Even a minor influence of the aggregation results in deviation of the absorption curves. Aggregates whose absorptions differ little from the monomer absorption are particularly tricky. Figure 2 shows the modification of the transitions $S_0 \rightarrow S_1$ when aggregation occurs. To simplify matters it is assumed that the transition moments M of aggregated molecules lie along their longitudinal axes. The van der Waals interaction W_1 leads to an energy level which is subjected to a Davidov splitting W_2. The allowed transition corresponds to the sum $M + M$, and the forbidden transition to the difference $M - M = 0$. The transition energy E depends on the orientation of the molecules in the aggregate; E is lowest for pure J aggregates ($\alpha = 0°$) and highest for pure H aggregates ($\alpha = 90°$). The function $W_2(\alpha)$ in Figure 2 illustrates that W_2 is zero at the magic angle ($\alpha = 54.73°$), which means there is no

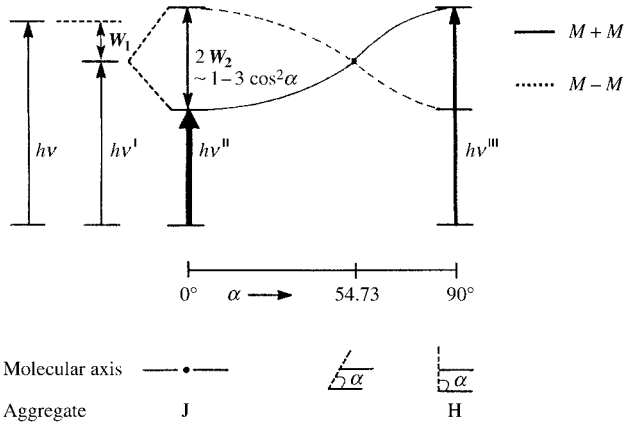

Figure 2. Electron transitions in aggregates, visualized for aggregated molecule pairs, whose transition moments M lie along the longitudinal molecular axis. The energy of the allowed transition (——) and of the forbidden transition (-----) depends on the stacking angle α. Jelley aggregates (J, $\alpha = 0$) exhibit a bathochromic shift ($\nu'' < \nu$) and H aggregates ($\alpha = 90°$) hypsochromic shifts ($\nu''' > \nu$).

discernible energy change. Aggregation can also lead to a steric effect, with the molecules less distorted and consequently absorb at longer wavelengths on aggregation.

The extension of conjugation by increasing numbers of repeat units n normally leads to a monotonously decreasing excitation energy $E(n)$ which converges towards E_∞.[18,37] The exponent a in Equation (10) determines the rate of convergence. Some time ago we found series of conjugated oligomers which show a monotonous hypsochromic effect.[25,38–41] Such a behavior is typical for certain π linkers (see Section 3.1) with strong donors D and strong acceptors A in the terminal positions. The convergence can then also be determined by an equation of the form (10) or (11). The energy $E_{DA}(n)$ [Eq. (13)] of an electron transition in D-π-A systems can be split into two parts; the first part $E_S(n)$ [defined by Eq. (14)] takes the extension of conjugation in the purely donor- or purely acceptor-substituted[42] system into consideration, the second term ΔE_{DA} [defined by Eq. (15)] is a correction term for the push-pull effect in series with terminal donor–acceptor substitution.[25]

$$E_{DA}(n) = E_S(n) - \Delta E_{DA}(n) \quad (13)$$

$$E_S(n) - E_\infty = [E_S(1) - E_\infty]e^{-a(n-1)} \quad (14)$$

$$\Delta E_{DA}(n) = [E_S(1) - E_{DA}(1)]e^{-\Delta a(n-1)} \quad (15)$$

$[E_S(n) - E_\infty]$ has a monotonously declining and $-\Delta E_{DA}(n)$ a monotonously rising fitting function. Both approach to zero for increasing numbers n of repeat units—clearly, this is also valid for their sum $[E_{DA}(n) - E_\infty]$. Figure 3 shows different cases of summation. A monotonously decreasing $E_{DA}(n)$ value results for type (a), which means such an oligomer series exhibits a uniform bathochromic effect: $E_{DA}(n) \geq E_{DA}(n+1) \geq E_\infty$. An oligomer series with a uniform hypsochromic effect is realized in type (b): $E_{DA}(n) \leq E_{DA}(n+1) \leq E_\infty$. The borderline case (a)/(b) between (a) and (b) is present for $E_{DA}(n) \approx E_\infty$, that is, when the energy of the

 © 2005 Wiley-VCH Verlag GmbH & Co. KGaA, Weinheim

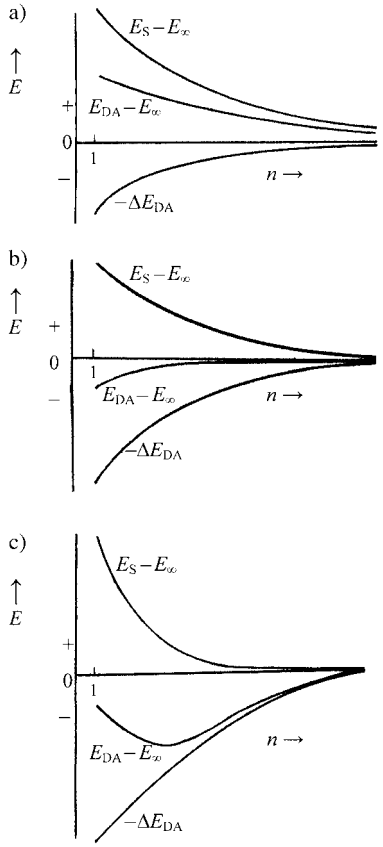

Figure 3. Variants for the convergence of excitation energies $E_{DA}(n) \rightarrow E_\infty$ of the long-wavelength electron transition in series of push-pull-substituted conjugated oligomers: a) uniform bathochromic behavior, b) uniform hypsochromic behavior, c) hypsochromic convergence after passing through a minimum of $E_{DA}(n)$.

electron transition is nearly independent of n (of the size of the chromophore). A rapidly decreasing term $[E_S(n) - E_\infty]$ with increasing numbers n can also lead to the fact that $E_{DA}(n)$ goes through a minimum before it approaches to E_∞ (type (c)). Examples of oligomer series D-π-A for the considered cases are given in the following sections; the theoretically imaginable case, in which $E_{DA}(n)$ goes through a maximum, is to my knowledge not unequivocally proven experimentally to date.

3. Push-Pull-Substituted Oligomers: Synthetic Concepts and Absorption Behavior

3.1. Linear Oligomers D-π-A

The push-pull effect has a strong influence on the long-wavelength electron transitions in conjugated oligomers with terminal donor–acceptor substituents (see Section 5). Table 1 shows as an example the *trans*-stilbenes **5a–f** (Scheme 4) which bear a branched dialkylamino group in the 4-position and various substituents R in the 4′-position.[21,25,39] Compared to **5a** with R = H, the compounds with acceptor groups R exhibit a bathochromic shift, which is more and more pronounced as the acceptor strength increases. Since the corresponding excitation $S_0 \rightarrow S_1$ is connected to an intramolecular charge transfer (ICT), the long-wavelength band is called a charge transfer band.

Table 1: Absorption in $CHCl_3$ and color of the crystals of the *trans*-stilbenes **5a–5f**.[a]

Compound **5**	R	λ_{max} [nm]	Crystal color
a[21,25]	H	366	colorless
b[21,25]	CN	401	yellow
c[21,25]	CHO	423	orange
d[21,25]	NO_2	461	red
e[39]	$HC{=}C(CN)_2$	525	dark red
f[39]	$C(CN){=}C(CN)_2$	670	blue

[a] Since the ε values are not known for many UV/Vis data discussed in this article, they are omitted completely.

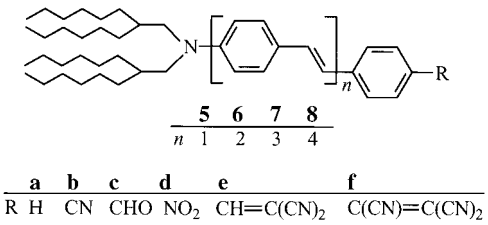

Scheme 4. Push-pull-substituted oligo(1,4-phenylenevinylene)s (OPVs) **5–8/b–f** and the comparitive series **5a–8a**.

An exciting question is how does the intramolecular charge transfer change when the distance between donor and acceptor groups increases, that is, when the number n of repeat units in the π linker is increased. Since dialkylamino groups with long alkyl chains have a solubilizing character, a systematic study of the oligo(1,4-phenylenevinylene)s (OPVs) **5a–e**, **6a–e**, **7a–e**, and **8a–e** could be performed.[21,25]

Compounds **5c–8c** were constructed from **9** by means of a Wittig–Horner reaction and a simple protecton strategy (Scheme 5). Phosphonate **10** served as an "extension reagent". After a condensation reaction in an alkaline medium, the deprotection of the masked formyl group in **10**

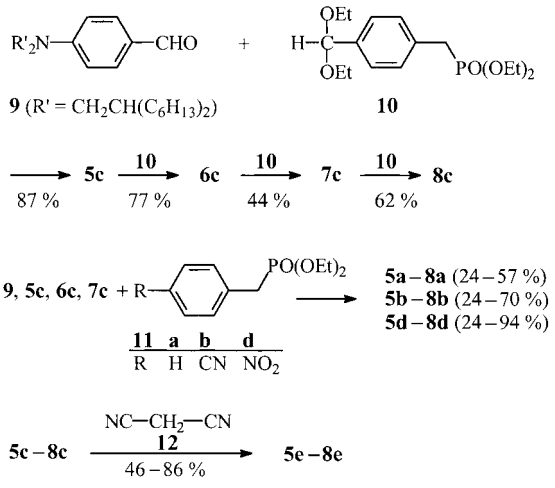

Scheme 5. Coupled convergent synthetic strategy for the OPV series **5–8/a–e**.

 © 2005 Wiley-VCH Verlag GmbH & Co. KGaA, Weinheim

occurred directly in the acidic work-up, so that a free aldehyde function was available for the next extension step. The compounds **9**, **5c**, **6c**, and **7c** were then reacted in an "end-capping process" with the phosphonates **11a**,**b**,**d** to give the series **5a–8a**, **5b–8b**, and **5d–8d**.[21,25] A condensation reaction of the aldehydes **5c–8c** with malononitrile **12** can be recommended for the "end capping" for the preparation of the series **5e–8e**.[39] It was possible to obtain the series of five oligomers through a minimum number of synthetic steps by applying this coupled, convergent synthetic strategy.

Figure 4 depicts the maxima of the long-wavelength absorptions of the OPVs **5–8a–e** measured in $CHCl_3$. A

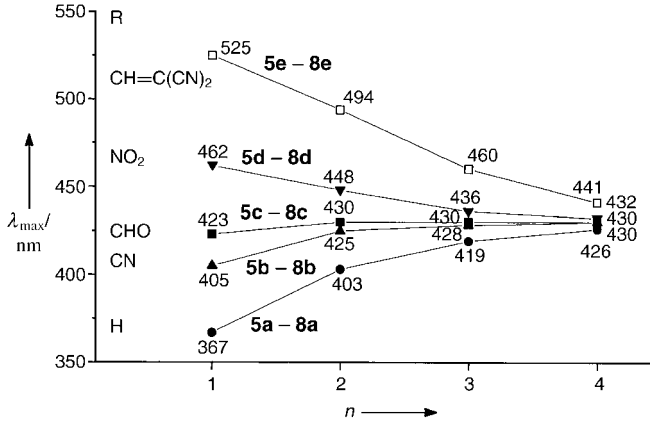

Figure 4. Maxima of the long-wavelength absorptions in the OPV series **5–8/a–e** in $CHCl_3$.

pronounced bathochromic effect can be realized for **5a–8a**, a decreased bathochromic effect for **5b–8b**, λ_{max} values of **5c–8c** which are fairly independent of the size of the chromophore, a hypsochromic effect for **5d–8d**, and an even stronger hypsochromic effect for **5e–8e**.

The evaluation according to Equations (13)–(15) is demonstrated in Figure 5. The extension of the conjugation leads

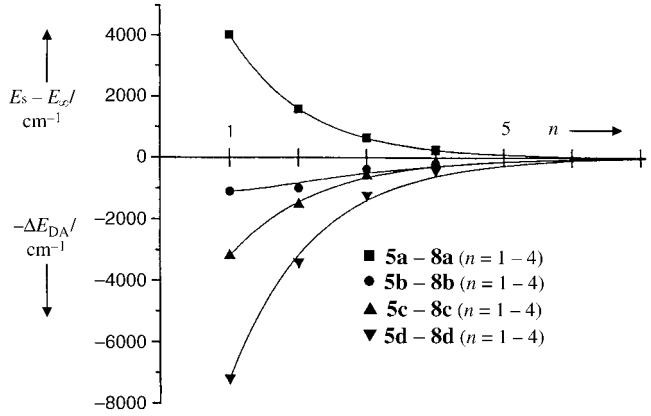

Figure 5. Partition of the energies of the electron transition $S_0 \rightarrow S_1$ into a term ($E_s - E_\infty$) which reflects the bathochromic shift caused by the extension of conjugation and a term $-\Delta E_{DA}$ which takes the decrease of the ICT and its consequence on the absorption into account. The measured data of **5–8/a–d** in $CHCl_3$ shown in Figure 4 are the basis for this distribution.[43]

to a bathochromic shift, which is shown by a decreasing difference of $E_S - E_\infty$ for the series **5a–8a**. The push-pull-substituted OPV series **5b–8b** bearing the relatively weak acceptor R = CN is characterized by a correction term $-\Delta E_{DA}$ which weakens the bathochromic shift. In the series **5d–8d**, with the nitro group as strong acceptor, the term $E_S - E_\infty$ is over-compensated by the term $-\Delta E_{DA}$; thus, a hypsochromic effect results. The two terms generally cancel each other out in **5c–8c** (formyl series), so that the absorption maxima are almost independent of the length of the chromophore.[43]

The compounds **5–8/a–e** show, without exception, positive solvatochromic effects, which originate from intramolecular charge transfer (ICT). As soon as the push-pull effect is suspended by protonation of the amino group, the bathochromic shift in the series **5b–8b** is strengthened and the hypsochromic shift in the series **5d–8d** is reversed to a bathochromic shift (Figure 6). However, the entire absorption

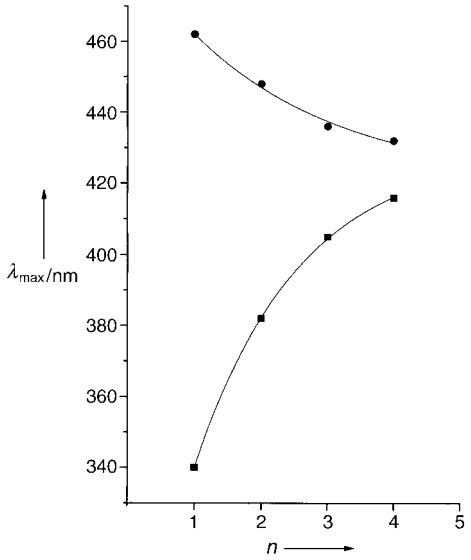

Figure 6. Absorption maxima in the OPV series **5d–8d** ($n = 1$–4); top curve: measurement in $CHCl_3$, bottom curve: measurement in $CHCl_3$/CF_3COOH (10:1).

range is located at essentially higher energy when the ICT is cancelled out (see Section 5).

An extension of conjugation in push-pull-substituted OPVs results in a bathochromic shift, but the decrease of the ICT and its effect on the absorption causes an opposite hypsochromic shift (see Section 5). Depending on the strength of the acceptor, a bathochromic or hypsochromic net effect results for systems with the same donor; this includes the case in which both effects cancel each other out. Exclusive bathochromic effects were found for OPV linkers with weaker donors, such as alkoxy groups. Compounds **13**[44–46] and **14**[46,47] in Scheme 6 illustrate this statement. Among the depicted variants $E(n)$ in Figure 3, the cases (a) and (b) as well as the borderline case (a)/(b) are realized in push-pull-substituted OPVs.

The *trans*-configured double bond in the repeat unit of **5–8/a–e** is replaced in the donor–acceptor-substituted oligo(1,4-phenyleneethynylene)s (OPEs) **15–18/a–e** shown in Scheme 7

 © 2005 Wiley-VCH Verlag GmbH & Co. KGaA, Weinheim

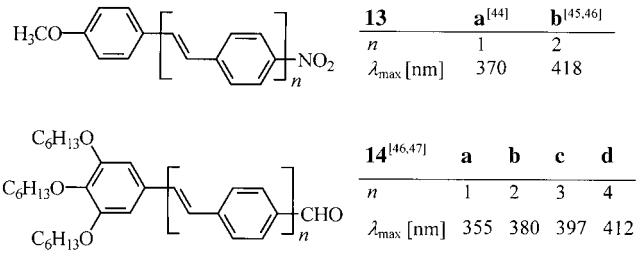

13	a[44]	b[45,46]
n	1	2
λ_{max} [nm]	370	418

14[46,47]	a	b	c	d
n	1	2	3	4
λ_{max} [nm]	355	380	397	412

Scheme 6. Push-pull-substituted OPVs with alkoxy groups as donor groups; absorption maxima in $CHCl_3$.

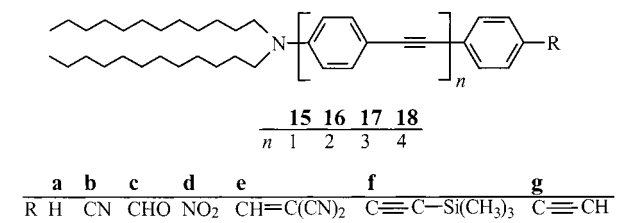

	15	16	17	18
n	1	2	3	4

a	b	c	d	e	f	g
R H	CN	CHO	NO_2	$CH{=}C(CN)_2$	$C{\equiv}C{-}Si(CH_3)_3$	$C{\equiv}CH$

Scheme 7. Push-pull-substituted OPE series **15–18/b–e**, comparitive series **15a–18a**, and precursors **15f–17f** and **15g–17g**.[41,48]

by a triple bond, and the didodecylamino group serves as a solubilizing donor function.[41] The preparation of the oligomer series **15–18/a–e** again takes place by a coupled, convergent strategy. The Sonogashira–Hagihara reaction and a simple protection strategy form the preparative basis.[41] Starting from **19** and **20**, the "auxiliary series" **15f–17f** and **15g–17g** were first prepared (Scheme 8). The extension

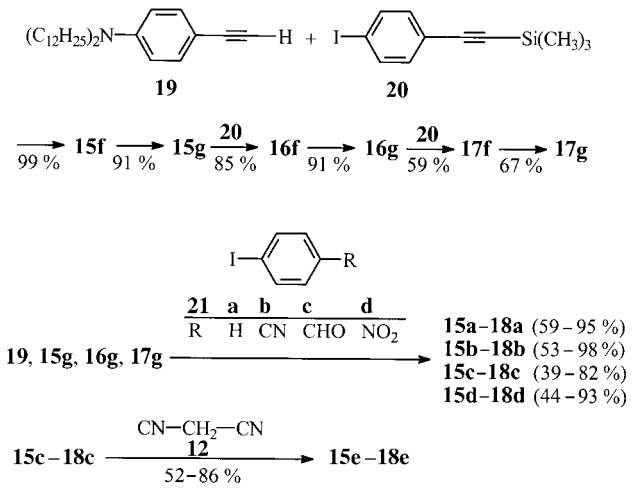

Scheme 8. Coupled convergent synthetic strategy for the OPE series **15–18/a–e** with the precursor series **15f–17f** and **15g–17g**.

reagent **20** was utilized for the Pd-catalyzed C–C coupling step; the subsequent alkaline deprotection left the ethynyl component open for the next extension step. The Sonogashira–Hagihara reaction with the corresponding iodobenzene, which contained the desired *p*-substituent (R = H, CN, CHO, NO_2), was used then as the "end-capping" step.[41] The OPE series **15e–18e** could be obtained by the condensation reaction of **15c–18c** and malononitrile.[46]

The long-wavelength absorption data for compounds **15–18/a–e** are summarized in Table 2.[41] The evaluation of the UV/Vis spectra is somewhat more difficult in the OPE series than in the OPV series because the long-wavelength absorption band ($S_0 \rightarrow S_1$) is superimposed by the higher energy electron transition $S_0 \rightarrow S_2$ (Figure 7 demonstrates this using

Table 2: Long-wavelength UV/Vis absorption of the OPE compounds **15–18/a–e** in $CHCl_3$.

Compound	n	$\tilde{\nu}_{max}$ [10^3 cm^{-1}]	λ_{max} [nm]
15a	1	29.33 ± 0.07	341
16a	2	26.74 ± 0.07	374
17a	3	26.28 ± 0.18	379[a]
18a	4	26.16 ± 0.30	378[a]
15b	1	25.84 ± 0.07	387
16b	2	25.84 ± 0.07	387
17b	3	25.97 ± 0.18	384[a]
18b	4	26.09 ± 0.30	379[a]
15c	1	25.00 ± 0.06	400
16c	2	25.64 ± 0.06	390
17c	3	26.00 ± 0.20	382[a]
18c	4	26.02 ± 0.25	388[a]
15d	1	23.15 ± 0.06	432
16d	2	24.81 ± 0.06	403
17d	3	26.15 ± 0.30	380[a]
18d	4	26.15 ± 0.30	382[a]
15e	1	20.45 ± 0.05	489
16e	2	22.62 ± 0.07	442
17e	3	24.75 ± 1.00	384[a]
18e	4	26.8 ± 0.30	373[a]

[a] The λ_{max} values differ in these cases from $1/\tilde{\nu}_{max}$ of the separated long-wavelength band because of the superposition of the bands.

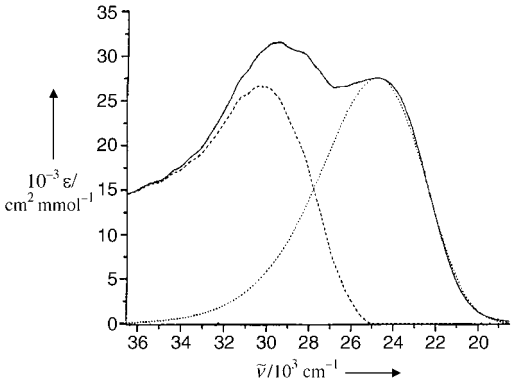

Figure 7. UV/Vis spectrum of **16d** in $CHCl_3$ (——) and its dissection into two bands according to Equations (16)–(18).[41]

16d as an example). A separation of the bands can be performed for example with an algorithm based on Gauss functions.[49] Since non-overlapping absorption bands at long wavelengths are also slightly unsymmetric in these series, exponential functions of type (16) proved to be a success.

$$\varepsilon(\tilde{\nu}) = \varepsilon_{max} \exp\left[-\left(\frac{\tilde{\nu}_{max}(\tilde{\nu}-\tilde{\nu}_{max})}{\tilde{\nu}\,\Delta\tilde{\nu}}\right)\right] \quad (16)$$

$$\text{with } \Delta\tilde{\nu} = |0.5(\tilde{\nu}_2 - \tilde{\nu}_1)| \quad (17)$$

$$\text{and } \varepsilon(\tilde{\nu}_1) = \varepsilon(\tilde{\nu}_2) = \varepsilon_{max}\, e^{-1} \quad (18)$$

 © 2005 Wiley-VCH Verlag GmbH & Co. KGaA, Weinheim

The evaluation of the data of **15–18/a–d** is visualized in Figure 8, which corresponds more or less to Figure 5 for the analogous donor–acceptor-substituted OPV systems **5–8/a–d**.[50] The interpretation of Figure 8 corresponds to the interpretation of Figure 5. The bathochromic effect resulting

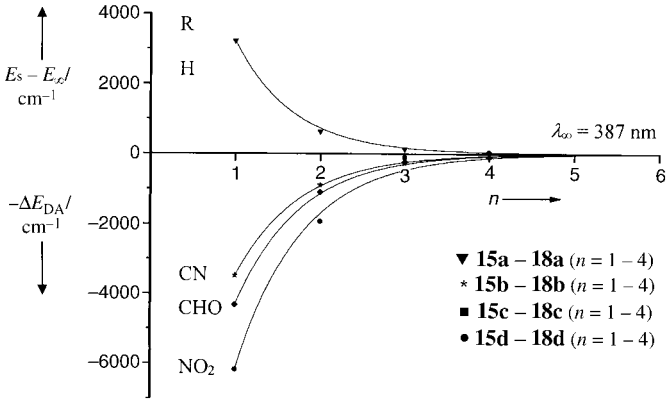

Figure 8. Partition of the electron transition energies ($S_0 \rightarrow S_1$) of **15–18/a–d** into a term ($E_S - E_\infty$) which reflects the bathochromic shift caused by the extension of conjugation and a term $-\Delta E_{DA}$ which takes the decrease of the ICT and its consequence on the absorption into account.

from the extension of conjugation is surpassed in the NO_2 series by the hypsochromic effect, which arises from the decrease in the ICT; the same is true to a lesser extent in the CHO series **15c–18c**; the two effects cancel themselves out almost completely in the CN series **15b–18b**. Altogether, the OPE linker is still somewhat more prone than the OPV linker to exhibit the unusual hypsochromic effect with increasing numbers *n*.[51] This situation has the consequence that even methoxy groups (as weaker donors) do not show a red-shift when in combination with strong acceptors such as NO_2. Compounds **22** and **23** in Scheme 9 are shown here as

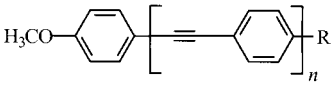

	R	*n*	λ_{max} [nm]
22a	CN	1	323
23a	CN	2	339
22b	NO_2	1	368
23b	NO_2	2	365

Scheme 9. Maxima of the long-wavelength absorptions of push-pull-substituted OPEs with methoxy groups as donors and CN or NO_2 groups as acceptors ($CHCl_3$ as solvent).

examples. Whereas $\lambda_{max}(2) - \lambda_{max}(1)$ amounts to +16 nm for **22a/23a**, a value of −3 nm was found for **22b/23b**.[46] The dialkylamino group (a strong donor) does not effect an inversion of the red-shift in the series **15g–17g** bearing the ethynyl group (a weak acceptor group).

Only single examples of push-pull-substituted oligoenes (OEs) of type **1** (polymethine dyes) or **24a,b–29a,b** ($n = 1,2,3, \ldots$) are known; an exception is represented by the aldehydes **24c–29c** ($R = CH_3$),[52a–c] which were prepared from the Zincke aldehyde by chain extensions with Grignard reagents and hydrolysis of the corresponding cyanines (Scheme 10).[52a]

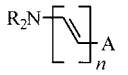

24–29	**a**	**b**	**c**
A	$CH=C(CN)_2$	CN	CHO

R = Alkyl

($n = 1,2,3, \ldots$)

	24c	**25c**	**26c**	**27c**	**28c**	**29c**
n	1	2	3	4	5	6
λ_{max} [nm]	283	362	422	462	492	513

Scheme 10. Push-pull-substituted oligoenes: Maxima of the long-wavelength absorption in CH_2Cl_2.

The absorption spectra of **24c–29c** measured in CH_2Cl_2 show a pronounced bathochromic shift for increasing numbers *n* of repeat units. Even the stronger electron-withdrawing dicyanovinyl group does not change this effect—nor when the *trans* double bonds are fixed in a transoid arrangement by incorporation in rings.[52d] Bathochromic effects were also observed by Lehn, Blanchard-Desce, Zyss, and co-workers in the series **30a–32a** and **30b–32b**, which contain carotinoid units as π linkers (Scheme 11). The synthesis of these com-

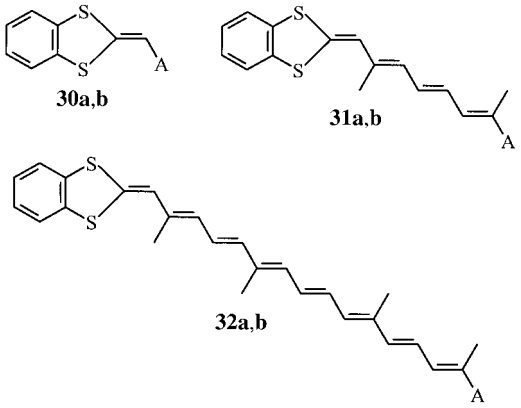

a A = CHO **b** $A = CH=C(CN)_2$

	30a	**31a**	**32a**		**30b**	**31b**	**32b**
λ_{max} [nm]	372	456	500	λ_{max} [nm]	446	562	588

Scheme 11. Carotinoid push-pull compounds and the maxima of their long-wavelength absorption in $CHCl_3$.[53–55]

pounds was performed by "one-sided" Wittig and Wittig–Horner reactions, respectively, of the carotinoid dialdehydes and the corresponding phosphorus reagents of 1,3-benzodithiole followed by subsequent condensation of the still-present aldehyde function with malononitrile.[53,54]

 © 2005 Wiley-VCH Verlag GmbH & Co. KGaA, Weinheim

The bathochromic shift for increasing length of the chromophore was also found by Blanchard-Desce, Barzoukas, Marder, and co-workers who studied the series **33–35**, which includes an aromatic or heteroaromatic ring in the π linker at the donor end (Scheme 12).[3,56,57] The synthetic strategy for **33–35** is depicted in Scheme 13. The aldehyde

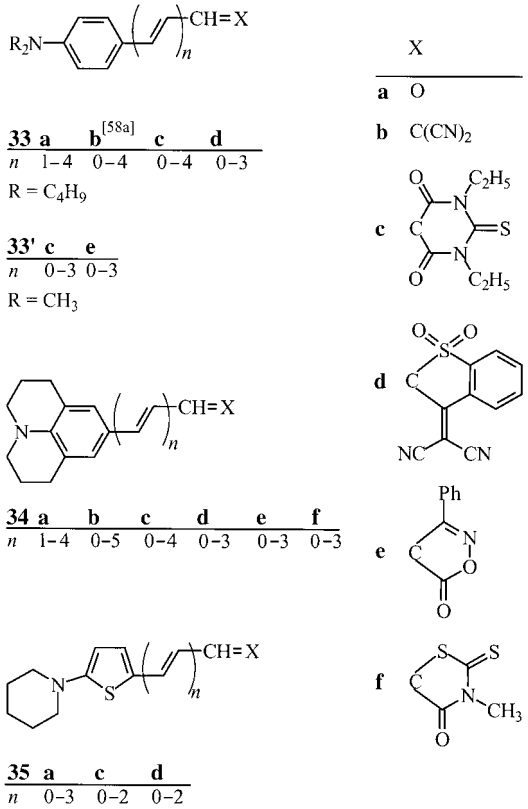

Scheme 12. Oligoenes with (hetero)aromatic rings as donors as well as various acceptors.

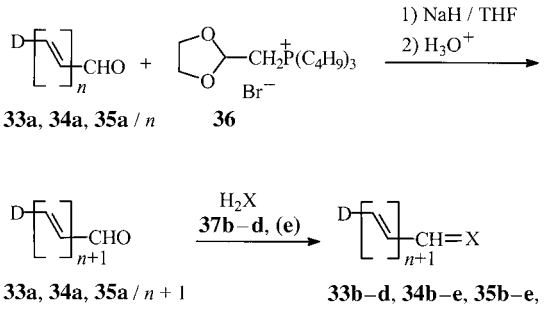

Scheme 13. Synthetic strategy for the series of compounds **33–35**.[57]

series **33a**, **34a**, and **35a** with the corresponding donor groups D acted as the central series and were constructed by means of the Wittig reaction with the extension reagent **36**. The condensation reaction with the active methylene components **37b–e** was then selected as the "end capping".[57] The maxima of the long-wavelength absorptions of a selection of compounds **33–35** are listed in Table 3. For constant values of n, the λ_{max} value becomes higher as the donor and acceptor

Table 3: Maxima of the long-wavelength absorption λ_{max} [nm] of the oligoenes **33b** (n = 0–4), **33d** (n = 0–3), **34a** (n = 1–4), **34b** (n = 0–5), **34f** (n = 0–3), and **35c** (n = 0–2) in $CHCl_3$.

n	**33b**[56]	**33d**[57]	**34a**[56]	**34b**[56]	**34f**[56]	**35c**[57]
0	443	603		458	494	512
1	507	695	413	531	542	619
2	540	773	446	572	556	710
3	571	826	469	594	566	
4	586		486	606		
5				613		

strength increases; $\lambda_{max}(n+1) > \lambda_{max}(n)$ is valid within each series. Analogous bathochromic effects were measured for series of compounds with 1,3-benzodithiole donor groups and carotinoid linkers which contain an aromatic or heteroaromatic ring (4-nitrophenyl, 4-cyanophenyl, 4-pyridyl) at the acceptor end.[53,55]

Push-pull-substituted oligoenes bearing aromatic rings at both chain ends[53,55,58b,59] show a diminished bathochromic effect. A comparison of the series **38a–41a** and **38b–41b** (Scheme 14) shows a characteristic result.[46,58b,59] Compounds

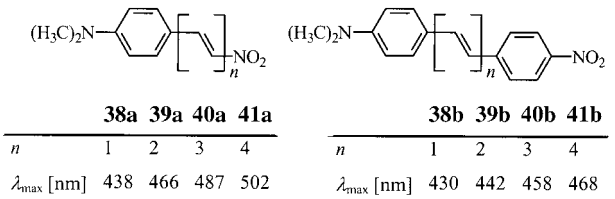

Scheme 14. Maxima of the long-wavelength absorption of oligoenes with terminal dimethylamino/nitro substitution, which include a benzene ring in the π linker on the donor side (**38a–41a**) as well as on the donor and acceptor sides (**38b–41b**); measured in $CHCl_3$.

analogous to **38b–40b**, but with a CN group instead of the NO_2 group, were investigated in the context of their dual fluorescence and twisted intramolecular charge transfer (TICT) states;[60–66] however, a discussion of these states is beyond the scope of the present Review.

Push-pull-substituted oligoynes (OIs) are scarcely reported in the literature to date.[67] The aminoketones **42** and **43** and the aminonitro compounds **44** and **45** are given here as examples (Scheme 15). Benzene rings at the ends of the π linker cause a hypsochromic effect for neither the push-pull-substituted oligoenes nor the corresponding oligoynes—in contrast with the accordingly substituted OPV and OPE systems.

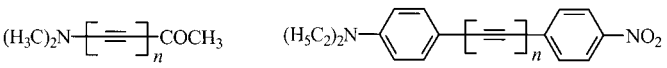

Compd	n	λ_{max} [nm]	Solvent	Compd	n	λ_{max} [nm]	Solvent
42[68]	1	277	CH_2Cl_2	**44**[70]	1	302	CH_2Cl_2
43[69]	2	330	CH_3CN	**45**[70]	3	450	CH_2Cl_2

Scheme 15. Maxima of the long-wavelength absorption of oligoynes with push-pull substitution.[68–71]

 © 2005 Wiley-VCH Verlag GmbH & Co. KGaA, Weinheim

Oligo(1,4-phenylene)s (OPs) differ from the OPVs, OPEs, OEs, and OIs discussed so far as a result of a strong torsion of the benzene rings along the chain. Torsional angles between 30 and 40° can be assumed, which considerably influence the conjugation and the ICT.[71,72] Since the resonance integrals do not only depend on the different atomic distances in the π linker but also on the torsion of the p orbitals, an acceleration of the convergence $E(n)\rightarrow E_\infty$ can in principal be expected for increasing torsion angles. A considerable planarization of the 1,4-phenylene chain by anelated five-membered rings results in a bathochromic shift;[71–73] Table 4 shows a comparision of biphenyls **46a–49a** and fluorenes **46b–49b** (see Scheme 16 for structures).

Table 4: Maxima of the long-wavelength absorption of the biphenyls **46a–49a** and comparison with the corresponding fluorenes **46b–49b**.[71,73]

R^1	R^2	Biphenyl drivatives	λ_{max} [nm]	Fluorene derivatives	λ_{max} [nm]
H	H	**46a**	252[a]	**46b**	262[a]
H	NO_2	**47a**	304[a]	**47b**	328[a]
$N(CH_3)_2$	H	**48a**	301[b]	**48b**	310[b]
$N(CH_3)_2$	NO_2	**49a**	390[b]	**49b**	417[b]

[a] Measurement in 1,4-dioxane. [b] Measurement in $CHCl_3$.

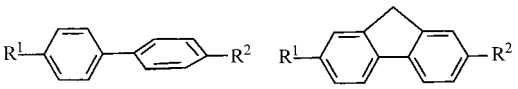

46a–49a **46b–49b**

Scheme 16. Planarization of the torsional angles of biphenyls in fluorenes (see Table 4 for R^1, R^2).

The synthetic strategy of oligo(1,4-phenylene)s is based on usual Pd-catalyzed aryl–aryl C–C coupling reactions such as the Suzuki, Negishi, Stille, Yamamoto, or Kumada reactions.[1k] The preparation of the series **54** with D = N-$(CH_3)_2$ and A = CN are described here as an example (Scheme 17). Negishi couplings of **50** with **51** led to the

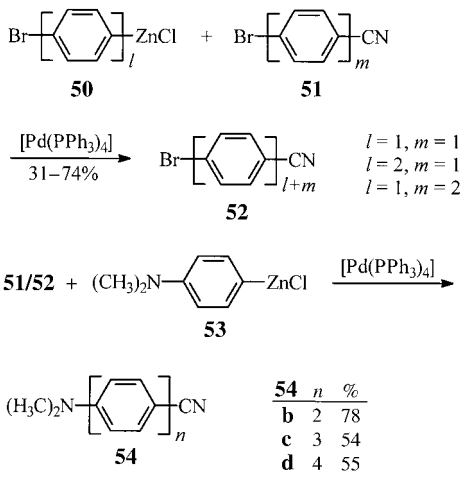

Scheme 17. Synthetic strategy for the construction of donor–acceptor-substituted OPs **54**.[74]

construction of the "auxiliary series" **52**. The primary insertion of the Pd into the C–Br bond of **51** is decisive for this step. Compounds **51** and **52** were then subjected to a cross-coupling reaction with **53**.[74]

Since the "range" of the ICT is considerably shorter than the conjugation (see Section 5), the continuous torsions along an oligo(1,4-phenylene) chain can lead to a fast decrease in the $E_D(n)-E_\infty$ value (see Figure 3c). Consequently, the energy $E_{DA}(n)$ for the electron transition $S_0\rightarrow S_1$ can pass through a minimum, and $\lambda_{max}(n)$ accordingly through a maximum (type (c), Figure 3)—in particular, when the correction term ΔE_{DA} of the ICT is large, that is, when a push-pull effect of a strong donor and a not too weak acceptor is present. This is realized for **54** and **55** (Table 5); the maximum

Table 5: Maxima of the long-wavelength absorption of donor–acceptor substituted oligo(1,4-phenylene)s D-[-C_6H_4-]$_n$-A: **54a–d**,[75] **55a–d**,[71,76] **56a–c**,[71] and **57a–c**.[46,77,78]

Compound	A	D	n	λ_{max} [nm]	Solvent
54a	CN	$N(CH_3)_2$	1	290	CCl_4
54b			2	342	CCl_4
54c			3	332	CCl_4
54d			4	314	CCl_4
55a	NO_2	NH_2	1	373	EtOH
55b			2	378	EtOH
55c			3	358	EtOH
55d			4	340	EtOH
56a	NO_2	OCH_3	1	302	1,4-dioxane
56b			2	332	1,4-dioxane
56c			3	340	1,4-dioxane
57a	CN	OCH_3	1	247	DMSO
57b			2	292	DMSO
57c			3	302	DMSO

value of λ_{max} is found in both cases for $n = 2$, but can be solvent dependent. When the amino function is substituted by the less-strong donor OCH_3, shifts to longer wavelengths are obtained for the series with A = NO_2 as well as for the series with A = CN with increasing values of n (type (a), Figure 3).

The introduction of thiophene or furan rings instead of benzene rings in the π linker results in the absorption maxima shifting to longer wavelengths (Scheme 18 shows some examples).[71] Push-pull-substituted oligomers whose π linkers consist exclusively of five-membered-ring heterocycles, were studied in particular for the thiophene series. Table 6 offers a comparison of bithiophenes with various donor and acceptor groups; it can be seen that the combination of a 1-pyrrolidine group and a nitro group in particular results in a far-red-shifted CT band. Thus, an interesting dependence of the absorption on the number n of repeat units can be expected for the push-pull-substituted oligothiophenes (OT; oligo(2,5-thienylene)s) studied by Effenberger and Würthner.[79–81] Table 7 shows a comparison of the methoxy-nitro series **66a–d** ($n = 1$–4) and the 1-pyrrolidino-nitro series **67a–d** ($n = 1$–4). Whereas a monotonous bathochromic shift with increasing n was found for **66a–d**, the λ_{max} value of **67a–d** passes through a maximum at $n = 3$.[82] Hence, the latter oligomer series belongs to type (c) in Figure 3 and resembles the corresponding OPs **54a–d** and **55a–d**. To date, there are

 © 2005 Wiley-VCH Verlag GmbH & Co. KGaA, Weinheim

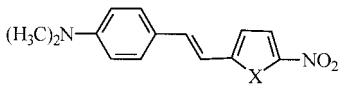

	X	λ_{max} [nm][71]
58	S	492 $CHCl_3$
59	O	478 $CHCl_3$
38b	CH=CH	430 $CHCl_3$

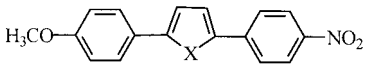

	X	λ_{max} [nm][71]
60	O	400 $CHCl_3$
56c	CH=CH	340 $CHCl_3$

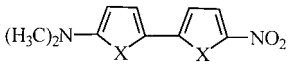

	X	λ_{max} [nm][79]
61	S	466 (*n*-hexane)
62	CH=CH	375 (*n*-hexane)

Scheme 18. Red-shift of the long-wavelength absorption band on replacement of the benzene rings in the π linker by thiophene or furan rings.

Table 6: Maxima of the long-wavelength absorption of donor–acceptor-substituted bithiophenes in *n*-hexane.[79,80]

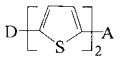

Compound	D	A	λ_{max} [nm]
63	OCH_3	CHO	372
64	$N(CH_3)_2$	CHO	421
65	SCH_3	NO_2	391
66b	OCH_3	NO_2	408
61	$N(CH_3)_2$	NO_2	466
67b		NO_2	499

Table 7: Maxima of the long-wavelength absorptions of the oligothiophenes **66a–d** and **67a–d** in *n*-hexane.[79–81]

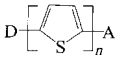

Compound	D	A	*n*	λ_{max} [nm]
66a	OCH_3	NO_2	1	340
66b			2	408
66c			3	442
66d			4	454
67a		NO_2	1	408
67b			2	499
67c			3	505
67d			4	497

few D-π-A series with repeat units consisting of thiophene rings and C–C double or triple bonds.[83] Oligo(2,5-thienylenevinylene)s (OTVs) which bear 4-diethylaminophenyl groups as the donor and NO_2, CHO, or $CH{=}C(CN)_2$ groups as the acceptor have to be mentioned in this context; all these cases correspond to "bathochromic series" (type (a)).[83a,b] The oligo(2,5-thienyleneethinylene)s (OTEs) **68a–c** and **69a–d**, which were recently prepared by a Sonogashira–Hagihara reaction, should also be mentioned (Scheme 19).[46] The series **68a–c** belongs to type (a) in Figure 3, whereas the series **69a–d** exhibits an $S_0 \rightarrow S_1$ transition, which is independent of the length of the chromophore.

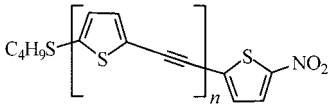

	n	λ_{max} [nm]
68a	1	413
68b	2	426
68c	4	428

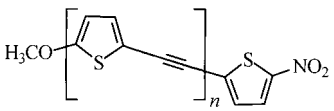

	n	λ_{max} [nm]
69a	1	431
69b	2	430 ± 5
69c	3	430 ± 5
69d	4	430 ± 10

Scheme 19. Maxima of the long-wavelength absorption of donor–acceptor-substituted oligo(2,5-thienyleneethynylene)s **68a–c** and **69a–d** (measured in $CHCl_3$).[46]

It remains to state at the end of this section that D-π-A systems can also be generated by protonation of suitable D-π-D systems. Not only does the protonation of terminal amino groups have to be considered, but also the thiophene ring itself, as demonstrated in Scheme 20. Protonation of **70a**,**b** in CD_2Cl_2/CF_3COOH leads to a shift of more than 200 nm to longer wavelengths.[84]

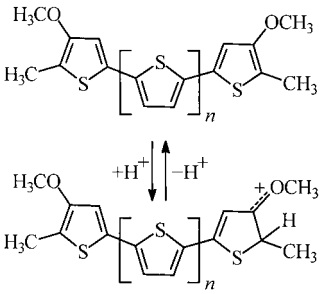

	n	λ_{max} [nm]
70a	1	386
70b	2	414

	n	λ_{max} [nm]
71a	1	590
71b	2	630

Scheme 20. Protonation of symmetrical oligothiophenes for the generation of D-π-A systems.

3.2. Oligomers with D-π-A-π-D or A-π-D-π-A Structures

Conjugated oligomers with a donor–acceptor–donor structure require bidentate acceptor groups in the center of the molecule. The presence of carbonyl and related groups in this position leads to cross-conjugation. An example is presented by Michlers ketone **72** ($m = n = 1$) and its higher homologues, though little is known about them.[85] Single examples of linearly conjugated D-π-A-π-D compounds exist in the series of azobenzenes **73**,[46,86–88] pyridazines **74**,[89] pyrazines **75**,[90] and 1,2,4,5-tetrazines **76**;[46,91] a systematic study was only performed for the squaraine series **77a–d**[92] (Scheme 21).

Compounds **77**, which are obtained by coupling the corresponding resorcinols and squaric acid, show an absorp-

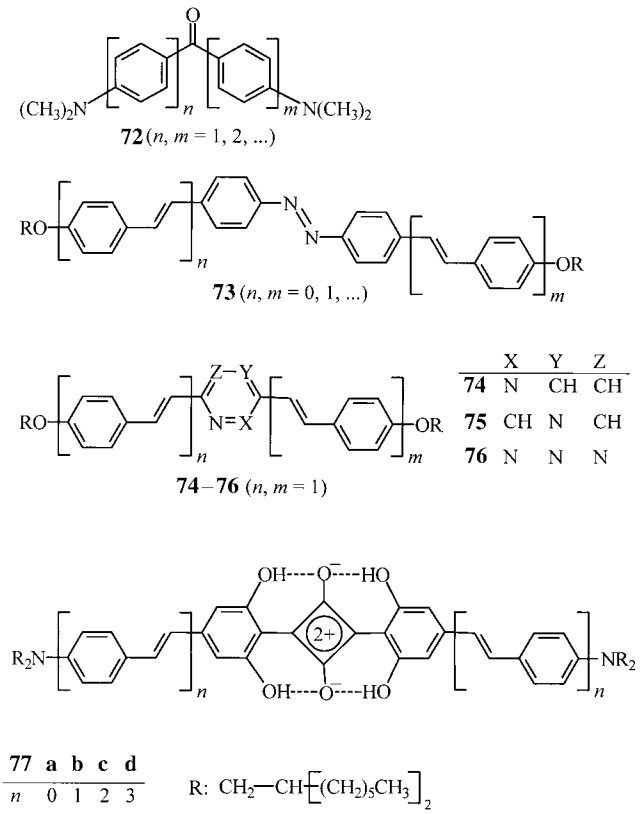

Scheme 21. Examples of D-π-A-π-D systems.

tion with a strong red-shift on going from $n=0$ to $n=1$; the blue dye **77a** is thereby converted into the NIR dye **77b**.[92] The electron transition which is predominantly localized in the squaraine ring[93] in **77a** becomes a transition in a push-pull-substituted stilbenoid compound and hence results in a pronounced hypsochromic effect for $n=2,3$.[92] This effect occurs only when the measurements are made in an organic solvent such as $CHCl_3$ (Figure 9)—when an acidic medium such as CF_3COOH is used, the amino groups become protonated and consequently lose their donor character; the generated cations then have an A-π-A-π-A structure and show the expected bathochromic shift (from $n=0$ to $n=3$).

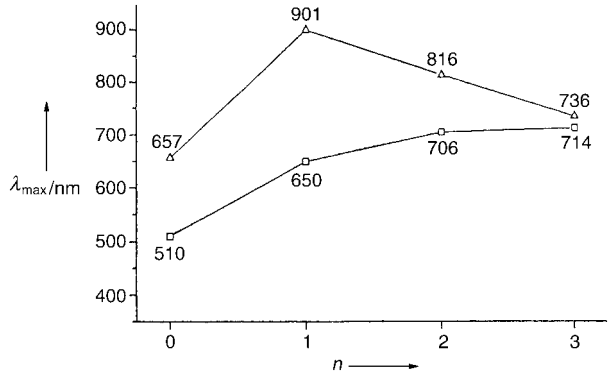

Figure 9. Maxima of the long-wavelength absorption of the squaraines **77a–d** ($n=0$–3) in $CHCl_3$ △ and in CF_3COOH □.

An extended planarization of the chromophore, in **77** through the formation of intramolecular hydrogen bridges, is an essential precondition for an efficient push-pull effect. Figure 10 shows, using compound **78** as an example, how the absorption is shifted from the NIR range to the UV range

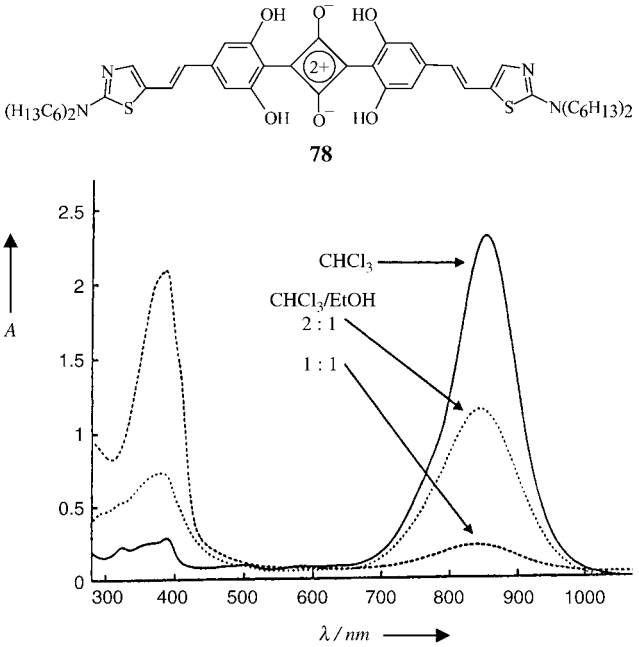

Figure 10. Absorption of squaraine **78** in $CHCl_3$ and in $CHCl_3$/EtOH mixtures.

($\Delta\lambda_{max} > 450$ nm) by the addition of ethanol which acts as a hydrogen bridge donor.[94] The benzene rings turn out of the plane of the squaraine rings when intermolecular hydrogen bridges are formed.

Compounds of the type A-π-D-π-A require bidentate donors such as O, S, or NH. No oligomer series of this type currently exists. Recently, the two first members ($n=1$, 2) of the series **79** (Scheme 22) with ferrocene as a strong donor were studied; they exhibit a bathochromic effect: $\lambda_{max}(2) > \lambda_{max}(1)$.[95]

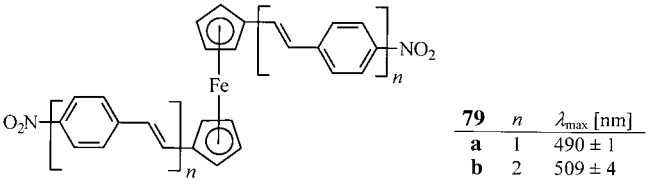

Scheme 22. Maxima of the long-wavelenth absorption of A-π-D-π-A compounds with ferrocene as the central donor (measured in $CHCl_3$).

3.3. Star-Shaped Compounds A-(π-D)$_3$ and D-(π-A)$_3$

Tridentate "cores" have to be considered in addition to the bidentate central acceptors or donors described in Section 2.3. Scheme 23 shows some central building blocks.

 © 2005 Wiley-VCH Verlag GmbH & Co. KGaA, Weinheim

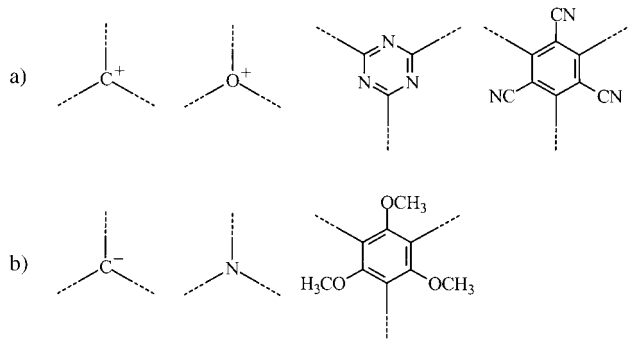

Scheme 23. Central building blocks for conjugated three-arm oligomers: a) acceptor groups for star-shaped compounds A-(π-D)$_3$, b) donor groups for star-shaped compounds D-(π-A)$_3$.

The series of methylium salts **80a–d** (Scheme 24) was prepared; they can be regarded as higher homologues of the well-known triphenylmethane dyes.[96] The synthesis of **80a–d** was realized from the corresponding carbinol bases, whose

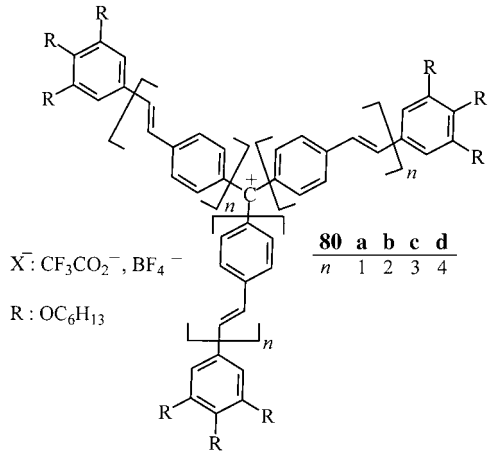

Scheme 24. Methylium salts with OPV chains which bear terminal donor groups.

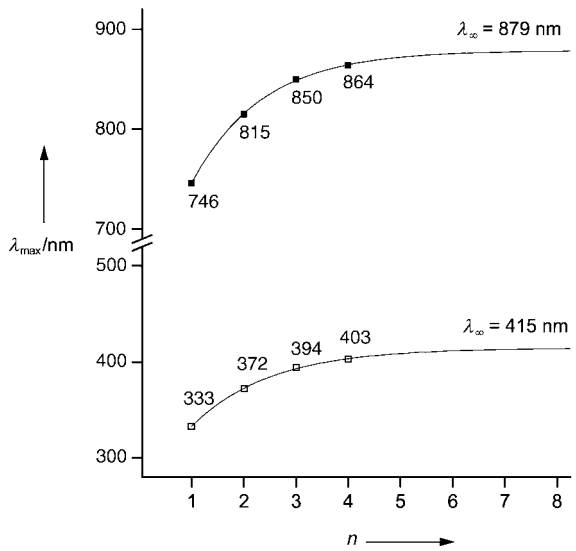

Figure 11. Maxima of the long-wavelength absorptions of the trifluoroacetates **80a–d** (n = 1–4) in $CHCl_3/CF_3CO_2H$ (7:3) and the corresponding carbinols (bottom curve) in $CHCl_3$. Extrapolation to λ_∞ by application of Equation (11).

Table 8: Maxima of the long-wavelength absorption of the colored salts **81a,b**, **82a,b**, and **83a–c**.

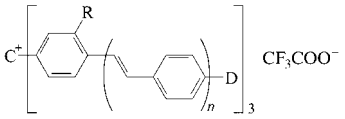

	R	D	n	λ_{max}[a] [nm]
81a[97]	H	OCH_3	1	718
81b[99]	CH_3	OCH_3	1	733
82a[97]	H	$N(CH_3)_2$	1	609
82b[99]	CH_3	$N(CH_3)_2$	1	615
83a[100]	H	$N[CH_2{-}CH(C_6H_{13})_2]_2$	1	622
83b[100]	H	$N[CH_2{-}CH(C_6H_{13})_2]_2$	2	740
83c[100]	H	$N[CH_2{-}CH(C_6H_{13})_2]_2$	3	790

[a] End values of λ_{max} at a high excess of CF_3COOH.

treatment with acid led to the elimination of the OH group bound on the central carbon atom. The cations **80a–d**, strictly as their carbinol bases, exhibit monotonously growing λ_{max} values with n—of course shifted by the push-pull effect from the UV/Vis region to the Vis/NIR region (Figure 11). The same is valid for methylium ions which are linked through polyene chains -(CH=CH)$_n$- to ferrocene as the terminal donor group; the λ_{max} value rises from 618 to 1187 nm on going from n = 2 to 14.[97]

In contrast to the weakly pH-dependent alkoxy-substituted color salts **80a–d** and **81a,b**, the dialkylamino compounds **82a,b** and **83a–c** (Table 8) exhibit absorptions which depend strongly on the concentration of H^+ ions.[98–101] The formation of the cations from the carbinols or their ethers on interaction with strong acids leads first to absorption maxima which are located far in the NIR region. A λ_{max} value of 1003 nm is found for **82b**,[100] and further addition of CF_3COOH induces a decrease in the intensity of this band and a slight blue-shift. Simultaneously, a new band appears at λ_{max} = 530 nm, which increases strongly and is red-shifted to 615 nm at high excess of CF_3COOH.[100] Table 8 shows the λ_{max} values at the "end of this titration" when all three terminal amino groups of **82b** are protonated. Hence, the push-pull character in the three arms is lost. Thus, it is understandable that the λ_{max} values of the methoxy compounds **81a,b** with n = 1 are higher than those of the dialkylamino compounds **82a,b** and **83a**.

Of the central acceptors for three-star oligomers shown in Scheme 21, the 1,3,5-triazines deserve special mention. The alkoxy-substituted compounds **84–86** and the dialkylamino compounds **87** and **88** were prepared by alkaline condensation reactions of 2,4,6-trimethyl-1,3,5-triazine with the corresponding aldehydes (Scheme 25).[101] The influence of the push-pull effect in **84** and the even stronger effect in **87** can be seen by comparison to the unsubstituted 2,4,6-tristyryl-1,3,5-triazine, which has a λ_{max} value of 327 nm. The absorption for

 © 2005 Wiley-VCH Verlag GmbH & Co. KGaA, Weinheim

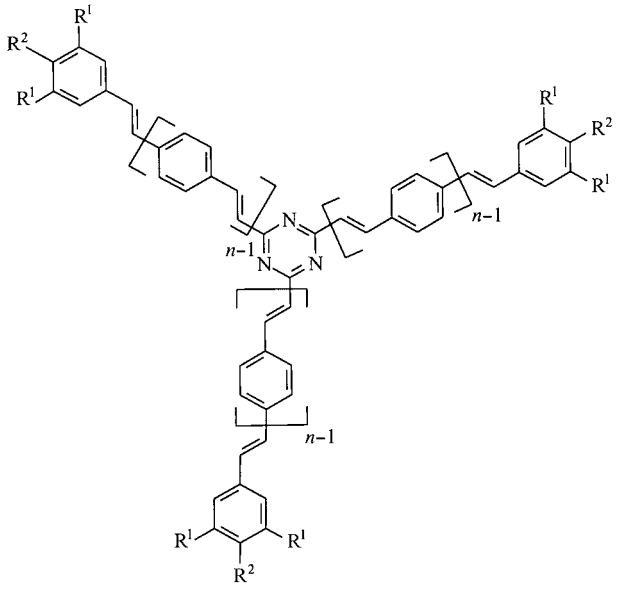

Compound	R^1	R^2	n	λ_{max} [nm]
84	H	OCH_3	1	356
85a	H	OC_6H_{13}	1	361
85b	H	OC_6H_{13}	2	400
86a	OC_6H_{13}	OC_6H_{13}	1	367
86b	OC_6H_{13}	OC_6H_{13}	2	398
86c	OC_6H_{13}	OC_6H_{13}	3	414
86d	OC_6H_{13}	OC_6H_{13}	4	420
87	H	$N(CH_3)_2$	1	427
88a	H	$N(C_{12}H_{25})_2$	1	445
88b	H	$N(C_{12}H_{25})_2$	2	458

Scheme 25. 1,3,5-Triazines with donor-substituted OPV chains and the maxima of their long-wavelength absorption (measurement of **84**–**86** in CH_2Cl_2, of **87** and **88** in $CHCl_3$).[101]

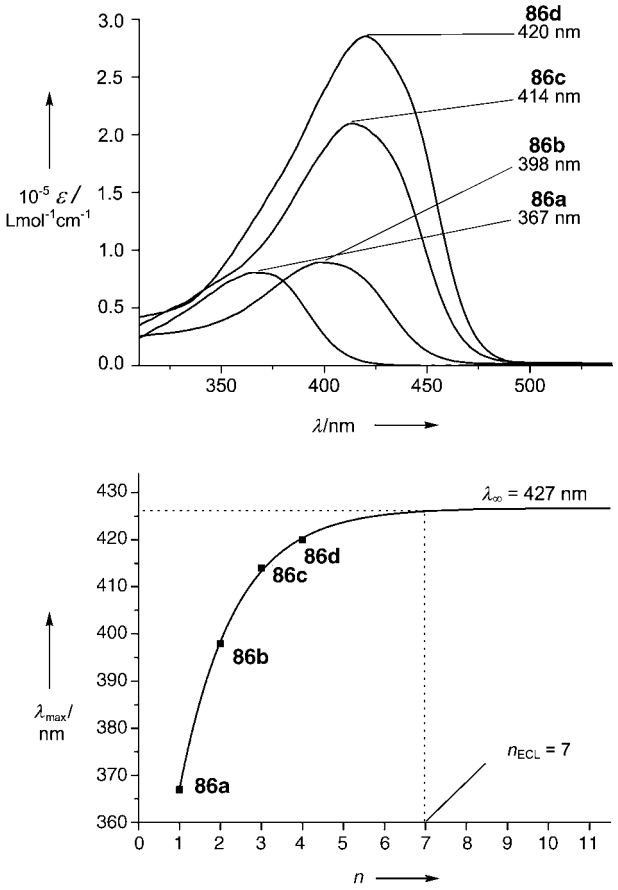

Figure 12. Top: long-wavelength absorption bands of the 1,3,5-triazines **86a**–**d** (n = 1–4) in CH_2Cl_2; bottom: extrapolation of the λ_{max} values according to Equation (11) and determination of the effective conjugation length according to Equation (12).

the series **86a**–**d** is red-shifted as the length of the conjugated arms increases. The absorption quickly approaches (n_{ECL} = 7) a limiting value of λ_∞ = 427 nm (Figure 12). An interesting feature is given by the "indicator behavior" of **87**. Unexpectedly, the first protonation on addition of trifluoroacetic acid occurs at the triazine ring, even though, for example, *N*,*N*-dimethylaniline has a higher basicity than 1,3,5-triazine. The yellow solution in $CHCl_3$ turns deep violet (λ_{max} = 549 nm). Further addition of CF_3COOH leads to a protonation of the terminal amino groups and the solution bleaches (λ_{max} = 365 nm).[102] The primary red-shift is based on an increase in the push-pull effect. However, as soon as the amino functions become protonated, their donor character is lost and an A-(π-A)$_3$ system is obtained.

Since the protonated 1,3,5-triazine ring is a strong acceptor and the amino group a strong donor, an extension of the chromophore should result in a hypsochromic effect. We established this relationship by comparing **88a** and **88b** (Figure 13). Compound **88a**, like **87**, shows a red-shift upon weak acidification, and afterwards a blue-shift on increased acidification. The higher homologue **86b** behaves in exactly the opposite way: the primary blue-shift is followed by a red-shift. The logical explanation is the following: the extension of the chromophore causes a bathochromic effect (445→458 nm) for **88** itself; a much stronger push-pull effect is present in the species with a protonated 1,3,5-triazine ring and the extension of the chromophore leads to a hypsochromic effect (551→394 nm); there is no push-pull effect in the completely protonated compounds; the normal extension of the conjugation then results in a bathochromic shift (368→459 nm).[103]

The benzene system seems to be the most interesting among the central donor groups listed in Scheme 23; however, until now only a few examples, such as **89a**,**b** (Scheme 26), have been prepared and studied.[104] Compound **89** and analogous benzene derivatives bearing three acceptor groups and three conjugated arms with terminal donor substituents (see Scheme 23) can be regarded as parent systems of hexasubstituted benzenes **91** having an octupolar character and therefore special significance for nonlinear optics.[70] Scheme 27 shows a synthetic approach to **91** based on the trimerization of alkynes. To my knowledge, series of conjugated compounds of type **91** with systematically extended π linkers are currently unknown.

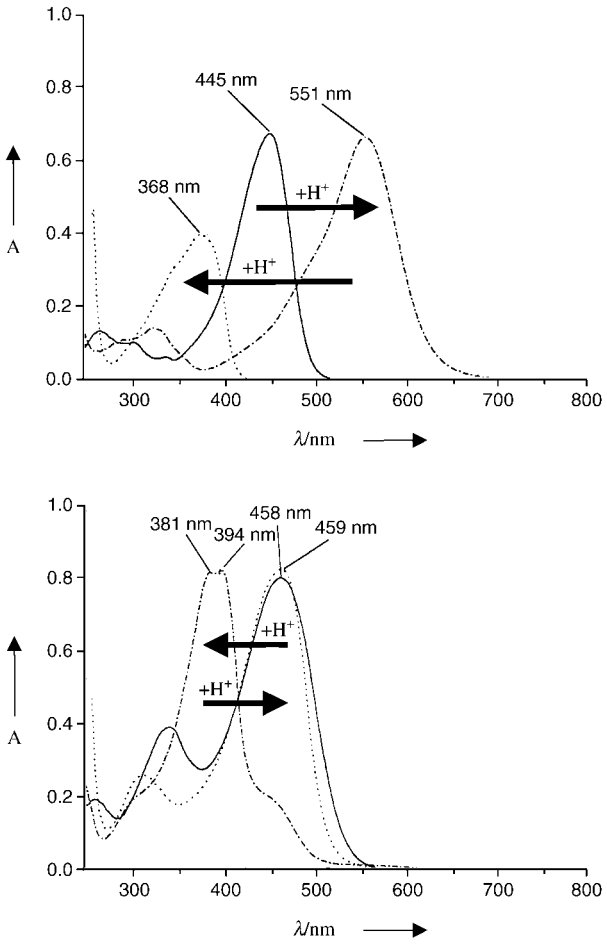

Figure 13. Top: bathochromic shift of the absorptions band of **88a** (——) by protonation of the 1,3,5-triazine ring (–•–•) and subsequent hypsochromic shift by complete protonation (•••••) in $CHCl_3$/CF_3COOH; bottom: hypsochromic shift of the absorption band of **88b** (——) by protonation of the 1,3,5-triazine ring (–•–•) and subsequent bathochromic shift by complete protonation (•••••) in $CHCl_3$/CF_3COOH.

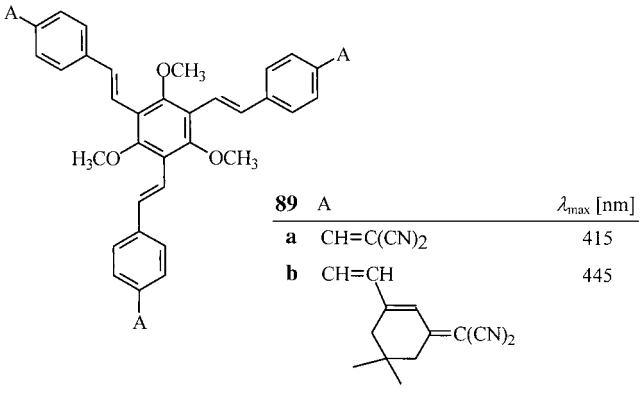

Scheme 26. Three-star compounds **89a**,**b** with central donor and terminal acceptor groups (absorption maxima in $CHCl_3$).

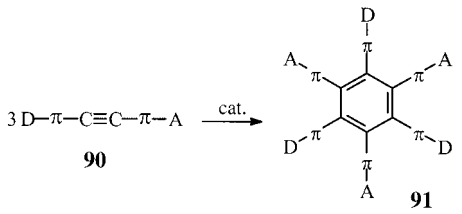

Scheme 27. Octupole **91** with a benzene core obtained by cyclotrimerization of alkynes **90** with push-pull character.

4. Nonlinear Optics in Series of Oligomers with Donor–Acceptor Substitution

Nonlinear optical properties (NLO) of organic materials are of great interest for optical data storage, data processing, and data transfer,[1p,105] and conjugated NLO chromophores with a pronounced push-pull character are of high significance. Figure 14[106] provides an explanation for this: if light is

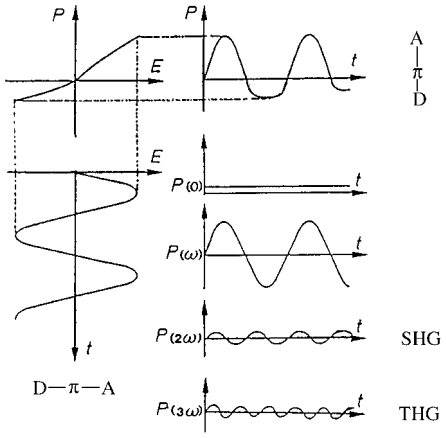

Figure 14. Description of nonlinear optics of D-π-A systems (SHG: second harmonic generation, THG: third harmonic generation).[106]

shining on a compound consisting of D-π-A molecules, the E vector causes a high polarization $P(E)$. The periodicity of $E(t)$ of the light wave corresponds to the periodicity $P(t)$; however, the function $P(t)$ is not a sine function. Its Fourier transformation leads to a progression (19), which contains the optical susceptibilities $\chi^{(n)}$ of nth order. For a single molecule, this corresponds to Equation (20) for the induced dipole moment.

$$P = \varepsilon_0 (\chi^{(1)} E + \chi^{(2)} E^2 + \chi^{(3)} E^3 + \ldots) \quad (19)$$

$$\mu_{\text{ind.}} = \alpha E + \beta E^2 + \gamma E^3 + \ldots \quad (20)$$

Apart from the linear polarizability α, there are hyperpolarizabilities β and γ (of first and second order, respectively) which are many magnitudes smaller. Since β and γ are very small (factors of 10^{10}, 10^{17}), high intensity laser light is needed to measure the frequency doubling and tripling. The advantage of donor–acceptor-substituted conjugated π systems arises from the fact that the shift of electrons from the

 © 2005 Wiley-VCH Verlag GmbH & Co. KGaA, Weinheim

donor to the acceptor is highly efficient (Figure 14); that becomes particularly apparent in the β values. Although D-π-A molecules are not centrosymmetric, they can crystallize in centrosymmetric space groups. The centrosymmetry must then also be valid for the function $P(E)$ [Eq. (21)]. This

$$P(-E) = -P(\mathrm{E}) \tag{21}$$

requires that $\chi^{(2)} = \beta = 0$ in the progressions (19) and (20). Many compounds with donor–acceptor substitution unfortunately crystallize in centrosymmetric crystal classes. Star-shaped systems of type **89** or **91** avoid this.

The influence of the substitution, in particular of the push-pull substitution, on β and γ becomes evident in the *trans*-stilbene derivatives in Table 9. Strong donors and strong acceptors enhance the β and γ values—in analogy to the dipole moment μ. However, a direct relationship between μ and β or γ does not exist, as the comparison of **13a** and **96** in Table 9 reveals.

Since strengthening the push-pull effect also shifts the CT band to higher λ_{max} values (see Section 3.1), a power law $\beta \sim \lambda_{max}^{k}$ or $\log\beta \sim \log\lambda_{max}$ seems to apply.[107] The second order hyperpolarizability γ of *trans*-stilbenes scales with β.[107] The push-pull compounds *N*,*N*-dimethyl-4-nitroaniline and (*E*)-4-dimethylamino-4′-nitrostilbene (DANS; **38b**) represent NLO standards that are often used.

Incorporation of a triple bond instead of a *trans*-configured double bond results in β and γ decreasing considerably and μ decreasing to a small extent. For 4-dimethylaminophenyl-4′-nitrophenylethyne $\beta = 46 \times 10^{-30}$ esu, $\gamma = 151 \times 10^{-36}$ esu, and $\mu = 6.1 \times 10^{-18}$ esu ($CHCl_3$).[71] The incorporation of benzene rings also proved to be unfavorable relative to equally extended π linkers consisting of olefinic double bonds (Scheme 28).

The β values, which were obtained, for example, by the EFISHG method (electric field induced second harmonic generation), depend somewhat on the applied wavelength. A simple correction to wavelength-independent, so-called static, β_0 values can be made on the basis of the two-level model[108,109] which works for D-π-A systems because of the domination of the CT transitions.[110]

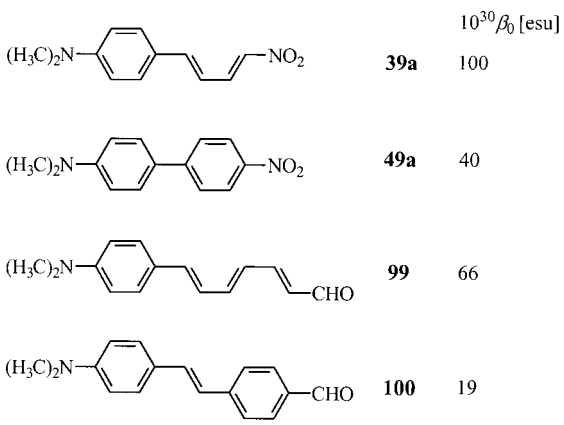

Scheme 28. Comparison of the β_0 values of D-π-A compounds having the same length of π linker but a different number of benzene rings.[58b]

The deterioration of the conjugation as a consequence of the torsion in oligo(1,4-phenylene)s (OPs) is already expressed in the λ_{max} values, but it is also noticeable in the hyperpolarizabilities β. Table 10 shows a comparison of biphenyls and the corresponding fairly planar fluorenes for this purpose. The correlation is much more complex for the γ values, as the comparison of **47a**,**b** and **56a**,**b** demonstrates.

Table 10: Comparison of dipole moments μ and hyperpolarizabilities β and γ of biphenyls and the corresponding fluorenes.[71]

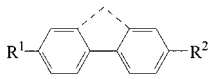

R^1	R^2	Biphenyl[a]	$10^{18}\mu$ [esu]	$10^{30}\beta$ [esu]	$10^{36}\gamma$ [esu]	Fluorene[a]	$10^{18}\mu$ [esu]	$10^{30}\beta$ [esu]	$10^{36}\gamma$ [esu]
H	H	**46a**	0	0	10	**46b**	0	0	
H	NO_2	**47a**	3.8	4.1	15	**47b**	4.1	5.1	29
OCH_3	NO_2	**56a**	4.5	9.2	39	**56b**	4.7	11	28
$N(CH_3)_2$	NO_2	**49a**	5.5	5.0	130	**49b**	6.0	55	

[a] Measurement of **46a**,**b**, **47a**,**b**, **56a**,**b** in 1,4-dioxane, of **49a**,**b** in $CHCl_3$.

Table 9: Dipole moments μ and hyperpolarizabilities β and γ of *trans*-stilbenes and their derivatives which bear a donor group in the 4-position and/or an acceptor group in the 4′-position.[107]

Compound	Solvent	4-R	4′-R	$10^{18}\mu$ [esu][a]	$10^{30}\beta$ [esu][a]	$10^{36}\gamma$ [esu][a]
92	$CHCl_3$	H	H	0	0	26
93	1,4-dioxane	$N(CH_3)_2$	H	2.1	10	64
94	1,4-dioxane	H	NO_2	4.2	11	61
38b	$CHCl_3$	$N(CH_3)_2$	NO_2	6.6	73	225
95	$CHCl_3$	NH_2	NO_2	5.1	40	147
13a	$CHCl_3$	OCH_3	NO_2	4.5	34	93
96	$CHCl_3$	SCH_3	NO_2	4.3	34	100
97	$CHCl_3$	$N(CH_3)_2$	CN	5.7	36	125
98	$CHCl_3$	OCH_3	CN	3.8	19	54

[a] esu: electrostatic units; μ: 10^{-30} Cm = 0.2998×10^{-18} esu = 0.2998 D; β: 10^{-50} $Cm^3V^{-2} = 2.694 \times 10^{-30}$ esu; γ: 10^{-60} $Cm^4V^{-3} = 8.078 \times 10^{-36}$ esu.

The extension of the π linker in D-OP-A systems can result in an increase in the β values;[71,111,112] similar to $\lambda_{max}(n)$, it is possible to pass through a maximum of $\beta(n)$. The first case is realized with **56a–c** (D = OCH_3/A = NO_2) and the latter with **55a–d** (D = NH_2/A = NO_2). The γ values always increase with increasing n. The effects are less pronounced in each case compared to the oligoenes **101** and **102** (Table 11)—even when the oligoenes bear benzene rings on one or both ends of the π linker. Consequently, oligoenes form the focus in NLO investigations of push-pull-substituted oligomers.[3,53,54,56,57,58a,b,71,113–119] Some examples are summarized in Table 12.

Analogous results are obtained for OEs with carotinoid linkers (see Section 3.1).[54,113,115,116,117,119] The incorporation of five-membered-ring heterocycles, such as furan or thiophene, in the π linker generates higher hyperpolarizabilities β than

 © 2005 Wiley-VCH Verlag GmbH & Co. KGaA, Weinheim

Table 11: Hyperpolarizabilities β and γ of push-pull-substituted oligo(1,4-phenylene)s (**55**, **56**) and oligoenes with one (**101**) or two terminal benzene rings (**102**).[3,71]

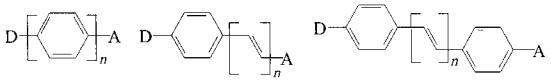

55a–d, **56a–c** **101a–c** **102a–d**

Compound	D	A	*n*	Solvent	$10^{30}\,\beta$ [esu]	$10^{36}\,\gamma$ [esu]
56a	OCH_3	NO_2	1	1,4-dDioxane	5.1	10
56b			2		9.2	39
56c			3		11.0	
55a	NH_2	NO_2	1	NMP	10	21
55b			2		24	96
55c			3		16	124
55d			4		11	133
101a	$N(CH_3)_2$	CHO	1	$CHCl_3$	30	63
101b			2		52	140
101c			3		88	257
102a	OCH_3	NO_2	1	$CHCl_3$	34	93
102b			2		47	130
102c			3		76	230
102d			4		101	

Table 12: Dipole moments μ and hyperpolarizabilities β_0 and γ of oligoenes.[56] (Structures shown in Scheme 12.)

Compound	*n*	μ [D]	$10^{30}\,\beta_0$ [esu]	$10^{36}\,\gamma$ [esu]
33b	0	8.8	74	
	1	9.3	195	378
	2	9.8	361	1724
	3	10	642	7363
	4	10	1229	
34b	0	9.7	63	
	1	9.0	195	395
	2	10.2	423	
	3	10.5	810	
	4	11	1043	
	5	11	1530	

for the corresponding benzene systems with comparable linker lengths, but lower β values than analogous compounds with diene building blocks. Table 13 shows comparisons of compounds **52**/**61**, **38b**/**59**/**58**, and **56c**/**60**/**66c**/**102b**.

Empirical laws were proposed many times on the basis of measured data for the hyperpolarizabilities β and γ. These laws reflect the influence of the substituents[71] and the influence of the number n of repeat units in the oligomers,[54,56,57,110,112,116,129] and include equations such as (22) and (24). Additional power laws derived on a theoretical or

$$\beta_0 \sim n^{k} \text{ or } \log\beta_0 \sim \log n \tag{22}$$

$$\text{e.g. } k = 1.9,^{[56]}\ 2.0,^{[110]}\ 2.4^{[54]} \tag{23}$$

$$\gamma \sim n^{\ell} \text{ or } \log\gamma \sim \log n \tag{24}$$

$$\text{e.g. } \ell = 4.2,^{[56]}\ 2.7^{[116]} \tag{25}$$

Table 13: Comparison of the hyperpolarizabilities β_0 of D-π-A compounds with and without heterocycles in the π linker.

Compound	Structural formula	$10^{30}\,\beta_0$ [esu]
52[79,81]	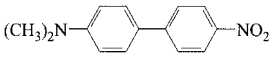	33
61[79,81]	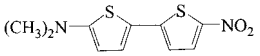	54
38b[71]	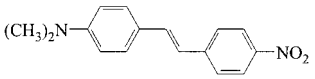	73
59[71]	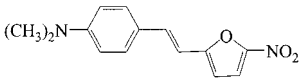	83
58[71]	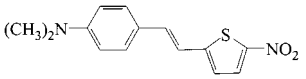	98
56c[71]	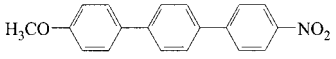	11
60[71]	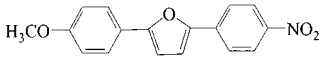	40
66c[81]	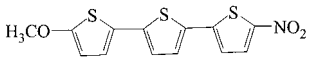	41
102b[71]	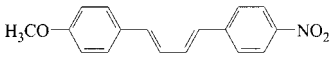	47

semitheoretical basis also exist.[23] The rare case in which the value of β does not increase monotonously with n, as for example in the OP series **55a–d**, cannot be covered by Equation (22). The individual exponents k und ℓ refer to the measurement of a certain series of donor–acceptor-substituted oligomers under certain conditions; moreover, they always refer to a narrow range of repeat units $1 \le n \le 5$. The expression $\ell > k$ is always valid for an oligomer series, which means that the γ values increase more strongly than the β values for increasing numbers n. The exponents k and ℓ should virtually be functions of n: $k(n)$, $\ell(n)$. However, an essential distinction arises from the fact that β_0 should approach a limiting value β_∞ for high numbers n, whereas this is only valid in the case of γ for $d\gamma/dn$.[23,24] A calculation (ZINDO, CEO) was performed for oligoene linkers up to $n = 40$.[120,121] Experimental values for such D-π-A systems do not exist, nor for systems which are nearly as large. The convergence problem of β and γ/n can be compared analogously to $\lambda_{max} \rightarrow \lambda_\infty$ by the aid of exponential functions.[122] Since the length L of the chromophore in conjugated oligomers is a linear function of n, $\beta(n)$ and $\gamma(n)$ can be described as functions $\beta(L)$ and $\gamma(L)$.

A simple calculation of β_0 can be made with the energy hc/λ_{max} of the long-wavelength transition $S_0 \rightarrow S_1$, the corresponding transiton moment μ_{01}, and the difference $\Delta\mu$ of the dipole moments $\mu(S_1)$ and $\mu(S_0)$[123] by applying the two-level model suggested by Oudar and Chemla.[108,109] Equation (26) provides the possibility to determine β_0 for the normally accessible region located away from the limiting value by normal absorption measurements of λ_{max} and μ_{01} as well as by

$$\beta_0 = \frac{6\mu_{01}^2 \Delta\mu \lambda_{max}^2}{h^2 c^2} \tag{26}$$

 © 2005 Wiley-VCH Verlag GmbH & Co. KGaA, Weinheim

electrooptical absorption measurements (EOAM) of $\Delta\mu$. If $\mu_{01}(n)$, $\Delta\mu(n)$, and $\lambda_{max}(n)$ all increase with n, it is also valid for $\beta_0(n)$.[79,81] The situation is more critical when $\mu^2{}_{01}\Delta\mu$ increases but λ^2_{max} decreases. We obtained β_0 values of 198, 287, and 346×10^{-50} Cm^3V for the series **5d**–**7d** ($n=1$–3), which means that the value of β_0 also increases in the case of a "hypsochromic series".[25] The fact that β_0 increases with n, irrespective of whether λ_{max} increases or decreases, reveals that a fitting function $\beta_0(\lambda_{max})$ is generally not meaningful. However, the linear function $\log\beta = f(\lambda_{max})$ can give evidence for substituent effects in compounds (for example, *trans*-stilbenes) which have the same π linker (see compounds in Table 9).[107] Substituent effects, but not necessarily the push-pull effect, have an effect on the size of γ. Hence, there are examples for which the γ values of D-π-A compounds are in between the γ values of D-π-D and A-π-A compounds.[116]

The power laws (27) and (28) suggested by Flytzanis and co-workers[124,125] only make sense when λ_{max} increases with the so-called delocalization length L_d.[126] The relation (27) is problematic for short π linkers with $L_d \approx n$[105a] and the correlation of $\chi^{(3)}$ or γ with λ_{max} is also not generally valid. In the "hypsochromic series" **15d**, **16d**, ..., $\lambda_{max}(n)$ decreases with growing n, but $\gamma(n)$ increases.[127] The relation (29) is

$$\chi^{(3)} \sim L_d^6 \text{ or } \log\chi^{(3)} \sim \log L_d \quad (27)$$

$$\chi^{(3)} \sim \lambda_{max}^6 \text{ or } \log\chi^{(3)} \sim \log\lambda_{max} \quad (28)$$

$$\gamma \sim n^{\mu} \text{ or } \log\gamma \sim \mu\log n \quad (29)$$

even reliable in such a case, in which $\mu(n)$ decreases with n and approaches the limiting value of 1.[105a] This convergence defines an effective conjugation length n'_{ECL}, which can, however, be different from n_{ECL} obtained from the convergence of the long-wavelength absorption. The absorption takes S_0 and S_1 into account, and an essential-state model of three, four, or more states is taken as the basis for the THG.

To summarize Section 4, the statement can be made that in addition to the substituent effects of D and A on γ and the push-pull effect on β, the nature of the π linker (type, length) plays a decisive role in the size of the β and γ values. Even the same linker has a different effect when its polarization is different with various D/A pairs. An explanation for this is provided in Section 5 in the context of VB theory.

5. VB and MO Models of D-π-A Systems

As already stated in Scheme 2, the model usually applied for D-π-A systems in the literature is a valence-bond model. It describes the ground state S_0 and the first electronically excited singlet state S_1 of such compounds by a linear combination of a zwitterionic **Z** and an electroneutral resonance structure **N** [Equations 30 and 31].

$$D^+\text{-}\pi\text{-}A^- \ (\mathbf{Z}) \leftrightarrow D\text{-}\pi\text{-}A \ (\mathbf{N}) \quad (30)$$

$$\psi(S_0) = c\psi_Z - \sqrt{1-c^2}\psi_N$$

$$\psi(S_1) = \sqrt{1-c^2}\psi_Z + c\psi_N \quad (31)$$

Several suggestions were made for the determination of the "weights" of the two limiting structures. Wortmann and co-workers[7–9] proposed the parameter c^2, which can be obtained by Equation (32); the participation of **Z** and **N** is

$$c^2 = \frac{1}{2}\left[1-\frac{\Delta\mu}{\sqrt{4\mu_{01}^2+\Delta\mu^2}}\right] \quad (32)$$

considered therein to be included in the difference in the dipole moments $\mu(S_1)-\mu(S_0)=\Delta\mu$ and the transition moment μ_{01}. Integration of the absorption curve or an approximation formula provide μ_{01}; $\Delta\mu$ is accessable for example by electro-optical absorption measurements (EOAM). The difference Δ of the dipole moments of **Z** and **N** is related to $\Delta\mu$ and c^2 according to Equation (33). Barzoukas et al.[6] used $\sin\theta/2$ instead of c in Equation (30) and defined the "mixed parameter" MIX as $-\cos\theta$ which corresponds to $(2c^2-1)$ in Equation (33).

$$\frac{\Delta\mu}{\Delta} = 1-2c^2 \quad (33)$$

Marder et al.[2–5] introduced the parameter BLA for the alternation of bond lengths in linear D-π-A chains. The parameter BOA for the alternating bond orders is closely connected to the alternation of bond lengths. BLA is accessible from X-ray data and is empiricly related to MIX [Eq. (34)].[6] However, BLA is not very useful if the π linker contains aromatic rings, because aromatic rings will keep their typical adjusted bond lengths.

$$\text{BLA (in Å)} = 0.11\,\text{MIX} \quad (34)$$

Table 14 shows the relationship between the polarizabilities α, β, and γ and the discussed parameters c^2, MIX, and BLA. The parameter f proposed by Lu, Chen et al.,[128] was also included in the table; f and MIX are connected by

Table 14: Dependence of the polarizabilities α, β, and γ on the parameters c^2, MIX, f, and BLA with the corresponding "weigths" of the resonance structures **Z** and **A**.

	c^2[a]	Weights **N**/**Z** or **Z**/**N**	MIX[b]	f[a]	Weights **N**/**Z** or **Z**/**N**	BLA[c] [Å]
α_{max}	0.5	50:50	0	0.5	50:50	0
$\beta=0$	0.5	50:50	0	0.5	50:50	0
$\lvert\beta\rvert_{max}$	0.211	79:21	$\pm\frac{1}{\sqrt{5}}$	0.5 ± 0.224	72:28	±0.049
$\gamma=0$			$\pm\frac{1}{\sqrt{5}}$	0.5 ± 0.224	72:28	±0.049
$\lvert\gamma_1\rvert_{max}$			$\pm\sqrt{\frac{3}{7}}$	0.5 ± 0.327	83:17	±0.072
$\lvert\gamma_2\rvert_{max}$			0	0.5	50:50	0

[a] $0<c^2<1$, $0<f<1$. [b] $-1<MIX<1$. [c] BLA is varied between the bond lengths $L(-C{=}C-)=1.34$ Å and $L(=C-C=)=1.45$ Å by about 0.11 Å; if Equation (33) is not used, optimum BLA values of 0.04 ± 0.01 Å and 0.06 ± 0.01 Å, respectively, are proposed for $\lvert\beta\rvert_{max}$ and $\lvert\chi_1\rvert_{max}$.[129]

 © 2005 Wiley-VCH Verlag GmbH & Co. KGaA, Weinheim

Equation (35). Moreover, for a better illustration, the "weights" **N**/**Z** (and equivalent **Z**/**N**) valid for c^2 and for

$$f = \frac{MIX + 1}{2} \qquad (35)$$

MIX and f are included in Table 14. The maximum of α is reached for a 50:50 ratio of **Z** and **A**, that is, for a complete equalization of the bonds (cyanine limit). Here, $\beta = 0$ (in reality β is very small). The maximum of β is reached for an **N**/**Z** ratio of about 3:1 (and its reciprocal); but then $\gamma = 0$. A parameter value close to the maximum of γ can be recommended for a simultaneous optimization of β and γ.[129]

The parameters proved to be successful for relatively short D-π-A systems with OE linkers. These parameters are not adequate when c^2 or f are close to 0 or 1 (MIX close to -1 or $+1$), and the VB model with the ψ functions (30) and (31) is generally not suitable for these cases.[21] An S_1 structure with predominant **Z** character ($1-c^2 \geq 0.9$) has a small probability for an extended chromophore which has a predominant **N** character in S_0 ($c^2 \leq 0.1$). The resonance structure **Z** should have a similar energy as the resonance structure **N** so that the resonance **Z**↔**N** is combined with a noticeable energy gain. The latter is certainly not realized when the π linker consists of repeat units which contain benzene rings or other aromatic ring systems.

An MO model appears to be much more suitable for such oligomers. In this model, partial dipole moments are present on the donor and the acceptor sides, and each partial moment is itself composed of an intrinsic part (μ_D, μ_A) and a part which is induced in each case by the dipole on the other chain end (μ_{Di}, μ_{Ai}). The induced parts become smaller with increasing separation of the donor and acceptor. The extent of the polarization from the ends of the chain in the direction of its center should rapidly decrease. This was also demonstrated by means of BLA values and partial charges obtained by a DFT/B3LYP/6-31G* calculation.[130]

Semiempirical methods need to be considered for the calculation of higher oligomers. We chose the AM1 method for the optimization of the geometry and the INDO/S method for the electron transitions.[21,22] Scheme 29 shows the polarization derived from AM1) calculations of the olefinic double bonds of the OPVs **5d**–**7d** and the corresponding triple bonds of the OPEs **15d**–**17d**—in each case expressed in terms of the charge differences Δq and $\Delta q'$, respectively. The positive and negative partial charges are related to the standards *trans*-stilbene and tolane, respectively.[131] The $\Delta\delta$ and $\Delta\delta'$ values reflect the differences in the chemical shifts of the ^{13}C nuclei of the double and triple bonds. A direct correlation can be seen: a large $\Delta q^{(\prime)}$ value results in a large $\Delta\delta^{(\prime)}$ value. The essential polarization can be found on the chain ends.[132] The effect decreases strongly towards the center of the chain. This trend of $\Delta q^{(\prime)}$ is even more pronounced for longer chains ($n \geq 4$).[21,22] ^{13}C NMR signals are a good indicator of partial charges. The correlations of the ^{13}C chemical shifts and their differences $\Delta\delta^{(\prime)}$ (obtained by the aid of the 2D HMBC technique) agree very well with the $\Delta q^{(\prime)}$ values, and therefore support nicely the MO model. The decreasing significance of the zwitterionic resonance structure **Z** with increasing distance of D and A can be also recognized in the compounds $(CH_3)_2N$-OE-CHO **24c**–**26c**, in which the rotational barrier of the C–N bond decreases strongly with increasing values of n.[52b,c]

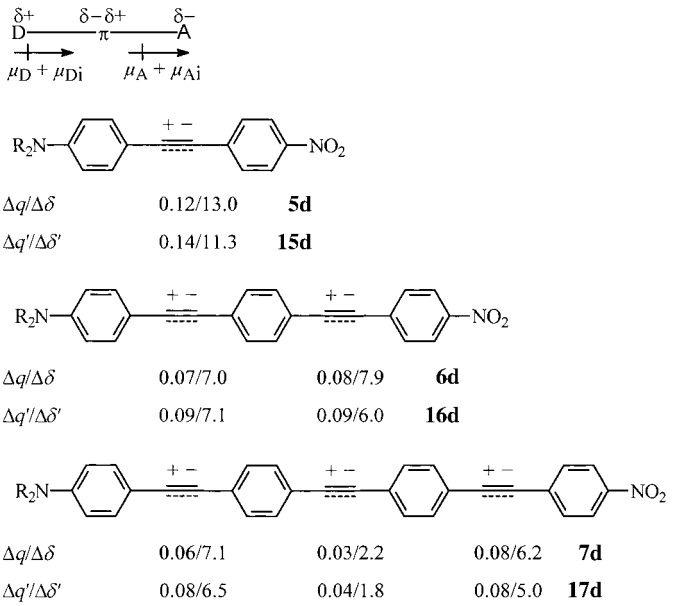

Scheme 29. MO model for conjugated oligomers with donor–acceptor substitution: Calculated charge differences Δq at the double bonds of the OPVs **5d**–**7d** ($n = 1$–3) and $\Delta q'$ at the triple bonds of the OPEs **15d**–**17d** ($n = 1$–3); the differences $\Delta\delta$ and $\Delta\delta'$ of the ^{13}C chemical shifts were measured in $CDCl_3$.[21,22]

Whereas the electron transitions $S_0 \rightarrow S_1$ in *trans*-stilbene and tolane are still almost pure HOMO→LUMO transitions, other orbitals mix in for the D-OPV-A and D-OPE-A systems, even for $n = 1$. The energy of HOMO−1 approaches constantly closer to the HOMO, and the LUMO+1 constantly closer to the LUMO, as n increases. The transitions HOMO−1→LUMO, HOMO→LUMO+1, and HOMO−1→LUMO+1 become more and more important for the long-wavelength absorption, especially since the overlap density of the HOMO and LUMO becomes smaller and smaller. Figure 15 shows as an example the OPEs **15d** ($n = 1$) and **18d** ($n = 4$), with the AM1-INDO/S calculation performed with dimethylamino groups instead of didodecylamino groups, which are necessary for solubilization. The HOMO→LUMO transitions are characterized by a strong intramolecular charge transfer (ICT) from the donor to the acceptor side. Figure 15 reveals that the ICT plays a very minor role in the other transitions. The long-wavelength absorption band (the charge transfer band) of D-π-A systems is essentially determined by the ICT.

D and A not only influence the orbital energies, they also alter the electron correlation. In terms of a self-consistent field (SCF) approximation, both the differences in the orbital energies ΔE_0 and also the configuration interactions of one-electron functions need to be considered for the excitation energies $E(S_0 \rightarrow S_1)$. Equation (36) contains the Coulomb

$$E = \Delta E_0 - J + 2K \qquad (36)$$

 © 2005 Wiley-VCH Verlag GmbH & Co. KGaA, Weinheim

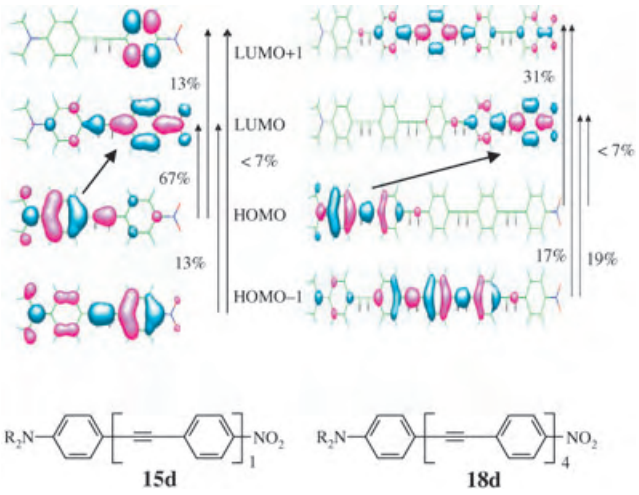

Figure 15. Calculation of the frontier orbitals of the OPEs **15d** and **18d** and their partipication in the electron transition $S_0 \rightarrow S_1$ by the AM1-INDO/S method.

repulsion integral J and the exchange integral K.[133] $E < \Delta E_0$ is always valid because $0 \leqq 2K < J$. A charge transfer within the chromophore diminishes the negative portion $(2K-J)$, because the overlap density decreases. Thus, E becomes smaller, which means that the band of the electron transition is shifted to longer wavelengths. A reduction in the ICT effects accordingly shifts the band to shorter wavelengths (see Figure 3). The classical example is given by anthracene and azulene. Although ΔE_0 is the same, the excitation energy E of the blue azulene is essentially smaller than E of the colorless anthracene because an ICT from the five-membered ring to the seven-membered ring takes place in the $S_0 \rightarrow S_1$ transition of azulene. This is not possible in the symmetric anthracene.[134] Figure 16 illustrates the relationship of Equation (36) in a simplified picture of a HOMO→LUMO transition.

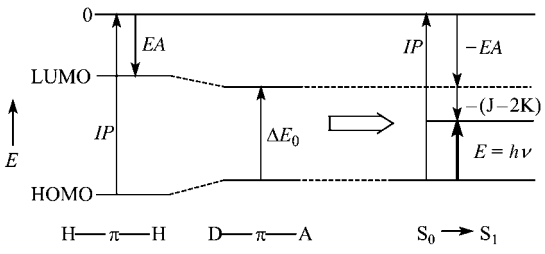

Figure 16. Influence of the donor–acceptor substitution in D-π-A systems on the energy of the long-wavelength electron excitation. (Exclusive regard of HOMO and LUMO, ΔE_0 as the difference of the ionization energy and negative electron affinity *EA* according to Koopmans theorem.)

The stronger the electron-releasing effect of D and the electron-withdrawing effect of A is, the lower is the transiton energy E $(S_0 \rightarrow S_1)$ of D-π-A systems with a constant number n of repeat units. The decrease of the ICT for increasing numbers n and a certain terminal D/A substitution is expressed in the $\Delta E_{DA}(n)$ term in Equation (13). Figure 17

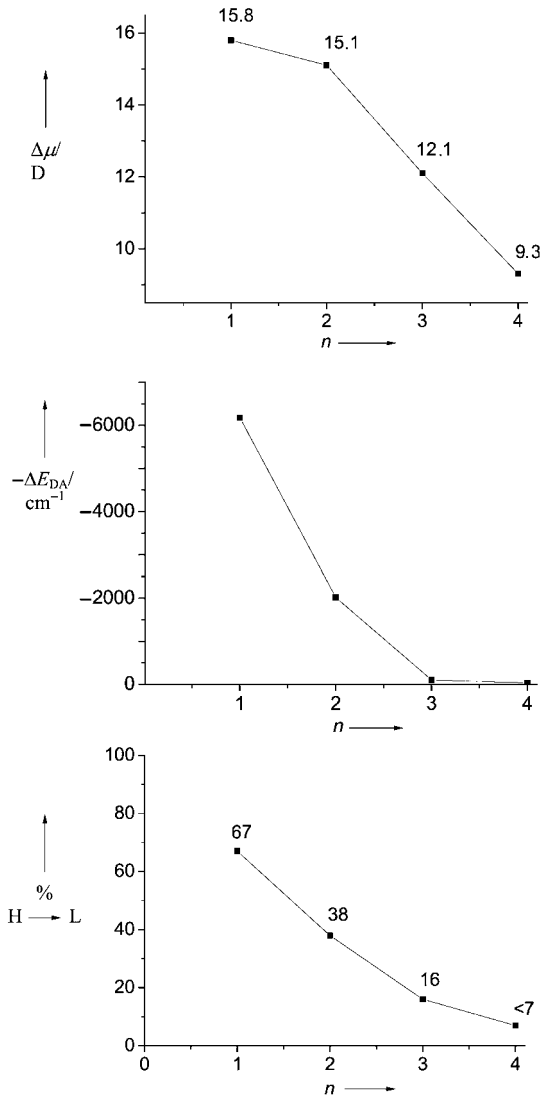

Figure 17. Bottom: partipication of the HOMO→LUMO transition in the long-wavelength absorption of **15d–18d** $(n = 1–4)$ calculated by AM1-INDO/S; middle: corresponding decrease in the term $-\Delta E_{DA}(n)$; top: decrease in the calculated difference of the dipole moments $\Delta\mu(n) = \mu(S_1) - \mu(S_0)$.

shows the calculated decrease of the HOMO→LUMO fraction of $S_0 \rightarrow S_1$ resulting from increasing numbers n in the series **15d–18d** $(D = N(CH_3)_2,\ A = NO_2,\ n = 1–4)$.[22] Simultaneously, the values of $\Delta E_{DA}(n)$ and $\Delta\mu = \mu(S_1) - \mu(S_0)$ decrease. As already explained in Section 2, the ΔE_{DA} term is able to diminish, cancel out, or reverse (to hypsochromic) the bathochromic effect in a series of conjugated oligomers.

Analogous results were obtained for compounds **5d–8d** with an OPV linker instead of the OPE linker.[21] Therefore, it is not necessary to show here a picture of the highest occupied and the lowest unoccupied orbitals.[21,25] The stronger the donor and acceptor are, the faster the participation of the HOMO→LUMO transition decreases for the long-wavelength absorption, the more the topology of the other involved orbitals determines the decrease of the ICT, and the more rapidly the ICT-affected correction term $\Delta E_{DA}(n)$ approaches zero (Figure 18).

 © 2005 Wiley-VCH Verlag GmbH & Co. KGaA, Weinheim

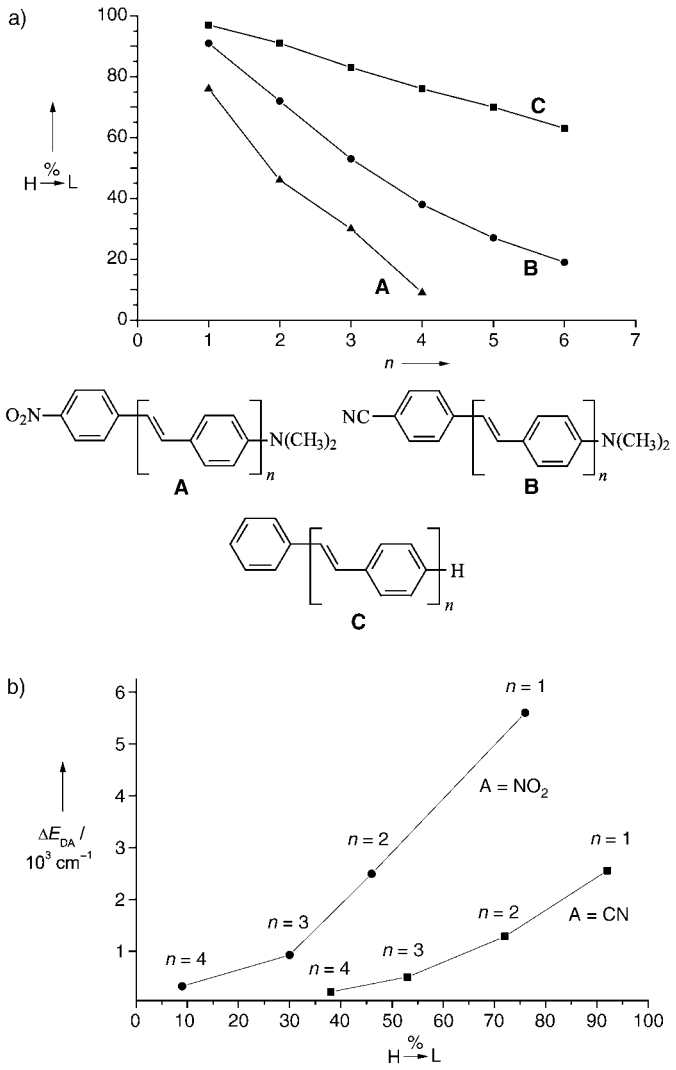

Figure 18. Partipication of the HOMO→LUMO transition in the long-wavelength absorption of OPVs with an increasing number *n* of repeat units (AM1-INDO/S calculation); b) dependence of the ICT term ΔE_{DA} on the fraction of H→L transition in the push-pull series $(H_3C)_2$N-OPV-NO_2 and $(H_3C)_2$N-OPV-CN.

6. Summary and Outlook

Conjugated oligomers with terminal donor–acceptor substitution are examples of "molecular wires"[135] which are predestinated to have special optical and optoelectronic effects. The preparation of such an oligomer series with an increasing number of repeat units in the π linker is best started on the donor side which bears solubilizing groups (such as NR_2, OR). The π linker is then extended by the application of an "extension reagent" and a protection group strategy until the acceptor group is attached in an end-capping step. This approach is recommended for the construction of parallel series with different acceptor groups to generate a central series from which other series are accessible by coupled, convergent syntheses.

The excitation of electrons in the linear or star-shaped oligomers of this type is characterized by an intramolecular charge transfer (ICT). The charge-transfer band reacts quite differently upon the extension of the chromophore, because a hypsochromic effect resulting from the decrease in the ICT is opposed to the bathochromic effect caused by the extension of the conjugation. This becomes apparent as soon as the number *n* of repeat units is increased, and consequently the distance between the donor and acceptor enhanced. The superposition of both influences leads to the variants for the $S_0 \rightarrow S_1$ transitions which are summarized in Table 15. In addition to the strength of donor and acceptor in the present D/A pair, the type of π linker plays a decisive role. Until now, exclusively bathochromic series exist for the oligoenes (D-OE-A) and oligoynes (D-OI-A; type (a): $\lambda_{max}(n) < \lambda_{max}(n+1) \leq \lambda_\infty$). In contrast, oligo(1,4-phenylenevinylene)s (D-OPV-A) and oligo(1,4-phenyleneethynylene)s (D-OPE-A) bearing strong donors and strong acceptors as end-groups can exhibit a hypsochromic behavior (type (b): $\lambda_{max}(n) > \lambda_{max}(n+1) \geq \lambda_\infty$). A certain weakening of the donor or acceptor strength may then give rise to a borderline case, in which the long-wavelength absorption is independent of the size of the chromophore (type (a)/(b): $\lambda_{max}(n) \approx \lambda_{max}(n+1) \approx \lambda_\infty$). OPV and OPE series with weak donors and weak acceptors show a bathochromic behavior. Oligo(1,4-phenylene)s (D-OP-A) and oligo(2,5-thienylene)s (D-OT-A) are special cases of type (c), in which $\lambda_{max}(n)$ passes through a maximum. Torsions along the π linker have a decisive influence on the CT band.[136] The fourth imaginable case, in which λ_{max} passes through a minimum, has not been unequivocally proven to date.[137] The number of investigated compounds of oligo(2,5-thienylenevinylene)s (D-OTV-A) or oligo(2,5-thienyleneethynylene)s (D-OTE-A) is too small for a reliable conclusion to be drawn.

The superposition of "conjugation effect" and opposite "ICT effect" can be rationalized by the superposition of two exponential functions (Figure 3); both effects exhibit a convergence behavior ($n \rightarrow \infty$). The intramolecular charge transfer diminishes the electron correlation, which is of special importance for the HOMO→LUMO excitation. However, semiemprical quantum mechanics (AM1, INDO/S) studies on D-OPV-A and D-OPE-A systems reveal that the HOMO→LUMO fraction of the long-wavelength absorption decreases continuously as *n* grows, that is, as the size of the chromophore grows (Figure 15). Together with this, $\Delta\mu = \mu(S_1) - \mu(S_0)$ and the correction term of the ICT in the absorption decrease (Figures 17 and 18).

The VB model D-π-A↔D^+-π-A^- often used in the literature is primarily suitable for the case in which short oligoenes are used as a π linker. This model with its zwitterionic resonance structure is not very useful for other π linkers, particularly not for π linkers which contain aromatic rings. In contrast, an MO model proved to be successful, which implies a decreasing polarization from the donor as well as from the acceptor side towards the center of the π linker (Scheme 29).

In the field of nonlinear optics (NLO), laws were often temptatively proposed that correlated the hyperpolarizabilites β and γ with λ_{max} values. This approach, however, fails for "hypsochromic series". Power laws or logarithmic functions can be used which contain the length *L* of the chromophores

 © 2005 Wiley-VCH Verlag GmbH & Co. KGaA, Weinheim

Table 15: Classification of the absorption behavior of series of donor–acceptor-substituted conjugated oligomers according to their dependence on the D/A combination and the π linker.

π linker	Monotonously batho-chromic series type (a)	Borderline type (a)/(b)	Monotonously hypso-chromic series type (b)	Series with an energy minimum type (c)
OPV	NR_2/CN OR/NO_2 OR/CHO OR/squaraine ferrocene/NO_2 OR/C^+ NR_2/1,3,5-triazine OR/1,3,5-triazine	NR_2/CHO	NR_2/NO_2 NR_2/CH=C(CN)$_2$ NR_2/squaraine NR_2/1,3,5-triazinium	
OPE	NR_2/C≡CH OR/CN	OR/NO_2 NR_2/CN	NR_2/NO_2 NR_2/CH=C(CN)$_2$ NR_2/CHO	
OE[a]	all investigated D/A combinations			
OI	NR_2/NO_2			
OP	OR/NO_2 OR/CN			NR_2/NO_2 NR_2/CN
OT	OR/NO_2			NR_2/NO_2
OTV[b]	NR_2/NO_2 NR_2/CH=(C(CN)$_2$			
OTE	SR/NO_2	OR/NO_2		

[a] D: NR_2, OR, SR, ferrocene, A: NO_2, CHO, CN, CH=CR_2 containing electron-withdrawing groups R, C^+; the OE linkers also include benzene or thiophene rings on one or both ends of the chain. [b] The OTV linker includes a terminal benzene ring on the donor side.

or the number n of repeat units in their argument. In contrast to λ_{max} and β, γ does not approach a limiting value for $n\rightarrow\infty$, but γ/n does.[23] The effective conjugation lengths n_{ECL} required for nonlinear optical properties are much greater than for linear optics. Therefore, an experimental proof of the convergence of β and γ/n is much more difficult.

Besides the selected D/A combination, the nature and length of the π linker are decisive for β and even to a greater extent for γ. 1,4-Phenylene units in an OP linker show a torsion along the chain which is unfavorable for large hyperpolarizabilities. On the whole, a comparison of β and γ values of various series D-π-A is essentially more difficult than a comparison of linear optical properties. The errors of the methods are considerably larger than, for example, for λ_{max} values, even when static, that is, wavelength-independent β_0 values and nonresonant γ values are used. Relative quantities related to a standard, which is measured at the same conditions, for example [Eq. (37)], are recommended for materials science applications.

$$\beta_{rel} = \frac{\beta_0(\text{compound})}{\beta_0(\text{4-nitroaniline})} \cdot \frac{\text{molecular mass (4-nitroaniline)}}{\text{molecular mass (compound)}} \qquad (37)$$

Altogether, considerable deficits can be recognized for the experimental determination of β and γ values of oligomer series. Numerous theoretical attempts have been made for their linear (Section 2) and nonlinear optics (Sections 4 and 5).[138,139] A new approach in the synthetic area is offered by star-shaped compounds (Section 3.3)[140] and dipolar structures such as **101**, in which—contrary to the resonance described in Scheme 3—the aromatic and dipolar resonance structures are compatible (Scheme 30).[141] The preparation of D-π-A structures tailored for certain electrooptical applications (molecular engineering) represent the final, highly promising goal.[142]

I am grateful to the Deutsche Forschungsgemeinschaft, the Volkswagen Foundation, the Fonds der Chemischen Industrie, and the Center of Materials Science of the University of Mainz for financial support of my own work cited in this article.

Received: July 1, 2004

[1] Selected monographs and reviews: a) H.-H. Hörhold, M. Helbig, D. Raabe, J. Opfermann, U. Scherf, R. Stockmann, D. Weiß, *Z. Chem.* **1987**, *27*, 126–137; b) J. L. Brédas, R. Silbly, *Conjugated Polymers*, Kluwer, Dordrecht, **1991**; c) K. Müllen, *Pure Appl. Chem.* **1993**, *65*, 89–96; d) W. R. Salaneck, I. Lundström, B. R. Rånby, *Conjugated Polymers and Related Materials*, Oxford University Press, Oxford, **1993**; e) J. M. Tour, *Chem. Rev.* **1996**, *96*, 537–553; f) R. Giesa, *J. Macromol. Sci. Rev. Macromol. Chem. Phys.* **1996**, *36*, 631–670; g) J. S. Moore, *Acc. Chem. Res.* **1997**, *30*, 402–413; h) L. Jones II, J. S. Schumm, J. M. Tour, *J. Org. Chem.* **1997**, *62*, 1388–1410; i) J. Roncali, *Chem. Rev.* **1997**, *97*, 173–205; j) A. Kraft, A. C. Grimsdale, A. B. Holmes, *Angew. Chem.* **1998**, *110*, 416–443; *Angew. Chem. Int. Ed.* **1998**, *37*, 403–428; k) *Electronic Materials: The Oligomer Approach* (Eds: K. Müllen, G. Wegner), Wiley-VCH, Weinheim, **1998**; l) T. M. Swager, *Acc. Chem. Res.* **1998**, *31*, 201–207; m) P. F. H. Schwab, M. D. Levin, J. Michl, *Chem. Rev.* **1999**, *99*, 1863–1933; n) U. Scherf, *Top. Curr. Chem.* **1999**, *201*, 163–222; o) R. E. Martin, F. Diederich, *Angew. Chem.* **1999**, *111*, 1440–1469; *Angew. Chem. Int. Ed.* **1999**, *38*, 1350–1377; p) J. J. Wolff, R. Wortmann, *Adv. Phys. Org. Chem.* **1999**, *32*, 121–217; q) U. H. F. Bunz, *Chem. Rev.* **2000**, *100*, 1605–1644; r) J. L. Segura, N. Martin, *J. Mater. Chem.* **2000**, *10*, 2403–2435; s) G. Hadziioannou, P. F. van Hutten, *Semiconductivity Polymers*, Wiley-VCH, Weinheim, **2000**; t) J. Roncali, *Acc. Chem.*

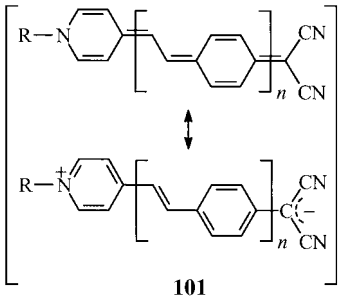

101

Scheme 30. Resonance forms of a quinoid, electroneutral, and an aromatic, zwitterionic resonance structure as an example that is opposed to the usual resonance of an aromatic, electroneutral, and a quinoid, zwitterionic limiting structure.

 © 2005 Wiley-VCH Verlag GmbH & Co. KGaA, Weinheim

Res. **2000**, *33*, 147 – 156; u) J. M. Tour, *Acc. Chem. Res.* **2000**, *33*, 791 – 804; v) A. Mishra, R. K. Behera, P. K. Behera, B. K. Mishra, G. B. Behera, *Chem. Rev.* **2000**, *100*, 1973 – 2011; w) H. E. Katz, Z. Bao, S. L. Gilat, *Acc. Chem. Res.* **2001**, *34*, 359 – 369; x) U. H. F. Bunz, *Acc. Chem. Res.* **2001**, *34*, 998 – 1010; y) S. Tretiak, S. Mukamel, *Chem. Rev.* **2002**, *102*, 3171 – 3212; z) S. Szafert, J. A. Gladysz, *Chem. Rev.* **2003**, *103*, 4175 – 4205.

[2] S. R. Marder, J. W. Perry, G. Bourhill, C. B. Gorman, B. G. Tiemann, K. Mansour, *Science* **1993**, *261*, 186 – 189.

[3] S. R. Marder, L. T. Cheng, B. G. Tiemann, A. C. Friedli, M. Blanchard-Desce, J. W. Perry, J. Skindhoj, *Science* **1994**, *263*, 511 – 514.

[4] S. R. Marder, C. B. Gorman, F. Meyers, J. W. Perry, G. Bourhill, J. L. Brédas, B. M. Pierce, *Science* **1994**, *265*, 632 – 639.

[5] S. R. Marder, C. B. Gormann, *Chem. Mater.* **1995**, *7*, 215 – 220.

[6] M. Barzoukas, C. Runser, A. Fort, M. Blanchard-Desce, *Chem. Phys. Lett.* **1996**, *257*, 531 – 537.

[7] R. Wortmann, C. Poga, R.-J. Twieg, C. Geletneky, C. R. Moylan, P. M. Lundquist, R. G. DeVoe, P. M. Cotts, H. Horn, J. E. Rice, D. M. Burland, *J. Chem. Phys.* **1996**, *105*, 10637 – 10647.

[8] F. Würthner, C. Thalacker, R. Matschiner, K. Lukaszuk, R. Wortmann, *Chem. Commun.* **1998**, 1739 – 1740.

[9] S. Beckmann, K.-H. Etzbach, P. Krämer, K. Lukaszuk, R. Matschiner, A. J. Schmidt, P. Schumacher, R. Sens, G. Seybold, R. Wortmann, F. Würthner, *Adv. Mater.* **1999**, *11*, 536 – 541.

[10] L. M. Tolbert, X. Zhao, *J. Am. Chem. Soc.* **1997**, *119*, 3253 – 3258.

[11] J. S. Craw, J. R. Reimers, G. B. Bacskay, A. T. Wong, N. S. Hush, *Chem. Phys.* **1993**, *176*, 407 – 420.

[12] C. Kuhn, *Synth. Met.* **1991**, *43*, 3681 – 3688.

[13] N. Tyutyulkov, F. Dietz, J. Fabian, A. Melhorn, A. Tadjer, *Theor. Chim. Acta* **1981**, *60*, 185 – 200.

[14] A. D. Kachkovskij, N. M. Kovalenko, G. A. Kachkovskii, *Theor. Exp. Chem.* **1999**, *35*, 205 – 210; A. D. Kachkovskij, N. M. Kovalenko, G. A. Kachkovskii, *Chem. Abstr.* **2000**, *132*, 195832x.

[15] A. D. Kachkovskij, O. A. Zhukova, *Theor. Exp. Chem.* **2001**, *37*, 283 – 287; A. D. Kachkovskij, O. A. Zhukova, *Chem. Abstr.* **2002**, *137*, 64534g.

[16] R. M. Abd El-Aal, *Dyes Pigm.* **2002**, *52*, 129 – 136.

[17] See for example ref. [1k] and [1o].

[18] H. Meier, U. Stalmach, H. Kolshorn, *Acta Polym.* **1997**, *48*, 379 – 384.

[19] H. Meier, D. Ickenroth, *Eur. J. Org. Chem.* **2002**, 1745 – 1749.

[20] D. Ickenroth, S. Weissmann, N. Rumpf, H. Meier, *Eur. J. Org. Chem.* **2002**, 2808 – 2814.

[21] H. Meier, J. Gerold, H. Kolshorn, B. Mühling, *Chem. Eur. J.* **2004**, *10*, 360 – 370.

[22] H. Meier, B. Mühling, H. Kolshorn, *Eur. J. Org. Chem.* **2004**, 1033 – 1042.

[23] a) C. Bubeck in ref. [1k], p. 449 and references therin; b) I. Ledoux, I. D. W. Samuel, J. Zyss, S. N. Yaliraki, F. J. Schattenmann, R. R. Schrock, R. J. Silbey, *Chem. Phys.* **1999**, *245*, 1 – 16.

[24] H. Meier, D. Ickenroth, U. Stalmach, K. Koynov, A. Bahtiar, C. Bubeck, *Eur. J. Org. Chem.* **2001**, 4431 – 4443.

[25] H. Meier, J. Gerold, H. Kolshorn, W. Baumann, M. Bletz, *Angew. Chem.* **2002**, *114*, 302 – 306; *Angew. Chem. Int. Ed.* **2002**, *41*, 292 – 295.

[26] W. Kutzelnigg, *Einführung in die Theoretische Chemie*, Wiley-VCH, Weinheim, **2002**, p. 269.

[27] H. Kuhn, *Fortschr. Chem. Org. Naturst.* **1958**, *21*, 169 – 205.

[28] H. Kuhn, *Fortschr. Chem. Org. Naturst.* **1959**, *22*, 404 – 451.

[29] G. Wenz, M. A. Müller, M. Schmidt, G. Wegner, *Macromolecules* **1984**, *17*, 837 – 850.

[30] G. Drefahl, G. Plötner, *Chem. Ber.* **1958**, *91*, 1280 – 1285.

[31] G. N. Lewis, M. Calvin, *Chem. Rev.* **1939**, *39*, 273 – 328.

[32] K. Hirayama, *J. Am. Chem. Soc.* **1955**, *77*, 373 – 379; K. Hirayama, *J. Am. Chem. Soc.* **1955**, *77*, 379 – 381.

[33] K. Hirayama, *J. Am. Chem. Soc.* **1955**, *77*, 382 – 383; K. Hirayama, *J. Am. Chem. Soc.* **1955**, *77*, 383 – 384.

[34] S. Dähne, R. Radeglia, *Tetrahedron* **1971**, *27*, 3673 – 3693; the power law suggested therein contains three parameters and hence can be adapted to individual series of oligomers, but it is not suitable for extrapolation.

[35] R. C. Johnson, *Pade Approximants and Their Applications* (Ed: P. R. Graves-Morris), Academic Press, London, **1973**.

[36] U. Stalmach, H. Kolshorn, I. Brehm, H. Meier, *Liebigs Ann.* **1996**, 1449 – 1456.

[37] H. Bässler in ref. [1k], pp. 403–431.

[38] H. Meier, R. Petermann, J. Gerold, *Chem. Commun.* **1999**, 977 – 978.

[39] H. Meier, J. Gerold, D. Jacob, *Tetrahedron Lett.* **2003**, *44*, 1915 – 1918.

[40] H. Meier, J. Gerold, H. Kolshorn, B. Mühling, *Chem. Eur. J.* **2004**, *10*, 360 – 370.

[41] H. Meier, B. Mühling, H. Kolshorn, *Eur. J. Org. Chem.* **2004**, 1033 – 1042.

[42] However, higher oligomers which contain exclusively a terminal acceptor group, such as the NO_2 group, are in most cases not accessible because they are insoluble. On the other hand, a possibility exists to introduce solubilizing groups R in purely donor-substituted series with NR_2 or OR groups.

[43] An analogous dissection for there series **5e**–**8e** requires the as yet unsynthesized OPV series with vinyl groups R.

[44] M. C. Flipse, R. de Jonge, R. H. Woudenberg, A. W. Marsman, C. A. van Walree, L. W. Jenneskens, *Chem. Phys. Lett.* **1995**, *245*, 297 – 303.

[45] G. Manecke, S. Lüttke, *Chem. Ber.* **1970**, *103*, 700 – 707.

[46] H. Meier, unpublished results.

[47] H. Meier, S. Kim, *Eur. J. Org. Chem.* **2001**, 1163 – 1167.

[48] Compare the series $(H_3C)_2$N-OPE-NO_2 with V. Francke, T. Mangel, K. Müllen, *Macromolecules* **1998**, *31*, 2447 – 2453.

[49] H.-H. Perkampus, *UV/Vis-Spektroskopie und ihre Anwendungen*, Springer, Berlin **1986**, p. 187.

[50] The dissection of the transition energies $E_{DA}(n)$ of **15e**–**18e** in the portions $E_S(n)$ and $\Delta E_{DA}(n)$ would require the until unknown series with R = vinyl.

[51] This is not valid if *ortho*-linked OPE units are used instead of the usual *para*-linked OPE chains; see M. S. Wong, J.-F. Nicoud, *Tetrahedron Lett.* **1994**, *35*, 6113 – 6116.

[52] a) S. S. Malhotra, M. C. Whiting, *J. Chem. Soc.* **1960**, 3812 – 3819; b) see also R. Radeglia, *Z. Phys. Chem. (Leipzig)* **1967**, *235*, 335 – 339; c) F. Würthner, S. Yao, J. Schilling, R. Wortmann, M. Redi-Abshiro, E. Mecher, F. Gallego-Gomez, K. Meerholz, *J. Am. Chem. Soc.* **2001**, *123*, 2810 – 2824; d) U. Lawrentz, W. Grahn, K. Lukaszuk, C. Klein, R. Wortmann, A. Feldner, D. Scherer, *Chem. Eur. J.* **2002**, *8*, 1573 – 1590.

[53] M. Blanchard-Desce, I. Ledoux, J.-M. Lehn, J. Malthête, J. Zyss, *J. Chem. Soc. Chem. Commun.* **1988**, 737 – 739.

[54] M. Barzoukas, M. Blanchard-Desce, D. Josse, J.-M. Lehn, J. Zyss, *Chem. Phys.* **1989**, *133*, 323 – 329.

[55] A. Slama-Schwok, M. Blanchard-Desce, J.-M. Lehn, *J. Phys. Chem.* **1990**, *94*, 3894 – 3902.

[56] V. Alain, L. Thouin, M. Blanchard-Desce, U. Gubler, C. Bosshard, P. Günter, J. Muller, A. Fort, M. Barzoukas, *Adv. Mater.* **1999**, *11*, 1210 – 1214.

[57] M. Blanchard-Desce, V. Alain, P. V. Bedworth, S. R. Marder, A. Fort, C. Runser, M. Barzoukas, S. Lebus, R. Wortmann, *Chem. Eur. J.* **1997**, *3*, 1091 – 1104.

[58] a) See also C.-F. Shu, Y.-C. Shu, Z.-H. Gong, S.-M. Peng, G.-H. Lee, A. K. Y. Jen, *Chem. Mater.* **1998**, *10*, 3284 – 3286; b) B. G.

Tiemann, L.-T. Cheng, S. R. Marder, *J. Chem. Soc. Chem. Commun.* **1993**, 735 – 737.
[59] D. M. Shin, D. G. Whitten, *J. Phys. Chem. A* **1998**, *102*, 2945 – 2956.
[60] Z. R. Grabowski, K. Rotkiewicz, W. Rettig, *Chem. Rev.* **2003**, *103*, 3899 – 4031, and references therein.
[61] S. A. Kovalenko, R. Schanz, T. A. Senyushkina, N. P. Ernsting, *Phys. Chem. Chem. Phys.* **2002**, *4*, 703 – 707.
[62] E. Abraham, J. Oberlé, G. Jonusauskas, R. Lapouyade, C. Rullière, *Chem. Phys.* **1997**, *214*, 409 – 423.
[63] E. Gilabert, R. Lapouyade, C. Rullière, *Chem. Phys. Lett.* **1988**, *145*, 262 – 268; E. Gilabert, R. Lapouyade, C. Rullière, *Chem. Phys. Lett.* **1991**, *185*, 82 – 87.
[64] J.-F. Létard, R. Lapouyade, W. Rettig, *J. Am. Chem. Soc.* **1993**, *115*, 2441 – 2447.
[65] J.-M. Viallet, F. Dupuy, R. Lapouyade, C. Rullière, *Chem. Phys. Lett.* **1994**, *222*, 571 – 578.
[66] R. Lapouyade, C. Czeschka, W. Majenz, W. Rettig, E. Gilabert, C. Rullière, *J. Phys. Chem.* **1992**, *96*, 9643 – 9650.
[67] On the contrary, oligoyne chains with CN as acceptor function on both chain ends are known up to eight repeat units: G. Schermann, T. Grösser, F. Hampel, A. Hirsch, *Chem. Eur. J.* **1997**, *3*, 1105 – 1112.
[68] K. Hafner, M. Neuenschwander, *Angew. Chem.* **1968**, *80*, 443 – 444; *Angew. Chem. Int. Ed. Engl.* **1968**, *7*, 459 – 460.
[69] U. Stämpfli, R. Galli, M. Neuenschwander, *Helv. Chim. Acta* **1983**, *66*, 1631 – 1637.
[70] B. Traber, J. J. Wolff, F. Rominger, T. Oeser, R. Gleiter, M. Goebel, R. Wortmann, *Chem. Eur. J.* **2004**, *10*, 1227 – 1238.
[71] L.-T. Cheng, W. Tam, S. R. Marder, A. E. Stiegman, G. Rikken, C. W. Spangler, *J. Phys. Chem.* **1991**, *95*, 10643 – 10652.
[72] P. C. Leung, J. Stevens, R. E. Harelstad, M. S. Spiering, D. J. Gerbi, C. V. Francis, J. E. Trend, G. V. D. Tiers, G. T. Boyd, D. A. Ender, R. C. Williams, *SPIE Proc.* **1989**, *1147*, 48 – 60; P. C. Leung, J. Stevens, R. E. Harelstad, M. S. Spiering, D. J. Gerbi, C. V. Francis, J. E. Trend, G. V. D. Tiers, G. T. Boyd, D. A. Ender, R. C. Williams, *Chem. Abstr.* **1990**, *112*, 207232d.
[73] See C. A. van Walree, A. W. Maarsman, A. W. Marsman, M. C. Flipse, L. W. Jenneskens, W. J. J. Smeets, A. L. Spek, *J. Chem. Soc. Perkin Trans. 2* **1997**, 809 – 820.
[74] C. Amatore, A. Jutand, S. Negri, J.-F. Fauvarque, *J. Organomet. Chem.* **1990**, *390*, 389 – 398.
[75] I. Ledoux, J. Zyss, A. Jutand, C. Amatore, *Chem. Phys.* **1991**, *150*, 117 – 123.
[76] R. W. H. Berry, P. Brocklehurst, A. Burawoy, *Tetrahedron* **1960**, *16*, 109 – 117.
[77] C. Combellas, H. Gautier, J. Simon, A. Thiebault, F. Tournilhac, M. Barzoukas, D. Josse, I. Ledoux, C. Amatore, J.-N. Verpeaux, *J. Chem. Soc. Chem. Commun.* **1988**, 203 – 204.
[78] A. Dulcic, C. Sauteret, *J. Chem. Phys.* **1978**, *69*, 3453 – 3457.
[79] F. Effenberger, F. Würthner, *Angew. Chem.* **1993**, *105*, 742 – 744; *Angew. Chem. Int. Ed. Engl.* **1993**, *32*, 719 – 721.
[80] F. Effenberger, F. Würthner, F. Steybe, *J. Org. Chem.* **1995**, *60*, 2082 – 2091.
[81] F. Würthner, F. Effenberger, R. Wortmann, P. Krämer, *Chem. Phys.* **1993**, *173*, 305 – 314.
[82] The hypsochromic shift $[\lambda_{max}(4)-\lambda_{max}(3)]$ amounts to 10 nm in toluene, 18 nm in THF, and 22 nm in CH_2Cl_2. It becomes more pronounced with increasing solvent polarity; F. Effenberger, private communication.
[83] a) V. P. Rao, A. K.-Y. Jen, K. Y. Wong, K. J. Drost, *Tetrahedron Lett.* **1993**, *34*, 1747 – 1750; b) A.K.-Y. Jen, V. P. Rao, K. Y. Wong, K. J. Drost, *J. Chem.* Soc. *Chem. Commun.* **1993**, 90 – 92; c) R. Hoss, O. König, V. Kramer-Hoss, U. Berger, P. Rogin, J. Hulliger, *Angew. Chem.* **1996**, *108*, 1774 – 1776; *Angew. Chem. Int. Ed. Engl.* **1996**, *35*, 1664 – 1666; d) J.-M. Raimundo, P. Blanchard, N. Gallego-Planas, N. Mercier, *J. Org. Chem.* **2002**, *67*, 205 – 218.
[84] Y. Yu, E. Gunic, L. L. Miller, *Chem. Mater.* **1995**, *7*, 255 – 256.
[85] W. Theilacker, W. Berger, P. Popper, *Chem. Ber.* **1956**, *89*, 970 – 983.
[86] H. Meier, F. Kosteyn, N. Hanold, H. Rau, G. Gauglitz, *Chem. Ber.* **1992**, *125*, 889 – 892.
[87] F. Kosteyn, G. Zerban, H. Meier, *Chem. Ber.* **1992**, *125*, 893 – 897.
[88] B. Weickhardt, A. E. Siegrist, *Helv. Chim. Acta* **1972**, *55*, 173 – 184.
[89] H. Meier, T. Lifka, K. Müller, *J. Inf. Rec. Mater.* **1994**, *21*, 457 – 460.
[90] M. Nohara, M. Hasegawa, C. Hosokawa, H. Tokailin, T. Kusumoto, *Chem. Lett.* **1990**, 189 – 190.
[91] T. Lifka, H. Meier, *J. Prakt. Chem. Chem.-Ztg.* **1995**, *337*, 641 – 646.
[92] H. Meier, R. Petermann, J. Gerold, *Chem. Commun.* **1999**, 977 – 978.
[93] R. W. Bigelow, H.-J. Freund, *Chem. Phys.* **1986**, *107*, 159 – 174.
[94] H. Meier, R. Petermann, *Helv. Chim. Acta* **2004**, *87*, 1109 – 1118.
[95] H. Meier, N. Hanold, B. Beile, unpublished results.
[96] H. Meier, S. Kim, *Eur. J. Org. Chem.* **2001**, 1163 – 1167.
[97] L. M. Tolbert, X. Zhao, Y. Ding, L. A. Bottomley, *J. Am. Chem. Soc.* **1995**, *117*, 12891 – 12892.
[98] D. Hellwinkel, H. Fritsch, *Chem. Ber.* **1989**, *122*, 2351 – 2359.
[99] C. Arbez-Gindre, C. G. Screttas, C. Fiorini, C. Schmidt, J.-M. Nunzi, *Tetrahedron Lett.* **1999**, *40*, 7413 – 7416.
[100] S. Sengupta, S. K. Sadhukhan, *J. Chem. Soc. Perkin Trans. 1* **2000**, 4332 – 4334.
[101] S. Kim, H. Meier, unpublished results.
[102] H. Meier, H. C. Holst, A. Oehlhof, *Eur. J. Org. Chem.* **2003**, 4173 – 4180.
[103] H. Meier, unpublished results.
[104] B. R. Cho, K. Chajara, H. J. Oh, K. H. Son, S.-J. Jeon, *Org. Lett.* **2002**, *4*, 1703 – 1706.
[105] See, for example: a) C. Bubeck in ref. [1k] p. 449–478; b) *Nonlinear Optical Properties of Organic Molecules and Crystals, Vol. 1 and 2* (Eds: D. S. Chemla, J. Zyss), Academic Press, New York, **1987**; c) P. N. Butcher, D. Cotter, *The Elements of Nonlinear Optics*, Cambridge University Press, Cambridge, **1990**; d) *Materials for Nonlinear Optics: Chemical Perspectives* (Eds: S. R. Marder, J. E. Solm, G. D. Stucky), ACS Symposium Series 455, ACS, Washington DC, **1991**; e) P. N. Prasad, D. J. Williams, *Introduction to Nonlinear Optical Effects in Molecules and Polymers*, Wiley, New York, **1991**; f) R. W. Boyd, *Nonlinear Optics*, Academic Press, Boston, **1992**; g) G. Zerbi, *Organic Materials for Photonics*, North-Holland, Amsterdam, **1993**; h) G. Zerbi, *Chem. Rev.* **1994**, *94*, 1 – 278; i) *Molecular Nonlinear Optics—Materials, Physics and Devices* (Ed: J. Zyss), Academic Press, San Siego, **1994**; j) M. W. Evans, *Modern Nonlinear Optics*, *Part 1–3*, Wiley, New York, **2001**.
[106] H. Meier, *Angew. Chem.* **1992**, *104*, 1425 – 1446; *Angew. Chem. Int. Ed. Engl.* **1992**, *31*, 1399 – 1420.
[107] L.-T. Cheng, W. Tam, S. H. Stevenson, G. R. Meredith, G. Rikken, S. R. Marder, *J. Phys. Chem.* **1991**, *95*, 10631 – 10643.
[108] J. L. Oudar, D. S. Chemla, *J. Chem. Phys.* **1977**, *66*, 2664 – 2668.
[109] J. L. Oudar, *J. Chem. Phys.* **1977**, *67*, 446 – 457.
[110] The correction consists of a dispersion factor $\beta_0\beta^{-1} = f(\lambda_L, \lambda_{max})$ which takes the λ_{max} value of the compound and its distance from the used laser wavelength λ_L into account; β_0 is in most cases considerable smaller than $\beta(2\omega)$. The γ value depends also to some extent on λ_L. The maximum of $\gamma(\lambda_L)$ corresponds to the resonance case γ_{res} for $\lambda_L = 3\lambda_{max}$.
[111] A. Dulcic, C. Flytzanis, C. T. Tang, D. Pépin, M. Fétizon, Y. Hoppilliard, *J. Chem. Phys.* **1981**, *74*, 1559 – 1563.

 © 2005 Wiley-VCH Verlag GmbH & Co. KGaA, Weinheim

[112] G. Berkovic, Y. R. Shen, M. Shadt, *Mol. Cryst. Liquid Cryst.* **1987**, *150*, 607 – 616.
[113] M. Blanchard-Desce, J.-M. Lehn, M. Barzoukas, I. Ledoux, J. Zyss, *Chem. Phys.* **1994**, *181*, 281 – 289.
[114] M. Blanchard-Desce, C. Runser, A. Fort, M. Barzoukas, J.-M. Lehn, V. Bloy, V. Alain, *Chem. Phys.* **1995**, *199*, 253 – 261.
[115] J. Messier, F. Kajzar, C. Sentein, M. Barzoukas, J. Zyss, M. Blanchard-Desce, J.-M. Lehn, *Nonlinear Opt.* **1992**, *2*, 53.
[116] G. Puccetti, M. Blanchard-Desce, I. Ledoux, J.-M. Lehn, J. Zyss, *J. Phys. Chem.* **1993**, *97*, 9385 – 9391.
[117] M. Blanchard-Desce, J.-M. Lehn, M. Barzoukas, C. Runser, A. Fort, I. Ledoux, J. Zyss, *Nonlinear Opt.* **1995**, *10*, 23 – 36.
[118] See also G. S. W. Craig, R. E. Cohen, R. R. Schrock, R. J. Silbey, G. Puccetti, I. Ledoux, J. Zyss, *J. Am. Chem. Soc.* **1997**, *119*, 115, 860 – 867.
[119] S. R. Marder, W. E. Torruellas, M. Blanchard-Desce, V. Ricci, G. I. Stegemann, S. Gilmour, J. L. Brédas, J. Li, G. W. Bublitz, S. G. Boxer, *Science* **1997**, *276*, 1233 – 1236.
[120] S. Tretiak, V. Chernyak, S. Mukamel, *Chem. Phys. Lett.* **1998**, *287*, 75 – 82.
[121] See also J. O. Morley, V. J. Docherty, D. Pugh, *J. Chem. Soc. Perkin Trans. 2* **1987**, 1351 – 1355.
[122] D. Li, M. A. Ratner, T. J. Marks, *J. Am. Chem. Soc.* **1988**, *110*, 1707 – 1715.
[123] J.-L. Oudar, J. Zyss, *Phys. Rev. A* **1982**, *26*, 2016 – 2027.
[124] C. Flytzanis in ref. [105b], Vol. II, **1987**, p. 121.
[125] G. P. Agrawal, C. Cojan, C. Flytzanis, *Phys. Rev. B* **1978**, *17*, 776 – 789.
[126] L_d is defined as the quotient $(\beta_2^2-\beta_1^2)\beta_2^{-1}$ for oligoenes with alternating double and single bonds and the corresponding resonance integrals $\beta_1 < \beta_2$; β-carotene has for example with $n = 11$ conjugated double bonds the value $L_d = 7.5 < n$. See also G. P. Agrawal, C. Flytzanis, *Chem. Phys. Lett.* **1976**, *44*, 366 – 370.
[127] C. Bubeck, K. Koynov, B. Mühling, H. Meier, unpublished results.
[128] D. Lu, G. Chen, J. W. Perry, W. A. Goddard III, *J. Am. Chem. Soc.* **1994**, *116*, 10679 – 10685.
[129] F. Meyers, S. R. Marder, B. M. Pierce, J.-L. Brédas, *J. Am. Chem. Soc.* **1994**, *116*, 10703 – 10714.
[130] M. C. Ruiz Delgado, V. Hernández, J. Casado, J. T. Lopez Navarrete, J.-M. Raimundo, P. Blanchard, J. Roncali, *Chem. Eur. J.* **2003**, *9*, 3670 – 3682.
[131] The quantum mechanical calculations were performed with dimethylamino groups.
[132] It depends on the donor and acceptor strength which of the two groups D and A causes the greater polarization; see Scheme 30 and ref. [130].
[133] See, for example: J. Michl, V. Bonačić-Koutecký, *Electronic Aspects of Organic Photochemistry*, Wiley, New York, **1990**, p. 35.
[134] J. Michl, E. W. Thulstrup, *Tetrahedron* **1976**, *32*, 205 – 209.
[135] M. D. Ward, *Chem. Ind.* **1996**, 568 – 571.
[136] P. C. Leung, J. Stevens, R. E. Harelstad, M. S. Spiering, D. J. Gerbi, C. V. Francis, J. E. Trend, G. V. D. Tiers, G. T. Boyd, D. A. Enders, R. C. Williams, *SPIE Proc.* **1989**, *1147*, 48 – 60.
[137] A DAOPE series, which is of interest for this case, was studied by Müllen and co-workers[48]: $\lambda_{max}(1) > \lambda_{max}(2) < \lambda_{max}(3)$. However, since additional hexyl side chains were introduced on going from $n = 1$ to $n = 2$, the minimum of λ_{max} for $n = 2$ could result from other effects.
[138] This also includes analyses of obtained vibrational bands in IR and Raman spectra.
[139] a) A. Bianco, M. Del Zoppo, G. Zerbi, *Synth. Met.* **2002**, *125*, 81 – 91; b) G. Zerbi, C. Castiglioni, M. Del Zoppo in ref. [1k], pp. 345–402.
[140] See also a) H. C. Holst, T. Pakula, H. Meier, *Tetrahedron* **2004**, *60*, 6765 – 6775; b) H. Meier, M. Lehmann, H. C. Holst, D. Schwöppe, *Tetrahedron* **2004**, *60*, 6881 – 6888.
[141] A. Abbotto, L. Beverina, S. Bradamante, A. Facchetti, C. Klein, G. A. Pagani, M. Redi-Alshiro, R. Wortmann, *Chem. Eur. J.* **2003**, *9*, 1991 – 2007.
[142] M. E. van der Boom, *Angew. Chem.* **2002**, *114*, 3511 – 3514; *Angew. Chem. Int. Ed.* **2002**, *41*, 3363 – 3366.

 © 2005 Wiley-VCH Verlag GmbH & Co. KGaA, Weinheim

Communications

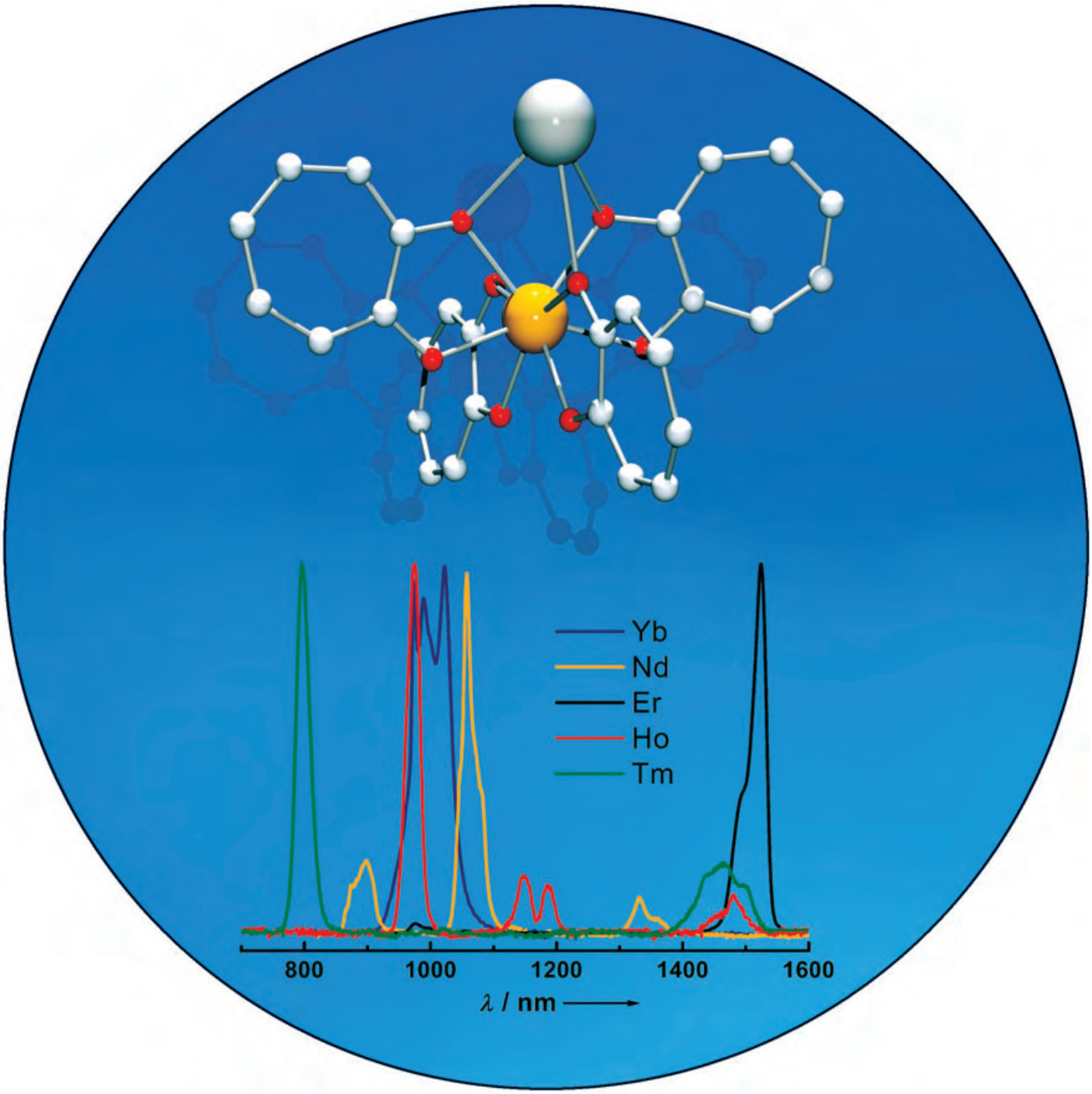

Bidentate tropolonate ligands coordinate lanthanide (Ln) cations to form $[Ln(tropolonate)_4]^-$ species in solution and sensitize the luminescence of the Ln ion. The structures of several such complexes with various Ln ions have been characterized. For more information, see the communication by S. Petoud and co-workers on the following pages.

 © 2005 Wiley-VCH Verlag GmbH & Co. KGaA, Weinheim DOI: 10.1002/anie.200463081

Luminescent Lanthanide Complexes

Sensitization of Near-Infrared-Emitting Lanthanide Cations in Solution by Tropolonate Ligands**

*Jian Zhang, Paul D. Badger, Steven J. Geib, and Stéphane Petoud**

The quest for luminescent reporters that emit in the near-infrared (NIR) domain is a target of prime importance, as NIR photons can penetrate deep into tissues without causing damage and without significant loss of intensity owing to the low absorption of NIR photons in such media.[1,2] Furthermore, the use of NIR light is one of the best strategies to obtain high-resolution pictures of deep tissues, as NIR light diffracts much less than visible light (diffraction is proportional to $1/(\lambda)^{SP}$, SP = scattering power).[3] NIR fluorescent organic dyes are the current candidates for such applications, but suffer from rapid photodecomposition when exposed to excitation light (photobleaching),[4] which prevents long exposure times or repetitive experiments and strongly limits the field of applications of these fluorophores. NIR luminescent lanthanide complexes are very promising reporters for detection in biological media for several reasons: 1) most lanthanide complexes do not photobleach,[5] 2) they display sharp emission bands that can be easily discriminated from background fluorescence,[6] and 3) they exhibit long luminescent lifetimes, which allow the removal of background fluorescence (autofluorescence) and increased assay sensitivity through time-resolved measurements.[7,8] Recent advances in technology allow such complexes to be excited in the NIR domain by using multiphoton excitation techniques.[9,10] So far, Nd and Yb complexes have been reported as NIR-luminescent reporters for these applications. However, there is still room for expanding the use of lanthanide complexes in biological applications. The molecules reported until now have limited luminescence output owing to low efficiency of intramolecular ligand-to-lanthanide energy transfer and/or insufficient protection of the metal ion against nonradiative deactivation processes. Furthermore, the sensitization of other lanthanide cations, such as Ho^{III} or Tm^{III}, is of high interest as supplementary emission wavelengths would then be also available. The narrow emission bandwidths of lanthanide cations allows for the simultaneous detection of several cations during the same experiment (multiplex assay). To obtain luminescent complexes for solution applications, the ligand(s) must harvest light and convert the resulting energy to the Ln^{III} ion (antenna effect),[11,12] as well as protect the Ln^{III} ion from nonradiative deactivations.[13] Oxygen-donor ligands that can efficiently absorb light are preferred because they also form strong bonds with lanthanide cations, which are hard Lewis acids.

We propose here a novel versatile approach to the development of lanthanide complexes that emit in the NIR based on tropolone as ligand. Upon deprotonation, tropolones (Figure 1) can be used as seven-membered ring,

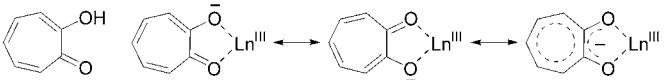

Figure 1. Structure of tropolone, and the coordination mode of tropolonate ligands with lanthanide (Ln^{III}) ions.

bidentate oxygen-donor chelators that allow direct coordination of the chromophoric group to the Ln^{III} cation. Their hard Lewis base character is suitable for forming strong bonds with Ln^{III}. Four tropolonate ligands are sufficient to complete the coordination number requirement of Ln^{III} (typically 8–12 in solution).[14,15] Tropolone has a good electronic structure to act as an antenna because the energy of its triplet state ($16\,800\ cm^{-1}$)[16] is compatible for efficient energy transfer to the low accepting levels of several Ln^{III} ions that emit in the NIR, such as Nd^{III}, Er^{III}, Ho^{III}, and Tm^{III}. For Yb^{III}, which has only one acceptor level ($^2F_{5/2}$) at $10\,200\ cm^{-1}$, the energy gap between the donor (ligand) triplet state and $^2F_{5/2}$ is quite large ($6600\ cm^{-1}$). Nonetheless, the phonon-assisted energy-transfer process could be used to explain the efficient energy transfer to Yb.[17] A large number of tropolone derivatives have been reported which allows for fine-tuning of the photophysical properties of the resulting lanthanide complexes. Herein we report the sensitization of several lanthanide cations that emit in the NIR (Nd^{III}, Er^{III}, Ho^{III}, Tm^{III}, and Yb^{III}) upon formation of the $[Ln(L)_4]^-$ complex (L = $C_7H_5O_2^-$; tropolonate) in aqueous and organic solutions.

Muetterties and Wright previously identified that tropolonate ions can form both ML_3- and ML_4-type complexes depending on the experimental conditions.[18] They prepared ML_4 complexes by using NH_4^+ and Na^+ as the counterions, but crystal structures of the complexes were not reported. Upon changing the counterion to K^+, we were able to isolate and analyze the crystal structures of $\{K[Ln(L)_4]\cdot DMF\}_\infty$ (Ln = Tb, Dy, Ho, Er, Tm, Yb, Lu; DMF = *N*,*N*-dimethylformamide) for the first time. The Ln^{III} ion is coordinated by the eight oxygen atoms of four tropolonate ligands. The bridging K^+ counterion has a coordination number of seven through interactions with six oxygen atoms from two molecules of the complex and one oxygen atom from a solvent (DMF) molecule. The K^+ ion seems to play a significant role in the packing pattern of the complex in the crystal. The crystal structures of the complexes formed with Dy, Ho, Er, Tm, Yb, and Lu are isostructural (triclinic, $P\bar{1}$, $Z = 2$; see Figure 2) and differ from the structure of the Tb complex by the relative position of the K^+ ion with respect to the Ln^{III} ion. In all cases, the coordination polyhedron around the lanthanide cation is

[*] J. Zhang, Dr. P. D. Badger, Prof. Dr. S. J. Geib, Prof. Dr. S. Petoud
Department of Chemistry
University of Pittsburgh
Pittsburgh, PA 15260 (USA)
Fax: (+1) 412-624-8611
E-mail: spetoud@pitt.edu

[**] The authors acknowledge financial support from the University of Pittsburgh.

Supporting information for this article is available on the WWW under http://www.angewandte.org or from the author.

 © 2005 Wiley-VCH Verlag GmbH & Co. KGaA, Weinheim

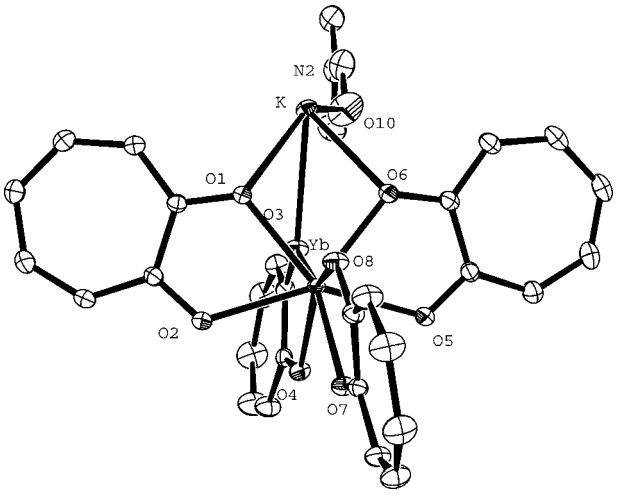

Figure 2. ORTEP drawing of K[Yb(L)$_4$]·DMF (50% probability level).

best described as a distorted dodecahedron (D_{2d}), one of the two most stable eight-coordinated polyhedra.

To confirm the stoichiometry of the complex in solution, an orientation spectrophotometric titration was performed by adding increasing amounts of Ln^{III} to a solution of the potassium salt of the tropolone ligand in DMSO. The absorption spectra recorded (see Supporting Information) reveal important changes upon addition of Ln^{III}. Preliminary treatment of these experimental data with SPECFIT software[19] indicates that four complexes are successively formed in solution (see Supporting Information); the calculated individual spectra of each of the four successive complexes ML_1, ML_2, ML_3, and ML_4 are uncorrelated.

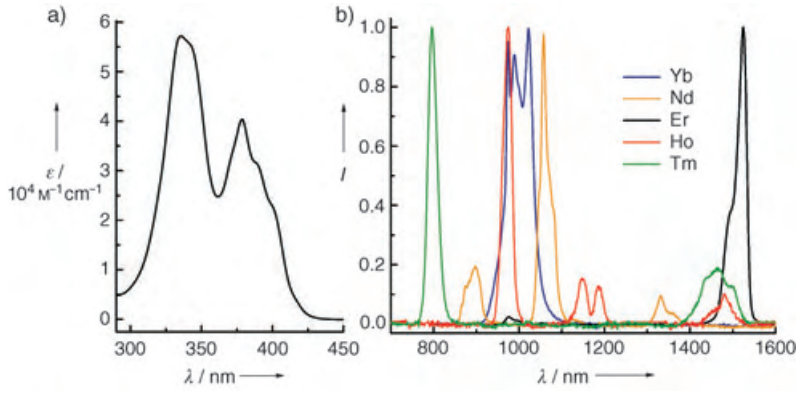

Figure 3. a) Absorption spectrum of [Yb(L)$_4$]$^-$ and b) normalized emission spectra of [Ln(L)$_4$]$^-$ with Ln = Yb, Nd, Er, Ho, and Tm (10^{-5} M in dimethylsulfoxide (DMSO)) in the NIR at 298 K upon ligand excitation at 340 nm using a Xenon lamp as excitation source.[20]

Upon formation of the corresponding ML_4 complexes, several lanthanide cations could be sensitized through the tropolonate ligands (Figure 3). Corresponding with ligand-to-metal energy transfer, the intensity of the fluorescence decreased for the tropolonate ligand which is centered in the visible region at 425 nm, while the luminescence of the corresponding lanthanide ion appeared as sharp emission lines in the NIR range. For the Nd complex, emission bands were observed at 897, 1056, and 1331 nm and are attributed to the $^4F_{3/2}\rightarrow{}^4I_{9/2}$, $^4F_{3/2}\rightarrow{}^4I_{11/2}$, and $^4F_{3/2}\rightarrow{}^4I_{13/2}$ transitions, respectively. For the Yb complex, there is only one emission band affected by crystal-field splitting which is assigned to the $^2F_{5/2}\rightarrow{}^2F_{7/2}$ transition. An observed emission band at 1524 nm is attributed to the $^4I_{13/2}\rightarrow{}^4I_{15/2}$ transition for Er. To the best of our knowledge, the emission of a holmium complex in solution is reported here for the first time: Four emission bands were observed. The emission bands at 975 and 1479 nm are assigned to $^5F_5\rightarrow{}^5I_7$ and $^5F_5\rightarrow{}^5I_6$ transitions, respectively. The emission bands at 1148 and 1187 nm are assigned to the same $^5I_6\rightarrow{}^5I_8$ transition split into two components. The emission bands of the Tm complex observed at 796 and 1465 nm are assigned to $^3F_4\rightarrow{}^3H_6$ and $^3F_4\rightarrow{}^3H_4$ transitions, respectively. The ligand-centered emission does not completely disappear when the lanthanide cation is added in any of these cases which indicates that the ligand-to-lanthanide energy-transfer process is not complete and that further optimization is possible.

The fact that the tropolonate ion can sensitize not only Yb, Nd, and Er but also Ho and Tm indicates that it is a very promising and versatile sensitizer for lanthanide cations that have acceptor levels located at relatively low energies. The narrow emission bands of lanthanide cations allow the simultaneous detection of several lanthanide cations during the same experiment by using a single excitation wavelength—a useful feature for multiplex assays.

To quantify the intramolecular ligand-to-lanthanide energy transfer as well as quenching processes that take place in the different lanthanide complexes, luminescence quantum yields upon ligand excitation were measured in various solvents (Table 1). Quantum yield values reported for the Yb^{III} complex compare well to those reported for other Yb^{III} complexes and are among the highest values.[21] There is a significant difference between measurements made in deuterated and non-deuterated solvents which indicates the presence of a nonradiative deactivation process. This dependency on the nature of the solvent suggests that the Ln^{III} cations are not completely protected from the solvent by the four tropolone ligands in solution. Nevertheless, the ligand-to-lanthanide energy-transfer process and the protection offered by the coordinated

Table 1: Absolute emission quantum yields (Φ) for [Ln(L)$_4$]$^-$ in organic and aqueous media.[a]

Ln	Solvent	Φ_{Ln}	Φ_{Ln} (deuterated solvent)
Yb	DMSO	$1.9\pm0.1\times10^{-2}$	$2.2\pm0.3\times10^{-2}$
Yb	MeOH	$1.3\pm0.2\times10^{-3}$	$1.6\pm0.2\times10^{-2}$
Yb	H_2O	$2.4\pm0.3\times10^{-4}$	$7.4\pm0.1\times10^{-3}$
Nd[b]	DMSO	$2.1\pm0.1\times10^{-3}$	$3.6\pm0.7\times10^{-3}$
Er[b]	DMSO	$1.7\pm0.1\times10^{-4}$	$3.2\pm0.4\times10^{-4}$
Tm[c]	DMSO	$3.8\pm0.2\times10^{-5}$	$5.7\pm0.2\times10^{-5}$
Ho[c]	DMSO	$2.3\pm0.2\times10^{-5}$	$2.4\pm0.1\times10^{-5}$

[a] λ_{ex} = 340 nm was used for quantum yield determinations. [b] Quantum yields were measured using [Yb(L)$_4$]$^-$ as standard. [c] Quantum yields were measured using [Er(L)$_4$]$^-$ as standard.

 © 2005 Wiley-VCH Verlag GmbH & Co. KGaA, Weinheim

ligands are sufficient to allow the measurement of the quantum yields of the Yb complex in water. The quantum yield values recorded for $[Ln(L)_4]^-$ with Ln = Nd, Er, Ho, and Tm are lower than those recorded with Ln = Yb, but are still easily measurable with a fluorimeter using a Xenon lamp as a source of excitation.

By using the formula established by Beeby et al.[13] and on the basis of the lifetimes (τ) of the Yb^{III} complexes recorded in H_2O and D_2O ($\tau_{H2O} = 0.75 \pm 0.01$ μs, $\tau_{D2O} = 10.03 \pm 0.11$ μs), we found that 1.1 molecules of water are directly bound to the lanthanide cation when the complex is in solution. The same result was obtained when the lifetimes measured in MeOH and CD_3OD ($\tau_{CH3OH} = 1.62 \pm 0.03$ μs, $\tau_{CD3OD} = 13.02 \pm 0.01$ μs) were used. This observation indicates that the structures observed in the solid state, in which no solvent molecules are bound to the lanthanide cation, are different from the structures of the lanthanide complexes in solution. The presence of nonradiative processes partially explains the low quantum yields observed for tropolonate complexes in water.

In conclusion, we have identified the structure of ML_4 complexes formed between bidentate tropolonate ligands and seven different lanthanide cations: Tb^{III}, Dy^{III}, Ho^{III}, Er^{III}, Tm^{III}, Yb^{III}, and Lu^{III}. The coordination geometry around the lanthanide cations is close to a dodecahedron. The intermolecular packing patterns are different between the Tb complex and the complexes formed with the other lanthanide cations reported here. Quantitative luminescence measurements indicated that tropolonate ligands are able to sensitize several lanthanide cations that emit in the near-infrared domain. Also, the luminescence of Ho^{III} in a lanthanide complex in solution is reported here for the first time. Quantum yields of the complexes formed with Yb^{III} are comparable to the highest reported quantum yields of other lanthanide complexes that emit in the NIR domain in organic solvents. In aqueous solution, water has a very strong deactivating effect on the luminescence of lanthanide ions owing to the coordination to Ln^{III} of water molecules, which were not present in the solid state.

Owing to the flexibility of the approach, limitations can be removed by preparing a multidentate ligand that connects several chelating tropolone units to a common backbone. The backbone will function 1) to improve protection of the lanthanide cation from nonradiative deactivation by preventing the access of water molecules to the metal ion and 2) to increase the stability of the complex in solution, a useful feature when the complex is used at low concentrations. Emission spectra of the complexes indicate that for all the studied lanthanide complexes here, there is a significant amount of residual ligand emission. This is an indication of incomplete energy transfer from the ligand to the lanthanide ion. The preparation of derivatives of tropolone ligands is underway to optimize this parameter.

Experimental Section

Tropolone, $LnCl_3 \cdot n H_2O$ (99.99%), and methanolic KOH (0.103 M) were purchased from Aldrich. The complexes were synthesized as follows: KOH (0.04 mmol) in methanol was added to a solution of tropolone (0.04 mmol) in methanol (10 mL). $LnCl_3 \cdot n H_2O$ (Ln = La, Pr, Nd, Sm, Eu, Gd, Tb, Dy, Ho, Er, Tm, Yb, and Lu; 0.01 mmol) in methanol (10 mL) was then added to the resulting solution. The precipitate was filtered, washed three times with methanol, and dried in vacuo over P_2O_5 for 48 h. Elemental analysis: calcd for $C_{28}H_{20}O_8KYb$ (%): C 48.28, H 2.89; found: C 48.47, H 2.92; ESI-MS: m/z: 736 $[M+K]^+$, 576 $[M-L]^+$, 416 $[M-2L-K]^+$. Single crystals of $\{K[Ln(L)_4]\cdot DMF\}_\infty$ were obtained by slow diffusion of diethyl ether into concentrated solutions of $[Ln(L)_4]^-$ in DMF.

Crystal data for $\{K[Yb(L)_4]\cdot DMF\}_\infty$: $C_{31}H_{27}KNO_9Yb$, $M = 769.68$, triclinic, $P\bar{1}$, $a = 7.2409(3)$, $b = 10.9079(4)$, $c = 19.8683(7)$ Å, $\alpha = 80.0870(10)$, $\beta = 84.1570(10)$, $\gamma = 78.8690(10)°$, $V = 1512.93(10)$ Å^3, $T = 298$ K, $Z = 2$, $\lambda Mo_{K\alpha} = 0.71073$ Å, 19668 reflections measured of which 10293 were unique ($R_{int} = 0.014$), 10027 observed reflections [$I > 2\sigma(I)$] were used in all calculations, $R(F) = 0.0209$, $R_w = 0.0544$. Crystal data for $\{K[Tb(L)_4]\cdot DMF\}_\infty$: $C_{31}H_{27}KNO_9Tb$, $M = 755.56$, monoclinic, $P2_1/n$, $a = 12.7566(12)$, $b = 13.2771(12)$, $c = 18.9393(18)$ Å, $\beta = 95.984(2)°$, $V = 3190.3(5)$ Å^3, $T = 298$ K, $Z = 4$, $\lambda Mo_{K\alpha} = 0.71073$ Å, 40368 reflections measured of which 11227 were unique ($R_{int} = 0.0588$), 6647 observed reflections [$I > 2\sigma(I)$] were used in all calculations, $R(F) = 0.0521$, $R_w = 0.1017$. CCDC 252899 ($\{K[Yb(L)_4]\cdot DMF\}_\infty$), 252900 ($\{K[Tb(L)_4]\cdot DMF\}_\infty$), 252901 ($\{K[Dy(L)_4]\cdot DMF\}_\infty$), 252902 ($\{K[Ho(L)_4]\cdot DMF\}_\infty$), 252903 ($\{K[Er(L)_4]\cdot DMF\}_\infty$), 252904 ($\{K[Tm(L)_4]\cdot DMF\}_\infty$), and 252905 ($\{K[Lu(L)_4]\cdot DMF\}_\infty$) contain the supplementary crystallographic data for this paper. These data can be obtained free of charge from the Cambridge Crystallographic Data Centre via www.ccdc.cam.ac.uk/data_request/cif.

FT-IR spectra were obtained from samples prepared as KBr pellets on a Perkin–Elmer BX spectrometer. Absorption spectra were recorded on a Perkin–Elmer Lambda 9 spectrophotometer coupled with a personal computer and by using software supplied by Perkin–Elmer. Emission and excitation (lanthanide luminescence) spectra were measured using a Jobin Yvon–Horiba Fluorolog-322 spectrofluorimeter equipped for measurements at both RT and 77 K (Hamamatsu R928 detector for the visible domain; DSS-IGA020L (Electro-Optical Systems, Inc.) detector for the NIR domain). Luminescence and excitation spectra were corrected for the instrumental function. Yb^{III} luminescence quantum yields were measured by using the $^4G_{5/2} \rightarrow {}^6H_{9/2}$ transition of a previously reported samarium–(2-hydroxyisophthalamide) macrobicyclic complex ($\Phi = 7.3 \times 10^{-4}$ in 0.01M TRIS buffer) as reference.[15] For convenience, the Yb complex was used as the standard for the quantum yield measurements of the Nd and Er complexes. The quantum yields for Tm and Ho complexes were measured by using the Er complex as the standard for better accuracy because of their comparable luminescence intensities. Detailed experimental setup and methods for photophysical measurements are described in the Supporting Information. Crystals for diffraction studies were attached to glass fibers with epoxy cement. X-ray data were collected on a Bruker Smart Apex CCD diffractometer by using graphite-monochromated $Mo_{K\alpha}$ radiation ($\lambda = 0.71073$ Å). Data processing, and structure solution and refinements were performed with the Bruker Smart, Saint, and SHELXTL program packages, respectively. All structures were solved by direct methods. All non-hydrogen atoms were refined anisotropically.

Received: December 28, 2004

Keywords: lanthanides · luminescence · near-infrared emitters · O ligands · sensitizers

[1] R. Weissleder, V. Ntziachristos, *Nat. Med.* **2003**, *9*, 123–128.
[2] S. Stolik, J. A. Delgado, A. Perez, L. Anasagasti, *J. Photochem. Photobiol. B* **2000**, *57*, 90–93.

 © 2005 Wiley-VCH Verlag GmbH & Co. KGaA, Weinheim

[3] S. Kim, Y. T. Lim, E. G. Soltesz, A. M. De Grand, J. Lee, A. Nakayama, J. A. Parker, T. Mihaljevic, R. G. Laurence, D. M. Dor, L. H. Cohn, M. G. Bawendi, J. V. Frangioni, *Nat. Biotechnol.* **2004**, *22*, 93 – 97.
[4] W. M. M. Yunus, C. K. Sheng, W. M. Z. W. Yunus, *J. Nonlinear Opt. Phys. Mater.* **2003**, *12*, 91 – 100.
[5] Z. Ye, M. Tan, G. Wang, J. Yuan, *Anal. Chem.* **2004**, *76*, 513 – 518.
[6] G. Mathis, *J. Biomol. Screening* **1999**, *4*, 309 – 313.
[7] I. Hemmila, V. M. Mukkala, *Crit. Rev. Clin. Lab. Sci.* **2001**, *38*, 441 – 519.
[8] J.-C. G. Bünzli, G. R. Choppin, *Lanthanide Probes in Life, Chemical, and Earth sciences: Theory and Practice*, Elsevier, Amsterdam, **1989**.
[9] K.-L. Wong, W.-M. Kwok, W.-T. Wong, D. L. Phillips, K.-W. Cheah, *Angew. Chem.* **2004**, *116*, 4759 – 4762; *Angew. Chem. Int. Ed.* **2004**, *43*, 4659 – 4662.
[10] G. Piszczek, B. P. Maliwal, I. Gryczynski, J. Dattelbaum, J. R. Lakowicz, *J. Fluoresc.* **2001**, *11*, 101 – 107.
[11] S. Petoud, J.-C. G. Bünzli, T. Glanzman, C. Piguet, Q. Xiang, R. P. Thummel, *J. Lumin.* **1999**, *82*, 69 – 79.
[12] N. Sabbatini, M. Guardigli, J. M. Lehn, *Coord. Chem. Rev.* **1993**, *123*, 201 – 228.
[13] A. Beeby, I. M. Clarkson, R. S. Dickins, S. Faulkner, D. Parker, L. Royle, A. S. de Sousa, J. A. G. Williams, M. Woods, *J. Chem. Soc. Perkin Trans. 2* **1999**, 493 – 503.
[14] D. Parker, R. S. Dickins, H. Puschmann, C. Crossland, J. A. K. Howard, *Chem. Rev.* **2002**, *102*, 1977 – 2010.
[15] S. Petoud, S. M. Cohen, J.-C. G. Bünzli, K. N. Raymond, *J. Am. Chem. Soc.* **2003**, *125*, 13 324 – 13 325.
[16] S. L. Murov, I. Carmichael, G. L. Hug, *Handbook of Photochemistry*, *2nd ed.*, Marcel Dekker, New York, **1993**.
[17] C. Reinhard, H. U. Güdel, *Inorg. Chem.* **2002**, *41*, 1048 – 1055.
[18] E. L. Muetterties, C. M. Wright, *J. Am. Chem. Soc.* **1965**, *87*, 4706 – 4717.
[19] H. Gampp, M. Maeder, C. J. Meyer, A. D. Zuberbühler, *Talanta* **1985**, *32*, 1133 – 1139.
[20] The emission spectra for NIR-emitting lanthanide complexes were normalized to display the different emission wavelengths of the individual lanthanide cations. Please refer to the quantum yield measurements in Table 1 for a comparison of the relative emission intensities.
[21] a) S. J. A. Pope, B. J. Coe, S. Faulkner, E. V. Bichenkova, X. Yu, K. T. Douglas, *J. Am. Chem. Soc.* **2004**, *126*, 9490 – 9491; b) T. J. Foley, B. S. Harrison, A. S. Knefely, K. A. Abboud, J. R. Reynolds, K. S. Schanze, J. M. Boncella, *Inorg. Chem.* **2003**, *42*, 5023 – 5032; c) G. A. Hebbink, L. Grave, L. A. Woldering, D. N. Reinhoudt, F. C. J. M. van Veggel, *J. Phys. Chem. A* **2003**, *107*, 2483 – 2491; d) F. R. Goncalves e Silva, O. L. Malta, C. Reinhard, H. U. Güdel, C. Piguet, J. E. Moser, J.-C. G. Bünzli, *J. Phys. Chem. A* **2002**, *106*, 1670 – 1677; e) M. Iwamuro, Y. Wada, T. Kitamura, N. Nakashima, S. Yanagida, *Phys. Chem. Chem. Phys.* **2000**, *2*, 2291 – 2296; f) M. H. V. Werts, J. W. Verhoeven, J. W. Hofstraat, *J. Chem. Soc. Perkin Trans. 2* **2000**, 433 – 439; g) A. Beeby, R. S. Dickins, S. Faulkner, D. Parker, J. A. G. Williams, *Chem. Commun.* **1997**, 1401 – 1402.

 © 2005 Wiley-VCH Verlag GmbH & Co. KGaA, Weinheim

Carbene Ligands

An Electron-Deficient Iridium(III) Dihydride Complex Capable of Intramolecular C–H Activation**

*Natalie M. Scott, Vincent Pons, Edwin D. Stevens, D. Michael Heinekey, and Steven P. Nolan**

Coordinatively unsaturated late-transition-metal hydride complexes are of significant importance in light of their vital role in many stoichiometric and catalytic reactions.[1] In particular, unsaturated cationic iridium hydride complexes have been shown to mediate a range of catalytic transformations, including alkane C–H bond activation.[2] Unsaturated cationic complexes are stabilized in many cases through the coordination of solvent molecules and/or by agostic interactions.[3] It has always been postulated that complexes coordinated with only sigma-bonding interactions, including agostic interactions, possess weak metal binding.[4] Thus, well-defined and characterized examples of these interactions are rare because of their high reactivity/poor stability.[5,6]

We recently reported the interactions of *N*,*N*′-di(*tert*-butyl)imidazol-2-ylidene (I*t*Bu) with $[\{Ir(coe)_2Cl\}_2]$ (coe = cyclooctene) leading to the formation of a doubly cyclometalated product $[Ir(I\mathit{t}Bu')_2Cl]$ (**1**; Scheme 1). Simple halide abstraction in **1** with $AgPF_6$ allows the preparation of a four-coordinate 14-electron complex $[Ir(I\mathit{t}Bu')_2](PF_6)$ (**2**) with a *cis* stereochemistry of the two vacant positions at the pseudooctahedral Ir center.[6]

The highly unsaturated nature of **2** led us to examine its reactivity with dihydrogen. Exposure of the deep-red solution of **2** in dichloromethane to H_2 gas resulted in the solution changing rapidly to pale yellow, and afforded a microcrystalline product **3** in excellent yield after work up in pentane [Eq. (1)].[7] The ^{1}H NMR spectrum of **3** at 298 K exhibits a single resonance in the hydride region at $\delta = -29.03$ ppm. A single sharp resonance at $\delta = 1.55$ ppm for the *t*butyl groups and a resonance at $\delta = 7.18$ ppm for the imidazole units were observed. The intensity ratio of the resonances for the hydride/*t*butyl/imidazole moieties is 2:36:4, which suggests **3** is a dihydride complex. Crystals of suitable quality for X-ray

[*] Dr. N. M. Scott, Prof. Dr. E. D. Stevens, Prof. Dr. S. P. Nolan
Department of Chemistry
University of New Orleans
New Orleans, LA 70148 (USA)
Fax: (+1) 504-280-6860
E-mail: snolan@uno.edu
Dr. V. Pons, Prof. Dr. D. M. Heinekey
Department of Chemistry
Box 351700, University of Washington
Seattle WA 98195-1700 (USA)

[**] The National Science Foundation is gratefully acknowledged for financial support of this work (through the Universities of New Orleans and Washington). Acquisition of the 750 MHz NMR spectrometer was supported by the National Science Foundation and the Murdoch Charitable Trust.

 © 2005 Wiley-VCH Verlag GmbH & Co. KGaA, Weinheim DOI: 10.1002/anie.200463000

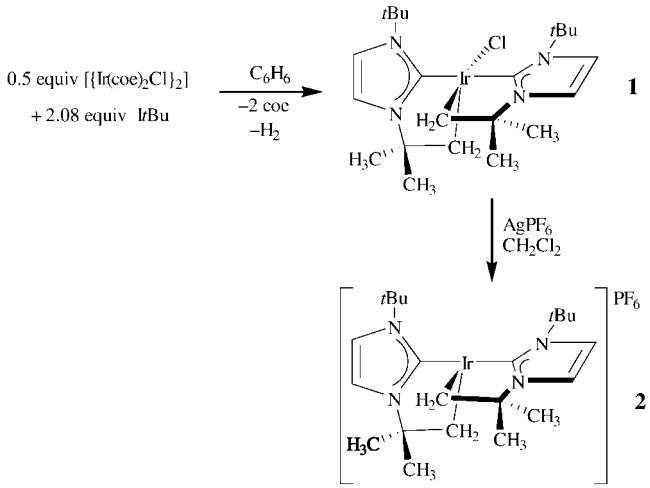

Scheme 1. Synthetic routes to **1** and **2**.

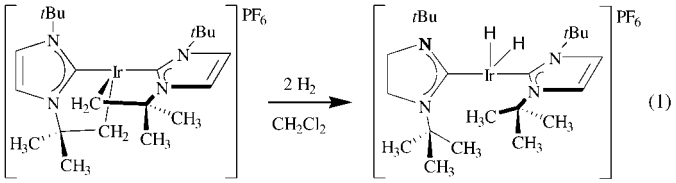

studies were grown by slow evaporation from a dichloromethane/pentane solution. The structure determination confirmed that **3** was the stable electron-deficient iridium(III) dihydride complex $[Ir(I\mathit{t}Bu)_2(H)_2](PF_6)$ (Figure 1).[8,9]

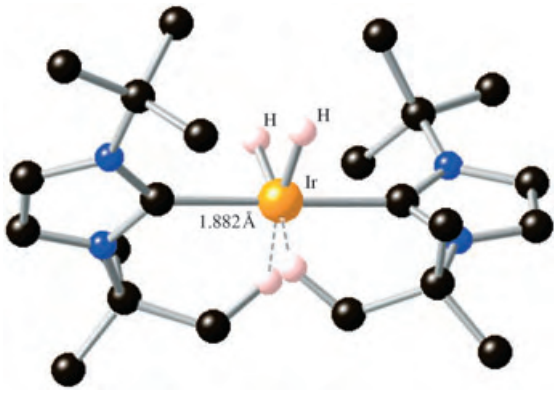

Figure 1. Ball-and-stick representation of $[Ir(I\mathit{t}Bu)_2(H)_2](PF_6)$ (**3**). The PF_6 counterion is omitted for clarity.

The solid-state structure possesses a twofold rotation axis and clearly shows a double agostic interaction between the *t*butyl groups and the iridium center with distances of 2.653 and 1.882 Å for each agostic interaction (Ir–C9 and Ir–H9A, respectively). The four-coordinate Ir^{III} complex adopts a pseudooctahedral environment with two vacant sites in a *cis* arrangement with the carbenic carbon atoms *trans* to each other but *cis* to the two *cis* hydride ligands. Furthermore, the two *cis* vacant positions are sterically protected by two agostic interactions with the nearby *t*butyl group. The structure of **3** provides a rare example of a "proposed" intermediate for an intramolecular C–H activation process. The I*t*Bu ligand apparently provides a unique stabilizing effect in coordinatively unsaturated iridium complexes.[10]

The X-ray structure of **3** indicates the presence of a double agostic interaction, but the NMR spectrum at ambient temperature indicates a highly symmetrical structure. The ^{1}H NMR spectra that were recorded over a range of temperatures (175–300 K) to probe for agostic interactions in solution revealed interesting dynamic behavior (Figure 2).

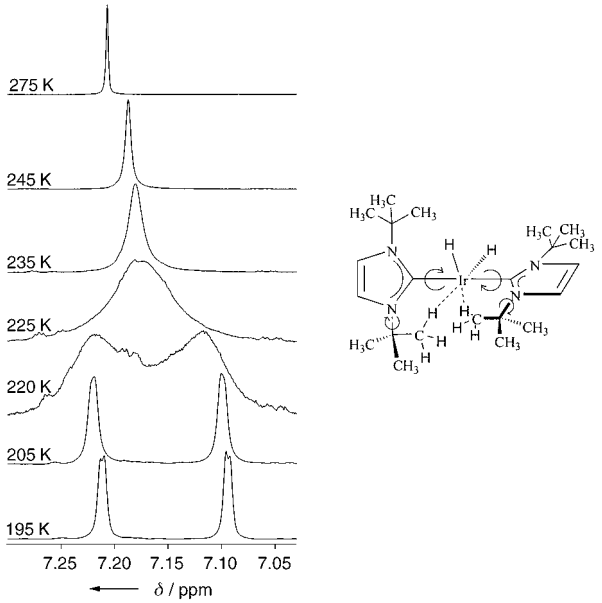

Figure 2. Imidazole region of the variable-temperature ^{1}H NMR spectra of **3** (500 MHz, CD_2Cl_2).

A dynamic process is frozen out at low temperature, which leads to two distinct environments for the *t*butyl and imidazole moieties. We attribute the appearance of the low-temperature spectra to a lower symmetry structure consistent with the solid-state structure. The switching of the *t*butyl groups between their free environments and undergoing agostic interactions is responsible for the changes in the NMR spectra with temperature (Figure 2). Lineshape analysis reveals that this process has $\Delta H^{\ddagger} = 7.68$ kcal mol^{-1}, $\Delta S^{\ddagger} = -11$ cal mol^{-1} per degree, and $\Delta G^{\ddagger}_{215} = 10.0$ kcal mol^{-1} thermodynamic parameters.

Reaction of **2** with D_2 gas was expected to lead to $[D_4]$**3** with D atoms incorporated in the hydride ligand and cyclometalated alkyl positions, in a manner analogous to the reaction of **2** with H_2 gas. Interestingly, rapid incorporation of D atoms into other *t*butyl C–H bonds was also observed. Extended exposure of **2** to D_2 gas led to complete deuteration in both the hydride ligands and the *t*butyl groups. Complex **3** can be completely regenerated by treatment with H_2 gas, which demonstrates that this D-atom exchange is fully reversible. A partially deuterated sample showed a very

 © 2005 Wiley-VCH Verlag GmbH & Co. KGaA, Weinheim

interesting range of 18 distinct resonances in the hydride region of the NMR spectrum from $\delta = -29.0$ to -29.15 ppm (an approximate span of 80 ppb; Figure 3).

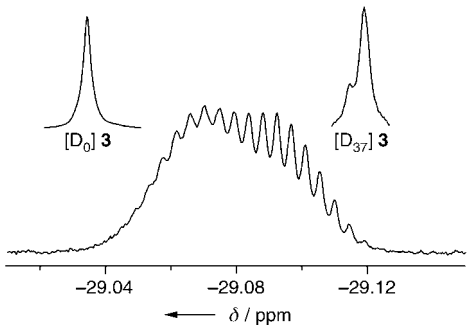

Figure 3. Partial ^{1}H NMR spectrum of [D$_n$]**3** (750 MHz, 298 K, CD_2Cl_2).

Experiments at different fields confirmed that none of these splittings arise from H–D coupling. We surmise that the 18 different resonances result from all the possible isotopomers of the two different deuterated *t*butyl groups. Two agostic interactions in **3**, with rapid equilibration of all C–H (C–D) bonds, are necessary for this conclusion to be correct. Our observations also require an unusual secondary-isotope effect on the chemical shift of a hydride ligand; however, the result of this isotope effect depends on whether the agostic interaction *trans* to the hydride ligand involves a C–H bond or a C–D bond. These interactions are rapidly averaged over all 18 C–H (C–D) bonds, thus leading to the resonance pattern in the NMR spectrum, with upfield shifts of approximately 5 ppb per deuterium center. These observations provide conclusive evidence that the double agostic interaction in the solid state is maintained in solution.

The highly unsaturated nature of **3** results in its rapid reaction with CO to form the previously reported dicarbonyl complex $[Ir(I\mathit{t}Bu')_2(CO)_2](PF_6)$.[6] Presumably, this complex is formed through intramolecular C–H activation and elimination of two equivalents of dihydrogen [Eq. (2)].[11]

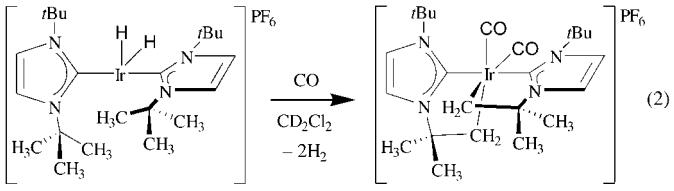

3 (2)

The reactivity of the presented iridium/N-heterocyclic carbene (NHC) system is unique[12] as its behavior is in stark contrast to that displayed by the iridium/phosphine system $[IrH(\eta^2\text{-}P\mathit{t}Bu_2Ph)(P\mathit{t}Bu_2Ph)][BAr'_4]$ ($Ar' = 3,5\text{-}(CF_3)_2C_6H_3$),[10] The iridium/phosphine system does not simply react with dihydrogen to form a dihydride complex but further reacts with H_2 gas to yield the 16-electron complex $[Ir(H)_2(H_2)(P\mathit{t}Bu_2Ph)_2][BAr'_4]$, which is observed at low temperature but is easily converted into $[Ir(H)_2(H_2)_2(P\mathit{t}Bu_2Ph)_2][BAr'_4]$ at higher temperature. No such dihydrogen binding is observed when **3** is subjected to atmospheric, or higher, pressures of H_2 gas. This lack of reactivity with excess H_2 gas to form a dihydrogen complex is further evidence of the strength of the agostic interactions within this electron-deficient Ir^{III} system in solution.

We performed a similar hydrogenation reaction with the related 14-electron rhodium(III) complex $[Rh(I\mathit{t}Bu')_2](PF_6)$.[13] Low-temperature NMR spectroscopic studies revealed the formation of a new hydride species; however, unlike **3**, the new hydride species has proven elusive and decomposes during attempted isolation. This instability may be associated with weaker M–H bonds in the case of rhodium complexes and nonoptimal positioning of the *t*butyl groups in the coordination sphere of the metal center, thus leading to weak agostic stabilization of the complex. Further exploration of the stabilization effects in this Rh system and other related Rh systems is ongoing.

We have described a remarkable electron-deficient cationic dihydride complex $[Ir(I\mathit{t}Bu)_2(H)_2](PF_6)$ (**3**) generated in high yield from reaction of a 14-electron complex $[Ir(I\mathit{t}Bu')_2](PF_6)$ (**2**) and H_2 gas. The reaction illustrates the reversibility of a double, intramolecular C–H activation process. Solid-state structural and low-temperature NMR spectroscopic studies involving **3** show a rare double agostic interaction present in a dihydride complex. Furthermore, reaction of **2** with D_2 gas did not lead to the expected [D$_4$]**3** compound but rather to complete deuteration of the hydride ligands and *t*butyl groups. Work is currently underway to exploit this specific reaction and invesitgate the action of **3** and its precursors in intermolecular substrate activation and functionalization.

Received: December 20, 2004
Published online: March 22, 2005

Keywords: agostic interactions · C–H activation · carbene ligands · coordination modes · iridium

[1] a) J. P. Collman, L. S. Hegedus, J. R. Norton, R. G. Finke in *Principles and Applications of Organotransition Metal Chemistry*, University Science, Mill Valley, CA, **1987**; b) W. A. Hermann, B. Cornils, *Angew. Chem.* **1997**, *109*, 1074–1095; *Angew. Chem. Int. Ed. Engl.* **1997**, *36*, 1048–1067.

[2] a) R. H. Crabtree, *Acc. Chem. Res.* **1990**, *23*, 95–101; b) G. Zassinovich, G. Mestroni, S. Gladiali, *Chem. Rev.* **1992**, *92*, 1051–1069; c) H. M. Lee, T. Jiang, E. D. Stevens, S. P. Nolan, *Organometallics* **2001**, *20*, 1255–1258; d) B. A. Arndtsen, R. G. Bergman, T. A. Mobley, T. H. Peterson, *Acc. Chem. Res.* **1995**, *28*, 154–162, and references therein; e) B. A. Arndsten, R. G. Bergman, *Science* **1995**, *270*, 1970–1973.

[3] a) S. H. Strauss, *Chem. Rev.* **1993**, *93*, 927–942; b) D. Huang, J. C. Huffman, W. E. Streib, J. C. Bollinger, O. Eisenstein, K. G. Caulton, *J. Am. Chem. Soc.* **1997**, *119*, 7398–7399; c) A. C. Cooper, E. Clot, J. C. Huffman, W. E. Streib, F. Maseras, O. Eisenstein, K. G. Caulton, *J. Am. Chem. Soc.* **1999**, *121*, 97–106; d) W. Baratta, E. Herdtweck, P. Rigo, *Angew. Chem.* **1999**, *111*, 1733–1735; *Angew. Chem. Int. Ed.* **1999**, *38*, 1629–1631; e) M. Brookhart, L. H. Green, L.-L. Wong, *Prog. Inorg. Chem.* **1988**, *36*, 1–124; f) S. S. Stahl, J. A. Labinger, J. E. Bercaw, *Angew.*

 © 2005 Wiley-VCH Verlag GmbH & Co. KGaA, Weinheim

Chem. **1998**, *110*, 2298 – 2311; *Angew. Chem. Int. Ed. Engl.* **1998**, *37*, 2181 – 2192.

[4] G. J. Kubas, *Metal Dihydrogen and σ-Bond Complexes: Structure, Theory and Reactivity*, Kluwer, New York, **2001**.

[5] a) R. Dorta, R. Goikhman, D. Milstein, *Organometallics* **2003**, *22*, 2806 – 2809; b) A. C. Cooper, W. E. Streib, O. Eisenstein, K. G. Caulton, *J. Am. Chem. Soc.* **1997**, *119*, 9069 – 9070; c) A. C. Cooper, E. Clot, J. C. Huffman, W. E. Streib, F. Maseras, O. Eisenstein, K. G. Caulton, *J. Am. Chem. Soc.* **1999**, *121*, 97 – 106.

[6] N. M. Scott, R. Dorta, L. Cavallo, E. D. Stevens, S. P. Nolan, *J. Am. Chem. Soc.*, **2005**, *127*, in press.

[7] **3**: A 500-mL Fischer–Porter vessel was charged with [Ir(I*t*-Bu′)$_2$](PF$_6$) (200 mg, 0.280 mmol) and dichloromethane (20 mL) in a glovebox. The vessel was taken out of the box, connected to a Schlenk line, and pressurized with H_2 gas (2.5 atm). The solution was then stirred for 3 days. The solvent volume was reduced to 3 mL and then pentane (10 mL) was added, which resulted in the immediate precipitation of a pale-yellow solid. The supernatant solution was decanted and the solid washed with pentane (3 × 5 mL) and dried in vacuo (186 mg, 95 % yield). ^{1}H NMR (750 MHz, CD_2Cl_2): $\delta = 7.18$ (s, 4H, CH-imidazole), 1.55 (s, 36H, $(CH_3)_3$), −29.03 ppm (s, 2H, H); ^{31}P NMR (161.90 MHz, CD_2Cl_2): $\delta = -138.67$ ppm (sept, $J = 710.4$ Hz); ^{19}F NMR (376.28 MHz, CD_2Cl_2): $\delta = -72.51$, −74.39 ppm ($J = 710.8$ Hz); ^{13}C NMR (100.56 MHz, CD_2Cl_2): $\delta = 168.14$ (C-carbene), 118.45 (C-imidazole), 58.68 ($C(CH_3)_3$), 29.66 ppm ($C(CH_3)_3$). Elemental analysis (%) calcd for $C_{22}H_{42}N_4F_6PIr$ (699.78): C 37.76, H 6.05, N 8.01; found: C 37.85, H 6.02, N 7.94.

[8] The number of electrons in **3** allows it to be described as a "14-electron" complex if the two M···H agostic interactions are simply considered as occupying the vacant sites in an ideal octahedral-metal environment. This observation is a matter of formalism and the words "electron deficient" are used to eliminate any ambiguity. For a 14-electron ruthenium complex, see: L. Watson, O. V. Ozerov, M. Pink, K. G. Caulton, *J. Am. Chem. Soc.* **2003**, *125*, 8426 – 8427.

[9] Crystal data for **3**: $C_{22}H_{42}F_6IrN_4P$, $M_r = 699.77$, orthorhombic *Pbcn*, $a = 9.8783(5)$, $b = 22.0515(12)$, $c = 12.4453(7)$ Å, 2711.0(3) Å^3, $T = 150(2)$ K, $Z = 4$, $\mu(Mo_{K\alpha}) = 0.711$ mm^{-1}, 23556 reflections collected (1779 independent), $R1$ [$I > 2\sigma(I)$] = 0.0334, $wR2$ (all data) = 0.0608. Towards the end of the refinement, the Fourier difference map showed all the hydrogen atoms associated with the I*t*Bu unit, as well as two peaks in positions consistent with the presence of two hydride ligands, which was in accordance with the NMR spectroscopic analysis. Therefore, the position of all the hydrogen atoms and hydride ligands were refined in the final least-squares cycles without constraints by using an isotropic temperature factor. The refined positional parameters gave an acceptable geometry and were left without correction. CCDC-255338 (**3**) contains the supplementary crystallographic data for this paper. These data can be obtained free of charge from the Cambridge Crystallographic Data Centre via www.ccdc.cam.ac.uk/data_request/cif.

[10] A. C. Cooper, O. Eisenstein, K. G. Caulton, *New J. Chem.* **1998**, *22*, 307 – 309.

[11] Identical ^{1}H, ^{13}C, ^{31}P, and ^{19}F NMR spectroscopic characterization to that already reported for [Ir(I*t*Bu′)$_2$(CO)$_2$](PF$_6$)[6] was obtained.

[12] A T-shaped 14-electron monohydride/platinum system stabilized by one agostic interaction has recently been reported: W. Barrata, S. Stoccoro, A. Doppiu, E. Herdweck, A. Zucca, P. Rigo, *Angew. Chem.* **2003**, *115*, 105 – 108; *Angew. Chem. Int. Ed.* **2003**, *42*, 105 – 108. The Pt(II) center preferentially adopted a 16-electron configuration, which is not the case for the Ir(III) center as it prefers an 18-electron environment.

[13] R. Dorta, E. D. Stevens, S. P. Nolan, *J. Am. Chem. Soc.* **2004**, *126*, 5054 – 5055.

 © 2005 Wiley-VCH Verlag GmbH & Co. KGaA, Weinheim

Structure Elucidation

Structural Studies of the System Na(saccharinate)·n H_2O: A Model for Crystallization**

*Rahul Banerjee, Prashant M. Bhatt, Michael T. Kirchner, and Gautam R. Desiraju**

Saccharin (*o*-sulfobenzimide; Hsac) and its salts have been used as sweeteners for 125 years.[1–3] Current annual worldwide consumption of sodium saccharin dihydrate, Na(sac)·2 H_2O (**1**, also referred to as soluble saccharin, saccharinum soluble, and crystallose) exceeds 30000 tons. The substance is 500-times sweeter than sucrose and finds extensive use as a noncalorific tabletop sweetener, in foods and beverages, in personal care products, and in a variety of nonfood applications. It is one of the most thoroughly tested of food ingredients and has the approval of the WHO (World Health Organization) after a century of safe use. During the course of recent work on the use of sac in pharmaceutical chemistry,[4] we determined the crystal structure of dihydrate **1**. This complex structure exhibits several unusual features, which could have implications for the mechanism of crystallization and which justify the consideration of crystallization as a supramolecular reaction.

The first unusual feature is that the structure of a highly crystalline small-molecule compound, which was first isolated in 1887, was not determined until 2004. Were earlier attempts made in this direction, and did they prove to be infructuous? Or were no attempts made? Was the structure determined in an industrial laboratory, but not published? It is difficult to examine such questions a posteriori, but it is known that Jovanovski and Kamenar crystallized **1** (prepared from sac and aqueous Na_2CO_3 by the method of Defournel[3]) from EtOH and determined the structure of the resultant triclinic hydrate, $Na_3(sac)_3$·2 H_2O (**2**).[5] Naumov et al., who crystallized **1** from water,[6] according to the method of Jovanovski et al.,[7] and obtained what they termed "another monoclinic form", further stated that "this (monoclinic) hydrate contains more than two molecules of water per formula unit and, therefore, cannot be considered a dihydrate". We obtained **1** routinely by crystallization of the commercial sample from water; indeed the commercial sample is identical to **1**, and crystals could also be selected easily from the commercial sample for X-ray crystallographic studies.

[*] R. Banerjee, P. M. Bhatt, Dr. M. T. Kirchner, Prof. G. R. Desiraju
School of Chemistry
University of Hyderabad
Hyderabad 500 046 (India)
Fax: (+91) 40-2301-0567
E-mail: gautam_desiraju@yahoo.com

[**] We thank the UGC for an SRF (R.B.), the CSIR for a JRF (P.M.B.), and the AvH Foundation for a Lynen Fellowship (M.T.K.). Financial assistance from the DST (IRPHA) and the UGC (UPE) is acknowledged.

Supporting information for this article is available on the WWW under http://www.angewandte.org or from the author.

 DOI: 10.1002/anie.200462967 © 2005 Wiley-VCH Verlag GmbH & Co. KGaA, Weinheim

The monoclinic crystals diffract well, and the structure was determined (Figure 1). Strictly speaking, the material is not even a dihydrate, but rather $Na_{16}(sac)_{16}\cdot 30\,H_2O$, which is equivalent to $Na(sac)\cdot 1.875\,H_2O$. The unit cell is large (15614 Å^3 at room temperature, $P2_1/n$, $Z=4$), and the above formula gives the number of species (362 atoms, 238 non-hydrogen atoms) in the crystallographic asymmetric unit. The asymmetric unit is not the largest reported,[8] but is still of substantial size and complexity. The 64 Na^+ cations, 64 sac^- anions, and 120 water molecules in the unit cell make this crystal structure one of the largest and most complex ever for ions/molecules that are as small and simple as these. Figure 1 shows that the structure may be demarcated into "regular" and "irregular" regions. In the regular domain, the saccharinate anions are nearly parallel and stacked, the Na^+ ions are hexacoordinated with water and sac^-, and the water molecules are efficiently hydrogen bonded. In the irregular region, there is disorder of sac^-, Na^+ (some of which is not necessarily hexacoordinated), and water (some of which is ill-resolved). The solution and refinement of the structure and the modeling of the disorder were not trivial, and we began to appreciate why perhaps this structure had remained undetermined for so long. However, the X-ray data obtained by us were good and extended to high resolution ($2\theta=52°$), there was no suggestion of modulation or superstructures, and with an R value of 0.045 and a satisfactory modeling of the disorder, we are confident of the quality of our analysis.[9]

The regular region of the structure consists of ten sac^- anions, which are arranged in a stack of five water-bridged hydrogen-bonded pairs, with an average plane···plane perpendicular distance of 3.69 Å (Figure 1). Two water molecules are involved in each saccharinate pair through strong O–H···N$^-$ hydrogen bonds ($d=2.85$ Å and $\theta=165.8°$). Cross-linking of the pairs occurs with octahedrally coordinated Na^+ ions (mean Na^+···O distance: 2.39 Å). The result is a compact, finite arrangement of sac^-, Na^+, and water molecules in the form of three supramolecular cubes and two half-cubes. Further connections with Na^+ and water in an elaborate network of hydrogen bonds and Na^+···O interactions complete the arrangement (see Supporting Information). In the irregular region, the six sac^- anions are no longer parallel. They, along with Na^+ and water, are positionally and/or orientationally disordered (see Supporting Information). There is a variation in the occupancies of these species from crystal to crystal and possibly between one temperature and another. All in all, we carried out structure determinations of four crystals at four different temperatures (total eight data sets collected at 100, 150, 200, and 298 K). The overall conclusion is that there is appreciable mobility of the species in this irregular region which leads to the second unusual feature of this crystal structure: A part of the structure, the regular region, resembles a conventional crystal, but another and adjacent part, the irregular region, has solution-like characteristics. We consider the structure to be in a state of "incipient crystallization".

The third unusual feature of structure **1** is that it can exist in equilibrium with water (Figure 2). When a crystal is placed in the proximity (10–12 mm) of a single drop of water in a

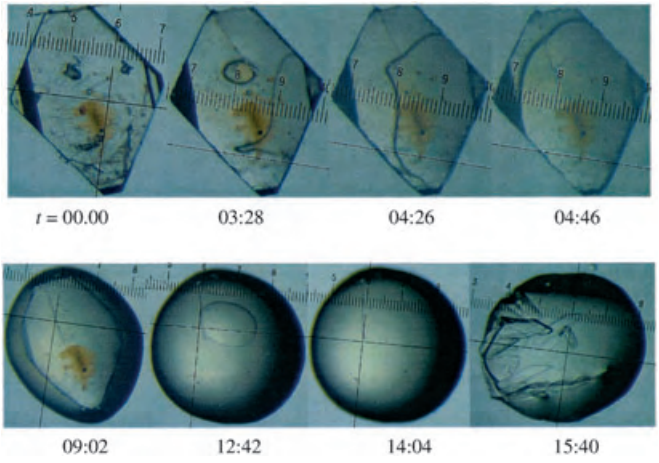

Figure 2. Rapid dissolution and recrystallization of dihydrate **1** in an environment saturated with water vapor (time recorded in minutes after closing the petri dish).

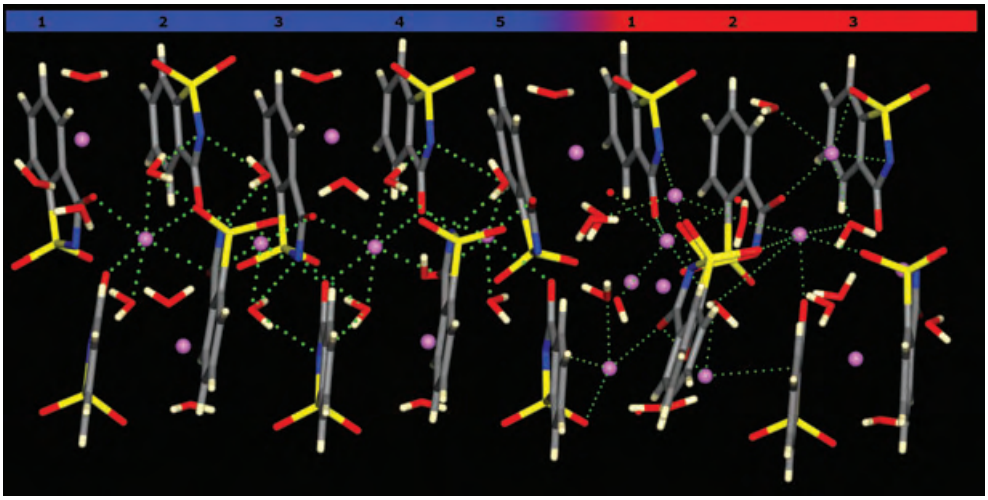

Figure 1. Crystal structure of dihydrate **1** (Na pink, O red, N blue, S yellow, C gray, H cream). The regular regions are on the left side, and the irregular regions are on the right. Note the finite supramolecular cube arrangement. The saccharin residues are numbered.

 © 2005 Wiley-VCH Verlag GmbH & Co. KGaA, Weinheim

closed environment (in a covered petri dish), it absorbs water rapidly (1–5 min). Further exposure to the vapor (5–15 min) results in dissolution of the crystal and is followed by rapid recrystallization if the water-saturated environment is absent (cover of petri dish removed). A crystal of **1** for which X-ray data were collected was exposed to water vapor for approximately 10 minutes and then remounted onto the diffractometer for data collection. Although the crystal shape was considerably altered, data collection proceeded normally and the structure obtained was as observed prior to this "watering" treatment. Interestingly, the orientations of the crystal axes before and after treatment with water do not differ by more than 3°, which indicates that this is not a case of dissolution and recrystallization, but rather that the crystal of **1** is bathed in the adhering saturated solution as shown in Figure 2.[10] The very easy solubility of **1** in water, the retention of crystallinity of the "watered" crystal, and the rapid recrystallization of the just-dissolved crystal, when taken along with the high water content of **1** and the presence of the irregular disordered domains in it indicate a crystal that is very close to the dissolution point. We note that the solubility of hydrate **1** at 27 °C is 120.3 g in 100 g water.[11] This is equivalent to a stoichiometry of Na(sac)·13 H_2O. Accordingly, the saturated solution of the substance contains only about seven times the amount of water as crystalline **1**.

The fourth unusual feature of crystalline **1** is that it also loses water readily. It is remarkable that a solid which is so deliquescent in a water-rich environment is so efflorescent in a water-deficient environment (dry N_2 flow, heating, standing in the open in the typically dry Hyderabad climate). TGA (thermogravimetric analysis) and DSC (differential scanning calorimetry) studies of **1** were carried out (see Supporting Information), and water loss was observed to occur in two stages. The first stage begins as low as 35 °C and is essentially complete by 50 °C to yield the Jovanovski–Kamenar hydrate **2**, the structure of which is shown in Figure 3 b. This structure was confirmed by X-ray powder diffraction studies. The second stage (**2** to anhydrate) occurs between 100 and 115 °C. The crystal structure of the anhydrate has not been reported hitherto. We obtained crystals by cooling a melt of the commercial sample, but these crystals were small and poorly diffracting, and the structural model we obtained (Figure 3 d) is of necessarily limited accuracy ($R = 0.19$). However, this model was confirmed with Rietveld refinement of the coordinates obtained in the single-crystal study against the X-ray powder spectrum of the anhydrate (see Supporting Information).[12] The resemblance of the packing of the anhydrate to that of hydrate **2** also provides confirmation of its structure.

A mixed Na/K water-deficient hydrate, $NaK_2(sac)_3 \cdot H_2O$ (**3**) has also been reported (Figure 3 c).[13] This structure has not been obtained for sodium saccharinate, but adopting the idea of a packing landscape,[14] we believe that it is a good model for the putative $Na_3(sac)_3 \cdot H_2O$. Finally, we obtained a potassium saccharinate salt $K_3(sac)_3 \cdot 2.33\,H_2O$ (**4**) when we crystallized a mixture of sac and K_2CO_3 from water.[15] The structure of **4** is shown in Figure 3 a, and in keeping with the theme of a packing landscape for the system Na(sac)·n H_2O, it would be a very good model for a water-rich pseudopolymorph of hydrate **2**. In summary, the four structures listed

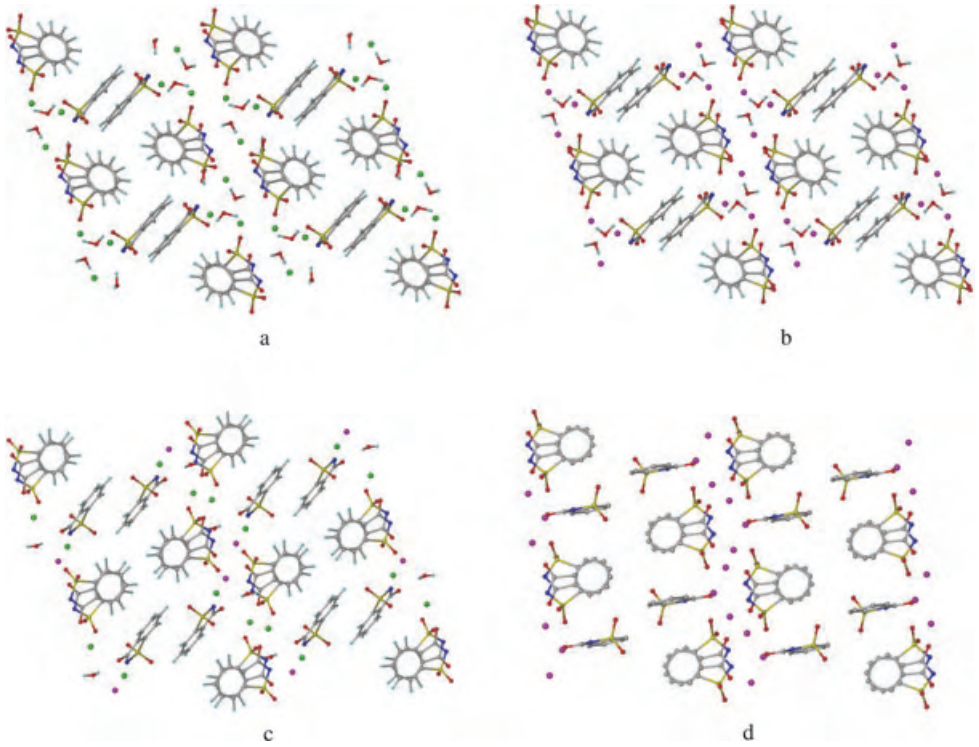

Figure 3. Packing landscape in the system (Na/K)(saccharinate)·n H_2O: a) Water-rich $K_3(sac)_3 \cdot 2.33\,H_2O$ (**4**), b) Jovanovski–Kamenar hydrate, $Na_3(sac)_3 \cdot 2\,H_2O$ (**2**), c) water-deficient $NaK_2(sac)_3 \cdot H_2O$ (**3**), and d) anhydrate Na(sac). Note the similarity in packing in these cases. Na^+/K^+ ions are shown as pink/green solid spheres.

 © 2005 Wiley-VCH Verlag GmbH & Co. KGaA, Weinheim

above (**2**, **3**, **4**, and anhydrate) are all very similar. In every case, the positions of Na^+/K^+ and sac^- ions are nearly the same and there are variable amounts of water, ranging from 0.78 molecules of water per formula unit of metal saccharinate in **4**, to 0.66 H_2O in hydrate **2**, to 0.33 H_2O in the mixed Na/K hydrate **3**, to zero in the anhydrate. The structure of dihydrate **1**, which has 1.875 formula units of water per formula unit of sodium saccharinate, is quite different from these four structures, which constitute a related set. Therefore, the transformation of structural significance is the loss of water from **1** to give the Jovanovski–Kamenar hydrate **2**.

Inspection of the crystal structures of **1** and **2** (Figure 3 and Figure 4) shows that while the sac^- residues in **1** are all nearly parallel, those in **2** occur in two groups that are

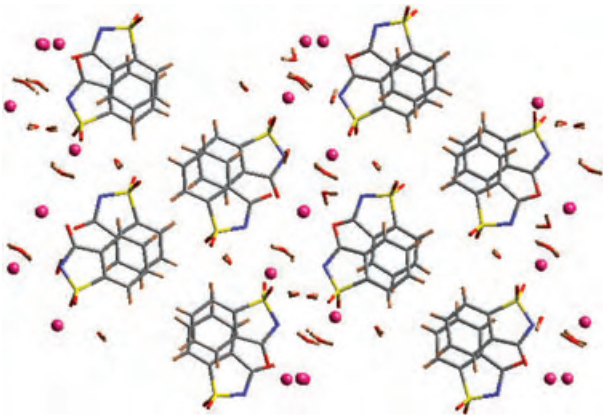

Figure 4. Crystal structure of dihydrate **1** looking down the stacking direction.

perpendicular to each other. The stacking of residues in the infinite stack down [001] bears a close resemblance to that in the regular domains of hydrate **1**. The residues that occur as discrete dimers in **2**, perpendicular to the infinite stack, are in a stoichiometry that is half that of the residues in the infinite stack. This 2:1 stoichiometry of residues in **2** is reminiscent of the 5:3 demarcation of sac^- residues in the regular and irregular regions of dihydrate **1** and suggests a possible mechanism for the conversion **1**→**2**.[16] Water loss from the infinite channels in water-rich **1** would allow for relative motion between stacks. While the regular domains are largely conserved,[17] the residues in the irregular domains might move into the empty regions created by the loss of water and also assume a perpendicular geometry. The cartoon depiction of events (Figure 5) is a good possibility because we propose that maximum movement of residues occurs in those regions of **1** where the arrangement is the least regular and where molecular motion is already expected to be facile.[18] Furthermore, we note that selected supramolecular synthons in dihydrate **1** are retained in the Jovanovski–Kamenar hydrate. The stacked synthons in the regular domains of **1** are preserved as mentioned above. Hydrogen-bonded synthons in the irregular domains of **1** are also conserved in **2** (Figure 6). The fact that these synthons are carried over into **2**, even as there is much structural reorganization, is in

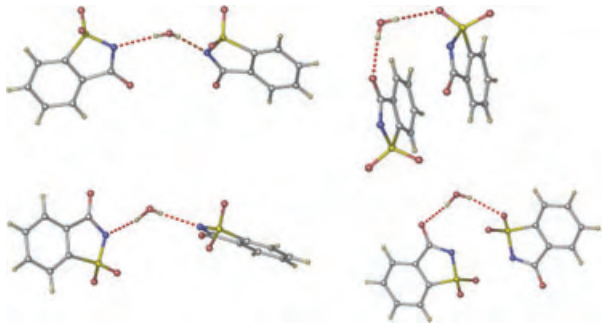

Figure 6. Conserved supramolecular synthons in dihydrate **1** (top) and the Jovanovski–Kamenar hydrate **2** (bottom).

keeping with the idea of synthons as kinetically significant units that are preserved through all stages of crystallization.[19]

Crystallization may be viewed as a supramolecular reaction, with nucleation likened to the transition state. The formation of a crystal from solution exemplifies a shift of the enthalpy–entropy balance. From the entropy-dominated situation in solution, order enters the putative crystal through the formation of a liquidlike cluster of solvent and solute.[20] The nucleation step is presumably accompanied by a critical increase in order and an entropically driven expulsion of solvent from the cluster into the bulk solution to yield the first crystals. Such a model explains why the majority of crystals of organic molecules do not contain solvent molecules of crystallization, unless there are specific enthalpic reasons

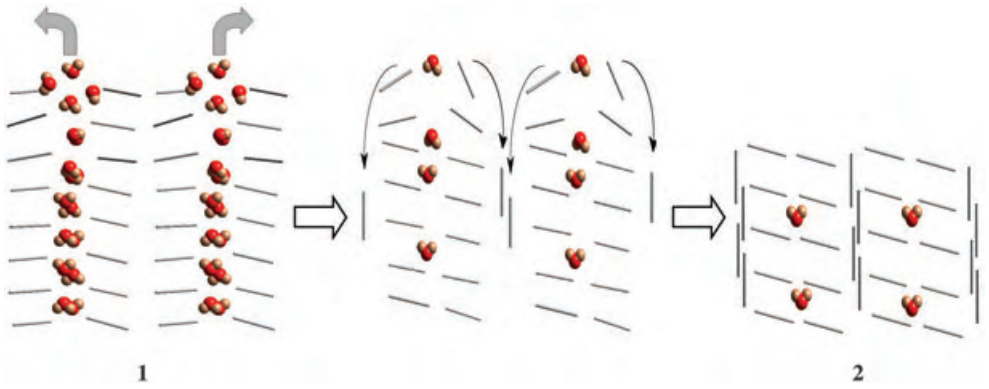

Figure 5. Transformation between hydrates, **1**→**2**. Note that all sac^- anions are nearly parallel in **1**, whereas they adopt two orientations in **2**.

 © 2005 Wiley-VCH Verlag GmbH & Co. KGaA, Weinheim

(hydrogen bonds, close packing) for solvent inclusion.[21] A crystal, in turn, represents the optimization of enthalpic factors through favorable intermolecular interactions. The appearance of certain robust interaction patterns, or supramolecular synthons, in crystal structures suggest that these patterns are kinetically favored, and they make their appearance even in the early stages of crystallization. It is instructive to view the crystal structure of **1** from the above viewpoint.

The structure of **1** is a good model for nucleation in the crystallization of the Jovanovski–Kamenar hydrate from water. Note that direct observation of a crystal nucleus through static diffraction methods will be difficult. A nucleus (like a transition state) is a high-energy intermediate, and it will only be possible to deduce ideas about its structure indirectly. However, there is enough in the structure of **1** that is unusual for us to believe that it represents as good an approximation of what a crystal nucleus looks like, as can be obtained presently. First, the unit cell and asymmetric unit are large. A large unit cell, in itself, is unexceptional, but for crystals in which the building blocks (molecules, ions, and solvent) are so small, such a large unit cell is noteworthy. A similar situation is obtained in the giant molybdate clusters studied by Müller and co-workers,[22] and one of us has stated elsewhere that the isolation of these structures provides a closer look at crystallization events.[23] We searched the Cambridge Structural Database for large unit cells and found 592 hits for which the volume of the unit cell is greater than 10000 $Å^3$. Of these, only a handful correspond to cases in which small molecules adopt low-symmetry space groups (typical examples are MACCID02, QOWDIP, and QULKOX). Dihydrate **1**, is therefore distinctive.

Second, the contents of the entire unit cell are not neatly organized, and there are regular and less-regular domains. One could even describe the irregular regions as "messy". The combination of these two events (large unit cell, regular and irregular domains) and also the excessive amount of solvent in the crystal is very suggestive of a crystallization reaction still in progress. Third, dihydrate **1** is evenly poised between solution and hydrate **2**. To our knowledge, there is no other reported example of a substance that gains and loses solvent so very easily. There is not much difference in water content between crystalline **1** and the saturated solution. Amazingly, the same compound loses water at 35 °C, and the resulting hydrate **2** does not gain water when exposed to the vapor. Once again, easy gain or loss of water would, in itself, be unexceptional. When it occurs for the same substance, it becomes significant and suggests that **1** is a bridge between the saturated solution and the stable Jovanovski–Kamenar hydrate; in other words, it is closer to the crystal nucleus of **2** than either of the extremes.

It is useful to consider just why this complex structure is even isolated. The finite supramolecular cube arrangement and the variation in the cube edges (2.312–2.595 Å) provide a hint. It is possible that the geometrical requirements for stacking of aromatic residues are not exactly in accord with the octahedral coordination of Na^+ ions (Figure 1), but it is clear that both these unconnected events are required to sustain the cube architecture. Accordingly, the regular domain cannot extend infinitely (if it did, **1** would become an ordinary, even somewhat commonplace, crystal). In trying to maintain the ring stacking, the Na^+ coordination is compromised or vice versa and the result is a blend of regular and irregular regions.[24] The regular regions, however, become the major portion of crystalline **2**, while the irregular regions undergo further evolution. This is a thermodynamic argument. On the kinetic side, it could be asserted that the main reason that one even observes a structure such as **1** is because the solvent involved is water. Enough has been said elsewhere about the ability of this remarkable solvent to sustain elaborate patterns of molecular recognition.[25] We have noted here that it plays a significant, even crucial, role in the supramolecular interactions in **1**. The energetics of these water interactions, to both sac^- and Na^+, may be sufficient to stabilize this essentially metastable species.

The liquidlike cluster of solvent and solute that precedes nucleation should contain solvent–solvent, solvent–solute, and solute–solute interactions. We note, however, that dihydrate **1** does not contain a single hydrogen bond between two water molecules. In keeping with the idea of crystallization as a supramolecular reaction and our description of dihydrate **1** as a supramolecular transition state, or at least a high-energy reaction intermediate, we apply the Hammond Postulate and conclude that **1** is an example of a late transition state. Large regions of **1** resemble the structure of **2**, and there are no solvent–solvent interactions. Elements of order have entered the crystal nucleus, the important supramolecular synthons are in place, if not exactly in the correct locations, and the product of crystallization (hydrate **2**) is a kinetic product. It is still a matter of conjecture that early transition-state crystal nuclei will have solution-like character and that they will lead to thermodynamic products (perhaps hydrate **3** or the anhydrate).

In conclusion, we have determined the crystal structure of the long-known sodium saccharinate dihydrate (**1**). This metastable structure relates both to solution and to the more-stable crystalline sodium saccharinate hydrates **2**–**4** and the anhydrate. It is truly ironic that a substance as unusual as **1** has been available on a scale of hundreds of tons for over a century, but has remained structurally uninvestigated until now. It is exceptional that a species which is in such delicate equilibrium with the solution is able to diffract so well. We believe that this property is because of the rigidity that is imparted to the system by several hydrogen bonds and $Na^+\cdots O$ interactions formed by water.[26] Indeed, the very existence and easy observation of this unique structure owe to the presence of the large excess of water in the crystal. We suggest that some degree of long-range order, essential for crystallinity, is already present in crystal nuclei, at least in those that correspond to late supramolecular transition states. In summary, dihydrate **1** appears to be a good model for the structure of a nucleus in the crystallization reaction.[27]

Received: December 16, 2004
Published online: March 22, 2005

Keywords: hydrogen bonds · nucleation · saccharin · transition states · water

 © 2005 Wiley-VCH Verlag GmbH & Co. KGaA, Weinheim

[1] C. Fahlberg, I. Remsen, *Ber. Dtsch. Chem. Ges.* **1879**, *12*, 469.
[2] C. Fahlberg, R. List, *Ber. Dtsch. Chem. Ges.* **1887**, *20*, 1597.
[3] M. H. Defournel, *Bull. Soc. Chim. Fr.* **1901**, *25*, 322.
[4] P. M. Bhatt, N. V. Ravindra, R. Banerjee, G. R. Desiraju, *Chem. Commun.* **2005**, 1073.
[5] G. Jovanovski, B. Kamenar, *Cryst. Struct. Commun.* **1982**, *11*, 247.
[6] P. Naumov, G. Jovanovski, S. Abbrent, L. Tergenius, *Thermochim. Acta* **2000**, *359*, 123.
[7] G. Jovanovski, O. Grupče, B. Šoptrajanov, *J. Mol. Struct.* **1990**, *219*, 61.
[8] S. E. Lister, I. R. Evans, J. A. K. Howard, A. Coelho, J. S. O. Evans, *Chem. Commun.* **2004**, 2540.
[9] Crystal data: Hydrate **1**, $Na_{16}(C_7H_4NO_3S)_{16}(H_2O)_{30}$, monoclinic, $P2_1/n$, $a = 18.5918(11)$, $b = 28.3628(16)$, $c = 29.0562(16)$ Å, $\beta = 93.560(2)°$, $V = 15291.7(15)$ Å^3, $Z = 4$, $T = 100(2)$ K, $\mu = 0.381$ mm^{-1}, 105833 reflections measured, 30081 independent, 21746 observed ($I > 2\sigma(I)$), 2385 parameters, $R1 = 0.0448$, $wR2 = 0.0719$ (for $I > 2\sigma(I)$). Hydrate **4**, $K_3(C_7H_4NO_3S)_3\cdot(H_2O)_{2.33}$, triclinic, $P\bar{1}$, $a = 7.6104(5)$, $b = 12.3049(8)$, $c = 15.4936(10)$ Å, $\alpha = 72.2780(10)$, $\beta = 86.5810(10)$, $\gamma = 81.2290(10)°$, $V = 1365.75(5)$ Å^3, $Z = 2$, $T = 298$ K, $\mu = 0.794$ mm^{-1}, 22602 reflections measured, 5369 independent, 5029 observed ($I > 2\sigma(I)$), 410 parameters, $R1 = 0.0312$, $wR2 = 0.0879$ (for $I > 2\sigma(I)$). Intensity data were collected on a Bruker Nonius Smart Apex CCD with graphite monochromated $Mo_{K\alpha}$ radiation at 100 K and 298 K. The structures were solved by direct methods and refined anisotropically by full-matrix least-squares method using the Shelxtl 6.14 software package. CCDC 258588 and 258589 contain the supplementary crystallographic data for this paper. These data can be obtained free of charge from the Cambridge Crystallographic Data Centre via www.ccdc.cam.ac.uk/data_request/cif.
[10] In hindsight, it is not clear if Naumov et al.[6] had examined (inadvertently) "watered" crystals when they stated that the dihydrate contains more than two molecules of water in the formula unit.
[11] M. L. Mitchell, R. L. Pearson, *Alternative Sweeteners* (Eds.: L. Nabors, R. C. Gelardi), Marcel Dekker, New York, **1991**. pp. 127–156.
[12] The Rietveld refinement was carried out with the program Powder Cell[2.3]. The refined coordinates are given in the Supporting Information.
[13] K. M. A. Malik, S. Z. Haider, M. A. Hossain, *Acta Crystallogr. Sect. C* **1984**, *40*, 1696.
[14] N. Blagden, R. J. Davey, *Cryst. Growth Des.* **2003**, *3*, 873.
[15] We performed this experiment to ascertain if a potassium analogue of dihydrate **1** could be obtained. It is hardly surprising that we could not and adds to the body of evidence which suggests that the structure of **1** is truly unusual. The water stoichiometry of 2.33 in this potassium salt, **4**, contrasts with the results of Jovanovski et al. (G. Jovanovski, B. Kaitner, O. Grupce, P. Naumov, *Cent. Eur. J. Chem.* **2004**, *2*, 254), who report the structure of $K_3(sac)_3\cdot 2H_2O$.
[16] In hindsight, it would appear that recrystallization of the commercial compound from EtOH by Jovanovski and Kamenar caused partial dehydration to **2**.
[17] Careful inspection of the packing diagrams will show that the registry of molecules in the stack changes in the conversion **1**→**2**, such that paired molecules in **1** have the SO_2 groups on the same side, while in **2** each pair has an SO_2 and a CO group on the same side. However, there is much reorganization in the transformation and we believe that such a registry change can be easily accomplished.
[18] This is strongly reminiscent of the dehydration mechanism in α-lactose monohydrate, see: S. Garnier, S. Petit, G. Coquerel, *J. Therm. Anal. Calorim.* **2002**, *68*, 489.
[19] G. R. Desiraju, *Stimulating Concepts in Chemistry* (Eds.: F. Vögtle, J. F. Stoddart, M. Shibasaki), Wiley-VCH, Weinheim, **2002**.
[20] G. R. Desiraju, *Nature* **2003**, *423*, 485.
[21] A. Nangia, G. R. Desiraju, *Chem. Commun.* **1999**, *7*, 605.
[22] a) A. Müller, S. Q. N. Shah, H. Bögge, M. Schmidtmann, *Nature* **1999**, *397*, 48; b) T. Liu, E. Diemann, H. Li, A. W. M. Dress, A. Müller, *Nature* **2003**, *426*, 59.
[23] G. R. Desiraju, *Nature* **2001**, *412*, 397.
[24] Our failure to obtain the potassium analogue of **1** supports this notion, but it is hardly proof. One might suggest that the K analogue occurs en route to crystals of **4**, and that it is a true transition state in contrast to **1**, which could be viewed as a high-energy reaction intermediate.
[25] Selected references include: a) L. J. Barbour, G. W. Orr, J. L. Atwood, *Nature* **1998**, *393*, 671; b) L. Infantes, J. Chisholm, S. Motherwell, *CrystEngComm* **2003**, *5*, 480; c) R. Ludwig, *Angew. Chem.* **2001**, *113*, 1856; *Angew. Chem. Int. Ed.* **2001**, *40*, 1808.
[26] Y. Sugawara, A. Nakamura, Y. Iimura, K. Kobayashi, H. Urabe, *J. Phys. Chem. B* **2002**, *106*, 10363.
[27] *Note added in proof:* While this paper was being refereed, the crystal structure of dihydrate **1** was published independently by another group, see: P. Naumov, G. Jovanovski, O. Grupèe, B. Kaitner, A. D. Rae, S. W. Ng, *Angew. Chem.* **2005**, *117*, 1277; *Angew. Chem. Int. Ed.* **2005**, *44*, 1251. The details of the crystal structure are essentially the same in both studies. However the remarkable aspect of the structure is that it touches upon the nature of what a supramolecular transition state might look like, and this interpretation is particular to our work.

 © 2005 Wiley-VCH Verlag GmbH & Co. KGaA, Weinheim

Miniaturization in Screening

A Microfluidic Approach for Screening Submicroliter Volumes against Multiple Reagents by Using Preformed Arrays of Nanoliter Plugs in a Three-Phase Liquid/Liquid/Gas Flow**

*Bo Zheng and Rustem F. Ismagilov**

Herein, we describe a simple, economical microfluidic method of screening a small volume (down to submicroliter volumes) of a solution against a large number of reagents on

[*] Dr. B. Zheng, Prof. R. F. Ismagilov
Department of Chemistry
The University of Chicago
5735 South Ellis Avenue, Chicago, IL 60637 (USA)
Fax: (+1) 773-702-0805
E-mail: r-ismagilov@uchicago.edu

[**] This work was supported by the National Institutes of Health (grant no. R01 EB001903) and by the Beckman Young Investigator Program and was performed at the MRSEC microfluidic facility funded by the National Science Foundation. We thank David Adamson for invaluable experimental assistance.

Supporting Information for this article is available on the WWW under http://www.angewandte.org or from the author.

 © 2005 Wiley-VCH Verlag GmbH & Co. KGaA, Weinheim DOI: 10.1002/anie.200462857

the nanoliter scale. The use of microfluidics to miniaturize chemical and biological screening is an important and active area of research in such diverse areas as biochemical assays, protein crystallization, and combinatorial chemistry.[1–7] Nanoliter aqueous plugs (droplets) transported through microchannels in an immiscible liquid have been used in a liquid/liquid flow system and allow miniaturization while eliminating dispersion,[8,9] accelerating mixing,[10] and providing control over the surface chemistry.[11] Applications of such systems to protein crystallization,[3,12] kinetic measurements,[10] assays,[13,14] DNA analysis,[8] and chemical synthesis[15] have been demonstrated.

Such plug-based microfluidic systems have been especially attractive for applications in which the concentrations of several reagents had to be varied. The concentrations were varied by rapidly changing the flow rates of the reagent streams as the droplets were formed.[3,12] Plug-based methods of that type require equipment for varying flow rates, and even though such equipment could be as simple as a few computer-controlled syringe pumps, this requirement presents a barrier to many potential users in chemical and biochemical laboratories. In addition, to increase the number of reagents that can be screened, both the number of the microfluidic channels in the device and the number of flow control devices have to be increased proportionally. Herein, we implement a complementary approach that uses preformed arrays of plugs to simplify the experiment for the user, relies on a liquid/liquid/gas three-phase flow system to ensure robustness, and allows a much larger number of reagents to be tested in a scalable fashion.

This approach consists of two steps. In the first step, an array of nanoliter plugs of many different reagents, separated and surrounded by a fluorinated carrier fluid, was generated inside a hydrophobic glass or plastic capillary (Figure 1a). The reagents in plugs may be stored inside sealed capillaries for months without evaporation or exposure to the ambient environment.[12] Such a two-phase system works well for fluids of matched viscosities. However, plugs may coalesce during subsequent use if the viscosity of the carrier fluid is very different from that of the aqueous solutions inside the plugs or if the viscosities within different plugs vary significantly. We used a three-phase liquid/liquid/gas system to enhance reliability in the manipulation and transport of these plugs: we separated the plugs by gas bubbles (Figure 1b,c) in addition to the carrier fluid. Formation of air bubbles in microfluidic devices has been previously described,[16] and gas bubbles have been used to separate liquid slugs of reagents in a liquid/gas two-phase flow, with applications for the synthesis of nanoparticles in microfluidic devices,[17,18] and have been used for actuation of steady microfluidic flow.[19] In addition, air bubbles have been widely used in biochemical analyzers.[20]

Herein, we use a liquid/liquid/gas three-phase flow system, in which the aqueous phase remains surrounded by the fluorocarbon, because the surface tension of the water–air interface ($\approx 70\ mN\,m^{-1}$) is significantly higher than both the surface tension of the water–fluorocarbon interface ($\approx 15\ mN\,m^{-1}$ with fluorosurfactants)[11] and the surface tension of the air–fluorocarbon interface. When there was only a wetting film of fluorocarbon between the air bubble and the aqueous plug (Figure 1c), and the osmotic pressures of the adjacent plugs were different, water transport between plugs was observed. Such water transport was prevented for several months when more fluorocarbon was used to separate the air bubbles and the plugs (Figure 1b).

In the second step, to perform the screening, the array was flowed from the capillary, through a funnel-shaped adapter (Figure 2a), into a microfluidic channel with a simple T-junction. The funnel-shaped adapter was used to couple the capillary with the microchannel. As the capillary was inserted into the adapter, a leak-proof connection was established without using any sealant. The microfluidic device could therefore be reused with experiments set up in multiple capillaries, one after another. As the array of plugs flowed into the microchannel, an aqueous target stream was allowed

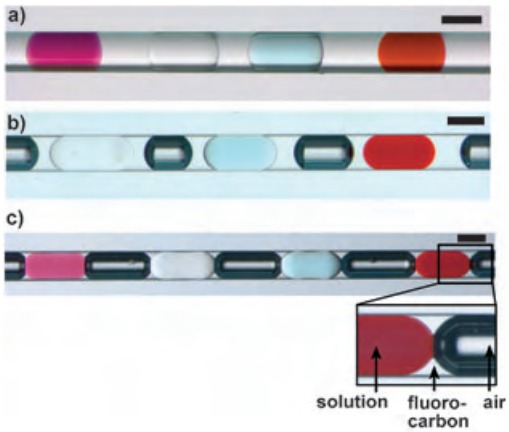

Figure 1. a) An array of plugs of four different reagents in a capillary. The plugs contain $KMnO_4$ (purple), NaCl (colorless), $CuSO_4$ (blue), and $Fe(SCN)_3$ (red), respectively. The colorless fluid is fluorocarbon. b,c) An array of plugs of different reagents formed in fluorocarbon and separated by air bubbles (dark) in a capillary. In (b) the aqueous plugs are separated from the air bubbles by a layer of fluorocarbon, thereby preventing cross-communication between the plugs. The scale bars are 200 μm.

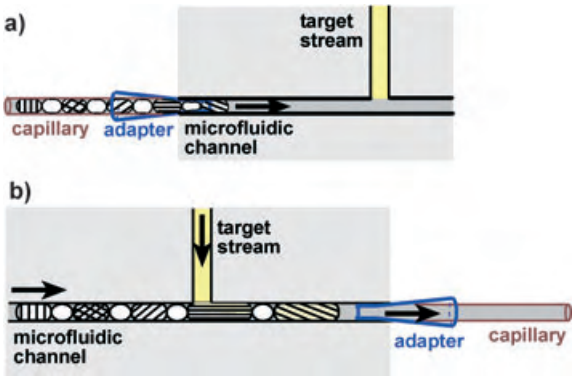

Figure 2. A schematic illustration of the process of utilizing an array of plugs for screening. a) The capillary containing the array of plugs is inserted into an adapter that is coupled with the inlet of the microfluidic channel. The array of plugs is then transported into the channel. b) As the array of plugs flows through the channel, each plug merges with a stream of the target solution, and the resulting plugs are collected in another capillary.

 © 2005 Wiley-VCH Verlag GmbH & Co. KGaA, Weinheim

to flow into the side channel of the T-junction. The plugs merged with the stream[15] to give larger plugs (Figure 2b), each containing one reagent from the array and the target sample. This merging has previously been characterized in detail.[15] Because of the surface tension at the gas/liquid interface and the elasticity of polydimethylsiloxane, the aqueous stream was not injected into small air bubbles, such as those shown in Figure 1b. The solutions were mixed in a volume ratio of 1:1, which was determined by the ratio of the two volumetric flow rates. A winding channel could be incorporated with the T-junction to accelerate mixing after merging, as demonstrated in nanoparticle synthesis in plugs in microchannels.[15] After merging, the plugs flowed into another capillary where they could be stored and monitored.

We illustrated this technique by performing a functional assay in which a set of enzymes was screened for phosphatase activity, by using a fluorogenic substrate, fluorescein diphosphate (FDP). Such an assay would be important for identifying a protein with the desired functional activity among thousands of proteins produced by the proteomics efforts. An array of plugs (≈15 nL) of alkaline phosphatase (AP), catalase, ribonuclease A (RNase), and lysozyme was first prepared in a capillary (Figure 3, see the Supporting Information for details). To eliminate potential false positives that result from the contamination of the substrate stream with an active enzyme, we separated every two neighboring enzyme plugs with two blank plugs containing phosphate-buffered saline (PBS; pH 7.4). Air bubbles were inserted between every two neighboring plugs. To assay the activity of the four enzymes on the FDP substrate, the array of plugs was merged with the solution of FDP at a T-junction (Figure 3a). The hydrolysis of FDP, which is catalyzed by AP, released fluorescein and was detected by fluorescence microcopy (Figure 3b). The plugs of the other three enzymes did not show any fluorescence, thereby confirming the lack of reactivity and the absence of contamination.

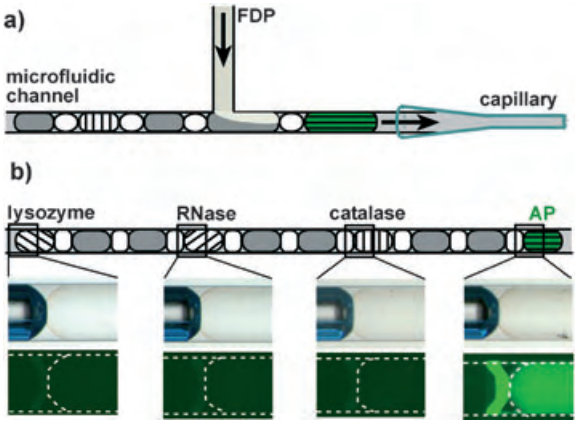

Figure 3. a) A schematic illustration of the assay of multiple enzymes against a single substrate (FDP). b) The result of the enzymatic assay. The drawing at the top illustrates the array of plugs. The plugs of PBS are in gray, the air bubbles are in white, and the plugs of enzymes are hatched. The microscope images in the middle are the bright-field micrographs of the plugs after merging. The images at the bottom are fluorescence micrographs of the corresponding plugs. In the rightmost fluorescence micrograph, the bright line is because of the reflection of the fluorescence of the AP plug from the edge of the air bubble. The dashed line indicates the outline of the capillary and the plugs.

Next, we demonstrated screening of a single protein against multiple crystallizing agents. We preformed plugs (≈15 nL) of 48 precipitants (numbered 1–48) from the crystal screen kit (Hampton Research) in a capillary. These plugs were merged with a stream of thaumatin, thereby giving rise to 48 crystallization trials. A total volume of less than 1.0 μL of thaumatin solution (60 mg mL^{-1} in 0.1 M *N*-(2-acetamido)-iminodiacetic acid buffer, pH 6.5) was used to fill the inlet tubing and the inlet of the microchannel, by using a syringe and tubing prefilled with carrier fluid to minimize waste of the protein solution. During the screening process, a volume of about 0.9 μL of thaumatin solution was consumed for screening and less than 0.1 μL remained in the channel. The merged plugs were transferred into the receiving capillary. Solutions of very different viscosities (from 1.0–33 cP)[21] were handled reliably in this system. Precipitation occurred during the merging of thaumatin with the plugs containing precipitant 30 (0.2 M $(NH_4)_2SO_4$/30 % poly(ethylene glycol)$_{8000}$). However, it did not interfere with the experiment because plugs are capable of transporting solids without allowing them to contact the walls of the microchannel.[15] After incubation for 36 h, we observed formation of crystals in plugs with precipitant 29 (0.8 M potassium sodium tartrate/0.1 M 2-[4-(2-hydroxyethyl)-1-piperazinyl]ethanesulfonic acid, pH 7.5) and no crystals in any other plugs, in agreement with experiments performed with microliter droplets. The screening results for three of the precipitants from the crystal screen kit are shown in Figure 4 (see the Supporting Information for experimental details).

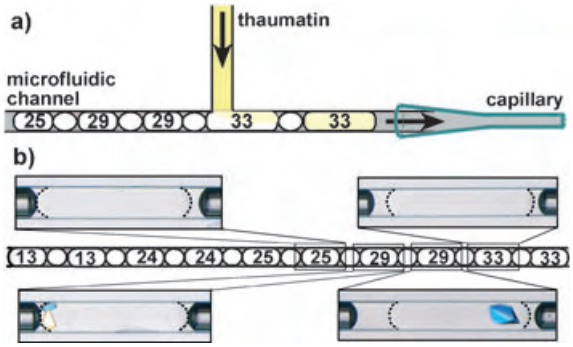

Figure 4. a) A schematic illustration of the screening of multiple precipitants for protein crystallization. b) The result of the precipitant screening. The drawing (middle) shows the merged plugs containing the precipitant and thaumatin, separated by the air bubbles. The numbers are the index numbers of the precipitants from the crystal screen kit. The four polarized-light micrographs show plugs that contain a mixture of thaumatin and precipitants 25, 29 (×2), and 33, respectively. Only the plugs containing precipitant 29 yielded crystals. The refractive index match between the fluorocarbon and the aqueous phases enables the observation of crystals at the edges of plugs, because the boundaries of the plugs are barely visible (shown with dashed lines).

 © 2005 Wiley-VCH Verlag GmbH & Co. KGaA, Weinheim

The approach described here is capable of screening microliter and submicroliter total volumes against multiple nanoliter volumes of reagents. We have demonstrated both screening of multiple proteins against a single reagent and screening of a single protein against many reagents. In the area of protein crystallization, this method enables sparse-matrix screening and is complementary to the methods for optimization of concentration that we developed previously.[3,12] It should be possible to use alternating plugs[12] to extend this method from the microbatch technique shown here to the vapor-diffusion technique.

This method has the following attractive features: 1) It is scalable—an increase in the number of reagents used in a screen does not require more complex fabrication, just a longer receiving capillary. 2) It is made reliable by the use of three-phase flow, in which a fluorinated carrier fluid provides protection of the plugs and control of surface chemistry, while gas bubbles prevent aqueous plugs from merging. 3) Arrays may be prefabricated by a range of methods, from simple methods with syringes to robotics.[22–24] Prefabricated arrays of plugs sealed in capillaries may be stored for months and could be made sterile or prepared under inert atmosphere, thereby expanding the range of potential applications. 4) The method is very simple for the end user—no sophisticated equipment is required at the user's end except a source of constant flow to drive the two streams to merge. A potential disadvantage of this method for some applications is that it is serial, rather than a parallel approach with multiple reagents against multiple substrates,[2,25] although some simple methods are quite effective even in serial format.[26] Overall, this method is attractive for applications in which reagents must be stored and used in a simple, reliable format, such as in diagnostics and detection. In addition, this method may find a wide range of applications in chemistry and biochemistry, by enhancing and miniaturizing current methods in which reagents are stored or distributed in 96- and 384-well plates, such as those in the fields of combinatorial chemistry, protein crystallization, and biochemical assaying.

A very interesting paper just appeared[27] that describes the use of preformed plugs in a cartridge for immunoassays. Microliter plugs were prepared in tubes by using a two-phase liquid/gas system, in which aqueous droplets were separated by air. By passing the droplets over surfaces loaded with antigens, immunoassays were conducted. The three-phase system described herein is different because, at least in our hands, it enables reliable transport of nanoliter volumes of aqueous solutions, prevents contact of aqueous solutions with the walls and eliminates dispersion, and prevents diffusion of water vapor from one aqueous plug to another. These differences are not essential for applications such as immunoassays—in fact the three-phase system may be less suitable for immunoassays or other reactions performed on the solid surface of a chip—but they are important in nanoliter enzymatic assays and protein crystallization. The two-phase system[27] is simpler to operate, because the flow rates do not need to be controlled at all, so the experiment may be performed even in the absence of electricity. This simplicity will be especially important for analysis in resource-poor settings.[27] Overall, the two approaches appear to be complementary in both their execution and their range of applications.

Received: December 9, 2004
Published online: March 22, 2005

Keywords: crystal growth · enzymatic arrays · microreactors · screening methods · three-phase system

[1] C. L. Hansen, E. Skordalakes, J. M. Berger, S. R. Quake, *Proc. Natl. Acad. Sci. USA* **2002**, *99*, 16531.
[2] J. Liu, C. Hansen, S. R. Quake, *Anal. Chem.* **2003**, *75*, 4718.
[3] B. Zheng, L. S. Roach, R. F. Ismagilov, *J. Am. Chem. Soc.* **2003**, *125*, 11170.
[4] P. Watts, S. J. Haswell, *Curr. Opin. Chem. Biol.* **2003**, *7*, 380.
[5] J. Kobayashi, Y. Mori, K. Okamoto, R. Akiyama, M. Ueno, T. Kitamori, S. Kobayashi, *Science* **2004**, *304*, 1305.
[6] A. Nagaki, K. Kawamura, S. Suga, T. Ando, M. Sawamoto, J. Yoshida, *J. Am. Chem. Soc.* **2004**, *126*, 14702.
[7] S. Suga, A. Nagaki, J. Yoshida, *Chem. Commun.* **2003**, 354.
[8] M. A. Burns, B. N. Johnson, S. N. Brahmasandra, K. Handique, J. R. Webster, M. Krishnan, T. S. Sammarco, P. M. Man, D. Jones, D. Heldsinger, C. H. Mastrangelo, D. T. Burke, *Science* **1998**, *282*, 484.
[9] O. D. Velev, B. G. Prevo, K. H. Bhatt, *Nature* **2003**, *426*, 515.
[10] H. Song, J. D. Tice, R. F. Ismagilov, *Angew. Chem.* **2003**, *115*, 792; *Angew. Chem. Int. Ed.* **2003**, *42*, 768.
[11] L. S. Roach, H. Song, R. F. Ismagilov, *Anal. Chem.* **2005**, *77*, 785.
[12] B. Zheng, J. D. Tice, L. S. Roach, R. F. Ismagilov, *Angew. Chem.* **2004**, *116*, 2562; *Angew. Chem. Int. Ed.* **2004**, *43*, 2508.
[13] B. Zheng, J. D. Tice, R. F. Ismagilov, *Anal. Chem.* **2004**, *76*, 4977.
[14] V. Srinivasan, V. K. Pamula, R. B. Fair, *Anal. Chim. Acta* **2004**, *507*, 145.
[15] I. Shestopalov, J. D. Tice, R. F. Ismagilov, *Lab Chip* **2004**, *4*, 316.
[16] P. Garstecki, I. Gitlin, W. DiLuzio, G. M. Whitesides, E. Kumacheva, H. A. Stone, *Appl. Phys. Lett.* **2004**, *85*, 2649.
[17] S. A. Khan, A. Gunther, M. A. Schmidt, K. F. Jensen, *Langmuir* **2004**, *20*, 8604.
[18] A. Gunther, S. A. Khan, M. Thalmann, F. Trachsel, K. F. Jensen, *Lab Chip* **2004**, *4*, 278.
[19] P. Marmottant, S. Hilgenfeldt, *Proc. Natl. Acad. Sci. USA* **2004**, *101*, 9523.
[20] H. Small, M. A. Langhorst, *Anal. Chem.* **1982**, *54*, A892.
[21] L. Ninni, H. Burd, W. H. Fung, A. J. A. Meirelles, *J. Chem. Eng. Data* **2003**, *48*, 324.
[22] P. Kuhn, K. Wilson, M. G. Patch, R. C. Stevens, *Curr. Opin. Chem. Biol.* **2002**, *6*, 704.
[23] R. Hui, A. Edwards, *J. Struct. Biol.* **2003**, *142*, 154.
[24] D. R. Meldrum, H. T. Evensen, W. H. Pence, S. E. Moody, D. L. Cunningham, P. J. Wiktor, *IEEE-ASME Trans. Mechatron.* **2000**, *5*, 212.
[25] R. F. Ismagilov, J. M. K. Ng, P. J. A. Kenis, G. M. Whitesides, *Anal. Chem.* **2001**, *73*, 5207.
[26] S. Suga, M. Okajima, K. Fujiwara, J. Yoshida, *J. Am. Chem. Soc.* **2001**, *123*, 7941.
[27] V. Linder, S. K. Sla, G. M. Whitesides, *Anal. Chem.* **2004**, *76*, 64.

 © 2005 Wiley-VCH Verlag GmbH & Co. KGaA, Weinheim

Mechanistic Models

A DFT Study on Hetero-Diels–Alder Reactions Catalyzed by Cobalt Complexes: Lewis Acidity Enhancement as a Consequence of Spin Transition Caused by Lewis Base Coordination

*Izumi Iwakura, Taketo Ikeno, and Tohru Yamada**

Among the various chiral Schiff base transition-metal complexes, the cobalt complexes with acacen- and salen-type ligands have been successfully employed as chiral Lewis acid catalysts, for example, for the enantioselective hetero-Diels–Alder reaction,[1] the carbonyl-ene reaction,[2] 1,3-dipolar cycloaddition of nitrones,[3] and ring opening of epoxides.[4] For these enantioselective catalyses, high efficiency and high stereoselectivity were realized, and specific catalytic activity of the cobalt complexes was achieved. Recently, theoretical analyses of reactions catalyzed by Schiff base complexes have attracted considerable attention,[5] but few analyses of the reaction pathways catalyzed by the Schiff base complexes as Lewis acids were performed. During our study on the catalyis of enantioselective cycloadditions and ene reactions by 3-oxobutylideneaminatocobalt complexes,[1a,b,2,3] we found that the enantioselectivity and reaction rate were improved when cationic Co^{III} complexes were used instead of Co^{II} complexes. Here we report on a theoretical analysis of cobalt-catalyzed hetero-Diels–Alder reactions, which revealed the crucial effect of aldehyde coordination as an axial ligand on the spin states and Lewis acidity of the cobalt complexes.

The hetero-Diels–Alder reaction catalyzed by the cobalt complex is depicted in Scheme 1; Danishefsky's diene[6] was replaced by a simple butadiene, and formaldehyde was adopted as the representative aldehyde. For the cobalt catalysts, complexes **1**–**3** were adopted as models. The unrestricted Becke three-parameter hybrid exchange functional combined with the Lee–Yang–Parr correlation functional (B3LYP)[7] was used with the LANL2DZ,[8] 6-31G(d), and 6-311G(d,p) basis sets for geometry optimizations and vibrational analyses.[9,10] Results with these basis sets were qualitatively quite consistent with our previous experimental results.[5d–f] The BP86 and BLYP methods were also examined

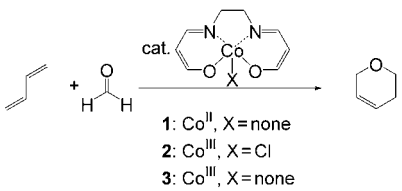

Scheme 1. Model system for hetero-Diels–Alder reaction.

at the 6-31G(d) level to check the validity of conclusions obtained by the B3LYP method.[10] For the cobalt(II) complexes, the doublet and quartet states were calculated, and for the cobalt(III) complexes, the singlet, triplet, and quintet states were examined. Reasonable rotational isomers were fully optimized, and the obtained energies were compared.[11] The total energy profiles for the catalytic cycle (single-point energies at B3LYP/6-31G(d)//B3LYP/6-31G(d)) are shown in Figures 1–3.[10]

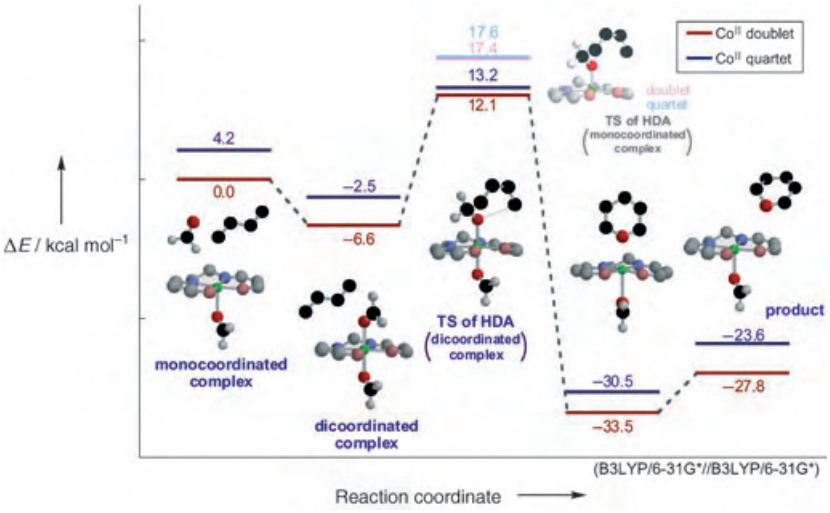

Figure 1. Energy profile for the catalytic cycle of the hetero-Diels–Alder reaction catalyzed by cobalt(II) complex **1**. Co green; N blue; O red, pink.

Calculation of the ground states of model complexes **1**–**3** revealed that Co^{II} complex **1** is in the doublet state, while Co^{III}-Cl complex **2** and cationic Co^{III} complex **3** are in the triplet state.

The effect of coordination of the aldehyde to cobalt complexes **1**–**3** was then examined. The structures of monocoordinated complexes Co^{II}-H_2CO and Co^{III}-H_2CO and dicoordinated complexes Co^{II}-2 H_2CO, Co^{III}-Cl-H_2CO, and Co^{III}-2 H_2CO were optimized. The Co^{II}-H_2CO and Co^{II}-2 H_2CO complexes are in the doublet state, and the Co^{III}-H_2CO and Co^{III}-2 H_2CO complexes in the triplet state, though for the dicoordinated Co^{III}-2 H_2CO complex, the energy difference between the triplet and singlet states was very small for some of the employed basis sets. On the other hand, Co^{III}-Cl-H_2CO is in the singlet state. This indicates that the spin transition is caused by coordination of the aldehyde for Co^{III}-Cl complex **2**. The dicoordinated complexes are more stable than the corresponding monocoordinated com-

[*] I. Iwakura, Dr. T. Ikeno, Prof. T. Yamada
Keio University
Department of Chemistry
3-14-1, Hiyoshi, Kohoku-ku, Yokohama 223-8522 (Japan)
Fax: (+81) 45-566-1716
E-mail: yamada@chem.keio.ac.jp

Supporting information for this article is available on the WWW under http://www.angewandte.org or from the author.

 © 2005 Wiley-VCH Verlag GmbH & Co. KGaA, Weinheim DOI: 10.1002/anie.200460836

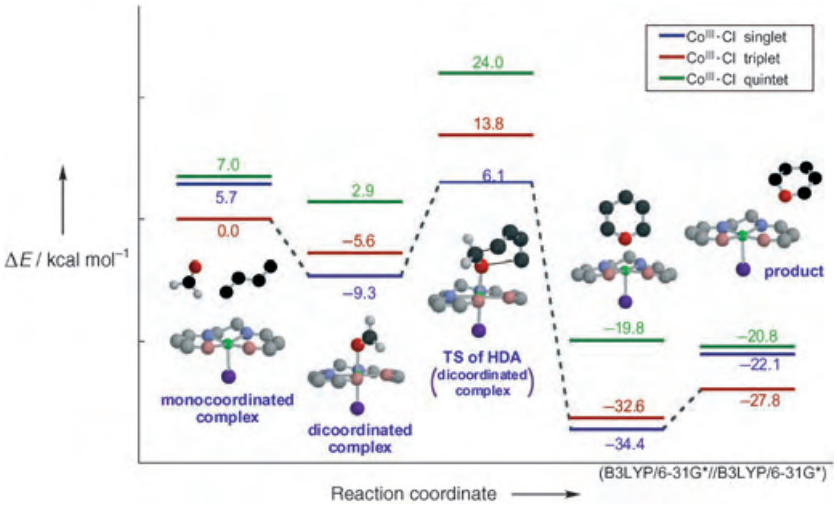

Figure 2. Energy profile for the catalytic cycle of the hetero-Diels–Alder reaction catalyzed by cobalt(III)-Cl complex **2**. Co green; N blue; O red, pink.

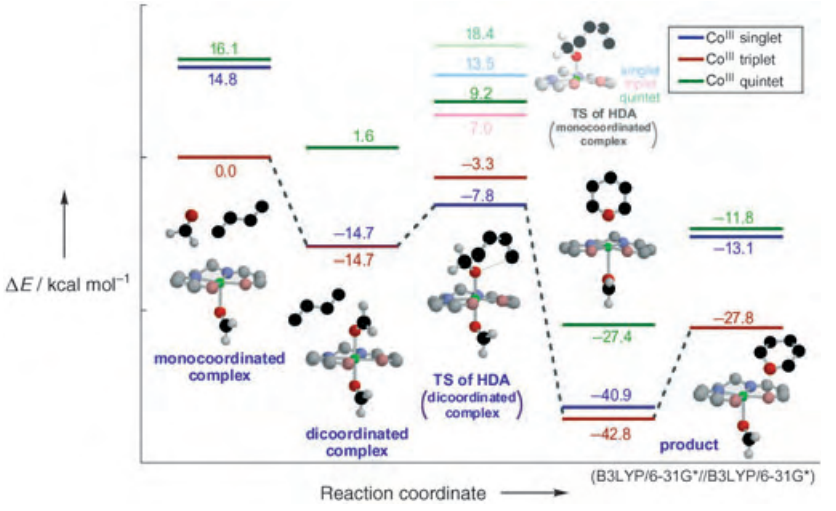

Figure 3. Energy profile for the catalytic cycle of the hetero-Diels–Alder reaction catalyzed by cobalt(III) complex **3**. Co green; N blue; O red, pink.

plexes.[12] For all the coordinated complexes, only structures in which a formaldehyde ligand is found on the same side as the O atoms of the ligand plane were obtained. It is reasonable to assume that the aldehydes should be located in a direction that negates the dipole moment of the cobalt complex. These results are well supported by the X-ray structure analysis of the salen cobalt(III) complex with two coordinated molecules of benzaldehyde.[1c]

By using all the coordinated complexes, the transition states (TS) of the hetero-Diels–Alder reaction with butadiene were calculated. Although the question of a concerted or stepwise process in Diels–Alder reactions has often been controversial, the present calculation concludes that the concerted pathway is more favorable than the stepwise pathway in the cobalt-complex-catalyzed hetero-Diels–Alder reaction.[13] These results are quite consistent with a recent analysis of the hetero-Diels–Alder reaction of butadiene and formaldehyde by CASSCF calculations[14] and with our experimental results.[1a,b]

Many rotational isomers involved in the direction of approach of the butadiene were obtained for the concerted pathway. The TSs with the attack of butadiene towards the two nitrogen atoms were higher in energy, though the energy differences of the other rotational isomers, in which butadiene approaches over the oxygen atom or bisects the two oxygen atoms, are small. All the obtained TS structures in the concerted pathway are very asynchronous, but the structures were not significantly affected by the cationic character (Table 1). In particular, the distance between the aldehyde oxygen and diene carbon atoms is very long (2.32–2.78 Å), while that between the aldehyde carbon and diene carbon atoms is relatively short (1.69–1.91 Å). For the TSs of the aldehyde Co complex with butadiene, the doublet and quartet states are close in energy for Co^{II} complex **1**, and the singlet states are the most stable for dicoordinated Co^{III}-Cl complex **2** and Co^{III} complex **3**. After the TS, the product is coordinated to the cobalt complex, and the calculation indicates that the singlet state is stable for the Co^{III}-Cl-product complex, while the stable spin state is a triplet for the Co^{III}-H_2CO-product complex. The ligand-exchange reaction of such types of Schiff base cobalt complexes proceed in a dissociative manner to release the product.[15] The monocoordinated cobalt complex is regenerated and the catalytic cycle completed. It has been concluded that the spin transition between the triplet and singlet states is caused by axial coordination of the aldehyde[16] in the cobalt(III) catalytic cycle by comparison with the monocoordinated cobalt(III) pathway.

Activation energies, representative bond lengths, and bond orders of the TSs are summarized in Table 1. The

Table 1: Activation energies [kcal mol^{-1}], bond lengths [Å], and bond orders of the transition states.[a]

Complex	Spin state	ΔE	Co–$O_{aldehyde}$	$C_{aldehyde}$–C_{diene}[c]	$O_{aldehyde}$–C_{diene}[c]
Co^{II}-H_2CO	doublet	17.4[b]	2.191	1.856 (0.66)	2.357 (0.62)
Co^{II}-2 H_2CO	doublet	18.7	2.289	1.906 (0.65)	2.315 (0.62)
Co^{III}-Cl-H_2CO	singlet	15.3	1.974	1.766 (0.61)	2.617 (0.61)
Co^{III}-H_2CO	triplet	7.0[b]	2.004	1.793 (0.76)	2.784 (0.57)
Co^{III}-2 H_2CO	singlet	6.8	1.903	1.685 (0.79)	2.566 (0.63)

[a] At the B3LYP/6-31G(d)//B3LYP/6-31G(d) level. [b] Activation energy for the monocoordinated Co^{II}-H_2CO and Co^{III}-H_2CO complexes, though these species are less stable than the dicoordinated complexes. [c] Bond orders in parentheses.

 © 2005 Wiley-VCH Verlag GmbH & Co. KGaA, Weinheim

activation energy clearly decreases in proportion to the cationic character of the cobalt complex (Co^{II} **1** > Co^{III}-Cl **2** ≫ Co^{III} **3**). These tendencies are quite consistent with previously reported experimental observations.[1a,b] It is noteworthy that by comparison with the ground states of the dicoordinated complexes, the Co–$O_{aldehyde}$ distance is shortened in the TS. (For the Co^{III}-2 H_2CO complex, the Co–$O_{aldehyde}$ distance changes from 1.93 to 1.90 Å in the singlet state and from 2.26 to 2.06 Å in the triplet state, while for the Co^{III}-Cl-H_2CO complex, it is shortened from 2.04 to 1.97 Å in the singlet state.) Since a diene is more electron rich than an aldehyde, delocalization of the electron from the diene to the aldehyde is favored in the TS, and this leads to stronger coordination of the aldehyde to the cobalt atom. Accordingly, the lower spin states are more favorable in the TS than in the ground states.

The length of the bond between the cobalt atom and the aldehyde indicates the Lewis acidity of the cobalt complex. It is generally considered that axial coordination of a Lewis base such as an aldehyde would decrease the Lewis acidity of complex catalysts. The present study conforms well with this hypothesis for the Co^{II} complex catalysts; the distance between the cobalt and aldehyde oxygen atoms in the TS is elongated from 2.19 to 2.29 Å by coordination of the aldehyde, since delocalization of an electron occurs from the lone pair of the oxygen atom into the antibonding orbital of the Co–$O_{aldehyde}$ bond. In contrast, spin transition from triplet to singlet for the Co^{III} complex overcomes the deactivation due to the coordination of the Lewis base, because there is no electron in the d_{z^2} orbital in the singlet state and the coordinative interaction between cobalt atom and aldehyde is stronger. Therefore, the distance is shortened from 2.00 to 1.90 Å (Figure 4).[17] It is generally considered that the closer the substrate approaches the metal center, the greater the enantioselectivity. Thus, in the Co^{III} complexes coordination of the aldehyde causes the Co–$O_{aldehyde}$ distance to shrink owing to the spin transition from the triplet to singlet in the TS, and hence the enantioselectivity is improved.

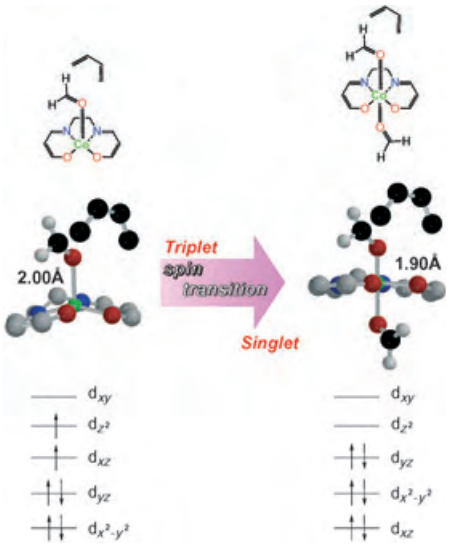

Figure 4. Coordination effect of aldehyde.

In summary, a theoretical analysis of the hetero-Diels–Alder reaction catalyzed by cobalt(II) and cobalt(III) complexes reveals the following results: 1) with increasing cationic character of the cobalt atom, the activation energy decreases; 2) spin transition between the triplet and singlet states occurs in the cobalt(III) catalytic cycle; and 3) axial coordination of an aldehyde plays a crucial role in the spin transition that enhances the Lewis acidity of the cobalt complex and improves the enantioselectivity.

Received: May 31, 2004
Revised: January 15, 2005
Published online: March 22, 2005

Keywords: cobalt · cycloaddition · density functional calculations · Lewis acids · spin crossover

[1] a) S. Kezuka, T. Mita, N. Ohtsuki, T. Ikeno, T. Yamda, *Bull. Chem. Soc. Jpn.* **2001**, *74*, 1333–1342; b) S. Kezuka, T. Mita, N. Ohtsuki, T. Ikeno, T. Yamada, *Chem. Lett.* **2000**, 824–825; c) Y. Huang, T. Iwama, V. H. Rawal, *J. Am. Chem. Soc.* **2002**, *124*, 5950–5951; d) L. S. Li, Y. K. Wu, Y. J. Hu, L. J. Xia, Y. L. Wu, *Tetrahedron: Asymmetry* **1998**, *9*, 2271–2277; e) Y. J. Hu, X. D. Huang, Z. J. Yao, Y. L. Wu, *J. Org. Chem.* **1998**, *63*, 2456–2461. Representative examples catalyzed by other metal Schiff base complexes: f) S. E. Schaus, J. Brånalt, E. N. Jacobsen, *J. Org. Chem.* **1998**, *63*, 403–405; g) K. Aikawa, R. Irie, T. Katsuki, *Tetrahedron* **2001**, *57*, 845–851.

[2] a) S. Kezuka, T. Ikeno, T. Yamada, *Org. Lett.* **2001**, *3*, 1937–1939; b) S. Kezuka, Y. Kogami, T. Ikeno, T. Yamada, *Bull. Chem. Soc. Jpn.* **2003**, *76*, 49–58.

[3] a) T. Mita, N. Ohtsuki, T. Ikeno, T. Yamada, *Org. Lett.* **2002**, *4*, 2457–2460; b) S. Kezuka, N. Ohtsuki, T. Mita, Y. Kogami, T. Ikeno, T. Yamada, *Bull. Chem. Soc. Jpn.* **2003**, *76*, 2197–2207.

[4] a) M. Tokunaga, J. F. Larrow, F. Kakiuchi, E. N. Jacobsen, *Science* **1997**, *277*, 936–938; b) S. E. Schaus, B. D. Brandes, J. F. Larrow, M. Tokunaga, K. B. Hansen, A. E. Gould, M. E. Furrow, E. N. Jacobsen, *J. Am. Chem. Soc.* **2002**, *124*, 1307–1315; c) H. Tanaka, Y. Kitaichi, M. Sato, T. Ikeno, T. Yamada, *Chem. Lett.* **2004**, *33*, 676–677.

[5] a) Recent examples: I. V. Khavrutskii, D. G. Musaev, K. Morokuma, *Inorg. Chem.* **2003**, *42*, 2606–2621, and the references therein; b) Y. G. Abashkin, S. K. Burt, *Org. Lett.* **2004**, *6*, 59–62; c) L. Cavallo, H. Jacobsen, *J. Org. Chem.* **2003**, *68*, 6202–6207; d) T. Ikeno, I. Iwakura, T. Yamada, *J. Am. Chem. Soc.* **2002**, *124*, 15152–15153; e) T. Ikeno, I. Iwakura, S. Yabushita, T. Yamada, *Org. Lett.* **2002**, *4*, 517–520; f) I. Iwakura, T. Ikeno, T. Yamada, *Org. Lett.* **2004**, *6*, 949–952.

[6] M. Bednarski, S. Danishefsky, *J. Am. Chem. Soc.* **1986**, *108*, 7060–7067.

[7] a) A. D. Becke, *J. Chem. Phys.* **1993**, *98*, 5648–5652; b) C. Lee, W. Yang, R. G. Parr, *Phys. Rev. B* **1988**, *37*, 785–789.

[8] P. J. Hay, W. R. Wadt, *J. Chem. Phys.* **1985**, *82*, 299–310.

[9] Gaussian 98 (Revision A.11), M. J. Frisch, G. W. Trucks, H. B. Schlegel, G. E. Scuseria, M. A. Robb, J. R. Cheeseman, V. G. Zakrzewski, J. A. Montgomery, Jr., R. E. Stratmann, J. C. Burant, S. Dapprich, J. M. Millam, A. D. Daniels, K. N. Kudin, M. C. Strain, O. Farkas, J. Tomasi, V. Barone, M. Cossi, R. Cammi, B. Mennucci, C. Pomelli, C. Adamo, S. Clifford, J. Ochterski, G. A. Petersson, P. Y. Ayala, Q. Cui, K. Morokuma, D. K. Malick, A. D. Rabuck, K. Raghavachari, J. B. Foresman, J. Cioslowski, J. V. Ortiz, B. B. Stefanov, G. Liu, A. Liashenko, P. Piskorz, I. Komaromi, R. Gomperts, R. L. Martin, D. J. Fox, T. Keith, M. A. Al-Laham, C. Y. Peng, A. Nanayakkara, C.

 © 2005 Wiley-VCH Verlag GmbH & Co. KGaA, Weinheim

Gonzalez, M. Challacombe, P. M. W. Gill, B. Johnson, W. Chen, M. W. Wong, J. L. Andres, C. Gonzalez, M. Head-Gordon, E. S. Replogle, J. A. Pople, Gaussian, Inc., Pittsburgh, PA, **1998**.

[10] In this manuscript, single-point energies at the B3LYP/6-31G(d) level are shown in Figures 1–3 and Table 1. The energy profiles (single-point energies, energies including ZPE corrections, and Gibbs energies) at the BLYP/6-31G(d), BP86/6-31G(d), B3LYP/LANL2DZ, B3LYP/6-31G(d), B3LYP/6-311G(d,p), B3LYP/6-311G(d,p)//B3LYP/6-31G(d), and B3LYP/6-311+G(d,p)//B3LYP/6-311G(d,p) levels are given in the Supporting Information. The Gibbs energies were calculated at 195 K (−78 °C) with a simple correction ($RT\ln V_{sol}/V_{gas}$: $T = 195$ K, $V_{gas} = 16\ \mathrm{L\,mol^{-1}}$, $V_{sol} = 1\ \mathrm{L\,mol^{-1}}$) from the gas phase to solution ($1\ \mathrm{mol\,L^{-1}}$). a) A. Ben-Naim, Y. Marcus, *J. Chem. Phys.* **1984**, *81*, 2016–2027; b) B. O. Leung, D. L. Reid, D. A. Armstrong, A. Rauk, *J. Phys. Chem. A* **2004**, *108*, 2720–2725. All the methods and basis sets led to the same conclusions.

[11] All structures of the rotational isomers around the Co–O axis (B3LYP/LANL2DZ and 6-31G(d)) are shown in the Supporting Information.

[12] After the BSSE correction, the complexation energies of Co^{II}-H_2CO, Co^{III}-Cl, and Co^{III}-H_2CO with H_2CO are 1.1, 4.8, and 11.0 $\mathrm{kcal\,mol^{-1}}$, respectively. Since the stabilization of the second coordination of the aldehyde to Co^{II}-H_2CO was very small, both mono- and dicoordinated TSs would be possible.

[13] The TSs of the stepwise pathway are shown in the Supporting Information.

[14] S. Sakai, *J. Mol. Struct.* **2003**, *630*, 177–185.

[15] a) G. Tauzher, R. Dreos Garlatti, G. Costa, *Inorg. Chim. Acta* **1983**, *75*, 145–148; b) R. Dreos Garlatti, G. Tauzher, G. Costa, *Inorg. Chim. Acta* **1986**, *121*, 27–32.

[16] a) D. Schröder, S. Shaik, H. Schwarz, *Acc. Chem. Res.* **2000**, *33*, 139–145; b) R. Poli, J. N. Harvey, *Chem. Soc. Rev.* **2003**, *32*, 1–8; c) C. Linde, B. Akermark, P.-O. Norrby, M. Svensson, *J. Am. Chem. Soc.* **1999**, *121*, 5083–5084.

[17] In the TS, the distance between the cobalt atom and the aldehyde in the triplet state of the Co^{III}-$2H_2CO$ complex is 2.063 Å, which is longer than that of the Co^{III}-H_2CO complex.

 © 2005 Wiley-VCH Verlag GmbH & Co. KGaA, Weinheim

Supramolecular Chemistry

A Trinuclear Eu^{III} Array within a Diastereoselectively Self-Assembled Helix Formed by Chiral Bipyridine-Carboxylate Ligands**

Olimpia Mamula, Marco Lama, Shane G. Telfer, Asao Nakamura, Reiko Kuroda, Helen Stoeckli-Evans, and Rosario Scopelitti*

Owing to their structural, magnetic, and emissive properties, complexes of lanthanide (Ln) ions with chiral ligands have found use as 1) asymmetric catalysts[1] and 2) probes for the characterization of ionic[2] or chiral environments.[3] However, in view of the lability and the weak coordination preferences of the Ln^{III} centers,[4] the synthesis of stable "true" enantiopure lanthanide coordination compounds, in which all the chirality sources (ligand, metal centers, supramolecular chirality) are fixed, represents a difficult goal. Indeed, only in a few cases has the synthesis of configurationally stable, mononuclear lanthanide complexes been achieved with high diastereoselectivity; these complexes were obtained from N-substituted 1,4,7,10-tetraazacyclododecane derivatives[5] or terpyridine-type chiral ligands.[6] With respect to complexes of higher nuclearity, solely the formation of dinuclear f–f helicates (from an enantiomerically pure ligand)[7] or d–f helicates (using a resolved triple-helical Cr^{III} complex, which preorganizes the ligand strands)[8] have been reported.

Bipyridine ligands that are derivatized with chiral pinene units have been found to be strong inductors of chirality for the stereocontrolled synthesis of complexes of transition-metal ions.[9] We sought to extend this range of ligands[10] to the stereoselective synthesis of supramolecular arrays of lanthanide ions. To this end, we designed ligand L^- (see Scheme 1), which features a carboxylate donor group appended to the pinene moiety to take advantage of the

[*] Dr. O. Mamula, M. Lama, Dr. R. Scopelitti
Institute of Chemical Sciences and Engineering
Ecole Polytechnique Fédérale de Lausanne
BCH 1403, 1015 Lausanne (Switzerland)
Fax: (+41) 21-693-9815
E-mail: olimpia.mamula@epfl.ch
Dr. S. G. Telfer, Dr. A. Nakamura, Prof. R. Kuroda
ERATO-SORST Kuroda Chiromorphology Project
Japan Science and Technology Agency
Komaba, Meguro-ku, Tokyo, 153-0041 (Japan)
Prof. H. Stoeckli-Evans
Institute of Chemistry
University of Neuchâtel
Bellevaux 51, 2000 Neuchâtel (Switzerland)

[**] This work was supported by the Swiss National Science Foundation (grant no. 2100-068077/200020-105320) and the EPFL. We thank the director of the laboratory, Prof. J.-C. G. Bünzli, for allowing the use of the laboratory infrastructure in the development of this independent project, and F. Nydegger for ES-MS measurements.

Supporting information for this article is available on the WWW under http://www.angewandte.org or from the author.

 DOI: 10.1002/anie.200500094 © 2005 Wiley-VCH Verlag GmbH & Co. KGaA, Weinheim

oxophilic character of Ln ions. Besides increasing the stability of the lanthanide complexes, the carboxylate group may also serve to enhance the transmission of the chiral information to the final supramolecular architecture. Herein we report the structure and chiroptical properties of the trinuclear array that results from self-assembly of L^- and Eu^{III} ions with complete diastereoselectivity. This complex displays a very interesting mode of helical chirality that originates from the propeller-like arrangement of the ligands around the trinuclear metal core.

The one-pot synthesis of the new carboxylic ligand (+)-HL (Scheme 1) is based on the known regio- and stereo-

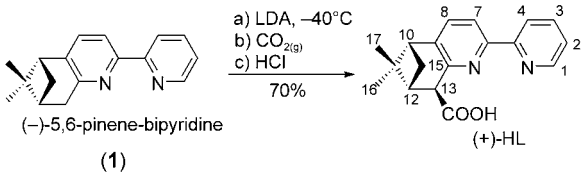

Scheme 1. Synthesis of the ligand (+)-HL, and its numbering scheme for NMR spectral assignments.

selective deprotonation of (−)-5,6-pinene-2,2′-bipyridine (**1**)[11] by lithium diisopropylamide (LDA).[12] Electrophilic attack of the anion with CO_2 generates a further chiral center (*S*). Final treatment of the product with HCl prevents decarboxylation[13] and yields the stable adduct (+)-HL·HCl. Treatment of $Eu(ClO_4)_3$ with two or more equivalents of (+)-HL·HCl in methanol in the presence of base (Et_3N or LiOH) instantaneously leads to the formation of a white precipitate. Crystals of this product could be grown from a solution in MeCN/MeOH, and X-ray crystallography[14] revealed the trinuclear assembly $[Eu_3\{(+)\text{-}L\}_6(\mu_3\text{-}OH)(H_2O)_3](ClO_4)_2\cdot 3H_2O$, as shown in Figure 1.

The assembly has crystallographically imposed C_3 symmetry (space group: *R*3), which relates the three Eu^{III} centers. The Eu–Eu distance is 3.915(1) Å, and the three metal ions are bridged by a hydroxide ion that lies slightly (0.84 Å) out of the plane defined by these ions. Six L^- ligands are incorporated into the overall array and these may be grouped into two sets of three symmetry-related ligands. The first set of three ligands, depicted in orange in Figure 1 and Figure 2, coordinate solely through their carboxylate groups, which bridge two Eu^{III} centers in a symmetrical μ^2-η^1:η^1 fashion. The uncoordinated bipyridyl units adopt an unusual *cis* conformation (dihedral angle: 4.1(8)°), which appears to be stabilized by hydrogen-bonding interactions with a water molecule of crystallization ($O_{H2O}\cdots N$ distance of 2.87(2) Å). These bipyridyl groups adopt a right-handed (*P*) helical arrangement in the solid state (Figure 2). The second set of three ligands, shown in green in Figure 1 and Figure 2, coordinate through both their carboxylate and bipyridyl donor groups. The carboxylate group links two Eu^{III} centers in a μ^2-η^2:η^1 fashion, while the bipyridyl group coordinates to one of the metal ions in a typical bidentate mode. This set of ligands adopts a left-handed (*M*) helical configuration which is manifest in the circular dichroism (CD) spectrum as

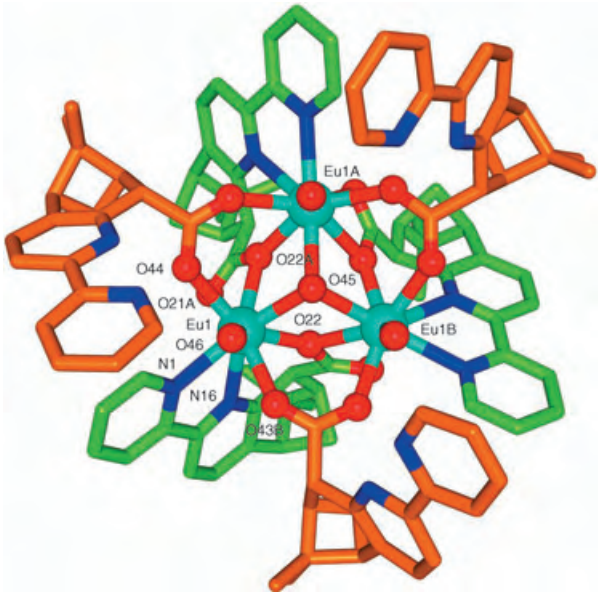

Figure 1. Crystal structure of $[Eu_3\{(+)\text{-}L\}_6(\mu_3\text{-}OH)(H_2O)_3](ClO_4)_2\cdot 3H_2O$ (O red, Eu turquoise, N dark blue; O-coordinated pinene-bipyridyl groups orange, N,O-coordinated pinene-bipyridyl groups green). View parallel to the crystallographic C_3 axis with a simplified labeling scheme. Hydrogen atoms, perchlorate counterions, and water molecules of crystallization have been omitted for clarity. Selected bond lengths [Å]: Eu1–N16 2.767(12), Eu1–O21A 2.667(10), Eu1–O22A 2.451(13), Eu1–O43B 2.333(9), Eu1–N1 2.508(14), Eu1–O22 2.297(11), Eu1–O45 2.411(5), Eu1–O46 2.504(6), Eu1–O44 2.379(9). Symmetry operations: a) $-y, x-y, z$; b) $-x+y, -x, z$.

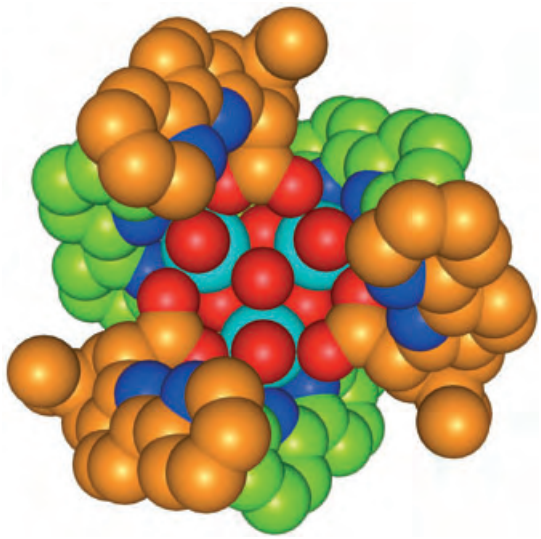

Figure 2. Space-filling representation of $[Eu_3\{(+)\text{-}L\}_6(\mu_3\text{-}OH)(H_2O)_3]^{2+}$ (O red, Eu turquoise, N dark blue). Ligands L^- coordinated only through their carboxylates groups are shown in orange; those coordinated through both the carboxylate and bipyridine moieties are shown in green.

discussed below. The coordination sphere of the europium ions is completed by a molecule of water, and the geometry at these centers is best described as a distorted, monocapped square antiprism. Preliminary results suggest that the trinu-

 © 2005 Wiley-VCH Verlag GmbH & Co. KGaA, Weinheim

clear assembly persists in the solution state, but further detailed investigations are necessary for a complete characterization of its behavior in solution.

The NMR spectra of the crude precipitate and dissolved crystals of the complexes were found to be identical. In the ^{1}H NMR spectrum, two sets of signals were observed in a 1:1 ratio spread over a range of almost 25 ppm (see Figure 3 and

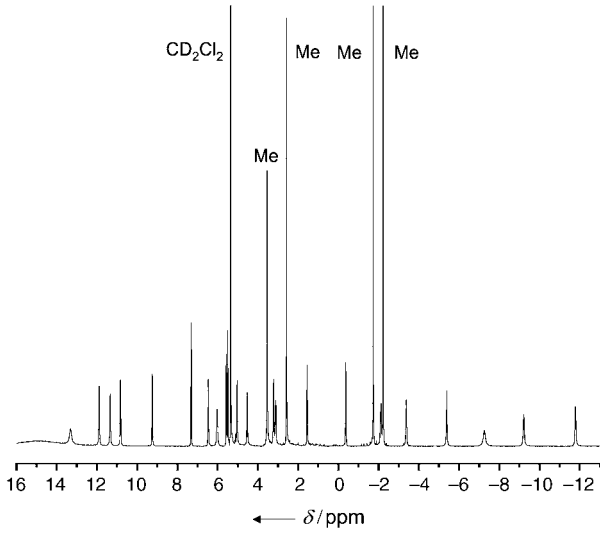

Figure 3. ^{1}H NMR spectrum of $[Eu_3\{(+)\text{-}L\}_6(\mu_3\text{-}OH)(H_2O)_3](ClO_4)_2\cdot 3H_2O$ in CD_2Cl_2 (400 MHz, RT).

Experimental Section). This observation indicates the existence of two magnetically distinct environments for the ligands in the complex, which may be related to the two distinct sets of ligands observed in the X-ray crystal structure of $[Eu_3\{(+)\text{-}L\}_6(\mu_3\text{-}OH)(H_2O)_3](ClO_4)_2\cdot 3H_2O$, as well as a high diastereoselectivity (d.e. $> 95\,\%$) of this self-assembly process.

The major peaks in the electrospray (ES) mass spectrum may be assigned to the molecular cation with loss of the coordinated water molecules, $[Eu_3L_6(OH)]^{2+}$, and its perchlorate adduct $\{[Eu_3L_6(OH)](ClO_4)\}^+$ (see Supporting Information). A third intense signal is attributed to $[Eu_3L_6(OH)(H_2O)]^{2+}$, which probably arises from the fragmentation processes in the gas phase.

The CD spectrum of $[Eu_3\{(+)\text{-}L\}_6(\mu_3\text{-}OH)(H_2O)_3](ClO_4)_2$ exhibits a bisignate curve centered around 320 nm (Figure 4). From the shape of this curve and the energy at which it appears, it is likely that it arises from the exciton coupling of the long-axis polarized π–π^* transitions of the bipyridine-type L^- ligands.[15] Of the two distinct sets of ligands in the overall array, the bipyridyl chromophores of the set that coordinate only through their carboxylate groups will rotate freely in solution, thus the average of their exciton-coupling interactions will be zero. On the other hand, the second set of ligands also coordinate through their bipyridine moieties and therefore will be rigidly held in a helical arrangement similar to that observed by crystallography (see Figure 5). Consequently, it is expected that exciton interactions between this set of chromophores will be entirely responsible for the low-

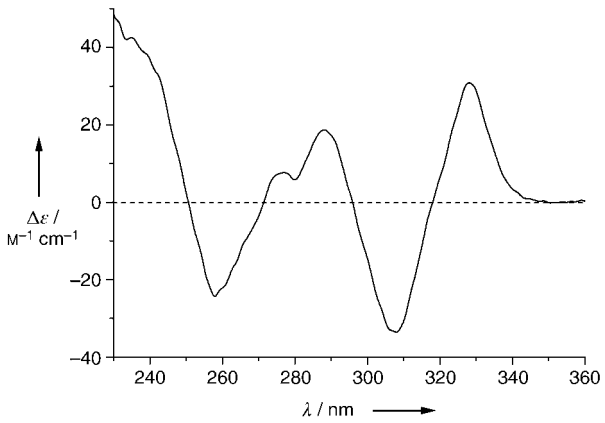

Figure 4. CD spectrum of $[Eu_3\{(+)\text{-}L\}_6(\mu_3\text{-}OH)(H_2O)_3](ClO_4)_2$ (10^{-4} M in CH_3CN).

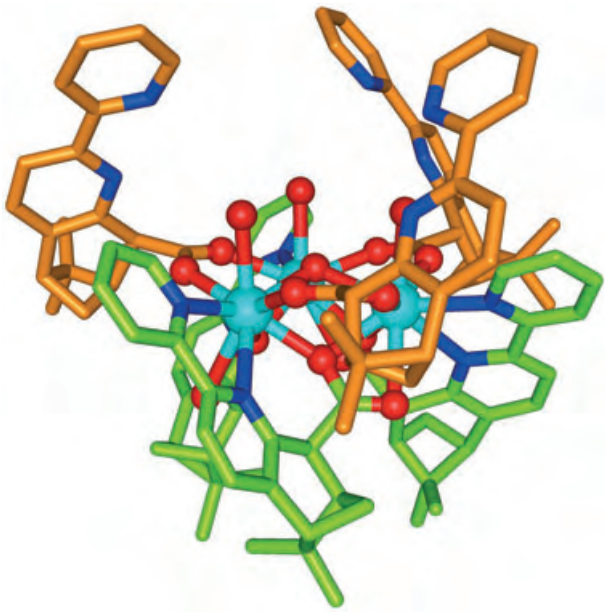

Figure 5. View perpendicular to the C_3 axis of the complex to highlight the ligands in the *M* configuration (green) that are responsible for the exciton coupling (O red, Eu turquoise, N dark blue).

energy exciton couplet. Exciton-coupling theory predicts that the left-handed (Λ) arrangement of these chromophores will give rise to a positive exciton couplet;[16] that is, a bisignate curve which is positive at lower energies. This prediction is in exact accord with the experimentally observed CD spectrum, but in the present case the three bipyridyl chromophores are coordinated to different metal centers, so the curve may be ascribed solely to internuclear exciton coupling.[17] These results underscore the importance of this phenomenon in metallosupramolecular chemistry.

Upon UV irradiation, the Eu^{III} array displays bright red luminescence in both solution (total emission quantum yield: $\phi_{tot}^{Eu} = 6.5\,\%$; lifetime: $\tau = 1.5$ ms in CH_3CN) and the solid state. These properties prompted us to investigate the chiroptical properties in the excited state by circularly polarized luminescence (CPL) spectroscopy. Excitation of

 © 2005 Wiley-VCH Verlag GmbH & Co. KGaA, Weinheim

the organic chromophore ($\lambda_{ex} = 315$ nm) gives rise to polarized emission bands that correspond to the Eu^{III}-centered $^5D_0 \rightarrow {}^7F_J$ transitions (Figure 6). The largest luminescence dissymmetry factor, defined as $g_{lum} = 2(I_L - I_R)/(I_L + I_R)$, in

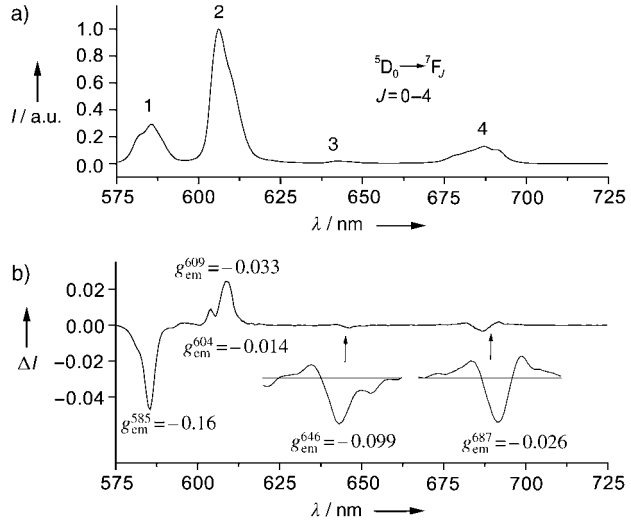

Figure 6. a) Total luminescence ($I_L + I_R$) and b) circularly polarized luminescence ($I_L - I_R$) spectra of the Eu^{III} complex (1.27×10^{-4} M in CH_3CN, 298 K).

which L and R denote left and right, respectively, is found for the magnetic-dipole allowed transition $^5D_0 \rightarrow {}^7F_1$. Its value of -0.16 ($\lambda = 585$ nm) is comparable to those of some reported mononuclear Eu^{III} complexes,[5c,18] and much higher than others.[5b,6] For the $\Delta J = 2$, 3, and 4 transitions, significantly lower absolute magnitudes of g_{lum} (0.09–0.01) were observed. CPL spectroscopy of polynuclear lanthanide complexes is still in its infancy, and the correlation of spectroscopic phenomena (transition type and sign sequence) with structural properties such as absolute configuration would require the systematic investigation of other enantiopure C_3-symmetric Ln^{III} complexes.

In summary, we have presented the diastereoselective self-assembly, structure, and chiroptical properties of a trinuclear Eu^{III} array, which exhibits an interesting mode of supramolecular helical chirality related to the arrangement of the ligands around the metallic core. This chirality is manifest in the CD spectrum of the trinuclear complex and lends strong support to a recently proposed internuclear exciton coupling model.[17] The new chiral bipyridine-carboxylate ligand discussed here successfully extends the family of pinene-derivatized bipyridine ligands to incorporate those capable of forming stable complexes with lanthanide ions. Preliminary investigations have shown that this ligand leads to similar trinuclear arrays with other lanthanide cations, including La^{III}, Gd^{III}, and Pr^{III}, through high-yielding self-assembly processes. Furthermore, the availability of both enantiomers of the ligand enables investigations of chiral discrimination phenomena in various energy-transfer processes.[19]

Experimental Section

Caution! Perchlorate salts are potentially explosive.[20] Tetramethylsilane (TMS) was used as internal reference for ^1H NMR experiments. The CPL spectrum was measured using a Jasco CPL-200 spectrophotometer (bandwidth: 2 nm).

(+)-HL·HCl·H_2O: ^1H NMR (400 MHz, CD_2Cl_2, TMS, 25 °C): $\delta =$ 8.97 (d, $^3J_{1,2} = 5.8$ Hz, 1H; H1), 8.40 (m, 2H; H3, H4), 8.13 (d, $^3J_{7,8} =$ 7.9 Hz, 1H; H7), 7.85 (dd, $^3J_{2,1} = 6.0$ Hz, $^3J_{2,3} = 6.0$ Hz, 1H; H2), 7.63 (d, $^3J_{8,7} = 7.9$ Hz, 1H; H8), 4.34 (d, $^3J_{13,12} = 2.5$ Hz, 1H; H13), 2.99 (dd, $^3J_{10,15a} = 5.6$ Hz; $^3J_{10,15b} = 5.6$ Hz, 1H; H10), 2.91 (ddd, $^2J_{15b,15a} = 9.6$ Hz, $^3J_{15b,10} = 5.8$ Hz, $^3J_{15b,12} = 5.8$ Hz, 1H; H15b), 2.74 (ddd, $^3J_{12,15b} =$ 5.8 Hz, $^4J_{12,10} = 5.8$ Hz, $^3J_{12,13} = 2.8$ Hz, 1H; H12), 1.60 (d, $^2J_{15a,15b} =$ 9.6 Hz, 1H; H15a), 1.52 (s, 3H; Me17), 0.72 ppm (s, 3H, Me16); UV/Vis (CH_3CN): λ_{max} (ε): 305 (10600), 250 nm (7500 $M^{-1}cm^{-1}$); CD (CH_3CN): λ ($\Delta\varepsilon$): 220 nm (5 $M^{-1}cm^{-1}$); $[\alpha]_D^{20} = +13.1$ deg $dm^2 mol^{-1}$ ($c = 6.9 \times 10^{-3}$ M in CH_3CN); HR-MS: m/z calcd for $C_{18}H_{19}N_2O_2$: 295.1442 $[M+H^+]^+$; found: 295.1441.

$[Eu_3\{(+)\text{-}L\}_6(OH)(H_2O)_3](ClO_4)_2$: Triethylamine (77 μL, 0.53 mmol, 2.3 equiv) was added to a solution of (+)-HL·HCl·H_2O (80 mg, 0.23 mmol) in MeOH (3 mL). A solution of $Eu(ClO_4)_3 \cdot 9H_2O$ (0.115 mmol, 0.5 equiv) in methanol (1.2 mL, 0.0487 M) was then dropped onto the stirring mixture. The white precipitate formed was collected by filtration, washed with cold MeOH, and dried (82 mg, 83% based on $[Eu_3\{(+)\text{-}L\}_6(OH)(H_2O)_3](ClO_4)_2 \cdot 5H_2O$). ^1H NMR (400 MHz, CD_2Cl_2, TMS, 25 °C): $\delta = 13.31$ (1H), 11.89 (1H), 11.33 (d, $J = 6.0$ Hz, 1H), 10.83 (dd, $J = 6.6$ Hz, $J = 6.6$ Hz, 1H), 9.25 (dd, $J =$ 6.9 Hz, $J = 5.0$, 1H), 7.31 (d, $J = 7.5$ Hz, 1H), 6.47 (dd, $J = 6.7$ Hz, $J =$ 6.7 Hz, 1H), 6.02 (1H), 5.58 (d, $J = 7.6$ Hz, 1H), 5.49 (d, $J = 7.6$ Hz, 1H), 5.03 (d, $J = 7.3$ Hz, 1H), 4.53 (d, $J = 6.7$ Hz, 1H), 3.53 (3H, Me), 3.23 (d, $J = 6.8$ Hz, 1H), 3.11 (1H), 2.57 (3H, Me), 1.55 (1H), −0.39 (1H), −1.69 (3H, Me), −2.15 (3H, Me), −2.11 (d, $J = 10.3$ Hz, 1H), −3.37 (1H), −5.38 (1H), −7.25 (1H), −9.21 (1H), −11.78 ppm (1H); ^{13}C NMR (100 MHz, CD_2Cl_2, 25 °C): $\delta = 228.9$, 190.1, 169.5, 160.7, 156.8, 154.4, 152.9, 152.2, 151.0, 147.4, 146.5, 141.9, 140.3, 136.0, 132.0, 128.3, 126.3, 124.9, 117.8, 105.4, 104.3, 93.1, 45.5, 43.3, 42.7, 41.9, 35.8, 30.1, 26.5, 23.3, 23.0, 21.2, 18.0, 1.1, −8.9, −40.5 ppm; IR: $\tilde{\nu} =$ 2935w, 1618s (COO^-), 1567m, 1454w, 1421s (COO^-), 1238w, 1094s (Cl–O), 860w, 792m, 753m; UV/Vis (CH_3CN, 1.8×10^{-6} M): λ_{max} (ε): 306 (67000), 278 (52500), 255 nm (48500 $M^{-1}cm^{-1}$); $[\alpha]_D^{20} =$ −97.3 deg $dm^2 mol^{-1}$ ($c = 1.1 \times 10^{-3}$ M in CH_3CN); ES-MS (10^{-4} M in CH_3CN): m/z (%): 1116.3 (100) $[Eu_3L_6(OH)]^{2+}$, 1107.3 (75) $[Eu_3L_6(OH)-H_2O]^{2+}$, 2331.4 (34) $[Eu_3L_6(OH)(ClO_4)]^+$, 1254.3 (15) $[Eu_3L_7]^{2+}$; Elemental analysis: calcd for $C_{108}H_{109}Eu_3N_{12}O_{23}Cl_2 \cdot 5H_2O$ (%): C 50.36, H 4.66, N 6.52; found: C 50.36, H 4.49, N 6.24.

Received: January 11, 2005
Revised: February 1, 2005
Published online: March 22, 2005

Keywords: chirality · helical structures · lanthanides · N,O ligands · supramolecular chemistry

[1] K. Mikami, M. Terada, H. Matsuzawa, *Angew. Chem.* **2002**, *114*, 3704; *Angew. Chem. Int. Ed.* **2002**, *41*, 3554.
[2] H. Tsukube, T. Yamada, S. Shinoda, *J. Alloys Compd.* **2004**, *374*, 40; R. S. Dickins, T. Gunnlaugsson, D. Parker, R. D. Peacock, *Chem. Commun.* **1998**, 1643.
[3] D. Parker, R. S. Dickins, H. Puschmann, C. Crossland, J. A. K. Howard, *Chem. Rev.* **2002**, *102*, 1977; H. C. Aspinall, *Chem. Rev.* **2002**, *102*, 1807.
[4] G. R. Choppin in *Lanthanide Probes in Life, Chemical, and Earth Sciences* (Eds.: J.-C. G. Bünzli, G. R. Choppin), Elsevier, Amsterdam, **1989**, chap. 1.
[5] a) R. S. Dickins, J. A. K. Howard, C. W. Lehmann, J. Moloney, D. Parker, R. D. Peacock, *Angew. Chem.* **1997**, *109*, 541; *Angew.*

 © 2005 Wiley-VCH Verlag GmbH & Co. KGaA, Weinheim

Chem. Int. Ed. Engl. **1997**, *36*, 521; b) R. S. Dickins, J. A. K. Howard, C. L. Maupin, J. M. Moloney, D. Parker, J. P. Riehl, G. Siligardi, J. A. G. Williams, *Chem. Eur. J.* **1999**, *5*, 1095; c) R. S. Dickins, J. A. K. Howard, J. M. Moloney, D. Parker, R. D. Peacock, G. Siligardi, *Chem. Commun.* **1997**, 1747; d) G. Bobba, R. S. Dickins, S. D. Kean, C. E. Mathieu, D. Parker, R. D. Peacock, G. Siligardi, M. J. Smith, J. A. G. Williams, C. F. G. C. Geraldes, *J. Chem. Soc. Perkin Trans. 2* **2001**, 1729; e) G. Bobba, Y. Bretonniere, J.-C. Frias, D. Parker, *Org. Biomol. Chem.* **2003**, *1*, 1870.

[6] G. Muller, J.-C. G. Bünzli, J. P. Riehl, D. Suhr, A. von Zelewsky, H. Mürner, *Chem. Commun.* **2002**, 1522.

[7] J. J. Lessmann, W. D. Horrocks, Jr., *Inorg. Chem.* **2000**, *39*, 3114.

[8] M. Cantuel, G. Bernardinelli, G. Muller, J. P. Riehl, C. Piguet, *Inorg. Chem.* **2004**, *43*, 1840.

[9] O. Mamula, A. von Zelewsky, G. Bernadinelli, *Angew. Chem.* **1998**, *110*, 301; *Angew. Chem. Int. Ed.* **1998**, *37*, 289; O. Mamula, T. Bark, A. von Zelewsky, G. Bernadinelli, *Angew. Chem.* **1999**, *111*, 3129; *Angew. Chem. Int. Ed.* **1999**, *38*, 2945; O. Mamula, A. von Zelewsky, *Coord. Chem. Rev.* **2003**, *242*, 87; L.-E. Perret-Aebi, A. von Zelewsky, C. Dietrich-Buchecker, J.-P. Sauvage, *Angew. Chem.* **2004**, *116*, 4582; *Angew. Chem. Int. Ed.* **2004**, *43*, 4482.

[10] M. Lama, O. Mamula, R. Scopelliti, *Synlett* **2004**, 1808.

[11] P. Hayoz, A. von Zelewsky, H. Stoeckli-Evans, *J. Am. Chem. Soc.* **1993**, *115*, 5111.

[12] P. Hayoz, A. von Zelewsky, *Tetrahedron Lett.* **1992**, *33*, 5165.

[13] W. von E. Doering, V. Z. Pasternak, *J. Am. Chem. Soc.* **1950**, *72*, 143.

[14] X-ray data for $[Eu_3\{(+)\text{-}L\}_6(\mu_3\text{-}OH)(H_2O)_3](ClO_4)_2\cdot 3H_2O$: $M_r = 2539.90$, rhombohedral, space group $R3$, $a = b = 17.3468(11)$, $c = 30.846(4)$ Å, $V = 8038.3(13)$ Å^3, $Z = 3$, $\rho_{calcd} = 1.574$ g cm^{-3}, $\mu(Mo_{K\alpha}) = 1.865$ mm^{-1}, $T = 140(2)$ K, $F(000) = 3858$, $2\theta_{max} = 50.1°$; 16262 reflections collected of which 6240 unique ($R_{int} = 0.1147$). Final R indices (3080 observed reflections, $I > 2\sigma I$): $R_1 = 0.0535$, $wR_2 = 0.0915$; final R indices (all data): $R_1 = 0.1049$, $wR_2 = 0.1189$. Highest residual electron density 1.242 e Å^{-3}. The structure was solved by direct methods using SIR97 ("SIR97, A new tool for crystal structure determination and refinement": A. Altomare, M. C. Burla, M. Camalli, G. L. Cascarano, C. Giacovazzo, A. Guagliardi, A. G. G. Moliterni, G. Polidori, R. Spagna, *J. Appl. Crystallogr.* **1999**, *32*, 115); refinement was performed using SHELXL-97 (G. M. Sheldrick, SHELXL-97, Program for the Refinement of Crystal Structures, University of Göttingen, Göttingen (Germany), **1997**) by the full-matrix least-squares technique. Hydrogen atoms were included in calculated positions and treated as riding atoms. No absorption correction was applied. CCDC-259970 contains the supplementary crystallographic data for this paper. These data can be obtained free of charge from The Cambridge Crystallographic Data Centre via www.ccdc.cam.ac.uk/data_request/cif.

[15] M. Ziegler, A. von Zelewsky, *Coord. Chem. Rev.* **1998**, *177*, 257; B. Bosnich, *Acc. Chem. Res.* **1969**, *2*, 266.

[16] A. Rodger, B. Norden, *Circular Dichroism and Linear Dichroism*, Oxford University Press, Oxford, **1997**.

[17] S. G. Telfer, N. Tajima, R. Kuroda, *J. Am. Chem. Soc.* **2004**, *126*, 1408; S. G. Telfer, N. Tajima, R. Kuroda, M. Cantuel, C. Piguet, *Inorg. Chem.* **2004**, *43*, 5302.

[18] N. C. Thompson, D. Parker, H. Schmitt-Willich, D. Suelzle, G. Muller, J. P. Riehl, *Dalton Trans.* **2004**, 1892.

[19] S. C. J. Meskers, H. P. J. M. Dekkers, *J. Phys. Chem. A* **2001**, *105*, 4589.

[20] W. C. Wolsey, *J. Chem. Educ.* **1973**, *50*, A335.

 © 2005 Wiley-VCH Verlag GmbH & Co. KGaA, Weinheim

Cluster Compounds

A Highly Unsaturated Platinum–Rhenium Cluster Complex that Adds an Unusually Large Amount of Hydrogen**

Richard D. Adams and Burjor Captain*

Important results continue to emerge from current research on polynuclear metal cluster complexes.[1] In recent studies we have shown that platinum and palladium groups containing the bulky tri-*tert*-butylphosphine ligand readily add to polynuclear metal cluster complexes to form adducts that are inherently electron deficient around the metal atoms.[2] Herein we present a new example of these complexes that exhibits an unusually high degree of electronic unsaturation that predisposes it to an addition reaction with an unusually large amount of hydrogen.

The new complex $[Pt_3Re_2(CO)_6(PtBu_3)_3]$ (**1**) was obtained in 18% yield from the reaction of $Pt(PtBu_3)_2$ with $[Re_2(CO)_{10}]$ in refluxing octane (125 °C). The compound was characterized by single-crystal X-ray diffraction methods (Figure 1). The

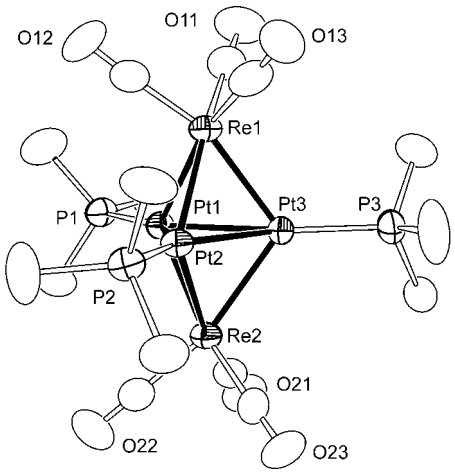

Figure 1. An ORTEP diagram of the molecular structure of **1**, thermal ellipsoids set at 30% probability. The methyl groups on the $PtBu_3$ ligands have been omitted for clarity. Selected bond lengths [Å]: Pt1-Re1 2.6275(7), Pt2-Re1 2.6728(7), Pt3-Re1 2.6431(7), Pt1-Re2 2.6690(7), Pt2-Re2 2.6158(7), Pt3-Re2 2.6617(7), Pt1-Pt2 2.7202(7), Pt1-Pt3 2.7104(7), Pt2-Pt3 2.7369(7).

[*] Prof. Dr. R. D. Adams, Dr. B. Captain
Department of Chemistry and Biochemistry
University of South Carolina
Columbia, SC 29208 (USA)
Fax: (+1) 803-777-6781
E-mail: adams@mail.chem.sc.edu

[**] We thank the Office of Basic Energy Sciences of the U.S. Department of Energy under Grant DE-FG02-00ER14980 and the USC NanoCenter for financial support. We thank Michael B. Hall and Charles Edwin Webster for discussions on the use of the Fenske–Hall program library, and Mark D. Smith for collecting the X-ray diffraction data for **2** at 100 K.

Supporting information for this article is available on the WWW under http://www.angewandte.org or from the author.

 DOI: 10.1002/anie.200500086 © 2005 Wiley-VCH Verlag GmbH & Co. KGaA, Weinheim

complex contains a trigonal bipyramidal cluster of five metal atoms. The equatorial plane of the cluster is defined by three Pt(P*t*Bu$_3$) groupings. The two {Re(CO)$_3$} units occupy the two apical positions. Compound **1** is electronically unsaturated by the amount of 10 valence electrons[3,4] Accordingly, the six Re–Pt bonds are unusually short, they range from 2.6158(7)–2.6728(7) Å. However, the Pt–Pt bonds are about normal, 2.7104(7)–2.7369(7) Å.

To understand the nature of the electronic unsaturation in **1** we have performed Fenske–Hall molecular orbital (MO) calculations.[5] The calculation was setup by using crystal coordinates for all non-hydrogen atoms, and assembling three {Pt(PH$_3$)} fragments in a trigonal planar arrangement and two {Re(CO)$_3$} fragments oriented perpendicular to that plane having overall an approximate D_{3h} symmetry. The calculations reveal the existence of five low-lying unoccupied molecular orbitals in the form of a degenerate pair at −3.28 eV having E″ symmetry (the lowest unoccupied molecular orbital; LUMO), a second degenerate pair (LUMO + 1) at −1.46 eV having E′ symmetry, and one nondegenerate orbital at −0.79 eV which has A_2'' symmetry. These five orbitals could accommodate the anticipated 10 "missing" valence bonding electrons. The highest occupied molecular orbital (HOMO) of A_1' symmetry lies at −4.65 eV. This orbital is dominated by Pt–Pt bonding in the Pt_3 plane, see Supporting Information for a diagram. The form of one of the degenerate E″ LUMOs is shown in Figure 2. The diagram shows that the contours of the orbital are oriented predominantly along the Re–Pt bonds.

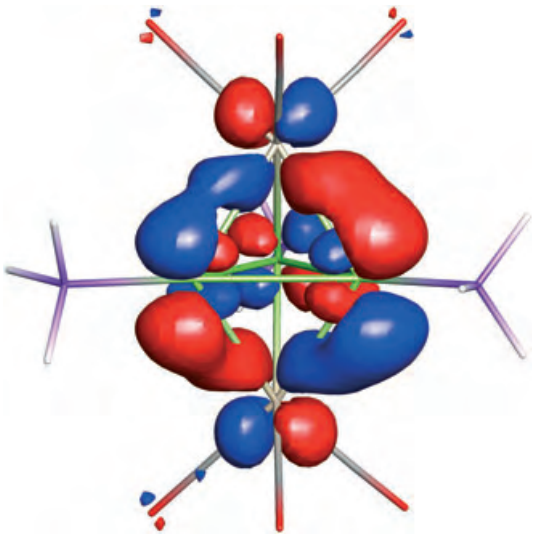

Figure 2. One of the two components of the E″ LUMO of **1**. Cluster shown as stick model; green Pt, brown Re, purple phosphine, red carbonyl.

We have found that **1** reacts with hydrogen, a convenient source of electrons, at room temperature to yield the hexahydrido complex [$Pt_3Re_2(CO)_6(P$*t*$Bu_3)_3(\mu\text{-}H)_6$] (**2**) in 90% yield. Compound **2** was also characterized by single-crystal X-ray diffraction (Figure 3). The metal cluster in **2** has

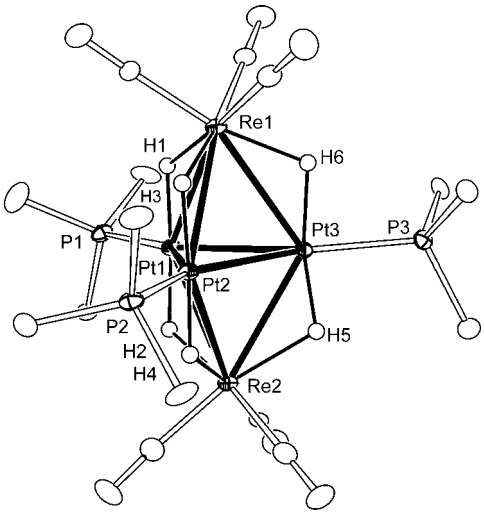

Figure 3. An ORTEP diagram of the molecular structure of **2**, thermal ellipsoids set at 50% probability. Selected bond lengths [Å]: Pt1-Re1 2.9202(3), Pt2-Re1 2.8989(3), Pt3-Re1 2.9004(3), Pt1-Re2 2.9170(3), Pt2-Re2 2.9134(3), Pt3-Re2 2.9050(3), Pt1-Pt2 2.7026(3), Pt1-Pt3 2.7095(3), Pt2-Pt3 2.7259(3), Pt1-H1 1.59(6), Pt1-H2 1.66(6), Pt2-H3 1.62(6), Pt2-H4 1.51(6), Pt3-H5 1.55(6), Pt3-H6 1.66(6), Re1-H1 1.91(6), Re1-H3 1.72(6), Re1-H6 1.89(6), Re2-H2 1.91(6), Re2-H4 1.97(6), Re2-H5 1.94(6).

a trigonal bipyramidal structure of five metal atoms similar to that of **1**, but it also contains six hydrido ligands arranged in a form having one bridging H ligand on each of the six Re–Pt bonds in the complex. Each of the six hydrido ligands was located and refined in the structural analysis by performing the intensity data collection at 100 K. As expected, the Re–Pt bonds have become significantly longer owing to the presence of the bridging hydrido ligands.[6] A Fenske–Hall MO calculation of **2**, analogous to that of **1**, shows an A_1' HOMO at −5.42 eV similar to that in **1**, but only one LUMO, an E′ that lies at −1.73 eV. The E″ and A_2'' orbitals in **1** are now filled bonding orbitals at −12.75 eV and −11.22 eV, respectively, and contain the six additional electrons that were supplied by the three equivalents of hydrogen. A correlation diagram showing the relationship between these orbitals in **1** and **2** is shown in Figure 4. The metal cluster of **2** is also electron deficient, but only by four electrons.

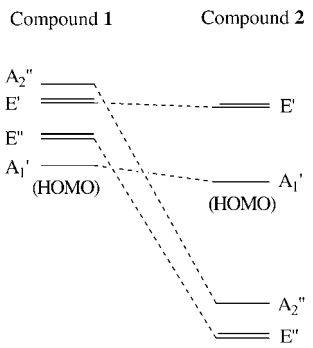

Figure 4. A correlation diagram of the Fenske–Hall MOs of **1** and **2** in D_{3h} symmetry.

 © 2005 Wiley-VCH Verlag GmbH & Co. KGaA, Weinheim

There are a few examples where metal complexes condense upon reaction with hydrogen to form polynuclear metal species that contain relatively large amounts of hydrogen,[7] but as far as we know this is the first example of the addition of three equivalents of H_2 by an intact molecular metal-cluster complex.

Platinum-containing bimetallic clusters on supports have recently been shown to exhibit superior properties for hydrogenation catalysis.[8] The addition of hydrogen to **1** under the unusually mild conditions reported herein (25 °C) suggest that it too might have applications as a hydrogenation catalyst. Compound **1** might also serve as a model for hydrogen storage although the addition of hydrogen to **1** is irreversible up to 151 °C.[9]

Experimental Section

1: $Pt(PtBu_3)_2$ (160.0 mg, 0.267 mmol) and $[Re_2(CO)_{10}]$ (29.0 mg, 0.044 mmol) were dissolved in octane (15 mL) and then heated to reflux for 3 h. The brown product was separated by thin layer chromatography (TLC; silica gel) using a 3:1 hexane/methylene chloride solvent mixture to give 13.9 mg (18 % yield). Spectral data for **1**: IR (in hexane): $\tilde{\nu}_{CO} = 1985$ (s), 1892 cm^{-1} (s). ^1H NMR (400 MHz, $[D_8]$toluene, 25 °C, TMS): $\delta = 1.63$ ppm (d, $^3J(P,H) = 13$ Hz, 81 H; CH_3); $^{31}P\{^1H\}$ NMR (162 MHz, $[D_8]$toluene, 25 °C, 85 % *ortho*-H_3PO_4): $\delta = 109.23$ ppm (m, 3 P). Crystal data for **1**: $Re_2Pt_3P_3O_6C_{42}H_{81}\cdot C_6H_{14}$, $M_r = 1818.82$, monoclinic, space group $P2_1/n$, $a = 13.9117(13)$, $b = 24.058(2)$, $c = 18.0919(17)$ Å, $\beta = 92.210(2)°$, $V = 6050.7(10)$ Å^3, $Z = 4$, $T = 296$ K, $Mo_{K\alpha} = 0.71073$ Å. The final $R1(F^2)$ was 0.0501 for 7040 reflections $I > 2\sigma(I)$.

2: Compound **1** (11.6 mg, 0.067 mmol) was dissolved in hexane (25 mL). Hydrogen gas was passed through the stirred solution at 25 °C for 4 h. The product was isolated by TLC (silica gel) using a 3:1 hexane/methylene chloride solvent to yield 10.5 mg (90 %) of orange **2**. Spectral data for **2**: IR (in hexane): $\tilde{\nu}_{CO} = 2009$ (s), 1914 cm^{-1} (vs). ^1H NMR (400 MHz, $[D_8]$toluene, 25 °C, TMS): $\delta = 1.50$ (d, $^3J(P,H) = 13$ Hz, 81 H; CH_3), −4.34 ppm (quartet, $^1J(Pt,H) = 723$ Hz, $^2J(P,H) = 4$ Hz, 6 H; hydrido); $^{31}P\{^1H\}$ NMR (162 MHz, $[D_8]$toluene, 25 °C, 85 % *ortho*-H_3PO_4): $\delta = 111.42$ ppm (m, 3 P). MS. ES$^+$/MS calcd for M+H, $[Re_2Pt_3P_3O_6C_{42}H_{87}+H]^+$, 1739, found 1739. Crystal data for **2**: $Re_2Pt_3P_3O_6C_{42}H_{81}\cdot C_6H_6\cdot {}^1/_2C_8H_{18}$, $M_r = 1873.92$, monoclinic, space group $P2_1/n$, $a = 14.7099(6)$, $b = 23.4704(9)$, $c = 17.7176(7)$ Å, $\beta = 91.0310(10)°$, $V = 6116.0(4)$ Å^3, $Z = 4$, $T = 100$ K, $Mo_{K\alpha} = 0.71073$ Å. The final $R1(F^2)$ was 0.0342 for 13055 reflections $I > 2\sigma(I)$. CCDC-260166 (**1**) and CCDC-260167 (**2**) contain the supplementary crystallographic data for this paper. These data can be obtained free of charge from the Cambridge Crystallographic Data Centre via www.ccdc.cam.ac.uk/data_request/cif.

Solutions of **2** in nonane were heated to reflux (151 °C) for 1 h. There was no spectroscopic evidence (infrared) for the formation of **1**.

Received: January 10, 2005
Published online: March 16, 2005

Keywords: cluster compounds · electron counting · hydrogen · platinum · rhenium

[1] P. J. Dyson, J. S. McIndoe, *Angew. Chem.* **2004**, *116*, 6152; *Angew. Chem. Int. Ed.* **2004**, *43*, 6028.

[2] a) R. D. Adams, B. Captain, W. Fu, M. B. Hall, J. Manson, M. D. Smith, C. E. Webster, *J. Am. Chem.* Soc. **2004**, *126*, 5253; b) R. D. Adams, B. Captain, W. Fu, P. J. Pellechia, M. D. Smith, *Inorg. Chem.* **2003**, *42*, 2094; c) R. D. Adams, B. Captain, W. Fu, M. B. Hall, M. D. Smith, C. E. Webster, *Inorg. Chem.* **2004**, *43*, 3921; d) R. D. Adams, B. Captain, M. B. Hall, J. L. Smith, Jr., C. E. Webster, *J. Am. Chem. Soc.* **2005**, *127*, 1007.

[3] A trigonal bipyramidal cluster of five metal atoms in which each of the metal atoms formally has an 18-electron configuration will have a total of 72 valence electrons.[4]

[4] D. M. P. Mingos, *Introduction to Cluster Chemistry*; Prentice Hall, Engelwood Cliffs, New Jersey, **1990**, chap. 2.

[5] a) M. B. Hall, R. F. Fenske, *Inorg. Chem.* **1972**, *11*, 768; b) J. Manson, C. E. Webster, M. B. Hall, JIMP Development Version 0.1.v117 (built for Windows PC and Redhat Linux 7.3), July 2004, Department of Chemistry, Texas A& M University, College Station, TX 77842, (http://www.chem.tamu.edu/jimp/); c) D. L. Lichtenberger, MOPLOT2: for orbital and density plots from linear combinations of Slater or Gaussian type orbitals; Version 2.0, June 1993, Department of Chemistry, University of Arizona, Tucson, Arizona 85721.

[6] R. G. Teller, R. Bau, *Struct. Bonding (Berlin)* **1981**, *41*, 1.

[7] a) M. J. Ingleson, M. F. Mahon, P. R. Raithby, A. S. Weller, *J. Am. Chem. Soc.* **2004**, *126*, 4784; b) T. H. Lemmen, K. Folting, J. C. Huffman, K. G. Caulton, *J. Am. Chem. Soc.* **1985**, *107*, 7774; c) G. V. Goeden, K. G. Caulton, *J. Am. Chem. Soc.* **1981**, *103*, 7354; d) D. Gregson, J. A. K. Howard, M. Murray, J. L. Spencer, *J. Chem. Soc. Chem. Commun.* **1981**, 716.

[8] a) J. M. Thomas, B. F. G. Johnson, R. Raja, G. Sankar, P. A. Midgley, *Acc. Chem. Res.* **2003**, *36*, 20; b) J. M. Thomas, R. Raja, B. F. G. Johnson, S. Hermans, M. D. Jones, T. Khimyak, *Ind. Eng. Chem. Res.* **2003**, *42*, 1563; c) R. Raja, T. Khimyak, J. M. Thomas, S. Hermans, B. F. G. Johnson, *Angew. Chem.* **2001**, *113*, 4774; *Angew. Chem. Int. Ed.* **2001**, *40*, 4638; d) J. M. Thomas, R. Raja, B. F. G. Johnson, T. J. O'Connell, G. Sankar, T. Khimyak, *Chem. Commun.* **2003**, 1126.

[9] a) L. Schlapbach, A. Züttel, *Nature* **2001**, *414*, 353; b) N. L. Rosi, J. Eckert, M. Eddaoudi, D. T. Vodak, M. O'Keerre, O. M. Yaghi, *Science* **2003**, *300*, 1127; c) X. Zhao, B. Xiao, A. J. Fletcher, K. M. Thomas, D. Bradshaw, M. J. Rosseinsky, *Science* **2004**, *306*, 1012.

 © 2005 Wiley-VCH Verlag GmbH & Co. KGaA, Weinheim

Glycopeptide Synthesis

Molecular Transporter Between Polymer Platforms: Highly Efficient Chemoenzymatic Glycopeptide Synthesis by the Combined Use of Solid-Phase and Water-Soluble Polymer Supports**

*Masataka Fumoto, Hiroshi Hinou, Takahiko Matsushita, Masaki Kurogochi, Takashi Ohta, Takaomi Ito, Kuriko Yamada, Akio Takimoto, Hirosato Kondo, Toshiyuki Inazu, and Shin-Ichiro Nishimura**

Polymer-supported synthesis is a practical and convenient method because it simplifies purification of the final products and makes combinatorial processes feasible. Chemical synthesis on solid-phase polymers made the automated synthesis of nucleotides (DNA/RNA) and peptides (proteins) possible,[1,2] and they are now indispensable devices for the investigation of the functional roles of genomes and proteins as well as the development of a variety of therapeutic reagents. Chemical synthesis of glycoconjugates, however, is a much more difficult task than the synthesis of nucleic acids or polypeptides because complex structures of glycoconjugates require extremely time-consuming and tedious procedures of regioselective protection and stereoselective glycosylation reactions. Although progress in solid-phase chemical synthesis meanwhile allowed the construction of a variety of oligosaccharides,[3] these methods still entail limitation of the target structures and technical difficulty for general biochemists or medical scientists. Enzymatic synthesis is a potential alternative to the chemical synthesis of complex oligosaccharides because of the specificities of both the stereochemistry and regioselectivity in the glycosylation reactions.[4] However, glycosyl acceptor substrates immobilized on solid supports are not suited for these enzymatic reactions in terms of efficiency and versatility in practical synthesis.

In the course of our studies of enzymatic synthesis, based on the cluster effect[5] of sugar-attached water-soluble polymers as multivalent acceptor substrates,[6] our interest has been focused on the efficient synthesis of glycopeptides as important signal molecules in cellular recognition.[7] To achieve a concerted and efficient glycopeptide synthesis based on a combined chemical and enzymatic strategy, we thought that the advent of an appropriate methodology to combine solid-phase peptide synthesis and liquid-phase carbohydrate synthesis was highly desirable.[4] Herein, we report a novel strategy of rapid and efficient synthesis of glycopeptides by using a convenient "molecular transporter" that interfaces two different polymer supports.

Our synthetic strategy is summarized in Figure 1 as follows: a) solid-phase synthesis of the photosensitive *O*-GlcNAc-peptides terminated by the molecular transporter **1**, b) deprotection and release of the transporter from the resin, c) chemoselective blotting of the molecular transporter that carries glycopeptide primers using a water-soluble polymer with alkoxyamino functional groups,[8] d) one-pot sugar elongation with glycosyltransferases, and e) release of full-length glycopeptides from the transporter on the polymer platform with a photoselective cleavage reaction.

The molecular transporter **1** was synthesized from L-proline, which was to be used as the N-terminal residue of the target peptide, by modification with a reactive ketone group with a photolabile linker moiety, 4-[4-(1-hydroxyethyl)-2-methoxy-5-nitrophenoxy]butyric acid[9] (see the Supporting Information).[10] This heterobifunctional linker acts as a transporter between the two different polymer platforms and allows both chemoselective blotting and photoselective cleavage (catch and release) of glycopeptides (Figure 1, steps c and e).

We demonstrated the feasibility of our method by constructing a dodecapeptide with a sialyl Lewis^X tetrasaccharide residue (**7**) as a model compound. Scheme 1 shows the solid-phase synthesis of a transporter molecule carrying an intermediate glycopeptide (**3**) on a Fmoc-Arg(Pbf)-NovaSynTGA resin using Fmoc-protected amino acids (Fmoc-AA) and Fmoc-Ser(Ac_3GlcNAcβ)-OH.[11] Next, the intermediate on the transporter (**3**) was blotted onto the water-soluble polyacrylamide derivative **4**[8] by chemoselective ligation of the ketone group of **3** with the alkoxyamino group of **4** without any purification process. We suggest that this blotting step using polymer **4**, which we proved is completed in three hours at room temperature under mild conditions (pH 5.0–5.5) by monitoring with reversed-phase (RP) HPLC (Figure 2), is crucial. As anticipated, polymer **4**

[*] Dr. H. Hinou, Dr. T. Ohta, Prof. S.-I. Nishimura
Glycochemosynthesis Team, Research Center for Glycoscience
National Institute of Advanced Industrial Science and Technology (AIST)
Sapporo 062-8517 (Japan)
Fax: (+81) 11-857-8441
E-mail: tiger.nishimura@aist.go.jp
T. Matsushita, Dr. M. Kurogochi, Prof. S.-I. Nishimura
Division of Biological Sciences, Graduate School of Science
Hokkaido University, Sapporo 001-0021, Japan
E-mail: shin@glyco.sci.hokudai.ac.jp
M. Fumoto, Dr. K. Yamada
Research Association for Biotechnology
Minato-ku, Tokyo 105-0003 (Japan)
M. Fumoto, T. Ito, Dr. A. Takimoto, Dr. H. Kondo
Shionogi & Co. Ltd.
Chuo-ku, Osaka 541-0045 (Japan)
Dr. K. Yamada
Hitachi High-Technologies Co.
Minato-ku, Tokyo 105-8717 (Japan)
Dr. T. Inazu
Department of Applied Chemistry, School of Engineering,
and Institute of Glycotechnology
Tokai University, Kanagawa 259-1292 (Japan)

[**] This work was partly supported by a grant for "Development of Methodologies and Databases for Structural Glycoproteomics" from the New Energy and Industrial Technology Development Organization (NEDO). We are grateful to Professor Y. Nakahara of Tokai University for valuable suggestions and comments. We also thank Ms. S. Oka, Ms. M. Kiuchi, and Mr. T. Hirose of the Center of Instrumental Analysis, Hokkaido University, for mass spectrometric measurements and amino acid analysis.

Supporting information for this article is available on the WWW under http://www.angewandte.org or from the author.

 © 2005 Wiley-VCH Verlag GmbH & Co. KGaA, Weinheim DOI: 10.1002/anie.200463065

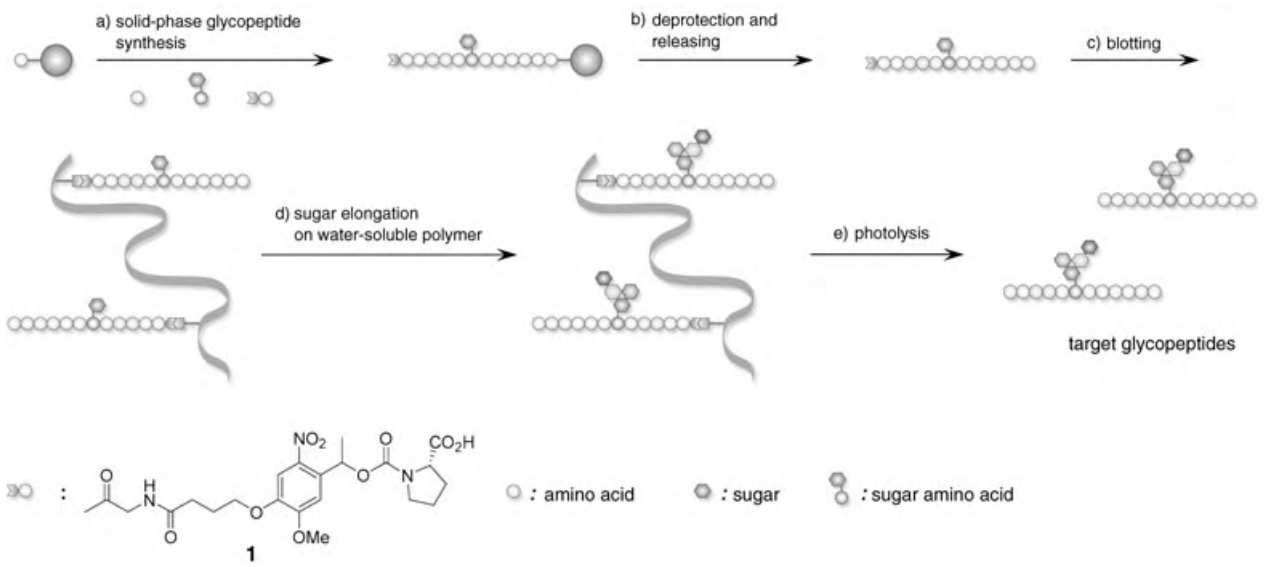

Figure 1. Glycopeptide synthesis using molecular transporter **1**.

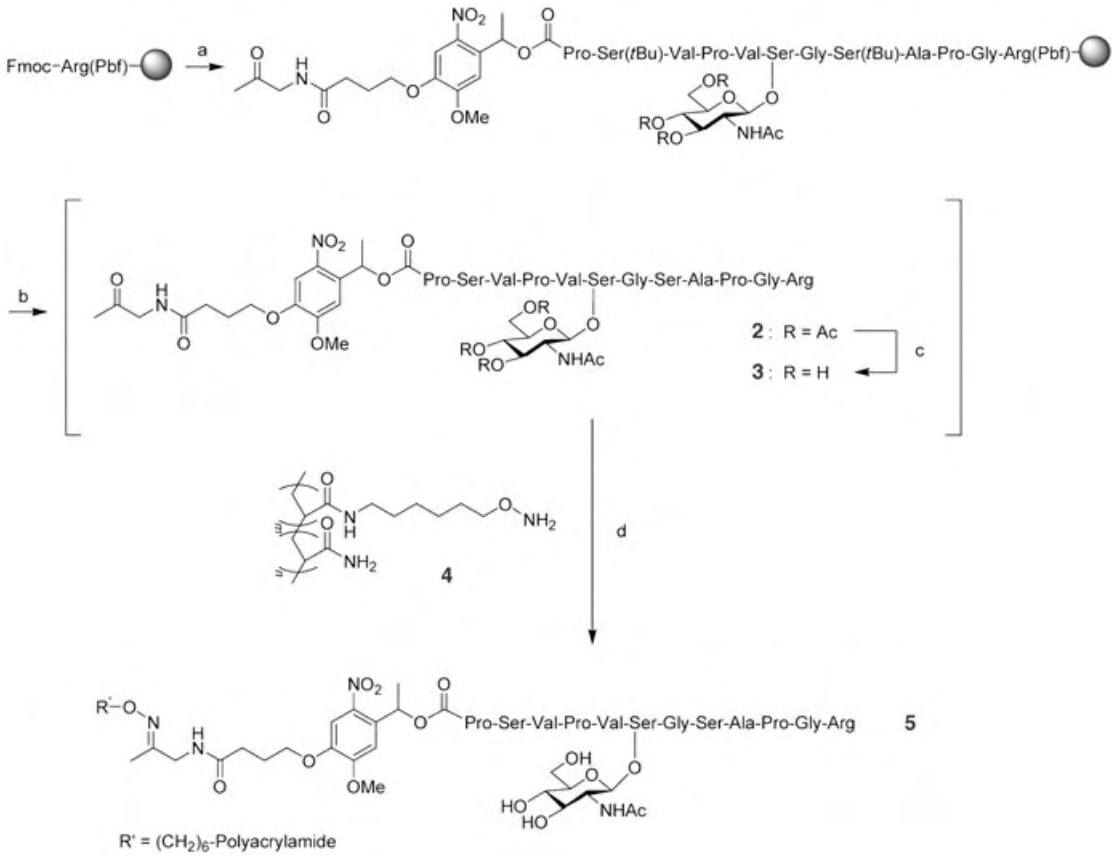

Scheme 1. a) 1. Piperidine, DMF; 2. Fmoc-AA or Fmoc-Ser(Ac_3GlcNAcβ)-OH or **1**, HBTU, HOBt, ethyldiisopropylamine, *N*-methylpyrrolidone/DMF; 3. Ac_2O, HOBt, ethyldiisopropylamine, DMF; b) 90% trifluoroacetic acid in water; c) NaOH, MeOH; d) AcOH/AcONa buffer (pH 5.0–5.5). DMF = dimethylformamide; HBTU = *O*-(benzotriazol-l-yl)-*N*,*N*,*N*′,*N*′-tetramethyluronium hexafluorophosphate; HOBt = 1-hydroxy-l*H*-benzotriazole. Pbf = 2,2,5,7,8-pentamethyldihydrobenzofurane-5-sulfonyl; Fmoc = 9-fluorenylmethoxycarbonyl; R′ = $(CH_2)_6$–polyacrylamide.

captured only the full-length peptide **3**, since free amino groups of the incomplete peptides were capped by acetylation prior to the removal of the Fmoc groups. After one-pot sugar elongation reactions by recombinant glycosyltransferases in the presence of sugar nucleotides as glycosyl donor substrates, selective cleavage reaction by photoirradiation at 365 nm proceeded smoothly and the target product **7** was obtained in 12% overall yield from the initial solid-phase synthesis (Scheme 2). As shown in Figure 3, the purity of the crude compound **7** released from the transporter was satisfactory

 © 2005 Wiley-VCH Verlag GmbH & Co. KGaA, Weinheim

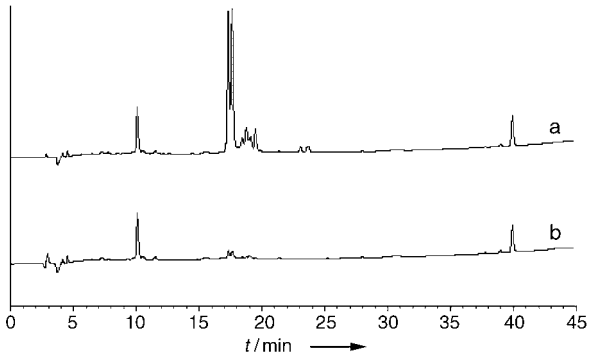

Figure 2. RP-HPLC analysis of the chemoselective ligation of the ketone group of compound **3** with the alkoxyamino group of polymer **4**. a) Chromatogram of the crude mixture of **3** before blotting; b) chromatogram after blotting for 3 h.

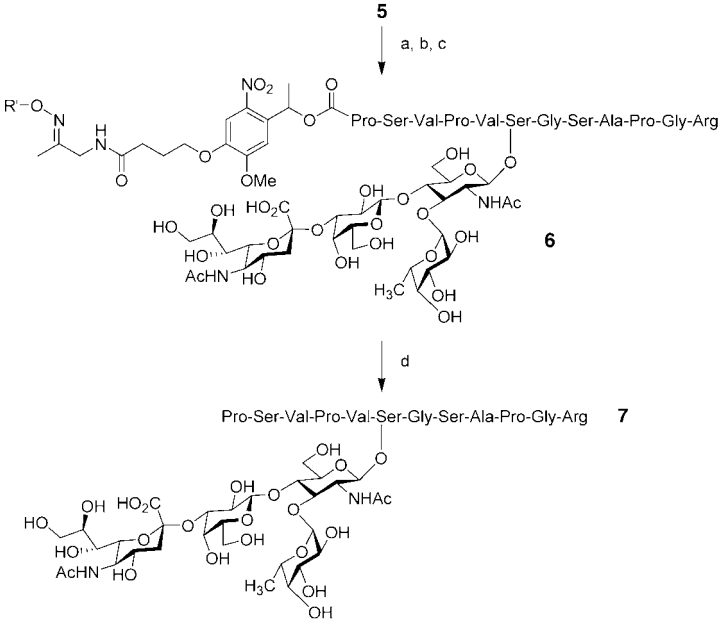

Scheme 2. a) UDP-Gal (5 mM), β-1,4-galactosyltransferase (100 mU mL^{-1}), $MnCl_2$ (10 mM), 0.1% BSA, HEPES buffer (50 mM, pH 7.0), 100%; b) CMP-NANA (5 mM), α-2,3-sialyltransferase (37 mU mL^{-1}), 0.1% BSA, HEPES buffer (50 mM, pH 7.0), 100%; c) GDP-Fuc (5–7 mM), α-1,3-fucosyltransferase (20–30 mU mL^{-1}), $MnCl_2$ (10 mM), 0.1% BSA, HEPES buffer (50 mM, pH 7.0), 100%; d) UV irradiation (365 nm). UDP = uracil diphosphate; BSA = bovine serum albumin; HEPES = *N*-(2-hydroxyethyl)piperazine-*N*′-2-ethanesulfonic acid; CMP-NANA = cytidine-5′-monophospho-*N*-acetylneuraminic acid sodium salt; GDP = guanosine diphosphate.

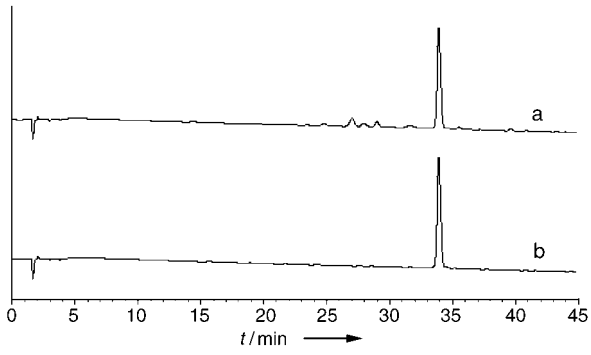

Figure 3. RP-HPLC analysis of glycopeptide **7**. a) Crude product **7**; b) product **7** purified by preparative-scale RP-HPLC.

enough for further biological assay, which suggests that blotting and one-pot glycosylation reactions on the water-soluble polymer mediated by molecular transporter **1** will become an efficient and versatile strategy for the high-throughput synthesis of a glycopeptide library.

Interestingly, it was also demonstrated that irradiation with a MALDI-TOF MS N_2 gas laser efficiently cleaved the transporter at its photosensitive position in the presence of 2,5-dihydroxybenzoic acid as matrix. The product-ion peaks can be used for monitoring and characterizing glycosylation reactions on the polymer support by subsequent precise structural analysis in the TOF/TOF mode.[12,13] As indicated in Figure 4, precise structural characterization of compound **7** was carried out by matrix-dependent selective fragmentation (MDSF)[12b] in the MALDI-TOF/TOF MS mode.

In conclusion, we have established a simple and efficient method for rapid glycopeptide synthesis by using a hetero-

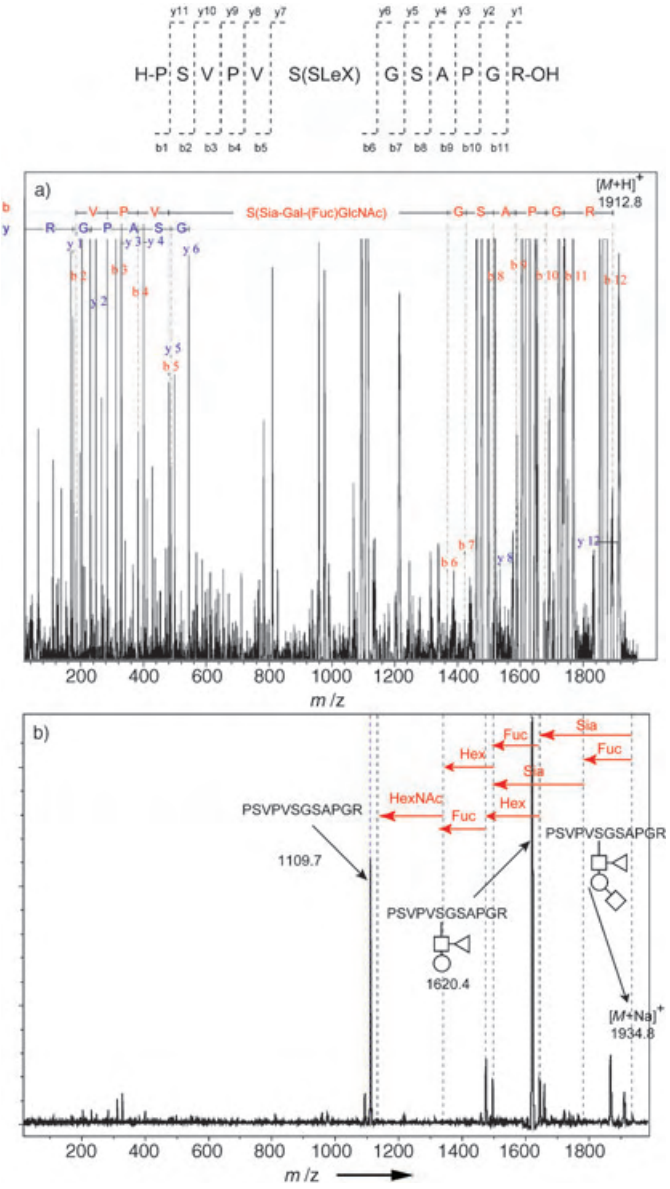

Figure 4. MALDI-TOF/TOF MS analysis of compound **7** by the MDSF method in the presence of a) 2,5-dihydroxybenzoic acid (DHB) or b) α-cyano-4-hydroxycinnamic acid as the matrix.

 © 2005 Wiley-VCH Verlag GmbH & Co. KGaA, Weinheim

bifunctional molecular transporter, which interfaces two types of polymer platforms for chemical and enzymatic synthesis. The merit of our strategy is evident: chemical blotting based on a terminal ketone group of the molecular transporter permits selective and quantitative transportation of a variety of products synthesized by general solid-phase synthesis. Moreover, the photoselective cleavage reaction of water-soluble polymers was suitable for an efficient and mild procedure to yield complex and unstable target compounds safely. The present two-dimensional synthetic scheme using a versatile molecular transporter will greatly accelerate both practical enzymatic synthesis with immobilized glycosyltransferases[14] and functional identification of biologically important glycopeptides.

Received: December 27, 2004
Published online: March 22, 2005

Keywords: enzymes · glycopeptides · polymers · solid-phase synthesis · synthetic methods

[1] a) R. B. Merrifield, *J. Am. Chem. Soc.* **1963**, *85*, 2149; b) R. B. Merrifield, *Angew. Chem.* **1985**, *97*, 801; *Angew. Chem. Int. Ed. Engl.* **1985**, *24*, 799.
[2] a) N. D. Sinha, J. Biernat, J. McManus, H. Köster, *Nucleic Acids Res.* **1984**, *12*, 4539; b) M. H. Caruthers, *Science* **1985**, *230*, 281.
[3] a) S. J. Danishefsky, K. F. McClure, J. T. Randolph, R. B. Ruggeri, *Science* **1993**, *260*, 1307; b) O. J. Plante, E. R. Palmacci, P. H. Seeberger, *Science* **2001**, *291*, 1523.
[4] For example: a) K. M. Koeller, C.-H. Wong, *Chem. Rev.* **2000**, *100*, 4465; b) M. Meldal, F.-I. Auzanneau, O. Hindsgaul, M. M. Monica, *J. Chem. Soc. Chem. Commun.* **1994**, 1849; c) O. Seitz, C.-H. Wong, *J. Am. Chem. Soc.* **1997**, *119*, 8766.
[5] Y. C. Lee, R. T. Lee, *Acc. Chem. Res.* **1995**, *28*, 321.
[6] For example: a) S.-I. Nishimura, K. Matsuoka, Y. C. Lee, *Tetrahedron Lett.* **1994**, *31*, 5657; b) S.-I. Nishimura, K. Yamada, *J. Am. Chem. Soc.* **1997**, *119*, 10555; c) K. Yamada, E. Fujita, S.-I. Nishimura, *Carbohydr. Res.* **1998**, *305*, 443.
[7] a) H. Herzner, T. Reipen, M. Schultz, H. Kunz, *Chem. Rev.* **2000**, *100*, 4495; b) P. M. St. Hilaire, M. Meldal, *Angew. Chem.* **2000**, *112*, 1210; *Angew. Chem. Int. Ed.* **2000**, *39*, 1162.
[8] S.-I. Nishimura, K. Niikura, M. Kurogochi, T. Matsushita, M. Fumoto, H. Hinou, R. Kamitani, H. Nakagawa, K. Deguchi, N. Miura, K. Monde, H. Kondo, *Angew. Chem.* **2005**, *117*, 93; *Angew. Chem. Int. Ed.* **2005**, *44*, 91.
[9] C. P. Holmes, *J. Org. Chem.* **1997**, *62*, 2370.
[10] For pioneering work on enzymatic oligosaccharide synthesis using polymers bearing a photolabile linker, see: U. Zehavi, S. Sadeh, M. Herchman, *Carbohydr. Res.* **1983**, *124*, 23.
[11] G. Arsequell, L. Krippner, R. A. Dwek, S. Y. C. Wong, *J. Chem. Soc. Chem. Commun.* **1994**, 2383.
[12] a) M. Kurogochi, T. Matsushita, S.-I. Nishimura, *Angew. Chem.* **2004**, *116*, 4163; *Angew. Chem. Int. Ed.* **2004**, *43*, 4071; b) M. Kurogochi, S.-I. Nishimura, *Anal. Chem.* **2004**, *76*, 6097.
[13] Meldal and co-workers also reported the feasibility of a photolabile linker for facile and efficient product characterization by MALDI-TOF MS in solid-phase glycopeptide synthesis: K. M. Halkes, C. H. Gotfredson, M. Grotli, L. P. Miranda, J. O. Duus, M. Meldal, *Chem. Eur. J.* **2001**, *7*, 3584.
[14] a) S. Nishiguchi, K. Yamada, Y. Fuji, S. Shibatani, A. Toda, S.-I. Nishimura, *Chem. Commun.* **2001**, 1944; b) A. Toda, K. Yamada, S.-I. Nishimura, *Adv. Synth. Catal.* **2002**, *344*, 61; c) N. Nagahori, K. Niikura, R. Sadamoto, M. Taniguchi, A. Yamagishi, K. Monde, S.-I. Nishimura, *Adv. Synth. Catal.* **2003**, *345*, 729.

 © 2005 Wiley-VCH Verlag GmbH & Co. KGaA, Weinheim

Supramolecular Chemistry

Calix[4]pyrrole: An Old yet New Ion-Pair Receptor**

Radu Custelcean, Lætitia H. Delmau, Bruce A. Moyer, Jonathan L. Sessler,* Won-Seob Cho, Dustin Gross, Gareth W. Bates, Simon J. Brooks, Mark E. Light, and Philip A. Gale**

In memory of Carlo Floriani

The development of ion-pair receptors, with the goal of achieving a higher level of control over recognition than that obtainable from simple ion binding, has intrigued researchers in supramolecular chemistry over the past decade.[1] Many reports have appeared during this period that describe the synthesis and study of very sophisticated receptor designs incorporating a range of electron-pair donor and acceptor groups. Most, if not all, of this work has been performed in the context of creating so-called ion-pair or salt hosts that will bind cation–anion pairs in homogeneous solution or enhance their extraction or transport under interfacial conditions. Whether the ditopic architecture in such systems confers real advantages over simpler combinations of single-ion receptors remains an open question. However, the utility of ion-pair receptors has been demonstrated in several systems incorpo-

[*] Dr. R. Custelcean, Dr. L. H. Delmau, Dr. B. A. Moyer
Chemical Sciences Division
Oak Ridge National Laboratory
P.O. Box 2008, Oak Ridge, TN 37831-6119 (USA)
Fax: (+1) 865-574-4939
E-mail: moyerba@ornl.gov

Prof. J. L. Sessler, W.-S. Cho, D. Gross
Department of Chemistry and Biochemistry
Institute for Cellular and Molecular Biology
University of Texas at Austin
1 University Station–A5300, Austin, TX 78712-0165 (USA)
Fax: (+1) 512-471-7550
E-mail: sessler@mail.utexas.edu

G. W. Bates, S. J. Brooks, Dr. M. E. Light, Dr. P. A. Gale
School of Chemistry
University of Southampton
Southampton SO17 1WD (UK)
Fax: (+44) 23-8059-3332
E-mail: philip.gale@soton.ac.uk

[**] The Southampton Group thanks the EPSRC/Crystal Faraday for a studentship to G.W.B. and the EPSRC for a DTA studentship to S.J.B. Additionally, we would like to thank Professor Mike Hursthouse and the EPSRC for access to the crystallography facilities at the University of Southampton. P.A.G. thanks the Royal Society for a University Research Fellowship. The work in Austin was supported by the US Department of Energy Office of Science (grant no. DE-FG02-04ER63741 to J.L.S.). The research at ORNL was sponsored by the Division of Chemical Sciences, Geosciences, and Biosciences, Office of Basic Energy Sciences, US Department of Energy, under contract no. DE-AC05-00OR22725 with Oak Ridge National Laboratory, managed and operated by UT-Battelle, LLC.

Supporting information for this article is available on the WWW under http://www.angewandte.org or from the author.

 DOI: 10.1002/anie.200462945 © 2005 Wiley-VCH Verlag GmbH & Co. KGaA, Weinheim

rating engineered steric constraints. Particular success has been encountered with receptors bearing cavities of limited dimensionality and directionality for contact ion pairs,[2] as well as with receptors that embody allosteric effects such that the binding of one ion organizes the receptor to accept the counterion.[3]

In spite of this progress, there remains a need to develop new ion-pair systems and to study the underlying effects that either promote or preclude concurrent anion–cation binding within a given receptor class. This need has prompted us to study the calix[4]pyrroles, a well-recognized class of anion receptors, in greater detail. We examined these systems as anion receptors for the extraction of cesium salts and observed anomalous behavior for the simple *meso*-octamethylcalix[4]pyrrole (**1**) which suggested exceptionally strong ion pairing of Cs^+ ions with complexes formed between **1** and Cl^- or Br^- ions in the organic phase. These anomalies could be best, and most interestingly, interpreted in terms of small halide ions organizing **1** into the cone conformation, which then in turn provides an electron-rich cup that putatively binds the Cs^+ ion.[4] Previous studies of ours have demonstrated that the binding of halide anions by **1** and other calix[4]pyrrole derivatives does indeed organize the receptors into the cone conformation.[5] However, this induced cup, or conelike cavity, has not yet been observed to serve as a receptor for electropositive species.

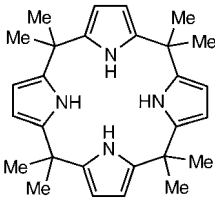

1

Although the solution chemistry remains under investigation, the exciting implication that **1** could function as a ditopic ion-pair receptor led us to study this easily prepared parent system in the solid state, in which any such potential behavior is expected to be most strongly manifested. Thus, we have carried out a crystallographic analysis of the anion-recognition behavior of calix[4]pyrrole in the presence of two large, polarizable cations, namely the cesium and imidazolium ions, and observed ditopic cation–anion binding in both cases.[6]

X-ray quality crystals of cesium halide/calix[4]pyrrole complexes were obtained by slow diffusion of a solution of cesium fluoride in ethanol into a solution of the calix[4]pyrrole in dichloromethane and by slow evaporation of solutions of cesium chloride or cesium bromide and calix[4]pyrrole in a dichloromethane/methanol mixture. The cesium fluoride/calix[4]pyrrole complex reveals that the cation is symmetrically included in the conelike cavity of the calix[4]pyrrole unit (Figure 1 a),[7] with an observed distance of 3.39 Å between the Cs^+ ion and the centroids of the pyrrole rings. The F^- ion is symmetrically bound to the four NH groups of the calix[4]pyrrole, with a distance of 2.79 Å for the N···F interaction (a similar distance to that observed previously in fluoride/calix[4]pyrrole complexes[5] and slightly shorter than those seen in a recently reported polyamide-based fluoride/cryptand complex[8]). The F^- ion is associated with the Cs^+ ion within the same complex (Cs···F contact distance of 3.69 Å), as well as with a Cs^+ ion in an adjacent complex (Cs···F contact distance of 2.77 Å), thus leading to the formation of a one-dimensional coordination polymer.

Likewise, the cesium chloride (Figure 1 b) and cesium bromide (Figure 1 c) salts are bound by the calix[4]pyrrole units as ion pairs in the solid state. The Cs^+ ion is tightly bound by the cone-shaped calix[4]pyrrole, with observed distances to the centroids of the pyrrole rings in the ranges 3.32–3.79 and 3.34–3.51 Å for the cesium chloride/calix[4]-pyrrole and cesium bromide/calix[4]pyrrole complexes, respectively. The Cl^- and Br^- ions are bound to the four NH groups of the calix[4]pyrrole by hydrogen bonds, with distances of 3.27–3.32 and 3.45–3.52 Å for the N···Cl and N···Br interactions, respectively. Like the cesium fluoride/calix[4]pyrrole complex, both the cesium chloride/calix[4]-pyrrole and cesium bromide/calix[4]pyrrole complexes form coordination polymers, with intermolecular Cs···X contact

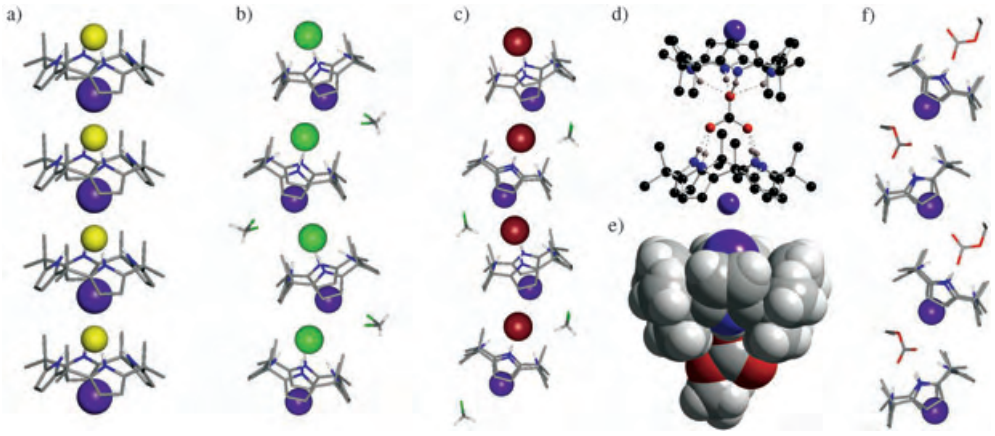

Figure 1. The X-ray crystal structures of a) the CsF, b) CsCl, and c) CsBr complexes of **1** showing inclusion of the Cs^+ ion in the cavity of the calix[4]pyrrole, thus leading to formation of a coordination network. d) The Cs_2CO_3 complex of **1** showing dimerization in the solid state (note that in this structure two different carbonate/calix[4]pyrrole binding modes exist). e) Space-filling representation of the $CsEtOCO_2$ complex of **1**, which illustrates inclusion of a Cs^+ ion in the calix[4]pyrrole cavity and f) the coordination network in this complex. The solvent has been removed for clarity in (d)–(f), and certain hydrogen atoms have been omitted for clarity in the non-space-filling representations. The Cs^+ ions are shown in purple, F^- ions in yellow, Cl^- ions in green, Br^- ions in orange/brown, O atoms in red, and C atoms in gray or black.

 © 2005 Wiley-VCH Verlag GmbH & Co. KGaA, Weinheim

distances of 3.38 and 3.59 Å for X = Cl and Br, respectively. However, dichloromethane is also included in the crystals for the bromide and chloride complexes, with solvent molecules associating with the cation in the chloride complex and both the cation and the anion in the bromide complex. The coordination chains adopt a zig-zag shape as a result.[9]

The attempted complexation of the calix[4]pyrrole with cesium hydroxide in an ethanol/dichloromethane mixture in air resulted in crystals of cesium carbonate and ethyl carbonate complexes being obtained, apparently by CO_2 fixation by the OH^- or EtO^- ions present in solution. Interestingly, the cesium carbonate/calix[4]pyrrole complex is a dimer consisting of a central anion bound through one oxygen atom to one calix[4]pyrrole unit (N···O separations of 2.82–2.89 Å) and through the other two oxygen atoms to the other macrocycle (in this case, each oxygen atom is bound by two hydrogen-bonding interactions, N···O distances of 2.78–2.84 Å). This dimer is of special interest because, to the best of our knowledge, it represents the first well-characterized "sandwich" complex reported to date[10] wherein a single anion serves to bridge two neutral pyrrole-based anion receptors. This complex is also of interest because the cesium counterions are found to reside in the cavity of each calix[4]pyrrole unit, thus balancing the charge (Figure 1d).

Similarly, the ethyl carbonate anion forms hydrogen bonds with the calix[4]pyrrole unit in two distinct ways: one $EtOCO_2^-$ ion is bound through one oxygen atom (N···O distances of 2.89–3.00 Å), while the second crystallographically different $EtOCO_2^-$ ion is bound by hydrogen bonds through two oxygen atoms (N···O distances of 2.87–3.04 Å). A space-filling representation of one of the two distinctive ethyl carbonate/calix[4]pyrrole pairs found in this structure is shown in Figure 1e, which illustrates the fit of the Cs^+ ion within the cuplike calix[4]pyrrole cavity. The ethyl carbonate anions in this structure act as a bridge between the four NH hydrogen-bond donors of one calix[4]pyrrole unit and a Cs^+ ion bound within the cavity of an adjacent complex (Cs···O contact distances of 2.84–3.17 Å). The net result of this anion–cation binding behavior is, once again, the formation of a one-dimensional coordination polymer in the solid state (Figure 1f).

High-quality crystals of the imidazolium salt complexes were prepared by evaporation of a solution of **1** in dichloromethane in the presence of 1-butyl-3-methylimidazolium chloride (**2**), 1-butyl-3-methylimidazolium bromide (**3**), 1-ethyl-3-methylimidazolium bromide (**4**), or 1,3-dimethylimidazolium methylsulfate (**5**).

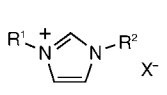

2: R^1 = *n*Bu, R^2 = Me, X = Cl^-
3: R^1 = *n*Bu, R^2 = Me, X = Br^-
4: R^1 = Et, R^2 = Me, X = Br^-
5: $R^1 = R^2$ = Me, X = $MeSO_4^-$

Complexes **1**·**2**·CH_2Cl_2·2 H_2O and **1**·**3**·CH_2Cl_2·2 H_2O were found to be isostructural. In the complex **1**·**2**, the Cl^- ion is bound by four NH hydrogen bonds from the pyrrole groups with N···Cl distances of 3.30–3.35 Å. The imidazolium cation is bound to the Cl^- ion by two CH···Cl hydrogen bonds (C31···Cl1 and C32···Cl1 distances are 3.47 and 3.66(3) Å). In the analogous bromide/calix[4]pyrrole complex, where NH···Br and CH···Br interactions were formed, the N···Br separations were 3.40–3.47 Å and the C31···Br1 and C32···Br1 separations were 3.52 and 3.71 Å, respectively. Interestingly, the imidazolium cations in these structures are included in the anion-induced cone-shaped cavity of an adjacent calix[4]pyrrole. The CH groups in the 4- and 5-positions of the imidazolium ring are close enough to have hydrogen-bonding interactions with the π-electron clouds of two of the pyrrole rings in the macrocycle. These interactions lead to the formation of one-dimensional chains in the solid state in **1**·**2** (Figure 2a) and **1**·**3** (see the Supporting Information).

Similarly, the anion binds to the four NH groups in the calix[4]pyrrole in the complex of **1** with **4**, with N···Br distances of 3.39–3.47 Å. In this case, two crystallographically distinct calixpyrrole complexes were observed in the solid-state structure. As in the structure of **1**·**2**, the imidazolium cation was found to reside in the calix[4]pyrrole cavity with the 4- and 5-positions of the imidazolium cation oriented within hydrogen-bonding distance of the π-electron clouds of two of the pyrrole rings. However, the orientation of the imidazolium cation differs slightly in the two crystallographically distinct complexes. In one of these calix[4]pyrrole complexes, the imidazolium cation is roughly symmetrically disposed with respect to the macrocycle (the H30···N10 and H31···N8 separations are 2.62 and 2.66 Å, respectively), whereas in the other calixpyrrole complex, the imidazolium cation is closer to one pyrrole ring than the other (the H64B···N2 and H65B···N4 distances are 2.71 and 2.43 Å, respectively). In contrast to the one-dimensional chains formed in **1**·**2** and **1**·**3** through imidazolium CH/anion interactions, the imidazolium CH group in the 2-position is within hydrogen-bonding distance of the π-electron cloud of one of the pyrrole rings of an adjacent calixpyrrole in this complex, as evidenced by the distance of 2.62 Å between the CH hydrogen (H32) and pyrrole nitrogen atoms (N2) (Figure 2b).

The structure of the 1,3-dimethylimidazolium methylsulfate complex of **1** (**1**·**5**) reveals that a bifurcated hydrogen bond is formed from the calix[4]pyrrole to the oxoanion guest. Three pyrrole NH groups form single NH···O hydrogen-bonding interactions with the O1 atom with separations of 2.95–3.07 Å. In contrast, the N4-H group forms two hydrogen bonds, one to the O1 atom (3.17 Å) and one to the O4 atom (3.36 Å). In this structure, a pendant methyl group (C33) was found to be encapsulated within the calix[4]pyrrole cavity. The imidazolium-ring CH groups and the other pendant methyl group are involved in hydrogen-bonding interactions to adjacent anions. As above, the net effect of these multiple interactions is the formation of a structure with long-range order, in this case a hydrogen-bonded sheet (C30···O2, C29···O3, and C32···O3 separations are 3.48, 3.39, and 3.05 Å, respectively; Figure 2c).

Preliminary studies on cesium- and imidazolium-cation inclusion in the conelike cavity of the chloride complex of **1** were conducted using ^{1}H NMR spectroscopic analysis in a variety of different solvents (for example, [D_5]nitrobenzene, [D_6]acetone/2% D_2O, and CD_2Cl_2). Significant shifts were

 © 2005 Wiley-VCH Verlag GmbH & Co. KGaA, Weinheim

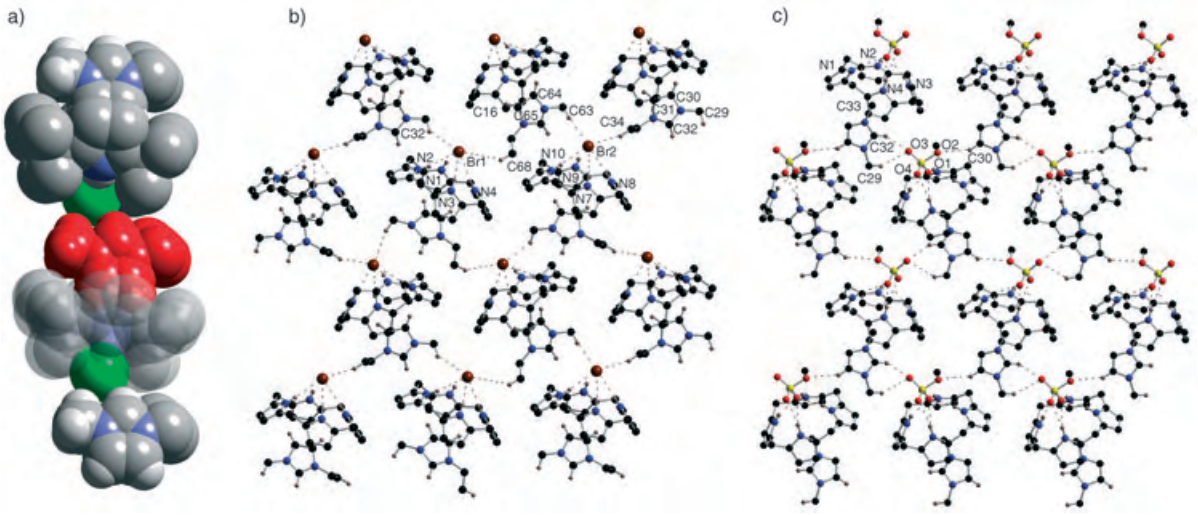

Figure 2. a) A space-filling representation of the coordination chain of **1·2**, which shows the imidazolium ring (4- and 5-positions) included in the calix[4]pyrrole cavity whilst the CH group at the 2-position and the pendant methyl group form a CH···Cl hydrogen-bonding interaction to an adjacent complex. One calix[4]pyrrole unit is rendered translucent and the included imidazolium cation is rendered red to illustrate the degree of penetration of the cation into the calix[4]pyrrole cavity. The non-acidic hydrogen atoms in the calix[4]pyrrole moiety and the solvent are omitted for clarity. Hydrogen-bonded network are formed in b) the **1·4** complex and c) the **1·5** complex (in this case, an imidazolium methyl group is included in the calix[4]pyrrole cavity). CH···O interactions from the imidazolium cation to the methylsulfate anion result in the formation of a two-dimensional sheet.

observed for the resonances of the pyrrole CH protons but not for the pyrrole NH protons on addition of $CsBPh_4$ or $CsClO_4$, and shielding of the imidazolium protons was also observed on addition of 1-butyl-3-methylimidazolium tetrafluoroborate to the chloride complex of **1**. These results are consistent with inclusion of the cations in the chloride/calix[4]pyrrole complex cavity in solution (see the Supporting Information). Investigations into the structure of the complexes formed in solution and quantification of the binding stoichiometry and thermodynamics under a range of experimental conditions are currently being carried out.

We believe that the present results open up a potentially new chapter in the chemistry of calix[4]pyrroles. We reported in 1996 that *meso*-octamethylcalix[4]pyrrole (**1**), a molecule known for over a century,[11] had hitherto unreported anion-complexation properties.[5] Herein, we have demonstrated that these easy-to-make macrocycles not only function as anion receptors but can act as ion-pair receptors. In particular, we have shown that in the solid state large diffuse cations, such as cesium and imidazolium ions, will occupy the electron-rich conelike cavity that is formed on anion binding to the NH portions of the calix[4]pyrrole core. These findings may inspire a range of new applications for calix[4]pyrroles, including their use as building blocks for crystal engineering and as possible receptors for anion–cation extractions. Studies of these and other possibilities are currently underway.

Experimental Section

1-CsF: $C_{28}H_{36}CsFN_4$, $M_r = 580.52$, colorless needles, $0.26 \times 0.08 \times 0.06\ mm^3$, tetragonal, space group $I4mm$, $a = b = 14.044(5)$, $c = 6.452(3)$ Å, $V = 1272.6(8)$ Å^3, $Z = 2$, $\rho_{calcd} = 1.515\ g\,cm^{-3}$, $F_{000} = 592$, Bruker SMART APEX, $Mo_{K\alpha}$ radiation, $\lambda = 0.71073$ Å, omega scan, $T = 173(2)$ K, $2\theta_{max} = 56.3°$, 6990 reflections collected, 894 unique ($R_{int} = 0.0258$). Final GOF = 1.105, $R1 = 0.0134$, $wR2 = 0.0330$, R indices based on 894 reflections with $I > 2\sigma(I)$, 50 parameters, 1 restraint. Lp and absorption corrections applied using SADABS, $T_{min} = 0.6987$, $T_{max} = 0.9161$, $\mu = 1.486\ mm^{-1}$. Residual electron density = 0.328 e Å^3. Absolute structure parameter = 0.00(3).

1-CsCl·CH_2Cl_2: $C_{29}H_{38}N_4Cl_3Cs_1$, $M_r = 681.89$, colorless needles, $0.33 \times 0.09 \times 0.03\ mm^3$, triclinic, space group $P\bar{1}$, $a = 10.669(4)$, $b = 15.300(6)$, $c = 20.543(8)$ Å, $\alpha = 110.882(7)$, $\beta = 95.529(7)$, $\gamma = 91.028(7)°$, $V = 3113(2)$ Å^3, $Z = 4$, $\rho_{calcd} = 1.455\ g\,cm^{-3}$, $F_{000} = 1384$, Bruker SMART APEX, $Mo_{K\alpha}$ radiation, $\lambda = 0.71073$ Å, omega scan, $T = 173(2)$ K, $2\theta_{max} = 56.7°$, 35439 reflections collected, 15354 unique ($R_{int} = 0.0302$). Final GOF = 1.225, $R1 = 0.0573$, $wR2 = 0.1100$, R indices based on 13655 reflections with $I > 2\sigma(I)$, 683 parameters, 0 restraints. Lp and absorption corrections applied using SADABS, $T_{min} = 0.6424$, $T_{max} = 0.9572$, $\mu = 1.471\ mm^{-1}$. Residual electron density = 1.724 e Å^3.

1-CsBr·2 CH_2Cl_2: $C_{30}H_{40}BrCl_4CsN_4$, $M_r = 811.28$, yellow plate, $0.31 \times 0.23 \times 0.02\ mm^3$, monoclinic, space group $P2_1/n$, $a = 10.501(4)$, $b = 15.659(5)$, $c = 20.982(7)$ Å, $\beta = 97.319(6)°$, $V = 3422(2)$ Å^3, $Z = 4$, $\rho_{calcd} = 1.575\ g\,cm^{-3}$, $F_{000} = 1624$, Bruker SMART APEX, $Mo_{K\alpha}$ radiation, $\lambda = 0.71073$ Å, omega scan, $T = 173(2)$ K, $2\theta_{max} = 56.7°$, 42059 reflections collected, 8488 unique ($R_{int} = 0.0409$). Final GOF = 1.036, $R1 = 0.0341$, $wR2 = 0.0870$, R indices based on 7009 reflections with $I > 2\sigma(I)$, 369 parameters, 0 restraints. Lp and absorption corrections applied using SADABS, $T_{min} = 0.5009$, $T_{max} = 0.9501$, $\mu = 2.588\ mm^{-1}$. Residual electron density = 1.361 e Å^3.

1$_2$-Cs_2CO_3·4 CH_2Cl_2: $C_{61}H_{80}Cl_8Cs_2N_8O_3$, $M_r = 1522.75$, colorless plates, $0.34 \times 0.23 \times 0.04\ mm^3$, monoclinic, space group $P2_1/n$, $a = 15.273(7)$, $b = 20.942(10)$, $c = 22.787(11)$ Å, $\beta = 105.769(9)°$, $V = 7014(6)$ Å^3, $Z = 4$, $\rho_{calcd} = 1.442\ g\,cm^{-3}$, $F_{000} = 3088$, Bruker SMART APEX, $Mo_{K\alpha}$ radiation, $\lambda = 0.71073$ Å, omega scan, $T = 173(2)$ K, $2\theta_{max} = 56.8°$, 86226 reflections collected, 17469 unique ($R_{int} = 0.0566$). Final GOF = 1.054, $R1 = 0.0595$, $wR2 = 0.1596$, R indices based on 13173 reflections with $I > 2\sigma(I)$, 755 parameters, 0 restraints. Lp and absorption corrections applied using SADABS, $T_{min} = 0.6492$, $T_{max} = 0.9465$, $\mu = 1.391\ mm^{-1}$. Residual electron density = 3.524 e Å^3.

1-CsEtOCO$_2$·0.5 EtOH: $C_{64}H_{88}N_8O_7Cs_2$, $M_r = 1347.24$, colorless plates, $0.20 \times 0.19 \times 0.03\ mm^3$, triclinic, space group $P\bar{1}$, $a = 10.606(5)$, $b = 15.618(7)$, $c = 20.147(9)$ Å, $\alpha = 95.107(8)$, $\beta = 98.914(8)$, $\gamma =$

 © 2005 Wiley-VCH Verlag GmbH & Co. KGaA, Weinheim

101.189(8)°, $V = 3210(2)$ Å^3, $Z = 2$, $\rho_{calcd} = 1.394$ g cm^{-3}, $F_{000} = 1388$, Bruker SMART APEX, $Mo_{K\alpha}$ radiation, $\lambda = 0.71073$ Å, omega scan, $T = 173(2)$ K, $2\theta_{max} = 56.7°$, 40329 reflections collected, 15892 unique ($R_{int} = 0.0339$). Final GOF = 1.048, $R1 = 0.0459$, $wR2 = 0.1284$, R indices based on 12142 reflections with $I > 2\sigma(I)$, 742 parameters, 0 restraints. Lp and absorption corrections applied using SADABS, $T_{min} = 0.7964$, $T_{max} = 0.9651$, $\mu = 1.192$ mm^{-1}. Residual electron density = 1.747 e Å^3.

1·2CH_2Cl_2·2H_2O: $C_{37}H_{57}N_6O_2Cl_3$, $M_r = 724.24$, pale-red prisms, $0.2 \times 0.2 \times 0.2$ mm^3, triclinic, space group $P\bar{1}$, $a = 10.4222(14)$, $b = 10.7682(11)$, $c = 17.993(2)$ Å, $\alpha = 74.664(11)$, $\beta = 81.603(13)$, $\gamma = 84.951(10)°$, $V = 1923.9(4)$ Å^3, $Z = 2$, $\rho_{calcd} = 1.250$ g cm^{-3}, $F_{000} = 776$, Bruker Nonius KappaCCD, $Mo_{K\alpha}$ radiation, $\lambda = 0.71073$ Å, phi and omega scans, $T = 120(2)$ K, $2\theta_{max} = 55.34°$, 41654 reflections collected, 8681 unique ($R_{int} = 0.0566$). Final GOF = 1.070, $R1 = 0.0519$, $wR2 = 0.1186$, R indices based on 8681 reflections with $I > 2\sigma(I)$, 484 parameters, 12 restraints. Lp and absorption corrections applied using TWINABS, $T_{min}/T_{max} = 0.763$, $\mu = 0.278$ mm^{-1}. Residual electron density = 1.288 e Å^{-3}.

1·3CH_2Cl_2·2H_2O: $C_{37}H_{57}N_6O_2Cl_2Br$, $M_r = 768.70$, colorless rods, $0.18 \times 0.05 \times 0.05$ mm^3, triclinic, space group $P\bar{1}$, $a = 10.5710(14)$, $b = 10.7800(11)$, $c = 18.082(2)$ Å, $\alpha = 74.528(11)$, $\beta = 81.155(13)$, $\gamma = 84.715(10)°$, $V = 1959.4(4)$ Å^3, $Z = 2$, $\rho_{calcd} = 1.303$ g cm^{-3}, $F_{000} = 812$, Bruker Nonius KappaCCD, $Mo_{K\alpha}$ radiation, $\lambda = 0.71073$ Å, phi and omega scans, $T = 120(2)$ K, $2\theta_{max} = 50.6°$, 21008 reflections collected, 6576 unique ($R_{int} = 0.1857$). Final GOF = 1.088, $R1 = 0.1113$, $wR2 = 0.2789$, R indices based on 6576 reflections with $I > 2\sigma(I)$, 467 parameters, 30 restraints. Lp and absorption corrections applied using TWINABS, $T_{min}/T_{max} = 0.563$, $\mu = 1.225$ mm^{-1}. Residual electron density = 1.208 e Å^{-3}.

1·4: $C_{34}H_{47}N_6Br$, $M_r = 619.69$, colorless blocks, $0.2 \times 0.05 \times 0.04$ mm^3, monoclinic, space group $P2_1/c$, $a = 21.238(3)$, $b = 17.043(4)$, $c = 18.287(4)$ Å, $\beta = 108.477(14)°$, $V = 6278(2)$ Å^3, $Z = 8$ (2 molecules), $\rho_{calcd} = 1.311$ g cm^{-3}, $F_{000} = 2624$, Bruker Nonius KappaCCD, $Mo_{K\alpha}$ radiation, $\lambda = 0.71073$ Å, phi and omega scans, $T = 120(2)$ K, $2\theta_{max} = 50.06°$, 54773 reflections collected, 11067 unique ($R_{int} = 0.1162$). Final GOF = 1.052, $R1 = 0.0885$, $wR2 = 0.2409$, R indices based on 11067 reflections with $I > 2\sigma(I)$, 749 parameters, 60 restraints. Lp and absorption corrections applied using SADABS, $T_{min}/T_{max} = 0.765$, $\mu = 1.343$ mm^{-1}. Residual electron density = 1.382 e Å^{-3}.

1·5: $C_{36}H_{52}N_6O_4Cl_4S$, $M_r = 806.70$, colorless plates, $0.4 \times 0.3 \times 0.05$ mm^3, monoclinic, space group $P2_1$, $a = 10.611(5)$, $b = 18.193(6)$, $c = 10.803(3)$ Å, $\beta = 106.36(2)°$, $V = 2001.0(12)$ Å^3, $Z = 2$, $\rho_{calcd} = 1.339$ g cm^{-3}, $F_{000} = 852$, Bruker Nonius KappaCCD, $Mo_{K\alpha}$ radiation, $\lambda = 0.71073$ Å, phi and omega scans, $T = 120(2)$ K, $2\theta_{max} = 55.54°$, 17479 reflections collected, non-merohedral twinned data—not merged. Final GOF = 1.173, $R1 = 0.1005$, $wR2 = 0.1831$, R indices based on 17479 reflections with $I > 2\sigma(I)$, 467 parameters, 5 restraints. Lp and absorption corrections applied using TWINABS, $T_{min}/T_{max} = 0.663$, $\mu = 0.394$ mm^{-1}. Residual electron density = 1.461 e Å^{-3}. Absolute structure parameters were not reliably determined because of twinning. All structures were solved with direct methods by using SHELXS 97, and refined on F^2 by using SHELXL 97.[12] Non-hydrogen atoms were refined anisotropically. H atoms were calculated and placed in idealized position by using a riding model. CCDC-257828–257832 and -258077–258080 contain the supplementary crystallographic data for **1**-CsF, **1**-CsCl·CH_2Cl_2, **1**-CsBr·2CH_2Cl_2, **1**$_2$-Cs_2CO_3·4CH_2Cl_2, **1**-CsEtOCO$_2$·0.5EtOH, **1**·3CH_2Cl_2·2H_2O **1**·2CH_2Cl_2·2H_2O, **1**·4, and **1**·5, respectively. These data can be obtained free of charge from the Cambridge Crystallographic Data Centre via www.ccdc.cam.ac.uk/data_request/cif.

Received: December 15, 2004

Keywords: calix compounds · crystal engineering · hydrogen bonds · ion pairs · supramolecular chemistry

[1] P. D. Beer, P. K. Hopkins, J. D. McKinney, *Chem. Commun.* **1999**, 1253–1254; S. Kubik, *J. Am. Chem. Soc.* **1999**, *121*, 5846–5855; M. D. Barboiu, N. D. Hovnanian, C. Luca, L. Cot, *Tetrahedron* **1999**, *55*, 9221–9232; A. Lutzen, A. R. Rebslo, C. A. Schalley, B. M. O'Leary, J. Rebek, *J. Am. Chem. Soc.* **1999**, *121*, 7455–7456; S. Kubik, R. Goddard, *J. Org. Chem.* **1999**, *64*, 9475–9486; S. L. De Wall, L. J. Barbour, G. W. Gokel, *J. Am. Chem. Soc.* **1999**, *121*, 8405–8406; E. S. Meadows, S. L. De Wall, L. J. Barbour, G. W. Gokel, *Chem. Commun.* **1999**, 1557–1558; N. Teramae, K. Shigemori, S. Nishizawa, *Chem. Lett.* **1999**, 1185–1186; M. J. Deetz, M. Shang, B. D. Smith, *J. Am. Chem. Soc.* **2000**, *122*, 6201–6207; T. G. Levitskaia, J. C. Bryan, R. A. Saclebon, J. D. Lamb, B. A. Moyer, *J. Am. Chem. Soc.* **2000**, *122*, 554–562; L. H. Uppadine, J. E. Redman, S. W. Dent, M. G. B. Drew, P. D. Beer, *Inorg. Chem.* **2001**, *40*, 2860–2869; S. Memon, M. Yilmaz, *J. Mol. Struct.* **2001**, *595*, 101–109; X. Shi, J. C. Fettinger, J. T. Davis, *Angew. Chem.* **2001**, *113*, 2909–2913; *Angew. Chem. Int. Ed.* **2001**, *40*, 2827–2830; G. J. Kirkovits, J. A. Shriver, P. A. Gale, J. L. Sessler, *J. Inclusion Phenom. Mol. Recognit. Chem.* **2001**, *41*, 69–75; J. L. Atwood, A. Szumna, *Chem. Commun.* **2003**, 940–941; G. Tumcharern, T. Tuntulani, S. J. Coles, M. B. Hursthouse, J. D. Kilburn, *Org. Lett.* **2003**, *5*, 4971–4974.

[2] J. M. Mahoney, A. M. Beatty, B. D. Smith, *J. Am. Chem. Soc.* **2001**, *123*, 5847–5848; J. M. Mahoney, R. A. Marshall, A. M. Beatty, B. D. Smith, S. Camiolo, P. A. Gale, *J. Supramol. Chem.* **2001**, *1*, 289–292.

[3] D. J. White, N. Laing, H. Miller, S. Parsons, S. Coles, P. A. Tasker, *Chem. Commun.* **1999**, 2077–2078; T. Tozawa, Y. Misawa, S. Tokita and Y. Kubo, *Tetrahedron Lett.* **2000**, *41*, 5219–5223.

[4] "Fluorinated Calixpyrroles Eliminate Anion Hofmeister Bias Selectivity": T. G. Levitskaia, T. Vercouter, B. A. Moyer, J. A. Shriver, J. L. Sessler, M. Marquez, Abstracts of the 27th International Symposium on Macrocyclic Chemistry, Park City, Utah (USA), June 23–27, **2002**.

[5] P. A. Gale, J. L. Sessler, V. Král, V. Lynch, *J. Am. Chem. Soc.* **1996**, *118*, 5140–5141; J. L. Sessler, A. Andrievsky, P. A. Gale, V. Lynch, *Angew. Chem.* **1996**, *108*, 2954–2957; *Angew. Chem. Int. Ed. Engl.* **1996**, *35*, 2782–2785; S. Camiolo, S. J. Coles, P. A. Gale, M. B. Hursthouse, J. L. Sessler, *Acta Crystallogr. Sect. E* **2001**, *57*, o816-o818; C. J. Woods, S. Camiolo, M. E. Light, S. J. Coles, M. B. Hursthouse, M. A. King, P. A. Gale, J. W. Essex, *J. Am. Chem. Soc.* **2002**, *124*, 8644–8652.

[6] Floriani and co-workers have published extensively on the metal coordination of deprotonated porphyrinogens. For an overview of their work, see: C. Floriani, R. Floriani-Moro in *The Porphyrin Handbook*, *Vol. 3* (Eds.: K. M. Kadish, K, M. Smith, R. Guilard), Academic Press, New York, **2000**, chap. 24, pp. 385–420.

[7] For an example of the inclusion of cesium ions in the aromatic cavity of a calix[4]arene, see: J. M. Harrowfield, M. I. Ogden, W. R. Richmond, A. H. White, *J. Chem. Soc. Chem. Commun.* **1991**, 1159–1161.

[8] S. O. Kang, D. VanderVelde, D. Powell, K. Bowman-James, *J. Am. Chem. Soc.* **2004**, *126*, 12272–12273.

[9] It is to be noted that the Cs···X distances of CsF, CsCl, and CsBr in the solid state are 3.004, 4.118, and 4.287 Å, respectively (W. P. Davey, *Phys. Rev.* **1923**, *21*, 143). The corresponding Cs···X intermolecular distances in the various **1**-CsX structures are shorter: 2.77, 3.38, and 3.59 Å for the F^-, Cl^-, and Br^- ions, respectively. These short intermolecular contacts are facilitated by the ion-pair binding of **1**, which leaves one side of the Cs^+ and X^- ions exposed. In the crystalline CsX salts, each ion interacts with six or eight counterions as imposed by the simple cubic (CsF) or body-centered cubic (CsCl and CsBr) symmetry, whereas the Cs···X interactions in **1**-CsX are limited to one

 © 2005 Wiley-VCH Verlag GmbH & Co. KGaA, Weinheim

dimension as a result of complexation by **1**. This arrangement leads to the shorter intermolecular contact distances observed in the **1**-CsX structures. Although these latter distances may appear short, they are, however, a simple consequence of crystal packing within one-dimensional coordination polymers. The binding of ion pairs within appropriate ditopic receptors can also lead to a shortening of the interionic distance relative to that seen in pure M^+X^- salts. For a particularly cogent example of this latter effect, see: J. M. Mahoney, R. A. Marshall, A. M. Beatty, B. D. Smith, S. Camiolo, P. A. Gale, *J. Supramol. Chem.* **2001**, *1*, 289–292, in which an NaCl ion pair is bound by an ion-pair receptor with a shorter interionic distance than that found in the NaCl crystalline lattice.

[10] For an example of an anion (sulfate) sandwich complex in a mixed amide/amine macrocycle, see: M. A. Hossain, J. M. Llinares, D. Powell, K. Bowman-James, *Inorg. Chem.* **2001**, *40*, 2936–2937; for an iodide sandwich complex of a cyclic peptide, see: S. Kubik, R. Goddard, R. Kirchner, D. Nolting, J. Seidel, *Angew. Chem.* **2001**, *113*, 2722–2725; *Angew. Chem. Int. Ed.* **2001**, *40*, 2648–2651.

[11] A. Baeyer, *Ber. Dtsch. Chem. Ges.* **1886**, *19*, 2184–2185.

[12] SHELXTL 6.12, Bruker AXS, Madison WI, **1997**.

 © 2005 Wiley-VCH Verlag GmbH & Co. KGaA, Weinheim

Bioconjugate Chemistry

Phototoxicity of Peptidoconjugates Modulated by a Single Amino Acid**

*Lisa M. Wittenhagen, Jay R. Carreon, Erin G. Prestwich, and Shana O. Kelley**

Oxidative stress resulting from the intracellular release of chemical oxidants or free radicals is known to exert deleterious effects on biological function. In cells, exposure to light or sensitizers can produce singlet oxygen ($^1O_2$), a highly reactive, mutagenic, and genotoxic species that induces oxidative stress.[1–3] These properties have been harnessed in photodynamic chemotherapy, an anticancer treatment that involves the photosensitization of $^1O_2$ to promote cell death within solid tumors.[4] Chemical modification of essential cellular components likely underlies the detrimental effects of $^1O_2$, as direct damage to DNA, proteins, and lipids is observed.[1,3,5–8] Given that the reaction of $^1O_2$ with DNA and amino acids generates transient species that are highly reactive (e.g. endoperoxides and peroxyl radicals),[8–10] cross-reactions between nucleic acids and bound proteins are probable.[11] Understanding and exploiting biomolecular cross-reactions that occur when $^1O_2$ is generated intracellularly may lead to new photodynamic therapeutics with enhanced potencies.

We have developed a strategy toward the study of oxidative cross-reactions promoted by $^1O_2$ between amino acids and DNA that relies on a family of DNA-binding peptidoconjugates bearing the photoactive intercalator thiazole orange (TO).[12,13] Upon photoexcitation, TO generates $^1O_2$, thus serving as an oxidant source and providing a DNA-binding anchor. We previously identified TO–dipeptide conjugates exhibiting DNA-photocleavage activity which depends on the composition of the peptide.[14] Conjugates that contain certain aromatic amino acids, particularly tryptophan (W) and tyrosine (Y), are capable of DNA photocleavage, whereas conjugates containing glycine (G) or phenylalanine (F) do not promote strand scission. An explanation for the DNA-cleavage activity was derived from previous research that identified a subset of protein residues (including tryptophan, cysteine, histidine, and tyrosine) which react with $^1O_2$ to form peroxides.[1,8–10] Peroxyl radicals are reasonable candidates as the active DNA-cleaving species, as precedent exists for strand scission through hydrogen abstraction from the DNA backbone by thermally-generated peroxides.[15] Indeed, studies of TO peptidoconjugates displaying strand-scission activity revealed that amino acid based peroxides are the active species that induce DNA cleavage.[14]

Herein we describe TO peptidoconjugates that access human cells and exhibit amino-acid-dependent phototoxicity. The TO conjugates feature a portion (residues 49–57) of the HIV-1 transactivator of transcription (Tat) peptide sequence, which was previously used by other research groups to deliver appended cargoes into cells.[16] Based on our previous findings, we wished to investigate whether cell-permeable TO peptidoconjugates are toxic to human cells upon photoexcitation, and to determine if toxicity can be triggered by the presence of specific amino acids, as previously demonstrated when the DNA strand scission activity was initially characterized.[14] Indeed, a TO–Tat peptidoconjugate containing tryptophan cleaves DNA in vitro and exhibits appreciable phototoxicity, whereas a glycine-containing analogue neither elicits significant DNA cleavage, nor causes cell death. These results present an example of novel peptide-containing photodynamic agents with activities that can be tuned through the manipulation of sequence composition.

TO–D-peptide conjugates **1a**–**2b** were prepared on Rink amide solid support, and the N terminus was capped with a TO derivative[14] by using standard solid-phase Fmoc chemistry.[14] Subsequent cleavage from the resin and purification by HPLC afforded TO peptidoconjugates **1a**–**2b** (Figure 1a). The non-natural D-peptide structure was used to impart resistance to proteolytic degradation.[17] The two versions of the Tat peptide, **1a** and **1b**, were prepared with glycine or tryptophan residues, respectively, positioned proximal to the

[*] L. M. Wittenhagen, J. R. Carreon, E. G. Prestwich, Dr. S. O. Kelley
Department of Chemistry
Eugene F. Merkert Chemistry Center, Boston College
Chestnut Hill, MA 02467 (USA)
Fax: (+1) 617-552-2705
E-mail: shana.kelley@bc.edu

[**] We acknowledge the NSF (CAREER award to S.O.K.) and the Sloan Foundation (Research Fellowship to S.O.K.) for funding. We also acknowledge generous access to fluorescence imaging facilities in the Biology Department at Boston College.

Supporting information for this article is available on the WWW under http://www.angewandte.org or from the author.

 © 2005 Wiley-VCH Verlag GmbH & Co. KGaA, Weinheim DOI: 10.1002/anie.200462836

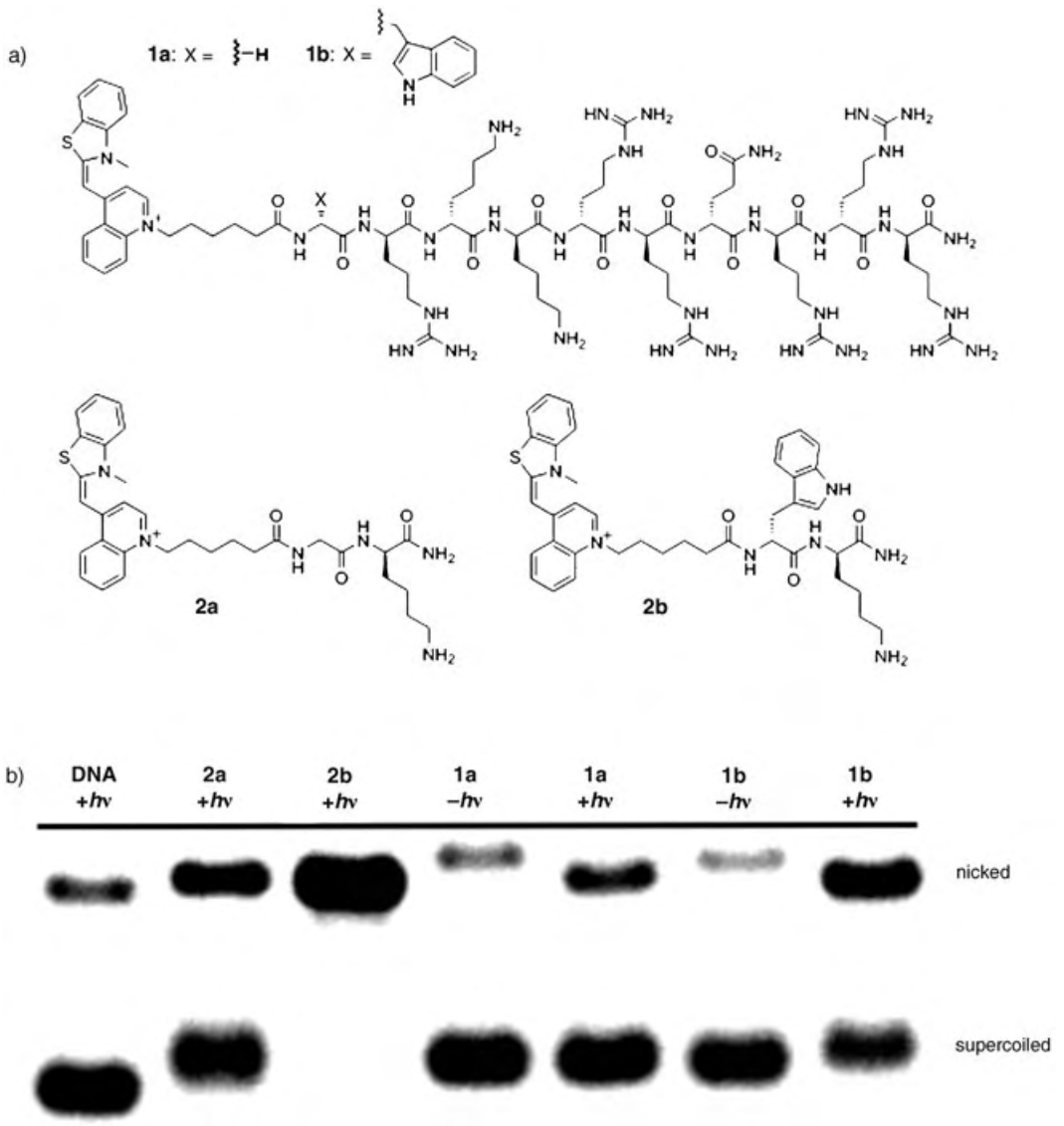

Figure 1. a) Structures of TO peptidoconjugates **1a** (TO–G–Tat), **1b** (TO–W–Tat), **2a** (TO–GK), **2b** (TO–WK); b) photocleavage of pUC18 plasmid DNA by TO peptidoconjugates analyzed by agarose gel electrophoresis. Solutions contained pUC18 (75 μM (base pairs)), sodium cacodylate (10 mM, pH 7), and TO peptidoconjugate (1 μM). Samples were irradiated ($\lambda = 501$ nm) for 30 min as indicated (+or−$h\nu$), and the conversion of supercoiled to nicked circular plasmid was monitored to evaluate DNA cleavage. (See Supporting Information for quantitation of cleavage efficiencies.)

dye to evaluate if selective DNA cleavage and phototoxicity could be observed. The TO–dipeptide conjugates **2a** and **2b** are analogous to L-amino acid containing conjugates previously reported,[14] and were synthesized to provide positive controls for DNA cleavage.

The photocleavage properties of the TO–Tat peptidoconjugates were investigated with a plasmid nicking assay. Upon irradiation with visible light, the tryptophan-containing conjugate **1b** caused high levels of strand scission (Figure 1b). The observation that **1b** yields greater DNA cleavage (induced by the tryptophan-based peroxide formed upon the production of $^1O_2$) than **1a** (which elicits only low-level cleavage from direct $^1O_2$-promoted damage) indicates that these TO conjugates exhibit photoreactivity analogous to that of their L-amino acid counterparts described previously.[14] Interestingly, **2b**, a control dipeptide conjugate comprised of D-amino acids, cleaved supercoiled plasmid DNA more efficiently than **1b**, thus demonstrating that tryptophan exhibits greater reactivity when presented to DNA within the context of a dipeptide rather than the Tat decapeptide.[18] This effect may arise from different tryptophan conformations that are induced by the two peptides. Nonetheless, these results indicate that the amino acid dependent DNA cleavage previously discovered and characterized[14] for dipeptide conjugates can be extrapolated to a more complex peptide structure. Furthermore, the TO–W–Tat peptidoconjugate, which should have good cellular uptake properties, is a suitable probe for studies inside cells.

Confocal fluorescence microscopy confirmed cellular uptake of the TO–Tat peptidoconjugates. As TO undergoes

 © 2005 Wiley-VCH Verlag GmbH & Co. KGaA, Weinheim

a dramatic increase in its fluorescence quantum yield when bound to DNA or RNA,[13] it can be used as an intrinsic probe for the location of the conjugates within cells. Both TO–Tat peptidoconjugates **1a** and **1b** exhibited identical localization patterns, indicating they were efficiently imported into living unfixed HeLa cells (Figure 2). Less than five percent of the cells were stained when treated with propidium iodide, a dye specific for dead cells, thus reflecting that the conditions used to evaluate uptake patterns of the peptidoconjugates did not induce cell death.

To further investigate the location of the TO–Tat peptidoconjugates within human cells, colocalization experiments were performed with two control dyes. SYTO-85 binds to nucleic acids and provides a marker for nuclear uptake, and mitotracker deep red-633 selectively stains mitochondria. Interestingly, the TO–Tat peptidoconjugates were found to enter both the mitochondria (Figure 3a–c) and the nucleoli (Figure 3d–f) of live cells.[19] This finding is in stark contrast to

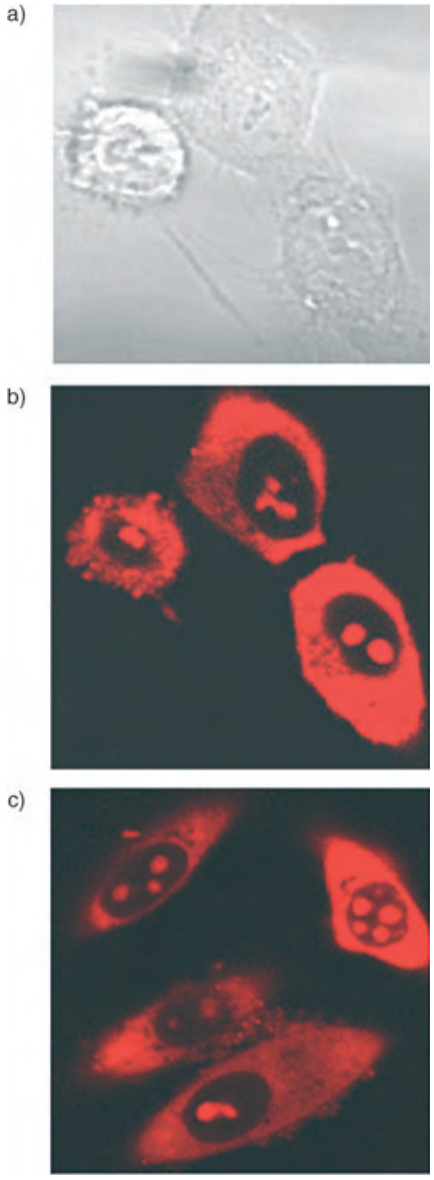

Figure 2. Confocal-microscopy images of unfixed living HeLa cells incubated for 1.5 h at 37 °C with TO–Tat peptidoconjugates (10 μM); a) transmission image of cells incubated with **1b**; b) red-fluorescence (λ_{ex} = 488 nm, λ_{em} = 500–571 nm) image of the same cells illustrates both cytoplasmic and nuclear uptake of **1b**; c) peptidoconjugate **1a** shows an identical internalization pattern to that of **1b**.

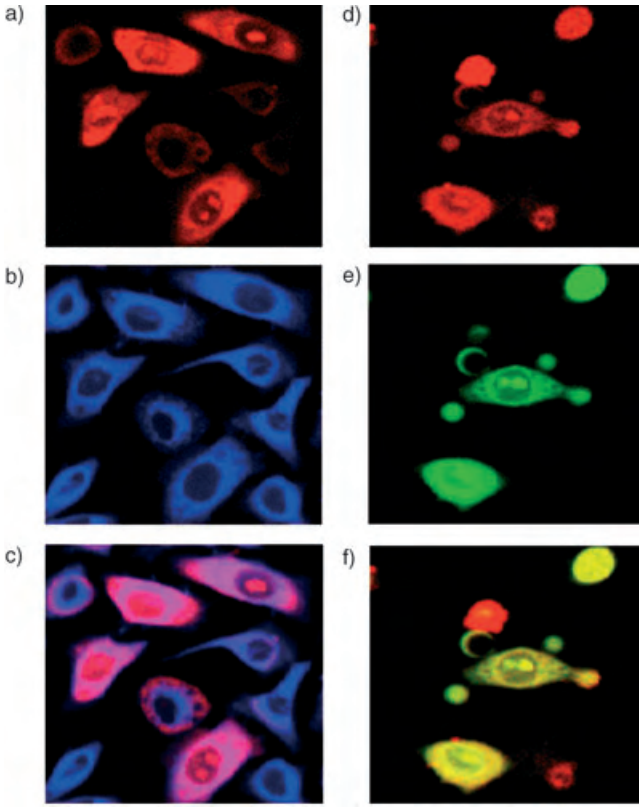

Figure 3. Localization profiles of TO–Tat peptidoconjugates. HeLa cells were incubated with **1a** (10 μM) and SYTO-85 (500 nM) or mitotracker red-633 (3 μM) for 1.5 h at 37 °C; a) and d) red-fluorescence image of cells stained with **1a**; b) visualization of mitotracker deep red-633 staining of the mitochondria; c) merged image of red- and blue-fluorescence images illustrating colocalization of **1a** with mitotracker deep red-633; e) green-fluorescence image illustrating nucleolar staining by SYTO-85; f) merged image showing that **1a** colocalizes with SYTO-85 in the nucleoli of these cells. Red fluorescence: λ_{ex} = 488 nm, λ_{em} = 500–571 nm; green fluorescence: λ_{ex} = 543 nm, λ_{em} = 556–648 nm; blue fluorescence: λ_{ex} = 543 nm, λ_{em} = 600–750 nm.[19]

the work of Ross et al., who found that the Tat sequence did not enter the mitochondria.[20] However, the peptide had been conjugated to a different dye (Oregon green); different cargoes can markedly change uptake and localization patterns.[16] The TO conjugates described herein are most emissive when bound to DNA. Therefore, as it is clear that the compounds have penetrated the nucleus, there may also be appreciable concentrations of the compounds in regions of the cell that appear dark in the images shown.

As the TO–Tat peptidoconjugates were shown to enter human cells efficiently, these probes presented an appropriate system for the analysis of phototoxicity. When incubated with HeLa cells and irradiated, the TO–W–Tat peptidoconjugate **1b** was significantly phototoxic to cells as a function of irradiation time, whereas cells exposed to the glycine-

 © 2005 Wiley-VCH Verlag GmbH & Co. KGaA, Weinheim

containing conjugate **1a** were unaffected (Figure 4). After irradiation, the cells were incubated with fresh media for 24 h before viability was analyzed to allow the effects of the compounds to be assessed. Cell death was not observed if cells

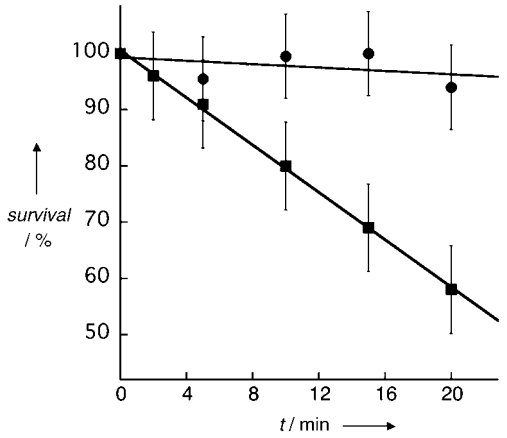

Figure 4. Phototoxicity of TO–Tat peptidoconjugates. Toxicity was evaluated 12 h after incubation (3 μM) and irradiation ($\lambda = 501$ nm) with **1a** (TO–G–Tat, ●) and **1b** (TO–W–Tat, ■) by CCK-8 assay. Data points show mean values; error bars show standard-deviation values. All assays were performed in triplicate, and three multiple, independent trials were conducted. Controls were performed in the dark to confirm that cell viability was maintained in the absence of photoexcitation. Light controls were also performed to confirm that the irradiation conditions did not harm the cells.

containing either conjugate were kept in the dark.[21] Interestingly, the Tat peptide was observed to effectively abolish the dark toxicity of the parent TO compound, as unmodified TO causes quantitative cell death even in the absence of light.

The correlation of phototoxicity with the DNA-photocleavage activity of the TO peptidoconjugates described herein strongly suggests that the tryptophan-based peroxides formed on TO conjugates containing this amino acid are responsible for this selectivity. Whereas it cannot be unequivocally proven that the decreased cell viability results from DNA cleavage, the location of the conjugates within the cellular compartments that contain genomic DNA presents the possibility that strand scission may underlie the toxicity described. This represents the first study in which designed Tat peptide sequences were used to induce selective DNA damage and to produce phototoxic agents.

Experimental Section

Dye–peptide conjugates: Solid-phase synthesis was performed with Rink amide resin (NovaBiochem). Couplings were performed with Fmoc-protected D-amino acid (4 equiv, Advanced ChemTech, Fmoc = 9-fluorenylmethyloxycarbonyl), HBTU (4 equiv, Advanced ChemTech, HBTU = *O*-(benzotriazol-l-yl)-*N*,*N*,*N*′,*N*′-tetramethyluronium hexafluorophosphate), and *N*,*N*-diisopropylethylamine (8 equiv, Acros) in *N*,*N*-dimethyl formamide (DMF) for 3 h. The Fmoc group was removed with piperidine (20% *v*/*v*) in DMF for 30 min. (To minimize diketopiperazine formation, dipeptides were deprotected with piperidine (50% *v*/*v*) in DMF for 5 min.) The deprotected N termini were capped with TO–COOH (4 equiv)[14] under standard coupling conditions as described above.[14] To minimize the formation of by-products resulting from Rink amide resin at high concentrations of trifluoroacetic acid (TFA), a two-step procedure for detachment/deprotection of the resin was performed as described.[22] The dye–peptide conjugates were detached from the resin by slurrying in TFA/CH_2Cl_2 (10% *v*/*v*) and transferred to a glass funnel with a fine sinter. The solvent was allowed to drip slowly through the resin bed and was washed with TFA/CH_2Cl_2 (5% *v*/*v*) and concentrated in vacuo. Deprotection was carried out by stirring the residue in TFA/TIS (95:5) at room temperature for 0.5–2 h (TIS = triisopropylsilane, Acros). The solution was concentrated in vacuo and Et_2O was added to precipitate the peptide. The resulting red solid was dissolved in TFA/H_2O (0.1% *v*/*v*) and purified by reversed-phase HPLC (H_2O/CH_3CN in TFA (0.1% *v*/*v*)). The products were isolated by lyophilization and characterized by MALDI-TOF MS. The purity of the peptides was >95% as determined by analytical reversed-phase HPLC (H_2O/CH_3CN in TFA (0.1% *v*/*v*)). A molar extinction coefficient of $\varepsilon = 63000\,M^{-1}cm^{-1}$ in H_2O ($\lambda = 500$ nm) was used to quantify TO–peptide conjugates.[13]

DNA photocleavage: TO–peptide conjugate (1 μM) was added to pUC18 (75 μM (base pairs)) in sodium cacodylate (10 mM, pH 7) in the dark. Irradiation was performed for 30 min ($\lambda = 501$ nm) with an Oriel Instruments spectral luminator tunable light source. The lamp intensity was 1.36 $mW\,cm^{-2}$. Cleavage efficiencies were evaluated by agarose gel (1%) electrophoresis visualized by ethidium bromide staining. Minimal cleavage was observed when identical samples were incubated in the dark, or when DNA samples were irradiated alone.

Cell culture: HeLa 229 cells (ATCC) were cultured as subconfluent monolayers on cell culture plates (25 or 75 cm^2) with vent caps (Corning) in 1 × minimum essential α medium (Gibco) supplemented with fetal bovine serum (10% *v*/*v*, ATCC) in a humidified incubator at 37 °C containing CO_2 (5%).

Confocal microscopy: HeLa cells that had been grown to subconfluence were dissociated from the surface with a solution of ethylenediaminetetraacetic acid (EDTA, 0.53 mM)/trypsin (0.05%) (2 mL, Cellgro) for 15 minutes at 37 °C. Aliquots of 1×10^5 cells were plated in four-well Lab-Tek glass-bottom coverslips (Nalge Nunc) and cultured overnight to allow cell adherence. The culture medium was removed, and the cells were rinsed in 1 × Ca^{2+}- and Mg^{2+}-free phosphate-buffered saline (PBS, pH 7.4, Cellgro). HeLa cells were incubated for 1.5 h at 37 °C with media (500 μL) containing **1a** or **1b** (10 μM). For colocalization studies, cells were incubated with **1a** (10 μM) and SYTO-85 (500 nM, Molecular Probes) or mitotracker deep red-633 (3 μM, Molecular Probes). Cells were washed three times for 5 min with PBS (1 mL). After washing, PBS (500 μL) was added and the cells were placed on ice. Images were taken with an inverted Leica TCS SP2 scanning confocal microscope with an oil immersion lens (40 ×). The images were analyzed with the Leica confocal software program.

Cells incubated with SYTO-85, mitotracker deep red-633, or **1a** were used to identify appropriate emission-collection parameters and to minimize bleed-through of the colocalized fluorophore. The excitation wavelength for both **1a** and **1b** ($\lambda_{ex\ max} = 501$ nm) was 488 nm, and emission was collected in the range of 500–571 nm. SYTO-85 ($\lambda_{ex\ max} = 567$ nm) and mitotracker deep red-633 ($\lambda_{ex\ max} = 644$ nm) were excited at 543 nm, and emissions were collected in the ranges of 556–648 and 600–750 nm, respectively. These parameters were used in all experiments. Cells were exposed to propidium iodide (MP Biomedicals) to determine the extent of cell death (<5%). Propidium iodide was excited at 488 nm, and emission was collected in the range of 550–700 nm. Cells that fluoresced brightly in subsequent experiments were assumed to be dead, and were not used in the evaluation of the conjugates.

Phototoxicity: HeLa cells were split as described above, and aliquots (100 μL) were seeded (1×10^4 cells) into 96-well clear flat-bottom microplates (Costar). After overnight incubation, the medium was replaced with new media (100 μL). Freshly prepared solutions of

 © 2005 Wiley-VCH Verlag GmbH & Co. KGaA, Weinheim

1a and **1b** (3 μM) were added to each well. Cells were incubated for 30 min in the dark at 37 °C, and then irradiated ($\lambda = 501$ nm) for 2, 5, 10, 15, and 20 min (UVA doses of 0.804, 2.01, 4.02, 6.03, and 8.04 $J\,cm^{-2}$, respectively) in triplicate with an Oriel Instruments spectral luminator tunable light source. The cell medium was replaced after the entire plate was irradiated. For the dark controls, fresh medium was also added.

Cells were analyzed with the cell counting kit-8 (CCK-8, Dojindo) to determine cell viability. After overnight incubation following irradiation, the medium was removed and fresh medium (90 μL) containing CCK-8 (10 μL) was introduced. After incubation at 37 °C for 1 h, the absorbance of each sample was measured ($\lambda =$ 470 nm) on a thermamax plate reader (Molecular Devices). The data for samples that contained only CCK-8 and medium were subtracted from all samples. Wells without conjugate were used as controls to determine the extent of cell death. Figure 4 represents an average of three separate trials.

Received: December 6, 2004
Published online: March 16, 2005

Keywords: amino acids · DNA cleavage · fluorescent probes · peptides · photooxidation

[1] M. J. Davies, *Biochem. Biophys. Res. Commun.* **2003**, *305*, 761 – 770.
[2] B. Epe, *Chem.-Biol. Interact.* **1991**, *80*, 239 – 260.
[3] H. Sies, C. F. Menck, *Mutat. Res.* **1992**, *275*, 367 – 375.
[4] D. E. Dolmans, D. Fukumura, R. K. Jain, *Nat. Rev. Cancer* **2003**, *3*, 380 – 387; b) M. R. Detty, S. L. Gibson, S. J. Wagner, *J. Med. Chem.* **2004**, *47*, 3897 – 3915; c) N. L. Oleinick, R. L. Morris, I. Belichenko, *Photochem. Photobiol. Sci.* **2002**, *1*, 1 – 21.
[5] H. Sies, *Mutat. Res.* **1993**, *299*, 183 – 191.
[6] A. Michaeli, J. Feitelson, *Photochem. Photobiol.* **1994**, *59*, 284 – 289.
[7] A. W. Girotti, W. Korytowski, *Methods Enzymol.* **2000**, *319*, 85 – 100.
[8] A. Wright, W. A. Bubb, C. L. Hawkins, M. J. Davies, *Photochem. Photobiol.* **2002**, *76*, 35 – 46.
[9] M. Tomita, M. Irie, T. Ukita, *Biochemistry* **1969**, *8*, 5149 – 5160.
[10] I. Saito, T. Matsuura, M. Nakagawa, T. Hino, *Acc. Chem. Res.* **1977**, *10*, 346 – 352.
[11] S. Gebicki, J. M. Gebicki, *Biochem. J.* **1999**, *338*, 629 – 636.
[12] M. Petersen, J. P. Jacobsen, *Bioconjugate Chem.* **1998**, *9*, 331 – 340.
[13] J. Nygren, N. Svanvik, M. Kubista, *Biopolymers* **1998**, *46*, 39 – 51.
[14] K. P. Mahon, Jr., R. F. Ortiz-Meoz, E. G. Prestwich, S. O. Kelley, *Chem. Commun.* **2003**, 1956 – 1957.
[15] T. A. Dix, K. M. Hess, M. A. Medina, R. W. Sullivan, S. L. Tilly, T. L. Webb, *Biochemistry* **1996**, *35*, 4578 – 4583.
[16] A. Joliot, A. Prochiantz, *Nat. Cell Biol.* **2004**, *6*, 189 – 196.
[17] P. M. Fischer, *Curr. Protein Pept. Sci.* **2003**, *4*, 339 – 356.
[18] The DNA cleavage observed with **1b** was comparable to that obtained with the TO–WK L-peptidoconjugate previously described.[14]
[19] Fluorescent images were assigned colors to maximize the ability to visualize the overlap between different fluorophores with the Leica confocal software. They do not reflect the emission properties of the fluorophore.
[20] M. F. Ross, A. Filipovska, R. A. Smith, M. J. Gait, M. P. Murphy, *Biochem. J.* **2004**, *383*, 457 – 468.
[21] Toxicities in the dark were negligible at 3 μM. However, as the concentrations of the conjugates approached 7 μM, significant toxicity in the dark was observed; therefore IC_{50} values could not be determined.
[22] NovaBiochem catalogue, **2004/5**, 3.15–3.16 (method 3 – 19).

 © 2005 Wiley-VCH Verlag GmbH & Co. KGaA, Weinheim

Cluster Compounds

Metal-Rich, Neutral and Cationic Organotin Clusters**

*Anne F. Richards, Barrett E. Eichler, Marcin Brynda, Marilyn M. Olmstead, and Philip P. Power**

With few exceptions, isolated clusters of the heavier Group 14 elements (Si–Pb) are of the Zintl (E_n^{x-}, $x = 2$, 3, or 4)[1,2] or organically substituted, that is, E_nR_m ($n = m$ or $n > m$; R = aryl, aryl, silyl, amide),[3,4] types. A notable feature of the two classes is that they rarely display a structural or electronic correspondence to each other. This situation is particularly evident in the structures of the element-rich[5] Group 14 organo clusters E_nR_m ($n > m$) such as $Sn_8\{Si(SiMe_3)_3\}_6$,[6] $Sn_8(Ar^{Mes_2})_4$[7] ($Ar^{Mes_2} = 2,6\text{-}Mes_2C_6H_3$; $Mes = 2,4,6\text{-}Me_3C_6H_2$), $Ge_8\{N(SiMe_3)_2\}_6$,[8] $Ge_6(Ar^{Mes_2})_2$,[9] $Sn_4Ge_2(Ar^{Mes_2})_2$[9] as well as the recently reported lead clusters $Pb_{10}R^*_6$ and $Pb_{12}R^*_6$ ($R^* = Si(SiMe_3)_3$).[10] These bear little stoichiometric or structural resemblance to the common E_5^{x-} or E_9^{x-} (E = Si–Pb) Zintl ions of these elements. A number of publications have shown that Zintl ion clusters, such as E_9^{x-}, can be derivatized with transition-metal or main-group fragments with preservation of the original framework.[11–15] Nonetheless, there is only one example (the anion $[Ge_9\{N(SiMe_3)_2\}_3]^-$)[16] of a derivatized Zintl cluster that can be synthesized without use of preformed E_5^{x-} or E_9^{x-} units. No stable examples of neutral clusters with structures analogous to the Zintl ions exist at present. Similarly, knowledge of cationic clusters of the Group 14 elements is extremely limited. For example, cationic Zintl clusters of these elements of any kind are currently unknown and the only well characterized stable cationic organo Group 14 cluster is the recently described silyl-substituted germanium species $[Ge_{10}(Si\mathit{t}Bu_3)_6I][B(C_6F_4H)_4]$.[17] Herein we report three new element-rich organo clusters of tin whose structures are analogous to, or derived from, the E_9^{x-} Zintl framework. These are the neutral $Sn_9(Ar^{Trip_2})_3 \cdot 4\,THF$ (**1**·4 THF; $Ar^{Trip_2} = 2,6\text{-}(2,4,6\text{-}\mathit{i}Pr_3C_6H_2)_2C_6H_3$) and the cationic clusters $[Sn_{10}(Ar^{Mes_2})_3]$ $[AlCl_4]$·PhMe (**2**·PhMe) and $[Sn_{10}(Ar^{Mes_2})_3][GaCl_4]$·PhMe (**3**·PhMe).

The neutral cluster $Sn_9(Ar^{Trip_2})_3$, which is paramagnetic and has 21 framework electrons, was synthesized by the thermolysis of $\{Ar^{Trip_2}Sn(\mu\text{-}H)\}_2$[18] in hot toluene and was isolated as dark red, almost black crystals. This method is a new synthetic route to tin clusters[19] that arose from exploring

[*] Dr. A. F. Richards, Dr. B. E. Eichler, Dr. M. Brynda, Prof. M. M. Olmstead, Prof. P. P. Power
Department of Chemistry, University of California
One Shields Avenue, Davis, CA 95616 (USA)
Fax: (+1) 530-752-8995
E-mail: pppower@ucdavis.edu

[**] The authors thank the NSF-CRC program for financial support. M.B. was supported by the Swiss National Science Foundation Grant 8220-067593.

Supporting information for this article is available on the WWW under http://www.angewandte.org or from the author.

 © 2005 Wiley-VCH Verlag GmbH & Co. KGaA, Weinheim DOI: 10.1002/anie.200500117

the decomposition of the hydride in an attempt to isolate the distannyne $Ar^{Trip_2}SnSnAr^{Trip_2}$.[20] Elimination of hydrogen does occur, but competing Sn–C bond cleavage results in ligand stripping to afford **1**. The arene HAr^{Trip_2} was also isolated from the reaction mixture. Compound **1** was characterized by X-ray crystallography and by EPR spectroscopy. The latter afforded a relatively broad signal with a *g* value near 2.031 in solution in toluene at room temperature. A representation of the structure of **1**[21] is shown in Figure 1. The Sn_9 framework

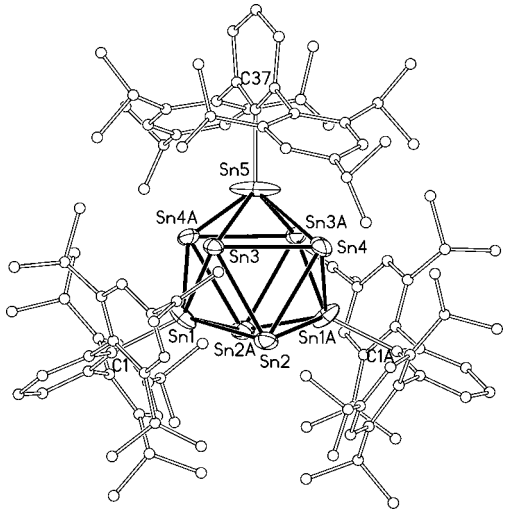

Figure 1. Schematic drawing of **1**. Selected bond lengths [Å] and angles [°]: Sn1-C1 2.21(2), Sn1-Sn2 2.944(2), Sn1-Sn3 2.967(2), Sn1-Sn4A 2.912(2), Sn2-Sn3 2.992(2), Sn2-Sn4 3.008(2), Sn3-Sn4 2.999(2), Sn3-Sn5 2.914(2), Sn4-Sn5 2.932(2), Sn5-C37 2.21(3); C1-Sn1-Sn2 122.9(4), C1-Sn1-Sn3 119.5(4), C1-Sn1-Sn4A 116.0(4), Sn2-Sn3-Sn4 60.27(4), Sn3-Sn2-Sn4 59.98(4).

has a tricapped, trigonal-prismatic, closo structure, which is similar to that first reported for the 21-framework-electron Zintl ion $[Sn_9]^{3-}$ by Corbett in 1983.[22] The most prominent structural features of trigonal-prismatic clusters of this type concern the Sn–Sn separations that define the height (h) and edge (e) of the trigonal prism and the distance from the capping to prismatic atoms.[23] In **1**, the average values for these distances are h = 4.12(4), e = 3.000(1), and capping distance 2.94(3) Å, respectively. These parameters afford an h/e value of 1.37, which is significantly higher than the range currently known (1.07–1.17) for $[E_9]^{3-}$ Zintl ions with 21 framework electrons.[2] The h/e value is closest to that recently observed for the anionic substituted germanium cluster $[Ge_9\{N(SiMe_3)_2\}_3]^-$ (h/e = 1.27),[11] which also has a closo structure despite the fact that it has 22 framework electrons for which a nido, monocapped square-antiprismatic arrangement is predicted by Wade's rules. Calculations[11] on the model species $[Ge_9H_3]^-$, however, yielded structural parameters close to those experimentally observed. In contrast, the derivatized Zintl ion $[Ge_9(BiPh_2)_2]^{2-}$[14] displays a nido Ge_9 framework that is consistent with its 22 framework electrons. The Sn–Sn bond length pattern in **1** is similar to that seen in closo $[E_9]^{3-}$ Zintl clusters where the shortest bonds (Sn–Sn bond lengths in the range 2.914(2)–2.967(2) Å) are observed to the tin atoms capping the rectangular prism faces, that is, the substituted Sn1, Sn1A, and Sn5 in **1**. DFT calculations[24] for Sn_9Me_3 model species for **1** afforded Sn–Sn bond lengths that resemble those experimentally observed, with the lengths calculated for the four-coordinate tin centers (average 2.935 Å) falling within the above-mentioned range. The calculated h/e value, 3.83 Å(avg)/3.25 Å(avg) ≈ 1.18 is not as great as that seen in **1**. However, it is greater than that in the $[Sn_9]^{3-}$ Zintl ion (h/e = 1.08).[22]

The cluster salts **2** and **3** were synthesized by the reduction of $Sn(Cl)Ar^{Mes_2}$ with one equivalent of KC_8 in the presence of 0.5 equivalents of $AlCl_3$ or $GaCl_3$. This synthetic approach arose out of attempts to isolate clusters with both Group 14 and Group 13 atoms in their frameworks. The inclusion of Group 13 elements was successful with use of the subvalent gallium (I) precursor "GaI",[25] but the use of $M^{III}Cl_3$ (M = Al or Ga) halides has not afforded "mixed" clusters to date. The products **2** and **3** were obtained as red–black hexagonal crystals. Although these crystals have a relatively high melting point, attempts at redissolving them result in decomposition with the deposition of elemental tin. Single-crystal X-ray diffraction established the structure that is illustrated for **2** in Figure 2. The Sn_{10} framework in the $[Sn_{10}(Ar^{Mes_2})_3]^+$ ion is almost identical in both compounds and the structure is based on a distorted octadecahedron. It may be viewed as being composed of Sn^{2+} ions (Sn5) capping Zintl-like $[Sn_9(Ar^{Mes_2})_3]^-$ moieties which are related to the neutral species **1** by a one-electron reduction. The existence of such monoanionic Zintl-like ions has precedence in the above-mentioned $[Ge_9\{N(SiMe_3)_2\}_3]^-$ ion.[16] The framework electron count for the Sn_{10}

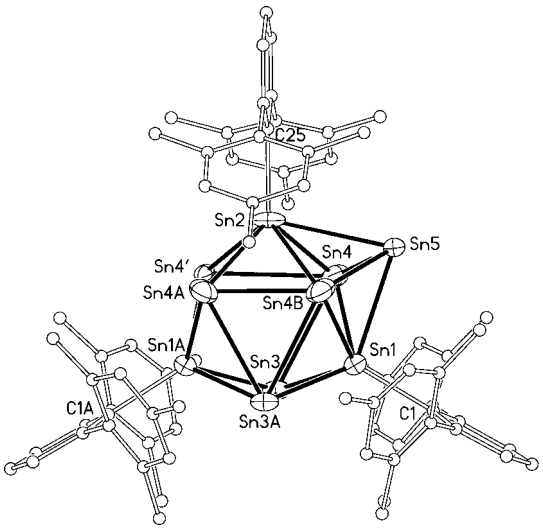

Figure 2. Schematic drawing of the cation in **2** (that in **3** is almost the same). Selected bond lengths [Å] and angles [°]. Sn1-C1 2.194(11), Sn2-C25 2.198(12), Sn1-Sn3 2.9174(8), Sn1-Sn4 3.010(1), Sn1-Sn5 3.000(1), Sn2-Sn5 3.118(1), Sn2-Sn4 3.122(1), Sn3-Sn4 3.087(1), Sn4-Sn5 2.9552, Sn4A-Sn4B 2.8929(2), Sn4-Sn4′ 3.185(2); C1-Sn1-Sn3 112.7(3), C1-Sn1-Sn4 115.2(3), Sn3-Sn1-Sn4 61.64(3), Sn4-Sn1-Sn5 57.91(3), Sn3-Sn1-Sn4 61.64(3), Sn4-Sn1-Sn5 57.91(3), Sn4-Sn1-Sn4B 96.14(5), C25-Sn2-Sn5 102.70(3), Sn4-Sn2-Sn5 56.52(2), Sn4A-Sn2-Sn4B 53.87(4), Sn4-Sn2-Sn4′ 65.22(6), Sn1-Sn3-Sn4 62.09(3), Sn1-Sn4-Sn5 61.66(3), Sn4′-Sn4-Sn5 114.45(3), Sn1-Sn5-Sn4 67.74(3), Sn2-Sn5-Sn4 61.82(3), Sn1-Sn5-Sn2 83.84(4).

 © 2005 Wiley-VCH Verlag GmbH & Co. KGaA, Weinheim

cation is 22, which is agreement with the view that it is derived from monocapping of the original trigonal-prismatic $Sn_9(Ar^{Mes_2})_3$ unit by a tin atom. This capping causes large distortions of the original trigonal-prismatic arrangement seen in the structures of **1** and the $[Ge_9\{N(SiMe_3)_2\}_3]^-$ ion. The original parallel trigonal Sn3 faces of the prism, which were separated by a relatively uniform "height" of approximately 4.0 Å between the respective pairs of tin atoms in **1**, become separated by 3.824, 3.946, and 4.594 Å in **2**; the longest distance (between Sn4 and Sn4B) in **2** is now bridged by the capping Sn5. Elsewhere within the cluster the Sn–Sn bond lengths are within the range 2.760(2)–3.185(2) Å.

In conclusion, we have isolated and characterized two new types of organotin clusters that are related structurally to the Sn_9^{x-} Zintl anions. The isolation of these compounds strengthens the notion that clusters of Group 14 elements can demonstrate a great variety of structural types and firmly establishes a relationship between the Zintl and organo clusters. The results suggest that further capping of the Sn_9^{x-} framework should lead to higher clusters. In addition, the ability of the terphenyl ligands to stabilize **1**–**3** as well as other clusters in which the majority of the metal atoms are unsubstituted[9] is noteworthy.

Experimental Section

All manipulations were carried out under an inert atmosphere in water-free conditions.

1: $\{Sn(\mu\text{-}H)Ar^{Trip_2}\}_2$ (0.601 g, 0.5 mmol) in toluene (30 mL) was heated to 100 °C in an oil bath for 1 h, during which time the initial blue color of the solution became dark red. The solution was cooled and filtered. The volume of the filtrate was reduced to saturation, but attempts to grow crystals for X-ray diffraction from toluene solutions were unsuccessful. With the addition of small quantities (ca. 5% volume) of THF, crystals of **1**·4 THF suitable for X-ray studies were obtained as red needles (0.052 g, 19%); m.p. desolvates at ca. 80°, dec > 100 °C. Elemental analysis (%) calcd for $C_{108}H_{147}Sn_9$: C 51.64, H 5.90; found: C 52.16, H, 6.03.

2: A solution of $Sn(Cl)Ar^{Mes_2}$ (0.467 g, 1 mmol) and $AlCl_3$ (0.67 g, 0.5 mmol) in THF (20 mL) was added dropwise to a well-stirred suspension of KC_8 (0.135 g, 1 mmol) in THF (20 mL) cooled in a dry-ice/acetone bath. The solution was allowed to reach room temperature within 12 h and filtered. The filtrate was collected, the volatile materials were removed under reduced pressure, and the residue was extracted with toluene (30 mL) and filtered. The filtrate was reduced in volume to incipient crystallization and stored at room temperature for one week to afford **2** as black (dark red in transmitted light) hexagonal crystals. (0.028 g, 12%); m.p. 144–146 °C. Elemental analysis (%) calcd for $C_{72}H_{75}Cl_4AlSn_{10}$: C 37.66, H 3.29; found: C 38.10, H 3.34.

3: The preparation of **3** was almost identical to that for **2** except that $GaCl_3$ was employed instead of $AlCl_3$. The product **3** was obtained as black (dark red in transmitted light) crystals (0.023 g, 10%); m.p. 185–186 °C. Elemental analysis (%) calcd for $C_{72}H_{75}Cl_4GaSn_{10}$: C 36.97, H 3.32; found: C 37.61, H 3.29.

Received: January 12, 2005
Published online: March 22, 2005

Keywords: cluster compounds · density functional calculations · structure elucidation · tin

[1] J. D. Corbett, *Angew. Chem.* **2000**, *112*, 682; *Angew. Chem. Int. Ed.* **2000**, *39*, 670.
[2] T. F. Fässler, *Coord. Chem. Rev.* **2001**, *215*, 347.
[3] A. Sekiguchi, S. Nagase, *The Chemistry of Organic Silicon Compounds*, *Vol. 2*, Part 1 (Eds.: Z. Rappaport, Y. Apeloig), Wiley, Chichester, **1998**, chap. 3, pp. 119–152.
[4] N. Wiberg, P. P. , Power, *Molecular Clusters of the Main Group Elements* (Eds.: M. Driess, H. Nöth), Wiley-VCH, Weineim, **2004**, chap. 25, pp. 188–208.
[5] A Schnepf, *Angew. Chem.* **2004**, *116*, 680; *Angew. Chem. Int. Ed.* **2004**, *43*, 664.
[6] N. Wiberg, H.-W. Lerner, S. Wagner, H. Nöth, T. Seifert, *Z. Naturforsch. B* **1999**, *54*, 877.
[7] B. E. Eichler, P. P. Power, *Angew. Chem.* **2001**, *113*, 818; *Angew. Chem. Int. Ed.* **2001**, *40*, 796.
[8] A. Schnepf, R. Köppe, *Angew. Chem.* **2003**, *115*, 940; *Angew. Chem. Int. Ed.* **2003**, *42*, 911.
[9] A. F. Richards, H. Hope, P. P. Power, *Angew. Chem.* **2003**, *115*, 4205; *Angew. Chem. Int. Ed.* **2003**, *42*, 4071.
[10] K. W. Klinkhammer, Y. Xiong, S. Yao, *Angew. Chem.* **2004**, *116*, 6328; *Angew. Chem. Int. Ed.* **2004**, *43*, 6206.
[11] B. W. Eichhorn, R. C. Haushalter, *J. Chem. Soc. Chem. Commun.* **1990**, 937.
[12] D. R. Gardner, J. C. Fettinger, B. W. Eichhorn, *Angew. Chem.* **1996**, *108*, 2867; *Angew. Chem. Int. Ed. Engl.* **1996**, *35*, 2852.
[13] J. Campbell, H. P. A. Mercier, H. Francke, D. P. Santry, D. A. Dixon, G. J. Schrobilgen, *Inorg. Chem.* **2002**, *41*, 86.
[14] A. Ugrinov, S. C. Sevov, *J. Am. Chem. Soc.* **2002**, *124*, 2442.
[15] A. Urgrinov, S. C. Sevov, *Chem. Eur. J.* **2004**, *10*, 3727.
[16] A. Schnepf, *Angew. Chem.* **2003**, *115*, 2728; *Angew. Chem. Int. Ed.* **2003**, *42*, 2624.
[17] A. Sekiguchi, Y. Ishida, Y. Kabe, M. Ichinohe, *J. Am. Chem. Soc.* **2002**, *124*, 8776.
[18] B. E. Eichler, P. P. Power, *J. Am. Chem. Soc.* **2000**, *122*, 8785.
[19] The assembly of the Pb_{10} and Pb_{12} clusters in ref. [10] is also believed to proceed through lead hydride intermediates.
[20] L. Pu, A. D. Phillips, A. F. Richards, M. Stender, R. S. Simons, M. M. Olmstead, P. P. Power, *J. Am. Chem. Soc.* **2003**, *125*, 11626.
[21] Crystal data for **1**·4 THF, **2**·PhMe, and **3**·PhMe obtained with $Mo_{K\alpha}$ ($\lambda = 0.7107$ Å) radiation at 90 K: **1**: monoclinic, *C*2/*c*, dark red needle, $a = 28.176(2)$, $b = 26.4492(2)$, $c = 16.673(1)$ Å, $\beta = 106.743(1)°$, $V = 11899.6(14)$ Å^3, $Z = 4$, $R1$(obs data) = 0.0826; $wR2$(all data) = 0.2296; **2**: orthorhombic *Cmme*, black hexagonal block, $a = 22.694(2)$, $b = 29.964(2)$, $c = 13.391(1)$ Å, $V = 9105.6(13)$ Å^3, $Z = 4$, $R1$ (obs data) = 0.0608; $wR2$ (all data) = 0.1913; **3**: orthohrombic *Cmme*, dark red block, $a = 22.622(2)$, $b = 29.917(3)$, $c = 13.376(1)$ Å, $Z = 4$, $R1$ (obs data) = 0.0645; $wR2$ (all data) = 0.1816. CCDC-259809–259811 contain the supplementary crystallographic data for this paper. These data can be obtained free of charge from the Cambridge Crystallographic Data Centre via www.ccdc.cam.ac.uk/data_request/cif. The structure of **1**·4 THF is disordered with respect to the twofold axis passing through Sn5 and C37. Division of the molecule into two parts was unsuccessful. But only the Sn atoms were assigned anisotropic thermal parameters. The half molecule of 2,6-$Trip_2C_6H_3$ was restrained using the SAME feature of SHELXL which relates its 1,2 and 1,3 positions to those of one-half of the organic moiety. Two molecules of THF are present, in the asymmetric unit. The molecules **2**·PhMe and **3**·PhMe are isostructural and were solved in the space group *Cmme* (No. 67, formerly *Cmma*). They consist of the cation $[R_3Sn_{10}]^+$ at a crystallographic site with mm symmetry, the anion $[AlCl_4]^-$ or $[GaCl_4]^-$ at a site of 222 symmetry and disordered PhMe at a site of 2/*m* symmetry. The anion is fully ordered, and PhMe was refined as a rigid group at the multiplicity of the site (0.25

occupancy) with isotropic thermal parameters. In the cation, there are two anomalies which lower the symmetry of the cluster. One of the Sn atoms (Sn5) is clearly at half occupancy and Sn4 occupies two sites in the ratio Sn4:Sn4′:0.75:0.25, which was established by refinement. The three atoms Sn4, Sn4A, and Sn4B are symmetry-related positions for the major atom of the site shared by Sn4 and Sn4′. The minor atom, Sn4′, is drawn such that it occupies the side of the cluster where Sn5 is absent to avoid unrealistically short bonds. In the average structure, Sn4′ would occupy all four positions related by *mm* symmetry, and Sn5 (which resides on a mirror plane) would be reflected to the opposite side as well. These various distortions in the cluster may be the cause of disorder in the R group beginning with the atom C1. The atoms that make up this group are disordered with respect to a mirror plane that passes through the *ipso* carbon C1 and the *para* carbon C4 of the C1 aryl ring. This gives the appearance of large thermal motions perpendicular to this plane. To better describe this group, the atoms C1 and C4 were shifted off the mirror and the remainder of the atoms in this group located from a difference Fourier map. Thus, the atoms C1–C24 were refined at 0.5 occupancy with isotropic thermal parameters and a SHELXL PART-1 statement.

[22] S. C. Critchlow, J. D. Corbett, *J. Am. Chem. Soc.* **1983**, *105*, 5715.

[23] T. F. Fässler, U. Schutz, *Inorg. Chem.* **1999**, *38*, 1866.

[24] The geometry optimizations of the model tin clusters Sn_9Me_3 and $[Sn_{10}Me_3]^+$ were performed using DFT with a hybrid B3LYP functional, including Becke's three-parameter nonlocal exchange potential and the nonlocal correlation functional of Lee–Yang–Parr . To reduce the computational costs without neglecting the relativistic effects, the effects of the core electrons on valence shell for Sn were represented by the quasi-relativistic effective-core potentials (ECPs). For this purpose two ECPs were used for tin atoms: Los Alamos LanL2DZ pseudopotential ECP with a valence basis (Sn 46 electrons core ECP, plus contracted (3s,3p)→[2s,2p]) and the large core CRENBL ECP augmented with polarization functions for C and Sn. Final optimization was also performed with an all electron 3-21g* basis set. The DFT calculations were carried out using the GAUSSIAN 03 package and the representations of the molecular structures and molecular orbitals were generated with the MOLEKEL program. The optimized geometrical parameters (interatomic distances [Å] and angles [°]) vary slightly with the basis set size; the Sn–Sn bond lengths are shorter by an average of 0.05–0.07 Å in the structure optimized at B3LYP/3-21g* level compared to the structure optimized using ECPs. These parameters obtained at B3LYP/3-21g* for Sn_9Me_3 and $[Sn_9Me_3]^+$ are in good agreement with those found in the crystal structure of **1** and **2**. Model of **1**, Sn_9Me_3: Sn1-Sn2 2.937, Sn1-Sn2A 2.937, Sn1-Sn3 2.935, Sn1-Sn4A 2.937, Sn2-Sn3 3.262, Sn3-Sn4 3.247, Sn2-Sn4 3.254; torsion angle Sn1A-Sn3A-Sn4-Sn5 33.4. Model of **2**, $[Sn_9Me_3]^+$: Sn1-Sn5 2.965, Sn1-Sn3 2.979, Sn1-Sn4 3.108, Sn4···Sn4B 4.852; Sn3-Sn1A-Sn4 69.4, Sn1-Sn3-Sn3A 50.8, Sn1-Sn4-Sn2 76.8, Sn1-Sn5-Sn2 81.3. Other relevant bond lengths and angles from the optimized structures are listed in the Supporting Information.

[25] A. F. Richards, M. Brynda, P. P. Power, *Organometallics* **2004**, *23*, 4009.

 © 2005 Wiley-VCH Verlag GmbH & Co. KGaA, Weinheim

Cluster Compounds

Synthesis and Characterization of the Nitrogen-Centered Trigonal Prismatic Clusters $[W_6NCl_{18}]^{n-}$ ($n = 1$–3)**

*Eric J. Welch, Chun Liang Yu, Nathan R. M. Crawford, and Jeffrey R. Long**

The extraordinarily rich chemistry of octahedral transition metal halide and chalcohalide clusters has begun to see use in a variety of applications, ranging from catalysis to chemical sensing.[1] In facilitating the design of such cluster-based materials, new synthetic methods for adjusting the core electronic character by atom substitution and for exchanging the six outer terminal ligands are of considerable value.[2] However, the prospect of utilizing a wholly different type of cluster unit arose very recently with the discovery of the molecular species $[W_6CCl_{18}]^{n-}$ ($n = 0$–3).[3] Instead of an octahedron, these clusters feature a carbon-centered W_6 trigonal prism surrounded by twelve edge-bridging chloride anions and six radially extended terminal chloride ligands. Such units are also known to exist within the one-dimensional compounds $A_3Nb_6SBr_{17}$ (A = K, Rb, Cs, and Tl),[4] suggesting that this trigonal-prism structure type may be quite pervasive. Noting that the electronic character of the centered, edge-bridged octahedral clusters $[Zr_6ZCl_{18}]^{n-}$ is highly dependent upon the interstitial atom Z, we attempted to replace the carbon atom in $[W_6CCl_{18}]^{2-}$ with other atoms.[5] Herein, we report the introduction of an interstitial nitrogen atom, which permits ready access to more electron-rich trigonal prismatic clusters.

Synthesis of the molecular salt $Na[W_6NCl_{18}]$ (**1**) parallels the low-temperature solid-state process employed for producing the original carbon-centered cluster phase,[3b] although with NaN_3 used in place of CCl_4. Elemental bismuth is known to be highly effective as a reducing agent in the formation of clusters such as $[W_6Cl_{14}]^{2-}$ and $[W_6O_{12}Cl_{12}]^{2-}$,[6] and is thought to act here according to reaction (1). A stoichiometric

$$6\,WCl_6 + NaN_3 + 6\,Bi \rightarrow Na[W_6NCl_{18}] + 6\,BiCl_3 + N_2 \qquad (1)$$

mixture of the reactants was sealed in an evacuated pyrex ampule and heated at 500 °C for 3 days. Bismuth chloride was then removed by sublimation, which left a black solid containing hexagonal plate-shaped crystals of **1**. Reactions performed with less or more than one equivalent of NaN_3 resulted in lower yields of **1**.

[*] E. J. Welch, C. L. Yu, N. R. M. Crawford, Prof. J. R. Long
Department of Chemistry
University of California
Berkeley, CA 94720-1460 (USA)
Fax: (+1) 510-642-8369
E-mail: jrlong@berkeley.edu

[**] This research was funded by DOE Grant No. DE-FG03–01ER15257.

Supporting information for this article is available on the WWW under http://www.angewandte.org or from the author.

 DOI: 10.1002/anie.200462585 © 2005 Wiley-VCH Verlag GmbH & Co. KGaA, Weinheim

X-ray crystallographic analysis[7] of **1** revealed the $[W_6NCl_{18}]^{1-}$ cluster (Figure 1), which has a structure fully analogous to that of the isoelectronic species $[W_6CCl_{18}]^{2-}$. The central $\{W_6N\}$ unit in the cluster is reminiscent of a fragment

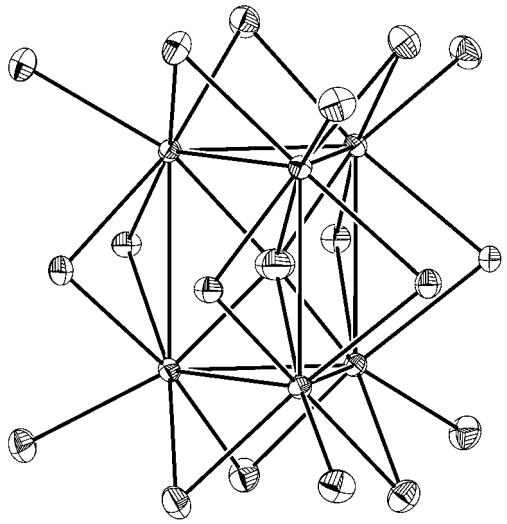

Figure 1. Structure of the nitrogen-centered trigonal prismatic cluster $[W_6NCl_{18}]^{1-}$ in **1**, with ellipsoids drawn at the 75% probability level. The lines connecting the W atoms are intended to emphasize the W_6 trigonal prism and do not necessarily represent full single bonds.[5b] Selected mean interatomic lengths [Å] and angles [°] for the $[W_6NCl_{18}]^{n-}$ ($n=1$–3) clusters in **1**, **2′**, and **3′**, respectively (Δ = triangle edge, | = longer rectangle edge, b = bridging, t = terminal): W-W$^{\Delta}$ 2.6518, 2.67(1), 2.69(6); W-W$^{|}$ 3.0705, 3.07(1), 3.0(1); W-N 2.1682, 2.173(7), 2.16(2); W-Cl$^{b\Delta}$ 2.382(1), 2.397(5), 2.408(13); W-Cl$^{b|}$ 2.448(3), 2.453(15), 2.46(2); W-Cl^{t} 2.409, 2.416(6), 2.440(8); W-N-W$^{\Delta}$ 75.39, 75(2), 77(2); W-N-W$^{|}$ 90.18, 89.8(7), 88(6); W-Cl$^{b\Delta}$-W 67.62, 67.6(4), 69(2); W-Cl$^{b|}$-W 77.63(12), 77.4(2), 75(3). For comparison, the corresponding mean bond lengths [Å] for the $[W_6CCl_{18}]^{2-}$ cluster in $(Bu_4N)_2[W_6CCl_{18}]$ are: W-W$^{\Delta}$ 2.667, W-W$^{|}$ 3.028, W-C 2.1595, W-Cl$^{b\Delta}$ 2.381(5), W-Cl$^{b|}$ 2.4585(5), W-Cl^{t} 2.443.[3b]

of WN, consisting of a nitrogen atom surrounded by a regular trigonal prism of tungsten atoms. The W–N bond length of 2.1682(4) Å in the cluster is very similar to the 2.188 Å bond length in WN,[8] but the latter possesses a trigonally compressed W_6 trigonal prism. Thus, the cluster exhibits a shorter W···W$^{\Delta}$ distance of 2.6518(6) Å within the W_3 triangles and a longer W···W$^{|}$ distance of 3.0705(7) Å along the remaining edges, while the corresponding bond lengths in WN are W–W$^{\Delta}$ = 2.893 and W–W$^{|}$ = 2.826 Å.[8] Note that these bond lengths are all somewhat longer than the W–W single bond distance of 2.607(4) Å observed in the face-capped octahedral cluster $[W_6Cl_{14}]^{2-}$.[9] The $\{W_6N\}$ unit in the cluster is surrounded by 18 chlorine atoms in a manner that preserves the D_{3h} symmetry, with one Cl atom bridging each triangular edge of the prism, two bridging each of the other edges, and one extending radially from each vertex. Interestingly, the structure of **1** is isotypic with that of W_6CCl_{18},[3a] featuring a hexagonal close packing of the clusters, but with Na^+ ions occupying the octahedral holes. Accordingly, compound **1** represents an expanded form of the NiAs structure.

Compound **1** is soluble in dilute HCl; however, the cluster undergoes a spontaneous one-electron reduction on work up, ultimately leading to formation of $(Bu_4N)_2[W_6NCl_{18}]$ (**2**). This behavior is consistent with the cyclic voltammogram of **2** in *N*,*N*-dimethylformamide (DMF), which displays a readily accessible $[W_6NCl_{18}]^{1-}/[W_6NCl_{18}]^{2-}$ couple at $E_{1/2} = 0.097$ V ($\Delta E_p = 63$ mV) versus the ferrocene/ferrocenium couple (Fc/Fc$^+$; Figure 2). Two further reduction events that correspond

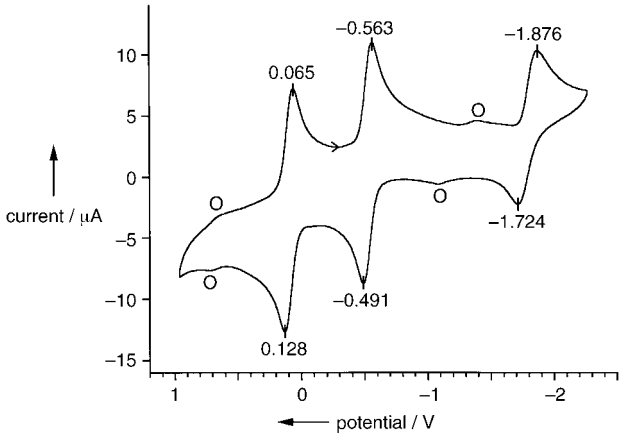

Figure 2. Cyclic voltammogram of **2** in DMF with potentials referenced to Fc/Fc$^+$. The measurements were performed on a platinum electrode at a scan rate of 100 mVs^{-1} with Bu_4NPF_6 (0.1 M) as the supporting electrolyte. Features marked with a circle appear only after the potential has been swept through the outermost couple on the right-hand side.

to a $[W_6NCl_{18}]^{2-}/[W_6NCl_{18}]^{3-}$ couple at $E_{1/2} = -0.527$ V ($\Delta E_p = 72$ mV) and a quasireversible $[W_6NCl_{18}]^{3-}/[W_6NCl_{18}]^{4-}$ couple at $E_{1/2} = -1.800$ V ($\Delta E_p = 152$ mV) are also apparent. Four additional peaks appear upon sweeping the potential past −1.8 V (as designated by circles in Figure 2). Presumably, these new smaller features are associated with the redox couples of cluster species wherein DMF has replaced one or more of the terminal chloride ligands, a process that should become more facile upon formation of $[W_6NCl_{18}]^{4-}$. In sum, the cyclic voltammetry results indicate that clusters with 24–27 $\{W_6N\}$-based valence electrons are chemically accessible. For comparison, the cyclic voltammogram of $(Bu_4N)_2[W_6CCl_{18}]$ in DMF shows four redox couples at $E_{1/2} = +0.974$, $+0.407$, -0.649, and -1.360 V versus Fc/Fc$^+$, indicating the accessibility of clusters having 22–26 $\{W_6C\}$-based valence electrons.[3b,10] Thus, the replacement of a carbon atom with a nitrogen atom in the cluster leads to significant stabilization of the species with higher electron counts, with the 24/25- and 25/26-electron couples shifting by $+0.746$ and $+0.833$ V, respectively.

DFT calculations[11] were performed on $[W_6NCl_{18}]^-$ to assess how these changes in electron count affect the electronic structure of the cluster (Figure 3). The results are consistent with the rich electrochemistry of $[W_6NCl_{18}]^-$ and indicate closely spaced frontier orbitals, with a HOMO–LUMO gap of 0.70 eV. The a_2'' HOMO is tungsten based, with bonding character within the two W_3 triangles and antibond-

 © 2005 Wiley-VCH Verlag GmbH & Co. KGaA, Weinheim

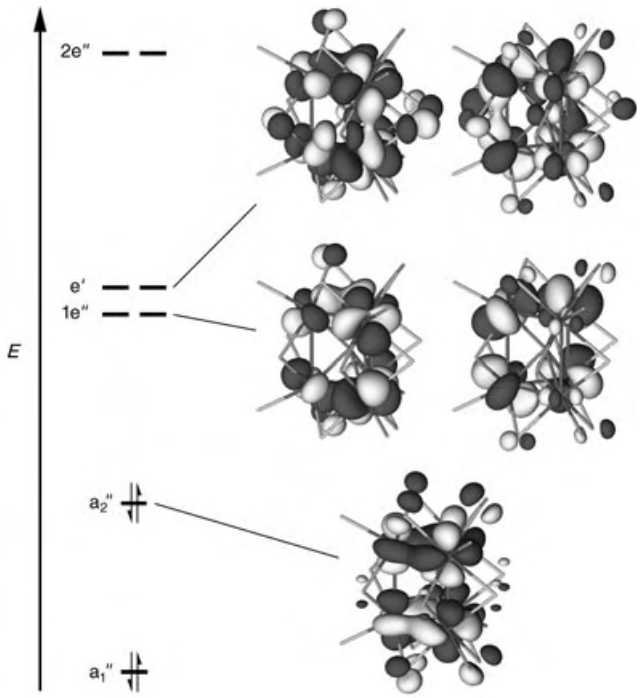

Figure 3. Frontier portion of the energy level diagram calculated for $[W_6NCl_{18}]^-$ along with depictions of selected molecular orbitals. Distortions observed in one- and two-electron-reduced clusters indicate that the added electrons populate the left-hand e′ orbital.

ing character between the triangles. The lowest unoccupied orbitals 1e″ and e′ are also mainly tungsten based and again feature a mixture of bonding and antibonding character. It is difficult to predict which one of these two pairs of orbitals would most readily accept an electron as they have an energy separation of just 0.099 eV; however, in either case a distortion away from the D_{3h} symmetry should occur upon reduction of the cluster by one electron. Depending upon the spin-pairing energy, further reduction by a second electron can then be expected either to amplify the distortion or give rise to a triplet ground state with reversion to the D_{3h} symmetry.

Crystallization of $(Bu_4N)[(Ph_3P)_2N][W_6NCl_{18}]$ (**2′**) afforded a structure[7] in which the 25-electron cluster $[W_6NCl_{18}]^{2-}$ exhibited no crystallographically imposed symmetry, thereby revealing the effects of the Jahn–Teller distortion. Most notably, two tungsten atoms are pinched together to give a shorter W···W$^{|}$ distance (3.0518(6) Å) relative to the structure of the 24-electron cluster. Furthermore, this shortened, right-hand edge of the trigonal prism is pulled slightly away from the opposing W_4 rectangle, thus resulting in longer W···W$^{\Delta}$ distances in the range 2.6585(6)–2.6835(6) Å (Figure 4b). The resultant structure has an approximate C_{2v} symmetry and is most consistent with population of the left-hand e′ orbital displayed in Figure 3. Although the magnitude of the distortion is somewhat less than that observed for the isoelectronic cluster $[W_6CCl_{18}]^{3-}$,[3b] it is comparable to that observed for octahedral Mo_6 and Re_6 clusters.[12]

Reduction of **2** with one equivalent of cobaltocene affords $(Bu_4N)_2(Cp_2Co)[W_6NCl_{18}]$ (**3**; Cp = cyclopentadienyl), which contains $[W_6NCl_{18}]^{3-}$, the first 26-electron cluster of its type. Subsequent crystallization as $(Bu_4N)_3[W_6NCl_{18}]\cdot MeCN$ (**3′**) gave a triclinic structure, in which the cluster geometry is again unconstrained by the symmetry of the crystal. The central $\{W_6N\}$ unit now exhibits a much more substantial form of the same distortion (Figure 4c). The two outermost tungsten atoms on the right-hand side are pinched together to give a short W···W$^{|}$ distance of 2.803(1) Å and are pulled away from the opposing $\{W_4\}$ rectangle to give elongated W···W$^{\Delta}$ distances in the range 2.730(1)–2.740(1) Å. Furthermore, a slight compression is evident in two edges of the opposing rectangle, thus resulting in shorter W···W$^{\Delta}$ distances of 2.592(1) and 2.606(1) Å. The overall nature of the distortion indicates pairing of the two added electrons in the left-hand e′ orbital in Figure 3, which is consistent with the observed diamagnetism of compound **3**. Interestingly, as the cluster is reduced and the average oxidation state of the tungsten centers changes from +3.33 to +3.17 to +3.00, the W···W$^{\Delta}$ and W···W$^{|}$ distances become more similar to (but certainly not identical to) the corresponding distances in WN (2.893 and 2.826 Å, respectively).[8]

Attempts to incorporate other transition metals and other interstitial atoms into trigonal prismatic clusters are currently underway. In particular, we are targeting fragments of solids, such as MoP and RuC, wherein the main group atoms are known to display a trigonal prismatic coordination geometry. Further efforts are directed toward exploring the ligand substitution chemistry of these clusters and developing solution-based methods for incorporating them within extended-framework materials.

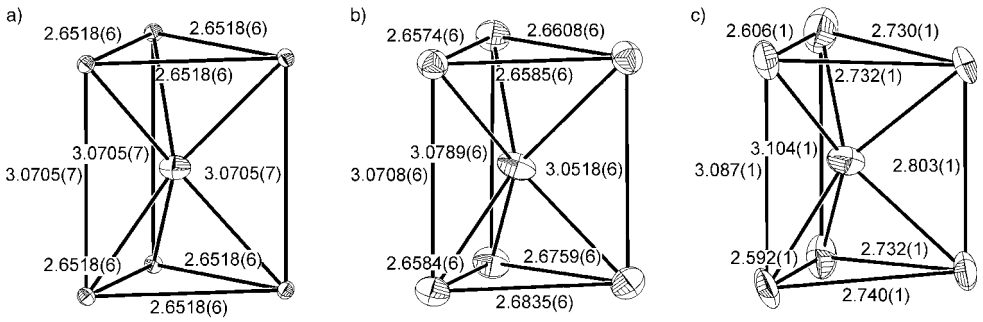

Figure 4. Central $\{W_6N\}$ units within the clusters: a) $[W_6NCl_{18}]^{1-}$, b) $[W_6NCl_{18}]^{2-}$, and c) $[W_6NCl_{18}]^{3-}$, as observed in the crystal structures of **1**, **2′**, and **3′**, respectively. Ellipsoids are drawn at the 50% probability level.

 © 2005 Wiley-VCH Verlag GmbH & Co. KGaA, Weinheim

Experimental Section

Dark-blue WCl_6 (99.9+ %, Aldrich) was purified prior to use by subliming away the usual impurity of red $[WOCl_4]$ at 140 °C under reduced pressure. The water used was distilled and deionized with a Milli-Q filtering system. Other reagents were used as received. UV/Vis absorption spectra were measured with a Hewlett–Packard 8453 spectrophotometer, and IR spectra were recorded on a Nicolet Avatar 360 FTIR spectrometer equipped with an attenuated total reflectance accessory. Mass-spectrometric measurements were performed in the negative-ion mode on a Micromass Quattro triple quadrapole mass spectrometer equipped with an electrospray ionization source or a Brüker Apex II 7 T actively shielded FTICR mass spectrometer equipped with an analytical electrospray ion source. Magnetic data were collected using a Quantum Design MPMSXL SQUID magnetometer and were corrected for diamagnetic contributions. Electrochemical measurements were conducted with a Bioanalytical Systems CV-50 potentiostat with platinum-disk working, platinum-wire auxiliary, and silver-wire reference electrodes. Samples were measured at a scan rate of 100 $mV\,s^{-1}$ in a supporting electrolyte of 0.1 M Bu_4NPF_6 in DMF. Ferrocene was added after each measurement as an internal reference.

1: A pyrex ampule (i.d. × o.d. × l = 21 × 25 × 260 mm) was loaded with WCl_6 (3.3 g, 8.4 mmol), NaN_3 (0.090 g, 1.4 mmol), and Bi powder (1.8 g, 8.4 mmol) in a nitrogen atmosphere and was then evacuated and sealed. The ampule was positioned in a tube furnace such that the end opposite to the reactants was located at the center of the furnace and elevated at an incline of approximately 30°. The furnace was heated up at a rate of 1 °C min^{-1} to 500 °C and maintained at that temperature for 3 days. The ampule was cooled to room temperature and then repositioned with the product-containing end in the center of the furnace. The colorless $BiCl_3$ was sublimed away by heating at 360 °C for 16 h. The remaining black solid contained hexagonal plate-shaped crystals of **1** (2.1 g, 84 %), which X-ray powder diffraction studies indicated to be the main crystalline product. Elemental analysis (%) calcd for $Cl_{18}NNaW_6$: C 0.00, H 0.00, N 0.77; found: C < 0.02, H < 0.02, N 0.56.

2: Compound **1** was pulverized and stirred in HCl (0.12 M, 50 mL) for 12 h to give a dark-purple solution. Addition of Bu_4NCl (0.50 g, 1.8 mmol) induced precipitation of an olive-green solid, which was collected by filtration, washed with water (3 × 20 mL), and dried in air. The solid was then stirred in acetonitrile (20 mL), which produced a dark-green solution that was collected by centrifugation and decantation. This process was repeated five times and then the supernatant solutions were combined and reduced to dryness under a stream of nitrogen gas. A solution of Bu_4NCl (0.25 g, 0.90 mmol) in water (30 mL) was added to the residue and the mixture was stirred for 5 min. The ensuing olive-green solid was collected by filtration, washed with water (3 × 20 mL), dried in air, and dissolved in acetonitrile (30 mL). Diffusion of diethyl ether vapor into the solution afforded black, octahedron-shaped crystals of **2**. The supernatant solution was decanted and the crystals were washed with diethyl ether (3 × 20 mL) and dried in air to yield 1.2 g (37 %) of product. Absorption spectrum (MeCN): λ_{max} (ε_M) 300 (sh, 17000), 432 (sh, 3060), 607 (sh, 948), 700 (sh, 852), 846 nm (sh, 515); ESMS (MeCN): *m*/*z* calcd for $[W_6NCl_{18}]^{2-}$: 877.5687, found: 877.5734; μ_{eff} = 1.63 μ_B at 298 K; elemental analysis (%) calcd for $C_{32}H_{72}Cl_{18}N_3W_6$: C 17.16, H 3.24, N 1.88; found: C 17.31, H 3.42, N 1.84. Plate-shaped crystals of **2′** were obtained by slowly cooling a hot acetonitrile solution (4 mL) of **2** (50 mg, 22 μmol) and $[(Ph_3P)_2N]Cl$ (26 mg, 45 μmol).

3: A solution of cobaltocene (43 mg, 0.23 mmol) in acetonitrile (10 mL) was prepared in a nitrogen atmosphere. An aliquot (2 mL) of this solution was added to a solution of **2** (0.10 g, 0.046 mmol) in acetonitrile (3 mL). Addition of diethyl ether (20 mL) produced a green–brown precipitate, which was collected by centrifugation and decantation, washed with diethyl ether (3 × 10 mL), and dried under a stream of nitrogen gas to yield 88 mg (81 %) of product as an olive-green powder. Absorption spectrum (MeCN): λ_{max} (ε_M) 262 (65600), 296 (sh, 15200), 565 (sh, 1810), 819 nm (sh, 497); ESMS: *m*/*z*: 877 ($[W_6NCl_{18}]^{2-}$); elemental analysis calcd for $C_{42}H_{82}Cl_{18}CoN_3W_6$: C 20.77, H 3.40, N 1.73; found: C 20.39, H 3.13, N 1.78. Brown needle-shaped crystals of **3′** were obtained by diffusing diethyl ether vapor into a solution of **3** (88 mg) in acetonitrile (4 mL).

Received: November 12, 2004
Published online: March 22, 2005

Keywords: cluster compounds · cyclic voltammetry · metal–metal bonding · nitrides · tungsten

[1] a) H. B. Gray, A. W. Maverick, *Science* **1981**, *214*, 1201; b) A. Simon, *Angew. Chem.* **1988**, *100*, 163; *Angew. Chem. Int. Ed. Engl.* **1988**, *27*, 159; c) J. H. Golden, H. B. Deng, F. J. DiSalvo, J. M. J. Fréchet, P. M. Thompson, *Science* **1995**, *268*, 1463; d) J. D. Franolic, J. R. Long, R. H. Holm, *J. Am. Chem. Soc.* **1995**, *117*, 8139; e) S. J. Hilsenbeck, R. E. McCarley, A. I. Goldman, G. L. Schrader, *Chem. Mater.* **1998**, *10*, 125; f) L. G. Beauvais, M. P. Shores, J. R. Long, *J. Am. Chem. Soc.* **2000**, *122*, 2763; g) J. C.-P. Gabriel, K. Boubekeur, S. Uriel, P. Batail, *Chem. Rev.* **2001**, *101*, 2037; h) B. K. Roland, H. D. Selby, M. D. Carducci, Z. Zheng, *J. Am. Chem. Soc.* **2002**, *124*, 3222; i) T. G. Gray, C. M. Rudzinski, E. M. Meyer, R. H. Holm, D. G. Nocera, *J. Am. Chem. Soc.* **2003**, *125*, 4755.

[2] E. J. Welch, J. R. Long, *Prog. Inorg. Chem.* **2005**, *54*, 1.

[3] a) Y.-Q. Zheng, H. G. von Schnering, J.-H. Chang, *Z. Anorg. Allg. Chem.* **2003**, *629*, 1256; b) E. J. Welch, N. R. M. Crawford, R. G. Bergman, J. R. Long, *J. Am. Chem. Soc.* **2003**, *125*, 11464.

[4] a) H. Womelsdorf, H.-J. Meyer, *Angew. Chem.* **1994**, *106*, 2022; *Angew. Chem. Int. Ed. Engl.* **1994**, *33*, 1943; b) H. Womelsdorf, H.-J. Meyer, *Z. Anorg. Allg. Chem.* **1996**, *622*, 2083.

[5] a) F. Rogel, J. D. Corbett, *J. Am. Chem. Soc.* **1990**, *112*, 8198; b) M. R. Bond, T. Hughbanks, *Inorg. Chem.* **1992**, *31*, 5015; c) D. Sun, T. Hughbanks, *Inorg. Chem.* **1999**, *38*, 992; d) X. Xie, T. Hughbanks, *Inorg. Chem.* **2002**, *41*, 1824.

[6] a) V. Kolesnichenko, L. Messerle, *Inorg. Chem.* **1998**, *37*, 3660; b) N. R. M. Crawford, J. R. Long, *Inorg. Chem.* **2001**, *40*, 3456.

[7] Crystallographic analyses: **1** ($Cl_{18}NNaW_6$): T = 160 K, space group $P6_3/m$, a = 8.8360(4), c = 17.840(2) Å, V = 1206.24(14) Å^3, Z = 2, ρ_{calcd} = 4.896 g cm^{-3}, R_1 = 0.0278, wR_2 = 0.0703 for 5253 data (719 independent), 44 parameters, 0 restraints. **2′** ($C_{52}H_{66}Cl_{18}N_3P_2W_6$): T = 162 K, space group $P2_1/c$, a = 21.782(2), b = 14.0432(10), c = 23.266(2) Å, β = 100.5410(10)°, V = 6996.8(9) Å^3, Z = 4, ρ_{calcd} = 2.408 g cm^{-3}, R_1 = 0.0420, wR_2 = 0.0613 for 40136 data (14322 independent), 734 parameters, 0 restraints. **3′** ($C_{50}H_{111}Cl_{18}N_5W_6$): T = 155 K, space group $P2_1/c$, a = 18.315(2), b = 23.131(3), c = 18.872(3) Å, β = 96.780(2)°, V = 7939(2) Å^3, Z = 4, ρ_{calcd} = 2.111 g cm^{-3}, R_1 = 0.0691, wR_2 = 0.1576 for 34645 data (13044 independent), 689 parameters, 0 restraints. Data were collected on a Brüker APEX diffractometer using graphite monochromated $Mo_{K\alpha}$ (λ = 0.71073 Å) radiation and were corrected for Lorentz, polarization, and absorption effects. Structures were solved by direct methods and refined against all data by using SHELXTL 5.0. The structure of **3′** exhibited disorder in the $(Bu_4N)^+$ ions, which was modeled by assigning appropriate peaks of electron density as partially occupied carbon atoms. Further details on the crystal structure investigations may be obtained from the Fachinformationszentrum Karlsruhe, 76344 Eggenstein-Leopoldshafen, Germany (fax: (+49) 7247-808-666; e-mail: crysdata@fiz-karlsruhe.de), on quoting the depository number CSD-414409 (**1**). CCDC-250473 and -250472 (**2′** and **3′**) contain the supplementary crystallographic data for this paper. These data can be obtained

 © 2005 Wiley-VCH Verlag GmbH & Co. KGaA, Weinheim

free of charge from the Cambridge Crystallographic Data Centre via www.ccdc.cam.ac.uk/data_request/cif.
[8] N. Schoenberg, *Acta Chem. Scand.* **1954**, *8*, 204.
[9] T. C. Zietlow, W. P. Schaefer, B. Sadeghi, N. Hua, H. B. Gray, *Inorg. Chem.* **1986**, *25*, 2195.
[10] Note that with just 22 {Nb_6S}-based valence electrons, the trigonal prismatic $Nb_6SBr_{18}^{4-}$ units in the one-dimensional compounds $A_3Nb_6SBr_{17}$ (A = K, Rb, Cs, and Tl) also have a lower electron count; see, Ref.[4]
[11] DFT calculations (HCTH407/LANL2DZ) utilized are HPCCG's NWChem, A Computational Chemistry Package for Parallel Computers, version 4.5; PNNL: Richland, WA, **2003**. See the Supporting Information for details.
[12] a) T. Saito, N. Yamamoto, T. Nagase, T. Tsuboi, K. Kobayashi, T. Yamagata, H. Imoto, K. Unoura, *Inorg. Chem.* **1990**, *29*, 764; b) S. A. Baudron, A. Deluzet, K. Boubekeur, P. Batail, *Chem. Commun.* **2002**, 2124.

 © 2005 Wiley-VCH Verlag GmbH & Co. KGaA, Weinheim

Solid-State Chemistry

Pillared Hybrid Solids with Access to Coordinatively Unsaturated Metal Sites: An Alternative Strategy**

Paul A. Maggard, Bangbo Yan, and Junhua Luo*

Porous solids that contain accessible, coordinatively unsaturated (open) metal sites within a rigid framework show great potential for applications in catalysis, absorption of gases (H_2 and CH_4), and small-molecule recognition,[1–4] as highlighted in recent reviews.[5,6] There is a growing interest to improve catalytic and gas-absorption selectivity through the immobilization of reactive transition-metal centers inside highly functionalized, size-selective pores. This is envisioned as an extension of the well-known catalysis mediated by zeolite solids and coordination compounds. However, only a few mixed examples of open-framework solids with access to open metal sites have been reported, including open Zn, Cu, and Tb sites in three distinct metal–organic frameworks,[3,4,7] and Ni and Co sites within separate metal–hydroxycarboxylate solids.[8,9] These open metal coordination sites are typically obtained post-synthesis upon removal of a terminal ligand (such as H_2O or pyridine) from the metal without irreversible destabilization or collapse of the pore structure. The carboxylate functional groups of the ligands convey much of the structural stability in the above examples.

[*] Prof. P. A. Maggard, Dr. B. Yan, Dr. J. Luo
Department of Chemistry, North Carolina State University
Raleigh, NC 27695 (USA)
Fax: (+1) 919-515-5079
E-mail: paul_maggard@ncsu.edu

[**] The authors acknowledge the assistance of C. Day and J. Folmer. This work was supported by the ACS Petroleum Research Fund (#40963-G10) and the NCSU Faculty Research and Professional Development Fund.

By contrast, our research efforts are directed toward the use of metal oxide/organic assemblies, in which a robust metal oxide layer serves as the general platform to both immobilize and help structurally stabilize the open metal sites. The general approach is shown in Scheme 1, and arose from the

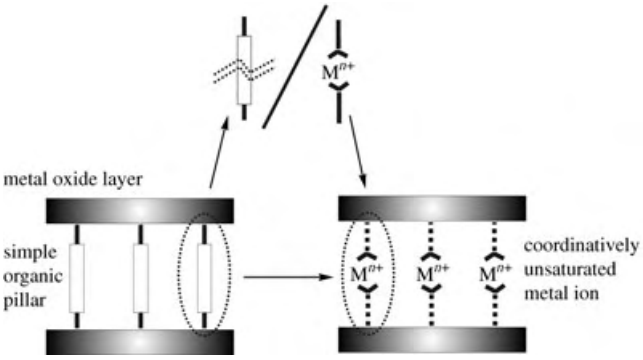

Scheme 1. The general strategy of substituting a symmetrical bridging ligand with an unsymmetrical ligand that results in access to open metal sites between metal oxide layers.

discovery and subsequent structural analysis of $Cu_2(pzc)_2(H_2O)_2ReO_4$ (pzc = 2-pyrazinecarboxylate),[10] which consists of $CuReO_4$ layers separated by pillars of $[Cu(pzc)_2(H_2O)_2]$. The strategy is based on substitution of the simple bridging ligand of a pillared solid for one that exhibits two different bonding preferences: one that favors attachment to the metal oxide layer and the other, to the desired transition metal. The ligand-bonding preferences can be used to entrain specific transition metals between the metal oxide layers. Furthermore, if the functional groups of the ligand satisfy the charge requirements of the transition metal (for example, two carboxylates for one M^{II}), then other neutral terminal ligands can be removed post-synthesis to yield open metal sites. The potential application of this synthetic strategy to immobilize open metal sites is also relevant to the large numbers of pillared layered phosphonates, sulfates, and hydroxide structures such as those reported earlier.[11–15] Herein we report the first description and application of this novel general strategy to target open Co and Ni sites stabilized between $AgReO_4$ layers.

The starting point of our synthesis was the simple, recently synthesized[16] $AgReO_4(pyz)$ (pyz = pyrazine) pillared solid shown in Figure 1a, which contains neutral $AgReO_4$ layers pillared by pyrazine. As suggested in Scheme 1, this synthesis was modified by using 2-pyrazinecarboxylate in place of pyrazine and adding Co^{II} and Ni^{II} for inclusion between the layers. Standard hydrothermal techniques were used and the reactants were heated at $\approx$110–140 °C for 24 h, followed by slow cooling for 24 h. Orange $Co(pzc)_2(H_2O)_2AgReO_4$ (**1**) and irregular platelike green crystals of $Ni(pzc)_2(H_2O)_2AgReO_4$ (**2**) were obtained and characterized by X-ray diffraction.[17] The reversible removal of coordinated H_2O was detected by thermogravimetric analysis (TGA).

The structures of both solids (Figures 1b and c) derive from that of $AgReO_4(pyz)$ in which $AgReO_4$ layers are bridged through pzc to interlayer Co or Ni centers in **1** and **2**,

 DOI: 10.1002/anie.200462715 © 2005 Wiley-VCH Verlag GmbH & Co. KGaA, Weinheim

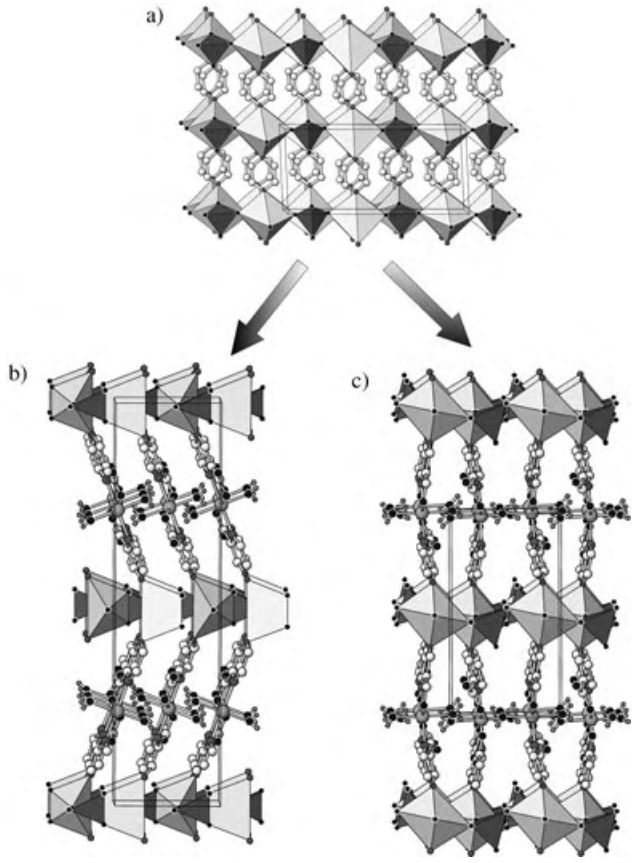

Figure 1. Layered structure views of a) $AgReO_4(pyz)$; b) $Co(pzc)_2(H_2O)_2AgReO_4$; and c) $Ni(pzc)_2(H_2O)_2AgReO_4$. $AgReO_4$ layers are illustrated with polyhedra; light polyhedra are Ag-centered, dark represent ReO_4^-; interlayer atoms: black = O, darkly shaded = N, white = C, and lightly shaded = Co and Ni.

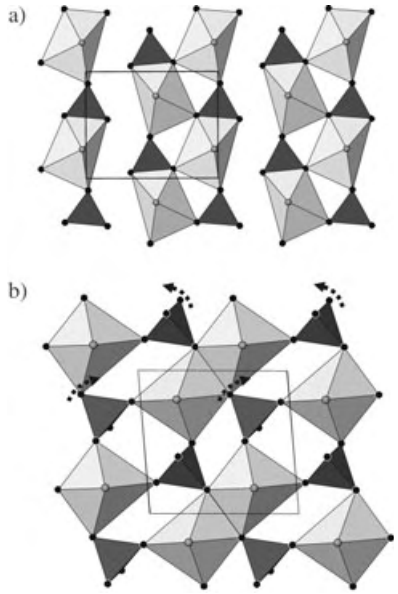

Figure 2. Polyhedral view normal to the $AgReO_4$ layers for a) **1** and b) **2**; dashed arrows denote rotations to interrelate the orientations of ReO_4^- tetrahedra between the two structures.

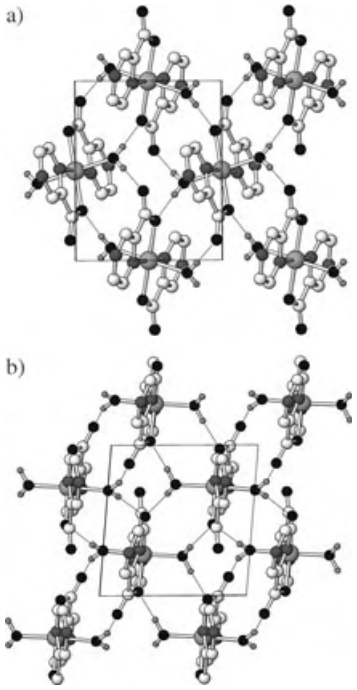

Figure 3. View of a single layer of $M(pzc)_2(H_2O)_2$ pillars drawn normal to the layer plane with the unit cell outlined: a) M = Co and b) M = Ni; interlayer atoms: black = O, darkly shaded = N, white = C, lightly shaded = Co and Ni, and gray = H.

respectively. The $[Co(pzc)_2]$ pillars in **1** are tilted with respect to the $AgReO_4$ layers, resulting in a relatively smaller interlayer spacing of $\approx$13.58 Å (*b*-axis/2), whereas the $[Ni(pzc)_2]$ pillars in **2** buckle only slightly with a *c*-axis layer spacing of $\approx$14.00 Å. The lone (*para*) N atoms of the pzc ligands bond preferentially to the Ag sites of the $AgReO_4$ layer with Ag–N bond lengths of 2.214(3) Å in **1** and 2.246(6) and 2.258(6) Å in **2**. Within the $AgReO_4$ layers of both structures, the ReO_4^- tetrahedra have regular Re–O bond lengths in the range of 1.680(6)–1.765(7) Å (Figure 2). The 2D packing of the $AgReO_4$ layers is structurally similar in **1** and **2**, with the ReO_4^- tetrahedra in approximately body-centered arrangements with Ag-centered polyhedra on the edges. However, in **2** there are two distinct sets of tetrahedral orientations that alternate, which causes the changes in local Ag atom environments. A rotation of each ReO_4^- tetrahedron in **2** by $\approx$20–25° that aligns them in a single direction brings this layer into closer similarity to the topology of **1** (Figure 2b).

The COO^- groups and N atoms of the pzc ligand preferentially coordinate to the equatorial positions of Co and Ni at the usual distances (2.026(5)–2.169(2) Å)[18,19] as shown in Figure 3. The COO^- groups and N atoms on opposing ligands arrange *trans* with respect to each other. The axial positions of the metals are bonded by H_2O, at distances of 2.060(2) Å for Co and 2.033(6) and 2.086(6) Å for Ni. In both **1** and **2**, each H_2O molecule forms H bonds (Figure 3, thin lines: OH···O) at distances of 1.75–2.13 Å to both O atoms of the carboxylate groups. However in **2**, an O atom of one carboxylate group has no H-bond contacts whereas the other has two. This difference results from the tilt of the $[Co(pzc)_2]$ pillars, in

 © 2005 Wiley-VCH Verlag GmbH & Co. KGaA, Weinheim

contrast to the nearly vertical pillars of $[Ni(pzc)_2]$. The metal-bridged pillars are bonded to the $AgReO_4$ layers, which structurally separate and hinder the Co/Ni sites from further bonding to free carboxylate groups as frequently occurs in metal–organic structures.[19,20] This feature also helps prevent structural collapse upon removal of coordinated H_2O from the Co/Ni centers.

TGA performed under flowing N_2 showed a mass loss that corresponds to the removal of coordinated H_2O (calcd, 5.1%; exptl, 5.2%) at 120°C for **1** and 170°C for **2**. TGA curves for both are shown as insets in Figure 4. Concomitant color changes were observed as lighter shades of orange and green for **1** and **2**, respectively. Further decomposition occurred at >300°C; the compounds exhibited a total range of stability close to 200°C. Both could be rehydrated with drops of H_2O on a glass slide, and subsequent TGA again revealed the characteristic 5% mass loss for all coordinated H_2O, an indication for porosity.[21] Full rehydration required only minutes for **1**, but up to 20 h for **2**. This is likely the result of the much larger crystal sizes of **2** (>×50, on average) and longer H_2O diffusion paths than present in **1**.

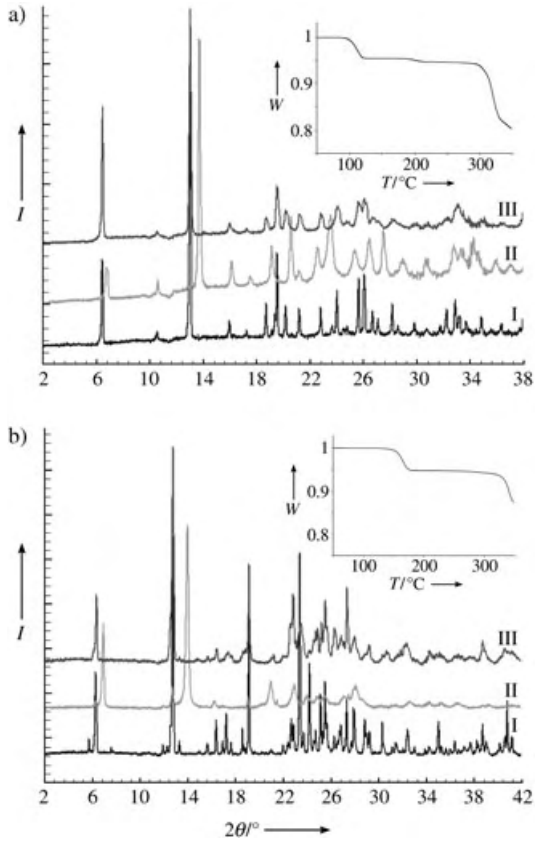

Figure 4. Powder X-ray diffraction results for a) **1**, and b) **2**; directly post-synthesis (I), after dehydration (II), and after rehydration (III); insets: respective TGA curves (w = mass fraction).

Powder X-ray diffractometry was used to monitor the rate and effect of rehydration and dehydration on both structures (Figure 4). After one cycle of dehydration/rehydration, **1** and **2** showed almost no change in peak position, and slightly less crystallinity. Shifts in peak position were noticeable upon dehydration, corresponding to decreases in the $AgReO_4$ interlayer spacing ($\approx$0.73 Å for the (020) and (040) planes for **1;** $\approx$1.34 Å for the (001) and (002) planes for **2**). The larger decrease in interlayer spacing for **2** is likely caused by the nearly vertical orientation of the $[Ni(pzc)_2]$ pillars in the hydrated state, which results in a more dramatic tilt (and compression) upon the removal of H_2O. Both dehydrated structures stabilize at a similar interlayer spacing of $\approx$12.8–13.0 Å.

The substitution of pyrazine for 2-pyrazinecarboxylate pillars between $AgReO_4$ layers, as diagrammed in Scheme 1, results in solids **1** and **2** that are predisposed to the formation of coordinatively unsaturated Ni and Co sites. Ongoing investigations of the Cu analogue show structural similarity, but a dehydrated and novel chiral framework that results from significant tilting of the pillars.[22] A recent synthesis of sulfate analogues suggest that strong coordination preferences of the organic pillars will be essential for the success of this strategy.[23] Notably, other examples of hybrid solids that use 2-pyrazinecarboxylate but contain tubelike structures have been reported; such hybrids exhibit porosity.[19] However, very few synthetic approaches are known that enable access to a similar diversity of open late-transition-metal sites within closely related hybrid solids.

Experimental Section

1: Product was obtained by hydrothermal reaction (1 g total) of Ag_2O (0.313 mmol), Re_2O_7 (0.313 mmol), 2-pyrazinecarboxylate (1.251 mmol), $Co(OH)_2$ (0.625 mmol), and distilled H_2O (31.26 mmol). All chemicals were used as received with stated purities of >99%. Reactants were loaded and sealed inside a teflon pouch, which was placed inside a teflon-lined stainless-steel reaction vessel (120 mL). The vessel was heated to and kept at 125°C for 36 h, and gradually cooled to room temperature over 24 h. The products consisted of large orange crystals and powder in typical yields of >90% based on Co.

2: Product was obtained by hydrothermal reaction of starting materials listed above for **1** in similar molar ratios and NiO (0.633 mmol) in place of $Co(OH)_2$. The reactants were heated at 140°C for 36 h, and gradually cooled to room temperature over 24 h. The products consisted of green crystals in >90% yield based on Ni.

Received: November 24, 2004
Published online: March 16, 2005

Keywords: cobalt · hydrothermal synthesis · microporous materials · nickel · solid-state structures

[1] N. Guillou, Q. Gao, P. M. Forster, J.-S. Chang, M. Nogues, S.-E. Park, G. Férey, A. K. Cheetham, *Angew. Chem.* **2001**, *113*, 2913; *Angew. Chem. Int. Ed.* **2001**, *40*, 2831.
[2] P. M. Forster, J. Eckert, J.-S. Chang, S.-E. Park, G. Férey, A. K. Cheetham, *J. Am. Chem. Soc.* **2003**, *125*, 1309.
[3] H. Li, C. E. Davis, T. L. Groy, D. G. Kelley, O. M. Yaghi, *J. Am. Chem. Soc.* **1998**, *120*, 2186.
[4] B. Chen, M. Eddaoudi, T. M. Reineke, J. W. Kampf, M. O'Keefe, O. M. Yaghi, *J. Am. Chem. Soc.* **2000**, *122*, 11559.
[5] P. M. Forster, A. K. Cheetham, *Top. Catal.* **2003**, *24*, 79.
[6] M. J. Rosseinsky, *Microporous Mesoporous Mater.* **2004**, *73*, 15.

 © 2005 Wiley-VCH Verlag GmbH & Co. KGaA, Weinheim

[7] T. M. Reineke, M. Eddaoudi, M. Fehr, D. Kelley, O. M. Yaghi, *J. Am. Chem. Soc.* **1999**, *121*, 1651.
[8] P. M. Forster, A. K. Cheetham, *Angew. Chem.* **2002**, *114*, 475; *Angew. Chem. Int. Ed.* **2002**, *41*, 457.
[9] S. O. H. Gutschke, D. J. Price, A. K. Powell, P. T. Wood, *Eur. J. Inorg. Chem.* **2001**, 2739.
[10] J. Luo, B. Alexander, T. R. Wagner, P. A. Maggard, *Inorg. Chem.* **2004**, *43*, 5537.
[11] A. Clearfield, *Chem. Mater.* **1998**, *10*, 2801.
[12] A. Clearfield, Z. Wang, *J. Chem. Soc. Dalton Trans.* **2002**, 2937.
[13] G. Alberti, R. Vivani, F. Marmottini, *J. Porous Mater.* **1998**, *5*, 205.
[14] a) A. Rujiwatra, C. J. Kepert, M. J. Rosseinsky, *Chem. Commun.* **1999**, 2307; b) A. Rujiwatra, G. J. Mander, C. J. Kepert, M. J. Rosseinsky, *Cryst. Growth Des.* **2005**, *5*, 183.
[15] K. Susumu, K. Ryo, *Comments Inorg. Chem.* **2002**, *23*, 101.
[16] P. A. Maggard, P. D. Boyle, unpublished results.
[17] Single-crystal data were collected on a Bruker Apex CCD area detector diffractometer with $Mo_{K\alpha}$ radiation ($\lambda = 0.71073$ Å). The data were solved and refined by using SHELXS97 and SHELXL97 within WINGX version 1.64.05.[24] Crystal data for **1**: orange ($0.066 \times 0.080 \times 0.110$ mm^3); $M_r = 699.22$; orthorhombic *Pnma* (no. 62); $a = 7.1029(6)$, $b = 27.160(2)$, $c = 8.7482(8)$ Å, $V = 1687.7(2)$ Å^3; $Z = 4$; $T = 293(2)$ K; $\rho_{calcd} = 2.752$ g cm^{-3}; $\mu = 9.337$. Crystal data for **2**: green ($0.18 \times 0.18 \times 0.03$ mm^3); $M_r = 699.00$; triclinic $P\bar{1}$ (no. 2); $a = 7.5795(9)$, $b = 7.8800(9)$, $c = 14.0052(9)$ Å, $\alpha = 83.271(2)$, $\beta = 89.660(3)$, $\gamma = 85.156(3)°$, $V = 827.75(15)$ Å^3; $Z = 2$; $T = 193(2)$ K; $\rho_{calcd} = 2.805$ g cm^{-3}; $\mu = 9.654$. For **1** and **2**, Final R/R_w on $|F^2|$ were 0.027/0.064 (2591 data) and 0.058/0.167 (5188 data) with GOF = 1.09 and 1.07, and max/min residual electron densities of 2.21/−0.7 and 4.75/−4.48. CCDC-257420 (**1**) and -257421 (**2**) contain the supplementary crystallographic data for this paper. These data can be obtained free of charge from The Cambridge Crystallographic Data Centre via www.ccdc.cam.ac.uk/data_request/cif.
[18] L.-M. Zheng, X. Wang, Y. Wang, A. J. Jacobson, *J. Mater. Chem.* **2001**, *11*, 1100.
[19] L.-M. Zheng, T. Whitfield, X. Wang, A. J. Jacobson, *Angew. Chem.* **2000**, *112*, 4702; *Angew. Chem. Int. Ed.* **2000**, *39*, 4528.
[20] S. K. Dey, B. Bag, K. M. Abdul Malik, M. S. El Fallah, J. Ribas, S. Mitra, *Inorg. Chem.* **2003**, *42*, 4029.
[21] Note: In general, uptake of structural water could also be the result of a dissolution/reprecipitation mechanism in which only subnanomolar concentrations in solution are required. However, powder X-ray diffraction patterns suggest a gradual structural change between the dehydrated and hydrated forms, in contrast to the dissolution mechanism.
[22] Unit cell: $P4_32_12$, $a = 7.612$, $c = 49.4945$ Å.
[23] P. A. Maggard, unpublished results.
[24] L. J. Farrugia, *J. Appl. Crystallogr.* **1999**, *32*, 837.

 © 2005 Wiley-VCH Verlag GmbH & Co. KGaA, Weinheim

Multivalent DNA Binding

High-Affinity Multivalent DNA Binding by Using Low-Molecular-Weight Dendrons**

*Mauri A. Kostiainen, John G. Hardy, and David K. Smith**

High-affinity binding between nanoscale objects is an essential prerequisite for "bottom-up" fabrication.[1] In recent years, interest has focused on the use of dendritic macromolecules as supramolecular nanoscale building blocks.[2] The branched superstructure of dendrons and dendrimers offers specific advantages, for example, enhancement of weak binding by using multivalent arrays of recognition units on the dendritic surface. This multivalency principle, in which organized arrays amplify the strength of a weak binding process, such as the binding of saccharides to proteins on cell surfaces, is now well established.[3]

DNA constitutes a particularly interesting target for nanotechnological exploitation.[4] High-affinity binding of DNA is useful for protecting DNA and ultimately for delivering genetic information into cells.[5] Noncovalent interactions between dendritic macromolecules and DNA are, therefore, of considerable current interest.[6] Polyamidoamine (PAMAM) dendrimers were the first systems to be investigated,[7] while dendritic poly(L-lysine)[8] and poly(propylene imine)[9] have also been studied recently. In general, higher-generation, or structurally fractured, systems are usually more effective for DNA binding and delivery. In an important recent study, however, Diederich and co-workers reported low-molecular-mass dendrons designed to self-assemble with DNA, which were capable of gene therapy.[10]

The interaction between a single protonated amine and the phosphate backbone of DNA is relatively weak and must compete with salt binding under biological conditions. Biology therefore uses tetraamines, such as spermine (Scheme 1), to achieve DNA binding.[11] Synthetic spermine derivatives are also widely used for applications in DNA binding and delivery.[12] However, although spermine is better than an isolated amine for binding DNA, the interaction is still relatively weak and the complex is mobile. Consequently, spermine struggles to compete with DNA-bound inorganic cations.[13]

[*] M. A. Kostiainen, J. G. Hardy, Dr. D. K. Smith
Department of Chemistry
University of York
Heslington, York, YO10 5DD (UK)
Fax: (+44) 1904-432-516
E-mail: dks3@york.ac.uk

[**] This work was supported through the Socrates–Erasmus European Exchange Scheme (M.A.K.) and by the Engineering and Physical Sciences Research Council and Syngenta through the CASE Scheme (J.G.H.). We acknowledge Ian Ashworth and Colin Brennan (Syngenta) for support and Meg Stark (Department of Biology, University of York) for assistance with TEM measurements.

Supporting Information for this article is available on the WWW under http://www.angewandte.org or from the author.

 © 2005 Wiley-VCH Verlag GmbH & Co. KGaA, Weinheim DOI: 10.1002/anie.200500066

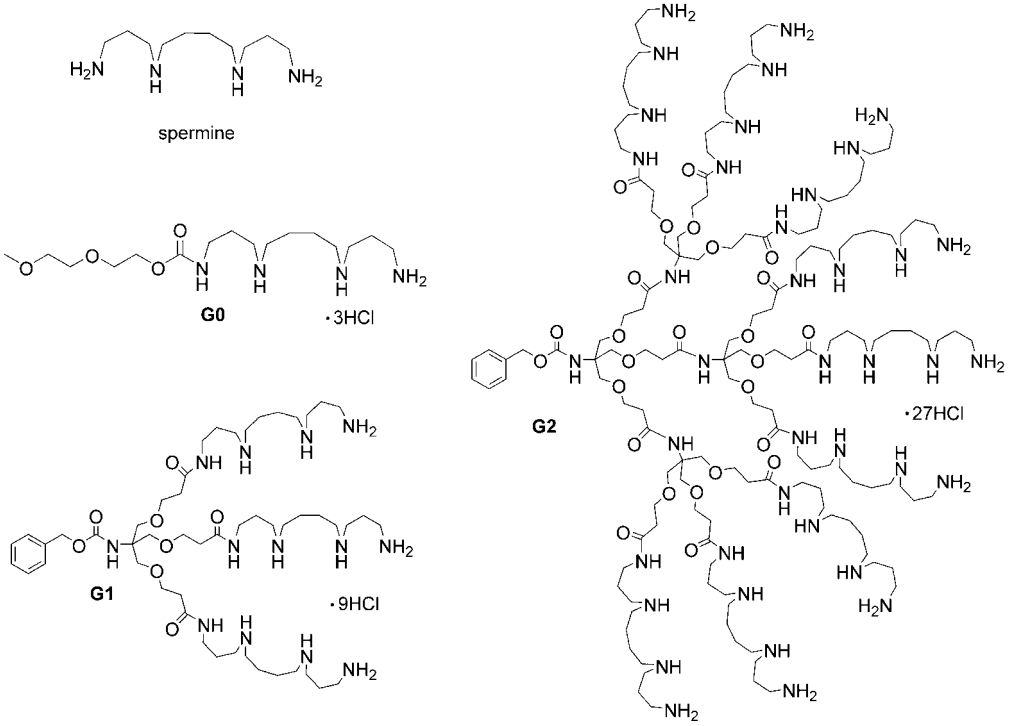

Scheme 1. Spermine and target spermine derivatives **G0**, **G1**, and **G2**.

We became interested in optimizing DNA binding and developing low-molecular-mass dendrons with very high affinities for DNA—such systems would be particularly useful for DNA encapsulation and protection.[14] We therefore decided to develop dendrons that express multivalent spermine arrays on their surfaces. Some previously reported multivalent spermine arrays comprised multiple spermine groups grafted onto dextran polymers;[15] however, we wanted to develop multivalent systems with well-defined molecular structures. Such monodisperse systems enable an understanding of structure–activity relationships and, in addition, have a greater chance of being licensed for therapeutic applications in the longer term. Herein, we report on multivalent dendritic spermine constructs with extremely high, salt-independent binding affinities for DNA.

We used a divergent synthetic approach to construct target compounds **G1** and **G2** (Scheme 1, details of the synthesis can be found in the Supporting Information). Newkome-type branching[16] was used as the dendritic scaffold, as such structures are readily synthesized[17] and should be biocompatible. After dendron synthesis, the surface was functionalized with spermine groups which had been appropriately protected by using the methodology of Blagbrough and Geall.[18] Deprotection of the spermine groups with HCl gas then yielded target compounds **G1** and **G2**. Model compound **G0** was constructed by using a similar approach (Scheme 1). All synthetic steps were high yielding and all target compounds and intermediates were fully characterized with standard methods (see the Supporting Information).

Initially, the binding of the spermine derivatives to DNA was studied by using an ethidium bromide displacement assay. This method is commonly used to study the binding of polyammonium compounds to DNA.[19] The displacement of ethidium bromide from its complex with DNA can be monitored because it has enhanced fluorescence when intercalated. This is a powerful comparative method, although the resulting data reflect a competition assay, rather than an absolute binding strength, and furthermore give no information about binding stoichiometry.

Fluorescence titrations were performed in buffered water at pH 7.2 using **G0**, **G1**, **G2**, and spermine itself. The resultant titration profiles are shown in Figure 1. At this physiologically relevant pH value, the spermine groups are largely protonated whilst the DNA is largely deprotonated, so electrostatic interactions are maximized.

The data can be presented in terms of C_{50} and CE_{50} values (Table 1). C_{50} values report the concentration of polyamine causing a 50% decrease in fluorescence intensity. CE_{50} values represent the "charge excess"[20] required to achieve the same

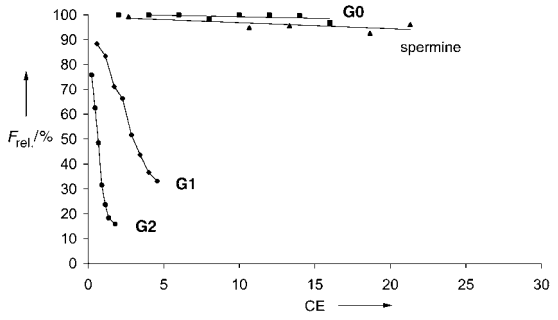

Figure 1. Fluorescence titration profiles for the addition of spermine, **G0**, **G1**, or **G2** to a solution of calf thymus DNA and ethidium bromide in buffered water (pH 7.2) in the presence of 150 mM NaCl.

 © 2005 Wiley-VCH Verlag GmbH & Co. KGaA, Weinheim

Table 1: Results for spermine, **G0**, **G1**, and **G2** from an ethidium bromide displacement assay.[a]

Compound	[NaCl] [mM]	Nominal charge	C_{50} [μM]	CE_{50}
spermine	9.4	4+	1.33	5.3
G0	9.4	3+	20	60
G1	9.4	9+	0.076	0.68
G2	9.4	27+	0.030	0.81
spermine	150	4+	390	1560
G0	150	3+	220	660
G1	150	9+	0.300	2.70
G2	150	27+	0.028	0.76

[a] Conditions: Measurements performed in buffered water at pH 7.2 (with 2 mM 2-[4-(2-hydroxyethyl)-1-piperazinyl]ethanesulfonic acid (HEPES) and 0.05 mM ethylenediaminetetraacetic tetraacetate (EDTA)). The calf thymus DNA (1 μM) and ethidium bromide (1.26 μM) concentrations were kept constant. The total added polyamine solution did not exceed 5% of the total volume; therefore, corrections were not made for sample dilution. Results are an average of at least three titrations. Experimental errors $\leq$10%.

50% reduction in fluorescence—the very best DNA binders should have CE_{50} values below 1.0. Spermine binds to DNA with moderate strength under low-salt (9.4 mM NaCl) conditions (C_{50} = 1.33 μM, CE_{50} = 5.3), but a very large charge excess would have been required at physiological salt concentrations (150 mM NaCl) in order to achieve 50% quenching of ethidium bromide fluorescence (C_{50} = 390 μM, CE_{50} = 1560). These results were in good agreement with literature data.[19a] Compound **G0** showed similar, if slightly weaker, DNA binding. This was expected, as one of the primary amines of spermine has been converted into an amide, which is incapable of protonation, and **G0** should therefore exhibit weaker electrostatic interactions with polyanionic DNA.

The dendritic systems **G1** and **G2** showed significantly enhanced DNA binding. Under low-salt conditions, **G1** effectively displaced ethidium bromide from DNA (C_{50} = 76 nM, CE_{50} = 0.68). Notably, the affinity for DNA is considerably more than three times higher than that of **G0**. This indicates that the organization of three spermine units on the dendritic framework enables DNA-binding activity that is more than the simple sum of its individual parts—the multivalency principle[3] in operation. Compound **G1** is somewhat affected by the increase in salt concentration but still shows reasonable binding under these conditions (C_{50} = 300 nM, CE_{50} = 2.70).

Compound **G2** shows a similar binding affinity to **G1** under low-salt conditions (C_{50} = 30 nM, CE_{50} = 0.81) but demonstrates its power at physiological salt concentrations, where the binding remains just as strong (C_{50} = 28 nM, CE_{50} = 0.76). The binding is therefore *salt independent*—a proactive dendritic effect. The multivalent system can therefore compete with Na^+ ions for binding sites on the surface of the DNA helix. Indeed, compound **G2** exhibits one of the best binding profiles reported by using this method, thereby proving that the strategy of organizing spermine units into a well-defined multivalent array has considerable power.

Gel electrophoresis was used to confirm the affinities of the dendrons for DNA in a direct binding assay. The dendritic constructs **G1** and **G2** retarded the electrophoretic mobility of DNA as a consequence of charge neutralization, whilst the spermine and **G0** analogues were ineffective (Figure 2). The CE values at which mobility was retarded were in agreement with the results of the ethidium bromide displacement assays.

Figure 2. Gel electrophoresis of plasmid DNA (250 ng per lane). Lane 1: Plasmid DNA. Lane 2: Plasmid DNA + spermine (250 ng). Lane 3: Plasmid DNA + **G0** (250 ng). Lane 4: Plasmid DNA + **G1** (250 ng). Lane 5: Plasmid DNA + **G2** (250 ng).

Finally, transmission electron microscopy (TEM) was used to image the complexes (Figure 3). The addition of spermine at CE = 1.8 to plasmid DNA in buffered water (pH 7.1, [NaCl] = 9.4 mM) prior to deposition on a carbon-coated copper grid gave rise to large unsymmetrical aggregates approximately 250 nm in diameter (Figure 3A). Compound **G0**, however, led to little or no compaction of DNA under the same conditions. On the other hand, use of **G1** or **G2** (CE = 2.7) gave rise to well-defined, approximately spherical nanoscale complexes (**G1**: approximately 100 nm in diameter; **G2**: approximately 400 nm in diameter) with no free plasmid being detected (Figures 3B,C). The size range of the aggregates formed was relatively large. Nonetheless, these observations indicate that compounds **G1** and **G2** efficiently bind DNA and condense it into approximately spherical complexes.

In summary, we have reported novel dendrons that bind DNA with remarkably high affinities. Notably, **G2** showed salt-independent DNA binding and it was a factor of ten more

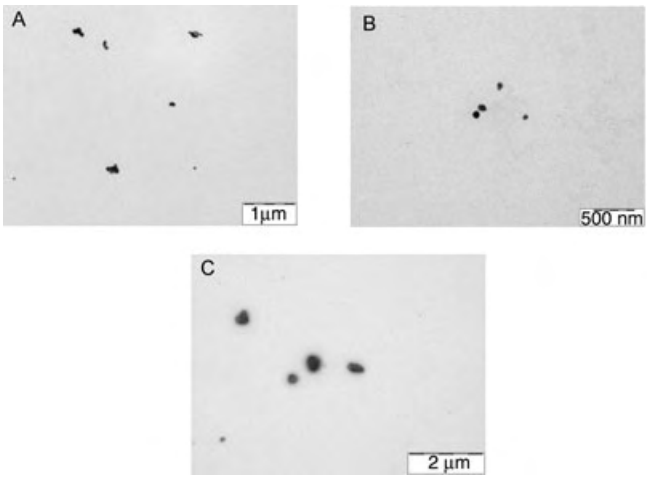

Figure 3. TEM images of DNA in the presence of A) spermine (CE = 1.8), B) **G1** (CE = 2.7), or C) **G2** (CE = 2.7). Samples were deposited from buffered water (pH 7.1).

 © 2005 Wiley-VCH Verlag GmbH & Co. KGaA, Weinheim

effective than the **G1** analogue under high-salt conditions, whilst **G1** was, in turn, significantly more effective than the **G0** analogue. It can be concluded that the expression of multiple spermine units, nature's own DNA binder, on the surface of a dendritic scaffold offers a powerful approach for achieving high-affinity DNA binding under physiological conditions. These molecules have potential for further synthetic variation, and in current and future work, we will be investigating the effect of structural modifications on DNA binding and nanoscale assembly, as well as looking at applications of the novel dendritic constructs in gene protection and delivery.

Received: January 7, 2005
Published online: March 22, 2005

Keywords: dendrimers · DNA · multivalency · nanochemistry · self-assembly

[1] a) G. M. Whitesides, B. Grzybowski, *Science* **2002**, *295*, 2418 – 2421; b) I. W. Hamley, *Angew. Chem.* **2003**, *115*, 1730 – 1752; *Angew. Chem. Int. Ed.* **2003**, *42*, 1692 – 1712.

[2] a) D. K. Smith, A. R. Hirst, C. S. Love, J. G. Hardy, S. V. Brignell, B. Huang, *Prog. Polym. Sci.* **2005**, in press; b) D. K. Smith, F. Diederich, *Top. Curr. Chem.* **2000**, *210*, 183 – 227; c) J. M. J. Fréchet, *Proc. Natl. Acad. Sci. USA* **2002**, *99*, 4782 – 4787; d) P. J. Gittins, L. J. Twyman, *Supramol. Chem.* **2003**, *15*, 5 – 23.

[3] a) S. Borman, *Chem. Eng. News* **2000**, *78*(41), 48 – 53; b) R. J. Pieters, *Trends Glycosci. Glycotechnol.* **2004**, *16*, 243 – 254; c) T. K. Lindhorst, *Top. Curr. Chem.* **2002**, *218*, 201 – 235; d) for a thermodynamic model, see: P. I. Kitov, D. R. Bundle, *J. Am. Chem. Soc.* **2003**, *125*, 16271 – 16284.

[4] H. Yan, S. H. Park, G. Finkelstein, J. H. Reif, T. H. LaBean, *Science* **2003**, *301*, 1882 – 1884.

[5] a) I. M. Verma, N. Somia, *Nature* **1997**, *389*, 239 – 242; b) D. Luo, M. Saltzmann, *Nat. Biotechnol.* **2000**, *18*, 33 – 37; c) T. Merdan, J. Kopecek, T. Kissel, *Adv. Drug Delivery Rev.* **2002**, *54*, 715 – 758.

[6] a) J. Dennig, *Top. Curr. Chem.* **2003**, *228*, 227 – 236; b) S. E. Stiriba, H. Frey, R. Haag, *Angew. Chem.* **2002**, *114*, 1385 – 1390; *Angew. Chem. Int. Ed.* **2002**, *41*, 1329 – 1334.

[7] a) J. Haensler, F. C. Szoka, *Bioconjugate Chem.* **1993**, *4*, 372 – 379; b) J. F. Kukowska-Latallo, A. U. Bielinska, J. Johnson, R. Spindler, D. A. Tomalia, J. R. Baker, *Proc. Natl. Acad. Sci. USA* **1996**, *93*, 4897 – 4902; c) M. X. Tang, C. T. Redemann, F. C. Szoka, *Bioconjugate Chem.* **1996**, *7*, 703 – 714; d) M. F. Ottaviani, F. Furini, A. Casini, N. J. Turro, S. Jockusch, D. A. Tomalia, L. Messori, *Macromolecules* **2000**, *33*, 7842 – 7851; e) J. H. Lee, Y. B. Lim, J. S. Choi, Y. Lee, T.-i. Kim, H. J. Kim, J. K. Yoon, K. Kim, J. S. Park, *Bioconjugate Chem.* **2003**, *14*, 1214 – 1221.

[8] a) J. S. Choi, D. K. Joo, C. H. Kim, K. Kim, J. S. Park, *J. Am. Chem. Soc.* **2000**, *122*, 474 – 480; b) M. Ohsaki, T. Okuda, A. Wada, T. Hirayama, T. Niidome, H. Aoyagi, *Bioconjugate Chem.* **2002**, *13*, 510 – 517.

[9] B. H. Zinselmeyer, S. P. Mackay, A. G. Schätzlein, I. F. Uchegbu, *Pharm. Res.* **2002**, *19*, 960 – 967.

[10] D. Joester, M. Losson, R. Pugin, H. Heinzelmann, E. Walter, H. P. Merkle, F. Diederich, *Angew. Chem.* **2003**, *115*, 1524 – 1528; *Angew. Chem. Int. Ed.* **2003**, *42*, 1486 – 1490.

[11] a) C. W. Tabor, H. Tabor, *Annu. Rev. Biochem.* **1984**, 740 – 790; b) V. Vijayanathan, T. Thomas, A. Shirahata, T. J. Thomas, *Biochemistry* **2001**, *40*, 13644 – 13651.

[12] For an overview, see: a) I. S. Blagbrough, A. J. Geall, A. P. Neal, *Biochem. Soc. Trans.* **2003**, *31*, 397 – 406; for further selected examples, see: b) G. Byk, C. Dubertret, V. Escriou, M. Frederic, G. Jaslin, R. Rangara, B. Pitard, J. Crouzet, P. Wils, B. Schwartz, D. Scherman, *J. Med. Chem.* **1998**, *41*, 224 – 235; c) A. J. Geall, M. A. W. Eaton, T. Baker, C. Catterall, I. S. Blagbrough, *FEBS Lett.* **1999**, *459*, 337 – 342; d) G. Ronsin, C. Perrin, P. Guédat, A. Kremer, P. Camilleri, A. J. Kirby, *Chem. Commun.* **2001**, 2234 – 2235; e) C. Boulanger, C. Di Giorgio, J. Gaucheron, P. Vierling, *Bioconjugate Chem.* **2004**, *15*, 901 – 908; f) T. Dewa, Y. Ieda, K. Morita, L. Wang, R. C. MacDonald, K. Iida, K. Yamashita, N. Oku, M. Nango, *Bioconjugate Chem.* **2004**, *15*, 824 – 830.

[13] a) N. Korolev, A. P. Lyubartsev, L. Nordenskiöld, A. Laaksonen, *J. Mol. Biol.* **2001**, *308*, 907 – 917; b) Y. Burak, G. Ariel, D. Andelman, *Curr. Opin. Colloid Interface Sci.* **2004**, *9*, 53 – 58.

[14] H. G. Abdelhady, S. Allen, M. C. Davies, C. J. Roberts, S. J. B. Tendler, P. M. Williams, *Nucleic Acids Res.* **2003**, *31*, 4001 – 4005.

[15] a) T. Azzam, H. Eliyahu, A. Makovitzki, M. Linial, A. J. Domb, *J. Controlled Release* **2004**, *96*, 309 – 323; b) H. Hosseinkhani, T. Azzam, Y. Tabata, A. J. Domb, *Gene Ther.* **2004**, *11*, 194 – 203.

[16] a) G. R. Newkome, X. Lin, *Macromolecules* **1991**, *24*, 1443 – 1444; b) G. R. Newkome, X. Lin, C. D. Weis, *Tetrahedron: Asymmetry* **1991**, *2*, 957 – 960; c) J. K. Young, G. R. Baker, G. R. Newkome, K. F. Morris, C. S. Johnson, Jr., *Macromolecules* **1994**, *27*, 3464 – 3471; d) J.-F. Nierengarten, T. Habicher, R. Kessinger, F. Cardullo, F. Diederich, V. Gramlich, J.-P. Gisselbrecht, C. Boudon, M. Gross, *Helv. Chim. Acta* **1997**, *80*, 2238 – 2276.

[17] C. M. Cardona, R. E. Gawley, *J. Org. Chem.* **2002**, *67*, 1411 – 1413.

[18] I. S. Blagbrough, A. J. Geall, *Tetrahedron Lett.* **1998**, *39*, 439 – 442.

[19] a) B. F. Cain, B. C. Baguley, W. A. Denny, *J. Med. Chem.* **1978**, *21*, 658 – 668; b) H. Gershon, R. Ghirlando, S. B. Guttman, A. Minsky, *Biochemistry* **1993**, *32*, 7143 – 7151.

[20] Charge excess is defined as the nominal "number of positive charges" of the polyamine divided by the "number of negative charges" present on the DNA. A molecular weight of 660 g mol^{-1} per base pair and one negative charge per nucleotide were assumed.

 © 2005 Wiley-VCH Verlag GmbH & Co. KGaA, Weinheim

N,P Ligands

A Ligand Composed of Dinitrogen and Methyldiphenylphosphane in a Cationic Molybdenum Complex**

*Tetsuro Murahashi, Christopher R. Clough, Joshua S. Figueroa, and Christopher C. Cummins**

It is well recognized that a reactive chemical fragment, which in its free state may be fleeting, not isolable, and difficult to observe, may sometimes be stabilized or trapped in an isolable form by coordination to a transition-metal center. Herein we report a unique ligand made of N_2 and PPh_2Me, which is stabilized in a cationic molybdenum complex. It does not seem likely that such a "diazophosphorane" $NNPR_3$ ligand[1] would be obtained simply by addition of PR_3 to a terminal metal–N_2 complex, because the β-N (terminal) atom of coordinated N_2 typically is at least moderately nucleophilic. Furthermore, the $NNPR_3$ moiety is expected to be thermodynamically unstable in view of the great stability of N_2 and PR_3. To the best of our knowledge, the diazophosphorane $NNPR_3$ unit has not been identified previously as a ligand in spite of the prevalent use of tertiary phosphines as ligands in N_2 coordination chemistry. However, the $NNPR_3$ moiety is found as a chemical fragment in some known phosphorus–nitrogen compounds such as $R_2C{=}N{-}N{=}PR_3$, $[R{-}N{=}N{-}PR_3]^+$, $CN{-}N{=}PR_3$, and $[NNNPR_3]^+$.[1,2]

As hinted at by the structures of these known compounds, we suggest that the $NNPR_3$ moiety has the potential for stabilization by binding with a metal center at its N-terminus. This study presents a rational construction of the surprising $NNPR_3$ ligand by stepwise functionalization of dinitrogen coordinated to a formally d^2 molybdenum center.[3] The X-ray structural analysis, as well as topological charge density analysis based on density functional calculations, indicate that the diazophosphorane ligand is stabilized effectively by equal contributions from the two following limiting resonance structures: (triorgano-phosphoranylidene)hydrazido(2−) $[Mo]^+(=N{-}N{=}PR_3)$ and (triorganophosphonio)diazenido $[Mo](N{=}N{-}^+PR_3)$; these are shown as **A** and **B**, respectively, in Scheme 1.

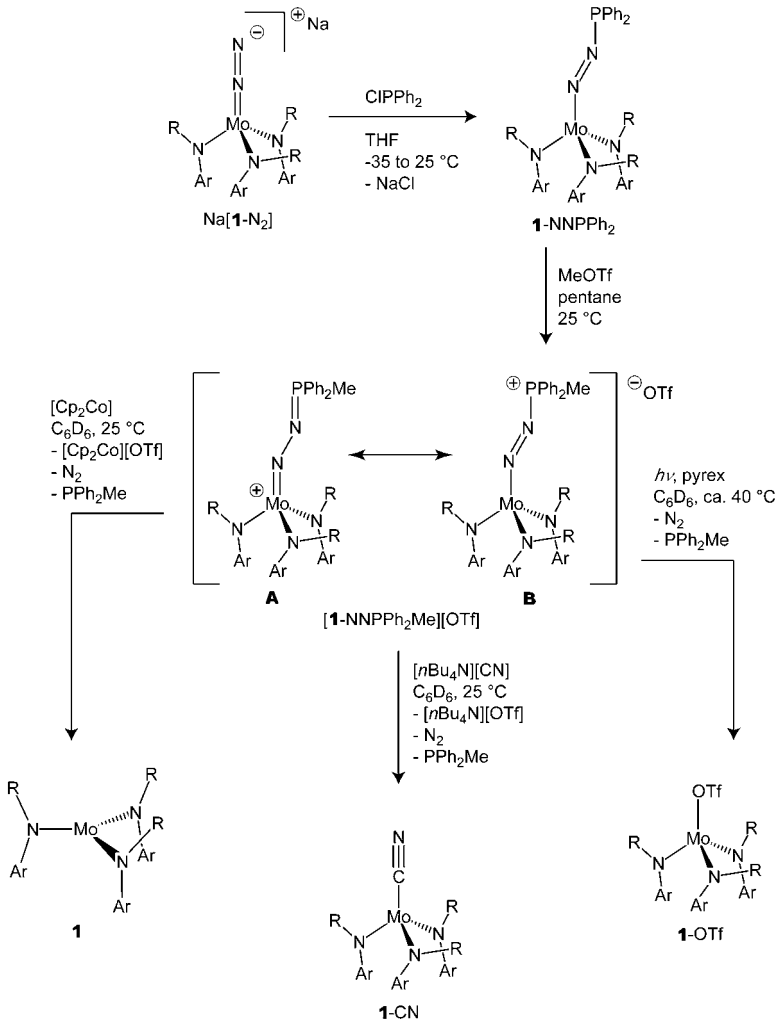

Scheme 1. Synthesis of [**1**-$NNPPh_2Me$][OTf], resonance structures, and reactivity. R = *t*Bu, Ar = 3,5-dimethylphenyl.

The anionic end-on dinitrogen complex $[(N_2)Mo\{N(t\text{Bu})Ar\}_3]^-$ $[\mathbf{1}\text{-}N_2]^-$ (Ar = 3,5-$Me_2C_6H_3$), which is conveniently obtained as its sodium salt by the reaction of $[Mo\{N(t\text{Bu})Ar\}_3]$ (**1**) with excess Na/Hg under 1 atm N_2,[4] was derivatized smoothly by reaction with Ph_2PCl in THF to afford the diphenylphosphinodiazenido complex **1**-$NNPPh_2$.[5] The $^{31}P\{^1H\}$ NMR signal of **1**-$NNPPh_2$ appears at $\delta = 67.3$ ppm as a singlet in C_6D_6. Monitoring of the reaction in C_6D_6 or $[D_8]$THF showed two major by-products: $[Mo\{N(t\text{Bu})Ar\}_3]$ (**1**) and Ph_2PPPh_2, with additional formation of $[ClMo\{N(t\text{Bu})Ar\}_3]$[5] in small quantities. The molar ratio of **1**-$NNPPh_2$/Ph_2PPPh_2 in C_6D_6 after 1 h at 23 °C was 78/22. The

[*] Dr. T. Murahashi,[+] C. R. Clough, J. S. Figueroa, Prof. Dr. C. C. Cummins
Department of Chemistry
Massachusetts Institute of Technology
77 Massachusetts Avenue, Room 2-227
Cambridge, MA 02139-4307 (USA)
Fax: (+1) 617-258-5700
E-mail: ccummins@mit.edu

[+] Permanent address:
Department of Applied Chemistry
Graduate School of Engineering
Osaka University
Suita, Osaka, 565-0871 (Japan)

[**] This work was supported by the United States National Science Foundation (CHE-0316823). Funding from the Japan Society for the Promotion of Science (JSPS) for Research Abroad (to T.M.) is also acknowledged.

 © 2005 Wiley-VCH Verlag GmbH & Co. KGaA, Weinheim DOI: 10.1002/anie.200463057

orange complex **1**-NNPPh$_2$ was isolated in 10% yield after repeated recrystallization from pentane at −35 °C. The low yield of isolated **1**-NNPPh$_2$ was due in part to the spontaneous decomposition of **1**-NNPPh$_2$ to [Mo{N(*t*Bu)Ar}$_3$],[6] Ph$_2$PPPh$_2$, and N$_2$ during the recrystallization. The structure of **1**-NNPPh$_2$ was determined by X-ray structure analysis (Figure 1). The N4–N5 (1.261(4) Å) and N5–P1 (1.736(4) Å)

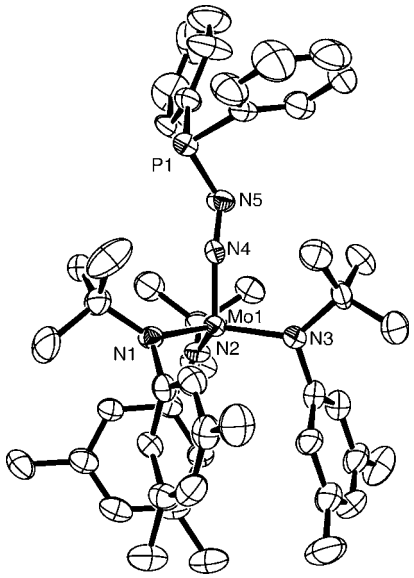

Figure 1. Molecular structure of **1**-NNPPh$_2$ with thermal ellipsoids drawn at the 50% probability level.

lengths are consistent with a N=N double bond and N–P single bond, respectively. Complex **1**-NNPPh$_2$ can thus be formulated as the phosphinodiazenido derivative [(Ph$_2$P–N=N)Mo{N(*t*Bu)Ar}$_3$].[7] The Mo1-N4-N5-P1 skeleton is bent at the N5 atom (N4-N5-P1 122.6(3)°). The Mo1–N4 length (1.753(3) Å) and Mo1-N4-N5 angle (171.1(3)°) are similar to those found for the related trimethylsilyldiazenido complex [(Me$_3$Si-N=N)Mo{N(*t*Bu)Ar}$_3$].[4] Strong multiple bonding between the α-N atom and Mo in these systems is indicated by the short bond length, the linear bond angle, and the isolobal relationship with nitrosyl complexes such as [(ON)Mo{N(*t*Bu)Ar}$_3$].[8] Because of the isolobal relationship between the quartet ground state Mo{N(*t*Bu)Ar}$_3$ fragment[6] and a ground state N atom, we recognize that nitrosyl [(ON)Mo{N(*t*Bu)Ar}$_3$] is isolobal with the triatomic N$_2$O molecule: both systems share a stable $(\pi_0)^4(\pi_1)^4$ configuration across linear MoNO and NNO moieties, respectively.

Treatment of **1**-NNPPh$_2$ with MeOTf (1 equiv) in C$_6$D$_6$ rapidly provided the triflate salt [(Ph$_2$MePNN)Mo{N(*t*Bu)Ar}$_3$][OTf] [**1**-NNPPh$_2$Me][OTf] of the desired cation, in essentially quantitative fashion at ambient temperature. No N-methylated product was observed, even when excess MeOTf was employed. In contrast, it has been reported that the reaction of Na[**1**-N$_2$] with MeOTf (2 equiv) afforded the doubly N-methylated product [(Me$_2$NN)Mo{N(*t*Bu)Ar}$_3$][OTf].[4] The yellow-orange complex [**1**-NNPPh$_2$Me][OTf] was isolated in 41% yield from Na[**1**-N$_2$] without purification of the intermediate **1**-NNPPh$_2$. The ^{1}H NMR resonance for the PPh$_2$(C*H*$_3$) moiety in [**1**-NNPPh$_2$Me][OTf] appears at $\delta =$ 3.03 ppm as a doublet ($^2J_{PH} = 13$ Hz). The ^{31}P{^{1}H} NMR spectrum of [**1**-NNPPh$_2$Me][OTf] shows a singlet at $\delta =$ 20.0 ppm. The structure of [**1**-NNPPh$_2$Me][OTf] was determined in a single-crystal X-ray diffraction study (Figure 2).

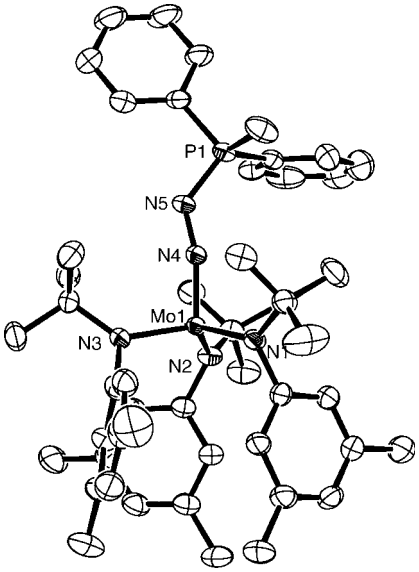

Figure 2. Molecular structure of cation [**1**-NNPPh$_2$Me]$^+$ with thermal ellipsoids drawn at the 50% probability level. The triflate counteranion is not shown.

The Mo1-N4-N5 angle (166.7(2)°) and N4-N5-P1 angle (129.2(2)°) in [**1**-NNPPh$_2$Me][OTf] differ only slightly from corresponding angles in **1**-NNPPh$_2$ (Figure 1). The system is thus still close to linear at the α-N atom and rather bent at the β-N atom. However, the N5–P1 interatomic distance (1.626(3) Å) is 0.11 Å shorter than the corresponding distance in **1**-NNPPh$_2$ (1.736(4) Å), and is similar to that found in a typical iminophosphorane (e.g. 1.602 Å for Ph-N=PPh$_3$).[9] Note also that the N4–N5 (1.299(3) Å) bond length is increased relative to **1**-NNPPh$_2$; in other words, greater activation of the N$_2$ unit has been triggered by the methylation reaction, although the N4–N5 distance in [**1**-NNPPh$_2$Me][OTf] is still considerably shorter than that observed for phosphoranylidene hydrazone systems such as Ph$_3$P=N–N=CPh$_2$ (N–N = 1.388 Å).[10] Of further interest: the Mo1–N4 (1.739(2) Å) bond length in [**1**-NNPPh$_2$Me][OTf] is slightly shorter than that found for precursor **1**-NNPPh$_2$.

The isolated salt [**1**-NNPPh$_2$Me][OTf] is stable in C$_6$D$_6$ solution in the dark for several days at ambient temperature and even at 50 °C for one day. Interestingly, degradation of the NNPPh$_2$Me ligand was observed when [**1**-NNPPh$_2$Me][OTf] was photoirradiated (Rayonet RPR-2537 Å lamps, Pyrex tube) in C$_6$D$_6$. After irradiation for 1 h at ca. 40 °C, approximately 50% of [**1**-NNPPh$_2$Me][OTf] was converted into the triflate complex [Mo{N(*t*Bu)Ar}$_3$(OTf)] (**1**-OTf) and PPh$_2$Me (ca. 90% based on the consumption of [**1**-NNPPh$_2$Me][OTf]) and presumably N$_2$. The purple triflate complex **1**-OTf was identified by an independent synthesis,

 © 2005 Wiley-VCH Verlag GmbH & Co. KGaA, Weinheim

that is, oxidation of [Mo{N(*t*Bu)Ar}$_3$] with AgOTf or [Cp_2Fe][OTf]. The reaction of [**1**-NNPPh$_2$Me][OTf] with [nBu$_4$N][CN] in C_6D_6 upon mixing afforded [(NC)Mo{N(*t*Bu)Ar}$_3$] (**1**-CN)[11] and PPh$_2$Me + N_2 almost quantitatively (Scheme 1). Treatment of [**1**-NNPPh$_2$Me][OTf] with cobaltocene (1 equiv) in C_6D_6 gave [Mo{N(*t*Bu)Ar}$_3$] (**1**) and PPh$_2$Me + N_2 again in almost quantitative yield. Thus, as expected, the fragile NNPPh$_2$Me ligand in [**1**-NNPPh$_2$Me][OTf] is subject to facile fragmentation to its PPh$_2$Me and N_2 components under exposure to some chemical or physical stimuli (Scheme 1).

To gain insight into the electronic structure of [**1**-NNPPh$_2$Me][OTf] we performed density functional calculations (ADF 2004.01, BP86/TZ2P) on the model compounds [(H$_2$PNN)Mo(NH$_2$)$_3$] (**1′**-NNPH$_2$) and [(H$_3$PNN)Mo(NH$_2$)$_3$]$^+$ ([**1′**-NNPH$_3$]$^+$).[12] A topological charge density analysis[13] was carried out with aid of the Xaim program,[14] based on the calculated charge density distributions. The electronic charge density value found at the (3,−1) critical point (ρ_b) of the N–N bond in [**1′**-NNPH$_3$]$^+$ (0.4016 e a_0^{-3}) was lower than that in **1′**-NNPH$_2$ (0.4586 e a_0^{-3}). The calculated bond order (n) is 1.6 for [**1′**-NNPH$_3$]$^+$ (cf. 1.9 for **1′**-NNPH$_2$); this estimation is derived from Bader's linear correlation between ρ_b values and N–N bond order (n).[13] These data indicate that the N–N bond in the cationic [Mo](NNPR$_3$) complex is intermediate between a single and a double bond.[15] The information obtained from computational analysis, combined with the experimental structural data, reveal that the bonding in cation [**1**-NNPPh$_2$Me]$^+$ is characterized by resonance between the hydrazido(2-) form **A** and the diazenido form **B** (Scheme 1). A similar pair of resonance structures was proposed in connection with the particular diazenylphosphonium salt [4-Et$_2$NC$_6$H$_4$NNPPh$_3$][BF$_4$] and its short P–N bond length (1.648 Å).[16]

In summary, this work demonstrates that the remarkable ligand NNPR$_3$ composed of dinitrogen and methyldiphenylphosphane can be obtained and is understandable in the context of a cationic molybdenum system. Because one-electron reduction of cation [**1**-NNPPh$_2$Me]$^+$ leads to fragmentation to the three known molecules PPh$_2$Me, N_2, and [Mo{N(*t*Bu)Ar}$_3$] (**1**), it may be said that this remarkable three-component system is bound together entirely by the absence of a single electron.

Experimental Section

1-NNPPh$_2$: A solution of Na[**1**-N_2] (500 mg, 0.740 mmol) in THF (6 mL) was combined with a solution of Ph$_2$PCl (133 μL, 0.740 mmol) in THF (2 mL) at −35 °C. After the reaction mixture had been stirred for 5 min, THF solvent was removed in vacuo. Then pentane (10 mL) was added, the mixture was filtered through Celite, and pentane was removed in vacuo. Repeated recrystallization from pentane gave analytically pure **1**-NNPPh$_2$ (62.8 mg, 10 % yield). ^{1}H NMR (C_6D_6): $\delta = 8.01$ (t, $J = 7.2$ Hz, 4H), 7.25 (t, $J = 8.4$ Hz, 4H), 7.10 (t, $J = 7.2$ Hz, 2H), 6.64 (s, 3H), 6.03 (s, 6H), 2.04 (s, 18H), 1.53 (s, 27H); ^{31}P{^{1}H} NMR (C_6D_6): $\delta = 67.3$ (s); Elemental analysis calcd C 68.80, H 7.70, N 8.36: found: C 69.03, H 8.19, N 7.96. Crystallographic data for **1**-NNPPh$_2$: $C_{48}H_{64}N_5PMo$, $M = 837.97$, space group $P2_1/c$, $a = 22.6095(19)$, $b = 10.5661(9)$, $c = 19.4732(16)$ Å; $\beta = 94.183(2)°$, $V = 4639.6(7)$ Å^3, $Z = 4$, $F(000) = 1776$, $\rho_{calcd} = 1.20$ g cm^{-3}, 542 parameters refined with 7280 reflections with $I > 2\sigma(I)$ to $R = 0.0516$.

[**1**-NNPPh$_2$Me][OTf]: A solution of Na[**1**-N_2] (600 mg, 0.888 mmol) in THF (6 mL) was combined with a solution of Ph$_2$PCl (159 μL, 0.888 mmol) in THF (2 mL) at −35 °C. After the reaction mixture was stirred for 5 min, THF solvent was removed in vacuo. Then pentane (10 mL) was added, the mixture was filtered through Celite, and pentane was removed in vacuo to give a crude material containing **1**-NNPPh$_2$ (387 mg). To a pentane solution of the crude product, MeOTf (55 μL, 0.49 mmol) was added, and the mixture was stirred for 5 min. Yellow powder was immediately generated. The liquid was decanted off, and the yellow powder was washed with pentane twice, and dried in vacuo. Recrystallization from CH_2Cl_2/Et$_2$O/n-hexane gave yellow-orange microcrystals of [**1**-NNPPh$_2$Me][OTf] (363 mg, 41 % yield from Na[**1**-N_2]). ^{1}H NMR (C_6D_6): $\delta = 8.19$ (dd, $J = 13.1$ Hz, $J = 8.4$ Hz, 4H), 7.32 (m, 4H), 7.15 (overlap with solvent residuals, 2H), 6.62 (s, 3H), 5.77 (br s, 6H), 3.03 (d, $J = 13.2$ Hz, 3H), 1.97 (s, 18H), 1.16 ppm (s, 27H); ^{31}P{^{1}H} NMR (C_6D_6): $\delta = 20.0$ ppm (s); FTIR (C_6D_6, KBr): $\tilde{\nu}_{NN} = 1586$ cm^{-1}. Elemental analysis calcd C 59.93, H 6.74, N 6.99; found: C 59.96, H 6.78, N 6.92. Crystallographic data for [**1**-NNPPh$_2$Me][OTf]: $C_{50}H_{67}N_5PSO_3F_3Mo$, $M = 1002.07$, space group $P2_1/n$, $a = 21.3981(17)$, $b = 10.8084(8)$, $c = 22.1557(17)$ Å; $\beta = 95.1550(10)°$, $V = 5103.4(7)$ Å^3, $Z = 4$, $F(000) = 2104$, $\rho_{calcd} = 1.304$ g cm^{-3}, 577 parameters refined with 11891 reflections with $I > 2\sigma(I)$ to $R = 0.0505$.

CCDC-258978 (**1**-NNPPh$_2$), CCDC-258979 ([**1**-NNPPh$_2$Me][OTf]) contain the supplementary crystallographic data for this paper. These data can be obtained free of charge from the Cambridge Crystallographic Data Centre via www.ccdc.cam.ac.uk/data_request/cif.

1-OTf: Mo(N[*t*Bu]Ar)$_3$ (**1**, 273 mg, 0.437 mmol) was dissolved in pentane (10 mL), and AgOTf (112 mg, 0.437 mmol) was added at room temperature. The mixture was stirred vigorously for 4 h. The color of the mixture changed to deep purple. Then the mixture was filtered through Celite, and the filtrate was concentrated. Crystallization from pentane at −35 °C gave deep purple microcrystals of **1**-OTf (43.8 mg, 13 % yield). ^{1}H NMR (C_6D_6): $\delta = 6.06$ (s, 3H), 5.94 (br s, 6H), 2.11 (s, 27H), 1.86 ppm (s, 18H); Elemental analysis calcd C 57.43, H 7.03, N 5.43; found: C 57.59, H 7.12, N 5.38. An NMR monitoring experiment of the reaction of [Mo{N(*t*Bu)Ar}$_3$] with [Cp_2Fe][OTf] (1 equiv) in C_6D_6/[D_8]THF (v/v = 9/1) showed quantitative formation of **1**-OTf.

Received: December 24, 2004
Published online: March 22, 2005

Keywords: diazenido ligands · dinitrogen ligands · molybdenum · N,P ligands · phosphine ligands

[1] The abbreviation R which appears in some general formulas in this paper is not necessarily identical to the R = *t*Bu as in **1** and complexes derived therefrom.

[2] Selected examples; a) H$_2$C=N–N=PPh$_3$: G. Wittig, W. Haag, *Chem. Ber.* **1955**, *88*, 1654; b) [Ph-N=N-PPh$_3$][BF$_4$]: R. Yamashita, K. Kikukawa, F. Wada, T. Matsuda, *J. Organomet. Chem.* **1980**, *201*, 463; c) CN–N=PPh$_3$: B. Weinberger, W. P. Fehlhammer, *Chem. Ber.* **1985**, *118*, 42; d) [NNNPPh$_3$][SbCl$_6$]: W. Buder, A. Schmidt, *Chem. Ber.* **1973**, *106*, 3812.

[3] It is known that some diazo compounds are stabilized by coordination to a d^2 metal center. For stabilization of terminal organoazido (NNNR) ligands; a) G. Proulx, R. G. Bergman, *J. Am. Chem. Soc.* **1995**, *117*, 6382; b) M. G. Fickes, W. M. Davis, C. C. Cummins, *J. Am. Chem. Soc.* **1995**, *117*, 6384; c) G. Proulx, R. G. Bergman, *Organometallics* **1996**, *15*, 684; d) G. Guillemot, E. Solari, C. Floriani, C. Rizzoli, *Organometallics* **2001**, *20*, 607. For stabilization of diazoalkane (NNCR$_2$) ligands; e) M. Dartiguenave, M. J. Menu, E. Deydier, Y. Dartiguenave, H. Siebald, *Coord. Chem. Rev.* **1998**, *178–180*, 623, and references therein.

 © 2005 Wiley-VCH Verlag GmbH & Co. KGaA, Weinheim

[4] J. C. Peters, J.-P. F. Cherry, C. Thomas, L. M. Baraldo, D. J. Mindiola, W. M. Davis, C. C. Cummins, *J. Am. Chem. Soc.* **1999**, *121*, 10053.
[5] A. Fürstner, C. Mathes, C. W. Lehmann, *J. Am. Chem. Soc.* **1999**, *121*, 9453.
[6] C. E. Laplaza, M. J. A. Johnson, J. C. Peters, A. L. Odom, E. Kim, C. C. Cummins, G. N. George, I. J. Pickering, *J. Am. Chem. Soc.* **1996**, *118*, 8623.
[7] A number of diazenido transition metal complexes are known; a) J. P. Collman, L. S. Hegedus, J. R. Norton, R. G. Finke, *Principles and Applications of Organotransition Metal Chemistry*, University Science Book, New York, **1987**; b) D. Sutton, *Chem. Soc. Rev.* **1975**, *3*, 443, and references therein. For synthesis from dinitrogen complex see c) J. Chatt, A. A. Diamantis, G. A. Heath, N. E. Hooper, G. J. Leigh, *J. Chem. Soc. Dalton Trans.* **1977**, 688; d) M. Hidai, Y. Mizobe, *Chem. Rev.* **1995**, *95*, 1115, and references therein.
[8] C. E. Laplaza, A. L. Odom, W. M. Davis, C. C. Cummins, *J. Am. Chem. Soc.* **1995**, *117*, 4999.
[9] E. Böhm, K. Dehnicke, J. Beck, W. Hiller, J. Strähle, A. Maurer, D. Fenske, *Z. Naturforsch. B* **1988**, *43*, 138.
[10] D. Bethell, M. P. Brown, M. M. Harding, C. A. Herbert, M. M. Khodaei, M. I. Rios, K. Woolstencroft, *Acta Crystallogr. Sect. B* **1992**, *48*, 683.
[11] J. C. Peters, L. M. Baraldo, T. A. Baker, A. R. Johnson, C. C. Cummins, *J. Organomet. Chem.* **1999**, *591*, 24.
[12] ADF Program Package (release 2004.1) was used. The optimized structures showed good agreement with the metrical parameters found in the crystal structure studies of **1**-$NNPPh_2$ and [**1**-$NNPPh_2Me$][OTf], except for the N-N-P angle in [**1**′-$NNPH_3$]$^+$ which appears marginally smaller compared to that found experimentally for [**1**-$NNPPh_2Me$][OTf]. Selected structural parameters of optimized **1**′-$NNPPH_2$ and [**1**′-$NNPH_3$]$^+$: for **1**′-$NNPH_2$: Mo–N 1.757, N–N 1.243, N–P 1.770 Å; Mo-N-N 174.6, N-N-P 120.94°; for [**1**′-$NNPH_3$]$^+$: Mo–N 1.735, N–N 1.295, N–P 1.627 Å; Mo-N-N 172.8, N-N-P 121.6°.
[13] R. F. W. Bader, *Atoms in Molecules, a Quantum Theory*, Oxford University Press, New York, **1990**. For calibration of linear ρ_b versus n relationship, we performed similar calculations on hydrazine, *trans*-diazene, and dinitrogen, the values of ρ_b(NN) for which are taken to represent $n = 1$, 2, and 3, respectively.
[14] J. C. Ortiz Alba, C. Bo Jane, *Xaim*, Universitat Rovira I Virgili, Tarragona, Spain.
[15] Analysis of the P–N bond revealed a substantially higher ρ_b value (0.1984 e a_0^{-3}) in [**1**′-$NNPH_3$]$^+$ than that in **1**′-$NNPH_2$ (0.1506 e a_0^{-3}). This is consistent with considerable iminophosphorane character in [**1**′-$NNPH_3$]$^+$. For the bonding on the iminophosphorane N=P bond see J. Koketsu, Y. Ninomiya, Y. Suzuki, N. Koga, *Inorg. Chem.* **1997**, *36*, 694, and references therein.
[16] F. W. B. Einstein, D. Sutton, P. L. Vogel, *Can. J. Chem.* **1978**, *56*, 891.

 © 2005 Wiley-VCH Verlag GmbH & Co. KGaA, Weinheim

Retraction

After the publication of this Communication the authors have noticed that the scale bars on some of the TEM images are wrong. The particle size data extracted from these images is thus incorrect and the conclusions drawn from this data are therefore invalid. Accordingly, all the authors withdraw this Communication. They apologize for these mistakes and that the readership of *Angewandte Chemie* has been misled by the publication of this Communication.

Design and Size Control of Uniform Zeolite Nanocrystals Synthesized in Adjustable Confined Voids Formed by Recyclable Monodisperse Polymer Spheres

X. Yang, Y. Feng, G. Tian, Y. Du, X. Ge, Y. Di, Y. Zhang, B. Sun, F.-S. Xiao* **2563–2568**

Angew. Chem. Int. Ed. **2005**, *44*

DOI 10.1002/anie.200462187

 © 2006 Wiley-VCH Verlag GmbH & Co. KGaA, Weinheim

Zeolite Nanocrystals

Design and Size Control of Uniform Zeolite Nanocrystals Synthesized in Adjustable Confined Voids Formed by Recyclable Monodisperse Polymer Spheres**

*Xiaoyu Yang, Yefei Feng, Ge Tian, Yunchen Du, Xin Ge, Yan Di, Yonglai Zhang, Bo Sun, and Feng-Shou Xiao**

Zeolite nanocrystals have attracted much attention because of their potential uses as active catalysts, effective membranes, low-*k* thin films, and model systems for fundamental studies of zeolite crystal growth.[1–16] For most of these applications, dispersible zeolite nanocrystals with controlled and uniform size are preferred.[1–20]

There are a number of examples of the preparation of zeolite nanocrystals.[21–32] For example, zeolite nanocrystals with small size and narrow distribution could be prepared by control of synthetic gel composition or crystallization temperature/time.[21–25] Addition of organic templates to synthetic gels can effectively reduce the size of the zeolites.[7,8,12–14,26–30] Space-confined synthesis by means of carbon black can be used to prepare zeolite nanocrystals, the sizes of which are generally controlled by the various types of carbon black.[31] Thermoreversible polymer hydrogels are novel media for the synthesis of zeolite nanocrystals, and the polymer hydrogels are recyclable.[32] However, design and size control of uniform zeolite nanocrystals is still not easy owing to the complexity of their synthesis and limitations of various synthetic routes.

Recently, uniform and monodisperse polymer spheres were synthesized, and there are voids between these polymer spheres in aqueous media.[33] Interestingly, these confined voids can be simply adjusted by the solid content and diameter of the polymer spheres. The adjustable confined voids formed by polymer spheres could potentially serve as micro- or nanoreactors for controlling zeolite growth. Moreover, these polymer spheres are stable in the temperature range 0–160 °C,[34] which is suitable for the synthesis of most types of zeolites. Furthermore, these polymer spheres can easily be transformed into polymer chains dissolved in an

[*] X. Yang, Y. Feng, G. Tian, Y. Du, X. Ge, Y. Di, Y. Zhang, B. Sun, Prof. F.-S. Xiao
Department of Chemistry & Key Laboratory of Inorganic Synthesis and Preparative Chemistry
Jilin University, Changchun 130012 (China)
Fax: (+86) 431-567-1974
E-mail: fsxiao@mail.jlu.edu.cn

[**] We thank Dr. U. Müller of BASF as well as Prof. B. Yang, Prof. Z.-C. Cui, Prof. D.-Z. Jiang, K. Zhang, H.-Y. Jia, M.-J. Li, J.-Y. Fang, H.-T. Li, and Dr. X. Chen of Jilin University for helpful suggestions and discussions. This work is supported by the NSFC (20373018, 20233030, and 20121103), BASF, the CNPC, the National High Technology Research and Development Program of China (863 Program), the State Basic Research Project (973 Program), and the Ministry of Education of China.

Supporting information for this article is available on the WWW under http://www.angewandte.org or from the author.

 DOI: 10.1002/anie.200462187 © 2005 Wiley-VCH Verlag GmbH & Co. KGaA, Weinheim

appropriate solvent, and the polymer chains can be transformed back into polymer spheres by evaporation of the solvent,[35,36] which allows convenient recycling of polymer spheres in zeolite synthesis.

Herein we report a simple route for the design and size control of uniform zeolite nanocrystals synthesized in confined voids formed by polymer spheres. Interestingly, the size (60–500 nm) of zeolite nanocrystals observed experimentally is in good agreement with that estimated from theoretical calculations. Moreover, the polymer spheres could be recycled during the synthesis of zeolite nanocrystals, which is an environmentally benign procedure. The general synthetic procedure is illustrated in Figure 1.

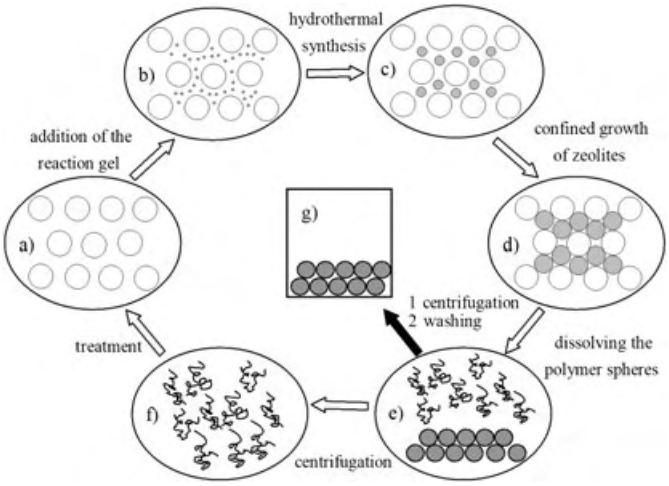

Figure 1. Schematic representation of the synthesis of zeolite nanocrystals in confined voids formed by polymer spheres: a) the emulsion with monodisperse polymer spheres, b) the aluminosilicate and titanosilicate gels are homogenously mixed with the emulsion, c) crystallization of zeolite nanocrystals, d) confined growth of zeolite nanocrystals in the voids controls the final size of the zeolite nanocrystals, e) the polymer spheres are dissolved to give a mixture of zeolite nanocrystals and polymer solution, f) separation of the polymer solution from the zeolite nanocrystals by centrifugation and washing, g) isolated zeolite nanocrystals, and (f)→(a) the solution of polymer chains is transformed into polymer spheres by evaporation of the solvent.

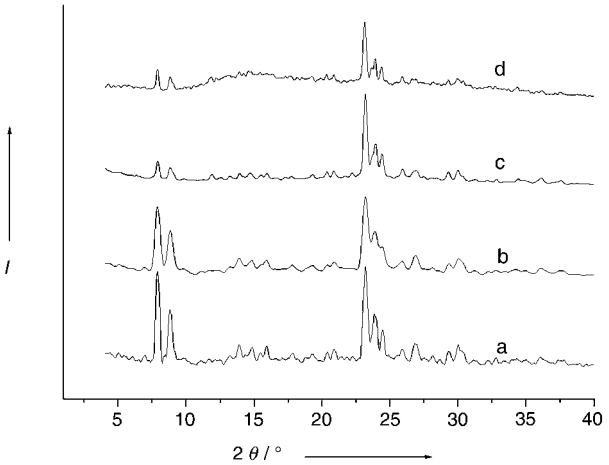

Figure 2. XRD patterns of nanosized a) ZSM-5(1.5), b) ZSM-5(3), c) ZSM-5(6), and d) ZSM-5(7.5) zeolites.

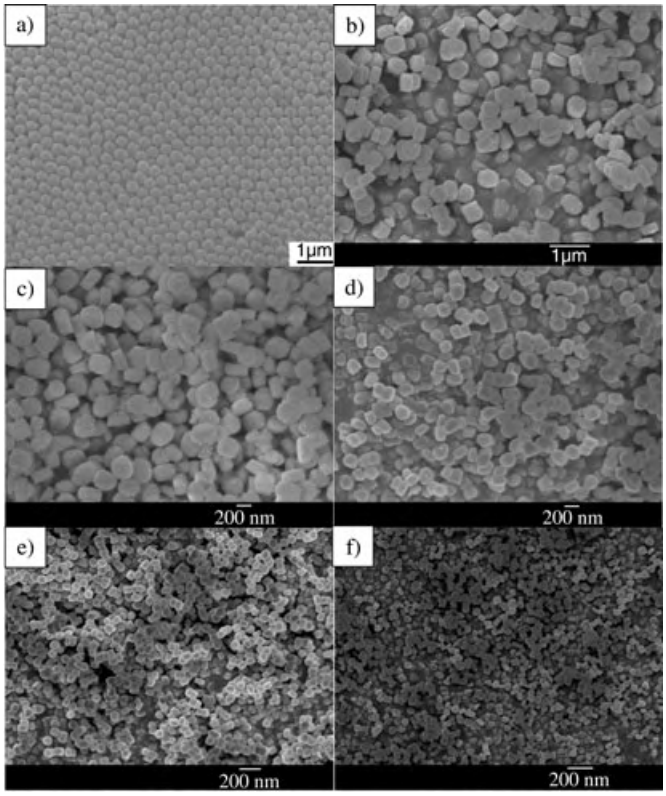

Figure 3. Field-emission SEM images of a) polymer nanospheres b) ZSM-5(1.5–500), c) ZSM-5(1.5), d) ZSM-5(3), e) ZSM-5(6), and f) ZSM-5(7.5) zeolites.

Figure 2 shows X-ray diffraction (XRD) patterns of ZSM-5 nanocrystals synthesized with various contents of polymer spheres. Notably, the XRD peaks of all samples are characteristic of ZSM-5 crystals, but the peaks become progressively weaker with increasing content of polymer spheres in the synthesis. This indicates that the size of the zeolite nanocrystals decreases with the increasing content of polymer spheres.

Figure 3 shows scanning electron microscopy (SEM) images of polymer spheres and ZSM-5 nanocrystals synthesized at various contents and diameters of polymer spheres. The zeolites have crystal sizes of around 60–500 nm (Figure 3b–f), and each zeolite sample has an almost uniform crystal size. For example, when the content of polymer spheres with a diameter of 340 ± 20 nm in the synthesis (see the Experimental Section) is 7.5 g, ZSM-5(7.5) has a crystal size of around 60 nm (Figure 3f), and when the content of the same polymer spheres is 1.5 g in the synthesis, ZSM-5(1.5) has a size of about 340 nm (Figure 3c). A content of polymer spheres with a diameter of 500 ± 30 nm of 1.5 g results in ZSM-5(1.5–500) with a size of around 500 nm (Figure 3b), and a content of the same polymer spheres of 3.0 g leads to ZSM-5(3–500) with a size of about 300 nm (see the Supporting Information). More importantly, the polymer spheres used for the synthesis of zeolite nanocrystals could be recycled.[36] (For an example of an SEM image of monodis-

 © 2005 Wiley-VCH Verlag GmbH & Co. KGaA, Weinheim

perse polymer spheres ($\approx$350 nm) synthesized from recovered polymer chains, see the Supporting Information).

Furthermore, transmission electron microscopy (TEM) studies of these zeolite samples confirm that they have uniform nanocrystals with high crystallinity. For example, a TEM image of ZSM-5(1.5) shows very uniform nanocrystals (see the Supporting Information).

Figure 4 shows N_2 adsorption/desorption isotherms of calcined ZSM-5 samples, and textural parameters are presented in Table 1. Notably, the samples exhibit a steep rise

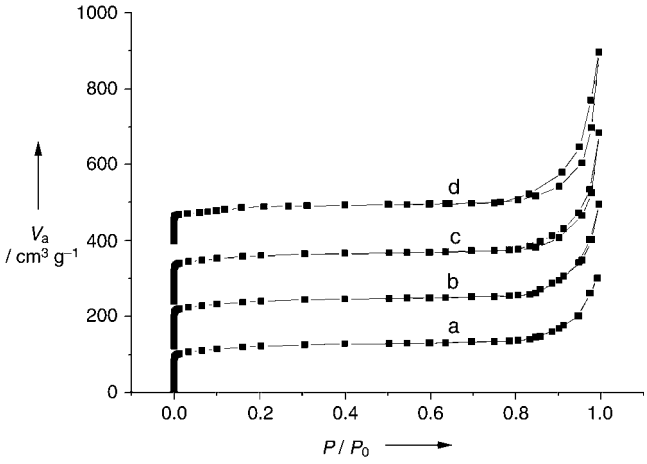

Figure 4. N_2 adsorption/desorption isotherms of nanosized a) ZSM-5(1.5), b) ZSM-5(3), c) ZSM-5(6), and d) ZSM-5(7.5) zeolites. Isotherms b), c), and d) are offset by 100, 220, and 390 cm^3 g^{-1}, respectively, along the vertical axis for clarity.

Table 1: Calculated and experimental size of zeolite nanocrystals synthesized in confined voids formed by polymer spheres.

Sample	Polymer content [g]	Exptl crystal size [nm][a]	Calcd crystal size [nm][b]	BET surface area [m^2 g^{-1}]
ZSM-5(1.5)	1.5	340 $\pm$ 30	340 $\pm$ 20	489
ZSM-5(3)	3.0	200 $\pm$ 20	200 $\pm$ 12	496
ZSM-5(6)	6.0	90 $\pm$ 8	89 $\pm$ 4	516
ZSM-5(7.5)	7.5	60 $\pm$ 6	58 $\pm$ 4	521
ZSM-5(1.5–500)	1.5	500 $\pm$ 40	500 $\pm$ 30	438
ZSM-5(3–500)	3.0	300 $\pm$ 30	294 $\pm$ 18	490

[a] Experimental crystal size was measured by SEM. [b] Calculated crystal size = 2 R_v (R_v is calculated by the equation $R_v = [2.29\, M_T^{-1/3} - 1]\, R_p$, in which M_T = polymer content and R_p = radius of a polymer sphere).

followed by flat curves at low partial pressures that are typical Langmuir curves. These results are reasonably assigned to complete filling of the micropores with N_2. Additionally, the samples also show quite narrow hysteretic uptakes at high partial pressures, which are assigned to mesopores formed by the aggregation of ZSM-5 nanocrystals. Interestingly, the BET surface area of the samples is relatively high compared with that of conventional ZSM-5 samples (Table 1). This further supports the fact that the zeolite ZSM-5 nanocrystals have small crystal sizes.

The synthesis of ZSM-5 nanocrystals of various sizes should be attributed directly to the use of various contents of polymer spheres because during synthesis all other parameters, such as temperature, time, template, pH value, and composition, are completely the same. Therefore, we suggest that the ZSM-5 nanocrystals crystallize in the confined voids, and the size of ZSM-5 nanocrystals should depend on that of the confined voids, which could be adjusted by the content of polymer spheres in the synthesis. The model of adjustable confined voids is proposed in Figure 5 (confined voids are

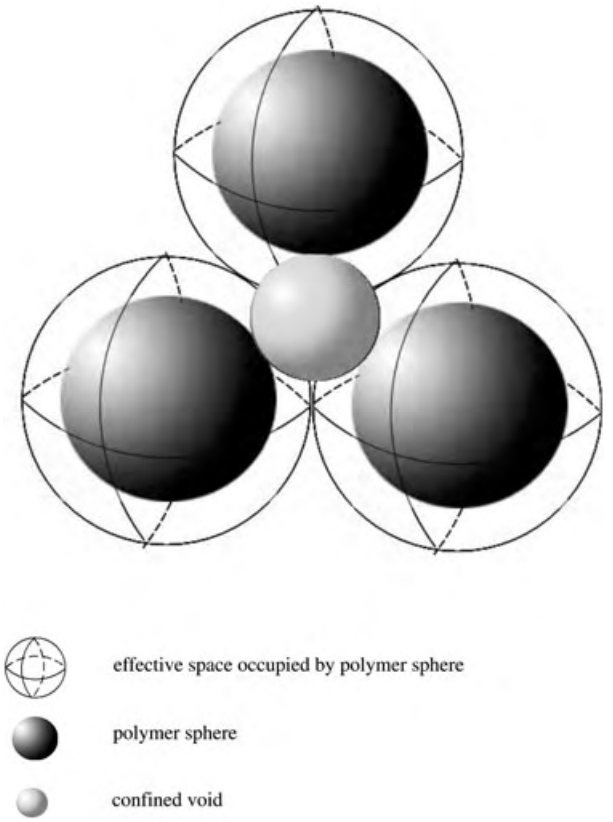

Figure 5. Proposed model of confined voids for crystallization of zeolite nanocrystals.

simplified as spherelike and polymer spheres are considered as hard, inflexible, and relatively actionless balls in the solution). According to this model, the relationship between the radius of a confined void R_v, the radius of a polymer sphere R_p, and the total weight of polymer spheres M_T is given by Equation (1).

$$R_v \approx [2.29\, M_T^{-1/3} - 1]\, R_p \quad [37] \qquad (1)$$

Clearly, the radius of the confined voids depends on the content and radius of the polymer spheres, and the confined voids can be designed and size-controlled by means of these parameters of the polymer spheres in the synthesis of zeolites. Figure 6 shows the good agreement between the size of zeolite nanocrystals calculated by Equation (1) and the experimental size of zeolite nanocrystals measured by SEM. This indicates that the size of zeolite nanocrystals can be simply designed and controlled by means of the adjustable voids formed by monodisperse polymer spheres.

 © 2005 Wiley-VCH Verlag GmbH & Co. KGaA, Weinheim

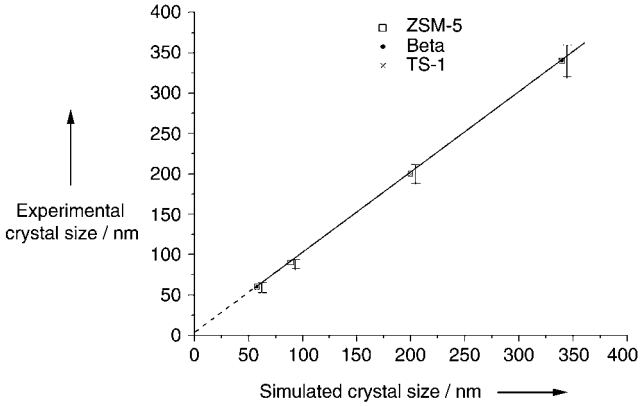

Figure 6. Plots of experimental crystal size of zeolite nanocrystals observed by SEM versus the simulated crystal size of zeolite nanocrystals estimated by a mathematical model of the confined voids (Figure 5 and the Supporting Information).

The synthesis of zeolite nanocrystals in confined voids is not limited to ZSM-5; zeolites such as A, X, Y, L, MOR, β, and TS-1 can also be synthesized. For example, samples of zeolite β with sizes of about 340 and 60 nm were synthesized at contents of polymer spheres of 1.5 and 7.5 g, respectively (Figure 7), and zeolite TS-1 with a size of around 200 nm was obtained at a content of polymer spheres of 3.0 g (see the Supporting Information). The strategy reported herein provides a unique, effective, and potentially general approach for the synthesis of zeolite nanocrystals and the other nanocrystals with controllable size under hydrothermal conditions.

Experimental Section

The monodisperse polymer spheres were supplied by BASF, and zeolite nanocrystals with various sizes were synthesized with varying contents of the polymer spheres.

Typical synthesis of ZSM-5 nanocrystals: 1) Aluminosilicate gel was prepared by mixing aqueous tetrapropylammonium hydroxide (TPAOH) solution (25%; 5 mL) with H_2O (5 mL), followed by addition of 0.3 g of $Al_2(SO_4)_3{\cdot}18H_2O$ (0.3 g) and tetraethyl orthosilicate (TEOS; 5 mL) with stirring (Al_2O_3/SiO_2/TPAOH/C_2H_5OH/H_2O molar ratio of 1.0:30:8:120:1500). The mixture was then aged at 140 °C for 3 h to form the aluminosilicate gel. 2) An emulsion (5 mL) containing 1.5, 3, 6, or 7.5 g of the polymer spheres with an average size of around 340 nm was mixed with the aluminosilicate gel (containing 60 mmol of SiO_2, 5 mL) obtained in step 1. The mixture was stirred at room temperature for 4 h, then transferred into an autoclave for further reaction at 140 °C for 96 h. 3) The crystallized product was treated with ethyl acetate, followed by washing by water, centrifugation, drying, and ultrasonic redispersion in water until the polymer was completely washed away. The final products are denoted ZSM-5(1.5), ZSM-5(3), ZSM-5(6), and ZSM-5(7.5), in which the number in parentheses is the content of polymer spheres in the synthesis. 4) The calcined samples were heated at 550 °C for 4 h to remove the TPA^+ template

Zeolite β(1.5) and β(7.5) samples were synthesized with polymer spheres (1.5 and 7.5 g) with a diameter of about 340 nm at a molar ratio of Al_2O_3/SiO_2/TEAOH/H_2O of 1.0:60:25:800, and TS-1(3) was prepared with polymer spheres (3.0 g) with a diameter of about 200 nm at a molar ratio of TiO_2/SiO_2/TPAOH/C_2H_5OH/H_2O of 1.0:30:8:120:375. Similarly, samples of ZSM-5(1.5–500), ZSM-5(3.0–500), and β(7.5–500) (see the Supporting Information) were synthesized with polymer spheres (1.5, 3.0, and 7.5 g) with a diameter of around 500 ± 30 nm.

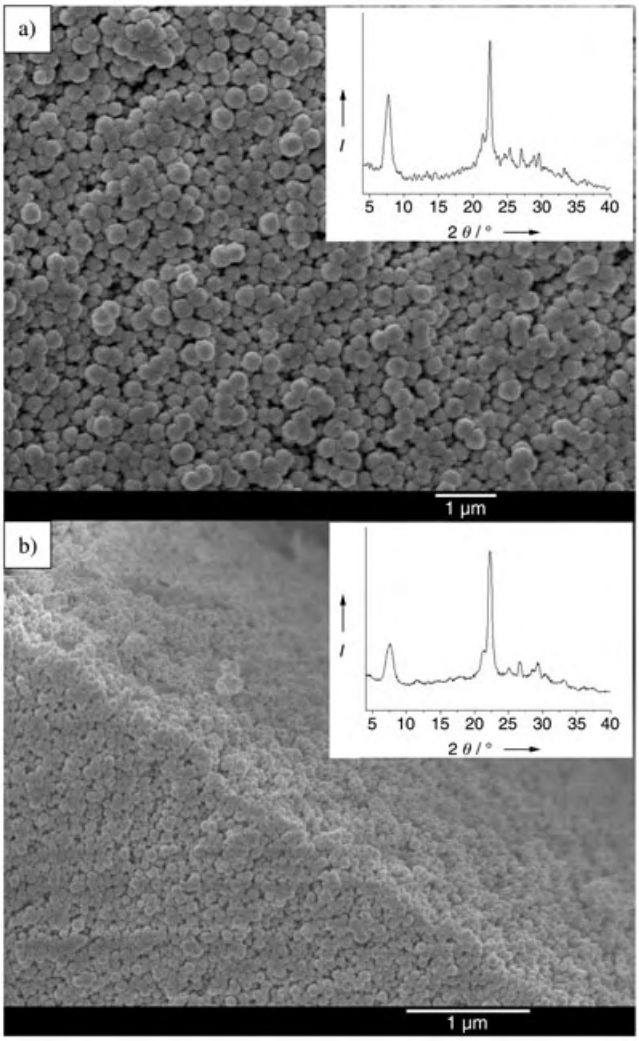

Figure 7. Field-emission SEM images and XRD patterns (inset) of nanosized a) β(1.5) and b) β(7.5) zeolites.

XRD patterns were obtained on a Siemens D5005 diffractometer by using $Cu_{K\alpha}$ radiation. SEM experiments were performed on a JSM-6700F electron microscope (JEOL, Japan). TEM experiments were performed on a JEM-3010 electron microscope (JEOL, Japan) with an acceleration voltage of 300 kV. The nitrogen adsorption and desorption isotherms at liquid-nitrogen temperature were measured on a Micromeritics ASAP 2020M system. The samples were degassed for 10 h at 300 °C before measurements. The Si/Al and Si/Ti ratios of the samples were measured on a Perkin-Elmer 3300DV ICP and by chemical analysis.

Received: October 2, 2004
Revised: December 18, 2004
Published online: March 22, 2005

Keywords: hydrothermal synthesis · nanocrystals · nanotechnology · polymers · zeolites

[1] K. Rajagopalan, A. W. Peters, G. C. Edwards, *Appl. Catal.* **1986**, *23*, 69–80.

 © 2005 Wiley-VCH Verlag GmbH & Co. KGaA, Weinheim

[2] M. A. Camblor, A. Corma, A. Martínez, F. A. Mocholí, J. P. Pariente, *Appl. Catal.* **1989**, *55*, 65 – 74.
[3] M. A. Camblor, A. Corma, A. Martínez, V. Martínez-Soria, S. Valencia, *J. Catal.* **1998**, *179*, 537 – 547.
[4] B. Notari, *Innovation in Zeolite Materials Science*, *Vol. 37* (Ed.: P. J. Grobet), Elsevier Science Publishers, Amsterdam, **1987**, pp. 413.
[5] O. Mitsui, K. Yohei (Asahi Kasei Comp), DE 3441072, May 23, **1985**; [*Chem. Abstr.* **1985**, *104*, 50589].
[6] A. J. H. P. van der Pol, A. J. Verduyn, J. H. C. van Hoff, *Appl. Catal.* **1992**, *92*, 113 – 130.
[7] L. C. Boudreau, J. A. Kuck, M. Tsapatsis, *J. Membr. Sci.* **1999**, *152*, 41 – 59.
[8] a) L. Huang, Z. Wang, J. Sun, L. Miao, Q. Li, Y. Yan, D. Zhao, *J. Am. Chem. Soc.* **2000**, *122*, 3530 – 3531; b) L. Huang, Z. Wang, H. Wang, J. Sun, Q. Li, D. Zhao, Y. Yan, *Microporous Mesoporous Mater.* **2001**, *48*, 73 – 78.
[9] A. G. Dong, Y. J. Wang, Y. Tang, N. Ren, Y. H. Zhang, J. H. Yue, Z. Gao, *Adv. Mater.* **2002**, *14*, 926 – 929.
[10] T. Wakihara, S. Yamakita, K. Lezumi, T. Okubo, *J. Am. Chem. Soc.* **2003**, *125*, 12388 – 12389.
[11] B. J. Zhang, S. A. Davis, N. H. Mendelson, S. Mann, *Chem. Commun.* **2000**, *9*, 781 – 782.
[12] M. H. Valkenberg, W. F. Holderich, *Catal. Rev. Sci. Eng.* **2002**, *44*, 321 – 374.
[13] a) C. T. Kresge, M. E. Leonowicz, W. J. Roth, J. C. Vartuli, J. S. Beck, *Nature* **1992**, *359*, 710 – 712; b) T. Yanagisawa, T. Shimizu, K. Kuroda, C. Kate, *Bull. Chem. Soc. Jpn.* **1990**, *63*, 988 – 992.
[14] C. E. A. Kirschhock, V. Buschmann, S. Kremer, R. Ravishankar, C. J. Y. Houssin, B. L. Mojet, R. A. van Santen, P. J. Grobet, P. A. Jacobs, J. A. Martens, *Angew. Chem.* **2001**, *113*, 2707 – 2710; *Angew. Chem. Int. Ed.* **2001**, *40*, 2637 – 2640.
[15] a) S. Mintova, N. H. Olson, J. Senker, T. Bein, *Angew. Chem.* **2002**, *114*, 2670 – 2673; *Angew. Chem. Int. Ed.* **2002**, *41*, 2558 – 2561; b) S. Mintova, N. H. Olson, V. Valtchev, T. Bein, *Science* **1999**, *283*, 958 – 960.
[16] B. J. Schoeman, J. Sterte, J. E. Otterstedt, *Zeolites* **1994**, *14*, 110 – 116.
[17] S. I. Zones, M. E. Davis, *Curr. Opin. Solid State Mater. Sci.* **1996**, *1*, 107 – 117.
[18] N. K. Raman, M. T. Anderson, C. J. Brinker, *Chem. Mater.* **1996**, *8*, 1682 – 1701.
[19] D. Y. Zhao, J. L. Feng, Q. S. Huo, N. Melosh, G. H. Fredrickson, B. F. Chmelka, G. D. Stucky, *Science* **1998**, *279*, 548 – 552.
[20] J. Y. Ying, C. P. Mehnert, M. S. Wong, *Angew. Chem.* **1999**, *111*, 58 – 82; *Angew. Chem. Int. Ed.* **1999**, *38*, 56 – 77.
[21] a) A. E. Persson, B. J. Schoeman, J. Sterte, J. E. Otterstedt, *Zeolites* **1994**, *14*, 557 – 567; b) E. F. S. Aguiar, A. Liebsch, B. C. Chaves, A. F. Costa, *Microporous Mesoporous Mater.* **1998**, *25*, 185 – 192; c) R. W. Corkery, B. W. Ninham, *Zeolites* **1997**, *18*, 379 – 386; d) M. Yamamura, K. Chaki, T. Wakatsuki, H. Okado, K. Fujimoto, *Zeolites* **1994**, *14*, 643 – 649.
[22] a) B. J. Schoeman, J. Sterte, J. E. Otterstedt, *J. Chem. Soc. Chem. Commun.* **1993**, 994 – 995; b) B. J. Schoeman, J. Sterte, J. E. Otterstedt, *Zeolites* **1994**, *14*, 208 – 216.
[23] P. A. Jacobs, E. G. Derouane, J. Weitkamp, *J. Chem. Soc. Chem. Commun.* **1981**, 591 – 593.
[24] M. A. Camblor, A. Corma, A. Mifsud, J. Pérez-Pariente, S. Valencia, *Stud. Surf. Sci. Catal.* **1997**, *105*, 341.
[25] Z. Gabelica, J. B. Nagy, G. Debras, E. G. Derouane, *Acta Chim. Hung.* **1985**, *119*, 275 – 284.
[26] M. E. Davis, *Nature* **2002**, *417*, 813 – 821.
[27] H. T. Wang, Z. B. Wang, Y. S. Yan, *Chem. Commun.* **2000**, 2333 – 2334.
[28] H. T. Wang, L. M. Huang, B. A. Holmberg, Y. S. Yan, *Chem. Commun.* **2002**, 1708 – 1709.
[29] H. T. Wang, B. A. Holmberg, Y. S. Yan, *J. Mater. Chem.* **2002**, *12*, 3640 – 3643.
[30] D. W. Breck, *Zeolite Molecular Sieves: Structure*, *Chemistry*, *and Use*, Wiley, New York, **1974**.
[31] C. Madsen, C. J. H. Jacobsen, *Chem. Commun.* **1999**, 673 – 674.
[32] H. Wang, B. A. Holmberg, Y. Yan, *J. Am. Chem. Soc.* **2003**, *125*, 9928 – 9929.
[33] a) B. T. Holland, C. F. Blanford, A. Stein, *Science* **1998**, *281*, 538 – 540; b) X. Chen, Z. Cui, Z. Chen, K. Zhang, G. Lu, G. Zhang, B. Yang, *Polymer* **2002**, *43*, 4147 – 4152.
[34] G. Zhang, Y. Yu, X. Chen, Y. Han, Y. Di, B. Yang, F.-S. Xiao, J.-C. Shen, *J. Colloid Interface Sci.* **2003**, *263*, 461 – 466.
[35] a) T. K. Bronich, A. V. Kabanov, V. A. Kabanov, K. Yu, A. Eisenberg, *Macromolecules* **1997**, *30*, 3519 – 3525; b) A. V. Kabanov, T. K. Bronich, V. A. Kabanov, K. Yu, A. Eisenberg, *J. Am. Chem. Soc.* **1998**, *120*, 9941 – 9942; c) S. V. Solomatin, T. K. Bronich, T. W. Bargar, A. Eisenberg, V. A. Kabanov, A. V. Kabanov, *Langmuir* **2003**, *19*, 8069 – 8076.
[36] In a typical process, the composite of polymer spheres and zeolite nanocrystals was treated with ethyl acetate to give a mixture of polymer chains and solid zeolite nanocrystals. After centrifugation of the mixture, pure polymer chains dissolved in ethyl acetate were obtained. Then, the polymer solution was slowly dripped into poly(vinyl alcohol) solution (0.5–2 wt%) or sodium dodecyl sulfate (SDS) solution (0.1–0.5 wt%) with stirring at room temperature to form an emulsion. After heating the emulsion at 40 °C for 24 h with stirring, highly dispersed polymer spheres formed, with release of the ethyl acetate in the emulsion.
[37] According to the model (Figure 5), the effective occupational space of each polymer sphere V_s can be calculated from the total volume of solution

$$V_T{:}V_s = k\,V_T/N \quad (2)$$

in which k is the density of a hexagonal close-packed structure (0.7405)[38] and N the number of polymer spheres. N can be calculated from the total weight of the polymer spheres M_T and the weight of a single polymer sphere

$$M_p{:}N = M_T/M_p \quad (3)$$

M_p can be calculated from the density of a single polymer sphere ρ_p and the volume of a single polymer sphere V_p, in which ρ_p is approximately equal to the density of polymer monomer, which could be measured.

$$M_p = \rho_p V_p \quad (4)$$

V_p can be calculated from the radius of a single polymer sphere R_p:

$$V_p = 4\pi R_p^3/3 \quad (5)$$

Combining Equations (2)–(5) gives the following expression for V_s:

$$V_s = k\,V_T \rho_p 4\pi R_p^3/3\,M_T \quad (6)$$

According to the mathematical model (see the Supporting Information), the radius of the confined voids R_v can be calculated from the radius of the effectively occupied space of a single polymer sphere R_s and R_p:

$$(R_v + R_p)/R_s = 2/3^{1/2} \quad (7)$$

$$R_s = (3\,V_s/4\pi)^{1/3} \quad (8)$$

 © 2005 Wiley-VCH Verlag GmbH & Co. KGaA, Weinheim

Combining Equations (6)–(8) gives the following equation:

$$R_v = [(2/3^{1/2})\,(k\,V_T\rho_p/M_T)^{1/3} - 1]\,R_p \quad (9)$$

in which $k = 0.7405$, $V_T = 10$ mL, and $\rho_p = 1.046\ \mathrm{mL\,g^{-1}}$. Therefore, the relationship between R_v, R_p, and M_T is:

$$R_v \approx [2.29\,M_T^{-1/3} - 1] \times R_p \quad (10)$$

[38] L. Pauling, *The Nature of Chemical Bond and the Structure of Molecules and Crystals*, Cornell University Press, **1960**.

 © 2005 Wiley-VCH Verlag GmbH & Co. KGaA, Weinheim

Bridging N,P Ligands

Stable, Water-Soluble Pta-Based Ru–Ag Organometallic Polymers**

Chaker Lidrissi, Antonio Romerosa, Mustapha Saoud, Manuel Serrano-Ruiz, Luca Gonsalvi, and Maurizio Peruzzini**

One of the latest trends in supramolecular chemistry is the quest for reproducible methods to achieve controlled self-organization of discrete units to form homo- and heterometallic coordination networks, aggregates, and polymers.[1] This development is based on the use of appropriate organic, inorganic, and organometallic building blocks that allow the synthesis of 1D linear or twisted chains, 2D squares and polygons, and 3D cubes and polyhedra.[2] Among the organic spacers, nitrogen-based aromatic heterocycles are the most widely used due to their good donor properties and rigidity. These ligands can act as corner units (bipy, phen)[3] and spacers (pyrazines,[4] terpy,[5] porphyrinates,[6] tetraazamacrocycles[7]). P-donor ligands as spacers have received less attention:[8] P_2 and P_5 ligands have been studied by Scheer and co-workers,[9] whereas the use of multidentate phosphanes has been reviewed recently.[10] To the best of our knowledge, the use of mixed N,P ligands as metal-coordinating spacers has not been reported to date.

Very few coordination polymers are water soluble, an example being the poly(ferrocenylsilane)-β-poly(aminomethacrylate) copolymer recently described by Manners and co-workers[11] as part of their ongoing study on metallocene-based polymers,[12] which can be prepared by ring-opening polymerization to afford either macromolecules with pendant ferrocenyl substituents in the polymer side chains[13] or poly(ferrocenylsilane)s.[14] Other examples of ligands that afford coordination polymers with various topologies and applications are ferrocenyl ligands bearing bipyridines[15] or carboxylates.[16]

Herein we describe the first known case of a water-soluble, air-stable, heterobimetallic polymeric structure based on two metal-containing moieties ($[CpRu]^+$ and $[AgCl_2]^-$) bridged by a cagelike, water-soluble monodentate phosphane, 1,3,5-triaza-7-phosphaadamantane (pta), in an unprecedented N,P coordinating mode.

We recently reported the synthesis and characterization of the water-soluble cyclopentadienylruthenium complex $[CpRuCl(pta)_2]$ (**1**), which is stabilized by the phosphaadamantane-like pta ligand, and described its catalytic and biological properties.[17] As part of our studies on new water-soluble organometallic derivatives based on the $[CpRu(pta)_2]^+$ moiety,[18] we treated **1** with one equivalent of AgOTf ($OTf = OSO_2CF_3$) in DMSO to remove the chloro ligand. Unexpectedly, no AgCl precipitated from the resulting orange solution, and neither did it contain the expected product $[CpRu(OTf)(pta)_2]$ (**2**), which was obtained by treatment of **1** with TlOTf.[19]

Intrigued by this apparently odd result, we repeated the experiment in an NMR tube. $^{31}P\{^1H\}$ NMR analysis in $[D_6]$DMSO indicated the formation of a 1:1 mixture of the new complex $[CpRu(pta)_2(dmso\text{-}\kappa S)]OTf$ (**3**; singlet at $\delta = -28.13$ ppm) and the bimetallic neutral coordination polymer $[\{CpRu(pta)_2(dmso\text{-}\kappa S)\}\{AgCl_2\}]_\infty$ (**4**; singlet at $\delta = -23.19$ ppm), as shown in Scheme 1.

Quantitative formation of **4** could be attained by adding one equivalent of NH_4Cl to a reaction mixture containing **1** and AgOTf. The elemental analysis and spectroscopic data are consistent with one molecule of DMSO being incorporated in the compound (see Experimental Section).

Upon repetition of the latter experiment in noncoordinating $CDCl_3$ instead of $[D_6]$DMSO, a similar Ru–Ag polymeric structure was obtained with the coordination sphere of Ru completed by an η^1-*O*-coordinated triflate anion, as suggested by the corresponding IR stretching frequency ν_{OSO} at $\tilde{\nu} = 1261\ cm^{-1}$ [20] and $^{19}F\{^1H\}$ NMR chemical shift at $\delta = -78.77$ ppm.[21] The negative charge of the repeating unit in this coordination polymer is likely to be balanced by the ammonium cation (Scheme 2). The complex $\{NH_4[\{CpRu(OTf)(pta)_2\}\{AgCl_2\}]\}_\infty$ (**5**) is characterized by a singlet at $\delta = -20.85$ ppm ($CDCl_3$) in the $^{31}P\{^1H\}$ NMR spectrum. When dissolved in DMSO, **5** is quantitatively converted into **4** with elimination of NH_4OTf.

[*] Dipl.-Chem. C. Lidrissi, Prof. Dr. A. Romerosa, Dr. M. Saoud, Dipl.-Chem. M. Serrano-Ruiz
Área de Quimica Inorganica
Universidad de Almería
04071 Almería (Spain)
Fax: (+34) 950-015-008
E-mail: romerosa@ual.es
Dr. L. Gonsalvi, Dr. M. Peruzzini
Consiglio Nazionale delle Ricerche
Istituto di Chimica dei Composti Organometallici (ICCOM-CNR)
Via Madonna del Piano snc, 50019 Sesto Fiorentino (FI) (Italy)
Fax: (+39) 055-522-5203
E-mail: mperuzzini@iccom.cnr.it

[**] Pta = 1,3,5-triaza-7-phosphaadamantane. A.R. thanks the DGICYT (Spain) for grants PPQ2000-1301 and PPQ2003-0133, and the PAI (Junta de Andalucía, FQM-317). This work was supported by the EC through the MCRTN program AQUACHEM (contract MRTN-CT-2003-503864) and the COST Actions D17 and D29. We are particularly indebted to Dr. Benjamín Sierra Martín, Ms. Lidia Rodriguez Maldonado, and Dr. Antonio Fernandez Barbero (Departamento de Física Aplicada, University of Almería) for performing the dynamic light-scattering measurements.

 © 2005 Wiley-VCH Verlag GmbH & Co. KGaA, Weinheim DOI: 10.1002/anie.200462790

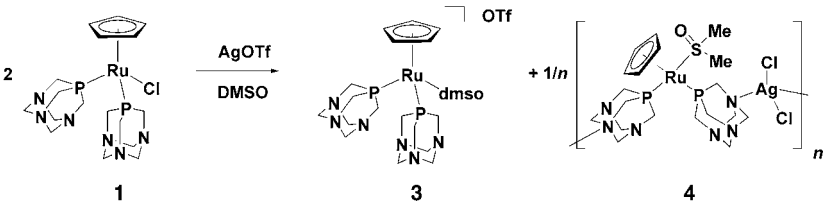

Scheme 1. Chloride abstraction from **1** with AgOTf leads to the soluble organometallic polymer **4**.

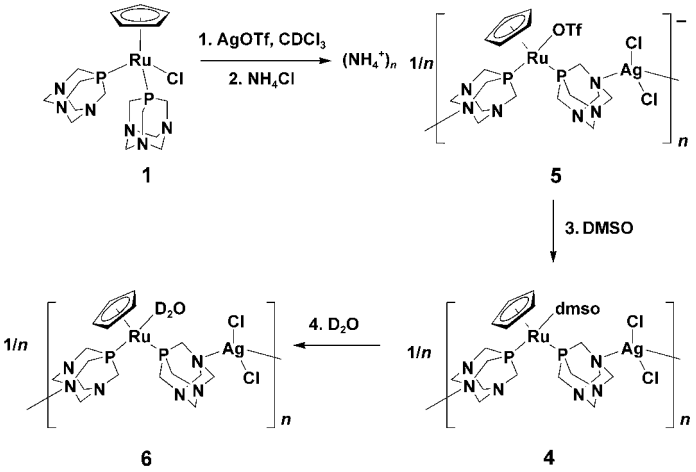

Scheme 2. Synthesis of the organometallic polymers **4**, **5**, and **6**.

Complex **4** is air stable both in the solid state and in solution, and dissolves in D_2O ($S_{25\,°C} = 12\ mg\,mL^{-1}$) with reversible exchange of the coordinated dmso ligand to yield the aquo complex $[\{CpRu(pta)_2(D_2O)\}\{AgCl_2\}]_\infty$ (**6**) (singlet at $\delta = -24.83$ ppm in D_2O in the ^{31}P NMR spectrum) as shown in Scheme 2. Slow crystallization of a dilute DMSO solution in air gave pale yellow crystals that were suitable for an X-ray diffraction study.[22] In the solid state **4** is a linear-chain polymer formed by alternating $[CpRu(dmso\text{-}\kappa S)]^+$ cations and $[AgCl_2]^-$ anions, with bridging pta ligands as tethering units between the two metal aggregates ($d_{Ru\cdots Ag} = 6.52(1)$ Å). Selected bond lengths and angles are provided in the caption of Figure 1.

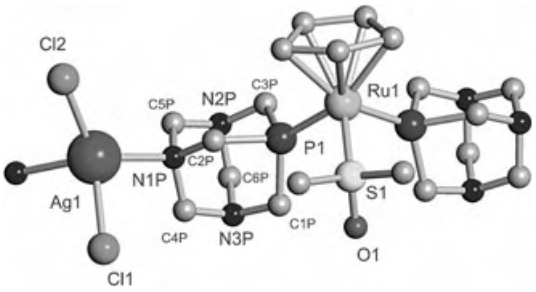

Figure 1. X-ray crystal structure of **4** (repeating unit). Selected bond lengths [Å] and angles [°]: Ru1–P1 2.285(2), Ru1–S1 2.248(3), Ru1–$Cp_{centroid}$ 1.925(1), S1–O1 1.482(7), Ag1–N1P 2.423(6), Ag1–Cl1 2.573(3), Ag1–Cl2 2.507(4); P1-Ru1-P1A 93.8(1), S1-Ru-P1 92.48(7), Cl1-Ag1-Cl2 124.07(12), Cl1-Ag1-N1P 98.15(14), Cl2-Ag1-N1P 98.50(17).

The crystal structure includes a molecule of water, which is kept in place by hydrogen bonding to an uncoordinated pta nitrogen atom belonging to a different polymer chain ($d_{O\cdots N} = 2.919(2)$ Å). The most striking feature of this solid-state structure is that pta is behaving for the first time as a bidentate ligand, bonded to the ruthenium center in the conventional way through the lone pair of the P atom and to the dichloroargentate(I) moiety through one of the three nitrogen atoms contained in the adamantane cage. The $[AgCl_2]^-$ moiety bridges two $[CpRu(pta)_2(dmso)]^+$ units to give a strongly distorted tetrahedron with the Cl1-Ag1-Cl2 angle opened up to 124.07° and the two N-Ag-Cl angles closed to about 98°. Crystallographically authenticated compounds containing $[AgCl_2]^-$ units are very rare; the average Ag–Cl distance for these complexes is 2.523 Å in a range between 2.097 and 2.915 Å.[23] The Ag–Cl distance in **4** is 2.540 Å (average value), which is near to the average Ag–Cl distance reported in the literature. The Ag–N distance (2.423(6) Å) is longer than that found for other diaminoargentato complexes (2.38 Å).[24]

The coordination geometry around ruthenium is more regular, with the Ru–$Cp_{centroid}$ distance (1.925 Å) slightly longer than in **1** (1.846 Å),[25] while the Ru–P separation (2.2856(19) Å) matches that found for the few other X-ray authenticated Ru–pta derivatives.[18,25,26] A symmetry plane in the molecule contains the atoms Ru1, S1, and O1, as well as one carbon atom of the Cp ring. The effects of the bridging pta phosphane, for which N-coordination to a transition metal is unprecedented,[27] are much more intriguing regarding the structural parameters of the ligand. The coordination of the dichloroargentate unit to the nitrogen atom of pta does not affect significantly the structural features of the cage with respect to other Ru–pta complexes.[17,18,25]

The Ru–Ag chains are kept together in a 2D array by electrostatic interactions between the $[CpRu(dmso)]^+$ and $[AgCl_2]^-$ units, with an interchain separation between the metal ions of 6.5673(9) Å (Figure 2). The 2D arrays are stacked in the lattice through a network of hydrogen bonds to water molecules that bridge a chlorine atom of one layer and a pta nitrogen atom of the adjacent one (Figure 3). The shortest hydrogen contacts between atoms in contiguous layers are 2.699(1) Å (Cl2–H17C) and 2.7382(11) Å (Cl1–H17B), which are longer than a normal hydrogen bond but shorter than the sum of the van der Waals radii. The Cp groups within adjacent layers alternate to minimize their steric interactions.[28]

Dynamic light-scattering (DLS) experiments[29] were carried out on **6** to determine the size of the particles in water and to verify whether the polymeric structure is retained in solution or shorter oligomeric substructures are formed.[30] The mean averaged diffusion coefficient was determined and the mean particle size calculated from the Einstein–Stokes equation.[31] The resulting hydrodynamic diameter indicates a monodisperse sample of about 500 nm, which suggests that the coordination polymer does not

 © 2005 Wiley-VCH Verlag GmbH & Co. KGaA, Weinheim

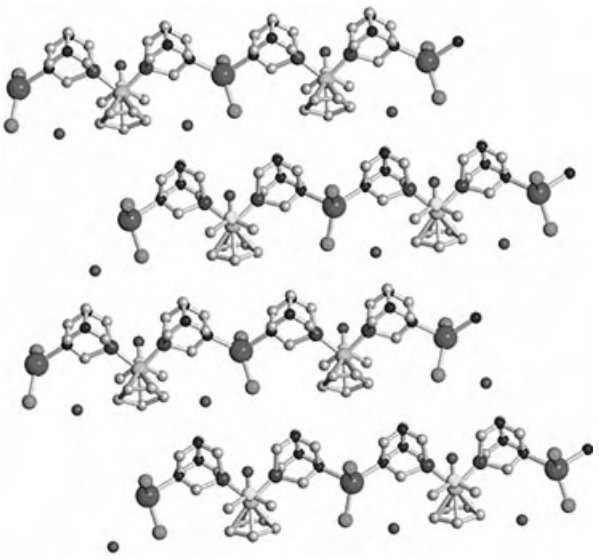

Figure 2. Spatial distribution of **4** showing the 2D arrangement formed by different polymeric chains intercalated by water molecules.

dissociate in water. DLS experiments were also performed with complexes **4** and **5**, both of which were obtained in situ as shown in Scheme 2. These measurements showed that the polymeric structure is also retained in $CHCl_3$ (**5**, 312 nm) and DMSO (**4**, 247 nm).

Macromolecular chains of organometallic species assembled into supramolecular structures by an extensive network of hydrogen-bonding interactions are rare,[8,32] and systems such as **4**–**6** that incorporate both half-sandwich cyclopentadienyl units and phosphanes have not been reported until now. Additionally, these coordination polymers are the first example of such organometallic macromolecules that are also water soluble.

Experiments are in progress to verify the N,P-coordination ability of pta with other transition-metal moieties and to establish the conductivity and electrochemical behavior of these organometallic polymers, as well as their chemical behavior in water.

Experimental Section

Complex **4** was obtained as pale yellow microcrystals from a DMSO solution (0.5 mL) of **5** (100 mg, 0.12 mmol) after standing at room temperature in the air for a week. Yield: 86 mg, 95%.

Alternatively, **4** was prepared by adding 0.5 mL of a DMSO solution of AgOTf (100 mg, 0.39 mmol) to a solution of **1** (201 mg, 0.39 mmol) and NH_4Cl (20.8 mg, 0.39 mmol) in the same solvent (0.5 mL). The reaction mixture was heated at 40 °C for 1 h. Addition of *n*-hexane (3 mL) gave **4** as a white powder, which was collected by filtration, washed with *n*-hexane (2 × 1.5 mL), and dried under vacuum. Yield: 283 mg, 96%. Elemental analysis (%) calcd for **4**·H_2O, $C_{19}H_{37}AgCl_2N_6O_2P_2RuS$ (753.96): C 30.24, H 4.95, N 11.14, S 4.24; found C 30.00, H 4.99, N 10.95, S 4.00. IR (KBr): $\tilde{\nu} = 1012\ cm^{-1}$ (S=O). ^1H NMR (300.13 MHz, 20 °C, $SiMe_4$, $[D_6]$DMSO): $\delta = 4.12$–4.19 (m, pta protons: PCH_2N + PCH_2NAg, 12H), 4.59, 4.82 (br, AB part of an ABCD spin system, $^2J_{H_AH_B} = 12.4$ Hz, $^4J_{H_AH_D} = 3.0$ Hz, pta protons: NCH_2NAg, 8H), 4.50, 4.71 (br, CD part of an ABCD system, $^2J_{H_CH_D} = 14.1$ Hz, $^4J_{H_AH_D} = 3.0$ Hz, pta protons: NCH_2N, 4H), 5.23 ppm (s, Cp, 5H); $^{13}C\{^1H\}$ NMR (75.47 MHz, 20 °C, $SiMe_4$, $[D_6]$DMSO): $\delta = 48.0$ (sept, $^1J_{C,D} = 21.4$ Hz, CD_3 of κS-coordinated $[D_6]$DMSO, exchange of coordinated DMSO with $[D_6]$DMSO takes place), 55.1 (brs, 2 × PCH_2N + PCH_2NAg), 71.1, 71.7 (partially overlapping brs, 2 × NCH_2N + NCH_2NAg), 83.6 ppm (s, Cp); $^{31}P\{^1H\}$ NMR (121.49 MHz, 20 °C, 85% H_3PO_4, $[D_6]$DMSO): $\delta = -23.19$ ppm (brs).

5: A solution of AgOTf (300 mg, 1.17 mmol) in 2 mL of $CHCl_3$ was added to a stirred solution of **1** (500 mg, 0.97 mmol) and NH_4Cl (54 mg, 1.0 mmol) in 5 mL of $CHCl_3$. The orange solution obtained after 1 h stirring at room temperature was filtered, and the solvent was removed from the solute under vacuum to afford **5** as an orange powder. Yield: 665 mg, 83%. Elemental analysis (%) calcd for $C_{18}H_{33}AgCl_2F_3N_7O_3P_2RuS$ (826.35): C 26.18, H 4.03, N 11.88, S 3.88; found C 25.90, H 4.19, N 11.46, S 3.40. IR (KBr): $\tilde{\nu} = 1260\ cm^{-1}$ $(OSO)_{OTf}$. ^1H NMR (300.13 MHz, 20 °C, TMS, $CDCl_3$): $\delta = 3.90$–4.22 (m, pta protons: PCH_2N + PCH_2NAg, 12H), 4.42–4.62 (m, pta protons: NCH_2N + NCH_2NAg, 12H), 4.86 ppm (s, Cp, 5H); $^{13}C\{^1H\}$ NMR (75.47 MHz, 20 °C, TMS, $CDCl_3$): $\delta = 55.9$ (brs, 2 × PCH_2N + PCH_2NAg), 70.5 (brs, 2 × NCH_2N + NCH_2NAg), 80.3 ppm (s, Cp), CF_3SO_3 not observed; $^{19}F\{^1H\}$ NMR (282.40 MHz, 20 °C, $CFCl_3$, $CDCl_3$): $\delta = -78.77$ ppm (s, CF_3SO_3); $^{31}P\{^1H\}$ NMR (121.49 MHz, 20 °C, 85% H_3PO_4, $CDCl_3$): $\delta = -20.85$ ppm (s).

Complex **6** was obtained quantitatively by dissolving **4** in D_2O. A pale cream powder was obtained after evaporating the solvent under vacuum. Yield: 92%. Elemental analysis (%) calcd for **6**·4D_2O, $C_{17}H_{29}AgCl_2D_8N_6O_4P_2Ru$ (739.35): C 27.61, H + D 6.13, N 11.37; found C 27.40, H + D 6.20, N 11.68. ^1H NMR (300.13 MHz, 20 °C, TMS, D_2O): $\delta = 4.15$–4.18 (m, pta protons: PCH_2N + PCH_2NAg, 12H), 4.59, 4.81 (br, AB part of an ABCD spin system, $^2J_{H_AH_B} = 12.4$ Hz, $^4J_{H_BH_D} = 1.1$ Hz, pta protons: NCH_2NAg, 8H), 4.51, 4.79 (br, CD part of an ABCD system, $^2J_{H_CH_D} = 13.1$ Hz, $^4J_{H_BH_D} = 1.1$ Hz, pta protons: NCH_2N, 4H), 5.37 ppm (s, Cp, 5H); $^{13}C\{^1H\}$ NMR (75.47 MHz, 20 °C, TMS, D_2O): $\delta = 54.4$–54.7 (brm, 2 × PCH_2N + PCH_2NAg), 70.6 (brs, 2 × NCH_2N + NCH_2NAg), 83.5 ppm (s, Cp);

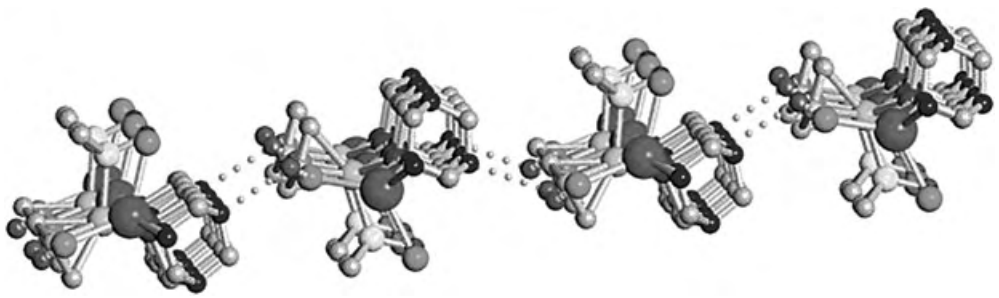

Figure 3. Spatial distribution of **4** showing the hydrogen-bonding network connecting the polymeric chains between a chlorine atom of one layer and a pta nitrogen atom of the adjacent one.

 © 2005 Wiley-VCH Verlag GmbH & Co. KGaA, Weinheim

$^{31}P\{^1H\}$ NMR (121.49 MHz, 20 °C, 85 % H_3PO_4, D_2O): $\delta = -24.83$ ppm (s).

Received: December 2, 2004
Published online: March 22, 2005

Keywords: bridging ligands · N,P ligands · organometallic polymers · ruthenium · silver

[1] a) J.-M. Lehn, *Supramolecular Chemistry*, Wiley-VCH, Weinheim, **1995**; b) R. Robson, B. F. Abrahams, S. R. Batten, R. W. Gable, B. F. Hoskins, J. Liu, *Supramolecular Architecture*, American Chemical Society, New York, **1992**, Ch. 19; c) A. J. Blake, N. R. Champness, P. Hubberstey, W. S. Li, M. A. Whitersby, M. Schröder, *Coord. Chem. Rev.* **1999**, *111*, 2798; d) P. J. Stang, B. Olenyuk, *Acc. Chem. Res.* **1997**, *30*, 502; e) D. Braga, F. Grepioni, G. R. Desiraju, *Chem. Rev.* **1998**, *98*, 1375; f) D. L. Caulder, K. N. Raymond, *Acc. Chem. Res.* **1999**, *32*, 975; g) S. Leininger, B. Olenyuk, P. J. Stang, *Chem. Rev.* **2000**, *100*, 853; h) M. Eddaoudi, D. B. Moler, H. Li, B. Chen, T. M. Reineke, M. O'Keefe, O. M. Yaghi, *Acc. Chem. Res.* **2001**, *34*, 319.

[2] a) M. Fujita, J. Yazaki, K. Ogura, *J. Am. Chem. Soc.* **1990**, *112*, 5645; b) G. F. Swiegers, T. J. Malefetse, *Coord. Chem. Rev.* **2002**, *225*, 91; c) Z. He, C. He, Z.-M. Wang, E.-Q. Gao, Y. Liu, C.-H. Yan, *Dalton Trans.* **2004**, 502; d) C. Janiak, *Dalton Trans.* **2003**, 2781.

[3] P. J. Hagrman, D. Hagrman, J. Zubieta, *Angew. Chem.* **1999**, *111*, 2798; *Angew. Chem. Int. Ed.* **1999**, *38*, 2638.

[4] D. L. Reger, K. J. Brown, J. R. Gardinier, M. D. Smith, *Organometallics* **2003**, *22*, 4973.

[5] a) M. Barboiu, G. Vaughan, R. Graff, J.-M. Lehn, *J. Am. Chem. Soc.* **2003**, *125*, 10257; b) A. M. Garcia, F. J. Romero-Salguero, D. M. Bassani, J.-M. Lehn, G. Baum, D. Fenske, *Chem. Eur. J.* **1999**, *5*, 1803.

[6] D. W. Smithenry, S. R. Wilson, K. S. Suslick, *Inorg. Chem.* **2003**, *42*, 7719.

[7] J. D. Chartres, L. F. Lindoy, G. V. Meehan, *Coord. Chem. Rev.* **2001**, *216–217*, 249, and references cited therein.

[8] X. L. Lu, W. K. Leong, T. S. A. Hor, L. Y. Goh, *J. Organomet. Chem.* **2004**, *689*, 1746, and references cited therein.

[9] a) J. Bai, E. Leiner, M. Scheer, *Angew. Chem.* **2002**, *114*, 820; *Angew. Chem. Int. Ed.* **2002**, *41*, 783; b) J. Bai, A. V. Virovets, M. Scheer, *Angew. Chem.* **2002**, *114*, 1808; *Angew. Chem. Int. Ed.* **2002**, *41*, 1737.

[10] S. L. James, X. Xu, R. V. Law, *Macromol. Symp.* **2003**, *196*, 187, and references cited therein.

[11] a) X.-S. Wang, M. Winnik, I. Manners, *Polym. Prepr. (Am. Chem. Soc., Div. Polym. Chem.)* **2002**, *86*, 93; b) X.-S. Wang, M. Winnik, I. Manners, *Macromol. Rapid Commun.* **2002**, *23*, 210.

[12] a) I. Manners, *Synthetic Metal-Containing Polymers*, Wiley-VCH, Weinheim, **2003**; b) I. Manners, *Science* **2001**, *294*, 1164.

[13] P. Nguyen, P. Gómez-Elipe, I. Manners, *Chem. Rev.* **1999**, *99*, 1515.

[14] a) D. A. Foucher, B. Z. Tang, I. Manners, *J. Am. Chem. Soc.* **1992**, *114*, 6246; b) Y. Ni, R. Rulkens, I. Manners, *J. Am. Chem. Soc.* **1996**, *118*, 4102.

[15] See for example: a) C. Bucher, C. H. Devillers, J. C. Moutet, G. Royal, E. Saint-Aman, *Chem. Commun.* **2003**, 888; b) E. Lindner, R. F. Zong, K. Eichele, U. Weisser, M. Ströbele, *Eur. J. Inorg. Chem.* **2003**, 705; c) D. M. Shin, I. S. Lee, Y. K. Chung, *Eur. J. Inorg. Chem.* **2003**, 2311; d) D. Braga, M. Polito, M. Bracaccini, D. D'Addario, E. Tagliavini, L. Sturba, F. Grepioni, *Organometallics* **2003**, *22*, 2142.

[16] a) I. S. Lee, D. M. Shin, Y. K. Chung, *Cryst. Growth Des.* **2003**, *3*, 521; b) G. Li, H. W. Hou, L. K. Li, X. R. Meng, Y. T. Fan, Y. Zhu, *Inorg. Chem.* **2003**, *42*, 4995; c) C. M. Zakaria, G. Ferguson, A. J. Lough, C. Glidewell, *Acta Crystallogr. Sect. B* **2002**, *58*, 786.

[17] D. N. Akbayeva, L. Gonsalvi, W. Oberhauser, M. Peruzzini, F. Vizza, P. Brüggeller, A. Romerosa, G. Sava, A. Bergamo, *Chem. Commun.* **2003**, 264.

[18] a) S. Bolaño, L. Gonsalvi, F. Zanobini, F. Vizza, V. Bertolasi, A. Romerosa, M. Peruzzini, *J. Mol. Catal. A* **2004**, *224*, 61; b) A. Romerosa, L. Gonsalvi, M. Peruzzini, unpublished results.

[19] Complex **2** was obtained as an orange microcrystalline compound by treating **1** with TlOTf in $CHCl_3$ (Yield: 85 %). Elemental analysis (%) calcd for $C_{18}H_{29}F_3N_6O_3P_2RuS$ (629.54): C 34.34, H 4.64, N 13.35, S 5.09; found C 34.10, H 4.30, N 12.94, S 4.69; IR (KBr): $\tilde{\nu} = 1261$, 1170, 1031 cm^{-1} (OTf); ^1H NMR (300.13 MHz, $CDCl_3$, 20 °C, Me_4Si): $\delta = 3.85$–4.58 (m, CH_2(pta), 24 H), 4.67 ppm (s, Cp, 5 H); $^{31}P\{^1H\}$ NMR (121.49 MHz, $CDCl_3$, 20 °C, 85 % H_3PO_4): $\delta = -15.47$ ppm.

[20] G. A. Lawrance, *Chem. Rev.* **1986**, *86*, 17.

[21] See for example: B. K. Bennett, S. Lovell, J. M. Mayer, *J. Am. Chem. Soc.* **2001**, *123*, 4336.

[22] Crystals of **4** were obtained by slow evaporation at room temperature of a DMSO solution of **5** in the air over one month. Crystal data for **4**: $C_{19}H_{37}AgCl_2N_6O_2P_2RuS$, orthorhombic, space group *Pnma* (no. 62), $a = 11.8733(9)$, $b = 12.9333(10)$, $c = 17.4306(13)$ Å, $V = 2676.7(4)$ Å^3, $Z = 4$, $\rho_{calcd} = 1.864$ Mg m^{-3}, final R_1 value 0.0495 for 1583 independent reflections ($I > 2\sigma(I)$). The data collection was performed at room temperature on a Bruker APEX CCD area-detector diffractometer, using $Mo_{K\alpha}$ radiation ($\lambda = 0.71073$ Å) by the ω scan method, within the limits $1.96 < \theta < 23.29°$. No empirical absorption correction was applied. The structure was solved by direct methods (SIR97) and refined by full-matrix least-squares on F^2 (SHELX 97). Anisotropic thermal factors were assigned to all the non-hydrogen atoms. The disordered O30 and Cl2 atoms were found and an average model was refined. The cyclopentadienyl C-atoms were statistically distributed around the Ru atom. All the H atoms except those bonded to O30 and the Cp carbon atoms were placed in calculated positions and not refined. All the diagrams were generated by using the SHELXL program. CCDC-241789 contains the supplementary crystallographic data for this paper. These data can be obtained free of charge from the Cambridge Crystallographic Data Centre via www.ccdc.cam.ac.uk/data_request/cif.

[23] a) G. Helgesson, S. Jagner, *Inorg. Chem.* **1991**, *30*, 2574; b) K. M. Lee, H. M. Wang, I. J. B. Lin, *J. Chem. Soc. Dalton Trans.* **2002**, 2852; c) G. Helgesson, S. Jagner, *J. Chem. Soc. Dalton Trans.* **1993**, 1069; d) Z. Xie, B.-M. Wu, T. C. W. Mak, J. Manning, C. A. Reed, *J. Chem. Soc. Dalton Trans.* **1997**, 1213; e) R. W. Turner, E. L. Amma, *J. Am. Chem. Soc.* **1966**, *88*, 3243; f) G. Exarchos, S. C. Nyburg, S. D. Robindon, *Polyhedron* **1998**, *17*, 1257; g) C.-W. Tsang, Q. Yang, E. T.-P. Sze, T. C. W. Mak, D. T. W. Cham, Z. Xie, *Inorg. Chem.* **2000**, *39*, 5851.

[24] Cambridge Structural Database (CSD): http://www.ccdc.cam.ac.uk/products/csd/ (October **2004**).

[25] B. J. Frost, C. A. Mebi, *Organometallics* **2004**, *23*, 5317.

[26] a) D. J. Darensbourg, F. Joó, M. Kannisto, A. Katho, J. H. Reibenspies, *Organometallics* **1992**, *11*, 1990; b) D. J. Darensbourg, F. Joó, M. Kannisto, A. Katho, J. H. Reibenspies, D. J. Daigle, *Inorg. Chem.* **1994**, *33*, 200; c) C. S. Allardyce, P. J. Dyson, D. J. Ellis, S. L. Heath, *Chem. Commun.* **2001**, 1396; d) D. J. Darensbourg, F. A. Beckford, J. H. Reibenspies, *J. Cluster Sci.* **2000**, *11*, 95.

[27] A. D. Phillips, L. Gonsalvi, A. Romerosa, F. Vizza, M. Peruzzini, *Coord. Chem. Rev.* **2004**, *248*, 955.

[28] The orientation of the Cp rings is predetermined by the symmetry operations in the space group of **4**.

[29] *Dynamic Light Scattering* (Eds. B. Bruce, R. Pecora), Wiley, New York, **1976**; B. J. Berne, R. Pecora, *Dynamic Light Scattering*

 © 2005 Wiley-VCH Verlag GmbH & Co. KGaA, Weinheim

with Applications to Chemistry, Biology, and Physics, Dover Publications, Dover, **2000**.

[30] Examples of solid poly(stannasiloxane)s that reversibly form smaller macrocycles in solution have been reported, see: J. Beckmann, K. Jurkschat, D. Schollmeyer, M. Schürmann, *J. Organomet. Chem.* **1997**, *543*, 229.

[31] A Malvern 4700 system operating with a 6328 Å-wavelength He–Ne laser was employed for recording the DLS measurement. The temperature was controlled with a precision of 0.1 K using both a Peltier thermocouple and an external bath. Light intensity was recorded at a fixed scattering angle, $\theta = 40°$. The time correlation function of the scattered intensity, $\langle I(0)I(\tau)\rangle$, was then calculated and the mean hydrodynamic diameter obtained by standard cumulated analysis. The sample temperature was equilibrated for 20 min before every measurement. Low particle concentrations were used for DLS measurements to diminish the effect of colloidal interactions as well as multiple scattering.

[32] a) L. Brammer, J. C. M. Rivas, R. Atencio, S. Fang, F. C. Pigge, *J. Chem. Soc. Dalton Trans.* **2000**, 3855; b) G. R. Desiraju, *Acc. Chem. Res.* **1996**, *29*, 441; c) D. L. Reger, R. F. Semeniuc, M. D. Smith, *J. Chem. Soc. Dalton Trans.* **2002**, 476; d) M. P. Thornberry, C. Slebodnick, P. A. Deck, F. R. Fronczek, *Organometallics* **2000**, *19*, 5352.

 © 2005 Wiley-VCH Verlag GmbH & Co. KGaA, Weinheim

Amplifying Fluorescent Polymers

Direct Synthesis of an Oligonucleotide–Poly(phenylene ethynylene) Conjugate with a Precise One-to-One Molecular Ratio**

*Chaoyong James Yang, Mauricio Pinto, Kirk Schanze, and Weihong Tan**

Conjugated polyelectrolytes have great potential in biochemical sensor applications[1–8] because of their unique light-harvesting[9,10] and superquenching[11–14] properties. Among them, water-soluble poly(phenylene ethynylene)s (PPEs) are attractive candidates in optical biosensing because of their facile synthesis and high fluorescence quantum yields in aqueous solution.[5,6,15] Highly sensitive bioprobes can be constructed with these polymers for selective target recognition. To achieve this objective, the polymer must be conjugated with a biomolecule such as a DNA strand, a peptide, or a protein. Such conjugation can be accomplished by coupling PPEs with pendant reactive groups to biomolecules with specific reactive moieties, for example, by formation of an amide bond between a PPE functionalized with a carboxylic acid group and an amine-functionalized biomolecule. Although some progress has been made in the coupling of PPEs to biotin,[11,16] there remains a clear need to develop new strategies for coupling PPEs to oligonucleotides and proteins. Effective strategies for coupling such biomolecules to conjugated polymers would have significant implications for a variety of fields, including bioanalysis and biomedical diagnostics.[17] Unfortunately, the coupling of PPEs to large biomolecules is fraught with difficulty. First, the introduction of reactive pendant groups can be challenging and may also change the polymer properties. Second, unfavorable steric and electrostatic interactions between the polymer and the target biomolecule result in a low coupling efficiency. Moreover, the coupled product has chemical and physical properties similar to those of the free polymer, which makes it difficult to separate the conjugated product from the unreacted polymer. Finally, the degree of coupling to the polymer is difficult to control because of the nature of the polymer, the poor coupling efficiency, and the lack of effective separation methods.

Herein, we introduce a versatile and effective synthetic method for coupling oligonucleotides to conjugated polyelectrolytes. Instead of synthesizing the polymer and oligonucleotide separately before coupling, we treat the oligonucleotide as an "end-capping" monomer in the Pd-catalyzed step-growth polymerization of a PPE-based conjugated polyelectrolyte. The oligonucleotide takes part in the polymerization process and is incorporated into the PPE chain as an end-capping unit. The oligonucleotide-functionalized monomer is bound to a controlled pore glass (CPG) solid support, thereby allowing the DNA–PPE conjugate to be easily separated by centrifugation. Furthermore, this method not only allows an oligonucleotide to be conjugated to a PPE chain, but it can also be extended to other biomolecules such as biotin by using a similar approach with biotin phosphoramidite.

Scheme 1 shows the process of making a DNA–PPE conjugate. On a CPG support, an oligonucleotide with a defined sequence was synthesized from the 3′ end to the 5′ end by using standard phosphoramidite chemistry (a). 5′-Dimethoxytrityl-5-iodo-2′-deoxyuridine 3′-[(2-cyanoethyl)-(*N*,*N*-diisopropyl)]phosphoramidite (5I-dU phosphoramidite) was used to introduce a 5I-dU residue as the last base of the oligonucleotide (b), which provided the functionalization necessary to render the oligonucleotide active as a monomer for the PPE. Under Sonogashira conditions, the 5I-dU base couples to terminal alkynes with high efficiency.[18,19] Without deprotection and cleavage from the CPG solid support, the 5I-dU-functionalized oligonucleotide was added to the PPE polymerization solution as an end-capping monomer, thereby allowing the polymer chain to cross-couple with the CPG-linked oligonucleotide (c). After polymerization, the CPG was washed and centrifuged several times until no PPE was detected in the supernatant. This procedure was followed by overnight incubation in ammonia to cleave the DNA–PPE

[*] C. J. Yang, Dr. M. Pinto, Prof. Dr. K. Schanze, Prof. Dr. W. Tan
Center for Research at the Bio/Nano Interface
Department of Chemistry
University of Florida
Gainesville, FL 32611-7200 (USA)
Fax: (+1) 352-846-2410
E-mail: tan@chem.ufl.edu

[**] This work is partially supported by National Institutes of Health grants and a National Science Foundation Nanoscale Interdisciplinary Research Teams (NIRT) grant. K.S.S. and M.R.P. acknowledge support from the US Department of Energy (DE-FG02-03ER15484). The authors also thank Dr. Jodie Johnson for his help with the ESI MS analysis.

Supporting Information for this article is available on the WWW under http://www.angewandte.org or from the author.

 © 2005 Wiley-VCH Verlag GmbH & Co. KGaA, Weinheim DOI: 10.1002/anie.200462431

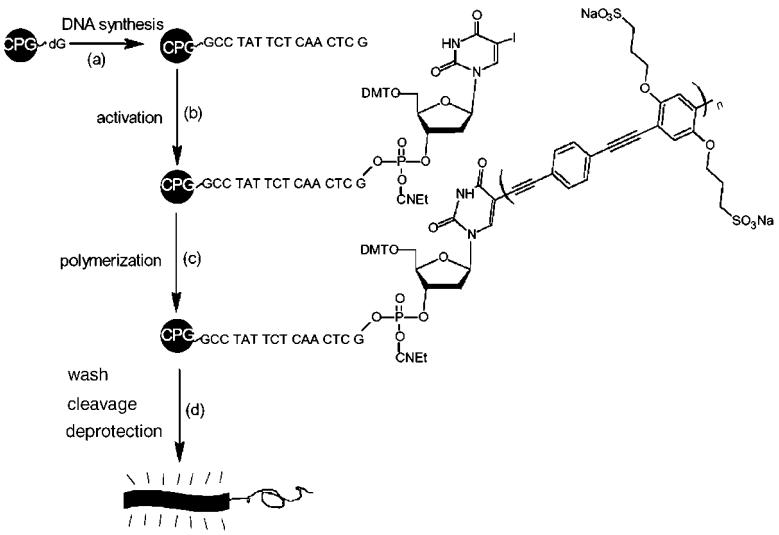

Scheme 1. Schematic representation of the solid-state synthesis of the DNA–PPE conjugate; for details see text. DMT = dimethoxytrityl.

conjugate from the solid support and to remove the protecting groups from the oligonucleotide bases. The product, DNA–PPE, was obtained after further desalting by means of ethanol precipitation (d).

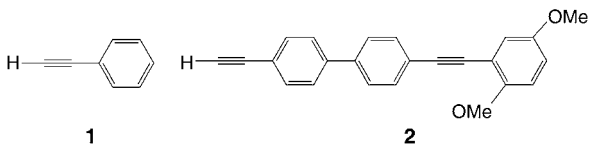

Scheme 2. Model molecules used to couple to the 5I-dU-functionalized oligonucleotide.

Two small organic molecules (Scheme 2) were used to demonstrate that the 5I-dU-modified oligonucleotide is able to conjugate to the polymer monomer and oligomer present in the polymerization reaction mixture. In one model reaction, ethynylbenzene (**1**) was coupled with the CPG-linked DNA. In a second reaction, 4-[(2,5-dimethoxyphenyl)-ethynyl]-4′-ethynyl-1,1′-biphenyl (**2**) was used to mimic a small PPE oligomer. The coupling products from both model reactions were analyzed with reversed-phase gradient HPLC/ESI MS. The molecular weights observed by mass spectrometry matched those calculated from the product structures, a result indicating that the CPG-linked oligonucleotide is able to undergo cross-coupling with terminal acetylenes under Sonogashira coupling conditions.

In the synthesis of DNA–PPE, the CPG from four CPG columns (1-μmol scale) containing the 5I-dU-modified oligonucleotide was transferred to a 100-mL round-bottomed flask containing dimethylsulfoxide (DMSO, 20 mL). The PPE monomers disodium 3-[2,5-diiodo-4-(3-sulfonatopropoxy)-phenoxy]propane-1-sulfonate (690 μmol) and 1,4-diethynylbenzene (694 μmol) were then added to the solution with stirring under a gentle flow of argon. The resulting solution was deoxygenated by several cycles of vacuum–argon degassing. Another solution comprising $[Pd(PPh_3)_4]$ (20 μmol) and CuI (20 μmol) in DMSO (10 mL) was likewise deoxygenated and subsequently added dropwise to the monomer solution. The final mixture was again deoxygenated and stirred at room temperature under argon for 24 h. The resulting solution was viscous and brown-yellow in color, and it exhibited an intense blue-green fluorescence under near-UV illumination. The solution was then centrifuged and the precipitated CPG was washed several times with DMSO and water until the supernatant was clear and colorless. After washing, the CPG was still yellow-green and highly fluorescent. The CPG was then incubated in ammonia at 55 °C to cleave the oligonucleotide from the CPG and to deprotect the bases. After overnight incubation, the CPG became white whereas the liquid phase turned yellow-green and fluoresced under UV illumination, thus indicating that the PPE coupled to DNA was cleaved from the CPG as a result of the cleavage of DNA from the support. A control synthesis was carried out by following the same procedures and experimental conditions, but a 16-mer DNA without the 5I-dU base was used. After three repeated rinses prior to cleaving DNA from the solid support, the control CPG became white, thus indicating no PPE coupled to the DNA in this control experiment. The solutions that resulted after ammonia incubation of the CPG derivatized with 5I-dU oligonucleotide and of the control CPG were desalted by ethanol precipitation, dried, and redissolved in deionized water. Figure 1 compares the fluorescence emission spectra of the DNA–PPE and control solutions. The DNA–PPE solution shows an emission band with a maximum at 520 nm, which is consistent with a previous report that this PPE emits at 520 nm in water (the emission is broad because the PPE is aggregated in water).[5] Deaggregation of the PPE, induced by the addition of a nonionic surfactant, dispersion into agarose gel, or changing to methanol as the solvent,[5] shifts its emission maximum to

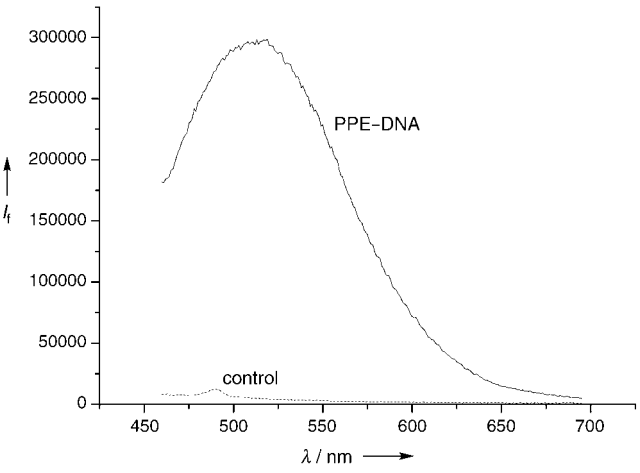

Figure 1. Fluorescence emission spectra of DNA–PPE and the control solution. I_f: fluorescence intensity.

 © 2005 Wiley-VCH Verlag GmbH & Co. KGaA, Weinheim

455 nm (see the Supporting Information). The strong fluorescence from the DNA–PPE solution and the lack of fluorescence from the control solution suggest that the PPE has been successfully coupled to the DNA.

Mass spectrometry analysis indicated that the DNA structure remained intact after exposure to the polymerization conditions (see the Supporting Information). Data from DNA hybridization experiments revealed no significant change in the binding capability of these oligonucleotides (see the Supporting Information).

The fact that the PPE is coupled to the 5I-dU-modified DNA was further confirmed by gel electrophoresis, in which a 0.5% agarose gel was used to analyze the DNA–PPE conjugate, the PPE, and the DNA obtained from the control synthesis. As shown in Figure 2, in the DNA lane (3), only one band is observed, while in the PPE lane (2), no DNA band exists. By contrast, there are two bands in the DNA–PPE lane (1), which suggests that at least two types of DNA are present. One is probably the "free" DNA (this band has a migration rate similar to that in lane 3), and the second is likely to be the DNA–PPE conjugate. The DNA–PPE band migrates very little in the agarose matrix; the reasons might be the rigid rod structure[7] of the PPE and the large molecular weight of the PPE–DNA conjugate. Quantitative analysis of the DNA–PPE lane revealed that the ratio of the overall intensity for the DNA band to that for the DNA–PPE conjugate band is about 1.2:1, a result that indicates a yield higher than 45% for the coupling reaction between the DNA strand and the PPE.

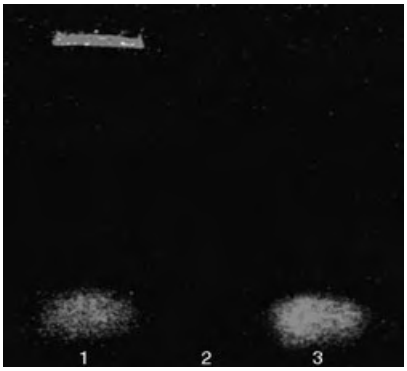

Figure 2. Gel electrophoresis of PPE–DNA (lane 1), PPE (lane 2), and DNA (lane 3) samples. Conditions: agarose (0.5%), 1× TBE buffer (0.089 M tris(hydroxymethyl)aminomethane (Tris), 0.089 M borate, and 2 mM ethylenediaminetetraacetate (EDTA), pH 8.2–8.4), 90 V for 20 min. The gel was prestained with ethidium bromide for DNA detection. Pictures were taken with a camera in fluorescence mode with a 540–640 nm band pass filter. This filter passes emission from ethidium bromide, thereby indicating the presence of oligonucleotide, while removing the emission for PPE under these conditions (PPE emits at 455 nm in agarose gel).

The successful establishment of this conjugation method allows us to construct a variety of biosensors with conjugated polymers, where precise control of the conjugation ratio of recognition molecule to polymer and complete separation of free conjugated polymer from biofunctionalized conjugated polymer are crucial. Our first attempt was to synthesize a molecular beacon with a conjugated polymer chain as its fluorophore. A molecular beacon[20,21] is a hairpin-shaped oligonucleotide with a fluorescent dye (Fl) at one end and a quencher (Q) at the other end. In the absence of the target DNA, the fluorescent dye and quencher molecule are brought close together by the self-complementary stem of the probe, and the fluorescence signal is suppressed. The perfectly matched DNA duplex is more stable than the single-stranded hairpin, so the molecular beacon readily hybridizes to its target sequence, thereby disrupting the stem structure, separating the fluorophore from the quencher, and restoring the fluorescence signal (Scheme 3a). Compared to a traditional molecular beacon, this new design uses a polymer chain as the fluorophore to amplify the fluorescence signal. When the molecular beacon is in its closed state, the polymer chain will be brought close to the quencher. It is expected that the fluorescence of the conjugated polymer will be strongly suppressed because of the superquenching property of the conjugated polymer. After target-DNA binding, the fluorescence of the conjugated polymer will be restored as a result of the increased separation distance between the conjugated polymer and the quencher (Scheme 3b).

The synthesis of the molecular beacon followed the same procedure as described above, except that a 3′-DABCYL-modified quencher CPG was used instead of a regular base CPG (Scheme 4; DABCYL = 4-(4-(dimethylamino)phenylazo)benzoic acid). As a universal quencher, DABCYL has been widely used as the quencher in molecular-beacon synthesis. Another reason why DABCYL was chosen was because its absorption overlaps with the PPE emission. Quenching experiments revealed that the Stern–Volmer quenching constant of DABCYL to PPE in free solution is about $4\times10^{6}\,\text{M}^{-1}$ (see the Supporting Information). The molecular-beacon sequence synthesized was 5′-PPE-CC TAG CTC TAA ATC ACT ATG GTC GCG CTA GG-DABCYL-3′. Theoretical calculations indicated that this sequence could form a stable hairpin structure.

Figure 3 shows the response of the molecular beacon labeled with the conjugated polymer to a fivefold excess of its target DNA. When a lower concentration of the target was

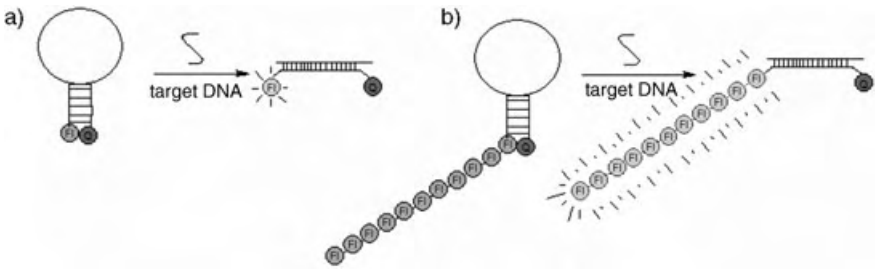

Scheme 3. Working principles of a molecular beacon (a) and a conjugated-polymer-labeled molecular beacon (b). In a regular molecular beacon, one fluorophore is used to report a target-binding event, whereas a chain of fluorophores is used in the polymer-labeled molecular beacon. Q = quencher, Fl = fluorophore.

 © 2005 Wiley-VCH Verlag GmbH & Co. KGaA, Weinheim

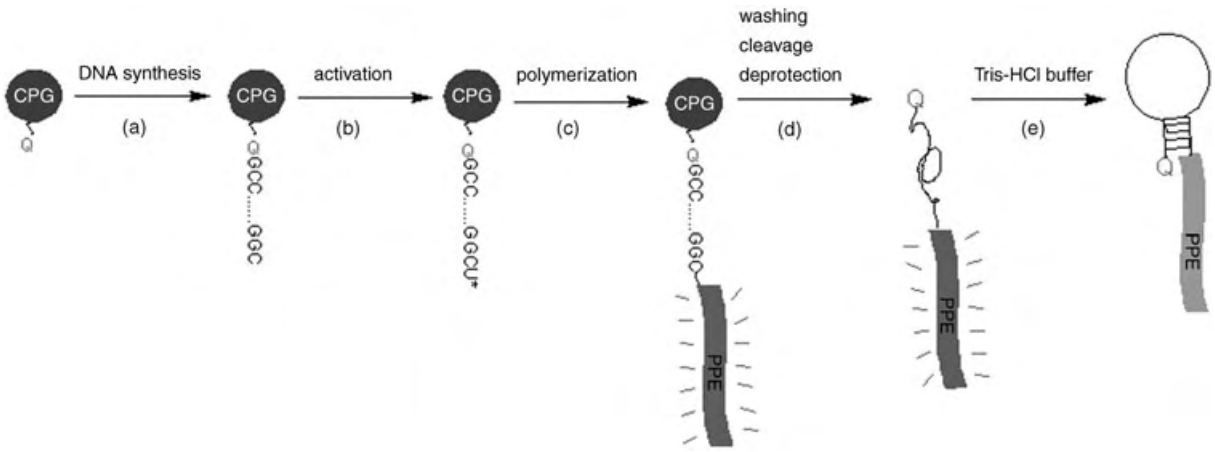

Scheme 4. Schematic representation of the solid-state synthesis of the PPE-labeled molecular beacon. Q stands for the DABCYL quencher.

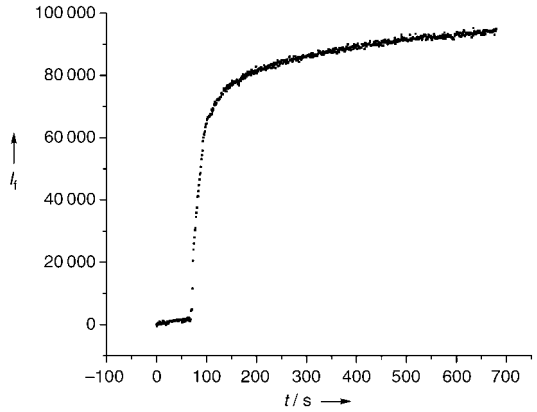

Figure 3. Response of the PPE-labeled molecular beacon synthesized according to Scheme 4 to its target DNA. Target sequence: 5′-GCG AC-CATA GTG ATT TAG A-3′. Buffer conditions: 20 mM Tris-HCl (pH 7.5), 50 mM NaCl, 5 mM $MgCl_2$, 0.1% Tween 20.

used, a slower reaction profile was observed. When a large excess of random-sequence DNA was added to the molecular-beacon solution as a negative control, no substantial change in the fluorescence intensity was observed. These hybridization results suggested that 1) the DABCYL molecule quenches the polymer chain when the molecular beacon is in the hairpin conformation and 2) the molecular beacon labeled with conjugated polymer functions as a normal molecular beacon that selectively hybridizes to its target DNA.

In conclusion, a novel synthetic method has been developed for the conjugation of a water-soluble PPE with an oligonucleotide. Coupling was achieved by carrying out the PPE polymerization reaction in the presence of a 5I-dU-terminated oligonucleotide linked to a CPG support. The DNA–PPE product can be easily separated from free PPE by centrifugation. The conjugation reaction is simple, fast, and easily controllable. The efficiency of the DNA–PPE coupling is high. Mass spectrometry analysis and the results of a DNA-hybridization study indicated that the polymerization conditions were so mild that the DNA exposed to them not only remained structurally intact but also kept its biorecognition capability. The new method has four distinct advantages: stoichiometric labeling of DNA to the polymer chain, easy separation to enable high purity of the desired final product, high yields for the DNA–PPE conjugation, and a stable product as a result of covalent conjugation between the biomolecules and the PPE. This new method makes it possible to efficiently couple a fluorescent amplifying polymer with biomolecules for bioanalysis and biosensor applications. As an example of using a conjugated polymer for DNA sensing, a molecular beacon with a conjugated polymer chain as the signaling element was prepared. Without the strategies described herein, the preparation of such a molecular beacon would be extremely difficult or even impossible. This molecular beacon gave a strong fluorescence signal specifically for the complementary sequence and showed promising results in bioanalysis. The physical, chemical, spectral, and biological properties of the DNA–PPE hybrid material are currently being investigated. The application of PPE-labeled molecular beacons to highly sensitive bioassays[22] is in progress.

Received: October 26, 2004
Published online: March 18, 2005

Keywords: biosensors · conjugated polymers · fluorescent probes · molecular beacons · oligonucleotides

[1] S. A. Kushon, K. Bradford, V. Marin, C. Suhrada, B. A. Armitage, D. McBranch, D. Whitten, *Langmuir* **2003**, *19*, 6456 – 6464.
[2] S. Wang, G. C. Bazan, *Adv. Mater.* **2003**, *15*, 1425 – 1428.
[3] D. T. McQuade, A. E. Pullen, T. M. Swager, *Chem. Rev.* **2000**, *100*, 2537 – 2574.
[4] B. S. Gaylord, A. J. Heeger, G. C. Bazan, *J. Am. Chem. Soc.* **2003**, *125*, 896 – 900.
[5] C. Y. Tan, M. R. Pinto, K. S. Schanze, *Chem. Commun.* **2002**, 446 – 447.
[6] M. R. Pinto, K. S. Schanze, *Proc. Natl. Acad. Sci. USA* **2004**, *101*, 7505 – 7510.
[7] U. H. F. Bunz, *Chem. Rev.* **2000**, *100*, 1605 – 1644.
[8] H. Huang, K. Wang, W. Tan, D. An, X. Yang, S. Huang, Q. Zhai, L. Zhou, Y. Jin, *Angew. Chem.* **2004**, *116*, 5753 – 5756; *Angew. Chem. Int. Ed.* **2004**, *43*, 5635 – 5638.

 © 2005 Wiley-VCH Verlag GmbH & Co. KGaA, Weinheim

[9] B. S. Gaylord, A. J. Heeger, G. C. Bazan, *Proc. Natl. Acad. Sci. USA* **2002**, *99*, 10954 – 10957.
[10] S. Wang, G. C. Bazan, *Adv. Mater.* **2003**, *15*, 1425 – 1428.
[11] S. A. Kushon, K. D. Ley, K. Bradford, R. M. Jones, D. McBranch, D. Whitten, *Langmuir* **2002**, *18*, 7245 – 7249.
[12] S. A. Kushon, K. Bradford, V. Marin, C. Suhrada, B. A. Armitage, D. McBranch, D. Whitten, *Langmuir* **2003**, *19*, 6456 – 6464.
[13] Y. Liu, S. J. Jiang, K. S. Schanze, *Chem. Commun.* **2003**, 650 – 651.
[14] R. M. Jones, T. S. Bergstedt, C. T. Buscher, D. McBranch, D. Whitten, *Langmuir* **2001**, *17*, 2568 – 2571.
[15] M. R. Pinto, K. S. Schanze, *Synthesis* **2002**, 1293 – 1309.
[16] J. N. Wilson, Y. Q. Wang, J. J. Lavigne, U. H. F. Bunz, *Chem. Commun.* **2003**, 1626 – 1627.
[17] P. S. Heeger, A. J. Heeger, *Proc. Natl. Acad. Sci. USA* **1999**, *96*, 12219 – 12221.
[18] S. I. Khan, M. W. Grinstaff, *J. Am. Chem. Soc.* **1999**, *121*, 4704 – 4705.
[19] M. Rist, N. Amann, H. A. Wagenknecht, *Eur. J. Org. Chem.* **2003**, 2498 – 2504.
[20] S. Tyagi, F. R. Kramer, *Nat. Biotechnol.* **1996**, *14*, 303 – 308.
[21] X. Fang, X. Liu, S. Schuster, W. Tan, *J. Am. Chem. Soc.* **1999**, *121*, 2921 – 2922; X. H. Fang, J. W. J. Li, J. Perlette, W. H. Tan, K. M. Wang, *Anal. Chem.* **2000**, *72*, 747A – 753A.
[22] X. H. Fang, W. H. Tan, *Anal. Chem.* **1999**, *71*, 3101 – 3105.

 © 2005 Wiley-VCH Verlag GmbH & Co. KGaA, Weinheim

Metathesis Catalysts

Alkenylcarbene Ruthenium Arene Complexes as Initiators of Alkene Metathesis: An Enyne Creates a Catalyst that Promotes Its Selective Transformation**

*Ricardo Castarlenas, Matthieu Eckert, and Pierre H. Dixneuf**

Alkene metathesis has become a powerful reaction in organic synthesis and polymerization as it allows new approaches for making crucial C–C bonds and thus reduces the number of steps in the synthesis to natural or biologically relevant compounds.[1] This is due to the discovery of well-defined alkylidene metal catalysts, of which those of ruthenium offer an especially good compromise between efficiency and tolerance to functional groups.[1d] The moderate stability of the coordinatively unsaturated ruthenium alkylidene catalytic species[2] can be compensated by high efficiency of the catalytic moiety, which allows transformation of a large quantity of substrate under mild conditions in a short time. Consequently, attempts are currently being made to generate highly active catalytic species in situ.[3,4]

Ruthenium arene complexes are effective precursors of catalytically active unsaturated alkylidene species.[3,5–8] Noels et al. showed that activation of $[\{RuCl_2(\eta^6\text{-}p\text{-cymene})\}_2]$ by addition of a bulky phosphane and (trimethylsilyl)diazomethane gives the highly active catalyst $[RuCl_2(=CHSiMe_3)(PCy_3)]$ for ring-opening metathesis polymerization (ROMP) of cycloolefins.[5] In situ introduction of a more electron-releasing N-heterocyclic carbene increases the catalytic performance.[6] Allenylidene ruthenium arene complexes promote alkene metathesis reactions,[1a,7] and their activity has been tremendously improved by protonation to generate a highly active indenylidene species.[8]

We now disclose the in situ generation of a new ruthenium alkene metathesis catalyst, namely, an alkenylcarbene ruthenium arene species generated from $[RuCl(\eta^6\text{-arene})(PCy_3)]X$ on activation of enynes. We show that the catalyst results from a metallo-retro-ene reaction involving a coordinated allyl or alkyl propargylic ether and allows the ring-closing metathesis (RCM) of enynes and dienes [Eq. (1)]. We present a remarkable example of a smart substrate: a propargyl ether that generates in situ a catalyst for its own selective transformation.

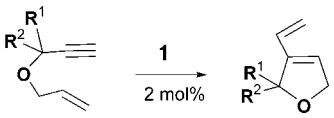

(1)

The 16-electron cationic complex $[RuCl(\eta^6\text{-}p\text{-cymene})(PCy_3)]CF_3SO_3$ (**1**), precursor of the allenylidene derivative $[RuCl(\eta^6\text{-}p\text{-cymene})(=C=C=CPh_2)(PCy_3)]CF_3SO_3$ (**2**),[7] does not show significant activity for the RCM of diallyl tosylamide (**3**; Table 1, entry 1). However, despite the fact that RCM of enynes is usually more difficult to perform than that of dienes, it was surprisingly found that complex **1** achieves excellent activity in the transformation of enynes into the corresponding alkenyl cycloalkenes under mild conditions [Eq. (1), Table 1, entries 2–6].[9] Thus, when allyl propargyl ethers **5–9** were treated with 2 mol% of **1** in CH_2Cl_2 at room temperature, alkenyl cycloalkenes **10–14** were selectively formed with a remarkable turnover frequency (TOF) of 12–47 h^{-1}. These results are just in the range of those obtained with other ruthenium-based olefin metathesis catalysts, as shown by Fürstner et al.[10] (1 mol% of catalyst, 80°C, 80–85% yield, 0.3–1 h) and Grela et al.[11] (1 mol% of catalyst, 0°C, 98% yield, 1 h). However, the lower catalytic activity for allyl propargyl tosylamide (**15**; Table 1, entry 7) confirms that allyl propargyl ethers play an important role.

It was first thought that the good catalytic activity observed was due to the fact that terminal enynes can react with **1** to form vinylidene species, as vinylidene ruthenium intermediates are moderate olefin metathesis initiators.[12]

[*] Dr. R. Castarlenas, M. Eckert, Prof. Dr. P. H. Dixneuf
Institut de chimie de Rennes
UMR 6509 CNRS-Université de Rennes
Organométalliques et Catalyse
Campus de Beaulieu, 35042 Rennes (France)
Fax: (+33) 2-2323-6939
E-mail: pierre.dixneuf@univ-rennes1.fr

[**] This work was supported by the CNRS, the Ministère de la Recherche, and the European Union through a Marie Curie Fellowship to R.C.

Supporting information for this article is available on the WWW under http://www.angewandte.org or from the author.

 © 2005 Wiley-VCH Verlag GmbH & Co. KGaA, Weinheim DOI: 10.1002/anie.200462865

Table 1: Diene and enyne RCM reactions promoted by **1** at room temperature.[a]

Entry	Substrate	Product	*t* [h]	Conv. [%][b]	TOF [h^{-1}]
1	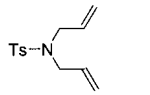 **3**	**4**	20	3	0.07
2	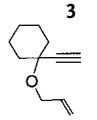 **5**	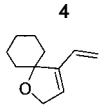 **10**	1	95	47.5
3	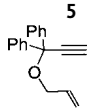 **6**	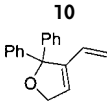 **11**	2.5	60	12.0
4	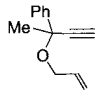 **7**	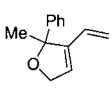 **12**	1	90	45.0
5	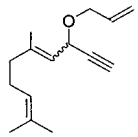 **8**	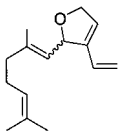 **13**	2	87	21.7
6	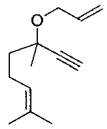 **9**	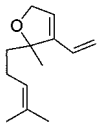 **14**	3	93	15.5
7	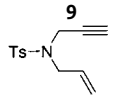 **15**	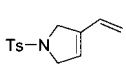 **16**	24	70	1.5

[a] [Monomer]/[Ru] = 50. [b] Determined by GC.

Table 2: Diene RCM reactions with 2% mol catalyst at room temperature.

Entry	Catalyst	Substrate	Product	*t* [h]	Conv. [%][a]	TOF [h^{-1}]
1	**17**	**3**	**4**	20	40	1
2	**18**	**3**	**4**	20	35	0.87
3	**20**	**3**	**4**	20	22	0.55
4	**21**[b]	**5**	**10**	1	99	49.50
5	**21**[b]	**3**	**4**	0.25	99	198
6	**24**[b]	**3**	**4**	0.25	95	190
7	**21**[b]	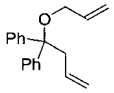 **25**	**28**	4	99	12.37
8	**21**[b]	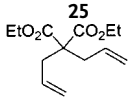 **26**	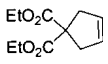 **29**	2	99	24.74
9	**21**[b]	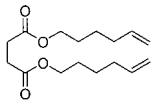 **27**	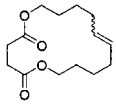 **30**	1	99	49.50

[a] Determined by GC. [b] Catalyst prepared in situ from **1** and **22** or **23**.

With the aim of confirming this hypothesis, new vinylidene derivatives [RuCl(η⁶-*p*-cymene){=C=CH(R)}(PCy_3)]CF_3SO_3 (R = Ph (**17**), CH_2Ph (**18**)) were synthesized from **1** and phenyl acetylene and benzyl acetylene, respectively [Eq. (2)].

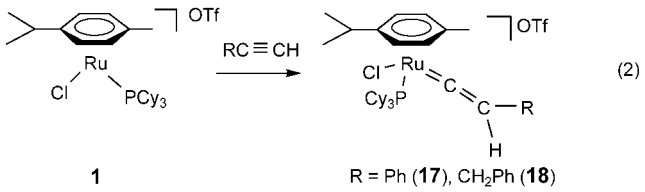

1 R = Ph (**17**), CH_2Ph (**18**) (2)

Complexes **17** and **18** are unstable at room temperature but were characterized at −30 °C. In the $^{13}C\{^1H\}$ NMR spectrum, the most interesting feature is the low-field doublets that appear at 358.3 ($^2J_{C,P}$ = 20.1 Hz, **17**) and 345.0 ppm ($^2J_{C,P}$ = 19.3 Hz, **18**), which correspond to the Ru=C carbon atom of the vinylidene moiety. However, **17** and **18** only slightly promote the RCM of diallyl tosylamide (TOF 0.87–1 h^{-1}, Table 2, entries 1 and 2) and therefore cannot explain the excellent catalytic activity displayed by complex **1** in the RCM of enynes **5**–**9**.

To elucidate the active species, a stoichiometric reaction between complex **1** and enyne **5** was carried out. After 5 min at room temperature, **5** was transformed into diene **10**, whereas cationic complex **1** apparently remained unchanged. This suggested that only a small amount of complex **1** was activated by **5** to form an undetectable highly active species that promotes RCM of the enyne. To increase the chances of observing the intermediate, the counteranion in **1** was exchanged with tetrakis[3,5-bis(trifluoromethyl)phenyl]borate (BAr^{F-}_4) to give the new cationic complex [RuCl(η⁶-*p*-cymene)(PCy_3)]BAr^F_4 (**19**; Scheme 1). The reaction of **19** with 1 equivalent of **5** was monitored by NMR spectroscopy at −30 °C. A new signal at δ = 48.1 ppm appeared in the $^{31}P\{^1H\}$ NMR spectrum showing the formation of a new complex which, on the basis of ^1H, ^{13}C, $^1H,^1H$ COSY, and $^1H,^{13}C$ HMQC and HMBC correlation experiments, was identified as alkenylcarbene complex [RuCl(η⁶-*p*-cymene){=CH−CH=$C(C_5H_{10})$}(PCy_3)]BAr^F_4 (**20**). Accompanying the signals for **20**, three multiplets at δ = 9.51, 6.25, and 6.10 ppm were observed and shown to correspond to the presence of acrolein.

A rational mechanism for the formation of the alkenylcarbene complex is proposed in Scheme 1. From the initially formed vinylidene species, a pericyclic retro-ene cleavage[13] generates the alkenylcarbene complex and acrolein. It has been shown that thermolysis of propargyl ethers at 350–450 °C leads to allenes and carbonyl compounds by a retro-ene transformation.[14] Mediation of a transition metal is expected to reduce the activation energy for the metallo-retro-ene reaction[15] and thus allow it to occur at low temperature (−30 °C).

The catalytic activity of the relatively stable BAr^{F-}_4-containing complex **20** in the transformation of diene **3** into **4** remains moderate (Table 2, entry 3), likely owing to the inhibition by BAr^{F-}_4. Indeed, the nature of the escorting anion

 © 2005 Wiley-VCH Verlag GmbH & Co. KGaA, Weinheim

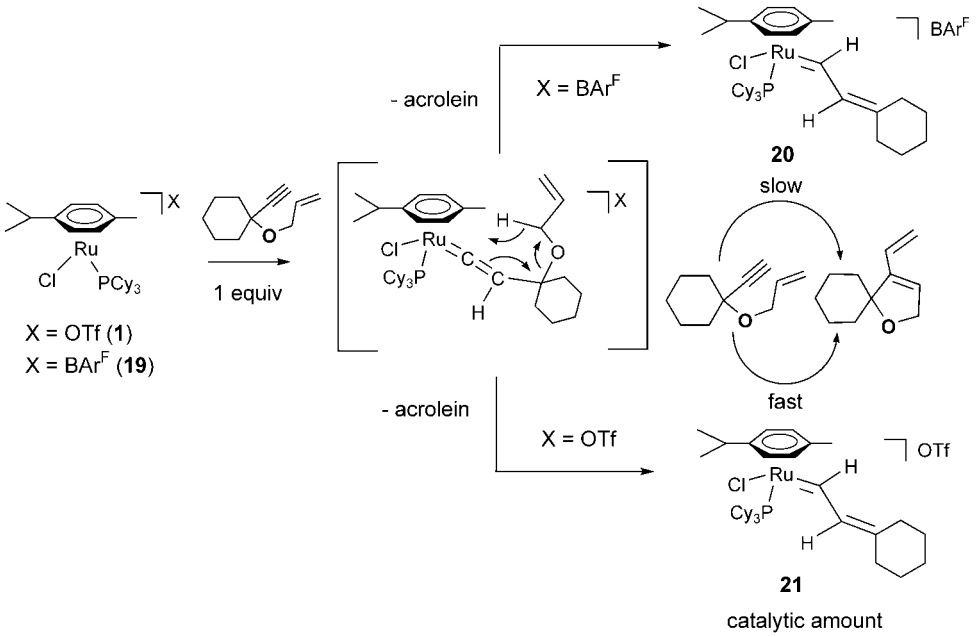

Scheme 1. Formation of ruthenium alkenylcarbene complexes by a metallo-retro-ene reaction.

in ruthenium allenylidene complex **2** drastically influences its catalytic activity in alkene metathesis according to the sequence $OTf^- > PF_6^- > BPh_4^- > BAr^{F-}_4$.[7]

Analogously to the formation of **20** from **19**, the reaction of triflate-containing complex **1** with enynes **5–9** is thus expected to generate ruthenium alkenylcarbene triflate catalyst **21**, which is much more active than the BAr^F_4 analogue **20** (Scheme 1). In fact, in this case the ruthenium alkenylcarbene **21** could not be isolated or characterized from the reaction of **1** with enyne **5**. To prove that the vinylcarbene intermediate can be generated by a retro-ene reaction independent of the enyne substrate, stoichiometric activation of the propyl propargyl ethers of type $CH_3CH_2CH_2OCR_2C{\equiv}CH$ ($R^2 = C_5H_{10}$ (**22**), R = Ph (**23**)), which cannot give rise to enyne RCM reactions, was attempted with **1**. At −30 °C in dichloromethane the reaction led in this case to formation of propanal and the triflate-containing alkenylcarbene complexes $[RuCl(\eta^6\text{-}p\text{-cymene})(=CH{-}CH{=}CR_2)(PCy_3)]CF_3SO_3$ ($R^2 = C_5H_{10}$ (**21**), R = Ph (**24**), Scheme 2). Both complexes **21** and **24** decompose at room temperature but could be characterised at −30 °C by NMR experiments. Note that

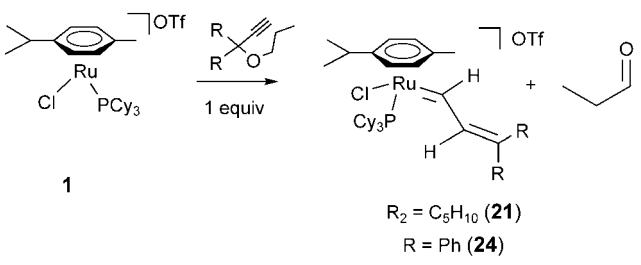

Scheme 2. Triflate alkenylcarbene catalysts generated from **1** and propyl propargyl ethers.

complexes **21** and **24** could not be observed on reaction of **1** with enynes **5** or **6** owing to their high catalytic activity toward these enynes.

Addition of enyne **5** to a catalytic amount of **21**, generated in situ by reaction of **1** and **22**, led over 1 h at room temperature to complete formation of **10** (Table 2, entry 4) and confirmed the formation of **21** from **1** and **5**.

These in situ generated catalyst systems **21** and **24** tremendously increase olefin metathesis activity for formation of **4** from diene **3** in comparison with parent complex **1** (Table 1, entry 1 versus Table 2, entries 5 and 6). Moreover, dienes **25–27**, which are almost inert in the presence of **1**, are completely converted into **28–30** by addition of 2 mol % of **21** at room temperature (Table 2, entries 7–9).

These new 18-electron, ionic alkenylcarbenes $[RuCl(\eta^6\text{-}p\text{-cymene})\{=CH{-}CH{=}CR_2\}(PCy_3)]X$ strongly differ in their nature and synthesis with the neutral, 16-electron $[RuCl_2(=CH{-}CH{=}CPh_2)(PCy_3)_2]$ complex arising from diphenyl cyclopropene[16] and diphenyl propargylic chloride.[17]

The above simple reaction of ruthenium complex **1** with allyl or propyl propargylic ethers is a simple and novel method of preparing ruthenium alkenylcarbene complexes and involves a metal-assisted retro-ene reaction. The catalytic transformation of allyl propargylic ethers is a remarkable example of a substrate that transforms in situ an inert ruthenium complex into an active catalyst that is then able to convert the parent enyne into a highly reorganized alkenylcycloalkene. This new method of generating an active alkene metathesis initiator from alkyl propargylic ethers has potential for the catalytic transformation of a variety of substrates by simple variation of propargyl ethers and electron-donor ligands in complex **1**.

 © 2005 Wiley-VCH Verlag GmbH & Co. KGaA, Weinheim

Experimental Section

Full experimental details and spectroscopic data are available in the Supporting Information. Coupling constants are given in Hz.

17, **18**: An orange solution of **1** (50 mg, 0.071 mmol) in CD_2Cl_2 (0.5 mL) in an NMR tube under argon atmosphere at 213 K was treated with phenylacetylene (9 μL, 0.081 mmol) or benzylacetylene (11 μL, 0.088 mmol). The color changed immediately to dark orange, and, after sealing the NMR tube, measurements were made. Selected data for **17**: ^{1}H NMR (300 MHz, CD_2Cl_2, 243 K): $\delta = 5.93$ ppm (s, 1H, =C=CH). ^{13}C{^{1}H} NMR (75.4 MHz, CD_2Cl_2, 243 K): $\delta = 358.3$ (d, $J_{C,P} = 20.1$, Ru=C), 118.4 ppm (s, Ru=C=*C*). Selected data for **18**: ^{1}H NMR (300 MHz, CD_2Cl_2, 243 K): $\delta = 5.17$ (dd, $J_{H,H} = 9.9$, 6.8, 1H, =C=CH), 3.95 (dd, $J_{H,H} = 14.6$, 6.8, 1H, =C(C*H*$_2$Ph)), 3.60 ppm (dd, $J_{H,H} = 14.6$, $J_{H,H} = 9.9$, 1H, =C(C*H*$_2$Ph)). ^{13}C{^{1}H} NMR (75.4 MHz, CD_2Cl_2, 243 K): $\delta = 345.0$ (d, $J_{C,P} = 19.3$ Hz, Ru=C), 112.1 ppm (s, Ru=C=*C*).

20: A violet solution of **19** (300 mg, 0.21 mmol) in CH_2Cl_2 (10 mL) at 243 K was treated with allyl 1-ethynylcyclohexyl ether (40 mg, 0.24 mmol), and the reaction mixture was stirred for 2 h. The resulting orange solution was evaporated to dryness below 243 K, and the residue was washed three times with cold pentane/diethyl ether (5/1 mL). The yellow solid was dried under vacuum (270 mg, 84% yield). Selected NMR data: ^{1}H NMR (300 MHz, CD_2Cl_2, 243 K): $\delta = 16.28$ (d, $J_{H,H} = 14.1$, 1H, Ru=CH), 8.12 ppm (d, $J_{H,H} = 14.1$, 1H, Ru=CH–C*H*=). ^{13}C{^{1}H} NMR, (75.4 MHz, CD_2Cl_2, 243 K): $\delta = 302.3$ (d, $J_{C,P} = 18.7$, Ru=C), 173.8 ppm (s, =*C*(C$_5$H$_{10}$)), 146.3 ppm (s, C–*C*H=C).

21, **24**: An orange solution of **1** (50 mg, 0.071 mmol) in CD_2Cl_2 (0.5 mL) in an NMR tube under argon atmosphere at 213 K was treated with propyl 1-ethynylcyclohexyl ether (**22**; 12 mg, 0.072 mmol) or propyl 1,1-diphenylethynyl ether (**23**; 18 mg, 0.072 mmol). Measurements were made immediately. Selected data for **21**: ^{1}H NMR (300 MHz, CD_2Cl_2, 243 K): $\delta = 16.12$ (d, $J_{H,H} = 13.8$, 1H, Ru=CH), 8.10 ppm (d, $J_{H,H} = 13.8$, 1H, Ru=CH–C*H*=). ^{13}C{^{1}H} NMR (75.4 MHz, CD_2Cl_2, 243 K): $\delta = 299.9$ (d, $J_{C,P} = 17.4$, Ru=C), 172.5 (s, =*C*(C$_5$H$_{10}$)), 147.2 ppm (s, C–*C*H=C). Selected data for **24**: ^{1}H NMR (300 MHz, CD_2Cl_2, 243 K): $\delta = 15.28$ (d, $J_{H,H} = 13.7$, 1H, Ru=CH), 8.56 ppm (d, $J_{H,H} = 13.7$, 1H, Ru=CH–C*H*=C). ^{13}C{^{1}H} NMR (75.4 MHz, CD_2Cl_2, 243 K): $\delta = 300.1$ (d, $J_{C,P} = 19.5$, Ru=C), 159.2 (s, =*C*Ph$_2$), 146.4 ppm (s, C–*C*H=C).

Received: December 9, 2004
Published online: March 22, 2005

Keywords: ene reaction · enynes · homogeneous catalysis · metathesis · ruthenium

[1] Recent reviews on alkene metathesis: a) R. Castarlenas, C. Fischmeister, C. Bruneau, P. H. Dixneuf, *J. Mol. Catal. A* **2004**, *213*, 31–37; b) R. R. Schrock, A. H. Hoveyda, *Angew. Chem.* **2003**, *115*, 4740–4782; *Angew. Chem. Int. Ed.* **2003**, *42*, 4592–4633; c) S. J. Connon, S. Blechert, *Angew. Chem.* **2003**, *115*, 1944–1968; *Angew. Chem. Int. Ed.* **2003**, *42*, 1900–1923; d) T. M. Trnka, R. H. Grubbs, *Acc. Chem. Res.* **2001**, *34*, 18–29.

[2] M. S. Sanford, J. A. Love, R. H. Grubbs, *J. Am. Chem. Soc.* **2001**, *123*, 6543–6554.

[3] a) B. Çetinkaya, S. Demir, I. Özdemir, L. Toupet, D. Séméril, C. Bruneau, P. H. Dixneuf, *Chem. Eur. J.* **2003**, *9*, 2323–2330; b) R. Castarlenas, I. Alaoui-Abdallaoui, D. Séméril, B. Mernari, S. Guesmi, P. H. Dixneuf, *New J. Chem.* **2003**, *27*, 6–8; c) A. Hafner, A. Mühlebach, P. A. van der Schaaf, *Angew. Chem.* **1997**, *109*, 2213–2216; *Angew. Chem. Int. Ed. Engl.* **1997**, *36*, 2121–2124.

[4] a) B. Schmidt, *Eur. J. Org. Chem.* **2004**, 1865–1880; b) J. Le Nôtre, A. A. Martínez, P. H. Dixneuf, C. Bruneau, *Tetrahedron* **2003**, *59*, 9425–9432; c) H. Li, W. F. Zhang, Y. Q. Wang, B. L. He, *Polym. Adv. Technol.* **2003**, *14*, 226–231; d) R. Castarlenas, C. Fischmeister, P. H. Dixneuf, *New J. Chem.* **2003**, *27*, 215–217; e) C. van Schalkwyk, H. C. M. Vosloo, J. M. Botha, *J. Mol. Catal. A* **2002**, *190*, 185–195.

[5] A. Demonceau, A. W. Stumpf, E. Saive, A. F. Noels, *Macromolecules* **1997**, *30*, 3127–3136.

[6] D. Séméril, C. Bruneau, P. H. Dixneuf, *Helv. Chim. Acta* **2001**, *84*, 3335–3341.

[7] A. Fürstner, M. Liebl, C. W. Lehmann, M. Picquet, R. Kunz, C. Bruneau, D. Touchard, P. H. Dixneuf, *Chem. Eur. J.* **2000**, *6*, 1847–1857.

[8] R. Castarlenas, P. H. Dixneuf, *Angew. Chem.* **2003**, *115*, 4662–4665; *Angew. Chem. Int. Ed.* **2003**, *42*, 4524–4527.

[9] For recent reviews on enyne metathesis, see a) S. T. Diver, A. J. Giessert, *Chem. Rev.* **2004**, *104*, 1317–1382; b) C. S. Poulsen, R. Madsen, *Synthesis* **2003**, 1–18; c) D. Séméril, C. Bruneau, P. H. Dixneuf, *Adv. Synth. Catal.* **2002**, *344*, 585–595.

[10] A. Fürstner, L. Ackermann, B. Gabor, R. Goddard, C. W. Lehmann, R. Mynott, F. Stelzer, O. R. Thiel, *Chem. Eur. J.* **2001**, *7*, 3236–3253.

[11] K. Grela, S. Harutyunyan, A. Michrowska, *Angew. Chem.* **2002**, *114*, 4210–4212; *Angew. Chem. Int. Ed.* **2002**, *41*, 4038–4040.

[12] a) T. Opstal, F. Verpoort, *J. Mol. Catal. A* **2003**, *200*, 49–61; b) H. Katayama, H. Urushima, F. Ozawa, *J. Organomet. Chem.* **2000**, *606*, 16–25; c) H. Katayama, T. Yoshida, F. Ozawa, *J. Organomet. Chem.* **1998**, *562*, 203–206.

[13] a) J. Dubac, A. Laporterie, *Chem. Rev.* **1987**, *87*, 319–334; b) W. Oppolzer, V. Snieckus, *Angew. Chem.* **1978**, *90*, 506–516; *Angew. Chem. Int. Ed. Engl.* **1978**, *17*, 476–486.

[14] a) P. Várnai, G. M. Keserü, *J. Org. Chem.* **1996**, *61*, 5831–5836; b) A. Viola, J. J. Collins, N. Filipp, *Tetrahedron* **1981**, *37*, 3765–3811.

[15] W. Oppolzer, *Angew. Chem.* **1989**, *101*, 39–53; *Angew. Chem. Int. Ed. Engl.* **1989**, *28*, 38–52.

[16] S. T. Nguyen, L. K. Johnson, R. H. Grubbs, J. W. Ziller, *J. Am. Chem. Soc.* **1992**, *114*, 3974–3975.

[17] T. E. Wilhelm, T. R. Belderrain, S. N. Brown, R. H. Grubbs, *Organometallics* **1997**, *16*, 3867–3869.

 © 2005 Wiley-VCH Verlag GmbH & Co. KGaA, Weinheim

Chelating Ligands

Self-Assembly of an Amphiphilic Iron(III) Chelator: Mimicking Iron Acquisition in Marine Bacteria

*Mariana Apostol, Paul Baret, Guy Serratrice, Jacques Desbrières, Jean-Luc Putaux, Marie-José Stébé, Dominique Expert, and Jean-Louis Pierre**

Iron is one of the most common elements on Earth, but its availability to living organisms is limited because of its extremely low solubility. Siderophores are low-molecular-weight iron(III) chelators that were evolved by microorganisms for the uptake of physiologically essential iron.[1] Among the mechanisms proposed for iron solubilization and transport into cells,[2] the self-assembly of amphiphilic siderophores from marine bacteria observed by Butler et al.[3] is a noteworthy process. Hydrophilic siderophores (marinobactins and aquachelins) with polar peptidic head groups and hydrophobic fatty acid tails are surface-active amphiphiles that form self-assembled structures. We thought that the biologically inspired use of this strategy might allow the resolution of the crucial problem of the hydrophilic/lipophilic balance encountered with abiotic siderophores designed for iron nutrition.[4] Amphiphilic iron chelators may also offer a new approach in iron chelation therapy.

Herein, we present a preliminary report on the self-assembly properties of amphiphilic chelators and their iron complexes, and discuss the first results concerning iron nutrition of *Erwinia chrysanthemi* and some mutants defective in the production of one or both of its siderophores. Three synthetic catechol-based chelators were investigated (Scheme 1).

The two monopodal ligands L^a and L^b were synthesized by reaction of 2,3-dimethoxybenzoyl chloride with dodecylamine and octylamine, respectively, followed by a deprotection step with BBr_3. The tripodal ligand L^T was obtained from our previously described[5] tripodal precursor 2,2,2-tris[3-(2,3-dimethoxybenzamido)propyl]acetic acid (by reaction of the acid chloride with hexadecylamine and then deprotection of the catechol groups). The ligands were characterized by mass spectrometry and ^1H and ^{13}C NMR spectroscopy (see Supporting Information). The pH-dependent equilibria of the ligand species and their ferric complexes were determined by potentiometric and spectrophotometric titrations to obtain their net charge at physiological pH, which tunes the amphiphilic properties.[6–8] The deprotonation constants of the ferric complexes $pK_{a,[Fe(LH)]}$, $pK_{a,[Fe(LH_2)]}$, and $pK_{a,[Fe(LH_3)]}$ are 7.9, 7.4, and 6.4, respectively (the fully deprotonated ligand is denoted L^{6-}), which indicates that $[Fe(L^TH)]^{2-}$ and $[Fe(L^TH_2)]^-$ are the major species at pH 7.4. The UV/Vis spectrum of the $[Fe^{III}(L^T)]$ system at pH 7.4 ($\lambda_{max} = 540$ nm, $\varepsilon = 4000\,M^{-1}cm^{-1}$) is similar to that for the $[Fe^{III}(CacCAM)]$ complex previously described,[5] which indicates a mixed salicylate (coordination with carbonyl and *o*-hydroxy oxygen atoms) and catecholate coordination. The pFe value of CacCAM is 27.5 at pH 7.4 ([L] = 10 μM, [Fe] = 1 μM). A similar value could be expected for ligand L^T, since we have shown that a change of backbone does not significantly alter the iron chelating efficiency of the ligand.[5] Notably, at pH 9 the spectral parameters ($\lambda_{max} = 490$ nm, $\varepsilon = 4300\,M^{-1}cm^{-1}$) indicate a tris-catecholate coordination. For ligands L^a or L^b, the spectrum of the ferric complexes at pH 7.4 ($\lambda_{max} = 540$ nm, $\varepsilon = 3300\,M^{-1}cm^{-1}$) is characteristic of a bis-salicylate coordination, which corresponds to the $[Fe(LH)_2]^+$ species. Despite an expected lower pFe value for ligands L^a or L^b compared with L^T (for example, pFe = 15 at pH 7.4, [L] = 10 μM, [Fe] = 1 μM for the dimethylamido derivative of catechol[9]), solutions of the ferric complexes of ligands L^a or L^b are very stable and no ferric hydroxide appears after several days.

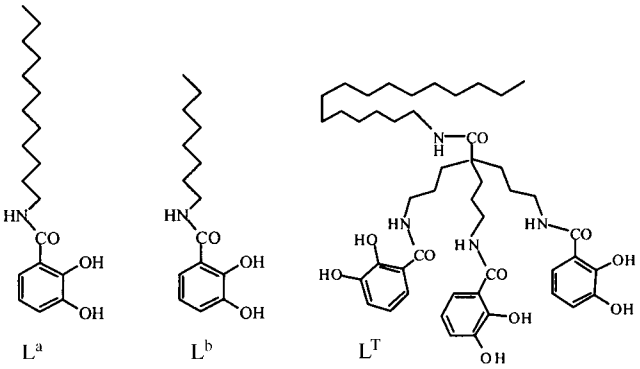

Scheme 1. Chemical formulae of the synthetic amphiphilic ligands.

In water/methanol (95/5, v/v) solution containing 3-(*N*-morpholino)propanesulfonic acid (MOPS) buffer at pH 7.4, the free ligands and their iron complexes exhibit tensioactive properties with a critical micelle concentration (CMC) of $< 10^{-5}$ M.[10] The low CMC values of the iron-free ligands are in the same range as that for marinobactin.[3a] Dynamic light-scattering studies[11] on solutions (10^{-4} M) of the Fe^{III} complexes of ligands L^a, L^b, and L^T in the same medium revealed the presence of spherical particles of diameter 200–250, 100–110, and 130 nm, respectively. In all cases the distribution is rather broad (polydispersity index of 0.2–0.3). The free ligands, which do not scatter light, are probably limited to micellar assembly. Similar observations have been made for the siderophores from marine bacteria.[3a] Cryo-transmission

[*] M. Apostol, Prof. P. Baret, Prof. G. Serratrice, Prof. J.-L. Pierre
LEDSS UMR CNRS 5616, Université J. Fourier
BP 53, 38041 Grenoble, Cedex 9 (France)
Fax: (+33) 4-7651-4836
E-mail: jean-louis.pierre@ujf-grenoble.fr
Prof. J. Desbrières, Dr. J.-L. Putaux
CERMAV UPR CNRS 5301, Université J. Fourier
BP 53, 38041 Grenoble, Cedex 9 (France)
Prof. M.-J. Stébé
SRSMC, UMR 7565 CNRS-UHP Nancy 1
BP 239, 54506 Vandoeuvre-les-Nancy cedex (France)
Dr. D. Expert
INRA/CNRS
16 rue Claude Bernard, 75231 Paris (France)

Supporting information for this article is available on the WWW under http://www.angewandte.org or from the author.

 © 2005 Wiley-VCH Verlag GmbH & Co. KGaA, Weinheim DOI: 10.1002/anie.200462841

electron microscopy (cryo-TEM) images of 1.4×10^{-3} M solutions of the Fe^{III} complexes showed polydisperse spherical particles with diameters ranging from 100 to 250 nm.[12] An example is given in Figure 1b for the $[Fe^{III}(L^T)]$ system. The

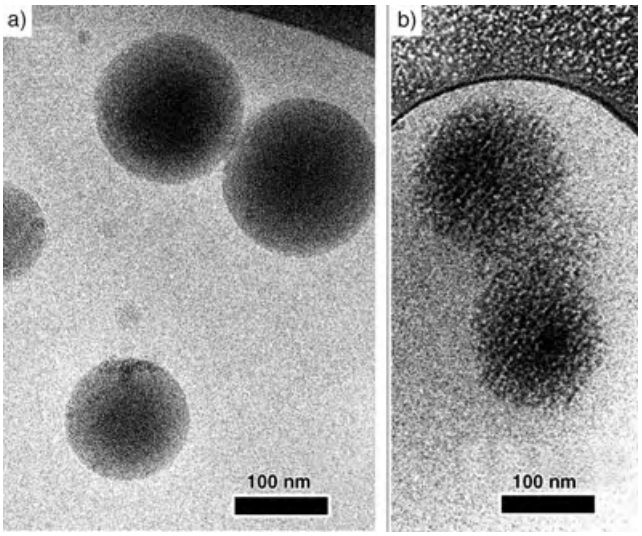

Figure 1. Cryo-TEM images of $[Fe^{III}(L^n)]$ complexes (10^{-3} M) in water/methanol (95/5, v/v) solution at pH 7.4 (MOPS buffer) embedded in vitreous ice;[10] a) ligand L^a 3 h after addition of 1% octanol and b) ligand L^T.

micrographs depicted in Figure 1 compare well with those of Fe^{III}-marinobactin vesicles.[3a] In the experiment depicted in Figure 1a, octanol (1 vol%) was added to the $[Fe^{III}(L^a)]$ solution to favor structuration of the particles. Successive cryoelectron micrographs allowed visualization of the evolution of the aggregates with time: vesicles of octanol first appeared at the surface of the aggregates (see Supporting Information) and after several hours perfectly spherical particles were observed. The contrast in the images of the particles (clear external surface and dark interior) suggests that they are filled. Furthermore, this observation indicates an aggregation of the molecules of the complexes, in agreement with an external hydrophilic surface as schematically depicted in reference [3a].

The ligands studied herein are good models for the physicochemical properties of the siderophores from marine bacteria. For a better understanding of the biological relevance of the self-assembly process (in correlation with the interesting discussion in reference [3a]), studies of bacterial iron nutrition were performed with *E. chrysanthemi*.[13–15] Preliminary results show that: 1) the iron aggregates allow nutrition; 2) the best results are obtained with the iron complex of ligand L^a; 3) the natural siderophore way is used when available (wild-type bacteria); and 4) nutrition is allowed in mutants without the siderophore way. Moreover, we showed that 70–75% of iron transport involves the TonB-dependent receptors Fct and/or 88 Da with Cbu for the inner membrane (see ref. [14] for a description of the iron transport system in *E. chrysanthemi*). For the remaining 25–30% of iron transport, it can be suggested that the aggregate merges with the outer membrane, which releases iron in the periplasm and then Yfe internalizes iron (Yfe is not TonB-dependent).

Further experiments are needed to reach more definite conclusions about the precise role of the self-assembly process in iron acquisition. This process, which is evidenced in marine bacteria, may allow new perspectives for applications in iron nutrition and for iron chelation therapy.

Received: December 7, 2004
Published online: March 16, 2005

Keywords: amphiphiles · iron · self-assembly · siderophores · vesicles

[1] J. B. Neilands, *J. Biol. Chem.* **1995**, *270*, 26723.
[2] A. Stinzi, C. Barnes, J. Xu, K. N. Raymond, *Proc. Natl. Acad. Sci. USA* **2000**, *97*, 10691.
[3] a) J. S. Martinez, G. P. Zhang, P. D. Holt, H.-T. Jung, C. J. Carrano, M. G. Haygood, A. Butler, *Science* **2000**, *287*, 1245; b) K. Barbeau, E. L. Rue, K. W. Bruland, A. Butler, *Nature* **2001**, *413*, 409; c) G. Xu, J. S. Martinez, J. T. Groves, A. Butler, *J. Am. Chem. Soc.* **2002**, *124*, 13408; d) J. S. Martinez, J. N. Carter-Franklin, E. Mann, J. D. Martin, M. G. Haygood, A. Butler, *Proc. Natl. Acad. Sci. USA* **2003**, *100*, 3754.
[4] a) D. Imbert, P. Baret, D. Gaude, I. Gautier-Luneau, G. Gellon, F. Thomas, G. Serratrice, J.-L. Pierre, *Chem. Eur. J.* **2002**, *8*, 1091; b) L. Yun-Ming, M. J. Miller, U. Möllmann, *Biometals* **2001**, *14*, 153; c) J. I. Wirgrau, A. L. Crumbliss, *Inorg. Chem.* **2003**, *42*, 5762.
[5] D. Imbert, D. Thomas, P. Baret, G. Serratrice, D. Gaude, J.-L. Pierre, J.-P. Laulhère, *New J. Chem.* **2000**, *24*, 281.
[6] The ligands and their ferric complexes have low solubilities in aqueous solution, therefore the potentiometric titrations were carried out in water/methanol (50/50, v/v; ligand concentration 0.5 mM) and the spectrophotometric titrations in water/methanol (95/5, v/v; ligand concentration 0.1 mM). The methods have been previously described.[4a] Data analysis of the potentiometric and spectrophotometric titrations was performed using the Hyperquad[7] and Letagrop[8] programs. The spectrophotometric titration of a mixture of Fe^{III} and ligands L^a or L^b in a 1:3 molar ratio was carried out over the pH range 5–12.
[7] P. Gans, A. Sabatini, A. Vacca, *Talanta* **1996**, *43*, 1739.
[8] a) L. G. Sillen, *Acta Chem. Scand.* **1964**, *18*, 1085; b) L. G. Sillen, B. Warnqvist, *Ark. Kemi* **1968**, *31*, 377.
[9] T. M. Garrett, P. W. Miller, K. N. Raymond, *Inorg. Chem.* **1989**, *28*, 128.
[10] Surface tension measurements were carried out with a drop tensiometer (Tracker; I.T. Concept, Longessagne, France) at 25 °C, which allowed the determination of the interfacial tension by analyzing the axial symmetric shape (Laplacian profile) of the rising air drop in solution. The CMC values were estimated from the intersection of the extrapolated linear portions of the plot of surface tension versus ligand or complex concentration.
[11] The size of the particles was measured by quasielastic light scattering. The movement of particles in suspension is characterized by a diffusion coefficient, and the particles undergo Brownian motion. A Malvern zetasizer 300HsA instrument was used at a scattering angle of 90°. This apparatus includes a 5-mW He–Ne laser that operates at a wavelength of 633 nm. The detector is an avalanche photodiode and the numerical correlator (type 7132CN with 256 channels) is controlled by the AutoSizer software version XY. The sample is contained in a flow-through cell kept at 23 °C. The data were analyzed by the CONTIN method. The translational diffusion coefficient is

 © 2005 Wiley-VCH Verlag GmbH & Co. KGaA, Weinheim

related to particle diameter using Stoke's diffusion law and the Einstein equation for Brownian motion.
[12] Thin liquid films of the suspensions were fast-frozen in liquid ethane at −171 °C with a method described by C. Poncet-Legrand, D. Cartalade, J.-L. Putaux, V. Cheynier, A. Vernhet, *Langmuir* **2003**, *19*, 10563. The samples were mounted in a Gatan 626 cryoholder at −180 °C, transferred into a Philips CM200 "cryo" transmission electron microscope, and observed under low-dose conditions at low temperature. Images were recorded on Kodak SO163 films.
[13] We used the Gram-negative *Erwinia chrysanthemi*, which produces two siderophores upon iron deficiency: chrysobactin (a monocatecholate) and achromobactin, which is produced only when chrysobactin synthesis is repressed.[14] The wild-type *E. chrysanthemi*, a chrysobactin-negative mutant, and a chrysobactin–achromobactin–tonB mutant were used. Iron complex solutions (0.5–50 mM) in culture medium were employed (iron complexes were added at the beginning of iron carency). The experimental protocol for iron nutrition is described in ref. [15].
[14] D. Expert, *Annu. Rev. Phytopathol.* **1999**, *37*, 307; and references therein.
[15] L. Rauscher, D. Expert, B. F. Matzanke, A. X. Trautwein, *J. Biol. Chem.* **2002**, *277*, 2385.

 © 2005 Wiley-VCH Verlag GmbH & Co. KGaA, Weinheim

Donor–Acceptor Systems

Circular Dichroism of a Chiral Tethered Donor–Acceptor System: Enhanced Anisotropy Factors in Charge-Transfer Transitions by Dimer Formation and by Confinement**

Tadashi Mori and Yoshihisa Inoue**

Charge-transfer (CT) interactions between a donor and an acceptor[1] are an important class of weak interactions that have been extensively exploited in molecular assemblies such as rotaxanes, catenanes, and molecular machines and devices.[2] A large number of tethered donor–acceptor pairs, or CT dyads, have been prepared[3] in the study of electron-transfer mechanisms and also in the development of molecular devices, such as nonlinear optical materials.[4] Chiral CT interaction is expected to be a useful tool not only for developing unique chiral molecular devices, but also for understanding and controlling molecular recognition phenomena, especially in solution. Therefore, optical rotatory dispersion and circular dichroism of optically active donor–acceptor complexes have already been examined for CT complexes that involve n–π* transitions.[5] Herein, we report the circular dichroism of intra- and intermolecular CT complexes with π–π* transitions, and also novel strategies for controlling the anisotropy factor by dimer formation and by confinement.

We chose 2,6-dimethoxynaphthalene and 4-cyano-*N*-methylpyridinium as a donor–acceptor pair, since these compounds possess low oxidation and reduction potentials ($E_{ox} = 1.1$–1.3 and $E_{red} = -0.64$ V versus the saturated calomel electrode (SCE), respectively)[6] and are expected to form a strong CT complex in solution. By linking these components with a trimethylene tether, we obtained CT dyad **1** as the BF_4^- salt, which was then subjected to electronic absorption (UV/Vis) and circular dichroism (CD) spectroscopy to study the CT complexation behavior and to elucidate the chiroptical properties of the representative CT complex(es) formed under a variety of conditions (Scheme 1).

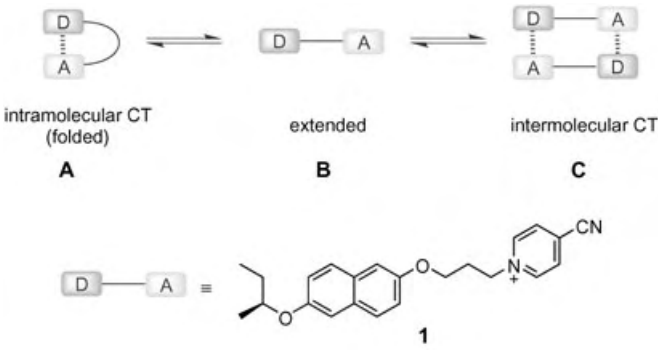

Scheme 1. Modes of CT complexation of the tethered chiral donor–acceptor dyad **1**.

The UV/Vis spectrum of dyad **1**, measured in dichloromethane at 25 °C, was almost superimposable on a sum of the spectra of the component donor and acceptor units, but exhibited a very weak band at 420 nm, which is assigned to a CT transition. An independent spectral titration of the intermolecular complex formation of 4-cyano-*N*-methylpyridinium with 2,6-dimethoxynaphthalene at varying concentrations also gave a CT band at comparative wavelengths. A Benesi–Hildebrand analysis[7] of the spectral titration results indicates the formation of a 1:1 complex with an association constant ($K_{CT} = 0.48\ M^{-1}$) and spectral properties ($\lambda_{max} =$ 420 nm, $\varepsilon_{CT} = 450\ M^{-1}cm^{-1}$) comparable to those reported for analogous nonchiral donor–acceptor pairs.[8] In contrast, the intensity of the CT band of **1** was linearly proportional to the concentration of **1** (at least up to 10 mM), which unequivocally indicated the intramolecular character of the CT complex observed. A face-to-face stacked complex with a

[*] Dr. T. Mori
Department of Molecular Chemistry
Graduate School of Engineering, Osaka University
2-1 Yamada-oka, Suita 565-0871 (Japan)
Fax: (+81) 6-6879-7923
E-mail: tmori@chem.eng.osaka-u.ac.jp
Prof. Dr. Y. Inoue
The Entropy Control Project
ICORP, JST
4-6-3 Kamishinden, Toyonaka 560-0085 (Japan)
Fax: (+81) 6-6836-1636
E-mail: inoue@chem.eng.osaka-u.ac.jp

[**] Financial support of this work by a Grant-in-Aid for Scientific Research from the Ministry of Education, Culture, Sports, Science, and Technology of Japan (No. 16750034, to T.M.) is gratefully acknowledged.

Supporting information for this article is available on the WWW under http://www.angewandte.org or from the author.

 © 2005 Wiley-VCH Verlag GmbH & Co. KGaA, Weinheim DOI: 10.1002/anie.200462071

folded structure (Scheme 1, folded monomer **A**) is probably formed upon the intramolecular CT interaction of **1**, as judged from the ROESY spectrum of **1** in CD_2Cl_2 at 25 °C (see the Supporting Information). A similar conformation was reported for the intermolecular CT complex of 2,6-dimethoxynaphthalene with methyl viologen in an X-ray crystallographic study.[9]

The UV/Vis spectrum of **1** showed a dramatic temperature dependence, particularly at temperatures lower than −50 °C; as the temperature decreased, a CT band at 480 nm became apparent. The dependency of the absorbance of the CT band on concentration (Figure 1), as well as the DFT calculations[10] (Figure 2), indicate that the origin of this CT band is the formation of an intermolecular 1:1 dimer in a head-to-tail orientation, in which two sets of donor–acceptor interactions are involved (Scheme 1, dimer **C**).

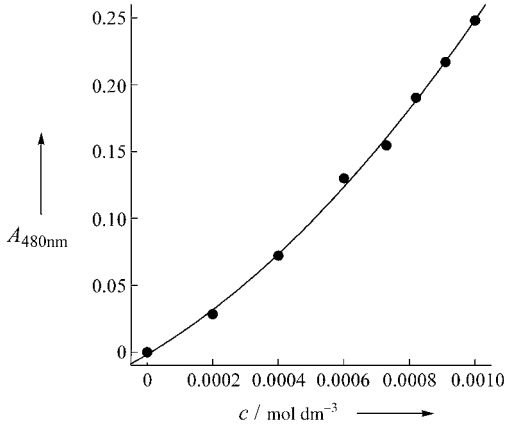

Figure 1. Experimental (●) and theoretical (——) concentration dependence of the absorbance of the CT band (at 480 nm) of dyad **1** in dichloromethane at −95 °C. The nonlinear least-squares fit revealed the dimeric nature of the CT complexation ($K = 3160\ M^{-1}$).

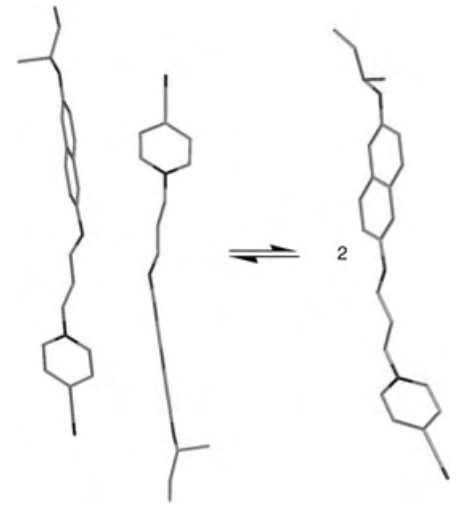

Figure 2. DFT-optimized structures of dimeric and monomeric dyad **1**. All calculations were performed with the Gaussian 98 package at the B3LYP/6-31G(d) level. Hydrogen atoms are omitted for clarity.

CD spectroscopy was also performed to elucidate the effects of the different conformation and association states **A**–**C** (Scheme 1) on the chiroptical properties of dyad **1**. A solution of **1** in dichloromethane (1 mM) showed only a weak positive CD for the ^1L_b transition of the naphthalene moiety at around 320 nm (Figure 3, trace a), which is in good agreement with the well-documented benzene sector rule.[11] The obtained *g* factor is extremely small, as low as 8×10^{-5}. However, this seems reasonable for such a chromophore that carries the smallest chiral auxiliary attached through a flexible ether linkage. Furthermore, no appreciable CT band was observed under the conditions employed. We may conclude,

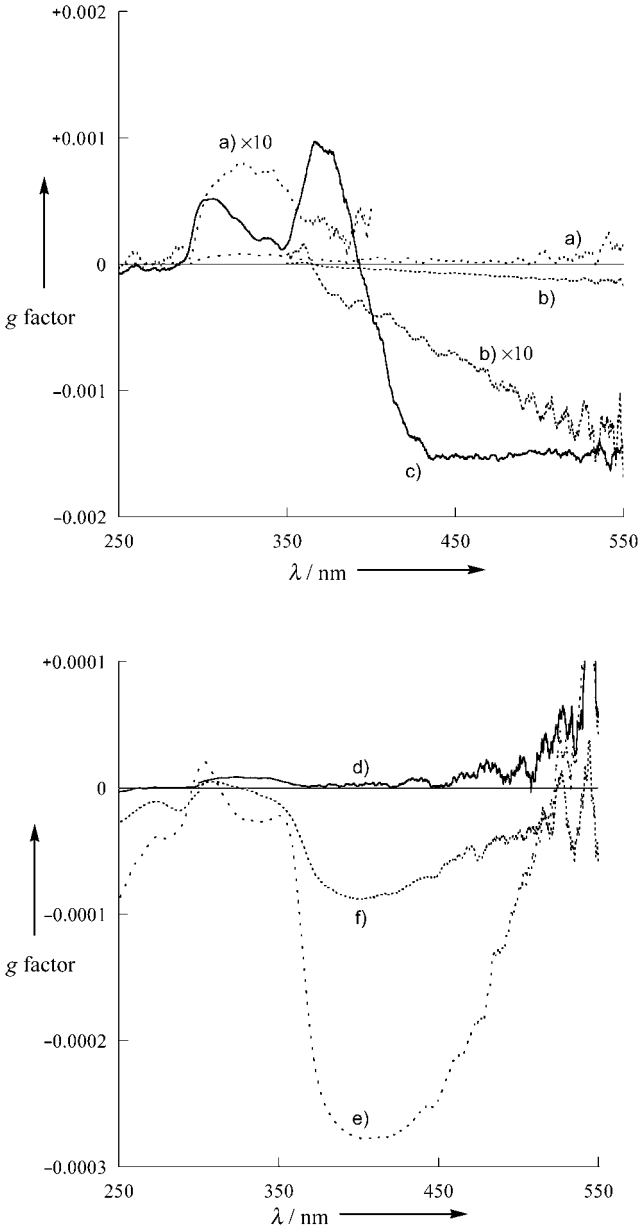

Figure 3. Anisotropy (*g*) factor profiles of **1** under different conditions: a) 1 mM in CH_2Cl_2 at 25 °C; b) 10 mM in MeCN at 25 °C; c) 1 mM in CH_2Cl_2 at −95 °C (intensities corrected for the actual concentration of dimeric species: 0.34 mM); d) 1 mM in MeOH at 25 °C, for comparison with (e) and (f); e) 1 mM in water containing 5 mM β-cyclodextrin at 25 °C; f) 1 mM in water containing 5 mM γ-cyclodextrin at 25 °C.

 © 2005 Wiley-VCH Verlag GmbH & Co. KGaA, Weinheim

therefore, that extended monomer **B** is the dominant species at a concentration of 1 mM at 25 °C.

At a higher concentration (10 mM in acetonitrile), the CD spectral behavior of **1** changed significantly; a very weak CD was observed in the ^1L_b region (300–350 nm) and an apparent negative CD in the CT transition region (Figure 3, trace b). Although we employed acetonitrile as the solvent of choice because of the lower solubility of **1** in less polar solvents, we have not observed so far a notable solvent dependence on the CD spectra of **1**. The contribution of the intramolecular CT complex **A** is probably enhanced to some extent under these conditions. The formation of the dimeric CT complex **C** was greatly promoted by reducing the temperature. Thus, a solution of **1** in dichloromethane (1 mM) exhibited a strong CD at 400–500 nm at −95 °C, along with a moderate CD in the ^1L_b region. As can be seen from Figure 3, trace c, the *g* factor reaches −0.0016 for the CT band (dimer **B**) and 0.0005–0.001 even at the shorter wavelengths. These values are at least one order of magnitude larger than the representative values reported for typical allowed transitions.[11] The anomalous *g* factors may be attributed to the conformational fixation caused by stronger interactions in the dimeric CT complex (see below).

The effects of conformational fixation caused by confinement on the chiroptical properties of the CT complex were further investigated by supramolecular interaction with cyclodextrin hosts. The host–guest interactions of **1** with cyclodextrins were first assessed by fluorescence spectroscopy. As can be seen from Figure 4, a solution of **1** in methanol (0.1 mM) showed fairly weak fluorescence at 330 nm (trace a) because of efficient intramolecular electron-transfer quenching, whereas much more intense fluorescence was observed upon the addition of β- or γ-cyclodextrin (0.5 mM) to an aqueous solution of **1** (0.1 mM; traces b and c). Similar behavior was previously reported for a variety of aromatic donor–viologen systems.[12] The fluorescent donor group is included in the cavity of β-cyclodextrin, so both intra- and intermolecular quenching by the pyridinium moiety and solvent molecules are greatly decelerated and the excited state is retained longer. In contrast, fluorescence enhancement is moderate in the case of γ-cyclodextrin (Figure 4, trace c). This result may be rationalized by a loose fitting of the donor group to a larger γ-cyclodextrin cavity, which can not completely prevent the quenching attack of the pyridinium moiety or solvent molecules. ^{1}H NMR spectroscopic analysis of the complexes also supports this conclusion, as the aromatic protons are much more deshielded in the presence of β-cyclodextrin than in the presence of γ-cyclodextrin (see the Supporting Information).

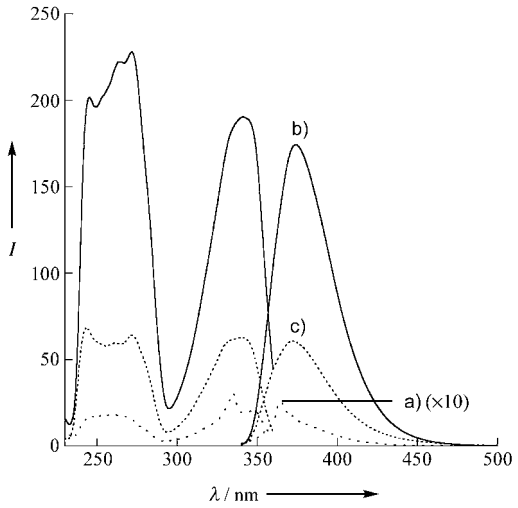

Figure 4. Fluorescence emission and excitation spectra of **1** (0.1 mM) at ambient temperature: a) in methanol (ten times expansion); in the presence of b) β- and c) γ-cyclodextrin (0.5 mM) in water.

Upon the addition of β- or γ-cyclodextrin (5 mM) to an aqueous solution of **1** (1 mM), large negative Cotton effects were induced in the ^1L_b (≈340 nm) and ^1L_a (≈240 nm) regions of the naphthalene chromophore (Figure 3, traces e and f). This result is consistent with the empirical rules[13] and indicates that the longer axis of the naphthalene moiety is parallel to the axis of the cyclodextrin cavity. Interestingly, the CT band exhibited larger negative Cotton effects with unusually large *g* factors of −0.00028 and −0.00008 for the β- and γ-cyclodextrin complexes, respectively. The strong CD for the CT band, particularly in the presence of β-cyclodextrin, is quite puzzling, since the cavity is formally fitted to the size of naphthalene and the included naphthalene moiety does not appear to form a CT complex even with the tethered pyridinium moiety. By combining all the results from the UV/Vis, fluorescence, NMR, and CD spectral examinations, we tentatively rationalize this interesting chiroptical behavior of the β-cyclodextrin complex of **1** as being a consequence of a shallow penetration or perching of the acceptor moiety into the β-cyclodextrin cavity, which is already occupied by the more hydrophobic naphthalene moiety, to afford a less face-to-face, twisted CT complex. It is thus inferred that the naphthalene moiety is accommodated in the β-cyclodextrin cavity and the remaining acceptor moiety is forced to form a tilted CT complex, which is closely located and/or twisted relative to the donor moiety and hence exhibits a stronger Cotton effect. However, the donor–acceptor pair is more face-to-face and less tightly packed in a larger γ-cyclodextrin cavity, which results in a less intense Cotton effect.

As formulated by Hush (mostly for transition-metal complexes), the electronic coupling element (H_{ab}) is related to the charge-transfer transition according to Equation (1),[14]

$$H_{ab}[cm^{-1}] = 0.0206(\nu_{max}\,\Delta\nu^{1/2}\,\varepsilon)^{1/2}/r \qquad (1)$$

in which ν_{max} and $\Delta\nu^{1/2}$ are the peak position and full width at half maximum (in wavenumbers) of the CT band, ε is the molar extinction coefficient at the CT-band maxima, and r is the effective separation of relevant redox centers in the complex.[15] The electronic coupling element H_{ab} was estimated for the CT transition of **1** under various conditions to give the values listed in Table 1. Notably, the CT interaction in the dimer is almost twice as large as that in the monomer. The H_{ab} value for the β-cyclodextrin complex is also appreciably larger than that of the uncomplexed monomer, probably as a result of the stronger intramolecular donor–acceptor interactions of **1** within the hydrophobic cyclodextrin cavities, or a slightly larger separation between donor and acceptor.

 © 2005 Wiley-VCH Verlag GmbH & Co. KGaA, Weinheim

Table 1: Anisotropy (g) factors and electronic coupling elements (H_{ab}) of monomeric and dimeric CT complexes and the β-cyclodextrin inclusion complex.

CT species	Conditions	H_{ab}[a]	λ_{max}[b]	g factor [$\times 10^3$]
A	[**1**] = 10 mM in MeCN, 25 °C	0.65	420	≈ −0.1
C	[**1**] = 1 mM in water, 25 °C	0.72	380	−0.3
B	[**1**] = 1 mM in CH_2Cl_2, −95 °C	1.23	480	−1.6

[a] Electronic coupling element [10^3 cm^{-1}], calculated by the Marcus–Hush equation [Eq. (1)], with the assumtion $r = 3.5$ Å. [b] Absorption maximum of the CT band [nm].

It has thus been demonstrated for the first time that donor–acceptor dyads, such as **1**, form both intramolecular monomeric and intermolecular dimeric CT complexes depending on the conditions employed, and that their CT bands give anomalously large g factors of up to 0.002. Such an enhancement in g factor upon CT interaction is of theoretical/mechanistic interest and also of practical use as a tool for enhancing the efficiency of absolute asymmetric synthesis with circularly polarized light.[16]

Received: September 22, 2004
Revised: January 21, 2005
Published online: March 22, 2005

Keywords: anisotropy · charge transfer · circular dichroism · cyclodextrins · donor–acceptor systems

[1] a) A. Foster, *Organic Charge-Transfer Complexes*, Academic Press, New York, **1969**; b) R. S. Mulliken, W. B. Person, *Molecular Complexes*, Wiley, New York, **1969**; c) R. Foster, *Molecular Complexes*, *Vol. 2*, Crane, Russak, New York, **1974**.

[2] a) Y.-H. Ko, K. Kim, J.-K. Kang, H. Chun, J. W. Lee, S. Sakamoto, K. Yamaguchi, J. C. Fettinger, K. Kim, *J. Am. Chem. Soc.* **2004**, *126*, 1932–1933; b) J. W. Lee, K. Kim, S. W. Choi, Y. H. Ko, S. Sakamoto, K. Yamaguchi, K. Kim, *Chem. Commun.* **2002**, 2692–2693; c) Y. J. Jeon, P. K. Bharadwaj, S. W. Choi, J. W. Lee, K. Kim, *Angew. Chem.* **2002**, *114*, 4654–4656; *Angew. Chem. Int. Ed.* **2002**, *41*, 4474–4476; d) S. A. Vignon, J. Wong, H.-R. Tseng, J. F. Stoddart, *Org. Lett.* **2004**, *6*, 1095–1098.

[3] a) T. P. Le, J. E. Rogers, L. A. Kelly, *J. Phys. Chem. A* **2000**, *104*, 6778–6785; b) A. Siemiarczuk, A. R. McIntosh, T. F. Ho, M. J. Stillman, K. J. Roach, A. C. Weedon, J. R. Bolton, J. S. Connolly, *J. Am. Chem. Soc.* **1983**, *105*, 7224–7230; c) E. A. Chandross, C. J. Dempster, *J. Am. Chem. Soc.* **1970**, *92*, 3586–3593; d) M. Itoh, *J. Am. Chem. Soc.* **1972**, *94*, 1034–1035.

[4] a) G. J. Simpson, *ChemPhysChem* **2004**, *5*, 1301–1310; b) H. Okubo, D. Nakano, S. Anzai, M. Yamaguchi, *J. Org. Chem.* **2001**, *66*, 557–563.

[5] a) G. Briegleb, H. G. Kuball, K. Henschel, W. Euing, *Ber. Bunsen-Ges. Phys. Chem.* **1972**, *76*, 101–105; b) G. Briegleb, H. G. Kuball, K. Henschel, *J. Physik. Chem. (Frankfurt)* **1965**, *46*, 229–249; G. Briegleb, H. G. Kuball, *Angew. Chem.* **1964**, *76*, 228–229; *Angew. Chem. Int. Ed. Engl.* **1964**, *3*, 307–308; see also: R. Gleiter, H. Hopf, *Modern Cyclophane Chemistry*, Wiley, New York, **2004**.

[6] a) C. Sato, K. Kikuchi, K. Okamura, Y. Takahashi, T. Miyashi, *J. Phys. Chem.* **1995**, *99*, 16925–16931; b) A. Zweig, A. H. Maurer, B. G. Robert, *J. Org. Chem.* **1967**, *32*, 1322–1329; c) K. Y. Lee, J. K. Kochi, *J. Chem. Soc. Perkin Trans. 2* **1992**, 1011–1017.

[7] a) H. A. Benesi, J. J. Hildebrand, *J. Am. Chem. Soc.* **1949**, *71*, 2703–2707; b) W. B. Person, *J. Am. Chem. Soc.* **1965**, *87*, 167–170.

[8] a) J. W. Verhoeven, I. P. Dirkx, T. J. de Boer, *Tetrahedron* **1969**, *25*, 3395–3405; b) A. S. N. Murthy, A. P. Bhardwaj, *Spectrochim. Acta* **1983**, *39A*, 939–942.

[9] K. B. Yoon, J. K. Kochi, *J. Phys. Chem.* **1991**, *95*, 3780–3790.

[10] DFT calculations were performed to search for the optimized structure in the folded conformation, but no energy minimum was found. This result is not very unexpected and could be rationalized, as DFT calculations (in the gas phase) underestimate the electronic interaction between donor and acceptor units. However, there is yet another possibility: that it is not the conventional through-space, but *through-bond* interactions in an extended conformation that give rise to the CT absorption, for which no face-to-face conformation is required. Indeed, the CT transition induced by through-bond interactions was reported for rigid donor–acceptor systems: a) J. W. Verhoeven, *Pure Appl. Chem.* **1986**, *58*, 1285–1290; b) A. J. De Gee, J. W. Verhoeven, W. J. Sep, T. J. De Boer, *J. Chem. Soc. Perkin Trans. 2* **1975**, 579–583. However, we do not have any conclusive evidence at present.

[11] H. E. Smith, *Chem. Rev.* **1998**, *98*, 1709–1740.

[12] a) J. W. Park, B. A. Lee, S. Y. Lee, *J. Phys. Chem. B* **1998**, *102*, 8209–8215; b) H. Yonemura, M. Kasahara, H. Saito, H. Nakamura, T. Matsuo, *J. Phys. Chem.* **1992**, *96*, 5765–5770; c) H. Yonemura, H. Nakamura, T. Matsuo, *Chem. Phys. Lett.* **1989**, *155*, 157–161; d) A. Toki, H. Yonemura, T. Matsuo, *Bull. Chem. Soc. Jpn.* **1993**, *66*, 3382–3386.

[13] a) K. Harata, H. Uedaira, *Bull. Chem. Soc. Jpn.* **1975**, *48*, 375–378; b) M. Kodaka, *J. Phys. Chem. A* **1998**, *102*, 8101–8103; c) M. Kodaka, *J. Am. Chem. Soc.* **1993**, *115*, 3702–3705.

[14] a) R. A. Marcus, N. Sutin, *Biochim. Biophys. Acta* **1985**, *811*, 265–322; b) N. S. Hush, *Coord. Chem. Rev.* **1985**, *64*, 135–157; c) N. S. Hush, *Electrochim. Acta* **1968**, *13*, 1005–1023; d) N. S. Hush, *Prog. Inorg. Chem.* **1967**, *8*, 391–444; e) N. S. Hush, *Trans. Faraday Soc.* **1961**, *57*, 557–580.

[15] We estimated the separation parameter r as 3.5 Å in the Hush equation from the molecular geometry on the basis of X-ray crystallographic and DFT-optimized structures of related charge-transfer complexes. However, an estimation of the value of r remains to be elucidated. a) H. Yoshikawa, S. Nishikiori, T. Ishida, *J. Phys. Chem. B* **2003**, *107*, 9261–9267; b) M.-S. Liao, Y. Lu, S. Scheiner, *J. Comput. Chem.* **2003**, *24*, 623–631.

[16] a) For a review, see: B. L. Feringa, R. A. van Delden, *Angew. Chem.* **1999**, *111*, 3624–3645; *Angew. Chem. Int. Ed.* **1999**, *38*, 3418–3438; see also: b) H. Nishino, A. Kosaka, G. A. Hembury, F. Aoki, K. Miyauchi, H. Shitomi, H. Onuki, Y. Inoue, *J. Am. Chem. Soc.* **2002**, *124*, 11618–11627; c) Y. Inoue, H. Tsuneishi, T. Hakushi, K. Yagi, K. Awazu, H. Onuki, *Chem. Commun.* **1996**, 2627–2628.

 © 2005 Wiley-VCH Verlag GmbH & Co. KGaA, Weinheim

Phenol Synthesis

Hydroxylation of Benzene to Phenol under Air and Carbon Monoxide Catalyzed by Molybdovanadophosphoric Acid**

*Masayuki Tani, Takao Sakamoto, Shuichi Mita, Satoshi Sakaguchi, and Yasutaka Ishii**

Phenols are one of the most important classes of raw materials in the chemical industry, and a variety of compounds are derived from them, such as resins, dyes, and pharmaceuticals.[1] In 2000, the worldwide production of phenol was 6.6 megatons. Most of this phenol is produced by the cumene process reported by Hock and Lang in 1944.[2] The direct conversion of benzene to phenol by hydroxylation with O_2 is the most desirable method among phenol syntheses. However, indirect phenol production through the formation of cumene hydroperoxide and oxidative decomposition of benzoic acid are currently employed. The direct synthesis of phenol from benzene and nitrous oxide has been described,[3] but this method is only cost-effective when nitrous oxide is available cheaply as a by-product.[4] Therefore, for a long time much attention has been paid to the direct synthesis of phenol by the hydroxylation of benzene with O_2, which is referred to as a dream oxidation in the chemical industry. There have been many attempts at the direct conversion of benzenes to phenols with H_2O_2[5] or O_2,[6] under the influence of a reducing agent, such as H_2[7] or CO[8] and transition metals, such as Cu, Pd, or Pt,[9] or heteropolyoxometalates.[10] Recently, Mizukami et al. reported a one-step conversion of benzene to phenol with O_2 and H_2 at a palladium membrane.[7]

In the course of our study on the coupling of benzene with acrylates in the presence of O_2 by $Pd(OAc)_2$ combined with molybdovanadophosphates, we found that a small amount of phenol is formed as a by-product.[11] Thus, our attention has been focused on the direct conversion of benzene (**1**) into phenol (**2**), and an efficient simple catalytic method for the synthesis of **2** from **1** using molybdovanadophosphoric acids as catalysts has been established [Eq. (1)].

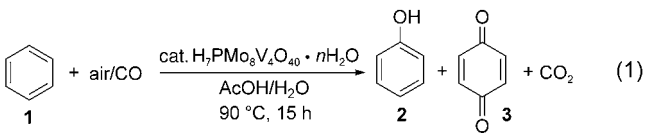

(1)

[*] M. Tani, T. Sakamoto, S. Mita, S. Sakaguchi, Prof. Y. Ishii
Department of Applied Chemistry
Faculty of Engineering and High Technology Research Center
Kansai University
Suita, Osaka 564-8680 (Japan)
Fax: (+81) 6-6339-4026
E-mail: ishii@ipcku.kansai-u.ac.jp

[**] This work was partially supported by MEXT.KAKENHI (No.15750095).

Supporting information for this article is available on the WWW under http://www.angewandte.org or from the author.

The reaction of **1** under air (15 atm) and CO (5 atm) with $H_7PMo_8V_4O_{40}\cdot n\,H_2O$[12] catalyst in acetic acid/water (9:1; 13.5/1.5 mL) at 90 °C for 15 h afforded **2** in 27.3 % yield (turnover number (TON) = 21.8), along with a small amount of 1,4-benzoquinone (**3**; 3.4 % yield), which was a further oxidation product of **2** (Table 1, run 2). About 70 % of the CO was recovered in this reaction, and the selectivity for **2** based on CO consumed was approximately 35 %. This is the first successful conversion of **1** into **2** in high yield by molybdovanadophosphoric acid under mild conditions.[13] It was found that the yield of **2** was influenced by the partial pressures of air and CO. For instance, the reaction under high air pressure (17.5 atm) and low CO pressure (2.5 atm) resulted in a decrease of the conversion of **1** into **2** (20.9 %; run 1). Under a CO pressure of 10 atm and an air pressure of 15 or 10 atm (runs 3 and 4, respectively), the results were almost the same as those for run 2. In the absence of CO, no reaction was induced (run 5). The reaction was considerably influenced by the amount of solvent mixture and the water content (runs 6–9). No reaction took place in anhydrous acetic acid (run 9). The reaction without sodium acetate resulted in a slight decrease in the yield of **2** (run 10). No reaction took place with a combination of air and H_2 in place of CO as the reducing agent (run 11). It is thought that CO, which can be easily obtained from abundant cheap carbon resources, such as asphalt and pitch, is a superior reducing agent to H_2 derived from methane and naphtha,[14] although the present method brought about the concurrent formation of phenol and a stoichiometric amount of CO_2.

Figure 1 shows the time-dependence of the hydroxylation of **1**. The production of **2** increased smoothly with time up to five hours and then continued at a constant level, while, **2** was slowly converted into **3** at the same time. The fact that **2** was converted into the overoxidized products including **3** by its individual exposure to CO and air in the presence of the catalyst supports this interpretation.

Table 1: Oxidation of benzene (**1**) to phenol (**2**) under air and CO by $H_7PMo_8V_4O_{40}$.[a]

Run	Air:CO [atm]	$AcOH/H_2O$ [mL]	Conv. [%][b]	Yield [%][c] **2**	**3**	TON [mol/mol]
1	17.5:2.5	13.5/1.5	33.0	20.9	3.2	16.7
2	15:5	13.5/1.5	41.6	27.3	3.4	21.8
3	15:10	13.5/1.5	47.4	28.1	4.0	22.4
4	10:10	13.5/1.5	44.5	25.9	2.8	20.7
5	20:0	13.5/1.5	n.r.			
6	15:5	18/2	41.4	26.9	3.5	21.5
7	15:5	9/1	41.0	21.0	3.7	16.8
8	15:5	4.5/0.5	44.7	18.1	4.1	14.5
9	15:5	15.0/0	n.r.			
10[d]	15:5	13.5/1.5	35.8	23.3	3.6	18.6
11[e]	15:5	13.5/1.5	n.r.			

[a] **1** (2 mmol) was reacted under air and CO in aqueous acetic acid in the presence of AcONa (0.1 mmol) with $H_7PMo_8V_4O_{40}\cdot n\,H_2O$ (25 μmol, 1.25 mol % based on $H_7PMo_8V_4O_{40}\cdot 24\,H_2O$) at 90 °C for 15 h. [b] n.r. = no reaction. [c] Based on **1** used. [d] Without NaOAc. [e] Air:H_2 = 15:5 (atm); H_2 was used instead of CO.

 © 2005 Wiley-VCH Verlag GmbH & Co. KGaA, Weinheim DOI: 10.1002/anie.200462769

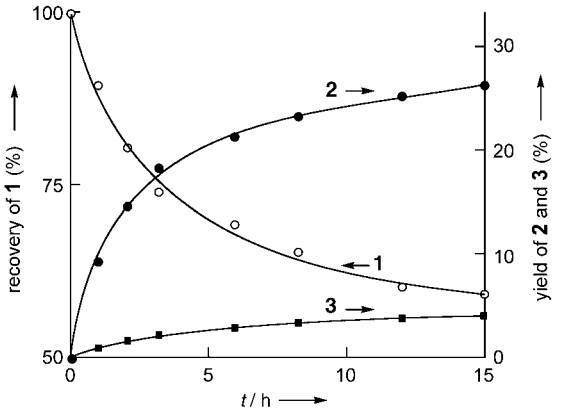

Figure 1. Time-dependence curve for the hydroxylation of **1** under the same conditions as run 6 in Table 1.

Table 2 shows the results of the hydroxylation of **1** in the presence of several molybdovanadophosphoric acids. The reaction was also promoted by $H_{3+n}PMo_{12-n}V_nO_{40}\cdot n\,H_2O$ ($n=$ 1–3)[12] to give **2** in yields of 13–22%, but $H_3PMo_{12}O_{40}\cdot n\,H_2O$, which lacked the vanadium atom, did not catalyze the hydroxylation. These results indicate that the vanadium species is a key element for the hydroxylation of benzene, although an active species is not identified because of the complexity of the molybdovanadophosphoric acids used as catalysts. Their ^{31}P NMR spectra (see Supporting Information) attest to the existence of many molybdovanadophosphoric acids that contain varying compositions of P, Mo, and V. However, no reaction occurred by using $[VO(acac)_2]$ (acac = acetylacetonate) as a catalyst (run 5). This result will be discussed later.

Table 2: Oxidation of benzene (**1**) to phenol (**2**) under air and CO catalyzed by several molybdovanadophosphoric acids.[a]

Run	Catalyst	Conv. [%]	Yield [%][b] **2**	**3**
1	$H_3PMo_{12}O_{40}$		n.r.	
2	$H_4PMo_{11}V_1O_{40}$	22.8	13.6	1.2
3	$H_5PMo_{10}V_2O_{40}$	36.8	21.3	3.0
4	$H_6PMo_9V_3O_{40}$	33.6	22.2	2.1
5	$VO(acac)_2$		n.r.	

[a] Reactions were carried out under the same conditions as those for run 2 in Table 1. [b] Based on **1** used.

From a practical synthetic viewpoint, reuse of the recovered catalyst is very important. Thus, the hydroxylation was repeated with recovered catalyst under the same conditions as those for run 2 in Table 1. The yields of **2** and **3** were almost the same throughout five runs, that is, 27–29% for **2** and 2–5% for **3**, in the 40–42% conversion of **1** (Table 3). The ^{31}P NMR spectrum of the recovered catalyst was only slightly different from that of the fresh one (see Supporting Information).

Two labeling experiments were carried out to obtain mechanistic information on the hydroxylation. The reaction using $H_2{}^{18}O$ in place of $H_2{}^{16}O$ afforded an 8:2 mixture of $Ph^{16}OH$ and $Ph^{18}OH$. This finding shows that a nucleophilic attack of $H_2{}^{18}O$ to form a cationic benzene intermediate seems to be unlikely as a major route to **2**. Second, the hydroxylation of **1** under CO and $^{18}O_2$ instead of $^{16}O_2$ in acetic acid and $H_2{}^{18}O$ was examined [Eq. (2)].

Table 3: Oxidation of benzene (**1**) to phenol (**2**) under air and CO by recovered catalyst.[a]

Run	Recovery	Yield [%][b] **2**	**3**
1	1st	27.5	4.3
2	2nd	27.5	5.3
3	3rd	28.5	2.0
4	4th	28.9	2.5
5	5th	28.0	3.2

[a] Reactions were carried out under the same conditions as those for run 2 in Table 1. [b] Based on **1** used. The conversion of **1** was 40–42%.

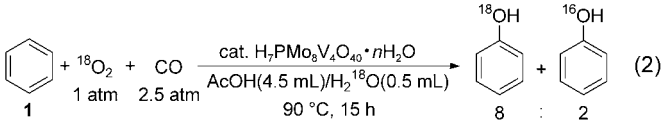

GC–MS measurement of the resulting phenol indicated that an approximate 8:2 mixture of $Ph^{18}OH$ and $Ph^{16}OH$ is formed. The preferential formation of $Ph^{18}OH$ indicates that gas-phase oxygen ($^{18}O_2$) serves as an oxygen source in this hydroxylation reaction. Also, it is likely that the ^{16}O atom in the $Ph^{16}OH$ comes from the oxygen in the $H_7PMo_8V_4O_{40}\cdot n\,H_2O$ structure. In fact, it was found that $H_7PMo_8V_4O_{40}$ was easily reduced with CO under these conditions. For example, when $H_7PMo_8V_4O_{40}\cdot n\,H_2O$ (0.5 mmol) in acetic acid was treated with CO (5 atm, ca. 11 mmol) at 90°C for 5 h, about 1 mmol of CO_2 was formed, and the color of the solution changed from orange to dark green. The formation of CO_2 and this color change of the catalyst solution suggest that $H_7PMo_8V_4O_{40}$ is easily reduced to $H_7PMo_8V_4O_{40-x}$, in which the oxygen is partially reduced as well. On the other hand, no such color change of the catalyst was observed when H_2 instead of CO was used for the reduction of $H_7PMo_8V_4O_{40}$. This is in agreement with the fact that the hydroxylation of **1** to **2** did not take place when H_2 was employed in place of CO (Table 1, run 11).

It may be assumed that the oxidation proceeds through a Fenton-type reaction of **1** with H_2O_2 generated in situ ($CO + O_2 + H_2O \rightarrow H_2O_2 + CO_2$), since H_2O_2 is reported to be formed with high turnover frequency from CO, O_2, and H_2O in the presence of a Pd catalyst.[15] Thus, we examined the hydroxylation of benzene with H_2O_2 catalyzed by molybdovanadophosphoric acid. Treatment of **1** with 35% H_2O_2 (1 equiv) in the presence of $H_6PMo_9V_3O_{40}$ in AcOH at 90°C for 8 h produced **2** in low yield (6–7%) based on the amount of **1** used. However, hydroxylation by H_2O_2 with $[VO(acac)_2]$ in place of the heteropoly acid afforded **2** in 3–4% yield, whereas the reaction under CO and air was not catalyzed by $[VO(acac)_2]$ at all (see Table 2, run 5). This fact

 © 2005 Wiley-VCH Verlag GmbH & Co. KGaA, Weinheim

may indicate that the formation of H_2O_2 from CO, O_2, and H_2O is unlikely in the present hydroxylation reaction. In addition, the reaction using $^{16}O_2$ and $H_2{}^{18}O$ gave an 8:2 mixture of $Ph^{16}OH$ and $Ph^{18}OH$ as shown above. If H_2O_2 is formed in this reaction, $H^{16}O^{18}OH$ would be generated from $^{16}O_2$ and $H_2{}^{18}O$, and as a consequence an approximate 1:1 mixture of $Ph^{16}OH$ and $Ph^{18}OH$ would be obtained. Therefore, the in situ generation of H_2O_2 is thought to be unlikely in the present hydroxylation reaction.

On the basis of these results, it can be concluded that O_2 is activated on the partially reduced $H_7PMo_8V_4O_{40-x}$ and that the activated oxygen reacts with **1** to eventually form **2**. In addition, since the reaction is not promoted by $H_3PMo_{12}O_{40}$, which lacks the V ion, it seems likely that O_2 is activated on the V species in $H_7PMo_8V_4O_{40-x}$.

In conclusion, we have developed a simple, direct synthetic method of producing phenol (**2**) from benzene (**1**) with air in the presence of CO by using molybdovanadophosphoric acids as catalysts. This method may provide a promising alternative route to **2** from **1** in place of the cumene process, which needs three reaction steps.

Experimental Section

Oxidation of benzene: in a typical procedure, the reaction was carried out in a teflon autoclave. Benzene (2 mmol) was added to a solution of $H_7PMo_8V_4O_{40}{\cdot}24H_2O$ (26.5 μmol) and AcONa (0.1 mmol) in AcOH (13.5 mL) and water (1.5 mL). The mixture was stirred at 90 °C for 15 h under air (15 atm) and CO (5 atm). After the reaction, GC and GC–MS analyses were performed. The conversions and yields of products were estimated from the peak areas, based on the GC internal standard technique.

Recovery of the catalyst: After the reaction, H_2O (5 mL) was added to the mixture, followed by extraction with iPr_2O (40 mL). The aqueous layer was washed with iPr_2O (40 mL), and the combined aqueous extracts were concentrated by evaporation under reduced pressure. The green solid obtained was dried in vacuo to give the recovered catalyst. The ^{31}P NMR spectra of the fresh and recovered catalysts were similar.

Received: December 1, 2004
Published online: March 22, 2005

Keywords: hydrocarbons · hydroxylation · oxidation · oxygen · synthetic methods

[1] a) R. A. Sheldon, J. K. Kochi, *Metal-Catalyzed Oxidations of Organic Compounds*, Academic, New York, **1981**; b) W. Jordan, H. Barneveld, O. van Gerlich, M. Kleine-Boymann, J. Ullrich in *Ullmann's Encyclopedia of Industrial Chemistry*, *Vol. A19*, VCH, Weinheim, **1991**, p. 307.

[2] H. Hock, S. Lang, *Ber. Desch. Chem. Ges.* **1944**, *B77*, 257.

[3] a) M. Iwamoto, J. Hirata, K. Matsukami, S. Kagawa, *J. Phys. Chem.* **1983**, *87*, 903; b) E. Suzuki, K. Nakashiro, Y. Ono, *Chem. Lett.* **1988**, 953; c) R. Burch, C. Howitt, *Appl. Catal. A* **1992**, *86*, 139; d) R. Burch, C. Howitt, *Appl. Catal. A* **1993**, *103*, 135; e) G. I. Panov, A. S. Kharitonov, V. I. Sobolev, *Appl. Catal. A* **1992**, *82*, 31; f) G. I. Panov, A. S. Kharitonov, V. I. Sobolev, *Appl. Catal. A* **1993**, *98*, 33; g) G. I. Panov, A. S. Kharitonov, V. I. Sobolev, *Appl. Catal. A* **1996**, *141*, 185; h) B. Liptakova, M. Hronec, Z. Cvengrosova, *Catal. Today* **2000**, *61*, 143.

[4] A. K. Uriarte, M. A. Rodkin, M. J. Gross, A. S. Kharitonov, G. I. Panov, *Stud. Surf. Sci. Catal.* **1997**, *110*, 857.

[5] a) C. Walling, *J. Am. Chem. Soc.* **1975**, *97*, 363; b) C. Walling, *Acc. Chem. Res.* **1975**, *8*, 125; c) J. R. L. Smith, R. O. C. Norman, *J. Am. Chem. Soc.* **1963**, *85*, 2897; d) N. A. Milas, *J. Am. Chem. Soc.* **1937**, *59*, 2342; e) H. Mimoun, L. Saussine, E. Daire, M. Postel, J. Fischer, R. Weiss, *J. Am. Chem. Soc.* **1983**, *105*, 3101; f) K. Nomiya, H. Yanagibayashi, C. Nozaki, K. Kondoh, E. Hiramatsu, Y. Shimizu, *J. Mol. Catal. A* **1996**, *114*, 181; g) L. W. Lee, W. J. Lee, Y. K. Park, S. E. Park, *Catal. Today* **2000**, *61*, 137; h) M. Stockmann, F. Konietzni, J. U. Notheis, J. Voss, W. F. Maier, *Appl. Catal. A* **2001**, *208*, 343.

[6] a) N. Herron, C. A. Tolman, *J. Am. Chem. Soc.* **1987**, *109*, 200; b) T. Kitano, Y. Kuroda, M. Mori, S. Ito, K. Sasaki, M. Nitta, *J. Chem. Soc. Perkin Trans. 2* **1993**, 981.

[7] S. Niwa, M. Eswaramoorthy, J. Nair, A. Raj, N. Itoh, H. Shoji, T. Namba, F. Mizukami, *Science* **2002**, *295*, 105.

[8] a) T. Jintoku, H. Taniguchi, Y. Fujiwara, *Chem. Lett.* **1987**, 1865; b) T. Jintoku, K. Takaki, Y. Fujiwara, Y. Fuchita, K. Hiraki, *Bull. Chem. Soc. Jpn.* **1990**, *63*, 438; c) T. Tsunami, M. Nakamura, H. Tominaga, *J. Chem. Soc. Chem. Commun.* **1992**, 1446; d) W. Laufer, J. P. M. Niederer, W. F. Hoelderich, *Adv. Synth. Catal.* **2002**, *344*, 1084.

[9] a) T. Kitano, T. Nakai, M. Nitta, M. Mori, S. Ito, K. Sasaki, *Bull. Chem. Soc. Jpn.* **1994**, *67*, 2850; b) T. Miyake, M. Hamada, Y. Sasaki, M. Oguri, *Appl. Catal. A* **1995**, *131*, 33; c) T. Miyake, M. Hamada, H. Niwa, M. Nishizuka, M. Oguri, *J. Mol. Catal. A* **2002**, *178*, 199; d) I. Yamanaka, T. Nabeta, S. Takenaka, K. Otsuka, *Stud. Surf. Sci. Catal.* **2000**, *130*, 815; e) T. Fukushi, W. Ueda, Y. Moro-oka, T. Ikawa, *Ind. Eng. Chem. Res.* **1989**, *28*, 1587; f) R. Hamada, Y. Shibata, S. Nishiyama, S. Tsuruya, *Phys. Chem. Chem. Phys.* **2003**, *5*, 956; g) H. Yamanaka, R. Hamada, H. Nibuta, S. Nishiyama, S. Tsuruya, *J. Mol. Catal. A* **2002**, *178*, 89; h) I. Yamanaka, S. Katagiri, S. Takenaka, K. Otsuka, *Stud. Surf. Sci. Catal.* **2002**, *130*, 809.

[10] a) K. Nomiya, K. Yagishita, Y. Nemoto, T. Kamataki, *J. Mol. Catal. A* **1997**, *126*, 43; b) L. C. Passoni, A. T. Cruz, R. Buffon, U. Schuchardt, *J. Mol. Catal. A* **1997**, *120*, 117; c) Y. J. Seo, Y. Mukai, T. Tagawa, S. Goto, *J. Mol. Catal. A* **1997**, *120*, 149.

[11] T. Yokota, M. Tani, S. Sakaguchi, Y. Ishii, *J. Am. Chem. Soc.* **2003**, *125*, 1476.

[12] a) G. A. Tsigdinos, C. J. Hallada, *Inorg. Chem.* **1968**, *7*, 437; b) L. Pettersson, I. Anderesson, A. Selling, J. H. Grate, *Inorg. Chem.* **1994**, *33*, 982; c) V. F. Odyakov, E. G. Zhizhina, R. I. Maksimovskaya, K. I. Matveev, *Kinet. Catal.* **1995**, *36*, 733; d) K. Nomiya, K. Yagishita, Y. Nemoto, T. Kamataki, *J. Mol. Catal. A* **1997**, *126*, 43; e) M. Vennat, P. Herson, J.-M. Brégeault, G. B. Shul'pin, *Eur. J. Inorg. Chem.* **2003**, 908.

[13] For example, the Pd-catalyzed synthesis of phenol from benzene under CO (5 atm) and O_2 (65 atm) in $H_2O/MeCOCH_2CHMe_2$ at 70 °C gave phenol in 3.2% yield based on benzene used: R. Tassiniari, D. Bianchi, R. Ungarelli, E. Battistel, R. D'Aloisio (Enichem S.P.A.), EP894783, **1999** [*Chem. Abstr.* **1999**, *130*, 155248].

[14] Evolution of about 0.9 kg of CO_2 is estimated to accompany the production of 1 m^3 of H_2 from CH_4.

[15] a) D. Bianchi, R. Bortolo, R. D'Aloisio, M. Ricci, *Angew. Chem.* **1999**, *111*, 734; *Angew. Chem. Int. Ed.* **1999**, *38*, 706; b) D. Bianchi, R. Bortolo, R. D'Aloisio, M. Ricci, S. Soattini (Enichem S.P.A.), EP808796, **1997** [*Chem. Abstr.* **1997**, *128*, 50358]; c) R. Vignola, E. Battistel, D. Bianchi, R. Bortolo, R. Tassinari (Enichem S.P.A.), EP861688, **1998** [*Chem. Abstr.* **1998**, *129*, 218223].

 © 2005 Wiley-VCH Verlag GmbH & Co. KGaA, Weinheim

Nanostructures

Polyol Synthesis of Platinum Nanostructures: Control of Morphology through the Manipulation of Reduction Kinetics**

*Jingyi Chen, Thurston Herricks, and Younan Xia**

A great deal of effort has been directed towards the synthesis of nanostructures that have well-controlled morphology.[1] It is generally accepted that the morphology (including dimensionality and shape) of a nanostructure may allow tuning that is as powerful as tuning with size for tailoring the electronic, optical, magnetic, and catalytic properties of a functional material. Herein we report a case study in which the morphology of Pt nanostructures could be readily controlled by manipulating the reduction kinetics of a polyol synthesis. More specifically, Pt nanostructures in the form of spheres, star-shaped particles, branched multipods, and uniform nanowires have been successfully synthesized by coupling the polyol reduction of a platinum precursor with the Fe^{II}/Fe^{III} redox pair and the adsorption of oxygen and nitrogen gases.

Platinum plays an important role in many industrial applications.[2] For example, it serves as a catalyst in the reduction of pollutant gases emitted from automobiles, the synthesis of nitric acid, oil cracking, and proton-exchange membrane (PEM) fuel cells.[3] All of these applications require the use of Pt as fine particles. It has also been established that both the reactivity and selectivity of Pt nanostructures in a catalytic reaction are highly dependent on the morphology and therefore on the crystallographic planes exposed on the surface of the nanoparticles.[4]

For these reasons, much effort has been devoted to the production of Pt nanostructures with monodispersed sizes and well-defined morphologies. Most of these studies, however, have been limited to Pt nanoparticles that could be easily synthesized by using a variety of chemical methods.[5] In general, such a synthesis involves the reduction of a Pt^{IV} or Pt^{II} precursor in the presence of a polymeric stabilizer by using reducing agents such as alcohol, sodium borohydride, or hydrogen gas. While the resultant nanoparticles may be considered monodisperse in size, they are often spherical or lack well-defined facets. The formation of well-faceted nanoparticles has only been demonstrated in a limited number of examples in which hydrogen gas was used as the reducing agent and sodium polyacrylate as the stabilizer.[6] Another chemical method of generating faceted Pt nanoparticles is based on the reduction of a Pt^{IV} precursor with sodium borohydride in water at 0 °C, followed by phase transfer of the reduced species to an organic solvent.[7] The mechanism responsible for the formation of these faceted nanoparticles has yet to be elucidated. In a different approach, nanorods and nanotubes of polycrystalline Pt have been fabricated by templating against channels in porous materials,[8] as well as Ag or Se nanowires.[9] Kijima et al. have also demonstrated the synthesis of Pt nanotubes by employing self-assembled structures of surfactants as the template.[10] Although template-based syntheses have proven to be straightforward and versatile, they are restricted by a number of drawbacks that include the requirement of template removal to obtain a pure product, the limited scope of morphological variation, and the polycrystallinity often associated with the product.

In a recent study,[11] we discovered that the addition of a trace amount of iron species (Fe^{II} or Fe^{III}) to a polyol process could significantly alter the growth kinetics of Pt nanostructures and thus induce the formation of Pt nanowires. These nanowires are characterized by uniform diameters and relatively high aspect ratios. Herein we demonstrate that the reduction kinetics can be further manipulated to obtain several other morphologies such as branched multipods. On the basis of our results from UV/Vis and X-ray photoelectron spectroscopy (XPS), we believe that the reduction of a Pt^{IV} precursor with polyol proceeds through two steps and involves a Pt^{II} intermediate (Figure 1).

After the reaction had proceeded in air at 110 °C for 1.5 h, all of the Pt^{IV} precursor was converted into a Pt^{II} species. When cooled down to room temperature and stored in a vial

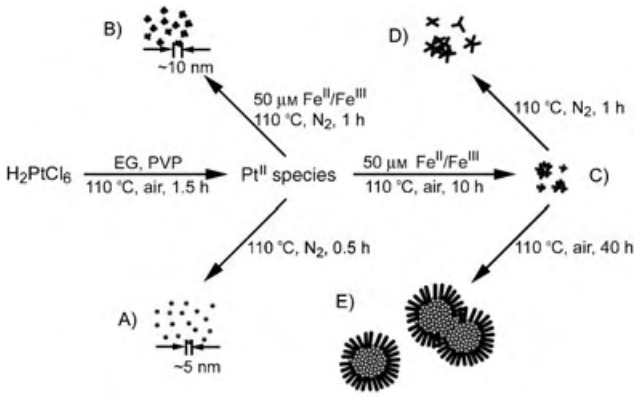

Figure 1. Four different ways to control the kinetics of polyol reduction and the corresponding morphologies observed for the Pt nanostructures. As the same amount of PVP was present in all four illustrated syntheses, the striking difference in morphology was not caused by PVP concentration. We believe that the PVP molecules in these syntheses only function as a stabilizer to prevent the resultant nanoparticles from aggregating into larger structures.

[*] J. Chen, T. Herricks, Prof. Y. Xia
Department of Chemistry
University of Washington
Seattle, WA 98195-1700 (USA)
Fax: (+1) 206-685-8665
E-mail: xia@chem.washington.edu

[**] This work has been supported in part by a DARPA–DURINT subcontract from Harvard University and a fellowship from the David and Lucile Packard Foundation. Y.X. is an Alfred P. Sloan Research Fellow and a Camille Dreyfus Teacher Scholar. J.C. and T.H. thank the Center for Nanotechnology at the University of Washington for a Nanotech Student Fellowship Award and an IGERT Fellowship Award (supported by the NSF, DGE-9987620), respectively. This work was performed in part at the Nanotech User Facility (NTUF), a member of the National Nanotechnology Infrastructure Network (NNIN) funded by the NSF.

Supporting information for this article is available on the WWW under http://www.angewandte.org or from the author.

 DOI: 10.1002/anie.200462668 © 2005 Wiley-VCH Verlag GmbH & Co. KGaA, Weinheim

under ambient conditions, the Pt^{II} intermediate could be left for more than one month without being further reduced to Pt^0. However, if the reaction was allowed to continue in air at 110 °C, the Pt^{II} species was fully reduced to produce spherical Pt nanoparticles of about 5-nm diameter within 1 h. In such a case, the reduction of the Pt^{II} species was greatly accelerated by an autocatalytic process once some Pt nuclei had formed in solution.[12] When this process was carried out under nitrogen atmosphere, the reduction of Pt^{II} species to Pt^0 became faster than in air, and spherical nanoparticles (Figure 1 A) were formed in the solution within 30 min. This observation implies that the adsorption of oxygen from air onto the surface of Pt nuclei was able to slow down the autocatalytic reduction of the Pt^{II} species.[13] Although the presence of oxygen could slow down this process, the reduction was still too fast to induce the formation of structures that deviated from the equilibrium shape.[14]

In contrast, the reduction of the Pt^{II} species could be retarded when an Fe^{II} or Fe^{III} species was introduced into the reaction mixture. In this case, Fe^{III} ions oxidized both Pt atoms and nuclei back to Pt^{II} species and thus significantly decreased the supersaturation of the Pt atoms (see Supporting Information). As the resultant Fe^{II} ions could be recycled back to Fe^{III} ions by aerial oxygen, only a small amount of Fe^{III} was needed in this synthesis. For the same reason, both Fe^{II} and Fe^{III} ions have the same function in controlling the reduction kinetics. The present work suggests that oxygen can slow down the growth through both surface adsorption and etching mechanisms when coupled with the Fe^{II}/Fe^{III} species. In general, it is hard to single out which mechanism is the dominant because both retardation effects have a strong dependence on the concentrations of oxygen and the Fe^{II}/Fe^{III} species. By taking advantage of these two mechanisms, the rate of reduction of the Pt^{II} species could be regulated; a range of products from A to E can be formed, with a slower reduction favoring the formation of E and a faster reduction favoring the formation of A. In general, as the reduction became slower, the growth of [111] planes increased, thus leading to the formation of highly anisotropic (branched and then 1D) nanostructures.

Figure 1 summarizes the major products that were observed when trace amounts of Fe^{II} or Fe^{III} species (with a final concentration of 50 μM) and/or nitrogen were introduced into the reaction system after the formation of the Pt^{II} species. Depending on whether the reaction was allowed to continue in air or under nitrogen, the Pt nanostructures were found to display different morphologies. Under a nitrogen atmosphere, star-shaped nanoparticles (Figure 1 B) were produced over a period of 1 h, while in air the reaction proceeded at a much slower rate and the nanostructures became more branched and subsequently assembled into submicrometer-sized agglomerates (Figure 1 C). Towards the end of this reaction, the Pt^{II} species were reduced at an extremely slow rate to generate uniform Pt nanowires (Figure 1 E) on the surface of each agglomerate. However, when nitrogen was applied, the reduction rate slightly increased and resulted in the formation of multipods with highly branched structures (Figure 1 D).

It is worth noting that the mechanism involved in the present work seems to be different from the model developed by Peng for CdSe nanostructures.[15] Highly anisotropic (branched and 1D) CdSe nanostructures were obtained at high monomer concentrations—and thus high reduction rates and supersaturations—and spherical CdSe nanoparticles were formed at low monomer concentrations.[15]. The trend that Peng observed for CdSe nanostructures is exactly the opposite of the trend we have observed as we found that highly anisotropic Pt nanostructures were only formed at extremely low supersaturations. If the reduction proceeded too quickly and hence the supersatuation was too high, only isotropic, spherical Pt nanoparticles were produced.

Figure 2 shows TEM and SEM images of the Pt nanostructures that correspond to the products illustrated in Figure 1. Consistent with the schematic drawing, the products

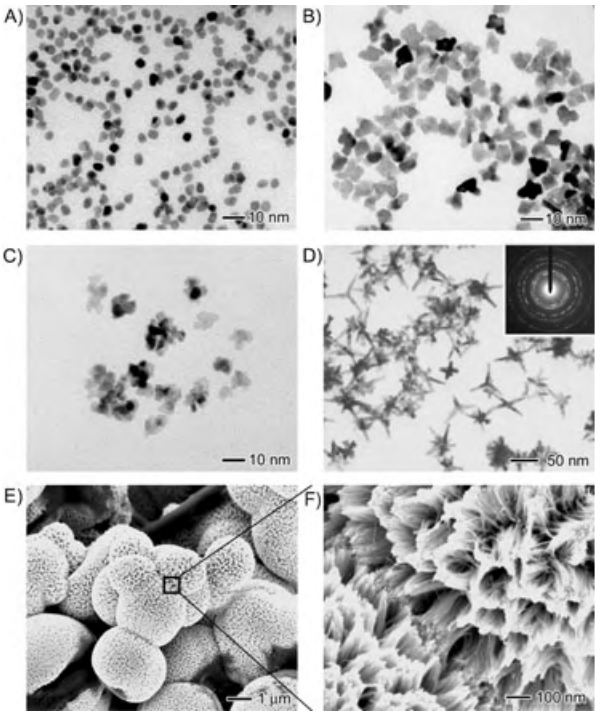

Figure 2. TEM (A–D) and SEM (E, F) images of Pt nanostructures that have been obtained by controlling the reduction rate of a polyol process. The products correspond to the morphology labeled A to E in Figure 1. The inset of (D) shows a typical electron-diffraction pattern of the branched nanostructures; F) enlarged section of the SEM image shown in (E) of the nanowires grown at the surface layer.

display a number of distinct morphologies depending on the experimental conditions. Figure 2 A shows a TEM image of the Pt nanoparticles when the reduction of the Pt^{II} intermediate was performed under nitrogen in the absence of an Fe^{II} or Fe^{III} species. The nanoparticles were roughly spherical in shape, with a mean diameter of about 5 nm. Note that the spherical shape is what we expect for a face-centered cubic metal formed under thermodynamic control.[16]

Figure 2 B shows a TEM image of the Pt nanoparticles that were obtained under conditions similar to those used in Figure 2 A, except that 50 μM Fe^{II} or Fe^{III} species had been added. In this case, the particles are larger and start to branch into a star shape. Figure 2 C shows a TEM image of a sample that was obtained by reducing the Pt^{II} intermediate in air for

 © 2005 Wiley-VCH Verlag GmbH & Co. KGaA, Weinheim

10 h. Due to the presence of oxygen, the reduction was much slower (relative to the reaction that resulted in particles of Figure 2B) and the product became more highly branched and eventually entangled into large agglomerates. Figure 2D shows a TEM image of the product that was obtained when the Pt^{II} intermediate was heated in air for 10 h, followed by the introduction of nitrogen for 1 h. The resultant nanostructures branch out to generate multipods with a diameter of around 50 nm. The inset shows a typical electron diffraction pattern recorded from an ensemble of such highly branched nanostructures which confirms that they are composed of pure face-centered cubic Pt.

Figure 2E shows an SEM image of the Pt structures when the iron-mediated reduction was carried out in air. Similar to that seen in a previous study,[11] the final product contained micrometer-scale agglomerates of Pt nanoparticles with their surfaces covered by a dense array of uniform nanowires. These agglomerates could further fuse into larger structures. Figure 2F gives a magnified view of the portion indicated by a box in Figure 2E. It is clear that the as-synthesized nanowires were monodisperse in size distribution and their averaged diameter was around 5 nm. Because the nanowires were loosely attached to the surface of each agglomerate, they could be readily released by brief sonication without breaking the agglomerates. As we have demonstrated before, the released nanowires could be recovered by centrifugation and then dispersed in ethanol or water without introducing additional surfactants.[11]

Figure 3 A–C show TEM images of a Pt multipod that were recorded by tilting the sample at different angles relative to the electron beam. The arrow in Figure 3A indicates the axis against which the TEM grid was rotated by either −45° (Figure 3B) or +45° (Figure 3C). From the images, we conclude that this Pt nanostructure is a tetrapod, with four "arms" of roughly equal length. Figure 3D shows a typical high-resolution (HR)TEM image of the end of an arm that reveals its single-crystalline structure and the ⟨111⟩ growth direction for each arm. The lattice spacing between the [111] planes, 0.23 nm, is consistent with that of the bulk crystal. In the current stage of development, the final product of each synthesis is usually a mixture of multipods that contain between two to six arms. Some of these products were single crystals and others contained twin defects.

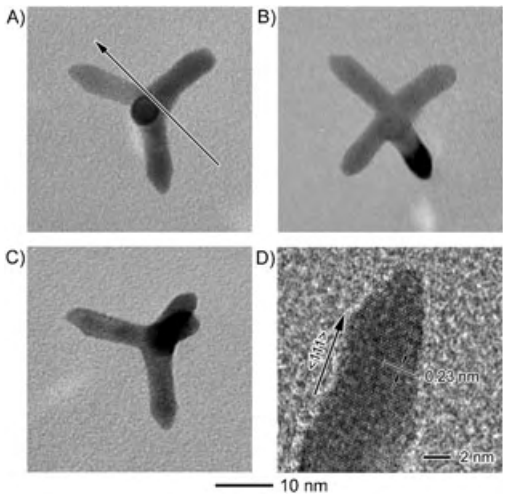

Figure 3. TEM images of a Pt tetrapod tilted at different angles to the axis indicated as an arrow: A) 0°, B) −45°, and C) 45°. The sample was taken from the product shown in Figure 1C. D) HRTEM image of one of the ends of this Pt tetrapod, which indicates that each arm was a single crystal with its growth direction along the ⟨111⟩ axis.

Figure 4 compares two types of four-armed nanostructures that we have observed: the first type is a tetrapod with a tetrahedral configuration (Figure 4A) whereas the second has a square-planar structure (Figure 4C). Their HRTEM images (Figure 4B and 4D, respectively) clearly indicate that the tetrapod is a single crystal and the square-planar structure has a twin plane in the middle of the nanostructure. As a result of this structural difference, the angles between adjacent arms are also substantially different. For the tetrahedral configuration, we believe that there was only one single-crystal seed involved and the four arms simply grew out of different sites (four of the eight corners) of the seed.

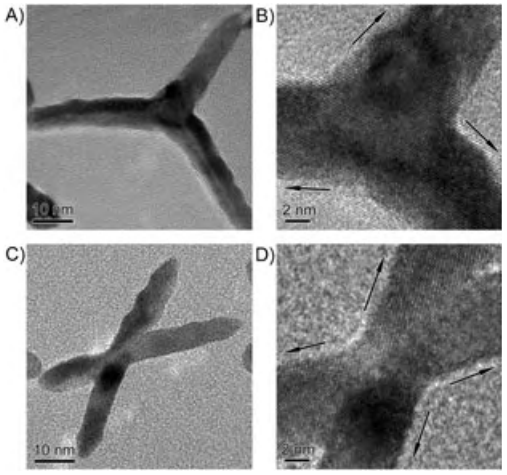

Figure 4. TEM and HRTEM images of two types of four-armed Pt nanostructures with different configurations: A), B) tetrahedral; C), D) square-planar. The HRTEM images indicate that all the arms grew along the ⟨111⟩ direction. While the square-planar structure has a twin plane in the middle, the tetrahedral structure is a single crystal because all four arms display the same fringe spacing and orientation.

In summary, we have demonstrated that Pt nanostructures with four different morphologies could be synthesized by controlling the reduction kinetics of a polyol process. The presence of both iron species and oxygen (or air) was found to be critical to the control of the reduction kinetics and hence morphology. Depending on the way the Fe^{II}/Fe^{III} redox pair and oxygen (from air) were supplied to the reaction system, Pt nanostructures in the form of spheres, star-shaped particles, branched multipods, and nanowires could be obtained as the major product for each run of synthesis. Although the strategy described here may resemble what has been widely explored in the general area of biomineralization,[17] the exact approaches are very different. In biomineralization, a biopolymer is used to mediate the diffusion rate of reactive species

 © 2005 Wiley-VCH Verlag GmbH & Co. KGaA, Weinheim

toward the surface of nuclei and thus to control the morphology. In the approach presented here, the growth of nuclei is retarded by blocking their surface with oxygen and/or by facilitating the dissolution of atoms from the nuclei. The net results of these two different approaches are the same: a reduction in supersaturation and the induction of morphologies that deviate from those favored thermodynamically.[18]

Although the reduction kinetics could also be controlled by varying other experimental conditions such as temperature, it seems that the introduction of Fe^{II}/Fe^{II} redox species and oxygen was the most convenient and versatile variable. For instance, we have also performed the synthesis at 100, 80, and 50 °C. While the reduction became notably slower at both 100 and 80 °C, it was still too fast to generate Pt nanostructures other than spherical particles. At 50 °C, the reduction of Pt^{II} species ceased and no Pt^0 species were observed after several days. We expected that these results will open the door to a systematic study on the control of shape and thus properties associated with metal nanostructures.

Experimental Section

In a typical synthesis, ethylene glycol (EG, J. T. Baker; 4 mL) was placed in a three-neck flask equipped with a reflux condenser and a magnetic stirring bar embedded in PYREX glass and heated in air at 110 °C for 1 h to remove any trace water. Hexachloroplatinic acid (H_2PtCl_6, 0.033 g; Aldrich) and poly(vinyl pyrrolidone) (PVP, $\bar{M}_W$ = 55000, 0.045 g; Aldrich) were dissolved separately in ethylene glycol (2 mL) at room temperature. The molar ratio between H_2PtCl_6 and the repeating unit of PVP was controlled at 1:5. These two EG solutions were then added dropwise simultaneously to the reaction flask within 1.5 min. The reaction mixture was heated at 110 °C in air for 1.5 h. The solution turned from golden orange to green–yellow, indicating the formation of Pt^{II} species as the intermediate. The reaction mixture was then heated in a nitrogen atmosphere and turned brown and finally dark brown in 1 h. For iron-mediated synthesis, the iron species (20 μL of 20 mM of $FeCl_3$ or $FeCl_2$ predissolved in EG; Aldrich) was introduced into the system after the reaction had proceeded in air at 110 °C for 1.5 h (or when the solution turned green–yellow). The resulting solution was colorless and a black precipitate settled at the bottom of the flask. When a nitrogen atmosphere was present for different periods of time during the iron-mediated reduction, products with different morphologies were obtained: 1) starlike nanoparticles were formed when a nitrogen atmosphere was supplied immediately after the formation of Pt^{II} species; 2) branched nanostructures were produced when a nitrogen atmosphere was supplied after the Pt^{II} species had been left in air and at 110 °C for 10 h. In general, the longer the Pt^{II} species were kept in air before application of nitrogen, the more the final product would agglomerate. In the last step, the product was collected by centrifugation, washed with ethanol several times to remove ethylene glycol and excess PVP, and characterized by SEM, TEM, and HRTEM. The SEM images were taken by using a field emission microscope (FEI, Sirion XL) operated at an accelerating voltage of 10–20 kV. The TEM images and diffraction patterns were obtained with a JEOL microscope (1200EX II) operated at 80 kV. The HRTEM images were captured on a Tecnai G^2 F20 operated at 200 kV.

Received: November 19, 2004
Revised: January 22, 2005
Published online: March 17, 2005

Keywords: kinetic control · nanostructures · platinum · reduction

[1] a) R. Narayanan, M. A. El-Sayed, *J. Phys. Chem. B* **2004**, *108*, 5726; b) Z. L. Wang, T. S. Ahmad, M. A. El-Sayed, *Surf. Sci.* **1997**, *380*, 302; c) D. J. Milliron, S. M. Hughes, Y. Cui, L. Manna, J. Li, L.-W. Wang, A. P. Alivisatos, *Nature* **2004**, *430*, 190; d) X. Peng, L. Manna, W. Yang, J. Wickham, E. Scher, A. Kadavanich, A. P. Alivisatos, *Nature* **2000**, *404*, 59; e) S.-M. Lee, Y.-M. Jun, S.-N. Cho, J. Cheon, *J. Am. Chem. Soc.* **2002**, *124*, 615; f) F. Kim, S. Connor, H. Sond, T. Kuykendall, P. Yang, *Angew. Chem.* **2004**, *116*, 3759; F. Kim, S. Connor, H. Sond, T. Kuykendall, P. Yang, *Angew. Chem.* **2004**, *116*, 3759; *Angew. Chem. Int. Ed.* **2004**, *43*, 3673; g) T. K. Tapan, C. J. Murphy, *J. Am. Chem. Soc.* **2004**, *126*, 8648; h) S. Chen, Z. Wang, J. Ballato, S. H. Foulger, D. L. Carroll, *J. Am. Chem. Soc.* **2003**, *125*, 16186; i) M. Pileni, *Nat. Mater.* **2003**, *2*, 145.

[2] For example: F. A. Cotton, G. Wilkinson, *Advanced Inorganic Chemistry*, 5th ed., Wiley, New York, **1988**, pp. 868.

[3] a) A. Rouxoux, J. Schulz, H. Patin, *Chem. Rev.* **2002**, *102*, 3757; b) K. R. Williams, G. T. Burstein, *Catal. Today*, **1997**, *38*, 401.

[4] a) R. Narayanan, M. A. El-Sayed, *Nano Lett.* **2004**, *4*, 1343; b) L. M. Falicov, G. A. Somorjai, *Proc. Natl. Acad. Sci. USA* **1985**, *82*, 2207.

[5] a) T. Teranishi, M. Hosoe, T. Tanaka, M. Miyake, *J. Phys. Chem. B* **1999**, *103*, 3818; b) S. Chen, K. Kimra, *J. Phys. Chem. B* **2001**, *105*, 5397; c) H. Wakayama, N. Setoyama, Y. Fukushima, *Adv. Mater.* **2003**, *15*, 742; d) X. Teng, D. Black, N. J. Watkins, Y. Gao, H. Yang, *Nano Lett.* **2003**, *3*, 261.

[6] T. S. Ahmadi, Z. L. Wang, T. C. Green, A. Heglein, M. A. El-Sayed, *Science* **1996**, *272*, 1924.

[7] S. Zhao, S. Chen, S. Wang, D. Li, H. Ma, *Langmuir* **2002**, *18*, 3315.

[8] a) Y. Sakamoto, A. Fukuoka, T. Higuchi, N. Shimomura, S. Inagaki, M. Ichikawa, *J. Phys. Chem. B* **2004**, *108*, 853; b) A. Husain, J. Hone, H. W. C. Postma, X. M. H. Huang, T. Drake, M. Barbic, *Appl. Phys. Lett.* **2003**, *83*, 1240; c) X. Fu, Y. Wang, N. Wu, L. Gui, Y. Tang, *J. Mater. Chem.* **2003**, *13*, 1192; d) H. J. Shin, R. Ryoo, Z. Liu, O. Terasaki, *J. Am. Chem. Soc.* **2001**, *123*, 1246; e) Y. Han, J. Kim, G. D. Stucky, *Chem. Mater.* **2000**, *12*, 2068.

[9] a) B. Mayers, X. Jiang, D. Sunderland, B. Cattle, Y. Xia, *J. Am. Chem. Soc.* **2003**, *125*, 13364; b) Y. Sun, B. Wiley, Z.-Y. Li, Y. Xia, *J. Am. Chem. Soc.* **2004**, *126*, 9399.

[10] T. Kijima, T. Yoshimura, M. Uota, T. Ikeda, D. Fujikawa, S. Mouri, *Angew. Chem.* **2004**, *116*, 203; T. Kijima, T. Yoshimura, M. Uota, T. Ikeda, D. Fujikawa, S. Mouri, *Angew. Chem.* **2004**, *116*, 230; *Angew. Chem. Int. Ed.* **2004**, *43*, 228.

[11] J. Chen, T. Herricks, M. Geissler, Y. Xia, *J. Am. Chem. Soc.* **2004**, *126*, 10854.

[12] J. M. Petroski, Z. Wang, T. C. Green, M. A. El-Sayed, *J. Phys. Chem. B* **1998**, *102*, 3316.

[13] T. Mallat, A. Baiker, *Catal. Today* **1994**, *19*, 247.

[14] T. Herricks, J. Chen, Y. Xia, *Nano Lett.* **2004**, *4*, 2367.

[15] X. Peng, *Adv. Mater.* **2003**, *15*, 459.

[16] Z. L. Wang, *J. Phys. Chem. B* **2000**, *104*, 1153.

[17] S. Mann, *Biomineralization: Principles and Concepts in Bioinorganic Materials Chemistry*, Oxford University Press, **2001**.

[18] A. Chernov, *Phys. Crystallogr.* **1972**, *16*, 734.

 © 2005 Wiley-VCH Verlag GmbH & Co. KGaA, Weinheim

Ethylene–Butadiene Copolymers

Alternating Copolymerization of Ethylene and Butadiene with a Neodymocene Catalyst**

*Julien Thuilliez, Vincent Monteil, Roger Spitz, and Christophe Boisson**

The introduction of unsaturated groups into the backbone of polyolefins is of interest for many applications, including the production of vulcanizable materials for the tire industry. The ideal would be to copolymerize conjugated dienes (butadiene, isoprene) with olefins, which are all cheap and readily available monomers. Since the discovery of Ziegler–Natta catalysts, research efforts have focused on the copolymerization of these two families of monomers. However, as the two classes of monomers polymerize according to different mechanisms, only a very limited number of catalysts are able to copolymerize them successfully.

Methods for producing alternating olefin–butadiene copolymers have been discussed in the literature for over 40 years. For instance, Natta et al. isolated this type of copolymer by extraction from a polymer mixture prepared at −25 °C using a vanadium-based system.[1] The disadvantage is that the catalysts must be prepared at very low temperature (−70 °C), and polymerization must be performed at low temperature (0 °C). Almost ten years later, Furukawa prepared similar polymers with a $TiCl_4/AlR_3$ catalyst system.[2] The polymerization temperature was slightly higher in this case (25 °C). $VO(OR)_2Cl/AlR_3$ catalysts, developed in the 1970s, can also be used to make alternating poly(ethylene-*co*-butadiene), as confirmed by Arnold et al. in 1991.[3] However, low polymerization temperatures are again required, since the proportion of 1,2-units increases with temperature and cross-linking reactions occur.[4] More recently, advances in the field of single-site catalysts have made possible the copolymerization of ethylene with butadiene by using Group 4 metallocene catalysts.[5] The difficulty here is that butadiene acts as a poison for the catalysts. Experimental studies have shown that activity decreases dramatically as the butadiene content increases.[6]

It appears that there are no Group 4 or vanadium-based catalysts that can be used for the copolymerization of conjugated dienes with olefins under acceptable conditions. Given this limitation, most industrial research groups have chosen an alternative route for the production of polyolefinic elastomers, namely, the terpolymerization of ethylene (E), propylene (P), and a diene monomer (DM) such as ethylenenorbornene, which is much more expensive than mainstream α olefins. However, compatibility problems, not expected with copolymers of olefins and conjugated dienes, have been observed during covulcanization of EPDM polymers with styrene–butadiene or natural rubbers. The copolymerization of olefins and conjugated dienes is therefore of significant interest from both scientific and economic points of view.

We have studied this reaction using organolanthanide catalysts. Previous studies have already resulted in efficient systems for the copolymerization of ethylene with butadiene, both in terms of activity and diene incorporation.[7] Recently, we described a new elastomer containing cyclohexane units obtained by intramolecular cyclization.[8] Since the ligand has a strong influence on the polymer microstructure, we extended our investigations to the silylene-bridged cyclopentadienyl fluorenyl neodymium complex $[\{Me_2Si(C_5H_4)(C_{13}H_8)\}NdCl]$ (**1**).

This complex was used in combination with butyloctylmagnesium (Bomag), an alkylating and transfer agent. To moderate the drift of polymer composition, copolymerization experiments were stopped at low conversion. Results are reported in Table 1. It is well known that the polymerization of ethylene is controlled by a reversible chain-transfer reaction between the dialkylmagnesium compound and the lanthanide complex until polymer precipitation.[9] After the precipitation of di(polyethenyl)magnesium, the molecular weight distribution generally broadens. As expected, the system **1**/Bomag leads to a high polydispersity index (PDI) in homopolymerization of ethylene (run 1). On the contrary, polymers with narrow molecular weight distribution were obtained in the presence of butadiene (Bd). Moreover, higher productivity was accompanied by an increase in molecular weight (compare runs 6 and 9). This interesting result can be simply explained by the fact that the copolymers remain soluble in the polymerization medium. Whereas only polymers of low molecular weight are accessible in the homopolymerization of ethylene, high-molecular-weight poly(ethylene-*co*-butadiene) can easily be prepared.

Table 1: Polymerization results.[a]

Run	Bd in feed [mol %]	*n*(Nd) [μmol]	Yield [g]	Reaction time [min]	M_n [g mol^{-1}] (PDI)
1	0	41	1.95	60	2700 (3.61)
2	5	41	1.20	20	2740 (1.36)
3	10	45	1.60	12	4230 (1.40)
4	20	43	2.50	12	5855 (1.62)
5	30	41	1.70	12	6695 (1.41)
6	50	41	1.95	20	7580 (1.52)
7	75	45	7.60	120	17660 (1.90)
8	100	43	1.50	720	6185 (2.30)
9	50	41	7.00	90	32500 (1.90)

[a] Polymerization conditions: $T = 80$ °C, toluene (200 mL), ratio [Mg]/[Nd] = 5.

[*] J. Thuilliez, Dr. V. Monteil, Dr. R. Spitz, Dr. C. Boisson
LCPP-CNRS/CPE Lyon UMR 140
Bât. 308F-B.P. 2077
43 Bd du 11 Novembre 1918, 69616 Villeurbanne (France)
Fax: (+33) 4-7243-1768
E-mail: boisson@lcpp.cpe.fr

[**] The authors thank the Manufacture Française des Pneumatiques Michelin for support, in particular Dr. Fanny Barbotin and Dr. Pierre Robert.

Supporting information for this article is available on the WWW under http://www.angewandte.org or from the author.

 DOI: 10.1002/anie.200462019 © 2005 Wiley-VCH Verlag GmbH & Co. KGaA, Weinheim

In the homopolymerization of ethylene or butadiene, the catalyst **1**/Bomag shows poor activities. In run 1, the activity was close to 50 kg mol^{-1} h^{-1}, which is lower than the activity of similar systems (for example, typical activities for $[(C_5Me_5)_2NdCl_2Li(OEt_2)_2]$/Bomag are close to 800 kg mol^{-1} h^{-1}).[10] Similarly, run 8 shows that only 1.50 g of polybutadiene was obtained after 12 h. Therefore, while the present system is not suitable for the preparation of homopolymers, it exhibits a novel and unexpected behavior in copolymerization reactions.

Mean activities were calculated for runs 1–8 (Figure 1). Activity increases considerably in the presence of butadiene, even at relatively high concentrations. The maximum value

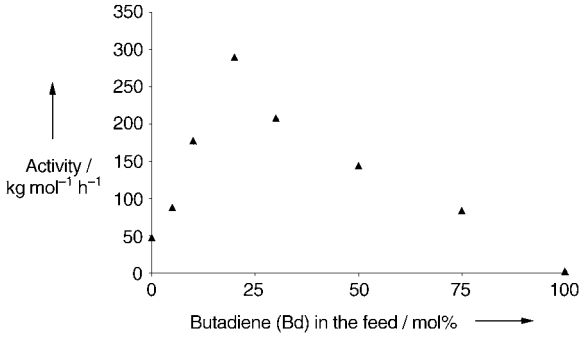

Figure 1. Average activity of **1**/Bomag in the copolymerization of ethylene and butadiene.

(around 300 kg mol^{-1} h^{-1}) was observed with a butadiene feed content of 20 mol%. To our knowledge, a system that is significantly more active in copolymerization than in homopolymerization has never before been observed with these kinds of catalysts; increasing the amount of butadiene usually decreases the activity.[5b]

Detailed stereochemistry of the polymers (determined by NMR spectroscopy) is reported in Table 2. Butadiene is mainly inserted in *trans*-1,4 configuration. ^{13}C NMR spectra also provide some important information on the sequence of the two monomers (Figure 2). The different copolymers have a strongly alternating character, as confirmed by run 6: TET triads are predominant, few TEE triads are observed, and no TEEE units are detected (T and E stand for *trans*-1,4-butadiene and ethylene units, respectively). The ability of the

Table 2: Polymer microstructure.

Run	Bd in feed [mol%]	Bd in polymer [mol%][a]	1,4-units (*trans*[b]) [mol%][a]	1,2-units [mol%][a]
2	5	24.5	96.3 (94.7)	3.7
3	10	34.3	97.6 (96.2)	2.4
4	20	41.5	96.9 (97.6)	3.1
5	30	45.2	96.6 (98.2)	3.4
6	50	48.3	95.6 (98.9)	4.4
7	75	52.4	93.8 (99.6)	6.2
8	100	100	84.1 (94.6)	15.9
9	50	49.4	94.5 (97.5)	5.5

[a] According to ^{1}H NMR spectroscopic data. [b] According to ^{13}C NMR spectroscopic data.

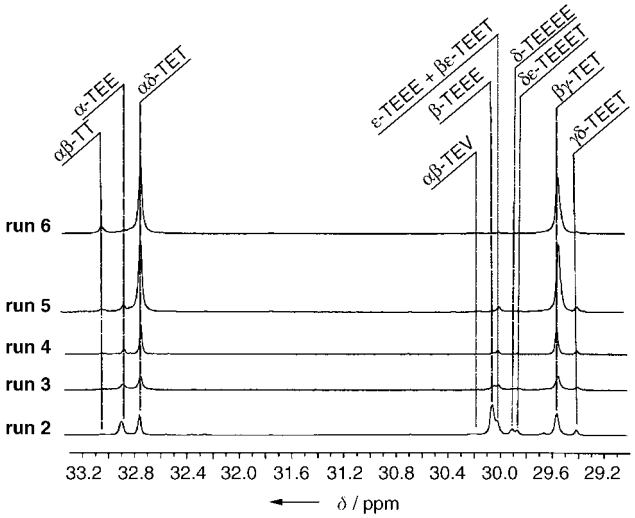

Figure 2. Comparison of the ^{13}C NMR spectra of ethylene–butadiene copolymers.

system to copolymerize ethylene with butadiene is confirmed, since the polymer prepared in run 9 shows the same alternating structure and has a molecular weight higher than 30000 g mol^{-1}. Differential scanning calorimetry revealed the typical thermal properties of poly(ethylene-*alt*-*trans*-1,4-butadiene) ($T_g = -70\,°C$, $T_m = 54\,°C$).[11] Furthermore, activity remains stable for long polymerization times.

Using the different ^{13}C NMR spectra, and assuming that butadiene units are mainly in *trans*-1,4 configuration, we calculated the reactivity ratio as $R_{Bd} = 0.07$ and $R_E = 0.09$ ($R_{Bd}R_E = 0.063$).[7b] Experimental data fit the theoretical composition diagram (Figure 3).

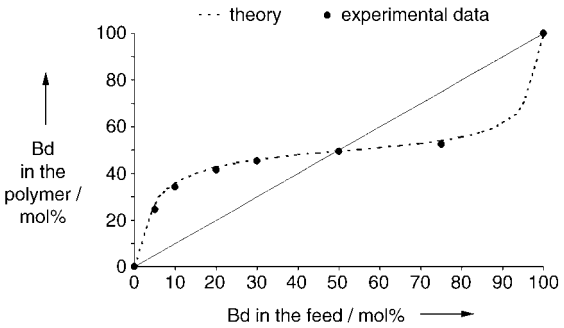

Figure 3. Composition diagram for the ethylene–butadiene copolymerization.

Copolymers prepared with **1**/Bomag exhibit the same alternating character as those obtained from vanadium-based catalysts.[1,3] The advantage of the neodymocene catalyst is that the polymerization is performed at high temperature (80 °C). In addition, high activities (one to two orders of magnitude higher than those of vanadium-based catalysts) are reached and there is no molecular-weight limitation with temperature.

The catalyst **1**/Bomag leads to good insertion of butadiene in *trans*-1,4 configuration. The mechanism for this positive

 © 2005 Wiley-VCH Verlag GmbH & Co. KGaA, Weinheim

result can be explained in the light of some of the more relevant theoretical studies presented in the literature. It has been reported that *cis*-1,4 stereoselectivity in the polymerization of butadiene is obtained by *s*-η^4-*cis*-butadiene insertion into a η^3-π-allylic metal–carbon bond.[12,13] Conversely, *trans*-1,4 units are commonly attributed to an *anti–syn* isomerization or to insertion of a η^2-coordinated *trans*-butadiene.[13] In a recent paper,[14] Wakatsuki and co-workers performed an interesting theoretical study on the coordination and insertion of butadiene into the Sm–H bond of the complex $[(C_5Me_5)_2SmH]$. It appears that η^2 coordination is widely favored because of steric effects.

Nevertheless, experimental evidence shows that bis(pentamethylcyclopentadienyl)lanthanide complexes give small amounts of butadiene insertion,[7a] an observation that is completely opposite to the efficiency of the catalyst **1**/Bomag ($R_E = k_{EE}/k_{EB} = 0.09$). Furthermore, Erker et al. isolated stable zirconocene and tantalocene complexes which involve *s-trans*-η^4-butadiene.[15] They suggested that *s-trans*-η^4-diene complexes can be postulated as intermediates responsible for the stereoselectivity in the polymerization of conjugated dienes.[15a] The experimental results reported herein can be explained by the existence of such an intermediate **A** (Scheme 1). In the case of the bridged complex **1**, the metal

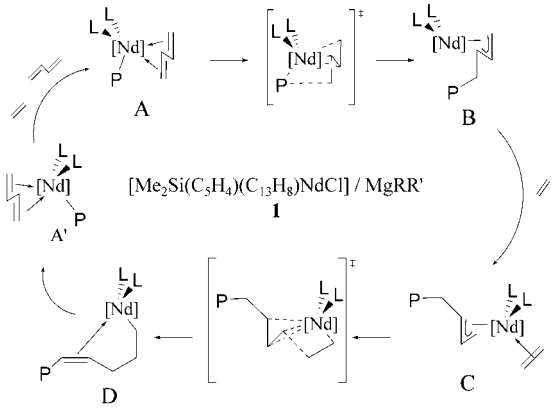

Scheme 1. Polymerization mechanism based on *s-trans*-η^4 coordination of butadiene. MgRR′ = butyloctylmagnesium.

is less hindered than in the structures "$(C_5Me_5)_2LnR$", and therefore more accessible. This then leads to the favorable reactivity of the diene in an *s-trans*-η^4 coordination mode. This hypothesis is also in agreement with a very low rate of subsequent diene insertion into the η^3-π-allylic metal–carbon bond ($R_B = k_{BB}/k_{BE} = 0.09$) and very low activity in the homopolymerization of butadiene. In fact, formation of an η^3-butenyl neodymocene complex impedes η^4 coordination of butadiene in the plane between the two Cp rings. For this reason the insertion of ethylene is preferred. This emphasizes another unexpected characteristic of the new catalyst for the alternating copolymerization of ethylene with butadiene: the system leads to a better insertion of ethylene into an η^3-π-allylic metal–carbon bond than into a σ metal–carbon bond ($k_{BE} > k_{EE}$). Assuming that insertions of monomers are first-order reactions, calculations based on kinetics using the slope of the curve in Figure 1 show that k_{BE}/k_{EE} is close to 10. This is illustrated by the unique activity increase observed in the presence of butadiene. We suggest that the formation of a η^3-allyl intermediate (**C**) modifies the electronic environment of the metal atom and assists the insertion of ethylene.

For the first time, alternating copolymerization of ethylene with butadiene has been performed with a metallocene-based single-site catalyst. The diene is mainly inserted in *trans*-1,4 configuration. In contrast with conventional systems which lead to similar polymers, the catalyst **1**/Bomag can be used at high temperature, and no gel formation is observed. The complex has useful activities in the range of 100–300 $kg\,mol^{-1}\,h^{-1}$, and high molecular weights were obtained. Furthermore, the catalyst shows an unprecedented behavior. In comparison with the homopolymerization of ethylene, a significant activity increase is observed when butadiene is added to the polymerization medium. With regard to the experimental results obtained with this bridged lanthanidocene-containing catalyst, it seems reasonable to assume an *s*-η^4-*trans* coordination mode of butadiene.

Experimental Section

All syntheses were performed under pure and dry argon by using standard Schlenk techniques or a glove box. Tetrahydrofuran was dried with sodium and distilled prior to use. Toluene and heptane were dried over 3-Å molecular sieves. Other reagents were purchased from commercial sources and used without any further purification. Complex **1** was prepared by reaction of $[\{Me_2Si(C_5H_4)(C_{13}H_8)\}Li_2(thf)_2]$ with $NdCl_3$ in THF, according to the procedure described by Qian et al.[16] No signal was observed by NMR spectroscopy because of the paramagnetism of neodymium.

Analytical techniques and polymerization procedures (250-mL glass reactor) are available in the Supporting Information.

Received: September 16, 2004
Revised: February 3, 2005
Published online: March 22, 2005

Keywords: butadiene · copolymerization · ethylene · homogeneous catalysis · lanthanides

[1] G. Natta, A. Zambelli, I. Pasquon, F. Ciampelli, *Makromol. Chem.* **1964**, *79*, 161.
[2] J. Furukawa, *J. Polym. Sci.* **1972**, *10*, 3027.
[3] M. Arnold, L. Wohlfahrt, W. Frank, G. Reinhold, *Makromol. Chem.* **1991**, *192*, 1017.
[4] M. Arnold, J. Reussner, L. Wohlfahrt, *Angew. Makromol. Chem.* **1992**, *196*, 37.
[5] a) S. Pragliola, G. Milano, G. Guerra, P. Longo, *J. Am. Chem. Soc.* **2002**, *124*, 3502; b) T. N. Choo, R. M. Waymouth, *J. Am. Chem. Soc.* **2003**, *125*, 8970.
[6] a) W. Kaminsky, M. Schlobohm, *Makromol. Chem. Macromol. Symp.* **1986**, *4*, 130; b) M. Marques, F. Coutinho, *Eur. Polym. J.* **1994**, *30*, 1055.
[7] a) F. Barbotin, V. Monteil, M.-F. Llauro, C. Boisson, R. Spitz, *Macromolecules* **2000**, *33*, 8521; b) M.-F. Llauro, C. Monnet, F. Barbotin, V. Monteil, R. Spitz, C. Boisson, *Macromolecules* **2001**, *34*, 3604.
[8] V. Monteil, R. Spitz, F. Barbotin, C. Boisson, *Macromol. Chem. Phys.* **2004**, *205*, 737.

 © 2005 Wiley-VCH Verlag GmbH & Co. KGaA, Weinheim

[9] S. Bogaert, T. Chenal, A. Mortreux, J.-F. Carpentier, *J. Mol. Catal. A* **2002**, *190*, 207.
[10] C. Boisson, V. Monteil, D. Ribour, R. Spitz, F. Barbotin, *Macromol. Chem. Phys.* **2003**, *204*, 1747.
[11] a) H. Utschick, J. Reussner, T. Wegner, G. Höhne, H. Fischer, M. Arnold, *J. Therm. Anal.* **1993**, *39*, 643; b) W. Gerum, G. Höhne, W. Wilke, M. Arnold, T. Wegner, *Macromol. Chem. Phys.* **1995**, *196*, 3797.
[12] a) S. Tobisch, *Acc. Chem. Res.* **2002**, *35*, 96; b) S. Tobisch, T. Nowak, H. Bögel, *J. Organomet. Chem.* **2001**, *619*, 24.
[13] a) S. Maiwald, H. Weissenborn, C. Sommer, G. Müller, R. Taube, *J. Organomet. Chem.* **2001**, *640*, 1; b) S. Maiwald, C. Sommer, G. Müller, R. Taube, *Macromol. Chem. Phys.* **2002**, *203*, 1029.
[14] S. Kaita, N. Koga, Z. Hou, Y. Doi, Y. Wakatsuki, *Organometallics* **2003**, *22*, 3077.
[15] a) G. Erker, J. Wicher, K. Engel, F. Rosenfeldt, W. Dietrich, *J. Am. Chem. Soc.* **1980**, *102*, 6344; b) H. C. Strauch, G. Erker, R. Fröhlich, *Organometallics* **1998**, *17*, 5746; c) M. Dahlmann, G. Erker, R. Fröhlich, O. Meyer, *Organometallics* **1999**, *18*, 4459.
[16] C. Qian, W. Nie, J. Sun, *Organometallics* **2000**, *19*, 4134.

 © 2005 Wiley-VCH Verlag GmbH & Co. KGaA, Weinheim

Organometallic Chemistry

Phenolate Complexes of Iron(II) in Different Spin States**

*Mark Wallasch, Gotthelf Wolmershäuser, and Helmut Sitzmann**

In 1996, [{^{4}CpFe(μ-Br)}$_2$] (**1a**, ^{4}Cp = η^5-C$_5$H(CHMe$_2$)$_4$) was reported as the first high-spin cyclopentadienyliron complex, but could not be prepared as single crystals.[1] With the tri(*tert*-butyl)cyclopentadienyl derivative [Cp‴Fe(μ-Br)]$_2$ (**1b**, Cp‴ = η^5-1,3,4-*t*Bu$_3$C$_5$H$_2$) structural information can now be obtained.[2] Because the alkylcyclopentadienyl ligands employed are bulky enough to hinder unwanted ligand redistribution reactions that result in ferrocene formation,[3] **1a**[1] and **1b** offer interesting synthetic possibilities. Reactions of complexes **1** with substituted phenolates reveal a delicate balance between different coordination modes (Scheme 1).

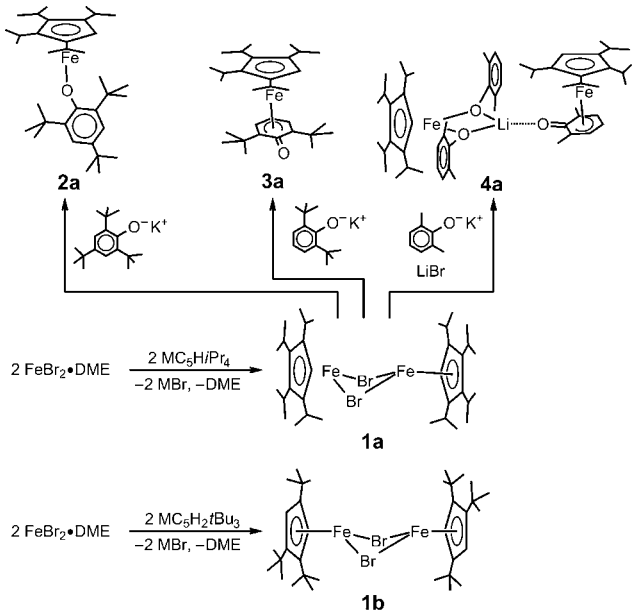

Scheme 1. Synthesis of complexes **1**–**4**; M = Li or Na.

Like **1a**, compound **1b** is a high-spin iron(II) species with four unpaired electrons and has a magnetic moment in solution of 5.09 μ$_B$ (**1a**: 5.15 μ$_B$[1]) The crystal structure of **1b** (Figure 1) shows a distance of 1.92 Å between the Fe centers

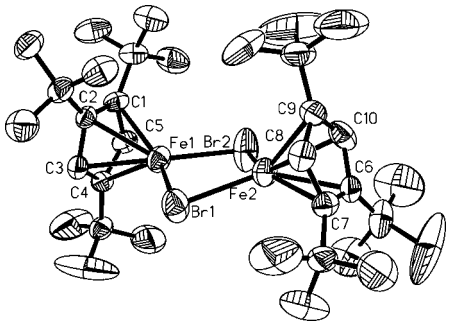

Figure 1. Crystal structure of the dimer **1b**. Selected interatomic distances [Å] and angles [°]: Fe-C 2.228(6)–2.302(6) Å, Fe1-Br1 2.5110(13), Fe1-Br2 2.4746(12), Fe2-Br1 2.4810(12), Fe2-Br2 2.5013, Fe-C$_5$ plane (^{4}Cp) 1.92, Fe···Fe 3.399(2), Br···Br 3.587(1); Br1-Fe1-Br2 92.01(4), Br1-Fe2-Br2 92.09(4), Fe1-Br1-Fe2 85.81(4), Fe1-Br2-Fe2 86.16(4).

and the ring planes, which is much longer than the value of 1.72 Å found in octaisopropylferrocene,[4] although octaisopropylferrocene is more sterically crowded.

Complexes **1** undergo smooth reactions with phenolates at ambient temperature (Scheme 1). Depending on the substituent pattern of the phenolate, the products are different in color, spectroscopic properties, and structure. With potassium 2,4,6-tri(*tert*-butyl)phenolate, **1a** yields red crystals, which are easily soluble in pentane and other aprotic solvents, extremely air-sensitive, and have a magnetic moment of 5.15 μ$_B$ in solution corresponding to the presence of four unpaired electrons. An attempted crystal-structure analysis provided evidence for a structure change. Unfortunately, the structure could not be resolved well but it shows the monomeric complex [(η^5-C$_5$H*i*Pr$_4$)Fe(OC$_6$H$_2$*t*Bu$_3$-2,4,6)] (**2a**) as drawn in Scheme 1. Since the Cp‴ derivative of **2a**, compound **2b**, was very similar and also did not give suitable crystals for X-ray diffraction, an experiment with 2,6-di(*tert*-butyl)phenolate was carried out in an attempt to obtain better crystals of the same type of complex.

From the reaction of **1a** with potassium 2,6-di(*tert*-butyl)phenolate, the diamagnetic compound **3a** was obtained in high yield as red-purple crystals, which are moderately air-stable. The NMR spectroscopic signals of **3a** (see Experimental Section) correspond to a sandwich complex with one tetraisopropylcyclopentadienyl and one oxocyclohexadienyl ligand. The crystal structure of **3a**[5] is shown in Figure 2. The distances between the iron atom and the two η^5-C$_5$ least-squares planes are 1.69 Å for the cyclopentadienyl and 1.64 Å for the oxocyclohexadienyl ligands. The angle between the least-squares planes is 6.6°. The carbon atoms of the six-membered ring show five bond lengths to the iron center ranging from 2.056(2) Å (Fe–C54) to 2.252(3) Å (Fe–C52) while the carbonyl carbon atom is found at a nonbonding distance of 2.414(3) Å from the iron center. The fold angle of the six-membered ring along the line C52···C56 is 9.5°, whereas for related complexes, fold angles of [Cp*Fe(η^5-C$_6$H$_5$O)] 1.6°,[6] (Cp* = η^5-C$_5$Me$_5$) for [Cp*Ir(η^5-C$_6$H$_5$O)]$^+$ 21°,[7] for [Cp*Rh(η^5-C$_6$H$_5$O)]$^+$ 14°,[8] for [Cp*Ru(η^5-C$_6$H$_5$O)] 4°,[9] for [Cp*Ru(η^5-2,6-*t*Bu$_2$OC$_6$H$_3$)] 19.1°[10] and for [(OC)$_3$Mn(η^5-C$_6$H$_5$O)] 21.3°[11] have been determined.

[*] Dr. M. Wallasch, Dr. G. Wolmershäuser, Prof. Dr. H. Sitzmann
FB Chemie der Universität Kaiserslautern
Erwin-Schrödinger-Strasse
67663 Kaiserslautern (Germany)
Fax: (+49) 631-205-2187
E-mail: sitzmann@chemie.uni-kl.de

[**] High-spin cyclopentadienyl complexes, part 5. This work was funded by Deutsche Forschungsgemeinschaft (DFG grant Si 366/9-1 and 9-2). We are grateful to Prof. Dr. O. J. Scherer for his generous support, and to Dr. G. Hornung for mass spectra. Part 4: H. Sitzmann, *Coord. Chem. Rev.* **2001**, *214*, 287–327.

 DOI: 10.1002/anie.200462153 © 2005 Wiley-VCH Verlag GmbH & Co. KGaA, Weinheim

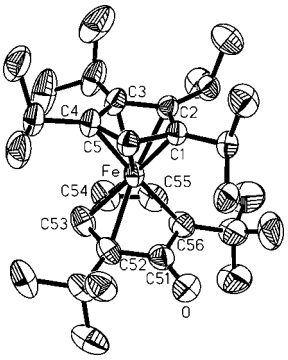

Figure 2. Crystal structure of **3a**. Selected interatomic distances [Å] and angles [°]: Fe-C (C1–C5) 2.074(2)–2.112(2), Fe-C (C52–C56) 2.056(2)–2.252(3), C51-O 1.246(3), Fe···C51 2.414(3); interplanar angle 6.6°.

The structure of **3a** suggests that a third alkyl substituent in the *para* position of the phenolate is necessary to stabilize the σ coordination of the phenolate found in **2a**. Among the oxocyclohexadienyl ligands mentioned above, the Ir[7] Rh,[8] and Ru[9,10] derivatives were formed in direct reactions from phenolate anions. For cyclopentadienyliron complexes with oxocyclohexadienyl ligands, indirect synthetic pathways had to be developed.[6,12]

Several reactions of complexes **1** with 2,6-dimethylphenolate gave oily product mixtures that could not be characterized. Only when the starting compound **1a** was prepared from lithium tetraisopropylcyclopentadienide (and contained a small amount of lithium bromide thereafter) and the reaction mixture with 2,6-dimethylphenolate was worked up after only 10 min of stirring at room temperature, could the paramagnetic complex **4a** be obtained in low yield by crystallization (Scheme 1).

The crystal structure of **4a** (Figure 3)[13] reveals a lithium cation[14] coordinated to the oxygen donor sites of one bis(μ,κ-O-2,6-dimethylphenolato)(tetraisopropylcyclopentadienyl)-ferrate(II) anion and the oxocyclohexadienyl part of another iron sandwich. Compound **4a** is the first example of a molecule in which two atoms of the same metal in the same oxidation state within the same molecule carry the same type

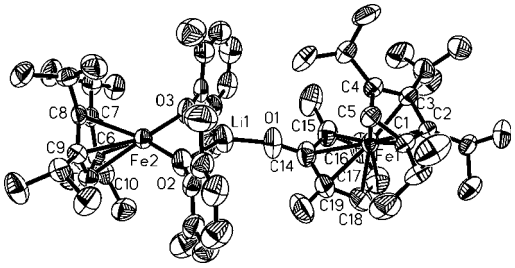

Figure 3. Crystal structure of **4a**. Selected interatomic distances [Å] and angles [°]: Fe1-C (C1–C5) 2.036(4)–2.093(4), Fe1-C (C15–C19) 2.051(5)–2.171(5), Fe1-dienyl plane (C15–C19) 1.58, Fe2-C (C6–C10) 2.276(4)–2.400(4), Li-O1 1.728(8), Li-O (O2–O3) 1.874(8) and 1.860(8), Fe2-O (O2–O3) 1.934(3) and 1.955(3); O2-Fe2-O3 83.97(11), Li-O-Fe (O2–O3) 93.3(2) and 93.6(3); sum of angles O-Li-O- 359.2

of cyclopentadienyl ligand and exhibit different spin states. The Fe–^{4}Cp (ring center) separation for the sandwich part is 1.68 Å, whereas the corresponding value for the other iron–ring-center separation is 1.97 Å, which is an increase of more than 17%. This result is comparable to the situation found in the low-spin and high-spin 1,1′-dimethylmanganocene (1.73 Å vs. 2.04 Å) by electron diffraction in the gas phase.[15]

Apart from the introduction of other nucleophiles, such as hydrocarbyl anions, it should be possible to oxidize the readily available complexes **1** and **2**, with their high-spin d^6 electron configuration, to Fe^{III} half-sandwich complexes of the as-yet unknown type $[CpFeX_2]$ with a d^5 electron configuration and without additional donor ligands.

Experimental Section

The extremely air-sensitive complexes were prepared and handled in a glove box (MBraun company, Garching) filled with argon. Measurement of magnetic properties in solution followed a modification[16] of Evans' method.[17] Complexes **1** were prepared as described for **1a** in ref. [1], obtained in 70–80% yield by evaporation of the filtered pentane extracts, and were used without further purification, see ref. [14]. Single crystals of **1b** were obtained from concentrated pentane solution at room temperature.

2a: A solution of $K(OC_6H_2tBu_3$-2,4,6) (246 mg, 0.82 mmol) in THF (5 mL) was added to a solution of **1a** (300 mg, 0.41 mmol (dimer)) in THF (5 mL). The solution was stirred for 12 h, then evaporated to dryness. The solid residue was extracted with pentane (10 mL) and the filtered extract evaporated to a volume of about 2 mL. At ambient temperature **2a** was obtained as red crystals in 252 mg (0.46 mmol, 56%) yield. Elemental analysis (%) calcd for $C_{35}H_{58}FeO$ (550.70): C 76.34, H 10.62; found C 75.43, H 10.60; EI-MS (70 eV): *m*/*z* (%): 550.2 (6) [M^+], 493.2 (5) [$M^+-C_4H_9$], 289.1 (1) [$Fe\{C_5H(CHMe_2)_4\}^+$], 262.2 (17) [$HOC_6H_2tBu_3^+$], 247.2 (100) [$HOC_6H_2tBu_3^+-CH_3$], 57.1 (88) [$C_4H_9^+$]; ^{1}H NMR (400 MHz, 298 K, C_6D_6): $\delta = 119.2$ ($\Delta\nu_{1/2}$ 395 Hz, 12H, $CH(CH_3)_2$), 72.9 ($\Delta\nu_{1/2}$ 935 Hz, 12H, $CH(CH_3)_2$), 28.9 ($\Delta\nu_{1/2}$ 404 Hz, 18H, *o*-$C(CH_3)_3$), −10.9 (9H, *p*-$C(CH_3)_3$), −106.0 ppm ($\Delta\nu_{1/2}$ 817 Hz, 12H, $CH(CH_3)_2$).Signals for the ring protons of both ligands could not be detected.

3a: A solution of $K(OC_6H_3tBu_2$-2,6) (200 mg, 0.82 mmol) in THF (5 mL) was added to a solution of **1a** (300 mg, 0.41 mmol) in THF (5 mL). The solution was stirred for 12 h, then evaporated to dryness. The solid residue was extracted with toluene (10 mL) and the filtered extract evaporated to a volume of about 2 mL. At ambient temperature **3a** was obtained as violet crystals in 257 mg (0.52 mmol, 64%) yield. Elemental analysis (%) calcd for $C_{31}H_{50}FeO$ (494.59): C 75.28, H 10.19; found C 74.20, H 10.19; EI-MS (70 eV): *m*/*z* (%): 522.3 (100) [$Fe\{C_5H(CHMe_2)_4\}_2^+$], 494.2 (3) [M^+], 438.2 (7) [$M^+-C_4H_9$], 289.1 (1) [$Fe\{C_5H(CHMe_2)_4\}^+$], 181.1 (3) [$OC_6H_3(CH_3)_2^+$], 57.1 (24) [$C_4H_9^+$], 43.0 (25) [C_3H_7]. ^{1}H NMR (400 MHz, 298 K, C_6D_6): $\delta = 5.31$ (d, ^3J(HH) = 6.0 Hz, 2H, meta), 4.90 (t, ^3J(HH) = 6.0 Hz, 1H, para), 4.49 (s, 1H, $C_5H(CHMe_2)_4$), 2.81 (m, 2H, $CHMe_2$), 2.70 (m, 2H, $CHMe_2$), 1.71 (s, 18H, $C(CH_3)_3$), 1.45 (br, 6H, $CH(CH_3)_2$), 1.17 (d, ^3J(HH) = 7.5 Hz, 6H, $CH(CH_3)_2$), 1.15 (d, ^3J(HH) = 7.5 Hz, 6H, $CH(CH_3)_2$), 0.95 ppm (d, ^3J(HH) = 6.6 Hz, 6H, $CH(CH_3)_2$). $^{13}C\{^1H\}$-NMR (100 MHz, C_6D_6): $\delta = 152.5$ (*C*O), 105.6, 102.1, 91.4, 83.6, 67.8, 65.8, 36.2 (CMe_3), 30.4 ($C(CH_3)_3$), 27.2 ($CH(CH_3)_2$), 26.9 ($CHMe_2$), 26.7 ($CH(CH_3)_2$), 24.2 ($CHMe_2$), 23.6 ($CH(CH_3)_2$), 23.2 ppm ($CH(CH_3)_2$).

4a: A solution of $K(OC_6H_3Me_2$-2,6) (131 mg, 0.82 mmol) in THF (5 mL) was added to a solution of **1a** (300 mg, 0.41 mmol) in THF (5 mL). The solution was stirred for 10 min, then evaporated to dryness. The solid residue was extracted with pentane (25 mL), the extract was filtered and evaporated to dryness. Crystals suitable for X-ray diffraction were grown by slow evaporation of a saturated pentane solution at room temperature, yield approximately 5 mg

 © 2005 Wiley-VCH Verlag GmbH & Co. KGaA, Weinheim

(0.0053 mmol, 1.3%) of green blocks immersed in an oily product mixture. (Observations and a comment on the crystallization of extremely soluble complexes from viscous solutions can be found in ref. [18]).

Received: September 29, 2004
Revised: December 21, 2004
Published online: March 22, 2005

Keywords: coordination chemistry · cyclopentadienyl complexes · iron · magnetic properties · phenolate

[1] H. Sitzmann, T. Dezember, W. Kaim, F. Baumann, D. Stalke, J. Kärcher, E. Dormann, H. Winter, C. Wachter, M. Kelemen, *Angew. Chem.* **1996**, *108*, 3013–3016; *Angew. Chem. Int. Ed. Engl.* **1996**, *35*, 2872–2874.

[2] Crystal structure analysis of **1b**, $Fe_2C_{34}H_{58}Br_2Fe_2$, $M_r = 738.32$: IPDS diffractometer with imaging system (Stoe), $Mo_{K\alpha}$ radiation, $\lambda = 71.073$ pm, $2\Theta_{max} = 51.36°$, 359 images with $0° \le \varphi \le 359°$ and $\Delta\varphi = 1.0°$, $T = 293(2)$ K, crystal dimensions $0.40 \times 0.24 \times 0.12$ mm^3, monoclinic, space group $P2_1/c$, lattice parameters:, $a = 13.9684(9)$, $b = 18.6529(16)$, $c = 15.1953(9)$ Å, $\beta = 113.680(7)°$, $V = 3625.8(4)$ Å^3, $Z = 4$, $\rho_{calcd} = 1.353$ g cm^{-3}, $\mu(Mo_{K\alpha}) = 30.24$ cm^{-1}, numerical absorption correction (ABST/PLATON 98), transmission factors 0.45615 to 0.70370, structure solution: direct methods (SIR97), full-matrix least-squares refinement based on F_o^2 (SHELXL-97), 46839 reflections, 6637 unique reflections, 361 parameters, 0 restraints, $R1(F_o > 2\sigma(F_o)) = 0.0459$, $wR2(\text{all}) = 0.1093$, residual electron density $+0.625$ to -0.335 e Å^{-3}, CH and CH_3 groups have been refined as rigid groups (C–H 0.96 Å) with variable torsion angles (C-C-H and H-C-H 109.5°). Further details on the crystal structure investigation may be obtained from the Fachinformationszentrum Karlsruhe, 76344 Eggenstein-Leopoldshafen, Germany (fax: (+49) 7247-808-666; e-mail: crysdata@fiz-karlsruhe.de), on quoting the depository numbers CSD-264484 **1b**, -264486 **3a**, and -264485 **4a**.

[3] K. Jonas, P. Klusmann, R. Goddard, *Z. Naturforsch. B* **1992**, *50*, 394–404.

[4] V. Quindt, D. Saurenz, O. Schmitt, M. Schär, T. Dezember, G. Wolmershäuser, H. Sitzmann, *J. Organomet. Chem.* **1999**, *579*, 376–384.

[5] Crystal structure determination of **3a** $FeC_{31}H_{50}O$ $M_r = 494.59$: IPDS diffractometer with imaging system (Stoe), $Mo_{K\alpha}$ radiation, $\lambda = 71.073$ pm, $2\Theta_{max} = 51.36°$, 359 images with $0° \le \varphi \le 359°$ and $\Delta\varphi = 1.0°$, $T = 293(2)$ K, crystal dimensions $0.60 \times 0.48 \times 0.24$ mm^3, monoclinic, space group $P2_1/n$, lattice parameters: $a = 9.7545(6)$, $b = 15.7666(8)$, $c = 18.2239(12)$ Å, $\beta = 91.063(7)°$, $V = 2802.3(3)$ Å^3, $Z = 4$, $\rho_{calcd} = 1.172$ g cm^{-3}, $\mu(Mo_{K\alpha}) = 5.58$ cm^{-1}, absorption correction with the multi-scan method (ABST/PLATON 98), transmission factors 0.74642 to 0.89045, structure solution: direct methods (SIR97), full-matrix least-squares refinement based on F_o^2 (SHELXL-97), 25361 reflections, 5245 unique reflections, 312 parameters, no restraints, $R1(F_o > 2\sigma(F_o)) = 0.0365$, $wR2(\text{all}) = 0.0977$, residual electron density $+0.221$ to -0.258 e Å^{-3}, CH and CH_3 groups have been refined as rigid groups with variable torsion angles (C–H 0.96 Å; C-C-H and H-C-H 109.5°).

[6] F. Moulines, L. Djakovitch, M.-H. Delville-Desbois, F. Robert, P. Gouzerh, D. Astruc, *J. Chem. Soc. Chem. Commun.* **1995**, 463.

[7] H. Amouri, J. Le Bras, J. Vaisserman, *Organometallics* **1998**, *17*, 5850.

[8] J. Le Bras, H. Amouri, Y. Besace, J. Vaisserman, G. Jaouen, *Bull. Soc. Chim. Fr.* **1995**, *132*, 1073.

[9] U. Koelle, M. J. Wang, G. Raabe, *Organometallics* **1992**, *11*, 2573.

[10] S. D. Loren, B. K. Campion, R. H. Heyn, T. Don Tilley, B. E. Bursten, K. W. Luth, *J. Am. Chem. Soc.* **1989**, *111*, 4712.

[11] S.-G. Lee, J. A. Kim, Y. K. Chung, T.-S. Yoon, N.-J. Kim, W. Shin, J. Kim, K. Kim, *Organometallics* **1995**, *14*, 1023.

[12] J. F. Helling, W. Hendrickson, *J. Organomet. Chem.* **1979**, *168*, 87–95.

[13] Crystal structure determination of **4a**, $Fe_2LiC_{58}H_{85}O_3$, $M_r = 948.90$, IPDS diffractometer with imaging system (Stoe), $Mo_{K\alpha}$ radiation, $\lambda = 71.073$ pm, $2\Theta_{max} = 51.36°$, 359 images with $0° \le \varphi \le 359°$ and $\Delta\varphi = 1.0°$, $T = 293(2)$ K, crystal dimensions $0.44 \times 0.44 \times 0.08$ mm^3, monoclinic, space group $P2_1/n$, lattice parameters: $a = 17.857(3)$, $b = 17.645(2)$, $c = 18.355(3)$ Å, $\beta = 111.407(18)°$, $V = 5384.5(15)$ Å^3, $Z = 4$, $\rho_{calcd} = 1.171$ g cm^{-3}, $\mu(Mo_{K\alpha}) = 5.79$ cm^{-1}, numerical absorption correction (ABST/PLATON 98), transmission factors 0.79820 to 0.95565, structure solution: direct methods (SIR97), full-matrix least-squares refinement based on F_o^2 (SHELXL-97), 73047 reflections, 9790 unique reflections, 610 parameters, 3 restraints, $R1(F_o > 2\sigma(F_o)) = 0.0435$, $wR2(\text{all}) = 0.0884$, residual electron density $+0.299$ to -0.194 e Å^{-3}, CH and CH_3 groups have been refined as rigid groups with variable torsion angles (C–H 0.96 Å; C-C-H and H-C-H 109.5°).

[14] When complexes **1**, isolated by pentane extraction, filtration, and evaporation, are redissolved in pentane, there is always a small amount of insoluble material left, which is presumably alkali halide carried into pentane solution. After two repetitions of this procedure a visible turbidity can still be observed upon redissolution. For the reactions described herein the material from the first pentane extract has been used.

[15] A. Almenningen, A. Haaland, S. Samdal, *J. Organomet. Chem.* **1978**, *149*, 219–229.

[16] K. Sur, *J. Magn. Reson.* **1989**, *82*, 169–173.

[17] D. F. Evans, *J. Chem. Soc.* **1959**, 2003.

[18] F. Baumann, E. Dormann, Y. Ehleiter, W. Kaim, J. Kärcher, M. Kelemen, R. Krammer, D. Saurenz, D. Stalke, C. Wachter, G. Wolmershäuser, H. Sitzmann, *J. Organomet. Chem.* **1999**, *587*, 267–283.

 © 2005 Wiley-VCH Verlag GmbH & Co. KGaA, Weinheim

Oligonucleotide Folding

Kinetics of Photoinduced RNA Refolding by Real-Time NMR Spectroscopy**

Philipp Wenter, Boris Fürtig, Alexandre Hainard, Harald Schwalbe, and Stefan Pitsch**

The catalytic and regulatory functions of RNA strongly depend on the reorganization of the tertiary structure and the refolding of secondary structures.[1] This dynamic diversity is illustrated by the frequent occurrence of multiple folding pathways,[2] as well as metastable[3] and coexisting ("bistable") conformations.[4] The folding of RNA from a denatured, non-native state has been studied extensively by a variety of techniques,[5] which have established a hierarchical folding pathway in which the rapid formation of secondary structural elements precedes the slower formation of tertiary elements.[6] In contrast, only a few time-resolved studies of RNA refolding from an unperturbed native state have been described.[7]

Herein we report a new method for the investigation of structure- and time-resolved RNA refolding that is based on the photolytic generation of preselected conformations in a nonequilibrium state, followed by the observation of refolding with real-time NMR spectroscopy. This method was applied to the detailed kinetic characterization of a bistable 20-base RNA sequence, which is known to adopt two coexisting hairpin-loop structures.[8]

The 20-base RNA sequence 5′-r[GACCGGAAG-GUCCGCCUUCC]-3′ forms two interconverting hairpin structures in a temperature-dependent equilibrium (Folds A and B, Figure 1b). To selectively destabilize the more stable Fold B, the selected guanosine groups that form base pairs in Fold B, but not in Fold A, were replaced by O^6-[(*S*)-1-(2-nitrophenyl)ethyl] guanosine ((*S*)-^{NPE}G, Figure 1a).[9] The bulky NPE group was expected to disrupt Watson–Crick G-C base-pair formation, thereby destabilizing associated secondary structures; upon subsequent photolytic cleavage, the base-pairing properties of the parent guanosine would be restored to allow refolding to take place.[10]

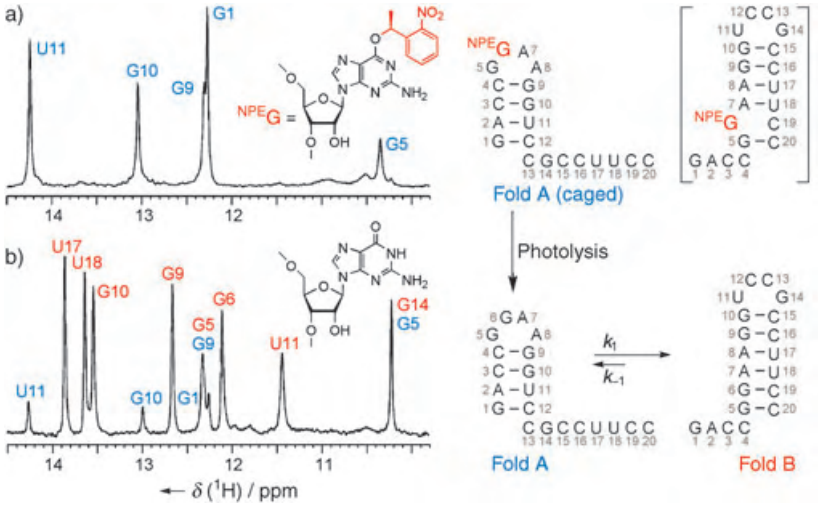

Figure 1. ^{1}H NMR spectra of imino protons and folding structures of the 20-base RNA sequence (c = 0.27 mM, 288 K) with color-coded signal assignments; imino proton NMR spectroscopy reveals individual signals for each proton involved in the central H bond of Watson–Crick base pairs. a) Spectrum of the sequence that is conformationally locked by the O^6-(*S*)-NPE modified guanosine at position 6 (^{NPE}G6, structure shown as inset); only the set of signals of Fold A are apparent. b) Spectrum obtained after photolytic removal of the NPE group by three laser pulses and subsequent equilibration for 1 h, which shows the two sets of signals of Folds A and B in a 1:5 ratio.

The RNA sequence 5′-r[GACCG($^{(S)\text{-NPE}}$G)AAG-GUCCGCCUUCC]-3′, which contains a single (*S*)-NPE modification on G6, showed the characteristic five imino proton signals exclusively for Fold A (Figure 1a and Figure S1, Supporting Information).[11] Further 2D-HSQC and HNN-COSY experiments on the same sequence labeled with ^{15}N at N(3) of C3 and N(1) of G10 showed that G10 is involved in only one base-pair interaction, and confirmed that its pairing partner is C3 (Figure S2, Supporting Information). These experiments unambiguously show that the introduction of only one photolabile NPE group leads to a complete shift of the conformational equilibrium towards the intrinsically less stable Fold A. The broadened imino proton signal of G9, however, indicates a perturbation of the hairpin-loop structure.

The imino proton spectrum shown in Figure 1b was generated from a sample of the $^{(S)\text{-NPE}}$G6-modified, ^{15}N-labeled RNA sequence (Figure 1a) photolyzed by three laser pulses directed into the NMR tube through a glass fiber and a pencil-like quartz tip,[12] and is identical to the spectrum of the unmodified sequence (Figures S1 and S2, Supporting Information); HPLC and MS analyses confirmed the clean and

[*] P. Wenter, A. Hainard, Prof. Dr. S. Pitsch
École Polytechnique Fédérale de Lausanne
Laboratory of Nucleic Acid Chemistry, EPFL-BCH
1015 Lausanne (Switzerland)
Fax: (+41) 21-693-9355
E-mail: stefan.pitsch@epfl.ch
B. Fürtig, Prof. Dr. H. Schwalbe
Johann Wolfgang Goethe University
Institute for Organic Chemistry and Chemical Biology
Center for Biological Magnetic Resonance
Marie-Curie Strasse 11, 60439 Frankfurt/Main (Germany)
Fax: (+49) 69-7982-9515
E-mail: schwalbe@nmr.uni-frankfurt.de

[**] We are grateful to Jens Wöhnert, Julia Wirmer, and Christian Richter for discussions, and to Rita Merz for conducting syntheses. The work was supported by the EPFL, the Swiss National Science Foundation (No. 2000-068090), the SFB 579 "RNA-Ligand-Wechselwirkung", and the "Studienstiftung des Deutschen Volkes" (B.F.).

Supporting information for this article is available on the WWW under http://www.angewandte.org or from the author.

 © 2005 Wiley-VCH Verlag GmbH & Co. KGaA, Weinheim DOI: 10.1002/anie.200462724

traceless removal (>98%) of the NPE group (Figure S3, Supporting Information).

Single-scan imino proton NMR spectra of the (*S*)-NPE-modified RNA sequence both before and 1 s after photolysis by a single laser pulse were nearly identical, which indicates that the sequence retained its preformed folded structure after release of the NPE group. To directly monitor the course of the cleavage reaction, identical experiments were carried out with a 1:1 mixture of two diastereomeric 20-base RNA oligomers that were obtained by the introduction of an (*R*/*S*)-NPE-protected guanosine residue. The imino proton signal splitting caused by the two configurations of the photolabile group (Figure 2a) collapsed to a single set within 1 s after photolysis by one laser pulse (Figure 2b). Clearly, the folded conformation initially imposed by the photolabile group was completely conserved immediately after its photolytic removal. Therefore, this method was successful for the selective preparation of one of the two folded structures that normally coexist for this sequence.

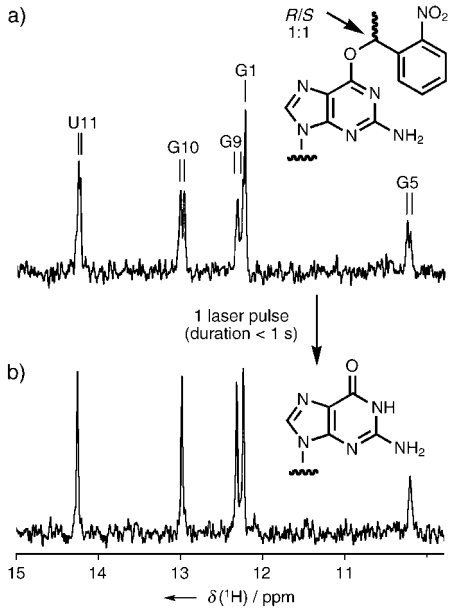

Figure 2. The course of the photolysis reaction at $c = 0.27$ mM, as monitored by single-scan ^{1}H NMR spectra of the 20-base RNA sequence initially modified at G6 with a 1:1 mixture of (*S*)- and (*R*)-NPE groups. a) Before photolysis; the peak splitting results from the two different NPE configurations. b) Immediately after a single laser pulse (duration <1 s); the initial peak splitting disappears as a result of the photolytic removal of the NPE group.

For the determination of kinetic parameters, two sets of experiments were carried out: one in which the RNA concentration was varied ($c = 0.17$, 0.26, and 0.34 mM; $T = 283$ K) and the other in which temperature was the variable ($T = 283$, 288, 293, and 298 K; $c = 0.26$ mM). After one laser pulse, 128 single-scan NMR spectra were recorded over a time period of 280 s during which equilibrium was established. The analysis was carried out with the resolved imino proton signals of U11/G10 and U17/G9; the former two correspond to the disappearing Fold A and the latter correspond to the appearing Fold B.

The equilibrium constants K were obtained from the relative intensities of the pairs of imino proton signals of U11/U17 and G9/G10. From the temperature dependence of the K values, which range between $K \approx 4$ at 298 K and $K \approx 7$ at 283 K, the values of $\Delta H = -5.9 \pm 0.5$ kcal mol^{-1} and $\Delta S = -17.0 \pm 1.9$ cal mol^{-1} K^{-1} were determined within a confidence interval (CI) of 90% (Figure 3c). The refolding rate constants k_1 were determined by fitting the normalized build-up and decay data for U17/G9 and U11/G10 signals, respectively, to the rate law for a reversible unimolecular reaction (Figure 3a,b; Figure S4, Supporting Information).

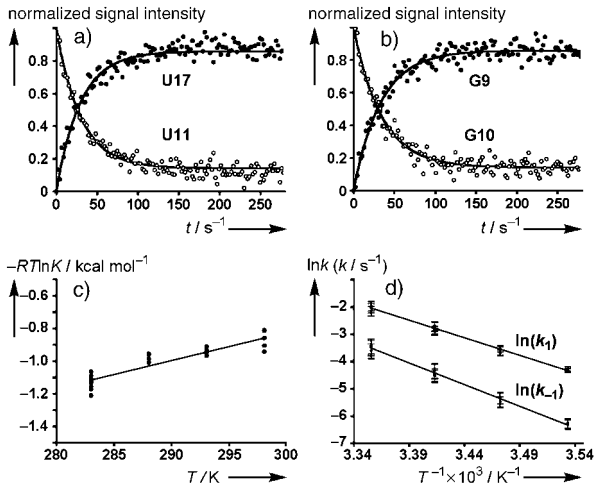

Figure 3. Kinetic analysis of the refolding reaction monitored through time-dependent single-scan NMR spectroscopic experiments with the photolyzed 20-base RNA sequence. a,b) Normalized imino proton signal intensities (U11/G10 from Fold A; U17/G9 from Fold B) as a function of time, recorded at 288 K after photolysis by a single laser pulse. The data curves were fit to the rate law of a reversible, unimolecular reaction (See Supporting Information for detailed procedures and fits at other temperatures). c) Linearized plot of $K = [\text{Fold B}]/[\text{Fold A}]$ according to $\Delta G = -RT\ln K = \Delta H - T\Delta S$. d) Arrhenius plot of k_1 and k_{-1} according to $\ln k = -\Delta H^{\ddagger}/(RT) + \ln A$; the error bars (shown at 99% CI) include the *K*-standard error of 10% and the curve-fit standard deviation.

The mean rate constants for the forward reaction ranged from $k_1 = 0.0136 \pm 0.0010$ s^{-1} at 283 K to $k_1 = 0.131 \pm 0.024$ s^{-1} at 298 K, and those for the reverse reaction from $k_{-1} = 0.0019 \pm 0.0002$ s^{-1} at 283 K to $k_{-1} = 0.031 \pm 0.006$ s^{-1} at 298 K (90% CI). These values were fit with the Arrhenius equation to yield the activation enthalpy $\Delta H^{\ddagger} = 25.5 \pm 3.1$ kcal mol^{-1} and the frequency factor $A = 10^{(17.8 \pm 1.2)}$ s^{-1} for the forward reaction within 90% CI. The respective values for the reverse reaction were $\Delta H^{\ddagger} = 30.6 \pm 3.1$ kcal mol^{-1} and $A = 10^{(20.9 \pm 1.4)}$ s^{-1} (Figure 3d). The rate constants determined at different concentrations were identical within 90% CI (for details, see Tables S5 and S6, Supporting Information).

These results suggest a pure first-order refolding mechanism. The activation enthalpy $\Delta H^{\ddagger} = 25.5$ kcal mol^{-1} amounts to about half the value for the entire base-pairing enthalpy

 © 2005 Wiley-VCH Verlag GmbH & Co. KGaA, Weinheim

$\Delta H = 55$ kcal mol^{-1}, which was determined by thermal denaturation studies.[8] This indicates that the rate-limiting step of the refolding mechanism involves disruption of about half the number of base pairs present.

Imino proton exchange rates with water were extracted from NOESY cross-peaks to obtain more information on the influence that global dynamics (interconverting folds) have on the local dynamic properties of individual base pairs.[13] These values were compared with those of the two corresponding truncated RNA hairpins that are conformationally locked to represent Fold A and Fold B, as they lack unpaired overhangs (Figure 4). In general, the individual water

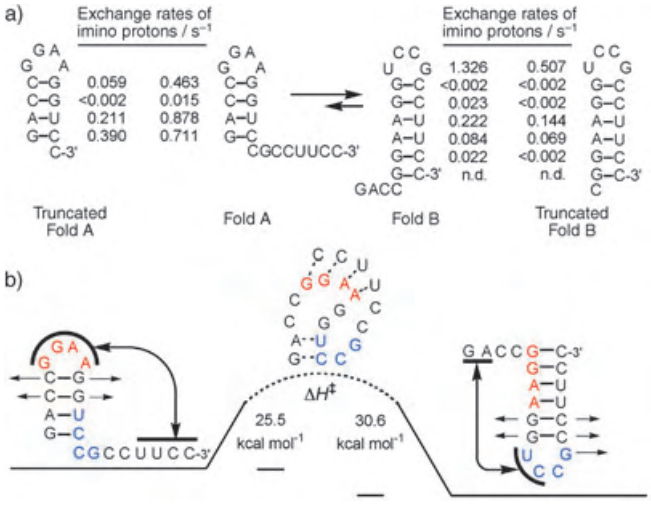

Figure 4. a) Exchange rates between base-pair imino protons and water, as determined in both folds of the bistable 20-base RNA sequence and the corresponding truncated, conformationally locked hairpin sequence; the detection level was 0.002 s^{-1} and the accuracy was estimated at ±5%; (n.d. = not detected).[13] b) Proposed associative refolding mechanism consistent with water exchange rates and kinetic parameters. During the course of refolding, which presumably involves several elementary steps,[14] transient structures could be formed in which the terminal base pairs of the stems of both Folds A and B are present simultaneously, as indicated schematically. The loop-forming nucleotides are indicated in color for clarity.

exchange rates within the bistable RNA sequence were significantly higher than the rates within the two truncated hairpin sequences (Figure 4a), which demonstrates that base pairs in the interconverting RNA structures are less rigid than the identical base pairs in the static structures. Interestingly, the increase in the water-exchange rates of the 20-base RNA sequence relative to those of the truncated hairpins became more important the closer the base pairs were to the loop region.

This result suggests an associative mechanism of refolding, which is proposed schematically in Figure 4b. In this mechanism, the refolding would be initiated by the formation of new base pairs between complementary nucleotides of the loop and the dangling ends, with a simultaneous detachment of the base pairs close to the loop.

With the method presented herein, we were able to accurately characterize the structure- and time-resolved refolding of a 20-base bistable RNA sequence. The refolding rate constants are at least four orders of magnitude less than those measured for hairpin formation in similar sequences from an unfolded state ($k = 10^4$–10^5 s^{-1}).[6] This new method might be extended toward the targeted preparation and kinetic characterization of distinct intermediates that are present along the complex folding pathways of larger RNA sequences.

Received: November 25, 2004
Published online: March 22, 2005

Keywords: kinetics · NMR spectroscopy · oligonucleotides · photolysis · RNA structures

[1] a) N. G. Walter, D. A. Harris, M. J. B. Pereira, D. Rueda, *Biopolymers* **2002**, *61*, 224–241; b) W. C. Winkler, R. R. Breaker, *ChemBioChem* **2001**, *2*, 1024–1032; c) P. Brion, E. Westhof, *Annu. Rev. Biophys. Biomol. Struct.* **1997**, *26*, 113–137.
[2] J. Pan, D. Thirumalai, S. A. Woodson, *J. Mol. Biol.* **1997**, *273*, 7–13.
[3] D. K. Treiber, M. S. Rook, P. P. Zarrinkar, J. R. Williamson, *Science* **1998**, *279*, 1943–1946.
[4] C. Höbartner, R. Micura, *J. Mol. Biol.* **2003**, *325*, 421–431.
[5] a) P. P. Zarrinkar, J. R. Williamson, *Science* **1994**, *265*, 918–924; b) X. Zhuang, L. E. Bartley, H. P. Babcock, R. Russell, T. Ha, D. Herschlag, S. Chu, *Science* **2000**, *288*, 2048–2051; c) B. Sclavi, M. Sullivan, M. R. Chance, M. Brenowitz, S. A. Woodson, *Science* **1998**, *279*, 1940–1943; d) J. Ravetch, J. Gralla, D. M. Crothers, *Nucleic Acids Res.* **1974**, *1*, 109–127; e) M. Menger, F. Eckstein, D. Porschke, *Biochemistry* **2000**, *39*, 4500–4507.
[6] a) D. Pörschke, *Mol. Biol. Biochem. Biophys.* **1977**, *24*, 191–218; b) D. M. Crothers, P. E. Cole, C. W. Hilbers, P. G. Shulman, *J. Mol. Biol.* **1974**, *87*, 63–88; c) D. Thirumalai, S. A. Woodson, *RNA* **2000**, *6*, 790–794; d) D. Thirumalai, N. Lee, S. A. Woodson, D. K. Klimov, *Annu. Rev. Phys. Chem.* **2001**, *52*, 751–762; e) I. Tinoco, Jr., C. Bustamante, *J. Mol. Biol.* **1999**, *293*, 271–281.
[7] a) T. C. Gluick, R. B. Gerstner, D. E. Draper, *J. Mol. Biol.* **1997**, *270*, 451–463; b) D. C. Lynch, P. R. Schimmel, *Biochemistry* **1974**, *13*, 1841–1852; c) D. C. Lynch, P. R. Schimmel, *Biochemistry* **1974**, *13*, 1852–1861.
[8] C. Höbartner, M. O. Ebert, B. Jaun, R. Micura, *Angew. Chem.* **2002**, *114*, 619–623; *Angew. Chem. Int. Ed.* **2002**, *41*, 605–609.
[9] The synthesis of the $^{(S)\text{-NPE}}$G-phosphoramidite is described in the Supporting Information; the *S* configuration of the NPE group was chosen arbitrarily. All RNA sequences were prepared from 2′-*O*-triisopropylsilyloxymethyl-protected phosphoramidites according to a) S. Pitsch, P. A. Weiss, L. Jenny, A. Stutz, X. Wu, *Helv. Chim. Acta* **2001**, *84*, 3773–3795; the synthesis of the ^{15}N-labeled phosphoramidites is reported in b) P. Wenter, S. Pitsch, *Helv. Chim. Acta* **2003**, *86*, 3955–3974.
[10] A similar approach for the selective destabilization of coexisting RNA secondary structures with O^6-(2,2,2-trichloroethyl)-modified guanosine was reported by C. Höbartner, H. Mittendorfer, K. Breuker, R. Micura, *Angew. Chem.* **2004**, *116*, 4012–4015; *Angew. Chem. Int. Ed.* **2004**, *43*, 3922–3925; however, removal of the Zn-labile trichloroethyl group is much slower than RNA refolding processes and thus prevents the determination of kinetic parameters.
[11] All NMR spectroscopic experiments were carried out with a Bruker AV 800 MHz spectrometer, equipped with 5-mm TXI-HCN cryogenic probes and *z*-axis gradients; detailed NMR spectroscopic methods are described in the Supporting Information; all experiments were carried out in H_2O/D_2O (9:1) and

 © 2005 Wiley-VCH Verlag GmbH & Co. KGaA, Weinheim

potassium arsenate buffer (25 mM, pH 7.0; identical results were obtained with sodium and potassium phosphate buffers in preliminary experiments). The 2D-HSQC and HNN-COSY spectra were recorded according to a) S. Mori, C. Abeygunawardana, M. O'Neil-Johnson, P. C. M. Vanzijl, *J. Magn. Reson. B* **1995**, *108*, 94 – 98 and b) A. J. Dingley, S. Grzesiek, *J. Am. Chem. Soc.* **1998**, *120*, 8293 – 8297.

[12] T. Kühn, H. Schwalbe, *J. Am. Chem. Soc.* **2000**, *122*, 6169 – 6174.

[13] Water exchange rates were extracted according to R. R. Ernst, G. Bodenhausen, A. Wokaun, *International Series of Monographs on Chemistry*, *Vol. 14*, Oxford University Press, **1987**; further details are given in the Supporting Information. In principle, overlapping signals at the resonance frequency of $^{1}H_{H_2O}$ could influence the intensity of the exchange-induced water–imino cross-peaks in the 2D NOESY experiment; however, the ribose protons are too far away from the imino protons. Hydroxy group protons are in exchange with water and could potentially contribute to the cross-peak intensity; again, the effect is made negligible by long distance. Base protons resonate upfield and cannot contribute to the cross-peak intensity.

[14] a) C. Flamm, W. Fontana, I. L. Hofacker, P. Schuster, *RNA* **2000**, *6*, 325 – 338; b) W. Zhang, S. J. Chen, *Proc. Natl. Acad. Sci. USA* **2002**, *99*, 1931 – 1936.

 © 2005 Wiley-VCH Verlag GmbH & Co. KGaA, Weinheim

DNA–Enzyme Conjugates

Covalent Hemin–DNA Adducts for Generating a Novel Class of Artificial Heme Enzymes**

*Ljiljana Fruk and Christof M. Niemeyer**

An important goal of nanobiotechnology is the generation of novel biomaterials with precise control at the nanometer scale.[1] DNA oligomers play an important role as structure-directing agents in the bottom-up fabrication of nanostructured functional devices, owing to their tremendous molecular recognition capabilities. The generation of semisynthetic DNA–protein conjugates makes it possible to combine the unique properties of DNA with the almost unlimited variety of functional components of proteins, which have evolved naturally to perform highly specific catalytic turnovers, energy conversions, or translocations.[2] However, to take advantage of the distinct functionalities of DNA–protein conjugates, one must face the challenge of developing synthetic strategies that permit control over both the stoichiometry and regioselectivity of DNA–protein coupling reactions.

Herein we report a novel approach toward well-defined and highly functional conjugates between DNA oligomers and enzymes that contain the hemin (iron protoporphyrin IX complex) prosthetic group. In the first step, covalent DNA–hemin adducts ($hemD_1$ and $hemD_2$; Scheme 1a) were synthesized on solid phase. After cleavage from the solid phase and purification, the hemD adducts were used to reconstitute apo-myoglobin (apo-Mb: myoglobin without its hemin prosthetic group).[3] Reconstitution of apo-Mb with $hemD_1$ and $hemD_2$ produced enzymatically active myoglobin that contained one or two DNA oligomers (MbD_1 and MbD_2, respectively; Scheme 1b) coupled to the enzyme in close proximity to the active site. To show that the DNA oligomers can be used as molecular handles for selective DNA-directed assembly, the MbD conjugates were hybridized to complementary capture oligomers immobilized on a solid support (Scheme 1c). Subsequent analysis of the enzymatic peroxidase activity revealed that the MbD conjugates are far more active than native myoglobin (Mb).

The oxygen storage protein Mb, which contains a non-covalently bound heme moiety, has been studied intensively over the past 30 years as a model system to investigate the functional role of the heme iron center,[4,5] long-range electron-transfer processes,[6] and the effects of metal exchanges or modifications of the heme side chains on the properties of the protein.[7,8] Although artificial Mbs have been prepared by site-directed mutagenesis,[9] the relative ease of heme removal and subsequent reconstitution of apo-Mb with functional porphyrin derivatives makes this system convenient for the design and study of artificial heme enzymes.[6] As an example, Hayashi and co-workers have shown that heme chemically modified with anionic groups at its propionate chains imparts Mb with enhanced peroxidase activity toward cationic substrates.[10]

Artificial Mb was chosen as an initial model system to investigate our concept of DNA conjugation (summarized in Scheme 1), as there is already a large body of knowledge about this protein. To this end, a 5′-alkylamino-modified 12-mer oligonucleotide (5′-amino-TCTCAACTCGTA) was synthesized with conventional phosphoramidite chemistry. Hemin was activated with *O*-(benzotriazol-1-yl)-*N*,*N*,*N*′,*N*′-tetramethyluronium hexafluorophosphate (HBTU) and *N*,*N*-diisopropylethylamine (DiPEA) in DMF/CH_3CN, and the resulting solution was injected into a DNA synthesizer to carry out the coupling reaction with the 5′-amino group of the oligomer. Following incubation for 30 min and deprotection under mild conditions (*tert*-butylamine, MeOH, H_2O), the oligonucleotide was purified with reversed-phase HPLC.[11] The two major products formed were identified by MALDI MS as hemin coupled with either one or two DNA oligomers ($hemD_1$ and $hemD_2$, respectively; Scheme 1a).

Both $hemD_1$ and $hemD_2$ were used in the reconstitution of apo-Mb to yield the conjugates MbD_1 and MbD_2, respectively (Scheme 1b). Chromatographic analysis of the reconstitution

[*] Dr. L. Fruk, Prof. Dr. C. M. Niemeyer
Fachbereich Chemie
Biologisch-Chemische Mikrostrukturtechnik
Universität Dortmund
Otto-Hahn Strasse 6, 44227 Dortmund (Germany)
Fax: (+49) 231-755-7082
E-mail: christof.niemeyer@uni-dortmund.de

[**] This work was supported by the Deutsche Forschungsgemeinschaft, the Alexander von Humboldt Foundation (research fellowship for L.F.), and the Fonds der Chemischen Industrie. We thank Joachim Müller for experimental assistance with peroxidase enzyme assays and Dr. Jens Müller for the provision of the DNA synthesizer.

Supporting information for this article is available on the WWW under http://www.angewandte.org or from the author.

 DOI: 10.1002/anie.200462567 © 2005 Wiley-VCH Verlag GmbH & Co. KGaA, Weinheim

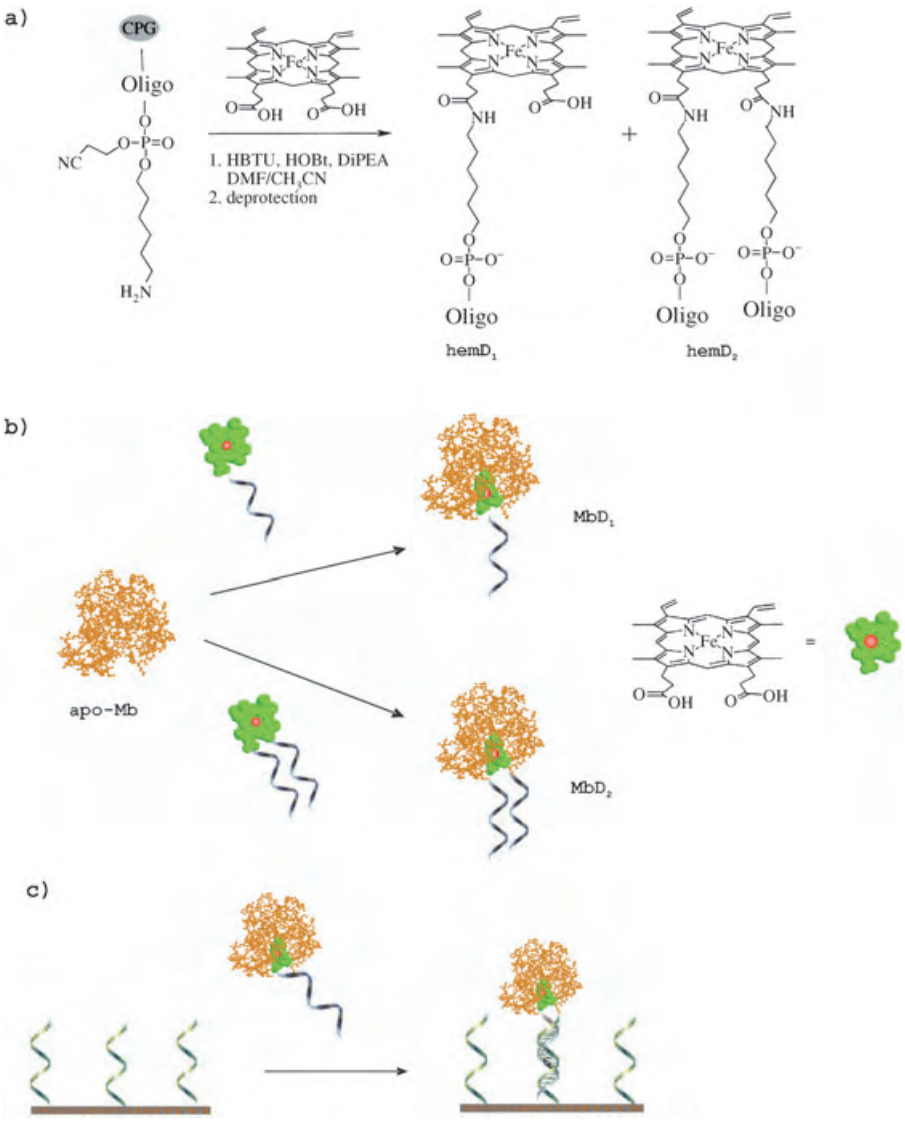

Scheme 1. Schematic representation of the synthesis and assembly of DNA–heme-enzyme conjugates; a) solid-phase synthesis of covalent DNA–hemin adducts $hemD_1$ and $hemD_2$, which contain one or two DNA oligomers, respectively; b) reconstitution of apo-Mb with hemin–DNA adducts leads to the formation of DNA–Mb conjugates MbD_1 and MbD_2; c) DNA-directed immobilization of the DNA–Mb conjugates. CPG = controlled pore glass; HOBt = 1-hydroxybenzotriazole.

by anion-exchange FPLC revealed that the uptake of $hemD_2$ was significantly slower than that of $hemD_1$ (36 and 24 h, respectively), which may be attributed to the greater steric bulk of $hemD_2$ which limits its diffusion into the heme-binding pocket of apo-Mb. Representative chromatograms of hemD purification (Figure 1) demonstrate the significant difference between the retention times of apo-Mb and the respective hemD and MbD conjugates, which enables fast and efficient purification. UV/Vis spectra of both MbD_1 and MbD_2 show an absorption maximum at 408 nm (sharp Soret band) and weak bands at 502, 543, and 632 nm (Q bands), which are in agreement with literature values for native Mb, as well as a broadened peak at 276 nm that arises from absorbance by proteins and DNA.[11]

To further characterize the semisynthetic MbD conjugates, the peroxidase activities of MbD_1 and MbD_2 were compared with that of native Mb.[12] To attain maximal assay sensitivity, Amplex UltraRed (Molecular Probes) was chosen as substrate, which, in the presence of H_2O_2, is converted into a fluorescent dye by peroxidase activity.[13] Figure 2a shows the increase in fluorescence from the enzymatic transformation of Amplex UltraRed by either native Mb, MbD_1, or MbD_2 (5 pmol in each case). It is evident that the activities of MbD_1 and MbD_2 are significantly higher than that of native Mb. Interestingly, MbD_2 shows an even higher activity than MbD_1 despite the greater potential for steric hindrance of the MbD_2 active site by the two bulky DNA moieties nearby. Although the reasons behind its enhanced activity remain unclear, MbD_2 was detectable in quantities as small as 0.1 pmol, whereas detection of native Mb reached a limit at 2 pmol. Further studies of the peroxidase activity, including investigations of other substrates, are currently underway.

To demonstrate that the DNA oligomers can indeed be used as recognition sites for selective binding to complementary oligonucleotides, we performed DNA-directed immobilization assays of MbD_1 and MbD_2 on solid phase (Scheme 1c). We have previously demonstrated that the DNA-directed immobilization of proteins proceeds with high efficiency and allows reversible, site-selective functionalization of solid substrates with proteins or other chemical functionalities.[14] Peroxidase activity was measured after MbD_1 and MbD_2 were immobilized to streptavidin-coated microplate wells functionalized with complementary biotinylated capture oligomers (5′biotin-TACGAGTTGAGA; Figure 2b). Again, the MbD_2 conjugates showed a significantly higher activity than MbD_1. Moreover, in control assays carried out in plate wells containing non-complementary capture oligomers, no enzymatic activity was detected. This indicates that the immobilization occurs exclusively by specific Watson–Crick base pairs formed between the Mb-bound DNA moieties and the capture sequences.

We have shown that novel artificial myoglobin proteins can be generated by reconstitution of apo-Mb with covalent DNA–hemin conjugates. Although we could clearly analyze the composition and chromatographic properties of these novel DNA–Mb conjugates, the elucidation of their particular catalytic properties reported herein has only just begun. Our future work will therefore focus not only on the peroxidase activity, but on characterizing the redox and electron-transfer properties of these conjugates as well.[17] Moreover, the highly specific binding properties of the DNA moiety will be studied in more detail by assembly of the DNA–Mb conjugates both

 © 2005 Wiley-VCH Verlag GmbH & Co. KGaA, Weinheim

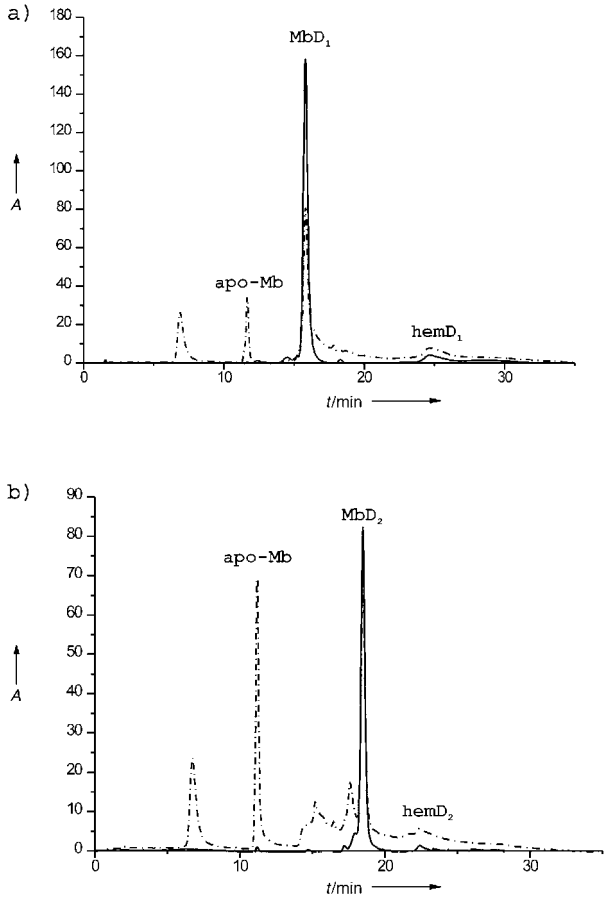

Figure 1. FPLC chromatograms of the reconstitution of apo-Mb with a) $hemD_1$ and with b) $hemD_2$; the dotted and solid lines indicate the absorbance measured at 280 and 405 nm, respectively.

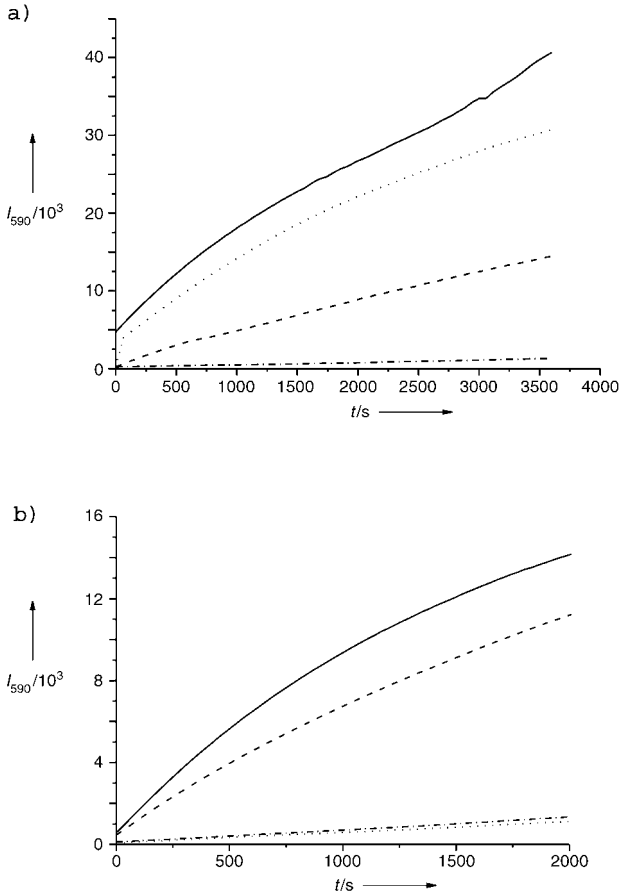

Figure 2. a) Peroxidase activity of 5 pmol native Mb (-----), MbD_1 (•••••), and MbD_2 (——) measured in solution with Amplex UltraRed as the substrate. A control reaction (–•–•) was carried out in the absence of peroxidase. b) Peroxidase activity of MbD_1 (-----) and MbD_2 (——) bound to microplate surfaces through DNA-directed immobilization. Control reactions with noncomplementary capture oligomers (••••• and –•–•) indicate the specificity of surface-capture events.

at the micrometer and nanometer length scales. Whereas the arrangements in the micrometer range should be useful for the generation of enzyme microarrays, the nanoscale assembly holds great potential for the fabrication of multifunctional protein constructs for applications in materials research[15] and life sciences.[2,16]

Notably, Mb served as a representative model system in this study for the seminal demonstration of our concept of generating well-defined DNA–heme-enzyme conjugates through the reconstitution of apo-enzymes with covalent hemin–DNA adducts. This method should transfer well to other heme enzymes, and we therefore anticipate that this approach will open the door to a large variety of novel redox catalysts. Through the programmable binding properties made possible by the specificity of DNA hybridization, such semisynthetic DNA–protein conjugates may be useful in a broad range of applications, from biocatalysts, sensors and transducer elements, to building blocks for micro- and nanostructured devices.

Received: November 10, 2004
Published online: March 18, 2005

Please note: Minor changes have been made to this manuscript since its publication in *Angewandte Chemie* Early View. The Editor.

Keywords: DNA · enzymes · heme proteins · immobilization · self-assembly

[1] C. M. Niemeyer, C. A. Mirkin, *Nanobiotechnology: Concepts, Methods and Applications*, Wiley-VCH, Weinheim, **2004**.
[2] C. M. Niemeyer, *Trends Biotechnol.* **2002**, *20*, 395–401.
[3] The reconstitution of apo-enzymes, in particular glucose oxidase with chemically modified flavin adenine dinucleotide (FAD) cofactors, has been used to generate artificial enzyme conjugates and to immobilize such enzymes to electrode surfaces. For examples, see: a) A. Riklin, E. Katz, I. Willner, A. Stocker, A. F. Buckmann, *Nature* **1995**, *376*, 672–675; b) M. Zayats, E. Katz, I. Willner, *J. Am. Chem. Soc.* **2002**, *124*, 2120–2121; c) M. Zayats, E. Katz, I. Willner, *J. Am. Chem. Soc.* **2002**, *124*, 14724–14735; d) Y. Xiao, F. Patolsky, E. Katz, J. F. Hainfeld, I. Willner, *Science* **2003**, *299*, 1877–1881; e) E. Katz, L. Sheeney-Haj-Ichia, I. Willner, *Angew. Chem.* **2004**, *116*, 3354–3362; *Angew. Chem. Int. Ed.* **2004**, *43*, 3292–3300, and references therein.
[4] T. Yonetani, H. R. Drott, J. S. Leigh, Jr., G. H. Reed, M. R. Waterman, T. Asakura, *J. Biol. Chem.* **1970**, *245*, 2998–3003.
[5] T. Yonetani, H. Yamamoto, G. V. Woodrow, *J. Biol. Chem.* **1974**, *249*, 682–690.

 © 2005 Wiley-VCH Verlag GmbH & Co. KGaA, Weinheim

[6] a) T. Hayashi, Y. Hisaeda, *Acc. Chem. Res.* **2002**, *35*, 35 – 43; b) T. Hayashi, H. Dejima, T. Matsuo, H. Sato, D. Murata, Y. Hisaeda, *J. Am. Chem. Soc.* **2002**, *124*, 11226 – 11227; c) H. Sato, T. Hayashi, T. Ando, Y. Hisaeda, T. Ueno, Y. Watanabe, *J. Am. Chem. Soc.* **2004**, *126*, 436 – 437, and references therein.

[7] T. Hayashi, T. Takimura, H. Ogoshi, *J. Am. Chem. Soc.* **1995**, *117*, 11606 – 11607.

[8] Y. Hitomi, T. Hayashi, K. Wada, T. Mizutani, Y. Hisaeda, H. Ogoshi, *Angew. Chem.* **2001**, *113*, 1132 – 1135; *Angew. Chem. Int. Ed.* **2001**, *40*, 1098 – 1101.

[9] L. Wan, M. B. Twitchett, L. D. Eltis, A. G. Mauk, M. Smith, *Proc. Natl. Acad. Sci. USA* **1998**, *95*, 12825 – 12831.

[10] T. Hayashi, Y. Hitomi, T. M. Ando, Y. Hisaeda, S. Kitagawa, H. Ogoshi, *J. Am. Chem. Soc.* **1999**, *121*, 7747 – 7750.

[11] UV/Vis data for $hemD_1$, $hemD_2$, MbD_1, and MbD_2 as well as MALDI MS spectra and details on the solid-phase coupling of DNA with hemin, the reconstitution of apo-Mb, and the enzyme activity assays are available in the Supporting Information.

[12] It is known that Mb reacts with H_2O_2 to form ferryl species that correspond to compound II of usual peroxidases.[10] Therefore, Mb has the potential to catalyze the oxidation of various substrates in the presence of H_2O_2. Notably, the peroxidase activity of Mb is much lower than that of other peroxidases such as horseradish peroxidase.

[13] The structure of Amplex UltraRed (Invitrogen A36006) is proprietary and undisclosed. However, according to information supplied by the manufacturer, the nonfluorescent Amplex UltraRed reacts similarly to Amplex Red reagent (10-acetyl-3,7-dihydroxyphenoxazine; Molecular Probes) in the presence of H_2O_2 at a stoichiometric ratio of 1:1 to produce a brightly fluorescent and strongly absorbing reaction product. The chemical structure and reaction path of Amplex Red are shown in the Supporting Information (Figure S4).

[14] a) C. M. Niemeyer, T. Sano, C. L. Smith, C. R. Cantor, *Nucleic Acids Res.* **1994**, *22*, 5530 – 5539; b) C. M. Niemeyer, L. Boldt, B. Ceyhan, D. Blohm, *Anal. Biochem.* **1999**, *268*, 54 – 63; c) C. M. Niemeyer, B. Ceyhan, *Angew. Chem.* **2001**, *113*, 3798 – 3801; *Angew. Chem. Int. Ed.* **2001**, *40*, 3685 – 3688; d) M. Lovrinovic, R. Seidel, R. Wacker, H. Schroeder, O. Seitz, M. Engelhard, R. Goody, C. M. Niemeyer, *Chem. Commun.* **2003**, 822 – 823; e) U. Feldkamp, R. Wacker, W. Banzhaf, C. M. Niemeyer, *ChemPhysChem* **2004**, *5*, 367 – 372; f) R. Wacker, C. M. Niemeyer, *ChemBioChem* **2004**, *5*, 453 – 459; g) R. Wacker, H. Schroeder, C. M. Niemeyer, *Anal. Biochem.* **2004**, *330*, 281 – 287; h) F. Kukolka, C. M. Niemeyer, *Org. Biomol. Chem.* **2004**, *2*, 2203 – 2206.

[15] C. M. Niemeyer, W. Bürger, J. Peplies, *Angew. Chem.* **1998**, *110*, 2391 – 2395; *Angew. Chem. Int. Ed.* **1998**, *37*, 2265 – 2268.

[16] C. M. Niemeyer, J. Koehler, C. Wuerdemann, *ChemBioChem* **2002**, *3*, 242 – 245.

[17] Previous work on electron transfer reactions occurring in a composite material prepared from myoglobin containing double-stranded DNA-modified hemin in poly(ethylene oxide) oligomers was carried out without characterization of the DNA-protein conjugate: K. Muneyasu, N. Y. Kawahara, H. Ohno, *Solid State Ionics* **1998**, *113 – 115*, 167 – 171.

 © 2005 Wiley-VCH Verlag GmbH & Co. KGaA, Weinheim

Cover Picture

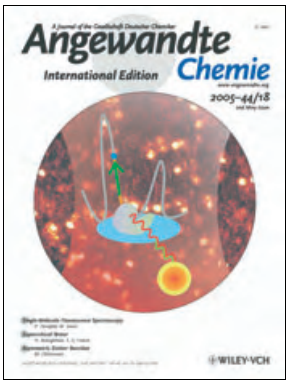

Philip Tinnefeld* and Markus Sauer*

Single-molecule fluorescence spectroscopy allows the direct observation of single receptor molecules in membranes and the identification of mRNA molecules in the nuclei of living cells. The cover picture shows the transcription centers (bright points) in a cell nucleus. The method can give information on the composition of the transcription centers, on the activity of polymerase, and on the synthesis of single-copy genes by the hybridization of a short dye-labeled oligonucleotide (green strand). M. Sauer and P. Tinnefeld describe the method and its uses in their Review on page 2642 ff.

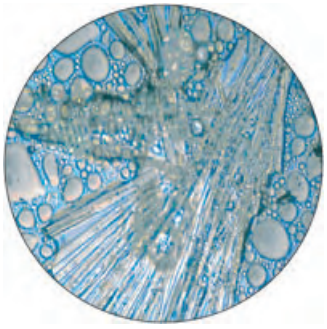

Supercritical Water
The properties of supercritical water and its mixtures with nonpolar, polar, and ionic materials, and the fundamental molecular processes involved are summarized by H. Weingärtner and E. U. Franck in their Review on page 2672 ff.

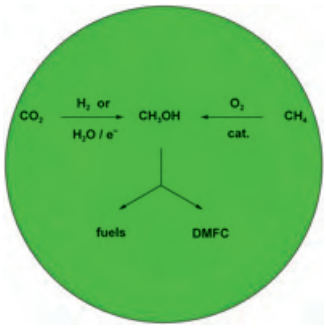

Methanol Economy
Finding efficient ways to store energy and produce convenient hydrocarbon-based fuels and products while mitigating global warming, and the role of methanol in this respect are the topics presented by Nobel Laureate G. A. Olah in his Essay on page 2636 ff.

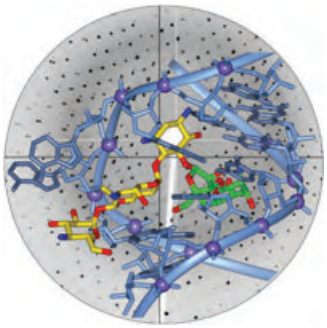

RNA-Target Recognition
Glycoside pseudo base pairs and triples are important for the recognition of the RNA target by the aminoglycoside apramycin, as shown by T. Hermann and co-workers in their Communication on page 2694 ff.

Contents

VIP *The following Communications have been judged by at least two referees to be "very important papers" and will be published online at www.angewandte.org soon:*

*R. Schiffmann, A. Heine, G. Klebe, C. D. P. Klein**
Metal Ions as Cofactors for Ligand Binding at Methionine Aminopeptidase: A Critical View on the Relevance of In Vitro Metalloenzyme Assays

*R. Shintani, A. Tsurusaki, K. Okamoto, T. Hayashi**
Rhodium–Chiral Diene Catalyzed Highly Chemo- and Enantioselective Arylative Cyclization of Alkyne-Tethered Electron-Deficient Olefins

E. Ruiz, G. Rajaraman, S. Alvarez, B. Gillon, J. Stride, R. Clérac, J. Larionova, S. Decurtins*
Symmetry and Topology Determine the Mo^{V}–CN–Mn^{II} Exchange Interactions in High-Spin Molecules

A. Fürstner, L. Turet*
Concise and Practical Synthesis of Latrunculin A by Ring-Closing Enyne–Yne Metathesis

*D. Wan, R. Tu, L. Zhang, H. Dai**
Deterministic One-to-One Synthesis of Germanium Nanowires and Individual Gold Nanoseed Patterning for Aligned Nanowire Arrays

*D. Cappel, S. Tüllmann, A. Krapp, G. Frenking**
Direct Estimate of the Conjugative and Hyperconjugative Stabilization in Diynes, Dienes, and Related Compounds

News

Destinctions for Materials Scientists Rao, Whitesides, and Langer ——— **2628**

Books

Organic Chemistry of Photography	Shinsaku Fujita	*reviewed by M. W. Tausch*	**2629**
Synthetic Multivalent Molecules	Seok-Ki Choi	*reviewed by J. Rojo*	**2629**

Highlights

Asymmetric Catalysis

M. Christmann* ——— **2632 – 2634**

New Developments in the Asymmetric Stetter Reaction

Highly active carbene catalysts have revitalized the interest in the asymmetric Stetter reaction as a method for the construction of 1,4-dicarbonyl compounds. With the latest generation of a catalyst developed by Rovis and co-workers (**1**, for example), products with quaternary stereocenters such as **2** can be generated in 85% yield and 99% *ee*.

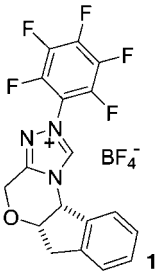

1

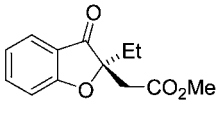

2
85% yield, 99% *ee*

Essays

Alternative Energy Sources

G. A. Olah* ——— **2636 – 2639**

Beyond Oil and Gas: The Methanol Economy

Methanol, a convenient liquid fuel and raw material for synthetic hydrocarbons, offers an alternative to depleting sources of fossil fuels and can be produced, for example, by reacting H_2 with CO_2 from industrial effluents or the atmosphere—good news with regards to global-warming concerns. This Essay discusses various aspects of current and alternative energy sources, with a particular focus on the "methanol economy" (see scheme).

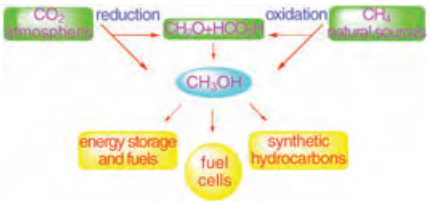

Reviews

One at a time, please: Advanced optical single-molecule techniques enable the monitoring of infectious pathways, the diffusion of single receptor molecules in membranes, and the detection and identification of single mRNA molecules in the nucleus of living cells (see picture). The article reviews recent progress in single-molecule fluorescence spectroscopy (SMFS) and outlines its future potential in combination with smart fluorescence-labeling strategies for successful applications in molecular and structural biology.

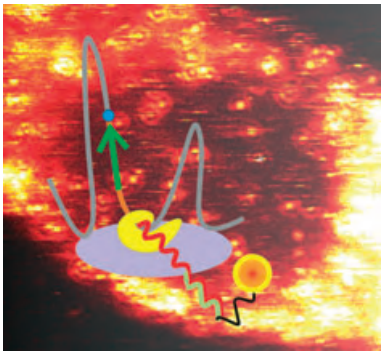

Single-Molecule Detection

P. Tinnefeld,* M. Sauer* ___ **2642 – 2671**

Branching Out of Single-Molecule Fluorescence Spectroscopy: Challenges for Chemistry and Influence on Biology

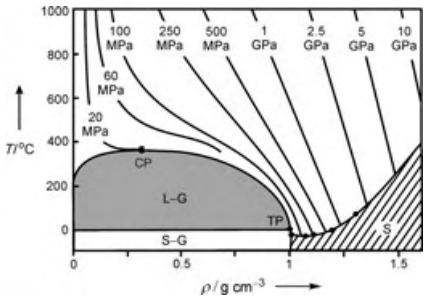

... and not a drop to drink. Water is not restricted to moderate temperatures and low pressures, but can exist at up to very high temperatures, far above its critical point (CP). In this supercritical regime water can be gradually compressed from gas-like to liquid-like densities (see picture; S = solid, L = liquid, G = gas, TP = triple point). The resulting dense supercritical states have tunable solvent properties which form the basis for innovative technologies.

Thermodynamics

H. Weingärtner,*
E. U. Franck _____ **2672 – 2692**

Supercritical Water as a Solvent

Communications

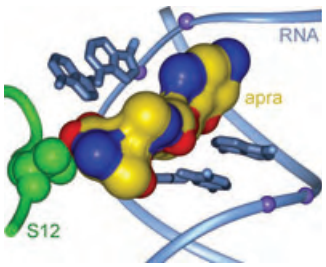

In the groove: The crystal structure of the bacterial decoding-site RNA in a complex with the antibiotic apramycin reveals how glycoside scaffolds participate in RNA recognition by natural products through the formation of pseudo base pairs and triples. The structure suggests that the inhibitory action of apramycin is based on interaction of the antibiotic with ribosomal protein S12 (see structural model), a control element of ribosome translocation.

Aminoglycoside Antibiotics

Q. Han, Q. Zhao, S. Fish, K. B. Simonsen, D. Vourloumis, J. M. Froelich, D. Wall, T. Hermann* _____ **2694 – 2700**

Molecular Recognition by Glycoside Pseudo Base Pairs and Triples in an Apramycin–RNA Complex

For the USA and Canada:
ANGEWANDTE CHEMIE International Edition (ISSN 1433-7851) is published weekly by Wiley-VCH PO Box 191161, D 69451 Weinheim, Germany. Air freight and mailing in the USA by Publications Expediting Inc. 200 Meacham Ave., Elmont, NY 11003. Periodicals postage paid at Jamaica NY 11431. US POSTMASTER: send address changes to *Angewandte Chemie*, Wiley-VCH, 111 River Street, Hoboken, NJ 07030. Annual subscription price for institutions: US$ 4948.00/4498.00 (valid for print and electronic / print or electronic delivery); for individuals who are personal members of a national chemical society, or whose institution already subscribes, or who are retired or self-employed consultants, print only: US$ 394.00. Postage and handling charges included. All Wiley-VCH prices are exclusive VAT.

 © 2005 Wiley-VCH Verlag GmbH & Co. KGaA, Weinheim

The best in chemistry –

for more than a hundred years

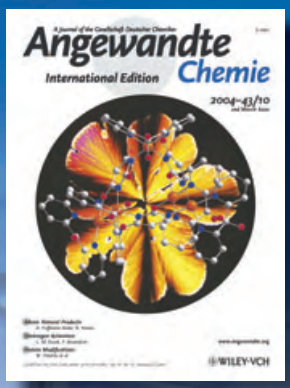

A Journal of the Gesellschaft Deutscher Chemiker

Angewandte International Edition **Chemie**

www.angewandte.org

1888: ***The beginning of a success story***

Constant Innovations

1962: *First issue of the International Edition*
1976: *Graphical abstracts*
1979: *Cover pictures*
1988: *Centenary of Angewandte*
1989: *Routine use of color*
1991: *New section: Highlights*
1992: *Computerized editorial tracking system*
1995: *Internet service for readers*
1998: *Regular press service; full-text online*
2000: *New section: Essays; EarlyView: Communications available online ahead of the printed version*
2001: *New section: Minireviews*
2002: *Online submission of manuscripts*
2003: *Weekly publication; new section: News; new layout*
2004: *Backfiles (1962-1997); ManuscriptXpress: Online system for authors and referees*

Angewandte's advisors...

Horst Kessler
Institut für Organische und Biochemie, Technische Universität München

» If you want to be recognized send your best papers to ***Angewandte Chemie****. The journal is scientifically of top quality; the layout makes the articles easy to read and contributes to the overall impact. An important step forward was the coverage in Medline making the life sciences community aware of the journal's content. Now the field of bioorganic chemistry is also becoming stronger in* ***Angewandte Chemie****. «*

Angewandte Chemie International Edition *is a journal of the German Chemical Society (GDCh)*

GDCh

WILEY InterScience® DISCOVER SOMETHING GREAT

WILEY-VCH

1831404_gu

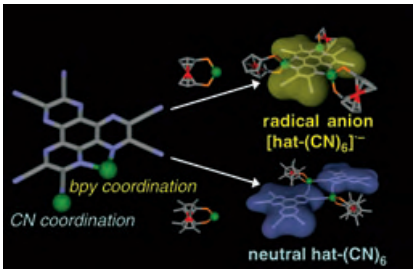

If the hat fits: The size of the ferrocene coligands used during the self-asssembly of hexaazatriphenylene hexacarbonitrile (hat-$(CN)_6$) with Cu^I ions determines the coordination mode of the hat-$(CN)_6$ ligand (bipyridine chelation or monodentate CN, see picture). The mode of coordination directly affects the oxidation state and the reduction potentials of the hat-$(CN)_6$ ligand.

Coordination Modes

S. Furukawa, T. Okubo, S. Masaoka, D. Tanaka, H.-C. Chang, S. Kitagawa* ——— **2700 – 2704**

Effect of the Metal-Assisted Assembling Mode on the Redox States of Hexaazatriphenylene Hexacarbonitrile

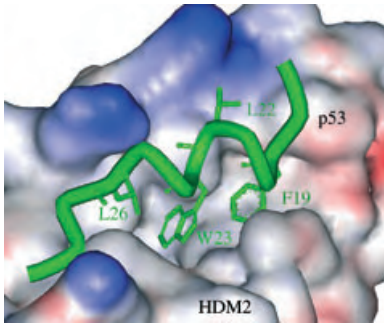

HDM2 regulates p53 by binding to its transactivation domain and promoting its ubiquitin-dependent degradation. Crystallographic analysis of the HDM2/p53 complex revealed that three hydrophobic residues (F19, W23, L26) along one face of the p53 helical peptide are essential for binding (see picture). Terphenyl-based antagonists mimic the α-helical region of p53 and disrupt HDM2/p53 complexation.

Protein–Protein Interactions

H. Yin, G.-i. Lee, H. S. Park, G. A. Payne, J. M. Rodriguez, S. M. Sebti, A. D. Hamilton* ——— **2704 – 2707**

Terphenyl-Based Helical Mimetics That Disrupt the p53/HDM2 Interaction

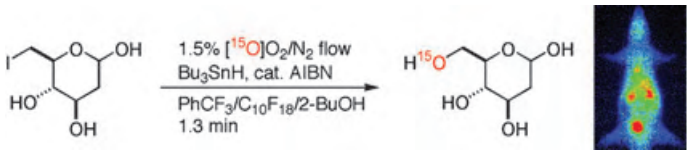

Make it quick! The oxygen isotope ^{15}O has a half-life of only 2 min, and was incorporated into a sugar through an ultrarapid radical hydroxylation of 2,6-dideoxy-6-iodo-D-glucose with labeled molecular oxygen to provide 6-[^{15}O]-2-deoxy-D-glucose (see scheme). The product accumulates in metabolically active organs of rats similarly to a ^{18}F-based tracer in common use, and represents a promising alternative for medical imaging.

Synthetic Methods

H. Yorimitsu, Y. Murakami, H. Takamatsu, S. Nishimura, E. Nakamura* ——— **2708 – 2711**

Ultra-rapid Synthesis of ^{15}O-Labeled 2-Deoxy-D-glucose for Positron Emission Tomography (PET)

Ferromagnetic or antiferromagnetic coupling? A theoretical study of complexes containing Mo^V–CN–Mn^{II} bridges reveals that a combination of local symmetry and molecular pseudosymmetry leads to a fascinating electronic structure that imposes antiferromagnetic interactions and results in a ferrimagnetic arrangement. The picture shows the spin density of the Mn_9Mo_6 complex studied.

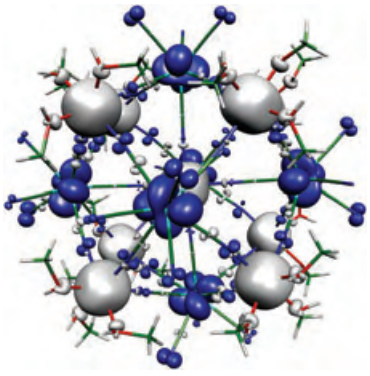

High-Spin Molecules

E. Ruiz,* G. Rajaraman, S. Alvarez, B. Gillon, J. Stride, R. Clérac, J. Larionova, S. Decurtins ——— **2711 – 2715**

Symmetry and Topology Determine the Mo^V–CN–Mn^{II} Exchange Interactions in High-Spin Molecules

 © 2005 Wiley-VCH Verlag GmbH & Co. KGaA, Weinheim

Contents

Lead(II) Detection

P. Chen, B. Greenberg, S. Taghavi, C. Romano, D. van der Lelie, C. He* ——— 2715 – 2719

An Exceptionally Selective Lead(II)-Regulatory Protein from *Ralstonia Metallidurans*: Development of a Fluorescent Lead(II) Probe

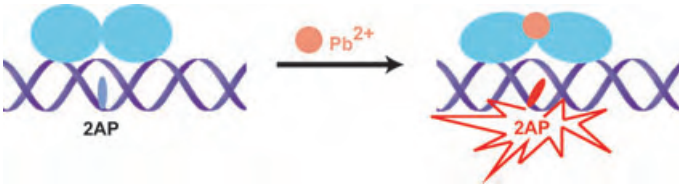

Lighting up lead: A Pb^{2+}-regulatory protein from *Ralstonia metallidurans* has been converted into a highly sensitive fluorescent Pb^{2+} probe (PbR691, turquoise circles in scheme). This fluorescent system reveals that the protein exhibits a surprisingly high binding selectivity towards Pb^{2+} ions over other metal ions.

Nonclassical Carbocations

P. Gutta, D. J. Tantillo* ——— 2719 – 2723

Proton Sandwiches: Nonclassical Carbocations with Tetracoordinate Protons

Exotic species: A number of unusual carbocations in which formally tetracoordinate protons are seemingly suspended between two C=C bonds were studied computationally. An example, the "proton sandwich" derived from 1,5-cyclooctadiene, is shown in the picture (C black, H white).

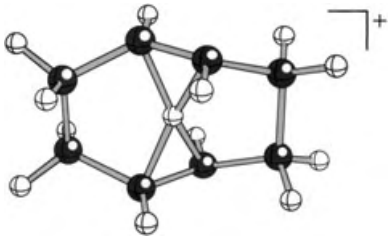

H Bonds in Carbohydrates

Q. Zhang, J. Jaroniec, G. Lee, P. E. Marszalek* ——— 2723 – 2727

Direct Detection of Inter-residue Hydrogen Bonds in Polysaccharides by Single-Molecule Force Spectroscopy

The elasticity of single amylose chains in solvents that promote or inhibit the formation of inter-residue hydrogen bonds was examined by AFM (see picture). Hydrogen bonds were found to rigidify the amylose chain in solvents of low dielectric constant, and the strength of inter-residue hydrogen bonds in sugars can be measured.

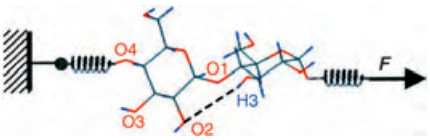

Host–Guest Systems

S. Hiraoka, K. Harano, M. Shiro, M. Shionoya* ——— 2727 – 2731

Quantitative Dynamic Interconversion between Ag^{I}-Mediated Capsule and Cage Complexes Accompanying Guest Encapsulation/Release

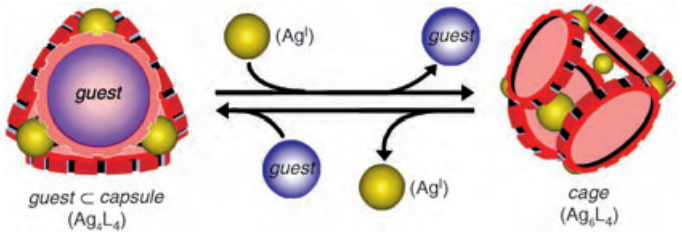

An accommodating host: Capsule- and cage-shaped complexes are formed from Ag^{I} and disk-shaped trismonodentate ligands in 1:1 and 1.5:1 concentration ratios, respectively; their interconversion is reversible. The capsule complex can entrap a small neutral molecule such as adamantane in the inner space, but the guest is released when the cage structure is adopted.

 © 2005 Wiley-VCH Verlag GmbH & Co. KGaA, Weinheim

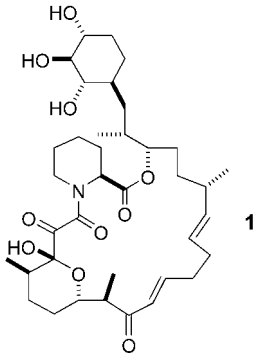

1

The structurally enticing antascomicin B (**1**), which exhibits potent immunosuppressant-antagonizing properties, has a complex polyketide structure. Key steps in its enantioselective total synthesis include a transannular catechol-templated Dieckmann reaction to assemble the challenging tricarbonyl functionality and a butanediacetal-directed allylation.

Natural Products Synthesis

D. E. A. Brittain, C. M. Griffiths-Jones, M. R. Linder, M. D. Smith, C. McCusker, J. S. Barlow, R. Akiyama, K. Yasuda, S. V. Ley* ——— **2732 – 2737**

Total Synthesis of Antascomicin B

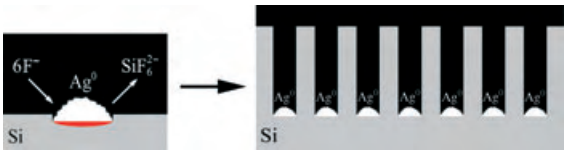

Neatly scratching the surface: A facile etching technique assisted by a silver-nanoparticle network to produce large-area 1D silicon nanostructure arrays with desired orientation and doping characteristics is demonstrated (see picture). A mechanism for the highly selective etching is proposed on the basis of experimental evidence.

Nanostructures

K. Peng, Y. Wu, H. Fang, X. Zhong, Y. Xu, J. Zhu* ——— **2737 – 2742**

Uniform, Axial-Orientation Alignment of One-Dimensional Single-Crystal Silicon Nanostructure Arrays

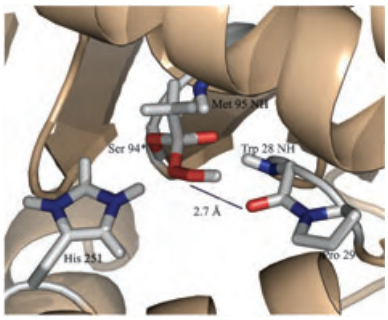

Changing substrates: A mutation that forms a *cis*-proline–peptide bond in a loop structure close to the active site of an aryl esterase from *Pseudomonas fluorescens* converts the enzyme into a perhydrolase (see picture). The switch in activity is explained by a new hydrogen bond formed between a backbone carbonyl oxygen atom and the peroxy deacylation intermediate.

Enzyme Catalysis

P. Bernhardt, K. Hult, R. J. Kazlauskas* ——— **2742 – 2746**

Molecular Basis of Perhydrolase Activity in Serine Hydrolases

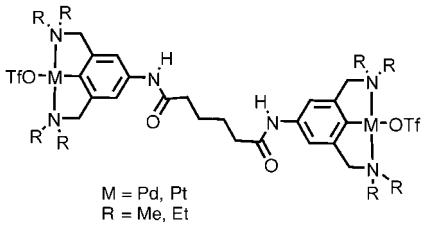

Hold on tight: The dynamics, rather than thermodynamics, of reversible cross-links are the primary determinants of bulk viscosities in a family of supramolecular networks. This result comes from a study in which a series of structurally similar pincer complexes (see picture, OTf = $CF_3SO_3^-$) that have different ligand-exchange dynamics is used to cross-link poly(4-vinylpyridine).

Cross-Linked Polymers

W. C. Yount, D. M. Loveless, S. L. Craig* ——— **2746 – 2748**

Strong Means Slow: Dynamic Contributions to the Bulk Mechanical Properties of Supramolecular Networks

 © 2005 Wiley-VCH Verlag GmbH & Co. KGaA, Weinheim

Contents

Phospholipid Monolayers

F. Gerber, M. P. Krafft,* T. F. Vandamme, M. Goldmann, P. Fontaine **2749 – 2752**

Preventing Crystallization of Phospholipids in Monolayers: A New Approach to Lung-Surfactant Therapy

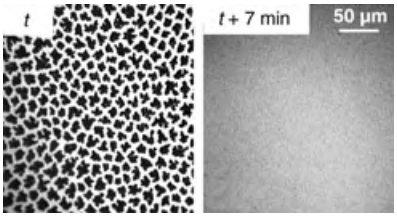

Control of phospholipid monolayer fluidity: A fluorocarbon gas (gFC) has a highly effective fluidizing effect on a semicrystalline monolayer of dipalmitoylphosphatidylcholine (DPPC, the main component of native lung surfactant), prevents it from crystallizing, and induces the dissolution of pre-existing liquid-condensed-phase domains (see fluorescence micrographs; left: without gFC, right: with gFC). The biocompatible FC may, therefore, prove useful in lung-surfactant therapy.

Asymmetric Catalysis

F. López, S. R. Harutyunyan, A. Meetsma, A. J. Minnaard, B. L. Feringa* **2752 – 2756**

Copper-Catalyzed Enantioselective Conjugate Addition of Grignard Reagents to α,β-Unsaturated Esters

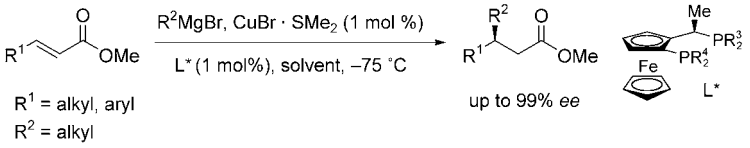

Stable dinuclear Cu complexes have been used to catalyze the conjugate addition of inexpensive and readily available Grignard reagents to acyclic α,β-unsaturated esters. The method provides the corresponding β-substituted optically active esters in high yields and with excellent enantioselectivities (see scheme). R^3 = cyclohexyl, R^4 = Ph or R^3 = Ph, R^4 = cyclohexyl.

Natural Products Synthesis

J. Uenishi,* M. Ohmi **2756 – 2760**

Total Synthesis of (−)-Laulimalide: Pd-Catalyzed Stereospecific Ring Construction of the Substituted 3,6-Dihydro[2*H*]pyran Units

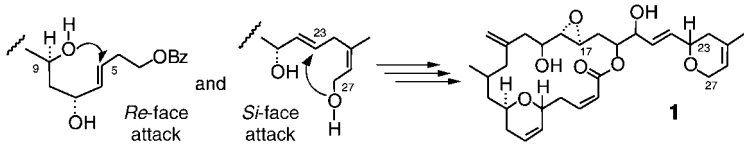

The potent anticancer agent (−)-laulimalide (**1**) was prepared through a versatile method that should allow access to other marine natural products. Key steps included a Pd-catalyzed 1,3 chirality transfer of an allylic alcohol. The *syn*-S_N2'-like processes occur stereospecifically in either 6-*endo*-trig or 6-*exo*-trig fashion to give the desired 3,6-dihydro[2*H*]pyran rings (see scheme).

Library Biosynthesis

A. Tavassoli, S. J. Benkovic* **2760 – 2763**

Genetically Selected Cyclic-Peptide Inhibitors of AICAR Transformylase Homodimerization

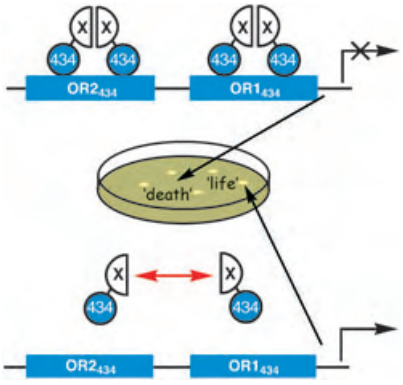

Finding the needle in a haystack need not be as troublesome as once thought. By coupling disruption of protein–protein (X–X) interactions to host-cell survival (see figure), inhibitors of ATIC (a key enzyme in the de novo purine biosynthetic pathway) were readily identified from a biosynthesized library of 10^7 small molecules. The activity and selectivity of nine cyclic peptides selected by this method were demonstrated in vivo and in vitro. AICAR=aminoimidazole-4-carboxamide ribonucleotide.

 © 2005 Wiley-VCH Verlag GmbH & Co. KGaA, Weinheim

Cofactors on the case: DNA detection by using an enzyme and its cofactor attached to an oligonucleotide is described. If the enzyme is functional only when the cofactor–oligonucleotide conjugate is not hybridized, substrate conversion monitored by fluorescence spectroscopy can be used as a reaction probe for hybridization (see scheme). Furthermore, as the enzyme turns over many copies of the substrate, the signal is greatly amplified.

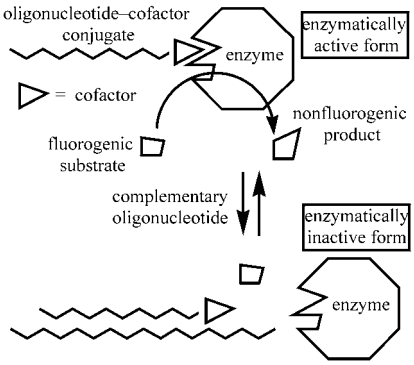

Fluorescence Spectroscopy

P. Simon, C. Dueymes, M. Fontecave,* J.-L. Décout* ——— **2764 – 2767**

DNA Detection through Signal Amplification by Using NADH:Flavin Oxidoreductase and Oligonucleotide–Flavin Conjugates as Cofactors

Dioxygen binds reversibly to the non-transition-metal complex **1** to form the spiroendoperoxide **2** (see scheme). Complexes **1** and **2** were characterized by NMR, IR, and UV/Vis spectroscopies, and their molecular structures were determined by X-ray crystallography.

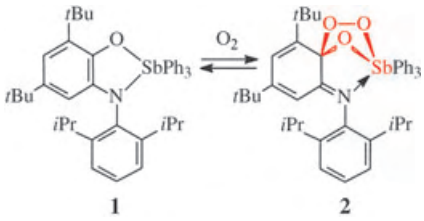

Main-Group Chemistry

G. A. Abakumov,* A. I. Poddel'sky, E. V. Grunova, V. K. Cherkasov, G. K. Fukin, Y. A. Kurskii, L. G. Abakumova ——— **2767 – 2771**

Reversible Binding of Dioxygen by a Non-Transition-Metal Complex

Removal of a single electron induced the extended conformers of bis(catecholacetal)s of acetylacetone to instantaneously fold into cyclophane-like π-stacked structures (shown schematically).

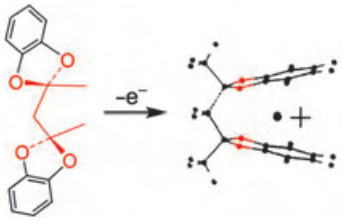

π Stacking

R. Rathore,* V. J. Chebny, E. J. Kopatz, I. A. Guzei ——— **2771 – 2774**

Redox-Induced Transformation from an Extended to a π-Stacked Conformer in Acyclic Bis(catecholacetal)s of Acetylacetone

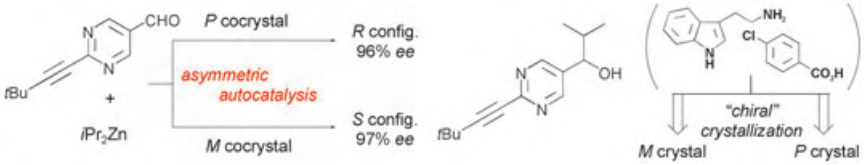

Enantioselective addition of diisopropylzinc to a pyrimidine-5-carbaldehyde was induced by chiral cocrystals of achiral two-component molecular crystals of tryptamine/*para*-chlorobenzoic acid (see scheme) and 3-indolepropionic acid/phenanthridine. This reaction, in conjunction with asymmetric autocatalysis, afforded a pyrimidyl alkanol in high enantiomeric excess.

Asymmetric Synthesis

T. Kawasaki, K. Jo, H. Igarashi, I. Sato, M. Nagano, H. Koshima, K. Soai* ——— **2774 – 2777**

Asymmetric Amplification Using Chiral Cocrystals Formed from Achiral Organic Molecules by Asymmetric Autocatalysis

 © 2005 Wiley-VCH Verlag GmbH & Co. KGaA, Weinheim

Contents

Natural Products Synthesis

A. Fürstner,* K. Radkowski, H. Peters _____ 2777 – 2781

Chasing a Phantom by Total Synthesis: The Butylcycloheptylprodigiosin Case

The dispute as to whether "butylcycloheptylprodigiosin" is a natural product or solely a misassigned structure lasted for more than a decade. This open question has now been answered by the first total synthesis of this tripyrrole alkaloid (see picture), which makes explicit use of the peculiarities of its highly strained *ortho*-anellated nine-membered ring.

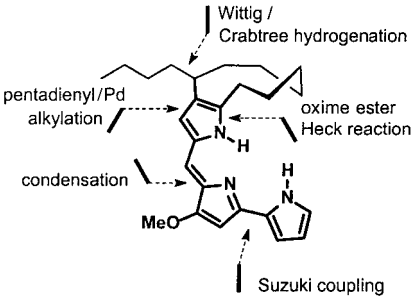

Materials Science

H. Deng, X. Li, Q. Peng, X. Wang, J. Chen, Y. Li* _____ 2782 – 2785

Monodisperse Magnetic Single-Crystal Ferrite Microspheres

Particularly uniform: Monodisperse ferrite microspheres can be synthesized to have diameters of about 200–800 nm (TEM image, left). High-resolution TEM analysis (image, right and inset) shows that each microsphere is a single crystal. Their hydrophilic and magnetic properties impart to the microparticles many potential uses in electronics and biomedicine.

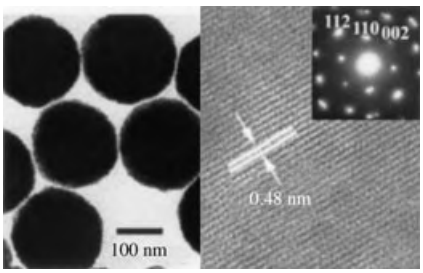

NMR Spectroscopy

C. M. Thiele* _____ 2787 – 2790

Scaling the Alignment of Small Organic Molecules in Substituted Polyglutamates by Variable-Angle Sample Spinning

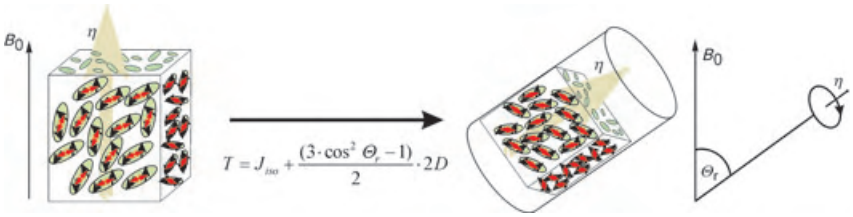

Residual dipolar couplings provide important information for the stereochemical assignment of moieties in small organic molecules. By spinning the liquid-crystalline sample at an angle Θ_r to the magnetic field, the anisotropic interactions can be scaled to meet the experimental requirements. This is shown here for strychnine in the liquid-crystalline phases of poly(γ-benzyl-L-glutamate) and poly(γ-ethyl-L-glutamate) in $CDCl_3$.

Heterogeneous Catalysis

M. Kurtz, J. Strunk, O. Hinrichsen,* M. Muhler, K. Fink,* B. Meyer, C. Wöll _____ 2790 – 2794

Active Sites on Oxide Surfaces: ZnO-Catalyzed Synthesis of Methanol from CO and H_2

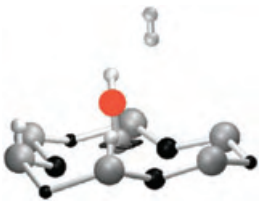

Is this place taken? A mechanism has been proposed for the formation of methanol from CO and H_2 on ZnO surfaces in which CO is adsorbed at oxygen vacancies on the heterogeneous catalyst (see picture: C red, H white, O gray, Zn black). The active sites are blocked when CO_2 is added to the gas mixture.

 © 2005 Wiley-VCH Verlag GmbH & Co. KGaA, Weinheim

Halides in control: Treating silver cyanide with CsCl, CsBr, or CsI, gives a zeolitic framework $\{[Cs]_5{}^3_\infty[Ag_4(CN)_4Cl]_2[AgCl_4]\}$ (**1**) of cross-linked, ropelike twisted five-fold helices, a layered polymer with a fishnet structure $[Cs]_6{}^2_\infty[Ag_{11}(CN)_{16}]$-$[Ag(CN)_2]\cdot 2\,CH_3CN$, or a simple double salt $Cs_5[Ag(CN)_2]_4I$. The existence of tetrachloroargentate(I) $[AgCl_4]^{3-}$ included into the channels of **1** is shown by a single-crystal structure for the first time (see picture).

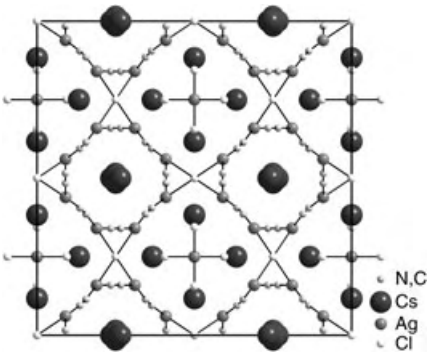

Silver(I) Compounds

V. Urban, T. Pretsch, H. Hartl* ——— **2794 – 2797**

From AgCN Chains to a Fivefold Helix and a Fishnet-Shaped Framework Structure

---

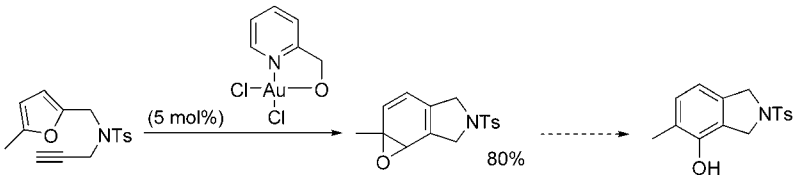

An elusive intermediate in the gold-catalyzed phenol synthesis was elucidated by modifying the energy profile of this process. Thus, the use of a ligand based on 2-hydroxymethylpyridine enabled the first observation of the intermediate arene oxide, which can be enriched to account for up to 80% of the material in the reaction mixture at room temperature (see scheme).

Reactive Intermediates

A. S. K. Hashmi,* M. Rudolph, J. P. Weyrauch, M. Wölfle, W. Frey, J. W. Bats ——— **2798 – 2801**

Gold Catalysis: Proof of Arene Oxides as Intermediates in the Phenol Synthesis

---

What is the design principle of a discotic liquid crystal? Up to now, such systems have involved a more or less rigid core surrounded by flexible side groups that point outward. Herein, shape-persistent macrocycles are introduced with flexible side chains that have intraannular positions (see picture).

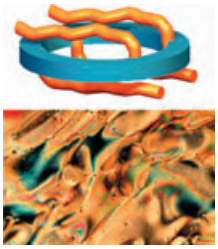

Liquid Crystals

S. Höger,* X. H. Cheng, A.-D. Ramminger, V. Enkelmann, A. Rapp, M. Mondeshki, I. Schnell ——— **2801 – 2805**

Discotic Liquid Crystals with an Inverted Structure

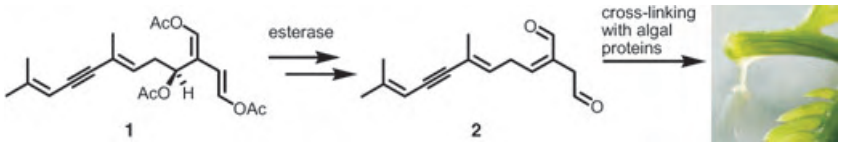

Rapid polymer formation under physiological conditions is triggered upon wounding of the unicellular macroalga *C. taxifolia*. This process is initiated by esterase-mediated deacetylation of caulerpenyne (**1**). The resulting 1,4-dialdehyde oxytoxin 2 (**2**) instantaneously reacts with nucleophilic groups from proteins to form a cross-linked biopolymer.

Biopolymers

S. Adolph, V. Jung, J. Rattke, G. Pohnert* ——— **2806 – 2808**

Wound Closure in the Invasive Green Alga *Caulerpa taxifolia* by Enzymatic Activation of a Protein Cross-Linker

 © 2005 Wiley-VCH Verlag GmbH & Co. KGaA, Weinheim

Sources

Product and Company Directory

You can start the entry for your company in "Sources" in any issue of *Angewandte Chemie*.

If you would like more information, please do not hesitate to contact us.

Wiley-VCH Verlag – Advertising Department
Tel.: 0 62 01 - 60 65 65
Fax: 0 62 01 - 60 65 50
E-Mail: MSchulz@wiley-vch.de

Service

Keywords ____ *2810*

Authors ____ *2811*

Preview ____ *2813*

Unique – New - Fascinating

2004. XV, 295 pages, 173 figures, 66 tables. Hardcover.
ISBN 3-527-30828-8
€ 129.- /£ 90.- /US$ 185.-

MASAKATSU SHIBASAKI and YOSHINORI YAMAMOTO, (eds.)

Multimetallic Catalysts in Organic Synthesis

The reference comprehensively covers this hot topic presenting the information hitherto scattered throughout smaller reviews or single book chapters to provide an introduction to this rapidly expanding field.
In ten chapters, the international team of expert authors treats asymmetric syntheses, new transformations, and organometallic reactions using homo- and hetero-bimetallic catalysts. Written for advanced researchers, this very timely publication is of significant benefit to organic and organometallic chemists in both academia and industry.

15710411_kn

Register now for the free
WILEY-VCH Newsletter!
www.wiley-vch.de/home/pas

WILEY-VCH • P.O. Box 10 11 61 • D-69451 Weinheim, Germany
Fax: +49 (0) 62 01 - 60 61 84
e-mail: service@wiley-vch.de • http://www.wiley-vch.de

WILEY-VCH

 © 2005 Wiley-VCH Verlag GmbH & Co. KGaA, Weinheim

C. N. R. Rao, G. M. Whitesides, and R. Langer Receive Dan David Prize: Future

The Dan David Prize has been awarded annually since 2002 in the categories Past, Present, and Future. The prize is financed by the Dan David Foundation and administered at Tel Aviv University. It will be presented on May 23. The review committee for the category Future includes the Nobel Laureates A. J. Heeger (Chemistry 2000) and L. Esaki (Physics 1973). The recipients must devote 10% of the prize money of US$ 1 million per category to aiding PhD students.

C. N. R. Rao

C. N. R. Rao is not only the recipient of the Dan David Prize, but also of the Indian Science Award to the value of US$ 62 500. Rao has also been appointed chair of the Scientific Advisory Council to the Indian Prime Minister. He has been recognized in particular for his research on transition-metal oxides. Focal points of his research are ceramic superconductors (La_2CuO_4), metal–insulator transitions, and colossal magnetoresistance. His Review published in 2001 on nanotubes[1a] is one of the five most downloaded articles from *ChemPhysChem* for 2004. He recently discussed metal carboxylates with open architectures in *Angewandte Chemie*[1b] and reported on InN nanocrystals, nanostrands, and nanotubes in *Small*.[1c] He is co-editor of a book on the chemistry of nanomaterials.[1d]

Chintamani Nagesa Ramachandra Rao completed his PhD at Purdue University (USA) and earned his DSc at the University of Mysore (India). From 1959 to 1994 he was a faculty member at the Indian Institute of Technology in Kanpur and at the Indian Institute of Science in Bangalore, and since 1989 has been associated with the J. Nehru Center for Advanced Scientific Research in Bangalore, where he is Linus Pauling Research Professor. Rao is a member of the Editorial Board of *Chemistry—A European Journal* and the Editorial Advisory Boards of *ChemPhysChem* and *Small*.

George M. Whitesides carries out research at the interface of bio- and nanotechnology. He recently reported in *Angewandte Chemie* the generation of monodisperse particles by using microfluidics.[2a] He is regarded as a pioneer in the field of self-organized monolayers. His Review on soft lithography[2b] from 1998 is one of the 10 articles most frequently accessed online since 2003 from *Angewandte Chemie*. In the special issue of *Advanced Materials* on the occasion of his 65th birthday, he contributed an article on the writing of scientific manuscripts.[2c] His thoughts on the future of chemistry[2d] and materials science[2e] were published in Essays in *Angewandte Chemie* and *Small*, respectively.

G. M. Whitesides

George M. Whitesides studied at Harvard University (USA) and completed his PhD in 1964 at the California Institute of Technology (USA) with J. D. Roberts. He was professor at MIT (USA) from 1963 to 1982, then transferred to the Department of Chemistry of Harvard University, where he is currently Mallinckrodt Professor of Chemistry. Whitesides is a member of the International Advisory Board of *Angewandte Chemie* and an honorary member of the Editorial Advisory Board of *Small*.

The award recognizes **Robert Langer** (MIT) for his research on biomaterials and tissue engineering, which focuses on biocompatible polymers for drug delivery and synthetic polymers, as well as polymers with shape memory and materials with switchable surfaces. In his most recent Communication in *Angewandte Chemie* he reported the semiautomated synthesis of a large library of degradable cationic polymers for gene delivery.[3a] In 2000 he discussed in a Review the use of microchips for the controlled release of drugs.[3b]

R. Langer

Langer studied chemical engineering and completed his bachelor's degree at Cornell University (USA) and doctorate at MIT. He was a member of the Science Board of the American Food and Drug Administration from 1995 to 2002, as Chairman from 1999 to 2002, and has received several honorary doctorates, for example, from the ETH Zürich (Switzerland) and the Technion in Haifa (Israel). Langer is a member of the International Advisory Board of *Angewandte Chemie*.

[1] a) C. N. R. Rao, B. C. Satishkumar, A. Govindaraj, M. Nath, *ChemPhysChem* **2001**, *2*, 78; b) C. N. R. Rao, S. Natarajan, R. Vaidhyanathan, *Angew. Chem.* **2004**, *116*, 1490; *Angew. Chem. Int. Ed.* **2004**, *43*, 1466; c) K. Sardar, F. L. Deepak, A. Govindaraj, M. M. Seikh, C. N. R. Rao, *Small* **2005**, *1*, 91; d) *The Chemistry of Nanomaterials* (Eds.: C. N. R. Rao, A. Müller, A. K. Cheetham), Wiley-VCH, Weinheim, **2004**.

[2] a) S. Xu, Z. Nie, M. Seo, P. Lewis, E. Kumacheva, H. A. Stone, P. Garstecki, D. B. Weibel, I. Gitlin, G. M. Whitesides, *Angew. Chem.* **2005**, *117*, 734; *Angew. Chem. Int. Ed.* **2005**, *44*, 724; b) Y. Xia, G. M. Whitesides, *Angew. Chem.* **1998**, *110*, 568; *Angew. Chem. Int. Ed.* **1998**, *37*, 550; c) G. M. Whitesides, *Adv. Mater.* **2004**, *16*, 1375; d) G. M. Whitesides, *Angew. Chem.* **2004**, *116*, 3716; *Angew. Chem. Int. Ed.* **2004**, *43*, 3632; e) G. M. Whitesides, *Small*, **2005**, *1*, 172.

[3] a) D. G. Anderson, D. M. Lynn, R. Langer, *Angew. Chem.* **2003**, *115*, 3261, *Angew. Chem. Int. Ed.* **2003**, *42*, 3153; b) J. T. Santini, Jr., A. C. Richards, R. Scheidt, M. J. Cima, R. Langer, *Angew. Chem.* **2000**, *112*, 2486; *Angew. Chem. Int. Ed.* **2000**, *39*, 2396.

 © 2005 Wiley-VCH Verlag GmbH & Co. KGaA, Weinheim DOI: 10.1002/anie.200501179

Asymmetric Catalysis

New Developments in the Asymmetric Stetter Reaction**

*Mathias Christmann**

Keywords:
asymmetric catalysis · carbenes · organocatalysis · Stetter reaction · umpolung

Processes mediated by small nucleophilic catalysts are currently experiencing a renaissance. In addition to competing with well-established metal-catalyzed reactions, there is a tempting opportunity to invert conventional reactivity patterns by exploiting the concept of polarity reversal (umpolung).[1] Following this strategy, aldehydes can be turned into acylanion equivalents[2] through covalent activation with suitable nucleophiles (Scheme 1). Among several catalysts, thiazolium salts **1** serve as precursors for nucleophilic carbenes **2**, which in turn are able attack aldehydes **3** to form the so-called Breslow intermediate **4**.[3,4] The 1,2-addition of this species with an acceptor aldehyde **5** is referred to as the benzoin condensation. In the early 1970s, Stetter and Schreckenberg extended this concept to conjugate acceptors **7**.[5] Since that time, the 1,4-addition of aldehydes to α,β-unsaturated carbonyl compounds has become commonly known as the Stetter reaction. If a prochiral acceptor is employed, chiral 1,4-dicarbonyl compounds such as **8** can be obtained, which are important intermediates in the synthesis of biologically active molecules.

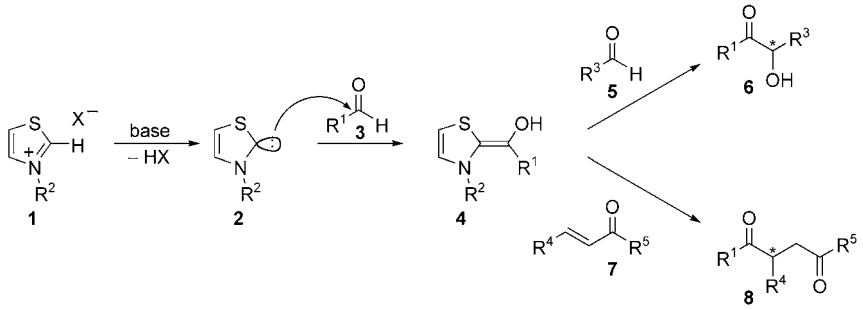

Scheme 1. Generation and reactions of acylanion equivalents.

In an effort to impart stereoselectivity to both the benzoin condensation and the Stetter reaction, various chiral catalysts have been developed over the past four decades. Inspired by the pioneering work of Sheehan and Hunneman on the asymmetric benzoin condensation,[6] many research groups have been involved in the development of chiral heteroazolium salt catalysts. The cyclization of the salicylaldehyde-derived substrate **9** to the corresponding chromanone **10** has become a benchmark for catalyst efficiency in intramolecular Stetter reactions (Scheme 2).

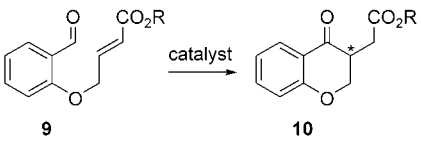

Scheme 2. Intramolecular Stetter reaction.

In 1996, Enders and co-workers reported the first asymmetric Stetter reaction. The key to their success was the increased reactivity of the triazolium salt **11** over that of previously used thiazolium salts.[7] With the triazolium unit embedded in the bicyclic framework of **12** (Bn = benzyl), Knight and Leeper[8] obtained high enantioselectivities in the benzoin condensation, which were further improved by Enders and Kallfass with catalyst **13**.[9] Recently, Rovis and co-workers have made significant progress in the asymmetric intramolecular Stetter reaction.[10]

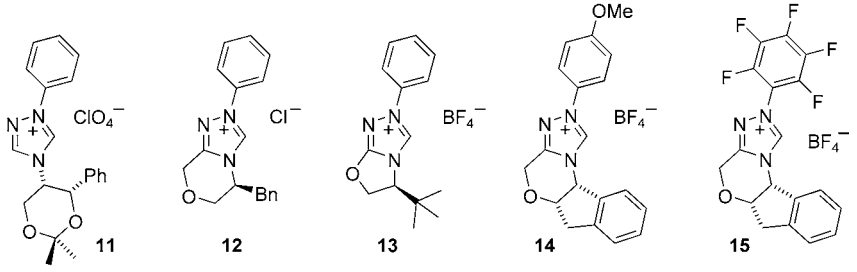

[*] Dr. M. Christmann
Institut für Organische Chemie
RWTH Aachen
Landoltweg 1, 52074 Aachen (Germany)
Fax: (+49) 241-809-2127
E-mail: christmann@oc.rwth-aachen.de

[**] The author thanks the Fonds der Chemischen Industrie for a Liebig fellowship.

 © 2005 Wiley-VCH Verlag GmbH & Co. KGaA, Weinheim DOI: 10.1002/anie.200500761

With 20 mol% of the aminoindanol-derived triazolium salt **14**, the intramolecular Stetter reaction of **9** (R = Et) proceeded smoothly to give the desired product **10** in 94% yield and 94% *ee*. With regard to the electronic nature of the phenyl ring on the triazole nitrogen, 4-methoxy substitution proved to be optimal. Catalyst **14** gave consistently high yields and percent *ee* values with substrates bearing a heteroatom in the γ position of the acceptor. In some cases, for example, with the aliphatic substrate **17**, the catalyst **16** was superior (Scheme 3).

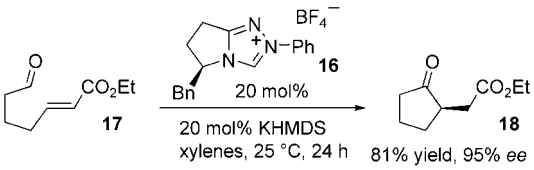

Scheme 3. Intramolecular Stetter reaction of aliphatic substrates. KHMDS = potassium hexamethyldisilazide.

Rovis also took on the challenge of generating quaternary stereocenters.[11] Analogous to the experience with **14**, the substitution pattern of the phenyl ring was found to be the decisive factor in the catalyst design. Surprisingly, the electron-deficient pentafluorophenyl catalyst **15** was the most effective in this case (up to 99% *ee*), suggesting mechanistic differences from β-monosubstituted substrates (Scheme 4).

A critical reader might interject that reactions with heteroazolium salts usually require as much catalyst as 20 mol%. Rovis notes that albeit with poorer selectivity, certain solvents can allow much lower catalyst loadings. For example, the reaction of **19** in the presence of triazolium salt **15** at 1 mol% in isopropanol affords the desired product **20** in 78% yield with 83% *ee*. This holds promise for catalysts with improved efficiency.

Bach and co-workers developed the axially chiral *N*-arylthiazolium catalyst **21**, which bears a menthol-derived backbone .[12] With this catalyst at 20 mol% they were able to isolate the Stetter product **10** (R = Me) in 75% yield with 50% *ee*. The low stereoselectivity was ascribed to an atropisomerization of the catalyst during the course of the reaction.

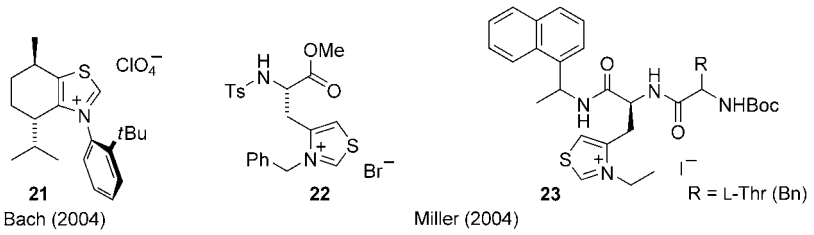

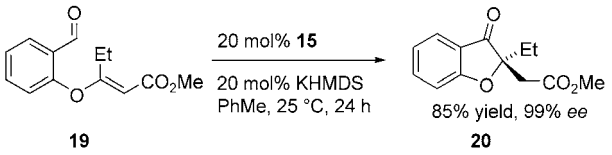

Scheme 4. Generation of quaternary stereocenters.

Following their elegant work on small peptide catalysts, the Miller research group also investigated the intramolecular asymmetric Stetter reaction.[13] For this purpose, the terminal histidine residue was replaced with thiazolylalanine (Taz) derivatives. An initial screen with **9** (R = *t*Bu) as the substrate and 20 mol% of the catalyst **22** (Ts = *p*-toluenesulfonyl) afforded the corresponding chromanone **10** in 40% yield and 80% *ee*. It was speculated that both yield and selectivity might be improved by the incorporation of Taz into small peptides. With catalyst **23** (Boc = *t*-butoxycarbonyl), the product **10** could be obtained in promising 67% yield and 73% *ee*.

In the intermolecular Stetter reaction, self-condensation of the donor aldehyde usually dominates over the conjugate addition, leading to benzoins as the major products. To circumvent this problem, Scheidt and co-workers[14] devised a strategy that employs acylsilanes as acylanion precursors.[15] As shown in Scheme 5, the reaction between acylsilane **24** and chalcone (**25**) as the conjugate acceptor, catalyzed by thiazolium salt **26**, proceeds smoothly to give 1,4-dicarbonyl product **27** in 77% yield.

In their mechanistic model, a carbene catalyst **1** adds to the acylsilane **28** to give—after 1,2-silyl migration (Brook rearrangement)—the intermediate **29** (Scheme 6). The alcohol is believed to induce a desilylation leading to the Breslow intermediate **4**. The conjugate addition predominates in this case as a result of the decreased electrophilicity of the acylsilane (in comparison with that of an aldehyde).

The 1,4-dicarbonyl products of Stetter reactions are ideal substrates for the Paal–Knorr synthesis. Müller and co-workers[16] as well as Bharadwaj and Scheidt[17] have developed efficient one-pot Stetter–Paal–Knorr protocols for

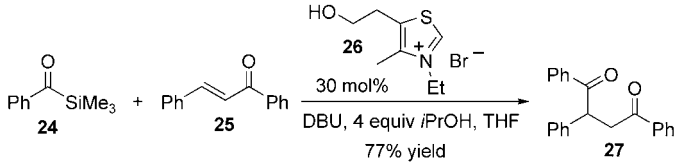

Scheme 5. Sila–Stetter reaction. DBU = 1,8-diazabicyclo[5.4.0]undec-7-ene.

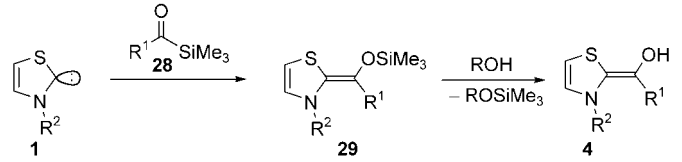

Scheme 6. Mechanistic proposal for the Sila–Stetter reaction.

 © 2005 Wiley-VCH Verlag GmbH & Co. KGaA, Weinheim

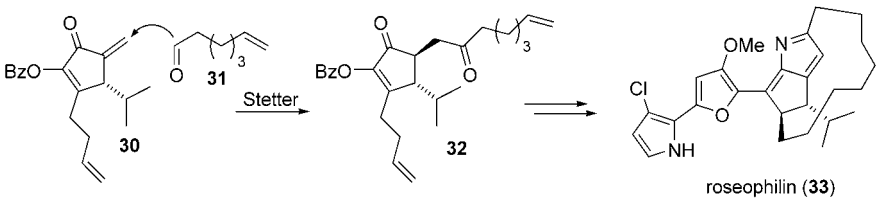

Scheme 7. Synthesis of roseophilin from Harrington and Tius. Bz = benzoyl.

the synthesis of highly substituted pyrroles.

Although the Stetter reaction can be carried out these days with very good yields and selectivities, only a few examples of its application toward the synthesis of natural products have been reported thus far.[18] Harrington and Tius employed a diastereoselective intermolecular Stetter reaction and a ring-closing metathesis reaction as the key steps in their elegant synthesis of roseophilin (**33**, Scheme 7).[19] The 1,4-dicarbonyl functionality in **32** serves as a precursor for the central pyrrole unit of the natural product.

The examples presented herein show that from the development of highly active catalysts and creative reaction design, asymmetric Stetter reactions have become a valuable addition to the repertoire of efficient C–C bond-forming reactions. It can be expected that these and other[20,21] umpolung reactions will stimulate chemists to dare new retrosynthetic disconnections in their synthetic strategies.

[1] D. Seebach, *Angew. Chem.* **1979**, *91*, 259; *Angew. Chem. Int. Ed. Engl.* **1979**, *18*, 239.

[2] J. S. Johnson, *Angew. Chem.* **2004**, *116*, 1348; *Angew. Chem. Int. Ed.* **2004**, *43*, 1326.

[3] a) T. Ukai, R. Tanaka, T. Dokawa, *J. Pharm. Soc. Jpn.* **1943**, *63*, 296; b) R. Breslow, *J. Am. Chem. Soc.* **1958**, *80*, 3719.

[4] For a review, see: D. Enders, T. Balensiefer, *Acc. Chem. Res.* **2004**, *37*, 534.

[5] a) H. Stetter, M. Schreckenberg, *Angew. Chem.* **1973**, *85*, 89; *Angew. Chem. Int. Ed. Engl.* **1973**, *12*, 81; b) H. Stetter, *Angew. Chem.* **1976**, *88*, 695; *Angew. Chem. Int. Ed. Engl.* **1976**, *15*, 639.

[6] J. C. Sheehan, D. H. Hunneman, *J. Am. Chem. Soc.* **1966**, *88*, 3666.

[7] D. Enders, K. Breuer, J. Runsink, J. H. Teles, *Helv. Chim. Acta* **1996**, *79*, 1899.

[8] R. L. Knight, F. J. Leeper, *J. Chem. Soc. Perkin Trans. 1* **1998**, 1891.

[9] D. Enders, U. Kallfass, *Angew. Chem.* **2002**, *114*, 1822; *Angew. Chem. Int. Ed.* **2002**, *41*, 1743.

[10] M. S. Kerr, J. Read de Alaniz, T. Rovis, *J. Am. Chem. Soc.* **2002**, *124*, 10298.

[11] a) M. S. Kerr, T. Rovis, *J. Am. Chem. Soc.* **2004**, *126*, 8876; b) T. Nakamura, O. Hara, T. Tamura, K. Makino, Y. Hamada, *Synlett* **2005**, 155.

[12] J. Pesch, K. Harms, T. Bach, *Eur. J. Org. Chem.* **2004**, 2025.

[13] S. M. Mennen, J. T. Blank, M. B. Tran-Dubé, J. E. Imbriglio, S. J. Miller, *Chem. Commun.* **2005**, 195.

[14] A. E. Mattson, A. R. Bharadwaj, K. A. Scheidt, *J. Am. Chem. Soc.* **2004**, *126*, 2315.

[15] X. Linghu, J. S. Johnson, *Angew. Chem.* **2003**, *115*, 2638; *Angew. Chem. Int. Ed.* **2003**, *42*, 2534.

[16] R. U. Braun, K. Zeitler, T. J. J. Müller, *Org. Lett.* **2001**, *3*, 3297.

[17] A. R. Bharadwaj, K. A. Scheidt, *Org. Lett.* **2004**, *6*, 2465.

[18] B. M. Trost, C. D. Shuey, F. DiNinno, S. S. McElvain, *J. Am. Chem. Soc.* **1979**, *101*, 1284.

[19] P. E. Harrington, M. A. Tius, *J. Am. Chem. Soc.* **2001**, *123*, 8509.

[20] For examples of conjugate umpolung, see: a) C. Burstein, F. Glorius, *Angew. Chem.* **2004**, *116*, 6331; *Angew. Chem. Int. Ed.* **2004**, *43*, 6205; b) S. S. Sohn, E. L. Rosen, J. W. Bode, *J. Am. Chem. Soc.* **2004**, *126*, 14370.

[21] For the related addition of aldehydes to acylimines, see: a) J. A. Murry, D. E. Frantz, A. Soheili, R. Tillyer, E. J. J. Grabowski, P. J. Reider, *J. Am. Chem. Soc.* **2001**, *123*, 9696; b) D. E. Frantz, L. Morency, A. Soheili, J. A. Murry, E. J. J. Grabowski, R. D. Tillyer, *Org. Lett.* **2004**, *6*, 843.

 © 2005 Wiley-VCH Verlag GmbH & Co. KGaA, Weinheim

Alternative Energy Sources

Beyond Oil and Gas: The Methanol Economy**

*George A. Olah**

Keywords:
environmental chemistry · hydrocarbons · hydrogen · methanol

Oil and natural gas together with coal, the main fossil fuels, not only remain our major energy sources but they are also the feedstocks for a great variety of manmade materials and products that range from gasoline and diesel oil to varied petrochemical and chemical products, including synthetic materials, plastics, and pharmaceuticals. What nature gave us as a gift, formed over the course of eons, is being used up rather rapidly. Fossil fuels continue to be significantly depleted and will become increasingly costly. Thus we need to search for new sources and solutions.

All fossil fuels are mixtures of hydrocarbons, which contain varying ratios of carbon and hydrogen. Upon their combustion, they are irreversibly used up: carbon is converted into carbon dioxide and hydrogen into water. On a related note, the increase of the CO_2 content of the atmosphere is considered a major manmade cause of global warming.

Coal and the Industrial Revolution

Coal is considered to have been formed during the so-called carboniferous period some 300 million years ago from the anaerobic decomposition of then-living plants. Its use for heating purposes began slowly and became more widespread in the 16th and 17th centuries mainly in England as a replacement for wood, which was becoming scarcer. Coal became dominant in the 18th century with the invention of the steam engine and the industrial revolution, which was also fueled by coal, that followed. In the 19th and 20th centuries, coal continued to satisfy the ever-increasing energy demand of mankind, and today it is used primarily for generating electricity.[1] Whereas our coal reserves may last for another two or three centuries, the mining of coal (except in areas suited for surface strip mining) is increasingly affected by socio-economical, safety, and environmental difficulties.

Oil and Natural Gas

Since the latter half of the 19th century, petroleum oil and natural gas have become increasingly important and dominant energy sources and raw materials for chemicals and manmade materials. They are certainly the most convenient fossil-fuel sources.

Much has been said over the years about the extent of our available oil and gas resources. At first glance, estimated world oil and gas reserves look impressive. These reserves seem not to have diminished in the last 50 years[2] owing to continuous developments and improved technologies that have allowed exploration, production, and recovery from increasingly difficult-to-access areas, such as the depths of the seas and inhospitable land areas from deserts to the Arctic. Conservation of energy and secondary and tertiary recovery from previously exploited fields are significant, but will not fundamentally change the long-range outlook.

Besides petroleum oil and natural gas (and also coal), we have additional sources of "heavy" hydrocarbons, such as heavy-oil deposits in Venezuela, oil shales in various geological formations including the US Rocky Mountains, and vast tar sand deposits in the Canadian province Alberta. The relatively stable hydrates of methane, as found under the Siberian tundras and along the continental shelves of the oceans, represent significant possibilities for natural gas deposits in the future. They will all eventually be exploited, although the difficulties and expense involved are extensive.

Besides the size of oil reserves (1–1.5 trillion barrels or some 200 billion metric tons), one must also consider our expanding world population, which exceeds 6 billion now and will probably approach 9–10 billion by the mid-21st century, as well as increasing standards of living and demand in countries such as China and India if one wants to predict how long the estimated oil reserves may last. Present estimates of our proven oil reserves reveal that they would last for some 40 years at the current rate of consumption. Natural gas reserves are comparable but somewhat larger. New developments and improved recovery methods, however, could extend these estimates significantly.

Alternative Energy Sources

To satisfy mankind's ever-increasing energy needs, one has to consider all feasible alternative energy sources. Hydro- and geothermal energy are used where Nature makes it feasible, but no

[*] Prof. Dr. G. A. Olah
Loker Hydrocarbon Research Institute and Department of Chemistry
University of Southern California
Los Angeles, CA 90089-1661 (USA)
Fax: (+1) 213-740-5087
E-mail: olah@usc.edu

[**] An identically titled monograph that discusses various aspects of the methanol economy is being published by Wiley-VCH.

 © 2005 Wiley-VCH Verlag GmbH & Co. KGaA, Weinheim DOI: 10.1002/anie.200462121

major new sources have been found. Energy from the sun and wind, and waves and tides of the seas all have real potential and are increasingly exploited, but their use on such a large scale so as to substitute fossil fuels is not likely to significantly affect our energy outlook in the foreseeable future.[3]

Atomic Energy

Probably the greatest technological achievement of the 20th century was to harness the energy of the atom. Regretfully, as it was first achieved by building the atomic bomb, in subsequent years public opinion increasingly turned against atomic energy, even for peaceful uses. Over the last few decades, relatively few new atomic power plants were constructed. There is even strong sentiment to close them down altogether in some countries, although others such as France depend on them for some 80% of their electricity needs. Progress has been made to limit the use of atomic energy to only peaceful uses and to improve its safety aspects, including the storage and disposal of radioactive waste. I believe that our society, which was able to build the atomic bomb, can and will solve these problems. In my opinion, the decline of the atomic energy industry is most regrettable. Whether or not one supports atomic energy, in the long term it is the most feasible and massive energy source for mankind.[4] Conservation and use of alternate energy sources are most desirable, but they cannot replace, by themselves, the "classic" energy sources in fulfilling mankind's enormous energy demand.

Energy Storage and Distribution

Despite their nonrenewable nature and diminishing resources, fossil fuels and particularly oil and gas will maintain their leading role as the most convenient source of transportation fuels and energy sources as long as they last. A vast infrastructure exists for their transport and distribution. As transportation fuels for our cars, trucks, and airplanes, they can be used in the form of their convenient products (liquid gasoline, diesel fuel) or as compressed natural gas. They are also the basic raw materials for chemical products and materials that are essential to our everyday life. However, the bulk of fossil fuels is utilized in power plants to generate electricity. From whatever source electricity is generated, its storage on a large scale is still unresolved; for example, batteries are inefficient and bulky. It is thus necessary to also find, besides new energy sources, efficient means to store and distribute energy.

The Hydrogen Economy and Its Difficulties

With our diminishing resources of fossil fuels, there is urgent need to develop feasible new and safe ways to store and distribute energy from whatever sources it is generated (atomic or alternate) as well as to produce efficiently manmade hydrocarbons.

One approach that was proposed and has been much discussed recently is the generation of hydrogen and its use as a clean fuel—the so-called "hydrogen economy". Hydrogen is not a natural energy source on earth as it is incompatible with the high oxygen content of our atmosphere. Whereas it is indeed clean burning to form water, its generation is a highly energy-consuming process, which itself is not necessarily clean. Presently it is mainly produced by the reforming of fossil fuels to give syngas (synthetic gas), a mixture of CO and H_2. The generated CO can also be used in the water gas shift reaction to yield more hydrogen. In this process, however, at least 20% of the energy of the fossil fuel is lost as heat. Hydrogen can also be produced by the electrolysis of water, a process that does not produce CO_2 nor involve a source of fossil fuels. Our oceans represent inexhaustible water sources that can be split by atomic energy or any of the alternate energies to produce hydrogen. Despite this, hydrogen is not convenient either as a means to store energy or for its subsequent use as a fuel. The handling of volatile (b.p.: −253 °C) and potentially explosive hydrogen gas necessitates special conditions: high pressure, use of special materials to minimize diffusion and leakage, and extensive safety precautions. Even so, any leaks could represent explosion hazards, which limits its potential use. Regardless, the U.S.[5] and other governments as well as major industries seem to be increasingly committing themselves to develop the hydrogen economy. Besides the mentioned difficulties of hydrogen storage and distribution, the development of the needed infrastructure for the hydrogen economy, in my view, is also economically prohibitive, although this infrastructure may eventually be developed. The volumetric power density of liquid hydrogen is also a drawback at only one-third of that of gasoline, while liquefying hydrogen requires considerable amounts of energy.[6]

The Methanol Economy and Its Advantages

Methanol, which is presently prepared from fossil-fuel-based syn-gas, can also be prepared by direct oxidative conversion of natural gas (methane) or reductive conversion of atmospheric carbon dioxide with hydrogen (Scheme 1). In this way, hydrogen can

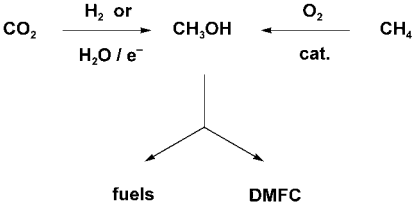

Scheme 1. Production of methanol from atmospheric carbon dioxide or from natural gas (methane), and its use as a fuel. DMFC: direct methanol fuel cell.

be stored by converting it into methanol—a convenient liquid fuel and raw material for synthetic hydrocarbons and their products—with carbon dioxide from industrial effluents or the atmosphere. This opens up the possibility of an alternative energy source to diminishing oil and gas resources and would lead to a feasible "methanol economy".

Owing to the serious limitations of the hydrogen economy, I have been proposing for some time now the methanol economy as a reasonable alternative.[7] Methanol provides an efficient means to store energy and can be used

 © 2005 Wiley-VCH Verlag GmbH & Co. KGaA, Weinheim

as a convenient fuel as well as a raw material for manmade hydrocarbons and their products.

Methanol is an excellent fuel in its own right and it can also be blended with gasoline, although it has half the volumetric energy density relative to gasoline or diesel. It is also used in the direct methanol fuel cell (DMFC) that we developed jointly with the Jet Propulsion Laboratory of Caltech.[8] In this electrochemical cell, methanol is directly oxidized with air to carbon dioxide and water to produce electricity, without the need to first generate hydrogen. This greatly simplifies the fuel-cell technology and makes it available to a wide scope of applications: for example, to provide power to cellular phones and computers (already under development) and eventually to motor scooters and cars, or even to use it in large electricity-generating facilities. It was also found that methanol can be conveniently converted into ethylene or propylene in the MTO (methanol-to-olefins) process (Scheme 2). In turn, these olefins can

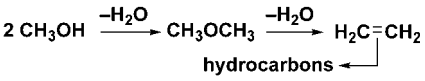

Scheme 2. Conversion of methanol into ethylene (or propylene) on the way to hydrocarbons and their products.

be used to produce hydrocarbon fuels and their products,[9] which are presently obtained from oil and gas. UOP, based on the earlier work of Jule Rabo and coworkers,[9d] developed an industrial process for the production of ethylene from methanol using acidic zeolite catalysts, and industrial plants based on this process are now under development.[9e]

In contrast to hydrogen gas, methanol is a convenient and safe liquid (b.p.: 64.7 °C). Whereas it is toxic when internally ingested and is frequently quoted as a poison, so are gasoline and diesel fuel. Some suggestions were made to use ethanol as a fuel as it can be made by fermentation from agricultural products. However, its use as a fuel has many drawbacks, and even Brazil is limiting its ambitious program to convert sugar cane into ethanol fuel. The overall economics to produce agriculture-based ethanol to replace fossil fuels is also not favorable. In fuel cells, ethanol encounters further difficulties as cleavage of C–C bonds is more difficult than cleavage of C–H bonds. Interestingly, it was Lenin that supported the industrial use of agricultural alcohol after the Bolshevik Revolution, but even the Russians resisted the "misuse" of their beloved vodka and the plan was abandoned.

At present, methanol is produced nearly exclusively from syn-gas, which is obtained by catalytic reforming of fossil fuels.[9b] As long as natural gas remains quite abundant, it seems reasonable to convert it directly (without first producing syn-gas) into methanol. In our research, much progress was made in the direct oxidative conversion of methane into methanol. As mentioned earlier, large resources of methane are tied up as gas hydrates in vast areas of sub-Arctic tundras and under the seas in the areas of the continental shelves.

Chemical Recycling of CO_2

As mentioned earlier, methanol can be also obtained by the reduction of carbon dioxide with hydrogen. Flue gases of coal- or fossil-fuel-burning power plants may be an abundant source of readily isolable carbon dioxide for the foreseeable future. Many industrial exhausts also contain considerable concentrations of carbon dioxide. Water can provide the required hydrogen. Instead of just sequestration, this process would recycle carbon dioxide into useful fuel and provide a source of hydrocarbons.

For the long-range solution to mankind's hydrocarbon needs as well as for efficient storage of energy that will eventually be generated from nonfossil fuel sources, the utilization of atmospheric carbon dioxide itself through its reduction to methanol offers a feasible new alternative. However, the content of carbon dioxide in the atmosphere is low at 0.037 %. Thus, new efficient ways to separate CO_2 are needed. One way is membrane separation technology, another is the use of selective absorption methods; here our ongoing research has led to significant advances to allow practical separation of atmospheric CO_2 from air. Besides, in the conversion of CO_2 to methanol, volatile hydrogen gas is converted into a convenient, safe liquid. If we can produce methanol efficiently on a large scale from atmospheric carbon dioxide and hydrogen, it could replace oil and gas both as a fuel and as a chemical raw material.

Atmospheric carbon dioxide is available to everybody on earth. The methanol economy thus eventually can liberate mankind from reliance on fossil fuels. The required hydrogen can be obtained from the electrolysis of water of the seas—an unlimited source. The electrical energy will be provided by atomic energy, which will be made safer and solved of problems pertaining to radioactive waste disposal, as well as by all suitable alternate energy sources (sun, wind, and hydroelectric). Alternatively, direct aqueous electrochemical reduction of CO_2 can be used,[7b] and photochemical reduction of CO_2 is also feasible. I believe that it is reasonable to consider the methanol economy as a practical and sensible approach to eventually replace fossil fuels. It can provide a feasible and safe way to store energy, to make available a convenient liquid fuel, and assure mankind an unlimited source of hydrocarbons, while at the same time mitigating the dangers of global warming owing to the greenhouse effect of carbon dioxide. In contrast to highly volatile hydrogen, methanol is a convenient liquid. Its use does not necessitate the development of a new and extremely costly and unproven infrastructure, nor does it suffer the great difficulties of safety as with the use of hydrogen.

The hydrogenation of carbon dioxide either by catalytic conversion with H_2 or by electrochemical reduction, including the reverse use of the direct methanol fuel cell,[7b] produces formic acid and formaldehyde besides methanol. It is possible, however, to further convert formic acid and formaldehyde into methanol and allow an overall high yield of methanol to be obtained. The direct oxidation of methane, which is still available from natural gas sources, into methanol also should be considered. This also always produces significant amounts of formaldehyde and formic acid. Higher selectivities to obtain methanol were reported only under low-conversion conditions.[10] With this in

 © 2005 Wiley-VCH Verlag GmbH & Co. KGaA, Weinheim

mind, we were successful in dramatically increasing the yields of methanol by the secondary conversion of formaldehyde/formic acid into methanol.

I suggest that carbon dioxide recycled by chemical reduction will provide an essential source of methanol for use as a fuel as well as a raw material for synthetic hydrocarbons and their products. Nature, of course, recycles carbon dioxide in the photosynthesis of plants by using water and solar energy in a process catalyzed by chlorophyll. However, the formation of hydrocarbons from plant life is a very slow process that requires hundreds of millions of years, although much faster bacterial conversion is feasible.

Methanol was suggested before as a fuel and a bridge to a renewable energy future,[11] however, these suggestions were never followed up by implementation. The reason, besides economic and practical factors, most probably was that methanol that originates from syn-gas generated from fossil fuel does not alleviate our dependence on fossil fuels.

The methanol economy through chemical recycling of carbon dioxide will eventually free mankind from dependence on diminishing natural fossil fuels. At the same time, recycling excess CO_2 from industrial gases and the atmosphere will mitigate a major man-made cause of global warming. The collection and sequestration of CO_2 in subterranean cavities or at the bottom of the seas is costly and does not provide a permanent solution, nor does it resolve our future needs for hydrocarbons. The still-controversial Kyoto agreement on global warming, which aims to limit CO_2 emissions, would be made more feasible by the availability of new technology, such as the chemical recycling of excess atmospheric carbon dioxide.

Ultimately all of our energy comes from the sun. As the sun will last for at least 4.5 billion years, there is an enormous amount of time for mankind to devise methods for harnessing its energy. We cannot in any way imagine advances of future generations. Discussion of what will happen beyond our present oil and gas economy relates to only the foreseeable future. Nevertheless, to find efficient ways to store energy and to produce convenient hydrocarbon-based fuels and products while mitigating global warming by recycling carbon dioxide is essential to our life and has long-range significance.

In the suggested methanol economy, methanol will be used as 1) a convenient energy-storage material, 2) a fuel, and 3) a feedstock to synthesize hydrocarbons and their products.

Published online: March 31, 2005

[1] B. Freese, *Coal, A Human History*, Perseus Publishing, Cambridge, **2003**.

[2] BP Statistical Review of World Energy, June 2004, to be found under http://www.bp.com/statisticalreview2004.

[3] *Energy Technologies for the 21st Century*, International Energy Agency, Paris, **1997**.

[4] R. C. Morris, *The Environmental Case for Nuclear Power*, Paragon House, St. Paul, MN, **2000**.

[5] National Hydrogen Energy Road Map, US Department of Energy, November 2002.

[6] a) "*Toward a Hydrogen Economy*", editorial and special issue: *Science* **2004**, *305*, 957; b) J. J. Romm, *The Hype About Hydrogen*, Island Press, Washington, **2004**.

[7] a) "The Search for New Technical Solutions for an Environmentally Sustainable Future: Recycling Carbon Dioxide into Useful Fuels": G. A. Olah in *Partnership for Global Ecosystem Management* (Eds.: I. Serageldin, J. Martin-Brown), *Proc. 5th Annual World Bank Conf.* (Washington DC) **1998**, p 65; b) G. A. Olah, G. K. S. Prakash, US patent 5928806, **1999**; c) G. A. Olah, *Chem. Eng. News* **2003**, *81* (38), 5; d) G. A. Olah, *Chem. Eng. News* **2003**, *81* (38), 42; e) G. A. Olah, *Catal. Lett.* **2004**, *93*, 1; f) G. A. Olah in *Chemical Research—2000 and Beyond: Challenges and Vision* (Ed.: P. Barkan), American Chemical Society, Washington DC, and Oxford University Press, Oxford, **1998**, pp. 40–54.

[8] a) S. Surumpudi, S. R. Narayanan, E. Vamos, H. Frank, G. Halpert, A. Laconti, J. Kosek, G. K. S. Prakash, G. A. Olah, *J. Power Sources* **1994**, *47*, 217; b) S. Surumpudi, S. R. Narayanan, E. Vamos, H. Frank, G. Halpert, G. K. S. Prakash, G. A. Olah, US Patent 6248460, **2001**; c) S. Surumpudi, S. R. Narayanan, E. Vamos, H. Frank, G. Halpert, G. K. S. Prakash, G. A. Olah, US Patent 5599638, **1997**; d) S. Surumpudi, S. R. Narayanan, E. Vamos, H. A. Frank, G. Halpert, G. A. Olah, G. K. S. Prakash, US Patent 6444343, **2002**; e) G. K. S. Prakash, M. C. Smart, Q. J. Wang, A. Atti, V. Pleynet, B. Yang, K. McGrath, G. A. Olah, S. R. Narayanan, W. Chun, T. Valdez, S. Surumpudi, *J. Fluorine Chem.* **2004**, *125*, 1217.

[9] a) G. A. Olah, H. Doggweiler, J. D. Felberg, S. Frohlich, M. J. Gridinia, R. Karpeles, T. Keumi, S. Inaba, W. M. Ip, K. Lammertsma, G. Salem, D. C. Tabor, *J. Am. Chem. Soc.* **1984**, *106*, 2143; b) J. B. Hansen in *Handbook of Heterogeneous Catalysis* (Eds.: G. Ertl, H. Knözinger, J. Weitkamp), VCH, Weinheim, **1997**, p. 1856; c) C. D. Chang in *Handbook of Heterogeneous Catalysis* (Eds.: G. Ertl, H. Knözinger, J. Weitkamp), VCH, Weinheim, **1997**, p. 1894, and references therein; d) J. A. Rabo in *Proc. 10th Int. Congress on Catalysis, Budapest* (Eds.: L. Guczi, F. Solymosi, P. Tétényi), Elsevier, Amsterdam, **1992**, *75A*, p. 1; e) "MTO: Meeting the Needs for Ethylene and Propylene Production", J. Andersen, S. Bakas, T. Foley, J. Gregor, B. Vora, S. Kvisle, H. Reier-Nilsen, T. Fuglerud, A. Grønvold, *ERTC Petrochem. Conf.* (Paris) 2003.

[10] H. Crabtree, *Chem. Rev.* **1995**, *95*, 987.

[11] a) C. L. Gray, Jr., J. A. Alson, *Moving America to Methanol*, University Michigan Press, Ann Arbor, **1985**; b) "Methanol": T. B. Reed, R. M. Lerner, *Science* **1973**, *182*, 1299; c) J. H. Perry, Jr., C. P. Perry, *Methanol: Bridge to a Renewable Future*, University Press of America, New York, London, **1990**; d) *Methanol as an Alternative Fuel Choice: An Assessment* (Ed.: W. L. Kohl), The John Hopkins Foreign Policy Institute, Washington, **1990**.

 © 2005 Wiley-VCH Verlag GmbH & Co. KGaA, Weinheim

Single-Molecule Detection

Branching Out of Single-Molecule Fluorescence Spectroscopy: Challenges for Chemistry and Influence on Biology

Philip Tinnefeld and Markus Sauer**

Keywords:
conformational dynamics · electron transfer · fluorescent labels · FRET (fluorescence resonance energy transfer) · single-molecule spectroscopy

Dedicated to Professor Jürgen Wolfrum on the occasion of his 65th birthday

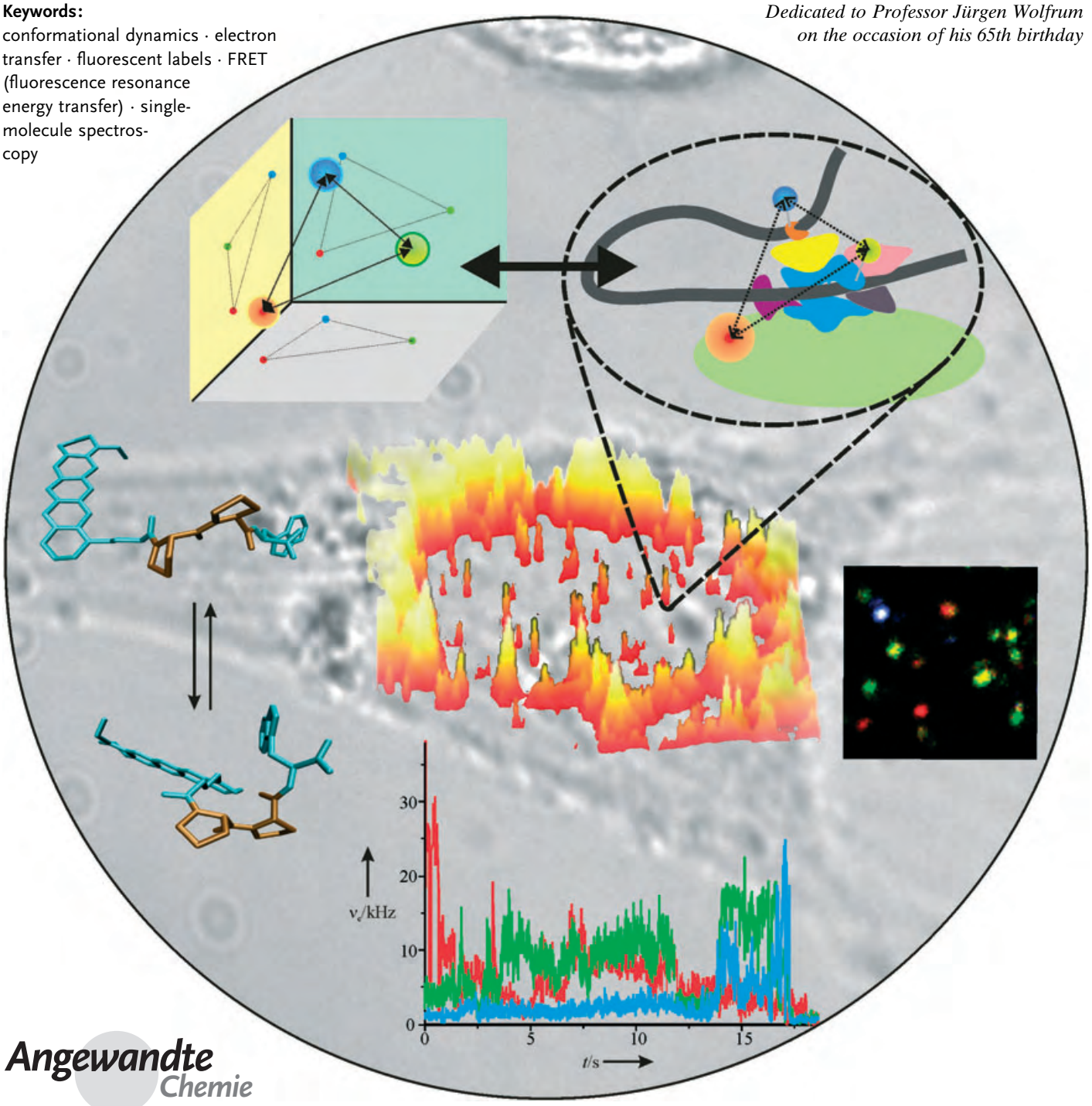

© 2005 Wiley-VCH Verlag GmbH & Co. KGaA, Weinheim
DOI: 10.1002/anie.200300647

In the last decade emerging single-molecule fluorescence-spectroscopy tools have been developed and adapted to analyze individual molecules under various conditions. Single-molecule-sensitive optical techniques are now well established and help to increase our understanding of complex problems in different disciplines ranging from materials science to cell biology. Previous dreams, such as the monitoring of the motility and structural changes of single motor proteins in living cells or the detection of single-copy genes and the determination of their distance from polymerase molecules in transcription factories in the nucleus of a living cell, no longer constitute unsolvable problems. In this Review we demonstrate that single-molecule fluorescence spectroscopy has become an independent discipline capable of solving problems in molecular biology. We outline the challenges and future prospects for optical single-molecule techniques which can be used in combination with smart labeling strategies to yield quantitative three-dimensional information about the dynamic organization of living cells.

From the Contents

1. Introduction 2643
2. Fundamentals and Technical Developments in SMFS 2645
3. Multiparameter SMFS, Photon Statistics and Analysis 2648
4. SMFS to Study Structure and Dynamics 2651
5. Use of SMFS to Study Photophysics in Multichromophoric Systems 2654
6. Molecular Photonic Wires 2655
7. SMFS in Biology 2657
8. Colocalization and Distance Measurements Between Single Molecules 2660
9. Summary and Outlook 2661

1. Introduction

Major technological breakthroughs and intensive efforts in pushing the detection limits of microscopic techniques in the last two decades have been the basis for fulfilling many scientists' dream: to detect, manipulate, and control matter on an atomic and molecular scale. Successful approaches to detect and study single atoms or molecules on surfaces have used near-field interactions with tunneling electrons or forces from sharp tips, in scanning tunneling microscopy (STM)[1] or atomic force microscopy.[2] On the other hand, optical methods enable the observation of single molecules from a certain distance unperturbed by tips. Moreover, advances in optical spectroscopy and microscopy have made it possible not only to detect and identify freely diffusing or immobilized fluorescent molecules, but also to realize spectroscopic measurements and monitor dynamic processes. Much of the fascination about single-molecule fluorescence spectroscopy (SMFS) stems from the fact that it provides the basis for a new and more direct scientific approach. That is, SMFS enables us to directly compare models, usually drawn from considerations of individual molecular systems, with experimental observations. In contrast to ensemble measurements which yield information only on average properties, single-molecule experiments provide information on individuals, such as distributions and time trajectories of properties that would otherwise be hidden. Whether each individual molecule has slightly different but constant properties (static disorder) or changes its properties over time (dynamic disorder), cannot be answered correctly by averaging the observable. Since in SMFS only one molecule is observed at a time, any synchronization procedure to induce, for example, a conformational change of the molecular structure is avoided. Therefore, SMFS represents a versatile tool to measure conformational dynamics in biopolymers, for example, protein folding or contact formation in peptides, on a wide range of time scales, extending from nanoseconds to seconds, at the single-molecule level.[3–5]

One of the most prominent and challenging examples that requires SMFS is the sequencing of a single DNA strand. In contrast to current DNA-sequencing schemes based on Sanger's enzymatic chain-termination method, fluorescence-based single-molecule DNA sequencing would allow a single fragment of DNA, several tens of kilobases or more in length, to be read at a theoretical rate of more than several hundred bases per second. The concept is to "watch" the stepwise incorporation of DNA bases by polymerase enzymes into a single DNA strand (Figure 1a).[6,7] If each base can be identified as it is incorporated into the DNA strand, the sequence can be obtained. Analogous to this approach, the reverse process could also be monitored, that is, an exonuclease could be used to degrade a single DNA strand base-by-base from one end while identifying each base after it is cleaved (Figure 1b).[8–11] Multiple DNA strands cannot be

[*] Dr. P. Tinnefeld, Prof. Dr. M. Sauer
Applied Laserphysics und Laserspectroscopy
Faculty of Physics
University of Bielefeld
Universitätsstrasse 25
33615 Bielefeld (Germany)
Fax: (+49) 521-106-2958
E-mail: tinnefeld@physik.uni-bielefeld.de
sauer@physik.uni-bielefeld.de

 DOI: 10.1002/anie.200300647 © 2005 Wiley-VCH Verlag GmbH & Co. KGaA, Weinheim

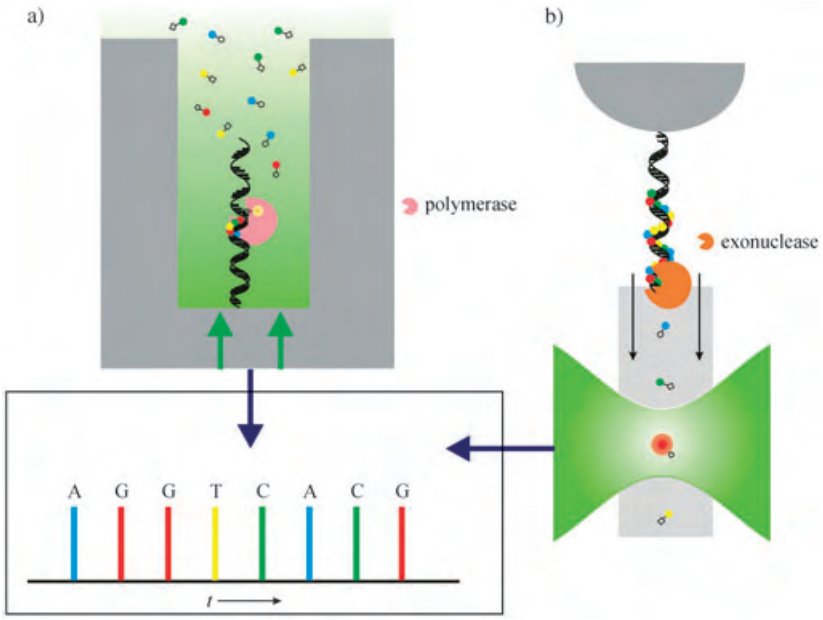

Figure 1. Illustration of the proposed procedure for polymerase-, and exonuclease-mediated sequencing of a single DNA molecule. a) Polymerase or DNA is immobilized in zero-mode waveguide nanostructures. The rapid decay of illumination incident to the entrance of such guides provides zeptoliter (10^{-21} L) effective observation volumes within the guides.[6] Zero-mode waveguides thereby enable single-molecule detection studies in the micromolar range, which is the concentrations required for efficient enzymatic DNA synthesis.[302] Owing to the small observation volume the typical residence time of freely diffusing single fluorescently labeled nucleotide molecules is in the range of a few microseconds. On the other hand, when recognized by the DNA polymerase and incorporated into the growing DNA strand, the residence time increases to several milliseconds, sufficiently long for its unequivocal fluorescence spectroscopic identification. b) In exonuclease-mediated sequencing, the DNA to be sequenced should be copied using a biotinylated primer, a DNA polymerase, and the four nucleotide triphosphates (dNTPs), each base type contains a different fluorescent label with distinct laser-induced fluorescence. The single DNA fragment is bound to a microsphere or other solid support and transferred into a flowing sample stream by mechanical micromanipulation or optical trapping. Upon addition of a 3′→5′ exonuclease, fluorescent nucleotide monophosphate molecules (dNMPs) will be cleaved and transported to the detection area down stream where they are identified based on their characteristic fluorescence properties.[9–11,82] In both schemes, the DNA sequence is directly retrieved from the detected signal sequence.

used because the different enzyme rates on the different DNA strands would result in rapid dephasing. This elegant alternative to common sequencing techniques requires the minimum conceivable starting material to obtain a sequence.

As simple as it sounds, the realization of single-molecule DNA sequencing constitutes one of the greatest challenges biologists, chemists, and physicists have confronted. From the biological point of view, major problems arise through the use of fluorescently labeled nucleotides. The bulky fluorescent dye attached to the nucleotide could hinder the polymerase- or exonuclease-mediated incorporation or degradation of nucleotides. Besides these problems, the well-defined selection of a single DNA strand and the detection and identification of each nucleotide through the spectroscopic characteristics of the fluorescent label with high accuracy are very demanding tasks. While the primary goal to sequence a single DNA fragment has not been achieved yet, each development step towards that goal is productive for the generation and improvement of analytic research systems capable of following biochemical processes (e.g., enzymatic activities) at the single-molecule level.

Current high-resolution methods, such as X-ray crystallography and NMR spectroscopy, have provided a vast array of structural detail for biological molecules, yet the output of these methods is limited by the static molecular description that they deliver and by ensemble averaging. Single-molecule methods provide an alternative set of approaches that will lead to a more direct view of the action of molecules without the need to infer functional processes from static structures. For example, many of the molecular machines that are essential for cell function and survival, such as replication, transcription, translation, and protein folding, are asynchronous and have different kinetic pathways. Biomolecular assemblies and machines can only be fully understood if the structure and function of the components of living systems is known. This discipline, known as structural biology, is in contrast to other fields of molecular biology an area of research where progress depends critically on sophisticated instruments and labeling strategies.

SMFS is now used in physics, chemistry, and biology and has already been elaborated in excellent reviews.[12–29] The

Philip Tinnefeld, born 1974, studied chemistry in Münster, Montpellier, and Heidelberg. In 2002, he received his PhD at the University of Heidelberg under the supervision of Prof. Jürgen Wolfrum. In 2001, he was recipient of a Schloessmann Award of the Max Planck Society for his ideas on the development of a molecular photonic wire. He carried out postdoctoral research with Prof. Shimon Weiss (UCLA) and with Prof. Frans C. De Schryver (Leuven) on the development of new single-molecule fluorescence techniques for the investigation of molecular interactions and dynamics. Since 2003 he is group leader in the department of Applied Laserphysics and Laserspectroscopy at the University of Bielefeld.

Markus Sauer was born 1965 in Pforzheim. He studied chemistry in Karlsruhe, Saarbrücken, and Heidelberg, and finished his PhD in physical chemistry at the University of Heidelberg in 1995 under the guidance of Prof. Jürgen Wolfrum. After a short-term visit at LBNL, Berkeley in the group of Prof. Shimon Weiss, he received the BioFuture award in 1998 to perform independent research on single-molecule handling, detection, and identification. In 2002 he finished his habilitation in Heidelberg at the Institute of Physical Chemistry. Since 2003 he is Professor for Applied Laserphysics and Laserspectroscopy at the University of Bielefeld.

 © 2005 Wiley-VCH Verlag GmbH & Co. KGaA, Weinheim

ongoing success of SMFS has been enabled not only by the development of optical single-molecule techniques but also through new refined organic-synthesis methods and the large repertoire of molecular-biology techniques. The ability to specifically label many different sites of macromolecules, for example, provides a great tool box for the application of spectroscopic techniques, such as fluorescence resonance energy transfer (FRET).[30] However, most biologically relevant SMFS studies have been performed in vitro, that is, the molecules under investigation were isolated and often immobilized to ease their observation and minimize background. The ultimate goal is to investigate these molecules in their natural environment, under native conditions, that is, in living cells. Only then can we observe them in their natural conditions and study the effect of molecular crowding, for example. Can SMFS successfully be utilized to study communication pathways, signaling cascades, or RNA polymerases during transcription inside the nucleus of a live cell?

Herein, recent advances of single-molecule spectroscopy and microscopy with emphasis on biological applications are reviewed. First, we will briefly explain the fundamentals for successful detection and spectroscopy of single fluorescent molecules. In particular, we will discuss the merits of wide-field and confocal microscopy. Then, we highlight various energy-transfer methods, capable of monitoring distance changes between single molecules, and demonstrate how multiparameter SMFS techniques combined with smart data analysis can be utilized to study and control complex multichromophoric systems and photonic wires and to quantitatively determine the number of interacting molecules and their relative orientations. Furthermore, we review new techniques, such as high-precision distance microscopy, to measure distances between single molecules well below the optical-resolution limit. Examples will be given how every accessible spectroscopic parameter can contribute to a better understanding of complex biological systems. Finally, we give some perspectives of how SMFS, in combination with optical tweezers, new labeling strategies, and other spectroscopic techniques, for example, surface-enhanced Raman spectroscopy, might be successfully adapted to live-cell analysis.

2. Fundamentals and Technical Developments in SMFS

Considering all the technical developments and scientific efforts that were required for the first successful detections of single fluorescent molecules in 1989[31] and 1990,[32] it is hard to imagine that it only takes a human eye, properly adjusted to the dark, and a microscope with high collection efficiency to detect single, ordinary fluorophores, such as a rhodamine molecule, by its fluorescence emission. To aid this detection, a variety of techniques have been applied to SMFS, of these wide-field microscopy using a state-of-the-art charge coupled device (CCD) detector is the simplest.

When the central player, usually a fluorophore, is illuminated by laser light it is excited from the ground-state, S_0, into high-lying vibrational levels of the first excited singlet-state, S_1. This state undergoes rapid, non-radiative, internal conversion to the lowest S_1 level. The optical saturation limit is the maximum rate that a dye molecule can be cycled between S_0 and S_1 and is dependent on the fluorescence lifetime of the dye, τ_f (Figure 2a). Several depopulation

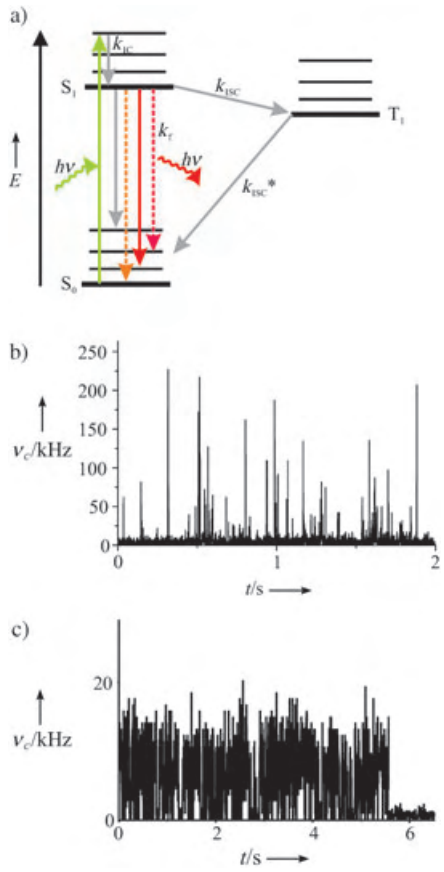

Figure 2. a) Three-electronic-state model describing the general photophysical behavior of single fluorescent molecules under laser illumination. b) Fluorescence signals observed in consecutive time windows (bins) of 1 ms from a 10^{-11} M aqueous solution of Cy5 molecules (count rate ν_c versus time t) using confocal fluorescence microscopy and a pulsed diode laser emitting at $\lambda = 635$ nm for excitation. When a molecule passes the observation volume, up to 200 photon counts are detected per millisecond. c) Fluorescence intensity trajectory of a single Cy5 molecule immobilized on a dry cover slide. One commonly observed source of single-molecule fluorescence-intensity fluctuations involves discrete intensity jumps from "on" (high intensity) to "off" (background) states arising from quantum jumps of the single molecule to non-emissive "dark" states, for example, triplet states. After approximately 5.6 s irreversible photobleaching occurs, reflected in a spontaneous drop of the fluorescence intensity to the background level.

pathways, such as intersystem crossing into the triplet state, compete with fluorescence emission, thus reducing the number of emitted photons. Furthermore, the number of photons that can be detected from a single fluorophore is limited by irreversible photobleaching, which is an intrinsic property of all conventional organic fluorophores. Common dye molecules can emit up to several 10^6 photons before irreversible photobleaching occurs. In general, the fluorescence signal is governed by the selection of appropriate

 © 2005 Wiley-VCH Verlag GmbH & Co. KGaA, Weinheim

fluorophores which exhibit a high extinction coefficient ε at the excitation wavelength λ, a high fluorescence quantum yield Φ_{fl}, and a high photostability. Additionally, the ideal fluorophore should have a fairly short fluorescence lifetime (i.e. in the nanosecond range) so that it can go through the excitation and emission cycle at high frequency and should not show fluorescence intermittencies (off states) as a result of, for example, triplet transitions (Figure 2).

The most important parameter in SMFS is the signal-to-noise ratio (S/N). With respect to the noise in the imaging signal, shot noise, or photon noise, is the most important contribution in that it poses the fundamental limit to the S/N ratio. Under real conditions the presence of background shot noise must also be considered. If the signal-to-background (S/B) ratio is large, nearly all detected photons represent image information, and the S/N ratio approaches the value $n^{1/2}$ (for a signal consisting of n photons). If the background contribution is large (small S/B ratio), the desired signal may become lost in the high background shot noise, resulting in an S/N ratio approaching zero. Background stems mainly from elastic (Rayleigh) and inelastic (Raman) scattering from solvent molecules as well as from autofluorescent impurities. While Rayleigh scattering can be efficiently suppressed by the use of suitable optical filters, the complete suppression of Raman scattering, which is directly proportional to the number of illuminated solvent molecules, is challenging because it occurs at least partly in the same wavelength range as the fluorescence signal. Autofluorescence from impurities strongly depends on the excitation, and detection wavelength. Especially in biological samples, luminescent impurities can decrease the sensitivity or even prevent the definite detection of individual fluorescent molecules. Therefore, it is desirable in single-molecule fluorescence experiments to work with fluorescent dyes that absorb and emit in the red region of the electromagnetic spectrum, this is because above 600 nm, there are only a few compounds known which show intrinsic absorption and emission.[33]

Since the contribution of background sources is directly proportional to the number of molecules in the excitation volume, the reduction of the excitation/detection volume is also key to a high S/N ratio. One SMFS method relies on hydrodynamic focusing of a sample stream in sheath-flow cuvettes down to a layer thickness $< 10\,\mu m$ in combination with pulsed excitation and time-gated detection to suppress Rayleigh and Raman scattering.[33] Further reduction of the excitation volume can be achieved using laser excitation in a 1) confocal, 2) evanescent, or 3) near-field configuration.

Near-field scanning optical microscopy (NSOM) has been developed primarily to break the optical diffraction limit, which restricts the spatial resolution of conventional optical measurements to approximately half of the wavelength of light.[34,35] In NSOM, subdiffraction spatial resolution on the order of 50–100 nm is achieved by bringing a sample to within 5–10 nm of a subwavelength sized optical aperture so that photons from the aperture do not have enough distance to experience diffraction (Figure 3a). Although NSOM offers advantages, such as the ability to correlate spectroscopic information with topographic information, it suffers from invasiveness and perturbation of the sample owing the nearness of the probe tip. NSOM also covers a huge field of research and is therefore beyond the scope of this review. Nevertheless, NSOM finds application in biology and enables simultaneous topographic and single-molecule fluorescence imaging on live cell membranes.[36–39]

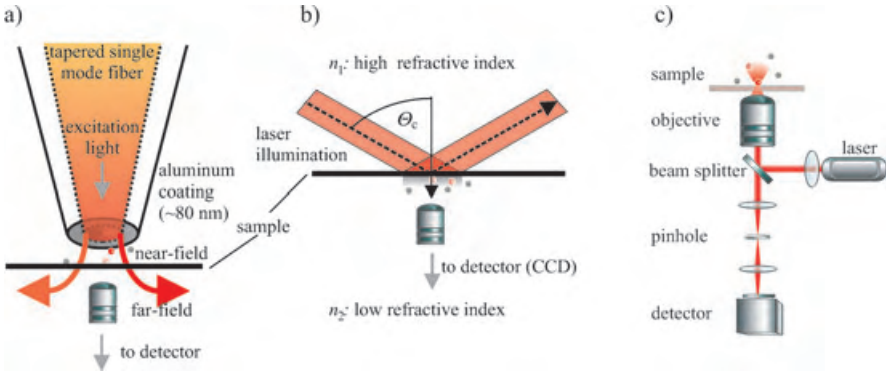

Figure 3. Schematic set-up of a) near-field scanning optical microscopy (NSOM), b) total internal reflection fluorescence microscopy (TIRFM), and c) confocal fluorescence microscopy.

In confocal microscopy, a laser beam is brought to near diffraction-limited focus in a sample by using an oil- or water-immersion, high numerical aperture (NA) objective.[40] The fluorescence is collected through the same objective and emission light is separated from excitation light by a dichroic mirror (Figure 3c). A small pinhole (50–100 μm in diameter) is placed in the image plane to reject light from out-of-focus regions. This arrangement defines a small spheroidal volume of 0.5–1.0 femtoliters in the sample. Rigler and co-workers were the first to exploit the use of confocal fluorescence microscopy for the detection of single-molecules.[41,42]

Using confocal optical arrangements and avalanche photodiodes (APDs) as detectors, individual fluorescent molecules can be easily detected with high S/N ratios. Confocal fluorescence microscopy has even been successfully employed in two-photon excitation (TPE) of individual fluorophores.[43–45] The principles of two-photon microscopy were first elucidated by Webb and co-workers.[46] TPE cross sections are extremely small, typically on the order of $10^{-50}\,cm^4\,s$ for most fluorophores, so that high intensity, short laser pulses (pulse widths of approximately 100 fs), for example, from a mode-locked Ti:sapphire laser, are required to achieve efficient TPE.[47,48] As a second-order, nonlinear process, the molecular excitation rate depends quadratically on the laser intensity. Since efficient excitation occurs only at the laser-beam focus, photobleaching of out-of-focus molecules is reduced. On the other hand, in-focus photobleaching is more pronounced so that TPE fluorescence count rates are generally lower. Since high fluorescence count rates are

 © 2005 Wiley-VCH Verlag GmbH & Co. KGaA, Weinheim

essential for SMFS, one-photon excitation represents the method of choice used in most applications. Furthermore, in some cases, the high excitation intensities required to generate fluorescence signals by TPE may lead to other nonlinear processes, for example, continuum generation in the solvent, which can increase the background and deteriorate fluorescence sensitivity. Nevertheless, TPE can be successfully utilized in two-color cross-correlation experiments to monitor colocalization of different dyes in the observation volume at the single-molecule level.[49] The main advantage of the two-photon technique is that the broadness of two-photon excitation spectra allows for dyes with different emission wavelengths to be excited by laser light of a single wavelength (so called spectral multiplexing).

In combination with fluorescence correlation spectroscopy (FCS), confocal fluorescence microscopy has found broad application, especially in the field of diagnostics and evolutionary biotechnology.[50] FCS uses Brownian motion to bring single or a few sample molecules through the confocal volume. By calculating the autocorrelation of the fluorescence intensity fluctuations, time-dependent dynamics can be followed in detail. However, since the emission bursts from many single molecules are used to calculate the autocorrelation function, differences between individuals are impossible to detect. Since the sensitivity of FCS affords nanomolar concentrations,[51] target molecules, such as specific DNA or RNA sequences, have to be amplified prior to the hybridization measurements.

Photon-counting histogram (PCH), and fluorescence-intensity distribution analysis (FIDA) are related techniques to differentiate between molecules with different fluorescence brightness. Both techniques measure photon counts in time intervals of fixed duration and fit these measurements to theoretical distributions.[52–54] Fluorescence-intensity multiple distributions analysis (FIMDA) uses a similar photon-counting histogram but with time intervals of varying duration, and can simultaneously extract information about diffusion and brightness.[55] The most recent autocorrelation method, photon arrival-time interval distribution (PAID) combines the autocorrelation approach of FCS with a photon-counting histogram to reveal information on multiple spectral channels.[56]

Wide-field CCD-array imaging does not have the high temporal resolution of an APD (ca. 100 ps) and does not achieve the best S/B ratio because more of the background from out-of-focus sources is collected and detected. On the other hand, wide-field imaging offers the advantage of parallel detection and the ability to acquire statistics rapidly on the millisecond behavior of hundreds of molecules individually and simultaneously.[57] This type of detection is particularly important in experiments where irreversible reactions are monitored, for example, the unwinding of immobilized DNA molecules upon addition of a helicase enzyme.[58] In this experiment, helicase molecules start unwinding of the DNA almost simultaneously and in a confocal setup only one molecule could be monitored for every sample preparation.

One possibility to obtain statistics with a low-temporal resolution but a high S/B ratio for a large number of molecules is total internal reflection (TIR) excitation of fluorescence near a dielectric interface (Figure 3b).[59,60] Usually, this evanescent wave excitation is achieved by prism-[61] or objective-type[62] TIR at a glass–-liquid or a glass–air interface. At the interface the optical electromagnetic field does not abruptly drop to zero but decays exponentially into the liquid or air phase. Molecules in a thin layer of approximately 200 nm thickness immediately next to this interface can still be excited by the rapidly decaying optical field. Hence, the illuminated volume is extremely thin thus providing very good S/N ratios. TIR-microscopy is particularly applicable for imaging single molecules at electromagnetic boundaries and has allowed the observation of fluorescently labeled myosin and kinesin molecules as well as individual adenosine-5′-triphosphate (ATP) turnover reactions.[61,63–65] Evanescent field excitation has been also successfully employed for two- and three-dimensional measurements of the structural dynamics of single myosin V motor protein complexes.[66]

In principal, single-molecule measurements can be subdivided into different categories depending on the experimental objective. In many single-molecule applications, such as DNA sequencing, it is necessary to classify the detected fluorescence signals of individual molecules or distinguish between single molecules. That is, the identification and analysis of static properties of freely diffusing or immobilized molecules. In other applications, individual molecules have to be observed over a long time to retrieve information about their mobility and trajectories. Single-molecule experiments are also utilized to study individual dynamics in a heterogeneous environment or conformational fluctuations of polymers or biomolecules.

Theoretically, several characteristic properties, such as 1) fluorescence intensity 2) fluorescence decay[67,68] 3) emission spectrum,[10,69] 4) diffusion coefficient (in solution),[70] and 5) fluorescence anisotropy,[71] can be used to identify an individual fluorescent molecule.[70] However, because the trajectory of each free individual molecule is given by Brownian motion and environmental factors, the number of detected fluorescence photons per molecule has a large statistical distribution. Although the entire fluorescence intensity distribution can be a well-defined characteristic for a species,[52,53,55,56] a single event is not. Therefore, fluorescence intensity alone is not an adequate parameter to identify a single molecule or to follow individual dynamics. There are many sources of intensity fluctuations other than those that are being investigated. Among these are orientation changes, blinking arising from photophysical or photochemical changes, or uncorrelated changes of the environment of the fluorophore.[72–79]

Fortunately, fluorescence photons deliver several measurable pieces of information that can help to transmit the changes of the molecules investigated to the experimenter. Besides the information that fluorescence lifetime, intensity, emission spectrum, and fluorescence anisotropy provide on the dynamics of the investigated system, it is important to remember that the number of photons emitted from a single fluorophore is limited. An elegant way to increase the information obtainable from a single fluorescent molecule is

 © 2005 Wiley-VCH Verlag GmbH & Co. KGaA, Weinheim

to monitor different fluorescence characteristics, if possible, in parallel.[80–82] In the static case, the parallel detection of different parameters can be used to improve the identification accuracy of single molecules,[71,82] to discriminate single fluorophores against background fluorescence, which is of particular interest in cells and tissues,[83] or to reveal heterogeneity in local environments.[76,84] The simultaneous recording of various spectroscopic parameters (so-called multiparameter analysis) provides the fundamental basis for improved single-molecule spectroscopic techniques that enable a refined understanding of spectroscopic dynamics and fluorophore interactions.[78,85–88] Furthermore, in contrast to ensemble fluorescence spectroscopy, SMFS offers an additional advantageous parameter, which is the photon statistic. Implementations for multiparameter SMFS and, in particular, this fifth, non-classical fluorescence parameter are explained in more detail in the following.

3. Multiparameter SMFS, Photon Statistics and Analysis

From the classical point of view, fluctuations in the number of photons detected cannot be reduced more than in a light field which obeys Poissonian statistics, that is, uncorrelated light. However, from the point of view of quantum mechanics, states are possible for which the photon-distribution is narrower than the Poisson distribution. These states have no classical analogue and are a direct manifestation of the corpuscular aspect of radiation. To achieve a sub-Poissonian distribution, photons must have the tendency to be separated in time. A simple system that can provide a light source for nonclassical or sub-Poissonian light is a single two-level quantum system, for example, a simplified model of a fluorophore. A fluorophore requires a certain time after emission of a photon to repopulate the excited state and emit the next photon. This can be visualized in a histogram in which the time lags between photons are represented. Under pulsed laser excitation with laser pulses that are significantly shorter than the excited-state lifetime of the fluorophore, no photon-pairs from the same molecule (coincidences) are detected within one laser pulse. On the other hand, according to Poissonian statistics, there is a probability of detecting two photons in two consecutive laser pulses. Similarly, for two molecules, the probability of detecting two photons within one laser pulse is one half that of detecting two photons in two consecutive laser pulses.[89,90] Consequently, for three molecules the probability is 0.67, and for four molecules 0.75, and so on, until the classical limit of one is approached for an ensemble. Accordingly, the ratio of the probability of detecting two photons within one laser pulse can be used to obtain information about the number of emitting species. Vice versa, if it is known that several fluorophores are present, the absence of any coincidences can indicate annihilation processes and can help to reveal molecular interactions in multichromophoric systems.[85,91]

Figure 4 depicts a schematic set-up used for multiparameter SMFS. Usually the sample is excited by a pulsed laser with a certain repetition rate defining the time-lag between consecutive laser pulses. The fluorescence signal is split by a dichroic mirror and detected on two single-photon counting avalanche diodes (APDs). The output TTL-pulses of the APDs are fed into specialized personal computer (PC) plug-in cards for time-correlated-single-photon-counting (TCSPC), nowadays with multidetector capability, high time-resolution, and low dead time (e.g. TimeHarp200 from Picoquant, or SPC-630 from Becker&Hickl). These boards are specially developed for single-molecule experiments. For each photon detected, three pieces of information are stored: 1) the macroscopic time, t_{macro} which is the arrival time after the beginning of the acquisition (resolution 50 ns), 2) the microscopic time, τ_{micro} which is the time delay between the laser pulse and the photon detection (resolution 8 ps), and 3) the channel (detector 1 (det1) or dectector 2 (det2)) from which each photon was detected. Because TCSPC cards have dead times in the range of 100–300 ns, it is necessary to apply an electronic delay to one of the two APD signals so that two fluorescence photons generated by the same laser pulse can both be registered. The ratio of fluorescence intensity detected at both APDs expressed as fractional intensity F_2 ($F_2 = I_{det2}/(I_{det1}+I_{det2})$) is a measure of the wavelength of the emission maximum of the fluorophore and enables the monitoring of spectral fluctuations. By exciting with linear-polarized light and monitoring the fluorescence signal in a perpendicular and parallel detection channel, the fluorescence anisotropy of single molecules can be measured. Applying linear-polarized laser light rotated in time by the help of an electrooptical modulator (EOM), delivers information about the number of absorbing species and their relative orientations.[85,91] From the time between consecutive photons registered at both APDs under circular polarization conditions, coincidence histograms can be constructed providing direct information about the number of emitting species (photon antibunching measurements).[90]

This arrangement allows the simultaneous construction of fluorescence intensity and lifetime trajectories for each detector. Plotting a histogram of the macroscopic arrival time in pre-selected time intervals, yields a so-called intensity trajectory of the fluorescence, which is used to visualize the intensity as a function of time (Figure 5). The histogram of the microscopic arrival times yields a fluorescence decay. This photon-by-photon detection mode allows the analysis of fluorescence intensity and lifetime trajectories in a sliding-scale fashion (Figure 5a),[92,93] or the construction of state-specific fluorescence decay curves (Figure 5b).[78] In a sliding-scale analysis, the signal trace of microscopic arrival times is plotted into a series of fluorescence-decay histograms with a constant number of events (e.g. 500 photon counts) which are subsequently analyzed by a maximum-likelihood estimator (MLE).[94–97] State-specific fluorescence decay curves are constructed from the microscopic arrival times with respect to the laser pulse by summing all the photon counts associated with certain intensity levels.

Although two channels give only a poor spectral resolution, this simple geometry can easily reveal spectral fluctuations on the millisecond time scale, and can substantially improve the identification accuracy of single fluorophores.[78,98] Two detectors are also required for photon

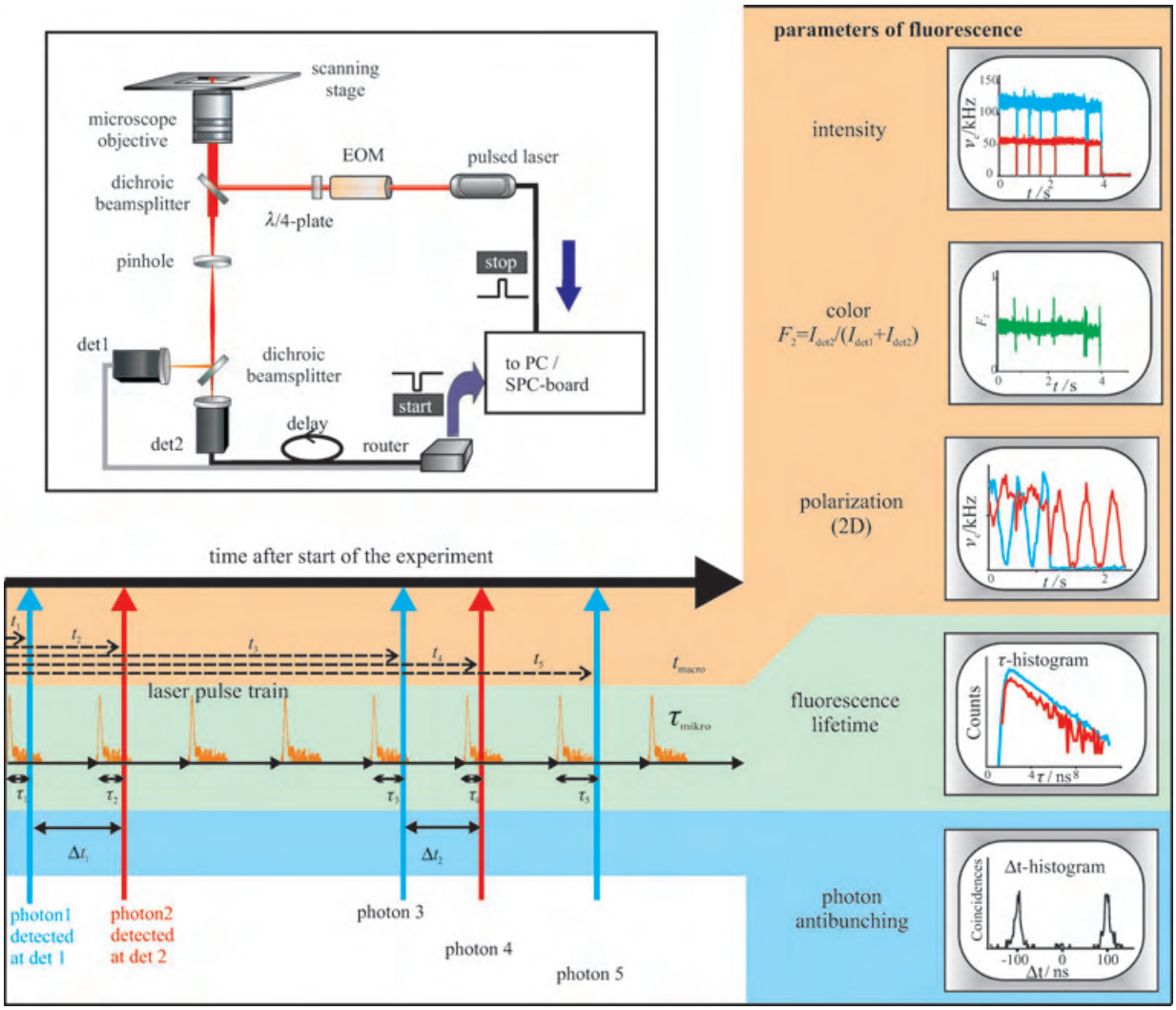

Figure 4. Set-up for multiparameter SMFS including photon antibunching, and polarization-modulated excitation spectroscopy.

antibunching measurement in a Hanbury–Brown and Twiss-type experiment.[99] In this case the sample is excited by circularly polarized light and the signal is split onto two APDs using either a 50:50 nonpolarizing beam splitter or a dichroic mirror. The time lag between consecutive photons are presented in so-called "interphoton times" histograms. The use of an appropriate delay for the signal of one of the two detectors enables the detection of quasi simultaneously arriving photons. This approach circumvents the dead time of the setup that comes from the detectors and data-acquisition electronics.

The interphoton-times histograms are corrected for the delay thus directly indicate photons that are associated with the same laser pulse at around zero interphoton time. As expected for an ensemble of molecules (a Poissonian light source), the peak pattern obtained clearly demonstrates the classical behavior of the radiation field emitted by an ensemble of molecules, that is, the central peak N_c is identical in intensity to the lateral (neighboring) peaks $\bar{N}_1$ (Figure 6b). In contrast, in case of a single molecule the central peak disappears since the probability of emitting more than one photon per laser pulse is negligible. Only a few background–background, background–signal, and signal–background events contribute to the central peak. With a background-count rate of approximately 2 kHz S/B ratios of 30–50 are obtained for single rhodamine derivatives adsorbed on a dry cover slide.[89] This situation results in high ratios of the area of the lateral peaks to the central peak (for example, 20 corresponding to an $N_c/\bar{N}_1$ ratio of 0.05 in Figure 6b). Previous photon antibunching studies used fluorophores under biologically irrelevant conditions,[100,101] or had to sample many molecules to obtain sufficient statistics for photon antibunching measurements.[102,103] Whereas, pulsed laser excitation experiments deliver a photon antibunching signal from single standard fluorophores immobilized on glass coverslides at room temperature in under one second.[89] The main advantage of pulsed photon antibunching experiments is that the desired saturation of the molecule's singlet transition can be achieved without high occupation of the triplet state, which is important as the triplet state is an intermediate for photo-

 © 2005 Wiley-VCH Verlag GmbH & Co. KGaA, Weinheim

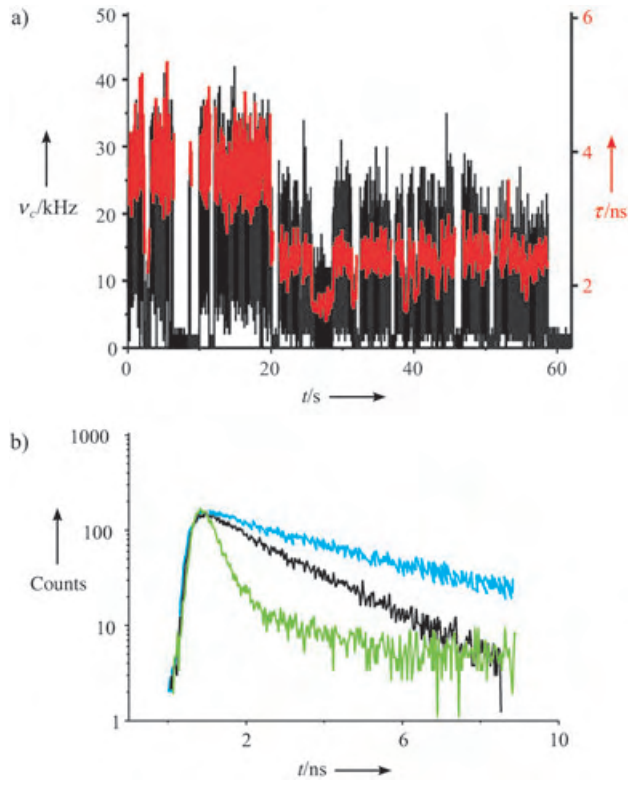

Figure 5. a) Fluorescence intensity (black), and lifetime (red) as a function of time (count rate ν_c versus time t) for a single oxazine molecule adsorbed on a cover slide and in the laser focus of a $\lambda = 635$ nm pulsed laser diode. Fluorescence lifetime categorization (binning) was accomplished using a sliding-scale analysis with a stepsize of 500 photon counts.[78] b) State-specific fluorescence decays of the three different intensity levels shown in (a) with $\nu_c > 22$ kHz (blue), 10–22 kHz (black), and 2–10 kHz (green).

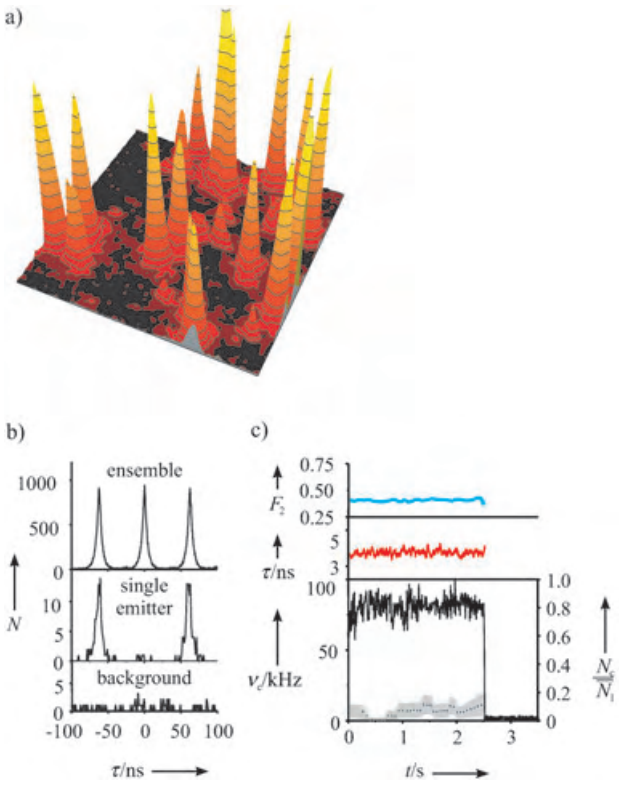

Figure 6. a) Confocal fluorescence image of a 6×6 μm area with an average density of approximately 0.5 rhodamine molecules per μm^2. By locating fluorescent molecules in the laser focus, fluorescence photons are generated at predetermined times, in this case, every 62.5 ns after excitation with the laser pulse (corresponding to the excitation frequency of 16 MHz. b) Histogram of interphoton times Δt recorded from an ensemble of rhodamine molecules in solution (10^{-8} M), from a single emitter, and from background. c) Multiparameter analysis of the data recorded from a single rhodamine molecule. Fluorescence intensity trajectory (black; count rate ν_c versus time t), fluorescence lifetime τ (red), and fractional intensity F_2 (blue) calculated from the intensities recorded after a dichroic beam splitter at detector 1 and detector 2, $F_2 = I_{det2}/(I_{det1}+I_{det2})$. Additionally, the antibunching signature as represented by the ratio of the area of the central peak to the area of lateral peaks ($N_c/\bar{N}_1$) is shown as dark gray dots. The stripe (light gray) indicates the statistical error of the $N_c/\bar{N}_1$ ratio.

destruction. Therefore, even dynamics in the radiation field emitted by the varying number of molecules in the laser focus can be studied as shown in Figure 6c (gray squares).[89,90] The almost constant $N_c/\bar{N}_1$ ratio of under 0.2 demonstrates that the photon probability distribution exhibits strong sub-Poissonian character throughout the whole experiment, that is, only one rhodamine molecule contributed to the detected light field.

Information about the orientations of transition dipoles of the fluorophores investigated can be obtained using different arrangements. Rotation of the linear polarization of the excitation beam using a combination of an EOM and a quarter-waveplate can reveal the orientation of fixed molecules from the phase shift of the emitted light.[76,79,91,104] Alternatively, measuring the polarization after excitation with circularly polarized light, for example, in a two-detector setup, can provide equivalent information. By using linearly polarized excitation light, the technique can be used to measure the polarization anisotropy of single molecules.[105]

As mentioned previously, imaging techniques can be used advantageously to observe multiple fluorescence parameters of single molecules in parallel. However, confocal geometries offer a higher time resolution (usually μs compared to ms in an imaging technique). Furthermore, not all the parameters are accessible to imaging, for example fluorescence lifetime and photon antibunching studies require confocal single-molecule spectroscopy. Although fluorescence lifetime imaging is possible using a time-gated intensified CCD-camera, it is in general not very practical at the level of single molecules because of long measurement times (required to shift the time-gate over the entire decay) and the limited photostability of conventional fluorophores. The other parameters, such as color and polarization are accessible by imaging, based on the dual-view concept originally developed by the Kinosita group.[106] Splitting the signal with regard to the property to be measured (e.g. a dichroic mirror for color and a polarizing beamsplitter for polarization) and subsequent imaging on different parts of the CCD-chip has proven to be a versatile approach for multiparameter imaging that has recently been extended to the simultaneous detection of color and polarization with a single CCD-Camera.[107]

 © 2005 Wiley-VCH Verlag GmbH & Co. KGaA, Weinheim

4. SMFS to Study Structure and Dynamics

One trend in SMFS is the investigation of multichromophore systems. These studies can be subdivided into two categories: exploring the fundamentals of molecular interactions on the level of individual molecules and the exploitation of energy transfer reactions to measure distances between molecules. To monitor, for example, conformational dynamics of biomolecules, such as protein folding, distance changes between certain amino acid or nucleic acid residues within the polymer chain have to be measured with high time resolution. From the spectroscopic point of view, any distance-dependent method, such as energy transfer, proton transfer, or photoinduced electron-transfer reactions, can be used to record conformational changes as long as they are reflected in alterations in the interaction with the probe molecules, for example, fluorophores. Very prominent in this context is the application of long-range dipole–dipole interactions, called fluorescence resonance energy transfer (FRET), to biological systems.

4.1. Fluorescence Resonance Energy Transfer (FRET)

Generally, FRET involves nonradiative transfer of electronic excitation from an excited donor, D* to a ground-state acceptor molecule A. The efficiency of this dipole–dipole interaction depends on the distance between the fluorophores, the spectral overlap of the donor emission and the acceptor absorption (the so-called overlap integral), the refractive index of the media, the donor quantum yield, and the relative orientation of the fluorophores. Förster type resonant energy transfer occurs for allowed singlet–singlet, and singlet–triplet transitions if the emission of D* and the absorption of A overlap significantly. For such transitions the Förster radius R_0 ranges from 20 to 80 Å. The Förster radius gives the separation at which the transfer efficiency equals 50%. Owing to the strong separation-dependence (the efficiency decays proportionally to the sixth power of the separation) FRET is ideally suited to obtain information about structure and structural changes of biologically important molecules.[108–114] In combination with SMFS, single-pair FRET (spFRET) is suited to reveal conformational changes in protein chains, and finds numerous applications in "dynamic structural biology".[115,116]

spFRET was first demonstrated in 1996 and has become one of the most popular tools in SMFS because the FRET-range covers the distance in which many important biological processes take place (Figure 7). The groups of Ha and Weiss in particular, demonstrated the potential of spFRET to reveal conformational dynamics in single biomolecules on the millisecond time scale showing, for example, unzipping of DNA by a single helicase molecule, magnesium dependent RNA dynamics, and protein folding.[116–124]

Deniz et al.[117] used spFRET to study protein folding of chymotrypsin inhibitor 2 (CI2), a small, single-domain protein, at the single-molecule level. CI2 was selected as a model system to study protein folding at the single-molecule level because it shows two-state folding. Folded and unfolded

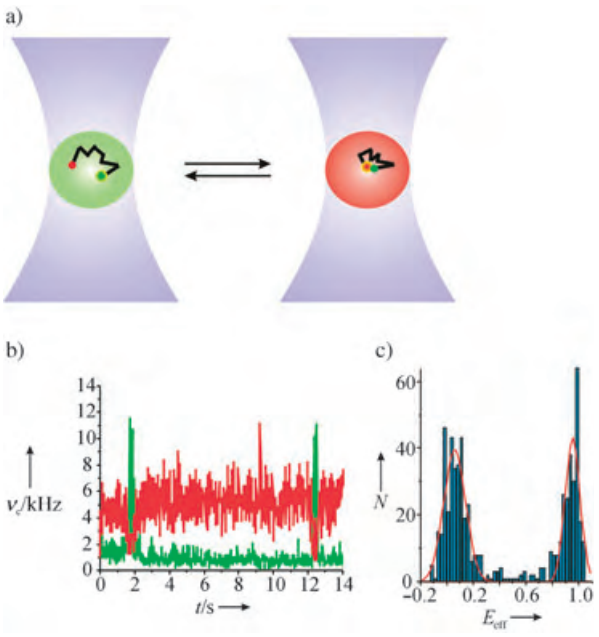

Figure 7. a) Principle of spFRET to study conformational dynamics in biomolecules. The molecule investigated is labeled site-specifically with a donor (green) and an acceptor dye (red). Depending on the donor–acceptor separation, the excited-state energy of the donor is transferred to the acceptor. b) Fluorescence trajectory (count rate, ν_c, versus time, t) of a single donor–acceptor labeled DNA hairpin (Cy3-5′-CCCCTA AGTAGTTCCTCAC T(Cy5)AGGGG-3′) immobilized in the laser focus by biotin–streptavidin binding. Structural changes, in this case opening and closing of the hairpin structure, are directly reflected in alterations in the FRET efficiency (e.g. at $t \approx 2$, and 12 s). c) FRET-efficiency, E_{eff} ($E_{eff} = I_A/(I_A+I_D)$) histograms (background corrected) extracted from individual fluorescence bursts of Cy3/Cy5 labeled double-stranded oligonucleotides (donor–acceptor separation: ca. 3.4 nm, corresponding to 10 base pairs) that are freely diffusing through the observation volume, and corresponding Gaussian fits. The large peak in zero energy-transfer efficiency arises from donor-only labeled DNA (nonhybridized Cy3 oligonucleotides), and premature photobleaching of the acceptor. The appearance of two maxima in the FRET-efficiency histogram instead of a broad distribution implies that conformational fluctuations between sub-states with different donor–acceptor orientations or separations are on average slower than the measurement time (typically 0.5–1 ms). If the conformational fluctuation rates were faster than the measurement time (which equals the diffusion time), the peak corresponding to high FRET efficiency would at least be broadened or gradually shifted to lower FRET efficiency.

subpopulations were revealed from measurements of freely diffusing single protein molecules. Different distance distributions between the donor and acceptor in the folded and the denatured state of the protein cause different FRET efficiencies. These subpopulations can be clearly resolved because only one molecule is probed at a time. Eaton and co-workers studied the equilibrium collapse of a polypeptide in the denatured state by monitoring spFRET efficiencies of unfolded populations as a function of denaturant concentration.[3] They could show that dynamic information, such as polypeptide reconfiguration times, can be extracted from the widths of single-molecule FRET efficiency distributions. The determination of barriers of reconfiguration times allows, in

 © 2005 Wiley-VCH Verlag GmbH & Co. KGaA, Weinheim

turn, the heights of free energy barriers of folding to be estimated. As a result of the availability of hundreds to thousands of events in only a few minutes, single-molecule studies in solution can easily differentiate between subpopulations of analyte molecules in heterogeneous ensembles (Figure 7c).[92,125,126] The kinetics of DNA hairpin–loop fluctuations is one of the fastest conformational fluctuations observed to date at the single-molecule level. By using a combination of FRET and FCS experiments, the rates for the opening and closing of DNA hairpins were determined to a few tens of microseconds, depending on the size and sequence of the loop and stem.[127–129]

To gain information about slower conformational dynamics of biopolymers, such as absolute values of transition rates between differently folded states, time trajectories of individual DNA, RNA, or protein molecules immobilized on a solid support have to be monitored in real time (Figure 7b). However, care must be taken to ensure that minimal perturbation of the molecules results from the immobilization on the modified glass surfaces.[130–132] Recently,[124] a new immobilization method was demonstrated that enables the observation of individual protein molecules, unperturbed by surface effects. Rhoades and co-workers monitored adenylate kinase molecules as they fold and unfold over many seconds. Individual, site-specific D/A-labeled proteins were trapped within surface-tethered lipid vesicles, thereby allowing spatial restriction without inducing any spurious interaction with the surface. By simultaneous measuring of donor fluorescence lifetime, intensity, and anisotropy the two main sources of error in FRET-based distance calculations (local quenching effects and restricted dye mobility) can be excluded.[105,133] In combination with refined labeling strategies, new multiparameter spFRET experiments enabled the direct observation of the proton-powered subunit rotation in single membrane-bound F_0F_1-ATP synthase molecules.[134]

These studies highlight that spFRET is a powerful tool to unravel the heterogeneity of conformational transitions in "dynamic structural biology" and to elucidate kinetic and static properties of biopolymers in both the folded and the unfolded states. Moreover, the choice of a suitable observable, such as the FRET-efficiency, allows for the motion of the biopolymer on its energy surface to be followed in real time.

4.2. Photoinduced Electron-Transfer Reactions

Other conformational dynamics with functional significance, for example in enzymes, often appear on much smaller spatial scales (down to several Ångströms). To monitor subnanometer conformational transitions of biopolymers, photoinduced chemical reactions of fluorescent dyes with molecular quenchers are of great interest. In contrast to FRET, photoinduced charge-transfer reactions require close proximity or even van der Waals contact between dye and quencher for fast and efficient conversion of electronic excited-state energy. To interpret fluorescence-quenching caused by photoinduced electron transfer, the transfer mechanism and its distance dependence has to be well understood. Generally, quenching of fluorophores in the first excited singlet state by electron donors or acceptors results in the formation of a radical ion pair $A^{\bullet-}D^{\bullet+}$, which returns to the ground state by charge recombination. The efficiency of charge separation is controlled by the relationship between the free energy of the reaction, the reorganization energy, and the distance between the donor and acceptor.[135,136]

Since efficient electron-transfer reactions usually require close proximity of donor and acceptor they are ideally suited to study small conformational changes in biomolecules, and to monitor, in particular, equilibrium fluctuations in proteins. For example, Chattopadhyay et al. coupled a fluorescein dye selectively to a hydrophobic cavity of an intestinal fatty acid binding protein and used FCS to study fluorescence fluctuations on the microsecond time scale.[137] Since fluorescein is efficiently quenched by several amino acids, in particular, by tryptophan residues[138,139] it is likely that the intensity fluctuations observed are caused by fluctuations in the interaction geometry of the fluorescein moiety and a tryptophan residue located in close proximity. Thus, small conformational changes, such as equilibrium fluctuations, can be directly reflected in the charge separation efficiency. Electron-transfer reactions enable the direct monitoring of subnanometer conformational fluctuations of a protein in its native state at the single-molecule level with microsecond time-resolution.

Very recently, Xie and co-workers used photoinduced electron transfer between a tyrosine residue and the flavin moiety as a probe for Ångström-scale structural changes in single protein molecules.[140] Correlation of the fluorescence lifetime fluctuations measured from single flavin molecules enabled the monitoring of conformational dynamics with submillisecond time resolution. Their data strongly suggest the existence of multiple interconverting conformers, a result which helps to explain the fluctuating catalytic activity of flavin reductase. Furthermore, the monitoring of sub-nanometer conformational changes at the single-molecule level under equilibrium conditions is advantageous because it allows the proteins conformational memory to be measured quantitatively at room temperature.

Alternatively, efficient photoinduced-electron transfer between fluorescent dyes and certain amino acids or DNA nucleotides can be used to record conformational fluctuations in peptides and oligonucleotides at the single-molecule level with sub-microsecond time-resolution.[5,141] The basic idea of the method is that the fluorescence of suitable fluorophores is selectively quenched by tryptophan or guanosine residues through photoinduced electron transfer, but only upon contact formation. Except for tryptophan and guanosine itself, all other amino acids and DNA bases quench with rates that are substantially smaller.[138,139,142–146] The general principle of this new method for measuring the kinetics of intramolecular contact formation in biopolymers is depicted in Figure 8a. A suitable fluorescent dye and a tryptophan or guanosine residue are incorporated into a peptide or oligonucleotide. The dynamics of the backbone will lead to conformations where the dye and the quenching residue come into contact (right structures in Figure 8a). After excitation of the dye molecule, it either emits a fluorescence

 © 2005 Wiley-VCH Verlag GmbH & Co. KGaA, Weinheim

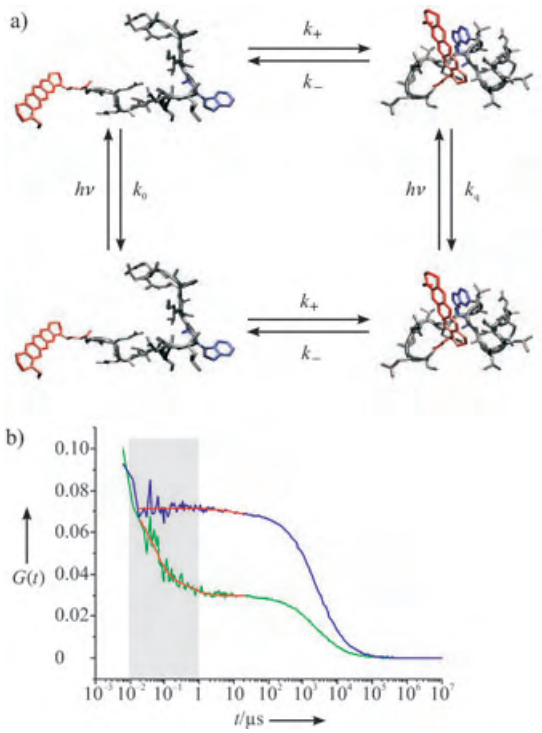

Figure 8. a) Principle for measuring the kinetics of intramolecular contact formation in peptides or oligonucleotides. The dynamics of the backbone will lead to conformations where the dye (red) and the tryptophan or guanosine residue (blue) come into contact. This contact formation results in complex formation and subsequent efficient fluorescence quenching by photoinduced charge separation from the ground-state tryptophan or guanosine to the first excited singlet state of the dye. Hence, the structures on the right can be considered to be non-fluorescent. b) FCS-curves measured from 10^{-9} M solutions of labeled peptides MR121-SQETFSDL**W**KLLPEN (green), and MR121-SQETFSDL**F**KLLPEN (blue) in PBS pH 7.4. Strong static quenching by photoinduced electron transfer upon contact formation between the dye and the tryptophan residue is reflected in the appearance of a short correlation term in the 10–1000 ns range (gray area). Abbreviations for the amino acid residues are: A alanine, D aspartic acid, E glutamic acid, F phenylalanine, G glycine, I isoleucine, K lysine, L leucine, N asparagine, P proline, Q glutamine, R arginine, S serine, T threonine, W tryptophan.

photon (dependent on the fluorescence quantum yield) or is quenched by an electron transfer reaction with the tryptophan or guanosine residue. Depending on the dye structure, quenching is dominated either by dynamic or static quenching.[139] If contact between the dye and the quenching residue results in complex formation in which there is a nearly coplanar stacking of quencher and dye, immediate efficient fluorescence quenching occurs. Thus, the right structure in Figure 8b can be considered to be essentially nonfluorescent. Hence, interphoton-times distribution analysis or FCS can be used to reveal the rate for contact formation (association rate), k_+, as well as the dissociation rate, k_-.

To demonstrate the potential of the method, the rate of contact formation between an oxazine dye (MR121) attached at the N-terminal end and a tryptophan residue, localized within the chain of two peptides with lengths of 15 and 20 amino acids, were investigated.[5] The peptides are flexible, linear fragments of the amino terminal transactivation domain of human p53, which is the target for several protein partners, such as the TATA box-binding protein (TBP), MDM2, or antibodies from the humoral immune response of cancer patients. Fast FCS on two detectors was used to measure the tryptophan-induced fluorescence quenching upon contact formation in 10^{-9} M peptide solutions. Association (contact formation) and dissociation rates in the range of a few hundred nanoseconds were measured for both peptides, consistent with data on the dynamics of unstructured peptides for which a different ensemble methodology was used.[147] The advantages of this fluorescence-quenching-based technique over other techniques are the ease of performing the experiments which can be carried out in water under air with single-molecule sensitivity. The exchange of the tryptophan by a phenylalanine residue results in the disappearance of the short correlation term in the 100 ns time range (Figure 8b).

The extraordinary sensitivity of the described fluorescence-based method is especially important for the application of "smart" fluorescent probes, used for the detection of minute amounts of target structures from biological samples. Both peptides used in the sub-microsecond kinetic studies discussed above are the target of p53 autoantibodies. These so-called epitopes for p53 autoantibodies, are known to be universal and highly specific tumor markers in cancer diagnosis.[148] Hence, both fluorescently labeled peptide-epitopes can be used as photoinduced electron-transfer (PET) biosensors to detect single p53 autoantibodies.[149] Upon specific binding to an p53 autoantibody the peptide chain adapts to the shape of the antibody cleft. Consequently, contact formation between tryptophan and MR121 is prevented. The resulting increase in fluorescence intensity can be used to signal binding events. The single-molecule sensitivity of the assay format allows for direct monitoring of p53 antibodies, present in blood serum samples of cancer patients.[146]

Selective quenching of oxazine dyes, such as MR121 and Atto655, by guanosine residues through electron transfer is also advantageous for the development of single-molecule-sensitive DNA or RNA probes, for example, DNA-hairpin sequences (Figure 9).[143] If quenching interactions between the dye coupled to one end of the hairpin stem and guanosine residues, located on the other end, are interrupted, for example, through binding of a complementary DNA sequence, or by cleavage by an endo- or exonuclease enzyme, fluorescence of the DNA hairpin is restored. DNA hairpin sequences labeled with a single oxazine dye at the 5′-end increase their fluorescence upon hybridization by up to 20-fold, which provides the basis for a cost-effective, and highly sensitive DNA–RNA detection method.[144] Other results have demonstrated that immobilized DNA hairpins modified for photoinduced intramolecular electron transfer from guanosine residues to excited fluorophores can be used to efficiently detect the presence of single target DNA or RNA molecules, even in the sub-picomolar concentration range in a reasonable time.[130] The method is therefore ideally suited to search for specific sequences in extremely low concentrations of target sequence.

 © 2005 Wiley-VCH Verlag GmbH & Co. KGaA, Weinheim

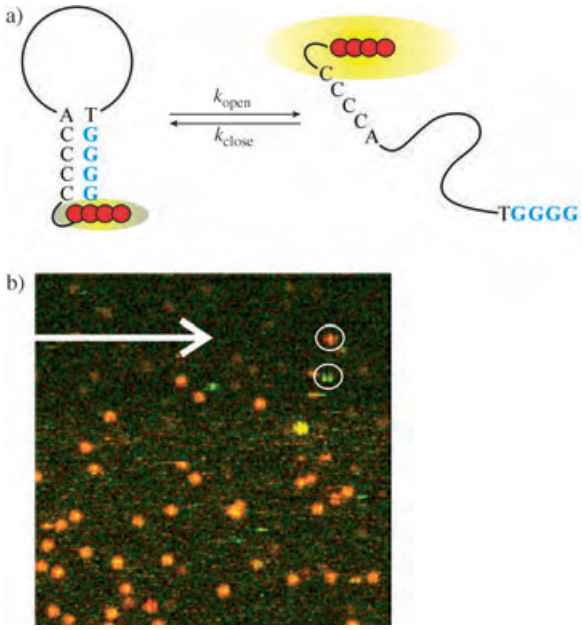

Figure 9. a) Schematic representation of the operation of a DNA hairpin modified for the selective guanosine quenching of fluorophores. The fluorophore (red) is attached to the cytosine containing 5′-end and quenched by guanosine residues (blue) by photoinduced electron transfer. Upon hybridization to the target sequence (complementary to the loop sequence), the fluorescence is restored as a result of a conformational reorganization that opens the stem. b) 3′-biotinylated hairpins (MR121-C6-5′-CCCCAT_{20}TGGGG-3′) labeled with the oxazine derivative MR121 were immobilized on a cover slide by biotin–streptavidin binding.[130] Scanning was performed from top left to bottom right using modulated excitation polarization. The confocal image (20×20 μm, 50 nm/pixel) shows fluorescence spots from single DNA hairpin molecules hybridized to their complementary target sequence (0–16 counts in 3 ms). The arrow indicates the addition of an excess of target sequence (oligo$(dA)_{30}$). Most fluorescent spots show a demodulated fluorescence intensity indicating freely rotating DNA hairpin molecules. The modulation stripes visible in the two spots marked by circles indicate rotationally stationary absorption dipoles of the fluorophores, that is, the fluorophores are stuck on the surface.

5. Use of SMFS to Study Photophysics in Multichromophoric Systems

With respect to single-molecule spectroscopic techniques, it should be pointed out that some characteristics, such as digital photobleaching or blinking, which have been generally accepted as characteristics of single chromophores have to be reconsidered. Single-molecule studies of molecular interactions in multichromophoric systems revealed the occurrence of fluorescence intermittences (off states) of several chromophores at the same time.[104,150–153] In multichromophoric systems various types of chromophore–chromophore interactions are possible depending on the interchromophore distance. Such interactions include Dexter energy transfer, dimer and excimer formation, electron-transfer reactions, photochemistry, and intermolecular quenching. Systems investigated to date include natural chromophores, such as the light harvesting complex LH2,[154,155] light harvesting proteins, such as phycoerythrins and allophycocyanine,[103,156,157] genetically encodable proteins, such as DsRed,[24,158–160] and artificial multichromophoric systems from simple dimers[161–163] to complex systems, such as light-emitting conjugated polymers[150–152,163,164] and well defined dendritic or linear systems.[85,91,104,156,165,166]

One prominent finding for many multichromophoric systems is the observation of collective blinking, that is, the complete fluorescence intermittency of all fluorophores simultaneously. Blinking of single molecules was one of the early phenomena observed and can be attributed to various processes. Most notable among the possible processes is triplet blinking, that is, the reversible transition to the triplet state through inter-system crossing.[167,168] SMFS has shed light on some of the mysteries why several molecules seem to undergo collective transitions to off-states. The common ground for explanations of collective blinking is that only one fluorophore undergoes a transition to an off state but that the nature of this off state is such that it quenches the fluorescence of the remaining fluorophores.[91,150,164] This principle is, for example, applicable for intersystem crossing where the molecule in the triplet state "absorbs" all the excitation energy from the other fluorophores by efficient Förster-type energy transfer.[91,104,156,163] Thus, the emission ($S_1 \rightarrow S_0$) of the fluorophores is in resonance with the $T_1 \rightarrow T_n$ transition of the fluorophore in the triplet state. This situation yields a molecule in a higher excited triplet state, T_n. The energy from T_n is rapidly dissipated thermally thus leaving the triplet fluorophore in T_1 again. The molecule in the triplet state can be rapidly cycled through T_1 and T_n until it returns to the singlet state by reverse intersystem crossing or phosphorescence.[163,169] The energy transfer from a fluorophore in the singlet state to a fluorophore in the triplet state is commonly called singlet–triplet (ST) annihilation because one S_1 excited-state-energy quantum appears to be annihilated.

Besides singlet–triplet annihilation, energy hopping between identical chromophores has to be considered in multichromophoric systems as well. Energy hopping is the transfer of excited-state energy from one molecule to another through weak dipole–dipole coupling (homo energy transfer),.[104,156] As a result of the different overlap of the corresponding spectra, different R_0 values and energy-transfer efficiencies are calculated for energy hopping and singlet–triplet annihilation in multichromophoric systems.

Recently, it was found that a third resonance energy transfer pathway with a third R_0 value has to be taken into account when studying chromophore interactions, this is singlet–singlet (SS) annihilation. In this case, two chromophores have to be excited almost simultaneously. Depending on the spectral overlap of the $S_1 \rightarrow S_0$ emission and $S_1 \rightarrow S_n$ absorption of the chromophores, energy transfer can occur. This transfer yields one chromophore in the ground state and the other in a higher excited state S_n. Internal conversion (nonradiative relaxation) rapidly converts the S_n state into the first excited singlet state. The net reaction is the "annihilation" of one exciton. As has been shown, singlet–singlet annihilation in multichromophoric systems is easily uncovered by photon antibunching experiments because all simultaneous excitations of more than one molecule in a multichromophoric system are annihilated.[85,91,170] Only when the

 © 2005 Wiley-VCH Verlag GmbH & Co. KGaA, Weinheim

multichromophoric system is significantly larger than the Förster radius for singlet–singlet annihilation does the vanished central peak in the interphoton-times histogram start to reappear.[171]

In summary, SMFS has shown that multichromophoric systems behave like single emitters in some regards, they show collective off states and photon antibunching. The basis of these processes are three Förster-type processes through which the fluorophores communicate, that is, energy hopping, singlet–singlet annihilation, and singlet–triplet annihilation (Figure 10). The efficiency of energy hopping and SS-annihilation can be determined by both ensemble and single-molecule time-resolved fluorescence experiments, for example, by lifetime, anisotropy, and antibunching measurements. On the other hand, ST-annihilation and its efficiency can only be measured at the single-molecule level by the analysis of collective off states.

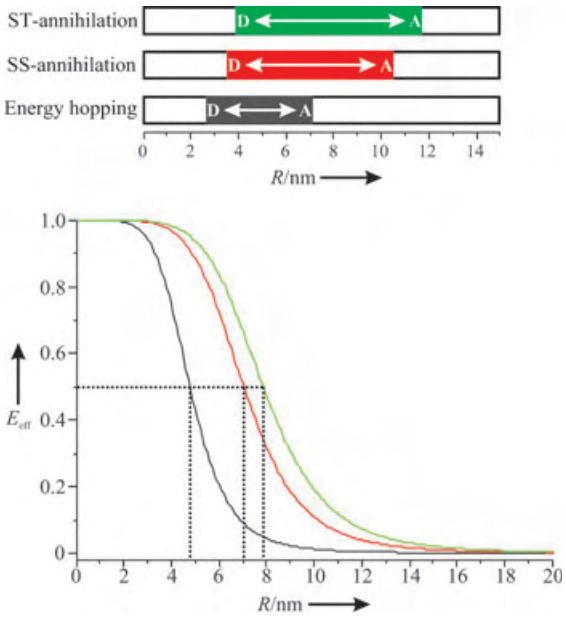

Figure 10. FRET efficiency, E_{eff}, versus donor–acceptor separation, R, calculated for three different Förster-type energy-transfer processes occurring between identical peryleneimide chromophores in rigid multichromophoric dendritic systems: energy hopping, singlet-singlet (SS)-annihilation, and singlet-triplet (ST)-annihilation.[91] R_0 values for the different transfer pathways were calculated from the absorption spectra S_0–S_1, S_1–S_n, and T–T_n and the corresponding emission spectra of the donor assuming an average κ^2 of 1.92 as computed from molecular mechanics calculations.[91]

As a result of the R^{-6} distance dependence, separations in the range 0.5 R_0 to 1.5 R_0, that is, with FRET efficiencies E_{eff} in the range 0.98 to 0.10, are suitable for FRET measurements. When using two peryleneimide chromophores this corresponds to distance changes of 2.39–7.05 nm for energy hopping, 3.52–10.56 nm for SS annihilation, and 3.93–11.79 nm for ST annihilation (Figure 10).[91] Thus, the use of two identical dyes enables the measurement of distances between 2 and 12 nm.[91,171] In addition, the synthesis of molecules equipped with two identical fluorophores is easier than the synthesis of compounds carrying two different fluorophores. In the case of stronger interactions, that is, beyond long-range FRET-interactions, other effects, such as alterations in the fluorescence spectrum and lifetime can be observed.[104,172]

6. Molecular Photonic Wires

The knowledge obtained from fundamental photophysical studies represents the basis for the future development of nanoscale optical devices, such as molecular photonic wires. In contrast to an electric wire, a photonic wire transports excited-state energy rather than electrons. On the level of molecular devices this is of great advantage because it circumvents the connection problem, that is, the bottleneck that occurs when trying to connect the molecular with macroscopic devices. In the case of a photonic wire, excited-state energy is induced into the wire by means of light, transported through the wire, and finally emitted at another wavelength and location or the energy is used for an electron-transfer reaction, that is, the conversion of excited-state energy into an electric charge. The basic idea of a photonic wire was first expressed by Lindsay et al.[173] and quite some effort was put into the synthesis of sophisticated porphyrins arrays. Besides problems that occur owing to energy sinks caused by local inhomogeneities throughout the strongly coupling porphyrins, these chromophores are hard to study by SMFS because of their low fluorescence and high triplet quantum yield.

On the other hand, it is clear that nanoscale devices have to be accessible for investigations on the level of the individual components. The ideal photonic wire consists of a very regular dye arrangement which allows for facile incoherent hopping but does not result in the alteration of photophysical properties of the individual dyes that leads to the formation of so-called energy sinks. Therefore an alternative strategy has recently been suggested which is based on 1) the use of conventional fluorophores with high quantum yields, 2) an energy cascade as the driving force for the excited-state energy to ensure unidirectionality, 3) an arrangement of the fluorophores such that strong interactions promoting dimer formation and quenching are prevented.[174,175] Thus, energy will be transferred through weak dipole–dipole induced chromophore interactions according to Förster theory.

From the synthetic point of view, this approach requires the development of a strategy to label a rigid scaffold in a well-defined manner with various fluorescent dyes. One possibility is the use of double-stranded DNA labeled with different chromophores. These transfer light, that is, energy, from donor to acceptor through several dipole–dipole induced energy-transfer steps using spectrally separated dyes. The chromophores have to form an energy cascade, that is, the input dye has the highest energy and the output dye has the lowest energy, ensuring the unidirectionality of the photonic wire (Figure 11 a). The optimal photonic wire, is the best compromise between unidirectional driving force and

 © 2005 Wiley-VCH Verlag GmbH & Co. KGaA, Weinheim

minimized loss of energy, for example, by the exploitation of homo-FRET processes for some energy-transfer steps.[175,176]

The unique features of double-stranded DNA make it an ideal building block in nanoscale molecular devices. With a persistence length of DNA of 50 nm, DNA constitutes a stiff scaffold to which chromophores can be attached.[177] In addition, the use of DNA offers many well developed labeling and post-labeling strategies for the introduction of a variety of different chromophores. The strength of this approach is the synthetic simplicity by which a large number of chromophores can be put into a well defined order. Starting from a single-stranded DNA fragment counter sequences that carry the desired chromophores can be hybridized to the single strand (Figure 11 b). Very recently, we demonstrated the synthesis and spectroscopic characterization of a unidirectional photonic wire based on four highly efficient energy-transfer steps between five spectrally different chromophores covalently attached to double-stranded DNA.[175] SMFS performed on four spectrally separated detectors uncovered subpopulations that exhibit overall energy-transfer efficiencies of up to 90% across a distance of 13.6 nm and a spectral range of approximately 200 nm. In the future it should be possible to define not only the distance between the chromophores but also their relative orientation. Such control might enable the use of fluorophores with smaller spacing thus allowing very fast energy-transfer through the Dexter mechanism. Approaches include the use of supramolecular chemistry possibly including template supports such as zeolites.[178]

A photonic wire however, is only one optoelectronic device complementary to nanoscale electronic devices. The next level of complexity is the insertion of a gate into a photonic wire. Recently, a single-molecule fluorescence photoswitch was developed by Irie et al.[179] They showed in a two color experiment that a fluorophore (bis(phenylethynyl)anthracene) connected to a switchable quenching unit (a diarylethene derivative) could be switched on and off by $\lambda =$ 488 nm and 325 nm light, respectively. UV light was used to activate the quencher while 488 nm light was used for deactivation of the quenching unit and probing the fluorescence of the fluorophore. Although, in general disadvantageous, the use of the same wavelength ($\lambda = 488$ nm) for probing and switching was possible because the deactivation

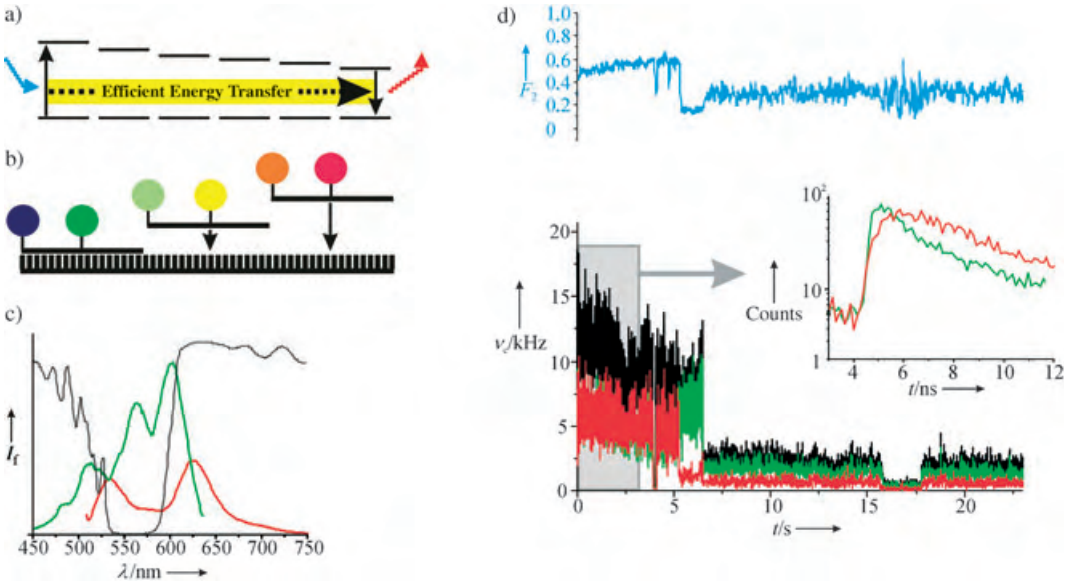

Figure 11. a) Principle of a unidirectional photonic wire. Excited-state energy is transferred by several energy-transfer steps from one end to the other. The chromophores used form an energy cascade to ensure the unidirectionality of the photonic wire. b) Synthesis strategy of a unidirectional photonic wire. To introduce different dyes in the correct order, short oligonucleotides labeled with two different dyes are hybridized to the complementary DNA strand. c) Ensemble excitation (green) and fluorescence emission (red) spectra (relative fluorescence intensity I_f, versus wavelength λ, of a DNA-based photonic wire carrying three dyes, rhodamine 110 (R110), tetramethylrhodamine (TMR), and ATTO 590 at interchromophore distances of 10 base pairs (ca. 3.4 nm). The transmission curve of the dichroic beam splitter used for SMFS of individual photonic wires is shown in gray. Calculation of the overall efficiency for energy transfer from the first donor R110 to TMR to the final acceptor ATTO 590 gives very different values depending on whether it is determined by the decrease in donor intensity (40%) or the relative intensities of the excitation spectrum (60%). On the other hand, it can be anticipated that owing to the size and complexity of the system, different conformational orientations of the chromophores, insufficient hybridization, and/or additional quenching pathways will generate an inhomogeneous broadening of the transfer efficiency observed form ensemble measurements. d) Fluorescence intensity trajectory recorded from a single photonic wire adsorbed on a cover slide by using spectrally resolved fluorescence lifetime imaging microscopy (SFLIM) with spectral detection windows from 520–590 nm (green) and 590–680 nm (red); overall intensity is shown in black.[78] During the first 5 s of the trajectory, the signal is dominated by the final acceptor ATTO 590 owing to efficient energy transfer. This result is also corroborated by time-resolved measurements. The fluorescence decay recorded during the first 3 s (gray area) on the short wavelength detector (green) shows distinct quenching while the decay measured on the long wavelength channel (red) shows a pronounced fluorescence rise time as a result of energy transfer and a long fluorescence decay time of about 4 ns as expected for the ATTO 590 dye. After 4 s a collective off state appears. After about 5 s the final acceptor ATTO 590 photobleaches which is reflected in an abrupt change in fractional intensity F_2 (blue) After photobleaching of the TMR dye at 7 s the F_2 value increases again slightly as a result of the fluorescence emission of the remaining R110 molecule and the transmission properties of the filter set used.

 © 2005 Wiley-VCH Verlag GmbH & Co. KGaA, Weinheim

(isomerization) is about 1000 times less efficient than the activation of the quenching unit. Thus, probing and isomerization can be controlled by the excitation light intensity. In a perfect photoswitch, however, switching should be completely independent of probing. Efficient quenching of the fluorophore by electron transfer is a more appropriate quenching mechanism for photoswitches. It could be possible to selectively address fluorophores within a photonic wire by the attachment of a switchable electron donor or acceptor (Figure 12). Ideally, these redox-photoswitches could be addressed by two different wavelengths at which the fluorophore does not absorb. A third wavelength is used for probing the state of the switch. Upon photoisomerization the unit should change its redox potential or alter the donor–acceptor interaction geometry such that it becomes a quencher of the fluorophore in one state while thermodynamics, kinetics, or the conformational state of the redox-photoswitch forbid the photoinduced electron-transfer reaction in the other (Figure 12).

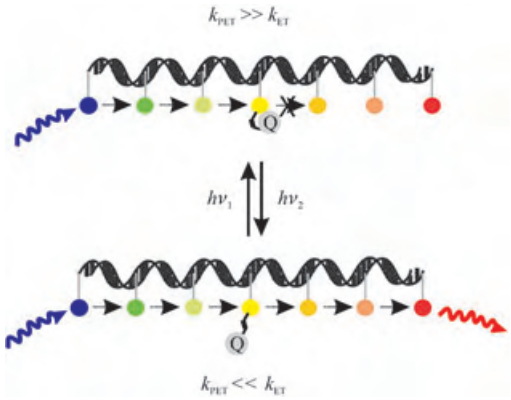

Figure 12. Idealized scheme of a unidirectional photonic wire controlled by a redox photoswitch. Photoisomerization of the linker of the electron-transfer quencher (Q) results in an altered interaction geometry between the fluorophore and the quencher. Switching of the wire is accomplished by excitation with a second and third wavelength ($\tilde{\nu}_1$, and $\tilde{\nu}_2$). In the off state (top) photoinduced electron transfer (PET) between one of the fluorophores and the quencher (Q) is much faster than intermolecular energy transfer (ET) to the next fluorophore ($k_{PET} \gg k_{ET}$). This arrangement allows selective switching of the photonic wire between the on and off state.

7. SMFS in Biology

In recent years, considerable progress has been made towards a better understanding of molecular machines, that is, highly organized self-assembled nanostructures, and their functions in living cells.[180–185] Although, rough data about the composition of biomolecular machines and their molecular interactions exist, much is still unknown about how nuclear metabolism, metabolic enzymes, and regulatory factors are organized. Furthermore, it is generally assumed that the multitude of cellular building blocks in many of these molecular machines do not act synchronously and might have different kinetic pathways. Since, for example, transcription factories containing polymerase II have a small size of approximately 40 nm and contain on average only around 8 active polymerase molecules in mammalian cells,[182] single-molecule sensitive detection methods are required to study the dynamic interplay of the cellular building blocks and their precise location and separations with high spatial and temporal resolution. Single-molecule fluorescence spectroscopic techniques are advantageous owing to the possibility to expand the analysis to three dimensions.[40] However, still single-molecule techniques seem too complicated to many researchers and in biology the number of genetic and electron-microscopic studies still outnumbers single-molecule fluorescence studies.

In the past few decades, in situ hybridization (ISH) and labeling methods have been optimized to such an extent that the microscopic detection of specific mRNA or protein molecules by using fluorescently labeled nucleic acid or antibody probes is possible.[186–189] Although a lot of effort is still being put into optimizing these procedures on fixed cells and tissue materials, there is an increasing demand for techniques that allow the visualization of proteins and RNAs in living cells. The reason for this interest in living-cell analysis is the concern that the observed localization patterns in fixed cells may not reflect the situation in living cells. Fixation and cell pretreatment may disturb localization patterns and to some extent deteriorate cell morphology.[190] In addition, information about the dynamics of DNA, RNA, or protein synthesis and transport can be obtained best when these processes are studied in living cells.

7.1. Fluorescence-Labeling Strategies for Cell Imaging

For the investigation of biologically relevant samples, target molecules have to be labeled with a fluorescent tag. A central issue for SMFS in cells is fluorescent labels, these have to fulfill special requirements, such as high biocompatibility, high photostability, and retention of biological function. The first problem, however, is site-specific labeling inside a living cell and some procedures have been reviewed recently.[23,191] In the simplest case the molecules to be investigated are prepared in vitro utilizing standard techniques for labeling biomolecules. Subsequently cell-loading is carried out by known chemical, electrical, mechanical, or vesicle-based procedures. To measure, for example, the localization of RNA in living cells the target sequence has to be labeled with a fluorescent complementary sequence. A problem that needs to be resolved in the fluorescence in vivo hybridization (FIVH) approach is the efficient delivery of probes to sites in a cell where they can hybridize with their target sequence. The most direct method to introduce probe molecules into a cell is by microinjection using micropipettes. Alternatively, liposomes can be used to introduce probe molecules into live cells.[192]

The microinjection technique is based on the use of a micropipette with a very small diameter tip and the application of a higher pressure at a predetermined time. However,

 © 2005 Wiley-VCH Verlag GmbH & Co. KGaA, Weinheim

this technique does not exhibit the necessary reproducibility required for SMFS, that is, the injection of only a few molecules per cell. Recently, fluorescently labeled oligonucleotides were microinjected into the cytoplasm and nucleus of living 3T3 mouse fibroblast cells using a micropipette.[83] Since, the micropipette used has an inner diameter of 500 ± 200 nm at the very end of the tip—comparable to the diameter of the confocal detection volume applied—almost all molecules leaving the micropipette were detected.[9,193,194] This situation means that the number of injected molecules is known. As a consequence, quantitative molecular information on a single cell level can be obtained.

Another very promising method is known as protein transduction. Several naturally occurring proteins have been found to enter cells easily, including the TAT protein from HIV.[195,196] Specific short sequences within the larger molecule account for the transduction abilities of these proteins. These arginine-rich peptides allow efficient translocation through the plasma membrane and subsequent accumulation in the cell nucleus. Therefore, they could be useful vectors for the intracellular delivery of various nonpermanent drugs including antisense oligonucleotides and peptides of pharmacological interest.[197] Cellular uptake of these cationic cell-penetrating peptides has been ascribed to a mechanism that does not involve endocytosis. Live-cell penetration studies (on HeLa cells and human foreskin kerantinocytes) without fixation, using fluorescently labeled, peptidase-resistant β-oligoarginines, demonstrate that longer-chain β-oligoarginines (8 and 10 residues) enter the cells and end up in the nuclei, especially in the nucleoli, irrespective of temperature (37 °C, and 4 °C) or pretreatment with NaN_3.[198,199]

In a related strategy, the high affinity between a target molecule and a smaller molecule, which can be prepared in vitro, is exploited. This strategy is more complicated than in vitro labeling as it requires a particularly high binding affinity between the partners to avoid unspecific binding inside the cell. Nevertheless, this method is advantageous when the investigated molecule is not available as a purified compound or when the location of the target can not simply be reproduced. An antibody or another specific ligand can perform this task of in situ labeling.[200] However, often it still remains a problem to target structures selectively with analyte concentrations in the range required for single-molecule spectroscopy (i.e. 10^{-10} M). Therefore in an improved version of the indirect labeling strategy the ligand senses the binding event and the fluorescence of the label is switched on only upon specific binding.[143,146] Alternatively, fluorescence can be activated in specific locations within the cell by using a label which is bound to a quencher by a photoactive linker. Cleavage of the quencher through photodissociation of the linker allows fluorescence of the chromophore. To monitor, for example, the synthesis of a protease enzyme, non-fluorescent protease substrates which fluoresce upon specific cleavage by the protease could be used.[201]

However, the most elegant way to specifically label proteins in vivo is genetic labeling. The fluorophore used is a genetically encoded protein, such as the green fluorescent protein (GFP) and its relatives. GFP from the bioluminescent jellyfish *Aequorea victoria* has revolutionized many areas of cell biology and biotechnology because it provides direct genetic encoding of strong visible fluorescence.[202,203] GFP can function as a protein tag because it tolerates N- and C-terminal linking to a broad variety of proteins, many of which retain their native function.[204,205] According to the method, the DNA sequence coding for GFP is placed immediately adjacent to the sequence coding for the protein of interest. During biosynthesis, the protein will be prepared as a GFP-fusion protein. GFP comprises 238 amino acids and has a barrel-like cylindrical structure where the fluorophore is highly protected, located on the central helix of the geometric center of the cylinder. These cylinders have a diameter of about 3 nm and a length of about 4 nm, that is, significantly larger than common fluorophores which are less than 1 nm. Although single-molecule studies of GFP- or yellow fluorescent protein (YFP)-fusion proteins were demonstrated in the membrane of living cells (GFP, and YFP are the brightest and most photostable candidates),[206–209] their complicated photophysics and low photostability renders their application in single-molecule measurements very difficult.[24,210–212]

The discovery of new fluorescent proteins from non-bioluminescent *Anthozoa* species,[213] in particular, the red-shifted fluorescent protein DsRed, opened new horizons for multicolor labeling and FRET applications. However, several major drawbacks, such as slow maturation and residual green fluorescence, need to be overcome for the efficient use of DsRed as an in vivo reporter, especially in SMFS applications.[158–160] To improve maturation properties, and to reduce aggregation, a number of other red fluorescent proteins and variants of DsRed have been developed, for example, DsRed2, DsRed-Express, eqFP611, or HcRed1.[214–216] Recently, the oligomerization problem of DsRed has been solved by mutagenetic means (mRFP1).[217] An elegant alternative to common FRET methods to study protein interactions in living cells is bimolecular fluorescence complementation. The new approach is based on complementation between two nonfluorescent fragments of the yellow fluorescent protein (YFP) when they are brought together by interactions between proteins fused to each fragment.[218]

7.2. SMFS in Living Cells

While individual fluorescent molecules can be detected in solution and on surfaces with good S/N ratios, a key question is whether single-molecule methods could be developed to study complex molecular processes in living cells. In contrast to clean and well-controlled conditions in vitro, the cellular environment contains a broad collection of biological macromolecules and fluorescent materials, such as porphyrins and flavins. This complex environment is known to produce intense background fluorescence, commonly known as autofluorescence. Therefore, often nanomolar or higher concentrations of fluorescently tagged proteins or oligonucleotides have been applied to enable measurement of intracellular and intranuclear diffusion by FCS.[219,220]

However, by using cells with very low expression levels, fluorescence signals of single diffusing EGFR-EGF fusion proteins in living cells could be detected.[221] Confocal

 © 2005 Wiley-VCH Verlag GmbH & Co. KGaA, Weinheim

fluorescence microscopy has been applied as well to detect fluorescence bursts of rhodamine-labeled oligonucleotide molecules in living cells.[222] To reduce the autofluorescence of the cell culture medium arising upon excitation in the green wavelength range, most measurements were performed in PBS (phosphate buffered saline). The first intracellular trajectories of single protein molecules labeled with several fluorophores was shown by Kubitscheck and co-workers.[223,224] Employing a laser video-microscope optimized for high sensitivity and high speed, single ribonucleoproteins were visualized and tracked at a spatial precision of 35 nm, and a time resolution of 30 ms.

Recently, Bräuchle and co-workers demonstrated the monitoring of the infection pathway of single viruses using real-time fluorescence imaging.[225] In a related study, pulsed laser excitation in the red region ($\lambda = 635$ nm), in combination with spectrally resolved fluorescence lifetime imaging microscopy (SFLIM), enabled the discrimination of fluorescence signals from individual fluorescently labeled oligonucleotides from autofluorescence signals. This discrimination was possible because of the characteristic fluorescence lifetime and spectral characteristics of the fluorophores used.[83] SFLIM images and fluorescence-intensity measurements obtained from living 3T3 mouse fibroblast cells containing approximately 100–1000 fluorescently labeled oligo(dT) 43 mer molecules showed that around 10–30% of the oligonucleotides cannot diffuse freely inside the nucleus but rather are tethered to elements of the transcriptional, splicing, and/or polyadenylation machinery. These results demonstrate that confocal imaging techniques in combination with real-time imaging microscopy allow transport pathways in intact biological systems to be studied, enable conclusions to be drawn from the underlying cellular architecture, and to analyze individual binding events as well as to observe mobility restrictions in living cells.

However, when tracking single molecules under native conditions they rapidly suffer from photobleaching. As a result, they can only be followed for a limited amount of time, which is often insufficient to obtain the desired information.[200] For in vitro studies of labeled molecules, methods have been worked out to increase photostability of the fluorophores so that they can be followed over minutes. In particular, the groups of Chu and Ha established the use of the glucoseoxidase–catalase system to remove oxygen under in vitro conditions, an approach which increases the photostability of cyanine dyes by orders of magnitude.[58,226] Unfortunately, such strategies can not be applied in live cells. In the future, new labels are required that are more photostable and still retain the biological functionality of the biomolecule under investigation. One class of fluorophores for which there are great expectations are semiconductor nanocrystals (NCs), such as core–shell CdSe/ZnS NCs.[227] Their unique optical properties—tunable narrow emission spectrum, broad excitation spectrum, high photostability, and long fluorescence lifetime (on the order of tens of nanoseconds)—make these bright probes attractive in experiments involving long observation times, multicolor, and time-gated detection. Furthermore, the relatively long fluorescence lifetime of CdSe nanocrystals could enhance imaging contrast and sensitivity in biological applications using time-gated detection.[228] Although NC biocompatibility was demonstrated few years ago,[227,229] the breakthrough in biological targeting was only achieved very recent.[230–236] These days, NCs can be easily functionalized, for example with streptavidin, to facilitate mild coupling to biotinylated biomolecules. Immunofluorescent labeling of cancer markers and other cellular targets on the surface of fixed and live cancer cells as well as staining of actin and microtubule fibers in the cytoplasm, and the detection of nuclear antigens inside the nucleus have been successfully demonstrated.[235] Due to these improvements it is anticipated that NCs will soon also play an important role for in vivo single molecule studies and first successful results have already been presented.[237,238]

Nevertheless, the use of NCs in biological applications of SMFS and fluorescence imaging does not represent the magic bullet. There are several problems associated with NCs which should not be underestimated. One disadvantage of NCs is the difficulty to engineer them with single binding sites that can be specifically conjugated to only one molecule of interest. Instead, during the labeling step, NCs tend to bind to several molecules simultaneously. Another problem is blinking,[239] which is strongly controlled by the excitation intensity (Figure 13a), and often obeys a power law.[240,241] Although, blinking of NCs is efficiently reduced in the presence of 1–10 mM sulfanylethanol (mercaptoethanol), the addition of reducing agents is not compatible with live cell imaging.[242] In addition, generally not all semiconductor particles are luminescent, but they can be photoactivated.[243]

Another issue is whether such particles, which are composed of toxic material, are well suited for in vivo studies and whether they impede biological functionality.[244] For example, besides their core–shell structure, commercially available NCs have a third layer—an organic surface coating—that gives them chemical and photophysical stability, inertness in different environments, buffer solubility, and facilitates the introduction of reactive groups for linking to biomolecules. Ultimately, this results in particle sizes of 15–25 nm in diameter, that is, about four to five-times larger than GFP and its derivatives, and 15 to 25-times larger than conventional fluorophores used to tag biomolecules. Another concern to be addressed is whether each of these particles contains only a single NC. Even though, this situation might be of minor importance for those users who are basically interested in the brightness of the fluorescence signal they obtain from a labeled biomolecule, it seriously renders the quantitative analysis of the fluorescence signal more complicated, for example, in applications where the number of molecules bound to a specific target molecule are of interest (Figure 13a).

We have used biotinylated polyarginine peptides (Arg_{10}-Lys) to afford the intracellular delivery of commercially available streptavidin-coated NCs (Qdot605 streptavidin conjugate) into HeLa cells. Fluorescently labeled NC-free polyarginines (Arg_{10}-Lys-fluorescein) enter the cell and accumulate in the nuclei, especially in the nucleoli (Figure 13b).[198,199] Streptavidin-coated NCs (10^{-8} M solution) are not taken up by HeLa cells neither do they stain the membranes of the cells even after 24 h exposure. On the

 © 2005 Wiley-VCH Verlag GmbH & Co. KGaA, Weinheim

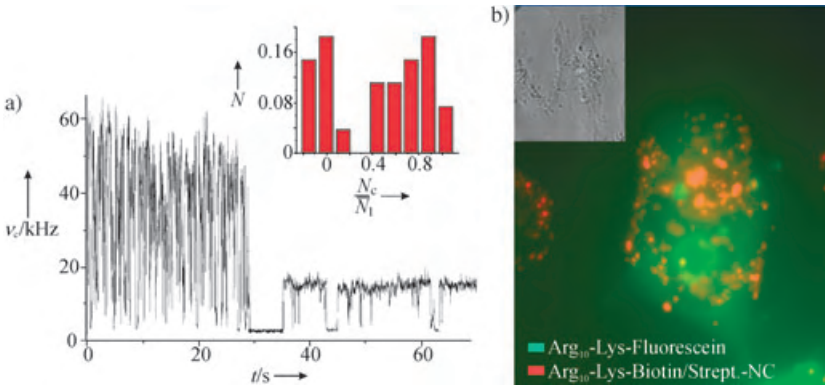

Figure 13. a) Fluorescence intensity trajectory (count rate, ν_c, versus time, t) of a single semiconductor NC (Qdot605–streptavidin conjugate) adsorbed on a bare glass surface under different excitation intensities (excitation at 488 nm using a frequency-doubled Ti:sapphire laser at a repetition rate of 3.8 MHz). After about 20 s, the shutter was closed and the average excitation intensity was changed from 1 to 0.2 kW cm^{-2}. Blinking of the NC is less frequent under lower excitation intensities. The inset shows a normalized histogram of the background-corrected ratios of the central to the lateral peaks, $N_c/\bar{N}_l$ measured from 60 single Qdot605–streptavidin conjugates adsorbed on a dry cover slide. The relatively high number of $N_c/\bar{N}_l$ ratios above 0.3 indicates that more than 50% of the NCs do not behave as a single emitter, possibly a result of aggregation of NC–streptavidin conjugates. b) Fluorescence image of a HeLa cell excited at 488 nm in PBS buffer. The inset shows a phase-contrast image of the cell. Cells were incubated with 10^{-8} M solution of Qdot605–streptavidin conjugates, 10^{-6} M biotinylated polyarginine (Arg_{10}-Lys), and 10^{-6} M fluorescently labeled polyarginine (Arg_{10}-Lys-fluorescein) for 20 min then washed. Whereas fluorescein labeled polyarginines (green) enter the cells and accumulate in the nucleoli,[198,199] streptavidin-coated NCs (red) covered with biotinylated polyarginine only bind on the membrane but do not enter the cells.

other hand, upon addition of an excess of biotinylated polyarginine peptides (10^{-6} M Arg_{10}-Lys-Biotin) NCs bind immediately and efficiently to the cell membrane but do not enter the cell. (Figure 13b). This result implies that the size and/or charge of the NCs used (15–20 nm) prevents their uptake by peptide specific pathways. Alternatively, the peptide recognition sequence (Arg_{10}) might be partly hidden in the streptavidin binding pocket.[195,199]

8. Colocalization and Distance Measurements Between Single Molecules

SMFS has open new avenues for investigating the three-dimensional cellular architecture and function of living cells. The information obtained to date has benefited from the small dimensions of a dye molecule. Since fluorophores are much smaller than the wavelength of light they emit, they act as point sources of light. The center of the resulting point-spread-function (PSF), that is, the response of the optical system, can be localized with high accuracy using the center-of-mass method or a Gaussian fit. The PSF describes the three-dimensional energy density in space measured from a point-like light-emitting object. This localization precision has been used to follow the motion of individual motor proteins,[64,245] the diffusional trajectories of labeled lipid molecules in membranes,[246,247] and the diffusion of molecules in gels.[248] The high positioning accuracy is also useful for the colocalization of the different building blocks of cellular molecular machines and for precision measurements of the distance between them. To close the resolution gap between far-field optical microscopy (> 200 nm) and FRET (ca. 2–8 nm) a single-molecule-sensitive colocalization technique with a resolution of a few tens of nanometers is required.

Recently, a relatively simple procedure, so-called single-molecule high-resolution imaging with photobleaching, was presented.[249] The method takes advantage of sequential photobleaching of two identical fluorophores to determine distances as small as 10 nm. Unfortunately, the method as described, can only be used to measure the two-dimensional projection of distances between pairs of molecules in the xy plane. Generally, colocalization of biomolecular building blocks is determined by staining the constituents with fluorescent labels that can be separated, at least partially, in their emission spectra. Quantitative three-dimensional fluorescence analysis is performed with multicolor confocal laser scanning microscopy (CLSM) and advanced image analysis techniques.[250,251] Spherical and chromatic aberrations in the excitation and detection paths diminish the attainable accuracy in established multicolor approaches.[252] To circumvent these problems, Lacoste et al. presented a new method for ultrahigh-resolution multicolor colocalization which relies on the use of luminescent nanoparticles that can be excited by a single laser wavelength but emit at different wavelengths.[253,254] In combination with multicolor confocal microscopy with "orthogonal" detection channels, the fluorescence of different emitters is separated and recorded independently. Because the same laser excites all emitters, chromatic aberrations in the excitation arm are eliminated. The method was demonstrated using two types of fluorescent nanoparticles: energy-transfer fluorescent beads (TransFluoSpheres) and semiconductor NCs. The large size (20–40 nm) of energy-transfer beads prevents their use for colocalization experiments in small molecular machines. As discussed above, NCs are somewhat smaller, exhibit bright fluorescence, and are far more stable than conventional dyes. However, the pronounced blinking of NCs deteriorates the quality of images and results in a reduced precision of localization.[254]

In 1995 Betzig recalled the fact that any optically distinguishable characteristic can be used for identification and isolation of a fluorophore.[255] As it has been shown that the fluorescence lifetime of single fluorescent dyes can be used as an unequivocal identification property,[9,68,256] colocalization of different emitters can also be performed by applying time-resolved fluorescence spectroscopy. The use of fluorescence lifetime as the sole identification criterion, for example, two dyes which exhibit similar absorption and emission characteristics but distinct fluorescence lifetimes, simplifies the experimental set-up drastically because only a single detector is required. By the use of appropriately selected fluorescent dyes, the method allows intermolecular distances down to the FRET range to be measured without chromatic aberrations.[257]

 © 2005 Wiley-VCH Verlag GmbH & Co. KGaA, Weinheim

In such distance measurements, there are two sources of error: 1) the detected photons have to be assigned to the corresponding emitter on the basis of their microscopic arrival time, 2) the two obtained PSFs have to be fitted to locate the emitters. To decrease the error in assigning the photons to the correct emitter, a combination of time and spectral information, such as that obtained by SFLIM, could be used. This approach would enable distance measurements to be made with nanometer accuracy between conventional single fluorescent dyes (Figure 14).

For the assignment of photons as well as for the localization accuracy, the selection of appropriate fluorophores is essential. Bodipy 630/650 and Cy5.5 are a suitable combination of dyes for high-precision distance measurements between single molecules as the two dyes exhibit a twofold difference in fluorescence lifetime (Bodipy 630/650 ca. 4 ns; Cy5.5 ca. 2 ns) and different fluorescence emission maxima (Bodipy 630/650 $\lambda \approx 660$ nm; Cy5.5 $\lambda \approx 700$ nm). When adsorbed on bare glass surfaces under dry conditions both of these dyes exhibit short off times in the micro- to millisecond range (that is, shorter than the integration time per pixel).[78,257] In addition, owing to the higher extinction coefficient of Cy5.5, the two chromophores can be excited at $\lambda = 635$ nm with comparable efficiency by using a single pulsed laser diode. Using a dichroic beam splitter at $\lambda = 685$ nm, the long fluorescence lifetime of Bodipy 630/650 is detected predominantly on the short-wavelength detector (det 1) while the shorter fluorescence lifetime of Cy5.5 is detected exclusively on the long-wavelength detector (det 2; Figure 14b). To demonstrate the feasibility and to evaluate the error of the method, precision distance measurements between the two dyes Bodipy 630/650 and Cy5.5 attached covalently to double-stranded DNA at separations varying between 10 and 200 base pairs are currently being carried out (Figure 14c).

To improve the spatial resolution of optical microscopy beyond the classical diffraction limit of light, several new methods have been developed. Among these are 4Pi microscopy,[258,259] near-field scanning optical microscopy (NSOM),[260,261] standing-wave fluorescence microscopy,[262–264] coherent optical dipole coupling of individual molecules at low temperature,[265] and point-spread-function (PSF) engineering by stimulated emission depletion (STED).[266–269] Among the new techniques, PSF engineering using STED is the most promising because it represents the first far-field method which, conceptually, has unlimited spatial resolution. In STED, a diffraction-limited fluorescence spot is sharpened by inhibiting the fluorescence through saturation. This is accomplished by quenching of the excited fluorophore at the rim of the focal spot by stimulated emission. STED has so far demonstrated a resolution of 28 nm with single molecules.[270] Since the excitation pulse is followed by a quenching pulse which acts on the excited state of the same molecule, the single-molecule experiments reported by Westphal et al. are the first single-molecule pump-probe experiments.[270] As they rely on saturated optical transitions, these methods are limited only by the attainable saturation level. As strong saturation should be feasible at low light intensities, nanoscale imaging ("nanoscopy") with focused light may be closer than ever.[268] Very recently, immunofluorescence imaging with an axial resolution of approximately 50 nm, corresponding to 1/16 of the irradiation wavelength of $\lambda = 793$ nm, has been achieved by stimulated emission depletion through opposing lenses (STED-4Pi).[269]

9. Summary and Outlook

It is beyond doubt that SMFS has increased our current understanding of biological macromolecules and their structure–function relations. Furthermore, ongoing single-molecule projects, such as the aim to sequence a single DNA fragment, have revealed unexpected behavior of biomolecules, such as DNA polymerases. In fact, most natural DNA polymerases and exonucleases have been found to discriminate against dye-labeled nucleotides; this may be due to steric hindrance at the active site of the enzyme as a result of the bulkiness of the label, and/or because the fluorescently labeled nucleotides typically have a net charge that differs from that of the natural substrates.[271,272] However, Brakmann and co-workers used the well documented power of direct evolution to identify mutant DNA polymerases that incorporate labeled nucleotides with high efficiency and retain a sufficient incorporation fidelity.[273] They discovered that a

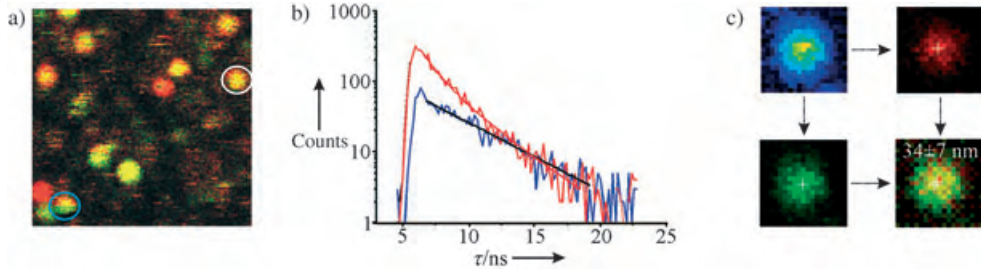

Figure 14. a) False-color SFLIM image of a double-stranded DNA (148 bp) labeled with Bodipy 630/650 at one terminus and Cy5.5 at the other and immobilized in agarose gel. Green spots are DNA molecules carrying only Bodipy and red spots are DNA molecules carrying only Cy5.5. Yellow spots are double-labeled DNA molecules. Photobleaching of Cy5.5 during the recording of the image is visible for the molecule circled blue. b) Fluorescence decays recorded on the long-wavelength (red), and short-wavelength channel (blue) for the spot circled white in (a). c) Colocalization of a Bodipy and Cy5.5 molecule with a separation of 34 ± 7 nm. Construction of the two separate fluorescence intensity images for the Bodipy (bottom left) and Cy5.5 dye (top right) was performed by pattern matching on the basis of the respective characteristic spectroscopic properties (F_2 value, and fluorescence lifetime).

 © 2005 Wiley-VCH Verlag GmbH & Co. KGaA, Weinheim

cloned natural polymerase, the unmodified exonuclease-deficient Klenow fragment of *Escherichia coli* DNA polymerase I polymerized 55 tetramethylrhodamine-4-dUTPs using an artificial (dA)55 template. Furthermore, the same enzyme was successfully used in an analogous reaction with a natural primer template with a length of 2700 base pairs, in which two of the natural substrates, dCTP and dTTP, were substituted by their rhodamine-labeled analogues.[274,275]

The fact that reaction pathways for different molecules are not predetermined, but still deliver the same product state represents another important result obtained by SMFS which has influenced the way in which we think about and model molecular systems. Dynamic structural studies showed that reactions proceed heterogeneously on multidimensional energy landscapes. That is, individual molecules follow different pathways on the energy landscape. Since these different pathways can occur on a wide range of time scales, extending from femtoseconds to seconds, individual reaction rates differ significantly. SMFS can be used to directly track the pathway of an individual molecule on its potential energy landscape on a broad range of time scales, under physiological conditions, and at equilibrium.[5,140,276] This was made possible by the use of dipole–dipole induced interactions and short-range electronic interactions between chromophores and naturally occurring amino acids, that is, photoinduced electron-transfer processes. With a distance dependence in the subnanometer range, electron-transfer reactions complement single-pair FRET measurements which are suited to longer distances. The new techniques enabled, for example, the monitoring of dynamic fluctuations in electron-transfer efficiency between amino acids and fluorophores on a submicrosecond time scale at the single-molecule level.[5] Thus, the monitoring of the conformational dynamics of individual biomolecules at equilibrium, under physiological conditions, with temporal resolutions comparable to those of new molecular dynamic simulations, is possible.[277]

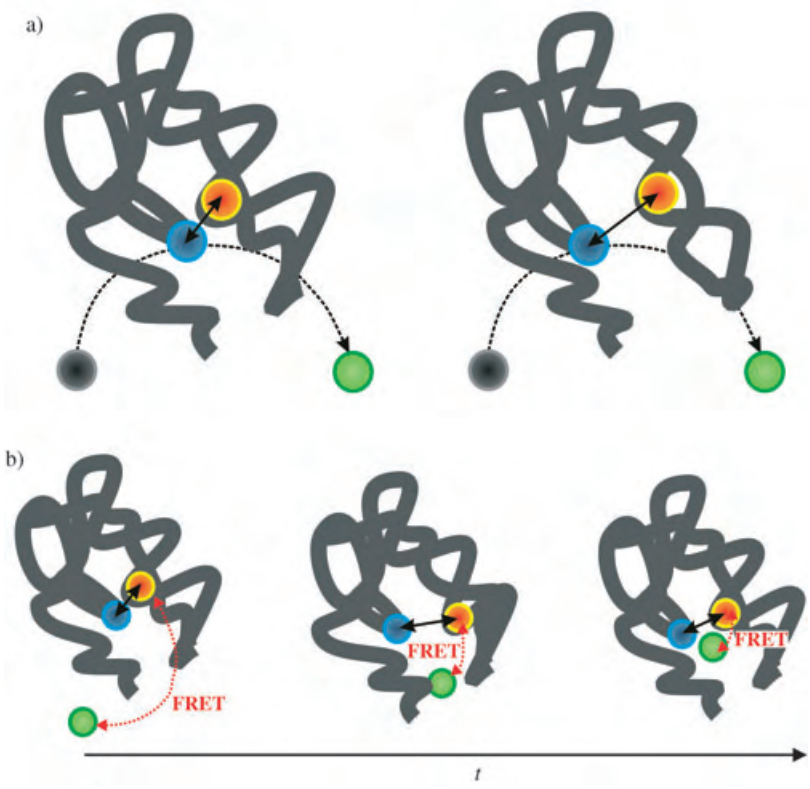

Figure 15. Outlook to possible future experiments correlating conformational dynamics to enzyme activity and the topography of energy landscapes. a) Conformational dynamics are monitored by the fluorescence intensity and lifetime of a fluorophore (red) which is quenched by an amino acid, for example, tryptophan (blue) through electron transfer. Simultaneously, the enzyme activity is recorded as a function of the conversion rate of a nonfluorescent substrate into a highly fluorescent product (green) at another excitation wavelength. b) Alternatively, a combined approach using electron transfer and spFRET could be applied. Time-resolved monitoring of the fluorescence intensity and lifetime of a red-absorbing fluorophore (red) specifically quenched through electron transfer by an amino acid residue (blue) reveals conformational dynamics. Fast switching of the excitation wavelength between the red fluorophore in the active site and a potential FRET donor coupled to the substrate (green) enables the simultaneous monitoring of distance changes occurring on the nanometer scale between the enzyme's active site and the substrate.

These results raise the hope that it might be possible to relate conformational dynamics directly with enzyme activity, for example, turnover rates (Figure 15). Such studies would require site-specific labeling of the active site of an enzyme with a fluorophore which is selectively quenched by an amino acid, for example, a tryptophan residue, in close proximity.[5,139,146,149] In addition, the fluorophore's conformational space has to be minimized, otherwise, the observed variation in electron-transfer efficiency could be masked by conformational fluctuations of the linker between the fluorophore and the quenching amino acid. Brownian motion results in subnanometer conformational changes in the active site of the enzyme, each conformation corresponds to a separate point on the potential energy surface, thus the conformational changes give rise to variations in electron-transfer efficiency, these are directly reflected in fluctuations of fluorescence intensity and lifetime. Depending on the time resolution achievable in such experiments, enzyme activity could be monitored simultaneously using, for example, a non-fluorescent substrate which is converted into a highly fluorescent product in the active site of the enzyme (Figure 15a).[278,279] Are specific reaction pathways related to the binding, reaction, and release of the substrate (Figure 15b)? An even more ambitious study will be to extract topographic information of the energy landscape by following the temporal order on which different conformations occur.

The application of spFRET experiments to biological questions has not exploited the full potential of this method yet. spFRET is not restricted to interaction measurements between two subunits of molecular machines or assemblies. Just like FRET was successfully used for the construction of a

 © 2005 Wiley-VCH Verlag GmbH & Co. KGaA, Weinheim

photonic wire, SMFS techniques have the potential to elucidate the interactions of more than two components simultaneously through multistep-FRET experiments. However, care has to be taken in the interpretation of colocalization and multistep-FRET data obtained from more than two differently labeled components. First, crosstalk in excitation and detection has to be reduced to a minimum to obtain unequivocal information. Second, to assign the lack of a FRET-signal to the absence of one molecule requires direct probing (excitation) of each component,[280] otherwise, misinterpretation of the data can easily occur. Nevertheless, by careful selection of the fluorophores and the excitation and detection technique used, multicolor experiments could be used to examine the interaction pathways in molecular assemblies as well as for the construction of 3D distance maps of the separations between differently labeled proteins in biomolecular assemblies.

First successful steps towards application of SMFS in live-cell imaging have been made. The pioneering technological breakthroughs achieved to date provide the basis for a variety of experiments which were unthinkable a few years ago. However, besides structural-dynamics studies, the ambition of single-molecule fluorescence spectroscopy must be to go beyond pure descriptive experiments and provide quantitative data on the biomolecular machines that are essential for cell function and survival. It is no longer enough to study just the colocalization of different biomolecules in specific compartments, rather we quest for measuring their absolute separations on the 0.1–200 nm length scale, their orientations, their subnanometer conformational fluctuations relevant for functioning, and importantly we are interested in the absolute number of interacting molecules. Furthermore, single-molecule techniques are at hand that could allow us to probe the local response of a cell upon specific stimuli (Figure 16). Using submicrometer pipettes in combination with scanning ion conductance microscopy (SICM) topographic images of living cells at high resolution under biological relevant conditions can be obtained.[281–283] The cell could be stimulated

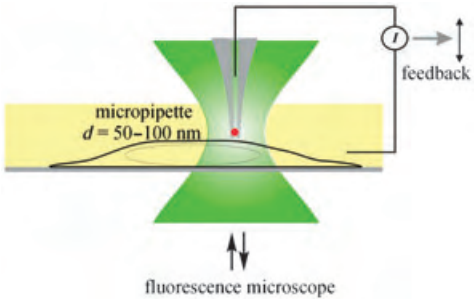

Figure 16. Possible application of SICM in combination with single-molecule fluorescence imaging to monitor local cellular dynamics. In SICM, an electrolyte-filled, glass micropipette is scanned over the surface of a sample bathed in an electrolytic solution.[281] The pipette–sample separation is maintained at a constant value by controlling the ion current that flows through the pipette aperture. The measured ion current is used to generate topographic features and/or images of the local ion currents flowing through pores on the sample surface. The spatial resolution achievable using SICM is dependent on the size of the tip aperture.

at well defined positions by injection into the cytoplasm or nucleus or delivering of individual fluorescently labeled molecules on the cell membrane while the response of the cell is measured at different locations by fluorescence scanning or imaging techniques.[284] Alternatively, SICM could be used to localize and measure the function of single ion channels in the membrane[285] while monitoring the binding of fluorescently labeled molecules at the inner or outer membrane.[286–288]

To extract quantitative information from SMFS data in living cells, such as the absolute number of polymerase molecules located in a transcription or replication foci and the distances between interacting molecules, several challenges need to be overcome. First, a technique is required which gives information about the number of molecules present in the laser focus. To date, in single-molecule studies in cells, several indirect methods have been used to confirm that the fluorescence observed is derived from only a single emitter, for example, photobleaching in a single, instantaneous step, or the observation of transient off states. On the other hand, polarization-modulated excitation spectroscopy or photon antibunching experiments can provide a more direct proof for the presence of a single molecule. Furthermore, the ratio of the number of coincident photon events to the number of noncoincident photon pairs in photon antibunching experiments gives a measure of the number of independently emitting fluorophores for a given time interval (Figure 17).[89,90,289] Therefore, photon antibunching measurements are well suited to count the number of fluorescent molecules present in the laser focus, as long as higher excited state interactions, such as singlet–singlet annihilation, can be neglected.[85] Besides the background which influences the ratio between the central and lateral peaks calculated from coincidence histograms, thus making counting harder, it will be more difficult to accurately determine the number of independent emitters when higher numbers of molecules ($>$ 4) are present.[90] Nevertheless, spectrally resolved fluorescence lifetime imaging microscopy (SFLIM) in combination with photon antibunching measurements are valuable tools for imaging and counting single molecules in cells (Figure 17). In addition, SFLIM is well suited to measure distances between single molecules although these separations are well below the optical resolution limit.[257] Consequently, the techniques are available that would enable a quantitative comprehension of biomolecular machines.

Since the well-defined labeling of biomolecules, for example, proteins, with a single fluorophore is the basis for quantitative measurements, new labeling strategies have to be developed: In general, proteins, for example, antibodies, are multiple labeled using fluorophore excess. The excess of free fluorophores is finally removed by gel filtration. Unfortunately, multiple-labeled antibodies cannot be used for the counting of molecules by photon antibunching. For example, the counting of the number of polymerase II molecules present in a transcription factory requires singly labeled antibodies. In principle, an average label degree of less than one can be easily obtained by reducing the fluorophore concentration in the labeling reaction. However, since the separation of labeled and unlabeled antibodies is almost

 © 2005 Wiley-VCH Verlag GmbH & Co. KGaA, Weinheim

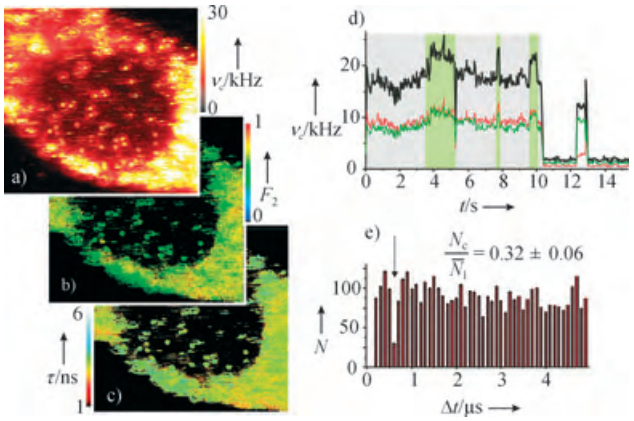

Figure 17. Confocal scanning fluorescence images of a fixed 3T3 fibroblast cell treated with 10^{-9} M solution of MR121-labeled oligo(dT) (40 mer) molecules (excitation at $\lambda = 635$ nm using a pulsed laser diode). Oligo(dT) can hybridize to the poly(A) tail of mRNAs.[186] a) Overall fluorescence-intensity image recorded with a SFLIM-microscope showing several bright spots in the nucleus with fluorescence count rates of up to 30 kHz.[78] b) and c) show the corresponding spectral image (F_2 image) and lifetime image (τ image) For the calculation of the F_2 and τ image, pixels containing less than 15 counts were discarded. Owing to the unequivocal spectroscopic characteristics of the MR121-labeled oligo(dT) molecules with fluorescence lifetimes of around 3 ns, and F_2 values of approximately 0.5, specific signals can be easily discriminated against autofluorescence.[83] d) Fluorescence-intensity trajectory (count rate, ν_c versus time, t in s) of a fluorescent spot in the nucleus of the fibroblast cell (traces: black overall intensity, green det 1, red det 2). With a background count rate of approximately 2 kHz, S/B ratios of about 9 are easily obtained in the nucleus. As several oligo(dT) molecules can bind to a single poly(A) tail of mRNA, it is not known whether the intensity fluctuations observed (compare gray and green areas) have a photophysical origin or are the result of a varying number of molecules contributing to the signal. d) The interphoton times (coincidence) histogram of all photons detected during the first 10 s of the trajectory give a $N_c/\bar{N}_1$ ratio of 0.32 ± 0.06. On the other hand, S/B considerations predict a $N_c/\bar{N}_1$ ratio of approximately 0.18 for a single emitter.[90] If however, interphoton-times histograms are constructed separately from the photons recorded in the higher intensity (green) and lower intensity parts (gray), two different $N_c/\bar{N}_1$ ratios of 0.55 ± 0.13 (for the green part) and 0.17 ± 0.05 (for the gray part) are obtained. This result demonstrates that the intensity fluctuations observed in the trajectory are caused by a varying number of fluorescing molecules present in the laser focus.

impossible, unlabeled antibodies would bind to polymerase molecules as well and prevent any quantitative statement. To circumvent these problems, Lewinska et al. described a novel method for the specific labeling of native proteins at a single, well-defined position using the commercial IgA protease to attach a non-natural peptidic moiety to the N terminus of the antibody. This natural peptidic moiety can be selectively modified.[290] We are currently developing a new labeling strategy for antibodies which guaranties that practically all the antibodies present in the sample carry a single fluorophore (with only a small number of double-labeled antibodies). The strategy comprises bridging of the fluorophore and antibody by a special linker, for example, a peptide, which binds specifically to its binding partner, for example, another antibody. Using, for example, an oligohistidine (6–12 histidine residues covalently attached by the N-terminal end to the fluorophore) as the linker and labeling conditions that ensure a very low degree of labeling, singly labeled antibodies can be obtained by the use of a His-tag purification column.

Finally, by combining SMFS measurements with single-molecule manipulation techniques, such as optical tweezers,[291] or other spectroscopic techniques, such as surface enhanced Raman scattering (SERS), it could be possible to monitor simultaneously several different observables of biological reactions in living cells. In common Raman spectroscopy the inelastically scattered light is used to identify molecules through their characteristic vibrational quantum states. SERS uses the fact that the rather weak Raman effect can be significantly strengthened (by a factor of up to 14 orders of magnitude) if the molecules are attached to nanometer-sized metal structures. The apparatus required for SERS, SMFS, and optical tweezers in cells are similar and comprise a laser that is focused into the cell by using a high magnification microscope objective. For example, Kneipp and co-workers deposited 60-nm gold particles inside cells as SERS-active nanostructures to measure the enhanced Raman signals of the chemical constituents of cells.[292] SERS mapping over a cell monolayer with 1 µm lateral resolution showed different Raman spectra at almost all places which reflects the very inhomogeneous constitution of the cells. The new spectroscopic method provides a tool for even more sensitive and structurally selective detection of chemicals inside a cell, and for monitoring their intracellular distributions.

Combinations of these new techniques, opens new opportunities for cell biology and biomedical studies. However, to combine SERS with optical tweezers and SMFS several challenges need to be overcome. First, optical trapping of metallic particles required for SERS is complicated.[293] Furthermore, absorption by the metal particle can cause a temperature rise and damage to living cells. This process has become known as opticution.[294] Even for refractory absorbing materials, the effects of heating can be a problem as bubble formation will disrupt trapping.[295] However, it could be possible to use standard microbeads for optical trapping if they are coated with a thin metal layer or some metal clusters are captured on the surface so that the optical excitation of a surface plasmon is supported but 3D optical trapping with minimal heating effects is still enabled. Several nanometers long water-soluble linkers, such as PEG linkers, have to be used to attach fluorescence sensors to the metal. This is because the fluorescence intensities are attenuated depending on the distance (up to tens of nm) between the fluorophores and the metal surfaces owing to fluorescence energy transfer to the metal.[296–298] In the future this combined approach could provide an elegant method to locally probe forces[299] and individual binding events with fluorescence sensors.[300] Simultaneously it could be possible to map the concentration of specific biomolecules in living cells by SERS.[292] In an extended version of the method, a single IR-laser line could be used simultaneously to trap the bead, generate the SERS signal, and excite the fluorophores by two-photon excitation.[301]

 © 2005 Wiley-VCH Verlag GmbH & Co. KGaA, Weinheim

Addendum (February 12, 2005)

Since the submission of this Review, scientific development has not been stagnant. The trend to address more sophisticated biological problems by single-molecule fluorescence spectroscopy continues. Examples include the improvement of the control of chemical approaches to meet the requirements of biological systems, the development and application of new techniques to investigate biomolecular dynamics, and the study of artificial light-harvesting or electron-transfer systems. In particular, it is clear that in contrast to previous SMFS studies which often had the character of feasibility studies more and more attention is focussed on the reliability of the results obtained, that is, methods have been further elaborated and characterized by controls and crosschecks.

Immobilization of biomolecules, for examples, has always been viewed with skepticism because the impact of the close surface on the properties of the molecule investigated is hard to exclude or to evaluate. Recent studies, however, show that surface perturbations can be minimized in such a way that they do not dominate the observed biomolecular dynamics. Okumus and co-workers, for example, compared the dynamics of ribozyme molecules directly tethered to the surface to those of ribozymes enclosed in immobilized vesicles and found no differences.[303] In addition, tethering strategies have been improved by comparing different immobilization schemes and a star-shaped poly(ethylene oxide) (PEO) has been found to be the least interfering in nature.[304]

While FRET is now an established SMFS technique which is applied to more complex problems, such as the investigation of translation,[305,306] and analyzing the reversible reaction pathway of the hairpin ribozyme,[307] new territory is entered when the interaction of more than two chromophores is investigated. The possibility to resolve FRET between three or even up to five chromophores, has recently been demonstrated[308–310] which opens up new vistas to visualize the interaction between more than two molecules or to correlate movements within a molecule or biomolecular complex. The understanding of FRET processes in multichromophoric model systems has led to a comprehensive level understanding of intersystem crossing and photobleaching,[311] so that the focus is now on the investigations of stronger interactions, such as the formation of excimer-states[312] and superradiance in strongly coupled tetraphenoxyperylenediimide trimers.[313] These new results are of interest in interpreting the photophysics of technological interesting molecules, such as π-conjugated polymers. [314]

Recent achievements demonstrate impressively that SMFS can supply important information on complex processes in living cells. For example, TIRFM has been successfully applied to visualize single-molecule processes in living cells, such as activation of the G protein Ras,[315] or exocytosis of IgG as mediated by the FcRn receptor.[316] Furthermore, transport through nuclear pore complexes could be directly monitored in permeabilized cells by single-molecule tracking. [317] More recently, the direct observation of the real-time catalysis and substrate kinetics of a single lipase enzyme (a single enzymatic turnover cycle) could be recorded for up to 2 h using nonfluorescent substrate molecules which are converted into highly fluorescent products upon hydrolysis, a method similar to that proposed in Figure 15 a.[318,319] Insights into the conformational fluctuations of the protein which are relevant for function could be obtained at the same time, if the enzyme were labeled site specifically with a suitable FRET-pair.

Other techniques which supply topographic information on the nanometer scale or other additional information about the systems being studied, such as AFM and electrical channel recording, are currently successfully combined with optical single-molecule techniques.[320,321] Biological applications of nanocrystals (NCs) are maturing with cytotoxic effects[322,323] and labeling strategies for live-cell applications at the forefront. [324–326] Recently, Lagerholm and co-workers described a strategy similar to that outlined in Figure 13 to deliver NCs into cells using arginine rich peptides on the surface of the NCs. Interestingly they find that cellular labeling occurs readily for suspended cells while, in agreement with our results, with supported cells, mainly the extracellular matrix is labeled.[325]

Improving the localization and colocalization accuracy of single biomolecules well below the optical resolution limit, remain one of the basic concerns of single-molecule spectroscopy. The potential of new methods, such as subsequent photobleaching of chromophores, STED microscopy, and spectrally resolved fluorescence lifetime imaging microscopy, to be of use in DNA mapping with very high resolution and for studying the motion of molecular motors, such as myosin V, has just begun to be explored.[327–333] In addition, scientists worldwide discuss the development of techniques that will enable the determination of the absolute 3D localization of individual molecules in living cells. This requires a kind of global positioning system (GPS) on a cellular level, a cellular positioning system (CPS) or molecular positioning system (MPS), and might be accomplished, for example, by labeling specific compartments within the cell with fluorophores of different spectral signature or by deposition of cells on 3D nanostructured surfaces at which at least three fixed points are selectively labeled with different dyes. Theoretically, this would enable the determination of the absolute position of each fluorescently labeled biomolecule with respect to the fixed points.

Although, the presented achievements represent a subjective selection they impressively demonstrate that SMFS is still a dynamic and emerging field that has not lost any of its fascination.

The authors are indebted to H. Barsch, V. Buschmann, A. Biebricher, F. C. De Schryver, S. Doose, K. H. Drexhage, J. Enderlein, M. F. Garcia-Parajo, K. T. Han, M. Heilemann, T. Heinlein, D.-P. Herten, J. Hofkens, J. P. Knemeyer, N. Marmé, C. Müller, H. Neuweiler, C. Roth, M. Rüping, C. W. Park, O. Piestert, P. Schlüter, A. Schulz, D. Seebach, C. A. M. Seidel, N. F. van Hulst, S. Weiss, K. D. Weston, J. Wolfrum, and C. Zander for their contributions and active support of the single-molecule fluorescence spectroscopy research in Heidelberg

 © 2005 Wiley-VCH Verlag GmbH & Co. KGaA, Weinheim

and Bielefeld. This work was supported by the BMBF, the VW-Stiftung, and the DFG.

Received: December 29, 2003

[1] G. Binnig, H. Rohrer, *Rev. Mod. Phys.* **1987**, *59*, 615 – 625.
[2] G. Binnig, C. F. Quate, C. Gerber, *Phys. Rev. Lett.* **1986**, *56*, 930 – 933.
[3] B. Schuler, E. A. Lipman, W. A. Eaton, *Nature* **2002**, *419*, 743 – 747.
[4] E. A. Lipman, B. Schuler, O. Bakajin, W. A. Eaton, *Science* **2003**, *301*, 1233 – 1235.
[5] H. Neuweiler, A. Schulz, M. Boehmer, J. Enderlein, M. Sauer, *J. Am. Chem. Soc.* **2003**, *125*, 5324 – 5330.
[6] M. J. Levene, J. Korlach, S. W. Turner, M. Foquet, H. G. Craighead, W. W. Webb, *Science* **2003**, *299*, 682 – 686.
[7] I. Braslavsky, B. Hebert, E. Kartalov, S. R. Quake, *Proc. Natl. Acad. Sci. USA* **2003**, *100*, 3960 – 3964.
[8] J. H. Jett, R. A. Keller, J. C. Martin, B. L. Marrone, R. K. Moyzis, R. L. Ratliff, N. K. Seitzinger, E. B. Shera, C. C. Stewart, *J. Biomol. Struct. Dyn.* **1989**, *7*, 301 – 309.
[9] M. Sauer, B. Angerer, W. Ankenbauer, Z. Foldes-Papp, F. Gobel, K. T. Han, R. Rigler, A. Schulz, J. Wolfrum, C. Zander, *J. Biotechnol.* **2001**, *86*, 181 – 201.
[10] K. Dorre, S. Brakmann, M. Brinkmeier, K.-T. Han, K. Riebeseel, P. Schwille, J. Stephan, T. Wetzel, M. Lapczyna, M. Stuke, R. Bader, M. Hinz, H. Seliger, J. Holm, M. Eigen, R. Rigler, *Bioimaging* **1997**, *5*, 139 – 152.
[11] J. H. Werner, H. Cai, J. H. Jett, L. Reha-Krantz, R. A. Keller, P. M. Goodwin, *J. Biotechnol.* **2003**, *102*, 1 – 14.
[12] W. E. Moerner, T. Basche, *Angew. Chem.* **1993**, *105*, 537 – 557; *Angew. Chem. Int. Ed. Engl.* **1993**, *32*, 457 – 476.
[13] X. S. Xie, *Acc. Chem. Res.* **1996**, *29*, 598 – 606.
[14] S. M. Nie, R. N. Zare, *Annu. Rev. Biophys. Biomol. Struct.* **1997**, *26*, 567 – 596.
[15] X. S. Xie, J. K. Trautman, *Annu. Rev. Phys. Chem.* **1998**, *49*, 441 – 480.
[16] W. P. Ambrose, P. M. Goodwin, J. H. Jett, A. Van Orden, J. H. Werner, R. A. Keller, *Chem. Rev.* **1999**, *99*, 2929 – 2956.
[17] W. E. Moerner, S. Weiss, J. K. Gimzewski, A. D. Mehta, *Science* **1999**, *283*, 1667 – 1695 (Single Molecule Special Issue).
[18] C. Zander, *J. Anal. Chem.* **2000**, *366*, 745 – 751.
[19] A. A. Deniz, T. A. Laurence, M. Dahan, D. S. Chemla, P. G. Schultz, S. Weiss, *Annu. Rev. Phys. Chem.* **2001**, *52*, 233 – 253.
[20] W. E. Moerner, *J. Phys. Chem. B* **2002**, *106*, 910 – 927.
[21] Y. Jung, E. Barkai, R. J. Silbey, *J. Chem. Phys.* **2002**, *117*, 10980 – 10995.
[22] M. Orrit, *J. Chem. Phys.* **2002**, *117*, 10938 – 10946.
[23] A. N. Kapanidis, S. Weiss, *J. Chem. Phys.* **2002**, *117*, 10953 – 10964.
[24] W. E. Moerner, *J. Chem. Phys.* **2002**, *117*, 10925 – 10937.
[25] X. Sunney Xie, *J. Chem. Phys.* **2002**, *117*, 11024 – 11032.
[26] R. A. Keller, W. P. Ambrose, A. A. Arias, H. Cai, S. R. Emory, P. M. Goodwin, J. H. Jett, *Anal. Chem.* **2002**, *74*, 316A-324A.
[27] U. Kubitscheck, *Single Mol.* **2002**, *3*, 267 – 274.
[28] M. Boehmer, J. Enderlein, *ChemPhysChem* **2003**, *4*, 792 – 808.
[29] W. E. Moerner, D. P. Fromm, *Rev. Sci. Instrum.* **2003**, *74*, 3597 – 3619.
[30] T. Förster, *Ann. Phys.* **1948**, *2*, 55 – 75.
[31] W. E. Moerner, L. Kador, *Phys. Rev. Lett.* **1989**, *62*, 2535 – 2538.
[32] E. B. Shera, N. K. Seitzinger, L. M. Davis, R. A. Keller, S. A. Soper, *Chem. Phys. Lett.* **1990**, *174*, 553 – 557.
[33] F. Zarrin, N. J. Dovichi, *Anal. Chem.* **1985**, *57*, 2690 – 2692.
[34] E. Betzig, R. J. Chichester, *Science* **1993**, *262*, 1422 – 1425.
[35] W. P. Ambrose, P. M. Goodwin, J. C. Martin, R. A. Keller, *Science* **1994**, *265*, 364 – 367.
[36] T. Enderle, T. Ha, D. S. Chemla, S. Weiss, *Ultramicroscopy* **1998**, *71*, 303 – 309.
[37] F. De Lange, A. Cambi, R. Huijbens, B. de Bakker, W. Rensen, M. Garcia-Parajo, N. Van Hulst, C. G. Figdor, *J. Cell Sci.* **2001**, *114*, 4153 – 4160.
[38] M. Koopman, B. I. de Bakker, M. F. Garcia-Parajo, N. F. van Hulst, *Appl. Phys. Lett.* **2003**, *83*, 5083 – 5085.
[39] A. Cambi, F. de Lange, N. M. van Maarseveen, M. Nijhuis, B. Joosten, E. M. H. P. van Dijk, B. I. de Bakker, J. A. M. Fransen, P. H. M. Bovee-Geurts, F. N. van Leeuwen, N. F. Van Hulst, C. G. Figdor, *J. Cell Biol.* **2004**, *164*, 145 – 155.
[40] J. B. Pawley, *Handbook of Biological Confocal Microscopy*, 2. Aufl., Plenum, New York, **1995**.
[41] R. Rigler, Ü. Mets, *Proc. SPIE-Int. Soc. Opt. Eng. Proc. SPIE* **1992**, 239 – 247.
[42] R. Rigler, Ü. Mets, J. Widengren, P. Kask, *Eur. Biophys. J. Biophys. Lett.* **1993**, *22*, 169 – 175.
[43] C. Xu, W. Zipfel, J. B. Shear, R. M. Williams, W. W. Webb, *Proc. Natl. Acad. Sci. USA* **1996**, *93*, 10763 – 10768.
[44] J. Mertz, C. Xu, W. W. Webb, *Opt. Lett.* **1995**, *20*, 2532 – 2534.
[45] L. Brand, C. Eggeling, C. Zander, K. H. Drexhage, C. A. M. Seidel, *J. Phys. Chem. A* **1997**, *101*, 4313 – 4321.
[46] W. Denk, J. H. Strickler, W. W. Webb, *Science* **1990**, *248*, 73 – 76.
[47] A. Fischer, C. Cremer, E. H. K. Stelzer, *Appl. Opt.* **1995**, *34*, 1989 – 2003.
[48] C. Xu, W. W. Webb, *J. Opt. Soc. Am. B* **1996**, *13*, 481 – 491.
[49] K. G. Heinze, M. Rarbach, M. Jahnz, P. Schwille, *Biophys. J.* **2002**, *83*, 1671 – 1681.
[50] M. Eigen, R. Rigler, *Proc. Natl. Acad. Sci. USA* **1994**, *91*, 5740 – 5747.
[51] S. Maiti, U. Haupts, W. W. Webb, *Proc. Natl. Acad. Sci. USA* **1997**, *94*, 11753 – 11757.
[52] Y. Chen, J. D. Müller, P. T. C. So, E. Gratton, *Biophys. J.* **1999**, *77*, 553 – 567.
[53] P. Kask, K. Palo, D. Ullmann, K. Gall, *Proc. Natl. Acad. Sci. USA* **1999**, *96*, 13756 – 13761.
[54] P. Kask, K. Palo, N. Fay, L. Brand, Ü. Mets, D. Ullmann, J. Jungmann, J. Pschorr, K. Gall, *Biophys. J.* **2000**, *78*, 1703 – 1713.
[55] K. Palo, Ü. Mets, S. Jäger, P. Kask, K. Gall, *Biophys. J.* **2000**, *79*, 2858 – 2866.
[56] T. A. Laurence, A. N. Kapanidis, X. Kong, D. S. Chemla, S. Weiss, *J. Phys. Chem. B* **2004**, *108*, 3051 – 3067.
[57] E. S. Yeung, *Chem. Rec.* **2001**, *1*, 123 – 139.
[58] T. Ha, I. Rasnik, W. Cheng, H. P. Babcock, G. H. Gauss, T. M. Lohman, S. Chu, *Nature* **2002**, *419*, 638 – 641.
[59] D. Axelrod, *Methods Cell Biol.* **1989**, *30*, 245 – 270.
[60] W. P. Ambrose, P. M. Goodwin, J. P. Nolan, *Cytometry* **1999**, *36*, 224 – 231.
[61] T. Funatsu, Y. Harada, M. Tokunaga, K. Saito, T. Yanagida, *Nature* **1995**, *374*, 555 – 559.
[62] M. Tokunaga, K. Kitamura, K. Saito, A. H. Iwane, T. Yanagida, *Biochem. Biophys. Res. Commun.* **1997**, *235*, 47 – 53.
[63] A. Yildiz, M. Tomishige, R. D. Vale, P. R. Selvin, *Science* **2004**, *303*, 676 – 679.
[64] A. Yildiz, J. N. Forkey, S. A. McKinney, T. Ha, Y. E. Goldman, P. R. Selvin, *Science* **2003**, *300*, 2061 – 2065.
[65] R. D. Vale, T. Funatsu, D. W. Pierce, L. Romberg, Y. Harada, T. Yanagida, *Nature* **1996**, *380*, 451 – 453.
[66] J. N. Forkey, M. E. Quinlan, M. A. Shaw, J. E. T. Corrie, Y. E. Goldman, *Nature* **2003**, *422*, 399 – 404.
[67] C. W. Wilkerson, P. M. Goodwin, W. P. Ambrose, J. C. Martin, R. A. Keller, *Appl. Phys. Lett.* **1993**, *62*, 2030 – 2032.
[68] M. Sauer, J. Arden-Jacob, K. H. Drexhage, F. Göbel, U. Lieberwirth, K. Mühlegger, R. Müller, J. Wolfrum, C. Zander, *Bioimaging* **1998**, *6*, 14 – 24.
[69] S. A. Soper, L. M. Davis, E. B. Shera, *J. Opt. Soc. Am. B* **1992**, *9*, 1761 – 1769.

 © 2005 Wiley-VCH Verlag GmbH & Co. KGaA, Weinheim

[70] A. Van Orden, R. A. Keller, *Anal. Chem.* **1998**, *70*, 4463 – 4471.
[71] J. Schaffer, A. Volkmer, C. Eggeling, V. Subramaniam, G. Striker, C. A. M. Seidel, *J. Phys. Chem. A* **1999**, *103*, 331 – 336.
[72] F. Stracke, C. Blum, S. Becker, K. Müllen, A. J. Meixner, *Chem. Phys. Lett.* **2000**, *325*, 196 – 202.
[73] A. J. Meixner, M. A. Weber, *J. Lumin.* **2000**, *86*, 181 – 187.
[74] K. D. Weston, S. K. Buratto, *J. Phys. Chem. A* **1998**, *102*, 3635 – 3638.
[75] H. P. Lu, X. S. Xie, *Nature* **1997**, *385*, 143 – 146.
[76] K. D. Weston, L. S. Goldner, *J. Phys. Chem. B* **2001**, *105*, 3453 – 3462.
[77] P. Tinnefeld, V. Buschmann, D. P. Herten, K.-T. Han, M. Sauer, *Single Mol.* **2000**, *1*, 215 – 223.
[78] P. Tinnefeld, D. P. Herten, M. Sauer, *J. Phys. Chem. A* **2001**, *105*, 7989 – 8003.
[79] T. Ha, T. Enderle, D. S. Chemla, P. R. Selvin, S. Weiss, *Phys. Rev. Lett.* **1996**, *77*, 3979 – 3982.
[80] M. Prummer, C. G. Hubner, B. Sick, B. Hecht, A. Renn, U. P. Wild, *Anal. Chem.* **2000**, *72*, 443 – 447.
[81] M. Prummer, B. Sick, A. Renn, U. P. Wild, *Anal. Chem.* **2004**, *76*, 1633 – 1640.
[82] D. P. Herten, P. Tinnefeld, M. Sauer, *Appl. Phys. B* **2000**, *71*, 765 – 771.
[83] J.-P. Knemeyer, D.-P. Herten, M. Sauer, *Anal. Chem.* **2003**, *75*, 2147 – 2153.
[84] D. S. English, E. J. Harbron, P. F. Barbara, *J. Chem. Phys.* **2001**, *114*, 10479 – 10485.
[85] P. Tinnefeld, K. D. Weston, T. Vosch, M. Cotlet, T. Weil, J. Hofkens, K. Müllen, F. C. De Schryver, M. Sauer, *J. Am. Chem. Soc.* **2002**, *124*, 14310 – 14311.
[86] C. Eggeling, S. Berger, L. Brand, J. R. Fries, J. Schaffer, A. Volkmer, C. A. M. Seidel, *J. Biotechnol.* **2001**, *86*, 163 – 180.
[87] R. Kühnemuth, C. A. M. Seidel, *Single Mol.* **2001**, *2*, 251 – 254.
[88] A. M. Kelley, X. Michalet, S. Weiss, *Science* **2001**, *292*, 1671 – 1672.
[89] P. Tinnefeld, C. Müller, M. Sauer, *Chem. Phys. Lett.* **2001**, *345*, 252 – 258.
[90] K. D. Weston, M. Dyck, P. Tinnefeld, C. Müller, D. P. Herten, M. Sauer, *Anal. Chem.* **2002**, *74*, 5342 – 5349.
[91] T. Vosch, M. Cotlet, J. Hofkens, K. Van Biest, M. Lor, K. Weston, P. Tinnefeld, M. Sauer, L. Latterini, K. Müllen, F. C. De Schryver, *J. Phys. Chem. A* **2003**, *107*, 6920 – 6931.
[92] C. Eggeling, J. R. Fries, L. Brand, R. Günther, C. A. M. Seidel, *Proc. Natl. Acad. Sci. USA* **1998**, *95*, 1556 – 1561.
[93] J. R. Fries, L. Brand, C. Eggeling, M. Köllner, C. A. M. Seidel, *J. Phys. Chem. A* **1998**, *102*, 6601 – 6613.
[94] J. Tellinghuisen, C. W. Wilkerson, Jr., *Anal. Chem.* **1993**, *65*, 1240 – 1246.
[95] J. Enderlein, M. Sauer, *J. Phys. Chem. A* **2001**, *105*, 48 – 53.
[96] J. Enderlein, P. M. Goodwin, A. Van Orden, W. P. Ambrose, R. Erdmann, R. A. Keller, *Chem. Phys. Lett.* **1997**, *270*, 464 – 470.
[97] M. Maus, M. Cotlet, J. Hofkens, T. Gensch, F. C. De Schryver, J. Schaffer, C. A. M. Seidel, *Anal. Chem.* **2001**, *73*, 2078 – 2086.
[98] T. Ha, T. Enderle, D. S. Chemla, P. R. Selvin, S. Weiss, *Chem. Phys. Lett.* **1997**, *271*, 1 – 5.
[99] R. Hanbury Brown, R. Q. Twiss, *Nature* **1956**, *178*, 1046 – 1048.
[100] T. Basche, W. E. Moerner, M. Orrit, H. Talon, *Phys. Rev. Lett.* **1992**, *69*, 1516 – 1519.
[101] L. Fleury, J. M. Segura, G. Zumofen, B. Hecht, U. P. Wild, *Phys. Rev. Lett.* **2000**, *84*, 1148 – 1151.
[102] W. P. Ambrose, P. M. Goodwin, J. Enderlein, D. J. Semin, J. C. Martin, R. A. Keller, *Chem. Phys. Lett.* **1997**, *269*, 365 – 370.
[103] M. Wu, P. M. Goodwin, W. P. Ambrose, R. A. Keller, *J. Phys. Chem.* **1996**, *100*, 17406 – 17409.
[104] J. Hofkens, M. Maus, T. Gensch, T. Vosch, M. Cotlet, F. Kohn, A. Herrmann, K. Müllen, F. De Schryver, *J. Am. Chem. Soc.* **2000**, *122*, 9278 – 9288.
[105] P. J. Rothwell, S. Berger, O. Kensch, S. Felekyan, M. Antonik, B. M. Wohrl, T. Restle, R. S. Goody, C. A. M. Seidel, *Proc. Natl. Acad. Sci. USA* **2003**, *100*, 1655 – 1660.
[106] K. Kinosita, Jr., H. Itoh, S. Ishiwata, K. Hirano, T. Nishizaka, T. Hayakawa, *J. Cell Biol.* **1991**, *115*, 67 – 73.
[107] L. Cognet, G. S. Harms, G. A. Blab, P. H. M. Lommerse, T. Schmidt, *Appl. Phys. Lett.* **2000**, *77*, 4052 – 4054.
[108] L. Stryer, R. P. Haugland, *Proc. Natl. Acad. Sci. USA* **1967**, *58*, 719 – 726.
[109] L. Stryer, *Annu. Rev. Biochem.* **1978**, *47*, 819 – 846.
[110] W. Veatch, L. Stryer, *J. Mol. Biol.* **1977**, *113*, 89 – 102.
[111] J. Szollosi, S. Damjanovich, L. Matyus, *Cytometry* **1998**, *34*, 159 – 179.
[112] F. Stühmeier, J. B. Welch, A. I. H. Murchie, D. M. J. Lilley, R. M. Clegg, *Biochemistry* **1997**, *36*, 13530 – 13538.
[113] K. M. Parkhurst, M. Brenowitz, L. J. Parkhurst, *Biochemistry* **1996**, *35*, 7459 – 7465.
[114] T. Tuschl, C. Gohlke, T. M. Jovin, E. Westhof, F. Eckstein, *Science* **1994**, *266*, 785 – 789.
[115] S. Weiss, *Nat. Struct. Biol.* **2000**, *7*, 724 – 729.
[116] T. Ha, *Methods* **2001**, *25*, 78 – 86.
[117] A. A. Deniz, T. A. Laurence, G. S. Beligere, M. Dahan, A. B. Martin, D. S. Chemla, P. E. Dawson, P. G. Schultz, S. Weiss, *Proc. Natl. Acad. Sci. USA* **2000**, *97*, 5179 – 5184.
[118] T. Ha, *Single Mol.* **2001**, *2*, 283 – 284.
[119] H. D. Kim, G. U. Nienhaus, T. Ha, J. W. Orr, J. R. Williamson, S. Chu, *Proc. Natl. Acad. Sci. USA* **2002**, *99*, 4284 – 4289.
[120] T. Ha, X. W. Zhuang, H. D. Kim, J. W. Orr, J. R. Williamson, S. Chu, *Proc. Natl. Acad. Sci. USA* **1999**, *96*, 9077 – 9082.
[121] X. Zhuang, L. E. Bartley, H. P. Babcock, R. Russell, T. Ha, D. Herschlag, S. Chu, *Science* **2000**, *288*, 2048 – 2051.
[122] E. Tan, T. J. Wilson, M. K. Nahas, R. M. Clegg, D. M. J. Lilley, T. Ha, *Proc. Natl. Acad. Sci. USA* **2003**, *100*, 9308 – 9313.
[123] M. Borsch, M. Diez, B. Zimmermann, R. Reuter, P. Graber, *FEBS Lett.* **2002**, *527*, 147 – 152.
[124] E. Rhoades, E. Gussakovsky, G. Haran, *Proc. Natl. Acad. Sci. USA* **2003**, *100*, 3197 – 3202.
[125] A. A. Deniz, M. Dahan, J. R. Grunwell, T. Ha, A. E. Faulhaber, D. S. Chemla, S. Weiss, P. G. Schultz, *Proc. Natl. Acad. Sci. USA* **1999**, *96*, 3670 – 3675.
[126] M. Sauer, K. H. Drexhage, U. Lieberwirth, R. Müller, S. Nord, C. Zander, *Chem. Phys. Lett.* **1998**, *284*, 153 – 163.
[127] G. Bonnet, O. Krichevsky, A. Libchaber, *Proc. Natl. Acad. Sci. USA* **1998**, *95*, 8602 – 8606.
[128] N. L. Goddard, G. Bonnet, O. Krichevsky, A. Libchaber, *Phys. Rev. Lett.* **2000**, *85*, 2400 – 2403.
[129] M. I. Wallace, L. Ying, S. Balasubramanian, D. Klenerman, *Proc. Natl. Acad. Sci. USA* **2001**, *98*, 5584 – 5589.
[130] O. Piestert, H. Barsch, V. Buschmann, T. Heinlein, J.-P. Knemeyer, K. D. Weston, M. Sauer, *Nano Lett.* **2003**, *3*, 979 – 982.
[131] M. A. Osborne, C. L. Barnes, S. Balasubramanian, D. Klenerman, *J. Phys. Chem. B* **2001**, *105*, 3120 – 3126.
[132] D. S. Talaga, W. L. Lau, H. Roder, J. Tang, Y. Jia, W. F. DeGrado, R. M. Hochstrasser, *Proc. Natl. Acad. Sci. USA* **2000**, *97*, 13021 – 13026.
[133] M. Margittai, J. Widengren, E. Schweinberger, G. F. Schroeder, S. Felekyan, E. Haustein, M. Koenig, D. Fasshauer, H. Grubmüller, R. Jahn, C. A. M. Seidel, *Proc. Natl. Acad. Sci. USA* **2003**, *100*, 15516 – 15521.
[134] M. Diez, B. Zimmermann, M. Boersch, M. Koenig, E. Schweinberger, S. Steigmiller, R. Reuter, S. Felekyan, V. Kudryavtsev, C. A. M. Seidel, P. Graeber, *Nat. Struct. Mol. Biol.* **2004**, *11*, 135 – 141.
[135] D. Rehm, A. Weller, *Isr. J. Chem.* **1970**, *8*, 259 – 271.
[136] R. A. Marcus, N. Sutin, *Biochim. Biophys. Acta* **1985**, *811*, 265 – 322.

 © 2005 Wiley-VCH Verlag GmbH & Co. KGaA, Weinheim

[137] K. Chattopadhyay, S. Saffarian, E. L. Elson, C. Frieden, *Proc. Natl. Acad. Sci. USA* **2002**, *99*, 14171 – 14176.
[138] R. M. Watt, E. W. Voss, Jr., *Immunochem.* **1977**, *14*, 533 – 551.
[139] N. Marme, J.-P. Knemeyer, M. Sauer, J. Wolfrum, *Bioconjugate Chem.* **2003**, *14*, 1133 – 1139.
[140] H. Yang, G. Luo, P. Karnchanaphanurach, T.-M. Louie, I. Rech, S. Cova, L. Xun, X. S. Xie, *Science* **2003**, *302*, 262 – 266.
[141] H. Neuweiler, M. Sauer, *Curr. Pharm. Biotechnol.* **2004**, *5*, 285 – 298.
[142] M. Sauer, K. T. Han, R. Müller, S. Nord, A. Schulz, S. Seeger, J. Wolfrum, J. Arden-Jacob, G. Deltau, N. J. Marx, C. Zander, K. H. Drexhage, *J. Fluoresc.* **1995**, *5*, 247 – 261.
[143] J. P. Knemeyer, N. Marme, M. Sauer, *Anal. Chem.* **2000**, *72*, 3717 – 3724.
[144] T. Heinlein, J.-P. Knemeyer, O. Piestert, M. Sauer, *J. Phys. Chem. B* **2003**, *107*, 7957 – 7964.
[145] A. C. Vaiana, H. Neuweiler, A. Schulz, J. Wolfrum, M. Sauer, J. C. Smith, *J. Am. Chem. Soc.* **2003**, *125*, 14564 – 14572.
[146] H. Neuweiler, A. Schulz, A. C. Vaiana, J. C. Smith, S. Kaul, J. Wolfrum, M. Sauer, *Angew. Chem.* **2002**, *114*, 4964 – 4968; *Angew. Chem. Int. Ed.* **2002**, *41*, 4769 – 4773.
[147] L. J. Lapidus, W. A. Eaton, J. Hofrichter, *Proc. Natl. Acad. Sci. USA* **2000**, *97*, 7220 – 7225.
[148] T. Soussi, *Immunol. Today* **1996**, *17*, 354 – 356.
[149] M. Sauer, *Angew. Chem.* **2003**, *115*, 1834 – 1837; *Angew. Chem. Int. Ed.* **2003**, *42*, 1790 – 1793.
[150] D. A. Van den Bout, W. T. Yip, D. H. Hu, D. K. Fu, T. M. Swager, P. F. Barbara, *Science* **1997**, *277*, 1074 – 1077.
[151] W. T. Yip, D. H. Hu, J. Yu, D. A. Van den Bout, P. F. Barbara, *J. Phys. Chem. A* **1998**, *102*, 7564 – 7575.
[152] T. Huser, M. Yan, L. J. Rothberg, *Proc. Natl. Acad. Sci. USA* **2000**, *97*, 11187 – 11191.
[153] J. D. White, J. H. Hsu, S. C. Yang, W. S. Fann, G. Y. Pern, S. A. Chen, *J. Chem. Phys.* **2001**, *114*, 3848 – 3852.
[154] M. A. Bopp, Y. W. Jia, L. Q. Li, R. J. Cogdell, R. M. Hochstrasser, *Proc. Natl. Acad. Sci. USA* **1997**, *94*, 10630 – 10635.
[155] M. A. Bopp, A. Sytnik, T. D. Howard, R. J. Cogdell, R. M. Hochstrasser, *Proc. Natl. Acad. Sci. USA* **1999**, *96*, 11271 – 11276.
[156] J. Hofkens, W. Schroeyers, D. Loos, M. Cotlet, F. Kohn, T. Vosch, M. Maus, A. Herrmann, K. Müllen, T. Gensch, F. C. De Schryver, *Spectrochim. Acta Part A* **2001**, *57*, 2093 – 2107.
[157] L. M. Ying, X. S. Xie, *J. Phys. Chem. B* **1998**, *102*, 10399 – 10409.
[158] B. Lounis, J. Deich, F. I. Rosell, S. G. Boxer, W. E. Moerner, *J. Phys. Chem. B* **2001**, *105*, 5048 – 5054.
[159] M. Cotlet, J. Hofkens, S. Habuchi, G. Dirix, M. Van Guyse, J. Michiels, J. Vanderleyden, F. C. De Schryver, *Proc. Natl. Acad. Sci. USA* **2001**, *98*, 14398 – 14403.
[160] M. F. Garcia-Parajo, M. Koopman, E. M. H. P. Van Dijk, V. Subramaniam, N. F. Van Hulst, *Proc. Natl. Acad. Sci. USA* **2001**, *98*, 14392 – 14397.
[161] T. Christ, F. Petzke, P. Bordat, A. Herrmann, E. Reuther, K. Mullen, T. Basche, *J. Lumin.* **2002**, *98*, 23 – 33.
[162] J. Hernando, M. van der Schaaf, E. M. H. P. van Dijk, M. Sauer, M. F. Garcia-Parajo, N. F. van Hulst, *J. Phys. Chem. A* **2003**, *107*, 43 – 52.
[163] P. Tinnefeld, V. Buschmann, K. D. Weston, M. Sauer, *J. Phys. Chem. A* **2003**, *107*, 323 – 327.
[164] J. Yu, D. H. Hu, P. F. Barbara, *Science* **2000**, *289*, 1327 – 1330.
[165] T. Gensch, J. Hofkens, A. Heirmann, K. Tsuda, W. Verheijen, T. Vosch, T. Christ, T. Basche, K. Müllen, F. C. De Schryver, *Angew. Chem.* **1999**, *111*, 3970 – 3974; *Angew. Chem. Int. Ed.* **1999**, *38*, 3752 – 3756.
[166] R. Gronheid, J. Hofkens, F. Kohn, T. Weil, E. Reuther, K. Müllen, F. C. De Schryver, *J. Am. Chem. Soc.* **2002**, *124*, 2418 – 2419.
[167] T. Basche, S. Kummer, C. Bräuchle, *Nature* **1995**, *373*, 132 – 134.
[168] J. Bernard, L. Fleury, H. Talon, M. Orrit, *J. Chem. Phys.* **1993**, *98*, 850 – 859.
[169] D. S. English, E. J. Harbron, P. F. Barbara, *J. Phys. Chem. A* **2000**, *104*, 9057 – 9061.
[170] C. G. Hübner, G. Zumofen, A. Renn, A. Herrmann, K. Müllen, T. Basche, *Phys. Rev. Lett.* **2003**, *91*, 093903/1 – 093903/4.
[171] J. Hofkens, M. Cotlet, T. Vosch, P. Tinnefeld, K. D. Weston, C. Ego, A. Grimsdale, K. Müllen, D. Beljonne, J. L. Bredas, S. Jordens, G. Schweitzer, M. Sauer, F. C. De Schryver, *Proc. Natl. Acad. Sci. USA* **2003**, *100*, 13146 – 13151.
[172] M. Lippitz, C. G. Hübner, T. Christ, H. Eichner, P. Bordat, A. Herrmann, K. Müllen, T. Basche, *Phys. Rev. Lett.* **2004**, *92*, 103001/1 – 103001/4.
[173] R. W. Wagner, J. S. Lindsey, *J. Am. Chem. Soc.* **1994**, *116*, 9759 – 9760.
[174] M. Heilemann, V. Buschmann, O. Piestert, P. Tinnefeld, K. D. Weston, M. Sauer, *Proc. SPIE-Int. Soc. Opt. Eng.* **2003**, *4962*, 38 – 46.
[175] M. Heilemann, P. Tinnefeld, G. Sanchez Mosteiro, M. F. Garcia Parajo, N. F. van Hulst, M. Sauer, *J. Am. Chem. Soc.* **2004**, *126*, 6514 – 6515.
[176] S. Vyawahare, S. Eyal, K. D. Mathews, S. R. Quake, *Nano Lett.* **2004**, *4*, 1035 – 1039.
[177] C. Bustamante, J. F. Marko, E. D. Siggia, S. Smith, *Science* **1994**, *265*, 1599 – 1600.
[178] G. Calzaferri, S. Huber, H. Maas, C. Minkowski, *Angew. Chem.* **2003**, *115*, 3860 – 3888; *Angew. Chem. Int. Ed.* **2003**, *42*, 3732 – 3758.
[179] M. Irie, T. Fukaminato, T. Sasaki, N. Tamai, T. Kawai, *Nature* **2002**, *420*, 759 – 760.
[180] D. L. Spector, *Annu. Rev. Cell Biol.* **1993**, *9*, 265 – 315.
[181] A. I. Lamond, W. C. Earnshaw, *Science* **1998**, *280*, 547 – 553.
[182] P. R. Cook, *Science* **1999**, *284*, 1790 – 1795.
[183] T. Cremer, C. Cremer, *Nat. Rev. Genet.* **2001**, *2*, 292 – 301.
[184] D. G. Wansink, O. C. Sibon, F. F. Cremers, R. van Driel, L. de Jong, *J. Cell Biol.* **1996**, *62*, 10 – 18.
[185] A. Pombo, D. A. Jackson, M. Hollinshead, Z. X. Wang, R. G. Roeder, P. R. Cook, *Embo J.* **1999**, *18*, 2241 – 2253.
[186] A. M. Femino, F. S. Fay, K. Fogarty, R. H. Singer, *Science* **1998**, *280*, 585 – 590.
[187] J. M. Levsky, S. M. Shenoy, R. C. Pezo, R. H. Singer, *Science* **2002**, *297*, 836 – 840.
[188] J. B. Lawrence, R. H. Singer, L. M. Marselle, *Cell* **1989**, *57*, 493 – 502.
[189] R. W. Dirks, *Histochem. Cell Biol.* **1996**, *106*, 151 – 166.
[190] R. W. Dirks, C. Molenaar, H. J. Tanke, *Histochem. Cell Biol.* **2001**, *115*, 3 – 11.
[191] J. Zhang, R. E. Campbell, A. Y. Ting, R. Y. Tsien, *Nat. Rev. Mol. Cell Biol.* **2002**, *3*, 906 – 918.
[192] A. R. Thierry, A. Dritschilo, *Nucleic Acids Res.* **1992**, *20*, 5691 – 5698.
[193] C. Zander, K. H. Drexhage, K. T. Han, J. Wolfrum, M. Sauer, *Chem. Phys. Lett.* **1998**, *286*, 457 – 465.
[194] W. Becker, H. Hickl, C. Zander, K. H. Drexhage, M. Sauer, S. Siebert, J. Wolfrum, *Rev. Sci. Instrum.* **1999**, *70*, 1835 – 1841.
[195] V. P. Torchilin, R. Rammohan, V. Weissig, T. S. Levchenko, *Proc. Natl. Acad. Sci. USA* **2001**, *98*, 8786 – 8791.
[196] S. R. Schwarze, A. Ho, A. Vocero-Akbani, S. F. Dowdy, *Science* **1999**, *285*, 1569 – 1572.
[197] E. Vives, P. Brodin, B. Lebleu, *J. Biol. Chem.* **1997**, *272*, 16010 – 16017.
[198] M. Rueping, Y. Mahajan, M. Sauer, D. Seebach, *ChemBioChem* **2002**, *3*, 257 – 259.
[199] D. Seebach, K. Namoto, Y. R. Mahajan, P. Bindschädler, R. Sustmann, M. Kirsch, N. S. Ryder, M. Weiss, M. Sauer, C. Roth,

S. Werner, H.-D. Beer, C. Munding, P. Walde, M. Voser, *Chem. Biodiversity* **2004**, *1*, 65 – 97.
[200] G. J. Schütz, V. P. Patuschenko, H. J. Gruber, H. G. Knaus, B. Pragl, H. Schindler, *Single Mol.* **2000**, *1*, 25 – 31.
[201] N. Marme, J. P. Knemeyer, J. Wolfrum, M. Sauer, *Angew. Chem.* **2004**, *116*, 3886 – 3890; *Angew. Chem. Int. Ed.* **2004**, *43*, 3798 – 3801.
[202] R. Y. Tsien, *Annu. Rev. Biochem.* **1998**, *67*, 509 – 544.
[203] G. S. Baird, D. A. Zacharias, R. Y. Tsien, *Proc. Natl. Acad. Sci. USA* **2000**, *97*, 11984 – 11989.
[204] S. L. Moores, J. H. Sabry, J. A. Spudich, *Proc. Natl. Acad. Sci. USA* **1996**, *93*, 443 – 446.
[205] K. R. Olson, J. R. McIntosh, J. B. Olmsted, *J. Cell Biol.* **1995**, *130*, 639 – 650.
[206] G. S. Harms, L. Cognet, P. H. M. Lommerse, G. A. Blab, T. Schmidt, *Biophys. J.* **2001**, *80*, 2396 – 2408.
[207] G. S. Harms, L. Cognet, P. H. M. Lommerse, G. A. Blab, H. Kahr, R. Gamsjäger, H. P. Spaink, N. M. Soldatov, C. Romanin, T. Schmidt, *Biophys. J.* **2001**, *81*, 2639 – 2646.
[208] R. Iino, A. Kusumi, *J. Fluoresc.* **2001**, *11*, 187 – 195.
[209] R. Iino, I. Koyama, A. Kusumi, *Biophys. J.* **2001**, *80*, 2667 – 2677.
[210] J. Widengren, B. Terry, R. Rigler, *Chem. Phys.* **1999**, *249*, 259 – 271.
[211] A. Zumbusch, G. Jung, *Single Mol.* **2000**, *1*, 261 – 270.
[212] M. Cotlet, J. Hofkens, M. Maus, T. Gensch, M. Van der Auweraer, J. Michiels, G. Dirix, M. Van Guyse, J. Vanderleyden, A. Visser, F. C. De Schryver, *J. Phys. Chem. B* **2001**, *105*, 4999 – 5006.
[213] M. V. Matz, A. F. Fradkov, Y. A. Labas, A. P. Savitsky, A. G. Zaraisky, M. L. Markelov, S. A. Lukyanov, *Nat. Biotechnol.* **1999**, *17*, 969 – 973.
[214] B. J. Bevis, B. S. Glick, *Nat. Biotechnol.* **2002**, *20*, 1159.
[215] J. Wiedenmann, A. Schenk, C. Rocker, A. Girod, K.-D. Spindler, G. U. Nienhaus, *Proc. Natl. Acad. Sci. USA* **2002**, *99*, 11646 – 11651.
[216] N. G. Gurskaya, A. F. Fradkov, A. Terskikh, M. V. Matz, Y. A. Labas, V. I. Martynov, Y. G. Yanushevich, K. A. Lukyanov, S. A. Lukyanov, *FEBS Lett.* **2001**, *507*, 16 – 20.
[217] R. E. Campbell, O. Tour, A. E. Palmer, P. A. Steinbach, G. S. Baird, D. A. Zacharias, R. Y. Tsien, *Proc. Natl. Acad. Sci. USA* **2002**, *99*, 7877 – 7882.
[218] C.-D. Hu, Y. Chinenov, T. K. Kerppola, *Mol. Cell* **2002**, *9*, 789 – 798.
[219] J. C. Politz, E. S. Browne, D. E. Wolf, T. Pederson, *Proc. Natl. Acad. Sci. USA* **1998**, *95*, 6043 – 6048.
[220] P. Schwille, F. J. Meyer-Almes, R. Rigler, *Biophys. J.* **1997**, *72*, 1878 – 1886.
[221] R. Brock, G. Vamosi, G. Vereb, T. M. Jovin, *Proc. Natl. Acad. Sci. USA* **1999**, *96*, 10123 – 10128.
[222] T. A. Byassee, W. C. Chan, S. Nie, *Anal. Chem.* **2000**, *72*, 5606 – 5611.
[223] T. Kues, A. Dickmanns, R. Luhrmann, R. Peters, U. Kubitscheck, *Proc. Natl. Acad. Sci. USA* **2001**, *98*, 12021 – 12026.
[224] T. Kues, R. Peters, U. Kubitscheck, *Biophys. J.* **2001**, *80*, 2954 – 2967.
[225] G. Seisenberger, M. U. Ried, T. Endreß, H. Büning, M. Hallek, C. Bräuchle, *Science* **2001**, *294*, 1929 – 1932.
[226] X. Zhuang, H. Kim, M. J. B. Pereira, H. P. Babcock, N. G. Walter, S. Chu, *Science* **2002**, *296*, 1473 – 1476.
[227] M. Bruchez, M. Moronne, P. Gin, S. Weiss, A. P. Alivisatos, *Science* **1998**, *281*, 2013 – 2016.
[228] M. Dahan, T. Laurence, F. Pinaud, D. S. Chemla, A. P. Alivisatos, M. Sauer, S. Weiss, *Opt. Lett.* **2001**, *26*, 825 – 827.
[229] W. C. W. Chan, S. M. Nie, *Science* **1998**, *281*, 2016 – 2018.
[230] B. Dubertret, P. Skourides, D. J. Norris, V. Noireaux, A. H. Brivanlou, A. Libchaber, *Science* **2002**, *298*, 1759 – 1762.
[231] J. K. Jaiswal, H. Mattoussi, J. M. Mauro, S. M. Simon, *Nat. Biotechnol.* **2003**, *21*, 47 – 51.
[232] B. M. Lingerfelt, H. Mattoussi, E. R. Goldman, J. M. Mauro, G. P. Anderson, *Anal. Chem.* **2003**, *75*, 4043 – 4049.
[233] E. R. Goldman, E. D. Balighian, H. Mattoussi, M. K. Kuno, J. M. Mauro, P. T. Tran, G. P. Anderson, *J. Am. Chem. Soc.* **2002**, *124*, 6378 – 6382.
[234] H. Mattoussi, J. M. Mauro, E. R. Goldman, G. P. Anderson, V. C. Sundar, F. V. Mikulec, M. G. Bawendi, *J. Am. Chem. Soc.* **2000**, *122*, 12142 – 12150.
[235] X. Wu, H. Liu, J. Liu, K. N. Haley, J. A. Treadway, J. P. Larson, N. Ge, F. Peale, M. P. Bruchez, *Nat. Biotechnol.* **2003**, *21*, 41 – 46.
[236] D. R. Larson, W. R. Zipfel, R. M. Williams, S. W. Clark, M. P. Bruchez, F. W. Wise, W. W. Webb, *Science* **2003**, *300*, 1434 – 1437.
[237] F. Pinaud, D. King, X. Michalet, S. Doose, S. Weiss, *Eur. Biophys. J.* **2003**, *32*, 261.
[238] M. Dahan, S. Levi, C. Luccardini, P. Rostaing, B. Riveau, A. Triller, *Science* **2003**, *302*, 442 – 445.
[239] M. Nirmal, B. O. Dabbousi, M. G. Bawendi, J. J. Macklin, J. K. Trautman, T. D. Harris, L. E. Brus, *Nature* **1996**, *383*, 802 – 804.
[240] M. Kuno, D. P. Fromm, H. F. Hamann, A. Gallagher, D. J. Nesbitt, *J. Chem. Phys.* **2000**, *112*, 3117 – 3120.
[241] M. Kuno, D. P. Fromm, H. F. Hamann, A. Gallagher, D. J. Nesbitt, *J. Chem. Phys.* **2001**, *115*, 1028 – 1040.
[242] S. Hohng, T. Ha, *J. Am. Chem. Soc.* **2004**, *126*, 1324 – 1325.
[243] S. R. Cordero, P. J. Carson, R. A. Estabrook, G. F. Strouse, S. K. Buratto, *J. Phys. Chem. B* **2000**, *104*, 12137 – 12142.
[244] W. J. Parak, R. Boudreau, M. Le Gros, D. Gerion, D. Zanchet, C. M. Micheel, S. C. Williams, A. P. Alivisatos, C. Larabell, *Adv. Mater.* **2002**, *14*, 882 – 885.
[245] I. Sase, H. Miyata, J. E. T. Corrie, J. S. Craik, K. Kinosita, *Biophys. J.* **1995**, *69*, 323 – 328.
[246] T. Schmidt, G. J. Schütz, W. Baumgartner, H. J. Gruber, H. Schindler, *J. Phys. Chem.* **1995**, *99*, 17662 – 17668.
[247] T. Schmidt, G. J. Schütz, W. Baumgartner, H. J. Gruber, H. Schindler, *Proc. Natl. Acad. Sci. USA* **1996**, *93*, 2926 – 2929.
[248] R. M. Dickson, D. J. Norris, Y. L. Tzeng, W. E. Moerner, *Science* **1996**, *274*, 966 – 969.
[249] M. P. Gordon, T. Ha, P. R. Selvin, *Proc. Natl. Acad. Sci. USA* **2004**, *101*, 6462 – 6465.
[250] A. Patwardhan, E. M. M. Manders, *Bioimaging* **1996**, *4*, 17 – 24.
[251] A. Esa, P. Edelmann, G. Kreth, L. Trakhtenbrot, N. Amariglio, G. Rechavi, M. Hausmann, C. Cremer, *J. Microsc.* **2000**, *199*, 96 – 105.
[252] A. M. van Oijen, J. Köhler, J. Schmidt, M. Müller, G. J. Brakenhoff, *Chem. Phys. Lett.* **1998**, *292*, 183 – 187.
[253] T. D. Lacoste, X. Michalet, F. Pinaud, D. S. Chemla, A. P. Alivisatos, S. Weiss, *Proc. Natl. Acad. Sci. USA* **2000**, *97*, 9461 – 9466.
[254] X. Michalet, T. D. Lacoste, S. Weiss, *Methods* **2001**, *25*, 87 – 102.
[255] E. Betzig, *Opt. Lett.* **1995**, *20*, 237 – 239.
[256] C. Zander, M. Sauer, K. H. Drexhage, D. S. Ko, A. Schulz, J. Wolfrum, L. Brand, C. Eggeling, C. A. M. Seidel, *Appl. Phys. B* **1996**, *63*, 517 – 523.
[257] M. Heilemann, D. P. Herten, R. Heintzmann, C. Cremer, C. Müller, P. Tinnefeld, K. D. Weston, J. Wolfrum, M. Sauer, *Anal. Chem.* **2002**, *74*, 3511 – 3517.
[258] S. Hell, E. H. K. Stelzer, *J. Opt. Soc. Am.* **1992**, *9*, 2159 – 2166.
[259] A. Egner, S. Jakobs, S. W. Hell, *Proc. Natl. Acad. Sci. USA* **2002**, *99*, 3370 – 3375.
[260] T. Enderle, T. Ha, D. F. Ogletree, D. S. Chemla, C. Magowan, S. Weiss, *Proc. Natl. Acad. Sci. USA* **1997**, *94*, 520 – 525.
[261] H. Gersen, M. F. Garcia-Parajo, L. Novotny, J. A. Veerman, L. Kuipers, N. F. van Hulst, *Phys. Rev. Lett.* **2000**, *85*, 5312 – 5315.

 © 2005 Wiley-VCH Verlag GmbH & Co. KGaA, Weinheim

[262] P. T. So, H. S. Kwon, C. Y. Dong, *J. Opt. Soc. Am. A* **2001**, *18*, 2833 – 2845.
[263] B. Albrecht, A. V. Failla, R. Heintzmann, C. Cremer, *J. Biomed. Opt.* **2001**, *6*, 292 – 299.
[264] V. Failla Antonio, U. Spoeri, B. Albrecht, A. Kroll, C. Cremer, *Appl. Opt.* **2002**, *41*, 7275 – 7283.
[265] C. Hettich, C. Schmitt, J. Zitzmann, S. Kuehn, I. Gerhardt, V. Sandoghdar, *Science* **2002**, *298*, 385 – 389.
[266] T. A. Klar, S. Jakobs, M. Dyba, A. Egner, S. W. Hell, *Proc. Natl. Acad. Sci. USA* **2000**, *97*, 8206 – 8210.
[267] V. Westphal, C. M. Blanca, M. Dyba, L. Kastrup, S. W. Hell, *Appl. Phys. Lett.* **2003**, *82*, 3125 – 3127.
[268] S. W. Hell, *Nat. Biotechnol.* **2003**, *21*, 1347 – 1355.
[269] M. Dyba, S. Jakobs, S. W. Hell, *Nat. Biotechnol.* **2003**, *21*, 1303 – 1304.
[270] V. Westphal, L. Kastrup, S. W. Hell, *Appl. Phys. B* **2003**, *77*, 377 – 380.
[271] Z. Zhu, J. Chao, H. Yu, A. S. Waggoner, *Nucleic Acids Res.* **1994**, *22*, 3418 – 3422.
[272] H. Yu, J. Chao, D. Patek, R. Mujumdar, S. Mujumdar, A. S. Waggoner, *Nucleic Acids Res.* **1994**, *22*, 3226 – 3232.
[273] S. Brakmann, P. Nieckchen, *ChemBioChem* **2001**, *2*, 773 – 777.
[274] S. Brakmann, S. Lobermann, *Angew. Chem. 2002*, *114*, 3350 – 3352; *Angew. Chem. Int. Ed.* **2002**, *41*, 3215 – 3217.
[275] S. Brakmann, S. Lobermann, *Angew. Chem.* **2001**, *113*, 1473 – 1476; *Angew. Chem. Int. Ed.* **2001**, *40*, 1427 – 1429.
[276] M. Orrit, *Science* **2003**, *302*, 239 – 240.
[277] C. D. Snow, H. Nguyen, V. S. Pande, M. Gruebele, *Nature* **2002**, *420*, 102 – 106.
[278] L. Edman, Z. Foldes-Papp, S. Wennmalm, R. Rigler, *Chem. Phys.* **1999**, *247*, 11 – 22.
[279] L. Edman, R. Rigler, *Proc. Natl. Acad. Sci. USA* **2000**, *97*, 8266 – 8271.
[280] A. N. Kapanidis, N. K. Lee, T. A. Laurence, S. Doose, E. Margeat, S. Weiss, *Proc. Natl. Acad. Sci. USA* **2004**, *101*, 8936 – 8941.
[281] P. K. Hansma, B. Drake, O. Marti, S. A. Gould, C. B. Prater, *Science* **1989**, *243*, 641 – 643.
[282] Y. E. Korchev, C. L. Bashford, M. Milovanovic, I. Vodyanoy, M. J. Lab, *Biophys. J.* **1997**, *73*, 653 – 658.
[283] Y. E. Korchev, M. Raval, M. J. Lab, J. Gorelik, C. R. W. Edwards, T. Rayment, D. Klenerman, *Biophys. J.* **2000**, *78*, 2675 – 2679.
[284] M. Ueda, Y. Sako, T. Tanaka, P. Devreotes, T. Yanagida, *Science* **2001**, *294*, 864 – 867.
[285] Y. E. Korchev, Y. A. Negulyaev, C. R. W. Edwards, I. Vodyanoy, M. J. Lab, *Nat. Cell Biol.* **2000**, *2*, 616 – 619.
[286] A. Sonnleitner, L. M. Mannuzzu, S. Terakawa, E. Y. Isacoff, *Proc. Natl. Acad. Sci. USA* **2002**, *99*, 12759 – 12764.
[287] G. S. Harms, G. Orr, M. Montal, B. D. Thrall, S. D. Colson, H. P. Lu, *Biophys. J.* **2003**, *85*, 1826 – 1838.
[288] T. Ide, Y. Takeuchi, T. Yanagida, *Single Mol.* **2002**, *3*, 33 – 42.
[289] C. Brunel, B. Lounis, P. Tamarat, M. Orrit, *Phys. Rev. Lett.* **1999**, *83*, 2722 – 2725.
[290] M. Lewinska, C. Seitz, A. Skerra, F. P. Schmidtchen, *Bioconjugate Chem.* **2004**, *15*, 231 – 234.
[291] A. Ashkin, J. M. Dziedzic, J. E. Bjorkholm, S. Chu, *Opt. Lett.* **1986**, *11*, 288 – 290.
[292] K. Kneipp, A. S. Haka, H. Kneipp, K. Badizadegan, N. Yoshizawa, C. Boone, K. E. Shafer-Peltier, J. T. Motz, R. R. Dasari, M. S. Feld, *Appl. Spectrosc.* **2002**, *56*, 150 – 154.
[293] M. Gu, D. Morrish, *J. Appl. Phys.* **2002**, *91*, 1606 – 1612.
[294] K. Svoboda, S. M. Block, *Annu. Rev. Biophys. Biomol. Struct.* **1994**, *23*, 247 – 285.
[295] K. C. Neuman, E. H. Chadd, G. F. Liou, K. Bergman, S. M. Block, *Biophys. J.* **1999**, *77*, 2856 – 2863.
[296] H. Kuhn, *J. Chem. Phys.* **1970**, *53*, 101 – 108.
[297] H. Imahori, H. Norieda, Y. Nishimura, I. Yamazaki, K. Higuchi, N. Kato, T. Motohiro, H. Yamada, K. Tamaki, M. Arimura, Y. Sakata, *J. Phys. Chem. B* **2000**, *104*, 1253 – 1260.
[298] H. Yokota, K. Saito, T. Yanagida, *Phys. Rev. Lett.* **1998**, *80*, 4606 – 4609.
[299] G. V. Soni, F. M. Hameed, T. Roopa, G. V. Shivashankar, *Curr. Sci.* **2002**, *83*, 1464 – 1470.
[300] M. J. Lang, P. M. Fordyce, S. M. Block, *J. Biol.* **2003**, *2*:6.
[301] H. Rubinsztein-Dunlop, T. A. Nieminen, M. E. J. Friese, N. R. Heckenberg, *Adv. Quantum Chem.* **1998**, *30*, 469 – 492.
[302] T. A. Laurence, S. Weiss, *Science* **2003**, *299*, 667 – 668.
[303] B. Okumus, T. J. Wilson, D. M. J. Lilley, T. Ha, *Biophys. J.* **2004**, *87*, 2798 – 2806.
[304] J. Groll, E. V. Amirgoulova, T. Ameringer, C. D. Heyes, C. Röcker, G. U. Nienhaus, M. Möller, *J. Am. Chem. Soc.* **2004**, *126*, 4234 – 4239.
[305] S. C. Blanchard, H. D. Kim, R. L. Gonzalez, Jr., J. D. Puglisi, S. Chu, *Proc. Natl. Acad. Sci. USA* **2004**, *101*, 12893 – 12898.
[306] S. C. Blanchard, R. L. Gonzalez, H. D. Kim, S. Chu, J. D. Puglisi, *Nat. Struct. Mol. Biol.* **2004**, *11*, 1008 – 1014.
[307] D. Rueda, G. Bokinsky, M. M. Rhodes, M. J. Rust, X. Zhuang, N. G. Walter, *Proc. Natl. Acad. Sci. USA* **2004**, *101*, 10066 – 10071.
[308] S. Hohng, C. Joo, T. Ha, *Biophys. J.* **2004**, *87*, 1328 – 1337.
[309] P. Tinnefeld, M. Heilemann, M. Sauer, *ChemPhysChem* **2005**, *6*, 217 – 222.
[310] J. P. Clamme, A. A. Deniz, *ChemPhysChem* **2004**, *5*, 1 – 4.
[311] P. Tinnefeld, J. Hofkens, D.-P. Herten, S. Masuo, T. Vosch, M. Cotlet, S. Habuchi, K. Müllen, F. C. De Schryver, M. Sauer, *ChemPhysChem* **2004**, *5*, 1786 – 1790.
[312] S. Masuo, T. Vosch, M. Cotlet, P. Tinnefeld, S. Habuchi, T. D. M. Bell, I. Oesterling, D. Beljonne, B. Champagne, K. Müllen, M. Sauer, J. Hofkens, F. C. De Schryver, *J. Phys. Chem. B* **2004**, *108*, 16686 – 16696.
[313] J. Hernando, J. P. Hoogenboom, E. M. H. P. van Dijk, J. J. Garcia-Lopez, M. Crego-Calama, D. N. Reinhoudt, N. F. van - Hulst, M. F. Garcia-Parajo, *Phys. Rev. Lett.* **2004**, *93*, 236404.
[314] F. Schindler, J. M. Lupton, J. Feldmann, U. Scherf, *Proc. Natl. Acad. Sci. USA* **2004**, *101*, 14695 – 14700.
[315] H. Murakoshi, R. Iino, T. Kobayashi, T. Fujiwara, C. Ohshima, A. Yoshimura, A. Kusumi, *Proc. Natl. Acad. Sci. USA* **2004**, *101*, 7317 – 7322.
[316] R. J. Ober, C. Martinez, X. Lai, J. Zhou, E. S. Ward, *Proc. Natl. Acad. Sci. USA* **2004**, *101*, 11076 – 11081.
[317] W. Yang, J. Gelles, S. M. Musser, *Proc. Natl. Acad. Sci. USA* **2004**, *101*, 12887 – 12892.
[318] K. Velonia, O. Flomenbom, D. Loos, S. Masuo, M. Cotlet, Y. Engelborghs, J. Hofkens, A. E. Rowan, J. Klafter, R. J. M. Nolte, F. C. de Schryver, *Angew. Chem.* **2005**, *117*, 566 – 570; *Angew. Chem. Int. Ed.* **2005**, *44*, 560 – 564.
[319] O. Flomenbom, K. Velonia, D. Loos, S. Masui, M. Cotlet, Y. Engelborghs, J. Hofkens, A. E. Rowan, R. J. M. Nolte, M. Van der Auweraer, F. C. de Schryver, J. Klafter, *Proc. Natl. Acad. Sci. USA* **2005**, *102*, ASAP.
[320] G. Harms, G. Orr, H. P. Lu, *Appl. Phys. Lett.* **2004**, *84*, 1792 – 1794.
[321] A. Sarkar, R. B. Robertson, J. M. Fernandez, *Proc. Natl. Acad. Sci. USA* **2004**, *101*, 12882 – 12886.
[322] A. M. Derfus, W. C. W. Chan, S. N. Bhatia, *Nano Lett.* **2004**, *4*, 11 – 18.
[323] C. Kirchner, T. Liedl, S. Kudera, T. Pellegrino, A. M. Javier, H. E. Gaub, S. Stoelzle, N. Fertig, W. J. Parak, *Nano Lett.* **2005**, *5*, 331 – 338.
[324] X. Michalet, F. F. Pinaud, L. A. Bentolila, J. M. Tsay, S. Doose, J. J. Li, G. Sundaresan, A. M. Wu, S. S. Gambhir, S. Weiss, *Science* **2005**, *307*, 538 – 544.

 © 2005 Wiley-VCH Verlag GmbH & Co. KGaA, Weinheim

[325] B. C. Lagerholm, M. Wang, L. A. Ernst, D. H. Ly, H. Liu, M. P. Bruchez, A. S. Waggoner, *Nano Lett.* **2004**, *4*, 2019 – 2022.
[326] A. M. Derfus, W. C. W. Chan, S. N. Bhatia, *Adv. Mater.* **2004**, *16*, 961 – 966.
[327] X. Qu, D. Wu, L. Mets, N. F. Scherer, *Proc. Natl. Acad. Sci. USA* **2004**, *101*, 11298 – 11303.
[328] T. Heinlein, A. Biebricher, P. Schlüter, C. Roth, D. P. Herten, J. Wolfrum, M. Heilemann, C. Müller, P. Tinnefeld, M. Sauer; unpublished results.
[329] E. Y. Chan, N. M. Goncalves, R. A. Haeusler, A. J. Hatch, J. W. Larson, A. M. Maletta, G. R. Yantz, E. D. Carstea, M. Fuchs, G. G. Wong, S. R. Gullans, R. Gilmanshin, *Genome Res.* **2004**, *14*, 1137 – 1146.
[330] L. Kastrup, S. W. Hell, *Angew. Chem.* **2004**, *116*, 6814 – 6818; *Angew. Chem. Int. Ed.* **2004**, *43*, 6646 – 6649.
[331] S. W. Hell, *Phys. Lett. A* **2004**, *326*, 140 – 145.
[332] S. W. Hell, M. Dyba, S. Jakobs, *Curr. Opin. Neurobiol.* **2004**, *14*, 599 – 609.
[333] L. S. Churchman, Z. Okten, R. S. Rock, J. F. Dawson, J. A. Spudich, *Proc. Natl. Acad. Sci. USA* **2005**, *102*, 1419 – 1423.

 © 2005 Wiley-VCH Verlag GmbH & Co. KGaA, Weinheim

Thermodynamics

Supercritical Water as a Solvent

Hermann Weingärtner and Ernst Ulrich Franck*

Keywords:
aqueous solutions · solvent properties · supercritical fluids · thermophysical properties · water

Angewandte Chemie

 © 2005 Wiley-VCH Verlag GmbH & Co. KGaA, Weinheim DOI: 10.1002/anie.200462468

Water is not restricted to moderate temperatures and low pressures, but can exist up to very high temperatures, far above its critical point at 647 K. In this supercritical regime, water can be gradually compressed from gas-like to liquid-like densities. The resulting dense supercritical states have extraordinary properties which can be tuned by temperature and pressure, and form the basis for innovative technologies. This Review covers the current knowledge of the major properties of supercritical water and its solutions with nonpolar, polar, and ionic compounds, and of the underlying molecular processes.

From the Contents

1. Introduction 2673
2. Supercritical Water 2674
3. Aqueous Mixtures with Nonpolar Compounds 2680
4. Aqueous Solutions of Electrolytes 2685
5. Conclusions 2689

1. Introduction

Water, in many respects, shows unique properties that are well characterized at ordinary conditions. Water can also exist, and has been investigated, at states far above its critical temperature of 647 K, where it can be gradually compressed from gas-like to liquid-like densities. The resulting dense supercritical states possess remarkable properties which differ largely from those at normal conditions.[1,2] Adopting a term from geochemistry, such supercritical, aqueous systems are often denoted as hydrothermal fluids.

Investigations of density variations are the key to understanding fluid behavior because such experiments allow the temperature dependence of the fluid properties to be separated from their volume dependence.[2] To achieve substantial density variations, pressures up to several hundred MPa are required. For example, for water at 773 K, a pressure of 1 GPa is needed to generate the ordinary liquid density of 1 $g\,cm^{-3}$. Under such conditions it is likely that water will corrode the vessels. Experiments must therefore contend with conditions of high temperature, high pressure, and high water corrosivity.

Under the conditions of interest, the molecular and electronic structures of most substances are not appreciably deformed, however, hydrogen bonds are highly sensitive to temperature and pressure. For example, the increase in the electrical conductance of fluid water at high temperatures and pressures indicates a transition from molecular to ionic states.[3,4] Moreover, it has long been suggested that by strong compression, the double-well potential of the hydrogen bond should degenerate into a single-well potential.[5] Recently, a high-pressure phase of ice with symmetrical hydrogen bonds has indeed been discovered.[6]

In many chemical and engineering applications supercritical water acts as a solvent or working fluid.[1] For example, in steam power plants, the liquid phase may extend up to more than 600 K, and superheated vapor can reach temperatures up to more than 900 K. Other applications include, gas and oil recovery, hydrothermal crystal growth, and high-temperature electrochemistry.[1] The exceptional properties of supercritical water also form major motives for searching for industrial utilization of it as an ecologically benign solvent in chemical reactions.[7] By tuning temperature and pressure, states can be achieved in which water becomes completely miscible with nonpolar compounds, while polar and ionic compounds remain highly soluble as well. In addition, the viscosity remains low, even at liquid-like densities, which enhances mass transfer and diffusion-controlled chemical reactions. There are many interesting reactions, such as the oxidation, pyrolysis, and hydrolysis of organic compounds, where supercritical water acts as a solvent or reactant or catalyst.[7]

Perhaps the most fascinating application is the destructive oxidation of organic waste in the supercritical water oxidation (SCWO) process.[8] At some conditions, organic waste, for example polychlorinated biphenyl compounds, is highly miscible with water. In the presence of oxygen, such compounds react to carbon dioxide, water, and some other small molecules. By careful choice of temperature and pressure, partial oxidation of organic molecules, for example of methane to methanol, can be achieved as well.[9] Because the dielectric constant increases with water density, high pressure favors the formation of polar over nonpolar oxidation products.

A phenomenon with considerable prospects is the production of combustion flames in a supercritical environment. Figure 1 shows a "hydrothermal" flame burning in a homogenous mixture of water and methane to which oxygen is injected from a nozzle.[8a] In this aqueous environment, spontaneous flame ignition occurs at 673 K, markedly below that of gaseous oxygen and methane mixtures. Such flames can burn for 30 min or even longer, and have been spectroscopically investigated[10] and modeled.[11]

Another field of major interest is geochemistry,[12,13] where supercritical water acts as a solvent for hydrothermal reactions, such as mineral formation, deposition, or dissolu-

[*] Prof. Dr. H. Weingärtner
Physikalische Chemie II
Ruhr-Universität Bochum
44780 Bochum (Germany)
Fax: (+49) 234-321-4293
E-mail: hermann.weingaertner@ruhr-uni-bochum.de
Prof. Dr. Dr. h.c. E. U. Franck[+]
Institut für Physikalische Chemie
Universität Karlsruhe
76128 Karlsruhe (Germany)
[+] Deceased

 DOI: 10.1002/anie.200462468 © 2005 Wiley-VCH Verlag GmbH & Co. KGaA, Weinheim

Figure 1. "Hydrothermal" flame, burning in a homogeneous supercritical aqueous mixture of 70 mol% water and 30 mol% methane at 100 MPa pressure and 713 K environmental temperature, observed through the sapphire windows of a high-pressure vessel.[8a] Oxygen is injected from below through a nozzle at a rate of 3 $mm^3 s^{-1}$. The height of the flame is about 3 mm. The "gas funnel" around and above the flame shows the upward flow of reaction products at higher temperatures and lower density, which generate a Schlieren contrast. There is no phase separation.

tion in the Earth's mantle. Water also participates in the formation of methane and heavier hydrocarbons of natural petroleum. Pressure increases in the Earth's mantle by about 1 GPa for every 30 km of depth, so geothermal brines typically have pressures above 100 MPa and temperatures above 500 K. Water at even more extreme conditions is present in the outer planets Neptune and Uranus, which contain a thick layer of "hot ices" between the outer atmosphere and the core.[14] In the laboratory, such conditions were mimicked in shock waves to pressures 180 GPa and 10000 K,[3] where the water density is 4 $g cm^{-3}$, that is, four times the normal liquid density.

In recent years, there has been great progress in the characterization of the properties of supercritical water and aqueous solutions, and the number of applications has rapidly increased. New experimental techniques now push the limits to extreme conditions of temperature and pressure, increase the experimental accuracy, and provide access to bulk and molecular properties previously not available. Theory and computer simulations greatly improve the understanding of these properties at the molecular level.

This Review covers these developments which are at the root of modern supercritical water technologies. To keep the Review manageable, we primarily focus on dense states with high solute concentrations, such as encountered in many chemical reactions in nature, the laboratory, and applications. In the literature, the main emphasis is on dilute aqueous solutions at moderate densities around 0.3 $g cm^{-3}$ which is near the critical point of pure water.[1] The solvent properties of dense supercritical water were first reviewed in 1961,[15] when the field was in its very infancy. The latter review may be consulted for the historical background.

2. Supercritical Water

2.1. Phase Diagram

Figure 2 shows the phase diagram of water in the temperature–density (T,ρ) plane. Isobars indicate the pressures. At

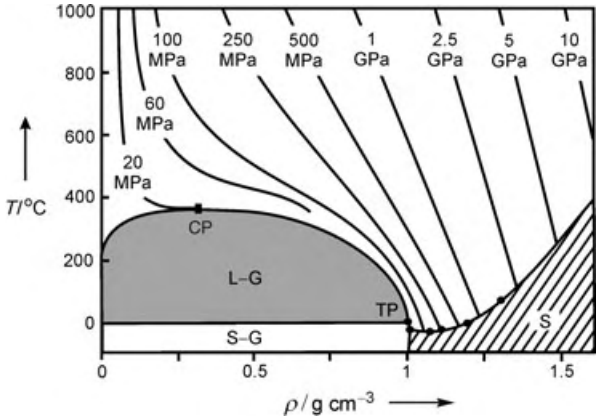

Figure 2. Temperature–density diagram of water with isobars.[23,24] Solid circles mark breaks in the melting line which arise from to phase transitions between the ice polymorphs. TP indicates the S–L–G triple point at 273.15 K. CP indicates the L–G critical point.

Ernst Ulrich Franck was born in 1920 in Hamburg. He received his doctoral degree in 1950 for work performed in the group of A. Eucken in Göttingen about transport phenomena in gases. Initiated by this work, and in contact with mineralogists at the University of Göttingen, above all with C. W. Correns, he established his research subject, the study of supercritical fluids. After his "Habilitation" in 1956 he spent a research fellowship at Oak Ridge. In 1961 he was appointed to the chair of Physical Chemistry at the University of Karlsruhe, where he stayed until his retirement in 1988, interrupted by many visiting fellowships. He received many scientific awards and was a member of several scientific academies. Ernst Ulrich Franck died on December 21, 2004, an obituary was published in ref [121].

Hermann Weingärtner was born in 1948 in Offenburg. He received his doctorate in 1976 for work carried out in the group of H. G. Hertz in Karlsruhe on nuclear magnetic resonance in electrolyte solutions. After his "Habilitation" in 1986 and after several research fellowships, among others at the Australian National University in Canberra, he was appointed, in 1995, to a professorship for Physical Chemistry at the Ruhr-University of Bochum. His major scientific activities are in the field of thermophysical properties and phase transitions of fluids.

 © 2005 Wiley-VCH Verlag GmbH & Co. KGaA, Weinheim

298 K, liquid water with a density of 0.997 $g\,cm^{-3}$ coexists with water vapor with a density of 2×10^{-5} $g\,cm^{-3}$. With increasing temperature, the density of the liquid decreases and that of the vapor increases. At the critical point both phases become identical and the dividing meniscus disappears. The critical temperature (T_c), pressure (P_c), and density (ρ_c) are:[16] $T_c=$ 647.1 K, $P_c=22.1$ MPa, $\rho_c=0.322$ $g\,cm^{-3}$. Applications typically use range from the critical density to liquid-like densities of about 1 $g\,cm^{-3}$.

The fluid range is encompassed by the melting line. Breaks in the melting line indicate transitions between several solid polymorphs of ice. Starting from the solid–liquid–gas (S–L–G) triple point at 273.15 K, where conventional ice I_h is stable, the melting line initially decreases (S, L, and G denote the solid, liquid, and gaseous phases, respectively). At 251 K and 220 MPa a new phase of ice (ice III) occurs, and the melting line turns to higher temperatures. There follow other polymorphs, the ices IV, V, and VI, until at 354.8 K and 2.17 GPa ice VII is formed. Ice VII is the only experimentally observed polymorph at equilibrium with supercritical water.

The observation of such high-pressure, high-temperature phase transitions is highly difficult. Great experimental progress has been achieved by the development of diamond anvil cells.[17] As schematically sketched in Figure 3, a small

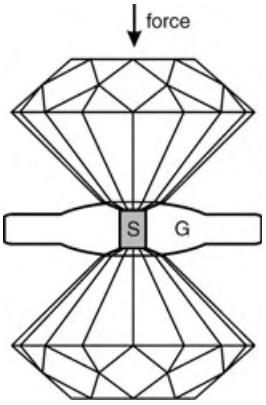

Figure 3. Schematic representation of the diamond anvil cell. The sample (S) in the gasket (G) is compressed by the flat-polished opposite faces of two diamonds.

amount of sample is held in a metal gasket between the flat-polished faces of two diamonds. The small volume of the sample enables very high pressures to be generated. Diamonds are transparent in the optical regime, thus allowing visual observation of the phase transitions. They are also transparent in many other spectral regions that are exploited by spectroscopic and scattering experiments. The pressure is usually determined by changes in the fluorescence spectrum of an added ruby. Recently, Loubeyre and co-workers[18] have exploited such techniques to monitor the course of the melting line of ice VII towards high temperatures. At the highest temperature reached, 751.5 K, the melting pressure is 13.1 GPa. Current data collections, such as the widely used Steam Tables,[19] still quote melting pressures obtained in from earlier work,[20] which, in part, are almost twice as high as those observed by Loubeyre and co-workers.

The continuation of the melting line to higher temperatures is of great interest in the geochemical sciences, but extrapolations are speculative because new solid phases (ice modifications) might occur. To some extent, experimentally inaccessible states of water can be explored by molecular dynamics (MD) simulations, in particular, if quantum-mechanical (ab initio) approaches are used. Ab initio MD simulations[21] indeed predict a further solid polymorph at coexistence with fluid water. In this "superionic" phase the proton jumps between the two equivalent positions along the O–O axis. By such simulations, the melting line was considered up to conditions in the interior of Neptune, and suggested that regime of "hot ices" in Neptune's interior is fluid rather than solid.[21]

2.2. P,V,T *Behavior*

Accurate pressure (P), volume (V), and temperature (T) data are not only of interest in itself, but also form a prerequisite for other studies because experiments are usually performed at given pressure and temperature, while they are easier understood as a function of volume and temperature. At moderate pressure, P,V,T data can be measured by static experiments, in which water is introduced into a pressure vessel, and the volume of water is determined at given temperature and pressure. Many years ago, Burnham et al.[22] and Franck and co-workers[23] pushed such experiments to 1273 K and 1 GPa, which forms the experimental limit of such techniques. It is believed that the uncertainties in the density values measured does not exceed 0.5%, but as P,V,T data enter into many analyses of other data, such a high accuracy is mandatory.

P,V,T data beyond these limits were derived from dynamic experiments using shock-wave techniques. Denoting the state prior to release of the shock wave by index "0", shocked states obey the Hugoniot relation for the internal energy U [Eq. (1)].

$$U-U_0=(P-P_0)(V-V_0)/2 \qquad (1)$$

Thermodynamic assumptions can be used to transcribe the measured U,P,V data into P,V,T data. More accurate temperature measurements can be made from the emission spectrum of the probe as determined by pyrometry. In this way, Nellis and co-workers determined P,V,T data up to 80 GPa and 5200 K.[24]

The regime between the static and dynamic data, typically between 1 and 10 GPa, is of great interest in geochemistry. Efforts are currently being made to bridge this gap by new experimental techniques. Diamond anvil cells are suited to generate these pressures, but do not provide direct volume information. Recently, P,V,T data up to 5 GPa and 673 K[25] could, however, be deduced indirectly from measurements of the speed of sound. Another remarkable method uses synthetic fluid inclusions, which are hydrothermally generated in healing fractures of quartz or corundum. After quenching to low temperature, the inclusions retain the properties of the fluid before trapping. By this technique,

 © 2005 Wiley-VCH Verlag GmbH & Co. KGaA, Weinheim

P,V,T data have been determined to 1873 K and 8 GPa.[26] There remain discrepancies among these various data sets, so that the *P,V,T* relation above 1 GPa is still uncertain.

2.3. Equations of State

The *P,V,T* surface of fluids is usually described by a pressure-explicit thermal equation of state $P(V,T)$. An appropriate theory would predict phase equilibria, *P,V,T* behavior, and other thermodynamic properties in the homogenous regime from a few physically significant input parameters. At present, no molecular-based equation of state fits these criteria.

In principle, simulations by Monte Carlo (MC) and molecular dynamics (MD) techniques can provide molecular-based equations of state, but are not yet accurate enough for applications. Moreover, there are considerable difficulties in simulations of supercritical water, because the success of simulations largely relies on the knowledge the intermolecular interaction potentials.[27] For water, a large number of model potentials have been suggested and parameterized with regard to properties at ordinary conditions. The parameterization depends however on temperature and pressure, and the experience gained at ordinary conditions cannot easily be transferred to supercritical states.[27] Moreover, in some cases, the subtleties of hydrogen-bonding may require ab initio MD simulations.[21]

Formulations of *P,V,T* behavior suited for applications rely on empirical or semi-empirical approaches, often with a large number of regressed parameters. The very properties that make supercritical fluids so useful, that is, the transition from gas-like to liquid-like behavior, render modeling efforts to be difficult. Because of their simplicity many workers prefer semi-empirical, "cubic" equations, which usually form descendents of the popular equations of van der Waals or Redlich and Kwong.[28] In addition, such cubic equations usually involve parameters of some physical significance, which facilitates data extrapolations. Many equations along these lines have been proposed for fluids in general,[1,28] but are often difficult to apply for supercritical water. For example, at very high pressures water remains much more compressible than can be captured by the typical repulsive terms in semi-empirical equations.[29] In addition, the non-analytical nature of some properties discussed in Section 2.4 largely complicates the design of accurate equations of state near critical points.

Increasing computer power now allows more general approaches, which comprise all kinds of thermodynamic data in a single equation for the Helmholtz energy $A(T,V)$ as a function of temperature and volume. Thermodynamic properties, including the *P,V,T* relation, then follow from partial derivatives of $A(T,V)$. The "International Association for the Properties of Water and Steam" (IAPWS), which coordinates research on thermophysical properties of water, recommends for accurate calculations an empirical equation by Wagner and Pruss[16] ("IAPWS-95") valid to 1273 K and 1 GPa.

It would be interesting to compare the equations of state for other simple hydrogen-bonded fluids with that of water. The *P,V,T* relations of ammonia[30] ($T_c = 461$ K) and hydrogen fluoride[31] ($T_c = 406$ K) have been recently reported to high pressures and temperatures, but no detailed comparison has been made that could single out possible peculiarities of water.

2.4. Critical Anomalies

Near liquid–gas (L–G) critical points some properties show divergences which obey asymptotic scaling laws of the form of Equation (2) where $\tau = |T - T_c|/T_c$ defines the temperature difference from the critical point, X_0 is a system-specific amplitude, and μ is a universal critical exponent.[32]

$$X = X_0 \tau^{\mu} + \ldots \quad \text{as } T \to T_c \tag{2}$$

Analytical equations of state can be expanded in a Taylor series everywhere, including the critical point, and by such expansions at the critical point the critical exponents of the various properties X turn out to be integers or rational fractions. For example, the L–G coexistence curve in Figure 2 obeys a scaling law of the form of Equation (3) where the so-called order parameter $\Delta\rho$ is given by the difference of the densities of the liquid (ρ_L) and gaseous (ρ_G) phases. Any analytical equation of state provides an exponent $\beta = 1/2$, which implies a parabolic coexistence curve.

$$\Delta\rho = \rho_L - \rho_G = B_0 \tau^{\beta} + \ldots \tag{3}$$

Analytical theories are denoted as "classical" or "mean-field equations. The term "mean-field" accounts for the fact that, in molecular theories, analytical expressions are obtained by assuming that the interaction of a particle with its neighbors can be represented by the mean field generated by its neighbors.

Experiments, however, provide critical exponents that do not conform to the mean-field values, they give irrational exponents and have a non-analytical behavior.[32] Instead, the critical behavior at the L–G transition can be by described the three-dimensional Ising spin 1/2 model.[33] This model was originally developed for describing the interactions of spins leading to ferromagnetic transitions. It considers the next-nearest neighbors of a particle only and presumes short-range interactions, typically with a r^{-6} separation dependence. Renormalization group theory allows the exact values for critical exponents to be computed.[33] The predicted value of the Ising exponent, $\beta = 0.326\ldots$, is confirmed by accurate data for L–G transitions in fluids. Among other things, this behavior implies that near the L–G critical point the coexistence curve in Figure 2 is approximately cubic, and much flatter than the parabolic shape predicted by analytical theories.

In the mean time, there is a widespread recognition that these anomalies give rise to considerable deficits in the traditional equations of state. In the best case the anomalies occur only close to T_c. These "weak anomalies" are indeed of little significance in chemical processes, and it is not crucial

 © 2005 Wiley-VCH Verlag GmbH & Co. KGaA, Weinheim

for applications to use a physically correct representation of the critical divergences. In the worst case the non-classical behavior extends over a wide temperature range. A prominent example for such a "strong anomaly" is the isobaric heat capacity C_P which goes to infinity at the critical point. About 30 K above T_c, the isothermal density dependence of C_P still shows a very pronounced maximum with a C_P value that is by an order of magnitude larger than that extrapolated from data taken far away from the critical point.[16,19] Even fully empirical equations, such as the IAPWS-95 equation mentioned earlier[16] include some non-analytical terms to obtain accurate descriptions of this behavior. In applications, the regime of large variations is difficult to control, and is usually avoided.

From the theoretical perspective, the anomalous phenomena close to T_c are now well understood. Large difficulties arise, however, from the need to account for the transition from asymptotic Ising-like behavior near critical points to mean-field behavior expected to prevail far away. This crossover forms the major reason for the large number of adjustable terms needed in accurate equations of state of the traditional form.[32] The need for a proper description of crossover has given rise to intense experimental and theoretical efforts. Sophisticated parametric crossover theories for fluids are now available,[32] and have been applied to water.[34] "Parametric" means that a physically plausible crossover function with a few adjustable parameters is used to interpolate between the mean-field and Ising limits. In comparison with fully empirical approaches with a large number of parameters, crossover theories are of similar precision, but are more difficult to implement and require more computer time. It is likely that the future increase in computer power will, however, favor crossover theories also with regard to applications.

2.5. Autodissociation

A key property in many applications is the dissociation equilibrium $H_2O \rightleftarrows H^+ + OH^-$, which is characterized by the equilibrium constant K [Eq. (4)] or the ion product K_W [Eq. (5)], where a refers to the activities of the species. At normal conditions, ion concentrations are sufficiently low to replace the activities by concentrations. Equations (4) and (5) are usually formulated with H_3O^+ rather than H^+, but at supercritical states such a formulation is by no means straightforward.

$$K = \frac{a(H^+)a(OH^-)}{a(H_2O)} \quad (4)$$

$$K_W = a(H^+)a(OH^-) \quad (5)$$

Because charged species are involved, the ion product can be studied by electrochemical methods, such as electrical conductance measurements. More than thirty years ago, Holzapfel and Franck[4] performed such measurements to 1273 K and 1 GPa. Later, shock-wave experiments pushed this limit to 180 GPa and 10000 K.[3] Figure 4 shows the

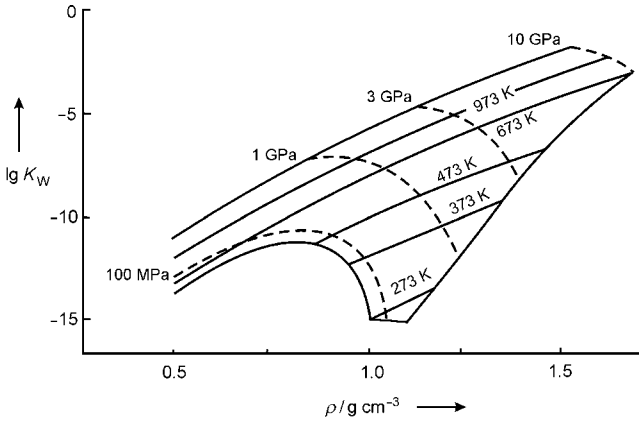

Figure 4. The ion product, K_W, of water up to temperatures of 1273 K and densities up to 1.5 g cm^{-3}.[35]

temperature- and density-dependence of the ion product, derived from the ion product tables of Marshall and Franck.[35] At normal conditions, $K_W = 1 \times 10^{-14}$, and the proton concentration possesses the familiar value of 1×10^{-7} mol L^{-1}. K_W increases with temperature and density. At 1273 K and liquid-like density, K_W is at least six orders of magnitude larger than at 298 K. This situation has dramatic consequences for hydrolysis and acid–base equilibria. For example, at 773 K and 200 MPa the equilibrium constant of the hydrolysis reaction $Cl^- + H_2O \rightleftarrows HCl + OH^-$ is by about nine orders of magnitude larger than at normal conditions, and the hydrolysis of alkali halides is comparable to that of acetates at normal conditions. Thus, corrosion will be greatly enhanced.

The increase in ionization is corroborated by recent shock-wave experiments to 180 GPa and 10000 K.[3] Near 1000 K and densities of about 2 g cm^{-3} the conductivity begins to level off a value of about 30 S cm^{-1}, which is comparable to that of molten hydroxides. Raman spectra of shock-compressed water indeed show the stretch vibration of the OH^- ion, but remarkably, no band for H_3O^+ is found.[36] The lack of a H_3O^+ band gives rise to the suspicion that the cation is H^+.[36] It has been noted[37] that these highly conducting states are of relevance for the interpretation of the large magnetic fields of the outer planets. At the high-temperature end of the shock-wave experiments, one may even be close to metallization of water, although no evidence for electronic contributions to the conductance was found.[3] Ab initio MD simulations locate the closure of the band gap at 7000 K near 300 GPa inside the fluid region.[21]

2.6. Transport Coefficients

Because all transport coefficients strongly depend on the viscosity of the medium, an accurate knowledge of the viscosity of supercritical water is mandatory. Figure 5 shows experimental data for the viscosity, η, to 823 K and 350 MPa.[38] The diagram is supplemented by low-pressure data[19] and by plausible extrapolations to 1273 K. Projected on the floor of the cube is the liquid–gas coexistence curve which indicates the two-phase regime.

 © 2005 Wiley-VCH Verlag GmbH & Co. KGaA, Weinheim

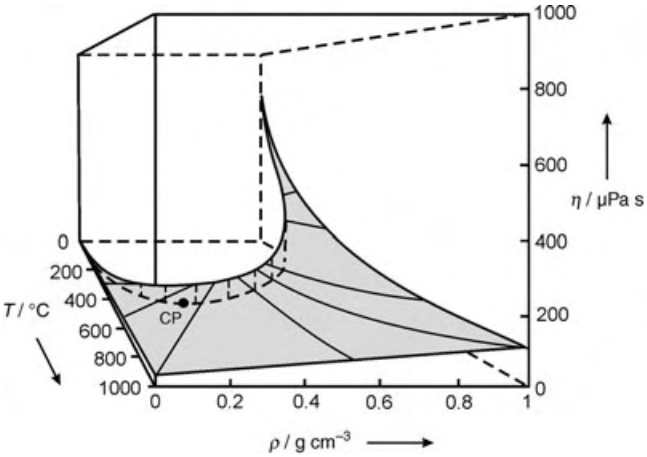

Figure 5. The viscosity, η, of water at temperatures up to 1273 K and densities up to 1 g cm^{-3}, constructed from experimental data to 823 K and 350 MPa,[38] in conjunction with plausible high-temperature extrapolations, and supplemented by low-pressure data.[19] The coexistence curve and critical point (CP) are shown at the floor of the cube.

At normal conditions the viscosities of gases and liquids differ by about two orders of magnitude. With increasing temperature at constant density, η increases slightly at gas-like densities and decreases markedly at liquid-like densities. The low-density behavior reflects translational momentum transfer and is well described by the kinetic theory of gases. In the high-density regime collisional momentum transfer prevails, which is not yet understood in detail. There is a wide range of densities, between 0.6 and 0.9 g cm^{-3}, where η depends only weakly on temperature and density. In this range, η amounts only to about one tenth of its value at normal conditions. This high fluidity is attractive in chemical processes because mass transfer and diffusion-controlled chemical reactions are largely enhanced.

The low viscosity reflects high molecular mobilities. The mean-square displacement $< r^2 >$ of a particle during time t is described by the self-diffusion coefficient $D = < r^2 > /6t$. At normal conditions $D \cong 2.3 \times 10^{-9}$ m^2 s^{-1}, at 973 K and liquid-like density $D \cong 10^{-8}$ m^2 s^{-1}.[39] A similar enhancement of molecular motions is found by nuclear magnetic[40] and dielectric[41] relaxation techniques which probe molecular rotations. Correspondingly, the thermal conductivity is high,[19,42] and thus exothermal chemical reactions can be controlled more easily.

In dense states a hydrodynamic approach is known to work quite well. Thus, the self-diffusion coefficient of a particle of effective radius r obeys the Stokes–Einstein relation [Eq. (6) where k_B is the Boltzmann constant].

$$D = \frac{k_B T}{6 \pi \eta r} \tag{6}$$

Equation (6) does not only apply to the self-diffusion of water, but also to the diffusion of traces of solutes in water. At decreasing water density, Equation (6) holds at least down to the critical density.[39] Thus, over a large range of conditions the factor $D\eta/T$ is almost constant, which facilitates predictions of solute diffusion. In the dilute gas limit, D is proportional to the ratio η/ρ of the viscosity and density, which differs drastically from the diffusion–viscosity relationship in dense phases.

In applications, mutual diffusion, often simply termed "diffusion", is of far greater importance than self diffusion. The mutual diffusion coefficient, D_{12}, describes mass flows driven by gradients in concentrations in mixtures, as described by Fick's laws. At the critical point, D_{12} goes to zero, which is known as "critical slowing-down". In the only study of mutual diffusion for supercritical aqueous mixtures so far conducted, Buelow and co-workers have demonstrated that critical slowing-down in concentrated solutions of $NaNO_3$ extends over a comparatively wide region.[43] Thus, diffusion-controlled reactions in concentrated solutions may be markedly slower than usually presumed. It can, however, be rigorously shown that critical slowing-down must disappear at infinite dilution of the solute. Therefore, in dilute solutions this phenomenon can probably be ignored.

2.7. Dielectric Properties

The relative dielectric permittivity ("dielectric constant"), ε, of water controls the solvent behavior and the ionic dissociation of salts. Accurate experimental data for ε over large regions of temperature and pressure are therefore necessary for many applications. Figure 6 shows the dielectric

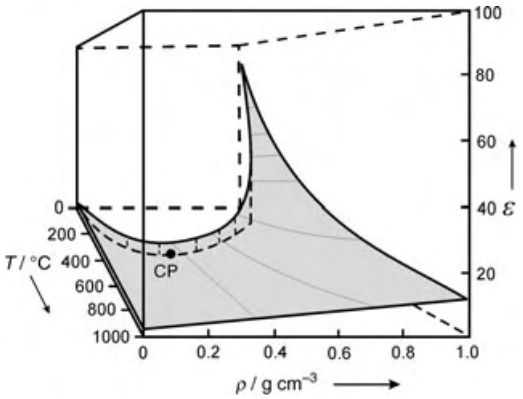

Figure 6. The dielectric constant, ε, of water up to 1273 K and densities up to 1 g cm^{-3}, constructed from experimental data to 823 K and 500 MPa,[44] in conjunction with high-temperature extrapolations based on model calculations to 1273 K.[45] The coexistence curve and critical point (CP) are shown at the floor of the cube.

constant to 1273 K and 1 g cm^{-3}, based on experimental data to 823 K and 500 MPa[44] and model calculations for higher temperatures.[45] ε decreases with increasing temperature and increases with increasing density. The familiar high value of $\varepsilon \cong 80$ occurs only in a small region at low temperatures. In a large supercritical region at high densities, the dielectric constant has values of the order of $\varepsilon = 10$–25. These values are similar to those of dipolar liquids, such as acetonitrile or

 © 2005 Wiley-VCH Verlag GmbH & Co. KGaA, Weinheim

acetone under ordinary conditions. These values are sufficiently high to dissolve and ionize electrolytes, but also enable miscibility with nonpolar solutes. At low densities the dielectric constant, and thus the ability to dissolve and ionize electrolytes, decreases rapidly. At the critical point $\varepsilon \cong 6$.[44]

The high values of ε at normal conditions result from preferred dipole orientations in the water structure. In molecular theory, non-random dipole orientations are described by the Kirkwood factor g_K, which in modern formulation is related to ε by Equation (7),[46] where N/V is the number density of the dipoles, μ the dipole moment of the isolated molecule, ε_∞ the high-frequency limit as a result of nuclear and electronic displacement polarizations. ε_0 is the permittivity of free space; g_K-values different from unity indicate preferred parallel ($g_K > 1$) or antiparallel ($g_K < 1$) dipole orientations.

$$\frac{(\varepsilon-\varepsilon_\infty)(2\varepsilon+\varepsilon_\infty)}{\varepsilon(\varepsilon_\infty+2)^2} = \frac{\mu^2 g_K}{9\varepsilon_0 kT}\left(\frac{N}{V}\right) \tag{7}$$

With regard to applications there is need for an accurate formulation that represents the dielectric constant over wide ranges of temperature and pressure,[47] which should be suitable for some extrapolation beyond the underlying range of experimental data. It has long been suggested that models for the Kirkwood factor may be simpler than for the dielectric constant itself.[15] Irrespective of the well-defined molecular meaning of g_K, all accurate data correlations of ε over wide ranges of pressure and temperature are, however, empirical. Some frequently used data correlations result, however, in quite different high-temperature and high-pressure extrapolations.[48] Because at high temperatures water looses its peculiarities, it may be more fruitful to exploit some solvable models of statistical mechanics as a guide for extrapolation. An attempt based on expressions for dipolar hard spheres seems promising.[45]

From the scientific perspective, the Kirkwood factor and the dielectric constant form useful targets for testing theories and simulations. Moreover, g_K may form a global measure of the water structure.[49] A physically significant computation of g_K through Equation (7), is however, a subtle problem.[50] Moreover, ab initio simulations suggest that the electric field induced by surrounding particles enhances the dipole moment of a hydrogen-bonded molecule, so that μ increases from the dilute gas to dense water.[51]

2.8. Hydrogen Bonding and Water Structure

At ordinary conditions the structure of water is dominated by a three-dimensional network of hydrogen bonds. It is a central question of any molecular approach to what extent these hydrogen-bonded structural patterns survive in the supercritical fluid. At the very outset, any such discussion requires a criterion for deciding when two neighboring molecules can be described as being hydrogen bonded. In simulations, hydrogen bonds are usually defined by energetic or structural properties of the molecular pair. Experimentalists resort to operational definitions, such as frequency shifts in spectra. The various criteria can lead to largely different estimates of the number of hydrogen bonds.[27]

In vibrational spectroscopy, hydrogen bonding leads to frequency shifts, changes in band contours, and the appearance of new bands. Infrared spectra to 823 K and 400 MPa were reported more than thirty years ago,[52] and were later supplemented by Raman data.[53] Figure 7 shows Raman spectra of the O–D symmetric stretch vibration of a solution of 5 mol% D_2O in H_2O. Deuterated samples are preferred because the O–D antisymmetric and symmetric stretch frequencies are far apart, while the O–H frequencies almost coincide. The possible hydrogen-bonded states give rise to complex multimodal spectra with overlapping component bands. Thus, spectral analyses is usually based on models. A major feature observed in going at liquid-like density from 298 K to 673 K, is that the band at 2450 cm^{-1} is gradually replaced by a band at 2650 cm^{-1}. If at 673 K the density is lowered, the band at 2650 cm^{-1} shifts to higher frequencies and approaches the limiting frequency of 2727 cm^{-1} of the highly dilute gas. Irrespective of details of data evaluation, it is clear that in dense supercritical water, at least at the temperatures considered, hydrogen bonding is retained to an appreciable extent.

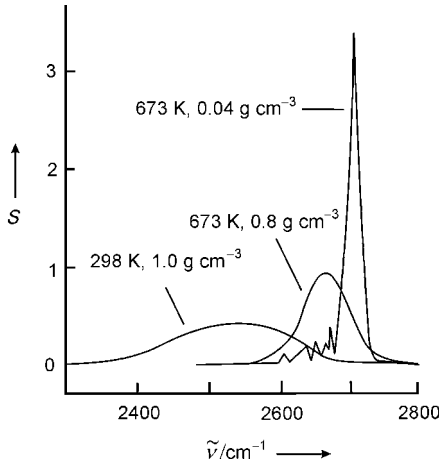

Figure 7. Isotropic Raman spectra of the O–D symmetric stretch vibration of 4.85 mol% D_2O in H_2O.[53] S is the spectral intensity in arbitrary units, $\tilde{\nu}$ is the wavenumber.

Another long established measure of hydrogen bonding is the chemical shift of the OH proton in the ^1H NMR spectrum, but only in 1997 were such data reported for supercritical water.[54] In contrast to vibrational spectroscopy, the longer time scale of the NMR experiments only provides an average degree of hydrogen bonding over the various configurations. The results of NMR and vibrational spectroscopy are consistent with one another.

Information on the water structure, and thus on hydrogen bonding, is also expected from scattering techniques. Neutron scattering is particularly suitable because, by using isotopically substituted samples, the distribution function of the intermolecular oxygen–hydrogen separation can be extracted.

 © 2005 Wiley-VCH Verlag GmbH & Co. KGaA, Weinheim

Difficult corrections and sophisticated numerical procedures are, however, required to evaluate the O–H-separation distribution functions from the raw scattering patterns. Thus, the interpretation of neutron scattering results for supercritical water has been controversial. A detailed discussion is given in a review by Chialvo and Cummings.[27] Herein we note only that, in contrast to earlier claims,[55] neutron scattering confirms the presence of hydrogen-bonded configurations in dense supercritical states.[56] While the experimental knowledge of the detailed water structure in the supercritical region is still far from being complete, the interplay between experiment and simulation has now singled out the major structural motifs.[27]

In summary, there is no doubt that hydrogen bonds are still present in dense supercritical water. This situation clearly reflects the fact that at the critical temperature the energy of the hydrogen-bond is still markedly larger than the thermal energy. The hydrogen-bonded configurations probably consists of dimers and small clusters.[27] The properties of water clusters are theoretically understood in great detail.[57] The extended network structure that is responsible for the unique properties of liquid water is, however, lost. It remains to exploit this knowledge in terms of models for thermophysical properties.

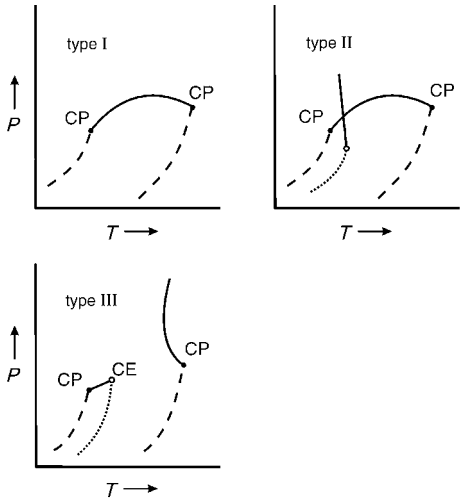

Figure 8. *P,T* projection of type I, II, and III phase behavior of the Scott–Konynenburg classification.[58,59] The projection shows the L–G critical curve (——), vapor-pressure curves of the pure components (– – –), and L-L-G three-phase line (••••). CP indicates the critical points of the pure fluids. CE is the critical end point.

3. Aqueous Mixtures with Nonpolar Compounds

3.1. General Topologies of Phase Diagrams

As a rule of thumb, water is a good solvent for electrolytes and hydrophilic substances, while it shows low solubilities for nonpolar substances. This behavior depends, however, on temperature and pressure. In the supercritical regime the solubility can be tuned by density, and thus by pressure, which opens many possibilities for using supercritical water as a solvent and reaction medium.

When a solute is added to water, the L–G critical point is displaced, giving rise to a locus of L–G critical points, the so-called critical curve. In addition, liquid–liquid (L–L) phase equilibria may occur and interfere with the L–G critical regime. For a full description of this broad variety of phase behavior a three-dimensional pressure–temperature–mole-fraction (P,T,x) diagram must be used. The composition is, for example, given in terms of the mole fraction x of one of the components. Often one resorts, however, to the projection of this diagram onto the P,T plane. A theory of Konynenburg and Scott[58] suggests six types of phase diagrams in the P,T projection. Albeit derived from an analysis of the simple van der Waals equation for mixtures, this topological scheme can also be applied to phase transitions in aqueous systems.[59] Three types of phase diagram of particular interest for supercritical aqueous solutions are depicted in Figure 8.

In the simplest cases, liquid–liquid immiscibility does not exist or does not extend into the gas–liquid critical region. In this sort of system, the vapor-pressure curves of the pure liquids are terminated by L–G critical points, which are connected by a continuous L–G critical curve for the mixtures. If the components are completely miscible at all conditions then the phase diagram is of type I shown in Figure 8. This type of behavior occurs for component molecules of similar shape and polarity. Examples are aqueous solutions of ammonia[60] and polar organic solutes, such as ethanol or acetone.[61]

For larger dissimilarities of the components L–L equilibria develop. These miscibility gaps are well-known phenomena in aqueous solutions of organic solutes. They result primarily from the hydrophobic nature of the solutes, which renders mixing with water entropically unfavorable. Schneider and collaborators have studied many L–L immiscibilities and their interference with L–G transitions,[62] recently also in diamond anvil cells to 2 GPa or higher.[63] For moderate hydrophobicity of the solute, the miscibility gaps are limited to low temperatures. In this case, the phase diagram has to account for the resulting L–L–G three-phase line, along which two liquid phases and the gaseous phase are in equilibrium. Additionally, there are one or more critical curves that describe the pressure dependence of the upper and/or lower temperatures of L–L demixing. In Figure 8 this behavior is exemplified for a so-called type II system. Actually, the possible phase behavior is much richer than shown.[59,62]

Most systems have, however, a disrupted critical curve. This interruption is crucial for understanding solubilities in supercritical water. In the following we presume that water is the less-volatile component of the binary mixture, as for example, encountered with inorganic gases and simple hydrocarbons. Then, in Figure 8 the water critical point is that at high pressure and high temperature. The reverse case, when water is the more-volatile component, for example, in mixtures with salts or minerals, will be discussed in Section 4.1.

Critical-curve interruption results from the fact that an increasing dissimilarity of the components displaces the L–L

 © 2005 Wiley-VCH Verlag GmbH & Co. KGaA, Weinheim

equilibria to higher temperatures. Eventually, the L–L–G three-phase line merges into the L–G critical line, and the type II phase diagram is transferred into other types, of which only type III behavior in Figure 8 is of relevance here. Aqueous mixtures with nonpolar inorganic gases and simple hydrocarbons are important examples of type III systems.

In the type III phase diagram, a L–G critical curve starts from the critical point of the volatile nonpolar component. Because of the low solubility of water in nonpolar fluids at low pressure, this branch of the critical curve is, however, rapidly interrupted by the L–L–G three-phase line at a so-called critical end point. This regime of traces of water in the nonpolar fluid at low pressures is scarcely of interest for applications. Rather, we focus on the high-pressure branch of the critical curve, whose origin is in the critical point of water. This branch runs either directly to higher temperatures and pressures, or more often, it moves initially towards lower temperatures and then passes a minimum. In both cases, phase separations occur in some regions even above the critical temperature of pure water. Because above the critical temperature, the fluid is loosely denoted as a gas, this behavior is sometimes denoted as "gas–gas (G–G) equilibrium".[59] This notion is somewhat misleading because the coexisting phases possess liquid-like densities.

Figure 9 shows a section of the *P*,*T*,*x* diagram for type III systems near the critical point of water, and includes isobars and isotherms. The shaded regime indicates the two-phase regions of isobaric segments. The heterogeneous regime rapidly broadens at lower temperatures, so that eventually, nonpolar solutes are soluble in water only in trace amounts, and vice versa. The critical curve connects the maxima of the isotherms and the isobars forming a border, to the high-temperature side of which, is a region of complete miscibility.

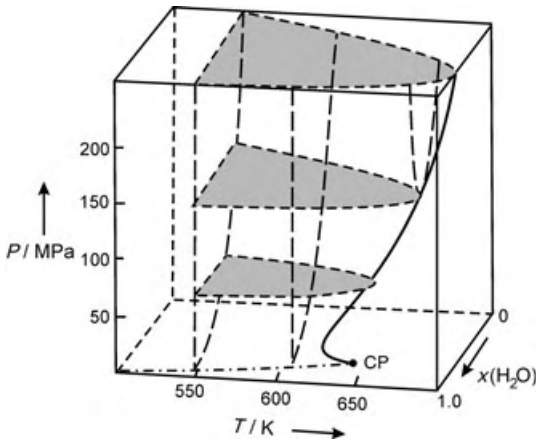

Figure 9. Schematic pressure–temperature–composition diagram with isotherms and isobars of a system composed of volatile nonpolar substances and water in the vicinity of the critical point of pure water. $x(H_2O)$ is the mole fraction of water. The shaded area indicates the two-phase regime. The critical curve (-----) connects the maxima of the isotherms and isobars, respectively, and limits the two-phase regime at high temperatures. The vapor-pressure curve of pure water (–•–•) is also shown which ends at the critical point CP.

3.2. Solubility of Nonpolar Solutes

The solubility of nonpolar, nonreacting inorganic and organic gases in water has often been studied by so-called synthetic or analytical techniques. In synthetic experiments, a mixture of known composition is introduced into the autoclave, and temperature and pressure are varied systematically. In simple cases the phase transition is observed visually. More generally, it manifests itself, for example, in breaks in *P*,*T* curves. The synthetic method gives not only *P*,*T*,*x* data, but can also be used to obtain volumetric data in the homogenous regime, thus providing the equation of state. In the analytical method, samples of the coexisting phases are extracted from the autoclave and their composition is analyzed. The analytical method is particularly useful in the range of low gas concentrations, but gives no volumetric data.

A variety of autoclaves have been devised for recording high-pressure, high-temperature phase equilibria. Figure 10 shows an autoclave[64] that enables both synthetic and

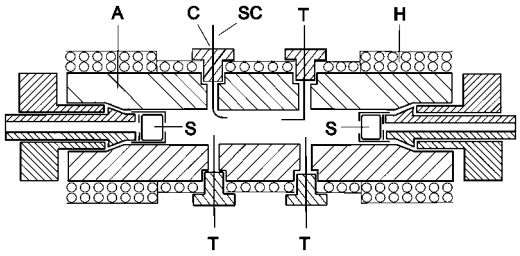

Figure 10. Autoclave for synthetic and analytical observation of high-pressure, high-temperature phase equilibria.[64] The autoclave (A) of 30-cm length, 6-cm outer diameter, and 2-cm internal diameter is made from a corrosion-resistant nickel alloy. There are three independent heating jackets (H) controlled by three thermo couples (T). Samples can be drawn through the connection (C) with a stainless steel capillary (SC) and a micrometric needle valve (not shown). The same connection (C) is used for filling, pressure transduction, and pressure measurement. The sample is magnetically stirred (not shown).

analytical experiments. The cylindrical autoclave (A) is made from a corrosion-resistant nickel alloy. On both ends, windows of synthetic sapphires (S) are mounted, which enable observation of the interior. On the outside there are several independent heat jackets (H). Temperature is controlled by three thermocouples (T). A thin stainless steel capillary (SC) enables extraction of samples through a needle valve. The same connection (C) is used for filling of the autoclave, pressure transduction, and pressure measurement.

Figure 11 shows experimental critical curves for aqueous solutions of representative nonpolar inorganic and organic solutes. The hatched lines indicate the side where the systems form two phases. At the high-temperature side the compounds are completely miscible. It is likely that these curves are terminated at very high pressures by solid–fluid equilibria. There is manifold interest in these critical curves in diverse field of applications. From the industrial perspective, such curves are of key importance as border lines, beyond which chemical reactions can be conducted in homogeneous phases with high concentrations of the reactants. The miscibility with

 © 2005 Wiley-VCH Verlag GmbH & Co. KGaA, Weinheim

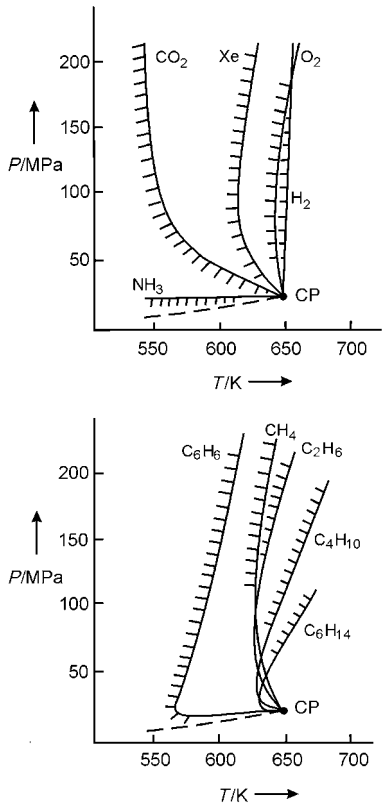

Figure 11. *P,T* projection of the critical curves for aqueous solutions of simple inorganic and organic solutes in the vicinity of the critical point of pure water. The dashed sides of the curves indicate the side of the two-phase regions. The line near the bottom left (– – –) represents the vapor-pressure curve of pure water which terminates in the critical point (CP). Data sources are given in the text.

solutes such as methane or carbon dioxide is of great importance in geochemistry.

With increasing attractive interactions between the components, the shapes of the critical curves change in a regular fashion. For the small, hard solute helium[65] the critical curve begins from the critical point of pure water with a positive slope. Hydrogen, a small and hard quadrupolar molecule, is accommodated in water with little change in the critical temperature.[66] For oxygen and nitrogen weak temperature minima develop, which in the large-scale plot of Figure 11 practically coincide.[64] At 298 K the solubility of oxygen is twice that of nitrogen, but this selectivity is lost at high temperatures. For stronger interactions, the minima become more pronounced, as observed for the higher rare gases,[67] and exemplified in Figure 11 for some lower homologues of the *n*-alkane series.[68,69] CO_2[70] and benzene[71] have strong quadrupole moments, and the homogenous range becomes large. Eventually, for highly polar solutes the critical curve is not interrupted. Notably, the limiting slopes of the critical curves at the critical point of water play a key role in the thermodynamics of highly dilute supercritical solutions.[72] Figure 11 shows, however, that the linear segments are small and not relevant for most applications considered herein.

With regard to hydrothermal solutions, the behavior of CO_2 is of particular interest. Early work on $CO_2 + H_2O$ has been reviewed by Tödheide.[13] Some discrepancies in the reported critical curves have been cured in more recent work by Mather and Franck.[70] CO_2 is miscible with water in all portions at temperatures more than 100 K below the critical temperature of pure water. There have been speculations that this enhanced miscibility reflects associated species, such as H_2CO_3, and their stepwise dissociation. The thermodynamic behavior as well as spectroscopic and conductimetric experiments give no evidence for such associated species.[13,73] Rather, the strong quadrupole moment of CO_2 seems to form the key for rationalizing its high solubility.

3.3. Critical Anomalies

There is much interest in nonclassical thermodynamic behavior. Critical anomalies do not only prevail at L–G transitions, but also apply to L–L equilibria. With regard to the study of critical anomalies it is, of course, easier to conduct experiments at L–L demixing (consolute) points, which often occur near room temperature.[59]

The scaling laws for pure liquids hold in an analogous form for liquid mixtures. In particular, for an L–L coexistence curve, Equation (3) can be reformulated as Equation (8) where the order parameter $\Delta\Phi$ is now given by the difference in composition of the coexisting phases.

$$\Delta\Phi = \Phi' - \Phi'' = B\tau^{\beta} + \ldots \tag{8}$$

The choice of the composition variable is a subtle problem, but there are good arguments that the difference $\Delta\Phi_1 = \Phi' - \Phi''$ of the volume fractions of the solute in the two phases is the most decisive quantity.[32,74] An analysis of L–L coexistence curves of binary mixtures shows Ising-like behavior with the same exponent $\beta \cong 0.326$,[74] as found for L–G equilibria of pure fluids. This is but one example for the principle of isomorphism of the critical anomalies of pure fluids and mixtures.

In the present context, the major importance of these results is that large Ising-type critical anomalies are significant for supercritical aqueous solutions. While some equations of state for mixtures explicitly include asymptotic Ising behavior,[75] crossover theories in analogy to that for pure water are lacking.[34] Even if the nature of the crossover in mixtures would be elucidated in detail, the formulation of such a global equation of state as a function of temperature, pressure, and composition would be an appreciable challenge. We therefore have to rely on classical approaches, and hope that they are flexible enough to absorb the effects of critical anomalies in their regressed parameters.

3.4. Equations of State

Because accurate experimental data are not easily acquired, it is desirable to have a predictive equation of state for supercritical aqueous solutions. The need for predictive power requires at least semi-empirical approaches with parameters of some physical meaning. As for one-

 © 2005 Wiley-VCH Verlag GmbH & Co. KGaA, Weinheim

component systems, a generalized formulation in terms of the Helmholtz energy $A(T,V,x)$ would provide the most appropriate form. In contrast, equations of state for mixtures usually begin with pressure-explicit relations of the form $P(V,T)$ for the pure fluids, which are then adapted to mixtures by introducing mixing rules.[1] The integration of these equations then allows chemical potentials, fugacities, or activities, to be calculated, which in turn, provide two- and three-phase lines by applying standard thermodynamic conditions for phase coexistence.[28]

Many equations of state have been derived for supercritical fluid mixtures in general,[1] but not all are suitable for describing aqueous solutions. Although at supercritical states the peculiar properties of liquid water no longer play an important role, the conditions for an appropriate equation are stringent, because the components have very different polarities. We consider a prototypical equation[76] which provides good descriptions of experimental phase diagrams and volumetric properties in the homogeneous regime, and has some predictive power.[68,76,77] This equation combines the popular Carnahan–Starling term for repulsive interactions[78] with an attractive term based on composition-dependent virial coefficients B_x and C_x of the square-well potential [Eq. (9)]. $\eta_x = (\pi/6)N_A\sigma_x^3$ is the packing fraction, calculated from an core diameter σ_x averaged over the core diameters of the components. The diameters σ_{ij} and depths ε_{ij} of the square-well potentials for the like-particle interactions ($i=j$) are derived from critical data of the pure components. Parameters for unlike-particle interactions ($i\neq j$) are determined by customary mixing rules: The energy parameter is estimated from the geometric mean, $\varepsilon_{12} = \xi(\varepsilon_{11}\varepsilon_{22})^{1/2}$, of the pure component parameters, the size parameter is estimated from the arithmetic mean, $\sigma_{12} = \zeta(\sigma_{11}+\sigma_{22})/2$. For accurate descriptions, the mixing rules are usually modified by adjustable parameters ξ and ζ, which makes them somewhat empirical. In practice, similar values of ξ and ζ may apply for homologous solutes. The approximations limit this equation of state, and many similar equations, to high temperatures. No accurate equation for aqueous solutions spans the total range from normal to supercritical conditions.

$$P = RT\frac{V_m^3 + V_m^2\eta_x + V_m\eta_x^2 - \eta_x^3}{V_m(V_m-\eta_x)^3} + RT\frac{B_x}{V_m^2 - V_m C_x/B_x} \qquad (9)$$

Many other equations of state have been suggested. As an interesting example, we quote a recent equation for binary and multicomponent mixtures by Duan, Møller, and Weare,[79] which was shown to rationalize data up to 2 GPa and 2000 K, even for aqueous multicomponent mixtures.[80] A particularly interesting feature is that this equation is calibrated, among others, against data from MD simulations.

3.5. Homogeneous Supercritical Solutions

There is much interest in the bulk and molecular properties of homogenous mixtures of water with nonpolar solutes, both with regard to applications and to the understanding of molecular interactions between water and nonpolar solutes. As noted in Section 3.2, some experimental techniques for measuring phase-transition curves also enable the determination of volumetric properties in the homogenous regime. Thus, many studies of phase transitions also report on the P,V,T,x relation.

Results of volumetric experiments are usually expressed in terms of excess molar volumes, $\bar{V}^E$, which reflect deviations from additive volume behavior of the components upon mixing at constant pressure and temperature (the bar over the symbol denotes molar quantities). Excess molar volumes of supercritical mixtures with nonpolar compounds are positive, which indicates a volume expansion upon mixing. Usually excess molar volumes decrease at high pressures.

If $\bar{V}^E$ is known, the excess molar Gibbs energy $\bar{G}^E$ is obtained by integration over the pressure starting from a known reference state [Eq. (10)].

$$\bar{G}^E(T,P,x) = \bar{G}^E(T,P_{ref},x) + \int_{P_{ref}}^{P} \bar{V}^E(T,P,x)\,dP \qquad (10)$$

Partial derivatives of $\bar{G}^E$ with respect to P, T, and x then allow the calculation of chemical potentials, and fugacity and activity coefficients, which control chemical equilibria and phase behavior. Owing to large non-ideal behavior an account of activity or fugacity coefficients in computations of chemical equilibria or phase equilibria is indispensable, even at the qualitative level.

In principle, such calculations do, however, not differ from routine calculations performed at normal conditions, where a plethora of excess Gibbs energy models is available for modeling.[28] There are, however, some pitfalls in treating highly dilute solutions near the critical point of pure water, where some properties, such as the chemical potential of the solute, show diverging behavior. This can result in counterintuitive behavior. These subtleties are a relatively new insight, and the literature is full of misinterpretations in terms of dramatic structural changes in supercritical aqueous solutions, when approaching high dilution. The problems can be cured by proper reformulation of the theory.[72]

Limiting the discussion to more concentrated solutions, where such subtleties can be ignored, the excess Gibbs energies of aqueous solutions of nonpolar solutes are large and positive, as illustrated in Figure 12 for $H_2O + O_2$.[64] Because the excess volumes are positive, this non-ideal behavior increases with increasing pressure. In most cases the observed values are far higher than the typical excess Gibbs energies of binary liquid mixtures at room temperature. In conventional interpretations such strongly positive excess Gibbs energies are attributed to strong self-aggregation and clustering of the like particles.

Spectroscopic data that could provide information on molecular clustering are completely lacking. Some important information comes, however, from dielectric-constant data for aqueous solutions of benzene.[44b] At 200 MPa and 673 K, the dielectric constant of pure water is $\varepsilon \cong 20$ which corresponds to that of many polar solvents at normal conditions. Figure 13 shows that, by adding benzene, ε decreases rapidly at constant pressure. The strong asymmetric shape of the

 © 2005 Wiley-VCH Verlag GmbH & Co. KGaA, Weinheim

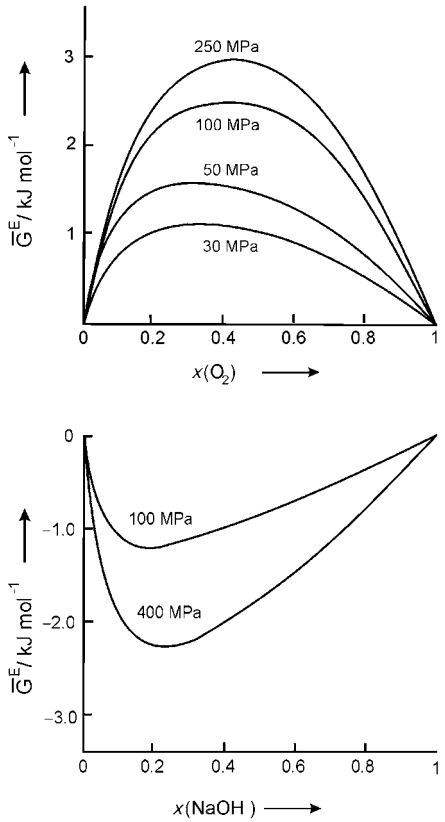

Figure 12. Excess molar Gibbs energies at 673 K of H_2O+O_2 (top)[64] and H_2O+NaOH (bottom)[108] as a function of the mole fractions of the solutes (O_2 and NaOH) at the pressures indicated in the Figure.

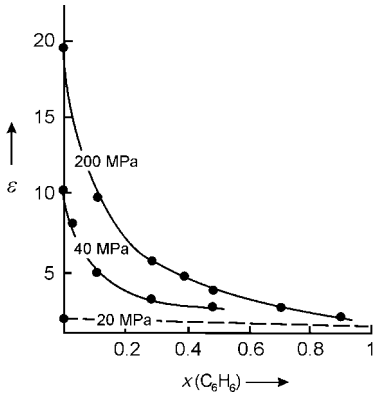

Figure 13. Dependence of the static dielectric constant, ε, of water + benzene mixtures on the mole fraction of benzene at 673 K and pressures of 200 and 40 MPa. The curve for 20 MPa is extrapolated from these data and data at additional pressures.[44b] $x(C_6H_6)$ is the mole fraction of benzene.

composition dependence is retained at lower pressures, until at 20 MPa and 673 K the dielectric constant of pure water no longer differs greatly from that of benzene. Goldman and Joslin[81] used a theory based on a density expansion of the dielectric constant to describe these data in terms of molecular aggregation.

3.6 Multicomponent Mixtures

Many systems of interest in chemistry, geochemistry, and engineering contain more than two components. Because the number of data points needed for the characterization of multicomponent systems is largely increased, theoretical efforts are even more profitable. Many equations of state can be extended to multicomponent systems in a straightforward way, and in favorable cases, information on the binary subsystems is sufficient to describe the behavior of ternary and multicomponent systems. Illustrative examples are studies dealing with the systems $H_2O+N_2+C_6H_{14}$,[82] $H_2O+N_2+C_6H_{14}+CO_2$,[82] or $H_2O+N_2+CH_4+CO_2$.[80] This success gives confidence for predictions made on systems where experimental data are scarce or absent. The system $H_2O+H_2+O_2$ is an important example of interest in diverse fields, for example, for modeling of jet propulsion. Figure 14 shows the computed phase diagram of at 644 K.[83] The side planes of the prism represent heterogeneous areas of the binary subsystems H_2O+H_2 and H_2O+O_2, for which some experimental data are available. Once the parameters of the binary subsystems are fixed, properties such as phase-transition curves of the ternary system, corresponding to states inside the prism, can be computed.

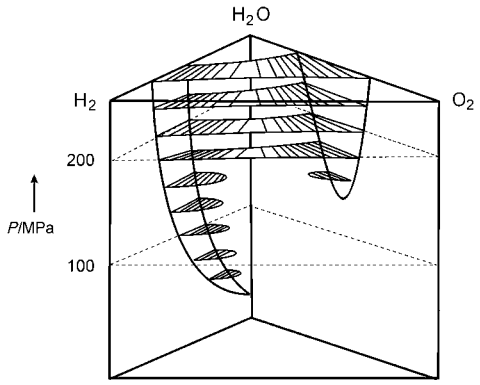

Figure 14. Computed pressure–composition phase diagram of the ternary system $H_2O+H_2+O_2$ at a constant temperature of 643 K. The side planes show the two-phase regions of the binary subsystems H_2O+H_2 and H_2O+O_2, which are fitted to experimental data.[64,66] Inside the prism the computed two-phase regions of the ternary mixtures are shown. (M. Neichel and E. U. Franck, unpublished results.)

A substantially different behavior is found if one of the components is a salt. The addition of salts to supercritical aqueous solutions leads to "salting-out" phenomena, which are, for example, of considerable interest for mineral formation in hydrothermal fluids. Figure 15 illustrates salting-out effects in H_2O+CO_2+NaCl.[84] It shows experimental phase boundaries for 4 and 48 mol% of CO_2 in water, and their displacement by NaCl. At 48 mol% CO_2 the addition of only 6 wt% of NaCl (relative to water) extends the heterogeneous regime by 100 K. Even larger shifts have been observed for methane.[85] As such experiments are extremely difficult and time-consuming, there seems to be no substitute for modeling. There are some promising results in this direction, for

 © 2005 Wiley-VCH Verlag GmbH & Co. KGaA, Weinheim

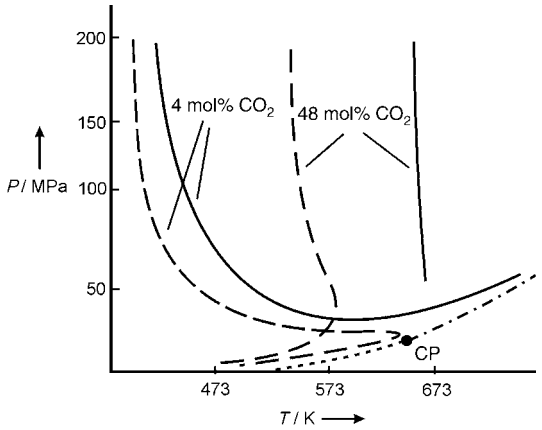

Figure 15. Phase-boundary curves of binary H_2O+CO_2 systems at mole fractions of CO_2 of 4 and 48% (– – –) and their displacement by NaCl (——).[84] The NaCl content relative to water is 6 wt%. The vapor-pressure curve of pure water (-----) and the initial part of the critical curve of the $H_2O+NaCl$ (–•–•) system near the critical point (CP) of pure water are also shown.

example for H_2O+CH_4+NaCl and $H_2O+CH_4+CO_2+NaCl$.[86] In principle, such modelings suffer, however, from the lack of information on interactions between salts and nonpolar substances. It is usually assumed that the solubility of salts in nonpolar fluids is completely negligible.

It is clear that many interesting applications of supercritical aqueous solutions concern geochemical problems.[12,13] Some geologically important hydrothermal fluids contain up to ten or more species at concentrations sufficiently high enough to influence phase transitions and thermodynamic properties. A fascinating example for the power of modern experimental technologies and theoretical modelings is the study of hydrocarbon genesis in the Earth's mantle. It is a common belief that the hydrocarbons of natural petroleum result from biotic organic materials under the pressure of deposited sediments. Recently, evidence has been reported that in the high-temperature, high-pressure hydrothermal solutions containing $CaCO_3$ and FeO, methane can be formed in an abiogenic pathway.[87] Scott et al.[88] have now demonstrated the formation of methane by in situ Raman spectroscopy in a diamond anvil cell at pressures between 5 and 11 GPa and temperatures between 500 K and 1500 K, a range which includes the typical conditions found in the Earth's mantle at a depth of about 30 km. The observations were further supported by thermodynamic calculations based on equations of state which were modified to allow for chemical reactions.[88] The results suggest that an abiogenic pathway may indeed contribute to the Earth's total methane budget. The potential exists for formation of heavier hydrocarbons in hydrothermal systems from methane as a precursor.

4. Aqueous Solutions of Electrolytes

4.1 Salt Solubility

Coulomb interactions between charged species are much stronger and of longer range than the interactions between uncharged species. Among others, these strong interactions lead to high critical temperatures for salts which cannot be reached by experiments. In contrast to the situation encountered with non-ionic fluids, water is then much more volatile than the solute. Even the temperatures of the normal melting points (S–L) and solid–liquid–gas (S–L–G) triple points of simple salts usually exceed the critical temperature of water. Thus, liquid–solid equilibria in supercritical water cannot be ignored and lead to complex phase diagrams, often involving more than one solid phase. Experiments are usually restricted to the water-rich regime.

For many applications it suffices to know the gross phase behavior. This behavior mainly depends on whether the vapor-pressure curve of the saturated solution, that is, the S–L–G three-phase line, cuts the L–G critical line (type 2) or does not cut it (type 1).[89] In the type 2 case salts are practically insoluble in dense supercritical water, in the type 1 case they are soluble. Even the type 1 electrolytes will precipitate, however, if the water density is decreased. Thus, instead of L–L equilibria, as encountered with non-ionic solutes, solid–liquid equilibria are now decisive for the fate of the L–G critical curve. Table 1 classifies some important salts according to their solubility behavior.[89] Soluble salts of type 1 includes most alkali and alkaline-earth halides and the hydroxides. The group of practically insoluble salts of type 2 includes, among others, the sulfates.

Table 1: Classification of salts according to their solubility behavior in supercritical water.[89]

Type 2 (insoluble)	Type 1 (soluble)
LiF, NaF	KF, RbF, CsF
	LiCl, NaCl, KCl, RbCl, CsCl
	LiBr, NaBr, KBr, RbBr, CsBr
CaF_2	$CaCl_2$, $CaBr_2$, CaI_2
BaF_2	$BaCl_2$, $BaBr_2$
Li_2CO_3, Na_2CO_3	K_2CO_3, Rb_2CO_3
Li_3PO_4, Na_3PO_4	K_3PO_4
Li_2SO_4, Na_2SO_4, K_2SO_4	Rb_2SO_4
$MgSO_4$, $CaSO_4$	

The most important example of a soluble salt is NaCl. Bischoff and Pitzer[90] have summarized the available work on the $NaCl+H_2O$ system and have discussed its phase behavior in detail. Today, the critical curve is known from fluid inclusion experiments to about 1100 K, corresponding to 30 wt% of NaCl.[91] At all compositions, the three-phase line S–L–G[92] runs sufficiently below the critical curve to avoid an interruption. Because liquid–liquid phase equilibria are absent as well, the critical curve of NaCl probably remains uninterrupted up to the critical point of NaCl above 3000 K. Rules of thumb developed for non-electrolytes predict an interruption whenever the ratio of the critical temperatures of the pure compounds exceeds a value of about 2–2.5.[58,59] For $NaCl+H_2O$ this ratio is 5. Clearly, electrolyte solutions do not obey this rule.

As an example for an insoluble type 2 salt, Figure 16 shows the three-phase line S–L–G of $MgSO_4$ as a function of the salt molarity m (mol per kg of water).[93] The key for

 © 2005 Wiley-VCH Verlag GmbH & Co. KGaA, Weinheim

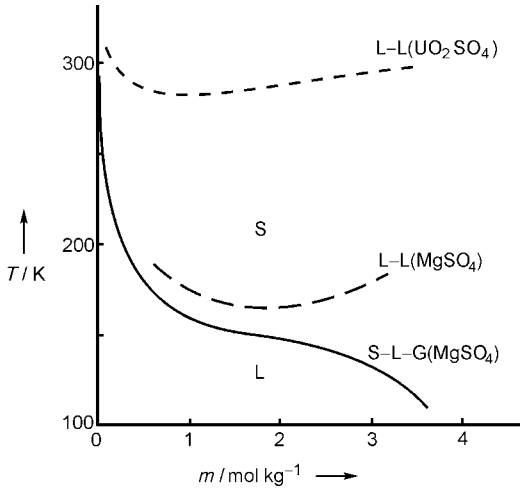

Figure 16. Three-phase line S–L–G of aqueous solutions of $MgSO_4$ at high temperatures (——). In the temperature range shown the retrograde solubility means that the solid regime (S) occurs above the liquid regime (L). The liquid–liquid coexistence curve (– – –) is estimated from pressure-jump experiments.[98] The experimentally observed liquid–liquid coexistence curve of $UO_2SO_4 + H_2O$ (-----)[95] is also shown.

understanding such phase equilibria is a negative temperature coefficient of the salt solubility at high temperatures. The solubility of $MgSO_4$ increases with increasing temperature up to about 343 K, but then decreases. This retrograde solubility implies that some salts of high solubility at ordinary conditions become sparingly soluble in hot water, so that in the segment of the phase diagram shown in Figure 16 the solid regime occurs at higher temperatures than the liquid regime. Salts such as Na_2SO_4 and Na_2CO_3 behave similarly. As a consequence the three-phase line will intersect the L–G critical line at a critical end point. Because at the critical end point the salt is present only in trace amount, this point is, in practice, indistinguishable from the critical point of pure water.

Many studies of such phase equilibria have been initiated by geochemists,[12,13] but there is considerable overlap with systems of interest in chemical or industrial applications. Low salt solubilities form, for example, a major problem for the industrial realizations of the SCWO process, because the salts may plug the reactor or connecting lines.[94] Transitions along homologous series should, however, be noted. For example, Table 1 shows that Na_2CO_3 is almost insoluble in dense supercritical water, but K_2CO_3 is highly soluble. Such details may be of great importance when faced with the choice of neutralizing an acidic feed of a reactor by NaOH or KOH. Of course, other properties, such the higher corrosivity of potassium salts, have to be considered as well.

4.2 Liquid–Liquid Phase Separations in Electrolyte Solutions

In principle, the possibility for critical-curve interruption by L–L equilibria in electrolyte solutions also exists. It is, however, a widespread belief that in electrolyte solutions such L–L phase equilibria are absent, because ion hydration stabilizes the solutions against such a decomposition. Actually, above 559 K the system $UO_2SO_4 + H_2O$ separates into two liquid phases.[95] For a long time, this demixing was attributed to disproportionation and hydrolysis of the uranyl ion. Today, it is known that it forms a generic feature of high-temperature aqueous solutions of multivalent ions, but is usually suppressed by the retrograde solubilities of the salts.[93,96,97]

Support for this conjecture has come from experiments with $MgSO_4$, which is an important constituent of natural solutions. The analysis of thermodynamic data suggests the appearance of an L–L equilibrium above the retrograde three-phase line S–L–G.[93] Figure 17 shows this behavior in a

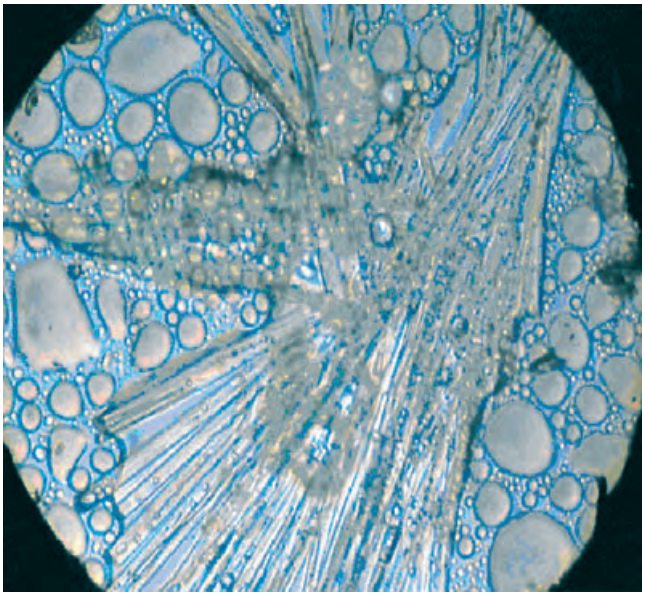

Figure 17. Liquid–liquid demixing and subsequent crystallization in an aqueous solution of $MgSO_4$ near 430 K after a pressure jump of about 0.5 GPa (generated in a gasket of 1-mm internal diameter of a diamond anvil cell). L–L demixing results in spontaneous formation of droplets. Needles of crystals indicate crystallization over a longer time scale.

diamond anvil cell.[98] A pressure jump near the retrograde three-phase line S–L–G results in a spontaneous liquid–liquid demixing, as indicated by droplet formation. Eventually, the formation of a solid phase gives a more stable state, so that on a longer time scale L–L demixing is followed by crystallization. The data indicate that the L–L coexistence curve is probably located 5–15 K above the retrograde three-phase line S–L–G. The estimated L–L coexistence curve is shown in Figure 16, that of $UO_2SO_4 + H_2O$ is given for comparison.

From the applications perspective, such L–L phase equilibria can be handled in reactors more easily than solid–liquid equilibria. It should, however, not be overlooked that L–L phase separation may generate very concentrated, highly corrosive solutions. Historically, technical and corrosion problems caused by L–L phase separation of $UO_2SO_4 +$

 © 2005 Wiley-VCH Verlag GmbH & Co. KGaA, Weinheim

H_2O were an important drawback for considering this system as a basis for an aqueous homogenous nuclear reactor.

From the scientific perspective, the L–L coexistence curves are of great importance for understanding electrolyte behavior, and can serve as important targets for testing electrolyte theories.[96,97] Theory shows that such equilibria are generic features of electrolyte solutions whenever the dielectric constant of the solvent is low. Thus, the phenomenon is not limited to high-temperature water, but is also present in non-aqueous solvents of low ε under ordinary conditions.[99] By well-known corresponding-states arguments,[97] such systems have been used to mimic properties of supercritical aqueous solutions that are difficult to study directly.

4.3 Critical Anomalies in Ionic Fluids

Another remarkable difference between ionic and non-ionic fluids concerns the near-critical behavior. It has been noted in Section 3.3 that the behavior of binary solutions should be isomorphous to that of pure fluids, and thus should exhibit Ising-like behavior. According to the renormalization group analysis,[33] Ising-like universality is a result of the short-range nature of molecular interactions. Thus, the Ising model applies to non-electrolyte interactions decaying with distance as $1/r^6$, but not to the $1/r$-dependent Coulomb potential.[100] The long-range nature of the Coulomb interactions could violate the critical point universality, and give rise to mean-field critical behavior. This problem provides an intriguing challenge for theory and experiment.[100] It is also relevant for applications[101] because the presence of mean-field behavior would remove many difficulties encountered in modeling non-ionic systems.

In assessing the problem, a look at the L–G critical behavior of metals may be fruitful. Early experiments for alkali metals suggested mean-field criticality, but more recently, highly accurate experiments by Hensel and co-workers for alkali metals and mercury have confirmed an Ising-like nature of the critical point.[102] A rationale is that the electrons screen the Coulomb interactions between the ionic cores to such an extent that they restore Ising-like behavior.[102,103]

In electrolyte solutions, the bare Coulomb interactions between a pair of ions are screened by the charges of the other ions. This effect is known as Debye-shielding. It enters, for example, into the Debye–Hückel-theory of dilute solutions, where it is accounted for by the concept of the "ion cloud".[104] The problem of the effect of Debye-shielding upon critical behavior has given rise to much recent theoretical and experimental work; see a comprehensive review by Weingärtner and Schröer.[96] From theory, a clear picture has not yet evolved because for sufficiently realistic models of an ionic fluid the necessary renormalization group analysis has not yet become feasible. Some experimental data for supercritical aqueous NaCl solutions seem to suggest mean-field behavior.[101]

Based on corresponding-states arguments, it seems possible to exploit L–L equilibria in non-aqueous electrolyte solutions as model systems for supercritical water systems. By clever choice of the salt and solvent, L–L critical points can be generated near ordinary conditions.[99] A much investigated system of this type is tetra-*n*-butylammonium picrate + *n*-dodecanol.[96,101,105] which has an upper critical point of 336 K. Taking the coexistence curve as a target, it is necessary to discriminate between the exponent $\beta = 1/2$ in the mean-field case and $\beta = 0.326$ in the Ising case. To a good approximation, the coexistence curve in Figure 18 is cubic in the asymptotic range;[105] for comparison a parabolic curve is also shown.

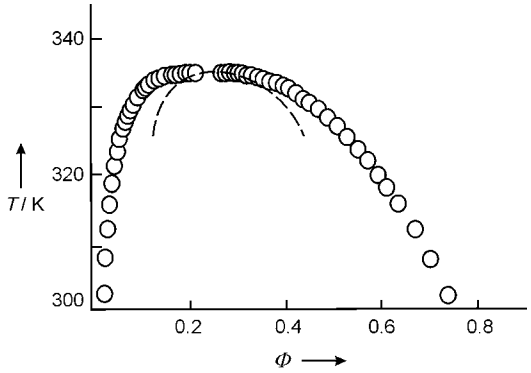

Figure 18. Experimental L–L coexistence curve of the model system tetra-*n*-butylammonium picrate + *n*-dodecanol,[105] which according to simple corresponding-states arguments mimics the critical behavior of L–L transitions in high-temperature aqueous electrolyte solutions. In the asymptotic range, the experimental points show essentially cubic behavior. The hypothetical parabolic curve of mean-field behavior is shown by the dashed line.

From such measurements[96,105] the issue of asymptotic critical behavior of ionic fluids may now be regarded as largely settled in favor of an asymptotic Ising-like critical character as found for non-ionic fluids. Applications usually involve states further away from critical points, where interesting differences between ionic and non-ionic solutes are indeed observed. Generally, crossover to mean-field behavior seems to be much faster for ionic than for non-ionic fluids.

4.4 Systems that are Continuously Miscible up to the Molten Salt

As in the case of non-ionic mixtures, there is great interest in characterizing the properties of salt + water systems over the complete miscibility range up to the molten salt. In practice, it is impossible to conduct such experiments at liquid-like densities with salts such as NaCl. At the normal melting temperature of NaCl of 1074 K, pressures higher than 1 GPa are necessary to compress water to a liquid-like density. Moreover, such states of high temperature and high density would be very corrosive. The equation of state of NaCl + H_2O only extends to 873 K, 400 MPa, and 25 wt % NaCl.[106] For NaCl a few additional fluid-inclusion data have been reported for higher temperatures and pressures.[107]

 © 2005 Wiley-VCH Verlag GmbH & Co. KGaA, Weinheim

Low-melting organic salts allow the transition from dilute electrolyte solutions to molten salts to be studied at ordinary conditions, but their solution properties are not typical for ionic behavior.[99] Moreover, the compressibility of such systems is too low to generate substantial density variations. A more suitable electrolyte is NaOH, which at normal pressure melts at 594 K. NaOH is completely miscible with high-density supercritical water, thus offering a broad homogeneous region for investigations. Volumetric data have been reported up to 673 K and 400 MPa.[108] In contrast to solutions of nonpolar solutes, the excess volumes are negative, which indicates significant volume contraction upon mixing.

The excess molar Gibbs energies $\bar{G}^E$ of $NaOH + H_2O$ in Figure 12 are negative, and exhibit a strongly asymmetrical shape for the concentration dependence with a minimum in the water-rich regime.[108] The data yield ionic activity coefficients that differ greatly from unity at all compositions. In modeling chemical or phase equilibria, the consideration of activity corrections is therefore mandatory. The difference to the positive $\bar{G}^E$ values of nonpolar solutes is striking. The negative values seem to reflect a dominance of ion hydration over other interparticle interactions. More detailed interpretations are, however, difficult because molten NaOH of low compressibility is mixed with highly compressible supercritical water.

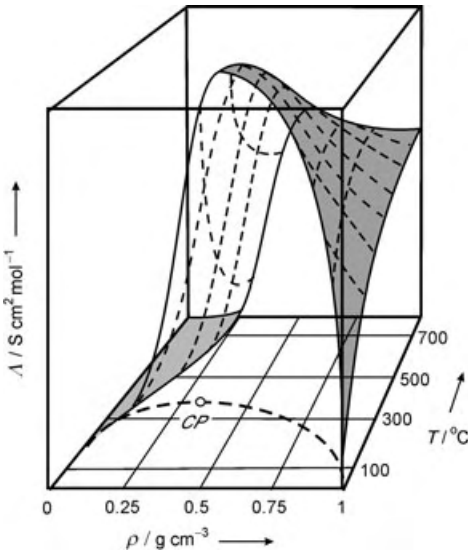

Figure 19. Schematic representation of the molar conductance, Λ, of alkali halides, strong acids, and hydroxides as a function of the density of water and the temperature at a constant mole fraction of the salt of approximately 2×10^{-5}, which corresponds to molar concentrations of 1 mmol L^{-1} at normal conditions. The maximum conductance is typically of the order of 1000–1500 $S\,cm^2\,mol^{-1}$, which is a factor of 8–10 higher than the molar conductance at normal conditions. The L–G coexistence curve and critical point (CP) of pure water are shown at the floor of the cube.

4.5 Electrical Properties

Since the first investigations of the electrical conductance of supercritical solutions of KCl, HCl, and KOH up to 1273 K and 1 GPa,[109] this subject has been of continuing interest.[110] Almost all conductance studies refer to dilute solutions, typically at molar concentrations of $c \approx 0.01$ mol L of the salt (referred to 298 K), which corresponds to a mole fraction of less than 2×10^{-4}. Figure 19 shows schematically the basic features of the molar conductance Λ of dilute solutions of alkali-metal salts, strong acids, and hydroxides plotted as a function of temperature and pressure.

Λ is almost zero at low water densities, where neutral ions pairs are stable. Above 0.2 $g\,cm^{-3}$ Λ begins to rise up to a maximum near 0.6 $g\,cm^{-3}$, where the dielectric constant of water is high enough to push the dissociation equilibrium almost entirely to the side of the free ions. The decrease of Λ at still higher densities reflects the increase in the viscosity of the solutions. The maximum conductivity is an order of magnitude higher than that at ordinary conditions. The "Grotthus mechanism" of rapid H^+ and OH^- ion transport via hydrogen bonds is less efficient at high temperatures.

For NaOH, conductance measurements have been performed up to the pure molten electrolyte.[111] Figure 20 shows an isotherm of the molar conductance at 623 K at liquid-like total density as a function of the mole fraction of NaOH. At dense states, water still has an appreciable dielectric constant, and the initial segment of the conductance curve shows the typical high values of dissociated electrolyte solutions, which rapidly decrease with increasing salt concentration. Above 20 mol % of salt, the gradual replacement of water by NaOH has only a limited influence, and the conductance behavior is already similar to that of a molten salt. Conductance equations for electrolyte solutions fail in describing this conductance behavior over the complete miscibility range, as do some familiar expressions based on an analysis of the conductance–viscosity ("Walden") product $\Lambda\eta$.

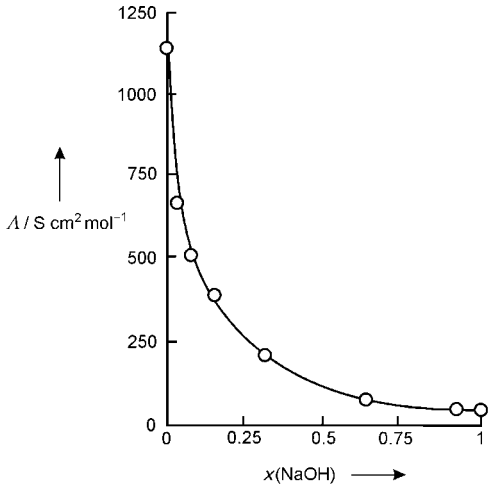

Figure 20. Isotherm of the molar conductance, Λ, of $H_2O + NaOH$ at 623 K and a total molar concentration of 50 mol L^{-1} as a function of the mole fraction of NaOH.[111]

If the water density is lowered, ion-pairing increases. The electrical conductance gives, however, no information on the configuration of the ion pairs. In favorable cases, Raman spectroscopy may provide such information, because intramolecular vibrations in molecular ions, such as NO_3^-, are

 © 2005 Wiley-VCH Verlag GmbH & Co. KGaA, Weinheim

influenced by contacts with other ions and by changes in hydration.[112] MD simulations may also contribute to the understanding of ion equilibria.[27] A broad range of ion configurations from contact ion pairs to solvent-separated ion pairs is usually found, but at low dielectric constant, contact ion pairs are preferably formed. Again, results for electrolyte solutions in non-aqueous solvents at normal conditions may indicate the phenomena to be expected in supercritical water.[97]

The high electrical conductance of supercritical aqueous solutions enables the electrolysis of water to H_2 and O_2. Such an electrolysis may, among others, be interesting for in situ generation of oxygen in oxidation processes. Experiments at supercritical conditions were performed in solutions of NaOH to 400 MPa and 803 K.[113] Figure 21 shows some results obtained with gold electrodes.

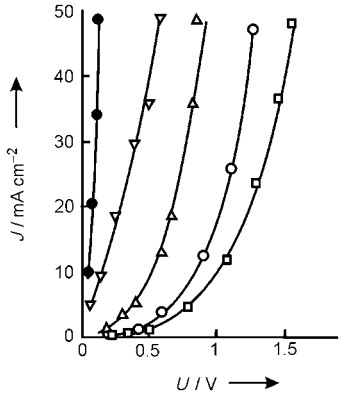

Figure 21. Electrical current density J as a function of potential U for aqueous solutions of NaOH of molar concentration 1 mol L^{-1} (referring to normal conditions) at 673 K (●), 573 K (▽), 473 K (△), 373 K (○), and 293 K (□).[113] The results are obtained with gold electrodes at a surface ratio of the cathode to anode of about 1:100. The pressure is 400 MPa in all cases.

At 298 K, the current-density–potential curves show a transition from low current densities below the decomposition potential to strongly increasing current densities above the decomposition potential. The equilibrium decomposition potential is $E^0 = 1.23$ V at 298 K and 0.1 MPa, but there are overpotentials. The equilibrium decomposition potential as well as the overpotentials decrease with increasing temperature. At high temperatures the potential curves become almost linear. The overpotential disappears, and current densities become very high. High temperatures reduce the influence of activation barriers, enhance transport processes, and reduce ion absorption at the electrodes. As a consequence, the electrodes is almost nonpolarizable above 673 K. The current densities of up to 35 A cm^{-2} obtained at cell voltages of about 2 V are two orders of magnitude higher than those obtained in industrial electrolyzers.

4.6 Transition-Metal Complexes

Knowledge of the ions present in solutions of transition-metal cations and of the stability regions of these aggregates is of particular interest in assessing the role of heavy-metal complexes in fields such as SCWO technology, metallurgy, or for understanding high-temperature corrosion. Spectroscopy in the visible (Vis) or ultraviolet (UV) range also provides a powerful means for investigating complex formation. For example, the hexaquo-complexes of Co^{2+} ions in aqueous $CoCl_2$ solutions at normal conditions give pink solutions, while at 573 K and a modest pressure of 35 MPa, the blue color of tetrahedral complexes prevails.[114] Similar changes in coordination have been found for other transition-metal cations by various spectroscopic methods,[112,114] and also by X-ray absorption fine structure (XAFS) experiments.[115] These changes of coordination number are intriguing because unsaturated metal centers may coordinate with organic ligands, thereby catalyzing the degradation of these molecules in supercritical water. It remains to be investigated whether high-temperature catalysts of practical use for such processes can be developed.

4.7 Equations of State

Under normal conditions the thermodynamics of aqueous electrolyte solutions has been developed to a mature state, and theories are well founded in statistical mechanics. Practically all these theories are built upon ideas developed by Debye and Hückel in their theory of dilute electrolyte solutions, which, among others, results in the famous limiting law for the mean ionic activity coefficient.[104] Treatments of concentrated solutions rely on extensions of Debye–Hückel theory. Above all, a semi-empirical approach developed in many studies from 1973 onwards by Pitzer and co-workers[116,117] is now widely used. Pitzer's theory combines a Debye–Hückel approach with a virial expansion for representing specific interactions.

Neither Pitzer's model nor other approaches are suited for extension to supercritical conditions. Some essential problems in applications are of a technical nature, and can be cured by reformulation of the theory.[118] A more fundamental problem is that all these approaches rely on a Debye–Hückel-type reference system of free ions immersed in the dielectric continuum of the solvent. A reference system based on interactions between free ions seems to be impractical in regions where most ions are paired. Anderko and Pitzer[119] have therefore gone a different way, by adopting a reference state based on dipolar hard spheres as models for ion pairs. This concept has been successfully applied to rationalize phase equilibria and P,V,T properties of binary and ternary supercritical systems.[119,120] A theory that spans the total range from normal to supercritical conditions requires the connection of this approach with the Debye–Hückel-type theories. Such a global approach is not yet available.

5. Conclusions

Dense supercritical water is a medium which provides an unusual variety of interesting phenomena. Continuous changes of thermophysical properties can be achieved by

 © 2005 Wiley-VCH Verlag GmbH & Co. KGaA, Weinheim

pressure variation, and result in transitions from "gas-like" to "liquid-like" behavior. With plausible extrapolations, the existing data base is sufficient to establish an equation of state to 1273 K and 1 GPa. From shock-wave experiments, there is even information on some properties of water at several thousand Kelvin and up to almost 200 GPa.

The ultimate aim is to explain macroscopic properties in terms of molecular interactions. In this regard, the advent of high-speed computers opens new ways. While simulations are not yet accurate enough for practical applications, they provide much insight into the molecular origin of the various phenomena. In this regard, the fluid structure of water and the underlying nature of the hydrogen bonds play a key role. It is now ensured by many experiments and simulations that hydrogen bonds exist in dense states far above the critical temperature of water.

The change in the thermophysical properties of supercritical water with temperature and density has dramatic consequences for its solvent behavior. At high-temperatures water looses the familiar high selectivity towards polar and ionic compounds, and in some range of temperature and pressure nonpolar compounds become highly miscible. Typically, at 673 K, all inorganic gases and simple organic compounds, if not destroyed, are completely miscible with water at pressures up to several 100 MPa. At high water densities some salts are highly soluble as well. This opens a window for generating homogeneous aqueous solutions with high concentrations of solutes of largely different polarity. This extraordinary behavior is, of course, impossible at ambient conditions, and forms the conceptual basis of innovative techniques such as SCWO technologies. Other interesting chemical applications can be conceived.

Because in many situations, one is fairly close to critical points, the challenge of incorporating the nonclassical critical nature of fluids into theories and data correlations still remains. There is now widespread recognition that such effects are not limited to the vicinity of the critical point, but in some cases extend to states far away. In this regard, many equations of state are deficient. In the best case, the critical anomalies are implicitly absorbed in adjustable parameters of the classical models. In the worst case, largely erroneous predictions are obtained. While the asymptotic scaling laws now allow an appropriate description near critical points, the understanding of crossover to classical behavior further away is still a challenge. A detailed understanding of this interplay between universal critical phenomena on the one hand and molecular interactions on the other remains a problem.

In this context it should be noted that the Coulomb interactions in ionic systems are much stronger and of longer range than van der Waals interactions in non-ionic fluids. This situation gives rise to substantial changes in phase behavior associated with the high critical temperatures and pressures and the high melting points of the salts. While in most supercritical solutions of nonpolar solutes phase behavior only fluid phase equilibria occur, in supercritical electrolyte solutions solid–fluid equilibria often play a decisive role. This fact has major consequences for industrial applications because salt precipitation in reactors is much more difficult to handle than fluid coexistence. Claims that the long-range nature of the Coulomb interactions even violates critical-point universality were, however, not confirmed by recent experiments.

As the strength of the Coulomb interactions crucially depends on their shielding by the dielectric constant of the solvent, a wide variety of ion configurations ranging from complete dissociation to complete association into neutral pairs can occur in supercritical water, which gives rise to large difficulties in formulating equations of state for supercritical aqueous electrolytes. For many transition metal ions, specific complex formation has to be considered as well. Pressure variation can lead to interesting changes in coordination which, in the light of possible prospects for catalysis, have yet to be explored in detail. Finally, the decisive role of supercritical solutions for geochemical processes should be emphasized again.

Received: October 29, 2004
Published online: April 13, 2004

[1] a) *Steam, Water and Hydrothermal Systems: Physics and Chemistry Meeting the Needs of Industry* (Eds.: P. R. Tremaine, P. G. Hill, D. Irish, P. V. Balakrishnan), NRC, Ottawa, **2000**; b) "Supercritical Fluids, Fandamentals and Applications": E. Kiran, P. G. Debenedetti, C. J. Peters, *NATO Sci. Ser. Ser. E* **2000**, *366*; c) *Supercritical Fluid Technology* (Eds. T. J. Bruno, J. F. Ely), CRC, Boca Raton, FL, USA, **1991**.
[2] a) E. U. Franck in ref. [1a], pp. 22–34; b) E. U. Franck in ref. [1b], pp. 307–322. c) E. U. Franck, *J. Chem. Thermodyn.* **1987**, *19*, 225 – 242; d) E. U. Franck, H. Weingärtner in *Chemical Thermodynamics. A Chemistry for the 21th Century Monograph*, (Ed. T. Letcher), Blackwell, London, **1999**, pp. 105 – 119.
[3] R. Chau, C. Mitchell, R. W. Minich, W. J. Nellis, *J. Chem. Phys.* **2001**, *114*, 1361 – 1365.
[4] W. B. Holzapfel, E. U. Franck, *Ber. Bunsen-Ges.* **1966**, *70*, 1105 – 1112.
[5] W. B. Holzapfel, *J. Chem. Phys.* **1972**, *56*, 712 – 715.
[6] a) P. Loubeyre, R. LeToullec, E. Wolanin, M. Hanfma, D. Hauserman, *Nature* **1999**, *397*, 503 – 506; b) M. Benoit, A. H. Romero, D. Marx, *Phys. Rev. Lett.* **2002**, *89*, 145501.
[7] a) D. Bröll, C. Kaul, A. Krämer, P. Krammer, T. Richter, M. Jung, H. Vogel, P. Zehner, *Angew. Chem.* **1999**, *111*, 3180 – 3196; *Angew. Chem. Int. Ed.* **1999**, *38*, 2998 – 3014; b) E. Savage, *Chem. Rev.* **1999**, *99*, 603 – 622.
[8] a) W. Schilling, E. U. Franck, *Ber. Bunsen-Ges.* **1988**, *92*, 631 – 636; b) R. W. Shaw, T. B. Brill, A. A. Clifford, C. A. Eckert, E. U. Franck, *Chem. Eng. News* **1991**, *69*, 26 – 39.
[9] T. Hirth, E. U. Franck, *Ber. Bunsen-Ges.* **1993**, *97*, 1091 – 1098.
[10] G. M. Pohsner, E. U. Franck, *Ber. Bunsen-Ges.* **1994**, *98*, 1082 – 1090.
[11] M. Sauer, F. Behrendt, E. U. Franck, *Ber. Bunsen-Ges.* **1993**, *97*, 900 – 908.
[12] See, for example, D. T. Rickard, F. E. Wickman, *Chemistry and Geochemistry of Solutions at High Temperatures and High Pressures*, Pergamon, Oxford, **1981**.
[13] K. Tödheide, *Ber. Bunsen-Ges.* **1982**, *86*, 1005 – 1016.
[14] B. Hubbard, *Science* **1997**, *275*, 1279 – 1280.
[15] E. U. Franck, *Angew. Chem.* **1961**, *73*, 309 – 322.
[16] W. Wagner, A. Pruss, *J. Phys. Chem. Ref. Data* **2002**, *31*, 387 – 535.
[17] a) G. J. Piermarini, S. Bloch, *Rev. Sci. Instrum.* **1975**, *46*, 973 – 979; b) J. D. Barnett, S. Bloch, G. J. Piermarini, *Rev. Sci. Instrum.* **1973**, *44*, 973, 1 – 9.

 © 2005 Wiley-VCH Verlag GmbH & Co. KGaA, Weinheim

[18] F. Datchi, P. Loubeyre, R. LeToullec, *Phys. Rev. B* **2000**, *61*, 6535 – 6546.
[19] L. Haar, J. S. Gallagher, G. S. Kell, *NBS/NRC Steam Tables: Thermodynamic and Transport Properties and Computer Programs for Vapour and Liquid States of Water in SI-Units*, US National Bureau of Standards, Gaithersburgh, **1984**.
[20] C. W. Pistorius, M. C. Pistorius, J. P. Blakey, L. J. Admiraal, *J. Chem. Phys.* **1963**, *38*, 600 – 602.
[21] C. Cavazzoni, G. L. Chiarotti, S. Scandolo, E. Tosatti, M. Bernasconi, M. Parinello, *Science* **1999**, *283*, 44 – 46.
[22] C. W. Burnham, J. R. Holloway, N. F. Davies, *Am. J. Sci. A* **1969**, *276*, 70 – 95.
[23] a) S. Maier, E. U. Franck, *Ber. Bunsen-Ges.* **1966**, *70*, 639 – 645; b) H. Köster, E. U. Franck, *Ber. Bunsen-Ges.* **1969**, *73*, 716 – 722.
[24] G. A. Lyzenga, T. J. Ahrens, W. J. Nellis, A. J. Mitchell, *J. Chem. Phys.* **1982**, *76*, 6282 – 6286.
[25] E. H. Abramson, J. M. Brown, *Geochim. Cosmochim. Acta* **2004**, *68*, 1827 – 1835.
[26] a) C. Withers, S. C. Kohn, R. A. Brooker, B. J. Wood, *Geochim. Cosmochim. Acta* **2000**, *64*, 1051 – 1057; b) J. P. Brodholdt, B. J. Wood, *Geochim. Cosmochim. Acta* **1994**, *58*, 2143 – 2148; c) D. J. Frost, B. J. Wood, *Geochim. Cosmochim. Acta* **1997**, *61*, 3301 – 3309.
[27] A. Chialvo, P. T. Cummings, *Adv. Chem. Phys.* **1999**, *109*, 115 – 205, and references therein.
[28] See, for example, J. M. Prausnitz, R. N. Lichtenthaler, E. Gomes de Azevedo, *Molecular Thermodynamics of Fluid-Phase Equilibria*, Prentice-Hall, Eaglewood Cliffs, **1986**.
[29] K. S. Pitzer, S. M. Sterner, *J. Chem. Phys.* **1994**, *101*, 3111 – 3116.
[30] A. Harlow, G. Wiegand, E. U. Franck, *Ber. Bunsen-Ges.* **1997**, *101*, 1461 – 1465.
[31] E. U. Franck, G. Wiegand, R. Gerhardt, *J. Supercrit. Fluids* **1999**, *15*, 127 – 133.
[32] M. A. Anisimov, J. V. Sengers in *Equations of State for Fluids and Fluid Mixtures* (Eds.: J. V. Sengers, R. F. Kayser, C. J. Peters, H. J. White), Elsevier, Amsterdam, **2000**.
[33] a) M. E. Fisher, *Rev. Mod. Phys.* **1998**, *70*, 653 – 681; b) "Scaling, Universality and Renormalization Group Theory": M. E. Fisher, *Lect. Notes Phys.* **1983**, *186*, 1 – 119.
[34] A. K. Wyczalkowska, Kh. S. Abdulkadirova, M. A. Anisimov, J. V. Sengers, *J. Chem. Phys.* **2000**, *113*, 4985 – 5002.
[35] W. L. Marshall, E. U. Franck *J. Phys. Chem. Ref. Data*, **1981**, *10*, 295 – 304.
[36] N. C. Holmes, W. J. Nellis, W. B. Graham, G. E. Walrafen, *Phys. Rev. Lett.* **1985**, *55*, 2433 – 2436.
[37] W. J. Nellis, D. C. Hamilton, N. C. Holmes, H. B. Radouski, F. H. Ree, A. C. Mitchell, M. Nicol, *Science* **1988**, *240*, 779 – 781.
[38] K. H. Dudziak, E. U. Franck, *Ber. Bunsen-Ges.* **1966**, *70*, 1120 – 1128.
[39] W. Lamb, G. A. Hoffman, J. J. Jonas, *J. Chem. Phys.* **1981**, *74*, 6875 – 6880.
[40] N. Matubayashi, N. Nakao, M. Nakahara, *J. Chem. Phys.* **2001**, *114*, 4107 – 4115.
[41] K. Okada, M. Yao, Y. Hiejima, H. Kohno, Y. Kajihara, *J. Chem. Phys.* **1999**, *110*, 3026 – 3036.
[42] F. J. Dietz, J. J. deGroot, E. U. Franck, *Ber. Bunsen-Ges.* **1981**, *85*, 1005 – 1009.
[43] T. J. Butenhoff, M. G. E. Goemans, S. J. Buelow, *J. Phys. Chem.* **1996**, *100*, 5982 – 5992.
[44] a) K. Heger, M. Uematsu, E. U. Franck, *Ber. Bunsen-Ges.* **1980**, *84*, 758 – 762; b) R. Deul, E. U. Franck, *Ber. Bunsen-Ges.* **1991**, *95*, 847 – 853.
[45] E. U. Franck, S. Rosenzweig, M. Christophorakos, *Ber. Bunsen-Ges.* **1990**, *94*, 199 – 203.
[46] J. G. Kirkwood, *J. Chem. Phys.* **1939**, *7*, 911 – 991.
[47] M. Uematsu, E. U. Franck, *J. Phys. Chem. Ref. Data* **1980**, *9*, 1291 – 1306.
[48] D. P. Fernandez, A. R. H. Goodwin, E. W. Lemmon, J. M. H. Levelt Sengers, C. R. Williams, *J. Phys. Chem. Ref. Data* **1997**, *26*, 1125 – 1166.
[49] Y. Marcus, *J. Mol. Liq.* **1999**, *81*, 101 – 113.
[50] H. Weingärtner, *J. Mol. Liq.* **2002**, *98–99*, 293 – 301.
[51] M. Boero, K. Terakura, T. Ikeshoji, C. C. Liew, M. Parrinello, *Phys. Rev. Lett.* **2000**, *85*, 3245 – 3248.
[52] E. U. Franck, K. H. Roth, *Discuss. Faraday Soc.* **1967**, *43*, 108 – 114.
[53] W. Kohl, H. A. Lindner, E. U. Franck, *Ber. Bunsen-Ges.* **1991**, *95*, 1586 – 1593.
[54] a) N. Matubayashi, C. Wakai, M. Nakahara, *Phys. Rev. Lett.* **1997**, *78*, 4309; b) N. Matubayashi, C. Wakai, M. Nakahara, *J. Chem. Phys.* **1997**, *107*, 9133 – 9140; c) M. M. Hoffman, M. S. Conradi, *J. Am. Chem. Soc.* **1997**, *119*, 3811 – 3817.
[55] R. H. Tromp, P. Postorino, G. W. Neilson, M. A. Ricci, A. K. Soper, *J. Chem. Phys.* **1994**, *101*, 6210 – 6215.
[56] a) A. Botti, F. Bruni, M. A. Ricci, A. K. Soper, *J. Chem. Phys.* **1998**, *109*, 3180 – 3184; b) K. Soper, F. Bruni, A. K. Ricci, *J. Chem. Phys.* **1997**, *106*, 247 – 254.
[57] R. Ludwig, *Angew. Chem.* **2001**, *113*, 1856 – 1876; *Angew. Chem. Int. Ed.* **2001**, *40*, 1808 – 1827.
[58] P. H. Van Konynenburg, R. L. Scott, *Discuss. Faraday Soc.* **1970**, *49*, 87 – 97.
[59] R. S. Rowlinson, F. L. Swinton, *Liquids and Liquid Mixtures*, Butterworths, London, **1982**.
[60] D. S. Tsiklis, L. R. Linhits, N. P. Goryunova, *Zh. Fiz. Khim.* **1965**, *39*, 2978 – 2981.
[61] W. L. Marshall, E. V. Jones, *J. Inorg. Nucl. Chem.* **1974**, *36*, 2319 – 2323.
[62] G. M. Schneider, *Phys. Chem. Chem. Phys.* **2002**, *4*, 845 – 852.
[63] a) R. Grzanna, G. M. Schneider, *Z. Phys. Chem.* **1996**, *192*, 41 – 47; b) H. Weingärtner, D. Klante, G. M. Schneider, *J. Solution Chem.* **1999**, *28*, 435 – 446.
[64] M. L. Japas, E. U. Franck, *Ber. Bunsen-Ges.* **1985**, *89*, 1268 – 1275; M. L. Japas, E. U. Franck, *Ber. Bunsen-Ges.* **1985**, *89*, 793 – 800.
[65] N. G. Sretenskaya, R. J. Sadus, E. U. Franck, *J. Phys. Chem.* **1995**, *99*, 4274 – 4277.
[66] T. M. Seward, E. U. Franck, *Ber. Bunsen-Ges.* **1981**, *85*, 2 – 7.
[67] Y. S. Wei, R. J. Sadus, E. U. Franck, *Fluid Phase Equilib.* **1996**, *123*, 1 – 15.
[68] M. Neichel, E. U. Franck, *J. Supercrit. Fluids* **1996**, *9*, 69 – 74.
[69] E. Brunner, *J. Chem. Thermodyn.* **1990**, *22*, 335 – 353.
[70] A. E. Mather, E. U. Franck, *J. Phys. Chem.* **1992**, *96*, 6 – 8.
[71] Z. Alwani, G. M. Schneider, *Ber. Bunsen-Ges.* **1969**, *73*, 294 – 301.
[72] J. M. H. Levelt Sengers in ref. [1c], pp. 1–56.
[73] R. Kruse, E. U. Franck, *Ber. Bunsen-Ges.* **1982**, *86*, 1036 – 1038.
[74] S. C. Greer, M. R. Moldover, *Annu. Rev. Phys. Chem.* **1981**, *32*, 233 – 265.
[75] J. C. Rainwater in ref. [1c], pp. 58–162.
[76] M. Christoforakos, E. U. Franck, *Ber. Bunsen-Ges.* **1986**, *90*, 780 – 789.
[77] M. Heilig, E. U. Franck, *Ber. Bunsen-Ges.* **1989**, *93*, 898 – 905.
[78] N. F. Carnahan, K. E. Starling, *J. Chem. Phys.* **1969**, *51*, 635 – 636.
[79] Z. H. Duan, N. Møller, J. H. Weare, *Geochim. Cosmochim. Acta* **1996**, *60*, 1209 – 1216.
[80] Z. H. Duan, N. Møller, J. H. Weare, *Geochim. Cosmochim. Acta* **2000**, *64*, 1069 – 1075.
[81] S. Goldman, C. Joslin, *Ber. Bunsen-Ges.* **1995**, *99*, 204 – 210.
[82] M. Heilig, E. U. Franck, *Ber. Bunsen-Ges.* **1990**, *94*, 27 – 35.
[83] E. U. Franck, M. Neichel, unpublished results.

 © 2005 Wiley-VCH Verlag GmbH & Co. KGaA, Weinheim

[84] M. Gehrig, H. Lentz, E. U. Franck, *Ber. Bunsen-Ges.* **1986**, *90*, 525 – 533.
[85] T. Krader, E. U. Franck, *Ber. Bunsen-Ges.* **1987**, *91*, 627 – 634.
[86] Z. H. Duan, N. Møller, J. H. Weare, *Geochim. Cosmochim. Acta* **2003**, *67*, 671.
[87] J. F. Kenney, V. A. Kutcherov, N. A. Bendeliani, V. A. Alekseev, *Proc. Natl. Acad. Sci. USA* **2002**, *99*, 10976 – 10981.
[88] H. P. Scott, R. J. Hemley, H.-K. Mao, D. R. Herschbach, L. E. Fried, W. M. Howard, S. Bastea, *Proc. Natl. Acad. Sci. USA* **2004**, *101*, 14023 – 14026.
[89] a) W. L. Marshall, *Chemistry* **1975**, *48*, 6 – 12; b) V. M. Valyashko, *Pure Appl. Chem.* **1997**, *69*, 2271 – 2280.
[90] J. L. Bischoff, K. S. Pitzer, *Am. J. Sci.* **1989**, *289*, 217 – 248.
[91] A. L. Knight, R. J. Bodnar, *Geochim. Cosmochim. Acta* **1989**, *53*, 3 – 8.
[92] K. G. Kravchuk, K. Tödheide, *Z. Phys. Chem.* **1996**, *193*, 139 – 150.
[93] H. Weingärtner, *Ber. Bunsen-Ges.* **1989**, *93*, 1058 – 1065.
[94] M. Hodes, P. A. Marrone, G. T. Hong, K. A. Smith, J. W. Tester, *J. Supercrit. Fluids* **2004**, *29*, 265 – 288.
[95] C. H. Secoy, *J. Am. Chem. Soc.* **1950**, *72*, 3343 – 3345.
[96] H. Weingärtner, W. Schröer, *Adv. Chem. Phys.* **2001**, *116*, 1 – 66.
[97] a) H. Weingärtner, W. Schröer, *Pure Appl. Chem.* **2004**, *76*, 19 – 27; b) H. Weingärtner, *Pure Appl. Chem.* **2001**, *73*, 1733 – 1748; c) H. Weingärtner, W. Schröer, in ref. [1a], pp. 320–327.
[98] H. Weingärtner, unpublished results.
[99] H. Weingärtner, T. Merkel, U. Maurer, J. P. Conzen, H. Glasbrenner, S. Käshammer, *Ber. Bunsen-Ges.* **1991**, *95*, 1579 – 1586.
[100] a) M. Fisher, *J. Stat. Phys.* **1994**, *75*, 1 – 36; b) G. Stell, *J. Stat. Phys.* **1995**, *78*, 197 – 338.
[101] K. S. Pitzer, *J. Phys. Chem.* **1995**, *99*, 13070 – 13077, and references therein.
[102] F. Hensel, *J. Phys. Condens. Matter* **1990**, SA33 – SA45.
[103] F. Hensel, W. C. Pilgrim, *Contrib. Plasma Phys.* **2003**, *43*, 206 – 210.
[104] a) P. Debye, E. Hückel, *Phys. Z.* **1923**, *24*, 185 – 206; b) R. A. Robinson, R. H. Stokes, *Electrolyte Solutions*, Butterworths, London, **1969**.
[105] M. Kleemeier, S. Wiegand, W. Schröer, H. Weingärtner, *J. Chem. Phys.* **1999**, *110*, 3085 – 3099.
[106] M. Gehrig, H. Lentz, E. U. Franck, *Ber. Bunsen-Ges.* **1983**, *87*, 597 – 600.
[107] R. J. Bodnar, *Pure Appl. Chem.* **1995**, *67*, 873 – 880.
[108] S. Kerschbaum, E. U. Franck, *Ber. Bunsen-Ges.* **1995**, *99*, 624 – 632.
[109] E. U. Franck, *Z. Phys. Chem.* **1956**, *8*, 92 – 106; E. U. Franck, *Z. Phys. Chem.* **1956**, *8*, 107 – 126; E. U. Franck, *Z. Phys. Chem.* **1956**, *8*, 192 – 206.
[110] P. Ho, D. A. Palmer, M. S. Kruszkiewicz, *J. Phys. Chem. B* **2001**, *105*, 1260 – 1266, and references therein.
[111] A. Eberz, E. U. Franck, *Ber. Bunsen-Ges.* **1995**, *99*, 1091 – 1103.
[112] a) D. E. Irish, T. Jarv, *Appl. Spectrosc.* **1983**, *37*, 50 – 55; b) P. D. Spohn, T. B. Brill, *J. Phys. Chem.* **1989**, *93*, 6224 – 6231.
[113] H. Boll, E. U. Franck, H. Weingärtner, *J. Chem. Thermodyn.* **2003**, *35*, 625 – 637.
[114] H. D. Lüdemann, E. U. Franck, *Ber. Bunsen-Ges.* **1967**, *71*, 455 – 460; H. D. Lüdemann, E. U. Franck, *Ber. Bunsen-Ges.* **1968**, *72*, 514 – 523.
[115] M. M. Hoffmann, J. G. Darab, B. J. Palmer, J. L. Fulton, *J. Phys. Chem. A* **1999**, *103*, 8471 – 8482.
[116] See, for example, K. S. Pitzer in *Activity Coefficients in Electrolyte Solutions* (Ed.: K. S. Pitzer), 2nd ed., CRC, Boca Raton, **1991**, pp. 75 – 153.
[117] K. S. Pitzer, *J. Phys. Chem.* **1973**, *77*, 268 – 277.
[118] J. M. H. Levelt Sengers, C. M. Everhart, G. Morrison, K. S. Pitzer, *Chem. Eng. Commun.* **1986**, *47*, 317 – 328.
[119] A. Anderko, K. S. Pitzer, *Geochim. Cosmochim. Acta* **1993**, *57*, 1657 – 1680.
[120] Z. Duan, N. Møller, J. H. Weare, *Geochim. Cosmochim. Acta* **1995**, *59*, 2869 – 2882.
[121] F. Hensel, *Angew. Chem.* **2005**, *117*, 1180; *Angew. Chem. Int. Ed.* **2005**, *44*, 1156.

 © 2005 Wiley-VCH Verlag GmbH & Co. KGaA, Weinheim

Communications

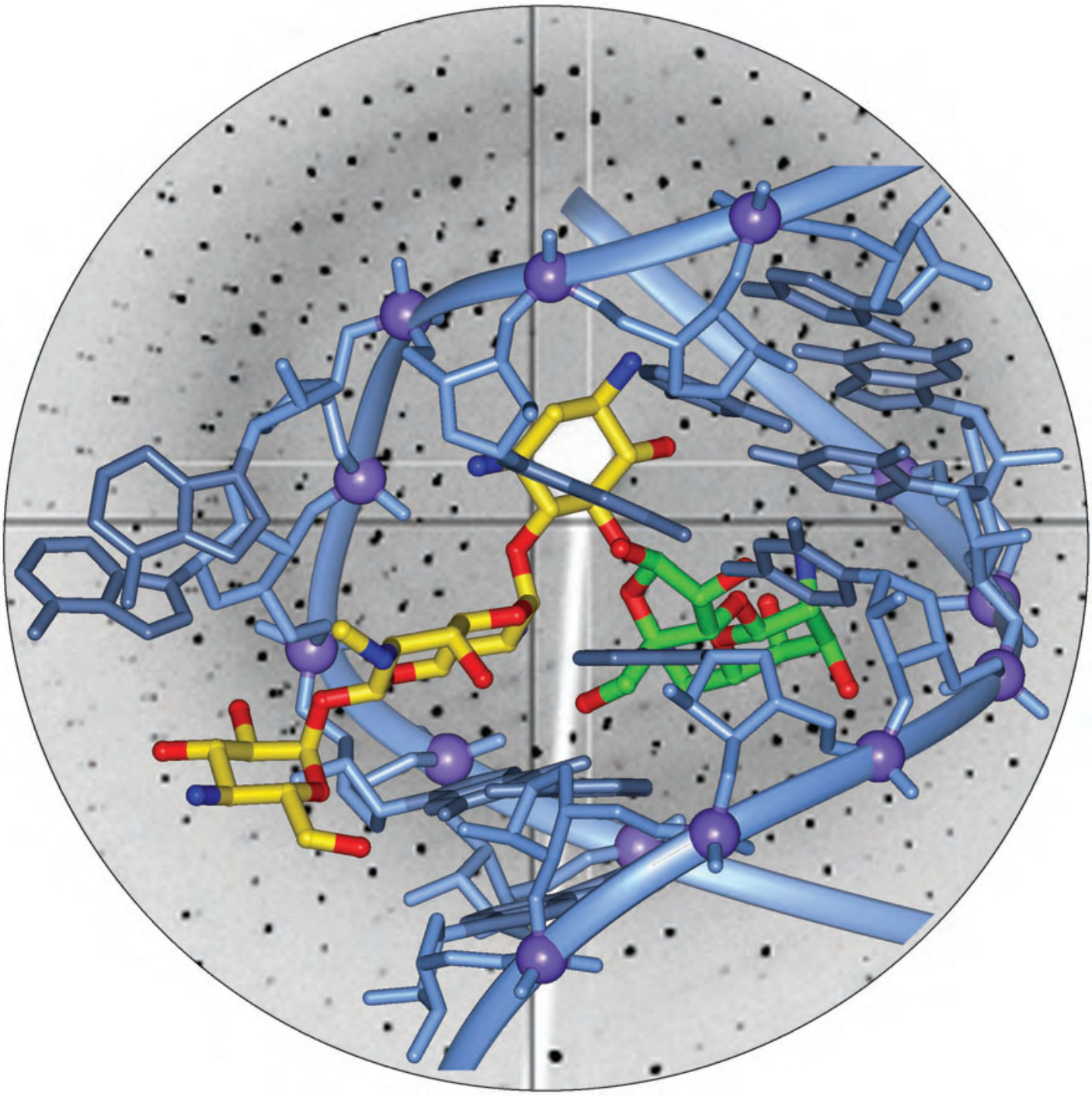

The aminoglycosides apramycin (yellow) and paromomycin (green) exploit different binding spaces at their target ribosomal decoding-site RNA although they share a common 2-deoxystreptamine scaffold (white center). More about these studies on molecular recognition can be found in the Communication by T. Hermann and co-workers on the following pages.

 © 2005 Wiley-VCH Verlag GmbH & Co. KGaA, Weinheim DOI: 10.1002/anie.200500028

Aminoglycoside Antibiotics

Molecular Recognition by Glycoside Pseudo Base Pairs and Triples in an Apramycin–RNA Complex**

*Qing Han, Qiang Zhao, Sarah Fish, Klaus B. Simonsen, Dionisios Vourloumis, Jamie M. Froelich, Daniel Wall, and Thomas Hermann**

The ribosome and its RNA components are targets for a diverse set of antibiotics, including the natural aminoglycosides, macrolides, and tetracyclins and the synthetic oxazolidinones, all of which interfere with bacterial protein synthesis.[1,2] Crystallographic analyses of ribosomal subunits and domains thereof in complex with antibiotics have demonstrated that the natural products interact almost exclusively with ribosomal RNA components (rRNA),[3] a result that lends support to earlier biochemical findings[4,5] and underlines the importance of RNA as a drug target.[6] Aminoglycoside antibiotics bind to 16S rRNA near the mRNA decoding site and thereby decrease the fidelity of translation by lowering the energetic cost of a conformational transition in the ribosome that is required for the discrimination between near-cognate and cognate tRNAs.[7,8] Insight into the molecular recognition of the decoding site by antibiotic ligands and the mechanics of translational fidelity are emerging from three-dimensional structures of aminoglycosides in complex with decoding-site oligonucleotides and whole 30S ribosomal subunits.[7,9–13]

Crystal structures have been determined for RNA complexed with two classes of aminoglycosides (Scheme 1). The three-dimensional structures of paromomycin (**5**) as well as tobramycin (**4**) and geneticin bound to the whole 30S ribosomal subunit and to small model oligonucleotides revealed a key role for the 2-deoxystreptamine (2-DOS) moiety in RNA recognition.[10–12,14] In all cases, the 2-DOS ring interacts with two consecutive base pairs of the decoding-site RNA, that is, C1407–G1494 and the non-Watson–Crick pair U1406○U1495 (Figure 1 a). Since these base pairs are conserved in both the bacterial and eukaryotic decoding site, molecular discrimination of the bacterial target by aminoglycosides is provided through a combination of sugar substituents at the 4- and 5- or the 4- and 6-positions of the 2-DOS moiety.

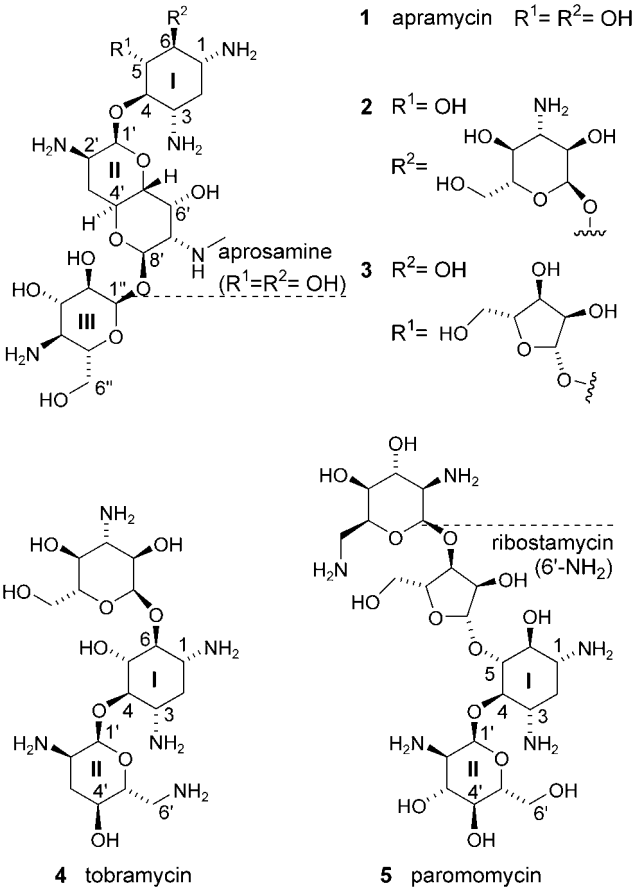

Scheme 1. Aminoglycoside antibiotics that bind to the bacterial decoding-site RNA. Apramycin (**1**), a unique 4-monosubstituted 2-deoxystreptamine, is described herein. Compounds **2** and **3** are semisynthetic apramycin derivatives.[35] Aprosamine is obtained from apramycin by acid hydrolysis of the terminal sugar (III) to leave a free hydroxy group at the 8′-position.[15] Crystal structures of decoding-site RNA complexed with tobramycin (**4**), a 4,6-disubstituted 2-deoxystreptamine, and paromomycin (**5**), a 4,5-disubstituted 2-deoxystreptamine, were described recently.[7,9–11] The 2-deoxystreptamine moiety shared by all structures is numbered I. The ring fragments numbered II are derived from glucose.

Apramycin (**1**) is unique among the aminoglycosides as it achieves antibacterial specificity by sugar substitution of the 2-DOS ring at the 4-position only (Scheme 1).[15–17] Chemical probing has been used to study binding of apramycin to the bacterial decoding site and has revealed specific interactions of the antibiotic with residues A1408 and G1494,[5] which also participate in the binding of the 4,5- and 4,6-disubstituted 2-DOS compounds.[10–12,14] In contrast to these aminoglycosides, which induce miscoding during translation, the primary effect of apramycin is inhibition of elongation by blocking ribosome translocation.[17] To decipher the molecular recognition of the bacterial rRNA target by apramycin, we have determined by

[*] Dr. Q. Han, Dr. Q. Zhao, S. Fish, Dr. T. Hermann
Department of Structural Chemistry
Anadys Pharmaceuticals, Inc.
3115 Merryfield Row, San Diego, CA 92121 (USA)
Fax: (+1) 858-527-1539
E-mail: thermann@anadyspharma.com
Dr. K. B. Simonsen,[+] Dr. D. Vourloumis
Department of Medicinal Chemistry
Anadys Pharmaceuticals, Inc. (USA)
J. M. Froelich, Dr. D. Wall
Department of Microbiology
Anadys Pharmaceuticals, Inc. (USA)
[+] Current address:
H. Lundbeck A/S
Copenhagen Valby (Denmark)

[**] This work was supported by the National Institutes of Health (Grant no. AI51104 to T.H.).

Supporting Information for this article is available on the WWW under http://www.angewandte.org or from the author.

 © 2005 Wiley-VCH Verlag GmbH & Co. KGaA, Weinheim

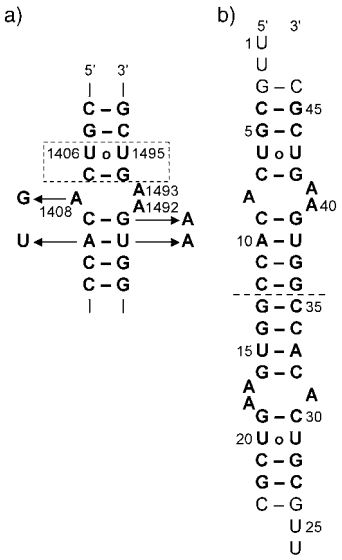

Figure 1. a) Secondary structure of the bacterial decoding-site internal loop in 16S rRNA. The four base changes of the eukaryotic sequence are indicated by arrows. The recognition site for the 2-DOS moiety of aminoglycosides is boxed. b) RNA construct used for cocrystallization with apramycin. Due to the self-complementarity of the single strands, two antiparallel decoding-site loops are formed. Residues that are specific to the bacterial decoding site are shown in bold.

X-ray crystallography the three-dimensional structure of apramycin complexed to the bacterial decoding site in an RNA model construct (Figure 1 b). Similar constructs have been used before for crystallographic structure determination of aminoglycoside–RNA complexes and were proved to represent authentic models of the ribosomal decoding site.[10–12,14,18]

In the crystal structure of the apramycin–RNA complex, both decoding-site internal loops are occupied by the aminoglycoside (see the Supporting Information). One of the ligand-binding sites participates in crystal-packing contacts, involving A 1492 and A 1493 in an interdigitated stacking arrangement with a neighboring RNA molecule, while the other decoding site is unperturbed by intermolecular contacts. As the geometry of the two ligand-binding sites is similar, we focus here on the analysis of the unperturbed site (Figure 2). The overall structure of the internal-loop RNA resembles the decoding-site complexes of paromomycin, tobramycin, and geneticin that were previously described.[10–12,14] The unpaired A 1408 residue is stacking between flanking base pairs and interacting with apramycin which spans the RNA helix from the interior at the deep (major) groove to the exterior at the shallow (minor) groove. The A 1492 and A 1493 residues are flipped out from the interior of the RNA helix, thereby creating an opening that accommodates the aminoglycoside (Figure 2 a).

The C 1407–G 1494 base pair and the U 1406○U 1495 non-Watson–Crick pair form both direct and water-mediated hydrogen bonds with the 2-DOS ring (I) of apramycin (Scheme 2 a). The hydrogen-bonding pattern and position of the apramycin 2-DOS ring relative to the RNA are similar to those of the 2-DOS moiety in the decoding-site complexes of other aminoglycosides (Figure 2 b and c).[10–12,14] The geometry of the U 1406○U 1495 pair most closely resembles the structure of this pair in the geneticin complex,[14] but with a relative translation of the residues that results in compression of the RNA helix diameter (9.3 Å C1′–C1′ distance, in comparison with 9.8 Å in the geneticin complex). It has been pointed out that a U 1406 A change confers resistance specifically to the 4,6-disubstituted 2-DOS aminoglycosides whose sugar substituent at the 6-position cannot be accommodated when a A 1406–U 1495 pair is present.[18] Apramycin, which does not carry substituents at either the 5- or 6-positions, can still bind to the U 1406 A decoding-site mutant. The 2-DOS interaction pattern in the apramycin complex is in agreement with susceptibility data for bacteria carrying a U 1406 A mutation, which show a fourfold hypersensitivity to this antibiotic.[19] Molecular modeling of an A 1406–U 1495

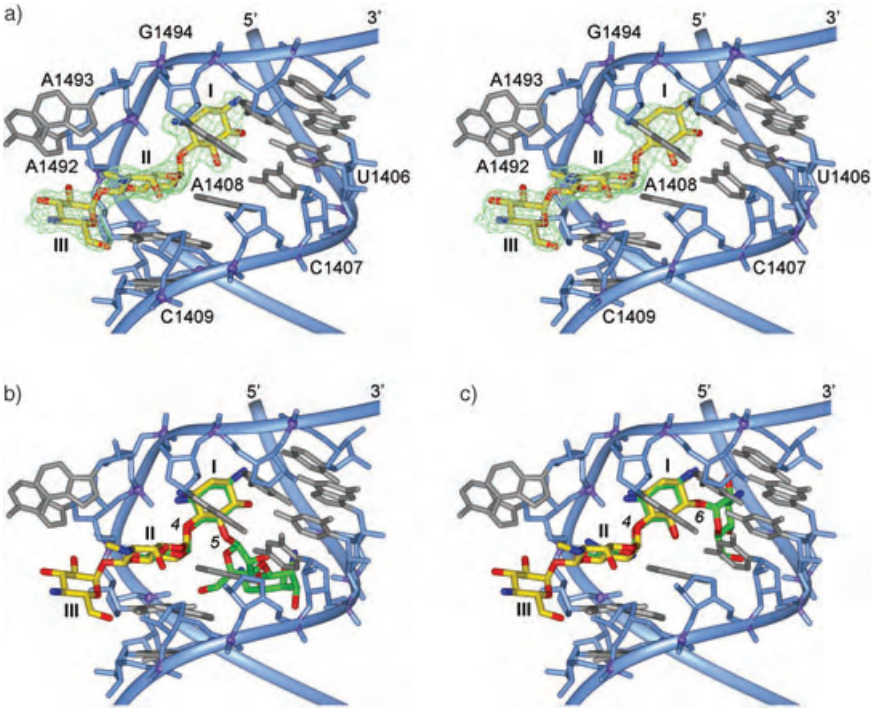

Figure 2. a) Stereoview of the apramycin–decoding-site RNA complex. Electron density ($2F_o-F_c$) is contoured at 1.0 σ around the aminoglycoside. Apramycin (yellow) ring fragments are numbered according to the sequence shown in Scheme 1. b) Superimposition (based on phosphate coordinates) of the complexes of apramycin (yellow) and paromomycin[10] (green) with the decoding site. Only the RNA of the apramycin complex is shown. The 4- and 5-substitution positions of the 2-DOS core in paromomycin are indicated. c) Superimposition (based on phosphate coordinates) of the complexes of apramycin (yellow) and tobramycin[11] (green) with the decoding site. The 4- and 6-substitution positions of the 2-DOS core in tobramycin are indicated. Base numbering follows the *Escherichia coli* sequence (see Figure 1).

 © 2005 Wiley-VCH Verlag GmbH & Co. KGaA, Weinheim

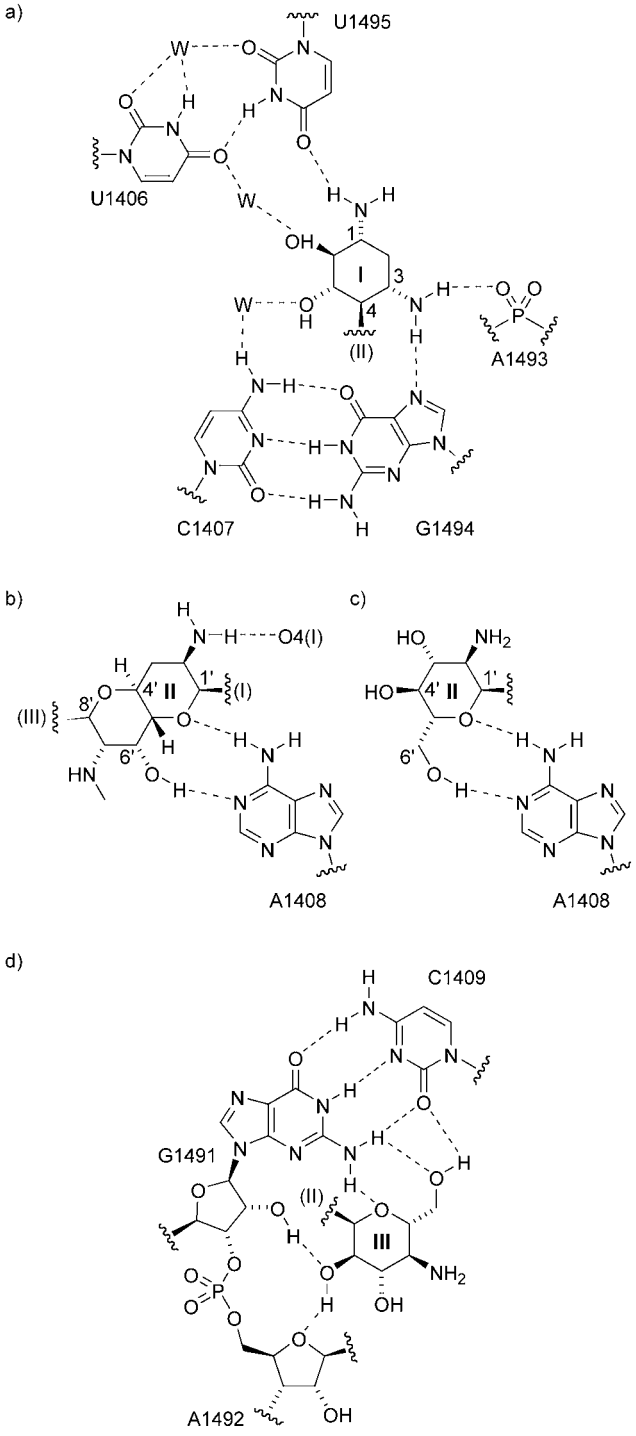

Scheme 2. a) Hydrogen-bonding interactions of the apramycin 2-DOS moiety with the decoding-site RNA target. Water molecules are indicated as W. b) Base-pair-like interaction of the bicyclic sugar (II) of apramycin with the A1408 residue. This can be compared with c) the interaction of the glucosamine moiety (II) of paromomycin with A1408.[10] d) Base-triple-like docking of the terminal sugar fragment (III) of apramycin to the minor-groove edge of a G–C pair. Base numbering follows the *Escherichia coli* sequence (see Figure 1).

Watson–Crick pair in the decoding-site structure shows that a water-mediated hydrogen bond could be formed between the 6-hydroxy group of the 2-DOS ring and the 4-amino substituent of A1406. This water-mediated interaction would adopt a more favorable geometry than the observed contact between the same 2-DOS hydroxy group and O4 of U1406 in the apramycin–wild-type RNA complex. Similar observations have been made for paromomycin and neomycin B,[19] 4,5-disubstituted 2-DOS aminoglycosides whose binding to the decoding site is positively affected by the U1406A mutation.[18]

The bicyclic sugar (II) of apramycin is stacking over the guanine base of the C1409–G1491 pair (Figure 2), aligned in a coplanar manner, and forming direct hydrogen-bond interactions with the A1408 residue (Scheme 2b). The ring connected to the 2-DOS moiety is located in a position similar to that of the glucosamine residue in other aminoglycosides bound to the decoding-site RNA (Figure 2b and c).[10–12,14] The hydrogen-bonding pattern between O1′ and O6′ of the apramycin sugar (II) and A1408 is identical to the interactions seen for the glucosamine ring in the paromomycin complex (Scheme 2c), and it gives rise to a geometry that has been described as a glycoside–adenine pseudo base pair.[14] The 2′-amino group of apramycin is involved in an intramolecular contact to O5 of the 2-DOS moiety. The interaction between the bicyclic sugar (II) of apramycin and A1408 explains susceptibility data for bacteria carrying an A1408G mutation or a methylated A1408 residue, either of which confers resistance to apramycin.[20,21] Methylation of the adenine exocyclic amino group or change to a guanine at residue 1408 prevents formation of the glycoside pseudo base pair with the apramycin sugar (II).

The terminal sugar (III) of apramycin is aligned at the shallow-groove edge of the C1409–G1491 pair and forms two direct hydrogen bonds to these bases, thereby resulting in an interaction that we termed a glycoside pseudo base triple (Scheme 2d). The geometry of the interaction closely resembles the arrangement of shallow-groove X·G–C base triples that occur in ribosomal RNA, such as the G2588·G2617–C2542 triple in 23S rRNA from *Haloarcula marismortui* and the A1085·G1055–C1104 triple in 23S rRNA from *Escherichia coli* (see also Figure S2 in the Supporting Information).[22,23] Shallow-groove recognition of RNA base pairs has frequently been observed in protein–RNA complexes, such as the ribosome, spliceosomal particles, and aminoacyl-tRNA synthetases.[24]

The 6″-hydroxy group of apramycin that participates in the interaction with the C1409–G1491 pair is located at a position that is occupied by a water molecule in the decoding-site complexes of tobramycin and geneticin.[11,12] Additional hydrogen bonds are formed between the 2″-hydroxy substituent of apramycin and the ribose moieties of G1491 and A1492. Aprosamine, which lacks the terminal sugar (III) of apramycin (Scheme 1),[15] still binds to the bacterial decoding-site RNA, albeit with a lower affinity that leads to a tenfold loss of potency in translation inhibition and bacterial growth suppression.[25] The interaction between the apramycin terminal sugar (III) and the C1409–G1491 pair is in agreement with bacterial resistance conferred by decoding-site mutations at these residues. Earlier investigations of *E. coli* strains carrying all possible nonlethal single and double mutations at the 1409 and 1491 residue positions showed that any change

 © 2005 Wiley-VCH Verlag GmbH & Co. KGaA, Weinheim

of the wild-type C–G pair results in 2- to 64-fold decrease in susceptibility to apramycin.[26]

Superimposition of the apramycin–RNA complex with the crystal structure of the 30S ribosomal paromomycin complex[7] shows that the orientation of the apramycin sugar (III) projects the 3″-hydroxy group into close proximity (<2 Å) with the T40 residue of ribosomal protein S12 (Figure 3). Recent functional studies of S12 have revealed

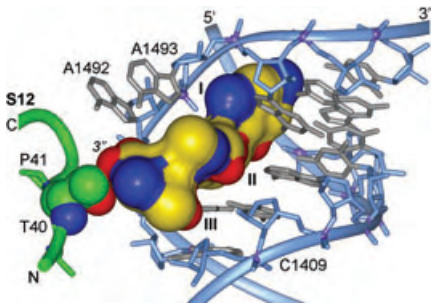

Figure 3. Superimposition (based on phosphate coordinates) of the apramycin–RNA complex with the decoding site in the crystal structure of the whole 30S ribosomal subunit complex with paromomycin.[7] The molecular surface of apramycin (yellow, dark blue, and red), the RNA of the apramycin complex (pale blue and gray), and a fragment of the ribosomal protein S12 (green) from the 30S subunit structure are shown. The 3″-hydroxy group of the terminal aminoglycoside ring (III) clashes with the side chain of the T40 residue (green and dark blue, labeled) within S12.

that it plays a key role as a control element for translocation of the mRNA–tRNA complex during translation.[27] Apramycin binding to the decoding site might interfere with the local conformation of S12 around the T40 residue, a possibility suggesting a hypothesis for the unique inhibitory action of apramycin on ribosome translocation.[17] Further support for this hypothesis comes from genetic studies of apramycin-resistant mutants of *E. coli*, which identified two genomic loci that conferred resistance to the aminoglycoside, *aprA* and *aprB*, both of which were mapped in the neighborhood of ribosomal gene *rpsL* (S12).[28]

The crystal structure of the apramycin–decoding-site complex reveals the molecular basis for the bacterial-target specificity of the aminoglycoside antibiotic. A pseudo-base-pair interaction of the bicyclic sugar (II) with A1408 and alignment of the terminal sugar (III) with C1409–G1491 in a pseudo base triple are key determinants of the bacterial-RNA complex which cannot form with the eukaryotic target. If the *E. coli* numbering scheme is applied, the eukaryotic decoding site carries G1408 and A1491 substitutions (Figure 1a), both of which would disrupt specific interactions with apramycin. In fact, the respective eukaryotic mutations, when introduced into the bacterial decoding site, confer resistance to apramycin.[20,26] Mass-spectrometric studies of aminoglycoside binding to RNA have produced somewhat contradictory results that suggest apramycin binds with comparable affinity to the wild-type bacterial decoding site and to A1408G mutants.[29] Crystallographic investigation of complexes between apramycin and eukaryotic decoding-site constructs indicates, however, that the aminoglycoside binds to the eukaryotic RNA in a fashion very distinct from its binding to the bacterial target; it is buried entirely inside the deep groove of the eukaryotic RNA and is shifted down toward the lower flanking stem of the adenine internal loop.[30] The biological significance of this interaction is currently not known. Apramycin has recently been shown to also bind with nanomolar affinity to stem loop I (SLI) of bacterial RepA mRNA, thereby disrupting a pseudoknot interaction that regulates translation of the protein.[31] Interestingly, aminoglycosides of the 4,5- and 4,6-disubstituted 2-DOS classes do not bind to the mRNA stem loop. The SLI RNA secondary structure shares little similarity with either bacterial or eukaryotic decoding-site RNA, a fact suggesting that a different binding mode for apramycin might exist for each of these targets.

The three-dimensional structures of aminoglycoside–decoding-site complexes,[7,9–13] including the apramycin–RNA crystal structure described here, illustrate a paradigm of RNA recognition by natural products derived from 2-DOS. Namely, the 2-DOS moiety is positioned face-on in the deep groove of RNA and serves as an "RNA-friendly" anchor scaffold that bridges adjacent base pairs.[32,33] Branching out from the central 2-DOS anchor are glycoside substituents that provide additional target-specific contacts by pseudo-base-pair and -triple interactions. A similar concept of base-pair-like interactions of glycosides with nucleobases has been proposed previously by Wong and co-workers who recognized the potential of 1,3-hydroxyamine motifs found in aminoglycosides for hydrogen-bonding alignment with the Hoogsteen face of guanosine.[34] The apramycin complex with the bacterial decoding site represents the first example of glycoside pseudo base pairs and triples simultaneously participating in RNA-target recognition by a small molecule.

Binding of the apramycin 2-DOS moiety to the decoding-site RNA at a position that is nearly identical to the 2-DOS arrangement in complexes with 4,5- and 4,6-disubstituted aminoglycosides[10–12,14] suggests that novel ligands might be created by attaching additional sugar moieties at the 5- or 6-positions of apramycin (Figure 2b,c). Indeed, the structural relationship between the 4-monosubstituted 2-DOS apramycin and aminoglycosides of the 4,5- and 4,6-disubstituted 2-DOS classes has been noted before and led to the synthesis of 6-*O*-(3-amino-3-deoxy-α-D-glucopyranosyl)apramycin (**2**, Scheme 1), an apramycin/tobramycin hybrid, and 5-*O*-(β-D-ribofuranosyl)apramycin (**3**, Scheme 1), an apramycin/ribostamycin hybrid.[35] Microbiological testing in a range of organisms revealed a generally two- to fourfold increase in potency of the large aminoglycoside hybrids **2** and **3** over apramycin.[35] One exception was the test against *Pseudomonas aeruginosa*, where the potency of **2** and **3** was less than that of the parent compound, possibly due to poor permeability of the large molecules.

In the past, our group and others have used structural information from decoding-site complexes of aminoglycosides to design novel synthetic ligands for the bacterial target.[33,36,37] The structure of the apramycin–decoding-site complex lends support to a design strategy that we suggested earlier, which aims to exploit interactions in the shallow groove of decoding-site RNA, specifically with C1409.[37]

 © 2005 Wiley-VCH Verlag GmbH & Co. KGaA, Weinheim

Experimental Section

RNA crystallization was performed with gel-purified and desalted oligonucleotides purchased from Dharmacon Research (Lafayette, CO). RNA was annealed by heating in buffer (50 mM sodium cacodylate (pH 6.5), 3 mM magnesium chloride, 0.05 mM ethylenediaminetetraacetate (EDTA)) at 75 °C for 1 min and cooling to room temperature. Apramycin was purchased as the sulfate (Sigma, St. Louis, MO) and prepared as a 1.5 mM stock solution in buffer (200 mM sodium cacodylate (pH 6.5), 300 mM potassium chloride). For crystallization, 0.25 mM RNA in buffer (1.5 μL), apramycin stock solution (1.5 μL), and a solution of 2.5% 2-methyl-2,4-pentanediol (MPD) and 2.5% glycerol in water (1.5 μL) were mixed and equilibrated against 65–80% MPD for hanging-drop vapor diffusion. Crystal plates of the apramycin–RNA complex grew within three days at 37 °C. For X-ray diffraction, crystals were flash-cooled in liquid nitrogen and transferred to a cold N_2 stream. Data sets were collected on beamline 14IDB at the Advanced Photon Source (APS) at Argonne National Laboratory (Argonne, IL). The crystals of the space group $P2_12_12_1$ diffracted to 2.7 Å resolution. Data were processed with the DENZO/SCALEPACK software.[38] Structures were solved by molecular replacement by using a published decoding-site RNA structure[10] as the initial model with the AMORE program[39] and were refined to R/R_{free} values of 0.24/0.30 with the CNX/CNS program (Accelrys, San Diego, CA).[40] For complete crystal data and refinement statistics, see the Supporting Information. Coordinates and structure factors have been deposited in the Protein Data Bank (accession code: 1YRJ).

Received: January 5, 2005
Published online: April 6, 2005

Keywords: antibiotics · glycosides · molecular recognition · RNA · structure–activity relationships

[1] C. Walsh, *Antibiotics: Actions, Origins, Resistance*, ASM Press, Washington, DC, **2003**.
[2] T. Hermann, *Biopolymers* **2003**, *70*, 4 – 18.
[3] T. Auerbach, A. Bashan, J. Harms, F. Schluenzen, R. Zarivach, H. Bartels, I. Agmon, M. Kessler, M. Pioletti, F. Franceschi, A. Yonath, *Curr. Drug Targets Infect. Disord.* **2002**, *2*, 169 – 186.
[4] D. Moazed, H. F. Noller, *Nature* **1987**, *327*, 389 – 394.
[5] J. Woodcock, D. Moazed, M. Cannon, J. Davies, H. F. Noller, *EMBO J.* **1991**, *10*, 3099 – 3103.
[6] a) T. Hermann, *Angew. Chem.* **2000**, *112*, 1962 – 1979; *Angew. Chem. Int. Ed.* **2000**, *39*, 1890 – 1904; b) T. Hermann, Y. Tor, *Expert Opin. Ther. Pat.* **2005**, *15*, 49 – 62; c) Q. Vicens, E. Westhof, *ChemBioChem* **2003**, *4*, 1018 – 1023.
[7] J. M. Ogle, D. E. Brodersen, W. M. Clemons, M. J. Tarry, A. P. Carter, V. Ramakrishnan, *Science* **2001**, *292*, 897 – 902.
[8] a) J. M. Ogle, A. P. Carter, V. Ramakrishnan, *Trends Biochem. Sci.* **2003**, *28*, 259 – 266; b) J. M. Ogle, F. V. Murphy, M. J. Tarry, A. P. Carter, V. Ramakrishnan, *Cell* **2002**, *111*, 721 – 732.
[9] A. P. Carter, W. M. Clemons, D. E. Brodersen, R. J. Morgan-Warren, B. T. Wimberly, V. Ramakrishnan, *Nature* **2000**, *407*, 340 – 348.
[10] Q. Vicens, E. Westhof, *Structure* **2001**, *9*, 647 – 658.
[11] Q. Vicens, E. Westhof, *Chem. Biol.* **2002**, *9*, 747 – 755.
[12] Q. Vicens, E. Westhof, *J. Mol. Biol.* **2003**, *326*, 1175 – 1188.
[13] a) D. Fourmy, M. I. Recht, S. C. Blanchard, J. D. Puglisi, *Science* **1996**, *274*, 1367 – 1371; b) S. Yoshizawa, D. Fourmy, J. D. Puglisi, *EMBO J.* **1998**, *17*, 6437 – 6448.
[14] Q. Vicens, E. Westhof, *Biopolymers* **2003**, *70*, 42 – 57.
[15] S. O'Connor, L. K. Lam, N. D. Jones, M. O. Chaney, *J. Org. Chem.* **1976**, *41*, 2087 – 2092.
[16] a) R. Ryden, B. J. Moore, *J. Antimicrob. Chemother.* **1977**, *3*, 609 – 613; b) J. R. Walton, *J. Antimicrob. Chemother.* **1978**, *4*, 309 – 313.
[17] S. Perzynski, M. Cannon, E. Cundliffe, S. B. Chahwala, J. Davies, *Eur. J. Biochem.* **1979**, *99*, 623 – 628.
[18] P. Pfister, S. Hobbie, Q. Vicens, E. C. Böttger, E. Westhof, *ChemBioChem* **2003**, *4*, 1078 – 1088.
[19] M. I. Recht, J. D. Puglisi, *Antimicrob. Agents Chemother.* **2001**, *45*, 2414 – 2419.
[20] M. I. Recht, S. Douthwaite, J. D. Puglisi, *EMBO J.* **1999**, *18*, 3133 – 3138.
[21] a) P. A. Skeggs, J. Thompson, E. Cundliffe, *Mol. Gen. Genet.* **1985**, *200*, 415 – 421; b) A. A. Beauclerk, E. Cundliffe, *J. Mol. Biol.* **1987**, *193*, 661 – 671.
[22] N. Ban, P. Nissen, J. Hansen, P. B. Moore, T. A. Steitz, *Science* **2000**, *289*, 905 – 920.
[23] a) B. T. Wimberly, R. Guymon, J. P. McCutcheon, S. W. White, V. Ramakrishnan, *Cell* **1999**, *97*, 491 – 502; b) G. L. Conn, D. E. Draper, E. E. Lattman, A. G. Gittis, *Science* **1999**, *284*, 1171 – 1174.
[24] a) D. J. Klein, P. B. Moore, T. A. Steitz, *J. Mol. Biol.* **2004**, *340*, 141 – 177; b) A. C. Cheng, W. W. Chen, C. N. Fuhrmann, A. D. Frankel, *J. Mol. Biol.* **2003**, *327*, 781 – 796; c) T. Hermann, E. Westhof, *Chem. Biol.* **1999**, *6*, 335 – 343.
[25] Biological activities: IC_{50} values of in vitro translation inhibition: 0.2 μM apramycin, 1.8 μM aprosamine; minimum inhibitory concentrations (MICs) against a standard *Escherichia coli* strain: 2 μg mL^{-1} of apramycin, 32 μg mL^{-1} of aprosamine. Assays were performed as described in: S. Barluenga, K. B. Simonsen, E. S. Littlefield, B. K. Ayida, D. Vourloumis, G. C. Winters, M. Takahashi, S. Shandrick, Q. Zhao, Q. Han, T. Hermann, *Bioorg. Med. Chem. Lett.* **2004**, *14*, 713 – 718.
[26] E. A. DeStasio, A. E. Dahlberg, *J. Mol. Biol.* **1990**, *212*, 127 – 133.
[27] A. R. Cukras, D. R. Southworth, J. L. Brunelle, G. M. Culver, R. Green, *Mol. Cell* **2003**, *12*, 321 – 328.
[28] B. Vasiljevic, D. Fira, L. Topisirovic, *J. Basic Microbiol.* **1993**, *3*, 47 – 51.
[29] R. H. Griffey, S. A. Hofstadler, K. A. Sannes-Lowery, D. J. Ecker, S. T. Crooke, *Proc. Natl. Acad. Sci. USA* **1999**, *96*, 10129 – 10133.
[30] T. Hermann, unpublished results.
[31] J. C. B. DeNap, J. R. Thomas, D. J. Musk, P. J. Hergenrother, *J. Am. Chem. Soc.* **2004**, *126*, 15402 – 15404.
[32] a) Y. Tor, T. Hermann, E. Westhof, *Chem. Biol.* **1998**, *5*, 277-283; b) S. J. Sucheck, Y.-K. Shue, *Curr. Opin. Drug Discovery Dev.* **2001**, *4*, 462 – 470; c) S. Yoshizawa, D. Fourmy, R. G. Eason, J. D. Puglisi, *Biochemistry* **2002**, *41*, 6263 – 6270.
[33] D. Vourloumis, M. Takahashi, G. C. Winters, K. B. Simonsen, B. K. Ayida, S. Barluenga, S. Qamar, S. Shandrick, Q. Zhao, T. Hermann, *Bioorg. Med. Chem. Lett.* **2002**, *12*, 3367 – 3372.
[34] a) M. Hendrix, P. B. Alper, E. S. Priestley, C.-H. Wong, *Angew. Chem.* **1997**, *109*, 119 – 122; *Angew. Chem. Int. Ed. Engl.* **1997**, *36*, 95 – 98; b) C.-H. Wong, M. Hendrix, D. D. Manning, C. Rosenbohm, W. A. Greenberg, *J. Am. Chem. Soc.* **1998**, *120*, 8319 – 8327.
[35] Y. Abe, S. Nakagawa, T. Naito, H. Kawaguchi, *J. Antibiot.* **1981**, *34*, 1434 – 1446.
[36] a) P. Alper, M. Hendrix, P. Sears, C.-H. Wong, *J. Am. Chem. Soc.* **1998**, *120*, 1965 – 1978; b) J. Haddad, L. P. Kotra, B. Llano-Sotelo, C. Kim, E. F. Azucena, M. Liu, S. B. Vakulenko, C. S. Chow, S. Mobashery, *J. Am. Chem. Soc.* **2002**, *124*, 3229 – 3237; c) D. Vourloumis, G. C. Winters, M. Takahashi, K. B. Simonsen, B. K. Ayida, S. Shandrick, Q. Zhao, T. Hermann, *ChemBioChem* **2003**, *4*, 879 – 885; d) K. B. Simonsen, B. K. Ayida, D. Vourloumis, G. C. Winters, M. Takahashi, S. Shandrick, Q. Zhao, T. Hermann, *ChemBioChem* **2003**, *4*, 886 – 890; e) D. Vourloumis,

 © 2005 Wiley-VCH Verlag GmbH & Co. KGaA, Weinheim

G. C. Winters, K. B. Simonsen, M. Takahashi, B. K. Ayida, S. Shandrick, Q. Zhao, Q. Han, T. Hermann, *ChemBioChem* **2005**, *6*, 58 – 65.
[37] K. B. Simonsen, B. K. Ayida, D. Vourloumis, M. Takahashi, G. C. Winters, S. Barluenga, S. Qamar, S. Shandrick, Q. Zhao, T. Hermann, *ChemBioChem* **2002**, *3*, 1223 – 1228.
[38] Z. Otwinowski, W. Minor, *Methods Enzymol.* **1997**, *276*, 307 – 326.
[39] J. Navaza, *Acta Crystallogr. Sect. A* **1994**, *50*, 157 – 163.
[40] A. T. Brünger, P. D. Adams, G. M. Clore, W. L. DeLano, P. Gros, R. W. Grosse-Kunstleve, J.-S. Jiang, J. Kuszewski, M. Niges, N. S. Pannu, R. J. Read, L. M. Rice, T. Simonson, K. L. Warren, *Acta Crystallogr. Sect. D* **1998**, *54*, 905 – 921.

 © 2005 Wiley-VCH Verlag GmbH & Co. KGaA, Weinheim

Coordination Modes

Effect of the Metal-Assisted Assembling Mode on the Redox States of Hexaazatriphenylene Hexacarbonitrile**

*Shuhei Furukawa, Takashi Okubo, Shigeyuki Masaoka, Daisuke Tanaka, Ho-Chol Chang, and Susumu Kitagawa**

Metal-directed self-assembly through several molecular recognition events on polydentate ligands with a suitable arrangement of binding sites has provided a route for the spontaneous but controlled generation of supramolecular architectures.[1] In particular, the properties of inorganic supramolecules with redox-active units are of intense interest with respect to their potential for application in sensors,[2] machines,[3] and electronic devices.[4] However, much less is known about the simultaneous control of both the assembly and the redox-state of these units. Organocyanides with low-lying π^* orbitals are particularly promising candidates for redox-active units because of their characteristic electronic structures, which are based on different, readily accessible oxidation states (neutral and anion radical states) and give rise to fascinating conductive and magnetic materials.[5] In addition, a metal-directed approach with these π-accepting molecules has the advantage not only of rational bottom-up construction, with its regulated coordination geometry, but also plays an important role in influencing the ligand-centered redox potential. A net charge transfer on complexation operates in metal/π ligand systems. This transfer gives rise to the "normal" effect,[6] which causes a large anodic shift because of the σ-polarization effect of coordination.[7] However, strong π back donation often occurs and overcompensates the σ-polarization effect, thus affording a cathodic shift.[8] Hence, we have focused on controlling the oxidation states of the ligand through metal-directed self-assembly.

Among the π-accepting organocyanides, hexaazatriphenylene hexacarbonitrile hat-$(CN)_6$ is an intriguing molecular unit[9,10] because of its characteristic electron-deficient heterocyclic core, which affords three reversible redox transitions as well as two possible modes of coordination: the bipyridine chelating (bpy sites) and the terminal nitrile N-binding sites (CN sites, Figure 1). Herein, we report two supramolecules of

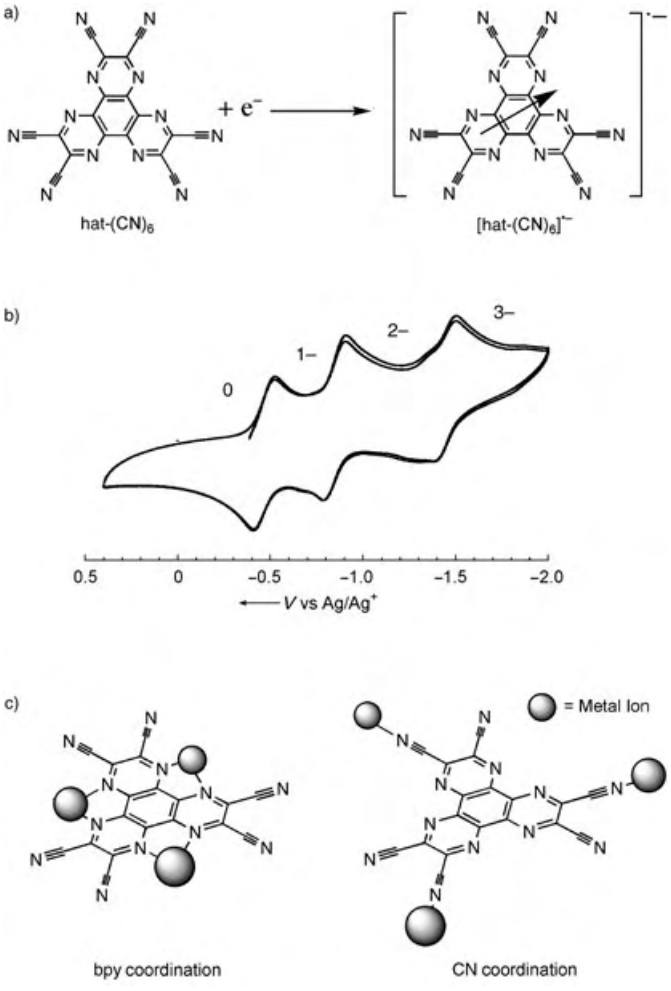

Figure 1. a) Two readily accessible different oxidation states of hat-$(CN)_6$: a neutral (left) and an anion radical form (right). b) Cyclic voltammogram of hat-$(CN)_6$ in THF showing three electrochemically reversible reduction waves. c) Two possible coordination modes of hat-$(CN)_6$: bpy (left) and CN (right) coordination modes.

[*] S. Furukawa, Dr. S. Masaoka, D. Tanaka, Dr. H.-C. Chang, Prof. Dr. S. Kitagawa
Department of Synthetic Chemistry and Biological Chemistry
Graduate School of Engineering
Kyoto University
Katsura, Nishikyo-ku, Kyoto 615-8510 (Japan)
Fax: (+81) 75-383-2732
E-mail: kitagawa@sbchem.kyoto-u.ac.jp
Dr. T. Okubo
School of Materials Science
Japan Advanced Institute of Science and Technology (JAIST)
Asahidai, Tatsunokuchi, Ishikawa 923-1292 (Japan)

[**] We would like to thank Prof. Dr. Takashi Kawamura and Dr. Ryo Kitaura for their help with the DFT calculations. This work was supported by a Grant-In-Aid for Science Research from the Ministry of Education, Culture, Sports, Science and Technology, Japan. S.F. is grateful to the JSPS Research Fellowships for Young Scientists.

Supporting information for this article is available on the WWW under http://www.angewandte.org or from the author.

 © 2005 Wiley-VCH Verlag GmbH & Co. KGaA, Weinheim DOI: 10.1002/anie.200462962

hat-$(CN)_6$, $[\{Cu(dppFc)\}_3\{hat\text{-}(CN)_6\}](PF_6)_2$ (**1**) and $[\{Cu(dppFc^*)\}_2\{hat\text{-}(CN)_6\}_2](PF_6)_2$ (**2**) (dppFc = 1,1′-bis(diphenylphosphino)ferrocene, dppFc* = 1,1′-bis(diphenylphosphino)octamethylferrocene), which possess different oxidation states; **1** contains the anion radical $[hat\text{-}(CN)_6]^{\bullet-}$ while **2** contains the neutral state hat-$(CN)_6$. Interestingly, the coordination mode of hat-$(CN)_6$ exerts a drastic effect on its reduction potentials through the "normal" effect of σ polarization.

The key to this synthesis was to design diphosphine coligands with ferrocene units on the secondary coordination sphere, namely dppX (X = Fc for **1** or Fc* for **2**; Fc = ferrocene, Fc* = octamethylferrocene). We used hat-$(CN)_6$ and $[Cu(CH_3CN)_4](PF_6)$ as the common assembling components, and dppX for modification of the mode of coordination. The overall process is shown in Scheme 1. Regardless of the ratio of the starting components (hat-$(CN)_6$, $[Cu(CH_3CN)_4](PF_6)$, and dppFc) the reaction proceeded at room temperature in dichloromethane/acetone to give a dark green solution. Single crystals of **1** were obtained by diffusion of hexane into a solution of the compound in dichloromethane. However, the use of dppFc* instead of dppFc under the same reaction conditions afforded a red solution. Crystals of **2** were obtained by diffusion of THF/hexane.

The electronic absorption spectrum of **1** in dichloromethane (see the Supporting Information) shows two intense characteristic bands at 715 and 805 nm which correspond to the π–π* transition band of the electrochemically generated anion radical $[hat\text{-}(CN)_6]^{\bullet-}$ (690 and 764 nm). In the case of **2**, no bands attributable to the anion radical form were observed, while one at 492 nm was detected, which was assigned to an MLCT transition from a copper(I) center to hat-$(CN)_6$. The vibration spectra of the complexes also supported the electronic characterization of hat-$(CN)_6$ deduced from the electronic absorption spectra. A single nitrile stretching band found at 2210 cm^{-1} for **1** was shifted to a lower energy region than that of free hat-$(CN)_6$ (at 2241 cm^{-1}). In contrast, compound **2** showed two bands at 2241 and 2194(sh) cm^{-1}, which were ascribed to the metal-free CN sites and the coordinated CN sites of the neutral hat-$(CN)_6$, respectively.[11]

The X-ray crystallographic structure of **1** (Figure 2) reveals a novel Cu_3Fc_3 hexanuclear supramolecule with a trianglar shape.[12] Complex **1** is composed of three $[Cu(dppFc)]^+$ units, with each of the copper(I) ions chelated by two P sites of dppFc (average Cu···P distance: 2.258(4) Å). The remaining two basal sites of the tetrahedral Cu coordination environment are occupied by two N atoms from bpy sites of $[hat\text{-}(CN)_6]^{\bullet-}$ which link three $[Cu(dppFc)]^+$ units (average Cu···N distance: 2.079(9) Å). Two PF_6^- counterions are accommodated in the cavities on each side of the planar $[hat\text{-}(CN)_6]^{\bullet-}$ that are created by the 12 phenyl groups of the three dppFc units.

The crystal structure of **2** shows a tetranuclear $Cu_2Fc^*_2$ complex[13] containing two hat-$(CN)_6$ molecules and two [Cu(dppFc*)] units (average Cu···P distance: 2.286(3) Å) as depicted in Figure 3. The remaining vacant sites on the tetrahedral copper(I) ions of each [Cu(dppFc*)] unit are occupied by two nearest-neighbor CN groups of each hat-$(CN)_6$ in two characteristic coordination arrangements: a linear arrangement (Cu···N distance: 1.999(7) Å, Cu-N-C angle: 175.2(7)°) and a bending arrangement (Cu···N distance: 2.115(7) Å, Cu-N-C angle: 147.3(7)°) which afford a dimer complex of hat-$(CN)_6$. It should be noted that the intramolecular π–π stacking interaction (3.31(1) Å) between the phenyl rings of dppFc* and hat-$(CN)_6$ compensates for the

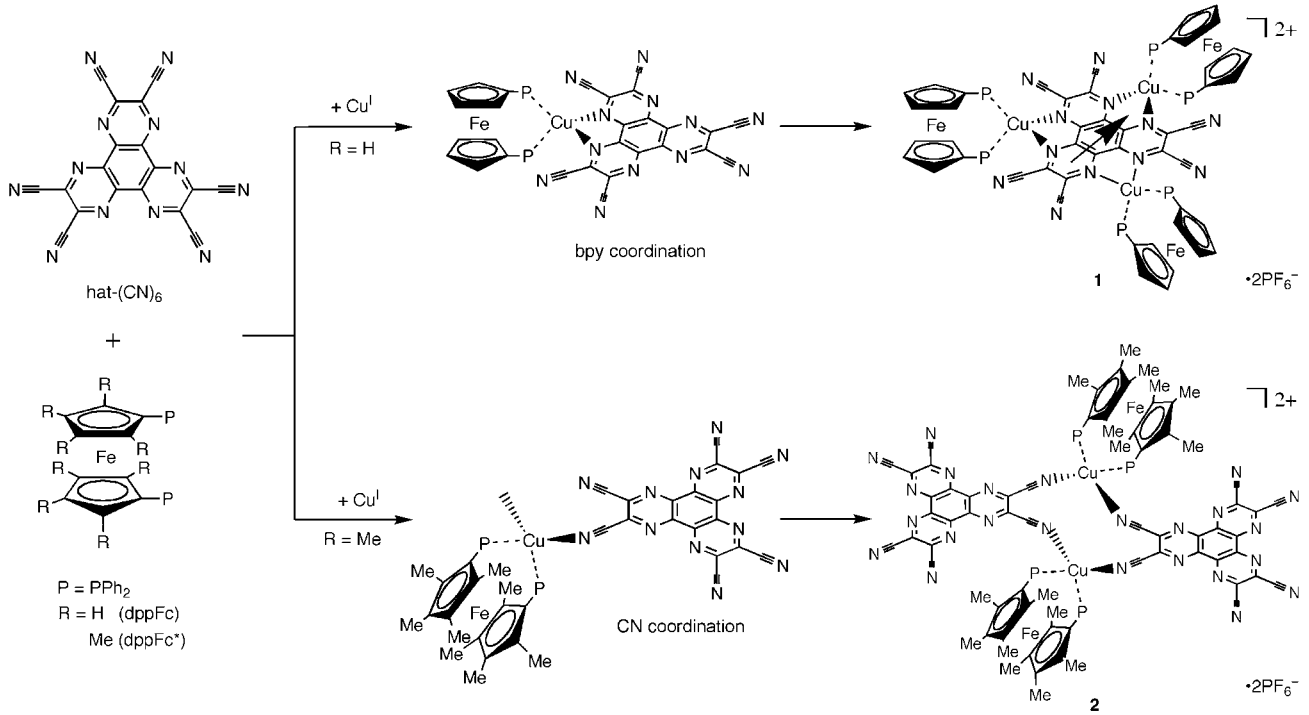

Scheme 1. Self-assembly of the hexanuclear complex **1** and the tetranuclear complex **2**.

 © 2005 Wiley-VCH Verlag GmbH & Co. KGaA, Weinheim

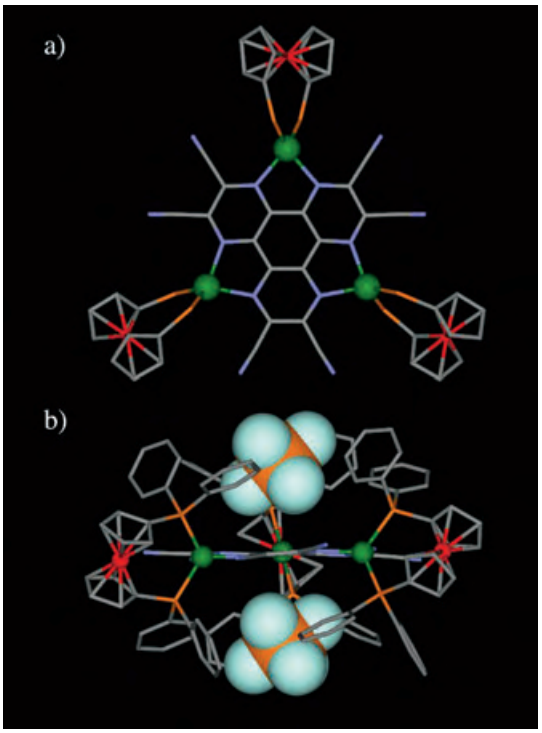

Figure 2. Molecular structure of the hexanuclear complex **1**. a) The top view of **1**. The phenyl groups of dppFc and the PF_6^- counterions are omitted for clarity. b) The side view of **1** with PF_6^- trapped within the cavities.

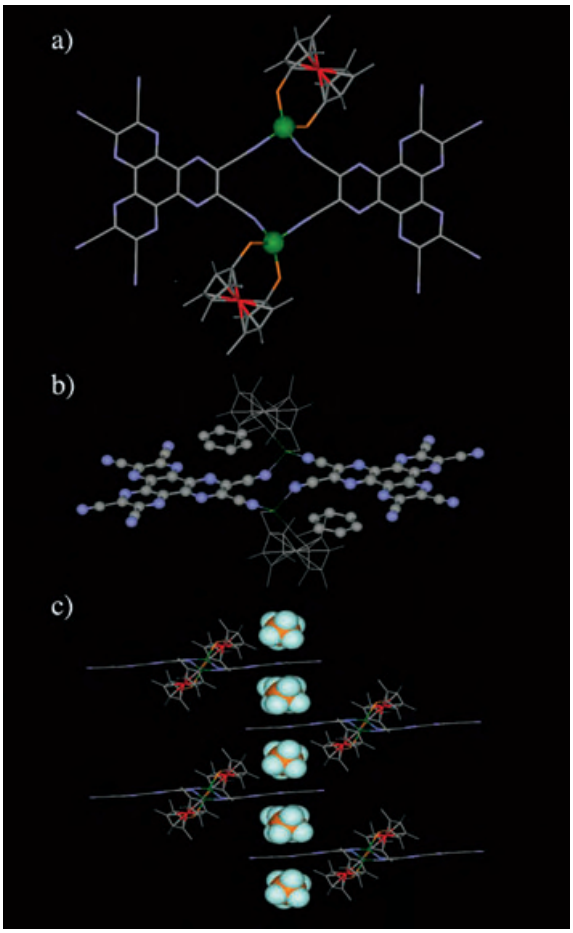

Figure 3. Molecular structure of the tetranuclar complex **2**. a) The top view of **2**. The phenyl groups of dppFc* and the PF_6^- counterions are omitted for clarity. b) The side view of **2** showing the intramolecular π–π stacking interactions between the one of the phenyl rings of dppFc* and hat-$(CN)_6$. c) Infinite structure of **2**. The alternating assembles of hat-$(CN)_6$ and PF_6^- afford the 1-D column structure.

weaker bending coordination, thus resulting in stabilization of the supramolecular structure (Figure 3b). Although the four noncoordinated CN sites of hat-$(CN)_6$ give a large remaining area, which allows for intermolecular π stacking, this interaction is hampered by the PF_6^- counterion located on the plane of the hat-$(CN)_6$ unit (Figure 3c). This situation arises because the electron-deficient heterocyclic core of hat may prefer the anion–π interaction[14] to intermolecular π-stacking interactions.

Although the spectroscopic and structural results indicate that the oxidation state of hat-$(CN)_6$ is dependent on its coordination mode, the results of the electrochemical studies are even more striking. The redox potentials and assignments of each electrochemical process for compounds **1**, **2**, and free hat-$(CN)_6$ are summarized in Figure 4 (see also the Supporting Information). Compared with the redox potentials of free hat-$(CN)_6$, those of the metal complexes encounter a more positive shift because of the "normal" effect.[15,16] The strength of this effect, illustrated by the value of $\Delta E_{1/2}$, highlights the significant difference between **1** and **2**; the process of hat-$(CN)_6$/[hat-$(CN)_6$]$^{\bullet-}$ for **1** ($\Delta E_{1/2} = +0.78$ V) is much larger than that for **2** ($\Delta E_{1/2} = +0.22$ V). The larger positive shift for **1** allows hat-$(CN)_6$ to be reduced to [hat-$(CN)_6$]$^{\bullet-}$ by an outer-sphere electron-transfer reaction involving the oxidation of copper(I) to copper(II).[17] The difference in the "normal" effect between **1** and **2** is ascribed to the cooperation of the number of coordinated copper(I) ions (three ions and one ion per hat-$(CN)_6$ molecule in **1** and **2**, respectively) and the coordination mode (bpy sites in **1** and

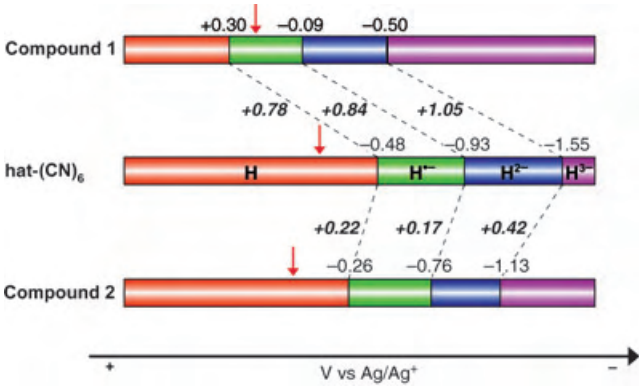

Figure 4. Schematic representation of redox potentials of hat-$(CN)_6$ (**H**) for **1**, **2**, and free **H**. The redox potentials of each compound are shown in normal fonts. The bold italic numbers indicate the difference in the potential of **1** or **2** from that of free **H**, ($\Delta E_{1/2} = E_{1/2}$(**1** or **2**) $- E_{1/2}$(free **H**)). The red arrow indicates the resting potential.

CN sites in **2**). Although studies of $[\{Ru(bpy)_2\}_n(hat)]^{2n+}$ ($n = 1$–3)[18] show that the larger positive shift of the reduction

 © 2005 Wiley-VCH Verlag GmbH & Co. KGaA, Weinheim

potentials of hat occurs with an increase in the number of coordinated metal ions, they also show that it is the coordination of the first metal ion, rather than the coordination of the second or third metal ion, that influences the reduction potentials of the hat ligand; the contribution of the first coordination is estimated to be half of the total shift for a trinuclear compound.[18,19] From this standpoint, the coordination of the ligand to the first copper(I) ion in **1** can be estimated as approximately +0.39 V,[19] which is much larger than the "normal" effect shown in complex **2** (+0.22 V). This result implies that the bpy coordination, rather than the terminal CN coordination, directly affects the electronic structure of the hat-$(CN)_6$ core.

Of the two possible coordination modes, coordination of the chelating bpy site is expected to be favored over coordination of the monodentate CN site. However, complex **2** is constructed by coordination of the CN groups, which implies that coordination to $[Cu(dppFc^*)]^+$ units at bpy sites is hampered. One of the most likely reasons for this is the steric repulsion between hat-$(CN)_6$ and the methyl groups of Fc*—the nearest distance between hat-$(CN)_6$ and dppFc in **1** is only 2.78 Å (estimated from the distance between the N atom of the CN groups and the H atom of the Fc moiety).[20] It is clear that the modification of Fc to Fc* causes the steric repulsion. In other words, hat-$(CN)_6$ recognizes the size of the Fc moieties on the bpy sites in the course of the self-assembling process, and chooses the preferable coordination mode for the metal centers.

In summary, this study demonstrates the effect of the coordination mode on the oxidation states of hat-$(CN)_6$ that can be achieved through a self-assembly process with copper(I) ions and ferrocene derivative coligands. The size of the ferrocene moieties plays a key role in determining the coordination mode, which causes a positive shift of reduction potentials of hat-$(CN)_6$ by net charge transfer. This approach paves the way not only to the accurate control of the oxidation state of redox-active ligands, but also to the close control of molecular and electronic structures of supramolecules.

Experimental Section

All operations were carried out in a nitrogen atmosphere by using standard Schlenk techniques. Hat-$(CN)_6$,[21] $[Cu(CH_3CN)_4](PF_6)$,[22] dppFc,[23] and dppFc*[24] were prepared according to literature procedures.

1: A solution of $[Cu(CH_3CN)_4](PF_6)$ (204 mg, 0.548 mmol) in acetone (5 mL) was added to a solution of dppFc (304 mg, 0.548 mmol) in CH_2Cl_2 (5 mL), and the resulting mixture was then added to a solution of hat-$(CN)_6$ (52.6 mg, 0.137 mmol) in acetone (10 mL). The reaction mixture immediately turned dark green. After the solvents had been removed in vacuo, the precipitate was washed with MeOH (5 mL) and THF (1 mL). The crystals were obtained by the diffusion method with CH_2Cl_2/hexane (30%). Although the composition obtained from the crystal structure is $\mathbf{1}\cdot 6\,CH_2Cl_2$, the elemental analysis is consistent with $\mathbf{1}\cdot 2\,CH_2Cl_2$. This difference arises because some solvent molecules are removed from the crystal on drying. Elemental analysis calcd for $C_{122}H_{88}Cl_4Cu_3F_{12}Fe_3N_{12}P_8$ ($\mathbf{1}\cdot 2\,CH_2Cl_2$): C 54.31, H 3.29, N 6.23; found: C 54.77, H 3.57, N 6.30.

2: This compound was prepared by a similar procedure as **1**, except that dppFc* was used as the starting material. The reaction mixture gave a red solution. After the solvents had been removed in vacuo, the precipitate was washed with EtOH (5 mL). The crystals were obtained by the diffusion method with THF/hexane (22%). Elemental analysis calcd for $C_{120}H_{88}Cu_2F_{12}Fe_2N_{24}P_6$ (**2**): C 57.22, H 3.52, N 13.35; found: C 56.72, H 3.70, N 12.34.

X-ray structure determination**:** Measurements were conducted on a Rigaku/MSC Mercury CCD diffractometer with graphite monochromated $Mo_{K\alpha}$ radiation ($\lambda = 0.71069$ Å). The structures were solved by Patterson methods (DIRDIF92/PATTY) and expanded using Fourier techniques. All calculations were performed using the teXsan crystallographic software package of Molecular Structure Corporation. CCDC-258214 (**1**) and CCDC-258213 (**2**) contain the supplementary crystallographic data for this paper. These data can be obtained free of charge from The Cambridge Crystallographic Data Centre via www.ccdc.cam.ac.uk/data_request/cif.

Received: December 16, 2004
Published online: March 14, 2005

Keywords: charge transfer · coordination modes · copper · N ligands · self-assembly

[1] a) J.-M. Lehn, *Supramolecular Chemistry-Concepts and Perspectives*, VCH, Weinheim, **1995**; b) *Comprehensive Supramolecular Chemistry*, *Vol. 9* (Eds.: J. L. Atwood, J. E. D. Davies, D. D. MacNicol, F. Vögtle, J.-M. Lehn), Pergamon, Oxford, **1996**; c) G. F. Swiegers, T. J. Malefetse, *Chem. Rev.* **2000**, *100*, 853; d) B. J. Holliday, C. A. Mirkin, *Angew. Chem.* **2001**, *113*, 2076; *Angew. Chem. Int. Ed.* **2001**, *40*, 253; e) M. W. Hosseini, *Coord. Chem. Rev.* **2003**, *240*, 157.

[2] a) P. D. Beer, P. A. Gale, *Angew. Chem.* **2001**, *113*, 502; *Angew. Chem. Int. Ed.* **2001**, *40*, 486; b) H. Piotrowski, G. Hilt, A. Schulz, P. Mayer, K. Polborn, K. Severin, *Chem. Eur. J.* **2001**, *7*, 3196.

[3] J.-P. Collin, C. Dietrich-Buchecker, P. Caviña, M. C. Jimenez-Molero, J.-P. Sauvage, *Acc. Chem. Res.* **2001**, *34*, 477.

[4] M. Ruben, J. Rojo, F. J. Romero-Salguero, L. H. Uppadine, J.-M. Lehn, *Angew. Chem.* **2004**, *116*, 3728; *Angew. Chem. Int. Ed.* **2004**, *43*, 3644.

[5] For discrete metal complexes of organocyanides such as TCNE, TCNQ, and related π acceptors, see: W. Kaim, M. Moscherosch, *Coord. Chem. Rev.* **1994**, *129*, 157 and references therein.

[6] W. Kaim, B. Olbrich-Deussner, R. Gross, S. Ernst, S. Kohlmann, C. Bessenbacher in *Paramagnetic Organometallic Species in Activation/Selectivity, Catalysis* (Eds.: M. Chanon, M. Julliard, J. C. Poite), Kluwer, Dordrecht, **1989**, p. 283.

[7] H. Hartmann, W. Kaim, I. Hartenbach, T. Scleid, M. Wanner, J. Fiedler, *Angew. Chem.* **2001**, *113*, 2927; *Angew. Chem. Int. Ed.* **2001**, *40*, 2842.

[8] M. Moscherosch, E. Waldhör, H. Binder, W. Kaim, J. Fiedler, *Inorg. Chem.* **1995**, *34*, 4326.

[9] For metal complexes with hat-$(CN)_6$, see: a) T. Okubo, S. Kitagawa, M. Kondo, H. Matsuzaka, T. Ishii, *Angew. Chem.* **1999**, *111*, 980; *Angew. Chem. Int. Ed.* **1999**, *38*, 931; b) T. Okubo, S. Kitagawa, S. Masaoka, S. Furukawa, M. Kondo, T. Noh, T. Isoshima, T. Wada, H, Sasabe, *Nonlinear Opt.* **2000**, *24*, 129; c) P. S. Szalay, J. R. Galán-Mascarós, R. Clérac, K. R. Dunbar, *Synth. Met.* **2001**, *122*, 535.

[10] For metal complexes with hat derivatives, see: a) S. Kitagawa, S. Masaoka, *Coord. Chem. Rev.* **2003**, *246*, 73; b) B. F. Abrahams, P. A. Jackson, R. Robson, *Angew. Chem.* **1998**, *110*, 2801; *Angew. Chem. Int. Ed.* **1998**, *37*, 2656; c) L. Latterini, G. Pourtois, C. Moucheron, R. Lazzaroni, J.-L. Brédas, A. Kirsch-De Mesmaeker, F. C. De Schryver, *Chem. Eur. J.* **2000**, *6*, 1331; d) P. N. W. Baxter, J.-M. Lehn, B. O. Knersel, G. Baum, D. Feske, *Chem. Eur. J.* **1999**, *5*, 113; e) J. R. Galán-Mascarós, K. R. Dunbar, *Chem. Commun.* **2001**, 217; f) S. Masaoka, S. Furukawa,

 © 2005 Wiley-VCH Verlag GmbH & Co. KGaA, Weinheim

H.-C. Chang, T. Mizutani, S. Kitagawa, *Angew. Chem.* **2001**, *113*, 3933; *Angew. Chem. Int. Ed.* **2001**, *40*, 3817.

[11] The related π-accepting organocyanides, TCNQ, show a similar tendency; see: a) S. A. O'Kane, R. Clérac, H. Zhao, X. Ouyang, J. R. Galán-Mascarós, R. Heintz, K. R. Dunbar, *J. Solid State Chem.* **2000**, *152*, 159; b) L. Ballester, A. Gutiérrez, M. F. Perpiñán, M. T. Azcondo, *Coord. Chem. Rev.* **1999**, *190–192*, 447.

[12] Crystal data for **1:** $C_{126}H_{96}Cl_{12}Cu_3F_{12}Fe_3N_{12}P_8$ (**1**·6 CH_2Cl_2), M_r = 3037.61, orthorhombic, space group *Pbcn* (no. 60), a = 30.80(5), b = 17.66(2), c = 23.66(4) Å, V = 12 869(33) Å^3, Z = 4, ρ_{calcd} = 1.568 g cm^{-3}, μ = 1.236 mm^{-1}. Data collection ($6.0 < 2\theta < 50.0°$) was performed at 223 K. Non-hydrogen atoms were refined anisotropically, whereas hydrogen atoms were introduced as fixed contributors. The structure was refined on F^2 and converged for 6233 unique reflections with $I > 3\sigma(I)$ and 794 parameters to give $R1$ = 0.1073 and $wR2$ = 0.2358.

[13] Crystal data for **2**: $C_{80}H_{44}O_5CuF_6FeN_{12}O_5P_3$ (**2**·10 THF), M_r = 1579.61, triclinic, space group $P\bar{1}$ (no. 2), a = 15.344(7), b = 17.443(11), c = 18.401(11) Å, α = 85.80(9), β = 68.33(8), γ = 65.41(7)°, V = 4142(5) Å^3, Z = 2, ρ_{calcd} = 1.266 g cm^{-3}, μ = 0.558 mm^{-1}. Data collection ($4.4 < 2\theta < 50°$) was performed at 163 K. The structure was refined on F^2 and converged for 7908 unique reflections with $I > 3\sigma(I)$ and 922 parameters to give $R1$ = 0.0886 and $wR2$ = 0.2636. Some of solvent molecules were refined isotropically, whereas other atoms were refined aniotropically. Hydrogen atoms were introduced as fixed contributors. One of the PF_6^- counterions was disordered, therefore it was refined as the disordered model.

[14] The closest distance between hat-$(CN)_6$ and PF_6^- is remarkably short (d = 2.80(1) Å). For recent articles on anion–π interactions, see: a) D. Quiñonero, C. Garau, C. Rotger, A. Frontera, P. Ballester, A. Costa, P. M. Deyà, *Angew. Chem.* **2002**, *114*, 3539; *Angew. Chem. Int. Ed.* **2002**, *41*, 3389; b) M. Mascal, A. Armstrong, M. D. Bartberger, *J. Am. Chem. Soc.* **2002**, *124*, 6274.

[15] Such a trend would be expected for metal complexes of conventional π-acceptor ligands such as bipyridines and their derivatives; see: a) A. Klein, C. Vogler, W. Kaim, *Organometallics* **1996**, *15*, 236; b) S. Berger, A. Klein, W. Kaim, J. Fiedler, *Inorg. Chem.* **1998**, *37*, 5664.

[16] Strongly π-accepting organocyanides such as TCNQ usually give negative shifts to the reduction potentials through π back donation,[10] with the exception of a tetranuclear rhenium complex.[9] Here, the "normal" effect dominates the reduction potentials of hat-$(CN)_6$.

[17] The possibility of dppFc acting as the reductant was also considered. However, since we have previously isolated the related compound with dppe,[11a] the copper(I) ion is the best candidate as the reducing agent.

[18] The reduction potentials of $[\{Ru(bpy)_2\}_n(hat)]^{2n+}$ are cited from the following reference (see also the Supporting Information): A. Masschelein, A. Kirsch-De Mesmaeker, C. Verhoeven, R. Nasielski-Hinkens, *Inorg. Chim. Acta* **1987**, *129*, L13.

[19] See the Supporting Information.

[20] DFT calculations on the model compounds also supports this steric effect by comparison of bpy coordination to [Cu(dppFc)] (**A**) and that to [Cu(dppFc*)] (**B**). As a result, the stabilization energy for the complexation to **B** is much smaller than that to **A**, about 49 kJ mol^{-1}, which indicates that the stable complexation is hampered by the methyl groups on Fc*. For details see the Supporting Information.

[21] a) J. T. Rademacher, K. Kanakarajan, A. W. Czarnik, *Synthesis* **1994**, 378; b) K. Kanakarajan, A. W. Czarnik, *J. Heterocycl. Chem.* **1998**, *25*, 1869; c) J. C. Beeson, L. J. Fitzgerald, J. C. Gallucci, R. E. Gerkin, J. T. Rademacher, A. W. Czarnik, *J. Am. Chem. Soc.* **1994**, *116*, 4621.

[22] a) P. Hemmerich, C. Sigwart, *Experientia* **1963**, *15*, 448; b) G. Kubas, *Inorg. Synth.* **1979**, *19*, 90.

[23] J. J. Bishop, A. Davison, M. L. Katcher, D. W. Lichtenberg, R. E. Merrill, J. C. Smart, *J. Organomet. Chem.* **1971**, *27*, 241.

[24] a) J. Szymoniak, J. Besançon, A. Dormond, C. Moïse, *J. Org. Chem.* **1990**, *55*, 1429; b) G. Trouve, R. Broussier, B. Gautheron, M. M. Kubicki, *Acta. Crystallogr. Sect. C* **1991**, *47*, 1966; c) M. Viotte, B. Gautheron, M. M. Kubicki, Y. Mugnier, R. V. Parish, *Inorg. Chem.* **1995**, *34*, 3465.

 © 2005 Wiley-VCH Verlag GmbH & Co. KGaA, Weinheim

Protein–Protein Interactions

Terphenyl-Based Helical Mimetics That Disrupt the p53/HDM2 Interaction**

*Hang Yin, Gui-in Lee, Hyung Soon Park, Gregory A. Payne, Johanna M. Rodriguez, Said M. Sebti, and Andrew D. Hamilton**

The p53 protein plays a key role in the apoptosis pathway.[1] Increased expression of wild-type p53 in stressed cells leads to cell-cycle arrest or apoptosis,[2] whereas in normal cells p53 is present at very low levels owing to regulation by human double minute 2 (HDM2), which promotes the degradation of p53 through an ubiquitin-dependent proteasome pathway.[3] The p53 protein is found in a mutated or inactive state in over 50% of cancerous tumors.[4] Moreover, overexpression of HDM2 has been implicated in the development of cancerous tumors, such as human osteogenic sarcomas and soft-tissue sarcomas,[5] as the overexpressed HDM2 abrogates the ability of p53 to induce cell-cycle arrest and apoptosis.[2] For these reasons, disruption of the p53/HDM2 interaction by using small-molecule agents has become an important goal for anticancer-drug development.[6]

HDM2 regulates p53 by complex formation that involves amino acid residues 18–102 of HDM2 and a helical region of p53 (amino acids 16–28).[7] Crystallographic analysis of the HDM2/p53 complex has revealed that three hydrophobic residues (F19, W23, L26) along one face of the p53 helical peptide are essential for binding (Figure 1a).[8] Several groups

[*] H. Yin, G.-i. Lee, H. S. Park, G. A. Payne, J. M. Rodriguez, Prof. A. D. Hamilton
Department of Chemistry, Yale University
P.O. Box 208107, New Haven, CT 06520-8107 (USA)
Fax: (+1) 203-432-6144
E-mail: andrew.hamilton@yale.edu
Prof. S. M. Sebti
Drug Discovery Program
H. Lee Moffitt Cancer Center and Research Institute
Departments of Oncology and Biochemistry and Molecular Biology
University of South Florida
Tampa, FL 33612 (USA)

[**] We thank the National Institutes of Health for support of this work (GM35208 and GM69850). The HDM2 pQE40 construct was kindly provided by Dr. Christian Klein (Hoffmann-La Roche, Inc.).

Supporting information for this article is available on the WWW under http://www.angewandte.org or from the author.

 © 2005 Wiley-VCH Verlag GmbH & Co. KGaA, Weinheim DOI: 10.1002/anie.200462316

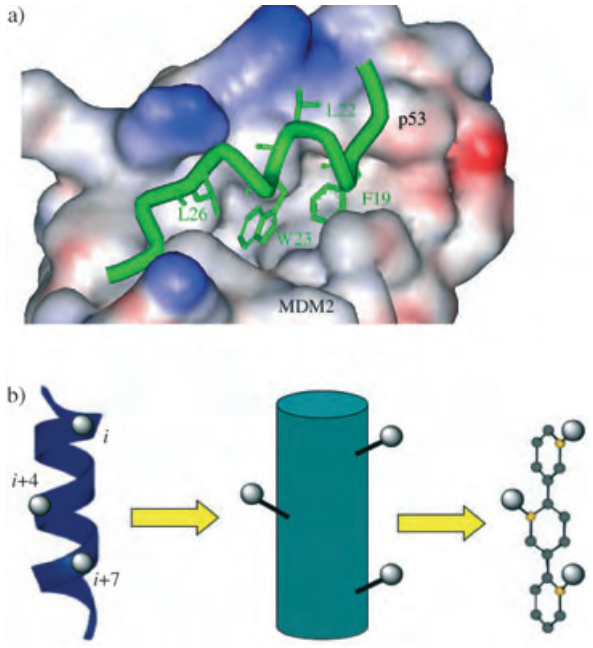

Figure 1. a) X-ray crystal structure of the HDM2/p53 complex. The key side chains of F19, W23, and L26 are shown in stick representation. b) α-Helical mimicry based on a terphenyl scaffold.

have reported small-molecule agents that disrupt p53/HDM2 dimerization. For example, Vassilev et al. identified *cis*-imidazoline analogues as low-molecular-weight antagonists of HDM2 in a high-throughput screening.[9] Most recently, peptidomimetics of the helical region of p53 based on a β hairpin[10] and 14-helix scaffolds[11] that disrupt the p53/HDM2 complexation were developed by the groups of Robinson and Schepartz, respectively. These studies serve as the proof-of-principle that the protein–protein interface of the HDM2/p53 complex provides a sound target for small-molecule agents.

Previously, we showed that terphenyl derivatives can mimic one face of a α-helical peptide (Figure 1b).[12] By substituting the appropriate alkyl or aryl substituents on the three *ortho*- positions of the terphenyl scaffold, the side chains are projected in an analogous way to the i, $i+4$, and $i+7$ residues of an α helix. Herein we report the use of this strategy in which a group of terphenyl-based antagonists mimic the α-helical region of the p53 peptide and disrupt the HDM2/p53 complexation.

We prepared an extensive library of terphenyl inhibitors through a synthesis involving sequential Suzuki couplings of the appropriate *ortho*-substituted methoxyphenylboronate and phenyltriflate. A previously reported fluorescence polarization (FP) competition assay with a fluorescein-labeled p53 peptide, which contains residues 15–31 of p53 with a cysteine residue appended to the C-terminus (SQETFSDLWKLLPENNVC), was used to assess the binding affinities of these terphenyl derivatives to HDM2.[11] Displacement of this probe through competitive binding of the terphenyl into the hydrophobic cleft of HDM2 leads to a decrease in its fluorescence polarization. Regression analysis was conducted to determine the K_i values by using the previously reported method.[13] To test the validity of this assay, we used non-labeled p53 peptide as the competitive inhibitor to bind HDM2, giving a K_i of 3.51 ± 0.11 μM, which closely matches the K_d value (3.02 ± 0.33 μM) obtained from saturation titration experiments.

Good in vitro inhibition potencies in disrupting the p53/HDM2 heterodimerization were observed for certain compounds within the terphenyl series (Table 1). The terphenyl **14** with an isobutyl, 2-naphthylmethylene, isobutyl side-chain sequence showed a K_i value of 0.182 ± 0.020 μM for displacing p53 binding to HDM2. Terphenyls **16**, **20**, **21** bear only some of the key side chains of **14**, and their affinities for HDM2 are significantly lower. These results confirmed the importance of all three key side chains. The role of these side chains is further emphasized by the weak binding of control compounds (**9** and **17**), which indicated that there is no nonspecific hydrophobic interaction between the terphenyl backbone and the protein surface. Comparison of **1** ($K_i = 3.83$ μM) and **4** ($K_i = 297$ μM), which have reverse side-chain sequences, indicated that the orientation of the terphenyl backbone is critical in the binding. The terphenyl compounds with 2′,6′-dimethyl substituents showed improved affinities, as seen in the comparison of **1** and **10**, which may be due to the increased rigidity of the terphenyl backbone and the lowered entropic penalty on binding.

The displacement of the p53 peptide from the surface of HDM2 in the fluorescence experiment strongly suggested that the potent terphenyl compounds bind to the same cleft on the HMD2 surface. This location of the binding domain was further confirmed by computational and NMR spectroscopy experiments. The binding surface of p53 is dominated by a triad of p53 amino acids (F19, W23, and L26) that interacts with a hydrophobic cleft on the HDM2 surface (Figure 1a).[8] In this classification, the F19-pocket is defined by R65, Y67, E69, H73, I74, V75, M62, and V93 residues of HDM2, the W23-pocket comprises S92, V93, L54, G58, Y60, V93, and F91, the L26-pocket is composed of Y100, T101, and V53. To study the binding mode of the terphenyl derivatives, we conducted computational simulations with the Autodock program.[14] The top-ranked docking results for terphenyl **14** (shown in Figure 2) suggested that the terphenyl compounds target the same surface area where p53 binds, inserting their side chains into the F19, W23, and L26-pockets.

We mapped the binding surface of the terphenyl compounds on HDM2 using ^{15}N HSQC NMR experiments. The chemical shift perturbation of the HDM2 amide backbone was monitored upon addition of six different terphenyl compounds: **1**, **3**, **6**, **11**, **12**, and **14** (results shown in Table 2). All six compounds consistently induced chemical-shift changes at residues V28, F55, G58, V93, and/or K94, which all lie in the p53-binding pocket (with an exception of V28, whose shift is possibly due to the global conformational change of the protein). The chemical-shift changes at these positions were also observed in the binding of the p53 peptide and HDM2,[15] demonstrating that these terphenyl derivatives recognize the protein surface in a similar manner to the p53 peptide. Further analysis of **3**, **12**, and **14** demonstrated that bulkier side chains at the R^2 position resulted in more-significant chemical shifts at the F55, L57, V93, and K94

 © 2005 Wiley-VCH Verlag GmbH & Co. KGaA, Weinheim

Table 1: Results of the fluorescence polarization assays.

Structure	Ligand	R^1	R^2	R^3	$K_i \pm$ S.D. [μM][a]
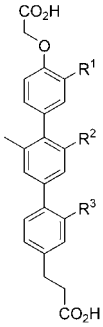	**1**	Bn	Me	Me	3.83 ± 0.70
	2	Me	Me	*i*Bu	35.3 ± 4.4
	3	*i*Bu	Me	*i*Bu	2.97 ± 0.15
	4	Me	Me	Bn	297 ± 92
	5	*i*Bu	Me	Bn	2.83 ± 0.63
	6	Bn	Me	Bn	2.17 ± 0.14
	7	Bn	Me	*i*Pr	13.1 ± 3.8
	8	Bn	Me	*i*Bu	6.25 ± 1.50
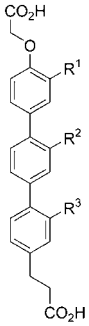	**9**	H	H	H	> 1000
	10	Bn	Me	Me	12.6 ± 2.1
	11	Bn	Bn	*i*Bu	0.978 ± 0.171
	12	*i*Bu	Bn	*i*Bu	3.50 ± 1.00
	13	*i*Bu	CH_2(1-Naph)	*i*Bu	25.7 ± 11.9
	14	*i*Bu	CH_2(2-Naph)	*i*Bu	0.182 ± 0.020
	15	CH_2(1-Naph)	*i*Bu	*i*Bu	11.6 ± 2.1
	16	*i*Bu	CH_2(1-Naph)	H	82.0 ± 8.6
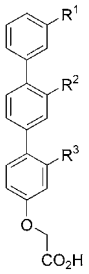	**17**	H	H	H	> 1000
	18	*i*Pr	Me	Me	> 1000
	19	*i*Pr	*i*Bu	*i*Bu	1.89 ± 0.30
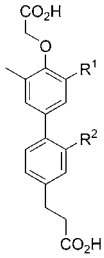	**20**	Bn	Me		70.8 ± 9.8
	21	Me	Me		479 ± 144

[a] The K_i and standard deviation (S.D.) values were obtained from three independent titrations.

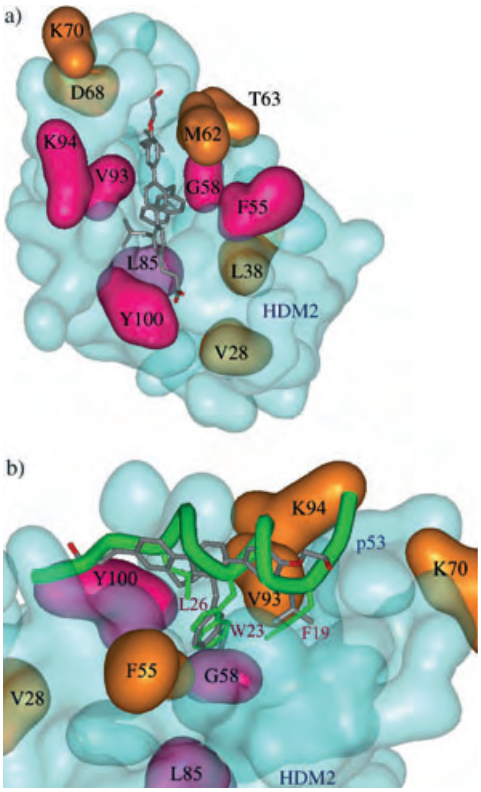

Figure 2. Results of the ^{15}N HSQC NMR spectroscopy and the molecular-docking experiments of terphenyl **14** binding to HDM2. a) The residues that showed significant and moderate chemical-shift changes upon addition of the terphenyl compounds are shown in magenta and orange, respectively. b) Overlay of the top-ranked docking result of **14** and the p53 peptide (green). The key hydrophobic side chains of F19, W23, and L26 are shown in stick representations.

positions. Terphenyl **14**, which shows the strongest binding ($K_i = 0.182 \pm 0.020$ μM), induced significant peak shifts for all these residues. In addition, a residue deep inside the W23 pocket, L85, is affected by **14**, suggesting that the 2-naphthylmethylene side chain inserts into the W23 pocket, thus resulting in a stronger binding (Figure 2b). Terphenyl **11**, which has a benzyl side chain at the R^1 position, clearly affected the residues M62 and H73 in the F19 pocket on HDM2, whereas **12** (*i*Bu at R^1) does not, which indicates that **11** inserts the benzyl side chain into the F19 pocket as p53 does. Taking all these results together, we concluded that the terphenyl derivatives are successful p53 mimetics and that these compounds present side chains into the F19, W23, and L26 binding pockets of HDM2.

A critical issue in the design of small-molecule α-helix mimetics is the selectivity of these compounds among different helix-binding proteins.[16] Nature frequently uses general secondary-structure modules, such as α helices, to recognize different protein targets and achieves high specificity through spatial and charge complementarity.[17] Previous studies have shown that the p53 peptide selectively binds to HDM2 over other oncogenic proteins, such as Bcl-x_L and Bcl-2, which both complex with the α-helical Bak BH3 domain.[18] In a similar manner to the p53/HDM2 interaction, the Bak peptide also projects key side chains at the *i*, *i* + 4, and *i* + 7 positions (V74, L78, and I81) into hydrophobic clefts on the targeted protein surfaces.[19] Comparison of terphenyl isomers **13** and **14,** which bear 1- and 2-naphthylmethylene side chains, respectively, on the middle phenyl rings, showed that terphenyl derivatives can selectively bind to different helix-binding proteins (Table 3).

 © 2005 Wiley-VCH Verlag GmbH & Co. KGaA, Weinheim

Table 2: Summary of the amino acid residues of HDM2 that showed chemical-shift changes upon addition of terphenyl inhibitors.

Ligand	Significantly shifted residues[a]	Moderately shifted residues[a]
1	S22, V28, F55, L57, G58, I61, K94, K98, Y104	T26, L35, E52, V53, D68
3	G12, T15, S22, V28, G58	R29, L35, F55, I74, S92, K94
6	V8, G12, S22, V28, K51, V53, Y56, M62, V93	L33, L35, E52, F55, T63, K70, H73, L82, L85, F91, S92, H96
11	G12, T15, V28, K51, G58, H73, F91, S92, V93	S22, K45, I61, M62, I74, V75, K94, K98, I99, L107
12	V8, T15, S22, V28, F55, L57, I74, F91, E95	R29, Y60, Y67, K70, S92
14	V8, G12, T15, S22, V28, F55, G58, K70, L85, V93, K94, Y100	L38, M62, T63, D68

[a] See Supporting Information.

Table 3: Comparison of terphenyl derivatives **13** and **14** in inhibition of different protein–protein complexes.

K_i [μM]	HDM2/p53	Bcl-x_L/Bak	Bcl-2/Bak
13	25.7	0.114	0.121
14	0.182	2.50	15.0

Terphenyl **14** binds to HDM2 over 100-fold more strongly than **13** and has a 14:82 fold selectivity over Bcl-x_L/Bcl-2. This is consistent with the deeper pocket in HDM2 for W23 at the $i+4$ position compared to the L78-pocket of Bcl-x_L or Bcl-2. These results confirm the generality of the terphenyl scaffold as a mimic of the side-chain-induced selectivity of α helices and provides a useful tool for the rational design of protein-binding agents. Evaluation of the inhibitory effects of terphenyl derivatives in whole cells is currently underway.

Received: October 15, 2004
Published online: March 14, 2005

Keywords: drug design · helical structures · inhibitors · protein–protein interactions · proteins

[1] D. P. Lane, *Nature* **1992**, *358*, 15.
[2] J. D. Chen, X. W. Wu, J. Y. Lin, A. J. Levine, *Mol. Cell. Biol.* **1996**, *16*, 2445.
[3] Y. Haupt, R. Maya, A. Kazaz, M. Oren, *Nature* **1997**, *387*, 296; R. Honda, H. Tanaka, H. Yasuda, *FEBS Lett.* **1997**, *420*, 25; M. H. G. Kubbutat, S. N. Jones, K. H. Vousden, *Nature* **1997**, *387*, 299.
[4] M. Hollstein, K. Rice, M. S. Greenblatt, T. Soussi, R. Fuchs, T. Sorlie, E. Hovig, B. Smithsorensen, R. Montesano, C. C. Harris, *Nucleic Acids Res.* **1994**, *22*, 3551.
[5] J. D. Oliner, K. W. Kinzler, P. S. Meltzer, D. L. George, B. Vogelstein, *Nature* **1992**, *358*, 80; C. Cordoncardo, E. Latres, M. Drobnjak, M. R. Oliva, D. Pollack, J. M. Woodruff, V. Marechal, J. D. Chen, M. F. Brennan, A. J. Levine, *Cancer Res.* **1994**, *54*, 794.
[6] P. Chene, *Nat. Rev. Cancer* **2003**, *3*, 102.
[7] J. D. Oliner, J. A. Pietenpol, S. Thiagalingam, J. Gvuris, K. W. Kinzler, B. Vogelstein, *Nature* **1993**, *362*, 857.
[8] P. H. Kussie, S. Gorina, V. Marechal, B. Elenbaas, J. Moreau, A. J. Levine, N. P. Pavletich, *Science* **1996**, *274*, 948.
[9] L. T. Vassilev, B. T. Vu, B. Graves, D. Carvajal, F. Podlaski, Z. Filipovic, N. Kong, U. Kammlott, C. Lukacs, C. Klein, N. Fotouhi, E. A. Liu, *Science* **2004**, *303*, 844.
[10] R. Fasan, R. L. A. Dias, K. Moehle, O. Zerbe, J. W. Vrijbloed, D. Obrecht, J. A. Robinson, *Angew. Chem.* **2004**, *116*, 2161; *Angew. Chem. Int. Ed.* **2004**, *43*, 2109.
[11] J. A. Kritzer, J. D. Lear, M. E. Hodsdon, A. Schepartz, *J. Am. Chem. Soc.* **2004**, *126*, 9468.
[12] O. Kutzki, H. S. Park, J. T. Ernst, B. P. Orner, H. Yin, A. D. Hamilton, *J. Am. Chem. Soc.* **2002**, *124*, 11838; J. T. Ernst, O. Kutzki, A. K. Debnath, S. Jiang, H. Lu, A. D. Hamilton, *Angew. Chem.* **2002**, *114*, 288; *Angew. Chem. Int. Ed.* **2002**, *41*, 278; B. P. Orner, J. T. Ernst, A. D. Hamilton, *J. Am. Chem. Soc.* **2001**, *123*, 5382.
[13] T. Wohland, K. Friedrich, R. Hovius, H. Vogel, *Biochemistry* **1999**, *38*, 8671; see the Supporting Information for the analysis protocol.
[14] R. Stoll, C. Renner, S. Hansen, S. Palme, C. Klein, A. Belling, W. Zeslawski, M. Kamionka, T. Rehm, P. Muhlhahn, R. Schumacher, F. Hesse, B. Kaluza, W. Voelter, R. A. Engh, T. A. Holak, *Biochemistry* **2001**, *40*, 336.
[15] O. Schon, A. Friedler, S. Freund, A. R. Fersht, *J. Mol. Biol.* **2004**, *336*, 197; O. Schon, A. Friedler, M. Bycroft, S. M. V. Freund, A. R. Fersht, *J. Mol. Biol.* **2002**, *323*, 491.
[16] J. W. Harbour, T. G. Murray in *Ophthalmic Surgery: Principles and Techniques* (Ed.: D. Albert), Blackwell Publishers, Maden, MA, **1998**, pp. 682.
[17] W. E. Stites, *Chem. Rev.* **1997**, *97*, 1233.
[18] J. W. Harbour, L. Worley, D. D. Ma, M. Cohen, *Arch. Ophtalmol.* **2002**, 120, 1341.
[19] M. Sattler, H. Liang, D. Nettesheim, R. P. Meadows, J. E. Harlan, M. Eberstadt, H. S. Yoon, S. B. Shuker, B. S. Chang, A. J. Minn, C. B. Thompson, S. W. Fesik, *Science* **1997**, *275*, 983.

 © 2005 Wiley-VCH Verlag GmbH & Co. KGaA, Weinheim

Synthetic Methods

Ultra-rapid Synthesis of ^{15}O-Labeled 2-Deoxy-D-glucose for Positron Emission Tomography (PET)**

*Hideki Yorimitsu, Yoshihiro Murakami, Hiroyuki Takamatsu, Shintaro Nishimura, and Eiichi Nakamura**

Positron emission tomography (PET) has gained importance in clinical diagnosis and in modern medicinal chemistry. In the former application, ^{18}F-labeled deoxyglucose ([^{18}F]FDG) is widely used for the analysis of glucose metabolism in vivo[1–5] and in the latter, PET is accelerating the pace of drug development.[6–8] Whereas efforts to develop PET tracer molecules has fallen largely in the area of ^{18}F labeling, development of a synthetic methodology suitable for more ubiquitous and natural elements is necessary, particularly for bioorganic and medicinal studies.[9] Oxygen is an attractive choice for labeling,[10] as it is ubiquitous in biologically active organic molecules. However, the 2-min half-life of the oxygen-15 isotope, which is much shorter than the half-lives of commonly used positron-emitting isotopes (^{11}C: 20 min; ^{13}N: 10 min; and ^{18}F: 110 min), has posed problems in synthesis, and the only successful target reported so far is ^{15}O-labeled butanol.[11] The short lifetime of ^{15}O is a potential advantage for repetitive PET measurements, as quicker and more reliable drug evaluation would be possible through the use of a variety of short-lived probes. Its potential disadvantages as a short-lived isotope have never been experimentally addressed, as suitably labeled molecules have not yet been accessible. In addition to the many potential applications of ^{15}O-labeled products, the synthesis of organic molecules with 2-min half-lives alone represents an exciting challenge in the efficiency of synthetic chemistry, in which yield and selectivity have been the central issues for a long time. Herein we report a single-step synthesis of 6-[^{15}O]-2-deoxy-D-glucose ([^{15}O]DG, **2**) from the corresponding iodide **1** as the proof-of-principle of our new ^{15}O-labeling methodology. Because of the mild and neutral nature of the radical conditions used, the synthesis can be performed without the protection of free hydroxy groups. This demonstrates that such labeling can be carried out as the last step in the synthesis of complex molecules, which would allow chemists to avoid carrying short-lived intermediates through a synthetic sequence.

Compound **2** was selected as the first target of our endeavor, as the initial rapid test of the labeled compound could be performed in an animal system with FDG as a reference standard. An attempted synthesis of an ^{15}O-labeled sugar from [^{15}O]H_2O (made from gaseous $^{15}O^{16}O$)[12] was published in a progress report in 1975; since then, no further mention of such an effort has been reported. Only several minutes are available for the synthesis and purification of **2**, which includes the time necessary for generation of ^{15}O from ^{15}N (a few minutes), mass transfer from the cyclotron ^{15}O generator to the chemical laboratory ($\approx$1 min), and transport from the chemical to the biological laboratory.

To handle the short-lived and radioactive compounds, the radical oxygenation reaction[13] that had been developed for ^{17}O and ^{18}O labeling of protected sugars (with air, alkyl halide, Bu_3SnH, and AIBN) was entirely remodeled (AIBN = azobis(isobutyronitrile)). The following nontrivial issues must be addressed for labeling with ^{15}O: 1) decreasing the reaction time from 10 h to a few minutes; 2) the lower rate of oxygenation that results from the low concentration $^{15}O^{16}O$ gas supplied (a mixture of O_2/N_2 (1.5:98.5), in contrast to the 1:4 ratio in air used previously); 3) a way to maximize the overall efficiency of the oxygen gas trapping (the absolute amount of ^{15}O supplied is too small ($^{15}O/^{16}O \approx 10^{-8}$:1) to be wasted in the synthetic operation); 4) the erratic induction time that is often observed in radical chain reactions; and 5) a variety of synthetic and operational issues related to radioactivity and automation. Given these limitations, we first had to forego use of the protected sugar that was employed in our ^{17}O and ^{18}O labeling studies, as there would be apparently no time for deprotection. As a technical approach, we discovered a mixture of $CF_3C_6H_5$/perfluorodecalin/2-butanol to be a good solvent for both molecular oxygen and unprotected sugar in a homogeneous solution.[14,15] Ordinary glassware was replaced with a special hot-air-jacketed reaction vessel equipped with a sintered glass bottom, through which oxygen gas was introduced as fine bubbles (Figure 1).

The synthesis of [^{15}O]DG (**2**) from 2,6-dideoxy-6-iodo-D-glucose (**1**) and putative intermediates of the reaction are shown in Scheme 1. The synthesis and purification were carried out with fully automated, computer-operated synthesis equipment.[16,17] The organic starting materials were simply introduced into the system, and after several minutes, a saline solution of the labeled sugar product **2** was retrieved for administration to test animals.

Figure 2 illustrates the synthetic operation system. Some details of the experimental procedure are described herein, as they are essential to reproducibility. Iodinated sugar **1** (274 mg, 1.00 mmol) in a 50-mL vial kept under nitrogen was first dissolved in 2-butanol (3.0 mL). The following were

[*] Dr. H. Yorimitsu, Prof. E. Nakamura
University of Tokyo, Department of Chemistry
Hongo, Bunkyo-ku, Tokyo 113-0033 (Japan)
Fax: (+81) 3-5800-6889
E-mail: nakamura@chem.s.u-tokyo.ac.jp
Dr. Y. Murakami, Dr. H. Takamatsu, Dr. S. Nishimura
Advanced Technology Platform Research Laboratory
Fujisawa Pharmaceutical Co. Ltd.
5-2-3, Tokodai, Tsukuba, Ibaraki 300-2698 (Japan)
and
The Medical and Pharmacological Research Center Foundation
Wo32, Inoyama-cho, Hakui, Ishikawa 925-0613 (Japan)

[**] This work was supported by a Grant-in-Aid for the 21st century COE Program for Frontiers in Fundamental Chemistry from the Ministry of Education, Culture, Sports, Science, and Technology of Japan (to E.N.), and by a postdoctoral research fellowship for SPD from the Japan Society for the Promotion of Science (to H.Y.). We thank Dr. Akihiro Noda for assistance with PPIS imaging and Dr. Masahiro Yamanaka and Dr. Cecile Savarin for their important previous contributions.

Supporting information for this article is available on the WWW under http://www.angewandte.org or from the author.

 © 2005 Wiley-VCH Verlag GmbH & Co. KGaA, Weinheim DOI: 10.1002/anie.200500044

Figure 1. Reactor for the radical hydroxylation. The numbers refer to lengths in mm.

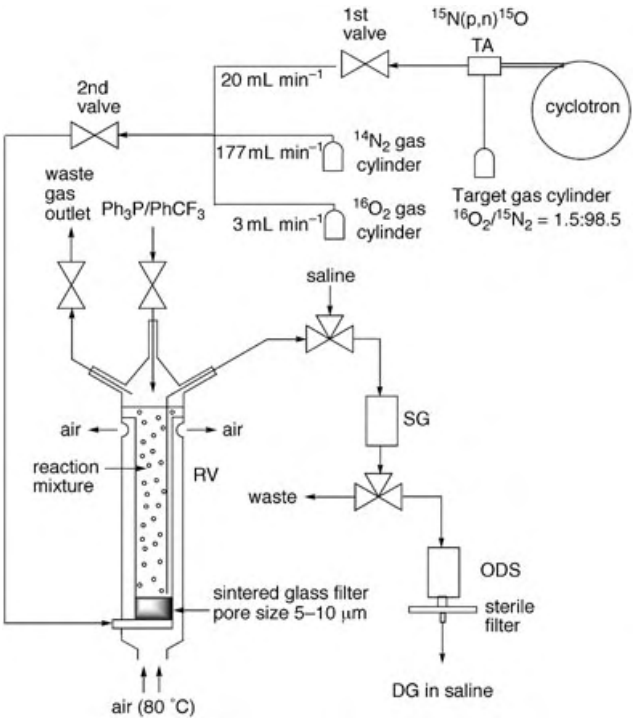

Figure 2. System diagram for synthesis of [^{15}O]DG (**2**): TA, target area (∅ 10 mm × 55 mm); RV, temperature-controlled reaction vessel (Figure 1); SG, Sep-Pak cartridge silica gel vac (3 cc) conditioned with $PhCF_3$ (10 mL); ODS, two Sep-Pak cartridges: C_{18} plus short in series conditioned with methanol (10 mL) and saline (10 mL); [^{15}O]O_2 reached RV without passing through soda lime and activated charcoal; valves are shown as triangle assemblies.

added to the solution in succession: α,α,α-trifluorotoluene (20.0 mL), perfluorodecalin (4.5 mL), and AIBN (4.0 mg, 0.025 mmol). Tributyltin hydride (807 μL, 3.00 mmol) was introduced with a microsyringe (100 μL) at room temperature, and the resulting homogeneous solution was transferred immediately with a syringe into the reaction vessel (RV) (Figure 1). The computer-controlled system was prepared for the following synthetic operations, and proton bombardment of the target gas was started at $t = 0$. At $t =$ 0.7 min, a supply of "cold" oxygen gas ($^{14}N_2 = 177$ mL min^{-1} and $^{16}O_2 = 3$ mL min^{-1}) was introduced to the reaction mixture simultaneously with the flow of temperature-controlled air (80 °C) in the RV jacket to initiate the radical chain reaction before the introduction of ^{15}O. Radical induction finished at $t = 2.2$ min, and the hydroxylation reaction started gradually to form [^{16}O]DG, peroxide **3,** and 2,6-dideoxy-D-glucose (**4**). At $t = 4.0$ min, as the rate of the chain reaction increased, the "hot" gas ([^{15}O]O_2/N_2) was released from the TA of the cyclotron (20 mL min^{-1}) through the first valve, mixed with cold O_2/N_2 gas through the second valve, and sent to the RV located in the room next to the cyclotron (200 mL min^{-1}). At $t = 4.7$ min, the "hot" gas arrived at the RV. At $t = 5.3$ min, the generation of ^{15}O in the cyclotron was stopped, yet the gas still continued to flow from the cyclotron. At $t =$ 6.0 min, both the "hot" gas [^{15}O]O_2/N_2 and the temperature-control (80 °C) air flows were stopped, for which the best timing was estimated reproducibly through a cold control experiment with the same reagents and setup. At $t = 6.1$ min, triphenylphosphine (262 mg, 1.00 mmol) in $C_6H_5CF_3$ (1.5 mL) was added to instantaneously convert any remaining hydroperoxide **3** into DG. At $t =$ 6.3 min, the reaction mixture was passed through the SG to allow retention of [^{15}O]DG on the silica gel and to elute most of the tin and phosphine compounds, as well as solvent. The adsorbed [^{15}O]DG was eluted with saline (3 mL), passed through the ODS to trap less polar contaminants, and finally a

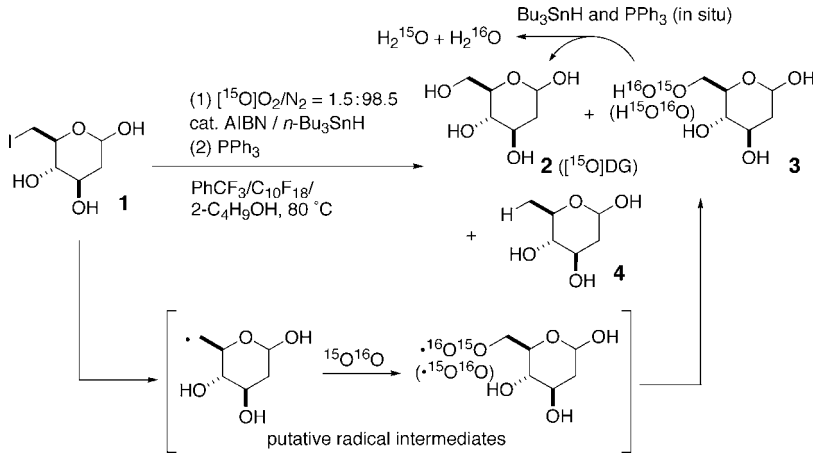

Scheme 1. Rapid synthesis of 6-[^{15}O]-2-deoxy-D-glucose from iodinated sugar **1** and a suggested reaction mechanism.

 © 2005 Wiley-VCH Verlag GmbH & Co. KGaA, Weinheim

sterile filter. Thus, at $t = 7.0$ min, [^{15}O]DG (**2**) was collected (0.04 mmol) in saline solution (3 mL). This sample was entirely free of tin and phosphine compounds, but contained 2,6-dideoxy-D-glucose (**4**, 0.04 mmol). As this latter compound does not contain ^{15}O, it does not affect the PET analysis. The mean radioactivity of the entire solution in the syringe for administration was reproducibly 0.7 GBq at $t =$ 8.0 min. The decay-corrected radiochemical purity was $\approx 70\,\%$, the remainder present as ^{15}O-labeled water (Scheme 1). The reproducibility depends critically on the duration of the induction period, which can be controlled through careful standardization of the chemical and instrumental details (Supporting Information). In experiments with "cold" $^{16}O_2$ gas, we synthesized, from 1.0 mmol starting compound (**1**), 0.27 mmol of the desired [^{16}O]DG and 0.71 mmol of 2,6-dideoxyglucose (**4**). The two products could be separated from each other readily by open chromatography purification (chloroform/methanol = 3:1).

The product-containing saline solution of [^{15}O]DG was a mixture of [^{15}O]DG and [^{15}O]H_2O (7:3; Supporting Information). The S_H2 reaction shown in Scheme 2[18] effects the

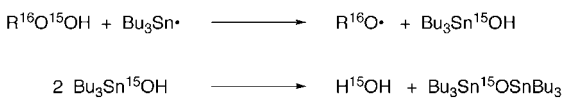

Scheme 2. Plausible mechanism for the formation of [^{15}O]H_2O.

production of [^{15}O]H_2O. Complete removal of this water remains a problem at this time but its resolution will be deferred, as it represents an issue of chemical engineering rather than one that is purely chemical. Taking into account the chemical yield in the cold control experiments, the mechanical loss during purification, the generation of 8 GBq of [^{15}O]O_2 at $t = 8.0$ min, and the fact that only half the ^{15}O in the $^{15}O^{16}O$ gas was incorporated into the sugar product (the remainder having gone into $H_2{}^{15}O$, $^{15}OPPh_3$, and $(Bu_3Sn)_2{}^{15}O$), we calculate that the yield of [^{15}O]DG based on hot oxygen gas was about 80 % before purification (Supporting Information).

The saline solution of [^{15}O]DG (3 mL) was administered to rats at $t = 8.1$–8.5 min. Figure 3a shows an image of a test animal based on the total gamma-ray capture in a planar positron imaging system (PPIS) between 15 and 30 min after injection. This image is essentially the same as that obtained with 2-deoxy-2-[^{18}F]fluoro-D-glucose ([^{18}F]FDG) (Figure 3b), which shows accumulation in the expected organs for the imaging of glucose metabolism: the heart, kidneys, and bladder. The image is different from that obtained by [^{15}O]H_2O imaging (Figure 3c), which indicates that the image in Figure 3a is the result of [^{15}O]DG rather than [^{15}O]H_2O. Taking advantage of the short lifetime of [^{15}O]DG, we were also able to perform sequential [^{15}O]DG–[^{15}O]H_2O–[^{18}F]FDG measurements at 5-min intervals to obtain similar images (Supporting Information). With these results in hand, we are currently developing new analytical protocols for ^{15}O-isotope metabolic analysis.[19]

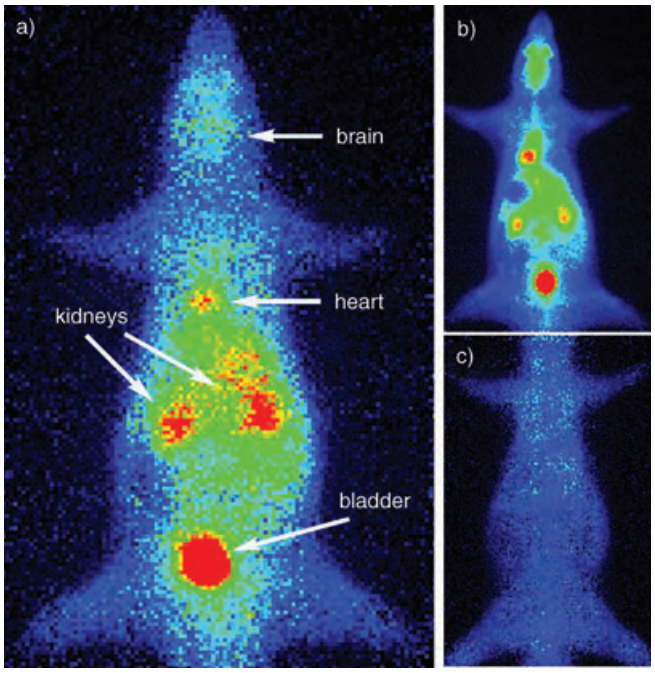

Figure 3. Representative planar positron images of the whole body distributions of 9-week-old male Wistar rats taken by PPIS with a) [^{15}O]DG (**2**), b) [^{18}F]FDG, and c) [^{15}O]H_2O; each image represents the accumulated images from 15 to 30 min after the beginning of intravenous injection of the tracer from a tail vein.

A practical quantity of an extremely short-lived radiopharmaceutical as complex as [^{15}O]DG has been synthesized for the first time. Particularly noteworthy is the simplicity of the oxygenation reaction,[13,20] which can be performed under full automation. The one-step synthetic operation is inherently simpler than ^{11}C labeling, which requires multiple-step operations that start with either ^{11}CO or $^{11}CO_2$.[9,21–23] With the proven synthetic merits of radical reactions in organic synthesis, the present method will be useful for labeling a variety of alcohols with ^{15}O, if the purification problems that depend on the specific compound at hand are set aside. This new ^{15}O-labeling methodology will allow investigations in both academic and industrial settings to focus on ^{15}O-labeled compounds of medicinal and bioorganic importance for the first time.

Received: January 6, 2005
Published online: April 12, 2005

Keywords: hydroxylation · imaging agents · isotopic labeling · radical reactions · radiopharmaceuticals

[1] B. M. Gallagher, A. Ansari, H. Atkins, V. Casella, D. R. Christman, J. S. Fowler, T. Ido, R. R. MacGregor, P. Som, C.-N. Wan, A. P. Wolf, D. E. Kuhl, M. Reivich, *J. Nucl. Med.* **1997**, *38*, 990–996.
[2] T. Ido, C.-N. Wan, V. Casella, J. S. Fowler, A. P. Wolf, *J. Labelled Compd. Radiopharm.* **1978**, *14*, 175–183.
[3] J. H. Greenberg, M. Reivich, A. Alavi, P. Hand, A. Rosenquist, W. Rintelmann, A. Stein, R. Tusa, R. Dann, D. Christman, J. Fowler, B. MacGregor, A. Wolf, *Science* **1981**, *212*, 678–680.

 © 2005 Wiley-VCH Verlag GmbH & Co. KGaA, Weinheim

[4] J. S. Fowler, A. P. Wolf, *Appl. Radiat. Isot.* **1986**, *37*, 663 – 668.
[5] P. Rigo, P. Paulus, B. J. Kaschten, R. Hustinx, T. Bury, G. Jerusalem, T. Benoit, J. Foidart-Willems, *Eur. J. Nucl. Med.* **1996**, *23*, 1641 – 1674.
[6] a) W. C. Eckelman, *Drug Discovery Today* **2003**, *8*, 404 – 410; b) A. M. J. Paans, *Drug Discovery Today* **2003**, *8*, 734; c) T. Jones, *Drug Discovery Today* **2003**, *8*, 734 – 735.
[7] E. O. Aboagye, P. M. Price, T. Jones, *Drug Discovery Today* **2001**, *6*, 293 – 302.
[8] Eds.: S. J. Gatley, F. I. Carroll, *Drug Dev. Res.* **2003**, *59 (2)*, Special Issue: PET and SPECT in Medication Development.
[9] *Radiopharmaceuticals for Positron Emission Tomography: Methodological Aspects* (Eds.: G. Stöcklin, V. W. Pike), Kluwer Academic Publishers, Dordrecht, **1993**.
[10] J. F. Maddaluno, K. F. Faull, *Appl. Radiat. Isot.* **1990**, *41*, 873 – 878.
[11] G. W. Kabalka, R. M. Lambrecht, M. Sajjad, J. S. Fowler, S. A. Kunda, G. W. McCollum, R. MacGregor, *Int. J. Radiat. Isot.* **1985**, *36*, 853 – 855.
[12] M. af Ugglas, E. Tóth-Pál, H. Beving, K.-Å. Pettersson, *Ann. Univ. Turku Ser. D* **1977**, *8*, 79 – 84.
[13] M. Sawamura, Y. Kawaguchi, E. Nakamura, *Synlett* **1997**, 801 – 802.
[14] E. P. Wesseler, R. Iltis, L. C. Clark, Jr., *J. Fluorine Chem.* **1977**, *9*, 137 – 146.
[15] A. Ogawa, D. P. Curran, *J. Org. Chem.* **1997**, *62*, 450 – 451.
[16] S. Nishimura, K. Yajima, N. Harada, Y. Ogawa, N. Hayashi, *J. Autom. Chem.* **1994**, *16*, 195 – 204.
[17] Y. Murakami, A. Kuroda, K. Osoda, S. Nishimura, *Tetrahedron Lett.* **2003**, *44*, 641 – 644.
[18] J. L. Brokenshire, K. U. Ingold, *Int. J. Chem. Kinet.* **1971**, *3*, 343 – 357.
[19] A. Noda, *The 44th Annual Meeting of The Japanese Society of Nuclear Medicine*, Nov. 4th-6th, 2004, Kyoto, Japan, 2VI333.
[20] E. Nakamura, T. Inubushi, S. Aoki, D. Machii, *J. Am. Chem. Soc.* **1991**, *113*, 8980 – 8982.
[21] R. R. MacGregor, J. S. Fowler, A. P. Wolf, C.-Y. Shiue, R. E. Lade, C.-N. Wan, *J. Nucl. Med.* **1981**, *22*, 800 – 803.
[22] M. Suzuki, R. Noyori, B. Långström, Y. Watanabe, *Bull. Chem. Soc. Jpn.* **2000**, *73*, 1053 – 1070.
[23] B. Långström, T. Kihlberg, M. Bergström, G. Antoni, M. Björkman, B. H. Forngren, T. Forngren, P. Hartvig, K. Markides, U. Yngve, M. Ögren, *Acta Chem. Scand.* **1999**, *53*, 651 – 669.

 © 2005 Wiley-VCH Verlag GmbH & Co. KGaA, Weinheim

High-Spin Molecules

Symmetry and Topology Determine the Mo^{V}–CN–Mn^{II} Exchange Interactions in High-Spin Molecules

Eliseo Ruiz, Gopalan Rajaraman, Santiago Alvarez, Béatrice Gillon, John Stride, Rodolphe Clérac, Joulia Larionova, and Silvio Decurtins*

The two conditions that the ground state of a compound must meet in order to behave as a single-molecule magnet[1] are a high spin and a significant anisotropy (i.e. a large uniaxial zero-field-splitting parameter). It is not surprising, therefore, that an increasing number of polynuclear transition-metal compounds are currently being reported in which the individual spins of the metal atoms are coupled through exchange interactions in such a way so as to produce a high total molecular spin. In this context, the highest spin proposed to date corresponds to $[Mn\{Mn(MeOH)_3\}_8(\mu\text{-}NC)_{30}\{Mo(CN)_3\}_6]\cdot 5\,MeOH\cdot 2\,H_2O$,[2] a compound that comprises Mo^{V} and Mn^{II} centers, abbreviated from here on as Mn_9Mo_6 (see Figure 1). In such a compound, a total spin of 51/2 would result from ferromagnetic interactions between the Mo and Mn ions through cyanide bridging ligands. However, for the analogous Mn_9W_6 compound,[3] a total spin of 39/2 has been postulated and is consistent with antiferromagnetic coupling between neighboring W and Mn atoms (i.e. an overall ferrimagnetic arrangement). In other compounds of varying

[*] Dr. E. Ruiz, Dr. G. Rajaraman,[+] Prof. S. Alvarez
Departament de Química Inorgànica
Centre Especial de Recerca en Química Teòrica (CeRQT)
Universitat de Barcelona, Diagonal 647, 08028 Barcelona (Spain)
Fax: (+34) 934-907-725
E-mail: eliseo.ruiz@qi.ub.es

Dr. B. Gillon, Dr. J. Stride[++]
Laboratoire Léon Brillouin
CEA-CNRS, UMR 0012, Centre d'Etudes de Saclay
91191 Gif-sur-Yvette (France)

Dr. R. Clérac
Centre de Recherche Paul Pascal
CNRS UPR-8641
115 Avenue Dr. Albert Schweitzer, 33600 Pessac (France)

Dr. J. Larionova
Laboratoire de Chimie Moléculaire et Organisation du Solide
UMR 5637, Université Montpellier II
Place E. Bataillon, 34095 Montpellier cedex 5 (France)

Prof. S. Decurtins
Department für Chemie und Biochemie
Universität Bern
Freiestrasse 3, 3012 Bern (Switzerland)

[+] Current address:
Department of Chemistry, University of Manchester
Manchester M13 9PL (UK)

[++] Current address:
Institut Laue-Langevin
6 Rue Jules Horowitz, BP156, 38042 Grenoble Cedex 9 (France)

Supporting information for this article is available on the WWW under http://www.angewandte.org or from the author.

 DOI: 10.1002/anie.200500129 © 2005 Wiley-VCH Verlag GmbH & Co. KGaA, Weinheim

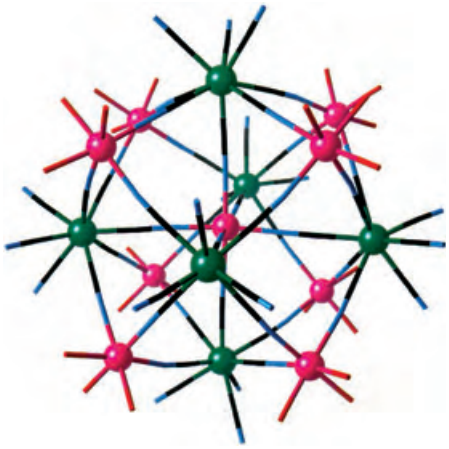

Figure 1. Molecular structure of the Mn_9Mo_6 complex (Mn magenta, Mo green; light blue, black, and red cylinders represent bonds to N, C, and O atoms, respectively). The carbon atoms of the methanol groups are omitted for clarity.

dimensionality based on Group 6 octacyanometallate(v) anions,[4–7] whose magnetic behavior is determined by the same type of $M^{V}\cdots Mn^{II}$ (M = Mo, W) exchange interactions, antiferromagnetism rather than ferromagnetism is observed in all cases (see Supporting Information for more details). All these compounds have in common the b_2^1 electron configuration for M in the $[M(CN)_8]^{3-}$ anion and $t_{2g}^3e_g^2$ for Mn^{II}, so it is not easy to explain why the cyanide-mediated exchange coupling is antiferromagnetic in all cases except Mn_9Mo_6, for which ferromagnetic coupling was assigned according to the available experimental data.

From a qualitative theoretical point of view,[8] the metal d orbitals that carry the unpaired electrons at each metal atom can interact through the π orbitals of the bridging cyanide groups to lead to an orbital gap, which should result in a significant antiferromagnetic contribution that tends to pair up the spins of the two types of metal ions. Although the proposed ferromagnetic behavior has been justified by using kinetic-exchange theory,[9] a qualitative molecular-orbital analysis supports the existence of only antiferromagnetic interactions.[7] Even if Mn_9Mo_6 is no longer the only known compound with a spin of 51/2 (a Mn_{25} complex with the same total spin has been reported recently[10]), clarification of the nature of the $M^{V}\cdots Mn^{II}$ exchange interaction is of importance, given the robustness and versatility of $[M(CN)_8]^{3-}$ anions[11] as building blocks for complex systems with high spin as well as the doubts that the attribution of an $S = 51/2$ spin state to the Mn_9Mo_6 complex have generated.[10] We therefore undertook a theoretical computational study based on density functional theory (DFT, B3LYP method; see Supporting Information for details) for dinuclear models as well as for the whole Mn_9Mo_6 complex to estimate the exchange-coupling constants in the cyano-bridged Mo^{V}–Mn^{II} compounds in an attempt to shed some light on their controversial magnetic behavior. Additionally, a polarized neutron diffraction experiment was performed on a single crystal of $[Mn\{Mn(MeOH)_3\}_8(\mu\text{-}NC)_{30}\{Mo(CN)_3\}_6]\cdot 5\,MeOH\cdot 2\,H_2O$ to offer unambiguous experimental evidence of the exact nature of the magnetic ground state of the Mn_9Mo_6 cluster.

The structure of Mn_9Mo_6 can be described as a centered cube of Mn^{II} cations, with the Mo^{V} ions capping its six faces (Figure 1) to thus form its dual octahedron. Such a geometrical compound, comprised of a cube and an octahedron as observed for the Mn_9Mo_6 core, appears as a member of the constellation of polyhedra in M. C. Escher's wood engraving "Stars" and can be seen at the upper left corner of Figure 2.

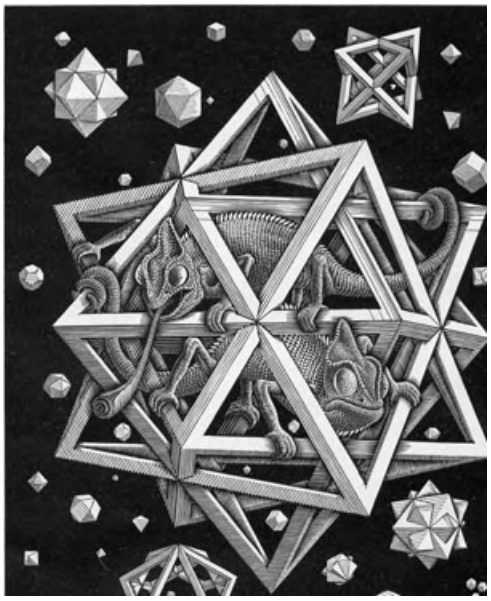

Figure 2. M. C. Escher's wood engraving "Stars" (1948), which shows the compound of a cube and an octahedron in the upper left corner. (Copyright 2005, The M. C. Escher Company, Holland. All rights reserved. www.mcescher.com).

The central Mn is radially bridged to the six Mo atoms by cyanide ligands, and the peripheral Mn atoms are bridged by tangential cyanides to three neighboring Mo atoms that form a triangular face of the Mo_6 octahedron. Furthermore, each Mo atom has three terminal cyano ligands that lead to octacoordinate Mo atoms, best described as triangular dodecahedra, as ascertained from continuous shape measures (CShM)[12] of the three independent $[Mo(CN)_8]^{3-}$ anions in the asymmetric unit of Mn_9Mo_6 (see Supporting Information). The central Mn atom is clearly octahedral, and the coordination spheres of peripheral Mn atoms, completed by methanol molecules, are also identified as octahedra from their CShMs. Remarkably, the Mn_9 and Mo_6 cores are very well described (see Supporting Information) as a centered cube and an octahedron, respectively, despite the low molecular symmetry (C_2) and even if the approximate D_{2d} symmetry of the MoC_8 dodecahedra and the octahedral pseudosymmetry of the metal cores are not in accord.

From the above description of the molecular structure, the following observations can be made with regards to the exchange-interaction pathways. Of the thirty cyano-bridged Mo···Mn interactions, six are associated with radial moieties and twenty-four with tangential Mo–CN–Mn moieties. The molecular symmetry (C_2 point group) reduces them to three radial and twelve tangential nonequivalent Mo···Mn interactions, whereas the approximate octahedral symmetry of the

 © 2005 Wiley-VCH Verlag GmbH & Co. KGaA, Weinheim

Mn_9Mo_6 core leaves only two types of exchange pathways, radial and tangential.

In an independent dodecahedral $[Mo(CN)_8]^{3-}$ anion, the unpaired electron resides in a d_{xy} orbital (Figure 3), as imposed by the local D_{2d} symmetry because all the ligands

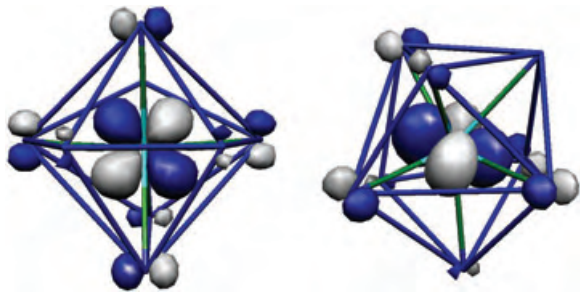

Figure 3. Representation of two different orientations of the molecular orbital that bears the unpaired electron for the mononuclear model $[Mo(CN)_8]^{3-}$, which corresponds to atom Mo3 in the Mn_9Mo_6 complex. Left: down the C_2 axis of the approximate D_{2d} symmetry; right: with the same orientation that the uppermost Mo atom has in Figure 1.

lie in its nodal planes, whereas the remaining d orbitals are all metal–ligand σ antibonding. From Figure 3 it is clear that the d_{xy} orbital is able to interact with the π-type orbitals of the cyano bridges of all eight ligands. However, in a dodecahedron there are four *equatorial* ligands that form angles of about 19° with the mean equatorial plane (perpendicular to the unique C_2 symmetry axis) and four *apical* ligands at approximately 39°. The former equatorial ligands are much better oriented to π-interact with the Mo d_{xy} orbital, and we should expect the exchange interaction to be more strongly antiferromagnetic when mediated by equatorial than by apical cyanide ligands. A careful analysis of the molecular structure tells us that each Mo^V ion is connected to the central Mn^{II} ion through an apical cyanide, to three peripheral Mn atoms through equatorial cyanides, and to a fourth Mn atom by means of an apical cyanide.

We calculated the exchange-coupling constants (J) of several representative dinuclear models extracted from the Mn_9Mo_6 molecule that present different types of exchange interactions from the point of view of the molecular (i.e. radial or tangential) and local (i.e. equatorial or apical) symmetries (Table 1). The calculated J values are all negative which suggests that all Mo···Mn exchange interactions in Mn_9Mo_6 are antiferromagnetic and that the whole molecule should be ferrimagnetically arranged with a net spin of 39/2. Furthermore, we see that all interactions through equatorial bridges are roughly twice as strong ($J \approx -20\ cm^{-1}$ in d–g) as those through apical cyanides ($J \approx -12\ cm^{-1}$ in a–c), as expected from overlap arguments. In contrast, neither the radial or tangential character of the interaction, nor the variations in the Mo-C-N and C-N-Mn bond angles (160–180° and 156–178°, respectively) seem to have a significant influence on the calculated values of J.

To verify our above conclusions, we performed calculations on dinuclear models of the chain compound Mn_3Mo_2,[5] which has three different Mo···Mn interactions per Mo atom. The three nonequivalent interactions present in this compound correspond to apical bridging cyanides, and the calculated J values for the corresponding dinuclear models (x–z, Table 1) are predicted to be about $-11\ cm^{-1}$, which consistently describe antiferromagnetic $Mo^V \cdots Mn^{II}$ interactions of the order of magnitude found for all apically bridged Mo–Mn pairs. In yet another compound, Mn_3W_2 with bipyridine,[4] the two different Mn–CN–W interactions correspond to apical positions of the W dodecahedra and the experimentally derived value of J is $-12.0\ cm^{-1}$, which remarkably coincides with our calculated values for Mn–CN–Mo apical interactions.

Table 1: Calculated exchange-coupling constants ($\boldsymbol{H} = -J\boldsymbol{S}_1\boldsymbol{S}_2$) for dinuclear models of the Mn_9Mo_6 compound (a–g) and the interactions in a Mn_3Mo_2 chain compound (x–z).[a]

Interaction	Metal atoms	Type	Bridge	J [cm^{-1}]
a	Mo1-Mn1	rad	ap	−12.4
b	Mo3-Mn1	rad	ap	−11.4
c	Mo1-Mn4	tang	ap	−12.2
d	Mo1-Mn5	tang	eq	−18.2
e	Mo1-Mn3	tang	eq	−21.6
f	Mo1-Mn2	tang	eq	−18.9
g	Mo2-Mn4	tang	eq	−22.8
x	Mo1-Mn2	–	ap	−9.9
y	Mo1-Mn1	–	ap	−10.7
z	Mo1-Mn1′	–	ap	−7.9

[a] $[Mo(CN)_7(\mu\text{-}CN)Mn(NC)_5]^{6-}$ is representative of the radial (rad) Mo–Mn pairs, and $[Mo(CN)_7(\mu\text{-}CN)Mn(NC)_2(MeOH)_3]^{3-}$ is representative of the tangential (tang) pairs. The apical (ap) or equatorial (eq) nature of the bridging cyanide relative to the dodecahedral coordination sphere of the Mo atom is also indicated.

The final theoretical evidence for antiferromagnetic exchange in Mn_9Mo_6 comes from calculations on the whole complex (2790 basis functions required) in three different spin configurations, with $S = 51/2$ (all spins up), $S = 41/2$ (the central Mn with spin down), and $S = 39/2$ (all Mo atoms with spins down). The $S = 39/2$ function appears to be lowest in energy which thus confirms the qualitative conclusion of our calculations on dinuclear models that antiferromagnetic Mo···Mn interactions are favored. If all interactions through apical cyanides are assumed to be approximately equal and likewise for all interactions through equatorial cyanides, we can obtain from the calculated energies average values for the corresponding coupling constants, $J_{ap} = -9.0\ cm^{-1}$ and $J_{eq} = -23.8\ cm^{-1}$, in excellent agreement with the results for dinuclear models.

The antiferromagnetic nature of Mn–Mo interactions in Mn_9Mo_6 is confirmed by the experimental results obtained from polarized neutron diffraction (PND) studies (see Supporting Information). Note that the single crystals of the cluster are extremely unstable in the absence of mother liquor and their exposure in air or argon atmospheres for a few minutes leads to a structural transformation. For this reason, a determination of the spin of the ground state for this compound is not easily obtained from the magnetic measurements. PND experiments performed on a single crystal of the Mn_9Mo_6 cluster within the mother liquor gives access to the experimental magnetic structure factors that are the Fourier components of the magnetization density. Owing to the small

 © 2005 Wiley-VCH Verlag GmbH & Co. KGaA, Weinheim

size of the crystal, a limited set of reflections was obtained. However, comparison of the experimental data and the three different models ($S = 51/2$, $S = 41/2$, and $S = 39/2$) unambiguously supports (Table 2) the ferrimagnetic model ($S = 39/2$).

Table 2: Experimental and calculated magnetic structure factors of the Mn_9Mo_6 compound for $S = 51/2$ (ferromagnetic), $S = 41/2$, and $S = 39/2$ (ferrimagnetic) models.

	Magnetic structure factor, $F_M(h,k,l)$ [μ_B]			
h,k,l	neutrons	$S = 51/2$	$S = 41/2$	$S = 39/2$
−2 2 1	15(8)	−1.4	8.9	18.2
2 0 2	−24(1)	−5.4	−7.2	−22.2
4 0 2	20(3)	38.7	−19.3	8.3
−2 0 4	27(2)	4.6	7.5	23.5
−12 0 6	67(8)	53.7	−21.5	47.6
0 6 8	−33(3)	−27.7	12.1	−26.6
1 5 9	36(8)	25.9	−13.6	25.6
	Reliability factors[a]			
$R(F_M)$[b]		0.47	1.19	0.26
$R_w(F_M)$[c]		0.84	0.89	0.22
GOF[d]		11.1	12.0	3.0

[a] The agreement factors, R and weighted R_w (with $w = 1/\sigma^2$), and the goodness of fit (GOF) are indicated. [b] $R(F_M) = (\sum_{hkl} ||F_M^o| - |F_M^c||)/(\sum_{hkl} |F_M^o|)$. [c] $R_w(F_M) = [(\sum_{hkl} w(|F_M^o| - |F_M^c|)^2)/(\sum_{hkl} w|F_M^o|^2)]^{1/2}$. [d] $GOF = [(\sum_{hkl} w(|F_M^o| - |F_M^c|)^2)]/(N_o - N_c)]^{1/2}$. N_o = number of reflections, N_v = number of parameters, w = weighting scheme.

In Table 2 are reported the results of the least-squares refinements performed on the basis of the experimental magnetic structure factor (F_M) values for the three different models. The absolute magnitudes of the manganese magnetic moments were fixed to $5\mu_B$ with sign arrangements that correspond to the three different models and the scale factor was refined. The best reliability factors were obtained for the $S = 39/2$ ferrimagnetic model ($R_w(F_M) = 22\,\%$), while the two other models led to weighted agreement factors greater than 80 %.

The calculated spin density for the single determinant ferrimagnetic state with $S = 39/2$ of Mn_9Mo_6 (Figure 4) offers us a wealth of information on the electronic structure and the mechanism of the exchange interaction. Characteristic features of this map can be interpreted as resulting from the interplay between spin delocalization and spin polarization,[13] notably the numerical values of atomic spin densities. Additionally, the following observations can be made about the three-dimensional shape of the spin density: 1) At each Mo atom, the spin density has the shape of the d_{xy} orbital, with the same orientation relative to the $Mo(CN)_8$ dodecahedron as with the independent monomer (Figure 3); 2) Although the spin densities at the C and N atoms of the bridging cyanides are opposite to those of the neighboring metal atom, which suggests a predominance of spin polarization over spin delocalization, this effect could also be attributed to a delocalization of the metal unpaired electrons through the π system of the cyanide mostly to the N atoms.[13] This effect is also seen in the significant spin population at the N atom but not at the C atom of the terminal cyanides; 3) The spin density on the cyanide ligands shows the form of p orbitals centered

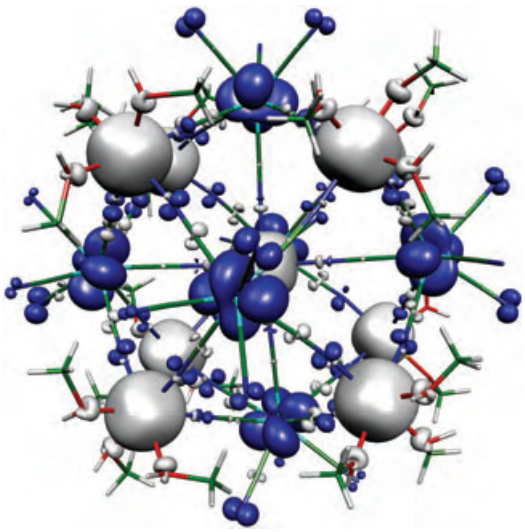

Figure 4. Representation of the spin density that corresponds to the $S = 39/2$ ground state of the Mn_9Mo_6 complex (clear and dark regions indicate positive and negative spin populations, respectively).

at the C and N atoms. Note that this p-orbital shape indicates that it is mostly the Mo^V cation that transfers spin density to the bridge, as its perpendicular π system, which interacts equally with Mn^{II} but not with Mo^V, shows no significant unpaired-spin population; 4) The shape of the spin density at the Mn atoms is nearly spherical, as expected for a set of five d orbitals with one unpaired electron each, even if slightly distorted toward cubes with the Mn–N bonds at the face centers. We recall that the t_{2g}^3 manifold is cubic whereas the e_g^2 manifold is octahedral,[14] and the combination of a cube and an octahedron should give a spherical spin density for a $t_{2g}^3e_g^2$ configuration. Slight deviation from sphericity at the Mn atoms results from the lesser spin density at the e_g orbitals relative to the t_{2g} orbitals owing to a significant delocalization of the former through σ bonding; 5) The σ delocalization of the Mn^{II} e_g electrons can be clearly seen at the O atoms of the terminal MeOH ligands by the approximate shape of an sp^3 hybrid orbital. Also the N atoms of the cyanide bridges present a small amount of positive σ-type spin density in the region of the Mn–N bonds which is consistent with the shape of an sp hybrid. The coexistence of positive σ and negative π spin density at the same metal atom is a remarkable feature of the complex electronic structure of Mn_9Mo_6.

Both the exchange-coupling constants and the spin-density map calculated for Mn_9Mo_6 show a fascinating interplay between the local symmetries of the building blocks and the topological symmetry of the molecular assembly. Hence, antiferromagnetic interactions between Mo^V and Mn^{II} are imposed by the d orbital pattern of the dodecahedral coordination sphere of the former rather than by the molecular symmetry, with apical and equatorial cyanides mediating exchange interactions of varying strengths that differ by a factor of approximately two. On the other hand, while the spin populations at the metal atoms conform to their approximate local symmetry, D_{2d} for Mo and O_h for Mn, they are repeated throughout the molecule with a topology that results from applying the symmetry operations

 © 2005 Wiley-VCH Verlag GmbH & Co. KGaA, Weinheim

of the approximately O_h-symmetric Mn_9Mo_6 core. On their side, the spin populations of bridging cyanides show the signature of their local $C_{\infty v}$ symmetry, disseminated throughout the molecule with the approximate O_h symmetry of the metallic framework. In summary, what is initially perceived from the molecular structure as one of the stars in the Escher galaxy, with the shape of a cube–octahedron compound, is revealed by an analysis of its magnetic structure to be a planetary system that orbits around the central Mn atom in which each Mo and Mn planet is surrounded by satellite ligands with dodecahedral and octahedral shapes, respectively.

Received: January 13, 2005
Published online: April 12, 2005

Keywords: density functional calculations · exchange coupling · manganese · molybdenum · spin density

[1] D. Gatteschi, *Angew. Chem.* **2003**, *115*, 278; *Angew. Chem. Int. Ed.* **2003**, *42*, 246; *Magnetism: Molecules to Materials*, *Vols. 1–4* (Eds.: J. S. Miller, M. Drillon), Wiley-VCH, Weinheim, **2001**–**2004**.
[2] J. Larionova, M. Gross, M. Pilkington, H. Andres, H. Stoeckli-Evans, H. U. Güdel, S. Decurtins, *Angew. Chem.* **2000**, *112*, 1667; *Angew. Chem. Int. Ed.* **2000**, *39*, 1605.
[3] Z.-J. Zhong, H. Seino, Y. Mizobe, M. Hidai, A. Fujishima, S.-I. Ohkoshi, K. Hashimoto, *J. Am. Chem. Soc.* **2000**, *122*, 2952.
[4] R. Podgajny, C. Desplanches, B. Sieclucka, R. Sessoli, V. Villar, C. Paulsen, W. Wernsdorder, Y. Dromzee, M. Verdaguer, *Inorg. Chem.* **2002**, *41*, 1323.
[5] D.-F. Li, l.-M. Zheng, W. X. Tang, *J. Chem. Soc. Dalton Trans.* **2002**, 2805.
[6] Y. Arimoto, S.-I. Ohkoshi, Z.-J. Zhong, H. Seino, Y. Mizobe, K. Hashimoto, *Chem. Lett.* **2002**, 832; T. Kashiwagi, S.-I. Ohkoshi, H. Seino, Y. Mizobe, K. Hashimoto, *J. Am. Chem. Soc.* **2004**, *126*, 5024; Z.-J. Zhong, H. Seino, Y. Mizobe, M. Hidai, M. Verdaguer, S.-I. Ohkoshi, K. Hashimoto, *Inorg. Chem.* **2000**, *39*, 5095.
[7] S. You, S.-I. Ohkoshi, Y. Arimoto, H. Seino, Y. Mizobe, K. Hashimoto, *Inorg. Chem.* **2003**, *42*, 1848.
[8] O. Kahn, B. Briat, *J. Chem. Soc. Faraday Trans. 2* **1976**, *72*, 1441; O. Kahn, B. Briat, *J. Chem. Soc. Faraday Trans. 2* **1976**, *72*, 268; O. Kahn, *Molecular Magnetism*, VCH Publishers, New York, **1993**; P. J. Hay, J. C. Thibeault, R. Hoffmann, *J. Am. Chem. Soc.* **1975**, *97*, 4884.
[9] L. Chibotaru, V. S. Mironov, A. Ceulemans, *Angew. Chem.* **2001**, *113*, 4561; *Angew. Chem. Int. Ed.* **2001**, *40*, 4429.
[10] M. Murugesu, M. Habrych, W. Wernsdorfer, K. A. Abboud, G. Christou, *J. Am. Chem. Soc.* **2004**, *126*, 4766.
[11] J. G. Leipoldt, J. S. Basson, A. Roodt, *Adv. Inorg. Chem.* **1993**, *40*, 241; K. R. Dunbar, R. A. Heintz, *Prog. Inorg. Chem.* **1997**, *45*, 283.
[12] In brief, if a set of atoms has a zero shape measure relative to a given polyhedron, this means that it has the exact shape of that polyhedron. Increasing values of the CShM indicate increasing degrees of distortion from the ideal polyhedron. H. Zabrodsky, S. Peleg, D. Avnir, *J. Am. Chem. Soc.* **1992**, *114*, 7843; S. Alvarez, D. Avnir, M. Llunell, M. Pinsky, *New J. Chem.* **2002**, *26*, 996; D. Casanova, M. Llunell, P. Alemany, S. Alvarez, *Chem. Eur. J.* **2005**, *11*, 1479.
[13] J. Cano, E. Ruiz, S. Alvarez, M. Verdaguer, *Comments Inorg. Chem.* **1998**, *20*, 27.
[14] C. Desplanches, E. Ruiz, A. Rodríguez-Fortea, S. Alvarez, *J. Am. Chem. Soc.* **2002**, *124*, 5197.

 © 2005 Wiley-VCH Verlag GmbH & Co. KGaA, Weinheim

Lead(II) Detection

An Exceptionally Selective Lead(II)-Regulatory Protein from *Ralstonia Metallidurans*: Development of a Fluorescent Lead(II) Probe**

*Peng Chen, Bill Greenberg, Safiyh Taghavi, Christine Romano, Daniel van der Lelie, and Chuan He**

Lead contamination is a serious threat to human health and the environment.[1,2] Lead poisoning is still one of the most common environmentally caused diseases in the world today.[3,4] Lead levels are typically measured by using atomic absorption spectroscopy or other related instrumental methods. Probes that can provide rapid, on-site evaluation of the lead content of a sample are very valuable for a variety of applications.[5] A primary challenge is to construct a "turn-on" probe that responds to lead(II) ions with a high selectivity over other heavy metal ions. This has not been achieved with chemically designed small molecules, despite some progress in the last decade.[5] Chemical probes have been developed for the detection of other small molecules, but with limited success for heavy metal ions and paramagnetic metal ions.[6]

An evolution strategy was elegantly applied by Lu and coworkers recently to construct Pb^{2+} probes based on a DNAzyme.[7] This system is surprisingly selective towards Pb^{2+} ions. We have adopted a different strategy that takes advantage of the function of metalloregulatory proteins. Nature has evolved numerous such proteins to control the concentrations of beneficial or toxic metal ions with unprecedented sensitivity and selectivity. If the biological sensory events of these proteins were reported with measurable signals, such as fluorescence, practical probes could be obtained for the detection of various metal ions.[8–10] We have recently invented a method to convert the MerR-family proteins into fluorescent reporters for the detection of Hg^{2+}

[*] Prof. P. Chen, C. Romano, C. He
Department of Chemistry
The University of Chicago
5735 S. Ellis Avenue, Chicago, IL 60637 (USA)
Fax: (+1) 773-702-0805
E-mail: chuanhe@uchicago.edu
B. Greenberg, Dr. S. Taghavi, Dr. D. van der Lelie
Biology Department, Building 463
Brookhaven National Laboratory
50 Bell Avenue, Upton, NY 11973-5000 (USA)

[**] This work was supported by the University of Chicago and a Searle Scholar award to C.H. P.C. is supported by the Burroughs Wellcome Fund Cross-Disciplinary Training Program (grant no.: 1001774C). The work by B.G., S.T., and D.v.d.L. was supported by Laboratory Directed Research and Development funds at the Brookhaven National Laboratory under contract with the US Department of Energy. We thank Dr. J. Piccirilli for the use of the DNA synthesizer, Dr. N.-S. Li, E. M. Duguid, and Y. Mishina for assistance with DNA synthesis, and the Biophysics Core Facility at the University of Chicago, and Dr. M. A. Yousef for help with fluorescence and isothermal titration calorimetry measurements.

Supporting Information for this article is available on the WWW under http://www.angewandte.org or from the author.

 DOI: 10.1002/anie.200462443 © 2005 Wiley-VCH Verlag GmbH & Co. KGaA, Weinheim

and coinage metal ions.[11] Herein we report the successful conversion of a novel Pb^{2+}-regulatory protein in *Ralstonia metallidurans* CH34 into a fluorescent reporter that exhibits high selectivity and sensitivity for Pb^{2+} ions. With the aid of this system, the binding of Pb^{2+} ions to the Pb^{2+}-regulatory protein was also characterized. A surprisingly high binding selectivity of the protein towards Pb^{2+} is revealed.

Ralstonia metallidurans is a Gram-negative, non-spore-forming bacillus that flourishes in millimolar concentrations of toxic heavy metals.[12] It is the only bacterium that has been shown to contain a lead-specific resistance pathway so far. The *pbr* operon is a unique operon, as it combines functions involved in uptake, efflux, and accumulation of Pb^{2+} ions.[13] All the resistance genes (*pbrTRABCD*) in the *pbr* operon are regulated by the PbrR protein, which mediates Pb^{2+}-inducible transcription from its divergent promoter (Figure 1). PbrR is

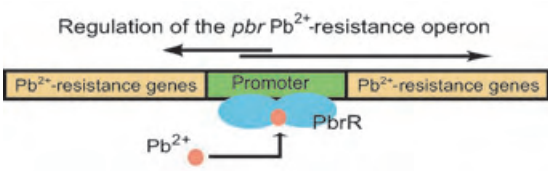

Figure 1. PbrR regulates the lead-resistance operon (*pbr*) in *Ralstonia metallidurans* strain CH34.

a member of the MerR family of metal-sensing regulatory proteins. It is the first protein to be discovered that can sense Pb^{2+} ions in nature.[13] PbrR691, another MerR-type protein that is encoded on the chromosome of *R. metallidurans* CH34, has been assigned as a homologue of PbrR (unpublished results);[14] however, its function has never been characterized. The binding of Pb^{2+} ions to PbrR and PbrR691 has not been studied in vitro. The concentration level of Pb^{2+} that triggers a response from these proteins is unclear. The selectivity and the molecular mechanism of the Pb^{2+} recognition have yet to be elucidated. We became very interested in studying these unique proteins, not only for developing Pb^{2+}-specific probes, but also to reveal strategies used by these proteins for recognizing trace levels of Pb^{2+} ions.

We applied a technique that we developed previously to convert the PbrR proteins into fluorescent reporters for Pb^{2+} ions.[11] The unique transcriptional activation mechanism used by the MerR proteins forms the basis for our approach.[15] A 25-mer duplex DNA containing the PbrR-binding sequence was prepared (**DNA-1** in Figure 2). In the central base pair of

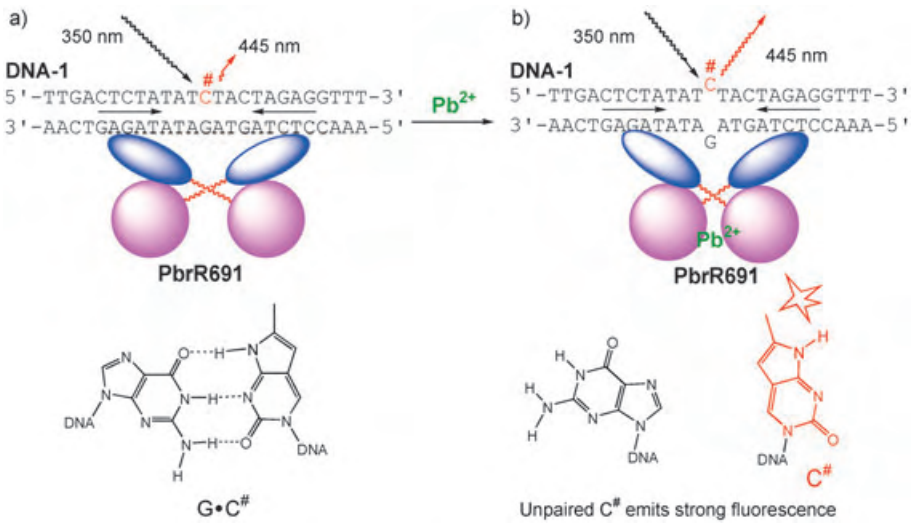

Figure 2. a) Pyrrolo-C ($C^{\#}$) can form a stable base pair with G. The fluorescence intensity of pyrrolo-C is quenched in the duplex DNA. The promoter sequence that PbrR691 binds is used to construct **DNA-1**; the dyad symmetrical sequence is marked with arrows. b) Binding of Pb^{2+} ions to PbrR691 induces base unpairing of pyrrolo-C, which emits strong fluorescence at $\lambda \approx 445$ nm upon excitation.

this sequence a fluorescent base, pyrrolo-C, was incorporated as the reporter. The addition of Pb^{2+} ions and PbrR should trigger a distortion of the duplex DNA to give an unpaired pyrrolo-C base, which will emit strong fluorescence at $\lambda \approx 445$ nm upon excitation at 350 nm. In the absence of PbrR and metal ions, **DNA-1** is expected to exhibit weak fluorescence.

The relevant genes for both PbrR and PbrR691 were cloned and expressed. PbrR showed a low solubility in aqueous solution. Fortunately, PbrR691 can be overexpressed as a soluble protein in large quantities. This protein was subsequently purified and used in this study (see the Supporting Information). The concentration of PbrR691 was determined by a bovine serum albumin (BSA) assay (Bio-Rad Laboratories, Inc.) that was calibrated by amino acid analysis (Protein Chemistry Laboratory, Texas A&M University).

The addition of PbrR691 to **DNA-1** did not cause noticeable changes in the fluorescence of the probe. However, the addition of one equivalent of Pb^{2+} ions per PbrR691 dimer triggered a significant fluorescence enhancement within seconds (Figure 3a). The probe is selective, as the addition of a 50-fold excess of Zn^{2+}, Co^{2+}, Hg^{2+}, Cu^{2+}, or Cd^{2+} caused less than 1/20th of the fluorescence increase at $\lambda = 445$ nm compared to that with Pb^{2+} ions (Figure 3b). We concluded that the fluorescence response of this PbrR691-based probe is over 1000-fold more selective towards Pb^{2+} ions than towards the other metal ions in this assay! Thus, PbrR691 appears to exhibit an unprecedented selectivity towards Pb^{2+} ions over other metal ions.

When we tried to perform an accurate analysis of Pb^{2+} binding to the protein by using this fluorescent system, we discovered that the fluorescence response from this probe is not optimum to give a quantitative assessment of Pb^{2+} binding to PbrR691. Instead, we employed 2-aminopurine (2AP), an analogue of adenine, as the fluorescent base. 2AP emits

 © 2005 Wiley-VCH Verlag GmbH & Co. KGaA, Weinheim

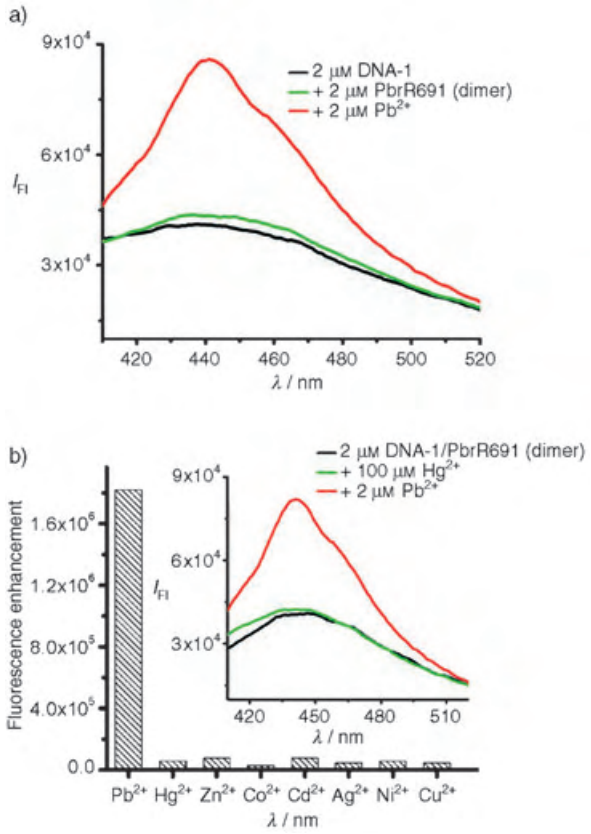

Figure 3. Responses of the PbrR691-based fluorescent probe towards different metal ions. a) Fluorescence spectra of the probe in the absence and presence of one equivalent of Pb^{2+} ions. b) The fluorescence enhancement integrated over $\lambda = 420$–500 nm in the presence of Pb^{2+} ions (2 μM) and other metal ions (100 μM). The inset presents the fluorescence spectra of the probe in the presence of Pb^{2+} (2 μM) and Hg^{2+} ions (100 μM).

fluorescence at $\lambda \approx 370$ nm when excited between $\lambda = 310$ and 320 nm. The incorporation of 2AP into DNA quenches its fluorescence. This quenching is attributed to stacking interactions with nearest neighbor nucleobases and to electron transfer to nearby bases.[16,17] When the base-pairing environment is perturbed, 2AP shows quantitatively enhanced fluorescence; this property makes 2AP an excellent fluorescent probe for studying the structural properties of the DNA duplexes. We incorporated a 2AP base into the central base pair of the PbrR-promoter DNA (**DNA-2**), as shown in Figure 4 a. The response of this new probe towards Pb^{2+} binding was tested.

The fluorescence of the 2AP-containing probe is quenched in double-stranded DNA. The addition of the apo-PbrR691 dimer to **DNA-2** did not give any significant fluorescence change. The addition of one equivalent of Pb^{2+} ions triggered a greater than threefold fluorescence enhancement. The intensity increase is reproducible and the response occurs at both 4 °C and room temperature. At room temperature, the detection limit can reach the nanomolar range (50 nM) for free Pb^{2+} ions in solution. The probe also shows higher selectivity towards Pb^{2+} ions than towards other metal ions (about 1000-fold, Figure 4 b). The binding of Pb^{2+} ions to PbrR691 appears to be reversible, as the addition of 10 μM ethylenediaminetetraacetate (EDTA) to the Pb^{2+}-bound probe restores the original spectrum of the metal-free probe.

This new 2AP-based Pb^{2+} probe has several advantages. It is sensitive and highly selective towards Pb^{2+} ions. It shows a quantitative response to various Pb^{2+} concentrations in solution. The fluorescent-reporter system also offers an opportunity to characterize the Pb^{2+}-binding properties of PbrR691. The binding of Pb^{2+} ions to PbrR691 was monitored by recording fluorescence spectra as a function of Pb^{2+} concentration, as shown in Figure 4 c. The metal-binding titration was fitted with a one-site binding model in the Origin program (Origin 7 SR2, OriginLab Corp., Northampton, MA). The fitting curve yielded a dissociation constant, K_d, of $1.98 \pm 0.16 \times 10^{-7}$ M (Figure 4 d). The fitting also indicated that PbrR691 forms a 2:1 complex with Pb^{2+} ions; thus, each PbrR691 dimer binds one Pb^{2+} ion.

To confirm the binding constant and the stoichiometry of the metal–protein complex in solution, we performed the continuous variation experiment (Job method; see the Supporting Information),[18] which unambiguously confirmed the formation of a 2:1 PbrR691:Pb^{2+} complex (Figure 4 e). This conclusion agrees with the fluorescence titration result. To verify the binding constant, isothermal titration calorimetry (ITC) was performed on the Pb^{2+}/PbrR691 system in a solution of 100 mM $NaNO_3$, 20 mM tris(hydroxymethyl)aminomethane/HNO_3 (Tris-HNO_3), and 5 % glycerol at pH 7.0.[19] The ITC data were fitted by the one-site binding model and they yielded the same 2:1 ratio between PbrR691 and Pb^{2+} ions (see the Supporting Information). The dissociation constant was calculated to be $2.07 \pm 0.14 \times 10^{-7}$ M, which is consistent with the fluorescence titration result.

Lastly, the Pb^{2+}-bound PbrR691 was prepared and analyzed. Excess amounts of $Pb(NO_3)_2$ (up to a final concentration of 500 μM) were added to a solution of PbrR691 (50 μM). The free and weakly bound Pb^{2+} ions were removed by consecutive dialyses with washing buffer (2 L). Inductively coupled plasma-mass spectrometry (ICP-MS) analysis of this sample showed 1.06 ± 0.02 equivalents of Pb^{2+} ions per PbrR691 dimer. When the protein solution was washed with EDTA (100 μM), almost no Pb^{2+} ions (0.008 equiv) were observed from the ICP-MS measurement. This observation further indicates the binding of one Pb^{2+} ion per PbrR691 dimer.

We have reported herein the characterization of a unique Pb^{2+}-regulatory protein, PbrR691. It shows a selectivity of over 1000-fold towards Pb^{2+} ions over other metal ions. By applying a mechanism-based approach, we have successfully converted this Pb^{2+}-sensory protein into a selective fluorescent Pb^{2+} reporter. This novel PbrR691-based Pb^{2+} probe has the potential to be used in practical applications after further improvements. The affinity and stoichiometry of the binding of Pb^{2+} ions to PbrR691 were also revealed with the aid of the fluorescent-reporter system and were further confirmed with other methods.

The development of a selective Pb^{2+} chelator for treating lead poisoning is an unachieved challenge.[1] We believe study of the molecular basis for selective Pb^{2+} recognition by

 © 2005 Wiley-VCH Verlag GmbH & Co. KGaA, Weinheim

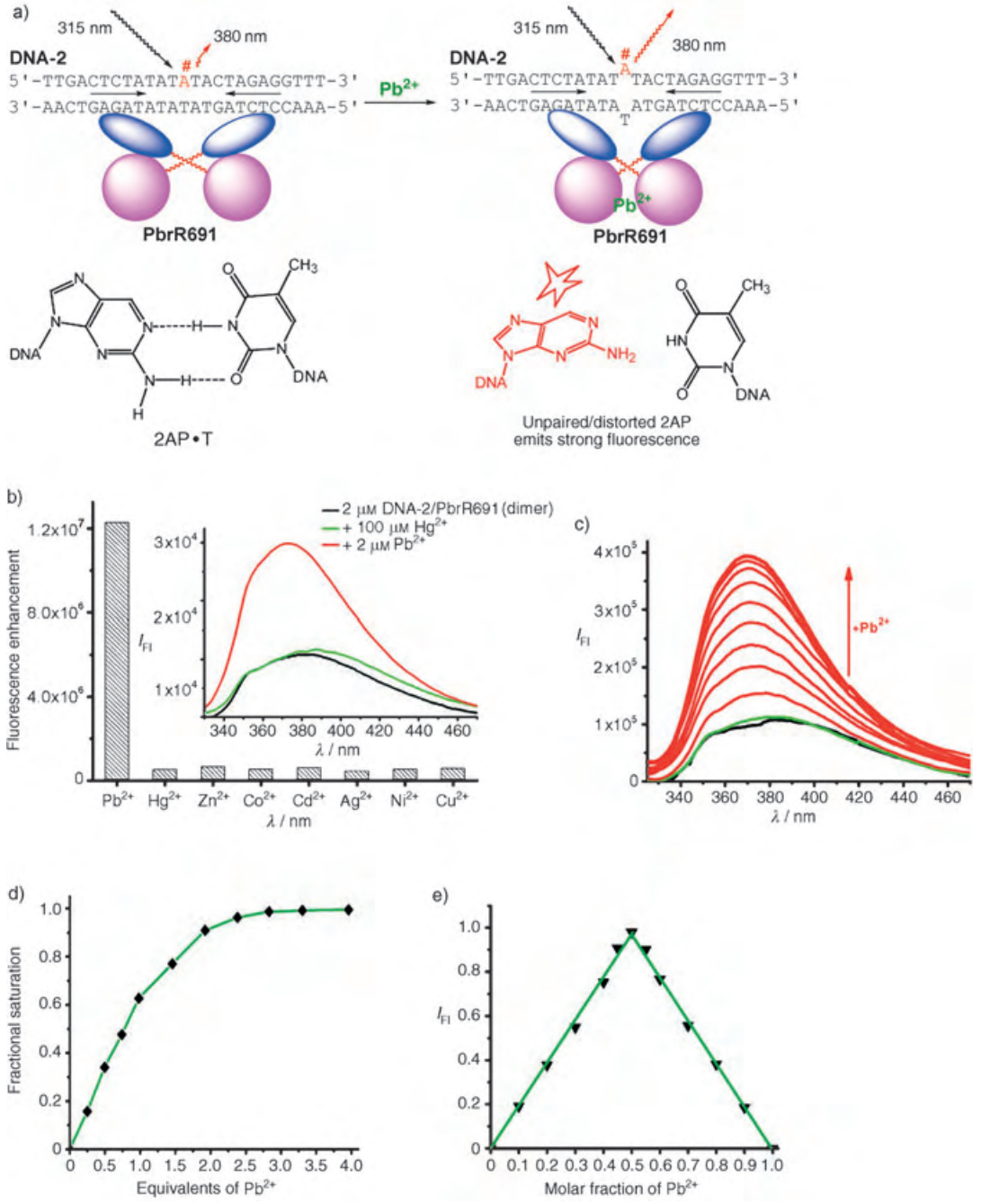

Figure 4. Binding of Pb^{2+} ions to PbrR691 as revealed by a 2AP-modified DNA probe (**DNA-2**). $A^{\#}$ = 2-aminopurine = 2AP. a) Binding of Pb^{2+} ions to PbrR691 induces base unpairing of 2AP, which emits strong fluorescence. b) The fluorescence enhancement integrated over λ = 350–420 nm in the presence of different metal ions. The insert presents the fluorescence spectra of the probe in the presence of Pb^{2+} (2 μM) and Hg^{2+} ions (100 μM). c) Fluorescence response of the PbrR691(dimer)/**DNA-2** complex to the addition of Pb^{2+} ions at pH 7.0. The initial concentrations of PbrR691(dimer) and **DNA-2** were both 2.0 μM (black: fluorescence of **DNA-2** only; green: fluorescence for the complex). Aliquots of 0.1 or 1 mM $Pb(NO_3)_2$ were added to yield final Pb^{2+} concentrations of 0.5, 1.0, 1.5, 2.0, 3.0, 4.0, 5.0, 6.0, 7.5, and 10.0 μM (red curves). d) The fractional saturation of the Pb^{2+}/PbrR691(dimer)/**DNA-2** complex as a function of Pb^{2+} ions added, based on the spectra presented in (c). e) Job plot of Pb^{2+} binding to PbrR691. The DNA concentration (**DNA-2**) was maintained at 4 μM. The sum of the concentration of PbrR691 and $Pb(NO_3)_2$ is 4 μM.

PbrR691 may provide fundamental knowledge for designing such agents in the future.

Keywords: fluorescent probes · lead · PbrR · regulatory proteins · sensors

Received: October 27, 2004
Revised: February 3, 2005
Published online: March 31, 2005

[1] E. S. Claudio, H. A. Godwin, J. S. Magyar, *Prog. Inorg. Chem.* **2003**, *51*, 1–144.
[2] H. A. Godwin, *Curr. Opin. Chem. Biol.* **2001**, *5*, 223–227.

 © 2005 Wiley-VCH Verlag GmbH & Co. KGaA, Weinheim

[3] P. J. Landrigan, A. C. Todd, *West. J. Med.* **1994**, *161*, 153 – 159.
[4] A. C. Todd, J. G. Wetmur, J. M. Moline, J. H. Godbold, S. M. Levin, P. J. Landrigan, *Environ. Health Perspect.* **1996**, *104*, 141 – 146.
[5] For examples, see: a) S. Deo, H. A. Godwin, *J. Am. Chem. Soc.* **2000**, *122*, 174 – 175; b) L. E. Kerper, P. M. Hinkle, *J. Biol. Chem.* **1997**, *272*, 8346 – 8352; c) U. Resch, K. Rurack, J. L. Bricks, J. L. Slominskii, *J. Fluoresc.* **1997**, *7*, 231S; d) M.-Y. Chae, J. Yoon, A. W. Czarnik, *J. Mol. Recognit.* **1996**, *9*, 297 – 301; e) R. T. Bronson, J. S. Bradshaw, P. B. Savage, S. Fuangswasdi, S. C. Lee, K. E. Krakowiak, R. M. Izatt, *J. Org. Chem.* **2001**, *66*, 4752 – 4758.
[6] Selected recent references: a) M. M. Henary, Y. G. Wu, C. I. Fahrni, *Chem. Eur. J.* **2004**, *10*, 3015 – 3025; b) C. Bargossi, M. C. Fiorini, M. Montalti, L. Prodi, N. Zaccheroni, *Coord. Chem. Rev.* **2000**, *208*, 17 – 32; c) S. C. Burdette, G. K. Walkup, B. Spingler, R. Y. Tsien, S. J. Lippard, *J. Am. Chem. Soc.* **2001**, *123*, 7831 – 7841; d) C. J. Chang, J. Jaworski, E. M. Nolan, M. Sheng, S. J. Lippard, *Proc. Natl. Acad. Sci. USA* **2004**, *101*, 1129 – 1134; e) T. Hayashita, D. Qing, M. Minagawa, J. C. Lee, C. H. Ku, N. Teramae, *Chem. Commun.* **2003**, 2160 – 2161; f) R. Krämer, *Angew. Chem.* **1998**, *110*, 804 – 806; *Angew. Chem. Int. Ed.* **1998**, *37*, 772 – 773; g) A. Ono, H. Togashi, *Angew. Chem.* **2004**, *116*, 4400 – 4402; *Angew. Chem. Int. Ed.* **2004**, *43*, 4300 – 4302; h) K. Rurack, M. Kollmannsberger, U. Resch-Genger, J. Daub, *J. Am. Chem. Soc.* **2000**, *122*, 968 – 969; i) M. Taki, J. L. Wolford, T. V. O'Halloran, *J. Am. Chem. Soc.* **2004**, *126*, 712 – 713; j) G. K. Walkup, B. Imperiali, *J. Am. Chem. Soc.* **1996**, *118*, 3053 – 3054; k) J. D. Winkler, C. M. Bowen, V. Michelet, *J. Am. Chem. Soc.* **1998**, *120*, 3237 – 3242; l) H. A. Godwin, J. M. Berg, *J. Am. Chem. Soc.* **1996**, *118*, 6514 – 6515; m) K. Hanaoka, K. Kikuchi, H. Kojima, Y. Urano, T. Nagano, *J. Am. Chem. Soc.* **2004**, *126*, 12470 – 12476; n) E. M. Nolan, S. J. Lippard, *J. Am. Chem. Soc.* **2003**, *125*, 14270 – 14271; o) E. Palomares, R. Vilar, J. R. Durrant, *Chem. Commun.* **2004**, 362 – 363; p) C. C. Y. Chang, A. Pralle, E. Y. Isacoff, C. J. Chang, *J. Am. Chem. Soc.* **2004**, *126*, 15392 – 15393.
[7] a) J. Li, Y. Lu, *J. Am. Chem. Soc.* **2000**, *122*, 10466 – 10467; b) J. W. Liu, Y. Lu, *J. Am. Chem. Soc.* **2003**, *125*, 6642 – 6643; c) J. W. Liu, Y. Lu, *Chem. Mater.* **2004**, *16*, 3231 – 3238.
[8] A. Miyawaki, J. Llopis, R. Heim, J. M. McCaffery, J. A. Adams, M. Ikura, R. Y. Tsien, *Nature* **1997**, *388*, 882 – 887.
[9] R. B. Thompson, B. P. Maliwal, V. L. Feliccia, C. A. Fierke, K. McCall, *Anal. Chem.* **1998**, *70*, 4717 – 4723.
[10] D. E. Benson, D. W. Conrad, R. M. de Lorimer, S. A. Trammell, H. W. Hellinga, *Science* **2001**, *293*, 1641 – 1644.
[11] P. Chen, C. He, *J. Am. Chem. Soc.* **2004**, *126*, 728 – 729.
[12] M. Mergeay, S. Monchy, T. Vallaeys, V. Auquier, A. Benotmane, P. Bertin, S. Taghavi, J. Dunn, D. van der Lelie, R. Wattiez, *FEMS Microbiol. Rev.* **2003**, *27*, 385 – 410.
[13] B. Borremans, J. L. Hobman, A. Provoost, N. L. Brown, D. van der Lelie, *J. Bacteriol.* **2001**, *183*, 5651 – 5658.
[14] Unpublished results.
[15] a) E. E. Z. Heldwein, R. G. Brennan, *Nature* **2001**, *409*, 378 – 382; b) A. O. Summers, *J. Bacteriol.* **1992**, *174*, 3097 – 3101; c) A. Z. Ansari, J. E. Bradner, T. V. Ohalloran, *Nature* **1995**, *374*, 371 – 375; d) C. E. Outten, F. W. Outten, T. V. O'Halloran, *J. Biol. Chem.* **1999**, *274*, 37517 – 37524; e) N. L. Brown, J. V. Stoyanov, S. P. Kidd, J. L. Hobman, *FEMS Microbiol. Rev.* **2003**, *27*, 145 – 163; f) L. M. Shewchuk, G. L. Verdine, H. Nash, C. T. Walsh, *Biochemistry* **1989**, *28*, 6140 – 6145.
[16] E. L. Rachofsky, R. Osman, J. B. A. Ross, *Biochemistry* **2001**, *40*, 946 – 956.
[17] J. M. Jean, K. B. Hall, *Biochemistry* **2002**, *41*, 13152 – 13161.
[18] C. J. Fahrni, T. V. O'Halloran, *J. Am. Chem. Soc.* **1999**, *121*, 11448 – 11458.
[19] M. M. Pierce, C. S. Raman, B. T. Nall, *Methods: A Companion to Methods in Enzymology* **1999**, *19*, 213 – 221.

 © 2005 Wiley-VCH Verlag GmbH & Co. KGaA, Weinheim

Nonclassical Carbocations

Proton Sandwiches: Nonclassical Carbocations with Tetracoordinate Protons**

*Pradeep Gutta and Dean J. Tantillo**

Nature makes an astonishing array of complex terpenoid natural products from only a few simple achiral, acyclic precursors such as farnesyl pyrophosphate.[1] Still, many details of terpenoid cyclization mechanisms are unknown. One outstanding issue is whether nonclassical carbocations are involved in these mechanisms,[1,2] and if so, then when, where, and why? During our ongoing theoretical studies on the mechanisms of terpenoid cyclizations, we encountered the unusual carbocation **1** (Figure 1).[3,4] In this complex cation, a formally tetracoordinate proton is seemingly suspended between two C=C bonds on opposite sides of a cyclooctadiene ring.

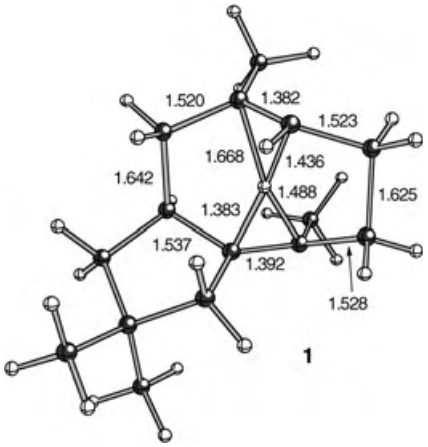

Figure 1. Optimized (B3LYP/6-31+G(d,p)) geometry of cation **1** (C black, H white). Selected bond lengths (Å) are shown.

Intrigued by this structure, we set out to explore simpler related species to see how common this structural motif might be. Initially we explored models based on 1,5-cyclooctadiene (**2**; Figure 2). Addition of a proton between its two C=C bonds followed by geometry optimization (using either B3LYP/6-31+G(d,p) or MP2/6-31+G(d,p)) led to cation **3** (Figure 3).[4] The geometry of cation **3**, which is D_2-symmetric,

[*] Dr. P. Gutta, Prof. D. J. Tantillo
Department of Chemistry
University of California, Davis
One Shields Avenue, Davis, CA 95616 (USA)
Fax: (+1) 530-752-8995
E-mail: tantillo@chem.ucdavis.edu

[**] We gratefully acknowledge the University of California, Davis, and the National Computational Science Alliance for support of this research, and we thank P. von R. Schleyer for helpful comments.

Supporting information, which includes coordinates and energies for all structures, for this article is available on the WWW under http://www.angewandte.org or from the author.

 DOI: 10.1002/anie.200461915 © 2005 Wiley-VCH Verlag GmbH & Co. KGaA, Weinheim

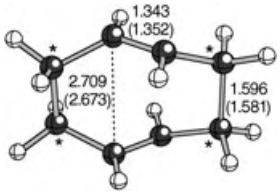

Figure 2. Structure of cyclooctadiene **2**. Selected bond lengths and distances (Å; B3LYP/6-31+G(d,p) (MP2/6-31+G(d,p) in parentheses)) are shown. * indicates carbon atoms of doubly allylic bonds.

is quite similar to the core of **1**.[5] The central proton of **3** is shared evenly by all four "alkene" carbon atoms at a distance of 1.48 Å (B3LYP level) or 1.46 Å (MP2 level) from each;[6] C···H distances in both cyclic[7] and acyclic[8] three-center, two-electron $[C\cdots H\cdots C]^+$ cations are less, typically around 1.3 Å. The double bonds in **2** appear to be well-preorganized to chelate a proton and are lengthened upon doing so as they share their electron density with the sandwiched proton. Overall, cation **3** can be viewed as a hybrid of the resonance structures shown in Scheme 1, a very unusual flavor of nonclassical cation[9] that boasts a five-center, four-electron bonding array.

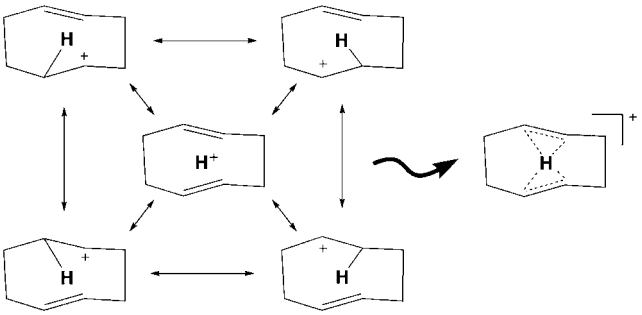

Scheme 1. Resonance structures for cation **3**.

Interestingly, both doubly allylic bonds (between carbon atoms marked with asterisks in Figure 2) of **2** are slightly lengthened upon addition of the proton, which indicates that they may help stabilize the four equivalent resonance structures shown in Scheme 1.[10] If the limiting resonance structure, which is shown at the left of Scheme 2 and consists of a proton sandwiched between two butadienes, is a significant contributor, then we arrive at the very unusual resonance hybrid shown at the right of Scheme 2, a nine-center, eight-electron species.[11,12]

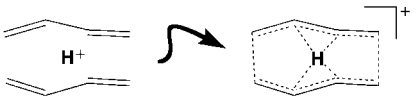

Scheme 2. Additional resonance structure (left; a proton sandwiched between two butadienes) and resulting resonance hybrid (right; a nine-center, eight-electron species) for **3**.

Let us now consider the distribution of charge throughout the molecule. Computed atomic charges[13] are shown in Figure 4a and the electrostatic potential of **3**,[14] mapped onto a surface that approximates the van der Waals surface of this species, is shown in Figure 4b. The central proton is the most positive atom in **3**, but positive charge is still delocalized over the molecule. In addition, it appears that access to the central proton is somewhat limited. The computed chemical shift of the central proton is also quite unusual with $\delta = +13.45$ ppm (GIAO/B3LYP/6-31+G(d,p) level) or $\delta = +13.33$ ppm (GIAO/MP2/6-31+G(d,p) level).[15,16] These chemical shift values are quite unlike those observed experimentally and computationally for protons in stable three-center, two-electron $[C\cdots H\cdots C]^+$ cations, which typically range from $\delta = -7$ to -3 ppm.[8,17] Clearly, whereas the hydrogens in $[C\cdots H\cdots C]^+$ cations are quite electron-rich (hydride-like), the hydrogen in cation **3** is quite electron-deficient.

One qualitative approach to constructing the molecular orbitals of the nine-center array in **3** is to build them from combinations of the π orbitals of butadiene and the s orbital of a proton. This leads to the orbitals shown at the center of Figure 4c. This qualitative picture is also reflected in the Kohn–Sham orbitals[18] from our B3LYP/6-31+G(d,p) calculations which are shown on the outside of Figure 4c. Wiberg bond indices[13c] for the C···H bonds, partial C=C double bonds, and doubly allylic C–C bonds are 0.21, 1.65, and 0.94, respectively, and these values are most consistent with the five-center, four-electron picture described above (see Scheme 1).

What are the limits on forming cations such as **3**?[12] Although cation **3** is highly delocalized, protonation of cyclooctadiene **2** on the "outside" actually leads to a more stable isomer, **4** (Figure 5).[19a] Structure **4** is approximately 40 kcal mol^{-1} lower in energy than **3** (39.6 and 40.3 kcal mol^{-1} at the B3LYP/6-31+G(d,p) and MP2/6-31+G(d,p) levels, respectively), perhaps, at least in part, because **4** allows an alternative nonclassical (three-center, two-electron) bonding array to form. The barrier for rearrangement of **3** to **4**, via the transition-state structure shown in Figure 6,[4b] is computed to be 2.8 kcal mol^{-1} at the B3LYP/6-31+G(d,p) level and

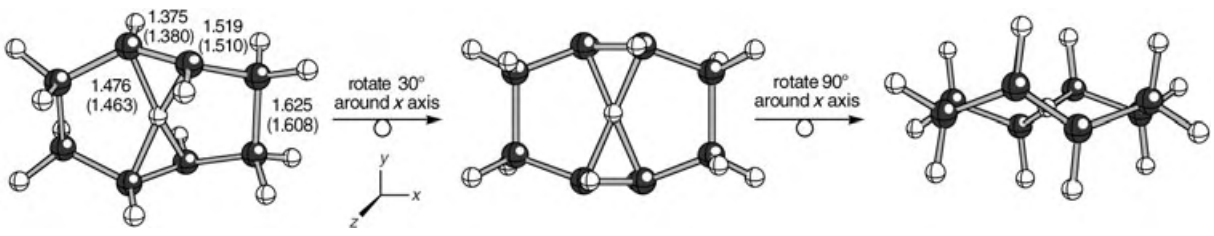

Figure 3. Three views of cation **3**. Selected bond lengths (Å; B3LYP/6-31+G(d,p) (MP2/6-31+G(d,p) in parentheses)) are shown.

 © 2005 Wiley-VCH Verlag GmbH & Co. KGaA, Weinheim

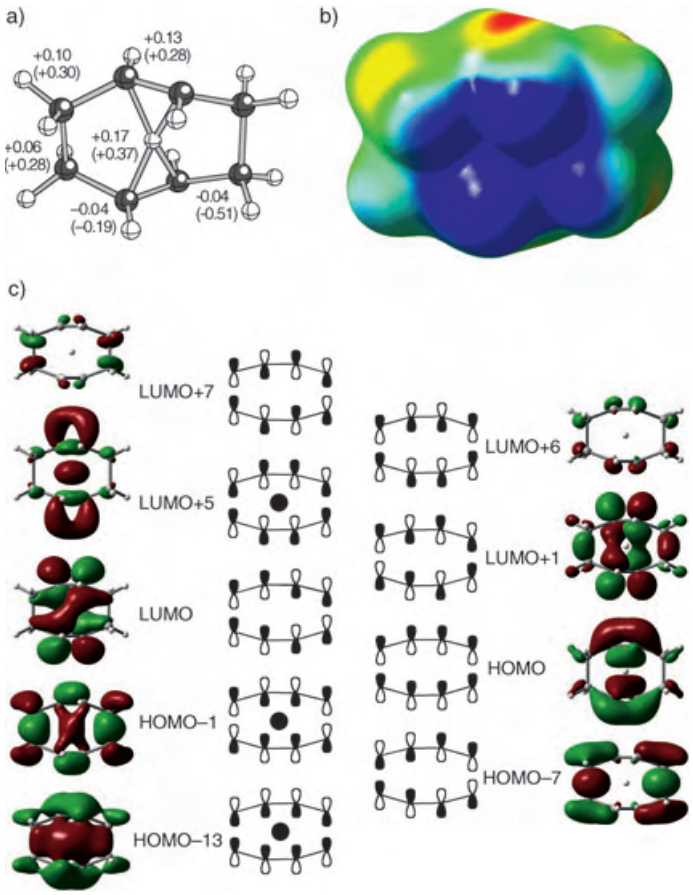

Figure 4. a) Computed atomic charges (B3LYP/6-31+G(d,p): CHelpG (NBO in parentheses)[13]), b) electrostatic potential surface constructed from the B3LYP density (blue is most positive and red is least positive), and c) qualitative and computed (B3LYP/6-31+G(d,p), isovalue = 0.04) molecular orbitals corresponding to the "butadienes + H" picture of bonding discussed in the text for cation **3**. Relative sizes of component atomic orbitals are not considered in the qualitative picture.

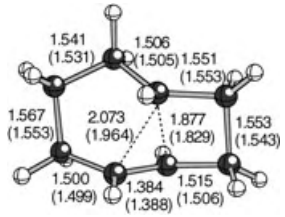

Figure 5. Computed geometry of the "out" protonated isomer **4**. Selected bond lengths and distances (Å; B3LYP/6-31+G(d,p) (MP2/6-31+G(d,p) in parentheses)) are shown.

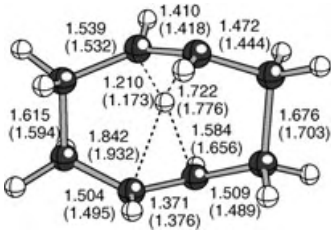

Figure 6. Computed geometry of the transition state for the isomerization of **3** to **4**. Selected bond lengths and distances (Å; B3LYP/6-31+G(d,p) (MP2/6-31+G(d,p) in parentheses)) are shown.

8.5 kcal mol^{-1} at the MP2/6-31+G(d,p) level.[19b] Note that, as expected for a very exergonic reaction, this is an early transition state, dominated by shifting of the proton. Note also that one of the doubly allylic bonds lengthens, which is indicative of hyperconjugative stabilization of the positive charge that builds up in its vicinity as the proton moves away from its central position. Whether or not suitably substituted systems that favor "in-protonation" or protect such "in-protonated" structures can be contrived is an open question.[20,21]

The propensities of other 1,5-cyclooctadiene isomers to form cations such as **3** were also explored.[12] First, there is another conformer of (*E*,*E*)-**2**. This structure, shown at the top of Figure 7, is less stable than **2** by

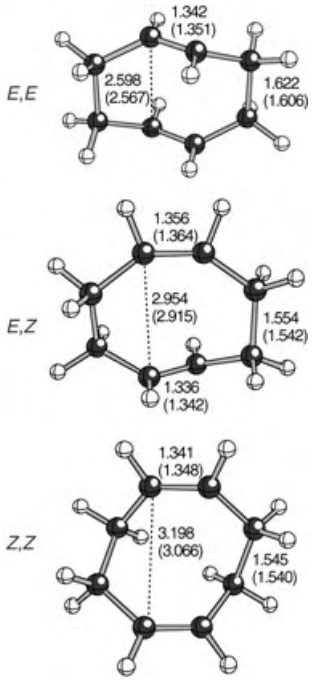

Figure 7. Computed geometries of cyclooctadienes. Selected bond lengths and distances (Å; B3LYP/6-31+G(d,p) (MP2/6-31+G(d,p) in parentheses)) are shown.

6.5 kcal mol^{-1} at the B3LYP/6-31+G(d,p) level and 7.9 kcal mol^{-1} at the MP2/6-31+G(d,p) level, and its two C=C bonds are parallel rather than "crossed" as they are in **2**. This arrangement is also suitable for sandwiching a proton, and C_{2h}-symmetric structure **5** is the energy-minimized structure of the resulting carbocation (Figure 8). Analogous delocal-

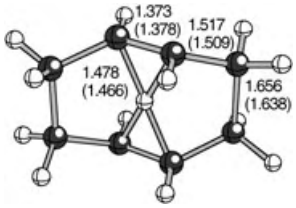

Figure 8. Geometry of cation **5**. Selected bond lengths (Å; B3LYP/6-31+G(d,p) (MP2/6-31+G(d,p) in parentheses)) are shown.

 © 2005 Wiley-VCH Verlag GmbH & Co. KGaA, Weinheim

ized cations could not, however, be located for *E*,*Z* and *Z*,*Z* isomers of **2** (Figure 7).[22] This finding is consistent with the fact that the *E*,*E* isomers seem to be better preorganized to share a proton; that is, they have shorter distances between their double bonds.

In summary, we have described a new type of nonclassical carbocation with a tetracoordinate proton. While exotic in their appearance, such species might be formed from suitable cyclooctadienes or by rearrangements of other cations and may even play a role in some biosynthetic terpenoid cyclizations. We are exploring both of these possibilities.[3] The prospect that such intermediates can lead to many different species through simple addition, rearrangement, or deprotonation reactions is particularly attractive from the perspective of reaction design.

Received: September 7, 2004
Revised: February 18, 2005
Published online: April 8, 2005

Keywords:
alkenes · carbocations · density functional calculations · protonation · terpenoids

[1] For leading references, see: a) D. E. Cane, *Chem. Rev.* **1990**, *90*, 1089 – 1103; b) K. U. Wendt, G. E. Schulz, E. J. Corey, D. R. Liu, *Angew. Chem.* **2000**, *112*, 2930 – 2952; *Angew. Chem. Int. Ed.* **2000**, *39*, 2812 – 2833; c) I. Abe, M. Rohmer, G. D. Prestwich, *Chem. Rev.* **1993**, *93*, 2189 – 2206; d) T. Hoshimo, T. Sato, *Chem. Commun.* **2002**, 291 – 301; e) D. E. Cane, *Acc. Chem. Res.* **1985**, *18*, 220 – 226.

[2] For leading references on proposed nonclassical intermediates in terpenoid biosynthesis, see: a) L. A. Wessjohann, W. Brandt, *Chem. Rev.* **2003**, *103*, 1625 – 1647; b) J.-L. Giner, P. Buzek, P. v. R. Schleyer, *J. Am. Chem. Soc.* **1995**, *117*, 12871 – 12872; c) H. K. Erickson, C. D. Poulter, *J. Am. Chem. Soc.* **2003**, *125*, 6886 – 6888; d) X. He, D. E. Cane, *J. Am. Chem. Soc.* **2004**, *126*, 2678 – 2679; e) M. J. S. Dewar, J. M. Ruiz, *Tetrahedron* **1987**, *43*, 2661 – 2674; f) G. A. Olah, *Angew. Chem.* **1995**, *107*, 1519 – 1532; *Angew. Chem. Int. Ed. Engl.* **1995**, *34*, 1393 – 1405; g) For leading references to older proposals by Djerassi, Arigoni, and Eschenmoser, see: J.-L. Giner, *Chem. Rev.* **1993**, *93*, 1735 – 1752.

[3] P. Gutta, D. J. Tantillo, unpublished results. Preliminary calculations indicate that **1** lies on the pathway between the farnesyl cation and pentalenene, a polycyclic terpenoid natural product, at least in the absence of a surrounding enzyme (see Ref. [1] for background on this and related terpenoid cyclizations).

[4] a) All calculations were performed with Gaussian 03 (Revision B.04), M. J. Frisch, G. W. Trucks, H. B. Schlegel, G. E. Scuseria, M. A. Robb, J. R. Cheeseman, J. A. Montgomery, Jr., T. Vreven, K. N. Kudin, J. C. Burant, J. M. Millam, S. S. Iyengar, J. Tomasi, V. Barone, B. Mennucci, M. Cossi, G. Scalmani, N. Rega, G. A. Petersson, H. Nakatsuji, M. Hada, M. Ehara, K. Toyota, R. Fukuda, J. Hasegawa, M. Ishida, T. Nakajima, Y. Honda, O. Kitao, H. Nakai, M. Klene, X. Li, J. E. Knox, H. P. Hratchian, J. B. Cross, C. Adamo, J. Jaramillo, R. Gomperts, R. E. Stratmann, O. Yazyev, A. J. Austin, R. Cammi, C. Pomelli, J. W. Ochterski, P. Y. Ayala, K. Morokuma, G. A. Voth, P. Salvador, J. J. Dannenberg, V. G. Zakrzewski, S. Dapprich, A. D. Daniels, M. C. Strain, O. Farkas, D. K. Malick, A. D. Rabuck, K. Raghavachari, J. B. Foresman, J. V. Ortiz, Q. Cui, A. G. Baboul, S. Clifford, J. Cioslowski, B. B. Stefanov, G. Liu, A. Liashenko, P. Piskorz, I. Komaromi, R. L. Martin, D. J. Fox, T. Keith, M. A. Al-Laham, C. Y. Peng, A. Nanayakkara, M. Challacombe, P. M. W. Gill, B. Johnson, W. Chen, M. W. Wong, C. Gonzalez, J. A. Pople, Gaussian, Inc., Pittsburgh, PA, **2003**; b) Geometries were optimized without symmetry constraints using B3LYP/6-31 + G(d,p) (A. D. Becke, *J. Chem. Phys.* **1993**, *98*, 5648 – 5652; A. D. Becke, *J. Chem. Phys.* **1993**, *98*, 1372 – 1377; C. Lee, W. Yang, R. G. Parr, *Phys. Rev. B* **1988**, *37*, 785 – 789; P. J. Stephens, F. J. Devlin, C. F. Chabalowski, M. J. Frisch, *J. Phys. Chem.* **1994**, *98*, 11623 – 11627) and MP2/6-31 + G(d,p) (C. Møller, M. S. Plesset, *Phys. Rev.* **1934**, *46*, 618 – 622). All structures were characterized by frequency calculations, and reported energies include zero-point energy corrections (unscaled). Intrinsic reaction coordinate (IRC) calculations (C. Gonzalez, H. B. Schlegel, *J. Phys. Chem.* **1990**, *94*, 5523 – 5527 and K. Fukui, *Acc. Chem. Res.* **1981**, *14*, 363 – 368) were also used to verify the identity of the transition structure associated with the interconversion of **3** and **4**; c) Extremely similar results (for both geometries and relative energies) were obtained by using the 6-311 + G(d,p) basis set. For example, for cation **3**, the biggest change in bond lengths on going from the double-zeta to triple-zeta basis set was 0.004 Å with both B3LYP and MP2, and predicted barriers for the **3**-to-**4** rearrangement changed by less than 0.5 kcal mol^{-1} for each. See Supporting Information for additional details; d) For recent reports that compare the B3LYP and MP2 methods for computing geometries and relative energies of small three-center, two-electron cations, see: I. V. Vrcek, V. Vrcek, H.-U. Siehl, *J. Phys. Chem. A* **2002**, *106*, 1604 – 1611 and D. Farcasiu, P. Lukinskas, S. V. Pamidighantam, *J. Phys. Chem. A* **2002**, *106*, 11672 – 11675; e) Structural drawings were produced by using Ball & Stick (N. Müller, A. Falk, Ball & Stick V.3.7.6—Molecular Graphics Application for MacOS Computers, Johannes Kepler University, Linz, **2000**).

[5] Many complexes of cyclooctadienes with transition metals are known. For structurally characterized complexes with simple metal cations, see: a) with Ag^+: A. Albinati, S. V. Meille, G. Carturan, *J. Organomet. Chem.* **1979**, *182*, 269 – 274; b) with Cu^+: M. Munakata, S. Kitagawa, H. Shimono, H. Masuda, *Inorg. Chem.* **1991**, *30*, 2610 – 2614.

[6] a) Computations on related complexes of protons with simple alkenes and alkynes were recently described. In these systems, the protons were shared quite unsymmetrically between the two π systems. See: S. J. Grabowski, W. A. Sokalski, J. Leszczynski, *J. Phys. Chem. A* **2004**, *108*, 1806 – 1812; b) A tricyclic tetraamine that complexes a proton by means of an array of four nitrogen lone-pairs has also been described. See: S. T. Howard, I. A. Fallis, *J. Org. Chem.* **1998**, *63*, 7117 – 7119; c) See also: J. W. M. Carneiro, C. A. Taft, C. H. T. P. Silva, J. G. R. Tostes, P. R. Seidl, P. S. S. Sinto, V. E. U. Costa, J. Alifantes, *Chem. Phys. Lett.* **2001**, *345*, 189 – 194.

[7] a) W. Quapp, D. Heidrich, *J. Mol. Struct.: THEOCHEM.* **2002**, *585*, 105 – 117, and references therein; b) J. W. de M. Carneiro, P. v. R. Schleyer, M. Saunders, R. Remington, H. F. Schaefer III, A. Rauk, T. S. Sorensen, *J. Am. Chem. Soc.* **1994**, *116*, 3483 – 3493; c) M. D. Bojin, D. J. Tantillo, unpublished results.

[8] a) R. Ponec, G. Yuzhakov, D. J. Tantillo, *J. Org. Chem.* **2004**, *69*, 2992 – 2996; b) J. E. McMurry, T. Lectka, *J. Am. Chem. Soc.* **1993**, *115*, 10167 – 10173; c) J. Cioslowski, *J. Am. Chem. Soc.* **1993**, *115*, 5177 – 5179.

[9] For leading references, see: a) C. A. Grob, *Acc. Chem. Res.* **1983**, *16*, 426 – 431; b) H. C. Brown, *Acc. Chem. Res.* **1983**, *16*, 432 – 440; c) G. A. Olah, G. K. S. Prakash, M. Saunders, *Acc. Chem. Res.* **1983**, *16*, 440 – 448; d) C. Walling, *Acc. Chem. Res.* **1983**, *16*, 448 – 454; e) H. C. Brown, *The Nonclassical Ion Problem*, Plenum, New York, **1977** (with comments by P. von R. Schleyer).

[10] Note that the doubly allylic bonds in **2** are already rather long, presumably as a result of through-bond coupling between the two alkenes. For leading references on through-bond coupling in

 © 2005 Wiley-VCH Verlag GmbH & Co. KGaA, Weinheim

related systems, see: a) H. Gan, M. G. Horner, B. J. Hrnjez, T. A. McCormack, J. L. King, Z. Gasyna, G. Chen, R. Gleiter, N. C. Yang, *J. Am. Chem. Soc.* **2000**, *122*, 12098 – 12111; b) R. Gleiter, W. Schäfer, *Acc. Chem. Res.* **1990**, *23*, 369 – 375.

[11] a) This species can also be thought of as a σ-polyacene with a proton sandwiched between its two polyene chains. For details on σ-polyacenes, see: D. J. Tantillo, R. Hoffmann, K. N. Houk, P. W. Warner, E. C. Brown, D. K. Henze, *J. Am. Chem. Soc.* **2004**, *126*, 4256 – 4263; b) In addition, **3** can be thought of as a protonated version of a suprafacial–suprafacial transition state for [4+4] dimerization of butadiene. For a recent discussion on the protonation of pericyclic transition structures, see: R. Hoffmann, D. J. Tantillo, *Angew. Chem.* **2003**, *115*, 6057 – 6062; *Angew. Chem. Int. Ed.* **2003**, *42*, 5877 – 5882.

[12] a) Addition of methoxy groups to all four carbon atoms of the doubly allylic bonds results in a structure which is similar to that of **3**, but with slightly lengthened (1.652 Å) doubly allylic bonds; b) The following structure, **6**, has also been shown to contain a tetracoordinate proton; P. von R. Schleyer, personal communication after this manuscript was submitted.

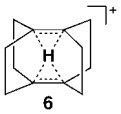

6

[13] Charge computations and NBO (natural bond orbital) analysis were carried out for the B3LYP/6-31 + G(d,p) structures. a) CHelpG: C. M. Breneman, K. B. Wiberg, *J. Comput. Chem.* **1990**, *11*, 361 – 373; b) NBO: A. E. Reed, L. A. Curtiss, F. Weinhold, *Chem. Rev.* **1988**, *88*, 899 – 926 and *"Natural Bond Orbital Methods"*, F. Weinhold in *Encyclopedia of Computational Chemistry*, *Vol. 3* (Eds.: P. v. R. Schleyer, N. L. Allinger, T. Clark, J. Gasteiger, P. A. Kollman, H. F. Schaefer III, P. R. Schreiner), Wiley, Chichester, **1998**, pp. 1792 – 1811; c) Wiberg bond indices: K. B. Wiberg, *Tetrahedron* **1968**, *24*, 1083 – 1096.

[14] a) C. K. Bagdassarian, V. L. Schramm, S. D. Schwartz, *J. Am. Chem. Soc.* **1996**, *118*, 8825 – 8836; b) G. Náray-Szabó, G. G. Ferenczy, *Chem. Rev.* **1995**, *95*, 829 – 847.

[15] Chemical shift calculations and geometry optimizations were performed at the same level of theory. For details on the methodology used, see: a) K. Wolinski, J. F. Hinton, P. Pulay, *J. Am. Chem. Soc.* **1990**, *112*, 8251 – 8260; b) K. Wolinski, R. Haacke, J. F. Hinton, P. Pulay, *J. Comput. Chem.* **1997**, *18*, 816 – 825; c) For a classic example of the use of computed chemical shifts in the characterization of carbocation structures, see: P. von R. Schleyer, K. Laidig, K. B. Wiberg, M. Saunders, M. Schindler, *J. Am. Chem. Soc.* **1988**, *110*, 300 – 301; d) For additional details on the successes and failures of DFT (density functional theory) in predicting magnetic properties, see: *Calculation of NMR and EPR Parameters: Theory and Applications* (Eds.: M. Kaupp, M. Bühl, V. G. Malkin), Wiley, New York, **2004**.

[16] The computed chemical shifts for all of the other protons in **3** ranged between $\delta = +3.08$ and $+6.16$ ppm at the B3LYP/6-31 + G(d,p) level ($+2.99$ and $+5.93$ ppm at the MP2/6-31 + G(d,p) level). All values are referenced to that for the protons in tetramethylsilane ($\delta = 0.00$ ppm).

[17] a) D. J. Tantillo, R. Hoffmann, *J. Am. Chem. Soc.* **2003**, *125*, 4042 – 4043; b) A referee suggested that the chemical shifts at $\delta = +13$ ppm might be indicative of antiaromaticity. The NICS(1) (nucleus-independent chemical shift at 1 Å above) value above the central proton is computed to be -5.4 ppm, and the NICS(0) and NICS(1) values at and above the centroid of the C···H···C rings are computed to be -41.4 and -3.3 ppm, all at the GIAO/B3LYP/6-31 + G(d,p) level. These values suggest that, if anything, this bonding array is slightly aromatic (the value at the centroid of the C-H-C rings is likely so large due to the proximity of the ring bonds). The NICS method is described in: P. von R. Schleyer, C. Maerker, A. Dransfeld, H. J. Jiao, N. J. R. v. E. Hommes, *J. Am. Chem. Soc.* **1996**, *118*, 6317 – 6318 and P. von R. Schleyer, M. Manoharan, Z.-X. Wang, B. Kiran, H. Jiao, R. Puchta, N. J. R. v. E. Hommes, *Org. Lett.* **2001**, *3*, 2465 – 2468.

[18] R. Stowasser, R. Hoffmann, *J. Am. Chem. Soc.* **1999**, *121*, 3414 – 3420.

[19] a) For an excellent review on "in–out" isomerism see: R. W. Alder, S. P. East, *Chem. Rev.* **1996**, *96*, 2097 – 2111; b) The possibility that tunneling may contribute to rearrangements of **3** was suggested by a referee. However, additional calculations will be required to test this proposition.

[20] Note that the computed proton affinity of **2** (to form **3**) is 182.8 kcal mol^{-1} at the B3LYP/6-31 + G(d,p) level, considerably larger than values for normal alkenes, which are typically around 165 kcal mol^{-1}. See Ref. [11b] as well as F. A. Carroll, *Perspectives on Structure and Mechanism in Organic Chemistry*, Brooks/Cole, Pacific Grove, **1998**, and references therein.

[21] There is also an analogy between **3** and the well-known bisamine "proton sponges" in that they both chelate protons. For reviews on "proton sponges", see: a) H. A. Staab, T. Saupe, *Angew. Chem.* **1988**, *100*, 895 – 909; *Angew. Chem. Int. Ed. Engl.* **1988**, *27*, 885 – 887; b) A. L. Llamas-Saiz, C. Foces-Foces, J. Elguero, *J. Mol. Struct.* **1994**, *328*, 297 – 323; See also Ref. [6].

[22] The energies of the *E*,*Z* and *Z*,*Z* isomers, relative to that of **2**, are -3.1 and -22.9 kcal mol^{-1} at the B3LYP/6-31 + G(d,p) level and $+1.1$ and -18.9 kcal mol^{-1} at the MP2/6-31 + G(d,p) level, respectively.

 © 2005 Wiley-VCH Verlag GmbH & Co. KGaA, Weinheim

H Bonds in Carbohydrates

Direct Detection of Inter-residue Hydrogen Bonds in Polysaccharides by Single-Molecule Force Spectroscopy**

*Qingmin Zhang, Justyna Jaroniec, Gwangrog Lee, and Piotr E. Marszalek**

Hydrogen bonds (H bonds) play important roles in determining the structure and function of biopolymers. For example, they are responsible for base pairing in nucleic acids, they contribute to the stability of proteins folds, and they control molecular recognition among proteins, DNA, and carbohydrates.[1] Polysaccharides, because of their abundance of hydroxy groups and oxygen atoms, are prone to form extensive networks of intra- and intermolecular hydrogen bonds.[2] The ubiquitous polysaccharide cellulose extensively

[*] Dr. Q. Zhang, J. Jaroniec, G. Lee, Prof. P. E. Marszalek
Center for Biologically Inspired Materials and Material Systems
Department of Mechanical Engineering and Materials Science
Duke University
Durham, NC 27708 (USA)
Fax: (+1) 919-660-8963
E-mail: pemar@duke.edu

[**] This work was supported by a grant from the National Science Foundation and by Duke University funds to P.E.M. We thank Prof. Yasuhiro Takahashi of Osaka University, Japan for a sample of amylose triacetate.

Supporting information for this article is available on the WWW under http://www.angewandte.org or from the author.

 DOI: 10.1002/anie.200462067 © 2005 Wiley-VCH Verlag GmbH & Co. KGaA, Weinheim

exploits intra- and intermolecular H bonds to form microfibrils that provide impressive mechanical strength to the cell wall in plants.[3] The existence of specific H bonds in biopolymers, including polysaccharides, is not always easy to detect directly. More typically H bonds are deduced based on the positions of putative H-bond donor and acceptor atoms, which are determined experimentally by X-ray/neutron diffraction or NMR spectroscopy,[2–5] or they are identified by computer modeling.[6,7] In solutions H bonds may be disturbed or eliminated altogether because their donors and acceptors may engage intermittently in hydrogen bonding with solvent molecules. Therefore, the existence of H bonds in a liquid phase is rather difficult to establish experimentally.

Herein we report a new approach to directly examine the propensity of polysaccharides to form inter-residue H bonds under various solvent conditions. This method involves single-molecule force spectroscopy[8,9] to measure the effect of H bonds on the elasticity of individual polysaccharide chains using the atomic force microscope (AFM). This technique was, for example, used to determine the role of water bridges in the helical structure of poly(ethyleneglycol)[9] and to measure the effect of H bonds on the elasticity of a modular protein, titin.[10]

In force spectroscopy, single polymer chains are attached at their extremities to a substrate and the AFM tip and are stretched vertically in solution to determine their force–extension relationships (force spectrograms). The force spectrogram of a simple polymer is typically described in the context of the entropic elasticity of the freely jointed chain (FJC) model.[11] However, the majority of the polysaccharides studied so far by AFM do not behave as FJCs.[8,12–14] Their force spectrograms display various enthalpic features that are mechanical fingerprints of force-induced conformational transitions, such as chair–boat transitions of the pyranose rings[12] and forced rotations of the hydroxymethyl group between various rotameric states.[13]

We propose that similar to force-induced conformational transitions, the existence of intramolecular hydrogen bonds should be revealed directly by force spectroscopy by registering their effect on the molecular elasticity. To test this hypothesis we measured force spectrograms of amylose, a linear 1→4-linked α-D-glucan with the known propensity to form inter-residue H bonds,[4,5] in various solvents. These solvents, by virtue of their widely different dielectric constants γ, were expected to either promote (low γ values) or inhibit (high γ values) the formation of intramolecular hydrogen bonds by controlling the electrostatic share of the bonding energy. Thus, by immersing amylose in solvents such as water ($\gamma = 80$) and dimethyl carbonate (DMC; $\gamma = 3.1$) we expected to control its hydrogen-bonding ability. The existence of H bonds could be then tested mechanically in single-molecule stretching measurements.

AFM stretching measurements were carried out on single amylose molecules in deionized water, dimethyl sulfoxide (DMSO, $\gamma = 47.2$), and dimethyl carbonate (DMC). The stretching of amylose in all these solvents is reversible (see the Supporting Information). Figure 1 compares typical force spectrograms of single amylose chains in these solvents. We recorded a total of 16 single-amylose force spectrograms in

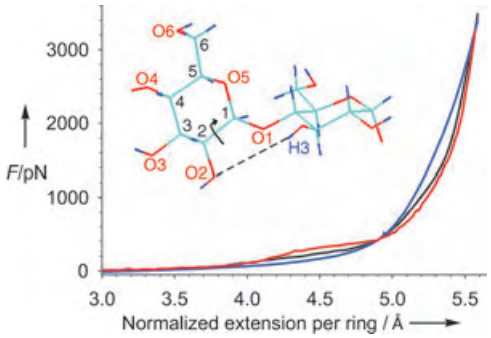

Figure 1. A comparison of typical force–extension relationships for amylose in H_2O (red trace), DMSO (black trace), and DMC (blue trace). The extensions were normalized by the molecules' length, measured at a common force of 3270 pN and then multiplied by the length of a single ring (O_4–O_1 distance) also determined at 3270 pN (see the Supporting Information). The inset shows the structure of maltose, a building block of amylose.

water, 11 in DMSO, and 11 in DMC, which displayed the same features as the respective spectrograms shown in Figure 1. From Figure 1 it is clear that the dielectric constant of the medium strongly affects the molecular elasticity of amylose. The difference between the recordings obtained in water and other solvents increases with the difference in their respective dielectric constants. The plateau feature, which is characteristic of the force spectrograms in water,[12] disappears progressively in the media of lower dielectric constant, and the slope of the force extension curves at higher extensions (> 5.0 Å per ring) increases abruptly relative to that determined in water. This behavior results in a crossover of the force–extension curves, which at low extensions (< 4.8 Å per ring) run below and at high extensions (> 5.0 Å per ring) above the trace obtained in water.

To clarify the effect of the dielectric constant of the medium on amylose elasticity we carried out molecular dynamics simulations of the stretching process using the steered molecular dynamics (SMD) protocol implemented in the program NAMD[15] and a new CHARMM-based force field for carbohydrates.[16] Similar SMD simulations performed on 1,6-linked glucans (pustulan and dextran), using the same force field, produced force–extension characteristics that agreed very well with our experimental AFM data.[13] In SMD one terminal of the molecule is fixed and the other is pulled by a Hookean spring, thus simulating AFM stretching experiments. The simulations were carried out on a chain composed of ten glucopyranose rings, and we used the simplest implicit solvent model, in which the solvent is represented solely by the fixed dielectric constant, γ, which normalizes all the electrostatic interactions. We carried out two 200-ns SMD simulations for two extreme cases, with $\gamma =$ 80 for water and $\gamma = 1$ for vacuum (Figure 2). We note that in both simulations the final conformation of the stretched pyranose rings is a skew boat (Figure 2a, inset). However, the force–extension curves obtained from these simulations significantly differ in a way that is consistent with our experimental data. Similar to the force–extension curve obtained in DMC, the curve obtained from the vacuum SMD ($\gamma = 1$) shows no hint of the plateau feature. In addition,

 © 2005 Wiley-VCH Verlag GmbH & Co. KGaA, Weinheim

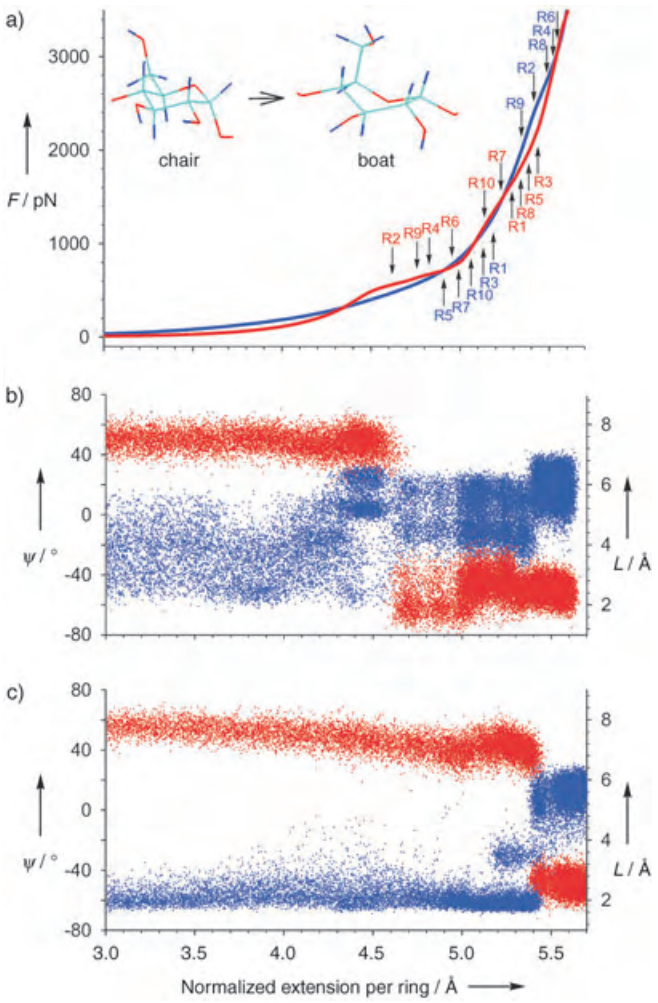

Figure 2. a) A comparison of force–extension curves of amylose obtained by 200-ns SMD simulations in water (red curve) and in vacuum (blue curve). The arrows indicate positions at which the individual rings flipped to a boatlike conformation. The inset shows the structures of the ring shortly before and after the conformational transition (generated using the program VMD[19]). b) SMD trajectories of the O2–H3′ distance (L) between rings 2 and 3 (blue trace, right axis) and of the ring dihedral angle ψ = O1-C1-C2-O2 (red trace, left axis) during the stretching process of amylose in water. c) Same as (b) but in a vacuum.

at intermediate extensions this curve runs under, and at higher extensions above, the curve obtained in the water SMD ($\gamma = 80$). Along the force–extension curves in Figure 2a we marked positions at which the individual rings underwent chair–boat transitions. It is evident that these transitions occurred later during the stretching in vacuum than in water, where 40% of the rings flipped to a boatlike conformation during the plateau phase. Our SMD result obtained in implicit water is similar to the result obtained for amylose using the quantum mechanics based SMD method and explicit water, where 50–60% of the rings changed their conformation during the plateau phase.[17] We conclude that in vaccum the forced chair–boat transitions are shifted to higher forces and thus require a higher energy input compared to the transitions in water.

In Figure 2b and c we monitor the behavior of the putative O2–H3′ hydrogen bonds (Figure 1, inset) between adjacent rings in water and in vacuum and analyze the trajectories of the ring conformation (dihedral angle ψ = O1-C1-C2-O2). In water (Figure 2b) the distance between O2 and H3′ varies greatly and oscillates between 2 and 5 Å before the chair–boat transition and between 3.5 and 6.5 Å after the transition. The transition itself, monitored as an abrupt change in ψ occurs at the normalized extension of $\approx$4.6 Å per ring at a force of $\approx$500 pN. Clearly, the O2–H3′ distance between the second and third pyranose rings, which is representative of other ring pairs as well, does not support a hydrogen bond between these rings.

In vacuum the O2–H3′ distance (Figure 2c) covers a much smaller range, 1.7–2.4 Å, which is consistent with a fairly strong hydrogen bond between these rings. Ring 2 flips to a skew-boat conformation at the normalized extension of 5.4 Å per ring, corresponding to a force of $\approx$2300 pN, close to the end of the stretching cycle. During this transition there is an abrupt increase in the O2–H3′ distance to $\approx$5 Å, which permanently breaks the hydrogen bond between these two rings. We conclude that in a medium of a low dielectric constant, strong hydrogen bonds between adjacent rings are formed in amylose, which involve the interaction between O2 and H3′ atoms. These bonds mechanically link adjacent rings and rigidify the amylose backbone. They must be broken before the rings can flip to an extended, skew-boatlike conformation. As a result, chair–boat transitions occur on average at higher extensions and forces and from already highly deformed and extended chair conformations, in which the O1–O4 distance is significantly greater than that in a relaxed chair. Therefore these transitions contribute relatively less to the chain contour length than those that occur at low forces (as in water). This effect eliminates the plateau feature from the force–extension curve.

We note that although the final conformations of the stretched pyranose rings in water and vacuum are similar (skew-boat), the conformational pathways leading to these conformations are different. In the case of a vacuum (or a medium of low dielectric constant) the stretching process, in addition to reducing the configurational entropy of the chain and flipping the rings to a skew-boat conformation, also breaks the inter-residue hydrogen bonds that are not permanently formed in water. Thus by comparing the experimental force extension curves obtained in water and in a low-dielectric-constant medium, it should be possible to estimate the strength of these hydrogen bonds. This can be done by calculating and comparing the increase in the free energy of the amylose chain ΔG when stretched to the same extension L_{max} in water and in DMC. ΔG can be calculated as the reversible work of the stretching force [Eq. (1)] This work can

$$\Delta G = \int_0^{L_{max}} F\,dx \qquad (1)$$

be measured by integrating the area under the force-extension curve. When the amylose extension x is normalized for one ring, as in Figure 1, ΔG represents the change in the

 © 2005 Wiley-VCH Verlag GmbH & Co. KGaA, Weinheim

free energy per ring and $\Delta G_{H\ bond} = \Delta G_{DMC} - \Delta G_{H_2O}$ corresponds to the strength of the inter-residue hydrogen bond per ring (see the Supporting Information). We find that on average $\Delta G_{H\ bond}$ is 1.5 kcal mol^{-1} (see the Supporting Information), which is a very reasonable estimate for the energy of a single hydrogen bond in maltose. Recently, Chen and Naidoo calculated the strength of this hydrogen bond in vacuum to be 4.99 kcal mol^{-1}.[7] If we assume that this energy scales inversely with the dielectric constant of the medium, we arrive at a value of 1.61 kcal mol^{-1} for DMC ($\gamma = 3.1$), which is very close to our estimate based on the AFM measurements.

Finally, if the interpretation of the results of our AFM measurements on amylose in terms of the hydrogen-bonding model is correct, eliminating the ability of amylose to form inter-residue H bonds altogether should make its elasticity solvent-independent. The ability to form H bonds can be abolished by replacing the hydroxy groups with the groups that cannot form H bonds, for example, acetates. In Figure 3

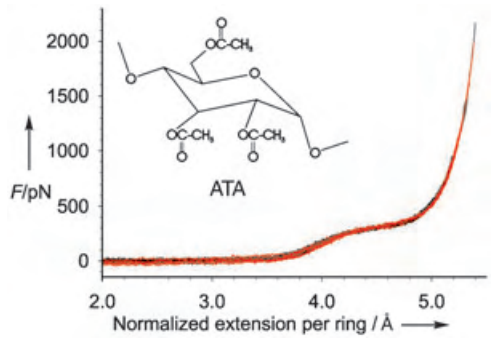

Figure 3. A comparison of AFM-determined force spectrograms of ATA in water (red curves, five different recordings) and in DMC (black traces, five different curves). The inset shows the structure of the ATA monomer.

we show the force–extension curves obtained by stretching single amylose triacetate (ATA)[18] molecules in water and in DMC. It is now clear that there is no difference between the recordings for ATA obtained in media of high and low dielectric constants, which corroborates our original conjecture. Moreover, all of the ATA curves (in DMC and water) look similar to the curves obtained on native amylose in water. This result suggests that: 1) water effectively eliminates inter-residue H bonds of amylose; 2) the acetate substituents do not affect the elasticity of amylose other than by eliminating H bonds; and 3) once the possibility to form inter-residue H bonds has been eliminated, the solvents play no significant role in amylose elasticity. The last conclusion also implies that the contributions to the force–extension relationship from changes in the interglycosidic torsion angles that accompany amylose stretching are similar in water and in DMC and therefore cannot explain the differences in the elasticity of native amylose observed in these solvents.

In conclusion, amylose can form strong inter-residue hydrogen bonds, which significantly rigidify the polymer, in solvents with a low dielectric constant. However, these H bonds are effectively eliminated in water. Single-molecule force spectroscopy is an ideal method for directly examining the hydrogen bonding in polysaccharides and accurately measuring their strength under various solvent conditions. The strength of our approach is in that once solubilized and adsorbed to a substrate, polysaccharides can be examined by AFM in a variety of solvents, including those they normally "do not like", because the AFM tip pulls the molecules into these solvents. As polysaccharide structures and functions are greatly affected by extensive networks of intra- and intermolecular hydrogen bonds, our method to directly detect and examine such bonds may find widespread application in the carbohydrate research and beyond.

Experimental Section

Force spectroscopy measurements on amylose were carried out in a PicoForce AFM (Veeco Metrology Group, Santa Barbara, CA) and a home-built force spectrometer.[12] Amylose (type III, from potato; Sigma-Aldrich) was dissolved in water at a concentration of 0.001–0.1 % (w/v) by heating (≈ 90 °C). A layer of polysaccharide molecules was created by drying a drop of these solutions onto glass coverslips, which had been cleaned by boiling in HCl and then in H_2O_2. Then the dehydrated sample was rinsed extensively with water to leave only those molecules that were tightly adsorbed to the glass surface.[14] After the substrate had been thoroughly dried and placed in the AFM, the liquid chamber was filled with an appropriate solvent for pulling measurements. To pick up amylose molecules, an AFM tip (Si_3N_4; Veeco) was pressed down onto the sample for 1–3 s at forces of 1–20 nN. Frequently, no molecule adhered to the tip, and no force extension curve (force spectrogram) was recorded in such a case. Occasionally, several molecules with various lengths adhered simultaneously to the tip, and a complicated force–extension pattern was recorded with several overlapping and irregular force peaks, which correspond to simultaneous stretching and sequential detachment of these molecules. Such recordings are difficult to interpret and are not included in this communication (see the Supporting Information). However, in ≈ 10 % of the recordings a quite distinct pattern, which can be attributed to individual amylose molecules, was registered. The unmistakable features of these single-amylose force spectrograms are: the characteristic plateau that always appears at a force of ≈ 270 pN in H_2O, full reversibility of the stretching process (forward and backward stretching traces are identical), and the overlapping of all the recordings after they have been normalized to a common extension (see the Supporting Information). The normalization procedure is important as it allows the comparison of force spectrograms obtained on molecular fragments that vary in length. This is a common procedure in AFM-based force spectroscopy, because AFM tip randomly picks up polymer fragments to be stretched (see the Supporting Information).[8,20]

Received: September 22, 2004
Revised: October 19, 2004
Published online: March 22, 2005

Keywords: carbohydrates · hydrogen bonding · molecular dynamics · scanning probe microscopy · solvent effects

[1] G. Gemmecker, *Angew. Chem.* **2000**, *112*, 1276–1279; *Angew. Chem. Int. Ed.* **2000**, *39*, 1224–1226.
[2] V. S. R. Rao, P. K. Qasba, P. V. Balaji, R . *Chandrasekaran, Conformation of Carbohydrates,* Amsterdam, Harwood Academic, **1998**.

 © 2005 Wiley-VCH Verlag GmbH & Co. KGaA, Weinheim

[3] a) Y. Nishiyama, J. Sugiyama, H. Chanzy, P. Langan, *J. Am. Chem. Soc.* **2003**, *125*, 14300 – 14306; b) M. Jarvis, *Nature* **2003**, *426*, 611 – 612.
[4] M. E. Gress, G. A. Jeffrey, *Acta Crystallogr. Sect. B* **1977**, *33*, 2490 – 2495.
[5] a) F. Takusagawa, R, A, Jacobson, *Acta Crystallogr. Sect. B* **1978**, *34*, 213 – 218; b) I. Tanaka, N. Tanaka, T. Ashida, M. Kakudo, *Acta Crystallogr. Sect. B* **1976**, *32*, 155 – 160; c) F. Brisse, R. H. Marchessault, S. Perez, P. Zugenmaier, *J. Am. Chem. Soc.* **1982**, *104*, 7470 – 7476; d) K. Gessler, I. Uson, T. Takata, N. Krauss, S. M. Smith, S. Okada, G. M. Sheldrick, W. Saenger, *Proc. Natl. Acad. Sci. USA* **1999**, *96*, 4246 – 4251.
[6] a) A. D. French, D. P. Miller, *ACS Symp. Ser.* **1994**, *569*, 235; b) S. Mendonca, G. P. Johnson, A. D. French, R. A. Laine, *J. Phys. Chem. A* **2002**, *106*, 4115 – 4124; c) R. A. Klein, *J. Am. Chem. Soc.* **2002**, *124*, 13931 – 13937; d) F. A. Momany, J. L. Willett, *J. Comput. Chem.* **2000**, *21*, 1204 – 1219; e) F. A. Momany, J. L. Willett, *Carbohydr. Res.* **2000**, *326*, 210 – 226; f) K. N. Kirschner, R. J. Woods, *Proc. Natl. Acad. Sci. USA* **2001**, *98*, 10541 – 10545; g) J. W. Brady, R. K. Schmidt, *J. Phys. Chem.* **1993**, *97*, 958 – 966; h) K. J. Naidoo, M. Kuttel, *J. Comput. Chem.* **2001**, *22*, 445 – 456.
[7] J. Y.-J. Chen, K. J. Naidoo, *J. Phys. Chem.* B **2003**, 107, 9558 – 9566.
[8] a) M. Rief, F. Oesterhelt, B. Heymann, H. E. Gaub, *Science* **1997**, *275*, 1295 – 1297; b) M. Grandbois, M. Beyer, M. Rief, H. Clausen-Schaumann, H. E. Gaub, *Science* **1999**, *283*, 1727 – 1730.
[9] F. Oesterhelt, M. Rief, H. E. Gaub, *New J. Phys.* **1999**, *1*, 6.1 – 6.11.
[10] P. E. Marszalek, H. Lu, H. Li, M. Carrion-Vazquez, A. F. Oberhauser, K. Schulten, J. M. Fernandez, *Nature* **1999**, *402*, 100 – 103.
[11] P. J. Flory, *Principles of Polymer Chemistry*, Cornell University Press, **1953**.
[12] a) P. E. Marszalek, A. F. Oberhauser, Y.-P. Pang, J. M. Fernandez, *Nature* **1998**, *396*, 661 – 664; b) P. E. Marszalek, Y.-P. Pang, H. Li, J. E. Yazal, A. F. Oberhauser, J. M. Fernandez, *Proc. Natl. Acad. Sci. USA* **1999**, *96*, 7894 – 7898; c) P. E. Marszalek, H. Li, A. F. Oberhauser, J. M. Fernandez, *Proc. Natl. Acad. Sci. USA* **2002**, *99*, 4278 – 4283.
[13] a) G. Lee, W. Nowak, J. Jaroniec, Q. Zhang, P. Marszalek, *Biophys. J.* **2004**, 87, 1456 – 1465; b) G. Lee, W. Nowak, J. Jaroniec, Q. Zhang, P. Marszalek, *J. Am. Chem. Soc.* **2004**, *126*, 6218 – 6219.
[14] H. Li, M. Rief, F. Oesterhelt, H. E. Gaub, *Adv. Mater.* **1998**, *10*, 316 – 319.
[15] L. Kalé, R. Skeel, M. Bhandarkar, R. Brunner, A. Gursoy, N. Krawetz, J. Phillips, A. Shinozaki, K. Varadarajan, K. Schulten, *J. Comput. Phys.* **1999**, 151, 283 – 312.
[16] M. Kuttel, J. W. Brady, K. J. Naidoo, *J. Comput. Chem.* **2002**, *23*, 1236 – 1243.
[17] Z. Lu, W. Nowak, G. Lee, P. E. Marszalek, W. Yang, *J. Am. Chem. Soc.* **2004**, *126*, 9033 – 9041.
[18] Y. Takahashi, S. Nishikawa, *Macromolecules* **2003**, *36*, 8656 – 8661.
[19] W. Humphrey, A. Dalke, K. Schulten, *J. Mol. Graphics* **1996**, 14, 33 – 38.
[20] P. E. Marszalek, H. Li, J. M. Fernandez, *Nat. Biotechnol.* **2001**, *19*, 258 – 262.

 © 2005 Wiley-VCH Verlag GmbH & Co. KGaA, Weinheim

Host–Guest Systems

Quantitative Dynamic Interconversion between Ag^{I}-Mediated Capsule and Cage Complexes Accompanying Guest Encapsulation/Release**

*Shuichi Hiraoka, Koji Harano, Motoo Shiro, and Mitsuhiko Shionoya**

Multicomponent self-assembly leading to discrete molecular architectures through reversible hydrogen bonding[1] or metal-coordination bonding[2] has attracted a great deal of attention. So far, many excellent examples of well-defined 3D structures, such as capsules,[3] cages,[4] boxes,[5] and tubes,[6] have been reported, and their inner spaces have been efficiently used as recognition[7] and reaction centers[8] for neutral molecules and ionic species. External stimuli-responsive supermolecules are considered as molecular devices in which conformational or configurational transitions of the molecules allow on–off switching of their functions such as motion, molecular recognition, and reaction control. However, to date, only a few examples have been reported on quantitative dynamic interconversions between differentiated self-assembled molecules formed from identical chemical components. To realize such a dynamic system, metal-mediated self-assembly has a great advantage in that the coordination number and geometry of transition-metal ions can be reversibly changed by their oxidation states[9] and concentration ratios of metal to ligand.[10,11] Such metal-centered changes should allow dynamic interconversion through metal–ligand exchanges between different kinds of metal-assembled structures.

Recently, we established an Ag^{I}-mediated interconvertible system with a disk-shaped trismonodentate ligand (L) in which three 2-benzimidazolyl rings and three methyl groups are alternately attached to the central benzene ring.[10] In this system, a structural interconversion between a capsule-shaped and a sandwich-shaped complex accompanies encapsulation/release of anionic molecules and was established by varying the metal-to-ligand ratio. In the study described herein, a disk-shaped trismonodentate ligand **1**, which has

[*] Dr. S. Hiraoka, K. Harano, Prof. Dr. M. Shionoya
Department of Chemistry, Graduate School of Science
The University of Tokyo
Hongo, Bunkyo-ku, Tokyo 113-0033 (Japan)
Fax: (+81) 3-5841-8061
E-mail: shionoya@chem.s.u-tokyo.ac.jp

Dr. M. Shiro
Rigaku Corporation, 3-9-12 Matsubaracho
Akishima, Tokyo 196-8666 (Japan)

[**] This work was supported by a Grant-in-Aid for The 21 st Century COE Program for Frontiers in Fundamental Chemistry and by Grants-in-Aid for Scientific Research (S) to M.S. (No. 16105001) and for Scientific Research on Priority Areas, "Dynamic Complexes" to S.H. (No. 420/16033215) from the Ministry of Education, Culture, Sports, Science, and Technology of Japan.

Supporting information for this article is available on the WWW under http://www.angewandte.org or from the author.

 DOI: 10.1002/anie.200462394 © 2005 Wiley-VCH Verlag GmbH & Co. KGaA, Weinheim

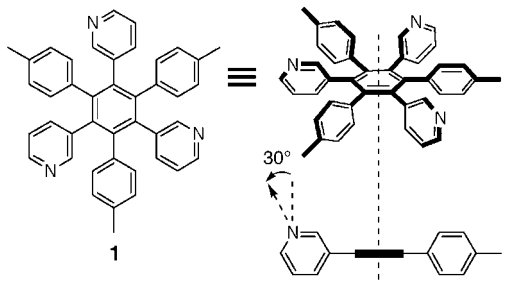

three 3-pyridyl and *p*-tolyl groups attached alternately to the central benzene ring, was designed with the aim of constructing larger capsule molecules that allow encapsulation/release of organic guest molecules. Each pyridyl ring is almost perpendicular to the central ring plane as a result of the steric hindrance between the neighboring pyridyl and *p*-tolyl groups. The coordination direction of each nitrogen donor atom of the 3-pyridyl groups is thereby somewhat distorted away from the central ring by 30°. From a molecular-modeling study, we expected that the combination of the ligand **1** with Ag^I, which can assume both a three-coordinate trigonal-planar and a two-coordinate linear geometry with monodentate ligands, should generate two different 3D structures with inner spaces when the metal-to-ligand ratios are 4:4 and 6:4.[12] Moreover, the quantitative, reversible structural interconversion between these two structures would provide an excellent molecular encapsulation/release system if only one of them binds preferentially to some given guest molecules.

Herein we present a quantitative interconversion between two Ag^I-containing molecular architectures, a capsule-shaped $[Ag_4\mathbf{1}_4]^{4+}$ and a cage-shaped $[Ag_6\mathbf{1}_4]^{6+}$ complex (Figure 1). These two complexes were self-assembled from trismonodentate disk-shaped ligands **1** and Ag^I by changing the **1**/Ag^I concentration ratios in the presence or absence of guest molecules. Indeed, the $[Ag_4\mathbf{1}_4]^{4+}$ capsule complex could accommodate a neutral organic molecule such as adamantane in the inner space with a high affinity. On the other hand, as soon as the capsule complex was converted into the cage-shaped counterpart, $[Ag_6\mathbf{1}_4]^{6+}$, the included guest molecule was immediately released. X-ray single-crystal analysis revealed a $[Ag_4\mathbf{1}_4]^{4+}$ capsule structure in which an adamantane molecule is trapped inside. Furthermore, the encapsulation and release of the guest molecule could be dynamically controlled by the quantitative Ag^I-dependent capsule↔cage interconversion.

^{1}H NMR titration experiments with ligand **1** and $AgPF_6$ in CD_3NO_2 revealed the quantitative formation of two different Ag^I complexes depending on the $[Ag^I]/[\mathbf{1}]$ ratios. Upon addition of an equimolar amount of $AgPF_6$ to a solution of **1** in CD_3NO_2 ($[Ag^I]:[\mathbf{1}] = 1:1$), the signals for metal-free ligand **1** completely disappeared and one set of new signals simultaneously appeared in a highly symmetrical pattern (Figure 2a). The signals for the *p*-tolyl ring moieties, H_e and H_f, are divided into two sets, which indicate that the Ag^I ions are placed only on one side of the disk-shaped ligand **1**. Notably, the signals for one of the *p*-tolyl protons (H_f) and for the methyl protons (H_g) are shifted upfield ($\Delta\delta = -2.0$ and -0.4 ppm for H_f and H_g, respectively). This is probably due to the shielding effects

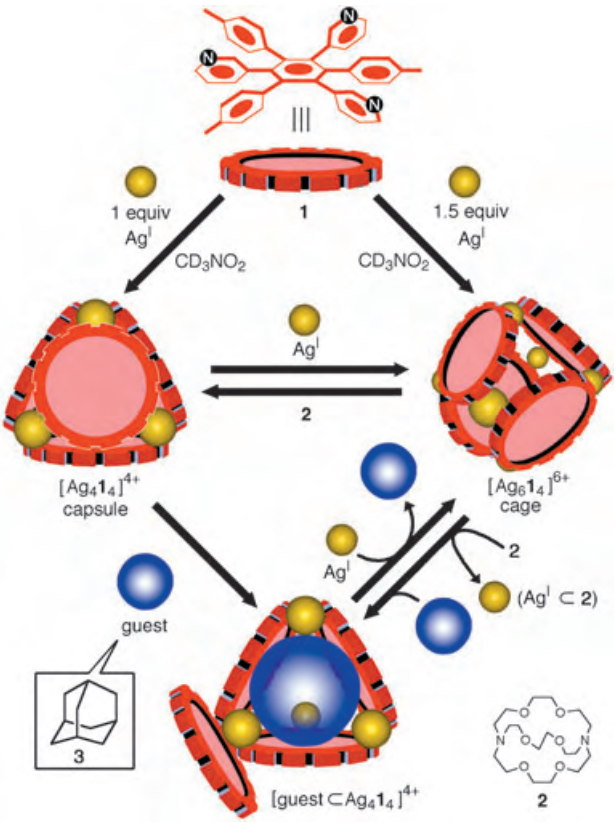

Figure 1. Schematic representation of the interconversion between $[Ag_4\mathbf{1}_4]^{4+}$ capsule and $[Ag_6\mathbf{1}_4]^{6+}$ cage complexes by changing the $[Ag^I]/[\mathbf{1}]$ ratio from 1:1 to 1.5:1. The $[Ag_4\mathbf{1}_4]^{4+}$ capsule complex can entrap a neutral organic molecule such as adamantane in the inner space, while the $[Ag_6\mathbf{1}_4]^{6+}$ cage complex cannot practically encapsulate the guest molecule. The encapsulation/release of the guest molecule is coupled with the reversible Ag^I-dependent capsule↔cage interconversion. A front disk is opened to show clearly a guest molecule encapsulated in the inner space of $[guest\subset Ag_4\mathbf{1}_4]^{4+}$.

of the Ag^I-bound aromatic ligands that form a self-assembled capsulelike structure.

On the other hand, when 1.5 equivalents of $AgPF_6$ were added ($[Ag^I]/[\mathbf{1}] = 1.5:1$), the ^{1}H NMR spectrum showed another set of highly symmetrical signals (Figure 2b), which indicate the quantitative formation of another Ag^I complex. In this case, the signals for the *p*-tolyl proton H_f do not shift upfield, which suggests that the ligand array should be different from that of a complex formed from a 1:1 mixture of Ag^I and **1**. These results demonstrated that two highly symmetrical structures were quantitatively formed from Ag^I and **1** in 1:1 and 1.5:1 ratios. The interconversion between these two thermodynamically stable complexes was fast and reached equilibrium within a few minutes after changing the Ag^I/**1** ratios.

ESI-TOF mass spectra confirmed the formation of $[Ag_4\mathbf{1}_4]^{4+}$ and $[Ag_6\mathbf{1}_4]^{6+}$ complexes with $[Ag^I]/[\mathbf{1}]$ ratios of 1:1 and 1.5:1, respectively (see Supporting Information). The ESI-TOF mass spectrum of a mixture of $AgPF_6$ and **1** in a 1:1 ratio showed a signal at $m/z = 965.2$, which was assigned to $[Ag_4\mathbf{1}_4{\cdot}PF_6]^{3+}$. In contrast, the spectrum of a mixture of $AgPF_6$ and **1** in a 1.5:1 ratio showed signals at $m/z = 814.1$ and 1133.9,

 © 2005 Wiley-VCH Verlag GmbH & Co. KGaA, Weinheim

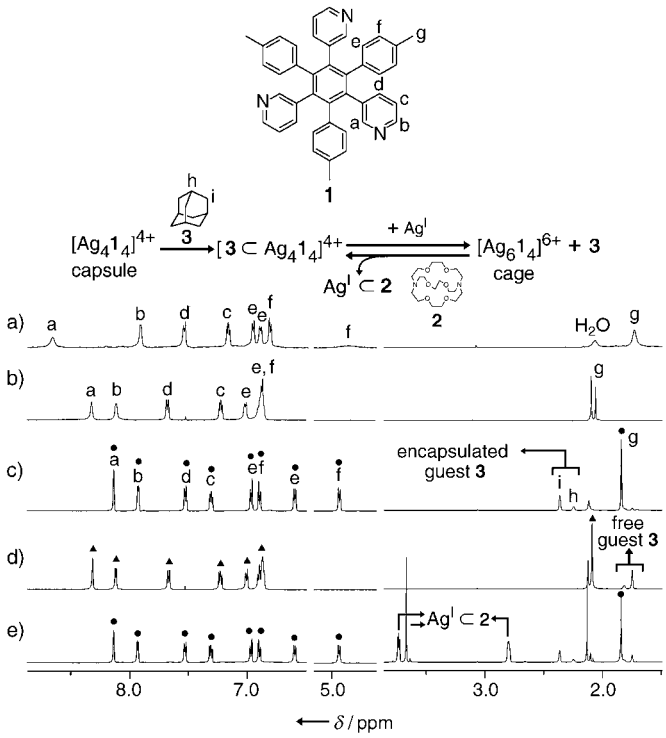

Figure 2. a)–b) ^{1}H NMR spectra (500 MHz) of $[Ag_4\mathbf{1}_4]^{4+}$ capsule and $[Ag_6\mathbf{1}_4]^{6+}$ cage complexes (CD_3NO_2, 293 K, [**1**] = 5.9 mM); a) $Ag_4\mathbf{1}_4\cdot(PF_6)_4$ and b) $Ag_6\mathbf{1}_4\cdot(PF_6)_6$. c)–e) Encapsulation of a guest molecule **3** in the $[Ag_4\mathbf{1}_4]^{4+}$ capsule complex and encapsulation/release of the guest molecule triggered by the capsule↔cage interconversion (^{1}H NMR (CD_3NO_2, 273 K, [**1**] = 10.8 mM)); c) $[\mathbf{3}\subset Ag_4\mathbf{1}_4]^{4+}$, $[Ag_4\mathbf{1}_4\cdot(PF_6)_4] = [\mathbf{3}] = 2.7$ mM. d) Upon addition of $AgPF_6$ (2.0 equiv) to the sample for (c), encapsulated **3** was released from inside as a result of the interconversion from the capsule into the cage. e) Upon addition of [2,2,2]cryptand **2** (2.0 equiv) to the sample for d), an $Ag_4\mathbf{1}_4$ capsule complex was formed and **3** was immediately encapsulated again in the capsule. Filled circles and triangles denote the inclusion complex $[\mathbf{3}\subset Ag_4\mathbf{1}_4]^{4+}$ and the $[Ag_6\mathbf{1}_4]^{6+}$ cage complex, respectively.

which are ascribable to $[Ag_6\mathbf{1}_4\cdot(PF_6)_2]^{4+}$ and $[Ag_6\mathbf{1}_4\cdot(PF_6)_3]^{3+}$, respectively. These mass spectral data and the symmetrical patterns of the ^{1}H NMR spectra overall suggest that the $[Ag_4\mathbf{1}_4]^{4+}$ complex should assume a trigonal-pyramidal, capsule-shaped structure in which four Ag^I ions are arranged in a tetrahedral fashion and three pyridyl nitrogen donor atoms coordinate to each Ag^I. Similarly, an octahedral structure was proposed for the $[Ag_6\mathbf{1}_4]^{6+}$ complex in which six two-coordinate Ag^I ions are arranged in an octahedral fashion so that half of the faces of octahedron are occupied by ligands **1** and the other half is opened to form an Ag^I-linked cage-shaped complex.[12]

From a molecular-modeling study in light of the ^{1}H NMR and ESI-TOF spectra, the Ag^I complexes should have the inner spaces for small molecules, and, in particular, the $[Ag_4\mathbf{1}_4]^{4+}$ complex was expected to have an enclosed space with an encapsulation function. Indeed, the investigation of the ability of $[Ag_4\mathbf{1}_4]^{4+}$ for molecular inclusion revealed that adamantane (**3**) is a suitable guest. The ^{1}H NMR spectrum of an equimolar mixture of **3** and the $[Ag_4\mathbf{1}_4]^{4+}$ capsule in CD_3NO_2 at 273 K gave rise to signals for **3** at $\delta = 2.4$ ppm and $\delta = 2.3$ ppm with downfield shifts of $\Delta\delta = +0.60$ and $+0.41$ ppm, respectively, as a result of the deshielding effect from the pyridyl and *p*-tolyl rings of the ligand part of the inclusion complex (Figure 2c). Under these conditions, approximately 91% of the guest molecules are included in the $[Ag_4\mathbf{1}_4]^{4+}$ complex and the guest **3** moves in and out of the interior slowly on the NMR timescale. The significant upfield shift of H_a ($\Delta\delta = -0.59$ ppm) upon inclusion suggests that the N–Ag^I distances are somewhat lengthened as the four ligands move slightly apart from each other as a result of the encapsulation of **3** accompanying an increase in the inner volume.[13] Evidence for the formation of the 1:1 inclusion complex, $[\mathbf{3}\subset Ag_4\mathbf{1}_4]^{4+}$, was provided by the ESI-TOF mass spectrum, which showed a signal that was assigned to $[\mathbf{3}\subset Ag_4\mathbf{1}_4]^{4+}$ at $m/z = 721.7$ (see Supporting Information). Thermodynamic parameters were determined for the encapsulation of **3** into the inner space of the $[Ag_4\mathbf{1}_4]^{4+}$ by variable-temperature ^{1}H NMR measurements.[14] The negative values of $\Delta H = -63.3$ kJ mol^{-1} and $\Delta S = -144$ J mol^{-1} K^{-1} in the encapsulation process indicate the great contribution of enthalpy-driven association to the stability through van der Waals contacts between the $[Ag_4\mathbf{1}_4]^{4+}$ capsule and the guest **3** as well as by the solvophobic effects on the process. The binding constant ($K = [\mathbf{3}\subset Ag_4\mathbf{1}_4]/([\mathbf{3}]\cdot[Ag_4\mathbf{1}_4])$; M^{-1}) was thus determined to be 3.8×10^4 M^{-1} at 273 K. A structurally similar 1-adamantanol was also encapsulated in the $[Ag_4\mathbf{1}_4]^{4+}$ capsule but the binding constant was decreased to 1.3×10^3 M^{-1}, which indicated that only 59% of 1-adamantanol was included under the same conditions. As for 1-chloroadamantane with a larger Cl group, only a slight binding affinity ($K < 1$ M^{-1}) was observed. These results indicate that the $[Ag_4\mathbf{1}_4]^{4+}$ capsule has a high selectivity for unsubstituted adamantane in the recognition of adamantane derivatives.[15,16] On the other hand, the $[Ag_6\mathbf{1}_4]^{6+}$ cage complex did not include any guest molecules tested, probably owing to its larger inner space, the absence of preferable interaction between the host and guest, and the presence of the openings in the cagelike structure.

The interconversion between the two Ag^I complexes was fast, as expected from the labile nature of the Ag^I-centered ligand exchange reactions. Furthermore, under the condition employed, the ratios of the two complexes were highly dependent on the $[Ag^I]/[\mathbf{1}]$ ratios (Figure 3a). This tendency was also observed when an adamantane was added to the solution, as shown in Figure 3b.

Similar results were obtained when silver trifluoromethanesulfonate (AgOTf) was used instead of $AgPF_6$ which indicated that counteranions have no significant influence on the interconversion process and on the encapsulation property of the cationic part, $[Ag_4\mathbf{1}_4]^{4+}$. Finally, X-ray analysis of the neutral inclusion complex $\mathbf{3}\subset Ag_4\mathbf{1}_4\cdot(TfO)_4$ revealed a capsule-shaped coordination structure in which one adamantane molecule is accommodated in the inner space (Figure 4). The capsule complex is composed of four pyridyl ligands **1** and four Ag^I ions, which are arranged 10.0 Å apart from each other in a tetrahedral fashion. Three pyridyl nitrogen atoms from three disk-shaped ligands (Ag–N: 2.29 Å (average)) and an oxygen atom of TfO^- coordinate to each Ag^I center (Ag–O: 2.50 Å (average)) in a distorted tetrahedral geometry. The mean deviation of the Ag^I from the N_3 plane is 0.391 Å. One

 © 2005 Wiley-VCH Verlag GmbH & Co. KGaA, Weinheim

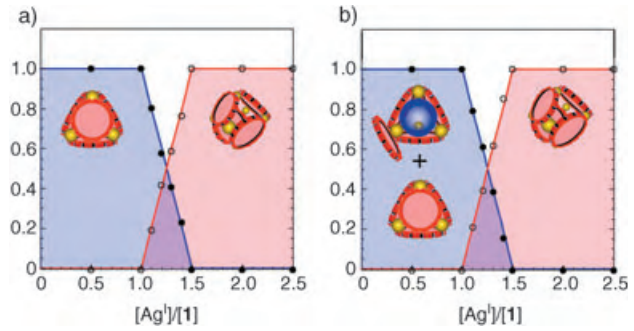

Figure 3. Effects of the presence of adamantane (**3**) on the interconversion between $[Ag_4\mathbf{1}_4]^{4+}$ and $[Ag_6\mathbf{1}_4]^{6+}$. a) Plot of $[Ag_4\mathbf{1}_4]/([Ag_4\mathbf{1}_4]+[Ag_6\mathbf{1}_4])$ (filled circles) and $[Ag_6\mathbf{1}_4]/([Ag_4\mathbf{1}_4]+[Ag_6\mathbf{1}_4])$ (open circles) against [Ag^{I}]/[**1**] determined from the ^{1}H NMR integral ratios. Solid lines are theoretically drawn for $[Ag_4\mathbf{1}_4]/([Ag_4\mathbf{1}_4]+[Ag_6\mathbf{1}_4])$ (blue) and $[Ag_6\mathbf{1}_4]/([Ag_4\mathbf{1}_4]+[Ag_6\mathbf{1}_4])$ (red) as a function of [Ag^{I}]/[**1**]. b) Plot of $([\mathbf{3}\subset Ag_4\mathbf{1}_4]+[Ag_4\mathbf{1}_4])/([\mathbf{3}\subset Ag_4\mathbf{1}_4]+[Ag_4\mathbf{1}_4]+[Ag_6\mathbf{1}_4])$ (filled circles) and $[Ag_6\mathbf{1}_4]/([\mathbf{3}\subset Ag_4\mathbf{1}_4]+[Ag_4\mathbf{1}_4]+[Ag_6\mathbf{1}_4])$ (open circles) against [Ag^{I}]/[**1**] determined from the ^{1}H NMR integral ratios. Solid lines are theoretically drawn as a function of [Ag^{I}]/[**1**]. A front disk is opened to clearly show a guest molecule in the inner space for the $[\mathbf{3}\subset Ag_4\mathbf{1}_4]^{4+}$ complex.

adamantane molecule is closely packed in the inner space and surrounded by the four ligands. The hydrogen atoms of **3** are close to *p*-tolyl H_e or pyridyl H_a within approximately 2.2–3.1 Å, as suggested by the ^{1}H NMR data for $\mathbf{3}\subset Ag_4\mathbf{1}_4\cdot(PF_6)_4$. The distance between H_h of **3** and the central benzene ring of **1** is 2.85 Å, thus indicating that there are no CH–π interactions between them.

As described above, the $[Ag_4\mathbf{1}_4]^{4+}$ capsule and the $[Ag_6\mathbf{1}_4]^{6+}$ cage complexes are totally different from each other in shape, volume, and internal structures, thus resulting in the large difference in their affinity for guest molecules. That is, an adamantane (**3**) is encapsulated in the $[Ag_4\mathbf{1}_4]^{4+}$ capsule with high affinity, whereas the $[Ag_6\mathbf{1}_4]^{6+}$ cage has practically no interaction with **3**. We exploited this switching system for the encapsulation/release of the guest molecule through the interconversion between the capsule- and cage-shaped structures. First, the $[Ag_4\mathbf{1}_4]^{4+}$ complex entrapped **3** into its inner space to form a 1:1 complex (Figure 2c). Upon addition of 2.0 equivalents of $AgPF_6$, the encapsulated **3** was immediately released to the bulk solvent as a result of the structural conversion from the $[Ag_4\mathbf{1}_4]^{4+}$ capsule into the $[Ag_6\mathbf{1}_4]^{6+}$ cage (Figure 2d). When 2.0 equivalents of [2,2,2]-cryptand **2** were added to the solution, two Ag^I ions of the $[Ag_6\mathbf{1}_4]^{6+}$ complex were trapped by **2**, and then the $[Ag_4\mathbf{1}_4]^{4+}$ capsule was reconstructed with simultaneous inclusion of **3** in the capsule (Figure 2e). This encapsulation/release cycle could be repeated at least three times without any loss of efficiency within a few minutes for each encapsulation/release cycle.[17]

In summary, we have developed an Ag^I-mediated structural on–off switching system in which the Ag^I-linked capsule ($[Ag_4\mathbf{1}_4]^{4+}$) and cage ($[Ag_6\mathbf{1}_4]^{6+}$) complexes are quantitatively interconverted, depending on the ratios of Ag^I to **1**. The capsule complex only has a large affinity for small neutral organic molecules such as adamantane, and its crystallographic analysis revealed the structure of the 1:1 inclusion

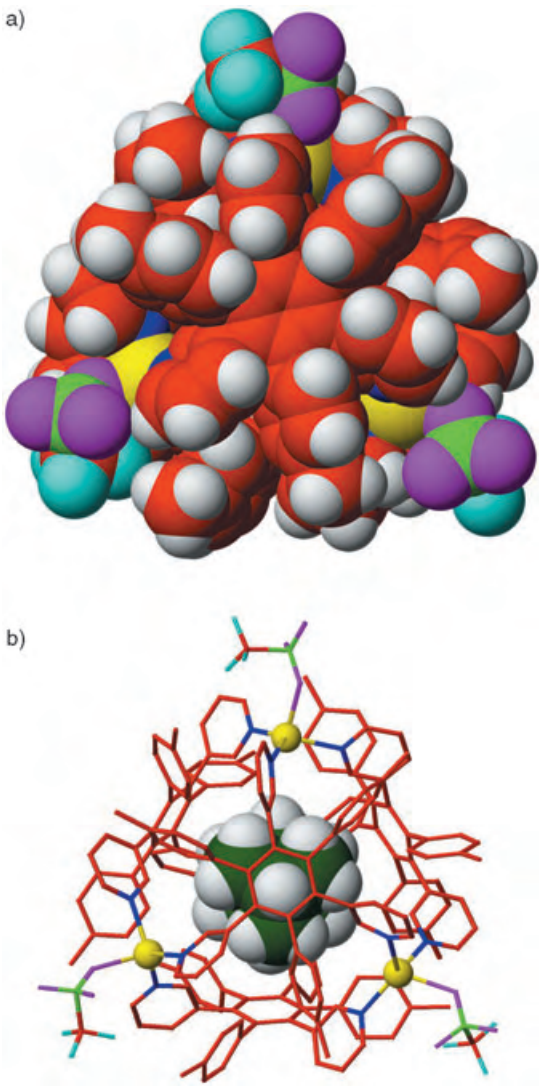

Figure 4. The crystal structure of $\mathbf{3}\subset Ag_4\mathbf{1}_4\cdot(TfO)_4$. Color labels: red (carbon), turquoise (carbon of **3**), blue (nitrogen), yellow (silver), purple (oxygen), light green (sulfur), cyan (fluorine), and white (hydrogen). a) A space-filling model; b) the capsule structure is depicted as a cylinder model. Hydrogen atoms of the $[Ag_4\mathbf{1}_4]^{4+}$ moiety are omitted for clarity.

complex with an adamantane molecule. Finally, we have established an excellent dynamic system for the encapsulation/release of guest molecules by the use of metal-mediated interconversion between the capsule and cage complexes constructed from trismonodentate ligands and Ag^I in a self-assembled manner. These results would open up prospects for exploiting nanocapsules for molecular transport systems. The construction of larger metallocapsules with dynamic properties is currently ongoing.

Experimental Section

$\mathbf{3}\subset Ag_4\mathbf{1}_4\cdot(TfO)_4$: A single crystal suitable for X-ray crystallographic analysis was obtained from a saturated solution of $Ag_4\mathbf{1}_4\cdot(TfO)_4$ and **3** (1:1 mixture) in CD_3NO_2 at 253 K. Crystallographic data ($C_{185}H_{173}Ag_4F_{12}N_{15}O_{26}S_4$): $M = 3810.18$, colorless, $0.20\times0.12\times$

 © 2005 Wiley-VCH Verlag GmbH & Co. KGaA, Weinheim

0.07 mm^3, orthorhombic, space group *Pccn*, $a = 16.414(11)$, $b = 32.34(2)$, $c = 37.30(2)$ Å, $V = 19800(21)$ $Å^3$, $Z = 4$, $R_1(I > 2\sigma(I)) = 0.1532$, $wR(F_o^2) = 0.4282$, GOF = 1.091; intensity data were measured at 93.1 K on a Rigaku RAXIS-RAPID Imaging Plate diffractometer with graphite monochromated $Mo_{K\alpha}$ ($\lambda_\alpha = 0.71075$ Å) radiation; structure solution was carried out with the program PATTY (P. Beurskens, T. Admiraal, G. Beurskens, G. Bosman, W. P. de Gelder, R. Israel, J. M. M. Smits, PATTY: The DIRDIF-94 Program System, Technical Report of the Crystallography Laboratory, University of Nijmegen, The Netherlands, **1994**). Considerably large R_1 and wR values might be due to the missing of one of four anions and a poor quality of the crystal used. CCDC-248984 contains the supplementary crystallographic data for this paper. These data can be obtained free of charge from the Cambridge Crystallographic Data Centre via www.ccdc.cam.ac.uk/data_request/cif.

Received: October 22, 2004
Published online: March 30, 2005

Keywords: cage compounds · host–guest systems · molecular recognition · self-assembly · silver

[1] a) F. Hof, S. L. Craig, C. Nuckolls, J. Rebek, Jr., *Angew. Chem.* **2002**, *114*, 1556–1578; *Angew. Chem. Int. Ed.* **2002**, *41*, 1488–1508; b) L. J. Prins, D. N. Reinhoudt, P. Timmerman, *Angew. Chem.* **2001**, *113*, 2690–2692; *Angew. Chem. Int. Ed.* **2001**, *40*, 2382–2426; c) L. R. MacGillivray, J. L. Atwood, *Angew. Chem.* **1999**, *111*, 1080–1096; *Angew. Chem. Int. Ed.* **1999**, *38*, 1018–1033.

[2] a) A. V. Davis, R. M. Yeh, K. N. Raymond, *Proc. Natl. Acad. Sci. USA* **2002**, *99*, 4793–4796; b) M. Fujita, K. Umemoto, M. Yoshizawa, N. Fujita, T. Kusukawa, K. Biradha, *Chem. Commun.* **2001**, 509–518; c) S. Leninger, B. Olenyuk, P. J. Stang, *Chem. Rev.* **2000**, *100*, 853–907; d) G. F. Swiegers, T. J. Malefetse, *Chem. Rev.* **2000**, *100*, 3483–3537.

[3] a) J. L. Atwood, A. Szumna, *J. Am. Chem. Soc.* **2002**, *124*, 10646–10647; b) J. L. Atwood, L. J. Barbour, A. Jerga, *Proc. Natl. Acad. Sci. USA* **2002**, *99*, 4837–4841; c) K. Umemoto, H. Tsukui, T. Kusukawa, K. Biradha, M. Fujita, *Angew. Chem.* **2001**, *113*, 2690–2692; *Angew. Chem. Int. Ed.* **2001**, *40*, 2620–2622; d) L. J. Prins, F. De Jong, P. Timmerman, D. N. Reinhoudt, *Nature* **2000**, *408*, 181–184; e) N. Takeda, K. Umemoto, K. Yamaguchi, M. Fujita, *Nature* **1999**, *398*, 794–796; f) B. Olenyuk, J. A. Whiteford, A. Fechtenkotter, P. J. Stang, *Nature* **1999**, *398*, 796–799; g) L. R. MacGillivray, J. L. Atwood, *Nature* **1997**, *389*, 469–472;

[4] a) R. Pinalli, V. Cristini, V. Sottili, S. Geremia, M. Campagnolo, A. Caneschi, E. Dalcanale, *J. Am. Chem. Soc.* **2004**, *126*, 6516–6517; b) C. J. Kuehl, Y. K. Kryschenko, U. Radhakrishnan, S. R. Seidel, S. D. Huang, P. J. Stang, *Proc. Natl. Acad. Sci. USA* **2002**, *99*, 4932–4936; c) A. Ikeda, H. Udzu, Z. Zhong, S. Shinkai, S. Sakamoto, K. Yamaguchi, *J. Am. Chem. Soc.* **2001**, *123*, 3872–3877; d) M. Fujita, D. Oguro, M. Miyazawa, H. Oka, K. Yamaguchi, K. Ogura, *Nature* **1995**, *378*, 469–471.

[5] a) Y. Yamanoi, Y. Sakamoto, T. Kusukawa, M. Fujita, S. Sakamoto, K. Yamaguchi, *J. Am. Chem. Soc.* **2001**, *123*, 980–981; b) R. H. Vreekamp, J. P. M. van Duynhoven, M. Hubert, W. Verboom, D. N. Reinhoudt, *Angew. Chem.* **1996**, *108*, 1303–1306; *Angew. Chem. Int. Ed. Engl.* **1996**, *35*, 1215–1218.

[6] a) D. T. Bong, T. D. Clark, J. R. Granja, M. R. Ghadiri, *Angew. Chem.* **2001**, *113*, 1016–1041; *Angew. Chem. Int. Ed.* **2001**, *40*, 988–1011; b) M. R. Ghadiri, J. R. Granja, R. A. Milligan, D. E. McRee, N. Khazanovich, *Nature* **1993**, *366*, 324–327; c) T. Yamaguchi, S. Tashiro, M. Tominaga, M. Kawano, T. Ozeki, M. Fujita, *J. Am. Chem. Soc.* **2004**, *126*, 10818–10819; d) M. Aoyagi, K. Biradha, M. Fujita, *J. Am. Chem. Soc.* **1999**, *121*, 7457–7458.

[7] a) M. Yoshizawa, M. Tamura, M. Fujita, *J. Am. Chem. Soc.* **2004**, *126*, 6846–6847; b) A. Scarso, L. Trembleau, J. Rebek, Jr., *Angew. Chem.* **2003**, *115*, 5657–5660; *Angew. Chem. Int. Ed.* **2003**, *42*, 5499–5502; c) J. M. C. A. Kerckhoffs, F. W. B. van Leeuwen, A. L. Spek, K. Kooijman, M. Crego-Calama, D. N. Reinhoudt, *Angew. Chem.* **2003**, *115*, 5895–5900; *Angew. Chem. Int. Ed.* **2003**, *42*, 5717–5722; d) J. L. Atwood, A. Szumna, *Chem. Commun.* **2003**, 940–941; e) A. Ikeda, M. Yoshimura, H. Udzu, C. Fukuhara, S. Shinkai, *J. Am. Chem. Soc.* **1999**, *121*, 4296–4297.

[8] a) D. Fiedler, R. G. Bergman, K. N. Raymond, *Angew. Chem.* **2004**, *116*, 6916–6919; *Angew. Chem. Int. Ed.* **2004**, *43*, 6748–6751; b) M. Yoshizawa, Y. Takeyama, T. Kusukawa, M. Fujita, *Angew. Chem.* **2002**, *114*, 1403–1405; *Angew. Chem. Int. Ed.* **2002**, *41*, 1347–1349; c) J. Kang, J. Rebek, Jr., *Nature* **1997**, *385*, 50–52; d) J. Kang, J. Santamaria, G. Hilmersson, J. Rebek, Jr., *J. Am. Chem. Soc.* **1998**, *120*, 7389–7390.

[9] a) M. C. Jiménez, C. Dietrich-Buchecker, J.-P. Sauvage, *Angew. Chem.* **2000**, *112*, 3422–3425; *Angew. Chem. Int. Ed.* **2000**, *39*, 3284–3287; b) M. C. Jimenez-Molero, C. Dietrich-Buchecker, J.-P. Sauvage, *Chem. Commun.* **2003**, 1613–1616.

[10] S. Hiraoka, T. Yi, M. Shiro, M. Shionoya, *J. Am. Chem. Soc.* **2002**, *124*, 14510–14511.

[11] a) S.-S. Sun, C. L. Stern, S.-B. T. Nguyen, J. T. Hupp, *J. Am. Chem. Soc.* **2004**, *126*, 6314–6326; b) M. Barboiu, E. Petit, G. Vaughan, *Chem. Eur. J.* **2004**, *10*, 2263–2270; c) C.-Y. Su, Y.-P. Cai, C.-L. Chen, M. D. Smith, W. Kaim, H.-C. zur Loye, *J. Am. Chem. Soc.* **2003**, *125*, 8595–8613; d) M. Barboiu, G. Vaughan, R. Graff, J.-M. Lehn, *J. Am. Chem. Soc.* **2003**, *125*, 10257–10265.

[12] The possibility of a sandwich-shaped $[Ag_3\mathbf{1}_2]^{3+}$ structure is ruled out because the coordination direction of pyridyl nitrogen atoms of **1** does not meet the requirements for the formation of $[Ag_3\mathbf{1}_2]^{3+}$, as suggested by its molecular-modeling study.

[13] The changes in the chemical shift of H_a signal of the $[Ag_4\mathbf{1}_4]^{4+}$ capsule complex should be affected by both the bonding nature of the Ag–N bonds and the deshielding effects of the *p*-tolyl rings in the neighboring ligands. Upon encapsulation of **3** in the $[Ag_4\mathbf{1}_4]^{4+}$ complex, the Ag–N bonds are lengthened so as to maximize van der Waals interaction between the $[Ag_4\mathbf{1}_4]^{4+}$ capsule and **3**. The movement of the four ligands away from each other with increasing Ag–N bond lengths of the $[\mathbf{3}\subset Ag_4\mathbf{1}_4]^{4+}$ should decrease the deshielding effects of the *p*-tolyl rings.

[14] The binding constant was determined by the ^1H NMR integral ratios of the $[\mathbf{3}\subset Ag_4\mathbf{1}_4]^{4+}$ and $[Ag_4\mathbf{1}_4]^{4+}$, and the thermodynamic parameters (ΔH and ΔS) were calculated from the ΔG values obtained at temperatures ranging from 273 to 333 K by the least-square method. Experimental data are shown in the Supporting Information.

[15] Several halogenated methanes were also encapsulated in the $Ag_4\mathbf{1}_4$ complex. Their binding constants K (M^{-1}) at 273 K are 7.5×10^2 (CBr_4), 1.0×10^2 (CBr_2Cl_2), 14 ($CFBr_3$), 18 ($CBrCl_3$), and 1.4 (CCl_4).

[16] ^{19}F NMR spectra of the $Ag_4\mathbf{1}_4$ capsule and $Ag_6\mathbf{1}_4$ cage complexes showed one set of signals similar to that of $AgPF_6$ or AgOTf which suggests that the counteranions should exist outside their inner space.

[17] An excellent example is reported in reference [7c] for the release of guest molecules in the hydrogen-bonded cage triggered by the change of their components. However, the reversible encapsulation/release process was not established by this system.

 © 2005 Wiley-VCH Verlag GmbH & Co. KGaA, Weinheim

Natural Products Synthesis

Total Synthesis of Antascomicin B**

*Dominic E. A. Brittain, Charlotte M. Griffiths-Jones, Michael R. Linder, Martin D. Smith, Catherine McCusker, Jaqueline S. Barlow, Ryo Akiyama, Kosuke Yasuda, and Steven V. Ley**

In 1996, a search for novel materials that might elicit similar biological effects to rapamycin and FK506 was initiated at Sandoz.[1] The immunophilin FKBP12 (the primary target for rapamycin and FK506) was used and the degree of binding to substrates in competition with FK506 was measured to evaluate metabolites from over 12000 strains of *Actinomycetes*. Alongside the known immunophilin-binding compounds rapamycin, ascomycin,[2] and meridamycin,[3] the novel antascomicin family was discovered.

It was found that, despite the strong levels of binding to FKBP12 of all these compounds, only rapamycin and ascomycin show immunosuppressive properties in vitro and in vivo, whereas meridamycin and the antascomicins show none.[1,3] Specifically, the antascomicins bind FKBP12 to the same degree as do FK506 and rapamycin (1.1 and 0.6 nM, respectively, in the same binding assay) and antagonize both immunosuppressants. It has been demonstrated by Schreiber and co-workers that it is the fate of the ligand–FKBP12 complex, rather than solely ligand binding to FKBP12, that determines the immunosuppressive effect.[4,5] Subsequently, the significantly higher levels of FKBP12 found in the brain, rather than in the immune system,[6] stimulated work on the effects of rapamycin and FK506 complexes with FKBP12 in the treatment of neurodegenerative diseases.[7] However, the immunosuppressive effects of these complexes became a liability,[8] thus pushing nonimmunosuppressive FKBP ligands to the fore. Further results demonstrated the ability of synthetic FKBP ligands to promote not only regrowth of damaged nerves in the peripheral nervous system, but also the regeneration of damaged neurons in the central nervous system.[9]

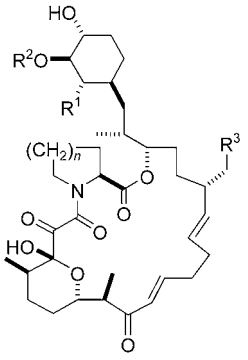

Antascomicin	R^1	R^2	R^3	n	FKBP12 binding IC_{50} (nM)
A	H	H	H	2	2.0
B	OH	H	H	2	0.7
C	OH	Me	H	2	1.0
D	H	H	H	1	5.2
E	H	H	OH	2	0.7

The wealth of biological and chemical attention attracted by other FKBP12 ligands prompted us to initiate a program aimed at the total synthesis of antascomicin B, as it combined both structural complexity and the most potent FKBP12 binding ability. Antascomicin B is an enticing target for the synthetic organic chemist as it has a complex polyketide structure that includes both lactol and lactam functionalities, 12 stereogenic centers, and a masked 1,2,3-tricarbonyl unit. A recent synthetic study described the stereoselective synthesis of the C18–C34 fragment of antascomicin A;[10] however, no total synthesis of any member of the antascomicin family has been disclosed. Examination of the structure of antascomicin B (**1**) suggested disconnection to three major fragments (Scheme 1).

Construction of the C10–C34 carbon framework was envisaged through the coupling of a C24 anion (via an intermediate sulfone on fragment **III**) with the epoxide functionality at C25 in fragment **II**, followed by esterification with pipecolic acid fragment **I**. The installation of all but two of the carbon atoms present in the natural product would then set the stage for the key macrocyclization and tricarbonyl-generation steps. Enone formation (C16) and deprotection would then be all that was required to complete the synthesis.

Fragment **II** could be constructed by a ring-closing metathesis of diene **2**, which could be derived by addition of the allyl stannane **4** to a butanediacetal-protected aldehyde **3** (Scheme 2).

By utilizing work developed in our group on the use of desymmetrized butanediacetal-protected tartrates as building blocks for *anti*-1,2-diols,[11–13] diacetal **6** was easily prepared from dimethyl D-tartrate **5** in large quantities and converted into protected aldehyde **3** via protected tetrol **7** (Scheme 3). It

[*] Dr. D. E. A. Brittain, Dr. C. M. Griffiths-Jones, Dr. M. R. Linder, Dr. M. D. Smith, Dr. C. McCusker, Dr. J. S. Barlow, Dr. R. Akiyama, Dr. K. Yasuda, Professor Dr. S. V. Ley
Department of Chemistry
University of Cambridge
Lensfield Road, Cambridge CB2 1EW (UK)
Fax: (+44) 1223-336-442
E-mail: svl1000@cam.ac.uk

[**] The authors would like to thank Novartis for the Novartis Research Fellowship (to S.V.L.), Trinity College, Cambridge for a Junior Research Fellowship (to D.E.A.B.), Pembroke College, Cambridge and the Royal Society for fellowships (to M.D.S.), the EPSRC (to C.M.G.-J., M.R.L., C.M., and D.E.A.B.), Tanabe Seiyaku Co., Ltd. for a postdoctoral fellowship (to K.Y.), and the Japanese Society for the Promotion of Sciences (to R.A.). The authors would also like to acknowledge the contribution of Prof. Hidenori Watanabe (University of Tokyo; Cambridge 1998–2000) whose studies on a related system were invaluable in the development of the macrocyclization method described herein.

Supporting information for this article is available on the WWW under http://www.angewandte.org or from the author.

 © 2005 Wiley-VCH Verlag GmbH & Co. KGaA, Weinheim DOI: 10.1002/anie.200500174

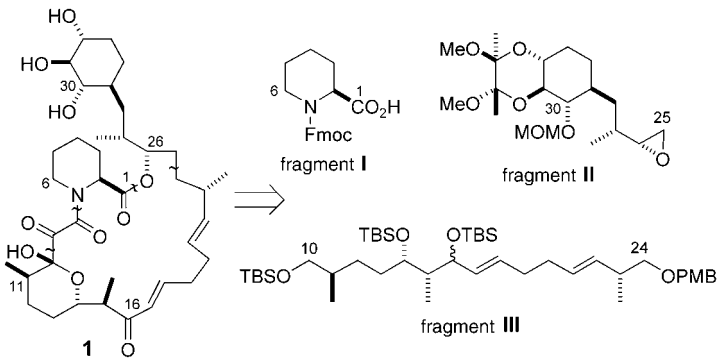

Scheme 1. Disconnection of antascomicin B. Fmoc = 9-fluorenylmethyloxycarbonyl; MOM = methoxymethyl; TBS = *tert*-butyldimethylsilyl; PMB = *p*-methoxybenzyl.

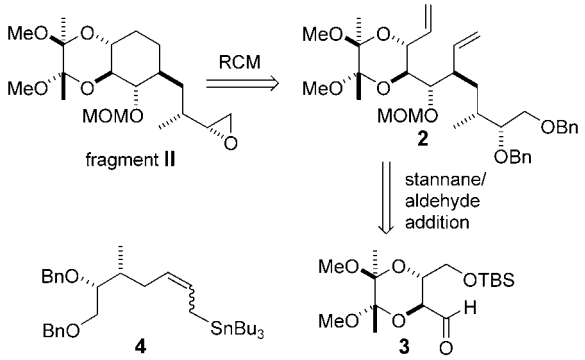

Scheme 2. Retrosynthetic analysis of fragment **II**. Bn = benzyl.

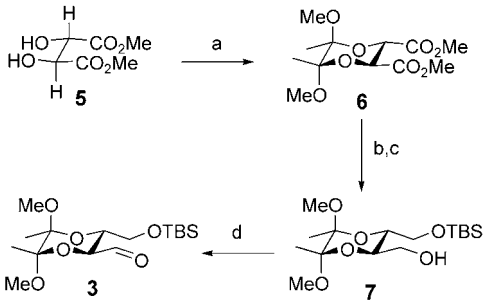

Scheme 3. Reagents and conditions: a) MeCOCOMe, CSA, $CH(OMe)_3$, MeOH, 68%; b) $LiAlH_4$, THF, 99%; c) NaH, TBSCl, 87%; d) $(COCl)_2$, DMSO, CH_2Cl_2, Et_3N. CSA = (+/−)-camphorsulfonic acid; DMSO = dimethyl sulfoxide.

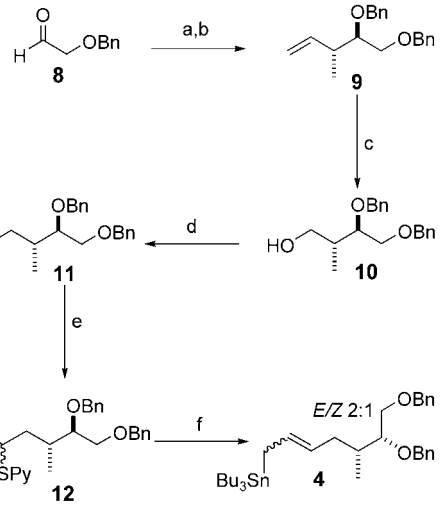

Scheme 4. Reagents and conditions: a) 1. (*E*)-Butene, KO*t*Bu, *n*-BuLi, THF, −78 °C; 2. (+)-$(Ipc)_2BOMe$, Et_2O, $BF_3{\cdot}OEt_2$, aldehyde, −78 °C; b) BnBr, NaH, DMF, 62% over two steps; c) 1. O_3, CH_2Cl_2, −78 °C; then PPh_3, 2. $NaBH_4$, MeOH, 90% over two steps; d) I_2, PPh_3, imidazole, CH_2Cl_2, 90%; e) allylpyridylsulfide, *t*BuLi, THF, −78 °C, 95%; f) Bu_3SnLi, CuBr, THF, −78 °C, 98%. Ipc = isopinocampheyl; DMF = *N*,*N*-dimethylformamide.

was found that butanediacetal-protected aldehyde **3** was most effective when used crude in subsequent reactions.

After some encouraging results with model studies on the addition of allyl stannanes to aldehyde **3**, work began on the synthesis of the fully substituted allyl stannane **4** (Scheme 4). The two stereogenic centers in allyl stannane **4** were installed through asymmetric crotylation of commercially available benzyloxyacetaldehyde (**8**) to give the secondary alcohol with 97% *ee*, under conditions originally developed by Brown and Bhat.[14] Benzylation to provide alkene **9** and reductive ozonolysis afforded primary alcohol **10**. Owing to the stability of the ozonide to reduction by sodium borohydride, it was necessary to form the aldehyde initially en route to the alcohol. This was achieved with triphenylphosphane, and the transformation remained a one-pot procedure. Subsequent conversion into iodide **11** and displacement by allylpyridylsulfide provided substrate **12**. The allyl stannane functionality was subsequently installed through an anionic cuprate procedure to give stannane **4**.[15]

A variety of conditions were examined for the aldehyde/stannane addition, with the optimum selectivity arising from the use of zinc iodide in CH_2Cl_2 to give **13** with near total diastereoselectivity at C30 and in a 7:1 ratio at C29 in favor of the desired isomer (Scheme 5). It was found that the *E*/*Z* ratio of the stannane had only a minor effect on the diastereoselectivity of the subsequent addition.

Modeling studies and precedent for stannane additions suggest the mechanism and transition state shown in Figure 1.[16,17] It is believed that chelation between the carbonyl group and the axial lone pair of electrons on the α-oxygen atom of the butanediacetal group through the Zn^{2+} permits attack of the stannane to occur onto only one face of the carbonyl group. The allyl stannane attacks in an antiperiplanar orientation, with the vinylic hydrogen substituent being placed over the chelate ring.

Protection of the newly formed hydroxy group as a MOM ether and removal of the TBS protecting group yielded alcohol **14**, which upon completion of a Swern–Wittig protocol, provided access to the ring-closing-metathesis precursor **2**. Portionwise addition of Grubbs second-generation imidazolidine catalyst[18] to the substrate in refluxing toluene enabled the substituted cyclohexene to be formed in 95% yield. Treatment with hydrogen in the presence of palladium on carbon resulted in the reduction of the C33–C34 double bond and the simultaneous removal of both benzyl

 © 2005 Wiley-VCH Verlag GmbH & Co. KGaA, Weinheim

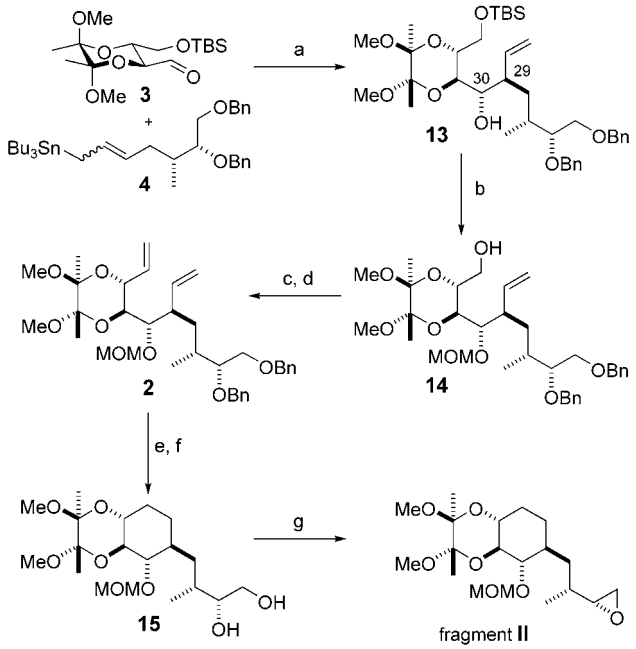

Scheme 5. Reagents and conditions: a) ZnI_2, CH_2Cl_2 −78 °C→RT, 85% over two steps, *syn*/*anti* 6:1 at C29–C30; b) 1. MOMCl, DIPEA, CH_2Cl_2; 2. TBAF, THF, 89% over two steps; c) $(COCl)_2$, DMSO, Et_3N, CH_2Cl_2; d) $MePPh_3Br$, BuLi, THF, −78 °C→RT, 87% over two steps; e) 1,3-(bis-(mesityl)-2-imidazolidinylidene) dichloro(phenylmethylene) (tricyclohexylphosphane) ruthenium (3×3.5 mol%), toluene, reflux, 95%; f) H_2, Pd/C, EtOH, 96%; g) NaH, 2-(2,4,6-triisopropylbenzenesulfonyl)-imidazole, THF, 88%. DIPEA = diisopropylethylamine; TBAF = tetrabutylammonium fluoride.

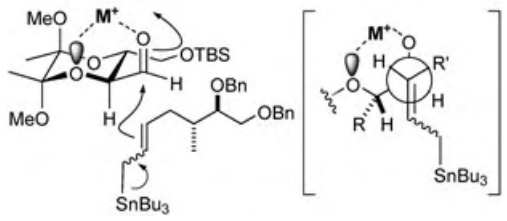

Figure 1. Suggested mechanism and transition state for stannane additions.

groups to give diol **15**, which was transformed in one step to the epoxide, fragment **II** (Scheme 5).

The synthesis of fragment **III** centered on the construction of aldehyde **16** and alkyne **17** and on their coupling through a hydrozirconation protocol to create the C10–C24 allylic alcohol (Scheme 6).

Synthesis of the C10–C16 aldehyde **16** started from iodide **18**, which is available in two steps from commercially available (*2S*)-3-bromo-2-methylpropan-1-ol by silylation and halide exchange. Displacement with allylmagnesium chloride in the presence of copper iodide gave the terminal olefin-bearing compound that underwent ozonolysis with reductive workup to afford the aldehyde **19** in an overall yield of 79% for the two steps (Scheme 7).

The C14–C15 stereogenic centers were introduced through an asymmetric aldol reaction by using the Evans

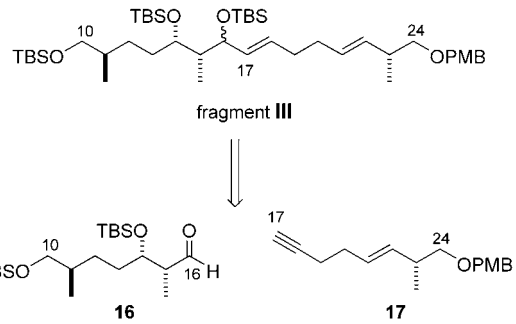

Scheme 6. Retrosynthetic analysis of fragment **III**.

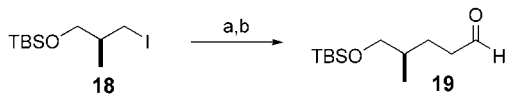

Scheme 7. Reagents and conditions: a) AllylMgCl, CuI, THF, 90%; b) O_3, CH_2Cl_2, −78 °C; then PPh_3, 88%.

chiral auxiliary.[19] Addition of the boron enolate of oxazolidinone **20** to aldehyde **19** gave aldol adduct **21** in high yield as a single diastereoisomer after recrystallization. Protection of the C14 hydroxy group as a silyl ether, and removal of the auxiliary via thioester **22**[20,21] gave the desired aldehyde **16** (Scheme 8).

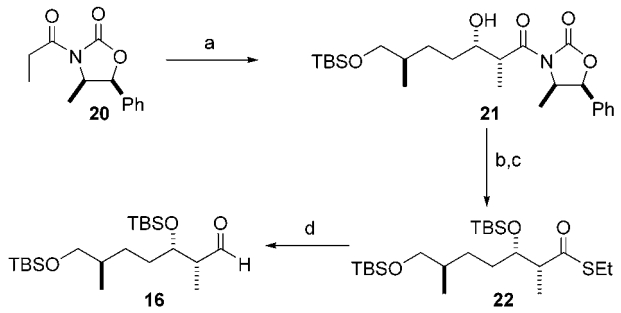

Scheme 8. Reagents and conditions: a) Bu_2BOTf, Et_3N, CH_2Cl_2, **19**, −80 °C, 60 h; then pH 7.2 phosphate-buffered MeOH, H_2O_2, 94% (single isomer); b) TBSCl, imidazole, DMF, 100%; c) EtSH, BuLi, THF, −78 °C, 99%; d) Et_3SiH, Pd/C, acetone, 99%. Tf = trifluoromethanesulfonyl.

The synthesis of alkyne **17** started from primary alcohol **23**, which is available in four steps from Roche ester ((*S*)-3-hydroxy-2-methylpropionic acid methyl ester). Swern oxidation followed by Wittig reaction was used to establish the C21–C22 *trans* olefin **24** with exceptionally high selectivity (Scheme 9). Reduction with DIBAL-H to alcohol **25** and conversion into bromide **26** enabled introduction of the alkyne functionality in its TMS-protected form to give protected alkyne **27** in 88% yield. A minor allene side product (8%), which arises from S_E2' attack of the TMS-propargyl organolithium reagent, was also isolated. Desilylation under basic conditions completed the synthesis of alkyne **17** in this high-yielding series of steps.

 © 2005 Wiley-VCH Verlag GmbH & Co. KGaA, Weinheim

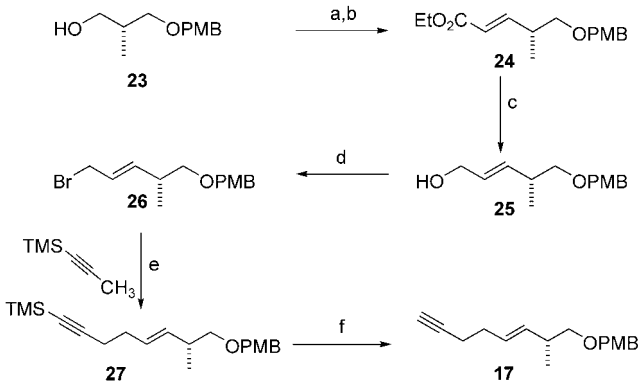

Scheme 9. Reagents and conditions: a) $(COCl)_2$, DMSO, Et_3N, CH_2Cl_2, 95%; b) Ph_3PCHCO_2Et, CH_2Cl_2, 0°C→RT, 2 days, 98%, *E*/*Z* 99:1; c) DIBAL-H, PhMe, −78°C, 1.5 h, 93%; d) Ph_3P, CBr_4, CH_2Cl_2, 95%; e) BuLi, THF, −78°C, 1 h, 88%; f) aqueous NaOH (10%), 2 days, 99%. DIBAL-H = diisobutylaluminum hydride.

Cis-specific hydrozirconation of alkyne **17** with freshly prepared Schwartz reagent[22] afforded a vinylzirconium species[23] that underwent silver perchlorate mediated addition to aldehyde **16** in 96% yield.[24,25] The resultant secondary alcohol **28** was formed as a 1:1 mixture of separable diastereoisomers; the stereoselectivity is unimportant at this stage as the alcohol functionality at C16 is ultimately oxidized. After separation (for analytical convenience), silylation of the secondary alcohol completed the synthesis of fragment **III** (Scheme 10).

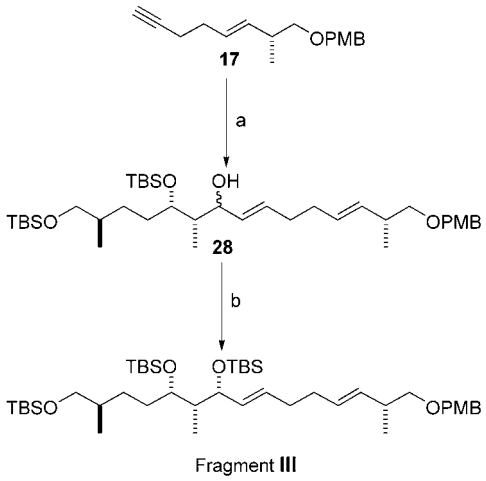

Scheme 10. Reagents and conditions: a) 1. $[Zr(Cp)_2(H)(Cl)]$, CH_2Cl_2, −78→0°C; 2. **16**, $AgClO_4$, CH_2Cl_2, 96%, (1:1 mixture, separable); b) 1. separation; 2. TBSCl, imidazole, DMF, 93%.

To couple with fragment **II**, the 16*R* diastereoisomer of fragment **III** was converted into the C24 sulfone (Scheme 11). Oxidative removal of the PMB protecting group and direct conversion into the sulfide was followed by selective oxidation of the sulfur function by using diphenyldiselenide and hydrogen peroxide to give sulfone **29**.[26] Addition of the α-lithiated sulfone to fragment **II** was then carried out in THF and HMPA to give two diastereoisomeric γ-hydroxysulfones,

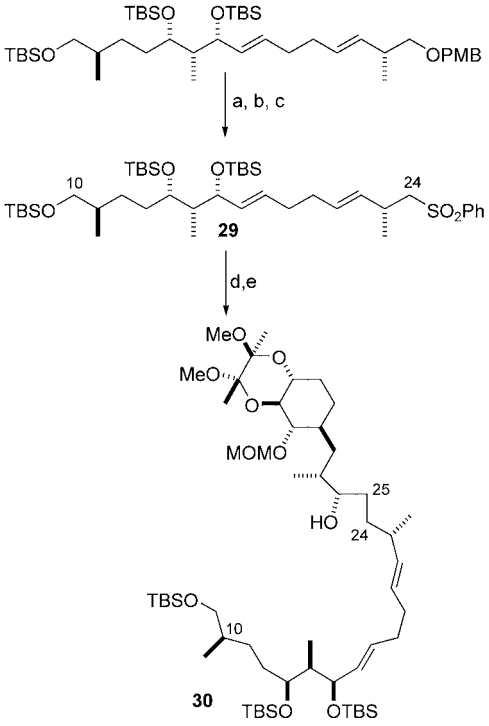

Scheme 11. Reagents and conditions: a) DDQ, CH_2Cl_2, H_2O; b) PhSSPh, PBu_3, py, 95% over two steps; c) PhSeSePh, H_2O_2, Et_2O, 88%; d) BuLi, HMPA, THF, −78°C; then fragment **II** at −20°C, 70%; e) lithium 4,4-di-*tert*-butylbiphenyl, THF, −78°C, 78%. DDQ = 2,3-dichloro-5,6-dicyano-*p*-benzoquinone; HMPA = hexamethylphosphoramide.

epimeric at C24, which were reductively desulfonylated with excess lithium in the presence of 1.5 equivalents of 4,4-di-*tert*-butylbiphenyl to give alcohol **30**.[27–29] This was subsequently esterified with *N*-Fmoc-protected pipecolic acid, fragment **I**, and the primary TBS group was removed by using camphorsulfonic acid in methanol to give late-stage intermediate **31a** (Scheme 12).

As this desilylation was not completely selective, a small proportion (25%) of bisdeprotected product **31b** was also formed. This was easily recycled by protection with TBSCl to regenerate the fully protected triol **30**. The C10-OH group was oxidized to carboxylic acid through a two-step TPAP[30]–Pinnick protocol[31] in 76% yield over two steps.

Despite employing a disconnection across the C9–C10 carbon–carbon bond, it was envisaged that macrocyclization could be effected by exploiting the relative ease of carbon–heteroatom bond formation and the entropic advantage of using a tether. With this in mind, the Fmoc group on the pipecolic acid moiety was removed to afford the free amine **32**, which was treated with benzo[1,4]dioxin-2-one to form amide **33** with the first carbon–heteroatom bond. High-dilution macrolactonization (0.001M) with EDCI then formed the second carbon–heteroatom bond to generate catechol-tethered macrocycle **34**. Treatment with LHMDS in THF led to the formation of the required C9–C10 bond, presumably through a kinetic C9 deprotonation followed by a transannular Dieckmann-type condensation onto the C10 ester to give macrocycle **35**. The effectiveness of this transformation

 © 2005 Wiley-VCH Verlag GmbH & Co. KGaA, Weinheim

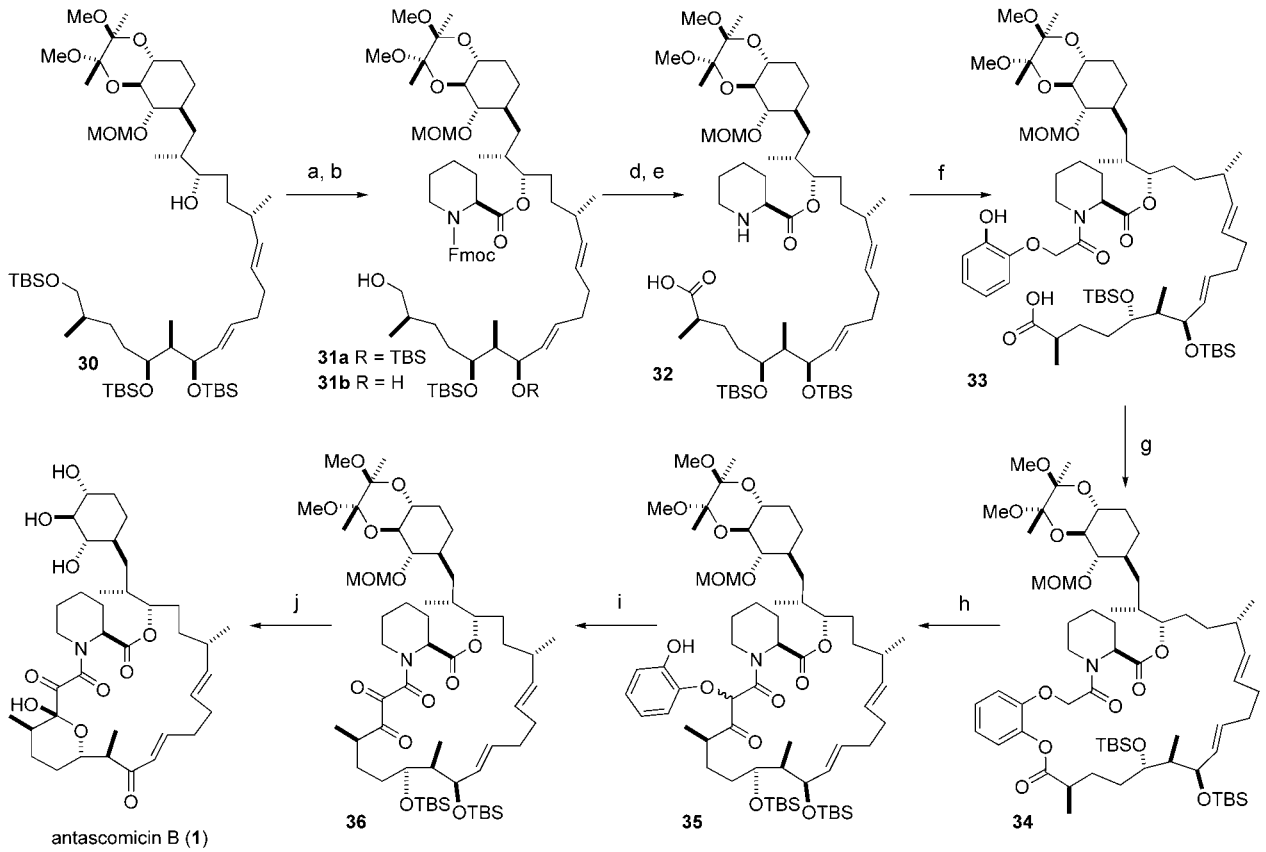

Scheme 12. Reagents and conditions: a) EDCI, DMAP, CH_2Cl_2, fragment **I**, −5 °C, 95%; b) CSA, MeOH, CH_2Cl_2, −15 °C 62%; c) TBSCl, imidazole, DMF, 98%; d) 1. TPAP, NMO, CH_2Cl_2, 2. $NaClO_2$, NaH_2PO_4, 2-methylbut-2-ene, *t*BuOH, 76% over two steps; e) piperidine, DMF; f) benzo-[1,4]dioxin-2-one, DMAP, CH_2Cl_2, 87% over two steps; g) EDCI, CH_2Cl_2, 71%; h) LHMDS, THF, 68%; i) DMP, H_2O, CH_2Cl_2, py, 80%; j) 1. HF·py, py, THF, 4 days; 2. DMP, CH_2Cl_2, py; 3. TFA, H_2O, 10 min, 13% over three steps. EDCI = 1-ethyl-3-[3-(dimethylamino)propyl]carbodiimide hydrochloride; DMAP = 4-dimethylaminopyridine, TPAP = tetra-*n*-propylammonium perruthenate; NMO = *N*-methylmorpholine *N*-oxide; LHMDS = lithium hexamethyldisilazide; DMP = Dess–Martin periodinane; TFA = trifluoroacetic acid.

lies in the simplified requirements of its six-membered transition state. Oxidation[32,33] with the Dess–Martin reagent[34] in the presence of water[35] cleaved the catechol tether and directly furnished the desired tricarbonyl **36**, which contains the complete carbon framework of antascomicin B (**1**). Medium-ring ketones have been synthesized by the Ohtsuka group in a related approach by using lactam sulfoxides followed by a reductive tether cleavage;[36–38] this method has been applied to the preparation of a taxane skeleton.[39]

Removal of the TBS protecting groups at C16 and C14 with pyridine-buffered HF·pyridine complex was slow but effective and led to the spontaneous formation of the six-membered C10 lactol. The C16 allylic alcohol was then oxidized under Dess–Martin conditions to generate the corresponding α,β-unsaturated carbonyl compound. Simultaneous deprotection of the MOM and butane diacetal groups under acidic conditions afforded the natural product, which was demonstrated to be identical to an authentic sample.[40,41–48]

The challenge posed by the total synthesis of antascomicin B has been met through the combination of established synthetic procedures and our research group methods, including the use of butanediacetal as both a protecting and a stereodirecting functionality, and the development of novel transformations including a transannular Dieckmann oxidation protocol to access the vicinal tricarbonyl functionality. Completion of the synthesis in a total of 52 synthetic steps from commercially available starting materials (longest linear sequence: 23 steps) demonstrates the utility of these methods in the synthesis of complex natural products.

Received: January 17, 2005
Published online: April 1, 2005

Keywords: macrocycles · natural products · oxidation · total synthesis

[1] T. Fehr, J.-J. Sanglier, W. Schuler, L. Gschwind, M. Ponelle, W. Schilling, C. Wioland, *J. Antibiot.* **1996**, *49*, 230.
[2] M. Morisaki, T. Arai, *J. Antibiot.* **1992**, *45*, 126.
[3] G. M. Salituro, D. L. Zink, A. Dahl, J. Nielsen, E. Wu, L. Y. Huang, C. Kastner, F. J. Dumont, *Tetrahedron Lett.* **1995**, *36*, 997.
[4] B. E. Bierer, P. K. Somers, T. J. Wandless, S. J. Burakoff, S. L. Schreiber, *Science* **1990**, *250*, 556.
[5] P. K. Somers, T. J. Wandless, S. L. Schreiber, *J. Am. Chem. Soc.* **1991**, *113*, 8045.

 © 2005 Wiley-VCH Verlag GmbH & Co. KGaA, Weinheim

[6] J. P. Steiner, T. M. Dawson, M. Fotuhi, C. E. Glatt, A. M. Snowman, N. Cohen, S. H. Snyder, *Nature* **1992**, *358*, 584.
[7] S. H. Snyder, D. M. Sabatini, M. M. Lai, J. P. Steiner, G. S. Hamilton, P. D. Suzdak, *Trends Pharmacol. Sci.* **1998**, *19*, 21.
[8] J. P. Steiner, M. A. Connolly, H. I. Valentine, G. S. Hamilton, T. M. Dawson, L. Hester, S. H. Snyder, *Nat. Med.* **1997**, *3*, 421.
[9] G. S. Hamilton, W. Huang, M. A. Connolly, D. T. Ross, H. Guo, H. L. Valentine, P. D. Suzdak, J. P. Steiner, *Bioorg. Med. Chem. Lett.* **1997**, *7*, 1785.
[10] H. Fuwa, Y. Okamura, H. Natsugari, *Tetrahedron* **2004**, *60*, 5341.
[11] J. S. Barlow, D. J. Dixon, A. C. Foster, S. V. Ley, D. J. Reynolds, *J. Chem. Soc. Perkin Trans. 1* **1999**, 1627.
[12] D. J. Dixon, A. C. Foster, S. V. Ley, D. J. Reynolds, *J. Chem. Soc. Perkin Trans. 1* **1999**, 1631.
[13] S. V. Ley, D. K. Baeschlin, D. J. Dixon, A. C. Foster, S. J. Ince, H. W. M. Priepke, D. J. Reynolds, *Chem. Rev.* **2001**, *101*, 53.
[14] H. C. Brown, K. S. Bhat, *J. Am. Chem. Soc.* **1986**, *108*, 5919.
[15] T. Takeda, S. Ogawa, N. Ohta, T. Fujiwara, *Chem. Lett.* **1987**, 1967.
[16] G. E. Keck, K. A. Savin, E. N. K. Cressman, D. E. Abbott, *J. Org. Chem.* **1994**, *59*, 7889.
[17] G. E. Keck, D. E. Abbott, E. P. Boden, E. J. Enholm, *Tetrahedron Lett.* **1984**, *25*, 3927.
[18] M. Scholl, S. Ding, C. W. Lee, R. H. Grubbs, *Org. Lett.* **1999**, *1*, 953.
[19] D. A. Evans, J. V. Nelson, E. Vogel, T. R. Taber, *J. Am. Chem. Soc.* **1981**, *103*, 3099.
[20] T. Fukuyama, S.-C. Lin, L. Li, *J. Am. Chem. Soc.* **1990**, *112*, 7050.
[21] D. A. Evans, W. C. Black, *J. Am. Chem. Soc.* **1993**, *115*, 4497.
[22] S. L. Buchwald, S. J. Lamaire, R. B. Nielsen, B. T. Watson, S. M. King, *Tetrahedron Lett.* **1987**, *28*, 3895.
[23] J. Schwartz, D. W. Hart, *J. Am. Chem. Soc.* **1974**, *96*, 8115.
[24] H. Maeta, T. Hashimoto, T. Hasegawa, K. Suzuki, *Tetrahedron Lett.* **1992**, *33*, 5965.
[25] K. Suzuki, T. Hasegawa, T. Imai, H. Maeta, S. Ohba, *Tetrahedron* **1995**, *51*, 4483.
[26] H. J. Reich, F. Chow, S. L. Peake, *Synthesis* **1978**, 299.
[27] M. Yus, *Chem. Soc. Rev.* **1996**, *25*, 155.
[28] M. Yus, R. P. Herrera, A. Guijarro, *Tetrahedron Lett.* **2001**, *42*, 3455.
[29] M. Yus, R. P. Herrera, A. Guijarro, *Chem. Eur. J.* **2002**, *8*, 2574.
[30] S. V. Ley, J. Norman, W. P. Griffith, S. P. Marsden, *Synthesis* **1994**, 639.
[31] B. S. Bal, W. E. Childers, Jr., H. W. Pinnick, *Tetrahedron* **1981**, *37*, 2091.
[32] M. J. Batchelor, R. J. Gillespie, J. M. C. Golec, C. J. R. Hedgecock, *Tetrahedron Lett.* **1993**, *34*, 167.
[33] C. M. Hayward, D. Yohannes, S. J. Danishefsky, *J. Am. Chem. Soc.* **1993**, *115*, 9345.
[34] D. B. Dess, J. C. Martin, *J. Org. Chem.* **1983**, *48*, 4155.
[35] S. D. Meyer, S. L. Schreiber, *J. Org. Chem.* **1994**, *59*, 7549.
[36] Y. Ohtsuka, T. Oishi, *Chem. Pharm. Bull.* **1983**, *31*, 443.
[37] Y. Ohtsuka, T. Oishi, *Chem. Pharm. Bull.* **1983**, *31*, 454.
[38] Y. Ohtsuka, S. Niitsuma, H. Tadokoro, T. Hayashi, T. Oishi, *J. Org. Chem.* **1984**, *49*, 2326.
[39] K. Takatori, Y. Takeuchi, Y. Shinohara, K. Yamaguchi, M. Nakamura, T. Hirosawa, T. Shimizu, M. Saito, S. Aizawa, O. Sugiyama, Y. Ohtsuka, M. Kajiwara, *Synlett* **1999**, 975.
[40] It has been demonstrated that natural products of this nature can exist as isomeric mixtures, corresponding to the six-membered lactol and a seven-membered lactol (derived by addition of the 14-OH group to the C9 carbonyl group.[41–48] The synthetic sample contained a second isomer of antascomicin B, which was identified as the corresponding seven-membered lactol; the 1H NMR is complicated by the natural product existing in $CDCl_3$ as a mixture of rotamers that do not interconvert on the NMR timescale. In a model study, it was demonstrated that treatment of authentic antascomicin A with catalytic trifluoroacetic acid in chloroform generates a second species (a seven-membered lactol) analogous to that observed in the synthetic sample of antascomicin B. Over time, this converts back into the original six-membered lactol system.
[41] K. Baumann, B. Oberhauser, M. A. Grassberger, G. Haidl, G. Schulz, *Tetrahedron Lett.* **1995**, *36*, 2231.
[42] K. Baumann, B. Oberhauser, G. Strnadt, H. Knapp, G. Schulz, M. A. Grassberger, *Synlett* **1999**, 877.
[43] F. P. Gailliot, T. K. Natishan, J. M. Ballard, R. A. Reamer, D. Kuczynski, G. J. McManemin, R. S. Egan, B. C. Buckland, *J. Antibiot.* **1994**, *47*, 806.
[44] Y. Namiki, N. Kihara, S. Koda, K. Hane, T. Yasuda, *J. Antibiot.* **1993**, *46*, 1149.
[45] Y. Namiki, A. Fujiwara, N. Kihara, S. Koda, K. Hane, T. Yasuda, *Drug Dev. Ind. Pharm.* **1995**, *21*, 809.
[46] P. Hughes, J. Musser, M. Conklin, R. Russo, *Tetrahedron Lett.* **1992**, *33*, 4739.
[47] P. Karuso, H. Kessler, D. F. Mierke, *J. Am. Chem. Soc.* **1990**, *112*, 9434.
[48] H. Kessler, R. Haessner, W. Schüler, *Helv. Chim. Acta* **1993**, *76*, 117.

 © 2005 Wiley-VCH Verlag GmbH & Co. KGaA, Weinheim

Nanostructures

Uniform, Axial-Orientation Alignment of One-Dimensional Single-Crystal Silicon Nanostructure Arrays**

*Kuiqing Peng, Yin Wu, Hui Fang, Xiaoyan Zhong, Ying Xu, and Jing Zhu**

Among the various nanostructures, one-dimensional (1D) single-crystal semiconducting nanostructures are considered to be the most critical building blocks for nanoscale optoelectronics.[1–4] Silicon, the most important semiconducting material in microelectronics, and its 1D nanostructures have attracted attention owing to their potential application in integrated optoelectronic nanodevices.[5–8] To date, various

[*] Dr. K. Peng, Y. Wu, H. Fang, X. Zhong, Y. Xu, Prof. J. Zhu
Department of Materials Sciences and Engineering
Tsinghua University
Beijing, 100084 (China)
Fax: (+86) 10-6277-2507
E-mail: jzhu@mail.tsinghua.edu.cn

Dr. K. Peng
Department of Physics and Materials Science
Center of Super-Diamond and Advanced Films (COSDAF)
City University of Hong Kong
Hong Kong SAR (China)

Y. Xu
Institute of Solar Energy Research
Beijing 100084 (China)

[**] This work was supported by the National Natural Science Foundation, National 973 Project of the People's Republic of China, and 985 Project of Tsinghua University.

Supporting information for this article is available on the WWW under http://www.angewandte.org or from the author.

 DOI: 10.1002/anie.200462995 © 2005 Wiley-VCH Verlag GmbH & Co. KGaA, Weinheim

methods including chemical vapor deposition (CVD),[9] laser ablation,[10,11] and other methods[12,13] have been developed to prepare 1D silicon nanostructures. These syntheses are quite accessible and well-controlled; for example, single-crystal silicon nanowires with controlled diameters have been prepared by using laser-assisted catalytic growth.

The axial crystallographic orientations of 1D silicon nanostructures are expected to influence their electronic structure (energy gap) as well as their physical properties (electron transport) according to previous theory calculations.[14,15] Holmes et al. reported a novel technique that employed supercritical solutions to prepare silicon nanowires with controlled thickness and orientations[13] and found that the wires formed at different pressures exhibited different preferential axial orientations. Their work opened the way to a new area of research: the orientation-controlled synthesis of 1D nanostructures. Accurate control over the axial crystallographic orientations of obtained silicon nanowires remains a challenge, both scientifically and technically. Therefore, to find simpler and quicker ways to produce 1D silicon nanostructures with desirable axial crystallographic orientation is still extremely desirable and of great importance to materials synthesis and future nanoscale optoelectronic devices that employ silicon.

We recently reported a chemical etching method to prepare large-area silicon nanowire arrays.[16,17] However, owing to the strong reaction between silicon and solutions of $HF/AgNO_3$ as well as the large quantities of silver dendrites produced by the galvanic displacement reaction, the exploration and understanding of the reaction mechanism is not easily accessible. Herein, we describe a simple and rapid metal-nanoparticle-assisted etching process to prepare large-area, highly oriented 1D silicon nanostructure arrays on single-crystal silicon wafers. The mechanism for the growth of 1D silicon nanostructures is also readily explored herein owing to the absence of large quantities of silver dendrites. More importantly, our detailed high-resolution electron microscopy (HREM) structural analysis indicates that single-crystal high-quality silicon nanowires (SiNWs) with desirable crystallographic orientation can be readily and controllably created by selecting silicon wafers with a corresponding crystallographic orientation. Optical reflection measurements also demonstrate that the obtained films of 1D silicon nanostructure arrays could suppress the optical reflection drastically over a wide spectral bandwidth. This remarkable characteristic makes it a promising candidate for antireflective surfaces over a large area on silicon wafers.

The production of our 1D silicon nanostructure arrays is quite simple and comprises three steps: 1) cleaning of the silicon wafers with cleaning solution, 2) electroplating the films of metal nanoparticles onto the cleaned silicon surface, and 3) immersion of the nanoparticle-covered silicon wafers into HF-based aqueous chemical etching solutions contained in sealed vessels and treatment for the desired time (at 20 to 60 °C, see Experimental Section). After the preparation process, the obtained samples were rinsed copiously in deionized water and dried at room temperature. The thickness of the films (or length of 1D silicon nanostructures) could be effectively controlled through adjusting the treatment time. The size of the films could be readily made as large as required and is ultimately limited only by the dimensions of the vessel.

Characterization of our as-synthesized samples by scanning electron microscopy (SEM) confirms that large-area highly oriented 1D silicon nanostructure arrays can be created on single-crystal silicon wafers around room temperature. Figure 1 shows the transmission electron microscopy

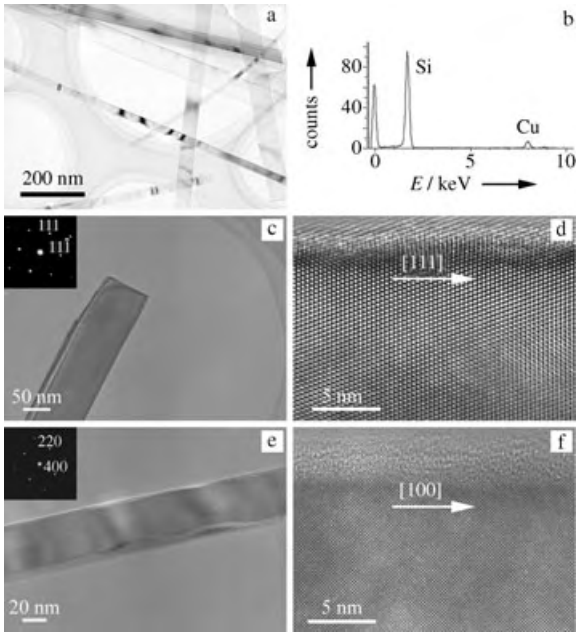

Figure 1. TEM images of as-synthesized 1D silicon nanostructures. a) Several nanowires and nanoribbons, b) an EDX spectrum recorded from one nanowire, c) an individual silicon nanoribbon synthesized from a p-type [111] silicon wafer (the inset shows its ED pattern recorded along the [$\bar{1}$10] axis), d) HREM image of the section of nanoribbon shown in part (c), e) an individual silicon nanowire synthesized from a p-type [100] silicon wafer, (the inset shows its ED pattern recorded along the [001] axis), and f) HREM image of the section of the nanowire shown in part (e).

(TEM) images of as-synthesized samples, which were prepared by deposition of a film of silver nanoparticles onto a silicon surface from a solution of $HF/AgNO_3$, followed by immersion of the treated silicon substrate into an aqueous solution of $HF/Fe(NO_3)_3$ at 50 °C for 30 minutes. 1D wire- and ribbonlike nanostructures can be clearly seen in Figure 1a. The electron diffraction (ED) patterns recorded from these 1D nanostructures show their single-crystal characteristics. Figure 1b is a representative energy-dispersive X-ray (EDX) spectrum for a nanoribbon sample and shows only a peak for silicon (the signal for copper originates from the supporting copper grid). Figure 1c is a TEM image of an individual nanoribbon prepared from a p-type silicon wafer with [111] orientation, and the inset is an ED pattern recorded from the nanoribbon, which could be indexed as the [$\bar{1}$10] zone axis of single-crystal silicon. Figure 1d shows the HREM image of the section of nanoribbon shown in Figure 1c. Analysis by ED and HREM indicate that the axial orientation of the nanoribbon is the [111] direction,

 © 2005 Wiley-VCH Verlag GmbH & Co. KGaA, Weinheim

which is the same as that of the initial silicon wafer. Figure 1e and f show the TEM images and ED pattern recorded from a nanowire prepared from a p-type silicon wafer with [100] orientation. Analysis of these TEM images clearly indicates that the nanowire grows along the [100] direction, which is identical to the orientation of the initial silicon wafer.

Further experiments confirmed that the axial crystallographic directions of as-synthesized 1D silicon nanostructures are determined by the orientation of the initial silicon wafers used. More specifically, 1D silicon nanostructures with desirable orientations could be created through selecting silicon wafers with identical orientations. Furthermore, the p- and n-type silicon wafers used in our experiments show near-identical behavior, thus 1D silicon nanostructures with desirable conduction type could also be readily obtained. Generally, etching generates regular or irregular etching pits. Here, however, it is surprising to see that the etched nanostructures are smooth and there is almost no diameter modulation along the long nanostructure axis for both types of wires. These results imply that smooth nanostructures may result from the special metal-nanoparticle catalytic etching process.

We named the as-synthesized samples "black silicon" owing to their black color, which also implies their potentially high antireflection property. Figure 2 shows a comparison of the hemispherical reflectance of 1D silicon nanostructure arrays and a polished silicon wafer. The reflectance of the films is drastically decreased relative to that of the polished silicon wafer over a broad spectral range (samples 1 and 2 are silver-treated silicon wafers treated in a solution of HF/$Fe(NO_3)_3$ for 50 and 30 min, respectively). The reflectance of the 1D silicon nanostructure films is less than 1.46% over the range 300–600 nm. This remarkable property suggests films of 1D silicon nanostructure arrays as candidates of antireflective surfaces. The ultralow reflectance of the 1D silicon nanostructure films may be a result of the high density of 1D silicon nanostructures and also the subwavelength-structured (SWS) surface, which could suppress reflection over a wide spectral bandwidth and a large field of view.[18]

The generally accepted growth mechanism of 1D silicon nanostructures is the vapor–liquid–solid (VLS) growth mechanism,[9,10] which is based on growth from a liquid metal seed particle. We suggest that the formation mechanism of the as-synthesized 1D silicon nanostructures is quite different from previously proposed mechanisms.[9,11,13,16,19] To clarify the formation mechanism of the 1D silicon nanostructures, detailed investigations were carried out on the silver-nanoparticle-assisted catalytic etching of silicon in a solution of HF/$Fe(NO_3)_3$.

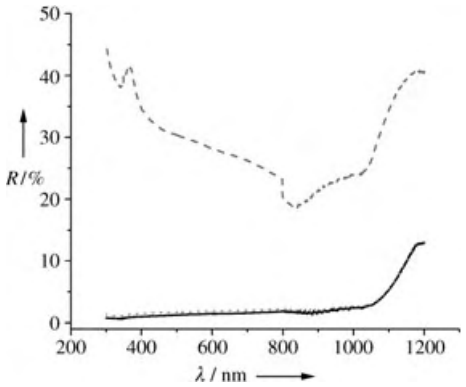

Figure 2. Reflectance (R) as a function of wavelength. Samples 1 (——) and 2 (----) were prepared by treating a silver-covered silicon wafer in an aqueous solution of HF/$Fe(NO_3)_3$ for 50 and 30 minutes, respectively. (Polished silicon: – – –).

Networks of silver nanoparticles were produced on silicon surfaces by the galvanic displacement reaction on treatment of the silicon wafer in a solution of HF/$AgNO_3$ for one minute (Figure 3a). Figure 3b–f show the morphological evolution process of a p-type [111] silicon wafer in HF/$Fe(NO_3)_3$ solution. With the elapse of treatment time, silver nanoparticle networks gradually sank into the bulk silicon and 1D silicon nanostructure arrays gradually emerged. Large-area oriented high-aspect-ratio 1D silicon nanostructure arrays could be produced on the silicon surface after immersion for 50 minutes in HF/$Fe(NO_3)_3$ solution (Figure 3f). This sinking behavior of silver nanoparticles could be seen clearly through

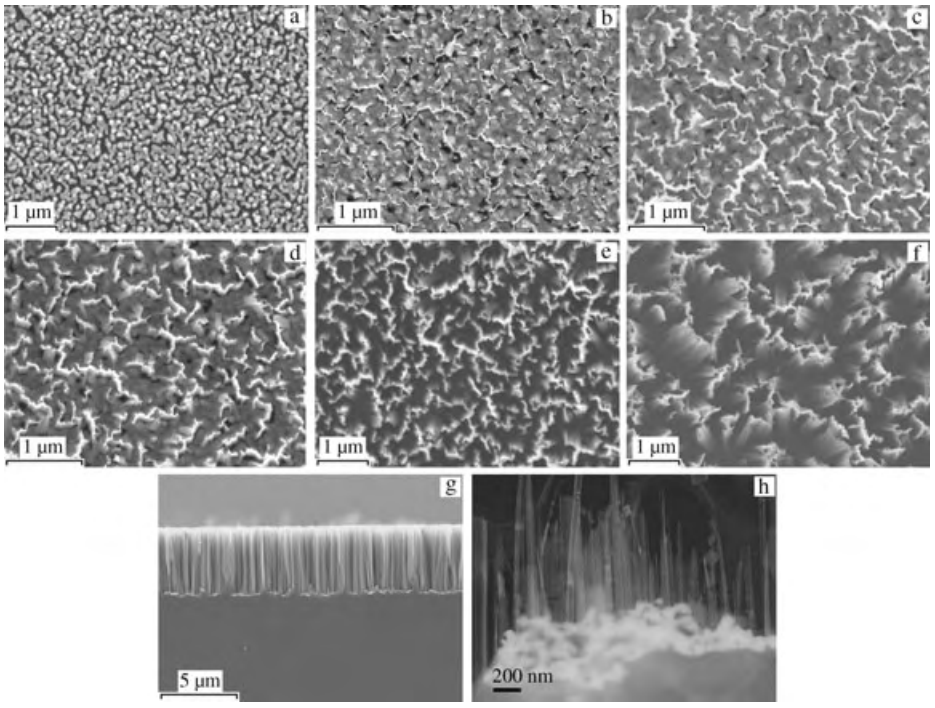

Figure 3. a–f) SEM images showing the morphological evolution of a silicon wafer in HF/$Fe(NO_3)_3$ solution at a) $t=0$, b) $t=2$, c) $t=5$, d) $t=10$, e) $t=20$, and f) $t=50$ min. g) SEM cross-section image and h) TEM image of the as-synthesized sample (silver nanoparticles can be clearly seen at the interface between the silicon substrate and the film of the 1D silicon nanostructure formed).

 © 2005 Wiley-VCH Verlag GmbH & Co. KGaA, Weinheim

an SEM cross-section image (Figure 3 g). Many silver nanoparticles can be seen at the interface between the silicon substrate and the formed film of 1D silicon nanostructures. A TEM image (Figure 3 h) more clearly shows the sunken silver nanoparticles situated at the interface between the silicon substrate and the formed 1D silicon nanostructure array.

These results imply that the collective sinking behavior of silver nanoparticle networks plays an important role in the formation of 1D silicon nanostructure arrays. Therefore, we propose a mechanism that accounts for the formation of 1D silicon nanostructures based on silicon etching and metal deposition electrochemistry in HF-based solution.[20–28] The mechanism of electroless silver deposition on silicon and silver-nanoparticle-catalyzed chemical etching process of silicon in $HF/Fe(NO_3)_3$ solution is shown in Figure 4.

Buriak and co-workers discovered that films of noble-metal nanoparticles could be deposited on germanium by the galvanic displacement reaction in the absence of toxic HF.[27] They suggested that the mechanism for the galvanic displacement reaction on germanium with gold, palladium, and platinum salts with highly positive equilibrium reduction potentials is expected to occur through hole injection into the valence band. They suggested that germanium–germanium bonds could supply the electrons used to reduce the metal salts on the surface, which leads to subsequent dissolution of the germanium substrate as the oxide. However, it remains to be determined if the oxidation and dissolution of the substrate occurs from beneath the metal deposits or alongside them.

In our experimental system, a similar electroless-deposition/semiconductor-etching process as that reported by Buriak for germanium occurs in the case of silicon, except that an etchant such as HF is necessary here because the silicon oxide produced must be etched away and dissolved into water. For the initial electroless deposition of silver from $HF/AgNO_3$ solution on silicon, simultaneous electrochemical processes including cathodic (silver-deposition reaction) and anodic reactions (silicon oxidation and dissolution) occur on the silicon surface. First, Ag^+ ions in the vicinity of the silicon surface capture electrons from the valence band (VB) of silicon and are deposited in the form of metallic silver nuclei (see Supporting Information). With the deposition and growth of silver nuclei, SiO_2 is formed simultaneously underneath the silver nanoparticles (Figure 4a,b). As the SiO_2 underneath the silver nanoparticles is etched away as SiF_6^{2-} by HF, then pits form immediately at the same positions (Figure 4c), so the silver nanoparticles sink into the pits as they form. This is consistent with our SEM observations, which confirmed that the oxidation and dissolution of the silicon substrate occurs from beneath the metal deposits.

In the solution of $HF/Fe(NO_3)_3$, the redox level of the Fe^{3+}/Fe^{2+} system lies well below the VB of silicon, so active kinetics are expected for the electron-capture process from the VB bonding electrons. However, contrary to fast reduction of Ag^+ ions, reduction of Fe^{3+} ions and oxidation of silicon proceed very slowly on the silicon surface in the absence of silver nanoparticles. When the silicon surface is covered with silver nanoparticles, reduction of Fe^{3+} ions and

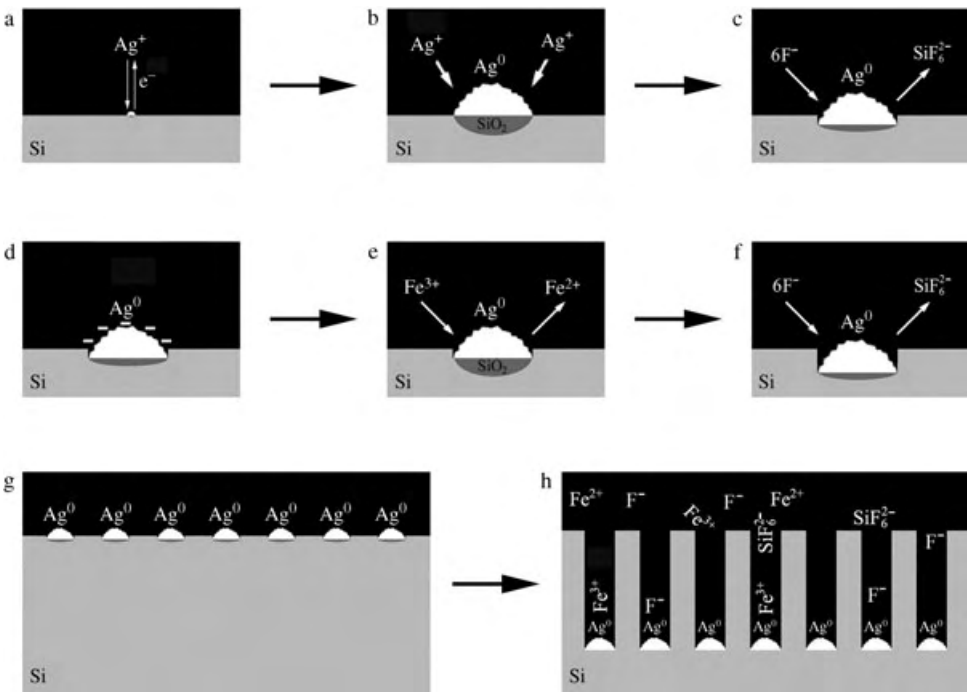

Figure 4. A model illustrating the electroless deposition of silver on silicon in $HF/AgNO_3$ solution and the silver-nanoparticle-catalyzed chemical etching of silicon in $HF/Fe(NO_3)_3$ solution. a–c) Nucleation and growth of silver nanoparticles on the silicon surface in $HF/AgNO_3$ solution: SiO_2 forms simultaneously underneath the silver nanoparticles, and pits form as a result of etching away of SiO_2 in HF solution. d–f) Reduction of Fe^{3+} ions, etching of silicon, and sinking of silver nanoparticles in $HF/Fe(NO_3)_3$ solution: deeper pits are created by the silver nanoparticles. g) Silver nanoparticle arrays form on the silicon surface. h) Deep pores form in the bulk silicon in $HF/Fe(NO_3)_3$ solution as a result of the continuous etching away of SiO_2 underneath the silver nanoparticles.

 © 2005 Wiley-VCH Verlag GmbH & Co. KGaA, Weinheim

oxidation of silicon is greatly enhanced. It is generally believed that metal nanoparticles adhered on a silicon surface have a higher electronegativity than silicon, so they could attract electrons from silicon to become negatively charged. These metal nanoparticles could then act as local microcathodes and enhance the cathodic reaction as a result of their catalytic activity.[24,26] Therefore, Fe^{3+} ions have the strong tendency to preferentially obtain electrons from silver nanoparticles and be reduced to Fe^{2+} ions, while the silicon underneath the silver nanoparticles is oxidized to SiO_2. The Ag^+/Ag system has a more positive redox potential than that of the Fe^{3+}/Fe^{2+} couple, so silver nanoparticles are stable and can continue to enhance the reduction of Fe^{3+} ions and the oxidation of silicon in the $HF/Fe(NO_3)_3$ solution. As the silver nanoparticles are pinned by the pits and cannot move horizontally on the silicon surface, selective etching occurs and deeper pits or pores finally form.

According to the above discussion, we suggest that initial shallow pits in silicon could be developed into deeper pores owing to the continuous etching away of SiO_2 and further sinking of silver nanoparticles upon prolonged immersion in the $HF/Fe(NO_3)_3$ solution (Figure 4d). The pores are simply the sinking tracks of silver nanoparticles. For spatially dispersive metal nanoparticles, separated deep pores should form. However, deposited silver nanoparticles have a strong tendency to form interconnected networks under the present silver-deposition conditions adopted. It can be easily understood that the collective sinking behavior of silver networks will cut the bulk silicon into freestanding 1D silicon nanostructures. We suggest that ordered pore arrays could be created if the silicon surface is patterned with ordered active metal-nanoparticle arrays.

Besides demonstrating the silver-nanoparticle-assisted formation of 1D silicon nanostructure arrays on silicon surfaces in $HF/Fe(NO_3)_3$ solution, we also investigated other noble-metal nanoparticles (Cu, Au, and Pt) deposited on silicon. The reduction of Fe^{3+} ions and oxidation of silicon could be greatly enhanced owing to the presence of these metal nanoparticles. However, only shallow pits were formed on the silicon surface for copper as a result of its high solubility, which is caused by its much lower redox potential relative to that of Fe^{3+}/Fe^{2+} in $HF/Fe(NO_3)_3$ solution. $AuCl_4^-/Au$ and $PtCl_6^{2-}/Pt$ have more-positive redox potentials than that for Fe^{3+}/Fe^{2+} (see Supporting Information), so gold and platinum nanoparticles are stable in the solution of $HF/Fe(NO_3)_3$. Gold nanoparticles have a strong tendency to form dense networks under our adopted deposition conditions. Oriented 1D silicon nanostructure arrays formed when gold-covered silicon wafers were treated in the $HF/Fe(NO_3)_3$ solution. In contrast, in the case of platinum, spatially dispersive nanoparticles formed on the silicon surface under these deposition conditions, but no nanoparticle networks were formed. According to our proposed mechanism, only separated deep pores could be created in bulk silicon, and the experimental results justify our model (see Supporting Information).

In conclusion, we have developed a facile metal-nanoparticle-assisted catalytic etching technique to produce large-area highly oriented 1D silicon nanostructure arrays with desirable axial crystallographic orientation. Exact control of the axial crystallographic orientation of 1D silicon nanostructures represents one significant step towards future nanoscale optoelectronic devices that employ silicon. The remarkable antireflection property of the 1D silicon nanostructure films also indicates its potential applicability as an antireflective surface for photovoltaic devices and optical detectors. A reasonable mechanism has been proposed on the basis of convincing experimental evidence. On the basis of our proposed mechanism, we believe that the metal-nanoparticle-assisted catalytic etching technique may also be extended to other materials, such as SiC and GaN.

Experimental Section

Preparation of nanostructure arrays: The synthesis of large-area oriented 1D silicon nanostructure arrays was conducted in a teflon-lined stainless steel autoclave. The production process comprised three steps: 1) cleaning the silicon wafers with cleaning solution—here we sequentially used acetone (5 min), ethanol (5 min), deionized water (2–3 times), and H_2SO_4/H_2O_2 (3:1 H_2SO_4 (97%)/H_2O_2 (30%), 10 min), then the wafers were thoroughly rinsed with deionized water (10 min) and dipped into a solution of HF (1 min); 2) electroplating the metal-nanoparticle films onto the cleaned silicon surface; and 3) immersion of the metal-nanoparticle-covered silicon wafers into HF-based aqueous chemical etching solutions contained in a sealed vessel and treated for the desired time (20–60 °C). After the preparation process, the obtained samples were rinsed copiously in deionized water and dried at room temperature.

All the experiments described here were performed at 50 °C. The thickness of films (or the length of 1D silicon nanostructures) could be effectively controlled through adjusting the etching time, and film sizes could be readily made as large as needed and are ultimately limited only by the vessel dimensions. The deposition of various metals and their influence on the etching morphologies of silicon were investigated. The concentrations of HF and $AgNO_3$ for the deposition of Ag nanoparticle films were 4.6 and 0.01 M, respectively, while the concentrations of HF and $Fe(NO_3)_3$ for etching the silver-nanoparticle-covered silicon wafers were 4.6 and 0.135 M, respectively.

Characterization: After preparation, the samples were studied by SEM (JEOL 6301F) and TEM (JEOL 2010F) equipped with an energy-dispersive X-ray spectrometer and a Gatan GIF 678 system. The samples for TEM were prepared by scraping the bulk sample with a knife, and then the scraping was collected and suspended in ethanol. A drop of this suspension was then placed on a carbon–copper grid and examined under a JEOL 2010F microscope. Optical reflectance measurements were performed with a Hitachi U-4001 UV/Vis spectrophotometer.

Received: December 20, 2004
Published online: April 6, 2005

Keywords: electrochemistry · nanostructures · semiconductors · silicon

[1] M. Law, J. Goldberger, P. D. Yang, *Annu. Rev. Mater. Res.* **2004**, *34*, 83.
[2] M. Law, D. J. Sirbuly, J. C. Johnson, J. Goldberger, R. J. Saykally, P. D. Yang, *Science* **2004**, *305*, 1269.
[3] X. F. Duan, Y. Huang, R. Agarwal, C. M. Lieber, *Nature* **2003**, *421*, 241.
[4] X. F. Duan, Y. Huang, Y. Cui, J. F. Wang, C. M. Lieber, *Nature* **2001**, *409*, 66.

 © 2005 Wiley-VCH Verlag GmbH & Co. KGaA, Weinheim

[5] X. Y. Zhao, C. M. Wei, L. Yang, M. Y. Chou, *Phys. Rev. Lett.* **2004**, *92*, 236805.
[6] D. D. D. Ma, C. S. Lee, F. C. K. Au, S. Y. Tong, S. T. Lee, *Science* **2003**, *299*, 1874.
[7] D. Y. Li, Y. Y. Wu, P. Kim, L. Shi, P. D. Yang, *Appl. Phys. Lett.* **2003**, *83*, 2934.
[8] Y. Cui, C. M. Lieber, *Science* **2001**, *291*, 851.
[9] J. Westwater, D. P. Gosain, S. Tomiya, S. Usui, H. Ruda, *J. Vac. Sci. Technol. B* **1997**, *15*, 554.
[10] A. M. Morales, C. M. Lieber, *Science* **1998**, *279*, 208.
[11] N. Wang, Y. F. Zhang, Y. H. Tang, C. S. Lee, S. T. Lee, *Appl. Phys. Lett.* **1998**, *73*, 3902.
[12] D. P. Yu, Z. G. Bai, Y. Ding, Q. L. Hang, H. Z. Zhang, J. J. Wang, Y. H. Zou, W. Qian, G. C. Xiong, H. T. Zhou, S. Q. Feng, *Appl. Phys. Lett.* **1998**, *72*, 3458.
[13] J. D. Holmes, K. P. Johnston, R. C. Doty, B. A. Korgel, *Science* **2000**, *287*, 1471.
[14] C. Delerue, G. Allan, M. Lannoo, *Phys. Rev. B* **1993**, *48*, 11024.
[15] H. Yorikawa, H. Uchida, S. Muramatsu, *J. Appl. Phys.* **1996**, *79*, 3619.
[16] K. Q. Peng, Y. J. Yan, S. P. Gao, J. Zhu, *Adv. Mater.* **2002**, *14*, 1164.
[17] K. Q. Peng, Z. P. Huang, J. Zhu, *Adv. Mater.* **2004**, *16*, 73.
[18] Y. Kanamori, M. Sasaki, K. Hane, *Opt. Lett.* **1999**, *24*, 1422.
[19] K. Q. Peng, Y. J. Yan, S. P. Gao, J. Zhu, *Adv. Funct. Mater.* **2003**, *13*, 127.
[20] N. Mitsugi, K. Nagai, *J. Electrochem. Soc.* **2004**, *151*, G302.
[21] P. Gorostiza, P. Allongue, R. Diaz, J. R. Morante, F. Sanz, *J. Phys. Chem. B* **2003**, *107*, 6454.
[22] L. Magagnin, R. Maboudian, C. Carraro, *J. Phys. Chem. B* **2002**, *106*, 401.
[23] J. S. Kim, H. Morita, J. D. Joo, T. Ohmi, *J. Electrochem. Soc.* **1997**, *144*, 3275.
[24] P. Gorostiza, R. Diaz, J. Servat, F. Sanz, J. R. Morante, *J. Electrochem. Soc.* **1997**, *144*, 909.
[25] G. J. Norga, M. Platero, K. A. Black, A. J. Reddy, J. Michel, L. C. Kimerling, *J. Electrochem. Soc.* **1997**, *144*, 2801.
[26] L. Teerlinck, P. W. Mertens, H. F. Schmidt, M. Meuris, M. M. Heyns, *J. Electrochem. Soc.* **1996**, *143*, 3323.
[27] L. A. Porter, H. C. Choi, A. E. Ribbe, J. M. Buriak, *Nano Lett.* **2002**, *2*, 1067.
[28] H. Morinaga, M. Suyama, T. Ohmi, *J. Electrochem. Soc.* **1994**, *141*, 2834.

 © 2005 Wiley-VCH Verlag GmbH & Co. KGaA, Weinheim

Enzyme Catalysis

Molecular Basis of Perhydrolase Activity in Serine Hydrolases**

*Peter Bernhardt, Karl Hult, and Romas J. Kazlauskas**

Catalytic promiscuity is the ability of one active site of an enzyme to catalyze several different chemical transformations.[1,2] Investigations and control of catalytic promiscuity are key to understanding the evolution of new enzymatic activities and the design of new enzyme-catalyzed reactions for synthesis. An example of a potentially useful catalytic process is the perhydrolase activity of esterases and lipases.[3,4] Herein we demonstrate a 2600-fold increase in the specificity of an esterase to catalyze perhydrolysis over hydrolysis. The procedures presented herein may be used for the design of other enzymes with altered nucleophile selectivities and that catalyze stereoselective oxidations.

Perhydrolases (previously known as metal-free haloperoxidases) contain a Ser–His–Asp catalytic triad and catalyze the reversible formation of peracids from carboxylic acids and hydrogen peroxide [Eq. (1)]. Perhydrolysis presumably takes

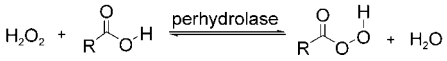

(1)

place with an esterase-like mechanism in which a carboxylic acid first reacts with the active site serine group to form an acyl-enzyme intermediate, which reacts with hydrogen peroxide to form a peracid.[5–9] The switch from water as the nucleophile to hydrogen peroxide could be considered a change in substrate selectivity, but the very different chemical reactivity of the respective products (carboxylic acid versus peroxycarboxylic acid) makes this an example of an alternate catalytic activity.

[*] M.Sc. P. Bernhardt, Prof. Dr. R. J. Kazlauskas
University of Minnesota
Department of Biochemistry, Molecular Biology and Biophysics,
The Biotechnology Institute, and
The Center for Microbial and Plant Genomics
1479 Gortner Avenue, St. Paul, Minnesota 55108 (USA)
Fax: (+1) 612-625-5780
E-mail: rjk@umn.edu

M.Sc. P. Bernhardt, Prof. Dr. K. Hult
School of Biotechnology, Department of Biochemistry
Royal Institute of Technology (KTH)
AlbaNova University Center
Roslagstullsbacken 21, 10691 Stockholm (Sweden)

[**] We thank the Swedish Foundation for International Cooperation in Research and Higher Education (STINT) and the University of Minnesota for financial support, the Minnesota Supercomputing Institute for computer modeling resources, C. Savile for advice and discussions, and M. Smith and J. Gosse for initial work.

Supporting information for this article is available on the WWW under http://www.angewandte.org or from the author.

 © 2005 Wiley-VCH Verlag GmbH & Co. KGaA, Weinheim DOI: 10.1002/anie.200463006

Perhydrolysis might be an inherent side activity of serine hydrolases;[10] esterases and lipases both catalyze slow perhydrolysis of carboxylic acids.[3,11] However, other evidence suggests that perhydrolase activity is distinct from hydrolase activity. The perhydrolase activity of lipases and esterases is much lower than their esterase activity, and, conversely, the esterase activity of perhydrolases is much lower than their perhydrolase activity. Some serine hydrolases (subtilisin, for example) do not exhibit perhydrolase activity which suggests that the Ser–His–Asp catalytic triad is not the only determinant for perhydrolase activity. Bugg recently proposed an alternate mechanism for perhydrolysis in which the catalytic serine stabilizes the carboxylic acid substrate with a hydrogen bond instead of forming an acyl-enzyme intermediate, but there is currently no experimental evidence for this proposal.[12]

Recent X-ray crystallographic structures of two enzymes from *Pseudomonas fluorescens*, an aryl esterase (PFE) that shows low perhydrolase activity[13] and a homologous perhydrolase (CPO-F), show similar active sites and no clear structural basis for distinguishing their different activities.[14] Initial work to convert PFE into a perhydrolase focused on the individual replacement of three amino acids that differ in PFE and CPO-F, each of which have C^{α} atoms within 14 Å of O^{γ} of the conserved Ser94 group: Met95 (C^{α}–O^{γ} = 4.5 Å), Tyr69 (C^{α}–O^{γ} = 14 Å), and Thr122 (C^{α}–O^{γ} = 9.9 Å). However, none of the mutant PFE forms showed a significant increase in perhydrolase activity. The Met95Thr mutation decreased esterase activity from 13.7 to 3.4 U mg^{-1} and perhydrolase activity to below the detection limit (< 0.02 U mg^{-1}). This decrease may result from a shift in the backbone amide of position 95, which forms part of the oxyanion hole. The esterase and perhydrolase activities of the Tyr69Met and Thr122Pro mutant forms are similar to those of the wild-type protein (Table 1).

As a direct structural comparison of PFE with CPO-F did not reveal a clear means to increase its perhydrolase activity, we aligned the amino acid sequences of six hydrolases and six perhydrolases to determine the essential residues for each activity. The alignment identified 15 amino acids common to most esterases and 57 amino acids common to most perhydrolases. Figure 1 summarizes the results in a Venn diagram similar to that used by Rothman and Kirsch to map conserved residues in related proteins.[15] Not surprisingly, PFE contains most of the amino acid residues common to esterases. However, PFE has amino acid substitutions at 14 positions out of the 57 amino acids common to most perhydrolases. We hypothesized that substitution of one or more of these 14 residues would provide an increase in perhydrolase activity and a decrease in esterase activity, and that the residues closest to the active site are those most important for catalytic activity. Three amino acid residues are within a sphere of 12 Å about the O^{γ} atom of catalytic Ser94: Pro29, Glu99, and Ile227. The Leu29Pro, Asp99Glu, and Phe227Ile mutants of PFE were obtained by site-directed mutagenesis with complementary mutagenic PCR primers. DNA sequencing confirmed the mutations and the three proteins were expressed and purified as described previously.[13]

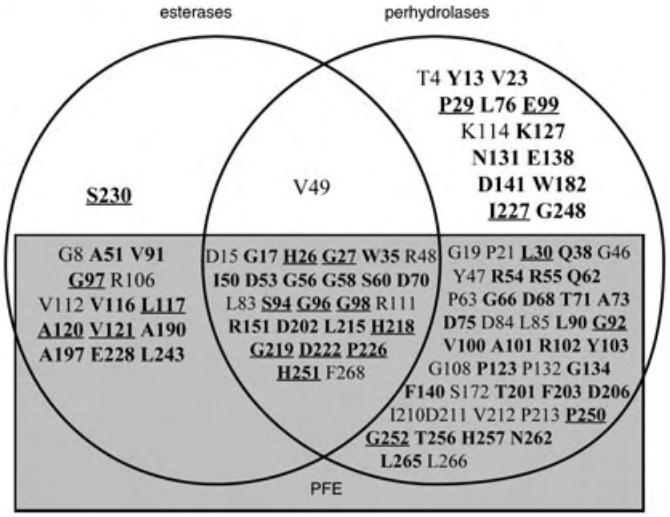

Figure 1. Conserved residues present either in esterases (left), or in perhydrolases (right), or shared between both enzyme types. Amino acids present in PFE are included in the gray box. All residues are numbered according to the primary sequence of PFE, and the kind of amino acid refers to the conserved group in the respective enzyme type. Residues are coded according to their distance from the O^{γ} of the conserved catalytic serine (underlined and boldface: < 12 Å; boldface: 12–20 Å; all others: > 20 Å).

Table 1: Rate of hydrolysis and perhydrolysis in PFE variants.

Enzyme	Hydrolysis [U mg^{-1}][a]	$\Delta\Delta G_{mut:wt}$ [kcal mol^{-1}][b]	Perhydrolysis [U mg^{-1}][c]	$\Delta\Delta G_{mut:wt}$ [kcal mol^{-1}][b]
wild-type	14	0	0.24	0
Leu29Pro	0.14	2.7	6.8	−2.0
Tyr69Met	18	−0.17	0.30	−0.13
Met95Thr	3.4	0.83	< 0.02	> 1.5
Asp99Glu	8.6	0.28	0.12	0.44
Thr122Pro	15	−0.062	0.18	0.17
Phe227Ile	38	−0.60	0.23	0.050

[a] Hydrolase activity assays were performed in *N*,*N*-bis(2-hydroxyethyl)-2-aminoethanesulfonic acid (BES) buffer (5 mM, pH 7.2) at 25 °C; 1 U = hydrolysis of 1 mmol substrate min^{-1} (*p*NPAc) and 1 mmol oxidized product min^{-1} (H_2O_2). [b] Energy equivalent of the rate change relative to wild-type PFE: $\Delta\Delta G = -RT(\ln x)$ for an *x*-fold rate change at T = 300 K. [c] Perhydrolase activity determined in acetate buffer (0.7 M, pH 5.5) at 25 °C; 1 U = consumption of 1 μmol substrate (monochlorodimedone) min^{-1}. The error limit for kinetic assays is estimated at 20%.

The Leu29Pro mutation shifted the behavior of the enzyme from esterase to perhydrolase activity. Under the conditions assayed (Supporting Information), perhydrolase activity increased 28-fold from 0.24 to 6.8 U mg^{-1} for the bromination of monochlorodimedone.[16] Furthermore, the hydrolytic activity toward *p*-nitrophenyl acetate (*p*NPAc) decreased 100-fold from 14 to 0.14 U mg^{-1} (Table 1). The level of perhydrolase activity was higher than that of a wild-type perhydrolase from *P. fluorescens* (3.8 U mg^{-1}), but lower than that of the perhydrolases from *P. putida* (12 U mg^{-1}) and *P. pyrrocinia* (47 U mg^{-1}).[14,8]

 © 2005 Wiley-VCH Verlag GmbH & Co. KGaA, Weinheim

The Asp99Glu and Phe227Ile mutants showed no increase in perhydrolase activity. For Asp99Glu, both the perhydrolase and hydrolase activities were lower than that of wild-type PFE: 0.12 and 8.6 U mg^{-1}, respectively (Table 1). The perhydrolase activity of Phe227Ile was statistically equivalent to that of the wild-type enzyme, whereas hydrolysis mediated by Phe227Ile (38 U mg^{-1}) was close to threefold higher than that catalyzed by the wild-type enzyme (14 U mg^{-1}; Table 1). Interestingly, residue 227 is at the periphery of the active site. The distance between O^{γ} of Ser94 and C^{α} of Phe227 is 11.5 Å; furthermore, the residue points toward the surface of the protein and is not part of the substrate-binding pockets.[13]

Kinetic characterizations of wild-type and Leu29Pro PFE showed that the major contributing factor to the observed perhydrolysis rate increase is V_{max}, which is 50-fold higher in the mutant (11 U mg^{-1}) than in the wild-type (0.22 U mg^{-1}). The perhydrolase reaction follows ping-pong kinetics with acetate and hydrogen peroxide. We measured the apparent kinetic constants for this reaction at a constant acetate concentration of 0.7 M. These values point to a 14-fold increase in catalytic efficiency (V_{max}/K_M) for perhydrolysis of acetic acid from 13 to 180 U mg^{-1}M^{-1}, which corresponds to a decreased activation-energy barrier of 1.6 kcal mol^{-1} at 300 K. The Leu29Pro mutation also caused a 50-fold decrease in V_{max} for the hydrolysis of *p*NPAc, whereas K_M increased threefold (Table 2). Altogether, this changed the catalytic efficiency 165-fold, which corresponds to an elevated activation-energy barrier for hydrolysis of 3.0 kcal mol^{-1} at 300 K.

Table 2: Kinetic parameters for *p*NPAc and apparent kinetic parameters for hydrogen peroxide.[a]

Enzyme, substrate	V_{max} [U mg^{-1}]	K_M [mM]	V_{max}/K_M [U mg^{-1} M^{-1}]
wild-type, *p*NPAc	143 ± 9	2.8 ± 0.4	51000
Leu29Pro, *p*NPAc	2.8 ± 1.1	8.9 ± 1.1	310
wild-type, H_2O_2	0.22 ± 0.02	17 ± 4	13
Leu29Pro, H_2O_2	11 ± 1	58 ± 12	180

[a] Reaction conditions as in Table 1.

The hydrolytic activity of Leu29Pro toward unactivated esters decreased much less dramatically, ranging from no change to an eightfold decrease (Table 3). The rate-determining step for hydrolysis may differ between activated esters (such as *p*NPAc) and unactivated esters. For activated esters, the acylation is most likely fast and deacylation would therefore be rate-determining.[17] For unactivated esters, the rates of acylation and deacylation are similar. The effect of the Leu29Pro mutation on the rate of hydrolysis of activated and unactivated esters suggests that the rate of *p*NPAc hydrolysis is lowered by a decrease in the rate of the deacylation step.

Molecular modeling was used to identify the molecular basis of the increase in perhydrolase activity caused by the Leu29Pro mutation. The model starting structure was prepared from the crystal structure of PFE (PDB ID: 1VA4). The Leu29Pro mutation was obtained by mutating position 29 of the wild-type structure scaffold. After energy minimization, an overlay of the proline residue in Leu29Pro PFE on the proline residue in CPO-F (PDB ID: 1A8S) confirmed identical conformations (results not shown). Assuming that perhydrolysis takes place with an esterase-like mechanism, we modeled the second tetrahedral intermediate to represent the transition state for hydrogen peroxide attack on the acyl enzyme. All modeled structures showed productive hydrogen bonds for catalytic triad residues and oxyanion-hole residues. In Leu29Pro PFE, a hydrogen bond was found between the carbonyl oxygen atom of Trp28 and the peroxide hydroxy group, with an O–O distance of 2.7 Å (O···H–O angle = 133°) (Figure 2a). Similarly, this hydrogen bond length in CPO-F was 2.7 Å (O···H–O angle = 127°). These distances are within the typical values for a hydrogen bond between the oxygen atom of a hydroxy group and a carbonyl oxygen atom: 2.8 ± 0.1 Å.[18] In contrast, the corresponding hydrogen bond in wild-type PFE is much weaker, with an O–O distance of 3.2 Å (O···H–O angle = 114°) (Figure 2b).

Table 3: Rate of hydrolysis and relative rates for several ester substrates.

Substrate	Wild-type [U mg^{-1}][a]	Leu29Pro [U mg^{-1}][a]	Fold rate change[b]
p-nitrophenyl acetate[c]	14	0.14	100
ethyl butyrate	1.3	0.16	8.1
ethyl valerate	0.65	0.083	7.8
propyl propionate	0.91	0.18	5.1
butyl propionate	0.57	0.14	4.1
ethyl propionate	0.75	0.19	3.9
methyl propionate	0.38	0.33	1.2

[a] Specific activity of ester hydrolysis determined in BES buffer (5 mM, pH 7.2) at 25 °C containing *p*-nitrophenol (0.51 mM) and substrate (5 mM); 1 U = 1 μmol protons generated from hydrolysis min^{-1} (Supporting Information). [b] The rate of hydrolysis by Leu29Pro over that of wild-type enzyme. [c] Experimental value, [*p*NPAc] = 0.3 mM.

Previous analysis of the CPO-F X-ray crystallographic structure found that Pro29 adopts a *cis*-peptide conformation, which may favor the reaction of hydrogen peroxide over water.[9] In that work, the perhydrolase activity of CPO-F was attributed to the difference in nucleophilic strength between hydrogen peroxide and water. Our results suggest that a hydrogen bond formed between the carbonyl oxygen atom of the enzyme and the peroxide nucleophile is the molecular basis for the increased perhydrolase activity. A peroxide hydroxy–carbonyl hydrogen bond could favor the perhydrolase reaction through orientation of the hydrogen peroxide substrate in a catalytically productive manner. The increased rate of perhydrolysis has an energy equivalent of 1.6 kcal mol^{-1}, which is consistent with a new hydrogen bond, as a hydrogen bond between a neutral donor/acceptor pair typically contributes 1–2 kcal mol^{-1} to substrate selectivity.[19,20]

To identify the molecular basis of the decreased hydrolytic activity of Leu29Pro toward *p*NPAc, we modeled the deacylation step of the hydrolysis. In wild-type PFE, modeling suggests that a water molecule can bridge the carbonyl oxygen

 © 2005 Wiley-VCH Verlag GmbH & Co. KGaA, Weinheim

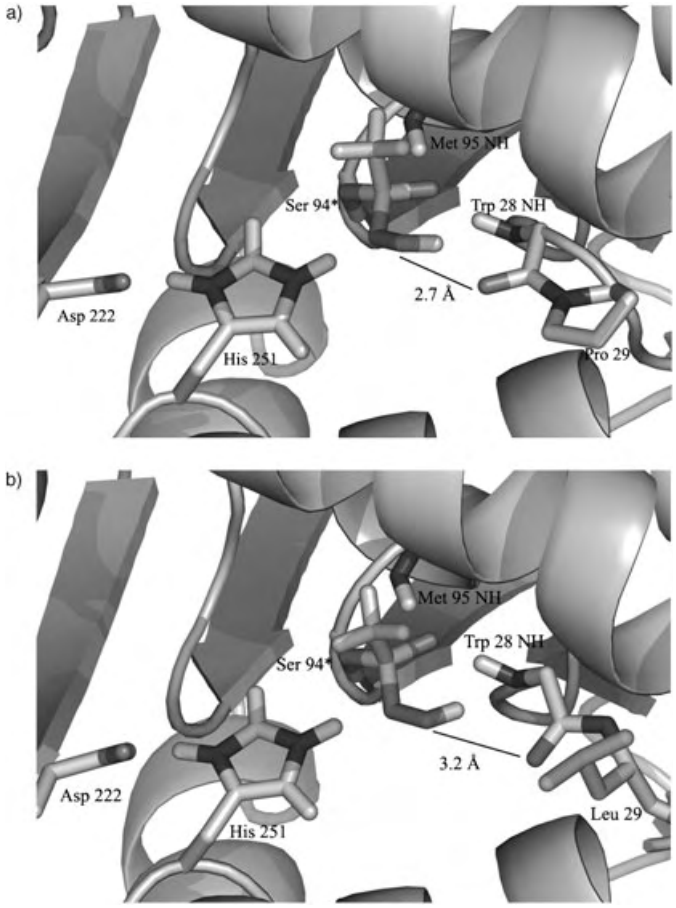

Figure 2. Models of the second tetrahedral intermediates of peracetic acid formation: a) Leu 29 Pro PFE has increased perhydrolase activity and a hydrogen bond between the backbone carbonyl oxygen atom of Trp 28 and the peroxide substrate hydroxy group (O–O = 2.7 Å, O···H–O angle = 133°); b) wild-type PFE has low perhydrolase activity and a weak hydrogen bond in the same location (O–O = 3.2 Å, O···H–O angle = 114°). Both structures show strong hydrogen bonds from the substrate to the catalytic histidine and in the oxyanion hole. The turn of residues 223–225, the side chains of residues 28 and 95, and the main chains of residues 29, 94, 222, and 251 are omitted for clarity.

of residue 28 and the hydroxy intermediate with hydrogen bonds, and thus lower the transition-state energy to facilitate deacylation. In Leu 29 Pro, the analogous space is insufficient for access of a water molecule and such stabilization is therefore missing (Supporting Information). As a result, the esterase activity for Leu 29 Pro was low for *p*NPAc because this change slowed the presumed rate-limiting deacylation step. Modeling suggests that the first tetrahedral intermediate for *p*NPAc showed no differences that could explain the large decrease in rate. The *p*-nitrophenyl moiety does adopt different configurations in wild-type and Leu 29 Pro PFE, but neither structure encounters significant steric strain.

In summary, the substitution of a single amino acid was sufficient to shift the hydrolase activity of PFE to make perhydrolysis the preferred reaction in aqueous solution. The catalytic activity is similar to that of naturally occurring perhydrolases. A molecular basis for the increase in perhydrolase activity is the presence of a carbonyl group in the vicinity of the active site that serves as a means to stabilize hydrogen peroxide attack on a putative acyl-enzyme intermediate (Figure 3). Modeling also shows that subtilisin, which also has a Ser–His–Asp catalytic triad but a different protein fold, lacks perhydrolase activity likely

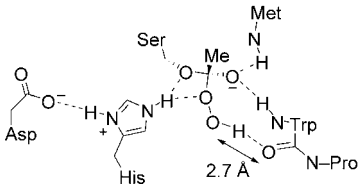

Figure 3. Proposed molecular basis of perhydrolase activity in an esterase from *P. fluorescens*: the formation of the second tetrahedral intermediate (after nucleophilic attack by the substrate peroxide) is facilitated and subsequently stabilized by a key hydrogen bond in the Leu 29 Pro mutant.

because the perhydrolysis tetrahedral intermediate lacks key hydrogen bonds (Supporting Information). A similar approach may be used to increase the perhydrolase activity of other serine hydrolases or to alter the preferred nucleophile to substrates other than water or hydrogen peroxide.

Received: December 21, 2004
Published online: March 31, 2005

Keywords: enzyme catalysis · hydrolases · molecular modeling · mutagenesis · peroxides

[1] P. J. O'Brien, D. Herschlag, *Chem. Biol.* **1999**, *6*, R91 – R105.
[2] U. T. Bornscheuer, R. J. Kazlauskas, *Angew. Chem.* **2004**, *116*, 6156 – 6165; *Angew. Chem. Int. Ed.* **2004**, *43*, 6032 – 6040.
[3] F. Björkling, H. Frykman, S. E. Godtfredsen, O. Kirk, *Tetrahedron* **1992**, *48*, 4587 – 4592.
[4] M. Picard, J. Gross, E. Lübbert, S. Tölzer, S. Krauss, K.-H. van Pée, A. Berkessel, *Angew. Chem.* **1997**, *109*, 1245 – 1248; *Angew. Chem. Int. Ed. Engl.* **1997**, *36*, 1196 – 1199.
[5] I. Pelletier, J. Altenbuchner, R. Mattes, *Biochim. Biophys. Acta* **1995**, *1250*, 149 – 157.
[6] K.-H. van Pée, G. Sury, F. Lingens, *Biol. Chem. Hoppe-Seyler* **1987**, *368*, 1225 – 1232.
[7] W. Wiesner, K.-H. van Pée, F. Lingens, *J. Biol. Chem.* **1988**, *263*, 13725 – 13732.
[8] N. Itoh, T. Kawanami, J.-Q. Liu, T. Dairi, M. Miyakoshi, C. Nitta, Y. Kimoto, *Biochim. Biophys. Acta* **2001**, *1545*, 53 – 66.
[9] B. Hofmann, S. Tölzer, I. Pelletier, J. Altenbuchner, K.-H. van Pée, H. J. Hecht, *J. Mol. Biol.* **1998**, *279*, 889 – 900.
[10] O. Kirk, L. S. Conrad, *Angew. Chem.* **1999**, *111*, 1031 – 1033; *Angew. Chem. Int. Ed.* **1999**, *38*, 977 – 979.
[11] O. Kirk, M. W. Christensen, T. Damhus, S. E. Godtfredsen, *Biocatalysis* **1994**, *11*, 65 – 77.
[12] T. D. H. Bugg, *Bioorg. Chem.* **2004**, *33*, 367 – 375.
[13] J. D. Cheeseman, A. Tocilj, S. Park, J. D. Schrag, R. J. Kazlauskas, *Acta Crystallogr. Sect. D* **2004**, *60*, 1237 – 1243.
[14] I. Pelletier, J. Altenbuchner, *Microbiology* **1995**, *141*, 459 – 468.
[15] S. C. Rothman, J. F. Kirsch, *J. Mol. Biol.* **2003**, *327*, 593 – 608.
[16] L. P. Hager, D. R. Morris, F. S. Brown, H. J. Eberwein, *J. Biol. Chem.* **1966**, *241*, 1769 – 1777.

 © 2005 Wiley-VCH Verlag GmbH & Co. KGaA, Weinheim

[17] H. Gutfreund, J. M. Sturtevant, *Biochem. J.* **1956**, *63*, 656 – 661.
[18] G. E. Schultz, R. H. Schirmer, *Principles of Protein Structure*, Springer, New York, **1984**, p. 35.
[19] A. R. Fersht, J.P Shi, J. Knill-Jones, D. M. Lowe, A. J. Wilkinson, D. M. Blow, P. Brick, P. Carter, M. M. Waye, G. Winter, *Nature* **1985**, *314*, 235 – 238.
[20] A. R. Fersht, *Biochemistry* **1988**, *27*, 1577 – 1580.

 © 2005 Wiley-VCH Verlag GmbH & Co. KGaA, Weinheim

Cross-Linked Polymers

Strong Means Slow: Dynamic Contributions to the Bulk Mechanical Properties of Supramolecular Networks**

*Wayne C. Yount, David M. Loveless, and Stephen L. Craig**

The desire to control rationally, through small-molecule synthesis, the properties of bulk materials has led to supramolecular approaches to, for example, polymers,[1,2] strong and weak organogels,[3] amphiphilic assemblies,[4] and liquid crystals.[5] In these materials, specific and well-defined interactions between molecules contribute to bulk material properties on two levels: structure and dynamics. Although the dynamic nature of the defining interactions is often the attribute that distinguishes supramolecular materials from their covalent counterparts,[6] direct mechanistic studies of the molecular contributions to the dynamic properties of materials are less abundant than structural studies.[7] Herein, we report that a simple structural variation in the networks of supramolecular sols and organogels provides a direct and quantitative measure of the relationship between molecular dynamics and macroscopic rheological properties. The approach is akin to a macromolecular "kinetic isotope effect", in that kinetic contributions to rate-determining processes are revealed by the differences in two isostructural systems. We find that it is the dynamics of molecular cross-links, much more so than their thermodynamics, which are specifically and quantitatively responsible for the bulk viscoelastic properties of the supramolecular networks.

The system under consideration is poly(4-vinylpyridine) (PVP) that is cross-linked by bis(M^{II}–pincer) compounds **1** (see Figure 2) derived from the work of van Koten[8] (M = Pd or Pt, Figure 1).[9] We recently reported that simple steric effects in the alkylamino ligands of **1** and related compounds change the rate of ligand exchange by approximately two orders of magnitude while leaving the thermodynamics of association effectively constant.[10] This independent control of dynamics is particularly significant; cross-linkers **1a** and **1b** (Figure 2) are structurally identical components within the network, and so their similar thermodynamics ensure that the extent and nature of cross-linking is essentially the same in the samples prepared from them. By extending the family of cross-linkers to the Pt^{II}–pincer molecules **1c** and **1d** (Figure 2) we are able to probe the effect of a wide range of molecular dynamics.

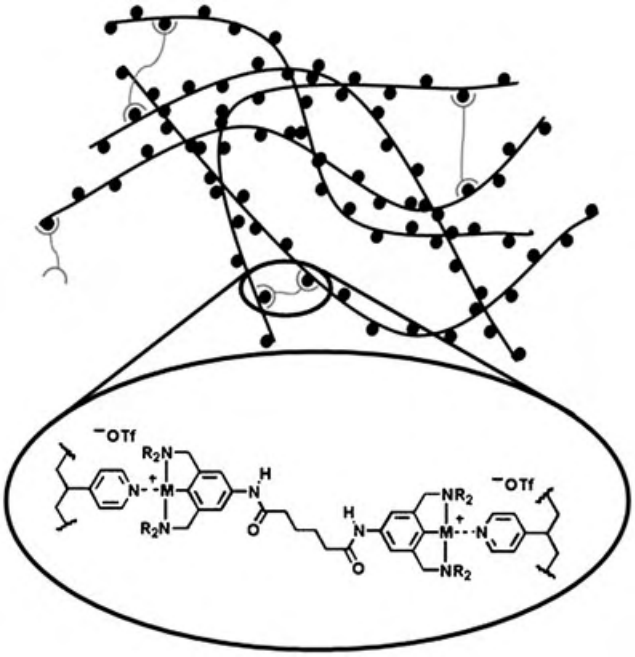

Figure 1. Schematic representation of reversible cross-links between poly(4-vinyl pyridine) through coordination with bis(M^{II}–pincer) complexes; OTf = $[CF_3SO_3]^-$.

The addition of 2% (by functional group) **1b** to a 100 mg mL^{-1} DMSO solution of PVP (Aldrich, M_r = 60000) gives rise to a clear, thick, deep yellow solution whose viscosity is approximately 2000-times greater than that of PVP alone (33 Pa s vs. 0.016 Pa s). Two control experiments confirm that the viscosity increase is due to coordinative cross-linking of the PVP by **1b**. First, the viscosity does not increase upon the addition of the same quantity of monomeric

[*] W. C. Yount, D. M. Loveless, Prof. S. L. Craig
Department of Chemistry and
Center for Biologically Inspired Materials and Materials Systems
P.M. Gross Chemical Laboratory
Duke University, Durham, NC 27708-0346 (USA)
Fax: (+1) 919-660-1605
E-mail: stephen.craig@duke.edu

[**] This work was supported by the Petroleum Research Fund of the American Chemical Society and Duke University. Partial support was provided by the North Carolina Biotechnology Center and Research Corp. D.M.L. is an NSF IGERT Fellow (DGE-0221632). S.L.C. gratefully acknowledges a DuPont Young Professor Award and a Camille and Henry Dreyfus New Faculty Award. We thank S. Zauscher for access to his rheometer, T. Ribiero for assistance with the dynamic NMR spectroscopy experiments, and T. Al-Tel for helpful conversations.

Supporting information for this article is available on the WWW under http://www.angewandte.org or from the author.

 © 2005 Wiley-VCH Verlag GmbH & Co. KGaA, Weinheim DOI: 10.1002/anie.200500026

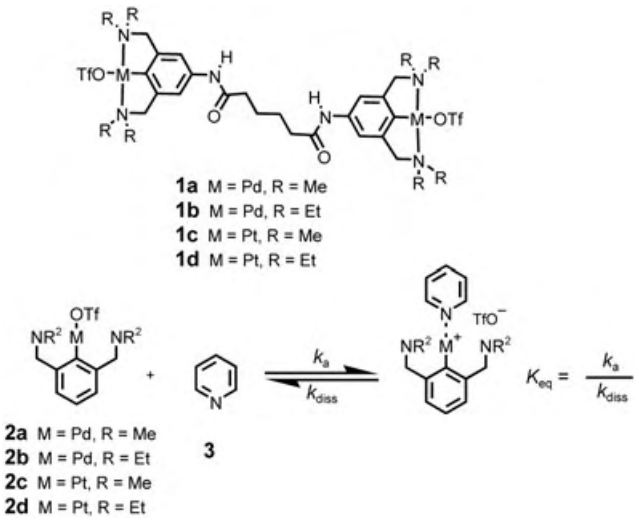

Figure 2. Structure of pincer-based dynamic cross-links **1a–d** and the model system **2** used to determine thermodynamic and kinetic parameters of pyridine coordination.

2b, so coordination to PVP alone is not responsible for the change in flow properties. Secondly, the viscosity of **1b**-PVP reverts back to that of a free-flowing solution with the addition of dimethylaminopyridine, which competes with the PVP side groups for the metal centers. The viscosity of the **1b**-PVP solutions depends on the concentration of **1b**. At constant total weight%, the solution viscosity increases monotonically with added **1b**, up to a viscosity of 550 Pa s at 5% functional group equivalents. These solutions are Newtonian, that is, their viscosities are independent of steady shear rate across the range examined (see Supporting Information).

The faster dynamics in cross-linker **1a** provide a mechanism by which to evaluate the dynamic contributions of ligand exchange to the properties of the network. The thermodynamics and kinetics in **1**-PVP are reported reliably by model system **2**-**3** (Figure 2; not accounting for cooperativity, the effects of which we assume to be equivalent in all systems),[10,11] and NMR spectroscopy measurements on **2a**-**3** and **2b**-**3** reveal nearly identical association constants of $35\,\text{M}^{-1}$ (**2a**-**3**) and $29\,\text{M}^{-1}$ (**2b**-**3**), in [D_6]DMSO. The effective concentration of pyridine in 100 mg mL^{-1} PVP is approximately 1M, and so $>97\%$ (higher if cross-linking is cooperative) of the metal sites are coordinated to PVP side groups. The ligand-exchange dynamics, however, are substantially different owing to increased steric bulk at the metal center of **2b**. For mixtures of 20 mM **3** and 10 mM **2**, the ^{1}H NMR spectrum of **2b**-**3** shows distinct signals corresponding to "free" (solvent-coordinated) and "bound" (pyridine-coordinated) metal centers, and the exchange between states is quantified by EXSY to be $15 \pm 1\,\text{s}^{-1}$. We expect the rate of exchange to be 70–100-times faster in **2a**-**3**, and, consistent with that expectation, the corresponding NMR signals are coalesced owing to fast exchange. The coalescence places a lower limit of $200\,\text{s}^{-1}$ on the exchange but does not permit an independent measurement. Thus the networks **1a**-PVP and **1b**-PVP are nearly identical in their equilibrium structure and extent of cross-linking, but they differ greatly in the dynamics of the interactions between the cross-linkers and the PVP backbone. The effect of those dynamics is dramatic. At 5% cross-linker, the viscosity of 100 mg mL^{-1} **1a**-PVP is only 6.7 Pa s—a factor of 80 less than that of the isostructural network **1b**-PVP. While the association constants are not identical, the effect of greater cross-linking in **1a**-PVP would be to increase the viscosity of **1a**-PVP relative to **1b**-PVP, the opposite effect to that observed. The dynamics dominate even the extent of cross-linking; 5% **1a**-PVP is less viscous, by a factor of 5, than 2% **1b**-PVP, despite having at least 2.5 times as many cross-links intact at any given instant.

The dynamic range of the experiments can be extended almost another five orders of magnitude by employing the platinum analogues **1c** and **1d** (Figure 2). The pyridine association constants of these compounds (again measured with the mononuclear analogues **2**) are greater than in **2a** and **2b** ($8000\,\text{M}^{-1}$ for **2c** and $4000\,\text{M}^{-1}$ for **2d**), but more importantly the rate constants for ligand exchange are 3–5 orders of magnitude smaller ($0.026 \pm 0.05\,\text{s}^{-1}$ for **2c** and $0.0006 \pm 0.0001\,\text{s}^{-1}$ for **2d**). These materials are gels at room temperature, and their viscosities are again correlated with molecular exchange dynamics, although absolute values for **1d**-PVP are outside the range accessible in our rheometer (Table 1).

Table 1: Absolute and relative thermodynamic, dynamic, and materials properties of pyridine coordination and the resulting supramolecular network solutions.[a]

Compound	K_{eq} [M^{-1}][b]	k_{ex} [s^{-1}][c]	η [Pa s][d]	K_{eq} [rel]	k_{ex}^{-1} [rel]	η [rel]
1a	35	$\approx$1100[e]	6.7	1.2	0.014	0.012
1b	29	15[f]	550	1	1	1
1c	8000	0.026[f]	240000	280	600	440
1d	4000	0.0006[g]	$>$240000[h]	140	25000	$>$440

[a] 100 mg mL^{-1} of **1**-PVP in DMSO, 5% functional group equivalent relative to poly(4-vinyl pyridine)). [b] Taken from model system **2**-**3**; 298 K; uncertainty $\pm$20%. [c] Taken from model system **2**-**3**; 298 K; unless otherwise stated, uncertainty $\pm$10%. See Supporting Information for details. [d] Taken from low-frequency plateau in oscillatory shear measurements; 293 K. [e] Extrapolated relative to **1b** using ref. [10]; estimated relative uncertainty $\pm$15%. [f] ^{1}H NMR EXSY spectroscopy; 298 K. [g] Ligand exchange monitored by ^{1}H NMR spectroscopy; 298 K. [h] more viscous than **1c**-PVP by inspection, value out of the range of the rheometer used.

The results offer mechanistic insights into the molecular origins of flow resistance in PVP supramolecular networks. The network responds to an applied stress through sequential, individual dissociation and re-association events, and these dynamics dominate over contributions from the intact supramolecular structure. It is noteworthy that the relationship appears to hold even when comparing **1b** and **1c**, where the association constants differ by a factor of approximately 300; relative viscosities are directly proportional to cross-link lifetime without considering the fraction of time for which the cross-links are dissociated. The entanglements that govern the viscoelastic response of these fluids are therefore specifically

 © 2005 Wiley-VCH Verlag GmbH & Co. KGaA, Weinheim

molecular in nature, rather than the result of increased friction owing to the size and/or physical entanglements of cross-link-induced aggregates. In this respect, the results described herein contrast with our previous study of linear polymeric assemblies defined by a similar coordination motif. In that work, the viscosities of the supramolecular polymer solutions reflected only the equilibrium structure of the assemblies without a measurable contribution from main-chain dissociation dynamics.[10]

van Esch and Feringa[12] and others[3] have described the importance of supramolecular organogels and the difficulty in probing the structural basis of their properties.[13] Reversible cross-linking, both specific[2,14] and nonspecific,[15] is well-known and is central to a range of fundamental and applied goals. In all cases, the intermolecular interactions contribute both to the equilibrium structure and the nonequilibrium dynamics of the materials. Herein we have shown that it is dynamics rather than the equilibrium structure that are paramount in determining the viscoelastic response of a family of cross-linked supramolecular polymers, a result that is in contrast to the behavior observed in linear analogues. The ability to address quantitatively the relative influence of dynamics and thermodynamics in supramolecular materials provides a mechanism to test the assumptions of old[16] and new[17] models of rheological behavior (e.g. transient network models, which appear to hold in this case) and to probe the role of cross-linking in important but challenging environments, such as grafted polymer brushes, thin films, composites and blends, and near the border of phase transitions. The results described above emphasize that under the nonequilibrium conditions of an applied mechanical stress, "strong" really means "slow". A quantitative understanding of when, where, and how molecular dynamics influence materials properties, therefore, provides an essential framework upon which organic chemists can contribute to materials engineering.

Received: January 4, 2005
Revised: January 24, 2005
Published online: April 1, 2005

Keywords: gels · mechanical properties · pincer complexes · polymers · supramolecular chemistry

[1] a) A. Ciferri, *Supramolecular Polymers*, Marcel Dekker, New York, **1998**; b) L. Brunsveld, B. J. B. Folmer, E. W. Meijer, R. P. Sijbesman, *Chem. Rev.* **2001**, *101*, 4071 – 4097; c) R. P. Sijbesma, F. H. Beijer, L. Brunseld, B. J. B. Folmer, J. H. K. Hirschberg, R. F. M. Lange, J. K. L. Lowe, E. W. Meijer, *Science* **1997**, *278*, 1601 – 1604; d) U. S. Schubert, H. Hofmeier, *Macromol. Rapid Commun.* **2002**, *23*, 561; e) S. J. Rowan, J. B. Beck, J. M. Ineman, *Polym. Prepr. Am. Chem. Soc. Div. Polym. Chem.* **2003**, *44*, 691 – 692; f) R. K. Castellano, R. Clark, S. L. Craig, C. Nuckolls, J. Rebek, Jr., *Proc. Natl. Acad. Sci. USA* **2000**, *97*, 12418 – 12421.

[2] J. M. Pollino, K. P. Nair, L. P. Stubbs, J. Adams, M. Weck, *Tetrahedron* **2004**, *60*, 7205 – 7215.

[3] a) P. Terech, R. G. Weiss, *Chem. Rev.* **1997**, *97*, 3133 – 3159; b) L. A. Estroff, A. D. Hamilton, *Chem. Rev.* **2004**, *104*, 1201 – 1217.

[4] a) J.-F. Gohy, B. G. G. Lohmeijer, S. K. Varshney, U. S. Schubert, *Macromolecules* **2002**, *35*, 7427 – 7435; b) U. Drechsler, R. J. Thibault, V. M. Rotello, *Macromolecules* **2002**, *35*, 9621 – 9623; c) X. Tang, F. Hua, K. Yamato, E. Ruckenstein, B. Gong, W. Kim, C. Y. Ryu, *Angew. Chem.* **2004**, *116*, 6633 – 6636; *Angew. Chem. Int. Ed.* **2004**, *43*, 6471 – 6474; d) Y. Liu, J. Xu, S. L. Craig, *Chem. Commun.* **2004**, 1864 – 1865.

[5] V. Percec, *Macromol. Symp.* **1997**, *117*, 267 – 273.

[6] A. V. Davis, R. M. Yeh, K. N. Raymond, *Proc. Natl. Acad. Sci. USA* **2002**, *99*, 4793 – 4796.

[7] For selected recent reports of kinetic contributions to properties of supramolecular assemblies, see: a) J. T. Davis, M. S. Kaucher, F. W. Kotch, M. A. Iezzi, B. C. Clover, K. M. Mullaugh, *Org. Lett.* **2004**, *6*, 4265 – 4268; b) A. Hori, K. Yamashita, M. Fujita, *Angew. Chem.* **2004**, *116*, 5126 – 5129; *Angew. Chem. Int. Ed.* **2004**, *43*, 5016 – 5019.

[8] For a recent review of pincer complex chemistry, see: M. Q. Slagt, D. A. P. van Zwieten, A. J. C. M. Moerkerk, R. J. M. K. Gebbink, G. van Koten, *Coord. Chem. Rev.* **2004**, *248*, 2275 – 2282.

[9] For other recent reports of pincer complexes in supramolecular chemistry, see: a) G. Rodriguez, M. Albrecht, J. Schoenmaker, A. Ford, M. Lutz, A. Spek, G. van Koten, *J. Am. Chem. Soc.* **2002**, *124*, 5127 – 5138; b) W. T. S. Huck, L. J. Prins, R. H. Fokkens, N. M. M. Nibbering, F. C. J. M. van Veggel, D. N. Reinhoudt, *J. Am. Chem. Soc.* **1998**, *120*, 6240 – 6246.

[10] W. C. Yount, H. Juwarker, S. L. Craig, *J. Am. Chem. Soc.* **2003**, *125*, 15302 – 15303.

[11] F. Basolo, J. Chatt, H. B. Gray, R. G. Pearson, B. L. Shaw, *J. Chem. Soc.* **1961**, 2207.

[12] "Gels": J. van Esch, B. L. Feringa in *Encyclopedia of Supramolecular Chemistry*, *Vol. 2* (Ed.: J. L. Atwood, J. W. Steed), Marcel Dekker, New York, **2004**, pp. 586 – 594.

[13] For a recent and thorough characterization of supramolecular networks, see: T. Vermonden, M. J. van Steenbergen, N. A. M. Besseling, A. T. M. Marcelis, W. E. Hennink, E. J. R. Sudholter, M. A. Cohen Stuart, *J. Am. Chem. Soc.* **2004**, *126*, 15802 – 15808.

[14] a) R. K. Schultz, R. R. Myers, *Macromolecules* **1969**, *2*, 281 – 285; b) M. Shibayama, F. Ikkai, R. Moriwaki, S. Nomura, *Macromolecules* **1994**, *27*, 1738 – 1743; c) Y. Zhao, J. B. Beck, S. J. Rowan, A. M. Jamieson, *Macromolecules* **2004**, *37*, 3529 – 3531; d) M. Shibata, Y. Kimura, D. Yaginuma, *Polymer* **2004**, *45*, 7571 – 7577.

[15] S. B. Ross-Murphy, *Polym. Networks* **1998**, 288 – 315.

[16] a) M. S. Green, A. V. Tobolsky, *J. Chem. Phys.* **1946**, *14*, 80 – 89; b) A. S. Lodge, *Trans. Faraday Soc.* **1956**, *52*, 120 – 130; c) M. Yamamoto, *J. Phys. Soc. Jpn.* **1956**, *11*, 413 – 421.

[17] a) R. H. W. Wientjes, R. J. J. Jongschaap, M. H. G. Duits, J. Mellema, *J. Rheol.* **1999**, *43*, 375 – 391; b) R. J. J. Jongschaap, R. H. W. Wientjes, M. H. G. Duits, J. Mellema, *Macromolecules* **2001**, *34*, 1031 – 1038.

 © 2005 Wiley-VCH Verlag GmbH & Co. KGaA, Weinheim

Phospholipid Monolayers

Preventing Crystallization of Phospholipids in Monolayers: A New Approach to Lung-Surfactant Therapy**

Frédéric Gerber, Marie Pierre Krafft, Thierry F. Vandamme, Michel Goldmann, and Philippe Fontaine*

We report that a fluorocarbon gas can have a highly effective fluidizing effect on a semicrystalline dipalmitoylphosphatidylcholine (DPPC) monolayer and can prevent it from crystallizing. DPPC monolayers are commonly being used as simplified models of lung surfactant.

The native lung surfactant (LS) is a complex mixture of lipids and proteins that forms a monolayer at the alveolus/air interface of mammalian species. This layer lowers the air/alveoli surface tension upon compression (that is, during expiration), reduces the work of breathing, and respreads easily on expansion (that is, during inspiration).[1–3] The main component of native LS is DPPC. It is accompanied by small amounts of other lipids and of four specific proteins, SP-A, SP-B, SP-C, and SP-D. SP-B and SP-C are amphiphilic proteins that were recently shown to play an important role in the surface activity of LS.[1,3] Although DPPC can generate near-zero surface tension at the air/water interface during compression, it is a poor LS when used alone. This is because it tends to form rigid, multilamellar structures in solution and, consequently, does not adsorb efficiently and rapidly at the air/water interface.

When compressed at an air/water interface at 25 °C, DPPC forms a monolayer that is in a liquid-condensed state at high surface density. It forms essentially two-dimensional crystalline domains at the interface.[1–3] Such crystallization opposes effective respreading of the phospholipid on the alveolar surface upon inspiration. It is believed that the unsaturated and anionic phospholipids (especially phosphatidylglycerol) and hydrophobic proteins present in the native surfactant compensate for these limitations (from the respiratory-function standpoint) of DPPC monolayers.[4] In particular, one of the proteins of LS, SP-B, was shown to induce a reversible folding transition at monolayer collapse, thereby allowing all the components of LS to remain at the interface during respreading.[3]

Over the past few years, several LS substitutes (for example, Curosurf (Chiesi Pharmaceutici, Parma, Italy) and Survanta (Ross Laboratories, Columbus, OH, USA)) have been developed that are now clinically used in the treatment of neonatal respiratory distress syndrome. These replacement LSs consist of phospholipidic fractions of bovine (Survanta) and porcine (Curosurf) lung surfactant. However, these natural extracts are not entirely devoid of inherent immunological risks and potential viral contamination. Other drawbacks include the limited supply of animal surfactant, the cost of the purification procedure, and the difficulty of achieving batch-to-batch consistency. Therefore, there is a clear need for alternative synthetic LS substitutes.[1–4]

We found that a fluorocarbon gas very effectively inhibits the crystallization of DPPC on compression and facilitates its respreading on decompression. Because of their high biological inertness, remarkable ability to solubilize oxygen, and extremely low solubility in water, fluorocarbons (FCs) have been investigated for various biological applications, especially intravascular oxygen transport[5,6] and the stabilization of gaseous microbubbles that are used as contrast agents in ultrasound imaging.[5,6] Partial liquid ventilation with FCs has been explored as a treatment for acute respiratory distress syndrome (ARDS).[7–10] Improved oxygenation and lung compliance were achieved.[7] Recently, delivery of vaporized FCs to oleic acid injured ARDS sheep has resulted in significant and sustained improvement in gas exchange and lung compliance.[11,12] Although these results suggest that FCs may be useful in pulmonary-disease therapy, no study aimed at determining the influence of FCs on lung surfactant or lung-surfactant models appears to have been reported.

We have investigated the effects of an FC gas (gFC) on the physical state of DPPC Langmuir monolayers upon compression. Langmuir monolayers provide useful model systems for studying the lung surfactant. Although great care is necessary when extrapolating Langmuir monolayer behavior to lung-surfactant behavior in vivo, general correlations between in vitro and in vivo behavior have started to emerge.[13] The behavior of surfactants in monolayers is characterized by surface pressure–molecular area (π–A) compression isotherms. Compression isotherms of DPPC monolayers were measured under an atmosphere saturated with various gFCs. Fluorescence microscopy (FM) and grazing incidence X-ray diffraction (GIXD) were used to determine the morphology and degree of order of the organized domains within the monolayers. Perfluorooctyl bromide (PFOB) was selected as the gFC because it is one of the most thoroughly investigated FCs for biomedical applications,[14] particularly for pulmonary applications. Both the ability of gPFOB to prevent the formation of crystalline DPPC domains and its ability to dissolve such domains once formed were determined.

[*] F. Gerber, Dr. M. P. Krafft
Institut Charles Sadron (CNRS UPR 22)
6 rue Boussingault, 67083 Strasbourg Cedex (France)
Fax: (+33) 388-414-099
E-mail: krafft@ics.u-strasbg.fr
F. Gerber, Dr. T. F. Vandamme
Laboratoire de Chimie Bioorganique (UMR 7514)
Université Louis Pasteur
74 Route du Rhin, 67401 Illkirch (France)
M. Goldmann, Dr. P. Fontaine
Laboratoire pour l'Utilisation du Rayonnement Electromagnétique (LURE, UMR 130)
Centre Universitaire Paris Sud, Bât 209D
91898 Orsay Cedex (France)
and
Institut des Nano-Sciences de Paris (INSP-UMR CNRS 7588)
Campus Boucicaut
140 rue de Lourmel, 75015 Paris (France)

[**] We thank Alliance Pharmaceutical Corporation (San Diego, CA, USA) for the gift of perfluorooctyl bromide.

 DOI: 10.1002/anie.200462978 © 2005 Wiley-VCH Verlag GmbH & Co. KGaA, Weinheim

Isotherms of DPPC monolayers compressed at 25 °C on a pure water subphase under an atmosphere of N_2 and under an atmosphere of N_2 saturated with PFOB (vapor pressure: 10.5 torr at 25 °C) are shown in Figure 1. When compressed

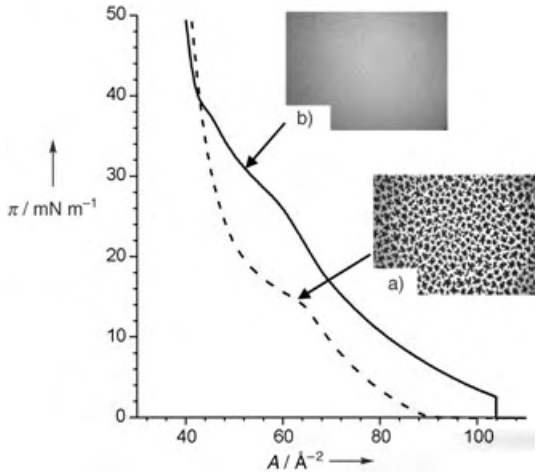

Figure 1. Compression isotherm of DPPC measured at 25 °C in an atmosphere of N_2 (dashed line) or N_2 saturated with PFOB (solid line). Insets: fluorescence images of a) the DPPC monolayer at $\pi = 15\ mN\,m^{-1}$ showing the crystalline domains and b) the DPPC monolayer in contact with PFOB ($\pi = 30\ mN\,m^{-1}$).

under pure N_2, DPPC undergoes a first-order phase transition from a liquid-expanded (LE) phase to a liquid-condensed (LC) phase at a surface pressure of $\pi \approx 13\ mN\,m^{-1}$. The LE/LC coexistence region is evidenced by the presence of a plateau on the isotherm and by the observation of discrete domains of LC phase within a continuous LE phase, as visualized with FM (inset (a) in Figure 1). This is in agreement with previous work.[15] When surface pressure increases, the LC domains increase in size, become more numerous, and progressively merge into a continuous LC phase.

Compressing the DPPC monolayer under an N_2 atmosphere saturated with gPFOB changes the phase behavior drastically. The transition at $\pi \approx 13\ mN\,m^{-1}$ (Figure 1) has disappeared. The new transition seen at $\pi \approx 28\ mN\,m^{-1}$ is no longer of the LE/LC type, as assessed from the fluorescence images, which are bright and featureless not only at $30\ mN\,m^{-1}$ (inset (b) in Figure 1) but throughout the whole range of π values. The fact that the dye remains soluble for all π values suggests the formation of two LE phases, with a transition through a collective tilt. This indicates that the DPPC monolayer in contact with gPFOB is in a homogeneous fluid LE phase throughout the range of surface pressures investigated. Below $\pi = 40\ mN\,m^{-1}$, the isotherm is shifted towards larger molecular areas, a fact indicating that some PFOB is incorporated into the DPPC monolayer. These experiments demonstrate that gPFOB molecules interact with DPPC molecules, prevent the formation of the LC phase, and hence induce a fluidizing effect in the monolayer.

To assess the effect of gPFOB on already formed crystalline DPPC domains, we have compressed DPPC monolayers at $\pi = 10\ mN\,m^{-1}$, thus causing the formation of LC domains. gPFOB-saturated N_2 was then allowed to flow into the gas-tight box enclosing the trough. The fluorescence images of Figure 2 show that five minutes after the introduction of gPFOB the LC domains have become significantly smaller. After three minutes, the domains have totally disappeared, a result indicating that the DPPC monolayer has become totally fluid.

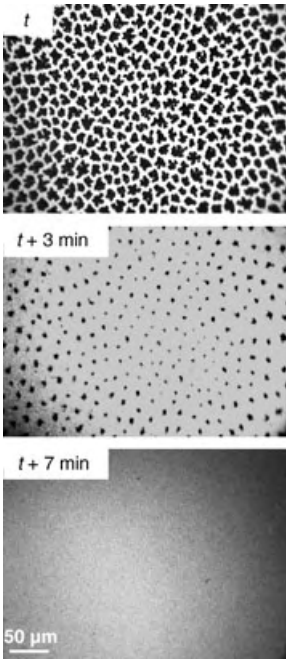

Figure 2. Fluorescence images of a DPPC monolayer compressed at $\pi = 10\ mN\,m^{-1}$ under N_2 (upper image). At time *t*, the atmosphere of N_2 above the monolayer started to be saturated with gPFOB. One can see that the LC domains progressively disappear with time. After 7 min, the monolayer is totally homogeneous and fluid.

To secure another unambiguous, independent assessment of any possible crystalline regions of the monolayer, we performed GIXD experiments. The X-ray beam hits the surface of water at an incidence lower than the critical angle of total external reflection for water (≈ 2.5 mrad at 7.7 keV). Under these conditions, an evanescent wave propagates along the air/water interface. If an ordered monolayer is present at the interface, the wave is diffracted and Bragg peaks are obtained. GIXD experiments thus provide information on the existence and structure of ordered zones within the monolayer.[16] N_2 is replaced by He gas to reduce the X-ray scattering by the gas phase, which can mask the surface-diffraction peaks.

Figure 3a shows the integrated diffracted X-ray intensity (I/I_0) as a function of the in-plane scattering wave vector q_{xy} of a DPPC monolayer compressed at $\pi = 20\ mN\,m^{-1}$. At this surface pressure, two Bragg peaks are obtained that indicate a rectangular unit cell (tilted L_{2d} phase). The calculated area per chain ($\approx 23\ Å^2$) and the tilt angle obtained from Bragg rod analysis are in agreement with published data.[17] When the He atmosphere is saturated with gPFOB, the diffraction

 © 2005 Wiley-VCH Verlag GmbH & Co. KGaA, Weinheim

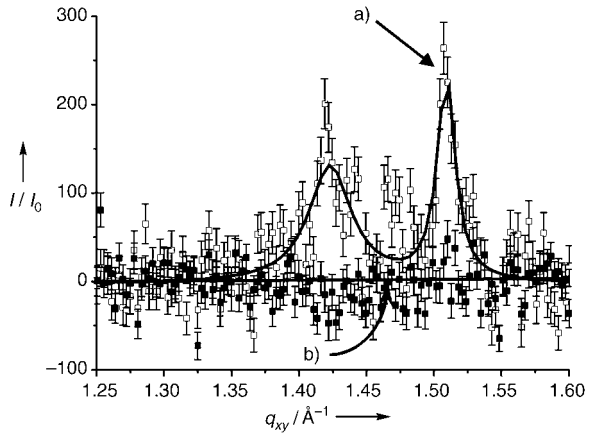

Figure 3. Diffracted intensity of the grazing X-rays I/I_0 as a function of the in-plane scattering wave vector q_{xy}. a) When compressed at $\pi = 20\ \mathrm{mN\,m^{-1}}$ under He, the DPPC monolayer shows the two Bragg peaks characteristic of the tilted LC phase at 1.42 and 1.51 Å^{-1}. b) When the helium is saturated with gPFOB, the peaks disappear rapidly.

peaks disappear within a few minutes, thereby indicating the dissolution of the LC domains, which allows the rapid respreading of the DPPC molecules. Furthermore, when pure He was subsequently allowed to sweep the gas-tight box while the compression of the DPPC monolayer was maintained at $\pi = 20\ \mathrm{mN\,m^{-1}}$, the two diffraction peaks were seen to slowly reappear, thereby showing reformation of the LC domains. This establishes the facts that PFOB molecules are adsorbed into the DPPC monolayer and that they inhibit the organization of the DPPC molecules into LC domains. When the inflow of gPFOB is stopped, while the flow of He gas is maintained, the PFOB molecules adsorbed at the interface are removed and the DPPC monolayer recovers its normal behavior, that is, crystallizes.

In conclusion, gaseous PFOB was found to suppress the LC phase of DPPC Langmuir monolayers and, hence, the formation of crystalline domains. When contacted with the gFC, the DPPC monolayer remains in the LE phase throughout the range of surface pressures investigated (up to $\pi = 40\ \mathrm{mN\,m^{-1}}$), as assessed by compression isotherms, FM, and GIXD experiments. It was also found that gFCs can induce the dissolution of pre-existing LC-phase domains, and hence facilitate the respreading of the DPPC molecules on the water surface, as shown by FM and GIXD; gPFOB, thus, demonstrated a highly effective fluidizing effect on the DPPC monolayer. Other fluorocarbons, including perfluorooctylethane, bis(perfluoroalkyl)ethanes, and perfluorodecalin, were also effective. The insights provided by this study suggest that some FCs, whose biocompatibility is well documented, in combination with DPPC, may prove useful in lung-surfactant-substitute compositions.

Experimental Section

L-α-1,2-Dipalmitoyl-*sn*-3-glycerophosphatidylcholine (DPPC) was obtained from Sigma in >99% purity. Spreading solutions of DPPC (1.0 mmol L^{-1} for minitrough experiments and 2.0 mmol L^{-1} for GIXD experiments) were prepared in chloroform (analytical grade). Water was purified by using a Millipore system (pH 5.5, surface tension = 72.1 mN m^{-1} at 20 °C, resistivity = 18 MΩ cm). The fluorescent dye (2-[6-(7-nitrobenz-2-oxa-1,3-diazol-4-yl)amino]hexanoyl-1-hexadecanoyl-*sn*-glycero-3-phosphocholine, NBDC$_6$-HPC) was purchased from Molecular Probes (Eugene, OR, USA), and used at a lipid mole ratio of 1%.

Surface pressure versus molecular area isotherms were recorded on a Langmuir minitrough (Riegler&Kirstein, Potsdam, Germany) equipped with two movable barriers (speed = 2.0 mm min^{-1}). The surface pressure was measured by using the Wilhelmy plate method. The trough was enclosed in a gas-tight box that was flushed either with pure N_2 or with N_2 saturated with gPFOB. In the latter case, N_2 was allowed to bubble at room temperature through the liquid fluorocarbon before being flushed into the gas-tight box. The flow rate of the gas phase (N_2 or PFOB-saturated N_2) was set to 1.2 L min^{-1}. The temperature was regulated to 25 ± 0.5 °C. DPPC solution (15 μL) was spread on the water surface. The errors in π and A were estimated as ±1 mN m^{-1} and ±1 Å^2, respectively.

Fluorescence microscopy was achieved with the above Langmuir balance equipped with an Olympus fluorescence microscope fitted with a 20×-power objective. An Olympus 100-W high-pressure mercury lamp was used for excitation. A dichroic mirror/barrier filter assembly was used to filter and direct the excitation light onto the monolayer (450–490 nm) and to filter out the emitted fluorescence (520 nm). The emitted fluorescence was collected by the objective and detected with a Hamamatsu intensified camera. The microscope was linked to the gas-tight box of the trough through an extensible gusset to allow easy control of the partial pressure of PFOB. The surface pressure was kept constant throughout the fluorescence microscopy experiments.

GIXD experiments were perfomed at the D41B beamline of the LURE-DCI synchrotron source (Orsay, France). The teflon Langmuir trough mounted on the diffractometer was equipped with a movable single barrier. The surface pressure π (as measured by the Wilhelmy plate method) was kept constant throughout a given scan. The trough was enclosed in a gas-tight box with kapton windows filled with water-saturated helium. The temperature was regulated to 20 ± 0.5 °C. Approximately 50 μL of DPPC solution were spread on the water surface. The film was compressed stepwise and Bragg peaks were recorded at each set pressure step. The X-ray wavelength, α = 1.646 Å, of the incoming X-ray beam was selected by using a focusing Ge(111) monochromator. The grazing angle of incidence (θ_i = 2.08 mrad) was set slightly below the critical angle for total external reflection of the X-rays at the air/water interface (about 2.8 mrad at 1.646 Å). For the acquisition of the diffracted intensity, we used a new set up composed of a two-dimensional detector and a single vertical slit positioned between the sample and the detector.[18] The q_{xy} resolution was 0.007 Å^{-1} for the q range explored. The total duration of a scan was typically 10 min. The shape of the Bragg rods gave information about the tilt angle τ and tilt azimuth φ.[19] In this study, the nearest-neighbor tilted phase (L_{2d}, $\tau \neq 0$, $\varphi = 0$) was observed, according to the nomenclature introduced in Ref. [17]. For this L_{2d} phase, the diffraction pattern exhibited two peaks. The peak located at low q_{xy} corresponds to the degenerate [11] and [$\bar{1}$1] out-of-plane reflections, and the other peak corresponds to the [02] in-plane reflection.

Received: December 17, 2004

Keywords: fluidizing effects · fluorocarbons · liquid crystals · monolayers · phospholipids

[1] J. A. Zasadzinski, J. Ding, H. E. Warriner, F. Bringezu, A. J. Waring, *Curr. Opin. Colloid Interface Sci.* **2001**, *6*, 506.

 © 2005 Wiley-VCH Verlag GmbH & Co. KGaA, Weinheim

[2] R. H. Notter, *Lung Surfactants: Basic Science and Clinical Applications*, *Vol. 149*, Marcel Dekker, New York, **2000**.
[3] J. Ding, D. Y. Takamoto, A. von Nahmen, M. M. Lipp, K. Y. C. Lee, A. J. Waring, J. A. Zasadzinski, *Biophys. J.* **2001**, *80*, 2262.
[4] R. Veldhuizen, K. Nag, S. Orgeig, F. Possmayer, *Biochim. Biophys. Acta* **1998**, *1408*, 90.
[5] J. G. Riess, *Chem. Rev.* **2001**, *101*, 2797.
[6] E. G. Schutt, D. H. Klein, R. M. Mattrey, J. G. Riess, *Angew. Chem.* **2003**, *115*, 3336; *Angew. Chem. Int. Ed.* **2003**, *42*, 3218.
[7] M. R. Wolfson, N. E. Kechner, R. F. Roache, J. DeChadarevian, H. E. Friss, S. D. Rubenstein, T. H. Shaffer, *J. Appl. Physiol.* **1998**, *84*, 624.
[8] M. Sukumar, M. Bommaraju, J. E. Fisher, F. C. Morin, M. C. Papo, B. P. Fuhrman, L. J. Hernan, C. L. Leach, *J. Appl. Physiol.* **1998**, *84*, 327.
[9] C. L. Leach, J. S. Greenspan, D. Rubenstein, T. H. Shaffer, M. R. Wolfson, J. C. Jackson, R. DeLemos, B. P. Fuhrman, *N. Engl. J. Med.* **1996**, *335*, 761.
[10] A. T. Rotta, B. Gunnarsson, L. J. Hernan, B. P. Fuhrman, D. M. Steinhorn, *J. Crit. Care* **2000**, *28*, 202.
[11] J. U. Bleyl, M. Ragaller, U. Tscho, M. Regner, M. Hübler, M. Kanzow, O. Vincent, M. Albrecht, *Crit. Care Med.* **2002**, *30*, 1340.
[12] K. von der Hardt, E. Schoof, M. A. Kandler, J. Dötsch, W. Rascher, *Pediatr. Res.* **2002**, *51*, 177.
[13] M. M. Lipp, K. Y. C. Lee, D. Y. Takamoto, J. A. Zasadzinski, A. J. Waring, *Phys. Rev. Lett.* **1998**, *81*, 1650.
[14] J. G. Riess in *Handbook of Fluorous Chemistry* (Eds.: J. A. Gladysz, I. Horváth, D. P. Curran), Wiley-VCH, Weinheim, **2004**, p. 521.
[15] M. Lösche, E. Sackmann, H. Möhwald, *Ber. Bunsen-Ges.* **1983**, *87*, 848.
[16] P. Fontaine, M. Goldmann, P. Muller, M.-C. Fauré, O. Kolovanov, M. P. Krafft, *J. Am. Chem. Soc.* **2005**, *127*, 512.
[17] V. M. Kaganer, H. Möhwald, P. Dutta, *Rev. Mod. Phys.* **1999**, *71*, 779.
[18] P. Fontaine, M. Goldmann, M. Bordessoule, A. Jucha, *Rev. Sci. Instrum.* **2004**, *75*, 3097.
[19] J. Als-Nielsen, D. Jacquemain, K. Kjaer, F. Leveiller, M. Lahav, L. Leiserowitz, *Phys. Rep.* **1994**, *251*, 246.

 © 2005 Wiley-VCH Verlag GmbH & Co. KGaA, Weinheim

Asymmetric Catalysis

Copper-Catalyzed Enantioselective Conjugate Addition of Grignard Reagents to α,β-Unsaturated Esters**

*Fernando López, Syuzanna R. Harutyunyan, Auke Meetsma, Adriaan J. Minnaard, and Ben L. Feringa**

The development of catalyst systems for the enantioselective conjugate addition of organometallic reagents to α,β-unsaturated compounds has been the subject of intensive research over the past few decades.[1] Whereas extraordinary advances have been made in asymmetric 1,4-additions to enones, lactones, and nitroalkenes,[1–5] in the case of acyclic α,β-unsaturated esters the progress has been limited,[6] despite the enormous synthetic potential of the resulting enantiopure β-substituted esters as building blocks for natural product synthesis.[7,8]

The lower intrinsic reactivity of α,β-unsaturated esters relative to that of enones,[9] and the challenge to control the different conformers present in acyclic unsaturated systems, may account for this paucity of versatile methodologies. To address these issues, several alternatives based on the use of different ester surrogates (i.e. oxazolidinones, pyrrolidinones, pyrazolidinones, acyl phosphonates, and imides), were developed successfully, with highly enantioselective Michael additions of soft nucleophiles resulting.[10] However, for alkyl metal compounds only an enantioselective conjugate addition of dialkyl zinc reagents to unsaturated *N*-acyl oxazolidinones has been reported to date.[11] Very recently, our research group described an alternative strategy based on a conjugate addition to alkylidene malonates that yields β-substituted esters after a decarboxylation step, but the method is restricted to the addition of dimethylzinc.[12,13] Therefore, despite these important achievements, general and efficient enantioselective conjugate additions of organometallic reagents to α,β-unsaturated esters remain a major challenge.

[*] Dr. F. López, Dr. S. R. Harutyunyan, A. Meetsma, Dr. A. J. Minnaard, Prof. Dr. B. L. Feringa
Department of Organic Chemistry and
Molecular Inorganic Chemistry
Stratingh Institute, University of Groningen
Nijenborgh 4, 9747 AG, Groningen (The Netherlands)
Fax: (+31) 50-363-4296
E-mail: b.l.feringa@rug.nl

[**] Financial support from the Dutch Ministry of Economic Affairs under the EET Scheme (grant nos. EETK97107 and EETK99104) and the Sixth Framework Programme of the European Community (Marie Curie Intra-European Fellowship to F.L.; contract no: MEIF-CT-2004-009767) is gratefully acknowledged. We thank T. D. Tiemersma-Wegman for technical support (GC and HPLC) and Dr. W. R. Browne for valuable discussions. We are grateful to Dr. H.-U. Blaser (Solvias, Basel) for a generous gift of josiphos ligands.

Supporting information for this article is available on the WWW under http://www.angewandte.org or from the author.

 © 2005 Wiley-VCH Verlag GmbH & Co. KGaA, Weinheim DOI: 10.1002/anie.200500317

Encouraged by the recent successful developments in the asymmetric addition of Grignard reagents to enones,[14] we decided to explore the conjugate addition to α,β-unsaturated acid derivatives and report herein the first highly enantioselective catalytic conjugate addition of organomagnesium reagents to this class of substrates.[15] The reactions are easy to execute, rigorously inert conditions are not required, and an air-stable (pre)catalyst has been identified that can be recycled and reused without any deterioration in yield or enantioselectivity.

Preliminary screening involved the crotonic acid derivatives **1a–d** (Scheme 1). The data obtained indicated that the catalyst complexes prepared from the ligands josiphos (**2a**) or

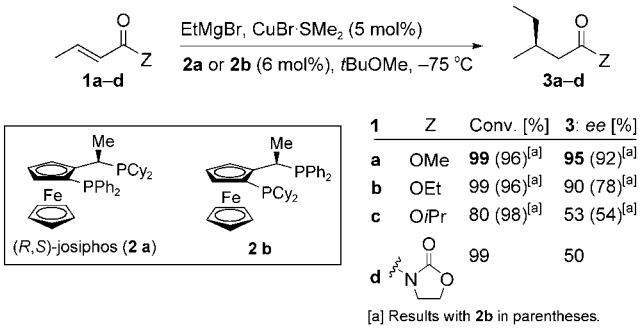

1	Z	Conv. [%]	3: *ee* [%]
a	OMe	**99** (96)[a]	**95** (92)[a]
b	OEt	99 (96)[a]	90 (78)[a]
c	O*i*Pr	80 (98)[a]	53 (54)[a]
d		99	50

[a] Results with **2b** in parentheses.

Scheme 1. Initial screening of catalysts and crotonic acid derivatives. Cy = cyclohexyl.

2b,[14,16] $CuBr{\cdot}SMe_2$, and EtMgBr were the most efficient. These complexes led to higher stereoselectivities than the other combinations of diphosphines, Cu sources, and ethylmagnesium halides tested. Remarkably, the use of sterically hindered esters (e.g. **1c**) to avoid the undesired 1,2-addition, or more reactive ester surrogates, such as the oxazolidinone **1d**, is not required. Indeed, the highest conversions and stereoselectivities were observed with methyl crotonate (**1a**).

The influence of the catalyst loading was investigated for the addition of EtMgBr to **1a**. The addition was equally effective with 1 mol% of the catalyst **2a**/$CuBr{\cdot}SMe_2$, and even with 0.2 mol% (substrate-to-catalyst ratio (S/C) of 500:1); the same conversion and enantioselectivity were observed (99% conversion, 95% *ee*).[17] No less significantly, the reaction proved to be very robust; reagent grade solvents were tolerated without the need for the rigorous exclusion of moisture and oxygen. This robustness led us to believe that a relatively air-stable catalyst could be participating in the process. After completion of the reaction, the addition of pentane to the crude residue led to the recovery, following filtration, of the dinuclear Cu complex **4a**.[18] The participation of this complex in the catalytic cycle is evident, as the reaction of **1a** with recovered **4a** (0.5 mol%) and EtMgBr afforded **3a** with the same yield and enantioselectivity. Furthermore, **4a** could be prepared independently as shown in Scheme 2 and proved to be air-stable, which significantly increased the simplicity of the procedure. Interestingly, the slow evaporation of a solution of **4a** in acetonitrile provided single crystals of the related mononuclear trigonal-planar Cu

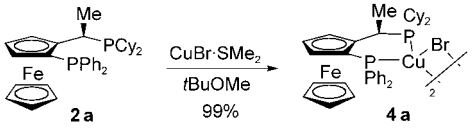

Scheme 2. Preparation of the copper catalyst **4a**.

complex **4a**′. The X-ray crystal structure obtained for this complex is shown in Figure 1.[19,20]

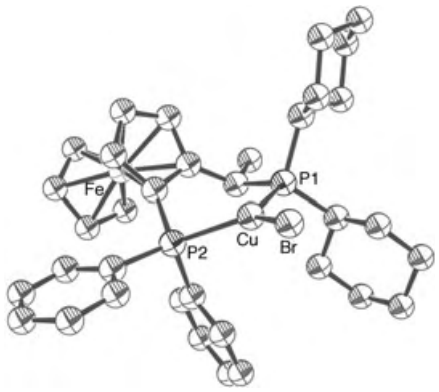

Figure 1. X-ray structure of **4a**′. Hydrogen atoms have been omitted for clarity.

Next, we analyzed the scope of the asymmetric conjugate addition to methyl crotonate **1a** with respect to the Grignard reagent. Reactions were typically carried out with 0.5 mol% of the copper catalyst **4a**, and conversion was complete within 2 h at −75 °C. As shown in Table 1, the method is suitable for the addition of several different Grignard reagents and provides exclusively the product of 1,4-addition (regioselectivity > 99:1) with high to excellent enantioselectivity.[21]

To determine the scope of the reaction with respect to the β substituent on the electrophile, a series of α,β-unsaturated esters were prepared in a single step by a Horner–Emmons

Table 1: Enantioselective conjugate addition of Grignard reagents RMgBr to methyl crotonate (**1a**).[a]

Entry	RMgBr	Product	Yield [%][b,c]	*ee* [%][d,e]
1	*n*PrMgBr	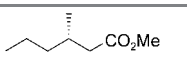	86	95 (*S*)
2	*n*BuMgBr	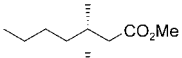	92	95 (*S*)
3	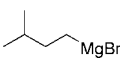	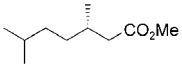	90	96
4	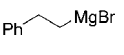	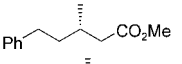	84	87
5	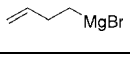	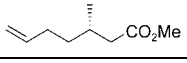	67	85 (*S*)

[a] Conditions: **1a** was added dropwise over 1 h to a solution of RMgBr (1.15–1.25 equiv) and **4a** (0.5 mol%) in *t*BuOMe. [b] Conversion > 98% (GC-MS) after 2 h in all cases. [c] Yield of isolated product. [d] Determined by GC on a chiral phase (G-TA for entries 1, 2, and 5; dex-CB for entry 3) or HPLC (chiralcel OD-H for entry 4).[22] [e] Absolute configurations were established by comparison with known compounds.

 © 2005 Wiley-VCH Verlag GmbH & Co. KGaA, Weinheim

reaction or through olefin cross-metathesis.[23] The results, summarized in Table 2, indicate that a broad range of unsaturated esters with different groups at the β position participate successfully in the enantioselective conjugate addition. As a general trend, less hindered α,β-unsaturated esters, without branching at the γ position (Table 2, entries 1–8), afforded better results with the complex **4a**, derived from josiphos (**2a**); the corresponding products were formed with complete regioselectivity and enantioselectivities in the range 86–95% *ee*. However, for substrates with bulky groups at the double bond (e.g. **5g** and **5h**), superior efficiency was observed when the ligand **2b**, in which the positions of the alkyl and aryl phosphine groups have been interchanged, was used instead of **2a** (Table 2, entries 9, 10).[24] Thus, the addition of EtMgBr to **5g** and **5h** (Table 2, entries 10, 12) proceeded smoothly at −75 °C to afford the desired products with nearly complete stereoselectivity (98–99% *ee*) and in excellent yields. To further demonstrate the potential of this method, the conjugate addition to **5g** was carried out on a 1-g scale (0.5 mol% catalyst); **6g** was afforded in 88% yield and with an excellent 98% *ee* (Table 2, entry 11). Interestingly, the study of the addition of MeMgBr to **5a** led us to find a practical limitation of the method: Although the product was formed with high enantioselectivity (93% *ee*), the reaction rate was prohibitively slow (19% conversion after 24 h; 37% conversion in the presence of TMSCl; Table 2, entries 13, 14).

Finally, we studied the addition to aryl-substituted α,β-unsaturated esters (Table 2, entries 15–22). As in the case of β-substituted hindered substrates, higher enantioselectivities were observed in these reactions when the Cu complex **4b** was used as the catalyst (e.g. Table 2, entries 15, 16 and 17, 18). The poor solubility at low temperature in aliphatic ethers of most of these substrates (**5j**–**n**) required the use of CH_2Cl_2

Table 2: Scope of the enantioselective conjugate addition of Grignard reagents to α,β-unsaturated esters.[a]

Entry		5	RMgBr	Product (**6**)	Catalyst (mol%)	Yield [%][b]	*ee* [%][c]
1	**a**	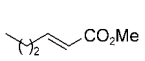	EtMgBr	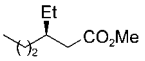	**4a** (0.5)	99[d]	93
2	**b**	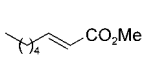	EtMgBr	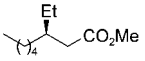	**4a** (0.5)	89	88
3	**c**	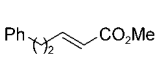	EtMgBr	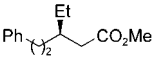	**4a** (0.5)	91	91
4	**c**	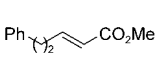	*n*BuMgBr	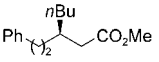	**4a** (0.5)	94	92
5	**d**	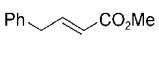	EtMgBr	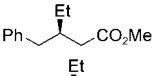	**4a** (0.5)	75	95
6	**e**	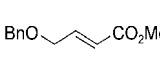	EtMgBr	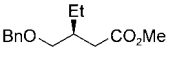	**4a** (2.5)	85	86
7	**f**	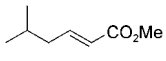	*n*BuMgBr	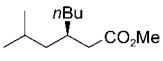	**4a** (0.5)	87	88
8					**4a** (2.5)	99[d]	92
9	**g**	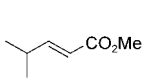	EtMgBr	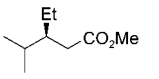	**4a** (2.5)	93[d,e]	87 (*S*)
10					**4b** (2.5)	99[d,e]	99 (*S*)
11					**4b** (0.5)	88[e]	98 (*S*)
12	**h**	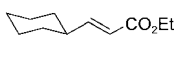	EtMgBr	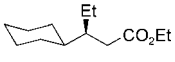	**4b** (2.5)	86[e]	98 (*S*)
13	**a**	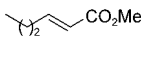	MeMgBr	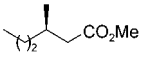	**4a** (2.5)	19[d]	93
14					**4a** (2.5)	37[d,g]	90
15	**i**	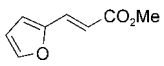	EtMgBr	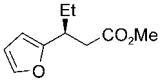	**4a** (2.5)	62[d,e]	86
16					**4b** (0.5)	90[e]	95
17	**j**	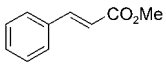	EtMgBr	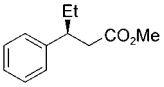	**4a** (2.5)	42[d–f]	75 (*S*)
18					**4b** (1.5)	94[e,f]	98 (*S*)
19	**k**	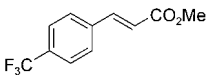	EtMgBr	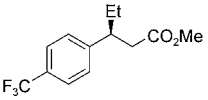	**4b** (1.5)	99[e,f]	96
20	**l**	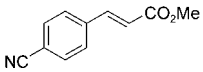	EtMgBr	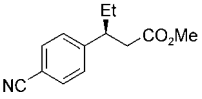	**4b** (5)	80[e,f]	88
21	**m**	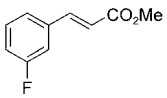	EtMgBr	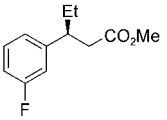	**4b** (1.5)	92[e,f]	97
22	**n**	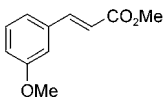	EtMgBr	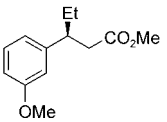	**4b** (1.5)	91[e,f]	97

[a] Conditions: **4** (see table), RMgBr (1.15 equiv), 0.35 M in *t*BuOMe, −75 °C, unless otherwise noted. [b] Yield of isolated product unless otherwise noted. [c] Determined by GC on a chiral phase (G-TA or dex-CB) or HPLC (chiralcel OD-H).[22] [d] Conversion (GC).[22] [e] RMgBr: 2.5 equivalents. [f] Reaction carried out in CH_2Cl_2, 0.25 M. [g] TMSCl (5.0 equiv) used. Bn = benzyl, TMS = trimethylsilyl.

 © 2005 Wiley-VCH Verlag GmbH & Co. KGaA, Weinheim

as the solvent to achieve complete conversions and to avoid undesired 1,2-addition products. Although slightly longer reaction times (3–5 h) were needed than for aliphatic substrates, the method proved to be highly effective and afforded exclusively the desired 1,4-addition products with enantioselectivities ranging from 88–98% *ee*. Finally, preliminary results indicate that aryl moieties that bear donor and acceptor substituents are tolerated, even those with potentially competitive groups, such as nitrile groups.

In conclusion, we have demonstrated that inexpensive and readily available Grignard reagents and stable dinuclear Cu complexes can be used for the first time in catalytic enantioselective conjugate addition reations to simple acyclic α,β-unsaturated methyl esters. These reactions provide access to highly valuable β-substituted chiral esters in good yields and with excellent enantioselectivities (up to 99% *ee*). Studies are underway to establish the full scope of this methodology, as well as to elucidate the reaction mechanism.

Received: January 27, 2005
Published online: April 11, 2005

Keywords: asymmetric catalysis · conjugate addition · copper · enantioselectivity · Grignard reaction

[1] For reviews, see: a) N. Krause, A. Hoffmann-Röder, *Synthesis* **2001**, 171–196; b) B. L. Feringa, R. Naasz, R. Imbos, L. A. Arnold in *Modern Organocopper Chemistry*, (Ed.: N. Krause), VCH, Weinheim, **2002**, pp. 224–258; c) B. L. Feringa, *Acc. Chem. Res.* **2000**, *33*, 346–353; d) A. Alexakis, C. Benhaim, *Eur. J. Org. Chem.* **2002**, 3221–3236; e) K. Tomioka, Y. Nagaoka in *Comprehensive Asymmetric Catalysis*, *Vol. 3* (Eds.: E. N. Jacobsen, A. Pfaltz, H. Yamamoto), Springer, New York, **1999**, pp. 1105–1120; f) K. Yamasaki, T. Hayashi, *Chem. Rev.* **2003**, *103*, 2829–2844.

[2] For recent advances with cyclic systems, see: a) M. Shi, C.-J. Wang, W. Zhang, *Chem. Eur. J.* **2004**, *10*, 5507–5516; b) T. Hayashi, K. Ueyama, N. Tokunaga, K. Yoshida, *J. Am. Chem. Soc.* **2003**, *125*, 11508–11509; c) I. J. Krauss, J. L. Leighton, *Org. Lett.* **2003**, *5*, 3201–3203.

[3] For recent advances with acyclic enones, see: a) A. P. Duncan, J. L. Leighton, *Org. Lett.* **2004**, *6*, 4117–4119; b) A. Alexakis, D. Polet, S. Rosset, S. March, *J. Org. Chem.* **2004**, *69*, 5660–5667; c) P. K. Fraser, S. Woodward, *Chem. Eur. J.* **2003**, *9*, 776–783; d) H. Mizutani, S. J. Degrado, A. H. Hoveyda, *J. Am. Chem. Soc.* **2002**, *124*, 779–781.

[4] For conjugate additions to lactones, see: a) M. T. Reetz, A. Gosberg, D. Moulin, *Tetrahedron Lett.* **2002**, *43*, 1189–1191; b) M. Yan, L.-W. Yang, K.-Y. Wong, A. C. S. Chan, *Chem. Commun.* **2000**, 115–116; c) M. Kanai, Y. Nakagawa, K. Tomioka, *Tetrahedron* **1999**, *55*, 3843–3854.

[5] For recent advances with nitroalkenes, see: a) A. Duursma, A. J. Minnaard, B. L. Feringa, *J. Am. Chem. Soc.* **2003**, *125*, 3700–3701; b) C. A. Luchaco-Cullis, A. H. Hoveyda, *J. Am. Chem. Soc.* **2002**, *124*, 8192–8193, and references therein.

[6] To date, only a Rh-catalyzed asymmetric conjugate addition of aryl boron reagents to α,β-unsaturated esters has been reported, but the method is intrinsically unsuitable for the direct addition of alkyl groups: a) S. Sakuma, M. Sakai, R. Itooka, N. Miyaura, *J. Org. Chem.* **2000**, *65*, 5951–5955; b) Y. Takaya, T. Senda, H. Kurushima, M. Ogasawara, T. Hayashi, *Tetrahedron: Asymmetry* **1999**, *10*, 4047–4056.

[7] For approaches to β-substituted esters based on chiral-auxiliary strategies, see: a) W. Oppolzer, H. J. Löher, *Helv. Chim. Acta* **1981**, *64*, 2808–2811; b) W. Oppolzer, T. Stevenson, *Tetrahedron Lett.* **1986**, *27*, 1139–1140; c) C. Fang, T. Ogawa, H. Suemune, K. Sakai, *Tetrahedron: Asymmetry* **1991**, *2*, 389–398; d) A. Alexakis, R. Sedrani, P. Mangeney, J. F. Normant, *Tetrahedron Lett.* **1988**, *29*, 4411–4414; for an example based on stoichiometric chiral additives, see: e) F. Xu, R. D. Tillyer, D. M. Tschaen, E. J. J. Grabowski, P. J. Reider, *Tetrahedron: Asymmetry* **1998**, *9*, 1651–1655.

[8] For a catalytic approach based on an asymmetric 1,4-hydrosilylation of α,β-unsaturated esters, see: a) B. H. Lipshutz, J. M. Servesko, B. R. Taft, *J. Am. Chem. Soc.* **2004**, *126*, 8352–8353; b) D. H. Apella, Y. Moritani, R. Shintani, E. M. Ferreira, S. L. Buchwald, *J. Am. Chem. Soc.* **1999**, *121*, 9473–9474.

[9] For an explanation of the reactivity of α,β-unsaturated carboxylic acid derivatives relative to that of enones on the basis of their respective LUMO energies, see: S. Matsunaga, T. Kinoshita, S. Okuda, S. Harada, M. Shibasaki, *J. Am. Chem. Soc.* **2004**, *126*, 7559–7570.

[10] For selected recent examples, see: a) M. S. Taylor, E. N. Jacobsen, *J. Am. Chem. Soc.* **2003**, *125*, 11204–11205, and references therein; b) D. A. Evans, K. A. Scheidt, J. N. Johnston, M. C. Willis, *J. Am. Chem. Soc.* **2001**, *123*, 4480–4491; for examples with heteroatom-based nucleophiles, see: c) C. D. Vanderwall, E. N. Jacobsen, *J. Am. Chem. Soc.* **2004**, *126*, 14724–14725; d) M. P. Sibi, N. Prabagaran, S. G. Ghorpade, C. P. Jasperse, *J. Am. Chem. Soc.* **2003**, *125*, 11796–11797, and references therein; e) see also references [1a] and [1e].

[11] A. W. Hird, A. H. Hoveyda, *Angew. Chem.* **2003**, *115*, 1314–1317; *Angew. Chem. Int. Ed.* **2003**, *42*, 1276–1279.

[12] J. Schuppan, A. J. Minnaard, B. L. Feringa, *Chem. Commun.* **2004**, 792–793.

[13] With other alkyl zinc reagents only modest selectivities were observed; see also: A. Alexakis, C. Benhaim, *Tetrahedron: Asymmetry* **2001**, *12*, 1151–1157.

[14] a) B. L. Feringa, R. Badorrey, D. Peña, S. R. Harutyunyan, A. J. Minnaard, *Proc. Natl. Acad. Sci. USA* **2004**, *101*, 5834–5838; b) F. López, S. R. Harutyunyan, A. J. Minnaard, B. L. Feringa, *J. Am. Chem. Soc.* **2004**, *126*, 12784–12785.

[15] a) For enantioselective additions of Grignard reagents to lactones, see references [14a] (5 mol% catalyst: 47–82% *ee*) and [4c] (32 mol% catalyst: 76–90% *ee*).

[16] H.-U. Blaser, W. Brieden, B. Pugin, F. Spindler, M. Studer, A. Togni, *Top. Catal.* **2002**, *19*, 3–16, and references therein.

[17] A further decrease in the catalyst loading to 0.05 mol% (S/C = 2000:1) still led to **3a** with a remarkable 86% *ee* and 70% conversion (GC-MS).

[18] Compound **4a** was recovered in 82% yield. For related achiral halogen-bridged dinuclear Cu species, see: a) E. D. Blue, A. Davis, D. Conner, T. B. Gunnoe, P. D. Boyle, P. S. White, *J. Am. Chem. Soc.* **2003**, *125*, 9435–9441; b) S. P. Neo, Z-Y. Zhou, T. C. W. Mak, T. S. A. Hor, *J. Chem. Soc. Dalton Trans.* **1994**, 3451–3458, and references therein.

[19] Alternatively, **4a′** can be prepared by mixing **2a** and $CuBr{\cdot}SMe_2$ in acetonitrile and converted into the dimeric complex **4a** by treatment with halogenated solvents. See Supporting Information for the characterization of **4a** and **4a′** and further information.

[20] CCDC 261573 contains the supplementary crystallographic data for this paper. These data can be obtained free of charge from the Cambridge Crystallographic Data Centre via www.ccdc.cam.ac.uk/data_request/cif.

[21] Sterically hindered Grignard reagents, such as *i*PrMgBr, and aryl Grignard reagents, such as PhMgBr, have provided poor results so far. (*i*PrMgBr: 26% conversion, 12% *ee*; PhMgBr: 55% conversion, 1% *ee*.)

 © 2005 Wiley-VCH Verlag GmbH & Co. KGaA, Weinheim

[22] See Supporting Information for details.
[23] For a Review on olefin cross-metathesis, see: a) S. J. Connon, S. Blechert, *Angew. Chem.* **2003**, *115*, 1944–1968; *Angew. Chem. Int. Ed.* **2003**, *42*, 1900–1923.
[24] A Cu complex **4b** obtained from **2b** and $CuBr{\cdot}SMe_2$ was prepared by the method shown in Scheme 2 and used in these reactions. The same results were obtained when **4b** was prepared in situ.

 © 2005 Wiley-VCH Verlag GmbH & Co. KGaA, Weinheim

Natural Products Synthesis

Total Synthesis of (−)-Laulimalide: Pd-Catalyzed Stereospecific Ring Construction of the Substituted 3,6-Dihydro[2*H*]pyran Units**

Jun'ichi Uenishi and Masashi Ohmi*

Laulimalide (**1**; Scheme 1) is a novel cancer-therapy agent isolated from the marine sponges *Hyattella* sp. and *Cacospongia mycofijiensis*.[1] Initially, **1** received considerable attention for its potent microtubulin-stabilizing profile, similar to that of taxol with a potency against multidrug-resistant cells at nanomolar concentrations.[2] Recently **1** received additional attention because it seems to have a binding site distinct from that of taxol at the tubulin polymers,[3a–c] which opens up the possibility of using it together with taxol as an enhanced treatment. Owing to its restricted natural supply and unique 18-membered structure, **1** has attracted the interest of synthetic organic chemists.[4] However, although several elegant total syntheses have been reported,[5] a more efficient and flexible synthesis is still required to provide further derivatives for biological evaluation. In particular, the 3,6-dihydro[2*H*]pyran unit is important not only in the synthesis of **1**, but also as a principal component in many biologically important marine natural products. Although these two 3,6-dihydro[2*H*]pyran rings of **1** have been elegantly constructed by olefin metathesis,[5a,c,e–h] hetero-Diels–Alder reaction,[5b,d,f,g] and a few other protocols,[5b,g] we sought a new and general synthetic method for the ring other than the previous methods, thus prompting us to investigate the synthesis of **1**.

Herein, we describe the total synthesis of **1** as well as a new preparation of the 3,6-dihydro[2*H*]pyran moiety based on Pd-catalyzed stereospecific ring formation. As illustrated in Scheme 1, the key reaction steps for our total synthesis of **1** involve the assembly of the two fragments **2** and **3** by Sakurai–Hosomi coupling and Yamaguchi macrolactonization as well as the stereospecific synthesis of two dihydropyran ring units by 6-*exo*-trig and 6-*endo*-trig cyclizations.

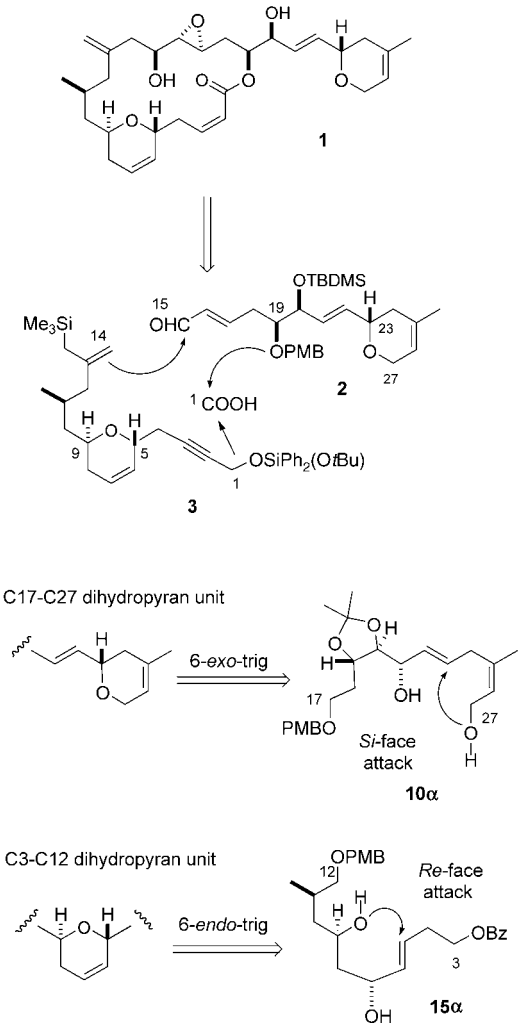

Scheme 1. Retrosynthetic analysis of (−)-laulimalide (**1**). TBDMS = *tert*-butyldimethylsilyl; PMB = *p*-methoxybenzyl; Bz = benzoyl.

The C17–C27 framework was readily prepared by Horner–Wadsworth–Emmons reaction of **4** with **5**, and successive diastereoselective reduction by $NaBH_4$ in the presence of $CeCl_3$ heptahydrate gave β-alcohol **6** in 56% yield in two steps (Scheme 2).[6] Mitsunobu reaction of **6** with benzoic acid gave a mixture of C21 and C23 α-benzoates **7α** and **7α′** in 81% yield as a 1:1 mixture with inversion of the configuration by S_N2 and S_N2' reactions. After cleavage of the TBDPS group with TBAF (nBu$_4$NF), the mixture of regioisomers was subjected to Pd^0-catalyzed intramolecular O-allylation with $[Pd_2(dba)_3]$ in the presence of neocuproine to furnish the desired (*S*)-**8** in 50% yield along with unconverted C21 benzoate **7α** in 44% yield.[7]

[*] Prof. J. Uenishi, M. Ohmi
Kyoto Pharmaceutical University
Misasagi, Yamashina, Kyoto, 607-8412 (Japan)
Fax: (+81) 75-595-4763
E-mail: juenishi@mb.kyoto-phu.ac.jp

[**] This research was supported (in part) by the 21st COE Program from the Ministry of Education, Science and Culture of Japan. We appreciate Dr. B. M. Gallagher, Jr. (Eisai Research Institute) for providing a copy of NMR charts for the seco acid **20** and (−)-laulimalide **1**.

Supporting information for this article is available on the WWW under http://www.angewandte.org or from the author.

 © 2005 Wiley-VCH Verlag GmbH & Co. KGaA, Weinheim DOI: 10.1002/anie.200500029

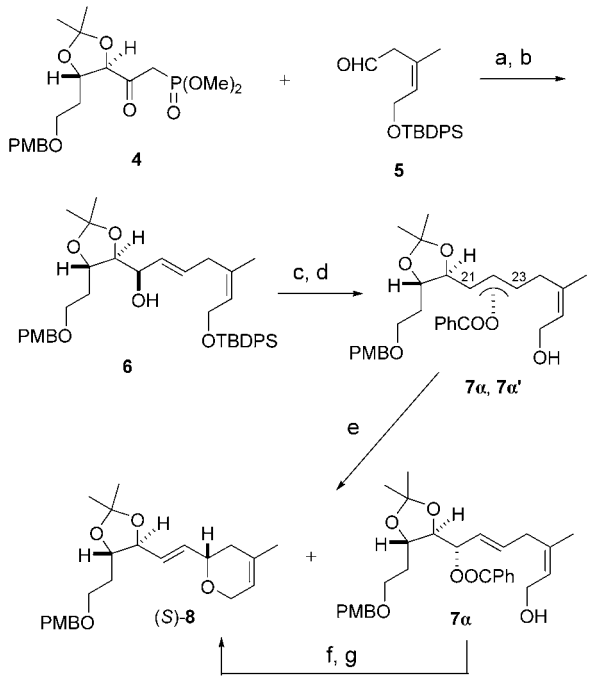

Scheme 2. Preparation of the C17–C27 unit. Reagents and conditions: a) K_2CO_3 THF/H_2O (1:1), room temperature, 70%; b) $NaBH_4$, $CeCl_3 \cdot 7H_2O$, MeOH, −78 °C→RT, 80%; c) DEAD, Ph_3P, PhCOOH, benzene, room temperature, 81%; d) TBAF, THF, room temperature, 86%; e) $[Pd_2(dba)_3]$ (20 mol%), neocuproine, toluene, room temperature, 89% (based on recovered **7α**); f) K_2CO_3, MeOH, room temperature, 97%; g) $[PdCl_2(CH_3CN)_2]$ (10 mol%), THF, 0 °C, 89%. DEAD = diethyl azodicarboxylate; TBAF = tetra-*n*-butylammonium fluoride; TBDPS = *tert*-butyldiphenylsilyl.

The results for the related Pd^0- and Pd^{II}-catalyzed ring formation of the C21 carbonates **9** and alcohols **10** are listed in Table 1. The reaction of **9α** and **9β** with $[Pd_2(dba)_3]$ proceeded stereospecifically to give the *syn*-S_N2'-reaction-type products (*S*)-**8** and (*R*)-**8** in 59% and 43% yield, respectively, by the net retention mechanism.[8] The reaction of **10α** with $[PdCl_2(CH_3CN)_2]$ gave the desired pyran (*S*)-**8** exclusively in 89% yield.[9] On the other hand, the β-diastereomer **10β** gave (*R*)-**8** stereospecifically in 77% yield.

The 1,3 chirality transfer took place with retention of the configuration by an internal *syn*-S_N2'-type attack of the oxygen nucleophile in an *exo*-trig fashion (Scheme 3). When a Pd π-complex **I** is formed selectively on the same side of the double bond as the hydroxy group, the oxygen nucleophile attacks the olefinic carbon center from the *Si* face by a *syn*

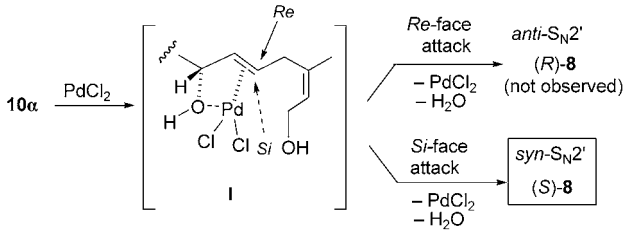

Scheme 3. Synthesis of (*S*)-**8** by *syn*-S_N2' reaction of **10α**.

addition and successive *syn* elimination of Pd(OH)Cl from the resultant Pd σ-complex to give (*S*)-**8**.[10] In contrast, when the oxygen nucleophile attacks the olefinic carbon center of **I** from the *Re* face by an *anti* addition, the diastereomer (*R*)-**8** is obtained.[11]

After cleavage of the acetonide of (*S*)-**8**, oxidation of the diol with DDQ gave *p*-methoxybenzylidene acetal **11** in 77% yield over the two steps (Scheme 4). Subsequently, silylation

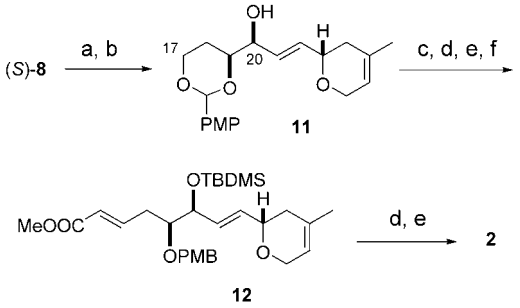

Scheme 4. Synthesis of **2**. Reagents and conditions: a) HCl, MeOH, room temperature, 89%; b) DDQ, molecular sieves (4 Å), CH_2Cl_2, 0 °C, 87%; c) TBDMSCl, imidazole, DMF, room temperature, 90%; d) DIBAL-H, CH_2Cl_2, −78 °C, 83%; e) DMP, 96%; f) $Ph_3PCHCOOMe$, benzene, room temperature, 92%; **12**→**2**: d) 98%; e) 94%. DDQ = 2,3-dichloro-5,6-dicyano-1,4-benzoquinone; DMF = *N*,*N*-dimethylformamide; DIBAL-H = diisobutylaluminum hydride; DMP = Dess–Martin periodinane.

Table 1: Pd^0- and Pd^{II}-catalyzed synthesis of (*S*)-**8** and (*R*)-**8**.

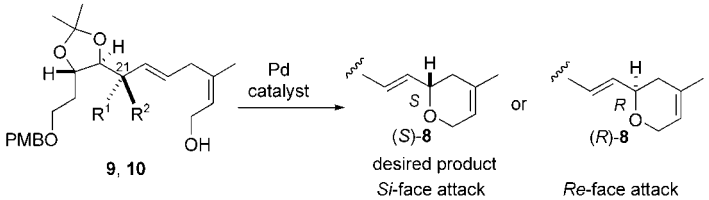

Entry	Compd.	R^1	R^2	Catalyst	**8** (*S*/*R*)	Yield [%]
1	**9α**	OCOOMe	H	$[Pd_2(dba)_3]$[a]	100:0	59[b]
2	**9β**	H	OCOOMe	$[Pd_2(dba)_3]$[a]	0:100	43[b]
3	**10α**	OH	H	$[PdCl_2(CH_3CN)_2]$[c]	100:0	89
4	**10β**	H	OH	$[PdCl_2(CH_3CN)_2]$[c]	0:100	77

[a] Toluene, 80 °C. Neocuproine was used as a ligand. [b] Triene was produced as a by-product. [c] THF, 0 °C.

of the C20 alcohol followed by reductive opening of the benzylidene acetal gave the C17 alcohol.[12] Oxidation of the primary alcohol to an aldehyde followed by a Wittig reaction gave α,β-unsaturated ester **12** in 66% yield over four steps. Reduction of the ester with DIBAL-H and oxidation with Dess–Martin periodinane afforded the desired aldehyde **2** in 92% yield over two steps. The product was identical to the aldehyde reported by Nelson et al.[5g]

The synthesis of the C1–C14 carbon chain commenced from allylic alcohol **13** (Scheme 5).[13] The routine three steps (silylation of the secondary alcohol, osmylation of the double bond, and cleavage of the diol) gave an aldehyde, which underwent Ni/Cr-pro-

 © 2005 Wiley-VCH Verlag GmbH & Co. KGaA, Weinheim

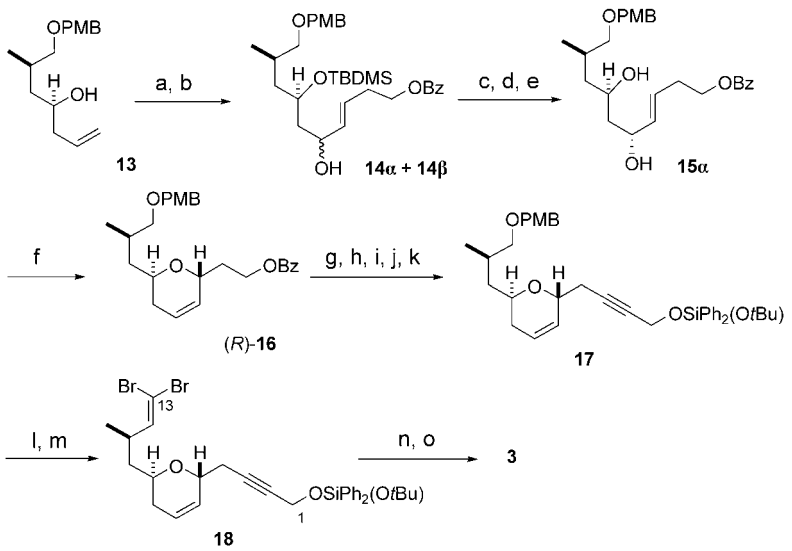

Scheme 5. Synthesis of **3**. Reagents and conditions: a) TBDMSCl, imidazole, DMF, room temperature, 97%; b) 1. OsO_4 (cat.), NMO, THF/H_2O (5:1), room temperature; 2. $NaIO_4$, THF/H_2O (5:1); 3. (*E*)-4-benzyloxy-1-iodo-1-butene, $NiCl_2/CrCl_2$ (cat.), DMSO, room temperature, 75%; c) DMP, 91%; d) BH_3·THF complex, (*S*)-CBS, THF, −40 °C, 99% (d.r. > 97:3); e) TBAF, THF, room temperature, 85%; f) $[PdCl_2(CH_3CN)_2]$ (15 mol%), benzoquinone, THF, −5 °C, 60%; g) K_2CO_3, MeOH, room temperature, 92%; h) DMP, 90%; i) CBr_4, PPh_3, CH_2Cl_2, 0 °C, 94%; j) *n*BuLi, THF, −78 °C; then $(HCHO)_n$, −78 → 0 °C, 83%; k) (O*t*Bu)Ph_2SiCl, Et_3N, CH_2Cl_2, room temperature, 99%; l) DDQ, CH_2Cl_2/buffer (pH 7) (10:1), room temperature, 87%; m) 1. DMP; 2. CBr_4, PPh_3, CH_2Cl_2, 0 °C, 78%; n) $Pd(OAc)_2$ (cat.), PPh_3, Me_3SiCH_2MgCl, THF, 50 °C, 86%; o) PPTS, THF/CH_3CN (9:1), room temperature, 99%. NMO = *N*-methylmorpholine *N*-oxide; DMSO = dimethyl sulfoxide; CBS = Corey–Bakshi–Shibata oxazaborolidine reagent; PPTS = pyridinium toluene-*p*-sulfonate.

moted addition[14] with (*E*)-4-benzoyloxy-1-iodo-1-butene to afford the allylic alcohols **14α** and **14β** as a mixture of diastereomers in 73% yield over four steps. Dess–Martin oxidation and enantioselective reduction of the enone with a combination of BH_3 and an (*S*)-oxazaborolidine ligand (CBS)[15] at −40 °C gave **14α** in 90% yield with high stereoselectivity (> 20:1). After removal of the TBDMS group, the diol **15α** was subjected to Pd^{II}-catalyzed ring formation in a 6-*endo*-trig fashion to give the desired pyran (*R*)-**16** exclusively in 60% yield.[16]

As shown in Table 2, pyran (*S*)-**16** was obtained from the alcohol (*S*)-**15β** in 56% yield under the same reaction conditions.[17] On the other hand, the Pd^0-catalyzed reaction of the corresponding carbonate did not undergo cyclization and gave mainly a diene.

Table 2: Pd^{II}- and Pd^0-catalyzed Synthesis of (*R*)-**16** and (*S*)-**16**.

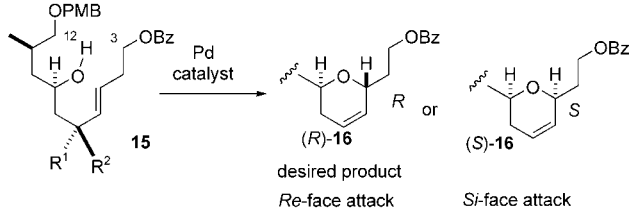

Entry	Compd.	R^1	R^2	Catalyst[a]	**16** (*R*/*S*)	Yield [%]
1	**15α**	OH	H	$[PdCl_2(CH_3CN)_2]$	100:0	60
2	**15β**	H	OH	$[PdCl_2(CH_3CN)_2]$	0:100	56
3	carbonate	OCOOMe	OH	$[Pd_2(dba)_3]$	–	–[b]

[a] Pd catalyst (15 mol%) was used in the presence of benzoquinone. [b] Diene was formed.

Interestingly, 6-*endo*-trig cyclization of **15α** occurs through a *syn*-S_N2' process to give the desired *trans*-(*R*)-dihydropyran ring; in this case, the hydroxy group attacks the *Re* face of the olefinic carbon atom (Scheme 6).

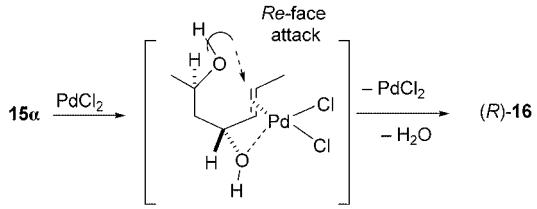

Scheme 6. Synthesis of (*R*)-**16** by *syn*-S_N2' reaction of **15α**.

As shown in Scheme 5, (*R*)-**16** was converted into **17** in 64% yield through the following five-step procedure: 1) deprotection of the terminal benzoate, 2) oxidation to the aldehyde, 3) homologation of the aldehyde to the 1,1-dibromoalkene, 4) debromination with *n*BuLi (2.4 equiv) and reaction of the generated lithioalkyne with paraformaldehyde, and 5) protection of the resultant alcohol with (*t*BuO)Ph_2SiCl as an orthogonal protecting group to TBDMS. The C12 PMB (*p*-methoxybenzyl) ether was transformed into a C14 allylsilane unit in five steps. Deprotection of the PMB ether with DDQ, oxidation to the aldehyde with Dess–Martin periodinane, dibromoolefination with carbon tetrabromide and triphenylphosphane gave **18** in 68% yield. The cross-coupling of the 1,1-dibromo-1-alkene **18** with Me_3SiCH_2MgCl catalyzed by 10 mol% $Pd(OAc)_2$ in the presence of triphenylphosphane gave the corresponding bis(trimethylsilylmethyl)alkene in 86% yield[18] which upon treatment with PPTS as a weak acid underwent protodesilylation to provide *exo* allylsilane **3** quantitatively.

Fragments **2** and **3** were assembled by Sakurai–Hosomi reaction promoted by $SnCl_4$ in 86% yield. Although the reaction gave a mixture of diastereomeric alcohols, oxidation of the alcohol to the enone with Dess–Martin periodinane and enantioselective reduction of the enone with BH_3 and (*R*)-CBS[15] gave the desired alcohol (*S*)-**19** in 79% yield as a single diastereomer (Scheme 7). Silylation of the alcohol and chemoselective cleavage of the (*t*BuO)Ph_2Si ether with K_2CO_3 in methanol gave propargyl alcohol in 88% yield. The C1 alcohol was converted into the seco acid in three steps: oxidation of the propargyl alcohol, deprotection of the PMB ether, and Kraus oxidation.[19] The seco acid **20**[5h] was obtained in 78% yield over the three steps. Yamaguchi lactonization, deprotection of the two silyl ethers, and partial reduction of the alkynyl group to the alkene afforded desoxylaulimalide (**21**)[5c] in 68% yield over three steps. Finally, Sharpless epoxidation with (+)-diisopropyl tartrate gave (−)-laulimalide (**1**) in 80% yield. All the physical and spectroscopic data of **1**, including specific rotation ($[\alpha]_D^{24} = -193$ ($c = 0.18$, $CHCl_3$)), are in perfect accord with those of

 © 2005 Wiley-VCH Verlag GmbH & Co. KGaA, Weinheim

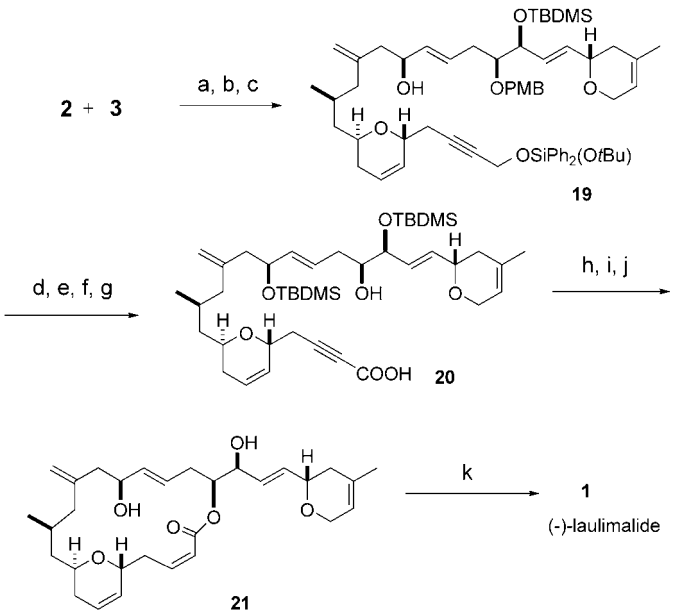

Scheme 7. Coupling of **2** and **3** and synthesis of **1**. Reagents and conditions: a) $SnCl_4$, CH_2Cl_2, −78 °C, 86%; b) DMP, 86%; c) BH_3·THF complex, (*R*)-CBS, THF, −40 °C, 92%; d) TBDMSCl, imidazole, DMF, room temperature, 95%; e) K_2CO_3, MeOH/THF (3:1), room temperature, 93%; f) 1. DMP; 2. DDQ, CH_2Cl_2/buffer(pH 7) (2:1), 0 °C, 80%; g) $NaClO_2$, 2-methyl-2-butene, NaH_2PO_4, THF/*t*BuOH (1:2), 0 °C, 98%; h) Yamaguchi lactonization, 88%; i) HF·py, CH_3CN, room temperature, quant. j) Lindlar cat., H_2, quinoline, EtOAc/1-hexene (1:1), room temperature, 77%; k) Sharpless epoxidation conditions, (+)-diisopropyl tartrate, 80%.

the natural product as well as those previously reported.[5a–c,h]

In conclusion, we have completed the asymmetric total synthesis of (−)-laulimalide based on the novel Pd^{II}- and Pd^0-catalyzed stereospecific ring formation of a 3,6-dihydro[2*H*]-pyran system. We believe that this method should be useful for the synthesis of not only **1** but also of a variety of other marine natural products that contain the 3,6-dihydro[2*H*]-pyran unit.

Experimental Section

3,6-Dihydro[2*H*]pyran formation (representative reaction): A mixture of **10** (1 mmol) and $[PdCl_2(CH_3CN)_2]$ (0.1 mmol) in THF (10 mL) was stirred for 3 h at 0 °C. After concentration, the residue was purified by chromatography on silica gel, eluted with EtOAc in hexane (20%) to give (*S*)-**8** as a colorless oil in 89% yield. $R_f = 0.36$ (20% EtOAc in hexane); $[\alpha]_D^{24} = -61.8$ ($c = 0.11$, MeOH); ^{1}H NMR (400 MHz, $CDCl_3$): $\delta = 1.40$ (3H, s), 1.40 (3H, s), 1.69 (3H, brs), 1.77–1.95 (3H, m), 1.99–2.08 (1H, m), 3.51–3.63 (2H, m), 3.80 (3H, s), 3.83 (1H, td, $J = 8.2$ and 4.0 Hz), 4.00–4.09 (2H, m), 4.11–4.22 (2H, m), 4.43 (2H, s), 5.41 (1H, brs), 5.70 (1H, ddd, $J = 15.6$, 7.5, and 1.3 Hz), 5.87 (1H, ddd, $J = 15.6$, 5.4, and 0.5 Hz), 6.86 (2H, d, $J = 8.8$ Hz), 7.25 ppm (2H, d, $J = 8.8$ Hz); ^{13}C NMR (100 MHz, $CDCl_3$): $\delta = 22.9$, 26.9, 27.2, 32.0, 35.6, 55.2, 65.6, 66.7, 72.6, 73.1, 77.8, 81.9, 108.6, 113.7, 119.6, 127.4, 129.2, 130.5, 131.3, 135.4, 159.1 ppm; IR (neat): $\tilde{\nu} = 1613$, 1514 cm^{-1}; MS (20 eV): *m*/*z* (%): 388 (0.4) [M^+], 370 (1), 209 (6), 160 (10), 136 (36), 121 (100); HRMS (20 eV): calcd for $C_{23}H_{32}O_5$: 388.2250, found: 388.2251. (*R*)-**8**: 77% yield; its physical and spectroscopic data is described in the Supporting Information.

Reaction of **15**: A mixture of **15** (3 mmol) and $[PdCl_2(CH_3CN)_2]$ (0.45 mmol) in THF (60 mL) was stirred for 1 h at −5 °C. After addition of benzoquinone (0.9 mmol), the mixture was stirred for 2 days at room temperature. The mixture was diluted with hexane (70 mL), and $NaBH_4$ (1 mmol) was added to decompose the remaining benzoquinone. The standard workup and purification by silica-gel column chromatography eluted with EtOAc in hexane (10%) gave (*R*)-**16** as a colorless oil in 60% yield. $R_f = 0.76$ (30% EtOAc in hexane); $[\alpha]_D^{24} = -29.5$ ($c = 0.74$, $CHCl_3$); ^{1}H NMR (400 MHz, $CDCl_3$): $\delta = 0.97$ (3H, d, $J = 6.8$ Hz), 1.23 (1H, ddd, $J = 14.1$, 9.5, and 3.5 Hz), 1.71 (1H, ddd, $J = 14.1$, 9.7, and 4.2 Hz), 1.89–2.13 (5H, m), 3.24 (1H, dd, $J = 9.1$ and 6.5 Hz), 3.33 (1H, dd, $J = 9.1$ and 6.0 Hz), 3.75–3.82 (1H, m), 3.79 (3H, s), 4.38–4.52 (3H, m), 4.43 (2H, s), 5.68–5.73 (1H, m), 5.82–5.88 (1H, m), 6.86 (2H, d, $J = 6.8$ Hz), 7.25 (2H, d, $J = 8.6$ Hz), 7.40–7.45 (2H, m), 7.52–7.57 (1H, m), 8.02–8.06 ppm (2H, m); ^{13}C NMR (100 MHz, $CDCl_3$): $\delta = 16.8$, 29.7, 31.3, 33.0, 39.4, 55.3, 61.9, 65.2, 69.2, 72.5, 75.9, 113.7, 124.8, 128.3, 129.0, 129.1, 129.6, 130.4, 130.9, 132.9, 159.0, 166.5 ppm; IR (neat): $\tilde{\nu} = 2955$, 2930, 1716, 1613, 1513, 1276, 1249, 1112, 1036 cm^{-1}; MS (20 eV): *m*/*z* (%): 424 (2) [M^+], 303 (2), 285 (3), 204 (11), 181 (44), 121 (100); HR-MS (20 eV): calcd for $C_{26}H_{32}O_5$: 424.2250; found: 424.2249. (*S*)-**16**: 56% yield; its physical and spectroscopic data is described in the Supporting Information.

Received: January 5, 2005
Published online: March 30, 2005

Keywords: diastereoselectivity · macrocycles · natural products · palladium · total synthesis

[1] a) E. Quinoa, Y. Kakou, P. Crews, *J. Org. Chem.* **1988**, *53*, 3642–3644; b) D. G. Corley, R. Herb, R. E. Moore, P. J. Scheuer, V. J. Paul, *J. Org. Chem.* **1988**, *53*, 3644–3646; c) C. W. Jefford, G. Bernardinelli, J. Tanaka, T. Higa, *Tetrahedron Lett.* **1996**, *37*, 159–162.

[2] S. L. Mooberry, G. Tien, A. H. Hernandez, A. Plubrukarn, B. S. Davidson, *Cancer Res.* **1999**, *59*, 653–660.

[3] a) D. E. Pryor, A. O'Brate, G. Bilcer, J. F. Diaz, Y. Wang, Y. Wang, M. Kabaki, M. K. Jung, J. M. Andreu, A. K. Ghosh, P. Giannakakou, E. Hamel, *Biochemistry* **2002**, *41*, 9109–9115; b) E. J. Gapud, R. Bai, A. K. Ghosh, E. Hamel, *Mol. Pharmacol.* **2004**, *66*, 113–121; c) O. Pineda, J. Farras, L. Maccari, F. Manetti, M. Botta, J. Vilarrasa, *Bioorg. Med. Chem. Lett.* **2004**, *14*, 4825–4829.

[4] An excellent review for (−)-laulimalide; see, J. Mulzer, E. Öhler, *Chem. Rev.* **2003**, *103*, 3753–3786.

[5] Total syntheses; see, a) A. K. Ghosh, Y. Wang, *J. Am. Chem. Soc.* **2000**, *122*, 11027–11028; b) I. Paterson, C. De Savi, M. Tudge, *Org. Lett.* **2001**, *3*, 3149–3152; c) J. Mulzer, E. Öhler, *Angew. Chem.* **2001**, *113*, 3961–3964; *Angew. Chem. Int. Ed.* **2001**, *40*, 3842–3846; d) P. A. Wender, S. G. Hegde, R. D. Hubbard, L. Zhang, *J. Am. Chem. Soc.* **2002**, *124*, 4956–4957; e) M. T. Crimmins, M. G. Stanton, S. P. Allwein, *J. Am. Chem. Soc.* **2002**, *124*, 5958–5959; f) D. R. Williams, L. Mi, R. J. Mullins, R. E. Stites, *Tetrahedron Lett.* **2002**, *43*, 4841–4844; g) S. G. Nelson, W. S. Cheung, A. J. Kassick, M. A. Hilfiker, *J. Am. Chem. Soc.* **2002**, *124*, 13654–13655; h) B. M. Gallagher, Jr., F. G. Fang, C. W. Johannes, M. Pesant, M. R. Tremblay, H. Zhao, K. Akasaka, X. Li, J. Liu, B. A. Littlefield, *Bioorg. Med. Chem. Lett.* **2004**, *14*, 575–579.

[6] J. Uenishi, M. Ohmi, K. Matsui, M. Iwano, *Tetrahedron* **2005**, *61*, 1971–1979.

[7] The compound **7α** was unreactive under these (and even harsher) conditions.

[8] A. Pfaltz, M. Lautens in *Comprehensive Asymmetric Catalysis*, *Vol. II* (Eds.: E. N. Jacobsen, A. Pfaltz, H. Yamamoto), Springer,

 © 2005 Wiley-VCH Verlag GmbH & Co. KGaA, Weinheim

Berlin, **1999**, pp. 833–884; J. Tsuji, *Palladium Reagents and Catalysts*, Wiley, Chichester, **1995**.

[9] For Pd^{II}-catalyzed intramolecular C–O bond-forming reaction, see: T. Hosokawa, S. Murahashi in *Handbook of Organopalladium Chemistry for Organic Synthesis*, *Vol. 2* (Ed: E.-i. Negishi), Wiley, New York, **2002**, pp. 2169–2192.

[10] If the alternative Pd π complex is formed as shown below, though it is unfavorable owing to allylic strain, and the oxygen nucleophile were to attack the olefinic carbon atom from the other side of the Pd π complex, the desired 23*S* stereogenic center would be generated. However, the successive *syn* elimination of Pd(OH)Cl would then afford the 21*Z* alkenyl product.

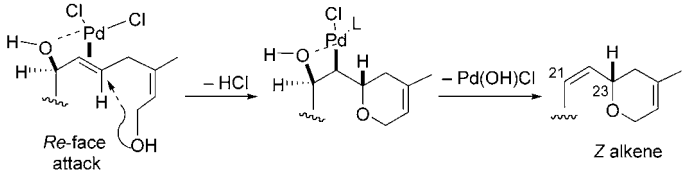

[11] Interestingly, Pd^{II}-catalyzed piperidine ring formation gave the opposite stereochemistry in an *anti*-S_N2'-type reaction: Y. Hirai, M. Nagatsu, *Chem. Lett.* **1994**, 21–22.

[12] Although the *O*-silyl group at C20 was desilylated partially under these conditions, acetylation of C17-OH followed by silylation of C20-OH with TBDMSCl and methanolysis of the acetate led to the primary alcohol in 80% yield over three steps.

[13] Compound **13** was prepared from methyl (*S*)-3-hydroxy-2-methylpropionate according to: A. Ahmed, E. K. Hoegenauer, V. S. Enev M. Hanbauer, H. Kaehlig, E. Öhler, J. Mulzer, *J. Org. Chem.* **2003**, *68*, 3026–3042.

[14] a) H. Jin, J. Uenishi, W. J. Christ, Y. Kishi, *J. Am. Chem. Soc.* **1986**, *108*, 5644–5646; b) K. Takai, M. Tagashira, T. Kuroda, K. Oshima, L. Utimoto, H. Nozaki, *J. Am. Chem. Soc.* **1986**, *108*, 6048–6050.

[15] For enantioselective reduction through CBS reduction, see: E. J. Corey, R. K. Bakshi, S. Shibata, *J. Am. Chem. Soc.* **1987**, *109*, 5551–5553; for the reduction of an enone with BH_3 and (*R*)- or (*S*)-2-methyl-oxazaborolidine, see: H. Motoyoshi, K. Ishigami, T. Kitahara, *Tetrahedron* **2001**, *57*, 3899–3908.

[16] For 5-*endo*-trig cyclization in dihydrofuran synthesis, see: S. Saito, T. Hara, N. Takahashi, M. Hirai, T. Moriwake, *Synlett* **1992**, 237–238.

[17] The stereochemistry of **15α** and **15β** was confirmed by NOE experiments after their conversion into acetonide derivatives.

[18] J. Uenishi, M. Ohmi, *Heterocycles* **2003**, *61*, 365–376.

[19] G. A. Kraus, B. Roth, *J. Org. Chem.* **1980**, *45*, 4825–4830.

 © 2005 Wiley-VCH Verlag GmbH & Co. KGaA, Weinheim

Library Biosynthesis

Genetically Selected Cyclic-Peptide Inhibitors of AICAR Transformylase Homodimerization**

*Ali Tavassoli and Stephen J. Benkovic**

The de novo purine biosynthetic pathway is used by virtually all organisms for the production of purine nucleotides. The final two steps of this pathway (Scheme 1) are catalyzed by aminoimidazole-4-carboxamide ribonucleotide transformylase/inosine monophosphate cyclohydrolase (AICAR Tfase/IMPCH), the two activities of a highly conserved 64 kDa bifunctional protein (ATIC) that possesses two distinct domains.[1] The C-terminal AICAR Tfase domain (residues 200–593) catalyzes the transfer of a formyl group from N_{10}-formyltetrahydrofolate (10-f-thf) to AICAR. The N-terminal IMPCH domain (residues 1–199) catalyzes the final step of the pathway.[2]

Cancer cells rely heavily on the de novo pathway for purine biosynthesis.[3] Thus, the inhibition of enzymes in this pathway is an attractive approach for the development of anticancer agents. As well as their potential uses in the treatment of malignant diseases, ATIC inhibitors are used in the treatment of inflammatory diseases, such as rheumethoid arthritis.[4]

The AICAR Tfase activity of ATIC is dependent on its homodimerization, whereas the IMPCH activity is not. The recently reported crystal structure shows ATIC as a dimer with an interface of ≈ 5000 Å^2.[2] There is much potential for the development of a new generation of therapeutic agents that act by inhibiting protein–protein interactions.[5] We chose genetic selection as the means to identify small molecules that specifically inhibit ATIC homodimerization and thereby inhibit AICAR Tfase activity. The selected approach utilizes whole cells as reporters of a designated intracellular event (interruption of a protein–protein interaction) by correlating host growth to the desired functional property of a small molecule. An advantage of this method is the selection of library members in vivo, which allows both affinity and selectivity to be assayed simultaneously.

Specifically, the combination of our split intein-mediated circular ligation of peptides and proteins (SICLOPPS) technology (Scheme 2)[6] with a bacterial reverse two-hybrid system (RTHS) provides a method with the above characteristics for the systematic identification of small-molecule

[*] Dr. A. Tavassoli, Prof. S. J. Benkovic
Department of Chemistry
The Pennsylvania State University
University Park, PA 16802 (USA)
Fax: (+1) 814-865-2973
E-mail: sjb1@psu.edu

[**] We thank A. R. Horswill, T. A. Naumann, S. W. Nelson, S. N. Savinov, and M. E. Webb for helpful discussions. This work was funded by National Institutes of Health grant GM24129-28.
AICAR = aminoimidazole-4-carboxamide ribonucleotide.

Supporting information for this article is available on the WWW under http://www.angewandte.org or from the author.

 © 2005 Wiley-VCH Verlag GmbH & Co. KGaA, Weinheim DOI: 10.1002/anie.200500417

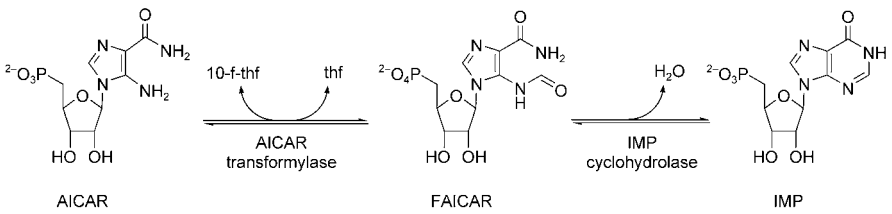

Scheme 1. Final two steps of the de novo purine biosynthetic pathway catalyzed by ATIC.

inhibitors of protein–protein interactions.[7] SICLOPPS allows the intracellular synthesis of libraries containing up to 10^8 cyclic peptides,[6] which is several orders of magnitude larger than those possible by conventional synthetic methods. The cyclization of peptides confers in vivo stability through the resulting resistance to degradation by proteases.[8]

Our bacterial RTHS[7] is based on the bacteriophage regulatory system,[9] which links the disruption of the fusion-protein homodimer to the expression of three reporter genes (Figure 1). HIS3[10] (imidazole glycerol phosphate dehydratase) and Kan^R (aminoglycoside 3′-phosphotransferase for kanamycin resistance) are two chemically tunable, conditionally selective reporter genes. The third reporter gene, LacZ (β-galactosidase), is used to quantify the protein–protein interaction through β-galactosidase assays.

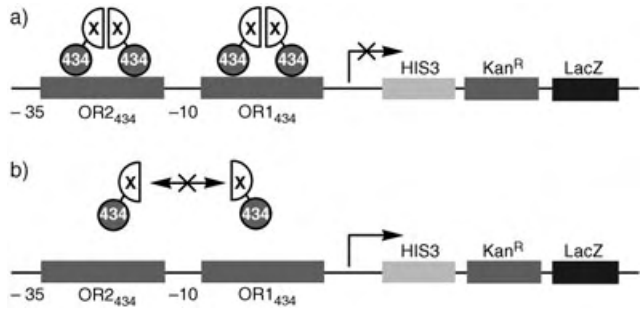

Figure 1. a) The protein fusions (X = target protein) associate (by binding to the 434 operator OR1 and OR2) to form a functional repressor of the promoter that directs expression of the reporter genes, thus inhibiting growth on minimal media. b) A small molecule inhibits the protein–protein interaction, thus restoring growth by the induction of HIS3 and Kan^R.

ATIC was cloned as a fusion with the DNA-binding domain of bacteriophage 434 repressor and placed under the control of an isopropyl-β-D-thiogalactoside (IPTG) inducible promoter. The fusion constructs showed IPTG-dependent repression of the reporter genes on selective media, thus confirming the formation of a functional repressor (Figure 1a). To improve the selection conditions, a new RTHS strain was constructed by integrating the ATIC fusion onto the chromosome. The level of IPTG that leads to optimal repression was determined to be 50 μM by β-galactosidase assays.

The first SICLOPPS library transformed into the selection strain encoded a hexapeptide with five random residues and a cysteine nucleophile. Approximately 10^7 transformants were plated onto histidine-free minimal media supplemented with arabinose (inducer for SICLOPPS), 3-amino-1,2,4-triazole (3-AT, competitive inhibitor of the HIS3 product), and kanamycin at a density of 10^6 per plate (100×15 mm). The plates were incubated until colonies were readily visible (approximately 1 in 10^5). A second library, which encoded an octapeptide with five random residues and an invariable SGW motif, was also tested (Scheme 2). Around 200 colonies were picked and screened for arabinose-dependent growth advantage and IPTG-dependent inhibition of growth to eliminate false positive results. The expected phenotype was further confirmed by isolating and retransforming the selected SICLOPPS plasmids into the selection strain. The 14 remaining cyclic peptides were then ranked for activity by spotting serial dilutions of the corresponding cells onto selective media; the conferred growth advantage was compared at each dilution level (Figure 2).

To assess the in vivo target specificity of the selected cyclic peptides, a new RTHS strain containing a 434 repressor DNA-binding domain fusion with the *Saccharomyces cerevisiae* GCN4 leucine zipper (LZ) on its chromosome was constructed. The SICLOPPS plasmids of the active selectants were transformed into the LZ RTHS strain and ranked by drop spotting. ATIC-specific cyclic-peptide inhibitors were expected to be inactive in the LZ strain (identical to the ATIC RTHS strain except for the LZ homodimer). Five of the 14 selectants conferred a growth advantage (arabinose-dependent) on the LZ RTHS strain and were therefore discarded.

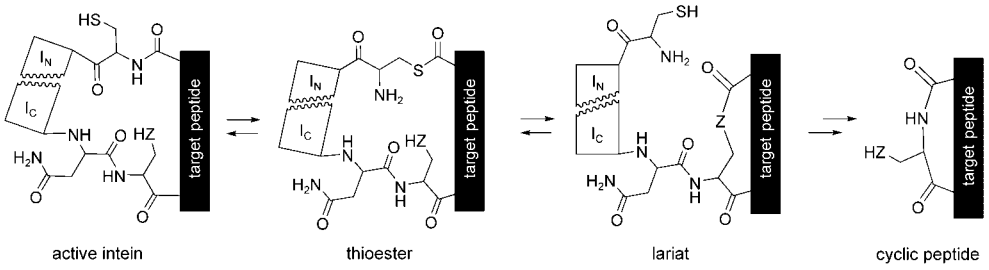

Scheme 2. An expressed fusion protein folds to form an active intein, which undergoes a series of rearrangements to generate a cyclic peptide. In this case the target cyclic peptide contains a series of randomly encoded amino acids to give libraries of $\approx 10^8$ members. Library 1: Z = S, target peptide = $CX_1X_2X_3X_4X_5$; library 2: Z = O, target peptide = $SGWX_1X_2X_3X_4X_5$ (X_n = random amino acid).

 © 2005 Wiley-VCH Verlag GmbH & Co. KGaA, Weinheim

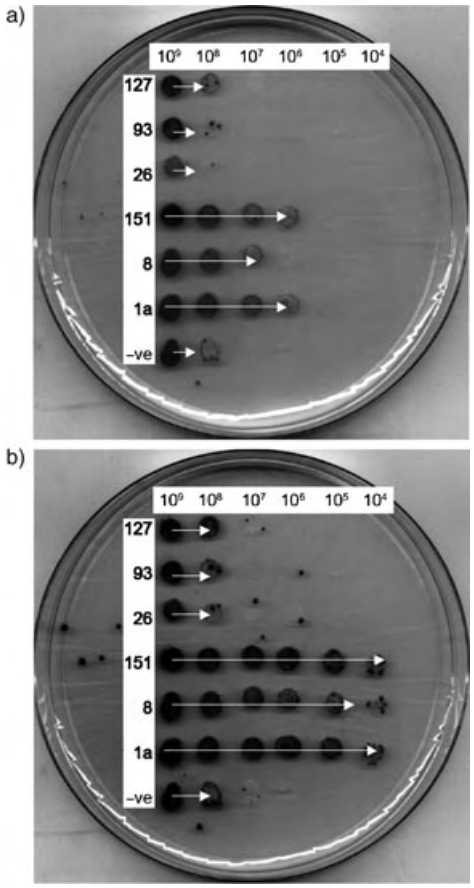

Figure 2. Determination of cyclic-peptide activity (rows) by drop spotting serial dilutions (2.5 μL of $\approx 10^n$ cells mL^{-1}) onto selective media containing arabinose and observing growth after 2 days (a) and after 4 days (b). In this case peptides **1a**, **8**, and **151** are active. Growth was not observed past the first column in the absence of arabinose (data not shown). −ve = control strain containing a blank SICLOPPS plasmid that does not express a cyclic peptide.

An inherent advantage of using genetically encoded libraries is the relative ease with which the structure of the active members can be determined (in contrast to deciphering synthetically derived libraries). Thus, DNA sequencing of the variable inserts present on the selected SICLOPPS plasmids readily revealed the amino acid sequence of the ATIC-specific cyclic-peptide inhibitors (Table 1).

There is considerable sequence homology in the genetically selected peptides. In general, arginine is favored in position 1, followed in position 2 by an aromatic amino acid (tyrosine or phenylalanine) in the more active, or an aliphatic amino acid (isoleucine, leucine, or valine) in the less active, cyclic peptides. The third random position is mainly occupied by leucine or phenylalanine. The three most active inhibitors contain an amino acid with an amide side chain (asparagine or glutamine) in position 4. The fifth amino acid is mostly valine or leucine.

Table 1: Sequence of the selected cyclic peptides in order of biological activity.

Activity rank	Name	Peptide sequence
1	**1a**	R Y F N V C
1	**151**	M F L N V SGW
2	**8**	R I L Q L C
2	**4**	R F F I C C
3	**6**	T V L M F C
3	**15**	S M M V L C
3	**5**	R I L V L C
3	**26**	P V L L L C
3	**25**	M L L I V C

As the AICAR Tfase activity of ATIC is dependent on its dimerization, disruption of the homodimer can be monitered in vitro by AICAR Tfase assays. The two most active cyclic peptides (**1a** and **151**) were synthesized chemically for in vitro testing. The synthesis of cyclic peptide **1a** involved the immobilization of the corresponding linear sequence on a modified amino polyethylene glycol acrylamide copolymer (PEGA) resin by forming a disulfide bond with its cysteine side chain.[7] The immobilized peptide was then cyclized and cleaved from the PEGA resin (Scheme 3a). The cyclization of linear peptide **151** was carried out in *N*,*N*-dimethylformamide (DMF) at high dilution to favor monomolecular cyclization (Scheme 3b).

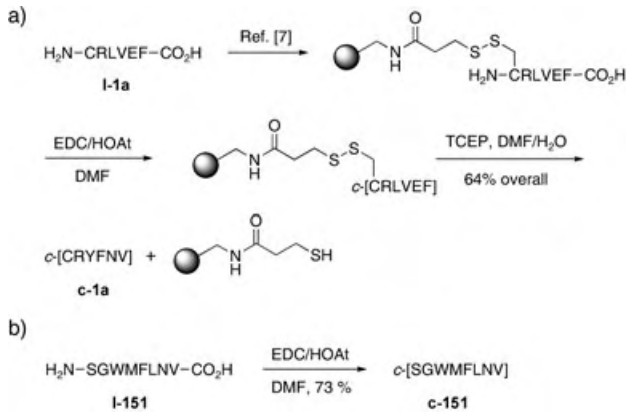

Scheme 3. Synthesis of cyclic-peptide inhibitors **c-1a** and **c-151**. In both cases the linear peptides are cyclized by treatment with 1-ethyl-3-(3′-dimethylaminopropyl)carbodiimide (EDC) and 1-hydroxy-7-azabenzotriazole (HOAt) in DMF. Peptide **c-1a** is cleaved from the resin with tris(2-carboxyethyl)phosphane (TCEP).

The cyclic peptides were purified by reversed-phase chromatography. The chemical nature of the peptides was confirmed by comparison with samples prepared biologically (SICLOPPS) by reversed-phase HPLC and electrospray-ionization mass spectrometry. Cyclic peptides **c-1a** and **c-151**, as well as their linear counterparts **l-1a** and **l-151**, were assayed against AICAR Tfase. The peptides were assumed to compete with f-10-thf, which binds to ATIC and stabilizes its dimerization. From the measured k_{cat} value of the enzyme ($1.1\ s^{-1}$) and K_m value of f-10-thf (33.9 μM), the equation for competitive inhibition was used to determine the K_i values (Figure 3).

Peptide **c-1a** was found to have a K_i value of 17 ± 4.2 μM, whereas its linear counterpart **l-1a** has a K_i value of 142 ± 22.5 μM. Inhibitor **c-151** has a K_i value of 59 ± 6.8 μM, and again the linear peptide **l-151** is less active with a K_i value of

 © 2005 Wiley-VCH Verlag GmbH & Co. KGaA, Weinheim

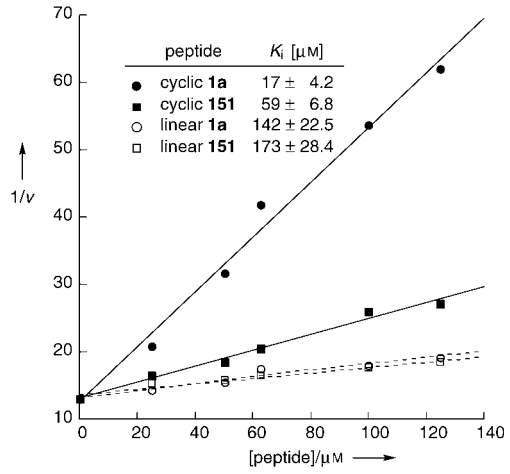

Figure 3. The K_i values of cyclic-peptide inhibitors **1a** and **151** and their linear counterparts as determined by assuming competitive inhibition with respect to 10-f-thf.

173 ± 28.4 μM. That both cyclic peptides are several times more potent than their linear counterparts confirms the superior activity of the genetically selected cyclic epitopes and demonstrates the inherent entropic benefit of a constrained scaffold. The cyclic peptides were also assayed against IMPCH and showed no inhibitory effects. IMPCH activity is not dependent on enzyme dimerization, which suggests that the compounds act by inhibiting ATIC dimerization.

The nature of the inhibition of the most active peptide, **c-1a**, was verified by progress-curve analysis.[11–14] The progress curves were fitted to a model in which the inhibitor binds a single protomer of ATIC, thereby preventing dimerization, as well as to the standard inhibition models (noncompetitive, uncompetitive, mixed, and competitive), by using DynaFit.[11] The data for peptide **c-1a** best fitted the nonstandard model (inhibition of enzyme dimerization) with respect to 10-f-thf and the noncompetitive inhibition model with respect to AICAR (see Supporting Information). This result is consistent with both the ordered binding observed for the enzyme and stabilization of the catalytic dimer by 10-f-thf.[15,16] Furthermore, the K_i value of **c-1a** obtained by this method (18 ± 8.6 μM) matches closely that obtained by assuming competitive inhibition with f-10-thf (17 ± 4.2 μM). The collective kinetic data confirm that cyclic peptide **1a** acts by inhibiting the dimerization of ATIC (as also indicated by the in vivo studies). We are currently attempting to evolve more-potent inhibitors by using second-generation SICLOPPS libraries (based on the selected sequences) and peptidomimetics.[17]

In summary, we have demonstrated a novel approach for the genetic selection of cyclic-peptide inhibitors of AICAR Tfase by combining the RTHS and SICLOPPS technologies. Nine cyclic peptides were selected from an intracellular library of 10^7 members and confirmed to function by selective disruption of the ATIC homodimer in vivo and in vitro. These compounds represent a striking structural departure from the antifolate-based inhibitors generally targeted against this enzyme.[18] The reported methodology allows rapid identification of small-molecule inhibitors of protein–protein interactions, and is thus a powerful and novel approach to drug discovery.

Received: February 3, 2005
Published online: April 13, 2005

Keywords: bioorganic chemistry · enzymes · inhibitors · library biosynthesis · peptides

[1] L. Ni, K. Guan, H. Zalkin, J. E. Dixon, *Gene* **1991**, *106*, 197.
[2] S. E. Greasley, P. Horton, J. Ramcharan, G. P. Beardsley, S. J. Benkovic, I. A. Wilson, *Nat. Struct. Biol.* **2001**, *8*, 402.
[3] R. C. Jackson, R. J. Harkrader in *Nucleosides and Cancer Treatment* (Eds.: M. H. N. Tattersall, R. M. Fox), Academic Press, Sydney, **1981**, p. 18.
[4] P. Gadangi, M. Longaker, D. Naime, R. I. Levin, P. A. Recht, M. C. Montesinos, M. T. Buckley, G. Carlin, B. N. Cronstein, *J. Immunol.* **1996**, *156*, 1937.
[5] R. Zutshi, M. Brickner, J. Chmielewski, *Curr. Opin. Chem. Biol.* **1998**, *2*, 62.
[6] C. P. Scott, E. Abel-Santos, A. D. Jones, S. J. Benkovic, *Chem. Biol.* **2001**, *8*, 801.
[7] A. R. Horswill, S. N. Savinov, S. J. Benkovic, *Proc. Natl. Acad. Sci. USA* **2004**, *101*, 15591.
[8] Y. Q. Tang, J. Yuan, G. Osapay, K. Osapay, D. Tran, C. J. Miller, A. J. Ouellette, M. E. Selsted, *Science* **1999**, *286*, 498.
[9] J. C. Hu, E. K. O'Shea, P. S. Kim, R. T. Sauer, *Science* **1990**, *250*, 1400.
[10] J. K. Joung, E. I. Ramm, C. O. Pabo, *Proc. Natl. Acad. Sci. USA* **2000**, *97*, 7382.
[11] P. Kuzmic, *Anal. Biochem.* **1996**, *237*, 260.
[12] S. R. Stone, H. J. Fromm, *Biochemistry* **1980**, *19*, 620.
[13] M. Bauer, H. Griengl, W. Steiner, *Biotechnol. Bioeng.* **1999**, *62*, 20.
[14] C. Frieden, *Trends Biochem. Sci.* **1993**, *18*, 58.
[15] J. M. Vergis, K. G. Bulock, K. G. Fleming, G. P. Beardsley, *J. Biol. Chem.* **2001**, *276*, 7727.
[16] K. G. Bulock, G. P. Beardsley, K. S. Anderson, *J. Biol. Chem.* **2002**, *277*, 22168.
[17] S. A. Andronati, T. L. Karaseva, A. A. Krysko, *Curr. Med. Chem.* **2004**, *11*, 1183.
[18] C. G. Cheong, D. W. Wolan, S. E. Greasley, P. A. Horton, G. P. Beardsley, I. A. Wilson, *J. Biol. Chem.* **2004**, *279*, 18034.

 © 2005 Wiley-VCH Verlag GmbH & Co. KGaA, Weinheim

Fluorescence Spectroscopy

DNA Detection through Signal Amplification by Using NADH:Flavin Oxidoreductase and Oligonucleotide–Flavin Conjugates as Cofactors**

Philippe Simon, Cécile Dueymes, Marc Fontecave, and Jean-Luc Décout**

Sensitive detection of DNA on the basis of hybridization to a complementary DNA probe and complex-specific signal (for example, fluorescence) detection, may be improved by molecular amplification methods.[1] DNA target amplification is one of the most widely used methods and is mainly based on the polymerase chain reaction (PCR). Recently, signal-amplification techniques based on catalytic reactions, which might be useful for PCR-independent detection of label-free DNA sequences, have also been investigated.[2–5] These methods allow each probe-hybridization event to be converted into many signal events because the catalyst (a chemical or an enzyme) turns over many copies of the sensing-reaction substrate. As a consequence, high sensitivity can be attained. For example, the insertion of ferrocene moieties or redox-active intercalators allows hybrids to catalyze electrochemical reactions that can be monitored either amperometrically or chemically.[2,3] Herein we propose an original and simple strategy that involves the cofactor of an enzyme as the catalytic species. In this system, the DNA probe is an oligonucleotide covalently attached to the cofactor, and the enzyme is selected on the basis of its ability to catalyze the cofactor-dependent conversion of a fluorogenic substrate into an optically silent product (Figure 1). If the enzyme is functional only with a single-stranded cofactor–oligonucleotide conjugate, and not when the latter is hybridized to its complementary strand, enzymatic conversion of the substrate, monitored by fluorescence spectroscopy, can serve as a tool to differentiate whether the probe is hybridized or not (Figure 1). Since the enzyme turns over many copies of the fluorogenic substrate, the difference in the fluorescence

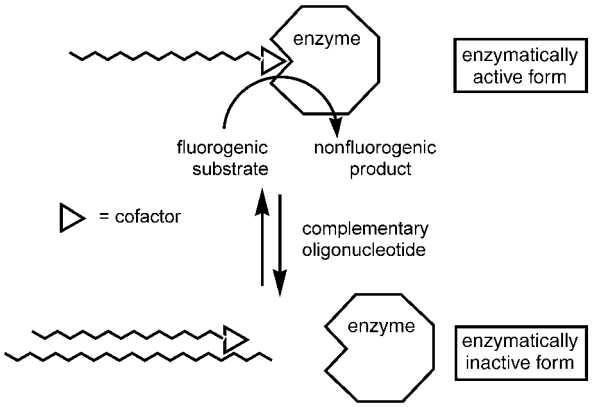

Figure 1. Schematic representation of DNA detection by using an enzyme and its cofactor conjugated to an oligonucleotide probe.

signals obtained with the free and the hybridized probes can be greatly amplified enzymatically.

This new concept is illustrated herein with an enzyme that catalyzes the oxidation of reduced pyridine nucleotides, either nicotinamide adenine dinucleotide phosphate (NADPH) or nicotinamide adenine dinucleotide (NADH), by molecular oxygen in the presence of a riboflavin, either flavin mononucleotide (FMN) or flavin adenine dinucleotide (FAD), as a cofactor. Such an enzyme is called an NAD(P)H:flavin oxidoreductase or flavin reductase.[6] We selected the flavin reductase from *Escherichia coli*, named Fre, which is soluble, monomeric, and very easy to purify in large amounts.[7,8] Structural, mechanistic, and substrate-specificity studies in our laboratory[9–12] have shown that Fre contains an active site which accomodates both the flavin and the reduced pyridine nucleotide and that the reaction proceeds in two steps (Scheme 1): first, a hydride transfer from NAD(P)H to the

$$\mathrm{NAD(P)H + H^+ + flavin_{ox} \longrightarrow NAD(P)^+ + flavin_{red}}$$

$$\mathrm{flavin_{red} + O_2 \longrightarrow flavin_{ox} + H_2O_2}$$

Scheme 1. The reaction catalyzed by Fre, an NAD(P)H:flavin oxidoreductase.

oxidized flavin and then an oxidation of the reduced flavin by molecular oxygen, thereby regenerating the cofactor for a new cycle. With small amounts of flavin it is thus possible to oxidize large excesses of NAD(P)H, a process that can be easily monitored spectrophotometrically since NAD(P)H absorbs light at 340 nm whereas $NAD(P)^+$ does not. The reaction can also be followed by fluorescence spectroscopy since NAD(P)H is fluorogenic ($\lambda_{excitation} = 340$ nm, $\lambda_{emission} = 460$ nm).

Fre was selected for its ability to interact with the flavin substrate exclusively through the isoalloxazine ring with a minor contribution of the ribityl chain, thus allowing a variety of modifications of the latter with moderate effect on the activity.[9] **Fl1** (Scheme 2), a riboflavin analogue in which the OH groups of the ribityl chain at positions 2–4 have been removed, and its 5′ conjugate to thymidine through a phosphate group, **Fl2**, which have previously been synthe-

[*] Dr. C. Dueymes, Prof. M. Fontecave
Laboratoire de Chimie et Biochimie des Centres Rédox Biologiques
UMR Université Joseph Fourier-CNRS-CEA 5047
CEA Grenoble
17 Avenue des Martyrs, 38054 Grenoble Cedex 9 (France)
Fax: (+33) 438-78-91-24
E-mail: mfontecave@cea.fr
P. Simon, J.-L. Décout
Chimie Bioorganique
Département de Pharmacochimie Moléculaire
UMR CNRS/Université Joseph Fourier 5063
FR CNRS 2607
BP 138, 5 Avenue de Verdun, 38243 Meylan (France)
Fax: (+33) 476-04-10-07
E-mail: Jean-Luc.Decout@ujf-grenoble.fr

[**] NADH = nicotinamide adenine dinucleotide, reduced form. This work was supported by the CNRS program "Puces à ADN".

Supporting information for this article is available on the WWW under http://www.angewandte.org or from the author.

 © 2005 Wiley-VCH Verlag GmbH & Co. KGaA, Weinheim DOI: 10.1002/anie.200461145

Conjugates:

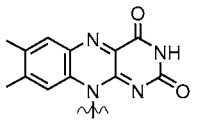

Fl

Fl—$(CH_2)_6$—OH **Fl1**

Fl—$(CH_2)_6$—O—P(=O)(O$^-$)—5'—d(T)$_n$ **Fl2**: n = 1; **1**: n = 11; **2**: n = 16

Fl—$(CH_2)_6$—O—P(=O)(O$^-$)—5'—d(CCCCCACCACTTCCCCTCTC) 3' **3**

Targets:

4: 5' d(CGTGT**(A)$_{11}$**GGCAGTAC) 3'

5: d(GCCTGAT**GAGAGGGGAAGTGGTGGGGG**AGACATAGCCCACC)

6: d(GCCTGAT**GAGAGGGGAAGTGGTGG**CCCAGACATAGCCCACC)

7: d(GCCTGAT**GAGAGGGGAAGTGG**ATTCCCAGACATAGCCCACC)

8: d(GCCTGAT**GAGAGGGGA**CT**TGGTGGGGG**AGACATAGCCCACC)

Scheme 2. Oligonucleotide–flavin conjugates and the corresponding targets. Fl designates the isoalloxazine ring.

sized,[13] are excellent substrates of Fre, as shown from a comparison of the obtained Michaelis constant (K_M) and maximal rate (V_{max}) values with those determined for the natural FAD cofactor (Table 1). Since the probes represented in Figure 1 are oligonucleotide–flavin conjugates, which should function as cofactors of the flavin reductase, we used conjugates **1**–**3** (Scheme 2) in which the 5′ end of the oligonucleotide is attached to the terminus of the side chain of **Fl1**. These conjugates, previously exploited in other applications, were prepared as previously described.[13,14] The broad specificity of Fre with regard to flavins was confirmed with the demonstration, for the first time, that macromolecular single-stranded oligonucleotide–flavin conjugates can also be used by the enzyme (Table 1). Since the enzymatic reduction of these compounds by NADH follows Michaelis–Menten behavior (not shown), it was possible to determine kinetic V_{max} and K_M parameters (Table 1). The data indicated that the K_M value is indeed only affected moderately by the covalent attachment of the 5′ end of an oligonucleotide to the lateral chain of the flavin. The V_{max} value is also only affected moderately. It is likely that recognition by Fre is possible because the spacing provided by the C_6 linker allows the redox-active isoalloxazine moiety to enter the active site. The three-dimensional structure of Fre in complex with riboflavin indeed shows that the ribityl chain is, to a great extent, exposed to the solvent.[12] Thus, oligonucleotide–flavin conjugates can be readily detected in solution from the oxidation of NADH in the presence of catalytic amounts of Fre. This reaction can be monitored on the basis of the decay of the intensity of either the absorption band at 340 nm or the fluorescence at 460 nm. The large excess of NADH with respect to the flavin (20:1–2000:1), as well as the lack of flavin fluorescence below 470 nm and the limited absorption of the flavin between 290–350 nm, prevents flavin absorption/fluorescence from interfering under the assay conditions used.[15,16] In Figure 2 is shown the effect on NADH oxidation at 25 °C of adding increasing amounts of **5**, a 41-mer oligonucleotide containing a 20-mer sequence complementary to that of **3**, to a 10 μM solution of conjugate **3**. We determined a melting temperature (T_m) value of 62 °C for the **3**:**5** duplex under the conditions of the assay and verified that the presence of Fre has no effect on this value. Whereas the addition of a twofold excess of **5** almost totally inhibited the reaction, the addition of a tenfold excess of a noncomplementary oligonucleotide had no effect on the enzyme activity (data not shown). Thus, **5** behaves as an efficient inhibitor of the reaction as a consequence of its ability to hybridize to **3** and to generate a duplex in which the flavin moiety is not recognized by Fre anymore, probably because of increased

Table 1: Oligonucleotide–flavin conjugates are cofactors of Fre, the NAD(P)H:flavin oxidoreductase from *Escherichia coli*.[a]

Flavin substrate	V_m [nmol min^{-1} mg^{-1}]	K_M [μM]
FAD	16000	1
Fl1	14000	2
Fl2	12000	1
1	8500	4
2	10000	6
3	12000	6

[a] Conditions: The oxidation of 250 μM NADH was monitored spectrophotometrically (λ_{max} = 340 nm; ε = 6220 mM^{-1} cm^{-1}) in the presence of 2 μg mL^{-1} Fre and 1–45 μM flavin substrate at 25 °C. The buffer was 50 mM tris(hydroxymethyl)aminomethane/HCl (Tris-HCl; pH 7.6) with 1 M NaCl (for **1** and **2**) or 10 mM NaCl (for **3**).

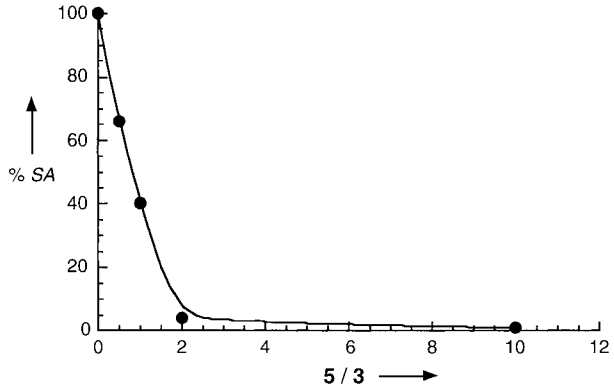

Figure 2. Inhibition of enzymatic oligonucleotide–flavin-dependent NADH oxidation by the complementary strand. The assay mixture contained 10 μM **3**, the flavin reductase (0.36 μg), 200 μM NADH in 50 mM Tris-HCl, and 10 mM NaCl buffer at 25 °C, as well as the complementary oligonucleotide **5** (Scheme 1) in increasing amounts. The activity is assayed on the basis of the oxidation of NADH as monitored spectrophotometrically at 340 nm. **5**/**3** designates the molar excess of oligonucleotide **5** with regard to **3**; %SA designates the percentage specific activity [nmol min^{-1} per mg protein] with 100% corresponding to an assay in the absence of **5**.

 © 2005 Wiley-VCH Verlag GmbH & Co. KGaA, Weinheim

steric hindrance. It is also possible that the isoalloxazine moiety is made less available because of specific interactions in the duplex, in agreement with the reported observation that the fluorescence at 520 nm of an oligonucleotide–flavin conjugate is almost totally quenched within a duplex and that the redox properties of the isoalloxazine ring in such a duplex are greatly modified.[17,18]

We propose that enzyme oxidation of NADH is a simple and sensitive method to detect a target DNA by using an oligonucleotide–flavin probe and catalytic amounts of Fre. The enzyme is crucial as it not only greatly accelerates the sensing reaction but it also allows a clear differentiation between the free and hybridized probes, since Fre recognizes only the former as a cofactor. The intensity of the signal (the difference between free and hybridized probes) can be made very large as a result of the possibility of consuming large concentrations of NADH when the probe is free (Figure 2). Mismatches in the complementary sequence of the target DNA could also be detected by this technique. Indeed, various degrees of inhibition of the flavin reductase activity were observed with targets of variable complementarity. The results (Table 2) indicate that Fre-activity measurements

Table 2: Inhibition of **3**-dependent NADH oxidase activity by hybridization.

Target DNA	Specific activity [%][a]
none	100
5	1
6	12
7	30
8	5

[a] 100% corresponds to 6000 nmol min^{-1} per mg protein. The assay was carried out in the presence of 10 equivalents of target DNA (**5**–**8**) with regard to oligonucleotide **3**, 200 μM NADH, and 3 μg mL^{-1} Fre in 50 mM Tris-HCl (0.1 mL, pH 7.6) with 10 mM NaCl.

make it possible to discriminate targets of slightly different sequences. Less inhibition occurs as a result of mutations at the 3′ part of the target facing the 5′ part of the probe **3** (compare **5** to **6** and **7**, Scheme 2 and Table 2) or of mutations in the interior of the DNA target (compare **5** to **8**, Scheme 2 and Table 2). This effect probably results from a combination of increased accessibility of the flavin moiety and decreased amounts of the hybridized probe at equilibrium and might have applications for the detection of mutated sequences in solution.

The experimental results shown in Figure 3 indicate that the enzymatic NADH oxidation reaction can be carried out in a standard 96-well plate containing the oligonucleotide–flavin probe **1** (0.5 μM, 7.5 pmol) and the enzyme in solution (15 μL), and monitored by a simple camera working at an excitation wavelength of 302 nm, which corresponds to radiation that is very little absorbed by the flavin. The reaction was initiated by the addition of 1 mM NADH, and fluorescence images of the plate were obtained after incubation for 15 min at 18°C. As shown in Figure 3, intense fluorescence was detected only in the well containing the complementary oligonucleotide **4** after the reaction (right column, middle well). No fluorescence was detected when the reaction was carried out in the absence of **4** or in the presence of a noncomplementary oligonucleotide (Figure 3). Finally, when the reaction was carried out at temperatures above 25°C, no difference was observed whether the oligonucleotide **4** was present or not, since at this temperature a large amount of **1** is not hybridized to **4** (the T_m value for **1**:**4** duplex is 27°C).

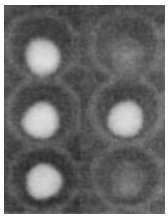

Figure 3. Fluorescence detection of DNA hybridization by using the oligonucleotide–flavin/flavin reductase technique. The image is obtained after incubation (15 min) of 0.5 μM **1** with 1 mM NADH, 100 mM NaCl, and Fre (1.5 μg) in 50 mM Tris-HCl (15 μL, pH 7.5) at 18°C in the presence or absence of the target **4** followed by UV illumination at 302 nm. Left: time zero; right: after 15 min. Top: **1** alone; middle: **1** in the presence of **4** (10 equiv); bottom: **1** in the presence of a noncomplementary 22-mer oligonucleotide (10 equiv).

In this work, no attempt at optimization in terms of sensitivity has been carried out and further investigation is required to reach the highest sensitivities recently reported for comparable systems.[2–4] Theoretically, enhanced sensitivity with this system can be achieved either by prolonging the reaction or by increasing the concentration of the enzyme. For example, the same image as that shown in Figure 3 was also obtained with 50 nM **1** (0.75 pmol in 15 μL) with the same enzyme concentration but with a reaction time of 2 h. In fact, one of the limitations resides in the K_m value for the flavin. Improvement of the system will depend on the development of oligonucleotide–flavin conjugates with smaller K_m values. Previous studies have shown that this goal is realistic.[9] Another limitation is the weak fluorescence of NADH, but this problem can be solved with more-fluorescent analogues, since we have shown that Fre also displays unique binding properties regarding reduced pyridine nucleotides, thereby allowing extensive modifications of the latter.[10]

In conclusion, the concept summarized in Figure 1 for DNA detection has been illustrated experimentally.[19] We have shown that single-stranded oligonucleotide–flavin conjugates are good substrates of an NAD(P)H:flavin oxidoreductase. The fact that hybridization to the complementary strand inhibits the enzyme reaction selectively provides the basis for an enzymatic amplification of nucleic acid sensing. The advantage of the method is the simplicity of the probe and of the sensing reaction.

Received: July 1, 2004
Revised: December 27, 2004
Published online: March 17, 2005

Keywords: DNA detection · flavins · fluorescence · oligonucleotides · oxidoreductases

 © 2005 Wiley-VCH Verlag GmbH & Co. KGaA, Weinheim

[1] B. Schweitzer, S. Kingsmore, *Curr. Opin. Biotechnol.* **2001**, *12*, 21 – 27.
[2] F. Pattolsky, Y. Weizman, I. Willner, *J. Am. Chem. Soc.* **2002**, *124*, 770 – 772.
[3] F. Patolsky, E. Katz, I. Willner, *Angew. Chem.* **2002**, *114*, 3548 – 3552; *Angew. Chem. Int. Ed.* **2002**, *41*, 3398 – 3402.
[4] S. Sando, T. Sasaki, K. Kanatani, Y. Aoyama, *J. Am. Chem. Soc.* **2003**, *125*, 15720 – 15721.
[5] A. Saghatelian, K. M. Guckian, D. A. Thayer, M. R. Ghadiri, *J. Am. Chem. Soc.* **2002**, *124*, 344 – 345.
[6] M. Fontecave, J. Covès, J. L. Pierre, *Biol. Met.* **1994**, *7*, 3 – 8.
[7] M. Fontecave, R. Eliasson, P. Reichard, *J. Biol. Chem.* **1987**, *262*, 12325 – 12331.
[8] P. Gaudu, D. Touati, V. Nivière, M. Fontecave, *J. Biol. Chem.* **1994**, *269*, 8182 – 8188.
[9] F. Fieschi, V. Nivière, C. Frier, J.-L. Décout, M. Fontecave, *J. Biol. Chem.* **1995**, *270*, 30392 – 30400.
[10] V. Nivière, F. Fieschi, J. L. Décout, M. Fontecave, *J. Biol. Chem.* **1996**, *271*, 16656 – 16661.
[11] V. Nivière, M. A. Vanoni, G. Zanetti, M. Fontecave, *Biochemistry* **1998**, *37*, 11879 – 11887.
[12] M. Ingelman, S. Ramaswamy, V. Nivière, M. Fontecave, H. Eklund, *Biochemistry* **1999**, *38*, 7040 – 7049.
[13] C. Frier, J.-L. Décout, M. Fontecave, *J. Org. Chem.* **1997**, *62*, 3520 – 3528.
[14] C. Frier, J. F. Mouscadet, J. L. Décout, C. Auclair, M. Fontecave, *Chem. Commun.* **1998**, 2457 – 2458.
[15] A. Schwögler, T. Carell, *Org. Lett.* **2000**, *2*, 1415 – 1418.
[16] A. Schwögler, L. T. Burgdorf, T. Carell, *Angew. Chem.* **2000**, *112*, 4082 – 4085; *Angew. Chem. Int. Ed.* **2000**, *39*, 3918 – 3920.
[17] C. Dueymes, J. L. Décout, P. Peltié, M. Fontecave, *Angew. Chem.* **2002**, *114*, 504 – 507; *Angew. Chem. Int. Ed.* **2002**, *41*, 486 – 489.
[18] S. Cosnier, C. Gondran, C. Dueymes, P. Simon, M. Fontecave, J.-L. Décout, *Chem. Commun.* **2004**, 1624 – 1625.
[19] This concept has been patented: Commissariat à l'Energie Atomique, FR 2001-9460, WO 2002-FR2482, **2002**.

 © 2005 Wiley-VCH Verlag GmbH & Co. KGaA, Weinheim

Main-Group Chemistry

Reversible Binding of Dioxygen by a Non-Transition-Metal Complex**

Gleb A. Abakumov, Andrey I. Poddel'sky, Ekaterina V. Grunova, Vladimir K. Cherkasov, Georgy K. Fukin, Yury A. Kurskii, and Ludmila G. Abakumova*

For decades, reversible binding of molecular oxygen to various organic and coordination compounds has remained one of the fundamental problems in chemistry because it concerns a number of biochemical and catalytic processes that occur with the participation of molecular oxygen.[1] Numerous examples of reversible binding of molecular oxygen to transition-metal complexes, thus modeling the active centers in biological oxygen carriers, are known.[2] In these complexes, the binding of oxygen is accompanied, in many cases, by the transfer of electrons from the metal center to the oxygen molecule, and thus the oxidation state of the metal atom changes.

A number of studies concern the problem of reversible binding of oxygen to condensed aromatic compounds to form endoperoxides.[3] Usually in these cases, dioxygen is bound and liberated in a singlet state from the adduct that is formed. Therefore, its activation requires a significant amount of excitation energy.

The reversible addition of molecular oxygen to non-transition-metal and nonmetal organoelemental compounds has not been reported to date. Herein, we describe the first example of reversible binding of dioxygen by a non-transition-metal complex: *o*-amidophenolatotriphenylantimony(v).

The starting complex [4,6-di-*tert*-butyl-*N*-(2,6-diisopropylphenyl)-*o*-amidophenolato]triphenylantimony(v) (**1**) was synthesized by the oxidative addition of 4,6-di-*tert*-butyl-*N*-(2,6-diisopropylphenyl)-*o*-iminobenzoquinone to triphenyl antimony(iii) (Scheme 1). Compound **1** was characterized by NMR, IR, and UV/Vis spectroscopies.

The molecular structure of **1** was determined by X-ray analysis (Figure 1). Single crystals of **1** suitable for X-ray analysis were obtained by slow recrystallization from toluene as a toluene solvate **1**·0.5 $C_6H_5CH_3$. The structure of **1** shows that atom Sb(1) has a distorted tetragonal-pyramidal coordination. The basal plane is formed by oxygen, nitrogen, and two carbon atoms, C(33) and C(39), of phenyl groups that are

[*] Prof. Dr. G. A. Abakumov, A. I. Poddel'sky, E. V. Grunova, Prof. Dr. V. K. Cherkasov, Dr. G. K. Fukin, Dr. Y. A. Kurskii, Dr. L. G. Abakumova
G. A. Razuvaev Institute of Organometallic Chemistry of Russian Academy of Sciences
Tropinina 49, 603950 Nizhny Novgorod GSP-445 (Russia)
Fax: (+7) 831-212-7497
E-mail: aip@imoc.sinn.ru

[**] This work was supported by the Russian Foundation for Basic Research (grant 04-03-32409) and the Russian President Grant supporting scientific schools (grant no. 1649.2003.3).

 DOI: 10.1002/anie.200462503 © 2005 Wiley-VCH Verlag GmbH & Co. KGaA, Weinheim

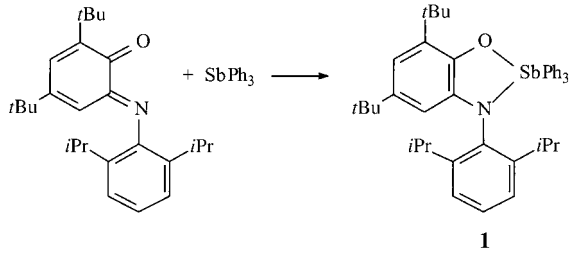

Scheme 1. The synthesis of **1**.

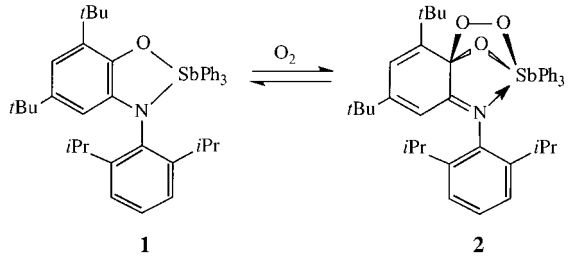

Scheme 2. The interconversion of **1** and **2**.

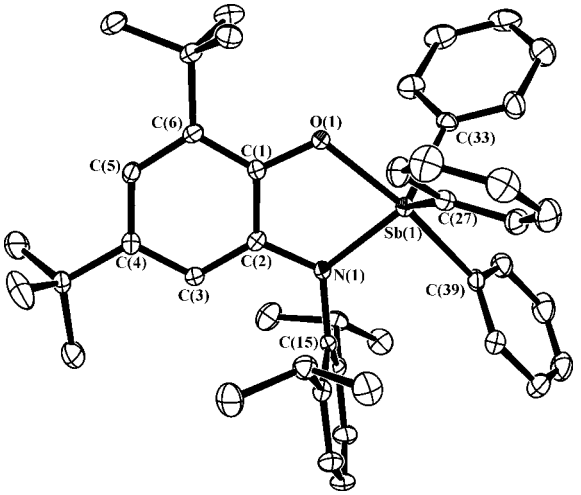

Figure 1. An ORTEP view of **1**, with 30% probability ellipsoids (H atoms are omitted for clarity). Selected bond lengths [Å] and angles [°]: Sb(1)-O(1) 2.074(2), Sb(1)-N(1) 2.041(3), Sb(1)-C(27) 2.128(4), Sb(1)-C(33) 2.138(4), Sb(1)-C(39) 2.137(4), O(1)-C(1) 1.351(4), N(1)-C(2) 1.408(4), N(1)-C(15) 1.441(4), C(1)-C(2) 1.406(5), C(2)-C(3) 1.382(5), C(3)-C(4) 1.385(5), C(4)-C(5) 1.388(5), C(5)-C(6) 1.396(5), C(1)-C(6) 1.395(5); N(1)-Sb(1)-O(1) 77.83(10), N(1)-Sb(1)-C(27) 116.19(14), O(1)-Sb(1)-C(27) 94.13(13), N(1)-Sb(1)-C(33) 134.40(14), O(1)-Sb(1)-C(33) 84.18(13), C(27)-Sb(1)-C(33) 106.52(16), N(1)-Sb(1)-C(39) 92.60(13), O(1)-Sb(1)-C(39) 164.81(13), C(27)-Sb(1)-C(39) 100.72(15), C(33)-Sb(1)-C(39) 94.56(15).

coordinated to the Sb center. The apical position is occupied by a carbon atom, C(27), of a third phenyl group. The dihedral angle between the C(33)-Sb(1)-C(39) and O(1)-Sb(1)-N(1) planes is 134.2°. The C–C bond lengths in the C(1)–C(6) carbon ring lie in the range 1.385(5)–1.406(5) Å, which indicates that the ring is aromatic. The C–N (1.408(4) Å) and C–O (1.351(4) Å) bond lengths are very close to those found in *N*-phenyl-*o*-amidophenolate ligands in other metal complexes (C–N, 1.38–1.39 Å; C–O, 1.35–1.36 Å)[4] and to that expected for C–O bonds in catecholates (1.35 Å).[5] The Sb–O (2.074(2) Å) and Sb–N (2.041(2) Å) interatomic distances are close to the covalent radii of the corresponding elements.[6] Thus, the structure determination unambiguously shows that the antimony(v) center in **1** is bound to an *o*-amidophenolate dianion and three phenyl groups; this structure is also supported by IR spectroscopic data.

Complex **1** is thermally stable (m.p. 170–171 °C) and air-stable in the solid state. However, in solution, **1** binds molecular oxygen to yield compound **2**, which contains a five-atom trioxastibolane ring (Scheme 2). After prolonged exposure of a solution of complex **1** to air, changes in the corresponding NMR and electronic absorption spectra are observed. In the ^{1}H NMR spectrum (Figure 2), the intensity

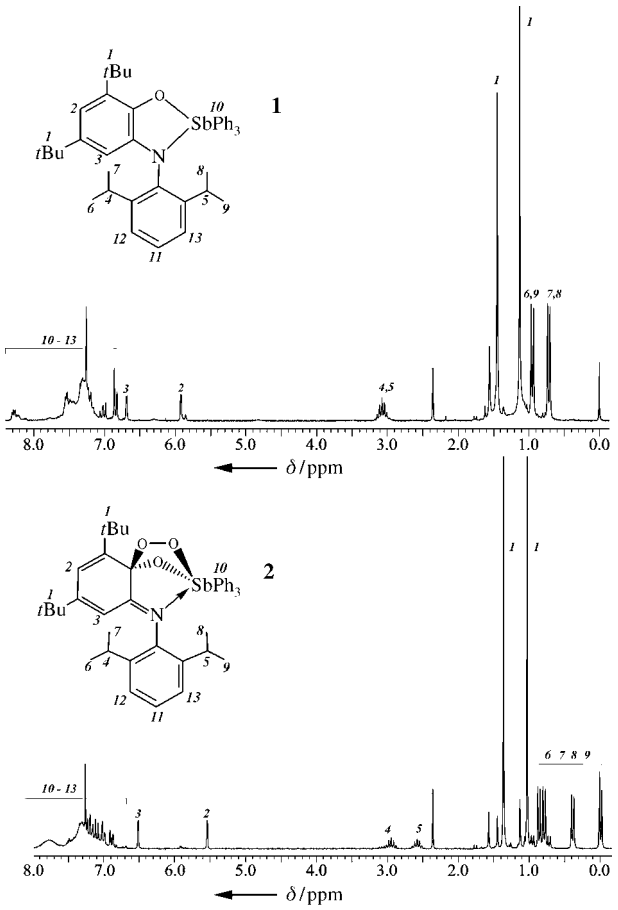

Figure 2. ^{1}H NMR spectra of **1** (top) and **2** (bottom) in $CDCl_3$ at 298 K.

of all proton resonances of **1** decreases, while the intensity of resonances related to **2** increases. Shifts of the signals attributed to the protons of the *tert*-butyl and aromatic groups of a distorted *o*-amidophenolato moiety are observed on addition of dioxygen. In $CDCl_3$, the *tert*-butyl protons of **1** correspond to two singlets at 1.13 and 1.44 ppm, whereas signals from the *tert*-butyl protons of **2** are found at 1.02 and 1.36 ppm. The signals from the aromatic protons in the amidophenolato ligand of **1** appear as doublets centered at 5.91 and 6.69 ppm ($^4J_{H,H} = 2.3$ Hz). The corresponding aro-

 © 2005 Wiley-VCH Verlag GmbH & Co. KGaA, Weinheim

matic protons of **2** give rise to doublet signals centered at 5.53 and 6.51 ppm ($^4J_{H,H} = 1.5$ Hz). Furthermore, in contrast to **1** the asymmetry of complex **2** makes the two methine protons and the protons of the four CH_3 groups of the isopropyl substituents at *N*-aryl nonequivalent. Two isopropyl methine protons of **1** appear as a septet centered at 3.07 ppm ($^3J_{H,H} =$ 6.8 Hz). However, the same methine protons in **2** appear as two septets centered at 2.58 and 2.94 ppm ($^3J_{H,H} = 6.8$ Hz). The signals for the isopropyl methyl groups of **1** are two doublets centered at 0.71 and 0.94 ppm ($^3J_{H,H} = 6.8$ Hz), but the same methyl protons of **2** appear as four doublets at −0.02, 0.38, 0.78, and 0.86 ppm ($^3J_{H,H} = 6.8$ Hz).

In the electronic absorption spectra of the reaction mixture, a new band ($\lambda_{max} = 338$ nm) appears while the intensity of the absorption band of **1** ($\lambda_{max} = 300$ nm) decreases.

Complex **1** was completely converted into **2** in [D_6]acetone (2×10^{-3} M) within two hours when the reaction mixture was stirred in air at 290 K. Spiroendoperoxide **2** was isolated from acetone as air-stable, yellow–orange crystals, which contained one solvate acetone molecule per molecule of complex. The molecular structure of **2** was established by single-crystal X-ray analysis (Figure 3). The O(2)–O(3) bridge, which binds the Sb(1) and C(1) atoms, is slightly shorter (1.461(3) Å) than the analogous bond (1.493(5) Å) in a similar Rh complex[7] and close to the O–O bond length in antimony endoperoxide 3,3-dihydro-5,5-dimethyl-3,3,3-triphenyl-1,2,4,3-trioxastibolane (1.468 Å).[8] The Sb(1) atom in **2** has a distorted octahedral coordination environment. The Sb(1)-O(1)-C(1)-C(2) metallacycle of the *o*-amidophenolato ligand is nonplanar. The dihedral angle between the Sb(1)-O(1)-C(1) plane and Sb(1)-N(1)-C(2)-C(1) plane is 125.6°; the O(1)-C(1)-C(2)-N(1) torsion angle is 34.9°. The C(1)–O(1) bond (1.369(4) Å) is typical for a single bond of a phenolate group,[4,5] whereas the C(2)–N(1) interatomic distance (1.287(3) Å) is close to that of a C–N double bond.[4,6] The C(1)–C(2,6) (1.527(4), 1.510(4) Å) bond lengths and angles around C(1) (102.9(2)–115.2(3)°) indicate sp^3 hybridization of the C(1) atom. The Sb–C (2.141(3)–2.144(3) Å) and Sb–O (2.032(2), 2.072(2) Å) bond lengths are typical for Sb^V compounds,[5,9] and the Sb(1)–N(1) separation (2.425(3) Å) is within the range expected for donor–acceptor Sb–N bonds.[6]

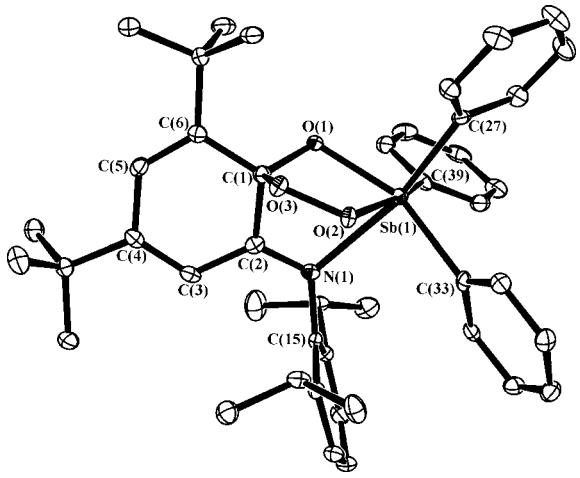

Figure 3. An ORTEP view of **2**, with 30% probability ellipsoids (H atoms are omitted for clariy). Selected bond lengths [Å] and angles [°]: Sb(1)-O(1) 2.032(2), Sb(1)-O(2) 2.072(2), Sb(1)-N(1) 2.425(3), Sb(1)-C(27) 2.141(3), Sb(1)-C(33) 2.144(3), Sb(1)-C(39) 2.144(4), C(1)-O(1) 1.369(4), C(1)-O(3) 1.479(4), N(1)-C(2) 1.287(4), N(1)-C(15) 1.447(4), C(1)-C(2) 1.527(4), C(2)-C(3) 1.433(4), C(3)-C(4) 1.342(5), C(4)-C(5) 1.471(5), C(5)-C(6) 1.347(4), C(1)-C(6) 1.510(4), O(2)-O(3) 1.461(3); N(1)-Sb(1)-O(1) 71.61(8), N(1)-Sb(1)-O(2) 72.77(8), N(1)-Sb(1)-C(27) 163.41(11), O(1)-Sb(1)-C(33) 158.88(10), O(2)-Sb(1)-C(39) 164.80(10), O(1)-Sb(1)-O(2) 79.27(8).

It is remarkable that the transformation of **1** into **2** is completely reversible. Moderate heating of solutions of **2** leads to the initial *o*-amidophenolate **1** by elimination of dioxygen. ^{1}H NMR spectroscopy shows that the conversion of **2** into **1** in [D_6]acetone solution (2×10^{-3} M) is effected by repeating a freeze–pump–warm (50 °C) cycle over 60 minutes. It is necessary to emphasize that **1** reacts with molecular oxygen in its triplet state. The reaction between **1** and O_2 occurs with identical rate under the natural light of the laboratory and in darkness.

Some examples of linear peroxo compounds of antimony are known.[9] The related antimony endoperoxide 3,3-dihydro-5,5-dimethyl-3,3,3-triphenyl-1,2,4,3-trioxastibolane[8] and antimony–oxygen clusters with μ-peroxo ligands have been described previously.[10] However, these compounds are prepared either by exchange reactions or with hydrogen peroxide, but not with dioxygen, and they are not able to eliminate the dioxygen.[8–10]

The unique ability of complex **1** to bind dioxygen reversibly is caused by the redox activity of the *o*-amidophenolate ligand. It is well known that dianions of *o*-aminophenoles, which are similar to catecholate dianions,[11] undergo reversible single-electron oxidation in the coordination sphere of the metal center, which results in the formation of an *o*-iminobenzosemiquinolate.[4,12] Such a transformation can occur by an intramolecular mechanism because of the change in oxidation state of the central atom[12a] or under the influence of an external oxidizer.[4]

We suggest two possible mechanisms for the binding of dioxygen by **1**. The first mechanism assumes a one-electron oxidation of the *o*-amidophenolato ligand by molecular oxygen, with the intermediate formation of an ion pair consisting of the molecular cation $\mathbf{1}^+$ and a superoxide anion (Scheme 3). At the next stage, the triplet diradical complex of antimony(v) that contains the *o*-iminobenzosemiquinonate and peroxo ligands is formed as the result of geminate recombination of ion pairs. Interspin conversion of a triplet state into a singlet state in this diradical is facilitated by the presence of the heavy antimony atom, which has a large spin–orbital interaction constant. The subsequent recombination of the radical centers in the singlet intermediate results in the formation of the final bicyclic endoperoxide **2**. Note that the homolytic substitution reaction on the antimony center with dioxygen takes place even if the electron-transfer stage is omitted. Such a substitution with stable radicals is typical for catecholate complexes.[13]

The second mechanism is similar to that proposed for the reversible binding of triplet dioxygen by bianthrene.[3b] It concerns the formation of a loosely bound complex of **1** and

 © 2005 Wiley-VCH Verlag GmbH & Co. KGaA, Weinheim

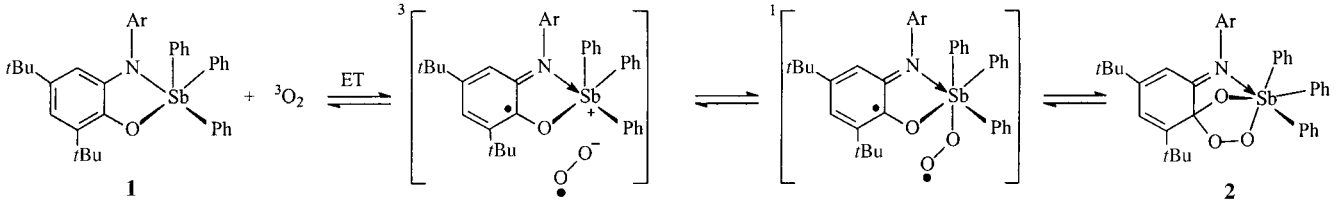

Scheme 3. Plausible mechanism for the reversible conversion of **1** into **2**. ET = electron transfer.

dioxygen, which then proceeds by a spin-forbidden step with charge transfer from **1** to dioxygen to form **2**. The available data do not allow us to distinguish between these two possible mechanisms. However, we suppose that the first mechanism is more probable. The biradical complex is also the key intermediate in the elimination of molecular oxygen. This biradical complex is formed in the first step by the homolytic splitting of the C–O bond. The essential factor that assists this process is the energy compensation because of the formation of an *o*-iminobenzosemiquinonate chelate ligand bonded to antimony.

Experimental Section

The starting materials used were from commercially available sources (Aldrich, Fluka, Strem) unless otherwise noted. 4,6-Di-*tert*-butyl-*N*-(2,6-diisopropylphenyl)-*o*-iminobenzoquinone was synthesized by using a reported method.[14] Synthetic procedures were carried out under vacuum (for **1**) with dried, distilled solvents. ^{1}H NMR spectra were obtained on a Bruker DPX-200 spectrometer (200 MHz). IR spectra (4000–400 cm^{-1}) were recorded on Specord M-80 in nujol. X-ray data were collected on a Bruker Smart Apex diffractometer.

1: A solution of 4,6-di-*tert*-butyl-*N*-(2,6-diisopropylphenyl)-*o*-iminobenzoquinone (0.76 g, 2 mmol) in toluene (30 mL) was added to a stirred solution of $SbPh_3$ (0.71 g, 2 mmol) in toluene (15 mL). The reaction was allowed to proceed over 3 h at room temperature, during which time the mixture gradually changed color from cherry red to orange. The resulting solution was concentrated to 15 mL and stored for a day at 0°C. The product was isolated by filtration and recrystallized over a longer period from toluene to yield yellow, X-ray-quality crystals (1.39 g, 89%); m.p. 170–171°C; Elemental analysis calcd (%) for $C_{47.5}H_{56}ONSb$ (778.72 g mol^{-1}): C 73.26, H 7.25, Sb 15.63; found: C 72.88, H 6.96, Sb 15.60; IR (Nujol): $\tilde{\nu}$ = 1580w, 1570m, 1450s, 1440s, 1430s, 1415m, 1390s, 1360m, 1330m, 1315w, 1290m, 1240s, 1060s, 1055w, 1025w, 995s, 895w, 865w, 850 m, 825w, 805w, 755w, 730s, 690s, 655m, 605w, 530w, 490w, 455m, 440m cm^{-1}.

^{1}H NMR of **1**·0.5 C_7H_8 (200 MHz, $CDCl_3$, 25°C, TMS): δ = 0.71, 0.94 (both d, $^3J_{H,H}$ = 6.8 Hz, both 6H; 2 CH(CH_3)$_2$), 1.13, 1.44 (both s, both 9H; 2 *t*Bu), 2.36 (s, 0.5 × 3H; CH_3 of toluene), 3.07 (sept, $^3J_{H,H}$ = 6.8 Hz, 2H; 2 CH(CH_3)$_2$), 5.91, 6.69 (both d, $^4J_{H,H}$ = 2.3 Hz, both 1H; C_6H_2 aromatic), 6.8–8.3 ppm (m, 20.5H; 18 protons of aromatic groups in **1** and 0.5 × 5 protons of toluene); ^{1}H NMR of **1**·0.5 C_7H_8 (200 MHz, [D$_6$]acetone, 25°C, TMS): δ = 0.78, 0.96 (both d, $^3J_{H,H}$ = 6.8 Hz, both 6H; 2 CH(CH_3)$_2$), 1.11, 1.42 (both s, both 9H; 2 *t*Bu), 2.32 (s, 0.5 × 3H; CH_3 of toluene), 3.16 (sept, $^3J_{H,H}$ = 6.8 Hz, 2H; 2 CH(CH_3)$_2$), 5.91, 6.70 (both d, $^4J_{H,H}$ = 2.3 Hz, both 1H; C_6H_2 aromatic), 6.9–7.8 ppm (m, 20.5H; 18 protons of aromatic groups in **1** and 0.5 × 5 protons of toluene).

Crystal data for **1**·0.5 C_7H_8: $C_{47.5}H_{56}NOSb$, M_r = 778.72, monoclinic, space group $P2_1/n$, a = 10.525(2), b = 14.861(3), c = 26.426(6) Å; β = 99.855(5)°, V = 4072.5(15) Å^3, Z = 4, ρ_{calcd} = 1.228 g cm^{-3}, T = 293(2) K, F(000) = 1566, λ(Mo$_{K\alpha}$) = 0.71073 Å, μ = 0.710 mm^{-1}. Yellow crystal, 0.50 × 0.04 × 0.04 mm^3, θ = 1.56–23.32°, 27208 reflections collected, 5866 independent reflections (R_{int} = 0.0808); GOF(F^2) = 1.029, R_1(I>2σ(I)) = 0.0455, wR_2 (all data) = 0.0963; largest diff. peak and hole 0.597/−0.350 e Å^{-3}.

2: Compound **1** (195 mg, 0.25 mmol) was dissolved in toluene and left in air for 2 h. The solvent was removed by slow evaporation and the residue was recrystallized from acetone over 3 days to yield yellow–orange crystals of **2**·C_3H_6O suitable for X-ray analysis which were collected and dried in air (144 mg, 80%); m.p. 173–176°C (decomp); IR (nujol): $\tilde{\nu}$ = 1715s, 1645s, 1600m, 1590m, 1570m, 1485s, 1435s, 1365s, 1315w, 1275w, 1260w, 1225s, 1180m, 1140s, 1080m, 1065m, 1030w, 1005w, 985w, 940w, 910m, 870m, 855w, 795 m, 760w, 745s, 730s, 705s, 665w, 625w, 570w, 545w, 535w, 490w, 460s cm^{-1}; ^{1}H NMR (200 MHz, $CDCl_3$, 25°C, TMS): δ = −0.02 (d, $^3J_{H,H}$ = 6.8 Hz, 3H; CH_3 of *i*Pr), 0.38 (d, $^3J_{H,H}$ = 6.8 Hz, 3H; CH_3 of *i*Pr), 0.78 (d, $^3J_{H,H}$ = 6.8 Hz, 3H; CH_3 of *i*Pr), 0.86 (d, $^3J_{H,H}$ = 6.8 Hz, 3H; CH_3 of *i*Pr); 1.02, 1.36 (both s, both 9H; 2 *t*Bu), 2.58, 2.94 (both sept, $^3J_{H,H}$ = 6.8 Hz, both 1H; 2 CH of 2 *i*Pr), 5.53, 6.51 (both d, $^3J_{H,H}$ = 1.5 Hz, both 1H; C_6H_2 aromatic), 6.8–7.6 ppm (m, 18H; aromatic); ^{1}H NMR (200 MHz, [D$_6$]acetone, 25°C, TMS): δ = 0.01 (d, $^3J_{H,H}$ = 6.8 Hz, 3H; CH_3 of *i*Pr), 0.43 (d, $^3J_{H,H}$ = 6.8 Hz, 3H; CH_3 of *i*Pr), 0.81 (d, $^3J_{H,H}$ = 6.8 Hz, 3H; CH_3 of *i*Pr), 0.88 (d, $^3J_{H,H}$ = 6.8 Hz, 3H; CH_3 of *i*Pr); 1.06, 1.36 (both s, both 9H; 2 *t*Bu), 2.68, 3.03 (both sept, $^3J_{H,H}$ = 6.8 Hz, both 1H; 2 CH of 2 *i*Pr), 5.60, 6.66 (both d, $^4J_{H,H}$ = 1.5 Hz, both 1H; C_6H_2 aromatic), 6.9–8.0 ppm (m, 18H; aromatic).

Crystal data for **2**·C_3H_6O: $C_{47}H_{58}NO_4Sb$, M_r = 822.73, monoclinic, space group $P2_1/n$, a = 13.2049(6), b = 21.8719(10), c = 14.8069(7) Å; β = 97.4860(10)°, V = 4240.0(3) Å^3, Z = 4, ρ_{calcd} = 1.289 g cm^{-3}, T = 100(2) K, F(000) = 1720, λ(Mo$_{K\alpha}$) = 0.71073 Å, μ = 0.693 mm^{-1}; yellow–orange crystal, 0.08 × 0.05 × 0.02 mm^3, θ = 1.67–25.00°, 23334 reflections collected, 7455 independent reflections (R_{int} = 0.0619); GOF(F^2) = 0.970, R_1(I>2σ(I)) = 0.0370, wR_2(all data) = 0.0727; largest diff. peak and hole 0.613/−0.417 e Å^{-3}.

CCDC 253414 (**1**) and 253415 (**2**) contain the supplementary crystallographic data for this paper. These data can be obtained free of charge from the Cambridge Crystallographic Data Centre via www.ccdc.cam.ac.uk/data_request/cif.

Received: November 3, 2004
Published online: March 31, 2005

Keywords: antimony · N,O ligands · oxo ligands · oxygen · peroxides

[1] a) H. Mimoun in *Comprehensive Coordination Chemistry*, *Vol. 6* (Eds.: G. Wilkinson, R. D. Gillard, J. A. McCleverty), Pergamon, Oxford, **1987**, pp. 317–410; b) L. I. Simándi, *Advances in Catalytic Activation of Dioxygen By Metal Complexes*, *Catalysis By Metal Complexes*, *Vol. 26*, Kluwer, Boston, **2003**.

[2] a) D. H. Busch, N. W. Alcock, *Coord. Chem. Rev.* **1994**, *94*, 585–623; b) A. Butler, M. J. Clague, G. E. Meister, *Coord. Chem. Rev.* **1994**, *94*, 625–638; c) R. A. Sheldon, J. K. Kochi, *Metal-Catalyzed Oxidations of Organic Compounds*, Academic Press, New York, **1981**; d) *Oxygen Complexes and Oxygen Activation by Transition Metals* (Eds.: A. E. Martell, D. T. Sawyer), Plenum, New York, **1988**.

 © 2005 Wiley-VCH Verlag GmbH & Co. KGaA, Weinheim

[3] a) J.-M. Aubry, C. Pierlot, J. Rigaudy, R. Schmidt, *Acc. Chem. Res.* **2003**, *36*, 668 – 675; b) M. Seip, H.-D. Brauer, *J. Am. Chem. Soc.* **1992**, *114*, 4486 – 4490; c) T. Sawada, K. Mimura, T. Thiemann, T. Yamato, M. Tashiro, S. Mataka, *J. Chem. Soc. Perkin Trans. 1* **1998**, 1369 – 1371.

[4] a) H. Chun, C. N. Verani, P. Chaudhuri, E. Bothe, E. Bill, T. Weyhermüller, K. Wieghardt, *Inorg. Chem.* **2001**, *40*, 4157 – 4166; b) H. Chun, P. Chaudhuri, T. Weyhermüller, K. Wieghardt, *Inorg. Chem.* **2002**, *41*, 790 – 795; c) K. S. Min, T. Weyhermüller, K. Wieghardt, *Dalton Trans.* **2004**, 178 – 186; d) X. Sun, H. Chun, K. Hildenbrand, E. Bothe, T. Weyhermüller, F. Neese, K. Wieghardt, *Inorg. Chem.* **2002**, *41*, 4295 – 4303; e) P. Chaudhuri, C. N. Verani, E. Bill, E. Bothe, T. Weyhermüller, K. Wieghardt, *J. Am. Chem. Soc.* **2001**, *123*, 2213 – 2223.

[5] a) S. R. Sofen, D. C. Ware, S. R. Cooper, K. N. Raymond, *Inorg. Chem.* **1979**, *18*, 234 – 239; b) R. R. Holmes, R. O. Day, V. Chandrasekhar, J. M. Holmes, *Inorg. Chem.* **1987**, *26*, 157 – 163; c) R. R. Holmes, R. O. Day, V. Chandrasekhar, J. M. Holmes, *Inorg. Chem.* **1987**, *26*, 163 – 168.

[6] J. Emsley, *The Elements*, Clarendon, Oxford, **1991**.

[7] S. Dutta, S.-M. Peng, S. Bhattacharya, *Inorg. Chem.* **2000**, *39*, 2231 – 2234.

[8] J. Bordner, G. O. Doak, T. S. Everett, *J. Am. Chem. Soc.* **1986**, *108*, 4206 – 4213.

[9] a) Z. A. Starikova, T. M. Shchegoleva, V. K. Trunov, I. E. Pokrovskaya, E. N. Kanunnikova, *Kristallografiya* **1979**, *24*, 1211 – 1215; b) V. E. Shklover, Yu. T. Struchkov, V. A. Dodonov, T. I. Zinov'eva, V. L. Antonovskii, *Metalloorg. Khim.* **1988**, *1*, 1140 – 1142; c) Z. A. Starikova, T. M. Shchegoleva, V. K. Trunov, I. E. Pokrovskaya, *Kristallografiya* **1978**, *23*, 969 – 973; d) W. Satoh, S. Masumoto, Y. Yamamoto, K. Akiba, *Heteroat. Chem.* **2001**, *12*, 431 – 443.

[10] a) H. J. Breunig, T. Krüger, E. Lork, *J. Organomet. Chem.* **2002**, *648*, 209 – 213; b) H. J. Breunig, T. Krüger, E. Lork, *Angew. Chem.* **1997**, *109*, 654 – 655; *Angew. Chem. Int. Ed. Engl.* **1997**, *36*, 615 – 617.

[11] a) C. G. Pierpont, *Coord. Chem. Rev.* **2001**, *216–217*, 99 – 125; b) R. M. Buchanan, C. G. Pierpont, *J. Am. Chem. Soc.* **1980**, *102*, 4951 – 4957; c) G. A. Abakumov, A. V. Lobanov, V. K. Cherkasov, *Dokl. Akad. Nauk USSR* **1982**, *266*, 361 – 363.

[12] a) D. Herebian, P. Ghosh, H. Chun, E. Bothe, T. Weyhermüller, K. Wieghardt, *Eur. J. Inorg. Chem.* **2002**, 1957 – 1967; b) P. Chaudhuri, M. Hess, K. Hildenbrand, E. Bill, T. Weyhermüller, K. Wieghardt, *Inorg. Chem.* **1999**, *38*, 2781 – 2790.

[13] A. I. Prokof'ev, T. I. Prokof'eva, I. S. Belostotskaya, N. N. Bubnov, S. P. Solodovnikov, V. V. Ershov, M. I. Kabachnik, *Tetrahedron* **1979**, *35*, 2471 – 2482.

[14] G. A. Abakumov, N. O. Druzhkov, Yu. A. Kurskii, A. S. Shavyrin, *Russ. Chem. Bull. Int. Ed.* **2003**, *52*, 712 – 717.

 © 2005 Wiley-VCH Verlag GmbH & Co. KGaA, Weinheim

π Stacking

Redox-Induced Transformation from an Extended to a π-Stacked Conformer in Acyclic Bis(catecholacetal)s of Acetylacetone**

Rajendra Rathore, Vincent J. Chebny, Erica J. Kopatz, and Ilia A. Guzei*

The design and synthesis of new π-stacked molecular arrays holds potential for the preparation of wirelike materials for applications in the ever-evolving area of molecular electronics and nanotechnology.[1] We have recently demonstrated that polyfluorenes adopt cyclophane-like π-stacked structures when woven at the alternating carbon atoms of the backbone of an acyclic alkane (Figure 1).[2] This π-stacked arrangement

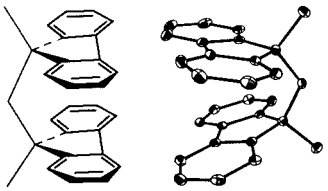

Figure 1. Molecular structure of a π-stacked bifluorene.

of the aromatic moieties in the depicted bifluorene (as well as its higher homologues) arises because of the disk-shaped structure of the fluorene moieties, as well as the *anti* arrangement of all the bonds in the alkane backbone, allow the π-stacked structure to be stabilized both in solution and solid state, as confirmed by NMR spectroscopy and X-ray crystallography.[2]

Our ongoing interest in such cofacially stacked polybenzenoid structures led us to hypothesize that a π-stacked arrangement should be feasible in the bis(catecholacetal) of acetylacetone (**1a**). This compound is readily available by the reaction of acetylacetone (a 1,3-diketone) with catechol in toluene in the presence of an acid catalyst [Eq. (1)].[3]

The molecular structures of various conformers of **1a**, calculated by density functional theory (DFT) at the B3LYP/6-31G* level, showed that both the π-stacked and extended conformers are accessible. The extended conformer **1aE** is only about 2.1 kcal mol^{-1} lower in energy than the π-stacked

[*] Prof. R. Rathore, V. J. Chebny, E. J. Kopatz
Department of Chemistry
Marquette University
P.O. Box 1881, Milwaukee, WI 53201-1881 (USA)
Fax: (+1) 414-288-7066
E-mail: rajendra.rathore@marquette.edu
Dr. I. A. Guzei
Molecular Structure Laboratory
Department of Chemistry, University of Wisconsin
Madison, WI (USA)

[**] We thank the National Science Foundation (Career Award) and the donors of the Petroleum Research Fund (AC12345), administered by the American Chemical Society, for financial support.

 DOI: 10.1002/anie.200463103 © 2005 Wiley-VCH Verlag GmbH & Co. KGaA, Weinheim

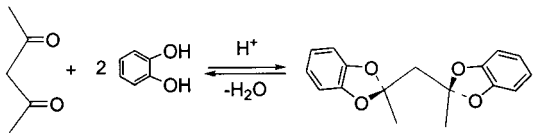

(1)

1a

conformer **1aS** (Figure 2). Interestingly, the energy optimization of the π-stacked conformer of bis(catecholacetal) of acetonoylacetone **2aS** (a 1,4-diketone) always resulted in the extended conformer **2aE** (Figure 3). This suggests that the stacked conformer is substantially higher in energy and not readily attainable.

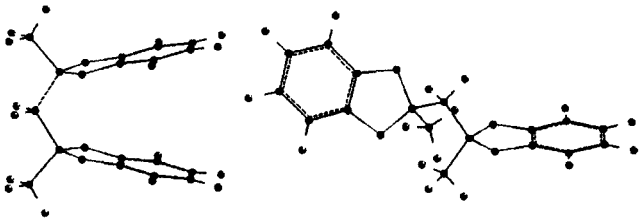

Figure 2. Structures of the π-stacked conformer **1aS** (left) and the extended conformer **1aE** (right).

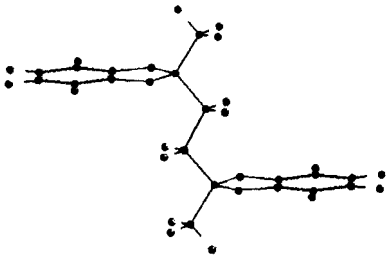

Figure 3. Structure of the extended conformer **2aE**.

Accordingly, herein, we will delineate that the extended conformers of *bis*-catechol acetals of acetylacetone (**1E**) undergo instantaneous folding into cyclphane-like stacked conformers (**1S**) upon one-electron oxidation by using electrochemistry and time resolved laser-flash photolysis as follows.

Various catechol acetals as well as the dimethylcatechol acetals **1**–**3** were readily synthesized by acid-catalyzed con-

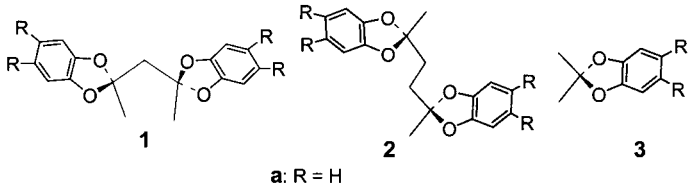

densation with the corresponding ketones in refluxing toluene.[3] An X-ray structure analysis confirmed that **1b** in the solid state exists exclusively as the extended conformer (Figure 4),[4] as expected based on DFT calculations

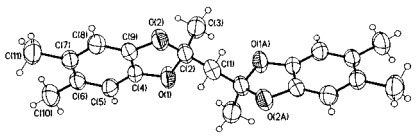

Figure 4. Molecular structure of **1b** in the solid state showing the extended conformer.

To demonstrate whether both the extended and the π-stacked conformers of **1** exist in solution, we examined the electron donor–acceptor (EDA) complexes of **1**–**3** with tetrachloro-*p*-benzoquinone (chloranil as an electron acceptor) by UV/Vis spectroscopy. It has been well established that the redox potentials (or π basicity) of the π-stacked cyclophane-like aromatic donors are significantly lower than that of their extended analogues.[5] The π basicity can be readily gauged by formation of the EDA complexes in solution according to the Mulliken theory.[6]

Interestingly, when colorless solutions of diacetals **1a** and **2a** as well as the monoacetal **3a** were exposed to a pale yellow solution of chloranil in CH_2Cl_2, they all instantaneously produced red solutions. Furthermore, the UV/Vis spectra showed a broad charge-transfer (CT) absorption band centered at $\lambda_{max} = 522 \pm 2$ nm. Similarly, the dimethylcatechol acetals **1b**, **2b**, and **3b** produced green solutions upon exposure to solutions of chloranil, and they each showed a charge-transfer absorption band centered at $\lambda_{max} = 608 \pm 2$ nm.[7] The identical CT transitions for various acetals in a given series suggests that the electron-donor strength is the same, and thus indicates that there is little or no contribution of the π-stacked conformer **1S** in solution. Moreover, the similarity of the chemical shifts for the aromatic and aliphatic protons in **1**–**3** (see the Experimental Section) further supports that **1a** and **1b** exist mostly as the extended conformer in solution. The variable temperature NMR analyses of **1** indicated that the postulated conformers **1E** and **1S** cannot be frozen out, even at −100 °C in CH_2Cl_2.

The cyclic voltammograms of **1a**, **2a**, and **3a** showed irreversible oxidation because of the presence of substitution-labile positions *para* to the oxygen atoms. On the other hand, the electrochemical oxidation of **1b**, **2b**, and **3b** at a platinum electrode in CH_2Cl_2 (containing nBu$_4$NPF$_6$ as the supporting electrolyte) was reversible at a scan rate of 25–400 mV s^{-1}; all anodic/cathodic peak current ratios were $I_a/I_c = 1.0$ (theoretical) at room temperature (Figure 5). Furthermore, both monoacetal **3b** and diacetal **2b** showed only a single reversible (CV) wave at a potential of $E_{ox} = 1.23 \pm 0.01$ V versus SCE. A quantitative evaluation of the CV peaks and peak currents with added ferrocene (as an internal standard, $E_{ox} = 0.45$ V vs. SCE) revealed that the reversible oxidations correspond to the production of monocation $\mathbf{3b}^{\bullet+}$ and dication $\mathbf{2b}^{2+}$ by transfer of one and two electrons, respectively. In contrast, dimethylcatechol acetal **1b** showed two reversible one-electron oxidation waves at $E_{ox} = 1.13$ and 1.50 V versus SCE (Figure 5).

The observation of a two-electron oxidation of **2b** at a single potential is consistent with the fact that it exists exclusively in the extended conformer, and thus the two dimethylcatechol rings in **2b** are not in electronic communi-

 © 2005 Wiley-VCH Verlag GmbH & Co. KGaA, Weinheim

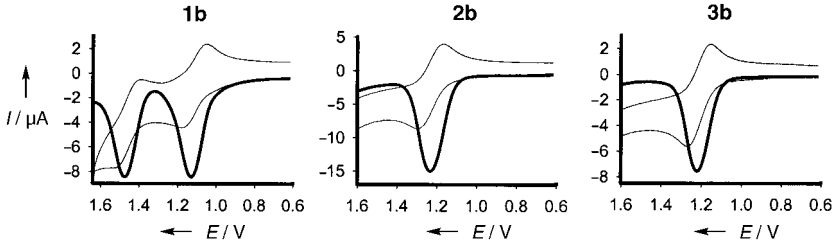

Figure 5. Cyclic voltammograms of **1b**, **2b**, and **3b** (5 mM) in CH_2Cl_2 measured at a scan rate of $\nu = 200\ mV s^{-1}$ at 25 °C. The corresponding square wave voltammograms are shown as bold curves. E = electric potential, I = current.

cation. On the other hand, the two well-separated one-electron oxidation waves in **1b** are easily explained by the following: Upon removal of a single electron the extended conformer transforms into the π-stacked conformer by a simple C–C bond rotation. This leads to cyclophane-like stabilization of the cationic charge in $\mathbf{1b}^{\bullet+}$ and thus renders the oxidation of the second dimethylcatechol ring more difficult (by about 370 mV; Scheme 1).[8]

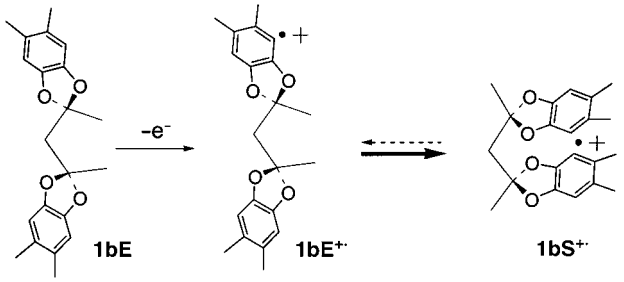

Scheme 1. Transformation of the extended conformer of **1b** into the π-stacked conformer upon one-electron oxidation.

As such, the effective electronic coupling between cofacially oriented aryl moieties in **1b** is readily judged by the reversible electrochemical oxidation at significantly (namely, 100 mV) lower potential as compared to the model electron donors **2b** and **3b**. Such through-space electronic coupling between cofacially stacked aryl moieties can also be seen in the electronic spectra of their radical cation, where characteristic charge-resonance transitions in the near-IR region are observed.[9] Accordingly, we generated the radical cations of **1**–**3** based on time-resolved absorption measurements upon diffusional electron-transfer quenching of photoexcited chloranil triplet as an oxidant ($E_{red} = 2.2$ V vs. SCE) using laser-flash photolysis.[10]

The transient spectrum obtained 100 ns after laser excitation (10 ns) of chloranil (5 mM) in the presence of **1a** (10 mM) in CH_2Cl_2/CH_3CN (1/1) showed an absorption band at $\lambda_{max} = 450$ nm with a shoulder at 420 nm, characteristic of a chloranil radical anion,[11] together with a broad absorption band centered at $\lambda_{max} = 1400$ nm (Figure 6a). The local absorption band of the catechol ether radical cations only have maxima at about 450 nm,[11] and thus lie within the envelope of the signal for the chloranil radical anion. Similarly, the radical cation $\mathbf{1b}^{\bullet+}$ showed an intense near-IR transition with a red-shifted absorption maximum at $\lambda_{max} \approx 1600$ nm (Figure 6b). The radical cations $\mathbf{2a}^{\bullet+}$, $\mathbf{2b}^{\bullet+}$, $\mathbf{3a}^{\bullet+}$, and $\mathbf{3b}^{\bullet+}$, generated similarly, lacked any absorption in the near-IR region. The observation of the charge-resonance transitions in the radical cations $\mathbf{1a}^{\bullet+}$ and $\mathbf{1b}^{\bullet+}$ (because of effective through-space electronic coupling) confirms a rapid transformation of the extended conformers into the π-stacked conformers upon one-electron oxidation (Scheme 1).

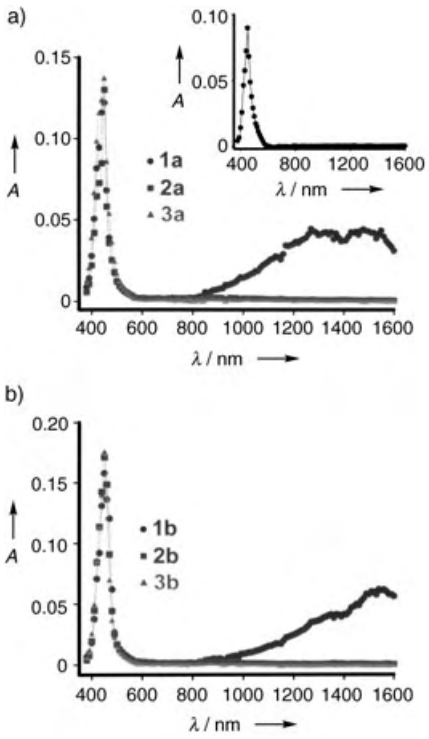

Figure 6. The transient absorption spectra of the radical ions formed from 0.005 M chloranil and 0.01 M **1a**, **2a**, and **3a** (a) or 0.01 M **1b**, **2b**, and **3b** (b) in a CH_2Cl_2/CH_3CN (1:1) following laser excitation at 355 nm for 10 ns. Inset in (a): The absorption spectrum of chloranil radical anion generated under identical conditions using 1,4-diazabicyclo[2.2.2]octane (DABCO) as an electron donor (the radical cation absorbs at $\lambda < 350$ nm).

In summary, we have demonstrated that catechol acetals of acetylacetone (**1**) in the neutral state exist exclusively as the extended conformers. However, the one-electron oxidation readily transforms these extended conformers into the folded π-stacked conformers. We are actively investigating the usefulness of such a redox-controlled molecular motion in readily available catechol acetals **1a** and **1b** as well as the design and synthesis of higher homologues of these electroactive materials.

Experimental Section

Compounds **1**–**3** were synthesized using standard literature procedures.[3] Their molecular structures were calculated with the aid of the

 © 2005 Wiley-VCH Verlag GmbH & Co. KGaA, Weinheim

"Spartan 02" graphics program. NMR spectra were recorded using a 300-mHz Varian spectrometer.

1a: M.p. 67–68 °C; ^{1}H NMR ($CDCl_3$): $\delta = 1.74$ (s, 6H), 2.60 (s, 2H), 6.75 ppm (sym m, 8H); ^{13}C NMR ($CDCl_3$): $\delta = 25.36$, 46.57, 108.80, 116.48, 121.42, 146.96 ppm; GC–MS: m/z 284 ([M^+] calcd for $C_{17}H_{16}O_4$); elemental analysis (%) calcd for $C_{17}H_{16}O_4$: C 71.82, H 5.67; found: C 71.91, H 5.72.

2a: M.p. 120–121 °C; ^{1}H NMR ($CDCl_3$): $\delta = 1.62$ (s, 6H), 2.15 (s, 4H), 6.77 ppm (m, 8H); ^{13}C NMR ($CDCl_3$): $\delta = 25.00$, 32.98, 108.54, 118.31, 121.21, 147.42 ppm; GC–MS: m/z 298 ([M^+] calcd for $C_{18}H_{18}O_4$); elemental analysis (%) calcd for $C_{18}H_{18}O_4$: C 72.47, H 6.08; found: C 72.57, H 6.10.

3a: Liquid; ^{1}H NMR ($CDCl_3$): $\delta = 1.69$ (s, 6H), 6.78 ppm (sym m, 4H); ^{13}C NMR ($CDCl_3$): $\delta = 26.25$, 108.75, 117.62, 121.27, 147.47 ppm; GC–MS: m/z 150 ([M^+] calcd. for $C_9H_{10}O_2$); elemental analysis (%) calcd for $C_9H_{10}O_2$: C 71.98, H 6.71; found: C 72.07, H 6.75.

1b: M.p. 139–140 °C; ^{1}H NMR ($CDCl_3$): $\delta = 1.70$ (s, 6H), 2.15 (s, 12H), 2.54 (s, 2H), 6.54 ppm (s, 4H); ^{13}C NMR ($CDCl_3$): $\delta = 20.02$, 25.28, 46.38, 110.21, 116.47, 128.88, 145.06 ppm; GC–MS: m/z 340 ([M^+] calcd for $C_{21}H_{24}O_4$); elemental analysis (%) calcd for $C_{21}H_{24}O_4$: C 74.09, H 7.11; found: C 74.14, H 7.17

2b: M.p. 181–182 °C; ^{1}H NMR ($CDCl_3$): $\delta = 1.57$ (s, 6H), 2.09 (s, 4H), 2.15 (s, 12H), 6.53 ppm (s, 4H); ^{13}C NMR ($CDCl_3$): $\delta = 19.90$, 24.96, 32.91, 109.81, 118.18, 128.52, 145.43 ppm; GC–MS: m/z 354 ([M^+] calcd for $C_{22}H_{26}O_4$); elemental analysis (%) calcd for $C_{22}H_{26}O_4$: C 74.55, H 7.39; found: C 74.61, H 7.42.

3b: Colorless liquid; ^{1}H NMR ($CDCl_3$): $\delta = 1.66$ (s, 6H), 2.18 (s, 6H), 6.56 ppm (s, 2H); ^{13}C NMR ($CDCl_3$): $\delta = 19.92$, 26.03, 109.95, 117.31, 128.51, 145.28 ppm; GC–MS: m/z 178 ([M^+] calcd for $C_{11}H_{14}O_2$); elemental analysis (%) calcd for $C_{11}H_{14}O_2$: C 74.13, H 7.92; found: C 74.17, H 7.99.

Received: December 30, 2004
Published online: March 30, 2005

Keywords: cyclic voltammetry · cyclophanes · photolysis · pi interactions · radicals

[1] a) *Introduction to Molecular Electronics* (Eds.: M. C. Petty, M. R. Bryce, D. Bloor), Oxford University Press, New York, **1995**; b) B. G. Maiya, T. Ramasarma, *Curr. Sci.* **2001**, *70*, 1523–1530; c) F. D. Lewis, R. L. Letsinger, M. R. Wasielewski, *Acc. Chem. Res.* **2001**, *34*, 159–170; d) A. R. Wartini, J. Valenzuela, H. A. Staab, F. A. Neugebauer, *Eur. J. Org. Chem.* **1998**, 139–148; e) W. Grimme, H. T. Kaemmerling, J. Lex, R. Gleiter, J. Heinze, M. Dietrich, *Angew. Chem.* **1991**, *103*, 215–217; *Angew. Chem. Int. Ed. Engl.* **1991**, *30*, 205–207; f) also, see: J. M. Tour, *Acc. Chem. Res.* **2000**, *33*, 791–804, and references therein.

[2] R. Rathore, S. H. Abdelwhaed, I. A. Guezi, *J. Am. Chem. Soc.* **2003**, *125*, 8712–8713.

[3] a) T.-S. Li, L.-J. Li, B. Lu, F. Yang, *J. Chem. Soc. Perkin Trans. 1* **1998**, 1561–3564; b) E. R. Cole, G. Crank, H. T. H. Minh, *Aust. J. Chem.* **1980**, *33*, 675–680.

[4] A suitable crystal ($0.37 \times 0.25 \times 0.16$ mm^3) of **1b** was obtained from CH_2Cl_2/CH_3OH at 23 °C. Crystal data for **1b**: $C_{21}H_{24}O_4$, $M_r = 340.4$, orthorhombic, space group *Pbcn*, $a = 119.591(4)$, $b = 10.5813(18)$, $c = 9.1146(15)$ Å, $\rho_{calcd} = 1.197$ Mg m^{-3}, $V = 1889.4(6)$ Å^3, $Z = 4$. Of 6523 total reflections measured, 1878 were symmetrically nonequivalent; $R1 = 0.0467$ and w$R2 = 0.1079$ for 1878 reflections with $I > 2\sigma(I)$. CCDC-247657 contains the supplementary crystallographic data for this paper. These data can be obtained free of charge from the Cambridge Crystallographic Data Centre via www.ccdc.cam.ac.uk/data_request/cif.

[5] a) D. J. Cram, R. H. Bauer, *J. Am. Chem. Soc.* **1959**, *81*, 5971–5977; b) L. A. Singer, D. J. Cram, *J. Am. Chem. Soc.* **1963**, *85*, 1080–1084; c) M. Taniguchi, S. Mataka, T. Thiemann, T. Sawada, K. Mimura, Y. Mitoma, *Bull. Chem. Soc. Jpn.* **1998**, *71*, 2661–2668.

[6] R. Rathore, S. V. Lindeman, J. K. Kochi, *J. Am. Chem. Soc.* **1997**, *119*, 9343–9404, and references therein.

[7] Veratrole (1,2-dimethoxybenzene) and 4,5-dimethylveratrole (1,2-dimethoxy-4,5-dimethylbenzene) show similar charge-transfer absorption bands at 518 and 606 nm, respectively, with chloranil as an electron acceptor in CH_2Cl_2.

[8] Compare: S. Mataka, K. Shigaki, T. Sawada, Y. Mitoma, M. Taniguchi, T. Thiemann, K. Ohga, N. Egashira, *Angew. Chem.* **1998**, *110*, 2626–2628; *Angew. Chem. Int. Ed.* **1998**, *37*, 2532–2534.

[9] a) S. F. Nelsen, *Chem. Eur. J.* **2000**, *6*, 581–588; b) B. Badger, B. Brocklehurst, *Trans. Faraday Soc.* **1969**, *65*, 2576–2588; c) B. Badger, B. Brocklehurst, *Nature* **1968**, *219*, 263–264; d) M. A. J. Rodgers, *J. Chem. Soc. Faraday Trans. 1* **1972**, *68*, 1278–1292; e) R. Rathore, C. L. Burns, S. A. Abdelwahed, *Org. Lett.* **2004**, *6*, 1689–1692.

[10] a) R. Rathore, S. M. Hubig, J. K. Kochi, *J. Am. Chem. Soc.* **1997**, *119*, 11468–11480; b) S. M. Hübig, R. Rathore, J. K. Kochi, *J. Am. Chem. Soc.* **1999**, *121*, 617–626.

[11] T. Shida, *Electronic Absorption Spectra of Radical Ions*, Elsevier, Amsterdam, **1988**.

 © 2005 Wiley-VCH Verlag GmbH & Co. KGaA, Weinheim

Asymmetric Synthesis

Asymmetric Amplification Using Chiral Cocrystals Formed from Achiral Organic Molecules by Asymmetric Autocatalysis**

*Tsuneomi Kawasaki, Kazumichi Jo, Hirotaka Igarashi, Itaru Sato, Masaki Nagano, Hideko Koshima, and Kenso Soai**

The origin and amplification of chirality leading to the overwhelming enantioenrichment of organic compounds, such as the L-amino acids and D-sugars on Earth, is a significant topic of interest.[1] One of the proposed mecha-

[*] Dr. T. Kawasaki, K. Jo, H. Igarashi, Dr. I. Sato, Prof. Dr. K. Soai
Department of Applied Chemistry
Faculty of Science, Tokyo University of Science
Kagurazaka, Shinjuku-ku, Tokyo 162-8601 (Japan)
Fax: (+81) 3-3235-2214
E-mail: soai@rs.kagu.tus.ac.jp
M. Nagano, Prof. Dr. H. Koshima
Department of Applied Chemistry
Faculty of Engineering, Ehime University
Matsuyama, Ehime 790-8577 (Japan)

[**] This work was supported by a Grant-in-Aid for Scientific Research from The Ministry of Education, Culture, Sports, Science, and Technology (MEXT).

 © 2005 Wiley-VCH Verlag GmbH & Co. KGaA, Weinheim DOI: 10.1002/anie.200462963

nisms for the origin of chirality is the generation of chiral crystals formed from achiral organic compounds, with each crystal exhibiting one of the two possible enantiomorphs.[2] Of the 230 possible space groups, 65 are chiral, and it is worth noting that among the five most common space groups of organic crystalline compounds, on the basis of a survey of approximately 29000 crystal structure determinations, about 18% of crystals belong to the two chiral space groups $P2_12_12_1$ and $P2_1$.[3] Moreover, the formation of chiral cocrystals of a quaternary ammonium salt from an equimolar solution of an achiral carboxylic acid with amine components has been reported.[4] These crystals belong to a typical chiral space group and have both clockwise (*P*) and counterclockwise (*M*) helicities.

Although examples of highly stereospecific reactions that use chiral crystals of achiral compounds have been reported, these reactions are limited as these chiral crystals were only used as reactants, and so that the amount of chirality did not increase (Scheme 1).[5–7] Amplification of the amount of chirality is required for significant quantities of the desired chiral compounds to be obtained. To the best of our knowledge, no highly enantioselective reactions using chiral crystals as chiral initiators (or catalysts) have been reported. Thus, a challenging problem to be addressed is the development of a highly enantioselective synthesis using chiral cocrystals formed from achiral organic molecules as chiral inducers or catalysts, whereby the enantioselective synthesis enables significant amplification of the amount of the chirality in the system (Scheme 1).

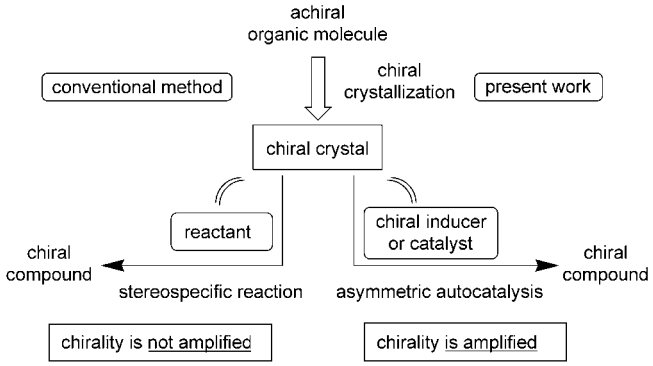

Scheme 1. A comparison of the concept of utilizing chiral crystals composed of achiral organic molecules as chiral inducers or catalysts in asymmetric autocatalysis with their conventional use as reactants in stereospecific reactions.

During our studies into asymmetric autocatalytic processes we found that the asymmetric autocatalysis of a 5-pyrimidyl alkanol in the enantioselective addition of diisopropylzinc to pyrimidine-5-carbaldehyde (**5**) proceeds with an amplification of enantiomeric excess.[8–10]

Herein, we report on a highly enantioselective addition of $i\mathrm{Pr}_2\mathrm{Zn}$ to **5** in the presence of chiral cocrystals of tryptamine/*para*-chlorobenzoic acid (**1**/**2**)[3c] and 3-indolepropionic acid/phenanthridine (**3**/**4**; Scheme 2)[3a] The enantioselective addition of $i\mathrm{Pr}_2\mathrm{Zn}$ to **5** in the presence of powdered *P* or *M* crystals gave the pyrimidyl alkanol **6** with high enantioselectivity in high yield. The absolute configuration of the corresponding 5-pyrimidyl alkanol **6** was controlled by the chirality of these cocrystals, which had been prepared from achiral organic molecules. The molar amount of the prepared chiral compounds in this reaction was increased by a factor of up to 30, which was calculated from the molar ratio of the chiral cocrystal and the resulting chiral 5-pyrimidyl alkanol **6**. Moreover, chiral 5-pyrimidyl alkanol **6** can be automultiplied by subsequent asymmetric autocatalysis, as we have previously reported.[8a]

The (*R*)-pyrimidyl alkanol **6** was obtained in a 90% yield and with 89% *ee* (Table 1, entry 1) when the reaction was performed in the presence of the *P* crystal of **1**/**2**. Repeated reactions in the presence of *P*-(**1**/**2**) led to (*R*)-**6** being obtained in 82–96% *ee*, thus showing that the results are reproducible (Table 1, entries 3, 5, and 7). On the other hand, the reaction between **5** and $i\mathrm{Pr}_2\mathrm{Zn}$ in the presence of the *M*-(**1**/**2**) crystal instead of the *P* crystal always gave (*S*)-**6** in 82–95% *ee* and 86–94% yield (Table 1, entries 2, 4, 6, and 8). Both reactions were performed using the same apparatus and gave the same results, thus excluding any effect other than that of the chiral cocrystal (Table 1, entries 7 and 8).

Next, we examined the addition of $i\mathrm{Pr}_2\mathrm{Zn}$ to **5** under the same conditions using the **3**/**4** chiral cocrystal. The enantioselective preparation of (*R*)-pyrimidyl alkanol **6** was induced in the presence of the *P* crystal of **3**/**4** and was obtained with 72–92% *ee* in 92–99% yield (Table 1, entries 9, 11, 13, and

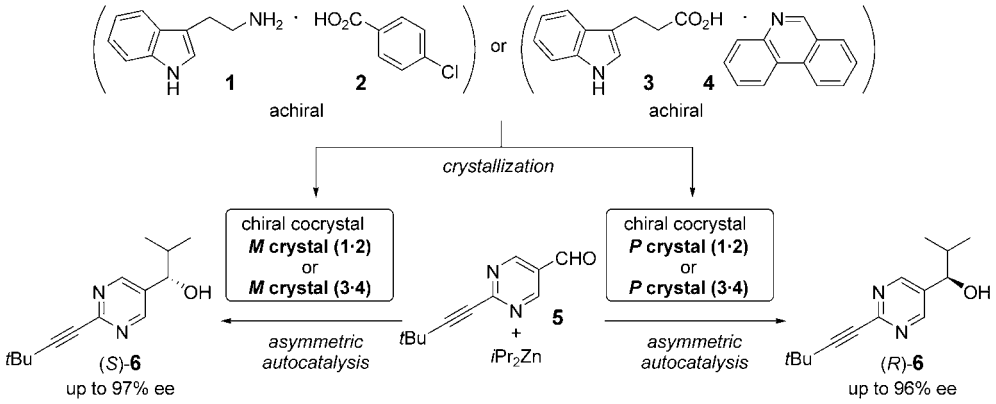

Scheme 2. Highly enantioselective asymmetric autocatalysis using chiral cocrystals **1**/**2** and **3**/**4**.

 © 2005 Wiley-VCH Verlag GmbH & Co. KGaA, Weinheim

Table 1: The highly enantioselective synthesis of pyrimidyl alkanols in the presence of chiral cocrystals **1/2** and **3/4**.

Entry[a]	Chiral cocrystal[b]	Pyrimidyl alkanol **6**		
		yield [%]	*ee* [%][c]	config.
1	*P*-(**1/2**)	90	89	*R*
2	*M*-(**1/2**)	86	89	*S*
3	*P*-(**1/2**)	92	87	*R*
4	*M*-(**1/2**)	88	82	*S*
5[d]	*P*-(**1/2**)	99	96	*R*
6	*M*-(**1/2**)	92	95	*S*
7[d,e]	*P*-(**1/2**)	88	82	*R*
8[e]	*M*-(**1/2**)	94	92	*S*
9	*P*-(**3/4**)	93	92	*R*
10	*M*-(**3/4**)	89	89	*S*
11	*P*-(**3/4**)	92	86	*R*
12	*M*-(**3/4**)	91	85	*S*
13	*P*-(**3/4**)	94	72	*R*
14	*M*-(**3/4**)	93	93	*S*
15[e]	*P*-(**3/4**)	99	87	*R*
16[e]	*M*-(**3/4**)	90	97	*S*

[a] The molar ratio used was cocrystal/**5**/iPr$_2$Zn = 0.05:1.55:3.25 unless otherwise noted. Compound **5** and iPr$_2$Zn were added in four separate portions. [b] The cocrystals were ground into a powder using a pestle and mortar. The chirality of the cocrystals was verified from solid-state CD spectra using nujol. The powder of cocrystal **1/2** was washed with diethyl ether and then with hexane several times and dried in vacuo before use. The powder of cocrystal **3/4** was washed several times using only hexane because of its solubility in diethyl ether. [c] The *ee* value was determined by HPLC on a chiral stationary phase (chiralcel OD column, eluent = 3% 2-propanol in hexane, flow rate = 1.0 mL min^{-1}, 254 nm UV detector, retention time = 18.1 min for (*S*)-**6**, 26.9 min for (*R*)-**6**). [d] The molar ratio used was cocrystal/**5**/iPr$_2$Zn = 0.05:1.05:2.25. Compound **5** and iPr$_2$Zn were added in three separate portions. [e] Each reaction was performed using the same apparatus to exclude any effect other than that of the chiral cocrystal.

15). On the other hand, the reaction between **5** and iPr$_2$Zn in the presence of the *M*-(**3/4**) cocrystal always gave (*S*)-**6** with 85–97% *ee* in 89–93% yield (Table 1, entries 10, 12, 14, and 16). Again, the same equipment was used in this series of reactions to exclude any effect other than that of the chiral cocrystal (Table 1, entries 15 and 16).

The enantioselectivity observed in this asymmetric reaction may be explained as follows: The initial reaction of the aldehyde **5** and iPr$_2$Zn proceeded on the chiral surface of the cocrystal so that a small enantiomeric excess was induced. Then, subsequent asymmetric autocatalysis with an amplification of chirality afforded alkanol **6** (as zinc alkoxide) in a high enantiomeric excess, and with the corresponding absolute configuration. Further mechanistic details are now under investigation.

In summary, the highly enantioselective addition of iPr$_2$Zn to pyrimidine-5-carbaldehyde (**5**) was achieved by utilizing the chirality of two-component molecular crystals of tryptamine/*para*-chlorobenzoic acid (**1/2**) and 3-indolepropionic acid/phenanthridine (**3/4**). These results clearly demonstrate that the chirality of the cocrystals **1/2** and **3/4** is responsible for the enantioselective addition of iPr$_2$Zn to **5**. We believe that the insight that chiral crystals composed of achiral compounds offer into the origin and evolution of chirality is significantly increased by asymmetric autocatalysis.

Experimental Section

A typical experimental procedure: A cocrystal (single crystal = 50 mg) was ground into a powder using a pestle and mortar (particle size estimated from SEM images = 2–10 μm). The two enantiomorphous *P* and *M* crystals of **1/2** and **3/4** were discriminated by solid-state circular dichroism (CD) spectroscopic analysis (nujol). The powder of **1/2** was washed with diethyl ether and hexane several times and then dried in vacuo before use.

iPr$_2$Zn (0.25 mmol, in solution with hexane (1.0 M, 0.25 mL)) was added dropwise at 0 °C to a finely powdered sample of cocrystal **1/2** (15.8 mg, 0.05 mmol). The hexane was immediately removed by distillation under reduced pressure (3.0 mm Hg, 5 min) to leave a white powder of cocrystal **1/2**, whose surface was coated with iPr$_2$Zn. A solution of **5** (9.4 mg, 0.05 mmol) in methylcyclohexane (1.5 mL) was then added over a period of 30 min at 0 °C and the mixture was stirred for 16 h at 0 °C. Toluene (0.7 mL), iPr$_2$Zn (0.2 mmol, in solution with toluene (1.0 M, 0.2 mL)), and a solution of **5** (18.8 mg, 0.1 mmol) in toluene (0.75 mL) were added successively, and the reaction mixture stirred at 0 °C for 3 h.

Then, toluene (5.0 mL), iPr$_2$Zn (0.8 mmol, 0.8 mL of a 1 M toluene solution), and a solution of aldehyde **5** (75.2 mg, 0.4 mmol) in toluene (2.0 mL) were added successively and the mixture was stirred at 0 °C for 1 h. Once again, toluene (14 mL), iPr$_2$Zn (2.0 mmol, in solution with toluene (1.0 M, 2.0 mL)), and a solution of aldehyde **5** (188.2 mg, 1.0 mmol) in toluene (5.0 mL) were added successively, and the mixture was stirred at 0 °C for 1 h. The reaction was quenched with hydrochloric acid (1 M, 5 mL) and neutralized with a saturated sodium hydrogen carbonate solution (15 mL). The mixture was then filtered through celite and the filtrate extracted with ethyl acetate (×3). The combined organic layers were dried over anhydrous sodium sulfate and evaporated in vacuo. Purification of the residue by thin-layer chromatography on silica gel (hexane/ethyl acetate, 2:1) gave the 5-pyrimidyl alkanol **6**.

Received: December 16, 2004
Published online: March 30, 2005

Keywords: asymmetric synthesis · autocatalysis · chirality · cocrystals · zinc

[1] a) B. L. Feringa, R. A. van Delden, *Angew. Chem.* **1999**, *111*, 3624–3645; *Angew. Chem. Int. Ed.* **1999**, *38*, 3418–3438; b) K. Mislow, *Collect. Czech. Chem. Commun.* **2003**, *68*, 849–864; c) C. Girard, H. B. Kagan, *Angew. Chem.* **1998**, *110*, 3088–3127; *Angew. Chem. Int. Ed.* **1998**, *37*, 2923–2959; d) A. Eschenmoser, *Science* **1999**, *284*, 2118–2124; e) H. Zepik, E. Shavit, M. Tang, T. R. Jensen, K. Kjaer, G. Bolbach, L. Leiserowitz, I. Weissbuch, M. Lahav, *Science* **2002**, *295*, 1266–1269; f) M. M. Green, J.-W. Park, T. Sato, A. Teramoto, S. Lifson, R. L. B. Selinger, J. V. Selinger, *Angew. Chem.* **1999**, *111*, 3329–3345; *Angew. Chem. Int. Ed.* **1999**, *38*, 3139–3154; g) W. A. Bonner, *Origins Life Evol. Biosphere* **1995**, *25*, 175–190; h) D. K. Kondepudi, K. Asakura, *Acc. Chem. Res.* **2001**, *34*, 946–954; i) J. S. Siegel, *Chirality* **1998**, *10*, 24–27; j) S. Mason, *Chem. Soc. Rev.* **1988**, *17*, 347–359; k) L. Keszthelyi, *Q. Rev. Biophys.* **1995**, *28*, 473–507; l) V. Avetisov, V. Goldanskii, *Proc. Natl. Acad. Sci. USA* **1996**, *93*, 11435–11442; m) M. Avalos, R. Babiano, P. Cintas, J. L. Jimenez, J. C. Palacios, *Tetrahedron: Asymmetry* **2000**, *11*, 2845–2874.

[2] a) J. Jacques, A. Collet, S. M. Wilen, *Enantiomers, Racemates, and Resolutions*, Wiley, New York, **1981**, p. 14; b) B. S. Green, M. Lahav, D. Rabinovich, *Acc. Chem. Res.* **1979**, *12*, 191–197; for chiral crystallization of inorganic sodium chlorate, see c) R. M. Pagni, R. N. Compton, *Cryst. Growth Des.* **2002**, *2*, 249–253;

 © 2005 Wiley-VCH Verlag GmbH & Co. KGaA, Weinheim

d) D. K. Kondepudi, R. J. Kaufman, N. Singh, *Science* **1990**, *250*, 975 – 977.
[3] M. Sakamoto, *Chem. Eur. J.* **1997**, *3*, 684 – 689.
[4] a) H. Koshima, E. Hayashi, T. Matsuura, K. Tanaka, F. Toda, M. Kato, M. Kiguchi, *Tetrahedron Lett.* **1997**, *38*, 5009 – 5012; b) H. Koshima, S. Honke, F. Fujita, *J. Org. Chem.* **1999**, *64*, 3916 – 3921; c) H. Koshima, M. Miyauchi, M. Shiro, *Supramol. Chem.* **2001**, *13*, 137 – 142; d) H. Koshima, M. Nagano, T. Asahi, *J. Am. Chem. Soc.*, **2005**, *127*, 2455 – 2463.
[5] Reviews: a) M. Hasegawa, *Chem. Rev.* **1983**, *83*, 507 – 518; b) V. Ramamurthy, K. Vebkatesan, *Chem. Rev.* **1987**, *87*, 433 – 481; c) J. R. Scheffer, M. Garcia-Garibay, *Photochemistry on Solid Surface* (Eds.: M. Anpo, T. Matsuura), Elsevier, Amsterdam **1989**, chap. 9, p. 501; d) K.-L. Ding, Y. Wang, Y.-J. Wu, H. Matsuura, *Youji Huaxue* **1996**, *16*, 1; e) H. Koshima, T. Matsuura, *Yuki Gosei Kagaku Kyokaishi* (*J. Synth. Org. Chem. Jpn.*) **1998**, *56*, 268 – 279; f) H. Koshima, T. Matsuura, *Yuki Gosei Kagaku Kyokaishi* (*J. Synth. Org. Chem. Jpn.*) **1998**, *56*, 466 – 477.
[6] a) M. D. Cohen, G. M. J. Schmidt, *J. Chem. Soc.* **1964**, 1996 – 2000; b) K. Penzien, G. M. Schmidt, *Angew. Chem.* **1969**, *81*, 628; *Angew. Chem. Int. Ed. Engl.* **1969**, *8*, 608 – 609; c) A. Elgavi, B. S. Green, G. M. J. Schmidt, *J. Am. Chem. Soc.* **1973**, *95*, 2058 – 2059.
[7] a) L. Addadi, M. Lahav, *J. Am. Chem. Soc.* **1978**, *100*, 2838 – 2844; c) L. Addadi, M. Lahav, *J. Am. Chem. Soc.* **1979**, *101*, 2152 – 2156; d) S. V. Evans, M. Garcia-Garibay, N. Omkaram, J. R. Scheffer, J. Trotter, F. Wireko, *J. Am. Chem. Soc.* **1986**, *108*, 5648 – 5650; e) M. Hasegawa, C.-M. Chung, N. Murro, Y, Maekawa, *J. Am. Chem. Soc.* **1990**, *112*, 5676 – 5677; f) A. L. Roughton, M. Muneer, M. Demuth, *J. Am. Chem. Soc.* **1993**, *115*, 2085 – 2087; g) F. Toda, K. Tanaka, *Supramol. Chem.* **1994**, *3*, 87 – 88; h) T. Suzuki, T. Fukushima, Y. Yamashita, T. Miyashi, *J. Am. Chem. Soc.* **1994**, *116*, 2793 – 2803; i) H. Koshima, K.-L. Ding, Y. Chisaka, T. Matsuura, *J. Am. Chem. Soc.* **1996**, *118*, 12059 – 12065.
[8] Reviews: a) K. Soai, T. Shibata, I. Sato, *Acc. Chem. Res.* **2000**, *33*, 382 – 390; b) K. Soai, I. Sato, T. Shibata, *Chem. Rec.* **2001**, *1*, 321 – 332; c) C. Bolm, F. Bienewald, A. Seger, *Angew. Chem.* **1996**, *108*, 1767 – 1769; *Angew. Chem. Int. Ed. Engl.* **1996**, *35*, 1657 – 1659; d) M. Avalos, R. Babiano, P. Cintas, J. L. Jiménez, J. C. Palacios, *Chem. Commun.* **2000**, 887 – 892; e) H. Buschmann, R. Thede, D. Heller, *Angew. Chem.* **2000**, *112*, 4197 – 4200; *Angew. Chem. Int. Ed.* **2000**, *39*, 4033 – 4036; f) M. H. Todd, *Chem. Soc. Rev.* **2002**, *31*, 211 – 222; g) K. Soai, T. Shibata, I. Sato, *Bull. Chem. Soc. Jpn.* **2004**, *77*, 1063 – 1073; h) K. Mikami, M. Yamanaka, *Chem. Rev.* **2003**, *103*, 3369 – 3400.
[9] a) K. Soai, T. Shibata, H. Morioka, K. Choji, *Nature* **1995**, *378*, 767 – 768; b) T. Shibata, T. Hayase, J. Yamamoto, K. Soai, *Tetrahedron: Asymmetry* **1997**, *8*, 1717 – 1719; c) T. Shibata, J. Yamamoto, N. Matsumoto, S. Yonekubo, S. Osanai, K. Soai, *J. Am. Chem. Soc.* **1998**, *120*, 12157 – 12158; d) K. Soai, S. Osanai, K. Kadowaki, S. Yonekubo, T. Shibata, I. Sato, *J. Am. Chem. Soc.* **1999**, *121*, 11235 – 11236; e) I. Sato, D. Omiya, T. Saito, K. Soai, *J. Am. Chem. Soc.* **2000**, *122*, 11739 – 11740; f) I. Sato, R. Yamashima, K. Kadowaki, J. Yamamoto, T. Shibata, K. Soai, *Angew. Chem.* **2001**, *113*, 1130 – 1132; *Angew. Chem. Int. Ed.* **2001**, *40*, 1096 – 1098; g) I. Sato, H. Urabe, S. Ishiguro, T. Shibata, *Angew. Chem.* **2003**, *115*, 329 – 331; *Angew. Chem. Int. Ed.* **2003**, *42*, 315 – 317; h) I. Sato, K. Kadowaki, Y. Ohgo, K. Soai, *J. Mol. Catal. A* **2004**, *216*, 209 – 214; i) I. Sato, T. Nakao, R. Sugie, T. Kawasaki, K. Soai, *Synthesis* **2004**, 1419 – 1428; j) I. Sato, M. Shimizu, T. Kawasaki, K. Soai, *Bull. Chem. Soc. Jpn.* **2004**, *77*, 1587 – 1588; k) I. Sato, R. Sugie, Y. Matsueda, Y. Furumura, K. Soai, *Angew. Chem.* **2004**, *116*, 4590 – 4592; *Angew. Chem. Int. Ed.* **2004**, *43*, 4490 – 4492; l) T. Kawasaki, K. Ishikawa, H. Sekibata, I. Sato, K. Soai, *Tetrahedron Lett.* **2004**, *45*, 7939 – 7941; m) T. Kawasaki, M. Shimizu, K. Suzuki, I. Sato, K. Soai, *Tetrahedron: Asymmetry* **2004**, *15*, 3699 – 3701.
[10] For studies on the mechanism, see: a) I. Sato, D. Omiya, H. Igarashi, K. Kato, Y. Ogi, K. Tsukiyama, K. Soai, *Tetrahedron: Asymmetry* **2003**, *14*, 975 – 979; b) I. D. Gridnev, J. M. Serafimov, J. M. Brown, *Angew. Chem.* **2004**, *116*, 4992 – 4995; *Angew. Chem. Int. Ed.* **2004**, *43*, 4884 – 4887; c) D. G. Blackmond, *Proc. Natl. Acad. Sci. USA* **2004**, *101*, 5732 – 5736; d) T. Buhse, *Tetrahedron: Asymmetry* **2003**, *14*, 1055 – 1061; e) Y. Saito, H. Hyuga, *J. Phys. Soc. Jpn.* **2004**, *73*, 33 – 35; f) G. Lente, *J. Phys. Chem. A* **2004**, *108*, 9475 – 9478.

 © 2005 Wiley-VCH Verlag GmbH & Co. KGaA, Weinheim

Natural Product Synthesis

Chasing a Phantom by Total Synthesis: The Butylcycloheptylprodigiosin Case**

Alois Fürstner, Karin Radkowski, and Hartwig Peters*

The deeply red-colored tripyrrole alkaloids of the "prodigiosin" series exert pronounced immunosuppressive activities at doses that are not cytotoxic.[1] Most notably, in vivo studies have shown that these pigments produced by various *Serratia* and *Streptomyces* strains act synergistically with cyclosporine A, FK 506, or rapamycin, which are presently the dominating drugs in clinical immunosuppressive regimens.[2,3] Since the availability of agents that can act at different stages along the T-cell activation pathway may improve therapeutic results, the prodigiosins constitute important new lead compounds in the search for supplementary drugs to prevent allograft rejection. These findings have rejuvenated interest in this class of pyrrole alkaloids, as evident from many recent studies mapping their biological profiles in great detail.[1]

During our program aimed at the total synthesis[4–7] and biochemical validation of various pyrrolic natural products,[8] our attention was drawn to a secondary metabolite called "butylcycloheptylprodigiosin".[9] It was originally isolated from *Streptomyces* sp. Y-42 and *Streptomyces abikoensis* (formerly, *Streptoverticillium rubrireticuli*). Gerber and Stahly assigned structure **1** to this then novel member of the prodigiosin family (Scheme 1).[10] Floss and co-workers later attributed the same structure to the "pink pigment" obtained from a culture broth of *Streptomyces coelicolor* mutants.[11]

[*] Prof. A. Fürstner, K. Radkowski, Dr. H. Peters
Max-Planck-Institut für Kohlenforschung
45470 Mülheim/Ruhr (Germany)
Fax: (+49) 208-306-2994
E-mail: fuerstner@mpi-muelheim.mpg.de

[**] Generous financial support from the Deutsche Forschungsgemeinschaft (Leibniz award program), the Fonds der Chemischen Industrie, and the Merck Research Council is gratefully acknowledged. We thank Dr. R. Mynott and C. Wirtz for their invaluable help with numerous NMR analyses and Prof. H. Floss for providing a copy of the ^{1}H NMR spectrum of his "pink pigment" for comparison.

 DOI: 10.1002/anie.200462215 © 2005 Wiley-VCH Verlag GmbH & Co. KGaA, Weinheim

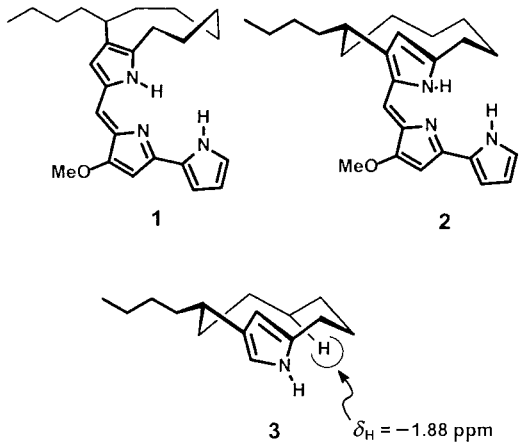

Scheme 1. The structures of butylcycloheptylprodigiosin (**1**) and its *meta*-bridged isomer streptorubin B (**2**); an illustration of the characteristic spectral fingerprint of *meta*-pyrrolophane **3**.

However, these assignments were questioned by Weyland and co-workers, who showed that their sample isolated from the actinomycete strain B 4358 was the *meta*-bridged isomer streptorubin B (**2**) rather than the *ortho*-annelated compound **1**, thus suggesting that the structure of the latter needed to be revised.[12] As these three research groups were investigating samples derived from different bacterial strains, it appeared to us that this conclusion might have been premature and that the available data deserved more scrupulous consideration.

A previous synthesis campaign by our research group had opened a concise route to product **2** and its congeners by a platinum-catalyzed cycloisomerization reaction.[4,13] All the *meta*-pyrrolophanes prepared showed a very characteristic "fingerprint" in their ^{1}H NMR spectra. Specifically, the rigidity of the bridging 10-membered ring forces one of the protons of the *ansa* chain to reside within the anisotropy cone of the aromatic pyrrole nucleus, thus causing a significant upfield shift of the corresponding signal to $\delta = -1.55$ ppm in **2** and $\delta = -1.88$ ppm in its core segment **3** (see Scheme 1).[4,12,14] Although the reported spectral data of the "pink pigment" isolated by the groups of Gerber and Floss are incomplete,[10,11] no such signal is documented. As it appears unlikely to us that such a conspicuous detail would have escaped the attention of two independent groups, we suspected that butylcycloheptylprodigiosin (**1**) is in fact a natural product distinct from **2** rather than a phantom. It was only through synthesis, however, that this open question could be answered.

To this end, the assembly of the pyrrolopyrromethane chromophore of **1** from building blocks **4**–**6** by successive condensation and cross-coupling reactions was envisaged (Scheme 2).[5,15] Since **5** and **6** are commercially available, the success of the project hinged on the efficient preparation of aldehyde **4**. Bearing in mind that (the ground-state as well as the transition-state) strain energy reaches its maximum with nine-membered cycles,[16] we preferred a strategy based on the annelation of the pyrrole nucleus to a *preexisting* cyclononane template over a late-stage cyclization of the medium-sized carbocycle.

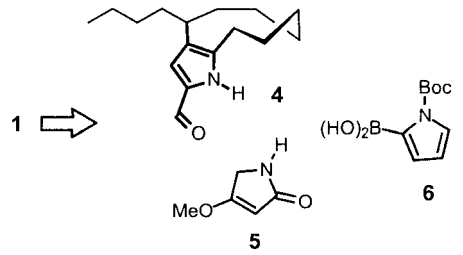

Scheme 2. Retrosynthetic analysis of **1**.

Intramolecular Heck-type reactions of unsaturated oxime esters pioneered by Narasaka and co-workers might serve this purpose well (Scheme 3).[17] In this rather unconventional

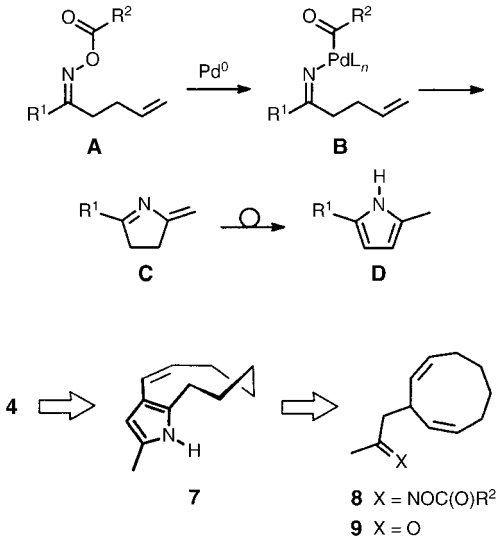

Scheme 3. The conversion of unsaturated oxime esters into pyrrole derivatives by a Narasaka–Heck reaction. Application of this transform to the preparation of the core segment of **1**.

transfomation, the Pd^0 catalyst inserts into a suitable oxime derivative **A** to give an iminopalladium intermediate **B**, which reacts with a suitably located olefin to give a pyrrole derivative **D** after isomerization of the methylenedihydropyrrole **C** initially formed. This reaction, however, is known to be very sensitive to seemingly minor changes in substrate and can be plagued by competing side reactions, such as Beckmann rearrangements, hydrolysis, or fragmentation.[17] To the best of our knowledge, no application to a total synthesis has been reported to date.

In the present context, this method might open a convenient entry to the core segment **4** of the butylcycloheptylprodigiosin skeleton. Cyclononadienylacetone (**9**) was considered to be the optimal substrate for this reaction because 1) the presence of two double bonds should increase the number of reactive encounters during the Narasaka–Heck cyclization of the derived oxime ester **8** and, hence, increase the yield; 2) the remaining double bond in the expected product **7** provides a handle for the introduction of the butyl side chain of the target; and 3) the symmetrical structure of **9** should facilitate the large-scale preparation of this strained compound.

 © 2005 Wiley-VCH Verlag GmbH & Co. KGaA, Weinheim

Our synthesis started from (*Z*,*Z*)-cyclononadienone (**10**).[18] 1,2-Reduction of the ketone group with diisobutylaluminum hydride (DIBAL-H) followed by acetylation of the resulting alcohol gave acetate **11** in almost quantitative yield (Scheme 4). Exposure of **11** to methyl acetoacetate in the presence of NaH and catalytic amounts of $[Pd(PPh_3)_4]$ afforded product **12** in 74% yield. This outcome is remarkable for various reasons: although one might expect that oxidative insertion of a Pd^0 center into the bisallylic acetate **11** engenders the formation of a pentadienylpalladium intermediate that then reacts with the nucleophile to give a conjugated diene product,[19] the double bonds are site-isolated in the major isomer **12**. Moreover, it is noteworthy that both of them are *Z* configured, although nine-membered rings are large enough to embody *E* alkenes without difficulty, and palladium catalysis is known to isomerize allylic systems effectively. This regio- and stereochemical outcome therefore advocates the notion that the two "allylic" sites in **11** remain uncoupled during the course of the Tsuji–Trost reaction as a result of the conformational peculiarities of the medium ring.[20]

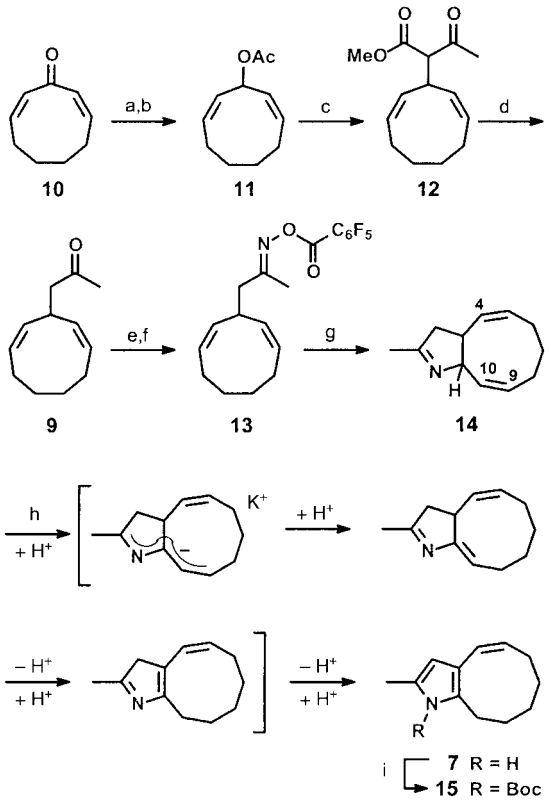

Scheme 4. Synthesis of the *ortho*-pyrrolophane core structure: a) DIBAL-H, CH_2Cl_2, 0°C, 97%; b) Ac_2O, Et_3N, DMAP (0.5 mol%), CH_2Cl_2, 97%; c) methyl acetoacetate, NaH, $[Pd(PPh_3)_4]$ (5 mol%), THF, 55°C, 74%; d) aq DMSO, 180°C, 99%; e) $H_2NOH{\cdot}HCl$, NaOAc, aq EtOH, 100°C, 97%; f) pentafluorobenzoyl chloride, Et_3N, Et_2O, −78°C→RT, 97%; g) $Pd(OAc)_2$ (12 mol%), $[P(o\text{-tolyl})_3]$ (12 mol%), Et_3N, DMF, 110°C, 54%; h) KH, 1,3-diaminopropane, 65%; i) Boc_2O, DMAP (10 mol%), MeCN, 50°C, 69%. DMAP = 4-dimethylaminopyridine, DMSO = dimethyl sulfoxide.

Krapcho decarboxylation[21] of **12** followed by conversion of the resulting cyclononadienylacetone (**9**) into the pentafluorobenzoyl oxime ester **13** under standard conditions proceeded smoothly, thus setting the stage for the envisaged Narasaka–Heck cyclization.[17] This key transformation was effected on a multigram scale by a catalyst formed in situ from $Pd(OAc)_2$ and $[P(o\text{-tolyl})_3]$ in DMF (*N*,*N*-dimethylformamide) at 110°C and delivered the unsaturated bicyclic imine **14** in 54% yield. Because of its exceptional sensitivity and unusual volatility, this compound must be treated with great care and should be elaborated without undue delay.[22]

Although Narasaka–Heck reactions of simple substrates usually deliver the corresponding pyrrole derivatives directly (see Scheme 3),[17] a method had to be found for the aromatization of product **14**. We comtemplated that deprotonation of this compound at the bridgehead position α to the nitrogen atom engenders the formation of a stabilized azapentadienyl anion that might be reprotonated to give the conjugated diene isomer preferentially, so compound **14** was treated with KAPA (potassium 3-aminopropylamide)[23] in 1,3-diaminopropane as the reaction medium at ambient temperature. In line with our expectations, the ensuing series of "thermodynamic" deprotonation/reprotonation events resulted in the *selective* shift of the 9,10-double bond in **14**, thus delivering the highly sensitive pyrrole **7**, which was immediately *N*-protected to give compound **15**.[22,24] Isomeric by-products formed under these conditions were separated after the subsequent oxidation step.

The only remaining double bond in **15** is suitably located for the introduction of the butyl side chain of the final target. However, all attempts to manipulate this olefin by means of a Wacker oxidation, a rhodium-catalyzed hydroboration, or an oxymercuration strategy were unsuccessful. Only the uncatalyzed hydroboration with $BH_3{\cdot}THF$ followed by stepwise oxidation with H_2O_2 (in the presence of excess Me_3N to protect the alkyl borane against proto-deborylation)[25] and Dess–Martin periodinane[26] allowed us to functionalize the alkene, thus furnishing ketone **16** and its anti-Markovnikov isomer in 65% overall yield (isomer ratio ≈5:1–2.5:1; 75% based on recovered starting material; Scheme 5). The anti-Markovnikov isomer and impurities derived from isomeric olefins (see above) could be removed at this stage by routine flash column chromatography. The severe steric shielding exerted by the cyclononyl skeleton also became evident in the subsequent Wittig olefination of **16**, which required forcing conditions but delivered product **17** in good yield and excellent purity. Its trisubstituted alkene moiety was hydrogenated with $[Ir(pyridine)(cod)(PCy_3)]PF_6$[27] (cod = 1,5-cyclooctadiene, Cy = cyclohexyl) as the catalyst to give **18** without reduction of the pyrrole causing any interference.

Pyrroles in general are known to be sensitive to oxidizing agents.[28] Therefore, the conversion of the methyl branch in **18** into the corresponding aldehyde was considered to be potentially troublesome. In fact, all classical reagents known to effect such benzylic oxidations failed in the present case. After some experimentation, however, a satisfactory solution for this problem was found by using cerium ammonium nitrate (CAN).[29] Key to success was the careful optimization of the reaction medium. Although previous reports recom-

 © 2005 Wiley-VCH Verlag GmbH & Co. KGaA, Weinheim

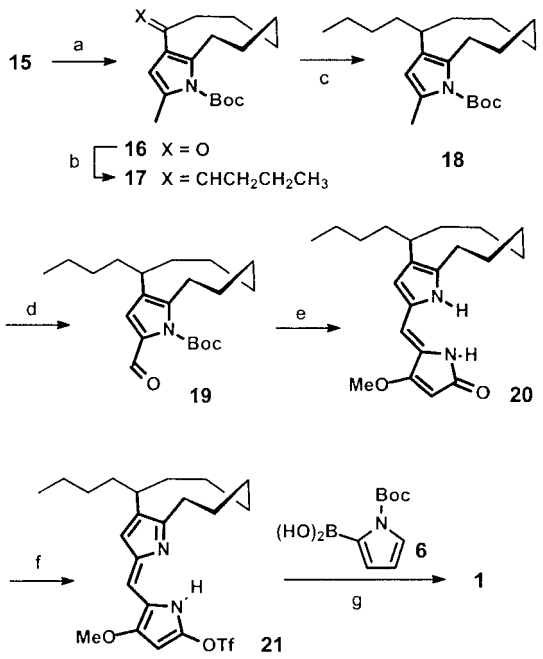

Scheme 5. Completion of the first total synthesis of butylcycloheptylprodigiosin (**1**): a) 1. BH_3·THF, THF, −10 °C; 2. H_2O_2, Me_3N·THF, aq NaOH (3 M), 0 °C; 3. Dess–Martin periodinane, 65 % (5:1–2.5:1 isomer ratio); b) $Ph_3P{=}CHCH_2CH_2CH_3$, toluene, reflux, 75 %; c) H_2 (1 atm), [Ir(pyridine)(cod)(PCy_3)]PF_6 (10 mol %), CH_2Cl_2, 90 %; d) CAN, $CHCl_3$/DME/H_2O, 60–65 %; e) **5**, aq NaOH, DMSO, 60 °C, 64–69 %; f) Tf_2O, CH_2Cl_2, 0 °C, 72–79 %; g) **6**, [$Pd(PPh_3)_4$] (8 mol %), LiCl, aq Na_2CO_3, DME, 80 °C, 70 %.

mended the use of CAN in aqueous THF/HOAc,[30] compound **18** was rapidly destroyed under these conditions, likely due to uncontrolled overoxidations. In an attempt to separate the reagent from the substrate and products, the oxidations were performed in biphasic media. In fact, the use of $CHCl_3$/H_2O furnished the desired aldehyde **19**, although the reaction rate was unacceptably low. Graftifyingly, the addition of small amounts of 1,2-dimethoxyethane (DME) as a "phase-transfer" agent led to a significant improvement and allowed the oxidation of **18** to proceed in only 30 minutes, thus affording the desired product **19** in respectable yields of 60–65 %. The generality of this novel method for benzylic oxidations of highly sensitive electron-rich arenes is subject to further studies in this laboratory.

Now that reliable access to the key building block **19** bearing the *ortho*-annelated medium-sized ring had been secured through a sequence of rather unconventional transformations, the assembly of the final target **1** could be pursued by following established routes.[5,8,15] To this end, the base-promoted condensation of aldehyde **19** with commercial lactam **5** was accompanied by cleavage of the *N*-Boc (Boc = *tert*-butoxycarbonyl) protecting group. Treatment of the resulting product **20** with Tf_2O (Tf = trifluoromethanesulfonyl) induced a reorganization of the π system and delivered triflate **21** as the substrate for the final Suzuki coupling.[31] Exposure of this compound to boronic acid **6** in the presence of catalytic amounts of [$Pd(PPh_3)_4$] and LiCl (3 equivalents) under previously optimized conditions[5a] afforded cycloheptylprodigiosin (**1**) in 70 % yield as a deeply red–pink colored solid. As expected, no signal from this compound is seen upfield of trimethylsilane (TMS) in the ^{1}H NMR spectrum. Although the spectrum is clearly different to that of the *meta*-bridged streptorubin B (**2**), the pattern signature is in accord with the signals reported for **1** (see Table 1 for the spectroscopic analysis).[10,11] A comparison with the spectrum of an authentic (although not entirely pure) sample of the "pink pigment" showed an excellent match. Therefore, it must be concluded that cycloheptylprodigiosin (**1**) is a natural product distinct from streptorubin B (**2**), as originally suggested by Gerber and Stahly[10] and Floss and co-workers.[11]

Table 1: Selected data for cycloheptylprodigiosin (**1**).[a]

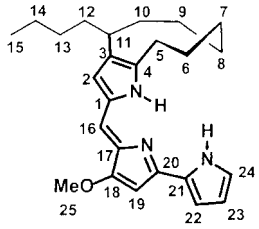

^{1}H NMR (600 MHz, CD_2Cl_2): δ = 6.82 (s, 1 H; 16-H), 6.72 (br s, 1 H; 24-H), 6.69 (dd, J = 3.6, 1.3 Hz, 1 H, 22-H), 6.34 (s, 1 H, 2-H), 6.20 (dd, J = 3.6, 2.6 Hz, 1 H, 23-H), 6.08 (s, 1 H, 19-H), 3.97 (s, 3 H, 25-H), 2.59 (m, 1 H, 11-H), 2.33 (br, 2 H, 5-H), 1.68 (m, 1 H, 6a-H), 1.62–1.50 (m, 4 H, 7a-H, 10a-H, 12-H), 1.41–1.15 (m, 9 H; 7b-H, 8-H, 9a-H, 10b-H, 13-H, 14-H), 1.00 (m, 1 H; 6b-H), 0.85 (t, J = 6 Hz, 3 H; 15-H), 0.83 ppm (m, 1 H; 9b-H); ^{13}C NMR (150 MHz, CD_2Cl_2): δ = 128.5 (s; C1), 118.6 (d; C2), 128.2 (s; C3), 142.9 (s; C4), 27.6 (t; C5), 27.7 (t; C6), 28.0 (t; C7), 28.1 (t; C8), 23.3 (t; C9), 38.0 (t; C10), 36.1 (d; C11), 37.1 (t; C12), 30.6 (t; C13), 23.2 (t; C14), 14.2 (q; C15), 116.2 (d; C16), 139.2 (s; C17)*, 169.2 (s; C18), 95.7 (d; C19), 159.6 (s; C20)*, 129.1 (s; C21), 112.6 (d; C22), 110.6 (d; C23), 122.3 (d; C24), 58.8 ppm (q; C25); IR (KAP): $\tilde{\nu}$ = 3322, 3103, 2921, 2852, 1738, 1618, 1577, 1552, 1449, 1361, 1333, 1285, 1221, 1148, 1116, 1086, 1057, 998, 954, 890, 767, 728 cm^{-1}; MS (EI) m/z (%): 391 [M^+], (100).

[a] All assignments are unambiguous (except those marked *, which might be mutually interchanged) and are based on 1D and 2D spectra. The multiplicity of the signals in the ^{13}C NMR spectrum refers to the geminal protons (DEPT). The insert shows the arbitrary numbering scheme.

Finally, it should be mentioned that aldehyde **19** can be used as a common building block for the preparation of a focused library of analogues by exploiting the late-stage flexibility inherent in the chosen synthetic route. A detailed mapping of the biochemical properties of the resuscitated alkaloid **1** (prepared in a 16-step sequence in approximately 1.5 % overall yield from cyclononadienone) and its congeners **22**–**25** (Scheme 6) are underway and will be reported in due course.

Received: October 6, 2004
Published online: March 30, 2005

Keywords: alkaloids · cyclophanes · medium-ring compounds · palladium · pyrroles

 © 2005 Wiley-VCH Verlag GmbH & Co. KGaA, Weinheim

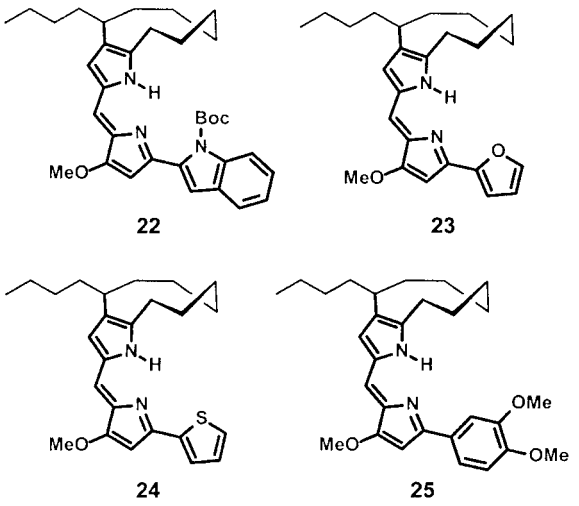

Scheme 6. Analogues of **1** prepared by diversion from the total synthesis route in the final cross-coupling step.

[1] a) A. Fürstner, *Angew. Chem.* **2003**, *115*, 3706 – 3728; *Angew. Chem. Int. Ed.* **2003**, *42*, 3582 – 3603; b) R. A. Manderville, *Curr. Med. Chem. Anti-Cancer Agents* **2001**, *1*, 195 – 218; c) R. Pérez-Tomás, B. Montaner, E. Llagostera, V. Soto-Cerrato, *Biochem. Pharmacol.* **2003**, *66*, 1447 – 1452.

[2] a) A. Nakamura, J. Magae, R. F. Tsuji, M. Yamasaki, K. Nagai, *Transplantation* **1989**, *47*, 1013 – 1016; b) J. Magae, M. W. Miller, K. Nagai, G. M. Shearer, *J. Antibiot.* **1996**, *49*, 86 – 90; c) S. M. Stepkowski, Z. S. Nagy, M.-E. Wang, F. Behbod, R. Erwin-Cohen, B. D. Kahan, R. A. Kirken, *Transplant. Proc.* **2001**, *33*, 3272 – 3273; d) S. M. Stepkowski, R. A. Erwin-Cohen, F. Behbod, M.-E. Wang, X. Qu, N. Tejpal, Z. S. Nagy, B. D. Kahan, R. A. Kirken, *Blood* **2002**, *99*, 680 – 689.

[3] a) R. D'Alessio, A. Bargiotti, O. Carlini, F. Colotta, M. Ferrari, P. Gnocchi, A. Isetta, N. Mongelli, P. Motta, A. Rossi, M. Rossi, M. Tibolla, E. Vanotti, *J. Med. Chem.* **2000**, *43*, 2557 – 2565; b) A. Mortellaro, S. Songia, P. Gnocchi, M. Ferrari, C. Fornasiero, R. D'Alessio, A. Isetta, F. Colotta, J. Golay, *J. Immunol.* **1999**, *162*, 7102 – 7109.

[4] A. Fürstner, H. Szillat, B. Gabor, R. Mynott, *J. Am. Chem. Soc.* **1998**, *120*, 8305 – 8314.

[5] a) A. Fürstner, J. Grabowski, C. W. Lehmann, *J. Org. Chem.* **1999**, *64*, 8275 – 8280; b) A. Fürstner, H. Krause, *J. Org. Chem.* **1999**, *64*, 8281 – 8286.

[6] a) A. Fürstner, H. Weintritt, *J. Am. Chem. Soc.* **1998**, *120*, 2817 – 2825; b) A. Fürstner, H. Weintritt, *J. Am. Chem. Soc.* **1997**, *119*, 2944 – 2945; c) A. Fürstner, T. Gastner, H. Weintritt, *J. Org. Chem.* **1999**, *64*, 2361 – 2366.

[7] a) A. Fürstner, H. Weintritt, A. Hupperts, *J. Org. Chem.* **1995**, *60*, 6637 – 6641; b) A. Fürstner, H. Krause, O. R. Thiel, *Tetrahedron* **2002**, *58*, 6373 – 6380; c) A. Fürstner, A. Hupperts, A. Ptock, E. Janssen, *J. Org. Chem.* **1994**, *59*, 5215 – 5229.

[8] a) A. Fürstner, J. Grabowski, C. W. Lehmann, T. Kataoka, K. Nagai, *ChemBioChem* **2001**, *2*, 60 – 68; b) A. Fürstner, E. J. Grabowski, *ChemBioChem* **2001**, *2*, 706 – 709; c) A. Fürstner, K. Reinecke, H. Prinz, H. Waldmann, *ChemBioChem* **2004**, *5*, 1575 – 1579.

[9] Note that this name is not very well chosen because compound **1** is not a cycloheptyl but a cyclononyl derivative.

[10] a) N. N. Gerber, *J. Antibiot.* **1975**, *28*, 194 – 199; b) N. N. Gerber, D. P. Stahly, *Appl. Microbiol.* **1975**, *30*, 807 – 810.

[11] S.-W. Tsao, B. A. M. Rudd, X.-G. He, C.-J. Chang, H. G. Floss, *J. Antibiot.* **1985**, *38*, 128 – 131.

[12] H. Laatsch, M. Kellner, H. Weyland, *J. Antibiot.* **1991**, *44*, 187 – 191.

[13] a) A. Fürstner, H. Szillat, F. Stelzer, *J. Am. Chem. Soc.* **2000**, *122*, 6785 – 6786; b) A. Fürstner, F. Stelzer, H. Szillat, *J. Am. Chem. Soc.* **2001**, *123*, 11863 – 11869; c) M. Méndez, V. Mamane, A. Fürstner, *ChemTracts* **2003**, *16*, 397 – 425.

[14] N. N. Gerber, A. G. McInnes, D. G. Smith, J. A. Walter, J. L. C. Wright, L. C. Vining, *Can. J. Chem.* **1978**, *56*, 1155 – 1163.

[15] R. D'Allessio, A. Rossi, *Synlett* **1996**, 513 – 514.

[16] C. Galli, L. Mandolini, *Eur. J. Org. Chem.* **2000**, 3117 – 3125.

[17] a) H. Tsutsui, M. Kitamura, K. Narasaka, *Bull. Chem. Soc. Jpn.* **2002**, *75*, 1451 – 1460; b) H. Tsutsui, K. Narasaka, *Chem. Lett.* **1999**, *28*, 45 – 46; c) S. Zaman, M. Kitamura, K. Narasaka, *Bull. Chem. Soc. Jpn.* **2003**, *76*, 1055 – 1062; d) H. Tsutsui, K. Narasaka, *Chem. Lett.* **2001**, *30*, 526 – 527; e) S. Chiba, M. Kitamura, O. Saku, K. Narasaka, *Bull. Chem. Soc. Jpn.* **2004**, *77*, 785 – 796.

[18] The preparation of **10** from the commercially available cyclononanone follows a literature method; an optimized procedure affording multigram quantities will be reported in a forthcoming full paper; see: a) E. W. Garbisch, Jr., *J. Org. Chem.* **1965**, *30*, 2109 – 2120; b) see also: R. Noyori, Y. Ohnishi, M. Katô, *Tetrahedron Lett.* **1971**, *19*, 1515 – 1518.

[19] For studies on metal-catalyzed alkylations of pentadienyl acetates, see: B. M. Trost, M.-H. Hung, *J. Am. Chem. Soc.* **1984**, *106*, 6837 – 6839.

[20] DFT optimization of the conformation of the presumed π-allylpalladium intermediate corroborate this interpretation.

[21] a) A. P. Krapcho, *Synthesis* **1982**, 805 – 822; b) A. P. Krapcho, *Synthesis* **1982**, 893 – 914.

[22] During the course of this synthesis, we noticed the exceptional volatility of many cyclononane derivatives even at fairly low temperatures, which renders the isolation of these compounds difficult and adversely affects the yields. This phenomenon is particularly pronounced in compounds **7** and **10**–**15**.

[23] C. A. Brown, P. K. Jadhav, *Org. Synth.* **1987**, *65*, 224 – 229.

[24] For a related aromatization reaction of a pyrrole with KAPA, see Ref.[4]

[25] M. Zaidlewicz, *J. Organomet. Chem.* **1985**, *293*, 139 – 146.

[26] a) D. B. Dess, J. C. Martin, *J. Org. Chem.* **1983**, *48*, 4155 – 4156; b) S. D. Meyer, S. L. Schreiber, *J. Org. Chem.* **1994**, *59*, 7549 – 7552.

[27] R. H. Crabtree, H. Felkin, T. Fillebeen-Khan, G. E. Morris, *J. Organomet. Chem.* **1979**, *168*, 183 – 195.

[28] A. Gossauer in *Methoden der Organischen Chemie (Houben-Weyl)*, *Vol. E6a*, 4th ed. (Ed.: R. P. Kreher), Thieme, Stuttgart, **1994**, pp. 556 – 798.

[29] Reviews: a) G. A. Molander, *Chem. Rev.* **1992**, *92*, 29 – 68; b) T.-L. Ho, *Synthesis* **1973**, 347 – 354; c) for a recent study, see: A. M. Khenkin, R. Neumann, *J. Am. Chem. Soc.* **2004**, *126*, 6356 – 6362, and references therein.

[30] a) T. Thyrann, D. A. Lightner, *Tetrahedron Lett.* **1995**, *36*, 4345 – 4348; b) J. B. Paine, D. Dolphin, *Can. J. Chem.* **1976**, *54*, 411 – 414.

[31] a) A. Suzuki, *J. Organomet. Chem.* **1999**, *576*, 147 – 168; b) N. Miyaura, A. Suzuki, *Chem. Rev.* **1995**, *95*, 2457 – 2483.

 © 2005 Wiley-VCH Verlag GmbH & Co. KGaA, Weinheim

Materials Science

Monodisperse Magnetic Single-Crystal Ferrite Microspheres**

*Hong Deng, Xiaolin Li, Qing Peng, Xun Wang, Jinping Chen, and Yadong Li**

It has been thought that many novel properties and potential applications would emerge from monodisperse materials with small dimensions. Therefore, the synthesis of monodisperse nanoparticles has been intensively pursued for their technological and fundamental scientific importance.[1–7] The synthesis of nanostructured magnetic materials has become a particularly important area of research and is attracting a growing interest because of the potential applications such materials have in ferrofluids, advanced magnetic materials, catalysts, colored pigments, high-density magnetic recording media, and medical diagnostics.[8–13] Spinel ferrites (MFe_2O_4; M = Fe, Mn, Zn, or Co) are among the most important magnetic materials and have been widely used in electronic devices, information storage, magnetic resonance imaging (MRI), and drug-delivery technology.[8,9,14] Magnetite (Fe_3O_4) has recently been considered an ideal candidate for biological applications, both as a tag for sensing and imaging, and as an activity agent for antitumor therapy.[15–17] For high performance in function-specific biological applications, magnetic particles must be spherical and have smooth surfaces, narrow size distributions, large surface areas (for maximal protein or enzyme binding), high magnetic saturation (σ_s) to provide maximum signal, and good dispersion in liquid media.[6,18,19]

After Sugimoto and Matijević reported the preparation of magnetite particles with a narrow size distribution in the early 1980s,[20] monodisperse ferrite has been fabricated by various chemistry-based synthetic methods, including coprecipitation, the reverse micelle method, microwave plasma synthesis, sol-gel techniques, freeze drying, ultrasound irradiation, hydrothermal methods, laser pyrolysis techniques, and thermal decomposition of organometallic and coordination compounds.[1,9,14,18,20–27] However, most of these approaches were focused on the synthesis of ferrite particles limited to diameters below 30 nm. There are no reports on the synthesis of well-crystallized ferrite nanoparticles with sizes similar to protein molecules. The development of a facile and economic synthetic strategy for the synthesis of hydrophilic, biocompatible magnetite nanoparticles would benefit their technical use in biomedical fields, especially for applications in vivo. Herein we report a general approach for the fabrication of monodisperse, hydrophilic, and single-crystalline ferrite microspheres by a solvothermal reduction method. To the best of our knowledge, this is the first report on the synthesis of single-crystalline magnetic microspheres. The ferrite spheres had monodisperse diameters that were tunable in the range of 200–800 nm. This work resulted in an important method for obtaining various monodisperse, magnetic, and single-crystalline microspheres, and provided an opportunity to further apply these promising materials.

Typical syntheses of Fe_3O_4 and ferrite microspheres were carried out in a solvothermal system by modified reduction reactions between $FeCl_3$ and ethylene glycol. We confirmed the production of Fe_3O_4 by conducting controlled oxidation reactions in which α- and γ-Fe_2O_3 were produced (Supporting Information).[1b,28–29] The crystalline structures of MFe_2O_4 were characterized by XRD. As shown in Figure 1, the

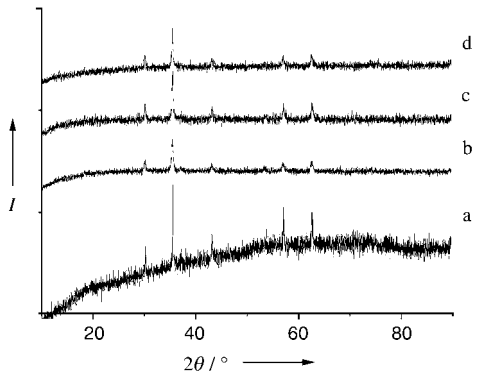

Figure 1. XRD patterns of Fe_3O_4, trace a; $MnFe_2O_4$, trace b; $ZnFe_2O_4$, trace c; and $CoFe_2O_4$, trace d.

patterns can be easily indexed to Fe_3O_4 (JCPDS 75-1609), $MnFe_2O_4$ (JCPDS 74-2403), $ZnFe_2O_4$ (JCPDS 22-1012), and $CoFe_2O_4$ (JCPDS 22-1068). The Fe_3O_4 sample was determined by X-ray photoelectron spectroscopy (Supporting Information).

The size and shape of the products were examined by TEM and scanning electron microscopy (SEM). Figure 2 shows representative images of the spinel ferrite compounds, which are spherical and have very narrow diameter distributions. The standard deviation for Fe_3O_4 particle diameters is ≈5%, excluding agglomerate particles (for diameter-distribution histograms of the MFe_2O_4 microspheres, see Supporting Information). Furthermore, the shape and size of the α-Fe_2O_3 and γ-Fe_2O_3 products remained unchanged from those of the Fe_3O_4 precursor. In a typical solvothermal process, the

[*] Dr. H. Deng, X. Li, Q. Peng, X. Wang, Prof. Y. Li
Department of Chemistry and the Key Laboratory of Atomic & Molecular Nanosciences
(Ministry of Education, China)
Tsinghua University, Beijing, 100084 (P.R. China)
and
National Center for Nanoscience and Nanotechnology
Beijing, 100084 (P.R. China)
Fax: (+86) 10-6278-8765
E-mail: ydli@tsinghua.edu.cn
Prof. J. Chen
Department of Physics
Peking University, Beijing, 100084 (P.R. China)

[**] This work was supported by the NSFC (90406003, 20401010, 50372030, 20025102, 20131030), the Foundation for the Author of National Excellent Doctoral Dissertation of the P.R. China, and the state key project of fundamental research for nanomaterials and nanostructures (2003CB716901).

Supporting information for this article is available on the WWW under http://www.angewandte.org or from the author.

 © 2005 Wiley-VCH Verlag GmbH & Co. KGaA, Weinheim DOI: 10.1002/anie.200462551

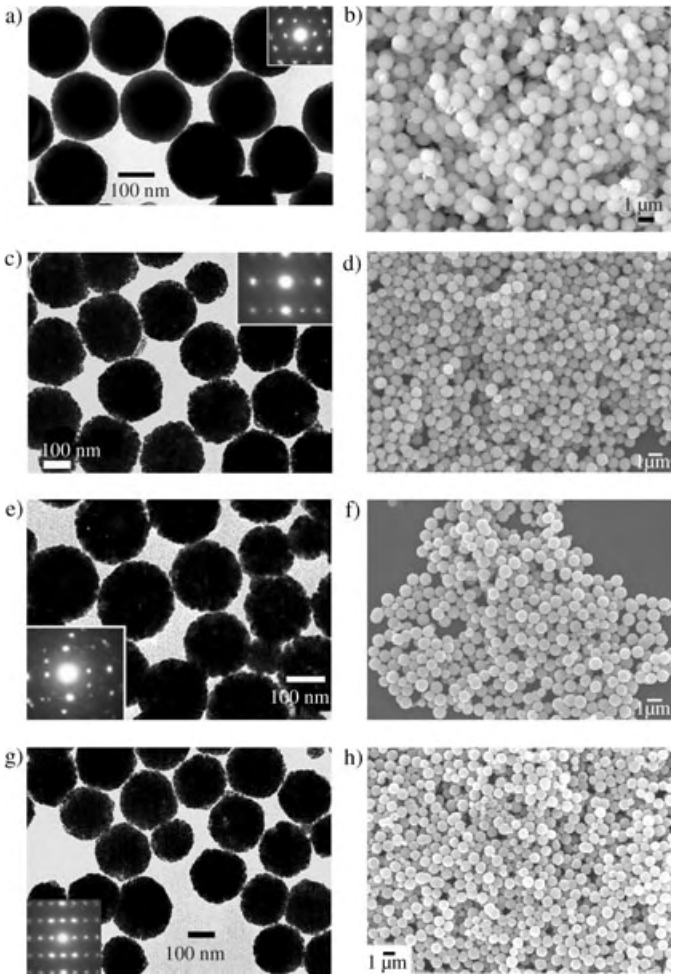

Figure 2. Representative TEM images (a, c, e, and g) and SEM images (b, d, f, and h) of microspheres of Fe_3O_4, (a and b); $MnFe_2O_4$, (c and d); $ZnFe_2O_4$, (e and f); and $CoFe_2O_4$, (g and h). Microsphere diameter is ≈800 nm in the SEM images, and ≈200 nm in the TEM images, in which the insets show the corresponding electron diffraction patterns.

diameters of the MFe_2O_4 ferrite microspheres were influenced by reaction time and the concentration of starting material. With precursor concentration (0.13 M) and temperature (200 °C) held constant, microsphere diameters were observed to be ≈200 nm at a reaction time of 8 h (Figures 2 a, c, e, and g), ≈400 nm at 48 h, and ≈800 nm at 72 h (Figures 2 b, d, f, and h). Likewise, microsphere diameters increased with an increase in precursor concentration. However, the complex nature of the growth process makes it difficult to obtain a straightforward correlation between particle diameter and changes in reaction time or precursor concentration. Electron-diffraction patterns taken from individual MFe_2O_4 microspheres revealed the single-crystalline nature of these samples. Energy-dispersive X-ray analysis (EDAX) was also measured to determine the chemical composition of the ferrite samples. Results from EDAX spectra from individual ferrite microspheres showed that samples contain only Fe and O for Fe_3O_4; Mn, Fe, and O for $MnFe_2O_4$; Zn, Fe, and O for $ZnFe_2O_4$; and Co, Fe, and O for $CoFe_2O_4$ (Supporting Information). The atomic ratio Fe/O for Fe_3O_4 was 3:4, and an analogous M/Fe/O ratio of ≈1:2:4 was observed for each of the other MFe_2O_4 products (M = Mn, Zn, Co), in agreement with the expected stoichiometry in each case.

High-resolution TEM (HRTEM) analysis provided more detailed structural information on the microspheres. A representative TEM image of the Fe_3O_4 microspheres is shown in Figure 3 a, in which the HRTEM image (boxed area) further supports the single-crystalline nature of the particles (Supporting Information). The interlayer distance was calculated to be ≈0.48 nm, which agrees well with the separation between the (101) lattice planes.

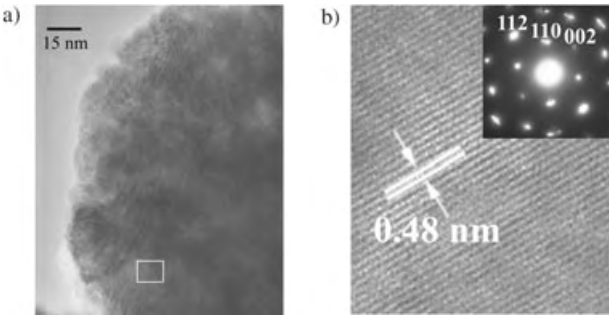

Figure 3. a) Representative TEM image of a Fe_3O_4 microsphere (diameter ≈200 nm); b) HRTEM image of the boxed region of part (a) and the electron-diffraction pattern of the individual Fe_3O_4 microsphere (inset).

Both the literature[6,7] and our own experimental evidence have led us to believe that ethylene glycol plays an important role in ferrite formation. Ethylene glycol is a strong reducing agent with a relatively high boiling point,[7] and has been widely used in the polyol process to provide monodisperse fine metal or metal oxide nanoparticles. However, magnetic spinel ferrite particles have a strong tendency to agglomerate during their formation in the liquid-phase process. To obtain monodisperse Fe_3O_4 particles, we designed a modified synthetic route in which three added features were found to be critical. First, NaAc was added for electrostatic stabilization to prevent particle agglomeration. Such benefits of NaAc were found in similar syntheses with Ru, Pt, and Rh particles.[30,31] In our system, NaAc was even more important, as its addition seems to assist in the ethylene glycol mediated reduction of $FeCl_3$ to Fe_3O_4. Control experiments showed that Fe^{3+} could not be reduced by ethylene glycol alone under the same reaction conditions. Second, polyethylene glycol was added as a surfactant and as an additional preventative measure against particle agglomeration. The third feature is the increased reaction temperature of 200 °C, which is necessary for the production of Fe_3O_4.

The magnetic properties of the ferrite microspheres were investigated with a vibrating sample magnetometer. Figure 4 shows the magnetization curves measured at 300 K for MFe_2O_4 microspheres with diameters of ≈200 nm. The magnetic saturation values are 81.9 emu g^{-1} for Fe_3O_4,

 © 2005 Wiley-VCH Verlag GmbH & Co. KGaA, Weinheim

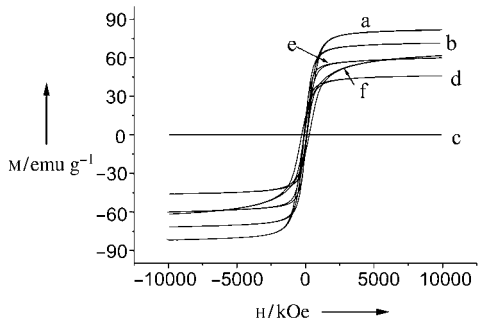

Figure 4. Room-temperature magnetization curves of ferrite microspheres (diameter ≈200 nm): Fe_3O_4, trace a; γ-Fe_2O_3, trace b; α-Fe_2O_3, trace c; $MnFe_2O_4$, trace d; $ZnFe_2O_4$, trace e; and $CoFe_2O_4$, trace f.

53.2 emu g^{-1} for $MnFe_2O_4$, 60.0 emu g^{-1} for $ZnFe_2O_4$, and 61.6 emu g^{-1} for $CoFe_2O_4$. More detailed investigations of the magnetic properties of these products are still in progress. The product of Fe_3O_4 oxidation in HNO_3 gave a σ_s value of 72 emu g^{-1} (Figure 4), which is close to the value of 74 emu g^{-1} determined from the analysis of commercial γ-Fe_2O_3 powder (Aldrich, 48-1-066-5), supporting the formation of γ-Fe_2O_3 under these conditions. After the Fe_3O_4 sample was oxidized in air at 400 °C for 3 h, the σ_s value of the product was negligible (Figure 4), which indicates that under these conditions Fe_3O_4 is transformed into α-Fe_2O_3.

To examine the colloid stability of ferrite samples, magnetic ferrite microspheres (20 mg) were dispersed in doubly distilled water (80 mL) by sonication. The magnetic particles remained in suspension for more than 1 day, which demonstrates that they can be well-dispersed in aqueous solution. Therefore, with the appropriate surface modifications, these microspheres may be suitable for clinical diagnosis and in the transport of drugs, proteins, viruses, or bacteria. The synthetic strategy developed in this study offers several important advantageous features for the technical application of microparticles. First, the ferrite spheres are magnetic, which means that they can be manipulated by an external magnetic field. Second, our strategy allows the direct production of highly crystalline, monodisperse, and hydrophilic spheres. Third, microsphere size is controllable, with diameters ranging from 200 to 800 nm. Finally, the raw materials are inexpensive and the yields are relatively high (92 %), which makes this process amenable to large-scale reactions for industrial needs.

In summary, the solvothermal reduction method has been used to successfully produce a series of ferrite MFe_2O_4 (M = Fe, Mn, Co, Zn) microspheres. This approach provides a one-step, simple, general, and inexpensive method for the preparation of monodisperse magnetic microspheres with a tunable diameter range of ≈200–800 nm. We believe that these hydrophilic and biocompatible microspheres will have important applications not only in advanced magnetic materials and ferrofluid technology, but also in biomedical fields such as biomolecular separations, targeted drug delivery, cancer diagnosis and treatment, as well as magnetic resonance imaging.

Experimental Section

Fe_3O_4 microsphere synthesis:[32] $FeCl_3 \cdot 6H_2O$ (1.35 g, 5 mmol) was dissolved in ethylene glycol (40 mL) to form a clear solution, followed by the addition of NaAc (3.6 g) and polyethylene glycol (1.0 g). The mixture was stirred vigorously for 30 min and then sealed in a teflon-lined stainless-steel autoclave (50 mL capacity). The autoclave was heated to and maintained at 200 °C for 8–72 h, and allowed to cool to room temperature. The black products were washed several times with ethanol and dried at 60 °C for 6 h.

The above process can be can be extended to the synthesis of MFe_2O_4 (M = Co, Mn, Zn) microspheres by coprecipitation of M^{II} and Fe^{III} chlorides ($M^{2+}/Fe^{3+} = 0.5$).[32] For example, a mixture of $MnCl_2 \cdot 4H_2O$ (0.50 g, 2.5 mmol) and $FeCl_3 \cdot 6H_2O$ (1.35 g, 5 mmol) under the same reaction conditions as used for the synthesis of Fe_3O_4 microspheres, produced microspheres of $MnFe_2O_4$.

All samples were characterized on a Bruker D8 Advance powder X-ray diffractometer with $Cu_{K\alpha}$ radiation ($\lambda = 1.5418$ Å). The TEM and HRTEM images were generated with a Hitachi H-800 transmission electron microscope and with a JEOL JEM-2010F high-resolution transmission electron microscope. SEM images were taken with a NORAN LDO 1530 apparatus. Magnetic studies were carried out on a Quantum Design SQUID magnetometer.

Received: November 9, 2004
Published online: March 30, 2005

Keywords: colloids · crystal growth · iron · magnetic properties · reduction

[1] a) S. Sun, C. B. Murray, D. Weller, L. Folks, A. Moser, *Science* **2000**, *287*, 1989 – 1992; b) S. H. Sun, H. Zeng, D. B. Robinson, *J. Am. Chem. Soc.* **2004**, *126*, 273 – 279; c) S. Sun, H. Zeng, *J. Am. Chem. Soc.* **2002**, *124*, 8204 – 8205; d) K. E. Elkins, T. S. Vedantam, J. P. Liu, H. Zeng, H. S. H. Sun, Y. Ding, Z. L. Wang, *Nano Lett.* **2003**, *3*, 1647 – 1649.

[2] R. Jin, Y. Cao, C. A. Mirkin, K. L. Kelly, G. C. Schatz, J. G. Zheng, *Science* **2001**, *294*, 1901 – 1904.

[3] a) S. U. Son, Y. Jang, J. Park, H. B. Na, H. M. Park, H. J. Yun, J. Lee, T. Hyeon, *J. Am. Chem. Soc.* **2004**, *126*, 5226 – 5227; b) S. U. Son, Y. Jang, K. Y. Yoon, E. Kang, T. Hyeon, *Nano Lett.* **2004**, *4*, 1147 – 1151; c) S. W. Kim, J. Park, Y. Jang, Y. Chung, S. Hwang, T. Hyeon, Y. W. Kim, *Nano Lett.* **2003**, *3*, 1289 – 1291; d) J. Joo, T. Yu, Y. W. Kim, H. M. Park, F. X. Wu, J. Z. Zhang, T. Hyeon, *J. Am. Chem. Soc.* **2003**, *125*, 6553 – 6557.

[4] a) F. Caruso, R. A. Caruso, H. Mohwald, *Science* **1998**, *282*, 1111 – 1114; b) F. Caruso, *Adv. Mater.* **2001**, *13*, 11 – 22; c) F. Caruso, *Chem. Eur. J.* **2000**, *6*, 413 – 419.

[5] a) X. G. Peng, *Adv. Mater.* **2003**, *15*, 459 – 463; b) Z. A. Peng, X. G. Peng, *J. Am. Chem. Soc.* **2001**, *123*, 1389 – 1395.

[6] a) Y. Sun, Y. Xia, *Science* **2002**, *298*, 2176 – 2179; b) Y. Lu, Y. Yin, B. T. Mayers, Y. Xia, *Nano Lett.* **2002**, *2*, 183 – 186; c) Y. L. Wang, Y. N. Xia, *Nano Lett.* **2004**, *4*, 2047 – 2050.

[7] a) Q. Peng, Y. J. Dong, Y. D. Li, *Angew. Chem.* **2003**, *115*, 3135 – 3138; *Angew. Chem. Int. Ed.* **2003**, *42*, 3027 – 3030; b) Q. Peng, S. Xu, Z. B. Zhuang, X. Wang, Y. D. Li, *Small* **2004**, *1*, 216 – 221; c) X. M. Sun, Y. D. Li, *Angew. Chem.* **2004**, *116*, 3915 – 3919; *Angew. Chem. Int. Ed.* **2004**, *43*, 3827 – 3831; d) X. M. Sun, Y. D. Li, *Angew. Chem.* **2004**, *116*, 607 – 611; *Angew. Chem. Int. Ed.* **2004**, *43*, 597 – 601; e) J. W. Wang, X. Wang, Q. Peng, Y. D. Li, *Inorg. Chem.* **2004**, *43*, 7552 – 7556; f) Y. Zhang, Y. D. Li, *J. Phys. Chem. B* **2004**, *108*, 17805 – 17811.

[8] F. Caruso, M. Spasova, A. Susha, M. Giersig, R. A. Caruso, *Chem. Mater.* **2001**, *13*, 109 – 116.

[9] a) T. Hyeon, *Chem. Commun.* **2003**, *8*, 927 – 934; b) T. Hyeon, Y. Chung, J. Park, S. S. Lee, Y. W. Kim, B. H. Park, *J. Phys. Chem. B*

 © 2005 Wiley-VCH Verlag GmbH & Co. KGaA, Weinheim

2002, *106*, 6831 – 6833; c) T. Hyeon, S. S. Lee, J. Park, Y. Chung, H. B. Na, *J. Am. Chem. Soc.* **2001**, *123*, 12798 – 12801.
[10] Y. Xiong, X. Xie, S. Chen, Z. Li, *Chem. Eur. J.* **2003**, *9*, 4991 – 4996.
[11] K. Woo, H. J. Lee, J. Ahn, Y. S. Park, *Adv. Mater.* **2003**, *15*, 1761 – 1764.
[12] a) X. Teng, H. Yang, *J. Mater. Chem.* **2004**, *14*, 774 – 779; b) Y. Wang, J. Wong, X. Teng, X. Lin, H. Yang, *Nano. Lett.* **2003**, *3*, 1554 – 1559; c) Y. Wang, X. Teng, J. Wang, H. Yang, *Nano. Lett.* **2003**, *3*, 789 – 793.
[13] A. Yu, M. Mizuno, Y. Sasaki, H. Kondo, *Appl. Phys. Lett.* **2002**, *81*, 3768 – 3771.
[14] a) S. Yu, M. Yoshimura, *Adv. Funct. Mater.* **2002**, *12*, 9 – 15; b) S. Yu, M. Yoshimura, *Chem. Mater.* **2000**, *12*, 3805 – 3810.
[15] a) J. M. Perez, T. O'Loughlin, F. J. Simeone, R. Weissleder, L. Josephson, *J. Am. Chem. Soc.* **2002**, *124*, 2856 – 2857; b) J. M. Perez, F. J. Simeone, A. Tsourkas, L. Josephson, R. Weissleder, *Nano Letter.* **2004**, *4*, 119 – 122; c) J. M. Perez, L. Josephson, T. O'Loughlin, D. Hogemann, R. Weissleder, *Nat. Biotechnol.* **2002**, *20*, 816 – 820.
[16] A. Y. Louie, M. M. Huber, E. T. Ahrens, U. Rothbacher, R. Moats, R. E. Jacobs, S. E. Fraser, T. J. Meade, *Nat. Biotechnol.* **2000**, *18*, 321 – 325.
[17] U. Häfeli, W. Schütt, J. Teller, M. Zborowski, *Scientific and Clinical Application of Magnetic Carriers*, Plenum, New York, **1997**.
[18] S. H. Gee, Y. K. Hong, D. W. Erickson, M. H. Park, *J. Appl. Phys.* **2003**, *93*, 7560 – 7562.
[19] K. Woo, J. Hong, S. Choi, H. Lee, J. Ahn, C. S. Kim, S. W. Lee, *Chem. Mater.* **2004**, *16*, 2814 – 2818.
[20] a) T. Sugimoto, E. Matijević, *J. Colloid Interface Sci.* **1980**, *74*, 227 – 243; b) E. Matijević, *Acc. Chem. Res.* **1981**, *14*, 22 – 29; c) T. Sugimoto, *Monodispersed Particles*, Elsevier, New York, **2001**.
[21] J. Jolivert, C. Chanéac, E. Tronc, *Chem. Commun.* **2004**, 481 – 487.
[22] F. Li, J. Liu, D. G. Evans, X. Duan, *Chem. Mater.* **2004**, *16*, 1597 – 1602.
[23] X. Chen, Z. Deng, L. Li, Y. Li, *Chin. J. Inorg. Chem.* **2002**, *18*, 460 – 464.
[24] L. A. Harris, J. D. Goff, A. Y. Carmichael, J. S. Riffle, J. J. Harburn, T. G. S. Pierre, M. Saunders, *Chem. Mater.* **2003**, *15*, 1367 – 1377.
[25] Z. H. Zhou, J. Wang, X. Liu, H. S. O. Chan, *J. Mater. Chem.* **2001**, *11*, 1704 – 1709.
[26] Y. Sahoo, M. Cheon, S. Wang, H. Luo, E. P. Furlani, P. N. Prasad, *J. Phys. Chem. B* **2004**, *108*, 3380 – 3383.
[27] Q. Song, Z. J. Zhang, *J. Am. Chem. Soc.* **2004**, *126*, 6164 – 6168.
[28] J. L. Lyon, D. A. Fleming, M. B. Stone, P. Schiffer, M. E. Williams, *Nano Lett.* **2004**, *4*, 719 – 723.
[29] R. M. Comell, U. Schwertmann, *The Iron Oxides: Structure, Properties, Reactions, Occurrences and Uses*, VCH, New York, **1996**.
[30] a) G. Viau, P. Toneguzzo, A. Pierrard, O. Acher, F. Fiévet-Vincent, F. Fiévet, *Scr. Mater.* **2001**, *44*, 2263 – 2267; b) G. Viau, R. Brayner, L. Poul, N. Chakroune, E. Lacaze, F. Fiévet-Vincent, F. Fiévet, *Chem. Mater.* **2003**, *15*, 486 – 494.
[31] K. R. Brown, D. G. Walter, M. J. Natan, *Chem. Mater.* **2000**, *12*, 306 – 313.
[32] Y. D. Li, H. Deng, Chinese Patent 200410009788.9, **2004**.

 © 2005 Wiley-VCH Verlag GmbH & Co. KGaA, Weinheim

NMR Spectroscopy

Scaling the Alignment of Small Organic Molecules in Substituted Polyglutamates by Variable-Angle Sample Spinning**

*Christina M. Thiele**

The determination of the relative configuration of small organic molecules by NMR spectroscopy usually relies on the analysis of NOE data and ^3J coupling constants. Recently the approach of using residual dipolar couplings (RDCs) has come into focus, as RDCs contain both distance and angle information. It is, for example, possible to assign all diastereotopic protons in strychnine simultaneously without the use of NOE data[1] and to determine the complete relative configuration of a fluorinated compound containing five stereocenters.[2] In order to observe residual dipolar couplings, however, it is necessary to induce partial alignment of the molecule in the magnetic field. Alignment media inducing weak alignment for organic molecules are still scarce. The liquid-crystalline polyglutamates[1,3–6] and deuterated PCBP (4-*n*-pentyl-4′-cyanobiphenyl)[7] are used for this purpose. Recently the use of crosslinked polystyrene (PS) and crosslinked poly(dimethylsiloxane) (PDMS) was described, and here the degree of alignment is dependent on the degree of crosslinking.[8–10]

The disadvantage of liquid-crystalline media is that below a minimum concentration of the liquid crystal in the solvent, the phase becomes isotropic and no longer induces alignment. Thus the degree of alignment can be adjusted within specific regions only. Scalability is possible with polymer sticks, although the degree of alignment cannot be adjusted after sample preparation, which might be problematic in the structure elucidation of natural products due to limited sample amounts. An alternative is provided by variable-angle sample spinning (VASS), where the liquid-crystalline sample is spun at an angle Θ_r to the magnetic field in order to reduce anisotropic interactions.[11–15] We present here a straightforward approach to scaling residual dipolar couplings in the chiral orienting media poly(γ-benzyl-L-glutamate)/$CDCl_3$ (PBLG) and poly(γ-ethyl-L-glutamate)/$CDCl_3$ (PELG) by applying variable-angle sample spinning.

If a liquid crystal with molecular positive magnetic anisotropy ($\Delta\chi_m > 0$) is spun at an angle Θ_r to the magnetic field which is smaller than the magic angle ($\Theta_r < 54.7°$) and with a spinning speed considerably higher than its critical spinning speed ω_c, then the director of the liquid crystal aligns parallel to the spinning axis. The anisotropic interactions of the solute (and the liquid crystal) are directly related to the angle Θ_r since they are proportional to the second Legendre polynomial ($P_2(\cos\Theta_r) = (3\cos^2\Theta_r - 1)/2$). Thus by changing the angle Θ_r the dipolar interactions can be scaled. The total spin–spin coupling constant T (also called the effective coupling constant J_{eff}) in spectra can obtained from Equation (1).[11]

$$T = J_{eff} = J_{iso} + \frac{3\cos^2\Theta_r - 1}{2}(2D + J_{aniso}) \quad (1)$$

Here, T is the total spin–spin coupling constant, Θ_r the angle to the magnetic field, J_{iso} the isotropic (scalar) coupling constant, D residual dipolar coupling, and J_{aniso} the anisotropy of the scalar coupling, which is usually neglected.

The two polyglutamates used in this study, PBLG and PELG, are commercially available, and the samples were prepared as described previously with strychnine[5,1] and other compounds.[16] The samples were checked for homogeneity in standard 5-mm liquid-state NMR tubes. If the lines of the solvent $CDCl_3$ displayed a sharp doublet in the deuterium spectrum due to quadrupolar splitting, the viscous liquid crystal was transferred into a 4-mm solid-state rotor and closed with a cap without a hole to limit solvent evaporation. The samples were spun at various angles relative to the magnetic field (at the same spinning speed). For this purpose a Bruker DRX-600 spectrometer equipped with a standard dual (^1H,^{13}C) Bruker HR-MAS probe with *z*-gradients was used. The deuterium spectra were recorded (using the lock channel) to get an estimate of the reduction in the observed couplings (Figure 1). As there is no goniometer on the probe, the angle was calibrated using the quadrupolar splitting of the solvent within the liquid crystal. To record spectra of the static case, the measurement was performed without rotation. In this case the liquid crystal aligns parallel to the magnetic field at whatever angle the rotor stands. For PBLG this was a spontaneous process; for PELG, however, equilibration within the probe for 20 min was necessary to get sharp lines. Care must be taken when adjusting the spinning speed. The spinning speed, which has to be exceeded to avoid spinning side bands and guarantee alignment of the director with the rotation axis, shows a square dependence on the magnetic field. In theory the alignment of the director parallel to the spinning axis should improve with higher spinning frequencies.[11] A different observation was made here, which is in accordance with results published by Lesot et al.,[17] where a second critical spinning speed was observed, above which the director is distributed at various angles towards the magnetic field. Therefore the spinning speed was chosen to be 1180 Hz for PBLG and 1002 Hz for PELG in order to stay within these two borders at a magnetic field strength of 14.10 T (corresponding to a ^1H NMR frequency of 600 MHz). At spinning speeds of less than 1000 Hz rotation was not stable with our HR-MAS probe, thus 1000 Hz was the lower limit. At spinning speeds of more than 1400 Hz for PBLG and

[*] Dr. C. M. Thiele
Institut für Analytische Chemie
Universität Leipzig
Johannisallee 29, 04103 Leipzig (Germany)
Fax: (+49) 341-97-36115
E-mail: thiele@chemie.uni-leipzig.de

[**] This work was supported by the Fonds der Chemischen Industrie. I thank Prof. Dr. S. Berger, Dr. P. Lesot, Dr. M. Zweckstetter, and Prof. Dr. D. Freude for their help.

Supporting information for this article is available on the WWW under http://www.angewandte.org or from the author.

 DOI: 10.1002/anie.200461532 © 2005 Wiley-VCH Verlag GmbH & Co. KGaA, Weinheim

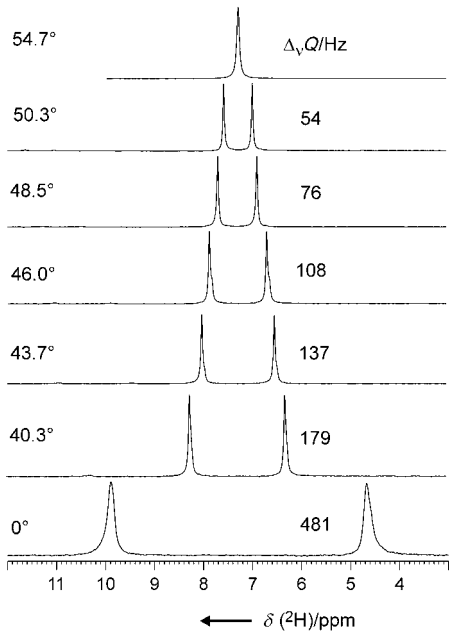

Figure 1. One-dimensional ^{2}H NMR spectra (92.09 MHz) of $CDCl_3$ in PBLG. Θ_r (on the left side of each trace) is varied to give $\Delta_\nu Q$ values between 0 Hz (top, magic angle) and 481 Hz (bottom, static case, 0°). Spinning speed 1180 Hz, temperature 298 K.

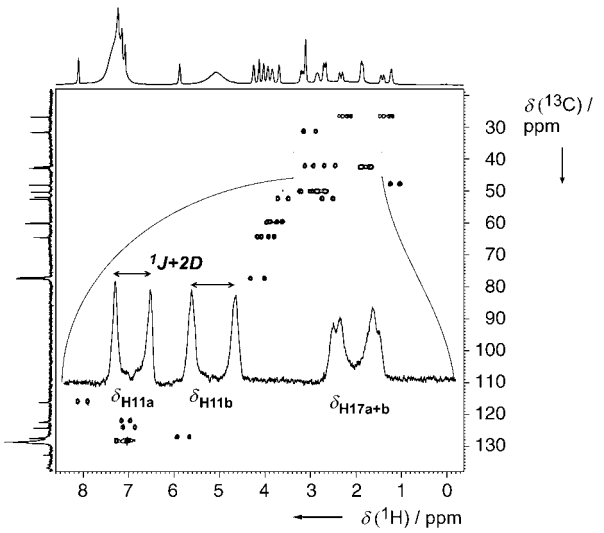

Figure 2. Two-dimensional HSQC spectrum of strychnine in PBLG/$CDCl_3$ at $\Theta_r = 50.3°$ recorded without ^{13}C decoupling during acquisition (1180 Hz, 298 K). As can be seen from the 1D slice at a ^{13}C chemical shift of 42 ppm the total spin–spin C–H couplings can be extracted easily. No signals of PBLG are seen in the 2D spectrum.

3500 Hz for PELG the behavior of the lines was the same as that described by Lesot et al.[17]

Two measurements were performed to extract one-bond ^{13}C-^{1}H RDCs. In one measurement an isotropic solution of strychnine was used to give the scalar coupling constant J (or the nematic sample is spun at the magic angle); the other measurement was conducted in the nematic phase using a solid-state rotor at an angle where the size of total couplings is convenient. The measurement of RDCs for strychnine at angles close to the magic angle (54.7–48.5° for PBLG and all angles used for PELG, respectively) HSQC spectra without decoupling during acquisition could be used without problems (see Figure 2), as the dipolar interactions remain small (as expected). At angles farther from the magic angle gated-decoupled carbon spectra were used to extract residual dipolar coupling. As can be seen from Figure 3b, ^{13}C-^{1}H RDCs can be scaled according to requirements. At the top the isotropic spectrum (spinning at the magic angle) is depicted, thus giving the scalar couplings. From top to bottom the degree of anisotropic interaction increases leading, for example, from a triplet for C15 (methylene group) in the isotropic case ($\Theta_r = 54.7°$) to a doublet of doublets ($\Theta_r = 40.3°$) with both D values smaller than J_{iso}. This then develops further to a doublet-like signal for C15 in the static case, where $-2\,D$ for one proton is equal to J_{iso}, giving a spin–spin coupling constant T of 0 Hz, and one D is of the size of -15.1 Hz giving a T value of 108.8 Hz for the other proton. The considerable broadening of the lines, due to among other things long-range C–H couplings, leads to large errors in D for the static case as described previously.[5] This example of the two protons on C15 clearly shows the power of this approach, as it was not considered advisable to extract couplings of this size from static spectra only.

For PELG the measurement of virtually all RDCs was possible at all chosen angles including the static case (see the Supporting Information). A linear correlation of the size of the dipolar coupling of the solute (D/Hz) vs. the quadrupolar splitting of the organic solvent $CDCl_3$ ($\Delta_\nu Q$/Hz) shows excellent fits (R^2 larger than 0.94) for 13 out of 22 couplings. Due to the limited amount of data for PELG (only three different angles were examined in addition to the static case) no statement can be made concerning the nine other couplings. An extrapolation of the values for the static case from those obtained by variable-angle sample spinning gives a good estimate of the size of all couplings. For PBLG, however, very few couplings could be measured for the static case as described previously.[5] Using the approach of variable-angle sample spinning virtually all couplings could be measured at the angles between 40° and 50°, and linear behavior for D vs. $\Delta_\nu Q$ was observed for most of the couplings (see Figure 4). The slope of this straight line can then be used to extrapolate the values for the static case; these values can be confirmed by the spectra (± 10 Hz is, for example, only 3 % error for C1 and C4) for 17 out of 22 couplings, thus also revealing earlier misinterpretations of the spectra.

The alignment tensors for strychnine in PBLG and PELG were calculated using the program package PALES using the modules "bestfit" and "addition of dipolar coupling noise"[18,19] Significant changes in the degree of alignment within each sample were found, which increased upon increasing degree of anisotropy introduced (increasing $\Delta_\nu Q$) as expected (Table 1).

The degree of orientation in PBLG and PELG is different, as previously described.[1] With these new experiments, however, the orientation of alignment for PBLG can be determined more reliably, thus revealing differences in the orientation of strychnine in PBLG and PELG. The x, y and z

 © 2005 Wiley-VCH Verlag GmbH & Co. KGaA, Weinheim

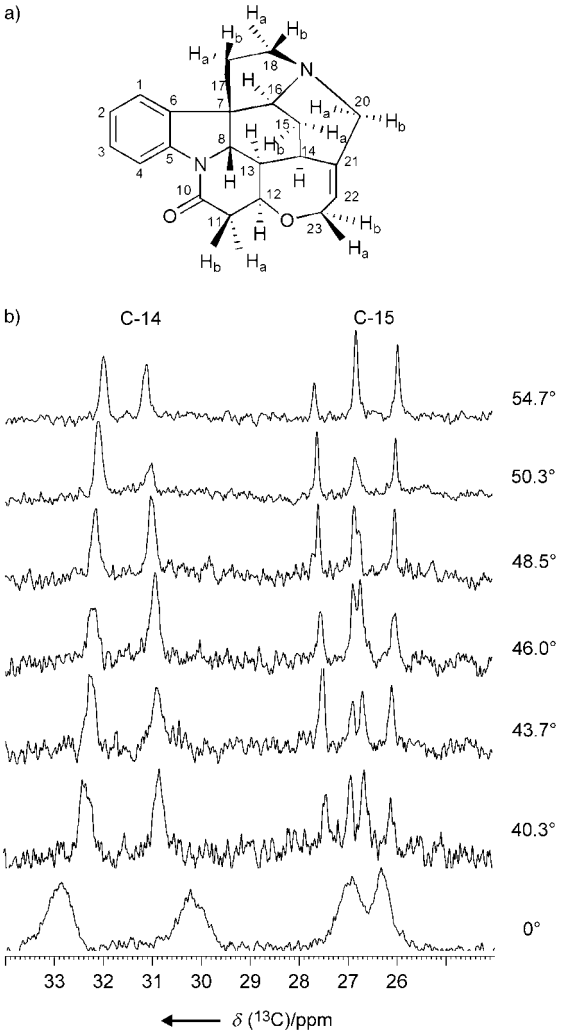

Figure 3. a) Structural formula of strychnine and numbering as used in the text. b) Part of ^{13}C gated decoupled 1D NMR spectra of strychnine (signal of carbon atoms denoted C14 and C15) in PBLG/$CDCl_3$ at a magnetic field strength of 14.1 T. Θ_r is varied from the magic angle (top) to 0°, the static case (bottom).

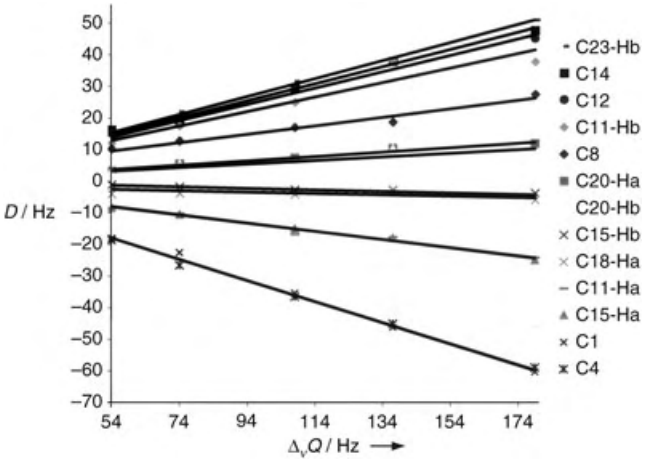

Figure 4. Plot of observed residual dipolar coupling constants D [Hz] of strychnine in PBLG vs. quadrupolar splitting $\Delta_\nu Q$ [Hz] of the solvent $CDCl_3$ (as a measure for Θ_r). Linear behavior can be observed for all RDCs (not all lines shown).

axes differ by 11°, 12° and 6°, respectively (see the Supporting Information for details). Whether this difference in the orientation of alignment is strong enough to consider these two alignment media as linearly independent remains to be seen. If this is indeed the case, they could then be used for the determination of the relative configuration at highly substituted stereocenters as well as for the study of dynamic processes, as has been shown impressively for biomolecules.[20–22]

In summary, we have demonstrated the usefulness of variable-angle sample spinning to scale partial alignment of small organic molecules. Extraction of RDCs becomes now convenient since it is possible to reduce the RDCs according to requirements from one single sample. Even the isotropic spectrum can be obtained from the anisotropic sample by spinning at the magic angle for the liquid crystals used here. One drawback might be the need for a probe that can be spun at different angles. We used a standard Bruker HR-MAS probe available to many organic chemistry groups; a specially built VASS probe is not required.

The alignment media used here induce orientations of the solute complimentary to those possible with the recently described PS sticks. This is important as it broadens the applicability of using RDCs in structure elucidation of small organic molecules, an approach that will certainly remove many ambiguities in the structure determination of natural products.

Received: August 4, 2004
Revised: January 10, 2005
Published online: March 30, 2005

Keywords: NMR spectroscopy · polyglutamates · residual dipolar couplings · structure determination

Table 1: Alignment properties of PBLG and PELG at various angles Θ_r[a]

	PBLG						PELG			
$\Delta_\nu Q$ [Hz]	54	74	108	137	179	481	37	70	122	456
Θ_r [°]	50.3	48.5	46.0	43.7	40.3	0	51.5	48.7	44.3	0
D_a [10^{-4} Hz]	2.16	2.55	4.05	4.93	6.52	19.6	0.52	0.99	1.83	6.09
D_r/D_a	0.65	0.63	0.41	0.63	0.66	0.53	0.46	0.59	0.60	0.66
n(RDC)	22	20	22	19	20	22	22	20	22	22
R	0.99	1.00	0.97	0.99	0.99	0.99	0.96	0.99	0.99	0.99

[a] D_a is the axial component and D_r/D_a the rhombicity of the alignment tensor. n(RDC) is the number of RDCs used for the calculation, R is Pearson's correlation coefficient of experimental versus back-calculated dipolar couplings within PALES.

 © 2005 Wiley-VCH Verlag GmbH & Co. KGaA, Weinheim

[1] C. M. Thiele, *J. Org. Chem.* **2004**, *69*, 7403 – 7413, and references therein.
[2] J. Yan, F. Delagio, A. Kaerner, A. D. Kline, H. Mo, M. J. Shapiro, T. A. Smitka, G. A. Stephenson, E. R. Zartler, *J. Am. Chem. Soc.* **2004**, *126*, 5008 – 5017.
[3] C. Aroulanda, V. Boucard, F. Guibé, J. Courtieu, D. Merlet, *Chem. Eur. J.* **2003**, *9*, 4536 – 4539.
[4] L. Verdier, P. Sakhaii, M. Zweckstetter, C. Griesinger, *J. Magn. Reson.* **2003**, *163*, 353 – 359.
[5] C. M. Thiele, S. Berger, *Org. Lett.* **2003**, *5*, 705 – 708.
[6] C. Aroulanda, P. Lesot, D. Merlet, J. Courtieu, *J. Phys. Chem. A* **2003**, *107*, 10911 – 10918.
[7] B. Bendiak, *J. Am. Chem. Soc.* **2002**, *124*, 14862 – 14863.
[8] B. Luy, K. Kobzar, H. Kessler, *Angew. Chem.* **2004**, *116*, 1112 – 1115; Angew. *Chem. Int. Ed.* **2004**, *43*, 1092 – 1094.
[9] J. C. Freudenberger, P. Spiteller, R. Bauer, H. Kessler, B. Luy, *J. Am. Chem. Soc.* **2004**, *126*, 14690 – 14691.
[10] Very recently published polymer alignment media for polar substances: J. C. Freudenberger, S. Knör, K. Kobzar, D. Heckmann, T. Paululat, H. Kessler, B. Luy, *Angew. Chem.* **2005**, *117*, 427 – 430; *Angew. Chem. Int. Ed.* **2005**, *44*, 423 – 426; P. Haberz, J. Farjon, C. Griesinger, *Angew. Chem.* **2005**, *117*, 431 – 433; *Angew. Chem. Int. Ed.* **2005**, *44*, 427 – 429.
[11] J. Courtieu, J. P. Bayle, B. M. Fung, *Prog. Nucl. Magn. Reson. Spectrosc.* **1994**, *26*, 141 – 169.
[12] R. R. Havlin, G. H. J. Park, T. Mazur, A. Pines, *J. Am. Chem. Soc.* **2003**, *125*, 7998 – 8006.
[13] G. Zandomeneghi, M. Tomaselli, P. T. F. Williamson, B. H. Meier, *J. Biomol. NMR* **2003**, *25*, 113 – 123.
[14] J. Courtieu, D. W. Alderman, D. M. Grant, J. P. Bayle, *J. Chem. Phys.* **1982**, *77*, 723 – 730.
[15] N. Lancelot, K. Elbayed, A. Bianco, M. Piotto, *J. Biomol. NMR* **2004**, *29*, 259 – 269.
[16] C. Aroulanda, M. Sarfarti, J. Courtieu, P. Lesot, *Enantiomer* **2001**, *6*, 281 – 287.
[17] P. Lesot, J. W. Emsley, J. Courtieu, *Liq. Cryst.* **1998**, *25*, 123 – 127.
[18] M. Zweckstetter, A. Bax, *J. Am. Chem. Soc.* **2000**, *122*, 3791 – 3792.
[19] M. Zweckstetter, A. Bax, *J. Biomol. NMR* **2002**, *23*, 127 – 137.
[20] J. Meiler, J. J. Pompers, W. Peti, C. Griesinger, R. Brüschweiler, *J. Am. Chem. Soc.* **2001**, *123*, 6098 – 6107.
[21] J. R. Tolman, *J. Am. Chem. Soc.* **2002**, *124*, 12020 – 12030.
[22] T. S. Ulmer, B. E. Ramirez, F. Delagio, A. Bax, *J. Am. Chem. Soc.* **2003**, *125*, 9179 – 9191.

 © 2005 Wiley-VCH Verlag GmbH & Co. KGaA, Weinheim

Heterogeneous Catalysis

Active Sites on Oxide Surfaces: ZnO-Catalyzed Synthesis of Methanol from CO and H_2**

Melanie Kurtz, Jennifer Strunk, Olaf Hinrichsen, Martin Muhler, Karin Fink,* Bernd Meyer, and Christof Wöll*

Chemical processes on metal oxide surfaces have been of great interest for a long time, mostly due to their relevance in the field of heterogeneous catalysis. Since "perfect" oxide surfaces usually show only little or no activity, it is widely believed that the high reactivity of oxide powders results from the presence of a small number of active sites.[1] Most of the models proposed for these active sites are based on oxygen vacancies or defects. There is literature consensus on the role of these active sites and the particular importance of oxygen vacancies. However, only a few case studies have been described in which for a specific reaction the geometric structure of an active site is not only specified, but also confirmed by theoretical calculations and validated by kinetic studies conducted in a reactor under conditions close to those applied industrially.

We have conducted such a study for the synthesis of methanol over ZnO powders. In a recently published theoretical paper,[2] an active site and a reaction mechanism were proposed but without a comparison to kinetic data. It was assumed that a Cu-free model for the active site is sufficient to explain the formation of methanol from a CO_2/H_2 mixture on an industrially applied $Cu/ZnO/Al_2O_3$ catalyst. In our extensive analysis we find—for an active site similar to that proposed—an energetically more favorable reaction pathway, in which it is not carbon dioxide acting as carbon source, as was assumed so far, but carbon monoxide, which is favored for thermodynamic reasons. On the ZnO-supported Cu-containing powder catalysts used at present for the industrial synthesis of methanol, another reaction mechanism with carbon dioxide as the carbon source is occurring. This was a point of controversy for a long time, but the mechanism

[*] Dr. M. Kurtz, Dipl.-Chem. J. Strunk, Prof. Dr.-Ing. O. Hinrichsen, Prof. Dr. M. Muhler
Lehrstuhl für Technische Chemie
Ruhr-Universität Bochum, 44780 Bochum (Germany)
Fax: (+49) 234-32-14115
E-mail: o.hinrichsen@techem.ruhr-uni-bochum.de

Dr. K. Fink, Dr. B. Meyer
Lehrstuhl für Theoretische Chemie
Ruhr-Universität Bochum, 44780 Bochum (Germany)
Fax: (+49) 234-32-14045
E-mail: karin.fink@ruhr-uni-bochum.de

Prof. Dr. C. Wöll
Lehrstuhl für Physikalische Chemie I
Ruhr-Universität Bochum, 44780 Bochum (Germany)

[**] This research was supported by the German Science Foundation within the framework of the Collaborative Research Center 558 "Metal–Substrate Interactions in Heterogeneous Catalysis".

 © 2005 Wiley-VCH Verlag GmbH & Co. KGaA, Weinheim DOI: 10.1002/anie.200462374

was finally clarified by experiments using isotope-labeled reactants.[3–7]

One of the major problems in the analysis of chemical processes on such active sites is their typically rather low concentration on the surface. Thus, the systematic analysis of precise data by the well-established methods of surface physics and chemistry is impossible or at least highly problematic. For example, it is not possible to determine experimentally the binding energy of CO on defect sites with reliability. Just recently, reliable information available concerning binding energies on perfect ZnO surfaces was reported.[8–11] In the present study, we have therefore chosen an approach in which we combine precise quantum chemical ab initio calculations—which had been validated beforehand by calculations on perfect systems and by a comparison with experimental data[12]—with detailed measurements under steady-state conditions close to those applied in industry. Based on these measurements and the quantum chemical results, we propose a reaction mechanism in which a CO molecule is bound in an unusual adsorption geometry and transformed into a formyl species.

The kinetic and characterization studies of several differently prepared ZnO powder samples presented in ref. [13] showed that methanol synthesis on ZnO is a structure-sensitive reaction; polar surfaces are distinguished by their high turnover frequencies. Figure 1 compares reactions per-

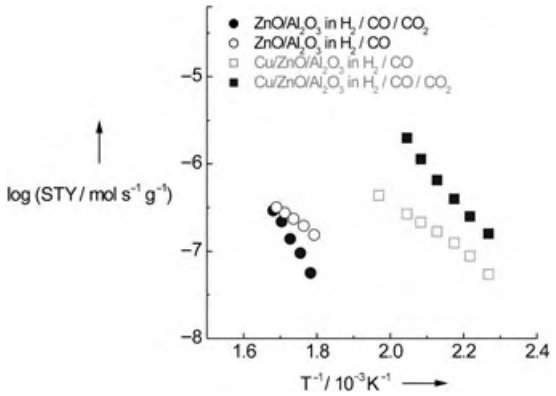

Figure 1. Comparison of the activity of the binary and ternary catalysts.

formed with a Cu-free binary ZnO/Al_2O_3 catalyst and a ternary Cu catalyst under near-industrial reaction conditions. The latter catalyst is applied technically in large-scale, low-temperature methanol synthesis. Under similar conditions it is much more active than the binary ZnO/Al_2O_3 catalyst, which is highly temperature-stable. When a CO/H_2 mixture is used, the space–time yield (STY) is already on the same order of magnitude as when the temperature is 100 K lower. The difference in the STYs is even more pronounced when gas mixture with another composition is employed. A synthesis gas containing CO_2 results in a drastic increase in activity for the ternary system but a decrease for the binary system.

The inhibiting effect of CO_2 was proven by the following experimental sequence: a gas mixture containing about 72% H_2, 10% CO, and 18% N_2 was passed over the ZnO/Al_2O_3 catalyst at a flow rate of 100 NmL min^{-1}. When the CH_3OH concentration was constant over time, 1% CO_2 was added to the synthesis gas. The concentrations of CO and H_2 were kept constant, and only the N_2 content was adjusted. After the system had again reached a steady-state CH_3OH content, the CO_2 fraction in the inlet flow was increased to 2, 3, 4, 6, and 8%. The activity plot thus determined experimentally (Figure 2) clearly shows that even an addition of CO_2 as low

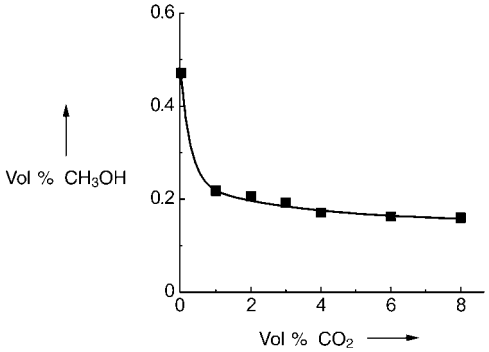

Figure 2. The activity of the coprecipitated ZnO/Al_2O_3 catalyst as a function of the fraction of CO_2 in the inlet flow. Experimental conditions: $\dot{V}=100$ NmL min^{-1}, $T=583$ K, $P=4.1$ MPa, $w_{cat.}=1.00$ g.

as 1% results in a strong decrease of the CH_3OH yield. Further addition of CO_2 continuously lowers the CH_3OH yield, but the effect is less pronounced. CO_2 therefore seems to act on the ZnO/Al_2O_3 catalyst as a catalyst poison. Since the catalytic activity of the ZnO/Al_2O_3 catalyst depends on the preset CO/CO_2 ratio, the working state of the active site under industrial conditions is of particular importance.

Even small amounts of CO_2 in the synthesis gas markedly lower the formation of CH_3OH on the ZnO/Al_2O_3 catalyst. This observation strongly supports the hypothesis that the active site of the ZnO/Al_2O_3 catalyst is an oxygen vacancy. In this case the number of active sites on the catalyst would increase in a highly reducing atmosphere (no CO_2, high level of CO). Supplementary measurements confirmed the formation of small amounts of CO_2 when the catalyst was exposed to a gas mixture with a high concentration of CO. These findings can be explained by a direct removal of oxygen from the ZnO lattice by CO, leading to the formation of CO_2. Inversely, addition of CO_2 to the synthesis gas would cause an oxidation of the vacancies and catalyst activity would drop.

To support these mechanistic ideas we performed quantum chemical ab initio calculations to determine the geometric structure and the energies of different intermediates for the reaction of CO with $2H_2$ over ZnO catalysts. An "embedded cluster" approach was used in which the surroundings of the active site are described by a cluster treated explicitly with quantum chemical methods while the cluster itself is embedded in an extended point-charge field.

As in the work of French et al.,[2] the polar O-terminated $ZnO(000\bar{1})$ surface was chosen as starting point for our calculations. To build a model for the active center we first investigated the atomic structure and chemical composition of the $(000\bar{1})$ surface under catalytic conditions. For a long time it was believed that the $(000\bar{1})$ surface of ZnO is

 © 2005 Wiley-VCH Verlag GmbH & Co. KGaA, Weinheim

unreconstructed and exhibits an ideal "truncated bulk" structure. Because of the polar character of the $(000\bar{1})$ surface inevitably partly occupied surface bands would be present in this case, leading to a vanishing band gap.[14,15] However, in the last years it was shown by experimental and theoretical work[11,12,16] that the $(000\bar{1})$ surface is stabilized by the formation of O vacancies or the adsorption of hydrogen, depending on the experimental conditions. The driving force behind these structural changes is the avoidance of partly filled surface bands. Assuming that the $ZnO(000\bar{1})$ surface is in thermodynamic equilibrium with H_2 and O_2 in the gas phase, Meyer[16] determined a surface phase diagram by using DFT slab calculations. At pressures and temperatures typically employed in methanol synthesis the most stable structure was found to be a surface with a hydrogen-atom surface coverage of 50% where all surface bands are filled.

The point-charge field used for the embedding of the ab initio cluster was generated by using the optimized structure of the hydroxylated $ZnO(000\bar{1})$ surface from ref. [16]. The active site with the O vacancy was obtained by removing an entire H_2O molecule from the surface in accordance with the tendency to avoid occupied surface states (Figure 3). As the first step, the adsorption geometries for different adsorbed intermediates were determined.[17] All atoms of the adsorbates and the positions of the three Zn ions together with the six surface O atoms (including the H atoms bound to these O atoms) next to the vacancy were relaxed. For the optimized structures the adsorption energies were calculated with the Bochum program package,[18–20] taking into account the dynamic correlation within the multiconfiguration coupled electron pair approximation (MCCEPA),[20] an approximate coupled-cluster method. We used TZVPP basis sets for the adsorbate molecules and the Zn and O ions of the first coordination shell of the active site. The basis set superposition error for the binding energy was corrected as proposed by Boys and Bernadi.[21] To compare the energies of the different intermediates it is important to correct all energies for zero-point vibrations, since they change dramatically during the reaction: for the gas-phase reaction $CO + 2H_2 \rightarrow CH_3OH$, by 64.7 kJ mol^{-1} (for experimental data see ref. [22]).

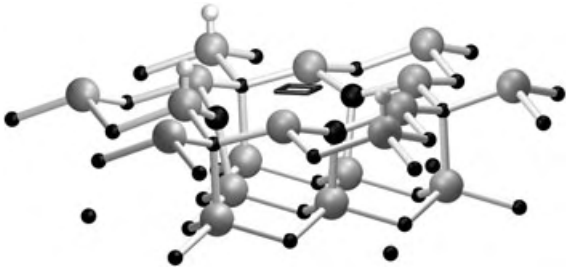

Figure 3. The ab initio cluster consists of the three Zn atoms of the first Zn coordination shell (black, big) next to the defect site (square), the nine O atoms of the first O coordination shell (six from the first and three from the second layer, gray), three O atoms from the third layer that are a short distance (4.567 Å) from the defect site, six further O atoms from the first layer (gray), all H atoms (white) bound to the cluster O atoms, and of all Zn atoms neighboring the cluster oxygen atoms (black, small).

Figure 4 shows the geometries and the relative energies of the most important steps in the reaction mechanism for the synthesis of CH_3OH from CO and H_2. The binding energies for the optimized structures are given in Table 1.

The combination of the results of the quantum chemical calculations and the kinetic measurements suggests the following model for the overall reaction: Over ZnO catalysts, methanol is formed mainly from adsorbed CO. At the active site CO is adsorbed perpendicularly to the surface and can be bound either through the C or the O atom. The binding energy for the C-bound configuration, 17.1 kJ mol^{-1}, is almost the same as for the O-bound adsorption within the accuracy of the calculations. Therefore, both situations should be present under catalytic conditions. CO adsorbed through the oxygen atom is more favorable for the subsequent hydrogenation steps. Hence, this configuration was considered in our calculations for the next steps. The calculated binding

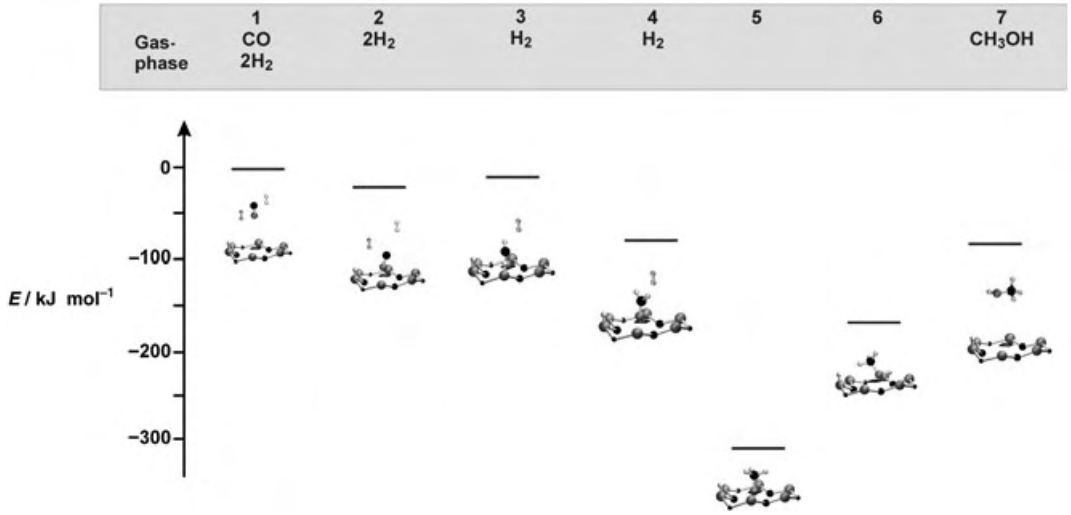

Figure 4. Potential energy diagram and adsorption geometries for formation of methanol from CO and H_2 catalyzed by ZnO. Cluster: Zn black, O gray, H white; Adsorbate: C black, O gray, H white.

 © 2005 Wiley-VCH Verlag GmbH & Co. KGaA, Weinheim

Table 1: Calculated energies [kJ mol^{-1}] of the intermediates relative to the energy of the starting compounds.

	Adsorbate(s)	Gas phase	ΔE(SCF)	ΔE(MCCEPA)	NPE [a]	E incl. NPE	d_O [Å][b]
1		$CO+2H_2$	0.0	0.0	66.2	0.0	
2	OC	$2H_2$	−12.0	−15.0	66.2	−15.0	0.90
3	CHO^-, H^+	H_2	3.4	3.1	61.5	−1.6	0.22
4	CH_2O	H_2	−91.2	−105.8	96.0	−76.0	0.53
5	CH_3O^-, H^+		−320.0	−344.0	102.6	−307.6	0.12
6	CH_3OH		−193.0	−226.1	134.2	−158.1	0.79
7		CH_3OH	−115.1	−143.7	134.2	−75.8	

[a] NPE: calculated zero-point energy. [b] d_O: distance of the O atoms from the position of the defect site.

energy for CO at the active site is much smaller than the CO_2 adsorption energy of 69.0 kJ mol^{-1} obtained by French et al.[2] Therefore, CO_2 in the synthesis gas can possibly block the active site for the CO reaction.

We expect the formation of a formyl species to be the next reaction step.[24–27] It is well known that H_2 adsorbs dissociatively at the O vacancies of the polar surfaces. Therefore, we assume that formyl is formed by the transfer of H^- to the carbon atom of the CO, adsorbed through the oxygen atom, at the active site, while a neighboring oxygen atom is protonated at the same time. In the energy diagram in Figure 4, the formyl species has about the same energy as the starting situation as a result of two compensating effects: The adsorption of the negatively charged formyl species is strongly stabilized in the Madelung field of the ZnO environment and leads in combination with the proton affinity of the cluster to strong binding at the active site. On the other hand, breaking the CO triple bond and dissociating the H_2 molecule cost a lot of energy.

Since the adsorption of CO on ZnO is weak,[12,29] we assume that the formation of formyl is the rate-determining step in methanol synthesis. The following stepwise hydrogenation of the formyl species with dissociatively adsorbed hydrogen leads to the methoxy species, which is also observed on ZnO in studies on intermediates.[27,30–32] The formyl species abstracts the proton of a neighboring OH group, rearranges to formaldehyde, and then reacts with a further H^- to give the strongly bound methoxy species. The methoxy ion is adsorbed such that the negatively charged oxygen atom is located at the defect site. In the last hydrogenation step, a proton of a neighboring OH group is transferred to the methoxy species forming methanol. The methanol molecule desorbs from the surface, the O defect is reestablished, and the catalytic cycle is completed. The catalyst is regenerated continuously, since in the presence of CO and H_2 at high temperatures small amounts of CO_2 and H_2O are always formed, leading to the formation of new active sites. This might be the reason why ZnO is very stable under reaction conditions and suitable as a catalyst for CO hydrogenation under industrial conditions.

Adding CO_2 to the CO/H_2 gas mixture leads to a change in the reaction mechanism in the ZnO-catalyzed methanol synthesis. In analogy to the mechanism described in ref. [2] for ZnO or to the redox mechanism postulated for Cu-containing catalysts,[33] the reaction path for the hydrogenation of CO_2 includes the formation of a formate and a methoxy species as intermediates. In the presence of CO_2, the formation of methanol is significantly slower. In contrast to the CO mechanism via a formyl species, the reaction path with CO_2 takes place preferentially under these reaction conditions because the formate intermediate is more stable than formyl. In our opinion, the activity of the Cu-containing catalyst is determined by the strong interaction between Cu and ZnO_{1-x} (x is equal to the number of O vacancies). The hydrogenation of CO_2 at the Cu-ZnO_{1-x} interface is favored over the conversion of CO.[34] For definite proof that methanol is formed by these two different reaction paths, spectroscopic analysis of the intermediates, calculation of transition states, and comparison of the results obtained by microkinetic modeling based on quantum chemical calculations with the data of kinetic measurements will be necessary.

Experimental Section

The catalysts were synthesized by the coprecipitation method. The hydroxycarbonate precursors were prepared by precipitation from metal nitrate solutions with sodium carbonate at pH 7. The concentrations of the nitrate solutions was adjusted to a nominal catalyst composition of 85 mol% ZnO and 15 mol% Al_2O_3 for the ZnO/Al_2O_3 catalyst. The resulting precipitate was aged in the mother liquor under continuous stirring for 2 h. The aged precipitate was filtered and washed with deionized water (6 × 20 mL). Drying was performed overnight at 393 K followed by calcination in synthetic air ($\dot{V}$ = 10 NmL min^{-1}) increasing the temperature from room temperature to 593 K at a heating rate of 2 K min^{-1} and maintaining the temperature for 3 h. The calcined precursor was pressed and sieved, yielding a grain fraction of 250–355 μm. The preparation of the ternary Cu/ZnO/Al_2O_3 catalyst with a nominal catalyst composition of 70 mol% Cu, 15 mol% ZnO, and 15 mol% Al_2O_3 followed the same procedure.

For the catalytic experiments, 1.00 g of the calcined precursor (250–355 μm) was used in a fixed-bed single-pass tubular reactor (bed length ca. 2.1 cm). For pretreatment, the sample was heated at a constant rate of 1 K min^{-1} to 448 K and held at this temperature overnight. A mixture of 2% H_2 in He ($\dot{V}$ = 60 NmL min^{-1}) was chosen as the pretreatment gas. Then the reactor temperature was increased at a constant rate of 1 K min^{-1} to 513 K and held at this temperature for 30 min. Then the pretreatment gas mixture was replaced with pure hydrogen ($\dot{V}$ = 60 NmL min^{-1}). The space-time yield (STY) was determined at 4.1 MPa and 453–583 K using synthesis gas mixtures containing H_2, CO, CO_2, and N_2 with the following composition: (○) 73.1% H_2, 10.8% CO, 16.1% N_2; (●) 72.3% H_2, 9.9% CO, 4.5% CO_2, 13.3% N_2; (□) 73.9% H_2 9.6% CO, 16.5% N_2; (■) 73.2% H_2, 9.5% CO, 4.6% CO_2, 12.7% N_2.

Received: October 20, 2004
Revised: January 18, 2005
Published online: April 4, 2005

Keywords: heterogeneous catalysis · kinetics · methanol synthesis · quantum chemistry · zinc oxide

 © 2005 Wiley-VCH Verlag GmbH & Co. KGaA, Weinheim

[1] V. E. Henrich, P. A. Cox, *The Surface Science of Metal Oxides*, Cambridge University Press, **1996**.
[2] S. A. French, A. A. Sokol, S. T. Bromley, C. R. A. Catlow, S. C. Rogers, F. King, P. Sherwood, *Angew. Chem.* **2001**, *113*, 4569; *Angew. Chem. Int. Ed.* **2001**, *40*, 4437.
[3] B. Denise, R. P. A. Sneeden, *CHEMTECH* **1982**, *108*.
[4] Y. B. Kagan, L. G. Liberov, E. V. Slivinskii, S. Loktev, G. I. Lin, A. Y. Rozovskii, A. N. Bashikov, *Dokl. Akad. Nauk SSSR* **1975**, *221*, 1093.
[5] G. H. Graaf, E. J. Stamhuis, A. A. C. M. Beenackers, *Chem. Eng. Sci.* **1988**, *43*, 3185.
[6] K. Klier, V. Chatikavanij, R. G. Herman, G. W. Simmons, *J. Catal.* **1982**, *74*, 343.
[7] G. Liu, D. Willcox, M. Garland, H. H. Kung, *J. Catal.* **1984**, *90*, 139.
[8] T. Becker, C. Boas, U. Burghaus, C. Wöll, *Phys. Rev. B* **2000**, *61*, 4536.
[9] T. Becker, C. Boas, U. Burghaus, C. Wöll, *J. Vac. Sci. Technol.* **2000**, *18*, 1089.
[10] T. Becker, M. Kunat, C. Boas, U. Burghaus, C. Wöll, *J. Chem. Phys.* **2000**, *113*, 6334.
[11] M. Kunat, S. Gil Girol, T. Becker, U. Burghaus, C. Wöll, *Phys. Rev. B* **2002**, *66*, 081 402.
[12] V. Staemmler, K. Fink, B. Meyer, D. Marx, M. Kunat, S. Gil Girol, U. Burghaus, C. Wöll, *Phys. Rev. Lett.* **2003**, *90*, 106 102.
[13] H. Wilmer, M. Kurtz, K. V. Klementiev, O. P. Tkachenko, W. Grünert, O. Hinrichsen, A. Birkner, S. Rabe, K. Merz, M. Driess, C. Wöll, M. Muhler, *Phys. Chem. Chem. Phys.* **2003**, *5*, 4736.
[14] A. Wander, F. Schedin, P. Steadman, A. Norris, R. McGrath, T. S. Turner, G. Thornton, N. M. Harrison, *Phys. Rev. Lett.* **2001**, *86*, 3811.
[15] B. Meyer, D. Marx, *Phys. Rev. B* **2003**, *67*, 035403.
[16] B. Meyer, *Phys. Rev. B* **2004**, *69*, 045416.
[17] The geometry optimizations were performed at the Hartree—Fock level with the program package TURBOMOLE: R. Ahlrichs, M. Bär, M. Häser, H. Horn, C. Kölmel, *Chem. Phys. Lett.* **1989**, *162*, 165.
[18] V. Staemmler, *Theor. Chim. Acta* **1977**, *45*, 89.
[19] U. Meier, V. Staemmler, *Theor. Chim. Acta* **1989**, *76*, 95.
[20] R. Fink, V. Staemmler, *Theor. Chim. Acta* **1993**, *87*, 129.
[21] S. F. Boys, F. Bernadi, *Mol. Phys.* **1970**, *19*, 553.
[22] T. Shimanouchi, *Tables of Molecular Vibrational Frequencies* **1972**, National Bureau of Standards.
[23] To obtaine the zero-point energies for the different reaction steps, the zero-point vibrations of the adsorbates and the molecules remaining in the gas phase were calculated in the harmonic approximation using B3LYP and a 6-31G* basis set: Gaussian 98 (Revision A.11), M. J. Frisch, G. W. Trucks, H. B. Schlegel, G. E. Scuseria, M. A. Robb, J. R. Cheeseman, V. G. Zakrzewski, J. A. Montgomery, R. E. Stratmann, J. C. Burant, S. Dapprich, J. M. Millam, A. D. Daniels, K. N. Kudin, M. C. Strain, O. Farkas, J. Tomasi, V. Barone, M. Cossi, R. Cammi, B. Mennucci, C. Pomelli, C. Adamo, S. Clifford, J. Ochterski, G. A. Petersson, P. Y. Ayala, Q. Cui, K. Morokuma, D. K. Malick, A. D. Rabuck, K. Raghavachari, J. B. Foresman, J. Cioslowski, J. V. Ortiz, B. B. Stefanov, G. Liu, A. Liashenko, P. Piskorz, I. Komaromi, R. Gomperts, R. L. Martin, D. J. Fox, T. Keith, M. A. Al-Laham, C. Y. Peng, A. Nanayakkara, C. Gonzalez, M. Challacombe, P. M. W. Gill, B. G. Johnson, W. Chen, M. W. Wong, J. L. Andres, M. Head-Gordon, E. S. Replogle, J. A. Pople, Gaussian, Inc., Pittsburgh, PA, **1998**.
[24] J. C. Lavalley, J. Saussey, T. Rais, *J. Mol. Catal.* **1982**, *17*, 289.
[25] J. Saussey, J. C. Lavalley, J. Lamotte, T. Rais, *J. Chem. Soc. Chem. Commun.* **1982**, *17*, 278.
[26] J. Saussey, J. C. Lavalley, T. Rais, A. Chakor-Alami, J. P. Hindermann, A. Kinnemann, *J. Mol. Catal.* **1984**, *26*, 159.
[27] C. Chauvin, J. Saussey, J. C. Lavalley, G. Djega- Mariadassou, *Appl. Catal.* **1986**, *25*, 59.
[28] S. A. French, A. A. Sokol, S. T. Bromley, C. R. A. Catlow, P. Sherwood, *Top. Catal.* **2003**, *24*, 161.
[29] H. H. Kung, *Catal. Rev. Sci. Eng.* **1980**, *22*, 235.
[30] A. Ueno, T. Onishi, K. Tamaru, *Trans. Faraday Soc.* **1971**, *67*, 3585.
[31] L. Chan, G. L. Griffin, *Surf. Sci.* **1985**, *155*, 387.
[32] S. Akhter, W. H. Cheng, K. Lui, H. H. Kung, *J. Catal.* **1984**, *85*, 437.
[33] J. B. Hansen in *Handbook of Heterogeneous Catalysis*, *Vol. 4* (Eds.: G. Ertl, H. Knözinger, J. Weitkamp), Wiley-VCH, Weinheim, **1997**, p. 1856 – 1876, and references therein.
[34] M. Kurtz, N. Bauer, H. Wilmer, O. Hinrichsen, M. Muhler, *Chem. Ing. Tech.* **2004**, *76*, 42; M. Kurtz, N. Bauer, H. Wilmer, O. Hinrichsen, M. Muhler, *Chem. Eng. Technol.* **2004**, *27*, 1146.

 © 2005 Wiley-VCH Verlag GmbH & Co. KGaA, Weinheim

Silver(I) Compounds

From AgCN Chains to a Fivefold Helix and a Fishnet-Shaped Framework Structure**

*Victoria Urban, Thorsten Pretsch, and Hans Hartl**

In a time when chemists have to find innovative and tricky ways to synthesize novel materials, sometimes very simple reactions yield unexpected compounds with surprising compositions and properties. One remarkable example is the unspectacular reaction of the cesium halides CsCl, CsBr, and CsI with silver cyanide in acetonitrile. Using the analogous reaction conditions and identical concentration ratios of reactants, the reactions lead to meshed cyanoargentates(I). This investigation was initiated by our attempts to segregate the linear chains of $^{1}_{\infty}$[AgCN] and $^{1}_{\infty}$[CuCN] within solid silver- and copper cyanide[1,2] by adding suitable reactants. The aim was to increase the coordination number at the silver and copper center,[3] or to link these chains to polymeric coordination compounds with zeolitic structures.[4,5] Microporous solids, which can, size- and shape-selectively occlude molecules and ions owing to the rigidity and stability of their networks, are of great importance as host lattices, ion exchangers and catalysts. The search for alternative coordination polymers is therefore of great interest.

The reaction of AgCN and CsCl in acetonitrile yields colorless, rod-shaped crystals of the composition $[Cs]_{5\infty}^{3}[Ag_4(CN)_4Cl]_2[AgCl_4]$ (**1**). The crystal structure of this com-

[*] V. Urban, T. Pretsch, H. Hartl
Institute of Inorganic and Analytical Chemistry
Freie Universität Berlin
Fabeckstrasse 34–36, 14195 Berlin (Germany)
Fax: (+49) 30-8385-43310
E-mail: hartl@chemie.fu-berlin.de

[**] We thank Mrs. Irene Brüdgam for performing the diffraction measurements.

 © 2005 Wiley-VCH Verlag GmbH & Co. KGaA, Weinheim DOI: 10.1002/anie.200462793

pound (Figure 1)[6] can be divided into three exceptional structural parts:

a) an anionic host lattice $^{3}_{\infty}[Ag_4(CN)_4Cl^-]$ with two channel-like cavities of different diameter, running parallel to each other,
b) cationic pillars $^{1}_{\infty}[Cs_4AgCl_4^+]$ in the wider channels and
c) chains of cesium cations in the narrower channels.

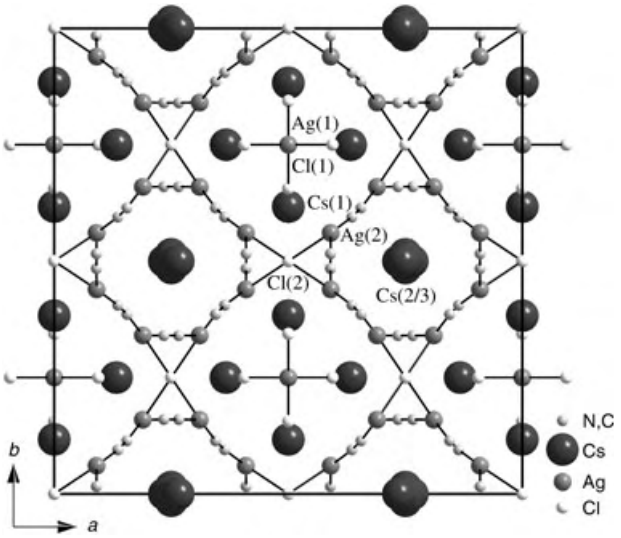

Figure 1. The crystal structure of **1** in the *ab* plane (selected bond lengths [Å]: Ag-C/N 2.113(6) and 2.120(7), C≡N 1.154(14)).

In the anionic lattice, five $^{1}_{\infty}[Ag(CN)]$-strings are wound to a rope with the symmetry 4_1 (Figure 2a and b). There is a channel-like cavity in the core of the rope. Disordered cesium cations fill these channels which have a diameter of approximately 8.5 Å (based on the Ag^I centers). One complete turn of a single string around the cesium chain takes four translational vectors *c* and eight AgCN units (Figure 2c). The, at first sight unusual, spiral-shaped winding of five single strings to a fivefold helix with a fourfold screw axis occurs because of the perfect superposition of neighboring strings along the *c* axis with a distance of one translational period *c*. The strings themselves are connected three dimensionally by μ_4-bridging chlorine atoms causing the coordination number of Ag(2) to increase from 2 to 3. The N/C-Ag-N/C angle is 151.4(3)° and the N/C-Ag-Cl angle 98.9(2)°. The Ag–Cl bond length is 2.763(1) Å with the chloride ion Cl(2) being planar coordinated by four Ag^I. This arrangement gives a second type of cylindrical tube (diameter about 9.9 Å based on the Ag^I centers), formed around $^{1}_{\infty}[Cs_4AgCl_4^+]$ columns consisting of closely packed cesium cations and tetrachloroargentate(I) ions $[AgCl_4]^{3-}$ (Figure 1). Compounds with $[AgCl_4]^{3-}$ ions have not been isolated before as attempted syntheses always yielded oligomeric or polymeric compounds with lower silver to chlorine ratios (Ag:Cl ≤ 3) thereby avoiding a high negative charge.

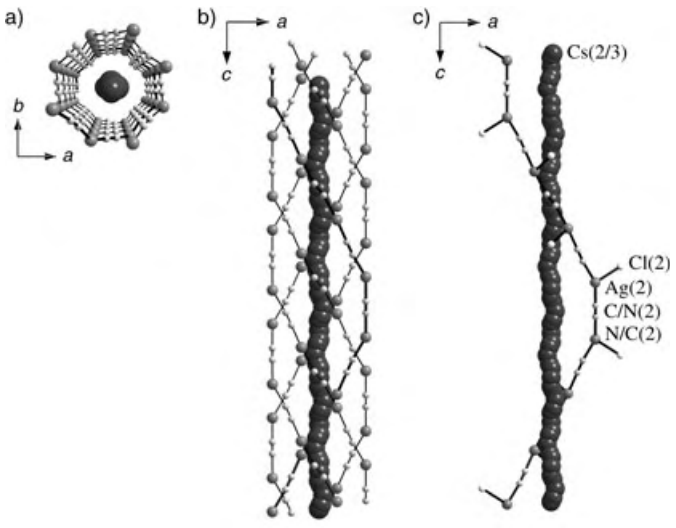

Figure 2. Crystal structure of **1**, a) AgCN fivefold helix with cesium ions, direction [001], b) AgCN-fivefold helix with trapped cesium ions, direction [010], c) single AgCN chain, which twists around disordered cesium ions, direction [010].

Through their inclusion in the zeolite-type cyanoargentate(I) host lattice, the $[AgCl_4]^{3-}$ ions are stabilized by forming a heterocubane-type Cs_4Cl_4 arrangement with the Ag^I ions in the center (Figure 3). The $[Cs_4AgCl_4^+]$ units are off set by 90° and stacked on top of each other so that vacant heterocubane-like Cs_4Cl_4 arrangements are formed. The arrangement $^{1}_{\infty}[Cs_4AgCl_4^+]$ can be described as columns cut out of the NaCl structure, in which every second center position of the Cs_4Cl_4 cube is occupied by an Ag^+ ion. The Ag–Cl bond length in the tetrahedral ion $[AgCl_4]^{3-}$ is 2.558(2) Å and the Cl-Ag(1)-Cl bond angles range from of 108.8(1)° to 110.9(2)°. The shortest contact between the chlorine atoms of the $[AgCl_4]^{3-}$ and the Ag(2) atoms of the channel walls is 2.948(2) Å. This separation is significantly longer than the corresponding values in $[AgCl_4]^{3-}$ or in $Rb_2{}^{1}_{\infty}[AgCl_3]$ (2.587–2.602 Å[7]).

Figure 3. Cationic column $^{1}_{\infty}[Cs_4AgCl_4]^+$ in **1**.

The reaction of AgCN and CsBr results in the formation of $[Cs]_6{}^{2}_{\infty}[Ag_{11}(CN)_{16}][Ag(CN)_2]\cdot 2\,CH_3CN$ (**2**).[6] In this compound, cesium cations, $[Ag(CN)_2]^-$ ions, and acetonitrile molecules are trapped in a two-dimensional cyanoargentate(I) network $^{2}_{\infty}[Ag_{11}(CN)_{16}{}^{5-}]$ and once again, undulating $^{1}_{\infty}[AgCN]$ strings form the polymeric network. The strings are tied to give a fishnet-like layer with large $(AgCN)_{16}$ meshes, in which the Ag^I atoms are alternatingly coordinated by two cyano ligands in a slightly distorted linear geometry or by four cyano ligands in a tetrahedral geometry. Half of the fourfold coordinate Ag^I atoms take part in the spiro-type cross-linking of the $^{1}_{\infty}[AgCN]$ chains, the other half is bound to the terminal $[Ag(CN)_2]^-$ units, which point thread-like out of the net (Figure 4). The very twisted 48-atom meshes are so large that three of these nets intertwine without cross-linking (Figure 5a) and form layers with a surface covered by terminal $[Ag(CN)_2]^-$ groups. The anionic layers are held

 © 2005 Wiley-VCH Verlag GmbH & Co. KGaA, Weinheim

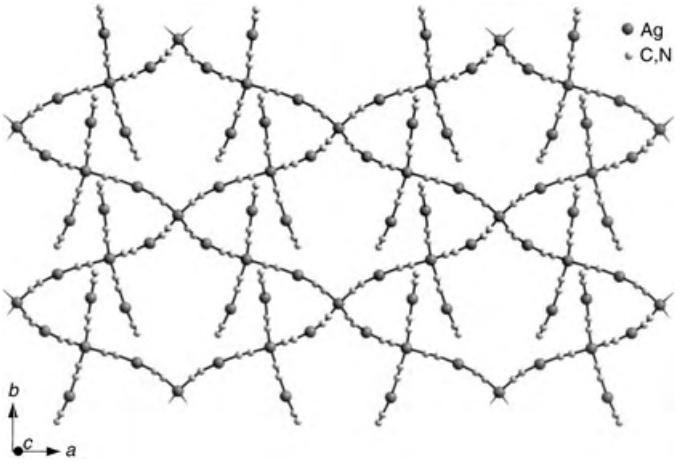

Figure 4. Fishnet made from $(AgCN)_{16}$ meshes with terminal $[Ag(CN)_2]^-$ units as part of the structure of **2**.

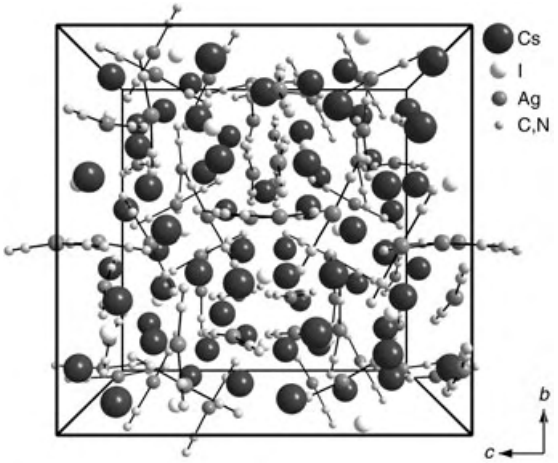

Figure 6. Perspective view of the unit cell of **3** in the [100] direction (selected bond lengths in $[Ag(CN)_2]^-$, [Å]: Ag–C 2.085(4) and 2.096(4), C≡N 1.104(5) and 1.118(5)).

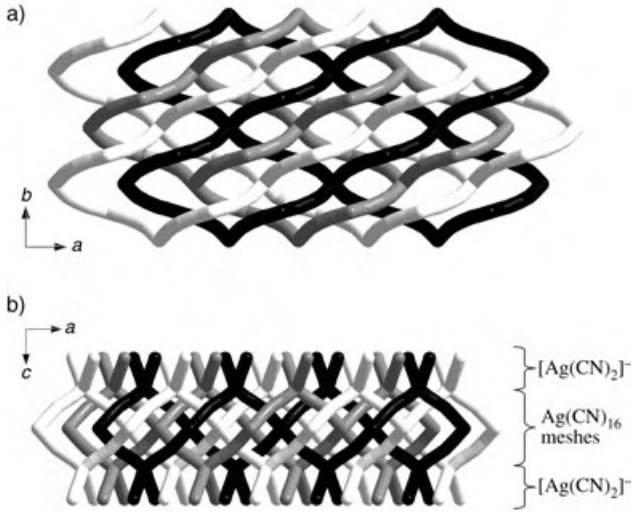

Figure 5. Wire model of three interpenetrating cyanoargentate(I) networks in **2**, a) direction [001], without $[Ag(CN)_2]^-$ units, b) direction [010], with $[Ag(CN)_2]^-$ units.

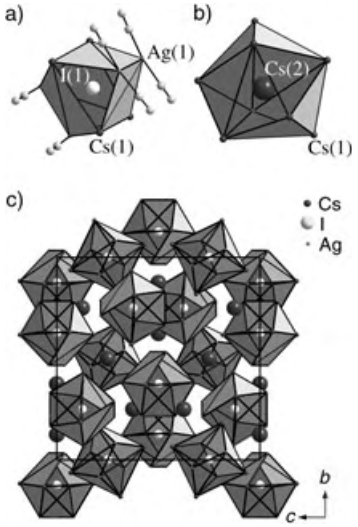

Figure 7. Coordination polyhedron around I^- and Cs(2) in **3**, a) environment of the iodide ions, b) triangulated dodecahedron of Cs cations around Cs(2) in **3**, c) packing of the $[I\{[Ag(CN)_2]_4Cs_4\}]^-$ ions around Cs(2) cations.

together by some of the cesium cations. The remaining cesium cations, the isolated $[Ag(CN)_2]^-$ ions, and disordered acetonitrile molecules fill the cavities of the cyanoargentate(I) framework.

Treating CsI with AgCN did not produce the polymeric cyanoargentate(I) framework but instead yielded the cubic crystallizing double salt $Cs_5[Ag(CN)_2]_4I$ (**3**)[6] featuring Cs^+, $[Ag(CN)_2]^-$, and I^- ions (Figure 6). The constitution of the crystal structure seems unsystematic at first, it contains one crystallographically independent Ag^+ and I^- ion as well as two Cs^+ and CN^- ions. However, the structure can be described using the coordination polyhedra around one of the two cesium cations (Cs2) and around the iodide ion. Both ions occupy positions of the symmetry $\bar{4} = S_4$. The iodide ion is surrounded by a square-planar arrangement of four cesium cations at a distance of 3.849(2) Å and a distorted tetrahedron of four silver atoms from the $[Ag(CN)_2]^-$ ions at a distance of 3.678(1) Å (Figure 7a and c). The uncommon arrangement of Cs and Ag atoms, is comparable with the arrangement of nitrogen and sulfur atoms in S_4N_4.[8] The CN^- ions turn away from the iodide ions resulting in a small deviation of the $[Ag(CN)_2]^-$ ions from linearity (C-Ag-C 170.0(2)°). The polyhedra $[I\{[Ag(CN)_2]_4Cs_4\}]^-$ on the other hand (Figure 7b) are grouped around the as yet unconsidered Cs^+ ion Cs(1) so that it is surrounded by a triangulated dodecahedron of eight Cs atoms at distances of 4.670(1) and 4.721(1) Å (Figure 7b van der Waals radius of Cs: 2.44 Å[9]).

Porous solids are commonly made with the help of organic templates. However, the larger alkaline cations as well as saltlike ion agglomerates can also be used for the formation of hybridlike networks of covalent and ionic sublattices.[10,11] By treating silver cyanide with CsCl, CsBr, or CsI, a zeolitic framework of cross-linked, rope-like twisted fivefold helices **1**, a layered polymer knotted like a fishnet **2**, or a simple

 © 2005 Wiley-VCH Verlag GmbH & Co. KGaA, Weinheim

double salt **3** is formed depending on the alkali halide used. All three reactions were carried out using analogous stoichiometric ratios in acetonitrile. The yield of compound **1**, which could also be isolated from acetone, can be increased by using an excess of AgCN.

The role of the halogenide in the formation of the varying product could be as follows: During the reaction of AgCN with CsCl, the sublattice, which consists of $^{1}_{\infty}[Cs_4AgCl_4]^+$ ions, could be the driving force for the development of the covalent chloro-cyano-argentate(I) network $^{3}_{\infty}[Ag_4(CN)_4Cl]^-$. Such a salt-template effect,[11] that is, the inclusion of saltlike structures in covalent networks, was to date only observed in molten salts.[10] In non-hydrous solvents of medium polarity, the tendency to form saltlike ionic clusters should be strongest for CsCl and decrease for CsBr and CsI, which is confirmed by the product formation of **1**, **2**, and **3**. Furthermore, the cross-linking of cyanoargentate(I) sublattices by Ag-Br-Ag and Ag-I-Ag-bridges hinders the formation of bromoargentates(I) and iodoargentates(I) as by-products.

Experimental Section

1: AgCN (1.5 g, 11.2 mmol) and CsCl (0.66 g, 3.9 mmol) in acetonitrile (200 mL) were heated under reflux and stirring for 21 h. To separate the insoluble residues, the solution was cooled slowly to room temperature and filtered. After two weeks at 4 °C, 0.5 g of colorless, rodlike crystals of **1** are obtained from the filtrate. The crystals are moderately stable when removed from their mother liquor. Decomposition: 161–163 °C. Elemental analysis calcd (%) for $C_8N_8Ag_9Cl_6Cs_5$: C 4.67, N 5.45, Cl 10.34; found: C 5.37, N 5.92, Cl 9.40. IR (KBr): $\tilde{\nu}$ = 2922 (m), 2853 (m), 2362 (w), 2336 (w), 2263 (w), 2137 (s), 1595 (w), 1510 (w), 1384 (m), 1266 (w), 1040 (m), 908 (w), 668 (w), 553 (m), 538 (m), 474 (m), 426 (m), 307 (w), 286 (w), 262 (w), 232 (w), 206 (m), 198 (m), 154 (m), 147 (m), 115 (s), 74 cm^{-1} (m).

2: AgCN (0.2 g, 1.5 mmol) and CsBr (0.32 g, 1.5 mmol) were heated under reflux for 24 h in acetonitrile (40 mL) while stirring. After concentrating the solution to 10 mL, the solution was cooled to room temperature and filtered. Within two weeks at 4 °C, 0.01 g of the air-stable, colorless, hexagonal crystals of **2** formed from the filtrate. Decomposition: 192–194 °C. Elemental analysis calcd (%) for $C_{18}N_{18}Ag_{12}Cs_6$: C 8.44, N 9.85; found: C 8.18, N 9.45. IR (KBr): $\tilde{\nu}$ = 2921 (m), 2852 (m), 2362 (w), 2336 (w), 2139 (s), 2120 (s), 1703 (w), 1650 (w), 1462 (w), 1384 (m), 1246 (w), 1164 (w), 1025 (w), 668 (w), 583 (w), 551 (m), 471 (s), 433 (m), 391 (s), 291 (m), 265 (m), 244 (m), 124 cm^{-1} (vs).

3: AgCN (1.5 g 11.2 mmol) and CsI (2.9 g, 11.2 mmol) were heated under reflux for 24 h in acetonitrile (200 mL) while stirring. The solution was cooled to room temperature and filtered. Within 24 h at 4 °C, 0.2 g of colorless, cubic crystals of **3** formed from the filtrate. Decomposition: 296–298 °C. Elemental analysis calcd (%) for $C_8N_8Ag_4Cs_5I$: C 6.71, N 7.83; found: C 6.76, N 7.96. IR (KBr): $\tilde{\nu}$ = 2923 (w), 2853 (w), 2362 (w), 2127 (s), 1626 (w), 1384 (w), 1032 (w), 668 (w), 569 (w), 551 (w), 473 (m), 379 (s), 306 (w), 297 (m), 279 (m), 243 (w), 206 (w), 121 (vs), 75 cm^{-1} (m).

Received: December 2, 2004
Published online: April 13, 2005

[1] G. A. Bowmaker, B. J. Kennedy, J. C. Reid, *Inorg. Chem.* **1998**, *37*, 3968–3974.
[2] S. J. Hibble, S. G. Eversfield, A. R. Cowley, A. M. Chippindale, *Angew. Chem.* **2004**, *116*, 638–640; *Angew. Chem. Int. Ed.* **2004**, *43*, 628–630.
[3] G. A. Bowmaker, H. Hartl, V. Urban, *Inorg. Chem.* **2000**, *39*, 4548–4554.
[4] T. Pretsch, I. Brüdgam, H. Hartl, *Z. Anorg. Allg. Chem.* **2003**, *629*, 942–944.
[5] T. Pretsch, H. Hartl, *Z. Anorg. Allg. Chem.* **2004**, *630*, 1581–1588.
[6] Crystal structure determination of compounds **1**–**3**: Data were collected at 173 K, Bruker-XPS diffractometer (CCD area detector, $Mo_{K\alpha}$ radiation, λ = 0.71073 Å), empirical absorption correction (SADABS), direct methods, least-squares refinement against F^2 (SHELX-97), all non-hydrogen atoms with anisotropic displacement parameters. An exact assignment of the carbon and nitrogen atoms of the 1,2-μ_2-bridging cyano ligands was not possible; these positions were occupied with one half C and one half N. The terminal cyano ligands are bound to Ag by the C atoms. The figures were produced with the program Diamond. **1**: M_r = 2056.24 g mol^{-1}, tetragonal, $I4_1/amd$ (No. 141), a = 22.418(2), c = 7.182(1) Å, V = 3612.4(5) Å^3, ρ_{calcd} = 3.781 g cm^{-3}, Z = 4, μ = 10.193 mm^{-1}, 17222 collected reflections, 1102 unique reflections [R_{int} = 0.0676], R Indices [$I > 2\sigma(I)$]: $R1$ = 0.0318, $wR2$ = 0.0745, R Indices (all data): $R1$ = 0.0498, $wR2$ = 0.0803. **2**: M_r = 2642.33 g mol^{-1}, orthorhombic, *Fddd* (No. 70), a = 9.581(5), b = 15.608(5), c = 66.050(20) Å, V = 9877(7) Å^3, ρ_{calcd} = 3.546 g cm^{-3}, Z = 8, μ = 9.043 mm^{-1}, 20965 collected reflections, 2864 unique reflections [R_{int} = 0.0728], R Indices [$I > 2\sigma(I)$]: $R1$ = 0.0636, $wR2$ = 0.1890, R Indices (all data): $R1$ = 0.0977, $wR2$ = 0.2098. **3**: M_r = 1431.07 g mol^{-1}, cubic, $I\bar{4}3d$ (No. 220), a = 20.059(1) Å, V = 8071.4(6) Å^3, ρ_{calcd} = 3.533 g cm^{-3}, Z = 12, μ = 10.692 mm^{-1}, 47513 collected reflections, 2064 unique reflections [R_{int} = 0.0217], Flack-Parameter: 0.01(2), R Indices [$I > 2\sigma(I)$]: $R1$ = 0.0144, $wR2$ = 0.0343, R Indices (all data): $R1$ = 0.0150, $wR2$ = 0.0345. Further details on the crystal structure investigations may be obtained from the Fachinformationszentrum Karlsruhe, 76344 Eggenstein-Leopoldshafen, Germany (fax: (+49) 7247-808-666; e-mail: crysdata@fiz-karlsruhe.de), on quoting the depository number CSD-414601 (**1**) and CSD-414602 (**3**). CCDC-257094 (**2**) contains the supplementary crystallographic data for this paper. These data can be obtained free of charge from the Cambridge Crystallographic Data Centre via www.ccdc.cam.ac.uk/data_request/cif.
[7] C. Hasselgren, S. Jagner, *Acta Crystallogr. Sect. C* **1999**, *55*, 1208–1210.
[8] B. D. Sharma, J. Donohue, *Acta Crystallogr.* **1963**, *16*, 891–897.
[9] A. Shih, *Phys. Rev.* **1974**, *9*, 1507–1514.
[10] Q. Huang, S.-J. Hwu, *Inorg. Chem.* **2003**, *42*, 655–657.
[11] Q. Huang, S.-J. Hwu, X. Mo, *Angew. Chem.* **2001**, *113*, 1754–1756; *Angew. Chem. Int. Ed.* **2001**, *40*, 1690–1693.

Keywords: coordination modes · cyanides · framework structures · silver · tetrachloroargentate(I)

 © 2005 Wiley-VCH Verlag GmbH & Co. KGaA, Weinheim

Reactive Intermediates

Gold Catalysis: Proof of Arene Oxides as Intermediates in the Phenol Synthesis**

A. Stephen K. Hashmi, Matthias Rudolph, Jan P. Weyrauch, Michael Wölfle, Wolfgang Frey, and Jan W. Bats*

The gold-catalyzed synthesis of highly substituted arenes **2** or benzofurans **3** from furans **1** has proved to be a powerful tool for organic synthesis (Scheme 1).[1] As reported previously, a number of other transition metals with a d^8 configuration also catalyze this transformation,[1b,2] but all are significantly less active than gold(III).[1b] We had obtained experimental evidence for an intramolecular migration of the furan oxygen atom (which becomes the phenol oxygen atom).[1a] Such a 1,2-transposition suggested the intermediacy of an arene oxide, but in our initial publication we only dared to propose a simple, organic-type mechanism (pathway I via **A** and **B**, Scheme 2).[1a]

Subsequently, Echavarren and co-workers conducted theoretical studies in which they compared pathways I and II (Scheme 2). According to their calculations, pathway II is favored, and side products observed in Pt^{II}-catalyzed reactions would also correspond to the hydrolysis of intermediate **D** of pathway II.[2] However, such side products do not necessarily stem from the catalytic cycle but can be generated in a competing side reaction. Furthermore, the gold-catalyzed reactions were highly selective, and such side products were never observed. Other conceivable pathways would proceed through alkynyl or vinylidene complexes (**I** or **J**, pathway IV), or, if the d^8 precatalyst was reduced in situ, the insertion of a d^{10} species into the $C(sp^2)$–O bond (as in the Felkin/Wenkert reaction;[3] pathway III), followed by insertion of the alkyne to give **F**.

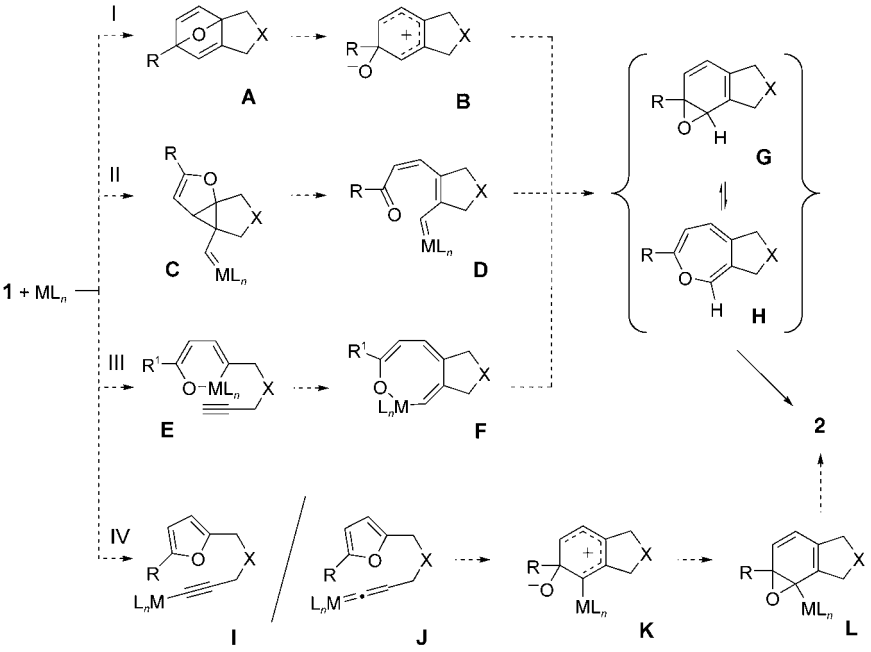

Scheme 2. Possible pathways for the transformation of **1** into **2**.

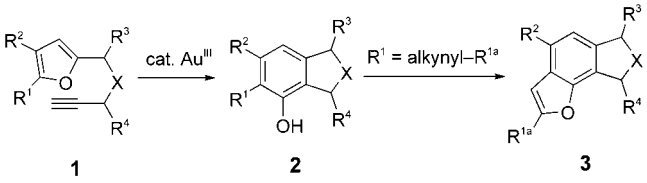

Scheme 1. The gold-catalyzed phenol synthesis. R^1–R^4 = alkyl, aryl, alkynyl; X = CR^5_2, NR^5, O (three atoms in the linker), $-CR^5_2NR^6-$ (four atoms in the linker).

Herein we describe how the arene oxides/oxepins **G**/**H** can be enriched and detected readily in the reaction mixture after modification of the energy profile of the reaction by variation of the ligand in the gold complex. Our efforts to gain further experimental mechanistic insight formed the starting point of these studies. Even experiments with substoichiometric amounts of $AuCl_3$ (30 mol%) led to no detectable concentration of an intermediate. When a mixture at −20 °C of $AuCl_3$ (5 mol%) and the substrate was warmed up gradually, either no reaction was observed by ^{1}H NMR spectroscopy, or the slow formation of **2** at 0 °C. The breaking of four bonds and the formation of four new bonds during the reaction is clearly not a single-transition-state elementary reaction, and thus the failure to detect any intermediates with $AuCl_3$ simply meant that the first step was the rate-limiting step. If the reaction proceeded by pathway IV, a primary kinetic isotope effect should be observable with **1** deuterated at the alkyne, but this effect was not observed.

To detect intermediates, it is necessary to change the energy profile of the whole reaction; a later step must have

[*] Prof. Dr. A. S. K. Hashmi, Dipl.-Chem. M. Rudolph, Dipl.-Chem. J. P. Weyrauch, M. Wölfle, Dr. W. Frey
Institut für Organische Chemie
Universität Stuttgart
Pfaffenwaldring 55, 70569 Stuttgart (Germany)
Fax: (+49) 711-685-4321
E-mail: hashmi@hashmi.de
Dr. J. W. Bats
Institut für Organische Chemie und Chemische Biologie
Johann Wolfgang Goethe-Universität
Marie-Curie-Strasse 11, 60439 Frankfurt am Main (Germany)

[**] This work was supported by the Fonds der Chemischen Industrie, in particular through a Chemiefonds-Doktoranden-Stipendium to J.P.W., and by the AURICAT EU-RTN (HPRN-CT-2002-00174).

Supporting information for this article is available on the WWW under http://www.angewandte.org or from the author.

 © 2005 Wiley-VCH Verlag GmbH & Co. KGaA, Weinheim DOI: 10.1002/anie.200462672

the highest energy of activation. When we used **1a** (R^1 = Me, R^2–R^4 = H, X = NTs; Ts = *p*-toluenesulfonyl) and the complex **4**[4] (X-ray crystal structure shown in Figure 1),[5] we indeed observed an additional species **5a**/**6a** (Figure 2).

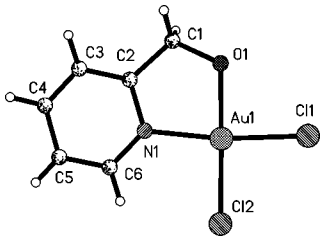

Figure 1. Crystal structure of **4**.

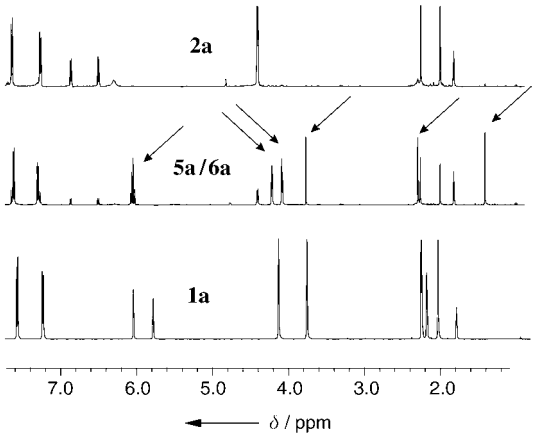

Figure 2. ^{1}H NMR spectrum of the transient species.

Under optimized conditions, **5a**/**6a** can be enriched to account for 80% of the material in the reaction mixture at room temperature (Figure 3) and shows long-term stability when cooled to −20°C. At room temperature **5a**/**6a** converts directly into **2a** (Scheme 3).

Two-dimensional NMR spectroscopy (H,H-COSY, HMQC) of the reaction mixture at −20°C strongly pointed towards the presence of an arene oxide structure **5a**. The direct isolation of **5a** failed, as the compound always

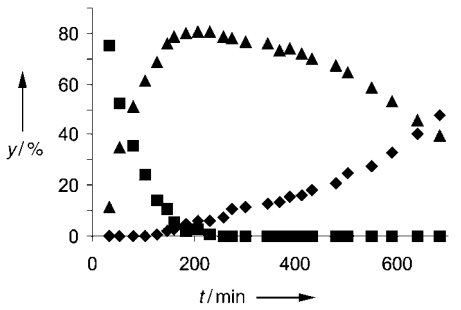

Figure 3. The amount *y* of the transient species as a percentage of the material present in the reaction mixture is plotted against time. The transient species can be accumulated to 80%. ◆ **2a**, ■ **1a**, ▲ **5a**/**6a**.

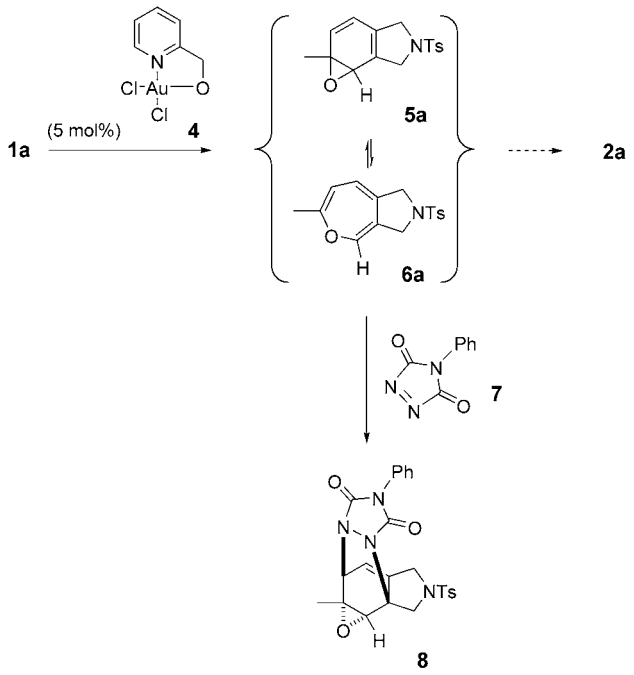

Scheme 3. Diels–Alder reaction of the transient species.

rearranged to **2a**. From the literature it was known that the 1,3-diene substructure of arene oxides can undergo Diels–Alder reactions with dienophiles such as **7** to provide stable derivatives.[6] By following this concept, **8** was isolated as a single diastereomer and could even be characterized by X-ray crystal-structure analysis (Scheme 3, Figure 4).[5]

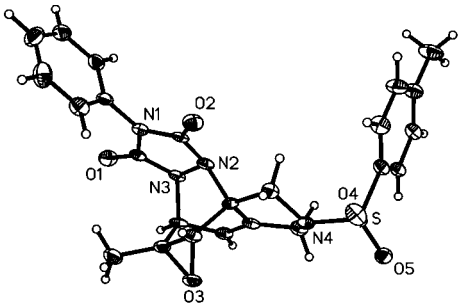

Figure 4. Crystal structure of **8**.

When other complexes, such as **9**,[7] **10**[8] (X-ray crystal structure shown in Figure 5),[5] **11**,[8] and even $PtCl_2$ or $[\{(cod)IrCl\}_2]$ (cod = cyclooctadiene), were used, small transient peaks of **5a** were also observed in the ^{1}H NMR spectra recorded during the reaction.

It is clear that **2a** is much lower in energy than **1a**. Density functional calculations (B3LYP/6-31G** including zero-point-energy (ZPE) correction) showed that even **5a** and **6a** are both 19 kcal mol^{-1} lower in energy than **1a**, and the reaction to give **2a** then sets free another 42 kcal mol^{-1}. On the other hand, the experimentally observed relative energies of **5a** and **6a** could not be reproduced at this level of theory: In the NMR spectra, the signals for the diastereotopic hydrogen atoms of both CH_2 groups adjacent to the tosyl-

 © 2005 Wiley-VCH Verlag GmbH & Co. KGaA, Weinheim

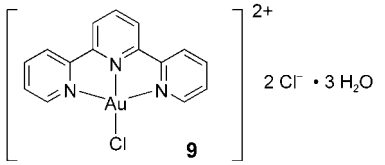

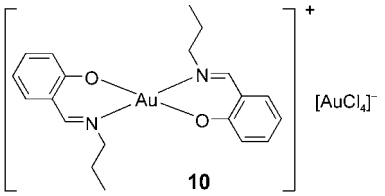

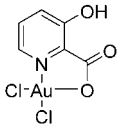

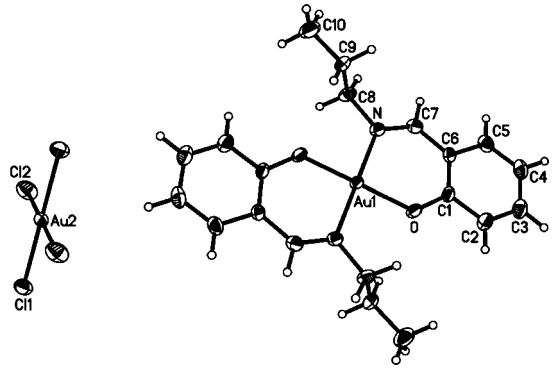

Figure 5. Crystal strucuture of **10**.

amide group suggest that **5a** is lower in energy than **6a** and that a possible equilibrium with low concentrations of **6a** must be slow on the NMR timescale; however, calculations with different basis sets (B3LYP/6-31G**, BLYP/6-31G**, or LMP2/6-31G**, each including ZPE correction) gave identical energies within the error of the method (a difference of less than 1 kcal mol^{-1}).[9,10]

Further support for an arene oxide structure was provided by the following characteristic ^{1}H NMR and ^{13}C NMR spectroscopic data, which are in good agreement with literature values for a substituted epoxide: The signal for the hydrogen atom on the epoxide is a singlet at $\delta =$ 3.87 ppm[11] with $^1J_{CH} = 184$ Hz;[12] the tertiary and quaternary carbon atoms of the oxirane ring give rise to signals at $\delta = 66.1$ and 69.5 ppm, respectively;[13] the signal for the hydrogen atoms on the methyl group is shifted to high field at $\delta =$ 1.52 ppm, thus indicating an sp^3-hybridized neighboring group.

Under the reaction conditions **5a** does not undergo interconversion into other constitutionally isomeric arene oxides, as is known from the "oxygen walk"[14] in the NIH shift reaction.[15] The possibility of enriching the intermediate seems to be quite general; other substrates, such as **2b** ($R^1 =$ mesityl, R^2–$R^4 =$ H, X = NTs), **2c** ($R^1 =$ Me, R^2–$R^4 =$ H, X = NNs; Ns = nosyl), **2d** ($R^1 =$ Me, R^2–$R^4 =$ H, X = O), **2e** ($R^1 =$ 4-Br-Ph, R^2–$R^4 =$ H, X = O), and **2f** ($R^1 =$ Me, R^2–$R^4 =$ H, X = $^-$CH(CH$_2$O–allyl)O$^-$) show the same chemical behavior.

In conclusion, we have provided the first direct experimental evidence for the formation of **2** via **5**. The lack of a primary kinetic isotope effect in the $AuCl_3$-catalyzed reactions is an argument against pathway IV, by which, furthermore, the isomerization of the metalated arene oxide **L** to the phenolate should be faster than a possible protodemetalation of **L**. Thus, of the many conceivable pathways, only those that proceed via **5**, such as pathways I–III, can be responsible for product formation. With a workup appropriate to the sensitivity of **5**, complex **4** might open a new entry to the entire chemistry[11] of **5** from simple, readily available starting materials. A further modification of the energy profile of the reaction by ligand variation might reveal even more details of the reaction mechanism.

Experimental Section

Synthesis of **8**: **1a** (45.0 mg, 150 μmol) was dissolved in CD_3CN, and **4** (2.70 mg, 7.50 μmol, 5 mol %) was added. The reaction was monitored at room temperature by NMR spectroscopy. After five hours, the solution was cooled to −40 °C, and **7** (26.4 mg, 150 μmol) was added. The red solution was stored in the freezer at −25 °C for four days; during this time it became colorless. After column chromatography of the crude material (petroleum ether/ethyl acetate (PE/EA) 3:1), **8** (31.3 mg, 44 % from **1a**) was obtained as a colorless solid. m.p. 158 °C; R_f (PE/EA 2:1): 0.23; ^{1}H NMR (500 MHz, CD_2Cl_2): $\delta = 1.55$ (s, 3H), 2.38 (s, 3H), 3.32 (s, 1H), 3.55 (d, $^2J = 11.6$ Hz, 1H), 3.70 (dd, $^2J =$ 14.6 Hz, 2.5 Hz, 1H), 4.00 (dd, $^2J = 14.6$ Hz, $^4J = 2.0$ Hz, 1H), 4.81 (d, $^2J = 11.6$ Hz, 1H), 4.92 (d, $^3J = 5.9$ Hz, 1H), 5.96 (dt, $^3J = 5.9$ Hz, $^4J =$ 2.25 Hz,[a] 1H), 7.32–7.36 (m, 5H), 7.40–7.43 (m, 2H), 7.68 ppm (d, $^3J = 8.2$ Hz, 2H); [a] only a mean coupling constant could be determined; ^{13}C NMR (126 MHz, CD_2Cl_2): $\delta = 16.35$ (q), 21.69 (q), 49.12 (t), 51.22 (d), 51.59 (t), 52.09 (q), 59.39 (d), 71.07 (s), 116.35 (d), 125.97 (d, 2C), 128.41 (d, 2C), 128.81 (d), 129.36 (d, 2C), 130.28 (d, 2C), 131.57 (s), 132.37 (s), 138.96 (s), 144.96 (s), 154.64 (s), 155.36 ppm (s); IR (neat): $\tilde{\nu} = 1767$, 1710, 1596, 1497, 1415, 1361, 1319, 1248, 1161, 1095, 1076, 1063, 1025, 993, 811, 782, 760, 712, 693, 666 cm^{-1}; MS (FAB(+), 3-nitrobenzyl alcohol): *m/z*: 479 $[M+H]^+$; MS (EI(−), 70 eV): *m/z* (%): 177 (42), 119 (64), 91 (100), 65 (22); $C_{24}H_{22}N_4O_5S$ (478.52).

Received: November 19, 2004
Revised: January 19, 2005
Published online: March 30, 2005

Keywords: arene oxides · density functional calculations · gold · homogeneous catalysis · N ligands

[1] a) A. S. K. Hashmi, T. M. Frost, J. W. Bats, *J. Am. Chem. Soc.* **2000**, *122*, 11553–11554; b) A. S. K. Hashmi, T. M. Frost, J. W. Bats, *Org. Lett.* **2001**, *3*, 3769–3771; c) A. S. K. Hashmi, T. M. Frost, J. W. Bats, *Catal. Today* **2002**, *72*, 19–72; d) A. S. K. Hashmi, L. Ding, J. W. Bats, P. Fischer, W. Frey, *Chem. Eur. J.* **2003**, *9*, 4339–4345; e) A. S. K. Hashmi, J. P. Weyrauch, M. Rudolph, E. Kurpejović, *Angew. Chem.* **2004**, *116*, 6707–6709; *Angew. Chem. Int. Ed.* **2004**, *43*, 6545–6547.

 © 2005 Wiley-VCH Verlag GmbH & Co. KGaA, Weinheim

[2] a) B. Martín-Matute, D. J. Cardenas, A. M. Echavarren, *Angew. Chem.* **2001**, *113*, 4890 – 4893; *Angew. Chem. Int. Ed.* **2001**, *40*, 4754 – 4757; b) B. Martín-Matute, C. Nevado, D. J. Cárdenas, A. M. Echavarren, *J. Am. Chem. Soc.* **2003**, *125*, 5757 – 5766.
[3] a) E. Wenkert, E. L. Michelotti, C. S. Swindell, *J. Am. Chem. Soc.* **1979**, *101*, 2246 – 2247; b) E. Wenkert, E. L. Michelotti, C. S. Swindell, M. Tingoli, *J. Org. Chem.* **1984**, *49*, 4894 – 4899; c) E. Wenkert, V. F. Ferreira, E. L. Michelotti, M. Tingoli, *J. Org. Chem.* **1985**, *50*, 719 – 721; d) P. Kocienski, N. J. Dixon, S. Wadman, *Tetrahedron Lett.* **1988**, *29*, 2357 – 2360.
[4] L. Canovese, L. Cattalini, G. Marangoni, M. L. Tobe, *J. Chem. Soc. Dalton Trans.* **1985**, 731 – 735.
[5] CCDC 256196 (**4**), 256266 (**8**), and 256267 (**10**) contain the supplementary crystallographic data for this paper. These data can be obtained free of charge from the Cambridge Crystallographic Data Centre via www.ccdc.cam.ac.uk/data_request/cif.
[6] a) M. P. Servé, D. M. Jerina, *J. Org. Chem.* **1978**, *43*, 2711 – 2713; b) J. R. Gillard, M. J. Newlands, J. N. Bridson, D. J. Burnell, *Can. J. Chem.* **1991**, *69*, 1337 – 1343; c) K. Nojima, C. Isogami, M. Hirobe, *Chem. Pharm. Bull.* **1993**, *41*, 2106 – 2108; d) A. P. Henderson, E. Mutlu, A. Leclercq, C. Bleasdale, W. Clegg, R. A. Henderson, B. T. Golding, *Chem. Commun.* **2002**, 1956 – 1957.
[7] L. S. Hollis, S. J. Lippard, *J. Am. Chem. Soc.* **1983**, *105*, 4293 – 4299.
[8] A. Dar, K. Moss, S. M. Cottrill, R. V. Parisch, C. A. McAuliffe, R. G. Pritchard, B. Beagley, J. Sandbank, *J. Chem. Soc. Dalton Trans.* **1992**, 1907 – 1913.
[9] We thank Dr. G. Rauhut and Prof. Dr. H. Stoll, Institut für Theoretische Chemie der Universität Stuttgart, for their continuous advice while we were carrying out the calculations.
[10] In reference [2b], Echavarren and co-workers even suggest that the oxepine is the ground state on the basis of PM3 calculations. The difference in energy was estimated to be 10.3–12.7 kcal mol^{-1}.
[11] a) E. Vogel, H. Günther, *Angew. Chem.* **1967**, *79*, 429 – 446; *Angew. Chem. Int. Ed. Engl* **1967**, *6*, 385 – 401; b) D. R. Boyd, N. D. Sharma, *Chem. Soc. Rev.* **1996**, *25*, 289 – 296; c) L. I. Belen'kii, *Comp. Heterocycl. Chem. II* **1996**, *9*, 45 – 66; d) S. von Angerer, W. Tochtermann, *Methoden Org. Chem. (Houben Weyl) 4th ed. 1952–*, *Vol. E9d*, **1998**, pp. 1 – 64.
[12] P. Laszlo, *Bull. Soc. Chim. Fr.* **1976**, *1*, 558 – 568.
[13] H. Günther, G. Jikeli, *Chem. Ber.* **1973**, *106*, 1863 – 1880.
[14] P. Y. Bruice, G. J. Kasperek, T. C. Bruice, H. Yagi, D. M. Jerina, *J. Am. Chem. Soc.* **1973**, *95*, 1673 – 1674.
[15] G. Guroff, J. W. Daly, D. M. Jerina, J. Renson, B. Witkop, S. Udenfriend, *Science* **1967**, *157*, 1524 – 1530.

 © 2005 Wiley-VCH Verlag GmbH & Co. KGaA, Weinheim

Liquid Crystals

Discotic Liquid Crystals with an Inverted Structure**

Sigurd Höger, Xiao Hong Cheng, Anne-Désirée Ramminger, Volker Enkelmann, Almut Rapp, Mihail Mondeshki, and Ingo Schnell*

Discotic liquid crystals, first described by Chandrasekhar and co-workers 25 years ago, can be used for a variety of optical and electronic applications.[1] For example, discotics in the columnar phase are interesting materials for photovoltaic applications, and discotic nematic liquid crystals can be used as compensation layers in display technology.[2,3] Furthermore, compounds based on macrocyclic mesogens are valuable candidates for the formation of tubelike superstructures.[4] The common design principle of all discotic liquid crystals is a more or less rigid core (disklike or macrocyclic) with peripheral flexible side groups that point outward. We recently reported the first indication that macrocycles composed of a rigid periphery and flexible side groups that point to the *inside* (inverted liquid crystals) also exhibit thermotropic mesophases.[5] This new design was derived from the X-ray single-crystal structure analysis of **1**, which adopts a solid-state conformation in which the long alkyl chains point inward. However, as these chains are located at the adaptable positions of the ring, which can be easily switched between different conformations, it is not clear whether the same conformation is retained in the liquid-crystal phase.[6] Herein we prove unambiguously that discotic liquid crystals with an inverted structure actually exist.

The key compounds for our investigations are nanometer-sized shape-persistent macrocycles **2**–**5** with flexible alkyl chains attached to the rigid backbone. The investigation of the thermal behavior of compound **2a** by differential scanning calorimetry (DSC) and optical microscopy (crossed polarizers) shows that it melts at 134 °C to form a mesophase that becomes isotropic (I) at 159 °C. The observed Schlieren texture (Figure 1, left) and the observation of only a broad

[*] Prof. S. Höger, Dr. X. H. Cheng[+]
Institute for Chemical Technology and Polymer Chemistry
University of Karlsruhe
Engesserstrasse 18, 76131 Karlsruhe (Germany)
Fax: (+49) 721-608-3151
E-mail: hoeger@chemie.uni-karlsruhe.de
A.-D. Ramminger, Dr. V. Enkelmann, Dr. A. Rapp,[++] M. Mondeshki, Dr. I. Schnell
Max Planck Institute for Polymer Research
Ackermannweg 10, 55128 Mainz (Germany)
[+] On leave from the School of Chemistry and Materials Engineering of Yunnan University, China.
[++] Present address:
Department of Chemical Engineering
Materials Research Laboratory
University of California, Santa Barbara, CA 93106 (USA)
[**] Financial Support by the Deutsche Forschungsgemeinschaft is gratefully acknowledged.

 DOI: 10.1002/anie.200462319 © 2005 Wiley-VCH Verlag GmbH & Co. KGaA, Weinheim

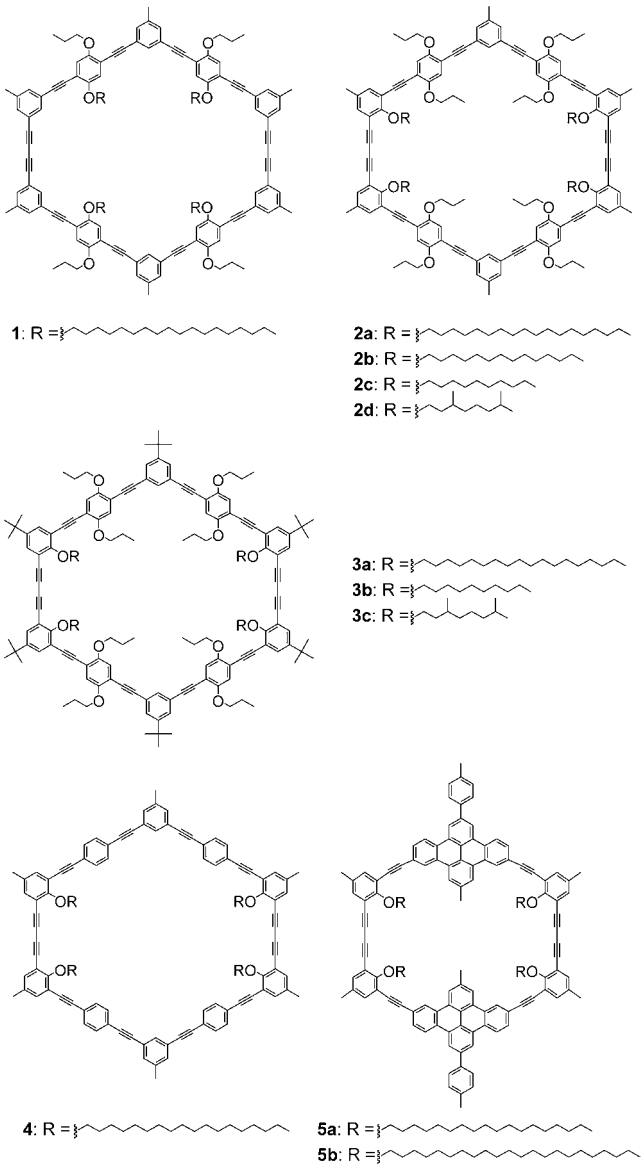

reflection at approximately 4.5 Å indicates the formation of a nematic phase (N), as also found for **1**. In contrast to **1**, however, the octadecyloxy side groups of **2a** have a fixed intraannular position and *cannot* flip to the outside. This means that **2a** is the first definite example of a liquid crystal with this new design: a rigid periphery acts as a frame for flexible side chains that point to the inside (inverted liquid crystal, Figure 1, right).

Figure 1. Left: Nematic Schlieren texture of **2a** at 150 °C. Middle: Design principle of conventional cyclic molecules capable of forming thermotropic mesophases. Right: Schematic presentation of the alkyl chain arrangement in **2a**.

The intraannular orientation of the alkyl chains in **2a** was also confirmed by X-ray single-crystal structure analysis (Figure 2).[7] As in the solid-state structure of **1**, the cyclic backbone of **2a** is not completely planar. As a result, the alkyl

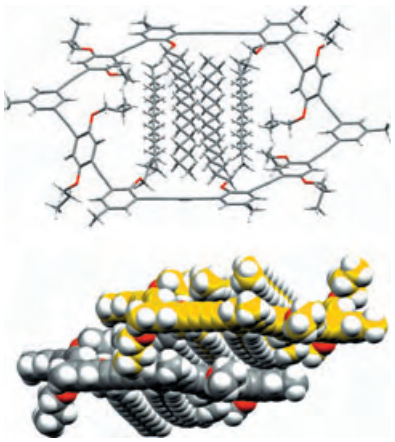

Figure 2. Top: Structure of **2a** in the crystal. Bottom: The packing behavior of the alkyl chains of **2a** in the crystal show that the flexible side chains form a dense alkyl packing (different shading is used for clarity).

chains are located alternately above and below the ring plane and form a dense alkyl packing with side chains of adjacent rings. Although short intermolecular contacts are present between the rigid portions of the macrocycle in **2a**, the alkyl chains melt upon heating and the molecules become mobile to form the liquid-crystalline phase by parallel arrangement. In the liquid-crystalline phase (at 145 °C) the dynamic order parameters for the macrocycles are on the order of $S = 0.1$–0.15 (as determined by solid-state NMR spectroscopy), and the mobility of the alkyl chains increases from the anchoring OCH_2 groups ($S \approx 0.1$) toward the chain ends ($S \rightarrow 0$).[8,9] This mobility increase is a well-known phenomenon, but in this case it does not occur in the usual gradual manner along the C_{18} chain. Instead, most of the CH_2 segments appear to exhibit similar dynamic behavior, which is reflected in a common order parameter of $S \approx 0.04$ that only drops to zero at the chain end.

One of the objectives of this investigation was to vary thermal parameters (T_m, T_i, ΔT) through changes in molecular structure. If the macrocycle is not to be changed, there are, in principle, two ways this can be done: 1) variation of the length and shape of the intraannular side chains and 2) introduction of bulky side chains at the periphery to control the distances (interactions) between rings. Transition temperatures and enthalpies for the macrocycles investigated herein are summarized in Table 1.[10] With all other molecular parameters kept constant, a side-chain length of approximately 14 carbon atoms is necessary to obtain mesophases with **2** in a temperature range in which no thermal decomposition is observed. Furthermore, the introduction of branched (dimethyloctyl) side groups does not influence this behavior significantly.[11,12]

Attempts to broaden the mesophase temperature range of these new discotics through the attachment of bulky groups at

 © 2005 Wiley-VCH Verlag GmbH & Co. KGaA, Weinheim

Table 1: Phase-transition behavior of the macrocycles **1**–**5**.

Compound	Phase-transition temperature [°C] (Enthalpy [kJ mol^{-1}])			
1	185 (152.7)	N	207 (0.73)	I
2a	134 (71.5)	N	159 (1.82)	I
2b	148 (94.7)	N	222 (3.52)	I
2c	247 (106.3)	N	[a]	
2d	266 (87.7)	N	[b]	
3a	157 (126.4)	I	[c]	
3b	266 (115.5)	I	[b]	
3c	267 (39.3)	I	[b]	
4	185 (44.5)	I		
5a	226 (65.1)	N	[a]	
5b	218 (21.0)	N	[a]	

[a] Isotropization temperature lies above the decomposition temperature. [b] Melting is accompanied by decomposition. [c] Solidifies upon cooling as a glass.

the ring peripheries were ineffective. We expected the *tert*-butyl-substituted macrocycles **3** to have a lower melting point owing to an increased separation between the rigid parts of the macrocycles, but in all cases we observed slightly higher melting points than those of the methyl analogue **2**.[11a] Unexpectedly, none of the macrocycles **3** were found to be liquid crystalline. However, the structures of **3a** and **3c** could be determined crystallographically (Figure 3).

Although a direct correlation between the crystal structures and organization of molecules in the mesophase is questionable, there are some significant differences between the crystal structures of the mesophase-forming macrocycles **1** and **2a**, and those of **3a** and **3c**, which do not form mesophases. We assumed that the alkyl chains of **3a** would also undergo dense alkyl packing as was observed for **2a** and **1**. On the contrary, however, the side chains in **3a** show no tendency at all to organize in one of the commonly observed alkyl-chain-packing motifs. They deviate from the expected *all-trans* conformation and instead orient themselves perpendicular to the ring plane such that one of the chains encloses the side of an adjacent ring (Figure 3, middle left).[13] Accordingly, in the crystalline state, the side chains in **3a** exhibit a gradual increase in segment mobility from the anchoring point at the macrocycle ($S \approx 0.6$ at $T = 54\,^{\circ}C$) toward the chain ends ($S \approx 0.3$), as determined by solid-state NMR spectroscopy. Such an increase of alkyl-chain flexibility is not observed in **2a** for which the chain segments show mobility that is substantially more uniform with a common (and higher) dynamic order parameter of $S \approx 0.65$ at $T = 54\,^{\circ}C$.

Furthermore, the macrocycles in the crystal lattice are locked by the large *tert*-butyl groups (Figure 3, bottom left). This implies that even if the alkyl chains become mobile upon heating, melting of the side chains does not interrupt the

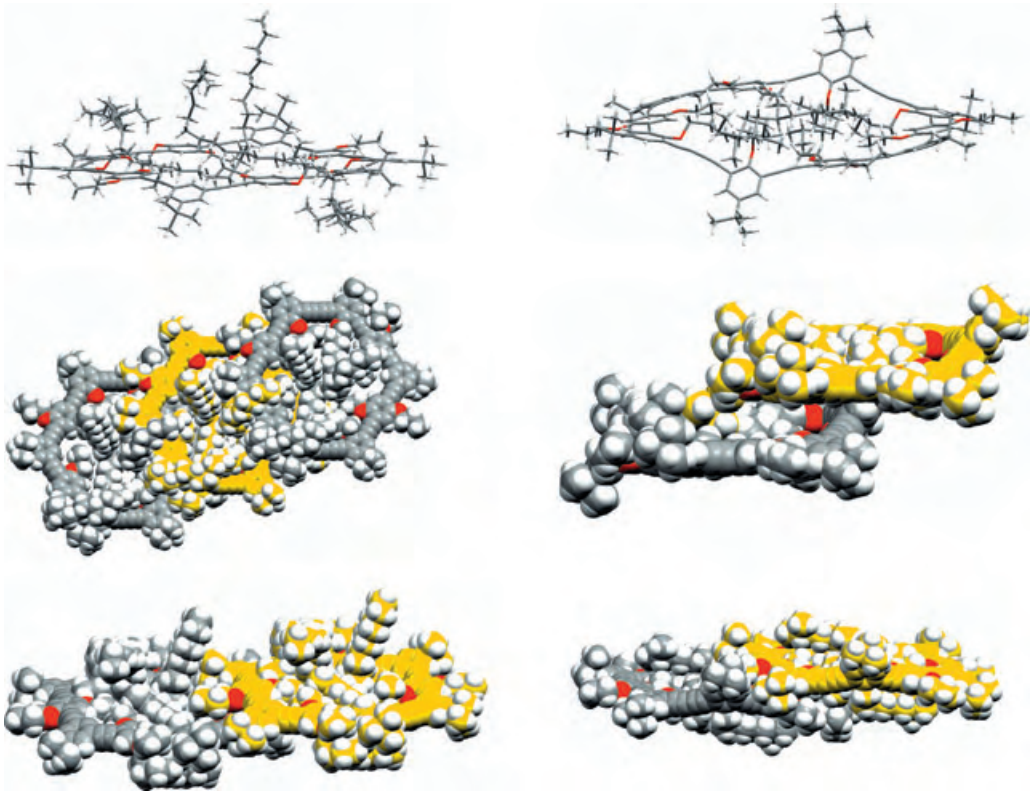

Figure 3. Top left: Structure of **3a** in the crystal. Middle left: Top view of three molecules of **3a** which shows the interlocking of the macrocycles. One C_{18} chain encloses the rigid side of an adjacent ring. Bottom left: The side view shows that the rigid parts of the rings are locked by the bulky *tert*-butyl groups at the corners of the ring. Notably, two of the four C_{18} side chains are disordered: the terminal 11 carbon atoms are found in two orientations, each of which is present with 50% probability (only one orientation is displayed for clarity). Top right: Structure of **3c** in the crystal. Middle right: Side view of two molecules of **3c** which shows that the *tert*-butyl group of the upper macrocycle dips deep inside the flexible alkyl interior of the other ring. Bottom right: Again, the side view shows that the rigid parts of the rings are locked by the bulky *tert*-butyl groups at the corners of the ring (different shading is used for clarity).

 © 2005 Wiley-VCH Verlag GmbH & Co. KGaA, Weinheim

extensive ring–ring interactions, and the mechanical coupling of the rings in **3a** does not break down before it is completely (isotropically) molten.

An ordered side-chain packing cannot be expected for **3c**. In this case the macrocyclic frame strongly deviates from planarity and two of the side chains are bent above and below the macrocycle (Figure 3, right). This leaves cavities in which the bulky *tert*-butyl groups located above and below the macrocycles can interdigitate. As also found for **3a**, *tert*-butyl groups lock adjacent molecules together so that an interruption of the ring–ring interaction is only possible when the material is completely molten. Additionally, the size of the bulky side groups leads to a more spherical shape of the molecule which can destabilize liquid-crystalline phases.[11a,14]

To investigate the influence of ring substituents on the thermal behavior of the compounds, macrocycle **4** was synthesized which lacks adaptable substituents on the rigid ring. The formation of a mesophase with **4** was also not observed. It is highly probable that removal of the adaptable side groups generates empty space within the macrocycles, and the resulting conflict between molecular anisotropy and empty space inside the rings destabilizes the formation of a thermotropic mesophase.[15] Alternatively, it is possible that adaptable, flexible side groups or small extraannular substituents are principally required to obtain liquid-crystal phases with these compounds. To address this issue, macrocycles that do not contain such groups, **5a** and **5b,** were investigated.[16] For both compounds a nematic mesophase could be observed.[17] Under the assumptions made above, it can be speculated that the polycyclic aromatic backbone decreases the size of the open cavity inside the rings, which prevents the molecules from interlocking with each other. Macrocycles **5a** could be crystallized as a solvate from tetrachloroethane (TCE) to give four TCE molecules per ring (Figure 4).

The relatively flat internal void of the macrocycle is already filled with the first few carbon atoms of the intraannular side groups. The remaining portions of the alkyl chains are located above and below the macrocyclic framework. Two of the C_{18} chains are oriented parallel to the ring and crystallize in pairs with alkyl chains from adjacent rings. These alkyl-chain pairs are sandwiched between two polycyclic aromatic units of the rigid macrocyclic backbone, separating them from each other. The remaining two alkyl chains deviate further from the ring plane and fill the lateral space between the rings. Interlocking of the molecules through entanglement of rigid and flexible parts between adjacent molecules cannot be observed, although close π–π contacts could be identified in this case. Furthermore, interlocking of the molecules through the extraannular substituents does not occur. Although **5a** could be crystallized only as solvate, the structure clearly shows that the internal void of each macrocycle is filled by its own alkyl chains. This means that the alkyl chains melt upon heating and the molecules can move sufficiently to form a mesophase before complete (isotropic) melting.[18] The mesophase formed by macrocycles **5a** and **5b** shows that the design principle described herein is not restricted to the phenylene–ethynylene backbone of macrocycles **1** or **2**. Moreover, it shows that substituents at the adaptable positions of macrocycles are not a prerequisite for the observation of a mesophase.

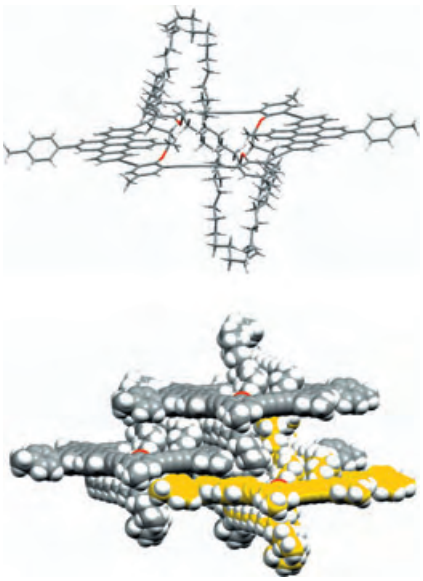

Figure 4. Top: Structure of **5a** in the crystal (solvent not shown). Bottom: Side view of four molecules of **5a** in the crystal which show that the polycyclic aromatic portions of the ring are separated by alkyl chains. Although a strong deviation of some of the alkyl chains from the ring plane is observed, interlocking of the molecules cannot be found. Furthermore, no interlocking of the rigid ring parts by the extraannular methyl or phenyl substituents can be observed (different shading is used for clarity).

In conclusion, shape-persistent rings with intraannular flexible side chains have been demonstrated as a hitherto unknown design principle for discotic liquid crystals. From investigations of their thermal behavior and the X-ray single-crystal structure analysis of these compounds, some preliminary guidelines for the synthesis of liquid crystals with an inverted structure can be deduced: 1) The formation of a mesophase is correlated to the possibility of the system to fill the interior space more or less with its own alkyl chains. 2) The molecules must not contain extraannular bulky substituents that cause the molecules to interlock and that also decrease molecular asymmetry. 3) The actual conformation of the alkyl chains in the solid state gives no apparent information about the thermal behavior of the macrocycles. Instead, it is important that no interlocking of the molecules occurs. Our investigations indicate that this design principle is rather general and that the presence of adaptable substituents is not a structural prerequisite. Therefore, a variety of different macrocycles with other aspect ratios are expected to exhibit liquid crystallinity as well.[19]

Received: October 15, 2004
Revised: January 14, 2005
Published online: March 30, 2005

Keywords: liquid crystals · macrocycles · mesophases · substituent effects · supramolecular chemistry

 © 2005 Wiley-VCH Verlag GmbH & Co. KGaA, Weinheim

[1] a) S. Chandrasekhar, B. K. Sadashiva, K. A. Suresh, *Pramana* **1977**, *9*, 471 – 480; b) S. Chandrasekhar in *Handbook of Liquid Crystals*, *Vol. 2B* (Eds.: D. Demus, J. Goodby, G. W. Gray, H.-W. Spiess, V. Vill), Wiley-VCH, Weinheim, **1998**, pp. 749 – 780; c) R. J. Bushby, O. R. Lozman, *Curr. Opin. Colloid Interface Sci.* **2002**, *7*, 343 – 354.

[2] a) D. Adam, P. Schuhmacher, J. Simmerer, L. Haeussling, K. Siemensmeyer, K. H. Etzbach, H. Ringsdorf, D. Haarer, *Nature* **1994**, *371*, 141 – 143; b) N. Boden, R. J. Bushby, J. Clements, B. Movaghar, *J. Mater. Chem.* **1999**, *9*, 2081 – 2086; c) L. Schmidt-Mende, A. Fechtenkötter, K. Müllen, E. Moons, R. H. Friend, J. D. MacKenzie, *Science* **2001**, *293*, 1119 – 1122.

[3] a) H. Mori, Y. Itoh, Y. Nishiura, T. Nakamura, Y. Shinagawa, *Jpn. J. Appl. Phys. Part 1* **1997**, *36*, 143 – 147; b) M. Okazaki, K. Kawata, H. Nishikawa, M. Negoro, *Polym. Adv. Technol.* **2000**, *11*, 398 – 403; c) S. Kumar, S. K. Varshney, *Angew. Chem.* **2000**, *112*, 3270 – 3272; *Angew. Chem. Int. Ed.* **2000**, *39*, 3140 – 3142.

[4] a) J. P. Behr, J.-M. Lehn, A.-C. Dock, D. Moras, *Nature* **1982**, *295*, 526 – 527; b) J.-M. Lehn, J. Malthete, A.-M. Levelut, *J. Chem. Soc. Chem. Commun.* **1985**, 1794 – 1796; c) J. Zhang, J. S. Moore, *J. Am. Chem. Soc.* **1994**, *116*, 2655 – 2656; d) O. Mindyuk, M. R. Stetzer, P. A. Heiney, J. C. Nelson, J. S. Moore, *Adv. Mater.* **1998**, *10*, 1363 – 1366.

[5] S. Höger, V. Enkelmann, K. Bonrad, C. Tschierske, *Angew. Chem.* **2000**, *112*, 3256 – 3258; *Angew. Chem. Int. Ed.* **2000**, *39*, 2268 – 2270.

[6] a) S. Höger, V. Enkelmann, *Angew. Chem.* **1995**, *107*, 2917 – 2920; *Angew. Chem. Int. Ed. Engl.* **1995**, *34*, 2713 – 2716; b) D. L. Morrison, S. Höger, *Chem. Commun.* **1996**, 2313 – 2314; c) S. Höger, D. L. Morrison, V. Enkelmann, *J. Am. Chem. Soc.* **2002**, *124*, 6734 – 6736.

[7] CCDC-252531–252534 contain the supplementary crystallographic data for this paper. These data can be obtained free of charge from The Cambridge Crystallographic Data Centre via www.ccdc.cam.ac.uk/data_request/cif. Selected crystal data: **2a** ($T = 250$ K): triclinic, $P\bar{1}$, $a = 14.888(1)$, $b = 17.448(1)$, $c = 18.262(1)$ Å, $\alpha = 71.501(1)$, $\beta = 75.386(1)$, $\gamma = 70.278(1)°$, $V = 4178.7(3)$ Å^3, $Z = 2$, $\rho_x = 1.056$ g cm^{-3}, 31555 independent reflections, 6336 reflections observed, $R = 0.0863$, $R_w = 0.1043$. **3a** ($T = 120$ K): triclinic, $P\bar{1}$, $a = 16.519(1)$, $b = 16.652(1)$, $c = 18.742(1)$ Å, $\alpha = 108.824(2)$, $\beta = 102.745(2)$, $\gamma = 103.448(2)°$, $V = 4494.5(3)$ Å^3, $Z = 2$, $\rho_x = 1.058$ g cm^{-3}, 17332 independent reflections, 6702 reflections observed, $R = 0.0730$, $R_w = 0.0761$. **3c** ($T = 120$ K): triclinic, $P\bar{1}$, $a = 13.707(2)$, $b = 17.783(2)$, $c = 17.952(2)$ Å, $\alpha = 62.568(2)$, $\beta = 87.979(2)$, $\gamma = 87.306(1)°$, $V = 3879.3(2)$ Å^3, $Z = 2$, $\rho_x = 1.060$ g cm^{-3}, 9887 independent reflections, 2856 reflections observed, $R = 0.0684$, $R_w = 0.0710$. **5a**·4TCE ($T = 220$ K): triclinic, $P\bar{1}$; $a = 15.9580(6)$, $b = 16.0040(7)$, $c = 17.7550(7)$ Å, $\alpha = 96.7810(12)$, $\beta = 103.2770(14)$, $\gamma = 102.9350(14)°$, $V = 4232.1(3)$ Å^3, $Z = 2$, $\rho_x = 1.213$ g cm^{-3}, 17818 independent reflections, 6577 reflections observed, $R = 0.0882$, $R_w = 0.0901$.

[8] The dynamic order parameters (S) discussed herein represent the residual anisotropy of a given molecular segment, as determined by NMR spectroscopy from the residual dipole–dipole coupling between two nuclei in the segment (^{1}H–^{1}H in CH_2, or ^{13}C–^{1}H in CH or CH_3). Formally, S can be expressed in the form of Equation (1) in which $P(\theta,\theta_0)$ is the distribution function of orientations θ adopted by a segment in the course of its motion starting from the initial orientation θ_0.

$$S(\theta_0) = \int_0^1 \tfrac{1}{2}(3\cos^2\theta - 1)\, P(\theta,\theta_0)\, d\cos\theta \quad (1)$$

If the samples are not macroscopically oriented (as in our case), the parameters $S(\theta_0)$ must be averaged over all possible initial orientations θ_0 to yield the dynamic order parameter [Eq. (2)]:

$$S = \langle S(\theta_0)/\tfrac{1}{2}(3\cos^2\theta_0 - 1)\rangle_{\theta_0} \quad (2)$$

These dynamic order parameters S should not be confused with the orientational order parameters that are often used for describing the degree of orientational order in liquid crystals. The two parameters are not identical, yet they are related: the dynamic order parameters are affected by both the local motions of molecular segments and the overall motions of the molecules. In contrast, only the overall molecular motions are relevant to the orientational order parameters, such that dynamic order parameters can be (and are, in our case) decreased by local segment motions relative to the orientational order of the molecules.

[9] a) I. Schnell, *Prog. Nucl. Magn. Reson. Spectrosc.* **2004**, *45*, 145 – 207; b) A. Rapp, I. Schnell, D. Sebastiani, S. P. Brown, V. Percec, H. W. Spiess, *J. Am. Chem. Soc.* **2003**, *125*, 13284 – 13297.

[10] Unless otherwise stated, mesophases were assigned on the basis of their textures.

[11] a) D. M. Collard, C. P. Lillya, *J. Am. Chem. Soc.* **1991**, *113*, 8577 – 8583; b) S. Kumar, D. S. S. Rao, S. K. Prasad, *J. Mater. Chem.* **1999**, *9*, 2751 – 2754.

[12] Thermogravimetric analysis (TGA) of **2d** shows no weight loss up to 300 °C. However, partial decomposition of the materials cannot be fully excluded above 230–250 °C.

[13] This unusual packing behavior may result from the increased ring width, which does not allow optimal space filling with all alkyl chains in the *trans* configuration.

[14] Assuming a similar packing behavior for **2d**, the smaller terminal methyl groups do not cause an interlocking of the molecules and allow mesophase formation.

[15] a) S. Höger, K. Bonrad, A. Mourran, U. Beginn, M. Möller, *J. Am. Chem. Soc.* **2001**, *123*, 5651 – 5659; b) M. Fischer, G. Lieser, A. Rapp, I. Schnell, W. Mamdouh, S. De Feyter, F. C. De Schryver, S. Höger, *J. Am. Chem. Soc.* **2004**, *126*, 214 – 222.

[16] X. H. Cheng, S. Höger, D. Fenske, *Org. Lett.* **2003**, *5*, 2587 – 2589.

[17] A transition for **5a** was observed at 194 °C ($\Delta H = 27.3$ kJ mol^{-1}) to another LC phase that is not yet assigned.

[18] Additionally, it can be assumed that the large polycyclic aromatic functions of the compound stabilize an orientation correlation of molecules in the mesophase: P. J. Collings, M. Hird, *Introduction to Liquid Crystals*, Taylor & Francis, London, **1997**, p. 83. Moreover, the flexibility of the macrocyclic backbone of **5** is likely to be less than that of the other macrocycles.

[19] K. Praefke, D. Blunk, D. Singer, J. W. Goodby, K. J. Toyne, M. Hird, P. Styring, W. D. J. A. Norbert, *Mol. Cryst. Liq. Cryst.* **1998**, *323*, 231 – 259.

 © 2005 Wiley-VCH Verlag GmbH & Co. KGaA, Weinheim

Biopolymers

Wound Closure in the Invasive Green Alga *Caulerpa taxifolia* by Enzymatic Activation of a Protein Cross-Linker**

*Sven Adolph, Verena Jung, Janine Rattke, and Georg Pohnert**

The injury to a multicellular organism is generally not fatal, as regenerative tissue can be formed adjacent to the wound. Therefore, a repair mechanism for the injured cells themselves is not required. In contrast, the survival of a unicellular organism upon injury is strongly dependent on processes that allow the cell to cope with physical damage. This is especially true for siphonous green algae such as *Caulerpa taxifolia*, which consist of a single polyploid (with multiple nuclei) cell that can reach up to several meters in length. *C. taxifolia* is an invasive tropical alga that has spread rapidly after its introduction into the Mediterranean Sea and the North American Pacific, and has thereby massively altered the native ecosystems of these regions.[1,2]

The success of *C. taxifolia* is based on high temperature and substrate tolerance, an efficient mechanism of chemical defense, and a remarkable method of asexual proliferation:[3–5] after mechanical disruption of the alga, the resulting fragments are sealed by a gelatinous external wound plug (EWP). Formation of the EWP occurs within seconds after injury, and prevents the remaining cytoplasm from coming into contact with the surrounding sea water (Figure 1a).[6] This initial wound response is followed by the deposition of insoluble material beneath the external polymer to form an internal wound barrier.[6–8] The resulting sealed-cell fragments bear the full genetic information of the original cell, and can establish new colonies independently.[7] Today, massive *C. taxifolia* patches that were generated from the introduced parent fragments are being reported in infected regions;[9] as a result of their reproductive strategy, most of the invading *C. taxifolia* specimens belong to a single clone. [10,11]

In our investigations of the wound response of *C. taxifolia* we found that an esterase is involved in the transformation of caulerpenyne (**1**), the major secondary metabolite of this alga, immediately after tissue disruption. The resulting 1,4-dialdehyde, which contains a conjugated double bond, is very reactive and can only be characterized indirectly by trapping methods (Scheme 1).[12] This dialdehyde was originally detected in mollusks that feed on *Caulerpa prolifera* and was termed oxytoxin 2 (**2**).[13]

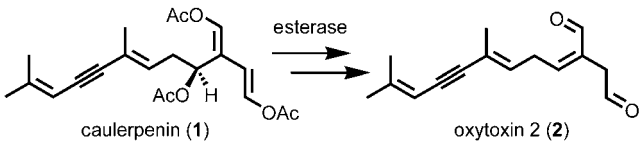

Scheme 1. Formation of oxytoxin 2 (**2**) by esterase-mediated deacetylation of caulerpenyne (**1**) and concomitant dehydration.

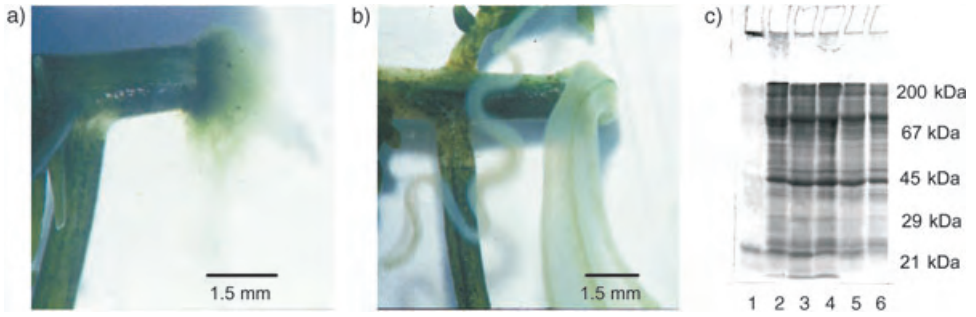

Figure 1. a) External wound plug of *C. taxifolia* formed 60 s after cleavage with a razor blade; b) wound plug formation is suppressed in the presence of lysine (100 mg mL^{-1} seawater); c) SDS-PAGE separation of *C. taxifolia* proteins: lane 1, protein content 5 min after wounding; lane 2, intact algae in which the esterase was inactivated by boiling the algal fragment before workup; lanes 3/4, wounded/intact alga + lysine (0.2 mmol (mg alga)$^{-1}$); lanes 5/6, wounded/intact alga + cysteine (0.2 mmol (mg alga)$^{-1}$); all samples were boiled in SDS/DTT before loading the gel (12%).

[*] Dipl. Chem. S. Adolph, Dr. V. Jung,[+] J. Rattke, Priv. Doz. Dr. G. Pohnert
Max Planck Institute for Chemical Ecology
Hans-Knöll-Strasse 8, 07745 Jena (Germany)
Fax: (+49) 3641-571-256
E-mail: pohnert@ice.mpg.de

[+] Present address:
Lonza AG, Walliser Werke
3930 Visp (Switzerland)

[**] We thank the Deutsche Forschungsgemeinschaft for funding. Prof. W. Boland is gratefully acknowledged for support, Dr. B. Schneider for help with NMR spectroscopic measurements, and A. Perner for HRMS measurements.

The concentration of deacetylated caulerpenyne, as monitored by HPLC–APCI MS, reaches a transient maximum within the first minutes after injury to the alga. Only four minutes later, this metabolite is no longer detectable (Figure 2). Moreover, with HPLC–MS, GC–MS, and NMR spectroscopy experiments, no products of low molar mass were detected which suggests that either oxytoxin 2 (**2**) degrades quickly or it is involved in the formation of a polymer. Interestingly, the decay kinetics of **2** matched those of the formation of the EWP.[8] As dicarbonyl compounds can act as crosslinking agents through reaction with nucleophilic functional groups of proteins,[14] the kinetic observations

 © 2005 Wiley-VCH Verlag GmbH & Co. KGaA, Weinheim DOI: 10.1002/anie.200462276

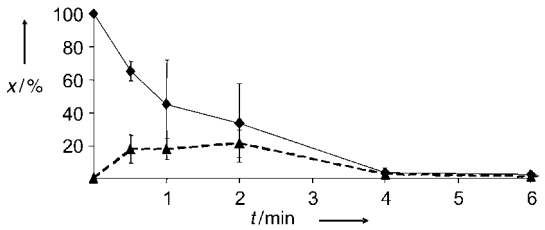

Figure 2. Caulerpenyne transformation (◆) and fate of the deacetylated product (▲) in wounded algae. After defined periods of time, samples of wounded *C. taxifolia* were extracted with hexane and immediately analyzed by normal-phase HPLC–APCI MS.[16] Relative amounts (x) to the internal standard (stilbene) are given. The deacetylated product was quantified by its molecular ion $[M+H]^+$ ($m/z = 231$); error bars are based on SD ($n = 3$). APCI = atmospheric pressure chemical ionization.

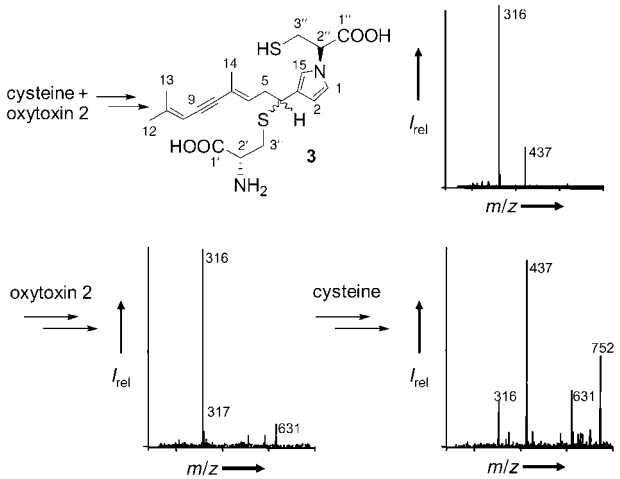

Figure 3. LC–MS analysis of extracts from *C. taxifolia* wounded in the presence of cysteine. The insert shows the APCI mass spectra of the identified cysteine adducts. The structure of cross-linking reaction product **3** was verified by HRMS and NMR spectroscopy. The mass spectra of additional signals from the LC–MS separation are given below. These can be tentatively assigned to the larger polymerization products of two oxytoxin 2 (**2**), and two or three cysteine units, respectively; UV/Vis and fragmentation patterns demonstrate that they are derived from oxytoxin 2 and cysteine.

prompted us to investigate the role of **2** as a putative mediator of polymer formation in the wound-closure process.

Analysis of the SDS-PAGE-separation patterns of protein extracts from both intact and wounded tissue samples revealed the first indications for protein crosslinking in injured *C. taxifolia*. As expected, distinct proteins can be detected from samples of intact algae. In contrast, five minutes after injury, tissue samples had a considerably lower amount of SDS-PAGE-separable proteins, and insoluble material was detected in the loading pockets of the gel (Figure 1c). This polymer remained insoluble after excessive boiling of the samples in sodium dodecyl sulfate (SDS) and dithiothreitol (DTT) which suggests that the material is assembled by covalent linkages. A similar reaction occurs when commercially available cross-linking reagents such as glutaraldehyde or enzymatically unmasked dialdehydes from higher plants are added to protein mixtures.[14,15]

We reasoned that externally added nucleophilic amino acids should be able to compete with the algal proteins for the reactive sites of oxytoxin 2 (**2**). Indeed, the presence of excess lysine suppressed formation of the EWP polymer, despite the fact that the *C. taxifolia* esterase remained uninhibited in transformation of caulerpenyne (**1**) as substrate (verified by GC–MS). Within the first minutes after injury in lysine-enriched seawater, the entire cell contents leaked into the surrounding medium (Figure 1b). The suppression of polymer formation by the nucleophilic amino acids lysine and cysteine was also documented by the fact that the protein-separation pattern in gel electrophoresis was similar to that of intact algae, in which the cross-linking reaction is absent (Figure 1c).

To elucidate further the processes involved in EWP formation, HPLC–APCI MS measurements of *C. taxifolia* extracts wounded in the presence of cysteine were performed. A series of products could be detected that were clearly derived from caulerpenyne (**1**), as they exhibited the characteristic UV/Vis spectroscopic signatures of the dienyne backbone. The molecular ions and characteristic fragments of these products indicated that cysteine–oxytoxin 2 adducts and crosslinked species were formed (Figure 3). The observed suppression of wound-plug formation in the presence of the nucleophilic amino acids is thus most likely caused by their reaction with dialdehyde **2**, which renders it unavailable for the natural formation of polymers with algal proteins.

As the matrix of wounded algae is very complex, it was not possible to conclude whether any additional factors are required for the formation of the EWP polymer. To obtain further insight into the underlying processes of the polymerization, we designed a simplified experimental setup in which pure caulerpenyne (**1**) was deacetylated with immobilized esterase. In the presence of cysteine, the same adducts and crosslinking products as shown in Figure 3 could be observed. This allowed the generation and purification of sufficient quantities of the first crosslinking product, **3**, for NMR spectroscopic analysis. 2D NMR spectroscopy results are in full agreement with the assigned structure, which could be formed by the Michael addition of a S nucleophile to the conjugated double bond and condensation of a N nucleophile with the 1,4-dialdehyde moiety (Figure 3).

This simplified setup demonstrates that only an esterase and caulerpenyne (**1**) are required to initiate the reaction with amino acid derived nucleophiles. Moreover, deacetylation of caulerpenyne in the presence of a model peptide with only one accessible nucleophilic group allowed identification of the resulting oxytoxin 2–peptide condensation product **4** (Figure 4). This result unambiguously demonstrates the reactivity of unmasked caulerpenyne toward peptide-bound N nucleophiles. This finding also reveals a potential application for the caulerpenyne (**1**)/esterase system in the targeted initiation of protein-crosslinking reactions.

Our results support previous investigations of the constituents of the EWP of *C. taxifolia*. Dreher et al. determined the carbohydrate and protein content of isolated viscoelastic material from different wounded *Caulerpa* spp. Interestingly, they found that 50–75% of the insoluble material consists of

 © 2005 Wiley-VCH Verlag GmbH & Co. KGaA, Weinheim

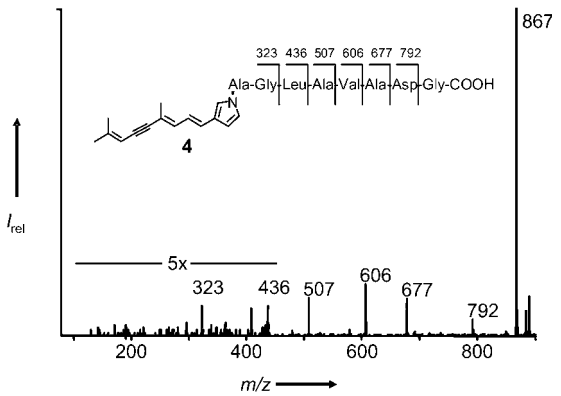

Figure 4. Esterase-mediated deacetylation of caulerpenyne (**1**) in the presence of the synthetic oligopeptide H-AGLAVADG-OH results in the formation of adduct **4**. The fragmentation of the peptide bonds in ESI MS is indicated. High resolution ESI MS for **4**: calcd for $C_{43}H_{62}N_8O_{11}Na$ [M+Na^+]: 889.4430; found 889.4398.

proteins of very high molar mass.[6] Our experiments lead to the assumption that upon wounding, proteins are recruited to the formation of this material through cross-linking reactions. These reactions are triggered by a fast esterase-mediated release of the reactive oxytoxin 2 (**2**) from caulerpenyne (**1**), a storage product stabilized by enol acetate functionalities. Thus, a controlled enzymatic process that may be initiated by the disruption of cellular compartments initiates the rapid self-assembly of a hitherto unknown type of biopolymer. With such a strategy, physical injuries can be exploited to generate new offspring which supports the fast proliferation of this invasive alga.

It is exceptional that such a viable cell function is based entirely on a secondary metabolite, but highly reactive esterases make this wound reaction reliable. Within minutes, they quantitatively transform caulerpenyne (present in over 1.3 % of the wet mass of the alga)[3,16] and release an excess of the protein-crosslinking reagent oxytoxin 2. Interestingly, caulerpenyne (**1**) fulfils a dual function as defensive metabolite and as a key reagent in the wound-sealing process.[3]

Numerous siphonous green algae contain terpenoid metabolites with the 1,4-bis-enoylacetate structural element found in caulerpenyne (**1**).[17] A deacetylation mechanism is involved in the transformation of halimedatetraacetate, a sesquiterpene from *Halimeda* spp.,[18] and caulerpenyne (**1**) from other *Caulerpa* spp.[16] This finding suggests that the new principle of wound closure identified herein may be universally distributed among those giant-celled algae.

Experimental Section

For model investigations with immobilized esterase, caulerpenyne (**1**) (28 mg, 10 mg mL^{-1} in MeOH) was treated with porcine liver esterase (2.8 g, immobilized on eupergit C, $\approx$500 U g^{-1}, Sigma), in Tris/TFA buffer (100 mM, pH 7.5) in the presence of cysteine (60.6 mg), or on a smaller scale with the synthetic oligopeptide H-AGLAVADG-OH (710 μg). The suspensions were shaken vigorously for 1 h, followed by the removal of the esterase by filtration. The filtrate was directly submitted to reversed-phase HPLC–APCI MS analysis or preparative reversed-phase HPLC. TFA = trifluoroacetic acid.

Analytical data for the major diastereomer of the first cross-linking product **3**: ^{1}H NMR (500 MHz, [D$_4$]MeOH): δ = 1.28 (s, 3H; 14-H), 1.79 (s, 3H; 12-H), 1.84 (s, 3H; 13-H), 2.66 (2H; 5-H, sp (sp = superimposed with minor diastereomer)), 2.85 (dd J = 15.0, 4.1 Hz, 1H; 3′-H$_b$), 3.15 (2H; 3″-H, sp), 3.24 (dd J = 15.0, 5.6 Hz, 1H; 3′-H$_a$), 3.60 (dd J = 5.6, 4.1 Hz, 1H; 2′-H), 3.85 (pseudotriplet J = 7.4 Hz, 1H; 4-H), 4.57 (1H; 2″-H, sp), 5.31 (s, 1H; 10-H), 5.74 (1H; 6-H, sp), 6.17 (1H; 2-H, sp), 6.82 (1H; 1-H, sp), 6.87 ppm (1H; 15-H, sp); ^{13}C NMR (125 MHz, [D$_4$]MeOH): δ = 18.3 (C14), 21.3 (C13), 25.1 (C12), 28.0 (C3″), 32.8 (C3′), 36.0 (C5), 45.3 (C4), 55.2 (C2′), 68.2 (C2″), 85.7 (C9), 95.8 (C8), 106.5 (C2), 106.9 (C10), 120.4 (C15), 121.3 (C7), 125.1 (C1), 127.1 (C3), 134.7 (C6), 148.8 (C11), 172.5 (C1′), 175.4 ppm (C1″); the chemical shifts were assigned with HMBC and HMQC, the spin systems 1-H–2-H; 4-H–6-H; 2′-H–3′-H and 2″-H–3″-H could be followed in H,H-COSY experiments; high-resolution ESI MS m/z: calcd for $C_{21}H_{29}S_2N_2O_4$ [M+H]$^+$: 437.1569; found: 437.1583.

Received: October 12, 2004
Published online: March 24, 2005

Keywords: aldehydes · biopolymers · biosynthesis · chemical ecology · proteins

[1] A. Occhipinti-Ambrogi, D. Savini, *Mar. Pollut. Bull.* **2003**, *46*, 542–551.
[2] J. Kaiser, *Science* **2000**, *289*, 222–223.
[3] P. Amade, R. Lemee, *Aquat. Toxicol.* **1998**, *43*, 287–300.
[4] A. Meinesz, L. Benichou, J. Blachier, T. Komatsu, R. Lemee, H. Molenaar, X. Mari, *Bot. Mar.* **1995**, *38*, 499–508.
[5] A. Meinesz, B. Hesse, *Oceanol. Acta* **1991**, *14*, 415–426.
[6] T. W. Dreher, D. B. Hawthorne, B. R. Grant, *Protoplasma* **1982**, *110*, 129–137.
[7] D. Menzel, *Protoplasma* **1988**, *144*, 73–91.
[8] T. W. Dreher, B. R. Grant, R. Wetherbee, *Protoplasma* **1978**, *96*, 189–203.
[9] C. M. Smith, L. J. Walters, *Mar. Ecol.* **1999**, *20*, 307–319.
[10] O. Jousson, J. Pawlowski, L. Zaninetti, F. W. Zechman, F. Din, G. Di Guiseppe, R. Woodfield, A. Millar, A. Meinesz, *Nature* **2000**, *408*, 157–158.
[11] O. Jousson, J. Pawlowski, L. Zaninetti, A. Meinesz, C. F. Boudouresque, *Mar. Ecol. Prog. Ser.* **1998**, *172*, 275–280.
[12] V. Jung, G. Pohnert, *Tetrahedron* **2001**, *57*, 7169–7172.
[13] G. Cimino, A. Crispino, V. Dimarzo, M. Gavagnin, J. D. Ros, *Experientia* **1990**, *46*, 767–770.
[14] S. J. Meade, A. G. Miller, J. A. Gerrard, *Bioorg. Med. Chem.* **2003**, *11*, 853–862.
[15] K. Konno, C. Hirayama, H. Yasui, M. Nakamura, *Proc. Natl. Acad. Sci. USA* **1999**, *96*, 9159–9164.
[16] V. Jung, T. Thibaut, A. Meinesz, G. Pohnert, *J. Chem. Ecol.* **2002**, *28*, 2091–2105.
[17] V. J. Paul, W. Fenical, *Bioorg. Mar. Chem.* **1987**, *1*, 1–29.
[18] V. J. Paul, K. L. van Alstyne, *J. Exp. Mar. Biol. Ecol.* **1992**, *160*, 191–203.

 © 2005 Wiley-VCH Verlag GmbH & Co. KGaA, Weinheim